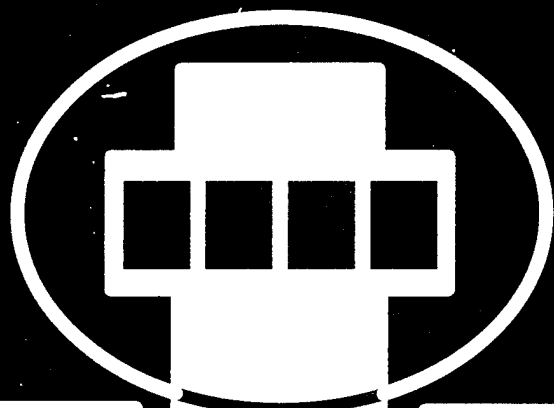


**Proceedings of the 1995
Particle Accelerator Conference
and International Conference
on High-Energy Accelerators**



PROCEEDINGS OF THE 1995
PARTICLE ACCELERATOR CONFERENCE
AND INTERNATIONAL CONFERENCE
ON HIGH-ENERGY ACCELERATORS
JULY 1-5, 1995
AT THE UNIVERSITY OF TEXAS AT AUSTIN





The
American
Physical
Society

Proceedings of the 1995 Particle Accelerator Conference

N00014-95-1-0791

Volume 4 of 5

Papers from the sixteenth biennial Particle Accelerator Conference, an international forum on accelerator science and technology held May 1-5, 1995, in Dallas, Texas, organized by Los Alamos National Laboratory (LANL) and Stanford Linear Accelerator Center (SLAC), jointly sponsored by the Institute of Electrical and Electronics Engineers (IEEE) Nuclear and Plasma Sciences Society (NPSS), the American Physical Society (APS) Division of Particles and Beams (DPB), and the International Union of Pure and Applied Physics (IUPAP), and conducted with support from the US Department of Energy, the National Science Foundation, and the Office of Naval Research.

19960705 128

PROCEEDINGS OF THE 1995 PARTICLE ACCELERATOR CONFERENCE

Abstracting is permitted with credit to the source. Libraries are permitted to photocopy beyond the limits of U. S. copyright law for private use of patrons those articles in this volume that carry a code at the bottom of the first page, provided the per-copy fee indicated in the code is paid through the Copyright Clearance Center, 222 Rosewood Drive, Danvers, MA 01923. Instructors are permitted to photocopy isolated articles for noncommercial classroom use without fee. For other copying, reprint, or republication permission, write to the IEEE Copyright Manager, IEEE Operations Center, 445 Hoes Lane, Piscataway, NJ 08855-1331. All rights reserved. Copyright © 1996 by the Institute of Electrical and Electronic Engineers, Inc.

IEEE Catalog Number: 95CH35843 (softbound)
95CB35843 (casebound)

Library of Congress Number: 88-647453

ISBN Softbound: 0-7803-2934-1
ISBN Casebound: 0-7803-2935-X
ISBN Microfiche: 0-7803-2936-8
ISBN CD-ROM: 0-7803-2937-6

Additional copies of this publication are available from

IEEE Operations Center
445 Hoes Lane
P. O. Box 1331
Piscataway, NJ 08855-1331 USA

Phone: 1-800-678-IEEE (1-800-678-4333)
1-908-981-1393
FAX: 1-908-981-9667
Telex: 833-233
e-mail: customer.service@ieee.org

The CD-ROM version is available from

Dan Rusthoy, PAC95 Treasurer
Los Alamos National Laboratory
P. O. Box 1663 - M/S H811
Los Alamos, NM 87545 USA

Phone: 505-667-2796
FAX: 505-667-0919
e-mail: drusthoy@lanl.gov

Volume 1

Plenary and Special Sessions

CEBAF Commissioning and Future Plans (Invited) — Hermann A. Grunder	1	MAD01
The Advanced Photon Source (Invited) — John N. Galayda	4	MAD02
Commissioning and Performance of the HIMAC Medical Accelerator (Invited) — S. Yamada	9	MAD03
Accelerator Field Development at Novosibirsk (History, Status, Prospects) (Invited) — A. Skrinsky	14	MAD04
A Personal Perspective of High Energy Accelerators (Invited) — Gustav-Adolf Voss	27	FPD01
Photon-Photon Colliders (Invited) — Andrew M. Sessler	30	FPD02
Transmutation and Energy Production with High Power Accelerators (Invited) — G.P. Lawrence	35	FPD03
The Large Hadron Collider (Invited) — L.R. Evans	40	FPD04
Frontiers of Particle Physics (Invited) — L. Okun	45	FPD05
R. R. Wilson Prize Lecture: Pretzels (Invited) — R. Littauer	manuscript not submitted	MXG01
Experimental Studies of Longitudinal Dynamics of Space-Charge Dominated Electron Beams (Invited) — D.X. Wang	48	MXG02
High-Energy High-Luminosity $\mu^+ \mu^-$ Collider Design (Invited) — Robert B. Palmer, Richard Fernow, Juan C. Gallardo, Y.Y. Lee, Yagmur Torun, David Neuffer, David Winn	53	MXG03
Cosmic Acceleration Mechanisms (Invited) — J. Arons	manuscript not submitted	MXG04

Accelerator Applications

Hadron Particle Therapy (Invited) — Jose R. Alonso	58	WPE01
Micromechanics via Synchrotron Radiation (Invited) — H. Guckel	63	WPE02
Radionuclide Production for the Biosciences (Invited) — Thomas J. Ruth	67	WPE03
X-Ray Lithography - Status and Projected Use (Invited) — W.A. Johnson	manuscript not submitted	WPE04
Microelectronic Applications for RF Sources and Accelerators (Invited) — Cha-Mei Tang	70	WPE05
A High-Gradient Electron Injector to an X-Ray Lithography Ring (Invited) — D. Yu	manuscript not submitted	FAG01
X-Ray Holography (Invited) — I. McNulty	manuscript not submitted	FAG02
Medical and Surgical Applications of FELs (Invited) — Benedikt Jean	75	FAG03
Medical Uses of Monochromatic X-Rays (Invited) — Frank E. Carroll	80	FAG04
Texas Regional Medical Technology Center — R. Sah, T.D. Cain, E.K. Cleveland, K. Saadatmand, M.E. Schulze, R.A. Winje	83	FAG05
A Proposed 100-400 MeV Beam Facility at Fermilab — C. Johnstone, C. Ankenbrandt, S. Bjerklie, D. Boehnlein, M. Foley, T. Kroc, J. Lackey, A. Lennox, A. Leveling, E. McCrory, M. Popovic, C. Schmidt, K. Vaziri	86	FAG06
Cyclotrons for Isotope Production — B.F. Milton, N.R. Stevenson	89	FAG07
European Heavy Ion ICF Driver Development — G. Plass	92	FAG08
A 3-Stage Cyclotron Complex for Driving the Energy Amplifier — P. Mandrillon, N. Fietier, C. Rubbia	95	FAG09
Accelerator-Based Gamma Neutron Transmutation of Radionuclides as a New Technology for the Nuclear Fuel Cycle — I.P. Ereemeev	98	FAG10
A High-Average-Power FEL for Industrial Applications — H.F. Dylla, S. Benson, J. Bisognano, C.L. Bohn, L. Cardman, D. Engwall, J. Fugitt, K. Jordan, D. Kehne, Z. Li, H. Liu, L. Merminga, G.R. Neil, D. Neuffer, M. Shinn, C. Sinclair, M. Wiseman, L.J. Brillson, D.P. Henkel, H. Helvajian, M.J. Kelley	102	FAG11
X-Ray Radiation by Relativistic Electrons in Condensed Media on Base of MSU Race-Track Microtron — V.K. Grishin, A.S. Chepurinov, K.A. Gudkov, B.S. Ishkhanov, S.A. Kosterin, E.V. Lasutin, S.V. Blazhevich, N.N. Nasonov	105	FAG12
Applications of MeV Proton and Deuteron Linear Accelerators — George H. Gillespie, Gerald E. McMichael	107	FAG13
Accelerator Requirements for Fast-Neutron Interrogation of Luggage and Cargo — B.J. Micklich, C.L. Fink, T.J. Yule	110	FAG14

Energy Varying Resonant Beam Extraction from the Synchrotron — K. Hiramoto, <i>M. Tadokoro, J.I. Hirota, M. Nishi, K. Noda.....</i>	113	TAB03
Radiotherapy Process Integration Using a Compact Photon Source Together with Fluence Control and Patient Imaging — D. Tronc, F. Dugardin, J.P. Georges, R. Letoumelin, <i>J.L. Pourre.....</i>	116	TAB04
A 1.5 GeV Compact Light Source with Superconducting Bending Magnets — A.A. Garren, <i>D.B. Cline, M.A. Green, D.E. Johnson, J.J. Kolonko, E.M. Leung, D.D. Madura,</i> <i>L.C. Schachinger.....</i>	119	TAB06
Applications of Industrial Electron Accelerators at Samsung Heavy Industries — <i>Bumsoo Han, Keeman Kim, Kihun Joh, Sungmyun Kim, Byungmun Kim, Heunggyu Park,</i> <i>Jongpil Park, Jinsoo Kim, Wongu Kang, Kyungwoo Kang, Yuri Kim, Sangil Lee, Younghee Kim</i>	122	TAB09
Application of Accelerated Electron Beams for Rubber and Polymer Modification — <i>A. Shalnov, B.Yu. Bogdanovich, A. Ignatyev, V. Senyukov.....</i>	125	TAB13
Status on Low Energy (10 MeV Range) X-band Linacs Developed Worldwide — <i>A.V. Michine.....</i>	128	TAB15
Linear Accelerator for Radiation Chemistry Research at Notre Dame — K. Whitham, <i>S. Lyons, R. Miller, D. Nett, P. Treas, A. Zante, R.W. Fessenden, M.D. Thomas, Y. Wang</i>	131	TAB17
IREN Status: New Electron Linac Driven Intense Resonance Neutron Source — A. Krasnykh	134	TAC01
A Cost Estimation Model for High Power FELs — George R. Neil	137	TAC03
Details of the Initial Part of the Tungsten Ion Linac for Particle Track Membranes Production — V. Kushin, T. Kulevoy, N. Nesterov, A. Oreshnikov, S. Plotnikov, D. Seleznev, <i>V. Zubovskiy.....</i>	140	TAC05
A Series of Ion Accelerators for Industry — B.N. Sukhina, N.I. Alinovskiy, I.L. Chertok, <i>S.N. Chumakov, N.S. Dikansky, A.D. Goncharov</i>	143	TAC06
A Pulsed Source of Neutron Focus for Fundamental and Applied Research in High-Energy Electron Accelerator Centres — I.P. Ereemeev.....	146	TAC11
Moderator/Collimator for a Proton/Deuteron Linac to Produce a High-Intensity, High- Quality Thermal Neutron Beam for Neutron Radiography — R.C. Singletary Jr., <i>G.R. Imel, G.E. McMichael</i>	149	TAC12
Experimental Set-up for Multiplication Coefficient Fluctuation Study vs Accelerator Parameter Deviations on the JINR Pulsed Accelerator Driven Neutron Source — <i>V. Belkovets, A. Ivanov, A. Kaminsky, A. Krasnykh, N. Malakhov, L. Menshikov, Yu. Popov,</i> <i>V. Piataev, N. Pilyar, V. Rudenko, L. Somov, A. Sumbaev, V. Tarabrin.....</i>	152	TAC16

Synchrotron Light Sources and Free Electron Lasers

European Synchrotron Radiation Storage Rings (Invited) — H. Zygier.....	155	TPG01
Development of the JAERI FEL Driven by a Superconducting Accelerator (Invited) — <i>E.J. Minehara, M. Sugimoto, M. Sawamura, R. Nagai, N. Kikuzawa.....</i>	159	TPG02
Status of New Light Sources in Russia (Invited) — G. Kulipanov	manuscript not submitted	TPG03
Free Electron Laser Research in China (Invited) — Jialin Xie.....	162	TPG04
Accelerator Physics Trends at the ESRF — A. Ropert, L. Farvacque, J. Jacob, J.L. Laclare, <i>E. Plouviez, J.L. Revol, K. Scheidt</i>	167	TPG05
Commissioning of the PLS 2 GeV Storage Ring — M. Yoon, J.Y. Huang, J.S. Jang, M. Kwon, <i>T. Lee, S.H. Nam.....</i>	171	TPG06
Femtosecond X-Rays from 90° Thomson Scattering — W. Leemans, R. Schoenlein, A. Chin, <i>E. Glover, R. Govil, P. Volfbeyn, S. Chattopadhyay, K.-J. Kim, C.V. Shank.....</i>	174	TPG07
Design of a Diffraction Limited Light Source (DIFL) — D. Einfeld, J. Schaper, M. Plesko	177	TPG08
Updated Pans for DIAMOND, a New X-ray Light Source for the UK — V.P. Suller, <i>J.A. Clarke, J.B. Fitzgerald, H.L. Owen, M.W. Poole, X. Queralt, S.L. Smith.....</i>	180	TPG09
Design Optimization for an X-Ray Free Electron Laser Driven by SLAC Linac — Ming Xie.....	183	TPG10

The FERMI FEL Project at Trieste — D. Bulfone, F. Cargnello, G. D'Auria, F. Daclon, M. Ferianis, M. Giannini, G. Margaritondo, A. Massarotti, A. Rindi, R. Rosei, C. Rubbia, R. Visintini, R.P. Walker, A. Wrulich, D. Zangrando, F. Ciocci, G. Dattoli, A. De Angelis, A. Dipace, A. Doria, G.P. Gallerano, F. Garosi, L. Giannessi, E. Giovenale, L. Mezi, P.L. Ottaviani, A. Renieri, E. Sabia, A. Segreto, A. Torre, M. Castellano, P. Patteri, S. Tazzari, F. Tazzioli, F. Cevenini, A. Cutolo.....	186	TPG11
Studies on a Free Electron Laser for the TESLA Test Facility — J. Rossbach.....	189	TPG12
MIT Microwiggler for Free Electron Laser Applications — P. Catravas, R. Stoner, J. Blastos, D. Sisson, I. Mastovsky, G. Bekefi, X.-J. Wang, A. Fisher.....	192	TPG14
DORIS III as a Dedicated Source for Synchrotron Radiation — H. Nesemann, W. Brefeld, F. Brinker, W. Decking, O. Kaul, B. Sarau.....	195	FAA02
Beam Lifetime and Beam Brightness in ALS — C. Kim, A. Jackson, A. Warwick.....	198	FAA03
Asynchronized Energy Ramping at SRRS Storage Ring — Gwo-Huei Luo, L.H. Chang, Y. Cheng, K.T. Hsu, C.C. Kuo, W.C. Lau, Ch. Wang, P.K. Tseng, Y.C. Liu.....	201	FAA04
Emittance Measurements in the ALS Booster Synchrotron — D. Massoletti, C.H. Kim, A. Jackson.....	204	FAA05
Compton Scattering in the ALS Booster — D. Robin, C. Kim, A. Sessler.....	207	FAA06
Beam Stability at SRRS Storage Ring — W.T. Weng, H.P. Chang, J.R. Chen, Y. Cheng, K.T. Hsu, C.C. Kuo, J.C. Lee, K.K. Lin, Y.C. Liu, G.H. Luo, K.L. Tsang.....	210	FAA07
Commissioning of the Duke Storage Ring — V.N. Litvinenko, Y. Wu, B. Burnham, J.M.J. Madey, F. Carter, C. Dickey, M. Emamian, J. Gustavsson, N. Hower, P. Morcombe, S.H. Park, P. O'Shea, R. Sachtshale, D. Straub, G. Swift, P. Wang, J. Widgren.....	213	FAA08
Pulsed VUV Synchrotron Radiation Source — S.H. Kim, Y.S. Cho, T.Y. Kim, K.H. Chung.....	216	FAA10
Merits of a Sub-Harmonic Approach to a Single-Pass, 1.5-Å FEL — W.M. Fawley, H.-D. Nuhn, R. Bonifacio, E.T. Scharlemann.....	219	FAA12
Operation of the ELETTRA Injection Linac in the FEL Mode — G. D'Auria, C.J. Bocchetta, M. Plesko, C. Rossi, L. Tosi, R.P. Walker, A. Wrulich.....	222	FAA13
Free Electron Laser - FEL - Study in Institute of Nuclear Physics of MSU — V.K. Grishin, B.S. Ishkhanov, T.A. Novikova, V.I. Shvedunov.....	225	FAA14
A Chirped-Pulse Regenerative-Amplifier FEL for the Gamma-Gamma Collider — K.C.D. Chan, J.C. Goldstein, D.C. Nguyen, H. Takeda.....	228	FAA16
Alignment and Magnet Error Tolerances for the LCLS X-Ray FEL — H.-D. Nuhn, E.T. Scharlemann, R. Schlüter.....	231	FAA17
Electron Transport and Emittance Diagnostics in CIRFEL — J. Krishnaswamy, I.S. Lehrman, R. Hartley, R.H. Austin.....	234	FAA19
Study on Accelerator Noise Effects on a Far-Infrared FEL Oscillator — Shinian Fu, Yinbao Chen, Zhibin Huang.....	237	FAA21
Status of the UCLA High-Gain Infrared Free Electron Laser — M. Hogan, C. Pellegrini, J. Rosenzweig, G. Travish, A. Varfolomeev.....	240	FAA23
Accelerator Design for the High-Power Industrial FEL — D.V. Neuffer, S. Benson, J. Bisognano, D. Douglas, H.F. Dylla, D. Kehne, J. Fugitt, K. Jordan, Z. Li, H.-X. Liu, L. Merminga, G. Neil, M. Shinn, C. Sinclair, M. Wiseman, M. Cornacchia.....	243	FAA25
Free Electron Laser Amplifier Experiment Based on 3.5 MeV Linear Induction Accelerator — Ding Bainan, Deng Jianjun, Hu Shenzong, Shi Jinsui, Zhu Wenjun, Li Qing, He Yi.....	246	FAA26
A High Duty Factor Electron Linac for FEL — T.D. Hayward, D.H. Dowell, A.M. Vetter, C. Lancaster, L. Milliman, D. Smith, J. Adamski, C. Parazzoli.....	248	FAA27
A Kilowatt Class Visible Free Electron Laser Facility — J.L. Adamski, D.H. Dowell, T.D. Hayward, C.G. Parazzoli, A.M. Vetter.....	251	FAA28
Self-Consistent Analysis of Radiation and Relativistic Electron Beam Dynamics in a Helical Wiggler Using Lienard-Wiechert Fields — M. Tecimer, L.R. Elias.....	254	FAA29
First Lasings at Visible and IR Range of Linac-Based FELs at the FELI — T. Tomimasu, E. Oshita, S. Okuma, K. Wakita, K. Saeki, A. Zako, T. Suzuki, Y. Miyauchi, A. Koga, S. Nishihara, A. Nagai, E. Tongu, K. Wakisaka, A. Kobayashi, M. Yasumoto.....	257	FAA30
The Northrop Grumman Compact Infrared FEL (CIRFEL) — I.S. Lehrman, J. Krishnaswamy, R.A. Hartley, R.H. Austin.....	260	FAA31
A Proposed NSLS X-Ray Ring Upgrade Using B Factory Technology — E.B. Blum.....	263	FAR01
A Low Emittance Lattice for the NSLS X-Ray Ring — J. Safranek.....	266	FAR02

Design of a 1.2 GeV Synchrotron Light Source for X-Ray Lithography at Samsung Heavy Industries — Keeman Kim, Bumsoo Han, Kihun Joh, Sungmyun Kim, Byungmun Kim, Heunggyu Park, Jongpil Park, Jinsoo Kim, Wongu Kang, Kyungwoo Kang, Yuri Kim, Sangil Lee, Youngee Kim.....	269	FAR03
ANKA, A Synchrotron Light Source for Microstructure Fabrication and Analysis — H.O. Moser, M. Ballauff, V. Bechtold, H. Bertagnolli, J. Bialy, P. v. Blanckenhagen, C. Bocchetta, W. Bothe, C. Coluzza, A.N. Danilewsky, K.D. Eichhorn, B. Eigenmann, D. Einfeld, L. Friedrich, M. Haller, N. Holtkamp, V. Honecker, K. Hümmer, E. Huttel, J. Jacob, V. Kashikin, J. Kircher, H. Klewe-Nebenius, A. Knöchel, A. Krüssel, G. Kumpe, K.D. Möller, J. Mohr, M. Nagaenko, F.J. Pantenburg, M. Plesko, J. Schaper, K. Schlösser, G. Schulz, S. Schuppler, H. Schweickert, I. Seidel, Y. Severgin, I. Shukeilo, L. Steinbock, R. Steininger, M. Svandrlík, G. Williams, K. Wilson, J. Zegenhagen.....	272	FAR06
An Undulator at PETRA II - A New Synchrotron Radiation Source at DESY — K. Balewski, W. Brefeld, U. Hahn, J. Pflüger, R. Rossmanith.....	275	FAR07
Electron Storage Ring, KSR for Light Source with Synchrotron Radiation — A. Noda, H. Dewa, H. Fujita, M. Ikegami, Y. Iwashita, S. Kakigi, M. Kando, K. Mashiko, H. Okamoto, T. Shirai, M. Inoue.....	278	FAR08
A Lattice for the Future Project of VUV and Soft X-Ray High Brilliant Light Source — H. Takaki, Y. Kobayashi, K. Matsuda, Y. Kamiya.....	281	FAR09
Millimeter Wave Coherent Synchrotron Radiation in a Compact Electron Storage Ring — J.B. Murphy, E. Blum, R. Heese, J. Keane, S. Krinsky.....	284	FAR10
Commissioning of the Argonne Positron Accumulator Ring — M. Borland.....	287	FAR11
APS Storage Ring Commissioning and Early Operational Experience — G. Decker.....	290	FAR13
New Specifications for the SOLEIL Project — M.-P. Level, P. Brunelle, A. Nadji, M. Sommer, H. Zyngier, J. Faure, P. Nghiem, J. Payet, A. Tkatchenko.....	293	FAR14
A Combined Magnet Lattice of the Synchrotron Light Source ISI-800 — I. Karnaukhov, S. Kononenko, A. Shcherbakov, V. Nemoshkalenko, V. Molodkin, A. Shpak.....	296	FAR16
Progress of the ISI-800 Project — E. Bulyak, S. Efimov, A. Gevchuk, P. Gladkikh, I. Karnaukhov, S. Kononenko, V. Kozin, V. Markov, N. Mocheshnikov, A. Mytsykov, A. Shcherbakov, Yu. Telegin, A. Zelinsky, V. Molodkin, V. Nemoshkalenko, A. Shpak.....	299	FAR17
Reduction of Open-Loop Low Frequency Beam Motion at the APS — G. Decker, Y.G. Kang, S. Kim, D. Mangra, R. Merl, D. McGhee, S. Sharma.....	303	FAR19
Horizontal-Vertical Coupling Correction at Aladdin — R.A. Bosch, W.S. Trzeciak.....	306	FAR20
One and a Half Years of Experience with the Operation of the Synchrotron Light Source ELETTRA — C.J. Bocchetta, D. Bulfone, F. Daclon, G. D'Auria, A. Fabris, R. Fabris, M. Ferianis, M. Giannini, F. Iazzourene, E. Karantzoulis, A. Massarotti, R. Nagaoka, N. Pangos, R. Richter, C. Rossi, M. Svandrlík, L. Tosi, R. Visintini, R.P. Walker, F. Wei, A. Wrulich.....	309	FAR21

Low and Intermediate Energy Accelerators

First Generation ISOL Radioactive Ion Beam Facilities (Invited) — D.K. Olsen.....	312	RPG01
Latest Developments in Superconducting Cyclotrons (Invited) — H.W. Schreuder.....	317	RPG02
Synchrotron-Driven Spallation Sources (Invited) — P.J. Bryant.....	322	RPG03
Heavy Ion Cooling Rings (Invited) — J.S. Hangst.....	manuscript not submitted	RPG04
Commissioning the MIT-Bates South Hall Ring — K. Jacobs, R. Averill, S. Bradley, A. Carter, G. Dodson, K. Dow, M. Farkhondeh, E. Ihloff, S. Kowalski, B. McAllister, W. Sapp, C. Sibley, S. Sobczynski, D. Tieger, C. Tschalaer, E. Tsentalovich, W. Turchinets, A. Zolfaghari, T. Zwart.....	327	RPG05
The AmPS Ring: Actual Performance and Future Plans — G. Luijckx, R. Bakker, H. Boer Rookhuizen, C. de Jager, F. Kroes, J. van der Laan, R. Maas, J. Noomen, Y. Wu.....	330	RPG06
Feasibility Study for Using the FNAL Antiproton Source as a Low Energy Proton-Antiproton Collider — Mike Church, Stephan Maury.....	333	RPG07
CIS, A Low Energy Injector for the IUCF Cooler — D.L. Friesel, S.Y. Lee.....	336	RPG08
The R&D Works on the High Intensity Proton Linear Accelerator for Nuclear Waste Transmutation — N. Ito, M. Mizumoto, K. Hasegawa, H. Oguri, J. Kusano, Y. Okumura, M. Kawai, H. Ino, H. Murata, Y. Touchi.....	339	RPG09
Development of the RFD Linac Structure — D.A. Swenson, K.R. Crandall, F.W. Guy, J.W. Lenz, A.D. Ringwall, L.S. Walling.....	342	RPG10

Proposed Upgrade of the NSCL — R.C. York, H. Blosser, T. Grimm, D. Johnson, D. Lawton, F. Marti, J. Vincent, X. Wu, A.F. Zeller	345	RPG11
ISAC-1: Radioactive Ion Beams Facility at TRIUMF — P.G. Bricault, R. Baartman, J.L. Beveridge, G.S. Clark, J. Doornbos, G. Dutto, T. Hodges, S. Koscielniak, L. Root, P.W. Schmor, H.R. Schneider	348	RPG12
First Beam Tests of the INS Split Coaxial RFQ for Radioactive Nuclei — S. Arai, A. Imanishi, K. Niki, M. Okada, Y. Takeda, E. Tojyo, N. Tokuda	351	RPG13
Accelerator Complex for a Radioactive Ion Beam Facility at ATLAS — J.A. Nolen	354	RPG14
The Lattice Design of Indiana University Cyclotron Facility Cooler Injector Synchrotron — D. Li, X. Kang, D.L. Friesel, S.Y. Lee, J.Y. Liu, A. Pei, A. Riabko, L. Wang	357	TAP03
Design Study of AntiProton Accumulation and Deceleration Ring in the KEK PS Complex — S. Machida, M. Yoshii, Y. Mori, N. Tokuda, Y. Ishi	360	TAP04
Feasibility Study of a 1-MW Pulsed Spallation Source — Y. Cho, Y.-C. Chae, E. Crosbie, M. Fathizadeh, H. Friedsam, K. Harkay, D. Horan, S. Kim, R. Kustom, E. Lessner, W. McDowell, D. McGhee, F. Mills, H. Moe, R. Nielsen, G. Norek, K.J. Peterson, A. Rauchas, K. Symon, K. Thompson, D. Warner, M. White	363	TAP05
ORIC Central Region Calculations — J.D. Bailey, D.T. Dowling, S.N. Lane, S.W. Mosko, D.K. Olsen, B.A. Tatum	366	TAP07
An Internal Timing Probe for Use in the MSU K1200 Cyclotron — J.D. Bailey, J. Kuchar, F. Marti, J. Ottarson	369	TAP08
Axial Injection and Phase Selection Studies of the MSU K1200 Cyclotron — J.D. Bailey	372	TAP09
Study and Redesign of the NSCL K500 Central Region — S.L. Snyder, F. Marti	375	TAP10
Heavy Ion Acceleration Strategies in the AGS Accelerator Complex -- 1994 Status Report — L.A. Ahrens, J. Benjamin, M. Blaskiewicz, J.M. Brennan, C.J. Gardner, H.C. Hseuh, Y.Y. Lee, R.K. Reece, T. Roser, A. Soukas, P. Thieberger	378	TAP11
Observation of Intensity Dependent Losses in Au(15+) Beams — M. Blaskiewicz, L.A. Ahrens, H.C. Hseuh, T. Roser, Y. Shoji, K. Zeno	381	TAP12
High Intensity Proton Operations at the Brookhaven — M. Blaskiewicz, L.A. Ahrens, E.J. Bleser, J.M. Brennan, C.J. Gardner, J.W. Glenn, R.K. Reece, T. Roser, M.J. Syphers, W. VanAsselt, S.Y. Zhang	383	TAP13
Fast Extracted Proton Beams at Low Energies in the CPS East Experimental Area — R. Cappel, L. Durieu, J.-Y. Hémerly, M. Martini, J.-P. Riunaud, Ch. Steinbach	386	TAP14
Ion-Optics Systems Of Multiply Charged High-Energy Ions For High Emittance Beams — V.O. Naidenov, L.A. Baranova, G.M. Gusinskii, A.V. Matyukov, S.Ya. Yavor	389	TAP16

High Energy Hadron Accelerators and Colliders

The Status of the Fermilab Main Injector Project (Invited) — D. Bogert, W. Fowler, S. Holmes, P. Martin, T. Pawlak	391	MPG01
Status and Future of the Tevatron (Invited) — V. Bharadwaj	396	MPG02
The RHIC Project - Status and Plans (Invited) — M. Harrison	401	MPG03
HERA Status and Plans (Invited) — R. Brinkmann	406	MPG04
The CERN Heavy Ion Accelerating Facility (Invited) — H.D. Haseroth	411	MPG05
UNK Status and Plans (Invited) — G. Gurov	416	MPG06
Reduction of Particle Losses in HERA by Generating an Additional Harmonic Tune Modulation — O.S. Brüning, F. Willeke	420	MPG07
Acceleration of Lead Ions in the CERN PS Booster and the CERN PS — F. Blas, P. Bossard, R. Cappel, G. Cyvoct, R. Garoby, G. Gelato, H. Haseroth, E. Jensen, D. Manglunki, K. Metzmacher, F. Pedersen, N. Rasmussen, K. Schindl, G.C. Schneider, H. Schönauer, L. Sermeus, M. Thivent, M. van Rooij, F. Völker, E. Wildner	423	MPG09
Highly Efficient Deflection of the Divergent Beam by Bent Single Crystal — V.I. Baranov, V.M. Biryukov, A.P. Bugorsky, Yu.A. Chesnokov, V.I. Kotov, M.V. Tarakanov, V.I. Terekhov, S.V. Tsarik, O.L. Fedin, M.A. Gordeeva, M.P. Gur'yev, Yu.P. Platonov, A.I. Smirnov	426	MPG10
Potential Accelerator Improvements Required for the Tevatron Upgrade at Fermilab — G. Jackson, G.W. Foster	428	MPG11
Beyond the LHC: A Conceptual Approach to a Future High Energy Hadron Collider — M.J. Syphers, M.A. Harrison, S. Peggs	431	MPG12

132 nsec Bunch Spacing in the Tevatron Proton-Antiproton Collider — <i>S.D. Holmes, J.A. Holt, J. Johnstone, J. Marriner, M. Martens, D. McGinnis</i>	434	WAP01
Aluminum Beam Tube for the Super Collider: An Option for No-Coating & No-Liner — <i>W. Chou</i>	437	WAP02
Variable Bunch Spacing in Super Collider — <i>W. Chou</i>	440	WAP03
Fermilab Collider Run 1B Statistics — <i>V. Bharadwaj, J. Crawford, R. Mau</i>	443	WAP04
Optimizing the Luminosity in the Tevatron by Independently Moving the Horizontal and Vertical Beta Stars Longitudinally — <i>M.A. Martens, G.P. Goderre</i>	446	WAP05
A Model of the Fermilab Collider for Optimization of Performance — <i>Elliot S. McCrory, Peter W. Lucas</i>	449	WAP06
Coupling in the Tevatron — <i>Norman M. Gelfand</i>	452	WAP07
Calculating Luminosity for a Coupled Tevatron Lattice — <i>J.A. Holt, M.A. Martens, L. Michelotti, G. Goderre</i>	455	WAP08
Remarks Concerning the γ-Production Probability of High Relativistic Dirac-Electrons in the Positron Bunch — <i>Huschang Heydari</i>	458	WAP09
Field Quality Evaluation of the Superconducting Magnets of the Relativistic Heavy Ion Collider — <i>J. Wei, R.C. Gupta, A. Jain, S.G. Peggs, C.G. Trahern, D. Trbojevic, P. Wanderer</i>	461	WAP10
High Intensity Proton Beams in a Multi-cycled SPS — <i>A. Faugier, X. Altuna, R. Bailey, R. Blanchard, T. Bohl, H. Burkhardt, P. Collier, K. Cornelis, N. Garrel, A. Hilaire, M. Jonker, R. Keizer, M. Lamont, T. Linnecar, G. de Rijk, G. Roy, H. Schmickler, J. Wenninger</i>	464	WAP12
The SPS as Accelerator of Pb^{82+} Ions — <i>A. Faugier, X. Altuna, R. Bailey, R. Blanchard, T. Bohl, E. Brouzet, H. Burkhardt, P. Collier, K. Cornelis, G. de Rijk, F. Ferioli, A. Hilaire, M. Lamont, T. Linnecar, M. Jonker, C. Niquille, G. Roy, H. Schmickler</i>	467	WAP13
Experimental Evidence for Multi-pass Extraction with a Bent Crystal — <i>B. Dehning, K. Elsener, G. Fidecaro, M. Gyr, W. Herr, J. Klem, W. Scandale, G. Vuagnin, E. Weisse, S. Weisz, S.P. Møller, E. Uggerhoj, A. Freund, R. Hustache, G. Carboni, M.P. Bussa, F. Tosello</i>	470	WAP14
Storage Ring for Enhanced Antiproton Production at Fermilab — <i>G. Jackson, G.W. Foster</i>	473	WAP16

Circular Electron Accelerators and Colliders

LEP Status and Plans (Invited) — <i>S. Myers</i>	476	WPG01
CESR Status and Plans (Invited) — <i>David L. Rubin</i>	481	WPG02
PEP II Status and Plans (Invited) — <i>John T. Seeman</i>	486	WPG03
KEKB Status and Plans (Invited) — <i>Shin-ichi Kurokawa</i>	491	WPG04
DAΦNE Status and Plans (Invited) — <i>G. Vignola</i>	495	WPG05
Electron-Positron Colliders at Novosibirsk (Invited) — <i>N. Dikansky</i>	500	WPG06
BEPC Status and Plans (Invited) — <i>Shu-Hong Wang</i>	506	WPG07
The First Attainment and Routine Use of Longitudinal Spin Polarization at a High Energy Electron Storage Ring — <i>D.P. Barber</i>	511	WPG08
Experiments with Bunch Trains in LEP — <i>O. Brunner, W. Herr, G. von Holtey, E. Keil, M. Lamont, M. Meddahi, J. Poole, R. Schmidt, A. Verdier, C. Zhang</i>	514	WPG09
Trapped Macroparticles in Electron Storage Rings — <i>F. Zimmermann, J.T. Seeman, M. Zolotarev, W. Stoeffl</i>	517	WPG10
A Compact-High Performance NLC Damping Ring Using High Magnetic Field Bending Magnets — <i>D.B. Cline, A. Garren, M. Green, J. Kolonko, D. Madura</i>	520	WPG11
Application of Precision Magnetic Measurements for Control of the Duke Storage Ring — <i>B. Burnham, V.N. Litvinenko, Y. Wu</i>	524	RAA01
Wiggler Insertion of the PEP-II B-Factor LER — <i>J. Heim, L. Bertolini, J. Dressler, O. Fackler, B. Hobson, M. Kendall, T. O'Connor, W. Stoeffl, T. Swan, A. Zholents, M.S. Zisman</i>	527	RAA03
Status of the High Energy Ring of the PEP II B-Factor — <i>U. Wienands, E. Reuter, J.T. Seeman, W. Davies-White, A. Fisher, J. Fox, L. Genova, J. Gracia, C. Perkins, M. Pietryka, H. Schwarz, T. Taylor, T. Jackson, C. Belser, D. Shimer</i>	530	RAA04
Design of the PEP-II Low-Energy Ring — <i>M.S. Zisman, R.B. Yourd, H. Hsieh</i>	533	RAA05
Injection Envelope Matching in Storage Rings — <i>M.G. Minty, W.L. Spence</i>	536	RAA06
A Mathematical Model for Investigating Chromatic Electron Beam Extraction from a Pulse Stretcher Ring — <i>Yu.N. Grigor'ev, A.Yu. Zelinsky</i>	539	RAA07

The Dynamical Aperture of ISI - 800 — <i>S. Efimov, I. Karnaukhov, S. Kononenko, A. Shcherbakov, A. Tarasenko, A. Zelinsky</i>	542	RAA08
The Influence of Residual Vertical Dispersion on LEP Performance — <i>P. Collier, H. Schmickler</i>	545	RAA10
Operational Procedures to Obtain High Beam-Beam Tune Shifts in LEP Pretzel Operation — <i>R. Bailey, P. Collier, T. Bohl, H. Burkhardt, K. Cornelis, G. De Rijk, A. Faugier, M. Jonker, M. Lamont, G. Roy, H. Schmickler, J. Wenninger</i>	548	RAA11
Synchrotron Phase Space Injection into LEP — <i>P. Collier</i>	551	RAA12
Systematic Studies of the LEP Working Point — <i>P. Collier, H. Schmickler</i>	554	RAA13
Modification of the LEP Electrostatic Separator Systems for Operation with Bunch Trains — <i>B. Balhan, A. Burton, E. Carlier, J.-P. Deluen, J. Dieperink, N. Garrel, B. Goddard, R. Guinand, W. Kalbreier, M. Laffin, M. Lamont, V. Mertens, J. Poole, H. Verhagen</i>	557	RAA15
Low Emittance Lattice for LEP — <i>Y. Alexahin, D. Brandt, K. Cornelis, A. Hofmann, J.P. Koutchouk, M. Meddahi, G. Roy, A. Verdier</i>	560	RAA17
Radiation Damping Partitions and RF-Fields — <i>M. Cornacchia, A. Hofmann</i>	564	RAA18
Experiments on Beam-Beam Depolarization at LEP — <i>R. Assmann, A. Blondel, B. Dehning, A. Drees, P. Grosse-Wiesmann, H. Grote, M. Placidi, R. Schmidt, F. Tecker, J. Wenninger</i>	567	RAA19
Measurements of Impedance Distributions and Instability Thresholds in LEP — <i>D. Brandt, P. Castro, K. Cornelis, A. Hofmann, G. Morpurgo, G.L. Sabbi, J. Wenninger, B. Zotter</i>	570	RAA20
A Preliminary Lattice Design of a Tau-Charm Factory Storage Ring in Beijing — <i>N. Huang, L. Jin, Y. Wu, G. Xu</i>	573	RAA21
Low Energy Ring Lattice of the PEP II Asymmetric B-Factor — <i>Y. Cai, M. Donald, R. Helm, J. Irwin, Y. Nosochkov, D.M. Ritson, Y. Yan, E. Forest, A. Zholents</i>	576	RAA22
Damping Rates of the SRRS Storage Ring — <i>K.T. Hsu, C.C. Kuo, W.K. Lau, W.T. Weng</i>	579	RAA23
Performance of the SRRS Storage Ring and Wiggler Commissioning — <i>C. Kuo, K.T. Hsu, G.H. Luo, W.K. Lau, Ch. Wang, H.P. Chang, L.H. Chang, M.H. Wang, J.C. Lee, C.S. Hsue, W.T. Weng, Y.C. Liu</i>	582	RAA24
Detector Solenoid Compensation in the PEP-II B-Factor — <i>Y. Nosochkov, Y. Cai, J. Irwin, M. Sullivan, E. Forest</i>	585	RAA25
Swamp Plots for Dynamic Aperture studies of PEP-II Lattices — <i>Y.T. Yan, J. Irwin, Y. Cai, T. Chen, D. Ritson</i>	588	RAA26
Lattice Design for the High Energy Ring of the SLAC B-Factor (PEP-II) — <i>M.H.R. Donald, Y. Cai, J. Irwin, Y. Nosochkov, D.M. Ritson, J. Seeman, H.-U. Wienands, Y.T. Yan</i>	591	RAA27
The APS Booster Synchrotron: Commissioning and Operational Experience — <i>S.V. Milton</i>	594	RAA28
A Preliminary Design for a Tau-Charm Factory — <i>J. Norem, E. Crosbie, J. Repond, L. Teng</i>	597	RAA29
A Spin Control System for the South Hall Ring at the Bates Linear Accelerator Center — <i>T. Zwart, P. Ivanov, Yu. Shatunov, R. Averill, K. Jacobs, S. Kowalski, W. Turchinets</i>	600	RAA31
Beam-Based Alignment of Sextupoles with the Modulation Method — <i>M. Kikuchi, K. Egawa, H. Fukuma, M. Tejima</i>	603	RAA33

Linear Colliders and Advanced Accelerator Concepts

The Stanford Linear Collider (Invited) — <i>Paul Emma</i>	606	WAG01
Options and Trade-Offs in Linear Collider Design (Invited) — <i>J. Rossbach</i>	611	WAG02
Test Facilities for Future Linear Colliders — <i>Ronald D. Ruth</i>	616	WAG03
Channel Guided Lasers for Plasma Accelerators (Invited) — <i>H.M. Milchberg, C.G. Durfee III, T.M. Antonsen, P. Mora</i>	621	WAG04
Inverse Cerenkov Accelerator Results (Invited) — <i>W.D. Kimura</i>	626	WAG05
Measurements of Plasma Wake-Fields in the Blow-Out Regime — <i>N. Barov, M. Conde, J.B. Rosenzweig, P. Schoessow, G. Cox, W. Gai, R. Konecny, J. Power, J. Simpson</i>	631	WAG06
Experimental Study of Electron Acceleration by Plasma Beat-Waves with Nd Lasers — <i>F. Amiranoff, F. Moulin, J. Fusellier, J.M. Joly, M. Juillard, M. Bercher, D. Bernard, A. Debraine, J.M. Dieulot, F. Jacquet, P. Matricon, Ph. Miné, B. Montès, R. Morano, P. Poilleux, A. Specka, J. Morillo, J. Ardonneau, B. Cros, G. Matthieussent, C. Stenz, P. Mora</i>	634	WAG07
A Broadband Electron Spectrometer and Electron Detectors for Laser Accelerator Experiments — <i>C.E. Clayton, K.A. Marsh, C. Joshi, C.B. Darrow, A.E. Dangor, A. Modena, Z. Najmudin, V. Malka</i>	637	WAG08

Photon Acceleration from Rest to the Speed of Light — C.H. Lai, T. Katsouleas, R. Liou, W.B. Mori, C. Joshi, P. Muggli, R. Brogle, J. Dawson.....	640	WAG09
A Constant Gradient Planar Accelerating Structure for Linac Use — Y.W. Kang, P.J. Matthews, R.L. Kustom.....	643	WAG10
Pulse to Pulse Stability Issues in the SLC — C. Adolphsen, R. Assmann, F.J. Decker, P. Emma, J. Frisch, L.J. Hendrickson, P. Krejcik, M. Minty, N. Phinney, P. Raimondi, M.C. Ross, T. Slaton, W. Spence, R. Stege, H. Tang, F. Tian, J. Turner, M. Woodley, F. Zimmermann.....	646	WAG11
HOM-Free Linear Accelerating Structure for e+e- Linear Collider at C-Band — T. Shintake, K. Kubo, H. Matsumoto, O. Takeda.....	649	WAG12
SLAC/CERN High Gradient Tests of an X-Band Accelerating Section — J.W. Wang, G.A. Loew, R.J. Loewen, R.D. Ruth, A.E. Vlieks, I. Wilson, W. Wuensch.....	653	WAG13

Linear Colliders

Performance of the 1994/95 SLC Final Focus System — F. Zimmermann, T. Barklow, S. Ecklund, P. Emma, D. McCormick, N. Phinney, P. Raimondi, M. Ross, T. Slaton, F. Tian, J. Turner, M. Woodley, M. Placidi, N. Toge, N. Walker.....	656	RPB01
Direct Measurement of Transverse Wakefields in the SLC Linac — P. Krejcik, R. Assmann, F.-J. Decker, S. Hartman, R. Miller, T. Raubenheimer.....	659	RPB02
Feedback Performance at the Stanford Linear Collider — M.G. Minty, C. Adolphsen, L.J. Hendrickson, R. Sass, T. Slaton, M. Woodley.....	662	RPB03
Vibration Studies of the Stanford Linear Accelerator — J.L. Turner, C. Adolphsen, G.B. Bowden, F.J. Decker, S.C. Hartman, S. Matsumoto, G. Mazaheri, D. McCormick, M. Ross, R. Stege, S. Virotek, M. Woodley.....	665	RPB04
SLAC Modulator Availability and Impact on SLC Operation — A.R. Donaldson, J.R. Ashton.....	668	RPB05
The SLC as a Second Generation Linear Collider — J.E. Spencer.....	671	RPB06
Status of the Design for the TESLA Linear Collider — R. Brinkmann.....	674	RPB07
The TESLA Test Facility (TTF) Linac - A Status Report — H. Weise.....	677	RPB08
The Infrastructure for the TESLA Test Facility (TTF) - A Status Report — S. Wolff.....	680	RPB09
The Status of the S-Band Linear Collider Study — N. Holtkamp.....	683	RPB12
The S-Band Linear Collider Test Facility — N. Holtkamp.....	686	RPB13
Beam Dynamics Studies for the SBLC — M. Drevlak, R. Wanzenberg.....	689	RPB14
S-Band HOM-Damper Calculations and Experiments — M. Dohlus, M. Marx, N. Holtkamp, P. Hülsmann, W.F.O. Müller, M. Kurz, H.-W. Glock, H. Klein.....	692	RPB15
The S-Band 36-Cell Experiment — B. Krietenstein, O. Podebrad, U. v.Rienen, T. Weiland, H.-W. Glock, P. Hülsmann, H. Klein, M. Kurz, C. Peschke, M. Dohlus, N. Holtkamp.....	695	RPB16

Volume 2

Linear Colliders (cont'd)

Parameters for the SLAC Next Linear Collider — T. Raubenheimer, C. Adolphsen, D. Burke, P. Chen, S. Ecklund, J. Irwin, G. Loew, T. Markiewicz, R. Miller, E. Paterson, N. Phinney, M. Ross, R. Ruth, J. Sheppard, H. Tang, K. Thompson, P. Wilson.....	698	RPC01
A Damping Ring Design for the SLAC Next Linear Collider — T.O. Raubenheimer, J. Byrd, J. Corlett, R. Early, M. Furman, A. Jackson, P. Krejcik, K. Kubo, T. Mattison, M. Minty, W. Moshhammer, D. Robin, B. Scott, J. Spencer, K. Thompson, P. Wilson.....	701	RPC02
A Bunch Compressor for the Next Linear Collider — P. Emma, T. Raubenheimer, F. Zimmermann.....	704	RPC03
A Final Focus System for the Next Linear Collider — F. Zimmermann, K. Brown, P. Emma, R. Helm, J. Irwin, P. Tenenbaum, P. Wilson.....	707	RPC06
Optimization of the NLC Final Focus System — F. Zimmermann, R. Helm, J. Irwin.....	710	RPC07
The SLAC NLC Extraction & Diagnostic Line — J. Spencer, J. Irwin, D. Walz, M. Woods.....	713	RPC08

CLIC - A Compact and Efficient High Energy Linear Collider — <i>H. Braun, R. Corsini, J.-P. Delahaye, G. Guignard, C. Johnson, J. Madsen, W. Schnell, L. Thorndahl, I. Wilson, W. Wuensch, B. Zotter</i>	716	RPC09
CLIC Test Facility Developments and Results — <i>R. Bossart, H. Braun, F. Chautard, M. Comunian, J.P. Delahaye, J.C. Godot, I. Kamber, J.H.B. Madsen, L. Rinolfi, S. Schreiber, G. Suberlucq, I. Wilson, W. Wuensch</i>	719	RPC10
Generation of a 30 GHz Train of Bunches Using a Magnetic Switch-Yard — <i>B. Autin, R. Corsini</i>	722	RPC11
A New Family of Isochronous Arcs — <i>G. Guignard, E.T. d'Amico</i>	725	RPC12
Updating of Beam Dynamics in the CLIC Main Linac — <i>G. Guignard</i>	728	RPC13
Improved CLIC Performances Using the Beam Response for Correcting Alignment Errors — <i>C. Fischer</i>	731	RPC14
Experimental Studies of a CERN-CLIC 32.98 GHz High Gradient Accelerating Structure Driven by the MIT Free Electron Laser Amplifier — <i>P. Volfbeyn, I. Mastovsky, G. Bekefi, I. Wilson, W. Wuensch</i>	734	RPC15
Design of a Relativistic Klystron Two-Beam Accelerator Prototype — <i>G. Westenskow, G. Caporaso, Y. Chen, T. Houck, S. Yu, S. Chattopadhyay, E. Henestroza, H. Li, C. Peters, L. Reginato, A. Sessler</i>	737	RPC16
Beam Dynamics Issues in an Extended Relativistic Klystron — <i>G. Giordano, H. Li, N. Goffeney, E. Henestroza, A. Sessler, S. Yu, T. Houck, G. Westenskow</i>	740	RPC17
Engineering Conceptual Design of the Relativistic Klystron Two-Beam Accelerator Based Power Source for 1-TeV Next Linear Collider — <i>L. Reginato, C. Peters, D. Vanecek, S. Yu, F. Deadrick</i>	743	RPC18
Design of Inductively Detuned RF Extraction Cavities for the Relativistic Klystron Two Beam Accelerator — <i>E. Henestroza, S.S. Yu, H. Li</i>	746	RPC19
Beam-Based Optical Tuning of the Final Focus Test Beam — <i>P. Tenenbaum, D. Burke, S. Hartman, R. Helm, J. Irwin, R. Iverson, P. Raimondi, W. Spence, V. Bharadwaj, M. Halling, J. Holt, J. Buon, J. Jeanjean, F. Le Diberder, V. Lepeltier, P. Puzo, K. Oide, T. Shintake, N. Yamamoto</i>	749	RPC20
Fermilab Contributions to the FFTB — <i>V. Bharadwaj, A. Braun, M. Halling, J.A. Holt, D. Still</i>	752	RPC21
HV Injection Phase Orbit Characteristics for Sub-Picosecond Bunch Operation with a High Gradient 17 GHz Linac — <i>J. Haimson, B. Mecklenburg</i>	755	RPC22

New Acceleration Techniques

Electron Acceleration in Relativistic Plasma Waves Generated by a Single Frequency Short-Pulse Laser — <i>C.A. Coverdale, C.B. Darrow, C.D. Decker, W.B. Mori, K.-C. Tzeng, C.E. Clayton, K.A. Marsh, C. Joshi</i>	758	RAB01
Theory and Simulation of Plasma Accelerators — <i>W.B. Mori, K.-C. Tzeng, C.D. Decker, C.E. Clayton, C. Joshi, T. Katsouleas, P. Lai, T.C. Chiou, R. Kinter</i>	761	RAB02
An Injector-prebuncher for a Plasma Electron Accelerator — <i>M. Lampel, C. Pellegrini, R. Zhang, C. Joshi, W.M. Fawley</i>	764	RAB03
Measurements of the Beatwave Dynamics in Time and Space — <i>A. Lal, K. Wharton, D. Gordon, M.J. Everett, C.E. Clayton, C. Joshi</i>	767	RAB04
A Novel Technique for Probing the Transverse Interactions Between an Electron Beam and a Plasma — <i>D. Gordon, A. Lal, C.E. Clayton, M. Everett, C. Joshi</i>	770	RAB05
Studies of Intense Laser Propagation in Channels for Extended Length Plasma Accelerators — <i>T. Katsouleas, T.C. Chiou, W.B. Mori, J.S. Wurtele, G. Shvets</i>	773	RAB08
UV Laser Ionization and Electron Beam Diagnostics for Plasma Lenses — <i>R. Govil, P. Volfbeyn, W. Leemans</i>	776	RAB10
Plasma Wakefield Acceleration Experiments in Overdense Regime Driven by Narrow Bunches — <i>T. Kozawa, T. Ueda, T. Kobayashi, M. Uesaka, K. Miya, A. Ogata, H. Nakanishi, T. Kawakubo, M. Arinaga, K. Nakajima, H. Shibata, N. Yugami, Y. Nishida, D. Whittum, Y. Yoshida</i>	779	RAB13
The Wake-Field Excitation in a Plasma-Dielectric Structure by a Sequence of Short Bunches of Relativistic Electrons — <i>I.N. Onishchenko, V.A. Kiseljov, A.K. Berezin, G.V. Sotnikov, V.V. Uskov, A.F. Linnik, Ya.B. Fainberg</i>	782	RAB15

A Beam Focusing System for a Linac Driven by a Traveling Laser Focus — A.A. Mikhailichenko.....	784	RAB18
2 x 2 TeV $\mu^+\mu^-$ Collider: Lattice and Accelerator-Detector Interface Study — N.M. Gelfand, N.V. Mokhov.....	787	RAB19
Muon Cooling and Acceleration Experiment at TRIUMF — S.A. Bogacz, D.B. Cline, P.H. Sandler, D.A. Sanders.....	790	RAB20
Helical Siberian Snakes — E. Ludmirsky.....	793	RAB21
Performance of Achromatic Lattice with Combined Function Sextupoles at Duke Storage Ring — V.N. Litvinenko, Y. Wu, B. Burnham, J.M.J. Madey, S.H. Park.....	796	RAB22

Accelerators and Storage Rings, Misc.

Matreshka High-Intensity Accelerator of Continuous Particle Beams — F.A. Vodopianov.....	799	TAR02
The Amplitude and Phase Control of the ALS Storage Ring RF System — C.C. Lo, B. Taylor, K. Baptiste.....	801	TAR03
Integral Dipole Field Calibration of the SRRRC Storage Ring Combined Function Bending Magnets — J.C. Lee, Peace Chang, C.S. Hsue.....	804	TAR04
Improved Mobile 70 MeV Race-Track Microtron Design — V.I. Shvedunov, A.I. Karev, V.N. Melekhin, N.P. Sobenin, W.P. Trower.....	807	TAR05
The Improvement of Energy Measurement in BTS Transport Line by Using Beam Tracing Method — M.H. Wang, J.C. Lee.....	810	TAR06
Design Study of PAL-Stretcher Ring — I.S. Ko, G.N. Kim, J. Choi, M.H. Cho, W. Namkung.....	813	TAR07
Thermomechanical Analysis of a Compact-Design High Heat Load Crotch Absorber — I.C. Sheng, S. Sharma, R. Rotela, J. Howell.....	816	TAR08
Novosibirsk Tau-Charm Factory Design Study — N. Dikansky, V. Parkhomchuk, A. Skrinsky, V. Yakimenko.....	819	TAR11
Development of a RAMI Program for LANSCE Upgrade — K.C.D. Chan, A. Browman, R.L. Hutson, R.J. Macek, P.J. Tallerico, C.A. Wilkinson.....	822	TAR12
Accelerator Waveform Synthesis and Longitudinal Beam Dynamics in a Small Induction Recirculator — T.J. Fessenden, D.P. Grote, W.M. Sharp.....	825	TAR13
Progress Toward a Prototype Recirculating Induction Accelerator for Heavy-Ion Fusion — A. Friedman, J.J. Barnard, M.D. Cable, D.A. Callahan, F.J. Deadrick, S. Eylon, T.J. Fessenden, D.P. Grote, D.L. Judd, H.C. Kirbie, D.B. Longinotti, S.M. Lund, L.A. Natrass, M.B. Nelson, M.A. Newton, T.C. Sangster, W.M. Sharp, S.S. Yu.....	828	TAR14
Three Dimensional Simulations of a Small Induction Recirculator Accelerator — D.P. Grote, A. Friedman, I. Haber.....	831	TAR15
A Dynamic Momentum Compaction Factor Lattice in the FERMILAB DEBUNCHER Ring — D.N. Olivieri, M. Church, J. Morgan.....	834	TAR16
Mechanical Design of Recirculating Accelerator Experiments for Heavy-Ion Fusion — V. Karpenko, J. Barnard, F. Deadrick, A. Friedman, D. Grote, S. Lund, J. Meredith, L. Natrass, M. Nelson, G. Repose, C. Sangster, W. Sharp, T. Fessenden, D. Longinotti, C. Ward.....	837	TAR17
The PEP-II Project-Wide Database — A. Chan, S. Calish, G. Crane, I. MacGregor, S. Meyer, J. Wong, A. Weinstein.....	840	TAR18
Chromaticity Compensation - Booster Sextupoles — S.A. Bogacz, K.-Y. Ng, J.-F. Ostiguy.....	843	TAR20
Overview of $\mu^+\mu^-$ Collider Options — D.B. Cline.....	846	TAR21
HIRFL Status and HIRFL-CSR Proposal — Ye Fang, Wang Yifang.....	850	TAR22

Particle Sources and Injectors

A Review of Polarized Ion Sources (Invited) — P.W. Schmor.....	853	MPE01
Sources for Production of Radioactive Ion-Beams (Invited) — Helge L. Ravn.....	858	MPE02
The TRIUMF High-Curent DC Optically -Pumped Polarized H⁺ Ion Source — A.N. Zelenski, C.D.P. Levy, K. Jayamanna, M. McDonald, P.W. Schmor, W.T.H. van Oers, J. Welz, G.W. Wight, G. Dutto, Y. Mori, T. Sakae.....	864	MPE03

Lifetime Test on a High-Performance DC Microwave Proton Source — J. Sherman, <i>D. Hodgkins, P. Lara, J.D. Schneider, R. Stevens Jr.</i>	867	MPE04
Performance Enhancement of a Compact Radio Frequency Ion Source by the Injection of Supplemental Electrons — R.F. Welton, G.D. Alton, D. Becher, G.D. Mills, J. Dellwo, <i>S.N. Murray</i>	871	MPE05
A High-Current Position Source — V.V. Gorev	874	MPE06
Polarized Electron Sources (Invited) — J.E. Clendenin	877	MPE08
High Brightness Electron Sources (Invited) — Richard L. Sheffield	882	MPE09
Polarization Studies of Strained GaAs Photocathodes at the SLAC Gun Test Laboratory — <i>P. Sáez, R. Alley, J. Clendenin, J. Frisch, R. Kirby, R. Mair, T. Maruyama, R. Miller,</i> <i>G. Mulhollan, C. Prescott, H. Tang, K. Witte</i>	887	MPE10
Experimental Results of the ATF In-line Injection System — X.J. Wang, T. Srinivasan-Rao, <i>K. Batchelor, M. Babzien, I. Ben-Zvi, R. Malone, I. Pogorelsky, X. Qiu, J. Sheehan, J. Skaritka</i>	890	MPE11
High Power Testing of a 17 GHz Photocathode RF Gun — S.C. Chen, B.G. Danly, J. Gonichon, <i>C.L. Lin, R.J. Temkin, S.R. Trotz, J.S. Wurtele</i>	893	MPE12
Analytical Model for Emittance Compensation in RF Photo-Injectors — L. Serafini, <i>J.B. Rosenzweig</i>	896	MPE13
Emission, Plasma Formation, and Brightness of a PZT Ferroelectric Cathode — <i>S. Sampayan, G. Caporaso, D. Trimble, G. Westenskow</i>	899	MPE14

Radio Frequency Guns and Linac Injectors

Design and Testing of the 2 MV Heavy Ion Injector for the Fusion Energy Research Program — W. Abraham, R. Benjergdes, L. Reginato, J. Stoker, R. Hipple, C. Peters, J. Pruyn, <i>D. Vanecek, S. Yu</i>	902	WPA01
K⁺ Diode for the LLNL Heavy Ion Recirculator Accelerator Experiment — S. Eylon, <i>E. Henestroza, F. Deadrick</i>	905	WPA02
A Single Bunch RFQ System for Heavy Ions — J. Madlung, A. Firjahn-Andersch, A. Schempp	908	WPA03
The Design of Low Frequency Heavy Ion RFQ Resonators — A. Schempp, H. Vormann, <i>U. Beisel, H. Deitinghoff, O. Engels, D. Li</i>	911	WPA04
A VE-RFQ-Injector for a Cyclotron — A. Schempp, O. Engels, F. Marhauser	914	WPA05
Fermilab Linac Injector, Revisited — M. Popovic, L. Allen, C.W. Schmidt	917	WPA06
New RF Structures for the Fermilab Linac Injector — M. Popovic, A. Moretti, R.J. Nobel	920	WPA07
High-Power RF Operations Studies with the CRITS RFQ — G.O. Bolme, D.R. Keffeler, <i>V.W. Brown, D.C. Clark, D. Hodgkins, P.D. Lara, M.L. Milder, D. Rees, P.J. Schafstall,</i> <i>J.D. Schneider, J.D. Sherman, R.R. Stevens, T. Zaugg</i>	923	WPA08
Beam Dynamics Studies of the Heavy Ion Fusion Accelerator Injector — E. Henestroza, <i>S.S. Yu, S. Eylon, D.P. Grote</i>	926	WPA09
First Tests at Injector for the S-Band Test Facility at DESY — M. Schmitz, W. Herold, <i>N. Holtkamp, W. Kriens, R. Walther</i>	929	WPA12
RF Phasing of the Duke Linac — Ping Wang, Nelson Hower, Patrick G. O'Shea	932	WPA13
Simulations and Measurements of the TTF Phase-1 Injector Gun — T. Garvey, M. Omeich, <i>M. Jablonka, J.M. Joly, H. Long</i>	935	WPA14
Experimental Studies on Cold Cathode Magnetron Gun — A.N. Dovbnya, V.V. Zakutin, <i>V.F. Zhiglo, A.N. Opanasenko, V.P. Romasko, S.A. Cherenshchikov</i>	938	WPA15
Secondary Emission in Cold-Cathode Magnetron Injection Gun — S.A. Cherenshchikov, <i>A.N. Dovbnya, A.N. Opanasenko</i>	939	WPA16
Design of a High Charge CW Photocathode Injector Test Stand at CEBAF — H. Liu, <i>D. Kehne, S. Benson, J. Bisognano, L. Cardman, F. Dylla, D. Engwall, J. Fugitt, K. Jordan,</i> <i>G. Neil, D. Neuffer, C. Sinclair, M. Wiseman, B. Yunn</i>	942	WPA17
CANDELA Photo-Injector Experimental Results With a Dispenser Photocathode — <i>C. Travier, B. Leblond, M. Bernard, J.N. Cayla, P. Thomas, P. Georges</i>	945	WPB01
A Multi-Cell RF Photoinjector Design — Sanghyun Park	948	WPB02
On the Frequency Scalings of RF Guns — Leon C.-L. Lin, J.S. Wurtele, S.C. Chen	951	WPB03
Waveguide Broad-Wall Coupling for RF Guns — Leon C.-L. Lin, S.C. Chen, J.S. Wurtele	954	WPB04

Charge and Wavelength Scaling of RF Photoinjectors: A Design Tool — J. Rosenzweig, <i>E. Colby</i>	957	WPB05
A Photocathode RF Gun Design for a mm-Wave Linac-Based FEL — A. Nassiri, T. Berenc, <i>J. Foster, G. Waldschmidt, J. Zhou</i>	961	WPB06
The RF Gun Development at SRRC — C.H. Ho, W.K. Lau, J.I. Hwang, S.Y. Hsu, Y.C. Liu	964	WPB07
Design and Construction of High Brightness RF Photoinjectors for TESLA — E. Colby, <i>V. Bharadwaj, J.F. Ostiguy, T. Nicol, M. Conde, J. Rosenzweig</i>	967	WPB08
Jitter Sensitivity in Photoinjectors — Patrick G. O'Shea	970	WPB09
Asymmetric Emittance Beam Generation Using Round Beam RF Guns and Non-linear Optics — G. Fiorentini, C. Pagani, L. Serafini	973	WPB10
The Argonne Wakefield Accelerator High Current Photocathode Gun and Drive Linac — <i>P. Schoessow, E. Chojnacki, G. Cox, W. Gai, C. Ho, R. Konecny, J. Power, M. Rosing,</i> <i>J. Simpson, N. Barov, M. Conde</i>	976	WPB11
Witness Gun for the Argonne Wakefield Accelerator — J. Power, J. Simpson, E. Chojnacki, <i>R. Konecny</i>	979	WPB12
Microwave Measurements of the BNL/SLAC/UCLA 1.6 Cell Photocathode RF Gun — <i>D.T. Palmer, R.H. Miller, H. Winick, X.J. Wang, K. Batchelor, M. Woodle, I. Ben-Zvi</i>	982	WPB13
Subpicosecond, Ultra-Bright Electron Injector — Bruce E. Carlsten, Martin L. Milder, <i>John M. Kinross-Wright, Donald W. Feldman, Steven Russell, John G. Plato, Alan Shapiro,</i> <i>Boyd Sherwood, Jan Studebaker, Richard Lovato, David Warren, Carl Timmer, Ronald Cooper,</i> <i>Ronald Sturges, Mel Williams</i>	985	WPB15
Energy Spread Compensation in an Electron Linear Accelerator — Yu.D. Tur, <i>A.N. Dovbnaya, V.A. Kushnir, V.V. Mitrochenko, D.L. Stepin</i>	988	WPB16
On Enhancement of Limited Accelerating Charge — Yu. Tur	990	WPB17
Magnetic Pulse Compression Using a Third Harmonic RF Linearizer — D.H. Dowell, <i>T.D. Hayward, A.M. Vetter</i>	992	WPB20
A Comparison of L-Band and C-Band RF Guns as Sources for Inline-Injection Systems — <i>Juan C. Gallardo, Harold G. Kirk, Thomas Meyer</i>	995	WPB21
Progress in the Study and Construction of the TESLA Test Facility Injector — R. Chehab, <i>M. Bernard, J.C. Bourdon, T. Garvey, B. Jacquemard, M. Mencick, B. Mouton, M. Omeich,</i> <i>J. Rodier, P. Roudier, J.L. Saury, M. Taurigna-Quere, Y. Thiery, B. Aune, M. Desmons,</i> <i>J. Fusellier, F. Gougnaud, J.F. Gournay, M. Jablonka, J.M. Joly, M. Juillard, Y. Lussignol,</i> <i>A. Mosnier, B. Phung, S. Buhler, T. Junquera</i>	998	WPB22

Particle Sources

Hollow Beam Profile in the Extraction System of ECR Ion Source — Y. Batygin, A. Goto, <i>Y. Yano</i>	1001	WPC01
Ion Sources for Use in Research and Applied High Voltage Accelerators — S. Nikiforov, <i>V. Golubev, D. Solnyshkov, M. Svinin, G. Voronin</i>	1004	WPC03
Direct Fast Beam Chopping of H⁻ Ion Beam in the Surface-Plasma H⁻ Ion Source — <i>K. Shinto, A. Takagi, Z. Igarashi, K. Ikegami, M. Kinsho, S. Machida, M. Yoshii, Y. Mori</i>	1007	WPC07
Emittance Measurements of the High Intensity Polarized Ion Source at IUCF — <i>V. Derenchuk, R. Brown, H. Petri, E. Stephenson, M. Wedekind</i>	1010	WPC08
Report on EBIS Studies for a RHIC Preinjector — E. Beebe, A. Hershcovitch, A. Kponou, <i>K. Prelec, J. Alessi, R. Schmieder</i>	1013	WPC09
Development of a Volume H⁻ Ion Source for LAMPF — D.R. Swenson, R.L. York, <i>R.R. Stevens Jr., C. Geisik, W. Ingalls, J.E. Stelzer, D. Fitzgerald</i>	1016	WPC10
Generation of High Purity CW Proton Beams from Microwave-Driven Sources — <i>David Spence, Keith R. Lykke</i>	1019	WPC11
Computational Studies for an Advanced Design ECR Ion Source — G.D. Alton, J. Dellwo, <i>R.F. Welton, D.N. Smith</i>	1022	WPC12
Pulsed Ion Sources of Duoplasmatron Type with Cold and Hot Cathodes — A. Glazov, <i>V. Krasnopolsky, R. Meshcherov, V. Masalov</i>	1025	WPC13
Double Pulse Experiment with a Velvet Cathode on the ATA Injector — G. Westenskow, <i>G. Caporaso, Y. Chen, T. Houck, S. Sampayan</i>	1027	WPC16

Emittance Measurements for the Illinois/CEBAF Polarized Electron Source — <i>B.M. Dunham, L.S. Cardman, C.K. Sinclair.....</i>	1030	WPC17
The NLC Positron Source — H. Tang, A.V. Kulikov, J.E. Clendenin, S.D. Ecklund, R.A. Miller, A.D. Yermian.....	1033	WPC18
Ferroelectric Cathodes as Electron Beam Sources — D. Flechtner, G.S. Kerslick, J.D. Ivers, J.A. Nation, L. Schächter.....	1036	WPC19
Studies of Linear and Nonlinear Photoelectric Emission for Advanced Accelerator Applications — R. Brogle, P. Muggli, P. Davis, G. Hairapetian, C. Joshi.....	1039	WPC20
A Derivative Standard for Polarimeter Calibration — G. Mulhollan, J. Clendenin, P. Sáez, D. Schultz, H. Tang, A.W. Pang, H. Hopster, K. Trantham, M. Johnston, T. Gay, B. Johnson, M. Magugumela, F.B. Dunning, G.K. Walters, G.F. Hanne.....	1043	WPC21
Analysis of Positron Focusing Section for SPring-8 Linac — A. Mizuno, S. Suzuki, H. Yoshikawa, T. Hori, K. Yanagida, H. Sakaki, T. Taniuchi, H. Kotaki, H. Yokomizo.....	1046	WPC22
R & D Activity on High QE Alkali Photocathodes for RF Guns — P. Michelato, A. Di Bona, C. Pagani, D. Sertore, S. Valeri.....	1049	WPC23
Development of an Accelerator-Ready Photocathode Drive Laser at CEBAF — S. Benson, M. Shinn.....	1052	WPC24

Linear Accelerators

Analytical Formulae for the Loss Factors and Wakefields of a Disk-loaded Accelerating Structure — J. Gao.....	1055	RPA03
Design Parameters for the Damped Detuned Accelerating Structure — K. Ko, K. Bane, R. Gluckstern, H. Hoag, N. Kroll, X.T. Lin, R. Miller, R. Ruth, K. Thompson, J. Wang.....	1058	RPA04
Operation of PLS 2-GeV Linac — W. Namkung, I.S. Ko, M.H. Cho, J.S. Bak, J. Choi, H.S. Lee.....	1061	RPA06
Radiation Measurements at the Advanced Photon Source (APS) Linear Accelerator — H.J. Moe, J.H. Vacca, V.R. Veluri, M. White.....	1064	RPA07
Positron Focusing in the Advanced Photon Source (APS) Linear Accelerator — Y.L. Qian, M. White.....	1067	RPA08
Bunch Length Measurements at the Advanced Photon Source (APS) Linear Accelerator — N.S. Sereno, R. Fuja, C. Gold, A.E. Grelick, A. Nassiri, J.J. Song, M. White.....	1070	RPA10
Performance of the Advanced Photon Source (APS) Linear Accelerator — M. White, N. Arnold, W. Berg, A. Cours, R. Fuja, J. Goral, A. Grelick, K. Ko, Y.L. Qian, T. Russell, N.S. Sereno, W. Wesolowski.....	1073	RPA11
TW Accelerating Structures with Minimal Surface Electric Field — O. Nezhevenko, D. Myakishev, V. Tarnetsky, V. Yakovlev.....	1076	RPA12
A 100 MeV Injector for the Electron Storage Ring at Kyoto University — T. Shirai, M. Kando, M. Ikegami, Y. Iwashita, H. Okamoto, S. Kakigi, H. Dewa, H. Fujita, A. Noda, M. Inoue, K. Mashiko.....	1079	RPA13
Phase Control and Intra-Pulse Phase Compensation of the Advanced Photon Source (APS) Linear Accelerator — A.E. Grelick, N. Arnold, K. Ko, N. Sereno, M. White.....	1082	RPA14
Error Sensitivity Study for Side Coupled Muffin Tin Structures using a Finite Difference Program — Warner Bruns.....	1085	RPA15
Design of Input Couplers and Endcells for Side Coupled Muffin-Tin Structures — Warner Bruns.....	1088	RPA16
Accelerator Archeology - The Resurrection of the Stanford MARKIII Electron Linac at Duke — P.G. O'Shea, F. Carter, C. Dickey, N. Hower, V.N. Litvinenko, R. Sachschaale, G. Swift, P. Wang, Y. Wu, J.M.J. Madey.....	1090	RPA17
Cold Model Test of Biperiodic L-Support Disk-and-Washer Linac Structure — Y. Iwashita, A. Noda, H. Okamoto, T. Shirai, M. Inoue.....	1093	RPA18
Compact Low Energy CW Linac with High Beam Current — A. Alimov, A. Chepurnov, O. Chubarov, D. Ermakov, K. Gudkov, B. Ishkhanov, I. Piskarev, V. Shvedunov, A. Shumakov.....	1096	RPA19
C-Band Linac RF-System for e+e- Linear Collider — T. Shintake, N. Akasaka, K.L.F. Bane, H. Hayano, K. Kubo, H. Matsumoto, S. Matsumoto, K. Oide, K. Yokoya.....	1099	RPA20
Initial Operation of the UCLA Plane Wave Transformer (PWT) Linac — R. Zhang, P. Davis, G. Hairapetian, M. Hogan, C. Joshi, M. Lampel, S. Park, C. Pellegrini, J. Rosenzweig, G. Travish.....	1102	RPA21

The UCLA Compact High Brightness Electron Accelerator — <i>P. Davis, G. Hairapetian, M. Hogan, C. Joshi, M. Lampel, S. Park, C. Pellegrini, J. Rosenzweig, G. Travish, R. Zhang</i>	1105	RPA22
A Semi-Automated System for the Characterization of NLC Accelerating Structures — <i>S.M. Hanna, G.B. Bowden, H.A. Hoag, R. Loewen, A.E. Vlieks, J.W. Wang</i>	1108	RPA23
SLAC Accelerator Operations Report: 1992-1995 — <i>R. Erickson, C.W. Allen, T.K. Inman, W. Linebarger, M. Stanek</i>	1111	RPA24
Beam Current Limitation in Microwave Accelerators — <i>A.V. Mishin, I.S. Shchedrin</i>	1114	RPA25
Installation and Commissioning of the e+/e- Injector for DAΦNE at Frascati — <i>K. Whitham, H. Amankath, J. Edighoffer, K. Fleckner, E. Gower, S. Lyons, D. Nett, D. Palmer, R. Sheppard, S. Sutter, P. Treas, A. Zante, R. Miller, R. Boni, H. Hsieh, F. Sannibale, M. Vescovi, G. Vignola</i>	1116	RPA26
Recent Studies of Linac for Production of Radioactive Beams in the INR — <i>I.N. Birukov, I.V. Gonin, D.V. Gorelov, A.N. Iljinov, V.A. Moiseev, P.N. Ostroumov, A.V. Tiunov</i>	1119	RPR01
RFQ Cold Model Studies — <i>P.G. Bricault, D. Joffe, H.R. Schneider</i>	1122	RPR02
Simulation of the TRIUMF Split-Ring 4-Rod RFQ with MAFIA — <i>P.G. Bricault, H.R. Schneider</i>	1125	RPR03
A Low-charge-state Injector Linac for ATLAS — <i>K.W. Shepard, J.W. Kim</i>	1128	RPR05
Progress of the Heidelberg High Current Injector — <i>C.-M. Kleffner, S. Auch, M. Grieser, D. Habs, V. Kößler, M. Madert, R. Repnow, D. Schwalm, H. Deitinghoff, A. Schempp, E. Jaeschke, R. von Hahn, S. Papureanu</i>	1131	RPR06
The New Concepts in Designing the CW High-current Linacs — <i>B.P. Murin, G.I. Batskikh, V.M. Belugin, B.I. Bondarev, A.A. Vasiljev, A.P. Durkin, Yu.D. Ivanov, V.A. Konovalov, A.P. Fedotov, I.V. Shumakov</i>	1134	RPR07
A Versatile, High-Power Proton Linac for Accelerator Driven Transmutation Technologies — <i>J.H. Billen, S. Nath, J.E. Stovall, H. Takeda, R.L. Wood, L.M. Young</i>	1137	RPR08
A Compact High-Power Proton Linac for Radioisotope Production — <i>H. Takeda, J.H. Billen, S. Nath, J.E. Stovall, R.L. Wood, L.M. Young</i>	1140	RPR09
Potentialities of Electron and Ion Beam Accelerators for Long-Lived Nuclear Waste Transmutation — <i>A. Shalnov, N. Abramenko, B. Bogdanovich, M. Karetnikov, A. Nesterovich, A. Puchkov</i>	1143	RPR10
RFQ Design for High-Intensity Proton Beams — <i>R. Ferdinand, J.-M. Lagniel, P. Mattei</i>	1146	RPR11
Methods for Increasing of Beam Intensity in Undulator Linear Accelerator — <i>E.S. Masunov</i>	1149	RPR12
Linac Integrated Scheme Using RF Energy Storage and Compression — <i>A.V. Smirnov</i>	1152	RPR13
Magnetic Field Influence on RF-Structures Electrodynamics Characteristics and Sparking Limit — <i>A. Shalnov, N. Abramenko, B. Bogdanovich, M. Karetnikov, A. Nesterovich, M. Tubaev</i>	1155	RPR15
Calculations on the Possibility of the Simultaneous Acceleration of Ions with Different Charge States in a RFQ — <i>H. Deitinghoff</i>	1158	RPR18
Phase-Scan Analysis Results for the First Drift Tube Linac Module in the Ground Test Accelerator: Data Reproducibility and Comparison to Simulations — <i>K.F. Johnson, O.R. Sander, G.O. Bolme, S. Bowling, R. Connolly, J.D. Gilpatrick, W.P. Lysenko, J. Power, E.A. Wadlinger, V. Yuan</i>	1161	RPR19
Accelerator Systems Optimizing Code — <i>C.C. Paulson, A.M.M. Todd, M.A. Peacock, M.F. Reusch, D. Bruhwiler, S.L. Mendelsohn, D. Berwald, C. Piaszczyk, T. Meyers, G.H. Gillespie, B.W. Hill, R.A. Jamison</i>	1164	RPR20
Unexpected Matching Insensitivity in DTL of GTA Accelerator — <i>V.W. Yuan, O.R. Sander, R.C. Connolly, J.D. Gilpatrick, K.F. Johnson, W.P. Lysenko, D.P. Rusthoi, M. Smith, R. Weiss</i>	1167	RPR22
Current Losses and Equilibrium in RF Linear Accelerators — <i>Nathan Brown, Martin Reiser</i>	1170	RPR23
MMF Linac Upgrade Possibilities for the Pulsed Neutron Source — <i>S.K. Esin, L.V. Kravchuk, A.I. Kvasha, P.N. Ostroumov, V.L. Serov</i>	1173	RPR24
Moscow Meson Factory DTL RF System Upgrade — <i>S.K. Esin, L.V. Kravchuk, A.I. Kvasha, V.L. Serov</i>	1175	RPR25

Pulsed and High Intensity Beams and Technology

Heavy Ion Fusion 2 MV Injector (Invited) — <i>S. Yu, S. Eylon, E. Henestroza, C. Peters, L. Reginato, D. Vanecek, F. delaRama, R. Hipple, J.D. Stoker, D. Grote, F. Deadrick</i>	1178	TAE01
Linac-Driven Spallation-Neutron Source (Invited) — <i>Andrew J. Jason</i>	1183	TAE02

High Average Power, High Current Pulsed Accelerator Technology (Invited) — <i>Eugene L. Neu</i>	1188	TAE03
Studies of Localized Space-Charge Waves in Space-Charge Dominated Beams (Invited) — <i>J.G. Wang, M. Reiser</i>	1193	TAE04
Design of the Jupiter Accelerator for Large X-ray Yields — J.J. Ramirez	1198	TAE05
Design and Power Flow Studies of a 500-TW Inductive Voltage Adder (IVA) Accelerator — <i>M.G. Mazarakis, J.W. Poukey, J.P. Corley, D.L. Smith, L. Bennett, J.J. Ramirez, P. Pankuch,</i> <i>I. Smith, P. Corcoran, P. Spence</i>	1201	TAE06
COBRA Accelerator for Sandia ICF Diode Research at Cornell University — David L. Smith, <i>Pete Ingwersen, Lawrence F. Bennett, John D. Boyes, David E. Anderson, John B. Greenly,</i> <i>Ravi N. Sudan</i>	1204	TAE07
Beam Injector and Transport Calculations for ITS — Thomas P. Hughes, David C. Moir, <i>Paul W. Allison</i>	1207	TAE08
Status of the AIRIX Induction Accelerator — Ph. Eyharts, Ph. Anthouard, J. Bardy, <i>C. Bonnafond, Ph. Delsart, A. Devin, P. Eyl, J. Labrousche, J. Launspach, J. De Mascureau,</i> <i>E. Merle, A. Roques, P. Le Taillandier, M. Thevenot, D. Villate, L. Voisin</i>	1210	TAE09
Pulse Modulators for Ion Recirculator Cells — T.F. Godlove, L.K. Len, F.M. Mako, <i>W.M. Black, K. Sloth</i>	1213	TAE10
A High Charge State Heavy Ion Beam Source for HIF — S. Eylon, E. Henestroza	1216	TAE11
Design and Operation of a 700kV, 700A Modulator — J.D. Ivers, G.S. Kerslick, J.A. Nation, <i>L. Schächter</i>	1219	TAE12
The 3 MEV, 200 KW High Voltage Electron Accelerator for Industrial Application — <i>N.G. Tolstun, V.S. Kuznetsov, A.S. Ivanov, V.P. Ovchinnikov, M.P. Svinjin</i>	1222	TAE13
Klystron Modulator for Industrial Linac — Yu.D. Tur, V.I. Beloglazov, E.A. Khomyakov, <i>V.P. Krivchikov, V.B. Mufel, V.V. Zakutin</i>	1225	TAE14
Optimization of High-Current Ion Beam Acceleration and Charge Compensation in Two Cusps of Induction Linac — Vyacheslav I. Karas', Nadya G. Belova	1227	WAA01
2,5-Dimensional Numerical Simulation of Propagation of the Finite Sequence of Relativistic Electron Bunches (REB) in Tenuous and Dense Plasmas — V.I. Karas', Ya.B. Fainberg, <i>V.D. Levchenko, Yu.S. Sigov</i>	1230	WAA02
Kinetic Simulation of Fields Excitation and Particle Acceleration by Laser Beat Wave in Non-Homogeneous Plasmas — V.I. Karas', Ya.B. Fainberg, V.D. Levchenko, Yu.S. Sigov	1233	WAA03
An Upgraded Proton Injection Kicker Magnet for the Fermilab MIR — J. Dinkel, R. Reilly	1236	WAA05
Fermilab Main Injector Abort Kicker System — C.C. Jensen, J.A. Dinkel	1239	WAA07
Analysis of the Electrical Noise from the APS Kicker Magnet Power Supplies — <i>J.A. Carwardine, J. Wang</i>	1242	WAA08
Design and Test Results of Kicker Units for the Positron Accumulator Ring at the APS — <i>J. Wang</i>	1245	WAA09
Development of a Modular and Upgradeable Fast Kicker Magnet System for the Duke Storage Ring — R.J. Sachtshale, C. Dickey, P. Morcombe	1248	WAA10
High Current High Accuracy IGBT Pulse Generator — V.V. Nesterov, A.R. Donaldson	1251	WAA11
Analysis and Design Modifications for Upgrade of Storage Ring Bump Pulse System Driving the Injection Bump Magnets at the ALS — G.D. Stover	1254	WAA14
Eddy Currents Induced in a Muon Storage Ring Vacuum Chamber Due to a Fast Kicker — <i>W.Q. Feng, E.B. Forsyth</i>	1257	WAA15
High Pulse Power Modulator for a S-Band Transmitter — J. DeCobert, B. Binns, R. Campbell, <i>A. Hawkins, D. Wang, A. Zolfaghari</i>	1260	WAA16
Modulator for Klystron 5045 — N.S. Dikansky, V. Akimov, B. Estrin, K. Gubin, I. Kazarezov, <i>V. Kokoulin, N. Kot, A. Novokhatsky, Yu. Tokarev, S. Vasserman</i>	1263	WAA17
High Voltage Nanosecond Generators for SIBERIA - 2 — A. Kadnikov, V. Deviatilov, <i>V. Korchuganov, Yu. Matveev, D. Shvedov</i>	1266	WAA18
High Gradient Insulator Technology for the Dielectric Wall Accelerator — S. Sampayan, <i>G. Caporaso, B. Carder, Y. Chen, C. Holmes, E. Lauer, D. Trimble, J. Elizondo, M. Krogh,</i> <i>B. Rosenblum, C. Eichenberger, J. Fockler</i>	1269	WAA19
Status of the First Stage of Linear Induction Accelerator SILUND-21 — A.A. Fateev, <i>G.V. Dolbilov, I.I. Golubev, I.N. Ivanov, V.V. Kosukhin, N.I. Lebedev, V.A. Petrov,</i> <i>V.N. Razuvakin, V.S. Shvetsov, M.V. Yurkov</i>	1272	WAA20

EMIR-M Installation in the Mode of Operation with Plasma Opening Switch —

V.P. Kovalev, V.M. Korepanov, B.M. Lavrent'ev, R.N. Munasyrov, B.A. Filatov..... 1274 WAA21

Magnet Technology**New Developments in Niobium Titanium Superconductors (Invited) — D.C. Larbalestier,**

P.J. Lee..... 1276 TPE01

Superconducting Magnets (Invited) — R. Perin..... 1282 TPE02**Assembly and Commissioning of the LHC Test String (Invited) — P. Faugeras**..... 1288 TPE03**Construction and Testing of Arc Dipoles and Quadrupoles for the Relativistic Heavy Ion**

**Collider (RHIC) at BNL (Invited) — P. Wanderer, J. Muratore, M. Anerella, G. Ganetis,
A. Ghosh, A. Greene, R. Gupta, A. Jain, S. Kahn, E. Kelly, G. Morgan, A. Prodel, M. Rehak,**

W. Sampson, R. Thomas, P. Thompson, E. Willen..... 1293 TPE04

Permanent Magnet Design for the Fermilab Main Injector Recycler Ring — G.W. Foster,

K. Bertsche, J.-F. Ostiguy, B. Brown, H. Glass, G. Jackson, M. May, D. Orris, Dick Gustafson..... 1298 TPE05

Recent Advances in Insertion Devices (Invited) — E. Gluskin, E.R. Moog..... 1301 TPE06**Permanent Magnet Beam Transport (Invited) — R.F. Holsinger**..... 1305 TPE07**Statistical Analyses of the Magnet Data for the Advanced Photon Source Storage Ring**

Magnets (Invited) — S.H. Kim, D.W. Carnegie, C. Doose, R. Hogrefe, K. Kim, R. Merl..... 1310 TPE08

The Magnet System for the BESSY II Injector Synchrotron — T. Knuth, D. Krämer,

E. Weihreter, I. Chertok, S. Michailov, B. Sukhina..... 1316 TPE09

Segmented High Quality Undulators — J. Chavanne, P. Elleaume, P. Van Vaerenbergh..... 1319 TPE10**Design of the PEP-II Low-Energy Ring Arc Magnets — T. Henderson, N. Li, J. Osborn,**

J. Tanabe, D. Yee, R. Yourd, W. Du, Y. Jiang, Y. Sun..... 1322 FAP01

Prototype Development of the BESSY II Storage Ring Magnetic Elements — T. Becker,

D. Krämer, S. Küchler, U. Strönisch, V. Korchuganov, N. Kuznetsov, E. Levichev..... 1325 FAP02

Design, Construction, and Procurement Methodology of Magnets for the 7-GeV Advanced

Photon Source — A. Gorski, J. Argyrakis, J. Biggs, E. Black, J. Humbert, J. Jagger,

K. Thompson..... 1328 FAP03

The Main Injector Trim Dipole Magnets — R. Baiod, D.J. Harding, D.E. Johnson, P.S. Martin,

S. Mishra..... 1331 FAP04

The Main Injector Chromaticity Correction Sextupole Magnets: Measurements and

Operating Schemes — C.M. Bhat, A. Bogacz, B.C. Brown, D.J. Harding, Si J. Fang,

P.S. Martin, H.D. Glass, J. Sim..... 1334 FAP05

Magnetic Field Measurements of the Initial Fermilab Main Injector Production

Quadrupoles — D.J. Harding, R. Baiod, B.C. Brown, J.A. Carson, N.S. Chester, E. Desavouret,

J. DiMarco, J.D. Garvey, H.D. Glass, P.J. Hall, P.S. Martin, P.O. Mazur, C.S. Mishra,

A. Mokhtarani, J.M. Nogiec, D.F. Orris, J.E. Pachnik, A.D. Russell, S.A. Sharonov, J.W. Sim,

J.C. Tompkins, K. Trombly-Freytag, D.G.C. Walbridge, V.A. Yarba..... 1337 FAP06

Magnetic Field Measurements of the Initial Fermilab Main Injector Production Dipoles —

D.J. Harding, R. Baiod, B.C. Brown, J.A. Carson, N.S. Chester, E. Desavouret, J. DiMarco,

J.D. Garvey, H.D. Glass, P.J. Hall, P.S. Martin, P.O. Mazur, S. Mishra, A. Mokhtarani,

J.M. Nogiec, D.F. Orris, J.E. Pachnik, A.D. Russell, S.A. Sharonov, J.W. Sim, J.C. Tompkins,

K. Trombly-Freytag, D.G.C. Walbridge, V.A. Yarba..... 1340 FAP07

The Fermilab Main Injector Dipole and Quadrupole Cooling Design and Bus Connections

— J.A. Satti..... 1343 FAP08

Design of the Fermilab Main Injector Lambertson — D.E. Johnson, R. Baiod, D.J. Harding,

P.S. Martin, M. May..... 1346 FAP09

Three-Dimensional End Effects in Iron Septum Magnets — J.-F. Ostiguy, D.E. Johnson..... 1349 FAP10**Design and B-field Measurements of a Lambertson Injection Magnet for the RHIC**

Machine — N. Tsoupas, E. Rodger, J. Claus, H.W. Foelsche, P. Wanderer..... 1352 FAP11

The APS Direct-Drive Pulsed Septum Magnets — S. Sheynin, F. Lopez, S.V. Milton..... 1355 FAP12**Development of the Pulse Magnets for the Booster Synchrotron of SPring-8 — H. Yonehara,**

H. Suzuki, T. Nagafuchi, M. Kodaira, T. Aoki, N. Tani, S. Hayashi, Y. Ueyama, T. Kaneda,

Y. Sasaki, H. Abe, H. Yokomizo..... 1358 FAP13

Magnetic Design of the LNL Transport Line — R.H.A. Farias, Liu Lin, G. Tosin..... 1361 FAP14**Construction and Characterization of Combined Function Quadrupoles — G. Tosin**..... 1364 FAP15

Dipole Magnets for the SLAC 50 GeV A-Line Upgrade — R. Erickson, S. DeBarger, C.M. Spencer, Z. Wolf.....	1366	FAP16
Design and Testing of the Magnetic Quadrupole for the Heavy Ion Fusion Program — R. Benjergdes, A. Faltens, W. Fawley, C. Peters, L. Reginato, M. Stuart.....	1369	FAP17
Design and Construction of a Large Aperture, Quadrupole Electromagnet Prototype for ILSE — M. Stuart, A. Faltens, W.M. Fawley, C. Peters, M.C. Vella.....	1372	FAP18
A Permanent Race-Track Microtron End Magnet — A.I. Karev, V.N. Melekhin, V.I. Shvedunov, N.P. Sobenin, W.P. Trower.....	1375	FAP19
Planar Permanent Magnet Multipoles: Measurements and Configurations — T. Cremer, R. Tatchyn.....	1378	FAP20
Temperature Considerations in the Design of a Permanent Magnet Storage Ring — K. Bertsche, J.-F. Ostiguy, W.B. Foster.....	1381	FAP21
3D Numerical Analysis of Magnets and the Effect of Eddy Current on Fast Steering — T. Nagatsuka, T. Koseki, Y. Kamiya, Y. Terada.....	1384	FAP22
MEB Resitive Magnets Prototypes Manufacturing — G. Batskikh, G. Mamaev, T. Latypov, I. Tenyakov, Y. Tereshkin.....	1387	FAP24

Volume 3

Magnet Technology (cont'd)

Quench Antennas for RHIC Quadrupole Magnets — T. Ogitsu, A. Terashima, K. Tsuchiya, G. Ganetis, J. Muratore, P. Wanderer.....	1390	FAQ02
Superconducting 8 cm Corrector Magnets for the Relativistic Heavy Ion Collider (RHIC) — A. Morgillo, J. Escallier, G. Ganetis, A. Greene, A. Ghosh, A. Jain, E. Kelly, A. Marone, G. Morgan, J. Muratore, W. Sampson, P. Thompson, P.J. Wanderer, E. Willen.....	1393	FAQ03
Superconducting Sextupoles and Trim Quadrupoles for RHIC — P. Thompson, M. Anerella, G. Ganetis, A. Ghosh, A. Greene, R. Gupta, A. Jain, E. Kelly, M. Lindner, G. Morgan, J. Muratore, W. Sampson, P. Wanderer, E. Willen.....	1396	FAQ04
Study of UNK Quench Protection System on the String of 4 UNK Superconducting Magnets — A. Andriishchin, O. Afanasiev, V. Gridasov, A. Erochin, E. Kachtanov, K. Myznikov, V. Sytchev, L. Vassiliev, O. Veselov, N. Yarygin.....	1399	FAQ06
Two Alternate High Gradient Quadrupoles; An Upgraded Tevatron IR and a "Pipe" Design — A.D. McInturff, J.M. van Oort, R.M. Scanlan.....	1402	FAQ07
Superconducting Focusing Solenoid for X-band Klystron — T. Ogitsu, T. Higo, H. Mizuno, Y. Imai, T. Inaguchi, T. Minato, T.H. Kim, T. Uemura, S. Yokoyama, Z. Wolf, D. Jensen, P. Radusewicz.....	1405	FAQ08
A High Gradient Superconducting Quadrupole for a Low Charge State Ion Linac — J.W. Kim, K.W. Shepard, J.A. Nolen.....	1408	FAQ09
Status of the High Brilliance Synchrotron Radiation Source BESSY-II — E. Jaeschke, S. Khan, D. Krämer, D. Schirmer.....	1411	FAQ12
Harmonic Generation FEL Magnets: Measured B-fields Compared to 3D Simulations — W.S. Graves, L. Solomon.....	1414	FAQ13
Measurement of Ramp Rate Sensitivity in Model Dipoles with Ebanol-Coated Cable — C. Haddock, V. Kovachev, D. Capone.....	1417	FAQ14
Combined Element Magnet Production for the Relativistic Heavy Ion Collider (RHIC) at BNL — S. Mulhall, H. Foelsche, G. Ganetis, A. Greene, E. Kelly, S. Plate, E. Willen.....	1420	FAQ15
Field Quality Control Through the Production Phase of the RHIC Arc Dipoles — R. Gupta, A. Jain, S. Kahn, G. Morgan, P. Thompson, P. Wanderer, E. Willen.....	1423	FAQ16
The Elliptical Multipole Wiggler Project — E. Gluskin, D. Frachon, P.M. Ivanov, J. Maines, E.A. Medvedko, E. Trakhtenberg, L.R. Turner, I. Vasserman, G.I. Erg, Yu.A. Evtushenko, N.G. Gavrilov, G.N. Kulipanov, A.S. Medvedko, S.P. Petrov, V.M. Popik, N.A. Vinokurov, A. Friedman, S. Krinsky, G. Rakowsky, O. Singh.....	1426	FAQ17
Results of Magnetic Measurements and Field Integral Compensation for the Elliptical Multipole Wiggler — D. Frachon, P.M. Ivanov, E.A. Medvedko, I. Vasserman, O. Despe, Y.G. Kang.....	1429	FAQ18

Status of ELETTRA Insertion Devices — <i>R.P. Walker, R. Bracco, A. Codutti, B. Diviacco, D. Millo, D. Zangrando</i>	1432	FAQ19
Expected Radiation Spectra of a 30-m Long Undulator in SPring-8 — <i>M. Takao, Y. Miyahara</i>	1435	FAQ20
Analytical Formulation of a Quasi-periodic Undulator — <i>M. Takao, S. Hashimoto, S. Sasaki, Y. Miyahara</i>	1438	FAQ21
High-Field Strong-Focusing Undulator Designs for X-Ray Linac Coherent Light Source (LCLS) Applications — <i>S. Caspi, R. Schlueter, R. Tatchyn</i>	1441	FAQ23
Wigglers at the Advanced Light Source — <i>E. Hoyer, J. Akre, D. Humphries, T. Jackson, S. Marks, Y. Minamihara, P. Pipersky, D. Plate, G. Portmann, R. Schlueter</i>	1444	FAQ24
Design of End Magnetic Structures for the Advanced Light Source Wigglers — <i>D. Humphries, J. Akre, E. Hoyer, S. Marks, Y. Minamihara, P. Pipersky, D. Plate, R. Schlueter</i>	1447	FAQ25
Passive End Pole Compensation Scheme for a 1.8 Tesla Wiggler — <i>L.H. Chang, Ch. Wang, C.H. Chang, T.C. Fan</i>	1450	FAQ26
Insertion of Helical Siberian Snakes in RHIC — <i>A. Luccio, F. Pilat</i>	1453	FAQ28
Modeling of WLS Field with Piecewisely Constant Magnets — <i>Zuping Liu, Aihua Zhao</i>	1456	FAQ29
A BESSY-1 6 Tesla WLS Effect Compensation Scheme — <i>Zuping Liu, Aihua Zhao</i>	1459	FAQ30
16 Tesla Block-Coil Dipole for Future Hadron Colliders — <i>Peter M. McIntyre, Weijun Shen</i>	1462	FAQ31
Automated Methods of Field Harmonic Signal Extraction and Processing for the Magnets in Superconducting Supercollider — <i>T.S. Jaffery, J. Butteris, M. Wake</i>	1465	FAQ32

Radio Frequency Technology

Review of the Development of RF Cavities for High Currents (Invited) — <i>J. Kirchgessner</i>	1469	FAE01
Performance of Normal Conducting Structures for Linear Colliders (Invited) — <i>Toshiyasu Higo</i>	1474	FAE02
High Gradient Superconducting RF Systems (Invited) — <i>J. Graber</i>	1478	FAE03
Development and Advances in Conventional High Power RF Systems (Invited) — <i>P.B. Wilson</i>	1483	FAE04
The Upgraded RF System for the AGS and High Intensity Proton Beams (Invited) — <i>J.M. Brennan</i>	1489	FAE05
Phase-Stable, Microwave FEL Amplifier — <i>Bruce E. Carlsten, Michael V. Fazio, W. Brian Haynes, Lisa M. May, James M. Potter</i>	1494	FAE06
1.2 MW Klystron for Asymmetric Storage Ring B Factory — <i>W.R. Fowkes, G. Caryotakis, E. Doyle, E. Jongewaard, C. Pearson, R. Phillips, J. Sackett, E. Wright, H. Bohlen, G. Huffman, S. Lenci, E. Lien, E. McCune, G. Miram</i>	1497	FAE07
Analysis of Multipacting in Coaxial Lines — <i>E. Somersalo, P. Ylä-Oijala, D. Proch</i>	1500	FAE08
An Accelerator Resonantly Coupled with an Energy Storage (ARES) for the KEKB — <i>Y. Yamazaki, K. Akai, N. Akasaka, E. Ezura, T. Kageyama, F. Naito, T. Shintake, Y. Takeuchi</i>	1503	FAE09
Non Integer Harmonic Number Acceleration of Lead Ions in the CERN SPS — <i>D. Boussard, T. Bohl, T. Linnekar, U. Wehrle</i>	1506	FAE10
Analysis and Results of the Industrial Production of the Superconducting Nb/Cu Cavities for the LEP2 Project — <i>E. Chiaveri, C. Benvenuti, R. Cosso, D. Lacarrere, K.M. Schirm, M. Taufer, W. Weingarten</i>	1509	FAE11
Performance Experience with the CEBAF SRF Cavities — <i>C. Reece, J. Benesch, M. Drury, C. Hovater, J. Mammoser, T. Powers, J. Preble</i>	1512	FAE12
Beam Test of a Superconducting Cavity for the CESR Luminosity Upgrade — <i>H. Padamsee, P. Barnes, S. Belomestnykh, K. Berkelman, M. Billing, R. Ehrlich, G. Flynn, Z. Greenwald, W. Hartung, T. Hays, S. Henderson, R. Kaplan, J. Kirchgessner, J. Knobloch, D. Moffat, H. Muller, E. Nordberg, S. Peck, M. Pisharody, J. Reilly, J. Rogers, D. Rice, D. Rubin, D. Sagan, J. Sears, M. Tigner, J. Welch</i>	1515	FAE13

Radio Frequency Power Sources

Development of Input & Output Structures for High Power X-Band TWT Amplifiers — <i>S. Naqvi, Cz. Golkowski, G.S. Kerslick, J.A. Nation, L. Schächter</i>	1518	TAQ01
Characterization of a Klystrode as a RF Source for High-Average-Power Accelerators — <i>D. Rees, D. Keffeler, W. Roybal, P.J. Tallerico</i>	1521	TAQ02
Choppertron II — <i>T.L. Houck, G.A. Westenskow, J. Haimson, B. Mecklenburg</i>	1524	TAQ03

The Resistive-Wall Klystron as a High-Power Microwave Source — Han S. Uhm.....	1527	TAQ04
Operating Conditions of High-Power Relativistic Klystron — Han S. Uhm	1530	TAQ05
Spurious Oscillations in High Power Klystrons — B. Krietenstein, K. Ko, T. Lee, U. Becker, T. Weiland, M. Dohlus.....	1533	TAQ06
In-House Repair of a 30 Megawatt S Band Klystron — R. Sachtschale, P.G. O'Shea, M. Ponds, G. Swift.....	1536	TAQ07
Development of a High Power 1.2 MW CW L-Band Klystron — K. Hirano, Y.L. Wang, T. Emoto, A. Enomoto, I. Sato	1539	TAQ08
Ultrarelativistic Klystron - a Future Super Power UHF Generator — F.A. Vodopianov	1542	TAQ10
A 200 KW Power Amplifier and Solid State Driver for the Fermilab Main Injector — J. Reid, H. Miller	1544	TAQ11
A 476 MHz RF System for the Storage Mode of the AmPS Ring — F. Kroes, P. de Groen, E. Heine, B. Heutenik, A. Kruijer, B. Munneke, R. Pirovano, T. Sluijk, J. Verkooyen.....	1547	TAQ12
Lifetime Experience with Low Temperature Cathodes Equipped in Super Power Klystrons — Rudolf Backmor.....	1550	TAQ13
Microwave System of PLS 2-GeV Linac — H.S. Lee, O.H. Hwang, S.H. Park, C.M. Ryu, W. Namkung	1553	TAQ14
Klystron-Modulator System Performances for PLS 2-GeV Linac — M.H. Cho, J.S. Oh, S.S. Park, W. Namkung.....	1556	TAQ15
Klystron Modulator Operation and Upgrades for the APS Linac — Thomas J. Russell, Alexander Cours	1559	TAQ16
Prospects for Developing Microwave Amplifiers to Drive Multi-TeV Linear Colliders — V.L. Granatstein, G.S. Nusinovich, J. Calame, W. Lawson, A. Singh, H. Guo, M. Reiser	1561	TAQ17
Design of 100 MW, Two-Cavity Gyroklystrons for Accelerator Applications — J.P. Calame, W. Lawson, J. Cheng, B. Hogan, M. Castle, V.L. Granatstein, M. Reiser.....	1563	TAQ18
Design of Three-Cavity Coaxial Gyroklystron Circuits for Linear Collider Applications — W. Lawson, G. Saraph, J.P. Calame, J. Cheng, M. Castle, B. Hogan, M. Reiser, V.L. Granatstein, H. Metz	1566	TAQ19
Numerical Simulation of Magnicon Amplifier — V. Yakovlev, O. Danilov, O. Nezhevenko, V. Tarnetsky.....	1569	TAQ21
RF-Power Upgrade Systems with Energy Compression for Electron Linacs — A. Shalnov, B.Yu. Bogdanovich, A. Ignatyev, V. Senyukov.....	1572	TAQ23
RF-Power Upgrade System with Resonant Loading — A. Shalnov, B. Bogdanovich, A. Ignatyev, V. Senyukov.....	1575	TAQ24
High-Power Test of Traveling-Wave-Type RF-Pulse Compressor — S. Yamaguchi, A. Enomoto, I. Sato, Y. Igarashi.....	1578	TAQ25
Active Radiofrequency Pulse Compression Using Switched Resonant Delay Lines — Sami G. Tantawi, Ronald D. Ruth, A.E. Vlieks.....	1581	TAQ26
Design of a Multi-Megawatt X-Band Solid State Microwave Switch — Sami G. Tantawi, Terry G. Lee, Ronald D. Ruth, A.E. Vlieks, Max Zolotarev	1584	TAQ27
Reduced Field TE01 X-Band Traveling Wave Window — W.R. Fowkes, R.S. Callin, S.G. Tantawi, E.L. Wright.....	1587	TAQ28
Design and High-Power Test of a TE11-Mode X-Band RF Window with Taper Transitions — Y. Otake, S. Tokumoto, H. Mizuno.....	1590	TAQ29
Feasibility Study of Optically Coupling RF-Power at mm Waves — B. Littmann, H. Henke.....	1593	TAQ30
A Low-Frequency High-Voltage RF-Barrier Bunching System for High-Intensity Neutron Source Compressor Rings — T.W. Hardek, D. Rees, C. Ziomek.....	1596	TAQ31
Temporal Evolution of Multipactor Discharge — R. Kishek, Y.Y. Lau, R.M. Gilgenbach.....	1599	TAQ32
Stabilizing a Power Amplifier Feeding a High Q Resonant Load — A.K. Mitra, R.L. Poirier, J.J. Lu, R. Hohbach.....	1602	TAQ33
Study of 14 GHz VLEPP Klystron With RF Absorbing Drift Tubes — G.V. Dolbilov, N.I. Azorsky, A.A. Fateev, N.I. Lebedev, V.A. Petrov, V.P. Sarantsev, V.S. Shvetsov, M.V. Yurkov.....	1605	TAQ34
24-MW, 24-μs Pulse RF Power Supply For Linac-Based FELs — E. Ohshita, Y. Morii, S. Abe, S. Okuma, K. Wakita, T. Tomimasu, I. Ito, Y. Miyai, K. Nakata, M. Hakota	1608	TAQ35
Initial Operation of an X-Band Magnicon Amplifier Experiment — S.H. Gold, A.K. Kinkad, A.W. Fliflet, B. Hafizi	1611	TAQ37

Superconducting RF

The Effects of Tuning and Terminating on the Operating Mode of Multi-Cell Coupled Cavity — Zubao Qian	1614	TPP01
Response of Superconducting Cavities to High Peak Power — T. Hays, H. Padamsee	1617	TPP02
Development of HOM Damper for B-Factor (KEKB) Superconducting Cavities — T. Tajima, K. Asano, T. Furuya, M. Izawa, S. Mitsunobu, T. Takahashi, N. Gamo, S. Iida, Y. Ishi, Y. Kijima, S. Kokura, M. Kudo, K. Sennyu, S. Tachibana, H. Takashina, N. Taniyama	1620	TPP03
Microscopic Examination of Defects Located by Thermometry in 1.5 GHz Superconducting Niobium Cavities — J. Knobloch, R. Durand, H. Muller, H. Padamsee	1623	TPP04
RF System for the NSLS Coherent Infrared Radiation Source — W. Broome, R. Biscardi, J. Keane, P. Mortazavi, M. Thomas, J.M. Wang	1626	TPP06
Development of TESLA-type Cavity at KEK — M. Ono, E. Kako, S. Noguchi, K. Saito, T. Shishido, M. Wake, H. Inoue, T. Fujino, Y. Funahashi, M. Matsuoka, T. Suzuki, T. Higuchi, H. Umezawa	1629	TPP07
Study of Luminous Spots Observed on Metallic Surfaces Subjected to High RF Fields — T. Junquera, S. Maïssa, M. Fouaidy, A. Le Goff, B. Bonin, M. Luong, H. Safa, J. Tan	1632	TPP09
Test Results for a Heat-Treated 4-Cell 805-MHz Superconducting Cavity — Brian Rusnak, Alan Shapiro	1636	TPP10
An Advanced Rotating T-R Mapping & its Diagnoses of TESLA 9-Cell Superconducting Cavity — Q.S. Shu, G. Deppe, W-D. Möller, M. Pekeler, D. Proch, D. Renken, P. Stein, C. Stolzenburg, T. Junquera, A. Caruette, M. Fouaidy	1639	TPP11
Improvements to Power Couplers for the LEP2 Superconducting Cavities — J. Tückmantel, C. Benvenuti, D. Bloess, D. Boussard, G. Geschonke, E. Haebel, N. Hilleret, S. Juras, H.P. Kindermann, J. Uythoven, C. Wyss, M. Stirbet	1642	TPP12
Arcing Phenomena on CEBAF RF-Windows at Cryogenic Temperatures — Tom Powers, Peter Kneisel, Ray Allen	1645	TPP13
Surface Scanning Thermometers for Diagnosing the TESLA SRF Cavities — T. Junquera, A. Caruette, M. Fouaidy, Q.S. Shu	1648	TPP14
Microwave Surface Resistance of YBaCuO Superconducting Films Laser-Ablated on Copper Substrates — J. Liu, K. Asano, E. Ezura, M. Fukutomi, S. Inagaki, S. Isagawa, K. Komori, S. Kumagai, H. Nakanishi, M. Tosa, K. Yoshihara	1652	TPP16

Room Temperature RF

Transverse Coupling Impedance Measurement Using Image Current — D. Sun, P. Colestock, M. Foley	1655	WPP01
Decreasing Transient Beam Loading in RF Cavities of U-70 Accelerator — O.P. Lebedev	1658	WPP02
RF System for Bunch Lengthening — R. Biscardi, G. Ramirez	1660	WPP03
Electromagnetic Field Vector Components Precise Measurements in Accelerating Structures — M.A. Chernogubovsky, M.F. Vorogushin	1663	WPP04
A New Tuning Method for Traveling Wave Structures — T. Khabiboulline, V. Puntus, M. Dohlus, N. Holtkamp, G. Kreps, S. Ivanov, K. Jin	1666	WPP05
RF Systems for RHIC — J. Rose, J. Brodowski, R. Connolly, D.P. Deng, S. Kwiatkowski, W. Pirkel, A. Ratti	1669	WPP07
A New RF System for Bunch Coalescing in the Fermilab Main Ring — J. Dey, I. Kourbanis, D. Wildman	1672	WPP08
Higher Order Modes of the Main Ring Cavity at Fermilab — J. Dey, D. Wildman	1675	WPP09
RF Measurements and Control of Higher Order Modes in Accelerating Cavities — V. Veshcherevich, S. Krutikhin, I. Kuptsov, S. Nosyrev, A. Novikov, I. Sedlyarov	1678	WPP10
RF System of VEPP-4M Electron-Positron Collider — E. Gorniker, P. Abramsky, V. Arbutov, S. Belomestnykh, A. Bushuyev, M. Fomin, I. Kuptsov, G. Kurkin, S. Nosyrev, V. Petrov, I. Sedlyarov, V. Veshcherevich	1681	WPP11
Storage Ring Cavity Higher-Order Mode Dampers for the Advanced Photon Source — Paul Matthews, Yoon Kang, Robert Kustom	1684	WPP12

Reduction of Multipactor in RF Ceramic Windows Using a Simple Titanium-Vapor Deposition System — K. Primdahl, R. Kustom, J. Maj	1687	WPP13
Cooling the APS Storage Ring Radio-Frequency Accelerating Cavities Thermal/Stress/Fatigue Analysis and Cavity Cooling Configuration — K. Primdahl, R. Kustom	1690	WPP14
RF Cavities for the Positron Accumulator Ring (PAR) of the Advanced Photon Source (APS) — Y.W. Kang, A. Nassiri, J.F. Bridges, T.L. Smith, J.J. Song	1693	WPP16
The Proposal of Complex Impedance Termination for Versatile HOM Damper Cavity — V.V. Paramonov	1696	WPP17
The Magnetron-Type Varactor for Fast Control in Accelerator RF Systems — M.I. Kuznetsov, V.V. Paramonov, Yu.V. Senichev, I.B. Enchevich, R.L. Poirier	1699	WPP18
The Distortion of the Accelerating Field Distribution in Compensated Structures due to Steady-State Beam Loading — V.G. Andreev, V.V. Paramonov	1702	WPP19
The Indiana University Cooler Injector Synchrotron RF System — A. Pei, M. Ellison, D. Friesel, D. Jenner, X. Kang, S.Y. Lee, D. Li, J. Liu, A. Riabko, L. Wang, K. Hedblom	1705	WPP20
The Indiana University Cooler Injection Synchrotron RF Cavity — A. Pei, M. Ellison, D. Friesel, D. Jenner, X. Kang, S.Y. Lee, D. Li, J. Liu, A. Riabko, L. Wang, K. Hedblom	1708	WPP21
Determination of Resonant Frequency and External Q Values for the Bessy II HOM-Damped Cavity — Frank Schönfeld, Bengt Littmann	1711	WPP22
106 MHz Cavity for Improving Coalescing Efficiency in the Fermilab Main Ring — J. Dey, I. Kourbanis, D. Wildman	1714	WPP23
On the Higher Order Mode Coupler Design for Damped Accelerating Structures — Jie Gao	1717	WPQ01
High Power Window Tests on a 500 MHz Planar Window for the CESR Upgrade — M. Pisharody, P. Barnes, E. Chojnacki, R. Durand, T. Hays, R. Kaplan, J. Kirchgessner, J. Reilly, H. Padamsee, J. Sears	1720	WPQ02
Operational Performances and Future Upgrades for the ELETTRA RF System — A. Fabris, A. Massarotti, C. Pasotti, M. Svandrlík	1723	WPQ04
X-Band High Power Dry Load for NLCTA — K. Ko, H. Hoag, T. Lee, S. Tantawi	1726	WPQ05
Development of a High-Power RF Cavity for the PEP-II B Factory — R.A. Rimmer, M.A. Allen, J. Saba, H. Schwarz, F.C. Belser, D.D. Berger, R.M. Franks	1729	WPQ06
A Design of Input Coupler for RF-Cavity — T. Nagatsuka, T. Koseki, Y. Kamiya, M. Izawa, Y. Terada	1732	WPQ07
Design of the KEKB RF System — K. Akai, E. Ezura, Y. Yamazaki	1735	WPQ08
RF Characteristics of ARES Cold Models — N. Akasaka, K. Akai, T. Kageyama, T. Shintake, Y. Yamazaki	1738	WPQ09
Design of Traveling Wave Windows for the PEP-II RF Coupling Network — N.M. Kroll, C.-K. Ng, J. Judkins, M. Neubauer	1741	WPQ10
Impedance Spectrum for the PEP-II RF Cavity — X.E. Lin, K. Ko, C.-K. Ng	1744	WPQ12
Measurement and Analysis of Higher-Order-Mode (HOM) Damping in B-Factory R-F Cavities — D.A. Goldberg, M. Irwin, R.A. Rimmer	1747	WPQ13
Planar Structures for Electron Acceleration — H. Henke	1750	WPQ14
Precise Fabrication of X-Band Detuned Accelerating Structure for Linear Collider — T. Higo, H. Sakai, Y. Higashi, T. Takatomi, S. Koike	1753	WPQ15
Development of a Beam-Pipe HOM Absorber for the ATF Damping Ring — F. Hinode, S. Sakanaka	1756	WPQ16
Development of a HOM-Damped Cavity for the KEK B-Factory (KEKB) — T. Kageyama, K. Akai, N. Akasaka, E. Ezura, F. Naito, T. Shintake, Y. Takeuchi, Y. Yamazaki, T. Kobayashi	1759	WPQ17
Possible Cavity Construction Techniques for the DIAMOND Storage Ring — D.M. Dykes, D.S.G. Higgins	1762	WPQ18
The Design of the 26.7 MHz RF Cavity for RHIC — J. Rose, J. Brodowski, D.P. Deng, S. Kwiakowski, W. Pirkel, A. Ratti	1765	WPQ19
A Design Upgrade of the RF Cavity and Its Power Window for High Current Operation of the NSLS X-Ray Storage Ring — P. Mortazavi, M. Thomas	1768	WPQ20
A Ferrite Loaded Untuned Cavity for a Compact Proton Synchrotron — J.I. Hirota, K. Hiramoto, M. Nishi, Y. Iwashita, A. Noda, M. Inoue	1770	WPQ21
On the Theory of Two Coupled Cavities — N.I. Aizatsky	1773	WPQ22

Measurement of Multipacting Currents of Metal Surfaces in RF Fields — D. Proch, <i>D. Einfeld, R. Onken, N. Steinhauser</i>	1776	WPQ24
Optimization of CLIC Transfer Structure (CTS) Design to Meet New Drive Beam Parameters — A. Millich	1779	WPQ25
A High-Power Multiple-Harmonic Acceleration System for Proton- and Heavy-Ion Synchrotrons — P. Ausset, G. Charruau, F.J. Etzkorn, C. Fougeron, H. Meuth, S. Papureanu, <i>A. Schnase</i>	1781	WPQ26
A Bunch Lengthening RF Cavity for Aladdin — K.J. Kleman	1785	WPR01
Design of a High-Power Test Cavity for the ATF Damping Ring — S. Sakanaka, F. Hinode, <i>M. Akemoto, S. Tokumoto, T. Higo, J. Urakawa, T. Miura, Y. Hirata, K. Satoh</i>	1788	WPR02
Design of an RF System for the ATF Damping Ring — S. Sakanaka, F. Hinode, M. Akemoto, <i>H. Hayano, H. Matsumoto, K. Kubo, S. Tokumoto, T. Higo, J. Urakawa</i>	1791	WPR03
Development of a Damped Cavity with SiC Beam-Duct — T. Koseki, M. Izawa, Y. Kamiya	1794	WPR04
HOM Absorber for the KEKB Normal Conducting Cavity — Y. Takeuchi, K. Akai, <i>N. Akasaka, E. Ezura, T. Kageyama, F. Naito, T. Shintake, Y. Yamazaki</i>	1797	WPR05
PEP-II B-Factory Prototype Higher Order Mode Load Design — R. Pendleton, K. Ko, C. Ng, <i>M. Neubauer, H. Schwarz, R. Rimmer</i>	1800	WPR07
High-Power RF Window and Coupler Development for the PEP-II B Factory — M. Neubauer, <i>K. Fant, J. Hodgson, J. Judkins, H. Schwarz, R.A. Rimmer</i>	1803	WPR08
Input Coupler for the KEKB Normal Conducting Cavity — F. Naito, K. Akai, N. Akasaka, <i>E. Ezura, T. Kageyama, T. Shintake, Y. Takeuchi, Y. Yamazaki</i>	1806	WPR09
Minimum Wakefield Achievable by Waveguide Damped Cavity — Xintian E. Lin, <i>Norman M. Kroll</i>	1809	WPR10
PLS RF System Operation During the Commissioning — M. Kwon, I.H. Yu, H.J. Park, <i>D.H. Han, M. Yoon, Y.S. Kim</i>	1812	WPR11
Acoustic Experimental Studies of High Power Modes in Accelerating Structure of Kurchatov SR Source — M. Gangeluk, A. Kadnikov, Yu. Krylov, S. Kuznetsov, V. Moiseev, <i>V. Petrenko, V. Ushkov, Yu. Yupinov</i>	1815	WPR13
Computer Simulations of a Wide-Bandwidth Ferrite-Loaded High-Power Waveguide Termination — J. Johnson, R. Rimmer, J. Corlett	1818	WPR14
Effects of Temperature Variation on the SLC Linac RF System — F.-J. Decker, R. Akre, <i>M. Byrne, Z.D. Farkas, H. Jarvis, K. Jobe, R Koontz, M. Mitchell, R. Pennacchi, M. Ross,</i> <i>H. Smith</i>	1821	WPR15
Broadband Coax-Waveguide Transitions — T. Rizawa, R. Pendleton	1824	WPR16
Rectangular Microtron Accelerating Structure — N.P. Sobenin, V.N. Kandrunin, <i>V.N. Melekhin, A.I. Karev, V.I. Shvedunov, W.P. Trower</i>	1827	WPR17
Investigation of the Biperiodic Accelerating Structure For The Free Electron Laser Buncher — N.P. Sobenin, S.N. Yarygin, D.V. Kostin, A.A. Zavadtsev	1830	WPR18
Ferromagnetic Cores Made from Amorphous Material for Broad-Band Accelerating System — I. Bolotin, V. Budilin, A. Glazov, V. Krasnopolsky, V. Skuratov	1833	WPR19
A New Structure with Continuous RF Acceleration and Focusing — J.J. Manca, M.C. Fallis, <i>J.P.J. Manca</i>	1835	WPR20
Spark Location in RF Cavities — Q. Kerns, M. Popovic, C. Kerns	1838	WPR21
RF System for the Duke 1 GeV Storage Ring — Ping Wang, Peter Morcombe, Ying Wu, <i>Grigori Kurkin</i>	1841	WPR22

Injection, Extraction and Targetry

Matching Section to the RFQ Using Permanent Magnet Symmetric Lens — M. Kando, <i>M. Ikegami, H. Dewa, H. Fujita, T. Shirai, H. Okamoto, Y. Iwashita, S. Kakigi, A. Noda,</i> <i>M. Inoue</i>	1843	WAQ01
Conceptual Designs of Beam Choppers for RFQ Linacs — Subrata Nath, Ralph R. Stevens Jr, <i>Thomas P. Wangler</i>	1846	WAQ02
The Role of Space Charge in the Performance of the Bunching System for the ATLAS Positive Ion Injector — R.C. Pardo, R. Smith	1849	WAQ03

Experimental Investigations of Plasma Lens Focusing and Plasma Channel Transport of Heavy Ion Beams — A. Tauschwitz, S.S. Yu, S. Eylon, L. Reginato, W. Leemans, J.O. Rasmussen, R.O. Bangerter.....	1852	WAQ04
A Low Energy Ion Beam Transport System with Variable Field Permanent Magnetic Quadrupoles — Y. Mori, A. Takagi, M. Kinsho, T. Baba, K. Shinto.....	1855	WAQ06
A Comparison of Two Injection Line Matching Sections for Compact Cyclotrons — T. Kuo, R. Baartman, L. Root, B. Milton, R. Laxadal, D. Yuan, K. Jayamanna, P. Schmor, G. Dutto, M. Dehnel, K. Erdman.....	1858	WAQ07
Stripping Injection Into the New Booster Ring at IUCF — K. Hedblom, D.L. Friesel.....	1861	WAQ08
Accurate Tuning of 90° Cells in a FODO Lattice — K. Bertsche, N. Mao.....	1864	WAQ09
Design Principles for High Current Beam Injection Lines — H. Liu, D. Neuffer.....	1867	WAQ11
Survey and Analysis of Line-Frequency Interference in the CEBAF Accelerator — M.G. Tiefenback, Rui Li.....	1870	WAQ12
Location and Correction of 60 Hz in the CEBAF Injector — R. Legg, D. Douglas, G.A. Krafft, Q. Saulter.....	1873	WAQ14
PEP-II Injection Transport Construction Status and Commissioning Plans — T. Fieguth, E. Bloom, F. Bulos, T. Donaldson, B. Feerick, G. Godfrey, G. Leyh, D. Nelson, M. Ross, D. Schultz, J. Sheppard, P. Smith, C. Spencer, J. Weinberg.....	1876	WAQ15
Beam Transport Lines at BESSY-II — D. Schirmer, M. v.Hartrott, S. Khan, D. Krämer, E. Weihreter.....	1879	WAQ17
Matching the Emittance of a Linac to the Acceptance of a Racetrack Microtron — R.W. de Leeuw, M.C.J. de Wijs, J.I.M. Botman, G.A. Webers, W.H.C. Theuws, C.J. Timmermans, H.L. Hagedoorn.....	1882	WAQ19
The Extraction Orbit and Extraction Beam Transport Line for a 75 MeV Racetrack Microtron — R.W. de Leeuw, H.R.M. van Greevenbroek, J.I.M. Botman, G.A. Webers, C.J. Timmermans, H.L. Hagedoorn.....	1885	WAQ20
Electromagnetic, Thermal and Structural Analysis of the Fermilab Antiproton Source Lithium Collection Lens — S. O'Day, K. Anderson.....	1888	WAQ22
A New Concept in the Design of the LHC Beam Dump — J.M. Zazula, M. Gyr, G.R. Stevenson, E. Weisse.....	1891	WAQ24
Loss Concentration and Evacuation by Mini-Wire-Septa from Circular Machines for Spallation Neutron Sources — H. Schönauer.....	1894	WAQ25
Status of the Radioactive Ion Beam Injector at the Holifield Radioactive Ion Beam Facility — D.T. Dowling, G.D. Alton, R.L. Auble, M.R. Dinehart, D.L. Haynes, J.W. Johnson, R.C. Juras, Y.S. Kwon, M.J. Meigs, G.D. Mills, S.W. Mosko, D.K. Olsen, B.A. Tatum, C.E. Williams, H. Wollnik.....	1897	WAQ26
A New Fast Rise Time Kicker System For Antiproton Injection Into The Tevatron — B. Hanna, J. Dinkel, C. Jensen, D. Qunell, R. Reilly, D. Tinsley, J. Walton.....	1900	WAR01
Design of the MI40 Beam-Abort Dump — C.M. Bhat, P.S. Martin, A.D. Russell.....	1903	WAR02
Study on the Metallic Coating of the Ceramic Chamber for the ATF Damping Ring Kicker Magnets — N. Terunuma, H. Nakayama, J. Urakawa.....	1906	WAR03
Prospect of the Fast Extraction from KEK-PS for the Long Base Line Neutrino Experiment — H. Sato, Y. Shoji, T. Kawakubo.....	1909	WAR04
Helium Beam Acceleration in the KEK Proton Synchrotron with a Newly Developed Injection System for Positive/Negative Ions — I. Sakai, A. Takagi, Y. Mori, S. Machida, M. Yoshii, T. Toyama, M. Shirakata, Y. Shoji, H. Sato.....	1912	WAR05
Fast and Reliable Kicker Magnets for the SLC Damping Rings — T.S. Mattison, R.L. Cassel, A.R. Donaldson, G. Gross.....	1915	WAR06
Status of the Nuclotron Slow Extraction System — V.I. Chernikov, I.B. Issinsky, O.S. Kozlov, V.A. Mikhailov, S.A. Novikov.....	1918	WAR09
The RHIC Injection Fast Kicker — E.B. Forsyth, G.C. Pappas, J.E. Tuozzolo, W. Zhang.....	1921	WAR10
The Active Filter Voltage Ripple Correction System of the Brookhaven AGS Main Magnet Power Supply — I. Marneris, R. Bonati, J. Geller, J.N. Sandberg, A. Soukas.....	1924	WAR11
The Injection Kicker System for the Muon G-2 Experiment — G.C. Pappas, E.B. Forsyth, W. Feng.....	1927	WAR12
The AGS Accelerator Complex with the New Fast Extraction System — M. Tanaka, E.J. Bleser, J.W. Glenn, Y.Y. Lee, A. Soukas.....	1930	WAR13
DESY III - Dump System with One Fast Kicker — J. Ruemmler.....	1933	WAR14

Utilizing a Pulsed Deflector for Extraction of Pulsed Beams from the TRIUMF Cyclotron — <i>R.E. Laxdal</i>	1936	WAR15
Requirements for a Beam Sweeping System for the Fermilab Antiproton Source Target — <i>F.M. Bieniosek, K. Anderson, K. Fullett</i>	1939	WAR17
Measurement and Reduction of Quadrupole Injection Oscillations in the Fermilab Antiproton Accumulator — <i>F.M. Bieniosek, K. Fullett</i>	1942	WAR18
Results from Experiments of Crystal Extraction of 900 GeV Proton Beams from the Tevatron Collider — <i>G. Jackson, D. Carrigan, D. Chen, C.T. Murphy, A. Bogacz, S. Ramachandran, J. Rhoades, A. McManus, S. Baker</i>	1945	WAR19
High Energy Beam Line Based on Bending Crystal — <i>V.M. Biryukov, Yu.A. Chesnokov, V.N. Greth, A.A. Ivanov, V.I. Kotov, V.S. Selesnev, M.V. Tarakanov, V.I. Terekhov, S.V. Tsarik</i>	1948	WAR20
Observation of the Influence of the Crystal Surface Defects on the Characteristics of the High Energy Particle Beam Deflected With a Bent Monocrystal — <i>V.I. Baranov, V.M. Biryukov, Yu.A. Chesnokov, V.I. Kotov, M.V. Tarakanov, S.V. Tsarik</i>	1949	WAR21
Beam Extraction with Using of Volume Reflection Effect in Crystals — <i>I. Yazynin</i>	1952	WAR22
Use of a Bent Crystal for Beam Extraction in a Slow Extraction Mode — <i>A.A. Asseev, M.Yu. Gorin</i>	1955	WAR23
Computer Simulation of the Tevatron Crystal Extraction Experiment — <i>Valery Biryukov</i>	1958	WAR24

Power Supplies

PEP-II Magnet Power Conversion Systems — <i>L.T. Jackson, A.H. Saab, D.W. Shimer</i>	1961	RPP01
The AGS Main Magnet Power Supply Upgrade — <i>J.N. Sandberg, R. Casella, J. Geller, I. Marneris, A. Soukas, N. Schumburg</i>	1964	RPP02
Performance of the Ramping Power Supplies for the APS Booster Synchrotron — <i>J.A. Carwardine, S.V. Milton, D.G. McGhee</i>	1967	RPP03
A Distributed Dipole Power Supply System for the EUTERPE Electron Ring — <i>A.H. Kemper, Boling Xi, R.W. de Leeuw, W.H.C. Theuws, J.I.M. Botman, C.J. Timmermans, H.L. Hagedoorn, R.G.J. Oude Velthuis</i>	1970	RPP04
A 20 Ampere Shunt Regulator for Controlling Individual Magnets in a Seriesed String — <i>E.J. Martin, N. Dobeck, G.S. Jones, M.K. O'Sullivan</i>	1973	RPP06
A Multi-Channel Corrector Magnet Controller — <i>G.E. Leyh, A.R. Donaldson, L.T. Jackson</i>	1976	RPP07
Advances in Power Supply and Control System for Electrostatic Accelerators — <i>S.N. Chumakov, A.D. Goncharov, A.N. Malygin, V.P. Ostanin, B.N. Sukhina, V.S. Tupikov</i>	1979	RPP08
Mode Analysis of Synchrotron Magnet Strings — <i>M. Kumada</i>	1982	RPP09
Autotransformer Configurations to Enhance Utility Power Quality of High Power AC/DC Rectifier Systems — <i>Sewan Choi, Prasad N. Enjeti, Ira J. Pitel</i>	1985	RPP11
Performance of a 2-Megawatt High Voltage Test Load — <i>D. Horan, R. Kustom, M. Ferguson</i>	1988	RPP12
Early Operating and Reliability Experience with the CEBAF DC Magnet Power Supplies — <i>W. Merz, R. Flood, E.J. Martin, M. O'Sullivan</i>	1991	RPP13

Cryogenics, Vacuum, Alignment and Other Technical Systems

CEBAF Cryogenic System (Invited) — <i>Claus H. Rode</i>	1994	RPE01
The Large Hadron Collider Vacuum System (Invited) — <i>B. Angerth, F. Bertinelli, J.-C. Brunet, R. Calder, F. Caspers, P. Cruikshank, J.-M. Dalin, O. Gröbner, N. Kos, A. Mathewson, A. Poncet, C. Reymermier, F. Ruggiero, T. Scholz, S. Sgobba, E. Wallén</i>	1999	RPE02
Large Medical Gantries (Invited) — <i>J.B. Flanz</i>	2004	RPE03
Alignment Considerations for the Next Linear Collider (Invited) — <i>Robert E. Ruland</i>	2009	RPE04
Reliability of the LEP Vacuum System: Experience and Analysis — <i>P.M. Strubin, J.-P. Bojon</i>	2014	RPE06
On the Electron Beam Lifetime Problem in HERA — <i>D.R.C. Kelly, W. Bialowons, R. Brinkmann, H. Ehrlichmann, J. Kouptsidis</i>	2017	RPE08
Design and Testing of a High Power, Ultra-High Vacuum, Dual-Directional Coupler for the Advanced Photon Source (APS) Linear Accelerator — <i>S.O. Brauer, A.E. Grelick, J. Grimmer, R.D. Otocky, Y.W. Kang, J. Noonan, T. Russell</i>	2020	RPE09
A Pulse Septum Magnet with Low Outgassing Rate — <i>Yuan Ji Pei, W.M. Li, D.M. Jiang, X.Q. Wang</i>	2023	RPE10

Surveying the Monument System at Lawrence Berkeley Laboratory's Advanced Light Source Accelerator — W. Thur, T. Lauritzen.....	2026	RPE12
Induced Radioactivity of Thick Copper and Lead Targets Irradiated by Protons, ^4He and ^{12}C Nuclei with Energy 3.65 GeV/Nucleon — A.A. Astapov, V.P. Bambalevski.....	2029	RPE13
The PEP-II High Power Beam Dumping System — A. Kulikov, J. Seeman, M. Zolotorev.....	2032	RPE14
Cryogenic Thermometry in Superconducting Accelerators — V.I. Datskov, J.A. Demko, J.G. Weisend, M. Hentges.....	2034	MPP01
Cryogenic Operation and On-line Measurement of RF Losses in the SC Cavities of LEP2 — G. Winkler, Ph. Gayet, D. Güsewell, Ch. Titcomb.....	2037	MPP02
Pressure Measurement for the UNK-1 Vacuum System — A. Kiver, V. Komarov, K. Mirzoev, V. Terekhov, A. Vasilevsky.....	2040	MPP03
Total Pressure Measurements in the ELETTRA Storage Ring According to the Performance of the Sputter-Ion Pumps — F. Giacuzzo, J. Miertusova.....	2042	MPP04
Insertion Device Vacuum Chamber for the ELETTRA Storage Ring — J. Miertusova, N. Pangos.....	2045	MPP05
Bellows Design for the PEP-II High Energy Ring Arc Chambers — M.E. Nordby, N. Kurita, C.-K. Ng.....	2048	MPP07
A Zero-Length Bellows for the PEP-II High-Energy Ring — M. Nordby, E.F. Daly, N. Kurita, J. Langton.....	2051	MPP08
Processing of O.F.E. Copper Beam Chambers for PEP-II High Energy Ring — E. Hoyt, M. Hoyt, R. Kirby, C. Perkins, D. Wright, A. Farvid.....	2054	MPP09
Stretchforming Vacuum Chambers for the PEP-II B-Factory High Energy Storage Ring — E.F. Daly, D. Bostic, A. Lisin, M. Palrang, C. Perkins, K. Skarpaas.....	2057	MPP10
Beam Vacuum Chambers for Brookhaven's Muon Storage Ring — H.C. Hseuh, L. Snyderstrup, W.S. Jiang, C. Pai, M. Mapes.....	2060	MPP11
Test Results of Pre-Production Prototype Distributed Ion Pump Design for the PEP-II Asymmetric B-Factory Collider — F.R. Holdener, D. Behne, D. Hathaway, K. Kishiyama, M. Mugge, W. Stoeffl, K. van Bibber, C. Perkins, E.F. Daly, E. Hoyt, M. Hoyt, M. Nordby, J. Seeman, D. Wright.....	2064	MPP12
Design of the PEP-II Low Energy Ring Vacuum System — D. Hunt, K. Kennedy, T. Stevens.....	2067	MPP13
The Vacuum Upgrade of the CERN PS and PS Booster — M. van Rooij, J.-P. Bertuzzi, M. Brouet, A. Burlet, C. Burnside, R. Gavaggio, L. Petty, A. Poncet.....	2069	MPP15
The Vacuum System for Insertion Devices at the Advanced Photon Source — E. Trakhtenberg, E. Gluskin, P. Den Hartog, T. Klippert, G. Wiemerslage, S. Xu.....	2072	MPP16
Test Results of a Combined Distributed Ion Pump/Non-Evaporable Getter Pump Design Developed as a Proposed Alternative Pumping System for the PEP-II Asymmetric B-Factory Collider — F.R. Holdener, D. Behne, D. Hathaway, K. Kishiyama, M. Mugge, W. Stoeffl, K. van Bibber, C. Perkins, E.F. Daly, E. Hoyt, M. Hoyt, M. Nordby, J. Seeman, D. Wright.....	2075	MPP20

Volume 4

Cryogenics, Vacuum, Alignment and Other Technical Systems (cont'd)

Ground Motion Measurements in HERA — V. Shiltsev, B. Baklakov, P. Lebedev, C. Montag, J. Rossbach.....	2078	TAA01
Alignment of Duke Free Electron Laser Storage Ring — M. Emamian, N. Hower, Y. Levashov.....	2081	TAA02
Beamline Smoothing of the Advanced Photon Source — H. Friedrich, M. Penicka, S. Zhao.....	2084	TAA03
Improvement of the Alignment System for the KEK 2.5-GeV Electron Linac — Y. Ogawa, A. Enomoto, I. Sato.....	2087	TAA04
A Mechanical Feedback System for Linear Colliders to Compensate Fast Magnet Motion — C. Montag, J. Rossbach.....	2090	TAA06
A Microstrip Based Position System for the Alignment of the TTF Cryostat — D. Giove, A. Bosotti, C. Pagani, G. Varisco.....	2093	TAA07
Beam-Based Magnetic Alignment of the Final Focus Test Beam — P. Tenenbaum, D. Burke, R. Helm, J. Irwin, P. Raimondi, K. Oide, K. Flöttmann.....	2096	TAA08

Alignment and Survey of the Elements in RHIC — <i>D. Trbojevic, P. Cameron, G.L. Ganetis, M.A. Goldman, R. Gupta, M. Harrison, M.F. Hemmer, F.X. Karl, A. Jain, W. Louie, S. Mulhall, S. Peggs, S. Tepikian, R. Thomas, P. Wanderer</i>	2099	TAA09
RF Radiation Measurement for the Advanced Photon Source (APS) Personnel Safety System — <i>J.J. Song, J. Kim, R. Otocky, J. Zhou</i>	2102	TAA11
Radiation Shielding of the Main Injector — <i>C.M. Bhat, P.S. Martin</i>	2105	TAA12
The Safety Interlock System of Synchrotron Radiation Research Center — <i>T.F. Lin, J.P. Wang</i>	2108	TAA14
Radiological Protection Policy Aspects Concerning the Preliminary Design and Operation Modus of the Athens RT Microtron Facility — <i>B. Spyropoulos</i>	2111	TAA15
SLAC Synchronous Condenser — <i>C. Corvin</i>	2114	TAA16
Printed-Circuit Quadrupole Design — <i>Terry F. Godlove, Santiago Bernal, Martin Reiser</i>	2117	TAA17
Microprocessor Controlled Four-Axis Goniometer — <i>A. Bortnyansky, M. Klopenkov, M. Pavlovets, M. Svinin, P. Kovach, J. Dobrovodsky</i>	2120	TAA18
Optically Induced Surface Flashover Switching for the Dielectric Wall Accelerator — <i>S. Sampayan, G. Caporaso, B. Carder, M. Norton, D. Trimble, J. Elizondo</i>	2123	TAA20
Measurements of Magnet Vibrations at the Advanced Photon Source — <i>V. Shiltsev</i>	2126	TAA21
The Vacuum System for the PEP II High Energy Ring Straight Sections — <i>U. Wienands, E. Daly, S.A. Heifets, A. Kulikov, N. Kurita, M. Nordby, C. Perkins, E. Reuter, J.T. Seeman, F.C. Belser, J. Berg, F.R. Holdener, J.A. Kerns, M.R. McDaniel, W. Stoeffl</i>	2129	TAA22
Compact X-band High Power Load Using Magnetic Stainless Steel — <i>Sami G. Tantawi, A.E. Vlieks</i>	2132	TAA27
Progress on Plasma Lens Experiments at the Final Focus Test Beam — <i>P. Kwok, P. Chen, D. Cline, W. Barletta, S. Berridge, W. Bugg, C. Bula, S. Chattopadhyay, W. Craddock, I. Hsu, R. Iverson, T. Katsouleas, P. Lai, W. Leemans, R. Liou, K.T. McDonald, D.D. Meyerhofer, K. Nakajima, H. Nakanishi, C.K. Ng, Y. Nishida, J. Norem, A. Ogata, J. Rosenzweig, M. Ross, A. Sessler, T. Shintake, J. Spencer, J.J. Su, A.W. Weidemann, G. Westenskow, D. Whittum, R. Williams, J. Wurtele</i>	2135	TAA28
Measurement of the Electric Field Uniformity in an Electrostatic Separator — <i>Weiran Lou, James J. Welch</i>	2138	TAA29
Analysis and Redesign of RF Filter Bar to Relieve Thermal Stresses — <i>E.G. Schmenk, K.W. Kelly, V. Saile, H.P. Bluem</i>	2141	TAA32
Loaded Delay Lines for Future R.F. Pulse Compression Systems — <i>R.M. Jones, P.B. Wilson, N.M. Kroll</i>	2144	TAA33

Controls and Computing

Integrating Industrial and Accelerator Control Systems (Invited) — <i>R. Saban</i>	2147	WAE01
Control System for Fermilab's Low Temperature Upgrade (Invited) — <i>B.L. Norris</i>	2152	WAE02
Databases for Accelerator Control - An Operations Viewpoint (Invited) — <i>J. Poole</i>	2157	WAE03
Taking an Object-Oriented View of Accelerators (Invited) — <i>Hiroshi Nishimura</i>	2162	WAE04
The CEBAF Control System (Invited) — <i>William A. Watson III</i>	2167	WAE05
MECAR (Main Ring Excitation Controller and Regulator): A Real Time Learning Regulator For The Fermilab Main Ring Or The Main Injector Synchrotron — <i>R. Flora, K. Martin, A. Moibenko, H. Pfeffer, D. Wolff, P. Prieto, S. Hays</i>	2172	WAE07
Framework for a General Purpose, Intelligent Control System for Particle Accelerators — <i>R.T. Westervelt, W.B. Klein, G. Luger</i>	2175	WAE08
Automatic Beam Steering in the CERN PS Complex — <i>B. Autin, G.H. Hemelsoet, M. Martini, E. Wildner</i>	2178	WAE09
Integrated On-Line Accelerator Modeling at CEBAF — <i>B.A. Bowling, H. Shoaee, J. van Zeijts, S. Witherspoon, W. Watson</i>	2181	WAE10
A Self-Describing File Protocol for Simulation Integration and Shared Post-Processors — <i>M. Borland</i>	2184	WAE11
Analytic Computation of Beam Impedances in Complex Heterogenous Accelerator Geometries — <i>S. Petracca, I.M. Pinto, F. Ruggiero</i>	2187	WAE12
Comparison of CONDOR, FCI and MAFIA Calculations for a 150MW S-Band Klystron with Measurements — <i>U. Becker, T. Weiland, M. Dohlus, S. Lütgert, D. Sprehn</i>	2190	WAE13

Controls

The BEPC Control System Upgraded — J. Zhao, X. Geng, Y. Yu, B. Wang, C. Wang, J. Xu, W. Liu, H. Luo, Y. Wang, M. Zhan.....	2193	MPA01
Control System of PLS 2-GeV Linac — I.S. Ko, W. Namkung.....	2196	MPA02
Control System of the Synchrotron Radiation Source SIBERIA-2 — A. Valentinov, A. Kadnikov, Y. Krylov, S. Kuznetsov, Y. Yupinov.....	2199	MPA04
Control System for the Holifield Radioactive Ion Beam Facility — B.A. Tatum, R.C. Juras, M.J. Meigs.....	2202	MPA05
Control System Design for KEKB Accelerators — S.-I. Kurokawa, T. Katoh, T.T. Nakamura, T. Mimashi, N. Yamamoto.....	2205	MPA06
Design of SPring-8 Linac Control System Using Object Oriented Concept — H. Sakaki, H. Yoshikawa, Y. Itoh, A. Kuba, T. Hori, A. Mizuno, H. Yokomizo.....	2208	MPA07
The Slow Control System of the Muon g-2 Experiment — Arnold Stillman.....	2211	MPA09
The Duke Storage Ring Control System — Y. Wu, B. Burnham, V.N. Litvinenko.....	2214	MPA10
EPICS at Duke University — C. Dickey, B. Burnham, F. Carter, R. Fricks, V. Litvinenko, A. Nagchadhuri, P. Morcombe, R. Pantazis, P. O'Shea, R. Sachschtale, Y. Wu.....	2217	MPA11
The Integration of Two Control Systems — M. Bickley, K. White.....	2220	MPA12
Upgrade of NSLS Timing System — O. Singh, S. Ramamoorthy, J. Sheehan, J. Smith.....	2223	MPA15
Accelerator Timing at Brookhaven National Laboratory — B. Oerter, C.R. Conkling.....	2226	MPA16
The RHIC General Purpose Multiplexed Analog to Digital Converter System — R. Michnoff.....	2229	MPA17
The Datacon Master - Renovation of a Datacon Field Bus Communications System for Accelerator Control — T.M. Kerner, R. Warkentien.....	2232	MPA18
Upgrade of the Controls for the Brookhaven Linac — W.E. Buxton.....	2235	MPA19
Commissioning Software Tools at the Advanced Photon Source — L. Emery.....	2238	MPR01
Rapid Application Development Using the Tcl/Tk Language — Johannes van Zeijts.....	2241	MPR02
Accelerator Operation Management Using Objects — H. Nishimura, C. Timossi, M. Valdez.....	2244	MPR03
Orbit Control at the ALS Based on Sensitivity Matrices — H. Nishimura, L. Schachinger, H. Ohgaki.....	2247	MPR04
Error Handling in the NSLS Control System — Susila Ramamoorthy, Pauline Pearson, John Smith.....	2250	MPR07
History Data Collection, Retriving and Display in the NSLS Control System — Y.N. Tang, J.D. Smith.....	2253	MPR08
Virtual Instrumentation Interface for SRRC Control System — Jenny Chen, C.H. Kuo, Gloria Huang, J.S. Chen, C.J. Wang, K.T. Hsu, G.J. Jan.....	2256	MPR10
User-Friendly Interface for Operator in the Controls of UNK Beam-Transfer Line. — Yu. Karshev, Yu. Fedotov, V. Komarov, I. Lobov.....	2259	MPR11
Macmon: A Monitoring Program for ELETTRA — Emanuel Karantzoulis, Mark Plesko.....	2262	MPR12
Device Control at CEBAF — S. Schaffner, D. Barker, V. Bookwalter, B. Bowling, K. Brown, L. Doolittle, T. Fox, S. Higgins, A. Hofler, G. Lahti, P. Letta, B. Montjar, N. Patavalis, J. Tang, W. Watson, C. West, D. Wetherholt, K. White, S. Witherspoon, M. Wise.....	2265	MPR13
Automated Frequency Tuning of SRF Cavities at CEBAF — M. Chowdhary, L. Doolittle, G. Lahti, S.N. Simrock, R. Terrell.....	2268	MPR14
Operational Monitoring of the CEBAF RF System — J. Karn, B. Dunham, M. Tiefenback.....	2271	MPR15
Operating Experience with the New TRIUMF RF Control System — K. Fong, M. Laverty, S. Fang.....	2273	MPR16
Managing Control Algorithms with an Object-Oriented Database — M. Bickley, W. Watson.....	2276	MPR19
Design of the Commissioning Software for the AGS to RHIC Transfer Line — C.G. Trahern, C. Saltmarsh, T. Satogata, J. Kewisch, S. Sathe, T. D'Ottavio, S. Tepikian, D. Shea.....	2279	MPR20

Computer Codes

A Relational Database for Magnets and Measurement Systems at the Fermilab Magnet Test Facility — J.W. Sim, B.C. Brown, H.D. Glass, D.J. Harding, C.S. Mishra, A.D. Russell, K. Trombly-Freytag, D.G.C. Walbridge.....	2282	MPB05
---	------	-------

Software for a Database-Controlled Measurement System at the Fermilab Magnet Test Facility — <i>J.W. Sim, R. Baiod, B.C. Brown, E. Desavouret, H.D. Glass, P.J. Hall, D.J. Harding, C.S. Mishra, J.M. Nogiec, J.E. Pachnik, A. Russell, K. Trombly-Freytag, D.G.C. Walbridge</i>	2285	MPB06
BBAT: Bunch and Bucket Analysis Tool — <i>D.-P. Deng</i>	2288	MPB08
MASTAC - New Code for Solving Three-Dimensional Non-linear Magnetostatic Problems — <i>M. Rojak, E. Shurina, Yu. Soloveichik, A. Grudiev, M. Tiunov, P. Vobly</i>	2291	MPB09
The Computer Code BPERM for Wakepotential & Impedance Calculations — <i>T. Barts, W. Chou</i>	2294	MPB10
RESOLVE at CEBAF — <i>Byung C. Yunn, Rui Li, Stefan Simrock</i>	2297	MPB11
New Graphic User Interface for the Charged Particle Beam Program PARMILA — <i>George H. Gillespie, Barrey W. Hill</i>	2300	MPB14
XWAKE 1.1: A New Impedance and Wake Field Software Package — <i>G.W. Saewert, T.G. Jurgens</i>	2303	MPB15
The Los Alamos Accelerator Code Group — <i>Frank L. Krawczyk, James H. Billen, Robert D. Ryne, Harunori Takeda, Lloyd M. Young</i>	2306	MPB16
Beam Simulation and Radiation Dose Calculation at the Advanced Photon Source with SHOWER, an Interface Program to the EGS4 Code System — <i>L. Emery</i>	2309	MPB17
An Interactive Version of the PBGUNS Program for the Simulation of Axisymmetric and 2-D, Electron and Ion Beams and Guns — <i>Jack E. Boers</i>	2312	MPB18
Vector Computer Used for Calculation of 3D Magnetostatic Fields — <i>E.P. Zhidkov, M.B. Yuldasheva, I.P. Yudin, O.I. Yuldashev</i>	2314	MPB19
Impedance Study for the PEP-II B-factory — <i>S. Heifets, A. Chao, E. Daly, K. Ko, N. Kurita, X. Lin, C. Ng, M. Nordby, C. Perkins, J. Seeman, G. Stupakov, U. Wienands, D. Wright, M. Zolotarev, E. Henestroza, G. Lambertson, J. Corlett, J. Byrd, M. Zisman, T. Weiland, W. Stoeffl, C. Bolser</i>	2317	MPC01
Pressure Stability under a Pump Failure — <i>S.A. Heifets, J. Seeman, W. Stoeffl</i>	2319	MPC02
Investigation of the Beam Impedance of a Slowly Varying Waveguide — <i>R.M. Jones, S.A. Heifets</i>	2321	MPC03
Optimal Transport of Low Energy Particle Beams — <i>Christopher K. Allen, Samar K. Guharay, Martin Reiser</i>	2324	MPC04
Simulation of the Space Charge Effect in RHIC — <i>G.F. Dell, S. Peggs</i>	2327	MPC05
Magnetic Shielding for the D0 Detector Solenoid Upgrade — <i>J.-F. Ostiguy, R. Yamada</i>	2330	MPC07
Trapped Modes in the PEP-II B-Factory Interaction Region — <i>E. Henestroza, S. Heifets, M. Zolotarev</i>	2333	MPC08
A Proof of Principle of a Storage Ring with Fifth-Order Achromatic Bending Arcs — <i>Weishi Wan, Martin Berz</i>	2336	MPC09
Analytic Electrostatic Solution of an Axisymmetric Accelerator Gap — <i>John K. Boyd</i>	2339	MPC13
3D-Finite Difference Analysis of Planar Loop Couplers as Beam Electrodes in Stochastic Cooling Systems — <i>R. Schultheis, H.L. Hartnagel, B. Franzke</i>	2342	MPC15
Some Remarks on the Location of Higher Order Modes in Tapered Accelerating Structures with the Use of a Coupled Oscillator Model — <i>G. Romanov, S. Ivanov, M. Dohlus, N. Holtkamp</i>	2345	MPC16
The New Possibilities of SuperLANS Code for Evaluation of Axisymmetric Cavities — <i>D.G. Myakishev, V.P. Yakovlev</i>	2348	MPC17
Transverse EM Fields in a Detuned X-band Accelerating Structure — <i>S.A. Heifets, S.A. Kheifets, B. Woo</i>	2351	MPC18
RF Cavity Computer Design Codes — <i>P.A. McIntosh</i>	2353	MPC19
Arbitrary Order Transfer Maps for RF Cavities — <i>Johannes van Zeijts</i>	2356	MPC20
The Computation of the Dynamic Inductance of Magnet Systems and Force Distribution in Ferromagnetic Region on the Basis of 3-D Numerical Simulation of Magnetic Field — <i>N. Doinikov, V. Kukhtin, E. Lamzin, B. Mingalev, Yu. Severgin, S. Sytchevsky</i>	2359	MPC21
Advanced Electromagnetic Design of Cavities for High Current Accelerators — <i>Frank L. Krawczyk</i>	2361	MPC22
Modified PARMILA Code for New Accelerating Structures — <i>H. Takeda, J.E. Stovall</i>	2364	MPC23
Tracking Particles with Wake Fields and Space Charge Effects — <i>A.J. Riche</i>	2367	MPC24
On the Importance of Fourth Order Effects on Wakefield Calculations for Short Bunches — <i>Zenghai Li, Joseph J. Bisognano</i>	2370	MPC25

Coupling Impedances of Muffin-Tin Structures with Closed and Open Sides — <i>M. Filtz</i>	2373	MPC28
Explicit Soft Fringe Maps of a Quadrupole — <i>John Irwin, Chun-xi Wang</i>	2376	MPC31

Instrumentation and Feedback

Bunched Beam Cooling for the Fermilab Tevatron (<i>Invited</i>) — <i>Ralph J. Pasquinelli</i>	2379	RAE01
Fast Digital Dampers for the Fermilab Booster (<i>Invited</i>) — <i>James M. Steimel Jr.</i>	2384	RAE02
Fast Feedback for Linear Colliders (<i>Invited</i>) — <i>L. Hendrickson, C. Adolphsen, S. Allison, T. Gromme, P. Grossberg, T. Himel, K. Krauter, R. MacKenzie, M. Minty, R. Sass, H. Shoaee, M. Woodley</i>	2389	RAE03
Instrumentation in Medical Systems (<i>Invited</i>) — <i>W.T. Chu</i>	2394	RAE04
Laser Diagnostics of a One-Dimensional Ordered Ion Beam — <i>R. Calabrese, V. Guidi, P. Lenisa, U. Tambini, E. Mariotti, L. Moi</i>	2399	RAE05
Determining Electron Beam Parameters from Edge Radiation Measurement Results on Siberia-1 Storage Ring — <i>O.V. Chubar</i>	2402	RAE06
Absolute Energy Measurement in e^-e^+ Linear Colliders — <i>Blaine E. Norum, Robert Rossmanith</i>	2405	RAE07
INR Activity in Development and Production of Bunch Shape Monitors — <i>S.K. Esin, A.V. Feschenko, P.N. Ostroumov</i>	2408	RAE08
Conceptual design of a Charged Particle Beam Energy Spectrometer Utilizing Transition Radiation Grating — <i>X.Z. Qiu, X.J. Wang, K. Batchelor, I. Ben-Zvi</i>	2411	RAE09
An Analysis of the Operational Performance of the Automatic Global Horizontal Beam Position Control System on the SRS at Daresbury — <i>J.B. Fitzgerald, B.G. Martlew, P.D. Quinn, S.L. Smith</i>	2414	RAE10
A Prototype Fast Feedback System for Energy Lock at CEBAF — <i>M. Chowdhary, G.A. Krafft, H. Shoaee, S.N. Simrock, W.A. Watson</i>	2417	RAE11
Operation and Performance of the PEP-II Prototype Longitudinal Damping System at the ALS — <i>D. Teytelman, R. Claus, J. Fox, H. Hindi, J. Hoeflich, I. Linscott, J. Olsen, G. Oxoby, S. Prabhakar, W. Ross, L. Sapozhnikov, A. Drago, M. Serio, J. Byrd, J. Corlett, G. Stover</i>	2420	RAE12
Commissioning of the ALS Transverse Coupled-Bunch Feedback System — <i>W. Barry, J. Byrd, J. Corlett, J. Johnson, G. Lambertson, J. Fox</i>	2423	RAE13
Operation of a Fast Digital Transverse Feedback System in CESR — <i>J.T. Rogers, M.G. Billing, J.A. Dobbins, C.R. Dunnam, D.L. Hartill, T. Holmquist, B.D. McDaniel, T.A. Pelaia, M. Pisharody, J.P. Sikora, C.R. Strohman</i>	2426	RAE14
Measuring and Adjusting the Path Length at CEBAF — <i>G.A. Krafft, M. Crofford, D.R. Douglas, S.L. Harwood, R. Kazimi, R. Legg, W. Oren, K. Tremblay, D. Wang</i>	2429	WXE01
Simulations of the BNL/SLAC/UCLA 1.6 Cell Emittance Compensated Photocathode RF Gun Low Energy Beam Line — <i>D.T. Palmer, R.H. Miller, H. Winick, X.J. Wang, K. Batchelor, M. Woodley, I. Ben-Zvi</i>	2432	WXE03
Small Gap Undulator Experiment on the NSLS X-Ray Ring — <i>P.M. Stefan, S. Krinsky, G. Rakowsky, L. Solomon</i>	2435	WXE04
Measurements of Longitudinal Dynamics in the SLC Damping Rings — <i>R.L. Holtzapple, R.H. Siemann, C. Simopoulos</i>	2438	WXE05
Single Bunch Collective Effects in the ALS — <i>J.M. Byrd, J.N. Corlett, T. Renner</i>	2441	WXE06
Experiments of Nanometer Spot Size Monitor at FFTB Using Laser Interferometry — <i>T. Shintake, K. Oide, N. Yamamoto, A. Hayakawa, Y. Ozaki, D. Burke, R.C. Field, S. Hartman, R. Iverson, P. Tenenbaum, D. Walz</i>	2444	WXE07
Transverse Electron Beam Size Measurements Using the Lloyd's Mirror Scheme of Synchrotron Light Interference — <i>O.V. Chubar</i>	2447	WXE08

Instrumentation

Charge Balancing Fill Rate Monitor — <i>J.L. Rothman, E.B. Blum</i>	2450	MPQ01
Sensitivity and Offset Calibration for the Beam Position Monitors at the Advanced Photon Source — <i>Y. Chung, D. Barr, G. Decker, K. Evans Jr., E. Kahana</i>	2452	MPQ03
An Sampling Detector for the RHIC BPM Electronics — <i>W.A. Ryan, T.J. Shea</i>	2455	MPQ04
RHIC Beam Position Monitor Characterization		

— P.R. Cameron, M.C. Grau, M. Morvillo, T.J. Shea, R.E. Sikora.....	2458	MPQ05
Duke Storage Ring Tune Measurements System using Razor Blade and Photomultiplier — V.N. Litvinenko, B. Burnham, N. Hower, P. Morcombe, Y. Wu	2461	MPQ06
The Development of Beam Current Monitors in the APS — X. Wang, F. Lenkszus, E. Rotela.....	2464	MPQ07
Overall Design Concepts for the APS Storage Ring Machine Protection System — A. Lumpkin, R. Fuja, A. Votaw, X. Wang, D. Shu, J. Stepp, N. Arnold, G. Nawrocki, G. Decker, Y. Chung	2467	MPQ08
Status of the Synchrotron Radiation Monitors for the APS Facility Rings — A. Lumpkin, B. Yang	2470	MPQ09
Initial Diagnostics Commissioning Results for the Advanced Photon Source (APS) — A. Lumpkin, D. Patterson, X. Wang, E. Kahana, W. Sellyey, A. Votaw, B. Yang, R. Fuja, W. Berg, M. Borland, L. Emery, G. Decker, S. Milton.....	2473	MPQ10
Initial Tests of the Dual-Sweep Streak Camera System Planned for APS Particle-Beam Diagnostics — A. Lumpkin, B. Yang, W. Gai, W. Cieslik.....	2476	MPQ11
A Transverse Tune Monitor for the Fermilab Main Ring — P.J. Chou, B. Fellenz, G. Jackson.....	2479	MPQ13
Recalibration of Position Monitors With Beams — Kotaro Satoh, Masaki Tejima.....	2482	MPQ14
Simulation of PEP-II Beam Position Monitors — C.-K. Ng, T. Weiland, D. Martin, S. Smith, N. Kurita.....	2485	MPQ15
Prototype Bunch Killer System At SRRC — G.J. Jan, Jenny Chen, C.H. Kuo, T.F. Lin, K.T. Pan, Glory Lin, K.T. Hsu.....	2488	MPQ16
Beam Diagnostics for the Amsterdam Pulse Stretcher AmPS — J.G. Noomen, H. Boer-Rookhuizen, N. Dobbe, J. v. Es, E. Heine, F. Kroes, J. Kuijt, J. v.d. Laan, A. Poelman, H. Nieuwenkamp, T. Sluijk.....	2491	MPQ17
Non-Destructive Beam Profile Measuring System Observing Fluorescence Generated by Circulating Beam — T. Kawakubo, E. Kadokura, T. Kubo, T. Ishida, H. Yamaguchi	2494	MPQ18
The Closed Orbit Measurement of SRRC Booster During Ramping — T.S. Ueng, K.T. Hsu, K.H. Hwu, K.K. Lin	2497	MPQ19
Lattice Function Measurement with TBT BPM Data — Ming-Jen Yang.....	2500	MPQ20
Optimal Placement of Profile Monitors in a Mismatched FODO Lattice — K. Bertsche	2503	MPQ21
SSRL Beam Position Monitor Detection Electronics — J. Sebek, R. Hettel, R. Matheson, R. Ortiz, J. Wachter	2506	MPQ22
Single-Turn Beam Position Monitor for the NSLS VUV Electron Storage Ring — R.J. Nawrocky, S.L. Kramer.....	2509	MPQ23
Design of the Button Beam Position Monitor for PEP-II — N. Kurita, D. Martin, S. Smith, C. Ng, M. Nordby, C. Perkins.....	2512	MPQ25
Study of Fast Electron Beam Profile Monitor System — Ian Hsu, C.I. Yu, C.C. Chu.....	2515	MPQ26
The Average Orbit System Upgrade for the Brookhaven AGS — D.J. Ciardullo, J.M. Brennan	2518	MPQ30
Feasibility Study of an Orbit Feedback System for the KEKB Facility — Y. Funakoshi, M. Tejima, H. Ishii	2521	MPQ31
Turn-by-Turn Beam Position Measurement for 1.3 GeV Booster Synchrotron — T.S. Ueng, K.T. Hsu, C.S. Fang, Y.M. Chang, K.K. Lin	2524	MPQ32
Beam Position Monitor for the LNSL UVX Synchrotron Light Source — F.S. Rafael, E.K.C.S. Hayashi	2527	MPQ33
Transition Radiation Electron Beam Diagnostic Study at ATF — X.Z. Qiu, X.J. Wang, K. Batchelor, I. Ben-Zvi.....	2530	TPB01
Machine Parameter Measurement of the Amsterdam Pulse Stretcher AmPS — Y.Y. Wu, R. Maas	2533	TPB03
Wire Setup Calibration of Beam Position Monitors — D. Wang, B. Binns, M. Kogan, A. Zolfaghari	2536	TPB04
Beam profile data analysis for the RHIC Injection Line — Ping Zhou.....	2539	TPB05
Energy Spread of Ion Beams Generated in Multicusp Ion Sources — M. Sarstedt, P. Herz, W.B. Kunkel, Y. Lee, K.N. Leung, L. Perkins, D. Pickard, M. Weber, M.D. Williams, E. Hammel.....	2542	TPB07
A 2 MHz 3-Port Analog Isolation and Fanout Module — Edward R. Beadle	2545	TPB08
A General Purpose Fiber Optic Link with Radiation Resistance — Edward R. Beadle	2548	TPB09
DSP Based Data Acquisition for RHIC — T.J. Shea, J. Mead, C.M. Degen.....	2551	TPB12

Ion-Chamber Beam-Loss-Monitor System for the Los Alamos Meson Physics Facility — <i>M. Plum, D. Brown, A. Browman, R. Macek</i>	2554	TPB13
Development of Beam Position Monitors for Heavy Ion Recirculators — F.J. Deadrick, <i>J.J. Barnard, T.J. Fessenden, J.W. Meredith, J. Rintamaki</i>	2557	TPB14
Laser Compton Polarimetry of Proton Beams — A. Stillman	2560	TPB15
Phase and Synchronous Detector Theory as Applied to Beam Position and Intensity Measurements — J.D. Gilpatrick	2563	TPB16
Testing Coaxial Switches of BPM using a High-Resolution RF Detector — Takao Ieiri	2566	TPB17
A Beam Size Monitor Based on Appearance Intensities for Multiple Gas Ionization — <i>T. Katsouleas, J. Yoshii, W.B. Mori, C. Joshi, C. Clayton</i>	2569	TPB18
Beam Profile Measurement in the Presence of Noise — K. Bertsche, J. Palkovic	2572	TPB19
Beam Shaping Using a New Digital Noise Generator — H. Stockhorst, G. Heinrichs, <i>A. Schnase, S. Papureanu, U. Bechstedt, R. Maier, R. Tölle</i>	2574	TPB20
The RHIC Transfer Line Cable Database — E.H. Scholl, T. Satogata	2577	TPB21
Characterization of Beam Position Monitors for Measurement of Second Moment — <i>S.J. Russell, J.D. Gilpatrick, J.F. Power, R.B. Shurter</i>	2580	TPB22
Beam Diagnostic Systems and Their Use in the New IUCF Beam Line — W.P. Jones, M. Ball, <i>J. Collins, T. Ellison, B. Hamilton</i>	2583	TPB24
Tomographic Method of Experimental Research of Particle Distribution in Phase Space — <i>V.V. Kalashnikov, V.I. Moiseev, V.V. Petrenko</i>	2586	TPB25
Design of the Beam Profile Monitor System for the RHIC Injection Line — R.L. Witkover	2589	TPB26
Beam Intensity Observation System at SRRC — C.J. Wang, C.H. Kuo, J.S. Chen, Jenny Chen, <i>K.T. Hsu, G.J. Jan</i>	2592	TPB29
Performance of the Advanced Photon Source (APS) Linac Beam Position Monitors (BPMs) with Logarithmic Amplifier Electronics — R.E. Fuja, M. White	2595	TPC01
Preliminary Calculations on the Determination of APS Particle-Beam Parameters Based on Undulator Radiation — A. Lumpkin, B. Yang, Y. Chung, R. Dejus, G. Voykov, G. Dattoli	2598	TPC03
Coherent Synchrotron Radiation Detector for a Non-Invasive Subpicosecond Bunch Length Monitor — G.A. Krafft, D. Wang, E. Price, E. Feldl, D. Porterfield, P. Wood, T. Crowe	2601	TPC04
A Beam Test of Button-Type Beam Position Monitor for the ATF Damping Ring — <i>F. Hinode, H. Hayano, M. Tejima, N. Terunuma, J. Urakawa</i>	2604	TPC05
Application of a Transverse Phase-Space Measurement Technique for High-Brightness, H- Beams to the GTA H- Beam — K.F. Johnson, R.C. Connolly, R.C. Garcia, D.P. Rusthoi, <i>O.R. Sander, D.P. Sandoval, M.A. Shinas, M. Smith, V.W. Yuan</i>	2607	TPC06
Precision Intercomparison of Beam Current Monitors at CEBAF — R. Kazimi, B. Dunham, <i>G.A. Krafft, R. Legg, C. Liang, C. Sinclair, J. Mammoser</i>	2610	TPC07
Damped Button Electrode for B-Factory BPM System — T. Obina, T. Shintake, Y.H. Chin, <i>N. Akasaka</i>	2613	TPC08
Beam Monitors for the S-Band Test Facility — W. Radloff, M. Wendt	2616	TPC09
Low Energy Regime for Optical Transition Radiation Emission — D. Giove, C. De Martinis, <i>M. Pullia, P. Mangili</i>	2619	TPC10
Recovery of CTF Beam Signals from a Strong Wakefield Background — Yan Yin, <i>Elmar Schulte, Tord Ekelöf</i>	2622	TPC11
A Low-Cost Non-Intercepting Beam Current and Phase Monitor for Heavy Ions — <i>J.M. Bogaty, B.E. Clift</i>	2625	TPC12
Transverse Emittance Systematics Measured for Heavy-Ion Beams at ATLAS — J.A. Nolen, <i>T.A. Barlow, K.A. Beyer, K.A. Woody</i>	2628	TPC13
Beam Position Monitors in the TESLA Test Facility Linac — R. Lorenz	2631	TPC14
Energy Measurement of Relativistic Electrons by Compton Scattering — Ian Hsu, C.-C. Chu, <i>C.-I. Yu, C.-I. Chen, A.-T. Lai, Y.-C. Liu, P.-K. Tseng, G.-Y. Hsiung, R.-C. Hsu, C.-P. Wang, R.-</i> <i>C. Chen</i>	2634	TPC15
Tests of a High Resolution Beam Profile Monitor — J. Norem, J. Dawson, W. Haberichter, <i>R. Lam, L. Reed, X.-F. Yang, J. Spencer</i>	2637	TPC16
Airix Alignment and High Current Beam Diagnostics — D. Villate, Ch. Bonnafond, A. Devin, <i>E. Merle</i>	2640	TPC17
A New Beam Intensity Monitoring System with Wide Dynamic Range for the Holifield Radioactive Ion Beam Facility — M.J. Meigs, D.L. Haynes, C.M. Jones, C.T. LeCroy	2643	TPC18

Diagnostic Beam Pulses for Monitoring the SLC Linac — <i>F.-J. Decker, M. Stanek, H. Smith, F. Tian</i>	2646	TPC20
Observation of Thermal Effects on the LEP Wire Scanners — <i>J. Camas, C. Fischer, J.J. Gras, R. Jung, J. Koopman</i>	2649	TPC21
CEBAF Beam Loss Accounting — <i>R. Ursic, K. Mahoney, C. Hovater, A. Hutton, C. Sinclair</i>	2652	TPC26
Nanometer Resolution BPM Using Damped Slot Resonator — <i>S.C. Hartman, T. Shintake, N. Akasaka</i>	2655	TPC29
An Automatic Tune-Measurement System for the CELSIUS Ring — <i>T. Lofnes</i>	2658	TPC31

Feedback

Software Architecture of the Longitudinal Feedback System for PEP-II, ALS and DAΦNE — <i>R. Claus, J. Fox, I. Linscott, G. Oxoby, W. Ross, L. Sapozhnikov, D. Teytelman, A. Drago, M. Serio</i>	2660	RPQ01
Digital I/Q Demodulator — <i>C. Ziomek, P. Corredoura</i>	2663	RPQ02
RF Feedback Simulation Results for PEP-II — <i>R. Tighe, P. Corredoura</i>	2666	RPQ03
TM0,1,5,0 Mode Cavity for Longitudinal Bunch Feedback Kicker — <i>T. Shintake</i>	2669	RPQ04
Low Level RF System Design for the PEP-II B Factory — <i>P. Corredoura, R. Claus, L. Sapozhnikov, H. Schwarz, R. Tighe, C. Ziomek</i>	2672	RPQ05
Experiment of the RF Feedback using a Parallel Comb Filter — <i>S. Yoshimoto, E. Ezura, K. Akai, T. Takashima</i>	2675	RPQ06
Digital Transverse Beam Dampers for the Brookhaven AGS — <i>G.A. Smith, V. Castillo, T. Roser, W. Van Asselt, R. Witkover, V. Wong</i>	2678	RPQ07
Design of the PEP-II Transverse Coupled-Bunch Feedback System — <i>W. Barry, J. Byrd, J. Corlett, M. Fahmie, J. Johnson, G. Lambertson, M. Nyman, J. Fox, D. Teytelman</i>	2681	RPQ08
Simulations of the PEP-II Transverse Coupled-Bunch Feedback System — <i>J.M. Byrd</i>	2684	RPQ09
Fermilab Booster Low Level RF System Upgrades — <i>Robert C. Webber</i>	2687	RPQ10
Energy Stability in a High Average Power FEL — <i>L. Merminga, J.J. Bisognano</i>	2690	RPQ11
Automated Beam Based Alignment of the ALS Quadrupoles — <i>G. Portmann, D. Robin, L. Schachinger</i>	2693	RPQ13
First Results with a Nonlinear Digital Orbit Feedback System at the NSLS — <i>Eva Bozoki, Aharon Friedman, Susila Ramamoorthy</i>	2696	RPQ14
Local Beam Position Feedback Experiments on the ESRF Storage Ring — <i>Y. Chung, E. Kahana, J. Kirchman, A. Lumpkin, J. Meyer, E. Plouviez, K. Scheidt, E. Taurel, A. Ando, S. Sasaki, A. Taketani</i>	2699	RPQ15
Implementation of the Global and Local Beam Position Feedback Systems for the Advanced Photon Source Storage Ring — <i>Y. Chung, D. Barr, G. Decker, J. Galayda, J. Kirchman, F. Lenkszus, A. Lumpkin, A.J. Votaw</i>	2702	RPQ16
The RHIC Accelerating Cavity Prototype Tuner — <i>A. Ratti, J.M. Brennan, J. Brodowski, E. Onillon, J. Rose</i>	2705	RPQ17
Ramp Tuning of the APS Booster Synchrotron Magnet Power Supplies — <i>S.V. Milton, J.A. Carwardine</i>	2708	RPQ18
Orbit Stability Improvements at the NSLS X-Ray Ring — <i>J. Safranek, O. Singh, L. Solomon</i>	2711	RPQ19
Digital Orbit Feedback Compensation for SPEAR — <i>J. Corbett, R. Hettel, D. Keeley, D. Mostowfi</i>	2714	RPQ21
Digital Orbit Feedback Control for SPEAR — <i>R. Hettel, J. Corbett, D. Keeley, I. Linscott, D. Mostowfi, J. Sebek, C. Wermelskirchen</i>	2717	RPQ22
Beam Position Feedback Systems for the PF Storage Ring — <i>N. Nakamura, K. Haga, T. Honda, T. Kasuga, M. Katoh, Y. Kobayashi, M. Tadano, M. Yokoyama</i>	2720	RPQ23
The New Booster Synchronization Loop — <i>E. Onillon, J.M. Brennan</i>	2723	RPQ25
Recent Progress in the Development of the Bunch Feedback Systems for KEKB — <i>E. Kikutani, T. Kasuga, Y. Minagawa, T. Obina, M. Tobiyama</i>	2726	RPQ26
60 Hz Beam Motion Reduction at NSLS UV Storage Ring — <i>Om V. Singh</i>	2729	RPQ27
The CEBAF Fiber Optic Phase Reference System — <i>K. Crawford, S. Simrock, C. Hovater, A. Krycuk</i>	2732	RPQ29
RF System Modeling for the High Average Power FEL at CEBAF — <i>L. Merminga, J. Fugitt, G. Neil, S. Simrock</i>	2735	RPQ30

Beam Positioning and Monitoring in the Racetrack Microtron Eindhoven — W. Theuws,		
<i>R.W. de Leeuw, G.A. Webers, J.I.M. Botman, C.J. Timmermans, H.L. Hagedoorn</i>	2738	RPQ31
Multi-Bunch Systems at DESY — Rolf-Dieter Kohaupt	2741	RPQ32

High Energy Accelerator Beam Dynamics

Results of Final Focus Test Beam (Invited) — V.A. Alexandrof, V. Balakin, A. Mikhailichenko,		
<i>K. Flöttmann, F. Peters, G.-A. Voss, V. Bharadwaj, M. Halling, J.A. Holt, J. Buon, J. Jeanjean,</i>		
<i>F. LeDiberder, V. Lepeltier, P. Puzo, G. Heimlinger, R. Settles, U. Stierlin, N. Akasaka,</i>		
<i>H. Hayano, N. Ishihara, H. Nakayama, K. Oide, T. Shintake, Y. Takeuchi, N. Yamamoto,</i>		
<i>F. Bulos, D. Burke, R. Field, S. Hartman, R. Helm, J. Irwin, R. Iverson, P. Raimondi, S. Rokni,</i>		
<i>G. Roy, W. Spence, P. Tenenbaum, S.R. Wagner, D. Walz, S. Williams</i>	2742	TAG01
Comparison of Measured and Calculated Dynamic Aperture (Invited) — F. Willeke	2747	TAG02
Ion Effects in Future Circular and Linear Accelerators (Invited) — T.O. Raubenheimer	2752	TAG03
Nonlinear Wave Phenomena in Coasting Beams (Invited) — P.L. Colestock, L.K. Spentzouris,		
<i>F. Ostiguy</i>	2757	TAG04
The Cure of Multibunch Instabilities in ELETTRA — M. Svandrlik, C.J. Bocchetta, A. Fabris,		
<i>F. Iazzourene, E. Karantzoulis, R. Nagaoka, C. Pasotti, L. Tosi, R.P. Walker, A. Wrulich</i>	2762	TAG05
Nonlinear Analyses of Storage Ring Lattices Using One-Turn Maps — Y.T. Yan, J. Irwin,		
<i>T. Chen</i>	2765	TAG06
Precise Determination and Comparison of the SPS Dynamic Aperture in Experiment and		
Simulation — W. Fischer, F. Schmidt	2768	TAG07
Coherency of the Long Range Beam-Beam Interaction in CESR — Alexander B. Temnykh,		
<i>James J. Welch</i>	2771	TAG08
Effect of Quadrupole Noise on the Emittance Growth of Protons in HERA — T. Sen,		
<i>O. Brüning, F. Willeke</i>	2774	TAG09
Nonlinear Mode Coupling Analysis in the Tevatron — S. Assadi, C.S. Mishra	2777	TAG10
Lattice Design for KEKB Colliding Rings — H. Koiso, K. Oide	2780	TAG11
Entropy and Emittance Growth — Patrick G. O'Shea	2783	TAG12
Analysis of Optical Stochastic Cooling Including Transverse Effects — K.-J. Kim	2786	TAG13

Volume 5

Linear and Nonlinear Orbit Theory

Reduction of Non Linear Resonance Excitation from Insertion Devices in the ALS —		
<i>D. Robin, G. Krebs, G. Portmann, A. Zholents, W. Decking</i>	2789	FAB01
Sum Betatron Resonances under Linear Coupling of Oscillations — P.N. Chirkov,		
<i>I.I. Petrenko</i>	2792	FAB02
Linear Orbit Parameters for the Exact Equations of Motion — G. Parzen	2795	FAB03
Tune Modulation Due to Synchrotron Oscillations and Chromaticity, and the Dynamic		
Aperture — G. Parzen	2798	FAB04
Normal Mode Tunes for Linear Coupled Motion in Six Dimensional Phase Space —		
<i>G. Parzen</i>	2801	FAB05
Fast Symplectic Mapping and Quasi-invariants for the Large Hadron Collider —		
<i>R.L. Warnock, J.S. Berg, E. Forest</i>	2804	FAB06
Nonlinear Dependence of Synchrotron Radiation on Beam Parameters — G.H. Hoffstätter	2807	FAB07
Effects of Imperfections on the Dynamic Aperture and Closed Orbit of the IPNS Upgrade		
Synchrotron — E. Lessner, Y.-C. Chae, S. Kim	2811	FAB09
Paraxial Expansion of a Static Magnetic Field in a Ring Accelerator — Lee C. Teng	2814	FAB10
Experimental Determination of Linear Optics Including Quadrupole Rotations —		
<i>J. Safranek</i>	2817	FAB11
Perturbation of Beam Energy Due to Steering and Pretzel Orbit — W. Lou, M. Billing,		
<i>D. Rice</i>	2820	FAB12
Lattice Studies for a High-Brightness Light Source — D. Kaltchev, R.V. Servranckx,		
<i>M.K. Craddock, W. Joho</i>	2823	FAB14

Transfer Maps Through Ideal Bends (Again?) — Leo Michelotti.....	2826	FAB15
Skew Chromaticity in Large Accelerators — S. Peggs, G.F. Dell.....	2829	FAB20
The Effect and Correction of Coupling Generated by the RHIC Triplet Quadrupoles — F. Pilat, S. Peggs, S. Tepikian, D. Trbojevic, J. Wei.....	2832	FAB22
The Beam Envelope Equation - Systematic Solution for a FODO Lattice with Space Charge — Edward P. Lee.....	2835	FAC01
Analytic Second- and Third-Order Achromat Designs — Chunxi Wang, Alex Chao	2838	FAC02
Measurement of Chromatic Effects in LEP — D. Brandt, P. Castro, K. Cornelis, A. Hofmann, G. Morpurgo, G.L. Sabbi, A. Verdier	2841	FAC03
The Lattice of the CERN Large Hadron Collider — W. Scandale, B. Jeanneret, J.- P. Koutchouk, X. Luo, F. Méot, R. Ostojic, T. Risselada, C. Rufer, T. Taylor, T. Trenkler, S. Weisz.....	2844	FAC04
Sorting Strategies for the LHC Based on Normal Forms — W. Scandale, M. Giovannozzi, R. Grassi, E. Todesco.....	2847	FAC06
Algorithms to get a Circulating Beam — André Verdier, Frank Richard.....	2850	FAC07
Non-Linear Chromaticity Correction with Sextupole Families — André Verdier	2853	FAC08
Simulation of Charged Particle Transport in Nonlinear Axisymmetrical Electrostatic Potential — I.P. Yudin, V.V. Andreev	2856	FAC09
Stochastic Effects in Real and Simulated Ion Beams — Jürgen Struckmeier.....	2860	FAC10
Magnetic Field Correction in Nuclotron — I.B. Issinsky, V.A. Mikhailov, V.A. Shchepunov.....	2863	FAC12
Effects of the CHESS Wigglers on a Beam with an Angular Offset — James J. Welch	2866	FAC14
Particle Tracking with Generating Functions of Magnetic Fringing Fields — Godehard Wüstefeld.....	2868	FAC16
Computation of Lattice Maps Using Modular BCH and Similarity Composition Rules — J. Irwin	2871	FAC18
Treatment of Wiggler and Undulator Field Errors in Tracking Codes — W. Decking, O. Kaul, H. Neemann, J. Roßbach.....	2874	FAC19
Experimental Study of the Duke Storage Ring Dynamic Aperture — Y. Wu, V.N. Litvinenko, B. Burnham, J.M.J. Madey	2877	FAC20

Beam-Beam Interaction and Beam Cooling

A New Model of the e⁺e⁻ Beam-Beam Interaction — K.D. Cromer, B.E. Norum.....	2880	RAP01
A Study of Beam-Beam Interactions at Finite Crossing Angles for a B-Factory — K. Hirata, K. Ohmi, N. Toge	2883	RAP02
Simulation of Beam-Beam Effects in Tevatron — C.S. Mishra, S. Assadi, R. Talman	2886	RAP03
The Dynamic Beta Effect in CESR — David Sagan.....	2889	RAP04
Lifetime and Tail Simulations for Beam-Beam Effects in PEP-II B Factory — D.N. Shatilov, A.A. Zholents	2892	RAP05
Gamma Ray Sources Based on Resonant Backscattering of Laser Beams With Relativistic Heavy Ion Beams — E.G. Bessonov, Kwang-Je Kim	2895	RAP06
Observations of the Effects of the Beam-Beam Interaction on the Orbits of Stored Beams in CESR — E. Young	2898	RAP07
Calculations on Depolarization in HERA due to Beam-Beam Effects — M. Böge, T. Limberg.....	2901	RAP08
A Map for the Thick Beam-Beam Interaction — J. Irwin, T. Chen.....	2904	RAP09
Transient Beam Loading in the SLC Damping Rings — M.G. Minty, R.H. Siemann.....	2907	RAP10
Studies of Halo Distributions Under Beam-Beam Interaction — T. Chen, J. Irwin, R.H. Siemann.....	2910	RAP11
The Effect of Phase Advance Errors Between Interaction Points on Beam Halos — T. Chen, J. Irwin, R.H. Siemann.....	2913	RAP12
Compensation of the "Pacman" Tune Spread by Tailoring the Beam Current — Miguel A. Furman	2916	RAP14
Disruption Effects on the Beam Size Measurement — P. Raimondi, F.-J. Decker, P. Chen.....	2919	RAP15
Flat Beam Spot Sizes Measurement in the SLC-Final Focus — P. Raimondi, F.-J. Decker	2922	RAP16
Polarization Correlations in the SLC Final Focus — F.-J. Decker.....	2925	RAP17
Supercooling of Bunched Beams by Coherent Synchrotron Radiation — M. Bergher.....	2928	RAP19

Analysis of the Tevatron Collider Beam Spectrum for Bunched Beam Stochastic Cooling — <i>G. Jackson</i>	2931	RAP20
Asymmetric Hopf Bifurcation for Proton Beams with Electron Cooling — <i>X. Kang, M. Ball, B. Brabson, J. Budnick, D.D. Caussyn, P. Colestock, G. East, M. Ellison, B. Hamilton, K. Hedblom, S.Y. Lee, D. Li, J.Y. Liu, K.Y. Ng, A. Pei, A. Riabko, M. Syphers, L. Wang, Y. Wang</i>	2934	RAP21
Space Charge Effects and Intensity Limits of Electron-Cooled Bunched Beams — <i>S. Nagaitsev, T. Ellison, M. Ball, V. Derenchuk, G. East, M. Ellison, B. Hamilton, P. Schwandt</i>	2937	RAP22
Stability Conditions for a Neutralised Electron Cooling Beam — <i>J. Bosser, S. Maury, D. Möhl, F. Varenne, I. Meshkov, E. Syresin, E. Mustafin, P. Zenkevich</i>	2940	RAP23
Neutralisation of the LEAR Electron-Cooling Beam: Experimental Results — <i>J. Bosser, F. Caspers, M. Chanel, R. Ley, R. Maccaferri, S. Maury, G. Molinari, G. Tranquille, F. Varenne, I. Meshkov, V. Polyakov, A. Smirnov, O. Stepashkin, E. Syresin</i>	2943	RAP24
Crystalline Beam Properties as Predicted for the Storage Ring ASTRID and TSR — <i>Jie Wei, Xiao-Ping Li, Andrew Sessler</i>	2946	RAP25

Instabilities and Cures

Impedance Matrix - an Unified Approach to Longitudinal Coupled-Bunch Feedbacks in a Synchrotron — <i>S. Ivanov</i>	2949	TPQ01
The Coupling Impedance of Toroidal Beam Pipe with Circular Cross Section — <i>H. Hahn</i>	2952	TPQ02
Bunch Lengthening Study in BEPC — <i>Z. Guo, Q. Qin, G. Xu, C. Zhang</i>	2955	TPQ03
Practical Criterion of Transverse Coupled-Bunch Head-Tail Stability — <i>S. Ivanov, M. Pozdeev</i>	2958	TPQ04
A Code to Compute the Action-Angle Transformation for a Particle in an Arbitrary Potential Well — <i>J. Scott Berg, Robert L. Warnock</i>	2962	TPQ07
Study of Longitudinal Coupled-Bunch Instabilities in the SRRC Storage Ring — <i>W.K. Lau, M.H. Wang, K.T. Hsu, L.H. Chang, Ch. Wang, C.C. Kuo</i>	2965	TPQ08
Suppression of the Transverse Oscillation in the SRRC Storage Ring by RF Knockout Method — <i>J.C. Lee, M.H. Wang, K.T. Hsu, R.J. Sheu, G. Lin, C.S. Hsue</i>	2968	TPQ09
The Observation of Longitudinal Coupled Bunch Motion on Streak Camera at SRRC — <i>M.H. Wang, K.T. Hsu, W.K. Lau, C.S. Hsue, H.J. Tsai, H.P. Chang, J.C. Lee, C.C. Kuo</i>	2971	TPQ10
Resistive-Wall Instability Experiment in Space-Charge Dominated Electron Beams — <i>H. Suk, J.G. Wang, M. Reiser</i>	2974	TPQ11
Mode-Coupling Instability and Bunch Lengthening in Proton Machines — <i>K.Y. Ng</i>	2977	TPQ12
Longitudinal Wakefield for Synchrotron Radiation — <i>J.B. Murphy, S. Krinsky, R.L. Gluckstern</i>	2980	TPQ14
Review of Beam Instability Studies for the SSC — <i>W. Chou</i>	2983	TPQ15
Collective Effects in the NLC Damping Ring Designs — <i>T. Raubenheimer, K.L.F. Bane, J.S. Berg, J. Byrd, J. Corlett, M. Furman, S. Heifets, K. Kubo, M. Minty, B. Scott, K.A. Thompson, P.B. Wilson, F. Zimmermann</i>	2986	TPQ16
Emittance and Energy Control in the NLC Main Linacs — <i>C. Adolphsen, K.L.F. Bane, K. Kubo, T. Raubenheimer, R.D. Ruth, K.A. Thompson, F. Zimmermann</i>	2989	TPQ17
Digital Signal Processing for the APS Transverse and Longitudinal Damping System — <i>D. Barr, W. Sellyey</i>	2992	TPQ19
Longitudinal Coupling Impedance of a Hole in an Infinite Plane Screen — <i>Yong-Chul Chae</i>	2995	TPQ20
Investigation of Resistive Wall Instability in the 7-GeV APS Storage Ring — <i>Yong-Chul Chae</i>	2998	TPQ21
Longitudinal Instability Analysis for the IPNS Upgrade — <i>K. Harkay, Y. Cho, E. Lessner</i>	3001	TPQ22
Transverse Instability Analysis for the IPNS Upgrade — <i>K. Harkay, Y. Cho</i>	3004	TPQ23
Longitudinal Emittance Measurements in the Fermilab Booster — <i>D.A. Herrup</i>	3007	TPQ25
Analog Dampers in the Fermilab Booster — <i>D.A. Herrup, D. McGinnis, J. Steimel, R. Tomlin</i>	3010	TPQ26
A Study of the Longitudinal Coupled Bunch Instability in the Fermilab Main Ring — <i>K. Junck, J. Marriner, D. McGinnis</i>	3013	TPQ28
Inference of Wake Field Structure by Driving Longitudinal Coupled Bunch Modes in Main Ring — <i>S. Assadi, K. Junck, P. Colestock, J. Marriner</i>	3016	WAB01
Simulation of Transverse Coupled Bunch Instabilities — <i>S. Khan</i>	3019	WAB03
The Transition Jump System for the AGS — <i>W.K. van Asselt, L.A. Ahrens, J.M. Brennan, A. Dunbar, E. Keith-Monnia, J.T. Morris, M.J. Syphers</i>	3022	WAB04

Measurements of Longitudinal Phase Space in the SLC Linac — R.L. Holtzapple, F.-J. Decker, R.K. Jobe, C. Simopoulos	3025	WAB05
Observation of Induced Beam Oscillation from Actively Displaced RF Accelerating Structures — John T. Seeman, Henk Fischer, William Roster	3028	WAB06
Measurement of the Effect of Collimator Generated Wakefields on the Beams in the SLC — K.L.F. Bane, C. Adolphsen, F.-J. Decker, P. Emma, P. Krejcik, F. Zimmermann	3031	WAB07
Beam Trajectory Jitter in the SLC Linac — Chris Adolphsen, Tim Slaton	3034	WAB08
Emittance Growth due to Decoherence and Wakefields — M.G. Minty, A.W. Chao, W.L. Spence	3037	WAB09
A Weak Microwave Instability with Potential Well Distortion and Radial Mode Coupling — Alex Chao, Bo Chen, Katsunobu Oide	3040	WAB10
Wake Field and the Diffraction Model Due to a Flat Beam Moving Past a Conducting Wedge — A.W. Chao, H. Henke	3043	WAB11
Operating Experience with High Beam Currents and Transient Beam Loading in the SLC Damping Rings — M.G. Minty, R. Akre, P. Krejcik, R.H. Siemann	3046	WAB12
Deflecting Forces for the Case of Multi Mode Beam - RF Cavity Interaction in Linear Accelerators — V.G. Kurakin	3049	WAB14
Photoelectron Trapping Mechanism for Transverse Coupled Bunch Mode Growth in CESR — J.T. Rogers	3052	WAB15
Electron Cooler Impedances — A. Burov	3055	WAB16
Wall Impedances for Low and Moderate Energies — A. Burov	3058	WAB17
Impedance Analysis of the PEP-II Vacuum Chamber — C.-K. Ng, T. Weiland	3061	WAB18
Microwave Instabilities in Electron Rings with Negative Momentum Compaction Factor — S.X. Fang, K. Oide, K. Yokoya, B. Chen, J.Q. Wang	3064	WAB20
Microwave Stability at Transition — J.A. Holt, P.L. Colestock	3067	WAC01
Experimental Observations of Nonlinear Coupling of Longitudinal Modes in Unbunched Beams — Linda Klamp Spentzouris, Patrick L. Colestock, Francois Ostiguy	3070	WAC02
Damping Rate Measurements in the SLC Damping Rings — C. Simopoulos, R.L. Holtzapple	3073	WAC04
Transverse Multibunch Instabilities for Non-Rigid Bunches — J. Scott Berg, Ronald D. Ruth	3076	WAC05
Simulations of Transition Crossing in the Main Injector — C.M. Bhat, J.A. MacLachlan	3079	WAC06
Impedance Budget for the KEK B-Factory — Y.H. Chin, K. Satoh	3082	WAC07
Single-Beam Collective Effects in the KEK B-Factory — Y.H. Chin, K. Akai, Y. Funakoshi, K. Oide, K. Satoh	3085	WAC08
Beam Transfer Function and Transverse Impedance Measurements in the Fermilab Main Ring — P.J. Chou, G. Jackson	3088	WAC09
Experimental Studies of Transverse Beam Instabilities at Injection in the Fermilab Main Ring — P.J. Chou, G. Jackson	3091	WAC10
Longitudinal Multibunch Feedback Experiment with Switched Filter Bank — A. Pei, M. Ball, M. Ellison, X. Kang, S.Y. Lee, D. Li, J. Liu, A. Riabko, L. Wang	3094	WAC12
Field Propagation Effects and Related Multibunch Instability in Multicell Capture Cavities — M. Ferrario, A. Mosnier, L. Serafini, F. Tazzioli, J.-M. Tessier	3097	WAC13
Cure of Transverse Instabilities by Chromaticity Modulation — T. Nakamura	3100	WAC14
A Fast Beam-Ion Instability — F. Zimmermann, T.O. Raubenheimer, G. Stupakov	3102	WAC15
Simulations of the Longitudinal Instability in the New SLC Damping Rings — K.L.F. Bane, K. Oide	3105	WAC16
High-Intensity Single Bunch Instability Behavior In The New SLC Damping Ring Vacuum Chamber — K. Bane, J. Bowers, A. Chao, T. Chen, F.J. Decker, R.L. Holtzapple, P. Krejcik, T. Limberg, A. Lisin, B. McKee, M.G. Minty, C.-K. Ng, M. Pietryka, B. Podobedov, A. Rackelmann, C. Rago, T. Raubenheimer, M.C. Ross, R.H. Siemann, C. Simopoulos, W. Spence, J. Spencer, R. Stege, F. Tian, J. Turner, J. Weinberg, D. Whittum, D. Wright, F. Zimmermann	3109	WAC17
Alignment Tolerance of Accelerating Structures and Corrections for Future Linear Colliders — K. Kubo, C. Adolphsen, K.L.F. Bane, T.O. Raubenheimer, K.A. Thompson	3112	WAC18
Refinements to Longitudinal, Single Bunch, Coherent Instability Theory — S.R. Koscielniak	3115	WAC19
Simulations of Sawtooth Instability — R. Baartman, M. D'Yachkov	3119	WAC20
Characterisation of a Localised Broad-Band Impedance Phenomenon on the SRS — S.F. Hill	3122	WAC21
Cavity-Beam Instabilities on the SRS at Daresbury — P.A. McIntosh, D.M. Dykes	3125	WAC22

Bunch Lengthening Thresholds on the Daresbury SRS — J.A. Clarke.....	3128	WAC23
Estimation of Collective Instabilities in RHIC — W.W. MacKay, M. Blaskiewicz, D. Deng, V. Mane, S. Peggs, A. Ratti, J. Rose, T.J. Shea, J. Wei.....	3131	WAC24
RHIC Injection Kicker Impedance — V. Mane, S. Peggs, D. Trbojevic, W. Zhang.....	3134	WAC25
KRAKEN, a Numerical Model of RHIC Impedances — S. Peggs, V. Mane.....	3137	WAC26
Lattice Design of Beijing Light Source — N. Huang, L. Jin, D. Wang, L. Wang, A. Xiao, G. Xu.....	3140	WAC27
A Theoretical Study of the Electron-Proton Instability in a Long Proton Pulse — Tai-Sen F. Wang.....	3143	WAC28
Recent Progress on Beam Stability Study in the PSR — T. Wang, P. Channell, R. Cooper, D. Fitzgerald, T. Hardek, R. Hutson, A. Jason, R. Macek, M. Plum, C. Wilkinson, E. Colton.....	3146	WAC29

Low Energy Accelerator Beam Dynamics

Halos of Intense Proton Beams (Invited) — Robert D. Ryne, Salman Habib, Thomas P. Wangler.....	3149	RAG01
Polarized Proton Beams (Invited) — T. Roser.....	3154	RAG02
Beam Dynamics in Heavy Ion Fusion (Invited) — Peter Seidl.....	3159	RAG03
Crystalline Beams (Invited) — John P. Schiffer.....	3164	RAG04
Injecting a Kapchinskij-Vladimirskij Distribution into a Proton Synchrotron — E. Crosbie, K. Symon.....	3167	RAG05
Halo of a High-Brightness Electron Beam — G. Haouat, N. Pichoff, C. Couillaud, J.P. De Brion, J. Di Crescenzo, S. Joly, A. Loulergue, C. Ruiz, S. Seguin, S. Striby.....	3170	RAG06
Studies on Halo Formation in a Long Magnetic Quadrupole FODO Channel First Experimental Results — P.-Y. Beauvais, D. Bogard, P.-A. Chamouard, R. Ferdinand, G. Haouat, J.-M. Lagniel, J.-L. Lemaire, N. Pichoff, C. Ruiz.....	3173	RAG07
Radial Mode Evolution in Longitudinal Bunched Beam Instability — S.Y. Zhang, W.T. Weng.....	3176	RAG08
Stability of a Breathing K-V Beam — Robert L. Gluckstern, Wen-Hao Cheng.....	3179	RAG09
Hamiltonian Formalism for Space Charge Dominated Beams in a Uniform Focusing Channel — A. Riabko, M. Ellison, X. Kang, S.Y. Lee, J.Y. Liu, D. Li, A. Pei, L. Wang.....	3182	RAG10
Simulation Studies of the LAMPF Proton Linac — R.W. Garnett, E.R. Gray, L.J. Rybarczyk, T.P. Wangler.....	3185	RAG11
Functional Dependence of Wakefunctions for $v < c$ — Zenghai Li, Joseph J. Bisognano.....	3188	RAG12
Betatron Transients Caused by Rapid Changes in the Closed Orbit — James J. Welch.....	3191	RAG13
Phenomenology of Crystalline Beams in Smooth Accelerators — A.F. Haffmans, D. Maletic, A.G. Ruggiero.....	3194	RAG14
Beam Dynamics in the 1.3 GeV High Intensity ESS Coupled Cavity Linac — M. Pabst, K. Bongardt.....	3197	TPA01
Final Bunch Rotation and Momentum Spread Limitation for the ESS Facility — K. Bongardt, M. Pabst.....	3200	TPA02
Design Criteria for High Intensity H⁻-Injector Linacs — K. Bongardt, M. Pabst.....	3203	TPA03
Measurements of Vacuum Chamber Impedance Effects on the Stored Beam at CESR — M. Billing, Z. Greenwald, W. Hartung, W.R. Lou, M. Pisharody, J. Rogers, D. Sagan, J. Sikora.....	3206	TPA04
The Study of Nonlinear Effects Influenced by Space Charge in High Intensity Linac — A.A. Kolomiets, S.G. Yaramishev, P.R. Zenkevich, A.P. Korolev.....	3209	TPA05
Beam Size Versus Intensity for Resonant Extracted Beam at the Brookhaven AGS — K.A. Brown, R. Thern, H. Huang.....	3212	TPA06
Review of Longitudinal Perturbation Formalism — S.Y. Zhang.....	3214	TPA08
Klystron Power Specifications Based on Transient Beam Loading Analysis in Damping Rings — M.G. Minty, R.H. Siemann.....	3217	TPA09
Transverse Combining of Four Beams in MBE-4 — C.M. Celata, W. Chupp, A. Faltens, W.M. Fawley, W. Ghiorso, K.D. Hahn, E. Henestroza, C. Peters, P. Seidl.....	3220	TPA10
Ion Core Parameters in the Bending Magnets of Electron Storage Rings — E. Bulyak.....	3223	TPA12
Ion Driven Effects in the Intence Electron Beam Circulating in Storage Rings — E. Bulyak.....	3226	TPA13
Disk-Loaded Waveguides for Accelerating High Intensity Short Pulse Electron Beams — N.I. Aizatsky.....	3229	TPA14
The Description of High Current Beam Dynamics Using Lie Algebraic Methods — A.I. Borodich, A.A. Khrutchinsky, V.I. Stolyarsky.....	3232	TPA15

Chaos, a Source of Charge Redistribution and Halo Formation in Space-Charge Dominated Beams — Jean-Michel Lagniel, David Libault	3235	TPA17
Transport of a Partially-Neutralized Ion Beam in a Heavy-Ion Fusion Reactor Chamber — Debra A. Callahan, A. Bruce Langdon	3238	TPR01
Emittance Growth from Rotated Quadrupoles in Heavy Ion Accelerators — John J. Barnard.....	3241	TPR02
Wakefield Effects on the Beam Accelerated in a Photoinjector: Perturbation Due to the Exit Aperture — J.-M. Dolique, W. Salah.....	3245	TPR04
Influence of the Photoinjector Exit Aperture on the Wakefield Driven by an Intense Electron Beam Pulse: a Theoretical Approach — J.-M. Dolique	3248	TPR05
Invariability of Intense Beam Emittance in Nonlinear Focusing Channel — Y.K. Batygin.....	3251	TPR06
Beam Transport for Uniform Irradiation: Nonlinear Space Charge and the Effect of Boundary Conditions — D. Bruhwiler, Yuri K. Batygin.....	3254	TPR07
Transport of Bunched Beams with Space Charge Through a Periodic Lattice — M.F. Reusch, D.L. Bruhwiler.....	3257	TPR08
Modeling Space Charge in Beams for Heavy-Ion Fusion — W.M. Sharp	3260	TPR09
Impedance of Periodic Irises in a Beam Pipe — Shicheng Jiang, Robert L. Gluckstern, Hiromi Okamoto	3263	TPR11
Frequency Dependence of the Polarizability and Susceptibility of a Circular Hole in a Thick Conducting Wall — Wen-Hao Cheng, Alexei V. Fedotov, Robert L. Gluckstern	3266	TPR12
Spatial-Temporal Hysteresis Effects in an Intense Electron Beam — A.V. Agafonov, A.N. Lebedev, V.S. Voronin	3269	TPR13
General Wave Equation in the Electrostatic Approximation — A.V. Agafonov.....	3272	TPR14
Space Charge Effects at KEK-Booster Synchrotron — Chihiro Ohmori, Toshikazu Adachi, Tadamichi Kawakubo, Motohiro Kihara, Isao Yamane	3275	TPR16
On the Relaxation of Semi-Gaussian and K-V Beams to Thermal Equilibrium — S.M. Lund, J.J. Barnard, J.M. Miller.....	3278	TPR18
Transverse-Longitudinal Energy Equilibration in a Long Uniform Beam — I. Haber, D.A. Callahan, A. Friedman, D.P. Grote, A.B. Langdon	3282	TPR19

Beam Dynamics, Misc.

Variants of Optics Schemes and Accelerator Configurations for Athens Microtron: Preliminary Considerations — A.V. Tiunov, V.I. Shvedunov, I.V. Surma, K. Hizanidis, C. Kalfas, C. Trikalinos, J. Tigelis.....	3285	RAQ01
Study of Beam Decoherence in the Presence of Head-Tail Instability Using a Two-particle Model — G.V. Stupakov, A.W. Chao.....	3288	RAQ02
Beam Distribution Function after Filamentation — T.O. Raubenheimer, F.-J. Decker, J.T. Seeman.....	3291	RAQ03
Measurement of the Interaction Between a Beam and a Beam Line Higher-Order Mode Absorber in a Storage Ring — W. Hartung, P. Barnes, S. Belomestnykh, M. Billing, R. Chiang, E. Chojnacki, J. Kirchgessner, D. Moffat, H. Padamsee, M. Pisharody, D. Rubin, M. Tigner.....	3294	RAQ04
A New Analytical Model for Axi-symmetric Cavities — D. Burrini, C. Pagani, L. Serafini.....	3297	RAQ05
Impurity Growth in Single Bunch Operation of PF — M. Tobiyama, A. Higuchi, T. Mitsuhashi, T. Kasuga, S. Sakanaka.....	3300	RAQ06
Coupling Impedance of a Periodic Array of Diaphragms — G.V. Stupakov.....	3303	RAQ09
Coupling Impedance of a Long Slot and an Array of Slots in a Circular Vacuum Chamber — G.V. Stupakov.....	3306	RAQ10
Dark Currents for CEBAF Linacs — Byung C. Yunn	3309	RAQ11
Improvements in Bunch Coalescing in the Fermilab Main Ring — J. Dey, I. Kourbanis, D. Wildman	3312	RAQ13
Slow Extraction of Particles Using a Thin Target for Driving for Resonance — Yu. Severgin, W. Belov, A. Makarov, M. Tarovik.....	3315	RAQ14
Properties of a Transverse Damping System, Calculated by a Simple Matrix Formalism — S. Koscielniak, H.J. Tran.....	3317	RAQ15
A Concept for Emittance Reduction of DC Radioactive Heavy-Ion Beams — J.A. Nolen, J.C. Dooling.....	3320	RAQ16

Measurements of the Octupole-Induced Amplitude-Dependent Frequency Shift in SPEAR — P. Tran, C. Pellegrini, J. Yang, M. Cornacchia, J. Corbett.....	3323	RAQ17
Radiation Damping in Focusing-Dominated Systems — Zhirong Huang, Pisin Chen, Ronald D. Ruth.....	3326	RAQ18
Colliding Crystalline Beams — A.F. Haffmans, D. Maletic, A.G. Ruggiero.....	3329	RAQ20
Helical Spin Rotators and Snakes for RHIC — V.I. Ptitsin, Yu.M. Shatunov, S. Peggs.....	3331	RAQ21
Effects of Enhanced Chromatic Nonlinearity during the AGS gt-Jump — J. Wei, J.M. Brennan, L.A. Ahrens, M.M. Blaskiewicz, D.-P. Deng, W.W. MacKay, S. Peggs, T. Satogata, D. Trbojevic, A. Warner, W.K. van Asselt.....	3334	RAQ22
Effect of Parametric Resonances on the Bunched Beam Dilution Mechanism — L. Wang, M. Ball, B. Brabson, J. Budnick, D.D. Caussyn, G. East, M. Ellison, X. Kang, S.Y. Lee, D. Li, J.Y. Liu, K.Y. Ng, A. Pei, A. Riabko, D. Rich, T. Sloan, M. Syphers.....	3337	RAQ23
Parametric Resonances and Stochastic Layer Induced by A Phase Modulation — J.Y. Liu, M. Ball, B. Brabson, J. Budnick, D.D. Caussyn, P. Colestock, V. Derenchuk, G. East, M. Ellison, D. Friesel, B. Hamilton, W.P. Jones, X. Kang, S.Y. Lee, D. Li, K.Y. Ng, A. Pei, A. Riabko, T. Sloan, M. Syphers, L. Wang.....	3340	RAQ24
Nonlinear Space Charge Effect of Gaussian Type Bunched Beam in Linac — Yinbao Chen, Shinian Fu, Zhibin Huang, Zhenhai Zhang.....	3343	RAQ25
Emittance Growth Caused by Bunched Beam with Nonuniform Distributions in Both Longitudinal and Transverse Directions in Linac — Zhibin Huang, Yinbao Chen, Shinian Fu.....	3346	RAQ26
The Envelopes of Beam Motion in the Charged Particle Cyclic Accelerator — Yu.P. Virchenko, Yu.N. Grigor'ev.....	3349	RAQ28
A Semi-analytical Approach to the Design of Low Energy Cylindrically Symmetric Transport Lines — Pedro F. Tavares.....	3352	RAQ29
Stability of Trapped Ions in Electron Storage Rings in View of Parametric Resonance — Y. Miyahara.....	3355	RAQ30
Entropy and Emittance of Particle and Photon Beams — K.-J. Kim, R.G. Littlejohn.....	3358	RAQ02
Effect of the Coupling Slots on Beam Dynamics in Accelerator Structure of Moscow CW RTM — V.I. Shvedunov, A.S. Alimov, A.S. Chepurinov, O.V. Chubarov, D.I. Ermakov, A.V. Tiunov, P.L. Tkachev.....	3361	RAQ04
The Electron Beam Orbit Sensitivity on the Photon Flux of the Photon Beam Line — Ian Hsu, G.H. Luo, K.L. Tsang, C.C. Chu, C.I. Yu, W.T. Weng, S.C. Chung.....	3364	RAQ05
Ground Motion in LEP and LHC — L. Vos.....	3367	RAQ07
Cosmic Particle Acceleration at Very High Energies — K.O. Thielheim.....	3370	RAQ09
Trapped Modes in the Vacuum Chamber of an Arbitrary Cross Section — Sergey S. Kurennoy, Gennady V. Stupakov.....	3373	RAQ11
A General Approach for Calculating Coupling Impedances of Small Discontinuities — Sergey S. Kurennoy, Robert L. Gluckstern, Gennady V. Stupakov.....	3376	RAQ12
Polarizabilities of an Annular Cut and Coupling Impedances of Button-Type Beam Position Monitors — Sergey S. Kurennoy.....	3379	RAQ13
The Effect of Coupling on Luminosity — D. Sagan.....	3382	RAQ15
RFQ-DTL Matching Solutions for Different Requirements — D. Raparia.....	3385	RAQ16
Low-Dispersion γ Jump for the Main Injector — K.Y. Ng, A. Bogacz.....	3388	RAQ17
Wakefields and HOMs Studies of a Superconducting Cavity Module with the CESR Beam — S. Belomestnykh, W. Hartung, G. Flynn, J. Kirchgessner, H. Padamsee, M. Pisharody.....	3391	RAQ18
Comparison of the Predicted and Measured Loss Factor of the Superconducting Cavity Assembly for the CESR Upgrade — S. Belomestnykh, W. Hartung, J. Kirchgessner, D. Moffat, H. Muller, H. Padamsee, V. Veshcherevich.....	3394	RAQ19
Control of Trapped Ion Instabilities in the Fermilab Antiproton Accumulator — Steven J. Werkema.....	3397	RAQ20
Longitudinal Emittance Oscillation in a Superconducting Drift Tube Linac — J.W. Kim, K.W. Shepard.....	3400	RAQ21
Electric Fields, Electron Production, and Electron Motion at the Stripper Foil in the Los Alamos Proton Storage Ring — M. Plum.....	3403	RAQ22
Electron Clearing in the Los Alamos Proton Storage Ring — M. Plum, J. Allen, M. Borden, D. Fitzgerald, R. Macek, T.S. Wang.....	3406	RAQ23

Advanced Photon Source Insertion Device Field Quality and Multipole Error Specification — <i>Yong-Chul Chae, Glenn Decker</i>	3409	RAR24
Study of Field Ionization in the Charge Exchange Injection for the IPNS Upgrade — <i>Yong-Chul Chae, Yanglai Cho</i>	3412	RAR25
Lattice Considerations for a Tau-Charm Factory — <i>L.C. Teng, E.A. Crosbie</i>	3415	RAR26
Effects of Vertical Aperture on Beam Lifetime at the Advanced Photon Source (APS) Storage Ring — <i>Hana M. Bizek</i>	3418	RAR27
Rebucketing After Transition in RHIC — <i>D.-P. Deng, S. Peggs</i>	3421	RAR29
Closed-Orbit Drifts in HERA in Correlation with Ground Motion — <i>V. Shiltsev, B. Baklakov,</i> <i>P. Lebedev, C. Montag, J. Rossbach</i>	3424	RAR30
Simulation of the Acceleration of Polarized Protons in Circular Accelerators — <i>Yu. Shatunov, V. Yakimenko</i>	3427	RAR31

GROUND MOTION MEASUREMENTS IN HERA

V. Shiltsev, B. Baklakov, P. Lebedev, Budker INP, 630090, Novosibirsk, RUSSIA
and C. Montag, J. Rossbach, DESY, 22603 Hamburg, GERMANY

Abstract

This article presents the results of ground motion measurements at DESY. Power spectral densities of vertical and horizontal ground motion were obtained in a frequency range from 0.003 Hz up to 140 Hz at some points of the HERA tunnel. The spectra of correlation were measured at a 30 m distance between seismic probes. Amplitudes of measured uncorrelated vibrations are compared with Linear Colliders tolerances.

I. Introduction

Vibrations of magnetic elements of particle accelerators due to the ground motion cause the distortion of beam orbits. At modern colliders with separated beam optics systems for each beam species (e.g. HERA, Linear Colliders), the cumulative effect of numerous perturbations produced by microscopic vibrations of quadrupoles manifest itself as beam-beam separation at the interaction point (in contrast to the majority of existing machines where both beams share the same guiding magnetic fields).

While the orbit distortions in the accelerators are sensitive to the uncorrelated quadrupole motion, the goals of the experiments at DESY were to investigate the spatial correlation and measure the amplitudes of the HERA tunnel vibrations under conditions of a working accelerator. A very broad frequency band of almost 5 decades from 0.003 Hz to 140 Hz is a distinctive feature of these experiments.

These measurements were done in the HERA Hall North (H1 detector area) and in the HERA Hall West at a depth of about 25 m. The measurements are described in detail in [1].

II. Instruments and Methods

Sensors for the ground motion were four SM-3KV type velocity meters (a pair of vertical and a pair of horizontal) which allow us to obtain the data in a 0.1 – 140 Hz frequency band with a sensitivity of about 80 mV/($\mu\text{m/s}$); and a pair of three component CMG-3T geophones made by Guralp Systems Co. with a flat velocity response of 0.75 mV/($\mu\text{m/s}$) in the band 0.003 Hz – 50 Hz.

The electrical signals from all the probes were digitized and developed by a CAMAC-based experimental set-up which includes two 10-bit and 4-channel ADCs, four 20-bit ADCs, differential amplifiers with low-pass frequency filters, and an IBM 486 personal computer. The signals were digitized simultaneously by the ADCs with a sampling frequency (variable by a timer from 0.1 Hz to 32 kHz) and then sent to the memory for storage. The maximum memory available for one channel is 64-K 24-bit words. It corresponds to 18 h of permanent measurement time with a sampling rate of 1 Hz or about 3 min with 400 Hz. For long-term measurements we used the low-pass filters at 0.5 Hz, 2 Hz or 20 Hz, for fast analyses the 200-Hz filter was applied.

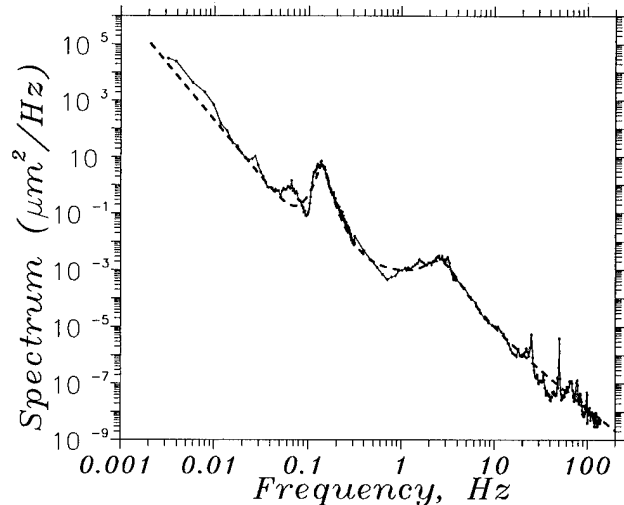


Figure 1. Spectrum of vertical vibrations.

As the ground motion is *noise*, its properties can be described by the *power spectral density* (PSD) $S_x(f)$. The dimension of the PSD is *power in a unit frequency band*, i.e., m^2/Hz for the PSD of displacement. The value of $S_x(f)$ relates to the rms value of the signal $X_{rms}(f_1, f_2)$ in frequency band from f_1 to f_2 as $X_{rms}(f_1, f_2) = \sqrt{\int_{f_1}^{f_2} S_x(f) df}$. The *normalized spectrum of the correlation* $K(f)$ of two signals $x(t)$ and $y(t)$ is defined as

$$K(f) = \frac{\langle X(f)Y^*(f) \rangle}{\sqrt{\langle X(f)X^*(f) \rangle \langle Y(f)Y^*(f) \rangle}}, \quad (1)$$

where the brackets $\langle \dots \rangle$ mean the time averaging over the different measurement data, and $X(f)$ and $Y(f)$ are the Fourier transformations of $x(t)$ and $y(t)$. Note, that correlation $K(f)$ is a complex function. The coherence of the two signals is equal to the modulus of $K(f)$. By the definition, the value of the coherence does not exceed 1.0.

III. Results

The PSD of the vertical ground motion measured 20-21.09.1994 in HERA Hall West at the tunnel depth is shown in Fig. 1 in a log-log scale. The spectrum can be approximated by the formula (see dashed line)

$$S_x(f)[\mu\text{m}^2/\text{Hz}] \approx \frac{2 \cdot 10^6}{(\frac{f}{0.001})^4} + \frac{10^{-3}}{1 + f^{5/2}} + \frac{5}{(1 + (\frac{f-f_m}{0.14 \cdot f_m})^2)^{3/2}} + \frac{2 \cdot 10^{-3}}{(1 + (\frac{f-f_c}{0.45 \cdot f_c})^2)^{3/2}}. \quad (2)$$

The first term in (2) fits the spectrum of the slow ground motion noise in a frequency range of 0.003 – 0.1 Hz, the second one describes a continual part of the spectrum from 4 Hz to 140 Hz, the third one represents the *microseismic waves* with the frequencies about $f_m=0.14$ Hz, and the last one corresponds to a broad peak around $f_c=2.5$ Hz, which is often referred to the manifestation of the resonances in an upper crust. Clearly visible peaks in the PSD at about 25 Hz and 50 Hz are not described in (2) because of their definitely technological origin. The horizontal ground motion was also measured simultaneously, and its amplitudes are the same as the vertical ones within a factor of 3.

During almost two months of observation in Hamburg the rms amplitude of the microseismic waves (the square root of integral of PSD around f_m) varied smoothly within the range of $0.1 \div 2 \mu\text{m}$, and their mean frequency f_m varied from 0.1 Hz up to 0.25 Hz. To determine the direction toward the sources of these waves, we set side by side a pair of the horizontal SM-3KV type geophones, so that their pendula were perpendicular to each other. Their signals passed through a 0.07 Hz – 0.5 Hz filter and were recorded for further processing [1]. Figure 2 presents the angular distribution of the 0.07-0.5 Hz signals for Sept. 2, 1994 data record when the probes were installed on the bottom of the H1 pit. The length of each ray in this Figure is proportional to the squared amplitude (energy) of waves which propagate in the direction of the ray. The main "leaf" of the diagram points to the North-North-West (the North-West coast of Denmark, or the southern coast of Norway) while a pair of smaller ones are directed to the closest coastal lines of the North Sea and the Baltic Sea. The ground motion at higher frequencies, that can not be properly treated as waves, shows practically uniform angular distribution.

The spectra of the coherence $Co(f)$ were measured in a frequency range of 0.01 – 140 Hz by a pair of the vertical SM3-KV probes and in the band of 0.003 – 20 Hz by the CMG-3T geophones. Usually, we made 63 FFTs of the signals (for $1 \div 1000$ s long records) because this allows us to reduce the statistical error of the coherence measurement down to $\approx 10\%$.

Initially, the probes were set together in a certain point of the HERA Hall West at the tunnel depth, and it was found that $Co(f) \approx 1.0$ over the whole frequency range (see solid line in Fig.3). Being displaced by $L=15$ m, the same probes showed a significant drop in the coherence at the frequencies higher than 5 Hz and below 0.05 Hz (see dashed line). The further increase in the distance up to $L=30$ m (maximum available distance in the Hall West pit) led to a larger decrease of the coherence as it is presented by a marked line in Fig.3.

It is seen that inspite of the tendency of smaller coherence at longer distances, there are some frequency regions with good coherence, namely, around 100 Hz, 50 Hz, 2 Hz and 0.2 Hz. As for the frequencies above 1 Hz, the decrease in the coherence at 30 m is well understood and was always observed earlier. Below 0.05 Hz, the fall of the coherence is somewhat surprising. While the internal noises of low-frequency CMG-3T type probes are smaller than a signal (it is proven experimentally because the coherence at $L=0$ m is close to 1.0), some external noises can explain the lack of the coherence ("floating" of the ground potential, fluctuations of pressure and temperature at different tunnel

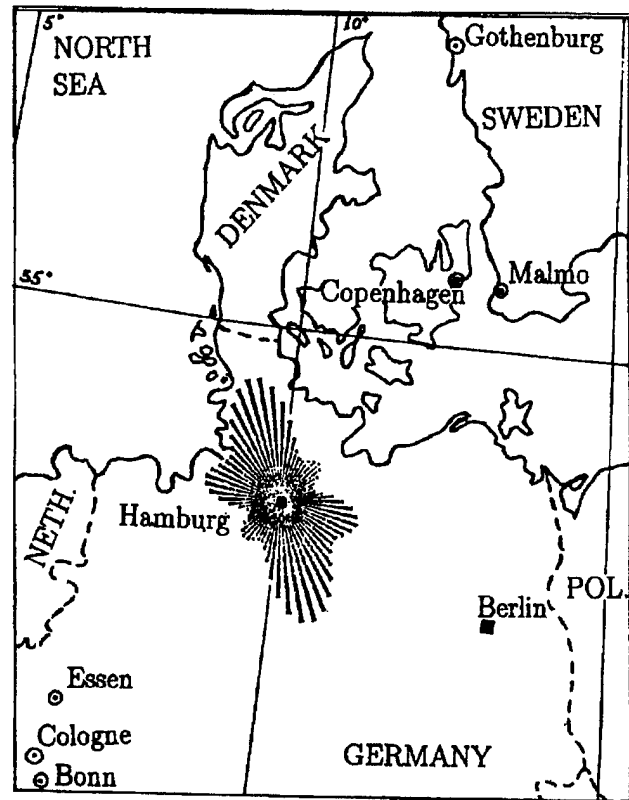


Figure 2. Directions of 0.07–0.5 Hz ground waves.

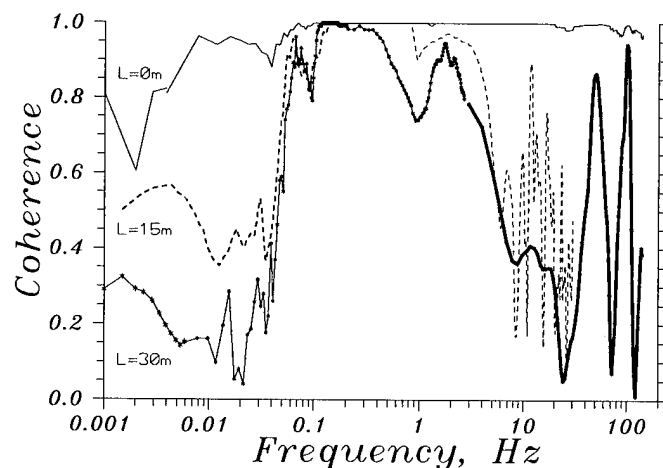


Figure 3. Spectra of coherence at 0, 15 and 30 meters.

points, cracks in the concrete, etc). Further investigations of the issue are necessary.

During almost two months of these experiments, we observed some dozen events with the amplitudes far above the ordinary ones. As Hamburg is rather quiet seismic site, these events were mostly the waves from remote earthquakes. Typically, they had 20 – 400 μm amplitude, a period of about 10-30 s, and their durations were up to 2000 s. The statistics of the events with large amplitudes allows us to approximate the mean time $T(A)$ between the events with amplitude more than A as $T(A)[\text{days}] \approx 10 * (A/100\mu\text{m})$. Having a very large wavelength of about a hundred of km, the earthquake waves can not produce beam orbit distortions in the accelerators built in elastic media, and we did not see any beam orbit distortions in the HERA collider during the quakes [1].

IV. Discussion and Summary

The quadrupole vibrations result in the beam degradation in Linear Colliders. These vibrations arise from the motion of the ground amplified by support systems, vibrations due to cooling flow turbulence, etc. Tolerances on uncorrelated jitter of the quadrupoles in the main linac vary for the different LC projects [2]: for vertical motion it is about 10 – 30 nanometers for small emittance designs (CLIC, VLEPP, JLC, NLC – X-band machines) and 50 – 100 nanometers for S-band and TESLA designs. Tolerances on the quads motion in a final focus system are about 10 times more severe. To reduce the effect of the ground motion, one can either use a beam-based feedback system or measure and correct the actual quad motion. The experience of using the SLC beam-based feedback has shown that the system operates effectively at the frequencies below $f_{rep}/30$ where f_{rep} is the repetition frequency of the linac. Therefore, the vibrations above that frequency are not correctable by the beam-base technique.

The data obtained in the HERA tunnel allow us to estimate the amplitudes of the vibrations at the frequencies above certain frequency f . Figure 4 shows the rms amplitudes $U_{30m}(f)$ of the uncorrelated ground motion at $L=30$ m in comparison with the rms amplitude of the absolute ground motion at both points $A(f)$ (dashed line) vs. the frequency f . These values were obtained according to the formula

$$U_{30m}(f) = \sqrt{\int_f^\infty (1 - C_{o30m}(f)) \cdot S_x(f) df} \quad (3)$$

and

$$A(f) = \sqrt{\int_f^\infty S_x(f) df}, \quad (4)$$

where $C_{o30m}(f)$ is the coherence spectrum at $L = 30$ m as shown in Fig.3 and $S_x(f)$ is the PSD of the vertical ground motion in the HERA tunnel (presented in Fig.1). One can see that the incoherent motion is noticeably smaller than the coherent motion only in a frequency range of 0.05 Hz – 2 Hz. It should be emphasized that the increase in the uncorrelated motion at the frequencies less than 0.05 Hz is due to the lack of coherence $C_{o30m}(f)$ in this range which should be checked more carefully.

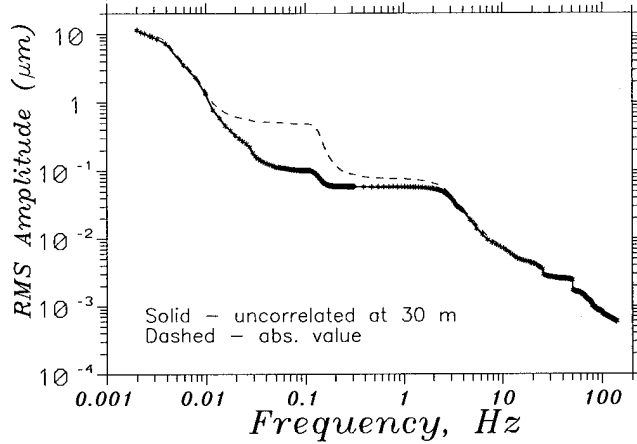


Figure. 4. RMS amplitude of vertical vibrations at frequencies higher than f vs. f

Table I

	$f_{rep}/30$, Hz	Jitter toler., nm	U_{30m} , nm
X-band	4-10	10-30	15-5
S-band	0.3-2	70	60

Finally, Table I compares our results on the uncorrelated ground motion with the requirements for the two groups of the LC projects.

From the Table I one can see that for all the projects the ground motion amplitudes measured in HERA are over or close to the tolerable levels.

We express our acknowledgement to Y. Soloviev, I. Shevyakov, S. Herb, M. Seidel, W. Radloff, M. Lomperski, S. Kazaryan (DESY), N. Dikanisky, V. Parkhomchuk, S. Sigmatulin, A. Chupira (INP) for their assistance in preparing the measurements in DESY. We would like to thank G.-A. Voss, F. Willeke (DESY) and A. Skrinsky (INP) for useful discussions.

References

- [1] V. Shiltsev *et al.*, to appear as DESY HERA Report, 1995; see also this conference.
- [2] *Proc. of Int. Workshop "Linear Colliders'95"*, KEK, 1995.

Alignment of Duke Free Electron Laser Storage Ring

M. Emamian, N. Hower

Duke Free Electron Laser Laboratory, Duke University, Durham NC 27706

Y. Levashov

Budker Institute of Nuclear Physics, Novosibirsk, Russia

Abstract:

At present, Duke Free Electron Laser Laboratory storage ring facilities consist of a 50 meter long RF powered linac and a 107 meter circumference storagering which is designed to store 1 A of electron beam at 1 GeV. In this report, specifications and procedures for alignment of over 200 magnets, most of which must be positioned to achieve efficient injection and to obtain storage time of several hours, will be discussed. In particular tolerances of better than ± 0.05 mm in transverse position of ring quads and ± 1 mm for the linac quads were achieved. Some redundancy measurements such as a stretched wire method for all straight section components, wire offset measurements for the arc magnets and an invar tape designed by the Budker Institute of Nuclear Physics (BINP) for the distances between the floor monuments were used to verify the accuracy of our alignment method.

I. INTRODUCTION:

The Duke Free Electron Laser (FEL) Laboratory is housed in a 5100 square meter building located on the west campus of Duke University in Durham, NC. The building was designed to house the Laboratory's advanced infrared, ultraviolet and x-ray FEL sources, linac sections, their accelerator drives, all bending and correcting magnets and the instrumentation and setup space required by the researchers using these light sources.

The building is laid out to provide a central 2200 square meter experimental area with attached office and shop space, and a 143 meter long underground tunnel to house the linac injector required by the FELs.

To satisfy the extraordinary stability requirements for research in the ultraviolet and x-ray regions, a 1 meter thick floor slab for the storage ring area is supported on a series of 32 closely spaced caissons extended to the underlying bedrock. The spacing of the caissons and the thickness of the slab were specified to limit the deflection of the slab to less than 0.12 mm under static and dynamic load.

II. ALIGNMENT INSTRUMENTS AND TOOLS:

Several optical instruments and alignment tools were used to accomplish the alignment of the Duke FEL Laboratory

storage ring. A list of these instruments and tools is as follows:

- Brunson 76-RH Telescopic transit square, used to align components in a vertical plane.
- Brunson 376-RHN Universal transit square, to perform the dual functions of telescopic transit square and line-scope to turn right angles.
- Kern electronic theodolite model E2, performs angle measurements in both horizontal and vertical planes.
- Wild precision sight level model N3, used to sight in horizontal plane and set elevations of components.
- Wild precision optical plummet model NL, used for nadir plumbing.
- Brunson 803 invar scale extension kit, to measure linear distances of less than 7 meters.
- BINP invar tape, to measure distances of less than 25 meters.
- Specially made tools such as:
 - "Meterstick" assembly: used to measure horizontal transverse positions of quadrupoles in the arcs.
 - "Mirror assembly": used to measure azimuthal rotation angles about a vertical axis of arc quadrupoles, through retroreflection.
 - stretched wire-related tools: used to support wires stretched between two known points and measure transverse distances between it and intermediate magnet. Stretched wire has been used to ascertain that the floor monuments are in one straight line.

III. FLOOR MONUMENT LAYOUT:

A. Ring Floor Monument Network:

27 floor monuments (designated as Duke floor monuments) are installed in an array of 9x3 (Fig. 1). The intervals between these floor monuments are 5 meters in longitudinal and 5.2 meters in transverse direction. Transit square was used to align the monuments in a straight line. Perpendicularity of the lines were set with a theodolite and a 376 transit square. Precise distances between these monuments were measured with invar rod kit. Relative elevations of these monuments were then measured with reference to monument Mcc using the precision sight level. In order to use the BINP invar tape for verifying the distances between the monu-

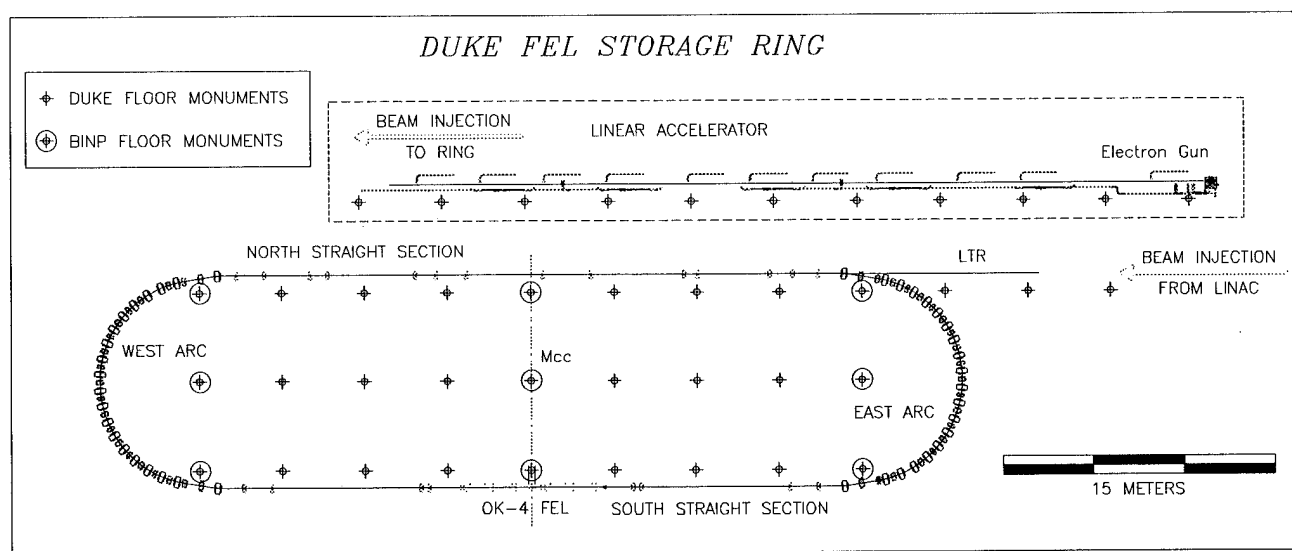


Figure 1

ments, a total of 9 specially made BINP floor monuments were adapted on the existing Duke floor monuments.

B. Linac to ring (LTR) and Injection linac Floor Monuments:

15 floor monuments are installed in a straight line as an extension from the north straight line of ring monuments at approximately 5 meter intervals. Distances and elevations of these monuments were evaluated with the same method as the ring monuments.

IV-NOMENCLATURE FOR ALIGNMENT POSITIONS AND ANGLES:

- X = Horizontal (transverse) position.
- X' = Angular Rotation about x axis (Pitch).
- Y = Vertical position.
- Y' = Angular rotation about Y axis, Yaw.
- Z = Longitudinal position (in beam direction).
- Z' = Angular Rotation about z axis (Roll).

V-ALIGNMENT TOLERANCES:

Installation tolerances on storage ring magnets:

	X mm	Y mm	Z mm	X' mr	Y' mr	Z' mr
Arc quads	.05	.05	.25	.5	.5	.5
Arc dipoles	.05	.05	.25	.5	.5	.5
Straight section quads	.05	.05	.25	.5	.5	.5

Installation tolerances on linac components:

	X	Y	Z	X'	Y'	Z'
Quads	.1	.1	.25	.5	.5	.5
Dipoles	.25	.25	.25	.5	.5	.5
Linac sections	.25	.25	.25			

VI. STORAGE RING ALIGNMENT

The alignment of the storage ring can be divided into 3 stages:

1. Injection Linac
2. Linac to Ring (LTR)
3. Ring

1. Alignment of Injection Linac:

At present the injection linac is comprised of 4 pairs of focusing and defocusing quadrupoles (quad doublets), 2 dipole magnets, 6 fluorescent screens, 4 current transformers, 6 steering magnets and eleven linac sections (linear accelerator sections). The theoretical electron beam path was transversely offset by 90.11 cm parallel the linac floor monuments. Relative positions and elevations of floor monuments were used as references for the alignment of the linac components. Quadrupoles and dipoles were aligned using fiducials near their extremities. Positions of these fiducials had been previously checked to a high accuracy. Linac sections were aligned in longitudinal direction with respect to fiducials that are placed at the entrance of RF input power and in X and Y direction using their outer ring and disk body.

2. Alignment of Linac to Ring (LTR):

LTR facilities begin at the end of the injection linac's high energy electron faraday cup and end at the entrance of the storage ring's septum magnet. It consists of 3 chicane (dipole) magnets, 5 quadrupoles and 6 steering magnets.

Basic principles of alignment of injection linac were applied to the LTR components.

3.- Alignment of the storage ring:

3a. Straight section alignment: The north and south straight sections consist of 22 quadrupoles, 14 steering magnets, a septum magnet, a kicker magnet and a 178 MHz RF cavity. In addition to the existing fiducials on these quads, a special BINP made fiducial is mounted on the side of each quad at exactly 25.40 cm away from its mechanical center. These fiducials are used as references for alignment of quads in the X direction. Initially, the first and the last quads on each straight section were aligned. To align these two quads in X, Z and Y' direction, A Brunson 376 transit square (placed at the nearest floor monument) and a conventional surveying scale with a proper length of invar rod were used. A Wild optical sight level and a highprecision alignment level were used to set the elevation Y, and checking the roll and pitch of each quad. Once these two quads were aligned, a thin (about .06 mm thick) wire was stretched between the BINP fiducials of the first and the last quads. This wire was then used as a reference line for alignment of the Intermediate quads in transverse direction. The first and the last quad were also used to position their neighboring quads in longitudinal direction and set their ψ angle. Optical sight level and precision alignment level were subsequently used to set the elevation, roll and pitch of these quads.

3b. Arc alignment: Each dipole was mechanically aligned with respect to its companion quadrupole by pushing both magnets tightly against an accurately machined positioning jig, and then bolting and pinning both to a common aluminum base plate. Subsequently only this base plate was moved, in six degrees of freedom. Three leveling screws were adjusted to set the elevation, pitch and roll of the magnet cluster, using the precision sight level and precision alignment levels in the conventional way.

Then the remaining coordinates ρ , θ , and ψ (refer to figure 2) were set for each cluster in turn using the specially made "invar meterstick" system, which takes advantage of the fact that in our arc lattice each focusing quadrupole is equidistant from a common "arc center" point. A heavy hollow steel post was erected over this point and its upper end centered over the arc center monument using an accurate optical plummet mounted on the upper end. The post's adjustable diagonal braces are spring loaded to eliminate backlash.

The polar angle θ to the center of each quadrupole is set by moving the cluster plate along the beam direction until a target at the quadrupole center lines up with the crosshairs of a theodolite whose angle has been preset at the desired value, relative to the ring's arc-to-arc axis, defined as $\theta=0$. The radial distance ρ is set using the invar-core meterstick pivoting about the center post. The tip of the micrometer head at the outer end of this "meterstick" contacts a hardened spherical button mounted on the inward-facing side of the quadrupole. The radius on this button was machined equal to the

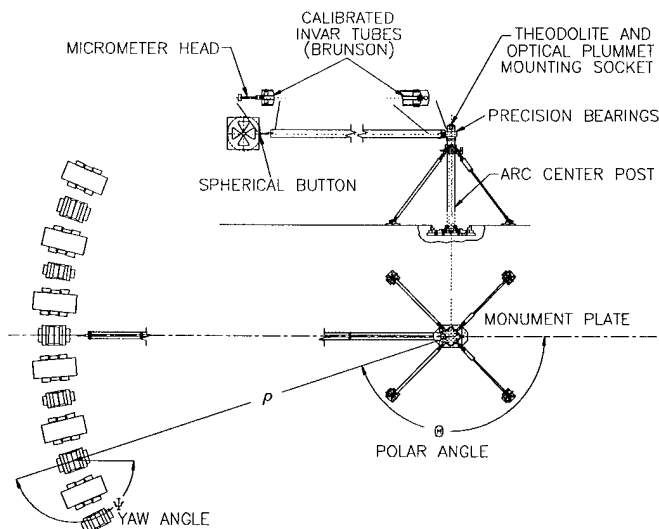


Figure 2

distance from the poletip center to the outer surface of the button, which means the meterstick is in effect measuring the distance to a sphere centered on the quadrupole. Thus the measured distance ρ is to first order independent of the Yaw angle, ψ , of the quadrupole.

This final coordinate ψ is then set to its desired value by setting the theodolite telescope's angle to the desired value, and rotating the cluster plate about a vertical axis through the quadrupole (which is possible due to the mechanical design of the cluster plate supports). This rotation is halted when the reflected image of the telescope's crosshairs line up with the crosshairs seen through the telescope. The reflection is off a plane mirror mounted on a fixture attached to the quadrupole in such a way that it is perpendicular to the flat end of the quadrupole. This perpendicularity is ensured using a pentaprism whose turning angle is specified to be within 3 arc-seconds (.015 mr) of a true 90 degree angle.

Beamline Smoothing of the Advanced Photon Source*

H. Friedsam, M. Penicka, S. Zhao
Argonne National Laboratory
9700 South Cass Avenue
USA - Argonne, Illinois 60439

Abstract

This paper outlines a general beamline smoothing concept based on the use of First Principle Component analysis. Beamline smoothing is commonly used for the detection of blunders in the positioning of beam elements and to provide a smooth particle beam path with the fewest adjustments to individual beam components. It also provides the data for assessment of the achieved positioning quality.

I. INTRODUCTION

During the last three years the Advanced Photon Source (APS) has been under construction at Argonne National Laboratory. The APS is a 7-GeV synchrotron light source which is being used for basic research in material science, chemistry, physics, biology, and medicine.

The APS consists of a 70m-long linear accelerator, a positron accumulator ring (PAR), a synchrotron ring (SY) with a circumference of 368m, and the storage ring (SR) with a circumference of 1104m (Fig. 1). The 40m electron linac uses 200-MeV electrons for the production of positrons. In the 30m-long linear accelerator section following the electron linac, the particles gain a mass of 450 MeV before entering the positron accumulator ring. From there the beam is injected into the booster synchrotron which accelerates the positrons from 450 MeV to 7 GeV before entering the storage ring. The storage ring can accommodate up to 68 x-ray beamlines.

II. ALIGNMENT TOLERANCES

The global alignment tolerance requires the positioning of all beam components within an envelop of $\pm 5\text{mm}$ of their ideal position. The circumference of the storage ring should be within $\pm 20\text{cm}$ of the nominal design value.

The most demanding relative alignment tolerance is required for the positioning of the storage ring multipoles. The maximum tolerable transverse and vertical displacements for these beam components must be within $\pm 0.15\text{mm}$ [1].

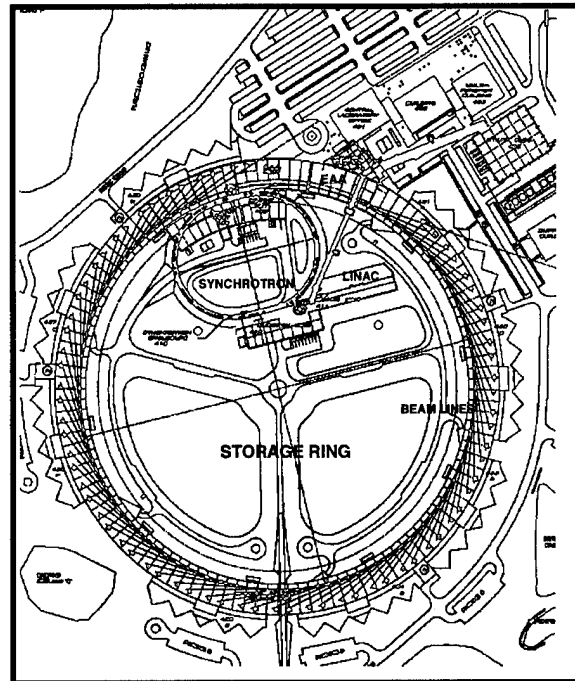


Fig. 1 APS site overview

III. THE BEAMLINE SMOOTHING CONCEPT

The global positioning accuracy for the beam components is determined by systematic and random errors. When performing least squares adjustments of the survey measurements, the data is assumed to be free of systematic errors; otherwise the concept of least squares is not applicable. Many precautions are taken to reduce the effects of systematic errors during the measurement process by applying special survey procedures [2].

Using error propagation for the measurements between two primary control points [3] yields the absolute positioning envelope as shown in Fig. 2.

The absolute error envelope is minimal in the vicinity of the connection to the primary control network points and reaches its maximum halfway between these points. The actual smooth beamline represented by the magnet fiducial marks meanders within the boundaries of the absolute error envelope as depicted by the dashed line in Fig. 2. The ideal reference line given by the lattice coordinates for each beam component is shown as a solid straight line connecting the two primary control points.

* Work supported by US DOE Office of Basic Energy Sciences under Contract No. W-31-109-ENG-38.

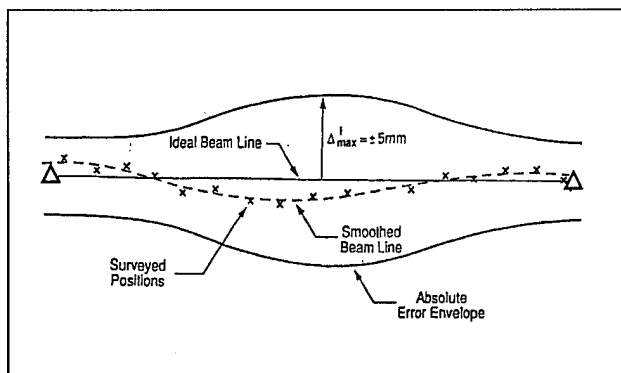


Fig. 2 Absolute error envelope

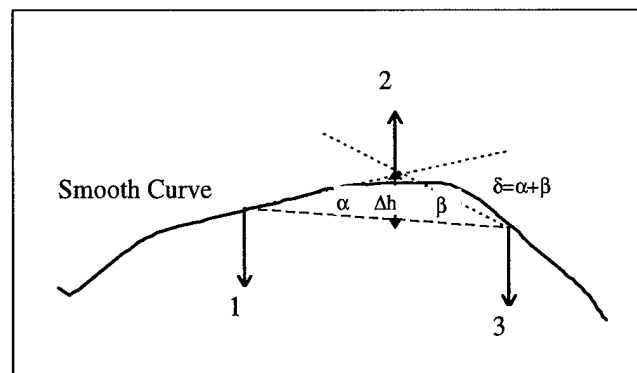


Fig. 3 Smoothness criteria

The task of the alignment team is to ensure a smooth particle beamline. It is of no importance to the operation of the accelerator whether this curve is identical to the ideal reference line or one of many smooth curves within the boundaries of the absolute error envelope as long as smoothness between adjacent beam components is guaranteed. Therefore the goal of the relative alignment step is to obtain a smooth beamline with a minimum number of required adjustments to individual beam elements.

Different concepts have been proposed to tackle this task. See for instance the approach taken by DESY to perform the relative alignment of HERA [4] or the route taken by CERN for smoothing the SPS beamline [5].

The approach used for smoothing the APS booster synchrotron and storage ring beamlines is based on a development originating at SLAC for the relative alignment of the SLC [6]. It is a general beamline smoothing concept based on First Principle Component analysis and is applicable to almost all beamlines independent of the beamline geometry. The beamline geometry is of no importance because the algorithm operates on the differences between the ideal and actual measured position of the beam component.

Principal curves are defined as smooth, one-dimensional curves passing through the middle of a p-dimensional data set, minimizing the sum of the perpendicular distances from the data points to the curve. The result is a non-parametric curve with a shape suggested by the data. The curves are found in an iterative process starting with the principal component line [7].

A smoothness criteria has to be defined that will stop the iteration process or the curve would approach each data point, thus defeating the purpose of smoothing. In the case of the APS, all multipoles are supposed to be aligned to $\pm 0.15\text{mm}$ relative to each other. That means that the middle component of three successive beam elements numbered 1, 2 and 3 in Fig. 3, should not deviate from a straight line connecting the end components by more than Δh , which is $\pm 0.15\text{mm}$ for the APS.

After the completion of the storage ring girder alignment the positions of all quadrupoles, sextupoles and dipoles were measured once more using laser trackers [8]. In order to obtain the connection between individual tracker setups, additional temporary control points were installed and measured. The data was analyzed using a bundle adjustment routine developed at SLAC. The differences between the resulting magnet positions from the bundle adjustment and the ideal locations were then subjected to the smooth curve fitting operation.

The results of the smoothing process can be seen in Figs. 4 and 5 for the transverse and vertical deviations from the ideal position. One can see that the smooth curve deviates from the ideal position by $\pm 4\text{mm}$, within the confines of the envelop for the absolute positioning of beam components.

Finally Figs. 6 and 7 show the histograms for the deviations of the multipoles from the smooth beamline. All components have been placed within the 2σ range. Out of 680 multipoles, only 3% in the transverse direction, and 2% in the vertical direction have been placed in the 1σ to 2σ range. The achieved relative position tolerances are $\pm 0.09\text{mm}$ transverse and $\pm 0.07\text{mm}$ vertical, well within the specified tolerance level.

V. SUMMARY

Considering that a relative positioning accuracy of $\pm 0.09\text{mm}$ in the transverse direction and $\pm 0.07\text{mm}$ in the vertical direction was achieved, and taking into account the standard deviation for the determination of the magnetic center versus the mechanical center of $\pm 0.075\text{mm}$, the position between magnetic centers is estimated to be within $\pm 0.125\text{mm}$ [9].

The successful alignment of the APS storage ring is also documented by the rapid progress in the commissioning program. Shortly after the start of the storage ring commissioning phase, the beam was transported around the whole ring using only four horizontal and three vertical correctors. Multiple turns have been recorded in the mean time and rf capture of the beam has been demonstrated.

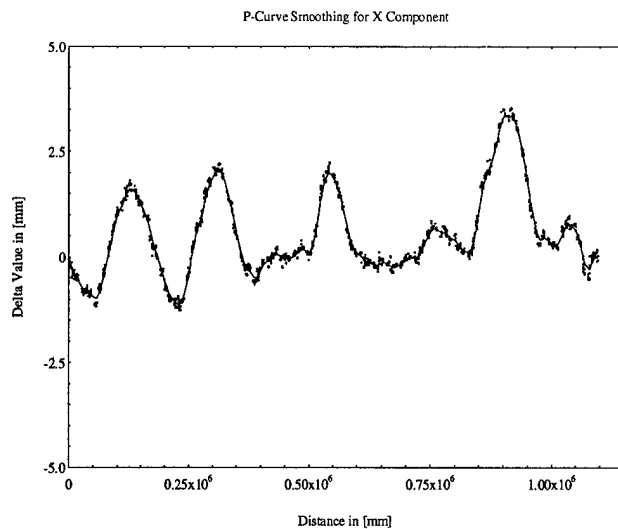


Fig. 4 Transverse displacements

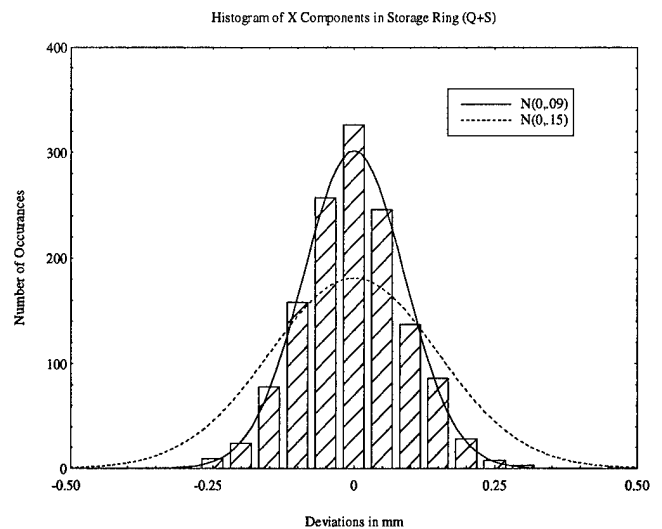


Fig. 6 Histogram of the transverse displacements of all storage ring multipoles

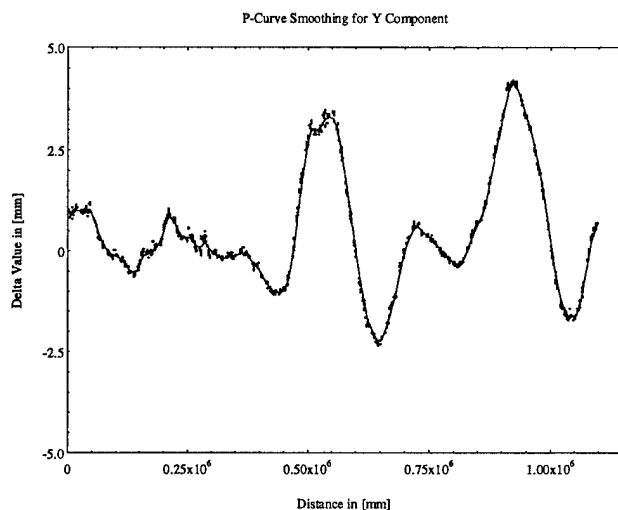


Fig. 5 Vertical displacements

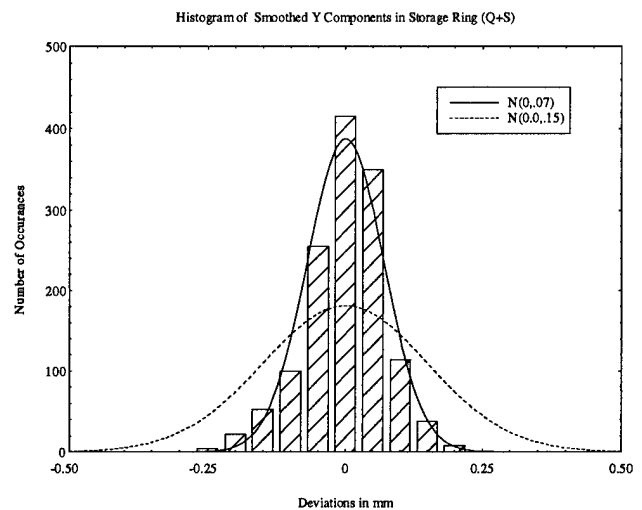


Fig. 7 Histogram of the vertical displacements of all storage ring multipoles

VI. REFERENCES

- [1] 7-GeV Advanced Photon Source Conceptual Design Report, Argonne National Laboratory, ANL-87-15, (1987).
- [2] R. Ruland, *Accelerator and Transport Line Survey and Alignment*, (Stanford Linear Accelerator Center, California, SLAC Pub.-5672, 1991).
- [3] H. Friedsam, J. Penicka, S. Zhao, *Survey and Alignment Report on the Primary Control Network for the APS*, Light Source Note LS-220, (1993).
- [4] W. Schwarz, *Die Justierung von Teilchenbeschleunigern*, (Allgemeine Vermessungs Nachrichten, Heft 1, 1990).
- [5] M. Mayoud, "Applied Metrology for LEP," in *CERN Accelerator School Applied Geodesy for Particle Accelerators*, (CERN, Switzerland, April 1987).
- [6] H. Friedsam, W. Oren, "The Application of the First Principal Curve Analysis Technique to Smooth Beamlines," in *Proceedings of the First International Workshop on Accelerator Alignment*, (Stanford Linear Accelerator Center, California, 1989).
- [7] Trevor Hastie, *Principal Curves and Surfaces*, (Stanford Linear Accelerator Center, California, SLAC Pub.-276, 1984).
- [8] H. Friedsam, "A New Accelerator Alignment Concept using Laser Trackers," in *Proceedings of the Fourth European Particle Accelerator Conference*, (London, England, 1994).
- [9] S. Kim, D. Carnegie, C. Doose, R. Hogrefe, K. Kim, R. Merl, "Statistical Analysis of the Magnet Data for the Advanced Photon Source Storage Ring Magnets," in *Particle Accelerator Conference*, (Dallas, Texas, 1995).

IMPROVEMENT OF THE ALIGNMENT SYSTEM FOR THE KEK 2.5-GEV ELECTRON LINAC

Y. Ogawa, A. Enomoto, and I. Sato, KEK, National Laboratory for High Energy Physics,
Tsukuba, Ibaraki, 305 Japan

The alignment system for the KEK 2.5-GeV electron linac was improved regarding several points: replacement of the large gas laser (He-Ne) with a compact diode-pumped solid laser (Nd:YAG), the introduction of a single-mode, polarization-maintaining fiber between the laser and the light-injection point into the alignment vacuum duct, and the use of new optics for realizing a diffraction-limited beam along the entire linac length of 460 m. The new system works satisfactorily and serves as a light source of good quality. A preliminary measurement of the system resolution for the KEK 2.5-GeV electron linac is reported as well as the main points concerning the improvements. A new design of the linac alignment system for the KEKB injector linac is also proposed.

I. INTRODUCTION

The stable acceleration of a high-current electron beam of good quality is one of the common requirements for modern large-scale electron accelerators, including linacs for a large yield of positrons, linacs for FEL, and future linear colliders. For realizing stable operation, transverse wake-field effects of high-current beams, which could cause a beam instability and degrade the beam quality, must be minimized in various ways. It has been recognized that the precise alignment of the accelerators is one of the key issues concerning the prevention of a wake-field instability.

In the KEKB injector linac [1] it is required that a large amount of positrons be produced effectively, for which a high-current, single-bunched primary electron beam of more than 10 nano Coulomb must be stably accelerated up to the positron production target (4 GeV). The alignment tolerances due to the transverse wake field have been calculated [2]; the misalignment errors of the accelerator components must be less than 0.1mm.

We have so far used the laser alignment system that was constructed about 14 years ago when the linac was commissioned. Since in recent years it had some troubles regarding optical systems, including the light source, and did not give the required resolution of alignment measurements, we planned to improve the alignment system for the KEKB injector linac. The key items of the improvement are the following:

1. light source and optical system
2. position-detection system
3. automatic alignment measuring system

By carrying out item (1) the beam quality of light is to become better, and the resolution of position

measurements will be improved. We describe here mainly the first item, which was successfully accomplished. Regarding items (2) and (3), a brief prospect is presented in connection with a practical design of the alignment system for the KEKB injector linac.

II. ALIGNMENT SYSTEM

Since the roundness effect of the earth is eminent in this kind of very long system, it is in principle impossible to align the system along the long beamline by the usual method using levels. A conceptual drawing of the laser alignment system is shown in Figure 1.

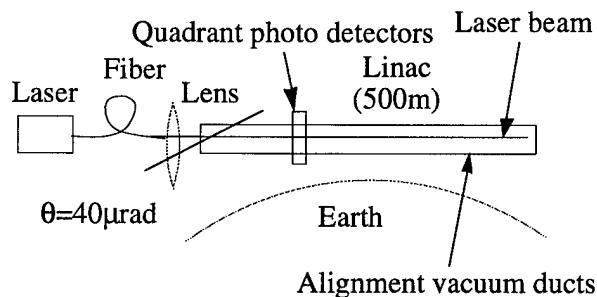


Figure. 1: Conceptual drawing of the laser alignment system.

A. Principle

The procedure of alignment is basically divided into two parts:

1. By using a laser beam as a reference line along the entire linac, the positions of each accelerator girder are measured with quadrant photo detectors set at the front and back ends of the girder. The light path is kept in a vacuum so that any index fluctuation effect on the laser beam can be avoided.
2. The accelerator girders are then aligned so that the positions become centered. The accelerator components are put on these girders with a mechanical precision of less than 0.1 mm.

This procedure signifies that the measurement resolution of alignment must be less than 0.1 mm, which satisfies the alignment tolerance calculated from the transverse wake-field effects. As a result, this alignment scheme should also work for the KEKB injector linac.

B. New Light Source

Since the laser beam is utilized as a reference line, it must be of good quality: the mode must have not only a

good Gaussian profile, but also a shorter wavelength for accomplishing a smaller beam size of the diffraction limit. The laser used so far is a He-Ne gas laser at a wavelength of 633 nm, which essentially suffers instability problems due to the characteristics of the gas used. The recent progress of laser-diode pumped solid lasers is prominent; a good beam quality is easily obtained compared with that of gas lasers. Besides, utilization of non-linear optical materials allows an effective generation of a laser beam having a shorter wavelength. We have adopted a laser-diode pumped Nd:YAG laser with subharmonic generation at a wavelength of 532 nm as a new light source. The characteristics of the laser are shown in Table I.

Table I. Parameters of the laser for alignment: a laser-diode pumped Nd:YAG laser with subharmonic generation (single longitudinal mode) [3].

Wavelength (nm)	532
CW Output Power (mw)	>10
Transverse Mode	TEM ₀₀
TEM ₀₀ Beam Diameter (mm)	0.32
TEM ₀₀ Beam Divergence (mrad)	2.2
Beam Pointing Stability (μ rad)	± 3 (measured @ 8hrs)
Stability of Output Power (%)	$< \pm 2$ (8hrs)
Noise (10Hz-1GHz) (% rms)	< 0.5
Polarization	linear
Inherent Line Width (kHz)	< 10 (1ms)
Jitter (kHz)	$< \pm 500$ (1s)

C. Fiber Optics

Although the laser shows a fairly good pointing stability of $\pm 3 \mu$ rad over 8 hours, it is not sufficient for our alignment system, since this angular variation causes a beam-position fluctuation of ± 1.5 mm at a distance of 500 m. In order to prevent this effect, we have introduced a single-mode polarization-maintaining optical fiber for transporting the laser beam from the laser to the alignment optical system. In this way, we could isolate the alignment optical system from the laser, so that it is not affected by the laser, itself. The pointing stability is improved by using a positioning system of high-precision and high-stability for the fiber output point. The mode shape is also improved by the mode-cleaning effect of the fiber, showing a good Gaussian form.

D. Alignment Optical System

Since the laser beam is used as a reference line, the beam size must be sufficiently small to permit the required measurement resolution. According to the characteristics of the quadrant photo detectors and the electric circuits, it has turned out that a beam size of less

of 50 μ m. From calculations based on Gaussian beam optics, if a diffraction-limited beam is established and the beam waist is located at a distance of 500 m from the beam-injection point, the beam size would be about 15-20 mm for a wavelength of 532 nm, which is satisfactory for our system.

For accomplishing this, we made special optics for a beam-size transformation that enables a diffraction-limited beam along the entire linac. The experimental results show that a laser beam with an initial size of 30 mm in diameter at the electron gun girder is successfully transported to the end of the linac, where the beam diameter is measured to be less than 15 mm ($1/e^2$). As a result, an alignment resolution of less than 50 μ m is expected.

III. PRELIMINARY MEASUREMENTS

In order to check the performance of the system, we carried out preliminary measurements of the alignment status of the KEK 2.5-GeV linac as well as a brief calibration of the measurements.

A. Calibration

Rough calibrations were performed at two representative points (first and last acceleration sections) in the linac in order to understand the position dependence of the calibration factors. By moving the quadratic photo detectors with a precision of 10 μ m, the detector outputs were measured. The results are shown in Figure 2. The errors due to beam-position fluctuations were sufficiently small during the measurements. The measurement resolution was estimated to be less than 50 μ m.

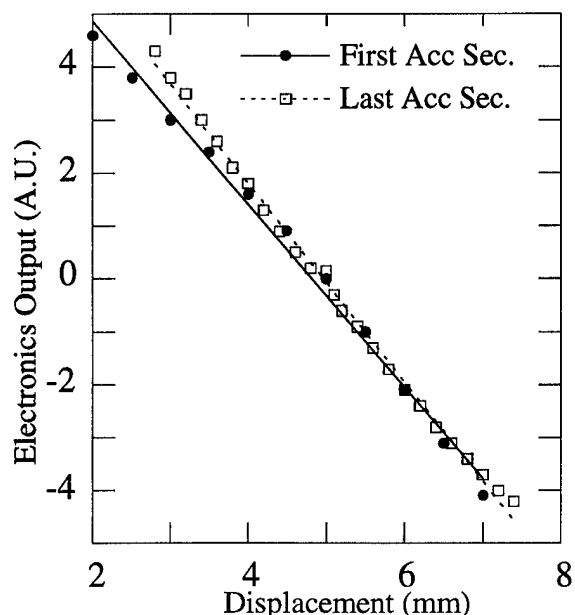


Figure 2: Calibration of the alignment system. The solid lines represent the linear fitting of the data.

The linearity is not bad in the measurement dynamic range of two or three millimeters, while the position dependence seems not to be large in this range of beam size. For a more precise calibration, however, it is necessary to measure at the same time the beam size at each calibration point. Therefore, the calibration factors obtained by the slopes of the fitted lines will have some errors due to the ambiguity of the beam sizes if they are used for positions other than the present calibration points.

B. Alignment Measurement

Figure 3 shows the alignment status of the KEK 2.5-GeV linac (preliminary). Since the calibration factors are not universal (as mentioned in the preceding section), the absolute amount of deviation seen in the graph will be revised. In any case, the results indicate that the linac is misaligned to some extent. We will therefore adjust the misalignment in the near future.

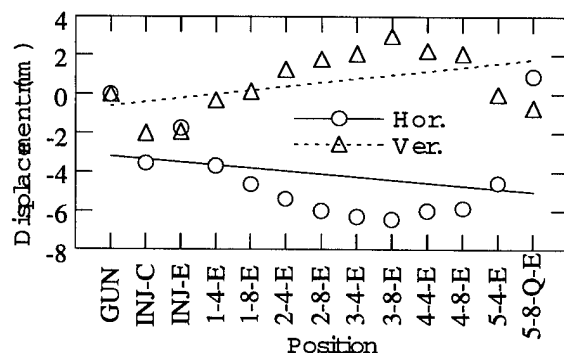


Figure 3: Alignment status of the KEK 2.5-GeV linac (preliminary).

IV. CONCLUSIONS AND DISCUSSIONS

The alignment measuring system of the KEK 2.5-GeV linac was improved regarding several points. A measurement resolution of 50 μm was achieved by installing a new laser and an alignment optical system comprising an optical fiber.

For further improvements, we plan to accommodate an automatic alignment measuring system, including an improvement of the position-detection system. This

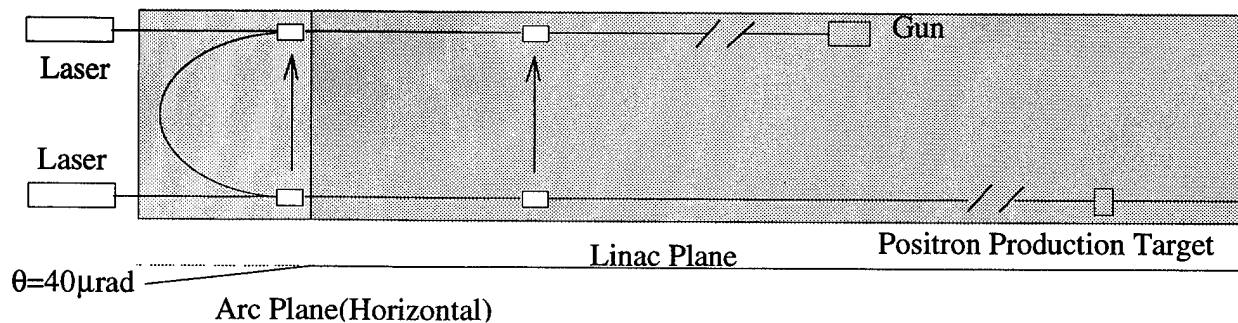


Figure 4: Alignment configuration of the KEKB injector linac.

system would be especially useful for real-time monitors of the alignment status of the KEKB injector linac, since it would help figure out one of the causes in case that the stable operation of the linac is disturbed by some unpredictable phenomena, such as earthquakes.

In the KEKB project, the linac has an arc section in order to utilize the present positron generator linac for increasing the total energy of the linac. Therefore, the alignment must be carried out in three parts: the up-stream linac, the arc, and the down-stream linac (Figure 4). We plan to align the three parts as follows:

1. Align the down-stream linac using the present alignment system with a precision of less than 0.1 mm.
2. Transfer the height of two separate points of the down-stream linac to corresponding points of the up-stream linac with a laser trigonometry or some other methods. In the up-stream linac, we employ a laser alignment system identical to that of the down-stream linac by using the two transferred points as references. For the horizontal directions perpendicular to the beam line, we use the usual levels. As a result, the plane of the down-stream linac is transferred to the up-stream linac.
3. Align the arc section with the usual levels. This signifies that the plane of the arc section is inclined to the others with an angle of about 40 μrad (Figure 1 and 4).

V. ACKNOWLEDGMENTS

The authors would like to thank T. Tanaka of Hakuto Co., Ltd and Y. Iino of Mitsubishi Heavy Industries, Ltd for their helpful collaboration.

VI. REFERENCES

- [1] A. Enomoto et al., Proc. of the 1994 International Linac Conference, Aug. 21-216, Tsukuba, Japan, p. 184.
- [2] Y. Ogawa et al., *ibid.* p. 535.
- [3] ADLAS diode laser pumped solid state laser, 532 nm cw, Nd:YAG, model 105.

A MECHANICAL FEEDBACK SYSTEM FOR LINEAR COLLIDERS TO COMPENSATE FAST MAGNET MOTION

C. Montag, J. Rossbach
DESY
Notkestrasse 85
D-22603 Hamburg

Abstract

For high luminosity, all linear collider schemes under study require very low emittance beams. When transverse beam dimensions of the opposing linacs become very small, high beam position stability is necessary to maintain high luminosity. For the 500 GeV c.m. S-band collider SBLC uncorrelated rms quadrupole vibrations must be smaller than some 70 nm and have to be reduced to 20 nm for the 1 TeV upgrade.

An inexpensive mechanical stabilization scheme based on geophones, piezocrystals and a digital feedback system has been successfully tested. It damps quadrupole motions in a frequency range of 2 – 30 Hz by factors up to 4, such that remaining magnet motions may be within tolerance limits. Based on a geophone with noise level below 1 nm, it is likely that this system may allow stabilization below the 10 nm level.

I. INTRODUCTION

To achieve a luminosity at least comparable to existing e^+e^- storage rings like LEP, all linear collider schemes currently under study require very low emittance beams focused to transverse beam dimensions of some 10 nm vertical and some 100 nm horizontal.

Since luminosity degradation should not exceed 3%, which corresponds to beam center positions being 0.25σ off center, tolerable quadrupole jitter amplitudes are limited to [1]

$$\sigma_q = 0.25 \cdot \sqrt{\frac{\epsilon_{\text{end}} \cdot \bar{\beta}_{\text{end}}}{N_{\text{quads}}}} \cdot \cos \frac{\mu}{2}, \quad (1)$$

where ϵ_{end} , $\bar{\beta}_{\text{end}}$ and N_{quads} are the actual emittance at the end of the linac, the beta function averaged over the last FODO cell and the number of quadrupoles, respectively. μ is the phase advance per cell. It can be shown that eq. 1 also holds if the beta function is scaled according to $\beta \propto \gamma^\alpha$ with arbitrary α between 0 and 0.8 [2].

Using SBLC parameters [3], this leads to $\sigma_q = 70$ nm and $\sigma_q = 20$ nm for the 500 GeV and the 1 TeV machine, respectively. Comparison with measured ground motion of HERA Hall West (see fig. 1) [4] shows that these limits are exceeded by ground motion amplitudes at frequencies below 6 Hz (20 nm limit) and 0.2 Hz (70 nm limit).

II. COMPENSATION SCHEMES

For ground motion compensation considerations, the frequency spectrum of this disturbance can be divided into two

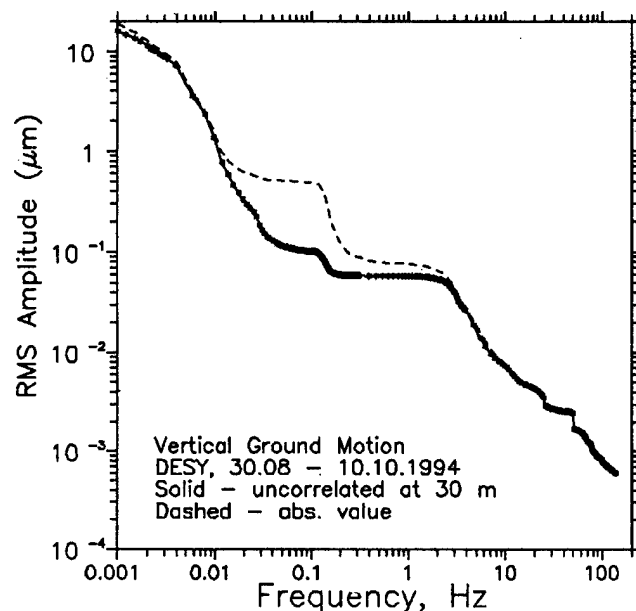


Figure 1. rms values of ground motion measured in HERA Hall West

parts, each of them requiring different compensation techniques. Due to the quite low repetition rate f_{rep} of nearly all linear colliders, beam based orbit correction schemes are applicable only to compensate very slow ground motion with frequencies not exceeding $0.05 \cdot f_{\text{rep}}$. For the SBLC with $f_{\text{rep}} = 50$ Hz, this leads to an upper limiting frequency for the application of beam based correction schemes of approximately 2 Hz. Therefore, ground motion with frequencies beyond this limit requires a different technique.

The simplest considerable attempt consists of some kind of "spring", acting as passively damping quadrupole support due to the $1/f^2$ characteristics for frequencies higher than the resonance frequency of the spring. To be able to damp frequencies as low as 2 Hz, a resonance frequency of some 1 Hz is required. This leads to a spring compression due to the magnet mass of 25 cm, which is unacceptable because of the high compliance of such a system. Therefore, passive damping is feasible only in the high frequency region ($f > 100$ Hz).

To compensate fast ground motion in the frequency band 2 Hz – 100 Hz, an active stabilization scheme consisting of a geophone measuring the velocity of the magnet motion on top of each quadrupole and a piezoelectric actuator tilting the magnet around its horizontal transverse axis in order to keep its center at rest has been built (figs. 2, 3).

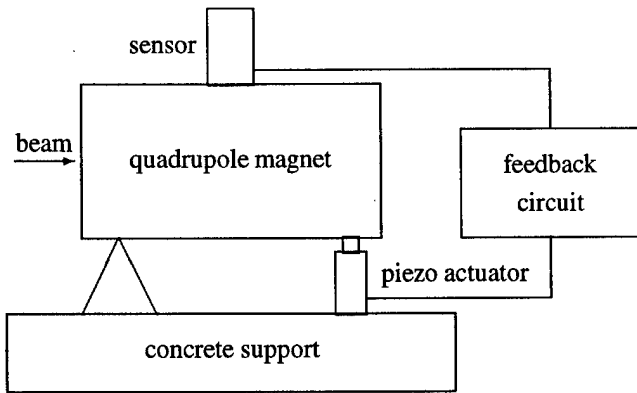


Figure 2. Schematic view of feedback system to compensate fast ground motion.

The internal noise of these sensors was obtained by measuring the output signals of two sensors responding to the same input signal (ground motion). Both signals were integrated in order to get the displacement. The averaged noise power spectrum $\bar{\Phi}_{nn}$ can then be calculated as

$$\bar{\Phi}_{nn} = \bar{\Phi}_{yy} - |H|^2 \bar{\Phi}_{xx}, \quad (2)$$

where $\bar{\Phi}_{xx}$ and $\bar{\Phi}_{yy}$ are the averaged power spectra of the two displacement signals $x(t)$ and $y(t)$, respectively. Note that here and in the following both x and y describe vertical motion. H is the ratio of the transfer functions of the two geophones. In our case of two identical sensors, it is assumed to be unity. For more details, see [5].

The internal noise σ_n^2 in the frequency band from a lower frequency f_0 to infinity can be calculated by integrating the noise power spectrum over this frequency range:

$$\sigma_n^2(f_0) = \int_{\omega_0=2\pi \cdot f_0}^{\infty} \bar{\Phi}_{nn}(\omega) d\omega. \quad (3)$$

Fig. 4 shows the measured rms noise level $\sigma_n(f_0)$ of this sensor type in the frequency band f_0 to infinity as a function of the lower frequency f_0 . As can be seen, the noise level in the frequency band above 2 Hz corresponds to approximately 1 nm.

III. RESULTS

The system described in section II has been successfully tested. With one sensor on the floor below the magnet support and the other on top of the magnet, motion signals have been obtained using a PC with 12 bit A/D board. These signals were integrated in order to get the displacement and Fourier transformed to get the power spectra Φ_{xx} and Φ_{yy} . From these power spectra, the rms value of the displacement in the frequency band from a lower frequency f_0 to infinity was calculated by integration over this frequency band:

$$\sigma_x^2(f_0) = \int_{\omega_0=2\pi \cdot f_0}^{\infty} \Phi_{xx}(\omega) d\omega. \quad (4)$$

Fig. 5 shows simultaneously measured rms values $\sigma_x(f_0)$ and $\sigma_y(f_0)$ of vertical motion on the floor (solid line, σ_x) and on

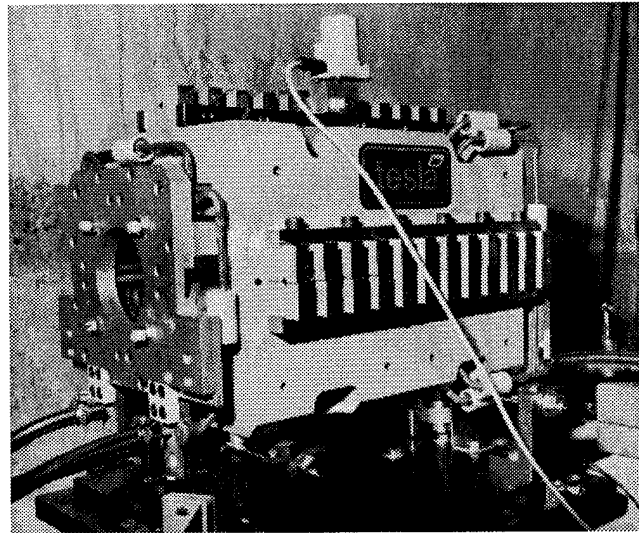


Figure 3. Active stabilization system, consisting of a geophone on top of the quadrupole and a piezo driver to tilt the magnet.

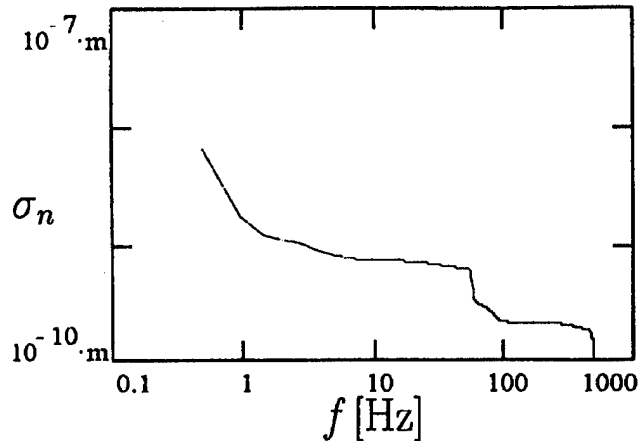


Figure 4. rms value σ_n of the internal noise of the geophone in the frequency band f_0 to infinity as function of the lower frequency f_0 .

top of the magnet (dashed line, σ_y) as function of the lower frequency f_0 .

These data were obtained under very noisy conditions in DESY hall 2, with a cooling water flow of 220 l/h (design value: 120 l/h). Fig. 6 shows the measured feedback gain of the system, calculated from the square root of the ratio of the power spectra simultaneously measured on the floor and on top of the magnet.

IV. CONCLUSION

It has been successfully demonstrated that active stabilization of mechanical quadrupole vibrations to levels necessary for linear collider operation is feasible even in noisy environments. For the whole linear collider, the costs of these ground motion compensation devices would not exceed 10 Mio US-\$. Therefore, fast ground motion considerations should not dominate the choice of the linear collider site.

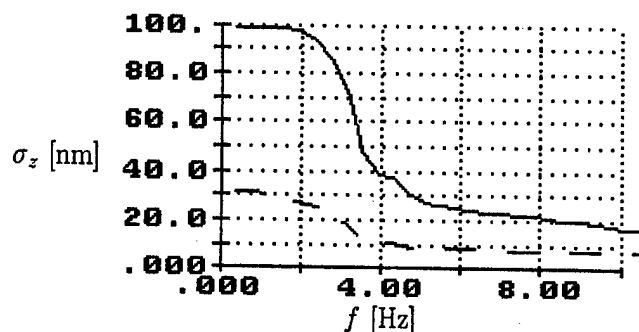


Figure. 5. rms values of motion signals in the frequency band f_0 to infinity as function of the lower frequency f_0 , simultaneously measured on the floor below the magnet (solid line) and on top of the quadrupole (dashed line).

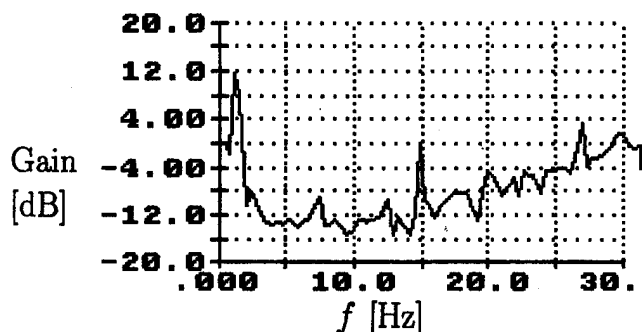


Figure. 6. Measured feedback gain of the active stabilization system.

V. ACKNOWLEDGEMENTS

We would like to thank G. Meyer and H. Kaiser for the excellent design of the magnet support and many helpful discussions.

References

- [1] T. O. Raubenheimer, SLAC report 387, 1991
- [2] J. Rossbach, Tolerance on uncorrelated Motion of Quadrupoles for Linear Colliders, DESY M/VM 93-01
- [3] N. Holtkamp et al., Status of the S-Band Linear Collider Study, DESY M-93-05
- [4] V. Shiltsev, B. Baklakov, P. Lebedev, C. Montag, J. Rossbach, Measurements of Uncorrelated Ground Motion at HERA, these proceedings
- [5] C. Montag, M. Lomperski, J. Rossbach, Studies of Measurement and Compensation Techniques of Magnet Motion for Linear Colliders, Proc. EPAC 94

A Microstrip Based Position System for the Alignment of the TTF Cryostat

D. Giove, A. Bosotti, C. Pagani and G. Varisco, INFN Milano
LASA, Via F.lli Cervi 201, Segrate (Mi), Italy

Abstract

The cryostat designed for the superconducting cavities of the Tesla Test Facility (TTF) is quite a complex structure with strict requirements on the alignment of the different components at the LHe temperature. A system able to measure on-line misalignments on the full length of the cryostat module (12 meters long) during cool down and operation procedures seems a very useful tool in order to verify structural analysis computation. A microstrip based system using a stretched wire has been designed for this purpose in our laboratory. Desy will provide the stretching system for the wire and the support system for the position transducers. In this paper we will present and discuss the design based on warm and cold tests on a prototype.

Introduction

The TTF facility will consist of four 12 m long cryounits each with eight 9-cell superconducting cavities operating at 1.3 GHz and one focusing quadrupole. Beam tests will be carried out at about 500 MeV.

The test program for TTF includes measures of the cryomodule alignment stability and reproducibility during cool-down/warm up operations.

In the TTF cryostat the cavities are suspended and aligned off a large 300 mm diameter helium gas return pipe. Three support posts, derived from the SSC magnet cryostat design, provide the warm to cold support transition from the outside of the cryostat to the helium gas header. Cavities are first assembled and aligned with a standard optical system in an alignment fixture. The required alignment tolerances for the elements inside a cryomodule are 0.5 mm for the RF cavities and 50 μ m for the quadrupole. After final assembly inside the cryomodule, the stability of the axis position will be on line monitored during thermal cycles with a resolution of 10 μ m.

Method

On line monitoring of the relative position of the different elements inside a cryomodule will be accomplished using a stretched wire alignment system. A detailed discussion of this method may be found in the literature, since it has been already used for the precise measurement of transport components in beam lines⁽¹⁾. Taking as a reference such an experience,⁽²⁾ we have designed a measuring instrument able to work at LHe temperature.

In our system two sets of 18 transducers, called WPMs (Wire Position Monitors), will be fixed along two straight sections inside the cryomodule to provide a complete 3D analysis of the displacements. They will be assembled on titanium support arms (designed by Desy), in order to bind their position to the cold mass (RF cavities and a quadrupole). Each WPM is similar to a beam position monitor. It contains 4 antennas and the differential signal strength received from opposite pairs is the quantity of interest. The WPMs receive their signal from a stretched wire excited by a 140 Mhz RF signal and centered inside a tube. The tube is the outer conductor in a coaxial structure which presents a constant impedance to the signal and which shields the signal from external interferences. The wire is stretched by means of an external system (designed at Desy) which will also provide the reference to the wire.

The design of the TTF system had to take into account a lot of constraints due to the peculiar operating conditions. The most important have been the wide range of temperature (from room temperature up to the operating one of 2°K), the need to contain the overall power consumption at 2°K (few Watts) and the fact that the system, after the final assembly, will be inaccessible.

Details of the apparatus

The main elements of the apparatus are the WPM, the wire and the coaxial tube, the RF cables from the WPM up to the exit connectors, the read out electronics and the data acquisition and analysis system. In the following we will describe the characteristic choices for each one of these elements. A more detailed description is available in Ref. 3.

The WPM

A schematic layout of two WPMs with their supporting frames, is shown in fig. 1. It is of the stripline kind with four electrodes matched to 50 Ω and symmetrically placed at 90° each other. The downstream end of each stripline (relative to RF propagation) is terminated to 50 Ω and the clear aperture is of 12 mm. The aperture has been imposed by the prevision about the displacement of the supports during the cool down: $\Delta y=1.6-1.8$ mm and $\Delta x=0.3-0.6$ mm respectively for cavities and quadrupole.

Striplines are 2.6 mm width and 64 mm long. The characteristic impedance of a stripline measured alone is 50 Ω (SWR has been measured less than 1.1 from room up to LHe temperature). The wire-stripline coupling and the

crosstalk between adjacent striplines have been measured as 39 dB and >55 dB respectively.

The choice of the material for the WPMs and for the electrodes has been the consequence of measurements on prototypes from room up to LHe temperature. Brass, titanium and aluminum has been tested. For thermal compatibility and weight considerations, the use of standard microstrip for electrodes has been discarded, while solid aluminum (copper and silver plated) has been chosen both for the WPM body and electrodes.

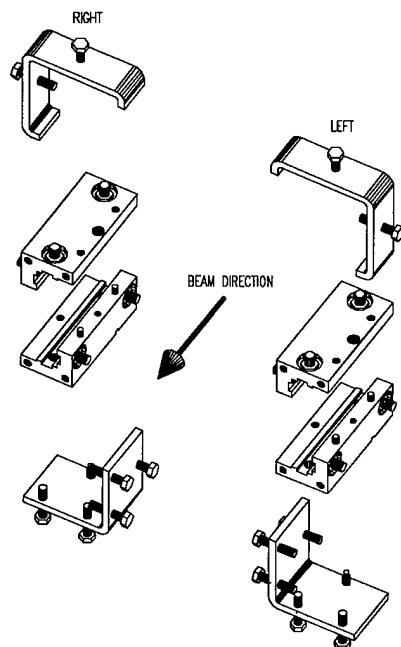


Fig. 1 Schematic layout of two WPMs with their supporting frames

The wire and the coaxial tube

The wire employed is a 0.5 mm diameter beryllium copper wire. The choice of the material has been imposed by the need to use amagnetic materials and the possibility to stretch the wire with an high tensile stress (of the order of 100 Kg/mm²). This will reduce, under the operating conditions, the overall sag of the wire at 2.07 mm. Power loss on the wire is of the order of 0.2 dB at room temperature and it will be negligible at LHe temperature.

The coaxial tube has an internal diameter of 12 mm and is made of copper.

RF coaxial cable and connectors

The choice of the connectors and RF coaxial cables to transport the signal from WPM to the external of the cryomodule has been a major technological challenge.

Radioactive environment have limited the choice of dielectric materials for connectors and cables. Capability to work at cryogenic conditions with low power loss at LHe

temperature (taking into account that the whole length of the coaxial cables inside a cryomodule will be of the order of 400 m) and good RF behavior have limited the choice of available cables.

The actual design has been based on a coaxial cable of 2.70 mm diameter with center conductor of copper clad stainless steel wire and dielectric of Kapton tape. Attenuation at room temperature is of 0.25 dB/m and operation up to -270°C has been proved. The computed heat load at 2 K for each cable is 18 mW. This figure will give an overall load of 2.6 W.

Connectors will follow a special mechanical design to fit to the cable.

50 Ω terminations will be fitted directly on the WPM. This would reduce the number of cables, and related problems. Terminations has been tested from room up to LHe temperature and negligible variations of SWR has been measured at 140 Mhz.

Read out electronics

The electronics which handle the signals coming from the WPMs has been designed according to the BPM electronics used at Sincrotrone Trieste ⁽⁴⁾.

The RF signal exciting the wire has a fixed frequency of 140 Mhz and a power of 10 dBm. The detector electronics is composed of three parts: the RF input, the IF/AGC/integrator and timing/ADC/DAC. Two main features of the detector are responsible for its stability and linearity. The first one is the choice to switch all the four inputs coming from a single WPM to a common readout electronics with a four channel PIN diodes multiplexer. The second one is the use of AGC circuitry in order to keep the highest electrode detected signal at the same output level in the full dynamic range. This guarantee the highest linearity and the best S/N ratio in ADC conversion (it has been measured of the order of 0.5 bit).

A characteristic of the whole design is that the electronics is completely controlled by an external CPU which provides gain control, synchronization signals and data handling capabilities. Such a feature reflects in a simpler analog electronics and provide an easier way to calibrate and control the board. The detector electronics has been developed according to the VXI format, in order to improve noise immunity and to take advantage of the larger board size. Each board will accommodate the components for the control of two WPMs. The interface toward the CPU (which is an Eltec Eurocomm 17, 68040 based @33 Mhz with FPU) is based on VME.

The amplitude detector (which has been modified with respect to the Trieste design, and is a XR 2208) has a very good linearity (< 0.1%) in a 20 dB range. An input amplifier stage has been added obtaining an RF signal sensitivity of -60 dBm with a dynamic range of 30 dB. The BPM detector cannot process the signal in less than 50 μ s, so the maximum rate of acquisition is of the order of 20 KHz for a single stripline. Under operating conditions the

acquisition rate is of 1 KHz, and the CPU performs an on line averaging of the readings. The algorithm has been designed to reject the natural oscillations of the wire (of the order of 4 Hz) and to control the rms deviation of the readings.

Data acquisition and analysis system

On line control of the detector electronics and handling of data acquisition from each one of the two structures is performed by a VME 68040 CPU fitted inside the VXI crate. Raw data acquisition, averaging and corrections with polynomial curve are performed at this level. A local hard disk stores data as a first level security.

Using an NFS based structure, data are transferred on a dedicated NFS server which provides functionalities of sharing data between consumer processes. These may be those of the consoles of the monitoring apparatus or, eventually, one of the control system of TTF.

Local consoles will be based on PCs employing LabVIEW as basic software. They will provide on line monitoring functionalities, with the capability to display displacement versus time for a whole structure or for a single WPM. Further data processing (frequency analysis, power spectrum of any instability, etc.) will be possible too. Data storage will be accomplished as a second security level.

Measures

A test fixture has been constructed for mapping the response of single WPM. The wire is mounted in a fixed position and the RF signal is applied to it. The WPM is assembled on a two axis translation stage and can be positioned anywhere within its aperture. The absolute accuracy of the positioning system is repeatable to about 4 μm . The structure is 1.2 meters long, with the WPM mounted between two sections of pipe which presents the correct boundary conditions.

The electronics reading chain is the same as the final one. The whole process is controlled by a LabVIEW dedicated program.

As expected, the dependence of the response with respect to the position of the wire can be described by a 3rd order polynomial, with a small coupling between the coordinate planes. The even and cross terms of the 2D polynomial expressions take into account mechanical tolerances and inter-electrode coupling. So doing accurate measurements over 50% of the mechanical aperture is guaranteed.

In order to determine the coefficients of the two bidimensional polynomial curves, which will characterize each WPM, a two steps mapping system has been followed. The first step provides two data sets from orthogonal axis through the electrical center of the WPM. Each data set refers to a back and forward path, in order to measure the absolute response and the repeatability of the system. Data have been taken every 10 μm over a range of ± 3 mm.

The second one provides measurements on square paths of

increasing distance from the electrical center of the WPM.

Using Mathematica, the data from previous measurements have been used to compute the coefficient of two dimensional polynomial curves. An excellent measure over a large portion of the WPM aperture has been obtained, as shown in fig. 2. Over the 50% of the aperture, we have got less than 10 μm of error, mainly due to mechanical uncertainty both for the x and for the y coordinate. The electronics contribution is less than 1 μm .

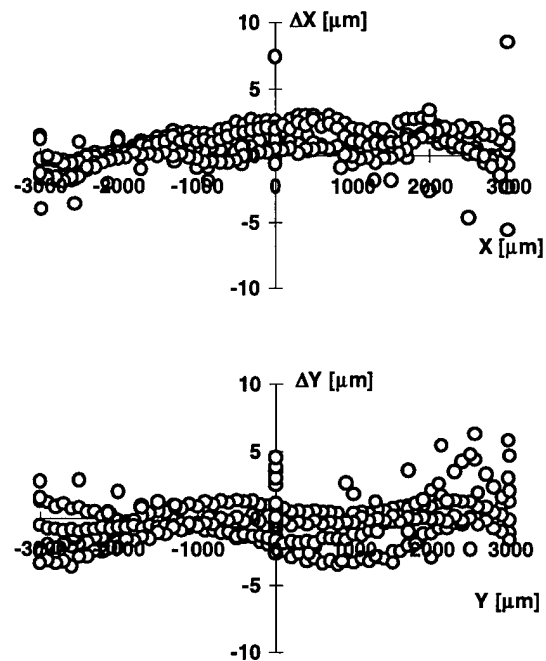


Fig. 2 Error in position measurements

Conclusions

We have developed a system able to measure displacements over a range of 6 mm with resolutions up to 10 μm . Components have been designed and tested for operation at 2°K. The final system is under construction and it will be ready for the installation in a TTF cryomodule by the end of July 1995.

Acknowledgments

We are particularly grateful to M. Bonezzi, D. Corti, M. Fusetti, P. Spada and S. Tizzoni for their contribution.

References

- [1] V.E. Bressler et al., Overview of the Final Focus Test Beam Alignment System, Proc. PAC 1991, p. 2736
- [2] F. Peters, private communication
- [3] D. Giove et al., The On Line Monitoring System for the Cold Mass of the TTF Cryostat, Tesla Report, to be published
- [4] R. De Monte et al., Elettra BPM System (Hardware and Software): First Results, Proc. EPAC 1994, pag. 1530

BEAM-BASED MAGNETIC ALIGNMENT OF THE FINAL FOCUS TEST BEAM*

P. Tenenbaum, D. Burke, R. Helm, J. Irwin, P. Raimondi
Stanford Linear Accelerator Center, Stanford University, Stanford, CA 94309 USA
K. Oide

National Laboratory for High Energy Physics, KEK, Tsukuba, Japan
K. Flöttmann

Deutsches Elektronen-Synchrotron, Hamburg, Germany

In order to optimize tunability and backgrounds in linear collider final focus systems, it is necessary to align strong quadrupole and sextupole magnets with beam-based measurements. Algorithms for alignment have been used successfully on the Final Focus Test Beam (FFTB) beamline at SLAC. Quadrupole magnets were aligned using a shunt technique, with resolutions from 50 microns down to 700 nanometers. Sextupole magnets were aligned by moving the magnets transverse to the beam and observing the kick on downstream beam position monitors. This procedure resulted in sextupole misalignment resolutions of 5 to 20 microns. All magnets were then moved into aligned positions via remote-controlled stages capable of sub-micron resolution. Details of the fitting algorithms, results of the measurement, and potential improvements in the system are discussed.

I. INTRODUCTION

Linear colliders operating in the TeV CM energy range are expected to have extremely tight *a priori* alignment tolerances on their quadrupole and sextupole elements. Misaligned quadrupoles generate dispersion, which can dilute the nanometer-sized focused spot; they can also cause the two beams to be steered out of collision, to such an extent that re-steering with correctors introduces unacceptable dispersion. Misaligned sextupoles can generate normal and skew quadrupole effects, resulting in waist shifts, dispersion, and coupling ($x'y$) at the IP. Finally, any significantly misaligned magnet can create detector backgrounds through aperture limiting in the element itself, or downstream via steering.

The Final Focus Test Beam (FFTB) is a prototype linear collider final focus designed to focus the 46.6 GeV SLAC beam to a vertical size of 60 nanometers. Tuning studies [1] have indicated that the spot size goal can be achieved if the RMS misalignments for quadrupoles and sextupoles do not exceed 100 microns in the horizontal and 30 microns in the vertical. In order to achieve these tolerances, we have developed a beam-based algorithm for measuring the misalignments of all strong quadrupole and sextupole magnets upstream of the Focal Point (FP). The magnets are then moved into aligned positions by remote-controlled stages. This eliminates the need to shut off the beam and enter the tunnel to correct alignment, reducing the concomitant risks from changes in the tunnel environment during positioning.

II. THE FINAL FOCUS TEST BEAM

*Work supported by the Department of Energy, contract DE-AC03-76SF00515.

The optics of the FFTB have been discussed elsewhere[2]. There are 30 strong quadrupoles upstream of the FP which are subject to beam-based alignment, and 4 sextupoles arranged in 2 families. The beamline contains 40 beam position monitors (BPMs) of a stripline design which are used in the alignment procedure[3]. Each quadrupole and sextupole magnet subject to beam-based alignment is mounted on a remote-controlled stage capable of independent x and y motion, with positioning accuracy of under 1 micron[4].

III. PREPARATION FOR ALIGNMENT

Prior to the beginning of beam-based alignment, the strong sextupole magnets are reduced to a nominal zero value. The entire line is then standardized. The magnets from the first bend magnet to the end of the line are set to their design values for small-spot operation. The matching quadrupoles upstream of the first bend are set to produce a low-divergence beam at the FP. This setting reduces the beam size throughout most of the FFTB, which eases constraints on the shunt range of the quadrupoles, and minimizes beam jitter and BPM background considerations. The FFTB enclosure is locked, and allowed to warm up to thermal equilibrium for several days.

IV. QUADRUPOLE ALIGNMENT

The quadrupole alignment procedure uses a shunt technique to measure the offset of the beam centroid from the magnetic center of each quad. Each quadrupole upstream of the FP is powered by a separate power supply, eliminating the need for shunt or boost supplies to change the quadrupole strength. The strength range of each quadrupole has been determined for the low-divergence optics by a series of simulation studies which optimize resolution and downstream aperture clearances at each setting of every quadrupole.

A. Data Acquisition

The beamline is aligned in segments, each of which contains between 3 and 6 consecutive magnets. For each segment, the alignment acquisition procedure is as follows:

1. Read in all FFTB-region BPMs for 100 orbits, average the positions at each BPM over the 100 orbits. This average constitutes the "reference orbit," which is subtracted from all subsequent BPM data at the beginning of the fit. This reduces the data used in fitting to differences from the reference orbit, which are correlated to quadrupole shunt

values to extract the misalignments. Despite extensive averaging, the reference orbit may still differ systematically from the nominal trajectory due to injection or energy offsets. The reference orbit is compared to several subsequent orbits to ensure its conformity before continuing acquisition.

2. Scan each quadrupole in the segment sequentially through its range of strengths. Three settings are used for each magnet, typically the nominal strength and (nominal \pm offset). At each setting, acquire readings from all FFTB BPMs for 8-10 pulses (not averaged). During this time, operators watch loss monitors, energy feedback signals, etc., to ensure that no errors occur which may contaminate the data. If so, the data for a quadrupole may be re-taken.
3. Once all data for a segment has been acquired successfully, the BPM and magnet strength data are submitted to a fitting routine, OPTFIT.

B. Fitting Algorithm -- OPTFIT

OPTFIT is an online program which combines first-order matrix formalism for centroid and/or beam matrix transport with MINUIT function minimization. It uses beamline data (magnet strengths, BPM readings, wire scanner measurements) to fit selected parameters of the line (magnet misalignments, strengths, incoming beam matrix).

The program takes as input the data acquired via the SLC data acquisition system; files describing the beamline devices and the transfer matrices between them; and a set of flags which indicate the parameters to be fit. Once this data has been passed to OPTFIT, the following steps are followed:

1. The reference orbit is subtracted from all other BPM data.
2. For each pulse, the energy variation from the reference orbit is determined. The FFTB extraction line contains BPMs on either side of a vertical permanent bend magnet, and these are used for this computation. The energy and energy uncertainty of each pulse are stored, and the BPM data used for this step are not used in the main fit.
3. For each pulse, the incoming jitter (x, x', y, y') relative to the reference orbit is determined. This is done using BPMs upstream of the first magnet whose alignment is to be fitted, i.e., in a region of non-varying transfer matrices. The fitted incoming coordinates and their error matrix are stored for each pulse, and the data used in this step are eliminated from the main fit. Because steps 2 and 3 are simple linear fits, matrix inversion (not MINUIT) is used.
4. The data between the last magnet to be fitted and the energy BPMs are subjected to quality tests. Because these BPMs are also in a region of invariant transport, the BPM readings can be fitted, pulse by pulse, to a "track" emanating from the downstream face of the last fitted magnet. The quality of fit to the "tracks" can indicate BPMs with excessive noise, individual bad readings, etc. These are eliminated from the fit.
5. The errors from fitting the incoming beam are propagated to each BPM used in the fit, and added in quadrature to the intrinsic BPM resolution.

6. MINUIT is called. The fit algorithm will then minimize χ^2 by changing the magnet positions and re-transporting each pulse (using the initial coordinates determined above), then comparing the results to the BPM data. The fitted misalignments are then returned, along with uncertainties, the normalized χ^2 , and the contribution to χ^2 from each BPM.

C. Refinements to the Procedure

Early experiments indicated that naively implementing the corrections recommended by OPTFIT was not satisfactory in all cases: frequently the misalignment of an upstream quadrupole served to kick the beam onto the line of the remaining magnets. In this case, simply moving the magnets would have forced us to move the entire FFTB line onto the arbitrary line of the incoming beam. A fit option was added in which the last quadrupole of a segment is defined to be "aligned," and a kick angle is fitted at the upstream end of the segment. This dramatically improved our ability to converge, especially in the beam matching region upstream of the first bend.

Other experiments showed that the quality of the fit was deteriorating as the area of interest moved downstream, as indicated by monotonically increasing normalized χ^2 values. This was traced to upstream magnets losing hysteresis, usually at the end of a scan (when set back to their original values). The magnets were then required to "mini-standardize," i.e., when the magnets are changed in a direction opposite to their hysteresis curves, the power supplies automatically overshoot the new set point by 5%, so the set point is approached from the correct direction. The dilution of fit quality was nearly eliminated by this refinement.

D. Results

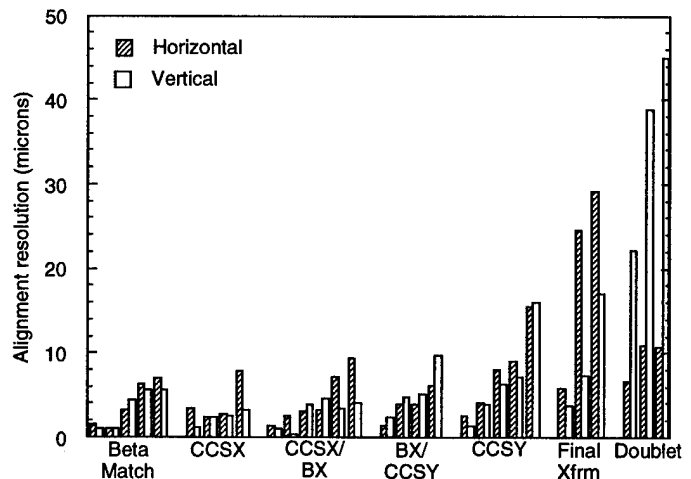


Figure 1. Resolution of quadrupole alignment technique for all FFTB magnets upstream of FP.

Figure 1 shows the achieved resolutions of the fitting procedure. These represent the resolution of the distance from the quadrupole center to the arbitrary line of the incoming beam. Each quadrupole in the segment introduces a kick to

the nominal trajectory, whose magnitude is uncertain due to the uncertainty in the quadrupole's alignment. The propagation of this kick is included in the fit of the downstream quadrupoles. Consequently, the resolution of the method degrades from upstream quadrupoles to downstream within a given segment. The monotonic loss of resolution from upstream segments to downstream segments is due to the decreasing number of BPMs downstream of the fitted magnets.

V. SEXTUPOLE ALIGNMENT

The SLC Final Focus performs CCS sextupole alignment by varying their sextupole families in strength and observing changes in waist, dispersion and coupling at the IP[5]. This technique relies on IP single-beam size monitors, which can be difficult to use in a linear collider final focus. The FFTB alignment technique, by contrast, relies only on BPMs and magnet movers, and can be completed before small-spot tuning begins.

Once all the quadrupoles have been aligned, the CCS sextupoles are turned on to a strong value (integrated second derivative = 33,000 kG/m). The sextupole is then scanned *in position*, via its mover, over the full range of the mover in either x or y. The thin lens kick of a sextupole magnet is of the form:

$$B_y = K_s (x^2 - y^2).$$

Consequently, the position on a downstream BPM will vary quadratically in x as a function of the mover (x or y) position. The downstream BPM values can then be fit to a parabola:

$$X_{\text{BPM}} = A(X_{\text{mover}} - B)^2 + C.$$

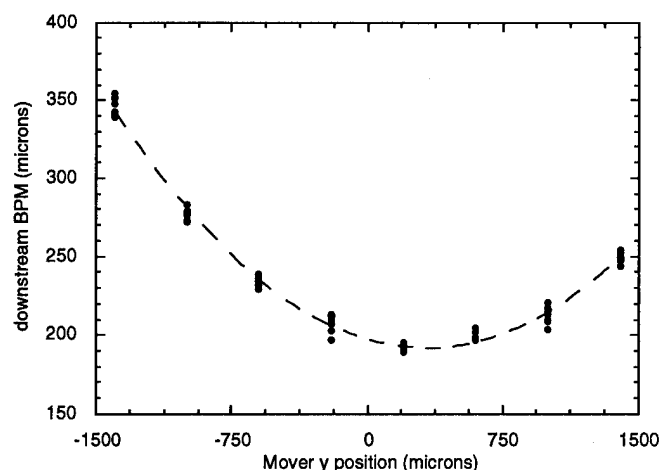


Figure 2. Reading of a downstream BPM vs sextupole mover position. Note that both x and y mover scans produce a quadratic horizontal kick at the downstream BPM.

The offset value, B, is the unambiguous center of the sextupole magnet, i.e., the point at which the magnetic gradient vanishes. The sextupole may then simply be set to this position. Figure 2 shows such a quadratic form for a BPM vs. sextupole mover scan, and Figure 3 shows the

achieved resolution of this procedure for all 4 FFTB CCS sextupoles.

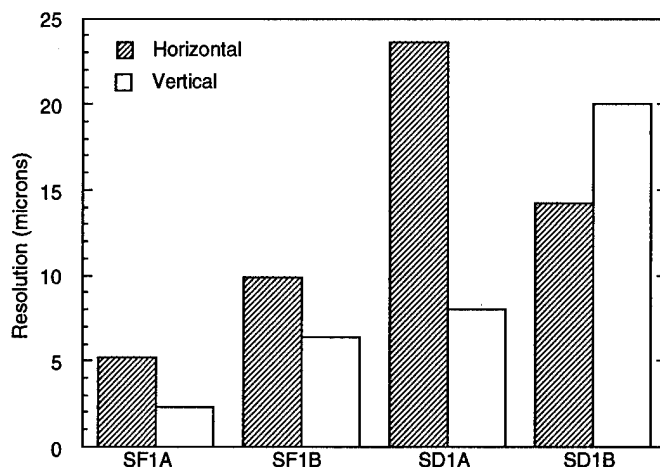


Figure 3. Resolution of sextupole alignment technique for all four CCS sextupoles.

VI. POSSIBLE IMPROVEMENTS

The incoming trajectories for the alignment of the upstream quadrupoles in the FFTB is determined by a pair of BPMs, separated by 85 meters. The first of these is a low-resolution device, rather than a high-resolution FFTB BPM. Replacing this BPM would improve convergence of these magnets. Since the upstream quadrupoles are used for beam matching and changing the IP divergence, this would be a significant improvement.

VII. ACKNOWLEDGMENTS

The authors would like to thank Lee Ann Yasukawa for writing the Quad Alignment interface software in the SLAC control system.

VIII. REFERENCES

- [1] K. Oide, "Design of Optics for the Final Focus Test Beam at SLAC," Proc. of the IEEE Part. Acc. Conf., 1989.
- [2] G. Roy, "Analysis of the Optics of the Final Focus Test Beam Using Lie Algebra Based Techniques." SLAC-Report-397 (1992).
- [3] H. Hayano *et al*, "High Resolution BPM for FFTB." Nucl. Inst. Methods A320:47-52 (1992).
- [4] G. Bowden *et al*, "Precision Magnet Movers for the Final Focus Test Beam," SLAC-PUB-6132 (1994).
- [5] P. Emma *et al*, "Beam-Based Alignment of the SLC Final Focus Sextupoles," Proc. of the IEEE Part. Acc. Conf., 1993.

Alignment and Survey of the Elements in RHIC *

D. Trbojevic, P. Cameron, G. L. Ganetis, M. A. Goldman, R. Gupta, M. Harrison, M. F. Hemmer, F. X. Karl, A. Jain, W. Louie, S. Mulhall, S. Peggs, S. Tepikian, R. Thomas, and P. Wanderer
Brookhaven National Laboratory
Upton, New York 11973, USA

Abstract

The Relativistic Heavy Ion Collider (RHIC) consists of two rings with cryogenic magnets at a 4.5K operating temperature. Control of positions of the dipole and quadrupole cold masses (iron laminations) and the beam position monitors (BPM's) during production and installation is presented. The roll of the dipoles is controlled by a combination of rotating coil measurements with the surveying measurements. The center of the quadrupole magnetic field is obtained by direct measurement of the field shape within a colloidal cell placed inside the quadrupoles. Special attention is given to the triplet quadrupole alignment and determination of the field center position.

I. Introduction

Two rings of RHIC cross each other in the horizontal plane at six interaction regions. Dipoles and corrector-quadrupole-sextupole (CQS) packages are installed inside the cryostats as they operate at a liquid helium temperature of 4.5K. During operation the magnet laminations are not accessible. In addition to collisions of heavy ions, the RHIC accelerators will do spin physics experiments with two proton beams. The spin physics puts additional constraints on the alignment of the RHIC magnets. The corrected closed orbit errors should be less than 1 mm. The quadrupole and dipole rolls should be less than 1 mrad.

II. The Global and Local Monument Networks in the RHIC Tunnel

The sixfold symmetry of the RHIC accelerators imposed the primary network of twelve survey monuments on the tunnel floor [1]. A clear line of sight from the twelve platforms is available via a penetration through the tunnel berm. An additional tower is located at the geometrical center of RHIC. Clear lines of sight are available from this tower to each of the twelve peripheral instrument platforms. Two accelerators in the RHIC tunnel lie in a horizontal plane of an orthogonal Cartesian coordinate system where in the center of the rings the vertical axis points upward along the local gravity. The survey results of the primary network showed the error ellipses for each of the twelve monuments to be between 0.32 mm and 0.70 mm on the major axis, and between 0.12 mm and 0.25 mm on the minor axis. The mean value on the major axis is 0.57 mm while the mean on the minor axis is 0.18 mm. The secondary network in the tunnel was established with the floor monuments located at each half cell with a distance of 14.1 meters between them. Surveying in RHIC is performed by using a combination of PC compatible

and Leica data collection hardware. Data collection is accomplished [2] using Zeos 386+ laptop computers with GeoNet software (ME5000.bas and DIRECT.bas), the Kern Mekometer for distance measuring and the Leica T3000K for direction observation. Vertical control is observed using the Leica NA3000 bar code level and recorded on board removable REC module. Data are passed on the REC module through a GIF12 reader connected to a PC on an RS232C standard COM port.

III. Control of the Dipole Center Positions During Production

RHIC dipoles are produced by the Northrop-Grumman Corporation in Bethpage, New York. Properties of the RHIC dipoles as well as other details of the dipole production are presented in other papers at this conference [3][4][5]. The dipole aperture center is located by a combination of the optical survey of the four fiducials with the mechanical survey during production. The presurveying of every element in the RHIC accelerator is executed with a portable Leica ManCat system using a Compaq 486c portable computer and T3000. Data are presently passed via floppy disk. Four fiducials are welded to the ends of the laminations - the "cold mass fiducials". The optical survey also locates the cold mass fiducial positions with respect to the outside cryostat fiducials as well as the relation to the horizontal gravitational base plane of the dipole supporting stands. The field angle of the dipoles is determined by the rotating coil ("mole") measurements with respect to the same gravitational plane. These measurements of the magnetic field angle are performed at room temperature for all dipoles. The first thirty dipoles, as well as every tenth dipole after that, are also measured at a superconducting temperature of 4.5 K with currents of 660 A, 1450 A, and 5000 A. A correlation between the cold and warm measurements of the field angle shows a standard deviation of 0.20 mrad. The error in measurements as well as reproducibility, is also estimated to be ± 0.2 mrad. The dipole field angle obtained from the harmonic probe measurements is set to be perpendicular to the RHIC horizontal plane in the tunnel by a rotation around the axis which crosses the radius of the dipole curvature at 1/3 of the average sagitta. The RHIC horizontal Cartesian plane perpendicular to the center gravitational vector is obtained after correction to the earth ellipsoidal curvature [1].

A. Production Control of CQS Assemblies

The three elements of the CQS assemblies are connected together inside the two welded "cold-mass" shells. The corrector, quadrupole, and sextupole vertical and radial positions are measured by the dial gauge indicator with electronic data transfer [5]. The quadrupole mechanical center is estimated from the measurements of the four upper and four lower notches in the

*Work performed under the auspices of the U.S. Department of Energy

laminations. The sextupole mechanical center is estimated from the positions of the two upper and two lower noches of the laminations close to the end of the sextupole. The cold masses are installed into the cryostat assemblies. Alignment of the CQS assemblies in the tunnel is based on the quadrupole center obtained by the ferrofluidic cell measurements.

B. Direct Measurement of the Quadrupole and Sextupole Centers by Ferrofluidic Cell at 4.5 K

The development and other details of the ferrofluidic measurements were presented earlier [6]. The centers of the first thirty quadrupoles and sextupoles will be obtained by direct optical measurements of the quadrupole and sextupole magnetic field shapes seen inside the colloidal cell at a temperature of 4.5 K. Figure 1 represents one of the results of the quadrupole center measurement with respect to the center line, related to the outside fiducials by the ManCat system.

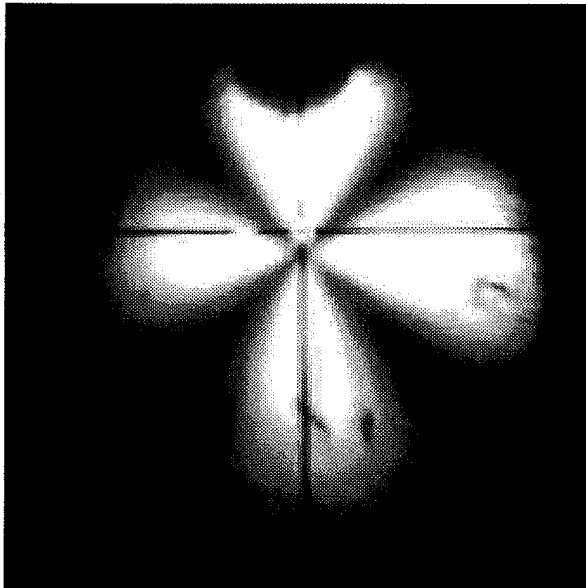


Figure 1. Quadrupole field pattern viewed during colloidal cell measurements at 4.5K. Current through the quadrupole is 5000A.

Two polarizers are crossed to each other (90°) and placed at the opposite ends of the CQS assembly. The collimated light can not be seen with the telescope if there is no magnetic field around the cell with the colloidal solution. A cylindrical glass cell is filled with ferrofluidic colloidal solution [6]. When the quadrupole field is present the small particles in the colloidal solution orient themselves along the magnetic field lines producing the field picture at the telescope. Figure 2 is obtained from the sextupole measurements at 4.5K with a current of 100A through the sextupole coils (operating current of the sextupoles is 30A). The accuracy of the quadrupole magnetic field center obtained by the colloidal cell is $\pm 50 \mu\text{m}$.

C. Results from the Colloidal Cell Measurements of the Quadrupole Center at Room Temperature

Most of the CQS assemblies will be measured at room temperature, by pulsing the superconducting coils with a current up

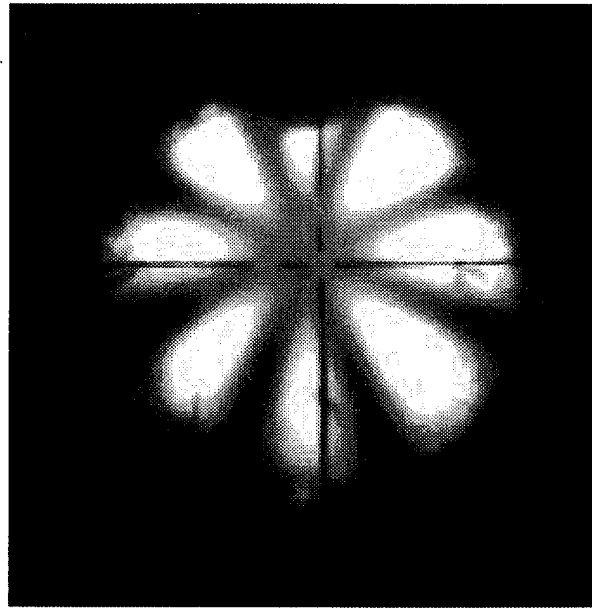


Figure 2. Field patterns viewed in the colloidal cell inside the sextupole magnet at 4.5K. Current through the sextupole coils is 100A.

to 300 A within 3 seconds. The colloidal cell quadrupole field shapes are obtained from the high resolution camera using the frame grabber. It takes 0.8 seconds for the ferrofluidic particles inside the colloidal solution to react to the outside magnetic field lines. Three pictures are taken during the 2 seconds flat top. Figure 3 shows the quadrupole field shape from the 300 A pulsing measurement. The calibration measurements at room temperature showed that one pixel is $50.8 \mu\text{m}$ long. The accuracy of determining the center of the magnetic field could be fraction of a pixel.

IV. Triplet Quadrupole Alignment

The collisions of the two beams at RHIC detectors "STAR" and "PHENIX" will have the maximum luminosity with the highest focusing of the triplet magnets. The twiss function $\beta^* = 1 \text{ m}$. At the storage conditions in RHIC the luminosity depends mostly on the magnetic field quality in the triplet quadrupoles as well as on the accuracy of their alignment. Special attention is given to the procedure and design of the triplet cryostat. Each quadrupole in the triplet cryostat will be aligned with an accuracy of $\pm 50 \mu\text{m}$ by using the colloidal cell technique. The triplet quadrupoles will be pulsed to produce a strong enough magnetic field to induce the field shape inside of the colloidal cell. The quadrupole field angle of the triplets is determined by the harmonic probe measurements with an estimated accuracy of $\pm 0.2 \text{ mrad}$.

V. The BPM Positions

The beam position monitors (BPM's) are located inside the CQS assemblies at the sextupole end. The BPM position with respect to the outside fiducials is determined by direct measurement of the center with a pulsed antenna. A high frequency signal of 50 MHz is sent to a rod placed close to the center of the

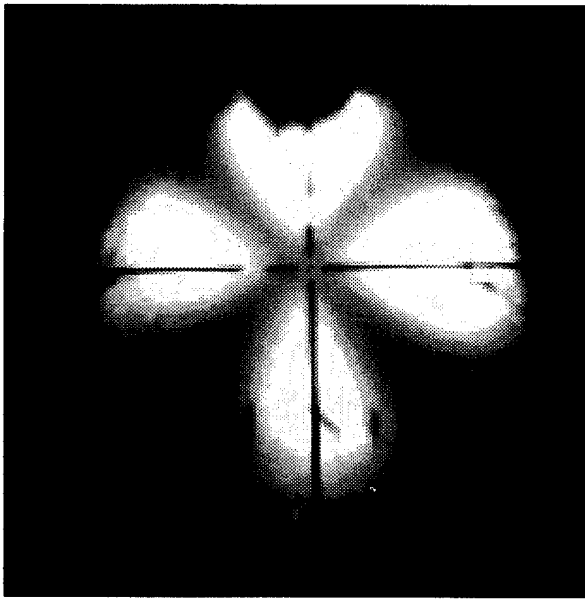


Figure 3. Quadrupole field shape viewed in the colloidal cell during a measurement with a current through the quadrupole of 300 A.

BPM. The BPM plates provide signals which determine the position of the rod with respect to the plates. Part of the rod outside the CQS vacuum flange has two fiducials. These are used to determine the rod position with respect to the outside cryostat fiducials by using the already mentioned ManCat system. The accuracy of the BPM position with respect to the outside fiducials is estimated to be ± 0.13 mm. During the calibration procedure it was found that the reproducibility and accuracy of the measurements was ± 50 μ m.

VI. Conclusions

The alignment errors of the RHIC arc quadrupole magnets in the RHIC accelerators are expected to be reduced to less than ± 0.25 mm due to the direct measurements of the quadrupole centers with respect to the outside cryostat fiducials by the optical colloidal cell measurements. The dipole and quadrupole magnetic field angles are obtained from harmonic probe measurements with an accuracy of ± 0.2 mrad. It is estimated that the rms roll errors of the dipoles will be less than 1 mrad and in the case of the quadrupoles less than 0.5 mrad. The prefiducialization of every magnet in RHIC is automated with direct electronic data transfer and analyses. The best possible positions of the RHIC elements in the tunnel are obtained by a combination of the optical survey measurements, mechanical measurements, and harmonic probe field angle measurements.

References

- [1] M.A. Goldman, "RHIC Reference Geometry", Brookhaven National Laboratory Internal Document, AD/RHIC/RD-43, August 1992.
- [2] M. Hemmer, "RHIC Electronic Data Collection and Survey and Alignment Database", Brookhaven National Laboratory Internal Document, August 1993.
- [3] P. Wanderer et al., "Construction and Testing of Arc Dipoles and Quadrupoles for the Relativistic Heavy Ion Collider (RHIC) at BNL", at this conference.
- [4] J. Wei et al., "Field Quality Evaluation of the Superconducting Magnets of the Relativistic Heavy Ion Collider", at this conference.
- [5] S. Mulhall et al., "Combined Element Magnet Production for Relativistic Heavy Ion Collider at BNL, at this conference.
- [6] M.A. Goldman, R.E. Sikora, and T.J. Shea, "Preliminary Studies on a Magneto-Optical Procedure for Aligning RHIC magnets", IEEE Proceedings 1993, Washington DC May 17-20, pp.2916-2918.

RF Radiation Measurement for the Advanced Photon Source (APS) Personnel Safety System*

J.J. Song, J. Kim, R. Ostocki and J. Zhou

Argonne National Laboratory
9700 South Cass Avenue
Argonne, IL 60439 USA

Abstract

The Advanced Photon Source (APS) booster and storage ring RF system consists of five 1-MW klystrons, four 5-cell cavities, and sixteen single-cell cavities. The RF power is distributed through many hundreds of feet of WR2300 waveguide with H-hybrids and circulators. In order to protect personnel from the danger of RF radiation due to loose flanges or other openings in the waveguide system, three detector systems were implemented: an RF radiation detector, a waveguide pressure switch, and a Radiax aperture detector (RAD). This paper describes RF radiation measurements on the WR 2300 waveguide system.

I. INTRODUCTION

As shown in Fig. (1), the APS personnel safety system consists of RF radiation monitors, X-ray radiation monitors, klystron shield switches, and waveguide air pressure gauges.

The RF radiation monitors are installed at the injection site, extraction wing, and the connecting corridor. Two cooling blowers are installed to provide air pressure in the WR2300 waveguide system. Three sets of photohelic meters are installed to monitor the air pressure in the waveguide and blowers. In case there is a gap in any of the waveguide flanges, the air pressure will drop and RF radiation will be generated from the gap. The RF system will be automatically shut down if the air pressure drops below the preset trip point. The trip point is set at a value based on the "air pressure - gap size" relationship. The purpose of this study is to develop a relation between the gap size and the amount of RF radiation which will allow a direct comparison between the pressure and the RF radiation in the waveguide system.

II. Measurement Setup

According to IEEE standards, the radiation threshold limit value (TLV) at 352 MHz is 3.52 mW/cm^2 . The APS high-power RF system consists of five 1-MW klystrons which operate at about 400-kW RF output power. Each cavity in the booster or storage ring receives about 100-kW RF power. We will use this input power level as the normalized power for RF radiation measurement.

The measurement setup is shown in Fig. (2). An HP 8753C network analyzer is used as the signal source, followed by a 100-W 50-dB power amplifier. An HP 8594E spectrum analyzer is used to monitor the signal in the waveguide, coupled through a 50-dB directional coupler. At the ends of the waveguide there

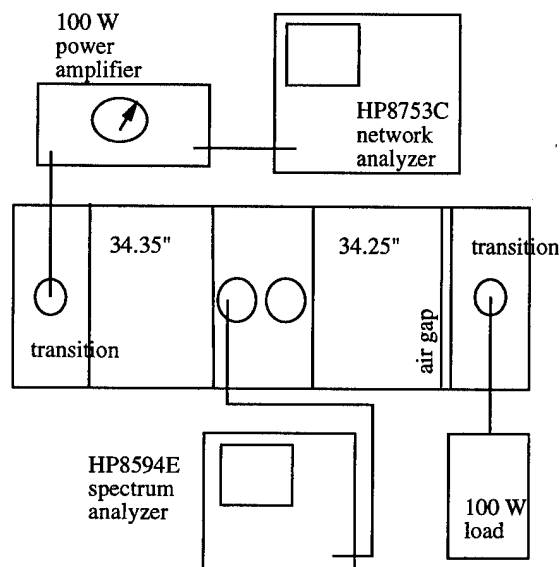


Figure 2. Measurement setup for the waveguide radiation test

are two coaxial transitions, one connected to the source and the other to a 100-W load.

A flange gap between the straight waveguide section and the transition section is created by placing washers between the flanges. The gap size is controlled by the number of washers used. The reflected power due to the gap and the load is also monitored by the output signal of the directional coupler.

The waveguide is placed in a position where one of the narrow walls is on the ground. The RF radiation is measured at two broad walls and one of the narrow walls facing upwards. The radiation is measured at different distances from the gap: one right at the gap with zero distance and the other one foot away from the gap. This practice is aimed at evaluating the reduction in radiation with respect to the increasing distance. The measuring instrument is a Narda RF radiation detector with probes.

III. Measurement Results

The frequency of the continuous wave (CW) signal is set at 351.93 MHz, which is the operating frequency of the APS booster and storage ring RF system. The input signal level in the waveguide is set at 17, 20, 47, and 50 dBm, respectively, corresponding to 50 mW, 100 mW, 50 W, and 100 W. The signal level in the waveguide is monitored by the spectrum analyzer connected to the coupler with a -50.5-dB coupling coefficient. The attenuation of the cable is 1.5 dB. Thus the correction factor is $50.5 + 1.5 = 52 \text{ dB}$. Fig. (3) gives the forward signal

*Work supported by U.S. Department of Energy, Office of Basic Energy Sciences under Contract No. W-31-109-ENG-38.

APS SR/RF Personnel Safety System Layout

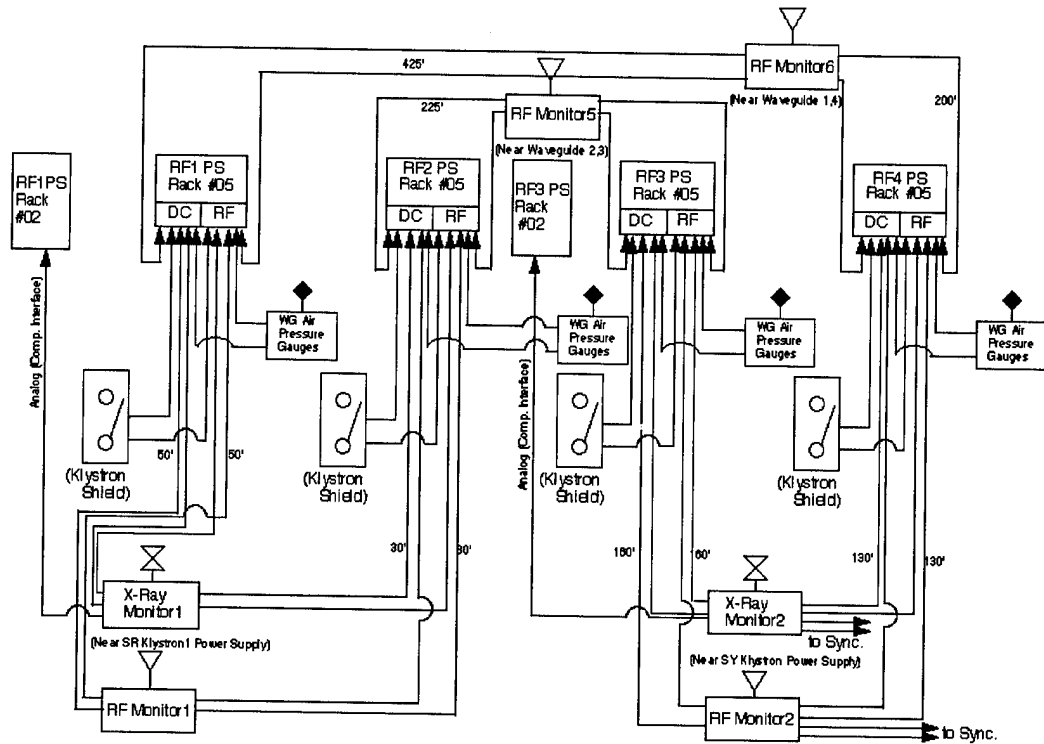


Figure. 1. APS Storage Ring Personnel Safety System

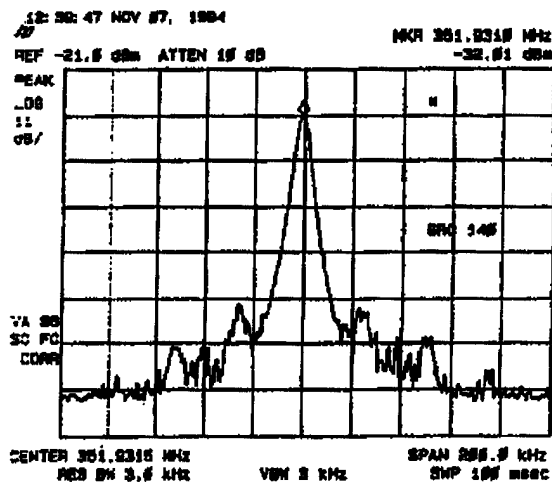


Figure. 3. Forward signal in the waveguide measured by the spectrum analyzer

measured from the spectrum analyzer with a gap size of 0.18 inch. In this case the signal level in the waveguide is given by $-32.01 + 52 = 20.01$ dBm. The reflected power is roughly 30 dB lower than the forward power, indicating the fact that even for a large flange gap, the reflected RF power is fairly small. Measurement results of RF radiation are given in Fig. (4). The top curve with a \diamond symbol is measured at the flange with 20 dBm in-

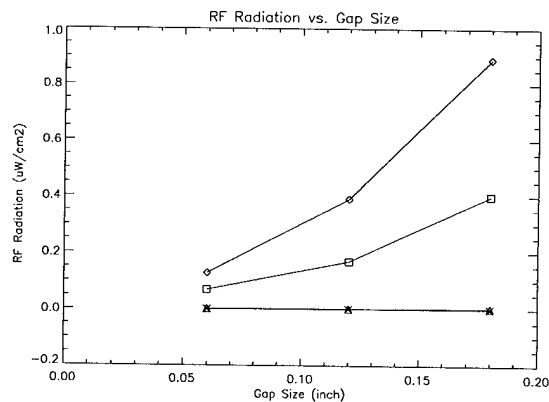


Figure. 4. RF Radiation vs. Gap Size.

put power; the middle curve with a box symbol is measured at the flange with 17 dBm input power; the bottom curves with a \times symbol is measured at one foot away from the flange with 20 dBm input power; and the bottom curve with a triangle symbol is measured at one foot away from the flange with 17 dBm input power. The input power mentioned above is the actual forward power in the waveguide.

In order to interpret these data in terms of the threshold limit value (TLV), we need to normalize these data to the input power

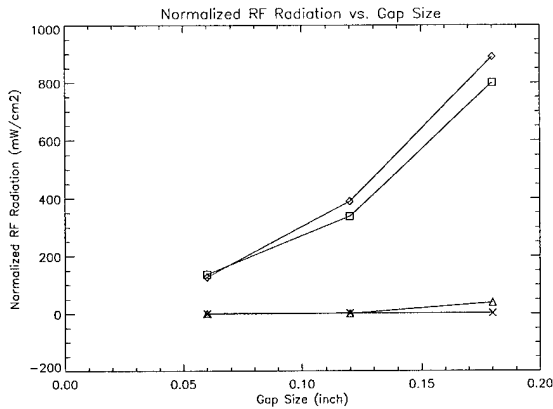


Figure 5. RF radiation vs. gap size normalized to 100 kW input power

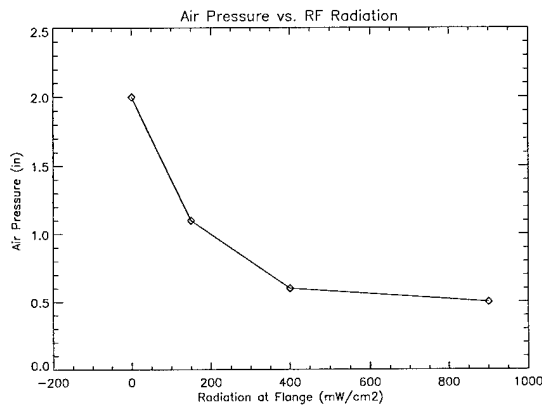


Figure 6. Air Pressure vs. RF Radiation

of 100 kW,

$$R_{site} = \frac{100kW}{P_{in}} \cdot R_{lab}, \quad (1)$$

where R_{site} is the projected radiation level with a 100-kW input power and R_{lab} is the measured radiation with P_{in} input power. From the measured result of Fig. (5) we can see that the radiation measured at the flange is much higher than the threshold limit value (TLV). But the radiation at one foot away falls below the TLV for a fairly large gap size of 0.12 inch. This indicates that special safety provisions may not be necessary if this procedure is a realistic simulation of what might occur in the APS RF system.

From the measured results of radiation versus gap size, and the air pressure versus gap size, we can find out a direct relationship between the radiation and air pressure, as depicted in Fig. (6). This curve can be used as a guideline to set the air pressure trip point for RF protection.

IV. The RAD System

An RF monitor can effectively detect RF radiation leaks, but it is a localized device which can only be located in a number of scattered places. In order to develop a cost effective way to detect RF radiation in a widely distributed system, the Radiax aperture detector system was proposed and is being implemented. Radiax cables with apertures on the outer conductor will

be installed along the waveguide system. Any RF radiation from waveguides will penetrate into the cable through the apertures and deliver a signal to the detector connected to the end of the cable.

V. Conclusions

RF radiation due to waveguide gap is measured. For a fairly large gap (0.12 inch), the projected radiation level from 100 kW input power falls below the threshold limit value ($3.52mW/cm^2$) at one foot away from the flange gap. A Radiax aperture detector system will be installed as a more cost-effective way to monitor RF radiation in a wide area.

RADIATION SHIELDING OF THE MAIN INJECTOR

C. M. Bhat and P.S. Martin

Fermi National Accelerator Laboratory*
P.O. Box 500, Batavia, IL 60510

Abstract

The radiation shielding in the Fermilab Main Injector (FMI) complex has been carried out by adopting a number of prescribed stringent guidelines established by a previous safety analysis[1]. Determination of the required amount of radiation shielding at various locations of the FMI has been done using Monte Carlo computations. A three dimensional ray tracing code as well as a code based upon empirical observations have been employed in certain cases.

I. Introduction

The Fermilab accelerator complex consists of a chain of four proton accelerators with a beam energy up to 800GeV for fixed target experiments and up to 2 TeV (center of mass energy) for collider experiments. The Fermilab Main Injector (FMI) which is being built in a separate enclosure, will replace the 150 GeV Main Ring (MR) accelerator which is currently being used as an injector to the Tevatron. FMI has many added advantages over the MR[2]. Having larger admittance both in the transverse and in the longitudinal phase space, the FMI is capable of providing more than $5E12$ protons/batch at 120 GeV for the antiproton production target and over $3E13$ protons/batch at 150 GeV for the fixed target operations. When such a high energy and high intensity facility is being built, it is necessary that proper care is taken regarding environmental protection as well.

II. Shielding Guidelines

The radiation safety is an important and mandated requirement for all Fermilab facilities. In order to meet this responsibility a number of guidelines have been provided in the FERMILAB RADIOLOGICAL CONTROL MANUAL and have been followed for designing the FMI. Many of the stated guidelines in this manual are more stringent than the DOE standards. A list of Fermilab standards which are relevant to the aspects of radiation shielding evaluation at the FMI, are given in Table I.

Table I. Fermilab standards for radiation shielding evaluations.

Operated by the Universities Research Association, under contracts with the U.S. Department of Energy

Description	Maximum Allowed Dosage
Visitors and public: Whole body	0.05 rem/year (i.e., 0.025 mrem/hr) (Unlimited Occupancy)
Non-radiation workers: Whole body	0.05 rem/year (i.e., 0.025 mrem/hr) (Unlimited Occupancy)
Radiation workers: (direct 'prompt' radiation)	1.5 rem/year (≤ 300 mrem / quarter)
Ground water activation ^a	20 pCi/ml-year (3H) 0.4 pCi/ml-y (^{22}Na)

^a These nuclides are of major concern to Fermilab. However care has been taken to meet the requirements of DOE order N0. 5400.5 for other radioactive nuclides causing contamination in the ground water.

Using the guide lines in Table I and the results of Monte Carlo calculations with CASIM[3] for some typical cases, the following shielding criteria have been developed[1]:

1. For unlimited occupancy we need soil equivalent shielding of 7.92 m (26 ft) for 150 GeV beam-lines enclosures, and a soil equivalent shielding of 7.46 m (24.5 ft) for the 8 GeV beam-lines and the FMI enclosures.

2. 0.305 m (1 ft) of steel[4] is a soil equivalent of 0.88 m (2.89 ft) and 0.305 m of heavy concrete (78% concrete with 22 % steel) is a soil equivalent of 0.46 m.

These are used very often in deciding the shielding thickness for radiation protections.

III. FMI Design, Beam Intensities and Beam-losses

FMI is located underground. The tunnel floor of the FMI is at an elevation of 217.47 m (713.5 ft) which is about 1.82 m lower than the Tevatron tunnel floor. It has a total circumference of 3319.41 m. A geometric layout of the FMI along with some critical area of interest from the radiation shielding point of view are shown in Fig. 1. For the purpose of injection and extraction

of the proton beams, a total of seven beam lines will be built. Some beam lines have varying elevations.

Each region of FMI and its beam-lines that poses potential radiation safety problems has a unique structure, so they have to be treated individually. For instance, the RF gallery near the MI60 straight section is one such area. The proton and the antiproton beams from the FMI will be injected in to the Tevatron near(under) this gallery. The two accelerators are at different elevations. A total of five beam lines originate in the vicinity of this region. The walls in the beam enclosure have a number of utility penetrations and alcoves. At the surface level (at an elevation of 226.31 m) there is the MI60 service building. Evaluating the radiation shielding for a region like this is very difficult task. We will briefly discuss the shielding aspects of this region later.

The beam in the FMI will be accelerated to 120 GeV and 150 GeV depending upon the application. The operating scenarios for the FMI are listed in Table II. The FMI is capable of operating in five different modes. The beam intensities shown in Table II are design goals.

Table II. The beam intensities for different operation scenarios of the FMI and beam loss terms.

FMI Mode of Operation	Proton Beam Intensity and Cycle time
pbar Production	5E12p/1.5sec @120GeV
Fast Resonant Extraction	3E13p/1.9sec @120GeV
Slow Resonant Extraction	3E13p/2.9sec @120GeV
Collider Injection	5E12p/5sec @150GeV
Tevatron Fixed Target	3E13p/30sec @150GeV
Beam-loss Scenario	Source Term
Operation Losses (Annual)	1E19 @8GeV 4.1E18 @120GeV
Accidental Losses	5.7E16 @8GeV 8.5E15 @120GeV

Defining the beam-loss term for an accelerator is a difficult task. Generally they are categorized into, a) normal operational beam-losses and, b) accidental beam losses. A conservative estimate for the FMI has been made based upon our past experience with the Main Ring operation and are listed in Table II. These beam-losses have been used as source terms for shielding evaluations. There is also an estimated annual proton beam abort

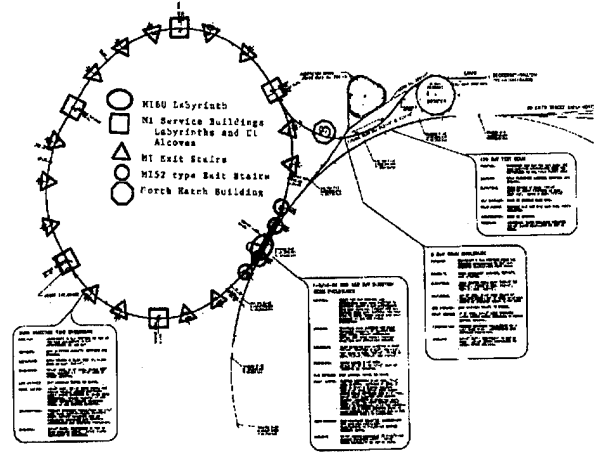


Figure 1: A geometric layout of the FMI. Ellipse : MI60 labyrinth, square:MI Service Buildings, Triangle : MI Exit Stairs, Circle : MI52 type Exit Stairs, Octagon : 8GeV North Hatch Building.

for the FMI which has been taken into account in designing the FMI beamdump[5].

IV. Shielding Calculations

After establishing the guidelines and beam-loss terms, radiation shielding calculations have been performed. When a high energy particle interacts with a material, a shower of particles mainly consisting of protons, neutrons and pions will be produced. These in turn interact further resulting in cascades of particles with angular distribution peaked in the forward direction. If the beam is lost in an energized magnet, the angular distribution need not be symmetric. The radiation dose at any point will be calculated using the number of stars produced at that location which depends upon the hadron flux, the energy, the angle and the shielding in between. When multi-GeV primary protons are lost in a target, the contributions to the prompt radiation dose in the transverse direction will be dominated by the low energy neutrons, while in the forward direction the muons (which are long-ranged) will dominate. For shielding purposes we have to consider both of them separately.

We have carried out shielding calculations for most of the locations around the FMI using Monte Carlo codes[3] CASIM (for hadrons) and MUSIM (for muons) in cylindrical geometry. The culverts are some of the locations of potential problems around the FMI which do not have cylindrical symmetry. In these cases, we have used a derivative of the code CASIM (called CASPEN [3]) and the required amount of steel under the culverts were determined. There are a number of locations with very complicated geometry around the FMI. The radiation shielding calculations for such locations using a Monte Carlo code is extremely difficult and time consuming. Therefore we developed a three dimensional ray tracing computer code with Monte Carlo results embedded in it. The CASIM calculation on a typical beam-line enclosure (with soil around) has shown that the shower maximum is occurring at an angle of 68° for 150

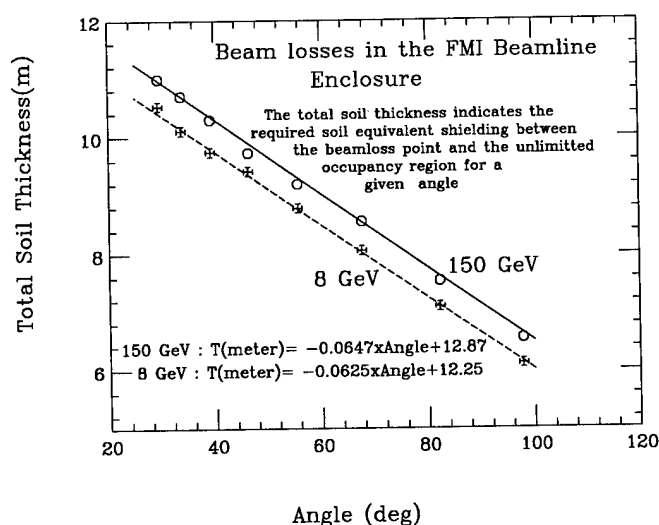


Figure 2: The soil equivalent shielding thickness as a function of angle adopted in the ray tracing computer code.

GeV beam loss. This has a total radial soil equivalent shielding of 8.4 m from the loss point to the unlimited occupancy region. Lower the angle larger will be the radial shielding thickness. The required soil equivalent shielding thickness for unlimited occupancy as a function of angle is shown in Fig. 2. We have adopted this scheme in our ray tracing code.

For exit stairs and penetrations we used EXIT2A which assumes that two successive legs in an exit stairs are at 90° to one another. This program was developed by using empirical observations in fixed target experiments[6]

V. Radiation Dose at Some Critical Locations

The estimated radiation doses near the unlimited occupancy regions for some critical locations of the FMI are listed in Table III. For many cases a combination of Monte Carlo calculations and EXIT2A or ray tracing computer programs were used. For example, for MI52 exit stairs the EXIT2A is used in combination with CASPEN because the MI beam-line enclosure is under one of the five legs. The shielding between the beam-line and this leg is only 0.6 m of concrete. Hence, the strength of the radiation source is evaluated using CASPEN and the attenuation terms are determined using EXIT2A. In order to achieve radiation dose ≤ 0.01 mrem/hr for normal operation beam losses we had to vary the lengths of each leg to get an optimum value. This gives a conservative estimate of radiation dose at MI52 exit stairs.

MI60 straight section is another complicated area as mentioned earlier. Here we used the ray tracing program to decide the required amount of shielding as a function of angle. For some locations CASIM calculations have been carried out with rectangular geometry to estimate the leakage due to edge scattering. For the entire straight section we achieved minimum of 7.92 m of soil equivalent shielding.

Description	Max. Dose Rate	
	operational (mrem/hr)	Accidental (mrem/acc.)
MI60 Labyrinths ^a	0.09	1.2
Labyrinths and Utility Alcoves in MI Service Buildings(5)	0.01	0.06
Exit Stairs (14)	0.01	.15
MI52 Exit Stairs (4)	≤ 0.01	0.05
North Hatch Building	≤ 0.01	0.43
Penetrations	≤ 0.01	0.09

^a Posting a caution sign is required.

VI. Summary

The radiation shielding evaluation has been carried out for FMI using previously set guidelines. The FMI beam-loss terms for different scenarios have been mentioned. The shielding evaluations have been carried out using Monte Carlo and a ray tracing computer code. For exit stairs calculations have been done with EXIT2A. For 8GeV beam lines and FMI enclosure we have achieved a minimum of 7.46 m soil equivalent shielding and, for the 120 and 150 GeV beam lines a minimum of 7.92 m soil equivalent shielding have been achieved.

Authors would like to acknowledge Dr. A. Van Ginneken, Dr. N.V. Mokhov and Mr. A. Leveling for useful discussions at various stages this work.

References

- [1] Preliminary Safety Analysis Report of MI, 1992
- [2] D. Bogert, W. Fowler, S. Holmes, P. Martin and T. Pawlak, 'The status of the Fermilab Main Injector Project' (these proceedings).
- [3] A. Van Ginneken CASIM Fermilab-FN272(1975), MUSIM Fermilab-FN594(1992), CASPEN (private communication).
- [4] P.H. Grabincius, Fermilab TM1719(1991).
- [5] C.M. Bhat, P.S. Martin and A. Russell, 'Design of FMI Beam-abort dump' (these proceedings).
- [6] C. Moore, EXIT2A (private communication)

The Safety Interlock System of Synchrotron Radiation Research Center

T. F. Lin, J. P. Wang
Synchrotron Radiation Research Center, Taiwan, R. O. C.

ABSTRACT

The Safety Interlock System (SIS) at the Synchrotron Radiation Research Center (SRRC) is introduced. SIS is designed to protect people from exposure to accidental high radiation. It is composed of three subsystems. The Access Control System (ACS) prevents people from being exposed to the extremely high radiation inside the booster and storage ring shielding housing (or called the interlock area) during machine operation. The Beamline Enable Controller (BEC) controls the operation of the main shutter of each beamline. The Hutch Interlock System (HIS) prevents users from exposed to the radiation present when the X-ray beamlines are operating. The interlock design principles, the system features, the safety logic and electronic circuits are described along with the operation procedures.

I. Introduction

The Safety Interlock System (SIS) is designed to protect personnel from exposure to radiation present when the synchrotron facilities are operating. SIS is a system that ensure certain conditions have been met, in a proper sequence, before the accelerator can be operated, the beam can be injected to the storage ring or a beamline can be used. In addition, any action that could potentially cause accidentally exposure will violate the SIS system and cause a fault. The result of a SIS fault will terminate the booster operation, cease the injection process, and eliminate all the stored electron beam in the storage ring.

SIS consists three subsystems. The upper part of SIS is the Access Control System (ACS). This system controls the operation of booster and storage ring. Access control, automatic broadcasting, search confirmation, injection warning, and emergency shut down are the basic functions of ACS. The middle part of SIS is the Beamline Enable Controller (BEC) which controls the open mechanism of the main shutter of each beamline. The lower part of SIS is the Hutch Interlock System (HIS). This system safeguards the operation of the wiggler X-ray beamline. The interlock design principles are set following the guidance of the up-to-date accelerator safety order[1]-[6]. The logic development, prototype construction, and real system installation are executed by SRRC staff. The system has been reviewed by the Safety Committee of SRRC and outside expertise.

II. Interlock Design Principles

The merit of an appropriate beam interlock system not only increases the degree of protection afforded individuals, but also reduces the technical and administrative burden. The fundamental philosophy is to make sure fail safe operation of the system, and to provide back-up functions in the event of

failure. SIS at SRRC is designed following the principles given below.

1. The system should be fail safe, redundant, unrestrictive, and testable.
2. Emergency-off and search confirmation buttons should be provided inside the interlock area, and be clearly visible, easily distinguishable, unambiguously labeled, and readily accessible.
3. Emergency exit mechanisms should be provided in entrance doors of interlock area, even when interlocked. Emergency entry features for interlocked doors are not precluded.
4. Clearly labeled status indicators reflecting actual conditions should be provided at entrance doors.
5. A reasonable search interval should be provided for each interlock area. An audible and visual warning interval should also be provided before the beam is introduced.
6. The main shutter of each beamline should be closed during injection, and the branch shutters (photon shutters) should not be opened before the open of the main shutter.
7. Once SIS fault is happened, there should have redundant devices to cease the injection process and dump all the stored electron beam.

III. System Description

SIS can be classified into three different control levels. The upper part is the ACS of the booster and storage ring. BEC and HIS are the middle and lower part respectively. All these three systems are tied into the injector and ring control systems. Any violation of these systems will cease the injection process and dump the stored beam. The principal components and operation logic of each subsystem are described in the following section.

1. Access Control System

ACS controls the operation of the booster and storage ring. The block diagram of this system is shown in Fig. 1. The principal components together with their functions are described below.

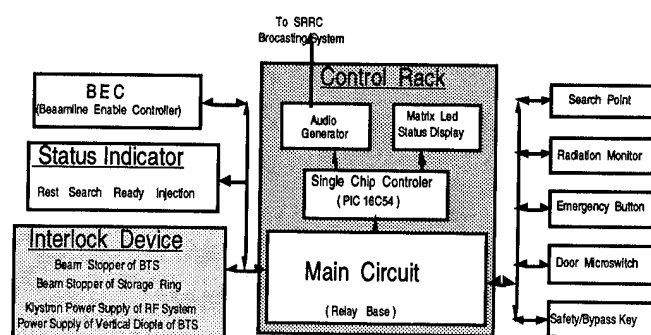


Fig 1 Access Control System (ACS) block diagram

(1). Control Rack

This is the main body of ACS. Signals from door micro-switches, search points, emergency buttons, radiation monitor, safety key and bypass key are processed here. Any emergency action been detected, it will send a command to the interlock devices to cease the operation of the machine. Status indication, automatic broadcasting, injection alarm and feedback monitor functions are also provided by this hardwired relay based control rack.

(2). Status Indicator

Status indicators are installed at entrance doors of interlock areas and some suitable positions to show the operation condition of the booster and storage ring. Each indicator receives command from the control rack and is able to show 4 different modes of operation.

Rest : Green light is shown in indicator. Beam is off, electrical hazard is also off.

Search : Yellow light is shown in indicator. Search procedure is going to be taken.

Ready : Red light is shown in indicator. Search is completed. Beam may be stored.

Injection : Flash red light is shown in indicator. Injection process is undertaking.

(3). Search Point

Search points are installed inside booster shielding room and storage ring shielding tunnel. Every search point should be activated sequentially in the search procedure. Violate the sequence or over the given search time period will cause the search invalid.

(4). Emergency Button

Emergency buttons are installed inside the interlock areas with clearly visible indicator and easily distinguishable color and labeling. Once someone being trapped inside the interlock area, emergency button provides the function to shutdown the machine operation immediately.

(5). Force In/Out

Force in/out mechanism is provided at every entrance door of the interlock areas. Should serious accident be happened, anyone could use the force in/out function to get in/out the interlock area to save the personnel or equipment in time. In ACS, force in/out process is treated as an emergency event.

(6). Interlock Device

The interlock devices linked to ACS are shown in table 1. Anyone of these devices can cease the operation of the injector, terminate the injection process and eliminated the stored beam. This configuration can fulfill the redundant requirement.

Table 1. Interlock Devices of ACS

Booster ACS	Storage Ring ACS
Gun Trigger of LINAC	Beam Stopper of BTS
Gun High Voltage of LINAC	Beam Stopper of Storage Ring
Modulator High Voltage of LINAC	Klystron Power Supply of RF System
Klystron Power Supply of RF System	Power Supply of Vertical Dipole of BTS

2. Beamline Enable Controller

BEC is located at the control room of storage ring and is controlled by the operator. It governs the operation of the main shutter of each beamline. Any one of the beamlines should get the enable signal issued from this device before it can lift the safety shutter and introduce the synchrotron radiation to the end station. When HIS fault is sensed, it will send a signal to ACS to turn off the klystron power supply of the storage ring RF systems. The stored beam will be eliminated in this situation.

The operation of BEC is interlocked with the two beam stoppers of the transport line (BTS). It will keep in disable state when any one of the beam stoppers of BTS is open. This design insures that no main shutter of beamlines will be open during the injection process. The high intensity injection caused bremsstrahlung radiation will always be shielded by the heavy metal shutter. Radiation protection objective can be achieved.

3. Hutch Interlock System

The design philosophy of HIS is nearly the same as that of ACS. However, its scale is reduced just to cover the area of a hutch. Most of the components described in ACS section are used in HIS. The introduction given below will focus on the unique features of HIS.

The electronic circuit of HIS is shown in Figs. 2. The final target of HIS is to open the photon shutter of the beamline. Before reaching this goal, enable signals issued from other systems should be received, emergency chain should be closed, search procedure should be performed, hutch door should be locked, hutch key should be returned to control panel, audible and visual alarm interval should be finished, and user control button should be activated. The enable signals are linked directly to the user control button and are independent with hutch related circuit. This make it possible to lessen the boring and unnecessary search procedure in the re-injection event after unexpected beam dump.

A safety key and a test key are also designed in HIS. The safety key controls one of the enable signals of the photon shutter. It is administered by the safety person. Not before all the safety concerns of the beamline being solved, can the safety key be delivered to enable user control button. The test key is designed for function testing. Through a safety application procedure, users can get the key to test the function of the photon shutter.

Once HIS fault is happened, i.e. emergency button been activated or hutch door been forced open, a signal will send to BEC for closing the main shutter and dumping the stored beam. A manual reset process is required before the hutch can reopen for synchrotron radiation experiment.

IV. Operation Procedure

Access to the interlock area is restricted, so as to prevent accidental operation, by means of mechanical locks, micro-

switches, search points and control keys. A search procedure is also needed for confirming the safe conditions inside the interlock area. Except for some insignificant differences, the procedures for accessing and searching the interlock area are same for both ACS and HIS. Followings are the summaries of HIS operation procedures.

1. Close photon shutter using the user control button on the control panel. Turn hutch key to "release" position and pull it out.
2. Open the hutch door using hutch key. When hutch door is open, photon shutter is disable. Users can work safely in the hutch.
3. After works being done, push the search point inside the hutch. This action activates a flashing lamp and an audible buzzer. A timer is also activated to stop the warning process and give user a predetermined time (30-60 sec) to search hutch, lock hutch door, return hutch key back to control panel, and turn it back to "lock" position.
4. Failure to comply with previously described action will cancel the procedure, search process must be re-tried.
5. Push the "search complete" button on the control panel. This action turns off the light inside the hutch for 10 to 15 seconds.
6. After the search process, the hutch is ready for beam on. If someone is still imprisoned in the hutch, he can force open the door or push the "emergency" button to cancel the open of photon shutter and dump the stored beam.

V. Summary

The safety interlock system at SRRC is established by the cooperation of instrument and control experts and safety people. The design logic of this system is fulfilled with the safety interlock principles. The successfully implementation of this system has increased the operation safety of SRRC facilities.

VI. References

- [1] Department of Energy, "Accelerator Safety Order, Guidance", (1991).
- [2] T. Dickinson, "Radiation Safety Systems at the NSLS", Proceedings of the 1987 IEEE Particle Accelerator Conference, 1605-1607, (1987).
- [3] Y. Satow, T. Kosuge and T. Matsushita, "Radiation Safety Interlock System for Photon Factory X-ray Beam Lines", Nucl. Instrum. Meth., Sect. A., (1986).
- [4] E. Benson, K. Crook, N. Ipe, G. Nelson, J. C. Liu, J. Cerino, R. Hettel and R. Yotam, "The Personnel Protection System for a Synchrotron Radiation Accelerator Facility : Radiation Safety Perspective", SLAC-Pub-5833, (1992).
- [5] R. C. McCall, W. R. Casey, L. V. Coulson, J. B. Mccaslin, A. J. Miller, K. F. Crook and T. N. Simmons, "Health Physics Manual of Good Practices for Accelerator Facilities", SLAC-Report-327, (1988).
- [6] K. Batchelor, "National Synchrotron Light Source Safety Analysis Report", BNL 51584, UC-28, (1982).

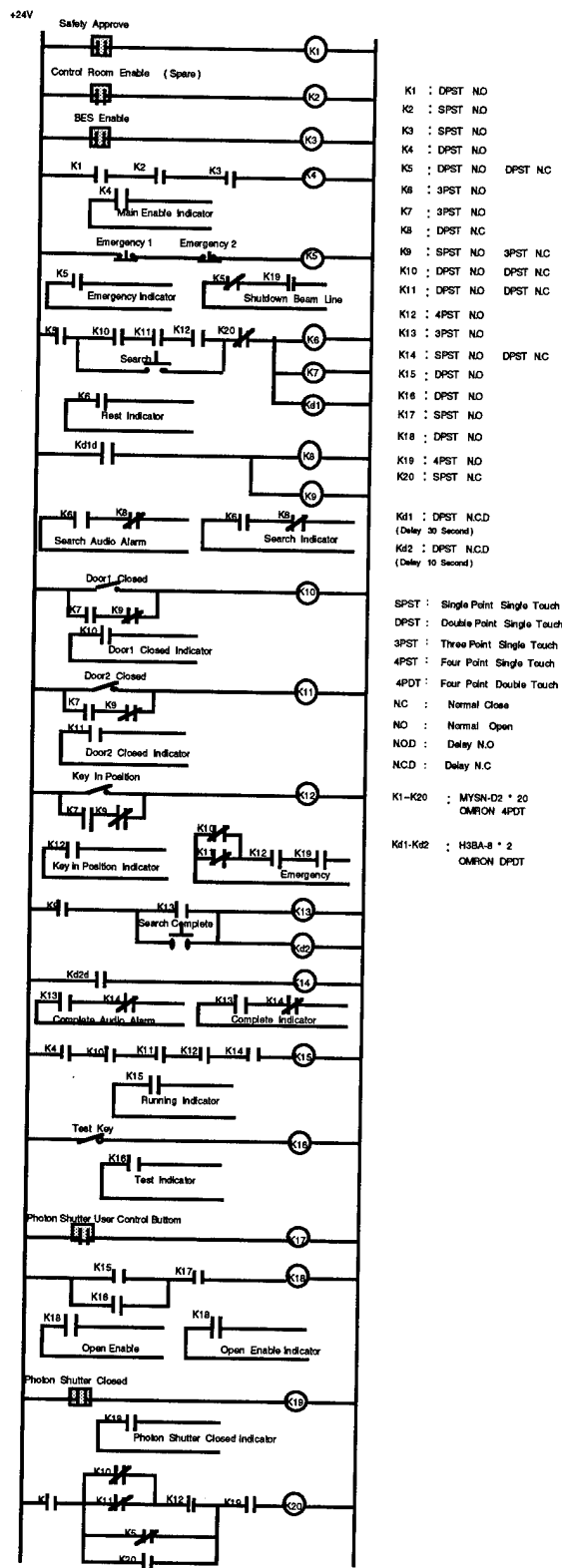


Fig 2 Hutch Interlock System (HIS) electronic circuit

Radiological Protection Policy Aspects Concerning the Preliminary Design and Operation Modus of the Athens RT Microtron Facility

B. Spyropoulos, Institute of Accelerating Systems & Applications
and Technological Education Institution of Athens, Athens, Greece

The 185 MeV Racetrack Microtron under installation in the Athens Institute of Accelerating Systems and Applications has been developed in a joint NIST/LANL project [3], in order to cover the need for CW Electron Accelerators for nuclear physics.

The features of the NIST/LANL RTM allow the use of the accelerator to drive a FEL, as well as, a wide range of applications in irradiation techniques (e.g. material science, radiobiology etc.).

I. THE RACE-TRACK MICROTRON FEATURES

The 185 MeV Racetrack Microtron main parameters are following:

Injection energy	5 MeV
Energy gain per pass	12 MeV
Number of passes	1-15
Output energy	7-185 MeV
Average current	10-550 μ A
Accelerating frequency	2380 MHz
End magnet field	1.0T
Peak current	< 65 mA
Micropulse length	3.5 psec
Micropulse frequency	2380 Mhz
Macroscopic duty factor	1.0
Energy spread	< 40 keV
Normalized emittance ($\beta\gamma\epsilon$)	<10 μ m

The accelerator comprises a 5 MeV Injector connected to a Racetrack Microtron by a 180 degree beam transport system. The Injector consists of an 100 keV, DC Electron Gun followed by a transverse emittance defining system, a Chopping and Bunching stage and a 5 MeV CW Linac.

In the RTM 5 MeV electrons from the Injector are recirculated for up to 15 passes through an 8 m long, 12 MeV, CW Linac for a total energy gain of up 180 MeV.

Microwave power is delivered from a single, 450 kW output cw Klystron (50 kW distribution system, 100 kW in the Injector Linac, 200 kW in the 12 MeV Linac.

The system uses 1.1 MW, of which 9% (100 kW) is converted into beam power [3]. With a floor area 5x16 m² the

RTM is extremely compact. The average beam power at full energy is 100 kW.

II. SITE PLANNING & RADIATION PROTECTION REQUIREMENTS

The Radiological Safety Aspects strongly influence the Site Planning. The major assumptions for the planning of the accelerator vault and the future extensions are following:

- The accelerator vault (9 x 36 m², 7.5 m height) will be buried, taking into account the natural features of the ground.
- Bulky items should be brought into the vault through a concrete (cross section:4x4 m²) radiation protection door, moving on rails. Tracks are approaching through a ramp.
- The RTM will be installed in the first part (9 x 21 m²) of the vault. An experimental hall (9 x 14 m²) will be formed through a removable (equipment radiation protection) modular concrete 1 m thick and 2.5 - 3.0 m high wall, transported by a wall mounted 15 - 25 tn crane.
- At the end of the vault a beam dump and activation experiment space (6 x 3 m², 3 m height) will be formed.
- The connection to the Auxilliary Building, which will include Control, Engineering, Laboratories etc., is done through a labyrinth, having a cross - section of 2 x 2 m². Several shapes of the maze (two, three or four legged) have been examined.
- Cables and pipelines are guided through the maze, which will also enable personnel access and equipment transportation, on behalf of a lift and a staircase.
- The lay - out of the future extension of the IASA including fence - posting, as far as location and orientation is concerned, has been influenced by the shielding needs, since soil will be the main shielding material.

III. MAIN ASPECTS AND POTENTIAL HAZARDS ENCOUNTERED

Concerning radiological safety, following aspects, as well as, potential hazards have been mainly encountered:

- High-energy electron interactions with matter and estimation of the associated radiation parameters.
- Shielding calculations, interlocks and accesibility.
- Components, air, dust and cooling water activation.
- Radiolytic reactions and noxious gases formation.
- Hazards due to potential sources beyond ionizing radiations.

The starting points and the approaching technique are presented for the most important aspects:

A. Electromagnetic cascade.

High - energy electron interactions with matter lead to an estimation of the associated radiation parameters. Relevant for radiation protection purposes at the energy range up to 185 MeV are [11]:

- Secondary photons (Bremsstrahlung)
- Photoneutrons, i.e. giant resonance ($E < 30$ MeV), quasi-deuteron effect ($30 \text{ MeV} < E < 140$ MeV) and photopion channels opening ($E > 140$ MeV).

B. Shielding calculation.

Shielding calculations have been based on the data of Alsmiller and Gabriel [1],[5]. Under the assumption of 2% lost power the first calculations result in following barriers thicknesses, taking into account possible future upgrading:

Structural Element Scheduled Construction

Ceiling	2 m concrete + 4 m soil
Wall (Northern)	11 m soil
Wall (Southern)	10 m soil
Wall (Western)	8 m soil
Door	3 m concrete
Dump (walls)	13 m soil
Dump (ceiling)	12 m soil
Dump (beam-stop direction)	20 m soil

For the design of the maze connecting the accelerator vault and the auxilliary building, the thermal neutron transmission curves of Maerker et al. [8] have been taken into account.

The beam dump will be an Al cylinder [4], filled with Al spheres, fluted by cooling-water and followed by a Cu block.

The expected dose rate, due to neutron skyshine at different distances d from the facility, will be between:

0.5 nSv/h ($d: 500$ m) - 12 nSv/h ($d: 100$ m)

or

0.001 mSv/y - 0.024 mSv/y.

C. Radioactivation by the electron beam.

Radioactivity may be induced in solid components of the accelerator, as well as, in air contained in the accelerator vault, experimental halls etc. and in water of the cooling systems [2],[7]. The most important radioactivity-inducing reactions are the (γ, n) and much less the $(\gamma, 2n)$ ones.

The components to be most suspected for activation are those that absorb most of the beam energy, in particular the beam dumps, targets, magnets and collimators.

For the nuclides relevant for the radiation protection, the corresponding saturation activities [9],[10] are between 22 (Al) and 2000 GBq/kW (Stainless steel). The expected dose-equivalent rates, at 1 m distance from suspicious stainless steel components will not exceed, 0.30 mSv/h, at time of accelerator turnoff.

Activation monitors will be installed near the door (sluice) and other critical points.

The interaction of Bremsstrahlung with air nuclei causes mainly production of radioactive gases above the production threshold i.e. 10.55 MeV, due to giant resonance reactions. These interactions produce mainly O-15 and N-13 in air with 2.1 min and 10 min half-lives respectively [12].

For the facility, in the extreme case of having full power (185 MeV, 0.1 mA) on a high Z target the radioactivity production rate would be approximately 44.4 kBq/s and the corresponding equilibrium radioactivity 37 MBq.

Taking into account the dimensions of the accelerator vault the maximum concentration expected will be aproximately 0.0114 Bq/cm³, since the maximum permissible concentration (MPC) according to the ICRP Recommendation is 0.074 Bq/cm³.

Radioactivity in water is mainly formed by the interaction of Bremsstrahlung, with the O-16 component of, water-cooled targets and beam dumps, as well as in ground water, outside the concrete shielding and especially around the beam dump.

The maximal total saturation activity expected in the primary cooling system, taking into account, that the maximum electron beam power will not exceed 18.5 kW, is expected to be 675 GBq, including 611 GBq of O-15, resulting in locally exposure rates of up to a few mSv/h which may easily be

shielded. The ground water level seems to be much deeper than the critical 11 - 13 m from the surface.

Noxious gases produced by ionizing radiation are ozone (O₃) and nitrogen oxides (NO_x). Ozone is the most toxic and might constitute a health hazard within the radiation room [13].

The saturation concentration of ozone, in the case of no ventilation is proportional to the effective decomposition time and the ozone production rate [6]. The expected saturation activity in the Microtron vault will be approximately five times less than the threshold limit value (0.1 ppm).

IV. ENVIRONMENTAL MONITORING PROGRAMME

Following measurement programme will be set up, in order to ensure an effective environmental monitoring:

- On line photon and neutron site monitoring (14 ionization chambers, several moderated BF-3 counters).
- Personnel and experimental site dosimetry (6LiF/7LiF albedo and polyethylene moderated doseimeters).
- Activation monitoring (locally survey meters, Ge - Multichannel Analyzer).
- Environmental monitoring and sampling system out of fence post.
- Background data acquisition.

A dedicated radiation protection and environmental monitoring laboratory will be provided in the auxiliary building of the Facility.

V. GENERAL SAFETY REQUIREMENTS.

Mechanical Hazards in the facility are related to the planning, installation and operation of overhead cranes, load elevators, machine tools, gas bottles [11], compressed air etc. Further hazards are related with the design and the operation of the massive radiation protection doors and partitions or even with the installation of heavy items, as magnets. Last but not least, cooling water or water processing unit pipelines as well malfunction or inadequate planning in rain-water drainage, could result in flood and an appropriate detection and pumping system should be installed.

Electrical hazards include the ones due to high voltage used in the klystron, the vacuum and beam-line monitoring instrumentation, short-circuit hazards concerning the high

current magnet power-supplies, as well as, the ordinary electrical hazards met in an industrial environment.

Disturbances caused by the high frequency on the RTM signal cables and monitoring equipment (e.g. to ionization chambers, if not RF-shielded), should also be considered.

Closely related to electrical hazards, is the threat of fire and the related fire-protection system of the facility including individual smoke detectors combined with Halon extinguishers, upon each major functional unit or ceiling mounted.

Finally, a general accident limitation operational policy, including all the remaining miscellaneous hazards (chemicals, toxic materials as lead, LASERS, intra-laboratory traffic etc.) should be worked out, on behalf of the architectural and functional features of the facility.

VI. REFERENCES

- [1]. Alsmiller R.G.Jr., Moran H.S., Electron - Photon Cascades Calculations and Neutron Yields from Electrons in thick Targets, ORNL-1502, 1967.
- [2]. Barbier M., Induced radioactivity, North-Holland, Amsterdam & John Wiley, New York, 1969.
- [3]. Debenham P.H. et al., The NIST/NRL Free Electron Laser facility, SPIE Vol. 1133 FEL II, (1989), 89.
- [4]. Dimmer D., Entwurf der Strahlfaenger fuer MAMI B, Diplomarbeit, IFK, J. Gutenberg Univ. Mainz, 1988.
- [5]. Gabriel T.A., Lillie R.A., Bishop B.L., Shielding Considerations for the 750 MeV Electron Accelerator at the University of Illinois, ORNL/TM-10036, 1986.
- [6]. George A.C. et al., Evaluation of the hazard from radioactive gas and ozone at Linacs, Brookhaven National Laboratory, USAEC, Rep. CONF-651109, (1969), 539.
- [7]. Fasso A. et al., Radiation problems in the design of the LEP, CERN 84-02, 1984.
- [8]. Maerker R.E., Clairborne H.C., Clifford C.E., Neutron attenuation in rectangular ducts, in: Engineering Compendium on Radiation Shielding, Vol. I, Springer Verlag, N. York, 1968.
- [9]. Saxon G., Radioactivity induced by high energy electrons, Rad.Prot.Acc.Envir., Proc.Conf.Rutherford Lab., Oxon, 1969.
- [10]. Stabler (de) H., Photon induced residual activity, SLAC, Report TN-63-92, 1963.
- [11]. Swanson W.P., Radiological safety aspects of the operation of electron linacs, TR-188, IAEA, Vienna 1979.
- [12]. Vialettes H., Gas and dust activation in the target room of the Saclay Electron Linac, Proc. 2nd Int. Conf. Acc.D osim. Exper., SLAC Rep. CONF-681101, 1969, 121.
- [13]. Willis C., Boyd A.W., Young M.J., Radiolysis of air and nitrogen - oxygen mixtures with intense pulses: determination of a mechanism by comparison of measured and computed yields. Can.J.Chem. 48. (1970). 1515.

SLAC SYNCHRONOUS CONDENSER

C. Corvin, Stanford Linear Accelerator Center, Stanford University, Stanford, CA 94309 USA

Abstract

A synchronous condenser is a synchronous machine that generates reactive power that leads real power by 90 degrees in phase. The leading reactive power generated by the condenser offsets or cancels the normal lagging reactive power consumed by inductive and nonlinear loads at the accelerator complex. The quality of SLAC's utility power is improved with the addition of the condenser. The inertia of the condenser's 35,000 pound rotor damps and smoothes voltage excursions on two 12 kilovolt master substation buses, improving voltage regulation site wide. The condenser absorbs high frequency transients and noise in effect "scrubbing" the electric system power at its primary distribution source. In addition, the condenser produces a substantial savings in power costs. Federal and investor owned utilities that supply electric power to SLAC levy a monthly penalty for lagging reactive power delivered to the site. For the 1993 fiscal year this totaled over \$285,000 in added costs for the year. By generating leading reactive power on site, thereby reducing total lagging reactive power requirements, a substantial savings in electric utility bills is achieved. Actual savings of \$150,000 or more a year are possible depending on experimental operations.

I. INTRODUCTION

Prior to May 1989, monthly electrical power billing at the Stanford Linear Accelerator Center (SLAC) included charges for energy and peak demand but no charges for power factor. The power factor in May 1989 was 0.79 and a penalty of \$1,850 was assessed. It was clear at that time that the penalty would go much higher. A project was initiated to correct the site's power factor using fixed nonswitching capacitors. The objective was to correct the SLAC base load power factor. By March 1990, the time the fixed capacitor project was approved, installed, and operational, the monthly power factor penalty had grown to \$31,600. The addition of the fixed capacitors immediately reduced the monthly penalty to a monthly average of \$13,800. With the capacitors operational, a second and more aggressive stage of power factor correction was initiated to correct the variable component of site loading above base load. This paper describes the SLAC synchronous condenser, a project approved in July of 1992, and made operational in June of 1994.

II. PROJECT OVERVIEW

Circuit analysis of the SLAC utility system from the previous capacitor project indicated that the base load power factor capacitor would be resonant at close to the eleventh harmonic of the fundamental of 60 hertz. Measurements following actual operation of the capacitor confirmed the previous circuit analysis. This analysis was again used for the synchronous condenser. The site base load was taken as 26 megawatts with the site peak load taken as twice that at 52 megawatts. To be cost effective the variable portion of the new power factor correction needed to achieve at least 0.90 power factor at 52 megawatts. A leading reactive source of 10 megavolt-amperes was necessary.

A rotating machine was selected as opposed to a system of thyristor-switched capacitors so as to reduce and attenuate switching transients and to also improve voltage regulation. Site load variations are comparatively slow as are existing 12 kilovolt voltage regulator tap changes. The 10 megavar rotating machine is a good match to the existing SLAC utility power system which has response times to slow voltage changes in the 10 second range. Fast voltage excursions on the 12 kilovolt substation bus see some degree of attenuation in the iron and windings of the machine but are otherwise ignored by the slower condenser power factor control system.

Existing master substation 12 kilovolt bussing and circuit breakers, as well as physical site building constraints, require that the machine be located near the SLAC master substation control building. To reduce costs, existing circuit breakers and a relocated portable building are used for the condenser and auxiliary systems. The 510 square foot portable building is designed to be lowered over the condenser to gain a substantial savings over fixed building costs. The condenser's 12 kilovolt circuit breaker and its potential transformers were located in a small new 150-square-foot building adjacent to the portable building.

The condenser is located in a region classified as a seismic zone 4 near the San Andreas fault. The foundation design for the 84,000 pound machine requires a three-foot thick concrete and steel base over undisturbed sandstone. The initial base level is to within 0.024 inches, end to end, along the rotor shaft. Three axis vibration sensors on the machine are designed to shut down the condenser during seismic events that exceed a 0.00375 inch excursion along any axis. Typical operating vibration is 0.0008 inches peak to peak.

III. TECHNICAL

The synchronous condenser is a 10 megavar, 12.47 kilovolt, 3 phase, 60 hertz, 900 rpm, wye connected machine with a solid state exciter mounted on the rotor shaft. The condenser is started with a 200 horsepower, 480 volt, 3 phase, 60 hertz, 1200 rpm induction motor driven by a pulse width modulated variable speed drive. The main rotor shaft is horizontal and is supported at each end by journal bearings with the exciter and starting motor on opposite ends directly coupled to the main shaft. A low pressure, low volume oil lubrication system pumps oil to the bearings. A 1200 psi high pressure oil system lifts the 35,000 pound main shaft to start the condenser from rest. The condenser is microprocessor-controlled for all functions.

Starting and synchronizing are accomplished without operator intervention. As the machine approaches synchronization, the starting drive motor overspeeds the condenser and then allows it to drift down through synchronous speed. Should the speed change, slip, be excessive, synchronizing is blocked and the rotor is accelerated again but with less energy added. The process repeats until slip is low enough to insure lock-in without pullout. The exact moment of pull-in is computed and considers the breaker contact travel time. The condenser motors when first energized. Only enough field current is present to insure pull-in. As a consequence, starting the condenser produces no discernible electrical system disturbances at the site. The total time for run-up and synchronizing is just over 6 minutes. A controlled shutdown requires 50 minutes to achieve a full stop and 15 minutes if the pulse width modulated starting drive is used for braking.

SLAC 12.47 kilovolt utility busses, numbers one and two, provide reference phase angle information to control the condenser. A desired power factor operating point of 0.90 is preset for a typical site load of 52 megawatts. A comparator circuit in the condenser power factor controller measures actual and preset power factors then produces a dc signal level that controls the condenser field and voltage regulators. The time constant for this control is a factor of 10 faster than the site 12 kilovolt distribution system voltage regulator so as to isolate site voltage control from site power factor control.

IV. SITE POWER QUALITY

Because revenue operations have taken priority over operations analysis, only a small number of samples to compare and evaluate utility waveform improvements have been taken. However, in all cases, the quality of the utility power has been better with the condenser operating than without it operating. Measurement to measurement differences have been attributed to site loading changes that alter the harmonic content of the waveform. The greatest changes are in the current waveforms which vary widely with various combinations of rectifier loads at the site. Table 1 describes a sample of condenser effects on the site utility waveforms.

	Without Condenser	With Condenser
% THD Voltage Neutral to Ground	40.7	39.6
% THD Current A Phase	44.0	1.0
% THD Voltage A Phase to Neutral	1.4	1.3

Table 1: Percent total harmonic distortion compared, with and without the synchronous condenser operating.

V. AVOIDED POWER COSTS

Operation of the synchronous condenser reduces power factor penalties by generating expensive kilovars from relatively inexpensive kilowatts. A typical kilowatt at SLAC is purchased for \$0.03 per kilowatt whereas depending on the power factor a kilovar can cost as much as \$1.38 per kilovar per kilowatt demand. The condenser has no flywheel or end shaft load so its primary load is windage. The machine moves 30,000 cubic feet of air a minute for cooling with a power consumption of only 150 kilowatts. It generates 10,000 kilovars at full output and will go to 11,500 kilovars for peaking on margins.

The Western Area Power Administration Rate Order 59 [1], distributes power factor penalties as indicated in Table 2. This table also notes the SLAC power factor level before and after the synchronous condenser project.

WAPA-59		SLAC pf
Power Factor	\$ Rate kvar/kw	Level
0.95	\$0.00	Jan '95
0.94	\$0.09	
0.93	\$0.17	
0.92	\$0.24	
0.91	\$0.32	
0.90	\$0.39	
0.89	\$0.46	
0.88	\$0.53	
0.87	\$0.60	
0.86	\$0.66	
0.85	\$0.73	Jun '92
0.84	\$0.79	
0.83	\$0.86	
-	--	
0.75 & below	\$1.38	

Table 2: WAPA rate order 59 [1], with SLAC power factors for Jan '95 and Jun '92.

During the months of November and December 1994, and January 1995, SLAC's average monthly power factor penalty, at 0.90 power factor and 47.4 megawatts, was \$18,486 per month with the synchronous condenser in full revenue operation. Site power factor in June, July, and August of 1992 was between 0.83 and 0.84. The 0.83 power factor of 1992 at today's WAPA rates would generate a power factor penalty of \$40,764 for 47.4 megawatts. Actual average monthly savings at SLAC in early 1995 have been just over \$20,000 a month during SLC operations with a polarized beam.

The total synchronous condenser project cost is \$686,971. For 10 months of full laboratory operation each year, the simple payback is 3.43 years. Maintenance costs are minor, being primarily for spectral analysis of oil and for vibration samples. Since the main shaft spins unloaded, the bearings will have long lifetimes with only infrequent maintenance.

VI. UPGRADES

With the operation of PEP-II loads beginning sometime in 1997, peak electrical demand at SLAC will exceed 70 megawatts. Additional power factor correction will be needed at that time. Based on experience thus far, either fixed or variable power factor correction can be employed.

VII. ACKNOWLEDGMENTS

I thank Pat Kobe and Don Lee for their superb technical support, especially during the start-up and run-in of the condenser. Also deserving thanks is Len Risse whose helped with the auxilliary systems, especially the oil system. Pran Kaul provided seismic expertise, rigging direction and designed the condenser foundation. The project combined the talents of many additional persons from a variety of disciplines. I thank them all.

VIII. REFERENCES

- [1] Western Area Power Administration, *Central Valley Project Notice of Rate Order* No. WAPA-59 (July 2, 1993). Federal Register, vol. 58, no. 126, pp. 35948-35949.

Printed-Circuit Quadrupole Design*

Terry F. Godlove, FM Technologies, Inc., Fairfax, VA
Santiago Bernal and Martin Reiser, University of Maryland, College Park, MD

I. INTRODUCTION

A printed-circuit quadrupole has been designed for low-energy electron beam research in the Institute for Plasma Research at the University of Maryland. Previously, solenoid focusing has been employed. Quadrupoles will allow more realistic beam studies to be performed in straight beams, and are necessary for a ring geometry currently under consideration. Applications include high-current, high-energy accelerators and heavy-ion inertial fusion.

Based on the quadrupole design, a scaled-up prototype has been built and the field measured. In this report we describe the design procedure and the measurements. The conductor geometry is similar to that described by Avery, Lambertson and Pike for printed-circuit steering coils [1]. Our goal was a very short quadrupole (length = diameter) for low fields, <30 G, but with good precision and linearity.

For such short quadrupoles the fringe fields dominate the behavior. Integrals of the field parallel to the z-axis must be used to check the linearity rather than the field itself. Also, attention must be paid to the external connections.

Three desktop computer programs were used in the design: (1) a spreadsheet to set up formulas which determine conductor location based on a few key input parameters and an algorithm; (2) a 3-D magnetics program to study the linearity of the magnetic field integrated along lines parallel to the beam axis at various radii, and (3) a CAD program to provide the file required by the printed-circuit fabricator. To save time in searching for optimum parameters, the spreadsheet program is designed to automatically generate the appropriate file needed for the magnetics program. It also generates the file required by the CAD program.

All of the conductors lie on the surface of a cylindrical mount concentric with the beam pipe. The printed circuit is made flexible to conform to the cylindrical mount.

II. DESIGN

The widely known method--using a current distribution that follows a $\cos(n\theta)$ distribution, where $n=2$ for a quadrupole and θ is the azimuthal coordinate--does not apply here. It applies when the active conductors have equal length. For a short, compact quadrupole the inactive return conductors should lie in planes perpendicular to the beam axis. Thus a practical quadrupole must employ gradually shorter active conductors. This leads to a small increase in current density with increasing angle rather than the normal cosine-like decrease, in order to compensate for the short conductors. This was recognized by Avery *et al* [1]. Their results encouraged us to apply the same ideas to quadrupoles.

A detailed analytical approach for conductors which require smooth bends at the coil ends (e.g., superconducting wire) has been given by Laslett, Caspi and Helm [2]. Our approach is to adopt a simple algorithm for our square-cornered geometry and search for a solution with the 3-D magnetics code. We chose twenty conductors for each 45° segment, sufficient for good linearity yet small enough for practical fabrication.

Coil Geometry

Figure 1 shows our final geometry, as printed by the CAD program. Four coils are shown, two on top and two on the underside of a thin, flexible insulating base. These represent half of the quadrupole, i.e., 0-180°. The other half, 180°-360°, is identical. Each coil has 20 turns and 40 active conductors--parallel to the axis--and 40 return, arc-shaped conductors in planes perpendicular to the axis. There are 640 conductors, all in series. The eight coils employ four different connections, arranged for minimum stray field due to the external leads and interconnections. This can only be done using both sides of the plastic base. Also, use of both sides doubles the magnetic field.

We adopted equal spacing for the return conductors. Linearity is optimized using the algorithm described below to locate the active conductors.

Computer Programs

The spreadsheet program has several major functions. Input parameters are the coil radius, R , axial length, L , the return conductor spacing, ΔL , and the spacing between the first two active conductors, $\Delta\theta$. The remaining active conductors are located using

$$\theta_{n+1} - \theta_n = \Delta\theta / (1 + \theta_n^2/k) \quad (1)$$

where $n=1$ to 20, $\theta_1 = \Delta\theta/2$, and k is an adjustable constant.

We studied the magnetic fields using the 3-D, iron-free magnetics program MAG-PC, a product of the Infolytica Corporation. The required input ASCII file which gives the location of all of the conductors is generated automatically in the spreadsheet. An additional parameter is required: the number which the magnetics program uses to divide up the arcs into straight segments for computation. We used 10 segments for trial runs and 16 segments for final runs.

It should be noted that, while Fig. 1 shows the connections required for a continuous coil, the field calculations are based on a series of interlocking rectangles. To obtain the CAD drawing one corner of every rectangle is shortened so that it connects to the adjacent inner rectangle. We expect the error introduced in this way to be negligible.

* Supported by the US Department of Energy.

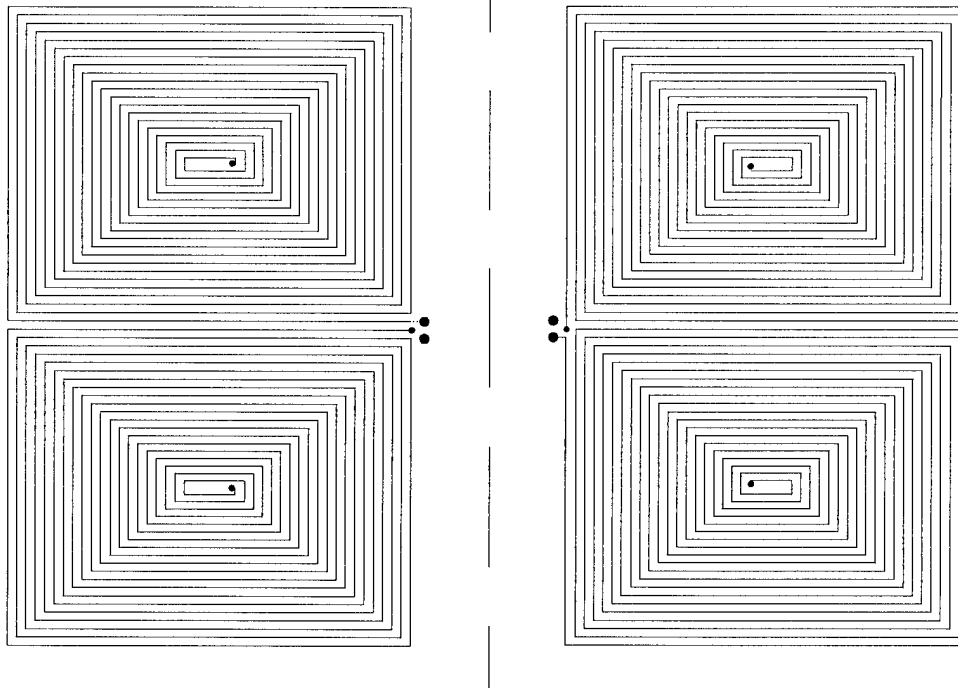


Fig. 1. Upper side (left) and underside (right) of the double-sided printed circuit. The beam axis is horizontal. One-half (0 to 180°) of the circuit is shown. The other half (180° to 360°) is identical. The dark spots are feedthrough connections. The external twisted pair is connected to the two largest spots.

The magnetics program computes the Biot-Savart law to calculate B_x , B_y and B_z for each line and segment of arc. The output B_y is summed to obtain the z-scan integral.

The final program is a CAD program, AutoSketch for Windows, from Autodesk, Inc., to generate the file--known as a .DXF file--given to the printed circuit fabricator. The entire file is programmed into the spreadsheet and generated automatically based on the input parameters. Separate files are required for the two sides because of the different end connections.

III. RESULTS

Table I shows the field integral results for the parameters found to yield the best linearity for a scaled-up quadrupole with $L = 2R = 100$ cm. Specifically, $k = 3.0$, $\Delta L/L = 0.023$, and $\Delta\theta = 2.34^\circ$. The scans are taken along lines parallel to the z-axis, at five radii and three polar angles.

Table I -- Deviations from Linearity for Scaled Coil
(100-pt. z-scan, 16-segment arcs, 3-digit output file)

Polar Angle	Relative Gradient	-----Deviations in % for $r/R =$ -----				
		0.2	0.4	0.6	0.7	0.8
0	558.1	-0.11	-0.10	+0.21	+0.58	+1.49
30°	557.4	+0.03	+0.08	-0.12	-0.33	-0.58
45°	557.3	+0.03	+0.02	-0.05	+0.17	+0.70

The relative field gradient at each angle (corrected for the angle) is the average of the gradients for the first three radii, i.e., $r/R = 0.2$, 0.4 , and 0.6 . Deviations from the average gradient at each angle are given in percent.

Computational accuracy in MAG-PC was checked by increasing the number of scan points, the number of segments used for the return arcs, and the number of decimals used in the output files.

The results indicate a deviation from linearity $<0.6\%$ for radii up to $r/R = 0.7$. Runs with slightly different parameters indicate the sensitivity. For example, scans performed with $k = 2.7$ and 3.3 gave deviations up to 1.4% for $r/R < 0.6$ and 3.3% for $r/R = 0.8$. Similarly, runs varying $\Delta\theta$ and $\Delta L/L$ indicate sensitivity of about 0.03° and 0.01 , respectively.

Prototype Quadrupole

A scaled model with radius $R = 12.8$ cm was built to check the calculations. A Hall probe was used to make z-axis scans at four different radii, $r/R = 0$, 0.2 , 0.4 and 0.6 . The vertical component of the earth's field was balanced with large Helmholtz coils and corrections were made for the small x-component. Care was taken in probe positioning and zero drift of the gaussmeter. A typical z-axis scan is shown in Fig. 2. The agreement between MAG-PC calculations and measurements is excellent.

Measurements indicated that the mechanical axis and the magnetic axis were coincident within about 1 mm. No

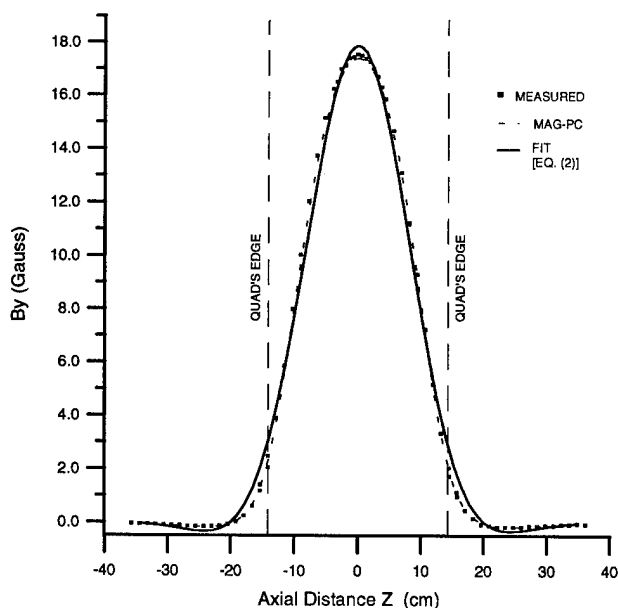


Fig. 2. Axial scan of prototype magnetic field B_y at $r=7.62$ cm ($r/R=0.60$), $\theta=0$ and $I=10$ A.

evidence was found of significant differences between the magnetic fields produced by the spiral geometry of Fig. 1 and the concentric-rectangle geometry used in MAG-PC.

Finally, the calculated transverse field $B_y(z)$ was fit to an analytical expression whose parameters were adjusted for optimum linearity of the axially-integrated magnetic field at four radii. The resulting empirical function is

$$B_y(r,z,\theta) = (B_0 r/a) \exp(-z^2/2\sigma^2) \cos(2\pi z/\lambda) \cos\theta \quad (2)$$

where $B_0/a = 2.34$ Gauss/cm, $\sigma = 10.2$ cm, and $\lambda = 80$ cm for the prototype. When these quantities are scaled to the printed-circuit quadrupole (quad radius/prototype radius = 0.172) we get $B_0/a = 7.93$ Gauss/cm, $\sigma=1.75$, $\lambda=13.75$ cm, and $I=1$ A. Eq. (2) is particularly useful for future particle-in-cell code simulations. Eq. (2) can be integrated using the expression below.

$$\int_{-\infty}^{\infty} \exp(-z^2/2\sigma^2) \cos(2\pi z/\lambda) dz = \sigma(2\pi)^{1/2} \exp[-2\pi^2(\sigma/\lambda)^2]$$

Lattice Design

For the final quadrupole we chose $L = 2R = 4.4$ cm to conform to our normal aperture. The integrated field from MAG-PC is 11.1 G-cm per Ampere at $r = 0.44$ cm, equivalent to a gradient of 7.93 G/cm for a 3.19-cm effective length, square-edged quadrupole. These values were then compared with solutions of the envelope equations for a space-charge dominated beam in a FODO lattice. For this purpose we used a convenient program developed by one of us for studying heavy-ion recirculating induction linacs [3].

For a moderately high beam current of 100 mA at 10 keV (generalized perveance = 1.5×10^{-3}), a normalized emittance of 8 mm-mrad, and a zero-current phase advance of 76° , a solution of the envelope equations is obtained with a

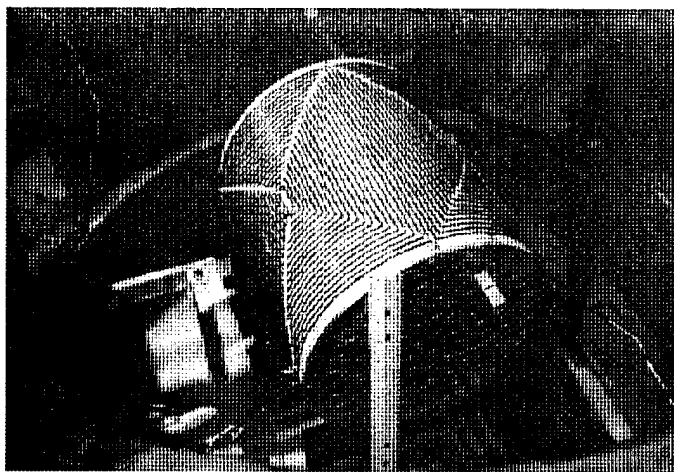


Fig. 3. Photograph of 25.6-cm diam prototype.

mean beam radius of 0.9 cm, depressed phase advance of 9° , and a half-lattice period of 15 cm. The quadrupoles occupy 29% of the axial space for this lattice. The beam clearance factor (aperture radius/mean beam radius) is 2.1. The solution is a compromise between the desire for a long lattice length and the desire to have a somewhat larger depressed phase advance.

Fawley *et al* studied space-charge dominated transport in large-aperture-ratio quadrupoles [4]. They found very little emittance growth for a well-matched beam when the beam radius/half-lattice-period < 0.1 . Our ratio, 0.06, satisfies this criterion.

The required gradient for the above solution is 9.4 G/cm, which means that the quadrupoles should be operated at 1.2 A circuit current, taking into account the factor of two from the double-sided circuit. From tables supplied by the printed-circuit fabricators, this will produce a temperature rise of about 15° C in the circuit for "2-ounce" copper plating. If necessary, the quadrupole can be pulsed.

A separate, general issue that must be faced is the use of low magnetic fields in the presence of stray fields and the earth's field. A combination of cancellation coils, magnetic shielding and precise steering corrections should be sufficient.

We thank A. Faltens for pointing out the 1971 LBL reference, L.K. Len for assistance with the computer programs, and J.G. Wang and W.M. Fawley for discussions.

- [1] Robert P. Avery, Glen R. Lambertson and Chester D. Pike, Proc. 1971 Part. Accel. Conf., p 885.
- [2] L. Jackson Laslett, S. Caspi and M. Helm, Particle Accelerators **22**, 1 (1987).
- [3] T.F. Godlove, Particle Accelerators **37-38**, 439 (1992).
- [4] W.M. Fawley, L.J. Laslett, C.M. Celata, A. Faltens and I. Haber, IEEE Cat. 93CH3279-7, 724 (1993).

MICROPROCESSOR CONTROLLED FOUR-AXIS GONIOMETER

A. Bortnyansky, M. Klopenkov, M. Pavlovets, M. Svinin
Efremov Research Institute of Electrophysical Apparatus, P.O. Box 42, 189631 St.
Petersburg, Russia

P. Kovach, J. Dobrovodsky
Department of Nuclear Physics and Technology Faculty of Electrical Engineering,
Slovak Technical University, 812 19 Bratislava, Slovak Republic

A four-axis vacuum goniometer for application in ion beam channeling is described. It has three axis of rotation and one translation stage for movement in horizontal direction. The error reproducibility has been found to be less than one step. The microprocessor controlled goniometer is driven by vacuum stepper motors that are located within the vacuum chamber. The control of four stepper motors may be executed either from the front panel of control unit or from the host computer across the serial port. The sample can be heated up to 900° C.

I. INTRODUCTION

To investigate the location of impurity atoms and nature and depth distribution of lattice disorder channelled Rutherford backscattering spectrometry (RBS) is widely used technique [1]. An use of the channeling effect impose the certain requirement both on the divergence of ions beam and on the precision orientation of the studied crystal target. Moreover, one must be able to vary the position and the orientation of the sample during the experiments within a wide angle range. Therefore a goniometer must be used which combines a wide angular range with the ability to move in very small steps about rotation axes. It is also important to execute all manipulation with crystal in automatic mode. The above considerations have led us to the design the microprocessor controlled goniometer described in the following.

II. THE GONIOMETER MECHANISM

A schematic diagram of the four-axis goniometer is shown in fig.1. The goniometer includes three independent motor driven angular rotations and one transverse Y-translation of the target stage. It is also necessary to allow for movement to another spot on the sample surface if damage occurs as a result of the irradiation.

The goniometer occupies the space of 240 mm diameter with height of 240 mm. It is mounted vertically on the bottom flange of a target chamber. The distance of the centre-line of the three axis from the top surface of the bottom flange is 185 mm. The vacuum stepper motors with the step of 3 deg. are placed inside a vacuum chamber. For the ease of installation of each axis and the inspection of the functionality and precision of the mechanical parts the reference scales for each movement are provided.

The first rotation takes place about the vertical axis Z, indicated in fig.1 by angle α and has the range of -10 to +70 deg. with a step of 0.004 deg. The stepper motor M1 drives the sample holder around Z-axis via two pairs of spur gears (Fig. 1, position 2 and 3) and worm and wheel assembly. These gears displace the motor rotation axis and the worm and wheel assembly (pos. 4) then drives the body of goniometer head (pos.17) around the Z-axis directly. The gear ratio of the reduction gear (pos. 2,3,4) is 750.

The second rotation, angle in the fig. 1, involves a tilt of target about the Y-axis and has the range of -20 to + 90 deg. with respect to the vertical with a step of 0.006 deg. The drive from stepper motor M2 to the Y-axis is realised via the worm and wheel assembly (pos. 6) and the pair of displacement spur gears (pos. 5). The gear ratio of the reduction gear (pos. 5,6) is 540.

The third rotation occurs about the surface normal (the azimuth angle β) and has the range of 360 deg. with a step of 0.028 deg. The sample is pivoted around X-axis by the stepper motor M3 through the worm and wheel assembly (pos.7) with the gear ratio of 108.

Besides the rotations there is a possibility for shifting the sample along the horizontal axis Y. This movement is implemented by means of the stepper motor M4 through the micrometer screw (pos. 8). One can shift the sample in this horizontal direction over a distance of 25 mm with a step of 0.004 mm and with an accuracy of 0.01 mm.

The accuracy of the reading and setting with aid of indicated scales for axes Z and Y have the magnitude not a worse than 0.025 deg. and for X-axis has one not a worse than 0.05 deg.

One sample with the diameter up to 80 mm or 21 samples of 10x10 mm² may be placed on the target holder. However, as comes out of possible horizontal motion, only the circle of 50 mm diameter can be investigated. The goniometer construction allows also another type of target holder to be used if necessary. For instance, to heat the sample the target holders with direct resistive heating are used. The sample with size up to 20 mm may be placed on those type of holder. The temperature to which a sample may be heated is limited by the heat loss from the oven and sample to its surroundings and may be reached up to 900 °C.

To compensate for difference in target thickness the additional manual control is included. This adjustment can be as large as 9 mm.

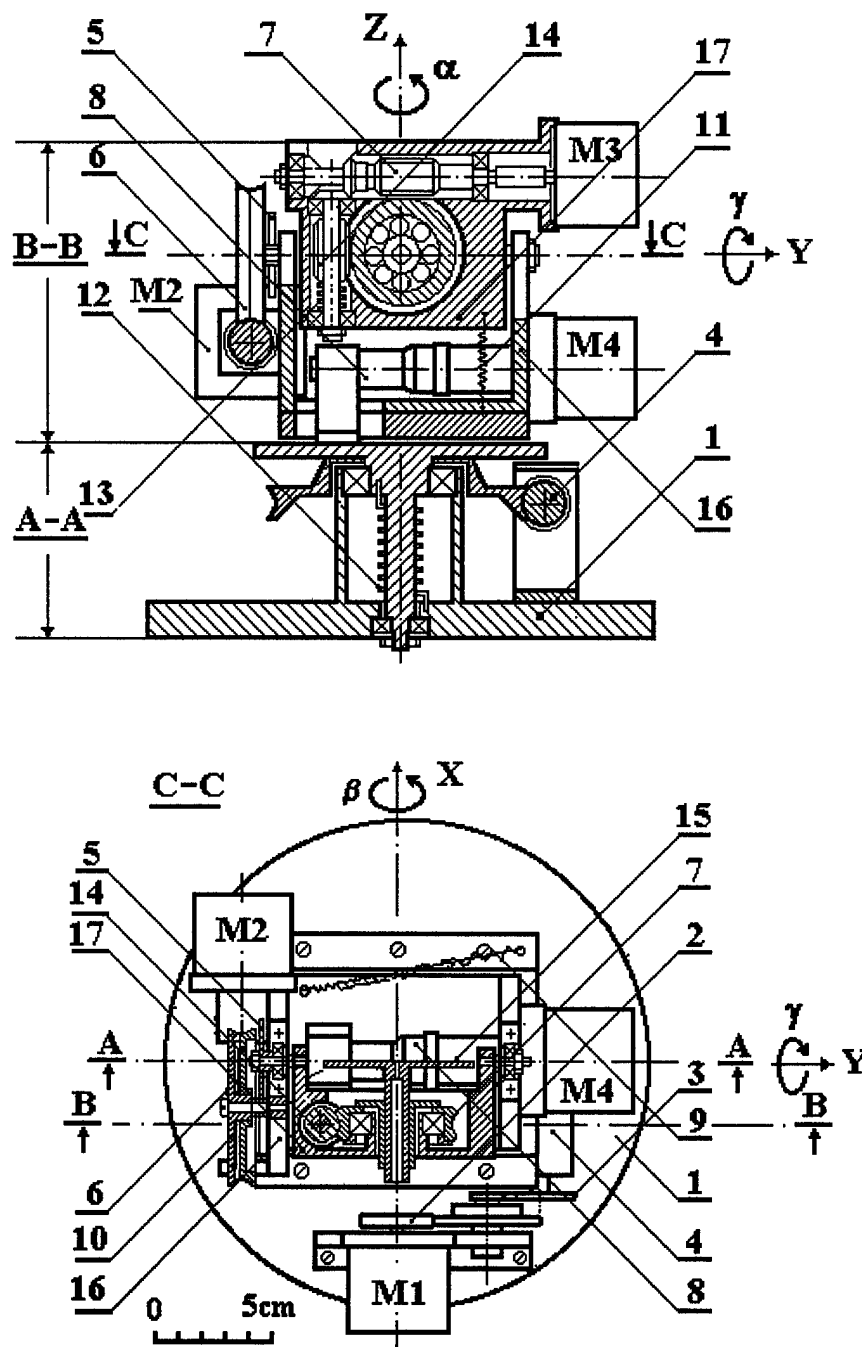


Fig. 1. Schematic diagram of the goniometer.

M1, M2, M3, M4 - stepper motors; 1 - the basis of the goniometer; 2 and 3 - two pairs of spur gears; 4 - worm and wheel assembly; 5 - displacement spur gears; 6 - worm and wheel assembly; 7 - worm and wheel drive; 8 - micrometer screw; 9, 10, 11, 12, 13 - anti-backlash springs; 14 - anti-backlash worm; 15 - target holder; 16 - basic support bracket of goniometer head; 17 - body of goniometer head.

All construction parts of the goniometer including ball bearings are made of stainless steel, the gears and worm wheels are made of bronze. As a gear lubricant the molybdenum disulphide is used.

III. CONTROL UNIT AND TEST RESULTS

To control the four stepper motors of goniometer the microprocessor based control unit was designed. Motors may be selected and operated either from the front panel switches or from host computer across the serial port, i.e. the control unit based on autonomy microprocessor performs the all control and exchange operation [2]. That kind of solution enable one to simplify the control algorithm of goniometer and to organize easily the inspection of the motors temperature, the the motors movement in the given limits, the display of angle and translation magnitudes, the connection with host computer.

Single-step or multiple-step operation with a controlled acceleration, retardation and preset repetition numbers are available. For the sake of excluding the error condition during the control of goniometer and to keep the axes co-ordinates in the storage there is the non-volatile memory and data protections in case of power turn off or any of supply voltages decreases under the limiting level. To exclude the data losses in case of power failure the check of data integrity and authenticity in internal RAM of control unit is carried. The setting of the initial co-ordinates is fulfilling from the front panel with the aid of automatic time switch within limits 0 and 9999 steps.

In the manual mode the all function of control unit is supported by the monitor subprogram stored in the internal ROM of control unit. The subprogram carries out a display on the indicators the co-ordinates and the state of the control unit. The operation beginning of selected motor is taking place only after the special command.

The remote control set up with the suitable switch on the front panel. In this mode the host computer is able to read the memory contents of control units and to set the rotation direction and the step number of acceleration and operating of the motor and also to put the selected motor into the operating and the stopping.

The reproducibility of the goniometer, developed for the target chamber of Ion Beam Laboratory at STU (Bratislava) [3], were tested by an optical method using a diode laser fixed on target holders. These measurements showed, that the settings on all three axes were reproducible to less than one step.

IV. CONCLUSION

The near surface analysis technique of RBS combined with channelling demands the user of a goniometer with a wide angular range that is also capable of being moved over small angles in an accurate series of steps. The microprocessor controlled goniometer described here fulfils these requirements. The goniometer construction allows to

investigate the samples with the diameter up to 80 mm or up to 20 mm with the heating.

This work has been supported by VAM Ltd (Bratislava, Slovak Republic).

REFERENCES

- [1] W.K. Chu, J.W. Mayer, M.A. Nicolet, Backscattering spectrometry (Academic Press, New York, 1978).
- [2] T. Kenjo, Stepping motors and their microprocessor controls (Clarendon Press, Oxford, 1984).
- [3] P. Kovach, M. Pavlovich, J. Dobrovodsky, Nucl. Instr. and Meth. B 85 (1994) 749-751.

OPTICALLY INDUCED SURFACE FLASHOVER SWITCHING FOR THE DIELECTRIC WALL ACCELERATOR*

S. Sampayan, G. Caporaso, B. Carder^{a)}, M. Norton, D. Trimble, Lawrence Livermore National Laboratory, Livermore, CA 94551 USA, and J. Elizondo^{b)}, Tetra Corporation, 3501 Hawkins Street NE, Albuquerque, NM, 87131 USA

Fast, low jitter command triggered switching is key to the successful implementation of the dielectric wall accelerator (DWA). We are studying a UV induced vacuum surface flashover switch for this purpose. We present our initial data using a Nd:YAG ($\lambda=1.06$ nm) laser incident onto a high gradient insulator surface at 1ω , 2ω , 3ω , and 4ω . Best 1σ jitter was <1 ns with no degradation of the switch after 500 shots.

I. INTRODUCTION

The dielectric wall accelerator (DWA) is a new accelerator concept particularly suited for short pulse (<10 ns) and high currents (>1 kA) [1]. A pulsed acceleration field is developed by a series of asymmetric Blumleins (i.e., pulse forming lines) incorporated into the insulator structure (Fig. 1). Combined with new high gradient vacuum insulator technology, short-pulse-high-gradients of greater than 20-30 MV/m may be possible [2,3].

The asymmetric Blumlein consists of two stacked pulse forming lines of different transit times (i.e., differing permittivities, ϵ_r) and ideally, of equal impedances (Fig. 2). When the conductor in common with both lines is charged to potential, V_0 , and shorted at the end opposite the accelerator beam tube, two reversed polarity wavefronts in each line move at velocities proportional to $\epsilon_r^{-0.5}$ toward the beam tube. For a fast pulse line length of time, τ , and a slow pulse line length of time, 3τ , an energy gain of $2V_0$ occurs across a single Blumlein structure into a matched beam load over the interval τ to 3τ .

For short pulse applications, fast, low jitter switching is required to preserve usable pulse width. Further, the switch must be capable of gradients at least comparable to that of the main accelerator structure. Potential technologies which

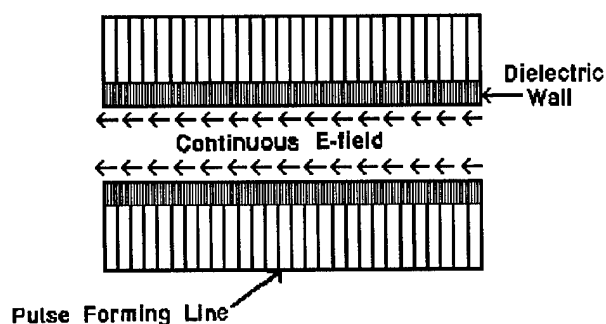


Figure 1. Dielectric Wall Accelerator (DWA).

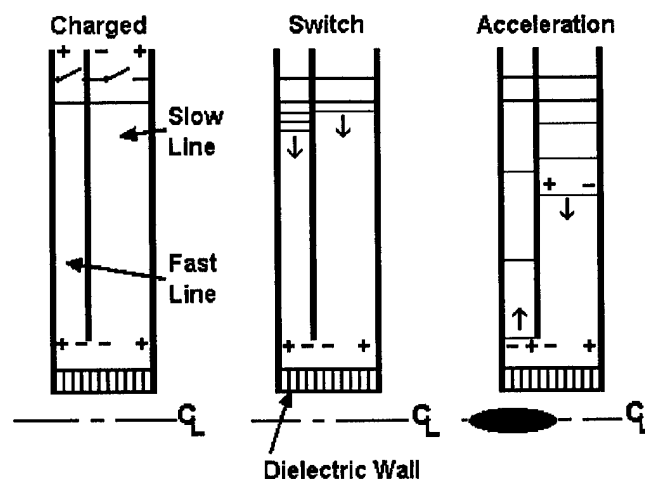


Figure 2. Asymmetric Blumlein operation.

meet this requirement include photo-conductive or electron beam induced solid-state switching (particularly those based on diamond films), high pressure gas, and liquid dielectric switches.

For the near term, vacuum surface flashover switching appears the simplest to implement. Such a switching technique relies on the initiation of a fast high current vacuum surface discharge on a moderately stressed insulator. Earlier work by others using field distortion triggering showed low jitter (order 1 ns) [4]. High current rate of rise ($dI/dt > 10^{13}$ A/s) appears possible based on data from surface flashover

*Performed under the auspices of the US Department of Energy by Lawrence Livermore National Laboratory under contract No. W-7405-Eng-48.

a)Consultant.

b)Present affiliation: Voss Scientific, 416 Washington Street NE, Albuquerque, NM 87108.

discharges [5]. Further, high gradients are possible with new insulator technology [2,3]. We present our initial results here.

II. APPARATUS

A diagram of the switch apparatus and optical layout is shown in Fig. 3. The laser was a Q-switched, Nd:YAG laser ($\lambda=1.06 \mu\text{m}$), with a 200 mJ output in an approximately 10 ns pulse. The switch substrate was a high gradient insulator sample 2.5 cm diameter by 0.59 cm thick. A 10 J "mini-Marx" generator which was used to develop a pulsed voltage of approximately 1.3 μs FWHM (3.0 μs base-to-base) and up to 250 kV amplitude across the sample.

To study the properties of switch closure at different wavelengths, three additional harmonics were generated at 2ω , 3ω , and 4ω ($\lambda=532 \text{ nm}$, 355 nm , and 266 nm , respectively). Type I doubling in CD*A was used to obtain 2ω . A BBO two crystal, Type I, walk off compensated scheme was used to produce 4ω from the second harmonic. 3ω was generated by summing the first and second harmonic in a KD*P Type II tripler. Maximum available output energies at 2ω , 3ω , and 4ω were 100 mJ, 40 mJ and 40 mJ respectively with pulse widths of approximately 6-8 ns.

Optical energy from the laser was delivered through a UV grade fused silica window. Energy delivered to the target was measured on each shot by sampling from an uncoated fused silica wedge with a cross calibrated joule meter. Temporal optical pulse shape was also measured with a fast rise-time (500 ps) pyroelectric detector. Fluence delivered to the target was determined from the measured energy and approximate beam area at the sample. The effects of a semicircular beam image and partial illumination were also

investigated.

The high gradient insulator was prepared by interleaving individual layers of 0.064 mm stainless steel and 0.127 mm polycarbonate film. The structure was slightly compressed between polished bare aluminum electrodes. The entire assembly was placed in a turbo-molecular pumped, stainless-steel chamber. Experiments were generally performed at 10^{-6} T .

II. EXPERIMENTAL RESULTS AND DISCUSSION

Our preliminary delay data for 3ω and 4ω (Figs. 4 and 5, respectively) shows a decreasing trend in the delay time and jitter with increased fluence. We define delay as the time from the 50% point in peak fluence to the 50% point in peak switch current. Statistics are based on a minimum of 8-10 pulses from the laser.

Delay varies only slightly from 30 ns at a fluence of 30 mJ/cm^2 to 19 ns at 230 mJ/cm^2 for 3ω and from 25 ns at a peak of 15 mJ/cm^2 to 6-11 ns at 100 mJ/cm^2 for 4ω . The 1σ jitter (error bars) decreased significantly from approximately 10 ns at a fluence of 30 mJ/cm^2 to 0.97 ns at 230 mJ/cm^2 for 3ω . And likewise, the 1σ jitter decreased significantly from approximately 10 ns at a fluence of 15 mJ/cm^2 to 0.80 ns at 100 mJ/cm^2 for 4ω . Representative data showing timing distribution at two fluences is shown in Fig. 6.

Delay time dependence on voltage, spot size, and spot shape was not evident within the statistics of the data nor was shot-to-shot degradation evident over the approximately 500 shots necessary to acquire the data.

Probability of closure is shown in Figure 7 as a function of fluence and incident wavelength. For a 20% closure prob-

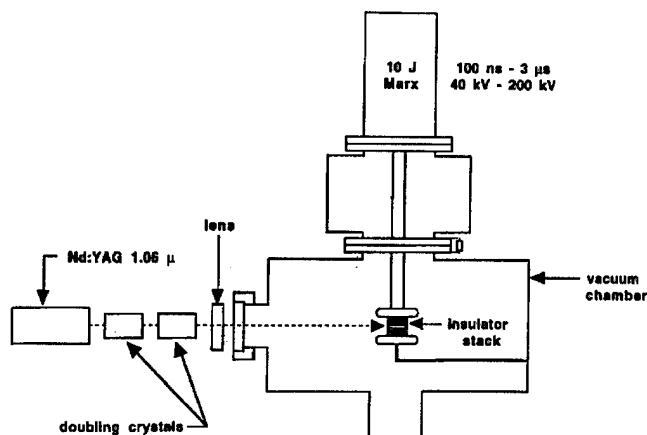


Figure 3. Experimental Apparatus (shown for 4ω).

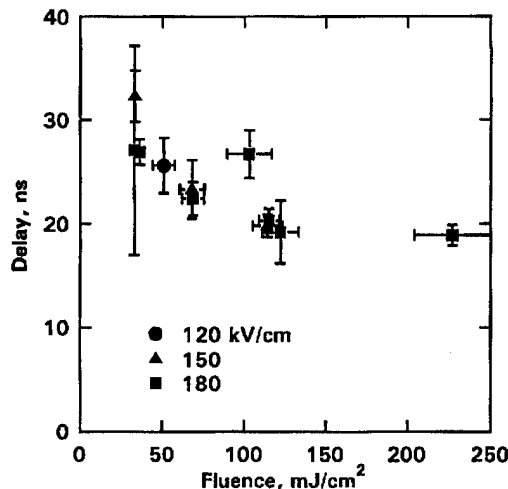


Figure 4. 3ω switch closure delay results.

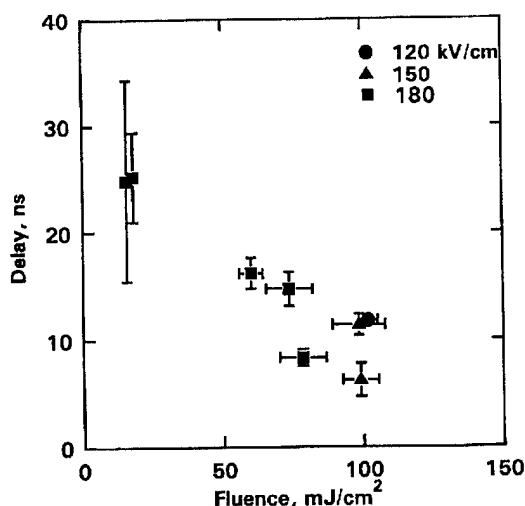


Figure 5. 4ω switch closure delay results.

ability, fluence requirements varied from 15-27 mJ/cm^2 . An increased fluence of 26-50 mJ/cm^2 resulted in an increased closure probability of 80%. Similar results taken at approximately 4ω were observed by others [6].

There was a decreasing fluence threshold trend above 3ω that cannot be explained based on the statistics of the data. As the sample was transparent in the visible, we speculate that a certain amount of focusing and internal reflection could have occurred. An increase in the fluence could have therefore resulted. Lastly, as can be seen from the data, a reasonable closure probability was possible for 1ω and 2ω . Delay times were from 75 ns to 225 ns for 1ω and 25 ns to 35 ns for 2ω . Significant scatter in the data was present, however.

IV. SUMMARY

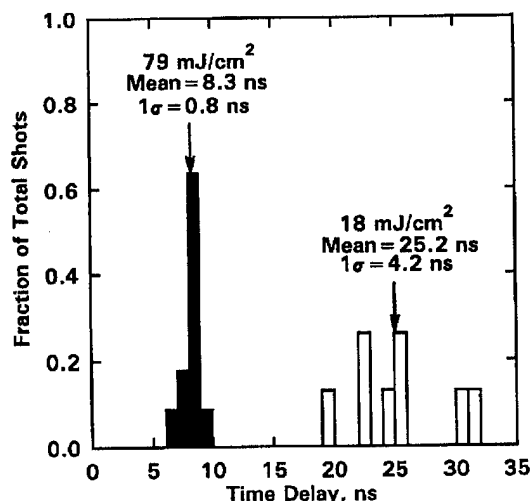


Figure 6. Typical distribution ($\lambda=266$ nm, $E=180$ kV/cm).

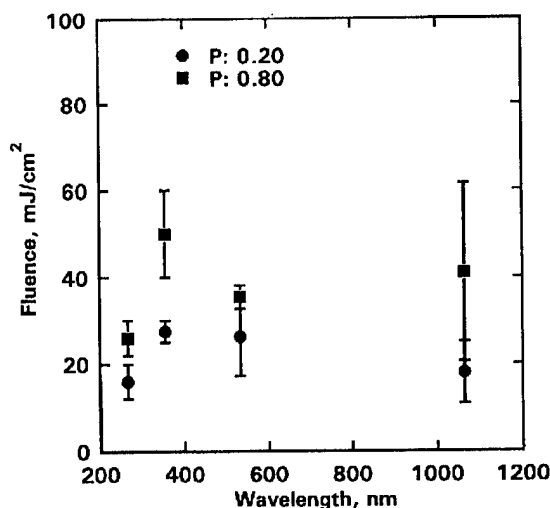


Figure 7. Closure probability.

We have performed initial testing of a laser initiated vacuum surface flashover switch. Experiments were performed with a Nd-YAG laser optical source ($\lambda=1.06$ μm) and a high gradient insulator. We observed that closure is possible at 1ω , 2ω , 3ω , and 4ω ; statistically meaningful data were only obtainable for 3ω and 4ω in our experiments. At elevated fluences, delay times were measured to be 6-19 ns, jitter was below 0.9 ns. Closure thresholds were measured and for 80% probability of closure, was found to be 26-50 mJ/cm^2 .

V. REFERENCES

- [1]G. Caporaso, presented at 1994 Joint Topical Course "Frontiers of Accelerator Technology" Maui, Hawaii, 1994.
- [2]S. Sampayan, et. al., presented at the 1995 Particle Accelerator Conference and International Conference on High Energy Accelerators, Dallas, Texas, 1995.
- [3]J. Elizondo and A. Rodriguez, in Proceedings of the 1992 15th International Symposium on Discharges and Electrical Insulation in Vacuum (VDE-Verlag GMBH, Berlin 1992), pp. 198-202.
- [4]I. Smith, G. Lauer, and M. Levine, in IEEE Conference Record of 1982 15th Power Modulator Symposium (IEEE, New York, NY 1982), pp. 160-163.
- [5]H. Miller, in Proceedings of the 1992 15th International Symposium on Discharges and Electrical Insulation in Vacuum (VDE-Verlag GMBH, Berlin 1992), pp. 165-174.
- [6]C. Enloe and R. Gilgenbach, IEEE Trans. on Plasma Science **16**, 379 (1988).

MEASUREMENTS OF MAGNET VIBRATIONS AT THE ADVANCED PHOTON SOURCE

V. Shiltsev, Budker INP, 630090, Novosibirsk, RUSSIA

Abstract

This article presents results of ground motion and magnet vibrations measurements at the Advanced Photon Source. The experiments were done over a frequency range of 0.1 – 100 Hz. Spectral power densities of vertical and horizontal motions of the APS hall floor and quadrupoles on regular supports were obtained. Magnet vibrations induced by designed cooling water flow and spectral characteristics of spatial correlation of the quadrupole vibrations at different sectors of the ring were also investigated. Amplitudes of the measured vibrations are compared with quad jitter tolerances in the APS.

I. Introduction

The Advanced Photon Source (APS) is a synchrotron radiation facility under construction at Argonne National Laboratory. It is based on 1.1-kilometer-circumference 7-GeV positron storage ring [1]. To obtain high brilliance X-ray radiation of the positron beam from dipole magnets and insertion devices at each of 40 sectors of the ring, the transverse beam sizes and angle divergencies should be rather small all around the circumference. Design values of horizontal and vertical beam emittances are $\epsilon_H = 10 \text{ nm}$ and $\epsilon_V = 1 \text{ nm}$, and corresponding the rms beam sizes are $\sigma_H \approx 300 \text{ } \mu\text{m}$, $\sigma'_H \approx 25 \text{ } \mu\text{rad}$ and $\sigma_V \approx 100 \text{ } \mu\text{m}$, $\sigma'_V \approx 10 \text{ } \mu\text{rad}$. These small dimensions result in the beam position being highly sensitive to vibrations of magnetic elements that produce jitter of the positron beam closed orbit and corresponding instability of synchrotron radiation beam angle and position. The issue arises from the fact that closed orbit distortion (COD) is a summation of all disturbances around the ring, i.e. many times larger than the amplitude of the distortion caused by a single magnet.

For uncorrelated displacements of quads, the summation over the APS lattice gives factors of COD magnification in comparison with amplitude of vibration of about 50 for horizontal and about 40 for vertical distortions [1]. If one assumes that 10% jitter of the effective beam emittance is not dangerous for the purposes of the X-ray users then maximum allowable amplitudes of quad horizontal and vertical vibrations are $\delta_H \approx 0.34 \text{ } \mu\text{m}$ and $\delta_V \approx 0.12 \text{ } \mu\text{m}$, respectively [1], [2]. Corresponding criteria for a single quadrupole vibration amplitude give maximum values of $\Delta_H \approx 2.2 \text{ } \mu\text{m}$ and $\Delta_V \approx 1.3 \text{ } \mu\text{m}$.

Another source of beam jitter (rarely considered in estimations) is a tilt of dipole magnets (across the beam orbit) $\delta\theta$ which produces a vertical kick acting on the beam equal to $\Delta\theta_{beam} = \delta\theta \cdot \theta_0$, where θ_0 is the bending angle of the orbit by the main field of the dipole (about 80 mrad for the APS). It's easy to calculate that the angular vibration $\delta\theta \approx (\delta_V/F)/\theta_0 \approx 0.25 \text{ } \mu\text{rad}$ will also cause 10% increase of the effective emittance. If one takes a dipole-to-floor distance of about 1.2 m, then such angular amplitude corresponds to a maximum allowable horizontal (across

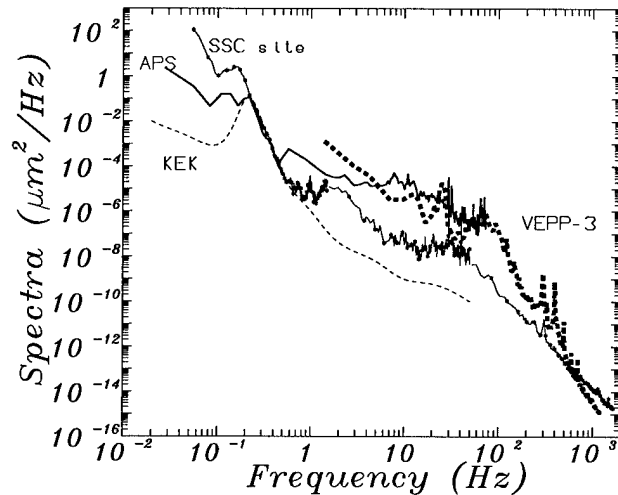


Figure. 1. Power spectral densities of vertical ground motion in the APS tunnel in comparison with data from SSC, VEPP-3, KEK.

the beam orbit) dipole vibration of about $1.2 \cdot 0.25 = 0.3 \text{ } \mu\text{m}$ – even a little smaller than for quads.

If the amplitudes of vibrations are above these conditions, some feedback system of beam position steering is necessary to keep X-ray beam positions all over the ring. The frequency band of the system should be larger than the band of concerned vibrations. Therefore it's very important to have the following information about a magnet's vibrations: (1) its spectral characteristics (power spectral densities) and (2) the spectral characteristics of spatial correlation of the vibrations (spectrum of correlation).

As the ground motion is *noise*, its properties can be described by the *power spectral density (PSD)* $S_x(f)$. The dimension of the PSD is *power in a unit frequency band*, i.e., m^2/Hz for the PSD of displacement. The value of $S_x(f)$ relates to the rms value of the signal $X_{rms}(f_1, f_2)$ in frequency band from f_1 to f_2 as $X_{rms}(f_1, f_2) = \sqrt{\int_{f_1}^{f_2} S_x(f) df}$. The *normalized spectrum of the correlation* $K(f)$ of two signals $x(t)$ and $y(t)$ is defined as

$$K(f) = \frac{\langle X(f)Y^*(f) \rangle}{\sqrt{\langle X(f)X^*(f) \rangle \langle Y(f)Y^*(f) \rangle}}, \quad (1)$$

where the brackets $\langle \dots \rangle$ mean the time averaging over the different measurement data, and $X(f)$ and $Y(f)$ are the Fourier transformations of $x(t)$ and $y(t)$. Note, that correlation $K(f)$ is a complex function. The coherence of the two signals is equal to the modulus of $K(f)$. By the definition, the value of the coherence does not exceed 1.0.

During our experiments we took these signals from two similar seismic probes distanced from each other. If the value of the coherence is close to zero in some frequency band, it means

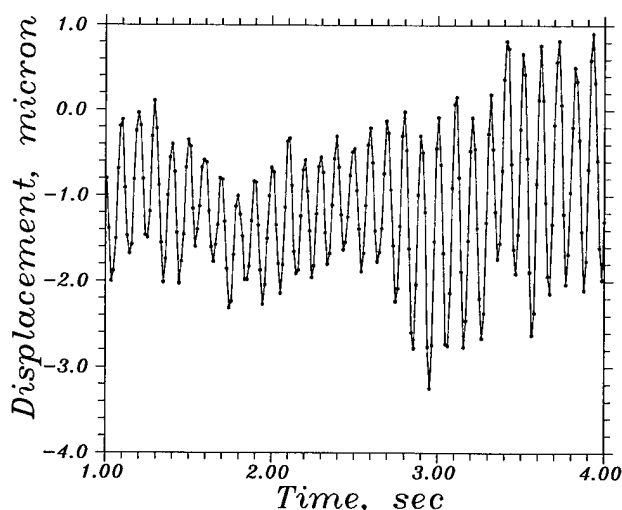


Figure 2. Horizontal vibration of the APS quad with cooling water flow rate 200 g/sec.

absence of any correlation between the vibrations; if two signals are well-correlated, the value of the coherence is close to 1.0.

II. Instruments and Methods

Measurements [3] were taken in the experiment hall of the APS building. Quadrupole vibrations were measured mainly at Sector 39 where the magnets were installed on regular girders and connected with pipes for cooling water. Some measurements were done at the Sector 19 floor just above the tunnel under the APS building, where we investigated the effect of traffic under the ring. At the time of experiments (19-26 of May 1994) there were no installed girders and magnets.

Sensors for the ground motion were two SM-3KV type velocity meters which allow us to obtain the data in a 0.1 – 140 Hz frequency band with a sensitivity of about 80 mV/($\mu\text{m/s}$).

The electrical signals from both probes were digitized and developed by a CAMAC-based experimental set-up which includes two 10-bit and 4-channel ADCs, four 20-bit ADCs, differential amplifiers with low-pass frequency filters, and an IBM 486 personal computer. The signals were digitized simultaneously by the ADCs with a sampling frequency (variable by a timer from 0.1 Hz to 32 kHz) and then sent to the memory for storage. The maximum memory available for one channel is 64-K 24-bit words. It corresponds to 18 h of permanent measurement time with a sampling rate of 1 Hz or about 3 min with 400 Hz. For long-term measurements we used the low-pass filters at 2 Hz or 20 Hz, for fast analyses the 200-Hz filter was applied.

The probes and set-up are described in detail in Ref.[4].

III. Results of Measurements

Let us consider vertical motion of the APS quadrupole magnet AQ-1 installed on a regular girder in Sector 39. Solid line in Fig.1 presents PSD of the vertical vibrations under conditions of magnet power supplies were switched off. The peak at about 0.1–0.2 Hz is due to the *microseismic waves* produced by ocean at the closest coastal line. The waves are well correlated over the wavelength of about 20 km and, therefore, they do not pro-

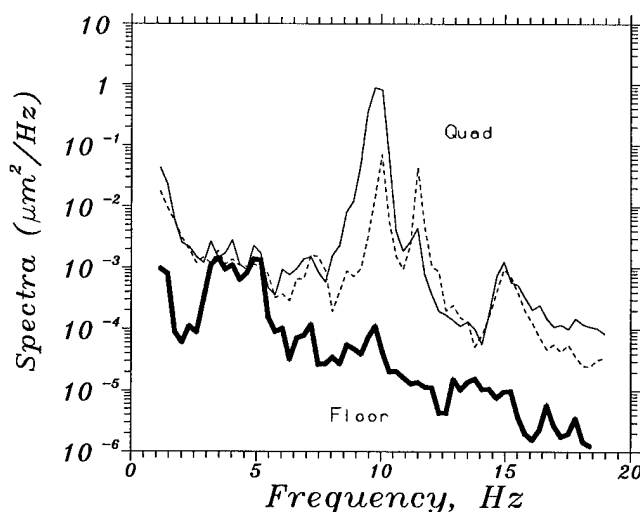


Figure 3. PSD of horizontal vibration of the APS floor (marked line), the APS quad with cooling water on (solid line), and the same quad with an additional wooden support installed (dashed line).

duce orbit distortions at accelerators (e.g. in HERA [5]). The continuum spectra out of microseismic peak frequency are due to ground motion noises.

It is interesting to compare the spectra of vertical vibrations at the APS (this work), at KEK [6], in the SSC tunnel [7], and in the hall of the VEPP-3 storage ring (Novosibirsk) [8] (see Fig.1). All data were obtained under “quiet” conditions (night or weekend). One can mention that all the spectra look rather similar, contain the microseismic peak at 0.07-0.2 Hz, and demonstrate the same “falling” character. A valuable difference occurs at frequencies 1-100 Hz where technical noise plays a major role. One can see that the APS spectrum is closer to the VEPP-3 spectrum (that storage ring was under operation during measurements) than to the data from KEK and SSC which were far away from additional sources of vibrations.

Our observations have shown that the motion of the quadrupole can be about 3 μm while a man was passing beside the magnet. This is twice above the allowable level for the APS. Another point of trouble is traffic under the ring, in a tunnel under Sector 19. The measurement of floor motion was done when a compact car drove through it and this resulted in 1.5 micron displacement.

Vibrations with higher frequencies (say, more than 1 Hz) are mostly due to technical noises; the strongest one is pressure fluctuations in flow of cooling water. Usually rms vertical amplitude of the quadrupole vibrations (frequency band 2-50 Hz) during our measurements was about 0.015 – 0.02 micron without water flow and as large as 0.06 – 0.09 micron with 200 g/sec cooling water flow. This is under the allowable levels for the APS and in rather well coincidence with previous measurements with *Tele-dyne Geotech* S-500 vibroprobes [9].

Horizontal vibrations of the AQ-1 quadrupole have rms values in band 2-50 Hz of about 0.02 – 0.04 micron in the absence of water flow. The 200-g/sec cooling water flow rate led to huge horizontal vibrations. (see a 3-sec record of the quad motion in Fig.2). The maximum peak-to-peak amplitude of the 10-Hz oscillations is up to 3 micron. The 10-Hz frequency is determined

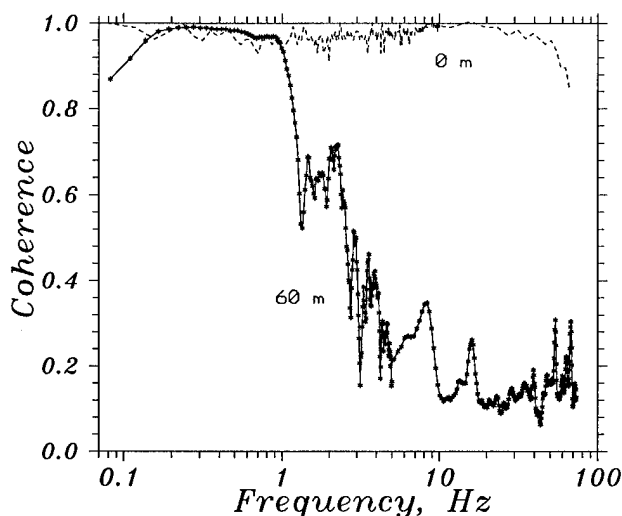


Figure 4. Coherence spectra of vertical motions of two APS quadrupoles distanced by two APS sectors (about 60 meters).

by the resonance of the girder support structure that is mechanically driven by coil and pipe vibrations due to the water flow.

Figure 3 presents the PSDs of the horizontal quad vibrations with cooling water on (solid line), and how the spectrum was changed after installation of a wooden stick between the quad and the wall of the hall (it improves rigidity and decreases the rms amplitude four times from 0.84 micron to 0.22 micron, see dashed line). The PSD of horizontal movement of the floor is marked by stars. One could conclude that something similar to an additional wooden support may be used to obtain horizontal vibrations below the acceptable level of about $0.3 \mu\text{m}$. Alternatively, other measures to damp the dangerous 10 Hz resonance should be applied.

The measured coherence spectra of vertical vibrations are shown in Fig.4. The dashed line shows that in the case when two SM-3KV type probes are set side by side, their signals are the same and the coherence is ≈ 1.0 in the frequency band of 0.08-70 Hz as it should be in the case when probes' internal noises are much less than signal. The marked line corresponds to the coherence of motions of two AQ-1 quadrupole magnets in different sectors of the APS ring (namely, Sector 39 and Sector 37, distance about 60 meters). One can surely say that quad motions are practically uncorrelated at frequencies above 1-2 Hz because the degree of coherence is less than 0.5. Below 1 Hz and down to 0.07 Hz the coherence is close to 1.0 because at these frequencies the microseismic waves (correlated over large distances, at least over 20 km wavelength) are the main contribution to motion of the ground and quadrupoles.

IV. Summary

Finally, let's summarize some results of the work:

- correlation measurements have shown that motion of magnets may be treated as uncorrelated in the high frequency part of the spectrum (above 1-2 Hz);
- rms values of uncorrelated vertical and horizontal magnet vibrations under quiet conditions are about 0.015-0.04 micron, i.e., below allowable level for the APS;

- cooling water flow rate of about 200 g/sec doesn't cause dangerous vertical vibrations of quadrupoles;
- 10 Hz mechanical resonance of the system "quadrupole-girder" driven by the water flow fluctuations leads to quadrupole vibration amplitudes some three times above acceptable limits and additional damping support is needed;

Author deeply appreciate the help of J. Galayda, G. Kulipanov, D. Mangra, P. Ivanov, E. Medvedko, S. Sharma, G. Decker, and J. Jendrzeczyk for their help in organization of these measurements. I am grateful to my colleagues from Budker Institute of Nuclear Physics (Novosibirsk) – V. Parkhomchuk, B. Baklakov, P. Lebedev, S. Sigmatulin and A. Chupiro for their assistance in the preparation of the equipment used at Argonne.

References

- [1] *7 GeV Advanced Photon Source: Conceptual Design Report*, ANL-87-15, April 1987.
- [2] J.A. Jendrzeczk and M.S. Wambsganss, *Proc. of 1991 Symp. on Optical Sci. and Eng.*, San Jose, CA.
- [3] V. Shiltsev, INP Preprint 94-71, Novosibirsk (1994).
- [4] V. Shiltsev, in book *AIP Conference Proceedings 326*, p.560 (1995).
- [5] V. Shiltsev, *et.al*, these conference.
- [6] Y.Ogava et al., KEK Preprint 92-104 and *Proc. of the 16th Int. Linac Conf.*, Ottawa, Canada, 1992.
- [7] V. Parkhomchuk, V. Shiltsev, H.J. Weaver, *Proc. of 1993 IEEE Part. Accel. Conf.*, Washington, DC.
- [8] V. Lebedev, P. Lebedev, V. Parkhomchuk, V. Shiltsev, INP Preprint 92-39, Novosibirsk (1992).
- [9] J.A.Jendrzeczk, private communication.

THE VACUUM SYSTEM FOR THE PEP II HIGH ENERGY RING STRAIGHT SECTIONS. *

U. Wienands, E. Daly, S.A. Heifets, A. Kulikov, N. Kurita, M. Nordby, C. Perkins E. Reuter, J.T. Seeman, SLAC, Stanford, CA; and
F.C. Belser, J. Berg, F.R. Holdener, J.A. Kerns, M.R. McDaniel, W. Stoeffl, LLNL, Livermore, CA

Abstract

The six straight insertions of the PEP II High Energy Ring (HER)[1] serve various functions: lattice tuning, beam injection and abort, providing space for rf cavities, longitudinal and transverse feedback, beam diagnostics and the interaction point. A stainless steel vacuum system has been designed; prototypes are currently being built. Cooling is required due to radiation coming from the last arc dipole and resistive losses in the vacuum chamber. Although the nominal beam current of the HER is 1 A the vacuum system is designed for 3 A to provide margin and an upgrade path.

I. DESIGN REQUIREMENTS

The PEP II Conceptual Design Report (CDR, Ref.[2]) calls for an average pressure in the straights of 3 nTorr, mainly determined by beam lifetime considerations. In order to achieve this pressure, about 3 m pump spacing would be required in the first 6-7 cells of each straight section due to the still significant synchrotron radiation at 3 A current. Initially, lower intensities are expected and, therefore, for first commissioning 220 l/s ion getter pumps will be provided at every quadrupole only (≈ 7 m pump spacing). Fig. 1 shows the pressure profile and gas load at

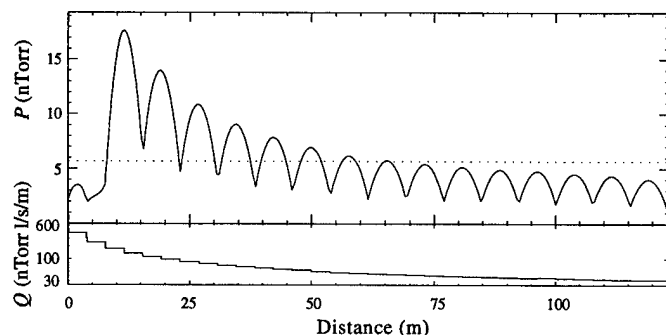


Figure 1. Pressure and gas load along an HER straight section

1 A beam current. For this calculation, a photon-induced desorption rate of $\eta = 2 \times 10^{-6}$ is assumed. To achieve this value, the vacuum components will be glow-discharge cleaned after chemical cleaning. Initially, η will be higher but the cleaning effect of synchrotron radiation will reduce η , especially so at the upstream end of the straight. Over time, η is expected to go down and eventually be less than 10^{-6} . If it is found that the pressure does not reach the required level, additional pumping tees and

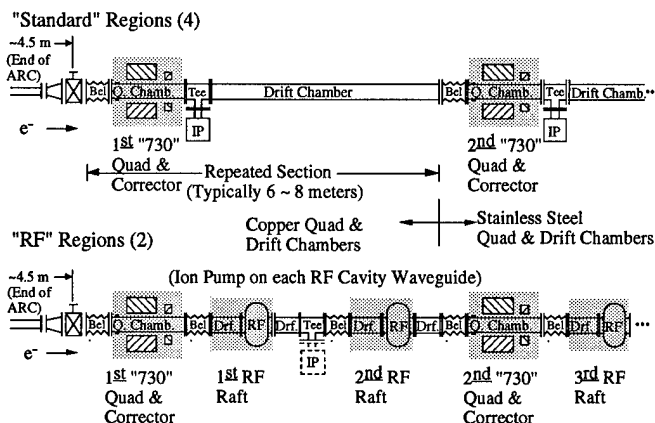


Figure 2. Layout of arc-straight transitions

pumps will be installed in the first cells. The vacuum system of each straight section can be separated from the adjacent arcs by gate valves located right after the transition in shape from the octagonal profile used in the arcs to circular pipe. The transition regions are shown in Fig. 2.

The expected distribution of the power deposition along the beam pipe for 3 A beam current is shown in Fig. 3. At the upstream end of each straight section it is dominated by the synchrotron radiation; this causes the pressure rise in Fig. 1. Additional power is being deposited by direct $I^2 R$ losses due to image currents and by losses arising from higher-order modes (HOM) traveling along the vacuum system, which will dissipate predominantly in the stainless steel walls. Cu extrusions will be used rather than stainless steel in the first 4.2 m using the same shape as in the dipoles of the arcs.[3], [4] The pump chamber provides

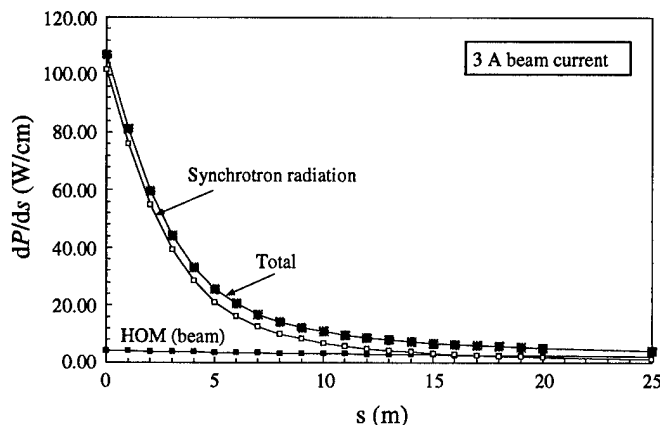


Figure 3. Power deposition along beam pipe

*Work supported by US Department of Energy under contract DE-AC03-76SF00515, DE-AC03-76SF00098, DE-AC03-81ER40050, DE-AS03-76ER70285 and W-7405-Eng-48

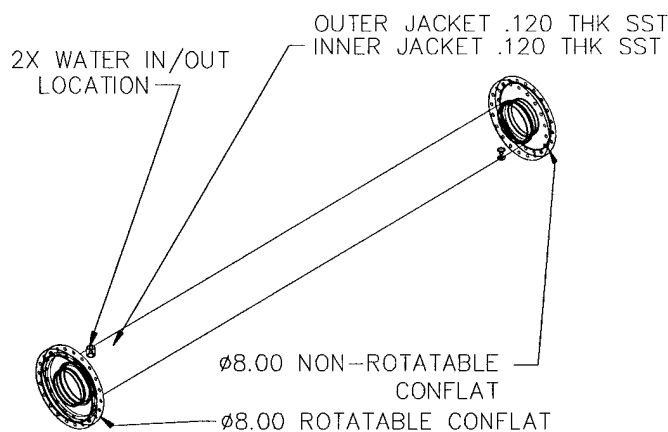


Figure 4. Drift chamber

a convenient, shielded area for four pump ports to hold NEG cartridges.

The heating of an uncooled beam pipe as a function of power can be calculated approximately. We have performed a test heating a 1 m long sample of ss pipe by direct current and measuring its temperature. Experiment and calculation are consistent and show that a linear power density of 1 W/cm along the pipe will lead to temperatures of about 70-80° C if not cooled; this would lead to undesirable outgassing.

Due to the high currents and short bunches, a strict impedance budget is enforced for the whole HER vacuum system. The total inductive impedance is limited by the bunch lengthening threshold to less than 200 nH for the whole ring. Narrow band impedance limits are frequency dependent; but the contribution of the vacuum system should be insignificant compared to that of the rf cavities. The existence of any gaps along the inner wall (e.g. at flanges) is being avoided. Care is being taken to avoid any possibility of mode trapping between adjacent shape transitions in the beam pipe. Almost every discontinuity is being tapered to less than 10° angle. An impedance committee has been set up to scrutinize every significant discontinuity and transition in the vacuum system.[5]

II. COMPONENT DESIGN

The straight section vacuum system is modular, with four basic components as shown in Fig. 2: Drift chamber, Quadrupole chamber, Pumping Tee and Bellows module. AISI 304L stainless steel is used throughout. The beam pipe is required to be seamless to avoid the possibility of seam-related problems. In addition, no welds at all are permitted to be within any of the magnetic elements as improperly carried out welds could change the μ of the material away from unity. The μ of the material has been specified to be less than $\mu_r = 1.05$ and will be inspected upon receiving of the pipe stock.

A. Drift Chamber

The drift chamber is designed using two concentric round ss pipes with a 1/16 in. gap for the cooling water. A sketch of the chamber is shown in Fig. 4. The concentric chamber design allows for fairly uniform cooling around the azimuth of and along the whole chamber; a wire coil inserted between chamber and

cooling jacket together with some extra spacers at the ends assists to this end. Conflat flanges are welded on at each end.

B. Quadrupole Chamber

The cooling-jacket concept used for the drift chamber can not be used for the quadrupole chamber. The 50 mm pole radius of the quadrupole magnets and the inner radius requirement of 44.5 mm or larger proved to be mutually exclusive unless expensive custom-made pipe stock be purchased. Therefore a different concept is being pursued using regular 44.5 mm inner radius "Schedule 10" piping (Fig. 5). The pipe is coated with a 1 mm copper layer and four 6.35 mm Cu cooling pipes will be soldered to the outside. The copper layer increases the heat conductance both from areas of the pipe not directly under the cooling channels. At each flange the cooling pipe will be wrapped around the beam pipe for increased cooling. In this way, margin is provided against vertical displacement of the synchrotron radiation fan and areas under the flanges receive adequate cooling as well.

C. Pumping Tee

The pumping tee module is shown in Fig. 6. The pump is attached to the 8 in flange welded to a plenum. A slotted Cu insert provides the rf shield necessary to reduce the impedance of the pumping tee. 8 in flanges are used rather than 6 in to avoid the need for blind-tapped holes. The conductance of the whole assembly is calculated to be about 470 l/s; this results in an effective pumping speed of 150 l/s for a 220 l/s pump. Those tees located near the upstream end of the straight sections have to be able to handle significant synchrotron radiation. In order to be able to do so, 1 cm wide strips at the side of the Tee are not slotted and a stainless cooling line is brazed to the insert.

The long slots are transparent to TE field modes emanating from the rf cavities and also generated by mode conversion of the TM fields associated with the beam. These can cause heating in the pumps and will therefore be screened by a thin Cu sheet with 5 mm wide slots orthogonal to the slots on the insert. The long slots also increase the effective diameter of the beam pipe and, thus, potentially can lead to trapped modes. To avoid this possibility the aperture will be slightly restricted in the region of the

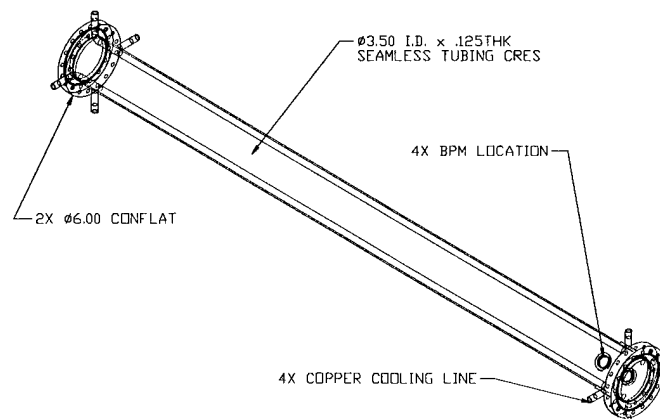


Figure 5. Quadrupole chamber

slots, by about 0.5 mm. MAFIA calculations confirm the effectiveness of this approach.

D. Bellows Module

The bellows module is the most challenging part of the vacuum system. The bellows themselves have to be protected from too much power dissipation and would present an unacceptable impedance to the beam; therefore, they will be shielded. The shield has to present as smooth a surface as possible to the beam to reduce the inductive broad-band impedance and has to do this over the full operational extension/contraction range of about 5 mm. In addition, it has to sustain a contraction of up to 19 mm without damage if *in situ* bake-out were to take place.

The shield uses a sliding-finger design with the fingers of the rf shield riding outside on the rim of a slightly conical stainless stub. Figure 7 shows a sketch of the bellows assembly. The fingers are straight where exposed to the beam to avoid creating a bulge in the crosssectional area that could act as a cavity. The total broad band impedance of all ≈ 100 straight-section bellows modules is about 4.5 nH which is acceptable. The fingers are made of dispersion-strengthened copper (GlidCop) rather than BeCu, for improved strength and thermal handling and will be silver coated. The stub, made of stainless, will be copper coated on the inside to reduce I^2R and HOM losses and will have a Rhodium coating at the contact area. A taper at the upstream end of the bellows protects the fingers and the stub from synchrotron radiation.

A test fixture has been built to test the stability of the fingers over at least 200000 compression-expansion cycles at operating temperatures. Contact resistance and dust production can be assessed in this way. A current of 2 A per finger can be injected into the fixture, but the frequency of 2 MHz is too low to fully test the current carrying ability of the fingers.

References

- [1] U. Wienands *et al.*, "Status of the High Energy Ring of the

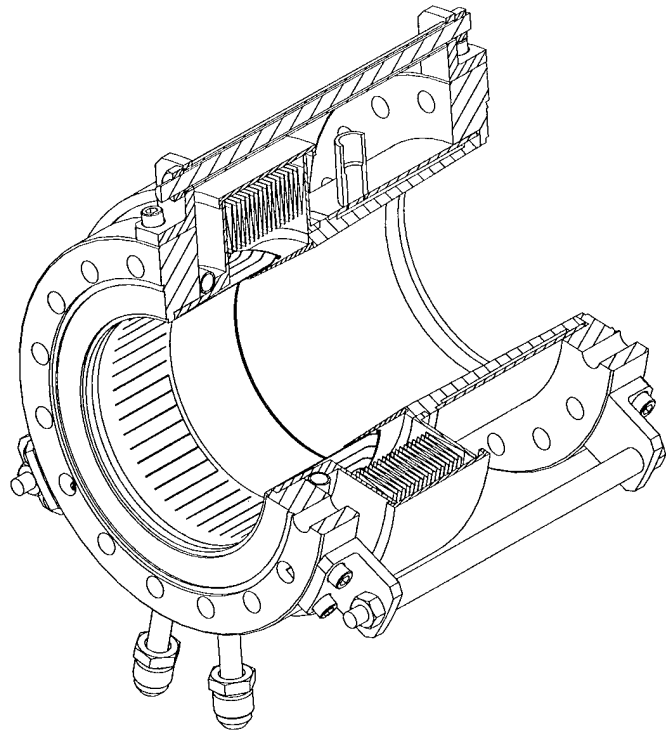


Figure 7. Bellows assembly

PEP II B-Factory", these proceedings.

- [2] M. Zisman, Ed., "PEP-II An Asymmetric B Factory", Conceptual Design Report, SLAC-416.
 [3] C. Perkins *et al.*, "Vacuum System of the PEP-II High Energy Ring", Proc. EPAC, London, UK, 1994.
 [4] E.F. Daly *et al.*, "Stretch Forming Vacuum Chambers for the PEP-II B-Factory High Energy Ring", these proceedings.
 [5] S.A. Heifets *et al.*, "Impedance Budget of the PEP II B-Factory", these proceedings.

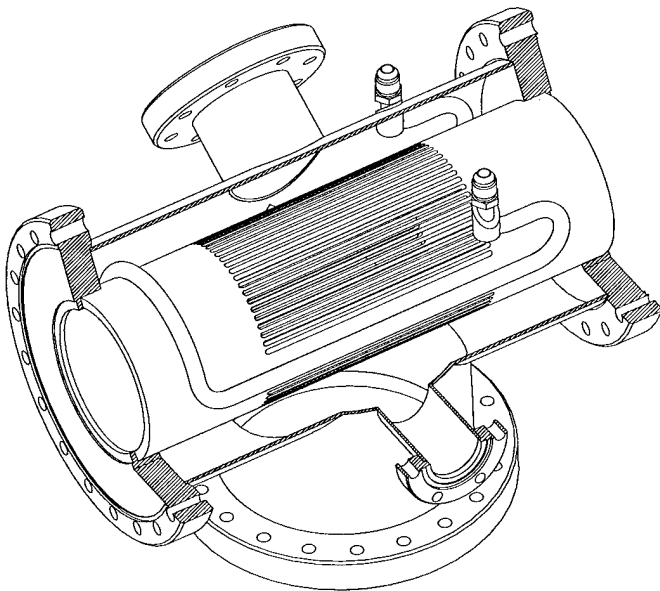


Figure 6. Pumping Tee

Compact X-band High Power Load Using Magnetic Stainless Steel *

Sami G. Tantawi†, and A. E. Vlieks
Stanford Linear Accelerator Center Stanford, CA 94309

Abstract:

We present design and experimental results of a high power X-band load. The load is formed as a disk-loaded waveguide structure using lossy, type 430, stainless steel. The design parameters have been optimized using the recently developed mode-matching code MLEGO. The load has been designed for compactness while maintaining a band width greater than 300 MHz.

I. INTRODUCTION

The high power rf system of the Next Linear Collider (NLC) contains several points where a high power rf load is required, namely, the output of the traveling wave accelerator, the output of the pulse compression system, and the output of the rf source. If the load is terminating the output of a pulse compression system it should be able to handle 400 MW of peak power for $t = 250$ nsec. On the other hand, it should be able to handle an average power of 22.5 kW based on an rf power source of 100 MW for a period of 1.25 μ sec, and a repetition rate of 180 Hz. The operating frequency is 11.424 GHz. Of course the power could be split into several ports and dissipated into several loads. However, for obvious reasons, the number of loads should be minimized.

High power water loads have been developed and at X-band. They are composed of "pill-box" windows with water circulating on the down stream side of the ceramic disk to dissipate the power. At very high power levels there is a danger of rf breakdown resulting in water leaking to the vacuum side if the ceramic window fails. Therefore, a vacuum compatible "dry" load is required.

A dry load made from a waveguide loaded with lossy ceramics is under development [2]. However, these loads are expensive because of vacuum compatible ceramics. They are, also, hard to make because of difficulties associated with brazing of ceramics to the copper waveguide walls.

Instead of using lossy ceramics one can use a waveguide made from magnetic stainless steel. This type of stainless steel is vacuum compatible and at the same time has a relatively high rf surface resistivity. However, the attenuation constant in rectangular guide is not enough to completely absorb the signal in a short length of waveguide. Such a load was built at X-band with a total length of approximately 1.5 meters [3]. An obvious remedy is to spiral the wave guide to reduce the size. Nevertheless, this long length of wave guide requires distributed pumping to guarantee good vacuum, and the resultant load is heavy and expensive.

Indeed, one can match, with a post, a short length of lossy guide terminated by a short circuit. However the resultant load would have a very narrow bandwidth. An

alternative is a series of a very low Q resonators. These resonators would absorb the power gradually in short distance while keeping the bandwidth relatively wide. A realization of this idea using a series of chokes in a circular waveguide is presented. The geometry is relatively simple and compact.

In Sec. II the design theory is presented. Simulations using both mode matching code MLEGO, and HFSS are compared with both theory and experiment. Finally we present the cold test results of our first experimental load

II. Theory

A. Basic Idea.

Figure 1 illustrates the basic structure of the load. It consists of several chokes placed in a circular waveguide. The circular guide is to be operated in the fundamental mode (TE_{11}).

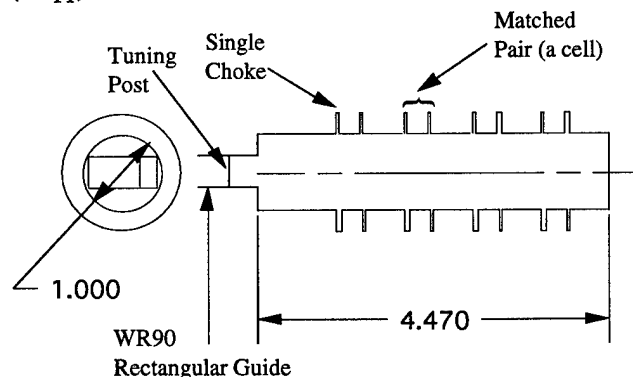


Figure 1. 430 Stainless Steel High Power Load Schematic Diagram (Dimensions are in inches)

If there are no losses and the chokes are tuned near their resonant frequency, i.e. the choke depth is $\sim \lambda/4$, each choke would have a very high reflection coefficient. However, since the structure is made from 430 stainless steel, there are considerable amounts of wall losses. Hence, each choke couple a considerable amount of power to the next one. On average, each choke has a transmission coefficient that is more or less is equal to the reflection coefficient. By adjusting the distance between two chokes it is possible to match the pair. We call such a pair a load cell. By proper design we can adjust each cell so that the power dissipated per cell is a constant.

Finally the input to the circular guide is matched to the standard WR90 rectangular guide using an inductive post. These type of junction has a relatively large bandwidth; hence, it will not be a limiting factor on the load bandwidth.

B. Single Choke Theory.

Consider treating the choke as a three port network with the third port terminated in a short circuit. We define ports one

*This work is supported by the U.S. Department of Energy under contract DE-AC03-76SF00515

†Also with Electrical Communications and Electronics Dept. Cairo University, Giza, Egypt.

and two as the circular waveguide ports and port three as the radial waveguide choke. If we initially assume that this is a lossless structure, then, the scattering matrix representing the structure is unitary and we can write

$$\underline{S} = \begin{pmatrix} \sin^2(\frac{\theta}{2}) & -\cos^2(\frac{\theta}{2}) & \frac{\sin \theta}{\sqrt{2}} \\ -\cos^2(\frac{\theta}{2}) & \sin^2(\frac{\theta}{2}) & \frac{\sin \theta}{\sqrt{2}} \\ \frac{\sin \theta}{\sqrt{2}} & \frac{\sin \theta}{\sqrt{2}} & \cos \theta \end{pmatrix}; \quad (1)$$

where θ is a parameter that completely defines the scattering matrix. The scattered rf signals \underline{V}^- is related to the incident rf signals \underline{V}^+ by

$$\underline{V}^- = \underline{S}\underline{V}^+; \quad (2)$$

where V_i^\pm represents incident/reflected rf signal from the i th port. We terminate the third port so that all the scattered power from that port is completely reflected; i.e., $V_3^+ = V_3^- e^{i\psi}$.

To account for losses in the choke, we write

$$V_3^+ = V_3^- \alpha e^{i\psi} \quad (3)$$

where α is the attenuation suffered by the radial wave during its round trip through the choke. One can show that

$$\alpha^2 = \exp\left\{\frac{2R_s}{0.637Z_0k_0t} \times \int_{k_0r_i}^{k_0r_o} [J_0^2(\rho) + J_2^2(\rho) + Y_0^2(\rho) + Y_2^2(\rho)] \rho d\rho\right\} \times (1 - \Delta) \quad (4)$$

Here, $J_i(\rho)$ and $Y_i(\rho)$ are the first and second kind Bessel functions of order i , R_s is the rf surface wall resistance, k_0 is the wave propagation constant in free space, r_i and r_o are the inner and outer radius of the choke, t is the choke thickness, Z_0 is the free space wave impedance, and the term $(1 - \Delta)$ accounts for the end wall losses. The term Δ is

$$\Delta = [(J_0(r_0k_0) - J_2(r_0k_0))^2 + (Y_0(r_0k_0) - Y_2(r_0k_0))^2] \frac{R_s r_0 k_0}{0.637Z_0} \quad (5)$$

The reflection coefficient and transmission coefficients are then, given by

$$R = \frac{(\alpha e^{j\psi} + 1) \sin^2(\theta/2)}{1 - \alpha e^{j\psi} \cos(\theta)}, \quad (6)$$

$$T = \frac{(\alpha e^{j\psi} - 1) \cos^2(\theta/2)}{1 - \alpha e^{j\psi} \cos(\theta)}; \quad (7)$$

and

$$e^{j\psi} = -\frac{H_1^{(2)}(r_0k_0)H_1^{(1)}(r_ik_0)}{H_1^{(1)}(r_0k_0)H_1^{(2)}(r_ik_0)} \quad (8)$$

where $H_1^{(i)}$ is the Hankel function of kind i and first order.

Finally, following the arguments found in [4], we can show that

$$\sin(\theta) \sim (k_0t)^{3/2} \left(1 - \left(\frac{1.841}{r_ik_0}\right)^2\right)^{1/4} |H_1^{(2)}(r_ik_0)| \quad (9)$$

III. SIMULATIONS

The basic design dimensions for the load were found using the above theory. We refined these dimensions using a mode matching code Mlego. In this code the structure is divided into several circular waveguides along the axial direction. The fields in each section are expanded in terms of circular waveguide modes. In finding these modes we assumed that the waveguide has a constant wall impedance Z_s given by

$$Z_s = \left(\frac{\omega\mu_0\mu_r}{2\sigma}\right)^{1/2} (1 + j) \quad (10)$$

where σ is the conductivity of the guide walls, and μ_r is the relative permeability of the walls. For a discussion of these mode and its orthogonality, the reader is referred to [5].

As usual we match the fields along the cross-sectional area between different waveguide sections. We also demand that the field on the walls along these cross-sectional area satisfy Eq. (10).

Figure 2. compares between the mode matching results HFSS simulations, and theory mode matching and HFSS agree well. However, for speed purpose, we used mode matching in our design.

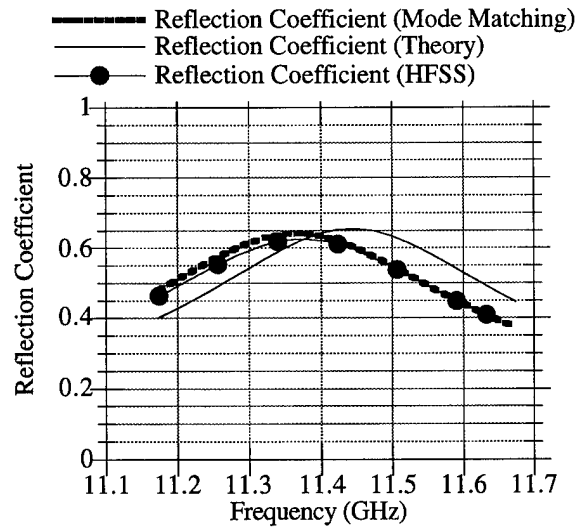


Figure 2a. Comparison between theory and different simulation methods for the reflection coefficient of single choke ($t=0.040''$, $r_i=0.5''$, and $r_o=0.755''$)

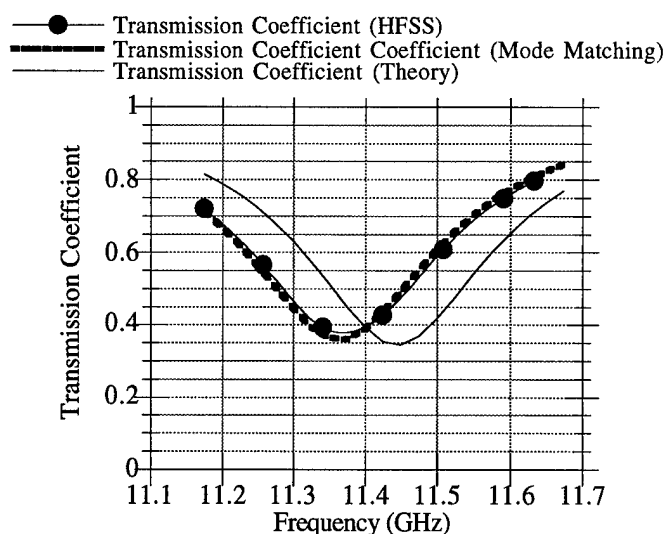


Figure 2b. Comparison between theory and different simulation methods for the transmission coefficient of single choke ($t=0.040$ ", $r_i=0.5$ ", and $r_o=0.755$ ")

IV. EXPERIMENTAL RESULTS

Based on results from the mode matching code we built a matched pair of slots. The distance between the centers of the two chokes is 0.310", and the two chokes have the same dimensions as those of Fig. 2. Figure 3 shows both the transmission and reflection coefficient of this matched pair.

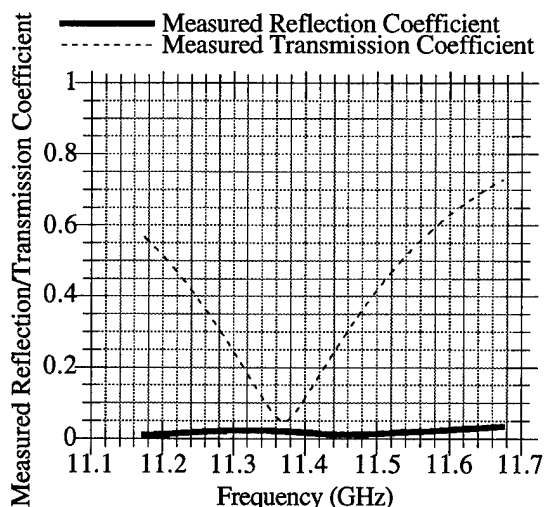
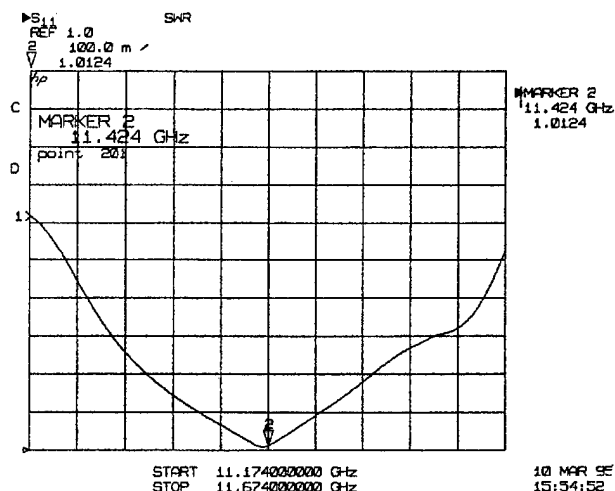


Figure 3. Experimental results of a matched pair of chokes

Finally, Fig. 4 presents the characteristics of a load made of four such cells (Fig. 1). Note that bandwidth is greater than 400 MHz for SWR < 1.5.



Measured SWR for a four cells load with the rectangular to waveguide junction matched with a post.

CONCLUSION

We describe the principles and simulation tools used in designing a compact broad band rf load made of 430 stainless. We also, presente a design theory. Simulations using mode matching and HFSS showed a good agreement. We, also, show agreement between simulation and experimental data. The load has a SWR of less than 1.5 for a 400MHz bandwidth.

V. ACKNOWLEDGMENT

The authors wishes to thank T. G. Lee for his contributions to the cold test setup.

VI. REFERENCES

- [1]W. R. Fowkes et. al, "High Power rf Window and Waveguide Component Development and Testing Above 100 MW at X-Band," presented at the Linac 92 Conf., Ottawa, Canada, August, 1992, also in SLAC-Pub 5877, Aug.,1992
- [2]K Ko, et. al., "X-band High Power Dry Load for NLCTA," This proceedings
- [3]W. R. Fowkes, private communications
- [4]R. E. Collin, "Field Theory of Guided Waves," Ch. 7, Sec. 7.3. McGraw Hill Inc, New York, 1960
- [5]S. F. Mahmoud, "Electromagnetic Waveguides Theory and Applications," Peter Peregrinus Ltd., 1991.

Progress on Plasma Lens Experiments at the Final Focus Test Beam*

P. Kwok², P. Chen¹³, D. Cline², W. Barletta⁴, S. Berridge¹⁴, W. Bugg¹⁴, C. Bula¹⁰, S. Chattopadhyay⁴, W. Craddock¹³, I. Hsu⁹, R. Iverson¹³, T. Katsouleas¹², P. Lai¹², W. Leemans⁴, R. Liou¹², K. T. McDonald¹⁰, D. D. Meyerhofer¹¹, K. Nakajima⁸, H. Nakanishi⁸, C. K. Ng¹³, Y. Nishida¹⁵, J. Norem¹, A. Ogata⁸, J. Rosenzweig², M. Ross¹³, A. Sessler⁴, T. Shintake⁸, J. Spencer¹³, J. J. Su⁷, A. W. Weidemann¹⁴, G. Westenskow⁵, D. Whittum¹³, R. Williams³, J. Wurtele⁶.

Abstract

The proposal to perform a series of plasma lens experiments at the Final Focus Test Beam at SLAC has been described earlier. We report on our progress towards validation of concepts involved in the experiments, including the laser ionized plasma production test, development of the supersonic gas jet as the plasma source, and study on focused beam size measurement techniques. Most importantly, the effects of background events due to plasma lenses in future linear collider detectors, such as that in the NLC, are studied in details and are shown to be within detector tolerances.

I. INTRODUCTION

Although the concept of plasma lens [1] has been reasonably verified in several low energy, low density experiments [2-4], the utility of the plasma lens in high energy physics has yet to be proven. It is necessary to further demonstrate plasma focusing in a setting close to the true high energy collider with negligible induced backgrounds to the detector. The proposal to perform the plasma lens experiments at the FFTB at SLAC has been described earlier [5]. Here we report on the substantial progress that has been made in verifying the key concepts of the experiments.

II. PLASMA PRODUCTION TEST

The plasma production test was performed at the Laboratory for Laser Energetics of the University of Rochester. Plasmas suitable for the plasma lens experiments at the FFTB, with lengths of 1 mm and electron densities of order 10^{18} cm^{-3} , were produced with transverse laser illumination. The high-powered laser system employed in the test is capable of delivering up to 1 J at 1 μm with a pulse

length of 1.3 ps, and is similar to the one installed at the FFTB for experiment E-144 [6]. The nominal focal spot size of the laser is $\sim 100 \mu\text{m}$ FWHM, which corresponds to a Rayleigh length of $\sim 3 \text{ mm}$. A cylindrical lens was added to produce the focusing for a 1 mm plasma.

Xenon, which has ionization potentials similar to hydrogen, was used for the test. Since xenon can have multiple charge states, a lower gas pressure can be used in the test chamber to obtain an electron density of 10^{18} cm^{-3} . The lower gas pressure minimized the defocusing of the ionization laser in the gas-filled chamber.

The plasma density was determined by measuring the recombination light with a photomultiplier tube (PMT) [7]. Dimensions of the plasma were measured using CCD image of the recombination light. With a 300 mJ laser pulse, a plasma with electron density of $0.8 \times 10^{18} \text{ cm}^{-3}$ and measures 1.1 mm transversely was produced (Figure 1).

The test has shown that plasma of extended size with electron density of order 10^{18} cm^{-3} can be produced using laser ionization. A hydrogen plasma with the appropriate properties should, hence, be available for the plasma lens experiments.

III. SUPERSONIC GAS JET DEVELOPMENT

In an effort to minimize background events, a supersonic hydrogen jet is under development for use with the plasma lens experiments at the FFTB. With the use of gas jets, the experimental design has been completely revised which eliminated all solid materials inside the beam pipe at the interaction point. Such gas jets offer the practical advantage during initial beam tuning, as well as suitability for application at high energy detectors.

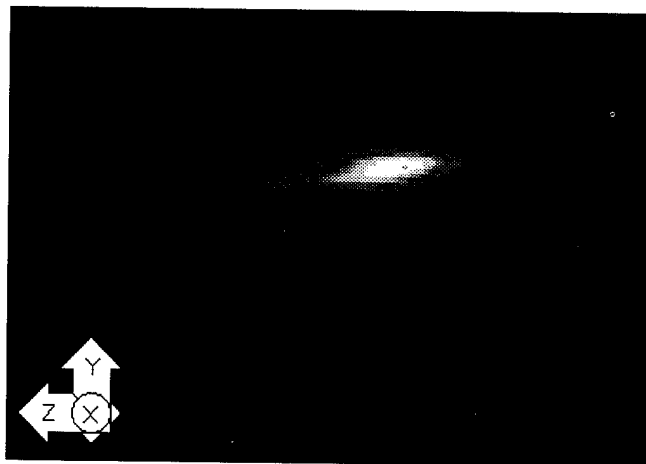


Figure 1: Artificially colored image of the plasma produced with a cylindrical lens. The laser travels in the Z-direction. The cylindrical lens was oriented to defocus the laser slightly in the Y-dimension to form a long focus.

*Work supported by Department of Energy contract DE-AC03-76SF00515 and grant DE-FG03-92ER40695.

¹Argonne National Laboratory, Argonne, Illinois

²University of California, Los Angeles, California

³Florida A & M University, Tallahassee, Florida

⁴Lawrence Berkeley Laboratory, Berkeley, California

⁵Lawrence Livermore National Laboratory, Livermore, California

⁶Massachusetts Institute of Technology, Cambridge, Massachusetts

⁷National Central University, Taiwan

⁸National Laboratory for High Energy Physics (KEK), Tsukuba, Japan

⁹National Tsing-Hua University, Taiwan

¹⁰Princeton University, Princeton, New Jersey

¹¹University of Rochester, Rochester, New York

¹²University of Southern California, Los Angeles, California

¹³Stanford Linear Accelerator Center, Stanford, California

¹⁴University of Tennessee, Knoxville, Tennessee

¹⁵Utsunomiya University, Utsunomiya, Japan

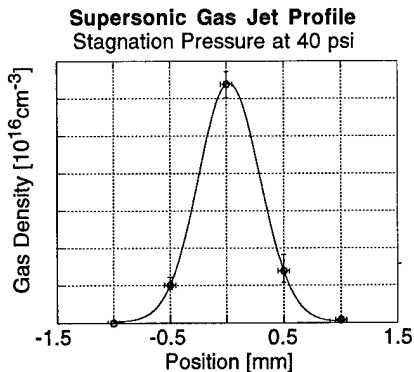


Figure 2: Transverse profile of the supersonic gas jet measured at Rochester.

The gas jet is delivered through a simple axis-symmetric converging/diverging nozzle with an opening angle of 10° and a throat diameter of $75 \mu\text{m}$. Continuous operation of the gas jet alleviates vibration problems associated with pulsed gas jets. Nominal operating pressure of the nozzle is designed to be 2,000 psia, which gives a gas density of $\sim 2.5 \times 10^{18} \text{ cm}^{-3}$ at the nozzle exit. The operating pressure can be substantially lowered with the use of liquid nitrogen pre-cooling.

The first generation nozzle design is based on a simple one-dimensional gas dynamics model that assumes an ideal gas in steady-state, isentropic flow [8]. A procedure was developed to produce the copper nozzle using conventional machining techniques combined with an extrusion process to achieve the final throat diameter.

Preliminary testing of the nozzle at low operating pressure (~ 40 psia) has been performed at the University of Rochester. The nozzle was moved relative to the laser so that a rough profile can be measured (Figure 2). Since the nozzle was not operating at its designed pressure, the gas density obtainable was far lower than 10^{18} cm^{-3} . However, the gas density attained agrees reasonably well with prediction.

Vacuum testing of the nozzle has started recently to check the vacuum pumping requirements for operating the gas jet in the FFTB. The nozzle was installed into a test system that approximates a differential beam line vacuum pumping system with two turbo molecular pumps giving a combined pumping capacity of 365 liter/sec. The gas from the nozzle is collected through an orifice by two mechanical pumps with a combined pumping capacity of 33 liter/sec. Initial results are not as positive as we have expected and are still under investigation. One of the concerns is the underexpansion of the gas jet due to a high exit pressure relative to the stagnation pressure, causing shock waves to disrupt the flow pattern [8].

IV. BEAM SIZE MEASUREMENTS

A. Laser-Compton Monitor

The Laser-Compton Monitor developed by Tsumoru Shintake [9] is installed in the FFTB and has been

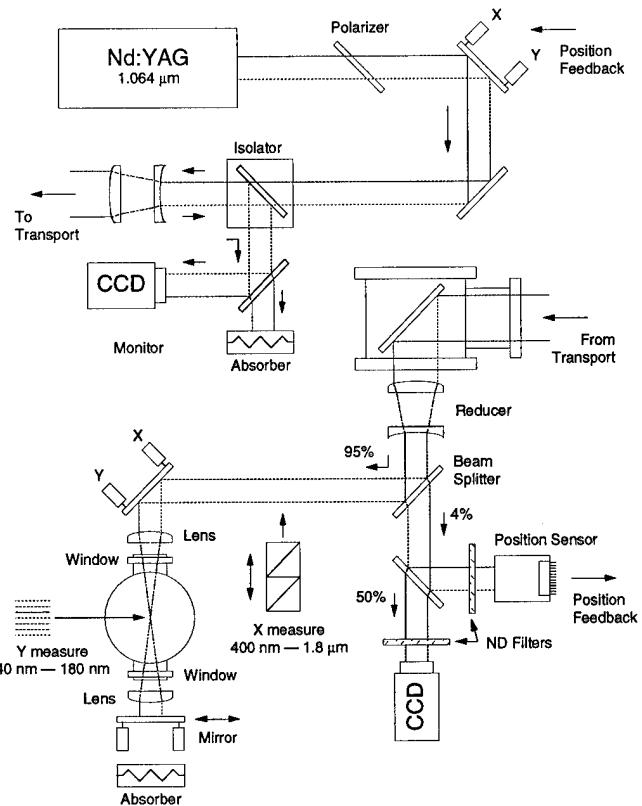


Figure 3: Schematic of the simplified version of the Laser-Compton Monitor.

successfully operated there [10] to measure beam sizes of less than 100 nm. For the plasma lens experiments, a simplified version of the monitor is being developed for installation at the plasma lens focus (Figure 3). The Compton-scattered photons will be observed by the same detector that measures the bremsstrahlung photons from the wire scanners.

B. Measurement of the Compton-Scattered Electrons

As a supplementary measurement to the Compton-scattered photons from the Laser-Compton Monitor, we intend to measure the spectrum of the Compton-scattered electrons using the existing E-144 Electron Calorimeter (ECal). The segmented calorimeter is located just downstream of the permanent dump magnets of the FFTB beam line, and provides a spectrometric analysis of the electrons.

ECal is a silicon calorimeter with tungsten as radiator, consisting of 23 layers of 3.5 mm tungsten, 1.04 mm air, and 0.300 mm silicon sandwiched between two pieces of 0.83 mm G10. The silicon wafers are subdivided into 1.6 by 1.6 cm² pads, where each layer has 4 such pads horizontally and 12 vertically. The silicon pads are ganged together in depth to form towers, where 4 longitudinal segments are read out separately for each tower. ECal sits on a stage which allows it to be moved up towards the beam line. Electrons from the beam will hit the center 2 (of 4) horizontal pads, so that the outer pads can possibly be used for backgrounds subtraction.

The modulation depth in the number of Compton-scattered electrons is determined by measuring the energies deposited in several rows of ECal both above and below the

Compton edge. Energies deposited would, after correction for background and shower sharing, be divided by an average energy to obtain a number of Compton electrons in the momentum range. The average energy of a selected row is determined by integrating the Compton cross section over its momentum bite.

C. Measurement with Bremsstrahlung Optics

Beam profile can be measured by converting the electron beam to bremsstrahlung photons using a thick radiator, and using collimators and slits to determine the size of the source of photons using a variant of pinhole optics [11]. The system has been tested at the MIT/Bates 1 GeV electron linear accelerator and can be used as a supplementary measurement for the plasma lens experiments.

V. DETECTOR BACKGROUNDS FROM PLASMA LENSES

Background sources for particle detectors from a plasma lens can be divided into three kinds, namely, electrons/positrons, protons, and photons. These backgrounds originate from different elementary physical processes underlying the interactions of the incoming electron or positron beams with the plasma near the interaction point. We have calculated the cross sections and angular distributions for all the processes responsible for the various sources of backgrounds [12], from which the number of background particles can be determined for any given machine parameters. Here we have chosen NLC as an example, with which the prospect of the application of plasma lenses in future linear collider detectors can be examined.

For our calculations, we have taken the NLC beam energy E_{beam} at 250 GeV, $N = 0.6 \times 10^{10}$, $\sigma_x = 300$ nm, $\sigma_y = 3$ nm, $\sigma_z = 100$ μ m, the hydrogen plasma density n_p is 10^{18} cm⁻³ and $L = 2$ mm. The number of bunches in a bunch train n_b is 90. The angular cut for the scattered particles into the detector is taken to be 150 mrad. Results of our calculations are summarized in Table 1.

Background Source	Partial Cross Section (cm ⁻²)	Vertex Detector	Drift Chamber
Bhabha & Møller	0	0	0
Elastic ep :			
electrons	0.103×10^{-45}	negligible	negligible
protons	0.613×10^{-39}	negligible	negligible
Inelastic ep :			
electrons	0.132×10^{-33}	negligible	negligible
charged hadrons	0.396×10^{-29}	0.23	0.23
Inelastic γp :			
charged hadrons	0.313×10^{-28}	1.8	1.8
Compton from:			
quadrupole	0.995×10^{-25}	2000 γ s	2600 γ s
plasma focusing	0.548×10^{-25}	990 γ s	1800 γ s
bremsstrahlung	0.119×10^{-24}	540 γ s	270 γ s

Table 1: Summary of background sources from plasma lens in NLC.

We have assumed that the resolution time for the detector is much longer than 1.4 ns, which is the separation between successive bunches in a bunch train. We have conservatively integrated the events over a train of 90 bunches, with a total time span of ~ 125 ns. Time separation between bunch trains is ~ 5 ms.

For vertex detectors, the serious range for background photons is between 4 keV and 100 keV. When imposing such energy cuts, the number of background photons is reduced to $\sim 3,600$. For drift chambers, only photons with energies greater than ~ 100 keV need to be considered, and the background photons total about 4,700. Drift chambers can tolerate about 10,000 incident photons, of which typically no more than 100 convert.

It can be seen from Table 1 that all the main components of the detector should survive from the plasma lens induced backgrounds. Therefore, the implementation of a plasma lens for luminosity enhancement in high energy e^+e^- collisions is feasible without hampering the normal performance of the detector.

VI. SUMMARY

Feasibility of the key concepts involved in the plasma lens experiments have been proven. The mild background events induced by beam-plasma interaction has been shown to be within tolerances for applications at high energy detectors. Further work is to be done on the supersonic gas jet, including the addition of a converging/diverging supersonic diffuser to control shock waves, as well as the development of an asymmetric (flat) supersonic gas jet to reduce vacuum pumping requirements and backgrounds.

VII. REFERENCES

- [1] P. Chen, Part. Accel. **20**, 171 (1987).
- [2] J. Rosenzweig *et al.*, Phys. Rev. Lett. **61**, 98 (1988).
- [3] H. Nakanishi *et al.*, Phys. Rev. Lett. **66**, 1870 (1991).
- [4] G. Hairapetian *et al.*, Phys. Rev. Lett. **72**, 2403 (1994).
- [5] W. Barletta *et al.*, Proceedings of the Particle Accelerator Conference 1993, 2638, Washington, DC (1993).
- [6] J. G. Heinrich *et al.*, "SLAC Proposal E-144," Stanford Linear Accelerator Center, Stanford, CA (1991).
- [7] L. Lompré *et al.*, J. Appl. Phys. **63** (5), 1791 (1988).
- [8] M. Saad, *Compressible Fluid Flow*, Prentice Hall, Englewood Cliffs, NJ (1985).
- [9] T. Shintake, Nucl. Inst. and Meth. **A311**, 453 (1992).
- [10] T. Shintake *et al.*, "First Beam Test of Nanometer Spot Size Monitor using Laser Interferometry," KEK Preprint 94-129, KEK, Tsukuba, Japan (1994).
- [11] J. Norem *et al.*, Nucl. Inst. and Meth., to be published.
- [12] C. Baltay, "Backgrounds in SLD due to the Proposed SLC Plasma Lens," SLD Internal Notes, unpublished.

Measurement of Electric Field Uniformity in an Electrostatic Separator

Weiran Lou and James J. Welch, *Cornell University, Ithaca NY**

Introduction

Electrostatic separators are used in several modern storage rings to generate large distortions of the closed orbit as a means of avoiding undesirable beam-beam collisions in the arcs. Unlike comparable magnetic elements, there is not a well developed technology to measure the electric field quality of electrostatic separators, so the ultimate field uniformity is largely left up to the conservatism and skill of the designers and fabricators of the devices. Measurements of the electric field integrate over the entire path of the particles, including end effects, and sense the effects of misalignments, warpage and other mechanical errors on individual units. This ability not only helps with quality control, but also to interpret machine studies where the results are sensitive to the nonuniformities of the electric field. In particular, electric field measurements can provide a better estimate of the tuneshift and sextupole moments as a function of beam position in the separators.

Description of Method

The basic technique we used for measuring the electric field is to stretch a long thin wire along a hypothetical particle trajectory between the electrodes and adjust the potential of the wire relative to the electrode potentials to zero out the net charge on the wire. The induced charge is observed by oscillating the electrode voltages so that the resulting induced currents can be seen on an oscilloscope. Once the wire potential is determined the wire can be translated a precise amount and the process repeated. The electric field is obtained by taking the derivative of the wire potential data with respect to the position of the wire. In practice the highest accuracy is obtained by first setting of the voltage divider which sets the potential of the wire relative to the electrodes, and then adjusting the position of the wire to zero out the induced signal.

One nice features of this method is that it uses a motionless wire; the field is oscillated to produce the signal. (An alternate arrangement is described in [1].) Also, the required equipment is quite modest: a potentiometer, a sinusoidal single source (eg. Wavetek), an ordinary transformer, two translation stages, an oscilloscope and wire, were all that we used. The overall accuracy depends mostly on the quality of the potentiometer.

To understand how this works, first imagine that the charge on the electrodes is unperturbed by the presence of charge on the wire, (See figure 1). The effect of the perturbation is negligibly small over the range of wire positions of interest because

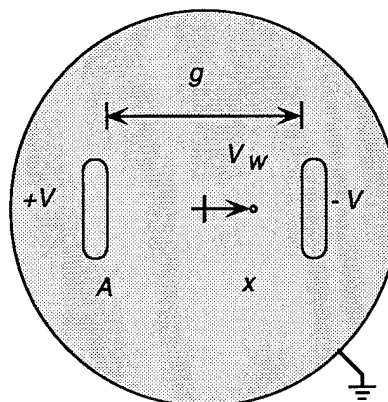


Figure 1: The measurement wire, electrodes, chamber and the voltages are shown schematically in this figure.

the induced net charge on the wire can be made essentially zero compared with the charge on the electrodes. We will call E_0 the electric field generated by the charge on the electrodes only. It is this electric field that we wish to measure.

Similarly imagine that the field generated by the charge on the wire is approximately the simple line charge field in free space (no electrodes or chamber) which in cgs units is

$$E_w(r) = \frac{2\lambda}{r}$$

where λ is the net charge per unit length on the wire and r is the distance from the wire center. The potential of the wire is maintained externally and determines the charge on the wire at each wire position. Clearly this latter approximation is not valid near the electrodes. Whatever the actual wire field is, we only require that it go to zero when the net charge on the wire is zero. This will not be true very close to the wire where polarization charges create a dipole field which cancel out the electrode field inside the wire. But the dipole field have very short range and will not affect the charge distribution on the electrodes and therefore do not change E_0 . Similarly it will not be true near the electrodes where image charges are induced, unless $\lambda = 0$.

Analysis

First we put $\pm V$ on the two electrodes and hold the wire at V_w . The wire is at position x . We will define the origin of the coordinate system such that for a wire at the origin there is no net

charge on the wire ($\lambda = 0$) when the wire is held at ground potential ($V_w = 0$). Normally, for a symmetric separator this would be exactly between the two electrodes, but due to imperfections could be different in practice.

$E = E_0 + E_w$ is the total electric field at any point, and A is the x coordinate of V electrode (approximately $-g/2$). Then

$$(V - V_w) = \int_A^x E dl \quad (1)$$

$$= \int_A^0 E_0 dl + \int_0^x E_0 dl + \int_A^x E_w dl \quad (2)$$

$$\approx \int_A^0 E_0 dl + \int_0^x E_0 dl + \int_{A-x}^{-\phi/2} \frac{2\lambda}{l} dl \quad (3)$$

From the definition of the origin we have

$$V = \int_A^0 E_0 \cdot dl \quad (4)$$

With this definition applied back to equation 3 we have

$$-V_w \approx \int_0^x E_0 dl + \int_{A-x}^{-\phi/2} \frac{2\lambda}{l} dl \quad (5)$$

Equation 5 can be used in the following manner. For each wire position adjust V_w to make $\lambda \approx 0$, record the wire position and voltage. Since $\lambda \approx 0$

$$V_w = - \int_0^x E_0 dl \quad (6)$$

so the electric field may be obtained from $E_0(x, y) = -\nabla V_w$.

Measurements

A prediction for the shape of the electric field in the gap was obtained from a 2D successive over-relaxation code written specifically for this separator. In the design of the electrodes considerable effort was expended to optimize the field quality by minimizing the nonuniformity of the electric field at the origin and nearby. If the uniformity of the field in the real separator was similar to the design there should be almost no observable beam dynamical effects due to the separator field.

A prototype for the new low impedance horizontal separators was measured. The electrode length is 2.5 m and the gap between the electrodes is about 10 cm.

Figure 2 shows the measured V_w/V versus the horizontal coordinate. Superposed on this is the calculated electric potential due 2D code. Clearly there are easily measurable deviations.

Figure 3 shows the deviation of a fourth order fit to the measured data from the calculated field. The linear and nonlinear field coefficients are tabulated in table 1.

It was found that the calculated kick at the origin agrees well the measured kick, (see the b_1 terms in table 1). However, the nonlinear fields of the prototype were much larger than those predicted for perfect 2D geometry. The discrepancy is easily seen in figure 2, but is more obvious in figure 3 where the theory is subtracted from the measured values. The theoretical voltage

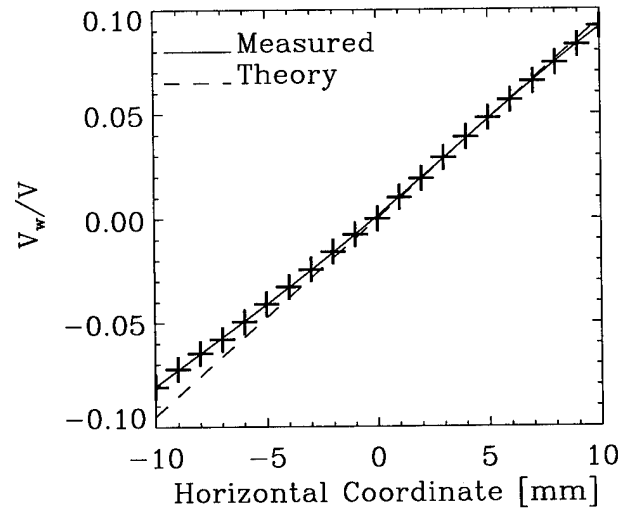


Figure 2: Measured V_w/V versus the horizontal coordinate is superposed with the results from a 2D electrostatic calculation.

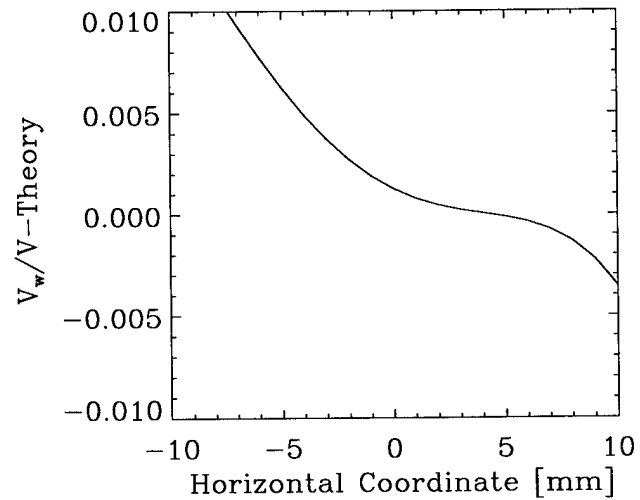


Figure 3: Plotted is the deviation of the fourth order fit to the measurements of V_w/V from the results from a 2D electrostatic calculation.

order	Laplace	Measurement
b_0	0.0	1.27×10^{-3}
b_1	9.46×10^{-3}	8.94×10^{-3}
b_2	0.0	8.18×10^{-5}
b_3	-1.41×10^{-8}	-3.39×10^{-6}
b_4	0.0	-4.10×10^{-7}

Table 1: Calculated and measured field coefficients up to the fourth order. There are defined by $V_w/V_{applied} = b_0 + b_1x + b_2x^2 + b_3x^3 + b_4x^4$ where x is in millimeters.

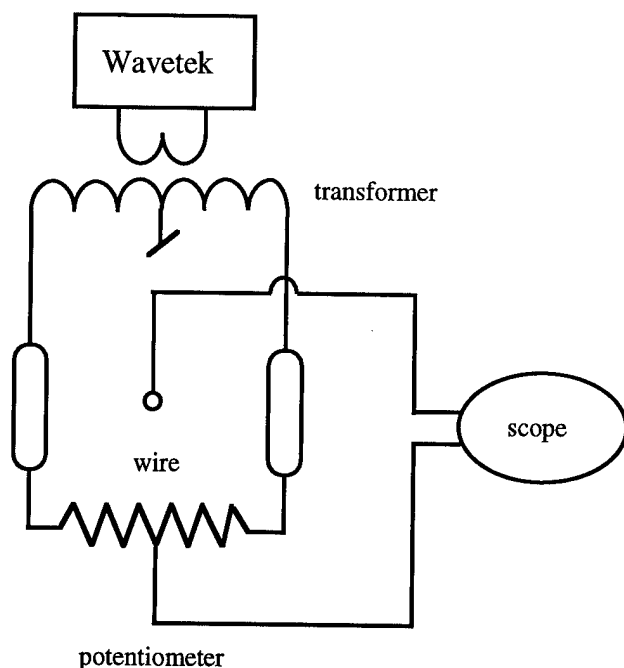


Figure 4: A somewhat simplified schematic of the circuit used to measure to excite the electrodes and measure the induced wire potential is shown.

must be antisymmetric about the mechanical center and therefore has only odd order coefficients in an expansion in x . The measured data has even order coefficients which are of comparable importance over the measurement range. Symmetry of the electrodes implies these even order coefficients cannot be accounted for by 3D end effects. One can therefore conclude that the error introduced by the 2D approximation is comparable or less than other errors. The apparent offset in figure 3 of the origin of the measured data can only be explained by the presence of even symmetry terms. In fact, it is almost entirely due to b_1 term and the nonzero b_0 term. Possible causes are electrode misalignments and unbalanced voltages on the electrodes. The voltage balance was set by the relative number of turns on two legs of the transformer and was not particularly accurate.

Technical Details

A simplified electrical schematic is given in figure 4. The center tap of an ordinary audio transformer is grounded to the separator vacuum chamber. A sinusoidal signal is generated by a Wavetek signal generator with a frequency between 400 and 4 kHz. This arrangement establish approximately equal and opposite voltages on the electrodes as they are normal powered. The wire is connected to a high impedance input of an oscilloscope with the common of the the scope input connected to the center tap of a good potentiometer. If there is any net charge induced on the wire it will oscillate with the applied field and cause current to flow in the high impedance input of the scope where it is easily observed. Referencing the common of the scope to the potentiometer center voltage effectively biases the wire to

the potentiometer voltage. In practice since only a limited range of positions is desired an accurate fixed resistance is placed on either side of the potentiometer thereby increasing the measurement resolution. The applied source frequency should be chosen carefully to get the best results. Higher frequencies will cause larger currents to flow into the scope for the same induced charge and provide a bigger signal. However, if there frequency is too high the capacitance of the cables and impedance of the scope input tends to average out the signal and sensitivity is lost. Another complication is that the main signal circuit resonates with a broad resonance center around 10 kHz. Thus the voltage being applied to the electrodes and consequently the charge induced on wire are strong functions of frequency in this range.

References

- [1] A.A. Mikhailichenko, *On the Measurement of Electric Fields Using a Rotating Probe*, Novosibirsk, Institute of Nuclear Physics preprint 84-126 (1984), In Russian

ANALYSIS AND REDESIGN OF RF FILTER BAR TO RELIEVE THERMAL STRESSES

E. G. Schmenk and K. W. Kelly, Department of Mechanical Engineering,
Louisiana State University, Baton Rouge, LA 70803
V Saile and H. P. Bluem, Center for Advanced Microstructures and Devices,
Baton Rouge, LA 70803

I. ABSTRACT

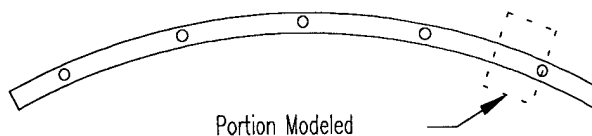
During operation of the electron storage ring at the Center for Advanced Microstructures and Devices (CAMD), high thermal stresses were induced in RF filter bars, causing the bars to deflect into the path of the emitted beams. Finite-element models (FEMs) were developed to model both the original and alternate RF filter bar designs. An improved filter bar design was implemented.

II. INTRODUCTION

Filter Bar Description

The ring at CAMD consists of eight segments with eight dipole-magnet vacuum chambers. Each dipole chamber bends the electron beam 45 degrees. As the electrons are turned, radiation is emitted in the horizontal plane tangential to the path of the electrons. The resulting fan-shaped beam of radiation passes between two horizontal RF filter bars.

As originally designed, each RF filter bar (Figures 1 and 2) was approximately 1.18 inches wide, 0.54 inches high and 92 inches long. It was curved to form an arc of 45 degrees to conform with the shape of the chamber. Each bar was suspended or supported by five posts. Four of the posts were in slots elongated by one-eighth of one inch to allow for differing thermal expansion during the vacuum bake-out cycle, while the center post was not free to move.



DRAWING NOT TO SCALE

Figure 1: RF Filter Top View

Problem Description

When the electron storage ring is properly aligned, virtually no radiation is absorbed by the RF filter bars. As the alignment becomes worse, a greater percentage of the emitted radiation strikes the filter bars, and the temperature of the bars increases. At CAMD, minor misalignments, coupled with an RF filter bar design that did not accommodate significant thermal expansion, resulted in the bars heating and bowing vertically into the path of the

radiation. To prevent recurrence of this event, an improved RF filter bar design was sought.

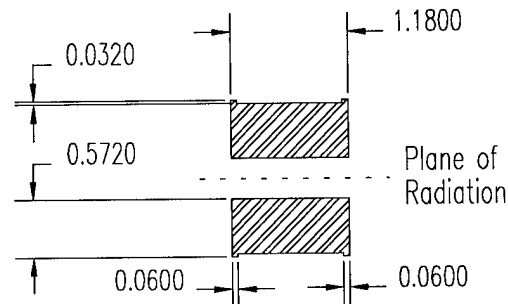


Figure 2: RF Filter Bars Side View

III. MODELING EFFORT

Model of Original RF Bar

A FEM of the original filter bar was developed using the commercial package ANSYS to predict the thermal stresses and deflections created when the bar absorbs a small percentage of the radiation emitted within one chamber. CAMD personnel provided the estimate that the original problem may have resulted from the bar absorbing as little as 200 watts of the 6000 watts generated in the chamber. The bar was modeled with three dimensional eight node elements. The assumptions used to model the problem are listed as follows:

- The synchrotron radiation striking the bar was completely absorbed.
- 200 watts of synchrotron radiation struck the bar at the bottom of the inside edge.
- The radiation was evenly distributed along the length of the bar.
- All surfaces of the bar had an emissivity of 0.5.
- The bars radiated to surroundings that were at a temperature of 535 deg. R (75 deg. F).
- There was no conduction heat transfer through the posts or through contact with the walls of the chamber.
- The bar had a rectangular cross section; the small ridges were ignored.
- Only elastic deformation was considered (even though stresses were above the elastic limit); plastic deformation and creep were ignored.

- The material properties of the bar were not affected by temperatures.
- All degrees of freedom are restrained at the posts.
- Because of symmetry, only one eighth of the bar needed to be modeled.

In the steady state case in which the bar absorbs 200 watts, thermal stresses in the bar were quite high, and the deformation in the vertical direction was significant.

Models of Alternate RF Bar Designs

A series of FEM models was built to predict the performance of different RF filter bar designs. The primary design criteria of the new designs are listed below:

1) The most important criteria of the new RF filter bars is that they be able to continuously absorb a small percentage of the emitted radiation (200 watts out of a possible 6000 watts) without deforming into the path of the radiation.

2) The decision was made by CAMD personnel to embed thermocouples in the new RF filter bars. The second design goal is that in the event all of the chamber radiation is absorbed by a bar, the embedded thermocouples should detect a rise in temperature of the front edge of the RF bar before the RF bar is damaged.

3) The capability of the bars to filter RF radiation should not be reduced.

Steady-State Solutions

Modeling results for a number of filter bar designs were obtained for the steady state case in which the bar absorbs 200 watts. In all cases, a primary design concept was that although bending in the vertical direction could not be allowed, some bending in the horizontal direction was considered acceptable. In the original design, the area moment of inertia resisting bending horizontally was about 4.8 times the value in the vertical direction, so the bar relieved compressive stresses by bending vertically into the radiation. In the first attempt to make the modeled bar bow horizontally, vertical notches were cut into the bar from the outside edge. A model was developed which predicted that the bar with notches would deflect significantly in the horizontal direction, but not in the vertical direction. The predicted horizontal deflection for the case in which the bar absorbs 200 watts is shown in Figure 3.

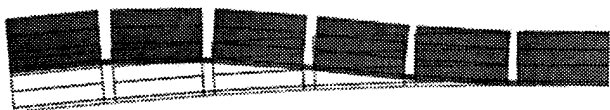


Figure 3: Bar Notched on One Side

A second proposed design involved cutting vertical notches into the bar from both the inside and outside edges. It was hoped that this design would relieve stresses by

allowing compression, somewhat like an accordion, without suffering a large change to its overall shape. The model confirmed this hypothesis. If 200 watts of energy were absorbed by the bar, the maximum remaining tensile stresses were predicted to be 57 kpsi when notches were cut on both sides as compared to 140 kpsi with notches only on the outside edge of the bar. The predicted deflections (Figure 4) are also much smaller.



Figure 4: Bar Notched on Both Sides

Yet another alternative involved building the RF filter bar out of four separate sections, each approximately one-fourth of the total length and held in place by a single pin. A gap would be left between the sections for purposes of thermal expansion. The finite element model was used to study how much the radius of curvature would change if the bar was struck by radiation. This alternative offers the advantage of almost guaranteeing no build-up of thermal stresses, but the installation procedure was thought to be too complex so this last option was not seriously considered.

Transient Thermal Models

To satisfy the second design criteria in which the bar is subjected to a sudden heat input equal to the output from one chamber (6000 watts), a second set of models was used. In these cases, only a two dimensional transient thermal analysis was required.

Transient thermal models were used to determine where thermocouples should be placed in the bar. The installation of the filter bars would be easiest if the thermocouples were centered in the posts used to suspend the bars, but there was a concern that if radiation suddenly struck the bar, substantial damage to the bar could occur before the thermocouples measured a rise in temperature. The transient thermal models allowed the prediction of the temperature profile across the cross section of the bar as a function of time. Modeling results showed that if the bar was made of stainless steel, the temperature of the lower corner would rise over 500 °R, where the radiative heat flux is applied, before the temperature in the middle of the bar changed. If the bar was made of copper, the temperature variation across the bar was decreased, due to the greater thermal conductivity of the bar. Figures 5 and 6 show the transient thermal response (for stainless steel and copper, respectively) when radiation striking the bar suddenly increases from 200 watts to 6000 watts. The conclusion of this modeling effort was that if the bar is made of copper, then the placement of the thermocouple is not crucial. However, if the bar is made of stainless steel, then the thermocouple should be placed as close as possible to the suspected region where the radiation is absorbed.

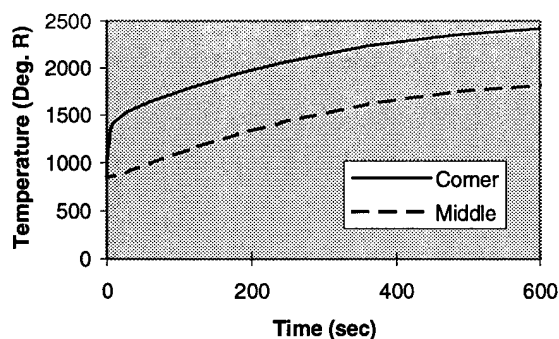


Figure 5: Thermal Response of a Steel Bar

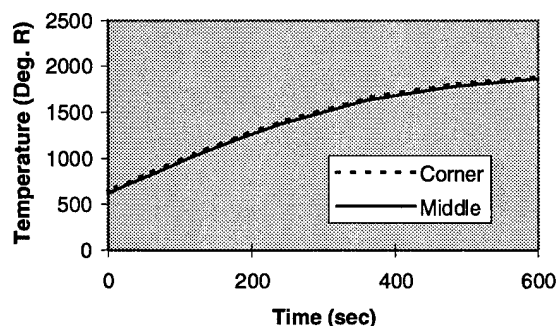


Figure 6: Thermal Response of a Copper Bar

IV. INSTALLATION

The dipole chamber with the most damaged RF filter bar was refitted with redesigned filter bars. The filter bars were removed and replaced by sliding them in and out of the ends of the chamber, instead of fully opening the chamber. This method minimized the required work on the chamber itself, but did not allow visual inspection of the filter bars before removal. It was noted however, that one of the posts supporting the upper bar had been deformed, indicating that it had been under severe shear stress while installed.

The new RF filter bars incorporated some of the ideas that had been tested using the finite element models (Figure 7). The new bars were made of four separate segments, each held by two pins in elongated slots. The slots are elongated to allow the pins to slide if necessary due to thermal expansion. Small gaps were left between the segments to prevent contact during any expansion. When the idea of subdividing the bar was originally modeled, each segment had been supported by only one pin, but two pins were used in the actual redesign to make installation easier. The additional pins were installed by drilling holes in the chamber, then welding the pins in place.

There was some concern that the pins would not slide in their slots due to cold welding, so notches were cut in the inside and outside edges of the bars similar to the notches that had been tested using the finite element program. It is hoped that

these notches will allow thermal stresses to be relieved, if the posts fail to slide, without the bar deflecting into the path of

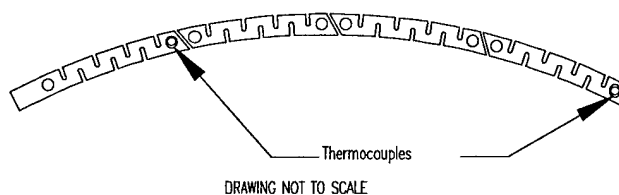


Figure 7: Redesigned RF Filter Bar

the light beams.

Thermocouples were installed in two of the posts holding the bar in place. It is hoped that high temperature readings from the thermocouples, as well as a decrease of vacuum in the chamber, will provide adequate warning if the bar is struck by excessive radiation.

The bars were made of stainless steel instead of copper because of the superior strength of the stainless steel. Since the chamber is also made of steel, the problem of welding two dissimilar metals was also avoided.

V. TESTING

The retrofitted chamber was installed on April 3, 1995. To date, the chamber is suffering from excessive photo-induced off-gassing, and no conclusive testing of the new design has been completed. The synchrotron radiation was directed onto a new RF filter bar once, and no symptoms of significant deflection of the bar were noted.

VI. CONCLUSIONS

The possibility that synchrotron radiation may accidentally strike the RF filter bars should be considered during the design of the equipment. Otherwise the bars may deflect into the normal path of the radiation due to thermal stresses caused by the radiation.

A finite element software package can be a useful tool while studying the alternate designs of the RF filter bars, and to predict what will happen when radiation strikes the bar.

An alternative filter bar design has been implemented in a dipole chamber at CAMD. Further testing is required to determine if the new bars can absorb radiation and heat up without affecting storage ring operability.

VII. REFERENCES

- [1] Pearce, Jorge and Sah, Richard "Analysis of Dipole-Chamber Problems", Maxwell Laboratories, Inc., Brobeck Division, 4905 Central Avenue, Richmond, CA 94804-5803, USA, December 3, 1993.

LOADED DELAY LINES FOR FUTURE R.F. PULSE COMPRESSION SYSTEMS[†]

R.M. Jones*, P.B. Wilson* & N.M Kroll^{^^}

*Stanford Linear Accelerator Center,

Stanford University, Stanford, CA 94309

^{^^}University of California, San Diego, La Jolla, CA 90732

Abstract

The peak power delivered by the klystrons in the NLCTA (Next Linear Collider Test Accelerator) now under construction at SLAC is enhanced by a factor of four in a SLED-II type of R.F. pulse compression system (pulse width compression ratio of six). To achieve the desired output pulse duration of 250 ns, a delay line constructed from a 36 m length of circular waveguide is used. Future colliders, however, will require even higher peak power and larger compression factors, which favors a more efficient binary pulse compression approach. Binary pulse compression, however, requires a line whose delay time is approximately proportional to the compression factor. To reduce the length of these lines to manageable proportions, periodically loaded delay lines are being analyzed using a generalized scattering matrix approach. One issue under study is the possibility of propagating two TE_{0n} modes, one with a high group velocity and one with a group velocity of the order $0.05c$, for use in a single-line binary pulse compression system. Particular attention is paid to time domain pulse degradation and to Ohmic losses.

I. INTRODUCTION & METHODOLOGY EMPLOYED

Electron-positron colliders in the TeV range will require microwave sources delivering power in the hundred megawatt range. The large power demands are alleviated to some extent through the use of pulse compression techniques in which the power of the pulse is enhanced at the expense of the time duration of the pulse.

In order to reduce the length of the delay lines necessary to store the energy for a pulse compression scheme the characteristics of a delay line periodically loaded with thick irises are investigated. In the SLED-II¹ system (SLAC energy development system using resonant lines), overmoded circular waveguides are used to store energy from the early portion of the output pulse from the klystrons. Once the line is charged the phase of the klystron is reversed, leading to a discharge of this energy at a reduced pulse width and enhanced overall pulsed power. To achieve a pulse of length 250 ns requires a delay line of length 36 m.

The length of the line can be reduced by loading it periodically with irises, in order to reduce the group

velocity of the wave. In BPC (binary pulse compression²), in which the peak power is doubled in successive stages. At each stage it is required to delay the progress of the wave from the first half of the pulse with respect to the last half, so that they arrive synchronously in time at the output of the stage. To achieve this end, either two lines are required, one with a low group velocity and one with a group velocity near c , or a delay line propagating two different modes simultaneously with widely differing group velocities. We explore this latter method with a TE_{01} mode and a TE_{02} mode propagating in a delay line consisting of a large number of inward and outward steps (thick irises)

The theoretical gain of a BPC system is 100% for a system consisting of components with infinite conductivity in which no mode conversion occurs at discontinuities. However, in reality the system possesses finite Ohmic wall losses which both degrade the shape of the pulse and reduce the overall system efficiency and finite mismatches occur at waveguide discontinuities. Ohmic wall losses are paid attention to by allowing the axial wavenumber to possess both a real and imaginary component (the latter corresponding to the wall losses) and also, by taking into account transverse wall losses in a multi-mode S-matrix analysis.

Our initial investigation in the area of multi-mode propagation down iris-loaded delay lines revealed that the highest order propagating mode can undergo significant reflection under resonance conditions (this is a choke mode), and that the mode below in frequency can also be delayed as a consequence of the avoided crossing in the characteristic dispersion curves of the waveguide. However, it is not possible to operate in a choke mode regime for lower order propagating modes. For this reason we chose the diameter of the waveguide to be 2.32 inches (the cut-off of the TE_{02} mode lies at 11.36GHz) and the outward radial step (negative iris) is chosen to be three times larger. The choice of the latter diameter dictates the group velocity and the point of avoided crossing in the dispersion curves.

II. APPLICATION OF MODE MATCHING METHOD TO THE DISPERSION CHARACTERISTICS OF LOADED DELAY LINES

The Brillouin diagrams for the loaded delay lines are calculated using a scattering matrix method involving

[†] Supported by Department of Energy, DE-AC03-76SF00515* and DE-FG03-92ER40759**

matching the electric and magnetic field at either side of the aperture region of a periodic structure. This mode matching method converges provided a sufficient number of modes is used to represent the field at transitions in the geometry of the waveguide.

Firstly, the *generalized* lossless S-Matrix of a single narrow to wide transition (NW) is calculated by matching the complete modally decomposed field at the transition:

$$\begin{pmatrix} S_{11} & S_{12} \\ S_{21} & S_{22} \end{pmatrix} = \begin{pmatrix} 2q_0^{-1} - I & 2q_0^{-1} p_0 \\ a(S_{22} + I) & aS_{21} + I \end{pmatrix} \quad (2.1)$$

where the q_0 and p_0 matrices are given in terms Y , the admittance matrix of the wide transition and \hat{Z} , the impedance matrix of the narrow transition:

$$q_0 = I + \hat{Z}a^t Y a, \quad p_0 = \hat{Z}a^t Y \quad (2.2)$$

The inner product matrix is given by:

$$a = \int_{S_{ap}} e \cdot \hat{e} dS \quad (2.3)$$

where the integral is performed over the aperture plane of the waveguide transition and the normalised mode functions e and \hat{e} correspond to circular waveguide mode functions³ of the wide section and the narrow section respectively. The NW matrix is cascaded with the wide to narrow (WN) transition to give the overall narrow to wide to narrow (NWN) scattering matrix for all modes (including evanescent modes). This matrix is converted into a multi-mode transmission or wave-amplitude matrix by applying the matrix relation:

$$\begin{pmatrix} T_{11} & T_{12} \\ T_{21} & T_{22} \end{pmatrix} = \begin{pmatrix} S_{21}^{-1} & -S_{21}^{-1} S_{22} \\ S_{11} S_{21}^{-1} & S_{12} - S_{11} S_{21}^{-1} S_{22} \end{pmatrix} \quad (2.4)$$

Finally, the eigenvalues of the multi-mode wave-amplitude matrix, for a given frequency, are of the form $\exp(j\Psi)$. Real values of Ψ correspond to modes within the pass-band of the Brillouin diagram. In practice twenty or more modes are necessary in order to adequately satisfy the boundary conditions. For a single waveguide mode propagating within the structure it is sufficient to consider a single mode wave-amplitude matrix (all modes are of course retained in the S-matrix calculation). However, for two propagating modes it is necessary to maintain the full-mode wave-amplitude matrix in the calculation of the eigenvalues.

Thus, the method proceeds with a search for real phase values as a function of frequency; the dispersion diagram is constructed by inverting the resulting phase dependence on frequency. Complex phase values of purely imaginary content are rejected as this represents waves within the stop-band region.

III. DISPERSION CHARACTERISTICS OF MULTIPLY LOADED DELAY LINES

The narrow and wide transition are .5 inches and .53 inches in length respectively. The latter dimension was chosen in order to allow at least one radial mode to propagate within the wide transition (i.e. the negative iris region). The radius of the narrow waveguide, viz, 1.16 inches, was chosen with a view to allowing two azimuthally symmetric TE modes to propagate in order to operate close to the cut-off of the upper band TE mode. The below fig. 1 shows the characteristic dispersion diagram for the chosen loaded delay line. The dashed line also indicated is the characteristic velocity of light line.

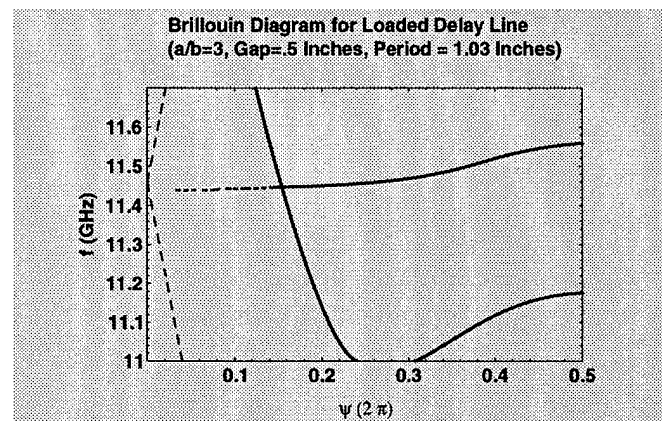


Figure 1: Brillouin Diagram for a Loaded Delay Line

The wide transition (i.e. the negative iris) has the effect of splitting the smooth wall dispersion curves. This avoided crossing in the dispersion curves allows one to have two waves propagating down the periodic structure. At a frequency of 11.503 GHz there is simultaneously a high group velocity wave of $-0.7c$ (i.e. a backward wave) and low group velocity wave of $0.05c$. This allows for the possibility of operating a binary pulse compression system in a single loaded delay line.

IV. PULSE PROPAGATION THROUGH SLED DELAY LINES

The progress of the pulse through the structure is monitored by the convolution of the input signal with the time response of the loaded delay line. To model the propagation of a pulse through the SLED delay lines we require the frequency response function of the loaded waveguide. The inverse transform of the product of the response function and the Fourier spectrum of the pulse allows the progress of the pulse through the structure to be monitored. The response function is obtained by evaluating the overall scattering matrix of the structure.

The effect of Ohmic losses is an important consideration. Wall losses are paid attention to using wavenumbers in which Ohmic losses are taken into account utilizing third order perturbation in the exact eigenvalues (the first order perturbation method is invalid close to the cut-off region of

the waveguide) and also by calculating the scattering matrix of each NW transition incorporating Ohmic losses due to the presence of the transverse wall. The generalized scattering matrix of a single transition is given by:

$$\begin{pmatrix} S_{11} & S_{12} \\ S_{21} & S_{22} \end{pmatrix} = \begin{pmatrix} 2q^{-1} - I & 2q^{-1}p \\ d^{-1}a(S_{22} + I) & d^{-1}(aS_{21} - 2I) + I \end{pmatrix} \quad (4.1)$$

where:

$$\begin{aligned} q &= I + \hat{Z}a^t\bar{Y}a, \quad p = \hat{Z}a^t\bar{Y}, \quad d = I + R_m w\bar{Y}, \\ \bar{Y} &= Yd^{-1}, \quad w = I - aa^t \end{aligned} \quad (4.2)$$

I is the unit matrix, a^t is the transpose of the matrix of inner products of the normalised mode functions, and R_m represents the wall resistance of the waveguide. In the limit of infinite wall conductivity (4.1) becomes (2.1). This scattering matrix is cascaded with succeeding matrices to give the overall matrix of the structure in the frequency domain.

The input trapezoidal pulse with of duration 250 ns and a sharp rise and fall time of 5 ns, together with the amplitude of its Fourier spectrum are illustrated in the below fig. 2.

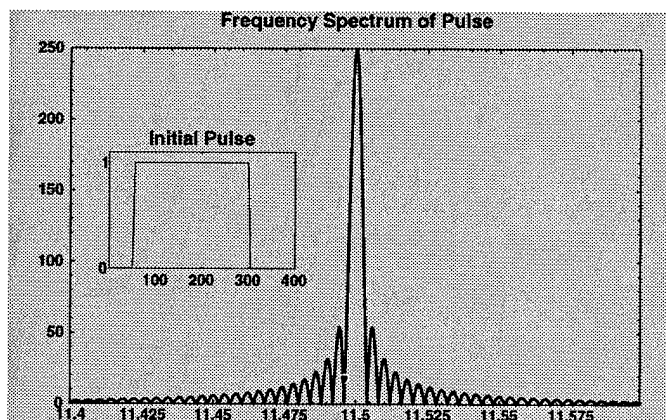


Figure 2: Input Waveform & Fourier Spectrum

Also shown in fig. 3 is the waveform corresponding to the propagation of a TE_{01} mode through one thousand and twenty four cells. The shape of the leading edge of the pulse is degraded by presence of the dispersive loaded delay line. However, even for this particularly large number of irises the overall shape of the pulse suffers remarkably little degradation. Ohmic wall losses of the system are of course unavoidable and this accounts for the diminished amplitude and overall area of the transmitted pulse. The TE_{02} suffers substantially larger Ohmic wall losses and to reduce these losses for multi-mode propagation one must use superconducting waveguide.

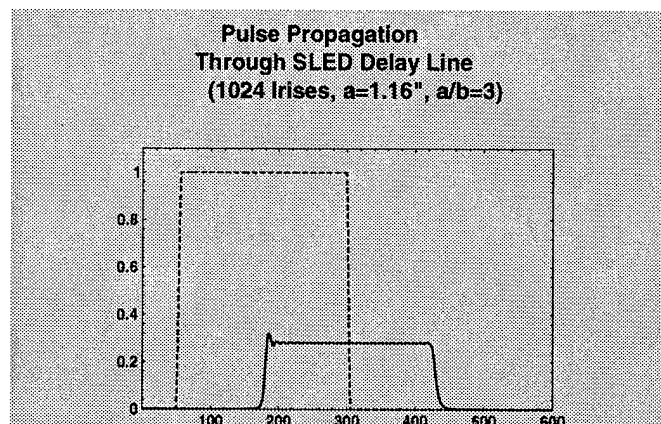


Figure 3: Pulse Propagation Through Loaded Delay Line

V. DISCUSSION

The concept of using a single-line iris-loaded waveguide to simultaneously delay the progress of two input pulses has been demonstrated, but the losses associated with the higher order mode (TE_{02} in this case) have been shown to be too high to be acceptable for practical purposes, unless one is prepared to utilize superconducting iris-loaded waveguide. However, a superconducting waveguide will impose a limit on the magnetic field that is tolerable and so limits the power transport through the system.

VI. REFERENCES

1. The original concept of SLED, developed by P.B. Wilson and Z.D. Farkas (Z.D. Farkas, H.A. Hogg, G.A. Loew, & P.B. Wilson, SLAC Pub-1453) as applied to a series of resonant lines is known as SLED-II: A. Fieberg and C. Schlieblich, EPAC, Rome, Italy, 1988
2. Z.D. Farkas, IEEE Trans MTT, **34**, 1036-1043, 1986
3. N. Marcuvitz, *Waveguide Handbook*, 1986 (Peter Peregrinus Ltd).

INTEGRATING INDUSTRIAL AND ACCELERATOR CONTROL SYSTEMS

R.Saban, AT Division, CERN, 1211 Geneva 23, Switzerland

ABSTRACT

The increasing presence of industrial control systems in high-energy physics laboratories raises the questions of their integration into the general control infrastructure and the organisation of the operation of the associated equipment. The method of integration is dictated by the adopted operation strategy; in turn, the latter determines the former. After an introduction to industrial control systems this paper describes different communication mechanisms with alien systems provided by manufacturers and reports on experience acquired at CERN. The major operation strategies in terms of level of coupling are described and their requirements on the integration methods are discussed.

I. INTRODUCTION

Commercial industrial control systems have entered high energy laboratory sites either as integral parts of large installations or as embedded controllers hidden in equipment which are largely used in industry [1,2]. While it was immediately obvious that the former (cryogenics, tunnel cooling and ventilation, etc.) needed to be monitored and partly controlled because of their tight coupling to accelerator operations, it took some time before it was felt there was a need for integrating the latter (water distribution, building heating, etc.). Furthermore, the picture was blurred by the fact that until recently, some of the installations and equipment were purchased without their control system and were equipped in-house with systems derived from accelerator control architectures. The general belief is that this practice should be abandoned in favour of turnkey systems; therefore the integration issue for all control systems is posed with an increased need of completeness.

II. CONTROLS IN INDUSTRY

Industrial control systems were created to automatize manufacturing industry. Broadly speaking, manufacturing processes are of two types: sequential processes (e.g. vehicle assembly) and continuous processes (e.g. oil cracking). This classification has given birth to two lineages in industrial control equipment both best adapted to the type of process to which they are applied: relay based logic gave birth to one and analogue regulators gave birth to the other. Because of the complexity and also the size of the plants, the most advanced techniques for supervision, communication, integration of alien equipment, remote control, etc. were developed by manufacturers of control systems for continuous processes.

Control equipment in industry is based on rugged networks, fieldbuses and digital computers equipped with input/output ports with or without dedicated processing power. They are designed to sustain the harsh factory or outdoor environment. Of their origin they have retained only the programming method: for sequential processes it is largely inspired from drawing relay based circuits (ladder logic) or representing finite state automata (sequential function chart) while for continuous processes it is based on blocks connected to each other by lines (function block).

Standardization efforts [3,4] in the field of industrial controls have led to a widely accepted model known as the Computer Integrated Manufacturing (CIM) pyramid. This model divides the industrial control of a factory into four levels with distinct functions and capabilities.

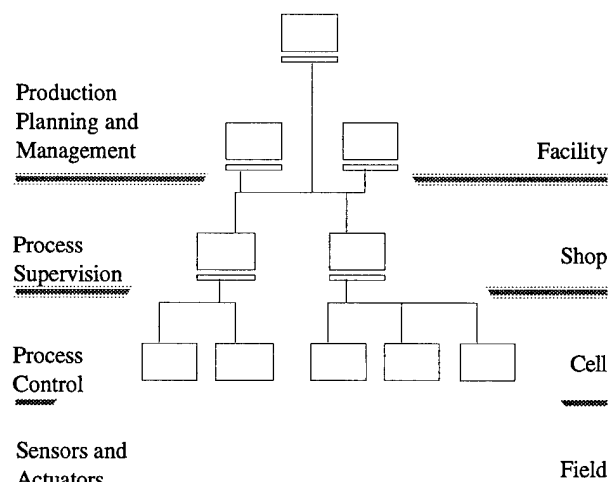


Figure 1

Manufacturers of control systems for industry offer a complete line of products which ranges from the programmable logic controllers (PLC) on the factory floor to the process supervision and advanced production management stations. Additionally, they provide communication mechanisms, supervision tools, archiving schemes, etc. Care must be taken to preserve this bundle of features when integrating an industrial control system, or part of it, in an accelerator control system.

Integration has always been a market penetration asset: in fact, all manufacturers were confronted with existing alien control equipment which needed to be connected to the *new* system which they were providing. A variety of solutions have been developed.

A. Integrating Industrial Subsystems

Because of their large use in the manufacturing industry, a number of important domains in controls are particularly well understood. These domains include for example motion

control, control mechanisms for feedback loops and others. Such systems are widely used in accelerator/collider control but despite the existence of a big commercial offer, they are almost always built around in-house developments. However, there are cases where such systems have been integrated into the accelerator control system.

The most common solution connects PLCs at the cell level via a proprietary protocol over RS-232C (see figure 2). While being simple and based on well-known technology, this approach provides little bandwidth and tends to overload the PLC. The latter, which is foreseen for process control, is tied up with tasks like protocol conversion and communication management.

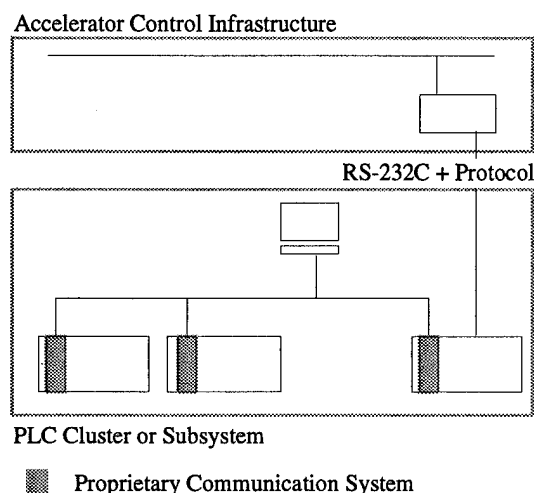


Figure 2

A variant of this is the integration of a cluster of PLCs acting as an industrial subsystem. This integration can be achieved either using the previous mechanism or exploiting the few other interfacing mechanism foreseen by the manufacturer: these include the porting of an industrial fieldbus to standard computer platforms.

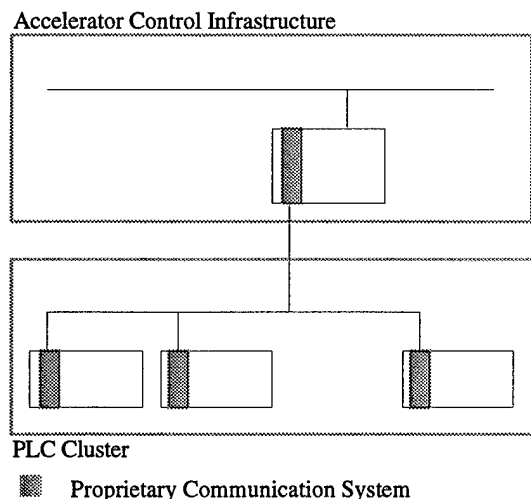


Figure 3

Another variant which has been implemented at CERN consists of using a commercial supervision package [5] which on one hand mediates the interaction with the PLC and on the other hand hosts a programming interface which disguises it in a member of the host control system.

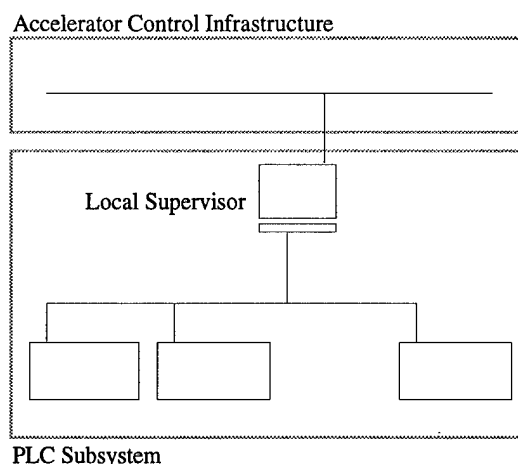


Figure 4

The major advantage of the latter types of integration is that the architecture of the host accelerator system is not altered by the presence of the alien system. The man-machine interface, alarm handling and logging, the communication mechanisms of the host system are used to control and monitor the industrial process below. However, all these facilities already foreseen by the manufacturer tend to be lost in this configuration.

B. Intra-PLC Communications

Communicating between PLCs of different brands has been made possible by the emergence of the Manufacturing Automation Protocol (MAP) standard [4,6]. This protocol has adopted ISO standards for all seven layers of the OSI model. At the highest level, called the Manufacturing Message Specification (MMS), an industrial automation controller is defined as a *Virtual Manufacturing Device* (VMD) with a number of properties and capabilities: upon the establishment of the service, a system which wants to use the associated equipment interrogates the controller about the particular type, the capabilities, the services, the power of the VMD and uses it accordingly.

A number of classes of devices have been described in companion standards to MAP; they range from Robot Control, Numerical Machines, Production Management to PLCs. The particular services offered by the latter companion standards include program invocation, variable exchange and executable image downloads. All these services are invoked by name and are independent of structures internal to the device or particular to a certain manufacturer.

In time critical applications this protocol is considered too heavy for intra-PLC communications. Therefore, all the PLC manufacturers that have developed proprietary communications mechanisms based on MAP never completely followed the MAP standard for communicating with their own PLCs: rather, they developed two different communication mechanisms running on the same hardware: one to be used with PLCs which they manufacture, the other with alien devices. The first implements a lighter, and

therefore more performant, version of MAP, while the second follows strictly the MAP standard [7,8]. Since with proprietary communications mechanisms care has been taken to follow the MAP standard at the uppermost layer compatibility, at the application program level, has usually been preserved.

C. Facility Level Integration

Manufacturers of large distributed control systems usually supply the process controllers, the supervision consoles and as well the communications infrastructure. The architecture usually includes a gateway to the control system situated in a production/facility management console which is often implemented using a general purpose computer platform. An application program library or a network server gives access to the parameters of the process which usually uses a local real-time database as a stepping stone between the requester of information and the field.

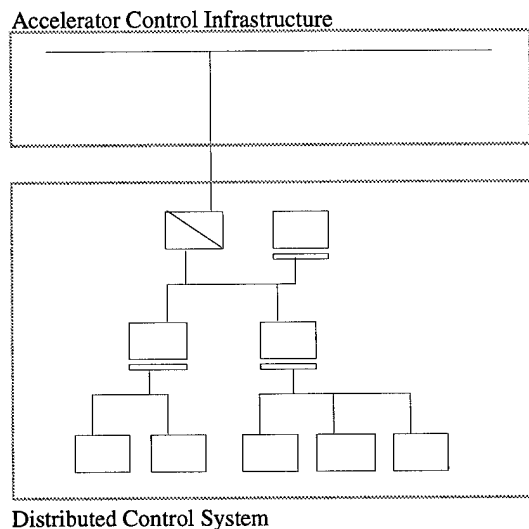


Figure 5

III. ORGANIZATION OF THE OPERATION OF FACILITIES

A number of large installations, thereafter referenced as *facilities*, have been integrated into the equipment of the large accelerator/collider installations of today. Not originating from high-energy physics, they provide essential services for the operation of the laboratory. The technology behind them is production oriented and was first developed or has been derived from conventional industrial processes of the same or smaller size. These facilities include air cooling, helium cryogenics, vacuum, ventilation, water distribution, etc. Not recognizing the common feature of their origin, different control strategies have been adopted in the past at CERN: some, like vacuum have completely followed the accelerator control strategy; others, like LEP ventilation and electricity distribution, have followed a mixed strategy and others, like LEP cryogenics, have followed a completely industrial strategy. With the exception of those facilities which are completely industrially controlled and therefore have their own control center, all have developed to a certain extent cryptic activity centers manned by experts. Outside normal

working hours, a first line service is provided by operators manning a Technical Control Room.

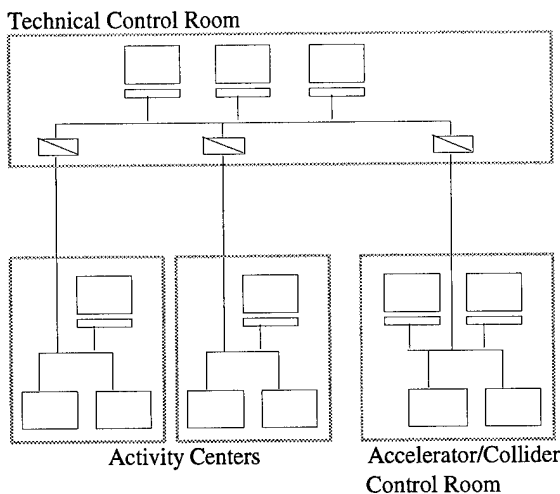


Figure 6

In case of equipment fault, the staff in the *Technical Control Room* follows a predefined procedure in order to re-establish normal operating conditions. If this fails, the facility is put, or falls by itself, into a safe stand-by state and an equipment specialist is called in to recover the facility. Indeed their complexity makes it hard to employ a team of general purpose operators: rather, in order to diagnose and recover from second level equipment faults, a team of experts in the particular trade is needed. This need becomes absolutely essential for equipment tuning and performance optimization.

In the *collider/accelerator control room*, the engineer in charge and the operators can do little with information on the speed of a turbine, the temperature in a helium vessel or the pressure in an air duct; rather, they need limited information on the facility as a whole, for example the answer to the question on whether or not they have enough cryogenic power to start an accelerating ramp.

The equipment specialist acts from an *activity center*; there he finds the tools which allow him to observe the system in depth and detail. He uses the tools which were made available and used during the commissioning of the facility, and are commonly in use by specialists in the same trade elsewhere; therefore, are most mature and suited for regular operation.

In order to achieve this operation strategy three major issues need to be resolved. First, a gateway needs to be programmed/configured in order to provide an access to the industrial system. This must be coherent with the accelerator control system architecture [9].

The second issue is related to network protocols. They should be able to traverse routers and bridges installed on the accelerator control system communication infrastructure and therefore be known by these devices.

The last, but not least important, issue is related to the way the industrial communication mechanisms load the network. In fact, some tend to consider the network as a private communication medium and use the full bandwidth. If this is the case, the demanding (real-time and volume) communications should be conveyed on a dedicated network (figure 7). The three issues have been addressed at CERN;

some of them have been solved by implementing particular solution; the protocol related issue is currently being investigated [10].

IV. EXPERIENCE AT CERN

A. Description

The cryogenics for the LEP2 project follow the *facility level integration* strategy. A turn-key distributed control system has been specified, purchased and installed in LEP. The CERN communication infrastructure has been used to connect remote sites.

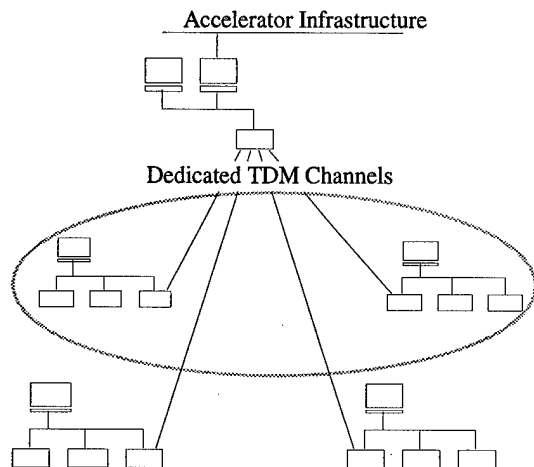


Figure 7

Regional control of the cryogenic installations is done from operator consoles situated at the four even points of LEP. The same control can be exercised remotely from the activity center. A production management system is situated in the activity center and is loosely connected to the accelerator control system.

The cooling and ventilation system of LEP was designed and manufactured by industry and controlled using industrial control systems. They are integrated as an *industrial subsystem* in the accelerator control system (Figure 2). While local control is possible in the four even points using industrial supervision consoles, the overall system is controlled and monitored via the accelerator control system. In this respect, the industrial subsystem is not different from any other subsystem of the accelerator. The overall cost for such a control system is around 200 SFr¹ per channel; this does not include the cost of in-house developments, but all the hardware and the software embedded in the PLCs.

Similarly, the control system of the vacuum for ISOLDE is implemented with a set of PLCs connected via a proprietary network interfaced to a front-end IBM PC compatible [11]. The latter performs the function of a gateway to the vacuum system and the protocol conversions. The recently commissioned access control system of the SPS, is in itself a complete industrial system. It has circumvented the integration problem by providing the supervision via operator consoles in the accelerator control room. The latter, for this

particular case, coincides with the activity center. The overall cost for such a control system is around 160 SFr per channel. It includes the hardware, the embedded and supervision software but does not include the cabling of the point-to-point links.

B. Discussion

From the integration exercises which were successfully conducted at CERN, a few important lessons can be learnt.

In order to keep under control the amount of the work associated to integrating industrial control systems, the number of manufacturers and therefore the number of different systems on the site can be minimized. The majority of the systems, both in volume and number, present on the CERN site are supplied by three major manufacturers. Although natural, this limit can be confirmed by stating the principle in the technical specifications. CERN is better armed for integrating these systems since in-house competence has been developed. The creation of a user group has encouraged people to choose large manufacturers already known at CERN thus contributing to this limitation.

The *facility integration strategy* which was adopted for the LEP2 cryogenics (figure 7), allowed the specification, purchase and installation of a turn-key commercial industrial control system [12]. This resulted in the full utilisation of all the features commonly used by people in the same trade elsewhere in industry. The major benefit of this was the large bundle of features purchased off-the-shelf and the relative maturity of the system purchased. The *loose integration* of this system into the accelerator control system was a non-issue because of the choice -by the manufacturer- of a commercial platform (VAX and later HP9000) to gateway its system. A program running under UNIXTM on a Hewlett-Packard HP9000 computer provides either a regularly refreshed data file or behaves as a data server connected via remote procedure calls or database query languages. This gateway is a delicate point which must be carefully dimensioned and used for what it was designed for: namely, giving access to process variables needed for accelerator operation.

The following two points should be emphasized:

- 1 For CERN, the tendering of the control system separately from the equipment has been a source of, often intractable, problems in understanding the equipment manufacturers and conveying the information to the control system suppliers. A different approach, namely the purchase of the equipment with its control system should be considered in the future.
- 2 Existing communication facilities (dedicated Time Division Multiplex channels, Ethernet, etc.) were made available to the control system supplier by CERN. A delicate issue of limits of responsibilities may arise in the future in case of equipment failure.

It is beyond doubt that this approach can only be adopted when the systems concerned are large and the equipment controlled is expensive: the overall cost for such a control system is around 700 SFr per channel. This includes the hardware and the software, from the field to the supervision console as well as the installation and the commissioning of the system.

The *industrial subsystem integration strategy* which was adopted for the LEP cooling and ventilation system (figures 2 and 4) allowed CERN to benefit partly of the experience of

¹ 1 US \$ \approx 1.3 SFr, Swiss Banking Corporation, December 1994

equipment and industrial control system manufacturer: in fact, only the process control part was completely dealt with by industrial PLCs. This put the suppliers into a familiar development environment. However, for monitoring and control, the communication mechanisms adopted were those of the host accelerator control system: this resulted in a total loss of the off-the-shelf features normally purchased with a commercial product: namely, intra-PLC communication, supervision, alarm handling, trends, etc. Some of these, absolutely necessary for the operation of the facility, had to be redesigned and, often painfully, integrated into the accelerator control system at a non negligible effort and cost. It is worthwhile mentioning that this approach, for such a big facility, results in an unnecessary tight coupling between the two control systems and the people who developed the interface. This mode of integration was not adapted to the size of the system.

V. CONCLUSION

The present technologies used by industrial control system manufacturers permit the easy integration of such systems at the highest level (figures 1 and 5). For large *facilities* this mode of integration is the most appropriate one because of technical advantages, better cost control and maturity of the products. The operation of such facilities by external teams provided via industrial support contract becomes feasible because of similarities with other industrial installations. In order to ease the integration of facilities following this strategy, the accelerator control system architectures must foresee alien systems and not alien subsystems only. Similarly, at an early stage of the project, the offer of the manufacturer must take into account the integration mechanisms available. The lack of standards probably implies that every system will require its own interface.

The use of industrial subsystems handling tasks widely present in industry like motion control, regulations, sequencing must be encouraged and in-house developments avoided. The inclusion of a limited number of interfaces like MAP and manufacturer dependent MMS implementations in the accelerator control system architectures will permit the natural integration of industrial subsystems.

Because of the size of the accelerator complex, the presence on the site of distributed control systems is unavoidable. The installation of private networks and other communications media have, so far, been avoided whenever this proved possible. In view of the evolution towards an increased number of industrial system and their associated communication mechanisms, it seems reasonable that high-energy physics laboratories foresee the integration of these mechanisms in the palette of network services offered by the laboratory and create a support structure with adequate competence and resources.

VI. ACKNOWLEDGEMENTS

The present paper is the result of a CERN-wide study that went on in CCIP² where people recognized the importance

and the benefits of adopting commercial solutions and using industrial control systems. I would like to thank in particular P.Ciriani, A.Guiard-Marigny, H-K.Kuhn, P.Liénard and M.Rabany who, with their work or through fruitful discussions, have complemented my knowledge on the subject.

VII. REFERENCES

- [1] M.Rabany, Interfacing Industrial Process Control Systems to LEP/LHC, ICALEPCS, Tsukuba 1991
- [2] R.Saban, P.Ciriani, A.Guiard-Marigny, H.Laeger, M.Rabany, A.Swift, Equipment industrially controlled, ICALEPCS, Berlin 1993
- [3] International Standard IEC 1131-3, Programmable controllers, 1993
- [4] A.Valenzano, C.Demartini, L.Ciminiera, MAP and TOP Communications - Standards and Applications, Addison-Wesley 1992.
- [5] F.Momal, D.Brahy, R.Saban, P.Sollander, Integrating a commercial industrial control system: a case study, ICALEPCS, Berlin 1993
- [6] International Standard ISO/IEC 9506, Industrial Automation Systems - Manufacturing Message Specification, 1990
- [7] Siemens, Communication Processor CP143, Users Manual Volume 1 and Volume 2, 1993
- [8] Telemecanique, TSX ETH 200 Coupleur OSI Ethernet, User's Manual, 1993
- [9] D.Brahy, Une passerelle entre le monde des automates programmables industriels et le contrôle des accélérateurs, Internal Technical Note AT-IC93-05, June 1993.
- [10] D.Brahy, P.Liénard, Private Communication, March 1995
- [11] D.Brahy, Mise en œuvre de réseaux locaux industriels SINEC au CERN, CERN Internal Technical Note, AT-IC95, April 1995
- [12] H.K. Kuhn, A.C.Juillerat, M.Rabany, J.C.Wolles, Specification, installation and commissioning of a large industrial control system for the LEP2 cryogenics, ICALEPCS, Berlin 1993

² *Coordination des Contrôles Industriels de Processus*, where specialists from different domains regularly meet around

topics related to industrial control systems and their manufacturers.

CONTROL SYSTEM FOR FERMILAB'S LOW TEMPERATURE UPGRADE

B.L. Norris, Fermi National Accelerator Laboratory, Batavia IL 60510*

Abstract

Fermilab recently upgraded the Tevatron Cryogenic Systems to allow for lower temperature operation. This Lower Temperature Upgrade grew out of a desire to increase the Colliding Beam Physics energy from 900 GeV to 1000 GeV. A key element in achieving this goal is the new cryogenic control system designed at Fermilab and installed in 24 satellite refrigerators and 8 compressor buildings. The cryogenic improvements and addition of hardware like cold compressors exceeded the capability of the original distributed controls package. The new distributed controls package uses a Multibus II platform and Intel's 80386 microprocessor. Token Ring is used as the link to the systems 6 primary crate locations with Arcnet used as the connection to the systems numerous I/O crates. I/O capabilities are double the capabilities of the original system. Software has also been upgraded with the introduction of more flexible control loop strategies and Finite State Machines used for automatic sequential control, like quench recovery or cold compressor pump down.

I. INTRODUCTION

Since the fall of 1993, a new cryogenic control system has been operational in Fermilab's Tevatron accelerator. This control system was one of numerous upgrades to assist with the lowering of the Tevatron magnet temperature from the original 4.45K 2 ϕ temperature to 3.56K. The need for a new control package was driven by the addition of a cold vapor compressor, the addition of instrumentation, and a need for upgraded software capabilities.

The project was broken into two parts referred to as Phase I and Phase II. Phase I resulted in the package being installed at each cryogenic site and operating with equivalent software to the old control system. Phase II is a period dedicated to enhancing the capabilities of the new controls system. These enhancements include imbedded software filters for analog channels used in control loops, development of multiple alarm scenarios for all devices, and ability to link real-time data to engineering software (for, example, helium property routines) to generate real-time cryogenic properties.

* Work supported by the U.S. Department of Energy under contract No. DE-AC02-76CH03000.

II. REVIEW OF TEVATRON CRYOGENIC SYSTEM

The Tevatron and the Cryogenic System, initially commissioned in 1983, now consists of two large liquefiers known as CHL I and CHL II and 24 satellite refrigerators. These satellite refrigerators are arranged in six sectors, each comprised of four refrigerator buildings and one compressor house. Equipment in each satellite includes a series of heat exchangers, two expansion engines, a valve box/dewar package with connection to the magnet system, a cold vapor compressor, electric valve actuators and a large array of cryogenic instrumentation. Compressor buildings include four 480 volt soft starters, four 300 kW motors and associated screw compressors, oil pumps, a water pump, and a wide variety of electric valve actuators and instrumentation.

The satellite refrigeration system is supplemented with liquid helium and liquid nitrogen transported around the 6.5 Km ring via a transfer line system connected to the CHL complex. Control of the CHL complex is completely separate from the satellites and is not discussed here.

III. LOW TEMPERATURE OPERATIONAL COMPLEXITIES

The mechanism for lowering the temperature of the Tevatron magnets is, at first glance, quite simple (see Figure 1). The details and impact to overall reliability issues are quite complex.

The backbone of the temperature reduction is a cold vapor compressor. This is a centrifugal machine manufactured by IHI of Japan. It is a high speed, gas bearing turbo machine capable of a maximum speed of 95,000 rpm with flow rates varying from 40-70 g/s and a minimum inlet pressure condition of 0.4 atmospheres. This machine is driven by a 1.5 kW induction motor.

First, operating a turbo machine under these conditions is non-trivial. Control loop algorithms must be chosen and tuned properly so that conditions of overcurrent, stall, or surge are avoided. Understanding the control requirements of this machine and integrating it into our PID control strategies has been key to achieving reliable operations. Transient conditions, such as quenches, translate to high outlet pressures for all 24 turbomachines. Control loops are adjusted for this and automatic sequential programs turnoff the machines at the quenching house. The cold compressor pumps on the gas head of a 130 liter dewar and must not be allowed to ingest liquid or liquid

droplets as damage may occur if it does. Special control loops (fill valve and dewar heater) are required to maintain dewar level. Automatic sequential algorithms are running all the time to sense such upsets such as a dewar overflow and in such a case, the cold compressor is turned off and a bypass valve is opened.

Second, using these machines adds heat of compression to each refrigerator's cycle. This can only be overcome by using more liquid helium supplied to each refrigerator via CHL and the transfer line. Conservation of CHL liquid helium usage is imperative since overuse of liquid helium will effect our ability to maintain constant, reliable lower temperatures and, in return, not allow higher energy operation. It is vitally important that refrigerators are tuned well and efficiency problems are recognized early. These issues have led us to consider global tuning concepts and have required meaningful engineering units (efficiencies, mass flow) to be available in real-time to cryogenic engineers. Phase II of this project addresses those needs.

Third, using the cold compressor to pump down from the original 4.5K state to a lower temperature requires sophisticated control strategies. As we begin to pump down and the 2 ϕ circuit gets colder, total refrigerator mass flow increases. If we make no corrections for this mass flow increase, we run a risk of running out of available warm compressor capacity and we also cause unnecessary pressure drop conditions leading to warmer magnet temperatures. This issue forces us to use complicated sequential programs in which we reduce the 2 ϕ pressure and compensate for higher mass flows by simultaneously closing the Joule-Thompson valves on each magnet string. All of this must be accomplished while maintaining adequate liquid level in the refrigerator dewar, an indication of refrigerator stability.

These and other issues have resulted in the control system described here.

IV. CONTROL SYSTEM HARDWARE DESCRIPTION

The new control system has been developed in a six sector configuration identical to the layout of the cryogenic hardware. A Multibus II platform using Intels 20 MHz 80386 processor is at the heart of each sector's system. Each Multibus II Crate can house as many as eight 80386's. A typical crate contains five processors, one for each refrigerator/compressor building in a sector. In the original Multibus I arrangement, each refrigerator/compressor building had a dedicated crate and processor which was interfaced to a CAMAC serial link.

The use of the Multibus II platform grew out of a project for an Upgraded Tevatron Front End [1]. Selecting this platform was based on having the right hardware and software people already in place to address the issues. The ability to easily interface to Fermilab's existing integrated

accelerator control system, and the need to design, build, and install a system in a very short time frame all led to the choice of this system. (The time period from initial funding request until completion of Phase I was three years.)

The main distributed network is Token Ring, connecting each sector's Multibus II crate. Ethernet and a Tevatron Clock Event system are supported at each crate as well. Ethernet is used to communicate to an embedded DOS PC which is, in turn, used for system initialization and diagnostics. An example of Ethernet usage is to download default files for control loops onto a local hard-drive.

Every sector uses an Arcnet local area network to communicate to the I/O subsystems located at each refrigerator and compressor building. Each refrigerator has 2 I/O subsystems, a Cryogenic Thermometry I/O and a Cryogenic Device I/O. (Compressors only use Cryogenic Device I/O.) Each subsystem I/O uses an Intel 16 MHz, 80C186 processor to control all the activity such as settings and readings.

The Device I/O subsystem provides support for transducer input, valve actuator controls, automatic control for magnet relief valves, power lead digital control, vacuum gauge readbacks, and various motor driven devices such as expansion engines or cold compressors. The Thermometry I/O subsystem provides support for 96 channels of pulsed current, resistance Thermometry and also acts as a link to the Tevatron Quench Protection system (QPM). A summary of the total Device I/O and Thermometry I/O hardware capabilities is outlined in Table 1.

It was recognized in the early specification stages of this project that some support for data acquisition greater than a 1 Hz rate was necessary. Although most cryogenic processes are slow (seconds to minutes), entering into the age of higher energy and lower temperatures created a number of questions about transient conditions such as quench analysis and cold compressor performance during upset conditions. These transient needs spawned a "snapshot" 16.3 second wide circular buffer operating at 1 KHz and capable of handling up to 16 channels. It is triggered by a programmed TCLK event or a dedicated digital input wired at the refrigerator/compressor building. With this board we have been able to analyze quench behavior of Tevatron magnets and reliefs at lower temperatures and higher energies to study the mechanical soundness of our system.

V. SOFTWARE DESCRIPTION

The 80386 processor software is a three tier system [2]. The chosen operating system is MTOS. The intermediate tier is OOC++ and is used for supporting standard ACNET communication. The final tier is the data acquisition tier. The data acquisition tier will be described here.

Table 1. Summary of Tevatron Refrigerator Input/Output Capabilities. ¹

Card Type	Analog Capabilities	Digital Capabilities	Max No. of Cards per Refrigerator
A/D Board	64 channels, 10 volt, 12 bit	—	2
Actuator Board	1 A/D channel, 10 volt, 12 bit, plus 24 volt DC drive control and LVDT instrumentation	4 T ² L Status	35
Engine Board	2 A/D channels, 10 volt, 12 bit plus 1 DAC channel	3 Momentary relays and 16 optical coupled status bits	6
Resistor Board	96 channels, 10 volt, 12 bit	Link to TeV QPM	1
Vacuum Board	12 channels, 10 volt, 12 bit	—	1
Relay Board	—	8 Latching relay and 8 T ² L status	4
Digital Board	—	30 T ² L Status	2

¹ The difference in the compressor I/O is a special board interfaces to the oil injection slider valves and Thermometry is not used.

The data acquisition tier of the 386 processor consists, in itself, of three layers. The first layer is a set of device drivers each built to support ACNET messages to that specific device. Types of messages include reading, setting, reading a setting, basic status, basic control, and both analog and digital alarms. With this layer we communicate to standard ACNET pages used for parameter display and application programs used for real physical control of equipment. The second layer is used as the primary control feature for cryogenic valves, engines, cold compressors, and motors. This layer is our closed loop control. Console applications allow cryogenic engineers to interface to this layer and effectively tune each cryogenic component. This second layer supports all combinations of PID control, operates at 1 Hz, and is set up so that each cryogenic loop is de-coupled from all others. As many as 32 control loops per house are supported.

The final and most powerful layer is the Finite State Machine layer. This software is used to handle routine procedures such as automatic cooldown, quench recovery, and cold compressor pump down to lower temperatures. These FSM's are coded at the console application level by Cryogenic engineers and then downloaded as necessary. There are 32 FSM's presently supported per refrigerator house. As will be described in the Phase II portion of this paper, FSM's are being used to expand our capabilities and make our system more flexible.

VI. PHASE I - INSTALLATION AND COST

The entire cryogenic control system had to be installed and made functional in a period from June 1, 1993 to Oct. 1, 1993. This included all refrigerators and the majority of compressor buildings. (Redundancy in compressors allowed us to do them at a slower pace.) This was a successful effort done by a combination of Accelerator Cryogenic and Accelerator Controls people. After initial installation, the month of October was used to shakedown system bugs. A significant amount of effort was required on the software end. By November, 27 new nodes were fully operational. Since that time, the remaining compressor houses have also been converted to the new scheme.

The total project cost for Phase I was approximately \$2232K. The breakdown for this cost is as follows:

Salaries & Fringes	1158K
Administration	23K
Hardware	857K
Software, Micro	185K
Software, Applications	93K
Cards, connectors, electronic components	542K
Enclosures, panels	109K
Multibus II crates, PC boards, assembly	187K
Electrician Labor	118K
Miscellaneous	118K

VII. PHASE II

Initially we felt it was too ambitious for us to attempt implementing entirely new control software that was not absolutely necessary. Phase II, which is an on-going project, was established to pursue to new specialized needs (mainly software oriented tasks). Although work continues on this phase, we have defined and begun implementation of a few of these new capabilities. These features include: 1) creation of software filters for use as control devices within loop algorithms, 2) creation of a mechanism to allow for multiple alarm states that are a function of the actual state the Tevatron Cryogenic System is in, and 3) the ability to link real time data to specialized engineering software to create, for example, thermodynamic or fluid calculations.

Filtering software has been created with two types of programmable filters, smoothing and Butterworth. These filters are created as a database device and defined via an ACNET application page. Filters can be used for process variable readbacks, analog output board settings, and read-ins for output devices such as motor or expander driver cards. All of these can be used in our normal control loop algorithms. Filters can be set, read, plotted and alarmed.

In an accelerator magnet cryogenic system it is quite often necessary to operate the system different than the steady state, powered condition. Events such as quenches, cryogenic maintenance, and shutdown periods make it necessary to handle temperature variations from 3.5K to 300K. This also requires a flexible alarm strategy. Until Phase II work was started, each cryogenic device had one alarm block associated with it (the operating state). In periods of non-operations, these alarms are sometimes masked and become useless. Created in Phase II is an automatic alarm strategy that understands the state a device is in and points to one of many alarm blocks residing in a tabloid on the refrigerator processor. A Finite State Machine is running on each refrigerator processor that determines which alarm state devices should be in. This alarm message, and messages for all refrigerator processors, are passed to a dedicated front end (Micro VAX that is referred to as a Virtual Machine Front-end) that checks the message for correctness, and then reflects back to a device resident in the refrigerator processor. This device, in turn, points to the proper alarm block. The Virtual Machine FE was used as a method for approaching global needs, such as disabling of the process or automatically choosing a specific alarm block independent of what a Finite State Machine is doing.

Another new feature is the ability to create real devices that have more meaningful engineering units. An example of this is helium mass flow in a refrigerator. It is typical in cryogenic systems to use a venturi that measures pressure drop as a measure of mass flow. Engineers find themselves using units that are mixed and not real meaningful to their system, e.g. In w or psid. If enough instrumentation and cryogenic fluid properties exist, more

meaningful units (to a cryogenic engineer) such as grams/second (or efficiencies) can be calculated. To accomplish this goal, we purchased "HEPAK" source code for helium properties from Cryodata, Inc. and are running it as part of a process named GLFRIG on a Micro VAX. This process can poll each refrigerator node every 2 seconds and provide data to console applications via a RETDAT process. The uses of this mechanism are enormous. It makes operating and diagnosing this system much easier and it allows us to start thinking in terms of global controls for overall refrigerator and compressor tuning. For example, at present an operator determines whether he has too little or too many 300 psig compressors operating. It takes daily attention and leads to us not optimizing our compressor usage. If we operate one compressor too many, we cost ourselves about \$150,000 over a year. These new control features should help us with issues of these sorts.

VIII. RELIABILITY

As stated earlier, completion of Phase I for 27 nodes was finished by November 1, 1993. On December 15, 1993 Colliding Beam Physics Run 1B began and is scheduled to continue until July 24, 1995. Accelerator downtime is tracked in an effort to understand problem areas. Since the beginning of this physics run the cryogenic control system has been charged with three hours of downtime occurring in a total of three events. This accounts for 2.5% of the total downtime charged to Cryogenic Systems. Two of the downtime events were caused by a loss of communication to a 386 processor and the third was a bad power supply in a Multibus crate. Other minor problems have occurred with I/O boards but none has led to an interruption in the physics program.

Besides the work on-going with Phase II, Fermilab controls personnel continue to work on problem areas of the design. Loss of communication via Token Ring has been one of two continuing problems. Because of the ability to continue local control of cryogenics during a Token Ring problem we have been able to survive numerous loss of communication situations. Controls personnel continue to work on this problem. The second continuing problem is a lack of reliability with Ethernet downloads. The problem has caused us the inability to download default files at times from a console. This reliability problem as well as a desire on our part to automatically update our default files on a daily basis are also being worked on.

IX. CONCLUSION

A new distributed cryogenic control system has been fully operational since November 1993. This system was specified, designed, built, and installed by Fermilab Controls and Cryogenic personnel. The system has operated well throughout Colliding Beam Physics Run 1B,

having been responsible for only three hours of downtime over a 18 month period.

This new system has given the Cryogenic system personnel much more flexibility than the original package. Hardware capabilities are double that of the original system and it has added such features as snapshot circular buffers to study transient conditions related to Low Temperature Operations.

X. ACKNOWLEDGMENTS

The author wishes to thank John Smolucha, Al Franck and Boris Lublinsky of the Fermilab Accelerator Division Controls Department as well as John Brubaker and Alex Martinez from the Accelerator Division Cryogenic Department for their dedicated efforts in this project.

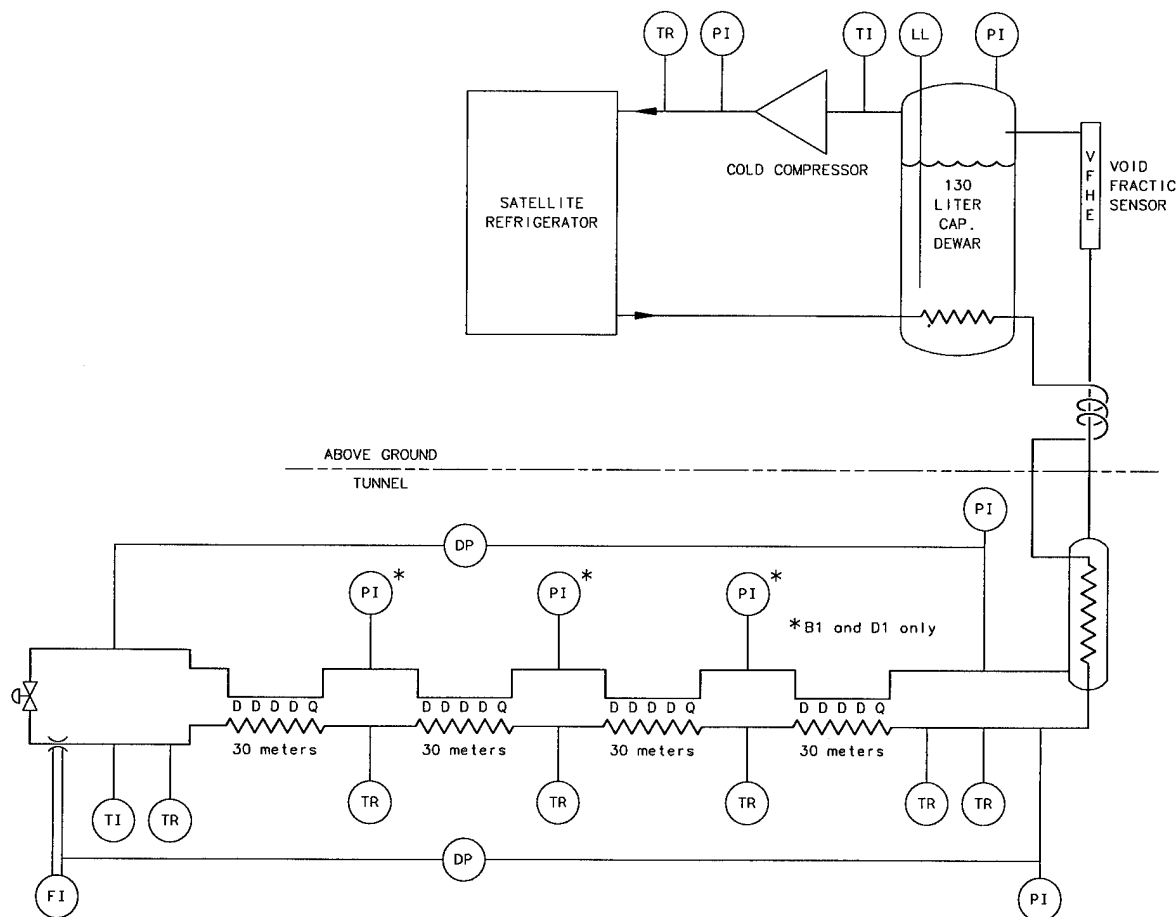


Figure 1: Satellite refrigerator layout after low temperature upgrade
Note: Only half of magnets shown (D=dipole magnet, Q= quadrupole magnet)

Software capabilities have been enhanced by adding more flexible PID control strategies, more versatile alarm blocks, and a method for creating real-time thermodynamic properties.

This control system has played and will continue to play a heavy role in Fermilab achieving higher energy operation.

XI. REFERENCES

- [1] M. Glass, J. Zagel, P. Smith, W. Marsh and J. Smolucha, "The Upgraded Tevatron Front End", Nuclear Instruments and Methods in Physics Research, A293 (1990) 87-92, North Holland.
- [2] B. Lubinsky, J. Firebaugh, J. Smolucha, "New Tevatron Cryogenic Control System", Proceedings of the Particle Accelerator Conference (1993), 1817-1819

DATABASES FOR ACCELERATOR CONTROL – AN OPERATIONS VIEWPOINT

J. Poole, CERN, Geneva, Switzerland

Abstract

The data in an accelerator control system is not only important for the control processes but also serves as the primary source of information required for the understanding of the accelerator's behaviour. The management of this resource is therefore fundamental to accelerator performance and in recent years there have been technological developments which have made new approaches feasible. This paper reviews the impact of database and related technologies on accelerator operation and performance, their implementation and the implications of their use.

I. INTRODUCTION

Operating databases for accelerator control has a scope much wider than the control system and accelerator operation. The constraints and relationships from outside the control system are such that the databases have to be considered in the wider context of the whole project: this view will be reflected in this paper.

The term database is commonly used to describe many different things including simple file systems. However, here the term 'database system' will be used to describe something which satisfies the following:

- a structured collection of data, held in computer storage, and the software which is used to access the data in a selective way. This means that the user can access the relevant data without having to know how or where the data is stored.
- a system which will allow concurrent and consistent manipulation of the data by multiple users.

This definition essentially limits the field to commercial DataBase Management Systems (DBMS).

The size of control systems and the complexity of the data associated with them has become a driving force behind the use of databases. Database technology has reached its teen age and in the last few years its performance (and that of the platforms it runs on) has increased by orders of magnitude, making their use in control systems a viable option.

The use of database systems inside a control system can reduce the maintenance burden, improve understanding of the machine's behaviour and lead to improved performance. Furthermore, the most fundamental benefit which comes with the introduction of database systems is derived from the creation of a unique source for the data and this has far reaching benefits for an organisation. In this paper, the way in which database systems are implemented and used will be reviewed and their impact on accelerator performance will be explored. The requirement for a coherent project-wide solution is stressed.

II. DATA MANAGEMENT

Inside every control system there is data describing the settings and performance of the machine; being able to analyse and

correlate it is fundamental to improving performance. A coherent solution to the data management problem is essential if many of the goals of accelerator operation are to be achieved.

Data is of little use if it cannot be accessed from a variety of places. At the same time, one requires tools to maintain and analyse it.

Today, commercial DBMS allow access from within control applications written in high level languages (C, Fortran etc.) and at the same time offer a variety of interfaces to commercial packages like data analysis tools and other databases.

Previously there were often many different data management systems at an accelerator site and this made control software difficult to develop and maintain because it involved diverse methods to access data. In a traditional system, a control program might have to address a power converter to find its current settings, an instrument to obtain a measurement and a database to obtain some calibrations: this could mean three completely different sets of routines within one small control program. The overheads in maintaining such software are very high: the individual systems all have to be maintained and when any one changes it implies changes to the control software as well.

Solutions based on databases where the access to the data is uniform can solve many of these problems. In addition, the peripheral problems like file management are greatly simplified. In some cases the advantage of lower maintenance overheads outweighs performance degradations arising from non-optimised systems. The database solution satisfies the requirement that a single data source is available to many users simultaneously in a heterogeneous environment and once this approach has been accepted, it leads to simpler systems which can be developed faster.

III. THE DATA UNIVERSE

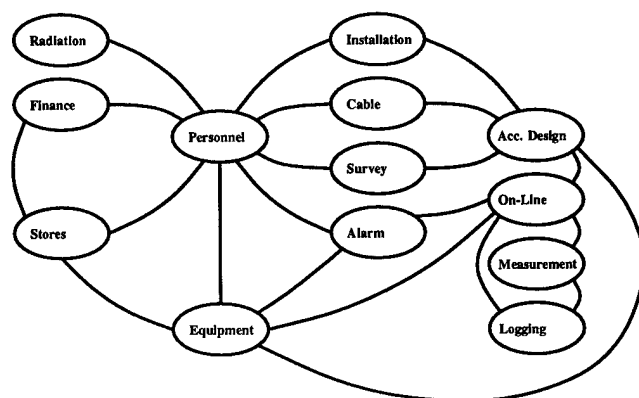


Figure. 1. A diagram representing some databases one would typically find at an accelerator laboratory and the links amongst them.

Although at many accelerator laboratories the database systems have evolved along with the various activities, the next generation of machines will feature project-wide, integrated database systems (see for example [1],[2]). In an accelerator laboratory there are gigabytes of data concerning personnel, finance, hardware and software and they are all inter-related; Figure 1 represents some of these inter-relationships, where the databases could possibly contain the following:

Radiation	Measurements, equipment (monitor) descriptions and calibrations
Finance	Purchasing, budgets, internal orders
Stores	Catalogue, suppliers
Personnel	Names, addresses, phone numbers, contractual details
Equipment	Inventory, procurement, testing, components, calibrations
Installation	Logistics, location of components, planning
Cables	Specifications, routing and connections
Survey	Position of elements and their evolution
Alarm	Descriptions, actions required, history, hierarchical information
Acc. Design	Accelerator components and assemblies, machine definition and historical evolution
On-line	Reference settings, actual settings, calibrations, data for applications
Measurement	Data from instrumentation updated at frequent intervals and kept for relatively short periods
Logging	Long term record of settings and measurements of the accelerator and its environment

The diagram illustrates the surprising links between conventional control system parameters and for example, personnel information. Such a link can be understood through the following example: a surveillance program detects an equipment fault; from the equipment data it can find the name of the person responsible; it can then deliver the phone numbers of this person to the accelerator operator who has to ensure that the fault is fixed.

The databases are separated according to the various functions of the laboratory and the different primary users of the information. This compartmentalisation is quite natural and necessary, particularly from the data maintenance aspect.

IV. SOCIOLOGY

The relationships among data at an accelerator facility cross many boundaries and it is a challenge to build systems in which these relationships can be exploited. The easiest way to achieve it, is for all databases to be implemented under the same DBMS or by having DBMS which can talk to each other. In a new project it is therefore important to reach an agreement on a common DBMS at an early stage so that developments in the different disciplines do not diverge.

Good design is a fundamental requirement for good performance from a DBMS and this in turn means that there must be a good initial information analysis. It has become generally accepted that flexible and reliable application software needs to be built by competent engineers who have been trained in appro-

priate methodologies. The same is true for databases but the technology is different and different expertise is required.

In order to achieve the goal of coherent database systems it is necessary to reach an agreement at project (or laboratory) management level on the policy. It is very easy for someone to believe that the data with which he is working is of no interest to anyone else and therefore he can use whatever system he has available to manage it; this inevitably leads to copies of files, inconsistencies and incompatibilities. Furthermore it is necessary to allocate adequate resources, not simply in terms of MIPS and DBMS licenses but also in personnel and their training.

Several categories of personnel are required to build and exploit databases: information analysts, database designers, software engineers and people who understand the particular system (personnel, hardware etc.). It is important that the people who understand the system are responsible for maintaining the data and therefore that they have some understanding of database technology. It is possible that one person could fulfill all roles for a particular system but it is unlikely that he could cover many more.

V. METHODOLOGY

A. Starting Point

Every new accelerator project starts with a computer simulation and this is an ideal point from which to start the data modeling and database implementation. The description of the new machine contains the names of the major components and the way in which they must be put together. This information is at the heart of nearly all other systems: the named components have some physical properties which form the basis for specifications for procurement; they have dimensions and positions which constrain the civil engineering; the components have to be connected to a control system and so on.

B. Analysis and Design

Many database instances have to be planned at an early stage in a project because they concern the hardware and contain information about procurement, construction, performance etc., others may come at a later date because they concern control data which are only needed by the application software. In both cases a detailed analysis of the information structures is essential before an effective database design can be established.

The analysis associated with the application software should be aimed at identifying the data which is necessary to define the states of the machine and software (evolution in time as well as snapshots). This leads to a better understanding of the machine behaviour [3]. The procedure requires formal methods like Structured Analysis and Structured Design (SASD) [4]. Powerful data modeling techniques are incorporated in SASD but they target the data involved in the software processes and therefore do not model the project-wide data. For information structures on the fringes of the control system, like the cable system, other techniques, such as the Nijssen Information Analysis Method (NIAM) [5], are more appropriate.

The fundamental point about this stage in the implementation is that analysis and design should be based on formal methods and supported by CASE tools. A good database design will lead

to robust application software which can be developed rapidly whilst on the other hand, a simple error in design can easily cause a DBMS to stop.

C. Object Technology

Object oriented methods have been a feature of accelerator control systems for many years but the majority of projects have been, or are being, built using conventional database technology. There is an increasing interest in using object databases because they fit well with current software developments. This new type of database system is a direction which is being exploited by most vendors and it is possible that the technology will have reached maturity in time to be used in the next generation of accelerators.

VI. IMPLEMENTATION ISSUES

A. Replication

Making copies of the unique source of data is dangerous and goes against the fundamental principles of database implementation but it is often necessary for at least some of the data. The latest generation of DBMS provide tools for data replication and in some cases facilities to re-integrate modified copies. This recent development is another feature which has helped the proliferation of DBMS in accelerator laboratories because it allows more control over the copied data and automatic procedures for maintenance.

B. Limitations

A DBMS will never be as fast as a data server purpose-built for a given application, but in many applications the DBMS will be fast enough. The advantages of the DBMS have led to an increased range of applications in accelerator control with only the high performance software requiring special data management. Even in these cases, non-volatile data is often down-loaded from a DBMS because it is easier to maintain the data there, and at the same time processed data is passed upwards to be stored in a DBMS.

C. Database Servers

The following is a list of requirements for database servers of various types:

- 24 hour availability
- Close to 100% reliability
- High performance query server
- Very large tables
- Mostly write or mostly query
- Multi-user, interactive or single user, batch
- Reliable production or flexible development environment

It is highly probable that in any project one will want to have a system with high reliability and availability, for control for example, and at the same time a development system which will almost certainly crash fairly often. When one adds other systems with further conflicting requirements it is clear that a single server is unsuitable and one must therefore plan to have several platforms, each tuned to satisfy the particular requirements.

VII. DBMS PERFORMANCE

A. Speed

For some years the speed of transactions has been at a level where the use of DBMS inside a control application has been possible. Today on a typical control system platform, it is possible to run simple transactions (query, update) at rates ~ 100 Hz against quite large tables ($> 10^4$ rows). This means that the use of the database is transparent to the operator for the majority of operations.

B. Size

Existing DBMS can comfortably handle ~ 100 Gigabytes and the next versions are targeting Terabytes. This development has enabled huge amounts of data to be stored and manipulated with ease, leading to interesting new possibilities for analysis and correlation.

The construction of such very large databases requires some special techniques [6] like filling all rows in a table at creation time (often $> 10^6$ rows) and only updating non-indexed rows. An interesting feature of correlation in very large databases where the rows in different systems do not have one-to-one relationships was reported in [6]: it is much more efficient to extract the relevant data and do the correlation in a separate program. Another difficulty with very large databases concerns backup: one has to copy a complete table even if only one row in several million has been updated. Commercial DBMS vendors see very large databases as an important market for the future and are therefore improving in these areas.

C. Reliability

In the 1980's one would not have considered using a DBMS in a mission-critical role in a control system because they were too slow and because they were not reliable. This situation has certainly changed: the whole of CERN's accelerator complex relies on RDBMS for operation. The PS and LEP share a database server for on-line control and the Z physics program in LEP relies on data being available in the logging database.

VIII. DISADVANTAGES

In a control system there are usually a number of different platforms and a DBMS may not run on all of them. This is a more serious problem in the larger machines where the number of platforms concerned tends to be larger. The result is that software running on the non-standard platforms cannot access the data directly and different methods (e.g. remote procedure calls or local files) have to be employed.

Unfortunately there is an overhead associated with the use of DBMS: a support infrastructure is required because the database kernel requires tuning, the disk space managing, backups have to be done and the developers need advice. Also, as with all commercial software, one is obliged to install the latest releases in order to maintain support from the manufacturer. When there are multiple platforms with new versions of their operating systems arriving from time to time, combined with evolving versions of the DBMS software, the system management is non trivial.

IX. IMPACT ON ACCELERATOR PERFORMANCE

A. More Efficient Software

With a well designed data model at the heart of the control system it is easy to build generic applications. In LEP, for example, a single application is used to make trims to 90% of the machine parameters. Another application controls the status of almost all of the equipment. This obviously reduces the resources required to build and maintain the applications and provides a simple interface for the operator.

The well designed data model also leads to simple solutions for many problems e.g. a particular set of orbit correctors will often perform more than one task, like closed orbit correction and a local orbit bump. Through an understanding of the processes it is possible to identify (and label) the data required to define the two separate functions and their states, and build structures to store them. Once these two aspects are separately identifiable it is possible to build a save-and-restore utility which will allow selective restore of the bump and/or orbit. A good database implementation also makes it possible to perform many complex actions and to easily accommodate new operational requirements throughout the accelerator's life cycle.

B. Settings Management

Every accelerator needs to store and re-create previous runs but this can rarely be achieved by re-loading a file containing a particular set of values. In a collider for example, the performance depends on the whole history of operations from the starting point before the first beam was injected through accumulation, acceleration, β -squeezing and so on. Being able to reproduce a previous run requires the re-construction of all the actions; improving it, requires one to be able to modify a subset. Partitioning the data and being able to identify the various components by function, state and when they were used, allows selective retrieval for re-loading in the machine – no more thumbing through the log book to find hand written values or file names.

C. Understanding the Physics

We can use the data to improve our understanding of the physics of the accelerator by looking at what we have asked the machine to do and comparing it with beam measurements. A simple example of this concerns the magnetic model: we set a given tune value which is converted to magnet strengths through the model and these in turn are converted to currents for the power converters through the magnet calibrations. Analysis of this process leads to refinement of the model and therefore better performance.

Correlation can also lead to a better understanding of the physics. A very good example of this was in LEP when there were unexplained variations in the beam energy: it was possible to demonstrate that the magnetic fields were stable but that there was a correlation with temperature variations in the tunnel.

D. Building on the Database

Once a database has been set up it becomes possible to build applications which use the data and to feed the data into vari-

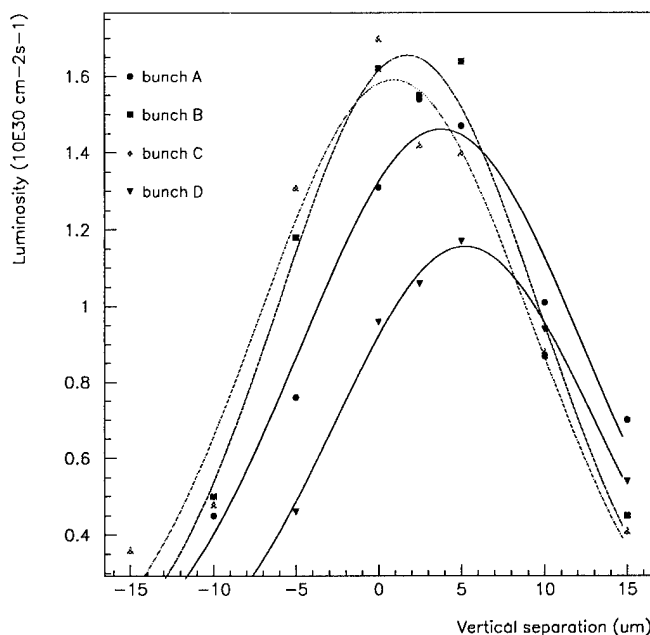


Figure 2. Plot of a Vertical Luminosity Scan of Bunch Trains derived from the LEP Measurement Database

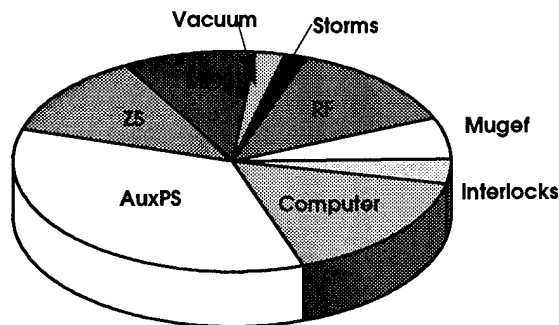


Figure 3. Analysis of faults in the SPS which caused loss of physics in LEP. The data was recorded in the SPS Database, selected with SQL and plotted using Excel

ous other packages for processing. The immediate spin off from a database containing up-to-date measurements from the instrumentation is the ability to make arbitrary displays of beam parameters for the operators. Furthermore, combining this and the control database in an application allows one to close feedback loops.

Figure 2 shows a typical plot of some data taken from the LEP Measurement Database [7]. The advantage of having a single repository for the measurement data is that the programmer does not have to know anything about the hardware or how to retrieve the data from it; he only has to access the database. In fact, a generic plotting facility based on the measurement database has been written, and the operator only has to specify what to plot.

Figure 3 is an example of a very different use of the data stored in the control system. It shows the result of an analysis of the fault history recorded in the SPS statistics database and demonstrates the usefulness to managers of the general availability of the data.

At LEP there have been many performance improvements which can be directly attributed to the database systems. Indeed

in the Proceedings of the LEP Performance Workshops [8] one can see that the percentage of graphs and tables derived from database data has increased from < 5% in 1993 to > 50% in 1995. People are able to access the data from many platforms and use their own favourite analysis package to process the data and this encourages them to study the data.

X. CONCLUSIONS

The commercial world has long regarded its information structures as corporate resources; in accelerator facilities this attitude is becoming more widely accepted. This implies a more global approach to information services and when properly implemented, leads to greater efficiency throughout the organisation.

It has been the improved performance of commercial RDBMS which has led to their proliferation in control systems. The speed and capability to handle large volumes of data is now adequate for many accelerator applications.

A coherent set of databases can be used for design, operation, maintenance and managerial applications. This approach leads to greater efficiency and improved accelerator performance whilst satisfying a wide variety of users but requires project-wide support and substantial resources.

Applying database technology in the way described above improves the understanding of the physics of an accelerator. At the same time managers can access performance data and analyse faults without having to search (or have someone else search) for data. Finally, the day-to-day operation of a machine becomes more reproducible and the complex functionality of an accelerator is better controlled.

XI. ACKNOWLEDGEMENT

I have drawn extensively on the experience of the people at CERN concerned with building the control databases for LEP and the SPS. The on-line control database was designed and built by P. Collier and M. Lamont; the logging and measurement databases by R. Billen, F. Bordry and E. Hatziangeli; the alarm database by M. Tyrrell and the vacuum by P. Strubin. I would also like to thank my colleagues at CERN and in the USA for their comments and ideas.

References

- [1] A. Chan et al., 'The PEP-II Project-Wide Database', this conference.
- [2] C.G. Trahern et al., 'Relational Databases for RHIC Design and Control', Proceedings of the Fourth EPAC, London, 1994, p. 1806.
- [3] R. Bailey et al., 'Development of the LEP High Level Control System using Oracle as an On-line Database', Proceedings of ICALEPCS, Berlin, Nucl. Instr. and Methods in Physics Research A 352 (1994), p. 430.
- [4] T. DeMarco, 'Structured Analysis and System Specification', Yourdon Press, New York, 1982.
- [5] G. Verheijen and J. Van Bakkum, 'NIAM: An Information Analysis Method', 1982.
- [6] R. Billen et al; 'LEP accelerator logging system using an on-line database', Proceedings of ICALEPCS, Berlin, Nucl.

Instr. and Methods in Physics Research A 352 (1994), p. 296.

- [7] M. Lamont, 'What has the Measurement System Given Us?', Proceedings of the Fifth Workshop on LEP Performance, CERN SL/95-08 (DI), February 1995, p. 23.
- [8] Proceedings of the Workshops on LEP Performance, CERN SL/93-19 (DI), CERN SL/94-06 (DI) and CERN SL/95-08 (DI).

TAKING AN OBJECT-ORIENTED VIEW OF ACCELERATORS*

Hiroshi Nishimura, Lawrence Berkeley Laboratory, University of California, CA 94720 USA

It was almost a decade ago that accelerator experts were introduced to the concept of object-oriented programming. This new methodology was expected to play a key role in solving various software problems. Today, there seems to be nothing that prevents us from taking advantage of this new technology. In fact, we are often forced to catch up with the computer industry's new *standards*. This is especially true for graphics programming.

While evaluating the benefits of using this new technology, we must also evaluate whether it is as effective as it was claimed. In this paper, we discuss these issues based on experiences at the Advanced Light Source[1].

I. INTRODUCTION

An accelerator project has a life cycle covering the design, construction and operation phases. Each stage needs various kinds of software supports. The role of software construction becomes successively more important from stage to stage.

The design phase is focused on specifications that determine when and how the actual construction starts and operates. Software construction has a procedure compatible with the structured approach, which is supported by structured programming and sometimes enforced by structured analysis and design. Sometimes the use of the structured approach is not directly related to software construction. When a project has specification-based procedures it indicates that the project management is structured.

The need for a structured approach is evident in hardware construction projects, such as buildings, magnets, and power supplies, because it is very difficult to modify them after they have been created. This need is not always as clear in software development, since software can allow for more flexibility. Using a structured approach may sacrifice the software's flexibility. In the early stages of a project the software specifications are in a conceptual state and tend to be incomplete especially for high level application programs. In addition, the rapid progress of computer technology may make a specification obsolete much earlier than expected.

Lack of flexibility also makes software management difficult in the normal operation phase. The duration of the accelerator operation is much longer than the use of specific software, so there is a continuous demand for the software modifications. This is particularly true for synchrotron light sources which have a wide variety of uses and operation modes. The software system must be designed to accommodate changes during the operation. This is a relatively new requirement.

* This work was supported by the Director, Office of Energy Research, Office of Basic Energy Sciences, Material Sciences Division of the U. S. Department of Energy under Contract No. DE-AC03-76SF00098.

Although the structured approach has improved software quality and productivity, a better method must be cultivated.

II. OBJECT-ORIENTED APPROACH

The situation described above is not limited to accelerators. Object-oriented programming (OOP) is believed to be panacea by many developers[2]. There are two approaches in OOP: a pure approach like Smalltalk and a hybrid approach like C++. Today, the hybrid approach, the most common of which is C++, has prevailed not only for accelerators, but in many other fields as well.

The merits of adopting OOP have been discussed frequently in the literature and are best described in "Object-Oriented Software Construction", by B. Meyer[3]. Since there are many aspects to OOP, we will discuss only a few.

A. Modularity

Increased modularity is the most immediate and natural result of OOP. It is analogous to the use of ICs in hardware circuits[4]. This feature encourages the separation of module developers and module users. Here a module means a class library. A developer can create modules without knowing the final requirements of the user. The user can utilize modules without knowing much about their implementation detail.

B. Flexibility

Software development is often limited by its complexity, but this can be significantly improved by more modularity. In addition, users have the freedom to customize the modules for their own purposes through an inheritance mechanism. This flexibility reduces the role of rigid software specifications and can provide more expandability and adaptability.

III. AREA OF OBJECT-ORIENTATION

OOP has become popular in the graphical user interface (GUI) field of programming. This has happened much earlier than in other fields because GUI is complex enough to encourage developers to adopt OOP. Although GUI plays an important role in accelerator-related programming, we have not discussed it here because it is not specific to our field. We have focused on the following items:

- A) Accelerator modeling and simulation
- B) Device control
- C) Machine studies
- D) Machine operations

A. Accelerator Modeling and Simulation

The most direct method of treating accelerator components, such as magnets, drift space and beam position monitors (BPMs), is as objects. This is because there are always real physical objects associated with them. By combining such elements or objects we can create a structured object to represent a beam-line as a series of the component objects. The circular ring can be a special type of a beam-line object. Accelerator modeling and simulation are very basic subjects for OOP.

Whether to use a beam object or not, becomes a design issue. There is not a lot of merit in treating a single particle as an object, but a bunch with multiple particles can be effectively simplified into an object.

Operator overloading does not always require the use of OOP, but can be supported efficiently by some of the OOP languages, such as C++. This mechanism has been popular with complex, vector and matrix calculations and is easily extendible to cover automatic differentiation or differential algebra (DA)[5]. In the same way, the accelerator-lattice definition can be simplified. Once we have found that the relationship between a lattice and its magnets is the same as that of a string and its characters. A string class can be extended to support the lattice definition.

B. Device Control

Device control involves the construction of a virtual device-class library on top of a device-access library that is not object oriented. A physical device is usually associated with multiple access channels. It is the application developer's task to deal with its details. A virtual device layer serves to hide the intrinsic complexity and provide flexibility through the inheritance mechanism.

C. Machine Study

Machine study is a special mode of machine operation performed by accelerator experts. Accelerator experts have a continuous need for software development and often become part of the study. In addition, accelerator experts who are not software developers will develop programs using whatever method they can use. Ideally they can share software resources as class libraries.

D. Machine Operation

Quite contrary to the case of machine studies, machine operation is carried out by operators. Programs for operation are provided by the control software experts. Therefore, it should be possible to adopt OOP and create class libraries. These class libraries will eventually provide a standard for the control programs.

The key issue is the execution management of the programs for operators. A control system is not a collection of individual programs, and there is a need for a mechanism to manage the overall operational context for the machine, for example, with regard to locking and unlocking devices, according to the operation mode. But this is not sufficient to accommodate very complex operation mode. One possible

approach is to recognize operations as objects. Then the problem becomes a run-time management of these operation objects. There is a possibility that we can reuse some kind of management scheme that has been created in other fields.

IV. OBJECT-ORIENTATION AT ALS

The ALS is small enough to adopt OOP, through a small number of software developers, at an early phase of its construction. OOP has been constantly used for GUI programming, modeling and simulation, and device controls since the ALS commissioning phase[6].

A. Accelerator Modeling and Simulation

As one of the first projects of the third generation light sources, the importance of accelerator modeling and simulation studies was strongly emphasized in the lattice design phase[7]. We have developed modeling and simulation programs, a 4x5 matrix code Tracy[8] and a full 6x6 code Gemini[9], using structured programming in Pascal. As these programs use the Pascal-S compiler[10] as the framework, users could freely program their procedures in Pascal to carry out simulation studies. The expandability and compatibility was not enough to develop a high level application program with the ALS control system[11].

During the commissioning phase, the kernel of Tracy was extracted and rewritten as a portable C library. Then OOP was applied by using Eiffel just on top of the C library[12]. Later, the library was completely redesigned in C++ to be compatible with the control system. This C++ class library is now called Goemon.[13]

Accelerator components such as magnets and BPMs are clearly separated from structures such as beam lines and rings. The component class has a class structure shown in Figure 1.

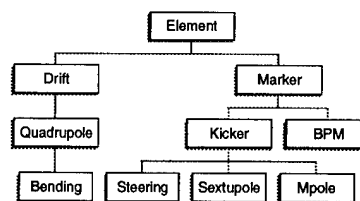


Figure 1. Goemon Component Class Library

Notice that a wiggler or an undulator is an exception, because it is represented either by a hard-edge model or a vertical quadrupole, and it is a composite component that is a beam line by itself.

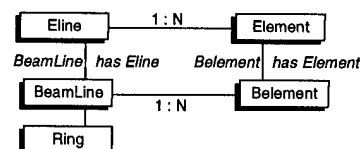


Figure 2. Goemon Structure Class Library

Figure 2 shows the Goemon structure class. Eline is a sequence of the Element objects used to define a lattice

structure by using an operator without using a parser as shown in Table 1. Element is the root of the component class.

```
DRIFT(L1,3.378695);
DRIFT(L2,0.434500);
.....
BEND( B,0.43257, 5.00, 3.00, 0.00, -0.810);
.....
Eline CELL=SYM+L1+2*QF+L2+2*QD+L3+B+L4+2*QFA
+L5+B +L5+2*QFA+L4+B+L3+2*QD+L2+2*QF+L1;
```

Table 1. Lattice Definition using Operator Overloading

Belement is one unit of a beam line that refers to Element and has storage for the optics functions and particle orbits at that location. BeamLine represents a beam-line and uses Eline to read the lattice structure and supports particle tracing and optics calculations.

Ring is a special BeamLine for circular accelerators. ALS structures are supported by derived classes with customized creators. The library also supports a full 6x6 tracking routine to simulate the effect of closed-orbit path-lengthening.

B. Device Control

Single-Device Control The ALS control system uses PCs that run Windows as operator consoles. The application programs were developed on them. Each physical device has one or more DMM channels. A DMM channel is a flat entry to the device-control channel-arrays. Each DMM channel has several subchannels to get and/or set process values, monitor values and Boolean values.

A DMM channel is wrapped with an object called DMMObj[14] that is a root class of single virtual devices. It was originally developed in Pascal with object support and rewritten in C++ on Windows 3.1. Then it was ported to Windows NT. Therefore, one device-class library could be kept for several implementations. Table 2 is an example for the declaration of a DMMObj in C++:

```
class DMMObj
{
public:
    UBYTE2 errCode;
    UBYTE4 index;
    DMMObj();
    DMMObj(char *aName);
    ~DMMObj();
    void findName(char *aName);
    virtual float getAM(void); // get monitor value
    virtual float getSP(void); // get process value
    virtual void setSP(float aSP); // set process value
    virtual int getBM(void); // boolean monitor
    virtual int getBC(void); // get boolean
    virtual void setBC(int OnOff); // set boolean
    // block transfer
    UBYTE2 getOffset(UBYTE2 Control);
    void getBytes(UBYTE2 Offset,UBYTE1*s,int n);
    void setBytes(UBYTE2 Offset,UBYTE1*s,int n);
};
```

Table 2. DMMObj Header in C++

The class structure under DMMObj is shown in Figure 3. Each physical device is supported by one of the classes in this family. Magnets, BPMs, and vacuum gauges are supported by corresponding classes that do not depend on the accelerator section where a single-device would be located. Undulators, DCCT beam-current monitor, and RF systems are supported

by specialized classes[15] at the device level.

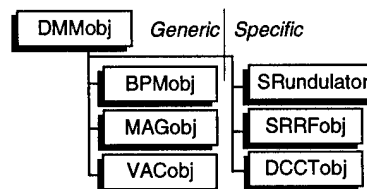


Figure 3. Single Device Class

Multiple-Device Control Multiple-device control is needed to control a group of devices collectively. Figure 4 shows the orthogonal relationship between a single-device class and a multiple-device class. For example, BPMObj supports an individual BPM in any accelerator section, and the multiple device class SRBPMS supports all the BPMs in the storage ring. A multiple device class is fully customized for the section it locates. In addition it supports quasi-synchronized, grouped device access and file access.

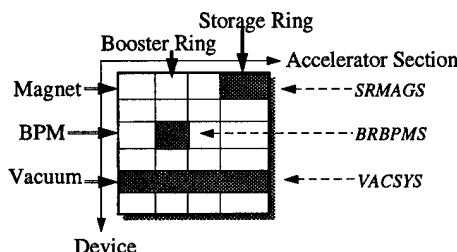


Figure 4. Single and Multiple Devices

Table 3 shows the header of SRBPMS in C++:

```
class SRBPMS
{
    float getXref(int n);
    float getYref(int n);
    float getXraw(int n);
    float getYraw(int n);
    public:
        // for data exchange
        void calcStat();
        void setRef();
        void setOffset();
        void clearRef();
        void write(FILE *f);
        void write(char * fname);
        void read(FILE *f);
        void read(char * fname);
        SRBPMSrec BPMrec;
        SRBPMS();
        ~SRBPMS();
        void getData();
        // access the n-th BPM
        float getX(int n);
        float getY(int n);
        float getXave(int n);
        float getYave(int n);
};
```

Table 3. SRBPMS Header in C++

The function getData() does a quasi-synchronized reading of all the storage-ring BPMs. As each BPM reading takes 2.0 msec to read X and Y, getData() takes about 200 msec for 96 BPMs. After using getData() functions getX(n) and getXave(n), etc., are available for access to individual data. This class also supports averaging and offset manipulation.

These device classes have been in daily use to support all the magnets, BPMs, and vacuum readings in the 1.5 GeV injection beam line and the storage ring. These magnets are still operated by using Pascal programs written during the commissioning phase. Other programs that involve BPMs were written in C++ and have been moved to Windows NT.

These multiple device classes must interface with other classes, such as the simulation class. Instead of pointing to

the other class, we use a data class to communicate indirectly. In the case of SRBPMS, this class called SRBPMrec. It is also shared by a simulation class and a graphics class.

EPICS Channel-Access Currently, all the machine devices are controlled by using the original DMM-based control system, except for the communication part of the undulator feedforward-programs[16]. This is because EPICS[17] channel access is used for the photon beam line control. Channel access has been ported to PCs running Windows NT and is supported as an object in C++[18].

C. Machine Studies

As machine studies are carried out on the PCs running Windows, there is a wide variety of software tools available for physicists and engineers who actually program. The tools actively used are LabView, MatLab, and compilers.

LabView is mainly used to control GPIB devices for instrumentation purposes[19], MatLab for the area where the algorithm itself has to be developed and compilers where high performance is required. The compiled applications are mostly written in C++ on Windows 3.1 or Windows NT 3.5.

D. Machine Operation

Although there are 3 insertion devices in the ALS storage ring, the operation is very stable. Currently real-time response is not required by the controls software. Therefore, most of the programs written in the commissioning phase are still in use, including those written in Toolbook, Excel and Visual Basic. They support a wide variety of fields: the saving and restoring of the machine-device status, the booster energy-ramp linearity-corrections, turning on and off devices in the injector section, timing setting, scraper and TV-paddle controls, and the storage-ring bunch-filling pattern controls. These do not require quick responses and some are complex. For these cases, the tools worked effectively on Windows.

But there are areas where high performance becomes an issue. These areas are covered by programs originally written in compilers. Most of them are object-oriented and use the DMMobj class-library. Many of them, especially those that support magnet operations, had to be updated several times when the operation scheme was changed. As OOP supports such evolution, these modifications were done efficiently. We have seen the benefit of OOP through such experiences.

An operational-context control is being developed. We have a device lock/unlock mechanism that uses shared memory, in the Intelligent Local Controller(ILC) to allocate registers, to count the "heart beat" of all magnet power supplies. We did not adopt a static semaphore because of the tolerance issue. Possible conflicts of magnet control, by multiple programs, are being prevented. But, this mechanism is at the device level and is not suitable to control complex operation modes.

A more advanced scheme to organize the machine operation has been investigated[20]. It uses a fully object-oriented approach including an object-oriented design tool

and an object-oriented database system. This combination looks very promising.

A model-based control can use both modeling objects and device objects, but it becomes usable only after a model is well calibrated. A model calibration itself is an important task at an early stage of the machine operation. There is a need to provide a model-free control scheme until the calibration is completed[21]. The commissioning of a model is an evolution process and OOP plays an important role.

V. LIMITATIONS OF OBJECT-ORIENTATION

We have confirmed that there are significant benefits from OOP, based on our experiences at ALS. The fields where OOP was applied, have also been functioning very well. To follow are some problems that cannot be ignored.

A. Lack of OO Developers

The first and most crucial problem is the lack of software developers in OOP. It has been said that it takes several months to train staff who already use C. This training period becomes a burden in many cases. Software developer training should be recognized as an important part of software development. Otherwise, it is impossible to set up a group of developers who can coherently work using objects. One example is the pioneering effort at the AGS Booster[22].

B. Reusability and Compatibility

OOP increases software reusability, which means the availability of reusable class libraries. But, a problem occurs as soon as we try to use several libraries. Compatibility among class libraries can be obtained either when they are designed to be compatible or when they are orthogonal to each other. As a result, most class libraries are grouped into families that are exclusive to each other. A very common situation is that the selection of a GUI class determines the family. Unfortunately, this is an inevitable result of the fact that GUI is event-driven, if it contains an application framework.

C. Lack of OO Standards

Class libraries are very useful if they are created according to an existing standard. We can implement standards without knowing the detail by using a reusable class prepared for it. In many cases, the class library becomes an exclusive standard. That is, the lack of reusability and compatibility is mainly due to lack of regulated standards. The reality is that standards are determined and provided by the manufacturer and they have not agreed on a standard, even in GUI classes, especially for UNIX Xwindows.

In addition, there is an intrinsic limit. By its very nature, OOP does not support persistency and concurrency. In other words, OOP itself does not cover databases, multitasking, or networking. They are outside of the language specification and as a result they are not supported by libraries that are not designed for OOP.

Relational databases have been popular, but most of them are proprietary and lack compatibility even with Structured Query Language (SQL). Very recently, SQL added a reasonably accepted interface standard called Open Database Connectivity (ODBC).

There are C++ classes available that wrap ODBC, but the performance of SQL itself will not be sufficient for accelerator control purposes. The standardization has not been sufficient in this field, even before we discuss its object-orientation. Networking has a similar situation. Both are usually treated as parts of various kinds of frameworks that are completely exclusive to each other.

D. Lack of the "Data Module" Concept

A data module is a NODAL[23] concept that lies between the system developers and their users, who are application programmers. It is a kind of software module that is similar to the object, but does not have the inheritance capability. The system developers create data modules as packages of routines. These data modules become new statements of the NODAL interpreter. The users access these modules as a part of the interpreter environment. In the case of Tracy and Gemini, we used a Pascal compiler for this purpose. But, it is not common in the modern GUI environment. Once a GUI application is created, it is not usually expandable. If a function needed by a user is not there, he may have to keep clicking buttons and menus endlessly to reach his goal.

The interface between the system developers and application users can be class libraries. Then the class users must recompile programs for any change they make. The programmability at run time is important and usually not being paid enough attention to by the providers. This is again a consequence of the structured approach, since it requires too much weight on the specifications in advance. OOP improves the situation considerably, but does not support the concerns of the data module concept.

VI. CONCLUSION

When OOP was discussed, the focus was on its benefits. Recently, pitfalls of OOP[24] are being pointed out. We have described the problems with OOP in respect to accelerators. But these are not serious enough for avoiding OOP. In our view the benefits are much greater. Remember that the most important thing in the software construction, for the accelerator project, is to provide programs on time using a reasonable amount of resources. Although we had to make some very practical compromises while using OOP, it improved productivity.

VIII. ACKNOWLEDGMENTS

The author wishes to thank the ALS Controls Section, especially C. Timossi for his continuous support for the device access, the Operators for their feedback on programs, and A. Jackson, R. Keller and K. Van Dongen for their time and advice.

IV. REFERENCES

- [1] LBL PUB-5172 Rev. LBL, 1986.
A. Jackson, IEEE PAC93, 93CH3279-7(1993)1432
- [2] G. Entsminger, "The Tao of Objects", M&T Books, CA, 1990.
- [3] B. Meyer, "Object-Oriented Software Construction", Prentice-Hall, NJ, 1988.
- [4] B. J. Cox, "Object-Oriented Programming", Addison-Wesley, MA, 1986..
- [5] M. Berz, SSC-152, 1988
Leo Michelotti, IEEE PAC89, CH2669-0(1989)839
N. Malitskey, A. Reshetov and Y. Yan, SSCL-659, 1994.
- [6] H. Nishimura, N.I.M. A 352, 379, 1994
- [7] A. Jackson, E. Forest, H. Nishimura and M. S. Zisman, IEEE PAC89, CH2669-0, 1752, 1989.
- [8] H. Nishimura, EPAC 88, (1989)803.
- [9] E. Forest and H. Nishimura, IEEE PAC 89, CH2669-0, 1304, 1989.
- [10] R.E. Berry, "Programming Language Translation", Ellis Horwood Ltd., England, 1981.
- [11] S. Magyary, IEEE PAC93, 93CH3279-7, 1811, 1993.
- [12] H. Nishimura, Comput. in Phys. 6, 456, 1992
- [13] H. Nishimura, LSAP-153, LBL Internal Report, 1993
- [14] H. Nishimura, LSAP-128, LBL Internal Report, 1992.
- [15] C. Kim, LSAP-165, LBL Internal Report, 1994.
- [16] G. Portmann and C. Timossi, LSEE-188, LBL Internal Report, 1994
- [17] L.R. Dalesio, M.R. Kraimer and A.J. Kozubal, ICALEPCS 91, KEK Proceedings 92-15, 278, KEK, Japan.
- [18] C. Timossi, LSEE 121, LBL Internal Report, 1995.
- [19] J. A. Hinkson, M. Chin, C. H. Kim, H. Nishimura, to be published in the proceedings of EPAC94.
O. Jones, private communication
- [20] H. Nishimura, C. Timossi, M. Valdez, these proceedings.
- [21] H. Nishimura, L. Schachinger and H. Ogaki, these proceedings.
- [22] J. F. Skelly, ICALEPCS 91, KEK Proceedings 92-15, 500, KEK, Japan.
- [23] M.C. Crowley-Milling and G.C. Shering, CERN 78-07, 1978.
- [24] B. E. Webster, "Pitfalls of Object-Oriented Development", M&T Books, NY, 1995.

The CEBAF Control System¹

William A. Watson III, Continuous Electron Beam Accelerator Facility,
MS 12H, 12000 Jefferson Av., Newport News, Virginia, 23606, USA

Abstract

CEBAF has recently upgraded its accelerator control system to use EPICS, a control system toolkit being developed by a collaboration among laboratories in the US and Europe. The migration to EPICS has taken place during a year of intense commissioning activity, with new and old control systems operating concurrently. Existing CAMAC hardware was preserved by adding a CAMAC serial highway link to VME; newer hardware developments are now primarily in VME. Software is distributed among three tiers of computers: first, workstations and X terminals for operator interfaces and high level applications; second, VME single board computers for distributed access to hardware and for local control processing (complex sequences, limit checking, some process control); third, embedded processors where needed for faster closed loop operation. In some cases, multiple VME processors transparently access a single serial highway for improved performance. This system has demonstrated the ability to scale EPICS to controlling thousands of devices, including hundreds of embedded processors, with control distributed among dozens of VME processors executing more than 125,000 EPICS database records. To deal with the large size of the control system, CEBAF has integrated an object oriented database, providing data management capabilities for both low level I/O (calibration, alarm limits, etc.) and high level machine modeling (optics properties, etc.). A new callable interface which is control system independent permits access to live EPICS data, data in other Unix processes, and data contained in the object oriented database (extensible to other sources).

INTRODUCTION

The Continuous Electron Beam Accelerator Facility

CEBAF is a 4 GEV electron accelerator in the process of commissioning in Newport News, Virginia, with the first experiments expected to run this summer. The unique features of this facility are its continuous beam and high luminosity -- ideal for experiments requiring large samples of events with minimal accidental coincidence rates.

The accelerator consists of two 0.4 GeV superconducting RF linacs connected by two 180° arcs. Each linac consists of 20 cryomodules, each containing 8 accelerating cavities. Beam is recirculated through the machine for up to 5 passes yielding an energy of 4 GeV. After any pass, the beam may be split and sent to any of the 3 halls, allowing simultaneous operation at the same or different (modulo 20%) energies. Two injectors

(one thermionic, one polarized) and a 3 slit chopper will allow different halls to receive different beam intensities and polarization.

Two of the three halls house conventional small solid angle spectrometers, and will use the full beam intensity (200 uA). Hall B will house the CEBAF Large Acceptance Spectrometer (CLAS), which will require beam currents 3 or 4 orders of magnitude lower. In Halls A and C, parity violation experiments will require measurements accurate to a part in 10⁷. This flexibility in beam delivery and constraints upon beam stability (both current and polarization) place complex demands upon the control system.

The control systems for both the accelerator and the experimental facilities are based upon EPICS -- Experimental Physics and Industrial Control System. [1] EPICS was selected as a replacement for the original control software when problems with scaling to the full machine were encountered nearly two years ago. The following discussion will describe the controls hardware at CEBAF, the use of EPICS in this system, and the higher level software being added above EPICS.

CONTROL SYSTEM ARCHITECTURE

Standard Model

The control system follows what has been referred to as the "standard model": a client-server system consisting of a collection of Unix workstations and X-terminals connected by a network to multiple servers running device control software. At CEBAF the network is a switched ethernet, which allows simple scaling to high bandwidths as needed. The server machines are VME single board computers running the EPICS real-time database. The client machines are HP workstations configured as two clusters for redundancy (Figure 1).

Conversion to EPICS

EPICS was selected as a replacement for the original CEBAF control system (TACL) when problems were encountered scaling it to over 25,000 control points. [2] The switch to EPICS was accomplished incrementally during machine commissioning, starting with the linacs and arcs a little over a year ago, and ending with the injector (except the gun) this past winter. The gun will be converted following an upgrade to its control hardware this summer.

The two systems were operated concurrently for much of the year, with information being exchanged between the systems. This co-existence was made easier by the fact that both EPICS and TACL are name based control systems -- applications address parameters in the machine by the name of the parameter, and not its hardware address.

¹ Work supported by the Department of Energy, contract DE-AC05-84ER40150. Work performed by the various groups at CEBAF and within the EPICS community.

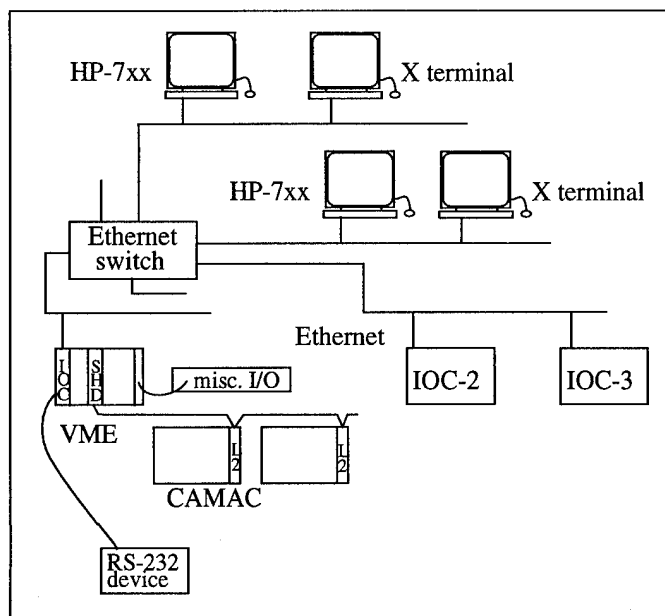


Figure 1: EPICS Architecture showing several displays and IOC's. CAMAC and other hardware is shown for one IOC.

The success of this conversion is evident in the success of machine commissioning. First beam on target (one pass) was delivered within 2 weeks of a date specified 7 years earlier! CEBAF has so far operated beam around 7 of the 9 arcs, and has delivered both pulsed and cw beam to Hall C for detector commissioning activities.

Hardware

In the previous control system, almost all of the machine hardware was interfaced to CAMAC. This investment in hardware has been preserved by replacing the GPIB interfaces to CAMAC with type L2 controllers, which are connected to VME via a serial highway -- with typically 2-8 crates per highway. Newer devices are interfaced directly to VME, or via standards such as GPIB, RS-232, and Arcnet. (Many other buses and interfaces are supported by EPICS at other sites).

Controlled Devices

The bulk of the control system deals with 3 types of devices: RF cavities (~350), magnets (~2000), and beam position monitors (~500). In addition, there are harps, beam viewers, beam loss monitors, gun and injector devices, and ancillary controls and monitoring.

Each RF cavity has a dedicated 8 MHz '186 embedded processor continuously (>20 Hz) adjusting setpoints of an analog feedback system. In addition, these processors monitor for certain critical faults, taking appropriate steps to protect the hardware. A CAMAC card provides an addressable 32 word buffer between the microprocessor and the VME processor, with interrupt support for messages to the '186. During the switch from TACL to EPICS, the embedded software was changed only slightly to support a message based communication protocol.

Embedded processors are also used for each magnet, but with much more limited functionality -- set the current and read the current. Communication with each magnet controller is via RS-485 serial lines, 32 controllers per line. At present, ramp functions are handled by the VME processor, but will be migrated to the embedded processors to improve response time for ramping large numbers of magnets.

Most of the remaining control system hardware is interfaced with commercial or custom CAMAC modules, with the exception of the newer beam position monitor electronics. These devices use a mixture of commercial and custom VME modules to support high speed acquisition of position information (easily tens of kilohertz). Personnel safety is handled by a completely separate PLC based system, and machine protection has both hardware and software components, with the software generally monitoring the state of the hardware.

Additional information about the migration of the low level device control from TACL to EPICS is given in a companion paper. [3]

EPICS

EPICS has been described in previous papers, [1,4] and is well documented on the World Wide Web, [5] so only a brief overview will be given here. EPICS provides a client-server architecture in which the server, called an IOC (I/O controller), executes a real-time database in which each record describes an input, an output, or a calculation.

Database Records

Each record contains a large amount of functionality; for example, an analog input record monitors its input, converts from raw counts to engineering units, compares the value to 2 upper and lower limits (more and less severe alarms), and may cause other records to process. In addition, the record detects significant changes (changes exceeding either of two pre-determined thresholds to support 2 classes of clients), and causes the clients to be notified. Alarms may additionally have hysteresis so that they don't oscillate when near the alarm limit. Simulation mode allows fetching a value from a location other than hardware.

Records may be processed periodically or in response to an external event -- either operator induced, hardware triggered, or software triggered. Records scanning at higher rates preempt slower records, improving real-time behavior.

Channel Access

Most fields within the record are accessible over the network (some read-only). An accessed field is referred to as a "channel", and the network protocol is correspondingly "channel access". [6] At present, channel access servers run only on the IOC, a VxWorks based system. A portable version of the channel access server is in development at LANL to allow any network process to be a server. [7]

The channel access application programming interface (API) is optimized for high performance applications, including buffering all requests and responses and containing support

for unlimited asynchronous replies (in the case of monitoring a value or an alarm status). Clients connect to servers by broadcasting the name of the desired channel (record.field), and broken connections are automatically re-established when a server becomes available again. Several hundred connections per second may be made to a single server, and monitoring several thousand changes each second produces a negligible load on a workstation (6% on an HP 715/50 for 2000 values/sec).

Algorithms

Control algorithms may be implemented via a number of techniques within EPICS. Database records, including subroutine and calc records, may be linked together to form an algorithm, with data transferred from one record to another. Most low level applications use this technique. More complex algorithms may in addition use a state machine sequencer, using a special language and compiler to facilitate this approach. A sequence runs as a channel access client, and may access both local and remote databases as well as any other resources on the VME system. High performance algorithms are implemented as tasks on the IOC, controlled and monitored through database records. This is the approach used for CEBAF's beam position monitors and fast feedback systems. [8] Finally, Unix applications (typically in C or C++) may interact with the EPICS database through channel access.

Utilities

EPICS includes several main general purpose client programs. (1) a save/restore utility, which includes basic check before restore and save-only capabilities; (2) general purpose operator interfaces (one X based, the other Motif); (3) an alarm manager to present alarm status organized into trees of arbitrary depth; (4) an archiver utility supporting 3 styles of data acquisition: (i) periodic sampling, (ii) record on significant change, and (iii) event driven sampling. In the third mode, a change in one channel can initiate recording of values for a set of other channels.

There are a wide variety of other general purpose clients including diagnostic utilities, a knob manager, a parameter page display -- with more being written each year.

EPICS also includes graphical and text based database creation tools, and scripts and other tools to facilitate building and managing the databases.

Integration with other software

EPICS has been integrated with a large number of other packages, including tcl/tk, PV-Wave, IDL, Mathematica, WingZ and others. In each of these packages, EPICS variables are accessible by name through channel access, so that channel access has functioned as a limited form of software bus.

CONTROL DEVICE API

One difficulty encountered with EPICS for high level applications is the fact that the implementation details of a low level algorithm are in many cases too visible: the high level application knows the names of the various records and fields. A change in the low level algorithm which adds or deletes

records (moving the needed information to other records) will invalidate the high level application.

A new layer (cdev, for control device) has been added above channel access to provide implementation hiding as well as several additional features. In this new API (defined by a team from all major EPICS sites), all I/O in the system is in the form of messages to devices such as *on* or *off* or *get current*. (Note: cdev builds upon ideas in earlier work done at ANL/APS [9]). In cdev, a device is a virtual entity potentially spanning multiple servers, and even multiple underlying services such as EPICS channel access, an archive data server, a host-based database, or a legacy control system.

The cdev layer routes messages to the appropriate service (such as channel access) based on the device name and the message. In this way, one can obtain the length of a magnet (from a static database) as easily as the current (from the real-time database). The application program is unaware of the source of the data: if the low level application is changed, it is only necessary to fix the mapping, and all high level applications using that information are correct. An architectural diagram of cdev is shown below. All services at the lowermost layer are dynamically loaded, and new services (interfaces to other systems) may be added without recompiling any other cdev sources (in fact without stopping the running application).

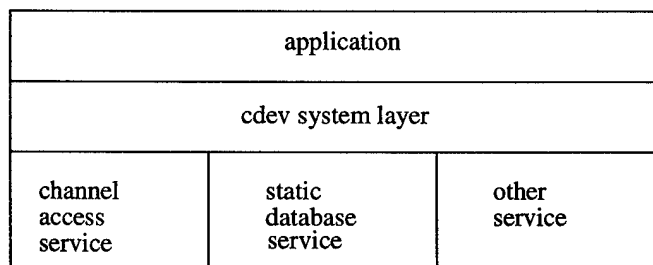


Figure 2: Block diagram of a cdev application with 3 services currently loaded.

An implementation of cdev in C++ has demonstrated that this additional layering introduces on the order of 10% additional I/O processing for both establishing connections and for receiving asynchronous replies. Advantages gained include a device abstraction, implementation hiding, access to a wider variety of data (including a centralized database, described below), wildcard query capability (not present in EPICS), and the ability to treat a collection of devices as a single device.

cdev Applications

A useful cdev demonstration application using tcl/tk for a windowing interface has been written at CEBAF. It allows selecting devices by regular expression, and can read/write/monitor device attributes.

A more sophisticated cdev application now in development will allow measuring correlations among parameters in the control system. This correlation package takes its inspiration from the SLAC Correlation Plot package, which was designed to "measure anything as a function of anything else".[10] Any number of parameters may be systematically

stepped, and at each step point, any number of other parameters may be measured. All I/O will be performed through cdev, making the package independent of EPICS or any other control system. In addition to device I/O, the package will support pop-up windows for operator input or prompting, and the ability to execute shell scripts (including tcl) at any point in the process.

In the long run, most of the general purpose EPICS applications will be re-written to run over cdev. This will decouple them from the EPICS database (giving record implementation independent request files) and allow them to be used in a wider variety of (non-EPICS) environments. For example, the EPICS display program DM (due to be converted this summer) could then be used to control or monitor the control systems of other non-EPICS laboratories -- the only integration expense will be in writing the cdev service layer. A template service will be available to facilitate this integration. Hopefully this ability to exchange utility programs will provide another opportunity to share software development among laboratories.

INTEGRATING AN OO DATABASE

Because of the large size of the control system (over 125,000 records), CEBAF decided a year ago to integrate the ObjectStore object oriented (OO) database with EPICS. Prior to this effort, EPICS contained no centralized database for tracking configuration parameters (hardware addresses, etc.), and operational parameters (alarms and limits, calibrations, etc.). The only tools available were the tools used to construct the databases, and the save/restore utility (smaller systems could also use a spreadsheet for save/restore). Database building tools are not easily used by operators and are generally only convenient for changing all instances of a parameter, for example the skew rate in a magnet. Using save/restore to manage these infrequently changing numbers is possible, but is cumbersome and increases the time to save the machine state.

With a centralized database, instance specific data is more easily managed. Information in the "static" (non-real-time) database is used to construct the real-time database at boot time. Access to this data at run time is through the higher performance IOCs. Persistent changes to these parameters may be made by writing to both the IOC and the oo database. In the future, support may be added for automatically migrating changes from the real-time systems to the static database.

An object oriented database was chosen because it avoids the costly step of table joins to link together dissimilar data, as in displaying relationships among records. Furthermore, the oodb is more naturally accessed by a C++ program in that objects in the database are handled the same way objects in memory are handled. A more detailed discussion of this project is contained in a companion paper. [11]

MODEL DRIVEN APPLICATIONS

High level accelerator control applications generally model the machine as an optical system, with the model parameters stored in a file, a database, or in memory; various applications access the shared parameters. At CEBAF these model

parameters will be maintained in memory by a dedicated server process. Access to the parameters of the model (twiss parameters, transfer matrices, etc.) will be by network calls using the cdev interface. [12]

A consequence of this level of integration of the model information and the rest of the control system is that parameters of the model may be displayed and manipulated by the general purpose display programs. Diagnostic information about the operation of the server process may also be monitored in this fashion.

Initially, high level accelerator control applications were developed using the scripting language tcl [13] and its associated packages. A tcl interface to channel access was written at CEBAF [14] which allows tcl to read, write, and monitor EPICS database fields. During the commissioning process, tcl based programs were produced to perform the following functions:

1. linac energy management (adjusts acceleration elements and quads based upon demand energy)
2. energy lock (slow feedback, about 1/2 Hz, to correct the linac energy based upon beam position in high dispersion region)
3. orbit lock (slow feedback from BPM's to magnets)
4. automated orbit centering in quads
5. automated arc steering
6. automated linac steering
7. optics (general diagnostic package)

Each of these applications used DIMAD [15] to calculate the relevant optics parameters; model information was obtained from a server process via RPC. As the new model server becomes available, the tcl based applications will be modified to use the new model server; programs requiring high performance will be written (or re-written) in C and C++.

SUMMARY

The migration of the control system at CEBAF from TACL to EPICS during a year of commissioning has been largely successful. EPICS is now successfully operating a system an order of magnitude bigger than any previous installation (APS has simultaneously scaled up to a comparable size), and shows every indication of being able to scale up another order of magnitude (with appropriate upgrades in network bandwidth). One can safely say that architecture is no longer an issue -- the "standard" model works.

New features are being added to facilitate the management of large control systems, including an object oriented database for device instance parameters.

CEBAF and others are now in the process of adding high level accelerator control applications above EPICS, with sufficient applications already in place to support commissioning. These new applications are being added in a way which preserves the open toolkit approach adopted by EPICS.

ACKNOWLEDGEMENTS

The conversion of the CEBAF control system was accomplished by deputy head Karen White and other members of the CEBAF controls department, with considerable debugging assistance from the CEBAF operations crew and technical support by visitors from LANL. Work on the cdev specification was done in collaboration with Claude Saunders and other members of the EPICS collaboration at APS, LBL, LANL, DESY, and Keck; the cdev implementation was done by Jie Chen in the Physics Data Acquisition Group, and by Walt Akers and Danjin Wu in the Controls Department. Development of high level applications was done by Hamid Shoaee (on sabbatical from SLAC), and by Johannes Van Zeijts and other members of the accelerator physics and accelerator performance groups.

REFERENCES

- [1] Leo R. Dalesio, et. al., "The Experimental Physics and Industrial Control System Architecture: Past, Present, and Future", *International Conference on Accelerator and Large Experimental Physics Control Systems*, Oct. 1993.
- [2] William A. Watson III, et. al., "The CEBAF Accelerator Control System: Migrating from a TACL to an EPICS Based System", op. cit.
- [3] Sally Schaffner, et. al., "Device Control at CEBAF", this conference.
- [4] Leo R. Dalesio, et. al., "The EPICS Architecture", ICALEPCS, 1991.
- [5] The web site for EPICS is <http://epics.aps.anl.gov>.
- [6] Jeff Hill, "Channel Access: A Software Bus for the LAACS," ICALEPCS, 1989.
- [7] Jeff Hill, private communication.
- [8] Mahesh Chowdhary et. al., "A Prototype Fast Feedback System for Energy Lock at CEBAF", this conference.
- [9] Claude Saunders, private communication.
- [10] L. Hendrickson et. al. "Correlation Plot Facility in the SLC Control System", ICALEPCS, 1991.
- [11] Matthew Bickley et. al. "Managing Control Algorithms with an Object-Oriented Database", this conference.
- [12] Bruce Bowling et. al., "Integrated On-Line Accelerator Modeling at CEBAF", this conference.
- [13] John Ousterhout, "Tcl and the Tk Toolkit" Addison-Wesley, 1994.
- [14] Johannes Van Zeijts, private communication.
- [15] R. V. Servranckx, User's Guide to the Program DIMAD, SLAC Report 285 UC-28 (A), May 1985.

MECAR (Main Ring Excitation Controller and Regulator): A Real Time Learning Regulator For The Fermilab Main Ring Or The Main Injector Synchrotron.

R. Flora, K. Martin, A. Moibenko, H. Pfeffer, D. Wolff, P. Prieto, S. Hays, Fermilab*, Batavia, IL 60510, USA

ABSTRACT

The real time computer for controlling and regulating the FNAL Main Ring power supplies has been upgraded with a new learning control system. The learning time of the system has been reduced by an order of magnitude, mostly through the implementation of a 95 tap FIR filter in the learning algorithm. The magnet system consists of three buses, which must track each other during a ramp from 100 to 1700 amps at a 2.4 second repetition rate. This paper will present the system configuration and the tools used during development and testing.

1. INTRODUCTION

The Fermi National Accelerator Laboratory Main Ring is used as an injector to either the Tevatron or the Antiproton Source. The Main Ring accepts 8 GeV beam from the Booster and accelerates the beam to either 150 GeV for use in the Tevatron or to 120 GeV for antiproton production. MECAR is an upgrade consisting of new computer hardware, current sensing equipment, and software.

The power system consists of three buses: one dipole bus with twenty-five power supplies and two quadrupole buses each having four supplies. Each power supply is a filtered 12 pulse SCR converter rated at ± 850 V and 3 KA. The dipole bus has a total inductance of 6 Henrys and a resistance of 6 Ohms. Each quad bus is .2 Henry and 1 Ohm. Both quadrupole buses are required to track the dipole bus while the current is ramped from 100 amps to either 1,360 (120 GeV) for the production of antiprotons, or 1,700 amps (150 GeV) for Tevatron injection. MECAR provides reference waveforms for all the power supplies and performs the real time current feedback for all three magnet buses. In addition, MECAR executes the cycle to cycle learning algorithms to further minimize regulation errors, and interfaces with the accelerator control system.

In about three years the Fermilab Main Ring will be upgraded to a new synchrotron known as the Main Injector. MECAR will be relocated to the Main Injector when needed and has been constructed to be compatible with both machines.

2. TRANSDUCTOR HARDWARE LAYOUT

Current signals are provided to MECAR through a set of DCCT's and subtraction electronics similar to other current regulation systems at Fermilab¹. These DCCT's are temperature stabilized and have an initial offset accuracy of <100 ppm with a long term drift stability of ≤ 10 ppm. Dual

transducers are installed for redundancy (see Figure #1). For the bend bus, a high resolution current error signal is generated by subtraction electronics taking the difference between the transducer signal and the output of a temperature stabilized D/A converter. With a gain of 100, this 21 bit equivalent signal is sent back to MECAR. The quadrupole current is measured with a difference transducer which subtracts the quad current from the bend current. This high resolution signal is used to regulate the quad bus current.

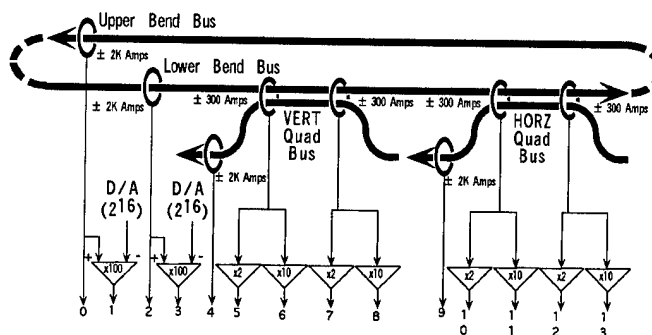


Figure #1 Bus Transducer Configuration

3. MECAR COMPUTER HARDWARE

The MECAR computer is made up of a 20-slot, 6U VME crate and various VME cards. A short description of the more important VME cards follows:

- Five CPU Boards: 25MHz 68040, 16MB RAM, ethernet
- Two Timer Boards: Clock decoding, timing and delay counters, 4 interrupt channels, in-house design
- Two Digital I/O Boards: 64-bit and 48-bit digital I/O boards, 8-bit programmable ports
- ADC Board: 16-bit, 64 Channel, 19uSec conversion time per channel, VME interrupt ability
- Power Supply Link Receiver and Transmitter Boards: 10Mbit, serial, unidirectional, proprietary data link, in-house design

It should be noted that some difficulty was encountered using the 68040 floating point processor in real time. Unmaskable interrupts are generated in response to simple underflows and overflows. These interrupts cause unacceptable performance degradation and even real time failure. The problem must be solved using explicit bounds checking throughout the real time signal processing.

4. MECAR SOFTWARE

4.1. Software Development Tools

* Work supported by the U.S. Department of Energy under contract No. DE-AC02-76CH03000.

Each of the CPU Boards are running Wind River Systems, Inc. VxWorks Real Time Operating System version 5.1.1. The VxWorks Development platform is an HP 9000 Model 735 Workstation. The version control for the C and 68k assembly language source code is done using the UNIX Source Code Control System (SCCS).

4.2. Subsystem Communication

Communication to MECAR is supported through two different mechanisms. The first is via Remote Procedure Calls (RPC), a protocol which is supported by VxWorks. An RPC driver Virtual Instrument (VI) interface was developed in-house for National Instrument Corp.'s LabVIEW®. LabVIEW's powerful and efficient environment was used extensively during development for reading and setting all manner of parameters. Many VI's have been made for engineering development, control, and diagnostics. Once MECAR becomes operational, LabVIEW VI's will only be used for engineering parameters and some debugging functions.

The second communication mechanism is the Accelerator Controls Network (ACNET). ACNET is a proprietary communication protocol which is used at Fermilab for all Control and Operational network communications. ACNET software is running in one of the five CPU boards in MECAR. Server RPC software written to support LabVIEW VI's during development is reused, whenever possible, by making client RPC calls from ACNET routines. Client RPC's are used by ACNET routines to communicate with the other four CPU boards in the MECAR VME crate. The RPC's use a Shared Memory Network supported by VxWorks, which is a TCP/IP network running over the VME backplane.

All real time communication between the CPU boards is done using shared memory over the VME bus.

4.3. MECAR Timing / Synchronization

The sample rate of the real-time code in MECAR is 1440Hz. The sampling interrupt is generated by a software controlled oscillator (SCO) which is phase locked to a 720Hz event on the accelerator clock system (TCLK). A phase-lock loop (PLL) is used to isolate MECAR from variations in the accelerator clock.

4.4. Signal Processing

A parallel 4 stage pipeline architecture is used for real time signal processing (see Figure #2). Assembly language is used to achieve 50% bandwidth utilization. The first stage is a hardware MADC triggered directly by the Phase Lock Loop (PLL). A VME interrupt from the MADC starts the second stage which executes in the System Program And Measure (SPAM) processor. System program information from the Accelerator Control System specifies all current waveforms. These programmatic signals are compared with transducer measurements from the MADC to determine the error in each of the 3 guide field buses.

These error signals are passed on to the third stage which executes in each of the 3 bus controller processors

(BEND, HORZ, and VERT) simultaneously and independently. Here regulation is accomplished with feedback and feedforward learning. The drive voltage is dispersed to successive tiers of power supplies in such a way as to minimize the voltage to ground seen by the magnets, and minimize reactive power, but allow sufficient slew time.

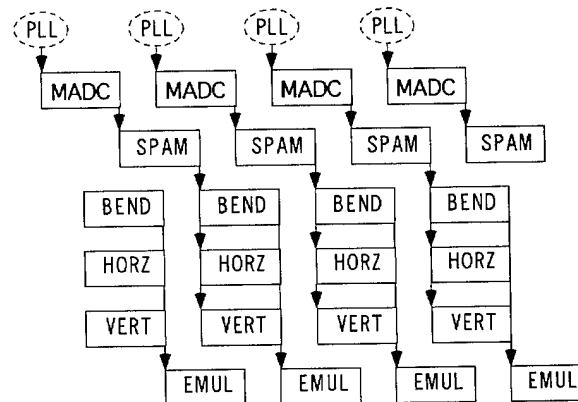


Figure #2 Execution Pipeline (time -->)

The last stage is used for development, diagnostics, and monitoring. Execution begins in the emulator (EMUL) processor after it has received an interrupt from each of the three Bus Controllers and basically emulates the response of the magnet load and power supply system for testing purposes. This load emulation has proven to be invaluable during development and commissioning.

4.5. Regulation

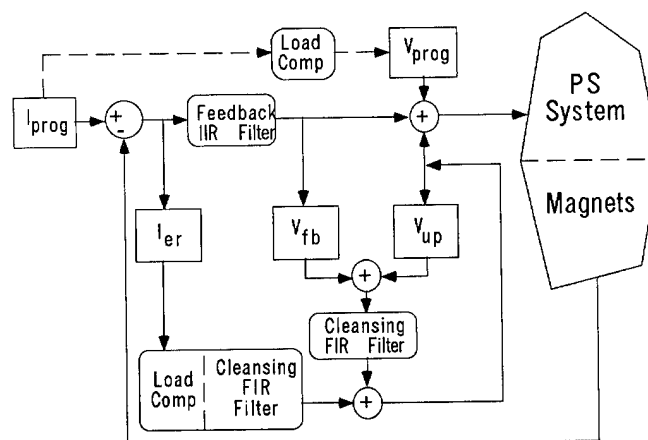


Figure #3 Control Signal Flow

A precalculated feedforward voltage program (V_{prog} in Figure #3) will drive the load to within $\pm 1\%$ of the reference waveform. The feedback loop (outer loop including the IIR filter in Figure #3) will bring it to within ± 500 ppm. The feedforward learning (inner part of Figure #3) further reduces the error to ± 30 ppm of maximum current. Feedforward learning is done by adding an "update" waveform, $V_{up}(t)$, to the power supply voltage drive. It is incremented each accelerator cycle by the sum of two signals: the real-time

voltage feedback applied during the previous cycle plus the voltage calculated to compensate for the measured current error. High frequencies of the new update waveform are attenuated for stability purposes with a FIR filter. Mathematically:

$$V'_{up}(t) = F_{FIR}(V_{up}(t) + V_{fb}(t) + L\dot{I}_{er}(t) + RI_{er}(t))$$

where the new update $V'_{up}(t)$ is calculated from the old update $V_{up}(t)$, the old feedback $V_{fb}(t)$, and the old error $I_{er}(t)$.

4.5.1. Feedback and Learning Interaction

Feedback can react to non-repetitive transient errors, but it can't anticipate errors; it has a finite phase delay. Feedforward learning, on the other hand, can anticipate errors, but only repetitive ones; it has no phase delay. When feedback and learning are connected properly, system stability separates into two domains: the time continuous domain for feedback, and the cycle to cycle iteration domain for learning. From a feedback stability point of view, the only effect of the learning is that the feedforward voltage program happens to be different on successive cycles. Within a cycle, on a time continuous basis, feedback stability is governed by classical theory. From a learning point of view, the new corrective learning signal is determined from the previous error signal. This error signal resulted while the previous feedback was present. Therefore, this new corrective signal must be applied with the previous feedback signal. The correction signal that is applied to the next cycle is the sum of the calculated voltage needed to correct the previously measured error and the corresponding previous feedback signal.

4.5.2. Feedforward Learning Stability

If the load is well behaved and completely predictable out to the Nyquist frequency, then a load compensation filter, if sufficiently accurate, will render the learning system absolutely stable. However, this is not the case with a large magnet system having multiple power supplies and stretching out over 4π kilometers. As different power supplies turn on during the ramp cycle, changing transmission line effects of the distributed magnet system make the high frequency behavior of the load intractable. Simply attenuating these frequencies in the load compensation and feedback signal is insufficient to make learning stable, because even the smallest error leakage will eventually accumulate in the updates and run away. The accumulated voltage correction must be "cleansed" of these frequencies on a regular basis. It can be shown that if transmission of the cleansing filter, $\alpha(f)$, satisfies:

$$\alpha(f) < \left| \frac{Z_{load}(f) + Z_{gain}(f)}{Z_{load}(f) - Z_{comp}(f)} \right|$$

for all frequencies at which the load is unpredictable, then the learning will be stable. Where $Z_{load}(f)$ is the actual load impedance, $Z_{gain}(f)$ is the feedback IIR filter and gain impedance, and $Z_{comp}(f)$ is the load compensation impedance.

4.5.3. Use of FIR Filters for Learning

Finite Impulse Response filters are ideal for feedforward learning because they can be implemented with absolutely no phase distortion or delay of any kind, by making them symmetric in the time domain. Currently a basic 95 tap FIR filter (see Figure #4) is being used to insure learning stability. A roll off at 30 Hz is chosen to match the frequency at which transmission line modes start to dominate in the bend bus.

5. TESTING

Due to the desire to maximize the physics output of the accelerator complex during the past six months, very little time has been available to test MECAR with the power supply system. However, with the time that has been available, MECAR has successfully operated and accelerated Main Ring beam. During these tests the learning algorithms have shown to be effective in 1 or 2 machine cycles. This represents a 10 fold decrease in learning time over the present system.

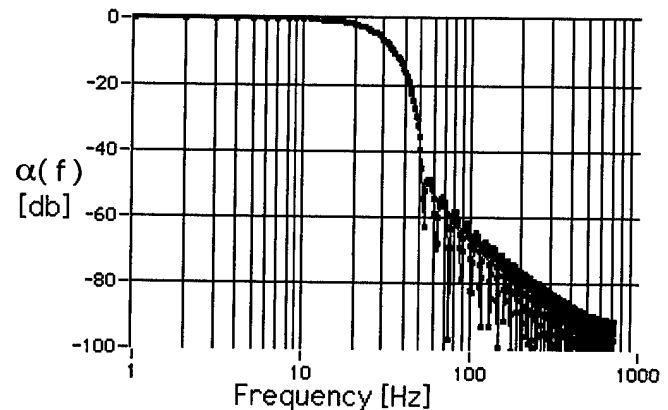


Figure #4 Cleansing FIR Filter Frequency Response

6. CONCLUSION

It has been proven that it is possible to build a feedforward learning controller that essentially learns in one repetition cycle. With attention to load filter accuracy and cleansing filter bandwidth, one can make such a system absolutely stable.

7. ACKNOWLEDGMENTS

We wish to acknowledge the very able help of the following people who built various components of the MECAR system: C. Briegel, B. Claypool, B. Lublinsky, O. Payne, K. Woodbury, and G. Wu.

8. REFERENCES

- ¹ S. Hays, D. Wolff and H. Pfeffer Fermilab, "Power Supply Regulation Systems Installed in the Fermilab Accelerators" IEEE Nuclear Science Symposium November 1991

Framework for a General Purpose, Intelligent Control System for Particle Accelerators

R. T. Westervelt, W. B. Klein

Vista Control System Inc., Los Alamos, New Mexico 87544

and

G. Luger

University of New Mexico, Albuquerque, New Mexico 87131

Abstract

Tuning and controlling particle accelerators is time consuming and expensive. Inherently nonlinear, the control problem is one to which conventional methods cannot satisfactorily be applied. Advanced information technologies such as expert systems and neural networks have been applied separately to the problem, with isolated success. Few, if any, of these advanced information technologies have been applied for general use or in a manner useful to multiple accelerator installations. We discuss results of coupling neural network and expert systems technology to solve several standard accelerator tuning problems based on realistic simulations. We also examine the effectiveness of additional heuristic search techniques such as genetic algorithms. Finally, we show the integration of this hybrid AI system with an existing general-purpose control system.

Project Overview

The goal of this project is to develop a very flexible, intelligent controller that can reduce the tuning time for a particle accelerator and can develop "better" tunes than are now achieved by human operators. Additionally, the intelligent controller should maintain the tune with smaller deviations than are currently exhibited. Various approaches have been taken to automate the control of accelerators [1,2,3], with varied degrees of success. Generally, most effort has been directed toward solving problems for a particular facility and little effort has been directed to developing more general solutions applicable to a number of different accelerator facilities. This paper reports the early status of this project after the first phase of the research.

The architectural framework for the controller is an expert system that guides more specialized controllers based on the state of the system and the tuning goal. We developed a realistic simulation environment to test the controller operation. We have examined several types of controllers, including back propagation neural networks, fuzzy logic controller, analytic based tuning by the expert system, and genetic algorithm tuners.

Steering, a standard zero-order problem, is one of the initial tasks of a beamline tuner. We first considered the basic situation in which steering was controlled by two steering magnets (SMs) separated by some distance. Two beam position monitors (BPMs) downstream of the steerers monitored the effect of the steerers. Steering must take into account beamline alignment, electronic offset and drift,

and downstream tuning requirements. In general, there is jitter in the initial beam coordinates with some frequency. Beam-source mechanical and electrical variation causes this jitter, which limits steering accuracy.

Another basic element of beam transport is the periodic line for focusing. Beam root mean square (rms) sizes are measured on profile monitors (PMs), which directly measure intensity distribution. These PMs, usually wire scanners, contain inherent inaccuracies due to beam fluctuation during measurement and component error. The relationship between quadrupole settings and beam profile is nonlinear, making accurate tuning difficult even for human operators.

Accelerator Simulation

We began by developing a program to simulate the steering scenario for initial prototyping of the intelligent controller. This test program was a linear model for beam deflection through the steering magnets. We ignored higher order effects of the steering magnets. The noise effects of beam variations, magnet variations, and measurement variations in the BPMs were all included in the simulation. Additionally, we included random device failures as an option in the simulation.

We interfaced TRANSPORT [4], a standard accelerator modeling program, to Vsystem, our commercial software product for developing control systems to provide a rich simulation environment. We modified TRANSPORT by adding additional input types to relate card deck elements to Vsystem database channels. We then modified TRANSPORT to automatically recalculate the simulation when any input parameters changed. Automatic recalculation effectively simulates the real world response of an accelerator.

We added realistic noise and error effects by filtering and varying the data as the data was stored in the Vsystem database. Random gaussian noise was added to data signals for monitoring devices. Noise characteristics were configurable from the Vsystem database. Time dependent device behavior was also included in the simulation.

Expert System

An expert system is a computer system that can help solve complex, real-world problems. Expert systems use large bodies of facts and procedures gathered from experts. These facts and procedures are usually domain specific knowledge gathered from real-world experience and not

necessarily equation-based constraints or foundational theorems. Expert systems use rules and facts to reason and make decisions, often using imprecise or incomplete information. Most expert systems also have the ability to explain their reasoning and decisions.

Our design used an expert system at the top level for reasoning and control. We developed the expert system was developed using the CLIPS package from NASA. Placing the expert system at the top level provided a controller to make large-scale decisions about how to solve the entire control problem, without considering detailed control issues. Details concerning how to solve subproblems were handled by lower level control modules. With direct access to the Vsystem control database, the expert system used all pertinent information to build a model for solving the system and to reason about specific components and more general tuning issues. This top-down approach reflects a true expert's knowledge in a large system, and it provides a good framework for building proper knowledge representations.

With the expert system in control, an object representation of the accelerator was necessary for reasoning about the beamline and for easy manipulation of structured objects reflecting the modularity of the beamline. Creating an object representation of the system within CLIPS enabled us to place knowledge about specific components within the component representation while maintaining a knowledge base representing facts and rules about the entire system. An object reasoning model allows appropriate encapsulation of knowledge with system objects, modularity of reasoning, and the possibility of distributed control. It is feasible with this system to make top level decisions and then provide control information to a distributed set of semi-autonomous control agents (objects).

Top-level control by an intelligent reasoning system facilitates breaking both problem and solution spaces down into well defined, easy to reason with subcomponents. We began by separating beamline components into groups by both functionality and control characteristics. By looking at the characteristics of each component, we can develop multiple partitions that imply certain types of solutions. Once the solution space has been well partitioned, an appropriate set of solutions is defined to operate on those partitions. The top level reasoning system can focus a particular partition and determine the best solution strategy for its resolution.

Neural Networks

A neural network is a group of individual processing elements, often divided into layers. The neural network passes the results of computations between layers and finally to an output layer. The individual processing elements, roughly analogous to biological neurons, combine inputs from multiple input paths and create an output using a transfer function. Neural processing elements can be combined into a variety of architectures and, along with associated training functions, can learn and recall non-linear functions and patterns. Neural networks have the

additional benefits of being able to function in the presence of incomplete or noisy input data, and processing inputs in parallel.

We chose a three-layer backpropagation network because of the simplicity of the task (learning a linear relationship in the presence of noise) and the straightforward representation. We were able to directly map network input and output nodes to BPMs and SMs respectively. The network was then trained to recognize causal relationships between changes in BPM readings and magnet adjustments. A fully trained network was given desired BPM changes as inputs. The network produced magnet adjustments that would cause the changes.

Because we wanted the neural network to learn relationships on the running beamline and to adjust its weights accordingly, we attempted to train the network on a run-time data set. We accomplished this task by allowing the system to make random adjustments to magnets on the beamline model and record the resulting BPM changes. This design produced a real-time training instance for the network. We then fed the BPM changes through the network to generate a set of predicted magnet adjustments. The system calculated the difference between predicted and actual magnet adjustments and backpropagated the error through the system.

While the neural network was able to learn SM/BPM relationships using limited training cycles, it was not able to converge on more complex problems. The neural network failed for two important reasons. The first reason was inadequate training data. Because the network attempted to gather real-time data about the current state of the system, it could not produce training data faster than it could evaluate SM/BPM changes in the system. While the network could typically improve its performance by continuing to take samples of the system and produce training instances, it would take too much on-line beam time to produce enough training data to adequately train the network.

Even if a training set were available, the network suffered from a greater problem. When the network generates training data as SM/BPM pairs and attempts to learn a causal relationship between random SM changes and resulting BPM changes, the network is not directed toward specific solution methods for adjusting BPMs. Potentially, a large number of SM adjustments could produce the same effect on BPM readings, given SMs in the same axis using separate power supplies.

Additional Control Methods

We also investigated several other control methods for these problems. These included an analytic control algorithm, fuzzy logic control and genetic algorithm searches.

The analytic technique for steering control relies on beamline behavior consistent with a simple linear model. After the expert system determines a set of components that make up a steering section, it measures the derivative between steering magnet power source currents and beam

monitor readings. The controller adjusted power to the SMs in the section and recorded resulting changes in BPM readings. The expert system then built an appropriate system of equations and solved them using gaussian elimination (reduction). The analytic method makes no attempt to filter noise or eliminate component errors. In general, the analytic method provides an accurate solution given large signal-to-noise ratio and properly functioning beamline components.

We cannot expect a purely analytic solution to adequately tune a beamline in most cases, especially during initial startup. One of the conditions that causes difficulty for tuning is beam fluctuation or jitter. Fuzzy logic is used in the beamline controller for reasoning about real-valued beamline data in the presence of noise or in situations where analytic methods have failed. The fuzzy logic steering solution used fuzzy rules about BPM relationships to follow a hill-climbing algorithm toward a good solution. Not only do fuzzy rules allow expert systems to reason about real-valued data without relying on specific values for rule boundaries, but they also allow reasoning about how data will be measured and evaluated. The expert system is able to modify the meaning of a set membership depending upon the specific problem being solved, the accuracy required, and the state of the system.

The fuzzy logic solution did a good job of quickly moving to an approximately correct solution, but tended to oscillate around a very accurate tune. We noticed that the accuracy of the fuzzy solution depended greatly on the quality of the knowledge we placed in the system. For example, a pure hill-climbing fuzzy system that only attempted to minimize BPM error tended to find local minima. When the rules were modified to evaluate BPM ratios and isolate specific magnets for adjustment, the fuzzy solution tended to find better solutions fairly quickly.

The genetic algorithm (GA) is an appropriate heuristic for focusing control because it can search large solution spaces in non-linear domains. The GA for steering control used genetic operators that modified magnet strengths according to a preset probability distribution. We implemented the focusing algorithm using fuzzy genetic operators which modified magnet strengths according to a fuzzy pattern. Fuzzy patterns eliminate the need for a priori determination of magnet adjustment strengths and patterns. The focusing GA was built with the realization that wire scanners cannot deliver real-time continuous feedback. Trial solutions for the algorithm are evaluated by actual testing on the simulated beamline. Since typical solution patterns can be determined for focusing, we used a special genetic operator to search the solution population for unwanted solution patterns (as determined by the expert system) and replace them with patterns representing good possible solutions. Fuzzy pattern matching and replacement guides the GA toward certain solutions and away from others, according to knowledge about typical solutions in the expert system. The algorithm can still perform a global search over the solution space, and it can still converge on a solution with a pattern differing from suggested "good" patterns. The guided solution was able to focus the periodic line in under 100 trials and to greater than expected accuracy.

Project Status

The first phase of this project is nearing completion. An application has been submitted for additional funding. Work is continuing to develop the next generation of the system based on the results of the first prototype. One of the major goals of the second phase of this project will be to test the controller at several operational accelerator facilities to determine successful it is under realistic conditions. The additional tests for the second phase of the project will be to expand the complexity of the simulated tuning problems to further stress the capabilities of the controller.

Using knowledge gained during the first phase of this project, we have prepared a clear plan for developing a full, intelligent control system for accelerators. In the most effective system, an expert system coordinates the activities of a set of independent processes controlling small subsystems of the accelerator. The expert system manages the overall tuning process by identifying and configuring subgoals based on the overall goal for the accelerator. These subgoals are then either subdivided further or are assigned to a suitable method, based on the goal and the operational situation. Provided with a varied set of methods, an expert system can overcome limitations in any particular control method by substituting a solution method well matched to the goal for a particular subsystem.

Acknowledgment

This work was supported by a grant from the DOE under the SBIR program. DOE Grant # DE FG05-94ER81897

We would also like to thank Andy Jason of AOT-1 at LANL for his invaluable assistance in developing the control scenarios and in his careful explanations of the underlying concepts involved.

References

- [1] S. Clearwater and W. Cleland, "A Real-Time Expert System for Trigger Logic-Logic Monitoring," *Proceedings of the International Conference on Accelerator and Large Experimental Physics Control Systems*, Vancouver, B.C. (November 1989)
- [2] D. Nguyen, and M. Lee, "Accelerator and Feedback Control Simulation Using Neural Networks," (SLAC-PUB-5503, May 1991)
- [3] D. Schultz, "The Development of an Expert System to tune a Beam Line," *Proceedings of the International Conference on Accelerator and Large Experimental Physics Control Systems*, Vancouver, B.C. (November 1989)
- [4] K. Brown et al. "TRANSPORT A Computer Program for Designing Charged Particle Beam Transport Systems," (SLAC-PUB-91 Rev 2, May 1977)

AUTOMATIC BEAM STEERING IN THE CERN PS COMPLEX

B. Autin, G.H. Hemelsoet, M. Martini, E. Wildner,
CERN, CH-1211 Geneva 23, Switzerland

Abstract

The recombination, transfer and injection of the four beams from the PS Booster to the PS Main Ring, have a high level of intricacy and are a subject of permanent concern for the operation of the PS Injector Complex. These tasks were thus selected as a test bench for the implementation of a prototype of an automatic beam steering system. The core of the system is based on a generic trajectory optimizer, robust enough to cope with imperfect observations. The algorithmic engine is connected to pick-up monitors and corrector magnets and its decision can be validated by the operator through a graphics user interface. Automatic beam steering can only be efficient if the beam optics is fully confirmed by experimental observations, a condition which forces the systematic elimination of errors both in hardware and software.

I. INTRODUCTION

Automatic steering in the PS complex has first been implemented in the transfer line TT2 which connects the 26 GeV synchrotron (PS) to the 300 GeV synchrotron (SPS). In this line, the beams have indeed to be carefully aligned [1] on secondary emission grid monitors for the precise measurement of the emittances which will be required for the Large Hadron Collider (LHC). The test revealed that the operation is considerably alleviated when it is aided by an "intelligent" software module and that the machine is fully reliable when the instrumentation and the correction systems respond as predicted by the classical theory of strong focusing machines [2]. In the context of the preparation of the PS for the LHC, the automation of various beam manipulations is the objective of the ABS project whose acronym stands for Automatic Beam Steering and Shaping. Among the numerous applications which are planned, priority has been given to the transfer from the 1 GeV booster (PSB) to the PS.

The physics process is schematically represented in Fig. 1. The beams circulating in each of the four booster rings are sequentially ejected towards individual transfer channels then merged in a common line [3] and finally injected into the PS. If no correction is applied, the momentum vectors of the four beams are different at the entry to the PS, the beams oscillate about the PS closed orbit and the beam emittances are degraded. The task of the corrections on the booster side consists of making the momentum vectors collinear. Once this is achieved, the common momentum vector is oriented tangent to the PS closed orbit by the PS injection system. The problem is much more complex than the simple alignment of a beam in a transfer line but the same correction architecture can be maintained if a generic procedure has been defined. The data acquisition whether it comes from SEM grids or electrostatic pick-ups is the same, the correction algorithm has always to solve a linear system, the graphics

interface is customized to the machine but its design is standard; the various modules are written in C or in *Mathematica* [4].

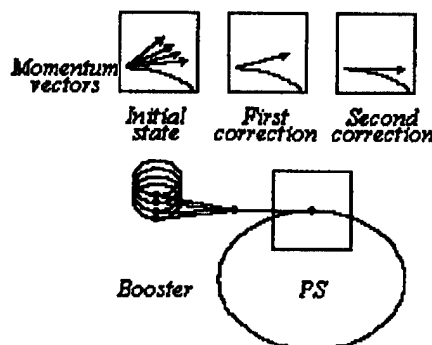


Figure 1. Transfer from PSB to PS

II. SYMBOLIC BEAM OPTICS

A. Machine modeling

The model of a machine is given by general purpose programs which can be numerical like *MAD* [5] or symbolic like *BeamOptics* [6], a package which will be included in the PS control system as soon as a data base containing the various characteristics of the machine components is available. Some technical aspects of the application of symbolic computing to beam optics are reported elsewhere [6]. It will only be said here that functionalities such as list processing, pattern recognition, object orientation through functional programming and linkage protocols in a UNIX environment have been found very efficient to write concise codes and integrate them in an existing control system.

B. Linear solver

Once the theoretical model of a machine is known, its adaptation to real experimental conditions resorts to perturbation techniques, the first order perturbations being by far the most frequently used. This is precisely the case of beam steering but also of tune adjustment, chromaticity, beam shaping in a final focus or geometrical aberrations. A first order perturbation is linear in the sense that the total perturbation is the sum of all the individual perturbations whether the perturbation is due to a dipolar, quadrupolar, sextupolar or any type of field. A primary element of generality is thus to get a linear solver which can be used for any kind of problem. The *Micado* algorithm [7] has been selected for this purpose and its main features are briefly summarized.

The algorithm solves a linear system iteratively in the presence of experimental errors or even breakdowns of the instrumentation or of the correcting elements. It consists basically of minimizing iteratively the norm of a residual vector

$$r = Ax + b \quad (1)$$

using a least squares method. b is a vector whose n components are the errors to be corrected, x is the correction vector which collects the m strengths to be applied to the correction magnets and $A(n, m)$ a matrix which represents the response of the beam to a set of correcting fields.

At each iteration, the first best magnet that yields the lowest residual r.m.s. distortion at monitor positions is selected and appended to the corrector set. Then, the residual distortion is re-analyzed and the next best magnet selected. All correctors from the previous iterations are kept but their strengths are recalculated. The method proceeds until the residual r.m.s. distortion is comparable with measurement errors.

The various steps of the calculation at the k -th iteration are:

1. Compute the corrector strengths as

$$x^{(k)} = - \left(A_i^{(k)T} A_i^{(k)} \right)^{-1} A_i^{(k)T} b \quad (2)$$

for all possible sub-matrices $A_i^{(k)}$ of A .

2. Compute the norm of the residual vector $r_i^{(k)}$ as

$$\|r_i^{(k)}\|^2 = b^T b + x_i^{(k)T} A_i^{(k)T} b \quad (3)$$

3. Select the corrector which minimizes the norm of the residual vectors

$$\|r_{i_k}^{(k)}\| = \min_i (\|r_i^{(k)}\|) \quad (4)$$

The method is fast and converges with a small number of correctors. It has been coded as a *Mathematica* package.

III. SPECIFIC ASPECTS OF BEAM STEERING

The theory of beam steering is well known for circular machines and transfer lines. However, hybrid cases occur when the position of the beam in a transfer line is modified by closed orbit distortion in an accelerator or when several transfer lines share a common section.

A. Transfer line

The correction of beam trajectories in transport channels requires a single trajectory measurement: the measurement vector is $b = \{u_i\}_{i=1 \dots n}$, where u_i is the beam position at the i -th pick-up. The components of the correction matrix A yield the trajectory deviations at the i -th pick-up due to a unit kick at the j -th corrector. For a transfer line, they are given by

$$a_{ij} = \begin{cases} \sqrt{\beta_i \beta_j} \sin(\mu_i - \mu_j) & \text{if } \mu_i > \mu_j \\ 0 & \text{if } \mu_i \leq \mu_j \end{cases} \quad (5)$$

where β and μ are the classical β -function and phase function.

B. Closed orbit

In a ring, the orbit distortion must satisfy cyclic boundary conditions and the expression of the matrix elements is

$$a_{ij} = \frac{\sqrt{\beta_i \beta_j}}{2 \sin \pi Q} \cos(-\pi Q + |\mu_j - \mu_i|) \quad (6)$$

where Q is the machine tune.

C. Combined closed orbit and transfer line

When the correctors of a circular machine affect the beam positions in an ejection line through a distortion of the ring closed orbit, the middle M of the fast extraction kicker is taken as a hinge point. The transfer matrix from the corrector to the pick-up is then the product of the closed orbit transfer matrix from corrector to M and of the channel transfer matrix from M to pick-up. After calculation it turns out that the expression of the correction coefficients is formally the same as for the closed orbit correction (Eq. 6) when the origin of the phases is taken at the point M .

D. Multiple transfer

When several transfer channels are connected to a same beam line the observations in the common channel are distinct for each beam whereas the common correctors act on all the beams. This situation is tackled by defining two correction matrices per beam: one, called $A^{(k)}$ is attached to the individual correctors; the other one, $A^{(c)}$ concerns the common correctors and is the same for all the beams. The global correction matrix can thus be written

$$A = \begin{pmatrix} A^{(1)} & 0 & \dots & 0 & A^{(c)} \\ 0 & A^{(2)} & \dots & 0 & A^{(c)} \\ \dots & \dots & \dots & \dots & \dots \\ 0 & 0 & \dots & A^{(N)} & A^{(c)} \end{pmatrix} \quad (7)$$

E. Two-turn injection

The coherent oscillations at injection may be corrected using two successive single turn trajectories measured shortly after injection and two correction magnets per plane [8].

The trajectory position at the i -th pick-up in machine turn number t can be expressed as

$$u_{i,t} = z_i + a \sqrt{\beta_i} \cos(\mu_i + \varphi + 2\pi(t-1)Q) \quad (8)$$

in which z_i is the closed orbit position at the i -th pick-up. The two unknowns of the problem are the coefficient a and the constant phase φ .

The closed orbit is eliminated by taking the trajectory difference between two successive turns. The result takes the form of a classical betatron oscillation after division by $2 \sin \pi Q$.

$$\frac{u_{i,t} - u_{i,t+1}}{2 \sin \pi Q} = a \sqrt{\beta_i} \times \cos(\mu_i + \varphi + 2\pi(t-1)Q + \pi(Q-1/2)) \quad (9)$$

The measurement vector b in Eq. 1 is thus

$$b = \left\{ \frac{u_{i,t} - u_{i,t+1}}{2 \sin \pi Q} \right\}_{i=1 \dots n} \quad (10)$$

and the correction matrix A is calculated using Eq. 5.

When the tune is unknown, the method can still be used: the *Mathematica* function which selects the best correction magnets and computes their strengths, searches in addition for the tune value Q which yields the minimum value of the norm of the residual vector.

IV. EXPERIMENTAL CORRECTIONS

A. Graphics user interface

For the operational application programs, standard graphics user interfaces have been integrated in the control system. Once the beam positions have been acquired and displayed, the operator can validate the measurements and choose the procedure of correction. The C program of the interface is connected to the *Mathematica* steering algorithm via the two way *MathLink* protocol. The development of the algorithm and its linkage to the control system are fully de-coupled.

An example of the organization of the interface is shown in Fig. 2 for the PS injection. The screen contains the display of the beam positions, the input to the correction algorithm and the calculated currents ready to be sent to the correction power supplies.

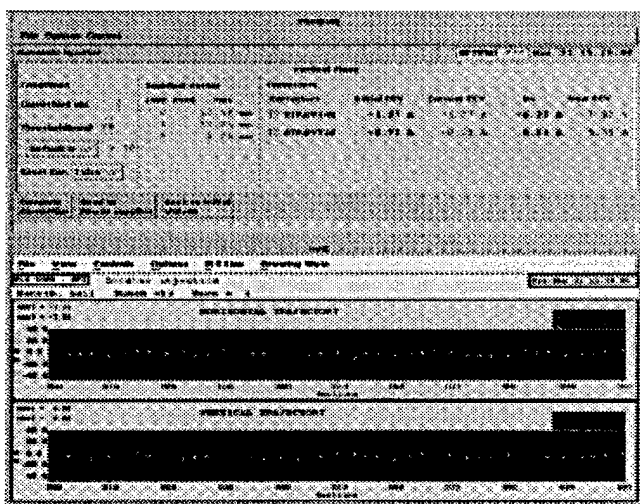


Figure 2. Graphics user interface for the PS injection

B. Correction of trajectories at PSB ejection

The procedure to correct the ejection trajectory of the PSB beam uses two dipoles in each ring and one steering magnet in the transfer line. For the vertical plane there are additional steering elements for the vertical recombination of the four rings. Downstream from the recombination point, the four beams are corrected in both planes to be aligned at the first PS injection steering element.

The automation of the ejection process did not converge when it was first applied. A systematic error tracing was then carried out and a major system deficiency was found to be the misalignment of the pick-ups with respect to the quadrupole axes. The measurements were filtered to take that misalignment into account and the correction became efficient. The position errors in each channel have typically been reduced to 2 mm after correction.

C. Correction of coherent oscillations at PS injection

The procedure has been implemented at the PS machine for the protons. The two-turn trajectories are observed with 40 pick-ups in each plane and there are two corrector magnets per plane. The performance of the correction procedure is closely related to the beam instrumentation. The quality of the observations has

been tested by comparing the experimental calibration factor of the correctors with their values deduced from magnetic measurements. As soon as the agreement between the two determinations of the calibration factors had been obtained, the correction of the coherent oscillations became reliable and the residual amplitude was of the same order as the errors in the injection line.

V. CONCLUSION

An automatic beam steering procedure has been successfully implemented for the correction of the PSB ejection trajectories and of the coherent transverse oscillations at PS injection. Central in the project is symbolic computing whose resources had not yet been thoroughly investigated for accelerator controls. Computer algebra which is the best known aspect of symbolic computing is a classical tool in theoretical applications and any algorithm produced with this technique can be made available for the machine operation without any delay. At the controls level, the list processing, pattern recognition and object orientation via functional programming used to treat mathematical expressions, fit the communication with equipment modules, graphics user interfaces or data bases. The experience gained on automatic beam steering in a special context will therefore be extended to other domains of the PS operation.

References

- [1] B. Autin, M. Arruat, F. diMaio, M. Martini, Beam Steering: A Test Bench for Generic Algorithms in Accelerator Controls, CHEP 94, San Francisco (1994).
- [2] E.D. Courant, H.S. Snyder, Theory of the Alternating-Gradient Synchrotron, Annals of Physics, vol. 3, p. 1-48 (1958).
- [3] J.P. Delahaye, La recombinaison des faisceaux issus des 4 anneaux du CERN PS Booster, CERN/PS/BR 79-12 (1979).
- [4] S. Wolfram, Mathematica - A System for Doing Mathematics by Computer, Addison-Wesley, Redwood City, 1991.
- [5] H. Grote, F.C. Iselin, The MAD Program - User's Reference Manual, CERN/SL/90-13 (AP) (1990).
- [6] M. Arruat, B. Autin, G.H. Hemelsoet, M. Martini, E. Wildner, Integration of Symbolic Computing in Accelerator Control, Proc. AIHENP95, Pisa (1995), to be published.
- [7] B. Autin, Y. Marti, Closed Orbit Correction of A.G. Machines Using a Small Number of Magnets, CERN ISR-MA/73-17 (1973).
- [8] M. Martini, J.P. Potier, T. Risselada, Automatic Injection Tuning Using Two Successive Single Turn Trajectory Measurements, Proc. EPAC 90, p. 1598-1600, Nice (1990).

INTEGRATED ON-LINE ACCELERATOR MODELING AT CEBAF

B. A. Bowling, H. Shoaee, J. Van Zeijts, S. Witherspoon, W. Watson
CEBAF, Newport News, VA 23606 USA

* An on-line accelerator modeling facility is currently under development at CEBAF. The model server, which is integrated with the EPICS control system, provides coupled and 2nd-order matrices for the entire accelerator, and forms the foundation for automated model-based control and diagnostic applications. Four types of machine models are provided, including design, golden or certified, live, and scratch or simulated model. Provisions are also made for the use of multiple lattice modeling programs such as DIMAD, PARMELA, and TLIE. Design and implementation details are discussed.

I. INTRODUCTION

CEBAF is a 4 GEV electron accelerator facility which is in the final stages of commissioning. It consists of two 400 MeV superconducting linacs with a 5 pass beam recirculation system. The facility is capable of simultaneously serving three experimental halls with beams of differing energies.

The goal of delivering high quality beams to experimenters requires the availability of appropriate control, diagnostics, and monitoring functions to direct the complex operation of the accelerator. In addition, the efficient operation of a complex accelerator requires the automation of as many routine machine functions as possible. This would assist in achieving the goal of operators acting as accelerator "pilots", rather than accelerator "mechanics".

An early decision in the design phase of the control system was to base all high level functions involving machine setup and operation on accelerator models rather than resorting to a "look-and adjust" method of operation. This was deemed particularly crucial during the commissioning phase of CEBAF, when it was required to reconcile the machine behavior with its model.

II. ARTEMIS MODEL ENVIRONMENT

The Accelerator Real Time Modeling Information Server (ARTEMIS), currently under development, will be a central Server/Client facility in the CEBAF accelerator control system, providing various model data (transfer matrices, twiss parameters, etc.) and supporting computations (e.g. quadrupole strength calculation for matching) for all model-driven facilities, including LEM (Linac Energy Management) software, beam steering, feedback, and beam diagnostic and optimization procedures [Fig. 1]. Centralizing the model calculations provides a uniform and consistent data collection for these and other applications, while eliminating the need for redundant calculations by different application software.

ARTEMIS will also be interfaced with on-line facilities such as Tcl/Tk and MATLAB, allowing for the rapid prototyping of model-based algorithms and applications before

they are made a permanent part of the control system.

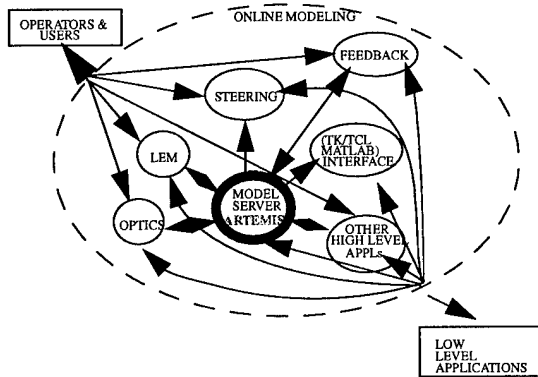


Figure 1: Modeling Environment Overview

Objectives

The main objective for ARTEMIS is to make available timely and accurate lattice information for use by any accelerator application software. Timeliness implies that the model must reflect changes in machine parameters at an acceptable rate. This is achieved through several updating mechanisms:

- Periodic updating of model(s) at a given rate.
- Model updates triggered by an external event.
- User initiated model calculations (on-demand modeling).

In addition, model accuracy demands correct treatment of all machine components, to the degree required by applications. ARTEMIS will provide availability of the following:

- Generation of first and second-order transfer functions.
- Provisions for inclusion of higher order models as needs dictate.
- Correct treatment of the acceleration process in the linac cavities, including effects of adiabatic damping and cavity focusing effects.
- Non-relativistic effects (handled by PARMELA interface).
- Spin polarization tracking.

Input to ARTEMIS will be the accelerator layout of all elements (using MAD standard for element definitions) including bends, quadrupoles, sextuples, correctors, BPMs, and viewers. This information includes device setpoints, position in accelerator coordinates, x, y and z, and path length. Commands supported by the server include:

- Retrieval of lattice functions.

*Supported by U.S. DOE Contract DE-AC05-84-ER40150

- General first and second-order transfer matrices.
- Retrieve hardware information, e.g. list of quadrupoles, BPMs, etc. in a given region, with the ability to use wildcards for specifying a list of devices.
- Update current model, i.e., using current setpoints, calculate machine parameters.
- Update the machine to reflect the desired model.

ARTEMIS will provide the capability to generate four distinct machine model classes:

- Golden model: this includes a consistent set of machine parameters that have been verified and deemed reasonable by an authorized expert. It is anticipated that this is the model that will be used by many control applications.
- Design model: this is a machine model based on the baseline design and setpoints of the accelerator.
- Current (pseudo-real-time) model: this is a machine model representing the latest or current accelerator setpoints, the update mechanism may be autonomous or user initiated. This form has utility for control codes which perform changes in lattice parameters.
- Simulation model: This model reflects the outcome of *what-if* scenarios as applied to the accelerator lattice. Possible applications include investigation of stray magnetic fields, focusing errors, injection errors, etc.

The objective of allowing ARTEMIS to exist in several distinct forms requires that the interface be available to all forms of software, preferably utilizing reusable code. This will be achieved by the EPICS Device API (known as *cdev*), currently under development at CEBAF. This layer provides any client access to the previously-defined model types, as well as to control system parameters (via channel access), database information, etc., all using a cohesive interface. ARTEMIS will act as a server process to the Device API.

III. THE MODEL DATABASE

The CEBAF beamlines are stored in an object oriented database. The commercial package chosen for use as the centralized database is ObjectStore. An object-oriented database was chosen over the more conventional relational form due to the decision to employ an object-oriented approach to the design and implementation on ARTEMIS. Typical accelerator beamlines lend themselves naturally to this approach, and most existing accelerator codes utilize the concepts of object-oriented design. For example, the definition of a FODO (Focusing-Defocusing) cell can be considered as an object, and many cells can be ordered together forming a collection known as a beamline, etc. One defines the classes, using inheritance, and these structures are used directly by the database. These same classes will be used in the actual ARTEMIS server, as well, exploiting reusability of code.

This database is automatically generated from the same set of input files that are used by CEBAF physicists to define and study the accelerator lattice. These files use the "standard" (MAD style) notation for defining beamline and element properties. The object-oriented class breakdown for ARTEMIS is as follows: an element is a generic beam line component that covers a physical entity on the beamline, such as a magnet, a beam position monitor, an accelerating cavity, a marker, a drift

space, etc. The elements attributes have been characterized as layout specific information, and conditional or calculated information.

Figure 2 illustrates the C++ classes defined for the input lattice definitions. The basic building block is the *beamElement* class, representing an element as defined above. The *beamElement* class inherits from the class *bmlnCondition* and references static information about a beam element via the *bmlnLayout* class. This class serves as a base class for each particular element type. The information contained in each element is dependent on element type.

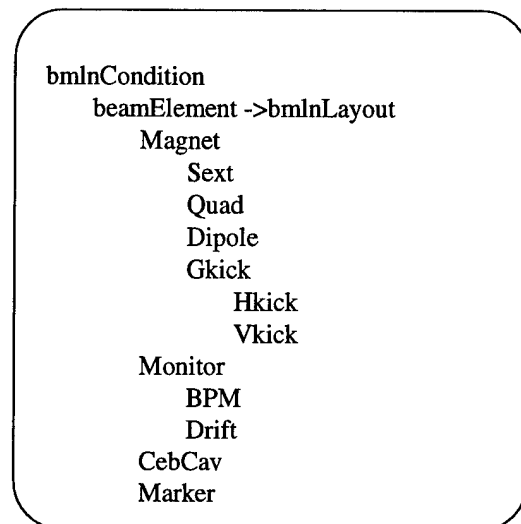


Figure 2: ARTEMIS Class Inheritance Structure

The *bmlnCondition* class is associated with every element. It maintains the "physics" of the element, such as lattice functions and transfer matrices, initial lattice conditions, element optical strength, beam momentum, etc. A matrix class is referenced here in order to take advantage of existing C++ matrix libraries.

The *bmlnLayout* class contains static information about an element defined in the lattice. The name field identifies the element to the model, and is unique throughout a section, which is defined as an ordered collection of elements. The class also maintains a unique EPICS *cntrlid* control system identifier. Physical information, such as element length, position, misalignment, etc., are also included in this class definition.

The smallest object that ARTEMIS server will operate upon is a beamline section, defined as an ordered collection of beam elements (*beamElement*). The beamline section class inherits from a *bmlnSet* collection of beam elements. Each section also includes a unique identifier used for access purposes. Initial conditions for matrix, Twiss, etc. are also maintained for the use of section matching.

The beamline class inherits from a *bmlnSet* collection of *beamSect*. This is an ordered collection of beam sections. ARTEMIS will have the ability to load and/or save beamlines, as well as sections. ARTEMIS can also create a beamline by joining beam sections.

Section method *madCr8db* is designed to download, to the database, a beam section from a MAD *hardware* output command. Drifts are concatenated and given unique names based on position in the accelerator in order to reduce unneeded elements. Complimentary, beamline method, *dbCr8mad*, can take

a beamline and construct a MAD input lattice deck for use with existing accelerator codes, such as DIMAD. The desire is to create an environment, using ObjectStore, which maintains all lattice information useful for the CEBAF project.

IV. MODEL SERVER

The server section of ARTEMIS is illustrated in figure 3. It consists of several subassemblies: a connection to the ObjectStore lattice database which performs the input-output lattice management for the server, a client communications section utilizing the EPICS Dev-API and ACE socket services, the actual server process ART, GenX model engine controller process, and CAUListener which provides the interface to EPICS network service. The specific global organization, object-oriented design approach, and use of C++ for implementation, was chosen for several reasons. The first is rapid server response to client connections and requests, which led to the use of multiple processes and the centralized shared memory segment. This arrangement allows GenX, the model engine process, to perform updates to model sections concurrently with ART server operations, improving client response time. Another benefit of the use of object-oriented approach during the design phase of ARTEMIS was that it allowed for independent design efforts for each object once the object interfaces were defined.

As stated above, GenX is used to perform the computationally intensive transfer matrices generation and propagation. The ARTEMIS server process performs the construction of Twiss parameters, sigma matrices, transfer matrix multiplication, ray propagation, polarization tracking, and response matrices, all of which pose a smaller computational burden, and can be built upon previously-calculated GenX transfer matrices.

ment of computed data objects, such as Twiss parameters.

The object-oriented approach also allows for the general reusability of existing accelerator codes. For example, the GenX process consists of classes for memory interface and communication, and an interface to a modeling engine. The engines chosen for CEBAF are DIMAD and PARMELLA, but the interface to GenX is sufficiently defined such that practically any modeling code can be interfaced. The class definitions provide constructor routines which handle many of the overhead functions usually performed by modeling codes, such as lattice generation and management, and model computation I/O. The addition of a new accelerator model would consist of creating the appropriate placeholders in the shared lattice objects, and providing the interface into GenX. An example is the concurrent use of PARMELLA for modeling the CEBAF injector region and DIMAD for the remainder of the machine, all under the control of one ARTEMIS server.

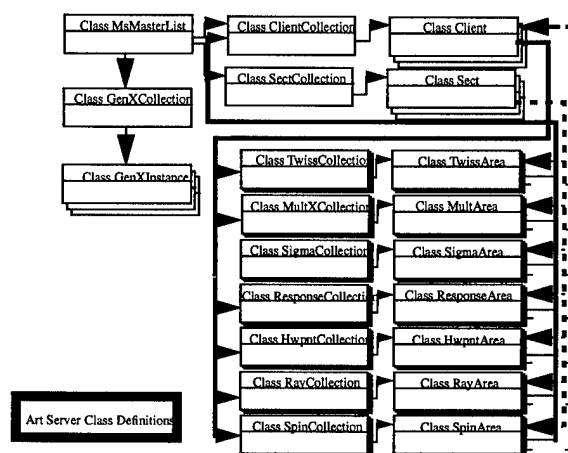


Figure 4: ARTEMIS Class Definitions

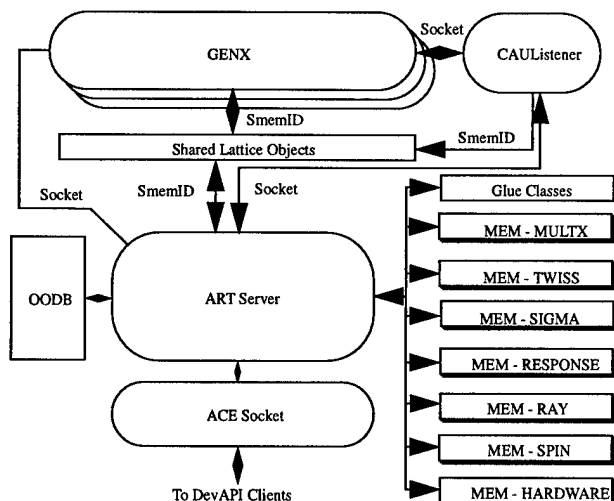


Figure 3: ARTEMIS Server Architecture

Figure 4 is a block diagram of the C++ classes used in the ARTEMIS server process. These structures maintain client connection information, GenX process control, management over the shared lattice objects (from ObjectStore), and manage-

V. ARTEMIS STATUS

Work is currently underway on implementation of the object-oriented database and the ARTEMIS server. First level testing is expected in June, 1995, which will include integration with DIMAD and the cdev device API.

V. REFERENCES

- [1] J. Kewisch et al., "Accelerator simulation and operation via identical operational interfaces," Proceedings of the fourteenth biennial Particle Accelerator Conference on Accelerator Science and Technology, May 1991, p. 1443.
- [2] M. Bickley et al., "Managing control algorithms with an object-oriented database," Proceedings of the sixteenth biennial Particle Accelerator Conference on Accelerator Science and Technology, May 1995.

A Self-Describing File Protocol for Simulation Integration and Shared Postprocessors*

M. Borland

Advanced Photon Source, Argonne National Laboratory
9700 South Cass Avenue, Argonne, Illinois 60439 USA

Abstract

A typical accelerator physics code uses a combination of text output, unformatted output, and special-purpose graphics to present results to the user. Most users must learn multiple graphics and postprocessing systems; many resort to manual extraction of data from text output, creation of customized postprocessing programs, and even modification of the simulation code. This situation slows research, results in duplication of effort, hampers unforeseen use of simulation output, and makes program upgrades potentially traumatic. This paper discusses the design and use of a self-describing file protocol that addresses these problems. An extensive toolkit of generic postprocessing programs, including sophisticated graphics, is available. This system has been used for most of the data collection for Advanced Photon Source (APS) commissioning, and is incorporated into a number of simulation codes.

I. INTRODUCTION

The structure of a typical accelerator physics code has changed little since the days when the only readily available output was the printout. Most codes still concentrate on this type of text-oriented output. The user wishing to postprocess a printout often ends up reading the data from paper or from a computer screen, and doing essentially manual computations, a procedure that is reminiscent of using tables of trigonometric functions and logarithms. A more sophisticated user may write a postprocessing program that reads the printout and performs computations. Unfortunately, the printout is almost necessarily either difficult to read or else difficult to parse. The printout typically mixes many types of data, making a robust postprocessor difficult to write. The user is frequently forced to resort to a text editor to extract the data of interest, which is time-consuming and error-prone. If the user succeeds in writing a postprocessor, he may find that it doesn't work with the next version of the simulation code, due to changes by the simulation's authors. This applies equally if the postprocessor is another simulation code, which explains why so few of the accelerator codes in existence today are able to use one another's output.

To make a bad situation worse, the user's effort to create a parser for a postprocessor must be duplicated for every code he uses, since there is no standardization of text or binary formats. If the user wishes to take advantage of the special features of two different simulation codes, he must write two different parsers. Many users find it easier to modify the simulation code itself rather than write a postprocessor. This again makes upgrades painful (since the modifications must be made to

each new version), and results in proliferation of nonstandard versions of the simulation code.

In an effort to solve some of these problems, code writers often supply a special-purpose postprocessor that does what they anticipate the user will need to do. This postprocessor may do little more than graphics, or it may do mathematical operations on the data; it is unlikely to be as sophisticated in these functions as commercially-available or generic packages. It is also unlikely to be compatible with similar postprocessors for other codes in terms of data formats or commands. These multiple postprocessors frequently duplicate each other's functions (e.g., graphics), which wastes effort. Further, the user is not free to exploit the special features of a particular postprocessor with data from an unrelated simulation. Finally, if the user needs to go beyond what the supplied postprocessor allows, he encounters the problems discussed above.

This paper discusses use of the "Self Describing Data Sets" (SDDS) file protocol to eliminate these problems.

II. SELF-DESCRIBING DATA

The concept of self-describing data starts from the recognition that a scientist typically associates a number of attributes with data: 1. The name by which the data is known. 2. The units of the data, if any. 3. The meaning of the data (i.e., a description). 4. A mathematical symbol to represent the data, if appropriate. 5. The type of data (e.g., floating-point).

A true self-describing file protocol (SDFP) should incorporate these attributes. The user of self-describing data obtains the data only by name. The user need not know, for example, which column of a table a quantity appears in or how the data is formatted. This is the crucial feature of self-describing data, as it enables one to avoid the above-mentioned pitfalls.

For the purpose of discussion, imagine some data that can be organized into a single table. For example, the data could be position, Twiss parameters, element name, etc., along an accelerator. Any program accessing the data would do so by name, using routines supplied by the creator of the SDFP. If the program needed only certain data (e.g., position and horizontal beta function), it would request only that data. The presence of additional data (e.g., dispersion), would be irrelevant. Further, the program need not know the source of the data—it could be from any source, from direct user input into a file to output from a simulation code.

If all of the presently-available accelerator codes that perform comparable computations employed the same SDFP for their output, users and programs could access data without regard for which code it was from. Programs would not need to be custom-designed to provide output to each other in order to work together. This would allow users to combine programs in ways not planned by the programs' creators. The only con-

* Work supported by U.S. Department of Energy, Office of Basic Energy Sciences, under Contract No. W-31-109-ENG-38.

straint would be that the codes used the appropriate names for quantities. (In practice, this restriction can be reduced by designing programs to request data under several different but equivalent names.)

The example of Twiss parameter output is illustrative for another reason. Most codes that compute Twiss parameters print the results in a single large table with 132-column lines. This forces truncation to (typically) three to six significant figures, in order to fit all of the data for each element on a single row of the table. Some programs provide a second output file that contains the data to full precision. Using an SDFP, neither the lack of precision nor the duplication of data would be necessary. Note that the user rarely looks at all of the columns present in a typical printout; for the user who requires a printout, a tool to take an SDFP file and create a customized printout containing only the columns of interest would be more satisfactory. Such a tool could be completely generic, so that it could be used with any program compliant with the SDFP.

III. THE SDDS DATA MODEL

The principles elucidated in the previous section have been implemented in the SDDS protocol. Any SDFP implementation makes assumptions about what type of data will be stored and how it will be arranged. These assumptions comprise the data model for the protocol. At the highest level, the SDDS model organizes data into a series of "data pages." Each page of any file must contain the same elements, but may contain different specific data. For example, each page could contain the Twiss parameters for a different accelerator, or for a different tuning of the same accelerator.

Within each page, the following classes of data are recognized: 1. Tabular data, consisting of an arbitrary number of rows of mixed-type data. The data in the table is referred to by the name of the column. The same columns are expected for each page of the file. 2. Array data, where each element is of fixed but arbitrary dimension (i.e., an arbitrary number of array indices is allowed). Arrays are accessed separately, but may be placed in groups. The size of an array may vary from page to page. 3. Parameter data, consisting of single values that may either be fixed throughout the file, or vary from page to page. A parameter is essentially an array containing a single value, but has simplified access.

Any element of these data classes may have one of the following C-language data types: float, double, short, long, char, and char *. These are, respectively, single and double-precision floating point, short and long integers, single characters, and character strings. All of these types may be mixed in the tabular data section, but each column must contain data of fixed type. Note that SDDS has no restrictions on the numbers of each type of element, on the length of the tabular data, on the dimension of arrays, on the size of arrays, or on the number of characters in string data elements.

To continue the example of storing Twiss parameters, one might create an SDDS file containing the following: 1. Parameters: The name of the lattice, the tunes, the chromaticities, the acceptances, etc. 2. Columns: The element name, the position,

the Twiss parameters, etc. 3. Arrays: The response matrix, matrices for tune and chromaticity adjustment, etc.

Other self-describing protocols are less restrictive than SDDS in that the data model is more flexible. While this is more powerful, it is considerably more complicated for both the program developer and user, which probably explains why existing SDFPs are not widely used. Experience with SDDS shows that there are very few instances where a more complicated model is required. At worst, the user may need to store disparate data in different, parallel files; this actually has the advantage of making the data easier to access. Some examples of data stored in SDDS at APS will be given in later sections.

Another advantage of SDDS over more complicated protocols is that the data may be either ASCII or unformatted (i.e., "binary"). The SDDS header (which describes the structure of the data pages), is in ASCII and has a familiar namelist format. It is a simple matter to create an SDDS file using print statements in a program, giving immediate access to a wide range of SDDS tools. The SDDS header has features to make it easy to convert existing text data into SDDS protocol; often, one merely creates a header and attaches it to the top of the file. These statements are not true of other SDFPs that I know of.

The SDDS header incorporates a protocol and version identification string, allowing determination that a given file is in SDDS protocol, and providing the version of the protocol. This permits upgrades of the protocol itself without disrupting users by making existing data or programs obsolete.

IV. THE SDDS TOOLKIT

A further break with traditional methods in accelerator simulation is the introduction of the toolkit concept for postprocessing [1]. A "toolkit" is a group of independent but cooperative programs. Traditionally, postprocessing has involved writing single- or few-purpose programs devoted to a single simulation code, in spite of the fact that the operations performed by many postprocessors are essentially identical. With the use of SDDS, it makes more sense to write generic programs that perform operations on data referred to by name.

While toolkit programs are shared by users, development is decentralized. The only requirement for an SDDS toolkit program is that it read and/or write SDDS files, so anyone may contribute programs. This is an advantage over "all-in-one" packages, which force the user to import data into a single program and work within a centrally-controlled environment. In contrast, toolkit programs are combined through use of the command shell and through command "scripts"; often, several programs are used sequentially on one or more data files. SDDS-compliant programs automatically work together by virtue of the common "language" of SDDS protocol, with little or no planning on the part of code developers.

The SDDS Toolkit is a growing group of about 35 programs that use SDDS files. Most accept SDDS input and produce SDDS output. In contrast to recent trends toward inefficient, tedious, and restrictive graphical user interfaces (GUIs), existing SDDS programs are accessed from the command line. While a GUI is sometimes helpful to the novice or

occasional user, it is rarely of benefit to the serious user except when the program is inherently graphical. Further, command-line tools can be included in scripts that require no user interaction. This permits assembly of custom postprocessing commands for repetitious tasks. Much of the data processing for APS commissioning is handled by such scripts [2].

Space permits mentioning only a portion of the Toolkit: **sddsplot** is a flexible, commercial-quality, device-independent graphics program. **sddscontour** is a graphics program for making contour and density maps of data. (Both of these are command-line driven, but bring up a GUI under X Windows.) **sdds2spreadsheet** and **sddsprintout** convert SDDS output to spreadsheet input or customized printouts. **sddsprocess** is a powerful data processing program that, among other features, permits computation, scanning, editing, statistics, and selection operations. **sddsgfit** and **sddsexpfit** do Gaussian and exponential fits. **sddsfft** does Fast-Fourier Transforms. **sddshist** and **sddshist2d** do one- and two-dimensional histogramming. **sddscorrelate** analyzes data for correlations, while **sddsoutlier** eliminates statistical outliers. **sddssort** sorts data by multiple user-specified criteria. **sddsxref** transfers data between files, with optional cross-referencing. **sddschanges** and **sddsenvelope** analyze data over multiple data pages. **sddsconvert** converts between binary and ASCII modes, as well as renaming and deleting elements.

V. SDDS-COMPLIANT SIMULATION CODES

A number of simulation codes have been converted to write and/or read SDDS files. Three distinct related programs are highlighted, with mention of how SDDS integrates them.

elegant [3] is an accelerator simulation code using matrix methods (up to second order), canonical integration, and numerical integration, with MAD-format lattice input. **elegant** provides up to 25 different SDDS output files containing widely varying types of data. While producing many separate files may seem cumbersome, it greatly simplifies the use of the data and the internal organization of the simulation. A typical simulation would result in the production of several of these.

For example, one could simulate a transport line with an arbitrary number of random perturbation sets. For each perturbation set, **elegant** could output the Twiss parameters and the transfer matrix, beam sizes and centroids from tracking, particle coordinates at specified locations, information on particles lost on apertures, trajectory predictions before and after correction, and more. **elegant** also accepts SDDS data as input. For example, if one asks for logs of random perturbations used during a simulation, one can have **elegant** read the perturbations for use in another simulation; one can generate the perturbation input by other means, e.g., from magnetic measurement or survey data. **elegant** will accept its own particle coordinate output as input, allowing multistage tracking; the same output can be postprocessed with any SDDS tool, or examined graphically with **sddsplot**.

shower [4] is a C program that provides an easy-to-use interface to the **EGS4** (Electron-Gamma Shower) program. **shower** not only produces SDDS output of multi-specie shower products, but will also read such output to allow multi-

stage simulation.

spiffe [5] is an electromagnetic field and particle-in-cell code used for rf gun simulation. Output includes snapshots of particle coordinates at constant time or position, electromagnetic fields at probe points, electromagnetic field maps, and the cavity boundary.

All three programs use only **sddsplot** and **sddscontour** for graphics. None requires any special-purpose postprocessing codes. **sddsprocess** can be used to translate the differing particle coordinate conventions of the three codes to permit tracking **shower** or **spiffe** output with **elegant**, or using **elegant** output as input to **shower**.

VI. SDDS-COMPLIANT EPICS APPLICATIONS

The control system used for the APS, known as the Experimental Physics and Industrial Control System (EPICS) [6], is used at a number of accelerator facilities in the United States. A number of "add-on" applications that use EPICS facilities have been developed, and are used for APS commissioning and operations. For example, **sddsexperiment** is a program that performs generic experiments on EPICS process variables (PVs); this includes changing PVs, reading back and analyzing PVs, and executing subprocesses. One use is measurement of response matrices. **sddsmonitor** and **sddsvmonitor** are EPICS monitoring programs, with sophisticated features like glitch- and event-triggered data logging.

With very few exceptions, SDDS is used for all accelerator commissioning data. For example, SDDS is used for: saving and restoring machine configurations; magnet conditioning instructions; GPIB device configurations; data from digital oscilloscopes and spectrum analyzers; machine history data; experimental data collected from process variables; data for generalized feedback on process variables [2]; and response matrices (from **elegant** or experiment) for orbit correction.

VII. OBTAINING CODE AND MANUALS

A distribution version of the SDDS library and Toolkit is expected to be available shortly after conference time. Manuals will be available as hypertext via World Wide Web, and in Postscript format. Details may be obtained by contacting the author at borland@aps.anl.gov.

VIII. REFERENCES

- [1] M. Borland, "A High-Brightness Thermionic Microwave Gun," Stanford Ph.D. Thesis, 1991, appendix A.
- [2] L. Emery, "Commissioning Software Tools at the Advanced Photon Source," these proceedings.
- [3] M. Borland, "Users Manual for **elegant**," APS LS-231, May 6, 1993.
- [4] L. Emery, "Beam Simulation and Radiation Dose Calculation at the Advanced Photon Source with **shower**, an EGS4 Interface," these proceedings.
- [5] M. Borland, unpublished program.
- [6] L. R. Dalesio, et. al., "EPICS Architecture," ICALEPS 1991, pp. 278-281, 1991.

ANALYTIC COMPUTATION OF BEAM IMPEDANCES IN COMPLEX HETEROGENOUS ACCELERATOR GEOMETRIES

S. Petracca, Dip. Fisica Teorica e S.M.S.A., Univ. of Salerno, IT;
I. M. Pinto, D.I.³E., Univ. of Salerno, IT; F. Ruggiero, CERN SL/AP, CH

Abstract

A general framework has been developed for computing longitudinal and transverse beam impedances in accelerator pipes consisting of several coaxial tubes with non simple transverse geometry, possibly made of composite materials and/or bearing special features like e.g. holes or slots, based on the combined use of Lorentz reciprocity theorem, Debye potentials, extended impedance boundary conditions, and generalized transmission line (waveguide) circuit concepts. The results are applied to the proposed LHC design.

I. INTRODUCTION

Rounded corners, multi-layered or composite walls, pumping holes, etc., make accelerator cross-sectional pipe geometries *not simple*. Beam coupling impedances must then be computed by numerical methods, analytic solutions being available only for simple (transverse) geometries where, e.g., the Laplacian is separable, and simple (e.g., perfect conductor) boundary conditions. Analytic, even approximate, solutions on the other hand are relatively appealing, as they provide an immediate insight into the role played by the design parameters.

In this paper we briefly summarize a general approach for the analytic computation of beam coupling impedances in complex structures, together with some representative results pertinent to the proposed LHC liner.

II. PERTURBED COUPLING IMPEDANCES

Stationary perturbative formulae for the beam (complex, frequency dependent) coupling impedances per unit length [1] of pipes with non-simple cross sections and/or boundary conditions can be obtained from the electromagnetic reciprocity (Lorentz) theorem, and relate the beam coupling impedance $Z_{||}^0$, Z_{\perp}^0 of a *simple, unperturbed* pipe assumed known, to that of another pipe differing from the former by some *perturbation* in the boundary geometry and/or constitutive properties [2], [3]¹. They read:

$$Z_{||} - Z_{||}^0 = \frac{\epsilon_0}{\beta_0 c Q^2} \left\{ Y_0 \oint_{\partial S} Z_{wall} E_{0n}^{*irr} \cdot [\beta_0 E_{0n}^{irr} + \beta_0^{-1} E_{0n}^{sol}] d\ell - \oint_{\partial S} E_{0z}^* E_{0n}^{irr} d\ell \right\}, \quad (1)$$

for the longitudinal impedance, and:

$$\bar{Z}_{\perp} - \bar{Z}_{\perp}^0 = \frac{\epsilon_0}{\beta_0 c Q^2 k} \lim_{\vec{r}_0, \vec{r}_1 \rightarrow 0} \left\{ Y_0 \oint_{\partial S} Z_{wall} \nabla_{\vec{r}_0} E_{0n}^{*irr}(\vec{r}, \vec{r}_0) \otimes \nabla_{\vec{r}_1} [\beta_0 E_{0n}^{irr} + \beta_0^{-1} E_{0n}^{sol}](\vec{r}, \vec{r}_1) d\ell + \right.$$

¹Equations (1) and (2) are accurate for suitably *small* perturbations; they are exact whenever the coupling impedances depend linearly on Z_{wall} .

$$\left. - \oint_{\partial S} [\nabla_{\vec{r}_0} E_{0z}^*(\vec{r}, \vec{r}_0) \otimes \nabla_{\vec{r}_1} E_{0n}^{irr}(\vec{r}, \vec{r}_1)] d\ell \right\} \quad (2)$$

for the transverse one². In (1) and (2) \vec{r} is the transverse position, $\nabla_{\vec{r}}$ is the transverse gradient, $\beta_0 = v_0/c$ =beam velocity/light velocity (in vacuum), ∂S is the pipe cross-section boundary, E_{0z}^{sol} , E_{0n}^{irr} are the (known, k -domain) solenoidal and irrotational parts (Helmholtz theorem) of the electric field, in the *simple, unperturbed* pipe, Q is the beam charge³, Y_0 is the free-space wave-admittance, Z_{wall} the (complex, frequency dependent) surface impedance describing the *local* properties of the pipe wall, and $k = \omega/\beta_0 c$.

The first integral on the r.h.s of (1) and (2) accounts for the effect of constitutive perturbations of the boundary, and thus is nonzero if and only if Z_{wall} is not identically zero on ∂S . The second integral on the r.h.s. of eq.s (1) and (2), on the other hand, accounts for the effect of geometrical perturbations of the boundary, and is non-zero if and only if the *unperturbed* axial field component E_{0z} is not identically zero on ∂S . Accordingly the second integral in (1) and in (2) effectively spans only the *geometrically perturbed* boundary subset $\partial S - \partial S_0$.

III. IMPEDANCE BOUNDARY CONDITIONS

Equations (1) and (2) are based on a simple Leontovich (impedance) boundary condition (BC), at the pipe wall [4]:

$$\vec{n} \times (\vec{n} \times \vec{E} - Z_{wall} \vec{H})|_{wall} = 0 \quad (3)$$

\vec{n} being the local normal unit vector. In the spirit of Leontovich BC, the penetration of EM fields from vacuum into *multilayered* lossy media can be viewed as lossy transverse electromagnetic (TEM) wave propagation in the direction (locally) normal to the interfaces.⁴

The equivalence between (TEM) waves in stratified media and voltage waves through cascaded transmission lines (TL) can thus be used to compute the wall impedance Z_{wall} at the inner surface of the beam screen, by repeated application of the impedance transport formula across a homogenous TL section with length ℓ characteristic impedance Z_c and propagation constant k :

$$Z_{in} = Z_c \frac{Z_{\ell} + j Z_c \tanh(j k \ell)}{Z_c + j Z_{\ell} \tanh(j k \ell)} \quad (4)$$

where Z_{ℓ} is the impedance connected to the output port, and Z_{in} is the impedance seen at the input port.

²Note that \bar{Z}_{\perp} is a tensor, in general. See [2], and references quoted therein.

³The impedances are obviously independent of Q , since the fields in (1) and (2) are proportional to Q .

⁴Leontovich BC can be applied provided: *i*) the magnitude of the relative index of refraction of the (first) medium where the field penetrates is large, and *ii*) the penetration depth is small compared to the (minimum) thickness of the medium and the curvature radius of its boundary [5].

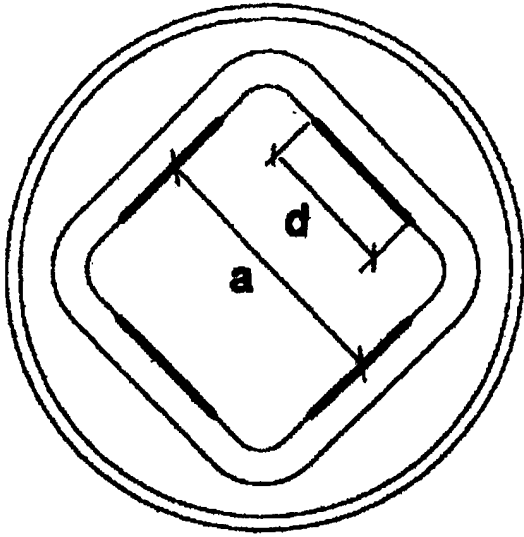


Figure 1. Tentative LHC design.

Even the boundary condition at a perfectly conducting screen bearing a regular array of holes can be modeled in terms of a wall impedance [6]:

$$Z_{wall} = -j \frac{Z_0 k_0}{s_t s_z} (\alpha_e + \alpha_m) \quad (5)$$

in agreement with [7], [8], where $\alpha_{e,m}$ are the (inside) electrical and magnetical polarizabilities of the holes (Bethe approximation implied, hole diameter \ll wavelength)⁵, and s_t, s_z are the inter-hole spacings in the transverse and longitudinal pipe directions, respectively.

IV. SOME RESULTS PERTINENT TO LHC

The tentative design of LHC is shown in Fig. 1⁶.

The main contribution to the beam impedances accordingly comes from the perforated stainless steel rounded corners of the beam screen. Using (1) and (2) and the exact solution for the fields produced by a relativistic particle traveling parallel to the axis of a perfectly conducting square-section pipe [10], one gets⁷:

$$Z_{||,\perp} - Z_{||,\perp 0} = C_{||,\perp} G_{||,\perp}^{(1)}(\xi) + D_{||,\perp} G_{||,\perp}^{(2)}(\xi), \quad (6)$$

where:

$$C_{||} = \frac{\epsilon_0^{-1} Y_0 Z_{wall}}{4\pi^2 c a} = k a^2 C_{\perp} \quad (7)$$

$$D_{||} = -j k \frac{(1 - \beta_0^2) \epsilon_0^{-1}}{4\pi^2 \beta_0 c} = k a^2 D_{\perp}, \quad (8)$$

The functions $G_{||,\perp}^{(1)}$ and $G_{||,\perp}^{(2)}$ are displayed in Figs 2⁸. The wall impedance on the rounded corners of the LHC liner (7) can be computed from the equivalent TL circuit shown in Fig. 3, by repeated application of eq. (4),

Its real part is accordingly displayed in Fig. 4.

⁵For a multi-coaxial pipe, the polarizabilities should be computed in the presence of the outer shells [6].

⁶A square beam-screen has been chosen in view of its better performance in terms of Laslett tune shifts [9].

⁷For the present case the transverse impedance is proportional to the unit dyadic \bar{I} , and can thus be described by a scalar.

⁸The second term in (6) related to boundary shape perturbation is imaginary, thus giving no contribution to power losses. As a space charge effect, it vanishes in the limit $\beta_0 \rightarrow 1$.

The longitudinal impedance can be used to compute the energy lost by the beam per unit pipe length (parasitic loss, $\Delta\mathcal{E}/L$ [1]). For a Gaussian bunch with r.m.s. length σ_z , using eq. (1), one has [6]:

$$\frac{\Delta\mathcal{E}}{L} = \frac{a^2}{Q^2 c Z_0} W\left(\frac{\sigma_z}{a}\right) G_{||}^{(1)}\left(\frac{d}{a}\right) \quad (9)$$

where for LHC $a^2 Q^{-2} c^{-1} Z_0^{-1} = 41.91 \text{ Joule m}^{-1}$, the function $G_{||}^{(1)}$ has been already defined, and:

$$W\left(\frac{\sigma_z}{a}\right) = Y_0 \int_{-\infty}^{+\infty} e^{-\frac{\sigma_z^2 y^2}{a^2 \beta_0^2}} \text{Re} \left[Z_{wall} \left(\frac{cy}{a} \right) \right] dy \quad (10)$$

is displayed in Fig. 5.

V. CONCLUSIONS

We introduced a general and systematic framework for computing beam coupling impedances and related quantities in possibly composite, multilayered, complex-shaped accelerator pipes, yielding accurate results in analytic form. We believe that the above could be a valuable tool for predicting the performance and optimizing the design of planned and/or existing accelerators.

References

- [1] A.W. Chao, *Physics of Collective Beam Instabilities in High Energy Accelerators*, J. Wiley & Sons, N.Y., 1993.
- [2] S. Petracca, Part. Acc., 1995, in print.
- [3] S. Petracca, CERN SL/Note 94-59 (AP), SL/Note 94-78, 1994.
- [4] R. Collin, *Field Theory of Guided Waves*, McGraw Hill, 1976.
- [5] T.B.A. Senior, IEEE Trans. AP-29, 826, 1981.
- [6] S. Petracca, CERN Rept. SL/AP 95, in preparation.
- [7] S.S. Kurennoy, SSCL-636, 1993; SSCL-650, 1993.
- [8] H. Okamoto et al., Phys. Rev. E50, 1501, 1994.
- [9] S. Petracca, Part. Acc., 48, 181, 1994.
- [10] S. Petracca, CERN Rept. SL/AP 93-13.
- [11] - *Design study of the LHC*, CERN 91-03.

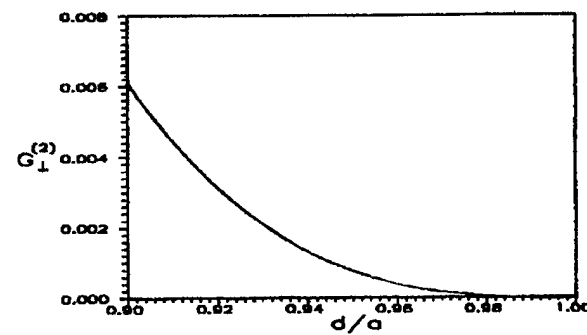
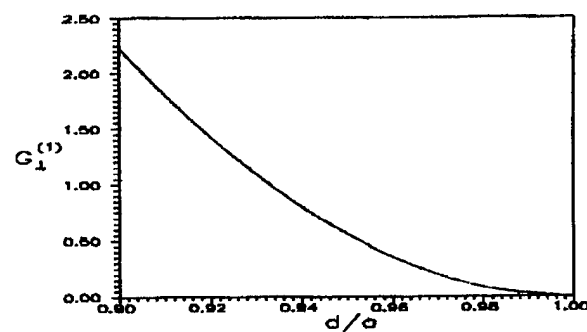
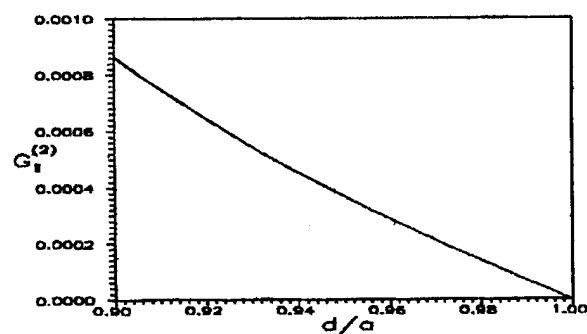
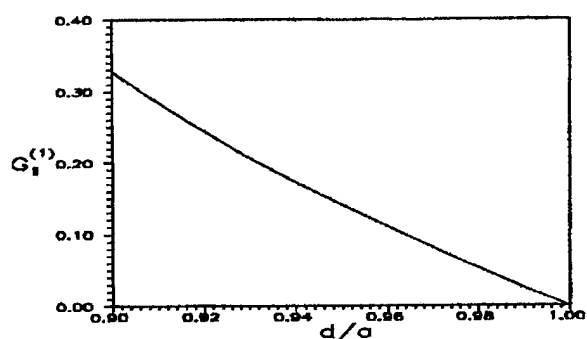


Figure 2. The functions $G_{||,\perp}^{(1)}$ and $G_{||,\perp}^{(2)}$.

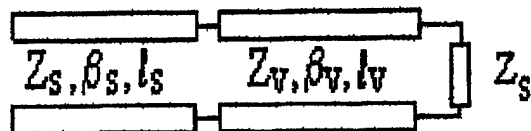
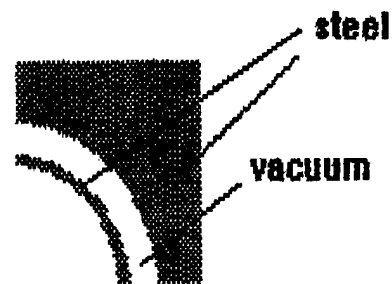


Figure 3. Multilayered wall and TL equivalent circuit.

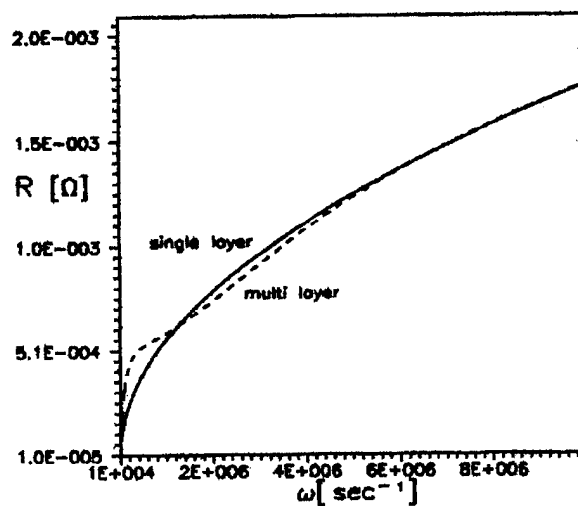


Figure 4. LHC wall impedance (rounded corners), realpart.

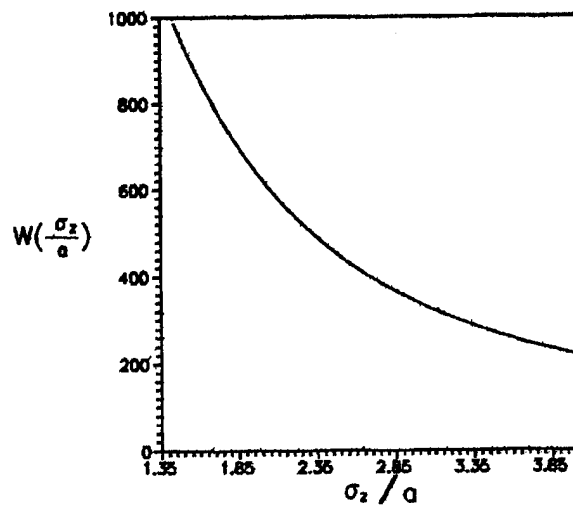


Figure 5. The function $W(\sigma_z/a)$.

COMPARISON OF CONDOR, FCI AND MAFFA CALCULATIONS FOR A 150MW S-BAND KLYSTRON WITH MEASUREMENTS

U.Becker, T.Weiland, TH-Darmstadt, Schlossgartenstr. 8, 64289 Darmstadt, Germany

M.Dohlus, DESY, Notkestr. 85, 22603 Hamburg, Germany

S.Lütgert, Philips, Stresemannallee 101, 22529 Hamburg, Germany

D.Sprehn, SLAC, Stanford, CA 94309, USA

Abstract

To facilitate the design of high power klystrons an investigation into the reliability and accuracy of three modern particle-in-cell codes was performed. A 150MW S-band klystron for which measurements were available was used for this comparison. The field calculations of the particle-in-cell codes are based on a finite difference time domain scheme, and use a port approximation to speed up the convergence to steady state. However they differ in many details (eg. calculation of E , B or A , ϕ ; space charge correction; 2D or 3D modelling of output cavity).

I. INTRODUCTION

The development of high power klystrons requires computer programs simulating the complex interaction of electrons with electromagnetic fields as realistic as possible. To analyse and verify the abilities of three modern codes (CONDOR, FCI and MAFFA) their calculations are compared with measurements at the 150-MW S-band klystron, which has been designed and built at SLAC [1] for the SBLC test facility at DESY. The design of the 7 cavity klystron is based on CONDOR calculations.

	design values	operation values
Beam voltage	535 kV	527 kV
Beam current	700 A	680 A
RF Pulsewidth, rep rate	3 μ s, 60 Hz	3 μ s, 60 Hz
RF output power	150 MW	> 150 MW
Saturated gain	55 dB	54 dB
Efficiency	≥ 40 %	42 %
Center frequency	2998 MHz	3002 MHz
Solenoidal focusing field	0.21 T	0.18 T

II. COMPUTER CODES

State of the art are two dimensional particle-in-cell (PIC) codes as CONDOR, FCI and MAFFA-TS2. These codes use the fact that with exception of input and output cavities most klystrons have a pure symmetry of revolution. In these codes the beam is simulated by macroscopic ring charges (macro particles) and their motion is integrated numerically (in 5D phase space). Therefore the electromagnetic fields or their potential representations are calculated in time-domain and take into account: electrostatic fields (eg. gun or dc beam), magnetostatic fields (eg. solenoid), resonant fields (cavities), transient processes and self-consistent field particle interactions. Problems are: the long simulation time (many periods until steady state), the noise caused by macro particles (gain > 55 dB), unphysical

properties of numerical field calculation and the space charge conservation. The first problem is solved by Yu's port approximation (PAP) [2]: only the beam pipe is simulated, the cavities are represented by their boundary fields, the fundamental mode of each cavity is simulated by an equivalent circuit while the higher modes are neglected. The amplitude of the circuit resonator is controlled by a predictor corrector technique to reach steady state in few rf periods. The effect of noise rises with simulation time and is therefore reduced by the fast turning on process. A further reduction is obtained by spatial filtering of fields and current densities and a systematic (not randomized) particle injection. To fulfil the continuity either the mapping of the particle motions to grid currents and the filtering have to be charge conserving (FCI, MAFFA) or the space charge has to be corrected from time to time (CONDOR).

A. CONDOR

The space charge correction in CONDOR is calculated as a correction potential. Poisson's equation for $\text{div} \vec{D} - \rho$ is solved and the correction is added every n th cycle where n is set by the user. In these calculations n was set between 1 and 3. The klystron is split into two segments (cavities 1 to 4 and 5,6,7). To transfer particles from one segment to the next, the particle data for the last rf periods are stored in a data dump and when the next segment is started the particles are reinjected periodically. To reduce the noise, the particle data were averaged over four periods. The fields are solved at the split-boundary using Neumann boundaries, no EM fields are dumped, and harmonics travelling in the drift tube are neglected. Therefore, it is best to divide the klystron at a point where the rf currents are relatively small. The output cavity is modelled directly in rz -coordinates (no PAP) whereby the dissipation of the output power is simulated by the r_{max} -boundary.

B. FCI

For the calculation [3] of the time dependent EM-fields, the wave equation for the scalar and vector potentials ϕ , A in the Lorentz gauge are employed rather than for fields E , B , because in the potential representation the Lorentz condition is consistent with the continuity equation for charge and current which is automatically satisfied in the simulation. The field distribution of the cavity modes in the drift tube is calculated by the FD method but using a refined mesh in the cavity region of the drift tube. Particle noise is controlled by a sophisticated filtering algorithm as well as by introducing a small damping term into Maxwell's equations. PAP is used for all cavities. Because the output cavity is of a pill-box type, the field calculation for this cavity has a reduced accuracy.

C. MAFIA

In the 2D simulations the steady state solution for all cavities is derived with the PAp. Therefore, for every dc voltage a special run is necessary to obtain the beam-loading conductances of the cavity modes which are later needed to perform the iteration process of the PAp. Unsymmetric effects and the excitation of higher order modes in the output circuit due to the strong coupling to the external waveguides ($Q_{ext} \approx 14$) are studied with a 3D PIC-simulation using MAFIA-TS3. The interface plane between the two and three dimensional simulation is located between cavity 6 and 7. There the periodic particle and electromagnetic field information is stored in the 2D run and reinitialized in the 3D run. The 3D simulation takes into account the cavity with all modes and the real broadband waveguides extracting the power. A detailed description of the interface and other characteristics of klystron simulation using MAFIA is given in [5].

III. INPUT PARAMETERS OF KLYSTRON CALCULATIONS

To ensure that the klystron simulations are based on the same operating conditions and to avoid differences caused by precalc. the following parameters have been chosen:

a) Coil Settings: the solenoid field can be adjusted with four independent coils:

coil	current dens. A/inch ²	z_{min}, z_{max} inch	r_{min}, r_{max} inch
bucking	-123.8	13.67, 17.00	7.97, 10.04
1	1656	21.0, 73.5	8.34, 9.34
2	1710	21.0, 73.5	9.84, 11.173
3	1224	59.55, 72.86	9.84, 11.173

In this z scale the cathod center is located at $z=14.415$ inch. (The field is plotted in [4] and [5].)

b) Beam Voltage and Current: the PIC-simulation starts right behind the gun region, where the DC-current is reinjected according to the particle properties calculated by the codes EGUN (for CONDOR and MAFIA) and SuperSAM (for FCI). The calculated perveances differ less than 2% from the measured values. For the simulations the current was scaled or extrapolated to the values printed in the $P_{out}(P_{in})$ -diagrams.

c) Cold Cavity Parameters: the parameters for the input and output cavity are design values and have been measured. The parameters of the other cavities have been calculated in good agreement by SUPERFISH, SuperLANS and MAFIA-E. The PIC simulations are very sensitive to the cavity parameters especially of cavity 2 and 3. Therefore the PAp is applied with identical cold cavity parameters in all three PIC-codes. Only the output cavity is simulated directly by MAFIA3D and CONDOR. The frequency and Q factor of the complete 3D discretization (including coupling slots and waveguides) have been verified in a separate 3D calculation.

cavity	frequency MHz	R/Q Ohm	Q_l	z_{center} inch
1	3000	87	127	27.775
2	3009.3	89	8200	33.195
3	3029	91	8300	39.665
4	3176.8	107	8900	55.765
5	3447.8	98	8700	62.695
6	3384.8	127	9500	66.015
7	2998	117	14	70.015

d) Changes: due to a late change of the geometrical description, the FCI calculation are done for a slightly different setup. The geometry of the bucking coil is: $z_{min}=13.3$ inch, $z_{max}=16.63$ inch, $r_{min}=7.9$ inch, $r_{max}=9.975$ inch. The cathod center is located at 14in, the center of the first cavity at 26inch while the distance between all other cavities is unchanged.

IV. MEASUREMENTS AND COMPARISON

A. Measurements

Only external parameters like input-, reflected-, output-power and the intercepted current could be measured directly. A parasitic oscillation ($f \approx 8.5$ GHz) was observed [1] and could be avoided by adjusting the solenoid field (see values in coil settings table). This instability cannot be predicted or analysed by the monopole monomode PAp model.

B. Comparison

a) Reflected Input Power: essentially the input power is either transferred to the beam or reflected. Neglecting wall losses, one can relate the cavity 1 voltage to the input power, reflection and cold cavity parameters:

$$V_1^2/P_{in} = 2(1+r)^2 Q_l R/Q,$$

which can be solved for r and compared:

I_b/A	480	495	511	523	527
measur.		0.179	0.190	0.187	0.183
CONDOR	0.169	0.216	0.179		0.219
FCI	0.046	0.046	0.058		0.059
MAFIA	0.176	0.184	0.193		0.206

The small reflection of the FCI calculation indicates an inaccurate simulation of the input cavity. The effect of this error is a reduced cavity 1 voltage and therefore a reduced gain (≈ -1 dB).

b) Linear Gain: the gains calculated by all programs are too high: CONDOR +7.6dB, FCI +4.8dB, MAFIA2D +2.1dB MAFIA3D +1.8dB at operation frequency. In the MAFIA calculation the maximum of the frequency response is shifted by at least 8MHz to the measurement.

c) Fourier Coefficients of Beam Current: for $U_b=511$ kV and identical cavity 1 voltage (3kV) the fourier components of the beam current and the cavity voltages are documented. In the range of the first three cavities the amplification of the cavity voltages and the 1st harmonic of the current are highest in CONDOR and lowest in MAFIA. The difference between CONDOR and FCI at the beginning is completely compensated to the end of the tube. The amplification along the last drift space is significantly higher in MAFIA so that the cavity 7 voltage is only 2.5% lower than by the other codes.

d) Output Cavity ($U_b=511\text{kV}$, $U_1=3\text{kV}$): even with very similar bunching and cavity 7 voltage the output power of CONDOR (155.1MW) and FCI (166.1MW) show a big difference. For these parameters MAFIA2D is in excellent agreement with CONDOR and MAFIA3D is further 10MW lower. The CONDOR/FCI differences and the MAFIA3D/2D differences of 10MW can only be explained by errors of the PAp. CONDOR (without PAp) and MAFIA2D (with PAp) give similar results because the cav. 7 voltage differs.

e) Numerical Effort:

	CONDOR	FCI	MAFIA 2D	MAFIA 3D ⁽¹⁾
$\delta r/\text{mm}$	0.88..0.87	1	1.5	1.6..2
$\delta x/\text{mm}$				1.6..2.5
$\delta y/\text{mm}$				1.6..2.5
$\delta z/\text{mm}$	0.88..0.91	2.5 ⁽²⁾	1.5	1.6..2
$\delta t/\text{ps}$	1.85	1.6 4.8 ⁽³⁾	1.57	1.57
rf-periods	60	45	42	15
particles/ rf-period	1240	556	1065	8520

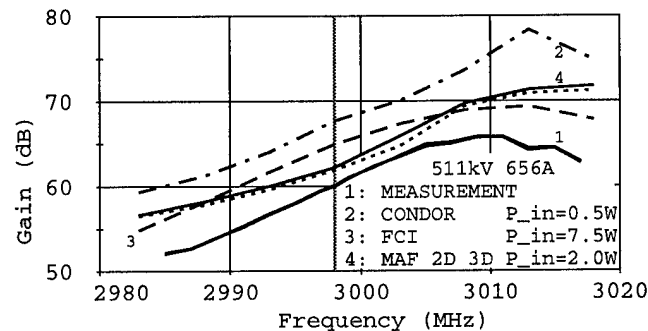
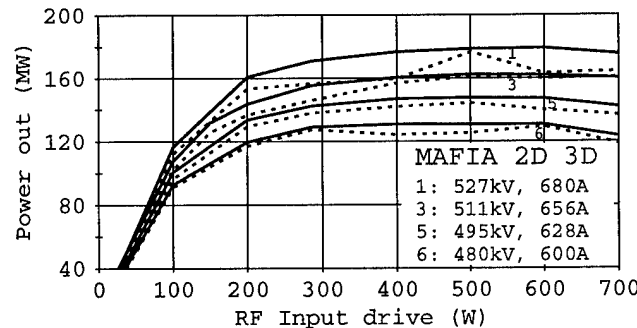
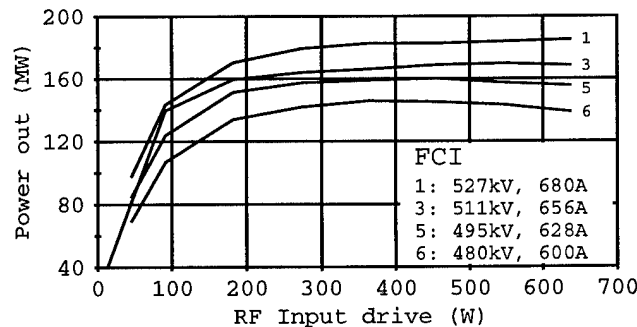
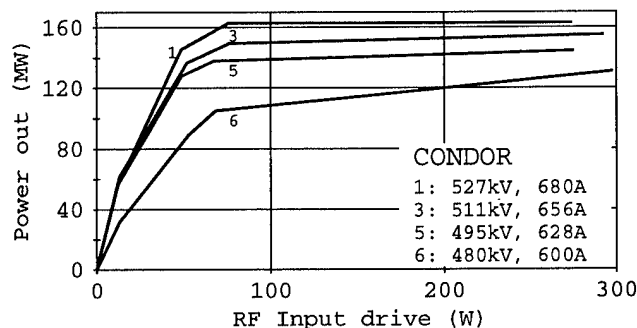
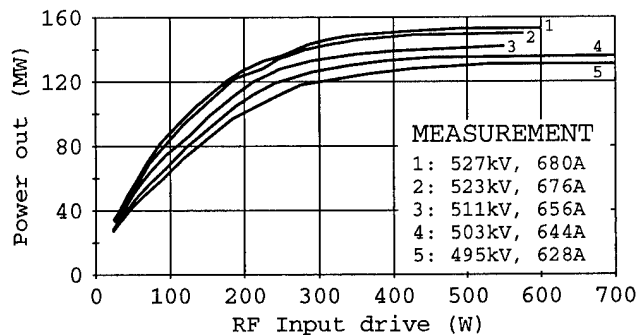
- (1) output cavity, (2) increased resolution in the cavity regions,
(3) integration of motion

V. SUMMARY

The measured input reflection coefficient indicates that the beam loading of the input cavity is not simulated precisely by FCI. All codes calculate overly high gains (especially CONDOR) and saturated output powers (especially FCI). The linear frequency characteristics are shifted upwards (especially by MAFIA). The port approximation causes significant errors in the output cavity.

References

- [1] D. Sprehn, R.M. Phillips, G. Caryotakis: "The Design and Performance of 150-MW S-Band Klystrons", SLAC-PUB-6677, Stanford Linear Accelerator Center, September 1994.
- [2] Simon Yu: "Particle-In-Cell Simulation of High Power Klystrons", SLAC-AP-34, September 1984.
- [3] T. Shintake: "High Power Klystron Simulations using FCI-Field Charge Interaction Code" KEK 90-3 A/D, May 1990.
- [4] S. Lütgert: "FCI Parameter Study for the 150 MW DESY Klystron", SBLC meeting at DESY, Hamburg, February 1995.
- [5] U. Becker, M. Dohlus, T. Weiland: "Three Dimensional Klystron Simulation", to be published in Particle Accelerators.



The BEPC Control System Upgraded

J. Zhao, X. Geng, Y. Yu, B. Wang
C. Wang, J. Xu, W. Liu, H. Luo, Y. Wang, M. Zhan
Institute of High Energy Physics, Chinese Academy of Sciences
P.O.Box 918-10, Beijing 100039, China
E-mail: zhaojj@bepc3.ihep.ac.cn

ABSTRACT

The upgrade of the BEPC control system has been finished one year ahead of the schedule and new system was put into use in October, 1994. The upgraded system adopts a distribution architecture based on DECnet. The workstations are used as console to replace the old hardware console, the new VAX computers carry out control jobs. Some dedicated adapters have been eliminated. Up to now, the new BEPC control system has been running safely and reliably for five months. The system upgrading is crowned success. What we have been finished is presented in this paper.

1. INTRODUCTION

The BEPC control system is a significant part of BEPC (Beijing Electron Positron Collider) which was built by the end of 1987. It adopted a centralized architecture copied from the new SPEAR control system because of the tight construction schedule, the system showed some obvious weak points during the long run.

The first weakness is the poor CPU power and the limited memory resource of the unique control computer VAX750. Another problem arises from the fact that some hardware adapters, such as VCC and the Grinnell controller, are old dedicated products from SLAC, which are no longer produced. This threatens the reliability of the control system.

As early as in 1990, we were planning to transform this system into a distributed one to make it faster in response and more reliable in performance. The upgrading work started in an all-round way in 1993, which carried out without interrupting the normal operation of BEPC. Therefore the low level CAMAC system was not changed. The main effort in upgrading the control system lies on software side. The upgrade of the BEPC control system has been finished and the new system was put into use in October, 1994, one year ahead of the schedule.

2. SYSTEM OVERVIEW

New console consists of two VAX4090 workstation and two X-terminals. Console manager based on X-window, which has a friendly man-machine interface and provides 12 graphic windows to display status of accelerator devices. We remain former style of the control panel to reduce training time of operator. The dedicated adapter Grinnell and VCC was eliminated, so that it is easy to maintain. Both VAX4500 and VAXII can independently control all BEPC equipment, or control the different devices separately. IEEE802.3 ethernet that connects all computers serves data communication. (see Figure 1)

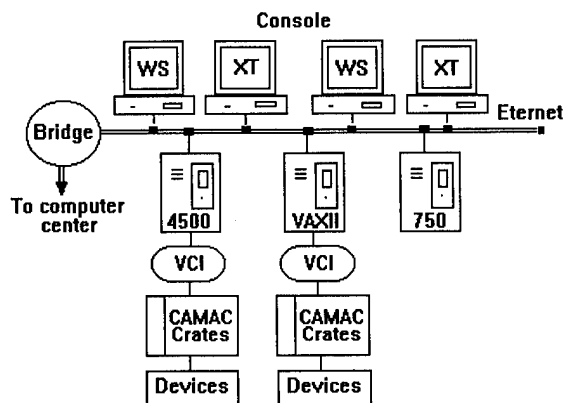


Fig. 1 The hardware structure of BEPC control system

The software is divided into three parts: console manager, network communication manager and real-time control jobs running on the control computers, such as local database, data acquisition programs, multi-task scheduler and about 23 accelerator application processes. (see Figure 2)

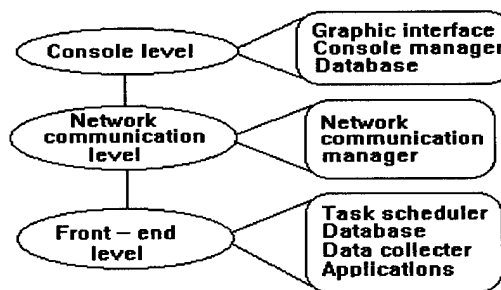


Fig. 2 Software structure

3. CONSOLE MANAGER

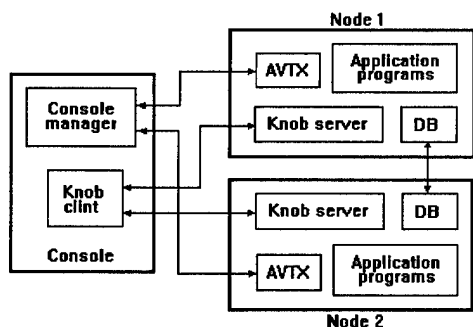
For the hardware console was substituted by software console under X-window environment, which carries out controlling and displaying. For that purpose, Console manager programs based on window were transplanted from SLAC. The principle of program is as follows: Create a window on VAX4090 and designate four areas (tile) simulating touchpanels and display devices. Though this programming ingeniously avoids great amount of work to improve the lower level program of the former control system, it still has some drawbacks:

(a) The weakness of XUI: it can not make perfect interface, and it is only able to quit and choose left or right touchpanel. (b) Serious shortcomings in operation: the size of "tile" can not be changed; because some "tile"s are too small and the text is overlapped, the operator can not observe the contents of both "tile"s simultaneously. So it is not

Because of the above-mentioned reasons, the program cannot be used in BEPC practical control. So we did a lot of work to analyze and regenerate it. Now we use Motif widget set. User Interface Language (UIL) is adopted in interface design to reduce the program crash caused by the mistake of interface design. Instead of former four areas (tile) divided in one window, six independent windows represent former console devices, and the windows can be reduced or enlarged independently to make full use of the limited screen and to make it possible for the operator to get information on several windows at the same time. The windows adopt Application Shell as their toplevel window, so that they can be turned into icon and stored in icon box when it was not used. All of the windows can be chosen to show on workstation or X-terminal. Thus the inconvenience of overlapping windows is avoided. In addition, the operator can acquire functions by using menus. The acknowledge windows can show operator some information. We have also developed knob control program by ourselves, which adopts client-server mode to control individual device.

4. NETWORK COMMUNICATION

DECnet for task to task non-transparent communication is adopted to develop network manager programs because it can realize data exchanging between programs running on different operating system and it provides more network functions, such as rejection of the network link request, synchronous or asynchronous termination of the netlink, management of net link multi-requests. etc.



The major procedure to make the network communication is Æ Requesting a logical link which creates a net control block, mail box or declares itself as a network object. Æ Accepting or rejecting a logical link request. Æ Sending and receiving data. Æ Terminating the link.

console manager. The second is between local databases on FEC's nodes, to carry out data exchange of the databases. There is a third network link between knob client program on console and knob server program on FEC. During the running time of BEPC, all of above network links keep opening. A library for network users has been established to let low level network operations be transparent for application programmers and to realize RPC (remote procedure call).

5. SCHEDULER PROGRAM

The upgrade system of BEPC is based on the DECnet. Program NEWAVTX is transplanted from SLAC. Because the associated graphic and touch panel will appear on X-window through the network, the NEWAVTX declares itself as a "network object" so that it can receive console commands and send out Grinnell commands through the network. The NEWAVTX gets the command and activates the proper application process. On the other hand, the related figure and touch panel files will be displayed on X-Window.

The upgraded structure of BEPC is different from that of SLAC in that our console node communicate with two nodes so two network links are created among those nodes. Thus the NEWAVTX has been improved . But when debugging , we found the touch panel “flashes “, Since the panel files from the two different computers simultaneously appear on the X-Window. In order to solve the problem, we corrected program NEWAVTX in VAXII, by setting a switch and putting it into database. As a result, the panel files in VAX-II are forbidden. Now, those programs work well and reach the expected goal.

6. UPGRADING DATABASE

For the distribution architecture of the new system, the original database has to be modified. First of all, we installed the database in each FEC computer with same data structure and records in the static area. To keep uniformity of the data records in those databases, the structure of the dynamic area has been changed, a new global index is created in each database when control system starts up. So that high level application programs can read the raw data with the global index and their source codes needn't any change. In addition, a shareable data pool was installed in the physical memory to exchange changed data by DBMS and manager of network communication. So the DBMS programs were modified to

manage the records in database and the shareable data pool. And a special network link serves transfer of the database records.

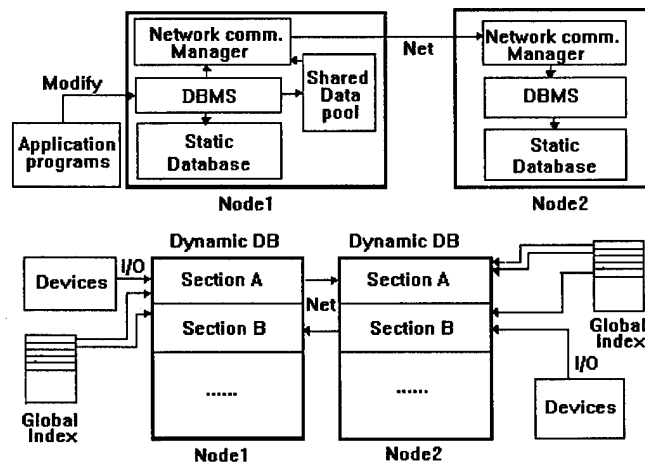


Fig. 4 The upgraded database

As figure 4 shown, when an application program or any one modifies a data record in node 1, the local DBMS sends the change to local database and the shareable data pool. And it notifies the network communication manager by event flag to fetch the data and send it to the node 2. The network communication manager in the node 2 receives the data and lets local DBMS put it in the local database. The raw data from devices in the dynamic area are refreshed each other once a second through network, so that the data in each database keep uniform.

7. DATA ACQUISITION

Data acquisition process XCAMAC refreshes the database at a rate of 2 times per second, and acquires about 4000 signals every time. What is more, the process also carries out the ramp operation of magnet power supply during particle acceleration of BEPC.

VAX-II/750 takes VCC as its Unibus-CAMAC interface, but in the improved system, VAX computers uses Qbus and their interface KSC2922/3922. KSC 2922 Computer Bus Adapter provides an interface between the DEC Q-Bus and up to eight 3922 dedicated crate controllers through a byte wide parallel bus. The 2922/3922 combination provides four DMA modes and a programmed transfer mode. DMA data rates up to 0.77 Mbytes per second can be achieved.

The format of data and command packet differs from that for VCC, therefore, the main work is changing the packet chains from VCC format to 3922 format. The other difference is data bit format. VCC require 16 high bits to be valid, but 2922 need 16 low bits.

Programs needing change include: packet creation program RPBZ, data I/O program XCAMAC, device on/off program DCOUT and beam position monitor program BPM. New packet organization program QPBZ acquires the CAMAC I/O address of every signal from the database, assembles them to CAMAC control words by calling 3922 software package subroutine and stores them in the database for CAMAC and other process to use. Since block transfer operation is need for acquiring analog signal by SAM module, so we wrote a new program for the organization of SAM packets. We find that the I/O speed of KSC2922/3922 is lower than that of VCC, so we

don't acquire device status information during the ramping of main PS to enhance the speed of it. In accordance with 3922 packet rules, the output data are placed in the packet chains and readback is mapped onto old VCC data area, so that the high level application programs reading raw data need no alteration.

8. CONCLUSION

The upgraded BEPC control system has been running safely and reliably for five months. The system upgrading is crowned with success. In the near future, some beam diagnostic, injection and Linac devices will be controlled by several PC/486 computers and connected to DECnet. With those done, the data needed by operator can be sent to the central console.

ACKNOWLEDGMENT

The author wishes to take this opportunity to thank Prof. Shi-yao Liu, who gave us a lot of advice. Our thanks also go to Prof. Shu-Ming Tang for her contribution to the upgrading plan. We would like to thank all the members of our control group.

REFERENCES

- [1] J. Zhao et al., Nucl. Instr. and Method in Phys. Res., (1994)A352.
- [2] X. Geng, Y. Yan, Nation Conf.
- [3] Y. Yu, J. Xu, Nation Conf.
- [4] J. Zhao, B. Wang, Int. Conf. on Elec.and Infor. Tech. (1994) 337
- [5] C. Wang et al., Int. Conf. on Elec. and Infor. Tech. (1994)112
- [6] J. Xu, Internal Report.

CONTROL SYSTEM OF PLS 2-GeV LINAC*

I. S. Ko and W. Namkung
Pohang Accelerator Laboratory, POSTECH
Pohang 790-784, Korea

The graphic-based realtime control system is developed and used for the normal operation of the PLS 2-GeV linac. Control and monitoring signals from local devices, such as magnet power supplies and modulators, are connected to the VME CPUs located in the field via special signal conditioning units. Data collected by these field CPUs are summarized and stored in the supervising VME CPUs located in the control room. Operators can control such devices simply by pointing and clicking with a mouse on the control panels which are X-windows loaded on a SUN workstation environment. Status and data to be monitored are displayed in terms of digital values and graphical presentations on individual status windows which are categorized functionally. Those windows are generated with the commercially available development software named RTworks. Every data transaction is done through a specified ethernet. There are four separate ethernets for effective data transactions. Fast signals, such as RF signals and modulator beam voltages, are captured by digital oscilloscopes and displayed in the control panel through the GPIB port. This paper presents main features and the general performance of the computer control system for the PLS 2-GeV linac.

I. INTRODUCTION

The Pohang Accelerator Laboratory (PAL) has recently completed the 2-GeV synchrotron radiation source named the Pohang Light Source (PLS). The PLS will serve as a low-emittance light source for various research such as basic science, applied science, and industrial and medical applications [1]. There is a 2-GeV linear accelerator as a full energy injector to the storage ring. This linac is consisted of 11 klystrons and modulators in the ground floor and 42 accelerating columns in the tunnel which is placed 6-m below the ground level. There are also many magnet power supplies (MPS), vacuum monitors, and various beam diagnostic devices. Furthermore, the linac control system includes the 96-m long beam transport line (BTL) and beam analyzing stations (BAS). These systems have various MPSs and diagnostic instruments. In order to accomplish fast and reliable control of the linac and BTL, the control system is divided into several subsystems, and these are linked to form a hierarchical structure.

The structure of the control system was finalized by January 1993, and actual S/W development started in May 1993 [2]. Before starting the major work, we made the signal list and the design manual for the linac control system [3,4]. At present, we complete the linac control system, and it plays a major role during the linac operation. It is obvious that the linac control system is continuously being upgraded based on operational experiences and

diagnostic equipment added.

II. CONTROL SYSTEM STRUCTURE

Our aim for the linac control system is to provide a reliable, fast-acting, distributed real-time system. The basic structure of the linac is shown in Fig. 1. There are three layers in the control hierarchy; device interface, data process, and operator interface layers. There are also three subsystems divided into their own functional characteristics; modulators and klystrons (MK), magnet power supplies and vacuum system (MG), and beam diagnostics (BM) subsystems. These are linked with four independent ethernets.

III. DEVICE INTERFACE LAYER

This layer is connected to the individual devices to be controlled and monitored. Each unit is consisted of an ELTEC E-16 CPU board, a 14" color graphic monitor, a draw-type keyboard, and appropriate I/O boards. The E-16 board includes a Motorola 68030 CPU, 4 MDRAM, an EGA compatible video port, and an ethernet port. The unit is operated under the realtime operating system OS-9. This computer is called the device interface computer (DIC). There are 11 units for the modulator and microwave system control, three units for magnet power supply control, two units for various diagnostic instruments. On-demand local computer control is available to all DICs. This feature is extremely useful for tests and the local commissioning of individual devices. All DICs are located in the klystron gallery.

A. MK Control

There are eleven MK stations placed next to the assigned modulator in the gallery. They control 11 modulators, 10 IPAs (isolator, phase shifter, and attenuator), and other equipment located adjacent to the MK station. In the first MK station, there is no IPA. Instead, the prebuncher and the buncher are controlled in this station. There are four RS422 ports to connect four step motor controllers to control the phase and the attenuation of the buncher and the prebuncher, respectively.

There is one 4-channel digital oscilloscope mounted on each MK station. The fast signals such as RF forward/reflect signals, an output signal of the pulse compressor, and modulator high-voltage signals can be seen by these oscilloscopes. The same data can be seen on the oscilloscope window in the main console via a GPIB port installed in the CPU board. There will be a 16x4 multiplexer to switch various signals to one of four input channel of the oscilloscope. These oscilloscopes are particularly useful to the maintenance crew to confirm the machine status by glancing the display panel.

* Work supported by Pohang Iron & Steel Co. and Ministry of Science and Technology, Korea

PLS Linac Control System

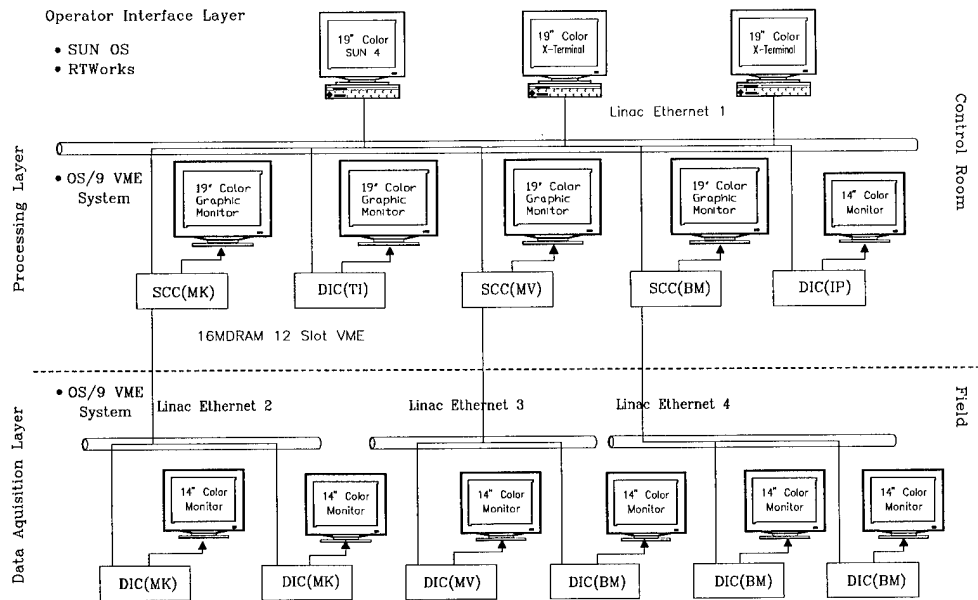


Figure 1: Schematic diagram for the PLS linac control system

B. MG Control

There are 100 power supplies for various magnets and solenoids in the linac and the BTL. These power supplies are grouped in three locations: 30 units for the preinjector placed near M1, 24 units for the rest of the linac placed near M8, and 46 units for the BTL placed in the BTL power supply room. Thus, there are 3 MG stations for the MPS control.

Each unit of six power supplies for dipole magnets in the BTL has an RS422 communication port that is connected to the VME CPU. However, the remaining power supplies are connected to the VME CPUs via special interfaces. In each MPS cabinet, there are one special interface unit with an RS422 port and four MPSs connected to the special interface unit through analog I/O channels. In this way, we can reduce the number of RS422 ports in the VME side and the cabling work drastically.

Even though there is one MG station assigned to the vacuum system, all the vacuum gauges are currently connected to IBM type PCs, and the vacuum pressures in the linac are displayed in the PC monitors. So, the vacuum related work is postponed to the future.

C. Beam Monitoring System

Various beam diagnostic instruments are used in the linac and the BTL for reliable machine operations.

There are 14 beam profile monitors (BPRM). This consists of a pneumatic actuator, a florescent screen, 4-way chamber and a viewing port, and a CCD camera. The BPRM is actually a destructive monitor, so we use them only to see the profile and rough location of the beam during the beam steering. The CCD camera control such as focusing and zoom in/out is done manually. Out of 14 BPRMs, 4 units are located in the linac, three (currently

two installed) units for the BAS, and 7 units in the BTL.

There are 13 beam current monitors (BCM): 7 in the linac, one for the BAS, and 5 for the BTL. The BCM consists of a ceramic vacuum chamber and a toroidal ferrite core to pick up the signal. At present, we use an analog oscilloscope to observe 2-ns pulses from the BCM. However, we have completed the signal peak holder to catch the BCM signals and to send them to the DIC. The circuitry is made on the VME board. It will be installed during the maintenance period in this summer.

There are also 57 beam loss monitors (BLM): 42 units in the linac and 15 units in the BTL and the BAS. The BLM is simply an ionization chamber to measure the ionization current due to the secondary emission. The signal integrator circuits have been completed after the commissioning period. It is installed in the NIM standard case. These units will be tested after completing data acquisition S/W.

In order to remove off-momentum particles, slit monitors are installed. One slit is placed just after the first bending magnet of the BTL. Another slit is placed in front of the 2-GeV BAS. The slit controller has an RS422 communication port connected to the VME CPU.

There are two BM stations: one for the linac placed near M7 and one for the BTL at the end of the linac gallery. The first BM station has one BPRM controller, one CCD camera controller, a VME CPU with BCM fast sample holders, and BLM signal integrators. Second BM station has one BPRM cable connection box, two slit controllers, a VME CPU with BCM fast sample holders, and BLM signal integrators. At present, all BPRMs are controlled from the first BM station.

IV. DATA PROCESS LAYER

A. Main System

In this layer, there are three CPUs called supervisory control computers (SCC). They are assigned to supervise MK stations, MG stations, and BM stations, respectively.

Each unit consists of an ELTEC E-7 board, a 19" monitor on the sub-control console, and a floppy and a hard disk for data storage. This Motorola 68040 based CPU board has two ethernet ports: one for data acquisitions and one for the operator interface layer. These units are installed in one cabinet. The cabinet is placed in the center of sub-control room which is next to the main control room only separated by large glass windows.

There is one more unit which is assigned to beam profile monitors. The beam profile image captured by a CCD camera is directly sent to the frame grabber (AVAL AVME-335). Image processing is done by the E-16 board. The beam profile is then displayed with x- and y-profiles directly from the AVAL-335 board. The refresh speed per 300x200 sized frame is about one-half second. A graphic monitor connected to the E-16 board is used to display beam profiles with the Gaussian fitting. It shows actual numeric numbers of beam sizes and deviations from the central trajectory. The graphic monitor is located on the main control console. This kind of configuration reduces massive traffics of image data drastically in the ethernet.

B. Backup System

There are three identical SCCs next to the main system as a backup system. Normally, these units are served as development stations without disturbing the main control system.

V. OPERATOR INTERFACE LAYER

A. Main Console

The operator interface computer (OIC) is actually a SUN-4 sparcstation with two X-terminals. The operating system is UNIX and the commercial S/W package named RTworks is intensively used to optimize graphics and data handling between the UNIX system and the OS-9 system. There are several windows for an operator to control and monitor individual components. Each window has a value display area and a control sub-window. All the control action can be made by selecting a specified area with a mouse or items from the pull-down menu. Two X-terminals and a SUN monitor are located in the main control console which is designed ergonomically. In front of the main console, there are two 19" CRTs and three color TV monitors hanging from the ceiling. One CRT displays current vacuum pressures and another one shows temperatures of cooling water circulating on accelerating columns in the tunnel. When the linac is not operating, three TV monitors are used to display several areas in the tunnel and the gallery. During the linac operation, these monitors are used to display information such as the beam lifetime and the beam current in the storage ring. They are broadcasted via cable TV channels from the storage ring control room.

B. Backup Console

There is a backup console in the sub-control room. Normally, this is used as a development station with backup SCCs. Since the main control room and the sub-control room are separated with large glass windows, the operators in the sub-control console can see the information displayed in the CRTs and TV monitors in the main control room.

VI. NETWORKS

There are four independent ethernets in the linac control system. Originally, the connection between the DICs and the SCCs was designed to use the MIL-STD-1553B protocol. However, it was replaced with three ethernets because of high cost and relatively slow data transaction rates. In addition to the ethernet between the OIC and the SCCs, there are three ethernets to MK, MG, and BM stations connecting to matching SCCs, respectively. This kind of configurations provides us highly flexible ways in writing schedule routines of the data process in the VME system.

VII. ACKNOWLEDGMENTS

We are grateful to thank to J. H. Kim, S. C. Kim, J. M. Kim, and G. S. Lee for their valuable efforts in developing the linac control system. We also thank to M. K. Kim, K. W. Kim, N. E. Sung, and H. S. Kang for their valuable comments based on their experiences on linac operations. Most of all, we would like to dedicated this achievement to late Dr. Hogil Kim, who established the PLS project.

VIII. REFERENCES

- [1]. Design Report of Pohang Light Source (revised ed.), Pohang Accelerator Laboratory, 1992.
- [2]. W. Namkung, et. al., "Progress of PLS 2-GeV Linac," Proc. of 1993 Particle Accelerator Conference, Washington, D.C., U.S.A., May 1993, pp581-583.
- [3]. I. Ko and W. Namkung, "Signal List for 2-GeV Linac," MA/LN-93001, Pohang Accelerator Laboratory, 1993.
- [4]. I. Ko, et. al., "Design Manual for PLS Linac Control System," MA/LN-93002, Pohang Accelerator Laboratory, 1993.

Control System of the Synchrotron Radiation Source SIBERIA-2.

A.Valentinov, A.Kadnikov, Y.Krylov, S.Kuznetsov, Y.Yupinov. Kurchatov Institute, Moscow 123182, Russia.

SIBERIA-2 is synchrotron radiation source at electron beam energy 2.5 GeV. The SIBERIA control system can be classed into three levels-- console, networking and data acquisition. This paper describes control hardware for magnet, RF and injection system; timing system; temperature and vacuum monitoring system; basic software. Control hardware consists of 36 CAMAC crates. The special software for automatic processes--beam accumulating, energy ramping were developed. Control systems are used in commissioning of accelerator complex.

1. INTRODUCTION

The control system is separated by 3 level schematically. The PC-network is presented upper-level for usage in the control rooms. The consoles are IBM PC 486 computers. 4 main control room computers are equipped with 19" color monitors and 8 Mbytes RAM. PCs run "MS-Windows for WorkGroups 3.11". Network Dynamic Data Exchange (NetDDE) between any tasks in several computers may be used. The single PC makes available the interconnection between the console network and the second level real-time control.

24-bit CAMAC-oriented computers use in the second real-time level of the control system [2]. At this level we have 8 computers in service. Each computer controls the specific part of accelerator complex (injection, main ring) or specific system (vacuum, beam diagnostic, termomonitoring, etc.). Switching center computer is equipped with 50 Mb HDD and provides communications to console network. Diskless peripheral computers connect to center by serial data links with 1 Mbit/sec physical rate. Real time computers are equipped with CAMAC system modules set: RS232 interface for local terminals, RAM, network interface, graphic adapter, peripheral crates driver. These run real-time multitasking "ODOS" operating system [3].

The I/O data acquisition and controlling CAMAC hardware is presented the low level of the control system. The peripheral crates are placed near the power supplies, RF, vacuum equipment and connected to control computers by serial data links. The distance between crates is 50-100 m. The coaxial cables used for convenience 1 Mbit/sec transmission rate. Total number of CAMAC crates is 36.

2. HARDWARE SOLUTIONS

2.1. General description

All CAMAC equipment for control system is designed and manufactured in the Budker INP (Novosibirsk). Control 24 bit computer is intellectual CAMAC crate controller. Architecture is suitable for width of CAMAC data bus and number of peripheral modules in crate. The LAM

manager and instruction for single/vector CAMAC exchanges are realized in firmware. Computer is equipped internal 64 kW RAM and used the CAMAC-bus in the capacity of I/O bus. The effective dedicated system software is designed in the Budker INP for real-time CAMAC applications. This computer allows to employ very simplify peripheral crate controllers and CPU-less CAMAC modules. The total number of CAMAC modules is more than 350. The set of modules includes the standard complex of ADC, DAC, input-output registers, timing generators.

2.2. Timing, synchronization and RF control

The synchronization system supports interprocess communications, automatic operations of accelerator; - and timing control for the slow pulsed elements and fast devices such as kickers and inflectors. In most cases we applied digital delay 8 channel 16 bit CAMAC module with programmable resolution 100 nsec - 12.8 microsec (maximum delay 6.5 msec- 828 msec). Main clocks for injection and acceleration processes are generated by slow digital timers with 20 msec resolution..

The special part is the synchronization between RF of main ring, RF of booster and fast inflectors in the injection process in main ring. The multi channel CAMAC programmable timing generators with the 0.4 ns resolution and 5.12 microsec maximum delay are used. The special programmable modules used for frequency matching and selection the number of bunch. Operator can select the number of bunch and control the phase of injection. The fast synchronization system allows to measure the time delay with 0.6 ns accuracy. The RF control includes 16 DAC channels for cavity voltage control, fider current setting and revolution frequency control

2.3. Power supplies control and measurement

Few types of power supplies are used for magnet elements: 1 ($I_{max} = 7200$ A) for bending magnets of main ring; 6 ($I_{max} = 1000$ A) for quadrupole lenses of main ring; 8 ($I_{max} = 25$ A) for sextupole, octupole lenses of main ring ; 168 ($I_{max} = 5$ A) for all correctors of main ring. Different DAC and ADC modules are employed, corresponding with the requirements of setting accuracy and stability. 20 bit DACs are used for main ring bending and quadrupole, these have the external synchronization input for ramping process realization. The integrated ADC with programmable resolution/conversion time is used for measurement main parameters of power supplies. This ADC has 1 input and controls the analog CAMAC mix for connection up to 256 channels. The most commonly used mode is the measurement of selected channels and stored these into on-

board ADC RAM, than information block can be reading by control computer. We employ the 14 bit/ 5 msec mode for correctors' power supplies measurement and connected to one ADC up to 128 channels (2 cabinets) and 16 bit/ 20 msec mode for high accuracy power supplies - up to 32 channels. Thus we can update information every 1 sec cycle. The 20 bit / 320 msec mode with stored up to 1024 samples may be applied for detailed investigation of selected power supply.

2.4. Temperature and vacuum monitoring

The building principles of monitoring systems are identical. Main functions are:

- all channel data acceptance with 1-5 sec working cycle;
- data handling - comparison with preventive and alarm levels, stored status and value information;
- control alarm devices and interlocks (adding to direct hardware control);
- graphic presentation- general status, history of selected channels.

The control computer supplies the feedback function of control except the termomonitoring system. This is based on intellectual ADC module, contained CPU, program ROM, RAM with warning limits. Module has 4 relay output for interlock communications. The interlocks used for power supplies alarm control.

2.5. Beam diagnostics

The DCCTs are used for beam current measurement in main ring. Signals after analog processing are accepted by integrated ADC, current history plotted at the color graphic monitor. The lifetime constant automatically displayed from the slope of decay. The set of 12 moveable scintillation probes is used for first turn diagnostic. Position of each probe is measurement using ADC with accuracy 0.2 mm. 24 horizontal and 24 vertical BPM are equipped in main ring. CAMAC set includes timer, integrated ADC and amplifier/filter dedicated modules. The 4 pickups and 4 fast ADC (internal RAM 1Kb, 8 bit, 1 sample /turn = 400 nsec) applied in the data handling system for diagnostic first 1000 turns. This system allows to optimize injection to main ring.

3. SOFTWARE

The applied software for control system includes the man-machine interface, intertask communications system, control of facility systems, beam diagnostics' programs. This software allows to achieve the working mode for booster and to start main ring operations.

Information about logical channel is stored in data-base, it includes : 1) logical channel name, dimension of value, limit of value, value-code factor; 2) name, address of corresponding CAMAC module, number of its channel, address of CAMAC crate; 3) comment for man-machine interface.

Applied software structure for control system of injection complex is shown in Fig1.

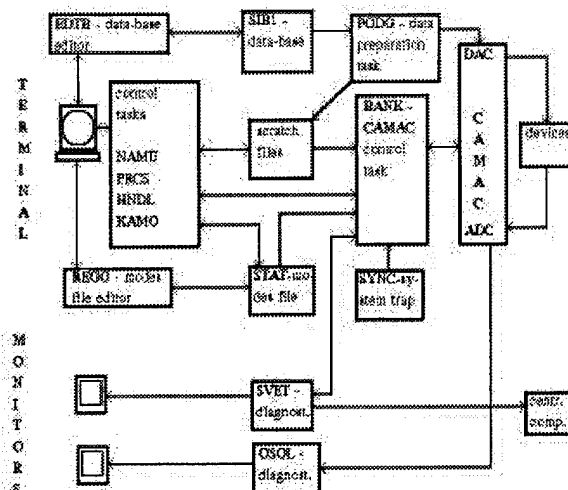


Fig. 1. Software structure for SIBERIA control.

Logical channels associated to same system integrate into logical elements and systems. There are following logical systems : linac, booster, beam transport line to main ring, pulsed system, magnet system. Their contents can intersect. The same data-base has a list of CAMAC crates and associated modules.

The data preparation program (named PODG) starts control system work cycle. It checks capability of channels, described in data-base, starts CAMAC modules, opens the scratch files. Than start a control program BANK, which executes command for CAMAC control.. This program receives a synchronous system trap generated by program SYNC with period 100 msec for injection facility and 300 msec for main ring. A code generated by control program is written in DAC with this period. The writing time for one channel is equal to 0.5 msec. The number of DAC-channels is equal 125 for injection facility and 250 for main ring respectively. Tact period is chosen so that BANK can write all DAC-channels in a time of period and some time remains for other programs. In each moment the program BANK executes only one inquires for control. Hence, when the program executes a long inquire, it does not control logical channels are absent in inquire. When the program of control receives a command to write a new code for a few channels in a few steps, BANK does a linear interpolation for each channel between current and wanted values, then writes all channels synchronous step by step. This process has the highest priority because non uniformity of the execution rules a beam loss (for example in acceleration). If the program BANK does not write by steps, it reads channels of measurements of all ADC at each 10-th tact.

Main control program NAMU forms a command, transmitted to BANK task for execution. There are following functions of program NAMU : controlling one or a group of channels; saving a present mode of CAMAC-modules in machine file named STAT and reading and listing of machine file; working with buffer. A user changes a wanted logical channel in the element and writes required value both a dimensional form and a shift of current value form or

percentage. The setting value transforms to code, transmitted to BANK program for execution. Inside logical element one can change a few channels simultaneously with any mutual coefficient. At each second the NAMU program updates values measured by ADC.

Program PRCS controls real-time process of changing of facility mode (for example beam accelerating). This program includes following functions: setting time expectation; external trap excitation and checking; setting the facility mode in desired number of steps. PRCS task gives a command to BANK program for execution. Now there are the following working cycle of accelerator facility: 1) injection in SIBERIA-1 and beam storing, 2) acceleration to 140 MeV in 50 steps, 3) acceleration to 240 MeV in 100 steps, 4) acceleration to 350 MeV in 100 steps, 5) beam transmission to SIBERIA-2, 6) return to the injection mode in 300 steps.

The status of facility systems is shown in control room monitors by special programs. One can see for example following two programs. Program SVET checks a magnet power supply. If difference between setting and reading values is more then tolerant value, associated symbol on the screen changes your color from green to yellow than red. The program shows three types of pictures: facility status, status of one of system, status of any fore channels. Program OSOL checks RF-power supply by 4-th channels CAMAC based digital oscilloscope. The program reads ADC, shows RF pulsed signals (screen copies see Fig. 2), saves 80 recent pictures. There are programs of control for pulsed power supply, vacuum monitoring, temperature and radiation checking system, which transmit the information to control room monitors.

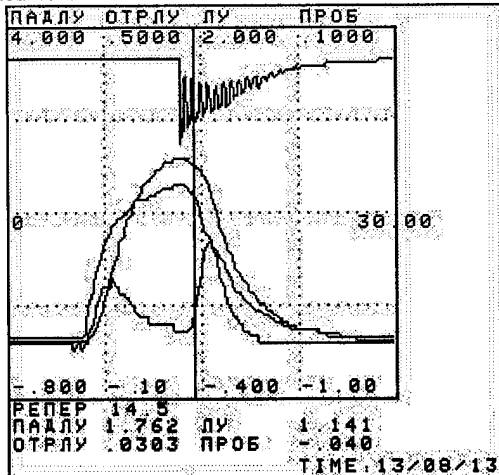


Fig. 2. RF generator control program screen copy.

There are few programs for automatically measurement of beam parameters. In injection and booster facility are following: RIPP - beam position in transport line

to main ring by second emission monitors, TOMN - stored current measurements by DCCT. In main ring are following: TOBN - stored current measurements by DCCT. One can see for example following two programs. Program RIPP reads CAMAC module of beam position monitor in transport line to SIBERIA-1 and shows to screen (see Fig. 3) transverse distribution, center-of-mass and width of beam.

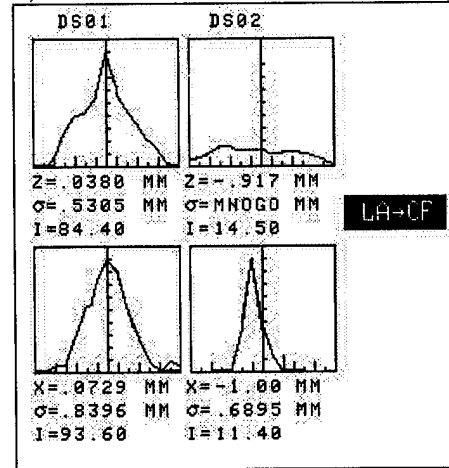


Fig. 3. Beam position monitor program screen copy. Program TOMN reads beam current monitor in SIBERIA-1, and shows (see Fig. 4) current value of stored beam, life time, beam energy and summary number of ampere * hour.

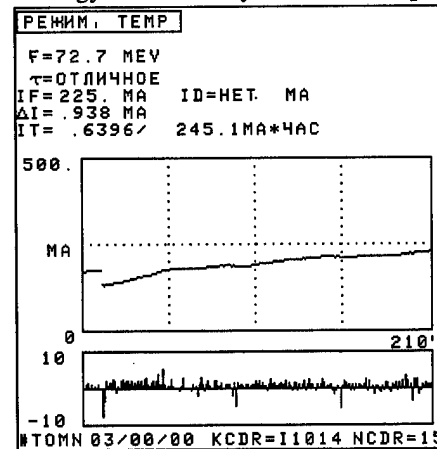


Fig. 4. Beam current measurements screen copy.

4. REFERENCES

- [1] V. Anashin et al., "The Dedicated Synchrotron Radiation Source SIBERIA-2", Proc. of EPAC'88, Rome, June 7-11, 1988 Vol.1 pp.380-382.
- [2] G. Piskunov, "24 bit CAMAC computer", Autometria, 1986 N4, pp. 32-38.
- [3] A. Aleshaev, "ODOS operating system", Preprint Budker INP 89-67, Novosibirsk 1989.

Control System for the Holifield Radioactive Ion Beam Facility

B.A. TATUM, R.C. JURAS, M.J. MEIGS

Oak Ridge National Laboratory [1], P. O. Box 2008, Oak Ridge, TN 37831-6368 USA

A new accelerator control system is being implemented as part of the development of the Holifield Radioactive Ion Beam Facility (HRIBF), a first generation radioactive ion beam (RIB) facility. The pre-existing accelerator control systems are based on 1970's technology and addition or alteration of controls is cumbersome and costly. A new, unified control system for the cyclotron and tandem accelerators, the RIB injector, ion sources, and accelerator beam lines is based on a commercial product from Vista Control Systems, Inc. Several other accelerator facilities, as well as numerous industrial sites, are now using this system. The control system is distributed over a number of computers which communicate over Ethernet and is easily extensible. Presently, implementation at the HRIBF is based on VAX/VMS, VAX/ELN, VME, and Allen-Bradley PLC5 programmable logic controller architectures. Expansion to include UNIX platforms and CAMAC hardware support is planned. Operator interface is via X-terminals. The system has proven to be quite powerful, yet it has been easy to implement with a small staff. A Vista users group has resulted in shared software to implement specific controls. This paper details present system features and future implementations at the HRIBF.

I. INTRODUCTION

Conversion of the Holifield Heavy Ion Research Facility (HHIRF) to the Holifield Radioactive Ion Beam Facility (HRIBF) [2] began in 1992. The HHIRF control system was a mixture of control technologies based on 1970's-vintage interface hardware and computing technology. The Oak Ridge Isochronous Cyclotron (ORIC) [3] and its associated beam lines were controlled through a combination of hardwired controls, an Allen-Bradley programmable logic controller (PLC) system, and a Modcomp real-time computer with CAMAC and "homemade" interface hardware. The tandem electrostatic accelerator control system was based on an Interdata computer system with a CAMAC hardware interface. These systems were not interconnected, were quite difficult to reconfigure, had non-graphical interfaces, and spare parts were either expensive or non-existent.

Both of the existing accelerators required considerable modifications in the facility reconfiguration. Additionally, existing beam lines had to be redesigned and reconfigured and new beam lines constructed. The major new addition to the facility was a 300 kV high-voltage platform system, referred to as the RIB injector [4], which houses a Target-Ion Source [5] and mass analysis system. The advent of

these changes and additions mandated a unified, modern, and easily extensible control system for the facility. The decision of which system to implement was not an easy one, but based on budgetary, scheduling, and manpower constraints, as well as flexibility and ease of operation, the control system manufactured by Vista Control Systems, Inc. was selected. The remainder of this paper details the implementation of this system at the HRIBF.

II. HARDWARE COMPONENTS

The Vista control system was, in 1993 when the HRIBF control system selection was made, purely based on the VAX/VMS/ELN architecture. The drawing utility VDRAW, the database generator VGEN, and the hardware interface code VACCESS all operate at the VMS level. Yet an advantage to Vista is an ability to expand the system by adding ELN nodes running just the VACCESS component. The conclusion for the HRIBF implementation was to distribute control with rt300 VAX processors in VME running the ELN operating system. Standard VME modules are used to provide an interface to existing Allen-Bradley programmable logic controllers (PLCs), serial interfaces, GPIB, ADCs, and DACs.

It was apparent that the hardware necessary to interface accelerator devices to Vista had to be as inexpensive and as flexible as possible. Most control functions were simple binary controls or analog control requiring at most 16 bits of resolution. Previously, ORIC beam line vacuum controls were implemented via an Allen-Bradley (A-B) PLC5 system which proved to be reliable and cost-effective. Devices are easily interfaced to the modules because of their terminal strip connectors. Additionally, Allen-Bradley manufactures a full line of ground-isolated ADC modules with resolutions of up to 16 bits and ground-isolated DAC modules with resolutions to 14 bits. Thus the majority of new devices in the HRIBF system are controlled via A-B PLCs. Scanner modules in VME link Vista to the A-B remote I/O link which can transfer data at a maximum rate of 115 kB. Analog and digital controls may be implemented in this manner directly through a remote I/O adapter residing in the PLC chassis. Thus the controls appear as "dumb I/O" to Vista. No PLC processor programming is required. A-B PLC5/20E ethernet processors were added to the system with chassis containing these processors tied directly to the 10-MB Ethernet rather than an A-B VME scanner module. Only discrete I/O are implemented in these chassis. (Analog I/O could be implemented, but block transfers would have to be programmed in the PLC ladder logic) Discrete I/O data tables can be read from and written to directly with Vista. An advantage to this scheme is that interlock functions for vacuum equipment, powers supplies, etc... can be programmed in ladder logic, thus minimizing wiring and

"The submitted manuscript has been authored by a contractor of the U.S. Government under contract No. DE-AC05-84OR21400. Accordingly, the U.S. Government retains a non-exclusive, royalty-free license to publish or reproduce the published form of this contribution, or allow others to do so, for U.S. Government purposes."

installation costs. Additionally, reliability is increased since the PLC processors continue to operate when the Vista system is not running and changes to interlock strings can be made quickly.

In addition to the A-B PLC hardware, a serial interface has been implemented through VME to provide both RS-232 and RS-485 interface to power supplies, teslameters, vacuum gauge and turbomolecular pump controllers. The VME Microsystems VMIC VME-6015 quad-serial interface card is presently being used. Each of the four ports may be individually configured.

Currently, four rt300 processors and corresponding VME chassis exist in the HRIBF system. Two of these chassis contain serial interface modules. All four chassis contain A-B scanner modules which have up to four PLC chassis attached to the remote I/O link. The total number of PLC chassis in the system presently connected in this manner is ten. Six A-B chassis containing PLC5/20E ethernet-connected processors are utilized. A schematic layout of the HRIBF control system is shown in Fig. 1.

III. SOFTWARE COMPONENTS

ASCII databases are developed which contain channels that specify parameters for device initialization and individual I/O points. Databases are thus easily created and changed. The Vista database generator, VGEN, is then used to compile the database. Once the databases are generated, they are mapped to various ELN nodes distributed on the ethernet. Quantity and organization of databases is at the user's discretion. In the HRIBF implementation, separate databases are used for each beamline and/or specific subsystem such as the target/ion source. Generally, each I/O point on a PLC module has a channel associated with it that contains, for example, address, initialization, priority, and scaling information.

Software has been written to integrate the Allen-Bradley PLC5 series hardware with Vista. Two Vsystem I/O scanner utilities provide updates of outputs based on "interest," which is a change in value of the database channel. Additionally, the utilities provide a time-based scanning of inputs with timing based on user specified clock ticks, a scan period, and a priority setting. The first of these utilities is an extension of Vaccess to ELN and runs on the rt300 VAXELN processors in VME. Its purpose is to provide interface via the A-B remote I/O scanner module in VME. The second utility is quite similar in operation to the first, but it runs under VMS and works in conjunction with A-B Interchange software to provide a means of accessing the PLC5/20E processors across the ethernet.

The serial interface program previously mentioned also runs on each rt300 VAXELN node, with a separate process for each of the four serial ports on each VME-6015 module.

IV. SYSTEM PERFORMANCE

Operational experience to date has been good. As with any newly implemented system, there is a learning process. This includes both familiarization with the system code and software specific to I/O. Timing with all A-B hardware has proven to be adequate thus far. If performance decreases with the addition of other components to the system, there are numerous ways to redistribute the hardware to improve throughput. For example, more A-B VME scanners can be added to an ELN node or more ELN nodes can be added.

Some basic problems exist. Timing and noise problems must be solved in conjunction with some serial devices. ELN nodes must be made independent of one another such that crashes or power loss in one node does not result in inadvertant crashes of other portions of the system. Support of additional hardware such as CAMAC will be necessary.

The operator interface is always an aspect which generates considerable debate. Vista is no exception to this because of the flexibility of screen creation with VDRAW. In subsequent months as routine facility operation resumes, operator training in the usage of Vista will take place and many improvements on screen design will evolve. The major request at this juncture is for knobs for beam tuning, and it is apparent that knobs will receive a high priority in future enhancements.

V. FUTURE IMPLEMENTATION

Presently, all aspects of the RIB injector and target/ion source are controlled through the new system, as are all aspects of the beam transport lines from ORIC to the RIB injector. The beam transport line from the RIB injector to the tandem and a transport line from the tandem to a new recoil mass spectrometer will be completed in late summer. All aspects of these beamlines will be controlled via Vista. Vista is also currently utilized to control the ORIC internal ion source and monitor the ORIC extraction system.

Many additions to the new control system must be accomplished in the coming months. The ORIC controls conversion will proceed as the next phase followed by the conversion of other existing beam transport lines, the tandem accelerator controls, and the stable beam injector controls. Knobs and additional handlers will be added to aid in beam tuning.

VI. SUMMARY

The Vista control system has been implemented for accelerator system control as part of the creation of the Holifield Radioactive Ion Beam Facility. This system has proven to be extremely flexible and reliable. Implementation of both hardware and software with a small controls group of three people has been straightforward and without great difficulty. Vista Control System personnel have provided outstanding support. To date, ORIC beam lines, some aspects of ORIC, the RIB injector,

and the tandem injection beam line are being controlled with Vista. Additional beam lines to be completed in FY95 will also be controlled through Vista as will additional ORIC components converted as time permits. A subsequent phase will be to convert the tandem controls to Vista, and add UNIX and CAMAC support. The culmination will be a versatile, distributed, and unified control system for the HRIBF.

VII. REFERENCES

[1] Research sponsored by the US Department of Energy under contract No. DE-AC05-84OR21400 with Martin Marietta Energy Systems, Inc.

[2] D.K. Olsen et al, Proc. Second Int Conf on Radioactive Nuclear Beams, Louvain-la-Neuve, Belgium, August 1991, ed. by Th. Delbar (Adam Hilger, Bristol, 1992), p. 131; A proposal for Physics with Exotic Beams at the Holifield Heavy Ion Research Facility, edited by J.D. Garrett and D.K. Olsen, February 1991.

[3] J.D. Bailey et. al., "ORIC Accelerator", ORNL Physics Division Progress Report, Document No. ORNL-6842, p. 1-10 (1994), Oak Ridge National Laboratory, P.O. Box 2008, Oak Ridge, TN 37831.

[4] D.T. Dowling et. al., "Status of the Radioactive Ion Beam Injector at the Holifield Radioactive Ion Beam Facility", paper RPR04 of this conference.

[5] G.D. Alton et. al., "The Electron Beam Plasma Target /Ion Source", ORNL Physics Division Progress Report, Document No. ORNL-6842, p. 1-26, (1994).

[6] P.F. Mantica et. al., "RIB 300 keV Diagnostics", ORNL Physics Division Progress Report, Document No. ORNL-6842, p. 1-24, (1994).

[7] G.D. Alton et. al., "The Charge Exchange Cell Project", ORNL Physics Division Progress Report, Document No. ORNL-6842, p. 1-31, (1994).

[8] M.J. Meigs et. al., "A New Beam Intensity Monitoring System With Wide Dynamic Range For The Holifield Radioactive Ion Beam Facility", paper TPC18 of this conference.

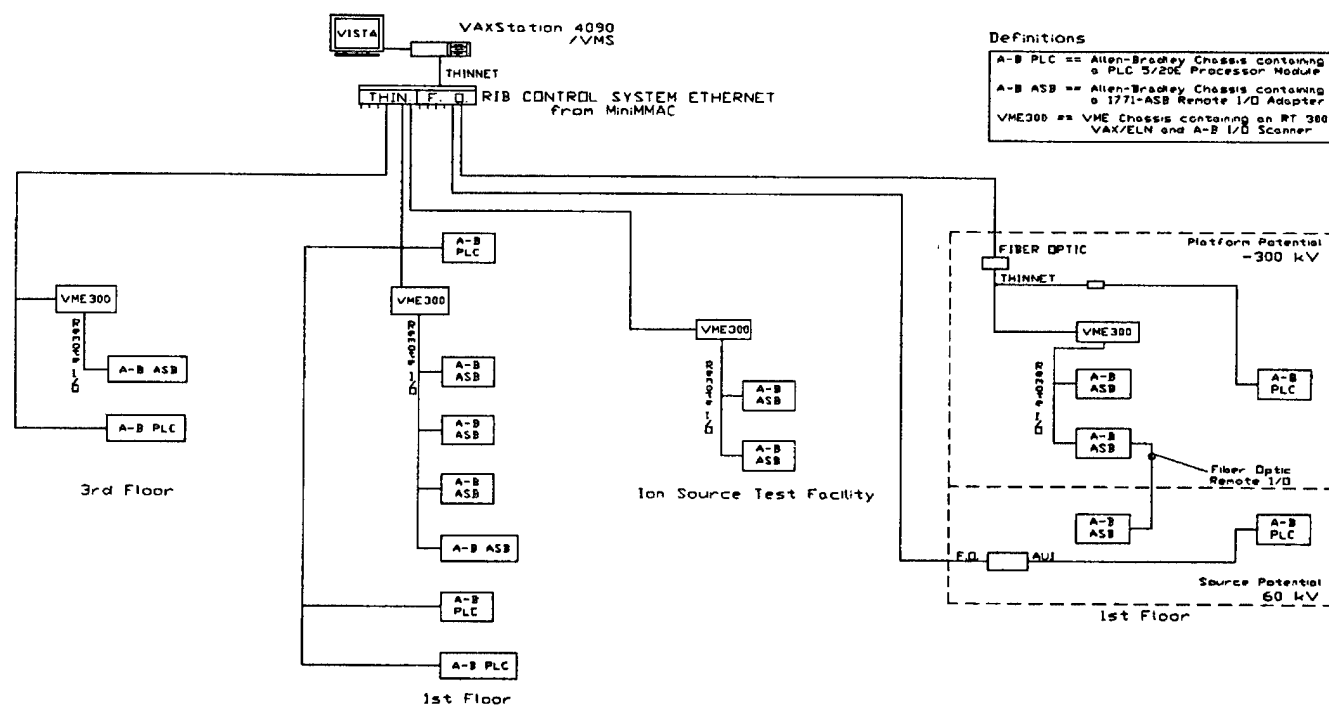


Figure 1: Schematic Layout of the HRIBF Control System

Control System Design for KEKB accelerators

S-I. Kurokawa, T. Katoh, T.T. Nakamura, T. Mimashi, N. Yamamoto
KEK, National Laboratory for High Energy Physics
1-1 Oho, Tsukuba, Ibaraki, 305 JAPAN

Abstract

The KEKB project, constructing an asymmetric electron-positron collider for B physics in Japan, has officially approved and has started in 1994. The goal of the KEKB accelerator control system is to provide a powerful, flexible, and extendible control system for both accelerator physicists, who need beam information and are not so patient, and operators, who control all equipment. To achieve this goal on schedule, we decided to use standard technology where it is applicable. We have studied some existing control systems based on "Standard Model" of the modern accelerator control systems, such as EPICS[1] or V-system[2], as a framework of the control system and have chosen the base of the control system according to this study. Another key issue in the KEKB accelerator control system is use of database management system for unified management of the information which the control system requires. Integration of control system with the modeling software, SAD[3], is also discussed.

I. The KEKB project

The KEKB[5] is the project to build an asymmetric, double ring $e^+ - e^-$ collider in KEK, Japan. The KEKB will be built inside the existing TRISTAN[4] main ring (MR) tunnel. The whole KEKB accelerator complex is shown in Figure 1. The high energy ring (HER) and the low energy ring (LER) will be installed side by side in the tunnel of the TRISTAN MR. To build the two rings equal circumferences, a cross-over zone is created in the Fuji section as shown in Figure 2.

The KEKB is designed for the detailed studies on B meson. Electrons accelerated up to 8 GeV by the upgraded LINAC will be stored in HER while LER stores positrons at 3.5 GeV. A low $\beta_y^* = 1$ cm, low emittance and a small emittance ratio should be maintained for sufficiently long period of time in order to achieve the design luminosity $1 \times 10^{34} \text{ cm}^{-2} \text{ s}^{-1}$ and to work as a B-factory for the high energy experiments.

The KEKB project was approved and started 1994. TRISTAN MR will be shut down at the end of 1995 and will be removed from the MR tunnel. Installation of the hardware in the tunnel will start at the end of 1996. The first commissioning of the KEKB is expected at the end of 1998. The control system should be installed at least one year before that time.

II. Design goal of the KEKB accelerator control system

A. Functional Requirements.

Before starting the design of KEKB accelerator control system, we reviewed functional requirements for the KEKB accelerator control system. In the process of the review, we find

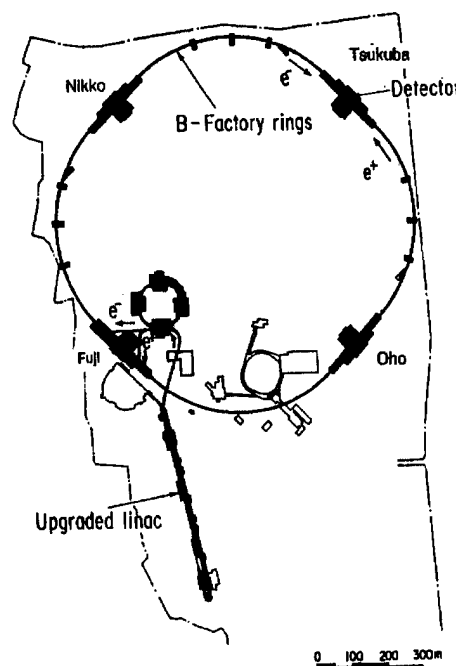


Figure 1. KEKB Accelerator Complex.

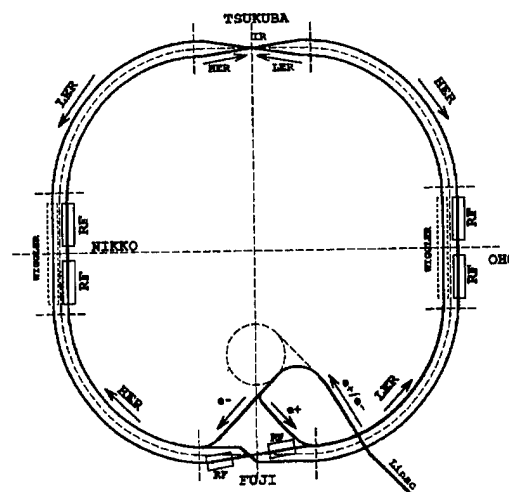


Figure 2. KEKB Accelerator Configuration.

that users of an accelerator control system consists of three groups. 1) *Hardware Group* : They will construct accelerator hardwares and need basic controls over their hardware, such as set/read/monitor/alarm/log data. 2) *Accelerator Operators* : They operate accelerators in a steady state. They initiate automated operation programs , monitor the performance of the machine and adjust some parameters to improve machine performance as required. They also respond to an alarm system and fix the problem pointed by the alarm system. 3) *Accelerator Physicist*: They use the accelerator as their experimental equipment. They collect data from the accelerator and analyze them to find a new knowledge on accelerator physics. Their effort will be resulted in a performance improvement of the machine, i.e. higher luminosity.

Each group has their own requirements for the accelerator control system.

1. *Hardware Group*:

- (a) Easy access to the hardware in a hardware interface development phase.
- (b) Standalone operation of the hardware subsystem independent from the other part of the accelerator.

2. *Operators*:

- (a) The control system should be operator-friendly.
- (b) Operator interfaces should have quick response, less than a few seconds.
- (c) All the operation should be recorded for later inspection.

3. *Accelerator Physicist*: Their basic requirement can be summarized as three principles,

- (a) All the data that are possible to take should be taken.
 - (b) All the data that are taken should be saved for later analyses.
 - (c) All the operation should be recorded for later inspection.
- Requirements to the control system for data analysis are,
- (a) Stored data should be easily extracted.
 - (b) The data should be easily analyzed.
 - (c) It should be possible to analyze data and the computer simulation result with the same tool.
 - (d) The programming system for application programs should be programmer-friendly.

The controls group itself has its requirements on the control system.

1. Easy integration of control sub-systems into the accelerator control system.
2. All the machine parameters and data about the machine components should be saved in the database.
3. Incremental upgrade and replacement should be possible.
4. Tight integration with the LINAC control system and the KEKB accelerator control system. It is important because of tight requirement on the beam injected to the KEKB rings.
5. CAMAC modules used and accumulated in the TRISTAN accelerator control system should be reused for economical and efficiency reason.

III. Basic Design Concepts

Considering requirements stated above, the basic concepts in KEKB accelerator control system are concluded as follows.

1. Design the system using so-called "Standard Model" of the accelerator control system.

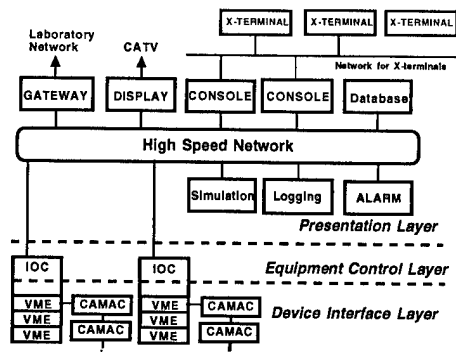


Figure. 3. KEKB Accelerator Control System Architecture

2. For the later upgrading or for maintenance, the interfaces between three layers should be well defined by using international standards.
3. As the interfaces between the control system and the equipment to be controlled, international standards such as CAMAC, VME, VXI and GPIB should be used.
4. To get quick response, high-speed networks should be used to connect computers.
5. To minimize man-power and efforts, the international collaboration or commercially available products should be applied.
6. For the application programmers, the object-oriented technique or abstraction should be fully utilized to hide the hardware behind.
7. Adopt the "Linkmen" system as in the construction of TRISTAN control system, where the linkmen make equipment database and code device drivers for the application programmers because they know the equipment best.

IV. KEKB Accelerator Control System Architecture

Our design of KEKB accelerator control system is based on EPICS[1]. The control system is divided into three layers; presentation layer, equipment control layer, and device interface layer, as shown in Figure 3. The first two layers are connected with each other through the high-speed network such as FDDI. To separate the network traffic between these layers from the traffic between console computers and X-terminals, another network and/or a network switch will be used.

A. *Presentation Layer*

The presentation layer includes operator's consoles, database manager, simulation computer, alarm generation/recording, data logging, display, and a gateway to KEK in site network. Workstations and/or CPU servers running UNIX operating systems are used in this layer. X-terminals with multiple displays will be used as operator consoles. The database manager keeps all the information concerning KEKB accelerators, for example machine parameters, equipment specifications, location, and so on. The simulation computer is used for accelerator physics calculations for such purpose as orbit correction. Failures of the equipment are monitored by each equipment computer and are reported to the alarm computer for broadcasting and recording purposes. The data logging computer collects data from various equipment

control computers for later analyses. The display computer displays data and transmits information over the KEKB site through the CATV network and other media. There is also a gateway computer which connects KEKB accelerator control computer network with the KEK laboratory network. The gateway computer makes it possible for staffs of accelerator department to reach KEKB accelerator equipment from their office. To avoid network jam caused by the access through the laboratory network, a proxy channel access(CA) server will be used on the gateway computer. This proxy CA server will intercept and bundle CA requests from the laboratory network.

The software environment required for this layer is very important in the whole system. The fundamental functions to display status and measured values graphically, to control each equipment, etc., should be supported from the beginning of installation of machine equipment. The programmer-friendly interfaces must be provided for the accelerator physicists to make application programs easily. And it is also important to have a very efficient data retrieval and analysis system from the database system.

B. Equipment Control Layer

The equipment control layer consists of computers that functionally control equipment of each hardware group, e.g. magnet, RF, beam monitor and so on. The equipment control computer, IOC(Input/Output Controller) in EPICS terminology, is a VME board-computer running real time operating system. In the VME bus, there will be CAMAC serial drivers and optional VME boards as the hardware interface between IOC and the device interface layers. The control computer may be replaced with the PC with VME bus interface for the maintenance reason.

C. Device Interface Layer

The lowest device interface layer consists of CAMAC crates and CAMAC modules inside the crates. We need to use VXI/VME interface for some hardwares, such as high speed BPM because of various reasons. The KEKB accelerator control system will also accept these interfaces. The CAMAC crates are connected by CAMAC serial highways or CAMAC branch highways corresponding to the characteristics required. For this layer, software drivers are provided on IOC's. These drivers are coded by the linkmen who have best knowledge of equipment to be controlled.

D. Data management

The database system is very important for the system. Any information related to the hardware components of the accelerators should be stored into the database system. Logging data, archived data and configuration data should also be accessible from the database system with same interface. Two commercial relational database software systems, ORACLE and SYBASE, are under evaluation.

V. Interface to the modeling program

The final goal of SAD[3] is to build a virtual accelerator on a digital computer. The user of SAD should be able to control this virtual accelerator through the same operator interface used

in a real accelerator. To realize this idea, we will develop an interface program between SAD and portable CA server, which will run on UNIX workstations. CA clients can access the virtual accelerator through this CA server using ordinal CA protocol.

VI. Conclusion

The conceptual design of the KEKB accelerator control system was presented. The detailed design is underway and will be finished soon. The construction will start then and will be finished by the second quarter of 1998. It is essential to use commercially available products and make use of software sharing to save required man-power and efforts. The system should be friendly to the accelerator physicists who make application programs. The database system will become the core of the KEKB accelerator control system and will make us possible to integrate all the sub-systems into one large system.

VII. Acknowledgement

The authors sincerely appreciate Dr. Jiri Navratil for his help in the evaluation of EPICS and a lot of interesting discussions.

References

- [1] L.R. Dalesio, et al., "EPICS Architecture", ICALEPCS 91, KEK Proceedings 92-15, (1992) pp.278-282., Dalesio, L., et al. "The Experimental Physics and Industrial Control System Architecture," ICALEPCS, Berlin, Germany, Oct. 18-22, 1993.
- [2] "Vsystem" is a product of Vista Control Systems Inc., Los Alamos, NM.
- [3] SAD is the accelerator design tool program developed at KEK.
- [4] Shin-ichi Kurokawa, et al., "The TRISTAN Control System", Nucl. Instr. and Meth., A247, (1986) pp. 29-36.
- [5] Shin-ichi Kurokawa, "Status of TRISTAN-II Project", Proceedings of the 1993 Particle Accelerator Conf, pp. 2004-2006, S-I Kurokawa, "KEKB status and Plans", presented in this conference, WPG04.

DESIGN OF SPring-8 LINAC CONTROL SYSTEM USING OBJECT ORIENTED CONCEPT

H.Sakaki, H.Yoshikawa, Y.Itoh, A.Kuba, T.Hori, A.Mizuno, H.Yokomizo
JAERI-RIKEN SPring-8 Project Team, Kamigori, Ako-gun, Hyogo 678-12 JAPAN

Abstract

At the present software technic, the methodology of Object Oriented Programming(OOP) has become the mainstream. Because it will be gave the efficient development of programming and the easy maintenance. OOP makes many parts of program that called Object, and these Objects are assembled into main program. When many Objects are reserved on the system development, so that the future development will be easy by using stored Objects.

On the accelerator, we consider the system as assembled parts. And it will always be improved or replaced. So OOP is suitable for the accelerator system [1], then we try for using OOP. First of all, all component of SPring-8 Linac were abstracted and modeled, and we designed a Super Class which is core of Object.

In this paper, the concept of our system and its present status are described.

I. STRUCTURE OF CONTROL SYSTEM

For the data acquisition and low level control of devices, we adopt the VME system. The hierarchy of control system have two layers. One is Control Process layer(VME), another is Operation Process layer(WS). These VMEs have MVME147s board(Motolara 68030 CPU) and run on OS-9 operating system. The WS is going to use HP9000 series. Table I shows I/O boards which are used in the VME system. All of them are commercial products. However device drivers that connect between OS and I/O boards were written by in-house staff. The VME system will locate in the second floor where is called the klystron gallery. And we will have many accidents at the control, because of the klystron EMI. Now we are examining about its [2].

Table I
SPring-8 Linac I/O boards

Name	Function	Number of boards
MVME147s	CPU(68030)	20
AVME9350	AI(16ch)	34
AVME9210	AO(6ch)	25
DVME-DIN3	DI(64ch)	53
DVME-DOU3	DO(64ch)	31
VPAK601	MotorControl(2ch)	55
EVME-GPIB21	GPIB	18

II. STRUCTURE OF SOFTWARE

A. Layout of Object

Fig 1 shows a layout of Objects in Linac. Objects in the VME system, as one to one projection of real devices. So that we can control as if the Object is a real device.

When a real device is replaced a new specifical device, the Object is only replaced the new Object, that's all. This is different from the conventional structured programming, therefore we can get high programming efficiency. On the Man Machine Interface(MMIF), now we are designing.

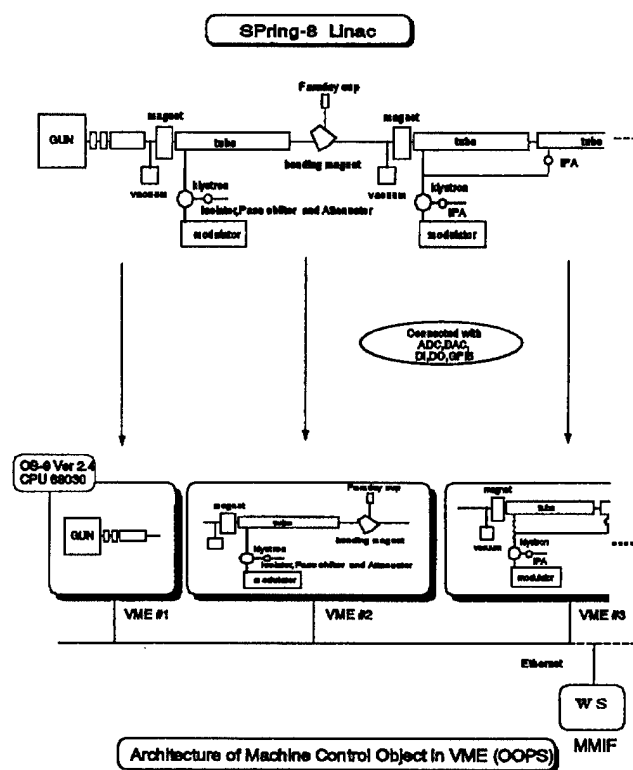


Figure 1. Layout of Object

B. Design of Super Class "MACHINE"

Assuming that Linac is constructed by similar simple components, we design the Super Class "MACHINE" that is core of Object. It has common characters of all devices.

Fig 2 shows the Super Class "MACHINE" and the Sub Classes of it. Main attributes of "MACHINE" are the "parameter and status" and the "Behavior". The "parameter and status" means common elements of Object, and the "Behavior" means the transitional status of Super Class (all Objects). Further, "Behavior" correspond to part of SPring-8 Linac machine Control Commands(SCC), the inter-Object message for SPring-8 Linac machine Control system, so that all Objects are became the "Behavior" status by SCC. On OS-9, Object Oriented Languages(like C++) have not been commercially available yet. So we have to use traditional C-Language for our Objects.

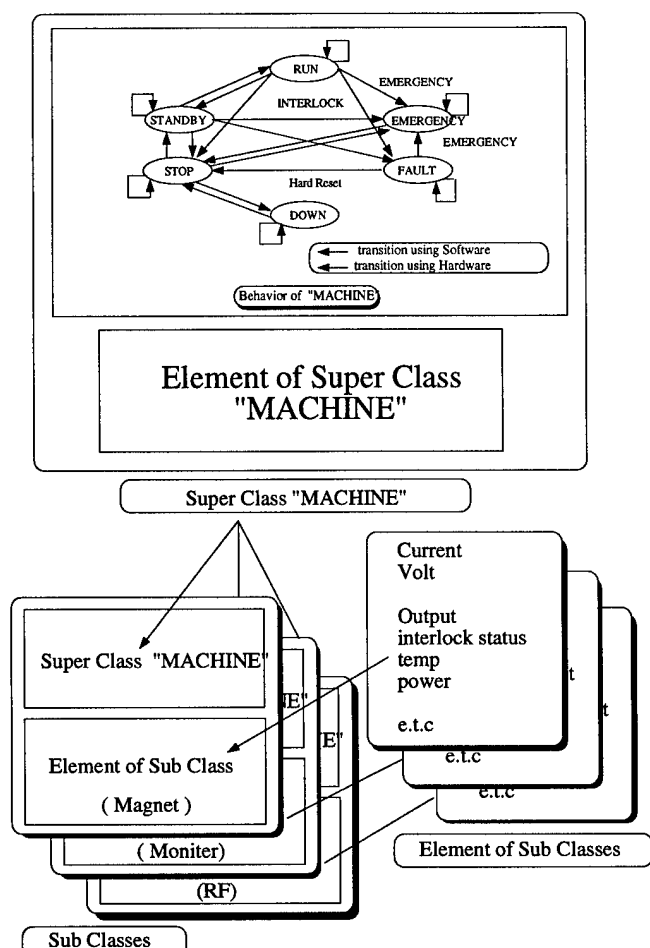


Figure 2. Design of Sub Class

C. SPring-8 Linac machine Control Datagram(SCD)

SCD means SPring-8 Linac machine Control Datagram [3]. The traffic of our network has single and rare fragmentation of data. Then we tried to find the suitable protocol for our requirement that it has to be standardized, be real-time feature and be matured as a reliable protocol.

But we could not find such a protocol, then we decided that TCP/IP is tentatively adapted to our protocol. Though, the connection-type service(typically TCP) should get down the efficiency of communication and take much CPU power for open/close connections. We want to reduce the over head of the communication service.

Other hands, the connectionless type service(UDP/IP) has smaller over head, and it is faster than connection-type service in our traffic condition. But it will happen that transport error, loss of packets and mistake, because of the ease of error check in UDP/IP. It is necessary to reinforce the error check. So it motivated us to develop the SCD protocol. The characteristics of SCD protocol are description follows.

- **Simple:** SCD is connectionless, open/close procedures are not needed, then the number of packets and the network traffic are reduced.
- **reliable:** The time-out sequence get higher reliability. The lower of protocol is UDP/IP which has enough reliability and is used all over the world.

- **flexible:** So MAR procedure is implemented, it is flexible to be adapted to the modification of the machine configuration.

SCD protocol is fifth layer as the session layer of OSI layer model(fig3). Data flows from upper layer to lower layer, and each layer build/divide the packet. In time domain, data is sent from head to tail.

(Hierarchy of OSI)

Structure of Packet

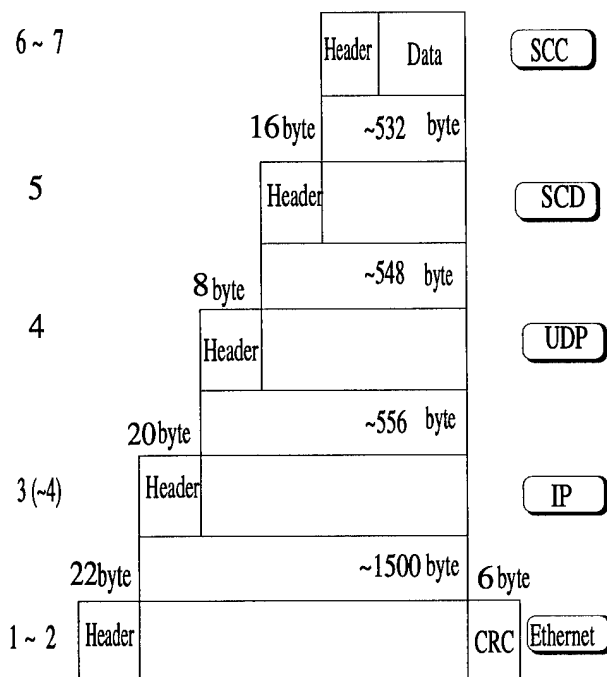


Figure 3. Layer of SCD

D. Communication Process

It is important for the machine control to pursue a data transfer speed. So, we designed the Communication Process following concepts on SCD.

- Using Object Oriented (different from Super Class "MACHINE")
- Self address learning type
- High flexibility

Fig 4 shows the Communication Process both WS side and VME side. This Process is implemented on HP-UX and OS-9. Between Communication Process and Objects, however, SCC is forwarded from Communication Process to Object by the Mailing system. When we want to send a parameter to Object, we can use API in the Communication Process. If we have never known the Object address, but Object name is known, Communication Process is able to search the address (MAR procedure) and to send SCC to the target Object. We never be worried about Object address. This looks like the Super Post Office.

This Process is also used Object Oriented concept and programming, so we will get a high maintainability.

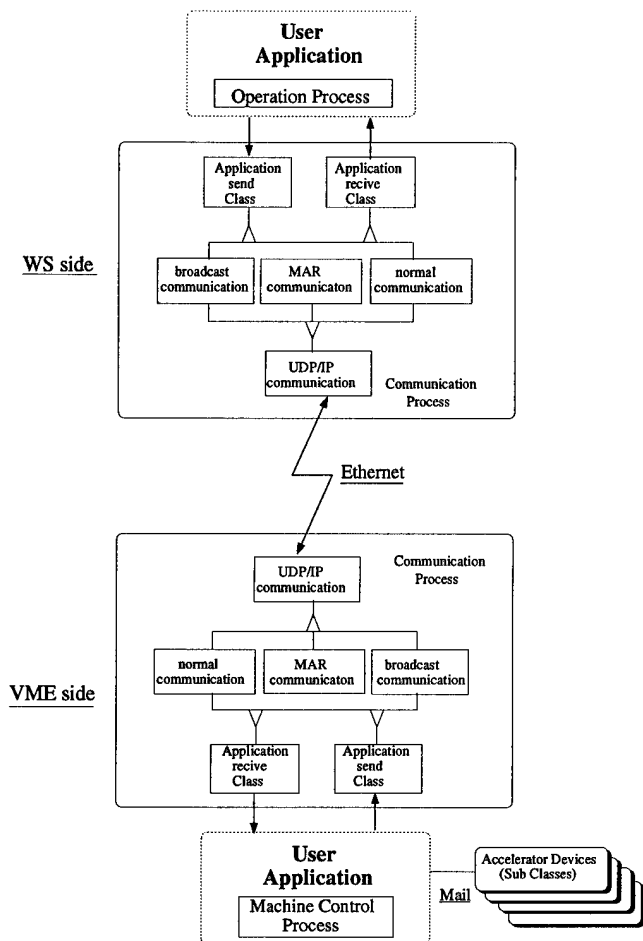


Figure 4. Layout of Communication Process

III. CONCLUSION

We designed the Super Class for SPring-8 Linac, so that we will be able to make the Sub Classes easily. However, as Object is written by traditional C-Language, it is felt slightly complex. Now, we are making all Objects on the VME system, and have to check the performance of our system. These Object are going to put together software and hardware on this year.

References

- [1] H.Nishimura, "Dynamic Accelerator Modeling Uses Objects in Eiffel", COMPUTERS IN PHYSICS, Vol.6, No.5, 1992,p456.
- [2] I.S.Ko et al., "CONTROL OF PLS 2-GeV LINAC", Presented at the 17th International Linac Conference, Tsukuba, Japan, August 21-26,1994
- [3] H.Yoshikawa et al., "Class structure of the Injector Linac control system of SPring-8", Nucl. Instr. and Meth. in Phys. Res. A352 (1994) 216-217

The Slow Control System of the Muon g-2 Experiment

Arnold Stillman* Brookhaven National Laboratory, Upton, NY 11973 USA

Abstract

The muon g-2 experiment (AGS E-821) will measure $a_\mu = \frac{1}{2}(g - 2)$, the anomalous magnetic dipole moment of the muon, in the world's largest superconducting solenoidal magnet. Since the magnet stores the muons during their lifetime, running the experiment is similar to running an accelerator, though on a much smaller scale and with fewer timing requirements. The slow control system for the experiment will provide real-time monitoring of the experimental parameters by means of industrial subsystems; commercial products comprise both the hardware and its interface. The industrial basis of the control system makes it quite easy to install, and provides a simple way of implementing rudimentary controls for most of the variables. Two independent networks isolate critical control functions from bookkeeping functions, yet still provide a degree of redundancy. Since commercial products form the bulk of the slow control software, there is a minimal programming requirement for tool development.

I. Introduction

Experiment 821 at the AGS will measure g-2 of the muon by storing a bunch of them in a magnetic field until they all decay. The magnetic field is a continuous circular dipole field, formed by four superconducting coils embedded in an iron yoke. The muons circulate in the magnetic field, but their decay electrons escape to smaller radii, entering calorimeters spaced radially about the inner circumference of the magnet. The muon precession frequency appears as a modulation of the decay electron spectrum. This implies that the data from the experiment is not a series of events, but rather the modulation impressed upon the energies of thousands of decay electrons. Running an experiment in this fashion almost approximates the running of a tiny accelerator with continuous extraction. There are a few differences, there is no extraction to external beamlines, there is no longitudinal acceleration (the relativistic γ of the muon is constant at a value known as the *magic* γ , to free the measurement from the effects of electrostatic focusing quadrupoles). Thus, there are no rf cavities or ramping magnetic fields. There is, though, weak electrostatic focusing with quadrupole electrodes embedded in the vacuum chamber. Since the experiment looks quite like an accelerator, there is a need for a more automatic presentation of device status, and a more central initiation of control signals, than is usually the case in a beam line. These requirements imply that the data acquisition systems for the hardware status, and the software for display, be fully integrated at the planning stages, rather than separately matched. An efficient way to take advantage of an integrated approach is to buy commercial plant-floor type monitors and their associated software packages. These customize easily to various industrial applications, and they seem to be applicable

to the muon storage ring as well, even though it is not quite like a plant floor.

There are architectural considerations in an experiment that one would not confront in industrial applications. These differences make the g-2 control system not quite a plug and play toy, but careful consideration of how various ring subsystems interact should make the continuous operation of the ring fairly painless. The main idea in this architecture is that all hardware subsystems operate in a high-priority, local control loop, but talk to the slow control system when they can. The slow control system then logs status information or trouble reports. The local control loops also have priority over control signals sent down to them from the slow control system. This is to prevent the human operator of a system from helplessly losing control to the slow control system.

At the level of the actual hardware, the slow control system will communicate to modular industrial controllers. These controllers are microcomputers, generally configured to operate scanning analog to digital converters or standard industrial signal conditioners. They exist as self-sufficient processors, and have the ability to run the local control functions easily. The ones that E-821 will use will be Allen-Bradley[1] PLC's (Programmable Local Controller's). They are nearly ubiquitous in plant floor environments, and they have sufficient communications ability to fulfill the reporting requirements for the slow control system. The newest versions also allow ethernet connections, which simplifies their integration into the existing BNL network.

The whole control system will use an ethernet network to communicate among its parts, and to communicate at a higher level to the data acquisition host. It will also have a hidden network strictly for automatic control purposes and free of any monitoring responsibilities. X-terminals will be the primary interface to humans. They will be running graphical applications strictly for control purposes.

II. The Local Controller Hardware

The controllers for the muon g-2 experiment will be Allen-Bradley PLC-5/E industrial controllers. These controllers have a small complement of memory with a battery backup, some communications ports, the ability to scan several hundred to several thousand input or output circuits, and options for EEPROM program backup. Basically, they are scanners that read to or write from a bank of circuits. Separate modules determine the identity of these circuits, and the types of signals they process. The controller simply reads channels and stores them in its memory. It then provides the channel information to a display, which can be just a screen with a display of status indicators, or a highly integrated front end of a control system.

The communications channels that the controllers use come in three types, two quite useful and one less so. There is the proprietary Data Highway, which connects all the PLC's, and which has a reasonably high capacity. There is an ethernet link,

*Work performed under the auspices of the U.S. Dept of Energy, Contract No. DE-AC02-76CH00016.

which exists independently of the Data Highway, and has about twenty times its transmission capacity. And finally, there is an RS-232 port, useful as a debugging tool, on each PLC.

The controller has all the characteristics of a small, dedicated computer. There is some data handling ability, interrupt capability, status flags, and the ability to run multiple control programs. Their use in E-821 will be to run local control loops for the major subsystems, and to pass news reports back up to the slow control host computer.

The controllers themselves do not have the ability to process raw input signals from various devices. Specialized input modules will handle these tasks. As an example, the controls for the liquid helium refrigerator require temperature readings from junction sensors. A specialized module linearizes and buffers these junction signals before passing them on to the processor, which likes to see only well-conditioned, standard industrial inputs (e.g. 20 ma. loop signals). Other electronic front ends perform similar conditioning in their respective environments.

This separated function design of the electronics also minimizes confusion in the field wiring to the processors. All wiring from the front end modules to the processors is on terminal strips, and is identical with respect to wire type and termination. The specialized input wiring we will segregate by function onto the appropriate electronics. This input bundling is easier to maintain and repair than just running wires in sequential channel order, heedless of their functions.

III. The Network

Devices and computers in the muon g-2 experiment will communicate with each other via an ethernet network. The PLC-5/E controllers have an internal ethernet interface, requiring, however, an external transceiver. Allen-Bradley software, running on the data acquisition/slow control host computer, will handle the communications between controller and the ethernet. This network should handle easily the data transmissions from ring subsystems and file transfers from the DAQ host.

In addition to the ethernet connections, the PLC's will communicate with each other via the proprietary Allen-Bradley Data Highway (actually, Data Highway+, or DH+), a custom network for their PLC interconnections. This second "shadow network" increases the slow control reliability by isolating the important control loops at the major subsystem level from the pure news-gathering functions of the ethernet. The Data Highway provides a way for automatic controls to function separately from the slow control system, though one could also activate devices through slow control, with the appropriate priority and privileges. Since the two networks share nothing, failure of the slow control system or the ethernet does not compromise the operation of the ring subsystems.

The Data Highway transmission rate is 57.6 kbaud, in contrast to the much faster ethernet rate of 10 Mbits/sec. However, the Data Highway carries much less in the way of actual data than the ethernet. The Data Highway interconnection is responsible for carrying the control signals, global flags, and small blocks of data among the PLC's. The detailed description of these transmissions among the PLC's is actually imbedded in the design of the subsystem control loops, which I will describe later. This "hidden" network remains invisible to the ethernet network, so

the ethernet must also carry some of the same information. This redundancy is fortuitous, increasing the reliability of the transmissions at no cost, since E-821 requires the ethernet and Allen-Bradley supplies the Data Highway as standard equipment.

IV. The General Architecture

The basic idea of a slow control system is to provide a monitor on the g-2 ring function. It should allow the free transfer of data from ring subsystems, unencumbering the extant automatic controls. These automatic controls and their self-linkages are not properly in the realm of the slow control system. However, there is a connection between automatic and slow control systems. It's probably best to describe the entire ring heirarchically, from the controller, at the base, to the slow control monitor, at the apex.

At the level of the hardware inputs, the PLC controllers share automatic control among themselves on the Data Highway, and they pass news reports up to the slow control host on the ethernet. Note that the only common point between the two networks is at the PLC. From there on, the networks separate permanently. The ethernet network includes the DAQ/slow control computer host, an HP9000.

The host computer runs the proprietary Allen-Bradley Interchange software, which allows the host to communicate directly to the PLC's over the ethernet. At this point, the slow control system has gotten access to data and/or news reports from the controllers. It is a collection of "unedited" data packages from the controllers. At this level, FactoryLink, a commercial software suite, takes over. FactoryLink integrates these reports graphically and stores the raw data in a proprietary database. The host computer monitor will display a picture or schematic of some subsystem, and variables or parameters that are changing will appear in graphical form. For example, the helium level in the cryostat would appear on the screen, if that screen were selected. The cryostat, filled with helium, would appear as part of a cartoon illustrating the refrigeration system.

The central tenet of the slow control system is that it monitor and control the E-821 subsystems without disrupting the local control or feedback of that subsystem. To achieve this non-interference, it is necessary to assign priorities to any operations which may affect the running of a particular subsystem. A local process, for instance, a power supply, has inherent feedback control, and may have setpoints and software controls, as well. These *Local Loops* have the highest priority, being interruptible only under conditions set forth by their designer. Next higher in priority are *Triggers* which represents a way that the slow control operator (i.e. an E-821 "Control Room" operator) could trigger a switch to control a device, or process. As a garish example, there could exist a "Crash" button, which would activate an energy dump from the magnet. Since these priorities are lower than the local loop priorities, the triggers are easy to disable intentionally at the hardware level.

At the lowest priority is the passing of reports up to the operator console, which displays them. The requirement here is for an update rate of perhaps once per second for preformatted reports. This should be slow enough that the PLC's have no problem keeping up with requests from the slow control system, even though they are executing their own set of instructions in the local loops. FactoryLink handles the initiation of requests and

processes the replies from the PLC's. No request for news ever slows down the automatic control system, since these requests are both of the lowest priority, and are travelling on the ethernet, not the Data Highway. The only mechanism for slowing any control functions will be the processing of requests by the PLC's, or the operation of triggers. If the news report from the PLC exists in a predetermined format, of constant length, the delay caused by its transmission becomes a bookkeeping problem. This just means that it becomes part of the local loop, simply another task for the PLC.

V. FactoryLink

FactoryLink is a product of USData Corp.[2] . It is an industrial plant-floor monitoring system made up of several software modules. Not all of the modules are necessary in any particular application, and, in fact, the g-2 experiment uses a subset of the full suite. FactoryLink, running on the host, gathers information from the PLC's and displays it in several ways. The primary mode is animation, whereby cartoon representations of subsystems respond to underlying tag values, which themselves are simply the readback signals from the hardware. A simple form of animation is a thermometer, for example, whose "mercury" rises and falls with the readback from a given thermocouple. FactoryLink also provides canned versions of strip chart recorders, linear scales, and color or gray-scale displays. There is a drawing tool for generating the screens that become animate, and a run manager that operates the screens once they are drawn.

FactoryLink also provides a database which is, in fact, central to its operation. This database is proprietary, though they do provide tools for accession and storage in standard formats (*e.g.* Sybase, dBaseIV, etc.).

References

- [1] Allen-Bradley, 100 Crossways Park West-Suite 202, Woodbury, NY 11797.
- [2] FactoryLink, USDATA Corporation, Industrial Products Division, 138 River Road, Andover, MA

The Duke Storage Ring Control System *

Y. Wu, B. Burnham, and V.N. Litvinenko

Duke FEL laboratory, Box 90319, Duke University, Durham, NC 27708-0319, USA

Abstract

The Duke storage ring is a dedicated facility for the UV-VUV FEL operation. The low level computer control system for the Duke storage ring is developed using EPICS. The control hardware employs several different architectures including CAMAC, GPIB, Allen Bradley, and VME. The high level control is implemented in Tcl-Tk scripts running on SPARCstations. Tcl-Tk provides the global control capabilities such as the energy ramping, the orbit compensation, and the tune and chromaticity control. The Duke storage ring control system was tested and operational for storage ring commissioning in Nov. 1994. During commissioning, additional control tools were developed to facilitate the operation.

I. INTRODUCTION

The Duke storage ring control system is based on the Experimental Physics and Industrial Control System (EPICS) [1]. EPICS was initially co-developed by Los Alamos National Laboratory and the Advanced Photon Source. Later, the co-development was joined by Lawrence Berkeley Laboratory (LBL), the Continuous Electron Beam Facility (CEBAF), and Deutsches Elektronen-Synchrotron (DESY).

EPICS is a tool-based control system. EPICS tools include the display manager, the alarm manager, the archiver, the sequencer, the channel access, and others. These tools are software modules with carefully defined layers and boundaries. The tool-based approach enables EPICS implementations to use completely different sets of tools, and allows independent development of EPICS at different sites.

The EPICS control system is also a distributed system comprised of operator interfaces (OPIs), input output controllers (IOCs) and local area network (LAN). Using EPICS, a sophisticated control system customized for a particular accelerator can be quickly implemented, tested and ready for operation, saving a tremendous amount of time and effort to develop a home-made control system.

The development of the EPICS control systems at Duke FEL lab is one of many success stories of the EPICS control system. Duke FEL lab was one of the early EPICS users. The first EPICS control system at Duke, the Mark III FEL control system, was completed and operational in September, 1993, under the direction of Dr. Ricardo Pantazis. In March, 1994, we started the major effort in developing the EPICS control system for the storage ring. On November 1, 1994, the basic functions of the control system were ready for storage ring commissioning.

Additional information about EPICS is found in [1], [2],[3], and their references. More information about the Duke storage ring commissioning, is found in [4].

II. REQUIREMENTS

The requirements of the Duke storage ring control system include the following:

- control for various hardware systems;
- functional control of a group of channels;
- control of beam instrumentation and diagnostic systems;
- machine modeling and intelligent controls.

In the first phase of the control system development, we concentrated on the hardware control and the functional control. Using EPICS we implemented controls on hardware systems, such as the magnet system, the RF system, the injection kicker, the vacuum system, the water cooling system, and diagnostic systems. Using Tcl-Tk we developed high level control tools to provide functional controls such as the energy ramping, the orbit compensation, and the tune and chromaticity control.

In addition, we implemented the EPICS alarm handler, archiver, and sequencer for the storage ring control system.

III. LOW LEVEL SOFTWARE DEVELOPMENT

Since serial CAMAC device-drivers were not available from EPICS when we began the control system development in March, 1994, we had to write our own device-drivers for serial CAMAC using the CEBAF low level CAMAC C library (developed by Marty Wise).

We have developed a standard driver for the serial CAMAC branch driver Hytec2992 to initialize CAMAC crates and to provide a uniform way for device codes to address CAMAC. We have also developed a set of device codes for DSP3016 (16-bit DAC), DSP2032 or BiRa5305 (16-bit ADC, SAM module), BiRa 2324/3224 (24-bit binary input and output modules), and Russian 20-bit ADC. In addition, we have developed a driver code for the GPIB-CAMAC interface board KS3388 and modified the standard EPICS driver for the Analogic DVX2502 to suit our application.

IV. HARDWARE SUBSYSTEMS

The Duke storage ring control system employs a mixed architectures of CAMAC, Allen Bradley, GPIB, and VME. The physical layout for the control system is shown in Fig.1.

The main control functionalities are implemented in CAMAC, because we have a large amount of CAMAC control hardware on hand. The CAMAC system includes the controls for dipoles, quadrupoles, and correctors, the readbacks for the dipoles, correctors, and the beam current monitor. Allen Bradley analog and binary modules are used to control the relatively slow subsystems, such as the water cooling, the vacuum, and the RF

*Work supported by U.S. Air Force Office of Scientific Research Grant F49620-93-1-0590 and U.S. Army Space & Strategic Defense Command Contract DASG60-89-C-0028.

cavity. The GPIB-CAMAC interface provides the communication between the CAMAC controller and the HP3458A multimeter. The HP3458A is used to precisely measure the quadrupole currents. The Analogic DVX 2502 board is used to read the quadrupole terminal voltages which are in turn used together with the quadrupole currents to calculate the quadrupole temperatures.

Overall, the present storage ring control system includes 278 analog inputs, 265 analog outputs, 48 binary inputs, and 23 binary outputs.

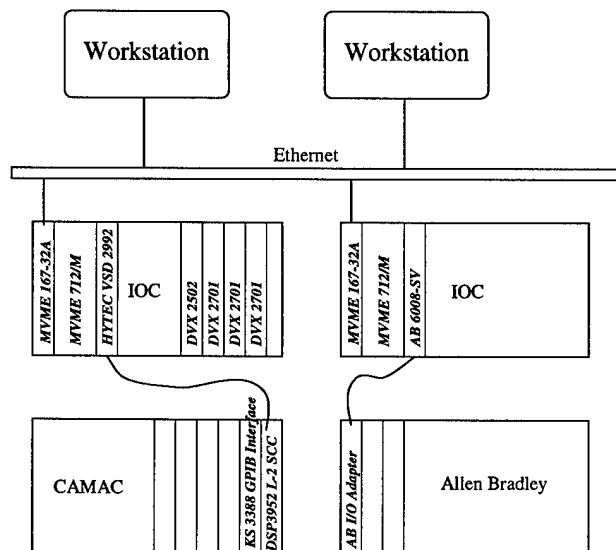


Figure 1. Hardware layout for the Duke storage ring control system.

V. IMPLEMENTATION OF EPICS

We implemented the storage ring control system based on EPICS release 3.11. The main effort has been devoted to developing and implementing the control database, the operator interface, the alarm handler, and the archiver.

Besides the regular analog and binary records, the control database contains a relatively large number of subroutine records. These records are used to accomplish complex control functionalities. One example is the magnet control. To utilize data from the magnetic measurements, we have analyzed the measured data and fit them to splines or high order polynomials which are later used in the subroutine records for the precision control of magnets (see [5]).

The storage ring operator interface is developed using the **edd/dm** tool. **edd/dm** has provided us an easy way to control and monitor the system. The alarm handler **ahl** is used to alarm abnormal quadrupole temperatures. We also have implemented the archiver, **ar**, to log the vacuum and beam current data for analysis.

VI. HIGH LEVEL CONTROL

The control of a physics application such as a storage ring requires a flexible means of handling the complex functional control of a group of hardware channels. However, when a change

is made in the EPICS device driver, database, or subroutine, an IOC reboot is needed to update the change. This approach limits the ability to construct new functional controls at run time, and diverts the effort of the application software development to the low level control debugging and implementation.

To avoid these problems, the scripting language – Tcl-Tk [6] can be used to build a dynamic, flexible and application oriented high level control.

A. Tcl-Tk

Tcl and Tk are software packages developed by Dr. John Ousterhout. Tcl (tool command language) is a scripting language for controlling and extending applications. Tk is an X window toolkit extension to Tcl, providing commands for building graphic user interfaces. Tcl is an *embeddable* language, which provides an easy way to incorporate other C procedures to extend the core Tcl features. Besides Tk, a number of other Tcl extensions have been developed including an interface to the EPICS control system – Tcl-CA (developed by Johannes van Zeijts at CEBAF).

Because of the nature of the scripting language, Tcl programs can be written and used interactively without compiling. This enables us to develop, test and debug control software on fly, saving a lot of time in code debugging, compiling and loading.

We have developed the Duke storage ring high level control using Tcl-Tk. An executable Tcl program with extensions such as Tcl-CA, TclX (an extended Tcl) and BLT (a graphic tool extension to Tk) is compiled and renamed as **epicswish**.

B. High Level Control

The high level control is made up of several Tcl scripts, including a control script, a kernel script, and a number of application scripts. The control script serves as a centralized control for the application loading and initialization. The kernel script, comprised of six procedures, provides basic communications between IOCs, workstations, and data files. The core of the functional control is implemented in various application scripts. The application scripts are summarized here:

1. a script to ramp the storage ring energy;
2. a script to control storage ring magnets and correctors — useful for magnet or corrector normalization;
3. a script to control dipole trim coils for closed orbit compensation;
4. a script to change tunes and chromaticities;
5. a script to take snapshot of or restore the control system configuration;
6. a script to modify a configuration file for use at a different energy and/or at a modified lattice configuration;
7. several Tk scripts to provide graphic interfaces to other application scripts.

A block diagram, Fig.2, summarizes the Duke storage ring high level control.

As an example, we illustrate the storage ring operation procedures in Fig.2. In an interactive **epicswish** window, we first load and initialize all related scripts by sourcing **control.tcl**. To prepare for injection, we call a **mod** procedure to modify an old snapshot **snp_03.01_95**. An editor is provided by **mod** to specify the injection beam energy, and changes in tunes, chromaticities,

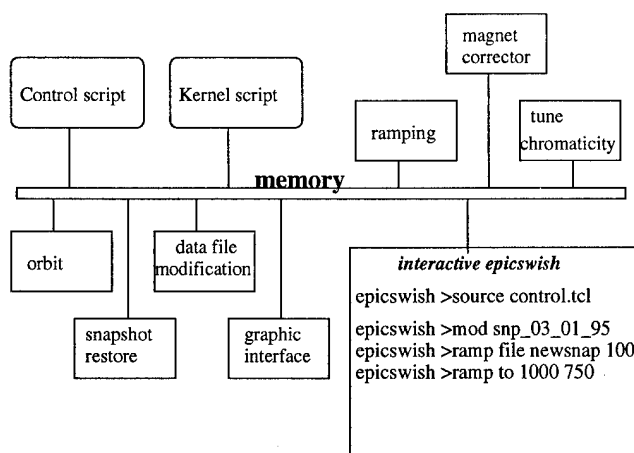


Figure. 2. Block diagram for the Duke storage ring high level control implemented in Tcl-Tk.

and/or the setting of a group of channels. Using standard lattice data files and interpolation methods, a new data file, named *newsnap*, is created. After ramping the storage ring to the new configuration (*newsnap*) in 100 steps, the ring is ready for injection. Finally, we ramp the stored beam current to 1000 MeV using standard configuration files in 750 steps.

As in this example, we successfully ramped the electron beam energy from an injection energy of 230–250 MeV to the designed 1100 MeV at the beginning of the storage ring commissioning [4].

VII. PERFORMANCE

The Duke storage ring control system consists of 614 I/O points and 1423 EPICS database records. The database records are distributed in two IOCs — "ring" and "ringmag". The "ring" IOC consisting of 195 records is lightly loaded, while "ringmag" IOC is heavily loaded with 1228 records, including 155 calculation records and 444 subroutine records. Since the beginning of commissioning in November, 1994, the storage ring control system has been practically trouble free, with only one IOC lockup due to a hung channel access process in the IOC.

The Tcl-Tk high level control has provided us with global functional control with reasonable performance. For example, the ramping script is capable of updating 240 control channels in about 0.5 second. Using this script, we are able to ramp electron beam from the injection energy of about 250 MeV to the design energy of 1000 MeV in about 6 minutes at 1 MeV per step.

VIII. CONCLUSION AND FUTURE DEVELOPMENT

Overall, the Duke storage ring control system is a stable, reliable, and easy to operate system. Using Tcl-Tk, we are able to continuously develop and improve high level control tools to meet the demands of the storage ring commissioning. With the combination of EPICS and Tcl-Tk, we were able to develop a sophisticated control system for the Duke storage ring within eight months with only two developers.

In the future, we intend to develop a fast ramping system by implementing a ramping mechanism in IOC. We also intend to improve the performance of the high level control by replacing

time consuming Tcl programs with C routines. At the same time, we will provide additional graphic interfaces to simplify storage ring operation.

In addition, the second phase of the control system development will focus on the development of beam instrumentation and diagnostic systems, as well as machine modeling and intelligent control.

IX. ACKNOWLEDGEMENTS

We are very thankful to Dr. Ricardo Pantazis for his work on the EPICS system implementation at Duke, as well as his early work in the storage ring control development. We would also like to thank Carl Dickey, Henry Goehring, Jim Meyer, and Owen Oakeley at Duke for their help in the control hardware implementation. We are very grateful to the EPICS community from which we obtained not only the EPICS control software, but also the constant support through its listserv on the net. We are especially thankful to the people at CEBAF: Chip Watson, Marty Wise, Johnny Tang, and Johannes van Zeijts for providing us with their low level CAMAC C library, CAMAC array input and output records, and Tcl-CA.

References

- [1] L. R. Dalesio, M. R. Kraimer, and A. Kozubal, "EPICS Architecture," Proceedings of ICALEPCS, KEK, Tsukuba, Japan, 1991, pp.278–282.
- [2] L. Dalesio, *et al.*, "The Experimental Physics and Industrial Control System Architecture," Proceedings of ICALEPCS, Berlin, Germany, Oct. 18–22, 1993.
- [3] W. McDowell, M. Knott, and M. Kraimer, "Status of the Advanced Photon Source and Its Accelerator Control System," ICALEPCS, Berlin, Germany, Oct. 18–22, 1993.
- [4] V.N. Litvinenko, *et al.*, "Commissioning of the Duke Storage Ring," these proceedings.
- [5] B. Burnham, *et al.*, "Application of Precision Magnetic Measurements for Control of the Duke Storage Ring," these proceedings.
- [6] J. K. Ousterhout, "Tcl and the Tk Toolkit," Addison-Wesley Publishing Co., Massachusetts, USA, 1994.

EPICS AT DUKE UNIVERSITY *

C.Dickey, B.Burnham, F.Carter, R.Fricks, V.Litvinenko,
A.Nagchaudhuri, P.Morcombe, R.Pantazis, P.O'Shea, R.Sachtschale, Y.Wu
Duke University, Free Electron Laser Laboratory
Box 90319 Durham, NC 27708-0319

Abstract

Since the last Particle Accelerator Conference, the Experimental Physics and Industrial Control System (EPICS) has been utilized for control system development and implementation on several accelerators that have recently been commissioned at the Free Electron Laser Laboratory which is operated under the auspices of the Physics Department at Duke University. The historic Mark III infrared free electron laser formerly located at Stanford University, a recently designed and constructed 280 MeV electron linear accelerator and a 1 GeV storage ring synchrotron are now operating under EPICS control. Commissioning of the new injection linac and the storage ring has gone extremely well.

The authors feel that through the employment of a standard controls development environment such as EPICS, considerable amounts of resources, both financial and human, have been saved. The authors note generally positive experiences with EPICS. The highlights of these experiences, as well as some suggestions for future improvements will be presented in the body of this report.

I. INTRODUCTION

In early 1992, EPICS was selected as the primary controls development environment for the injection linac and storage ring synchrotron projects at Duke. EPICS was decided upon due to various factors such as cost, availability, architecture, and funding structure: EPICS was provided at no cost to Duke by the AOT-8 Group at Los Alamos. The AOT-8 Group graciously pledged to help get EPICS established at Duke. EPICS' architecture conformed to what has been called the Standard Model of Control Systems [1]. Furthermore, the U.S. Army Space and Strategic Defense Command supported both the development of EPICS at Los Alamos and the development of the electron beam controls at Duke. By June 1992, the Ground Test Accelerator Control System (GTACS), the predecessor of EPICS, was being employed at Duke for control system development.

II. ARCHITECTURE

Although, the essential architecture of GTACS and EPICS has been discussed in many other papers [2], a brief description is probably necessary for those who may be unfamiliar with these systems. From the hardware standpoint, the systems are based around an Input/Output Controller (IOC). Although other options are available, the IOC's employed at Duke are of the most

common type; VME crates with Motorola MVME-167 CISC based single board microprocessors running Windriver's Vx-Works real-time kernel. User interfaces are displayed at Duke using Sun SPARCstations, although ports to other UNIX operated workstations are used at other laboratories. High level communication employs TCP/IP over Ethernet. Thus far, we have not separated the control machines from the Laboratory's business and scientific network. EPICS provides the means to interface to a variety of other I/O buses at the IOC layer. We have chosen to employ VME, CAMAC, GPIB and Allen-Bradley Industrial I/O as the locally supported I/O bus types, but many other buses are in use at other laboratories.

From a software standpoint, EPICS can be divided into various functional subsystems. These subsystems include; a distributed database, a display manager, an alarm handler, a data archiver, a sequencer, and channel access. The distributed database provides local control at the IOC level for data acquisition, data conversion, alarm handling, interlocking and control. A database configuration tool is used to configure the IOC. New device drivers and scan tasks can be added fairly easily to the distributed database to extend the supported hardware, I/O buses, and functionality in a modular form called a 'record type'. A subroutine record type can be used to implement complicated new devices or algorithms. Higher level control functionality can be established by interfacing various applications such as TCL/TK running on workstations with the channel access 'software bus' of EPICS.

During the months that followed the initial establishment of GTACS at Duke, several representative tasks were selected for controls development. These systems included controls for; the facility's de-ionized water system, the storage ring vacuum system, and the storage ring dipole magnet system. Initially, these systems were controlled and data was acquired using a mix of VME and Allen-Bradley Industrial I/O hardware. Eventually, these GTACS based applications were transferred to EPICS control. During the Summer of 1993, several new drivers were written for various CAMAC function modules that were already on-hand and plentiful. Our initial CAMAC interface was done with the CES Model CBD 8210 Parallel Branch Driver. Early benchmarking of throughput using the Motorola MVME-167A with the CES CAMAC Branch Driver revealed data rates in excess of 10kBytes per second. As it would turn out, the development of this new CAMAC support was quite fortuitous.

III. THE MARK III FEL

The Mark III FEL was originally constructed at Stanford and moved to Duke where it has been rebuilt [3]. It is a broadly tunable infrared source and is in high demand by a diverse users group. The Mark III essentially consists of an electron gun with

*This work at Duke was supported by the United States Air Force Office of Scientific Research, 10/01/93-09/29/96 Contract: F49620-93-0590, and the U.S. Army Space and Strategic Defense Command, 03/31/89-03/30/95 Contract: DASG60-89-C-0028

a thermionic cathode of lanthanum hexa-boride, a single Stanford linear accelerating section, a spectrometer, beam diagnostics, beam dump, the free electron laser assembly, and related support equipment. In the early Fall of 1993, a number of problems developed with the existing control system. We realized that we had just completed the necessary drivers for the CAMAC modules that were used in the Mark III control system and we also were testing the CES Parallel Branch Driver on a development IOC. Upon approval from management, a database translator routine was written to move much of the information from the original database into the EPICS database. Two Physics graduate students were given two days of training on EPICS. We moved our development IOC into place near the Mark III CAMAC crate and borrowed an A-2 crate controller and cable from a neighboring laboratory. Within two weeks the transfer of the Mark III to EPICS control was essentially complete. The Mark III was in full operation by the beginning of the third week. Improvements have continued to take the Mark III beyond the original operational capability. To date we have implemented 432 database records on the Mark III. It is expected that the Mark III control system will continue to grow at a steady rate during the coming years. The present records are a mix of analog input and output, and digital input and output for both data acquisition and control structures. Availability and reliability of the EPICS controls for the Mark III have proved to be truly excellent. Initially, we operated the Mark III for over a year without any EPICS related problems at all. However, immediately after the Storage Ring and Injection Linac control systems were commissioned, we experienced two IOC crashes on the Mark III in a period of several weeks. We eventually isolated the cause of these crashes; an unshielded Ethernet drop cable located in the storage ring near the injection kicker. Since replacing this cable with a shielded drop several months ago, we have experienced no further problems with the Mark III controls. Overall, the availability and reliability of the EPICS based controls on the Mark III are essentially one hundred percent.

IV. THE INJECTION LINAC

The Injection Linac [4] essentially consists of an electron gun that is very similar to the one used on the Mark III, eleven Stanford linear accelerating sections, low and high energy spectrometers, beam diagnostics and related support equipment. In the Winter of 1994 it was noted that a high level of overall similarity was present between the Mark III and the Injection Linac from the instrumentation and controls standpoint. The prior existence of the Mark III proved to greatly simplify the requirements definition task and provided a model for our application developers to build upon. From the instrumentation and controls standpoint, most of the work on the Injection Linac was begun and completed during the Summer of 1994. Eventually, 626 database records were established for the Injection Linac. These were again a mix of analog and digital inputs and outputs. The Injection Linac hardware configuration consists of one IOC and three remotely located CAMAC crates. We are using the Hytek VSD 2992 Serial Highway Driver in Bit Serial Mode for this application. We are indebted to the CEBAF Controls Group for sharing their initial development work freely with us. We feel that this is an example of one of the great advantages of

collaborative controls development.

As we began to commission the Injection Linac, the control system went through a period of rapid evolution. For a period of perhaps two months, changes were made to the configuration practically everyday. One problem that we noticed, was that it was extremely difficult to find rather minor database entry errors that would cause the system to either slow down, or even occasionally crash. We therefore recommend that tools be developed to efficiently locate such errors for rapid correction. Overall though, these were relatively minor irritations that were perhaps magnified somewhat by the rush of commissioning.

During the past eight months, we have experienced three crashes of the Injection Linac IOC. The cause of these crashes was traced to the same unshielded drop cable that was previously discussed regarding availability and reliability of the Mark III controls. Since this unshielded drop was replaced, we have experienced no further problems with the Injection Linac controls. The availability and reliability of the EPICS based controls on the Injection Linac are essentially one hundred percent.

V. THE STORAGE RING SYNCHROTRON

Due to the high degree of complexity of the Storage Ring controls, a paper in this proceedings is devoted entirely to this topic [5]. Therefore the description of this system will be kept brief. The Duke Storage Ring is built in a racetrack configuration with long straight sections that will soon be filled with free electron lasers and other sources [6]. The storage ring is energized with a radio frequency cavity of Russian design that utilizes a commercial radio frequency transmitter. The cavity tuners, transmitter, vacuum system, dc current transducer, beam position diagnostics, dipole, quadrupole, and trim power supply systems, photomultiplier tubes, de-ionized water system, and other support systems are now under EPICS control. To date roughly 1500 database records have been established. Higher level physics type control structures are implemented with TCL/TK. The Storage Ring employs two IOC's, four CAMAC crates, and four Allen-Bradley crates. The Storage Ring system employs a CAMAC Byte Serial Highway using the Hytek VSD 2992 modules.

During the past eight months, we have experienced perhaps two crashes of the Storage Ring IOC's. As with the other machines, these crashes were traced to the same unshielded communications drop mentioned earlier in this report. Again, since the drop cable was replaced, availability and reliability have been essentially one hundred percent.

VI. CONCLUSION

The authors feel that the utilization of EPICS at the Duke FEL Laboratory has saved much time and money. How much has been saved is very difficult to quantify due to a number of complicating factors such as the scope of the Instrumentation and Control Group's responsibilities which is quite broad at Duke, the effect of pre-existing equipment on estimates, differences in scale and requirements from one laboratory to another, and various other uncertainties.

From a functional standpoint we feel that we have implemented an advanced capability that would probably not have

been possible had we designed and constructed our own system from scratch given the modest financial and human resources associated with this project.

We wish to emphasize various areas that we feel should be addressed by the International EPICS Collaboration in the future:

- Improved Documentation
- Tools to Efficiently Locate Database Errors
- Reduce Implementation Costs
 - Reduce VxWorks License Cost for EPICS Users (Some reductions have already been realized)
 - Realize PC Based Implementation Capability (Perhaps with Linux)
- Establish a Purpose Funded Version Control and Support Group

VII. ACKNOWLEDGEMENTS

The authors wish to direct recognition to the contributions made by the following individuals and groups: Susan Alberts, Doris Albright, Dr. Genny Barnett, Dr. Steve Bensen (CEBAF), Rob Cataldo, Gerald Detweiler, Mark Emamian, Joe Faircloth, Denise Gamble, Hank Goehring, James Gustavsson, Nelson Hower, Marty Johnson, Len Kennard, Dr. Chad McKee, Humberto Mercado, Jim Meyer, Owen Oakeley, Janet Patterson, Dr. Harold Rose, Dr. Karl David Straub MD, Gary Swift, Dr. Eric Swarnes, Rick Taylor, Ping Wang, Jim Widgren, and our Director, Professor John Madey. We would like to thank the AOT-8 Group at Los Alamos National Laboratory and especially Bob Dalesio and Mike Thuot. We would like to thank the Controls Group at Argonne National Laboratory's Advanced Photon Source, and especially Marty Kraimer, John Winans, and Gregory Nawrocki. We would like to thank the Controls Group at CEBAF, especially Chip Watson. We would like to thank the Budker Institute of Nuclear Physics, especially Grigori Kurkin. We would like to thank Fermilab, especially Brian Chase, Joe Brown, John Sachtschale and Robert Trendler. Finally we would like to thank the entire International EPICS Collaboration for providing much so support, encouragement, and of course the source.

References

- [1] Control System Architecture: The Standard and Non-Standard Models - M.E. Thuot, L.R. Dalesio, The Proceedings of the 1993 Particle Accelerator Conference, Washington, D.C., USA
- [2] EPICS Architecture - L.R. Dalesio, M.R. Kraimer, and A.J. Kozubal, The Proceedings of the 1991 International Conference on Accelerator and Large Experimental Physics Control System, KEK Tsukuba, Japan
- [3] A Review of the Stanford Mark III FEL Program - S.V. Bensen, et al., Nuclear Instruments and Methods A296, 110 (1991)
- [4] Accelerator Archeology - The Resurrection of the Stanford MKIII Electron Linac at Duke - P.G. O'Shea, C. Dickey, R. Sachtschale, G. Swift, P. Wang, J.M.J. Madey, This Proceedings, Dallas, TX, USA
- [5] The Duke Storage Ring Control System - Y. Wu, B. Burnham, This Proceedings, Dallas, TX, USA
- [6] The Duke Free-Electron Laser Facility - P.G. O'Shea, V.N. Litvinenko, J.M.J. Madey, K.D. Straub, This Proceedings, Dallas, TX, USA

THE INTEGRATION OF TWO CONTROL SYSTEMS*

M. Bickley, K. White, Continuous Electron Beam Accelerator Facility, Newport News, VA 23606 USA

During the past year the Continuous Electron Beam Accelerator Facility (CEBAF) has installed a new machine control system, based on the Experimental Physics and Industrial Control System (EPICS). The migration from CEBAF's old control system, Thaumaturgic Automated Control Logic (TACL), had to be done concurrently with commissioning of the CEBAF accelerator. The smooth transition to EPICS was made possible by the similarity of the control systems' topological design and network communication protocol. Both systems have operator display computer nodes which are decoupled from the data acquisition and control nodes. The communication between display and control nodes of both control systems is based on making named requests for data, with data being passed on change of value. Due to TACL's use of a central communications process, it was possible to integrate both control systems' network communications in that process. This in turn meant that CEBAF did not require changes to any other software in order to support network communication between TACL and EPICS. CEBAF implemented the machine's control under EPICS in an evolutionary, controlled manner.

I. TACL NETWORK

TACL adheres to the "classic" control system model, with distributed front-end computers performing data acquisition and control, and dedicated console computers for operator displays. The front-end computers are Hewlett-Packard UNIX workstations communicating with CAMAC crates through a GPIB port on each workstation. Client processes execute on HP workstations, typically displaying machine data in a graphical format. Communication between the front-end computers and client processes utilizes a "Star" process, which mediates communications between all front-end computers and clients of the control data originating on the front-ends, Figure 1 [1]. Communication between the Star and other processes is based on named data. Availability of data on the front-end computers is made known to the Star by name, and when client processes wish to obtain data values they make that request by name. A data request sets up a logical stream for the data. On first request the data value is sent, and subsequently only changes in data value are passed to the requester. The data stream remains in place until either the client dies or terminates the stream.

II. EPICS NETWORK

The Experimental Physics and Industrial Control System (EPICS) also follows the "classic" control system model. In

*Supported by U.S. DOE Contract DE-AC05-84-ER40150

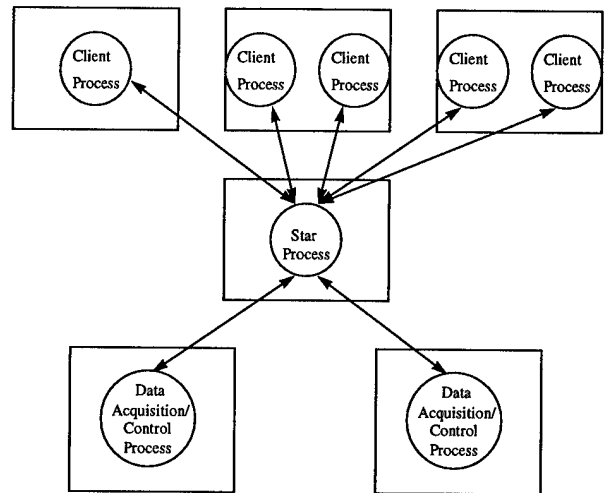


Figure 1: Communication Links in TACL

EPICS, distributed single-board computers serve as front ends, acquiring data and executing control algorithms. EPICS uses independent workstations that function as operator displays. The single-board computers are typically M68040-based, and execute the operating system VxWorks. Client processes can execute on a wide variety of platforms, from Sun and HP machines running UNIX to VMS-based VAX computers and even machines running WindowsNT.

There is no mediation between client processes and front-end computers in EPICS, Figure 2. A client broadcasts a data request by data name, and the front-end computer which is the source for that data responds. As with TACL, each data request is a logical stream, and data is passed on change.

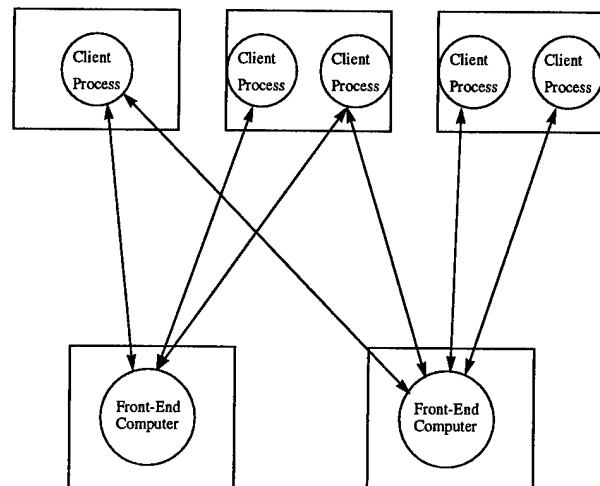


Figure 2: Communication Links in EPICS

III. INTEGRATION TECHNIQUE

In TACL, the Star is a point source for failure of the control system. While the existence of such a failure mode is generally indicative of a poor system design, it made the integration of the two control systems quite manageable. The Star served as the focal point for all inter-control system communications, and made accelerator operations feasible while CEBAF used a hybrid of both control systems.

The migration was evolutionary, so that operators could continue to use the TACL display tools with which they were familiar, even though some of the data they viewed originated on a different control system. From the point of view of the Star process, all of EPICS was treated as a single TACL front-end computer, figure 3. This meant that small pieces of the control system could be moved to EPICS independently, without altering client processes in the TACL part of the system. If a TACL client process made a request for a channel which came from a TACL front end, the TACL system worked as before. If the channel came from EPICS, the Star established a logical data stream with the appropriate EPICS front-end computer. When data updates were provided to the Star from EPICS, the data was forwarded to the client process. The source of the data, either TACL or EPICS, was transparent to the client.

There was no development effort to support EPICS clients obtaining values of data directly from TACL. This decision was based on the philosophy that the hybrid system was purely a stopgap while CEBAF developed expertise in using EPICS, and completed development of the control system applications. There was a management decision that the significant effort required to provide this functionality was not worth the limited benefit, since operators would always be able to operate on the EPICS portion of the control system using EPICS displays.

In TACL, the Star is made known of the names of existing data on front-end computers dynamically, when the comput-

ers establish communication with the Star. It was not possible to duplicate this functionality with EPICS. Instead a disk file was used to define which channels were available from EPICS. This was a limitation, because the addition of new data channels to the EPICS side meant that changes to the channel definition file were also required. This procedure was automated to simplify the burden on software developers. A side benefit of this technique, however, was that it enabled the development of name aliases for EPICS fields. Without the aliasing, additional EPICS records would have been required to map CEBAF's flat naming convention onto the EPICS 2-dimensional namespace (`<record>.<field>`).

Pushing Data into EPICS

CEBAF needed a mechanism to support EPICS control applications which obtained information from TACL front-ends. An example of this is the viewer system, which has components sprinkled around the entire accelerator. Viewers give machine operators immediate feedback regarding the characteristics of the beam at the viewer insertion point. However, in order to prevent their destruction, viewers can only be inserted when the electron gun is in a current-limited state. The current-limited control was implemented in TACL (as was the rest of the gun control software), but the control algorithm to manage individual viewers could be in EPICS, depending on the viewers' locations. In order to insert a viewer, the individual control had to obtain from TACL an authorization that the gun was in fact current-limited.

It would have been very difficult to make the Star process act like an EPICS front-end computer. While this solution would have made the two control systems completely transparent to each other, the time required to implement this was on the order of 1 man year. Instead, a different approach was used. In effect, the Star process was told to push particular TACL data values into the EPICS control system, creating a virtual client process which was the entire EPICS control system. Once the data was in EPICS it could be distributed to oth-

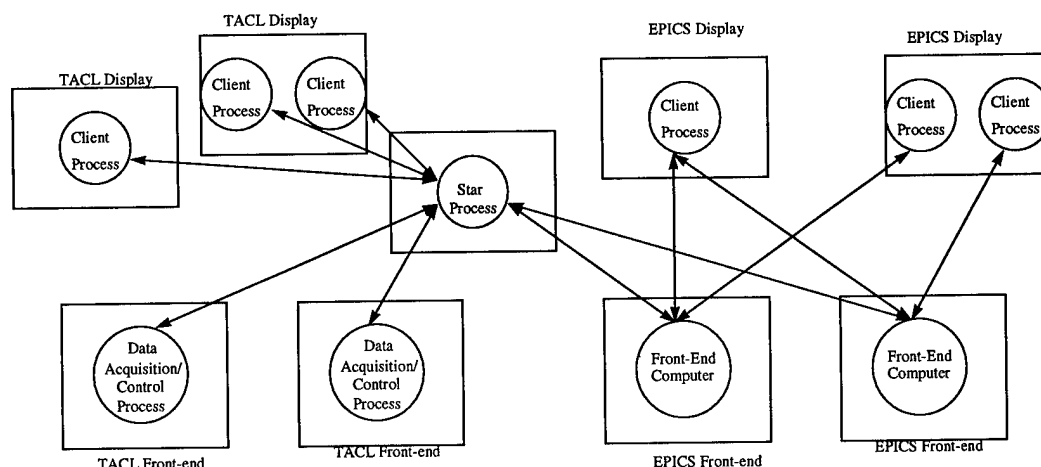


Figure 3: A Combined TACL and EPICS Control System

er EPICS front-end computers using standard tools available with that control system.

IV. MIGRATION PROCESS

CEBAF began the process of migrating the control system from TACL to EPICS by converting the existing low level applications running on HP workstations to run on EPICS IOCs. The conversion was planned as a phased implementation with the Star allowing TACL and EPICS to peacefully co-exist.

In the first phase, the low level controls for the RF application were converted. The TACL local computer devoted to control of two full cryomodules in the injector was replaced with an EPICS IOC, and the TACL logic was replaced by an EPICS database. The GPIB crate controller used for TACL were replaced with an L2 crate controller attached to a Serial Highway. The EPICS data was passed through the STAR to allow the TACL user interface to remain in place during testing. Once this proof of principle project was shown to work, the RF control database was replicated for the other 40 RF zones throughout the accelerator and was used for commissioning. The TACL screens were then replaced with EPICS screens.

As soon as the RF control of two cryomodules was functioning in EPICS, work was begun on the conversion of control algorithms for CEBAF's magnets and other diagnostic hardware. For most hardware the effort was devoted to simply reproducing the functionality of the TACL control system in EPICS. The devices in this category include harps, BPMs, BLMs, FSD, viewers, vacuum and valves. CEBAF took advantage of the control system changeover, however, to extend the capability of the magnet control software and add some long-desired features. The added functionality included automatic hysteresis and concurrent runtime control of magnets in units of either BDL or current. All of the diagnostic databases were installed on operational EPICS IOCs, first in the linacs and later in the arcs.

The devices mentioned above are duplicated and installed in many locations in the accelerator. Because control of these

duplicates is identical for all copies (other than hardware addresses), it was possible to replicate in short order their control algorithms throughout the accelerator control system, as TACL local computers were replaced with new EPICS IOCs. The conversions and installations took place during CEBAF commissioning and with the exception of a few short scheduled downtimes for hardware installation, the control system was operational during the entire migration process.

After EPICS was put into use in the linacs and arcs, the CEBAF injector was converted. Changeover of this region of the accelerator involved converting control algorithms for several unique devices, so opportunities for algorithm replication were limited.

Currently, the CEBAF accelerator is running under EPICS control. The Central Helium Liquefier (CHL) remains under TACL control. A "spy" program is used to allow communication between the two systems, through the Star. Work is in progress to convert the CEBAF Cryogenic Test Facility to EPICS, which will serve as a first step to converting the CHL. Due the high reliability need for CHL and CEBAF's operating schedule, it is anticipated this conversion will not take place immediately, but will be phased in over time.

V. REFERENCES

- [1] M. Bickley and J. Kewisch. "The Star, a Dynamically Configured Dataflow Director for Realtime Control." *Conference Record of the 1993 Particle Accelerator Conference*.
- [2] S. Schaffner, et. al, "Device Control at CEBAF." These proceedings.
- [3] W. Watson, et. al., "The CEBAF Accelerator Control System: Migrating from a TACL to an EPICS Based System." *International Conference on Accelerator and Large Experimental Physics Control Systems*, Oct., 1993
- [4] K. White, et. al., "The Migration of the CEBAF Accelerator Control System from TACL to EPICS." Internal CEBAF document, May 1994

UPGRADE OF NSLS TIMING SYSTEM *

O. SINGH, S. RAMAMOORTHY, J. SHEEHAN, J. SMITH

National Synchrotron Light Source, Brookhaven National Laboratory, Upton, NY 11973

I. ABSTRACT

We report on the progress of the new NSLS timing system. There are three types of requirements for NSLS timing system: clocks, synchronization and trigger circuits. All ring revolution frequency clocks are generated using ECL and high speed TTL logic. The synchronization circuits allows to fill both storage rings with any bunch pattern. The triggers are generated by using commercially available digital delay generators. The delay unit's outputs are ultrastable, with a resolution of 5 ps, and are programmed by computer via IEEE 488 interface. The block diagrams, description of all major timing components and the present status are provided in this paper.

II. INTRODUCTION

Electrons are injected into the NSLS storage rings from a 750 Mev booster synchrotron fed by a 120 Mev linac [1]. Each injection cycle populates one bunch into the booster, which then is extracted into either storage ring. The multibunch fill is achieved by sequencing the injection/extraction cycle to all bunches, one bunch at a time.

The NSLS timing system was commissioned in 1979 [2], which did not include the control for the single bunch transfer. In 1982, this function was added as an add-on timing system (single bunch transfer system [3]) which is controlled by its own microprocessor [4]. Although, this hybrid timing system has provided single bunch transfer operation, routinely, but it has become complex and difficult to maintain. The reliability has been poor and, occasionally, the timing jitter has been high.

The new timing system is simple and integrated; and is described in the following sections. Following data are useful in understanding the timing system:

UV rf frequency = 52.8856 Mhz
X-ray rf frequency = 52.8875 Mhz
Booster harmonic number = 5
UV harmonic number = 9
X-ray harmonic number = 30.

* Work performed under the auspices of the U.S. Dept. of Energy

III. CLOCKS

The figure 1 provides the block diagram for clock generating circuits. The storage ring harmonic counters are free running and generate UV revolution clock (uvrf/9) and X-ray revolution clock (xrxf/30). The booster ring harmonic

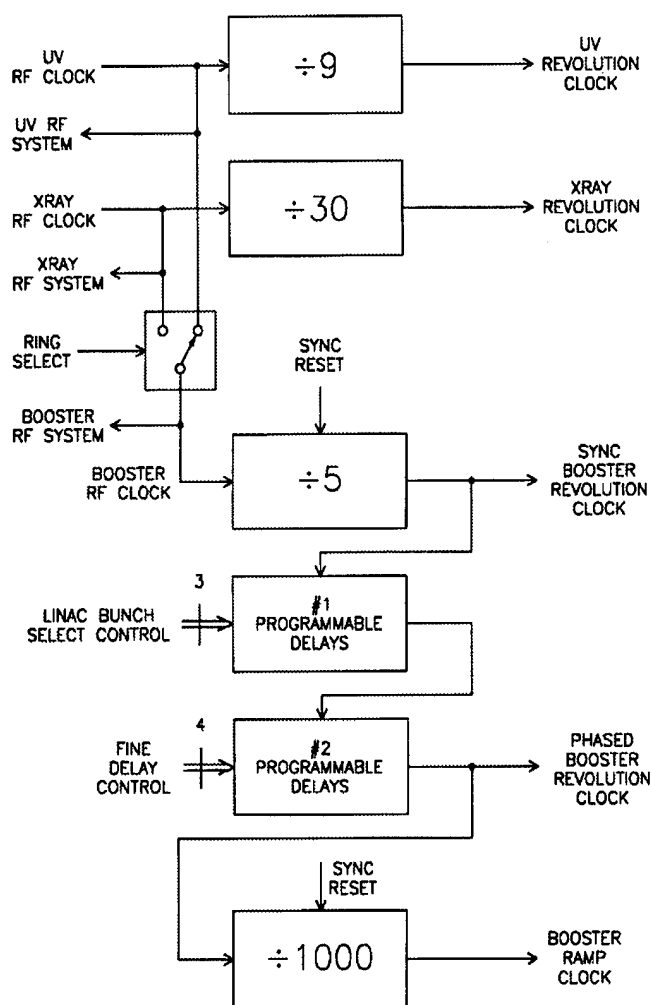


Figure 1 - Block Diagram for Clocks Circuits

counter generates booster revolution clock (brf/5) which is synchronized to the storage ring bunch marker (brf/90) by a sync reset signal. This synchronization, discussed more later, is necessary because when a new ring is selected to fill (changing the rf clock to the counter), the sync is lost.

Next, this clock ($\text{sync brf}/5$) is sent to the programmable delay (# 1) which provides 5 equally spaced delays. Each delay step is equal to the rf time period and it allows to select all five phases of $\text{brf}/5$ clock, precisely. Further, this clock is fine tuned by another programmable delay (#2). The setting resolution of this delay is ~ 1 nsec, which allows to tune the phased $\text{brf}/5$ clock to the linac.

The last counter (/1000) generates ~ 10 khz clock, which is used by booster ramping power supplies.

IV. SYNCHRONIZATION

The synchronization circuits consist of one delay unit DG535, few flip-flops and gates, as shown in figure 2. The delay section A generates injection repetition clock (Trep), with time period selectable in increment of $1/60$ sec. A 60 hz line signal triggers this delay section, while the delay is programmed to few msec less than desired repetition rate. Two additional clocks, Tphase1 and Tphase2, are generated from Trep. Tphase1 clock, delayed by ~ 20 msec from Trep, is synchronized with the storage ring bunch marker ($\text{brf}/90$), generating sync reset. Tphase2 clock, delayed by ~ 1 msec from

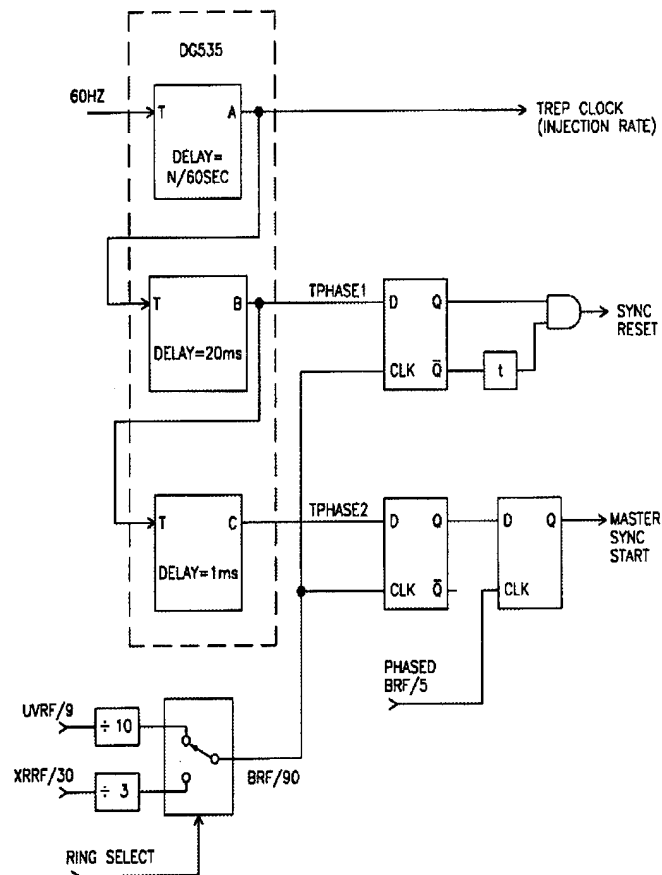


Figure 2 - Synchronization circuits

Tphase1, is synchronized with the storage ring bunch marker ($\text{brf}/90$), as well as, with the linac bunch clock (phased $\text{brf}/5$). This generates a master sync signal, which is used to trigger all other triggers as described in the "TRIGGER" section. This ensures that all trigger output are in phase with the linac bunch.

The storage ring bunch marker clock ($\text{brf}/90$), is generated as shown in the synchronization circuits.

Figure 3 shows the relative timings of above described signals and the sequence of events occur as follows: the Trep clock generates a flag for the computer, signaling, that it has next 20 msec for loading any new delay values into the injection delay units. Also, during this time, the booster bunch is selected, when computer selects one of five programmed delays in delay # 1 shown in the figure 2. Sync reset signal, generated by Tphase1 is used to reset the booster counter. The master sync signal, sequenced by Tphase2 signal, is used to trigger all delay units described in the TRIGGER section.

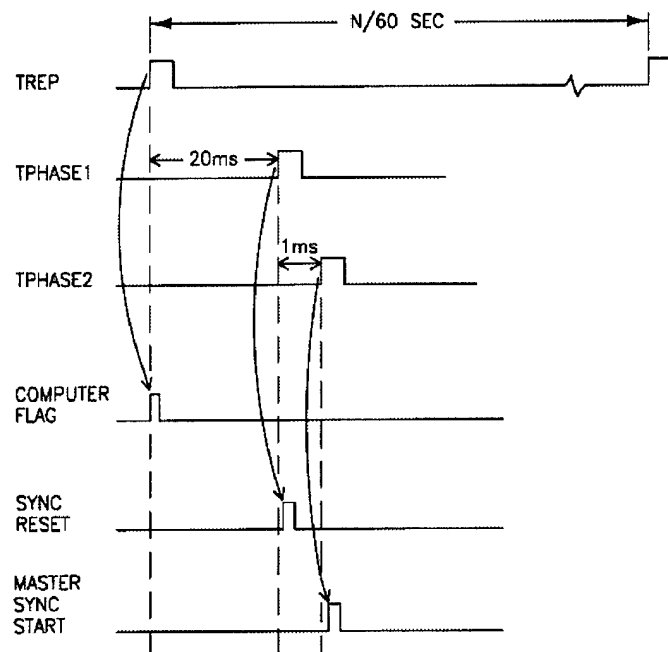


Figure 3 - Timing diagrams

V. TRIGGERS

All triggers are generated by ultrastable, low jitter programmable delay units. These delay units (DG 535 - Stanford Research Systems) are available, commercially, and the output delays can be set via IEEE 488 interface. Each delay unit is programmed to trigger from an external signal and provides upto four independent programmable outputs (A,B,C and D). The output jitter is lower than 0.5 ns and each

delay can be set with a resolution of 5 psec, if needed.

Figure 4 shows the layout of 6 delay units, which are grouped based on functions. The master sync signal, generated by sync circuits, triggers the top delay unit generating three START triggers: start of linac (TSOL), start of booster (TSOB) and start of ejection (TSOE). TSOL output triggers a group of two delay units providing signals used for linac gun, klystrons and linac to booster injection bumps/kickers. TSOB output triggers one delay unit providing signals for starting ramps for booster power supplies. TSOE output triggers another group of two delay units generating all trigger timings for ejection bumps and kickers.

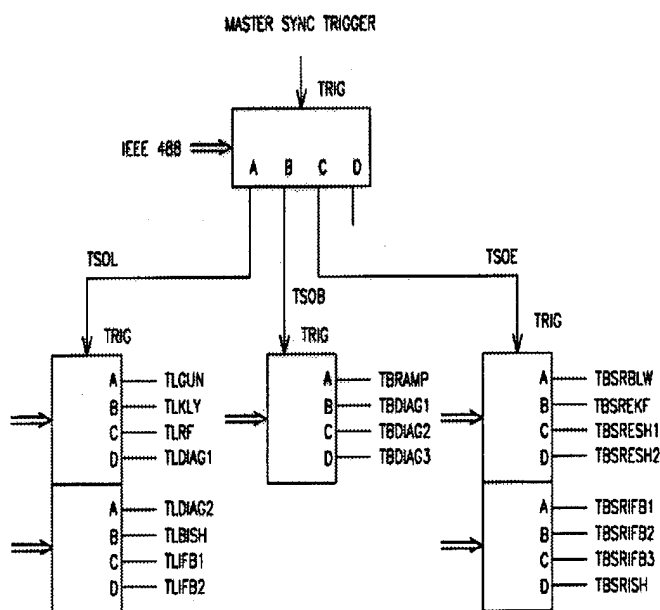


Figure 4 - Triggers block diagram

VI. STATUS

The computer interface to four delay units has been tested with an update request rate of 2 hz. The test has been successful and have demonstrated that all delays, required for injection/ejection, can be updated in less than 20 ms. The synchronization logic and clock circuits have been built and are being tested. The fast trigger distribution amplifiers are under construction, which will be used for driving triggers at their locations. The preliminary test on the complete system will start within a month and it is expected that the new system will be operational soon after that

VII. ACKNOWLEDGEMENTS

We would like to thank G. Frisbie for constructing and testing prototypes. He will also be involved in installing the complete timing system. Also, we would like to thank E. Meier for assisting in the design of the fast trigger distribution amplifier.

VIII. REFERENCES

- [1] E. Blum - NSLS Linac/ Booster normal operation, private communication
- [2] J. Sheehan - NSLS timing system - NSLS Technical note # 025 - 1979.
- [3] J. Sheehan, O. Singh, W. Rambo - Single Bunch transfer system at NSLS - Proc. of the 1983 Part. Acc. Conf.
- [4] S. Ramamoorthy, J.D. Smith, O. Singh - Multibunch controls, NSLS Technical note # 170 - 1985

ACCELERATOR TIMING AT BROOKHAVEN NATIONAL LABORATORY*

B. Oerter & C.R.Conkling Brookhaven National Laboratory, Upton, NY 11973 USA

Abstract

Accelerator timing at Brookhaven National Laboratory has evolved from multiple co-axial cables transmitting individual pulses in the original Alternating Gradient Synchrotron (AGS) design, to serial coded transmission as the AGS Booster was added. With the implementation of this technology, the Super Cycle Generator (SCG) which synchronizes the AGS, Booster, LINAC, and Tandem accelerators was introduced. This paper will describe the timing system being developed for the Relativistic Heavy Ion Collider (RHIC).

I. INTRODUCTION

A modern accelerator must synchronize the operations of equipment over a wide area. In the early days of the AGS, the timing system consisted of a group of master clocks which generated clock trains, and a few key timing pulses. The clock trains were resynchronized to the start of each main magnet cycle. Clocks were distributed to equipment locations on individual co-axial cables using 16 to 20 V transformer isolated pulses known as an AGS standard pulse. This signal level was chosen to guarantee the signal would be reliably detected in electrically noisy environments.

Delays necessary for sequencing systems were created using counters that counted down using one of the master clock trains. Timing triggers required in multiple locations were distributed from location to location using the same co-axial cable and AGS standard pulses.

The drawback of this system was the large number of cables to the many equipment locations. Another was the energy of the AGS pulse level. Low level analog and

digital circuits suffered from the ground bounce at the receiver.

II. AGS Booster

With the design of the Booster, additional requirements were imposed on the timing and control system. Pulse to Pulse Modulation (a term originally used at CERN) is an operating mode which permits changing the setup of the accelerator from cycle to cycle. To accomplish this, a Super Cycle Generator was designed to schedule the LINAC, Booster, AGS and Tandem Van de Graff. Multiple "users" are defined for each machine. Scheduling of active users is accomplished via timing signals initiated by the central timing system. Naturally, if each timing pulse was transmitted on a separate cable (there are currently 60 timing events identified for the Booster) the number of cables required to support Booster operations would be prohibitive.

The cabling issue was overcome by a system first developed at Fermilab. Pulses on individual cables were replaced with digital codes transmitted on a single serial link. This technique permits multiplexing of timing information on a single cable. The event codes are transmitted using a serial modified Manchester code (bi-phase mark). The transmission rate is 10 Mbits/sec, and 1.2 usec are required to transmit an event code. The event link transmits a continuous bi-phase-mark "ones" transmission during idle periods. A restriction of using a serial link is, since only one event can be transmitted at a time, they must be prioritized.

The Booster has used the serial timing distribution scheme since it was commissioned in 1989. Because of the rapid cycling nature of the Booster (7.5 Hz) the central timing generator for this

* Work performed under the auspices of the U.S. Department of Energy.

accelerator is table driven. Multiple tables permit rapid switching of timing setups. Each table contains an ordered list of events to be broadcast and the times at which they must be transmitted. The basic resolution of the system is 1 μ s. Software precludes contention by scheduling events at least 2 μ s apart. One limitation of the present design is that no provision currently exists to generate single occurrences of events or generate events from external (hardware generated) timing pulses.

III. RHIC Collider

The RHIC collider, currently being designed and built, requires a slightly different timing approach. The RHIC cycle is expected to be up to 10 hours long. During collision mode, timing events are more likely to be of an asynchronous nature, which is not well suited to table driven scheduling. Timing events and clocks from this link will be used to initiate hardware operations including changes in settings, state changes, and data acquisitions. Events may also be required by software running on systems not directly coupled to accelerator hardware. A standard clock frequency of 10 MHz, as is presently used in the AGS and Booster, provides adequate resolution for timing events in the RHIC acceleration and collision processes.

Event sequences to initiate waveforms and acquire data during the acceleration cycle, tune measurements, etc., will be implemented by cascading programmable delays. Clocks that are of a general interest, such as the line locked 720 Hz clock, generated by the main magnet power supply system, will also be available on the RHIC event link. Externally generated events may also come from other systems sensing unusual conditions with the beam. In the case of a beam abort, the abort event can be utilized to freeze circular buffers in data acquisition systems for post-mortem analysis.

An example of a software generated event would be one to synchronously activate new settings after they have been

loaded and verified. Software generated events may also provide a convenient way to commission new systems.

The probability exists that event requests could occur overlapped in time. Since only one event can be processed at a time, priority resolution will be an integral part of the central encoding facility. Event contention is handled in hardware with highest priority given to input 0 and lowest given to input 255. It should be pointed out, however, that lower priority events being processed will not be interrupted by the arrival of a higher priority event request.

The RHIC central event encoder its input modules, and supporting host computer interface occupy a single 21 slot VME chassis.

The event system interconnections are point-to-point, differential TTL, isolated at the receiving end by transformer coupling.

Interbuilding transmission to remote RHIC equipment locations is via single mode fiber optic transmitters and receivers.

At each RHIC equipment location, the optical transmission is converted back to electrical and buffered as differential TTL. A fanout/repeater is used to produce multiple outputs. General purpose decoder/delay modules may be located in these remote locations, as well as other specially designed modules having direct event link inputs (e.g., the waveform generator).

RHIC event codes can be permanently assigned without regard to their event link transmission priority level. This allows an event code trigger priority level to be adjusted relative to other event codes without changing the event code.

EVENT ENCODER MODULE

The event encoder module provides event code translation, computes the parity and encodes the event into a bi phase mark serial data stream for transmission on the RHIC timeline. As the code is serialized, a "zero" start bit is added, and code parity (even) is generated. The

output of the bi-phase-mark converter is transmitted over the RHIC event link.

The encoder module is connected to a 16-position event input module bus. At the end of the event code transmission, the encoder allows the event input module priority system time to determine the next event trigger (if any) to be transmitted by the encoder module, and maintain minimum headway. The event trigger with the lowest numeric value has the highest priority. The event encoder module converts event trigger inputs into RHIC event codes in a translation table. The translation table can be read and written via the VME interface.

INPUT MODULES

Each event input module accepts up to 16 event trigger inputs, and determines their relative priority. If other event input modules have been triggered, the event input module must have position priority (closest to the encoder module) in order to place its event trigger code on the bus. Sixteen input modules are required to support 256 events.

Event triggers can originate from software initiated commands to an input modules CSR or hardware generated pulses.

There is a 1.3 μ s event code transmission delay built into system. This assures that very high priority events will be transmitted with minimum time jitter. It is possible for a low priority trigger to be delayed by higher priority triggers. In this case there may be several transmission increments (1.2 usec/increment) from the trigger until the event is transmitted on the RHIC event link.

V102 DECODER/DELAY MODULE

The RHIC V102 module is a general purpose decoder/delay module that can be used to provide timing to systems and equipment not having a direct connection to the RHIC event link. The form factor is a 4hp X 6U VME module. The V102 includes a direct connection to the event link and has a VME interface for setting

up and configuring each delay channel. Each module contains eight output channels with flexible triggering and delay options. Delay clocks can be either internal or external.

V102 Module Functions

The V102 derives a 10 MHz clock from the RHIC event link carrier. Internal clocks are divided down from the 10 MHz clock. The divider chain may be synchronized to a user specified event code.

Each of the delay channels can be triggered from event link event(s) or, the preceding event channel (an external trigger coupled by an external cable in the case of channel 1), or an external trigger input.

A separate delay is provided for each channel. The delay is developed in a 32-bit counter, programmed to count down. The minimum delay is 1 count. The channel delay clock may be selected from the 10 MHz or 1 MHz internal clock or the external clock input. If an external clock is used, the maximum frequency is 5 MHz.

The output pulse width is controlled by a 16 bit counter, programmed to count down. The minimum pulse width is one delay clock period. The clock rate selected for the delay function is used for the pulse width counter.

Event channel outputs are available on the front panel and rear VMEbus P2 user pins. All triggers, event link event, VMEbus, or external are synchronized to the selected clock (external or internal) before the delay count down begins. Each decoder/delay module is completely self supporting, once initialized.

Acknowledgement

A special thanks to R. Ducar and the Fermilab controls staff for their help in understanding the TCLK timing system.

THE RHIC GENERAL PURPOSE MULTIPLEXED ANALOG TO DIGITAL CONVERTER SYSTEM*

R. Michnoff, Brookhaven National Laboratory, Upton, NY 11973 USA

ABSTRACT

A general purpose multiplexed analog to digital converter system is currently under development to support acquisition of analog signals for the Relativistic Heavy Ion Collider (RHIC) at Brookhaven National Laboratory. The system consists of a custom intelligent VME based controller module (V113) and a 14-bit 64 channel multiplexed A/D converter module (V114). The design features two independent scan groups, where one scan group is capable of acquiring 64 channels at 60 Hz, concurrently with the second scan group acquiring data at an aggregate rate of up to 80 k samples/second. An interface to the RHIC serially encoded event line is used to synchronize acquisition. Data is stored in a circular static RAM buffer on the controller module, then transferred to a commercial VMEbus CPU board and higher level workstations for plotting, report generation, analysis and storage.

I. DATA ACQUISITION REQUIREMENTS FOR ACCELERATORS

The most unique requirement for a data acquisition system for accelerators is that sampling of data must be synchronized to accelerator system timing. At the workstation level, data acquired from multiple locations, must be time correlated for plotting and analysis. Another critical requirement for the RHIC system is to provide a historical data buffer, where all data is stored in a continuous circular buffer at a relatively slow acquisition rate (typically 60 Hz) until a critical event such as a beam abort occurs. Selected historical data may then be viewed for analysis, and to determine conditions that caused the critical event. While data is being stored in the historical data buffer, the system must be capable of concurrently scanning a few selected channels at a much faster sampling rate for a snapshot period of time.

II. BACKGROUND

Based on the above requirements and after researching commercially available hardware, it was determined that a custom hardware solution was necessary. Various design options and system architectures were considered, and the finalized design is discussed herein.

III. SYSTEM ARCHITECTURE

A block diagram of the overall system architecture is shown in figure 1, and the front panel layout for each module is shown in figure 2.

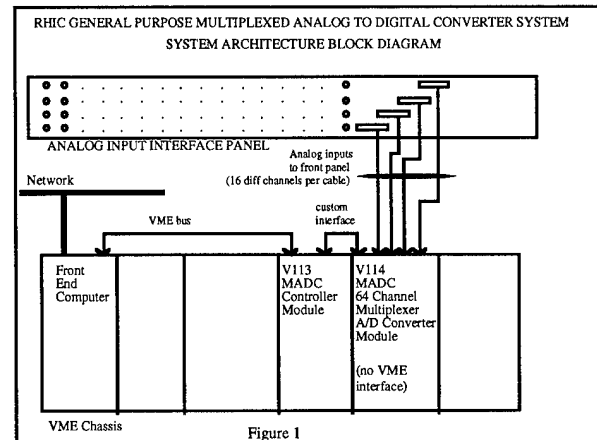


Figure 1

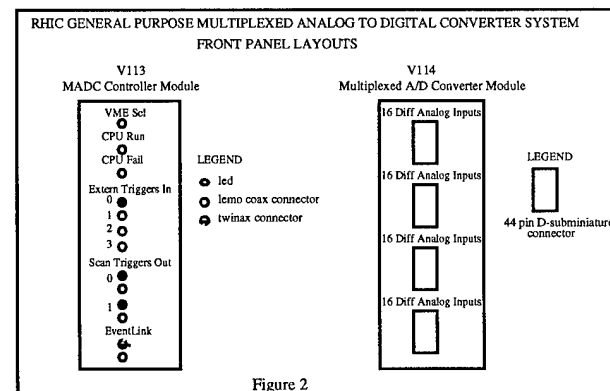


Figure 2

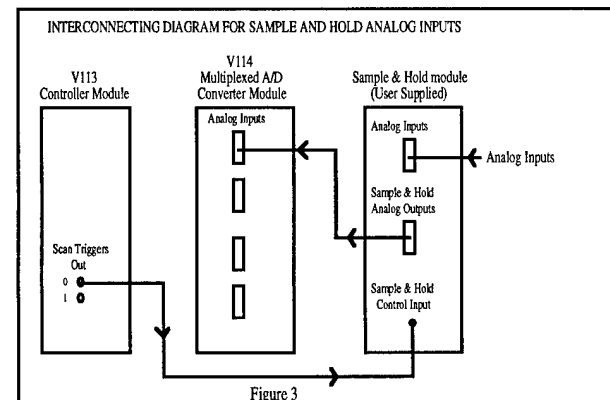
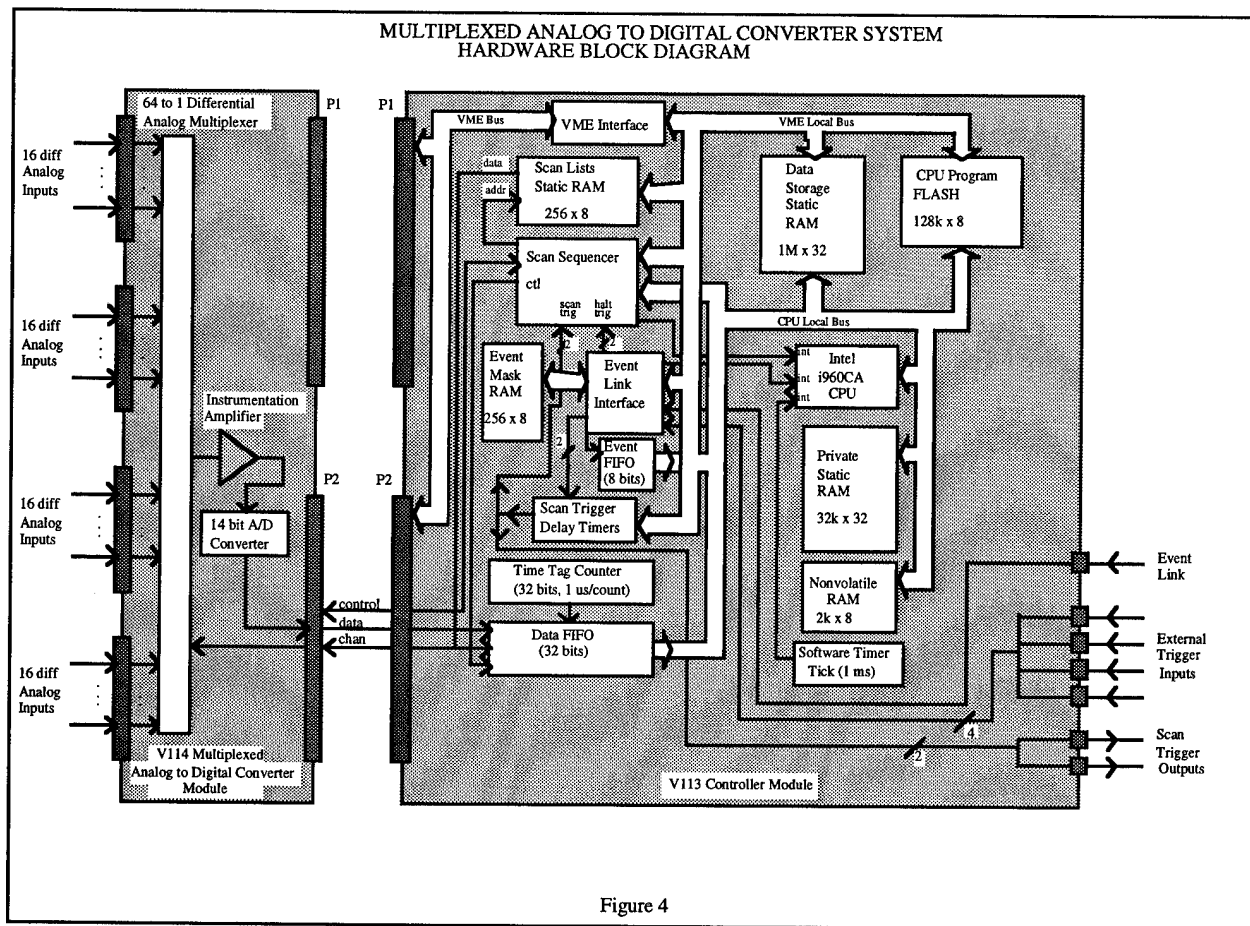


Figure 3

* Work performed under the auspices of the U.S. Dept. of Energy.



The RHIC multiplexed analog to digital converter system also provides the capability to be interfaced with a user supplied sample and hold module. The sample and hold analog outputs connect to the analog input connector on the V114 module. The sample and hold control is generated by the scan trigger output on the V113 module, as shown in figure 3.

A hardware block diagram for the V113 and V114 modules is provided in figure 4. The V113 controller module contains the VME bus interface, RHIC event link interface, data storage memory and all of the data acquisition system real-time intelligence. The V114 converter module contains the analog multiplexers, instrumentation amplifier, A/D converter, and a custom interface to the controller module through user defined pins on the VME bus P2 connector.

IV. SYSTEM FEATURES

A summary of the system's capabilities is detailed below.

A. Scan Groups

Two identical scan groups are provided. Each scan group is configured with the following information.

- a. Scan list containing all the channels to be scanned.
- b. Arm trigger setup.
- c. Halt trigger setup.
- d. Scan trigger setup.

Typically scan group 0 will contain all defined analog inputs, and will be configured to continuously scan at a rate of 60 Hz for use as a history buffer. Data acquisition will be configured to halt on a specified system event for postmortem analysis of beam aborts. The front end computer reads this buffer to obtain the most recent data for each analog input.

Scan group 1 will normally be used to acquire data according to application specific channel selection and timing requirements.

The following parameters are programmable for each scan group.

Arm/halt trigger source

One source is used for both the arm and halt trigger. This is configurable to be one of the following.

- a. Single event or logical OR of group of system events.
- b. External trigger.

Scan trigger source

The scan trigger source is configurable to be one of the following.

- a. Single event or logical OR of group of system events
- b. External trigger.

Arm trigger setup

The arm trigger is defined as the condition that causes data samples to begin being stored in the data buffer. After the arm trigger occurs, data samples will be acquired and stored on every scan trigger until the halt trigger occurs. The arm trigger is configurable to be one of the following.

- a. Arm immediately on start command from front end computer
- b. Arm on arm/halt trigger source
- c. Arm on ms delay after arm/halt trigger source

Scan trigger setup

The scan trigger is defined as the condition that causes a single acquisition of all channels in the scan group. Scan triggering will occur only when scanning is armed as defined by the arm trigger. The scan trigger is configurable to be one of the following.

- a. Scan on every period of programmable on-board clock (μ s resolution)
- b. Scan on scan trigger source.
- c. Scan on n th scan trigger source
- d. Scan on programmable delay after scan trigger source (μ s resolution)

Halt trigger setup

The halt trigger is defined as the occurrence of a condition that causes data acquisition to halt. After the halt trigger occurs, data acquisition will stop and an interrupt will be sent to the front end computer. The halt trigger is configurable to be one of the following.

- a. Scan continuously until front end computer commands stop
- b. Halt when data buffer full
- c. Halt on arm/halt trigger source
- d. Halt on ms delay after arm/halt trigger source
- e. Halt on number of scans after arm/halt trigger source

Reset at end of scan

Each scan group may be configured to reset the arm/halt trigger and the scan enable at the end of each complete scan.

B. On-board Data Buffer Memory

Data buffer memory is typically divided into two buffers, one for the scan group 0 and one for the scan group 1. The data buffer size is programmable in number of full scans. A full scan consists of one reading for each channel in the scan group. Data will be stored in a circular fashion, where the oldest data is overwritten as new data is acquired.

The V113 module may be populated with 1, 2, 3, or 4 Mbytes of data storage memory. The entire data storage memory is mapped to VME A32 space on a switch selectable 4 Mbyte boundary (A31..A22). VME data transfers supported include D32, D16, D08(E0), and BLT (block mode transfer).

Event mask RAM (256 bytes), scan list RAM (256 bytes), program FLASH (128 Kbytes), and configuration registers are mapped to VME A24 space on a switch selectable 256 Kbyte boundary (A23..A18). VME data transfers supported for this area are D08(E0) only.

C. Maximum Scan Rates

Maximum scan rates supported are as follows:

64 chans at 60 Hz for one scan group simultaneously with an aggregate rate of 80 KHz for the second scan group (1chan at 80 KHz, 2 chans at 40 KHz, etc).

Maximum continuous throughput from the V113 controller module to the front end computer, then to the higher level workstation is dependent on the network bandwidth. The goal is to provide a continuous update of 6 channels at 720 Hz to the requesting workstation. This translates to a network bandwidth requirement of:

$$720 \text{ scans/sec} * 6 \text{ samples/scan} * 2 \text{ bytes/sample} \\ = 8640 \text{ bytes/sec}$$

Faster acquisition will be provided with a snapshot mode, where the data acquisition is halted while the front end computer passes data to the higher level workstation.

V. ACKNOWLEDGEMENTS

Thank you to K. Seino, M. Shea, A. Franck, J. Gomilar, and J. Smedinghoff of Fermi National Accelerator Laboratory for describing the architecture, functionality and operational capabilities of the existing and future analog input systems at Fermi Lab during a trip in July 1993. Similar concepts were applied to the design of the BNL RHIC Multiplexed Analog to Digital Converter System.

THE DATACON MASTER - RENOVATION OF A DATACON FIELD BUS COMMUNICATIONS SYSTEM FOR ACCELERATOR CONTROL*

T. M. Kerner, R. Warkentien, AGS Department, Brookhaven National Laboratory
Upton, NY 11973-5000 USA

Abstract

The Datacon Master (V110) is a custom-designed VMEbus SBC event driven serial communications engine featuring a superscaler RISC 32-bit Intel i960 CPU. The V110 and a commercial VMEbus host CPU running vxWorks with an Ethernet LAN connecting UNIX workstation consoles, make up the real time control system. Five V110 and three host CPUs will replace and upgrade PDP10 and PDP8 Datacon AGS front end computers. Five V110s will support twenty Datacon field busses with some 2600 devices. The V110 firmware is written in C. An accelerator event time link interface and μ S timestamp are built-in. Each Datacon field bus supports up to 256 devices on a multidrop RG62A/U coaxial cable with up to 2000 feet between repeaters. Each V110 drives up to four full Datacon field busses at 1 MHz bandwidth.

I. INTRODUCTION

The Datacon system is a serial coaxial transformer isolated communication field bus system used to control and monitor accelerator remote devices. The Datacon field bus has been a BNL accelerator standard since its initial use in 1965.

A. Why Renovate?

The forcing factor to renovate was the inability to repair the aging PDP-8E and PDP10 computers. The maintenance on this aging system was costly and the large number of accelerator devices dependent on the Datacon system could not be converted in a reasonable period of time to a new modern field bus.

B. Upgrading to a Real Time Object Oriented Solution

The changeover to a new system had to be done quickly and cleanly. With as many as 2600 existing accelerator devices to control and monitor, a compatible and well-defined solution was required which could literally plug into the existing Datacon field bus coaxial cables. The limited time available during maintenance cycles was all that was available to change over to and qualify a new system. A well vetted and low risk system architecture [1] and strategy had to be developed. As a control system was being designed for the Relativistic Heavy Ion Collider (RHIC), the decision to merge this real-time object-oriented architecture with the Datacon field bus was reached.

C. The Solution

A commercial VMEbus host CPU mated with a custom designed VMEbus SBC event driven serial communications engine featuring a superscaler RISC 32-bit Intel i960 CPU met the design challenge. The commercial VMEbus host runs the vxWorks [2] real-time operating system and connects to UNIX workstations over a Ethernet [3] LAN. The V110

Datacon Master is the custom designed front end computer that integrates an accelerator event link system [4] with accelerator devices for up to 8 users adding new capabilities. The V110, with multiple user capability, increased bandwidth, shorter latency and overhead, would outpace the original system in functionality and performance by at least an order of magnitude. Great improvements came from a robust set of supported network protocols allowing even engineering PCs to be used to develop and test complex control system components. As communications improved and performance issues were no longer the limiting factor driving accelerator devices, a jump in controls effectiveness and efficiency could be realized.

II. SYSTEM COMPONENT DESCRIPTION

The Datacon Master System is divided into five functional parts.

A. The Commercial VMEbus Front End Computer

A Motorola MVME 162-222 was selected for use in the Datacon Master System for compatibility with the large quantities of this SBC previously selected for the new RHIC control system. The MVME162-222 with the vxWorks real-time operating system provided an adequate platform for the FEC functionality required to support Datacon Master functionality as well as being well positioned to make best use of resident programming skills.

B. The V110 Datacon Master Serial Communications Engine

The V110 is a single board VMEbus compatible custom designed communications engine. The V110 includes an accelerator event link decoder, a μ S time stamp counter, 4 parallel ports for 4 individual Datacon field busses, a full featured VMEbus interface which includes block transfer capability, 2 Mbytes of fast static RAM, a 33 MHz 32-bit Intel i960 RISC superscaler μ P, five large custom designed Altera programmable logic devices and 32-bit fast burst access PROM.

C. The P110 P2 Buffer Board

The P2 Buffer Board connects the VMEbus back plane to a ribbon cable assembly via buffers to allow high speed signals to travel over ribbon cable assemblies to the T110 Datacon Master Transition Module.

D. The T110 Datacon Master Transition Module

The T110 Datacon Master Transition Module contains 4 large Altera programmable logic devices that provide the serialization from a 32-bit wide multiplexed high speed data bus to the relatively slow 1 MHz serial data stream. The Altera devices send and receive TTL level serial differential data to the Datacon Driver.

*Work Performed under the auspices of the U.S. Department of Energy.

E. The DD110 Datacon Driver

The DD110 Datacon Driver converts the differential serial TTL level data found on the T110 DCM Transition Module into the ± 15 Volt levels transmitted and received on the Datacon field bus coaxial cables. The DD110 is located in its own rack mountable enclosure with its own power supply to isolate Datacon electrical noise from the rest of the Datacon Master system.

III. SYSTEM OPERATIONAL REQUIREMENTS

The renovated system must be compatible with all accelerator devices that predated it. There are approximately 28 device types. A recent survey found 2616 active addresses. Some of the 28 device types are power supply controls, stepping motor positioning systems, collimator jaw positioners, beam profile monitors, scalers, autodets, analog signal acquisition, video multiplexing, function generators, and chipmunk radiation monitors. A comprehensive plan to port over drivers and integrate the new real-time operating system was devised. Creation of a test platform with real Datacon devices and loop back testing would answer most of the compatibility issues facing the cut-over to the new system. Persistence of software objects would have to be added to the new system for power dips or outages. Integration with the new accelerator event link would require some development and coordination in both hardware and software. The firmware for the V110 Datacon Master would have to be developed jointly between the hardware designers and the software group. A specification for the host front end computer to the V110 Datacon Master had to be developed which was flexible and broad enough to accommodate both single user machines such as RHIC and multiple user machines such as the LINAC, the BOOSTER, and the AGS. The Datacon Master was designed to allow modular additions to the existing Datacon field bus controls. Up to 8 V110 Datacon masters accommodating 32 Datacon field lines could be accommodated in a single VME chassis. Power savings over the original main frame PDP10 and PDP8 computers with two 20-ton and one 5-ton air conditioning units would not be insignificant.

A. Integration Testing

A series of stress tests were created to run the new Datacon Master system at full bandwidth in conjunction with a test set that looped back transmissions for testing the error rate and qualifying both hardware and software. Tests were devised which were event link controlled as well as load and go immediately. The insertion and extraction of devices from chains of linked lists was tested using the host and Datacon Master firmware. Thousands of operations could be tested with the loop back features while looking for data failures or scheduling failures or overlaps. The event link code table acts as an event code filter and is maintained by the Datacon Master μ P. Codes designated as active are downloaded from the host front end computer. Any and all codes may be used as an event code, fiducial, or user change. The interpretation of the codes is completely under tabular program control. Connection to the real event link line demonstrated the proper dispatching of chained commands. Active event link codes are stored in a FIFO such that any code arrival rate can be handled properly. A Workstation was used to dispatch and display the reply messages with μ S arrival time stamps and

any DNA (Did Not Answer) status for unconnected devices after a preset μ S time-out period. Time-out periods were preset and observed on a line by line basis. On board non-volatile RAM may be used to safeguard against power interruption. The Datacon Master re-initializes within 1 second of power restoration.

B. Throughput or Performance

No significant degradation in system performance will be permitted with 4 lines simultaneously operating at the highest permissible bandwidth supported by the Datacon Line Specification [5]. All overhead for processing and time sharing with the VMEbus must be included in the serial shift out time of the Datacon transmission. Latency time from an event occurrence to the beginning of a Datacon transmission shall not exceed 25 μ S with 4 lines operating at maximum bandwidth. The Datacon Master was designed to modularly replace the Transition Module with a fiber optic driver such that upgrading to fiber can be accomplished with minimal impact on system design.

The time-out may be individually tuned to each line to provide the fastest possible turnaround time in the presence of a missing device. The time-out period is a function of line length, number of repeaters used, and device requirements.

The main memory consists of 2 Mbytes of high speed static RAM. This is enough RAM to support several users with long chained sequences of command and response messages. The memory is dual ported between the μ P and the VMEbus. Bus arbitration logic grants the μ P access to the SRAM on a priority basis before the VMEbus, which still allows enough time to complete all VMEbus cycles during idle μ P bus times. VMEbus block transfer capability to SRAM provides adequate VMEbus bandwidth when multiple Datacon Masters are inserted in a VME chassis. Eight general purpose registers are dual ported to the μ P and to the VMEbus for passing semaphores and status. Global and module switch registers are used to interrupt the local processor from the VMEbus.

IV. SYSTEM ARCHITECTURE

A. EPROM

The 64 Kbytes of EPROM are arranged 32-bits wide by 16 K deep. The EPROM is a burst access variety that makes use of the pipelined burst access mode of the i960. This is a high throughput memory region programmed with zero wait states for 132 Mbyte per second transfer rates, the highest performance available in a commercial μ P at the time of the Datacon Master design.

B. Superscaler RISC Processor

The Intel A80960CA-33 is a 33 MHz μ P with superscaler technology that enables the μ P to execute up to three instructions per clock cycle. The μ P has a two-way set associative 1 Kbyte 32-bit wide zero wait state internal instruction cache, a 32-bit wide 1 Kbyte zero wait state internal data RAM, 5-15 set register cache, and a high speed vector cached interrupt controller. The bus control unit allows the main external static RAM region to be configured as big endian for compatibility with dual porting to the VMEbus, while keeping μ P specific externals such as EPROM and its firmware little endian for compatibility with Intel compilers and software development tools.

C. 2 Mbytes SRAM

The 2 Mbytes of SRAM is configured as 32-bit wide by 500 K deep. It is in a pipelined burst memory region with one wait state. The SRAM is dual ported with bus arbitration to the VMEbus and is configured as big endian for compatibility with 68000 addressing.

D. Accelerator Event Link Decoder Filter

The event link decoder filter is set up as 8 pages in static RAM to accommodate 8 possible users. The memory table may be updated by the local μ P and then page swapped on the arrival of an event link fiducial code that signifies a user change.

E. Priority Interrupt Control Logic

To efficiently prioritize incoming Datacon line data available, parity error and time-outs for the 4 Datacon lines serviced plus VMEbus requests and VMEbus register interrupts, VMEbus error, and event link interrupts, custom interrupt control logic was designed to allow maximum throughput with minimum latency.

F. Event Link FIFO

Accelerator events may arrive back to back or 1.2 μ S apart. To handle this possibility, an event link FIFO temporarily stores each event until the μ P can service the interrupts that nominally take a few μ S.

G. NVRAM

NVRAM is available for storing volatile data to handle power dips. The Datacon Master finishes initialization after a power dip in about 1 second. This avoids the long host computer boot up time lag.

H. I/O Functions, Watchdog, Time Stamp

A watchdog monitors the voltage on the Datacon Master power planes. If the voltage should dip to 4.5 volts the watchdog reinitializes the local μ P, which then reinitializes the on board logic and VMEbus interface. This ensures an orderly power on reset as well as power dip reset. An early AC fail condition interrupts the μ P at the highest priority and saves volatile data. The watchdog is pinged by the local μ P as part of normal firmware operation. Should the μ P halt or hang, the watchdog would reset the μ P and reinitialize the board.

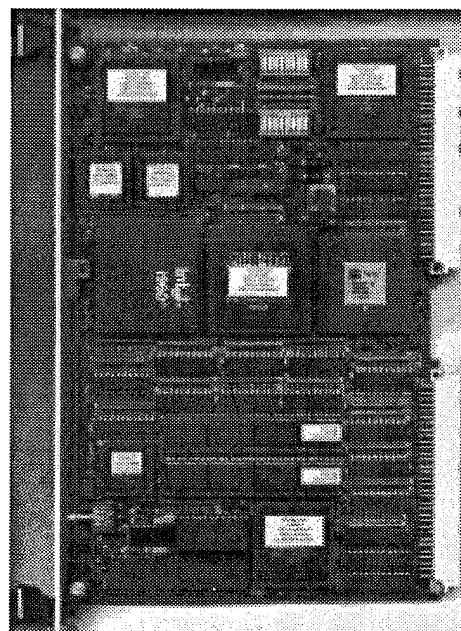
I. Timer Counters

Four timer counters are used to control the time-outs for each Datacon line. The 1 μ S clock on the timer counters provides delays up to 512 μ S programmed in 2 μ S increments. These counters ensure minimal turnaround time should a field device be disconnected or fail.

V. FIRMWARE

The Datacon Master protocol defines four types of information blocks: Input Request Blocks, Message Descriptor Blocks, Source Message Blocks, and Reply Message Blocks. IRBs are created by an off board host and are used to append or delete SMBs via a linked list of pointers in the MDB. IRBs contain a PPM user, accelerator event code,

Datacon line number, and MDB pointer. The MDB chains together SMB and RMBs that are executed on the same accelerator event. MDBs contain a forward and backward linking pointer, a SMB element count, a RMB repeat index, a SMB pointer and RMB pointer(s). SMBs and RMBs are therefore dynamically linked which gives rise to an efficient method for making modifications with little overhead. This technique allows multiple buffering, and complex triggering sequences to be created. MDB may be efficiently cut and pasted using the linked list of pointers. RMBs contain a start time stamp, end time stamp, reply message, and status code. The off board host is responsible for memory management and is required to secure exclusive use of sufficient memory space for each of the SMBs and RMBs that the host creates. For space reasons this protocol description has been oversimplified.



V110 Datacon Master

VI. ACKNOWLEDGMENTS

The authors are indebted to J. Skelly for driver software development and his ideas and contributions toward the design specification, and to T. Clifford and B. Oerter for their helpful discussions on system implementation. Special thanks to N. Schumberg for his contributions to the DD110 and T110 designs and R. Warkentien for firmware development.

VII. REFERENCES

- [1] L.T. Hoff, J.F. Skelly, "Accelerator Devices as Persistent Software Objects," BNL-48757, ICALEPCS, Berlin, Germany, October 18-22, 1993.
- [2] vxWorks is a registered trademark of Wind River Systems.
- [3] Ethernet is a registered trademark of Xerox Corp.
- [4] B.R. Oerter, C. R. Conkling Jr., "Accelerator Timing at Brookhaven National Laboratory," these proceedings.
- [5] "Specification for Datacon Signal Standards," Brookhaven National Laboratory, Upton, NY. 11973 SPEC. AGS-734, September 2, 1975.

UPGRADE OF THE CONTROLS FOR THE BROOKHAVEN LINAC*

W.E. Buxton

AGS Department, Brookhaven National Laboratory
Upton, New York 11973-5000 USA

Abstract

The control of the magnets, rf system, and other components at the Brookhaven Linac uses a system that was developed at Brookhaven in the late 1960's. This system will be retired in the summer of 1995.

The Linac controls are being upgraded using modern VME-based hardware compatible with RHIC generation controls, and an existing serial field bus. The timing for the Linac will also be upgraded and will use components developed for RHIC. The controls in general, the timing for the Linac, and the modules developed will be described.

I. INTRODUCTION

The control for most of the Brookhaven 200 MeV Linac is a system developed at Brookhaven over 25 years ago. This system derives reference voltages from motor-driven potentiometers which can be set via computers. This system is robust but is inflexible in that seconds are required to reconfigure the Linac control parameters. Also, the computers to control the potentiometers and acquire readbacks are obsolete and no longer supported [1]. Because of this, the PDP10 and PDP8 computers used to control the Linac are scheduled to be retired this summer. It was decided that since a new generation of VME based distributed controls for RHIC are being developed, the Linac controls should also be VME based to take advantage, as much as possible, of the RHIC development work.

II. LINAC CONTROL SYSTEM

The new controls for the Linac consist of RHIC style VME control chassis located in the Linac control room with local control and readback devices distributed along the Linac at the rf stations. The VME chassis is in turn connected to the accelerator control network (Ethernet). Workstations on the network provide the user interface. The VME controls are centralized and the distributed local controls for the more than 400 Linac devices are interfaced to the VME controller via a field bus called Datacon. Datacon is a bit serial bi-phase communication system developed at BNL in the 1970s. Although an old system, Datacon is extremely robust and noise immune. Datacon is a multidrop, transformer isolated serial bus that can operate over 2000 ft. of coaxial cable. It uses a simple protocol that is easily implemented in gate

arrays and is, therefore, relatively inexpensive. Because of its simplicity, the need for embedded microprocessors in remote Datacon devices is eliminated. This makes Datacon ideal for use in electrically hostile environments.

At the heart of the Datacon field bus system is the VME Datacon master [2]. This device was developed using field programmable gate Array (FPGA) and risk processor technology. The Datacon master supports multiple Datacon channels, each capable of addressing the full Datacon address space. The Datacon master has an on board direct interface to the accelerator serial timing link and local memory so that all Datacon transactions can be preloaded into tables, executed on selected timing events, and data returned and stored without intervention by the VME processor. This has resulted in a many fold increase in data throughput compared to older Datacon implementations.

As mentioned above, Datacon is a simple, inexpensive, and noise immune protocol. Due primarily to operation of high power rf devices, the electrical environment at the control points along the Linac is noisy. Because of this the decision was made to use the Datacon field bus and custom modules there and centralize the computing and storage functions in a quieter environment. Therefore, the VME chassis is located in the Linac control room. Residing in the chassis is a Datacon master module that communicates to fifteen remote Datacon chassis on four field busses. The Datacon chassis are installed at the quadrupole/rf stations and at other areas in which power supplies and other Linac devices have to be controlled. The Datacon chassis contain modules that control the state of, provides voltage references for, and returns digitized analog signals and statuses from the various Linac devices.

At each quadrupole/rf station there will be one or, in some cases, two Datacon chassis containing dual channel Datacon power supply control modules. Each Datacon field bus will service a number of quadrupole/rf stations such that all readbacks can be returned and all new setpoints updated within 100 ms. Thus, the Linac control parameters can be reconfigured between Linac beam pulses allowing full pulse-to-pulse modulation (PPM) of the Linac.

Each Datacon control chassis has several quadrupole magnet power supplies whose state is controlled in common. For example, the 30 tank 1 quadrupole magnet power supplies are turned on or off by a single Datacon command sequence. Each RF station has a separate command sequence to control the state of the high voltage power supply and a separate command sequence to turn the rf pulsing on or off. State

* Work performed under the auspices of the U.S. Department of Energy.

control of the quadrupole power supplies and the rf control is done on a non-PPM basis.

Returned with the various analog readbacks is the status of the state of the quadrupoles and the rf systems and the state of various interlocks and system faults. Distributed along the Linac are nine sector vacuum valves. Each Datacon chassis located at the quadrupole/rf stations will have a Datacon power supply control module dedicated to providing a command line and a status line for the valve control and status. The valve statuses and the valve state commands will also be non-PPM devices. There are also vacuum gauges that are distributed along the Linac. Each gauge has an analog output that represents the vacuum read by that gauge. A Datacon power supply control module will provide control and status for the sector valves and will read the vacuum gauges on a non PPM basis. Finally, two Datacon chassis will be located at the Linac vacuum-ion pump panel to control and monitor the vacuum pumps and vacuum pump power supplies. These will also be non-PPM devices.

The Datacon control chassis located at each of the Linac quadrupole/rf stations are commercially manufactured chassis that are similar to standard commercial VME chassis. The Datacon card cage uses the standard P1 and P2 connector configuration in the 21 available card slots as the VME chassis. Although not a VME implementation, it uses the P1 VME bus structure to control the Datacon power supply control modules in the chassis via a Datacon crate controller module. The chassis has a 6u x 220 mm card cage in the front for the control modules and crate controller and a 6u x 100 mm card cage in the rear for transition modules. P2 of the 220 mm card cage and P2 of the 100 mm card cage are connected via ribbon cables supplied and installed by the chassis manufacturer. Transition modules are used to adapt the Datacon power supply control module's generic outputs to the particular needs of the Linac control. Therefore, there is no hand wiring or configuration of the chassis needed. The modules plug in and the chassis is ready for service. Each of the control chassis has the following complement of modules.

1. Datacon crate controller - The Datacon crate controller accepts the Datacon bi-phase encoded serial transmission and decodes several data fields that are used by Datacon modules in general and the power supply control module in particular. For example, the power supply control module uses the following standard Datacon fields. The magnitude field that represents the required analog setpoint. The command field that represents the required state of the device controlled or the state of the Datacon power supply control module's analog I/O. Finally the address field to select the correct Datacon power supply control module to respond to the Datacon transmission. These fields along with a clock are sent to the control modules in the chassis via the VME bus structure. When a Datacon power supply control module in the chassis recognizes its address and finishes its task it then sends a reply back to the crate controller where it is encoded and returned to the source. The reply consists of (for the Linac) a digitized voltage readback and several status bits.

Older asynchronous implementations of the Datacon crate controller required that several one-shots be adjusted to establish proper pulse widths, clock trains, and delays. This required periodic adjustments as the module aged. The redesigned crate controller incorporates synchronous FPGA technology and requires no adjustments.

2. Datacon Power Supply Control module - A general purpose power supply control module was designed for digital control, digital status readbacks, analog output, and analog input. The Datacon power supply control module was also designed using FPGA technology. The module has two channels per module with each channel having the following features.

- a. Eight status inputs.
 - b. Four command lines. Each command line can be active low, active high, pulsed high, or pulsed low. The commands are encoded in the Datacon command field as described above.
 - c. An analog input that can be configured to be either - +/- 10 V or 0-10 V. The input is differential. The A/D converter can be triggered either by a Datacon transmission or by external timing pulses. Each channel is independently triggered.
 - d. An analog output that can be configured to be either +/- 10v or 0-10v. The output is single ended. The analog output powers up at 0 volts and remains at 0 volts until a Datacon command packet is sent to that channel. The power up condition is reported in the Datacon status field. The output of the D/A can be looped back to the A/D or a 1/2 scale reference can be read into the A/D via a command encoded into the Datacon command field.
3. Timing input module. This is a simple module that interfaces the read time trigger pulses which are AGS standard pulses (20 volts at 1 μ s) and converts them to TTL level. The read pulses are then fanned out to the power supply control modules via P1b bus lines to trigger the A/D conversion. Eventually this module will be replaced by a timeline interface module in which events to trigger the A/D conversion will be directly decoded from the Fiber Optic Linac timeline. This module will be capable of placing events on any of the eight P1b bus lines that are reserved for timing signals. The Power supply control module can then be set up to select one of eight possible sources to trigger the A/D conversion. The timeline interface module will also route the selected timing pulses on the front panel connectors for use as triggers or inputs to Linac devices.

III. LINAC TIMING

As in all modern accelerators, equipment operation at the Linac must be synchronized. In the past this synchronization was accomplished by individual timing pulses on coaxial cables distributed throughout the Linac. Adding signals to this system was difficult since new cable distributions were

required for each signal added. The next generation Linac timing system was designed and installed during the Booster Project and is based on the AGS and Booster timing systems. A fiber optic serial link is used, which has encoded timing events and clocks that are generated and transmitted on the cable from a central location. Timing events are then decoded at the place they are needed, converted to electrical pulses, and fanned out as required. Changes and additions to the timeline are not as difficult as in the original system but require programmable logic device changes to add and change events encoded onto the timeline.

The new Linac timing system will be an encoded timeline as before but will use the RHIC generation VME timing system modules [3,4]. The V100 event encoder module will be used to encode and transmit event codes on the Linac timeline. The V100 is interfaced via a bus structure to V101 event input modules that each input 16 event triggers and determines their relative priority. Event triggers can originate from two sources, either external triggers or the event input can have a trigger written to it via the VME processor. The timing system will also use the V104, V102 decoder/delay modules. These modules connect directly to the timeline and provide decoded pulses from events or can provide delayed outputs from an event. The events to decode and the delay from these events are fully programmable through the VME processor. These signals can then be used to trigger other devices such as scopes or can be conditioned by external circuitry and the results put onto the timeline via a V101 event input module channel.

Using the RHIC timing system modules, a Linac timeline can be built without hard wiring or hard coding. The timeline can be changed by command from computers on the accelerator control network and/or by cable changes between modules at the generator. The timeline generator will be located in the Linac control room and the encoded timeline will be distributed along the linac via fiber optic cables. .

[3] RHIC Event Timeline System, C.R. Conkling Jr. and B.R. Oerter BNL AD/RHIC/RD-61.

[4] Accelerator Timing At Brookhaven National Laboratory, B.R. Oerter and C.R. Conkling Jr., these proceedings.

IV. ACKNOWLEDGMENTS

The Author wishes to thank the following Brookhaven people for their support and assistance in the development and construction of the new Linac controls: J.G. Alessi, B. Briscoe, J. Czachor, W. Jappe, V. LoDestro, J. Skelly, B. Venegas.

V. REFERENCES

[1] Upgrade of the AGS H linac, J.G. Alessi, W. Buxton, A. Kponou, V. LoDestro, M. Mapes, A.J. McNerney, D. Raparia, Proc. of 17th International Linac Conf., Tsukuba, Japan, August 1994 (in press).

[2] The Datacon Master - Renovation of a Datacon Field Bus Communications System for Accelerator Control, T. Kerner, these proceedings.

Commissioning Software Tools at the Advanced Photon Source*

L. Emery

Argonne National Laboratory
9700 So. Cass Ave., Argonne, IL 60439

Abstract

A software tool-oriented approach has been adopted in the commissioning of the Advanced Photon Source (APS) at Argonne National Laboratory, particularly in the commissioning of the Positron Accumulator Ring (PAR). The general philosophy is to decompose a complicated procedure involving measurement, data processing, and control into a series of simpler steps, each accomplished by a generic toolkit program. The implementation is greatly facilitated by adopting the SDDS [1] (self-describing data set) protocol, which comes with its own toolkit. The combined toolkit has made accelerator physics measurements easier. For instance, the measurement of the optical functions of the PAR and the beamlines connected to it have been largely automated. Complicated measurements are feasible with a combination of tools running independently.

I. INTRODUCTION

There generally occur two types of control room activities during commissioning of an accelerator. One is letting the beam "go" as far as it can, and tweaking all manner of possibly relevant "knobs" to improve performance. The other is carefully measuring the beam properties, optical functions, etc. in order to deduce sources of limitations, or simply to verify that the accelerator performance is within specification. Since beam studies time is highly valued, an efficient and flexible system of software tools for collecting, processing, and displaying of data was developed at APS. These tools have been in use since the beginning of the commissioning of the APS PAR, and have greatly aided accelerator physics personnel in the control room.

This paper briefly introduces the toolkit concept, then gives an overview of the accelerator physics tools written so far. Specific examples of applications of beam control and measurements are presented afterwards.

II. SDDS TOOLKIT

A toolkit is a set of generic and cooperative programs whose actions may be combined to produce a more complicated action. The motivation of implementing a toolkit is to eliminate the repetition of graphics and data processing programming work among computer codes. At APS, M. Borland had already developed the SDDS toolkit [1] for postprocessing and plotting output from many accelerator physics codes. This toolkit requires the use of the SDDS self-describing file protocol [1] for data files. Data files are organized in "pages" consisting primarily of tables of data. The most useful feature of the protocol is attributing names, units, and descriptions to the data by way of a file header. Thus columns in the data tables can be operated upon by listing their names as part of an option of a tool command line. For instance, suppose that an SDDS data file, `aps.twi`, contains the Twiss parameters of the APS ring

with columns `s`, `betax`, and `betay` defined at every element. Then the data can be plotted with the `sddsplot` tool: `sddsplot -col=s, (betax,betay) aps.twi`. Data from any SDDS data file can be plotted in a similar way. A consistent data file protocol is the common thread that makes it possible for the members of the toolkit to work together. Thus, to take advantage of the SDDS toolkit, our control system tools read and output SDDS protocol compliant data files.

If one didn't use a toolkit approach, one would typically end up with data and graphics postprocessors that work only for the output of one physics code. Examples of these situations are too numerous to list.

The SDDS toolkit will not be explained in detail in this paper, as the toolkit is too extensive to fit. However, some of the SDDS tools will be mentioned later.

III. EPICS TOOLKIT

The control system at APS is the Experimental Physics and Industrial Control System (EPICS) [2]. In EPICS, a database record is known as a process variable (PV), a term we'll generalize to mean any accelerator data obtained from EPICS.

Below is a list of EPICS tools in frequent use in beam studies:

- **burtb, burtwb, burtmath** (Back-Up and Restore Tool): Save and restore accelerator configurations, respectively, in SDDS files.
- **sddsmonitor, sddsvmonitor, sddswmonitor**: Log PV data at regular intervals. Optionally, the conditions for a glitch or an oscilloscope-style trigger on a PV can be specified for the logging of data in a time window around those events. These tools are extremely useful for correlating data and diagnosing problems.
- **sddsexperiment, sddsvexperiment**: Vary PVs, and measure PVs with averaging. These tools require an input file of `namelist`-type commands describing the PVs to vary and measure. The results are written to a file which can, for example, be plotted directly using the `sddsplot` SDDS tool or be processed by one of the SDDS least-squares-fit tools.
- **sddscontrollaw**: Analogous to the term in control theory, this program uses a matrix and a list of PV readbacks (outputs) as a vector to calculate new setpoints of PVs (actuators). Suppose that R_i is a vector made from the list of readbacks at time index i , M is the correction matrix, and S_i is the vector of setpoints at time index i , then **sddscontrollaw** computes the new setpoints with $S_{i+1} = S_i - MR_i$. (The minus sign is present to indicate a correction.) The procedure can be repeated at a specified time interval.
- **squishPV**: Tweaks a list of PVs (e.g. correctors) to minimize the sum of another list of PV values (e.g. BPM readbacks). An SDDS input file provides the lists of PVs. The program tweaks one PV at a time, and leaves the tweaked PV at the value that gives the smallest sum for the readback PVs' absolute values. The procedure is naturally slower than **sddscontrollaw**'s which utilizes a correction matrix. However, the **squishPV** method is more robust in that it

*Work supported by U.S. Department of Energy, Office of Basic Energy Sciences under Contract No. W-31-109-ENG-38.

works in the presence of gross readback offsets and errors, and in ignorance of response matrices.

These tools are very general. They don't even presume that an *accelerator* is being controlled. Scripts of command-line tools written to work for one accelerator at APS have been easily adapted to work with another.

The SDDS and EPICS toolkits are accessed through the command line and do not use graphical user interfaces (GUIs), and for good reason. In our experience, the alternate use of mouse operations and keyboard input, the hallmark of GUI, is an impediment rather than an advantage to accomplishing any serious work. In addition, sequences of command lines can be put into a script, which isn't possible with GUIs.

The usefulness of these tools emerges when a few applications are given in the next section.

IV. APPLICATIONS

A. Optical Function Measurements

In commissioning a beamline or storage ring, one verifies that the optics matches the model by making beam response measurements, that is, measuring the response of BPM readings as a function of steering magnet settings.

In the PAR, such measurements have been used to improve the optical model [3]. In the storage ring, a first turn trajectory beam response measurement has so far been used to identify grossly problematic quadrupole magnet supplies.

The beam response measurement starts with **sdds-experiment** with BPM readbacks as the measured PVs and a corrector power supply current setpoint as a variable PV. The slopes of the **sddsexperiment** output data—obtained with the tool **sddsslopes**—give the beam response.

The PAR measurement will be demonstrated as an example. The command which runs **sddsexperiment** for the PAR corrector P1H1 is "**sddsexperiment P1H1.exp**" where the command input file P1H1.exp is shown below.

```
&measurement    control_name = "P1P1:x",
                  column_name="P1P1:x", units=mm
                  number_to_average = 5,
&end
&measurement    control_name = "P1P2:x",
                  column_name="P1P2:x", units=mm
                  number_to_average = 5,
&end
... (repeat the above for the rest of BPMs)
! do first corrector in PAR
&variable control_name = "P1H1:CurrentA0",
           column_name="P1H1", units="A",
           relative_to_original=1,
           index_number = 0, index_limit = 5,
           initial_value = -2.0, final_value = 2.0,
&end
&execute
           outputfile = "P1H1.sdds"
           post_change_pause=3
           intermeasurement_pause=0.5
&end
```

The measurement command requires the fields *control_name* and *column_name*. The *control_name* field gives the name of the PV (i.e. P1P1:x) that is read. The name of the *column_name* field will be given to the measurement data in the

output file. Having the flexibility of naming data columns is useful when a PV name is not very descriptive. The other fields are self-explanatory. The variable command shown here has four additional fields. They instruct the program to vary the PV P1H1:CurrentA0 from -2 A relative to the original value to +2 A relative to the original value in five equal steps. The **execute** command specifies the SDDS output file and the pause time in seconds between measurements and variable changes. The output file contains column definitions for all measured or varied PVs and additional columns for the standard deviations, if requested in the measurement definitions. The data file consists of one data page with one row of data for each variable step.

The beam response to one corrector is obtained with a command as simple as: "**sddsslopes P1H1.sdds P1H1.slopes -independentVariable=P1H1**".

As an aside, **sddsexperiment** allows the variation of more than one variable at a time. Variables can be varied on a multi-dimensional grid by assigning increasing integer values for *index_number*, starting with 0, for each independent variable. This feature has been used in making a longitudinal phase space scan of the injection efficiency into the PAR.

Another feature of **sddsexperiment** is the shell execution of scripts in between measurements or changes to a PV. In general, these scripts prepare some accelerator system for measurement or change. This allows the design of a relatively complex experiment. For example, a script can be used to capture and process beam images for beam size measurements.

B. Generalized Feedback Control

A generalized feedback control was required to compensate the drift in the energy of the linac beam feeding into the PAR. For many months of running, the linac beam energy drift exceeded or was equal to the energy aperture of the PAR ($\pm 1\%$). As a result, the injection efficiency into the PAR varied with time, and this made beam studies difficult. Since the energy drift was SLED cavity temperature related and therefore slow, the compensation was done with the program **sddscontrollaw** running on a workstation.

The first step of the general procedure is to identify the readback PVs and the control PVs related to the control problem. Then a linear response matrix of the readback PVs as a function of control PVs is measured, as described in the last section. The correction matrix required by **sddscontrollaw** is the inverse of this response matrix, and is computed by **sddspseudoinverse**, a generalized matrix inverter using the SVD method. The program **sddscontrollaw** is then applied with the correction matrix.

These steps are applied to the linac energy control. There are four BPMs in the beamline (LTP) transporting the linac beam to the PAR. Three of these are in non-zero dispersion locations (there is one bending magnet in the LTP following the first BPM). With all these BPMs, one can determine both the energy offset and the trajectory error, and correct for both. In controlling the linac beam energy there are many direct "knobs" available, such as pulse forming network voltage and rf drive. However, they have a slow response because they are motor driven. They are non-linear as well. Therefore we selected the SLED phase reversal timing variable for one of the linac sectors because this variable is roughly linear within its useful range, and its effect is prompt. In choosing the correctors for trajectory correction, we eliminate those that mimic the energy knob, such

as the LTP bending magnet, and any horizontal corrector close to it.

The following UNIX shell script was used to produce the correction matrix for the horizontal plane in the LTP:

```
#!/bin/csh
set correctorlist = \
  (LTP:H1 LTP:H2 LTP:H4 L5:SledTiming)
foreach corrector ($correctorlist)
  sddsexperiment $corrector.exp
  slopes $corrector.sdds $corrector.slopes \
    -independentVariable=$corrector \
    -excludeColumns=Time,$corrector
end
sddscombine *.slopes LTP.R12.trans -merge
sddsconvert LTP.R12.trans \
  -rename=col,IndependentVariable=CorrectorNames
sddstranspose LTP.R12.trans LTP.R12
sddsconvert LTP.R12 -rename=col,RowLabels=BPMNames
# calculate inverse
sddspseudoinverse LTP.R12 LTP.InvR12 \
  -minimumSingularValue=0.01
sddsconvert LTP.InvR12 \
  -rename=col,RowLabels=CorrectorNames
exit
```

The response of the LTP BPMs to the correctors and the SLED phase reversal timing variable were measured with **sddsexperiment**. The files ending in .exp are user-supplied and are similar to the file P1H1.exp in the previous subsection. The data was processed by **sddsslopes** to produce files of slopes with respect to the actuator setpoints. The tool **sddscombine** combines these files to form a 4x4 matrix file. Renaming of columns (with **sddsconvert**) after some toolkit operations is necessary so that the user can keep track of the physical significance of the data. With the minimumSingularValue option in **sddspseudoinverse**, one can throw away singular values that are small relative to the largest one.

The command that executes **sddscontrollaw** is "**sddscontrollaw** LTP.InvR12 R12-feedback.out -timeInterval=6 -steps=30000 -gain=0.75 -controlQuantityDefinition=LTP:H.def -testValues=LTP:H.tests". R12-feedback.out is an SDDS file logging all PV values during the execution. The gain value is the fraction of correction to be applied at every step. The option control_quantity_definition requires a user-defined file which has cross references of column names to the actual PV names. This file is usually generated by an instruction in the **sddsexperiment** command file whence the correction matrix column names originate. To add robustness to **sddscontrollaw**, an input file describing tests for a list of PV values can be specified on the command-line to suspend **sddscontrollaw** temporarily. The file LTPH.tests contains tests of beam intensity and of rf power to the linac sections.

C. Orbit Correction

sddscontrollaw can be used for conventional orbit correction. In this case, the number of steps only needs to be a few. For PAR, the correction matrix was first derived from a measured beam response matrix rather than the model response matrix since, early in the commissioning period, we were uncertain of the tunes and of the calibration of the BPMs. By view-

ing the beam response data with **sddsplot** we were able to detect bad BPMs and correctors, which were then easily removed from the response matrix data file by referring to their names using SDDS utilities. The orbit in the PAR was corrected very quickly with hardly any beam time wasted on debugging the simple scripts and command files.

D. Other EPICS Applications

Mention should be made of other EPICS applications that have been written, not as tools, but as specialized programs to solve specific problems, such as the program controlling and correcting errors of the APS booster ramping power supplies [4]. These applications write out SDDS-protocol compliant data files, in order to take advantage of the SDDS toolkit.

V. ACKNOWLEDGEMENT

Though the EPICS tools described here have many authors, most described here were conceived or written by M. Borland. All APS commissioning team members contributed to these tools by their suggestions for improvements and options.

VI. REFERENCES

- [1] M. Borland, "A Self-Describing File Protocol for Simulation Integration and Shared Postprocessors," these proceedings.
- [2] L. R. Dalesio, M. R. Kramer, A. J. Kozubal, "EPICS Architecture," in *ICALEPS*, pp. 278-281, 1991.
- [3] M. Borland, "Commissioning of the Argonne Positron Accumulator Ring," these proceedings.
- [4] J. A. Carwardine, S. V. Milton, and D. G. McGhee, "Performance of the Ramping Power Supplies for the APS Booster Synchrotron," these proceedings.

Rapid Application Development Using the Tcl/Tk Language*

Johannes van Zeijts, CEBAF, 12000 Jefferson Avenue, Newport News, VA 23606

Abstract

During the last year high level applications at CEBAF were written using the Tcl/Tk scripting language [1]. This language is rapidly gaining in popularity, in part due to the ease of constructing programs with X11 graphical user interfaces, and in part due to the ease of adding compiled user code for specialized purposes. Extensions to the language provide object oriented programming [2], [3], which was used to develop a hierarchy of classes relevant for high level accelerator control.

We describe the basic language features, some 3rd party add-on packages, and local additions to the toolbox. Next we describe the features of the accelerator object hierarchy, and finally describe applications written using this toolbox such as the ModelServer prototype, Slow Orbit and Energy Lock, the Linac Energy Management System, and other applications.

I. Introduction

Tcl is an interpreted scripting language with only one data type: strings. The language is not intended for number crunching but rather to provide scripting control to user contributed compiled packages. Tk is one such package written by the author of Tcl. Tk provides a way to create spectacular X-11 graphic user interfaces in a minimal amount of time without any knowledge of underlying GUI library packages [4], [5]. Interface elements are simply addressed by a string name and can be placed on the screen and configured by scripts or interactively. A rich set of commands is available for event driven programming.

Locally developed code provides access to control system information, lattice simulation codes, and matrix calculations [6]. Additionally we use the 'expect' extension [7] to provide a programmed interface to existing 3rd party programs like Mathematica and Matlab, and the 'blt' extension [8] to provide line and bar graph support. Finally the Tcl-DP extension [9] was used for the network connections between server and client programs.

The goal of the object oriented approach in this context is to provide a set of classes with a well defined interface to allow non-expert users to create high level applications without having knowledge about the implementation of any of the lower level functionality. We provide two sets of class hierarchies, one for beam line elements like correctors and beam position monitors, and one for applications like orbit and energy lock, and autosteering. Additionally, the object oriented extensions provide a clean way to produce and maintain large amounts of code.

II. Accelerator Objects

Accelerator beam line elements are well described in a hierarchical way. An 'Element' class has placeholders for properties common to all beam line elements like position and lattice function information. 'Magnet' and 'Bpm' classes specialize the

Element class and add element specific information. 'Dipole', 'Corrector', and 'Quad' classes are again a specialization of the 'Magnet' class. Tables with live information about beam line elements can be generated with just a few lines of code. Here we show the beam position panel (1) and the corrector panel (2). User defined columns can be easily created and filled.

BPM		Actions		Selections	
Name	on	pos	beam status	gold	
IPM1E02	<input checked="" type="checkbox"/> x	0	-666	0.0066	}
0	<input checked="" type="checkbox"/> y	0.00	No Beam	0.0415	
IPM1A01	<input checked="" type="checkbox"/> x	0	-666	-0.2253	}
0.00	<input checked="" type="checkbox"/> v	0.00	No Beam	0.1482	

Figure 1. Beam Position Monitor Panel

Corrector		Actions		Selections	
Name	on	bdl	kmol	angle	
MBT1L03H	<input type="checkbox"/> h	0.000	<input checked="" type="checkbox"/>	0.0	}
MBT1L03V	<input checked="" type="checkbox"/> v	82.243	<input type="checkbox"/>	0.394585	
MBT1L04H	<input checked="" type="checkbox"/> h	20.836	<input type="checkbox"/>	0.0789287	}
MBT1L04V	<input type="checkbox"/> v	0.000	<input checked="" type="checkbox"/>	0.0	
MBT1L05H	<input type="checkbox"/> h	0.000	<input checked="" type="checkbox"/>	0.0	}
MBT1L05V	<input checked="" type="checkbox"/> v	87.455	<input type="checkbox"/>	0.255759	
MBT1L06H	<input checked="" type="checkbox"/> h	-8.469	<input type="checkbox"/>	-0.0206492	}
MRT1L06V	<input type="checkbox"/> v	0.000	<input checked="" type="checkbox"/>	0.0	

Figure 2. Corrector Magnet Panel

III. Application Classes

Application classes are less obvious. In this case we have decided to provide a basic 'BpmLock' class which handles all basic actions of high level application which concern bpms, like selecting, reading gold values, beam loss checks, etc. The 'CorrectorLock' class inherits all this from the bpmlock class and adds all actions concerning correctors. At this level virtual functions are introduced for building response matrices, solving for new correctors, checking solutions, setting correctors, and communication with the Matlab based compute server. These methods

*This work was supported by the U.S. Department of Energy, under contract No. DE-AC05-84ER40150.

provide the basic functionality needed for an orbit lock application but are redefined in more specific classes like 'autosteering'. At the same level, inheriting from the bpmlock class, we provide a class for controlling cavities. This one provides the basic functionality needed for an energy lock application. New high level applications like Quad Centering simply define a new class deriving from the correctorlock class and add their specific methods [10]. A new autosteer program for the CEBAF arcs was brought on line in a very short time by inheriting from the existing autosteer class and only redefining a very limited number of methods responsible for the correction algorithm [11].

IV. Linac Energy Management

This application is required to calculate gradients for the RF Cavities in the CEBAF linacs given a requested energy increase. After successfully setting the gradients, the program is to set the quadrupoles in the linac to provide either a 60 or 120 degree fodo lattice. The main extra input to the program is a 'fudge factor' which accounts for non-crested cavities and gradient calibration errors. The program has been operational for more than a year, with only slight adjustments to the exception handling over this period. Figure (3) gives the main control panel.

Mon Apr 24 14:13:57 1995	Actions	Selections	Quit
Injector Energy	North Linac Increase	Total Energy	
45.00	+	445.0	
Fudge factor	400	Sum of GSET's/2	
1.015	*	406.0	
East Arc is set up for: 444.99925267062		Sum of DRVHop =	426.8325

Figure 3. Linac Energy Management Control Panel

V. Model Server

All optics related information at CEBAF is concentrated in a 'Model Server' application. This application is to store all relevant beam line element information and is to serve up transfer and response matrices between two arbitrary points in the machine to requesting client applications on the control network. The optics calculations are usually performed by Dimad [12] but hooks are available to include space charge and polarization codes.

Applications connect to the model server by declaring a 'Model Client' object. This object supports query calls to retrieve beam line elements and provides methods to retrieve response matrices. It is also the conduit through which beam line elements get element specific information from the model server like layout and lattice functions. As an example we provide the code used to produce figure (1):

```
ModelClient new
Bpm :: addlist [new elements bpms arc1]
Bpm :: on pos
Bpm :: Window .b
.b on pos status gold
```

The model server does not have a graphic user interface, but a 'model sniffer' application is available in the control room

to update the information after lattice changes, see figure (4). Producing the model server in Tcl with lattice information for

Do not Kill me, I am the GOLD model server		
ModelServer gold		
inj	5.5	45
linac1	45	445
arc1	445	
linac2	445	845
arc2	845	
arc3	1245	
arc4	1645	
arc5	2045	
arc6	2445	
arc7	2845	
arc8	3245	
arc9	3645	
c	4045	

Figure 4. Model Server Status Panel

the whole machine turned out to be a bit of a challenge due to the memory overhead of the '[incr tcl]' object package. Process sizes routinely reached the machine limit. For this and other reasons the model server application was the first chosen to be converted to C++ [13]. That application will maintain the existing model server in functionality and interface, and is expected to improve memory usage and data throughput by a significant amount.

VI. Slow Orbit and Energy Lock

One of the most important high level applications produced were the slow feedback loops. Their task is to provide a means to obtain reproducible results for the setup of linacs and arcs. They maintain a 'golden' orbit at certain beam position monitors and maintain the design energy by obtaining an energy offset value from the beam position monitors throughout the arcs. On start up, response matrices are collected from the model server and dispatched to the matrix package. Singular value decomposition is used to obtain correction values for orbit and energy while at the same time protecting against singular equations. A 'memory' factor is introduced to facilitate the running of several locks simultaneously without introducing spurious oscillations. Figure (5) shows the control panel for the energy lock.

VII. Auto Steering

Linac autosteering is required to on demand steer the beam to golden values while maintaining small corrector values. The algorithm is identical to the orbit lock application and the corrector

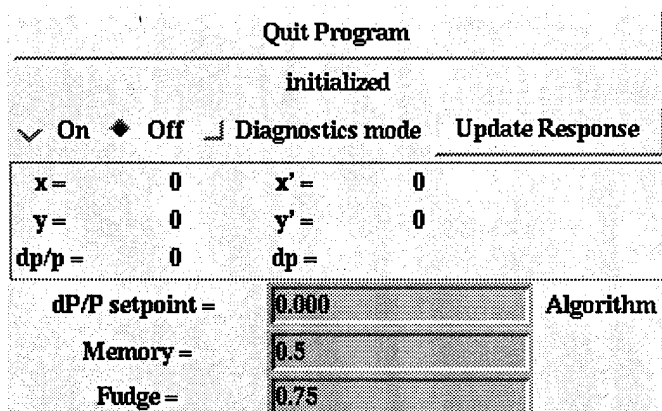


Figure 5. Control Panel for slow Energy Lock

goal has been achieved by only using correctors at positions with large beta functions. As usual the main exceptions are in detecting and handling of malfunctioning beam position monitors. A typical resulting corrector pattern is given in figure (6). The Arc Auto Steering algorithm is based on the linac steering but uses a much more complex algorithm [11], executed by Mathematica. A typical corrector change chart is shown in figure (7).

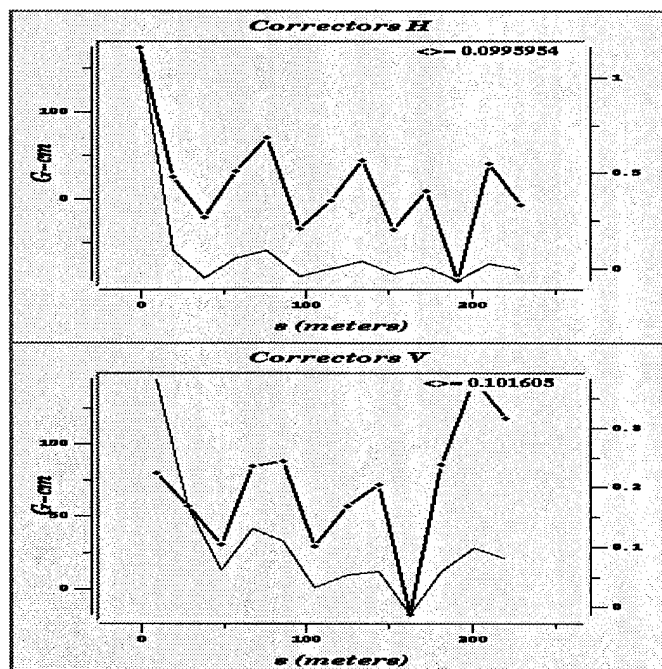


Figure 6. Corrector Display, in Gauss-cm and mrad

VIII. Conclusion

We have found the Tcl/Tk environment to be an ideal tool for rapidly producing fully functional prototypes of high level applications. Emphasis of application development can be put on the physics of the problem and on the exception handling, since long learning curves for windows programming are cut out of the process.

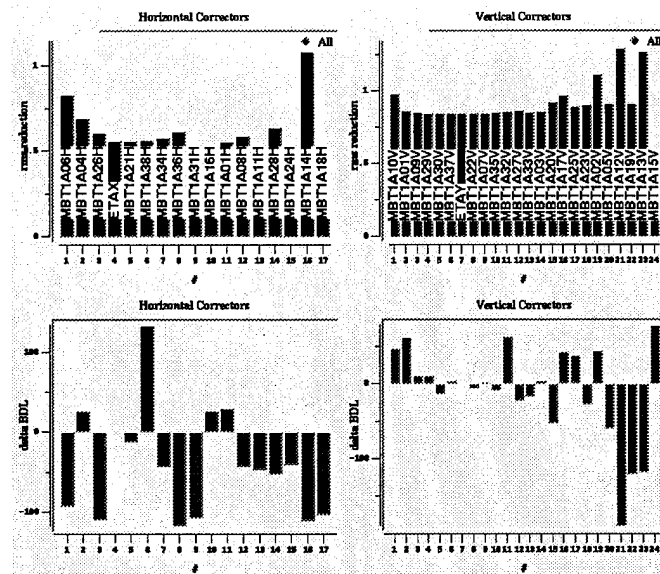


Figure 7. Arc AutoSteering corrector change barcharts

References

- [1] J. K. Ousterhout, *Tcl and the Tk Toolkit*, Addison-Wesley Professional Computing Series (1994)
- [2] M. J. McLennan, *[incr Tcl]: Object-Oriented Programming in Tcl*, Proceedings of the Tcl/Tk Workshop, UCB, June 10-11, 1993.
- [3] IXI Limited, *Object Tcl*, <http://www.x.co.uk>
- [4] B. Welch, *Practical Programming in Tcl and Tk*, Prentice Hall (1995)
- [5] Tcl/Tk is available from <ftp.aud.alcatel.com/tcl>
- [6] J. van Zeijts, *High Level Application Prototyping*, CEBAF-TN-94-038
- [7] D. Libes, *Exploring Expect: A Tcl-based Toolkit for Automating Interactive Programs*, O'Reilly and Associates, Inc. (1995)
- [8] G. Howlett, *Bacon, Lattice and Tomato graphs for Tcl*
- [9] L. A. Rowe et al., *Tcl Distributed Programming*
- [10] R. Li, *Quad Centering*, CEBAF MCC procedure
- [11] Y. C. Chao, *An Orbit Correction Algorithm for General Beam Lines*, submitted to N.I.M.
- [12] R. Servranckx et al., *DIMAD manual*
- [13] B. Bowling et al., *Integrated On-Line Modeling at CEBAF*, these proceedings.

ACCELERATOR OPERATION MANAGEMENT USING OBJECTS*

H. Nishimura, C. Timossi, M. Valdez, Lawrence Berkeley Laboratory, Berkeley, CA 94720 USA

Conflicts over control of shared devices or resources in an accelerator control system, and problems that can occur due to applications performing conflicting operations, are usually resolved by accelerator operators. For these conflicts to be detected by the control system, a model of accelerator operation must be available to the system. We present a design for an operation management system addressing the issues of operations management using the language of Object-Oriented Design (OOD). A possible implementation using commercially available software tools is also presented.

I. THE PROBLEM OF OPERATION MANAGEMENT

The Advanced Light Source (ALS) [1] is a facility operated at Lawrence Berkeley Laboratory to produce light for researchers. The facility, composed of an accelerator surrounded by optical beamlines, operates in many states such as start-up and shut-down, injection, and production with light being used by experimenters. Many activities or operations are typically in progress during each of these states; the danger is, that they may conflict. For example, when the storage ring is filling it is not appropriate for the control system to perform closed orbit correction. Conversely, during production, orbit correction should be active but it should have exclusive control of resources on which it depends, such as corrector magnets. Also, depending on the state of the accelerator, certain operations should not be allowed at all. Certainly, calibrating beam position monitors while orbit correction is active, could result in the unwanted loss of beam. Ultimately, these types of conflicts are prevented by the good sense of the operations crew, but it seems reasonable that a system that had knowledge about the operation of the accelerator could prevent these conflicts.

II. THE DESIGN PROCESS

Before starting the design, we first had to decide on the requirements but we were also very interested in methods and tools for supporting object-oriented design. We looked at two methodologies and tools.

A. Requirements

The Operation Management System is configured with a set of accelerator operations, and each operation having a list of necessary resources. The system must not allow conflicting operations to occur. There are essentially two types of conflicts: operational and resource. Resource conflicts occur when two operations attempt to control or lock the same resource (e.g., a bend magnet.) Operational conflicts do not occur on a resource level, but rather when one operation is able to affect another. If an attempt is made to start a conflicting operation, the system will identify the source of the conflict but will not attempt to preempt any of the active operations. When any type of conflict occurs the system will identify the source of the conflict by computer host name, operation name, and, if necessary, resource name. Since control operations are performed across a network of heterogeneous computers, the system must also operate in this environment.

B. Object-Oriented Design

Although there are slight differences in OOD methodologies, our design process was typical. First we identified the objects and their relationships (referred to as the static model). Next we examined typical scenarios for the system to determine the objects' methods (referred to as the dynamic model). Finally, we repeated the preceding steps until a model spanning a useful number of scenarios is complete. In fact, we are still iterating through this process.

C. Software Tools

We started the design wanting to take advantage of one of the new OOD tools which would not only aid in the design phase, but also in the implementation phase with its ability to generate C++ code. Since much of our existing application code is in C++, code generation was certainly useful in a tool. We worked with two methodologies described by: Rumbaugh [2], and Booch [3]. Also, we used two different software tools: OMTool [4] and Rational Rose/C++ [5]. Our choice of the Booch methodology for this design, was driven by our preference for Rational Rose (both the tools and the methodologies are going to be merged). We chose the ObjectStore Object Oriented Database [6] for storing persistent data because of its transparency in C++ programming, its support of data models we wanted to use

* Work supported by the Director, Office of Energy Research, Office of Basic Energy Sciences, Material Sciences Division, U.S. Department of Energy, under Contract No. DE-AC03-76SF0098

(e.g., lists and sets), and its locking model that we hoped to use to support resource locking.

III. THE DESIGN: CONCEPT

During the design phase, we attempt to model the behavior of the operations management system. The modeling process consists of first identifying the classes and then examining operational scenarios to make sure the model is complete.

A. The Object Model

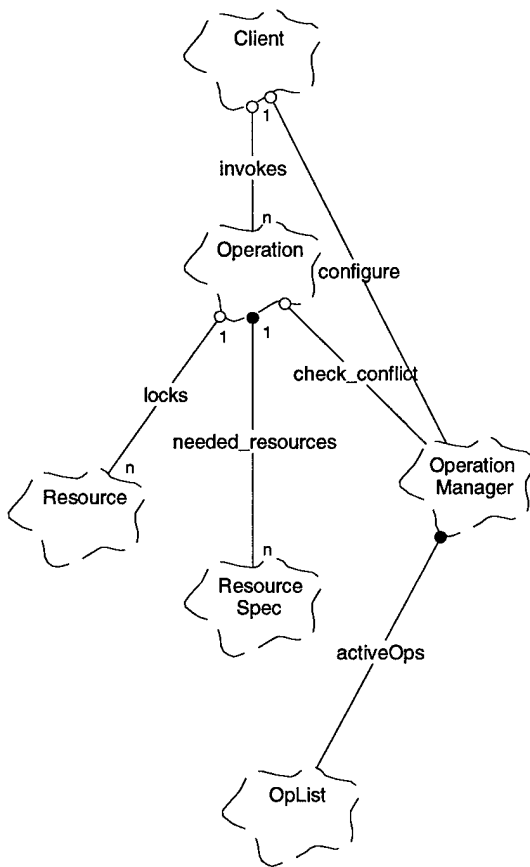
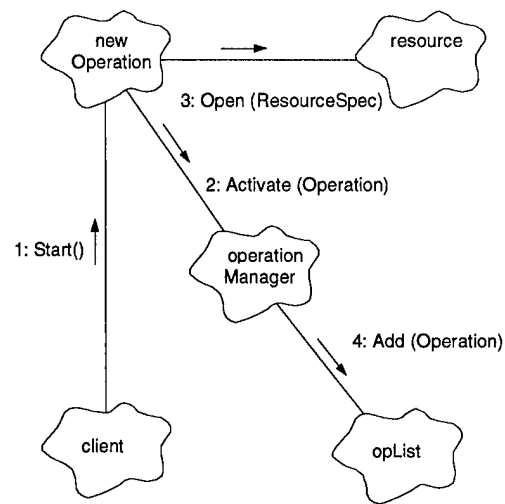


Figure 1: Class Diagram

Figure 1 is the class diagram (*static model*) of the system in Booch notation. Briefly, the broken clouds represent the *classes* (usually the nouns in the statement of the problem). We used the convention of capitalizing only class names and not objects. The lines name the relationships between the classes. These lines are adorned with circles denoting the type of relationship (open represents *uses* and closed represents *has-a*) and numbers representing the cardinality. Figure 1 reads: exactly one **Client** (class) uses *n* (many) **Operations** along with an **Operation Manager**. One **Operation** uses many **Resources**, contains many **Resource Specs** and uses one **Operation Manager** which contains an **OpList**.

B. Starting an Operation



Starting a new operation:

- 1: The client starts the operation.
- 2: If the operation doesn't conflict with another operation
- 3: and it can open the resources it needs,
- 4: then operation is added to the list of active operations.

Figure 2: Object Diagram

Figure 2 is the object diagram (*dynamic model*) of the particular scenario in which a new operation is invoked. The (closed) clouds represent specific instances of objects, with the lines representing messages flowing between the objects. The arrow points to the receiver of the message, and is labeled with the method that is invoked in the receiver. Figure 2 reads: A **client** (object) does a **Start()** on a **new Operation**. The **new Operation** asks the **operation Manager** to **Active()** it. The **operation Manager** determines if an operational conflict exists with the currently active operations contained in the **opList** object and the **new Operation**. If none exist then the **new Operation** is added to the **opList** object. If **Activate()** returns successfully, the **new Operation** then attempts to **Open()** its resources. If the **Open()** succeeds, then the **client** can manipulate its resources and continue.

IV. THE DESIGN: DETAIL

A. Operation

An operation object contains a unique identifier and a list of Resource Spec objects. Each of which identifies some resource that is needed for the operation to begin. When an new operation starts, it uses the Operation Manager to check for conflicting operations. It then uses its Resource Spec list to identify the resources it needs and attempts to lock them.

B. Operation Manager

The Operation Manager object contains the information needed to check for operational conflicts. This data is structured as a table of allowed operations stored in an ObjectStore database. This database is pre-configured with the allowed operations for a given state. The operation manager also contains the list of active operations in progress.

C. Resource Spec

The Resource Spec objects contain the resource information needed by the operation. Each Resource Spec object is maintained in a database and includes a resource name and the default settings or parameters for that particular resource. Because the default parameters or settings are included in the Resource Spec objects and not the Resource object itself, an operation can easily have variances of itself.

D. Resource

The Resource objects are used by the operation simply to provide a way in which accelerator resources can be locked. The Resource objects are maintained in a database pre-configured with the available accelerator resources. In some cases, exclusive write access to a resource is required, due either to the nature of the operation or to the nature of the resource. In either case, the resource is marked with the identifier of the operation with exclusive access. Also the host computer of the locking client and client information is kept in this object as well. This is useful for knowing which client on which computer is holding what devices. In general, the identifier of each operation using the resource is kept in the resource object as well as the host computer that the client is located.

E. Starting an Operation

To startup successfully, an operation must be able to mark each resource object in the database to indicate that it is in use by the operation. If one of the resources cannot be marked, because another operation has an exclusive lock, the operation must give up and restore the database to its initial state. Further, race conditions between operations simultaneously marking resources must be prevented. These requirements are implemented using ObjectStore transactions and the locking model; both features are designed to assure the database has a consistent state. The new operation first opens a transaction to the resource database. It can then read to see if any other operation is using the resources it needs. If the resource is free, the operation can put its signature in the object, thus enabling other operations to see which client on what host is using a particular resource. The write to a resource object will either put a write lock on the database, preventing any other operations from writing to it, or will

block until the lock can be obtained. Next, if all the resources are available, the transaction is closed, the database is updated, and the write lock is removed. If all the resources are not available, the transaction is abandoned, the write lock is removed, the client is notified of the failure, and no change is made to the database.

V. STATUS AND DISCUSSION

A. Object-Oriented Design

Both the methodologies and the tools are evolving (the Rumbaugh and Booch methods are merging for instance). They are new enough that changes are still coming rapidly, but they are stable enough that some useful principals and tools are present. Certainly, the tools are already worth the investment in time to learn to use them. At worst, they produce quality documentation for a design, at best they generate, and regenerate code and documentation as the design changes. We have also found that the simple principle of separating the design into static and dynamic models provides a useful approach to the design, at least for small systems. Although this system is not yet complete, the process which allows us to expand and eventually complete it remains the same.

B. Future Work

The current model lacks the ability to identify operations that only partly conflict. This means that operations that do not necessarily operationally conflict throughout their whole extent are forced to avoid each other. For example, suppose Operation A and Operation B both conflict only in the beginning of their operations. This model would not allow them to be active together regardless of where they were within their own operational extent.

VI. REFERENCES

- [1] "1-2 GeV Synchrotron Radiation Source, Conceptual Design Report," LBL PUB-5172 Rev. LBL, 1986. A. Jackson, "Commissioning and Performance of the Advanced Light Source", IEEE PAC93, 93CH3279-7(1993)1432.
- [2] James Rumbaugh et al. *Object-Oriented Modeling and Design*. Prentice Hall. 1991.
- [3] Grady Booch. *Object-Oriented Analysis and Design*. Benjamin/Cummings. 1994.
- [4] OMTTool, GE Advanced Concepts Center, King of Prussia, PA.
- [5] Rational Rose/C++, Rational Software Corporation, Santa Clara, CA.
- [6] ObjectStore, Object Design Inc., Burlington, MA.

ORBIT CONTROL AT THE ALS BASED ON SENSITIVITY MATRICES*

H. Nishimura, L. Schachinger and H. Ohgaki**

Lawrence Berkeley Laboratory, University of California, CA94720 USA

I. INTRODUCTION

A third-generation synchrotron-light source storage ring requires accurate orbit correction because its lattice is very sensitive to magnet imperfections and misalignments. If model-based control is used, calibration of this model is required in advance. Therefore, it is preferable to prepare some kind of model-free orbit control scheme that is complementary to model-based control. A sensitivity matrix (Smatrix) works effectively as the kernel of a model-free orbit control system for a given optics of a lattice. This paper describes recent efforts in this respect at Advanced Light Source (ALS)[1].

II. SMATRIX

A. Definition

An Smatrix, $S = (S_{ij})$, represents the effect of each steering magnet on each beam position monitor (BPM) around the ring as $\delta Z_i = \sum S_{ij} \delta K_j$, where δZ_i is a change in the position at the i -th BPM and δK_j is the deflection given by the j -th steering magnet.

B. Calculation and Measurement

A direct way of calculating a theoretical Smatrix is to use a program that can calculate either a closed orbit or linear optics. Measuring is also a straightforward method. An automated Smatrix measurement, in the ALS Storage Ring, takes about 40 minutes horizontally and 30 minutes vertically, and a quicker version is presently being tested so we can measure the matrices in both planes in 10 minutes.

C. Analysis

An Smatrix contains information, at BPM and Steering Magnet locations, of the linear optics contributions under which it was measured or calculated. Therefore, it is possible to reconstruct the lattice optics from it. This is usually a time-consuming and complex calculation. During the ALS commissioning period, our first effort was made in collaboration with BESSY[2]. A more complete analysis has been going on in collaboration with SSRL at SLAC[3].

In this paper, we will only discuss a simple analysis to check the validity of a measured Smatrix, by checking the symmetry of the ring it reflects. Let N and M be the number of BPMs and steering magnets per sector, respectively. Then symmetry requires the relation $S_{i+p, j+p} = S_{ij}$ where p is an integer. Assume there are errors in the calibration-factor set

(c_i, d_j) such that $\delta Z_i = c_i \delta Z_{oi}$ and $\delta K_j = d_j \delta K_{oj}$, where δZ_{oi} and δK_{oj} are ideal values. Then a least-square fit gives (c_i, d_j) .

If there is good symmetry with $c_i = d_j = 1.0$ the Smatrix can be taken as valid. In this case, all the BPMs and steering magnets are working properly during the measurement and the calibration factors are due to device-calibration errors and beta-function beat at the device locations. The beta-beat can be measured by other methods[4] and it is possible to extract the device-calibration errors. In the case of the ALS storage ring, it turned out that the calibration errors of BPMs and steering magnets are negligibly small and all the calibration factors are essentially caused by the beta-beat.

III. SMATRIX-BASED ORBIT CONTROL

The measured Smatrices at the ALS storage ring indicate that there is a beta-beat in the order of a few percent around the ring that is relevant for a model-based orbit control. Therefore, we have been working on an Smatrix-based orbit control.

With a fixed lattice configuration, it is possible to use Smatrices to set up parameters for several kinds of orbit correction schemes, including those that use local bumps or the singular value decomposition (SVD) method[5]. Figure 1 shows the components of our Smatrix-based orbit control.

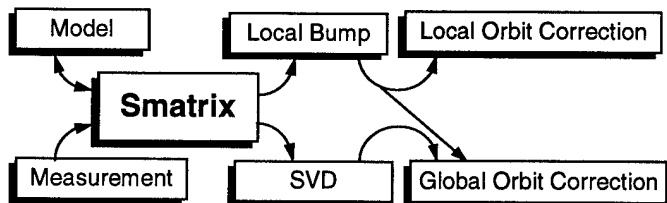


Fig.1. Smatrix-based orbit control.

This scheme does not exclude the use of a model, since one can calculate and analyze Smatrices with a model. A model-based control is indispensable when insertion devices and their compensation change the lattice configuration considerably.

Going through the process of Smatrix-based orbit control helps to calibrate the model parameters at the early stage of machine operation. The most primitive, yet important, calibration is the calculation of the BPM read-out values and the determination of the transfer functions of the steering magnets done by comparing the measured and calculated Smatrices on an assumed model. The transfer function of a

* This work was supported by the Director, Office of Energy Research, Office of Basic Energy Sciences, Material Sciences Division of the U. S. Department of Energy under Contract No. DE-AC03-76SF00098.

** Electrotechnical Laboratory, Tsukuba-shi, Ibaraki 305, Japan.

steering magnet is a current-to-field factor that can be influenced by other magnets in its neighborhood, if the magnets are close together. This evaluation task is numerically simple, but it does not fix the model qualitatively. For example, it is a separate task to determine the effective edge angles of a bending magnet.

IV. LOCAL ORBIT CORRECTION

An Smatrix contains the complete information to construct a local bump. Even if a model can calculate local bumps directly, it is a good idea to calculate an Smatrix first, then transfer it to the routine of building bumps. By creating an orbit correction algorithm, not by using a model directly, but using an Smatrix as shown in Figure 2, we can simulate the algorithm very accurately. This is because the same Smatrix is used to calculate both the changes in steering magnet settings and the expected read-out values of the BPMs.

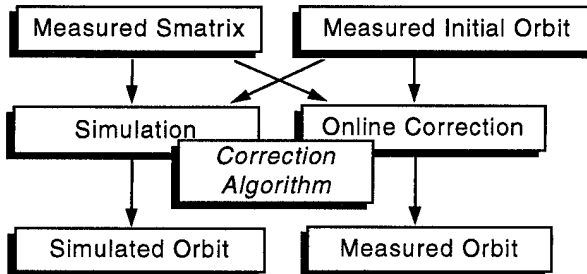


Figure 2. Measurement and simulation

This approach works very well with local orbit corrections using local bumps. Since the calibration factors are common to the measurement and the application of the Smatrix the local bumps derived from it are very precise.

At the ALS, we use local bumps to fine-tune the orbit at the light source-points, on top of the globally corrected orbit. There are a pair of horizontal and vertical local bumps for the bending beam line to control its angles, and two pairs for each undulator beam line to control its angles and positions. This activity is supported by the program IDbump[6] implemented on a PC running Windows.

For local bumps that are not too short, the accuracy has been enough for daily machine operation. However, short bumps with large orbit excursion require very accurately measured Smatrices.

Smatrixes are also used to compensate for residual dipole kicks caused by insertion devices[7]. This is also a kind of local orbit correction.

V. GLOBAL ORBIT CORRECTION

We use two kinds of global orbit correction schemes: an overlapped local-bump (OLB) method and an SVD method. Both schemes were started on SUN workstations in the commissioning period[8] and we recently started using these schemes on PCs. In this paper, we focus on the recent developments in C++ on PCs running Windows NT 3.5.

We have carried out an on-line orbit correction and an off-line simulation for both schemes. Inputs are the measured initial orbit and the measured Smatrix. Outputs are the simulated orbit and the actual, measured orbit, as shown in Figure 2.

A. OLB Method

The OLB method creates local bumps using 3 correctors around the ring in a magnet pattern 1-3-5, followed by the pattern 2-4-6 and so forth. This is to avoid short bumps that require strong kicks.

B. SVD Method

The SVD method is another popular method widely used for global orbit correction, and the subroutine package is readily available[9]. The selection of the number of eigenvalues requires caution. Using a large number of the eigenvalues can improve the orbit but the corrector strengths can be too strong for practical use.

C. Result

The simulations and the calculations were carried out using all 96 BPMs and all correctors: 94 horizontal and 70 vertical ones. The results of simulation and actual on-line orbit correction are summarized in Table 1.

	x-rms	y-rms	x-max	y-max
Initial	0.544	0.545	1.88	1.74
OLB sim.	0.227	0.189	0.866	0.964
OLB exp.	0.225	0.188	0.920	0.971
SVD sim.	0.381	0.189	1.44	0.975
SVD exp.	0.383	0.218	1.54	1.06

Table 1. Residual orbits [mm] after global orbit corrections

D. Discussion

OLB Method A model calculation shows that the residual closed-orbit distortion (COD) is estimated to be under 200 [μ m]. The results of the actual on-line corrections and off-line simulations are given in Table 1. The maximum kick angle was limited to 1.0 mrad horizontally and 0.5 mrad vertically. OLB was carried out in only 3 iterations around the ring because it saturates in further iteration steps, maintaining the rms error and slowly lowering the maximum value. This is considered to be the effect of the lengthening of the closed-orbit path. This lengthening effect is currently being investigated.

The agreement between the measured orbit and the simulation is extremely good, as shown in Figure 3. The maximum error is less than 100 μm horizontally and 50 μm vertically. Average deviations are 30 μm and 20 μm in both planes respectively.

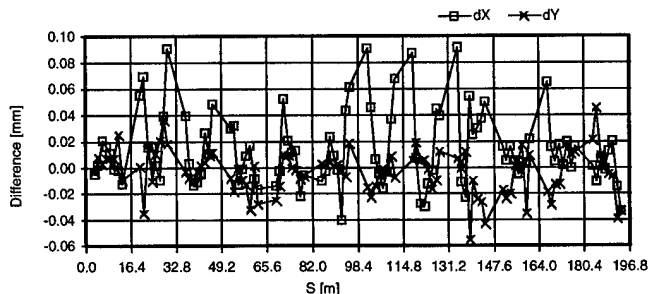


Figure 3. Difference between measurement and simulation with the OLB method

SVD Method The values in Table 1 obtained with the SVD methods are the result of using 40 eigenvalues and 3 iterations. Figure 4 shows the difference between the measured orbit and the simulation. Average deviations are 30 μm and 120 μm in both planes respectively. In the vertical plane this difference is six times larger than the one obtained with the OLB method. The reason for this large difference comes from the fact that the SVD method makes use of the whole S-matrix to correct the orbit. But, the agreements between simulation and measured orbit in rms values and maximum displacements are good.

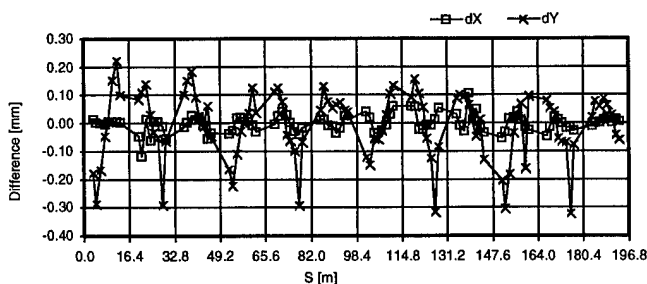


Figure 4. Difference between measurement and simulation with the SVD method

VI. DISCUSSION

An Smatrix-based orbit control is model-free and works accurately for a fixed lattice configuration. The off-line simulation can be done very accurately. It is complementary to a model-based orbit control and crucial in the early phases of operation. The technique also serves to calibrate the model used for a model-based orbit control which is the required operation mode when lattice configurations change.

VII. ACKNOWLEDGMENTS

The authors thank all the members of the ALS Accelerator Group and of the Controls Section, especially D. Robin and G. Portmann, for technical discussions. We also thank C. Timossi and M. Valdez for their software support, and the ALS Operators for their help in carrying out machine studies. We particularly appreciate the helpful advice from A. Jackson, R. Keller and K. Van Dongen.

VIII. REFERENCES

- [1] "1-2 GeV Synchrotron Radiation Source, Conceptual Design Report," LBL PUB-5172 Rev. LBL, 1986.
- [2] A. Jackson, "Commissioning and Performance of the Advanced Light Source", IEEE 93PAC, 93CH3279-7, 1432, 1993.
- [3] P. Kuske, LSAP-137, LBL Internal Report, 1993
- [4] J. Safranek, M.J. Lee, SLAC-PUB-6442, Feb.
- [5] L. Schachinger, LSAP-188, LBL Internal Report, 1994.
- [6] H. Nishimura, LSAP-185, LBL Internal Report, 1994.
- [7] D. Robin, private communication.
- [8] K. J. Kleman, "Beam Diagnostics and Control at Aladdin", Nuclear Inst. and Meth., A266, 172, 1988.
- [9] Y. Chung, G. Decker, and K. Evans, Jr., J. Safranek, I. So, Y. Tang, W.J. Corbett, and R. Hettel, "Global DC Closed Orbit Correction Experiment on the NSLS X-ray Ring and SPEAR", IEEE PAC, p.2275, 1993.
- [10] H. Nishimura, LSAP-182, LBL Internal Report, 1994.
- [11] G. Portmann and C. Timossi, LSEE-188, LBL Internal Report, 1994
- [12] L. Schachinger, LSAP-183, LBL Internal Report, 1994.
- [13] W.H. Press, B.P. Flannery, S.A. Teukolsky, W.T. Vetterling, Numerical Recipes in C, Cambridge University Press, P60, 1989.

ERROR HANDLING IN THE NSLS CONTROL SYSTEM

Susila Ramamoorthy, Pauline Pearson and John Smith

National Synchrotron Light Source, Brookhaven National Laboratory, Upton, NY 11973

Abstract

The error handling software is an important component of the NSLS control system and has been in use since 1982. Following the major control system upgrade, the error processing software has been improved at both micro and workstation levels. This note describes strategies used in error detection and reporting and the workstation software used for display and analysis of error messages.

I. INTRODUCTION

The control system at the National Synchrotron Light Source Facility has been upgraded to meet the increasing demands on the data acquisition speed and CPU power. The upgraded system has a two-level distributed architecture consisting of HP workstations for the host-level and VME-based microprocessor systems for the equipment level. The communication link is ethernet[1,2]. The VME micros are responsible for the hardware control and data acquisition. The Error handling system, initially installed in 1982, has been modified to work with the upgraded system. A lot of effort has been put into the error detection and error reporting software to make the Error Handler System a useful diagnostic tool for the operation of the facility.

II. OVERVIEW

The micros continuously monitor the associated hardware for error/alarm conditions and send error messages to an Error Processor which is itself a real-time micro system. The Error Processor displays the messages as they are received, on a console in the control room. In addition, the error messages are stored in memory. An Error Logger running as a background process on the main workstation periodically retrieves the error messages from the Error Processor micro and saves them on a disk. Figures 1 and 2 represent the physical layout of the Error Processor system and the data flow respectively. In the following sections, the micro software for error reporting, the Error Processor micro and the workstation software packages for error analysis are described.

III. MICRO SOFTWARE

All the VME micros are driven by a real-time operating system referred to as NSLS Control Monitor [3]. The monitor consists of a set of system tasks and interrupt handlers, built around a commercial real-time kernel (RTUX by Emerge Sys-

*Work performed under the auspices of the U.S. Dept. of Energy under contract no. DE-AC02-76CH00016.

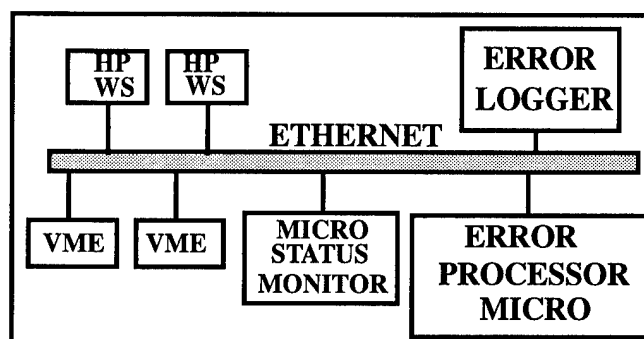


Figure 1. Physical Layout of the Error Handler System.

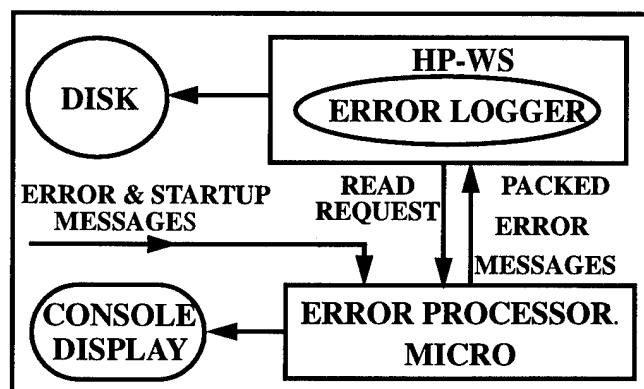


Figure 2. Data flow in the Error Handler System.

tems Inc.) and application/device-specific modules. The system software which is standard for all micros, manages communications, command decoding, displays, etc. It provides a utility library and services for error detection and reporting. The device-specific tasks are unique to each micro and are dictated by the hardware associated with it. The monitor views the hardware as a set of logical devices with unique names. A logical device is a software data object defining the data structure and the commands for a hardware or software parameter controlled by a micro. It responds to a standard set of commands from the workstations. One logical device can be mapped to one physical device or one logical device can represent multiple physical devices or vice versa. A standard format is used for all logical devices.

The relevance of the logical device concept in the current discussion is that the device structure contains all information necessary for error detection. The device-specific tasks scan the device hardware at 10 Hz or higher for alarm conditions and report errors using the services provided by the system part of the monitor.

The types of errors depend on the function of the logical

device. Following is the list of alarm conditions the software looks for:

1. Tolerance error for analog input-output devices when the difference between the set-point and read-back is not within the specified tolerance range. (e.g. The difference between the desired current for a power supply and the actual current exceeds the tolerance limit).
2. Alarm conditions when the monitored data falls out of the safe limits. (e.g. The data monitored by a radiation monitor is out of the specified range).
3. Time-out conditions observed while controlling an instrument or while acquiring the data from an instrument. (e.g. No reply is received when an instrument is read/controlled via an RS-232 serial port).
4. Invalid state error when the state of the digital device is different from the commanded state. (e.g. A shutter is commanded to open but status indicates closed).
5. Fault state of a digital input bit device. (e.g. Water flow error, RF cavity fault etc.).

The following features of the micro software help to identify true error or alarm conditions and prevent notification of meaningless and redundant messages:

1. Proper strategy is exercised for error checking and reporting. For all devices when a set command is received, alarm checking is inhibited until the command is executed and the hardware it represents settles. The settling time may vary from millisecond to seconds. The device is marked In-Process until the settling time has elapsed.
2. Alarm/fault states are not recognized unless valid conditions are satisfied or the hardware is in a particular state. As an example, a number of power supplies can be controlled by a power controller. In this case, tolerance error check is invalid unless the controller is on. The software checks this condition before monitoring the power supplies. Another example is the various faults associated with an RF amplifier. The "filament_under_current" or "plate_under_voltage" conditions are not real alarms unless the RF amplifier has been commanded "ON". The software uses the appropriate logic before checking for errors.
3. After detecting a fault, an error message is sent asynchronously to the Error processor. The message contains all information about the device such as the micro name, logical device record number, message code, time stamp and all pertinent data. The types of error (tolerance, time-out, etc.) are stored in the auxiliary status bytes of the record.

4. The error flag is latched in the device record to prevent error storms. No errors will be reported for the device until the error status is cleared.

5. Errors can be reset in a number of ways. For devices that accept "SET" commands, the monitor resets the errors when a SET command is received. The operators at a workstation can issue a clear command to any device or a global clear error command to a micro. When the error flag is cleared, if the device is still in error, an error message is generated again. If the device is out of alarm state, an Error Reset message is sent to the error processor micro. The monitor keeps updating the count of devices that are in error.

6. Disabling of error reporting can be done by simple commands from the host level computers. The error detection and error latching are still effective and the error status of the device can be obtained by reading the device record from a host level computer. This feature is useful when a particular hardware is known to be malfunctioning and the operator wants to shut off the alarms for those devices associated with the hardware. Error reporting can be re-enabled from the workstations. Error reporting can be disabled on a micro basis by selecting the configuration switch in the micro. This is required during the maintenance period when hardware is being checked out.

Alarm parameters such as tolerance value, limits for alarm level 1 and alarm level 2 can be modified by authorized personnel from any host level computer. Similarly the calibration values for read-backs can be changed to accommodate aging or changes in hardware. These parameters are saved in non-volatile memory and can be retrieved even if the micro is re-booted. The software also provides the option to restore the original or default values on re-boot.

In addition to the alarm/error messages, the micro sends a start up message when it is reset or powered down. The micro determines whether it is a COLD start or a WARM start and sends the appropriate message to the error handler. A cold start indicates that a micro has been powered down; a warm start indicates that a micro has been reset.

IV. ERROR PROCESSOR MICRO

This is similar to any other real-time micro in the system. All micros send error or informative messages using the micro to micro communication utility software in the monitor. The messages have protocols identical to those from workstations. The messages are similar to the "Set Data Array" packages from the workstations. The Error Processor decodes the message and generates a scrolling display on a console in the control room. Each message is displayed as a line and contains the micro name, the device name, description of the error or information with time stamp. Every 2 minutes, a blank line is written to scroll old messages off the display to ensure that the new messages can capture the operators attention. In addition, a

beep is generated for each message to alert the operators. The messages are stored in a ring buffer in chronological order. These messages are retrieved by the Error Logger process on a workstation.

Another key system is a Micro Status Monitoring micro. This periodically polls all the micros and generates a TV display of all micro names in green. If a micro fails to reply, the name is highlighted in red. The TV display has been extremely useful since one can immediately notice the failure of any micro and fix it. This reduces the loss of History data collected by the History programs on the workstation. Also, the micro can be fixed before the next beam injection into the storage ring thereby reducing the machine down time. Following a power dip, all micros automatically re-boot themselves. Any micro that does not re-boot can be identified immediately and reset manually.

V. ERROR LOGGER

This process runs in background on a workstation. Every 5 seconds, it collects the error message packets from the Error Processor micro and stores them in binary files on a disk. A new file whose name extension has the encoded date-time stamp is created at 00:00 hours every day and the messages for that day are stored in the file. If the error logger is restarted for any reason and a file for that day does not exist, a new file is created.

VI. WORKSTATION SOFTWARE

All workstation programs are X window Motif based. A set of tools is available for analysis and display of error messages and to monitor the network message rate.

Using standard data acquisition programs [4], one can get all parameters of a logical device. If a device is in error, the error field will be highlighted.

One of the packages referred to as Microstatus retrieves the Current Status array from all or a specified micro and displays the total number of devices in error, spurious bus interrupts, version number, the time elapsed since last re-boot, the list of devices in error etc, at any time.

Another important package is the error display and analysis program. This program can be run on any workstation. The program displays a menu bar with various options (Figure 3). By selecting the "FILE" menu one can get the list of the error log files and select the one for the required day. Old error files can be deleted by authorized members using this program. One can view the entire day file or a given time slot. The messages will be displayed with the micro name, device name, time-stamp, type of message and all the relevant data at the time the alarm was captured. There is also an option to view the current messages as they are logged on to disk. Other options allow one to get different types of summary: 1. Sort devices that are in error in the alphabetical order of micro names, 2. Summary of total number of error for all micros, 3. Number of errors for each device in a micro. One can get a hard copy of all the dis-

No.	Micro	Device	Errors	Error Resets
1	bxdm	bxd	2	1
2	butranm	bud3	18	9
3	butranm	bud4	2	1
4	xrfl2m	xrfl125kwp1teon	1	0
5	xrfl2m	xrfl125kwsrnon	1	0
6	xrfl2m	xrflrftnt1	2	1

Total Errors for ALL Micros = 26

Figure 3. Error Analysis and Display

plays using the print menu button.

A network test program allows one to send messages to any micro as fast as it can respond and prints out the communication rate, count of lost or timed-out messages, retries etc. This data helps one to identify the hardware problem (in the network or in the micro) or software problems (some unpredictable delay in an interrupt handler etc.).

VII. CONCLUSION

With the exercise of proper strategies in error detection and reporting in the micro software, meaningless errors have been eliminated and the error handling system has become a useful diagnostic tool both from the operations and engineering point of view. A number of hardware failures have been identified and fixed. Following a problem, one can often reconstruct the events that led to the failure. The micro status monitoring micro with a TV display has been extremely useful in minimizing the down time and loss of history data. The future plan is to incorporate the micro status monitoring function in the error micro itself. In future, the workstation programs would be able to send messages to the Error Processor to notify error or warning messages to the operators and to log them into the error message file.

VIII. REFERENCES

- [1] J.Smith, et al. Proc. IEEE Part. Acc. Conf. (1993), 1852.
- [2] J.Smith, S.Ramamoorthy and Y.Tang, Nucl. Instr. and Meth. in Phys. Res. A352((1994) 114-117.
- [3] S.Ramamoorthy and J. Smith, Proc. IEEE Part. Acc. Conf. (1993),1849.
- [4] Y.N.Tang et al., Proc. IEEE Part. Acc. Conf. (1993),1846.

History Data Collection, Retrieving and Display in the NSLS Control System *

Y.N. Tang and J.D. Smith, National Synchrotron Light Source, Brookhaven National Laboratory, Upton, NY 11973

Abstract

This paper presents the history data collection, retrieve and presentation subsystem of our control system. We made every effort to make the software friendly, convenient and robust. It is widely used and has become a very valuable diagnostic tool. Anyone may start and stop his own history at any data rate up to 20 Hz. The data can be periodically written to disk files or stored in a cyclic ring buffer and dumped to a disk file upon request. All the history data files use the self-contained and self-explanatory standard format. One graphical display program displays all the history data files because of their standard format. In addition to the standard features of a plot program, this display program can display up to 16 devices on both axis, take differences with a reference point, browse the data file by pages or a scroll bar, zoom-in and zoom-out any portion of the plot, do many types of analyses, etc.

I. INTRODUCTION

The history data archiving and retrieving is a very important subsystem in every accelerator control system. When we started to upgrade our control system several years ago, we decided to revamp this subsystem and we paid most of our attention to:

- It should be very flexible and easy to use to make this subsystem available and accessible to everyone;
- It should have a convenient and powerful program to display and browse the history data graphically.
- The history data should be readily available to other programs such as the orbit analysis program set.

In our old DG-based control system, we also had the history data collection processes running all the time. However, in order to look at the huge data set, one had to print it out. It was very time-consuming and tedious to check a thick stack of printed text papers. The limited display capability severely limited its use.

With the successful completion of our control system upgrade, the newly designed and developed history data subsystem has realized our design goals and become a very valuable tool in the daily operations and diagnostics. It plays an important role in the determination of the causes of beam dumps and other unexpected beam movements. The people in the RF group, power supply group, radiation and safety group, interlock group, Vacuum group and other groups use the history data to do different kinds of analysis, get the daily radiation doses for many locations, evaluate equipment performance, and detect equipment problems etc.

The following are the key elements of the history data system:

- a self-contained and self-explanatory standard file subsystem;
- two data collection programs: one for the normal history and the other for the fast history;

- a general graphical display program to browse and plot the history data. It also converts the data files of standard format to other formats used by commonly-used packages and data analysis programs.

II. TWO TYPES OF HISTORY DATA COLLECTION PROCESSES

Generally speaking, the history data collection processes produce huge data sets. In order to save disk space, we have two types of history data collections.

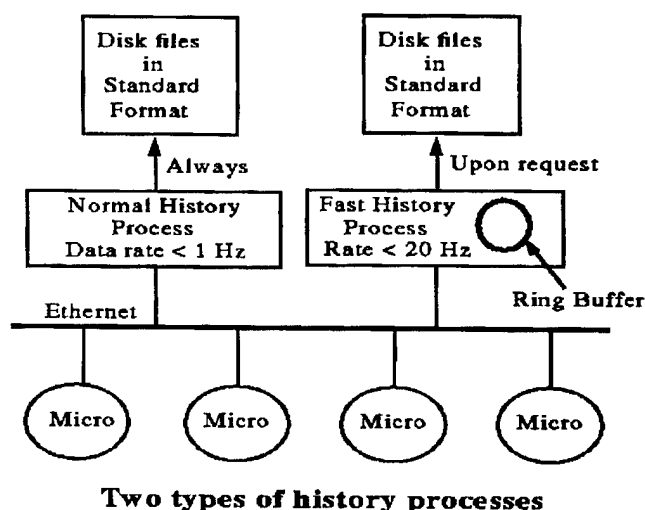


Figure 1. Two types of history data collections: the slow history and the fast history.

- The fast history collects data in a ring buffer, which is then dumped to a disk file upon request. Its collection rate can be as fast as 30 Hz. For example, the X-ray and VUV orbit is tracked by two fast histories at 5 to 10 Hz rate.
- The slow history collects and writes data to disk files at the required rate. The max rate is 1 Hz. Each slow history writes data to a specific subdirectory in the history disk, generates one file per day and uses the date as file names such as Mar1595.

All the data files generated by both fast and slow histories use the standard file format.

III. THE STANDARD FILE FORMAT

When we started to upgrade our control system, we designed and developed a so-called "self-contained and self-explanatory NSLS standard file subsystem" (we call it STF in the following text). At the beginning, we planned to apply this file format to all the applications. If done so, every application could read/write any files produced by other applications without the prior knowledge of the file format and structure. It has been proved that our

*Work performed under the auspices of the U.S. Department of Energy

plan was a little bit too ambitious. Yes, it could be done. But it needs too much effort. However, the STF has made our history data collection and display subsystem a real success. Without the STF, it would not be possible.

The STF subsystem contains:

- a set of carefully designed formats and rules for the file;
- a library containing functions to open/read/write/search the file. There should be functions to read/write anywhere in the file.

An STF file has a file header followed by several segments. Each segment has a segment header followed by the data. The file header consists of several sections and segment headers consist of a parameter section and several blocks. Some blocks are mandatory and some are not. Programmer may add their own blocks into these headers. Generally speaking, these headers have all the information needed to read/write the STF files.

As a matter of fact, the STF files are similar to database tables with the exception that an STF file may have many segments and each segment has its own table. Usually the numbers of rows and columns are different from segment to segment in an STF file. In the header of each segment, one may assign a label, display format, data physical type such as setpoints, limits etc for each column in the segment. Any data types including structures are allowed to form a column.

In the STF function library, one could

- get all the information in the file header and segment headers. For example, one may call *stfgetlabel* to get the labels of the columns in a data segment. These labels could be device names.
- read/write any columns by column index, by label, by physical type etc.
- read any portion of a segment. This is very useful when an application is browsing the file back and forth and zooming a section of data.
- update any portion of an existing segment or append data to the end of a segment.
- insert columns and/or rows to an existing segment.
- delete columns and/or rows from a segment.

Though it sounds that this is a very complicated system, in fact is not. We paid most of our attention to its efficiency. Because the history data files are generally large files (most are of several megabytes, some of them more than 20 megabytes), the display and browser program has to search back and forth many times through these files to display them. Therefore, the efficiency is one of the most important considerations.

We use one program *hbrowse* to display and plot all the history data. When *hbrowse* opens a history data file, it fetches all the device names (column labels) whose data are recorded in the file from the segment header. Then *hbrowse* presents these devices and asks the user to select devices to display. In addition to it, the program *hbrowse* fetches all the necessary information from the file and segment headers to read them correctly. Therefore, one program can display all the history data files.

IV. THE HISTORY DATA COLLECTION

We have two programs to start the history data collection. One is for the slow history and the other for the fast history. To start a history is a very simple matter: the major task is to make the

input data file to the history program. The file contains all the needed information including the data rate, device names, the data fields of interest etc.

Now we have about 20 history processes running at different data rates (from 0.01 Hz to 20 Hz). Most of them are started by ring managers, physicists, technicians and engineers.

V. THE HISTORY DATA BROWSE AND DISPLAY

There are two keys to the success of the history data subsystem. One is the standard file format, the other is the general graphical display program *hbrowse*.

History processes produce big sets of data. In order to make the history system really useful, how to display and present these huge data sets is essential.

In addition to all the common features of a plot program, the program *hbrowse*

- has two y-axes. Each y-axis can display up to 8 devices.
- uses time or any other device data such as the beam current as the x-axis.
- zooms any portion of the display by click and drag.
- displays any portion of the data set including the whole data set. To select the desired portion of data, use the mouse to move the line-marker on the picture.
- selects any point as the reference point to display the difference.
- uses push buttons or slider to browse through the whole file.
- provides filters and statistics calculation facilities.
- translates and rescales the picture.
- converts the history data files to other formats used by other programs and packages. For example, it generates data files for c-plot and orbit correction and analysis programs.

There are many other features not listed here. We have three sample displays. Figure 2 is the radiation history display. One may see the radiation increases during injections and whenever the booster is on. The top-right text panel gives the total radiation counts of the day. Note that it plots the difference with the reference point at the start of the day. Figure 3 presents a picture of a portion of a fast history, from which we detected the cause of a beam dump in the early morning of Jan 31, 1995. The cause is that X17 (wmainamp) tripped. The data of wmainamp, the X-ray current and three PUEs are plotted. Figure 4 is another format to display the radiation data.

VI. ACKNOWLEDGEMENTS

We would like to thank Sam Krinsky, Norman Fewell, Steve Kramer and other people in the NSLS for their many helpful suggestions. The commercial package XRT/Graph was used in the program *hbrowse*, which made the development much easier for us.

References

- [1] Y.N. Tang and J.D. Smith, NSLS Technotes, W-7, W-35, W-36 and W-37, 1990-1994.
- [2] J.D. Smith, S. Ramamoorthy and Y.N. Tang, Proceedings, ICALEPCS 1993.

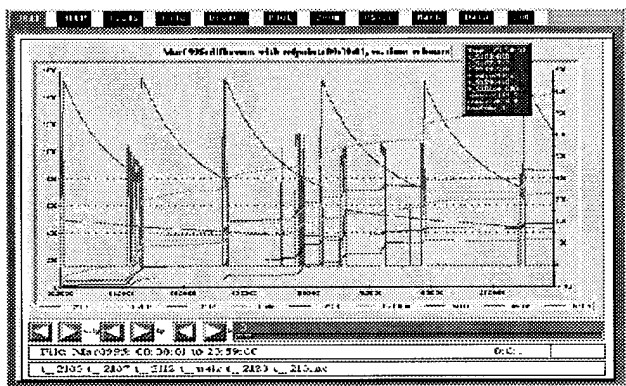


Figure. 2. The radiation history display

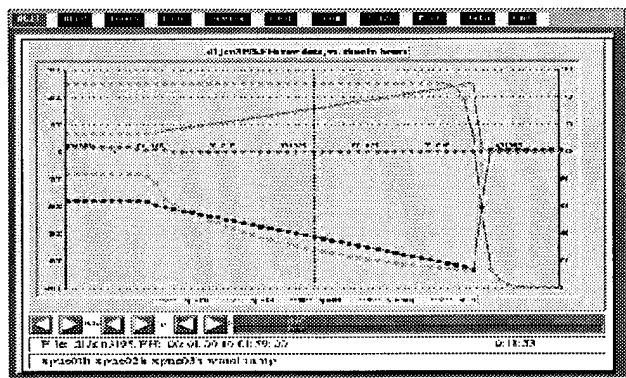


Figure. 3. The beam dump caused by x17 trip

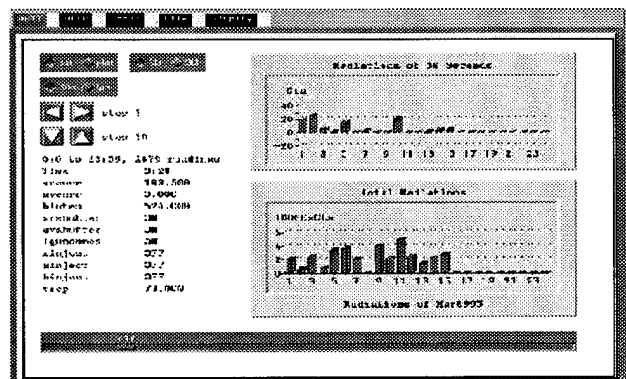


Figure. 4. Display history data in a bar chart

Virtual Instrumentation Interface for SRRC Control system

Jenny Chen, C. H. Kuo, Gloria Huang, J. S. Chen, C. J. Wang, K. T. Hsu, and G. J. Jan*

Synchrotron Radiation Research Center, Hsinchu 30077, Taiwan, R.O.C.

*Department of Electrical Engineering, National Taiwan University, Taipei 10764, Taiwan, R.O.C.

ABSTRACT

Virtual instrumentation system has been developed for the control system of SRRC. Almost of the measurement instruments are to provide IEEE-488 interface, they are distributed around the accelerator facilities, the virtual instrumentation system connects these instruments by local area network, Ethernet, to GPIB adapter. The man-machine interface developed by using LabVIEW, which is running at Sun's workstation. The workstation to be played as an instrument server, the operator can access remote instruments simply by point and click operation. The information provided by instruments can be analyzed and extracted the desire machine parameters at workstation. The main control system can access these parameters by standard network protocol. The major goals of the virtual instrumentation interface are to provide the automatic measurement of the machine parameters and to minimize the interlude of the machine physicists and operators. Machine parameters, such as tune, beam spectrum, filling pattern, bunch length, can be on-line displayed at main control panel or archived for various applications.

I. INTRODUCTION

A two-level hierarchical computer system is implemented for the control system of SRRC [1,2]. The control system can access any type of accelerator device. There are still missing link information sources, such as wave form as well as spectrum cannot be accessed from the control system at this moment. A few instruments support Ethernet interface, but most of them provide standard interface, such as GPIB, RS232,...etc. To fill this gap, the solution was to connect control system and variety instruments that have IEEE-488 interface to a control network (Ethernet) which is also distributed throughout the facility. Commercially available tool kit LabVIEW was used to develop the user interface that reduces large amount loading of programming [3,4,5]. LabVIEW provides an icon-based graphical programming environment that offers high productivity in development phase.

II. SYSTEM STRUCTURE

Almost of the measurement instruments provide IEEE-488 interface, they distributed around the accelerator facilities, the virtual instrumentation system connects these instruments by local area network via ethernet to GPIB adapter. Operator and machine physicist will have the flexibility to control the instruments from the computers in their offices. This system was built on standardized networking protocols and implemented with the measurement server concept. The system may configure to connect 8 GPIB-ENET adapters to drive GPIB devices. One GPIB-ENET adapter can drive 15 GPIB devices or expand

to 31 devices. The man-machine interface is developed by using LabVIEW, which is running at Sun's workstation. The workstation is played as an instrument server, the operator can access remote instruments simply by point and click operation. The application programs executed on the workstation analyze and extract the machine parameters from the information provided by the instruments. Users may access these parameters from control system through the standard network protocol.

The system configuration of the Ethernet-based virtual system is shown in figure 1. The figure shows there are two level computer systems connected by control network. The instrument's server is running on a Sun's SPARCstation.

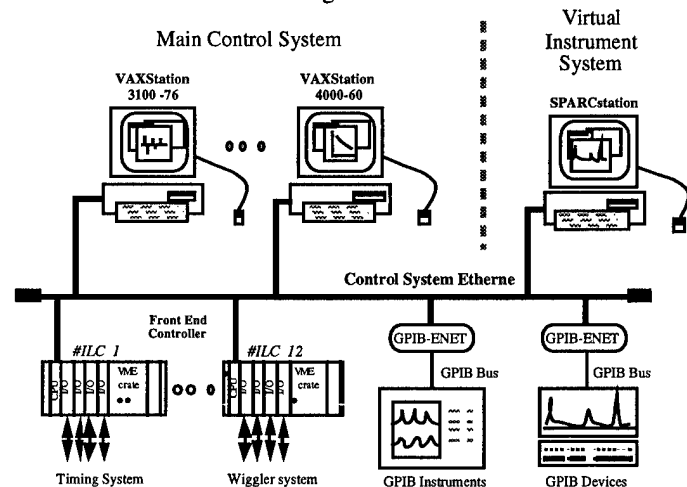


Figure 1. Ethernet based virtual instrumentation system

III. SOFTWARE STRUCTURE

According to our control system design [1,2], many workstations for control devices have the same configuration. The dynamic database and static database are the same on each computer. The main control system software was developed on VAX/VMS computer system. Relations between processes are shown in figure 2. A server process running on a control computer serves data access from non-database client. It can serve reading, setting requests, static database fields access and receive the results from some special measuring system then write into the part of dynamic database (DDB) that is not refreshed by ILC. ILCs upload their DDB at 10Hz, the dynamic data receiving process refreshes the console's DDB area. The refreshed area for each ILC was set to 1400 bytes. But on console level computer we configured the size of dynamic database for each ILC to 1500 bytes. Then there are 100 bytes are not refreshed by the ILC. Those special measured results were written into 1400 to 1500 bytes' area. There is another process responds to broadcast those results or

receive the broadcast data and write into the part of DDB to keep the consistency of control system. The device setting request is limited to the specified hosts that are listed in a file to provide security of control. The requests are built by string, it is simple for any computer system to communicate with each other that stands on UDP/IP protocol. The server creates the channel of data accessing between any computer system to main control system. By the channel, the measured results can be archived to files daily by an archiving process started on a specified computer that has large harddisk space. The same, they can be accessed by any control process from any control computer, they are base on the same database system. From the results we may understand more about the extracted machine parameters related to the effected devices, for example.

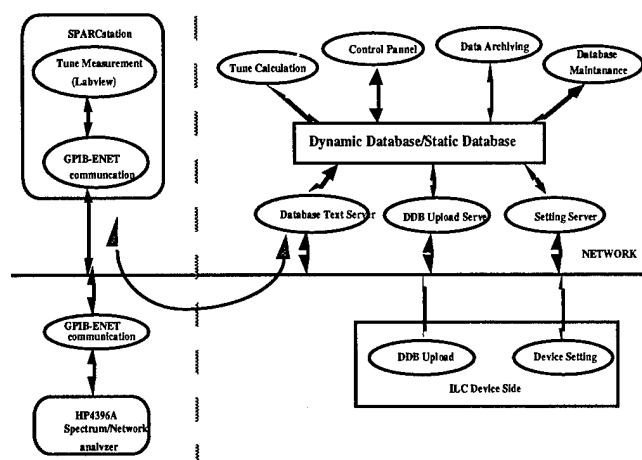


Figure 2. Relationship between processes

IV. USER AND CONTROL SYSTEM INTERFACE

The LabVIEW programming environment provides enough user-interface objects to build applications. The control program of LabVIEW is called Virtual Instrument. One VI program has two parts, control panel and diagram. The control panel provides user interface, the diagram is the execution body. It also supports Code Interface Nodes (CIN) function to link C program. It may be necessary if it is difficult to build functions by using LabVIEW objects. It should be careful to manipulate the passing variables to and from CIN functions. They are only passed by address, the data types of the variables cannot be checked, the error data type passing may cause fatal error at run time. During the command and data exchange between VI program and GPIB devices, the GPIB-ENET device translates the messages from Ethernet to GPIB bus signals that stands on TCP/IP protocol.

V. TYPICAL APPLICATIONS

We have developed several applications at this moment. The detailed of several applications are present here. These applications include spectrum analyzer

interface, optical sampling oscilloscope interface and sampling oscilloscope interface, etc.

A. Spectrum Analyzer And Tune Measurement

The spectrum and tune are measure by using HP 4396A spectrum and network analyzer. To make the tune measurement simplified, two reference values of tunes are calculated by a tune calculation process on a control computer.

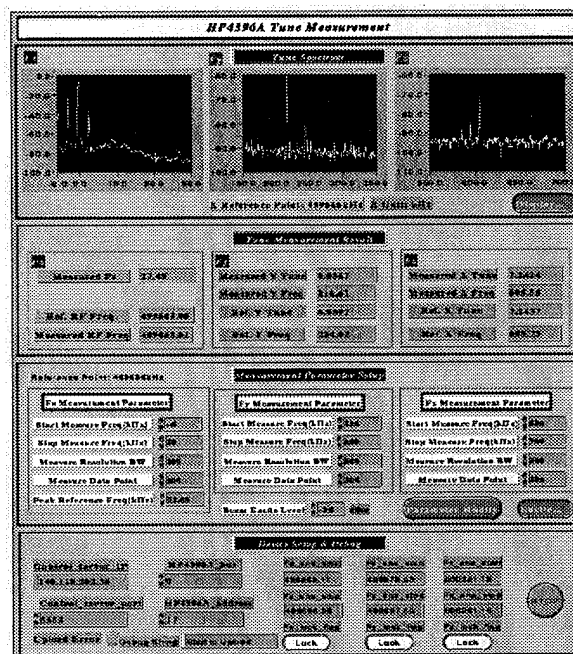


Figure 3. Tune measurement virtual instrument interface

The process calculates the tunes according to the machine lattice. Using the channel supported by the server, the reference values can be accessed and the measured results can be updated by the tune measuring process that is developed on a Sun UNIX computer. The tune measuring process uses the reference values to set analysis range to identify peaks. If the specified range cannot find tune peak then the analysis range of getting peaks will be set wider till the peak found or the range is set to the spectrum measuring boundary. If the tune is found the peak analysis range will be set to be close to the peak to avoid error locking. It also may excite the beam if the peak cannot be identified. The difference between measured tune and calculated tune value is about several kHz. HP4936A spectrum/network analyzer can be set to several sweeps ranges to do spectrum analysis. From our requirement it is set to 3 pieces of sweep range. The first is to get synchrotron frequency and the fundamental frequency to calculate tunes, the second is to get vertical tune v_y and the third is to get horizontal tune v_x . Then one sweep cycle we may get 4 peaks according to the peak analysis ranges.

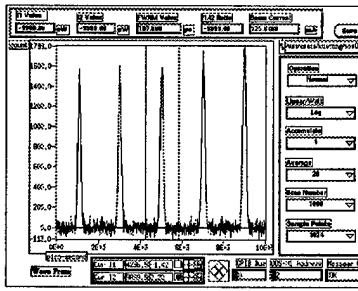


Figure 4. Optical sampling oscilloscope virtual instrument interface

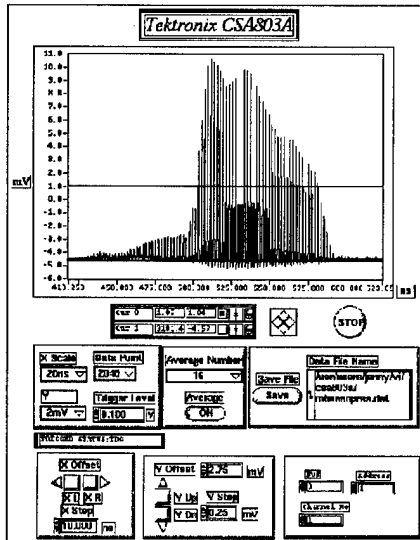


Figure 5. Oscilloscope virtual instrument interface

B. Optical sampling oscilloscope virtual interface

The averaged bunch length of the storage ring is measured by Hamamatsu OOS-01/VIS optical sampling oscilloscope that is located at synchrotron radiation diagnostic port, the location is about 150 meters far from control room. The device connects to Ethernet through GPIB-ENET adapter. The operator as well as machine physicists can access the bunch length on the control room on bunch length. The averaged bunch length is also stored on the machine database, it is valuable for analysis bunch length versus parameter of the machine. For example, beam intensity versus bunch length relation can be record automatically.

C. Oscilloscope Interface

Oscilloscopes are the most important instruments for the diagnostic and operate of the accelerator system. The virtual instrument system connects the oscilloscope through GPIB-ENET adapter. On the workstation, the operator can operate the oscilloscope as to the operate the real front panel of the oscilloscope.

VI. FUTURE PROSPECTIVE

The usability of the virtual instrument system has been demonstrated. But, present system is still in its infancy. There are many problems need to be solved. The major issue includes improve response time of the system, connect more equipment and find a better way to bridge the virtual instrument system with the existing control system database. The trend of the future instrument systems will use standard computer network protocols. Bring instrument server concept [5] and updated virtual instrumentation system for the control system of SRRC is the major activity of the near future.

VII. ACKNOWLEDGMENTS

The authors express their thanks the staff of the instrumentation and control group. The helps from Mr. H.P. Chang, Dr. C. C. Kuo and K. K. Lin are also highly appreciated. Very thank to Mr. K. H. Hwu for his kindness help.

VIII. REFERENCES

- [1] G. J. Jan, et al., "Computer control and instrumentation system at the SRRC", Nucl. Instr. and Meth. in Phys. Res. A 352 (1994) 33-39.
- [2] C. J. Wang, et al., "The design schemes of graphic user interface database and intelligent local controller in the SRRC control system", Nucl. Instr. and Meth. in Phys. Res. A 352 (1994) 300-305.
- [3] R. Jamal, "Graphical object-oriented programming with LabVIEW", Nucl. Instr. and Meth. in Phys. Res. A 352 (1994) 438-441.
- [4] J. A. Hinkson, M. Chin, C. H. Kim, H. Nishimura, "Automated Tune Measurements in the Advanced Light Source Storage Ring Using a LabVIEW Application", in European Accelerator Conference 1994.
- [5] N. Barnholt, "Future Test Systems Will Use Standard Network Protocols", Electronic Design, Jan 10, 1994.

USER-FRIENDLY INTERFACE FOR OPERATOR IN THE CONTROLS OF UNK BEAM-TRANSFER LINE

Yu. Karshev, Yu. Fedotov, V. Komarov, I. Lobov, IHEP, Protvino, Moscow Region, 142284, Russia

The beam-transfer line (BTL) was commissioned in March 1994 [1]. BTL has to inject proton beam from the existing 70 GeV accelerator (U-70) into the 600 GeV one (UNK-I [2]) under construction. An operator user-friendly interface for UNK BTL controls is described. Interface is equipped with sufficient means allowing to operator by customary terms to interact with technological process. Working in real-time regime program gives the possibilities: to control the BTL power supplies currents; to see the beam trajectory and profile along BTL; to compare real and computed through the measured emittance beam dimensions; to store archive data, etc. Working with statistical data of power supply current instabilities and beam trajectory displacements, program allows to do an estimation of partial contributions of every element in the beam position instabilities.

I. MAGNETIC STRUCTURE AND EQUIPMENT OF BTL

The injection channel of UNK [3] consists of three main parts: beam extraction system from U-70, beam-transfer line to UNK-I, and beam injection system into UNK-I. The extraction system consists of two full-aperture kicker-magnets KM-14 and KM-16, two septum-magnets SM-62 and SM-64, one quadrupole lens Q-66 for preliminary focusing, and two correction magnets in horizontal and vertical planes.

The line-of-route correction in every plane is made by eight correction stations disposed regularly along the line length. Each of the stations consists of two pick-ups and two correctors, the distance between them being a one-cell period. In total, the injection channel embeds 52 bending dipoles, 88 quads and 56 various correctors.

The beam diagnostic system comprises 3 current monitors, 46 pick-ups, 26 beam profile monitors as well as beam loss and halo monitors and 3 TV-screens.

II. BTL CONTROL SYSTEM

The BTL control system [4] is divided into four functional subsystems:

- magnet power supplies control;
- beam diagnostics;
- synchronization and dynamic interlock;
- vacuum control.

Each of these subsystems has its own console computer IBM PC 386 at the user's working place. The console computers are linked through serial communication lines to subsystem multiplexers situated in three BTL technological buildings. Each multiplexer combines subsystem controllers, which serve the corresponding technological equipment.

The control system has three software levels:

- software of controllers and multiplexers providing real-time procedures of the equipment;
- resident programs of the console computers;
- high-level applications which represent the control system shell and consist of programs set with convenient graphic interface.

The third-level software is installed on one computer IBM PC 386, linked to the console computers by LAN "Ethernet".

III. BTL CONTROL USER INTERFACE

The control system software was developed specially for the injection channel and was supposed to make the equipment on-line operation maximally convenient for the operator. The high-level user interface of the BTL control system allows the operator:

- to observe the physical structure of the whole transfer line with current data of the beam position and profile, magnetics elements parameters;
- to scroll the last measurement data from the power supply (PS) controllers and to change references of these supplies. These data are presented as physical values;
- to make a quick simulation of the beam trajectory and to correct the trace and focusing of the beam, using the measurement data;
- to accumulate and process statistical data from the beam diagnostic devices and the PS. Statistics can be viewed in form of tables and graphics.

The interface programs are written in "C" language using "Graphics Windows" package. It is presented in the form of graphic windows set like that of "Windows" system. Each window shows definite information by graphic or by table. In open windows the information is automatically renewed after each beam transfer cycle. In the windows there are horizontal and vertical menus and buttons. In order to change the menu, to switch between windows or to change the information in a window one should only press the standard set of function keys or use the mouse. If it is necessary, the operator can call the "Help window" with the description of commands.

Fig.1 shows the window with BTL fragment. The graphic images as icons of all magnets and beam diagnostic devices are given in this scheme. Near the beam position monitors there are indications to show the measurement data in form of adjustable resistors. "Invisible" buttons are hidden under the profile monitors and magnets images. By pressing those buttons with mouse one can open windows either with the beam profile or with the parameters of these magnets.

Magnets parameters table is given on fig.2. It contains the calculated fields and gradients and corresponding PS currents references, really measured PS currents and corresponding calculated magnets fields. Just after initialization the program calculates the fields and gradients of the magnets for a chosen energy, changes them into currents and sends as a data package

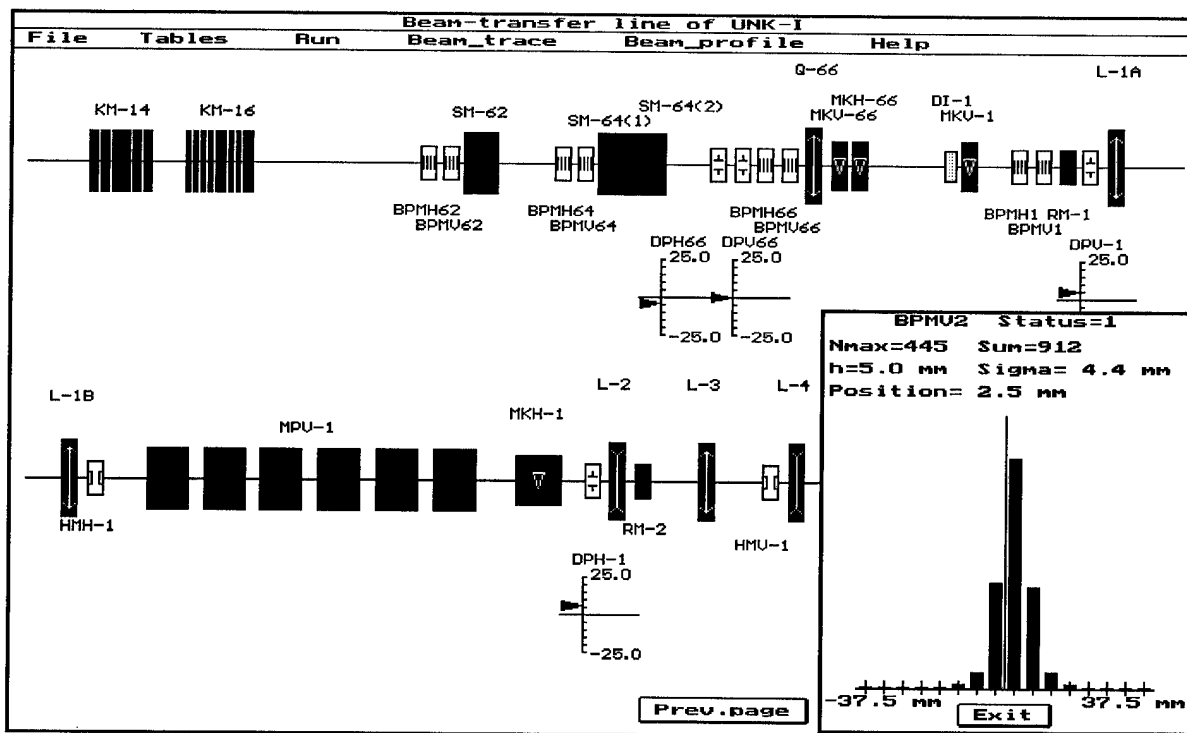


Figure 1: Window with the fragment of BTL.

to the console computer connected with the PS control. There they are processed and written in the PS controllers. The magnetic fields-into-PS-currents conversion is carried out by using the magnetic measurement results from the object-oriented BTL data base. The table also represents relative deviations of the real field in the magnets from calculated values.

The operator can change manually the magnetic fields or corresponding PS current sets by typing their new values on the keyboard. In this case the program watches for correctness of the user's action in order to keep the current deviations within the tolerances.

The program permanently receives (apart from the operator's action) data from the beam diagnostics and power supplies, processes them and accumulates the statistics, calculates correlation coefficients between PS and beam position instabilities. The PS currents changes from cycle to cycle are displayed in the form of graphic in window "Power supplies statistics". The statistics of the chosen PS is given.

The window "Beam trace" presents the beam trajectory along the whole channel in horizontal and vertical planes. The trace is drawn according to the measured data of the beam position, profile and halo monitors.

The beam trace is corrected only by operator's command in the window "Trace correction". Fig.3 shows this window. The table contains all correction dipoles, their status, corresponding monitors and correlation coefficient between the corrector current and beam position. Each corrector can be switched off (status "OFF"), switched on automatic mode (status "AUTO") or switched on manual control (status "HAND"). According to the operator's command the program calculates magnetic fields of

the correctors switched on automatic control mode. If it is necessary the operator switches some of the correctors on manual control and sets the corrector magnetic field by hand in the window "Parameters of magnet". By simulation the operator can view a expected trace after correction and write new current references in the PS controllers.

During calculations the program watches for the variation range of currents and polarity of the correction dipoles. If it is necessary to change the polarity the program informs the operator about it.

The convenience and visuality of the interface have made the user work more efficient. This fact allowed one to launch successfully the UNK beam transfer line in 1994.

IV. REFERENCES

- [1] A.A. Ageev et al. *Commissioning of the Beam-Transfer Line to UNK*. In Proceed. of EPAC'94, London, England, June 1994.
- [2] *IHEP 3000 GeV Accelerating-Storage Complex (UNK)*. IHEP Preprint 93-27, Protvino, 1993 (in Russian).
- [3] V.T. Baranov et al. *Beam-Transfer Line of UNK*. IHEP Preprint 92-118, Protvino, 1992 (in Russian).
- [4] A.I. Ageev et al. *Present Status of the UNK Control System at IHEP*. In Proceed. of ICALEPCS'93, Berlin, Germany, October 1993 (to be published).

Parameters of magnets						
Magnets	Theory	Work		Real		
	Field/grad	Field/grad	Current(A)	Field/grad	Current(A)	dB/B(%)
SM-62	2.553571	2.55357	1762.0	2.55137	1760.4	-0.086
SM-64(1)	-8.060000	-8.06000	-5561.4	-8.05002	-5554.5	-0.124
SM-64(2)	-8.060000	-8.06000	-5561.4	-8.06582	-5565.4	0.072
Q-66	4.249596	4.24960	294.0	4.24247	293.7	-0.168
MKV-66	0.0	0.93110	50.0	0.93417	50.2	9.342
MKH-66	0.0	0.00000	0.0	0.00000	0.0	0.000
MKV-1	0.0	0.00000	0.0	0.00000	0.0	0.000
L-1A	0.686271	0.68627	824.0	0.68618	824.4	-0.014
L-1B	0.686271	0.68627	824.0	0.68695	824.4	0.098
MPV-1(1)	-5.231856	-5.23186	-1236.8	-5.21772	-1233.4	-0.270
MPV-1(2)	-5.231856	-5.23186	-1237.0	-5.21081	-1231.9	-0.402
MPV-1(3)	-5.231856	-5.23186	-1236.0	-5.23670	-1237.2	0.092
MPV-1(4)	-5.231856	-5.23186	-1235.9	-5.23859	-1237.5	0.129
MPV-1(5)	-5.231856	-5.23186	-1234.3	-5.23226	-1234.4	0.008
MPV-1(6)	-5.231856	-5.23186	-1235.0	-5.23527	-1235.8	0.065
MKH-1	0.0	0.17078	40.0	0.17020	39.9	2.885
L-2	0.699207	0.69921	829.4	0.69899	829.1	-0.031
L-3	0.574665	0.57467	681.3	0.57563	682.5	0.168
L-4	0.768870	0.76887	925.6	0.76936	926.2	0.064
L-5	0.984593	0.98459	1170.8	0.98225	1168.0	-0.238

Energy: 65.00 GeV Reset Prev. page Next page Exit

Figure 2: Window with the fragment of table "Parameters of magnets".

Trace correction							
Correc.dipoles		Monitors		Correc.dipoles		Monitors	
Name	Status	Name	r m12(mm/A)	Name	Status	Name	z m12(mm/A)
MKH-66	AUTO	BPMH1	0.0 -0.166	MKV-66	AUTO	BPMU1	0.1 0.062
MKH-1	AUTO	BPMH2	0.3 0.140	MKV-1	AUTO	BPMU2	0.5 -1.715
MKH-2	HAND	BPMH3	0.9 4.420	MKV-2		BPMU3	0.5 -1.468
MKH				U-3	AUTO	BPMU3	0.5 3.698
MKH				U-4		BPMU4	-0.2 -0.046
MKH				U-5		BPMU4	-0.2 -3.146
MKH				U-6		BPMU4	-0.2 -3.147
MKH				U-7		BPMU4	-0.2 0.059
MKH				U-8		BPMU5	1.1 -3.152
MKH				U-9		BPMU5	1.1 0.058
MKH				U-10		BPMU5	1.1 0.067
MKH				U-11		BPMU5	1.1 3.147
MKH-12	AUTO	BPMH5	0.6 -3.157	MKV-12	AUTO	BPMU5	1.1 3.151
MKH-13	AUTO	BPMH6	-0.7 3.772	MKV-13	AUTO	BPMU6	-0.9 -3.633
MKH-14	AUTO	BPMH8	0.9 -6.366	MKV-14	AUTO	BPMU7	0.8 6.041
MKH-15		BPMH9	0.6 -3.309	MKV-15	AUTO	BPMU8	1.4 6.045
MKH-16	AUTO	BPMH9	0.6 -6.033	MKV-16	AUTO	BPMU9	1.3 6.024
MKH-17	AUTO	BPMH10	-0.4 -5.293	MKV-17	AUTO	BPMU10	0.9 5.457
MKH-18	AUTO	BPMH12	-0.4 -5.474	MKV-18	AUTO	BPMU13	0.5 3.420
MKH-19	AUTO	BPMH13	0.4 -3.621				

Parameters of magnet: MKH-2

MKH Theory field(kGs): 0.000000

MKH Work field(kGs): 0.104988

MKH Work current(A): 0.650

MKH Polarity: 1 Stat.OFF

MKH r: 6.05 mm z: -0.38 mm

MKH rd(BPMH3): 0.91 mm

MKH m12: 4.4198 mm/A

Reset Close Exit

Calculate Reset Run Exit

Figure 3: Window "Trace correction".

Macmon: A Monitoring Program for ELETTRA

Emanuel Karantzoulis and Mark Plesko*
Sincrotrone Trieste, Padriciano 99
34012 Trieste, Italy

* Josef Stefan Inst., Univ. of Ljubljana, Slovenia

Abstract

Macmon is a program entirely developed at ELETTRA that monitors and stores all the relevant machine parameters like beam position, beam current, vacuum, rf, injection, insertion devices, magnets current etc. during machine runs. Storage and retrieval of the data, their graphical display and correlations are some of the tasks that Macmon successfully performs. The methods used, its performance and some results are presented and discussed.

1. INTRODUCTION

ELETTRA is a third generation synchrotron light source situated at Trieste (Italy) operating at a variable beam energy from 1.0 to 2.3 GeV [1]. Operational aspects concerning the synchrotron can be found elsewhere [2], here need only be mentioned that currently 25% of the time is dedicated to machine studies while the rest is allotted to the users.

To facilitate machine studies and operation reliability we have developed a machine monitoring program that not only monitors a wide choice of machine parameters but also stores, analyses and compares them. Thus useful correlations can be found and interesting conclusions can be drawn leading towards a better understanding of the machine and consequently increasing its reliability.

The program, Macmon (Machine Monitoring), has been entirely developed at ELETTRA. The program is written in C, the data analysis part utilises the Motif (Toolkit) widgets and it is installed in the ELETTRA control system environment on the control room level workstations.

2. THE PROGRAM

Macmon can mainly be divided into two parts (A better understanding may be obtained from Fig. 1 below) A "low" level part that performs the data acquisition and storage and a "high" level part with the graphical user interface that deals with data reading, analysing and comparing. Additionally some high level software programs used to control and/or to measure from the machine are equipped with routines that can also store data in the Macmon storage files.

The low level Macmon is monitoring the following machine parameters: machine current, lifetime, injection rate, accumulated current, tunes, beam position in all 2x96 beam position monitors, beam size, rf frequency, voltage and temperature for each individual rf cavity, injection elements voltage and time delays, vacuum in each vacuum sector, insertion devices gap opening, power supplies current read and set values, scraper positions and radiation.

Additional information stored in Macmon from application/control programs is: dispersion, chromaticity and actions like the file name used to load the machine power supply currents, cycling and ramping.

3. THE LOW LEVEL PART

This part of the program is used for the data registration and storage. Our approach to the problem is by using separate programs that write on separate files at predetermined but independent time intervals. This way one may save much space rendering high flexibility to the system. Wherever it makes sense, groups of parameters are acquired and stored together. In order to save disk space, the acquired parameters are only written if at least one of them differs from its previously stored value by a predefined threshold. Further disk

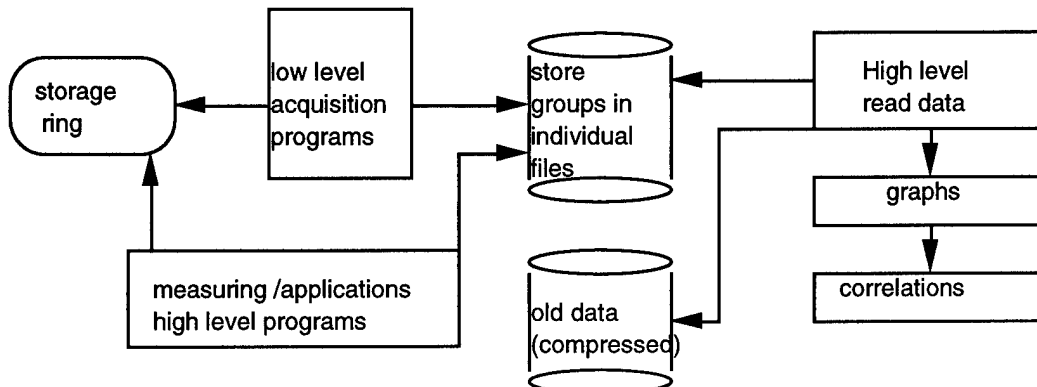


Figure 1: The main features of the ELETTRA Machine monitoring concept.

space saving is achieved by compressing data from previous runs. The decompression is handled transparently by the high level part of Macmon.

The programs run independently from each other, therefore even in the case of one program crashing or being locked up due to the hardware not responding, the others continue the data taking, minimising thus the loss of data. All programs have been written in the same fashion, based on the very successful high level software data structure and functions, developed for ELETTRA [3,4].

A particular group of the low level routines reside directly in some application and control programs which affect the settings of the machine. Therefore when and only when one of these programs change a parameter, this is recorded by Macmon.

4. THE HIGH LEVEL PART

This part of Macmon deals with the data manipulation e.g. retrieval and reading. It furthermore analyses the data in a effective way producing graphs while correlations between two machine parameters are also possible (e.g. see Fig. 2).

The program is user friendly and starts in the "running mode" -real time- namely reads the last line of the currently used monitoring files. For the display the user has to open the logbook window where all the aforementioned parameters are shown. A concise version of the logbook also exists which shows only the most important of the registered parameters. The history of those parameters can also be exported into tables for further analysis and printing.

To see the history of one or more parameters the user has simply to enter the start time and the end time. This is possible either directly or by opening a machine file catalogue that permits the user to target the time of a special action like loading a machine file, cycling or ramping. After the time interval is set the user opens the plot window where one

chooses the item to be plot. The plot pops out as a separate widget equipped with scale and save/print buttons.

In order to monitor quickly changing parameters, e.g. in the case of power supply oscillations, a trend routine is available, which logs one parameter as fast as possible and plots its history over the last few minutes.

5. CONCLUSIONS

The program has been successfully used since its first version one year ago and has provided much valuable information. It has been continuously upgraded and increased in performance over the past year. New structures and parameters could be added without major changes, due to the modular structure of the program and of the high level software of ELETTRA. In the figures 2 and 3 below one can see some characteristic pictures out of Macmon's imbedded graphic routine.

6. ACKNOWLEDGEMENT

We thank R. Sauro for patiently using the application since its initial stage and for his many comments and suggestions.

REFERENCES

- [1] A. Wrulich, "ELETTRA Status Report", proc. EPAC 1994, London, (1995)57
- [2] C.J. Bocchetta et al, "One and a Half Year of Experience with the Operation of the Synchrotron Light Source ELETTRA", these Proceedings.
- [3] M. Plesko, "A complete Data Structure for the High Level Software of ELETTRA", proc. EPAC 1994, London, (1995)1773.
- [4] M. Plesko et al, "The High Level Software of ELETTRA", proc. EPAC 1994, London, (1995)1776.

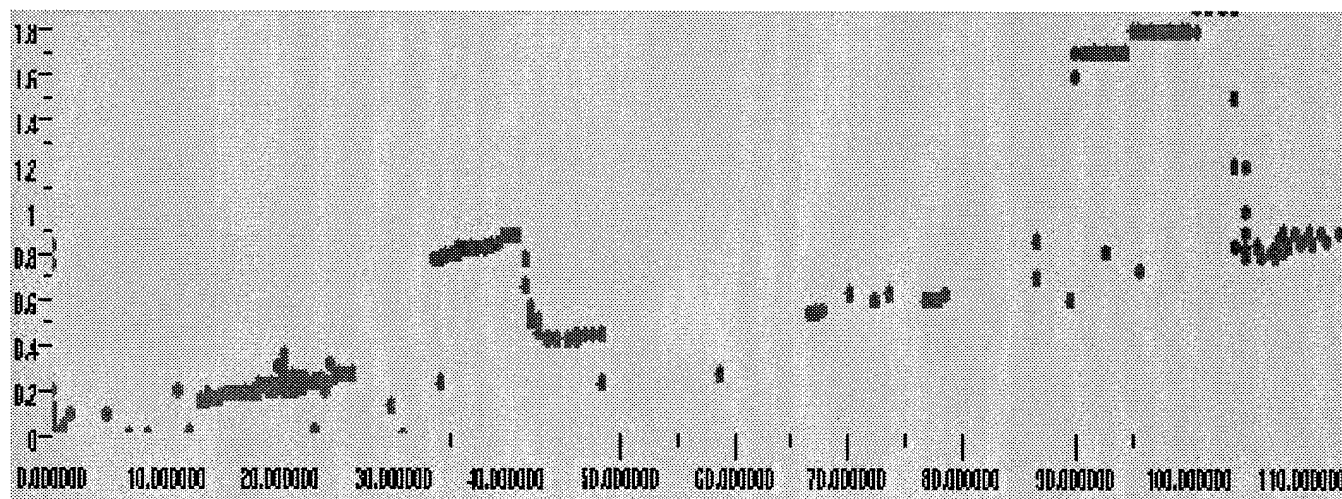


Figure 2: A Macmon correlation graph between pressure (pBar, y-axis) and beam current (mA, x-axis) over four days. As the storage ring was running both at 1 GeV and 2 GeV one can see the two main trends as straight lines.

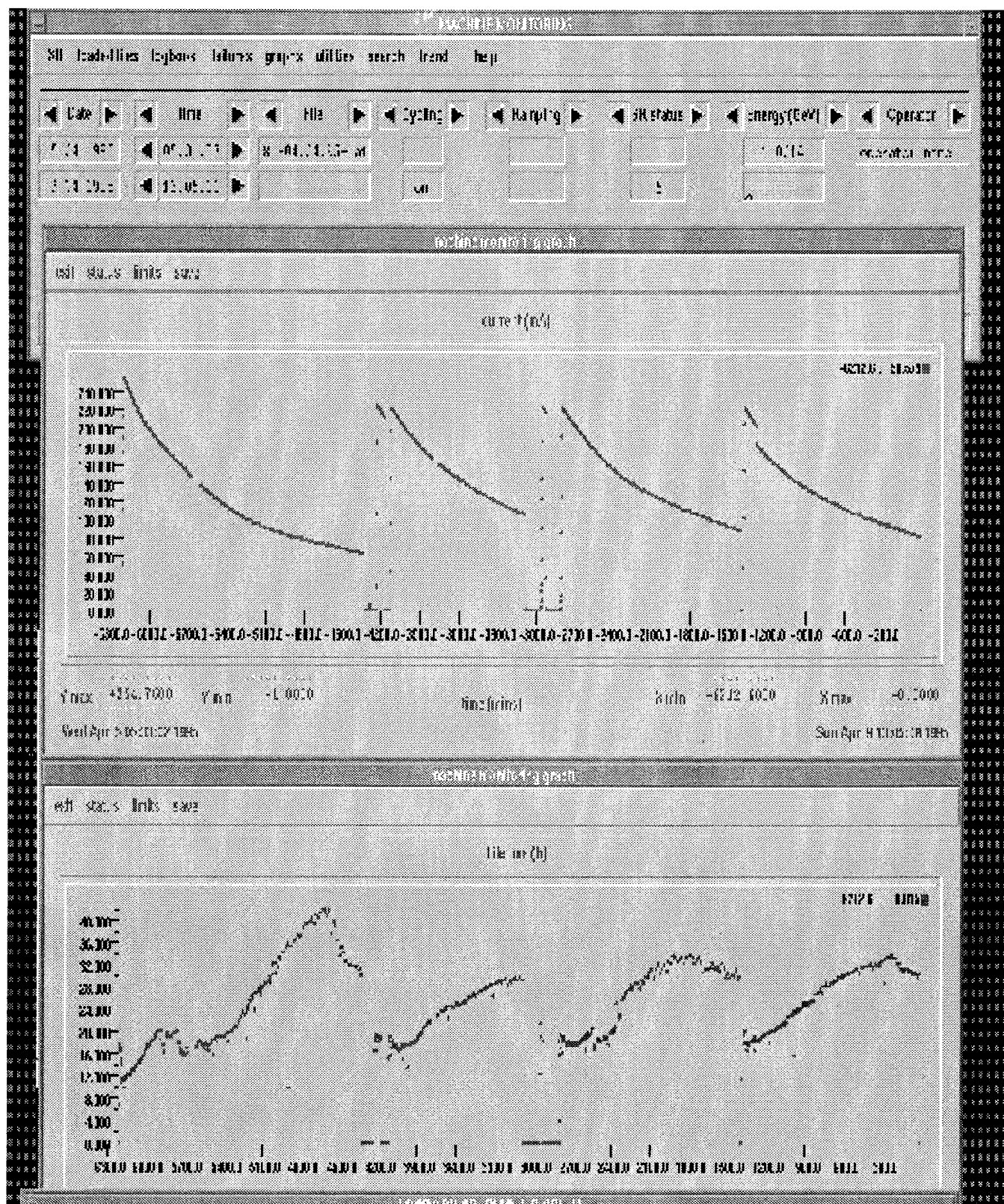


Figure 3: A classic picture of the machine current (mA, above) and lifetime(hours, below) on two independent graphic windows, for a period of four days and one injection per day. On the top it can be seen the main panel of the interface.

DEVICE CONTROL AT CEBAF*

S. Schaffner, D. Barker, V. Bookwalter, B. Bowling, K. Brown, L. Doolittle, T. Fox, S. Higgins, A. Hofler, G. Lahti, P. Letta, B. Montjar, N. Patavalis, J. Tang, W. Watson, C. West, D. Wetherholt, K. White, S. Witherspoon, and M. Wise, Continuous Electron Beam Accelerator Facility, Newport News, VA, USA

CEBAF has undergone a major conversion of its accelerator control system from TACL to EPICS, affecting device control for the RF system, magnets, the machine protection system, the vacuum and valves, and the diagnostic systems including beam position monitors (BPMs), harps, and the camera and solenoid devices (beam viewers, faraday cups, optical transition radiation viewers, synchrotron radiation monitor, etc.). Altogether these devices require approximately 125,000 EPICS database records. The majority of these devices are controlled through CAMAC; some use embedded microprocessors (RF and magnets), and newer interfaces are in VME. The standard EPICS toolkit was extended to include a driver for CAMAC which supports dual processors on one serial highway, custom database records for magnets and BPMs, and custom data acquisition tasks for the BPMs.

I. Differences Between TACL and EPICS

The systematic differences between TACL and EPICS have been well-documented, see [1 & 2]. From the standpoint of the low-level application developers at CEBAF involved in the conversion of the control system, a few key differences stand out.

A. Hardware Control

In TACL, control algorithms were stored as elements in a logic grid where different subsystems were distinguished by location in the grid. This inhibited independent development because only one subsystem at a time could access the grid to work on its control algorithm. In EPICS, the control algorithms are stored in independent databases which are not combined until the system is loaded onto the input-output controller (ioc).

Another difference is the frequency with which logic elements or database records are processed. Because TACL ran on UNIX machines, processing frequency was non-deterministic. EPICS runs on processors which use a real-time kernel, therefore the rate at which EPICS database records are processed is deterministic.

In TACL the logic grid was processed sequentially from left-to-right and cycled at a rate determined by the size of the logic grid and the speed of the processor. EPICS has a greater variety of execution options including differential scan rates, passive processing (records process only when triggered by another record), and software and hardware event-triggered processing. EPICS also provides a tool which makes it easy to set up finite state machines (sequencers) which give a finer degree of control over how database records are processed.

In TACL, predefined defaults could be set for signals coming from a remote computer when communication between two computers was lost. In EPICS, signals retain the last known value before communication was lost.

TACL provided predefined logical operators like OR, AND, NAND, and inverter as well mathematical operators including transcendental functions. TACL also provided digital logic elements such as Flip Flops, multiplexers/demultiplexers, comparators, and words-to-bits, bits-to-words convertors. The number of inputs and outputs for these elements could be easily set by the application developer. EPICS does not provide these operators in a pre-defined manner. It is not easy in EPICS to expand the number of inputs and outputs to a database record.

B. Operator Interface

The operator interface (OPI) portion of the control system in EPICS is fully integrated into the XWindows system while the TACL OPI was built using a proprietary graphics system that ran only on HP workstations. One impact is that in TACL, the OPI was limited to a single window per workstation while in EPICS the OPI can display multiple windows. In TACL, display screens tended to contain a lot of information and became very crowded. In EPICS, it is possible to modularize the information presented to operators which makes it easier to focus on a specific task.

The EPICS OPI does not have the same concept of a push-button as did TACL. In TACL it was possible to tie two signals to a single push-button so that the operator could set one signal and read back the results on a separate signal. In EPICS, push-buttons are tied to a single signal only. Also, the TACL OPI had a predefined symbol that interacted with the word-to-bits and bits-to-words logic element which would allow an operator to set and/or monitor individual bits. A pair of word-to-bits and bits-to-words records were added to EPICS at CEBAF early in the conversion process but a matching symbol was not added to the OPI until much later. Even now, it is not easy to set individual bits from the OPI in EPICS.

II. Conversion From TACL to EPICS

C. RF Prototype and CAMAC Driver

The first system to be converted was the RF system which supplies the power needed to accelerate the beam. The RF system is distributed across 350 modules and each module is controlled by a microprocessor. The microprocessors communicate to the control system via CAMAC buffer cards. Some additional control and monitoring functions are provided by CAMAC cards which are not integrated into the microprocessor system.

*Supported by U.S. DOE contract DE-AC05-84ER40150.

In TACL, the CAMAC interface to the control system was via GPIB into the HP computers. In EPICS the CAMAC interface goes through a HYTEC VSD 2992 Serial Highway Link Driver via the VME bus into the ioc. Initially EPICS did not possess drivers for CAMAC that were useful for CEBAF. Nor were drivers available to handle I/O to the RF microprocessors through the CAMAC buffer card. But due to the open architecture philosophy of EPICS it was possible to extend the EPICS toolkit to include drivers for standard CAMAC devices and a special driver to handle the buffered information to and from the RF microprocessors. The CAMAC driver also includes support for multiple processors on one serial highway, a feature which was not previously available in EPICS.

A parallel effort to the development of driver support was the conversion of the RF application from TACL to EPICS. The method used was to directly translate the TACL logic array, user processes and user functions, and state machine into EPICS database records, subroutine records and state machines. For the most part, the missing logic functions (logic gates, boolean operators, etc.) could be replaced with EPICS calculation and subroutine records. It was necessary to add two records to the standard EPICS library: bits-to-words and words-to-bits. TACL user functions and processes could be translated directly using standard EPICS records.

Translating the RF state machine proved to be slightly more difficult because the TACL version relied on the cyclical nature of execution of the logic grid and on the locations of some sets of logic elements relative to other sets in the logic grid, i.e., it was guaranteed that certain logic elements would process before other logic elements. In EPICS, the application developer has more flexibility to control the flow of processing but also more responsibility to make sure database records get processed in the correct order and at the correct time.

On the whole the conversion for the RF system went extremely well. It took the RF prototype team 3 months to produce a useable RF control system in EPICS. The major problems were the slow learning curve and the lack of novice oriented documentation for EPICS. Expert assistance from Los Alamos aided the prototype effort and allowed the CEBAF programmers on the prototype team to gain enough experience with the system to help others in the next phase of the conversion.

D. Vacuum and Valves and Harps

Once the CAMAC driver and device support were added to EPICS most low-level applications could be converted using only the available features of the standard EPICS toolkit. The simplest systems to convert were the beamline vacuum and valves and harps. The vacuum and valve system measures the vacuum in the beamline and provides control for valves which shut off sections of the beamline if contaminants are detected. The harps are diagnostic beam profile wire scanners. The conversion strategy for these systems was to take the existing TACL logic sets and find corresponding EPICS records. The vacuum and valve systems in TACL made heavy use of the JK Flip Flop logic element which has no matching record in EPICS. It turned out to be easy to model the behavior of this logic

element with an EPICS subroutine record. The harps required the addition of a sequencer to replace a TACL user function used to control a stepper motor. The first operational tests for these applications were completed within 3 months of the initial testing of the RF prototype.

E. Machine Protection System

The machine protection system (MPS) is used to detect and prevent operating conditions which are potentially dangerous to the accelerator due to beam power and/or beam loss. The MPS control software allows operators to determine the status of all the MPS elements in the accelerator at a glance as well as the ability to enter high voltage set points and read back voltages and currents. The first conversion of this system was operational within two months of first operations with the RF prototype. Again the conversion strategy was a direct translation from TACL to EPICS. Later iterations of this system preserved the functionality but took advantage of EPICS features that did not exist in TACL (such as differential scan rates). Future releases of EPICS will also permit security so that only operators in the control room can change selected parameters.

F. Solenoid and Camera Devices

The solenoid and camera system consists of solenoid driven devices such as faraday cups and retractable slits, solenoid and camera devices, mainly beam viewers, and some remote video monitoring devices, like experimental hall target chamber video. A single button selection of any one of these devices performs all functions for that device. For example, beam viewers cannot sustain high average beam currents without shattering, so the viewer control system must make sure that the thermionic gun parameters are lowered prior to insertion of a viewer. Some viewers are positioned such that they share the same physical location in the beamline as other devices so the viewer control software must make sure that these devices are retracted before a viewer is inserted. Also, since several viewers are connected to a single camera via a switcher only one can be viewed at a time. The software must retract a viewer which is currently inserted if another viewer is requested.

These systems are fairly simple as far as the hardware interface is concerned. One device has at most two limit switch readbacks, one solenoid control, and one camera control. All of these control points can be manipulated using standard EPICS records. The complexity of this system comes from the single button interface and the interfaces between other systems. In particular, it was possible to implement the mutual exclusion requirement very easily in TACL using logic gates with expandable numbers of inputs and outputs and a very simple user function. In order to duplicate this functionality in EPICS a fairly complex sequencer program had to be written.

G. Magnets

The CEBAF accelerator uses over 2000 magnets of various types. The use of EPICS allowed features to be incorporated in the control software that were not easily available under TACL. One of these features is the ability to write to hardware

only on request, which limits the possibility of writing noise to magnets causing them to go off hysteresis. Other features are: selectable control modes to track setpoint commands and initiate hysteresis cycling in the event that a setpoint command would violate the hysteresis curve; ability to control magnets by current or by field; control of the rate at which the current is requested to change; ability to maintain a constant field in magnets while doing maintenance in local mode.

It was not practical to implement all of these features using standard records from the EPICS toolkit; custom records were used instead. Since EPICS was designed as an open system that is easily extensible this did not present a real problem although, the effort was again hampered by the lack of good novice users documentation. But once the process was understood, extending EPICS to incorporate new record types was not a difficult task.

H. Beam Position Monitors (BPMs)

The CEBAF accelerator contains approximately 500 BPMs. Two different types of electronics are used to acquire data for these BPMs. In addition, some of the BPMs are multiplexed so that up to five BPMs share the same set of electronics. The most common type of BPM electronics are interfaced to CAMAC (the 4-channel BPMs); some of these BPMs are multiplexed and the multiplexer controller sits on the VME bus. The rest of the BPMs use switched electrode electronics (SEE) and are interfaced directly to the VME bus.

In theory, the 4-channel BPMs could have used the CAMAC driver support connected to the standard set of EPICS records. This proved not to be practical. The 4-channel BPMs need to acquire data at 60 Hz and the maximum cycling rate in EPICS is 10 Hz. This rate could be set higher, but some iocs control 40 BPMs and the overhead involved in database record processing made it impossible to acquire and process data for each BPM individually at a fast enough rate. The solution to this problem was to utilize the fact that EPICS allows an external process to event-trigger database processing. A data acquisition task was designed to acquire multiple data points for all the BPMs in a CAMAC crate, distribute the data to custom BPM records in the database and then trigger these records to process.

The data acquisition requirements for the SEE BPMs are even higher. These devices are controlled directly from VME and offer much greater performance and processing capabilities than the 4-channel BPMs. The same processing strategy was adopted for the SEE BPMs. This structure allows operators to control both types of BPMs electronics with the same set of global controls and presents a common interface to high level applications.

It was also necessary to write new EPICS VME driver support for the multiplexer controller since this board was developed in-house. It was possible to attach this driver to existing EPICS records.

III. Advantages of EPICS as a Control System

EPICS is both an open system and a modular system. At

the lowest level, the toolkit uses a real-time OS kernel and at the higher level, it uses X-Windows. It is easy to integrate new device support and to extend the system to include new record types. EPICS has very flexible control options such as settable, differential scan rates and event-triggered processing. Integrated tools are available to aid in development, database management, debugging, and operations. Since CEBAF began its conversion effort the novice documentation has been improved considerably and is available on the World Wide Web.

I. Scale of CEBAF Control System

Some idea of the size of the CEBAF accelerator control system can be summarized by the following table:

Table 1: Size of CEBAF Control System

System	# EPICS Records	# Control Points
RF	72034	28205
Vacuum and Valves	916	743
Harps	5281	3323
Machine Protection	3024	1773
Magnets	26849	8479
Solenoid and Camera	4336	419
BPMs	12625	4892
Total	125065	47834

The number of control points is defined to be the number of analog inputs and outputs plus the number of command bit inputs and outputs that communicate directly with the hardware.

The original TACL system controlled approximately 25% of the CEBAF accelerator. The current EPICS control system is operating the entire machine and is still growing. EPICS has proven to be a system which scales well and which provides good tools to aid application developers.

IV. References

- [1] William A. Watson III, et. al., "The CEBAF Accelerator Control System: Migrating from a TACL to an EPICS Based System", *International Conference on Accelerator and Large Experimental Physics Control Systems*, Oct., 1993.
- [2] Karen S. White, et. al., "The Migration of the CEBAF Accelerator Control System from TACL to EPICS", *CEBAF Control System Review*, May, 1994.

AUTOMATED FREQUENCY TUNING OF SRF CAVITIES AT CEBAF*

M. Chowdhary, L. Doolittle, G. Lahti, S.N. Simrock, R. Terrell,
Continuous Electron Beam Accelerator Facility, Newport News, VA 23606, USA

Abstract

An automated cavity tuning procedure has been implemented in the CEBAF control system to tune the superconducting RF (SRF) cavities to their operating frequency of 1497 MHz. The capture range for coarse tuning algorithm (Burst Mode) is more than 20 cavity bandwidths (5 kHz). The fine tuning algorithm (Sweep Mode) calibrates the phase offset in the detuning angle measurement. This paper describes the implementation of these algorithms and experience of their operation in CEBAF control system.

I. Introduction

The 338 superconducting RF cavities that populate the linear accelerator at CEBAF need their resonance frequencies tuned to within a few Hertz of the site's 1497 MHz reference oscillator. The resonance frequency of cavities change due to factors such as change in ambient temperature and helium pressure variation. These cavities are tuned using an automated process, known as Autotune, which involves a series of steps: Burst Mode is used to coarsely tune the cavity, starting as much as 5 kHz from center to within ± 160 Hz of the operating frequency. Next, Sweep Mode measures the phase offset in the detuning angle measurement to within $\pm 3^\circ$. Finally, Autotrack mode brings the operating detuning angle to within $\pm 3^\circ$ of the measured center frequency, and maintains it within $\pm 10^\circ$ in the presence of system drifts. Various modules of Autotune software run as a single or multiple copies of a Unix process executing on a cluster of HP 9000-7xx workstation(s).

II. Coarse Tuning (Burst Mode)

In this procedure, a bandwidth limited, pseudo-random phase modulated drive signal (noise burst) is sent to the cavity and the response of a 360° phase detector is measured and recorded. A signal from the master oscillator $V_1(t) = |V_1|e^{-i\omega_0 t}$ is sent to a vector modulator where it is modulated by a pseudo random signal $x(t) = e^{i\phi(t)}$ such that power spectrum of $x(t)$ is a positive constant for frequencies within ± 5 kHz and zero outside this range. The output signal from the vector modulator is amplified and sent to the cavity. The cavity acts like a filter on the noise signal and transmits the frequency components close to its resonance. A pickup probe in the cavity responds to the accelerating field, $V_c(t)$, in the cavity. This

signal is fed into the 360° phase detector where it is multiplied by a second reference signal, $V_2(t) = |V_2|e^{i\omega_0 t}$, from master oscillator to produce a baseband output signal $y(t) = V_2(t)V_c(t)$. The cavity resonance frequency can be determined by proper processing of the power spectrum of the output signal $y(t)$ as described in Ref [1]. The Fourier transform of $y(t)$ is

$$Y(\omega) = \int_0^T y(t) e^{-i\omega t} dt$$

and it can be shown from reference[1] that

$$|Y(\omega)|^2 = \int_{-T_M}^{T_M} e^{-i\omega\tau} T_M \left(1 - \frac{|\tau|}{T_M}\right) \langle R_{yy}(\tau) \rangle_T d\tau$$

$$\approx \int_{-\infty}^{\infty} W_{T_M}(\omega - \omega') S_{yy}(\omega') d\omega'$$

where $\langle R_{yy}(\tau) \rangle_T$ is the finite time correlation function and $S_{yy}(\omega')$ is the power spectrum of the output process $y(t)$. The above expression of $|Y(\omega)|^2$ corresponds to viewing the actual power spectrum through a spectral window W_{T_M} . When the resolution of $|Y(\omega)|^2$ is within the bandwidth of ± 5 kHz the power spectrum of the input process, $S_{xx}(\omega)$ is smoothed resulting in a clean well behaved peak of $|Y(\omega)|^2$ which is centered around the cavity resonance frequency. Fig 1 shows an example of one such power spectrum obtained while tuning a cavity which was detuned by approximately 2 kHz. The implementation of this technique is described in this section below.

The communication and control of a single SRF cavity is done by an embedded RF microprocessor [2]. This microprocessor is controlled by an EPICS state machine. In Autotune procedure, a preparatory setup of the RF system is completed and 200 Watts of forward power is established before the noise burst is sent down to excite the selected cavity.

The functionality of Burst Mode is described below:

- Send a trigger signal to the RF microprocessor to generate the noise burst in selected cavity(ies). Wait for acknowledge signal indicating successful completion of Burst Mode.
- Once the acknowledgment has been received, upload the data from the RF microprocessor to analyze it and determine the cavity resonance frequency.
- Initiate the tuner stepper motor movement in order to move the cavity resonance frequency closer to the operating frequency.
- Repeat steps b) through d) until the cavity resonance frequency is within ± 160 Hz of the operating frequency of

Supported by U.S.DOE Contract DE-AC05-84-ER40150

1497 MHz.

- e) Constantly check that RF power stays on while going through steps a) to d). If RF power is shut off (due to interlock trips) or if RF module becomes unavailable to the tuning process or if the cavity response signal is lower than the noise threshold ($4mV/\sqrt{Hz}$) then stop the tuning process after raising appropriate error flags.

The hardware presently used allows the measurement of cavity frequency in a range of up to ± 5 kHz from the operating frequency. If the cavity is detuned by several bandwidths, the detuning angle cannot be determined accurately due to low signal to noise ratio of the detuning angle phase detector (i.e. transmitted power is low). A typical Burst mode power spectrum is shown in figure 1. This cavity was detuned by approximately 2 kHz.

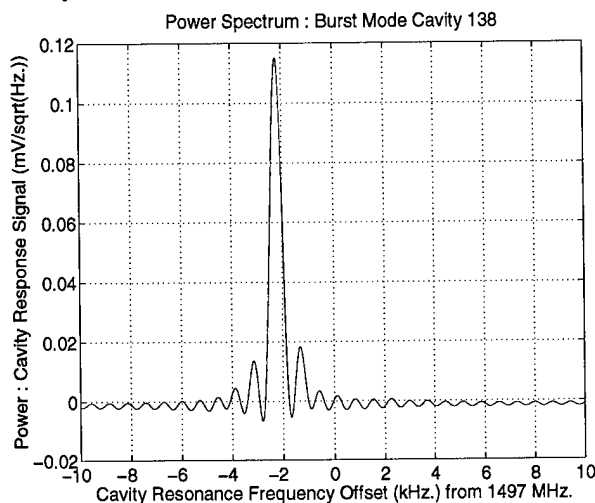


Fig 1

III. Fine Tuning (Sweep Mode)

In this procedure an analog feedback loop stabilizes the accelerating gradient in the cavity at 3 MV/m. A single side band modulation of the operating frequency is generated using the phase offset vector modulator. The phase offsets both in X and Y direction are set using $V_x = V_0 \sin(2\pi f_m t)$ and $V_y = V_0 \cos(2\pi f_m t)$. Ten points in one period of the modulating frequency are sufficient to suppress the lower order harmonics. The time interval between two DAC settings is given by $dt = 1/(f_m \times n)$, where n is the number of points in one 360° period. The detuning angle is constantly measured during the sweep process, and averaged to suppress dependence on microphonic noises. The modulating frequency is swept over the range of ± 200 Hz in steps of 5 Hz

The detuning angle measurement and the modulating frequency sweep are related as described by

$$\phi_{meas} = \text{atan}\left(2 \times Q_L \times \frac{f_m}{f_o}\right) + \phi_{off}$$

where, ϕ_{off} is the offset between measured detuning angle

from the hardware and the actual detuning angle. Q_L is the loaded quality factor for the cavity. The frequency sweep of ± 200 Hz in steps of 5 Hz takes 80 seconds. The sweep data is then uploaded from the RF microprocessor for analysis. The uploaded sweep data contains the detuning angle measurement from the hardware versus the modulating frequency data. A nonlinear curve fit is performed on this data to extract the detuning angle offset, the loaded quality factor and the cavity operating frequency. If the curve fit does not succeed to within the specified tolerances, then an alarm is raised and tuning process is terminated. A plot of the measured detuning angle data versus the modulating frequency and a nonlinear curve fit is shown in figure 2.

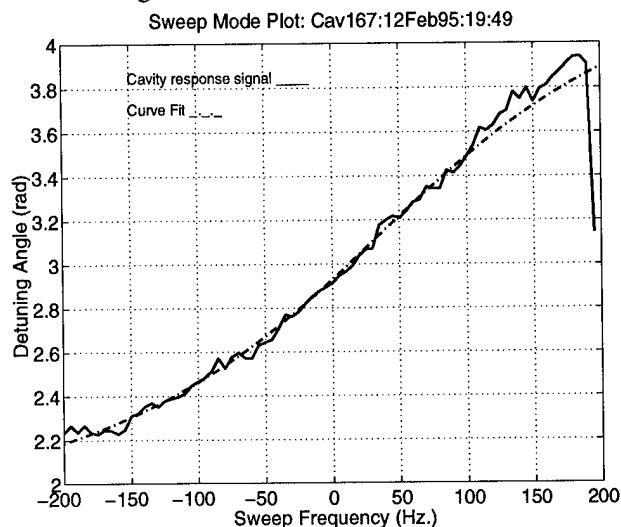


Fig 2

The detuning angle offset determined by the Sweep Mode is passed on to another process called Autotrack, which maintains a tuned cavity on resonance. Autotrack constantly monitors the measured detuning angle. A non-zero detuning angle means that cavity has drifted. The sign of the angle is an indication of which direction the stepper motor should be moved to compensate for the drift. Autotrack starts to move the stepper motor when it detects a detuning angle of greater than $\pm 10^\circ$ and continues to move the stepper motor until the detuning angle is within $\pm 3^\circ$. The response speed of the Autotrack feedback loop is designed to minimize the chances of overshoot, since recovering from overshoot involves unwinding the gear train backlash. One goal is to minimize the total motion of the stepper motor, since there are reliability concerns for the vacuum feedthrough that carries the drive shaft to the superconducting helium bath.

IV. Operational Experience

The Autotune routine has been used to tune SRF cavities at CEBAF since April 1994. Prior to availability of this facility, the cavities were tuned manually using a network analyzer and a stepper motor controller box. The cavity to be tuned was

subjected to a frequency sweep using the network analyzer and the amplitude of measured gradient signal from field probe in the cavity was observed to detect the cavity resonance frequency. Then the tuner stepper motors were moved using the controller box to tune the cavity to a resonance frequency of 1497 MHz. This process was not considered practical for long term routine use for a full complement of 338 cavities.

All of the cavity tuning now is done using the Autotune routine. The user interface for Autotune is based on the EPICS display tool MEDM. A diagnostic user interface is also provided, which is based on Tcl/Tk programming language. The diagnostic interface provides the ability to view the power spectra during Burst mode tuning and the sweep mode plot and the progress messages that are generated during the tuning process.

Performance statistics for Autotune routine were obtained from the logfiles that are created during the tuning process. The Autotune facility was used 1933 times during a three month period of 1/95 to 4/95. CEBAF has 338 SRF cavities. Thus, on an average a cavity was tuned approximately 6 times during this three month period.

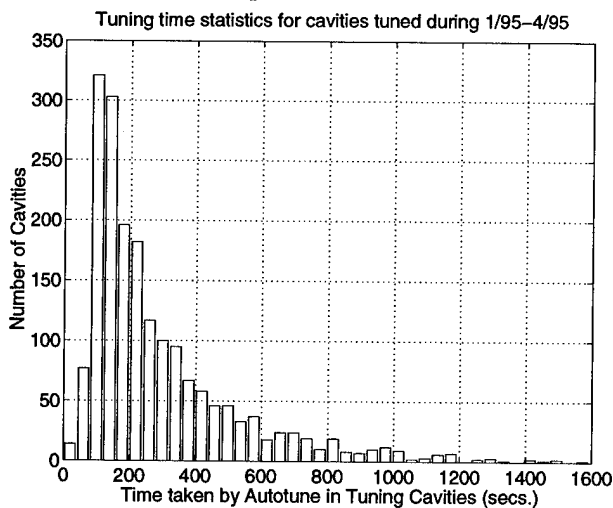


Fig 3

The figure 3 shows a histogram of the time taken by the tuning process. A majority of the cavities were tuned within ± 160 Hz of operating frequency in less than 150 seconds. A few cavities took as long as 1600 seconds to be tuned. Some of these cavities are known to have a considerable backlash in the gear train driven by the stepper motor to squeeze or expand the cavities. A few other cavities have sticky gear trains. The tuning time is also proportional to the amount of offset between cavity resonance frequency and the desired operating frequency. Some of the cavities that took a long time to tune were detuned by almost 5 kHz.

Figure 4 shows a histogram of detuning offset in cavity resonance frequency before Burst Mode tuning. A majority of cavities were detuned by -0.5 kHz. Burst Mode detected a few

cavities within a range of ± 10 kHz which exceeds the specification on operating range of Burst Mode set at ± 5 kHz.

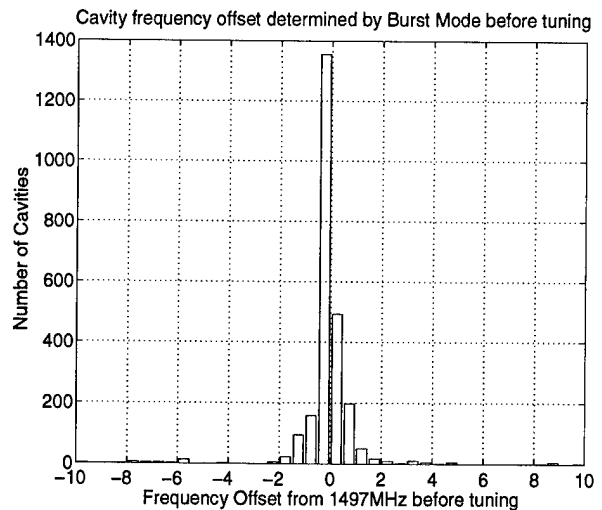


Fig 4

Figure 5 shows a histogram of the cavity resonance frequency offset from the operating frequency after Burst Mode tuning was completed. All the cavities were tuned to within ± 160 Hz specification for coarse tuning. A majority of cavities tuned appear to have been detuned by negative offset. This can be attributed to positive pressure fluctuations in the helium pressure during cryogenic testing that took place during this three month period.

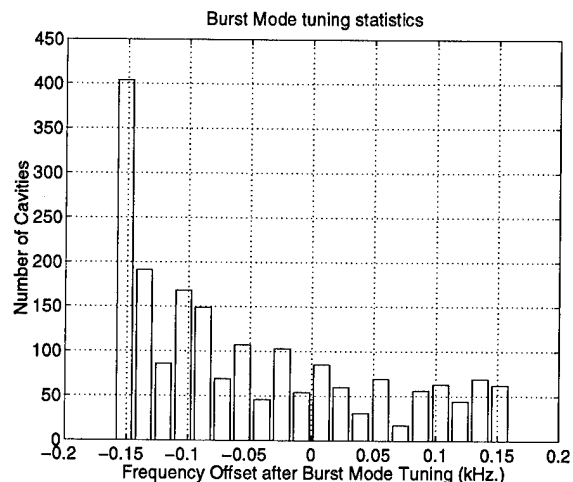


Fig 5

VI. REFERENCES

- [1] "Automated Measurement of Cavity Frequency and Cavity Tuning at CEBAF," R. Li, S.N. Simrock, and B. Yunn, CEBAF PR-93-011
- [2] "Microprocessor Support for CEBAF RF Control Module," I. Ashkenazi and G.E. Lahti, Proceedings of 1989 PAC Conference, pp 1861
- [3] "Software Requirements for RF Autotune," M. Chowdhary, J. Tang, Controls Software Group Requirements Document, CEBAF, 22 February 1994.

Operational Monitoring of the CEBAF RF System

J. Karn, B. Dunham, and M. Tiefenback*, The Continuous Electron Beam Accelerator Facility
Newport News, Virginia USA

An EPICS-based control interface has been developed which enables effective monitoring of the 338 independent RF systems that drive CEBAF's superconducting cavities. Visual screens allow the operator to quickly identify cavities that have faulted, or which are operating out of specification. These screens allow the operator easy access to automated routines for clearing faults, routines for documenting and tracking hardware problems, and expert screens for immediate correction of RF problems. The combination of visual screens and automated scripts has greatly decreased the time required to identify and recover from RF problems, significantly increasing operational uptime.

I. Introduction

CEBAF is a 4 GeV electron accelerator undergoing commissioning to produce a CW beam for nuclear physics research. The accelerator consists of a 45 MeV injector and two parallel 400 MeV linacs that utilize a total of 338 superconducting cavities. The cavities are grouped into 42 cryomodules each containing eight cavities, plus one two-cavity cryostat. The beam is recirculated through both linacs four additional times to achieve a total energy of 4 GeV.

II. RF Status Screens

Two display screens were constructed to show the status of the RF system of all cavities in each linac. Figure 1 shows the screen to monitor CEBAF's Injector and North Linac. The square indicator for each cavity is a composite of seven signals that describe the status of the cavity. These signals are listed in Table 1. The seven signal indicators are layered so that the higher priority signals cover the lower priority signals. Special characters were imbedded in the various indicators to make them distinguishable on non-color printers.

1. RF on
2. RF off
3. Klystron bypassed
4. Gradient set to zero
5. Autotrack process is not running
6. Autotrack process is faulted
7. Gradient lock feedback loop is not stable

Table 1 - Cavity RF Status Signals

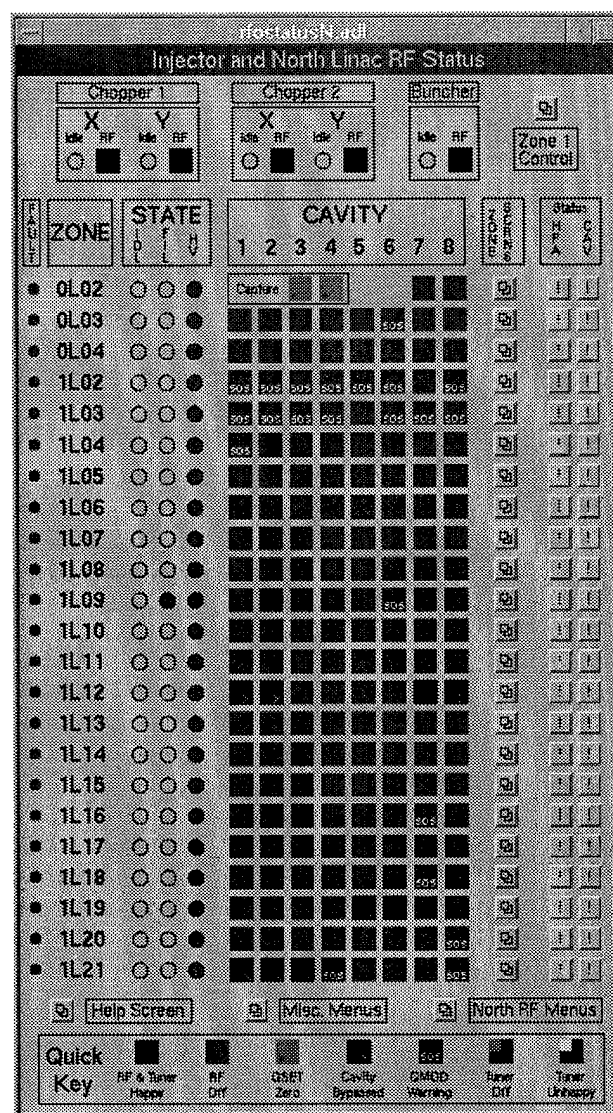


Figure 1 - Linac RF Status Screen

In addition to showing the status of RF in the individual cavities, the status screens also provide:

- The state of the High Voltage Power Supply that feeds the eight klystrons for a given cryomodule.
- Buttons to access expert control screens for diagnosing problems in specific cavities.
- Buttons to access automated routines for documenting changes made to a RF cavity or High Power Amplifier (described in Section III.)
- Buttons to access automated routines for clearing common faults (described in Section IV).

* Supported by DOE Contract # DE-AC05-84ER40150.

III. RF Operability Database Utility

A routine was developed using the TCL/TK Tool Kit¹ to allow operations personnel to document changes made in the status of individual cavities and High Power Amplifiers. Such changes could occur when a problem cavity is bypassed by an operator or when a cavity is restored to operation by the RF Group. The database would specify:

- status of the cavity's klystron (good or bad)
- status of the cavity's autotrack system (good or bad)
- status of the High Voltage Power Supply
- additional details or comments
- date and time stamp

This database provides two separate groups, the Accelerator Operations Group and the RF Group, an accurate way to communicate and track changes in a common system. Further, the RF Group can identify and correct recurring problems by tracking the history of each cavity's RF system.

In addition to tracking a cavity's RF history, the database provides a template for other control system utilities that interface with the RF system. An example is the CEBAF Linac Energy Management² utility that optimizes the gradients of all cavities in a linac to produce the required linac energy. This routine searches the RF Operability Database to determine which cavities are operational before calculating and changing cavity gradients.

IV. RF Fault Recovery Utility

A routine was developed using the TCL/TK Tool Kit to provide a fast and intelligent method of clearing a RF fault and restoring RF to the cavities. In addition to fault-induced RF trips, this utility is also useful for restoring RF following a planned maintenance downtime or after a tunnel access when all RF has been turned off. The utility attempts to bring the hardware configuration into agreement with the RF Operability Database, so that only designated cavities are operating and only the proper cavity tuning processes are activated. The control screen allows the operator to select individual cryomodules (all eight cavities) or an entire linac.

V. Future Applications

Future applications will use the RF Operational Database as part of their configuration input. A RF utility presently being tested provides a non-destructive method of matching the RF phase of each cavity to the phase of the beam. The mechanism for passing information between operations and maintenance personnel is proving very effective for the RF system, and is being applied to the beam position monitor system (550 monitors) of the CEBAF accelerator.

VI. Conclusion

The combination of visual screens and automated scripts has greatly decreased the time required to identify and recover from RF problems, significantly increasing operational uptime. In addition, these tools provide the Operations Group and the RF Group a common method for monitoring the 338 independent RF systems and for communicating any changes made in the operability of specific systems. These techniques are being expanded to new RF utilities as well as to other accelerator hardware systems.

References

- [1] J. K. Ousterhout, *Tcl and the Tk Toolkit*, Addison-Wesley Professional Computing Series (1994)
- [2] J. van Zeijts, *Rapid Application Development Using the Tcl/Tk Language*, these proceedings.

OPERATING EXPERIENCE WITH THE NEW TRIUMF RF CONTROL SYSTEM

K. Fong, M. Laverty, S. Fang, TRIUMF, 4004 Wesbrook Mall, Vancouver, B.C., Canada V6T 2A3

Abstract

The 23 MHz rf control of the TRIUMF cyclotron has been replaced by a new VXI control system based on digital signal processing. It provides amplitude and phase regulation of the cyclotron dee voltage, as well as other functions such as power-up sequencing, spark and high VSWR protection. Modularity of the hardware is achieved by the VXI architecture, and in the software by Object Oriented Programming. It is expected that this will result in a considerably longer MTBF, and shorter fault diagnosis and repair times, than the equipment it replaces. The new system has now been in operation for over two months. The results of commissioning, testing, and early operating experience are presented.

I. INTRODUCTION

The system described here represents the first major upgrade of the original TRIUMF cyclotron main rf control system [1], and is an outgrowth of earlier systems developed at TRIUMF. Its most recent predecessor is a VME-based system used for control of a 92MHz booster cavity [2]. Moving to a VXI platform allows much more functionality to be incorporated in each module. Also, the level of shielding inherent to VXI permits the incorporation of low-level analog as well as rf elements in the rack modules. This results in a high level of integration and fringe benefits such as much reduced fault diagnosis and repair times.

Preliminary test results using a resonator test facility were reported at EPAC'94 [3]. This system has now been installed and commissioned in the cyclotron. This paper offers a brief review of the noteworthy features of the new control system, together with data and observations collected in the course of commissioning and early operation.

II. SYSTEM OVERVIEW

A photo of the VXI control rack which contains virtually all of the active electronics is shown in Figure 1. Of the 13 available VXI slots, the first two (starting from the left) are occupied by the system controller. This is an embedded PC compatible which provides the VXI-bus interface and timing, the local operator interface, as well as most of the intelligence of the system. The second module, like the first, is a commercially available unit. It provides an interface for the safety interlock signals to the VXI bus. The remaining

modules were designed at TRIUMF to meet the requirements of this application. The first of these is the diagnostics module. This module provides analog data capture and data logging from various test points throughout the system via the VXI analog bus. The next module is the amplitude/phase controller. It provides high speed A/D and D/A conversion, as well as a pair of digital signal processors which implement the respective amplitude and phase control algorithms. The DSP's are programmed for Proportional-Integral-Differential feedback and run autonomously. Communication between the DSPs and the VXI interface is needed only when updating the PID parameters, and opening and closing the feedback loop.

Next to the amplitude/phase controller and coupled to it via the backplane is the rf module. This is the module where most of the low-level rf processing takes place. It includes the amplitude/phase modulator, the amplitude and phase detectors, and an rf switch to select between driven and self-resonant modes of operation. From the rf module, the rf signal goes to the preamp module. Here the signal is amplified to a level of about 5W before being output to the driver amplifiers. This module also performs VSWR detection, generating an interrupt to the DSP module when the reflected power exceeds a programmed limit. The direct digital frequency synthesizer module resides in the next slot, and provides a program controlled reference frequency for the driven mode of operation. Direct digital synthesis was chosen due to its ability to change frequency without generating amplitude and phase glitches. The frequency can also be set via remote or local soft pots.

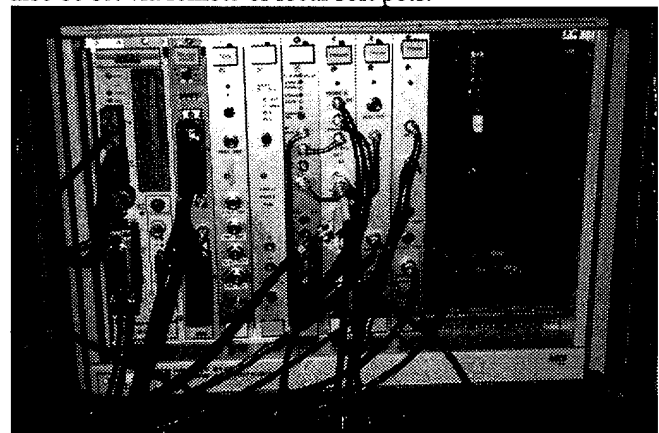


Figure 1 - VXI System Rack

The next module, the tuner controller, also uses a DSP. In this case convenience, rather than bandwidth, is the main

consideration. The tuning system uses modulation of the cooling water pressure to effect a change in resonator frequency, and has a bandwidth of the order of 1 Hz. . The last of the modules is the AIDC [4]. For the purposes of this system, it provides SDLC communications with the control room computers.

The system software was designed using the object-oriented constructs of the C++ language. A generic VXI interface is used as a parent object for all the register-based VXI modules. Higher level objects such as DSP interfacing inherit the functionality of this VXI object. Together with additional communication and control software for the DSP, it forms the parent for the three different DSP module interfaces. The state of every hardware module is updated every 0.05 sec and, for diagnostic purposes, this can be displayed in a dialog window. All the relevant information and controls necessary for normal running are duplicated and grouped into one single dialog window. The same information is sent to the central control system via the AIDC module, and displayed in an X-window on the operator console. Commands from the central control system are interpreted and acted upon. State changes and their causes are sent to a printer for logging.

III. SYSTEM INTEGRATION

Installation of the new control system was arranged to take place about one week prior to a planned cyclotron shutdown. This allowed for comparative testing with the old rf system, without the complications of shutdown related problems. Initial testing was accomplished in a series of stages, beginning with low power open-loop operation, and continuing on to full power close-loop operation. A control system analyzer was employed to measure parameters such as loop gain and noise spectra under open and closed loop conditions. A sample of the measured open loop frequency response is shown in Figure 2. The resulting curve shows almost single pole behavior, where the loop gain falls off at 20 dB/decade, until the unity gain point is reached. The low frequency pole is due to the integral component of the control algorithm. A second pole is located at about 3 kHz, which is due to the bandwidth of the cyclotron resonator. This pole is canceled by a zero at about 8 kHz, which arises from the proportional component of the control algorithm. The system group delays begin to dominate above 20 kHz. Loop gain at 10 Hz exceeds 60 dB. Phase margin is 130° at 9 kHz, and gain margin is 20 dB at 80 kHz. If necessary, the integral gain can be increased by factors of more than 10 to improve regulation below 3 kHz, and the proportional gain can be increased by a factor of 3 to improve regulation above 3 kHz, and still have sufficient gain and phase margin for stability.

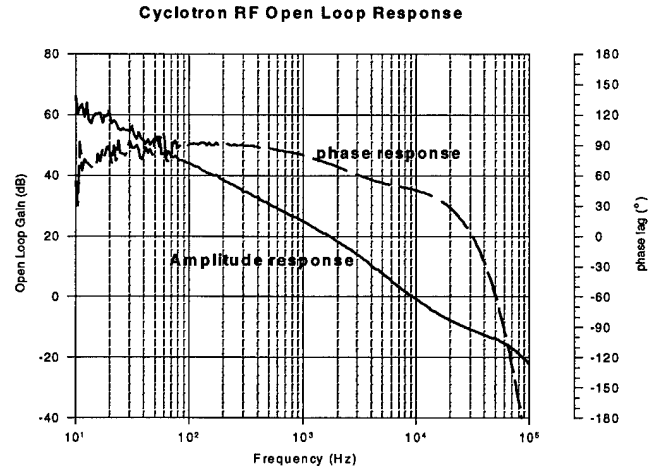


Figure 2 - Amplitude Loop Frequency Response

Similar measurements of the tuner control system produced the curve of Figure 3. The mechanics of this system result in a number of poles located at about 1 Hz. This puts a severe upper limit on the bandwidth which can be achieved, but does not cause any actual problems in practice, as this system's main purpose is to deal with thermal drift of the resonator frequency.

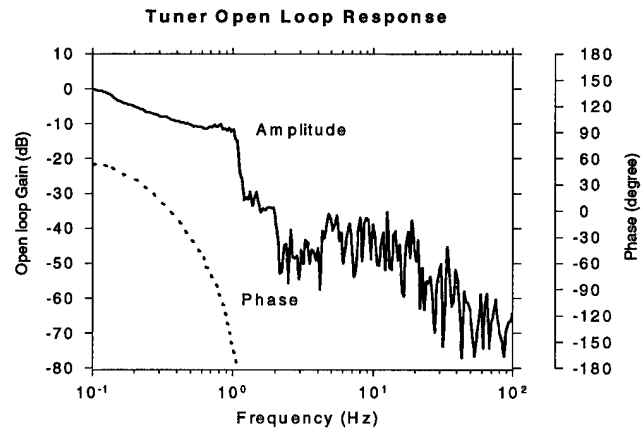


Figure 3 - Tuner Loop Response

Final test and integration had to await the end of the shutdown. This included testing of the control room operator interface software, as well as further testing and optimizing of the controls. One item in particular which had to wait for rf startup was optimization of the spark detector. The spark detector monitors the rf level, its fall time, as well as the reflected power in the main transmission line. This detector operates on the log of the resonator voltage. If the resonator voltage drops below 10 kV for more than 10μs, the drive is shut off. This is classified as a 'level trip'. Figure 4 shows an example of a level trip after the dee voltage has been decimated by a medium spark. The log amplitude signal is

also differentiated, and the resulting signal passed to three comparators. These are adjusted to detect three different rf decay rates, corresponding to small, medium, and large sparks in the resonator. Figure 5 shows the relative magnitude of these signals and their associated fall times. If the fall time of the dee voltage is such that it drops to less than 10% of its nominal value in less than 4 μ s, it is classified as a 'large spark trip' and the drive is shut off. The power amplifier is also protected against high reflected power. If the output of the reflected power detector in the preamp module exceeds a safe threshold value, the preamp module interrupts the DSP module via a local bus line. The amplitude DSP responds by reducing the output drive by a predetermined step and opening the feedback loop, if it is closed. As long as the reflected power exceeds the threshold, the output drive continues to decrease. If the problem corrects itself, the controller can rapidly ramp the drive up to full power again.

Characteristics of a medium spark

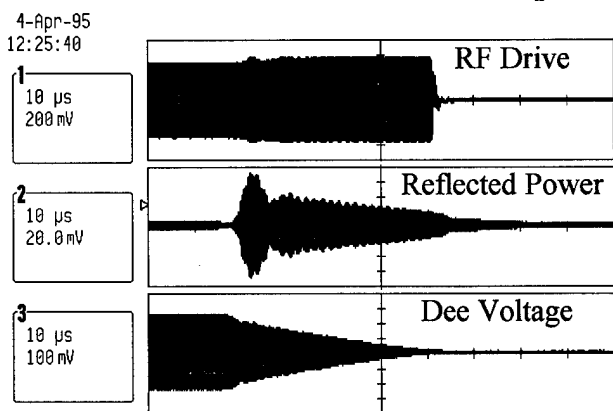


Figure 4 - Medium Spark

IV. CONCLUSION

Owing to careful preparatory work, the installation of the new system went relatively smoothly, considering the magnitude of the changes. As a precaution, the original system was left intact and ready to be reconnected if required. This option was not needed, however, and no significant downtime has been attributed to the new controls or the minor changes which have been required to date. As an example, one change which proved necessary was to increase the gain parameters to accommodate the effects of beam loading at high beam currents. This was readily accomplished via the local operator interface without interrupting the operation of the rf or the beam. Further work is being done to reduce the downtime of the system by fine tuning of the spark detection parameters, better diagnostic

data logging, and improved data exchange with remote computers.

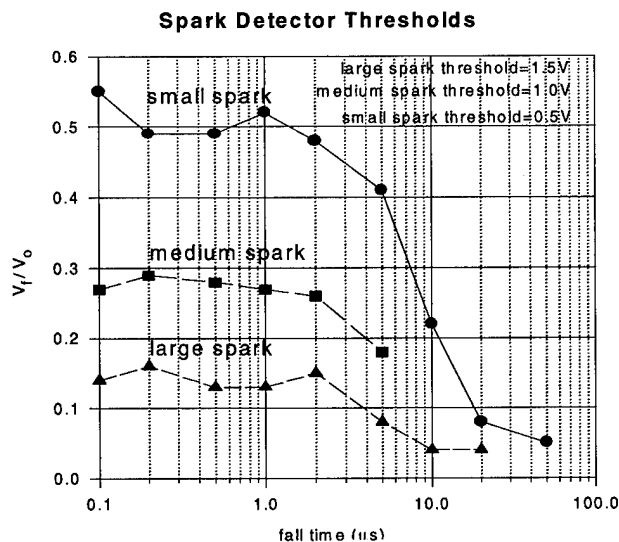


Figure 5 Spark Detector Thresholds

V. REFERENCES

- [1] R.H.M. Gummer, "RF Accelerating Voltage Control and Stabilization in the TRIUMF Cyclotron", IEEE Transactions on Nuclear Science, NS-22, No. 3, 1257, June 1975.
- [2] K. Fong, M. Lavery, S. Fang, "RF Control System Upgrade at Triumf", European Particle Accelerator Conference Proceedings, London, June 1994, pp. 1842-1844.
- [3] K. Fong, M. Lavery, "RF Control System for TRIUMF Booster Cavity", European Particle Accelerator Conference Proceedings, Berlin, Mar 1992, pp. 1176-1178.
- [4] D. Bishop, G. Waters, D. Dale, T. Ewart, D. Harrison, J. Lam, R. Keitel, "Development of an autonomous 32-bit intelligent device controller", Proceedings of the Third International Conference on Accelerator and Large Experimental Physics Control Systems, Berlin, Oct 1993, pp. 236-238.

MANAGING CONTROL ALGORITHMS WITH AN OBJECT-ORIENTED DATABASE*

M. Bickley, W. Watson, Continuous Electron Beam Accelerator Facility, Newport News, VA 23606 USA

The Continuous Electron Beam Accelerator Facility (CEBAF) uses the Experimental Physics and Industrial Control System (EPICS) for accelerator control [1]. In EPICS, the atomic element of a control algorithm is a record. Records are grouped together to form generic applications, for example to control a single magnet. The generic applications are then instantiated for each specific item of machine hardware. Instantiated applications are executed on one of the 30 data acquisition and control computers that are used in the control system. There are roughly 125,000 unique, instantiated records at CEBAF, each associated with a specific piece of hardware[2]. Management of these records in a database simplifies the task of application developers by allowing them to concentrate on algorithmic development instead of instantiation details. In addition, it decouples algorithmic development from the specification of operational parameters, allowing responsibility for those parameters to pass to machine operations staff. CEBAF needed an environment to provide support for development of EPICS database management tools. An object-oriented database (OODB) was chosen for two reasons: higher performance and the ability to smoothly manage objects of different types.

I. INTRODUCTION

A requirements analysis of the control system was performed, to determine CEBAF's data management needs. The analysis illuminated some limitations in the existing system and pointed the way to a solution. This section briefly introduces EPICS, and points out some of the problems that were presented to CEBAF.

EPICS provides a solid footing on which to base an accelerator control system. In EPICS, single-board computers using the real-time operating system VxWorks execute control algorithms coded as EPICS "databases". Each database consists of a number of records, which are executed according to rules of association specified prior to downloading of the database to its execution engine. The kinds of rules that are specified include execution order, prioritization of execution of the records and data communication between records.

Despite the solid execution environment that EPICS provides, its application development tools give little assistance in managing large projects like CEBAF. The developmental tools do not provide for data management outside of the application development framework, or for replication of EPICS databases. It is incumbent on each site that uses EPICS to provide its own mechanism for reproducing control algorithms. The typical solution at most EPICS sites is the use of UNIX-

based text processing tools to do replication, and incorporation of instance-specific record definition data either during replication or afterwards. These solutions are not typically well integrated into the operational control system, and make it difficult to manage large numbers of records.

When CEBAF first started using EPICS, application developers also chose to use text-processing tools. Developers used a schematic editor tool to create generic control algorithm templates for a particular piece of hardware, such as an RF module. Specific instances, corresponding to pieces of real hardware, were generated from the generic algorithms by making four passes with different tools through successive ASCII files. Complete processing of some of the larger generic files, associated with CEBAF's RF system, took more than five minutes on an unloaded HP-700 series machine. This processing time adds significantly to the burden of developers during the debugging and testing phases of application development.

Another drawback to this style of producing EPICS databases is the lack of management tools. For example, there is no mechanism to prevent different records from having the same name. Such name conflicts are typically found at record execution time (if at all). Other limitations include the inability to perform wild-card queries on the names of records, to identify from a record name the front-end computer on which it resides, or to quickly query the attributes of a particular record.

II. OBJECT ORIENTED DATABASES

CEBAF had a clear need for a data management package to organize the 125,000 operational EPICS records. A requirements analysis of the management problem illustrated the need for support in two areas, machine operations and application development. The requirements analysis supported the choice of an object-oriented database (OODB) system for its speed and flexibility.

Operational Support

The requirements analysis indicated that the data management package had to provide tools for operations staff to manage accelerator operational data. In the past, developers have been forced to maintain operational data in their algorithms. This has principally been because of a lack of tools for non-developers to manage the data. Using a commercial database as a repository for EPICS record information enables the development of those data management tools. This in turn allows developers to release control of operational parameters to the CEBAF operations staff. Once that is done, developers can concern themselves principally with algorithmic function-

*Supported by U.S. DOE Contract DE-AC05-84-ER40150

ality without worrying about operational detail.

For example, common attributes of most EPICS records are the upper and lower operational limits of the record's value. Those limits are typically used for graphical displays, and serve no algorithmic purpose. Once accelerator operations staff assume responsibility for the display limits, changes to the underlying algorithm should not result in the loss of the limit data. If the application developers add new records to the control algorithm, or delete old one, the display limit values set by the operations staff must propagate correctly into the new algorithm. For situations where propagation cannot be automated, the developer should be provided with tools to make the data propagation straightforward.

The current technique for managing operational data uses a program which backs up and restores large numbers of field values from data files. This program is capable of providing some of the same functionality as a database. Using this tool, however, just moves the data management problem from the application developers to the maintainers of the backup/restore data files. Further, the tool only operates on the operational accelerator: it does not provide methods for modifying EPICS records in a non-operational system. Finally, the backup/restore software does not provide tools to perform database-style actions on the information stored in its data files, such as queries, wildcarding and versioning.

Development Support

The data management package also had to provide tools to assist application developers, and improve their efficiency. While it would not be a part of run-time control algorithms, it would be integral to the development cycle of EPICS databases. A short turnaround time, from modification of a schematic to execution of the new algorithm, facilitates development and testing. It also shortens accelerator downtime in the event of algorithmic bugs in operational code.

The management package had to enable replication of generic applications into specific applications. In the interest of alleviating the management burden on developers, they should be able to define a generic control algorithm and rules to produce specific instances of it. Data management tools must be able to follow the specified rules and then produce new, specific applications from the generic algorithm. Then, the addition of a device for which a control algorithm already exists would require no additional work of any developers. The replication also must be fast, to shorten the time from completion of testing to operational readiness with the new control algorithm. For example, at CEBAF a single RF control application, controlling one zone of RF cavities, uses roughly 3300 records, and is instantiated 20 times. The database must be able to perform the instantiation in a reasonable time, on the order of minutes.

The management package to be used for EPICS record management had to meet other data management needs for the operation of the accelerator. At the time this development was being planned there were no clear requirements for database tools in other areas. It was clear, however, that a such a need would develop eventually.

The management package had to support heterogeneous data. Each of the more than 40 EPICS record types have different sets of attributes. The package of choice would have to be able to support this variety, which traditional relational databases cannot. We decided, therefore, to use an object-oriented database (OODB). We specifically chose to use Object Design's database, ObjectStore. It is tightly integrated into the C++ language with function overloading, and is extremely fast due to its use of virtual memory to support database references.

III. DATABASE DESIGN

The database design was intended to take advantage of the way that EPICS records are used, to save space and speed up the access of data within the database. Each record has from 50 to 200 attributes, known as fields. Within the record execution environment, in the memory of a single-board computer, records can require anywhere from 500 to more than 4000 bytes of storage. A database which has storage space for all fields of all operational records at CEBAF would have to be more than 100MB in size. This does not take into account the need for support for a development environment, or the desire to support versioning of operational software within the database. A better data design was required.

The organization of EPICS records leads naturally to a layout which minimizes the size of the management database. In EPICS, each record type is defined to include a set of fields, and the definition includes default values for each field. By including the record and field definition in the database a baseline can be established for all records. Every operational record can then be compared against the default for that type, and only non-defaulted field values stored in the database. Typically, only 5 to 10 fields have values other than the default, yielding a tenfold space savings. For example, there is a gradient setpoint record for each RF cavity. That record, of type "ao," has 100 defined fields. When used as a gradient setpoint record, however, only 7 field values are non-defaulted. These include high and low operational limits, maximum and minimum settable value, engineering units of the record, precision of the record, output hardware address and an inter-record connection.

The same rationale can be extended to provide even more space savings. During instantiation of the generic application, not all of the fields will have values that are different for that specific instance. In fact, typically very few of the fields have values other than the generic value. Therefore, by including for each instantiated application only those field values which are both non-defaulted and different from the generic, there is a further space savings. For example, the generic RF gradient record described before, with 8 non-default values in the generic form, has only two values which are different for specific instances of the record: the inter-record connection and the hardware address associated with this record.

In general, the space savings factor is between 2 and 3 times. The reduced size of the instantiated applications yields

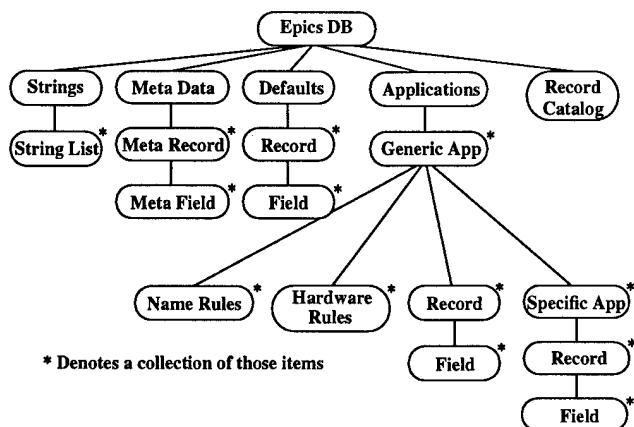


Fig 1. Schematic representation of the database structure

benefits in other ways besides the space savings. Replication of the generic applications is faster, since fewer fields must be created. Further, because each instantiated application is smaller, it can be stored more easily in the memory of workstations accessing the database. This greatly speeds up interaction with the database when queries are being generated.

Figure 1 shows a graphical representation of the organization of the EPICS database within the OODB. In the description below, italicized words refer to objects in the figure. The OODB representation, which includes all record information needed to manage all the EPICS records at CEBAF, is stored in an *Epics DB*, which is a collection of five different objects: *strings*, *meta data*, *defaults*, *applications* and a *record catalog*.

Strings: Some EPICS fields can only take on values which match one in a series of strings. The *strings* object, a collection of *string lists*, serves to support those fields. Each *string list* is in turn a collection of strings, where each string in the list is one of the possible values for a specific field. For example, every EPICS record has a field named "SCAN", which indicates the period with which the record should be executed. Some possible SCAN field values are "1 second", ".1 second" and "10 second". When a non-default value for a SCAN field is specified, the value stored with the field is not the string itself, but a pointer to the appropriate element of the SCAN string list. This format saves space, since only four bytes of storage are required for the pointer, rather than the 12 bytes that would be required for each use of the SCAN field. The *string lists* are also a convenient mechanism to verify the value of a field. If a user tries to specify a value for a field which uses a *string list*, and the value is not on the appropriate list, the user can be warned.

Meta data: The *meta data* object is a collection of *meta records*, with each *meta record* a collection of *meta fields*. Descriptive information about every field of every EPICS record is stored within the *meta data* object. This information includes, for example, the data type of the field value and a prompt string when querying a user for a value for this field. Gathering all of the *meta data* here makes it possible to keep other database objects as

small as possible. Every field in the *Epics DB* includes a pointer to its associated *meta field*. If meta information for a field is needed by a database tool, a pointer dereference provides access to it.

Defaults: The *defaults* object is a collection of *records*, with each *record* a collection of *fields*. Each *field* holds a pointer to its meta data description, and a field value. This value is the default value for the field. When a specific instance of a *field* does not specify a field value, this is the value that is used by EPICS.

Applications: The *applications* object is a collection of *generic application* objects. Each *generic application* is made up of a collection of *naming rules*, a collection of *hardware rules*, a collection of generic *records* and a collection of *specific applications*, which are instantiations of the *generic application*.

The *naming rules* are a series of strings that specify substitutions to be performed on each generic *record* and generic *field* value as they are instantiated into specific *records* and *fields*. The *hardware rules* are a collection of record name/hardware address pairs which are used to associate each instantiated *record* with a particular crate, slot and channel. *Hardware rules* are only needed for those records which perform hardware input or output. The *record* object associated with a *generic application* is a collection of the generic EPICS records that make up the control algorithm for that piece of hardware. Each *record* is a collection of those *fields* which have taken on a non-defaulted value.

Finally, the *specific applications* are each made up of a collection of *records*, one *record* for every *record* in the parent *generic application*. The names of each *record* in the *specific application* have been converted according to the *name rules* associated with the *generic application*. Each *record* is a (usually small) collection of *fields*. The *fields* in each *record* are those which have a value different than the default value, and also different than the value in the generic *record* from which it was instantiated. Some *field* values refer to other *records*, so those values are processed according to the *name rules* for the *generic application*.

Record catalog: The *record catalog* object is a collection of names of all *records* in the database, and pointers to the *records*. This provides a means for performing wild-card searches on all *records* in the *Epics DB* without having to navigate through each *generic application* and *specific application*.

IV. REFERENCES

- [1] W. McDowell et. al. "Status and Design of the Advanced Photon Source Control System", *Proceedings of the 1993 Particle Accelerator Conference*
- [2] S. Schaffner et. al. "Device Control at CEBAF", these proceedings
- [3] W. Watson et. al. "The CEBAF Accelerator Control System: Migrating from a TACL to an EPICS Based System", these proceedings

DESIGN OF THE COMMISSIONING SOFTWARE FOR THE AGS TO RHIC TRANSFER LINE*

C. G. Trahern, C. Saltmarsh[†], T. Satogata, J. Kewisch,
S. Sathe, T. D'ottavio, S. Tepikian, D. Shea
Brookhaven National Laboratory, P.O. Box 5000
Upton, New York 11973

Abstract

RHIC accelerator physicists and engineers have collaboratively specified the control system software for the commissioning of the AGS to RHIC transfer line (ATR) to occur in the fall of 1995. This paper summarizes the design and progress to date. We discuss the basic physics/engineering device model that we use to understand process and data flows, and describe the architecture and tools we will use to build the application level software.

I. INTRODUCTION

The AGS to RHIC transfer line will be commissioned in the fall of 1995. In preparation for the commissioning of RHIC in 1999, prototypes for some parts of the RHIC control system are being prepared to commission the transfer line.

The basic assumptions in our design effort are 1) the use of object oriented (OO) coding throughout, both at the embedded systems/hardware level as well as in physics level applications, and 2) a sequencing and interprocess communication protocol implemented using a program known as *glisch* [1]. Given these assumptions, the design of the control system has proceeded in two stages. In the first stage we took the list of requirements for the commissioning test and made a general analysis of the data and process management needed to meet these goals. In the second stage we have prioritized the requirements and organized the work of the accelerator physics and control groups to implement the relevant systems.

II. ACCELERATOR PARAMETER OBJECTS

High-level requirements for ATR commissioning range from the ability to control currents on individual power supplies to adjusting steering corrector elements in concert to produce the desired orbit deviation as measured by an assembly of beam position monitors (BPMs). In order to conceptualize the entire range of applications, a set of data models was created. For each accelerator parameter we define an object which contains the following data:

Parameters (e.g., tune, chromaticity, magnet current, etc.) are the set points that describe the desired state of the accelerator. Parameters are functions of time. The parameter value at any time is obtained by specifying the values at *step-stones* and using an appropriate interpolation method. In most cases the step-stones will coincide with the events on the accelerator event line. The control system can modify future step-stones, while present and past step-stones are not changeable.

All quantities that prescribe the state of the accelerator are parameters. The parameters are therefore redundant. A system of processes ensures that the parameters are consistent. This allows the operator to describe his goal directly. He can set any parameter and leave the task of finding the corresponding hardware settings to the control system.

Measurements are the actual readings from the machine hardware. (For most parameters a direct measurement is not available.) They are independent of the parameters with the same name. Although some hardware devices include the setting and measurement of an accelerator parameter in one module, this is the exception.

Trims are changes to the accelerator parameters that enforce desired behavior. Trims are only used in objects where a measurement is available. Ideally, trims make the value of the parameter and the measurement the same.

Method data are data that determine how to convert dependent parameters. Methods often change during operations. For example, given the desired orbit the method data describes which correction dipoles are used to move the orbit.

Accelerator knowledge is configuration information about the accelerator. This data changes only when the machine or the control system is reconfigured. Examples are lattice information, host names, power supply names and magnet data.

In order to describe the idea we resort to the methodology of data flow diagrams[2]. The general picture is shown in Figure 1 and a more complete discussion of this model can be found in [3]. In the figure processes are defined which perform the following data transformations:

1. Calculation of all dependent parameters, if the new parameter is changed.
2. Update of the new parameter if a parameter on which the new parameter depends changes.
3. Measurement of the parameter, if possible, and generation of an alarm if outside limits.
4. Prediction of trims.

A set-request from the operator or sequencer or a higher level object is first checked for semantics and for range in the "validate and sequence" process. Method data is used for this check.

If the request is valid, the parameter is set in the parameter data store. The "validate and sequence" process administers the step-stones in the parameter store. The parameter is passed on to the "calculate lower parameter" process. Method data is used to determine which lower level parameters are used to do the change. The process may also use other parameters and accelerator knowledge for the calculation.

The calculated parameters are sent to appropriate object(s) which internally have the same structure as this object: the de-

*Work performed under the auspices of the U. S. Department of Energy

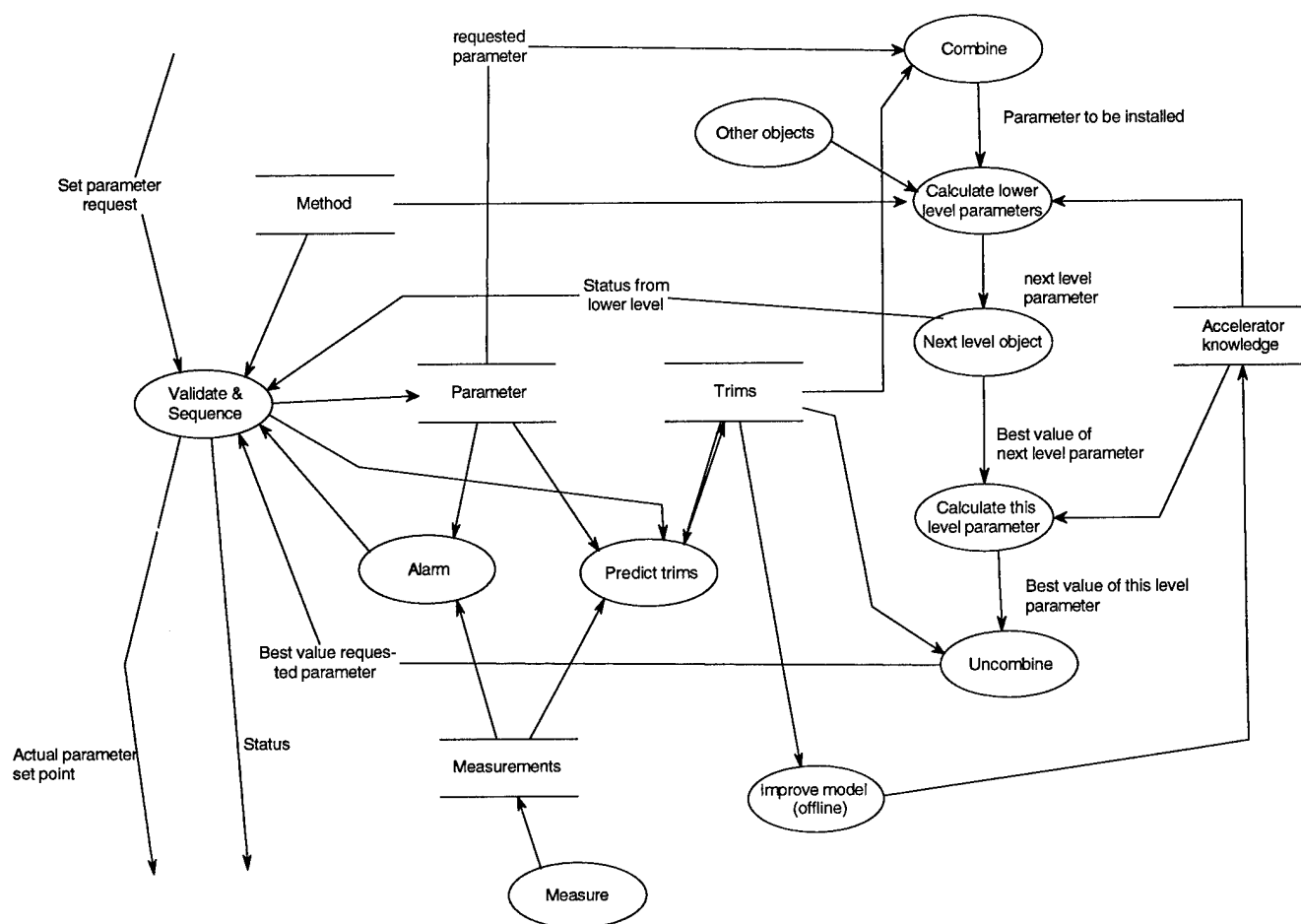


Figure 1. Data Flow Diagram for Parameter Object

sign is recursive. The lower level object returns the set parameter or, in the case of error, an error message and the best achievable parameter value which is passed to the validate and sequence process.

The validate and sequence process checks the success of the set operation and fields asynchronous errors. It updates the parameter value in the data store and returns the value or best value to the next higher level.

The "model" of the accelerator resides in the "calculate lower level parameter" and "calculate this level parameter" processes. It is important that these modeling processes occur on each level and are by design independent from each other. This allows implementation of new parameters and extensions of the model in a flexible way. In implementation the same program or process might be used at different levels. For example, an optics calculation process might be set up as a "persistent" service for different parameter objects.

The accelerator knowledge data store provides the basic information for the model. It contains lattice information, magnet data, etc. Although this data changes rarely, it is a part of the data flow.

The recursive design suggests that parameters can be organized as a tree, where each object is a node with all internally used objects as leaves. However, it turns out that there is no natural structure for this tree. Whatever parameter is set by

the operator or sequencer is the top level. The tree structure must therefore be dynamically configured for each operator or sequencer command.

The system described so far allows the generation of a consistent set of redundant parameters. If the model used is correct, the parameters give a complete description of the machine. Unfortunately, real life is often different, and the measurements of parameters differ from their desired values. The parameter object therefore contains measure and trim processes.

In addition to the parameter store the parameter object contains a trim store. The goal of operations is to predict the best trim, so that the machine behaves as described by the parameter. The trim is predicted on the basis of past experience. A "Predict Trim" process calculates the trim for the future step-stone from the measurement of the past or present and the parameters and trims that lead to those measurements. The "combine" process combines the parameter value and the trim value into a "parameter to be installed" value. (In most cases the combination means just adding the two values, but more complicated combinations are possible.) Instead of the desired (requested) parameter, this "parameter to be installed" is passed to the "calculate lower parameter" process. The returned values from the dependent parameter objects need to be "un-combined" from the trims before they are sent to the validate and sequence process for interpretation.

III. IMPLEMENTATION

C++ will be used for the programs that control the front end electronics, global beam-level applications and monitoring systems. Consequently, complex data structures can be developed with all the useful inheritance features of the language. Configuration data for all of these structures will be organized using both relational database management systems and UNIX file systems[4]. The transport of these data structures from one independent process to another will be managed by a program context known as *glish*. Client processes interconnected in a *glish* environment need no knowledge of other processes or their data structures. Events, defined as a name-value pair, are directed to various clients by the *glish* interpreter. When these named events occur in some process, the interpreter recognizes the event and passes the value data onto appropriate clients. This environment enables significant modularization of code as well as the distribution of processes over an extended network.

The architecture for the control system implied by the parameter object design would allow a hierarchy of software systems communicating with each other without a "hard" line between the front end and global beam-level control systems. For example, in principle the orbit correction algorithm could address hardware by passing the appropriate data structure via the *glish* interpreter directly to the front end computers. However, this functionality of *glish* will not be used during the commissioning test. A protocol/class library known as the Accelerator Device Object Interface or ADOIF will mediate between the global control systems and the front end modules. The front end electronics is controlled by VME based computers using the VxWorks[5] operating system. The conceptual design for the front end systems has been described elsewhere[6]. A *glish* client built around ADOIF will receive a *glish* event and forward it to the appropriate front end. Information from the front ends will pass back to the global systems analogously. Depending on the need to cache the readback information from hardware for use by various processes, device managers, also *glish* clients, will sit between the ADOIF *glish* client and the beam-level applications. These manager processes would be responsible for absorbing the data from front end computers and making it available to generic *glish* clients.

All processes are designed to be independent of any graphical user interface as a data source. Whether the local data of a process is output to the screen or not, the process will be addressable via the *glish* event sequencer. Generic device input follows the same principle. There will be button/menu driven parameter pages available though a graphical interface, but the same parameters will also be adjustable via the event interpreter.

IV. CONCLUSIONS

The commissioning software for the AGS to RHIC transfer line will be a model for the RHIC control system. We will test the ideas and principles outlined here in September 1995. After the test a thorough review of both the systems and design will be carried out. We are committed to "throwing away" code as well as a re-conceptualization of the system design in order to avoid future problems. The construction of the control system requires the close collaboration of both the accelerator physics and con-

trols groups. The outlook of the physics group tends to focus on the beam-level systems and that of the control group at the level of the front end computers. Making the transition between the two domains a smooth one is not a trivial task. We believe that the experience gained from the upcoming test will provide enough information to make whatever changes are needed for RHIC commissioning.

References

- [1] Vern Paxson, "The *Glish* 2.4 User's Manual", RHIC AP note 30.
- [2] T. DeMarco, *Structured analysis and system specification*, Englewood Cliffs, New Jersey, Prentice Hall, 1979.
- [3] T. D'Ottavio, et. al., "ATR Commissioning Software Task Force Report", RHIC AP note 53, 1994.
- [4] C. G. Trahern, et. al. "Relational Databases for RHIC Design and Control", EPAC proceedings, 1994.
- [5] VxWorks, Wind River Systems, Inc., 1010 Atlantic Ave., Alameda, California 94501-1147.
- [6] L. T. Hoff, J. F. Skelly, "Accelerator Devices at Persistent Software Objects", Nuclear Instruments and Methods in Physics Research A, 352 (1994) 185-188.

† Current address: Flat 4, 89 Belvedere Road, London SE19 2HX England, email: salty@crapeau.demon.co.uk

A RELATIONAL DATABASE FOR MAGNETS AND MEASUREMENT SYSTEMS AT THE FERMILAB MAGNET TEST FACILITY

J.W. Sim, B.C. Brown, H.D. Glass, D.J. Harding, C.S. Mishra, A.D. Russell, K. Trombly-Freytag, D.G.C. Walbridge, Fermi National Accelerator Laboratory* Batavia, IL 60510

Abstract

A magnet measurement system based on relational database technology has been developed for use at the Fermilab Magnet Test Facility (MTF). Results of magnetic field strength and field shape measurements are stored in the database for use in understanding accelerator and beamline operation. In addition to measurement results, the database is used to store measurement history and the commands which prescribe measurement sequences along with supporting parameters that control how each measurement is performed.

The system contains more than 200 tables with more than 1500 columns. The design of the tables is documented in the form of diagrams, design documents, as well as through tables which store, within the database itself, descriptions of each table and column.

I. SOFTWARE ENVIRONMENT

Software for a magnet measurement system[1],[2] has been created at Fermilab. This paper describes the database design and implementation which supports that system and provides access to the measurement results as well as the complete description of the measurement environment. We use the Sybase¹ relational database system, employing features of the standard relational model plus additional vendor specific features which have reduced implementation effort. The measurement system was developed primarily to support testing of magnets for the Fermilab Main Injector Project[3], but it also has been used to measure magnets for other applications.

II. DATABASE DESIGN OVERVIEW

There are several distinguishing features in the MTF database design including:

- Tables with closely related functionality are grouped together into "virtual databases." For example, measurement data obtained by rotating a coil in the field are stored in the "harmonics" virtual database, while measurement data obtained by scanning and measuring the field at various points are stored in "pointscan."
- Data are grouped into related tables based on natural hierarchies derived from data collection (points, runs, sequences) and data processing (raw, reduced, analyzed) relationships.
- Special procedures called *triggers* are executed to enforce the integrity of the relationships between data entered into the various database tables.

- To simplify referencing data in different tables, unique serial numbers are generated and used as the primary key for data that is cross-referenced in other tables.
- The database is used to store not only the results of measurements, but the prescription for how each measurement is performed and the history of measurements performed on each test subject.

III. VIRTUAL DATABASES

Tables with related information are grouped together into "virtual databases." The Sybase *data owner* concept is used to implement the virtual databases by creating a pseudo-user of the same name to own each "virtual database." There are two categories of virtual databases, those containing measurement results and those containing measurement commands and support data. Each of the virtual databases and its purpose is identified in the following subsections.

A. Measurement Results Virtual Databases

The following virtual databases are implemented for storing results of magnet measurements:

harmonics: contains tables for storing the data obtained when a magnet's field strength or field shape is measured by rotating a coil.

flatcoil: contains tables for storing the data obtained when a magnet's field strength or field shape is measured by ramping the magnet while measuring flux with a stationary coil, or by translating the coil within the field.

pointscan: contains tables for storing the data obtained when a magnetic field is measured at individual points, using either a Hall element or an NMR probe, or both.

currents: contains tables for storing the magnet current measured during a measurement.

results: contains tables for storing the measured magnet properties. Data in these tables are derived from data stored in the other Measurement Results Virtual Databases after applying appropriate data selection, analysis and perhaps fitting techniques.

B. Measurement Support Virtual Databases

Virtual databases in this category are used to store information that supports measurements, as opposed to storing actual results of magnet measurements. The virtual databases in this category include:

admin: identifies personnel involved in measurements, documents describing measurements; serial numbers generated by the system are also stored here.

subjects: identifies magnets tested or available for testing, information about the components used in assembling the

*Work supported by the U.S. Department of Energy under contract No. DE-AC02-76CH03000

¹Sybase, Inc. 6475 Christie Ave., Emeryville, CA, 94608

magnet, and which magnet design group each magnet belongs to.

calibrations: contains information about how data obtained from readout devices is converted into appropriate engineering units of interest. Also stores an historical record of what calibration constants were used to convert data.

facilities: identifies and provides details about test stands, readout devices, measurement probes, *etc.* that are used in measurements.

instruments: identifies the collection of devices used to perform each measurement.

logbook: stores checklists, which prescribe the sequence of steps performed during a measurement. Provides an historical record of activities performed during testing (e.g., when magnet was mounted on the stand, when and by whom each measurement was performed, *etc.*).

ramps: stores the list of currents at which each measurement is performed, along with details about how to accomplish the ramps.

quality control: stores values against which measurement results can be compared to determine whether magnetic properties are within expected ranges.

IV. MEASUREMENT RESULTS ORGANIZATION - RAW AND REDUCED DATA

Data points are the set of measurement results which characterize a given state of the magnet and measurement apparatus, such as a probe angle and flux, or a probe location and NMR field measurement. Data points are collected in sets called runs in which data are grouped by the measurement system operations used to acquire the data. Examples of runs include a magnet current excitation sequence, or a transverse probe movement (scan). For convenience of both programming and measurement specification, runs are grouped into related sets called sequences. A sequence normally carries out the operations required to measure a specific magnet property such as its strength vs. magnet current.

Data obtained from magnet measurements are stored with three levels of processing. Raw data consists, as nearly as possible, of direct instrument readings. Raw data for a measurement are stored with minimal conversions, thus permitting reprocessing effort to begin from the basic information. Reduced data are stored after all conversions to engineering units and all processing which can be done on a per run basis have been completed. Wherever possible, the reduced data describes the measurement results to be evaluated at measurement time. When further analysis is useful or required, the resulting analyzed data are also stored in the database.

The structures used to store measurement results reflect the measurement and reduction structure based on sequences, runs and points by using a related hierarchy of (master-detail) tables for sequences, runs and points for both raw data and reduced data. This design is repeated for the 'flatcoil', 'harmonics', and 'pointscan' measurement styles, with variations reflecting only the fundamental differences between the measurement techniques

Further analysis may combine more than one run, may involve

different measurement styles and perhaps utilizes knowledge of physical properties of the magnets under measurement. The output from this analysis is less dependant on measurement system specifics and therefore of more general interest. The 'results' virtual database tables store these analyzed data. Properties measured by complementary techniques are stored here, allowing cross-checks to be performed on the data.

V. THE SERIAL NUMBER GENERATOR

Sybase provides a feature called a stored procedure by which Structured Query Language (SQL) commands which are stored in the database. Triggers cause the execution of these stored procedures when specified database events, such as the insertion of a data row, occur. This feature is utilized to create a 'serial number' as a primary key for most of our tables. The insertion trigger code obtains the value to be stored as the primary key from the 'serial_generator' stored procedure which provides a unique integer value and records the table for which it has been requested. The commonality provided by the frequent use of 'serial numbers' as foreign keys permits us to create most of our trigger code for relational integrity automatically[4]. Since a single data type is used for most primary keys, a single column can reference a row in almost any table. Using a single comments table, comments are linked to almost any object defined within the database.

VI. SUPPORT TABLES - AN EXAMPLE

We will use the design of the *subjects* virtual database to illustrate some of the ways we use the relational model to capture the data we use about magnets and their components. Figure 1 illustrates this design graphically. The database design assumes that test subjects are identified products from a production series. It implements the usual "parts explosion" paradigm common to engineering design. The series table labels the design of the series of objects and the properties of that series are stored in the *series_attributes* and *series_text_attributes* tables. The nature of these properties is stored in the *series_attributes_defn* table. Individual subjects are identified in the *subjects* table and are identified as an instance of the series using a foreign key to the *series* table.

The hierarchical structure that defines the parts which are specified in the series design is stored using the *series* table to store the labels of the parts and the *series_components* table to declare their relation to the object (series) of which they are a part. The identity of a specific component of a subject is defined in the *subjects* table while the relationship to the base object in the *series/series_component* hierarchy is made specific in a *subjects/subject_components* hierarchy. This design permits us to identify and store a complete parts list in a compact form.

For the Main Injector magnets, the magnet, the yoke parts (two half cores), and coil parts (2 dipole or 4 quadrupole main coils and 4 quadrupole trim coil windings) are stored. Information which tracks parts in more detail can be stored here but at this time is not. Note that the column *series_components.component_role* defines the way a part is used in a magnet.

Note: All primary key columns of sntype (serial numbers) are foreign keys to the table "admin.serials"

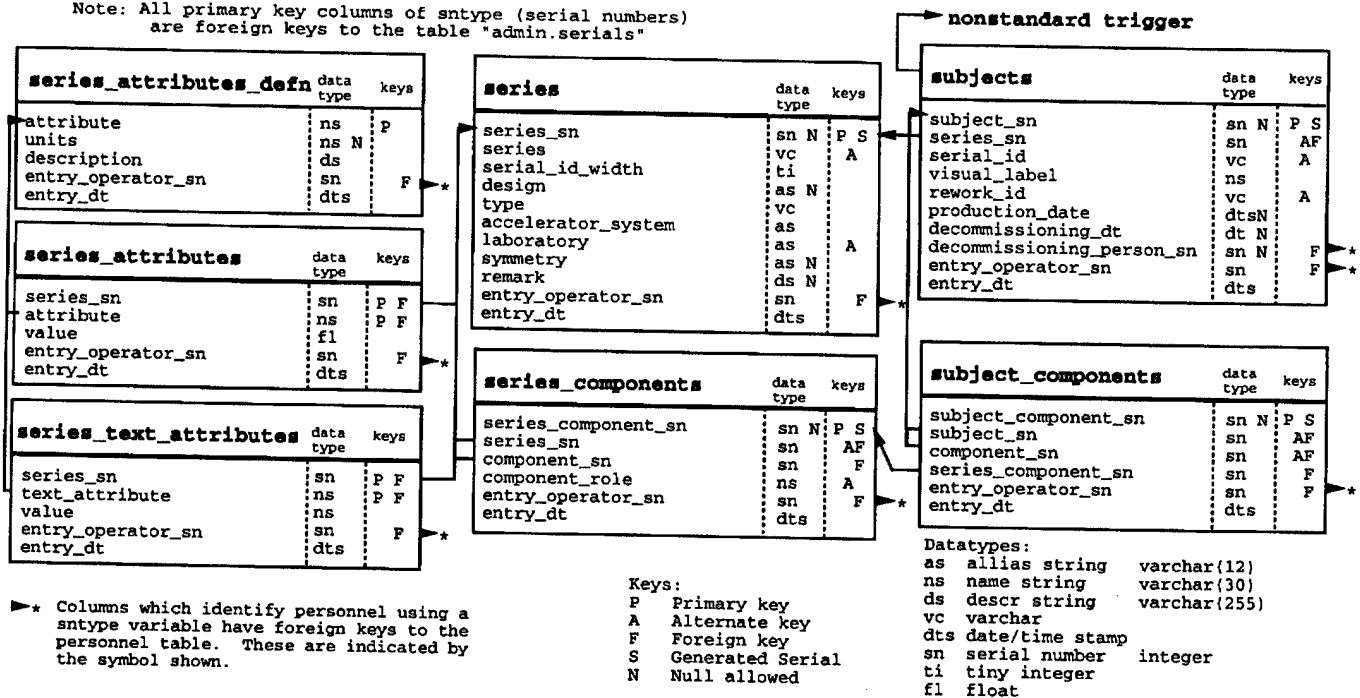


Figure 1. Graphic representation of the *subjects* virtual database which stores magnet and magnet component information.

VII. DOCUMENTATION

The system of documentation which is used to record this design[5] includes the use of a tool (TOT²) to record the table definitions, primary and foreign keys as well as descriptions of each table and column. This information is summarized graphically as illustrated in Figure 1. In addition, each virtual database is documented with a report which explains overall purposes and all special design considerations.

VIII. CONCLUSIONS

A database has been designed and implemented for magnet measurements which allows a single set of database tools to be used to access the measurement command structure, control and conversion parameters, raw, reduced and analyzed measurement results, and measurement history along with the list of measured objects, and a comment and assessment system. Measurements of more than 85 magnets have been recorded with the current system. The format is suitable for incorporating results from previous measurement systems into the same data storage structure.

References

- [1] J.W. Sim et al. Software for a Database-Controlled Measurement System at the Fermilab Magnet Test Facility. In *Proceedings this conference*.
- [2] B. C. Brown et. al. Software Design for a Database Driven System for Accelerator Magnet Measurements. In *Conference Record of the 1991 IEEE Particle Accelerator Conference, San Francisco, May 6-9, 1991*, page 2134. Institute of Electrical and Electronic Engineers, 1991.

- [3] D. Bogert. The Fermilab Injector Complex. In *Proceedings this conference*.
- [4] B.C. Brown et. al. Table of Tables – A Database Design Tool for SYBASE. TM 1707, Fermilab, January 1991.
- [5] B.C. Brown et. al. Overview of a Database System for Magnet Measurements. Technical Report MTF-92-0003 1.3, Fermilab, July 1992.

²This tool also generates SQL code that supports table creation and management.

SOFTWARE FOR A DATABASE-CONTROLLED MEASUREMENT SYSTEM AT THE FERMILAB MAGNET TEST FACILITY

J. W. Sim, R. Baiod, B. C. Brown, E. Desavouret, H. D. Glass, P. J. Hall, D. J. Harding, C. S. Mishra, J. M. Nogiec, J. E. Pachnik, A. Russell, K. Trombly-Freytag, and D. G. C. Walbridge,
Fermi National Accelerator Laboratory, P.O. Box 500 Batavia, IL 60510 USA*

Abstract

A software system has been developed for use in measuring the magnetic properties of accelerator magnets at the Fermilab Magnet Test Facility. Key features of the system include:

- Storage of measurement data in a relational database.
- Use of database tables to define the individual steps that occur during a measurement.
- Use of an "electronic logbook" to store an historical record of important measurement details within the database.
- A graphical user interface for measurement technicians and data analysts to use in acquiring and analyzing data.

Other papers describe the preliminary software design [1], the design of the database tables [2], and the results of measurements obtained using this system [3] [4]. This paper describes the final software system design, with particular emphasis on the data acquisition subsystem.

Currently, the system supports 3 test stations and has been used to measure approximately 85 magnets. It is used for both production measurements and R & D studies of prototype magnets.

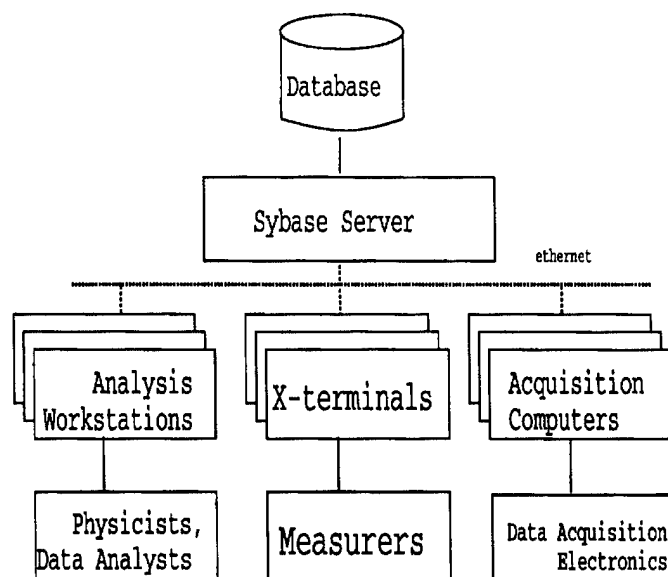


Figure 1. System Overview

I. SYSTEM OVERVIEW

As shown in Figure 1, the system consists of a network of distributed computers. A commercial relational database system, Sybase¹, is at the center of the system. Sybase is based on the client/server computing model. The Sybase server, which runs on a workstation that is dedicated for that purpose, manages the storage of data into and retrieval of data from the database. Requests for storage and retrieval of data come from client programs, which run on other workstations in the network.

Three types of client programs are used to access the database:

- General Purpose Clients provided as part of the Sybase relational database system. These clients allow for report generation, data entry, table browsing, etc.; they run on any of the analysis workstations.
- Data Acquisition Clients, written at the Fermilab Magnet Test Facility, which control data acquisition electronics and store measurement data into the database. These clients run on the acquisition computers.
- Data Analysis Clients, written at the Fermilab Magnet Test Facility, which perform post-acquisition data reduction and comparison of final results with expected results, storing the final results into the database. These clients run on any of the analysis workstations.

A. HARDWARE ENVIRONMENT

The workstations shown in the system overview are SPARCstations²; these are used by physicists and data analysts in an office environment. X-terminals are used by the measurement technicians to interact with the system; they were chosen over workstations to minimize system administration, and to avoid potential problems with the use of disk-based computers in a testing environment that includes dust and strong magnetic fields. The data acquisition computers are diskless implementations of Sun SPARC computers contained on a single-wide VME board.

The acquisition electronics consists of a mixture of VME, VXI and GPIB data acquisition and control devices.

B. SOFTWARE ENVIRONMENT

All of the computers used in the measurement system run SunOS (Solaris 1.1). The X-windows/Motif environment is used to provide a graphical interface as well as text-based windows for interacting with the system. Plotting of data is achieved us-

*Work supported by the U.S. Department of Energy under contract No. DE-AC02-76CH03000

¹Sybase, Inc. 6475 Christie Ave., Emeryville, CA, 94608

²Sun Microsystems, Inc. 2550 Garcia Avenue, Mountain View, CA, 94043

ing programs that provide plotting capability in the X-windows environment (PAW³, gnuplot⁴).

Code developed at Fermilab for this system is written almost exclusively in C; a few computational subroutines are written in FORTRAN.

Programs that access the database do so, at their lowest level, through Sybase's Open Client C programming interface. To simplify the programming interface, however, a layer of subroutines is built on top of the Open Client C interface. These subroutines, which allow reading data from the database, inserting data into the database, and updating data in the database, use variable argument list processing to provide access to data in tables of widely different format and content.

II. THE DATA ACQUISITION PROGRAM

The data acquisition program reads and controls measurement electronics, displays data plots, solicits required input from measurement technicians and stores acquired data into the database.

The data acquisition program is designed to achieve the following goals:

- allow varying measurement control parameters for different types of magnets or for special R & D test requirements. Examples of measurement control parameters include: the devices used for a given measurement, the list of currents at which to perform measurements, the range of probe positions at which to perform measurements, etc.
- allow exact repetition of a previous measurement, either for purposes of measuring similar magnets in an identical manner, or to verify the validity of a previous measurement.
- provide an historical record of important measurement parameters, such as the devices used in each measurement and the calibration parameters used to convert data to engineering units.
- store measurement results in a well-organized, efficient format, allowing data analysts to discern trends in measurement results or to detect problems with measurement electronics.

The database is used as a framework for achieving these goals. It is used to store not only the data obtained as a result of measuring a magnet, but also the prescription for and record of how the measurement is performed.

To accomplish the first two objectives listed above, a measurement must be decomposed into a sequence of steps, e.g.: ramp the magnet current, change probe position, measure field, store data. Once the individual steps are identified, a mechanism for assembling the steps in different combinations must be provided. To ensure that a given measurement can be repeated exactly, a means of storing the combination of steps used for a measurement must be provided.

The data acquisition program uses the database to store the list of steps that prescribe a given measurement. Each step is called a "checkitem", and the combination of steps is called a "checklist". A checklist can be either a collection of steps executed together in a specific order, or a list of steps in which a single measurement parameter is varied (in the manner of a programming

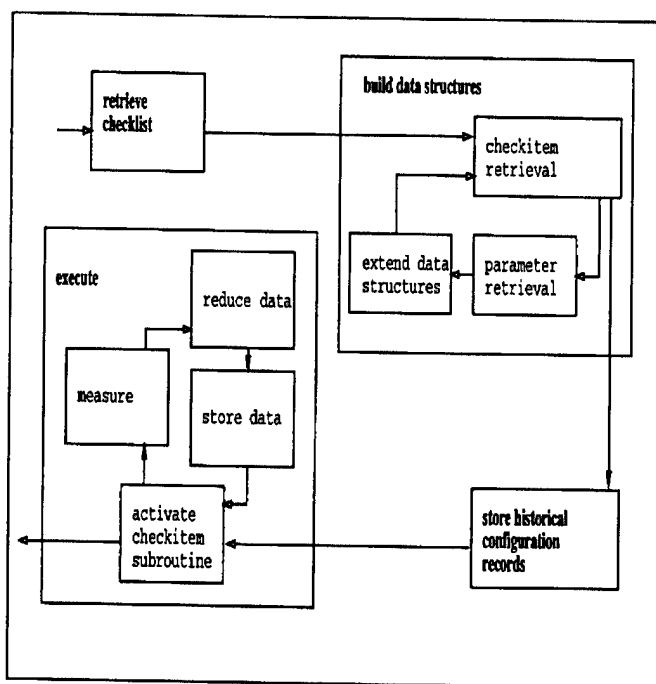


Figure 2. State Diagram of Data Acquisition Process

loop). A checklist can itself be a checkitem in another checklist, which allows for nesting of steps as well as reuse of a collection of steps.

Figure 2 illustrates the states that the data acquisition program executes while performing a measurement. It begins by retrieving the checklist from the database. As the checklist is retrieved, data structures are built in program memory to contain various items required to control how the measurement proceeds. These data structures include:

- a linked list of structures identifying the steps (checkitems) taken to perform the measurement.
- a linked list of structures specifying the instruments used to accomplish the measurement. An instrument is a collection of measurement devices designed to measure or control a single measurement variable, such as field strength or magnet current.
- structures associated with each device that identify the method of converting data from the raw output of the measurement devices (volts, counts, etc.) to more meaningful engineering units (Amperes, Tesla, etc.).

Once these data structures are constructed, the program creates entries in appropriate database tables to provide an historical record of:

- which checklist was used to acquire the data.
- which instruments were used during the measurement.
- which sets of calibration parameters were used during the measurement.
- any special comments entered by the measurement technician to describe the measurement.

At this stage, the data acquisition program is ready to execute the sequence of measurement steps prescribed by the individual checkitems in the checklist. Each type of checkitem has a sub-

³R. Brun et al., Physics Analysis Workstation (PAW) Reference Manual, CERN preprint Q121, 1989

⁴Colin Kelley, Thomas Williams, et. al available via ftp from dartmouth.edu

routine that performs the processing requested by that type of checkitem. The program runs the measurement by working its way through the linked list of measurement checkitems and calling the appropriate subroutine for servicing each checkitem, until the measurement is complete.

As the measurement proceeds, data is recorded into tables organized to separate "raw" data (as output from readout devices) from reduced data (data converted to engineering units). Data collected under a specific set of measurement conditions are stored in the database as "runs", while a set of runs taken under similar conditions is stored in the database as a "sequence".

The data obtained and stored by the data acquisition program may require further processing to provide useful information for physicists examining the data. Data analysis programs, which are described in the next section, perform this processing.

III. DATA ANALYSIS PROGRAMS

Data analysis programs are used to derive measurement results in the form most meaningful to the physicists who study the data and to store the derived results into the database. They also provide a means of testing the measurement data against the expected results for the type of magnet tested.

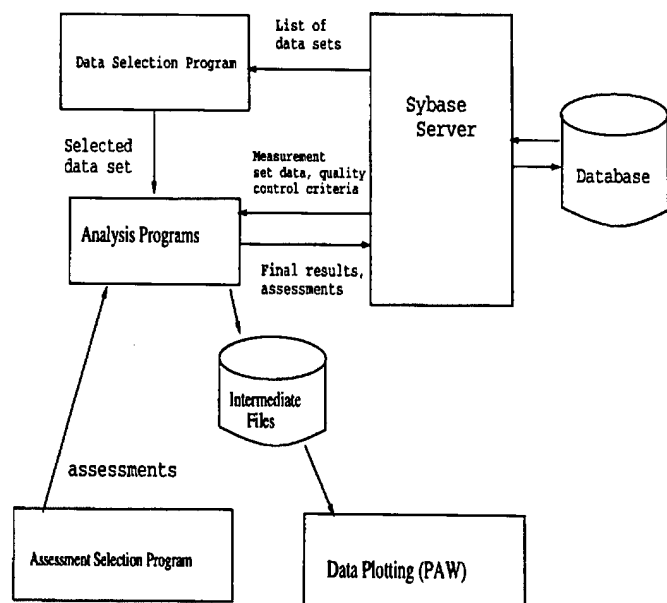


Figure 3. Block Diagram of Analysis Programs

Figure 3 shows a block diagram of the programs that participate in data analysis. The data selection program is an X-windows application that queries the database for a list of measurement sets to analyze and allows the measurement technician to select a data set from the list. The data selection program then activates one of several analysis programs, passing an identifier for the selected data set.

The analysis programs retrieve measurement data sets, using the set identifier to locate the data in the database. After retrieving the data, the analysis programs process the data into the appropriate form, write intermediate data files, and start up the data

plotting program, PAW, to present the data in a graphical format. Another program, the assessment selection program, is started at the same time as the data plotting program. This assessment selection program allows the measurer to provide an assessment of the quality of the data while viewing the data plots.

Once all of the data has been assessed, quality control criteria are retrieved from the database. The quality control criteria identify the expected results of measurements; measurement results are compared to the quality control criteria to determine whether there is a problem with the magnet or with the measurement. Results are stored into the database, along with a summary report of the measurement results that fail the quality control comparisons.

IV. CONCLUSION

A measurement system based on a relational database has been developed and used to test magnets for the Fermilab accelerator. The system provides:

- database-driven measurements, eliminating the need to develop new code when measurement steps change.
- flexibility in meeting the requirements of R & D measurements of prototype magnets as well as routine measurements of a variety of production magnets.
- integrated storage of measurement results, measurement control parameters and commentary information in a relational database, enabling better interpretation of the effects of measurement procedures on measurement results.
- efficient measurement of magnets, allowing testing to keep pace with magnet production as well as providing timely feedback to the magnet production process.

References

- [1] B.C. Brown et al. Software Design for a Database Driven System for Accelerator Magnet Measurements. In *Conference Record of the 1991 IEEE Particle Accelerator Conference, San Francisco, May 6-9, 1991*, page 2134. Institute of Electrical and Electronic Engineers, 1991.
- [2] J.W. Sim et al. A Relational Database for Magnets and Measurement Systems at the Fermilab Magnet Test Facility. In *Proceedings this conference*.
- [3] D.J. Harding et al. Magnetic Field Measurements of the Initial Production Main Injector Quadrupoles. In *Proceedings this conference*.
- [4] D.J. Harding et al. Magnetic Field Measurements of the Initial Production Main Injector Dipoles. In *Proceedings this conference*.

BBAT: bunch and bucket analysis tool*

D.-P. Deng

Relativistic Heavy Ion Collider

Brookhaven National Laboratory Upton, NY 11973-5000

Abstract

BBAT ['bat] is a graphical package, written in C, tcl/tk and BLT, to analyze bunch and bucket properties in the longitudinal phase space for a single and double rf system (Dr. BBAT) interactively. Its usage is detailed fully.

I. Introduction

BBAT is written to meet the need of an interactive graphical tool to explore the longitudinal phase space. It is driven for testing new ideas or new tricks quickly. It is especially suitable for machine physicists or operation staff as well both in the control room during machine studies or off-line to analyze the data. The heart of the package contains a set of c-routines to do the number crunching. The graphics part is wired with scripting language tcl/tk and BLT. The c-routines are general enough that one can write new applications such as animation of the bucket as a machine parameter varies via a sliding scale.

BBAT deals with single rf system. For double rf system, one can use Dr. BBAT, which stands for **D**ouble **r**f **B**unch and **B**ucket **A**nalysis **T**ool. One usage of Dr. BBAT is to visualize the process of bunch coalacing and flat bunch creation.

II. Layout of BBAT

The layout of BBAT has basically four parts, see Figure 1, parameter editing, basic derived parameters, plotting and phase space position. In the parameter editing part, Naturally, this part has two sections, one for the machine parameters and one for the beam parameters. In the machine parameters section, one needs to input the machine, the change rate of main dipole magnets, the energy, the rf gap volts and the rf harmonic numbers. In the beam parameter section, one needs to input the ion species, the charge state and the bunch size either the bunch length or the bunch area. Some parameters have multiple choices. In such cases, the multiple choices are arranged in buttons. In the **Machine** button, one can choose to work with different machines, where *AGS*, *Booster* and *RHIC* are built in machines, for other machines, one is prompted to enter some basic machine parameters. In the **Energy** button, one has a choice of the dipole magnet strength, the gamma value or the momentum or the kinetic energy of the beam. Then in the **Species** button, one can choose from a set of ions or inputting new ones.

Some basic derived parameters are displayed in the second part. These are the synchronous phase angle, stationary bucket area the moving bucket area, the small amplitude synchrotron frequency, bunch area and bunch length. The calculation on bunches is based on the calculation on the buckets, one is expected to redo the calculations on the buckets if the machine pa-

rameters are to be changed. The button **More Results** will pop up a window displaying more related parameter values.

In the third part: plotting, a bucket and a bunch is shown. By pointing the cursor in the plotting region, the position of the cursor in the phase space is displayed in the fourth part. The cursor itself has a horizontal hair which measures the vertical axis and a vertical hair which measures the horizontal axis. The phase space parameters displayed are the phase, bunch length, energy dE and momentum dP and fractional energy and momentum $\frac{dE}{E}$, $\frac{dP}{P}$, and the fractional radius or frequency changes $\frac{dR}{R}$, $\frac{df}{f}$, synchrotron frequency at any amplitudes and the difference with respect to that of small amplitudes. The last parameter displayed is the rf gap volts, which is the matching voltage for a bunch whose energy and phase are determined by the cross hairs of the cursor.

III. Layout of Dr. BBAT

The layout of Dr. BBAT, see Figure 2 is closely followed to BBAT. The first part is parameter editing. The parameters are the gap volts for the fundamental and high harmonic rf system, and the harmonic number which is not restricted to integer, the phase shift between the two rf systems, synchronous phase angle. The second part is basically the same as in the first part, slide scales are used instead of text entry. The third part is a plotting area, where the buckets, bunch, synchrotron potential, the combined rf waveform are displayed. The phase space parameters are displayed in the fourth part, which are the phase, bunch length, energy dE and momentum dP and fractional energy and momentum $\frac{dE}{E}$, $\frac{dP}{P}$, and the fractional radius or frequency changes $\frac{dR}{R}$, $\frac{df}{f}$, synchrotron frequency at any amplitudes. The bucket and bunch areas are also displayed, notice there could be multiple buckets.

IV. Usages

The main usages of BBAT are, not exclusive, follows:

- Bucket sizes, such as the bucket height, width, are easily calculated and graphically displayed. The relationship between the bucket and bunch can be visualized.
- Bunch area can be calculated by knowing the bunch length, and visa versa. The bunch height and synchrotron frequency spread is also easily shown just by moving the cursor to any where of the user's interests. In the plotting area, you can create new bunches by simply click of the cursor, new bunch length is automatically chosen and the bunch is updated.
- Matching a bunch in two machines, such as matching bunch from *Booster* to *AGS*, is easily accomplished by placing the cursor at the right height and length of the injected bunch in the *AGS*, the required matching voltage is automatically shown. The user can explore different matching scheme. If

*Work performed under the auspices of the US DoE.

mismatch, the user can easily find out how much dilution has incurred.

- If it's desired to move the orbit by certain amounts, the amount of changes in the rf frequency can be read off from the screen directly.

The main usages of Dr. BBAT are, not exclusive, follows:

- Dr. BBAT makes the very complicated bucket size calculations in a double rf system easy.
- The user can animate the process of bunch coalacing by changing the relative gap volts of the two system via a sliding scale.
- The user can also visualize the creation of a flat bunch.

V. Acknowledgement

The author would like to extend his thank to M. Brennan, J. Rose and A. Ratti for using the package and reporting bugs and suggestion for improvements.

References

- [1] Hofmann, A., Myers, S., Beam Dynamics in a Double RF System, Proc. XIth International Conference on High Energy Accelerators, CERN (1980).

Quit Refresh Print Config Second RF Help	
Editing machine and beam parameters	
Machine	ags
B dot (T/s)	0.1
Gamma	5.0
RF voltage/turn (kV)	100
RF harmonic number	8
--W	Bucket OK
Species	
Charge State	1
Bunch Length (ns)	100
--W	Bunch OK
Synchronous phase (deg)	
Stationary Bucket Area (eVs/u)	3.95103
Moving Bucket Area (eVs/u)	16.1872
Synchrotron frequency (Hz)	13.8438
Bunch Area (eVs/u)	312.595
Bunch Length (ns)	2.54011
More Results	

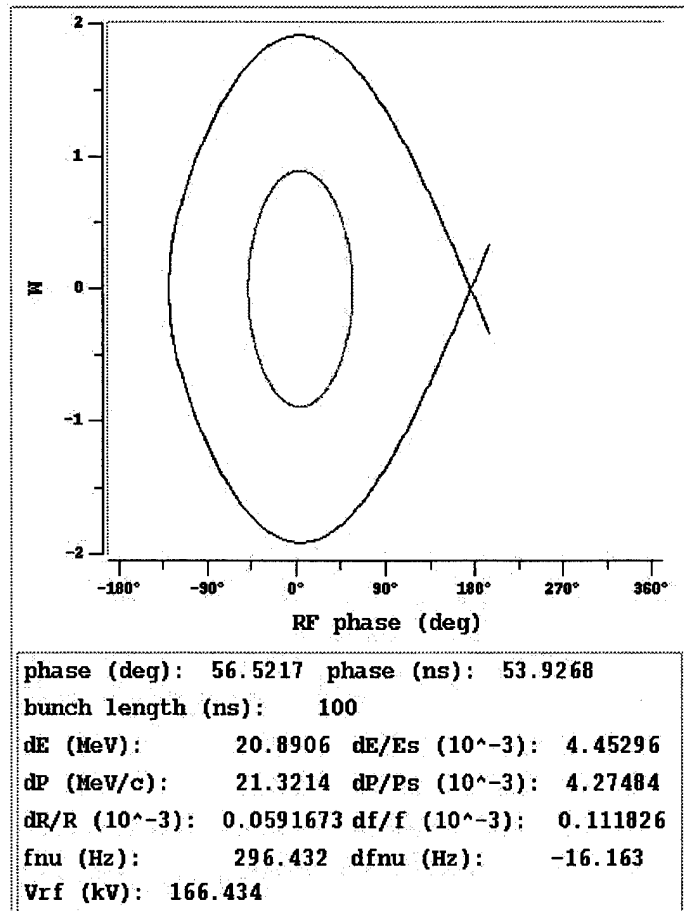


Figure. 1. A snapshot of BBAT.

Quit Redraw V Print Help

Editing RF parameters

Vrf100

Vn100

n2

Theta (deg)86

Vn/Vrf1.0

Phis (deg)4

Phi2s=(phis+theta) (deg)90

phis_14

V_1100

V_n100

theta86

k0

refresh

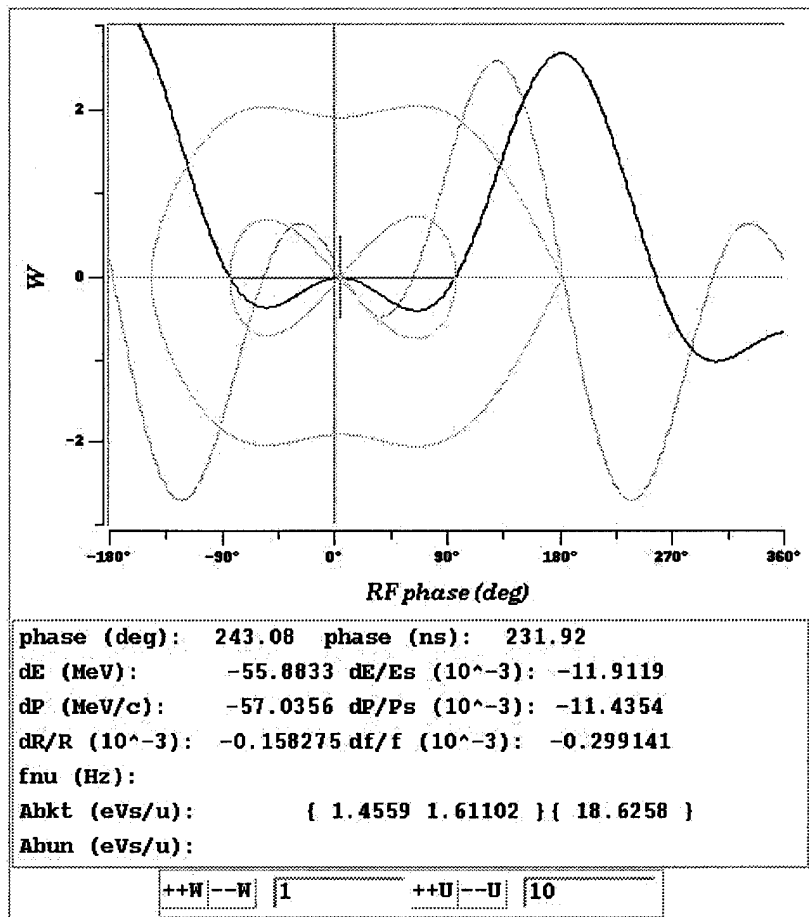


Figure. 2. A snapshot of Dr.BBAT

MASTAC - New Code for Solving Three-dimensional Non-linear Magnetostatic Problems

M. Rojak, E. Shurina, Yu. Soloveichik
Novosibirsk State Technical University

Novosibirsk 630092, Russia

A. Grudiev, M. Tiunov, P. Vobly
Budker Institute of Nuclear Physics
Novosibirsk 630090, Russia

Abstract

A new computer code MASTAC was developed for 3-D magnetic field calculations of different electromagnetic devices contained ferromagnetic, permanent magnet materials and current coils. The methods and algorithms developed in it allow to calculate magnetic field using a personal computer. The results of the calculations of a real magnet and the comparison them with the results of the magnetic measurements are presented.

I. Methods and algorithms

The method of solving three dimensional magnetostatic problems which is based on the use of two scalar potentials [1]: total in magnetic material and reduced in the rest of the region has been realized in computer code MASTAC. The potential difference at the boundary between the total and reduced potentials is calculated on the basis of functional minimization instead of integration. Such the approach permits to decrease significantly the time needed to calculate the potential difference.

The total and reduced potential calculations are performed by the finite element method on irregular tetrahedral mesh. The method of reproduced sections is used to construct a finite element mesh. The basic mesh is constructed with the algorithm of Delaunay triangulation [2]. This method permits to automate the process of tetrahedral mesh generation.

The magnetic field of currents is represented as a superposition of the fields from tetrahedrons on which the currents is divided. The vector of current density is of a constant value and the same direction in every tetrahedron. The field from a separate tetrahedron is calculated by analytical integration. The methods and algorithms applying to dividing of currents on tetrahedrons are similar to the methods and algorithms used for the construction of a finite element tetrahedral mesh.

A special smooth procedure is used for the calculation of magnetic induction.

II. Input and Output for MASTAC

The pre-processor gives an opportunity to fulfil all procedures concerning the entering of magnet geometry by means of a cursor driven by a mouse or with the help of a keyboard. During the enter of the magnet geometry its shape is continuously shown on the screen of a display. This allows to immediately see and correct the mistakes in shape of the magnet design. The control of the pre-processor is also realized with a mouse, that originates

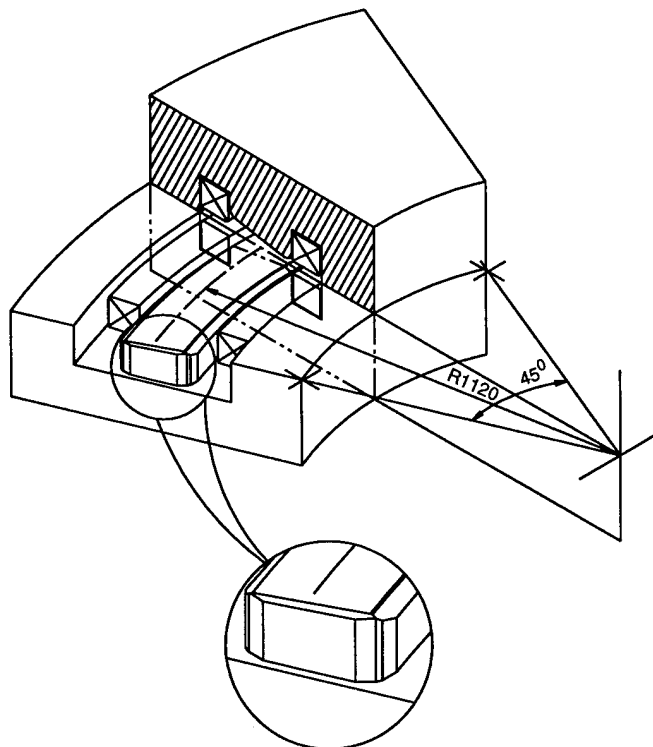


Figure. 1. General design of the dipole magnet.

a very convenient and friendly interface during the work with the computer code.

The graphic means developed in MASTAC allow to construct arbitrary objects in the base section, to put the nodes with local thickening or rarity of the mesh, to edit and deform the local section without changing their topology during the replication of the basic section along an arbitrary vector or arc. In such a manner, one can build a non-surplus mesh for magnets and current coils of curved complicated configuration.

The post-processor allows to take out a potential, magnetic permeability of the ferromagnetic materials, three components and the magnetic induction modulus in the form of graphs, coloured maps and isoclinical lines in an arbitrary cross-section of the magnet.

III. An example of magnetic field calculation

The precision of magnetic field calculations, its dependence on the number of mesh nodes and the capability of the pre-processor

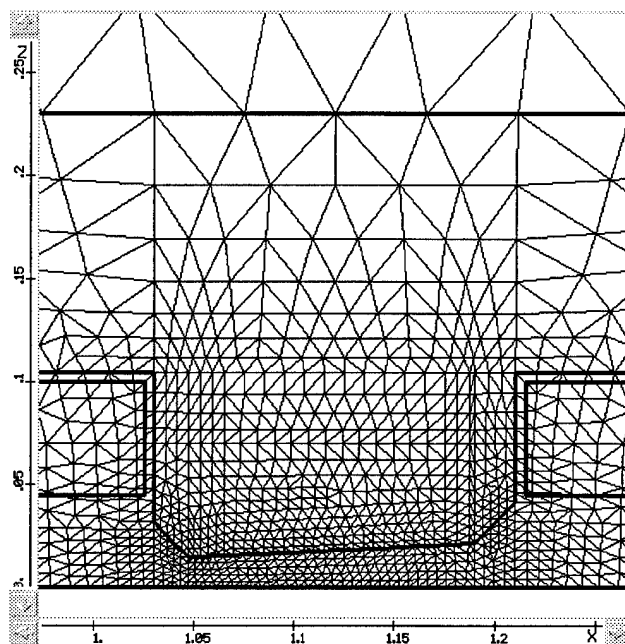


Figure 2. A mesh fragment in the base section of the magnet.

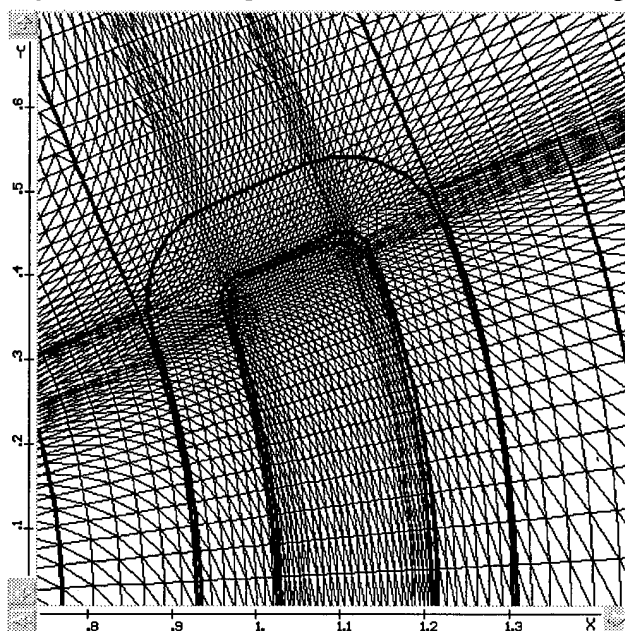


Figure 3. A mesh fragment in the horizontal section of the magnet.

to enter the magnet geometry are illustrated by magnetic calculations of a real magnet sketched in Fig. 1. It is a 45° curvilinear dipole magnet with a radius of curvature of 1.12 m and the complicated profile of poletips, which provides the field index $n=2.7$ in the 1.2-1.6 T range of magnetic fields. Besides the complicated profile, the poletips have lateral and face chamfers for the reduction magnetic induction in the neck and small chamfers at the corners for a more close fitting of current coils.

As it may be seen from Figs. 2 and 3, the graphic means of the pre-processor as well as the methods and algorithms used in it have allowed to describe, with high accuracy, the complicated

shape of curvilinear poletips and generate automatically of the 3-D tetrahedral mesh (64000 nodes).

The results of magnetic field calculations in the longitudinal and transversal sections of the working aperture, their dependence on the number of mesh nodes are presented in Figs. 4, 5, 6 and 7 together with the results of the magnetic field measurements. In this figures: dash line - calculation results (16000 nodes), solid line - (64000 nodes), " \diamond " - experimental results.

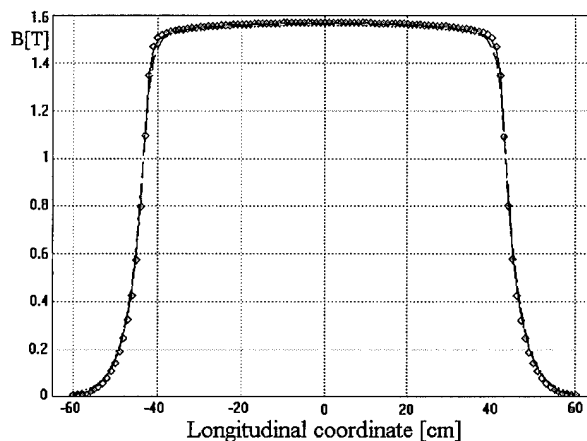


Figure 4. Field distribution of the vertical component in the midplane of the magnet.

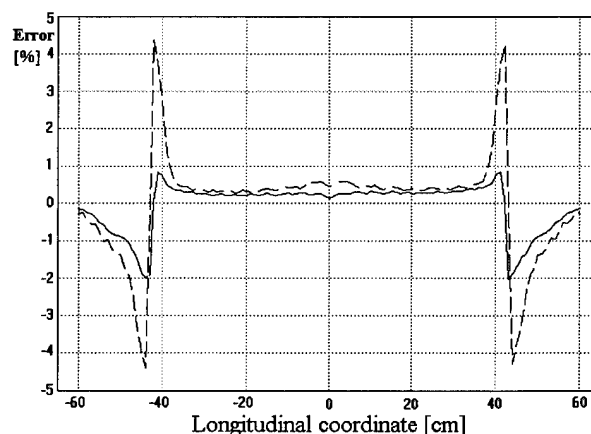


Figure 5. Error in the computed solution as a percentage of the central field.

The calculation times (PC 486DX2-66, 16 MB) depending on the number of mesh nodes are shown in the Table:

Number of nodes	16000	64000
Calculation time	2 h. 30 min.	11 h. 30 min.

IV. Conclusion

A new computer code MASTAC was written for 3-D electromagnetic field calculations. The graphic means of the pre-processor allow to enter easily the magnet geometry of arbitrary shape. The use of effective methods and algorithms in computer

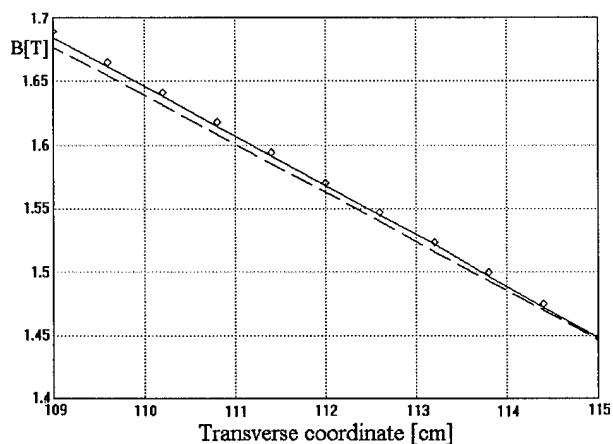


Figure. 6. Field distribution of the vertical component in the midplane of the magnet (middle section).

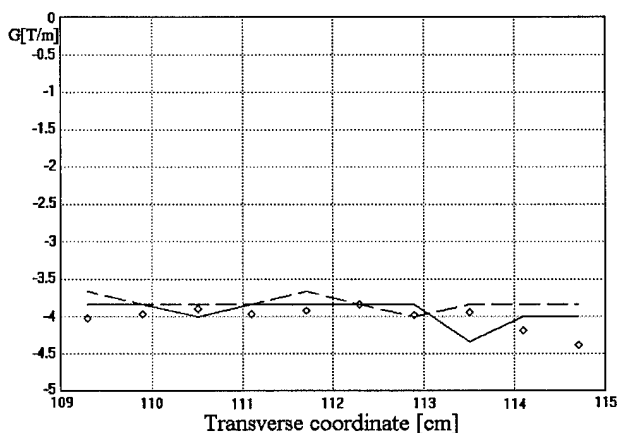


Figure. 7. Gradient distribution of the vertical component in the midplane of the magnet (middle section).

code MASTAC allow to have high precision of magnetic field calculations of any magnets on personal computers.

References

- [1] J. Simkin and C. W. Trowbridge, "Three dimensional non-linear electromagnetic field computations using scalar potentials," *Proceedings of the IEE*, vol. 127, no. 6, 1980.
- [2] B. Delaunay, "Sur la sphere vide," *Izvestiya Akademii Nauk, USSR, Math and Nat Sci Div*, No. 6, p. 793, 1934.

THE COMPUTER CODE BPERM FOR WAKEPOTENTIAL & IMPEDANCE CALCULATIONS

T. Barts, SSC Laboratory,* 2275 Highway 77 North, Waxahachie, TX 75165, USA
W. Chou, Fermilab,† P.O. Box 500, Batavia, IL 60510, USA

Abstract

The program **bperm** is a 2-dimensional code for wakepotential and impedance calculations based on an analytic method of boundary perturbation. It can be employed for periodic structures with rotational symmetry and is useful for structures with small discontinuities such as shielded bellows and valves, tapered transitions, weldments, etc. One principle used in developing the code is portability. It is written in Fortran 77 and is entirely self-contained, with no machine-dependent calls and with simple file input not relying on the namelist extension. The post-processor **gnuplot** has been used for plotting.[1] The code runs on UNIX as well as on VMS computers. It is currently stored on the Common File System (CFS) at the National Energy Research Supercomputer Center (NERSC). A user's guide can be found in Reference [2].

I. INTRODUCTION

The computer code **bperm** is a generalized version of an earlier code using the boundary perturbation method for calculating wakepotentials and impedances for periodic structures.[3] The fundamentals of this method can be found in References [3-6] and are briefly introduced below.

When a rigid Gaussian bunch of rms length σ traverses a periodic structure of period length L and mean radius b_0 , the longitudinal and transverse wakepotentials calculated by the boundary perturbation method are, respectively,

$$W_{||}(s)^{m=0}(V/pC) = -1.8\pi \sum_{p=1}^{\infty} p |2c_p|^2 \cdot \sum_{n=1}^{\infty} k_{0n} \operatorname{Re} \left[\frac{1}{2} e^{-s^2/2\sigma^2} w \left(\frac{k_{0n}\sigma}{\sqrt{2}} - j \frac{s}{\sqrt{2}\sigma} \right) \right], \quad (1)$$

$$W_{\perp}(s)^{m=1}(V/pC \cdot m) = -\frac{360\pi}{b_0^2} \sum_{p=1}^{\infty} p |2c_p|^2 \cdot \sum_{n=1}^{\infty} \left\{ \frac{1}{1-x_{1n}^2} \operatorname{Im} \left[\frac{1}{2} e^{-s^2/2\sigma^2} w \left(\frac{k'_{1n}\sigma}{\sqrt{2}} - j \frac{s}{\sqrt{2}\sigma} \right) \right] - \operatorname{Im} \left[\frac{1}{2} e^{-s^2/2\sigma^2} w \left(\frac{k_{1n}\sigma}{\sqrt{2}} - j \frac{s}{\sqrt{2}\sigma} \right) \right] \right\}, \quad (2)$$

in which s is the distance between the bunch head and the point where the wakepotentials are being calculated, w the complex error function, and

$$k_{mn} = \frac{\pi p}{L} + \frac{L x_{mn}^2}{4\pi p b_0^2}, \quad (3)$$

$$k'_{mn} = \frac{\pi p}{L} + \frac{L x'_{mn}{}^2}{4\pi p b_0^2}, \quad (4)$$

where x_{mn} and x'_{mn} are the n^{th} root of the Bessel functions J_m and J'_m , respectively. All the lengths on the r.h.s. of Eqs. (1)-(4) are in centimeters. The parameter c_p is the Fourier coefficient of the given periodic structure. For a simple geometry it may have an analytic expression. For example, for the structure shown in Figure 1, one has

$$c_p = -j \frac{2\epsilon}{\pi b_0} \frac{\sin(p \frac{\pi q}{L})}{\frac{\pi q}{L}} \frac{1}{p^2} \quad \text{for } p = \pm 1, \pm 3, \dots \quad (5)$$

$$= 0 \quad \text{otherwise.}$$

But in general, c_p has to be computed by a Fast Fourier Transform (FFT), as is done in the code **bperm**.

In order to convert the wakepotentials computed by Eqs. (1) and (2) to impedances, one needs to set the time origin correctly. For this purpose, the code shifts the time zero point from the bunch head to the bunch center, and moves the part of the wakepotentials between the bunch head and center to the tail of the wake. The shifted wakepotentials are then Fourier-transformed to impedances.

Since the code is based on analytical formulae, it consumes much less CPU and memory than that by numerical integration codes such as TBCI or ABCI.[7,8] In addition, it can be applied to more general types of geometries (provided that the perturbation is not too big) than some other analytical methods (e.g., the field matching method).

II. CODE DESCRIPTION

The program **bperm** is a 2-dimensional code and can be employed for periodic structures with rotational symmetry. The input is one complete period of the structure described in the **r** (radial) and **z** (axial) plane as an array of points, which are assumed to be connected with straight segments. Input data for **bperm** is in an ASCII file named **bperm.in**. It contains seven keywords: **dataset**, **title**, **pmax**, **smax**, **sigma**, **shape**, and **end**. They are explained in Table 1. The required ones are **shape** and **end**. The former is followed by the **r** and **z** coordinates of the structure, one pair of numerical values per line with the **r** and **z** value separated by either a comma or a space, while the latter ends the geometry description. The other keywords will use the default values if not specified. All

*Operated by the Universities Research Association, Inc., for the U.S. Department of Energy under Contract No. DE-AC35-89ER40486.

†Operated by the Universities Research Association, Inc., for the U.S. Department of Energy under Contract No. DE-AC02-76CHO3000.

Table 1. Input file keywords

Keyword	Description
shape	Start of shape (structure) data
end	End of shape data
sigma	RMS bunch length in cm (default 1.75)
pmax	Total number of interpolated coordinates used for the structure (default 128)
smax	Region of the wakepotential calculation in units of sigma (min 6, max 140, default 10)
dataset	Name of the output files (default bperm)
title	Plot subtitle
!	Flag for comments

keywords can be either upper, lower, or mixed cases. Any number of problem cases can be included in one input file, but each problem case must be separated from the next with the keyword **end**. Output of **bperm** is seven ASCII files including five files with plotting data for the structure, wakes and impedances, an information file and a **gnuplot** command file that will generate 13 plots. Output files are listed in Table 2.

Table 2. Output files

Name	Description
bperm.sh	Structure data
bperm.lw	Longitudinal wake
bperm.tw	Transverse wake
bperm.lz	Longitudinal impedance
bperm.tz	Transverse impedance
bperm.out	Information file
bperm.gp	Input file for gnuplot with commands produced by bperm
bperm.ps	Postscript file with 13 plots of the structure, wakes and impedance generated by gnuplot

Portability was the major principle in the development of **bperm**. The entire code is written in Fortran 77 and is self-contained, with no machine-dependent calls and with simple file input not relying on the namelist extension.

On a UNIX system, the command for creating the plots (which can be displayed on a X11 color window) and the postscript file **bperm.ps** is:

```
gnuplot bperm.gp
```

Because the post-processor **gnuplot** on a VAX/VMS does not execute properly with a load file created with the Fortran 77 compiler, a file named **bplot.com** is provided by the authors to fix this problem. The command for generating the plots is:

```
@bplot bperm.gp
```

Even though the code is designed to use **gnuplot** for post processing, any plotting package that uses columns of ordinates and abscissas could be substituted. Also the **gnuplot** input file can be modified to open a display terminal other than X11.

It needs to be noted that all output files are opened with the status 'unknown.' This increases user-friendliness on UNIX

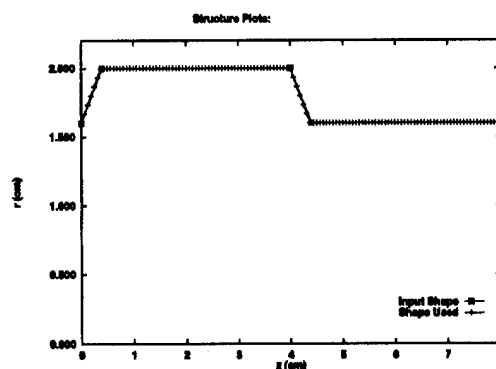


Figure 1. The structure in the example.

workstations by overwriting existing files with the same names. This overwriting also takes place when running **bperm** on a VAX/VMS. The VAX/VMS user needs to be very aware of this feature so that files that need to be saved have names changed before **bperm** makes subsequent runs with identical output dataset names.

III. EXAMPLE

Following is an input file **bperm.in** for the structure shown in Figure 1.

```
dataset=test
smax=10 sigma=1.75
title=bperm Test Problem
pmax=128 ! pmax stays at the
        default
shape
1.6 0.0
2.0 0.4
2.0 4.0
1.6 4.4
1.6 8.0
end
```

Figs. 2 and 3 are plots of the wakepotentials calculated with **bperm** for this input, plotted with **gnuplot**. As a comparison, the wakes obtained from the MAFIA code, **t3210**, are also plotted. It is seen that, in the range $[-5\sigma, 2\sigma]$, the two codes give similar results. The differences begin to show up beyond that region. This is probably due to the different boundary conditions used in the two codes — **bperm** assumes a periodic boundary, while MAFIA/**t3210** assumes an open boundary.

Figs. 4 and 5 are plots of the real and imaginary longitudinal impedances, and Figs. 6 and 7 the transverse ones.

IV. CODE DISTRIBUTION

Complete packages for **bperm** are available from the CFS at the NERSC and also via anonymous ftp from `gateway.ssc.gov`, in the `/pub` directory. The file **bperm.tar.Z** is the UNIX compressed tar file and **bperm.bck.Z** is the VMS save set. Both distributions include the **bperm** source code, either a **makefile** or a command file **make.com**, inputs and outputs for examples and complete

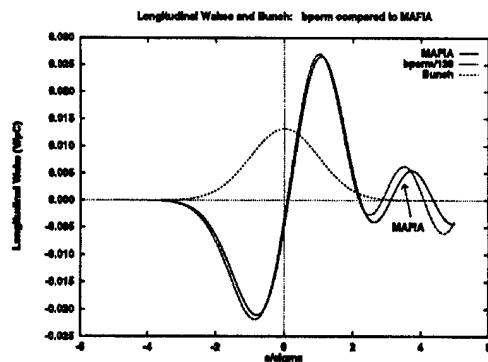


Figure 2. The longitudinal wakepotential.

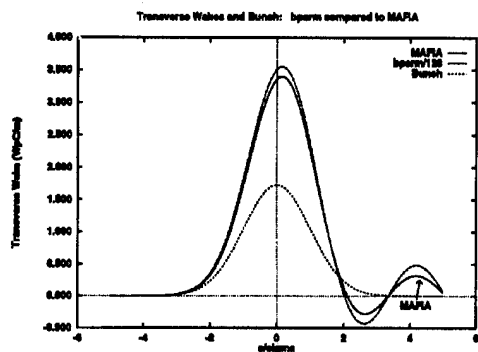


Figure 3. The transverse wakepotential.

documentation including a PostScript file of the User's Guide (i.e., Reference [2]).

References

- [1] The **gnuplot** software is available via anonymous ftp from dartmouth.edu in the /pub/gnuplot directory in the file gnuplot3.5.tar.Z.
- [2] T. Barts and W. Chou, SSCL-MAN-0035, SSC Laboratory (June 1994).
- [3] W. Chou, Light Source Note LS-149, Argonne National Laboratory (1990).
- [4] Z. H. Zhang, Acta Physica Sinica, V 28, p 563 (1979).
- [5] M. Chatard-Moulin and A. Papiernik, Proc. Particle Accelerator Conference, San Francisco, 1979, IEEE Trans Nucl. Sci. V 26, p 3523 (1979).
- [6] R. K. Cooper, S. Krinsky and P. L. Morton, Particle Accelerators, V 12, p 1 (1982).
- [7] T. Weiland, "MAFIA Release 3.1," D6100 Darmstadt, Germany (1991).
- [8] Y. Chin, "User's Guide for New ABCI Version 6.2," LBL-33091, CERN SL/92-49 (AP).

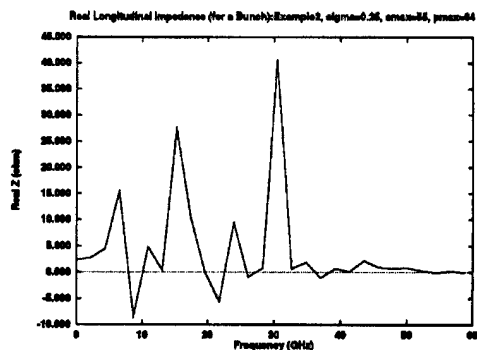


Figure 4. The real longitudinal impedance.

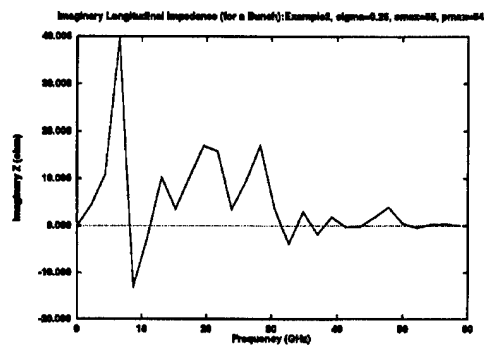


Figure 5. The imaginary longitudinal impedance.

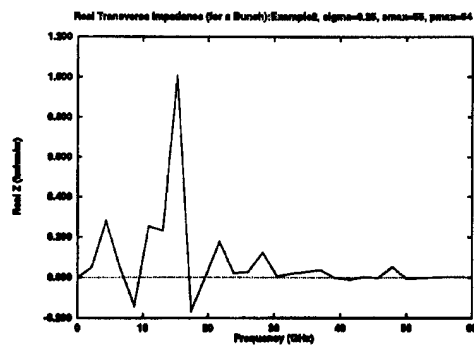


Figure 6. The real transverse Impedance.

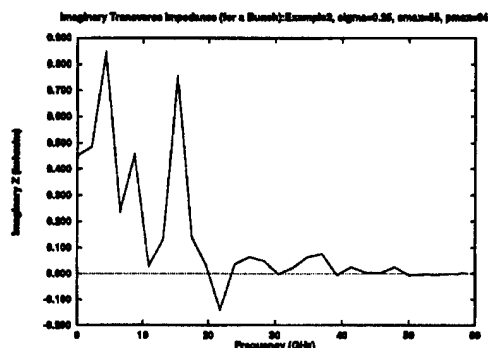


Figure 7. The imaginary transverse impedance.

RESOLVE AT CEBAF*

Byung C. Yunn, Rui Li, and Stefan Simrock
Continuous Electron Beam Accelerator Facility
12000 Jefferson Avenue, Newport News, VA 23606, USA

Abstract

M. Lee's program RESOLVE[1] has recently been in extensive use at CEBAF to help identify and correct optics problems in recirculation arcs and in linac beamlines encountered during the commissioning of the 4-GeV accelerator. We describe the integration of the program with our machine applications software package. A significant vertical focusing error in one of the recirculation arcs, which is attributed to edge focusing of dipole magnets, was found from the analysis of difference orbit measurement data. A corrective measure has been successfully implemented. Optics checks in the spreader and recombiner regions are discussed along with linac optics and 60Hz jitter.

I. INTRODUCTION

RESOLVE is a generic beam simulation code (up to second order in the transfer matrix) which can be used to find the possible causes of trajectory errors with multi-track data fitting capabilities. Usually, alignment errors and/or focusing errors of beam line magnets cause particle trajectories to deviate from the nominal path. Errors also show up when the beam energy is different from the design value. Finding and correcting sources of such errors quickly in the commissioning stage of a machine (CEBAF is currently commissioning a 4 GeV CW electron accelerator) is extremely helpful.

II. PREPARATION OF RESOLVE DECKS

Most CEBAF accelerator beamlines are designed with the optics code DIMAD[2] and a layout of any beamline must agree exactly with a corresponding DIMAD deck. The accelerator is divided naturally into 18 beamline units (45 MeV injector, two linacs - North and South, nine arcs - Arc 1 to 9, five beam switch yard lines, three experimental hall lines - Hall A, B, and C). A conversion program from a DIMAD deck to a RESOLVE deck has been written to help preparing RESOLVE decks for these beamlines. For all beamline elements except a cavity, a straight forward translation of conventions and formats adopted in DIMAD to those of RESOLVE is required for the conversion. Currently, a cavity element in RESOLVE is supposed to simulate a traveling wave linear accelerator as in TRANSPORT with an energy gain proportional to the length of the element. However, we find that CEBAF cavity provides significant transverse focusing in both directions to low energy electron beam. This is especially true in the first two cavities of the 45 MeV injector where the beam energy changes from 500 keV to 5 MeV. A quite elaborate cavity handling routine[3] has been incorporated into the DIMAD being used at CEBAF in order to model transverse cavity focusing also into a cavity element. Consequently, the North

Linac model in RESOLVE is likely to predict a slightly different trajectory in the beginning section for the first pass beam compared to DIMAD. However, the modeling difference should be negligible in the North Linac at higher passes and in the South Linac at all passes. Our RESOLVE decks start from the 45 MeV beamline known as the Injector Chicane to minimize effects of cavity modeling presently available in the code.

III. DATA TAKING AND READING

RESOLVE runs on a VAX system while machine control is by UNIX based computers at CEBAF. We have developed a fully interactive and easy to use RESOLVE data handling process integrated into CEBAF machine control system. The program is written in Tcl scripts since most high level optics control software such as orbit correction and energy and orbit locks programs are presently also written in Tcl[4] which is a very powerful scripting language based on a library of C procedures for developing GUI applications. From an operator console we can pull up an optics menu and initiate a data taking procedure. Fig. 1 shows the main window for a data taking. A click on SelectBeamline brings a menu of beamlines made of the 18 basic beamline units described in the previous section. One then assembles a beamline of interest concatenating several units selected from the menu.

```
Select Beamline

Your directory:      /usr/user2/mccops/tcl_apps/DataLog

Open Data File

Enter data file name      29MarArc1
Enter Reference Energy (MeV)      445
Make a note before taking each data
Note:      MBT1A01H
Take Data      1

Close Data File

View Data Info

Get Absolute Orbit from i-th Data Set
Get Difference Orbit from i-th and j-th Data Set
Clear data before opening another file
Clear Data

Quit
```

Figure 1. A menu for data taking.

*This work was supported by the U.S. Department of Energy, under contract No. DE-AC05-84ER40150.

Usually a corrector is chosen to provide a kick to the beam by a specified amount and then all beam position monitor(BPM) readings are recorded along with magnet settings and cavity gradients for future reference. After collecting all necessary data one can close a data file and quit or continue to prepare BPM input files required for the RESOLVE program with a click on either the GetDifference or GetAbsolute button. Data files taken previously are converted into .bpm files with a data read procedure written also in Tcl. Data analysis is performed with RESOLVE after transporting .bpm files to a VAX.

IV. OPTICS CHECK WITH RESOLVE

During the machine commissioning, we have systematically checked optics of beamline components with RESOLVE to ensure proper transport of the beam through the accelerator.

A. X-Y Coupling in Linacs

Data shown in Fig. 2 agree well with the linac model in the second(South) Linac, where the 1st pass beam with an initial energy of 445 MeV gains 400 MeV in energy. As expected, BPM data for the 1st pass beam in the first(North) Linac cannot be fitted with the model as a whole as a result of cavity focusing in the front end of the North Linac. An interesting feature seen in Fig. 2 is the existence of x-y coupling due to a skew quadrupole component of the fundamental accelerating mode of CEBAF superconducting cavity. A numerical calculation[5] predicts a total integrated gradient of the skew quad component, which is well localized at the location of higher order mode couplers, to be approximately 4 gauss when a single 5-cell cavity is powered at 5 MV/m gradient. Furthermore, it is shown that the skew quad component from each cavity of linacs (we have 180 cavities in each linac) adds when cavities are phased for acceleration. BPM data in Fig. 2 are for the beam motion initiated by kicking

the beam horizontally (top figure) at the entrance of the South Linac. The x-y coupling in cavities induces the motion in the vertical plane (bottom figure). The strength of skew quadrupoles used for the fit agrees with the numerically estimated value. We should also mention that an experiment to measure the skew quad component of a CEBAF cavity has been performed[6] at the first cryomodule of the North Linac and results qualitatively confirmed the theoretical estimate.

B. Arc Optics

Each arc is an isochronous 2nd order achromat, consisting of 3 distinct optical units called spreader, recombiner and arc proper. The nine arcs allow for 5 passes through the linacs.

In higher energy arcs starting from Arc 5 we find that difference orbit data at spreader/recombiner modules generally fit well with the models, while BPM data clearly deviate from the models at spreader/recombiner modules in the Arc 1 and 3. However, the agreement between the model and data is excellent in the spreader region of Arc 2 as shown in Fig. 3.

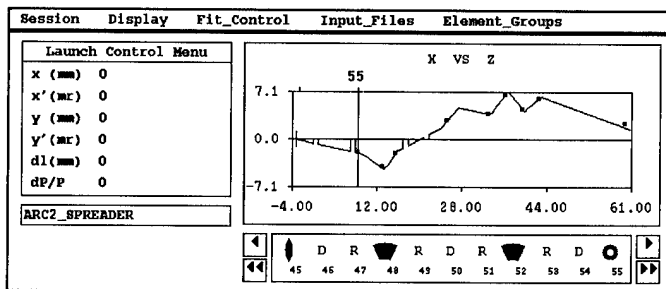


Figure 3. A difference orbit in 845 MeV Arc 2 spreader region.

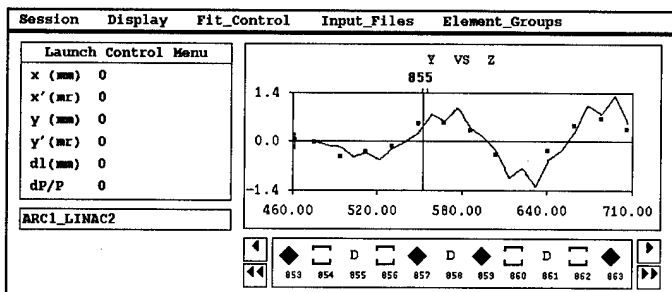
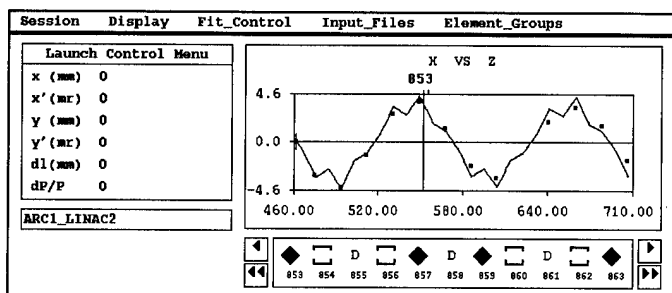


Figure 2. Fit of BPM data with model in S. Linac for the 1st pass beam. Phase advance per cell is set to 60 deg for this run.

BPM data in the Arc 1 shown in Fig. 4 clearly indicate that the vertical phase advance across the arc proper is more than the design value. RESOLVE finds that with a 2.7 % reduction in the strength of all 16 vertically focusing quadrupoles at the arc proper, the data agree well with our Arc 1 model as shown in the bottom figure of Fig. 4. Initially, we implemented this solution into the machine to correct arc optics and proceeded to the next Arc 2 expecting a similar optics problem. However, difference orbit data in Arc 2 proper agreed well with the Arc 2 model in both horizontal and vertical planes. This was a puzzle because Arc 2 appears optically almost identical to Arc 1. However, arc dipoles are not shimmed in general except in Arc 1. (All spreader and recombiner dipoles are shimmed.) In the 445 MeV Arc 1 beamline, an arc dipole is a 1-m long parallel faced magnet with a bending radius $\rho = 5.10m$ and with a bending angle $\theta = 11.25^\circ$. With the nominal shimming, the angle of inclination $\beta_1 = 5.625^\circ$ of the entrance face and the angle of inclination $\beta_2 = 5.625^\circ$ of the exit face, the dipole is vertically focusing with an edge focal length $f_y = 51.89m$. As a result of shimming the beam following the reference trajectory now traverses the arc dipole with $\beta_1 = \beta_1 = 7.165^\circ$. An added edge focusing changes f_y to 40.65 m. One must compensate an extra phase advance introduced by reducing the strength of a vertically focusing quadrupole (with a nominal focal length $f_q = 6.72m$) located next to the dipole. Consequently, we expect a change in f_q to 6.93 m which amounts to a 3.2% change, qualitatively explaining the discrepancy seen

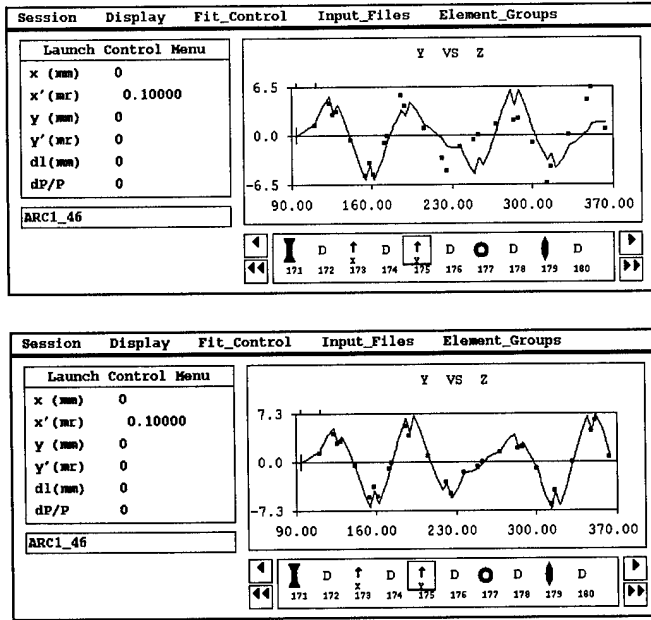


Figure 4. BPM data in Arc 1(top). The data fit nicely after vertical focusing correction(bottom).

between the model and data. The vertically focusing quadrupole family now has a strength in complete agreement with the value found with RESOLVE after DIMAD refitting Arc 1 optics with the shimmed dipoles.

C. 60Hz Perturbations

When a pulsed beam was line synchronized, BPM data were collected through each section as a function of time delay from the AC zero crossing in order to identify distributed 60Hz perturbations[7]. To describe an algorithm employed to analyze data, we start by introducing the initial beam vector incoming to beamline $R_0 = (x_0, x'_0, y_0, y'_0, \delta_0)$, the BPM reading $X = (x^{(1)}, x^{(2)}, \dots, x^{(m)})$ (We use only x readings for the simplicity of illustration.), and

$$M = \begin{pmatrix} M_{11}^{(1)} & M_{11}^{(2)} & \dots & M_{11}^{(m)} \\ M_{12}^{(1)} & M_{12}^{(2)} & \dots & M_{12}^{(m)} \\ \dots & \dots & \dots & \dots \\ M_{16}^{(1)} & M_{16}^{(2)} & \dots & M_{16}^{(m)} \end{pmatrix},$$

where $x^{(i)}$ is the horizontal position at the i th monitor, $M_{jk}^{(i)}$ is the transfer matrix from the start of the beamline to the i th monitor. These are related as $X = R_0 M$. A good fit requires terms upto the 3rd harmonic in the Fourier decomposition of 60Hz perturbed quantities. For example,

$$x(t) = x(0) + \sum_{n=1}^{n=3} [S_n \sin(2\pi n f_0 t) + C_n \cos(2\pi n f_0 t)],$$

where $f_0 = 60\text{Hz}$. Each element in the vectors X and R_0 can be Fourier expanded yielding the vector coefficients S_{xn} and C_{xn} for the expansion of X , and S_{0n} and C_{0n} for the expansion of R_0 . Assuming the transfer matrices are static, and using the orthogonality of sinusoidal functions, we get $S_{xn} = S_{0n} M$, $C_{xn} = C_{0n} M$

($n=1,3$). This suggests that the propagation of the Fourier coefficients can also be treated by RESOLVE as difference orbits with respect to the time independent orbit (or the orbit averaging over time). Therefore, for each S_{xn} and C_{xn} ($n=1,3$) a RESOLVE difference orbit can be obtained, and the incoming beam vector can be constructed by fitting S_{0n} and C_{0n} . A localized kick generated by a 60Hz field perturbation can be simulated as an additional $\delta R = (0, \delta x', 0, \delta y', 0)$ at its location. One can decompose δR with coefficient vectors $S_{\delta n}$ and $C_{\delta n}$. For a given n , the coefficients $S_{\delta n}$ and $C_{\delta n}$ behave just like kickers in the RESOLVE difference orbits for the corresponding S_{xn} and C_{xn} . As a consequence, we can quantify the distributed 60Hz kicks by resolving the difference orbits obtained from the coefficients of the frequency components of all the position monitors in the beamline.

As fully described in [7], a 60Hz kick of approximately 5 microradian in the path length adjusting "dogleg" region for the first pass was identified using RESOLVE. This is consistent with a measurement which shows that a malfunction in the dogleg magnet supplies generates ripple of approximately the same magnitude.

V. ACKNOWLEDGEMENTS

We thank Martin Lee for graciously providing his program RESOLVE and Joe Bisognano, Andrew Hutton, and Hamid Shoaee for many helpful suggestions.

References

- [1] M. Lee, "RESOLVE User's Guide".
- [2] R. Servranckx *et al.*, "Users Guide to the Program DIMAD," SLAC report 285 (1985).
- [3] D. Douglas, private communication.
- [4] J. K. Ousterhout, *Tcl and the Tk Toolkit*, Addison Wesley Professional Computing Series (1994).
- [5] Z. Li, "Beam Dynamics in the CEBAF Superconducting Cavities," Ph.D. thesis, The College of William and Mary, 1995.
- [6] M. G. Tiefenback, Z. Li, and B. C. Yunn, "Emittance Measurement and Transverse Cavity Transfer Matrix in the CEBAF Nuclear Physics Accelerator," unpublished, 1993.
- [7] M. G. Tiefenback and R. Li, "Survey and Analysis of Line-Frequency Interference in the CEBAF Accelerator," this conference.

NEW GRAPHIC USER INTERFACE FOR THE CHARGED PARTICLE BEAM PROGRAM PARMILA

George H. Gillespie and Barrey W. Hill
G. H. Gillespie Associates, Inc., P.O. Box 2961, Del Mar, CA 92014, U.S.A.

ABSTRACT

An advanced graphic user interface (GUI) has been developed for use with the PARMILA program. PARMILA (Phase and Radial Motion in Ion Linear Accelerators) is a multiparticle simulation program that provides a detailed description of the evolution of the beam in a linear accelerator. We have ported the Los Alamos Accelerator Code Group's Cray version of PARMILA to the Macintosh and integrated it with the Shell for Particle Accelerator Related Codes (S.P.A.R.C.) GUI environment. Problem set up is accomplished graphically. The configuration of a PARMILA beamline is defined by selecting icons representing transport elements from a palette and dragging them to a window. All input parameters are set using unique Data Tables built into multiple-pane windows. Rule-of-thumb upper and lower guidance limits for each parameter are displayed to assist users in problem specification. The graphic interface is described and examples using this new approach to running PARMILA are illustrated.

I. INTRODUCTION

PARMILA [1] has been the standard program used to model drift tube linacs since the program was originally developed by Swenson and coworkers in the mid 1960's at the Midwestern Universities Research Association [2]. It is also now utilized in the design of a variety of high-current beam transport lines and several related programs have been developed from the original code for application to other accelerator structures. While the program has been in widespread use for many years, the user interface has remained largely unchanged. Setting up problems is still time consuming and, with the increased complexity created by the incorporation of many advancements and improvements over the years, is often confusing as well. We have developed a new approach to using PARMILA by integrating it with a GUI, called the Shell for Particle Accelerator Related Codes (S.P.A.R.C.), designed specifically to support particle beam simulation and analysis programs. The S.P.A.R.C. GUI provides a unique software environment customized to the needs of the accelerator community [3]. The Los Alamos Accelerator Code Group's Cray version of PARMILA [4] has been integrated into this new software environment using an approach similar to that adopted for the integration of the TRACE 3-D program into S.P.A.R.C. [5]. The emphasis is placed upon the "front end" requirements for the GUI, concentrating on the initial problem set up, while retaining the PARMILA output in a form similar to that which users are accustomed to seeing.

II. DEFINING A BEAMLIN

Accelerator beamlines are defined graphically through a mouse-driven "drag and drop" user interface. Figure 1 illustrates the interface screen developed for PARMILA. Three primary elements of the interface are shown: a Menu Bar, Palette Bar, and two Document Windows. The Menu Bar contains standard items, associated with the operating system, as well as specific menu items used to support PARMILA. Examples of these menu items are discussed below. The Document Window and Palette Bar are the primary interface components for setting up a beamline. A Document Window contains all the information associated with a particular beamline problem. Up to six Document Windows may be open simultaneously; Figure 1 illustrates two. The Palette Bar contains icons representing all of the transport components, DTL tanks, and other elements available in PARMILA, as well as icons for setting up the initial beam and for identifying the stop point of a calculation. The configuration of a PARMILA beamline is defined by selecting icons from the Palette Bar and dragging them to the Model Space Pane of a Document Window. When dropped onto the Model Space Pane, each icon "snaps" into place at the end of the beamline. Elements may also be inserted into the middle of a beamline by dragging the appropriate icon to the connection line between any two adjacent icons on the Model Space Pane. The front Document Window in Figure 1 (Document Window 1) shows a beamline consisting of a low energy beam transport (LEBT) matching section, followed by one 350 MHz DTL tank. The Document Window 1 beamline is one of several [6] being used to test and evaluate the integrated PARMILA-GUI package. Document Window 2 shows a 425 MHz DTL matching section. The (Document Window 2) beamline is from the PARMILA documentation [4] and is also being used for testing.

The components of a beamline on the Model Space Pane may be rearranged using the Work Space Pane of the Document Window. Any icon representing a transport element, or any group of icons representing a segment of the beamline, may be selected and moved to the Work Space for temporary storage. Icons or groups of icons on the Work Space may then be inserted into, or placed on either end of, the beamline on the Model Space. The Work Space Pane may also be used for other purposes, such as temporarily storing alternate designs for a given beamline segment. Figure 1 shows a FODO cell on the Work Space Pane of Document Window 1.

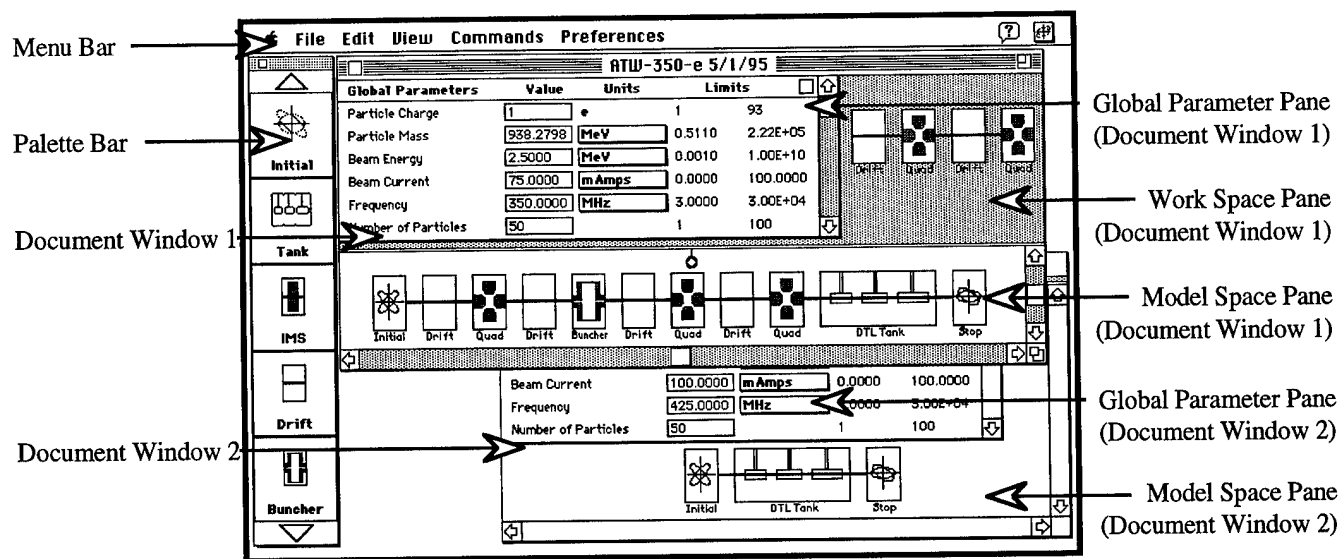


Figure 1. The PARMILA graphic user interface showing two Document Windows open, each with a different beamline.

III. EDITING INPUT PARAMETERS

Parameters are input using Data Tables. The Global Parameter Pane shown in Figure 1 illustrates the most common type of Data Table, which contains five fields for each parameter. These fields provide the parameter name, a value input box, the units of the parameter, and two user guidance limits for the parameter value. The lower and upper guidance limits can incorporate expert system type rules-of-thumb [5,7] to assist the user in setting up problems. The user may select different options for the units of a parameter, including unique "smart units" [3,5], via pop-up menus in the units field. The guidance limits, as well as the current value, are immediately displayed in the selected units.

The Global Parameters include all of the top level beam parameters, such as the particle charge and mass, the initial beam energy and current, etc. Data Tables for inputting parameters for each of the beamline elements are accessed via Piece Windows. The Piece Window for any beamline component is displayed on the computer screen by "double clicking" the corresponding icon in the Document Window. Figure 2 illustrates a Piece Window and Data Table for a PARMILA transport element. Certain parameters, such as those used to specify output for the element, have a finite number of options. In these cases, the value input and units fields are combined into a pop-up menu, and no user guidance limits are needed. For beamline elements requiring a large number of inputs, such as a DTL tank, multiple pane Piece Windows are utilized that allow the user to flip between different sets of parameters [8].

The S.P.A.R.C. GUI also provides other powerful beamline editing features. For example, beamline segments, such as the FODO lattice shown in Figure 1, may be copied from one Document Window and pasted into another. This is especially useful when examining similar beamline designs.

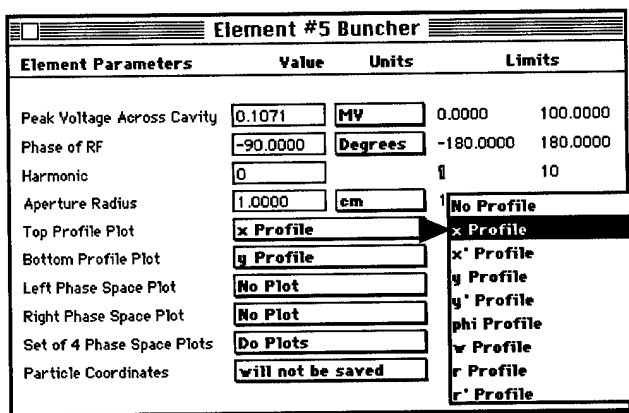


Figure 2. Piece Window, with parameter input Data Table, for the radiofrequency buncher element of PARMILA. Use of a pop-up menu for selection of a profile plot is illustrated.

IV. SELECTING OUTPUT DISPLAYS

Several run-time output display options are available using the interface we have developed. Profile plots and a variety of phase space plots may be displayed on-screen. These plots are the same as those normally generated from PARMILA data output files using a graphics post-processor. In a standard PARMILA input file, the user specifies the output to be generated for each transport element individually by setting a series of six two-digit codes on the data line for every element. The same specification of output options for each individual transport element may be also done using our interface, by selecting from among the options provided by the pop-up menus illustrated in Figure 2. The interface keeps track of the selections and generates the necessary series of two-digit codes for PARMILA. It is frequently desirable to use the same options for all transport elements,

which can be tedious to set up for a long transport line. Our interface provides an automated procedure for doing this.

Figure 3 illustrates a special window (accessed from the Preferences menu item shown in Figure 1) used to specify that the same Profile Plot options be applied to all elements in a section of the beamline. The window shown in Figure 3 is one of several unique input windows that can be used to specify the output displays to be created during a run.

Figure 3. Selecting beam profile display options.

Figure 4 shows two profile plots, for the DTL through cell 100 of the (Document Window 1) beamline illustrated in Figure 1. The plot parameters were specified using the window shown in Figure 3. Results may be viewed, as the PARMILA beam dynamics calculation proceeds, using a new interactive mode that allows users to "step through" the beamline and display profile plots, coordinate scatter plots and other output at specified locations.

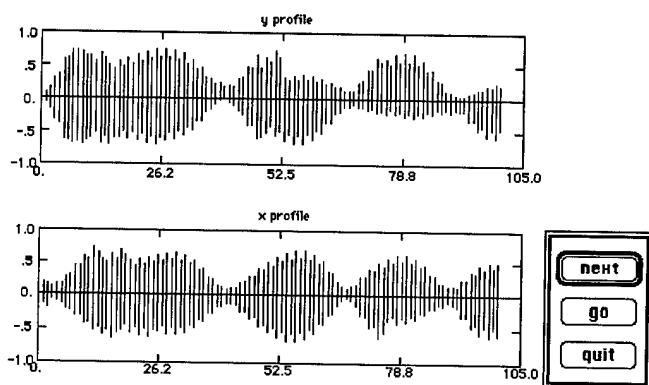


Figure 4. Vertical and horizontal beam profile displays for the interactive running of PARMILA from the interface. The profiles shown are for a severely mismatched beam being injected into the "ATW-350-e" DTL of Figure 1.

Scatter plots, of the two dimensional projections of the particle distributions, may also be displayed during a run. Locations in the beamline, where displays are to be shown during a run, may be set using pop-up menus in the Data Tables for each transport element (Figure 2) or using other special phase space output selection windows (similar to Figure 3) available from the Preferences menu (Figure 1).

V. SUMMARY

The integrated PARMILA-GUI package is a useful new tool for accelerator design and analysis. The program provides an interactive and intuitive package for designing transport lines and drift tube linacs. Both experienced and new users of PARMILA should realize increased productivity.

VI. ACKNOWLEDGEMENTS

The authors are indebted to Robert A. Jameson of the Los Alamos National Laboratory for constructive comments and for providing example problems to test our software. The assistance of James S. Gillespie in developing several parts of the S.P.A.R.C. interface are gratefully acknowledged.

VII. REFERENCES

- [1] G. P. Boicourt "PARMILA - An Overview," AIP Conf. Proc. **177**, 1-21 (1988).
- [2] B. Austin, T. W. Edwards, J. D. O'Meara, M. L. Palmer, D. A. Swenson and D. E. Young, "The Design of Proton Linear Accelerators of Energies up to 200 MeV," MURA-713, Appendix B "Computer Program for Linac Particle Dynamics," 115-129 (1965).
- [3] G. H. Gillespie, "The Shell for Particle Accelerated Related Codes (SPARC) - A Unique Graphical User Interface," AIP Conf. Proc. **297**, 576-583 (1993).
- [4] G. Boicourt and J. Merson, "PARMILA Users and Reference Manual," Los Alamos National Laboratory Report No. LA-UR-90-127, Revised, 141 pages (1992).
- [5] G. H. Gillespie and B. W. Hill, "A Graphical User Interface for TRACE 3-D Incorporating Some Expert System Type Features," 1992 Linear Accelerator Conference Proceedings, AECL-10728, 787-789 (1992).
- [6] R. A. Jameson, private communications (1994).
- [7] G. H. Gillespie, P. K. Van Staagen and B. W. Hill "Knowledge Rule Base for the Beam Optics Program TRACE 3-D," Proceedings of the 1993 Particle Accelerator Conference, Vol. 1, 86-88 (1993).
- [8] G. H. Gillespie, B. W. Hill and J. S. Gillespie, "Making PARMILA Easy to Use - Really Easy to Use!" Proceedings of the 10th International Conference on High Power Particle Beams, NTIS Report No. PB95-144317, Vol. 2, 626-633 (1994).

XWAKE 1.1: A NEW IMPEDANCE AND WAKE FIELD SOFTWARE PACKAGE

G. W. Saewert and T. G. Jurgens, Fermi National Accelerator Laboratory, Batavia, IL 60510 USA

Abstract

This paper outlines the novel features found in Xwake 1.1. This release of Xwake is a body of revolution (BOR) conformal finite difference time domain (FDTD) code written to model longitudinal and transverse wake fields and impedances. The package is capable of accurately modeling slowly tapered structures as well as devices containing dielectric and permeable media. A state of the art perfectly matched layer (PML) absorbing boundary condition (ABC) provides the ability to truncate the computational grid immediately at a device's beam pipe openings, increasing the computational efficiency of the package. The program includes automatic mesh generator, field solver and post processor plotting modules all integrated with an intuitive graphical user interface. Since the package is written with ANSI-C and the Motif widget set, Xwake 1.1 is portable across UNIX environments. The use of dynamic memory allocation enables the program to automatically scale itself to the problem size without resorting to code recompilation.

I. INTRODUCTION

Xwake is a computer code that computes the impedance of particle accelerator beam line structures. As with present codes, this is accomplished by driving a body of revolution finite difference electromagnetic field solver [1] with a rigid relativistically moving particle bunch. The fields produced by the bunch are integrated to get wake potential and impedance. However Xwake overcomes limitations of current codes.

Xwake includes numerous features to make it easy to use. Its graphical user interface (GUI) was designed to be intuitive and is built with the popular X/Motif widgets. This along with strict adherence to ANSI-C give it portability across UNIX platforms. Xwake allocates the memory it needs dynamically at run time, thus the problem size it can handle is limited only by the installed computer memory.

II. XWAKE 1.1 FEATURES

The upcoming summer 1995 1.1 release of Xwake incorporates the following advanced features: the ability to model permeable, dielectric and lossy material, conformal modeling of an object's shape, and a state of the art broadband absorbing boundary condition (ABC). In addition, Xwake 1.1 can perform both monopole and dipole calculations, whereas Xwake 1.0 did monopole calculations only.

Xwake can model materially inhomogeneous objects with arbitrary permeability, permittivity and conductivity. Codes commonly used in accelerator physics such as ABCI [2] and TBCI [3] are limited in their ability to represent the material composition. The only material other than a vacuum they can model is a perfect electrical conductor.

Xwake deforms the shape of computational cells so that they conform to and therefore preserve the shape of the material in-

terface [4]. Only cells immediately adjacent to the interface are deformed from the original rectangular cell shape. This means that the cost of utilizing the contour FDTD method over conventional FDTD methods is asymptotically negligible. Traditionally used codes use either a rectangular cell approximation (TBCI), or a diagonal unit cell approximation (ABCI) to describe the structure's shape. This level of geometrical accuracy is sufficient for the efficient computation of some structures, particularly when the media interfaces coincide with computational cell boundaries. However, previously reported results from Xwake 1.0 [5], showed a 64-fold savings in computer memory and a 512-fold savings in computer run time over ABCI to obtain equal accuracy in the modeling of a slowly tapered beam pipe.

The Xwake ABC is an extension [6] of Berenger's PML ABC. The ABC reflection coefficient is routinely below -80 db for arbitrary wave angles and a broad range of frequencies. This means multiple beam pipe modes will be simultaneously absorbed, thus lowering the computational lattice noise due to spurious mode reflections. This contrasts with the (single) mode matching technique used in other codes. Additionally this means that the beam pipe can be truncated closer to the region of interest. This decreases the use of computer resources.

To use the program first describe the problem in a text file, then run Xwake to input the text file and subsequently obtain solutions. Options for executing the mesh generator, solver/post processor and plot creator are provided by the controls of the GUI, enabling the user to make repeated calculations at will with different parameters without leaving the program. The user meshes the problem with either a stepped edge or contour approximation. Wake potentials and impedances are calculated by the solver using six user adjustable parameters with default values predetermined for convenience, likewise with the plotting options. Plots can be saved to a PostScript file or sent directly to a PostScript printer.

III. RESULTS

This section presents modeling results produced by Xwake 1.1. The examples chosen illustrate the salient features of the code.

A. Radial Transmission Line

The first structure modeled is a shorted radial transmission line. Both an empty and a ferrite loaded version are investigated. Figure 1 illustrates the problem at hand. The transmission line is 5 cm wide with a depth of 20 cm. The ferrite occupies the upper 15 cm of the transmission line. The beam pipe radius is 10 cm. The radial and longitudinal discretization lengths are 5 mm. The (hollow) beam radius coincides with the beam pipe and has an rms length of 2 cm. Figure 2 displays the monopole longitudinal impedance of the empty transmission line. An equivalent ABCI simulation provides similar results. Figures 3 and 4 show the dipole longitudinal and transverse wake potentials of the empty transmission line. Figure 5 is a plot of the dipole wake potentials

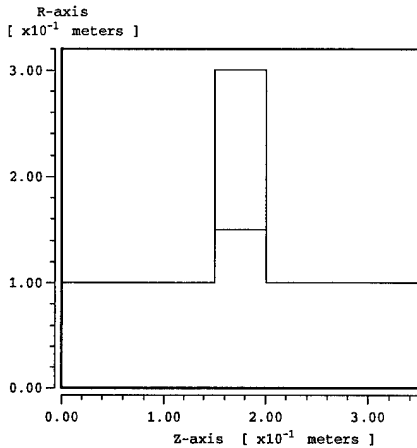


Figure 1. Radial Transmission Line Geometry

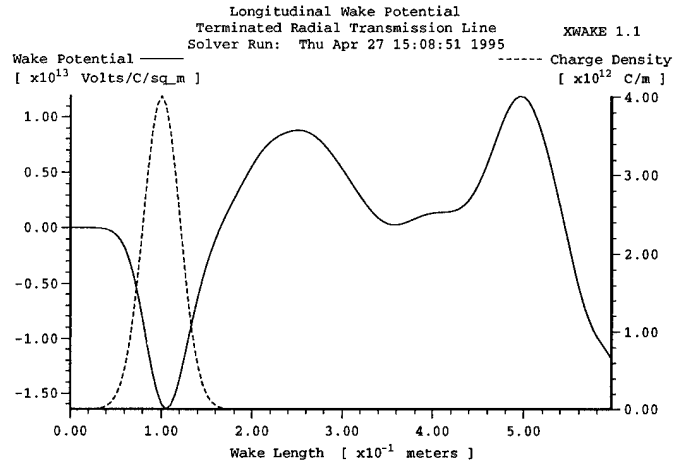


Figure 3. Dipole Longitudinal Wake Potential

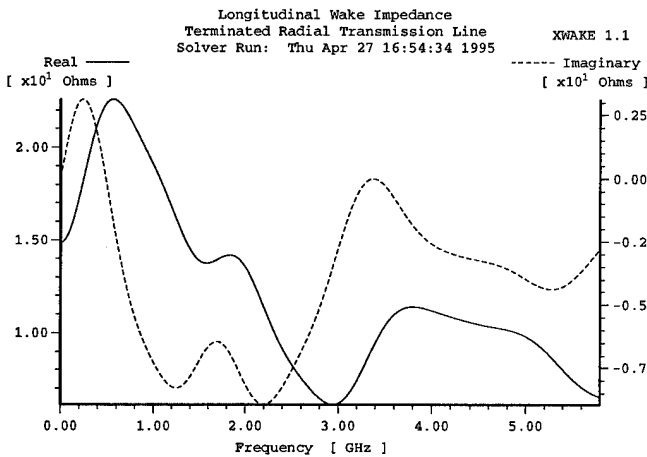


Figure 2. Monopole Longitudinal Impedance

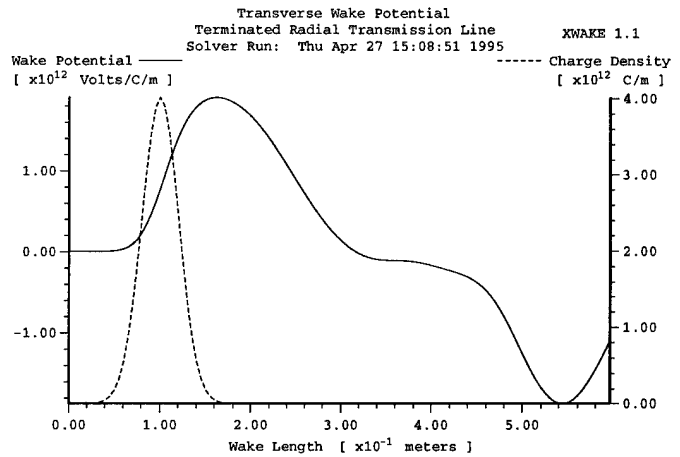


Figure 4. Dipole Transverse Wake Potential

calculated by ABCI version 8.8 for the same geometry, beam parameters and grid discretization lengths as modeled with Xwake. The Xwake and ABCI results are virtually identical. Note that the media interfaces coincide with the rectangular computational cell boundaries, which assures an accurate shape representation without deforming the cells.

Figure 6 is a graph of the monopole longitudinal impedance of the radial transmission line, this time loaded with a ferrite with a relative permeability of $\mu_r = 10$.

B. Beam Line Bellows

This example illustrates the advantage gained in using a contour geometry approximation over using a stepped approximation. Figure 7 depicts a ten convolution beam line bellow with outer and inner radii of 3.8 cm and 2.7 cm. The beam and beam pipe radii are also 2.7 cm. The radial and longitudinal discretization lengths are 0.5 mm and the beam rms length is 1 cm. Figure 8 shows a comparison of the Xwake computed monopole longitudinal wake potential using the contour cell and the rectangular cell (stepped) approximations. The contour FDTD model has converged and that is the contour data set plotted. The stepped FDTD data shown has a discretization of 0.5 mm, however it has

ABCI 8.8 Computed Wake Potentials

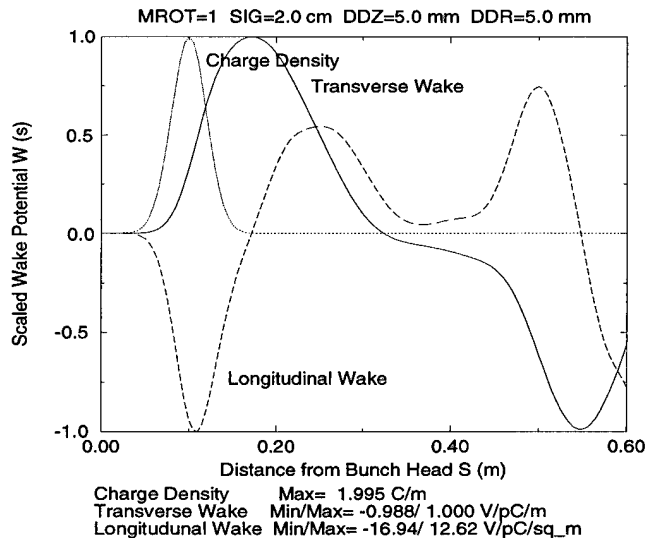


Figure 5. ABCI Calculated Dipole Wake Potentials

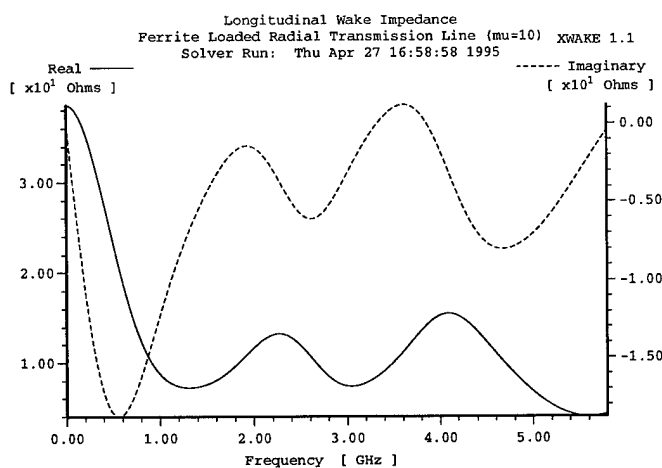


Figure 6. Monopole Longitudinal Impedance of Ferrite Loaded Radial Transmission Line

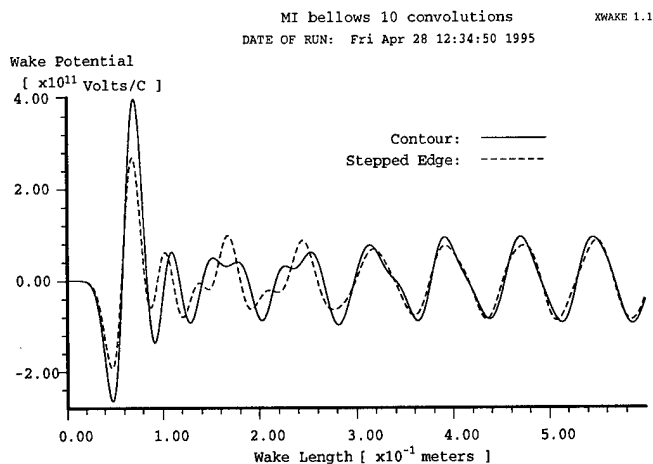


Figure 8. Bellows Stepped and Contour Wake Comparison

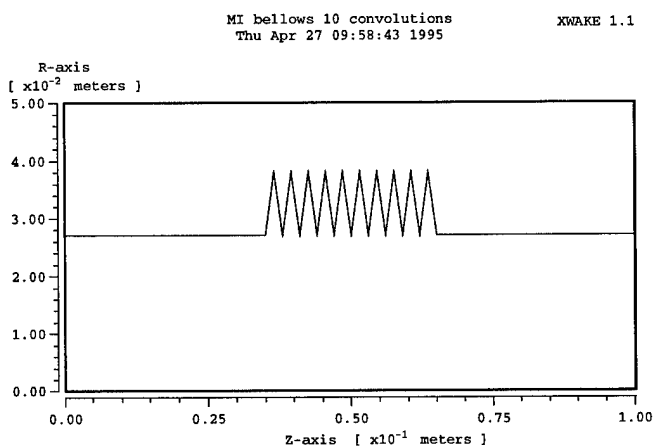


Figure 7. Bellows Geometry

not converged. The stepped discretization must be reduced to 0.125 mm for convergence. Hence, contouring provides a saving factor of four in memory and sixteen in time.

IV. SUMMARY

The salient features of the upcoming 1.1 release of Xwake were discussed. Four features which differentiate Xwake from other codes are: arbitrary inhomogeneous material modeling, contour FDTD geometry modeling, the use of a low noise broadband ABC and implementation of a GUI. Results and validations for both monopole and dipole simulations were presented.

Xwake 1.1 and its users' manual can be obtained via anonymous ftp from Fermilab. For more information contact either author at:

t.jurgens@ieee.org

saewert@crusher.fnal.gov

References

- [1] T.G. Jurgens and G.W. Saewert, "The Body of Revolution FDTD Algorithm", Chapter 12 in "Computational Electrodynamics: The Finite Difference Time Domain Method", by Allen Taflov, Artech House, 1995.

- [2] Y. H. Chin, "ABCI User's Guide", Version 8.8, February 1994.
- [3] T. Weiland, "On the Numerical Solution of Maxwell's Equations and Applications in the Field of Accelerator Physics", Particle Accelerators, 15, pp. 245-292, 1984.
- [4] T. G. Jurgens and A. Taflov, "Three-Dimensional Contour FDTD Modeling of Scattering from Single and Multiple Bodies", IEEE Trans. Antennas and Propagat., vol. 41, no. 12, pp. 1703-1708, 1993.
- [5] T. G. Jurgens, G. W. Saewert and F. A. Harfoush, "Xwake 1.0: A New Tool for Wakefield and Impedance Calculations", in 1994 European PAC Conference Proceedings, London, UK, May 1994.
- [6] T. G. Jurgens, "A Broadband Absorbing Boundary Condition for the FDTD Modeling of Circular Waveguides", 1995 IEEE MTT-S Intl. Microwave Symp., Orlando, FL, May 15-19.

THE LOS ALAMOS ACCELERATOR CODE GROUP *

Frank L. Krawczyk, James H. Billen, Robert D. Ryne, Harunori Takeda, Lloyd M. Young,
AOT-1, MS H817, Los Alamos National Laboratory, Los Alamos, NM 87545 USA

Abstract

The Los Alamos Accelerator Code Group (LAACG) is a national resource for members of the accelerator community who use and/or develop software for the design and analysis of particle accelerators, beam transport systems, light sources, storage rings, and components of these systems. Below we describe the LAACG's activities in high performance computing, maintenance and enhancement of POISSON/SUPERFISH and related codes and the dissemination of information on the INTERNET.

I. POISSON/SUPERFISH

The LAACG supports the PC version of POISSON, SUPERFISH and PANDIRA, currently used by several hundred people. POISSON/SUPERFISH is a collection of programs for calculating static magnetic and electric fields and radio-frequency electromagnetic fields in either 2-D Cartesian coordinates or axially symmetric cylindrical coordinates. The programs generate a triangular mesh fitted to the boundaries of different materials in the problem geometry. The original version of POISSON/SUPERFISH was written in the early 1970s by R. F. Holsinger from theory developed by Klaus Halbach[2]. An older UNIX version of these codes is also still available, but this version has not had any significant development in the past few years. At PAC93 [1] we described a new SUPERFISH root finder and some other improvements that we had implemented in the PC version.

During the past two years, we have made about 120 changes in the codes which include new features, bug fixes, and other improvements. The most significant of these changes include

- Run-time memory allocation of all mesh-point arrays and temporary data,
- A more robust meshing algorithm in AUTOMESH,
- A new field-interpolation algorithm that satisfies boundary conditions for rf, magnetostatic, and electrostatic problems,
- Automation and mouse support in the plotting program VGAPLOT,
- HPGL and PostScript graphics support in all plotting codes,
- Configuration options in file SF.INI,
- Up to 10-line problem descriptions for better record keeping,
- A utility program for examining contents of the solution file,
- For program developers, a linkable field-interpolation module for use in user-developed post processors and source code for reading the solution files.

Run-time memory allocation means that the computer's available memory is the only limit on the maximum problem size.

*Work supported by the U.S. Department of Energy, Office of High Energy Physics, Office of Scientific Computing, and Office of Nuclear Physics

The codes require 3 MB or more of memory. The more memory available, the larger the number of mesh points the codes can use to solve problems. We recommend at least 8 MB of installed RAM plus at least 100 MB of disk space for temporary data storage. If there is insufficient RAM, SUPERFISH and PANDIRA write temporary data to disk. The size of the temporary file depends upon the number of mesh points and the shape of the problem geometry.

The code distribution now includes the programs PANDIRA, a direct solver version of POISSON that also can handle permanent-magnet materials, and FORCE for calculating the force on coils and iron elements in magnetostatic problems. We hope to add the optimizing code MIRT to the package later this year. The complete PC SUPERFISH distribution contains 26 executable codes, 25,000 lines of on-line documentation, plus input files for about 50 sample problems. These examples include all of the sample problems from the Reference Manual and User's Guide [3]. Documentation specific to the PC version resides on disk. Programs are provided to display the documentation or produce indexed, paginated files suitable for printing. The installation requires about 13 MB of disk space. The codes are compiled from approximately 590,000 lines of FORTRAN source code.

We distribute the PC package, which includes an installation program, by internet FTP or, upon request, on either 3.5-inch or 5.25-inch floppy diskettes. Postage for mailing diskettes and printed manuals is paid by Los Alamos National Laboratory. Customs charges, if any, are paid by the recipient. Registered users receive notification of updates and bug fixes by Email. New users can register and request access to our FTP server by sending their postal address, phone and fax numbers to SUPERFISH@LANL.GOV.

II. HIGH PERFORMANCE COMPUTING

Accelerator-driven technologies are now being proposed to solve problems of national and international importance. These technologies have both economic and environmental implications. They include Accelerator Production of Tritium (APT), Accelerator Transmutation of Waste (ATW), Accelerator Based Conversion of plutonium (ABC), accelerator-driven production of spallation neutrons for materials science and biological-science research, accelerator driven production of neutrons for fusion-materials testing, and accelerator-driven fission-energy systems. All of these projects require next-generation linear accelerators that operate with extremely low beam loss. A maximum beam loss in the accelerator of roughly 10 parts per million is required to assure hands-on maintenance capability. Beam loss at this low level is due to the presence of a very low density beam halo at large transverse distances from the core. In order to predict beam halo with confidence, one must perform numerical simulations of unprecedented resolution. For example, to have a

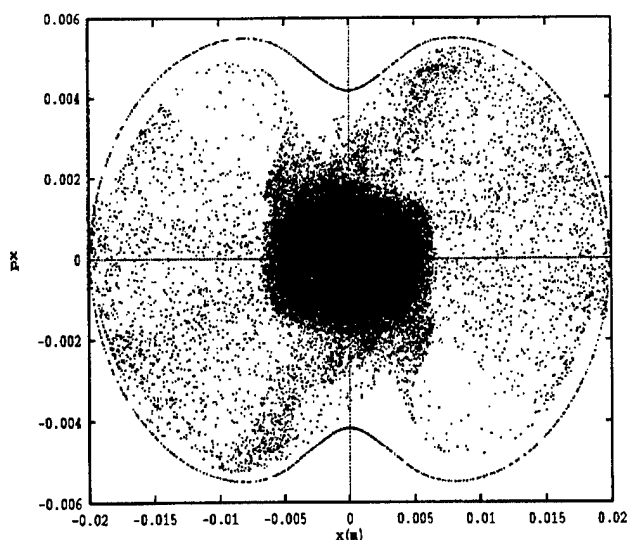


Figure 1. Beam phase space from a 2 million particle simulation on the CM-5 (65536 points are plotted). The outer peanut-shaped set of points were obtained from the particle-core model.

10% confidence in the number of halo particles, one would need to perform a simulation that resulted in roughly 100 particles in the halo; but if the halo accounted for 10 parts per million, this would mean that the simulation would require a total of 10 million particles. This is a major step beyond the linac simulations of the 1980s that typically used only 10,000 particles.

The LAACG has had much success in developing such a high-resolution accelerator-modeling capability[4]. Starting in 1994, we began using the massively parallel CM-5 at the Advanced Computing Laboratory at LANL to perform beam-halo simulations. The tools we are developing to model next-generation accelerators provide us with a means to test new designs, test theoretical models, and optimize our designs.

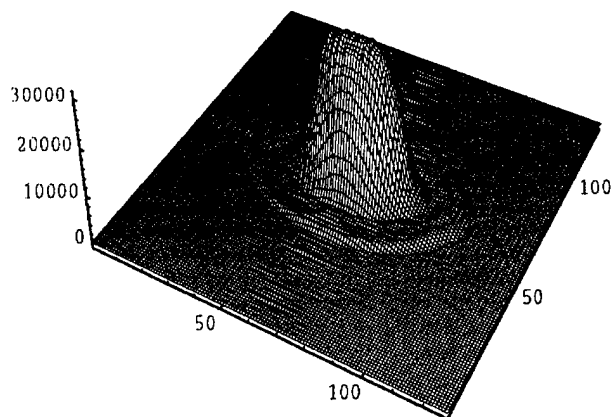


Figure 2. Output from a direct Vlasov/Poisson simulation. The 4-dimensional distribution function was integrated over p_x and p_y to obtain the beam density on a 128×128 grid.

We have developed and used a two-dimensional Particle-In-Cell code to model long beams in a variety of focusing systems. Using our code, we routinely perform simulations with several to ten million particles. One of our early applications was to model a mismatched KV beam in a constant focusing channel. We found that when the beam was unstable the

charge redistributed itself in such a way that, though a halo was formed, it was bounded, and furthermore the extent of the halo was in excellent agreement with a theoretical model called the particle-core model of halo evolution in mismatched beams. This is shown in Figure 1. We have also performed simulations that dealt with the controversial issue of whether or not quadrupole focusing can cause significant halo formation for matched beams. Our results indicate that breathing due to quadrupole focusing will not be a problem in the physics regime of the projects described above, where the tune depression is at worst approximately 50%. Besides developing particle simulation codes we are also studying other approaches to modeling and predicting beam halo. For example, we have developed a two-dimensional (four-dimensional phase space) direct Vlasov-Poisson simulation code. We have performed very high resolution simulations on a $128 \times 128 \times 128 \times 128$ grid, for a total of 268 million grid points. A typical simulation of a beam in a quadrupole channel is shown in Figure 2.

At present multi-million particle simulations are the best means we have to quantitatively predict extremely low beam loss, so they are crucial to lending support to the validity of proposed designs.

Since all of our codes are written in the CM FORTRAN program language (a FORTRAN90-like language), it will be easy to port them to other platforms that support the data parallel paradigm. So far our activities have emphasized two-dimensional modeling. Our future goals are aimed at modeling three-dimensional (i.e. bunched) beams including acceleration.

III. INFORMATION RESOURCES FOR THE ACCELERATOR COMMUNITY ON THE INTERNET

In October 1994 the LAACG began making information available via the World Wide Web (WWW). The documents can be accessed at the address:

<<http://www.atdiv.lanl.gov/doc/laacg/codehome.html>>. The published documents provide a variety of information of interest to the accelerator as well as other scientific communities. The documents include:

- information about the LAACG and its services,
- general information of interest for the accelerator community,
- extensive list of links to accelerator laboratories and institutes worldwide (approximately 100),
- information related to the field of electromagnetic field calculations and information on other computational tools for accelerator physics,
- online versions of the previously published Accelerator Code Compendium from 1990 and a new up-to-date Code Compendium,
- excerpts from the user-documentation of the codes distributed by the LAACG,

an online information service for the 1995 Particle Accelerator Conference in Dallas, Texas.

This new service is well accepted by the scientific community. This is documented by an average number of 235 accesses per month with an approximate monthly use of 1800 documents. 64 % of the accesses are from within the USA and Canada. The rest is predominantly from Europe and Japan (based on activities before April 19, 1995).

Table 1: Most Frequently Used Services

	Service	accesses
1.	PAC-Conference	1242
2.	Code Group Services	419
3.	Electromagnetics	297
4.	List of Accelerators	224
5.	General information	209
6.	POISSON/SUPERFISH	163
7.	Old Code Compendium	156
8.	P/S Userguide	119
9.	New Code Compendium	109

We encourage the community's interaction to help us improve the services provided on the WWW. Our major interest lies in the extension of a new online Code Compendium. The last printed version is from May 1990. With the rapid development of codes and computers this compendium is outdated. For this new compendium, the LAACG needs the community's input. At the conference questionnaires are available to enter new codes and update information on entries in the old compendium.

We also set up a FTP-server that allows the community to get the codes distributed by the LAACG over the network without extensive interaction with us. We still recommend subscribing to the POISSON/SUPERFISH mailing list. This is the only way to become aware of bugs, code corrections or code upgrades. The FTP-address can be obtained from the new WWW online Code Compendium.

Another activity of the code group on the INTERNET in mid 1993 led to the creation of a USENET discussion group on accelerator physics. The group *sci.physics.accelerators* is a discussion forum on accelerator physics, beam physics and general contacts between researchers.

Lastly, at the request of the LAACG an electronic preprint service centered on accelerator physics has been created. Such forums allow access to preprints of publications before they are available in paperbound journals. This service is available on the WWW at the URL: <<http://xxx.lanl.gov/>> as well as by electronic mail and FTP.

References

- [1] J. H. Billen and L. M. Young, "POISSON/SUPERFISH on PC Compatibles," Proceedings of the 1993 Particle Accelerator Conference, Vol. 2, p. 790.
- [2] K. Halbach, R.F. Honsinger, "SUPERFISH - A Computer Program for Evaluation of RF Cavities with Cylindrical Symmetry", Particle Accelerator 7(4), 213-222 (1976)
- [3] Reference Manual for the POISSON/SUPERFISH Group of Codes, Los Alamos National Laboratory Report LA-

UR-87-126 (1987); and User's Guide for the for the POISSON/SUPERFISH Group of Codes, Los Alamos National Laboratory Report LA-UR-87-115 (1987).

- [4] R. Ryne and T. Wangler, "Recent Results in Analysis and Simulation of Beam Halo," International Conference on Accelerator Driven Transmutation Technologies and Applications, Las Vegas, NV (July 1994)

Beam Simulation and Radiation Dose Calculation at the Advanced Photon Source with *shower*, an Interface Program to the EGS4 Code System*

L. Emery
Argonne National Laboratory
9700 So. Cass Ave., Argonne, IL 60439

Abstract

The interface program *shower* to the EGS [1] Monte Carlo electromagnetic cascade shower simulation code system was written to facilitate the definition of complicated target and shielding geometries and to simplify the handling of input and output of data. The geometry is defined by a series of namelist commands in an input file. The input and output beam data files follow the SDDS [2] (self-describing data set) protocol, which makes the files compatible with other physics codes that follow the same protocol. For instance, one can use the results of the cascade shower simulation as the input data for an accelerator tracking code. The *shower* code has also been used to calculate the bremsstrahlung component of radiation doses for possible beam loss scenarios at the Advanced Photon Source (APS) at Argonne National Laboratory.

I. Introduction

The APS consists of a linear accelerator, a positron accumulator ring (PAR), a booster, and a storage ring (SR) which provide synchrotron radiation for users. These accelerators are (mostly) above ground and require heavy shielding to protect personnel from radiation produced by electron or positron beam loss. The shielding has been designed [3] in a conservative way using empirical formulas [4] of bremsstrahlung and neutron production for various loss scenarios. However, from a physicist's point of view, it is desirable to obtain a more accurate value of radiation dose, say from running a Monte Carlo electromagnetic cascade shower code such as EGS [1]. Only when comparing an actual radiation dose measurement with a realistic calculation can one conclude whether the shielding performs as expected.

Another important calculation is the simulation of beams through foils, targets, or any other medium where the beam emerging on the other side requires further tracking. An accelerator code tracks particles before reaching the medium, then a program like EGS tracks particles within the medium, and the accelerator code tracks the emerging particles afterwards. In general, a program is written as a stand-alone unit, with no thought of its output being used by another program. Fortunately, the structure of EGS allows users to write their own interface to input and output files. I wrote the *shower* interface program for EGS with a newly defined protocol for data files [2] in mind, which makes *shower* data files compatible with the accelerator tracking code *elegant* [5] which uses the same protocol.

The paper will present the *shower* interface to the EGS system of code, and some applications to APS.

II. Interface to EGS

The code system EGS is a tried-and-true Monte Carlo shower code used by the health physics community and the high energy

physics detector community. EGS simulates electromagnetic showers by tracking individual particles with random discrete scattering events through regions filled with material. By summing up the energy losses in regions simulating human tissue, one can calculate the absorbed dose for humans.

In EGS, the user must specify one subroutine which defines the geometry of the problem and another for handling the output of data. The main routine is also user-provided and controls the calling of the main EGS routine. EGS users have traditionally written these subroutines in MORTRAN which requires a preprocessor to convert the code into FORTRAN. As I am dissatisfied with MORTRAN and FORTRAN, I decided to write these subroutines in C in order to use essential features of C such as structures and pointers. These subroutines and other supporting C subroutines form the interface. The FORTRAN physics core of EGS is left unchanged and linked to the C interface with no difficulty.

shower's command line requires two input files: a geometry file describing regions of material, and a particle coordinate file for the incident beam. The command line requires the naming of a summary file into which energy deposition and radiation dose information of each region is written. Other command line options control the random number generator seed, multiple sampling of the input beam, trajectory recording, input or output particle type filtering, particle splitting across boundaries, actions taken when particles go out of bounds or enter an undefined region, etc.

The geometry file contains namelist-type commands that define material regions shaped as blocks or cylinders with an optional output file specification for writing coordinates of particles crossing the material boundary. For example, the following lines define a 7-mm-thick tungsten target and a region where particle coordinates are recorded, possibly for further tracking.

```
&cylinder label="W target" material="W"
  r'lower'cm=0 r'upper'cm=2
  z'lower'cm=0 z'upper'cm=0.7 &end
&cylinder label="Output volume"
  material="Vacuum"
  outputfile="target-products"
  r'lower'cm=0 r'upper'cm=1
  z'lower'cm=0.7 z'upper'cm=1.0 &end
```

With variables such as *x'slices*, one can generate multiple regions divided equally along one or more spatial coordinates. This is useful for calculating radiation dose in a material as a function of one or more spatial coordinates. If a region definition overlaps a previously defined region, then the volume in common keeps the previous material definition. Thus, complicated geometries can be generated.

All beam data files and the summary file comply with the SDDS self-describing data file protocol [2] developed at APS. Once such a protocol is adopted, one can immediately draw on the SDDS toolkit for graphics and data postprocessing. SDDS-protocol files are organized in "pages" consisting primarily of

*Work supported by U.S. Department of Energy, Office of Basic Energy Sciences under Contract No. W-31-109-ENG-38.

tables of data. Each page may have non-tabular values, such as parameters, associated with it. The particularly useful feature of the protocol is the attribution of names, units, data type, and descriptions to the data by way of a file header. Thus, columns in the data tables and parameters can be operated upon by listing their names as part of an option of an SDDS toolkit command line. For instance, suppose that we want to filter data, histogram the filtered data, and plot the results. We assume that the data file `target-products` exists and has at least a data column named `Energy` and a parameter called `Type` giving the particle type as a string. Then one issues the following three self-explanatory SDDS commands:

```
sddsprocess target-products target.positrons
-match=parameter,Type=positrons,
sddshist target.positrons
target.positrons.hist -dataColumn=Energy,
and
sddsplot -column=Energy,frequency
target.positrons.hist
where target.positrons and
target.positrons.hist are SDDS files.
```

The columns defined in the particle coordinate files are `Energy`, `x`, `y`, `z`, `u`, `v`, `w`, where the last three are direction cosines. Each data page has a string parameter `Type` assigned one of `electron`, `positron`, or `photon`. Therefore, if a **shower** run produces the three types of particles, then at least three data pages are created in the output file, one for each type. **shower** does not presently support neutron creation or transport. However, if neutrons were included in the simulation, one would simply introduce the particle type `neutron`. The structure of the data file is unaffected.

The summary file contains data related to each region defined, such as the coordinates of the center of the region, the volume, the energy deposited from each type of particles, and absorbed dose. In the case of a region defined with human tissue, the absorbed dose is taken to be the dose equivalent for biological damage.

The availability of a toolkit permits the design of a lean interface program. One does not have to build in graphics or data processing into the code itself. The beam data can be written to a file for later processing, and one doesn't have to anticipate or implement all possible ways of presenting data in a physics code. Referring to the examples above, the tool **sddshist** can histogram any variable in the beam data files, a preferable method than imbedding histogram routines inside **EGS** or **shower**. Another tool in frequent use is **sddsprocess** which uses the data to perform mathematical calculations and other general processing functions such as filtering.

III. Applications

A. Beam Loss at Undulator Chamber

The APS ring will have Al undulator chambers with small vertical aperture to accommodate narrow gap undulators. A tapering Cu transition connecting the undulator chamber to the regular storage ring extruded chamber will be the most probable location of beam loss. Copper is a relatively heavy target that may generate a shower in a short distance, which tends to concentrate the dose. Most of the radiation will be directed forward into the curving storage ring high-density concrete tunnel at a small incident angle, thus giving a large effective depth. However the portion of radiation directed sideways, though relatively weaker, travels through only the 0.56 m of concrete. The **shower** calculation for this situation can confirm the amounts

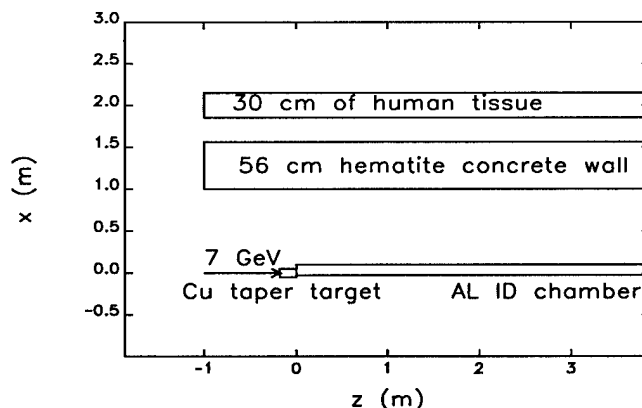


Figure 1: Top view of the material layout for beam loss at the undulator chamber

of extra shielding required.

It is commonplace to use empirical formulas to estimate dose rates for situations such as this one. In this case, the empirical formulas give dose rates that are about 10 times that calculated by **shower**. This factor is due mostly to the treatment of the attenuation of photons in the shielding. Part of the factor is the sometime erroneous assumption that the electromagnetic shower expends itself in a short distance compared to the distance from the source to the dose point.

Figure 1 shows the layout of the radiation dose calculation. The human tissue region used in the calculation is split into smaller regions along the z direction so that the average dose in each section can be obtained as a function of z .

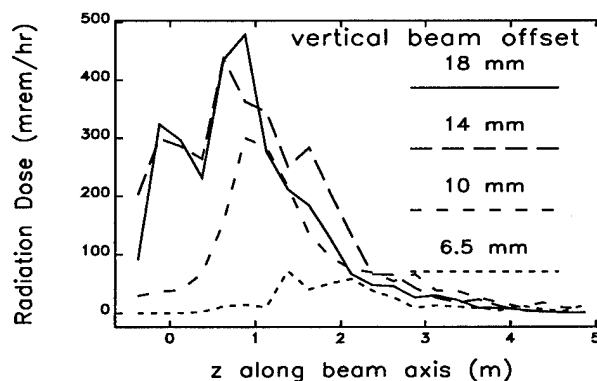


Figure 2: Calculated radiation dose profile outside the shielding wall along the beam direction for a 308-W injected beam loss with concrete shielding only.

Figure 2 shows the dose profile outside the shielding wall with no extra shielding for various injected beam vertical steering errors. The variation between profiles is due to the varying amount of Cu material through which the 7-GeV beam travels.

B. Beam Loss at Booster

In a possible worst-case radiation exposure incident in the booster, the fully accelerated 7-GeV positron beam hits the vacuum chamber inside a booster magnet below a 1-m-thick concrete ceiling in the extraction area. A fraction of the shower

products will spray upwards through the ceiling, and into an area that may be occupied by people.

For the beam loss location, I selected a focusing quadrupole where both a loss and the largest dose outside shielding is likely to occur. Though it would seem that any focusing quadrupole is as good as any other, I took one followed by an substantial accelerator component, like an rf cavity, so that the increase in dose outside the shielding due to additional scattering may be taken into account.

In the modeling of the geometry, all the material shapes have been generated by adding blocks of materials and vacuum. For instance, the elliptical vacuum chamber is modeled as a 1-mm-thick rectangular chamber of the same outer dimensions as the elliptical one. Similar changes to the quadrupole poles were made. The rf cavities were approximated by copper boxes of the same outer dimensions as the real ones. The calculation does not include any additional shielding that may eventually be installed to reduce the dose rate. The dose rate profile of the worst case of incident angle and position is shown in Figure 3.

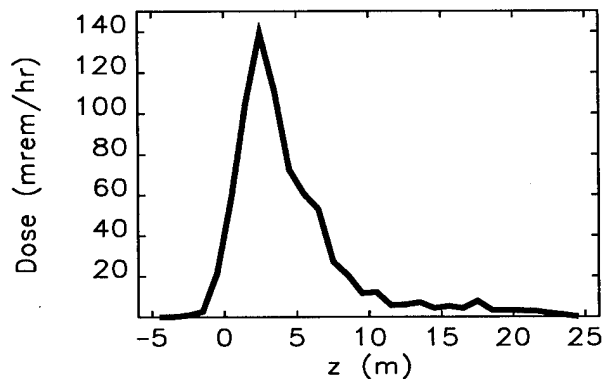


Figure 3: Calculated radiation dose profile above the booster ceiling along the beam direction for a 308-W booster beam loss with concrete shielding only.

C. Gas Bremsstrahlung Photon Scattering

The collisions between 7-GeV positrons of the APS stored beam and residual gas atoms in the ring 15-m straight sections produce x-ray photons ($E > 1$ MeV) which propagate down the x-ray beam pipe in the same direction as those of insertion device (ID) device x-rays ($E < 10$ keV). These photons are separated thirty meters downstream by a 1.3-m copper mirror which externally reflects the ID photons by 0.3 degree (5.2 mrad). About half of the bremsstrahlung photons hit the mirror and get absorbed or scattered. The other half hit an absorber or an absorbing wall behind the mirror. A very small fraction of high-energy photons scatters from the mirror and into beam the small solid angle acceptance of the ID photon collimators. These high-energy photons get scattered further downstream at an x-ray stopper inside a shielded beam pipe located in the experiment hall. Since the shielding surrounding these scatterers is designed for ID photons, and since these photons have energies of the order of MeVs (a thousand times the ID photons), one must make sure that this shielding is sufficient.

The geometry of the problem is somewhat complicated, as there are five scatterers, some widely spaced: a 15-m length of STP N₂ which simulates, with proper pressure scaling, the effect of few nT-pressure residual gas ($z=0$ m); a Cu mirror ($z=30$

m); a Pb collimator ($z=37.5$ m); a x-ray W stopper ($z=41$ m); and a lead-sandwich shielding beam pipe ($z=41$ m).

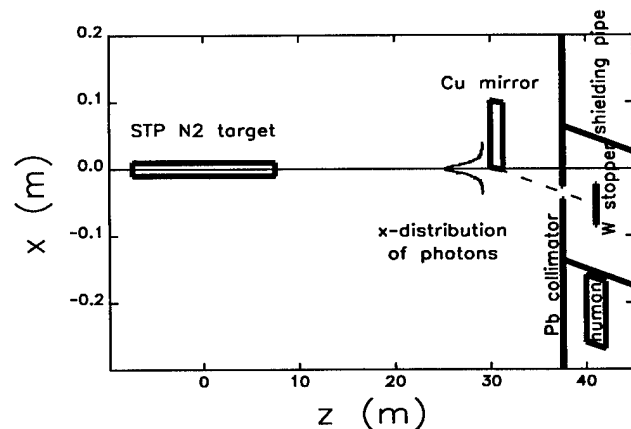


Figure 4: Top view of the material layout for bremsstrahlung photon propagation

Figure 4 lays out the geometry of the problem with an expanded horizontal scale.

The problem is split into four shower runs, about one per scatterer. Particle data are available after every run. Thus, particle fluxes and intensity distributions can be analyzed or plotted for selected points along the z axis. One such distribution appears in Figure 4.

For this situation, the radiation dose near the x-ray beam-line from gas bremsstrahlung is given in mrem/hr by $2 \times 10^{-3} (E[\text{GeV}]/7) I[\text{A}] P[\text{nT}]$ where E is the energy of the stored beam (normally 7 GeV), I is the stored current (0.1 A or 0.3 A), and P is the residual gas pressure (a few nT). The typical radiation dose is a few microrem/hr, a very small value.

IV. Acknowledgement

I thank H. Moe for guidance on the subject of radiation production. I thank M. Borland for advice on data and program organization.

V. References

- [1] W. R. Nelson, H. Hirayama, and D. W. O. Rogers, "The EGS4 Code System," SLAC 265, SLAC, December 1985.
- [2] M. Borland, "A Self-Describing File Protocol for Simulation Integration and Shared Postprocessors," these proceedings.
- [3] H. J. Moe, "Advanced Photon Source: Radiological Design Considerations," APS LS-141, revised, ANL, July 1991.
- [4] W. P. Swanson, "Radiological Safety Aspects of the Operation of Electron Linear Accelerators," Technical Report Series N 188, IAEA, 1979.
- [5] M. Borland, "User's Manual for elegant," APS LS-231, ANL, May 1993.

An Interactive Version of the PBGUNS Program for the Simulation of Axisymmetric and 2-D, Electron and Ion Beams and Guns.

Jack E. Boers
Thunderbird Simulations
626 Bradfield Drive, Garland, TX 75042-6005 USA

Abstract

PBGUNS, a program for the simulation of ion and electron beam extraction systems has been modified to permit their interactive design on an IBM-PC. The program can be interrupted after any relaxation cycle and its electrode configuration, and most other parameters, modified. A graphical interface is used in the modification of the electrodes on the screen without exiting the program or having to save (or restore) binary data. The program uses previous results to speed convergence of the new configuration and is quite tolerant of significant changes in electrodes and/or potentials. It is written in FORTRAN 77 (with DOS extenders) and can be run on any high end PC with at least 16 MBytes of memory.

I. INTRODUCTION

PBGUNS, a relaxation program including space charge and some thermal effects, was originally described at the 1993 ICOPS (Vancouver). It simulates virtually any type of axisymmetric or 2-D, relativistic or non-relativistic electron or, positive or negative, plasma, thermal, or sputter source ion extraction system. The program has been considerably refined and improved over the past two years to solve these types of problems faster and more accurately. The program has always had the capability of saving binary data and then restarting on the next run. As the program has improved it was found that it became more tolerant of changes in parameters and electrode shapes on restarts.

The electrodes are defined with quadratic line segments. The segments are connected head to tail around the electrode and may extend from boundary to boundary or may close around the electrode. The input data describe the line segments using their endpoints (and center and radius for circles) for each electrode.

While running designs of various beam systems it became evident that the process could be significantly speeded if the program could be interrupted, modified and restarted without exiting and restarting. Initial work permitted the interactive modification of the electrode shapes and parameters by changing the values on the input file and then resuming execution with the new values. This led to errors that were not obvious when they were introduced and would occasionally terminate the run catastrophically.

The greatest problem came with changing the electrode configuration where modest changes in an electrode could bomb the program if not carried out properly. It was necessary to develop a graphical interface to the interactive

routines so that errors in the configuration would be evident on the screen (and could still be corrected before resuming execution) while making changes in the electrodes.

The 25,000 line FORTRAN program currently runs on an 80386 or better, IBM-PC or clone, with at least 16 MBytes of memory, using DOS extenders. NDP-FORTRAN and NDP-PLOT (from Microway) are used for the compiler and the plotting capability. It will run small problems (100x50 arrays) in as little as 10 minutes, but may require several hours for very large problems (450x200) arrays, (about the limit for 16 MBytes of memory) on a MHz 486 PC. Obviously larger memories would permit larger simulations and faster processors would require less time. All calculations are done in double precision (8 byte) arithmetic.

The potentials are solved on a two dimensional array using Poisson's equation in rectangular or axisymmetric configurations. The beam is simulated by computing representative trajectories (up to 7000) through the device. Space charge is computed from the trajectories and stored on a matrix identical to the voltage array. The cathode or plasma region for extraction problems is simulated on a second (and usually finer) matrix so that greater accuracy and resolution can be obtained, most importantly at the cathode or plasma surface. Thermal effects, which can be very important for either electron or ion extraction, can be simulated including skew (azimuthal) angular distributions.

II. INTERACTIVITY

At the end of each voltage relaxation-trajectory computation cycle it is possible to switch to the interactive routines. Here it is possible to change either the electrodes or many of the parameters, such as voltages, electron or ion temperatures or densities, or both. After the initial relaxation of 10 to 15 cycles the program will generally require only 3 or 4 cycles to approach a new convergence. This can require from 1 to 15 minutes depending on the speed of the processor and the size of the matrix. It is usually not necessary or desirable to wait for a complete convergence before starting the modifications again.

The graphical routines permit the easy changing of the voltage, shape, deletion, addition, moving, or the replication of an electrode. The arrow keys are used to move a cursor on the screen and to define end points of the lines to 4 decimal places, and the center of circles to 5 decimal places. Circles are defined by their endpoints and the location of their center using the cursor to determine both. Cursor motion is followed from point to point by a rubber-band line

so that the changes are immediately seen, and exact numerical location of the cursor location also appears on the screen. The next version of the code may permit the use of the mouse, but it must also enable the same accuracy as the above routine.

Electrodes can be modified by moving, deleting, or adding line segments. One or both ends of a line segment can be moved with the cursor. If a segment is deleted the new connection for the preceding and succeeding line segments can be made with the cursor. Adding a new line segment is accomplished by specifying the segment after which it is to be inserted. Preceding and succeeding segment endpoints are then automatically adjusted to make a continuous surface.

It is also possible to generate an entirely new electrode using this same cursor technique. For more elaborate electrode shapes the circle drawing routines are especially useful for creating smooth contours. If an electrode is to be extensively modified it may be desirable to delete it and then generate a new electrode.

Fairly extensive changes can be made in the anodes without unduly destabilizing the program but one needs to be careful in the emission region where high space-charge density beams are being extracted. The space-charge densities from preceding cycles, which can be very large near an emission surface, can cause large transients in the calculations. Indeed, extensive changes in the cathode will require restarting the program. If one plans ahead it is possible to make relatively large adjustments in the plasma region of an ion beam.

One of the most useful features is the ability to generate a large number of electrodes by replicating a given electrode so that the potentials can be varied along the axis of the beam. One can adjust the voltages on the electrodes over a small section of the beam line until the desired beam is obtained. Usually the multiple electrodes can then be combined into larger electrodes and the process continued up the column. The interactive routines also permit the extension (or contraction) of the matrix (axially or radially) as one progresses down the line. The ability to change the voltages and immediately see the effect can sometimes lead to surprising results, especially when you try things you do not expect to work.

Electrodes may be moved axially and/or radially by specifying the distance to be moved or arbitrarily using the cursor. The most frequent use of this is to adjust the axial position of the electrodes to modify focussing or extraction effects.

If the matrix is expanded radially all lines that reach the top of the mesh are extended in a straight line to the new radial limit. Some care must be taken if these lines should cross in the extended region.

Parameters used in the simulation can be viewed and modified on the screen.

III. RESULTS

Results obtained with the interactive routines have been very encouraging. Problems that would have taken days

saving and restoring data, have in some cases been reduced to a few hours (and sometimes minutes) by using the interactive routines. Complex electrode shapes are easier to develop on the screen, using the interactive routines, than they are trying to do them by hand. With a few simple configurations to start only a basic knowledge of how the program works should be necessary to use it.

Making detailed improvements in an already good design are made easy by making small changes in the configuration and observing the changes in a very short time. The effects of raising or lowering a voltage or moving an electrode back and forth are rapidly observed.

The program has become very tolerant of large changes in the electrodes and seldom fails. Results are saved as the program executes so that recovery is frequently possible

IV. FUTURE DEVELOPMENT

The next version of the program will require the faster processors, such as the Pentium, Alpha or Power PC, and probably a better resolution screen so that actual results can be shown in separate windows on the screen while the program runs. All input will be from the screen so that mistakes will become nearly impossible. All modifications will be handled from the screen and virtually no knowledge of the programs inner workings will be required.

V. REFERENCES

- [1] Boers, J.E., "PBGUNS: a Digital Computer Program for the Simulation of Electron and Ion Beams on a PC", *Conference record, 1993 ICOPS, Vancouver, BC, 7-9 June 1993*.

VECTOR COMPUTER USED FOR CALCULATION OF 3D MAGNETOSTATIC FIELDS *

E.P.Zhidkov, M.B.Yuldasheva, I.P.Yudin, O.I.Yuldashev

Joint Institute for Nuclear Research, Dubna, Moscow region, 141980, Russia

Abstract

In this communication we describe the results of computations of 3D nonlinear magnetic field for a dipole magnet. Computations were carried out on vector computer CONVEX C120 by means of program MSFE3D [1].

I. FORMULATION OF THE PROBLEM

We consider the differential formulation of the magnetostatic problem for two scalar potentials [2], total – ψ and reduced – ϕ . Let Ω_F be a region with ferromagnetic material. We choose some region Ω , which contains Ω_F . Let Γ_0 be a boundary of the region Ω and $\Omega_A = \Omega \setminus \Omega_F$. Γ is a boundary between Ω_F and Ω_A . Then we have equations

$$\operatorname{div}(\mu \nabla \psi) = 0, \quad x \in \Omega_F; \quad (1)$$

$$\operatorname{div}(\nabla \phi) = 0, \quad x \in \Omega_A; \quad (2)$$

with the boundary conditions

$$\mu(\partial \psi / \partial n) = \partial \phi / \partial n - \mathbf{n} \cdot \mathbf{H}^S, \quad x \in \Gamma; \quad (3)$$

$$\psi = \phi + \phi^S, \quad x \in \Gamma; \quad (4)$$

$$\phi \approx 0, \quad x \in \Gamma_0. \quad (5)$$

Function $\mu = \mu(|\nabla \psi|)$ is given from the closed interval $1 \leq \mu_* \leq \mu \leq \mu^*$ where μ_* and μ^* are known constants. Vector \mathbf{H}^S is computed by the Biot-Savart's law

$$\mathbf{H}^S(x_0) = \frac{\mu_0}{4\pi} \int_{\Omega_S} \mathbf{J} \times \nabla \frac{1}{|x - x_0|} d\Omega_S,$$

where Ω_S is a source region, \mathbf{J} is a known vector of current density, μ_0 is the permeability of free space, $|x - x_0|$ is the distance between points x and x_0 . Potential ϕ^S is defined from the Laplace equation in the region Ω_F

$$\Delta \phi^S(x) = 0, \quad x \in \Omega_F, \quad (6)$$

with the boundary conditions

$$\frac{\partial \phi^S}{\partial n} = -\mathbf{n} \cdot \mathbf{H}^S, \quad x \in \Gamma, \quad \int_{\Gamma} \mathbf{n} \cdot \mathbf{H}^S ds = 0. \quad (7)$$

It is known that the generalized solutions of the formulated boundary value problems exist. The generalized solution of nonlinear problem (1)-(5) is unique, and the generalized solution of Neumann problem (6) - (7) is defined with constant. Finite element approximations converge to the exact generalized solutions.

*Work supported in part by the Russian Fund of Fundamental Investigations under grants 95-01-01467a and 95-01-00737a.

II. USING THE FINITE ELEMENT METHOD

As a finite element $\bar{\Omega}_j$, we choose convex hexahedron. Let us divide Ω by the finite elements so that $\bar{\Omega} = \cup \bar{\Omega}_j$, $\bar{\Omega}_i \cap \bar{\Omega}_j = \emptyset$, when $i \neq j$, supposing also, that every face of element $\bar{\Omega}_j$ is either a subset of Γ_0 , or a face of the other element, and the boundary Γ is formed by faces of the chosen elements.

We introduce in space with Cartesian coordinate system related to variable $\xi = (\xi_1, \xi_2, \xi_3)$, the linear shape functions N_m^e for cube $[-1, 1]^3$

$$N_m^e(\xi) = (1/8)(1 + \sigma_{m1}\xi_1)(1 + \sigma_{m2}\xi_2)(1 + \sigma_{m3}\xi_3),$$

$$m = 1, \dots, 8,$$

where the coefficients σ_{mk} are chosen as 1 or -1 so that N_m^e is equal to 1 in the vertex with number m and 0 in any other vertex. In view of that the cube $[-1, 1]^3$ turns into the element $\bar{\Omega}_j$ under the use of the transformation [3]

$$x_k = \sum_{m=1}^8 x_k^{j,m} N_m^e(\xi), \quad k = 1, 2, 3,$$

where $x_k^{j,m}$, $k = 1, 2, 3$ are coordinates of the element $\bar{\Omega}_j$ vertex with number m , the base functions $N_m(\xi(x))$, $m = 1, \dots, 8$ on element $\bar{\Omega}_j$ may be obtained. We shall find the solutions of the problems (1)-(5) and (6)-(7) in the form

$$\psi(x) = \sum_j \psi_j N_j(x), \quad x \in \bar{\Omega}_F;$$

$$\phi(x) = \sum_j \phi_j N_j(x), \quad x \in \bar{\Omega}_A; \quad (8)$$

$$\phi^S(x) = \sum_j \phi_j^S N_j(x), \quad x \in \bar{\Omega}_F,$$

where $\psi_j, \phi_j, j = 1, \dots, M$ and $\phi_j^S, j = 1, \dots, M_S$ are unknown potentials values in nodes of the space mesh, which is obtained as a result of partitioning the region $\bar{\Omega}$. Substituting the expressions for ψ and ϕ from (8) into generalized formulation of problem (1)-(5) and taking the boundary conditions into account, we perform the equation

$$\begin{aligned} & \sum_{x^j \in \bar{\Omega}_F} \psi_j \int_{\Omega_F} \mu \nabla N_i \cdot \nabla N_j d\Omega + \sum_{x^j \in \Gamma} \psi_j \int_{\Omega_A} \nabla N_i \cdot \nabla N_j d\Omega + \\ & + \sum_{x^j \in \Omega_A} \phi_j \int_{\Omega_A} \nabla N_i \cdot \nabla N_j d\Omega = - \int_{\Gamma} N_i \mathbf{n} \cdot \mathbf{H}^S dS + \\ & + \sum_{x^j \in \Gamma} \phi_j^S \int_{\Omega_A} \nabla N_i \cdot \nabla N_j d\Omega, \quad i = 1, \dots, M. \end{aligned} \quad (9)$$

Potential ϕ^S is found from the equation

$$\sum_{x^j \in \bar{\Omega}_F} \phi_j^S \int_{\Omega_F} \nabla N_i \cdot \nabla N_j d\Omega = - \int_{\Gamma} N_i \mathbf{n} \cdot \mathbf{H}^S dS, \quad (10)$$

$$i = 1, \dots, M_S.$$

Note that there is no need to solve this equation in whole Ω_F , because $\mathbf{H}^S = -\nabla \phi^S$ is orthogonal to gradients of the functions which are equal to 0 on the boundary of Ω_F [4]. I.e. it is enough to solve equation (10) in some situated near boundary volume of the region, completing the boundary conditions.

The integrals over regions Ω_F, Ω_A in (9) - (10) are computed by summation of the contributions from separate elements $\bar{\Omega}_j$. In such an element μ is a constant, its argument is computed in the centre. The centre is the point, every coordinate of which is the arithmetic mean of coordinates of hexahedron vertices.

III. SOLVING THE NONLINEAR SYSTEM

Let us write the discretized system of the nonlinear algebraic equations (9) with sparse matrix as

$$F(\mu)y = f, \quad \mu = \mu(y). \quad (11)$$

Usually for solving such a system some linearization is used and then the finding of the solution of system (11) reduces to the sequential solving of the linear problems. General iterative scheme for solving the nonlinear equation (11) has the form

$$B_n \frac{y_{n+1} - y_n}{\tau_n} = -(F_n y_n - f), \quad n = 0, 1, \dots, \quad (12)$$

where y_0, F_0, τ_0 are given. Two kinds of this process are usually used:

1. $B_n = F_n, \tau_n \equiv 1$;
2. $B_n = F'_n$, where F'_n is Jacobi matrix.

We use iterative scheme (12) for $B_n \equiv F_n$ and $\tau_n \in (0, 1]$. The parameter τ_n is chosen depending on behaviour of μ on every iteration. Note that the general theory of the iterative process (12) for self-adjoint, positive definite operator F is given in book [5].

Independently of B_n form, the linearized system of equations on every iteration should be solved

$$Az = b, \quad (13)$$

where A — symmetric, positive definite sparse matrix. Usually for this purpose the incomplete Cholesky decomposition with conjugate gradient method is used [6]. The special algorithms developed by authors in [7] are used for solving the equation (13) on the vector computer CONVEX C120.

IV. EXAMPLE OF 3D MAGNETOSTATIC FIELD CALCULATION

As an example of 3D magnetostatic field calculation we present here the computed results for dipole magnet of the setup EXCHARM. More information about this computations was published in [4,8]. The setup EXCHARM is a forward-spectrometer for investigation of hadron production of charmed particles and the indication of the narrow resonances in neutron-

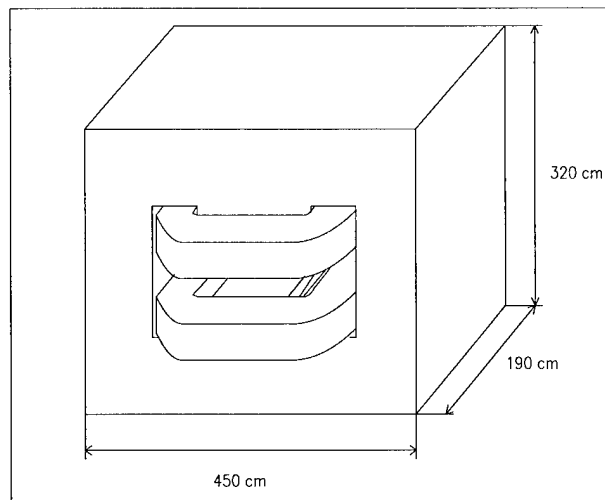


Figure 1. Schematic view of the SP-40 magnet.

nucleus interactions on the U-70 accelerator, at IHEP, Serpukhov, near Moscow. It is a further development of spectrometer BIS-2 [9]. The spectrometer includes the following basic elements: the SP-40 magnet, proportional chambers, a charged particle identification system, a Cherenkov shower detector, scintillation hodoscopes, an electronic system for event preselection and data acquisition.

The spectrometer magnet is a dipole with external dimensions $450 \times 320 \times 305 \text{ cm}^3$, with aperture $274 \times 48 \text{ cm}^2$. The length of the magnet is 190 cm and the working magnitude of magnetic field is 0.75 T. The schematic picture of the magnet is shown in fig.1.

All computed results are presented here in figures as the relations to the required magnetic field value B_0 in the magnet centre, where B_0 is equal to 0.75 T. The comparison of the computed (42800 nodes) and experimental curves for the relative main field component $B_y(z)/B_0$, has shown (fig.2) that inside the magnet the difference is not more than $\approx 10^{-3}$. In fig.3 the computed and experimental results are presented for the relative main component of the magnetic field for $x = 0 \text{ cm}$, $y = 19 \text{ cm}$.

In fig.4 the main field component at the end region of the magnet are given for $y = 0 \text{ cm}$. The computations have shown that the absolute values of the field components B_x/B_0 and B_z/B_0 in this region are not more than 2,7 % and 4 % accordingly.

Acknowledgments. Authors thank Dr. V.K.Balashov for useful discussion of Unix peculiarities.

References

- [1] M.B.Yuldasheva, O.I.Yuldashev, "The program complex MSFE3D for computations of three-dimensional magnetostatic fields. Version 1.2," JINR, P11-94-202, Dubna, 1994 (russian).
- [2] J.Simkin, C.W.Trowbridge, "Three dimensional non-linear electromagnetic field computations using scalar potentials," Proc. IEE, vol. 127, Pt. B, N 6, pp. 368-374, 1980.
- [3] A.R.Mitchell and R.Wait. The Finite element method in partial differential equations. Moscow: Mir, 1981 (russian).
- [4] E.P.Zhidkov, M.B.Yuldasheva, I.P.Yudin, O.I.Yuldashev, "Mathematical simulation of 3D magnetic field for spec-

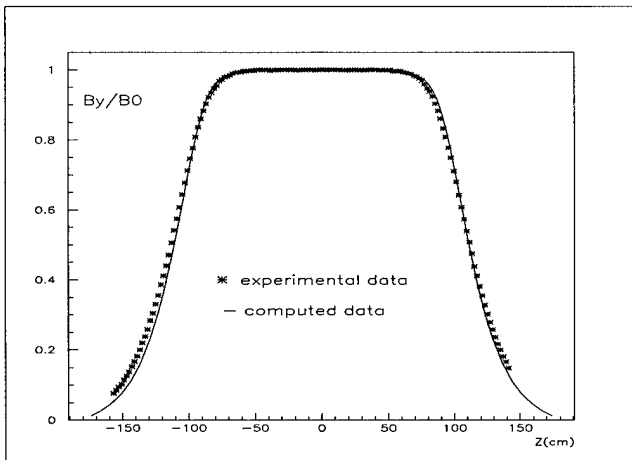


Figure 2. The comparison of computed and experimental data for relative field component B_y/B_0 for $x=0$ cm., $y=1$ cm.

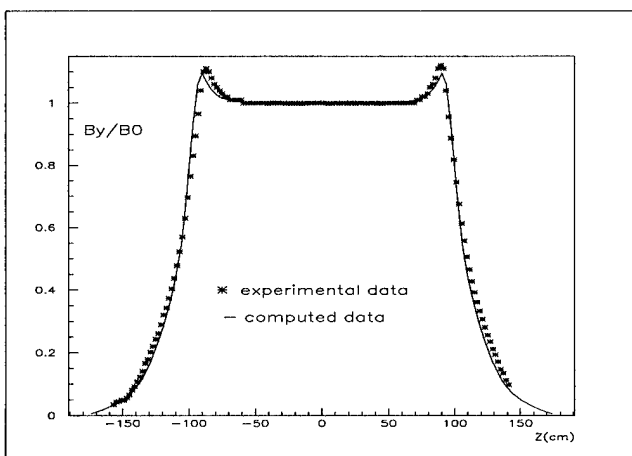


Figure 3. The comparison of computed and experimental data for relative field component B_y/B_0 for $x=0$ cm., $y=19$ cm.

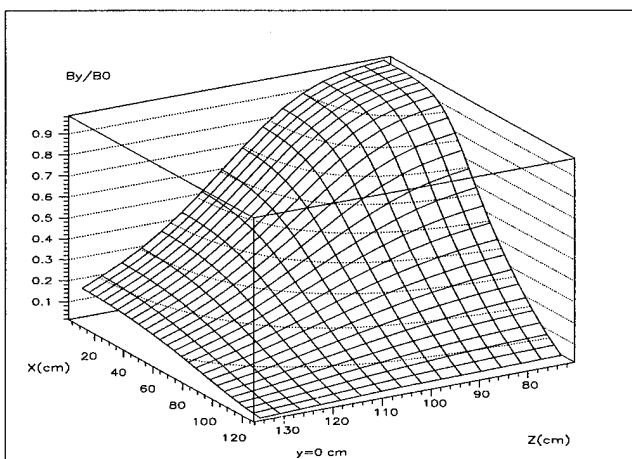


Figure 4. B_y/B_0 field component distribution at the end region of the magnet for $y=0$ cm.

trometer magnet SP-40," JINR, 11-94-160, Dubna, 1994 (russian).

- [5] A.A.Samarskii, E.S.Nikolaev, Methods of Solving the Mesh Equations. Moscow: Nauka, 1978 (russian).
- [6] D.S.Kershaw, "The incomplete Choleski-conjugate gradient method for the iterative solution of systems of linear equations," J. Comp. Phys., v. 26, pp. 43-65, 1978.
- [7] E.P.Zhidkov, M.B.Yuldasheva, O.I.Yuldashev, "Vector algorithms for solving 3D nonlinear magnetostatic problems", Mathematical Modeling, v.6, N 9, pp.99-116, 1994 (russian).
- [8] E.P.Zhidkov, M.B.Yuldasheva, I.P.Yudin, O.I.Yuldashev, "Computation of the magnetic field of a spectrometer in detectors region," JINR, E11-94-397, Dubna, 1994.
- [9] A.N.Aleev et al. JINR, P1-89-854, Dubna, 1989 (russian).

IMPEDANCE STUDY FOR THE PEP-II B-FACTORY*

S. Heifets, A. Chao, E. Daly, K. Ko, N. Kurita, X. Lin, C. Ng, M. Nordby, C. Perkins,
J. Seeman, G. Stupakov, U. Wienands, D. Wright, and M. Zolotarev

Stanford Linear Accelerator Center, Stanford University, Stanford, CA 94309 USA

E. Henestroza, G. Lambertson, J. Corlett, J. Byrd, and M. Zisman

Lawrence Berkeley Laboratory, Berkeley, CA 94720 USA

T. Weiland, TH-Darmstadt, D-64289 Darmstadt, Germany

W. Stoeffl and C. Bolser, Lawrence Livermore National Laboratory, Livermore, CA 94550 USA

The paper summarizes results of the impedance studies of the components of the B-factory. The prime goal of this activity was to support the design of the vacuum chamber and, at the same time, to get reasonable model of the machine impedance, which can be used later for detail studies of collective effects.

Coherent effects impose certain limitations on the magnitude of the impedance. The potential well distortion may give 10% bunch lengthening for the inductance $L = 225$ nH or $Z/n = 0.2 \Omega$ for the HER at the nominal 1A current. The microwave longitudinal and transverse instability set the limit on the effective impedance which is higher than the nominal machine currents. The transverse mode-coupling can be more dangerous but seems that we have a safety factor of the order of two. More serious limitations come from coupled bunch instabilities. Comparison with the damping time gives conservative limits on the impedance at a frequency f , the rms bunch length σ_B , and the nominal parameters of the rings:

$$\left(\frac{f}{\text{GHz}}\right)\left(\frac{\text{Re}Z}{k\Omega}\right)e^{-(2\pi f\sigma_B/c)^2} < 19.5 \text{ (HER)}; < 4.1 \text{ (LER)},$$

$$\frac{\text{Re}Z_{\perp}}{K\Omega/m}e^{-(2\pi f\sigma_B/c)^2} < 119.8 \text{ (HER)}; < 26.6 \text{ (LER)}.$$

The power deposited in the beam pipe by an uncorrelated train of bunches is $P = 4.16$ kW for the loss factor of $\kappa_l = 1$ V/pC.

The impedance generating elements are similar in both rings. They are mostly inductive, their contributions are summarized in the Table. The impedance of the LER ante-chamber replaces the impedance of the DIP screen, and wigglers give an additional contribution to the LER impedance budget.

The dominant contribution to the impedance comes, of course, from the damped RF cavities. The main longitudinal monopole and transverse dipole modes has been found

numerically with the code URMEL and measured on a prototype cavity. The maximum narrow-band (NB) impedance of a single cavity is larger than the limit of stability requiring a feedback system. Optimization of the vacuum chamber should be considered, in this context, as an attempt to minimize the requirements on the feedback system. The same is true for the dipole modes.

The longitudinal antechamber was measured and modeled with MAFIA. Calculations carried out with different length, height and width of the entrance slot, and different depth of the ante-chamber. In all cases, the wakefield is inductive and small. No trapped modes were found.

The beam abort system requires a long and deep vacuum chamber under the beam, which is terminated with a dump. To minimize the impedance, the chamber is screened with shallow RF tapers (down and back up to the beam pipe). The minimal angle of the taper-up is limited by the radiation length and the thickness of the screen. MAFIA calculations of the tapers give an inductive wakefield with no narrow-band trapped modes found.

The interaction region is a complicated 3-D set of masks and tapers was modeled with MAFIA as a whole structure. The main issue for the IR is heating which comes from the trapped modes in the central Berillium pipe ± 20 cm around the IP. The power deposition within the Berillium pipe depends on the loaded Q -factor of the modes. We estimate $Q_{ext} = 1200$ for a typical $f_m = 5.7$ GHz. In this case, only 10% of the power loss goes to the Berillium pipe wall. In principal, detuning from a resonance can be done by heating of the Berillium pipe. The power loss is enhanced for a train of bunches with bunch separation S_b for the resonance frequencies $\omega_{rSB}/(2\pi c) = \text{integer}$. The frequency spectrum of a train of bunches also has frequencies at the multiples of the revolution frequency ω_0 but the total loss of the coherent modes is smaller than the uncorrelated power loss P_0 .

The injection port generates impedance due to a slot in the tapered beam pipe wall and the taper. The impedance calculated with MAFIA was found to be mostly inductive with no indication of the trapped modes found.

* Work supported by Department of Energy contract DE-AC03-76SF00515.

The kicker ceramic has a thin titanium coating. The wakefield generated by the ceramic section is mostly resistive and is described by $R_\Omega = 5.7 \Omega$, and the loss factor $k_l = 0.04$ V/pC.

The final version of the BPM uses a round button with $a = 1.5$ cm diameter. Such a design, as MAFIA calculations show, satisfies requirements for sensitivity, heating, and power output to the cables. Measurements confirmed the results of MAFIA simulations quite well. For a 4-button BPM and 3A current the sensitivity is defined by the impedance 0.5Ω at 1 GHz. Power output to a cable is found by direct calculations of the fields at the port. The 1 cm beam offset in the direction to a button can increase the power to the cable by a factor of 2. The power absorbed in the ceramic, and in the thin Ni layer are small. The Q factor given by these losses is $Q_0 = 534$. The loaded Q_L determined by MAFIA and confirmed in wire measurements on a BPM prototype is much smaller ($Q_L \simeq 60$). Theory and measurements predict that most of the power is radiated back to the beam pipe. It is too low to enhance the power loss in a train of bunches. Some enhancement (by a factor of 6.2) may occur if a button cable is accidentally disconnected. The effects of the button recess was studied and found to be insignificant.

The design of the bellows module uses fingers outside of the beam pipe and does not use large synchrotron radiation masks. Instead, the beam pipes are offset horizontally by a few mm and the transitions are tapered to produce sufficient protection from synchrotron radiation. The impedance of the quadrupole/dipole transition with the tapered beam pipe offset was modeled with MAFIA. No trapped modes were found. The impedance of the bellows module is generated by finger slots, slots in the bellows corners, small tapers of the synchrotron radiation masks, and the RF seals. All contributions are small and correspond to an inductive impedance. The estimate of the impedance of the RF bellows seals is valid also for the flange gap-rings. The main issue for the bellows is not the beam impedance but the heating and operational reliability of the fingers. Heating by radiation through the slots and by coupling to the eigen modes in the bellow cavity outside the fingers have been considered.

Ports of the lumped vacuum pumps are screened with a grid of long and narrow slots. The potential problem here is the possibility to have trapped modes. The theory predicts a trapped mode at the grid of the vacuum port in the arcs with quite high shunt impedance. To eliminate trapping, the beam pipe at the vacuum port may be recessed with the recess volume equal or slightly larger than the polarizability of the slots. Numerical simulations with MAFIA confirmed this statements. A mesh of small holes on the pump side should be used to prevent propagation of TE modes to the pumps.

The longitudinal and transverse kickers for PEP-II are modeled after those designed and measured for the ALS.

The misaligned beam pipes can generate additional impedance. It was estimated with empirical formulas and confirmed by ABCI. The tolerance for the misalignment is 2 mm. The impedance of the synchrotron radiation is suppressed exponentially and gives negligible contribution for the PEP-II impedance budget.

The cross-talk between spatially close components has been considered, modeled, and designed to avoid mode trapping.

The main contributions to the impedance of PEP-II come from the RF cavities and the resistive wall impedance. Components giving the main contribution to the inductive part of the impedance are summarized in Table 1. The transverse impedance is dominated by the modes of the RF cavities, and resistive wall estimated above. The rest of the ring gives small a contribution and, therefore, it may be suffice to have an estimate of such a contribution based on results for the longitudinal impedance.

Table 1. The PEP-II HER inductive impedance

Parameter	L (nH)	k_l (V/pC)
Dipole screens	0.10	
BPM	11.	0.8
Arc bellow module	13.5	1.41
Collimators	18.9	0.24
Pump slots	0.8	
Flange/gap rings	0.47	0.03
Tapers oct/round	3.6	0.06
IR chamber	5.0	0.12
Feedback kickers	29.8	0.66
Injection port	0.17	0.004
Abort dump port	0.23	0.005
Total	83.3	3.4

PRESSURE STABILITY UNDER A PUMP FAILURE*

S. A. Heifets,* J. Seeman,* and W. Stoeffl[°]

*Stanford Linear Accelerator Center, Stanford University, Stanford, CA 94309 USA

[°]Lawrence Livermore Laboratory, Livermore, CA 94550 USA

Ions produced by a beam on the residual gas induce desorption from the beam pipe wall and may lead to a runaway pressure build up. The main mechanism of ion production is usually inelastic collisions of the beam particles. It may not be true for PEP-II where the combination of high energy and high beam current leads to MWs of the total power P_0 in synchrotron radiation. The photoeffect on the residual gas may produce more ions than produced in the inelastic collisions due to a much larger cross-section of the photoeffect σ^γ at low photon energies $h\omega$ where the number of photons $dP(\omega)/h\omega$ is maximum.

The total cross-section $\sigma_t = (1 + \Delta)\sigma_e$, where σ_e is the cross-section of the inelastic collision and correction Δ , which is the ratio of number of ions produced by photoeffect to the number of ions produced in inelastic collisions, can be estimated as

$$\Delta = \frac{N^\gamma}{N^e} = 0.84\alpha\gamma\sqrt{\frac{b}{\rho}} \int \frac{d\omega}{\omega} \left(\frac{\omega}{\omega_c}\right)^{1/3} \frac{\sigma^\gamma(\omega)}{\sigma^e}. \quad (1)$$

Here ω_c is the critical frequency of the synchrotron radiation, and $\alpha = 1/137$.

The cross-section of the photoeffect on a K-shell electron of a hydrogen-like atom with the charge Z is well known. To describe the low-energy photoeffect we scale it according to the Thomas-Fermi model, replacing parameters of a hydrogen-like atom by the parameters of an atom with the ionization potential I_0 . That gives

$$\sigma^\gamma = 0.23Z \frac{a_0^2}{Z^{2/3}} \left(Z^{4/3} \frac{I_0}{h\omega} \right)^4 \frac{e^{-4[\nu \arccot \nu - 1]}}{1 - e^{-2\pi\nu}}, \quad (2)$$

where $I = Z^2 I_0$, $\nu = (h\omega/I - 1)^{1/2}$, $I_0 = 13.6$ eV, and $a_0 = 0.5 \times 10^{-8}$ cm are parameters of a hydrogen atom. Numerical calculations give

$$\int \frac{d\omega}{\omega} \left(\frac{\omega}{\omega_c}\right)^{1/3} \frac{\sigma^\gamma(\omega)}{\sigma^e} = 0.094Z^{7/9} \left[\frac{I_0}{h\omega_c} \right]^{1/3} \left(\frac{a_0^2}{\sigma^e} \right). \quad (3)$$

For the parameters of the PEP-II HER and $Z = 28$, $\Delta = 1.35$, and the total cross-section is larger than the inelastic cross-section by the factor 2.35.

The pressure $P(z)$ along the pipe in the straight sections is found to be

$$P(z) = \frac{q_{sr}L}{4W} \frac{1}{\psi^2} \left[-1 + \frac{\cos(\Omega z - \psi)}{\cos \psi - (2W/S)\psi \sin \psi} \right], \quad (4)$$

where q_{sr} is the ion induced outgassing rate per unit length in (torr l/m/sec) induced by synchrotron radiation, $q_i = \eta\sigma_t(I/e)$

*Work supported by Department of Energy contract DE-AC03-76SF00515 (SLAC).

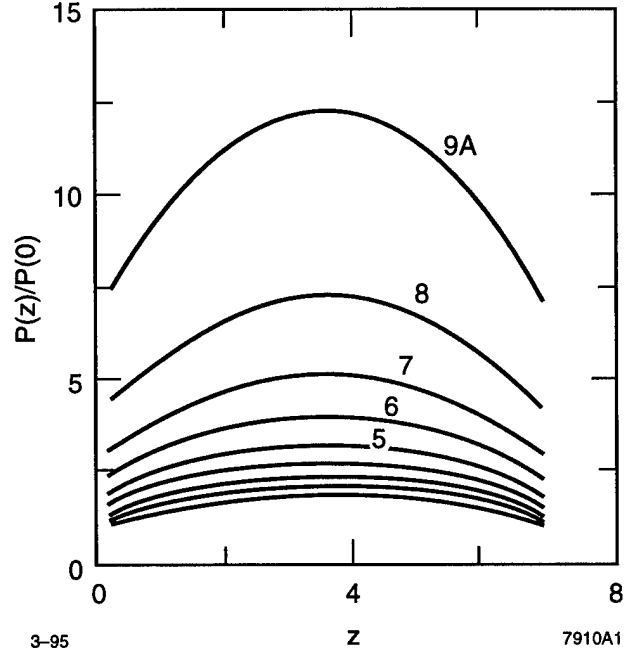


Figure 1. Pressure profile between pumps separated by 7 m for the beam current from 1 A to 9 A. The ion induced threshold current is $I_{th} = 10.469$ A for $W = 24.8$ l/sec, and $S = 68$ l/sec.

is the outgassing induced by the ions produced in collisions with the residual gas, I is the average beam current, $\psi = \Omega L/2$, $\Omega = \sqrt{q_i/LW}$, L is the pump separation, S is the pumping speed in (l/sec), and W is the pipe conductance in (l/sec). The desorption coefficient η , the number of outgassed molecules per ion, depends on the ion mass, energy, material and treatment of the wall, and can change in the wide range from $\eta \simeq 0.01$ to $\eta \simeq 10$.

Equation 4 shows that $P(z)$ goes to infinity if $\psi \tan \psi = S/2W$, defining the threshold current I_{th} at which pressure instability takes place. For the parameters: $\sigma^E = 2 \times 10^{-18}$ cm², $W = 24.8$ l/sec, $S = 68$ l/sec, and $\eta I_{th} = 10.47$ A. Figure 1 shows the pressure profile for $\eta = 1$ and the current in the range from 1 A to 9 A.

Consider now a situation when a pump at $z = 0$ fails doubling the pumping distance. The pressure profile in this case for the range $-L < z < L$ is

$$P(z) = \frac{q_{sr}L}{4W} \frac{1}{\psi^2} \left[-1 + \frac{\cos(\Omega z) \cos \psi}{\cos 2\psi \cos \psi - \frac{W}{S}\psi \sin 3\psi} \right], \quad (5)$$

giving the maximum pressure at $z = 0$.

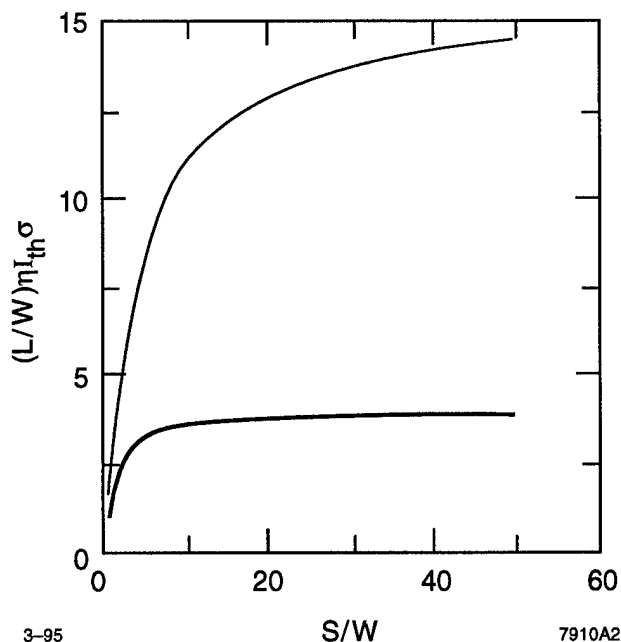


Figure 2. Parameter in the LHS of Eq. (7) versus S/W .

The solution describes substantial increase of the pressure at $z = 0$ (by a factor $\simeq 4$) compared to Eq. (4) and predicts the runaway situation at the current defined by

$$\psi \frac{\sin 3\psi}{\cos 2\psi \cos \psi} = \frac{S}{W}. \quad (6)$$

The lowest root of this equation defines the threshold current

$$\frac{L}{W} \eta I_{th} \sigma_c = 6.4 \psi^2, \quad (7)$$

where L is in meters, W is in l/sec, I_{th} in amperes, and σ_c is in units 10^{-18} cm^2 . This function is shown in Fig. 2 for the normal case (low curve) and with pump failure (upper curve). The right-hand side goes to a maximum value of 3.9 at large S/W giving $\eta I_{th} = 4.96 \text{ A}$ for the pipe $r = 5 \text{ cm}$, $L = 7 \text{ m}$, and $\sigma_c = 2 \cdot 10^{-18} \text{ cm}^2$. The threshold current is reduced from 10.47 A to 4.75 A for the parameters used above.

The conductance calculated from local conductances (M. Sullivan, private communication) is $W = 84 \text{ l/s}$ and $S = 400 \text{ l/s}$ for the interaction region $\pm 2.45 \text{ m}$ from IP. That gives quite high $\eta I_{th} = 27.4 \text{ A}$.

The threshold current is given by the pumping speed s of the distributed ion pumps for the HER arcs: $\eta I_{th} \sigma_c = 1.6 * s$ where s is in l/sec, σ_c is in 10^{-18} cm^2 , and I_{th} in A is very high for $s = 120 \text{ l/m/sec}$.

The situation is less obvious for the wiggler vacuum chamber (under design).

The estimate shows that PEP-II should not have a problem with a pressure instability at nominal pumping speed provided that η remains small, $\eta < 1$.

INVESTIGATION OF THE BEAM IMPEDANCE OF A SLOWLY VARYING WAVEGUIDE

R.M. Jones & S.A. Heifets, Stanford Linear Accelerator Center,
Stanford University, Stanford, CA 94309

A perturbation method is used to obtain analytic expressions for the multipole longitudinal and transverse beam impedance for an arbitrary waveguide whose radius is slowly varying and for the specific case of a symmetric small-angle taper. This method is also applicable for a particle in a wiggler undergoing periodic motion.

I. INTRODUCTION AND BASIS OF THE METHOD

In linear colliders, the particle beam traversing the structure will tend to possess a corona of stray particles with large transverse amplitudes. In order to minimize the deleterious effects of these particles on the luminosity of the beam a scraper is often used to disassociate them from the main beam. However, the scraper may lead to an enhanced transverse wake-field and hence lead to a diminishing of the beam emittance.

The method delineated below to calculate the beam impedance, relies on the angle of the taper being small, as is also required in practice to minimize beam degradation. In order that the expansion remain valid it is required that $k_0 b \ll 1$ and $k_0 b b' \ll 1$ (where $b' = db/dz$). The local change in $b(z)$, is required to be small, however the overall change may be large¹.

II. APPLICATION OF METHOD TO THE MONOPOLE LONGITUDINAL IMPEDANCE

In the frequency domain the electric and magnetic field is expressed in terms of \mathbf{A} , the vector potential:

$$\left. \begin{aligned} \mathbf{E} &= -jZ_0(k_0 + k_0^{-1}\nabla\nabla)\mathbf{A} \\ \mathbf{H} &= \nabla \times \mathbf{A} \end{aligned} \right\} \quad (2.1)$$

where k_0 is the free space wavenumber, Z_0 is the impedance of free space and the vector potential, for monopole a mode, lies along the axis of the structure, $\mathbf{A} = zA_z$. The wave equation, upon applying the Lorentz condition, for a charge Q traveling with a velocity $v_z (= c/\beta_z)$ offset from the axis by r_0 , becomes:

$$\left(\frac{1}{r} \frac{\partial}{\partial r} r \frac{\partial}{\partial r} - 2jk_0 \frac{\partial}{\partial z} + \frac{\partial^2}{\partial z^2} \right) y = -\frac{\delta(r-r_0)}{r} \quad (2.2)$$

Here terms of order γ^2 have been neglected, and the enhanced wavenumber and axial potential are given by:

$$\left. \begin{aligned} \hat{k}_0 &= k_0 / \beta_z = k_0 c / v_z \\ 2\pi A_z &= Qye^{-jk_0 z} \end{aligned} \right\} \quad (2.3)$$

The wave equation, (2.2), is solved iteratively using the perturbation procedure outlined in the previous section. Performing iterations about the zero order equation allows the following equations to be obtained for the first order and n-th order iterations:

$$\left. \begin{aligned} \nabla_r^2 y^0 &\equiv \frac{1}{r} \frac{\partial}{\partial r} r \frac{\partial}{\partial r} y^0 = -\frac{\delta(r-r_0)}{r} \\ \nabla_r^2 y^n &= 2jk_0 \frac{\partial}{\partial z} y^{n-1} - \epsilon_n^1 \frac{\partial^2}{\partial z^2} y^{n-2} \end{aligned} \right\} \quad (2.4)$$

where $\epsilon_n^1 = 1 - \delta_n^1$ and δ_n^1 is the Kronecker delta function. The Green's function for the left hand side of the zero order part of (2.4), viz, $G(r, r') = r' \ln(r/r')$, allows the general solution to the above equation to be developed as:

$$y^{(n)} = \int_0^r dr' \left\{ 2jk_0 \frac{\partial}{\partial z} y^{n-1} - \epsilon_n^1 \frac{\partial^2}{\partial z^2} y^{n-2} \right\} G(r, r') + a_n(z) \quad (2.5)$$

where $a_n(z)$ is a constant of integration and the quantity in parentheses is evaluated at $r=r'$. Thus the zero order, and first order solution are obtained as:

$$\left. \begin{aligned} y^{(0)} &= a_0(z) - \ln(r/r_0) \theta(r-r_0) \\ y^{(1)} &= a_1(z) + jk_0 r^2 a_0'(z) \end{aligned} \right\} \quad (2.6)$$

where θ is the unit step function. The $a_n(z)$ functions are obtained upon consideration of the boundary condition that the electric field along the taper is zero along the plane of the transition:

$$E_z + b'(z)E_r = 0 \quad (2.7)$$

The above boundary condition is applied successively at each iteration:

$$\frac{d}{dz} y^n + \frac{\partial}{\partial z} y^n = \frac{\epsilon_n^0}{jk_0} \frac{d}{dz} \left[\frac{\partial}{\partial z} y^{n-1} \right] \quad (2.8)$$

In the above, the total derivatives are evaluated taking into account $b(z)$ variation. This allows the wave equation to be solved in powers of k_0 . The longitudinal impedance is given by the inverse Fourier transform of the wake field and this is readily rewritten in terms of the electric field as:

$$Z_L = -\frac{1}{Q} \int_{-\infty}^{+\infty} dz E_z(k_0) \exp(jk_0 z) \quad (2.9)$$

This is transformed into:

$$Z_L = j \frac{Z_0}{Q} \int_{-\infty}^{+\infty} dz \left(k_0 + k_0^{-1} \frac{\partial^2}{\partial z^2} \right) A_z \quad (2.10)$$

and integrating by parts enables the impedance to be obtained as:

$$Z_L = \frac{Z_0}{\pi} \sum_{i=1}^n y^{(i)} \quad (2.11)$$

The impedance resulting from the application of this method up to third order in k_0 is given by:

$$Z_L = \frac{jk_0 Z_0}{4\pi} \int_{-\infty}^{+\infty} dz \left[b'^2 + \frac{5}{24} b'^4 + b'^2 b''^2 \left(\frac{1}{8} - \frac{k_0^2 b^2}{12} \right) \right] \quad (2.12)$$

Comparing the above with the impedance obtained by Yokoya² it is evident that the first term in parentheses corresponds to his result and all additional terms are higher order corrections.

Applying this method to the impedance of a symmetric cosinusoidal taper, $b(z) = b_0 - d \cos^2(\frac{\pi z}{2g})$ gives³:

$$Z_L = \frac{jk_0 g \alpha^2}{4\pi} \left\{ 1 - \frac{1}{2} \left(\frac{\pi b_0}{2d} \right)^2 (\tilde{z}_1 + \tilde{z}_3) \right\} \quad (2.13)$$

where the three parameters, \tilde{z}_1 , \tilde{z}_3 and α are given by:

$$\left. \begin{aligned} \tilde{z}_1 &\equiv 1 - \frac{d}{b_0} + \frac{3}{4} \left(\frac{d}{b_0} \right)^2, \quad \alpha \equiv \frac{\pi d}{g}, \\ \tilde{z}_3 &\equiv \frac{2k_0^2 b_0^2}{3} \left[1 - \frac{2d}{b_0} + \frac{21}{8} \left(\frac{d}{b_0} \right)^2 + \frac{13}{72} \left(\frac{d}{b_0} \right)^3 + \frac{1052}{1536} \left(\frac{d}{b_0} \right)^4 \right] \end{aligned} \right\} \quad (2.14)$$

Thus, it is evident that for $k_0 b_0 \ll 1$ the first term of (2.14) is sufficient for the calculation of the impedance. However, in the opposite limit higher order terms must be retained.

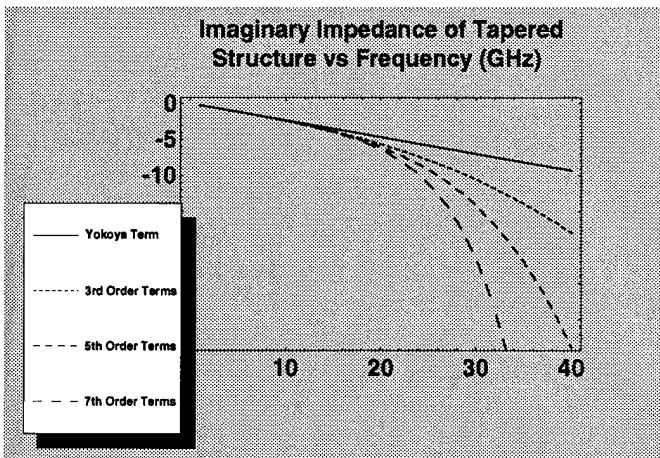


Figure 1

Curves of the impedance function, given by (2.13) up to third order in free space wavenumber, for $b_0 = 1\text{cm}$, $d = .3\text{cm}$, and $g = 6\text{cm}$, are illustrated in figure 1 (where additional terms up to seventh order in k_0 are also included). The linear functional dependence on frequency is indeed sufficient at large wavelengths. However, increasing the frequency rapidly gives rise to significant non-linearity in the dependence of the impedance on k_0 . Indeed, for frequencies in the neighborhood of 30 GHz the perturbation scheme is no longer valid as is revealed upon inspecting higher order perturbations.

III. EVALUATION OF THE TRANSVERSE IMPEDANCE

The transverse impedance is evaluated by solving the wave equation for a vector potential, which in the frequency domain, has components:

$$\mathbf{A} = \sum_{i=-\infty}^{+\infty} e^{jm\phi} \left[A_r \hat{r} + A_\phi \hat{\phi} + A_z \hat{z} \right] \quad (3.1)$$

The wave equation for a harmonic m , is transformed into:

$$\left. \begin{aligned} \left[\nabla_r^2 - \left(\frac{m}{r} \right)^2 \right] y_z &= -\frac{\delta(r-r_0)}{r} + \left[2jk_0 \frac{\partial}{\partial z} - \frac{\partial^2}{\partial z^2} \right] y_z \\ \left[\nabla_r^2 - \left(\frac{m \pm 1}{r} \right)^2 \right] y_{\pm} &= \left[2jk_0 \frac{\partial}{\partial z} - \frac{\partial^2}{\partial z^2} \right] y_{\pm} \end{aligned} \right\} \quad (3.2)$$

where the harmonics of the vector potential are given by:

$$\left. \begin{aligned} A_z &= \frac{Q}{2\pi} y_z e^{-jk_0 z} \\ A_r \pm A_\phi &= \frac{Q}{2\pi} y_{\pm} e^{-jk_0 z} \equiv \frac{Q}{2\pi} (y_r \pm y_\phi) e^{-jk_0 z} \end{aligned} \right\} \quad (3.3)$$

Using the Green's function for the left hand side of (3.2) viz

$$\left. \begin{aligned} G_z(r, r') &= \frac{r'}{2m} \left[\left(\frac{r}{r'} \right)^m - \left(\frac{r'}{r} \right)^m \right] \\ G_{\pm}(r, r') &= \frac{r'}{|m \pm 1|} \left[\left(\frac{r}{r'} \right)^{|m \pm 1|} - \left(\frac{r'}{r} \right)^{|m \pm 1|} \right] \end{aligned} \right\} \quad (3.4)$$

the wave equation is solved for the m -th order harmonic of the vector potential, expanding about the zero order solution enabling the n -order equation to be obtained in the form:

$$\left. \begin{aligned} y_z^n &= \int_0^r dr' G_z(r, r') f_z + a_z^n(z) (r/r')^{|m|} \\ y_{\pm}^n &= \int_0^r dr' G_{\pm}(r, r') f_{\pm} + a_{\pm}^n(z) (r/r')^{|m \pm 1|} \end{aligned} \right\} \quad (3.5)$$

where the functions within the integrals are evaluated at $r=r'$ and are given by:

$$\left. \begin{aligned} f_z &= -\delta_n^0 \frac{\delta(r-r_0)}{r} + \epsilon_n^0 \left[2jk_0 \frac{\partial}{\partial z} y_z^{n-1} - \epsilon_n^1 \frac{\partial^2}{\partial z^2} y_z^{n-2} \right] \\ f_{\pm} &= \epsilon_n^0 \left[2jk_0 \frac{\partial}{\partial z} y_{\pm}^{n-1} - \epsilon_n^1 \frac{\partial^2}{\partial z^2} y_{\pm}^{n-2} \right] \end{aligned} \right\} \quad (3.6)$$

This enables the zero order solution to be obtained as:

$$\left. \begin{aligned} y_z^{(0)} &= a_z^0(z) \left(\frac{r}{r_0} \right)^{|m|} - \theta(r-r_0) \left[\left(\frac{r}{r_0} \right)^{|m|} - \left(\frac{r_0}{r} \right)^{|m|} \right] \\ y_{\pm}^{(0)} &= a_{\pm}^0(z) \left(\frac{r}{r_0} \right)^{|m \pm 1|} \end{aligned} \right\} \quad (3.7)$$

Further, iterations proceed using (3.5) and the remaining constants of integration, $a_z^n(z)$ and $a_{\pm}^n(z)$ are evaluated by applying the condition that both the tangential electric field and the azimuthal electric field are zero along the boundary:

$$\left. \begin{aligned} \hat{D}y &= -\frac{jk_0 b'}{2} (y_+ + y_-) - \frac{d}{dz} (y_z + jk_0^{-1} \hat{D}y) \\ y_z &= -\frac{j}{k_0} \hat{D}y + \frac{jk_0 b}{2m} (y_+ - y_-) \end{aligned} \right\} \quad (3.8)$$

Here \hat{D} operating on y is defined by:

$$\hat{D}y = \left\{ \frac{1}{r} \frac{\partial}{\partial r} r(y_+ + y_-) + \frac{m}{2r} (y_+ - y_-) + \frac{\partial}{\partial z} y_z \right\} \quad (3.9)$$

This completes the calculation of the total field excited by the m -th harmonic of the charge traversing the structure.

The longitudinal impedance is given by:

$$\hat{Z}_L \equiv Z_L(r_0)^m = -\frac{Z_0}{Q} \int_{-\infty}^{+\infty} dz E_z(\omega) e^{jk_0 z} \quad (3.10)$$

and in terms of the vector potential:

$$\begin{aligned} \hat{Z}_L &= \frac{jZ_0}{2\pi} \int_{-\infty}^{+\infty} dz \left[k_0 y_z + e^{jk_0 z} k_0^{-1} \frac{\partial}{\partial z} (\hat{D}y - jk_0 y_z) e^{-jk_0 z} \right] \\ &= -\frac{Z_0}{2\pi} \int_{-\infty}^{+\infty} dz \hat{D}y \end{aligned} \quad (3.11)$$

where (2.1) has been used and an integration by parts has been performed. Further, in cylindrical coordinates the Panofsky-Wenzel theorem⁴ may be applied, enabling the transverse impedance to be obtained as:

$$Z_T = -\frac{m}{k_0} Z_L \quad (3.12)$$

This facilitates the transverse impedance to be obtained up to zero order in k_0 as:

$$Z_T = \frac{jZ_0 m}{\pi(1+m)} \int_{-\infty}^{+\infty} dz \left[\frac{b'}{b^m} \right]^2 \quad (3.13)$$

Here the transverse impedance has been doubled to convert from an exponential variation to a cosinusoidal harmonic. Additional higher order corrections, up to second order in k_0 are readily included for the dipole mode ($m=1$):

$$Z_T = \frac{jZ_0}{\pi} \int_{-\infty}^{+\infty} dz \left\{ \left[\frac{b'}{b} \right]^2 + \frac{1129}{8640} k_0^2 b'^4 \right\} \quad (3.14)$$

IV. DISCUSSION

The perturbation technique is an accurate method to evaluate the impedance of slowly varying accelerator structures consisting of waveguide with a sufficiently slowly varying radius and for a restricted frequency range. For the specific taper under consideration a first order perturbation is augmented with additional higher order terms with increasingly large frequencies up to the point at which the perturbation scheme is no longer valid.

Additional work is in progress on extending the frequency range in which the technique is valid and this is achieved by enhancing the method with a higher order perturbational technique. In this case (2.2) becomes:

$$\left(\frac{1}{r} \frac{\partial}{\partial r} r \frac{\partial}{\partial r} - 2jk_0 \frac{\partial}{\partial z} \right) y = -\frac{\delta(r-r_0)}{r} - \frac{\partial^2}{\partial z^2} y \quad (4.1)$$

The zero order part of (4.1) corresponds to setting the right hand side to zero. Utilizing this method enables the back-scattered wave to be taken into account and this enables the real component of the impedance to be evaluated. Further work is also in progress on applying this technique to investigate the beam impedance of a FEL wiggler.

V. REFERENCES

1. For a harmonic oscillator, driven at a frequency substantially below its natural frequency a perturbation about the zero order (obtained by setting all time derivatives to zero), gives an accurate solution for the amplitude of the oscillation. The method described herein is the spatial analogue of the time-dependent perturbation of a simple harmonic oscillator.
2. K. Yokoya, CERN SL/90-88, AP, (1990)
3. This result, up to third order in b_0/g , has exactly the same coefficients as obtained by B Warnock, SLAC-PUB-6038, 1993
4. W.K.H. Panofsky & W.A. Wenzel, Rev. Sci. Instrum., **27**, 967 (1956)

OPTIMAL TRANSPORT OF LOW ENERGY PARTICLE BEAMS*

Christopher K. Allen, Samar K. Guharay, and Martin Reiser
Institute for Plasma Research
University of Maryland, College Park, MD 20742

The transport and matching problem for a low energy transport system is approached from a control theoretical viewpoint. We model the beam dynamics and transport section using the KV envelope equations. To this model we apply the principles of optimal control to formulate techniques which aid in the design of the transport and matching section. The techniques are applied to the example of an H- beam transport and matching system.

I. INTRODUCTION

The design of particle beam transport and matching systems has typically been accomplished in much the same way an experiment is run. A computer program is used to simulate the behavior of the beam in a given transport system. The knobs of this simulated system are then adjusted until a satisfactory solution is obtained. This can be a lengthy and arduous process. The progress of such a procedure relies completely upon the experience, judgement, and intuition of the designer.

It is the goal of this work to utilize the principles of optimal control theory to aid in the design of beam transport and matching systems. We have developed an automated technique which determines the optimal lens strengths to match the beam envelope to a prescribed final state. In this paper, we consider beams with elliptical symmetry and apply the results to example Low Energy Beam Transport (LEBT) sections where space charge plays a dominant role.

II. MATHEMATICAL MODEL

A. Beam Dynamics

We model the particle beam using the KV envelope equations. In the two-dimensional steady-state case these equations model a uniform density beam with elliptical cross-section. Let $X(z)$ and $Y(z)$ represent the beam envelope semi-axes in the x and y planes, respectively. This system may be described by the system of coupled differential equations [1]

$$\begin{aligned} X'' + \kappa_x(z)X - \frac{2K}{X+Y} - \frac{\epsilon_x^2}{X^3} &= 0, \\ Y'' + \kappa_y(z)Y - \frac{2K}{X+Y} - \frac{\epsilon_y^2}{Y^3} &= 0, \end{aligned} \quad (1)$$

where the prime indicates differentiation with respect to z , K is the generalized beam perveance, and ϵ_x and ϵ_y are the effective emittances of the beam in the x and y planes, respectively. The functions $\kappa_x(z)$ and $\kappa_y(z)$ represent the

action of the transport section in the x and y planes, respectively. They are usually referred to as the focusing or control functions. These equations also describe the behavior of the r.m.s. beam envelope for any beam with elliptical symmetry in the xy plane [1,2].

B. The Transport System

The physical transport section consists of N discrete focusing lenses cascading axially. One of the most important assumptions we make in the paper is that the action of each lens is independent of the others. That is to say that while the beam propagates through a lens, no other lens affects it. This is not always physical, since we know that, in the case of electrostatic or magnetostatic quadrupole lenses, the fields of one lens tend to leak into the regions of any adjacent lenses. Typically, however, we may neglect any small coupling of this type and still acquire accurate results. Consequently, for each lens the focusing function is nonzero only on a finite interval of the z axis.

C. Boundary Conditions (Matching)

We are given initial conditions for the beam envelope at the transport section's entrance position, $z=z_i$. Label these initial conditions (X_i, X_i') for the x plane and (Y_i, Y_i') for the y plane. In the case of a transport and matching system we are also given desired final conditions at $z=z_f$, the exit location of the transport section. We will call these conditions (X_f, X_f') and (Y_f, Y_f') for the x and y planes, respectively. Thus, we must satisfy the following boundary conditions along with Eq. (1):

$$\begin{aligned} X(z_i) &= X_i, & X(z_f) &= X_f, \\ X'(z_i) &= X_i', & X'(z_f) &= X_f', \\ Y(z_i) &= Y_i, & Y(z_f) &= Y_f, \\ Y'(z_i) &= Y_i', & Y'(z_f) &= Y_f', \end{aligned}$$

D. Cost Functional

Let $X(z)$ and $Y(z)$ represent the x and y envelopes of some desirable reference trajectory for the system (these functions would be chosen by the designer). If the pair $[X(z), Y(z)]$ is the actual solution to Eq. (1) for a given system, then a plausible merit functional J for the solution trajectory is given by

$$J[X(z), Y(z)] = \frac{1}{2} \int_{z_i}^{z_f} \left[(X(z) - \bar{X}(z))^2 + (Y(z) - \bar{Y}(z))^2 \right] dz. \quad (3)$$

*Supported by DOE and ONR

This functional, in essence, measures the distance between the solution trajectory $[X(z), Y(z)]$ and the reference trajectory $[X_f(z), Y_f(z)]$.

The boundary conditions of Eq.'s (2) may be included in the functional J with the addition of a boundary term Φ

$$\Phi[X(z_f), Y(z_f)] = \frac{1}{2}[X(z_f) - X_f]^2 + \frac{1}{2}[Y(z_f) - Y_f]^2. \quad (4)$$

Thus, the functional which we actually minimize is $J[X(z), Y(z)] + \Phi[X(z_f), Y(z_f)]$.

III. OPTIMIZATION TECHNIQUE

Since the lens actions are independent, the focusing function $\kappa(z)$ may be subsectioned into N discrete parts, one for each lens. Denote the focusing function for lens n as $\kappa_n(z)$. Also the functional profile for each $\kappa_n(z)$ is known from the geometry of the lens. Therefore, only the amplitude of each $\kappa_n(z)$ remains variable (we do not vary the axial placement of each lens). Denote these amplitudes u_n . We are left with a linear cascade of discrete lenses which act on the beam, in succession, according to Eq. (1). The beam is steered solely by adjusting the set of controls $\{u_n\}$. This situation is referred to in the literature as a multistage control network [3]. The formal control problem is stated as: *find the sequence of controls $\{u_n\}$ which steers the system state from $[X_p, Y_p]$ to $[X_f, Y_f]$ according to the dynamics of Eq. (1) and which minimizes the merit functional of Eq. (3).*

We employ two different techniques from optimal control theory to solve this problem. The first is dynamic programming which has been outlined in a previous paper [4]. The technique works well for axisymmetric systems but usually becomes too CPU intensive for the two dimensional KV equations. Rather, in this situation note that Eq. (1) yields $X(z)$ and $Y(z)$ as implicit functions of the u_n 's. Therefore the functional J may also be regarded as a function of the u_n 's. The next logical step to this method of representation would be to take the gradient of J with respect to the u_n 's. Once we have this gradient, we may use nonlinear programming to search for the minimizing set of lens amplitudes [5]. This approach constitutes the second technique for solving the control problem. Fortunately, this control problem has a rich mathematical structure which may be exploited for computation of the gradients. It is possible to find them using only numerical integration, rather than differentiation. This yields a more accurate and a more stable search algorithm.

The major advantage of the second approach is that it is substantially faster than dynamic programming. So much so that the algorithm usually converges in a matter of minutes (dynamic programming for the fully two dimensional case typically has run times on the order of a day). The major disadvantage is that the technique searches out only local minima. Consequently, it is necessary to pick a starting point for the algorithm. That is, the designer must choose a

set of starting values for the u_n 's. Once started, the algorithm will pick out local minima in the vicinity of this starting set. This is quite unlike dynamic programming, which is a global technique not requiring any differentiability conditions.

IV. EXAMPLE

Both the algorithms discussed above have been implemented in a computer-aided design program called **Spot**, which runs on the PC under Microsoft Windows. It is an environment where the designer interacts with the optimizer in order to steer it in the desired direction. In this way the designer may quickly obtain local solutions to the optimal control problem using the nonlinear programming technique. Once found, the result may be checked using dynamic programming.

A. LEBT System

We consider the case of a Low Energy Beam transport (LEBT) section for high-current, high-brightness H⁻ beam currently under study at the University of Maryland [6]. The system is composed of six electrostatic quadrupole lenses (ESQ's) sandwiched between grounding shunts. We model the action of each lens using the "hard-edge" approximation. A detailed description of the system can be found in reference [6]. We list below the relevant parameters.

I (mA)	V (keV)	ϵ_x, ϵ_y (m-rad)	X_i & Y_i (mm)	X_i' & Y_i' (mrad)
30	35	5.56×10^{-5}	1.25	50

Table 1: Beam Parameters

Lens No.'s	Aperature Radius(mm)	Length (mm)	Spacing (mm)
1 & 6	15.0	25.0	6.0
2 & 5	22.0	59.0	6.0
3 & 4	22.0	47.0	6.0

Table 2: LEBT Parameters

B. Design Guidelines

Our goal is to match the beam to the final state $X_f = Y_f = 1.25\text{mm}$, $X_f' = Y_f' = -50\text{mrad}$. We have the design guidelines that the beam excursions through the ESQs should not exceed 75% of the aperture radius; this requirement will minimize spherical aberrations. Also, the lens voltage seen at the beam envelope should not exceed 10% of the beam voltage in order to minimize chromatic aberrations. In the following figures the controls $\{u_n\}$ are plotted, rather than the actual ESQ voltages. In our nonrelativistic situation, the conversion formula is given as

$$V_n = u_n V_b a^2 \quad (5)$$

where V_n is the ESQ voltage, V_b is the beam voltage and a is the ESQ aperture radius.

The reference trajectory we have chosen is a piecewise linear function of z (we let $X(z)=Y(z)=R(z)$).

$$\bar{R}(z) \equiv \begin{cases} 0.00125 + 0.100z & \text{if } z \in [0, 0.062] \\ 0.01335 & \text{if } z \in [0.062, 0.233] \\ 0.01335 - 0.100z & \text{if } z \in [0.233, 0.354] \end{cases} \quad (6)$$

In this way the reference trajectory levels off to 60% of the aperture radius of lenses 2,3,4, and 5 while remaining well within the requirements of lenses 1 and 6. The reference trajectory is shown in the following figures along with the corresponding solutions.

Figure 1 depicts the solution obtained by the nonlinear programming technique without any constraints imposed upon the lens voltages. The beam is essentially "bounced" off of these two lenses. Clearly this is an unacceptable solution since the beam envelope is comparable to the lens aperture. The situation is remedied by imposing constraints on the lens voltages in the nonlinear programming problem.

It was found that the current ESQ system cannot strictly meet the criteria for minimization of chromatic aberrations. A feasible solution was found when holding the lens voltages seen at the beam envelope to 15% of the beam voltage. This solution is shown in Figure 2. Note that the beam focusing is distributed more evenly across the lenses.

We wish to compare these solutions with that obtained previously without any automation. Figure 3 shows a solution obtained strictly by trial and error with the aim of achieving the same design guidelines. Both show similar characteristics. However, the trial and error solution violates more of the design guidelines. The most notable violations occur at the first lens, where the beam envelope fills 85% of the ESQ aperture and the lens voltage at the envelope is 20% of the beam voltage. This solution also fails to meet the boundary conditions exactly; the convergence is only -40mrad. We also mention that the solution of Figure 3 was found over several hours by an experienced designer while that of Figure 2 was found in less than half an hour.

V. CONCLUSION

The optimization techniques discussed here provide the basis for a useful computer aided design tool. When implemented as above, the designer may interactively guide the optimizer to desirable solutions. These solutions may then be checked against the dynamic programming scheme. This saves a substantial amount of time in the design phase and also allows for the exploration of many design alternatives.

VI. REFERENCES

- [1] M. Reiser, *Theory and Design of Charged Particle Beams* (Wiley, 1994), Sect. 4.4.2, 5.3.4.
- [2] F. R. Sacherer, "RMS Envelope Equations with Space Charge", *IEEE Trans. Nucl. Sci.* NS-18, 1105 (1971).
- [3] A.E. Bryson and Y.C. Ho, *Applied Optimal Control* (Wiley and Sons, 1975), Chapt. 2.

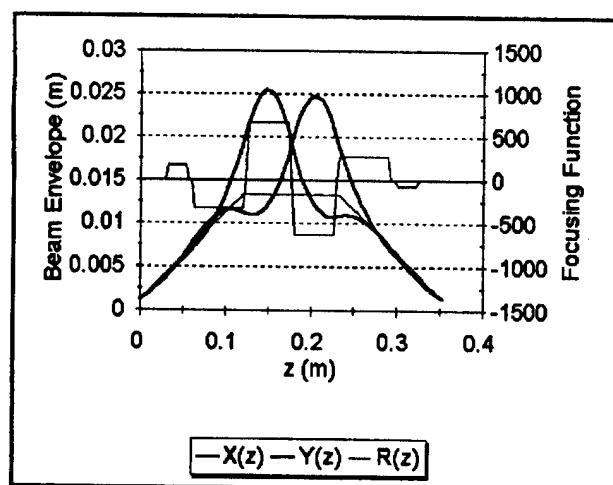


Figure 1: Unconstrained Optimal Solution

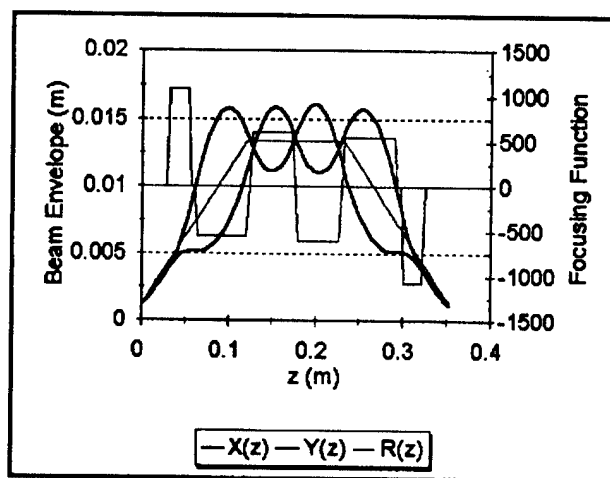


Figure 2: Constrained Optimal Solution

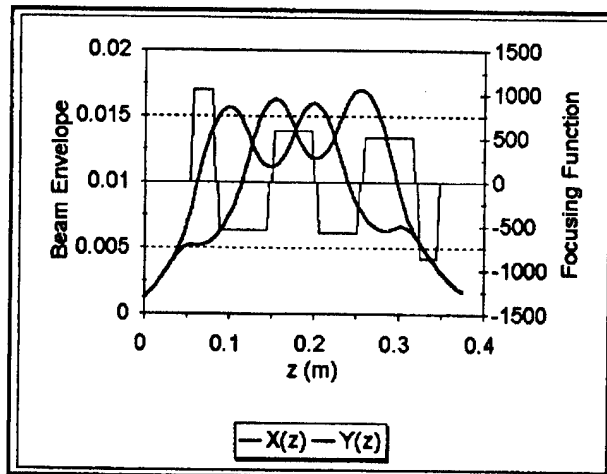


Figure 3: Trial and Error Solution

- [4] C.K. Allen, S.K. Guharay, and M. Reiser, "Optimal Control of Low Energy Particle Beams", *Proceedings Beams 94 Conf.*, San Diego, pp. 540-543.
- [5] D. Luenberger, *Linear and Nonlinear Programming: Second Edition*, (Addison-Wesley, 1984) Chapt.'s 8 and 9.
- [6] S. K. Guharay, C. K. Allen, and M. Reiser, *Nucl. Instr. and Meth. in Phys. Res.*, A 339 (1994), pp. 429-438.

Simulation of the Space Charge Effect in RHIC *

G.F. Dell and S. Peggs
Brookhaven National Laboratory
Upton, New York 11973, USA

Abstract

Space charge forces, representing the weak-strong case, are simulated by kicks from a line charge having a 2D-Gaussian transverse charge distribution. A series of particles having initial coordinates consistent with the dimensions of the injected beam are tracked sequentially, and tunes are obtained from analysis of the coordinates, x , x' , y , and y' , at the end of each turn. Stability is tested using 30K turn tracking runs during which the momentum error δ varies as $\delta = \hat{\delta} \sin(2\pi Q_s t)$.

I. INTRODUCTION

RHIC will have 57 bunches of 10^9 Au ions with a spacing of 67.3 m. There is a 9.8 m region on either side of the interaction point in which the colliding beams will be collinear. They will then be separated by the DX dipoles. With this geometry there are no parasitic beam-beam collisions. Hence the tune shift from beam-beam forces is limited to head on beam-beam collisions at the interaction points and is small.

The tune shift from the space charge is expected to be ~ 0.021 . As RHIC will operate between the 5th and 6th integer resonances at nominal tunes of $\nu_x = 28.190$ and $\nu_y = 29.180$, the anticipated space charge tune shift may drive particles on the edge of the beam to the 5th integer resonances at 28.200 and 29.200. The present study was made to explore possible limitations to the dynamic aperture caused by space charge forces.

The beam has transverse dimensions much smaller than the bunch length and is treated as a line charge having a transverse charge distribution represented by a 2-dimensional Gaussian. Test particles at an arbitrary displacement from the axis of the beam experience kicks attributed to the space charge force. The tunes of small amplitude betatron motion are depressed by as much as 0.021, and the arc quadrupoles are adjusted to restore the tunes to the nominal values of 28.190, 29.180. However, particles with large amplitudes experience little space charge force and have tunes that can approach or cross the 5th integer resonances at $\nu_x = 28.200$ and $\nu_y = 29.200$. Information on tune and amplitude growth of the motion is obtained by tracking on a grid with initial displacements defined by the action $J_t = (n\sigma)^2/2\beta = J_x + J_y$ with $0.5 \leq n \leq 7$.

II. THEORY

The electric field from a 2D-Gaussian charge distribution at a point (x,y) has been expressed in terms of the complex error function by Bassetti and Erskine [1]

$$E_x = \frac{Q}{2\epsilon_0\sqrt{\pi S_{xy}}} \text{Im}[W(\frac{z}{\sqrt{S_{xy}}}) - e^{-(\frac{x^2}{2\sigma_x^2} + \frac{y^2}{2\sigma_y^2})} W(\frac{z_1}{\sqrt{S_{xy}}})] \quad (1)$$

$$E_y = \frac{Q}{2\epsilon_0\sqrt{\pi S_{xy}}} \text{Re}[W(\frac{z}{\sqrt{S_{xy}}}) - e^{-(\frac{x^2}{2\sigma_x^2} + \frac{y^2}{2\sigma_y^2})} W(\frac{z_1}{\sqrt{S_{xy}}})] \quad (2)$$

The above expressions are valid when $\sigma_x > \sigma_y$, where:

$$S_{xy} = 2(\sigma_x^2 - \sigma_y^2), \quad (3)$$

$$z = x + iy, \quad (4)$$

$$z_1 = x \frac{\sigma_y}{\sigma_x} + iy \frac{\sigma_x}{\sigma_y}, \quad (5)$$

and

$$W(z) = e^{-z^2} [1 + \frac{2i}{\sqrt{\pi}} \int_0^z e^{u^2} du] \quad (6)$$

is the complex error function.

Okamoto and Talman [2] have used Pade approximations for rapid evaluation of the complex error function. This formalism has been incorporated in Teapot [3] to evaluate the beam-beam force. The calculation of the kick is divided into three cases according to the profile of the beam cross section: 1). when σ_x and σ_y are within one part in 10^4 of being equal, a radial Gaussian dependence, $(1 - e^{-r^2/2\sigma^2})$ is used, 2). when $\sigma_x > \sigma_y$, Eqn.1 - Eqn.6 are used, and 3). when $\sigma_y > \sigma_x$, x and y are interchanged in Eqn.1 - Eqn.6. Elements of class "beambeam", one of the Teapot elements with "extended allowed parameters", are used to generate kicks from the charge distribution. These elements are intended for calculation of the beam-beam force and are usually placed at the interaction points.

In the present study we use 144 of these elements to simulate the space charge force and have distributed them smoothly at the SF and SD sextupoles in all six arcs. The different optical functions at SF, where $\sigma_x > \sigma_y$, and SD, where $\sigma_y > \sigma_x$, require two families, and the number of particles/bunch as well as the local values of σ_x and σ_y must be specified for each.

Keil [4] considers the beam-beam force and points out the electric and magnetic components differ by a factor of β^2 . The magnitude of the kick given to the test particle depends upon whether the test particle is travelling with, or against, the beam. For the head on beam-beam effect the test particle travels against the beam, and the electric and magnetic fields add as $(1 + \beta^2)$. For space charge the test particle travels with the beam, and the

*Work performed under the auspices of the U.S. Department of Energy

electric and magnetic fields subtract as $(1 - \beta^2)$ and contribute a $1/\gamma^2$ factor to the space charge force.

We make use of the transverse dependence of the two dimensional charge distribution given by the beam-beam formalism in Teapot. Compensation for the difference between tune shifts from beam-beam and space charge forces can be made by adjusting the number of particles per bunch until the observed tune shifts equal the Laslett tune shift, Eqn.7. However, for the present study where kicks are present at all SF and SD sextupoles, the observed tune shifts are sufficiently close to the Laslett tune shift that no change of N_b is necessary.

$$\Delta\nu = -\frac{N_b r_p R_0 Z^2}{2\sqrt{2}\pi\beta^2\gamma^3\epsilon_{rms}\sigma_L A} \quad (7)$$

Where $N_b = 10^9$ is the number of gold ions per bunch, $r_p = 1.510^{-18} m$ is the classical proton radius, $R_0 = 610.18 m$ is the average radius of RHIC, $\gamma = 12.89$ at injection, $\epsilon_{rms} = \sigma^2/\beta = 1.29710^{-7} m$, $\sigma_L = 0.9961 m$, is the *rms* bunchlength, and $Z=79$, $A=197$ are the charge and mass number. For fully stripped gold, $\Delta\nu = -0.021$.

III. ERRORS

A. Position

Errors assigned to dipole position are $\sigma_x = \sigma_y = 0.5$ mm and to dipole orientation are $\sigma_\theta = 1$ mradian. Determination of the center and orientation of the fields in quadrupoles using colloidal cells[5] justifies using $\sigma_x = \sigma_y = 0.25$ mm and $\sigma_\theta = 0.5$ mradian for the position and orientation errors of all quadrupoles.

B. Magnetic

Magnetic harmonic errors[6], a_n and b_n with $1 \leq n \leq 9$, were obtained from magnetic measurements on 34 arc dipoles and 36 arc quadrupoles. Harmonic errors for special insertion magnets, D0 (10 cm) and DX(18cm) dipoles and the 13 cm triplet quadrupoles are based on a combination of magnet calculations and measurements of test magnets.

IV. SIMULATION

Tracking at constant momentum errors of $\delta = 0$ and $\pm 0.11\%$ ($\pm 2.5\sigma_p/p$) is performed for test particles with initial displacements defined by $J_t = J_x + J_y = (n\sigma)^2/2\beta$ for $0.5 \leq n \leq 7$ with values of the initial x and y satisfying $J_x/J_t = 0.96, 0.75, 0.50, 0.25$ and 0.04 . Each particle is tracked for 512 turns, and the values of x, x', y , and y' relative to the closed orbit are written to a file for post processing from which the tunes at each amplitude are obtained.

Stability is determined using 30K turn tracking runs during which the momentum error δ varies as $\delta = \delta \sin(2\pi Q_s t)$. As a line charge is assumed, there is no longitudinal variation of the charge density in a bunch.

Four different seeds are used to initiate the generation of random displacements, rotations, and magnet field errors. In each case two families of skew quadrupoles are used to globally decouple the betatron motion, and the arc quadrupoles are adjusted to obtain the desired tunes.

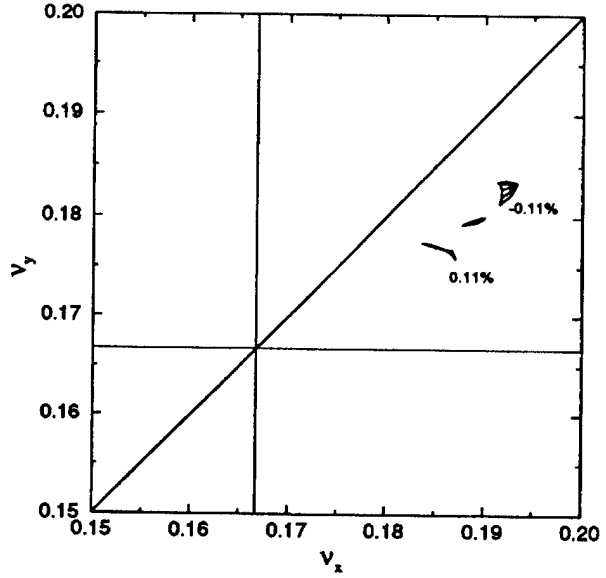


Figure. 1. Dependence of tune on δ , J_t , and aspect ratio x/y with all magnetic field and random positioning and orientation errors included. The nominal tunes are $\nu_x = 28.190$, $\nu_y = 29.180$, and at injection, below transition, the chromaticities $\xi_x = \xi_y = -3$.

V. RESULTS

Tunes are obtained by averaging the phase advance per turn in each plane, and the results are plotted in tune space with one set of lines connecting particles with equal action and another set of lines connecting particles having the same ratio of x/y . Test particles were located wherever two or more lines intersect. "Leafprints" showing the dependence of ν_x and ν_y on amplitude and aspect ratio x/y are shown in Figure 1 when only magnetic, positioning, and orientation errors are present. In general the tunes decrease as the amplitude increases. The addition of the space charge force depresses the tunes of particles at small amplitudes. The "leafprint" in Figure 2 includes the effect of space charge. The arc quadrupoles have been adjusted to restore tunes at small amplitude to the nominal tunes. The leaves for $\delta \neq 0$ are distorted; the tunes at large amplitude include shifts from magnetic field errors, while the tunes at small amplitudes also show a non-linear chromatic dependence. This feature results from the test particle oscillating around a closed orbit that is displaced by $\eta_x \delta$ from the center of the charge distribution.

Figure 3 shows results of a finer scan intended to search for tune distortion near the resonances. The test is most sensitive for the 2σ and 3σ lines and shows no peculiarities.

The stability of particles has also been tested by tracking all particles in the mesh for 30K turns. Figure 4 shows survival plots for four particles representing different error distributions. Solid lines connect data without space charge forces and dashed lines connect data with space charge forces included. The dynamic aperture is consistent with 10σ and the plateau shows that all particles having initial amplitudes $\leq 10\sigma$ survived the requested 30K turns. There is no significant decrease of the maximum dynamic aperture when space charge forces are included. As mentioned above, the regions most sensitive to perturbations

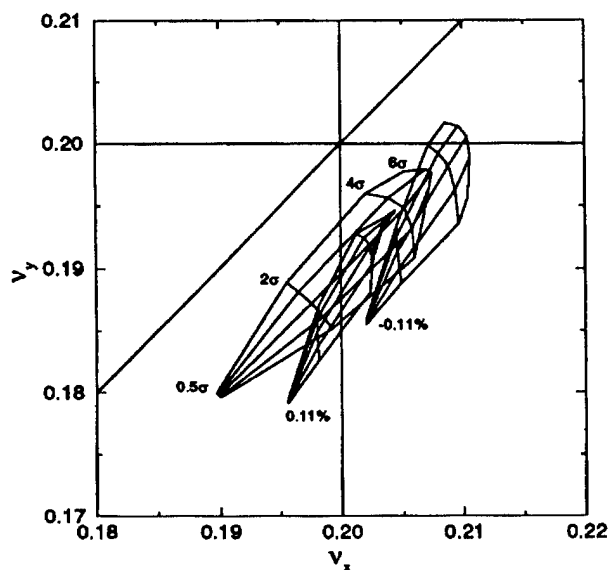


Figure 2. "Leafprint" when space charge forces are added to the configuration used in Figure 1. The nominal tunes have been shifted to $\nu_x = 28.210$, $\nu_y = 29.200$ to restore the tune at small amplitudes to $\nu_x = 28.190$, $\nu_y = 29.180$.

from the 5th integer resonances are $2 \leq n \leq 3$ for $\nu_x = 28.200$ and $n \geq 4$ for the $\nu_y = 29.200$ resonance. The plateau in Figure 4 shows that all particles having initial amplitudes in these ranges survived for the requested 30K turns and that, at the level of 30K turns, their stability is not limited by the 5th integer resonances.

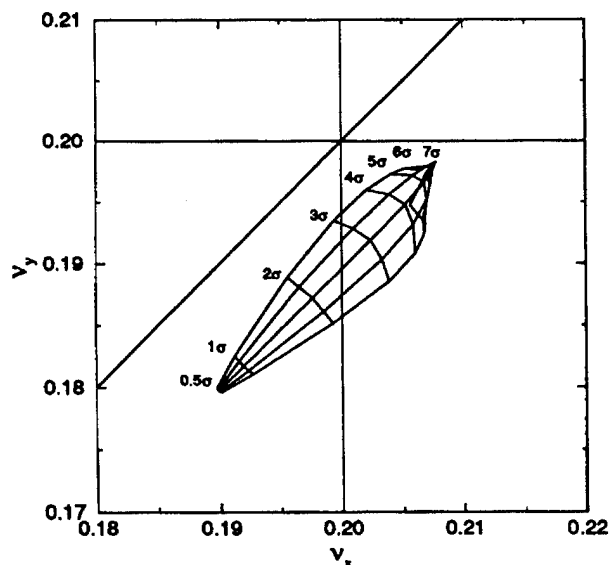


Figure 3. "Leafprint" at $\delta = 0.0\%$ using a finer mesh to explore the 5th integer resonances.

References

- [1] M. Bassetti and G.A. Erskine, "Closed expression for the electrical field of a two-dimensional Gaussian charge", CERN-ISR-TH/80-06, (Unpublished).

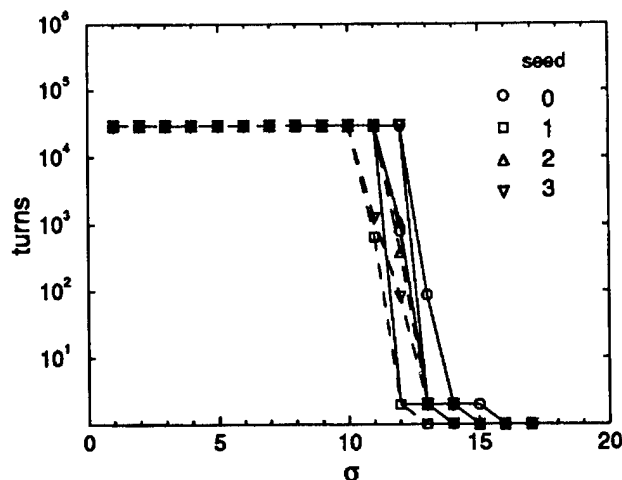


Figure 4. Comparison of dynamic aperture with (dashed) and without (solid) space charge at $\delta = 0.0\%$.

- [2] Y. Okamoto and R. Talman, "Rational Approximation of the Complex Error Function and the electric field of a Two-dimensional Gaussian Charge Distribution", Report CBN 80-13, Cornell University, Sept. 1980.
- [3] L. Schachinger and R. Talman, "Manual for the Program Teapot", Cornell Univ., (November 20, 1994).
- [4] E. Keil, CERN Accelerator School, Rhodes, Greece, Sept. 20 - Oct. 1, 1993, Report CERN SL/94-78 (AP).
- [5] D. Trbojevic et al., "Alignment and Survey of the Elements in RHIC", these proceedings.
- [6] J. Wei et al., "Field Quality Evaluation of the Superconducting Magnets for the Relativistic Heavy Ion Collider", these proceedings.

MAGNETIC SHIELDING FOR THE D0 DETECTOR SOLENOID UPGRADE

J.-F. Ostiguy and R. Yamada, Fermilab

Fermi National Accelerator Laboratory *, P.O. Box 500, Batavia, IL 60510

Abstract

A proposal to add a superconducting solenoid to the D0 detector at Fermilab has recently been approved. During collider operations, the detector is currently traversed by beams from both the Tevatron and the Main Ring. The Main Ring beam is accelerating protons for antiproton production, while the Tevatron beams are colliding. In the event where the D0 solenoid upgrade would be completed before the Main Injector – a replacement ring for the Main Ring, located in a separate tunnel – the Main Ring beam would have to be shielded from the solenoid leakage flux. Using 3D calculations, we estimate that it would be feasible to keep the stray field along the Main Ring beam at level that would not cause orbit control or beam stability problems. We estimate the mechanical forces both on the solenoid and on the magnetic shield.

Introduction

In the present mode of operation, the Main Ring simultaneously accelerates protons used for antiproton production while the Tevatron proton and antiproton beams are colliding. In order to minimize detector background, a special Main Ring overpass was built for CDF, the first detector put in service. For various reasons, which include high cost and additional complexity introduced by vertical bends, no elaborate overpass was built for D0, the second of the two detectors. As a result, the Main Ring beam now circulates through D0 approximately 2 m above the Tevatron beam and the interaction region (Figure 1). All problems and inconveniences resulting from this state of affair will be eliminated as soon as the Main Injector – a new machine, housed in a completely separate tunnel – is put into service. This is scheduled to happen in January 1999.

A decision was made this year to upgrade the D0 detector by the addition of a 2 Tesla superconducting solenoid. There is a small possibility that the D0 detector would have to take data with the new solenoid in before the Main Injector is ready. As shown in Figure 2, if no special precautions are taken, the magnetic field due to the solenoid along the Main Ring beam path is expected to be on the order of 200-500 Gauss. Since almost all available volume inside the detector is already occupied by calorimeters, it is not possible to use a large iron structure to channel the return flux of the solenoid. We have therefore investigated the possibility of magnetically shielding the Main Ring beam with a soft iron pipe.

Effects of Stray Magnetic Fields

It is sufficient to consider separately the effect of the longitudinal and transverse components of the magnetic field. While the longitudinal component of the field introduces a small amount

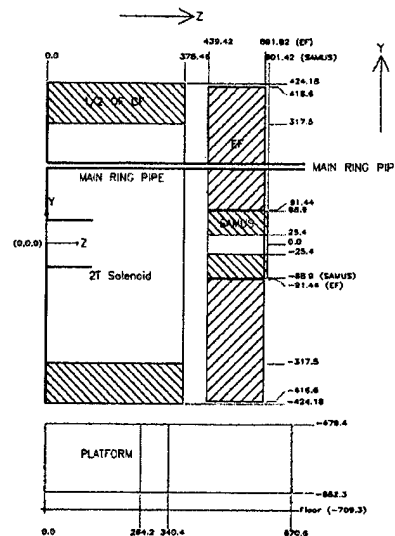


Figure 1. Side view of the D0 detector. Only one half of the detector is shown. All dimensions are in cm.

of coupling of between the horizontal and vertical motion, the transverse component deflects the beam. Using Ampere law, it is not difficult to show that along the beam path, $\int_{-\infty}^{\infty} B_z dz = 0$. With the origin at the center of the detector, $z = 0$ one has by symmetry, $B_y(-z) = -B_y(z)$ and therefore, no net angular deflection. Nevertheless, the net closed orbit distortion does not vanish. For a practical solenoid, any residual coupling due to the longitudinal field is expected to be extremely small and easily correctable. The main function of the magnetic shield is therefore to minimize

$$I = \left| \int_{-\infty}^{\infty} \left[\int_{-\infty}^z B_{\perp}(z') dz' \right] dz \right|$$

$$= \left| \int z B_{\perp}(z) dz \right|$$

To limit the background due to halo particles hitting the beam pipe and Main Ring operation, a rough estimate shows that I should be kept below $0.01 \text{ T}\cdot\text{m}^2$.

Field Calculations

Three-dimensional magnetic field calculations were performed with TOSCA, a well established finite element code. Only the effect of the 2 T solenoid was considered. The flux originating from the toroid excitation coils has been ignored. Although this is not exactly the case, the Main Ring beam pipe was assumed to be centered horizontally in order to take advantage of symmetry to reduce the problem

* Operated by the Universities Research Association, Inc., under contract with the U.S. Department of Energy.

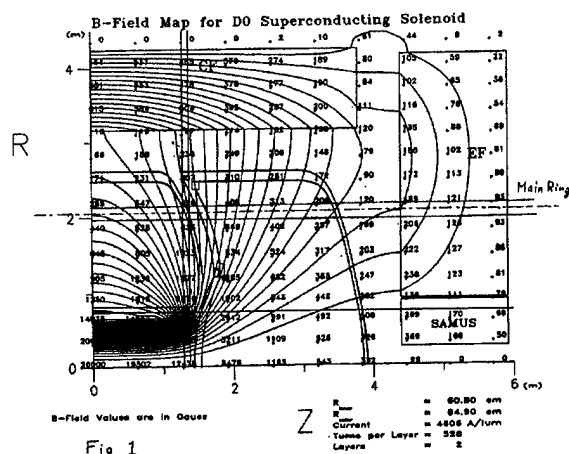


Fig. 1

Figure 2. Magnetic field map of the D0 detector solenoid. 1/4 of the detector is shown. The toroids are not excited.

size. The field distribution of the axial component B_z along the path of the Main Ring beam is presented in Figure 3 and the corresponding transverse component B_y is shown in Figure 4.

Figures 5 and 6 demonstrate the effect of the magnetic shield. The latter is a 6 cm inner radius, 2 cm thick, 8 m long soft iron pipe which is magnetically isolated from the EF toroid. Calculations show that the shield is fairly saturated (≈ 1.6 T) and not surprisingly, the longitudinal component of the field is not significantly reduced. However, the transverse component is reduced by approximately an order of magnitude and so is the integral I . No significant variation in the field are observed for small variations in the transverse position of the beam. The two sharp peaks at $z = \pm 390$ cm in Figure 5 are caused by fringing in the gap between the shielding pipe and the EF toroid. In practice, it would be important to pay attention to the method used to support the shielding pipe in order to minimize high order multipole contribution from the gap region. Although this does not appear to be necessary, the longitudinal field could be reduced by using small bucking solenoids around the shielding pipe. Figure 7 and 8 illustrate the effect of three 200 A solenoids located in the center and at both extremities of the shielding pipe. Note that the transverse field is not affected significantly.

By integrating the Maxwell stress tensor over a surface enclosing the shield, we estimate the attractive force between the solenoid and the shield to 2000 N. The shield mass is approximately 525 kg, so this represents roughly half of the gravitational force.

Conclusions

Although this is a preliminary analysis, we conclude that it is technically feasible to shield the Main Ring beam and operate the D0 detector with a 2 T solenoid. A more detailed analysis would require the inclusion of the toroid coils in the magnetic field calculations. Although it is probably unimportant, the distortion of the solenoidal field in the vicinity of the interaction region caused by the presence of the shield should probably be investigated.

Acknowledgments

The authors would like to thank John Marriner and Glenn Goderre for their valuable comments.

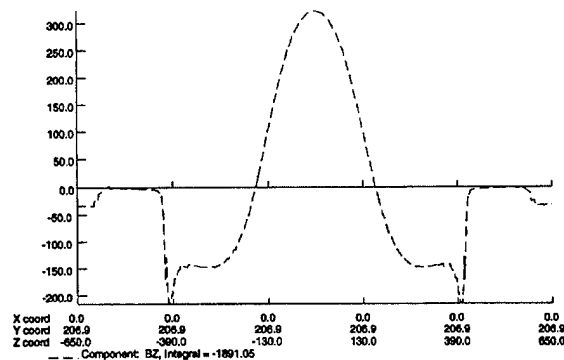


Figure 3. Longitudinal field along the Main Ring beam path. No shielding.

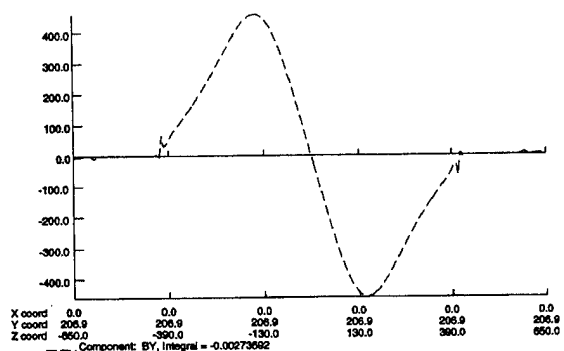


Figure 4. Transverse field along the Main Ring beam path. No shielding.

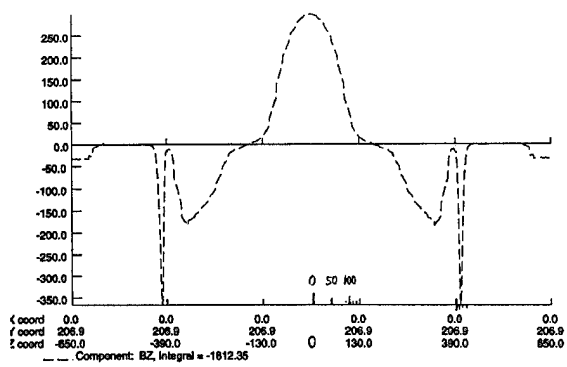


Figure 5. Longitudinal field along the Main Ring beam path. 2 cm thickness soft iron shield.

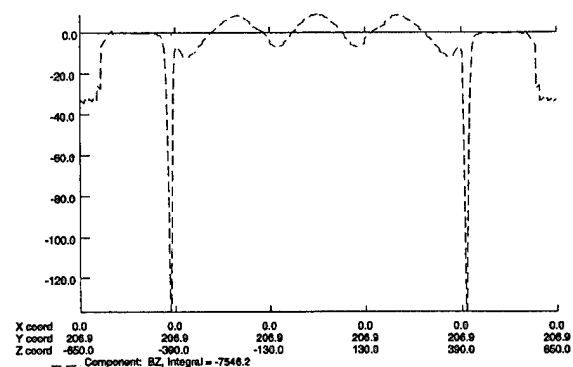


Figure 7. Longitudinal field along the Main Ring beam path. 2 cm thickness soft iron shield and 3 bucking solenoids.

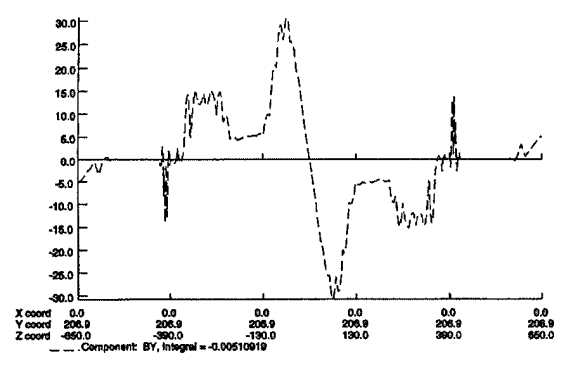


Figure 6. Transverse field along the Main Ring beam path. 2 cm thickness soft iron shield.

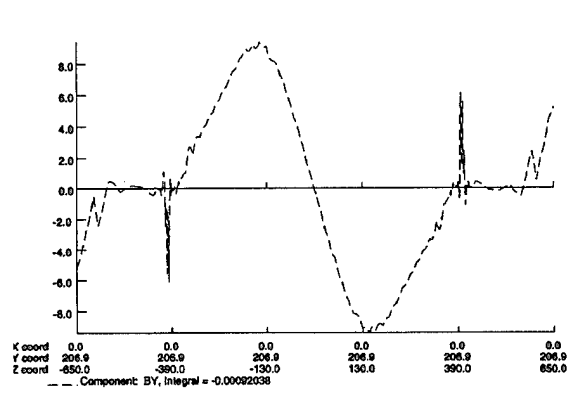


Figure 8. Transverse field along the Main Ring beam path. 2 cm thickness soft iron shield and 3 bucking solenoids.

TRAPPED MODES IN THE PEP-II B-FACTORY INTERACTION REGION*

E. Henestroza
Lawrence Berkeley Laboratory
University of California
Berkeley, California 94720

S. Heifets and M. Zolotarev
Stanford Linear Accelerator Center
Stanford University
Stanford, California 94309

ABSTRACT

The design of the PEP-II B-Factory Interaction Region is based primarily on beam-stay-clear requirements and on synchrotron radiation background considerations (masks are required to shield the detector beam pipe from all sources of synchrotron radiation). A complicated 3-dimensional structure results from these requirements. A high intensity beam traversing this structure will generate wake fields that lead to energy deposition on the beam pipe, as well as to decelerating and deflecting forces acting back on the beam. Computation of wake fields and impedances in frequency-domain and time-domain using 2-D and 3-D electromagnetic codes revealed the existence of trapped modes in the interaction region, which if not controlled could enhance the higher order mode heating of the beam pipe. We will present the simulation results and the design strategy to avoid resonant conditions between these trapped modes and the bunch train frequency.

I. INTRODUCTION

The PEP-II B-Factory, a high-luminosity, asymmetric electron-positron collider that will operate in the 10 GeV center-of-mass energy regime, is under construction at SLAC. The collider consists of a 9 GeV high-energy storage ring (HER), and a 3.1 GeV low-energy storage ring (LER). The average currents in the rings are 1 Amp. for the HER and 2.14 Amps. for the LER. The storage rings are designed to accommodate a large number of bunches, up to 3316 in buckets separated by 2.1 ns (476 MHz RF).

To achieve high luminosities in an asymmetric collider the beams have to collide head-on and be separated magnetically afterwards. Separating the unequal-energy beams by the use of bending magnets

and offset quadrupoles generates several fans of synchrotron radiation.

Several sources must be considered in the investigation of synchrotron radiation background including direct synchrotron radiation (primary masks must be placed to prevent such radiation from striking the detector beampipe, at the same time keeping the number of photon striking their tips to an acceptable level), photons that scatter through a mask tip, sources of synchrotron radiation from elements far upstream of the interaction region, and sources of backscattered photons from downstream surfaces.

Since the collider has to maintain an acceptable detector background condition, the design of the PEP-II B-Factory Interaction Region (IR) is based primarily on beam-stay-clear requirements and on synchrotron radiation background considerations. A complicated three-dimensional structure results from these requirements.

II. THE INTERACTION REGION

The proposed dimensions [1], in the horizontal and vertical planes, for a beam pipe design ± 1 m from the Interaction Point (IP) are shown in Figs. 1 and 2, in a reference frame in which the collision axis of the beams is the primary axis. The masks (highlighted in those figures as shaded areas) must shield the detector beam pipe from all sources of synchrotron radiation.

The interaction region (IR) is a three-dimensional structure, composed of a number of offset tapers with elliptical cross section, asymmetrically placed in the horizontal and vertical planes. A high intensity beam traversing this structure will generate wake fields that lead to energy deposition on the beam pipe, as well as to decelerating and deflecting forces acting back on the beam.

*Work supported by the U.S. Department of Energy under Contract DE-AC03-76SF00098 and DE-AC03-76SF00515.

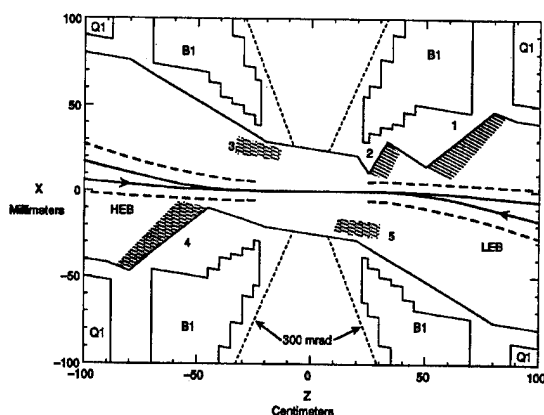


Figure 1: Horizontal plane, for a beam pipe design ± 1 m from the Interaction Point, in a reference frame in which the collision axis of the beams is the primary axis.

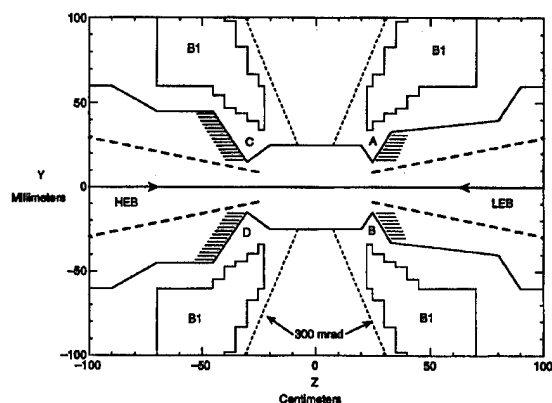


Figure 2: Vertical plane, for a beam pipe design ± 1 m from the Interaction Point, in a reference frame in which the collision axis of the beams is the primary axis.

III. WAKEFIELDS

The wakefield and impedance of the IR were calculated with the time-dependent electromagnetic codes MAFIA [2] and ABCI [3].

MAFIA calculations in three-dimensions showed that to a good approximation one could consider the interaction region as an axisymmetric structure, neglecting the beam pipe offsets and deformations, as well as the beam offsets from the main centerline. A cylindrically symmetric structure was obtained by rotating the layout of the real structure in the vertical plane.

The wake potentials for a gaussian bunch ($\sigma = 1$ cm), calculated for the real (3D) structure, are shown in Figure 3. The transverse wake is due to the asymmetry of the structure in the x-direction. Similar longitudinal

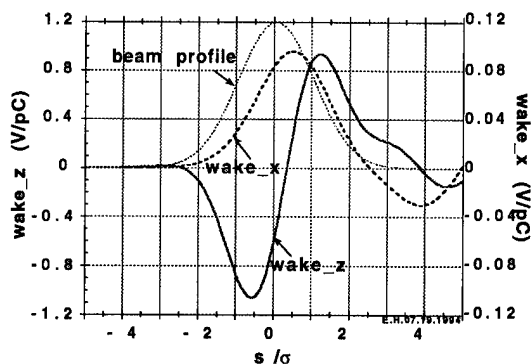


Figure 3: Wake potentials for the B-Factory Interaction Region. The distance is in units of the bunch length.

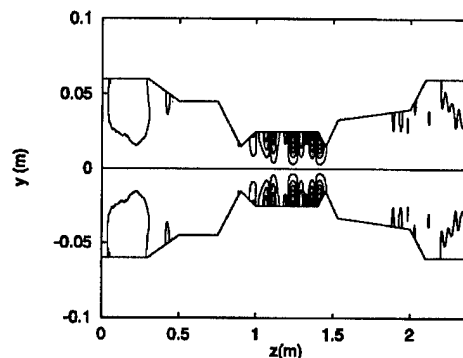


Figure 4: Electric field lines left by the beam in the IR after several beam transit times.

wake potential is obtained for the axisymmetric case. The broadband impedance is approximately inductive with $L \approx 5$ nH, corresponding to a $Z(n)/n \approx 5$ m Ω . The narrow-band impedance has a resonance at a frequency around 6 GHz. The loss factor of the total structure is $k_l = 0.12$ V/pC. Most of the lost power propagates downstream and is absorbed outside the IR.

The effect of the IR discontinuities on beam dynamics is negligible. The main issue for the IR is heating. The heating from the propagating high order modes (HOM) is small and the potential problem comes from the trapped modes in the central Beryllium pipe, ± 20 cm from the IP. The energy deposition could be enhanced substantially if there were trapped modes in the IR, provided their wave length were a multiple of the bunch spacing.

As shown in Fig. 4, the existence of trapped modes in the Be pipe is suggested from a long term calculation of the wake fields by the ABCI code.

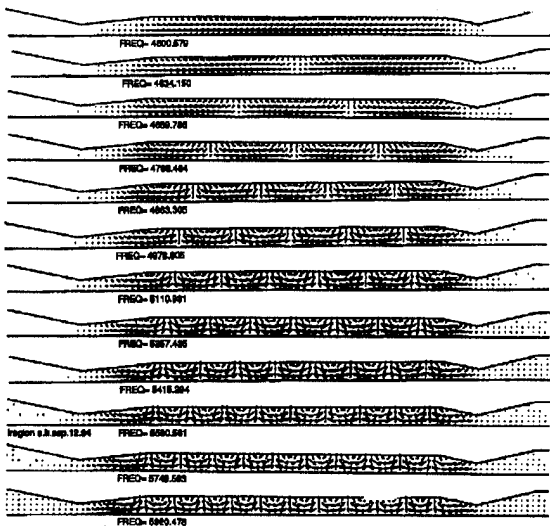


Figure 5: Electric field configuration of the trapped modes in the Be pipe of the B-Factory IR.

IV. TRAPPED MODES

The resonant modes of the axisymmetric structure, obtained by rotating the layout of the real structure in the vertical plane, were calculated using the frequency-domain code SUPERFISH [4]. A number of trapped TM_{01} modes, with frequencies ranging from 4.60 to 5.92 GHz, were found in the cavity-like confinement formed by the Be pipe and the adjacent masks. As expected, all these modes are the TM_{01} eigenmodes of a cylindrical pipe of radius $a=2.5$ cm. The frequency interval at the low frequency end is about 50 MHz and increases to 150 MHz at the upper frequency end. Figure 5 shows the electric field configuration of the normal modes. The total contribution to the loss factor from all the modes shown is $k_1 = 0.012$ V/pC.

Both beams excite the modes simultaneously. The power deposition within the Be pipe depends on the Q -factor of the modes. The Q_{ext} is due to the coupling of the trapped modes to the propagating modes in the adjacent beam pipes with larger radii. We estimate $Q_{ext} \approx 1200$ for a typical $f_m = 5.7$ GHz. Since the resistive wall $Q \approx 12000$, only 10% of the power loss goes to the Be pipe wall.

The total power deposition in the IR by two beams is given by $P_{tot} = ek_1(I_1^2 N_1 + I_2^2 N_2)$, where e is the electron charge, k_1 the loss factor, and I and N are the current and number of particles for each bunch respectively. With the average currents specified for the two rings we get $P_{tot} = 480$ W. In principle, detuning from a resonance can be done by heating the Be pipe. The frequency shift for the mode at the upper end of the frequency range is comparable with the width of the resonance.

The power loss is enhanced for a train of bunches depending on the detuning of the mode frequency from the resonance frequencies: $\omega_{rs} B / (2\pi c) = \text{an integer}$. If only 3 out of every 12 trapped modes are resonant, the power loss is $P = 3 * (1/12) * 480 \text{ W} * D_{max} = 1.92 \text{ kW}$, where we have estimated an enhancement factor $D_{max} \approx 16$. The power dissipated into the wall itself in this case is $P_{wall} = 192 \text{ W}$.

The Ohmic loss is much smaller. It depends on the rms bunch length, the skin depth of the wall, and the conductivity. For the B-Factory IR parameters, the power deposition per unit length is of order of 10 W/m, for a total of 4 W of ohmic loss into the Be pipe.

The frequency spectrum of a train of bunches also has frequencies at the multiples of the revolution frequency ω_0 but the total loss of the coherent modes is smaller than the uncorrelated power loss P_0 .

V. CONCLUSION

The total loss factor of the IR is relatively small and, by itself, is not a problem. The main concern for the HOMs at the IR is heating of the central Be pipe due to the localized trapped modes. Simulation shows that such modes indeed exist in the range between 4 and 6 GHz being separated by 50-100 MHz. A potential enhancement of the energy loss in a bunch train under resonance conditions is a problem but may be avoided by careful choice of the geometry and by controlled heating of the Be pipe, which detunes the modes differently for low and high frequency modes. Further 3D numerical calculations of the Q_{ext} , and measurements with a prototype structure are needed to study and to avoid the resonances.

VI. ACKNOWLEDGEMENTS

We are indebted to T. Weiland and Y. H. Chin for helpful discussions about their codes, and to M.K. Sullivan for information about the design of the IR.

VII. REFERENCES

- [1] "PEP-II : An Asymmetric B Factory", Conceptual Design Report, LBL-PUB-5379, June 1993.
- [2] The Mafia Collaboration, "User's Guide, MAFFIA Version 3.x". Darmstadt, Germany, 1992.
- [3] Y.H. Chin, Report CERN-SL/92-49 (AP), Geneva, Switzerland, 1992.
- [4] K. Halbach, and R.F. Holsinger, *Particle Accelerators*, Volume 7, 1976, pp. 213-222.

A Proof of Principle of A Storage Ring with Fifth-Order Achromatic Bending Arcs

Weishi Wan and Martin Berz

Department of Physics and Astronomy, and
National Superconducting Cyclotron Laboratory
Michigan State University, East Lansing, MI 48824

Abstract

The design of a storage ring consisting of two identical 180-degree bending arcs and two short straight sections is presented. Each of the bending arcs is a four-cell fifth-order achromat designed according to a recently developed theory about arbitrary-order achromats. Instead of repetition of cells, which is widely used in achromat design based on normal form theory, we utilize cells which are obtained from the original ones through mirror imaging about the x - y plane, which corresponds to a reversion. In our design, the second cell is the reversion of the first one. The third and fourth cells are identical to the first and second ones, respectively. Long term stability is studied through high-order tracking using code COSY INFINITY [1].

1 Introduction

In the past few years, various third-order achromatic systems containing at least seven repetitive identical cells have been found using normal form theory [2] [3] [4]. The number of bending magnets needed ranges from 7 to 300. Each solution requires a specific number of cells depending on the choice of the tunes of a cell.

By introducing mirror symmetry into the consideration, we developed a new theory which requires only four cells and as few as one bend per cell to obtain achromats of, in principle, arbitrary orders [5] [6]. The use of mirror symmetry enables us to choose from four kinds of cells, namely the forward cell (F), the cell in which the order of elements is reversed (R), the cell in which the direction of bend is switched (S), and the cell where reversion and switching is combined (C). According to the theory, the minimum number of conditions required for a four-cell fifth-order achromat with an arbitrary forward cell are five for the first order, four for the second order, fifteen for the third and the fourth orders and thirty nine for the fifth order. The optimal four-cell systems which require only the minimum number of conditions are listed in Table 1, together with the first-order requirements.

One of the possible applications of high-order achromats is achromatic bending sections of accelerators. In this report, a storage ring with two fifth-order achromatic bending arcs is pre-

Systems	Linear Conditions
F R S C	$(a \delta) = 0, (x a) = (a x) = 0$
F R F R	$(a \delta) = 0, (x x) = (a a) = 0$
F C S R	$(x \delta) = 0, (x a) = (a x) = 0$
F C F C	$(x \delta) = 0, (x x) = (a a) = 0$

Table 1: The optimal four-cell systems Additional linear conditions are $(y|y) = (b|b) = 0$ or $(y|b) = (b|y) = 0$ for each one.

sented. The detail of the design is discussed in Section 2. In Section 3, the repetitive stability is studied through tracking. Conclusions are given in Section 4.

2 Design of the Achromat

2.1 First- and Second-Order Design

In order to design an achromatic bending arc, no switched (S) or switched-reverse (C) sections can be used. Thus, the only choice is FRFR. The first-order layout should avoid large changes in the beta functions in order to minimize nonlinear aberrations; furthermore, there should be room for the insertion of correction multipoles. Another consideration is that, if possible, the number of first-order conditions should be further reduced through symmetry arrangements inside a cell.

The result of these thoughts is shown in Figure 1, where the 180-degree bending arcs are achromatic. The forward cell itself also consists of two parts, where one is the reversion of the other. This guarantees that at the end of it, $(x|x) = (a|a)$ and $(y|y) = (b|b)$. The building block of the arc is a FODO cell consisting of a defocusing quad, a 5.625° bend, and a focusing quad. All four FODO cells within one part of a cell are identical except the last one, which has an extra quadrupole for dispersion correction. So there are three knobs for the first-order design which can zero $(x|x)$, $(a|a)$, $(y|y)$, $(b|b)$, $(x|\delta)$ and $(a|\delta)$ at the same time. Figure 2 shows that the beam moves around the arc in a quite uniform manner avoiding large ray excursions and beta functions.

According to the arbitrary-order theory, four independent sextupoles are required to obtain a second-order achromat. However, because of the fact that to the first order, the cell R

This work was supported by the U.S. National Science Foundation, Grant No. PHY 89-13815, and the Alfred P. Sloan Foundation.

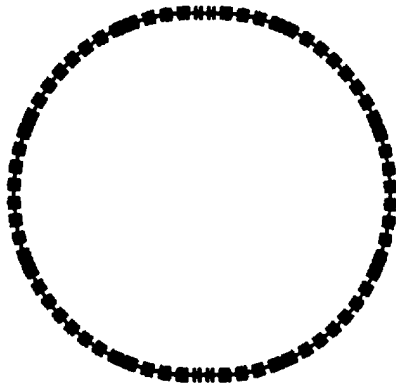


Figure 1: The layout of a storage ring with fifth-order achromatic bending arcs; the circumference is 1451.06 m; the tunes are $T_x = 0.03654$, $T_y = 0.03721$.

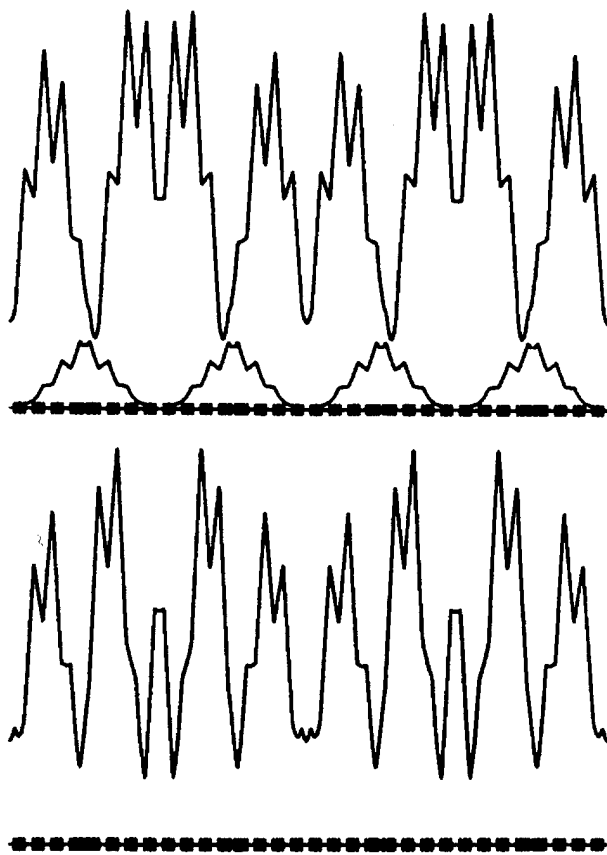


Figure 2: The beam envelope and the dispersive ray of the horizontal (top) and vertical (bottom) motion; emittance: 10π mm mrad (horizontal and vertical); $\Delta E/E$: 0.1%.

is identical to the cell F, a simplification is possible based on Brown's theory of second-order achromats ([7] [8]). In this theory, it is shown that a second-order achromat can be achieved by placing two pairs of sextupoles in dispersive regions and cancelling one chromatic aberration in each transverse plane. Therefore, a second-order achromat can be achieved on the arc using two sextupoles per cell. In our case, it turns out to be advantageous to split the sextupoles into symmetrically excited

pairs to ensure that up to the second order the second cell (R) still is the reversion of the first.

2.2 Higher-Order Design

After the investment in a careful first-order layout, the third-, fourth- and fifth-order corrections actually turn out to be conceptually straightforward, even though they are computationally more demanding. In the whole process of nonlinear optimization, only two aspects seem to be worth considering. First, the required multipole strengths are quite sensitive to the average distance among multiples of the same order. So, in order to keep their strength limited, it is important to dimension the total size of the ring and the dispersive region sufficiently large, as done in the previous section, and distribute multipoles of the same order roughly uniformly.

Secondly, all the decapoles have to be placed in regions with sufficient dispersion because all the fourth-order aberrations remaining after third-order achromaticity is achieved are of chromatic type. Thus it is advantageous to use a substantial dispersive region.

The combination of these considerations results in reasonably weak multipole strengths for third-, fourth- and fifth-order corrections. Table 2 shows that a fifth-order achromat is achieved.

1.00	0.000E+00	0.000E+00	0.000E+00	0.0000E+00	100000
0.000E+00	1.00	0.000E+00	0.000E+00	0.0000E+00	010000
0.000E+00	0.000E+00	1.00	0.000E+00	0.0000E+00	001000
0.000E+00	0.000E+00	0.000E+00	1.00	0.0000E+00	000100
0.000E+00	0.000E+00	0.000E+00	0.000E+00	1.000	000010
0.000E+00	0.000E+00	0.000E+00	0.000E+00	33.63	000001
0.000E+00	0.000E+00	0.000E+00	0.000E+00	-38.31	000002
0.000E+00	0.000E+00	0.000E+00	0.000E+00	-11044	000003
0.000E+00	0.000E+00	0.000E+00	0.000E+00	-2.124E+05	000004
0.000E+00	0.000E+00	0.000E+00	0.000E+00	0.9870E+09	000005

Table 2: The fifth-order map of the arc (Zero means smaller than $2E-01$.)

3 Repetitive Stability

With the arc at hand, a storage ring is designed, which contains two identical achromatic arcs and short straight sections. Each of the straight sections consist of two FODO cells with weak quads (less than 0.1 kG/cm as opposed to 1 kG/cm in the arc), which means that the quads only produce weak nonlinearities.

To study the repetitive stability of the ring, a 7th-order one-turn map is generated by COSY INFINITY and used for tracking. To be specific, we analyze the 10,000-turn dynamic behavior for both horizontal and vertical motions through the inspection of phase space plots. As an example, Figure 3 depicts the horizontal motion of on-energy particles up to 10,000 turns.

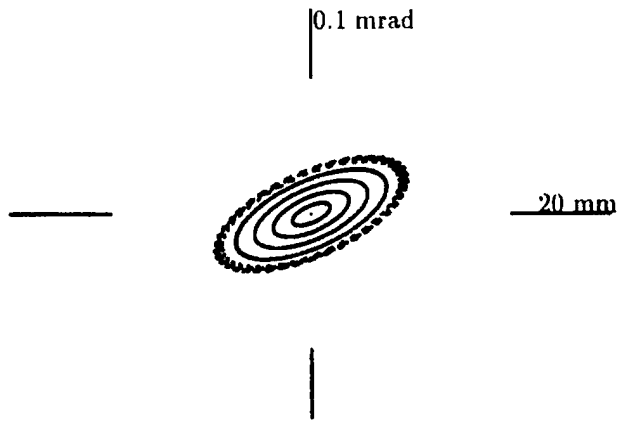


Figure 3: The 10,000-turn tracking of the x - a motion of on-energy particles

4 Conclusion

It has been shown that it is possible to design fifth-order achromatic bending arcs. Careful first-order considerations allow the use of relatively weak correction elements, and thus also weak nonlinearities beyond the orders that can be corrected. A storage ring containing the achromatic arcs is presented, and the repetitive stability is studied.

References

- [1] M. Berz, *COSY INFINITY Reference Manual Version 6*, Technical Report MSUCL-869 (1993).
- [2] A. J. Dragt, *Nucl. Instr. Methods* A258 (1987) 339.
- [3] F. Neri, in *Proc. Workshop on High Order Effects*. M. Berz and J. McIntyre (Eds.), Technical Report MSUCL-767 (1991).
- [4] F. Neri, private communication.
- [5] W. Wan and M. Berz, in preparation
- [6] W. Wan, *Theory and Applications of Arbitrary-Order Achromats*, Ph.D. Thesis, Michigan State University, (1995).
- [7] K. L. Brown, *IEEE Transactions on Nuclear Science*, Vol. NS-26, No. 3, p3490, 1979.
- [8] David C. Carey, *Nucl. Instr. Methods* 189 (1981) 365-367.

Analytic Electrostatic Solution of an Axisymmetric Accelerator Gap*

John K. Boyd

Lawrence Livermore National Laboratory, P.O. Box 808
Livermore, California 94550, USA

Introduction

Numerous computer codes calculate beam dynamics of particles traversing an accelerating gap. In order to carry out these calculations the electric field of a gap must be determined [1,2]. The electric field is obtained from derivatives of the scalar potential, which solves Laplace's equation and satisfies the appropriate boundary conditions. An integral approach [3,4] for the solution of Laplace's equation is used in this work since the objective is to determine the potential and fields without solving on a traditional spatial grid. The motivation is to quickly obtain forces for particle transport, [5] and eliminate the need to keep track of a large number of grid point fields. The problem then becomes one of how to evaluate the appropriate integral. In this work the integral solution has been converted to a finite sum of easily computed functions. Representing the integral solution in this manner provides a readily calculable formulation and avoids a number of difficulties inherent in dealing with an integral that can be weakly convergent in some regimes, and is, in general, highly oscillatory.

Formulation of the Scalar Potential Integral

The Laplace equation to be solved in cylindrical coordinates for an accelerator gap is,

$$\frac{1}{r} \frac{\partial}{\partial r} \left(r \frac{\partial \phi_{\text{total}}}{\partial r} \right) + \frac{\partial^2 \phi_{\text{total}}}{\partial z^2} = 0 \quad (1)$$

with the value of the potential prescribed at radius a . For axisymmetry in cylindrical coordinates, a Green's function is obtained by first expressing the delta function in terms of a trigonometric expansion [6]. The Green's function is then expanded in terms of the same functions used for the delta function expansion, but with an unknown radial function $g_m(r, r')$.

$$G(\tilde{x}, \tilde{x}') = \left(\frac{1}{2\pi^2} \right) \sum_{m=-\infty}^{\infty} \int_0^{\infty} dk e^{im(\theta - \theta')} \cos[k(z - z')] g_m(r, r') \quad (2)$$

The equation solved by the radial function after specializing to axisymmetry, $m = 0$, is as follows.

$$\frac{1}{r} \frac{\partial}{\partial r} \left(r \frac{\partial g_0}{\partial r} \right) - k^2 g_0 = - \frac{4\pi}{r} \delta(r - r') \quad (3)$$

The homogeneous version of Eq.(3) is the equation for the

modified Bessel functions. It is thus solved by a linear combination of $I_0(kr)$ and $K_0(kr)$ that satisfy the zero boundary condition at $r = a$ and the derivative discontinuity condition. Inserting the appropriate $g_0(r, r')$ into Eq.(2), a G is found which satisfies the necessary properties and is specialized to a region with a fixed radial boundary and thus a Dirichlet boundary condition appropriate to an accelerator gap.

$$G = \left(\frac{2}{\pi} \right) \int_0^{\infty} dk \cos k(z - z') \frac{I_0(kr_{<})}{I_0(ka)} (I_0(ka) K_0(kr_{>}) - K_0(ka) I_0(kr_{>})) \quad (4)$$

In Eq.(4) $r_{<}$ is the minimum of r, r' , $r_{>}$ is the maximum of r, r' , and both I_0 and K_0 are zero order modified Bessel functions.

Before the accelerator gap the wall potential is ϕ_1 and after the gap the potential is ϕ_2 . The total potential is thus constructed as the sum of a constant and an unknown scalar function which is odd in z ,

$$\phi_{\text{total}} = \frac{1}{2} (\phi_1 + \phi_2) + \phi \quad (5)$$

where ϕ now solves Eq.(1). The integral solution for ϕ is,

$$\phi(\hat{r}, \hat{z}) = \frac{2}{\pi} \int_0^{\infty} dx \frac{I_0(x\hat{r})}{I_0(x)} \sin x \hat{z} \int_0^{\infty} dz' \phi(1, z') \sin x z' \quad (6)$$

where Eq.(6) is a surface integral, $\phi(1, z')$ is the value of the potential on the wall, and pipe radius normalized variables are used, $x = ak$, $\hat{r} = r/a$, $\hat{z} = z/a$, and the normalized gap width is $\hat{w} = w/(2a)$. Along the wall beyond the gap $\hat{z} > \hat{w}$ the potential is constant with a boundary condition of $\phi(1, \hat{z}) = (\phi_2 - \phi_1)/2$. For complete generality the boundary condition in the gap where $\hat{z} < \hat{w}$ is written as a Fourier expansion,

$$\phi(1, \hat{z}) = (\phi_2 - \phi_1) \sum_{n=1}^{\infty} A_n \sin(C_n \hat{z}) \quad (7)$$

where $C_n = n\pi/(2\hat{w})$. Using Eq.(7) in Eq.(6) it is found that

$$\phi(\hat{r}, \hat{z}) = (\phi_2 - \phi_1) (\phi_0 + \sum \phi_n) / \pi \quad \text{where,}$$

$$\phi_0 = \int_0^{\infty} dx \frac{I_0(x\hat{r})}{I_0(x)} \cos x \hat{w} \left(\frac{\sin x \hat{z}}{x} \right) \quad (8)$$

is derived from the part of Eq.(6) having $\hat{z} > \hat{w}$ and ϕ_n is

* Work performed for the US Department of Energy by Lawrence Livermore National Laboratory under contract W-7405-ENG-48.

from the gap where $\hat{z} < \hat{w}$,

$$\phi_n = A_n \int_0^{\infty} dx \frac{I_0(x\hat{r})}{I_0(x)} \sin x\hat{z} \left[\frac{\sin[(C_n - x)\hat{w}]}{C_n - x} - \frac{\sin[(C_n + x)\hat{w}]}{C_n + x} \right] \quad (9)$$

From the definition $\tilde{E} = -\nabla\phi$ the field solution requires derivatives of ϕ_0 and ϕ_n .

$$\frac{d\phi_0}{d\hat{r}} = \int_0^{\infty} dx \frac{I_1(x\hat{r})}{I_0(x)} \cos x\hat{w} \sin x\hat{z} \quad (10)$$

$$\frac{d\phi_0}{d\hat{z}} = \int_0^{\infty} dx \frac{I_0(x\hat{r})}{I_0(x)} \cos x\hat{w} \cos x\hat{z} \quad (11)$$

$$\frac{d\phi_n}{d\hat{r}} = A_n \int_0^{\infty} dx \frac{I_1(x\hat{r})}{I_0(x)} x \sin x\hat{z} \left[\frac{\sin[(C_n - x)\hat{w}]}{C_n - x} - \frac{\sin[(C_n + x)\hat{w}]}{C_n + x} \right] \quad (12)$$

$$\frac{d\phi_n}{d\hat{z}} = A_n \int_0^{\infty} dx \frac{I_0(x\hat{r})}{I_0(x)} x \cos x\hat{z} \left[\frac{\sin[(C_n - x)\hat{w}]}{C_n - x} - \frac{\sin[(C_n + x)\hat{w}]}{C_n + x} \right] \quad (13)$$

The complete gap solution can now be written in terms of ϕ_0 , ϕ_n and their derivatives.

$$\phi_{\text{total}} = \frac{(\phi_1 + \phi_2)}{2} + \frac{\phi_2 - \phi_1}{\pi} \left[\phi_0 + \sum_{n=1}^{\infty} \phi_n \right]$$

$$E_r = -\frac{\phi_2 - \phi_1}{\pi a} \left[\frac{d\phi_0}{d\hat{r}} + \sum_{n=1}^{\infty} \frac{d\phi_n}{d\hat{r}} \right]$$

$$E_z = -\frac{\phi_2 - \phi_1}{\pi a} \left[\frac{d\phi_0}{d\hat{z}} + \sum_{n=1}^{\infty} \frac{d\phi_n}{d\hat{z}} \right] \quad (14)$$

Integral Approximation Technique

The integrals needed to specify the solution in Eq.(14) are given in Eq.(8)-(13). All the required integrals in Eq.(8)-(13), have integrands consisting of a ratio of Bessel functions multiplying trigonometric functions. The method of obtaining the integrals in this work is to first approximate the ratio of Bessel functions and then integrate the resulting expressions. The form of the ratio which is useful for ϕ_0 , ϕ_n , $d\phi_0/d\hat{z}$ and $d\phi_n/d\hat{z}$ comes from the following expression,

$$\frac{I_0(x\hat{r})}{I_0(x)} = e^{-sx} \left[1 + \left(e^{sx} \frac{I_0(x\hat{r})}{I_0(x)} - 1 \right) \right] \quad (15)$$

where $s = 1 - \hat{r}$. The right side of Eq.(15) is an equivalent but more advantageous way of representing the ratio of Bessel functions, since the expression in parenthesis is a function that begins at zero and rises to an asymptotic value. Consequently, the approximation is to express the Bessel function ratio in terms of a finite sum of exponentials raised to a negative power.

$$\frac{I_0(x\hat{r})}{I_0(x)} = e^{-sx} \left[1 + A_{\text{sym}}^{(1)} \left(1 + \sum_{l=1} \gamma_l^{(1)} e^{-\delta_l^{(1)} x} \right) \right] \quad (16)$$

In like manner the form of the Bessel function ratio for $d\phi_0/d\hat{r}$ and $d\phi_n/d\hat{r}$ comes from the following expression.

$$\frac{I_1(x\hat{r})}{I_0(x)} = e^{-sx} \left[e^{sx} \frac{I_1(x\hat{r})}{I_0(x)} \right] \quad (17)$$

Again the approximation is to express the Bessel function ratio in terms of a finite sum of exponentials.

$$\frac{I_1(x\hat{r})}{I_0(x)} = e^{-sx} \left[A_{\text{sym}}^{(2)} \left(1 + \sum_{l=1} \gamma_l^{(2)} e^{-\delta_l^{(2)} x} \right) \right] \quad (18)$$

To illustrate what has been gained by the approximation, the new form of ϕ_0 is examined in detail. Substituting Eq.(16) into Eq.(8) yields,

$$\phi_0 = \int_0^{\infty} dx e^{-sx} \left[1 + A_{\text{sym}}^{(1)} \left(1 + \sum_{l=1} \gamma_l^{(1)} e^{-\delta_l^{(1)} x} \right) \right] \cos x\hat{w} \frac{\sin x\hat{z}}{x}$$

where now ϕ_0 is expressed in terms of a sum of integrals. The

fundamental integral is,

$$I^{(1+)}(s, \hat{w}, \hat{z}) = \int_0^{\infty} dx e^{-sx} \cos x \hat{w} \left(\frac{\sin x \hat{z}}{x} \right) \quad (19)$$

which depends on the normalized gap width, radial and axial position. The important observation to make is that Eq.(22) is the Laplace transform of $\cos x \hat{w} (\sin x \hat{z}/x)$. If an auxiliary integral having a well known Laplace transform is defined,

$$I^{(1)}(s, \hat{z}) = \int_0^{\infty} dx e^{-sx} \left(\frac{\sin x \hat{z}}{x} \right) = \text{atan} \left(\frac{\hat{z}}{s} \right) \quad (20)$$

it can be seen the parameter shifting property of the Laplace transform gives,

$$\begin{aligned} I^{(1+)}(s, \hat{w}, \hat{z}) &= \frac{(I^{(1)}(s - i\hat{w}, \hat{z}) + I^{(1)}(s + i\hat{w}, \hat{z}))}{2} \\ &= \frac{1}{2} \left[\text{atan} \frac{\hat{z} + \hat{w}}{s} + \text{atan} \frac{\hat{z} - \hat{w}}{s} \right] \end{aligned} \quad (21)$$

Consequently ϕ_0 can be written entirely in terms of $I^{(1+)}(s, \hat{w}, \hat{z})$.

$$\begin{aligned} \phi_0 &= \left(1 + A_{sym}^{(1)} \right) I^{(1+)}(s, \hat{w}, \hat{z}) \\ &+ A_{sym}^{(1)} \sum_{l=1} \gamma_l^{(1)} I^{(1+)} \left(s + \delta_l^{(1)}, \hat{w}, \hat{z} \right) \end{aligned} \quad (22)$$

In an identical manner to the treatment of ϕ_0 , the Eq.(16) and (18) approximations are inserted into Eq.(9) to Eq.(13) to give approximations to those functions. In order to obtain these functions it is necessary to compute integrals similar to Eq.(19). As before these integrals can be derived from an auxiliary integral. In general there is a similar relation for the plus and minus superscript integrals.

$$I^{(n+)} = \frac{[I^{(n)}(s - i\hat{z}, \hat{w}) + I^{(n)}(s + i\hat{z}, \hat{w})]}{2} \quad (23)$$

$$I^{(n-)} = \frac{[I^{(n)}(s - i\hat{z}, \hat{w}) - I^{(n)}(s + i\hat{z}, \hat{w})]}{2i} \quad (24)$$

Determination of constants for series expressions

Having specified the integrals needed to calculate the functions in Eq.(9) to Eq.(13), the gap solution in Eq.(14) is known when the A_{sym} , γ_l , and δ_l constants required by the fit functions in Eq.(16) and Eq.(18) are determined. There are actually two sets of constants that need to be determined, however each set is obtained in the same manner, so the solution procedure will only be discussed for the $A_{sym}^{(1)}$, $\gamma_l^{(1)}$, and $\delta_l^{(1)}$ constants. By solving a non-linear set of equations, both the $\gamma_l^{(1)}$,

and $\delta_l^{(1)}$ constants can in principle be determined. The difficulty with obtaining this solution is that the $\delta_l^{(1)}$ constants can be imaginary rather than strictly real. As a consequence, the fit function then becomes exponentials multiplied by sine and cosine functions, and this causes the fit function to be rippled. To avoid this problem the $\delta_l^{(1)}$ constants are specified to be known positive real numbers. Heuristically the large values of $\delta_l^{(1)}$ determine the fit near zero and smaller values tend to have an effect over an extended range. The set of equations that then has to be solved for a particular radius is,

$$\sum_{l=1}^N \gamma_l^{(1)} e^{-\delta_l^{(1)} x_i} = \left(\frac{f(x_i, \hat{r})}{f(100, \hat{r})} \right) - 1 \quad (25)$$

which is just N equations in N unknowns. In Eq.(25) the asymptotic value is defined to be at $x = 100$, and,

$$f(x, \hat{r}) = e^{sx} \frac{I_0(x\hat{r})}{I_0(x)} - 1$$

The solution procedure for Eq.(25) is to first solve for a standard lower, upper matrix decomposition. This result only depends on already specified $\delta_l^{(1)}$ constants and is only done once. It is then multiplied times the right hand side of Eq.(25) for particular \hat{r} values that can vary. In principle Eq.(25) can be symbolically solved to obtain $\gamma_l^{(1)}(\hat{r})$, however the expressions rapidly get unwieldy for $N > 4$.

Conclusions

The solution of Laplace's equation has been formulated in an integral form using a cylindrical coordinate Green's function. The integral form of the solution has been converted into a finite sum of readily calculable functions. This derived solution avoids the difficulties of the original, weakly convergent infinite integral with an oscillatory integrand. The main approximation that has been used in the derived solution is to write the finite sum in terms of Laplace integrals. In this framework the solution is formulated for an arbitrary variation of the electric field in the gap.

References

- [1] P. Grivet, Electron Optics, (Pergamon Press, Oxford, 1972) p.164
- [2] C.L. Chang et. al., Proc. Conf. Computer Codes and Linear Accelerators, (LANL, LA-11857-C, January, 1990) p.27
- [3] C.K.Allen, S.K. Guhary, and M.Reiser, Proc. Computational Accelerator Physics, (AIP Proc 297, Los Alamos, NM, 1993) p. 568
- [4] A.B. El-Kareh, J.C. El-Kareh, Electron Beams, Lenses and Optics, Vol I, (Academic Press, New York, 1970) p. 28
- [5] J.K.Boyd, et. al., Nuc. Instr. Meth. Phys. A272(1988)p.590
- [6] J.D. Jackson, Classical Electrodynamics, (John Wiley, New York, 1975) p.118

3D-FINITE DIFFERENCE ANALYSIS OF PLANAR LOOP COUPLERS AS BEAM ELECTRODES IN STOCHASTIC COOLING SYSTEMS

R. Schultheis, H.L. Hartnagel and B.Franzke*,

Institut fuer Hochfrequenztechnik, Technical University Darmstadt,
64283 Darmstadt, Merckstr.23, Germany, E-mail: dg05@hrz.th-darmstadt.de

*GSI, Darmstadt

Abstract

Loop couplers are used for the interaction with the beam as pickups and kickers in stochastic cooling systems. This paper presents a new planar loop coupler based on Al_2O_3 as dielectric substrate and discusses both the signal-beam interaction and the scattering behaviour of the coupler working as a kicker. The planar concept is analyzed by means of a 3-d full-wave finite-difference method in the frequency domain and the results are compared to the image current approach, which is commonly used for coupler design.¹

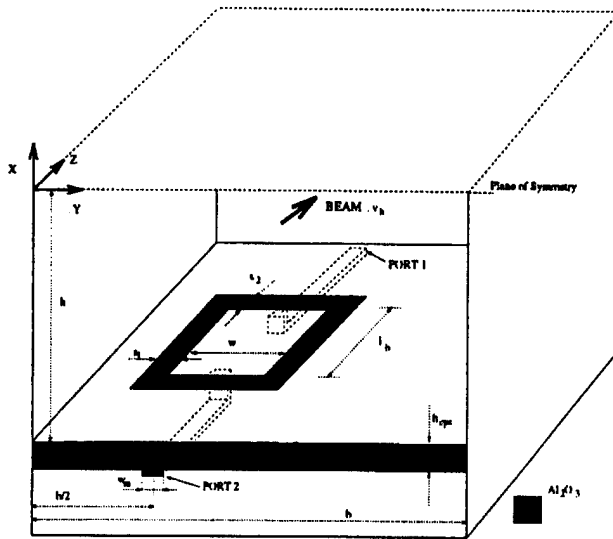


Figure. 1. Lower Half of a Planar Loop Coupler Doublet with $b = 70\text{mm}$, $h = 15\text{mm}$

I. INTRODUCTION

In the stochastic cooling system of GSI, Darmstadt both for detection and deflection of the beam conventional loop couplers [1] will be used as pickup and kicker device, respectively. In order to ensure sufficient efficiency an array of 16 coupler quadrupoles has to be incorporated into the storage ring. Their main drawback is the rather complicated mechanical fabrication.

First experiments already were performed on so-called planar loop couplers [2] for a system frequency range of 4-8GHz and on teflon as dielectric material. Their main advantage is the ease

of fabrication, since standard techniques of planar transmission lines for high-frequency circuit applications can be used.

This paper presents results on a planar loop coupler, which is designed particularly for the environment of the stochastic cooling system in the particle storage ring of GSI (frequency range: 0.9-1.6GHz, $f_{\text{mid}}=1.25\text{GHz}$). Thus, in order to satisfy the UHV requirements Al_2O_3 is used instead of teflon [2].

II. METHOD OF ANALYSIS

For analysis on one hand the 'doublet configuration' as shown in fig. 1 is considered, which consists of two planar couplers placed above and below the beam. Connecting two doublets with the distance l_d (coupler to coupler) of a microstrip on the back-side of the substrate in series leads to the 'super-doublet configuration', which is also under investigation.

The simulation itself is restricted to kicker operation for longitudinal beam cooling (even mode operation), when the coupler is fed at the upstream microstrip port 1 since, based on this analysis, both to the signal-beam interaction for vertical cooling and for pick-up operation can be derived [3].

The interaction of the deflecting electromagnetic field and the particle beam is described by means of a so-called kicker constant $\vec{K}(\omega, x_b, y_b)$, which assumes the beam to be a single charge travelling in position (x_b, y_b) along the z -axis and takes into account different beam and signal velocities (v_b and v_s , respectively).

$$\vec{K}(x_b, y_b, \omega) = \int_{-\infty}^{+\infty} (\vec{E}(x_b, y_b, z, \omega) + \vec{v}_b \times \vec{B}(x_b, y_b, z, \omega)) e^{j \frac{\omega z}{v_b}} dz \quad (1)$$

The electromagnetic field is calculated by means of a full-wave analysis applying the 3-d finite-difference method in the frequency domain. Thus, in contrast to the common image current approach effects such as field fringing at the end and beginning of the coupler, are taken into account. Furthermore, the same fieldtheoretical approach leads to the reflection and transmission coefficients of the complete 3-d configuration (S_{11} and S_{21} , respectively).

III. IMAGE CURRENT APPROACH

For the design of conventional loop couplers the image current approach is often applied, which analyzes the pick-up instead of the kicker. This approach can also be used for planar couplers, if one takes into account different beam and signal paths along the coupler:

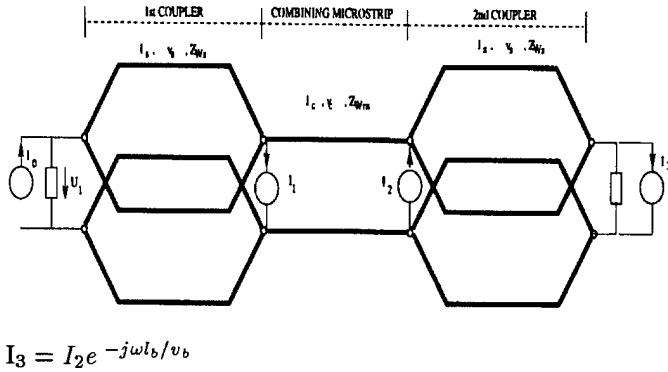
¹This work is supported by GSI

- while the beam is travelling parallel to the z-axis along the coupler (length l_b) the signal is running along two bent parallel slot lines each of length $l_s = l_b + w$ (see fig. 1).

Thus, to determine the frequency dependent coupling between the beam and the microstrip ports the single coupler can be replaced by two slot lines in parallel. Since the beam exits an image current on the surface of the coupler, the slot lines are driven by current sources, which differ only by a factor $e^{-j\omega l_s/v_b}$.

Following this principle the equivalent circuit of a super-doublet configuration can be derived (see fig. III) and the respective output voltage on the downstream port 2 can be determined (Eqn. 2).

Figure. 2. Equivalent Circuit of two planar couplers in series with distance l_d combined by a microstrip line of length l_c (Super-Doublet); with $I_1 = I_0 e^{-j\omega l_b/v_b}$, $I_2 = I_1 e^{-j\omega l_d/v_b}$, $I_3 = I_2 e^{-j\omega l_b/v_b}$



$$U_1 \sim \sin\left(\frac{\omega l_s}{2v_s} + \frac{\omega l_b}{2v_b}\right) \cos\left(\frac{\omega l_c}{2v_c} + \frac{\omega l_d}{2v_b} + \frac{\omega l_s}{2v_s} + \frac{\omega l_b}{2v_b}\right) \quad (2)$$

In Eqn. 2 the first factor represents the frequency dependent coupling of a single electrode, while the second one includes the typical characteristic due to the combination of two couplers in series.

The design of a super-doublet configuration is generally governed by the objective to ensure maximum interaction at mid-band frequency f_{mid} . As can be seen from Eqn. 2, this will be reached if the length l_b of the single coupler is given by:

$$l_b = \left(\frac{v_s}{2f_{mid}} - w\right) / \left(1 + \frac{v_s}{v_b}\right) \quad (3)$$

ensuring optimum coupling of the single coupler at f_{mid} and, furthermore, if the length l_c of the combining microstrip is given by:

$$l_c = \frac{v_c}{f_{mid}} - \left(\frac{v_c l_g}{v_b} + \frac{v_c l_s}{v_s} + \frac{v_c l_b}{v_b}\right) \quad (4)$$

which doubles coupling efficiency at f_{mid} .

The trick of this approach is the possibility to derive the coupling behaviour without any fieldtheoretical simulations and only by means of the transmission line characteristic, which can be taken from standard books dealing with analysis of transmission lines (e.g.: [4]). However, it should be pointed out, that this approach generally neglects both fringing fields due to the 3-d structure of the coupler and displacement currents.

IV. FIRST DESIGN

Considering the single coupler as succeeding junctions from microstrip- to slot- to microstrip-line minimum reflection requires matching of the respective characteristic impedances:

$$Z_{W_m} = \frac{1}{2} Z_{W_s}$$

wherein Z_{W_s} refers to the characteristic impedance of this slotline part which runs parallel to the z-axis.

Therefore, assuming a particular substrate height h_e and the restriction of Z_{W_m} to 50Ω both the microstrip width and slotwidth were determined by means of a 2-d finite difference analysis. On the other hand several 3-d simulations were necessary to optimize first the length l_b of a doublet and then the length l_c of the combining microstrip line of the super doublet configuration in order to ensure maximum coupling at f_{mid} .

For this first design uniform slotwidths were assumed, i.e.: $s_{s1} = s_{s2}$ (see fig. 1).

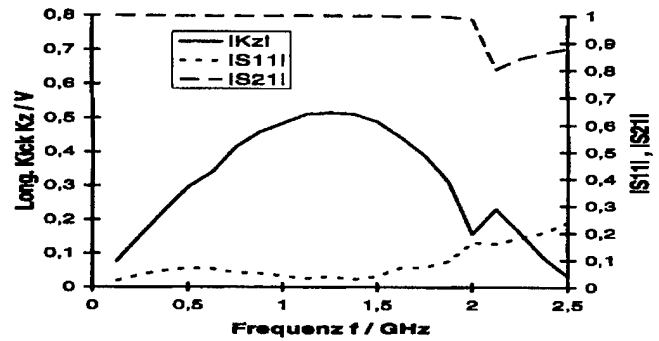


Figure. 3. Doublet in even mode operation with $(x_b, y_b) = (0, (b/2))$, $s_1 = s_2 = 3.0\text{mm}$, $w_m = 2.0\text{mm}$, $h_e = 2.5\text{mm}$, $l_b = 26\text{mm}$

Fig. 3 and Fig. 4 present the results of the 3-d fullwave simulations.

They demonstrate that an electrode length of $l_b = 26\text{mm}$ and a length of the combining microstrip $l_c = 38\text{mm}$ lead to a very good optimization of the maximum coupling at midband frequency f_{mid} for the doublet and super-doublet configuration, respectively. In comparison, applying the image current approach (Eqn. 3, Eqn. 4) gives the respective length dimensions as:

$$l_b = 23.6\text{mm}, l_c = 32.6\text{mm}$$

and leads to a deviation from the 3-d simulation of less than 15%.

On the other hand figs. 3 and 4 also demonstrate the weak scattering behaviour, particularly of the super doublet:

- at the upper frequency limit of the system frequency band $f_{up} = 1.6\text{GHz}$ 33% of the power fed into the upstream microstrip port of the super-doublet is reflected.

V. REDESIGN

In order to reduce the reflection coefficient S_{11} a redesign had to be performed. In the first design the characteristic impedance of the microstrip line was matched to the characteristic impedance of the part of the slotline which runs in parallel

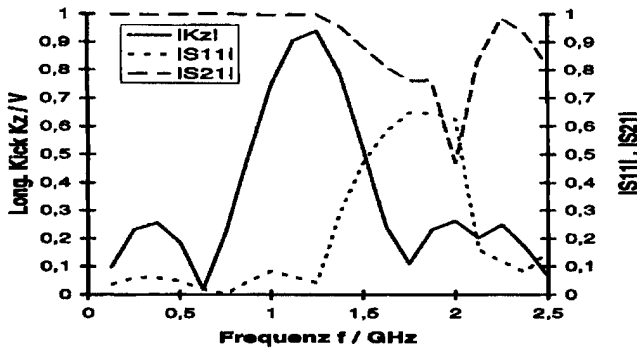


Figure 4. Super-Doublet in even mode operation with $(x_b, y_b) = (0, b/2)$, $s_1 = s_2 = 3.0\text{mm}$, $w_m = 2.0\text{mm}$, $h_e = 2.5\text{mm}$, $l_d = 28\text{mm}$, $l_c = 38\text{mm}$, $l_b = 26\text{mm}$

to the z-axis. From this point of view the part of the slot line, which is in parallel to the y-axis can be considered - in combination with the via hole - as a discontinuity which might cause additional reflections.

Therefore, in the redesign the constraint of equal slot dimensions was dropped and the optimum width of the horizontal slot s_2 for minimum reflection was investigated.

Furthermore in the first design the length of the combining microstrip l_c between the couplers in series was chosen to be larger than the coupler-coupler distance including substrate height ($l_c > l_d + 2h_e$). This causes further reflections, since the combining microstrip has to be bent. Thus, to minimize the number of bends in the redesign the combining microstrip was chosen to

$$l_c = l_d + 2h_e. \quad (5)$$

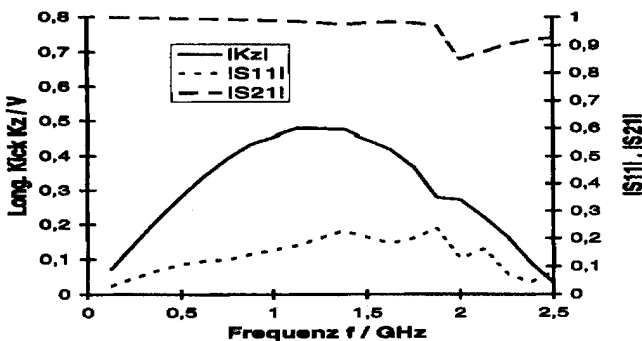


Figure 5. Doublet in even mode operation, with $(x_b, y_b) = (0, b/2)$, $s_1 = 3.0\text{mm}$, $s_2 = 1.75\text{mm}$, $w_m = 1.6\text{mm}$, $h_e = 2.0\text{mm}$, $l_b = 28\text{mm}$

As can be seen from fig. 5, the maximum coupling of the single coupler is exactly adjusted to midband frequency if the electrode length l_b is equal to 28mm. In comparison the image current approach Eqn.3 deviates less than 15% ($l_b = 24.9\text{mm}$) from the fullwave analysis.

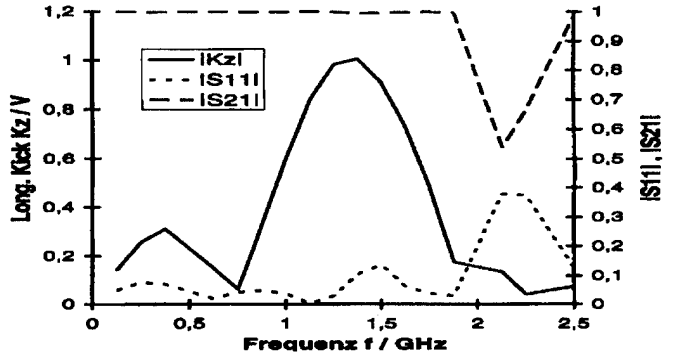


Figure 6. Super-Doublet in even mode operation; with $(x_b, y_b) = (0, b/2)$, $s_1 = 3.0\text{mm}$, $s_2 = 1.75\text{mm}$, $w_m = 1.6\text{mm}$, $h_e = 2.0\text{mm}$, $l_d = 20\text{mm}$, $l_c = 24\text{mm}$, $l_b = 28\text{mm}$

On the other hand the maximum coupling of the super doublet is reached at a higher frequency than f_{mid} . This deviation is due to a slight mismatch of the length of the combining microstrip l_c and the distance between the two couplers l_d , but seems to be still acceptable.

However, both fig. 5 and fig. 6 show a strongly reduced reflection of the power fed into the upstream port, i.e.: at the maximum, 2% of the power is reflected in the redesigned coupler within the system frequency band.

VI. CONCLUSION

The fullwave analysis of planar loop couplers using Al_2O_3 as substrates show that the following design aspects are to be taken into account to avoid reflections:

1. Different slot dimensions have to be used ($s_1 \neq s_2$)
2. Bends of the combining microstrip of super-doublets are to be avoided leading to Eqn.(5)

Furthermore, it was shown that the design of the planar coupler applying a modified image current approach is to be considered as a useful first approach. The error due to neglected fringing fields was found to be less than 15%.

References

- [1] Raabe P., Heinrich W., Hartnagel H.: Rigorous Computer Analysis of High Frequency Pickup and Kicker Devices for ESR Stochastic Cooling. Conf. Proc. EPAC 1992 (Berlin); pp919-921.
- [2] McGinnis D.; et.al.: Design of 4-8GHz Bunched Beam Stochastic Cooling Arrays for the Fermilab Tevatron. Conf.Proc. IEEE PAC 1991, pp.1389-1391
- [3] Lambertson G.: Dynamic Devices - Pickups and Kickers. AIP Conf.Proc. 153, New York (1987), pp.1414-1427.
- [4] Hoffmann R.K.: Integrated Microwave Circuits. Springer Verlag 1983.

Some Remarks on the Location of Higher Order Modes in Tapered Accelerating Structures with the use of a Coupled Oscillator Model

G.Romanov, INR, Moscow, Russia

S.Ivanov, MPEI, Moscow, Russia

M.Dohlus and N.Noltkamp, DESY, Hamburg, Germany .

ABSTRACT

This work is an attempt to overcome the difficulties which electrodynamic codes meet when calculating of RF characteristics of long accelerating structures consisting of cells of different geometry. The model of coupled oscillators (a kind of network model) seems to be an useful instrument in this case and may at least improve our understanding of higher order mode behavior in long tapered structures. The parameters of the model of multiple coupled oscillators (MCO) were determined on the basis of MAFIA calculations of the high order mode characteristics.

The frequency spectra, field distribution along the structure and normalized loss factor for the first band of HOMs in S-band accelerating section have been calculated. A comparison of the results of MCO calculations with the experimental data and the results of certain MAFIA calculations are presented.

1. INTRODUCTION

One of the most powerful and most general methods for numerical investigations of accelerating structures is the methods of moments. For example the modal field matching technique (or orthogonal expansion) and the finite element method can be derived from it. Both methods have to solve large algebraic systems - even in a case of a single resonator. The problem gets much more difficult for the calculation of accelerating structures consisting of a large number of coupled cells with different geometry. For example the calculation of the S-band Linear Collider (SBLC) structure with 180 different cells is out of the range of volume discretizing methods like FD- and FE-methods and needs a high computational effort for the modal field matching technique. To overcome this, it is reasonable to use resonant field itself as a basis function so that the discretization is much more effective and only one or a few unknowns per cell have to be evaluated. This method expressed in the terms of a network model and based mostly on an analogy is well known and used successfully very often (see for example [1]). In this work we develop the approach in more general form to establish more clear relations between electrodynamic values and model parameters. A particular goal of the work was to use the method for investigation of HOM in a long tapered S-band accelerating section and to get an information about their location (resonant frequencies of HOM, which ones of them and where are trapped inside the section etc.).

2. THE IDEA OF THE MULTIPLE COUPLED OSCILLATOR (MCO) TECHNIQUE

The electrodynamic eigenvalue problem is given by Maxwell's equation:

$$\frac{1}{\epsilon} \nabla \times \frac{1}{\mu} \nabla \times \mathbf{E} = \omega^2 \mathbf{E} . \quad (1)$$

Let us divide the resonator into some subvolumes and suppose that the fields may be expressed in each subvolume by some eigenfunctions \mathbf{E}_i . These eigenfunctions need not to fulfill the same boundary conditions (on the surfaces of the subvolumes) and we can use eigenfunctions of different sets of subvolumes. The major purpose of these eigenfunctions is to serve as a basis functions so that the total field can be approximated by a linear combination

$$\mathbf{E} = \sum x_j \mathbf{E}_j . \quad (2)$$

By substituting this into the eigenvalue equation (1) we find the residuum function

$$\mathbf{r} = \sum x_j \left[\frac{1}{\epsilon} \nabla \times \frac{1}{\mu} \nabla \times \mathbf{E}_j - \sum x_j \mathbf{E}_j \right] \quad (3)$$

and can apply the Galerkin test method:

$$r_i = \int \mathbf{E}_i \mathbf{r} dV = \sum x_j \int \mathbf{E}_i \left[\frac{1}{\epsilon} \nabla \times \frac{1}{\mu} \nabla \times \mathbf{E}_j - \sum x_j \mathbf{E}_j \right] dV = \sum x_j \int \mathbf{E}_i \mathbf{E}_j dV \quad (4)$$

Finally we claim that the tested residuum functions vanish and get a matrix eigenvalue problem:

$$\mathbf{A} \mathbf{x} = \omega^2 \mathbf{B} \mathbf{x} \quad (5)$$

with

$$(\mathbf{A})_{ij} = \int \mathbf{E}_i \left[\frac{1}{\epsilon} \nabla \times \frac{1}{\mu} \nabla \times \mathbf{E}_j \right] dV \text{ and } (\mathbf{B})_{ij} = \int \mathbf{E}_i \mathbf{E}_j dV . \quad (6)$$

The equation (5) can be interpreted in the terms of a network model, a mechanical system of pendulums and springs and so on. But a nature of the model is not that important, so we may constraint themselves by a following physical meaning of matrix elements - the ratios $((\mathbf{A})_{ij}/(\mathbf{B})_{ij})^{1/2}$ are the eigenfrequencies of some oscillators associated with given eigenfunctions (or subvolumes) and $(\mathbf{A})_{ij}$ and $(\mathbf{B})_{ij}$ ($i \neq j$) are the couplings between them. Eigenvector \mathbf{x}_n describes a field distribution along an accelerating section at resonant frequency ω_n .

One of the fundamental problems with this method is, that the eigenfunctions \mathbf{E}_i have to be calculated numerically and there may occur some difficulties with singularities in the

coefficient integrals $(A)_{ij}$. Therefore the elements of matrices **A** and **B** are mostly calculated by indirect methods.

3. A CHAIN OF IDENTICAL CELLS.

To build a model for a tapered accelerating section we have at first to determine a structure of MCO matrixes and then to calculate MCO parameters for the cells of every geometry separately. A basis for the calculation is a frequency spectra (calculated or measured) of the modes under interest of a section consisting of the identical cells of given geometry. We are interested in the first dipole band (TM-like modes) which is considered to be the most dangerous for a beam stability. But the second dipole band (TE-like modes) is very close to the first one and they combine a common spectra, so we have to take into account both of them. The same problem arisen at the time of investigation of DAW structure and a biperiodical chain of oscillators described by 5-diagonal symmetrical matrixes suggested in that work has been chosen as a model [2].

Let's associate the odd oscillators with TE-like modes and the even oscillators with TM-like modes. Following [3,4] we can derive a 2×2 matrix dispersion equation. Using this equation, given frequency spectra and some relations originating from the properties of HOMs we can calculate all MCO parameters for a cell of given geometry. In principle we get two solutions (two sets of MCO parameters) because the chain is biperiodical, but a choice of a right set is obvious and can be included in the procedure beforehand. A set of MCO parameters can be checked with the use of analytical solution of the matrix dispersion equation.

In Fig.1 the dispersion curves calculated by MCO for the cells N1 and N10 of a test S-band section [5] are given as an example together with MAFIA calculations.

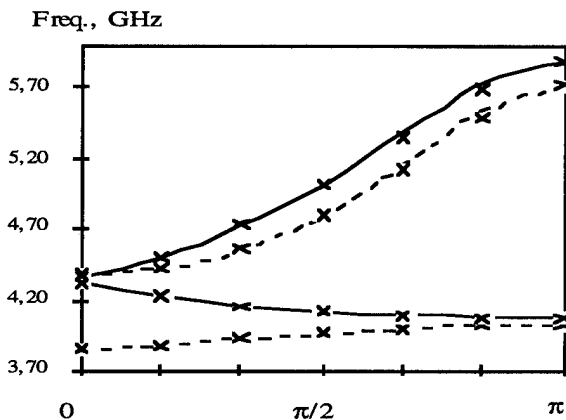


Fig.1. Dispersion curves for the cells N1 (dashed) and N10 (solid) of the test S-band structure calculated by MCO. Points - MAFIA calculations.

For magnetic walls inside end-irises E_z in centers of cells is described by $E_{0z}(\theta)\sin[(n-1/2)\theta]$. Even elements of vector x_0

are $a(\theta)\sin[(i-1)\theta/2]$. (Here θ - phase advance per cell, n - number of cell, i - even). Fig.2 demonstrates $E_{0z}(\theta)$ and $a(\theta)$ for lower branch of dispersion curve of cell N1 calculated by MAFIA (2 mm apart the structure axis) and MCO. Vectors are normalized as $xx = 1$, E_{0z} is normalized by stored energy, both amplitudes at $\theta = \pi$ are chosen equal to 1.

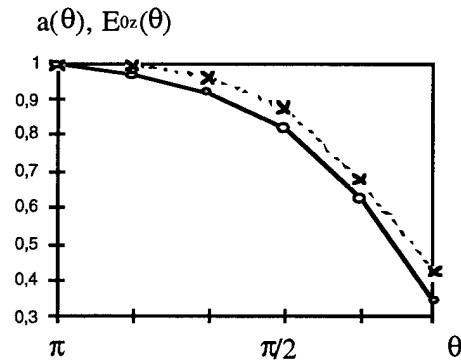


Fig.2. Amplitudes $a(\theta)$ and $E_{0z}(\theta)$ for lower branch of dispersion curve of cell N1. MAFIA - dashed, MCO - solid.

So, more or less accurate relation between absolute values of $E_{0z}(\theta)$ and $a(\theta)$ can be calculated.

4. A CHAIN OF TAPERED CELLS.

A real S-band section for Linac-II at DESY consisting of 148 cells has been chosen as an example of tapered accelerating section by two reasons: it is close to SBLC section by its parameters and the measurements of it were available.

To form the matrixes for a such long section a following procedure has been used: the MCO parameters for the separate cells (NN 1,26,50,76,100,126 and 148) have been calculated, the parameters of intermediate cells have been found by approximation and then all oscillators have been combined into full matrixes.

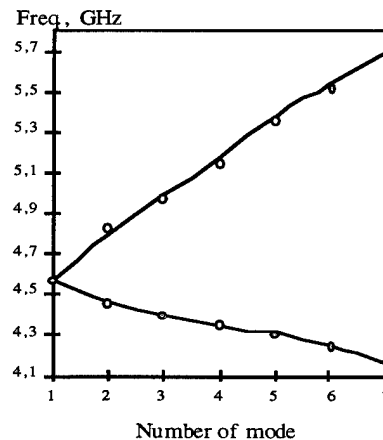


Fig.3. "Dispersion curve" of 6-cell strongly tapered section. Line - MCO, points - MAFIA.

To check the model a short strongly tapered section consisting of cups mentioned above was calculated by MAFIA and the results were compared to MCO calculations. Fig.3 shows a "dispersion curve" of the short strongly tapered structure.

5. RESULTS OF CALCULATIONS AND EXPERIMENTS

The MCO model of 148-cell Linac-II section was made and the resonant frequencies and field distributions for all modes were calculated. The results shown that the main part of modes, including dangerous ones with π -like distribution pieces, are not trapped inside section and can be excited through the first cell or even input coupler. This had been used when the spectra measurements and bead-pull field distribution measurements were performed in Linac-II section. Fig.4 shows calculated "dispersion curve" of the section and experimental resonant frequencies. Fig.5 shows a field distribution (calculated and measured) along structure of one of the modes.

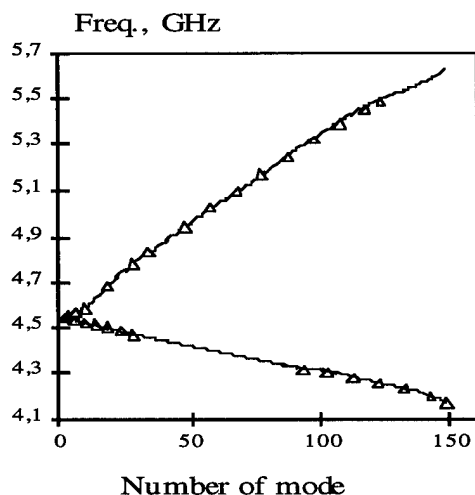


Fig.4. "Dispersion curve" of full 148-cell Linac-II S-band section. Lines - MCO calculations, points - measurements.

Calculations of loss factor parameter was done for the first band of Linac-II section on a basis of MCO data. Absolute values of E_z wasn't calculated, so a curve in Fig.6 should be considered just as normalized and qualitative.

6. CONCLUSION.

The comparison of the MCO calculation results to the experimental data and the test MAFIA calculations shows that this model can be useful and sufficiently accurate instrument for investigation of long tapered structures and in other cases, which require high computational efforts by other methods. Also it should be mentioned that MCO technique gives a possibility to investigate accelerating structure properties in analytical form.

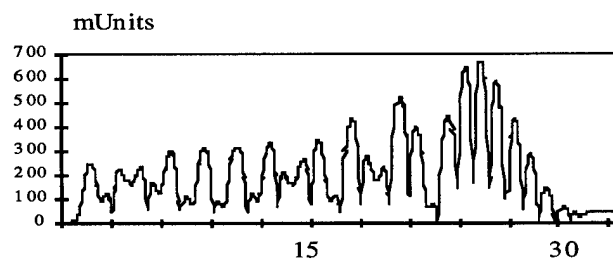
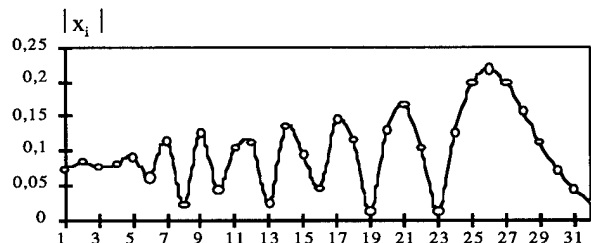


Fig.5. Distribution of E_z against number of cell of mode 138 of lower branch. Lower drawing - experimental data.

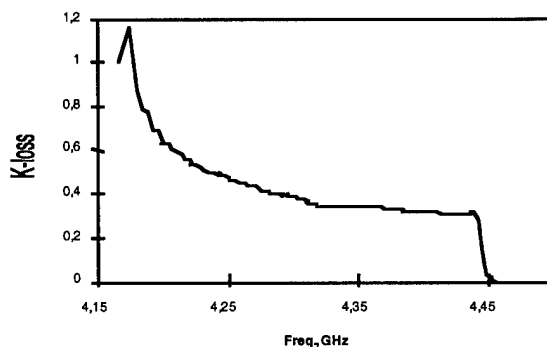


Fig.6. Normalized loss-factor for lower band of Linac-II S-band section.

REFERENCES

- [1] E.A.Knapp, B.C.Potter and J.M.Potter. "Standing Wave High Energy Linear Accelerator Structures". Rev. Sci. Instr., **39**, 1968.
- [2] L.V.Kravchuk, G.V.Romanov. "Stability of Field Distribution in Coupled Cavity Structures". Proc. of the 1990 Linear Accelerator Conference, Albuquerque, New Mexico, USA, 1990.
- [3] G.V.Romanov. Preprint INR R-0563, Moscow, 1987, (in Russian).
- [4] G.V.Romanov. Preprint INR R-0461, Moscow, 1986, (in Russian).
- [5] B. Krietenstein et al. "The S-band 36-cell Experiment". RPB16 this conference.

THE NEW POSSIBILITIES OF SUPERLANS CODE FOR EVALUATION OF AXISYMMETRIC CAVITIES

D.G.Myakishev, V.P.Yakovlev, Budker INP, 630090 Novosibirsk, Russia

The new versions of the SuperLANS code for evaluation of monopole modes in axisymmetric cavity with lossy filling and of multipole modes in axisymmetric cavity with inhomogeneous ferrite and dielectric filling are presented.

I. INTRODUCTION

The code SuperLANS [1] is developed in two directions:

- a code CLANS is made to calculate monopole modes in axisymmetric cavities with partial lossy dielectric and ferrite filling;
- a code SLANS2 is made to calculate multipole modes in axisymmetric cavities with partial dielectric and ferrite filling.

II. CLANS

Being the new version of SuperLANS, the code CLANS is developed to calculate monopole modes in axisymmetric cavities with lossy dielectric and ferrite filling, providing:

- evaluation of a cavity with dielectric and ferrite with loss tangent $\text{tg}\delta \leq 1$;
- solution of self-consistent problem for frequency dependent dielectric permittivity and magnetic permeability.

A. Mathematical formulation

To describe lossy filling with loss tangent $\text{tg}\delta \leq 1$, the complex permittivity and permeability are used. The electric and magnetic fields are also complex. The equation for the magnetic field, for example, for TM wave, is the same one as for SuperLANS [1]:

$$\frac{1}{\epsilon}(\Delta \vec{H})_{\varphi} + \omega^2 \epsilon_0 \mu_0 \mu \cdot \vec{H}_{\varphi} = 0 \quad (1)$$

The equation of such form provides the boundary condition on the dielectric and ferrite surfaces [2]. We use the coordinate system $(z, r^2/4)$ as in SuperLANS to improve solution near axis.

B. Solution method

The equation (1) is solved by the finite element method. We use four corner eight nodes isoparametric elements. Algebraic system of equations for node field values is produced by Galerkin method. To find several modes simultaneously in arbitrary spectrum domain, we use subspace iteration method with frequency shift.

If the permittivity and permeability of lossy filling depend on frequency, the self-consistent problem is solved. The iteration is produced in the next way. The solution for fixed permittivity and permeability is used as an initial approach. Then for this frequency the new values of

permeability and permittivity are chosen. Using this values of permittivity and permeability, we find the new frequency by the method of inverse iteration with frequency shift, which provides the effective separation of searched mode. We use the frequency of the previous iteration as a shift. As a rule, several iterations are enough to obtain the self-consistent solution. Iterations are produced automatically, if a file with permittivity and permeability frequency dependencies is prepared.

There are two versions of code for PC and VAX at present.

C. Results.

The code was tested on pillbox cavity with homogeneous losses filling. For cavity with sizes $r=1\text{cm}$ and $l=1\text{cm}$ with filling material permittivity and permeability $\epsilon=1, \mu=1$ and loss tangent $\text{tg}\delta=1$, with mesh 5×5 the fundamental mode frequency calculation accuracy is 0.01%.

The VAX version of the code is used for calculation of superconducting cavity with ferrite HOM damper in Cornell University [3]. The force lines of real and image parts of electric field for fundamental modes are shown on Fig. 1 and Fig.2. The force lines of real and image parts of electric field for "ghost" mode are shown on Fig.3 and Fig.4. This mode is obtained as a solution of self-consistent problem and connects to ferrite loading.

III. SLANS2

The code SLANS2 is developed to calculate the multipole modes in axisymmetric cavities with partial dielectric and ferrite filling.

A. Mathematical formulation

Unlike the scalar problem for monopole modes the problem of multipole mode calculation is a vector problem. In our case we can write usual wave equation, for example, for magnetic field:

$$\text{rot} \frac{1}{\epsilon} \text{rot} \vec{H} - \omega^2 \epsilon_0 \mu_0 \mu \cdot \vec{H} = 0 \quad (2)$$

To eliminate spurious modes we additionally use the equation:

$$\text{grad} \cdot \text{div}(\mu \vec{H}) = 0 \quad (3)$$

Combining (2) and (3), we obtain the following equation for partially homogeneous filling:

$$\frac{1}{\epsilon}(\text{rot} \cdot \text{rot} \vec{H} - \text{grad} \cdot \text{div} \vec{H}) - \omega^2 \epsilon_0 \mu_0 \mu \cdot \vec{H} = 0 \quad (4)$$

Rewriting this equation for field components and excluding ϕ -component using (3), we obtain two equations for H_z and H_r without the potential solutions [4], [5].

Boundary conditions for tangential and normal components of magnetic field on a metallic surface have the following form [6]:

$$\frac{\partial H_r}{\partial n} + K \cdot H_r = 0, \quad H_n = 0 \quad (5),$$

where K - is surface curvature in the axial cross section.

Solving eigen value problem for two transverse components of magnetic field we can reconstruct ϕ component of magnetic field and all components of electric field from Maxwell's equations.

SLANS2 also permits to solve eigen value problem for transverse components of electric field. In this case equations have the same form, except boundary conditions on a metallic surface, which have the following form [6]:

$$\frac{\partial E_n}{\partial n} + (K + \frac{n_r}{r})E_n = 0, \quad E_r = 0 \quad (5'),$$

where n_r is a radial component of the unit vector normal to the boundary.

Unlike SuperLANS and CLANS, we use the usual coordinate system (z, r) for SLANS2.

B. Solution method

To produce finite element mesh, we used the same mesh generator as for SuperLANS. Galerkin method is used to obtain the algebraic system. Unlike SuperLANS the matrix of system is not symmetric, so we must store the whole band of matrix.

To satisfy the boundary condition on a metallic surface (5) we use the method described in [6]. We rewrite discrete equations on metallic surfaces for normal and tangential field components: H_n , H_r or E_n , E_r . For this, we use a local matrix of rotation for the node field values on metal.

On ferrite or dielectric surfaces the problem of satisfying the boundary condition is more complicated. Only the tangent field components H_r and E_r are continuous and the normal components H_n and E_n have break. So we rewrite the discrete equations for B_n , H_r or D_n , E_r on ferrite or dielectric surfaces to satisfy the boundary conditions. This method permits to use a regular finite element mesh as in SuperLANS.

To calculate several modes simultaneously in arbitrary spectrum domain, we use the subspace iteration method.

C. Results

The spherical cavity with concentric spherical dielectric or ferrite insertion was used as a test. The convenience of this test is that it is possible to compare calculation results of SuperLANS and SLANS2, because monopole modes of SuperLANS are dipole modes of SLANS2 rotated by 90° . For the same meshes the differences between SuperLANS and SLANS2 results are less than 0.015%.

The code SLANS2 is used to calculate cavities for RF generator Magnicon [7]. The operating modes in this device are multipole. The field maps for two different modes for Magnicon penultimate cavity are shown on Fig.5 and Fig.6.

The code was also used to calculate a variant of the waveguide window for VLEPP klystron [8]. The window consist of a ceramic disk, which attached to a rectangular waveguide by the conical parts. The dipole modes are excited in such axisymmetric cavity. The field maps for two different modes are shown on Fig.7 and Fig.8: the first one is the "ghost" mode, which exist in the ceramic disk only, the second mode is one of the propagation modes.

IV. CONCLUSIONS

The codes CLANS and SLANS2, which are the advancement of the SuperLANS code for axisymmetric cavities, have proven to be very powerful tools for the analysis of many RF design problems.

Futher development will be creation of the code for calculation of multipole oscillation in cavities with lossy filling.

V. REFERENCES

- [1] D.G.Myakishev, V.P.Yakovlev, "An Interactive Code SuperLANS for Evaluation of RF-cavities and Acceleration Structures", in *IEEE Particle Accelerator Conf. Rec.*, 1991, vol.-5, pp.3002-3004.
- [2] M.M.Karliner, Yu.A.Sokulin, V.P.Yakovlev, "Calculation of azimuthal oscillation in axisymmetric cavities with nonhomogeneous ferrite and dielectric filling," preprint Budker INP 82-149 (in Russian).
- [3] S.Belomestnykh, W.Hartung, G.Flynn, H.Padamsee, M.Pisharody, "Wakefields and HOMs Studies of a Superconducting Cavity Module with the CESR Beams", report at present conference.
- [4] M.M.Karliner, B.M.Fomel, V.P.Yakovlev, "LANS2 - code for calculation of azimuthally nonhomogeneous oscillation in axisymmetric." preprint Budker INP 83-114 (in Russian).
- [5] M.S.Kaschiev, V.A.Kaschieva, I.V.Puzynin, V.V.Gusev, A.I.Fedoseev, I.V.Gonin, V.V.Paramonov, "Calculation of the total oscillation spectrum in axisymmetrical RF cavities and periodic structures", in *Proc.IX All-Union Conf. Particle Accelerators*, Dubna, USSR, 1984, vol. I, pp.137-141 (in Russian).
- [6] Yu.Portugalov, "Method of eigen electromagnetic field calculation in cavities of arbitrary shape", preprint IHEP 83-2, Serpukhov (in Russian).
- [7] O.A.Nezhevenko, "The magnicon: A new RF power source for accelerators" in *IEEE Particle Accelerator Conf. Rec.*, 1991, vol.-5, pp.2933-2942.
- [8] V.Shemelin, "A choice of high power RF window sizes", Int.Workshop on Pulsed RF Power Sources for Linear Colliders, Dubna-Protvino, 1993, BINP July 1993, pp. 369-372.

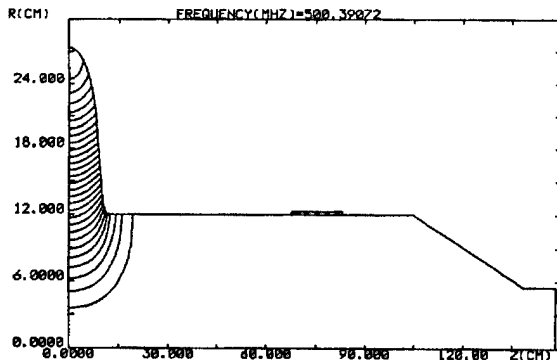


Figure 1: Real part of electric field of the operating mode of superconducting cavity.

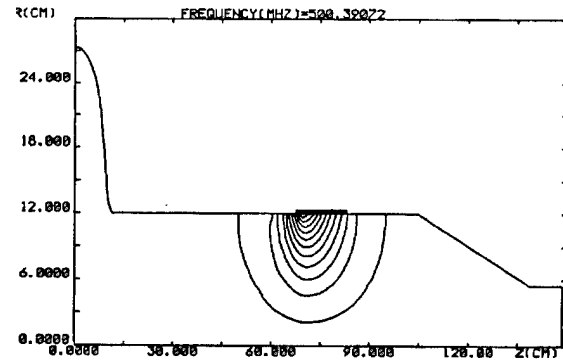


Figure 2: Imaginary part of electric field of the operating mode of superconducting cavity.

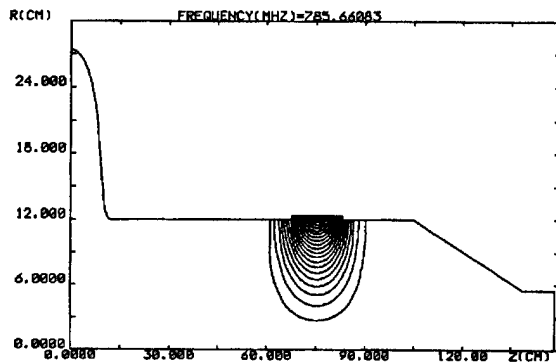


Figure 3: Real part of electric field of the "ghost" mode of superconducting cavity.

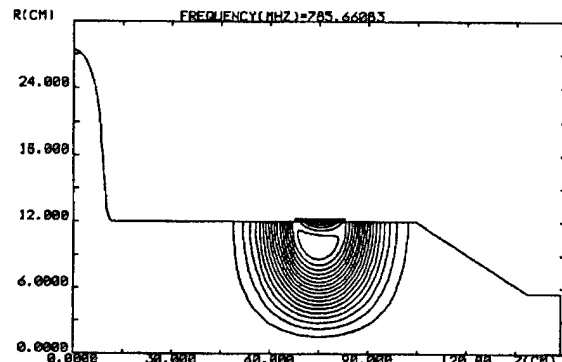


Figure 4: Imaginary part of electric field of the "ghost" mode of superconducting cavity.

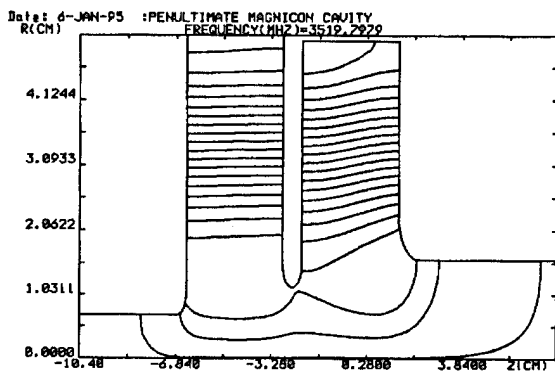


Figure 5: Field map of cophasal mode of the Magnicon penultimate cavity.

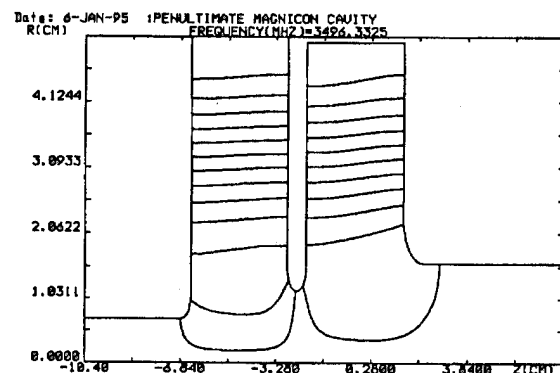


Figure 6: Field map of counterphasal mode of the Magnicon penultimate cavity.

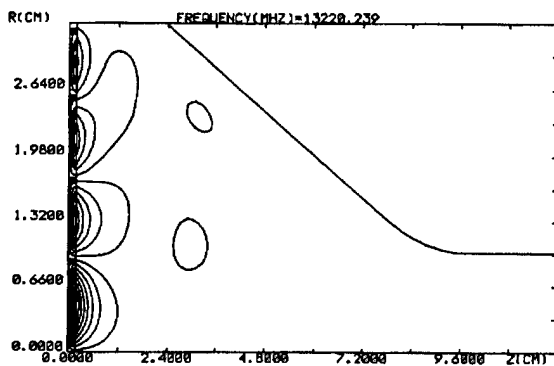


Figure 7: Field map of "ghost" mode in RF-window.

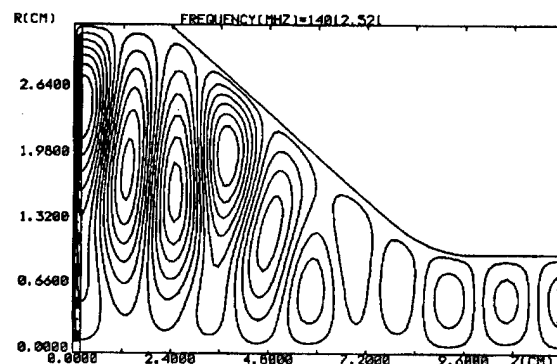


Figure 8: Field map of propagation mode in RF-window.

TRANSVERSE EM FIELDS IN A DETUNED X-BAND ACCELERATING STRUCTURE*

S. A. Heifets, S. A. Kheifets, and B. Woo

Stanford Linear Accelerator Center, Stanford University, Stanford, CA 94309 USA

Abstract

Results are presented of a study of the dipole EM fields in detuned accelerating sections excited by a point-like bunch. The transverse coupling impedance, the kick factors, and the wake functions are found.

The detuned accelerating structure^{[1][2]} has been designed to decrease the transverse wake field. Here we present the results of a study of the deflecting dipole fields for the structure excited by a pointlike charge using the computer code PROGON^[3]. The code is based on the field-matching technique for the frequency harmonics of the EM traveling waves. The geometry of the considered section—built out of 204 cells—can be found in Ref. 3. For each coupled-cell mode, including the trapped ones, the EM fields, the group velocity, and the stored energy are calculated. The computer time needed to calculate these quantities for the 204 cell structure (a cell is a cavity and an iris) is approximately 15 minutes on the IBM RISC 6000 workstation. The calculations take into account 16 space harmonics in the cavity region and 30 space harmonics in the iris region. Using the calculated EM fields of the structure, we calculate the transverse impedance, kick factors, and the transverse wake function. The results are matched quite well with the previous results^{[4][5][6]} based on the field-matching technique.

Figure 1 shows a comparison of the dispersion curves for the dipole passbands obtained in our calculations (symbols) with the program TRANSVRS (solid lines for the first and dashed lines for the second dipole passbands, respectively). The dispersion curves are calculated for a periodic structure corresponding to the parameters of the three cells taken at the beginning, in the center, and at the end of the structure. The three cases are labeled by the symbols C, D, and E, respectively. The radii of the iris and the cavity were measured in cm: C) 0.5250 and 1.112; D) 0.4625 and 1.083; and E) 0.4000 and 1.058. The results of our code are shown by full circles for the structure C, diamonds for the structure D, and squares for the cell-type E. Results of the code URMEL are shown with open circles.

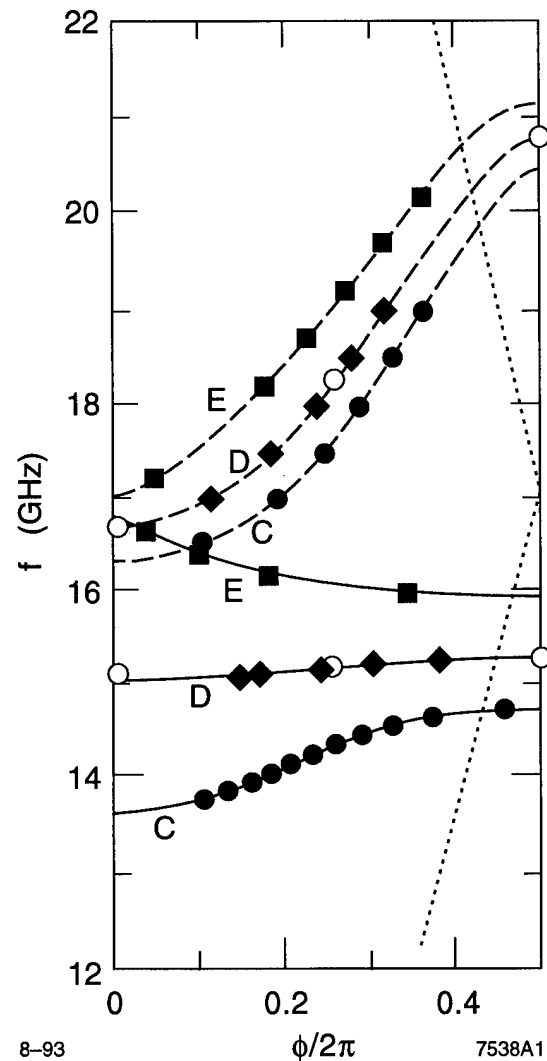


Figure 1. Comparison of dispersion curves for the dipole passbands.

Figure 2 depicts the real part of the impedance (in arbitrary units) calculated by integrating the field of each cell of the detuned structure at the frequencies shown at the top of the plot. The impedance is plotted versus the cell number. Results illustrate the mode trapping.

* Work supported by Department of Energy contract DE-AC03-76SF00515.

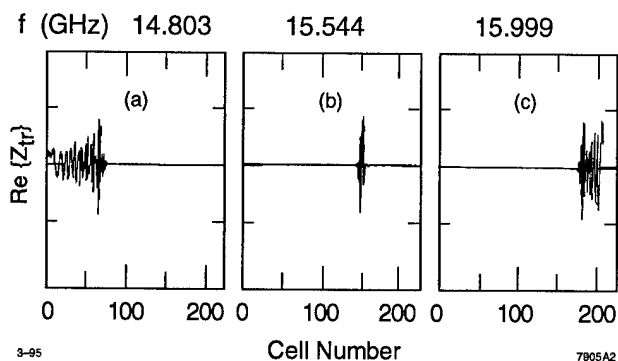


Figure 2. The real part of the impedance.

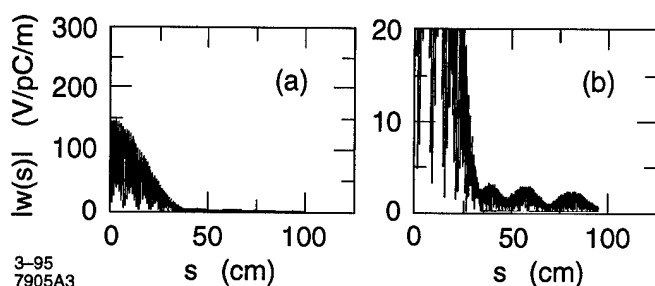


Figure 3. Absolute value of the short-range wake functions.

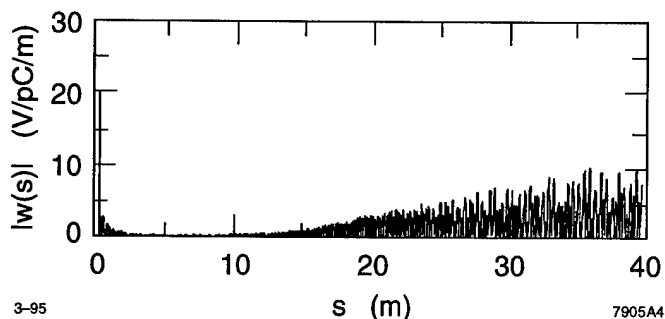


Figure 4. Absolute value of the long-range wake functions.

Figures 3 and 4 show the absolute value of the short-range and the long-range wake functions, respectively, calculated by direct integration of the EM field of the structure. The deflecting field, acting on a bunch travelling at the distance of about 40 cm behind the leading bunch, is reduced by a factor of 100, as has been found in Ref. 3.

Analysis of the different methods of calculation of the kick factors, propagation of the rf pulse in the detuned structure, and other results may be found in publications^{[7] [8]}.

REFERENCES

1. J.W. Wang, B.W. Littmann, Design Study on Qausi-Constant Gradient Accelerating Structure, SLAC Report AP-32, 1991.
2. K.L.F. Bane, R.L. Gluckstern, The Transverse Wakefield of a Detuned X-band Structure, SLAC-PUB-5783, 1992.
3. S.A. Heifets, S.A. Kheifets, Longitudinal EM fields in an Aperiodic Structures, SLAC-PUB-6124, 1992.
4. H.G. Beyer, et al., "Modal Field Matching in Tapered Multicell Structures," *Proc. XVth Intern. Conf. on High Energy Accel.*, Hamburg, Germany, July, 1992. *Int. J. Mod. Phys. A.* (World Scientific, Singapore) pp. 845-847.
5. U. van Rienen, "High Order Mode Analysis of Tapered Disc-Loaded Waveguides using the M-Mode Matching Technique," *Part. Accel.* 41, 1993, pp. 173-201.
6. W. Bruns, "Beam Coupling Impedance of Axial Symmetric Structures," Technische Universitaet Berlin, private communication, 1993.
7. S. A. Heifets, S. A. Kheifets, B. Woo, "Transverse Electromagnetic Fields in a Detuned X-band Accelerating Structure," SLAC-PUB-6336, 1993.
8. S. A. Heifets, S. A. Kheifets, "RF pulse Transmission through an Accelerating Section," SLAC Note AAS-74, 1992.

RF CAVITY COMPUTER DESIGN CODES.

P A McINTOSH, Daresbury Laboratory, Daresbury, Warrington WA4 4AD, UK.

Abstract

Computer simulation tools for RF cavity design have become a necessity in many laboratories around the world. There is a need for accurate predictions of fundamental frequency, Q factor, accelerating voltage requirements and longitudinal and transverse higher order mode impedances, all of which are of paramount importance when the price of manufacture of these cavities is so great but their influence on beam behavior is critical. There are numerous 2D and 3D simulation codes available at the moment which aid accurate modelling of accelerating structures but this paper focuses on three: MAFIA, URMEL-T and SuperLANS.

I. INTRODUCTION

The design of RF cavity geometry has become highly dependent on the use of computer design packages, whether it is 2D or 3D. There are many commercially available packages [1] on the market at the moment which give accurate geometry solutions to particular design criteria. The three packages which are the subject of this paper, are a small selection of those currently available and have been employed at Daresbury for several years. It is the intention of this paper to outline the internal functioning of these packages and to illustrate the computational resources required to operate them.

II. COMPUTER SIMULATION CODES

A. MAFIA v2.04, release 22/1/90. [2]

MAFIA is a 3D simulation code used for the design of RF cavities and other electromagnetic structures, including electrostatic and magnetostatic devices. It is an acronym for the solution of MAXwell's equations using the Finite Integration Algorithm. MAFIA comprises of a suite of programs which use the Finite Integration Technique to produce a set of finite-difference equations for the electric and magnetic field vectors for a particular geometry under investigation. The solutions to these equations provide time and frequency solutions to Maxwell's equations. The programs have dedicated functions which interact on the proceeding program (Table. 1) i.e. the output from a particular program is partly used as input to the following program.

Program	Description
M3	Mesh Generator
R3	Equation Generator
E31,E32	Eigenvalue Solvers
T3	Time Domain Solver
P3	Post Processor

Table 1. MAFIA subroutines and their function.

MAFIA uses a rectangular mesh generation routine which is flexible enough to model even the most complex geometries. The routine allows the user to specify the "coarseness" of the mesh in a particular area of interest.

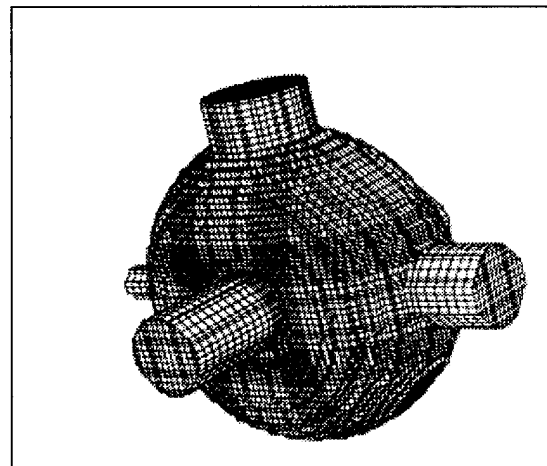


Figure 1. MAFIA 3D Mesh Generation.

MAFIA has been used quite extensively at Daresbury since its release under the auspices of the MAFIA collaboration, which comprised DESY,LANL and KFA in 1987. It is run on a Silicon Graphics Indigo² compute server, comprising: MIPS R4400 CPU at 140MHz, 128Mb RAM and is the only 3D simulation code presently available for RF cavity design at Daresbury.

Program	Real (secs)	User (secs)	Sys (secs)
M3b	82.52	71.77	0.51
R3	222.21	149.51	15.37
E31	3631.01	2906.27	33.64
P3b (list)	81.63	31.69	7.58

Table 2. Typical execution times for an optimised nose-coned cavity with 180,000 mesh points.

URMEL-T is a 2D simulation package which evaluates electromagnetic properties of cylindrical symmetric accelerating structures in the frequency and time domain. It uses a triangular mesh geometry (see Fig. 2) to give good approximation of the accelerating structures. By transforming Maxwell's equations into a linear algebraic eigenvalue problem, the frequency solutions are found in ascending order and "no modes are missed". URMEL-T not only allows for the solutions of longitudinal modes but it also has the ability to solve for Dipole (or transverse) modes.

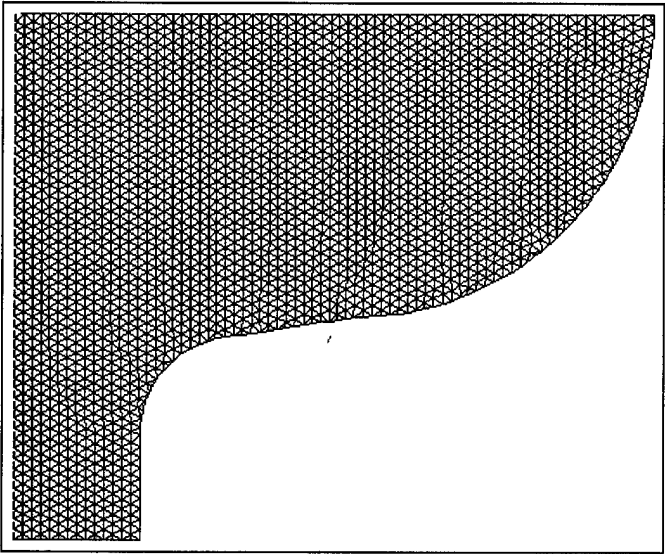


Figure 2. Finite Difference Mesh Generation in URMEL-T.

URMEL-T uses triangular mesh generation techniques, as opposed to its predecessor URMEL which used rectangular methods, which gives URMEL-T a greater flexibility at being able to closely map quite complex cavity geometries. Similarly, URMEL-T is run on a Silicon Graphics Indigo² workstation and typical execution times for an optimised spherical cavity with 3922 mesh points are:

Program	Real (secs)	User (secs)	Sys (secs)
URMEL-T	111.68	46.58	0.58

Table 3. Typical URMEL-T execution times.

C. SuperLANS. [4]

SuperLANS is a comparatively new finite element code which is used for the calculation of azimuthal homogeneous modes in axisymmetrical periodic structures and also for the calculation of critical frequencies in long homogenous waveguides. The code is used on an IBM compatible PC (with co-processor) and consists of a number of dedicated

sub-routines, rather like MAFIA, which interact on the proceeding routine. The code can either be run interactively or in batch mode, Fig 3. shows the sub-routine hierarchy.

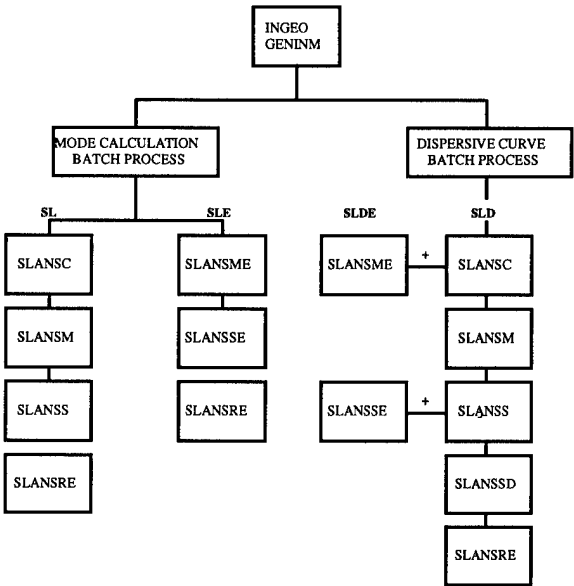


Figure 3. Sub-routine Hierarchy of SuperLANS Program

Whereby each routine performs the following function;

Routine	Description
INGEO	Input geometry
GENINM	Mesh generation
SLANSC	Definition of calculation parameters.
SLANSM	Matrix calculation
SLANSS	Definition of the cavity spectrum.
SLANSRE	Output of results.
SLANSD	Calculation of dispersive curves.
SLANSME	Matrix calculation for coordinated resultants.
SLANSSE	Calculation of coordinated resultants.

Table 4. SuperLANS Program list.

SuperLANS has the facility, whereby the geometry can be modified and interactively, the program will display the new resonant frequency (plus a specified number of HOM's), giving the user the ability to move the HOM spectrum away from potentially dangerous modes whilst maintaining the required resonant frequency.

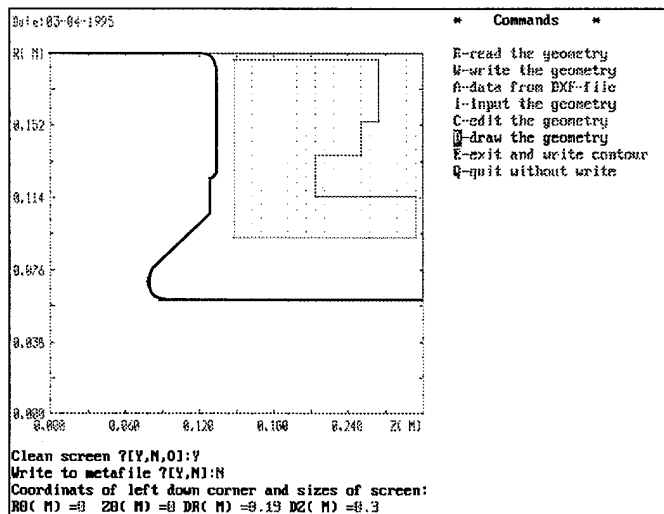


Figure 4. Geometry Manipulation Interface for SUPERLANS.

III. OTHER CODES

It is Daresbury's intention to broaden its use of RF cavity design codes and evaluation is planned for SuperFISH [5] which has been installed on an IBM compatible PC. A thorough evaluation of this code will be carried out by computing geometries already analysed by the aforementioned codes. It is also planned to evaluate the 3D version when it becomes available.

IV. CONCLUSIONS

For the accurate prediction of HOM frequencies of a real structure, a full 3D code is essential. Nevertheless a lot of useful work can be done with 2D codes, particularly in the early stages of the design of a structure. The increase in computational power of workstations and desktop PC's, means that it is no longer essential to have access to mainframe computers for this work.

V. ACKNOWLEDGMENTS

The author would like to thank B. Obradovic for his assistance in carrying out the SuperLANS computations.

VI. REFERENCES

- [1] Computer Codes for Particle Accelerator Design and Analysis: A Compendium, H.S. Deaven and K.C.D. Chan, LA-UR-90-1766 (1990).
- [2] MAFIA User Guide, The MAFIA Collaboration: DESY, LANL and KFA, May 1988.
- [3] URMEL and URMEL-T User Guide, U. Laustroer, U van Rienen and T. Weiland, DESY, Feb 1987.
- [4] The Code SUPERLANS, D.G. Myakishev, Novosibirsk-90, 630090, Russia, Jan 1993.

[5] PC Version of Poisson/SuperFISH Code Series, Version 4.12, Judith Coleman, Brookhaven National Laboratory, Upton, NY 11973, USA.

Arbitrary Order Transfer Maps for RF Cavities*

Johannes van Zeijts CEBAF, 12000 Jefferson Avenue, Newport News, VA 23606

Abstract

Current modeling of transfer maps for superconducting RF cavities at CEBAF includes only linear effects [1], [2]. Here we extend the transfer mapping modeling capability to include arbitrary order field information generated from the MAFIA field data. We include coupler kicks, normal and skew quadrupole focussing and higher order effects.

I. Introduction

Use of a Hamiltonian and associated conjugate variables is a prerequisite in the correct treatment of higher order effects and ensuring that the resulting transfer maps are symplectic. Much effort has been spent on creating realistic transfer maps for different magnets in the fixed energy case [3], [5], [6]. Here we present an extension of this work to the case where the design energy changes due to RF cavities.

The first part of this paper gives an introduction to the deviation variables and Hamiltonian used in the construction of transfer maps in the energy dependent case. The second part of the paper introduces the fields and the transfer map calculations for RF cavities. Finally we show how to derive transfer maps for elements that change the design energy, and give some examples for the CEBAF cavities.

II. Hamiltonian in Deviation Variables

Using standard techniques [4], [5] we derive the Hamiltonian in cartesian coordinates (x, y, t) with z as the independent variable as

$$K = -qA_z - \sqrt{\frac{pt^2}{c^2} - m^2c^2 - ((p_x - qA_x)^2 + (p_y - qA_y)^2)}. \quad (1)$$

We introduce deviation variables wrt. the design orbit and the $(z$ -dependent) design energy:

$$p_i^1(z) = -\sqrt{m^2c^4 + p_1^2(z)c^2} = -\gamma(z)mc^2, \quad (2)$$

where $p_1(z) = \beta(z)\gamma(z)mc$ is the design momentum, and wrt. the time of flight of the design orbit:

$$t_1(z) = \int \frac{1}{\beta(z)c} dz. \quad (3)$$

The scaling variables are wrt. a fixed momentum p_0 , usually chosen to be the final momentum. This leads to the transverse deviation variables:

$$X, P_x = \frac{p_x}{p_0}, Y, P_y = \frac{p_y}{p_0}, \quad (4)$$

and for the temporal phase space deviation variables:

$$\tau = c(t - t_1(z)), P_\tau = \frac{pt - p_i^1(z)}{p_0c}. \quad (5)$$

Using this the Hamiltonian with arbitrary vector potential entries becomes, using $B_\rho^1 = p_1/q$ and $f = \frac{\beta(z)\gamma(z)}{\beta_0\gamma_0}$

$$H = \frac{\gamma}{\beta_0\beta\gamma_0} - \frac{\tau}{\beta_0\gamma_0} \frac{\partial\gamma}{\partial z} - \frac{P_\tau}{\beta} - \frac{A_z}{B_\rho^0} - f \sqrt{1 - \frac{2P_\tau}{f\beta} + \frac{P_\tau^2}{f^2} - \left(\left(\frac{P_x}{f} - \frac{A_x}{B_\rho^1}\right)^2 + \left(\frac{P_y}{f} - \frac{A_y}{B_\rho^1}\right)^2\right)}. \quad (6)$$

Arbitrarily complicated magnetic fields can be handled by inserting the appropriate vector potentials. From Hamilton's equation we have, assuming $A_x(0, z, t) = A_y(0, z, t) = 0$

$$\dot{P}_\tau|_{\text{design}} = \frac{\partial H}{\partial \tau}|_{\text{design}} \equiv 0 \Rightarrow \frac{\partial\gamma}{\partial z} = -\frac{q}{mc} \frac{\partial A_z(0, z, t)}{\partial \tau}, \quad (7)$$

which gives the equation for the energy increase.

III. Simple RF Fields

Here we consider standing-wave fields in a cavity with axial symmetry i.e. we only get the angle independent TM modes. following [7] an appropriate expansion for E_z is

$$E_z(r, z, t) = \sum_{n=1}^N a_n I_0(k_n r) \cos\left((2n - n_0) \frac{\pi z}{2d}\right) \sin(\omega t + \phi_0), \quad (8)$$

with

$$k_n^2 = \beta_n^2 - \left(\frac{\omega}{c}\right)^2 = \left((2n - n_0) \frac{\pi}{2d}\right)^2 - \left(\frac{\omega}{c}\right)^2. \quad (9)$$

The condition $n_0 = 1$ corresponds to the condition that $E_z(r, d, t) = 0$. An equivalent expression for the time independent vector potential $A(r, z, t) = A(r, z) \cos(\omega t + \phi_0)$ is:

$$A_z(r, z) = \frac{1}{\omega} \sum_{n=1}^N a_n I_0(k_n r) \cos(2n - n_0) \frac{\pi z}{2d}, \quad (10)$$

and

$$A_r(r, z) = \frac{1}{4df} \sum_{n=1}^N \frac{a_n}{k_n} (2n - n_0) I_1(k_n r) \sin(2n - n_0) \frac{\pi z}{2d}. \quad (11)$$

The energy gain of the reference particle is given by the differential equation

$$\frac{\partial\gamma}{\partial z} = \frac{q}{mc^2} E_0(z) \sin(\omega t_1(z) + \phi_0), \quad (12)$$

where $E_0(z)$ is the on axis gradient given by

$$E_0(z) = \sum_{n=1}^N a_n \cos\left((2n - n_0) \frac{\pi z}{2d}\right). \quad (13)$$

*This work was supported by the U.S. Department of Energy, under contract No. DE-AC05-84ER40150.

In practice RF cavities are phased to achieve maximum energy gain for a given field amplitude. In our approach a working point is found by using a two-dimensional Newton method where we vary the field amplitude and the phase to find a given energy increase which is to first order independent of the phase.

IV. RF Multipole Fields

Following standard techniques [8] here we consider the general RF field expansion inside a cylinder. TM and TE mode multipole fields starting with dipole terms are handled. The terms $m = 0$ correspond to the fields in the previous section, the term $m = 1$ correspond to a dipole field, the terms $m = 2$ correspond to quadrupole fields, etc. Since cavities are no longer assumed to be mirror symmetric we have to use both $\cos(\beta_n z)$ and $\sin(\beta_n z)$ terms in the Fourier series expansion. In this case we need a total of 8 independent terms per mode (n, m) to describe the fields adequately.

A. TM and TE modes

An appropriate expansion for E_z becomes

$$E_z(r, \theta, z)_{nm} = I_m(k_n r) E_z(\theta, z)_{nm} \quad (14)$$

where

$$E_z(\theta, z)_{nm} = \cos(\beta_n z) (A_{nm}^{TM} \sin(m\theta) + B_{nm}^{TM} \cos(m\theta)) + \sin(\beta_n z) (C_{nm}^{TM} \sin(m\theta) + D_{nm}^{TM} \cos(m\theta))$$

The TE modes are derived from

$$B_z(r, \theta, z)_{nm} = \frac{1}{c} I_m(k_n r) B_z(\theta, z)_{nm} \quad (15)$$

where

$$B_z(\theta, z)_{nm} = \cos(\beta_n z) (A_{nm}^{TE} \sin(m\theta) + B_{nm}^{TE} \cos(m\theta)) + \sin(\beta_n z) (C_{nm}^{TE} \sin(m\theta) + D_{nm}^{TE} \cos(m\theta))$$

We omit the full expansions for the fields $E_\theta^{TM}(r, \theta, z)_{nm}$, $E_r^{TM}(r, \theta, z)_{nm}$, $E_\theta^{TE}(r, \theta, z)_{nm}$ and $E_r^{TE}(r, \theta, z)_{nm}$, they are given in [9].

B. Vector potentials

The vector potentials become

$$A_z(r, \theta, z) = \frac{1}{\omega} \sum_{n,m} E_z(r, \theta, z)_{nm}, \quad (16)$$

and

$$A_\theta(r, \theta, z) = \frac{1}{\omega} \sum_{n,m} (E_\theta^{TM}(r, \theta, z)_{nm} + E_\theta^{TE}(r, \theta, z)_{nm}), \quad (17)$$

and

$$A_r(r, \theta, z) = \frac{1}{\omega} \sum_{n,m} (E_r^{TM}(r, \theta, z)_{nm} + E_r^{TE}(r, \theta, z)_{nm}). \quad (18)$$

V. Transfer Maps for RF Cavities

In this section we describe how to obtain the arbitrary order transfer map for RF cavities in the deviation variables

$$x, P_x, y, P_y, \tau, P_\tau. \quad (19)$$

Given the requested energy increase and phase set point, the transfer map will be derived as a Taylor series and transformed into Lie algebraic form for use in lattice design and tracking codes.

We start by expanding all fields in cartesian coordinates

$$r \rightarrow \sqrt{x^2 + y^2}, \quad (20)$$

and

$$\omega t \rightarrow \frac{2\pi\tau}{\lambda} + \omega t_1(z). \quad (21)$$

The vector potential in cartesian coordinates is

$$A_x = \frac{x A_r - y A_\theta}{\sqrt{x^2 + y^2}}, \quad (22)$$

and

$$A_y = \frac{y A_r + x A_\theta}{\sqrt{x^2 + y^2}}. \quad (23)$$

For general m the expansion of the Bessel functions is

$$I_m(kr) = r^m \left(\frac{1}{2}\right)^m k^m \left[\frac{1}{m!} + \frac{k^2 r^2}{4(1+m)!} + \dots \right] \quad (24)$$

The expansion of the angular parts are

$$\sin(m\theta) = \frac{\Im(x + Iy)^m}{r^m}, \quad (25)$$

and

$$\cos(m\theta) = \frac{\Re(x + Iy)^m}{r^m}. \quad (26)$$

The terms r^m cancel in the product of these expansions as expected. The time dependent part is expanded in τ . Finally the expansions are inserted in the Hamiltonian (6), which is expanded analytically in the deviation variables to high order, using a symbolic manipulation program. The procedure to generate a transfer map from a Hamiltonian is described in [10], this basically involves integrating a set of ordinary differential equations for the coefficients of the Taylor series expansion. The system of ode's is extended by one for integrating $\gamma(z)$ and one for integrating $ct_1(z)$.

VI. CEBAF Cavities

As a first application of this approach we use the longitudinal electric field on axis for a typical CEBAF RF cavity. This field has been calculated using SuperFish and the coefficients in the expansion of $E_0(z)$ are presented in the table below. We have $\lambda = 0.2$ m, $f = 1497$ Mhz. The data is normalized to give a gradient of 1 MeV/m, and $d = 0.35$ m. Furthermore we present the data in Figure 1. In Figure 2 we plot the incremental energy increase (eq. 12) for the reference particle with the assumption that $\beta = 1$ and where we have chosen $\phi_0 = \pi/2$.

Work is in progress to apply the full power of the machinery presented in this paper to realistic cavities. For that purpose, the coefficients of the TM and TE modes are obtained by a Fourier transform of the MAFIA field data to high order [9].

n	a_n
1	0.2287767
2	-.5776482
3	0.7384962
4	1.396168
5	0.3219303
6	-.1126080
7	0.01861268
8	0.003110609
9	0.008141764
10	-.02498009
11	-.06243902
12	-.01799315
13	0.007256913
14	-.001471598

Table I
Expansion coefficients a_n for $E_0(z)$.

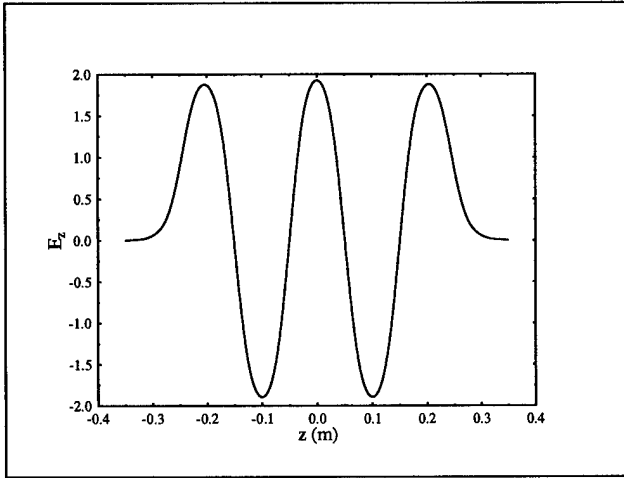


Figure 1. Longitudinal electric field on axis for a CEBAF cavity.

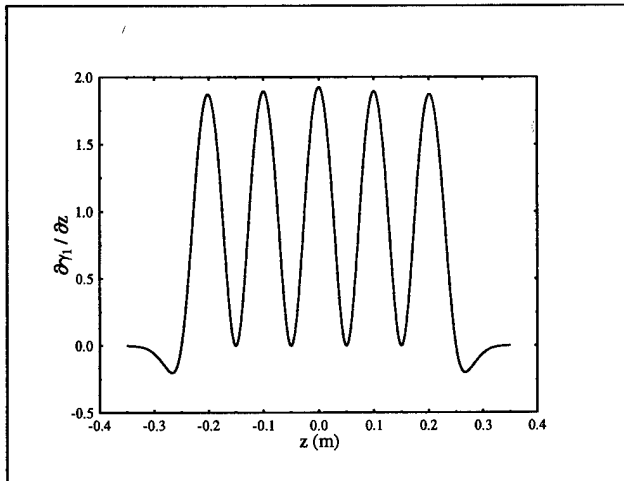


Figure 2. $\partial E_z / \partial z$ with $\beta = 1$ and $\phi_0 = \pi/2$.

VII. Conclusion

We have shown, in the Hamiltonian context, how to derive symplectic transfer maps in the presence of acceleration. Subsequently we have shown how to derive transfer maps for realistic RF cavities. The method is general purpose and able to handle RF quadrupole and higher multipoles, limited only by the availability of Fourier coefficients of the expansion coefficients.

Acknowledgments

I would like to thank Hongxiu Liu for pointing out reference [7] and for providing the expansion coefficients of the basic RF field, Zenghai Li for pointing out some errors in the multipole expansion and for providing the coefficients for CEBAF cavities from MAFIA data, Filippo Neri and David Douglas for discussions initiating this approach.

References

- [1] R. Servranckx et. al., *DIMAD manual*
- [2] G. A. Krafft, J. Jackson and D. Douglas, *First Order Focusing and Steering of Misaligned Cavities*, CEBAF TN 90-287.
- [3] A. J. Dragt et. al., *Marylie 3.0, A Program for Charged Particle Beam Transport Based on Lie Algebraic Methods*
- [4] J. M. Jowett, *Electron Dynamics with Radiation and Non-linear Wigglers*, CERN Accelerator School 87-03 (1987).
- [5] A. J. Dragt, *Numerical third-order transfer map for solenoid*, N.I.M. A298 (1990) 441-459.
- [6] A. J. Dragt, F. Neri, J.B.J. van Zeijts and J. Diamond, *Numerical third-order transfer map for combined function dipole*, N.I.M.
- [7] K. T. McDonald, *Design of the Laser-Driven RF Electron Gun for the BNL Accelerator Test Facility*, Princeton University preprint, Appendix A (1988).
- [8] J.D. Jackson, *Classical Electrodynamics*
- [9] Z. Li, *Beam Dynamics in the CEBAF Superconducting Cavities*, Ph.D. Thesis, College of William and Mary, March 1995.
- [10] J. van Zeijts, *New Features in the Design Code Tlie*, CAP'93 proceedings and CEBAF-PR-93-003.

The Computation of the Dynamic Inductance of Magnet Systems and Force Distribution in Ferromagnetic Region on the Basis of 3-D Numerical Simulation of Magnetic Field

N. Doinikov, V. Kukhtin, E. Lamzin, B. Mingalev, Yu. Severgin, S. Sytchevsky,
The D.V.Efremov Scientific Research Institute of Electrophysical Apparatus,
189631, St.-Petersburg, Russia

Static and dynamic inductances are ones of the main technical parameters of magnet systems at the designing stage. Ponderomotive force distribution is required for mechanical stress calculations.

The static inductance is used for evaluations of the stored energy, magnetic flux linkage in coils at instantaneous currents. The dynamic inductance allows to define the interrelation between the instantaneous flux linkage and currents determining a transient process in coils.

In the given paper a technique for determination of the dynamic inductance for magnet systems on the assumption of no eddy currents in ferromagnetic elements of a construction is proposed. This technique necessitates the evaluation of magnetic energy at two rather close values of current in a coil on the magnetization curve, i.e. static parameters of a magnet system are applied for the determination of the dynamic inductance. As, at present, magnet systems are more frequently designed on the basis of a magnetic field distribution analysis, obtained as a result of numerical simulation, the calculation of magnet energy involves no difficulties.

Algorithmic aspects of numerical simulation of specific and surface ponderomotive force loads for practical needs for designing electrophysical devices are given.

I. DETERMINATION OF THE DYNAMIC INDUCTANCE

The total magnetic energy W can be determined as follows [1], [2]

$$\begin{aligned} W &= \frac{1}{2} \int (\vec{B} \cdot \vec{H}) dV = \frac{1}{2} \int (\vec{A} \cdot \vec{j}) dV = \\ &= \frac{1}{2} \sum_k \int (\vec{A} \cdot \vec{j}_k) ds_k dl_k \\ &= \frac{1}{2} \sum_k I_k \int (\vec{A} \cdot d\vec{l}_k) j_k / I_k ds_k = \\ &= \frac{1}{2} \sum_k I_k \int ((\nabla \times \vec{A}) \cdot d\vec{S}_k^{(j)}) j_k / I_k ds_k = \\ &= \frac{1}{2} \sum_k I_k \int (\vec{B} \cdot d\vec{S}_k^{(j)}) j_k / I_k ds_k = \\ &= \frac{1}{2} \sum_k I_k \int \vec{j}_k j_k / I_k ds_k = \frac{1}{2} \sum_k \Psi_k I_k, \end{aligned}$$

where \vec{B}, \vec{H} - are the magnetic induction and strength vectors;

\vec{A} - is the vector potential ($\vec{B} = \text{rot} \vec{A}$);
 \vec{j}, I_k, Ψ_k - are the density vector, total current and flux linkage of the k -th coil;

$S_k^{(j)}$ - is the transverse cross-section of the k -th coil;
 l_k - is the loop of an elementary current filament with S_k cross-section.

In the general case the dynamic inductance of a current coil is known [4] to determine the velocity of the magnetic flux linkage with this coil

$$\frac{d\Psi_i}{dt} = L_{din,ik} \cdot \frac{dI_k}{dt}$$

Let us define:

$$\frac{\partial W}{\partial I_k} = \frac{1}{2} \sum_i^N \left(\frac{\partial \Psi_i}{\partial I_k} \cdot I_i + \Psi_k \right) = \frac{1}{2} \sum_i^N I_i (L_{din,ik} + L_{st,ik}),$$

where $L_{st,ik}$ - is the static inductance.

Without limitation of the commonness let us consider the case of one coil ($N = 1$). Then

$$\frac{dW}{dI} = \frac{1}{2} (L_{din} + L_{st})$$

The final expression for L_{din} is the following:

$$L_{din} = \frac{2dW}{dI} - L_{st}, \quad (1)$$

where

$$L_{st} = \frac{\Psi}{I} = \frac{2W}{I^2}$$

The determination of L_{din} according to (1) necessitates the two-fold computation of the problem for a magnet system to define the energy increment ΔW . However, due to a small current increment ΔI in a coil the results of the previous numerical simulations are rather well initial approximation for subsequent computations. The efficiency of a similar procedure is substantially increased, if determination of $L_{din} = L_{din}(I)$ dependency is needed.

In the case, when $W_1 = W(I_1)$ and $W_2 = W(I_1 + \Delta I)$ are known, L_{din} can be defined using the central difference of the form

$$L_{din}(I_1 + 0.5\Delta I) = 4 \frac{W_2 - W_1}{(k^2 - 1)I_1^2} - \frac{W_2 + k^2 W_1}{k^2 I_1^2}, \quad (2)$$

where

$$k = 1 + \frac{\Delta I}{I_1}$$

For the case of N coils, matrix of the dynamic inductances is calculated in the similar way to (2).

II. PONDEROMOTIVE FORCE SIMULATION

The problem of ponderomotive force determination has been discussed in [1], [6], [3], [7].

In using the finite element method for spatial magnetic field simulation it is assumed that magnetic permeability μ to be constant in each finite element. Such an approach permits a required accuracy of calculations of magnetic induction components and magnetic intensity ones, as well as field, energy, inductance and so on. In this case it is naturally to use a linear dependence between magnetic inductance B and magnetic intensity H for calculations of the ponderomotive force. Thus, detailed distribution of "the equivalent density" of ponderomotive force in ferromagnetic [1] can be constructed by using the "Maxwell Stress", $B^2 / 2\mu_0$. In the given model all of the finite element sides are "strong break surfaces" [6] in electromagnetic field. For real geometry of magnet systems such surfaces are interfaces, on which the surface density of ponderomotive force has physical sense [6].

Defining the outward normal from media "1" to media "2" one can obtain the expression for the ponderomotive force density, acting upon the interface

$$\vec{f} = \frac{1}{\mu_0}(B_{2n}\vec{H}_2 - B_{1n}\vec{H}_1) - \frac{1}{2\mu_0}(B_2H_2 - B_1H_1)\vec{n} \quad (3)$$

Thus, an algorithm of ponderomotive force calculations permits to find the specific ponderomotive force density, as well as the surface one, acting upon the interfaces of electromagnetic value break. Also it is possible to find the resultant force applied to the whole body, as well as to the part of the body taking into account small construction gaps. Such an approach has been used and appropriate software FERROPON (Finite Element, FERromagnet continua, PONderomotive force distribution) has been developed. Though this software is a part of the KOMPOT program package [5], it can be easily used separately for ponderomotive force calculations for available distribution of magnetic field.

References

- [1] I.E.Tamm. The Foundations of The Electricity Theory. M.: Nauka, 1976, p.616.
- [2] H.Buchholz. Elektrische und magnetische Potentialfelder Springer-verlag, 1957
- [3] J. Simkin. Recent developments in field and force computation. *Jorn. de Physique, c 1, v 45, No 1, 1984*
- [4] L.R.Neiman, K.S. Demirchyan. The Theoretical Foundations of Electrical Engineering. V.2. L.: Energia, 1975, p.407.
- [5] Doinikov N.I, Lamzin E.A., Sytchevsky S.E. On Computation of 3-D Magnetostatic Fields of Electrophysical Apparatus Magnet Systems. *IEEE Trans. on Magnetism*, V. 28, No. 1, Jan. 1992, pp. 908-911.
- [6] L. I. Sedov. Mechanics of continua. v. I, M.: Nauka, 1983, p.528.
- [7] A. V. Ivanov-Smolensky. Electromagnetic forces and energy transformation in electrical machines. M.: Vishaia shkola, 1989, p.312.

ADVANCED ELECTROMAGNETIC DESIGN OF CAVITIES FOR HIGH CURRENT ACCELERATORS *

Frank L. Krawczyk, AOT-1, MS H817, Los Alamos National Laboratory, Los Alamos, NM 87545 USA

Abstract

For high-current accelerators such as those proposed for transmutation technologies or spallation sources, preconstruction numerical modeling has a high importance. Non axisymmetric cavities require a full 3-D modeling. A complex analysis of structures beyond tuning and the calculation of Q and shunt impedance is required and also the interaction with the mechanical properties of the structures has to be taken into account. This paper reports on recent work done at LANL for proposed beam funnels, a new normal-conducting medium-energy structure (CCDTL) and superconducting cavities for medium energy. The electromagnetic calculations have been done with MAFIA, Rel 3.2 [1], the thermal and stress analysis results reported come from the ABAQUS engineering code.

I. THE COUPLED-CAVITY DRIFT TUBE LINAC STRUCTURE

A. General

In the velocity range of $0.1 \leq \beta \leq 0.5$ the drift tube linac (DTL) usually is selected as accelerating cavity. Jim Billen recently proposed a new structure with high shunt impedance and a good field stability in this velocity range [2]. This coupled-cavity drift tube linac structure (CCDTL) combines features from a regular DTL and the coupled-cavity linac (CCL), a commonly used structure for high energy protons. A detailed description of the CCDTL's mode of operation is given in [2].

A major part of the cavity design (to get nose, drift-tube and cavity geometries) has been done in 2-D, neglecting the influence of stems and asymmetrically positioned coupling slots. For a study on the feasibility of the CCDTL cavity a full 3-D modeling is needed (see Fig. 1). This should yield the full mode spectrum, the expected rf wall losses, resulting mechanical stresses and the required cooling.

B. Stem Modes and Losses

The first 3-D effect investigated was the introduction of modes by the stem(s) holding the drift tubes. This was done to confirm that no stem-related modes close to the accelerating mode exist. Table 1 lists the MAFIA-calculated frequencies of the lowest stem-related modes for different relative stem positions. These have been calculated for angles between stems from 0° (single stem) to 180° . The frequencies far exceed the 1400 MHz of the accelerating mode. Calculations for β up to 0.5 indicate that nowhere in this range these modes pose a problem.

Table 1. Nearest Stem-Related Modes for $\beta = 0.283$.

*Work supported by the U.S. Department of Energy, Defense Programs

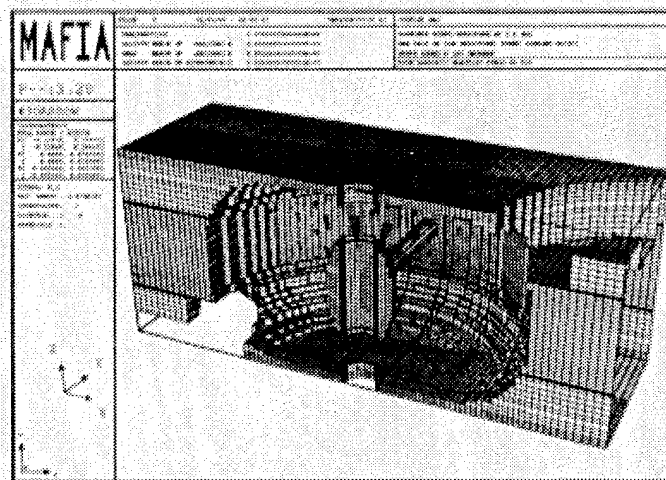


Figure 1. One half of a CCDTL structure with a single drift-tube and two stems 180° apart (only one stem is shown) 90° from the coupling slots. Only part of the coupling cells is shown, but full cells have been used for calculation. The cones indicate the accelerating electric field.

angle (degree)	frequency [GHz]
0	2.055
60	2.090
90	2.132
120	2.161
180	2.207

The second 3-D effect investigated was the power dissipation near the CCDTL cavity's coupling slots.

Figure 2 indicates the losses due to the rf fields around one of the coupling slots. The nonsymmetric distribution of losses will be taken into account in the cooling scheme for this structure.

The different curvatures meeting at the coupling slots pose some problem for the reliable determination of peak power densities in this area. Here a recalculation of the structure with a finer mesh combined with some smoothing of the obtained loss data is necessary. This helps to distinguish between real "hot spots" in the structure and those artificially introduced by discretization errors. Such a procedure has been successfully demonstrated for the structures in beam funnels [3]. We also consider testing electromagnetic field calculation codes based on a finite element formulation, that would be more compatible with the structural analysis codes. But such codes for rf problems still have to prove their general reliability.

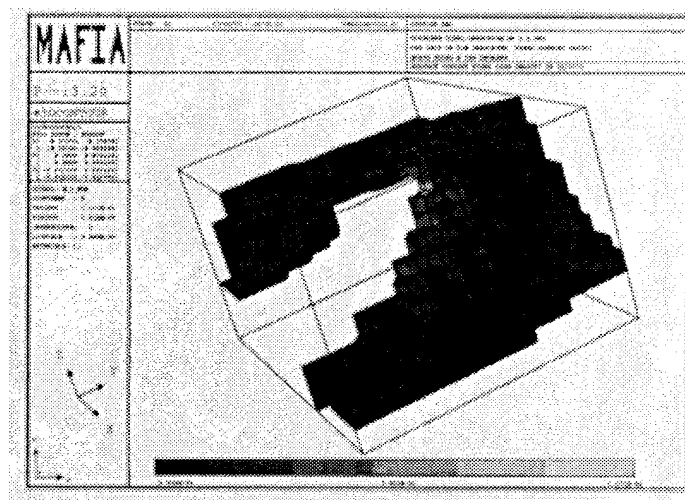


Figure 2. A close-up look at the rf-induced wall losses around one half of a coupling slot. Regions of higher losses are indicated by lighter shading.

II. DEFLECTOR CAVITIES FOR FUNNELING DEVICES

A. General

Funnels are key components of proton linacs when very high currents are required. The limits imposed by high space-charge forces at the low-energy end of a linac can be bypassed by starting with two beams of half the desired current. The bunches in these two beams from identical ion sources are formed 180° apart. In a funnel they are merged into a single beam. This is accomplished by a suitable arrangement of conventional accelerator components like lenses and buncher cavities together with a special non-axisymmetric rf deflector cavity.

B. The Simple Deflector Cavity

The complete design of a deflector cavity (see Fig. 3) was done for the proposed Accelerator Performance Demonstration Facility (APDF) at a beam energy of 20 MeV [3]. In this design the bunch length of the protons entering the deflector was small enough to see a fairly homogeneous deflecting rf field.

The combined electromagnetic and thermal/stress analysis of the cavity indicates that such a structure can be built and operated. However, the mechanical stresses as determined from the rf wall losses seem to be challenging; the forces on the deflector electrode reach 85 % of the copper yield strength.

The choice of a funneling energy of 20 MeV was determined primarily from beam dynamics considerations. Calculations for the deflector cavity of the European Spallation Source (ESS) [4], which is designed to operate at 5-7 MeV and a 10% duty factor show significantly less thermal stress. Here we explore a design at 12 MeV to examine the possibility of reducing the thermal stress in our deflector cavity.

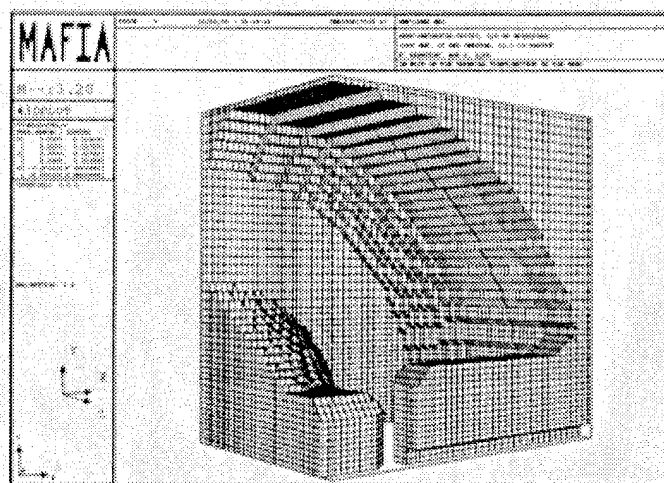


Figure 3. This is one eighth of the simple deflector cavity at 350 MHz, as modeled with MAFIA. On the left is one quarter of one of the two deflecting electrodes. On the right is one quarter of a nose-like structure, concentrating the deflecting fields near the center of the cavity.

C. The Deflector Cavity for a Combined First and Third Harmonic Deflection

At 12 MeV the longitudinal bunch size is wider than at 20 MeV. This accentuates the difference in the deflection seen by the center and the ends of the bunches. This problem can be reduced by an improved deflector cavity that uses the combined deflection of the first and third harmonic deflecting modes. If the proper phase and

relative amplitude between the two modes are chosen, the temporal variation of the deflecting field will be closer to a desired rectangular deflection pulse than can be obtained with just the fundamental mode. Figure 4 shows a modified deflector that has an additional deflecting mode at 1.05 GHz. The cavity shape variation has been chosen to (1) minimally affect the fundamental mode and (2) add surfaces at locations with low magnetic field amplitude to minimize the introduction of additional wall losses. The cavity represented here is not yet optimized but already indicates a significant improvement in terms of rf losses (see Table 2).

Table 2. Comparison of Some Data for the 20 MeV and 12 MeV Deflectors

	20 MeV Cavity	12 MeV Cavity
Gap Field	24 MV/m	20 MV/m
RF-Losses	48 kW	34 kW
Peak Loss-Dens.	68 W/cm ²	60 W/cm ²

In Fig. 5 the deflecting pulses from the fundamental and the combined harmonics are compared. The combined deflection pulse stays at a high level for a longer portion of the rf period and then drops off faster than the fundamental. The third harmonic field has a phase difference of 180° at the center of the gap and an amplitude of 1/10 with respect to the fundamental.

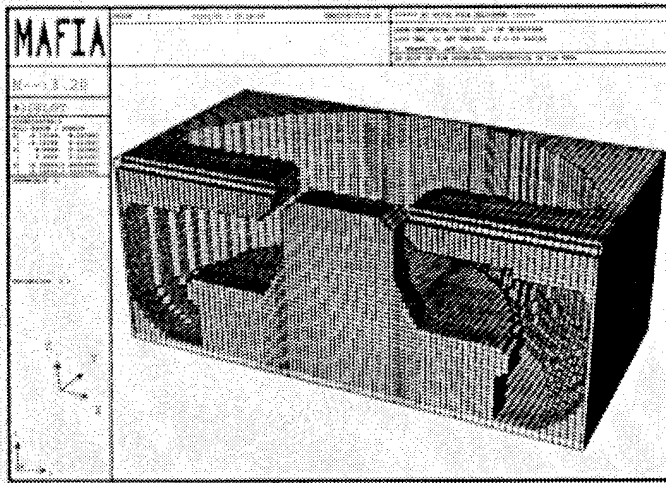


Figure 4. The combined first and third harmonic deflector. The pedestal added at the bottom of the electrodes decreases the frequency of a higher mode with a deflecting component to 1.05 GHz. The fundamental mode is hardly affected. Also the magnetic field amplitudes of the fundamental and the third harmonic in this part of the structure are low.

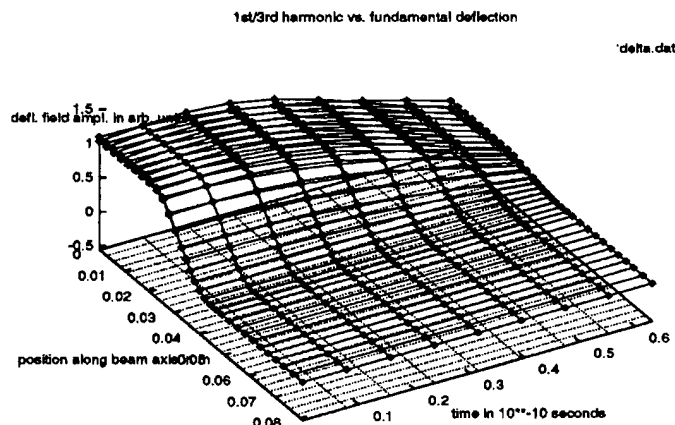


Figure 5. Comparison of the change in deflecting field with time for the fundamental and the combined deflection. The two deflecting surfaces nearly coincide, the combined deflection shows the maximal effect.

III. SUPERCONDUCTING CAVITIES FOR MEDIUM ENERGY PROTONS

A. General

Cost-saving issues in the design of high current proton accelerators raise the question of using superconducting cavities. Low risk and the need for only little technical development favor the use of elliptical cavities at high energies. At lower energies a good candidate seems to be the spoke structure, first proposed by J. Delayen et al. [5]. Figure 6 shows an eight-cell spoke cavity with a cross-bar structure at 7 MeV for 350 MHz.

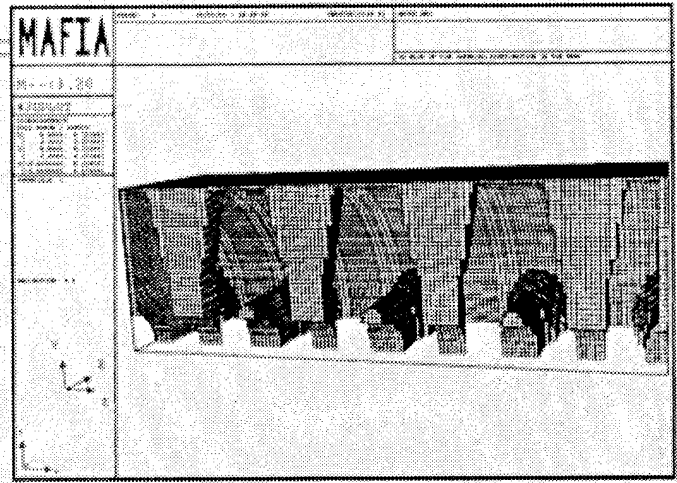


Figure 6. Eight-cell spoke cavity with cross-bar structure at 350 MHz and 7 MeV. This is one quarter of the cavity as discretized with MAFIA. The spoke shape can be further improved, but did already help to evaluate some general properties of this new structure. The beam-axis coincides with the z-axis.

This is still a non-optimized geometry that needs improvements. But it already hints that it seems suitable for several reasons:

- It has a higher mechanical stability at low β than an elliptical cavity,
- The bore size can be freely chosen, without affecting the coupling,
- The mode spectrum indicates that there are no problematic modes that should mix with the accelerating π -mode.
- It has a high ZT^2/Q (800 Ω/m or more).

Ratios of E_{peak}/E_0T of the order of 5 seem to be achievable at the energy of 7 MeV. This will improve with higher β . Our spoke model especially needs further improvement to achieve more reasonable ratios of H_{peak}/E_0T . These are predominantly determined by the geometry of the spoke base, where it meets the outer cavity wall.

References

- [1] M. Bartsch et al. "Solution of Maxwell's Equations", Computer Physics Comm. 72, 22-39 (1992)
- [2] James H. Billen et al. "A New Rf Structure for Intermediate-velocity Particles", Proc. of the 1994 International LINAC Conference, Vol I, p. 341
- [3] Frank L. Krawczyk, Nathan K. Bultman, K.C. Dominic Chan, Rick L. Martineau, Subrata Nath, Lloyd M. Young "Design of RF-Cavities in the Funnel of Accelerators for Transmutation Technologies", Proc. of the ADTT Conference, Las Vegas, Nevada, July 1994
- [4] Frank L. Krawczyk, "Comments on the ESS Funnel Cavity Design", LANL Memo AOT-1:94-171, 1994
- [5] Jean R. Delayen, Cort L. Bohn and C. T. Roche, Proceedings of the 1990 Linear Accelerator Conference, p 82.

MODIFIED PARMILA CODE FOR NEW ACCELERATING STRUCTURES*

H. Takeda and J. E. Stovall, Los Alamos National Laboratory, Los Alamos, NM 87545 USA

The PARMILA code was originally developed as a numerical tool to design and simulate the beam performance of the drift-tube linac (DTL). We have extended PARMILA to the design of both the coupled-cavity linac (CCL) and the coupled-cavity drift-tube linac (CCDTL). We describe the new design and simulation features associated with these linac structures and improvements to the code that facilitate a seamless linac design process.

PARMILA and New Accelerator Architectures

PARMILA stands for Phase And Radial Motion in Ion Linear Accelerators. This computer code originated in the 1960's to study DTL structures¹ and it has been widely used in the accelerator community. This popular code has benefited from years of use and improvements. It has been the basis of many successful linac designs and has been rigorously studied and tested. In recent years, we have seen the development of high-energy RFQ linacs and the CCDTL, a new rf structure² that extends the operating range of the CCL down to the output energy of the RFQ. These developments have motivated work to generalize the PARMILA code for various accelerator architectures.

A CCDTL cavity contains one or more drift tubes. Unlike the conventional DTL, the CCDTL drift tubes usually contain no focusing elements. Quadrupole lenses between cavities or between multi-cavity tanks provide the transverse focusing just like the arrangement in CCL structures. The section of PARMILA that generates the linac now also calculates the lengths of the inter-cavity drift spaces containing the quadrupole lenses. The input stream has several new options that describe the new cavity geometries and their associated focusing requirements. The cavity periodicity and the type of focusing lattice (e.g. FODO) are among the new input-stream entries. To make room for beam-line diagnostic equipment, quadrupole lenses can be either upstream, downstream, or centered in the inter-cavity drift space.

Cavity Configuration Options

PARMILA treats each accelerating gap and the adjacent drift distances as a "cell." A cavity can contain one or more cells. For example, DTL cells have length $\beta\lambda$, where β is the synchronous particle velocity and λ is the rf wavelength. The accelerating gap is in the middle of this cell. Previous versions of the code assumed that the quadrupole magnets were inside the drift tubes of the DTL. We have extended the linac-design and the beam-dynamics-simulation parts of PARMILA to accommodate new cavity structures as well as external quadrupole magnets. CCLs and CCDTLs consist of tanks containing one or more cavities with the focusing

magnet between tanks. CCDTL cavities always contains two or more cells. In the CCDTL, a cell extends from the center of one drift tube to the center of the next one or to the start of a drift space between cavities. Individual cell lengths in a CCDTL cavity differ depending on whether the cell abuts a cavity outside wall or another drift tube. Figure 1 shows short sections of CCDTL and CCL structures. The length of a CCDTL internal cell is $\beta\lambda$, while the length of an end cell is $3\beta\lambda/4$. The gap is not centered in this end cell. Each CCL cell has length $\beta\lambda/2$.

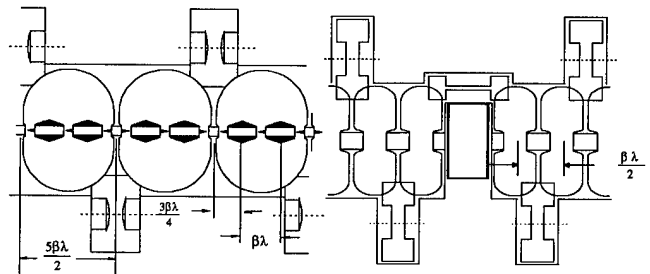


Figure 1. Short sections of CCDTL (left) and CCL (right). The coupling cells above and below the accelerating cells are nominally unexcited in the $\pi/2$ structure mode. The CCL shows a dead space between accelerating sections containing a quadrupole magnet.

The code stores a unique length for each cell in a cavity. For the CCDTL, this generality allows asymmetric cavities, though we expect most designs to use symmetric cavities. The cell geometry as well as the electric fields are treated differently in cavities containing single and multiple drift tubes. To calculate the individual cell geometry the cell generator uses multiple transit-time-factor tables for each type of cell tabulated as a function of β . The code interpolates intermediate values as required. The user supplies these tables as part of the input stream.

PARMILA designs each cell so that the beam maintains synchronism with the time-varying rf fields. The algorithm³ used to derive the cell lengths is the same for all types of linac. The code divides each gap at its midpoint and calculates the length of each side separately using the synchronous particle velocity before and after applying an energy kick. In CCL and CCDTL structures, the electric fields in adjacent cavities are 180° out of phase. The electric field for all cells within a CCDTL cavity are in phase. Most linac designs use a transverse focusing period that changes gradually with β . If a quadrupole lens is inserted between two cavities, additional multiples of $\beta\lambda$ may be needed to maintain synchronism with the drifting beam.

In our recent linac designs, we start with two-drift-tube CCDTL structures at low β and later switch to single-drift-tube CCDTL. This procedure uses each cavity type where it has high shunt impedance. In these $\pi/2$ -mode structures,

*Work supported by the US Department of Energy.

conventional TM_{010} -mode coupling cells provide the usual phase shift of π radians between accelerating cavities. Adjacent gaps in such a structure must be $\beta\lambda/2$ apart. Longer coupling cells can add odd-integer multiples of $\beta\lambda/2$ between active structures to create additional space for focusing lenses and diagnostics while still maintaining synchronism. By reorienting the coupling cavity (see Fig. 1 for the CCL), the designer can provide a 2π phase shift between cavities. This technique allows integer multiples of $\beta\lambda$ between cavities. Long spaces between active structures may require a bridge coupler when the length of a coupling cell approaches a full wavelength. Bridge couplers contain excited and unexcited cells placed off the beam axis to allow space for longer focusing elements or diagnostic devices. Using these techniques, the drift length between tanks can be tailored to practically any value of $n\beta\lambda/2$, where n is an integer. In PARMILA, these adjustments can be specified globally or for individual tank junctions. These options are controllable from the input stream. The code divides the space charge calculation in the connecting drifts into steps corresponding to a distance of about $\beta\lambda$.

PARMILA accepts input data for either FODO or FOFODODO lattices. It assumes, as a default, a constant magnetic field gradient for all focusing lenses. The designer can specify each quadrupole gradient individually or automatically ramp the gradient linearly with accelerator length, or as $1/\beta$. If part of the accelerator is turned off (for example, to produce a beam of lower energy than the nominal design), the code can compensate for the over focusing using the automatic ramping feature.

Tables of Transit-Time Factors

An important addition to the code has been expansion of the transit-time data tables to account for different boundary conditions at the ends of cells. A section of linac might require up to three separate tables of data from a cavity design code such as SUPERFISH. Each table includes transit-time factors and other properties of representative cells tabulated by particle β . One table includes data for internal cells that are symmetric about the gap center. This type of cell includes the usual DTL cell or CCL cells, each with the appropriate boundary conditions. DTL cells have Neumann boundaries between cells and CCL cells have Dirichlet boundaries. A second table defines end cells of a cavity that have a Neumann boundary on one side and a Dirichlet boundary on the side adjacent to the next cavity. A third table corresponds to cells at the end of an accelerating structure. Neither Neumann nor Dirichlet boundaries are appropriate for one end of this type of cell. The fields penetrate into the inter-tank drift space and attenuate exponentially because the resonant frequency is below the cut-off frequency of the bore tube. Single-drift-tube CCDTL structures use only the second and third tables. A CCL would use the first and third tables. In multi-gap cavities such as in a CCDTL, the voltage gain across gaps may vary for a nominal cavity excitation. The field distribution depends upon the detailed cavity geometry.

New table entries include the relative electric field strength for each type of cell.

PARMILA calculates each cell length using the transit-time factor and electric-field data interpolated from the supplied data tables. The code stores each cell geometry, the data interpolated from the tables, plus cavity power losses estimated from the shunt impedance contained in the tables. It saves this information in a separate file for each run. The present PARMILA generates only graded- β linacs, so unlike many existing CCLs, every cell has a different length. In a future version we plan to implement tanks of constant length cells.

Longitudinal Phase Space Considerations

To adjust the longitudinal acceptance, the user can manipulate both the synchronous phase ϕ_s and the spatially averaged electric field E_0 . Two types of ramping schemes are provided. A static ramp varies either ϕ_s or E_0 linearly with real-estate length. A dynamic ramp varies these parameters as a function of β . Another feature allows the designer to maintain a constant synchrotron oscillation frequency or constant longitudinal phase advance per cell. Additional ramping options based on cell number and active cavity length will be added to give the designer more flexibility.

The input stream includes the distribution of E_0 for designing the linac. For DTLs, E_0 can be ramped linearly with tank length. This type of ramped field distribution is relatively easy to achieve in an actual cavity. When an accelerator design varies E_0 in a CCDTL, the ramp applies only cavity to cavity. The cells within each cavity will have the relative field strength determined by a code such as SUPERFISH. For example, the center gap of a two-drift-tube cavity may in general have a different voltage gain from the end gaps. Designers will usually avoid longitudinal ramps within a cavity, because of the way it would complicate the cavity-to-cavity coupling.

The actual phase of the field in the cavities, of course, is fixed by the resonant rf mode. But, as seen by the beam, arbitrary phase shifts between cavities are possible by adjusting drift lengths between cavities. Using this feature we can create flexible longitudinal bunching and matching sections between different linac structures, for example between a RFQ and a CCDTL.

Simulation Studies

Like previous versions of PARMILA, the new code designs the linac and simulates its performance with beam in the same run. The design process involves generating cells of the appropriate length for the synchronous particle's increasing velocity. For the particle dynamics simulation, PARMILA treats each cell as a drift-gap-drift sequence of elements. For DTLs, this sequence can also include the half quadrupole lenses in the drift tubes. To continue a simulation into a linac section with a different cavity type, the code uses quadrupole half lenses on the end to complete a lattice period.

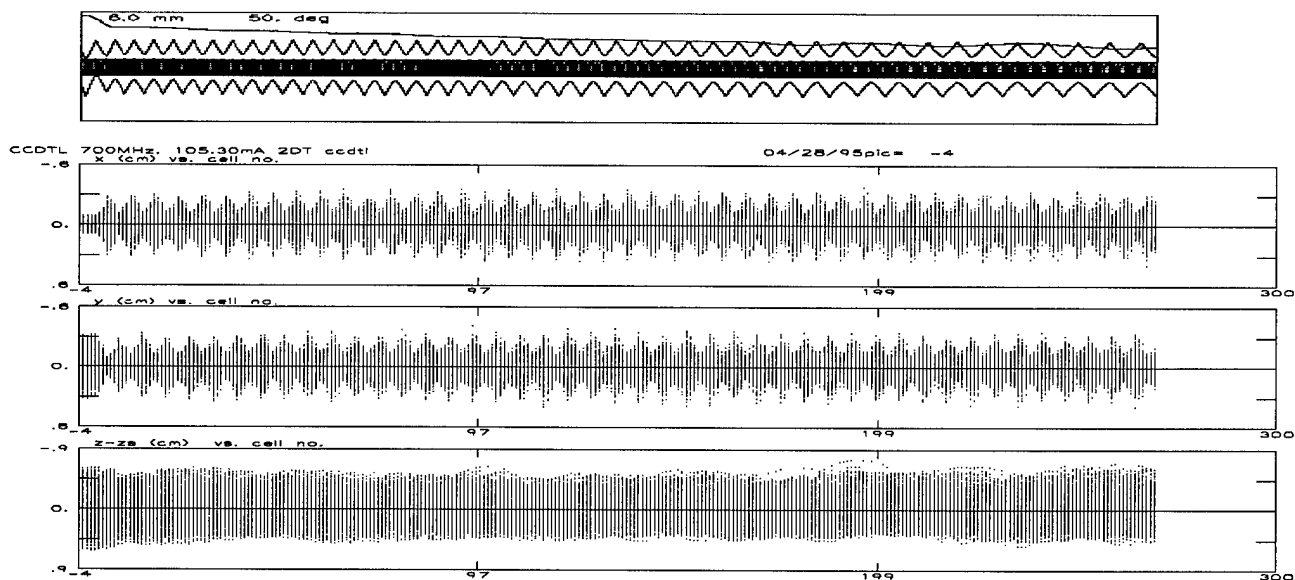


Figure 2. Sample output from a beam simulation study. The upper plot shows the beam envelope from a TRACE 3-D calculation. The other three plots are the X, Y, and Z beam profiles after each cell from a 1000-particle PARMILA run.

It writes the entire particle distribution to a data file. The next run reads the particle distribution and starts with another quadrupole half lens. PARMILA also can read the particle distribution produced by PARMTEQ at the RFQ exit and use it as the input distribution for a dynamics simulation. These features facilitate the design of a linac comprised of several different types of accelerating structures and provides a true end-to-end simulation capability.

During the simulation part of the calculation, the code reports after each cell several parameters of interest to the designer. The bunching is characterized by two bucket filling factors. These factors measure the distance of the beam from the separatrix. Also calculated is the synchrotron wavelength. These three parameters are used as the tools for manipulating the longitudinal match. A post processor program DTLPROC creates plots of the beam envelope and particle distributions. These plots are available at the end of each cell and at the centers of the external quadrupole lenses. Besides the standard geometrical quantities, PARMILA also lists other parameters associated with the new structures, including CCDTL and CCL cell lengths, cavity spacing, and the external quadrupole-magnet characteristics.

Figure 2 shows sample profiles for a proton beam in a CCDTL between 7 and 20 MeV. The beam first goes through a matching section made of three CCDTL cavities and four quadrupole lenses. The next section ramps the accelerating gradient and the synchronous phase. The ramp stops at an energy of about 12 MeV. After the ramping section, the beam is accelerated to 20 MeV at a fixed accelerating gradient and synchronous phase. For a seamless design process, PARMILA can write a TRACE 3-D⁴ input file that contains all the linac beam-line elements. TRACE 3-D calculates a variety of useful matching conditions. For the example shown in Fig. 2, PARMILA used matched parameters that were determined by an earlier TRACE 3-D run.

Summary

PARMILA can now design DTL, CCL, and CCDTL linacs and simulate their beam dynamics performance. The code designs a single structure per run. Separate runs of each linac structure can be linked together to design and simulate the entire accelerator. At the time of this conference (May, 1995), documentation for the new code is still in preparation. We plan to announce the release of the code and its on-line documentation on the World Wide Web. Interested users can consult the home page of the Los Alamos Accelerator Code Group⁵ (URL:<http://www.atdiv.lanl.gov/doc/laacg/codehome/html>) for the latest information on PARMILA.

References

- ¹D. A. Swenson, D. E. Young, and B. Austin, "Comparison of the Particle Motions as Calculated by Two Different Dynamics Programs," Proceedings of the 1966 Linear Accelerator Conference, Los Alamos National Laboratory report LA-3609, p. 229 (1966).
- ²J. H. Billen, F. L. Krawczyk, R. L. Wood and L. M. Young, "A New Structure for Intermediate-Velocity Particles," Proceedings of the 17th International Linac Conference, Tsukuba, Japan (August, 1994).
- ³A. Carne, B. Schnizer, P. Lapostolle, and M. Promé in *Linear Accelerators*, edited by P. M. Lapostolle and A. L. Septier, North Holland Publishing Company, p. 747 (1970).
- ⁴K. R. Crandall and D. P. Rusthoi, *TRACE 3-D Documentation*, Los Alamos National Laboratory report LA-UR-90-4146 (1990).
- ⁵F. L. Krawczyk, J. H. Billen, R. D. Ryne, H. Takeda, and L. M. Young, "The Los Alamos Accelerator Code Group (LAACG)," this conference.

TRACKING PARTICLES WITH WAKE FIELDS AND SPACE CHARGE EFFECTS

J. A. Riche, CERN Meyrin, CH-1211 Geneva 23, SWITZERLAND

A simple and precise way to account for beam cavity interactions is the use of delta wake potentials known from RF calculations or measurements. When this procedure is introduced in a tracking program following super-particles such as in PARMELA, besides the effect of the space charge, the evolution of the charge distribution within the bunches of a train can be determined. The interesting application is for non-rigid bunches at intermediate or low energy, as for the study of Compact Linear Collider beams in the CLIC Test Facility at CERN.

I. INTRODUCTION

Beam dynamics can be calculated with 'self consistent' codes with corresponding determination of the fields and of the movement during successive steps of time, as in MAFIA [1]. Available memory space and computing time restrict the application to short distances.

Other codes, as DTRACK and MTRACK [2,3] can follow a beam sliced longitudinally allowing for the study of transverse displacements, wake field effects and their cancellation along a very long beam path. With the code PARMELA [4], a number of different 'external' electromagnetic fields can be taken into account with specialized routines. The self field due to the space charge and its effect can be calculated, the charge being distributed in super-particles with equal charges.

This paper discusses the implementation which was made for the effects of the wakefields created by interaction of these super-particles with corrugated cavities. The force on a particle can be calculated by summing the actions of the one particle wakefield (delta or Green's function) due to the particles in front. When using the modal description of the delta wake, the frequencies and the loss factors are characteristics of a segment of the tube and may be referenced to the longitudinal geometry of the line as is done for any other type of fields. Then part of the problem is to find these constants for a given segment.

A. The one particle wake field

The measurements or the calculations can be made in the time domain or in the frequency domain.

$$w_{L\delta}(t) = \int_0^\infty 4 \operatorname{Re}(Z_L(\omega)) \cos(\omega t) d\omega$$

$w_{L\delta}(t)$ and $Z_L(\omega)$ are the longitudinal delta wake field and impedance, as defined in [5].

Isolating the contribution of discrete frequencies in the expression of the longitudinal delta wake:

$$w_{L\delta}(t) = \sum_n \cos(\omega_n t) \int_{\omega-\epsilon}^{\omega+\epsilon} 4 \operatorname{Re}(Z_L(\omega)) d\omega$$

This corresponds to the modal description of the longitudinal delta wake in mode 0:

$$w_{L\delta}(t) = \sum_n 2 k_{\delta n} \cos(\omega_n t)$$

The expressions for the transverse wake are similar, but with a sine function, and the transverse delta wake for the dipole mode in a structure with cell iris radius a is:

$$w_{T\delta}(t) = \sum_n 2 k_{\delta n} (c/\omega_n) a^{-2} \sin(\omega_n t)$$

B. The programs giving the modal loss factors

In some cases the analytic expressions for $w_{\delta}(t)$ and $Z(\omega)$ are known, as for the resistive wall of a circular pipe [6]. For a corrugated structure with rotational symmetry, several codes are available. KN7C and TRANSVRS, requiring a simplified geometry have been used for obtaining the ω_n and $k_{\delta n}$ for the CLIC structure [7]. Time domain code ABCI [8] includes a Fourier transform of the time domain wake fields giving the impedance versus frequency variation, from which the discrete series of parameters of the modal description can be derived. For the 3D CLIC transfer structure, MAFIA gives the effective wake fields for a given gaussian bunch length [9]. The deconvolution giving $w_{\delta}(t)$ is much easier when the lowest modes are dominant.

C. Computing time limitations and the number of modes

Because the bunches are assumed to be non rigid, the delta wake field is calculated many times in the tracking program.

Short range

The number of modes necessary for describing the short range wake fields can be limited by using an integral equivalent of the summation on the upper modes, (optical resonator model), and, as this should be done at each time step, spline functions are prepared in advance for further interpolations depending on the structure type. Another approximation has been proposed [10], from considering the asymptotic behaviour of the loss factor for a gaussian bunch when its length tends to 0. The total loss factor as a function of the gaussian distribution rms value, and the delta wake as a function of distance s to the particle, can be written:

$$k_L(\sigma) = \sum g_n \sigma^{b_n} \quad \text{and} \quad w_{L\delta}(s) = \sum a_n s^{b_n}$$

with the same exponent b_n , and a_n depending on g_n and b_n .

The total loss factor is not necessarily known, but if the effective wake is known for a gaussian bunch, a deconvolution can provide the coefficients for b_n and a_n , leading to a description of the wake field near the particle with a sum of very few terms. This is shown in Fig. 1 for the CLIC longitudinal delta wake field and on Fig. 2 for the transverse one, for an approximation with 3 terms only.

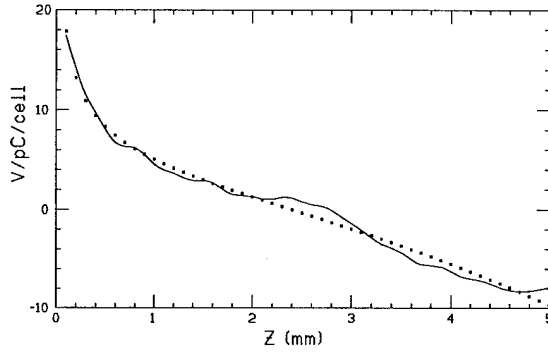


Fig. 1: CLIC longitudinal δ wake field (200 modes) and short range approximation

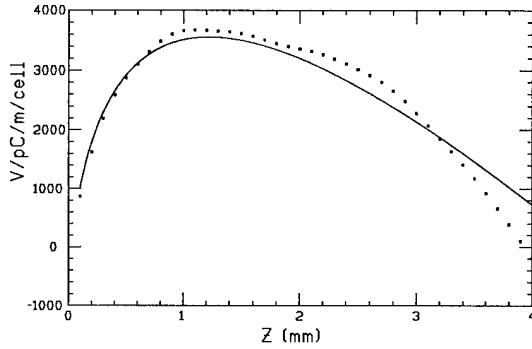


Fig. 2: CLIC transverse δ wake field (200 modes) and short range approximation

Long range

For the long range wake, the cancellation of the effects of the higher modes because of the frequency distribution is such that enough precision is attained when using only the first of them, as shown Fig. 3, where the longitudinal wake for CLIC obtained with 200 modes is compared with the one obtained with one mode only. For 9 modes, the difference is hardly visible at the same scale.

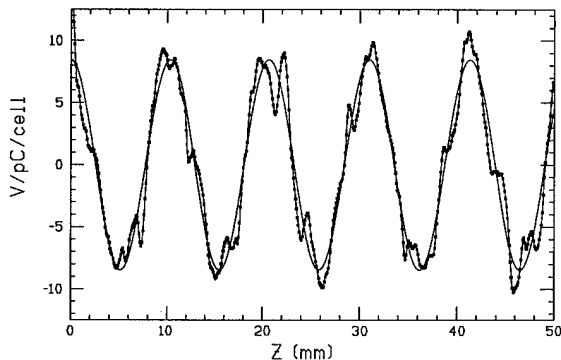


Fig. 3: CLIC longitudinal wake from 200 modes and long range description with one mode only

II. IMPLEMENTATION IN PARMELA.

The input file for the code is prepared in a very similar way to the operation without wake fields, but another file is given concerning the successive segments of the beam path where wake fields are considered, with references to different lists of frequencies, modal loss factors and group velocities.

All the particles are transported in each of the successive (and constant) intervals of time. The space charge forces are calculated for the distribution of the particles at a given time, and the kicks resulting from these forces are applied in advance for n_s basic time steps. The effect is therefore superimposed on the one due to the action of the external electromagnetic fields, calculated at each basic time step.

The action of the wake fields is superimposed in a similar way. They are also calculated for the distribution of the particles at a given time, and the resulting kicks applied on all particles for n_w successive basic time intervals.

Routines for the space charge and for the wake field are separated from those for the external fields and independent, which helps for implementation and for disconnecting the effects. By choosing the time interval, the precision can be adapted to the amount of charge, the energy and the degree of interaction with the walls. The simplicity of the kick formulation counterbalances the inconvenience of having many short time steps.

A. Logic of the code

When a particle position coincides with a zone with wake field, some of its parameters are recorded or updated at the previous limit of the zone. This is used to calculate the time separation between the particles, and the transverse coordinates all the particles in front had when passing by the same position as the considered one. Using the coordinates of the other particles at the same time could be misleading because the change in the parameters, specially the transverse coordinates of the particles far ahead can be significant.

If the group velocity v_g of the energy flow has been indicated as different from c in the data for the wake fields, the particle at a distance z from the entry of the structure is influenced only by the particles ahead distant by less than :

$$z (c - v_g) / v_g \quad [11].$$

This complicates the logic of the code, but it is the price to pay for tracking particles in non rigid bunches, that is even at low energy, with longitudinal crossing allowed. Particles are assembled into bunches at the input of the beam line. There is no limitation except available space for the total number of particles and available computer time.

B. Example of the output

As an example of the output, 2 gaussian bunches with $\sigma = 0.7$ mm, separated by 1 cm (360° of 30 GHz pulsing) are represented after 10 cm drift in the CLIC structure and 5 cm free drift. Initial energy is 60 MeV, charge per bunch 20 nC. The space charge effect is disconnected. The second bunch is represented shifted by 360° . An initial y transverse displace-

ment of 1 mm of both bunches at the input and the transverse wakes are the source of the divergence y_p of the particles recorded at the end. Initial emittance in y_p , and initial dispersion in momentum were chosen zero to exhibit the pure effect of the wakes. The grouping of macro particles close to the centres of the bunches comes from the initial gaussian distributions. The envelopes are shown for both bunches for 100% and 90% of the particles.

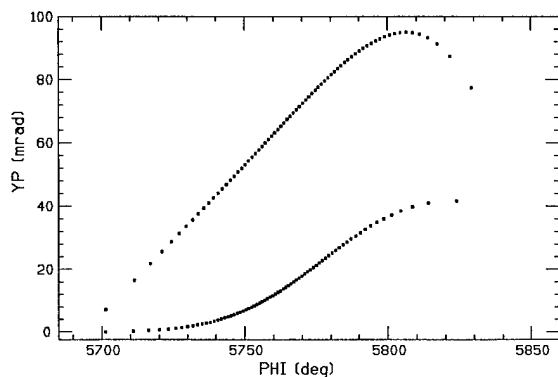


Fig. 4: Divergence induced by transverse wakes on 2 bunches

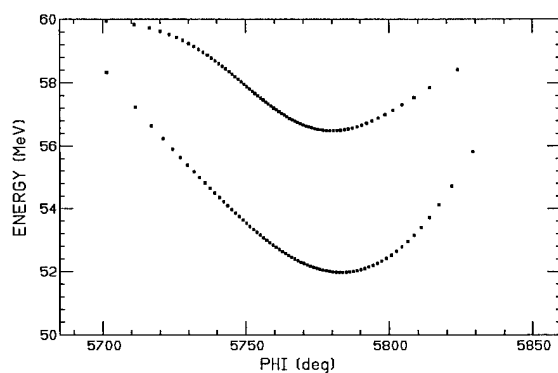


Fig. 5: Energy dispersion from longitudinal wakes on 2 bunches

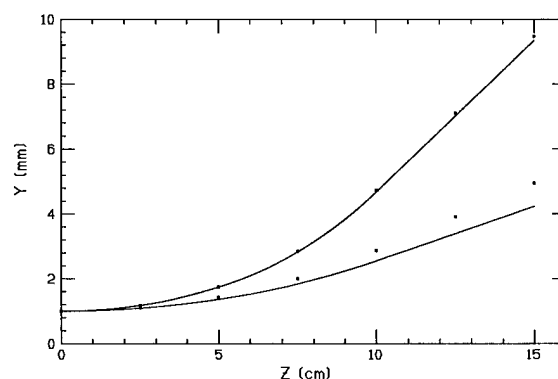


Fig. 6: Transverse envelope resulting from the wake field for 2 bunches

III. CONCLUSIONS

PARMELA has been transformed to treat carefully the action of the wake fields, using the modal description or the delta wake or another approximation. The version thus modified is called PARMTRACK [12]. All the existing parts of the code for treating accurately the action of the space charge and of the external fields have been kept unchanged.

Thanks go to G. Guignard for showing the need for a tracking program combining space charge and wake fields.

IV. REFERENCES

- [1] R. Klatt, F. Krawczyk, W.R. Novender, C. Palm, T. Weiland, B. Steffen, T. Barts, M.J. Browman, R. Cooper, C.T. Mottershead, G. Rodenz, S.G. Wipf, MAFIA, a 3D Electromagnetic CAD system for Magnets, RF Structure and Transient Wake Fields Calculations 1986 Linac Conf., SLAC 303, p. 276-278.
- [2] G. Guignard, Beam Stability Simulations in the Two CLIC Linacs, Int. Conf. on H.E.Accel., Hamburg 1992, p. 894-896.
- [3] G. Guignard, Tracking Codes for Bunchlets Trains in a Drive Linac, Int. Conf. on H.E.Accel., Hamburg 1992, p. 891-893.
- [4] B. Mouton, The PARMELA Program, (LAL/SERA 93-455, ORSAY). The version we have used is a combination of codes written at Los Alamos (D.A. Swenson, L. Young, K. Crandall, R. Mills, J. Stovall), BNL (K. Mc Donald), SLAC, IHEP, Beijing (H.Liu) compiled by B. Mouton.
- [5] B. Zotter, Electromagnetic Fields, Impedances and Wakes, AIP Conf. Proceedings 153, 1987, p. 664-696.
- [6] O. Henry, O. Napoly, The Resistive-Pipe Wake Potential for Short Bunches, CLIC Note 142, CERN, and DPhN-STAS/91-R08, CE SACLAY.
- [7] A. Millich, Computation of Wakefields for the CLIC Disk Loaded Waveguide, CLIC Note 137, CERN, and CERN/SL 91-27 (CO).
- [8] O. Napoly, Y.H. Chin, B. Zotter, A Generalized Method for Calculating Wake Potentials, CERN SL/AP 93-1.
- [9] A. Millich, CLIC Transfer Structure Simulation Using MAFIA, 1993 Particle Accel. Conf., Washington, p. 965-967.
- [10] A. Mosnier, Longitudinal and Transverse Wakes for the TESLA Cavity, CENS SACLAY, DAPHNIA-SEA, 9206.
- [11] L. Thorndahl, 30 GHz Longitudinal Wake and Compressed Pulse of the CLIC Transfer Structure (CTS), CLIC Note 218, CERN, and SL-RF/LT, Feb. 94.
- [12] J.A. Riche, PARMTRACK, a Program to Track Particles in Fields with the Effects of Space Charge and Wake Fields, CLIC Note 265, CERN.

ON THE IMPORTANCE OF FOURTH ORDER EFFECTS ON WAKEFIELD CALCULATIONS FOR SHORT BUNCHES*

Zenghai Li and Joseph J. Bisognano
CEBAF, 12000 Jefferson Avenue, Newport News, VA 23606

Abstract

The second-order FD-TD algorithm developed by Yee has been successful in wakefield calculations. However, unphysical results can be obtained in wakefunction calculations of very short bunches. A detailed study of this problem is presented in this paper. It is found that the truncation error inherent in the second-order Yee algorithm of standard codes is frequency dependent and is inadequate for wakefield calculations of short bunches which produce wakefields with high frequencies. A fourth order approach extending the work of J. Fang is presented, which reduces the truncation error two orders of magnitude. The results of the wakefunctions calculated by use of this fourth-order FD-TD algorithm are presented and compared with the results of the second-order FD-TD algorithm.

I. INTRODUCTION

Wakefunctions describe energy loss and transverse momentum change which a particle experiences when passing through a structure. Numerical calculations typically use a linear finite-difference time-domain (FD-TD) algorithm, known as the Yee [1] algorithm, to solve the Maxwell's equations. The algorithm has second order accuracy and has been widely used in numerical modeling of electromagnetic wave (microwave) interactions with arbitrary structures and beam-cavity interactions. The algorithm usually gives very good results by choosing an appropriate mesh and time step size. In the application of modeling microwave structures, good accuracy can be obtained by having the mesh size one tenth of λ_{min} [2]. In the application of wakefields calculations, good accuracy can be obtained by having the mesh size one fifth of σ , where σ is the rms bunch length of the driving particles, assuming a gaussian distribution.

Problems arise when the fields have high frequency components. These were encountered in the wakefields evaluations of the CEBAF 5-cell cavities. The CEBAF beam has very short bunch length. The spectrum of the current carried by the bunch contains very high frequency components. The wakefunctions calculated by use of TBCI and ABCI have unphysical oscillations even if the mesh size is one fifth of the rms bunch length.

It is found that these unphysical oscillations are due to the accuracy of the Yee algorithm and are frequency dependent. To solve the problem, we, extending J. Fang's work [3], developed a fourth-order finite-difference formalism in the cylindrical coordinate system. This formulae have accuracy to the forth order.

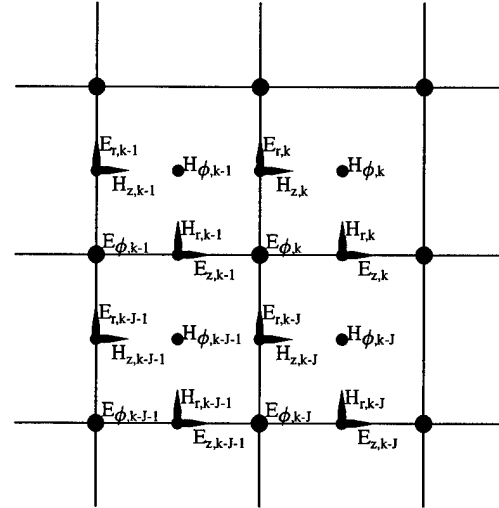


Figure. 1. The fields defined in the $r - z$ plane.

II. THE SECOND-ORDER FD-TD ALGORITHM

In this section, we present the FD-TD formulae in the cylindrical coordinate system used in TBCI [4]. The second-order FD-TD algorithm approximates the first-order time and spatial derivatives by linear finite differences. On the time axis, the H fields are evaluated a half time step ahead of the E fields, which gives a centered-difference analog to the time derivatives. Let the H fields be evaluated at times $n\Delta t$ and the E fields at times $(n + 1/2)\Delta t$, $n = 1, 2, 3, \dots$. The Maxwell's equations become

$$\mathbf{H}^{n+1} = \mathbf{H}^n - \frac{\Delta t}{\mu_0} \nabla \times \mathbf{E}^{n+1/2} \quad (1)$$

$$\mathbf{E}^{n+3/2} = \mathbf{E}^{n+1/2} + \frac{\Delta t}{\epsilon_0} \nabla \times \mathbf{H}^{n+1} - \frac{\Delta t}{\epsilon_0} \mathbf{J}^{n+1} \quad (2)$$

The fields are treated analytically in the ϕ coordinate, and are discretized in the $r - z$ plane as shown in Fig. 1. The first order derivatives in the curl operators in Eqs. (1) and (2) are replaced by linear finite differences

$$\frac{\partial(E, H)}{\partial x_i} \rightarrow \frac{(E, H)_{j+1} - (E, H)_j}{\Delta x_i} \quad (3)$$

The arrangement of the E and H fields in Fig. 1 provides a natural geometry which fulfills the centered-difference analog to the spatial derivatives of the curl operators in Maxwell's equations. The centered-difference scheme has accuracy to the second order.

To calculate the wakefield of a particle bunch, the fields are initially set to zero, $\mathbf{E}^{1/2} = 0$, $\mathbf{H}^0 = 0$, $\mathbf{J}^0 = 0$. The total electromagnetic fields can be calculated iteratively over these difference equations through the leapfrog process set forth by the centered-difference in the time axis.

*This work was supported by the U.S. Department of Energy, under contract No. DE-AC05-84ER40150.

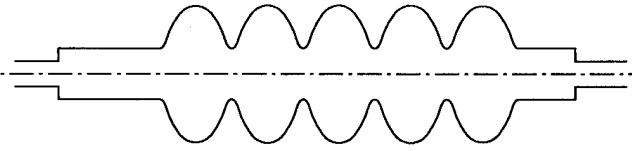


Figure 2. The cross section of the CEBAF 5-cell cavity.

The wakefunctions of the CEBAF superconducting cavity are calculated to demonstrate the shortcomings of the second-order FD-TD algorithm. The cross section of the CEBAF 5-cell cavity is as shown in Fig. 2. The mesh size used in the calculations is one fifth of the rms bunch length. The beam is on the axis. The wake is integrated at the beam pipe radius. The dashed line in Fig. 3 shows the longitudinal wakefunction of mode $m = 0$ for a 0.5 mm (rms) beam. The dotted line is the charge distribution. The wakefunction has strong oscillations starting from the tail of the bunch. These oscillations are unphysical since the strength is stronger than the wakefunction in the bunch region. The wakefunction calculated by TBCI for a 3 mm (rms) beam does not have the same problem, Fig. 4. This suggests that the error is bunch length dependent.

III. FOURTH-ORDER FD-TD ALGORITHM

Further studies showed [5] that the unphysical oscillations of the wakefunction in Fig. 3 is due to the truncation error of the second-order FD-TD algorithm. In principle, the problem can be solved by using a finer mesh. This may be impractical due to the limitation of computer memory. In this section, we derive a fourth-order FD-TD algorithm in the cylindrically symmetric coordinate system. The Yee lattice is used to define the fields. Fourth order accuracy is accomplished by including up to the third order derivatives of the fields in the Taylor expansions.

A. Fourth-order FD-TD algorithm

Expanding the E and the H fields to third order in time, we have

$$H^{n+1} = H^n + \Delta t \frac{\partial H^{n+1/2}}{\partial t} + \frac{\Delta t^3}{24} \frac{\partial^3 H^{n+1/2}}{\partial t^3} + O(\Delta t^5) \quad (4)$$

$$E^{n+3/2} = E^{n+1/2} + \Delta t \frac{\partial E^{n+1}}{\partial t} + \frac{\Delta t^3}{24} \frac{\partial^3 E^{n+1}}{\partial t^3} + O(\Delta t^5) \quad (5)$$

Replacing the time derivatives in Eqs. (4,5) by the curl operators defined by the Maxwell's equations, we have

$$H^{n+1} = H^n - \frac{\Delta t}{\mu_0} \nabla \times E^{n+1/2} - \frac{\Delta t^3 c^2}{24 \mu_0} \nabla \times \nabla^2 E^{n+1/2} + \frac{\Delta t^3 c^2}{24} \frac{\partial}{\partial t} (\nabla \times J^{n+1/2}) + O(\Delta t^5) \quad (6)$$

$$E^{n+3/2} = E^{n+1/2} + \frac{\Delta t}{\epsilon_0} \nabla \times H^{n+1} + \frac{\Delta t^3 c^2}{24 \epsilon_0} \nabla \times \nabla^2 H^{n+1} - \frac{\Delta t}{\epsilon_0} J^{n+1} + \frac{\Delta t^3}{24 \epsilon_0} \left(c^2 \nabla \times \nabla \times J^{n+1} \right.$$

$$\left. - \frac{\partial^2 J^{n+1}}{\partial t^2} \right) + O(\Delta t^5) \quad (7)$$

The first order derivatives involved in the curl operators are evaluated to the fourth order finite-difference as

$$\frac{\partial H_{z,k+1/2}}{\partial z} = \frac{H_{z,k+1} - H_{z,k}}{\Delta z} - \frac{\Delta z^2}{24} \frac{\partial^3 H_{z,k+1/2}}{\partial z^3} + O(\Delta z^4) \quad (8)$$

B. Frequency dependence of the higher-order terms

For a given mode, assuming that the fields have $e^{-j\omega t}$ time dependence, the third order terms in Eq. (6) have the following form (similarly for the E field in Eq. (7))

$$\Delta \left(\frac{\Delta H}{\Delta t} \right) = -j \frac{\Delta t^2 \omega^3}{24} H - \frac{\Delta z^2}{24 \mu_0} \left(\frac{\partial^3 E_\phi}{\partial z^3} r_0 - \left(\frac{\partial^3 E_r}{\partial z^3} - (k_r^2 + \frac{2}{r^2}) \frac{\partial E_z}{\partial r} + \frac{k_r^2}{r} E_z \right) \phi_0 - \left((rk_r^2 - \frac{1}{r}) \frac{\partial E_\phi}{\partial r} + 2k_r^2 E_\phi \right) z_0 \right) \quad (9)$$

Except for the phase difference, the third order derivatives respect to z can be written as $k_z^3(E, H)$ and the first order derivative respect to r is approximately $k_r(E, H)$. These higher-order terms are, therefore, proportional to $\omega(k\Delta z)^2$, or, $\omega(\frac{\Delta z}{\lambda})^2$. In general, $(\Delta z/\lambda)^2$ is small and is usually used as a measure of the magnitude of the contributions from the terms related. The situation here now is different, the coefficients of $(\Delta z/\lambda)^2$ linearly increase with the frequency. At high frequencies, these terms may not be "small" any more. Furthermore, the accumulated effects of these terms scale as $L_{cavity} \omega(k\Delta z)^2$ in the wakefunction calculation. The higher-order terms thus become more important in the wakefunction calculation of long structures.

In the second-order Yee algorithm, these terms are the lowest order truncation errors and are frequency dependent. Consider the case of wakefields driven by a gaussian bunch; the profile of the frequency spectrum of such a bunch is also gaussian. Frequencies that have lower magnitudes in the spectrum excite wakefields with lower amplitudes. The wakefields excited by the frequencies higher than a certain frequency will be negligibly small. Assuming this rolloff frequency is the frequency with a magnitude of 1% in the spectrum. The corresponding wave length of this frequency is $\lambda = 2\sigma$. Let the mesh size be one fifth of σ , that is $\Delta z/\lambda = 0.1$. This is the typical number suggested in [2] for numerical simulations of microwave propagation and in [4] for wakefield calculations. This number has been accepted as a general rule in the discretization of Maxwell's equations so that the meshes would have enough frequency resolution. This works fine in the calculation of the wakefields of long bunches where the rolloff frequency of the excitation of the wakefields is low. Good accuracy can be obtained with the choice of $\Delta z = \sigma/5$. In the calculation of wakefields of short bunches, the fields contain higher frequency components. The quantity $T\omega(\frac{\Delta z}{\lambda})^2$, where T is the total integration time, may no longer be small even if $\Delta z = \sigma/5$ or $\Delta z/\lambda = 0.1$ is retained since it depends linearly on the frequency and the integration time. The

rule of $\Delta z = \sigma/5$ is no longer valid. This is what we have seen in the examples studied in section II. Using smaller mesh size can improve the accuracy. But reducing the mesh size will increase the number of mesh points by many fold, for example 4 fold in the 2-D problem and 8 fold in the 3-D problems if the mesh size is halved. Computer memory becomes a problem.

The fourth-order FD-TD algorithm can reduce the truncation error to the fourth order

$$\omega \left(\frac{\Delta z}{\lambda} \right)^4 \quad (10)$$

Even though it is also linearly proportional to the frequency, the extra powers of $\Delta z/\lambda$ would greatly reduce the magnitude of the error. If the highest frequency of the excitation is not very high, the terms of the fourth order and higher of $\Delta z/\lambda$ are small.

C. Wakefunctionss calculated by fourth-order FD-TD algorithm

The fourth-order FD-TD algorithm was implemented in TBCI for testing. The results of the wakefunctions of the CEBAF 5-cell cavity of a 0.5 mm bunch are shown in Fig. 3 by the solid lines. The dashed lines are the results of the second-order FD-TD algorithm. The same mesh size is used, which is $\sigma/\Delta z=5$. No oscillations are observed in the fourth order result. The errors are suppressed.

IV. CONCLUSION

Higher-order truncation errors depend linearly on the frequency, and accumulate with time. The fourth-order FD-TD algorithm reduces these errors and is good for calculating the wakefields of sub-millimeter bunches. The fourth-order FD-TD algorithm takes more than six times longer CPU time than the second-order Yee algorithm. In exchange, there is no extra computer memory required.

References

- [1] Kane S. Yee, "Numerical Solution of Initial Boundary Value Problems Involving Maxwell's Equations in Isotropic Media," IEEE Trans. Antennas Proragat., vol. AP-14, pp. 302-307, May 1966.
- [2] A. Taflove, "Review of The Formulation and Applications of the Finite-difference Time-domain Method for Numerical Modeling of Electromagnetic Wave Interactions with Arbitrary Structures," Wave Motion, p547-582, 1988
- [3] J. Fang, Time Domain Finite Difference Computation for Maxwell's Equations, Ph.D. thesis, University of California at Berkeley, 1989.
- [4] T. Weiland, "Comment on Wake Field Computation in Time Domain," Nucl. Inst. and Meth. 216 p31-34, 1983.
- [5] Z. Li, Beam Dynamics in the CEBAF superconducting cavities, Ph.D. thesis, The College of William and Mary, 1995.

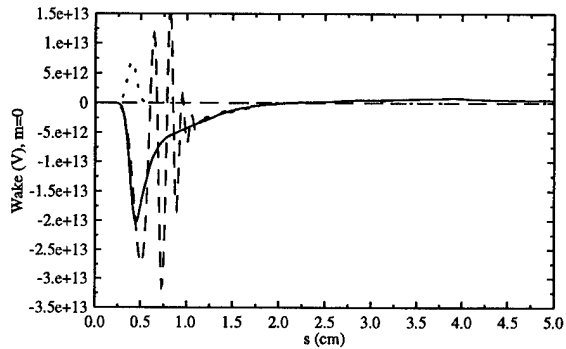


Figure 3. Wakefunction of the CEBAF 5-cell cavity, $\sigma = 0.5$ mm. Dashed line: the result of the second-order FD-TD algorithm; Solid line: the result of the fourth-order FD-TD algorithm.

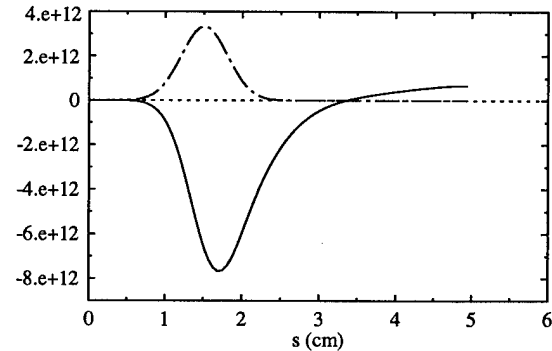


Figure 4. Wakefunction of the CEBAF 5-cell cavity, $\sigma_z = 3$ mm, second-order FD-TD algorithm.

COUPLING IMPEDANCES OF MUFFIN-TIN STRUCTURES WITH CLOSED AND OPEN SIDES

M. Filtz

Technische Universität Berlin, EN-2, Einsteinufer 17, D-10587 Berlin

Abstract

In a previous work the eigenmodes of a muffin-tin structure limited with lateral electric walls were calculated using the mode matching technique. Now a modulated off axis beam is introduced and the beam induced fields, as well as the longitudinal coupling impedances are calculated. Furthermore, in order to get the fields in case of the open structure, the discrete set of modes in the field expansions was replaced by a continuous spectrum. The appearing Fourier integrals are determined by means of the residuum calculus.

I. INTRODUCTION

In [1] an analytical solution based on the mode matching technique was proposed for calculating the fields in a periodic muffin-tin structure. In order to obtain a discrete set of modes in the drift region, a closed structure with electric walls at $x = \pm(w+d)/2$ was assumed. If one chooses the distance d large enough, the influence may be negligible for the resulting accelerating mode, but not for the deflecting mode, i.e. the dispersion relation for the deflecting mode depends strongly on the position of the electric walls. For example, if $d \rightarrow \infty$ one can expect that the cut-off frequency goes to zero. The purpose of the present paper is the extension of the previous analysis to an open structure (Fig. 1). Due to the lack of boundary conditions in x -direction, the fields in the drift region are now represented by a continuous spectrum of waveguide modes. The solution of this problem can be derived by utilizing the Fourier transform in combination with the mode matching technique.

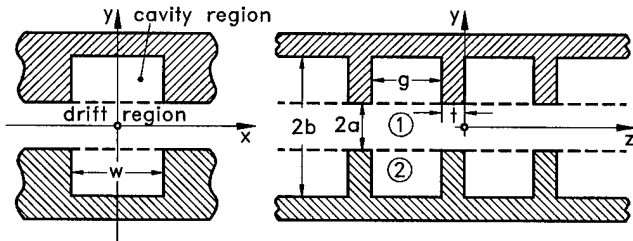


Figure 1. Transverse and longitudinal cut of the structure under consideration.

II. SOURCE FIELD IN THE DRIFT REGION

In order to determine the beam coupling impedances, we now introduce a charged particle $Q/2$ travelling off axis at $x = \delta x$, $y = \delta y$ with constant velocity $\mathbf{v} = \beta c \mathbf{e}_z$ in a parallel-plate waveguide. In the plane $y = 0$ we furthermore assume magnetic or electric boundary conditions (Fig. 2).

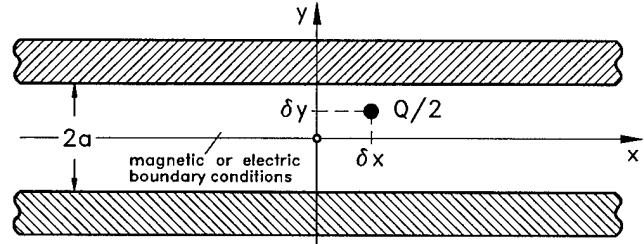


Figure 2. Charge $Q/2$ travelling in a parallel-plate waveguide.

In the frequency domain the magnetic field produced by this charge at $y = a$ can be written as the Fourier integral

$$H_x^{(s)} = -\frac{Q}{4\pi} e^{-j\frac{k}{\beta}z} \int_{-\infty}^{\infty} e^{j\xi(x-\delta x)} \frac{e^{\eta\delta y} \pm e^{-\eta\delta y}}{e^{\eta a} \pm e^{-\eta a}} d\xi \quad (1)$$

$$\eta = \sqrt{\left(\frac{k}{\gamma\beta}\right)^2 + \xi^2}, \quad \gamma^2 = \frac{1}{1-\beta^2}, \quad k = \frac{\omega}{c}$$

where the upper sign is valid for magnetic and the lower for electric boundary conditions at $y = 0$. Solving the Fourier integral by means of the residuum calculus one gets a different formulation

$$H_x^{(s)} = \frac{Q}{2a} e^{-j\frac{k}{\beta}z} \sum_i (-1)^i \left\{ \begin{array}{l} \cos p_i \delta y \\ \sin p_i \delta y \end{array} \right\} e^{-\lambda|x-\delta x|} \quad (2)$$

$$\lambda = \sqrt{p_i^2 + \left(\frac{k}{\gamma\beta}\right)^2}, \quad p_i = \left\{ \begin{array}{ll} (2i-1)\pi/2a, & \text{ma.} \\ i\pi/a, & \text{el.} \end{array} \right.$$

which will be used as a source term in the following.

III. THE SCATTERED FIELD PRODUCED BY THE CAVITIES

The field in the cavities can be determined in terms of standing wave functions as was done in [1]. Hence, in this paragraph we will only discuss the field expansion in the drift region 1, which can be written in the form

$$\mathbf{E}_t^{(1)} = \frac{Z_0 Q}{2\pi} \sum_n \int_{-\infty}^{\infty} \mathbf{F}_n(\xi, x, z) V_n(\xi, y) A_n(\xi) d\xi \quad (3)$$

$$\mathbf{e}_y \times \mathbf{H}_t^{(1)} = \frac{Q}{2\pi} \sum_n \int_{-\infty}^{\infty} \mathbf{F}_n(\xi, x, z) V_n'(\xi, y) A_n(\xi) Y_n^{(1)} d\xi$$

$$V_n(\xi, y) = \frac{-V_n^+(\xi, y) \mp V_n^-(\xi, y)}{V_n^+(\xi, a) \pm V_n^-(\xi, a)}, \quad V_n' = \frac{-j}{K_n^{(1)}(\xi)} \frac{\partial V_n}{\partial y}$$

$$V_n^\pm(\xi, y) = \exp \left\{ \mp j K_n^{(1)}(\xi) y \right\}, \quad K_n^{(1)}(\xi) = \sqrt{k^2 - \beta_n^2 - \xi^2}$$

$$Y_n^{(1)}(\xi) = \begin{cases} K_n^{(1)}(\xi)/k & , TE_y \\ k/K_n^{(1)}(\xi) & , TM_y \end{cases}, \quad \beta_n = \frac{k}{\beta} + \frac{2\pi n}{g+t}$$

$$\mathbf{F}_n(\xi, x, z) = j e^{-j(\beta_n z + \xi x)} \begin{cases} \beta_n \mathbf{e}_x - \xi \mathbf{e}_z & , TE_y \\ -\xi \mathbf{e}_x - \beta_n \mathbf{e}_z & , TM_y \end{cases}$$

As can be seen, the field is again decomposed in space harmonics with phase constants β_n and splitted into transverse electric (TE_y) and transverse magnetic (TM_y) components w.r.t $y = a$. The upper sign in V_n corresponds to a magnetic wall and the lower to an electric wall in $y = 0$. The main difference in Eq. (3) and the analogous field expansion in [1] is, that we now have to deal with an unknown continuous spectrum $A_n(\xi)$.

Due to lack of space, we will give only a brief summary of our analysis without mathematical details. Using the identity

$$\begin{aligned} \int_0^{g+t} \int_{-\infty}^{\infty} \mathbf{F}_n(\xi, x, z) \cdot \mathbf{F}_\nu^*(\xi', x, z) dx dz = \\ = 2\pi(g+t) \{ \beta_n^2 + \xi^2 \} \delta(\xi - \xi') \delta_\nu^\nu \end{aligned} \quad (4)$$

and satisfying the boundary condition for the electric field, one can express the unknown spectrum $A_n(\xi)$ in terms of the discrete coefficients of the field expansion in the cavity region 2. Substituting this spectrum into the Fourier integral of the magnetic field this integral can be written in the form

$$\begin{aligned} I_\nu = (-1)^m I_\nu^I - I_\nu^{II} = \\ = (-1)^m \int_{-\infty}^{\infty} f_\nu(\xi) e^{-j\xi(x - \frac{g}{2})} d\xi - \int_{-\infty}^{\infty} f_\nu(\xi) e^{-j\xi(x + \frac{g}{2})} d\xi. \end{aligned} \quad (5)$$

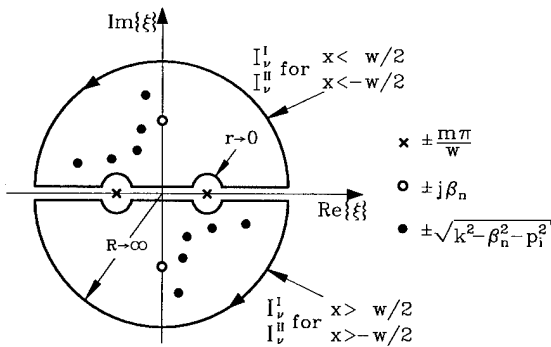


Figure 3. The location of poles in the complex plane.

The function $f_\nu(\xi)$ has poles at $\xi = \pm \frac{m\pi}{w}$, $\xi = \pm j\beta_n$, $\xi = \pm \sqrt{k^2 - \beta_n^2 - p_1^2}$. It can easily be shown, that the poles $\xi = \pm j\beta_n$ do not contribute, because they cancel each other after summing TE_y and TM_y modes. Fig. 3 shows the location of poles in the complex plane, and the integration path, where a complex wave number k with a small imaginary part was assumed. After solving the integral Eq. (5) by means of the residuum calculus, and satisfying the required continuity of the magnetic field, one finally gets a system of linear equations for the field coefficients in the cavity region.

IV. FINITE NUMBER OF CELLS

The analysis described above is valid for an infinite periodic structure. With a little modification however, we can use it to get results for a structure consisting of any finite number of cells. If we rotate the direction of the beam travelling along the structure by an angle of 90° around the y -axis, and if we choose zero phase advance per cell, i.e. $\beta_n = 2\pi n/(g+t)$, then we obtain the fields produced by one single cell (Fig. 4).

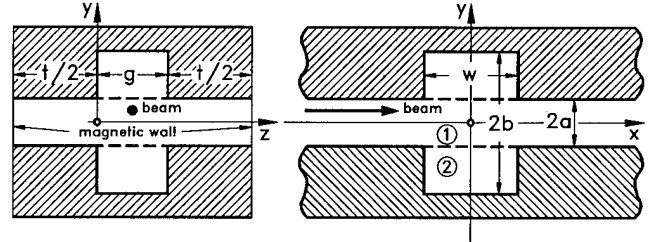


Figure 4. Changing the beam direction

As can be seen in Fig. 4, this manipulation leads to magnetic boundary conditions in the planes $z = -t/2$ and $z = g + t/2$, if the beam is located at $z = g/2$, $y = \delta y$. Of course, the meaning of dimension g has to be exchanged by w and vice versa. Adding more cells in x -direction is straightforward and leads to an increase of the number of linear equations by a factor of N , where N is the number of cells. Clearly, the structure is not exactly open. But it supports a TEM-wave, which radiates in beam direction and causes losses similar to those in a fully open structure.

V. NUMERICAL RESULTS

After solving the system of linear equations for the unknown field coefficients the integral

$$-Q Z(\omega) = \int_{z_1}^{z_2} E_z^{(1)}(x = \delta x, y = \delta y, z) e^{-j\frac{k}{\beta} z} dz \quad (6)$$

giving the longitudinal coupling impedance was evaluated, where $z_1 = 0$, $z_2 = g + t$ for an infinite periodic structure and $z_{1,2} = \mp\infty$ for a finite number of cells. Varying $\beta = v/c$ and looking for the peaks in Eq. (6), one obtains the dispersion relation which is plotted in Fig. 5 for the first deflecting mode, and compared to the closed structure analyzed in [1]. Obviously, the cut-off frequency goes to zero and there is no beam environment interaction for $\beta = 1$. Fig. 6+7 show the impedance of one single cell with electric or magnetic boundary conditions in $y = 0$, respectively. Below the cut-off frequency three sharp resonances can be observed. The following table gives their values in comparison to results from the FD computer code GDFIDL [3].

$\frac{f}{\text{GHz}}$ (analytic)	120.0	223.4	243.1
$\frac{f}{\text{GHz}}$ (GDFIDL)	120.1	223.2	241.8

The low frequency behaviour of the impedance in case of electric boundary conditions in $y = 0$, which allow the excitation of a TEM field, is similar to that calculated in [2] for a coaxial TEM structure, i.e. the imaginary part goes nearly linear with frequency and is much greater than the real one. Finally, in Fig. 8 the splitting up of the lowest cavity resonance

in a ten cell structure is demonstrated, where a small imaginary part of the wavenumber $k = \omega\sqrt{\epsilon\mu} + j \cdot 10^{-4}$ was assumed. As can easily be recognized, the strongest resonances occur at about 122 GHz, which agrees very well with the $\frac{2\pi}{3}$ accelerating mode from the dispersion relation in [1].

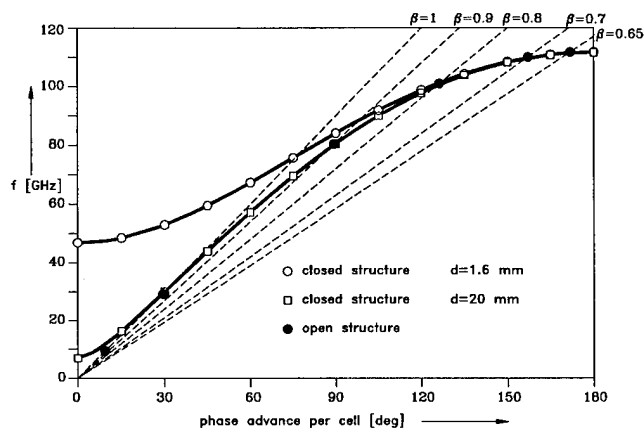


Figure 5. Dispersion relation for the first deflecting mode in a closed and open structure. ($a = 0.3$ mm, $b = 0.9$ mm, $w = 1.8$ mm, $g = 0.633$ mm, $t = 0.2$ mm)

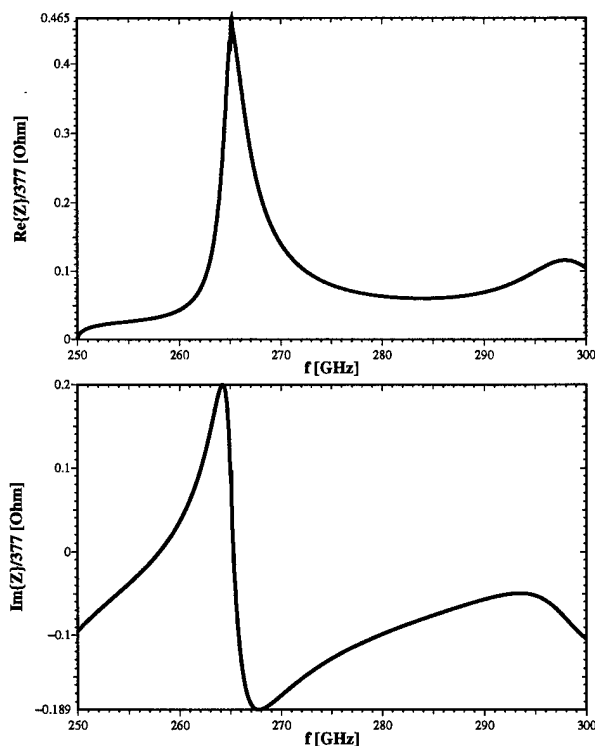


Figure 6. Longitudinal impedance of one single cell with no beam offset $\delta x = \delta y = 0$ and above cut-off frequency $f = 250$ GHz. ($a = 0.3$ mm, $b = 0.9$ mm, $w = 1.8$ mm, $g = 0.633$ mm, $d = 1.6$ mm)

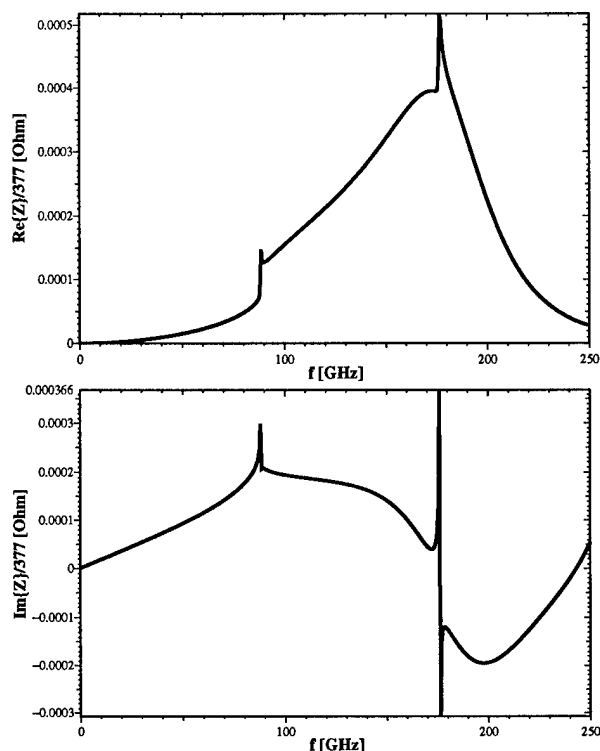


Figure 7. Longitudinal impedance of deflecting modes for a single cell with beam offset $\delta y = 0.01$ mm. ($a = 0.3$ mm, $b = 0.9$ mm, $w = 1.8$ mm, $g = 0.633$ mm, $d = 1.6$ mm)

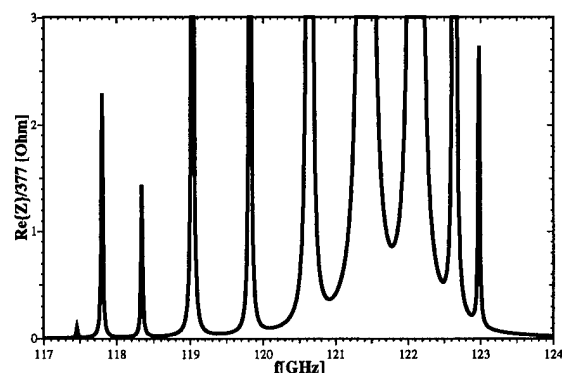


Figure 8. Real part of the longitudinal impedance per resonator for a ten cell structure with no beam offset. ($a = 0.3$ mm, $b = 0.9$ mm, $w = 1.8$ mm, $g = 0.633$ mm, $t = 0.2$ mm, $d = 1.6$ mm)

References

- [1] M. Filtz, "Analytical Calculation of Waves in a Muffin-Tin Structure", Proc. of European Particle Accelerator Conf., London 1994, pp.1271-1273
- [2] M. Filtz and T. Scholz, "Impedance Calculations for a Coaxial Liner", Proc. of European Particle Accelerator Conf., London 1994, pp.1333-1335
- [3] W. Bruns, "GDFIDL: A Finite Difference Program for Arbitrarily Small Perturbations in Rectangular Geometries", to be presented at the COMPUMAG 95, Berlin

EXPLICIT SOFT FRINGE MAPS OF A QUADRUPOLE

John Irwin and Chun-xi Wang

Stanford Linear Accelerator Center, Stanford University, Stanford, CA 94309 USA

Abstract

The analytic linear and nonlinear zero-length fringe maps are calculated explicitly for a normal quadrupole up to 6-th order generators. A very simple leading term is found for the linear fringe map. The 4-th order leading term is the L. Whiting's hard edge result as expected. No significant leading term at the 6-th order are found. Our results should be useful to estimate the significance of the soft fringe of a quadrupole to beam dynamics. The method used in this calculation can be used to compute the soft fringe maps of various magnets.

I. INTRODUCTION

Fringe fields exist for all kinds of magnets. They are an important source of nonlinearity in beam dynamics. Although maps including fringe fields can be calculated numerically using program like MARYLIE [3], [6], they are often neglected due to either their weak effects or the difficulties to handle them. It should be useful to have handy analytic fringe maps to estimate the significance of the fringe fields at various orders. An analytic map will be physically more meaningful also. There are some analytic results for hard-edge fringe maps[4], [10] but none for soft-fringe maps. In this paper, we calculate the linear and nonlinear symplectic maps of a normal quadrupole fringe field. For simplicity, we consider only the geometric nonlinearity. The authors would like to thank A. Dragt for calculating fringe maps numerically using his MARYLIE.

II. POSITION DEPENDENT HAMILTONIAN

For an on-momentum particle in a normal quadrupole, the Hamiltonian reads

$$\begin{aligned} H(x, P_x; y, P_y; z, \delta) \\ = -\frac{eA_z}{P_0} - \left[1 - (P_x - \frac{eA_x}{P_0})^2 - (P_y - \frac{eA_y}{P_0})^2 \right]^{\frac{1}{2}} \\ \simeq -\frac{eA_z}{P_0} + \frac{1}{2} \left[(P_x - \frac{eA_x}{P_0})^2 + (P_y - \frac{eA_y}{P_0})^2 \right] \end{aligned} \quad (1)$$

where P_x, P_y are the normalized momenta with respect to P_0 , and $\delta = \Delta P/P_0$; \vec{A} is the vector potential of the magnetic field. In the last step we dropped the kinematic nonlinear terms also. In fact, even the kinematic nonlinearity is significant for the whole quadrupole, it may not be important (at least at the 4-th order) in the fringe map we are considering because of the shortness of the fringe region.

For a magnetic field with cylindrical symmetry, its vector potential can be obtained from the on-axis field [5], [9]. In a conveniently chosen gauge, the non-zero components of a normal multipole are

$$A_r = \frac{\cos m\theta}{m} r \frac{\partial}{\partial z} \phi_m, \quad A_z = -\frac{\cos m\theta}{m} r \frac{\partial}{\partial r} \phi_m \quad (2)$$

where

$$\phi_m(r, z) = \sum_{l=0}^{\infty} \frac{(-1)^l m!}{2^{2l} l! (m+l)!} C_m^{(2l)} r^{m+2l}.$$

For a normal quadrupole with an on-axis gradient $G(s)$, $m = 2$ and $C_2 = \frac{1}{2} G(s)$. From the expansion of the vector potential, we can expand the Hamiltonian keeping up to 6-th order terms. This yields the approximate position dependent Hamiltonian to be used in our map calculation

$$\begin{aligned} H(s) = & \frac{1}{2} (P_x^2 + P_y^2) + \frac{1}{2} k(s) (x^2 - y^2) - \\ & \frac{1}{4} k'(s) (x P_x + y P_y) (x^2 - y^2) - \frac{1}{12} k''(s) (x^4 - y^4) \\ & + \frac{1}{32} k'^2(s) (x^4 - y^4) (x^2 - y^2) \\ & + \frac{1}{48} k'''(s) (x P_x + y P_y) (x^4 - y^4) \\ & + \frac{1}{256} k^{(4)}(s) (x^4 - y^4) (x^2 + y^2) + O(X^8) \end{aligned} \quad (3)$$

where $k(s) = \frac{e}{P_0} G(s)$ is the position dependent quadrupole strength.

If the quadrupole is long compared to its fringe field region, its strength approaches a constant $k_0 \equiv k(0)$ inside the quadrupole. We will treat the fringe field part as perturbation, i.e.

$$H(s) = H_0(s) + \tilde{H}(s) \longrightarrow H_0(s) \quad \text{outside fringe} \quad (4)$$

The perturbation term is chosen in two ways. In the nonlinear fringe map section, we use

$$H_0(s) = \frac{1}{2} (P_x^2 + P_y^2) + \frac{1}{2} k(s) (x^2 - y^2) \quad (5)$$

$$\tilde{H}(s) = H(s) - H_0(s) = \text{nonlinear terms in Eq.(3)}$$

In the linear fringe map section, we choose $H_0(s)$ a piece-wise constant Hamiltonian of an ideal quadrupole

$$H_0(s) = \begin{cases} \frac{1}{2} (P_x^2 + P_y^2) + \frac{1}{2} k_0 (x^2 - y^2) & s \leq s_0 \\ \frac{1}{2} (P_x^2 + P_y^2) & s > s_0 \end{cases} \quad (6)$$

and $\tilde{H}(s) = \frac{1}{2} \tilde{k}(s) (x^2 - y^2)$, where

$$\tilde{k}(s) = \begin{cases} k(s) - k_0 & s \leq s_0 \\ k(s) & s > s_0 \end{cases} \quad (7)$$

$s_0 = \frac{1}{k_0} \int_0^\infty k(s) ds$, the effective "magnetic length". Our results will be expressed in terms of the moments of $\tilde{k}(s)$

$$\begin{aligned} I_0 = \int_{s_0}^\infty k(s) ds, \quad I_1 = \int_{-\infty}^\infty \tilde{k}(s) (s - s_0) ds \\ I_2 = \int_{s_0}^\infty k(s) (s - s_0)^2 ds, \quad I_3 = \int_{-\infty}^\infty \tilde{k}(s) (s - s_0)^3 ds \end{aligned} \quad (8)$$

$$\begin{aligned}
\text{and } K &= \int_{-\infty}^{\infty} k'(s)^2 ds, \quad K_0 = \int_{-\infty}^{\infty} \tilde{k}(s)^2 ds \\
K_1 &= \int_{-\infty}^{\infty} k'(s)^2 (s - s_0)^2 ds \\
K_2 &= \int_{s_0}^{\infty} ds \int_s^{\infty} ds' k(s) k(s') (s' - s) \quad (9)
\end{aligned}$$

We assumed that $\tilde{k}(s)$ is anti-symmetric about the edge s_0 . It is nature to characterize the fringe width via the rms width σ of the bell-shaped function $k'(s)$ as

$$\sigma^2 = \frac{\int_0^{\infty} k'(s)(s - s_0)^2 ds}{\int_0^{\infty} k'(s) ds} = \frac{2I_1}{k_0} \quad (10)$$

3σ is a good measure of the half width of fringe region.

III. NON-LINEAR FRINGE MAP

Consider the map from the center of the quadrupole $s_1 = 0$ to a point s_2 that is far outside the fringe field region. Our goal is to find a symplectic fringe map \mathcal{Q}_f which represents the fringe field effects so that the map $\mathcal{M}(s_1 \rightarrow s_2)$ can be written as

$$\mathcal{M}(s_1 \rightarrow s_2) = \mathcal{M}_Q(s_1 \rightarrow s_0) \mathcal{Q}_f \mathcal{M}_{drift}(s_0 \rightarrow s_2) \quad (11)$$

where \mathcal{M}_Q is the map of an ideal quadrupole of strength k_0 and length $s_0 = L_{eff}$; \mathcal{M}_{drift} is the drift map from s_0 to s_2 . (They may contain kinematic nonlinearity even though we neglect it in our calculation of \mathcal{Q}_f . This approximation may not be good at the 6-th order)

Before working on Eq.(11), we concentrate on the non-linear part, i.e. considering

$$\mathcal{M}(s_1 \rightarrow s_2) = \mathcal{R}_-(s_1 \rightarrow s_0) \tilde{\mathcal{Q}}_f \mathcal{R}_+(s_0 \rightarrow s_2) \quad (12)$$

where \mathcal{R}_{\pm} are exact linear maps. To calculate this, we choose the perturbation $\tilde{H}(s)$ as in Eq.(5), slice the time dependent Hamiltonians into pieces and move all the linear map before and after s_0 to the left and right side respectively using similarity transformation. This process is exact. Then we concatenate all the nonlinear pieces into a perturbation map $\tilde{\mathcal{Q}}_f$ via 2nd order BCH formula. Since we are concerned with up to 6-th order generators, 3rd and higher order BCH terms do not contribute in this case. Therefore

$$\tilde{\mathcal{Q}}_f = e^{-\int_{s_1}^{s_2} ds \tilde{H}(s) + \frac{1}{2} \int_{s_1}^{s_2} ds \int_{s_1}^{s_2} ds' [\tilde{H}(s), \tilde{H}(s')]} \quad (13)$$

where $\tilde{H}(s) = \tilde{H}(s, R(s_0 \rightarrow s)X)$; X represents the phase space variables and $R(a \rightarrow b)$ is the exact linear matrix from a to b .

To carry out the integrations in Eq.(13), usually we need to know the exact linear matrix $R(s_0 \rightarrow s)$. However, since the fringe region is expected to be very short, we can Taylor expand $R(s_0 \rightarrow s)X$ about s_0 and truncate at a suitable order of $\Delta s = s - s_0$. The coefficients of the series involve the derivatives of $k(s)$ and the dynamical variables at location s_0 , which can be obtained via the Hamiltonian equations. This is a unique point in our approach. It is also possible to get exact results via integrals involving sine-like and cosine-like orbits as was done in [10], [7].

There is a subtlety about the convergence of this approach. Although in principle it should converge because the linear orbit

is a well behaved function, convergence could be slow due to cancellations among various orders. Fig.1 shows the deviation of the various order expansions in Δs from the exact linear orbit in the fringe region. We see that though the approximations inside the fringe region are getting better, they become worse outside. Fortunately, the fringe region is short. Therefore, the expansion needs to be good only within a certain window covering the fringe, and the integrations in Eq.(13) is over that window. This will suppress the high order moments and help convergence. The low order moments will not change much when the window is sufficiently large to maintain the original boundary conditions.

The 4-th order generators of $\tilde{\mathcal{Q}}_f$ result from the integration of Hamiltonian only. Expansion up to Δs^5 is used.

$$\begin{aligned}
F_4 \simeq & \frac{k_0}{12} [P_x(x^3 + 3xy^2) - P_y(y^3 + 3yx^2)] \\
& - \frac{1}{72} [6k'(s_0)I_1 + k'''(s_0)I_3](x^4 + 6x^2y^2 + y^4) \\
& - \frac{k(s_0)I_1}{6} (5x^3P_x + 9xP_xy^2 + 9yP_yx^2 + 5y^3P_y) \\
& + \frac{I_1}{2} (xP_x + yP_y)(P_x^2 - P_y^2) \quad (14)
\end{aligned}$$

The first term is the well-known hard-edge result; in which case $I_1 = I_3 = 0$. The other terms are due to the soft edge; the correction is usually quite weak. However, the effect of the pseudo-octupole term on tune shift has been observed[8]. The coefficient of this term can also be given by a slightly more accurate form $(k_0I_0 + K_0)/12$. A quick estimate of the coefficient I_1 can be done via Eq.(10).

The 6-th order generators of $\tilde{\mathcal{Q}}_f$ result from integrations of the 6-th order terms in \tilde{H} (up to Δs^3) and the Poisson bracket (up to Δs^2) of the 4-th order terms in \tilde{H}

$$\begin{aligned}
F_6 \simeq & -\frac{K}{288} (x^2 + y^2)(x^4 + 14x^2y^2 + y^4) \\
& + \frac{k_0k'(s_0)}{384} (x^2 + y^2)(x^4 + 10x^2y^2 + y^4) \\
& - \frac{5K_1k(s_0)}{96} (x^2 - y^2)(3x^4 + 2x^2y^2 + 3y^4) \\
& - \frac{K_0 - 2k_0I_0}{8} (x^2 - y^2)^3 \\
& + \frac{k_0k(s_0)}{48} (2P_x x^5 + 3P_y x^4 y + 11P_x x^3 y^2 + 11P_y x^2 y^3 \\
& \quad + 3P_x x y^4 + 2P_y y^5) \\
& + \frac{5K_1}{96} (15P_x^2 x^4 - P_y^2 x^4 - 8P_x P_y x^3 y - 6P_x^2 x^2 y^2
\end{aligned}$$

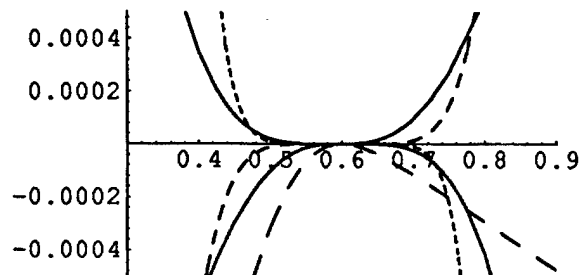


Figure 1. Deviations of expansions from exact linear orbit

$$\begin{aligned}
& -6P_y^2x^2y^2 - 8P_xP_yxy^3 - P_x^2y^4 + 15P_y^2y^4) \\
& - \frac{K_0 - 2k_0I_0}{24}(9P_x^2x^4 + 2P_y^2x^4 + 18P_xP_yx^3y + 3P_x^2x^2y^2 \\
& + 3P_y^2x^2y^2 + 18P_xP_yxy^3 + 2P_x^2y^4 + 9P_y^2y^4) \\
& + \frac{k_0}{96}(-5P_x^3x^3 + 7P_xP_y^2x^3 - 3P_x^2P_yx^2y + 9P_y^3x^2y \\
& - 9P_x^3xy^2 + 3P_xP_y^2xy^2 - 7P_x^2P_yy^3 + 5P_y^3y^3) \quad (15)
\end{aligned}$$

At 6-th order, there are no dominant term like the hard-edge term at 4-th order. The nonlinear fringe map in Eq.(12) is

$$\tilde{Q}_f = e^{iF} \quad \text{with} \quad F = F_4 + F_6 \quad (16)$$

IV. LINEAR FRINGE MAP

To obtain the fringe map Q_f in Eq.(11), we still need to work out the linear maps in Eq.(12). Now the Hamiltonians are given by Eq.(6). We use the same approach to treat the linear perturbation term and factor out a linear perturbation map at the edge s_0 . Since we are dealing with 2-nd order terms, all terms in the BCH series are the same order. Therefore it may be necessary to sum an infinite series. However, the second order BCH formula yields very good approximation due to the weakness of fringe perturbation.

The two linear maps in Eq.(12) are found to be

$$\begin{aligned}
\mathcal{R}_-(s_1 \rightarrow s_0) &= \mathcal{M}_Q(s_1 \rightarrow s_0) e^{if_2^-} \\
\mathcal{R}_+(s_0 \rightarrow s_2) &= e^{if_2^+} \mathcal{M}_{drift}(s_0 \rightarrow s_2) \quad (17)
\end{aligned}$$

$$\begin{aligned}
\text{with } f_2^- &\simeq \frac{I_0}{2}(x^2 - y^2) - \frac{I_1}{2}(xP_x - yP_y) + \frac{I_2}{2}(P_x^2 - P_y^2) \\
& - \frac{k_0I_2}{2}(x^2 + y^2) - \frac{k_0I_3}{3}(xP_x + yP_y) + \frac{K_2}{2}(x^2 + y^2) \quad (18)
\end{aligned}$$

$$\begin{aligned}
\text{and } f_2^+ &\simeq -\frac{I_0}{2}(x^2 - y^2) - \frac{I_1}{2}(xP_x - yP_y) \\
& - \frac{I_2}{2}(P_x^2 - P_y^2) + \frac{K_2}{2}(x^2 + y^2) \quad (19)
\end{aligned}$$

It is easy to concatenate the two linear fringe maps via 2-nd order BCH formula and get the total linear fringe map

$$\mathcal{R}_f = e^{if_2^-} e^{if_2^+} = e^{if_2} \quad (20)$$

f_2 has a significant leading term generating the matrix $\text{diag}\{e^{I_1}, e^{-I_1}, e^{-I_1}, e^{I_1}\}$, which yields a scale change of the phase space. The order of this effect is given by the dimensionless parameter I_1 .

To finish our calculation of the fringe map Q_f , we combine Eqs.(11, 12, 16, 17) and obtain

$$Q_f = e^{if_2^-} \tilde{Q}_f e^{if_2^+} = \mathcal{R}_f \exp\{e^{-if_2^+} F : \} \quad (21)$$

V. PEP-II Q1 MAGNET SOFT FRINGE FIELD EFFECTS

As an example, we will show the fringe field effects of the PEP-II Q1 magnet. It is a permanent magnet with the on-axis gradient $G(s)$ given by [1]

$$B_r \left[\frac{5}{8}z \left(\frac{v_1}{r_1^2} - \frac{v_2}{r_2^2} \right) + \frac{3}{8} \frac{1}{z} \left(\frac{1}{v_1} - \frac{1}{v_2} \right) + \frac{z}{8} \left(\frac{v_1^3}{r_1^2} - \frac{v_2^3}{r_2^2} \right) \right] \Big|_{z=s-L}^{z=s+L}$$

where $v_{1,2} = [1 + (\frac{z}{r_{1,2}})^2]^{-\frac{1}{2}}$. $s = 0$ is at the center of the quadrupole. L is half of its physical length. $r_{1,2}$ are the inner and outer radius. B_r is the remanent field of the permanent magnetic material. The parameters used are [2] $r_1 = 8.7$ cm, $r_2 = 16.6$ cm, $L = 60.0$ cm, $B_r = 1.05$ T, $G(0) = 10.64$ T/m. Also positron momentum $P_0 = 3.1$ GeV/C of the low energy ring is used. These yield the quantities defined in Eqs.(8,9) as

$$\begin{aligned}
k_0 &= 1.029\text{m}^{-2}, \quad L_{eff} = 0.60\text{m}, \quad I_0 = 2.28 \times 10^{-2}\text{m}^{-1}, \\
I_1 &= 1.85 \times 10^{-3}, \quad I_2 = 7.56 \times 10^{-5}\text{m}, \quad I_3 = 1.95 \times 10^{-5}\text{m}^2, \\
K &= 5.65\text{m}^{-5}, \quad K_0 = 0.0127\text{m}^{-3}, \quad K_1 = 0.00678\text{m}^{-3}, \\
K_2 &= 1.05 \times 10^{-5}\text{m}^{-1}
\end{aligned}$$

We calculated our fringe map generator coefficients and checked them against MARYLIE, which shows agreement at 4-th order and terms of 6-th order with momentum power less than 2(e.g. xP_xy^4 , x^6). The disagreement may be due to the kinematic terms. The four coefficients in F_4 is 0.086 , 4.4×10^{-4} , -1.5×10^{-4} , 8.6×10^{-4} . For beam dynamics, more useful figures are the coefficients in the normalized coordinates ($x = \sqrt{\beta}\hat{x}$, $P_x = (\hat{P}_x - \alpha\hat{x})/\sqrt{\beta}$). At Q1, $\beta \simeq 100$ and $\alpha \simeq 40$. The coefficients read 340 , 4.4 , 0.6 , 0.3×10^{-3} . The largest normalized coefficient in F_6 is the order of 2×10^4 .

References

- [1] G. B. Bowden, ABC technical note, no. 046, 1991
- [2] PEP-II conceptual design report, 1993, P.278
- [3] A. Dragt, et al, MARYLIE 3.0 user's manual,
- [4] E. Forest, J. Milutinovic, SSC report no.142
- [5] E. Forest, Ph.D thesis
- [6] G. H. Hoffstatter, M. Berz, Proceedings 1993 conference on computational accelerator physics.
- [7] B. Hartmann, M. Berz and H. Wollnik, NIM A208, 343(1990)
- [8] P. Krejeik, Proceedings of the 1987 IEEE particle accelerator conference, p.1278
- [9] M. Reiser, Theory and design of charged particle beams, New York, Wiley 1994
- [10] L. Whiting, NIM 83(1970) 232-244

Bunched Beam Cooling for the Fermilab Tevatron

Ralph J. Pasquinelli, Fermilab*, Batavia, IL. 60510 USA

ABSTRACT

Fermilab has been working on bunched beam transverse stochastic cooling in the Tevatron since 1990. In that time much progress has been made in understanding the difficulties of making such a system work with reasonable cooling times. Problems with common mode rejection of longitudinal signals, wide band GHz signal transmission using fiber optics, and specialized optical techniques of recursive notch filters have been researched and employed. Specialized planar loop pickup and kicker arrays were developed. Signal suppression has been observed. Efforts are underway to eliminate the coherent signals that dominate the Schottky spectrum.

I. INTRODUCTION

Emitance blow up in the Tevatron has been a cause of decreased integrated luminosity during the history of collider runs. The motivation for using stochastic cooling to reduce emitances and increase integrated luminosity has been reported earlier.¹ The success of stochastic cooling for DC coasting beams has been proven for over a decade. To date, limited stochastic cooling success has been achieved with bunched beams.² The cooling of high energy beam (900 GeV in the Tevatron) has not yet been successful. Four cooling systems have been designed in the 4-8 GHz band, one each for horizontal and vertical proton and antiproton beams. The intention of this paper is to present a progress report and current status of the systems at Fermilab.

II. HARDWARE

A. Pickups and Kickers

When the bunched beam cooling project started in 1990, it was clear that a new type of pickup electrode would be beneficial. The three dimensional designs that have been in use in the Antiproton Source did not have the mechanical tolerances required for this project. A new planar loop array was designed and built.³ The necessity of high common mode signal rejection required mechanical tolerances of the arrays to several mils. The arrays used for the current systems are a second generation planar array that no longer requires the use of via holes on the circuit card to connect the loops to the combiner board. The new design has been used successfully not only for this project, but for all cooling upgrades at 1-2 GHz, 2-4 GHz and 4-8 GHz in the Fermilab Antiproton Source. Variation in beam size during acceleration necessitated the design of plunging arrays to avoid aperture restriction. Initial tests using a connectorized microwave hybrid for subtracting the lab test signals indicated that the reproducibility of connections was not satisfactory for

optimal common mode rejection. It was decided to design the arrays on a single circuit card that would also include the differencing hybrid. (figure 1) The hybrid is a patented design⁴ developed at Fermilab that provides better than 0.2 dB amplitude balance and 2 degrees phase balance across the 4-8 GHz band. When signals are properly timed, this hybrid provides 40 dB minimum of common mode rejection in the difference output port. An added feature to improve common mode rejection is the use of inchworm motors (piezo electric) on one half of the array. These motors have the ability to move one array longitudinally with respect to the other by approximately 0.25 inch. This is in effect an adjustable delay that allows for precision timing of the signals prior to the subtraction in the hybrid.

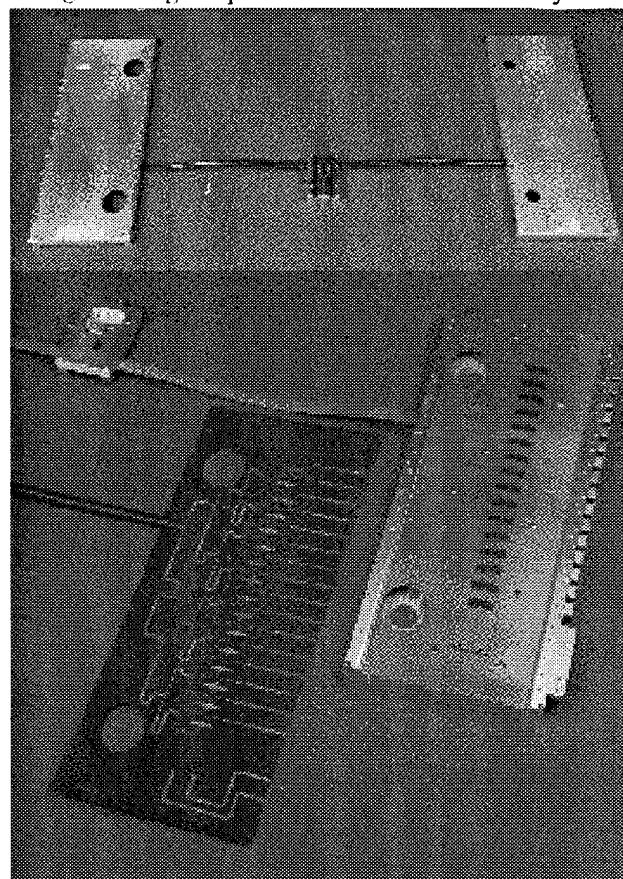


Figure 1: Teflon circuit board with planar 4-8 GHz pickup/kicker arrays. Differencing hybrid is part of circuit board making a connectorless array to hybrid assembly. Shown here laid out flat, the two sides of the array are folded to meet each other in a horizontal or vertical plane.

B. Gating

Early in the project it was discovered that gating of the feedback system was imperative. The location of the pickups and kickers in the TEVATRON are approximately 100 meters apart. The evanescent modes propagating down the beam pipe were of sufficient amplitude to cause a system oscillation. The gain of the cooling system is in

*Operated by Universities Research Association under contract to the United States Department of Energy.

excess of 150 dB. Gating interrupts the feedback path of the signal long enough to suppress the instability. An added benefit of the gating is that it improves the signal to noise ratio of signals for diagnostic monitoring. Fast PIN switches controlled by the Tevatron clock system provide the gating in the microwave feed back electronics. Rise times of 10 nanoseconds are typical. Special microwave cutoff devices were also added between the pickups and kickers in order to suppress modes in the beam pipe.

As the beam is only under the kicker for a short portion of the 21 microsecond revolution period, gating also reduces the duty cycle of power delivered to the kickers. This is important in reducing dissipated heat in the structure and minimizes cooling requirements.

C. Signal Transmission

The beam transit time of the Tevatron is 20.958595 microseconds. Due to limited space for locating the pickup and kickers in the lattice and the requirement for an odd multiple of 90 degree phase advance for betatron cooling, the delay is in excess of one turn. In order to keep the system phasing correct for cooling, time delay must be kept better than 5 picoseconds out of 21 microseconds. This corresponds to a phase error of 15 degrees at 8 GHz, the top frequency of the cooling bandwidth.

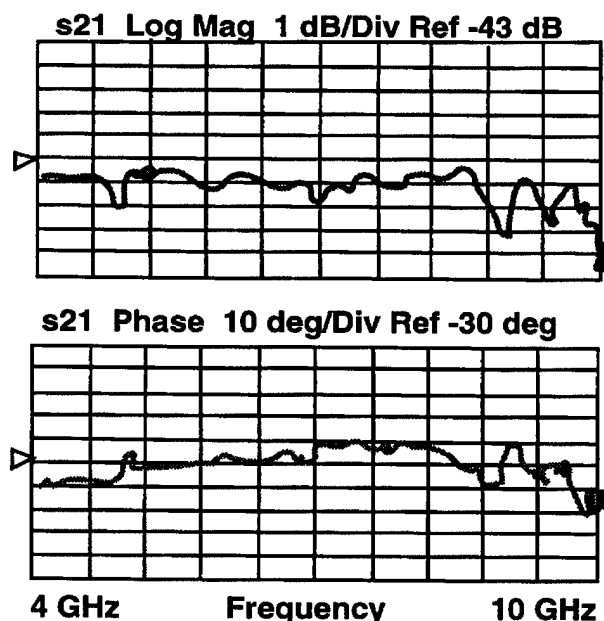


Figure 2: Response of Ortel Fiber Optic Transmission link 4-10 GHz with 6 km (31.613 usec) of single mode fiber.

Due to the long delay, coaxial cables would not be practical as the insertion loss for such a cable would exceed 1400 dB. The dispersion of such a transmission line would account for many 360 degree phase rotations. This is clearly the regime where optical fiber techniques are mandated. Broad band optical links⁵ have been available and used previously for stochastic cooling notch filters.⁶ These links provide the required bandwidth with a flat gain and phase profile (figure 2). The problem still exists that the delay tolerance is stringent. Normal fiber optic cable has a temperature coefficient of 30 ppm per degree

Centigrade. An optical fiber produced by Sumitomo of Japan⁷ is manufactured by depositing a liquid crystal polymer film on the outside cladding of the fiber. The effect is temperature compensation of the fiber as shown in figure 3. This 4.2 kilometer fiber is oven stabilized to better than 0.1 degree Celsius. Delay stabilization to better than a few picoseconds has been achieved. Unfortunately, the Sumitomo corporation is halting production of this fiber due to lack of demand.

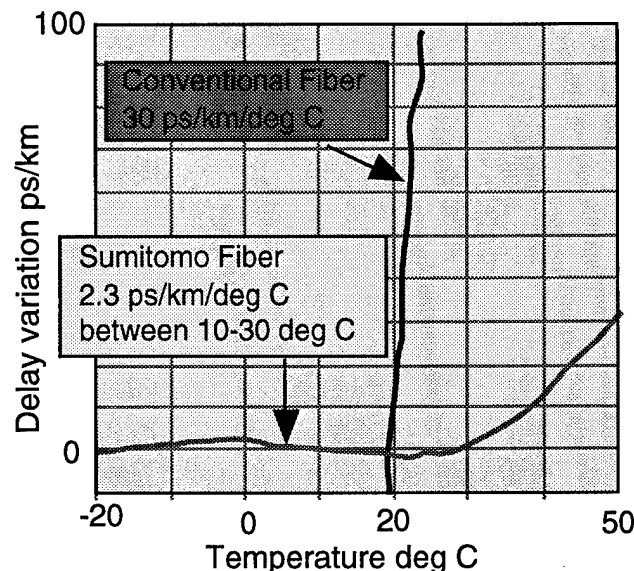


Figure 3: Temperature coefficient of Sumitomo vs. standard single mode optical fiber.

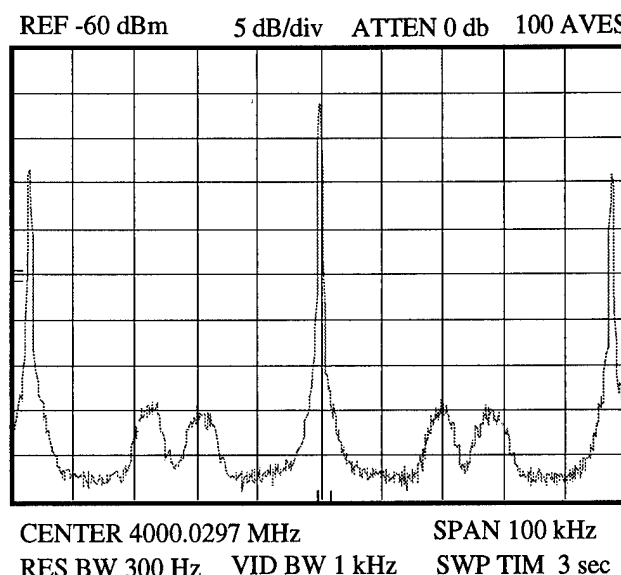
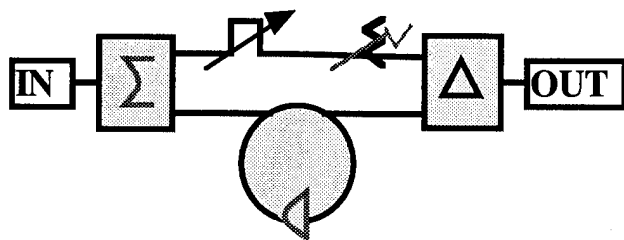


Figure 4: Schottky signal spectrum with gating showing the ratio of coherent to Schottky signal. Intensity is 3.3×10^{10} per bunch at 900 GeV.

D. Notch Filter

Shortly after the first observation of Schottky signals, it became clear that the longitudinal coherent portion of the spectrum would overpower the transverse signal, figure 4.

IIR Notch filter Block Diagram



Optical Storage Ring

Figure 5. Block diagram of IIR optical notch filter.

It was decided that a recursive notch filter needed to be developed.⁸ (figure 5) The width of the Schottky signals occupy a large percentage of the 47 KHz spacing between the revolution harmonics. In order for stochastic cooling to operate, the feedback phase of the system gain would have to be better than 45 degrees across the band, the 3 dB point. A normal correlator notch filter has a phase excursion of 180 degrees between revolution lines with an additional 180 phase jump at the notch. If such a filter were to be used, the heating and cooling would offset each other with no effective cooling resulting. A new type of filter was developed that employs an optical storage ring. The intent is to produce an infinite impulse response filter (IIR) that can have a "brick wall" amplitude response. (figure 6) This filter is also recursive with a 360 degree phase rotation each revolution harmonic, but due to the infinite impulse response of the storage ring, 340 of the 360 degree phase rotation takes place within 4 KHz of the notch repetition bandwidth of 47 KHz.

Amplitude 5 dB/Div



Phase 5 deg/Div



Figure 6. Response of IIR optical storage ring notch filter amplitude (top), phase (bottom). Center freq. 5 GHz

This filter is implemented with a fiber optic link similar to the transmission link described earlier. It was

very important to use a Fabry Perot type laser transmitter as opposed to a distributed feedback laser (DFB). When the filter was constructed using a DFB, the long coherence length of the laser created an interferometer in the storage ring. A Fabry Perot laser has a short enough coherence length to avoid this problem. The loss in single mode fiber optics is very low, typically less than 0.35 dB per kilometer. The delay for the optical storage ring must equal the transit time of the particles in the ring.

The resulting 4.2 kilometer fiber along with couplers and other required connections exceeds 2 dB of optical insertion loss. A source of optical gain is required to make up the loss. Amplifiers that provide gain completely in the optical domain have recently become available in the marketplace. Their development has been spurred by the advancement of fiber optic communications and the desire to minimize the required number of repeaters for transoceanic communications links. Two main types of amplifier are available commercially, laser type solid state amplifiers at 1310 nanometers⁹ and erbium doped fiber amplifiers at 1550 nanometers. Due to the fact that the broad band optical links operate at 1310 nanometers, the choice was limited to the solid state type. Gains of the order of 10 to 15 dB are typical. The erbium amplifiers have better gain and noise characteristics. The solid state amplifier is basically a laser below threshold and is hence a source of noise that varies with bias current. (figure 7) A very important consideration is the use of a polarization insensitive amplifier. The slightest variation in temperature or mechanical position of single mode fiber will cause polarization rotation. If an amplifier has variable gain as a function of polarization, a unity gain storage ring would be impossible to build. The Q or sharpness of the shape factor of the filter can be adjusted by varying the bias current of the amplifier figure 8.

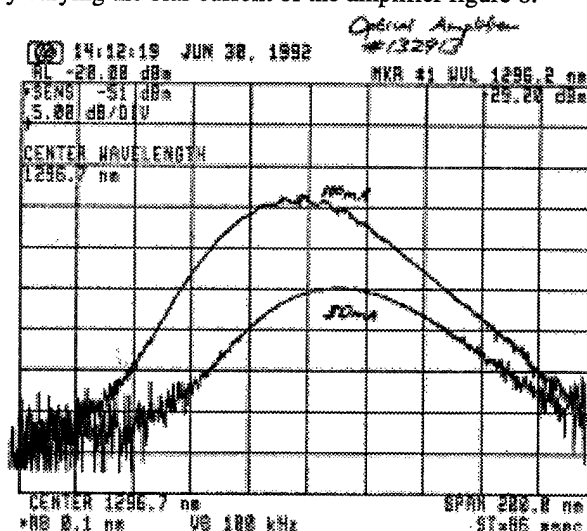


Figure 7: Solid-state optical amplifier optical noise spectrum vs. bias current. Top bias @ 100 mA, bottom @ 50 mA

One additional subtlety is the delay of the optical storage ring must be precisely the revolution frequency of the Tevatron at flattop to better than a picosecond. Because the signal path is totally optical, a delay mechanism had to be developed that could optically vary the delay. An optical "trombone" using a piezo electric cylinder with single mode fiber wrapped around it would provide a voltage variable optical delay. Such a trombone was designed and built with a 15 cm diameter piezo cylinder¹⁰ and provides about 10 picoseconds of delay variation per kilovolt of applied voltage. Because of the difficulty of cutting a 4 plus kilometer fiber to the length accuracy of fractions of a millimeter, regular single mode fiber was used. As described earlier, the temperature coefficient of regular fiber allows for temperature control of the bulk delay time. An oven with feedback is used to tune the coarse length of the fiber (this length fiber has a temp coefficient of 119 picoseconds per degree C) while the piezo trombone does the fine adjustment.

Optical Storage Ring Q vs Gain

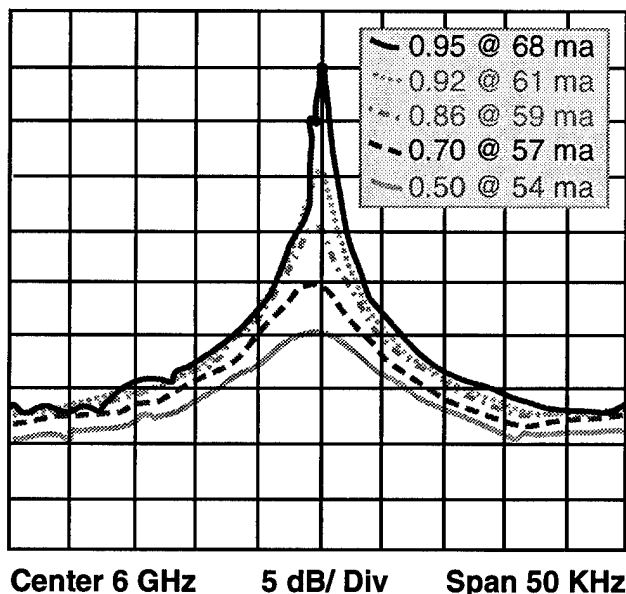


Figure 8: Q or sharpness of response of optical storage ring as a function of optical amplifier bias current. Unity gain is unstable. Gain variation for above curves was 9-12 dB.

III. EXPERIMENTAL RESULTS

If one were to examine the bunch structure of the 900 GeV beam, it would appear that the 2-4 nanosecond bunch length should not contain any frequency components above 2 GHz. This is unfortunately not the case. It is believed that the coherent signal is a result of micro bunch microwave structure of the beam. Efforts of reducing the signal via varying the RF voltage were unrewarded as a minimum of RF voltage is required to keep the beam bunched.

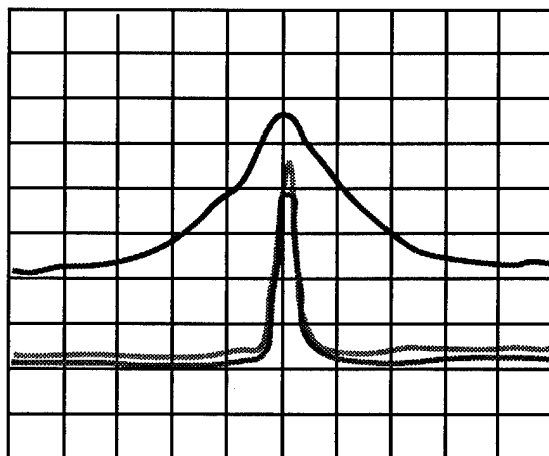
The large coherent spikes of the revolution harmonics account for about 99% of the kicker power. Attempts to reduce this line are the function of the notch filter. The notch filter has a dynamic range of approximately 50 dB

which is adequate. Unfortunately, the filter must be put in the electronic feedback as early as possible to avoid saturation of amplifiers downstream. The signal is pulsed due to the fact that the beam is bunched. The peak power of the signal causes saturation of amplifiers very early in the gain chain. The earliest in the gain chain that it can be located is right after the first preamplifier. At this stage, the signal to noise ratio of the beam signal does not exceed that of the filter itself due to the noise of the optical amplifier. (figure 9) A lower noise source of optical amplification would be required such as erbium, but then there is the incompatibility of the transmission link.

We have abandoned the use of the filter on the front end and have successfully measured transverse transfer functions. (figure 10) The system was timed and signal suppression was observed for the proton vertical plane. (figure 11) It is difficult to estimate the cooling time of such a system as further investigation of signal suppression across the band is necessary. The original requirement of a 20 hour cooling time has not been realized.

The coherent longitudinal spectral lines have also been observed at the ACOL at CERN.¹¹ Successful attempts at damping the line using a stochastic cooling system configured as a damper have been successful on the 3.6 GeV beam at CERN. Attempts to measure a longitudinal transfer function of the 900 GeV Beam in the Tevatron have not been possible to date. The amount of volts necessary to "tickle" the very stiff 900 GeV beam is beyond the capability of installed TWT power.

Ref lev -80 dBm, 5 dB/div



Cen Freq=4 GHz, Span=50 KHz, RB=1KHz

Figure 9: Top trace Schottky output of notch filter, spectrum dominated by optical amplifier noise resulting in microwave noise. Middle trace, coherent signal output of notch filter with optical leg turned off. Bottom trace coherent beam signal input to filter.

The end of the current collider run will be sometime later in the summer of 1995. The current initial luminosity record for a single store is 2.3×10^{31} . The original estimates for cooling performance were not based on the beam parameters of present operation which are more intense by about a factor of four. The time remaining before the fixed target physics run begins is limited. Due

to different Tevatron operating tunes during fixed target, major hardware changes would be required to continue bunched beam cooling experiments. That coupled with lack of extended stores during fixed target would severely cripple any progress. It is imperative to complete our work in the next few months.

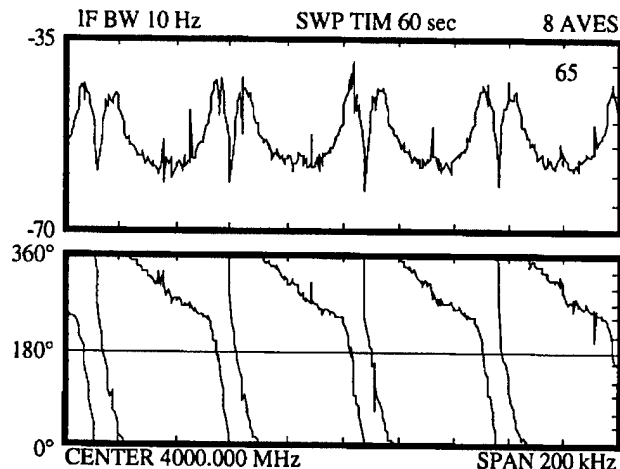


Figure 10: Open loop transfer function measurement. Top, amplitude, showing betatron sidebands. Bottom, phase response. Intensity was 3.1×10^{10} .

As it turns out, a new storage ring is being proposed within the Main Injector tunnel for recycling and storing antiprotons.¹² If bunched beam cooling proves to be inadequate in the Tevatron, all the hardware can easily be transferred to the new storage ring for coasting beam stochastic cooling.

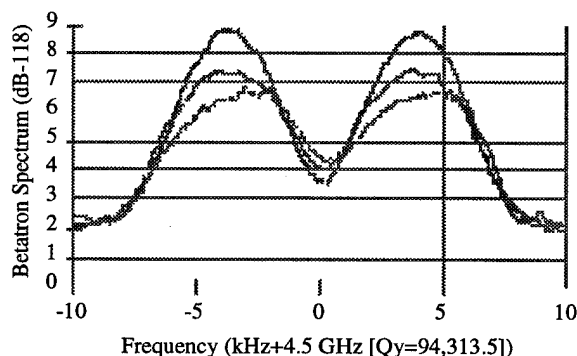


Figure 11: Measurement of signal suppression. Top, signal heating; Middle, open loop; Bottom, Signal Suppression.

IV. ACKNOWLEDGMENTS

A large number of people have contributed their talents to this project. Although cooling of high energy bunched beams has not yet been successful, many spin-offs from the developed technology have been used in other accelerator systems at Fermilab. The pickup/kicker electrode design is the brain child of Dave McGinnis with the expert help of Pat Hurh, Jim Budlong, and Don Poll. The "super hybrid" was designed by Jeff Petter. The optical technician extraordinaire was Ernie Buchanan.

Microwave systems and support were provided by the ace team of Ken Fullett, Dave Peterson, Wes Mueller, Pete Seifrid, Pat Sheahan, and Bob Vargo. John Marriner for his stochastic cooling expertise. Last but not least was the guidance of Gerry Jackson who started this project as a Wilson Fellow.

V. REFERENCES

- [1] G. Jackson, "Bunched Beam Stochastic Cooling", Conf. Record IEEE PAC, San Francisco (1991), p. 2532-2536.
- [2] J. Marriner, G. Jackson, D. McGinnis, R. J. Pasquinelli, D. Peterson, and J. Petter, "Bunched Beam Cooling in the FNAL Antiproton Accumulator", Eur. Part. Acc. Conf., Nice (1990), p. 1577.
- [3] D. McGinnis, "Theory and Design of Microwave Planar Electrodes for Stochastic Cooling of Particle Beams", Microwave and Optical Technology Letters, October 1991, Vol. 4/ Num. 11, p. 439-443.
- [4] J. Petter, "Planar Slot Coupled Microwave Hybrid", Patent #5,075,647; Dec. 24, 1991.
- [5] Ortel Corporation, 5515B optical link, Alhambra, CA.
- [6] R. J. Pasquinelli, W. Kells, D. Peterson, "Optical Correlator Notch Filters for Fermilab Debuncher Betatron Stochastic Cooling", Proc. IEEE PAC, Chicago (1989), p. 694-696.
- [7] Sumitomo Electric Industries, Thermally Stabilized Single Mode Fibers, Yokohama, Japan.
- [8] R. J. Pasquinelli, "Electro-Optical Technology Applied to Accelerator Beam Measurement and Control", Proc. IEEE PAC, Washington DC, (1993), p. 2081-2085.
- [9] BT&D Technologies, SOA3200 Polarization Insensitive Optical Amplifier, Wilmington, DE.
- [10] Channel Industries Inc., C5400 piezo cylinder, Santa Barbara, CA.
- [11] Private communications with Fritz Caspers. CERN.
- [12] G. Jackson, G. W. Foster, "A Storage Ring for Enhanced Antiproton Production at Fermilab", Proc. this conference IEEE PAC, Dallas, TX (1995).

FAST DIGITAL DAMPERS FOR THE FERMILAB BOOSTER

James M. Steimel Jr.
Fermi National Accelerator Laboratory*
P.O. Box 500, Batavia, IL 60510 USA

Abstract

As the intensity levels of the Fermilab Booster are pushed higher, it becomes necessary to have greater control over beam instabilities. One way to control these instabilities is with bunch-by-bunch active beam damping. This kind of damping imposes a very tight tolerance for the electrical delay from the detector to the deflector. The electrical delay must match the bunch revolution time, and the revolution time changes by 685ns in a period of 25ms in the booster. One way to track this delay is with a fast, time varying digital delay which is synchronized with the RF feedback system. A working prototype of a wide-band transverse digital damper system has been developed and tested on the Fermilab Booster. This paper will discuss the design, features, and results of the damper as well as problems associated with designing dampers for fast frequency sweeping accelerators.

I. INTRODUCTION

The upgrade of the Fermilab Linac from 200MeV to 400MeV has reduced the losses in the Booster due to space charge effects [1], but the increased beam current causes greater coupled bunch mode instabilities [2]. The challenges associated with designing a coupled bunch mode damper for the Booster are a large dynamic range, a fast sweeping RF system, and a large spread in tunes through the cycle. A digital system is ideal for handling these problems; therefore, digital bunched beam dampers were designed.

The damper configuration is shown in Figure 1. It consists of a common mode rejection front-end, digitizing units, fast memory, a D/A unit, and power amplifiers. All of the components, except for the power amplifiers, are VXI compatible and can be controlled with a personal computer or any other VXI control system. This paper will show why these functions are necessary to perform bunch-by-bunch damping in a fast sweeping accelerator and also show how the current Booster system satisfies these requirements.

II. DIGITIZERS AND MEMORY

Most of the problems associated with bunch-by-bunch damping in a fast sweeping accelerator can be addressed in the design of the digitizers and memory. The sampling process of the digitizers provides a natural rejection of the large common mode RF input signal. Delay and tune tracking

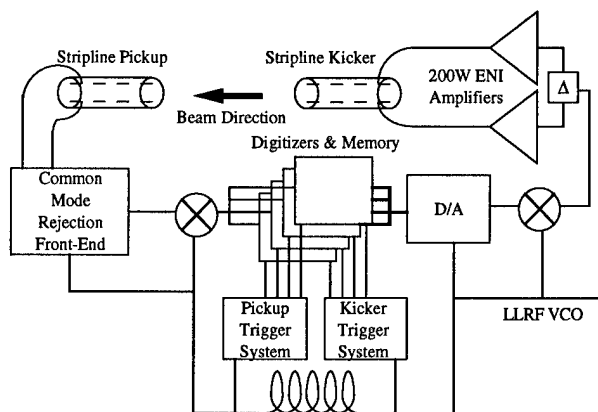


Figure 1: Block diagram of Fermilab Booster transverse digital damper system.

can be implemented in the triggering and digital processing. A block diagram of the digitizer is shown in Figure 2.

A. Components of Digitizer

The beam signal is mixed down with the RF frequency, filtered, and enters an A/D converter. The converter is triggered with a signal derived from the accelerator VCO

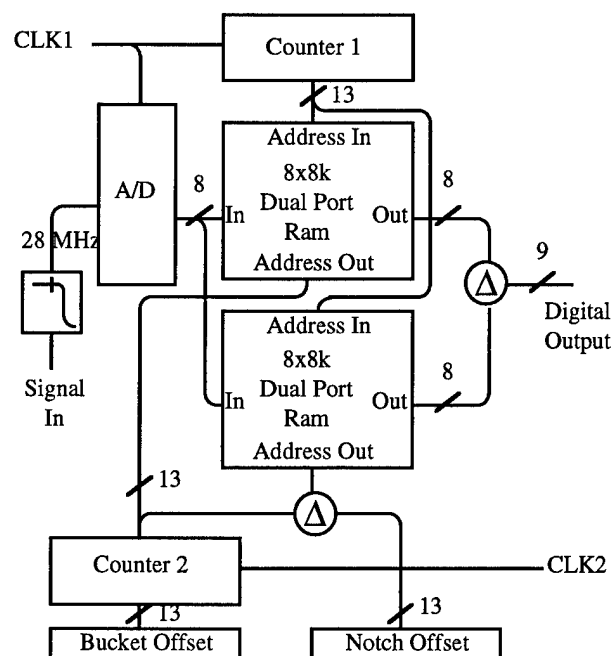


Figure 2: Block diagram of digitizer.

*Operated by the University Research Association, Inc. under contract with the US Department of Energy.

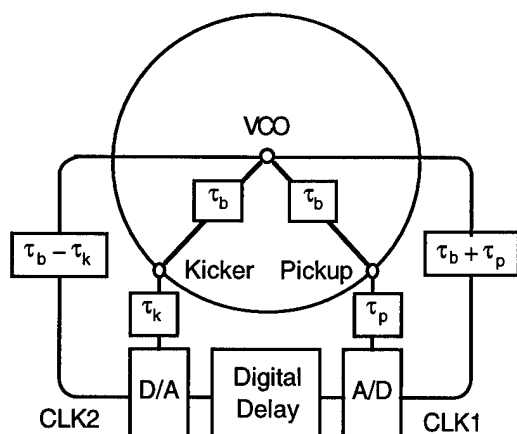
which remains locked to the frequency of the beam. This VCO signal drives a trigger system [3] which interleaves the digitizers according to the number of digitizers in the system and the number of beam occupied buckets in the accelerator. Although the A/D is capable of running at the RF frequency, the bit noise is significantly reduced by reducing the sampling rate.

From the converter, the data is stored in two fast dual port memories at the address specified by the top counter. The data is then output when the bottom counter matches the data's memory address. Counter 2 is set so that the combination of the delay in the memory plus the fixed cable delay is an integer number of beam revolutions, usually one revolution.

B. Delay Tracking

The RF accelerating voltage in the Booster must ramp from a frequency of 37MHz to 53MHz in a cycle time of 33ms, and the non-linear frequency ramp has a peak slope of 1GHz/s near the beginning of the cycle. The revolution period varies from 2.8μs to 1.59μs. To maintain feedback on the proper bucket, the processing system must handle 1.21μs of delay change quickly.

As long as the initial bucket delay is set correctly, taking into account beam velocity and fixed delay, the digital system will remain locked to the beam and provide proper bucket delay [4]. Figure 3 shows the timing conditions for the system. As the beam accelerates, more of the bucket delay is stored in the fixed cable delays, τ_p and τ_k . The bucket delay of the digital delay must be reduced. Because of the difference in delay from the VCO to the A/D trigger and the output trigger, an increase in frequency will trigger the output counter more than the A/D counter according to:



τ_b = Delay from VCO to Beam
 τ_k = Delay from D/A to Kicker
 τ_p = Delay from A/D to Pickup

Figure 3. Transverse Damper Timing Diagram.

$$\int_0^t f_{rf}[t' + \tau_k]dt' - \int_0^t f_{rf}[t' - \tau_p]dt' \quad (1)$$

The number of buckets stored in the fixed delay increases by the exact same amount so that the bucket delay stays matched.

C. Digitizer Common Mode Rejection

The output of the digitizers is the difference between the input delayed by the bucket delay and the input delayed by the notch delay. The response of this difference is given by:

$$H(\omega) = 2je^{-j\frac{n\omega}{2f_{rf}}} \sin\left(\frac{n\omega}{2f_{rf}}\right) \quad (2)$$

where n is the notch delay in number of buckets and f_{rf} is the accelerator VCO frequency. A plot of this response is shown in Figure 4 for $n = h$, the harmonic number of the accelerator. Notice that the amplitude response at the revolution frequencies is zero, and this will be true for a notch offset equal to any multiple of the harmonic number. Thus, this system reduces the output power requirements by eliminating the power due to unequal bunch population and low frequency synchrotron motion.

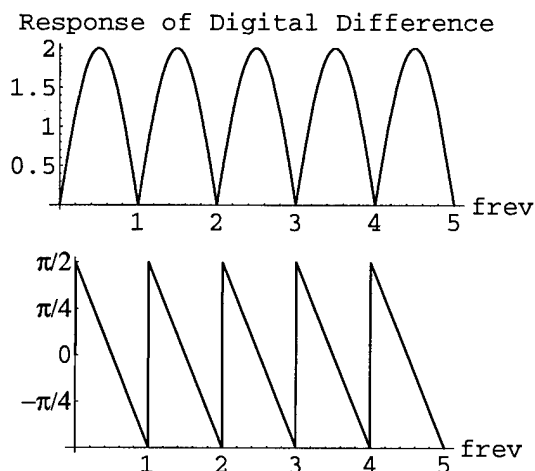


Figure 4: Response of the digital difference for $n=h$. The upper graph is the linear magnitude of the response and the lower graph is the phase in radians. The horizontal scale is in units of the revolution frequency.

D. Tune Tracking

Both the amplitude and phase responses of the system are important for good damper operation. One of the problems with the phase response of the system is the betatron phase advance from pickup to kicker. Ideally, this phase advance would be 90° [5], but due to physical limitations or changing tunes, this may not always be possible. Some dampers avoid this problem by having two pickups which are 90° apart in

phase advance and summing the two signals with variable attenuators until the phase advance between the new signal and the kicker is 90° . The variable attenuators are controlled by a fixed program or feedback of some kind [6].

Another way around this problem is to use the phase properties of the notch filter itself. The difference between the betatron phase advance and 90° appears as a phase offset in the response of the damper system to the upper betatron sideband. The lower betatron sideband sees an equal but opposite phase offset [7]. The notch delay can be adjusted until the phase slope caused by the notch compensates for the difference in phase between the two sidebands. The notch delay has been designed to vary as a function of time in the cycle. It reads a look-up table which is programmed to follow the changing tune of the machine.

III. COMMON MODE REJECTION

The gain of a damper system determines the instability damping rate [8]. With the maximum output power fixed, the maximum gain of the damper is determined by the amount of undampable signal which saturates the power amplifiers. This signal includes noise, RF harmonics, rotation harmonics, and synchrotron motion (for a transverse system). The digitizing system will almost eliminate all these signals except for random noise, but these signals will still cause problems for the digitizer input. The Booster digitizers have 8-bits of precision, and a maximum input signal of 10dBm. This means that all signals above 10dBm saturate the digitizer, and all signals below -38dBm at the digitizer fall below the noise floor. It has limited dynamic range and acts as a large source of noise. There must be some kind of common mode rejection before the inputs to the digitizers.

A. Cable Matching

The Fermilab Booster uses a directional stripline pickup to detect the transverse error signal for the damper. The signals from the two plates (top and bottom for vertical; inner and outer for horizontal) are combined in a 180° hybrid. One way to reduce the common-mode signal is to match the delay and amplitude of each leg of the hybrid perfectly, moving the electrical center of the pick-up to the position of the beam closed orbit. Unfortunately, this will not track the beam as the closed orbit changes.

B. Down Conversion and AC Coupling

The fundamental RF signal is about 55dB greater than an undamped, stimulated betatron instability signal. By down-converting the signal and AC coupling, the fundamental RF can be eliminated, but the second harmonic of the fundamental is still 43dB greater than the stimulated instability signal. Some method of tracking the closed orbit of the beam must be devised to reduce the second harmonic of the fundamental RF frequency.

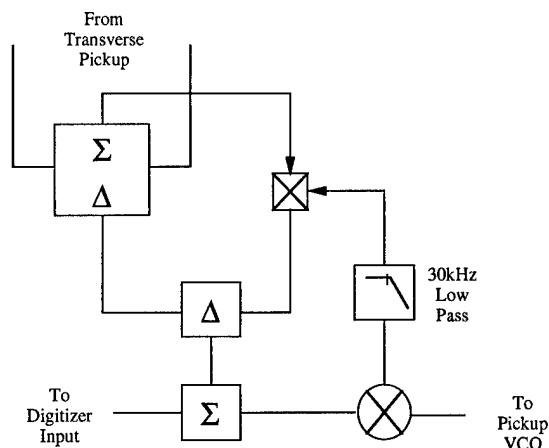


Figure 5: Booster transverse auto-zero circuit.

C. Closed Orbit Feedback

The method used for tracking the closed orbit in the Booster is shown in Figure 5. The signal from the hybrid is mixed down, amplified, and low-pass filtered. This filtered signal drives a fast, linear multiplier, and the other port of the multiplier is driven by the sum of the opposing plates. This multiplied sum signal is then subtracted from the hybrid signal to provide a tracking common-mode rejection. Signal associated with unequal bunch population is also reduced with this method since it effectively centers the beam between the plates. The only undesired signals it cannot reduce are longitudinal coupled bunch modes. These signals must be filtered by the digitizers.

D. Bandwidth Limiting

Information about all of the coupled bunch modes are contained in a bandwidth of half the RF frequency [9]. By limiting this bandwidth with filters, a majority of the aperture jitter noise that is inherent in the A/D converters can be reduced. A 28MHz low-pass filter is used just before the input to the digitizer to reduce the noise as well as help reduce the second harmonic of the fundamental RF.

IV. D/A AND AMPLIFIERS

The outputs of the digitizers are connected to the D/A through a 9-bit bus line. The kicker trigger system mediates the bus while the D/A triggers at the RF frequency. A block diagram of the D/A system is shown in Figure 6. The data from the bus enters a dual port RAM look-up table. This look-up table has many pages and is used to provide a digital gain coefficient for the system. After the table, the signal enters a 10-bit D/A converter. The signal from the converter is filtered to reduce overshoot noise and upconverted for a better response to the hybrid and amplifiers.

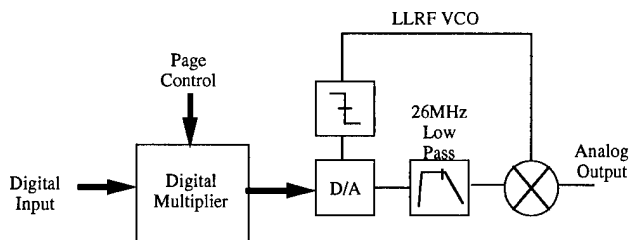


Figure 6: D/A block diagram.

The upconverted signal is split with a 180° hybrid and is then input in to two 200W ENI amplifiers. The amplifiers' bandwidth ranges from 100kHz to 150MHz and the electrical delays of these amplifiers are matched to better than 1ns. Each amplifier drives one plate of a stripline kicker to complete the circuit.

V. SYSTEM CONTROL

All of the components for the Booster damper system, except for the power amplifiers, are VXI compatible. This system uses a Macintosh computer with a National Instruments VXI-NuBus adapter and LabView® software for control. The control system is capable of adjusting the phase of the RF for upconverting and downconverting, adjusting the synchronization and patterns of the trigger systems, changing bucket and notch delays, and reading from and writing to the digitizer memory. Given only the information about the number of buckets and bunches in the machine and the desired bucket and notch delays, the computer is capable of setting all the components for effective damping. Once the system has been configured for damping, it can run independently from the computer. The computer can also be used to program the system for many different configurations. Examples are read only mode for measuring instabilities, write only mode for resonating a betatron instability, and transfer function measurement mode for measuring the system response.

VI. SYSTEM RESPONSE

A simplified diagram of the closed loop damper response is shown in Figure 7. The formula for this response is:

$$\frac{R(s)}{N(s)} = \frac{G(s)}{1 - H(s)G(s)} \quad (3)$$

As long as the real part of $H(s)G(s)$ remains less than +1, the system will be stable for all frequencies [10]. One way to check the response of the system is to measure the $H(s)G(s)$ product directly by opening the feedback path, stimulating the beam, and measuring the damper output.

The most common way for measuring the $H(s)G(s)$ product for a fixed frequency synchrotron is to place a network analyzer between the output of the low level damper system and the power amplifiers. It can be difficult to locate

the frequencies where the beam has a detectable response because the beam can have a very high Q at the betatron frequencies. However, once the response is located at two frequencies, the remaining betatron responses are very easy to locate because they must differ by an integral multiple of the revolution frequency.

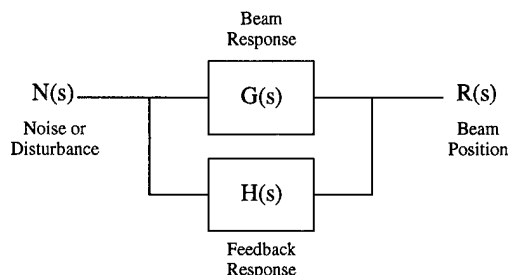


Figure 7: Block diagram of closed loop response for a damper system.

If the frequency of the synchrotron is not fixed, it becomes impossible to measure the response of the $H(s)G(s)$ product with a network analyzer. The revolution frequency will change significantly during the time it takes to resolve the betatron response causing a smearing of the response. For a sweeping frequency, it is better to use the digital damper system itself for making the transfer function measurements. The digitizer memories can be loaded with a sine-wave pattern and played on to the beam. While the pattern is being played, the system can be storing the response from the

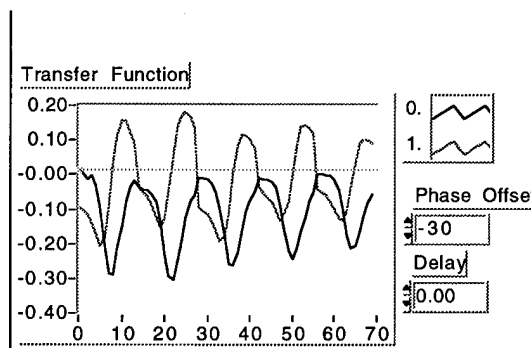


Figure 8: Plot of response measurement for many betatron modes. This plot shows modes 0, 1, 2, 3, and 5. The vertical axis shows the linear value of the real and imaginary response, and the horizontal axis shows the number of data points. The delay and phase offset are adjusted for most negative real response.

pickup right behind it. Once all the memory has been played, the response is compared to the stimulus pattern with the proper compensation for the system delay. Figure 8 shows a response measurement of many betatron modes. Since the system tracks the changing delay, the only way the signal will look smeared is if the tune changes significantly during the

measurement. With the ability to measure the response of the system, the bucket delays and notch delays can be tuned for damping throughout the entire Booster cycle.

VII. RESULTS OF DAMPER SYSTEM

The Fermilab Booster currently has one operational horizontal damper system. Although the system has the proper phase response through the entire cycle, the beam does not have any horizontal instabilities above the noise floor at the beginning of the cycle. The dampers do, however, have a profound effect on instabilities at the end of the cycle. Figure 9 shows a comparison between dampers on and dampers off for beam which is kicked horizontally during the last half of the Booster cycle. A vertical system is under construction and should be operational very soon.

VIII. ACKNOWLEDGMENTS

The author would like to thank Kerry Woodbury and Craig McClure for their work in designing the triggering system for the dampers. I would also like to thank Hengjie Ma for his design of the down-converting circuits, Ken Koch for his work in building the processing equipment, and a special thanks to Dave McGinnis for his support and inspirations for this project.

IX. REFERENCES

- [1] D. P. McGinnis, "Status of the Fermilab Booster After the 400 MeV Upgrade," *Proceedings of the Fourth European Accelerator Conference*, pp. 497-498.
- [2] A. W. Chao, *Physics of Collective Beam Instabilities in High Energy Accelerators*, pp. 349-352.
- [3] K. Woodbury, et al., "VXIbus Universal Clock Decoder Manual VXI-UCD," *Controls Hardware Release No. 91.0*.
- [4] J. Steimel and D. P. McGinnis, "Damping in the Fermilab Booster," *Proceedings of the 1993 Particle Accelerator Conference*, 2101.
- [5] L. Vos, "Transverse Feedback System in the CERN SPS," *Conference Proceedings of the 1991 AIP Accelerator Instrumentation Workshop*, 184.
- [6] J. M. Byrd, et al., "Design of the ALS Transverse Coupled-bunch Feedback System," *Proceedings of the 1993 Particle Accelerator Conference*, pp. 2109-2110.
- [7] S. van der Meer, "A Different Formulation of the Longitudinal and Transverse Beam Response," *CERN/PS/AA/80-4*, 9.
- [8] D. P. McGinnis, "Coupled Bunch Mode Instabilities Measurement and Control," *Conference Proceedings of the 1991 AIP Accelerator Instrumentation Workshop*, 78.
- [9] Ibid., pp. 69-70.
- [10] J. D. Fox, et al., "Feedback Control of Coupled - Bunch Instabilities," *Proceedings of the 1993 Particle Accelerator Conference*, 2077.

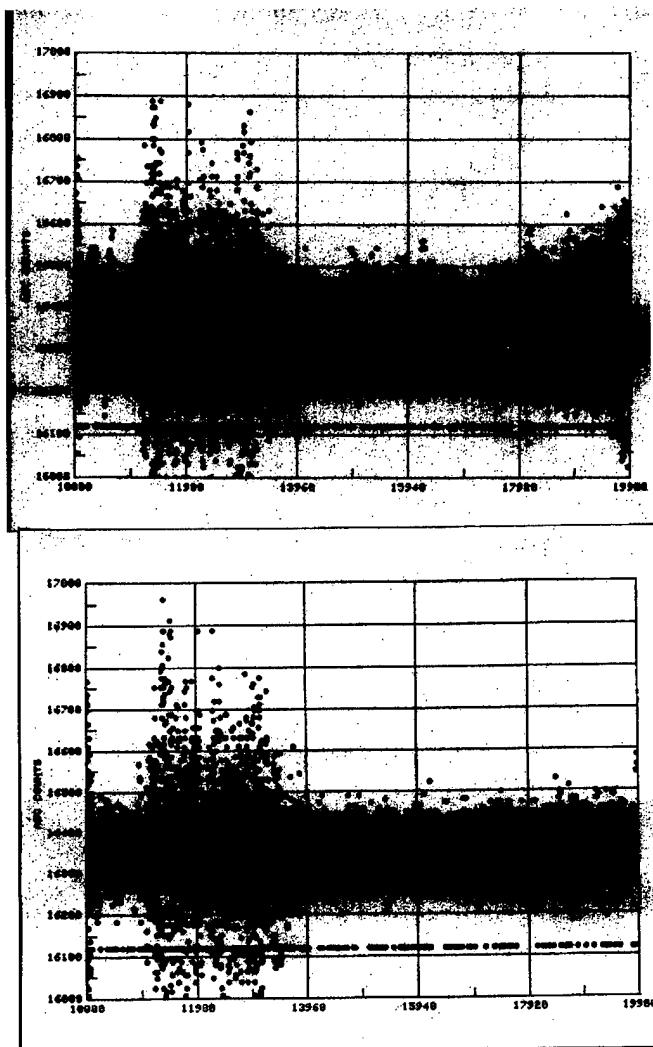


Figure 9: Plots of turn-by-turn horizontal position of Booster beam for the last half of the cycle. The top plot shows data with the dampers off, and the bottom plot shows data with the dampers on. The noise at the beginning of the plot is caused by synchrotron oscillations.

FAST FEEDBACK FOR LINEAR COLLIDERS

L. Hendrickson, C. Adolphsen, S. Allison, T. Gromme, P. Grossberg, T. Himel, K. Krauter,
R. MacKenzie, M. Minty, R. Sass, H. Shoaee and M. Woodley

*Stanford Linear Accelerator Center, Stanford University, Stanford, California 94309 **

*work supported by the Dept. of Energy, contract DEAC03-76SF00515

ABSTRACT

A fast feedback system provides beam stabilization for the SLC. As the SLC is in some sense a prototype for future linear colliders, this system may be a prototype for future feedbacks. The SLC provides a good base of experience for feedback requirements and capabilities as well as a testing ground for performance characteristics. The feedback system controls a wide variety of machine parameters throughout the SLC and associated experiments, including regulation of beam position, angle, energy, intensity and timing parameters. The design and applications of the system are described, in addition to results of recent performance studies.

INTRODUCTION

In four years of operation, the SLC feedback system has expanded from an originally-planned eight linac launch loops to nearly 50 control loops in every major area of the SLC as well as special experiments and diagnostic loops. Due to the database-driven design, new control loops are easily implemented usually without requiring software changes. The system, described more fully elsewhere[1], is generalized and supports the use of existing control system elements, usually without requiring the addition of dedicated hardware. The control algorithm is based on the state space formalism of digital control theory [6].

The pulsed electron and positron bunches in the SLC are generated at 120 Hertz. While some of the feedback loops operate at the full beam rate, others run at lower rates (typically 20 Hertz) mainly due to CPU and beam position monitor (BPM) limitations. The real-time functions run on Intel 80386 and 80486 microcomputers (micros) which are distributed geographically. In the SLC control system, the

micros do not ordinarily communicate with each other; to facilitate intermicro communication for the feedback system, a specialized point-to-point network was added[3].

The design is based on linear control, although some special-purpose nonlinear capabilities have been added. Matrices used by the real-time software are calculated offline in advance, usually incorporating data from the accelerator model with a design noise spectrum. The typical design corrects a step function with an exponential time-constant of 6 feedback iterations. The control algorithm does not include online adaption to changes in the machine response or noise spectrum. A "cascade" capability was added to the feedback system as a later enhancement; it is designed to eliminate overcorrection from a series of linac launch loops using adaptively calculated transport matrices.

The user interface to the feedback system provides a rich variety of control, diagnostic and analysis capabilities. Displays summarize the status of all feedback loops in selected geographical areas of the machine as well as details of specified loops. Calculated parameters may be studied on a pulse to pulse basis and over longer periods. Diagnostics such as beam jitter estimates and goodness-of-fit calculations enable operators and physicists to study long-term changes in the machine. From touch panels, users enter control parameters such as setpoints, gain factors, limits and filtering cuts.

APPLICATIONS

Applications of the system have far exceeded those originally planned. Figure 1 provides an overview of the types and locations of controls for the SLC. In addition there are control loops for special projects such as the Final Focus Test Beam, fixed target experiments and the polarized gun lab, as well as many diagnostic compute-only loops. Several more loops are planned for the new laser wire beam size monitor and for the PEP-II project.

Launch loops stabilize the beam positions and angles in the linac, injector, damping rings, positron return line,

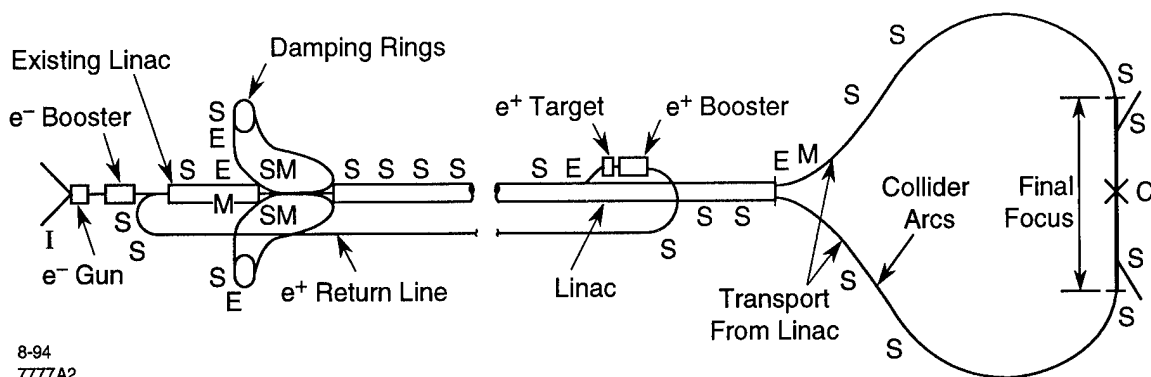


Figure 1: SLC schematic with fast feedback locations shown. S = steering loop; E = energy control; I = intensity/gun control; C = special purpose loop to maintain beam collisions; M = minimization

collider ARCs and final focus areas using BPM measurements and corrector magnet control. While the system was originally designed for this purpose, it was generalized in order to support a wide variety of measurement and control devices, including measurements of gated ADCs, and actuators such as amplitude controls, klystron phases and timing delays. With the addition of the polarized gun to the SLC, several feedback loops were added to control intensity of the YAG and Ti Sapphire lasers, gun extraction timing, and monitoring of gun-related parameters such as the polarization asymmetry.

The feedback algorithm is based on linear matrix calculations, but in some cases there is a need to control actuators which are not linear with the controlled states. This is accomplished by designing matrices to control an imaginary device which responds linearly. In the real-time software, the matrix equations determine a setting for the imaginary actuator and estimate its effect on the states. Given a requested setting for the imaginary actuator, the special purpose software then calculates what is needed for the real, nonlinear actuators in order to accomplish the required control. Control of the beam energy is provided in five SLC locations, some of which require nonlinear actuator calculations. For example, the energy control for the electron bunch which is extracted from the linac to make positrons, is accomplished with an interface to a hardware-based feedforward system. The feedforward controls the klystron phases for two linac sectors and is designed to compensate the energy for intensity variations detected in the damping ring. The feedback system controls the energy indirectly by varying amplitude controllers which are part of the feedforward. These amplitudes represent quadratic fit coefficients for energy versus klystron phase.

Energy control for the electron and positron beams in the linac requires nonlinear control of the klystron phases for two sectors. In order to provide independent energy control for the two beams, this was recently extended to control the timing of the 261 linac klystrons and subboosters, called the PSK time. The calculated PSK time is broadcast over a specialized network, received by all of the linac micros, and added to the nominal trigger timing for each klystron and subbooster.

At the interaction point, the beam deflection angles are controlled to keep the beams in collision. The beam behaviour is characterized by an S-shaped deflection curve. The slope of the linear portion of the curve (corresponding to small beam-beam separations), along with measurements of the beam deflections and intensities, is used in the special-purpose feedback calculations. Since the slope changes with beam size it is periodically determined by an external process which scans one beam across the other before downloading updated parameters to the feedback system. For small separations, the feedback controls optimally, within the central linear portion of the curve. In those cases where large disturbances bring the beam-beam separation out to the nonlinear portions of the curve, the feedback response is slower, but it controls correctly and collisions are successfully maintained.

MINIMIZATION

Minimization is an extension to the feedback system which applies where measurements respond parabolically with actuator movement. In these cases, given a single raw measurement such as a BPM reading, there is not enough information for a feedback to tell which way to move the actuator, because it may be on either side of the parabola. One way to obtain this information is to move the actuator and observe the measurement change. For the SLC

optimization packages, the actuator is scanned through a range of values and a parabolic fit is performed; but this is an invasive procedure. An alternate method implemented in the feedback system is called "dithering" [5]. This involves perturbing the actuator by a tiny amount above and below its nominal setting while taking synchronous beam measurements. After many pulses, an average slope is calculated for the measurement versus the actuator change. The slope of the parabola is linear with the actuator, so the linear feedback calculation is formulated with the calculated slope as a measurement. Minimization is accomplished by keeping the slope set at zero, but the feedback system is generalized so that the slope can be kept to any requested setpoint. In the SLC, generalized capability for dithering and minimization has been developed and demonstrated. The system has been able to perform dithering and control the beam to a stable point on the parabola. Unfortunately, use of the dithering system has proven to be invasive; the smallest dithering bit sizes cause unacceptable beam disturbances.

However, a noninvasive minimization feedback has been implemented and commissioned. The kicker timing feedback loop relies on the natural jitter of the ring extraction kick time (measured with a TDC) to produce slope calculations of BPM measurements versus kick time; dithering is not needed. In order to provide a reasonable slope estimate, 10,000 pulses of data are averaged; at a BPM measurement rate of 60 Hertz, it takes almost 3 minutes to produce a single calculation. Commissioned only a few days before the end of the last SLC run, the loop has already been shown to improve machine performance.

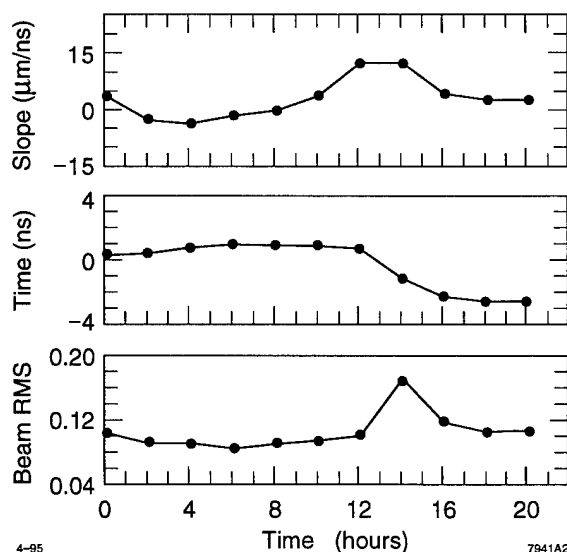


FIGURE 2: Minimization kicker timing feedback improves the RMS beam jitter

Figure 2 shows the feedback response to changing ring extraction conditions; the RMS beam jitter (calculated by a downstream feedback loop) increases until the feedback corrects the kicker timing, which reduces the jitter to its normal value. Note that the feedback response is slow due to an intentionally conservative initial design.

PERFORMANCE ISSUES

In the past year, progress has been made in identifying and analyzing SLC feedback performance issues[4]. Of particular interest is the response in the linac. There was concern that imperfections in the feedback modeling and the large number of loops may result in amplification of beam noise for some frequencies. However, with the finite sampling rate used in the feedback system, even ideal conditions would result in noise amplification for some frequencies. Techniques were developed to analyze the feedback response for both single loops and for the linac system as a whole. Several sources of feedback imperfection were identified and studied.

The matrices for a launch loop incorporate a transport model for that area of the accelerator, including transport elements between BPM readings, beam positions and angles, and corrector settings. In some cases, the online model does not accurately reflect the accelerator response, so feedback calibration is needed. This is accomplished by moving each corrector one at a time through a range of values and measuring the fitted beam positions and angles for each setting. The slopes of these states versus the corrector settings are incorporated into new feedback matrices. Recent software improvements have made the calibration system easier to use, but it remains an invasive procedure for which it is difficult to get sufficient beam time. In a few areas of the machine, the model is so poor that the feedback cannot be used without calibration. In marginal cases, imperfect modeling simply degrades the feedback performance.

Another performance consideration is the time response of the correctors. The design for linac loops assumes that corrector changes are implemented with a delay of three feedback iterations; one iteration is allowed for calculations and communication, with two additional iterations for the magnetic field to change. Recent measurements indicate that typical linac correctors can move from 10 to 90% of a requested change within about 9 120-Hertz pulses. For most of the linac loops, which run at 20 Hertz, the response is close enough to that used in the feedback design. However, for the last loop in the linac, which was upgraded to run at 60 Hertz, the corrector response is relatively slow and not adequately modeled. Simulations for the standard feedback design, shown in

figure 3, indicate that when corrector response is slow compared to the design feedback control of 6 pulses, there is performance degradation. Furthermore, the response becomes more sensitive to other factors such as imperfect modeling. Near the end of the last SLC run, attempts were made to design matrices with a better model of the slow corrector response. Tests of the new design showed improved feedback response, but other problems made it operationally unacceptable. Additional work is needed.

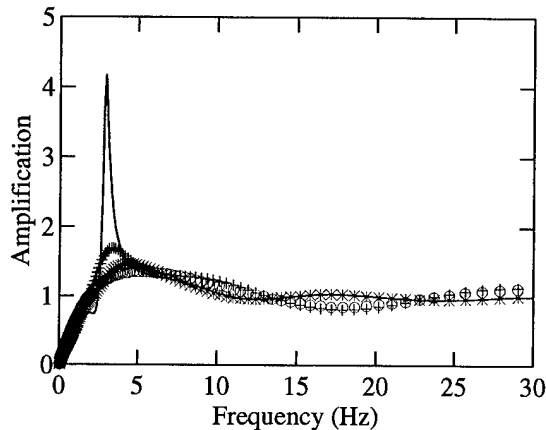


Figure 3: Simulations of feedback response with slow corrector speeds and imperfect calibrations. Plots shown are for the ideal case (o), slow correctors (*), poor modeling (+), and the combination of slow correctors with poor modeling (-).

Figure 4 shows estimates of feedback response for the series of linac launch loops. The response is measured by inducing a step function upstream of the linac, first with the feedbacks on and then with the feedbacks off. Fitted beam position data for both cases is acquired for several hundred consecutive pulses. The FFTs for both data sets are calculated and the ratio is plotted. Unfortunately this measurement is noisy. An alternate technique involves inducing sine waves over a range of known frequencies and measuring the resulting amplitudes with feedback on and off. The sine wave technique produces cleaner results less invasively, but it is more time-consuming. Also shown in figure 4 are simulations for feedback performance. Note that the "ideal" simulation assumes that the accelerator model is perfect, correctors are as fast as modeled, that all of the loops are operating with gain factors of 1.0 and that the cascade system is working perfectly. This is identical to the ideal simulation for a single loop. An initial attempt at a more realistic simulation includes effects of imperfect modeling, low gain factors and imperfect cascade

performance. More work needs to be done to measure, simulate and hopefully to optimize the performance of the linac loops as a system.

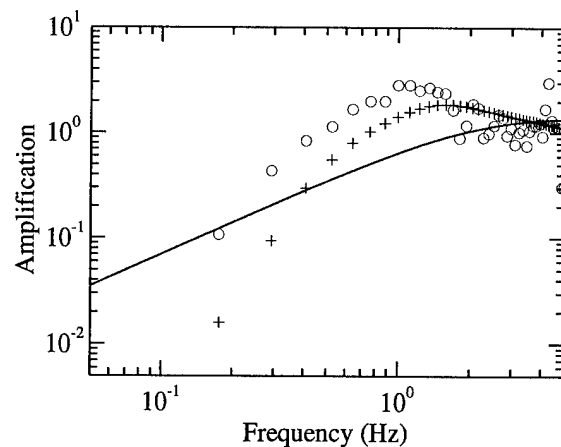


Figure 4: Measurement and simulations of feedback response (on/off) for the system of linac loops. Plots shown are for the ideal case (-), measured data taken from a ratio of FFTs (o), and an attempt at a realistic simulation (+).

"CASCADED" FAST FEEDBACK

As shown in figure 1, steering in the SLC linac is controlled by a series of feedback loops. In the original system, these loops were all controlling the same parameters; this resulted in problems with overcorrection of upstream perturbations and amplification of beam noise. This effect was predicted in the initial feedback design simulations and the cascade system was designed to correct this problem. Now, after receiving new measurements on each beam pulse, each linac loop sends its calculated states to the next downstream loop, and receives the current states from its upstream neighbor. The downstream loop performs corrections based on the differences between the states of the upstream and downstream loops. Therefore each loop should correct only the perturbations initiated immediately upstream of it. These corrections depend upon a reliable method for mathematically transporting the positions and angles at one point to the downstream location. The model is not good enough over these distances, so adaptive methods are used to dynamically update the transport matrices. The adaption calculations are based upon the SEquential Regression (SER) algorithm[7], adapted for use in the SLC feedback system[2].

Cascade performance can be characterized by rejection ratios. This is the fraction of an incoming perturbation which is seen and corrected by each feedback loop.

Ideally, for a loop immediately downstream of a perturbation, the rejection ratio should be one, and for the further-downstream loops the rejection ratio should be zero. Poor rejection ratios are an indication that the adaptively-calculated transport matrices do not perfectly model the actual beam transport.

Initially when the cascade system was commissioned, the rejection ratios for downstream loops indicated excellent response; typical downstream rejection ratios were 10%. In the past year, cascade performance has been revisited; recently the rejection ratios ranged from very good (10-25%) up to more than 50% for some cases. If all of the feedback loops ran with the full corrections, this would result in overshoot and ringing; as a result, the gain factors have been lowered so that each loop only performs a fraction of the required correction on each pulse.

Several possibilities were investigated in attempts to understand the cascade performance. If the machine were dominated by phase jitter instead of betatron jitter, this would produce incorrect transport, since the adaptive process relies on correlations of perturbations between loops. Furthermore, at recent SLC beam intensities, wakefields cause nonlinear transport effects which have been shown to be a significant problem for the cascade system. In one case, the transport magnitude from one feedback loop to the next varied by 50% for different perturbation source locations, both in simulation and from beam measurements. Finally, during low current studies, poorer BPM resolutions appeared to degrade the adaption results by introducing uncorrelated noise which pulls the adaptively-calculated transport magnitudes toward zero. Further study is needed in this area. However, analysis of the wakefield effect indicates that perfect cascade performance cannot be achieved with this architecture under current SLC conditions, since the beam transport is dependent on the source location of a perturbation and the implemented cascade design does not provide this information.

CONCLUSIONS

The fast feedback system has become essential for successful operation of the SLC. While its performance characteristics require further study and improvement, it provides many positive contributions for operations. The large number of feedback loops decouples the various areas of the SLC, supporting machine studies by allowing downstream loops to compensate for incoming disturbances. In the linac, beam emittance is optimized by moving feedback setpoints to produce closed orbit bumps. With the feedback system, machine reproducibility is improved and smoother startup after outages is seen.

Efficiency was improved by a factor of two in the first year of feedback operation. Operators steer much less often and there is a significant decrease in operator adjustments. This allows the operators time for more subtle tuning and contributes to increased luminosity.

It is hoped that future colliders will benefit from the substantial base of beam experience with the SLC feedback system. Comparable or superior capabilities are likely to be required; realistic feedback performance estimates as well as designs for future systems should include consideration of the challenges faced in the SLC system.

ACKNOWLEDGEMENTS

The SLC feedback system has benefitted from the contributions of many operators and physicists as well as hardware and software engineers. We are grateful to Chris Traller for preparation of the manuscript.

REFERENCES

- [1] L. J. Hendrickson et al. "Generalized fast feedback system in the SLC". In *Proceedings of the International Conference on Accelerators and Large Experimental Physics Control Systems*, Stanford Linear Accelerator Center, November 1991. SLAC-PUB-5683.
- [2] T. Himel et al. "Adaptive cascaded beam-based feedback at the SLC". In *Proceedings of the IEEE Particle Accelerator Conference*, Stanford Linear Accelerator Center, May 1993. SLAC-PUB-6125.
- [3] K. Krauter and D. Nelson. "SLC's Adaptation of the ALS high performance serial link". In *Proceedings of the IEEE Particle Accelerator Conference*, Stanford Linear Accelerator Center, May 1991.
- [4] M.G. Minty et al. "Optimization of feedback performance at the Stanford Linear Collider". In *Proceedings of this Conference*, Stanford Linear Accelerator Center, May 1995.
- [5] M.C. Ross, T. Himel, L.J. Hendrickson, and E. Miller. "Precise system stabilization at SLC using dither techniques". In *Proceedings of the IEEE Particle Accelerator Conference*, Stanford Linear Accelerator Center, May 1993. SLAC-PUB-6102.
- [6] F. Rouse, T. Himel, L.J. Hendrickson, and H. Shoaee. "Use of digital control theory state space formalism for feedback at SLC". In *Proceedings of the IEEE Particle Accelerator Conference*, Stanford Linear Accelerator Center, May 1991. SLAC-PUB-5470.
- [7] Bernard Widrow and Samuel D. Stearns. *Adaptive Signal Processing*. Prentice-Hall, Inc. 1985.

Instrumentation in Medical Systems

W. T. CHU

Lawrence Berkeley Laboratory, University of California, Berkeley, CA 94720

ABSTRACT

The demand for clinical use of accelerated heavy charged-particle (proton and light-ion) beams for cancer treatment is now burgeoning worldwide. Clinical trials are underway at more than a dozen accelerators. Several hospital-based accelerator facilities dedicated to radiation treatment of human cancer have been constructed, and their number is growing. Many instruments in medical systems have been developed for modifying extracted particle beams for clinical application, monitoring the delivery of the treatment beams, and controlling the treatment processes to ensure patient safety. These in turn demand new developments of instruments in controlling beam extraction, beam tuning, and beam transportation at the medical systems.

I. INTRODUCTION

There occur about 1.25 million new cancer patients annually in the US, and about 50% of them get radiation therapy in the course of their treatments. There are more than 3000 practicing radiation oncologists in the US, who rely mainly on electron linacs (~10-25 MeV) as radiation sources, which provide photon and electron beams for cancer treatment. Electrons, being light and therefore easily scattered, deposit their energy over a broad peak with ill-defined distal edge. The energy deposited by photons is characterized by an exponentially decreasing absorption with penetrating depth. In treating a deep-seated tumor, the entrance dose is always larger than the target dose, which is followed by a very gradually decreasing exit dose. These shortcomings may be overcome to a certain extent by using newly developed treatment schemes, such as three-dimensional conformal therapy [1] or tomotherapy [2], in which multiple ports of variable apertures and intensities are used to concentrate the dose inside an irregularly-shaped target volume, while spreading out, thereby diluting, the entrance and exit doses over larger surrounding tissues.

Now, consider mono-energetic heavy charged particle (proton or heavier ion) beams, which have sharp penumbrae and a definite range with a sharp Bragg peak followed by well-defined distal falloffs. By manipulating the energy (or range) of the beams, we can place a tumorcidal dose inside an irregularly shaped target volume while sparing the surrounding healthy tissues and critical organs.

If we can place a higher dose inside the target, than what was possible with conventional radiations, while keeping the doses in the surrounding tissues the same, we can expect an enhanced tumor control. If we reduce the doses in the surrounding tissues, we can expect reduced complications. Using proton beams, we can place 10% or more higher dose

inside a target without increasing the dose in surrounding tissues. Fig. 1 shows simplified description of the situation.

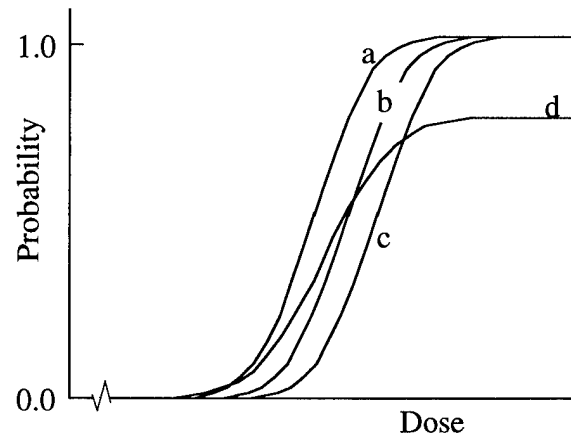


Fig. 1. For idealized treatments using conventional radiations, (a) the tumor control probability (TCP), and (b) the complication probability. If a new modality, such as protons, can shift the complication curve to (c), one can achieve the same TCP with smaller complication probability, or a larger TCP for a given complication probability. The curve (d) schematically depicts a TCP for an inaccurately delivered treatment.

For idealized treatments using conventional radiations, the curve (a) represents the tumor control probability (TCP), and (b) the complication probability. For a given dose, the difference between (a) and (b) represents the probability of tumor control without complication. Typically, the displacement of (b) from (a) is only ~5% of the dose. The sharp penumbrae and the sharp distal dose falloffs of protons help reducing the doses in surrounding critical organs, and move the complication probability curve to (c). Therefore, using a proton beam, one can achieve the same TCP with a smaller complication probability, or a larger TCP for a given complication probability than for conventional radiations. Here, the sharpnesses in penumbrae and distal dose falloffs are measured in millimeters, and small improvements makes a big difference in achieving a larger probability of tumor control without complications. The curve (d) schematically depicts a TCP for an inaccurately delivered treatment.

The conclusion is that a therapy plan using a few (2 to 4) proton ports can produce therapeutic effectiveness which is equal to, or better than, that by a three-dimensional conformal therapy plan employing a dozen different photon ports. It is an important point as the radiotherapy delivery is labor intensive, especially in therapy planning and treatment beam

delivery. Proton therapy will be cost-effective when compared with the three-dimensional conformal photon therapy.

Fifty years ago, working at the Radiation Laboratory of the University of California, Berkeley, the forerunner of the Lawrence Berkeley Laboratory (LBL), Robert R. Wilson worked out the rationale for applying accelerated heavy charged-particle beams for radiation treatment of human cancer [3]. Soon after at the 184-Inch Synchrocyclotron Cornelius A. Tobias and John H. Lawrence performed the first therapeutic exposure of human to protons, deuteron, and helium-ion beams [4]. During the ensuing half century, many clinical trials were performed using proton and light-ion beams at accelerators originally developed for physics uses. There are at least sixteen physics laboratories worldwide where clinical trials using accelerated protons are now performed, and the number is growing each year [5].

In recent years, there has been heightened interest in the medical community throughout the world to build dedicated medical accelerators. In 1991 Loma Linda University Medical Center in Loma Linda, CA commissioned a first *hospital-based* proton medical accelerator (a 250-MeV proton synchrotron) facility [6], and in 1993 the National Institute for Radiological Sciences in Chiba, Japan commissioned the Heavy Ion Medical Accelerator in Chiba (HIMAC, with dual synchrotrons, each capable of accelerating ions as heavy as Ar to an energy per nucleon of 800 MeV) [7]. These accelerator facilities were specifically built for the dedicated purpose of treating human cancer patients within the clinical centers. The second dedicated proton medical facility is now under construction at the Massachusetts General Hospital in Boston, MA [8], and another contraction plan is well under way at Waxahachie, TX [9]. Various accelerator types, including synchrotrons, cyclotrons, and linacs, will be used for hospital-based proton facilities dedicated to therapy.

The medical accelerator facility is a misnomer as the cost of the accelerator is only ~10–15% of the total construction cost. The remaining cost is distributed over the beam transport system, the clinical beam delivery systems with dosimetry and control systems (patient treatment nozzles), rotating gantries, patient positioners, and other conventional facilities.

II. CLINICAL REQUIREMENTS ON MEDICAL SYSTEMS

The design of an accelerator is normally decided by its user requirements. For physics machines, the most important accelerator parameters may be the attainable particle energy (to explore the new regions of interactions) and the beam intensity (for higher luminosity). Medical systems are no exception; the clinical requirements drive their designs. But, for medical systems the capital cost, reliability, and maintainability rate highly together with the machine performances. These characteristics are, of course, important for physics machines also; but the levels of requirements for them are far more stringent for medical machines. For example, a reliability of 85% may be considered excellent for a physics facility, but such a reliability is not even acceptable for a medical facility,

which requires a reliability better than 95%. The high capital cost of physics machines has been justified by the importance of the anticipated scientific discoveries and the potential values of their long-term trickle-down technologies, until recently when the social relevance came into being used to gauge the immediate cost-benefit relationship of scientific investments. The medical community has been more pragmatic. No hospital will build a medical accelerator facility unless there is a reasonable assurance of amortizing the investment during its useful life.

A recent LBL report reviewed clinical requirements of a proton therapy accelerator facility, which place stringent specifications on the accelerator and proton-beam parameters [10]. Many specialized instruments have been developed to satisfy these diverse and stringent clinical requirements, which are discussed in several recent review papers [11, 12]. These papers mainly dealt with instrumentation developed to modify (and monitor) heavy charged-particle beams extracted from accelerators to be suitable for treatment of human cancer. This paper discusses how these instruments placed constraints on medical systems, and consequently what new instrument developments must be made for medical systems.

III. BEAM TUNING

(a) Beam Emittance

In treating small targets, such as an arteriovenous malformation (AVM), a particle beam with a small cross-section and small divergence is needed. For example, in treating an AVM of $5 \times 5 \times 5 \text{ mm}^3$ at a depth of 10 cm, the multiple scattering will spread out the beam laterally by $\sigma_y = 0.23 \text{ mm}$, or the emittance of an "ideal" pencil beam will grow to $\sim 1.2 \times 10^2 \text{ mm-mrad}$. A typical transverse emittance of the beam obtained through resonant extraction from a synchrotron is $\epsilon \approx 5\pi \text{ mm-mrad}$ unnormalized, at 200 MeV proton energy, measured at the accelerator exit. Such an emittance is an order of magnitude smaller than the scattering effect inside the patient body, and therefore acceptable.

The beam intensity (number of protons/cm²/sec) needed for such a small-target treatment is only a very small fraction of a typical synchrotron output current. It allows the beam emittance to be made arbitrarily small through collimations as needed. On the contrary, if the treatment time is limited to two minutes, the beam particles cannot be thrown away by collimation for treating large areas, up to $40 \text{ cm} \times 40 \text{ cm}$. Even for large fields, the small beam emittance must be preserved if the field is produced using, for example, a pencil-beam scanning system. The emittance should be measured immediately upstream of the scanning magnets.

The beam emittance determines the gap sizes of the transport magnets. This implication becomes very acute for those magnets on a rotating gantry, because the total weight of the magnets on it drives the gantry structure and therefore its cost. An H^- synchrotron has been seriously considered for a medical application because its transverse emittance of the beam obtained through charge-exchange extraction is small, $\epsilon \approx 0.1\pi \text{ mm-mrad}$ [9]. (The idea was dropped because the

expected difficulties in maintaining the required high vacuum ($<10^{-10}$ torr) needed for a H^- synchrotron in a hospital setting. Accelerator physicists contended that such a vacuum could easily be maintained if a knowledgeable expert were around. A hospital cannot afford such an expert, and a medical system must be designed to operate without the need of resident experts except in cases of major repairs.)

(b) Beam Optics

A rotating gantry is needed to satisfy the clinical requirement that the treatment beams must be brought into the patient, usually in horizontal position, from any angle (4π sterad). The beam optics of a gantry takes a horizontally transported beam and bends it 180, 270, or even 360 degrees depending on the gantry design. When the gantry is rotated, the x- and y-axis of the beam optics are also rotated and mixed. As the clinical beam delivery system on the gantry demands a circularly symmetric beam (emittance $\epsilon_x = \epsilon_y$), the beam focusing elements on the gantry should be designed to preserve the circular beam spot of the incident beam ($\epsilon_x = \epsilon_y$) at any gantry angle and at any proton energy. At a physics facility, such a problem will be solved by providing a 6-dimensional phase-space detector at each crucial point in the beam transport system. In a medical system, we need the instrumentation that not only to ascertain the correct conditions routinely (*i.e.*, without physicists), but also correct the beam automatically, quickly and reliably. Any failure to achieve the correct beam configurations by the control system must be automatically reported to the treatment technologists.

The usual beams extracted from an accelerator are pencil beams, which have to be laterally broadened to cover the targets, which can be as large as 40 cm \times 40 cm. The beam can be broadened by scattering. The scattered beams usually result in two-dimensional Gaussian-like distributions, which must be further flattened to meet the clinical specification on the dose uniformity of $\pm 2.5\%$. "Contoured filters" are used at many proton therapy centers to flatten the scattered beams. For a contoured filter to work properly, the beam spot must be tuned to be circular ($\epsilon_x = \epsilon_y$), centered on the filter axis, and also the beam tuned parallel to it. An off-axis misalignment of 1-mm will result in an unacceptable lateral variation of dose to $\pm 7\%$. In medical systems, instrumentation should be provided to verify the correct tuning of the beam spot size and shape, beam position, and beam angular orientation.

The dynamic beam delivery systems, *e.g.*, wobblers or scanners, are developed to overcome the undesirable necessity of scattering materials in the beam. But the real benefit is their insensitivity to small misalignments of the beams. If the beam is misaligned by 1 mm, the entire scanned field will be shifted by 1 mm, which will be compensated by the patient collimation. As long as the incident beams into the scanner do not move during the scan, the desired uniformity will be achieved.

(c) Beam energy

The clinical requirement is to provide variable ranges in steps of 0.1 g/cm², and 0.05 g/cm² for ranges <5 g/cm², between and during treatments. It may be accomplished in

several ways. For a synchrotron, the beams may be extracted at different energies, and transported to the patient. As discussed above, this implies the tracking of all transport magnets and preserving the desired beam emittance and beam spot size and shape throughout the transport system including the gantry optics. The energy switch should be accomplished and ascertained within 2 minutes without an intervention of human operators. When a dynamic beam delivery, such as beam scanning, is used, the beam energy switching must be accomplished from pulse to pulse of the extracted beams (*e.g.*, 2 Hz). For a cyclotron, the beam may be extracted at the full energy, and degraded and momentum analyzed before transported to the patient. The magnet tracking requirements are the same as for synchrotrons as the degrader is placed near the cyclotron and far away from the treatment rooms to reduce the background radiation. In medical systems, we need the instrumentation to tune globally the accelerator, beam transport system, and the patient beam delivery system such that the correct beam geometry is established quickly and reliably.

(d) Energy Spread, $\Delta E/E$

The width of a Bragg peak of a mono-energetic heavy charged-particle beam extracted from an accelerator and stopping in water (or tissue) originates from the energy straggling in the absorbing medium and from the energy spread, $\Delta E/E$, of the incident beams. For example, a truly mono-energetic 150-MeV proton beam will show a width of 1.6 mm at the end of a 15-cm range in water due to the energy straggling. If the beam is extracted from a typical synchrotron, the energy spread in the beam in one extraction pulse is $\Delta E/E \approx 10^{-4}$ (representing 0.015-mm spread in water), and $\Delta E/E \approx 10^{-3}$ (0.15-mm spread in water) for the energy spread among several pulses (a treatment requires always more than several pulses). In this case, the energy straggling in the absorbing medium (patient body) is the major contributor in broadening the width of the Bragg peak. The particle beams from cyclotrons have about an order of magnitude larger $\Delta E/E$ within a pulse and among several pulses than those for synchrotron pulses. An energy spread among several extracted pulses of $\Delta E/E \approx 10^{-2}$ will contribute a comparable range spread as the range straggling inside the absorbing medium. The particle beams from a cyclotron are extracted at the full energy, and subsequently degraded to obtain lower energies. Therefore, to satisfy the clinical requirement that the distal dose falloff be not more than 1 mm over the straggling in water, it is important to momentum analyze an energy-degraded beam to obtain a smaller $\Delta E/E < 10^{-3}$. There should be provided an instrumentation to measure the energy spread of the beams.

IV. BEAM EXTRACTION CONTROL

(a) Uniform spill

The clinical requirement on the dose compliance is that the delivered dose should be within $\pm 2.5\%$ of the prescribed dose over treatment fields, which can be as large as 40 cm \times 40 cm. The requirement may be achieved by dynamic beam delivery, *e.g.*, wobbling or scanning. A constant scan speed will

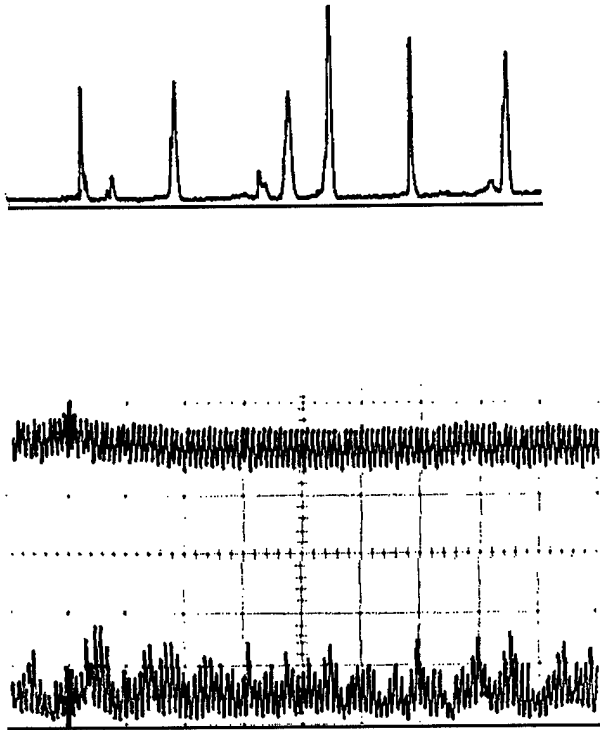


Fig. 2. (a) Top trace: The beam intensity distribution as a function of time (0.2 msec per division) obtained by a resonant extraction with no feedback. (b) Middle trace: The spill control signal used as the feedback. (c) Bottom trace: The uniform beam intensity distribution obtained through the spill control algorithm. The total number of particles under the peaks in (a) and (c) are the same. The vertical scale in (a) is greatly reduced compared to that of (c).

produce a uniform dose across the scan field if the intensity of the scanned beam is held constant during the scan. At the LBL Bevatron, a flat-top extraction (800-msec long) was used for a raster scanning scheme of 40 Hz in x direction and 0.5 Hz in y direction. As shown in Fig. 2(a), the resonance extraction used by nuclear physics experiments provided the beam spills whose peak-to-average flux ratio was $>30/1$, which was totally unacceptable for beam scanning. A uniform extraction intensity distribution was obtained through a feedback signal (b) resulting in the peak-to-average flux ratio of $\approx 3/1$ as shown in (c). The intensity output signal was from an annular scintillator surrounding the beam pipe looking at the halo of the extracted beam (called Beam Frequency Detector or BDF). Depending on the requested extraction level and the level attainable by the total number of circulating particles, the spill intensity reference (REF) was set for pulse-to-pulse to within a factor of $\approx 2-3$. This reference was set using a set of attenuators at the injector (mechanical sieves), which had a dynamic range of 1000:1. The feedback signal (b) was formed by a linear combination of three signals, namely, an integral of (BDF-REF) for an overall long-term control, the immediate real-time signal of (BDF-REF), and a sawtooth signal with a

two-times the spill frequency. A spill control chassis using this feedback signal controlled the ramping of the perturbing magnet (S1 extraction magnet) located upstream of the septum magnet. The attained uniformity of the extracted beam intensity was quite acceptable for the raster scanner system. The time structures in intensity over 10 kHz were not resolved by the raster scanned field and therefore tolerated, but the structures under ≈ 1 kHz had to be reduced as much as possible. A uniform intensity extraction is more readily achieved from a cyclotron. The linac's low duty factor in beam spills makes it not practical to use the beam scanning.

(b) Intensity control

One method of providing a spread-out peak is through range stacking, in which the beams are extracted from an accelerator at various predetermined energies, and different ranges are stacked inside the target depth. To save the energy steps, the width of the Bragg peak may be moderately spread out (e.g., 5 mm in water), and these 'mini-peaks' are stacked to cover the entire depth of the target. To obtain a desired slope of spread-out peak, an appropriate fluence (number of particles/cm²) of particles must be deposited at each range. This method of range stacking by varying the extraction energy is conceptually simple, but hard to implement as it requires not only changing the extraction energy pulse-to-pulse, but also accurately tracking all the beam transport elements from the accelerator to the patient so that the beam spots of different energies do not wander around. The energy precision needed is $< \pm 0.4$ MeV over the entire range of the extraction energy.

(c) Intensity modulation

In a pencil beam scanning method, high spatial modulation of deposited fluence at each range is needed, to obtain a dose compliance of better than $\pm 2.5\%$ of the prescribed dose across the field [13]. The dynamic range needed for spatial fluence modulation is about a factor of 20. Such spatial modulations may be achieved in any of the following three ways: by a raster scanner with variable scan speeds relying on uniform beam-extraction intensities, a raster scanner with a constant scan speeds using extractions with modulated intensities, or a raster scanner with variable scan speeds and modulated-intensity beam extractions. At LBL Bevatron, using the feedback system, an intensity modulation of a dynamic range of 7 with a time constant of 5 kHz was achieved.

(d) Beam gating

Instead of a range-modulating propeller, a wheel with several concentric annular tracks, divided into various absorber thicknesses, may be used to make various widths and slopes of spread-out peaks. The desired results are achieved by rotating the wheel and turning the beams on and off synchronously with the angular position of the wheel. For a cyclotron the beam gating with a 50 μ sec time constant can be provided by turning on and off the ion source current.

Large treatment fields may be achieved using a pixel scanner, in which the beam spot is moved to a predetermined position and an appropriate particle fluence is deposited, then the beam spot is moved to the next position, and the process repeats [14]. Often, it is impractical to gate the extraction or

injection using the detectors located in or near the treatment rooms, which are 50-100 meters away. In the pixel scanning system, the beam is shut off by a fast kicker magnet (50 μ sec response time) located next to the scan magnet, which moved the beam into a collimator jaw, while moving the beam spot to the next position.

(e) Beam cutoff

There are many occasions that call for accurate beam cutoffs. At the end of a treatment, when the prescribed dose is achieved, the beam into the patient must be immediately cut off. At LBL Bevatron, at the beginning of each dosimetry cycle (the Bevatron extraction), a set of preset scalars, connected to dose detectors, were loaded, and the one reaching the 'preset' first initiated the beam abort procedure by clamping the extraction magnets, stopping the beam within 50 μ sec. The beam abort procedure proceeded outside the computer-based control system. The backups was also accomplished completely outside the control system. At the beginning of each treatment, a set of manual preset scalars were set to 2% above the prescribed counts, which would initiate the beam abort procedure if the other systems were to fail.

(f) Instantaneous intensity

An extremely large instantaneous intensity ($>10^{12}$ protons/cm²/sec) should be avoided for various reasons. Ionization chambers using air or nitrogen gas at the atmospheric pressure may start saturating due to ion recombinations at about 10^{12} protons/cm²/sec. If the local dissolved oxygen in the tissue were depleted by a high instantaneous dose rate, a different biological response to the radiation will take place, and the translation of physical dose to biological dose becomes uncertain. Some accelerators have tendencies to spill accidentally an entire circulating beam during a slow extraction. Such accidental spills will have adverse consequences, especially in dynamic beam delivery, such as in pencil beam scanning.

V. SUMMARY

To achieve a full potential of proton treatment, further technological developments are needed to reduce local failures. Pencil-beam scanning technology must be developed to achieve three-dimensional dynamic conformal therapy. Beam scanning imposes stringent requirements on the accelerator facility performance, such as beam-energy variability, energy step size and switching time, beam emittance, beam position and angular precision and stability, duty factor of the extracted beams, beam intensity control as a function of time, uncontrolled intensity fluctuations, and control systems in order to assure patient safety. In order to operate effective medical systems, reliable and cost-effective instrumentation must be developed to monitor and control these parameters.

ACKNOWLEDGMENTS

The author wishes to thank Tim Renner, Bernhard Ludewigt, Krista Marks, Mark Nyman, R. P. Singh, and Ron Stradtner for making important contributions in the

development of many instruments described in this article. This work is supported by the Director, Office of Energy Research, Energy Research Laboratory Technology Transfer Program, of the U.S. Department of Energy under Contract No. DE-AC03-76SF00098.

REFERENCES

1. Smith, A. R. and Purdy, J. A. (guest editors), *Int. J. Radiat. Oncol. Biol. Phys.* 21, 1991.
2. Macker, T. R., *et al.*, *Med. Phys.* 20, 1709-1719, 1993.
3. Wilson, R. R. *Radiological Use of Fast Protons.* *Radiology* 47, 487-491, 1946.
4. Tobias, C. A., Roberts, J. E., Lawrence, J. H., Low-Beer, B. V. A., Anger, H. O., Born, J. L., McCombs, R. and Huggins, C. *Irradiation hypophysectomy and related studies using 340-MeV protons and 190-MeV deuterons* 1-95-106 Geneva, 1955.
5. For an up-to-date information on proton therapy trials, contact Janet Siserson, Harvard Cyclotron Laboratory, SISTERTSON@HUHEPL.Harvard.edu.
6. Coutrakon, G., *et al.*, *Study of the Loma Linda Proton Medical Accelerator.* *Medical Physics* 21, 1994.
7. Yamada, S. *Commissioning of the Medical Synchrotron HIMAC, Abstracts for the Thirteenth Int. Conf. on the Application of Accelerator in Research & Industry, Denton, Texas, Nov. 7-10, 1994 (1994).*
8. Flanz, J. *Overview of the MGH Northeast Proton Therapy Facility Plans and Progress, Abstracts for the Thirteenth Int. Conf. on the Application of Accelerator in Research & Industry, Denton, Texas, Nov. 1994 (1994).*
9. "The TERA Project and the Centre for Oncological Hadrontherapy", edited by U. Amaldi and M. Silari, *Progetto ADROTERAPIA, Istituto Nazionale di Fisica Nucleare, (1994).*
10. Chu, W. T., Staples, J. W., Ludewigt, B. A., Renner, T. R., Singh, R. P., Nyman, M. A., Collier, J. M., Daftari, I. K., Kubo, H., Petti, P. L., Verhey, L. J., Castro, J. R. and Alonso, J. R. *Performance Specifications for Proton Medical Facility, March 1993, LBL-33749, (1993).*
11. Chu, W. T., Ludewigt, B. A. and Renner, T. R. *Instrumentation for Treatment of Cancer Using Proton and Light-Ion Beams. Reviews of Scientific Instrument, 64, 2055-2122, 1993.*
12. Chu, W. T. *Instrumentation for Medical Beams. Proc. of the Beam Instrumentation Workshop, October 2-6, 1994, Vancouver, Canada (to be published in AIP Conference Proceedings), 1995.*
13. Brahme, A., Källman, P. and Lind, B. K. *Optimization of proton and heavy ion therapy using an adaptive inversion algorithm. Radiotherapy and Oncology* 15, 189-197, 1989.
14. Pedroni, E., Blattmann, H., Böhringer, T., Coray, A., Lin, S., Scheib, S. and Schneider, U. *Voxel Scanning for Proton Therapy. Proc. of the NIRS International Workshop on Heavy Charged Particle Therapy and Related Subjects, July 1991, Chiba, Japan, 94-109, 1991.*

LASER DIAGNOSTICS OF A ONE-DIMENSIONAL ORDERED ION BEAM.

R. Calabrese, V. Guidi*, P. Lenisa, U. Tambini, University of Ferrara, 44100 Ferrara, Italy
E. Mariotti and L. Moi, University of Siena, 53100 Siena, Italy

A novel method to detect ordering within a one-dimensional ion beam is proposed. The method exploits detection of fluorescence induced by two laser beams which simultaneously cross the ion beam. Appearance of correlation in fluorescence signal while moving the distance between the laser beams is indication of ordering in the beam.

I. INTRODUCTION

The possibility to observe ordered structures within an ion beam has met the interest of the community of accelerator people [1]. One of the crucial problems in this new research field is the diagnostic of an eventual ordered state for the ion beam. Experiments carried out in ion traps have shown that a record of crystallization is achieved by observing the fluorescence signal of ions through CCD camera [2]. Unfortunately, this technique cannot be applied straight away to accelerators since ions are traveling at relatively high velocity.

It is the purpose of this paper to show a method to detect ordering of an ion beam for one-dimensional ion structures.

II. THE DIAGNOSTICS DEVICE

Consider the simplest structure that is expected to be formed in a storage ring: a string of ions [3]. Typical values of interparticle spacing for the string configuration lie between $s=10-100 \mu\text{m}$; for the following we shall assume $s=50 \mu\text{m}$.

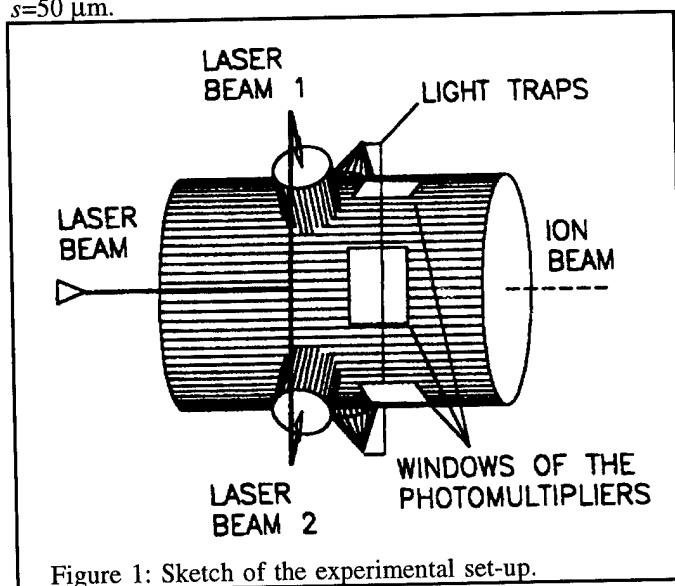


Figure 1: Sketch of the experimental set-up.

A pulsed laser - resonant with the traveling ions - is split in two parts, which simultaneously cross the ion beam at right angle at two nearby positions along the storage ring (see Figs. 1,2). This laser-to-ion crossing area is followed by four photomultipliers, which detect the photons emitted by the ions that have previously been excited by the laser beams.

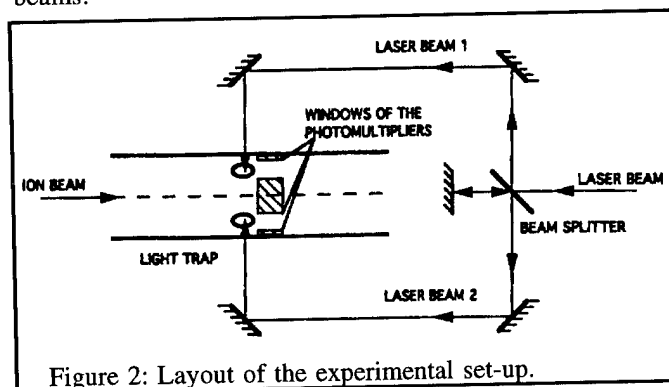


Figure 2: Layout of the experimental set-up.

The signals recorded by the photomultipliers are analyzed when one laser beam is moved with respect to the other one. In the absence of ordering, no correlation in fluorescence signals should be recorded while changing the relative distance of the two laser beams. On the contrary, if a string were obtained as a result of cooling, a strong correlation between the signals should be observed. Suppose that one of the four photomultipliers detects the fluorescence of an ion excited by one of the laser beams. If one of the other three photomultipliers detects a simultaneous fluorescence signal, it means that the other laser has interacted with another ion in the string, in turn indicating that the distance between the two ion-to-laser crossing points is an integer multiple of the string interparticle spacing. Then, by slightly moving the second laser beam, the correlation signal should vanish. A sort of periodical dependence on the distance between the laser beams should appear.

At non-zero temperature, ions are expected to oscillate both in the transverse and longitudinal directions (incoherent motion). Moreover, for a string longitudinal oscillations of equilibrium positions can also occur (coherent motion) through long-range waves. For the diagnostic system concerned through this paper the distance between the two laser beams can be chosen to match interparticle spacing of the string. In this case, the effect of coherent motion is ineffective as the nearest-neighbor spacing is relatively uniform. The effect of long wavelength on interparticle oscillations is negligible for a relative distance of a few lattice steps. An analytical evaluation of this effect can be found in Ref. [4]. Short

*Corresponding author.

wavelengths mostly affect the fluctuations in interparticle spacing, δs . Based on Ref. [4], a rough estimate holds: $\langle \delta s^2 \rangle / s^2 \sim 1/\Gamma$, where Γ is the plasma parameter for the ion beam (ratio between average neighboring ions Coulombic energy and thermal one). When the ion beam is being cooled δs becomes even lower than s ; as an example, at $\Gamma = 100$, $\delta s = 5 \mu\text{m}$. As distance between the laser beams increases, the correlation signal becomes progressively weaker.

The configuration of the diagnostic device can also compensate for a possible influence of transverse oscillations. Since the laser beams cross the string perpendicularly and their spots are small enough that they do not overlap, the ions suffering transverse oscillations in the direction of the laser can always be resonant, irrespective of their coordinates along that axis. Ion oscillations in direction orthogonal to both the laser and the string could in principle move the target ion outside the laser beam spot. To avoid this effect - and the consequent less efficiency - the laser beam can be focused by a cylindrical lens. This optical element can be arranged to produce a focal segment orthogonal to the directions of both the laser and the string. In this way the locations where the laser beams impinge on the string are two thin regions; these can be as wide as several hundreds of microns in one dimension without overlap between them. Transverse oscillations of a very cold ion beam are expected to be lower than this value.

A single ion of the beam interacts with the laser beam for very short time, t_{int} . The probability of excitation to the upper level $P(t_{\text{int}})$ is:

$$P(t_{\text{int}}) = \left(\sin \frac{\omega_R t_{\text{int}}}{2} \right)^2$$

where ω_R is Rabi frequency for the transition under consideration, which is proportional to the square root of the laser intensity. Thus, a reasonable interaction probability requests a sufficiently high laser intensity to make up for the short interaction time. This is not a problem since pulsed lasers are several times as intense as the saturation intensity for the ions that could be laser-cooled and a good excitation probability ($\sim 1/2$) can be achieved. Moreover the focusing lens increases the intensity of the laser beam at the interaction point.

III. MONTE CARLO SIMULATION

A Monte Carlo simulation was specifically developed to show the feasibility of the method. The simulation includes all the physical processes involved, such as excitation probability by the two laser beams, probability of spontaneous decay, geometrical acceptance of the detector system, filtering and quantum efficiency of the photomultipliers. Also considered are the finite size of the laser beams at the focalization points and the dynamic behavior of the system due to non-zero temperature of the ions in the beam.

For more details about the Monte Carlo simulation and the detection system see Ref. [5].

As a first example we shall consider the case of a string of $^{22}\text{Mg}^+$ ions circulating in the ASTRID Storage Ring (Aarhus) at $\Gamma = 100$ with $s = 50 \mu\text{m}$. Ion velocity is $\beta = 0.003$, which corresponds to a time of about 56 ps taken by an ion in the beam to travel a distance as big as interparticle spacing. A duration of 2 ps was chosen for the laser pulse. Figure 3 illustrates the fluorescence response as a function of the distance between the two laser beams. Appearance of fluorescence peaks is visible in the figure when the distance between the laser beams is an integer multiple of the string spacing. Also the results of simulation for a disordered beam with the same density as the string is shown; in this case a totally uncorrelated pattern is achieved and the fluorescence signal is related only to stray counting of the photomultipliers.

It is remarkable that a clear firm of ordering within the ion beam can be achieved with only 1 s acquisition time, i.e. much less than beam lifetime in the storage ring.

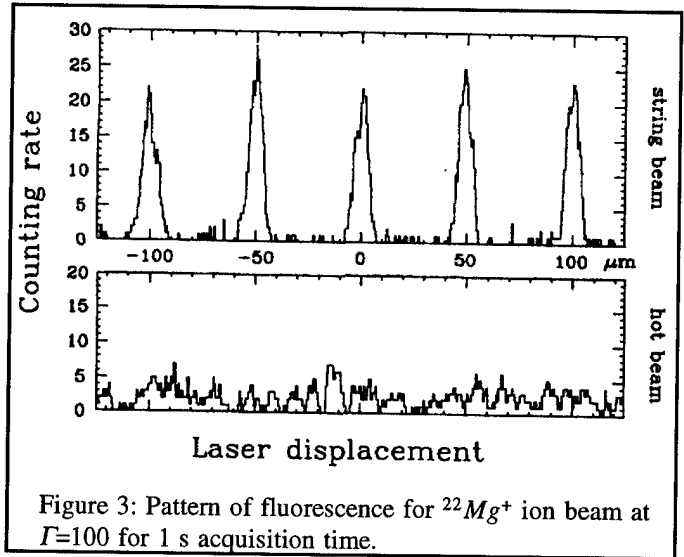


Figure 3: Pattern of fluorescence for $^{22}\text{Mg}^+$ ion beam at $\Gamma = 100$ for 1 s acquisition time.

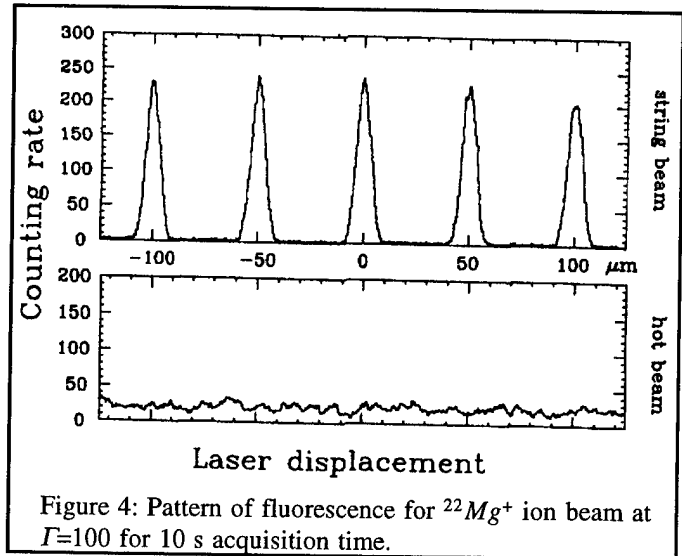


Figure 4: Pattern of fluorescence for $^{22}\text{Mg}^+$ ion beam at $\Gamma = 100$ for 10 s acquisition time.

The same simulation was carried out with the laser and beam parameters as for Fig. 3 but with a longer acquisition time (10 s). In this case correlation peaks have become more neat due to counting over a longer interval (Fig. 4).

A higher temperature of the beam, i.e. a lower plasma parameter, implies wider oscillations of interparticle positions.

As an example, Fig. 5 shows the correlation response at $\Gamma=50$.

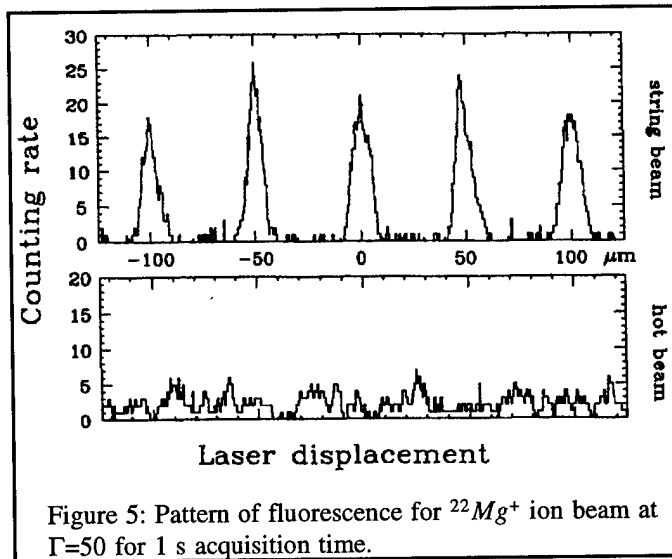


Figure 5: Pattern of fluorescence for $^{22}\text{Mg}^+$ ion beam at $\Gamma=50$ for 1 s acquisition time.

The simulation was carried out also for the case of $^7\text{Be}^+$ ion beam at TSR (Heidelberg) at $\Gamma=100$. Ion velocity is higher for this storage ring ($\beta=0.05$) and therefore one should resort to still shorter pulse duration for the laser. A commercially available 200-fs pulsed laser with some nJ/pulse was considered in the Monte Carlo and results are shown in Fig. 6. Correlation peaks are shorter, with respect to the case of $^{22}\text{Mg}^+$, due to lower quantum efficiency of photomultipliers and to the more complicated level structure of $^7\text{Be}^+$.

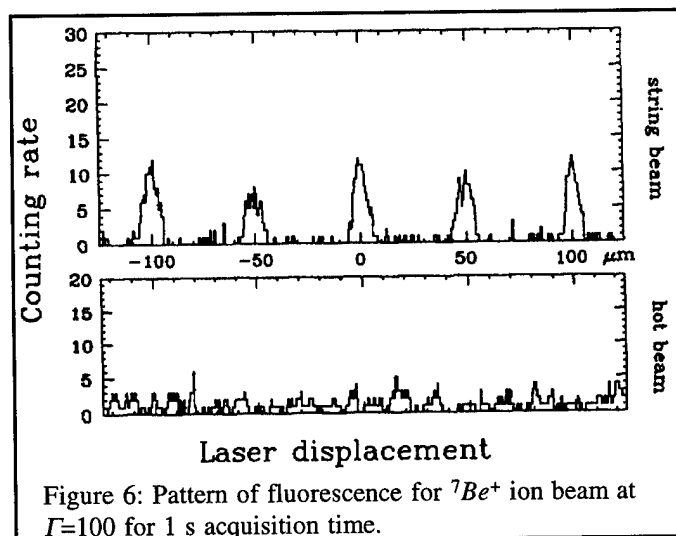


Figure 6: Pattern of fluorescence for $^7\text{Be}^+$ ion beam at $\Gamma=100$ for 1 s acquisition time.

Table I summarizes the important parameters for the previous cases.

Table I: *Important parameters for the simulation*

Storage ring	TSR	ASTRID
β	0.05	0.003
ion species	$^7\text{Be}^+$	$^{22}\text{Mg}^+$
wavelength	313 nm	280 nm
upper state lifetime	8.7 ns	3.5 ns
lower state lifetime	groundstate	groundstate
laser repetition rate	50 MHz	50 MHz
pulse duration	200 fs	2 ps

IV. DISCUSSION

It has been shown that the method is useful as a diagnostic tool to detect ordering in one-dimensional systems. The method enables to resolve the single-ion structure of the beam. Finally we wish to point out that all components of the system are commercially available and that the diagnostics could be easily implemented in one of the existing storage rings.

V. REFERENCES

- [1] J.P. Schiffer and P. Kienle, Z. Phys. A **321** (1985) 181.
- [2] I. Waki, S. Kassner, G. Birkel, and H. Walther, Phys. Rev. Lett. **68** (1992) 2007.
- [3] R.W. Hasse and J.P. Schiffer, Ann. Phys. **203** (1991) 419.
- [4] V.V. Avilov and I. Hofmann, Phys. Rev. E **47** (1993) 2019.
- [5] R. Calabrese, V. Guidi, P. Lenisa, U. Tambini, E. Mariotti and L. Moi, "Stroboscopic Laser Diagnostics for Detection of Ordering in One-Dimensional Ion Beam", submitted.

DETERMINING ELECTRON BEAM PARAMETERS FROM EDGE RADIATION MEASUREMENT RESULTS ON SIBERIA-1 STORAGE RING

O. V. Chubar, Russian Research Center KURCHATOV INSTITUTE, Moscow, 123182, RUSSIA

The paper deals with practical application of the method for electron beam diagnostics by means of edge radiation (ER) [1] on the Siberia-1 storage ring. In this application, each measurement of the ER intensity distribution allows one to determine a linear combination of three second-order moments of particle density distribution in transverse phase space. It is shown that, when combining data on the storage ring magnet lattice with the results of two ER intensity distribution measurements (performed at different distances from bending magnet edges), the totality of beam parameters, including horizontal and vertical RMS transverse sizes, angular divergences, energy spread, emittances and mixed moments can be determined.

I. INTRODUCTION

A possibility to determine angular divergences, transverse sizes and emittances of electron beam in a storage ring from measured intensity distributions of the edge radiation (i.e., the radiation generated at bending magnet edges) was stated in former related works [1] - [3].

Logical foundation of the ER-based method for electron beam diagnostics is very simple. The ER and the radiation emitted within elements of electron beam optics in storage rings was found to be very sensitive to angular divergences and transverse sizes of the electron beam [1]. Therefore, if one can measure the ER intensity distributions and perform precise calculation of the corresponding distributions for particular magnet lattice and measurement system, at different values of the beam parameters, then one can determine the real beam parameters as a result of fitting the measured and computed ER intensity distributions.

In Refs. [1], [2] general attention was paid to methods for effective computation of the ER intensity distributions in view of electron beam parameters, the methods being elaborated especially for the electron beam diagnostics. In Ref. [3] an emphasis was done on experimental equipment for the ER-based diagnostics. Though precise computation and measurement of the ER intensity distributions are very important for the beam diagnostics method concerned, these still are not sufficient for the "full-scale" implementation of the method. The main subject of this paper is treatment of the ER measurement results in order to determine electron beam divergences, transverse sizes and emittances.

In this paper, general attention is paid to the case of "empty" straight section between bending magnet edges (when no hard focusing elements are located within the straight section). This case was chosen for consideration due to two reasons: first, it is more simple for understanding the

main features of the ER-based method, and second, the situation takes place in the Siberia-1 450 MeV electron storage ring (Kurchatov Synchrotron Radiation Source, Moscow), where the experimental part of this work was done. The main distinctions from the case concerned one should keep in mind when applying the ER-based method to hard-focusing machines, are discussed at the end of the paper.

II. MEASURING AND FITTING THE ER INTENSITY DISTRIBUTIONS

Scheme of the ER measurement system installed on the Siberia-1 storage ring is shown in Figure 1. The system allows one to measure the ER intensity distributions simultaneously at two different distances from the middle of straight section, $y_1 < y_2 = y_{21} + y_{22}$. One can see from consideration presented in the next chapter that for optimal layout, the reference value separating y_1 and y_2 should be the value of horizontal beta-functions in some point within the straight section: $y_1 < \beta_x < y_2$. In this case the ER intensity distribution at y_1 is more sensitive to beam transverse size, and vice versa, the distribution at y_2 "feels" beam divergence better than the transverse size.

It can be shown analytically and numerically, that in the case of "empty" straight section (see note above) the ER

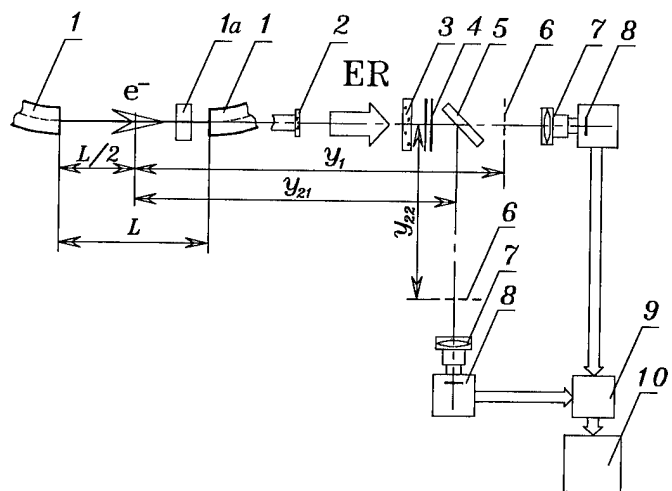


Figure 1: Scheme of the ER measurement system on the Siberia-1.

1- bending magnet; 1a- steering magnet; 2- extraction window; 3- neutral filters; 4- interference filter; 5- semitransparent mirror; 6- object plane; 7- lens; 8- CCD-matrix camera; 9- interface; 10- computer.

intensity distributions depend on RMS electron beam divergences $\sigma_{x'}$, $\sigma_{z'}$ and transverse sizes σ_x , σ_z in combinations:

$$\begin{cases} \sigma_{x'eff}^2 \equiv \sigma_{x'}^2 + \sigma_x^2/y^2 + 2M_{xx'}/y; \\ \sigma_{z'eff}^2 \equiv \sigma_{z'}^2 + \sigma_z^2/y^2 + 2M_{zz'}/y, \end{cases} \quad (1)$$

where $M_{xx'}$, $M_{zz'}$ are second-order central mixed moments of particle density distribution in transverse phase space, y is distance from some "initial point" within straight section or at bending magnet edges, to detector. The values of $\sigma_{x'}$, $\sigma_{z'}$, σ_x , σ_z , $M_{xx'}$, $M_{zz'}$, $\sigma_{x'eff}$, $\sigma_{z'eff}$ refer to the initial point (in most cases, it is more convenient to set the point in the middle of the straight section). It is worth mentioning that the feature is valid for large as well as for small distance y (as compared with the straight section length).

According to the preceding, one value of $\sigma_{x'eff}$ and one value of $\sigma_{z'eff}$ can be potentially determined from the ER intensity distribution measured at one distance y . Actual possibility to determine $\sigma_{x'eff}$ or $\sigma_{z'eff}$ depends on the straight section length L , bandwidth $\Delta\lambda$ of the monochromatic filter used, beam energy, detector dynamic range. Approximately, one can show that for the straight section large enough and the standard commercially available CCD detector, $\sigma_{z'eff}$ can be determined with appropriate precision if it takes place $\sigma_{z'eff} > \sqrt{\Delta\lambda/(2L)}/4$.

Figure 2 illustrates the fitting of measured and computed ER intensity distributions performed to determine $\sigma_{x'eff}$ and $\sigma_{z'eff}$.

III. DETERMINING ELECTRON BEAM PARAMETERS

Each of the two Eqs. (1) has three unknown beam parameters: $\sigma_{x'}$, σ_x , $M_{xx'}$ ($\sigma_{z'}$, σ_z , $M_{zz'}$). Therefore, formally, one can perform three independent measurements of the ER intensity distributions, at three different distances y , determine three values of $\sigma_{x'eff}$ ($\sigma_{z'eff}$) and solve non-homogeneous system of three algebraic equations with three unknowns: $\sigma_{x'}^2$, σ_x^2 , $M_{xx'}$ ($\sigma_{z'}^2$, σ_z^2 , $M_{zz'}$).

From the procedure described, vertical beam emittance ϵ_z can be readily determined: since vertical dispersion is negligible in most cases, then

$$\epsilon_z = (\sigma_z^2 \sigma_{z'}^2 - M_{zz'}^2)^{1/2}. \quad (2)$$

However, due to horizontal dispersion, the corresponding equation is not valid for horizontal motion (formally, one can find the value $(\sigma_x^2 \sigma_{x'}^2 - M_{xx'}^2)^{1/2}$, yet it is not integral of motion). Besides, some practical problems may take place when realizing the procedure described: it may appear not to be convenient to perform three independent measurements of the ER intensity distributions simultaneously or, if differences between distances y used are not large enough, the errors of the parameters determined may appear to be too large.

In Ref. [3], we used an additional assumption that $M_{xx'} = M_{zz'} = 0$ in the middle of the straight section. This allowed us to use two simultaneous ER measurements instead of three ones. Though rather judicious, the assumption still reduced the precision of data on beam parameters we obtained.

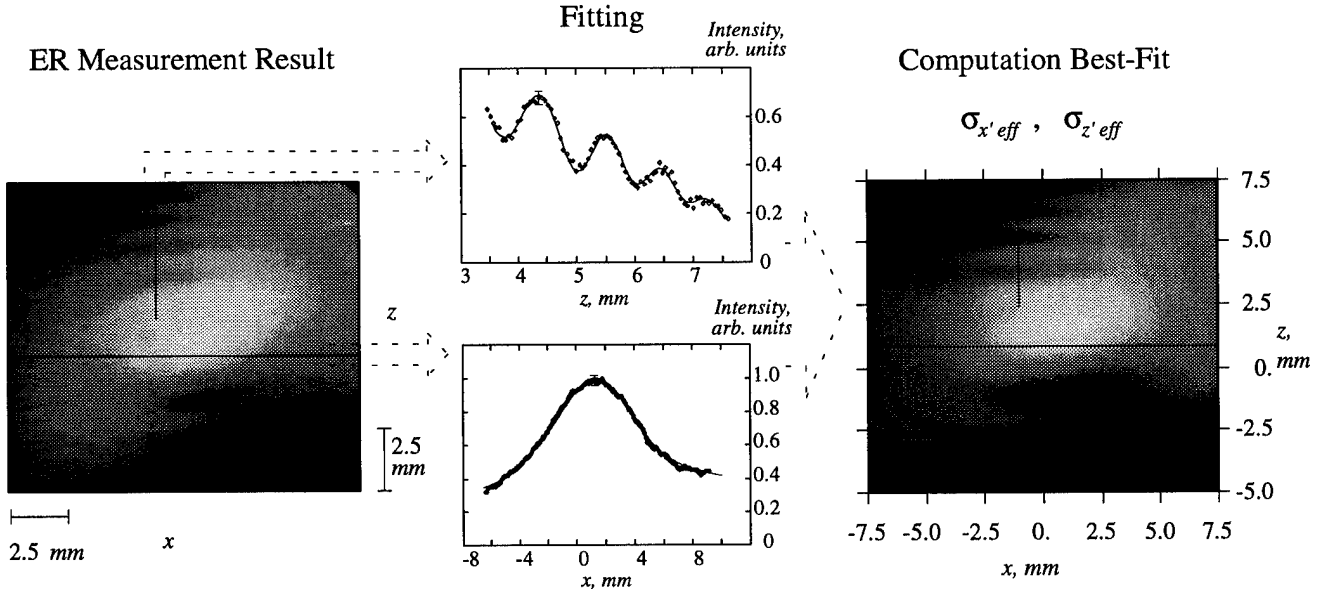


Figure 2: Fitting of measured and computed ER intensity distributions in order to determine $\sigma_{x'eff}$ and $\sigma_{z'eff}$.

◊ - experiment; — - computation best-fit.

The measurements were done at electron energy $E = 400$ MeV, wavelength $\lambda = 648 \pm 2$ nm, $y = 199$ cm.

Intensity distribution along horizontal line passing through global maximum allows one to determine: $\sigma_{x'eff} = 0.90 \pm 0.07$ mrad; the distribution along vertical line crossing interference oscillations far from the pattern center gives: $\sigma_{z'eff} = 0.068 \pm 0.007$ mrad.

More efficient way to determine the electron beam parameters from the ER measurement results is to use more information on the magnet structure. One can use the well-known expressions representing the second-order central moments through Twiss functions and beam emittance (the expressions can be readily obtained, for example, with the Moment method). This approach gives for vertical motion:

$$\begin{cases} \sigma_z^2 = \varepsilon_z \beta_z; \\ \sigma_{z'}^2 = \varepsilon_z \gamma_z; \\ M_{zz'} = -\varepsilon_z \alpha_z; \\ \sigma_{z'eff}^2 = \sigma_{z'}^2 + \sigma_z^2 / y^2 + 2M_{zz'} / y. \end{cases} \quad (3)$$

Here we have a non-homogeneous system of four algebraic equations with four unknowns ($\sigma_{z'}^2$, σ_z^2 , $M_{zz'}$ and ε_z); this system should have one solution. In Eqs. (3) the values of the Twiss functions α_z , β_z , γ_z should refer to the same "initial point" as y and $\sigma_{z'eff}$ (practically, it may be more convenient to use representations of α and γ through β and its derivative). According to Eqs. (3), only one measurement of the ER intensity distribution is sufficient to determine vertical parameters of the beam.

For horizontal motion, we have a non-homogeneous system of five algebraic equations with five unknowns ($\sigma_{x'}^2$, σ_x^2 , $M_{xx'}$, horizontal emittance ε_x and squared relative RMS energy spread $(\sigma_E/E)^2$):

$$\begin{cases} \sigma_x^2 = \varepsilon_x \beta_x + (\sigma_E/E)^2 \eta^2; \\ \sigma_{x'}^2 = \varepsilon_x \gamma_x + (\sigma_E/E)^2 \eta'^2; \\ M_{xx'} = -\varepsilon_x \alpha_x + (\sigma_E/E)^2 \eta \eta'; \\ \sigma_{x'eff1}^2 = \sigma_{x'}^2 + \sigma_x^2 / y_1^2 + 2M_{xx'} / y_1; \\ \sigma_{x'eff2}^2 = \sigma_{x'}^2 + \sigma_x^2 / y_2^2 + 2M_{xx'} / y_2, \end{cases} \quad (4)$$

where η and η' are values of dispersion function and its derivative at the initial point. Thus, with two measurements of the ER intensity distributions (at two different distances y_1 and y_2) we have not only horizontal divergence, transverse size and mixed moment $M_{xx'}$, but also the horizontal emittance and energy spread, the two last values being integrals of motion. Analysis of the system (4) allows one to see that better precision is attainable when $y_1 < \beta_x < y_2$ (as it was already mentioned in chapter II).

When applied to the Siberia-1 main mode of operation at $E = 450$ MeV, the edge radiation method and the experimental data treatment based on Eqs. (3) and (4) gave us the following electron beam parameters (see Table 1). In the Table 1, the values of $\sigma_{x'}$, σ_x , $M_{xx'}$, $\sigma_{z'}$, σ_z , and $M_{zz'}$ refer to the middle of the straight section we used. The values

Table 1. Siberia-1 transverse beam emittances and related parameters at $E = 450$ MeV.

ε_x	330 ± 30 nm	ε_z	8.1 ± 1.0 nm
σ_x	2.5 ± 0.3 mm	σ_z	0.11 ± 0.01 mm
$\sigma_{x'}$	0.46 ± 0.05 mrad	$\sigma_{z'}$	0.073 ± 0.009 mrad
$M_{xx'}$	3.2 ± 0.5 nm	$M_{zz'}$	0.0 nm
σ_E/E	$(1.2 \pm 0.2) \cdot 10^{-3}$		

of beam parameters are in gratifying agreement with those published earlier [4].

In presence of strong beam focusing elements within the straight section between bending magnet edges, some corrections should be introduced to the above consideration. In this case, due to different emission conditions for particles at different transverse coordinates, one can not say that the ER intensity distributions depend on beam parameters in combinations given by Eqs. (1). Nevertheless, the ER-based method is supposed to be applicable in this case too, as far as the ER distributions still can be precisely computed in terms of the magnet lattice and beam parameters [1], [2]. The presence of strong quadrupoles could allow one to determine $\sigma_{x'}$, σ_x , $M_{xx'}$, $\sigma_{z'}$, σ_z , $M_{zz'}$ directly from the fitting of measured and computed intensity distributions. Further on, at least two of three first Eqs. (4) should be used to determine horizontal emittance and energy spread in this case.

IV. ACKNOWLEDGEMENTS

I would like to thank all the Kurchatov Synchrotron Radiation Source staff for help and support.

V. REFERENCES

- [1] O.Chubar, E.Masunov, "Electron Beam Diagnostics by Means of Edge Radiation", Proceedings of the PAC-93, vol. 3, p. 2474.
- [2] O.V.Chubar, "Precise Computation of Electron Beam Radiation in Non-uniform Magnetic Fields as a Tool for the Beam Diagnostics", Fifth International Conference on Synchrotron Radiation Instrumentation SRI-94 (Stonybrook, New York, July 18-22, 1994), TuE9, to appear in Proceedings (Rev. Sci. Instrum., 1995, Vol. 66).
- [3] O.V.Chubar, I.M.Nagornyykh, Yu.V.Krylov, "Edge Radiation Based System for Beam Diagnostics on Siberia-1 Electron Storage Ring", Proceedings of the EPAC-94 (London, June 27 - July 1, 1994), vol. 2, p. 1673.
- [4] A.N.Artemyev et. al., "Development of the first phase of the specialized synchrotron radiation source Siberia-1", Nucl. Instr. and Meth., 1987, vol. A261, p. 18-21.

ABSOLUTE ENERGY MEASUREMENT IN $e^- e^+$ COLLIDERS*

Blaine E. Norum, University of Virginia, Charlottesville, USA
Robert Rossmanith, DESY, Hamburg, Germany

Abstract

A technique based on the Compton scattering of linearly polarized visible light is proposed for measuring the absolute energy of an electron beam in a linear collider. In the vicinity of 90 degrees in the rest frame of the electron the ratio of the cross-section for different linear light polarizations depends strongly on the absolute energy of the beam. This is especially true when the backscattering rates with light polarized perpendicular to the scattering plane is compared with light polarized in the scattering plane. As a result, the absolute energy of the beam can be determined to a high degree of precision by measuring the ratio of two counting rates. Using a strong laser field (e.g. that in a Fabry-Perot resonant cavity), the measurement can be performed in a fraction of a second. Examples of possible practical arrangements are given.

I. TECHNIQUES FOR MEASURING ENERGY

The energy of a stored electron beam can be measured both elegantly and accurately by depolarization.

In linacs, however, a similarly elegant method does not exist.

Up to now the energy of a linac beam could be measured in several ways.

a.) The standard way is to measure the deflection angle of the beam in a magnetic field. In order to obtain the absolute energy both $\int B \cdot dl$ and the deflection angle have to be measured.

b.) Several modifications of this technique exist, e.g. by using synchrotron light. A single line of the spectrum is selected and the intensities at various angles are compared [1].

The ratio of the intensity at these two angles varies when the energy changes. The technique can be modified by using two magnets of different strengths. In order to measure the absolute energy the field strength at the emission point has to be measured [2]. This has a clear advantage over a.) since the magnitude $\int B \cdot dl$ no longer has to be known. Only the absolute field strength at the emission point has to be measured using an absolute measuring device such as an NMR.

In a.) and b.) magnets are involved which deflect the beam. By using the Compton effect the energy of the beam can be measured without deflecting the beam. In most of the proposals the energy of the backscattered photons is measured. By measuring the energy of the backscattered photons with the highest energy, γ can be calculated. Unfortunately, it is very difficult to measure the energy of high energy photons with high accuracy. Therefore two concepts were developed.

c.) A laser with low energy photons is used as the source. If the electrons have relatively low energy (less than 5 GeV), the backscattered photons are in the keV range where detectors can measure the energy with high accuracy [3].

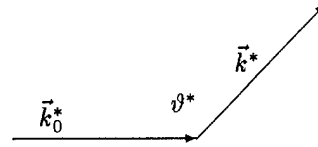


Figure 1. Scattering geometry in the rest frame

d.) Instead of optical photons RF photons are used. The beam traverses a cavity and produces visible photons. The energy of the backscattered visible photons can be analyzed by well known optical techniques [4].

Many variations of this technique exist: for instance, it is possible to use a wiggler instead of a cavity in d.). c.) and d.) only work well when the electron energy is relatively low.

Despite these deficiencies, the Compton effect is a very attractive method for performing energy measurements since only two particles (the photon and the electron) are involved in this process.

II. THE BASIC FORMULAS

The Klein-Nishina formula describes the Compton scattering cross-section for arbitrary electron and photon polarization. The formula is usually used in the rest frame of the electron. In the formula, all energy values are normalized to the rest mass of the electron ($m_0 c^2$). The normalized energy k of the incoming photon is $E_{phot}/m_0 c^2$. α is the crossing angle between the electron and the laser beam. In the rest frame of the electron the incoming photon has the energy

$$k_0^* = \gamma k (1 + \cos \alpha) \quad (1)$$

Magnitudes with an "*" refer to the rest frame. In the rest frame the laboratory angle α becomes α^* .

$$\sin \alpha^* = \frac{1}{\gamma} \frac{\sin \alpha}{1 + \cos \alpha} \quad (2)$$

After scattering, the energy of the scattered photon changes to

$$k^* = \left(1 - \cos \vartheta^* + \frac{1}{k_0^*} \right)^{-1} \quad (3)$$

The definitions of the magnitudes can be found in Fig. 1.

The polarization of the photon is described in the Klein-Nishina formula by a 3-dimensional vector (Stokes parameters): (ξ_1, ξ_2, ξ_3) . For an electromagnetic wave

$$\begin{aligned} E_x &= E_0 a_x \exp(i(kx - \omega t + \Delta_x)) \\ E_y &= E_0 a_y \exp(i(ky - \omega t + \Delta_y)) \end{aligned} \quad (4)$$

*This work was partly supported by the US Department of Energy

with

$$a_x^2 + a_y^2 = 1$$

the Stokes parameters are

$$\begin{aligned}\xi_1 &= a_x^2 - a_y^2 \\ \xi_2 &= 2a_x a_y \cos(\Delta_x - \Delta_y) \\ \xi_3 &= 2a_x a_y \sin(\Delta_x - \Delta_y)\end{aligned}\quad (5)$$

For linearly polarized light in the direction of the x or y axis $\vec{\xi} = (\pm 1, 0, 0)$, for linearly polarized light under 45° $\vec{\xi} = (0, 1, 0)$ and for unpolarized light $\vec{\xi} = (0, 0, 0)$.

The spin of the electron $\vec{\zeta}$ in the Klein-Nishina formula is a 3-dimensional vector with spin components oriented along the axes x, y and z.

In the rest frame of the electron the differential cross-section for Compton scattering is

$$\frac{d\sigma}{d\Omega} = \frac{r_0^2}{2} \left(\frac{k^*}{k_0^*} \right)^2 (\Phi_0 + \Phi_1 + \Phi_2) \quad (6)$$

r_0 is the classical electron radius.

$$\begin{aligned}\Phi_0 &= (1 + \cos^2 \vartheta^*) + (k_0^* - k^*)(1 - \cos \vartheta^*) \\ \Phi_1 &= \xi_1 \sin^2 \vartheta^* \\ \Phi_2 &= -\xi_3 (1 - \cos \vartheta^*) \vec{\zeta} (\vec{k}_0^* \cos \vartheta^* + \vec{k}^*)\end{aligned}\quad (7)$$

Φ_1 depends on linear polarization. In the following only linearly polarized or unpolarized light is taken into account: Φ_2 is zero.

In the rest frame $d\Omega$ is

$$d\Omega = \sin \vartheta^* d\vartheta^* d\varphi \quad (8)$$

φ is the azimuthal angle and frame independent.

The rest frame magnitudes can be transformed into the lab frame in the following way

$$\begin{aligned}k_x &= k_x^* \\ k_y &= \gamma(k_y^* - k^*) \\ k_z &= k_z^*\end{aligned}\quad (9)$$

And finally the scattering angle in the lab system is

$$\sin \vartheta = \frac{1}{\gamma} \frac{\sin \vartheta^*}{1 - \cos \vartheta^*} \quad (10)$$

In the following the basic idea of the measurement is introduced. For a scattering angle of 90 degrees ($\cos \vartheta^* = 0$, $\sin \vartheta^* = 1$) and linearly polarized light

$$\begin{aligned}\Phi_0 &= 1 + (k_0^* - k^*) \\ \Phi_1 &= \pm 1\end{aligned}\quad (11)$$

The cross-sections for the two different light polarizations are:

$$\begin{aligned}\left(\frac{d\sigma}{d\Omega} \right)_{\perp, 90^\circ} &\approx 2 + \frac{k_0^{*2}}{1 + k_0^*} \\ \left(\frac{d\sigma}{d\Omega} \right)_{\parallel, 90^\circ} &\approx \frac{k_0^{*2}}{1 + k_0^*}\end{aligned}\quad (12)$$

For unpolarized light and light with a polarization vector of 45 degrees relative to the x and y axis

$$\left(\frac{d\sigma}{d\Omega} \right)_{unpol, 90^\circ} \approx 1 + \frac{k_0^{*2}}{1 + k_0^*} \quad (13)$$

The ratio

$$\left(\frac{d\sigma}{d\Omega} \right)_{\perp, 90^\circ} / \left(\frac{d\sigma}{d\Omega} \right)_{\parallel, 90^\circ} = \frac{2 + 2k_0^* + k_0^{*2}}{k_0^{*2}} \quad (14)$$

depends only on the energy of the electrons and the energy of the photons: $k_0^* = 2\gamma k$ for $\alpha = 0$.

In a similar way cross-section ratios at 90° can be obtained which have a less complicated dependence on k_0^* :

$$\begin{aligned}\left[\left(\frac{d\sigma}{d\Omega} \right)_{\perp, 90^\circ} - \left(\frac{d\sigma}{d\Omega} \right)_{unpol, 90^\circ} \right] / \left(\frac{d\sigma}{d\Omega} \right)_{\parallel, 90^\circ} = \\ \frac{1}{k_0^{*2}} = \frac{1}{4\gamma^2 k^2}\end{aligned}\quad (15)$$

These formulas show the principle of the idea. By measuring ratios of counting rates with the Compton effect, the energy can be determined. Since most modern accelerators have Compton polarimeters the measurement can be performed using existing equipment. Energy measurement and polarization measurement with the Compton effect are very similar.

III. PRACTICAL DESIGN

From a practical point of view the flux measurement of photons emitted under 90 degrees is rather difficult. The detector of a polarimeter is usually a shower counter with a limited energy resolution. Thus, only photons within a certain energy range can be measured.

Fig. 2 shows the ratio defined in equation (14) for the energies 40 and 40.4 GeV and a photon energy of 2.5 eV in the vicinity of the 90 degree rest frame angle. Within any given energy interval the cross-section ratio and therefore the counting rate ratio differ significantly within any given energy interval both on the right hand side and left hand side of the minimum. If single photons can be detected and their energy evaluated the absolute energy of the beam can be easily determined when the energy resolution of the shower counter is well known.

The speed of the measurement is determined by the statistical error from the photon flux. The speed of the measurement is clearly a nonlinear function of the energy deviation: strong deviations produce a higher counting rate difference than do smaller ones. Fig. 2 calculated for a 10% energy deviation, produces a ratio which differs by more than a factor of 2 in the vicinity of 20 GeV.

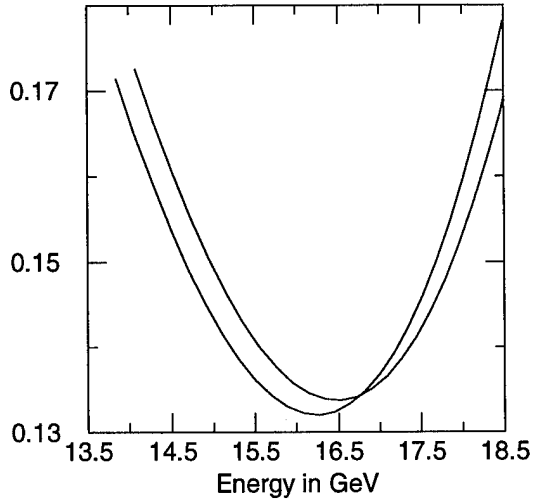


Figure 2. The ratio equation (14) for 2 electron energies, 40 and 40.4 GeV. The cross section ratio is plotted for photon energies in the vicinity of 90° (rest frame of the electron)

In order to measure the energy with an accuracy of 10^{-3} , 10^6 photons have to be collected by the detector. With a single photon technique the measuring time would be too long.

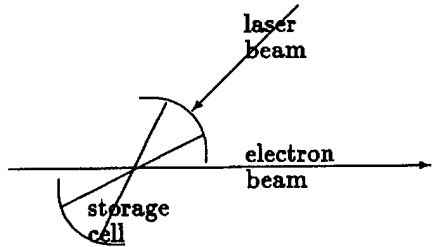


Figure 3. Principle of the storage cell laser-electron beam interaction. The intensity of the incoming laser beam is amplified by the Fabry-Perot cavity.

In order to increase the backscattering rate, the use of so-called storage cells was proposed. The idea was first used in gravity wave detectors. Two mirrors surround the electron beam as shown in Fig. 3. The beam is reflected forwards and backwards between the two mirrors. A typical intensity enhancement factor is 10^4 . In laboratory tests enhancement factors of 3×10^4 are obtained. In almost all accelerators the typical backscattering rate in a polarimeter without a storage cell is in the order of 1 kHz. With the storage cell this rate can be increased to 10^7 Hz. With this technique, the energy (as well as the polarization) can be measured with an accuracy of greater than 10^{-3} in less than one second. An accuracy of 10^{-4} can be obtained in approximately 10 sec.

It is obvious that this energy measuring device can be used as a sensor in a feedback loop in order to overcome drifts in the net gradients of the cavities. A storage cell is now under development at the University of Virginia, Charlottesville. First beam tests are expected to take place at the beginning of next year [5].

The practical problems connected with the detector design for the backscattered photons are very similar to the calibration problems connected with polarimeters. According to equation (10) the rest frame scattering angle is converted into an angle of $1/\gamma$ in the lab frame. For a 50 GeV beam this angle is $10 \mu\text{rad}$, for 500 GeV $1 \mu\text{rad}$. The laser interaction zone and the detector have to be several 100 meters apart from each other. The effect is also smeared out by the emittance. The influence of the emittance on the effect can be determined in a practical way by measuring the spectrum of the backscattered photons and then comparing it with calculations. Systematic detector and aperture errors can be eliminated by changing the direction of the linear polarization.

IV. ACKNOWLEDGEMENTS

The authors want to thank Prof. Ivan Karabekov from the Yerevan Physics Institute (YERPHI) for the many discussions and stimulating comments. Without his permanent engagement in precise beam energy measurement and his enthusiasm in this field this paper would not have been written. One of the authors (RR) also wishes to thank Prof. G.-A. Voss and Prof. B. Wiik, both at DESY, for having given him the opportunity to work on this subject at DESY.

References

- [1] I. P. Karabekov, D. L. Egikian and C. Yang, Measurement of the absolute value of mean energy of particles in collider beams, Nucl. Instr. Meth. A286(1990)37
- [2] I. P. Karabekov and R. Rossmanith, High resolution absolute energy measurement for CEBAF, Proc. XVth Internat. Conf. on High Energy Accelerators, Hamburg 1992, Int. J. Mod. Phys. A (Proc. Suppl.) 2B(1993)
- [3] T. P. Welch and R. Ent, Energy measurement of electron beams by Compton scattering, CEBAF, unpublished, 1994
- [4] W. Barry, P. K. Kloeppel and R. Rossmanith, Absolute measurement of beam energy by Compton Scattering, Proc. Third European Particle Accelerator Conf., Berlin, 1992, Editions Frontiere
- [5] B. E. Norum and T. P. Welch, An intense polarized photon source at CEBAF Hall B, Letter of Intent L01-93-105, CEBAF 1993 (unpublished)

INR ACTIVITY IN DEVELOPMENT AND PRODUCTION OF BUNCH SHAPE MONITORS

S.K.Esin, A.V.Feschenko, P.N.Ostroumov, Institute for Nuclear Research, 117312 Moscow, Russia

Precise measurements of the longitudinal profiles of ion beams with ~ 10 ps temporal resolution became available with the help of a Bunch Shape Monitor (BSM) developed and used at the INR. A number of BSMs have been developed, fabricated at the INR and tested with a beam at several laboratories during last 3 years. The upgraded BSM-Bunch Length and Velocity Detector (BLVD)-can measure not only longitudinal profile but also absolute beam velocity. A 3D-BSM is a further improvement of the monitor which allows a three-dimensional density distribution of the bunched beam to be measured.

I. INTRODUCTION

The BSMs are normally used to measure a bunch longitudinal density distribution at present. In these monitors the temporal structure of the beam under study is coherently transformed into that of low energy secondary electrons and then into a spatial structure by RF modulation. The first proposal to use low energy secondary electrons for this purpose was made in the early sixties [1]. To obtain a phase dependent separation of the electrons it was suggested that their velocity be modulated transversally in two perpendicular directions by a circular scan. The first real device was proposed and created in the mid seventies [2]. In this device an RF field was used to obtain longitudinal or energy modulation of the electrons. Phase separation of the electrons was obtained using a magnetic field.

In order to improve the phase resolution, a monitor with transverse modulation of the velocity of the electrons has been developed and built at the INR. In this monitor, the velocity of the electrons is transversally modulated by an RF sweep field in one direction providing a phase dependent separation after a drift space [3]. This device has been installed in the INR linac and is being used successfully to tune the accelerator and to test the beam quality. Monitors of this type have found application in a number of accelerators. Two devices have been developed and designed with our assistance at Fermilab [4]. Recently, four monitors have been built at INR for the SSC linac [5,6]. We have just completed development and design and have began fabrication of two BSMs for the DESY proton linac.

The devices mentioned above can be considered as traditional ones. A number of ideas have been proposed recently for the improvement of the traditional monitor. The BLVD provides a measurement of the average beam velocity as well as the bunch shape [7]. This detector has been developed, designed and built at the INR for the CERN Heavy Ion Linac [8]. Detectors of this type have been developed and are being fabricated for the DESY proton linac as well as for

the INR linac. The traditional BSM can be modernized to measure longitudinal and transverse distributions of beam bunches including two component beams [9]. A further improvement of the monitor is a 3D-BSM - a detector, which allows the measurement of the charge density distribution in a 3-dimensional space [10]. This monitor is being fabricated now at INR for the CERN proton linac.

II. BUNCH SHAPE MONITORS

The arrangement of the BSM with transverse modulation of low energy secondary electrons is reported elsewhere [3,11]. A BSM consists of the following main elements: a target, an input collimator, an electrostatic lens, an RF deflector, an output collimator and, following a drift space, an electron current detector.

Table 1

Deflector type	f, MHz	Lab
two coupled $\lambda/2$ coaxial	594.6	INR
two coupled $\lambda/2$ coaxial	202.56	DESY
$\lambda/4$ parallel wire line	427.6	SSCL
$\lambda/4$ parallel wire line	202.56	CERN
$5\lambda/4$ parallel wire line	1282.8	SSCL
$\lambda/2$ parallel wire line	991	INR
$\lambda/2$ parallel wire line	810.24	DESY

The general configuration of all of the BSMs we have developed is practically the same but specific features and designs differ and are determined by mechanical and electrical requirements as well as by beam parameters. The main component of a BSM is the RF deflector.

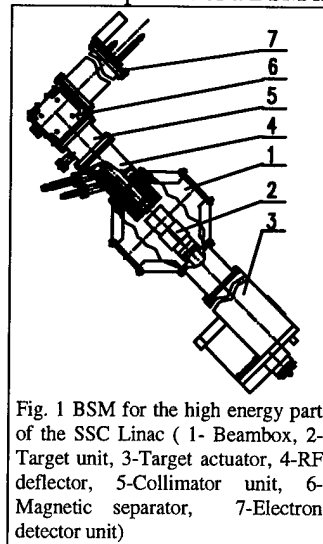


Fig. 1 BSM for the high energy part of the SSC Linac (1- Beambox, 2-Target unit, 3-Target actuator, 4-RF deflector, 5-Collimator unit, 6-Magnetic separator, 7-Electron detector unit)

Since 1992 we have used an RF deflector combined with electrostatic lenses in a single unit [9]. This combination allows improvement of the monitor parameters and avoids multipactor discharge due to the HV focusing potential applied to the deflecting plates. A number of RF deflectors have been developed (see Table 1). All of the deflectors consume ~ 10 W RF power to provide a nominal value of deflecting field. Fig. 1 shows one of the four BSMs built for the SSC

Laboratory. The devices fit into the standard beam box with a dimension along the beam line 80 mm. The monitor shown was intended to be used in the high energy section of the

accelerator. It utilizes an additional magnetic separator to prevent the influence of the electrons stripped from H ions. The DESY BSMs have been designed to be installed into the ports of the existing intertank sections.

The main parameter of the BSM is its phase resolution which depends upon a number of factors. A resolution of 1 degree for frequencies up to 400 MHz can be achieved.

III. BUNCH LENGTH AND VELOCITY DETECTORS

Time of flight methods have been used to measure the average velocity of beams with an RF bunch structure. Either two monitors installed a known distance apart [12] or a single movable one [13] can be used for this purpose. A BSM can be used as a movable detector [7]. When moving the BSM in a longitudinal direction one can observe a change in the bunch phase shape location by a value $\Delta\phi_0 = 2\pi d/\beta\lambda$, where β is the relativistic velocity of the beam, λ is the wavelength of the deflector RF field and d is the distance of the monitor displacement. By measuring $\Delta\phi_0$ and d one can find beam velocity. An improved monitor capable of measuring the average velocity, the BLVD, has been developed and built at INR for the CERN Heavy Ion Linac [8]. A general view of the BLVD is shown in fig. 2. The detector was used for Pb^{+27} ions with $\beta=0.02$ and $\beta=0.09$ and provided energy measurements with an accuracy of about 0.15% and 0.3% respectively.

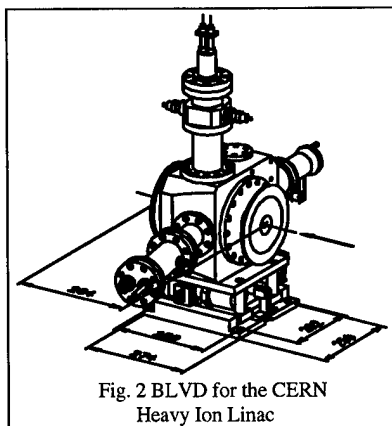


Fig. 2 BLVD for the CERN Heavy Ion Linac

The best accuracy is obtained when the value of the detector translation is exactly equal to $\beta\lambda$. If the translation equals $\beta\lambda/2$ the accuracy suffers a slight degradation but only half as much mechanical translation is required. For a high β it is expedient to use a

higher harmonic for the deflecting field. The BLVD for the DESY Linac, for which the design has recently been completed, will operate at the fourth harmonic, $f=810.24$ MHz. For the 50 MeV protons the value of the detector translation, $\beta\lambda/2$, is 60 mm.

IV. DETECTORS TO MEASURE THREE DIMENSIONAL DENSITY DISTRIBUTION

The name of the device, Bunch Shape Monitor, is not exactly correct. In the main, it is intended for the measurement of the longitudinal distribution of only those particles which impinge on the wire but not of a real bunch shape which is a function of the three coordinates.

To measure a three dimensional charge density distribution one can use the fact that the target is thin with respect to its distance from the deflector. A schematic diagram of the 3D-BSM is shown in fig. 3. The target is surrounded by a grounded shield. The target, shield, and collimator are moved in the y-direction simultaneously. In addition, the collimator can be moved independently in the x-direction with the help of the pusher. The width of the collimator, along the target, is much smaller than the beam transverse dimension. Thus the intensity of the electrons, passed through the collimator, is proportional to the intensity of the primary ions at a definite point of the transverse (x,y) plane. By moving the collimator horizontally, one can get information about the beam for different x-coordinates. Information for other y-coordinates can be obtained by moving the target, shield, and collimator vertically. By measuring the longitudinal distribution for each vertical location of the target and each horizontal location of the collimator one can obtain a 3-coordinate charge density distribution function. Spatial resolution in the x-direction depends upon a number of parameters and was estimated to be about 1 mm. To decrease the total duration of the measurements, the longitudinal distribution is measured within one beam pulse with the use of a multichannel collector.

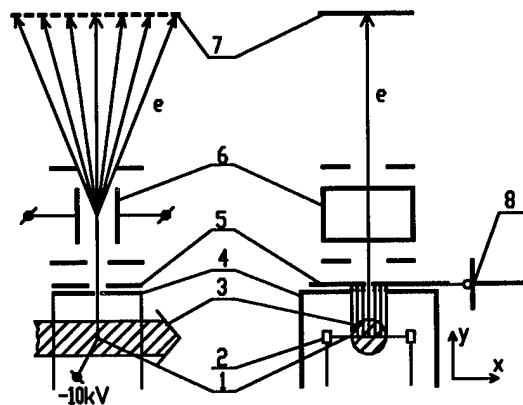


Fig. 3 Schematic diagram of the 3D-BSM (1-target, 2-target holders, 3-beam under study, 4-shield, 5-movable collimator, 6-RF deflector, 7-multichannel collector, 8-pusher)

The variable distance between the input collimator and the RF deflector entrance is transversed by the electrons with a constant and well known velocity thus enabling a simple restoration of the relative phase locations of longitudinal distributions measured for different y-coordinates. A slight variation of phase resolution due to changed focusing of the electrons for different target locations is a relatively small deficiency of the configuration. This configuration was selected for the 3D-BSM which we are now developing for the CERN Linac 2.

V. APPLICATION OF GAS TARGET

To measure high intensity ion beam parameters a gas target can be used as a source of secondary electrons. The molecular gas jet must have small transverse dimensions. A uniform electrostatic field, ~ 10 kV/cm, must be applied to

Table 2

Proton energy	100 MeV
Peak current	10 mA
Pulse length	100 μ s
Beam diameter	1 cm
Gas jet size	1 mm
Distance from the jet to the zero potential plane	2 cm
Magnetic spectrometer resolution $\Delta p/p$	10^{-2}
Concentration of air molecules in the target	10^{13} cm $^{-3}$

accelerate the detached electrons. The contribution of the finite jet size on the electron time-of-flight and energy spread can be compensated by using a magnetic spectrometer similar to the one shown in fig. 1. For the

parameters listed in Table 2 the number of electrons at the entrance of the electron collector is $\sim 10^4$ when the RF deflector is off. For a continuous gas flux and a 10^7 torr pressure a 1400 l/s pumping speed is required. This value can be reduced to a reasonable one if a pulsed bleed-in is used.

VI. SENSITIVITY OF BSM

The sensitivity of the BSM becomes of importance during the measurement of a low intensity beam or a longitudinal halo of a relatively high intensity beam.

Normally electron multipliers are used in BSMs to detect secondary electrons. Typical values of the maximum gain of the multipliers for different types of the devices are $\sim 10^5$ - 10^8 and can be adjusted over three to four orders of magnitude by varying the HV. The multipliers can detect individual electrons so, as a matter of principle, by increasing the duration of the measurements it is possible to measure longitudinal parameters of extremely low intensity beams. Practically, the sensitivity is limited in any specific case. Our experience allows us to distinguish the following cases:

1. Detection of the low intensity longitudinal halo of a relatively high intensity (about 10 mA) beam. In this case the sensitivity is limited by radiation background because of beam losses including inevitable losses due to interaction with the target. Regular measurements at the exit of the low energy section (100 MeV) of the INR linac have shown that it is relatively easy to detect longitudinal halo on the relative level of 10^{-3} . To detect halo on the level of 10^{-4} a special measurement procedure must be performed. The effect under consideration depends upon a number of factors: beam energy, type of particles, beam dimensions, etc.

2. Detection of longitudinal parameters of a low intensity beam. The minimum beam peak current we have made measurements with at the exit of the low energy section of the INR linac was about 3 μ A. In this case, the statistical nature of the signal is observed and amplitude resolution deteriorates due to the relatively small number of detected electrons. Integration of the signal within a beam pulse (80 μ s) provides an acceptable amplitude resolution. A further decrease of

intensity will result in the necessity to detect individual electrons. Measurements at the CERN Heavy Ion Linac have been made for the 0.25 MeV/amu (exit of the RFQ) and 4.2 MeV/amu (exit of the accelerator) Pb^{+27} 10 μ A beams [8]. At the exit of the accelerator a background signal originated from positive ions impinging on the negative potential target which was synchronous with the RF in the IH accelerating tanks. Due to this effect, the beam current to be analyzed has been limited to 1 μ A.

VII. CONCLUSION

A number of BSMs and modified detectors have been developed and built or are being built at INR for several laboratories. The devices have extremely high resolution and sensitivity. Due to differing beam parameters, frequencies, and mechanical and electrical requirements an individual approach to the research, development, and design of each monitor is necessary. Modern detectors like the BLVD can be used in place of conventional bulky and expensive diagnostic installations yet provide information otherwise inaccessible, e.g. by a 3D-BSM.

VII. REFERENCES

- [1] I.A.Prudnikov et al. A Device to Measure a Bunch Phase Length of Accelerated Beam. USSR invention license, H05h7/00, No.174281 (in Russian).
- [2] R.L.Witkov. A Non-Destructive Bunch Length Monitor For a Proton Linear Accelerator, NIM, 137 (1976), pp. 203-211.
- [3] A.V.Feschenko and P.N.Ostroumov. Bunch Shape Monitor and Its Application for an Ion Linac Tuning. Proc. of the 1986 Linac Conf., Stanford, June 2-6, pp. 323-327.
- [4] E.S.McCrory, C.W.Schmidt and Use of an INR-Style Bunch Length Detector in the Fermilab Linac. Proc. of the Linac-92, Ottawa, August 24-28, 1992, pp. 662-664.
- [5] J.M.Hurd et al. Bunch Shape Monitor for SSCL Linac. Proc. of the 1993 PAC, Washington, 1993, pp. 2426-2428.
- [6] S.K.Esin et al. Development and Fabrication of Bunch Shape Monitors For SSCL Linac. Reported at the 14th All Russia Meeting on Particle Accelerators. Protvino. October 25-27, 1994. Be published. (In Russian)
- [7] P.N.Ostroumov. Average Velocity Measurement of Accelerated Beam by Means of an Upgraded Bunch Length Detector. INR Preprint-812/92, May 1993.
- [8] Yu.V.Bylinsky et al. Bunch Length and Velocity Detector and Its Application in the CERN Heavy Ion Linac. Proc. of the EPAC-94, London, June 27-July 1, 1994.
- [9] A.V.Feschenko, A.A.Men'shov, P.N.Ostroumov. A Detector to Measure Longitudinal and Transverse Distributions of a Two Component Ion Beam. Proc. of the EPAC-92, Berlin, 24-28 March, 1992, V.2, pp. 1073-1075
- [10] S.K.Esin, A.V.Feschenko. Detector of Three Dimensional Charge Distribution in Linear Ion Accelerator. Reported at the 14th All Russia Meeting on Particle Accelerators. Protvino. October 25-27, 1994. Be published. (In Russian)
- [11] A.V.Feschenko. Bunch Shape Monitors Using Low Energy Secondary Electron Emission. AIP Conf. Proc. No. 281, Particles and Fields, Series 52, Accelerator Instrumentation Forth Annual Workshop, Berkeley, Ca. 1992, p.185-193.
- [12] Linear Ion Accelerators. Ed. by B.P.Murin, V.2, Atomizdat, 1978 (in Russian)
- [13] A.V.Feschenko et al. Precise Energy Measurement of the Continuous Proton Beam. Proc. of the 1989 IEEE Particle Acc. Conf., Chicago, 1989, V.2.

CONCEPTUAL DESIGN OF A CHARGED PARTICLE BEAM ENERGY SPECTROMETER UTILIZING TRANSITION RADIATION GRATING*

X.Z. Qiu, X.J. Wang, K. Batchelor and I. Ben-Zvi

National Synchrotron Light Source, Brookhaven National Laboratory
Upton, N.Y., 11973

Abstract

A new technique of measuring the energy spectrum of a charged particle beam using optical transition radiation is presented in this paper. The charged particle beam energy spectrum can be studied by analyzing the optical spectrum of the optical transition radiation produced in a multi-foil configuration. This type of energy spectrometer can have a very large energy acceptance which can not be matched by a simple conventional magnetic dipole spectrometer. The theory of transition radiation from a single boundary and from a foil with finite thickness are reviewed. Multi-foil transition radiation theory and its application for charged particle beam energy spectrum measurement are presented. The practical issues which might affect the performance of a multi-foil transition radiation energy spectrometer are discussed.

I. INTRODUCTION

A new charged particle beam energy spectrometer using transition radiation is presented in this paper. The spectrometer measures the electron beam energy spectrum by observing the interference effect of a multi-foil transition radiator. The energy acceptance of such a spectrometer can be extremely large.

We will review the basic physics for optical transition radiation from a single foil and a large number of parallel foils. With proper arrangement of the foil thickness and foil spacing, a strong interference can occur between radiation from different foils. The consequence will be the appearance of sharp interference peaks both in angular and spectral distributions. The angular and spectral locations of these peaks critically depend on the energy and the incoming angle of the radiating particle. The angular spread and spectral width of the OTR reflect the energy and angular distribution of the charged particle beams. This property of the OTR can be used for charge particle beam energy spectrum measurement.

Finally, the major factors that may affect the performance of the energy spectrometer discussed.

II. SINGLE-FOIL AND MULTI-FOIL TRANSITION RADIATION

A relativistic particle of charge e traveling in vacuum is entering foils with index of refraction η , as shown in figure 1. To simplify our discussion and illustrate the interesting physics, we

*This manuscript has been authored under contract number DE-AC02-76CH00016 with the U.S. Department of Energy. Accordingly, the U.S. Government retains a non-exclusive, royalty-free license to publish or reproduce the published form of this contribution, or allow others to do so, for U.S. Government purposes.

make the following assumptions. We assume that $|\eta - 1| \gg \gamma^{-2}$. The foils considered are produced so thin that the absorption of radiation in the foil can be ignored. Finally, we assume the particle is so energetic that the change in the particle trajectory due to Coulomb scattering is negligible.

When the particle crosses interface 1, transition radiation will be produced in both forward and backward direction. We are only interested in the forward radiation. For $\theta \ll 1$, the intensity is given by, [1]

$$\frac{d^2 I_1}{d\omega d\Omega} = \frac{e^2}{\pi^2 c} \frac{\theta^2}{(\gamma^{-2} + \theta^2)^2} \quad (1)$$

where θ is the angle between the direction the particle velocity and the observation direction, γ is the Lorentz factor.

After the particle has passed through the foil and crosses the interface 2, it will again produce transition radiation in the forward direction. The magnitude of the radiation is the same as that produced at interface 1, but is 180° out of phase. The combined intensity is then,

$$\frac{dI_{12}^2}{d\omega d\Omega} = \frac{e^2}{\pi^2 c} \frac{\theta^2}{(\gamma^{-2} + \theta^2)^2} \times 4 \sin^2 \left\{ \frac{\pi L_{12}}{2\lambda} [\eta(\gamma^{-2} + \theta^2) + 2(1 - \eta)] \right\} \quad (2)$$

where L_{12} is the thickness of the foil.

As the particle continues to travel through the foils. The total forward radiation is just the sum of the forward radiation from each foil,

$$\frac{d^2 I}{d\omega d\Omega} = \frac{d^2 I_{12}}{d\omega d\Omega} \times \frac{\sin^2(N\phi_{13}/2)}{\sin^2(\phi_{13}/2)} \quad (3)$$

where N is the number of foils and ϕ_{13} is the phase delay of the radiation from interface 3 relative to that from interface 1, is given by

$$\phi_{13} = \frac{\pi L_{12}}{\lambda} [\eta(\gamma^{-2} + \theta^2) + 2(1 - \eta)] + \frac{\pi L_{23}}{\lambda} (\gamma^{-2} + \theta^2) \quad (4)$$

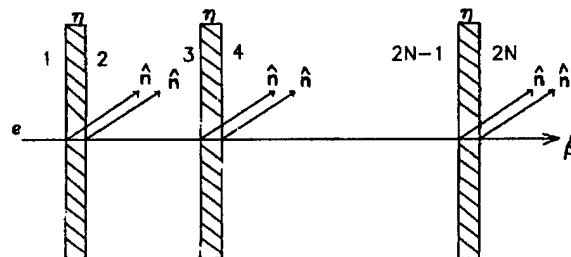


Figure 1. A charged particle travels through parallel foils.

Table I
Particles energy and spectrometer geometry

γ	94,96,98,100,102
	104,106,108,110,112
N	100
θ_0	0.01 rad
η	1.5
L_{12}	100 nm
L_{23}	10 mm
K_e	2

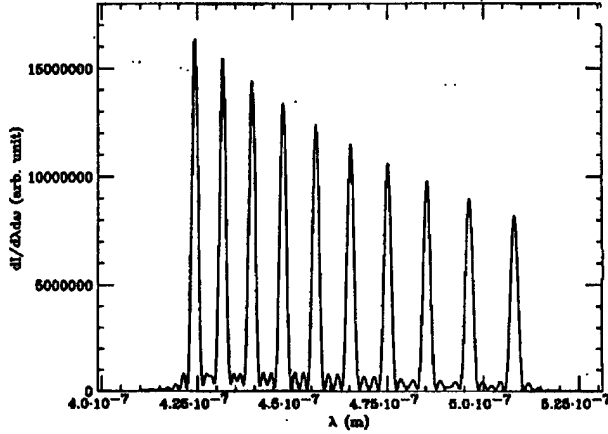


Figure 2. OTR spectrum for 10 particles with different energy

The total intensity per unit frequency per unit solid angle can be written as, In analogy to an optical grating, if the conditions

$$\phi_{13} = 2K_e\pi, \quad K_e = \text{integer} \quad (5)$$

$$N \gg 1 \quad (6)$$

are satisfied, sharp interference peaks will appear in the angular distribution for a particular wavelength of radiation and in the radiation spectrum for a particular observation angle. The spectral or angular location of these peaks can be used to determine the energy and incident angle of the radiating particle. We will concentrate on using the spectrum to determine the particle energy at a fixed observation angle.

As an example the transition radiation spectrum produced by 10 particles with the parameters given in Table 1 is plotted in Fig.2.

Normalization taking into account of the dependence of intensity on energy and the nonlinear relationship between wavelength and energy has to perform in order to recover the energy spectrum. The recovered energy spectrum is given in Fig.3.

The finite width of the peaks due to the finite number of foils will contribute to the uncertainty in energy. The uncertainty in energy determination due to the finite width of the peak is inversely proportional to the number of foils, and given by,

$$\frac{\delta\gamma_e}{\gamma_e} = \frac{1}{N} \times \frac{\gamma_e^2 \lambda_e}{L_{23}} \quad (7)$$

In order to achieve good resolution in the energy determination, large number of foils are used. It is difficult for the ra-

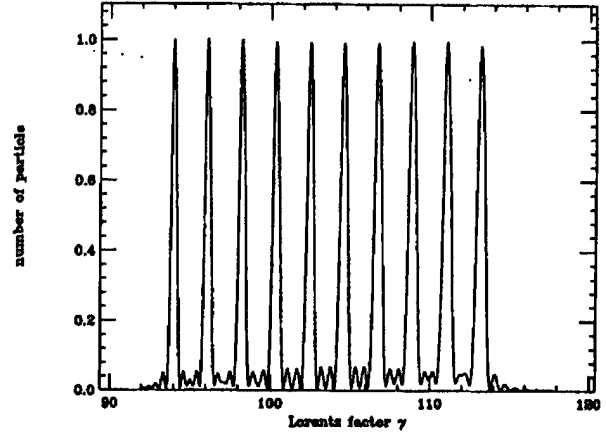


Figure 3. Normalized particle energy spectrum.

diation from the front and end foils to interfere if a large observation angle is used. This makes it necessary to observe the radiation at a smaller angle, even at a zero degree observation angle. For a perfect parallel charged particle beam, no radiation would be observed at this angle. However, the divergence of the beam and scattering of the particles in the foils will cause radiation in this direction.

The energy acceptance of a TRG energy spectrometer is quite large. In the case of a zero degree observation angle, if very thin foils are used, an energy acceptance of $\gamma \rightarrow 1.4\gamma$, which is about $\pm 20\%$, would be achievable. If relative thicker foils are used, acceptance of $\gamma \rightarrow 2\gamma$, which is about $\pm 50\%$, or higher should be achieved.

III. PRACTICAL ISSUES CONCERNING A TRG SPECTROMETER

There are many factors that may affect the performance of TRG spectrometer. We will discuss some of them in this section.

In order to maintain the desired energy resolution, the spread of interference peak due to the spread in observation angle should be smaller than the uncertainty in energy measurement. For observation angle θ_0 other than zero degree, we must have

$$\sigma_{x'} < \frac{1}{\gamma_e} \times \frac{\delta\gamma_e}{\gamma_e} \times \frac{1}{\theta_0 \gamma_e} \quad (8)$$

where γ_e is the Lorentz factor of the particle under measurement, $\sigma_{x'}$ is the rms beam divergence projected in the plane of observation. For the geometry in the example, $\sigma_{x'}$ must be smaller than $100 \mu\text{rad}$ for 1% energy measurement resolution.

In order to relax the tolerance of the measurement due to beam divergence, one can use a small observation angle. When $\theta_0 = 0^\circ$, the spread in energy measurement due to finite beam divergence is given by the curve,

$$I(\gamma, \gamma_e) \propto \gamma_e^4 \sigma_{x'}^2 \times u e^{-u} \quad (9)$$

where

$$u = \frac{\gamma - \gamma_e}{\gamma_e^3 \sigma_{x'}^2}, \quad 0 < u < \infty \quad (10)$$

The curve has its maximum at $u = 1$. Therefore there will be a systematic shift of $\delta\gamma = \gamma_e^3 \sigma_{x'}^2$ in the energy spectrum measurement, which has to be corrected in the calibration. Notice

that the signal is zero when $\sigma_{x'}$ is zero. 9 has a width of about $\delta u \approx 1$, so the divergence of the beam must satisfy,

$$\sigma_{x'} < \frac{1}{\gamma_e} \times \sqrt{\frac{\delta\gamma_e}{\gamma_e}} \quad (11)$$

Note the square root dependence on the desired energy resolution. For the geometry given in the example, if $K_e = 1$ is used, the upper limit of $\sigma_{x'}$ is about 1 mrad for 1% resolution.

The total rms scattering angle of the particle in the foils and the rms angular alignment error of the foils should also satisfy Eq. 8 or Eq. 11. In the case of estimating scattering, special care has to be taken when designing a TRG spectrometer for an electron beam. Because the foils will be used in a TRG spectrometer are very thin, the Highland form of the empirical formula for multiple scattering tends to overestimate the scattering effect. Using the formula given by Lynch and Danl [2], we estimate the rms scattering angle for a 50 MeV electron beam passes through 100 pieces of 100-nm-thick Carbon foils is about 1.13 mrad, which is comparable to the requirement for achieving 1% resolution.

When application of TRG spectrometer for heavy particle beams, like proton beams, the scattering is about three order of magnitudes smaller than electron beams with the same γ factor. So in these cases, scattering can be ignored.

The foil thickness and spacing tolerance is given by,

$$\delta L_{23} < \frac{2\gamma_e^2 \lambda_e}{N} \quad (12)$$

$$\delta L_{12} < \frac{\lambda_e}{|1-\eta|N} \quad (13)$$

For the geometry given in the example, we must have,

$$\delta L_{23} < 100\mu m \quad (14)$$

$$\frac{\delta L_{12}}{L_{12}} < 10\% \quad (15)$$

IV. CONCLUSION

We have discussed the basic operational principle for a TRG spectrometer. By proper selection of foil thickness and spacing, energy acceptance on the order of 50 percent or larger with resonable resolution can easily be achieved. We have also considered major factors may affect the performance of the energy spectrometer.

V. ACKNOWLEDGEMENTS

The authors wish to thank Dr. R. Fernow and Mr. S. Ulc for providing useful information about thin foils, and the entire ATF staff for their continuous support.

References

- [1] L. Wartski, S. Roland, J. Lasalle, M. Bolore, J. Appl. Phys., **46**, 3644 (1975).
- [2] G. Lynch and O. Danl, Nucl. Instr. And Meth., **B58**, 6 (1991).

AN ANALYSIS OF THE OPERATIONAL PERFORMANCE OF THE AUTOMATIC GLOBAL HORIZONTAL BEAM POSITION CONTROL SYSTEM ON THE SRS AT DARESBUURY

J. B. Fitzgerald, B. G. Martlew, P. D. Quinn and S. L. Smith
Daresbury Laboratory, Warrington WA4 4AD UK

The performance of the global feedback system for horizontal orbit position control, now in regular use at the Daresbury SRS second generation light source, is assessed in the light of operational experience. The success of the system in suppressing horizontal orbit shape changes is described, and current experimental and theoretical investigations of possible causes of residual orbit errors and approaches for their reduction are discussed.

I. INTRODUCTION

Since the advent of the high-brightness lattice [1] for the Daresbury SRS, a 2 GeV electron storage ring light source, beam position control has assumed increased importance. A range of techniques has proved successful in optimisation of electron and photon beam stability, for example the local vertical feedback system [2], now in operation on several beamlines.

A system of automatic global horizontal position control (HPC) has been used to correct the horizontal orbit during operational running. The system reads the orbit at each of 16 electron beam position monitors (BPMs) and applies corrections at 16 horizontal steering magnets (HSTRs). The correction strengths are determined by a least-squares optimisation using the steering magnet response matrix. Typically, the orbit is read and, where necessary, correction applied, every 30 seconds. The resolution of the BPM system is better than 5 μm . The hardware and software developed for the HPC system are described elsewhere [3].

II. PERFORMANCE OF THE HPC SYSTEM

Automatic global horizontal position control has been used routinely in operational running at the SRS since November 1994, and a database of around 100 user fills, each of typically 24 hours duration, has been collated. The correction software automatically records the measured beam position at each of the 16 BPMs as well as the 16 applied HSTR corrector magnet currents. Since the corrector response matrix (i.e. the effect at each of the 16 BPMs per unit current applied at each of the 16 HSTRs) is known, and indeed used by the HPC software to calculate the applied corrector strengths, the effect of the correction currents at each BPM can be back-calculated to derive the equivalent "uncorrected" beam position. Characteristics of the reconstructed data are in excellent agreement with trends typically observed in data collected during running without the HPC system in operation.

The observed electron beam position at each of 4 typical BPMs is shown in figure 1, along with the reconstructed

uncorrected position, which would have been seen without HPC, for comparison. The data show a dramatic improvement in measured beam stability at the BPMs. The large and widely differing drifts of typically $\sim 200 \mu\text{m}$ in the "uncorrected" data are reduced to a uniform drift of only about $\sim 70 \mu\text{m}$ over the same period (about 24 hours) after correction. This residual drift is identical for all BPMs, within the resolution of the measurement system, and is known as the "offset". This is the change in measured average horizontal orbit at the BPMs. This offset could in principle be corrected at the BPM either by applying a uniform change to all HSTRs or by changing the wavelength of the radio frequency system, according to the cause of the variation in offset. Because this is not yet unambiguously determined, the correction system aims only to reduce changes at each BPM relative to the offset. Since the residual movement at each BPM, after correction, is equal (within the limits of experimental uncertainty) to the offset, the HPC system can thus be said to be functioning ideally.

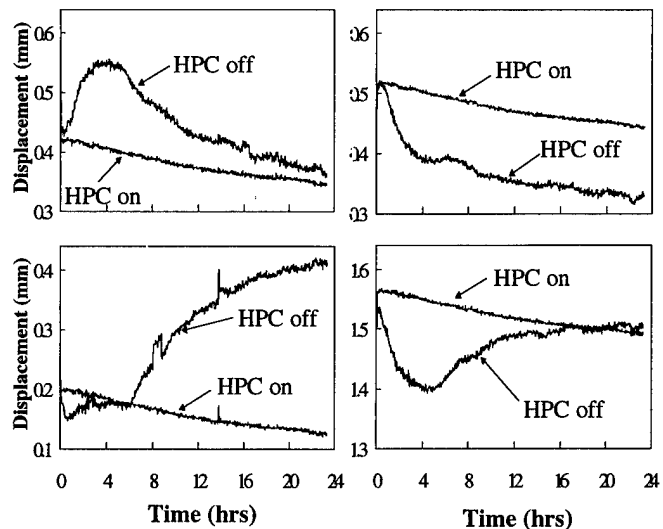


Figure 1: Typical variations of electron beam position with and without HPC

In addition to longer term drifts, sudden changes can occur. The correction of one such change is illustrated in figure 2. A step change is seen in a single BPM (fig. 2a), and the correction system responds promptly to apply an appropriate correction (fig. 2c), leaving a single-valued "spike" in the corrected BPM reading (fig. 2b). After a period of about an hour the step change is reversed, and the HSTR again adjusts. Thus a change in beam position at a BPM has been transferred into a change in applied HSTR corrector.

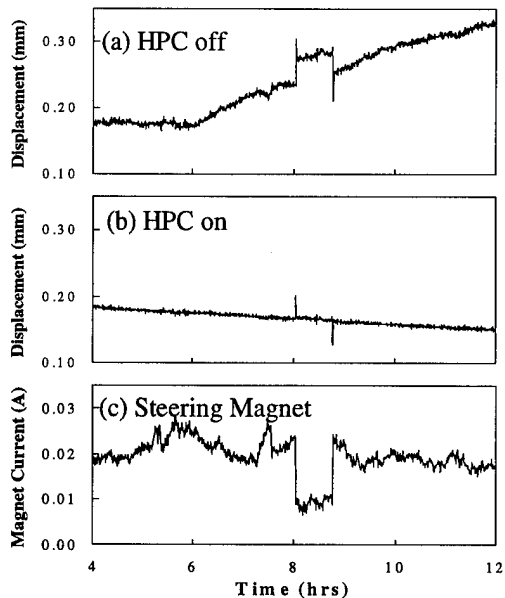


Figure 2: Correction of a step change at a single BPM

The efficacy of the HPC system in suppressing deviations from the average orbit is demonstrated in figure 3. The histograms show the rms deviation of each of the 16 BPMs from the offset (average) value over a particular fill of the storage ring. The upper part (fig. 3a) shows relatively large and widely varying deviations in the (reconstructed) uncorrected beam positions, while the lower part (fig. 3b) shows dramatically reduced rms deviations in the corrected beam position.

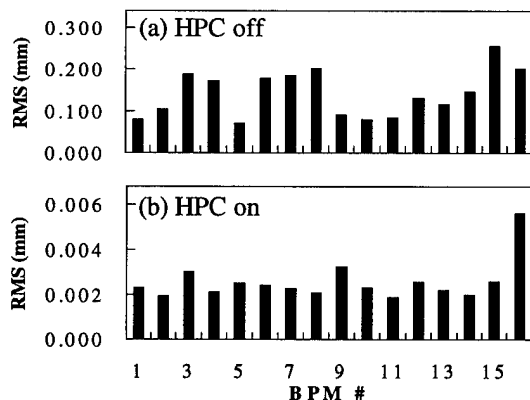


Figure 3: Typical RMS deviation from offset without (a) and with (b) HPC (Note different scales)

III. ORBIT CHANGES - CAUSES AND SOLUTIONS

It has been shown that HPC applied at the SRS is extremely effective in suppressing the build-up of orbit shape distortion or "ripple", greatly reducing beam movement at a BPM to the residual "offset". It is pertinent to seek the causes of both the evolution of orbit ripple and the observed offset

drift, and, where possible, identify approaches to minimise both.

Figure 4 shows the Fourier amplitudes of components of order $k=0-8$ ($k=0$ represents offset drift) in the change in orbit at the 16 BPMs around the ring over a half-hour period, obtained for data without (fig. 4a) and with (fig. 4b) automatic position correction. The uncorrected data show that the $k=6$ component dominates. This is close to the horizontal tune value $Q_h=6.18$, and indeed further examination reveals that the relative amplitudes of the components reflect the Fourier magnification factor $Q^2/(Q^2-k^2)$ [4]. This is the result expected for so-called "random" magnet errors, whereas changes in position measurements due, for example, to movement of the BPMs themselves would not lead to selective enhancement of the components close to the horizontal tune. The corresponding Fourier amplitudes derived from data taken with automatic global correction in operation show that all components other than offset drift are effectively suppressed (to within the accuracy of the measurement system), but that the offset drift is, as expected, unchanged.

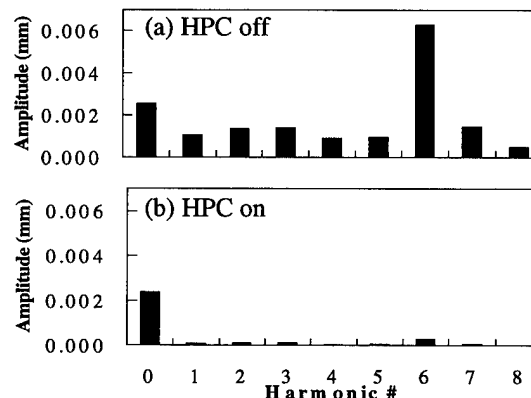


Figure 4: Relative amplitudes of Fourier harmonic components without (a) and with (b) HPC

The variation in average orbit or offset is shown in figure 5a for a typical fill. A moderately rapid increase in orbit offset is seen after injection, followed by a more gradual decline over the remainder of the fill. The plot shows the variation in offset both with position correction and after subtraction of the calculated effect of the applied corrector magnets; these are identical within the uncertainties of the measurement, giving confidence in the procedure used to reconstruct the "uncorrected" position data.

It turns out that the trends in offset as a function of time bear a resemblance to measured movements of the SRS vacuum vessel and magnets over a fill (see fig. 5b). These movements can be explained by temperature changes arising from the high magnet currents and from synchrotron radiation heating. The cycling of magnets at injection leads to increases in vessel temperature over the first few hours of each fill, while the decaying beam current leads to a slow decrease in temperature over the latter part of the fill. Measurements of movements of F-quadrupole magnets (those

causing the largest beam movements due to the high horizontal β -values at FQUDs) and of the BPMs have been made for specific elements of the SRS (see for example [5]) and theoretical models used to make predictions of closed orbit changes arising from variations in magnet position. The observed variations of beam position at the BPM are consistent with predicted effects of measured vessel and magnet movements. In the light of the successful application of HPC, a more extensive programme of investigations is now in progress.

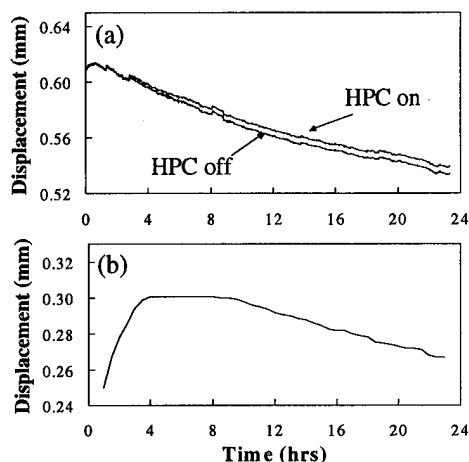


Figure 5 : Offset drift (with and without HPC) and typical vessel movement over a fill

It should be noted that the correction of apparent position changes due to BPM movements will also lead to effective magnet errors via the introduction of spurious "corrections", giving rise to orbit distortion. Thus it is critical, when operating automatic global horizontal position control, to minimise movements not only of magnets but also of the beam position monitors themselves.

First steps have already been taken to reduce movement of storage ring components, with encouraging success. In late November 1994, the "hot fill" procedure was introduced. Whenever possible, after beam dump, the magnets are maintained at the 2 GeV (full energy) currents until the moment of injection when 0.6 GeV levels are set. The magnet "down time", during which the magnet and the vessel temperatures drop sharply, is therefore minimised and the ensuing thermal cycling of storage ring components minimised.

The measured average offset drift since the introduction of "hot fills" has shown a marked decrease (see fig. 6). It is also of interest to note that the largest offset drifts follow periods of shutdown or several hours downtime before refill. It is clear that effective temperature stabilisation is of crucial importance in achieving stable horizontal orbit conditions.

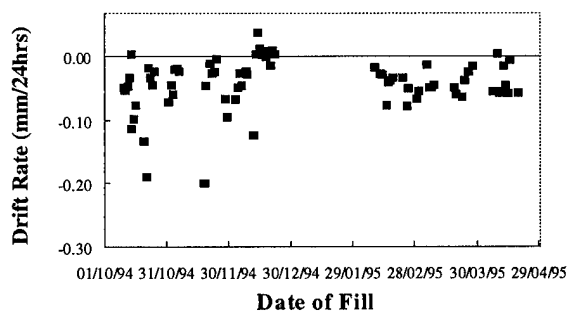


Figure 6: Average offset drift rates measured over fills

IV. CONCLUSIONS

The system of automatic global horizontal position control, used routinely at the Daresbury SRS since November 1994, has achieved a dramatic reduction in variations in the measured beam position (the orbit "ripple") at 16 beam position monitors around the ring. The comparatively small drifts in the residual "offset", or average orbit, which is determined by the RF synchronous condition, are not treated by the present approach. The dominant factor in offset drift is believed to be movement of storage ring elements caused by thermal fluctuations over the fill cycle. A programme of investigations aimed at gaining a better understanding of these effects, and of possible correction techniques, is now under way.

V. REFERENCES

- [1] V.P. Suller *et al.*, "SRS-2: Performance and Achievements", Proceedings of Particle Accelerator Conference, Chicago, 1989, pp467-469
- [2] J.A. Clarke *et al.*, "High Resolution Stabilisation of the Vertical Position of Photon Beams in the SRS Beam Lines", Proceedings of European Particle Accelerator Conference, London, June 1994, pp125-127
- [3] B.G. Martlew, R.J. Smith, S.L. Smith, "Development of Global Feedback for Beam Position Control in the Daresbury SRS Storage Ring", Proc. European Particle Accelerator Conference, London, June 1994, pp1574-1576
- [4] E.D. Courant and H.S. Snyder, "Theory of the Alternating-Gradient Synchrotron", Ann. Phys. **3**(1958)1-48
- [5] P.D. Quinn and T. Ring, "Developements in Orbit Control at the SRS at Daresbury", ABI Conference Proceedings, KEK, Tsukuba, Japan, April 1991

A PROTOTYPE FAST FEEDBACK SYSTEM FOR ENERGY LOCK AT CEBAF*

M. Chowdhary, G. A. Krafft, H. Shoaee, S. N. Simrock, W. A. Watson,
Continuous Electron Beam Accelerator Facility, Newport News, VA 23606 USA

The beam energy of CEBAF must be controlled accurately against phase and gradient fluctuations in RF cavities in order to achieve a 2.5×10^{-5} relative energy spread. A prototype fast feedback system based on the concepts of Modern Control Theory has been implemented in the CEBAF Control System to function as an energy lock. Measurements performed during the pulsed mode operations indicate presence of noise components at 4 Hz and 12 Hz on beam energy. This fast feedback prototype operates at 60 Hz rate and is integrated with EPICS. This paper describes the implementation of the fast feedback prototype, and operational experience with this system at CEBAF.

I. INTRODUCTION

The CEBAF accelerator consists of 45 MeV injector, two side-by-side superconducting linacs, and 9 recirculation arcs that recirculate the beam through the linacs up to 5 times for 4 GeV total energy. The energy spread in the emerging beam is determined by the bunch length, which is tightly controlled at CEBAF, and by the stability of the amplitude and phase of the RF fields in the superconducting cavities. The design specification for energy spread is $\sigma_E/E = 2.5 \times 10^{-5}$. A measurement of beam position in a high dispersion region of the arc can determine the relative energy of the beam to this precision. Then, the measured energy can be stabilized by changing the RF control settings in a feedback loop.

A prototype system has been built to test the techniques and ideas that will ultimately be used to develop an accelerator-wide generic fast feedback facility based on concepts of modern control theory. The energy and orbit lock applications are the first applications in this development.

II. DESIGN CONCEPTS

The primary objective for this feedback loop is to eliminate variations in the beam energy in the injector region up to 10 Hz rate. The measurement of beam energy fluctuations is obtained from Beam Position Monitors (BPMs) located in high dispersion region in the injection chicane. The correction required in the beam energy is achieved by modulating the accelerating gradient in selected corrector cavities upstream of the BPMs. The control input signal for modulating the accelerating gradient is calculated using the BPM measurements of current sample instant and the state of the system at previous

sample instant. The controller design is based on Linear Quadratic Gaussian [1] controller/estimator design. The optimal controller is designed based on system dynamics model, process and measurement noise statistics.

III. CONTROLLER/ESTIMATOR DESIGN

The description of the system in state space formalism is given by

$$x(k+1) = \Phi x(k) + \Gamma u(k) + w(k) \quad EQ 1$$

$$y(k) = Hx(k) + v(k) \quad EQ 2$$

$x(k)$ is the state vector which contains the attributes of the system that are dynamically significant, Φ is the system dynamic matrix which takes system from state k to state $k+1$, Γ is the control input matrix which takes the control inputs to the state vector, $u(k)$ is the vector of control inputs to the system, $w(k)$ is the process noise vector. $y(k)$ is vector of measurements, H is the measurement matrix which takes the measurements to states, $v(k)$ is the measurement noise vector

For this energy lock system, the state vector is $x = [X_o, X_o', Y_o, Y_o', \Delta E/E]$ which contains the beam position and angle in X and Y directions and $\Delta E/E$ is the energy variation at a reference point coming into the chicane. The H matrix contains the transfer matrix terms $R_{11}, R_{12}, R_{33}, R_{34}$ for the BPMs from a reference point.

A Kalman filter is used to estimate the states from the BPM measurements. The measurement update from sample instant k is obtained using

$$\hat{x}(k) = \bar{x}(k) + L(y(k) - H\bar{x}(k)) \quad EQ 3$$

and the time update that takes the state vector from sample instant k to $k+1$ using

$$\bar{x}(k+1) = \Phi \hat{x}(k) + \Gamma u(k) \quad EQ 4$$

Here $\hat{x}(k)$ is the estimated state vector and $\bar{x}(k+1)$ is the predicted state vector for sample instant $k+1$ obtained from the estimated state at time instant k . The controller equations that are used for the feedback loop can be obtained by combining the above two equations and are described as

$$\bar{x}(k+1) = \Phi \bar{x}(k) + \Gamma u(k) + \Phi L(y(k) - H\bar{x}(k)) \quad EQ 5$$

$$\hat{y}(k) = (H - HLH) \bar{x}(k) + HLy(k) \quad EQ 6$$

$$u(k) = -K \cdot \hat{x}(k) \quad EQ 7$$

L is the state estimator gain matrix and K is the output gain

matrix. The equation 5 is used to estimate the state vector at next sample instant $k+1$. This equation contains three terms. The first term uses the system dynamic matrix Φ and the state vector at time k and calculates new state. The second term which uses the control input matrix Γ puts in the effect of actuator settings on the state. The third term is the correction term between estimated and actual states obtained from the measurements. Equation 7 is used to calculate the actuator setting based on current state estimate using negative state feedback through an optimal gain matrix K .

K and L matrices are computed off-line using Matlab [5] from the solution to an algebraic Riccati Equation [1]. This equation is obtained from minimization of a functional for the chosen performance criteria for this system. Satisfactory response of controller and estimator is verified by performing simulations of the closed loop system using Simulink [5]. If the response controller and estimator for system performance specification is found satisfactory, the calculated matrices are stored in a file which is read at the time of feedback loop initialization.

IV. IMPLEMENTATION

The control hardware for the energy lock BPMs and the corrector cavities is located in 2 separate buildings, Fig 1, and is therefore controlled by two different I/O controllers (IOC-Motorola 68040) which are linked by Ethernet.

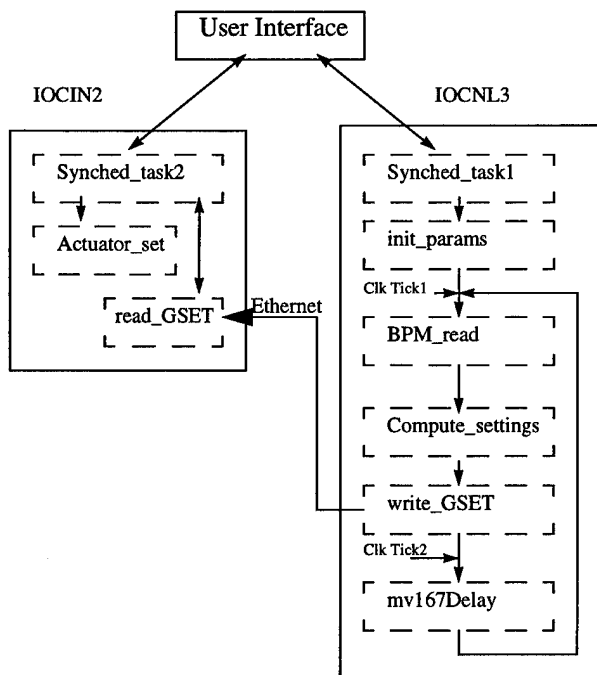


Fig 1

The energy variations are measured using 4 BPMs in the Injection Chicane. BPM data is obtained from the B0007 board (specialized data acquisition module for BPMs) resident

in a CAMAC crate on a serial highway loop that is controlled by a diagnostics IOC (IOCINL3). The accelerating gradient set-point on two corrector cavities is modulated in order to correct for energy fluctuations. The computed corrective signals are sent through a DAC as a ± 5 V signal to the analog offset inputs on RF control module. The DAC card is resident in a CAMAC crate close to the RF control module. This CAMAC crate is on a serial highway loop controlled by an RF IOC (which is IOCIN2). The communication between these two IOCs is done over Ethernet.

The feedback loop software is divided in two parts: EPICS [2] software and VxWorks [3] software. EPICS software manages the Graphical User Interface (GUI) for the feedback loop, triggers the appropriate modules of VxWorks software as required, and monitors the status of the loop. The organization of the VxWorks software is described using Fig 1. The *Synched_task1* and *Synched_task2* routines synchronously execute the various modules on two IOCs as shown in Fig 1. These routines are triggered ON/OFF when the user turns the energy lock loop ON/OFF. During the pulsed mode operation, the synchronization for sampling and correction for the feedback loop is done using the beam synchronization pulse signal.

Upon start-up, the *init_params* routine initializes the various parameters and matrices used by the feedback loop such as the controller gain matrix K , the estimator gain matrix L , the transfer matrix H for 4 BPMs, the BPM hardware constants and previously saved reference orbit settings. After initialization, the *Synched_task1* routine polls for the LAM signal; once the LAM has been received and reset, the *BPM_read* module is called. In order to obtain the BPM measurements at 60 Hz rate the B0007 hardware is accessed directly rather than obtaining these signals from the accelerator control system. The *BPM_read* module performs CAMAC reads to obtain the beam position data in X and Y planes from the B0007 card for individual BPMs. The beam position is calculated from the wire signals using calculations described in Ref. [4]. Then, *Compute_settings* uses the energy variation measurements obtained from the BPM data and computes the correction signal using equations described in previous section. The correction signal is sent to the IOCIN2 over Ethernet. A client/server set-up of TCP/IP protocol is used for data transfer over Ethernet. Communication between two IOCs through client and server stream sockets is set up at the time of IOC initialization.

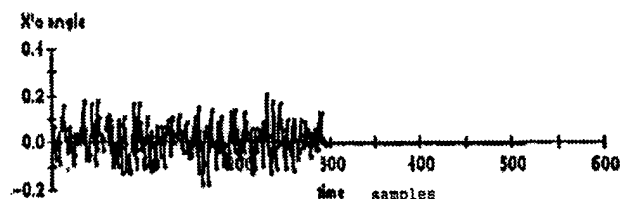
In every cycle of the measurement, computation of settings and actuation, two time measurements, Fig 1, are done using the auxiliary system clock on the IOC. From these two time measurements, the amount of time *Synched_task1* has to sleep before next sampling instant is computed and *mv167Delay* routine is used to effect it.

Synched_task2 on the IOCIN2 calls *read_GSET* to obtain the gradient setpoint correction signal. Once this data has been

received, *Actuator_set* is called to send the gradient setpoint signal to the vernier cavities. *Actuator_set* performs CAMAC writes to the DAC card to effect the correction signal.

V. RESULTS

One of requirements on the state estimator for this system is that the estimator should be able to distinguish between position changes caused by energy variations and that caused by betatron oscillations. Since there is no coupling in the X and Y planes a change in X position should not affect the Y position at the reference point. A series of open loop tests were performed to study the estimator response to position and energy changes. The results of these tests indicate a satisfactory response of state estimator. For the first part, a change in energy of 0.2 MeV was introduced by changing the accelerating gradient in two cavities upstream of energy lock location. The state estimator converged within 2-3 samples to the actual energy error introduced while X, X', Y, Y' were not affected.



Y'

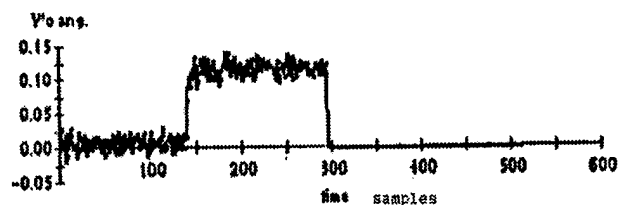


Fig 2

Next, a vertical corrector near the reference point was changed by 15 G.cm to introduce an angular change of 0.1 mrad in the Y' estimate. The estimator learned (Fig 2) of this change within 2-3 samples without affecting other states. A similar test for X' state was done using a horizontal corrector and similar results were observed. Initial tests of closed loop system response indicate that the energy lock loop is functional and it is able to lock the energy of beam against step changes in the energy introduced by changing the accelerating gradients of the cavities upstream of energy lock location. Fig 3a shows the $\Delta E/E$ after the step change in the energy was introduced and before the loop was closed. Fig 3b shows the $\Delta E/E$ after the loop was closed. Due to machine commissioning constraints we have had minimal closed loop testing time. More beam time is needed in order to collect data for producing a Bode plot of closed loop system response.

Ethernet has been used for transfer of correction signal

between two IOCs at 60 Hz rate. Initial data obtained indicates that Ethernet can be successfully be used to run the feedback loop at higher rate of 240 Hz reliably.

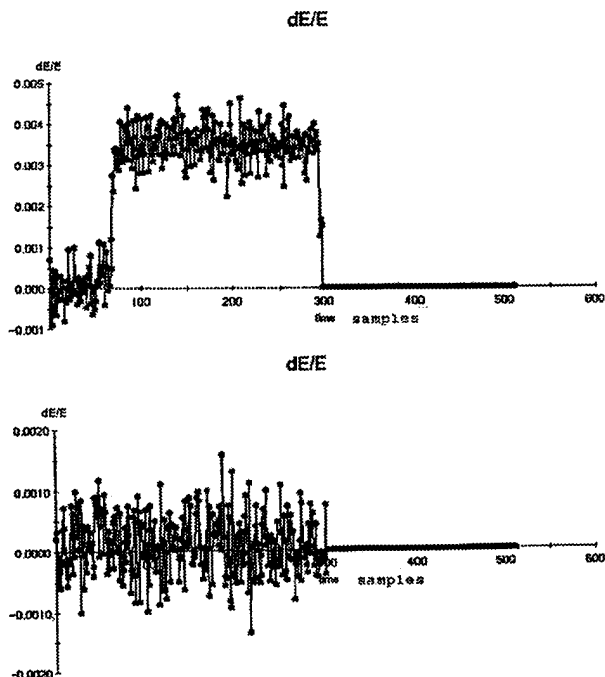


Fig 3

VI. CONCLUSIONS

Implementation of this feedback loop indicates that control design techniques based on concepts of Modern Control Theory can be successfully used for applications at CEBAF. A fast orbit lock controller designed using these techniques will be implemented in the Injector region at CEBAF shortly. Experience gained from implementation of these two loops will be used in developing a generic fast feedback facility for CEBAF.

VI. REFERENCES

- [1] B. Friedland, "Control System Design," McGraw-Hill Book Company, New York, 1986
- [2] Leo R. Dalesio, et. al. "The Experimental Physics and Industrial Control System Architecture: Past, Present, and Future," International Conference on Accelerator and Large Experimental Physics Control Systems, October 1993.
- [3] VxWorks Reference Manual, Copyright Wind River Systems, Inc., 1984-1993
- [4] A. Hofler, et al., "Performance of the CEBAF Arc Beam Position Monitors," Proceedings of 1993 PAC Conference, pp 2298-2300
- [5] Matlab reference Manual, Copyright The MathWorks, Inc., 1984-1993

Operation and Performance of the PEP-II Prototype Longitudinal Damping System at the ALS*

D. Teytelman, R. Claus, J. Fox, H. Hindi, J. Hoefflich, I. Linscott, J. Olsen, G. Oxoby, S. Prabhakar, W. Ross,
L. Sapozhnikov
Stanford Linear Accelerator Center, Stanford, CA 94309, USA
A. Drago, M. Serio
INFN-LNF, Frascati, Italy,
J. Byrd, J. Corlett, G. Stover
Lawrence Berkeley Laboratory, Berkeley, CA 94720

Abstract

A modular programmable longitudinal feedback system has been developed as a component of the PEP-II R+D program. This system is based on a family of VME and VXI packaged signal processing functions which implement a general purpose digital feedback controller for accelerators with bunch spacings of 2 ns. A complete PEP-II prototype system has been configured and installed for use at the LBL Advanced Light Source. The system configuration used for tests at the ALS is described and results are presented showing the action of the feedback system. Open and closed loop results showing the detection and calculation of feedback signals from bunch motion are presented and the system is shown to damp coupled-bunch instabilities in the ALS. Use of the system for accelerator diagnostics is illustrated via measurement of grow-damp transients which quantify growth rates without feedback, damping rates with feedback, and identify unstable modes

1. PEP-II Longitudinal Prototype

The PEP-II longitudinal prototype is a modular bunch-by-bunch processing system designed to implement longitudinal feedback signal processing [1]. The system is composed of several processing modules in VME and VXI formats. The analog-to-digital and digital-to-analog functions are implemented in a pair of VXI processing modules which are capable of sampling bunch motion and generating correction signals at a 500 MHz rate, which allows the system to operate with bunch spacings of 2 ns. The 500 MHz A/D functions are incorporated in the Downsampler module, which is a programmable sequencer capable of controlling the sampling of up to 2048 bunches with downsampling factors up to 32. The 500 MHz D/A is contained in the hold buffer VXI module, whose buffer memory contains the most recent kick value for each bunch in the system. A VXI packaged QPSK modulator (which generates a kicker carrier signal which spans 1 to 1.25 GHz) and a Timing module (which generates several ECL clock signals from the ring RF master oscillator) complete the digital signal processing VXI modules [2].

The signal processing algorithms are implemented as programs coded on AT+T DSP 1610 microprocessors. These single-chip 16 bit processors are organized into groups of four,

with four processors on each VME packaged DSP module. A system configuration for a particular accelerator requires 3 to 20 of the DSP modules, depending on the machine synchrotron frequency, revolution frequency and number of bunches. Each sampling interval the Downsampler module sends bunch data to a particular DSP board (based on the downsampler program) and the DSP board sends computed results to the Hold buffer module. Figure 1 is a photograph of the system configured for testing at the ALS, which uses 10 DSP modules total. The system is configured and downloaded via a set of control programs which specify the operating configuration of the system and generate coefficients for the DSP algorithms. An EPICS based user interface allows a single control interface from a master workstation, which communicates with several commercial VXI/VME processor modules which act to control the VME and VXI bus systems [3].

The analog and microwave components of the system are the same as implemented for the Longitudinal Quick Prototype. The processing bandwidth of the system can be seen in figure 2, which shows an oscilloscope record of the baseband correction signal (updated at the 500 MHz bunch crossing rate) and the resulting kicker drive signal. The risetime of the baseband signal is seen to be 320 ps.

2. ALS Results

A complete 4 processor feedback system (the longitudinal Quick Prototype) has been installed at the ALS since September 1993 [4]. It has been used to develop feedback algorithms and accelerator diagnostics, and is capable of controlling up to 90 bunches in the ALS machine. During the past six months this system has been used with a wideband longitudinal kicker structure and a 200 watt TWT power amplifier for a series of feedback tests and system development [5].

The system has been operated in conjunction with the transverse feedback system successfully for storage ring currents up to 320 mA [6]. The operation of the longitudinal system has been shown to increase the intensity of emitted undulator radiation by a factor of 2.5 (figure 3).

One of the attractive features of the programmable DSP architecture is the flexibility of the system. Because the signal processing is determined by software programs, it is easy to implement many accelerator diagnostic and machine physics measurements in the feedback processing. An example of an instability growth rate measurement is illustrated in figure 4. This grow-damp transient measurement is made by a DSP program which can turn off the longitudinal feedback output of

*Work supported by Department of Energy, contract DE-AC03-76SF00515

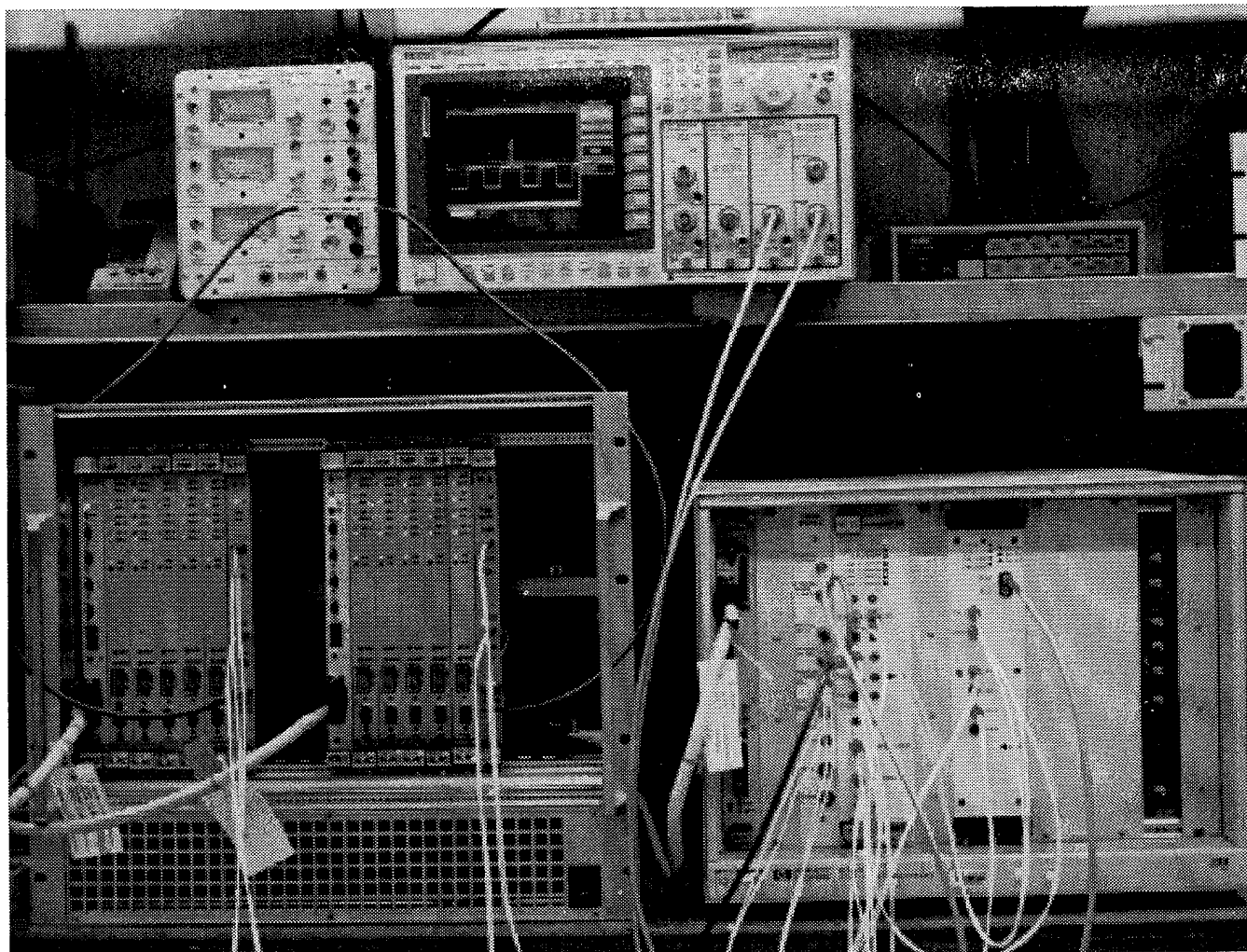


Figure 1. Photograph of the assembled system. The VME crate contains ten DSP modules, while the VXI crate contains the 500 MS/sec Down sampler and Hold Buffer Modules

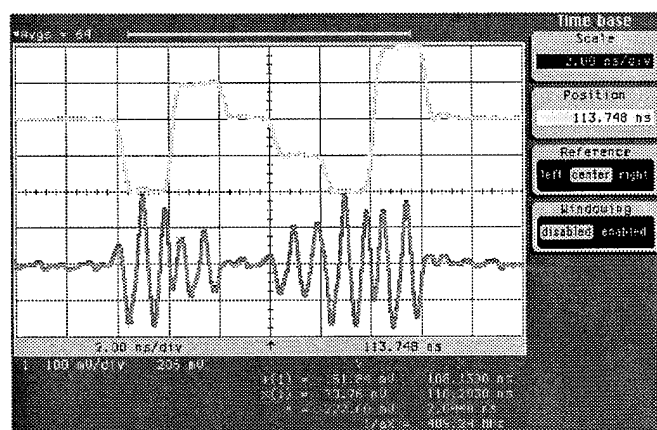


Figure 2. Oscilloscope photo of the baseband correction signal and the resulting amplitude modulated QPSK signal. Signals for 6 consecutive bunches are shown for 2 ns bunch spacing (2 ns/div scope speed). Note the 1 - 1.25 GHz kicker signal phase inverts for the negative correction values.

selected bunches for a user-programmed interval, and then restore control by turning the output signals back on. During this transient the DSP processors store the oscillation coordinates of the bunches. The transient begins from the stabilized state and reveals the growth rate of an instability via the structure of the envelope of the synchrotron oscillations. The damp-

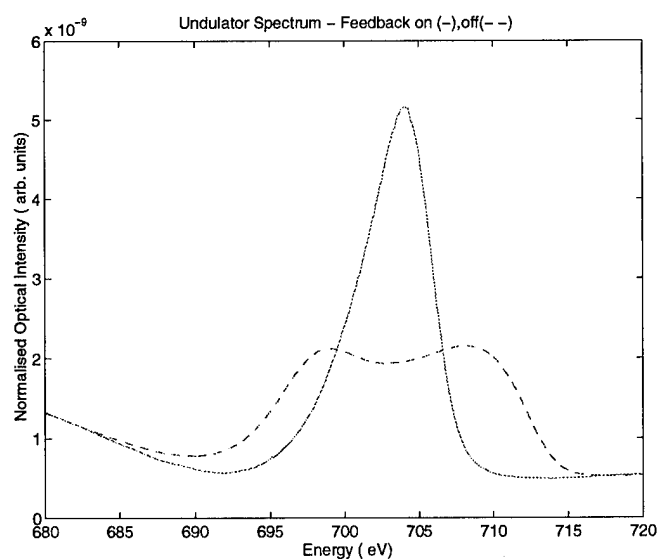


Figure 3. Undulator output spectrum taken at the ALS. The action of the feedback system reduces the linewidth and increases the intensity of the emitted radiation.

ing rate provided by the feedback system is seen in the second portion of the envelope. The figure shows the motion of a single bunch (out of 40).

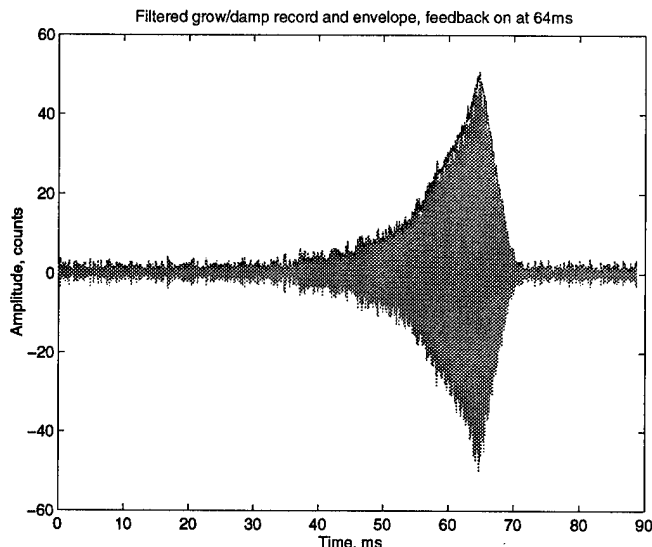


Figure 4. Grow-Damp Transient showing the growth of unstable motion when the feedback is turned off, followed by damping when the feedback is turned back on. The damping rate is seen to be -1.6 ms, while the growth rate is 9.8 ms.

This growth rate measurement can be made for various accelerator parameters. Figure 5 shows such growth rates as a function of current for several fill patterns and RF cavity tunings in the ALS. Note the linear scaling of inverse growth rate with current (as would be expected from theoretical considerations). Also note the sensitivity of the growth rate to cavity temperature. These measurements allow the feedback system effectiveness to be quantified and the selection of an accelerator operating point to be made. Such trade-offs are very significant in determining the required output power of the feedback system.

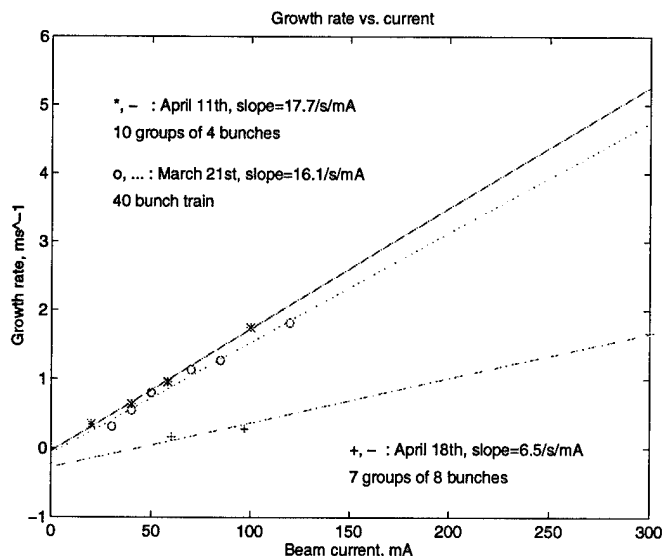


Figure 5. Figure of growth rate vs. current for various fill patterns and cavity temperature at the ALS.

3. SUMMARY

A general purpose digital signal processing system has been developed to control longitudinal multi-bunch instabilities. The system is flexible and operates at sampling rates up to 500 MHz. The operation of the downsampled processing system has been demonstrated at the Advanced Light Source and has been used to control longitudinal instabilities at operating currents up to 320 mA. Ongoing system development of operational software and measurement techniques is continuing, and the prototype PEP-II system will be commissioned for routine ALS operations in 1995.

4. ACKNOWLEDGMENTS

The authors thank the PEP-II Group and the SLAC Technical Division for their support, and thank the ALS staff and ALS Operations group for their hospitality and interest in this development program.

5. REFERENCES

- [1] Oxoby, et al., "Bunch by Bunch Longitudinal Feedback System for PEP-II," Proceedings of the 1994 European Particle Accelerator Conference.
- [2] Teytelman, et al., "Operation and Performance of a Longitudinal Feedback System Using Digital Processing", Proceedings of the 1994 Beam Instrumentation Workshop
- [3] Claus, et al., "Software Architecture of the Longitudinal Feedback System for PEP-II, ALS and DAPHNE", this conference (PAC 95)
- [4] Fox, et al., "Operation and Performance of a Longitudinal Damping System Using Parallel Digital Signal Processing", Proceedings of the 1994 European Particle Accelerator Conference).
- [5] Corlett, et al., "Longitudinal and Transverse Feedback Kickers for the ALS" Proceedings of the 1994 European Particle Accelerator Conference
- [6] Barry, et al., "Commissioning and Operation of the ALS Transverse Coupled-Bunch Feedback System", this conference (PAC 95)

COMMISSIONING OF THE ALS TRANSVERSE COUPLED-BUNCH FEEDBACK SYSTEM*

W. Barry, J. Byrd, J. Corlett, J. Johnson, G. Lambertson, Lawrence Berkeley Laboratory, Berkeley, CA 94720, and J. Fox, Stanford Linear Accelerator Center, Stanford, CA 94309.

Commissioning results of the ALS transverse coupled-bunch feedback system are discussed. New test results concerning baseband quadrature processing, heterodyne/homodyne detection, and simultaneous operation of the transverse and longitudinal systems¹ are presented.

I. INTRODUCTION

The LBL Advanced Light Source is a third generation 1.5 GeV electron storage ring for producing synchrotron radiation in the .5-10000 eV range². The ring is designed to support a moderately high average beam current (400 mA) and a large number bunches, up to 328 in buckets separated by 2 nsec. As a result, a broad and dense spectrum of transverse coupled-bunch modes can be excited by higher-order RF cavity resonances and the transverse resistive wall impedance.

In order to control growth of this coupled-bunch motion, a 250 MHz bandwidth bunch-by-bunch feedback system has been designed and is presently undergoing testing and commissioning at ALS. The feedback system design and specifications as well as early test results are given in previous references^{3,4,5}. In this paper, recent results emphasizing the simultaneous operation of the transverse and longitudinal systems are addressed. In addition, a brief overview of the system is presented for orientation.

II. SYSTEM OVERVIEW

A block diagram of the ALS transverse feedback system is shown in figure 1. The system utilizes two sets of button pickups for detecting beam moment, $I\Delta x$. By summing the moment signals from the two sets of pickups in proper proportion, a correction signal that is 90 degrees out of phase with beam position at the kickers can be obtained. This quadrature condition results in optimal damping and can be adjusted to accommodate changes in tune.

The moment signals are detected at the sixth harmonic of the 1.5 GHz RF frequency (3 GHz) in order to exploit the good sensitivity of the button pickups at this frequency. The button signals are differenced and summed to produce true x and y moment signals that are subsequently demodulated to baseband (150 kHz - 250 MHz). As reported previously, the receiver electronics supports two types of detection, heterodyne and homodyne. The nominal detection mode, heterodyne, utilizes a 3 GHz local oscillator that is phase-locked to the storage ring RF to amplitude demodulate

the moment signals. In the absence of the longitudinal feedback system, the transverse system operated necessarily in the presence of large synchrotron oscillations. In this case, the oscillating arrival time of the bunches with respect to the fixed-phase local oscillator causes a reduction and a possible sign change in the average feedback gain⁶. For this operating scenario, homodyne demodulation which employs a local oscillator signal derived from the sum of the four button signals was used. The homodyne technique however is less desirable than heterodyne detection because it results in a feedback gain that is proportional to the square of the bunch current. Presently, with the prototype longitudinal feedback system running at ALS, heterodyne detection may be used exclusively for the transverse system.

The baseband moment signals are proportionally mixed with variable attenuators and a summing hybrid to produce the quadrature kick signal. Other baseband processing includes simple two-tap coaxial notch filters for rejecting orbit harmonic signals and simple coaxial timing delays. Finally, four 150 W, 10 kHz - 220 MHz, Class-A, commercial amplifiers are used to drive each electrode of each kicker separately (300 W per kicker). The amplifier/kicker combination provides per-turn kicks ranging from 2.3 kV at 100 kHz to 1.6 kV at 220 MHz. At the nominal betatron tunes, these voltages and frequency range are sufficient to control any expected transverse coupled-bunch motion.

III. RECENT COMMISSIONING RESULTS

Recent commissioning and test results have involved the simultaneous operation of the longitudinal and transverse feedback systems. As indicated above, with the reliable operation of the prototype longitudinal system, heterodyne detection for the transverse system has been tested and shown to be superior to homodyne detection. The successful demonstration and adoption of heterodyne detection for transverse feedback is a major milestone in the commissioning of the ALS system and the design of the PEP-II system⁷ which is modeled after the ALS system.

When transverse coupled-bunch modes are driven by resonant impedances such as higher-order modes in the RF cavities, large synchrotron oscillations can have a strong damping effect. Basically, this effect is the same as the gain dilution effect in the heterodyne demodulation technique. That is, the oscillating arrival time of a bunch at the impedance causes the phase of the excitation to be different on every turn resulting in a reduction in the average kick received by the

*Supported by the US Department of Energy under Contract number DE-AC03-76SF00098 (LBL) and DE-AC03-76SF00515 (SLAC)

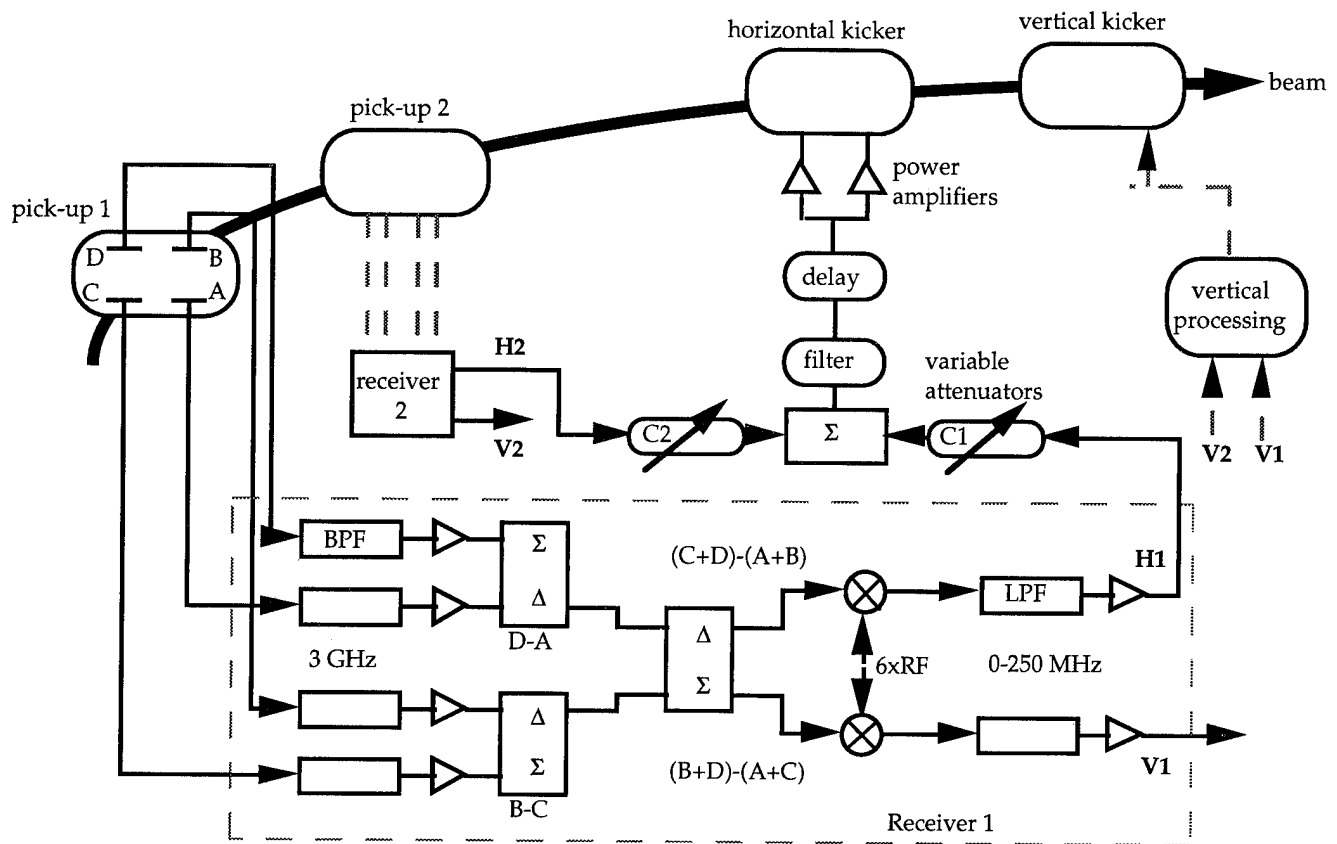


Figure 1. ALS transverse feedback system

bunch. In addition, with non-zero chromaticity, energy oscillations cause a bunch-by-bunch spread in tune which weakens bunch-to-bunch coupling in the transverse plane. If the synchrotron oscillations are large enough, these effects can cause a significant decrease in the growth rates of transverse modes and possibly prevent growth of modes which would otherwise be unstable.

These effects have been clearly seen at ALS during testing of the longitudinal feedback system. At moderate currents (> 70 mA), strong betatron sidebands are present when the longitudinal system has damped the longitudinal coupled-bunch motion. In the absence of longitudinal damping, these lines are weak or not present at all. Therefore, the ultimate test of the transverse system is its performance in conjunction with the longitudinal system.

Presently, efforts are under way to characterize the simultaneous performance of the longitudinal and transverse systems. Previously, as reported in reference [5], transverse coupled - bunch motion has been controlled in the presence of the longitudinal system as evidenced by the disappearance of betatron lines as detected by a spectrum analyzer. Recently, a synchrotron light monitor facility has been installed at beamline 3.1 at the ALS. With this facility, it is now possible to monitor the effects of the feedback systems on beam spot size.

Figure 2 shows the beam spot for a 175 mA beam consisting of 10 groups of 4 bunches (bunches separated by 4 nsec) equally spaced around the ring. In this case the

longitudinal system is controlling the synchrotron oscillations. As shown, strong vertical betatron oscillations cause a blowup in the vertical spot size. With the vertical

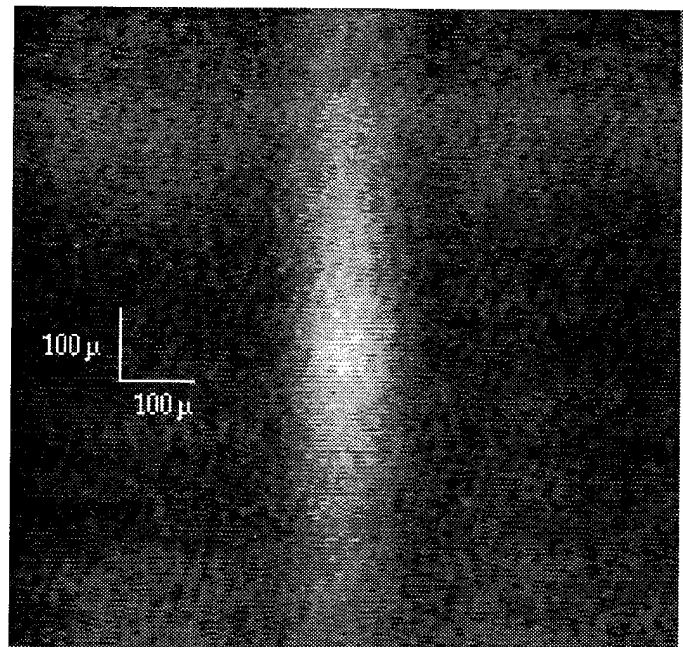


Figure 2. Beam spot with vertical feedback off.

feedback turned on, betatron oscillations are suppressed and the spot size is dramatically reduced as shown in figure 3. In both

bandwidth capabilities of the transverse system (operation with every bucket full) will be addressed.

V. ACKNOWLEDGMENTS

The authors wish to thank the many members of the LBL/SLAC-ALS/PEP-II feedback systems collaboration for many enlightening discussions and useful suggestions. In addition, we thank Tim Renner for the use of and assistance with ALS beamline 3.1.

VI. REFERENCES

- [1] J. Fox, et al., "Operation and Performance of the PEP-II Prototype Longitudinal Damping System at the ALS", These Proceedings.
- [2] "1 - 2 GeV Synchrotron Light Source", CDR, LBL Pub - 5172 Rev., July, 1986.
- [3] W. Barry, J. Byrd, J. Corlett, J. Hinkson, J. Johnson, and G. Lambertson, "Design of the ALS Transverse Coupled-Bunch Feedback System", Proceedings of the 1993 IEEE Particle Accelerator Conference, Washington DC, May, 1993.
- [4] W. Barry, J. Byrd, J. Corlett, G.R. Lambertson, and C.C. LO, "Transverse Coupled-Bunch Feedback in The Advanced Light Source (ALS)", Proceedings of the 1994 European Particle Accelerator Conference, London, England, June 27 - July 1, 1994.
- [5] W. Barry, J. Byrd, and J. Corlett, "The LBL Advanced Light Source Transverse Coupled - Bunch Feedback System - Recent Commissioning Results", Proceedings of the 1994 Beam Instrumentation Workshop, Vancouver, Canada, October 2 - 6, 1994.
- [6] W. Barry, "Stability of a Heterodyne - Based Transverse Feedback System in the Presence of Synchrotron Oscillations", CBP Tech Note - 58, LBL, July, 1994.
- [7] W. Barry, J. Byrd, J. Corlett, M. Fahmie, J. Johnson, G. Lambertson, M. Nyman, J. Fox, and D. Teytelman, "Design of the PEP-II Transverse Coupled - Bunch Feedback System", These Proceedings.

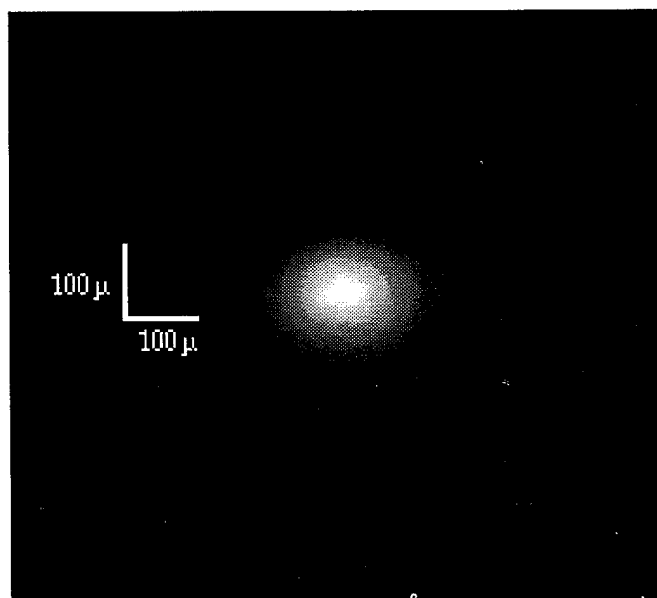


Figure 3. Beam spot size with vertical feedback on.

cases, the horizontal feedback was controlling a significantly smaller amount of horizontal betatron motion.

It should be noted that the prototype longitudinal system can control only specific bunch patterns with a minimum bunch spacing of 4 nsec (every other bucket). In this case, only half the bandwidth of the feedback systems is exercised. With the arrival of the final longitudinal system in the near future, the ability of both systems to damp coupled - bunch modes with every bucket full can be evaluated.

Finally, initial tests of the two - pickup quadrature system indicate that the transverse system can be operated in modes ranging from resistive to reactive as evidenced by amplitude reduction or frequency shift, respectively, of driven betatron lines on a spectrum analyzer. The remaining task is to determine the amplitude settings of each of the two pickups that minimize the deviation from linear phase of the feedback path over the entire baseband. This adjustment is expected to become critical when operating with every bucket full.

IV. CONCLUSION

A broadband feedback system for controlling transverse coupled-bunch instabilities in the LBL ALS is presently undergoing testing and commissioning. Most recently, the system has been tested in conjunction with the longitudinal system with excellent results. In particular, large vertical coupled - bunch motion has been controlled resulting in a dramatic decrease in beam spot size. Present efforts are being directed towards the optimum phasing of the two - pickup quadrature system. In addition, when the final longitudinal system is installed and operating, the full

OPERATION OF A FAST DIGITAL TRANSVERSE FEEDBACK SYSTEM IN CESR*

J.T. Rogers, M.G. Billing, J.A. Dobbins, C.R. Dunnam, D.L. Hartill, T. Holmquist, B.D. McDaniel, T.A. Pelaia, M. Pisharody, J.P. Sikora, and C.R. Strohmman,
Laboratory of Nuclear Studies, Cornell University, Ithaca, NY 14853 USA

Abstract

We have developed a time domain transverse feedback system with the high bandwidth needed to control transverse instabilities when the CESR e^+e^- collider is filled with trains of closely spaced bunches. This system is based on parallel digital processors and a stripline driver. It is capable of acting on arbitrary patterns of bunches having a minimum spacing of 14 ns. Several simplifying features have been introduced. A single shorted stripline kicker driven by one power amplifier is used to control both counter-rotating beams. The desired feedback phase is achieved by sampling the bunch position at a single location on two independently selectable beam revolutions. The system adapts to changes in the betatron tune, bunch pattern, or desired damping rate through the loading of new parameters into the digital processors via the CESR control system. The feedback system also functions as a fast gated bunch current monitor. Both vertical and horizontal loops are now used in CESR operation. The measured betatron damping rates with the transverse feedback system in operation are in agreement with the analytical prediction and a computer simulation developed in connection with this work.

I. INTRODUCTION

The Cornell Electron Storage Ring (CESR) is being upgraded to allow collisions of short trains of electron and positron bunches [1]. CESR is now operating with nine trains of two bunches each. We plan to operate with nine trains of as many as five bunches in the near future. A transverse coupled bunch instability [2] in CESR requires the use of active feedback. Before the present work, a time-domain horizontal feedback system based on a coaxial cable delay line and ferrite kicker magnet was used to stabilize the beam [3]. The use of bunch trains requires a redesigned transverse feedback system with higher bandwidth.

We chose to build a time domain feedback system because of the large number of coupled bunch modes that need to be damped. The minimum bunch spacing compatible with efficient injection fixes its sampling rate at 71.4 MHz. We further required that the feedback system accommodate a dynamic beam motion of ± 3 mm and arbitrary changes in tune, produce an error signal normalized to beam current, and provide a damping rate of 1000 s^{-1} .

Transverse feedback damping operates by sensing the beam position and applying a deflection to the beam proportional to its sensed position after its betatron phase has advanced by $\pi/2 + n\pi$. Because of signal processing delays the deflection cannot be applied to the beam on the same turn as the position is sensed.

The error signal must be delayed by at least one turn. The $2.56 \mu\text{s}$ revolution period of CESR implies a delay-bandwidth product of approximately 500 for the error signal. It is difficult to achieve this product by purely analog means, so we chose to delay the error signal digitally, and to implement the current normalization and other signal processing functions digitally as well.

II. SIGNAL PROCESSING

Figure 1 shows a block diagram of one digital feedback loop. The beam position signal is derived from the button electrodes used by the CESR orbit measurement system. The signals from opposite pairs of electrodes are summed in hybrid combinars. The remainder of the signal processing is done outside the CESR tunnel for access to the electronics during storage ring operation.

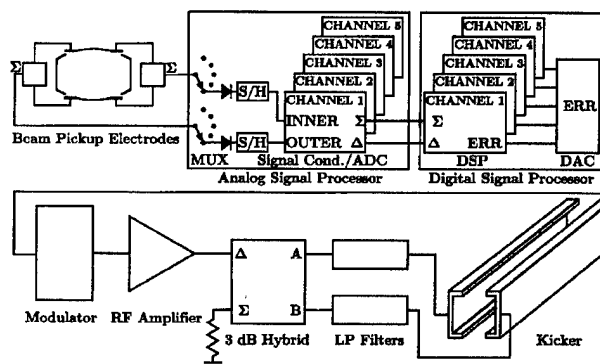


Figure 1. Block diagram of one digital feedback loop.

The receiver for the beam signal consists of a GaAs SPDT switch that serves as a fast gate, a diode rectifier which traps the signal as a charge on a capacitor, and an FET switch which discharges the capacitor before the next time the GaAs switch closes. Five parallel channels are needed (a sixth is left unused) because of the limited sampling rate of a commercially available 10 bit ADC.

The remainder of the signal processing occurs in five parallel channels. The sum and difference of the receiver signals from opposite pairs of electrodes are formed by a pair of operational amplifiers. These contain information about the bunch current and the product of the bunch current and beam displacement, respectively. These sum and difference signals are then digitized by a pair of 10 bit ADCs.

The position of the beam is reconstructed from the digitized sum and difference signals. The eight most significant bits of the sum word and the 10 bits of the difference word form an 18 bit address for a lookup table that stores a 12 bit beam position word. The contents of the lookup table can be tailored to produce

*This work has been supported by the National Science Foundation.

a damping rate that is any desired function of bunch current. It can also be used to compensate the position nonlinearity of the button electrodes, although we have not made use of this feature.

We delay the position word by an integer number of turns in FIFO memory and subtract it from the current position. The resulting number is the 10 bit error word, which is insensitive to static displacements and has a partially suppressed response to low frequency motions such as synchrotron oscillations. Another FIFO memory is used to delay the error word by an integer number of turns before it is used to deflect the beam, with the number of turns chosen to provide the correct $\pi/2 + n\pi$ betatron phase advance. Both of these delays are established in software and can be easily modified to accommodate changes in the storage ring optics, tunes, or feedback hardware location. A 10 bit DAC common to all five channels converts the error word to a voltage.

The digital signal processor is constructed of cards which plug into a VME backplane. Four feedback loops are needed for the horizontal and vertical stabilization of the electron and positron beams. For each of these loops a motherboard is used to provide the internal timing signals and data paths. Each motherboard holds five daughterboards, each of which performs the signal processing functions described above. Each daughterboard in turn holds a board which contains the analog sum and difference circuits and the associated pair of ADCs. Figure 2 shows a photograph of the feedback motherboard assembly containing the five daughterboards and ADC boards. A microprocessor in the VME crate runs the program which is used to enable or disable channels, load the lookup tables, and initialize the system so that it starts in a well-defined state. This program also calculates the current in each bunch by scaling and averaging the data from the 10 bit sum word. This current measurement is used in the CESR control room display and the automated injection procedure. An Xbus to VME interface is used for communication between the control system and the feedback microprocessor. External signals from the CESR ultrafast timing system are used by the feedback processor to generate its own internal timing.

III. RF ELECTRONICS

To drive the stripline kicker, we require a wideband RF amplifier with a flat phase response, the ability to drive a shorted line stably, and tolerance for some beam induced power reaching its output. After a survey of commercially available amplifiers, we chose a 200 W amplifier with a 0.25 to 150 MHz band¹. Because the lowest transverse mode frequencies fall below this amplifier's range, we upconvert the DAC output in a modulator. A trigger supplied by the digital feedback motherboard generates a 14 ns long bipolar pulse within the modulator. This bipolar pulse is then multiplied by the DAC output in a double balanced mixer. The modulator output is used to drive the power amplifier. There is some ringing in the mixer, so an improved modulator based on a fast four quadrant multiplier has been designed. A prototype of this modulator does not display this ringing and has improved frequency response.

A 180° 3 dB hybrid² located at the stripline kicker splits the amplifier output into a differential drive for the kicker. The hy-

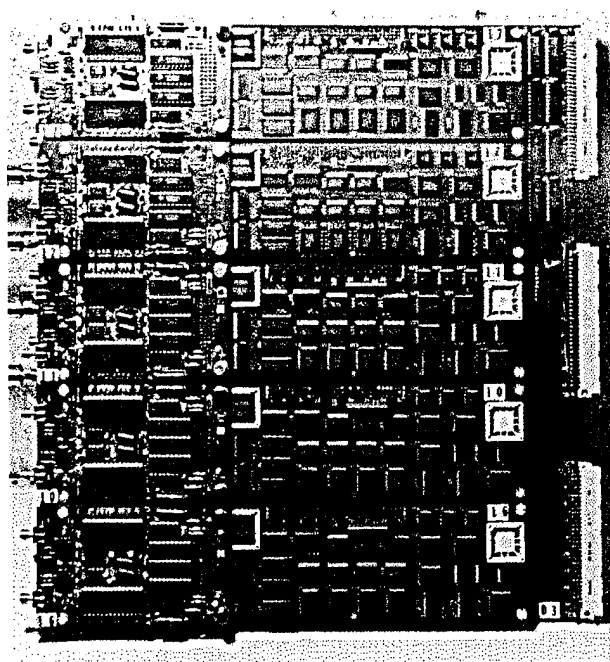


Figure 2. Feedback motherboard with five digital processor daughterboards. Each daughterboard holds an ADC board at its left.

brid is protected from the beam induced power from the stripline by matched low-pass filters. To avoid high frequency resonances in the striplines, the filters need to be purely resistive. They are implemented as water-cooled ferrite-loaded coaxial lines.

IV. STRIPLINE KICKERS

We use stripline kickers because of their high bandwidth. Each kicker contains two electrodes which act as 50 Ω transmission lines. Each electrode is shorted at one end, which spoils the directionality of the kicker, and allows the use of a single kicker driven by a single RF amplifier for both e^+ and e^- beams. The transverse deflection, voltage induced by the beam at the kicker terminals, and the beam impedance of the shorted kicker are the same as those of a kicker with striplines terminated in their own characteristic impedance [4].

The stripline electrodes are formed from OFHC copper sheet, and have a lip on each side to improve field uniformity and mechanical rigidity. Two flat copper ground electrodes are placed in the midplane between the stripline electrodes. These have the effect of conducting a substantial fraction of the beam image current, which reduces the longitudinal coupling of the kickers to the beam, and hence their beam impedance, while leaving the intended transverse coupling unaffected. The stripline and ground plane electrodes are cooled by water flowing in 5/16 in. O.D. copper tubing welded along their length.

The stripline electrodes and ground plane electrodes are assembled on one of the endplates of the kicker vacuum chamber. This endplate also contains the cooling water tubes and one type HN RF vacuum feedthrough for each stripline electrode. Ceramic spacers maintain a vacuum gap between the end of the stripline electrode and an extension of the beam pipe into the kicker chamber. This gap is designed to produce a 10 pF shunt

¹Model 3200L, ENI, Rochester, NY

²Model H3099, Werlatone, Inc., Brewster, NY

capacitance to prevent arcing in the RF feedthroughs and external RF components when CESR is operated with high bunch currents. This shunt capacitance is the limitation on the bandwidth of the kicker.

At the other end of the kicker the stripline and ground plane electrodes are welded into a square frame which is surrounded by beryllium copper spring finger contacts. During assembly this frame slides into a square ground contact on the other chamber end flange. The assembly process is shown in Fig. 3.



Figure 3. Stripline kicker during assembly. The RF feedthroughs are on the lower endplate in this photograph.

The aperture between the electrodes is larger than the the wide axis of CESR beampipe so that synchrotron radiation does not intercept the electrodes. Stainless steel transitions from the square opening of the kicker chamber to the approximately elliptical beampipe are provided with water-cooled copper absorbers to intercept the synchrotron radiation at a grazing angle. The stainless steel vacuum chamber has its own ion pump.

V. OPERATION

All four loops (e^+ and e^- , vertical and horizontal) of the digital transverse feedback system have been in operation since November, 1994. It is routinely used to stabilize bunch trains in high energy physics operation. Both the digital current normalization and digital phase adjustment have proven successful. In open-loop tests the shorted stripline kickers produced the calculated deflection for both e^+ and e^- beams, and the measured damping rate agrees with the calculated rate. Figure 4 shows a control room display of the amplitude of the $f_0 - f_h$ (182 kHz) horizontal coupled bunch mode as a function of time. The horizontal feedback has been momentarily gated off, then on again, restoring rapid damping of the instability.

Table 1 summarizes the digital feedback parameters.

VI. ACKNOWLEDGMENTS

The authors wish to thank M. Tigner, N. Kazarinov, D. Rubin, and the members of the CESR operations group for invaluable

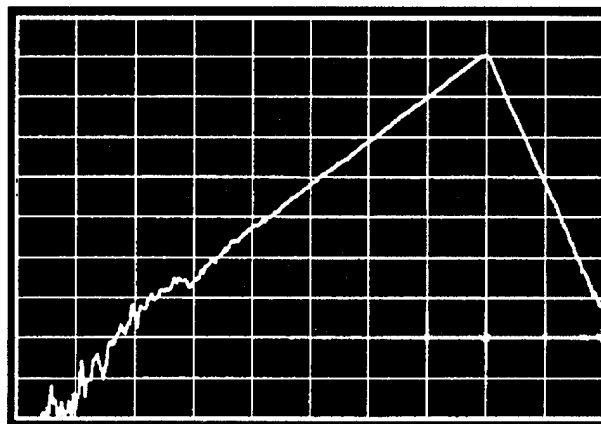


Figure 4. Amplitude of horizontal betatron motion vs. time. The feedback has been gated off during the first 8 divisions, then on again. The vertical scale is 5 dB/div. and the horizontal scale is 2.56 ms/div.

Table 1: Feedback parameters in current operation

L	Stripline electrode length	116 cm
w	Stripline electrode width	17.5 cm
b	Stripline electrode gap	12.0 cm
Z_C	Stripline impedance	50 Ω
k	Stripline HOM loss factor	0.018 V/pC
V_{peak}	Max. amplifier voltage	143 V
p	Beam momentum	5.3 GeV/c
β_x, β_y	Beta function at kicker	25.6, 18.2 m
x_{max}, y_{max}	Dyn. range ref. to pickup	5, 5 mm
α_x, α_y	Measured damping rate	2.4, 0.58 ms^{-1}

discussions. We gratefully acknowledge the efforts of the LNS technicians, machinists, and operators. Special thanks are due R. Meller for many useful suggestions and for providing the fast timing system.

References

- [1] D. Rice, *Proc. 1993 Particle Accelerator Conf.*, 1978 (1993).
- [2] L.E. Sakazaki, *et al.*, *IEEE Trans. Nucl. Sci.* **32** 2353 (1985).
- [3] R. Littauer, Cornell LNS note CON 87-19 (1987).
- [4] J.T. Rogers, Cornell LNS note CBN 95-4 (1995).

MEASURING AND ADJUSTING THE PATH LENGTH AT CEBAF*

G. A. Krafft, M. Crofford, D. R. Douglas, S. L. Harwood, R. Kazimi, R. Legg, W. Oren, K. Tremblay, and D. Wang, Continuous Electron Beam Accelerator Facility, 12000 Jefferson Avenue, Newport News, VA 23606 USA

Accurately setting the path length around the machine is central to the proper operation of the CEBAF accelerator. The CEBAF main accelerator consists of two recirculating superconducting linacs operating at 1497 MHz fundamental frequency. The electron beam can recirculate up to five times through the two linacs before it is extracted to the experimental halls. In order to obtain maximum energy gain and minimum energy spread through the linacs, all passes should arrive at the beginning of the linacs in phase at the crest of the RF cycle. In this paper we explain how the arrival times of higher pass beams are measured with respect to the first pass to less than one degree of RF phase and how the path length around the machine is adjusted.

Following a brief introduction to the CEBAF design and some local nomenclature, these topics will be discussed: differential RF phase measurement of time delay, the energy method of cresting the higher pass beams, results obtained with the measurement techniques, future plans and improvements to the devices, and finally, a set of conclusions.

I. INTRODUCTION

The CEBAF accelerator consists of a 45 MeV injector, two side-by-side 400 MeV superconducting linacs, 9 recirculation arcs that shuttle the beam through the linacs up to 5 times for 4 GeV total energy, and three experimental halls. In this paper the arcs will be labelled, Arc1-9, in the order that the beam passes through the arcs to the highest energy.

In the so-called extraction region of each of the arcs, three "dogleg" bend magnets are installed. By adjusting the excitation of this dogleg chicane, the path length of that arc is adjusted. If the path length of a given arc is adjusted, it is clear that the time of arrival of the microbunches through any higher pass through the linacs is phase shifted.

At CEBAF two types of measurements are used to set the proper recirculation path lengths. The first method, which will be called the energy maximization method, uses the fact that by finding the maximum energy gain through each pass of the linacs one assures that the time of arrival of all the passes is the same, modulo the RF wavelength of 20 cm. This method suffers from the fact that measurements must proceed sequentially, from the lower energy passes to the higher energy passes, to assure that all passes through the linac are properly crested.

A more global method of measuring the phase is to measure the time of arrival of the microbunches on the separate passes using fast RF diagnostics. This method is potentially much quicker than the former, because errors can be localized to individual arcs in a single measurement, and because the individual measurements occur in a single step, in contrast to the first method, where it takes at least three steps to establish a single cresting phase.

Both methods have been pursued at CEBAF with the following results. First setup of an arc is usually most easily accomplished with the time of arrival method. Within two or three measurement and adjustment cycles, the path length of the arc is set within a few degrees of the energy cresting phase. After being adjusted, the beam will fairly easily pass on through the next arc, at which time, it becomes possible to complete the energy maximization measurement easily. Usually, the machine is left in a configuration that maximizes the energy of a pass. As will be seen later, comparing with measurements using the time of arrival method yields discrepancies of order one degree. The time of arrival method has much higher precision than the cresting method. The remainder of the paper will describe in more detail why.

II. MEASUREMENT DEVICES

The path lengths of the arcs are determined using precision phase detectors to obtain relative time information about the electron beam bunches. As is seen in Fig. 1, the phase of a beam derived signal, obtained from a longitudinally polarized pickup cavity tuned to 1497 MHz, is compared with an RF signal derived from the master phase reference system through a mixer. The measurement proceeds by first establishing a 3.8 μ sec beam pulse. Because the total recirculation time is 4.2 μ sec, each of the passes separately excites the cavity. The variable phase shifter is used to calibrate the measurement by adjusting the phase shifter so that the first pass beam output is maximized and by recording the resulting voltage maximum.

The time of arrival measurement is done by adjusting the phase shifter so that the first pass output is zero; any output from the higher pass beams is attributable to relative time phase shifts between the individual passes. The electronic noise of the measurement allows a precision about 0.15° , or about 83μ m. When the measurement is complete, the path length may be changed using the dogleg chicane.

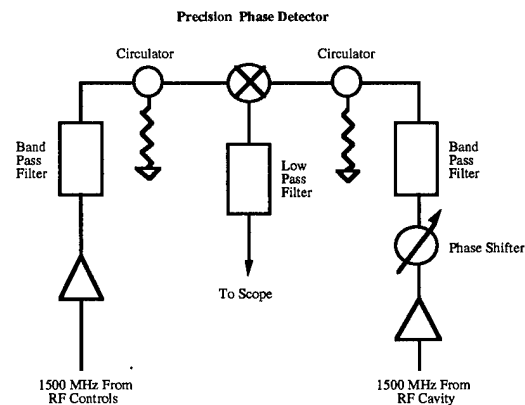


Fig.1 Precision Phase Detector

* Supported by U.S. DOE contract DE-AC05-84ER40150.

III. RESULTS

During the most recent commissioning run at CEBAF, the path length of a given arc was usually set by the energy maximization method, i.e. the dogleg magnets controlling the path length of an arc are adjusted so that the beam energy out the linac is maximized. Very precise relative energy information is obtained, at 10^{-4} energy resolution, using the succeeding arc as an energy monitor. For example, Arc 5 is used as an energy monitor when the dogleg of Arc 4 is set.

Even in the most optimistic case of the second pass through the north linac, with a relative energy resolution of $\delta E/E \approx 10^{-4}$ one obtains a phase set precision of about one degree using a measurement procedure based on dithering the arrival phase around the crest value. The relative precision degrades in proportion to the number of linac segments passed through.

Toward the end of our most recent running period, data like that appearing in Figs. 2 through 5 were collected, under conditions where the path length of Arcs 1 through 6 were adjusted by the energy maximization method. Figures 2 and 3 are oscilloscope traces using the north linac phase detector and Figures 4 and 5 were, within minutes, similar traces from the south linac phase detector. The beam conditions were a pulse length of 3.8 μsec and a beam current within the pulse of about 12 μA .

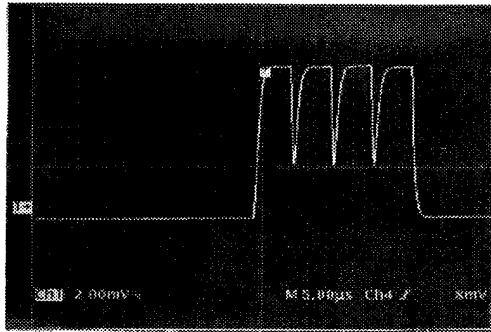


Fig.2 Phase Detector output in North Linac, Crest phase

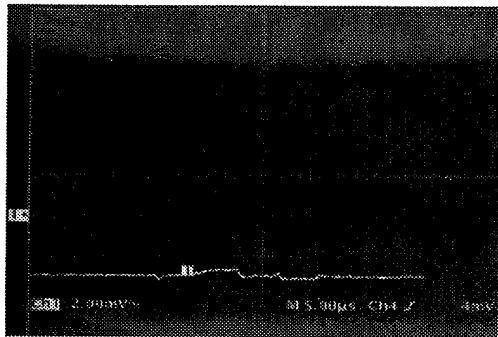


Fig. 3 Phase Detector output in North Linac, Zero crossing phase

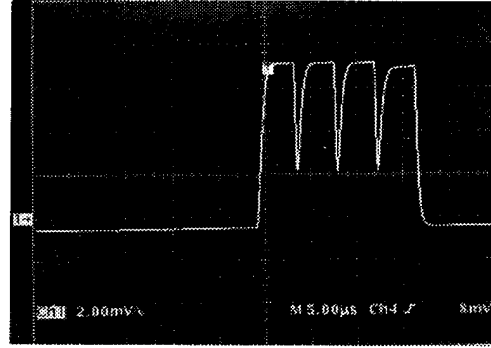


Fig. 4 Phase Detector output in South Linac, Crest phase

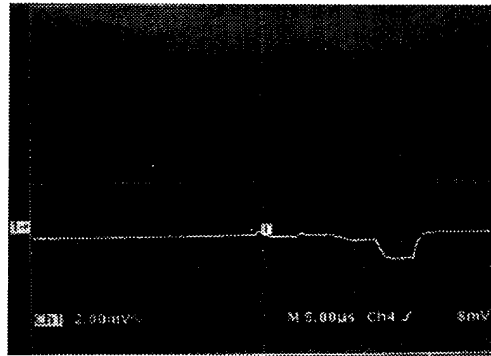


Fig. 5 Phase Detector output in South Linac, Zero crossing phase

Several comments are obvious from Figures 2 and 4, where the phase shifter is adjusted so that the phase detector output from the first pass beam is maximized. First, the rise time of the pulse, limited by the rise time of the detector cavity, is approximately 200 nsec. This allows data taking in the flat part of the curve of duration about 3 μsec . Second, it is clear that each separate pass of the beam is distinguished in the output of the phase detector. Third, knowing that the beam phase is within a few degrees of crest for all four passes of the north linac, one concludes that there is above 98% transmission of the beam through four passes of the north linac because the output voltages are the same within 2%. In Fig. 4, the fact that south linac pass four appears lower in voltage means that either there is beam loss in Arc 7, or the path length of Arc 7 produces a phase shift, visible in Fig. 5 and discussed below. Finally, by recording the maximum output from the first pass beam, V_1 , one has calibrated the phase detector.

Figures 3 and 5 result when the phase shifter of the phase detector is adjusted so that the first pass beam is at the zero crossing (i. e., at zero output voltage). Now the output voltages from the phase detector give the phase shifts of the higher pass beams relative to the first by

$$\Delta\phi = \sin^{-1} (V_i/V_1) \approx V_i/V_1, i = 2, 3, 4, 5$$

where V_1 is the calibration output voltage. The shown data yield the phase shifts of Table 1. In Fig. 4, most of the decrease in the phase detector output in pass 4 is due to the fact that the path length of Arc 7 is off by 9.5° , not because of transmission loss.

Table 1 :Relative Phase Shifts for Four Passes

North Linac	
$\Delta\phi_{12}$	0.7°
$\Delta\phi_{13}$	-1.1°
$\Delta\phi_{14}$	-1.7°
South Linac	
$\Delta\phi_{12}$	1.0°
$\Delta\phi_{13}$	-2.0°
$\Delta\phi_{14}$	-9.5°

Typically, when such a large phase shift is observed, new settings for the dogleg are computed and loaded into the machine. Usually, the adjustment yields the correct phase shift within a degree or two, allowing a precise arc spectrometer measurement to be completed.

Care must be taken that the amplifiers before the mixer are not in saturation, as otherwise the phase shifters are not necessarily calibrated properly. This possibility is overcome in the phase detector assembly by employing a variable attenuator before the mixer.

IV. FUTURE PLANS

There are several enhancements that will be pursued in the near term. They are related to computer control and analysis of measurements, coupled with automatic update of the dogleg magnets. An externally triggered 10 MHz A/D card is being purchased to digitize the phase detector outputs. The card will acquire data for 50 microseconds after the arrival of the first pass beam at each detector cavity. During the interval between beam pulses, the data (about 500 numbers) will be dumped into a control system IOC, where five sets of data in the flat region of the phase detector output (about 3 microsecond or thirty numbers), will be selected for averaging to reduce the noise in the measurement. Signal levels from each of the five passes will then be used to compute the time of arrival of the higher pass beams relative to the first pass beam.

Once the relative arrival times of the different passes have been determined, it is simple to compute an update for the path length doglegs, including the sign. Each of the arcs may be updated in parallel, in contrast to the situation when the arc is used as a spectrometer, where sequential cresting of the energy must proceed from the lower energy arcs to the higher energy ones. Consequently, operational time for path length adjustment is decreased substantially. For the precision work that CEBAF will reach in the future, it will be necessary to understand the reasons for the degree level discrepancies between the two methods. When the causes are understood, the measurement noise should allow cresting of the higher pass beams to 0.05 degrees of RF phase. This is twenty-five microns in path length or

100 femtoseconds in time. In the far future, regulating the path length in a feedback arrangement is possible.

Calibration of the measurement will proceed in the same way as that it occurs for the CEBAF bunch length measuring system [1,2]. The phase shifter will be automatically varied until a maximum value is obtained for the first pass beam signal using a non-linear optimization routine. After recording the maximum voltage, the phase shifter will then be adjusted to the zero crossing of the phase detector where calibrated phase measurements may proceed. The calibration process takes under one minute.

V. CONCLUSIONS

A path length measurement and adjustment scheme has been installed and commissioned at CEBAF. The system is based on measuring the time of arrival of the individual microbunches by measuring the phase of a beam generated field in an RF cavity tuned to a longitudinal mode, and on changing the path length of the individual arcs with dogleg magnets. Experimentally, when the beam energy is crested out of each arc individually, the beam phase as measured by the phase detector is found to be the same as the first pass beam phase within a degree at 1497 MHz. The one degree discrepancies between the arrival time measurement method and the energy cresting measurements are not fully understood. However, the noise floor of the time of arrival method is considerably better than the energy cresting method, especially for the higher passes.

Already, the time of arrival method of setting the beam phase is preferred when large phase shifts are to be corrected, both because it is possible to locate the arc in error quickly, and because the arc acceptance usually limits the energy cresting method when large errors are to be corrected. When both methods of setting the path length are a bit better understood, it is anticipated that the time of arrival method of beam phase determination will become standard, as its noise characteristics are better, and because the measurement takes much less time than cresting the arcs individually. Also, this monitor has been extremely useful in providing a quick indicator of beam loss, when the phase detector is set to maximize output.

VI. REFERENCES

- [1] G. A. Krafft, "CEBAF Status", *Proc. of the 1994 Linac Conference*, pgs. 3-7
- [2] C. G. Yao, "A New Scheme for Measuring the Length of Very Short Bunches at CEBAF", *Proc. of the 1990 Beam Instrumentation Workshop*, AIP Conference Proceedings No. 229, pgs. 254-259
- [3] Y. Chao, *et al.*, "Commissioning and Operation Experience with the CEBAF Recirculation Arc Beam Transport System", *Proc. of the 1993 Particle Accelerator Conference*, pgs. 587-589

Simulations of the BNL/SLAC/UCLA 1.6 Cell Emittance Compensated Photocathode RF Gun Low Energy Beam Line*

D. T. PALMER, R. H. MILLER AND H. WINICK

Stanford Linear Accelerator Center

Stanford University, Stanford CA 94309

X.J. WANG, K. BATCHELOR, M. WOODLE AND I. BEN-ZVI

Brookhaven National Laboratory Accelerator Test Facility

Upton, NY 11973

Abstract

A dedicated low energy (2 to 10 MeV) experimental beam line is now under construction at Brookhaven National Laboratories Accelerator Test Facility (BNL/ATF) for photocathode RF gun testing and photoemission experiments. The design of the experimental line, using the 1.6 cell photocathode RF gun developed by the BNL/SLAC/UCLA RF gun collaboration is presented. Detailed beam dynamics simulations were performed for the 1.6 cell RF gun injector using a solenoidal emittance compensation technique. An experimental program for testing the 1.6 cell RF gun is presented. This program includes beam loading caused by dark current, higher order mode field measurements, integrated and slice emittance measurements using a pepper-pot and RF kicker cavity.

I. Introduction

To produce the high-brightness electron beams needed for short wavelength FEL's [1], a photocathode RF gun with emittance compensation [2] is required. A 1.6 cell photocathode RF gun capable of producing a normalized rms emittance of, $\epsilon_{n,rms} \approx 1 \pi \text{ mm mrad}$, has been designed by the BNL/SLAC/UCLA RF gun collaboration to minimize multipole modes [3]. Beam dynamics simulations of the gun, with emittance compensation, are presented with and without acceleration. These simulations are used to define the physics requirements of the low energy beam line being built at BNL/ATF. A schematic diagram of the low energy beam line is presented along with the planned program of experimental beam dynamics studies.

II. Emittance Compensation

In solenoidal magnetic emittance compensated systems, the electron bunch is usually accelerated up to large γ quickly to freeze in the $\epsilon_{n,rms}$. The new ATF low-energy experimental beam line employs only an RF gun with no linac to freeze in the $\epsilon_{n,rms}$ produced by the emittance compensation scheme. We have designed a low energy beam line to measure $\epsilon_{n,rms}$ over a continuous range of positions downstream of the gun where simulations show the electron bunch attains an emittance minimum, ϵ_{min} , for accelerating gradients ranging between 100 – 140 MV/m.

*Work supported by the Department of Energy, contracts DE-AC03-76SF00515 and DE-AC02-76CH00016

Total Charge	1 nC
Number of particles	10K
Cathode Spot Size	1 mm radius
Longitudinal Profile	Flat Top
Transverse Profile	Flat Top
Initial Cathode KE	.5 eV
Initial Thermal Emittance, ϵ_o	$0 \pi \text{ mm mrad}$
$E_{Full Cell}/E_{Half Cell}$	1.00
$E_o \text{ at Cathode}$	100-140 MV/m

Table I

Electron Bunch Parameters used in Parmela

Parameters from table I were used in PARMELA [4] simulations for section II-A and II-B. Instead of using Fourier coefficients for the RF field calculations in the gun region [5], all simulations for 1.6 cell gun were performed using a field map generated by SUPERFISH. We further improved the magnetic field accuracy of the solenoid magnets by using a field map from POISSON [6]. This improvement was made necessary since each of the two solenoidal magnets, that comprise a bucking pair, is made up of nine 1001 steel laminations with eight current coils sandwiched between them. The magnetic field calculated in parmela using coil cards is accurately represented.

All simulations assume both the electron beam and RF fields are cylindrical symmetric. Space charge was included in all parmela simulations. The thermal emittance, ϵ_o , was not considered in these simulations. The total emittance $\epsilon_{n,rms}$ can be expressed as [7],

$$\sqrt{(\epsilon_{parmela}^2 + \epsilon_o^2 + \epsilon_{mp}^2)} \leq \epsilon_{n,rms} \leq (\epsilon_{parmela} + \epsilon_o + \epsilon_{mp})$$

where ϵ_{mp} is emittance growth due to the multi-pole fields and ϵ_o is the initial transverse emittance of the beam as it is produced off the cathode.

In the following subsections the emittance compensated photocathode RF injector performance with and without accelerating sections are discussed. The former case has application to the proposed RF photocathode gun test stand at SSRL, the DUV-FEL or ATF linac at BNL while the later case is for the low energy beam line at BNL/ATF.

A. With Acceleration

As part of the 1.6 cell photocathode RF gun development program a detailed design study of an 1.6 cell RF gun emittance compensated injector was conducted. The starting point for our simulations is the physical layout of the ATF in-line injector.

The parameter space that an in-line RF gun operates in is multi-dimensional. Examples of accelerator section parameters are cathode to input coupler distance, accelerating gradient, and input coupler RF phase. The emittance compensation magnetic parameters are magnet field strength, $\frac{\partial B_x}{\partial z}$ and the location of B_{max} . Electron bunch and gun parameters used in these simulations are found in table I. It should be noted that the laser injection phase was set to maximize the electron bunch energy on the output of the gun, which also minimizes the energy spread to 1%. Figure 1 is a plot of $\epsilon_{n,rms}$ versus z for an optimized parameter set. A halo is developed around the core of the bunch, in which 2% of the particles contributes 15% of the $\epsilon_{n,rms}$.

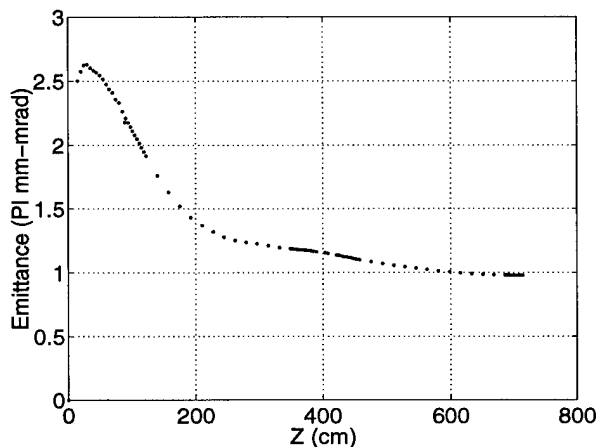


Figure 1. Parmela Simulations of Emittance Compensation with Acceleration

B. Without Acceleration

The initial testing of the BNL/SLAC/UCLA 1.6 Cell Emittance Compensated Photocathode RF Gun will be conducted on the Low Energy Beam Line at the ATF. Figure 2 is a representative plot of $\epsilon_{n,rms}$ versus z for an accelerating gradient of 100 MeV/m. An important features that stands out are the two local minima in the emittance. A possible cause of the double local minima is dissimilar space charge forces in the core and tails of the beam. This would cause different slices of the beam to be compensated for at different locations down the beam line. Simulations are on underway to understand this phenomenon.

III. The ATF Low Energy Experimental Beam Line and Experimental Characterization of the RF Gun

Figure 3 is the schematic diagram of the ATF low energy experimental beam line. The main components of the experimental beam line are the 1.6 cell photocathode RF gun and a pair of bucking solenoidal magnets. These are followed by a S-band RF kicker cavity operating at TM_{120} mode and a X-axis transla-

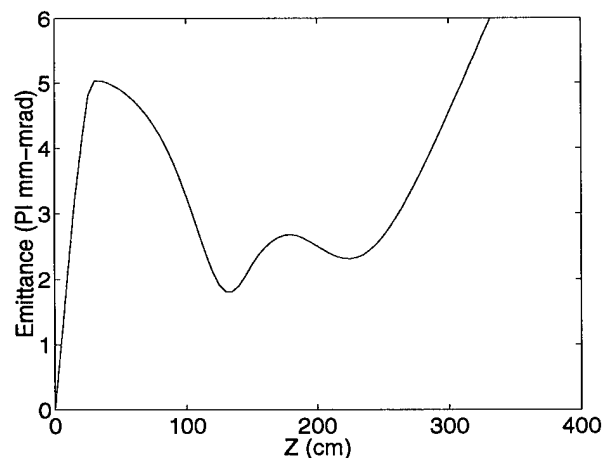


Figure 2. Parmela Simulations of Emittance Compensation without Acceleration

tional achromate which consist of two 90° sector magnets and a quadrupole triplet.

The nominal operating field for the 1.6 cell RF gun is 100 MV/m, therefore a significant amount of field emission current (dark current) will be present. This dark current causes beam loading in the RF gun. The beam loading effect will be experimentally studied using a six-pot reflectometer [8] located in the waveguide feeding the 1.6 cell RF gun.

The diagnostic devices installed on the low energy beam line consists of a RF kicker cavity, energy spectrometer, beam profile monitors and pepper-pots. The pepper-pot located in-line with the gun will be mounted on a z -translation stage, which will allow the mapping of the integrated $\epsilon_{n,rms}(z)$, with a z range of 100 cm.

When the RF kicker is used in conjunction with the z -translation pepper-pot, slice emittance studies of the double local minima seen in figure 2 can be conducted. This will allow full reconstruction of the transverse phase space of the beam along the electron bunch. The RF kicker and beam profile monitor will also be used for electron bunch length measurements.

The major improvement of the 1.6 cell gun over the original BNL 1.5 cell gun [9] is the elimination of all field asymmetries in the gun cavity. The manifestation of a field asymmetry is the presence of multi-pole spatial modes in the RF gun. Experimental measurements of the dipole and quadrupole modes will accomplished by shaping the laser profile on the cathode [10] and observing the transverse electron bunch profile down stream of the gun, as illustrated in figure 4.

The aperture of the 1.6 cell RF gun was increased by 0.5 cm to increase the cell to cell coupling. A secondary benefit is that larger aspect ratio beams can be transported thru the RF gun. Removal of the emittance compensation solenoids and installation of a quadrupole triplet will be accomplished after cylindrical symmetric emittance compensation studies are completed. This will facility flat beam experimental studies, which have applications to XLC type RF gun designs [11].

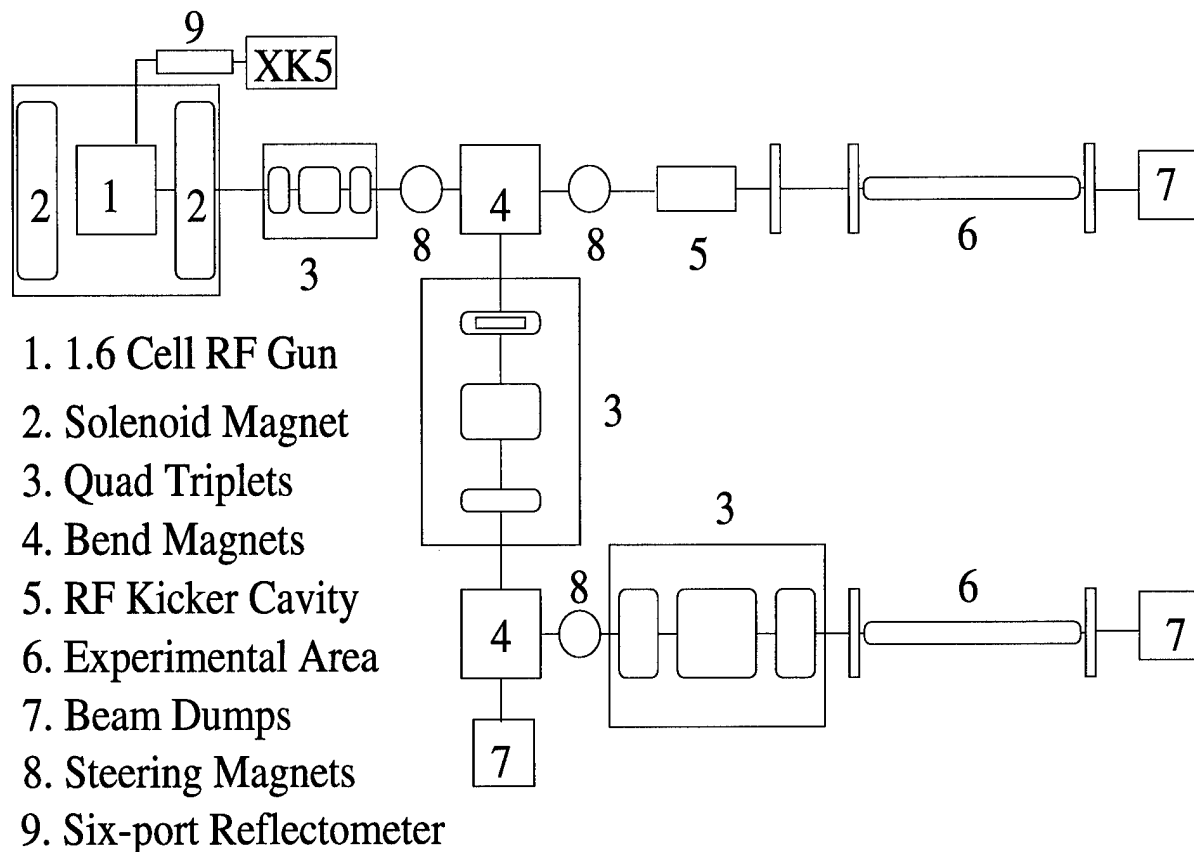


Figure 3. Low Energy Beam Line Design

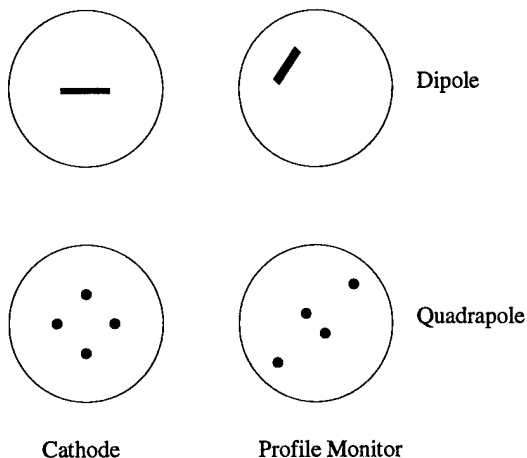


Figure 4. Dipole and Quadrupole Field Effects

IV. Conclusions

An emittance compensated photo-injector based on the BNL/SLAC/UCLA 1.6 cell photocathode RF gun is capable of producing $\epsilon_{n,rms} \approx 1 \pi mm mrad$ with a peak current of 100 Amps. We have outlined an experimental program to test the 1.6 cell RF gun at the ATF low energy experimental beam line. Beam loading will be studied using a six-port reflectometer. Integrated and slice emittance measurements will enable us directly study the emittance compensation process. The z translation stage pepper-pot will allow mapping of $\epsilon_{n,rms}(z)$. Using

the kicker cavity in conjunction with the z -translation pepper-pot will allow for the study of the double local minima in figure 2, which will increase our understanding of the emittance compensation process.

References

- [1] H. Winick *et al.*, *NIM*, **A347**, 199-205 (1994)
- [2] B. E. Carlsten, *NIM*, **bf A285**, 313 (1989)
- [3] D. T. Palmer *et al.*, these proceedings
- [4] L. M. Young, private communications
- [5] J. C. Gallardo and H. Kirk, *Proceeding PAC93*, 3615-3617 (1993)
- [6] K. Halbach and R. F. Holsinger, *Particle Accelerators*, **7**, 213 (1976)
- [7] K. J. Kim, *NIM*, **A275**, 201-218 (1989)
- [8] C. M. Fortgang *et al.*, *Rev. Sci. Instrum.*, **Vol. 61, No. 11**, 3405 (November 1990)
- [9] K. Batchelor *et al.*, *Proc. of 1990 EPAC* 541 - 543
- [10] Z. Li, private communications
- [11] X. J. Wang *et al.*, *RF Gun Studies*, CAP-ATF-TECH #11, 1991

SMALL-GAP UNDULATOR EXPERIMENT ON THE NSLS X-RAY RING

P.M. Stefan, S. Krinsky, G. Rakowsky and L. Solomon

NSLS-Brookhaven National Laboratory, P.O. Box 5000, Upton, NY 11973-5000

ABSTRACT

We report results of an on-going experiment being carried out in the X13 straight section of the NSLS X-ray Ring which explores the limits of the operation of small-gap undulators. In particular, we discuss measurements of stored electron beam lifetime as a function of the vertical aperture presented by a 4-jaw scraper or a variable-aperture vacuum vessel. At an electron beam current of 300 mA the variable-aperture vacuum chamber was closed to an inner aperture of 3.8 mm with no effect on the electron beam lifetime. Measurements of the output radiation spectrum of a 16 mm period undulator at a magnet gap of 7.5 mm are also described.

I. INTRODUCTION

The limits of operation of small-gap, short-period undulators are being explored in the X13 low- β straight section of the NSLS X-ray Ring. Measurements of stored electron beam lifetime as a function of vertical aperture were made using both a 4-jaw scraper assembly and the variable-aperture vacuum vessel of the NSLS Prototype Small-Gap Undulator (PSGU). Some potential limitations on the electron beam aperture, and hence the undulator gap, are Coulomb scattering lifetime, transverse impedance of the vacuum chamber, vacuum pressure in the low-conductance region of the small aperture chamber, and possible ion trapping in this region.

II. STUDIES OF BEAM LIFETIME VS. ELECTRON BEAM APERTURE

A. 4-jaw Scraper:

While design and fabrication of the variable-aperture vacuum chamber were in progress, an existing 4-jaw scraper assembly was refurbished and installed in the X13 straight section of the X-ray Ring. The vertical blades of the scraper were located about 150 mm upstream of the X13 straight section centerline ($\beta_y=0.4\text{m}$). The 4 scraper blades (2 horizontal, 2 vertical) were each 5 mm thick of uncooled copper and each was individually-controlled. Only a single blade was used at a time. Data were taken by moving one blade of the scraper in small steps and measuring the beam lifetime which resulted. Lifetimes were calculated by the change in amplitude of a stripline sum signal over time, which was monitored at 53 MHz using a spectrum analyzer.

Fig. 1 presents results taken using both the upper and lower scraper blades. The initial stored beam was 21 mA at 2.584 GeV, in 25 bunches and used the conventional vertical-beam-size optics

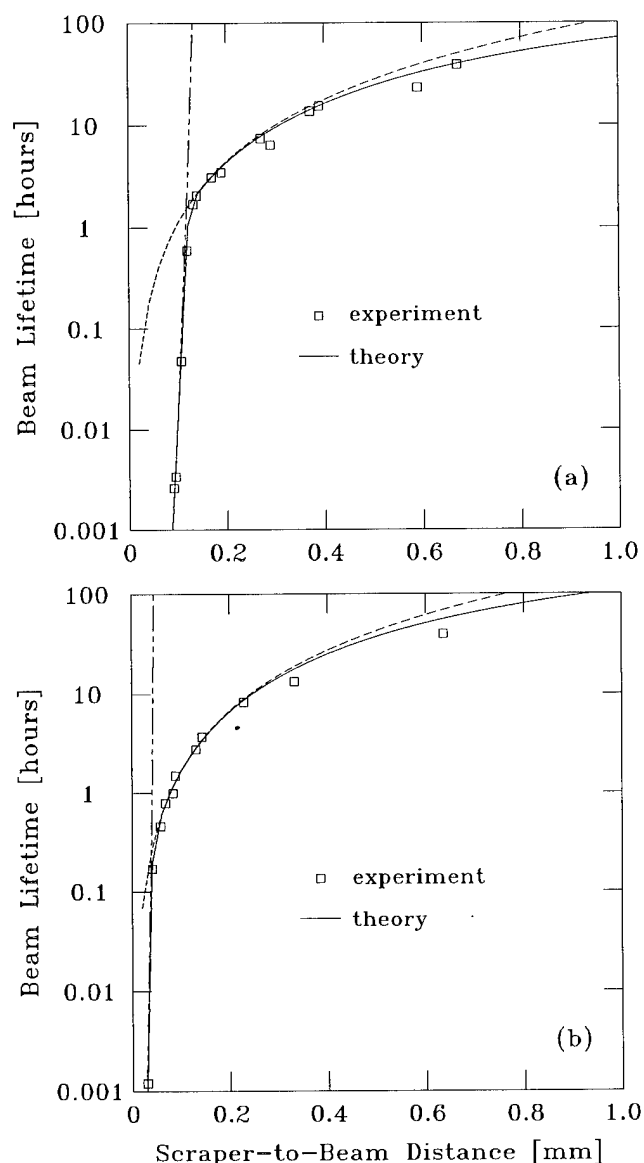


Figure 1: Vertical scraper results at low current: 21mA at 2.584 GeV. Two components of the theory curve are also illustrated, the quantum lifetime (section line) and the nuclear Coulomb scattering lifetime for the vertical (dashed line). (a) $\sigma_y=20 \mu\text{m}$; (b) $\sigma_y=7 \mu\text{m}$.

(a) and the small beam size optics (b) [1]. The theory curve [2] contains four contributions: the quantum lifetime, the nuclear Coulomb scattering lifetime for both horizontal and vertical apertures, and the nuclear bremsstrahlung lifetime. Of these, only the quantum and the vertical Coulomb components depend on the vertical beam aperture, and are illustrated in the figure using the section line and dashed line, respectively. One observes that Coulomb scattering dominates at longer lifetimes, but short

lifetimes are dominated by the quantum lifetime. The theoretical curve was fit to the data using a number of adjustable parameters. The experimental points from the upper blade were offset along the abscissa by a constant [(a) 130 μ m; (b) 185 μ m] due to the lack of absolute position calibration of the scraper blades, while the points taken using the lower blade were reflected about the origin and offset as a group to overlay the other points. The storage ring pressure was adjusted in the formulas for best fit where the vertical Coulomb scattering dominates [(a) 0.23 n torr; (b) 0.15 n torr], and the vertical beam size was similarly adjusted for best fit for lifetimes below 1 hour [(a) $\sigma_y = 20\mu$ m; (b) $\sigma_y = 7\mu$ m]. Of these adjustable parameters, the resulting ring pressure seems somewhat too low, but the other parameters seem reasonable. These results, together with other data taken at low current and high current, suggest that the full ring lifetime is attained at a full aperture of about 2 mm. This result is about half the minimum aperture expected from scaling the aperture at the β -max by the square-root of the beta function, and suggests the possibility that the PSGU might operate down to a 2.5mm aperture without lifetime degradation.

B. PSGU Variable-Aperture Vacuum Chamber

The NSLS Prototype Small-Gap Undulator is comprised of three major components: a variable-aperture vacuum chamber with drive system, a pure-permanent-magnet small-period undulator with an independent drive system, and an elevator base stage upon which all of the above components are supported. The design concept of the variable-aperture chamber has been described elsewhere [3], and is summarized in Fig. 2.

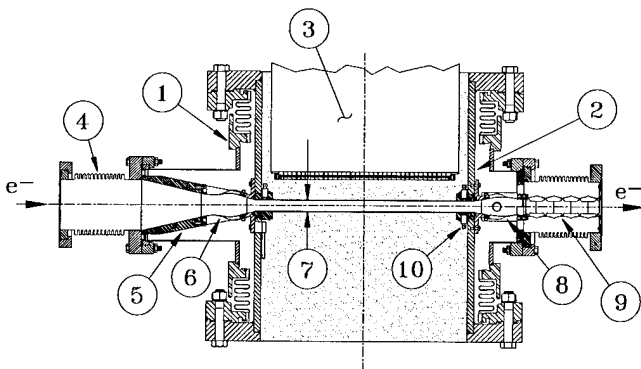


Figure 2: Elevation cross section of the variable-aperture vacuum chamber, with the electron beam in the plane of the page. See text for detailed description.

The figure presents an elevation cross section of the vacuum chamber, with the electron beam contained in the plane of the page. Deep wells, from the top and bottom flanges, extend towards the stored beam and can be moved closer together or farther apart by means of top and bottom bellows. The central section of the chamber(1), between the bellows, is fastened through legs to the elevator base stage below. Actuators attached between the two flanges control the electron beam aperture. The portions of the

wells near the stored beam(7) are thinned to 1 mm, and the magnet arrays of the undulator(3) are inserted into the wells, up near the thinned region. The chamber(1) is cylindrical, about 460 mm in diameter, with its axis oriented vertically. For these experiments, the electron beam aperture (7) could vary between 14 mm and 3.8 mm, and the minimum-aperture region is 104 mm wide and 390 mm long. PSGU is located in the X13 straight section of the NSLS X-ray Ring, with the axis of the vacuum chamber(1) 15 mm downstream of the straight centerline.

Further details of the vacuum vessel are also shown in Fig. 2. The beam enters the minimum-aperture region through an 89 mm diameter hydroformed-type bellows(4), a solid round-to-rectangular transition(5), and a set of flexible sheet-metal transitions(6). It exits through a similar sheet-metal transition(8), followed by a rectangular sheet-metal bellows liner(9). The vertical location of the electron beam within the minimum aperture is detected using pairs of pick-up electrodes(10) located at the upstream and downstream ends of the movable wells.

The implications of the 4-jaw scraper results were verified with the PSGU variable-gap vacuum chamber. When centered on the electron beam and closed to the minimum aperture of 3.8 mm, no change in the storage ring lifetime was observed. This was true not only for low beam currents, but also for 300 mA at 2.584 GeV, which is above the limits for present normal operations. No instability from vacuum chamber impedance was observed, confirming expectations from theory [4] and impedance measurements [5].

To reduce the electron beam aperture below 3.8 mm, the small-aperture region was offset from its initial position (centered on the electron beam) by use of the elevator base stage. The results appear in Fig. 3. The stored beam conditions were essentially the

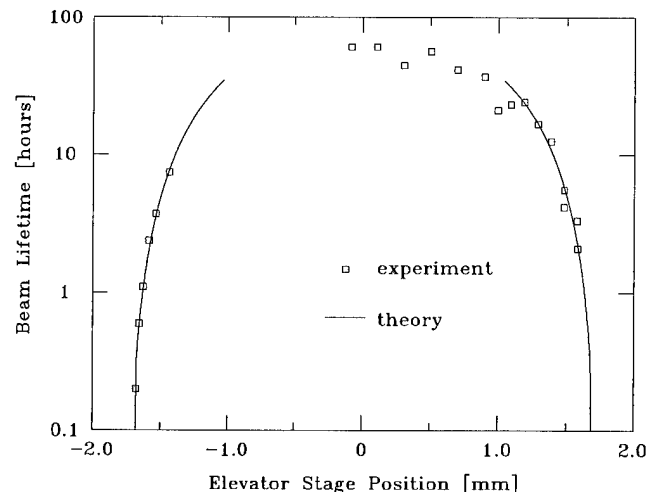


Figure 3: Results of vertical translation of the 3.8 mm minimum-aperture region. These results suggest that a minimum full aperture of 2 to 3 mm might be used without lifetime degradation.

same as for the scraper results presented in Fig. 1b, and utilized the small-vertical-beam-size optics [1]. The theory curve was

generated as in the previous case, but offset to match the data, and reflected about the 0 mm position. The adjustable parameters required were 0.3 ntorr for the pressure and $\sigma_y = 8.5 \mu\text{m}$. The quantum lifetime dominates the theory curve for lifetimes below 0.1 hours; otherwise, the Coulomb scattering lifetime is dominant. The lifetime with the aperture centered on the electron beam was about 61 hours, as can be seen from Fig. 3. It is seen that the aperture can be offset by more than 0.5 mm before there is any lifetime degradation, suggesting that a full aperture of between 2.8 mm and about 1.8 mm may be imposed with long lifetimes. This strongly motivated a re-work of the vacuum chamber to achieve reduced apertures while centered on the electron beam.

III. MEASUREMENT OF UNDULATOR RADIATION

Following installation of the PSGU magnet and drive system, the X13 beamline was modified and a simple single-crystal x-ray spectrometer was installed to measure the radiation spectrum. The result [6] appears in Fig. 4.

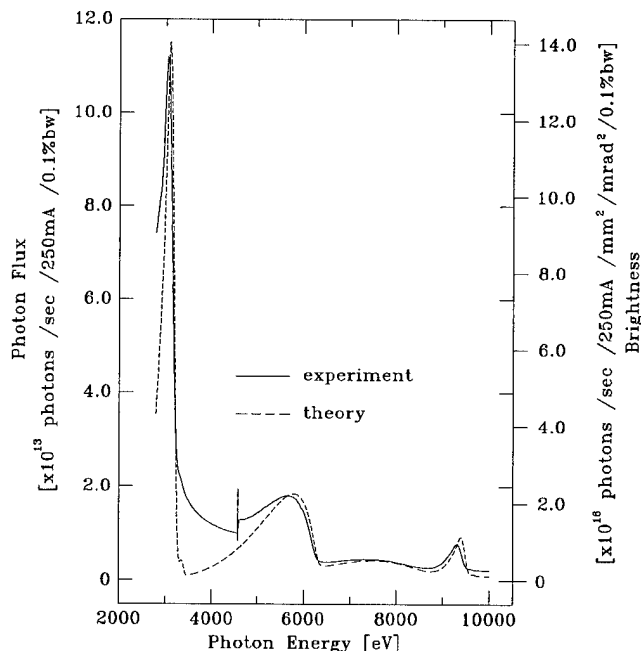


Figure 4: Spectrum measured for the 16 mm period undulator at a magnet gap of 7.5 mm, $K = 0.716$, at 2.584 GeV, 26 mA, with a minimum aperture of 3.8 mm. The theory curve was obtained using the URGENT [7] code.

The beam current was kept low to prevent overheating of the beamline Be window. The theory curve was obtained from the URGENT code [7], by specifying the basic undulator and storage ring parameters, the undulator K-parameter, and the location and size of the spectrometer slit. The processing of the experimental data involved almost no adjustable parameters. The absorption of the Be window and of the spectrometer gas (either He or N_2) was

removed, and the absolute efficiency of the ion chamber was calculated using absorption coefficients and the chamber dimensions. Finally, the bandwidth of the Si(III) analyzer was included. There was a significant scattered background from the analyzer crystal in the detected signal, especially in the case with He gas. In the He data, a constant background was subtracted to bring the lowest part of the curve back to zero. In Fig. 4, the short vertical line in the experiment curve at about 4.6 KeV is the splice point between the data taken with He gas (to lower energies) and that taken with N_2 gas (higher energies). Good agreement is seen between the theory and the experimental results.

IV. CONCLUDING REMARKS

We have successfully operated a small-gap undulator with a full vertical electron beam aperture of only 3.8mm, with no degradation of beam lifetime. Measurements carried out using the elevator stage strongly suggest that successful operation will be possible for a vertical beam aperture less than 3mm. In order to verify this, we have re-worked the PSGU vacuum chamber to permit a minimum aperture of 1 mm. Following the re-installation of the system in May 1995, we believe we will be able to achieve the design goal of a 6 mm magnet gap.

V. ACKNOWLEDGEMENT

We have benefited from discussions with E. Hoyer, J. Hastings, J. Galayda, H.C. Hseuh, G. Decker and E. Blum, and the contributions of D. Lynch, S. Hanna, J. Aloia, C. Stelmach, M. Radulescu, R. Freudenberg, D. Klein, C. Nielson, J. Dabrowski, L.E. Berman and D.P. Siddons. Work performed under the auspices of U.S. Department of Energy, under Contract DE-AC02-76CH00016.

VI. REFERENCES

- [1] J. Safranek and S. Krinsky, Proc. 1993 IEEE Part. Accel. Conf., Washington, DC, (1993), p. 1491.
- [2] Our analysis benefits from earlier work of G. Decker, unpublished, who used the scraper when it was located at a position where $\beta_y = 7\text{m}$.
- [3] P.M. Stefan, L. Solomon, S. Krinsky and G. Rakowsky, Proc. 1991 IEEE Part. Accel. Conf., San Francisco, CA, (1991) p. 1096.
- [4] K. Bane and S. Krinsky, Proc. 1993 IEEE Part. Accel. Conf., Washington, DC., (1993), p. 3375.
- [5] S. Hanna and P. Stefan, unpublished.
- [6] P.M. Stefan, S. Krinsky, G. Rakowsky and L. Solomon, in "A Festschrift in Honor of Klaus Halbach", LBL PUB-754, p. 161.
- [7] R.P. Walker and B. Diviacco, Rev. Sci. Instrum., 63(1), 392, (1992).

Measurements of Longitudinal Dynamics in the SLC Damping Rings*

R.L. Holtzapple, R.H. Siemann, and C. Simopoulos

Stanford Linear Accelerator Center, Stanford University, Stanford, CA 94309 USA

I. Abstract

Measurements of longitudinal beam properties in the Stanford Linear Collider (SLC) damping rings have been made using a Hamamatsu, model N3373-02, 500-femtosecond streak camera[1]. The dependence of bunch length on current and accelerating RF voltage was measured. The energy spread dependence of current was also measured. The turbulent instability threshold for the SLC damping ring is at the current of $I=1.5-2.0 \times 10^{10}$ particles per bunch.

II. Data Analysis and Systematic Errors

The measurements were performed on either the SLC electron or positron damping ring when the opportunities for beam time became available. We are not aware of any differences in the performance of these rings that would affect the results.

The streak camera uses synchrotron light produced in a bend magnet to determine the longitudinal bunch distribution. The light optics is described in reference 2. Longitudinal profiles of the beam distribution are fitted to an asymmetric Gaussian function given by

$$I(z) = I_0 + I_1 \exp \left\{ -\frac{1}{2} \left(\frac{(z - \bar{z})}{(1 + \text{sgn}(z - \bar{z})A)\sigma} \right)^2 \right\}$$

where I_0 =pedestal, I_1 =peak of the asymmetric Gaussian. The term $\text{sgn}(z - \bar{z})A$ is the asymmetry factor which parameterizes the shape of the asymmetric Gaussian. A chi-square minimization is performed on each streak camera picture.

The systematic errors addressed using the streak camera are: 1) dispersion in the light optics, 2) the slit width of the camera, and 3) the space charge effect at the photo cathode.

Dispersion in the glass elements of the optics can be minimized by using a narrow band interference filter. The peak spectral response of the streak camera is 500nm, and the interference filter used is centered at 500nm with a 40nm full width half maximum acceptance.

The slit width contributes to the resolution of the streak camera, by choosing 200 μ m or less this contribution is negligible.

To eliminate the intensity effects on the photo cathode, the multichannel plate gain was set to its maximum setting

* Work supported by Department of Energy
contract DE-AC03-76SF00515

and the incident light was filtered until the bunch length measurement was stable over a range of light intensities. Figure 1 exhibits the intensity effects on bunch length measurement and in this example the light is filtered by 50% to eliminate this effect.

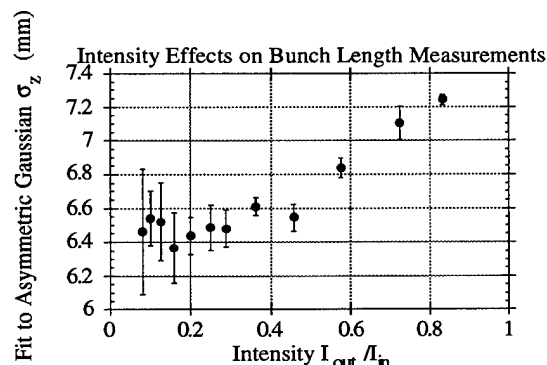


Figure 1. The bunch length dependence on light intensity measured at the damping ring with a current of $I=3.6 \times 10^{10}$.

In addition, beam related background light is detrimental to the signal to noise ratio of the streak camera. A light chopper, triggered on the same beam pulse as the streak camera, is used to reduce the background to acceptable levels.

III. Single Particle Properties

A number of beam properties depend on single particle behavior. They are calculable and can be used to validate the potential of the camera. They are: 1) the longitudinal damping time, 2) the dependence of bunch length on gap voltage, and 3) the synchrotron period.

The longitudinal emittance in the damping ring damps exponentially. The bunch length versus time elapsed since injection can be used to determine the longitudinal damping time. After the beam is injected the streak camera is triggered on damping ring turn 5000 where ten measurements of the bunch length are made. Each subsequent 1000 turns the measurement is repeated until the bunch length is fully damped. The mean bunch length is computed for each time setting, and the data was fit to the function

$$\sigma^2(t) = \sigma_{eq}^2 + \exp \left(-\frac{2t}{\tau_\delta} \right) (\sigma_{inj}^2 - \sigma_{eq}^2)$$

where the points are weighted by the root mean error squared. The fitting parameters are σ_{eq} the equilibrium bunch length, σ_{inj} the injected bunch length, and the

longitudinal damping time τ_δ . The measured damping time for the positron damping ring is $\tau_\delta = 1.87 \pm 0.13$ msec.

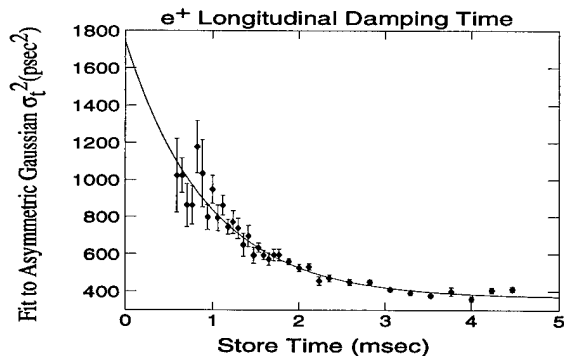


Figure 2. The longitudinal damping time in the damping ring. The solid line is a fit to the data.

The theoretical longitudinal damping time can be calculated by knowing the beam energy and magnetic field strengths of the magnets. The calculated value is $\tau_\delta = 1.79$ msec[3] which is in agreement with the measured value.

The equilibrium (low current) bunch length in a storage ring is inversely proportional to the square root of the RF accelerating gap voltage.

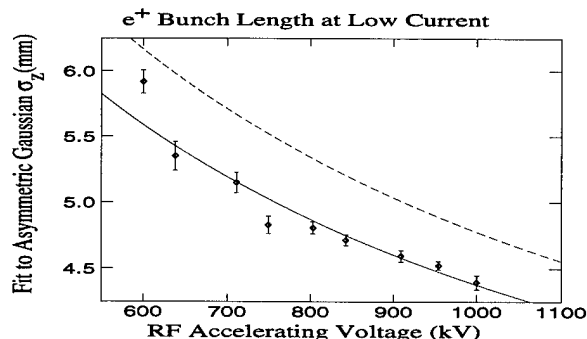


Figure 3. The equilibrium bunch length dependence on RF accelerating voltage for the damping ring at a low current of $I = 0.6 \times 10^{10}$.

Twenty-five streak camera pictures were taken at each RF accelerating voltage. The mean and root mean error were calculated at each RF voltage setting. Fitting the data to the function $\sigma_z = A(V_{RF})^m$ gives a value of $m = -0.48 \pm 0.03$ which is in good agreement with the expected value. In figure 3 the solid line is the fit to the data and the dashed line is the expected curve based on damping ring accelerator parameters.

After injection, the bunch length oscillates in size, and fitting the bunch length to the function

$$\sigma(t) = \sigma_0 + B \sin(\Omega t + \phi_0)$$

the synchrotron period $T_s = \frac{4\pi}{\Omega}$ can be determined. The time scale of longitudinal damping and filamentation is much longer than the 400 damping ring turns over which the measurement was performed, so they can be ignored.

The bunch length is measured 3 times every 10 turns starting at injection. The fit to the data is the solid line in figure 4. The measured synchrotron period is $T_s = 9.835 \pm 0.012$ μ sec which agrees with the expected value of $T_s = 9.834$ μ sec.

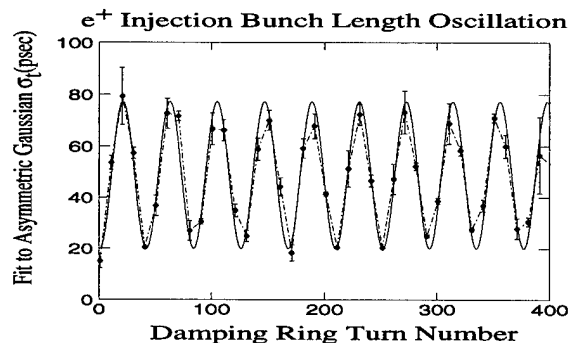


Figure 4. The bunch length oscillation in the damping ring as a function of damping ring turn number for the first 400 damping ring turns.

These results prove the usefulness of the streak camera for measuring longitudinal properties of the damping ring beam.

IV. High Current Measurements

The energy spread was measured as a function of current using a wire scanner in the transport line of the extracted beam. Given the dispersion, emittance, and beta function at the wire scanner the energy spread can be calculated from

$$\frac{\sigma_E}{E} = \frac{1}{\eta_x} \sqrt{\sigma_{xwire}^2 - \beta_x \epsilon_x}$$

where $\eta_x = -0.5667$ m, $\beta_x = 5.41$ m, $\gamma \epsilon_x = 4 \times 10^{-5}$ m rad, and the energy is $E = 1.19$ GeV.

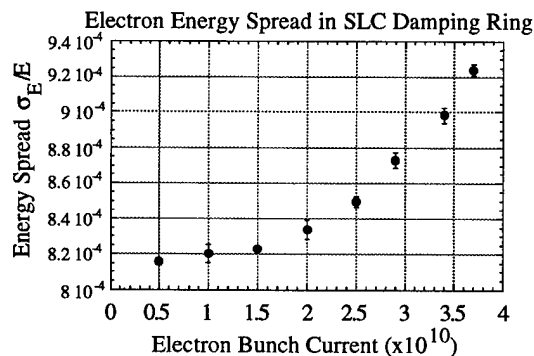


Figure 5. The energy spread as a function of current for the electron damping ring with $V_{RF} = 945$ kV.

The measurement shows an increase in energy spread (fig. 5) at a current of $I=1.5-2.0 \times 10^{10}$. This is due to the onset of a turbulent instability.

At high current the bunch length dependence on RF accelerating voltage changed due to the potential well distortion and the turbulent instability. Repeating the bunch length versus RF accelerating voltage experiment at high current and fitting the data (fig. 6) to the function $\sigma_z = A(V_{RF})^m$ gives the value of $m = -0.25 \pm 0.02$.

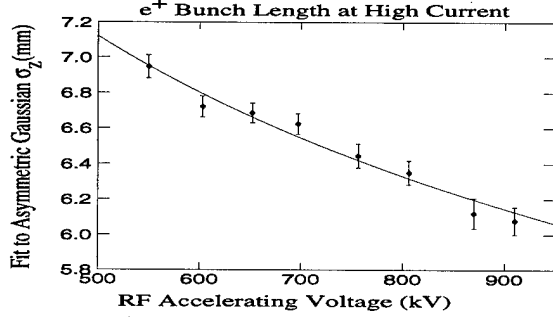


Figure 6. The bunch length dependence on RF accelerating voltage in the damping ring at a current at $I=3.3 \times 10^{10}$.

The bunch length increases and the distribution changes as the current increases. This is shown in figure 7.

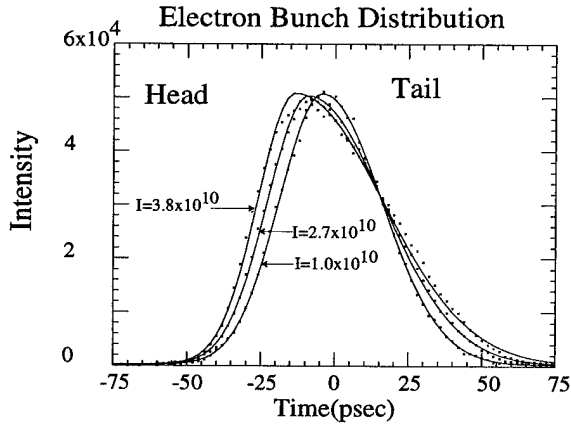


Figure 7. The bunch distribution for different currents (1.0 , 2.7 , and 3.8×10^{10}) in the damping rings. The plots are a sum of 25 pictures superimposed with the mean of the distributions shifted to a common origin.

Bunch length results are presented in figure 8. There is significant bunch lengthening due to potential well distortion below the turbulent threshold current of $1.5-2 \times 10^{10}$. This bunch lengthening continues above threshold

The asymmetry factor in the fitting function measures the departure from a Gaussian. Results are presented in figure 9. There is some asymmetry at low current that increases steadily due to potential well distortion. The bunch is highly asymmetric in the turbulent regime, but the dependence on current is not as strong.

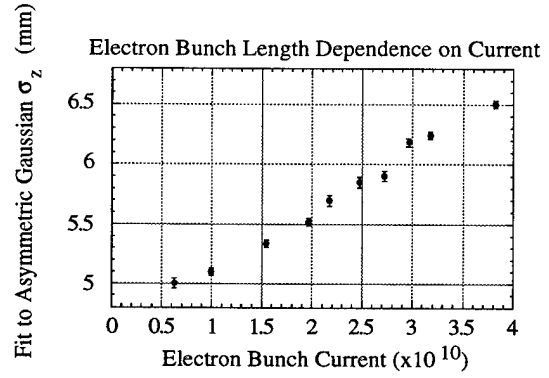


Figure 8. The bunch length dependence on current in the damping ring with $V_{RF} = 820$ kV.

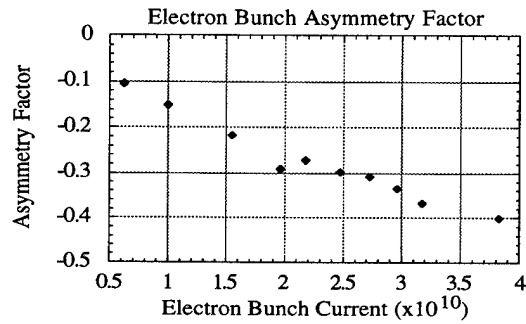


Figure 9. The asymmetry factor as function of current.

V. Conclusion

The longitudinal damping time and synchrotron tune measurement are in excellent agreement with theoretical calculations for damping rings.

The measurements of bunch length versus intensity and gap voltage provide a basis for testing our understanding of the damping ring impedance. These measurements combined with our knowledge of the impedance and other studies of the damping ring behavior serve as a guideline for the design of next generation damping rings.

The authors would like to thank K. Bane, F-J. Decker, P. Krejcik, M. Minty, M. Ross, and J. Spencer for valuable discussions and helpful suggestions

VI. REFERENCES

- [1] Hamamatsu Photonic Systems Corp., 360 Foothill Rd., Bridgewater, NJ 08807-6910.
- [2] C. Simopoulos, R.L. Holtzapple, "Damping Rate Measurements in the SLC Damping Rings", SLAC-PUB-95-6813, 1995.
- [3] R. Early et al., "Proposed Emittance Upgrade for the SLC Damping Rings", SLAC-PUB-6559, 1994.

Single Bunch Collective Effects in the ALS*

J. M. Byrd, J. N. Corlett, and T. Renner
Lawrence Berkeley Laboratory
Berkeley, CA 94720 USA

Abstract

We present a summary of measurements of single bunch collective effects in the Advanced Light Source (ALS). These effects include bunch lengthening, energy spread increase, HOM loss measurements, head-tail damping rates, current dependent tune shifts, and transverse mode coupling instability threshold. The longitudinal measurements are consistent with a broadband impedance $|Z_{||}/n|_{eff} = 0.22 \pm 0.07 \Omega$ and transverse measurements indicate broadband impedances of $Z_{y,eff} = 155 k\Omega/m$ and $Z_{x,eff} = 58 k\Omega/m$.

I. Introduction

The ALS is a 1.5-1.9 GeV electron storage ring optimized for producing high brightness synchrotron radiation. General parameters are given in Table I.

Collective effects in a storage ring describe the interaction of the beam with the surrounding vacuum chamber via the electromagnetic wakefields of the beam. Single bunch effects are generated by wakefields which persist over the length of bunch but generally decay before arrival of the next bunch. In the frequency domain, these wakefields are referred to as the broadband impedance. Bench impedance measurements of ALS vacuum chamber components have been conducted and are described elsewhere [1], [2]. Other collective effects in the ALS are described elsewhere [3], [4].

Single bunch currents up to 70 mA have been stored in the ALS, despite onset of the mode coupling instability (MCI) threshold in the vertical plane at ~28-30 mA. The vacuum chamber in one of the undulator straight sections was modified in December 1994, reducing the full height from 18 to 10 mm. Following this modification, the single bunch current was limited to 28 mA, probably because the reduced vertical aperture no longer contained the beam at the onset of the vertical MCI.

II. Longitudinal Measurements

A. Bunch Length and Energy Spread

Changes in the natural bunch length can typically be attributed to a combination of potential well distortion and the microwave instability (MWI). The former yields an increase or decrease in the bunch length and the latter an increase in the energy spread with a corresponding increase in the bunch length. The measurements shown below indicate that bunch lengthening in the ALS is dominated by growth of the energy spread via the MWI.

We used a technique for estimating the bunch length from the broadband frequency spectrum of a single button BPM which

Parameter	Description	Value
E	Beam energy	1.5 GeV
C	Circumference	196.8 m
f_{rf}	RF Freq.	499.654 MHz
σ_e	RMS $\delta E/E$	$7.1e-4$
h	Harmonic Number	328
I_0	Bunch current	1-2 mA
α	momentum compaction	$1.594e-3$
Q_s	Synchrotron tune	0.006
σ_t	RMS natural bunch length	5-10 mm
$Q_{x,y}$	Betatron tunes (x,y)	14.28, 8.18

Table I
Nominal ALS parameters.

was designed to have a broadband response. Although it is very difficult to make an absolute measurement of the bunch length or longitudinal bunch distribution using this technique because the detailed response of the pickup/cable is unknown, one can make good measurements of the relative change in bunch length assuming that the longitudinal distribution remains Gaussian and that the bunch length is known at some current. In this case, the ratio of the bunch spectra is given by

$$ratio = \frac{S_2(\omega)}{S_1(\omega)} \propto e^{-\omega^2(\sigma_2^2 - \sigma_1^2)} \quad (1)$$

where $S(\omega)$ is the signal as a function of frequency observed on the spectrum analyzer.

We assumed that the bunch length at low currents (<1 mA) was given by the natural bunch length and extracted the bunch length by fitting the ratio of the bunch spectra out to ~6-7 GHz. Recently, a fast photodiode has become available and is beginning to be used for bunch length measurements. It shows good agreement with the bunch spectrum technique. Results of bunch length measurements for $E = 1.52$ GeV and $Q_s = 0.0075$ are shown in Figure 1. Fitting the data to a power law yields

$$\sigma_t(cm) = (0.36 \pm 0.03) I_b(mA)^{(0.33 \pm 0.02)} \quad (2)$$

Changes in the energy spread were extracted from measurements of the transverse beam profile at a point of dispersion in the lattice. The transverse profile is measured from synchrotron light in the UV range illuminating a BGO crystal. A video image of the profile is fit to a Gaussian. The dispersion was measured at the source point and the beta functions at the source point were extrapolated from measured values at nearby quadrupoles. The energy spread data is shown in Figure 2. Although an increase in the energy spread vs. current is apparent, there is no clear threshold visible.

*This work was supported by the Director, Office of Energy Research, Office of Basic Energy Sciences, Materials Sciences Division, of the U.S. Department of Energy under Contract No. DE-AC03-76SF00098.

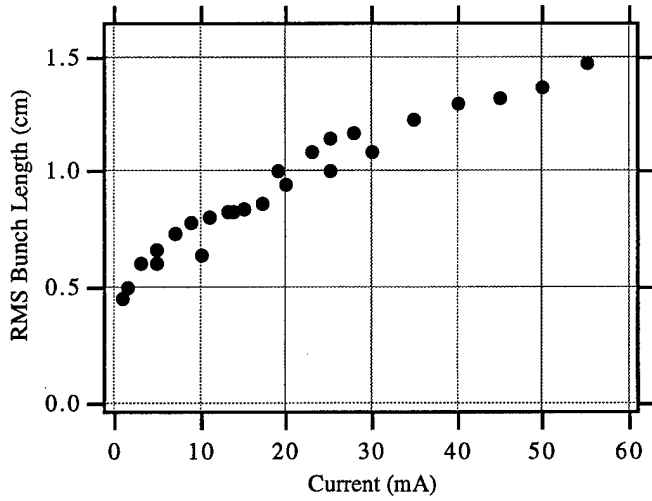


Figure 1. Measured RMS bunch length vs current for $E = 1.52$ GeV and $Q_s = 0.0075$.

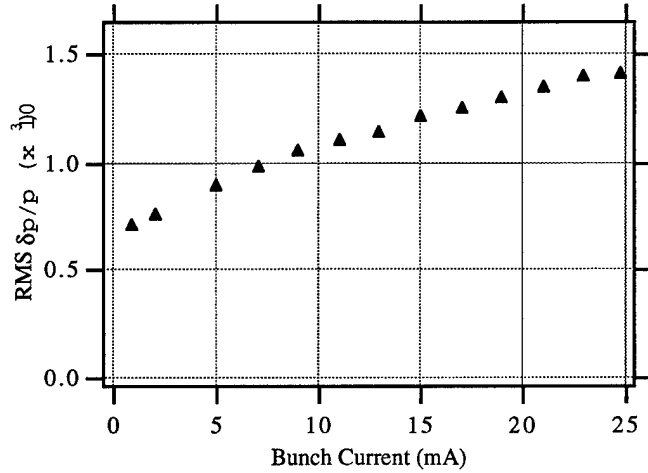


Figure 2. Measured RMS energy spread vs current extracted from a transverse profile monitor.

The increase in the energy spread indicates that the bunch lengthening is at least partially due to the MWI. Assuming that the bunch length changes due to potential well distortion are negligible, the bunch length above threshold as a function of current is given by

$$\sigma_l^3 = \frac{\alpha R^3}{2\pi(E/e)Q_s^2} \left| \frac{Z_{||}}{n} \right|_{eff} I_b \quad (3)$$

The power law dependence found from the bunch length data supports the assumption that the bunch lengthening results from the MWI. From this, we calculate $|Z_{||}/n|_{eff} = 0.22 \pm 0.07 \Omega$. The data from Figure 1 is shown on a log-log scale in Figure 3, along with the calculated bunch length dependence from Eq. 3 using the above value of $|Z_{||}/n|_{eff}$, corresponding to a threshold value of 2.2 mA.

B. Higher Order Mode Loss

We have attempted to probe the resistive part of the broadband impedance by measuring a shift in the synchronous phase angle vs. bunch current. A cavity probe signal and a BPM sum signal were compared using a vector voltmeter. No shift was measure-

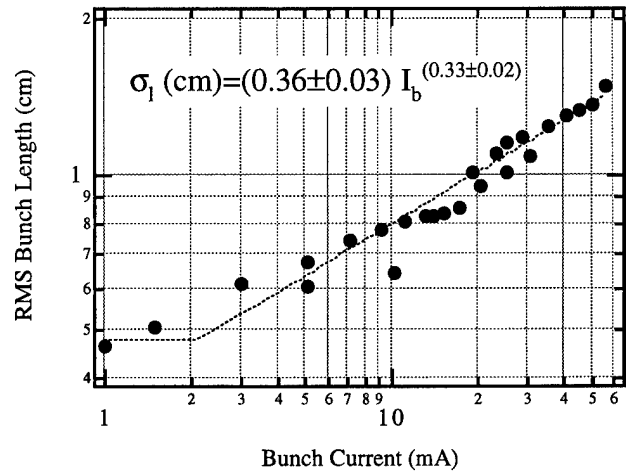


Figure 3. Measured RMS bunch length vs current showing 1/3 power law dependence.

able up to 12 mA with an accuracy of 1 degree. This yields an upper limit on the loss parameter of $k < 2.2 \text{ V/pC}$. The loss parameter estimated from the bench measurements of vacuum chamber components is $\sim 3.8 \text{ V/pC}$. The beam measurement was made prior to the vacuum chamber modification.

If the impedance is assumed to be a $Q=1$ resonator with a cut-off frequency of $f_r = 2.8 \text{ GHz}$, the average cutoff of the vacuum chamber, the loss parameter yields a broadband impedance of $|Z/n|_{||,eff} < 0.2 \Omega$.

III. Transverse Measurements

The effective transverse broadband impedance is found from the measured single bunch betatron tune shift vs. bunch current and the head-tail damping rate vs. bunch current and chromaticity. We measured tunes using signals from standard button BPMs with the beam driven by stripline kickers. The damping rates were measured on a spectrum analyser in tuned receiver mode using the transient from an injection bump. Unfortunately, we were not able to reliably produce measureable vertical transients. We made an effort to minimize the influence of decoherence on the damping rates by measuring the transients at the lowest possible kick amplitude.

The tune shift measurements are summarized in Figure 4. They yield values of $dQ_x/dI = -4.9 \pm 0.6 \times 10^{-5}/\text{mA}$ and $dQ_y/dI = -1.71 \pm 0.05 \times 10^{-4}/\text{mA}$. Following the modification of the vacuum chamber, the vertical tune shift vs. current increased to $dQ_y/dI = -2.29 \pm 0.05 \times 10^{-4}/\text{mA}$. (Measurements before and after the modification are referred to as pre- and post-VC in Figure 4.)

The transverse tune shift of the dipole mode vs. current is related to the effective impedance by[5]

$$\frac{dQ_{\perp}}{dI} = \frac{R}{4\sqrt{\pi}(E/e)\sigma_l} \beta_{\perp} Z_{\perp,eff} \quad (4)$$

where β_{\perp} is the average β -function in the lattice. We find values of $Z_{y,eff} = 155 \pm 4 \text{ k}\Omega/\text{m}$ and $Z_{x,eff} = 58 \pm 7 \text{ k}\Omega/\text{m}$. We believe the ratio of vertical to horizontal impedance results from the combination of the beampipe aspect ratio and relative β functions.

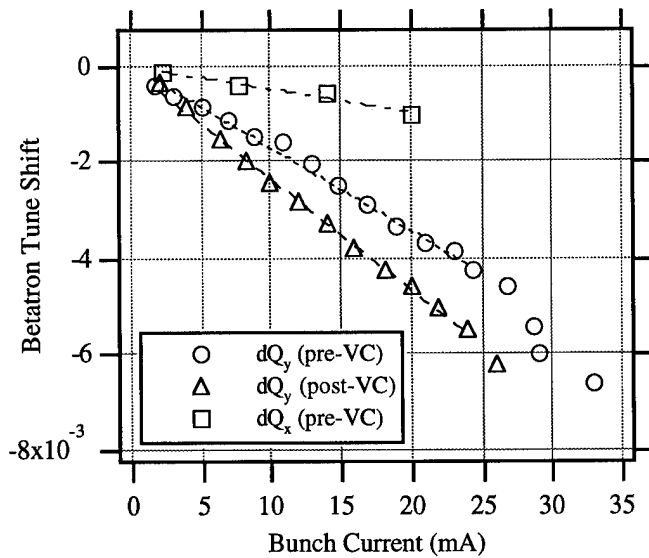


Figure 4. Transverse tune shifts vs. current. A reduction of the vertical aperture from 18 to 10 mm in one of the straight sections resulted in a 33% increase in the effective vertical impedance.

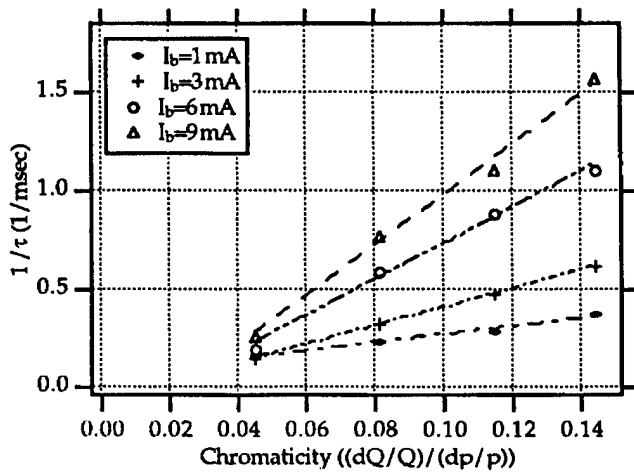


Figure 5. Horizontal damping rates vs. chromaticity at several current levels.

The head-tail damping rate measurements are summarized in Figure 5. They yield a value $d(\tau_x^{-1})/dI d\xi_x = 1.34 \pm 0.04/\text{msec}\cdot\text{mA}$, where the chromaticity $\xi \equiv dQ/Q/dE/E$. The range of chromaticity values corresponds to a chromatic frequency shift of $f_\xi = \xi \frac{Q_e}{\alpha} f_0 = 2 \text{ GHz}$. A cursory check did not indicate any dependence of the damping rate on bunch length. It is difficult to interpret these measurements in terms of an effective impedance without having a model of the frequency dependence of the actual impedance. We are awaiting further measurements under a wider variety of conditions before we do this analysis.

We observe a strong steady-state blowup in the vertical beam size at 25 mA which we associate with the threshold of the mode coupling instability, which agrees well with threshold calculated from the value of the vertical impedance found from the tune shift measurements. We cannot accumulate current higher than $\sim 28 \text{ mA}$. The threshold appears to be independent of chromatic-

ity (positive values only) and proportional to changes in the synchrotron frequency. We are not able to observe any synchrotron sidebands of the betatron tunes before the instability threshold, typically associated with the first head-tail modes. Prior to the change in the vacuum chamber described above, the onset of the instability occurred at 28 mA but did not limit the beam current. The instability appears to be self-limiting, probably due to nonlinearities in the betatron motion, but at amplitudes which now exceed the vertical acceptance of the vacuum chamber. There also appears to be some hysteretic behavior in the blowup with beam current. After the onset of the instability, we must drop the current several milliamps below the threshold before it returns to its nominal size.

IV. Conclusions and Acknowledgements

Bunch length and energy spread measurements indicate the MWI as the mechanism for bunch lengthening although further measurements under different conditions are needed to check the scaling. The effects of narrowing vacuum chambers for decreasing gaps for insertion devices shows a measureable increase in the transverse impedance, effectively decreasing the maximum single bunch current. The authors would like to thank the ALS Operations Group for assisting in the measurements.

References

- [1] J. N. Corlett, R. A. Rimmer *Impedance Measurements of Components for the ALS, Proceedings of the 1993 PAC*, May 1993.
- [2] J. Corlett, J. Byrd *Measurement and Computation of the Higher Order Modes for the ALS 500 MHz Accelerating Cavities, Proceedings of the 1993 PAC*, May 1993.
- [3] J. Byrd, J. Corlett *Measurements of Collective Effects in the ALS, Proceedings of the 1994 EPAC*, May 1994.
- [4] J. Byrd, J. Corlett *Spectral characterization of longitudinal coupled-bunch instabilities at the Advanced Light Source*, to be published in *Particle Accelerators*, May 1995.
- [5] F. J. Sacherer, *Transverse Bunched Beam Instabilities—Theory*, in *Proceedings of the 9th International Conference on High Energy Accelerators*, Stanford, 1974.

EXPERIMENTS OF NANOMETER SPOT SIZE MONITOR AT FFTB USING LASER INTERFEROMETRY

T. Shintake, K. Oide, and N. Yamamoto

KEK: National Laboratory for High Energy Physics, Oho, Tsukuba, Ibaraki 305 Japan

A. Hayakawa, and Y. Ozaki

KHI : Kawasaki Heavy Ind. Ltd., Akashi, 673 Japan

D. Burke, R. C. Field, S. Hartman, R. Iverson, P. Tenenbaum, and D. Walz

SLAC: Stanford Linear Accelerator Center, Stanford CA 94309, USA

The nanometer spot size monitor based on the laser interferometry has been developed and installed in the final focus test beam (FFTB) line at SLAC. The beam experiments started in September 1993, the first fringe pattern from the monitor was observed in the beginning of April 1994, then the small vertical spot around 70 nm was observed in May 1994. The spot size monitor has been routinely used for tuning the beam optics in FFTB. Basic principle of this monitor has been well proved, and its high performance as a precise beam monitor in nanometer range has been demonstrated.

I. INTRODUCTION

In order to prove the feasibility of TeV-scale electron-positron linear colliders, the FFTB beam line has been constructed at SLAC under the international collaborations[1]. This specially designed focusing system aims to focus a low-emittance electron beam to a tiny flat beam of 1 μm in horizontal and 60 nm in vertical sizes. To achieve the design spot of FFTB, many new instrumentations have been developed and applied[2].

Among these developments, measurement of the extremely small spot size is one of challenges in this project. In 1990, a new method was devised by the author which utilizes Compton scattering of photons in a laser interference fringe[3]. Figure 1 shows schematic diagram of this monitor. A laser beam is split into two beams and folded onto itself to produce an interference fringe pattern in space. The electron beam is scanned across this pattern to yield a modulated rate of Compton-scattered photon in the forward direction. The depth of the modulation corresponds to the spot size.

The spot size monitor system was developed by KEK and KHI, and installed in the focal point of FFTB line in August 1993[4]. This monitor has six laser beam lines in one interferometer table. By choosing a set of two laser beam lines, this monitor can produce three different measuring ranges: $0.8 \mu\text{m} < \sigma_x < 4 \mu\text{m}$, $150 \text{ nm} < \sigma_y < 750 \text{ nm}$, and $40 \text{ nm} < \sigma_y < 200 \text{ nm}$.

The monitor has been commissioned in April 1993, and routinely used for the beam tuning. In the beam operation, we found several problems, such as, low signal to noise ratio of γ -ray, laser beam position drift, laser pulse timing drift, and laser beam position pulse-to-pulse jitter. To settle these problems, we improved the hardware and also

software in this system. In this paper, practical operation method, example results, and also the hardware improvements are described.

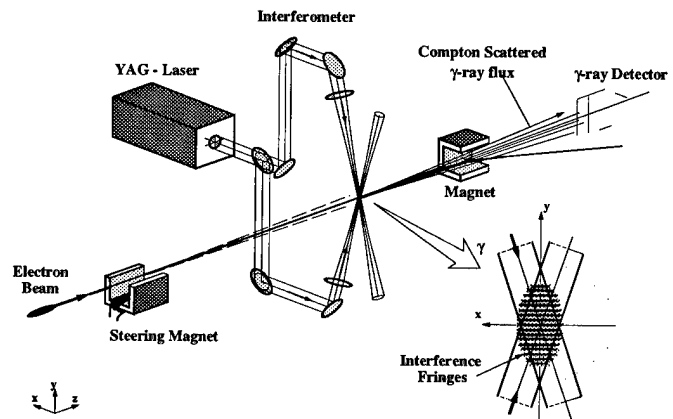


Fig.1 Schematic diagram of the spot size monitor using laser interferometry.

II. MEASUREMENT PROCEDURE

A. z-axis alignment

For z-axis alignment of the laser beams, we prepared a slit scanner. We insert the slit of 0.5 mm width at the focal point, and scan the z-position of laser beam by the mirror mover. We measure the transmitted laser power through the slit using a photo-detector at opposite side. From this measurement, we can determine the center of the slit looking from laser beam and set the mirror position to this center. By repeating this process for all laser beam lines, we can align all laser beam lines in one plane.

B. xy-axis alignment

For xy-axis alignment, we use γ -ray signal from the electron beam. By scanning the electron beam trajectory along x or y axis, we look for a γ -ray peak of the laser beam. By adjusting x or y axis of each mirror, we can align each laser beam to the center (electron beam axis).

C. Q-switch timing adjustment

The laser has pulse length of 10 nsec. We have to adjust the laser pulse timing just on the electron beam timing. To do this, we measure the γ -ray signal from one laser beam by scanning the Q-switch timing to find out the laser peak.

Since we use a seeding laser in YAG-laser system, the timing of laser peak is sensitive to temperature variation in laser system (because the oscillator axis is sensitive to temperature change). We are preparing a thermo-controller to keep the air temperature within ± 0.5 deg. C.

D. Spot Size Measurement

After the laser beam alignment, we choose fringe type (by choosing a set of two beam lines from the six beam lines), and scan the electron beam across the fringe pattern. We take 18 shot data in one point, in which 6 data are Laser_ON data, and 12 data are Laser_OFF data, we subtract the averaged Laser_OFF data from the averaged Laser_ON data to eliminate the background baseline shift.

III. MEASUREMENT EXAMPLE

Scanning the electron beam trajectory with fine step, we observe a periodic intensity modulation in the γ -ray data as shown in Fig. 2(a). The vertical axis is the averaged and noise-subtracted γ -ray counts (ADC counts). The solid curve is a least-mean-square fit of analytical function:

$$Y = A + B \sin\left(\frac{2\pi}{d}y + C\right) \quad (1)$$

where d is a period of the fringe pattern(dark-to-dark distance). We use theoretical value of $d = \lambda_0/2\sin(\theta/2)$, where λ_0 is wavelength of laser, θ is crossing angle of laser beams, in this case, $\lambda_0 = 1064$ nm, $\theta = 174$ deg., and $d = 533$ nm. From the fitting, $A = 106.7$, $B = 72.6$, and the modulation depth is $B/A = 0.68$. From this we calculate the spot size as follows.

Assuming a Gaussian beam, the modulation depth is related to the spot size:

$$M = B/A = |\cos\theta| \cdot C_p \cdot C_\beta \cdot \exp(-2k_y^2 \sigma_y^{*2}) \quad (2)$$

where $|\cos\theta|$ is a correction factor for a traveling wave component in the fringe. For $\theta = 174$ deg., it becomes 0.9945. C_p is a correction factor for power imbalance of two laser beams:

$$C_p = \frac{2\sqrt{P_2/P_1}}{1 + P_2/P_1} \quad (3)$$

In the present case, the power ratio P_2/P_1 is 1.26, and the correction factor is 0.993. C_β is a correction factor for laser beam depth in z-direction:

$$C_\beta = \frac{1}{\sqrt{1 + (k_y \sigma_y^* w_0 / \beta^*)^2}} \quad (4)$$

where k_y is the wave number of laser beam in y-direction:

$$k_y = k_0 \cdot \sin(\theta/2) = 2\pi/\lambda \cdot \sin(\theta/2) = 5.90 \mu\text{m}^{-1}. \quad (5)$$

w_0 is a laser waist size at the focal point. Since this correction factor is also a function of the spot size, eq. (2) can not be simply solved. Because of this reason, in a first

step, letting $C_\beta = 1.0$, we calculate a raw spot size from eq.(2). In this example, the spot size is $\sigma_y^* = 73.2$ nm.

Figure 2 (b) shows the distribution of the measured raw spot size in the last 3 hours of the run in May 1994. The distribution shows that the beam line of FFTB has the stability of $\sigma_y^* = 70 \pm 7$ nm.

For the 70 nm spot size, the correction factor C_β for laser beam depth in z-direction becomes 0.92, where we put $w_0 = 100 \mu\text{m}$, $\beta^* = 100 \mu\text{m}$. With this correction, the spot size in Fig. 2 (b) becomes $\sigma_y^* = 65 \pm 7$ nm.

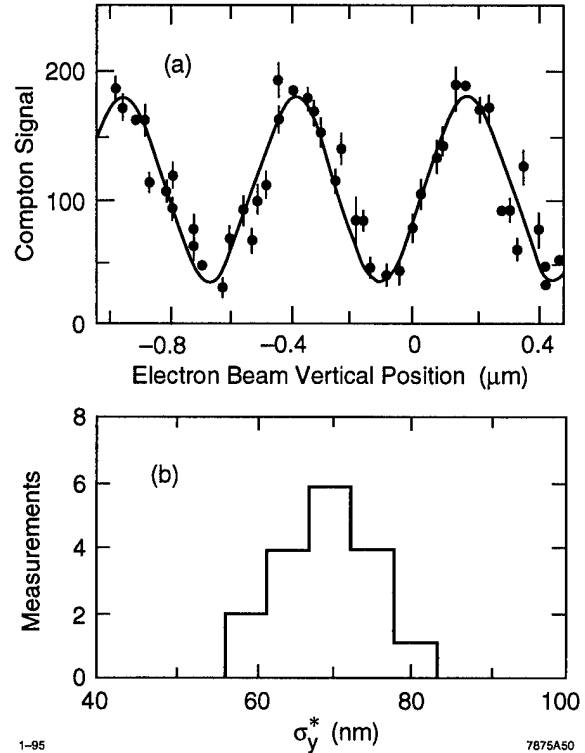


Fig. 2. (a) Measured fringe pattern in the Compton scattered γ -ray. Solid curve is the least-square-fit of sine-function. (b) Spot size distribution for 3 hours measurement.

IV. HARDWARE IMPROVEMENTS

Figure 2 (b) shows the spot size distribution of the measured in the last 3 hours of the run in May 1994. This distribution shows that the beam line of FFTB has the stability of 70 ± 7 nm. However, the stability includes possible fluctuations in the spot size monitor. In order to resolve the electron beam stability from the spot size monitor stability, we started improvement work right after the run. Some of the improvement has been done before the September run in 1994, and tested. They are summarized below.

A. YAG-Laser

We use pulsed Nd: YAG-laser, which emits Q-switched pulse light at 1064 nm of infrared wavelength, pulse length 10 ns, pulse energy of 200 mJ and repetition rate at 10 pps. A seeding laser is implemented to keep the

coherency better than 3 m, which is quite enough to our measurement. We always monitor the laser light timing to make sure the pulsed laser light is on timing to the electron bunch. With this monitoring, also we can confirm that the laser is fully locked to the seeding source(in case of out-of-locking, the timing shift back 30 nsec). The unwanted circular polarization component, and the perpendicular component are eliminated by means of high power polarizers.

In the September-1993 run, we observed a discrepancy in measured IP spot size. One of the possible error sources is beam pointing pulse-to-pulse jitter of laser beam. This phenomena is related to (a) fluctuation of stored energy of the seeding laser, (b) jitter of the flash-lamp pumping power, (c) cavity-axis fluctuation in the oscillator due to mechanical vibration, and (d) unwanted mirror tilt due to piezo mover in seeding system. Inspection of these items and improvements are anticipated for the next run.

B. Laser Beam Transport System

In order to avoid beam position fluctuation due to unstable refraction in the air, the laser beam is transported in vacuum about 30 meters from the laser building to the interferometer inside the FFTB tunnel. The YAG-laser has a big pointing drift (0.5 mrad max.) due to temperature change in cooling water of YAG-rod and ambient air temperature change. In order to eliminate the beam position movement, a feedback loop is implemented, which keeps the laser beam position at the entrance on the interferometer to the center by controlling the mirror angle in front of the YAG-laser.

However, in the September-1993 run, it was found that a mirror in the transport line was moving due to the sun light heating the concrete roof of FFTB tunnel, and the laser beam position at the focal-point was always moving around about a few tens of μm . In the spot size measurements, we frequently needed to check the position and trim the final mirrors.

In order to eliminate this drift, another feedback loop has been implemented. In the present system, one feedback loop keeps the incoming laser beam to the center at the interferometer entrance, and the second loop keeps the focused beam at IP to the center. In the recent beam run at March-1995, the stability has been quite improved, no beam position drift was observed.

C. Noise Background Subtraction

Since the spot size is determined by the modulation depth in the Compton scattered γ -ray data, i.e., the ratio of AC to DC components, for accurate measurements it is very important to eliminate the effect of the noise background. To do this, a synchronous detection technique is used. When the electron beam runs at 30 Hz, the laser is fired at 10 Hz. That is, for each electron beam pulse the laser beam is fired alternatively: ON_OFF_OFF_ON_OFF_OFF... The laser-ON γ -ray data is averaged for six pulses, and the noise-background (laser-OFF) γ -ray

data is averaged for twelve pulses, then the noise-background data is subtracted from the laser-ON data.

D. Interferometer Optics

In order to measure the spot size accurately, we have to overlap two laser beams precisely at the focal point. If the laser beam diameter at the focal point is larger, the alignment tolerance becomes looser. However, if the laser beam diameter is larger than the β -function at IP, it becomes difficult to directly measure the minimum spot size at electron beam waist. Also the γ -ray count per pulse becomes lower, which is inversely proportional to the laser beam diameter. On the other hand, if the laser beam diameter becomes smaller, we can get good γ -ray count and we can measure the spot size with good S/N ratio. However, the alignment tolerance becomes severe.

In the initial design, we chose the laser beam diameter to the upper limit, that is, $\sigma_L = 50 \mu\text{m}$. The alignment was easy, but the S/N ratio was as low as 3 : 1. We changed the laser beam optics, and made the beam size smaller: $\sigma_L = 30 \mu\text{m}$, then the S/N ratio was improved twice.

V. SUMMARY

Nanometer beam was produced in FFTB and whose transverse dimensions were successfully measured by the spot size monitor based on the laser interferometry. This success is a big milestone toward the electron-positron linear collider R&D project. In an actual linear collider, we use a short wavelength laser such as 5th harmonic radiation of Nd: YAG-laser at 213 nm. Fully utilizing the synchronous-noise-background-subtraction technique and using a stable laser oscillator, it will be possible to measure the modulation amplitude up to 95% or more. The spot size of 3~4 nm at interaction point can be measured with enough accuracy based on this method.

VI. ACKNOWLEDGMENTS

We gratefully acknowledge the additional members of FFTB collaboration and all who contributed to this project, whose various support was key to its success.

VII. REFERENCES

- [1] M. Berndt et al., "Final Focus Test Beam Design Report, SLAC-REF-376(1991).
- [2] V. A. Alexandrof, et al., "Results of Final Focus Test Beam", in these proceedings.
- [3] T. Shintake, "Proposal of a nanometer beam size monitor for e^+e^- linear colliders", Nucl. Instrum. and Meth. in Physics Research A311 (1992) 453-464.
- [4] T. Shintake, H. Hayano, A. Hayakawa, Y. Ozaki, M. Ohashi, K. Yasuda, D. Walz, S. Wagner and D. Burke, "Design of Laser-Compton Spot Size Monitor", proc. XVth Int. Conf. on High Energy Accelerators, Hamburg, Germany July 1992, pp. 215-217
- [5] V. Balakin et al., "Focusing of Submicron Beams for TeV-Scale e^+e^- Linear Colliders", Phys. Rev. Let. Vol. 74, 27 March 1995, pp. 2479-2492

TRANSVERSE ELECTRON BEAM SIZE MEASUREMENTS USING THE LLOYD'S MIRROR SCHEME OF SYNCHROTRON LIGHT INTERFERENCE

O. V. Chubar, Russian Research Center KURCHATOV INSTITUTE, Moscow, 123182, RUSSIA

Method for horizontal and vertical electron beam size measurements using the Lloyd's Mirror with monochromatic synchrotron light is presented. The use of the interference scheme with synchrotron light may result in fringes of the light intensity distribution, the way it takes place in the case of point light sources. Dimensions of the interference pattern and the fringes contrast are found to essentially depend on transverse size of the emitting electron beam. The resulting light intensity distributions can be calculated analytically. This allows one to determine the transverse size of electron beam immediately from the results of the intensity distribution measurements. Analytical expressions for the intensity distributions of synchrotron light in the Lloyd's Mirror interference scheme are given. Beam size measurement results on the Siberia-1 storage ring by the method concerned are presented.

I. INTRODUCTION

Interference of light is known to be very powerful research instrument in modern physics. In a wide range of experiments and measurements, interferometry normally provides very high precision unattainable with other methods. This paper describes an attempt to use the high information potential of the interference patterns to determine transverse size of electron beam in a storage ring.

It is well-known that "quality" of interference pattern (for example, its visibility or contrast) in most interference schemes essentially depends on characteristics of emitting light source [1]. For a finite-size source, the smaller is the source size, the better is the visibility of the interference pattern. Just this simple feature, with electron beam as a source emitting the synchrotron radiation (SR), is used in the method to be described.

In practice, precise calculation of interference patterns in view of the emitting beam and interference scheme parameters is needed to determine actual values of the beam parameters. Advantageously, SR intensity distributions in the patterns produced with simple interference schemes can be calculated to a very high accuracy. With that, the procedure of determining the beam transverse sizes consists of measuring the intensity distributions concerned and fitting the measured and calculated distributions by varying "guess values" of the actual beam transverse sizes.

Formally, the method under discussion is similar to the edge radiation (ER) based method [2] - [3]: in both cases interference effects are used and the procedures of determining beam parameters consist of very similar steps. Yet there is essential difference between the two methods. In the case of ER, the interference of light appears due to specific emission conditions of the electron beam. Meanwhile, in the

method under discussion, standard bending magnet SR is used, and the interference is a result of applying specific scheme for propagation and detection of the light. An important consequence of the difference is discussed in the following chapter among other aspects.

To measure horizontal and vertical size of electron beam, the simplest "Lloyd's Mirror" interference scheme [1] was chosen. We used two modifications of the scheme (see Figures 1 and 2), the one with vertical mirror located at small distance h_x from optical axis as shown in Figure 1-a (to determine horizontal size of electron beam), and one with horizontal mirror shifted by small distance h_z from median plane as shown in Figure 1-b (to determine vertical size).

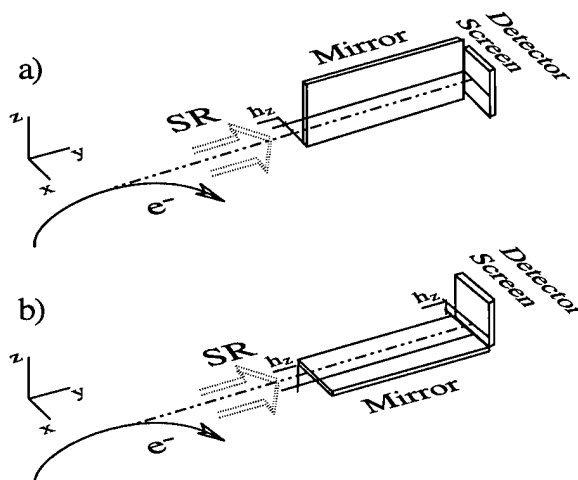


Figure 1. Lloyd's Mirror schemes of synchrotron light interference:

- a) vertical mirror (to determine horizontal beam size);
- b) horizontal mirror (to determine vertical beam size).

II. ANALYTICAL DESCRIPTION OF SYNCHROTRON RADIATION INTERFERENCE IN LLOYD'S MIRROR SCHEME

To describe the SR intensity distribution to appear at detector screen in the Lloyd's Mirror interference scheme, one should take into account synchrotron light coming to the screen from electron beam directly, as well as the reflected light. Also, one should keep in mind that the radiation emitted by single electron is coherent, whereas the light by different particles of the beam is dominantly incoherent (as in most cases in electron storage rings).

The following expressions can be obtained for spectral angular distribution of synchrotron light emitted by the total electron beam in the Lloyd's Mirror schemes (in terms of photon flux per unit solid angle per unit relative spectral interval), for the vertical mirror:

$$\frac{dN_1}{dtd\Omega(d\lambda/\lambda)} = \frac{8\alpha I}{e} \cdot p \cdot \left[\text{Ai}'^2(Z) + p\zeta^2 \text{Ai}^2(Z) \right] \times \left[1 - \cos(4\pi h_x \xi / \lambda) \cdot \exp(-8\pi^2 \sigma_x^2 \xi^2 / \lambda^2) \right]; \quad (1)$$

and for the horizontal one:

$$\frac{dN_2}{dtd\Omega(d\lambda/\lambda)} = \frac{4\alpha I}{e} \cdot p \cdot \left\{ \text{Ai}'^2(Z_+) + \text{Ai}'^2(Z_-) + p\zeta_+^2 \text{Ai}^2(Z_+) + p\zeta_-^2 \text{Ai}^2(Z_-) - 2[\text{Ai}'(Z_+) \text{Ai}'(Z_-) - p\zeta_+ \zeta_- \text{Ai}(Z_+) \text{Ai}(Z_-)] \right\} \times \cos(4\pi h_z \zeta / \lambda) \cdot \exp(-8\pi^2 \sigma_z^2 \zeta^2 / \lambda^2); \quad (2)$$

where

$Z = p(\gamma^{-2} + \zeta^2)$; $Z_{\pm} = p(\gamma^{-2} + \zeta_{\pm}^2)$; $p = (\pi\rho/\lambda)^{2/3}$; $\xi = x^*/y^*$; $\zeta = z^*/y^*$; $\zeta_{\pm} = (z^* \pm h_z)/y^*$; Ai and Ai' are the Airy function and its derivative respectively, α is the fine-structure constant, e the charge of electron, I the electron current, γ the reduced energy of electrons, λ the radiation wavelength, ρ bending magnet radius; σ_x is horizontal size of the electron beam, σ_z its vertical size; y^* is distance from "radiation point" to detector screen, x^* and z^* are horizontal and vertical coordinates of the observation point (belonging to the detector screen).

Eqs. (1) and (2) are valid with the constraints $\gamma \gg 1$; $|\xi| \ll 1$; $|\zeta| \ll y^*/\rho$; $|\zeta_{\pm}| \ll 1$; $\lambda > \lambda_c$; $\sigma_z \ll (\lambda/\rho)^{1/3}$; $\sigma_x \ll 1$; $\sigma_z \ll y^*(\lambda/\rho)^{1/3}$; $\sigma_z \ll h_z \ll y^*$; $\sigma_x \ll h_x \ll y^*$,

where σ_x' and σ_z' are horizontal and vertical angular divergences of the electron beam, λ_c the critical wavelength of synchrotron radiation.

The well-known Fresnel formulae for the reflected wave [1] were taken into account when deriving Eqs. (1) - (2), and the mirrors' reflectivity was assumed $\approx 100\%$ (the latter being quite realistic assumption for the grazing incidence taking place in the case under consideration).

As one can see from Eqs. (1) and (2), the angular distribution of monochromatic SR in the case of vertical mirror depends on the horizontal beam size σ_x , and in the case of horizontal mirror the distribution depends on the vertical size σ_z . In both cases the finite size of the beam suppresses visibility of the interference fringes (or fringes' contrast). With that, the fringes' width depends on distance from the mirror plane to the beam (h_x, h_z), but not on σ_x, σ_z . The latter is beneficial for the beam size measurements: for a reasonable range of the horizontal and vertical beam size values, there is a possibility to set such values of h_x and h_z that make the beam size measurements realizable in practice. Besides, there is no need in precise geodetic installation of the mirrors before the measurements; the actual values of h_x and h_z can be determined together with σ_x and σ_z , as a result of fitting the expressions (1) and (2) to measurement results.

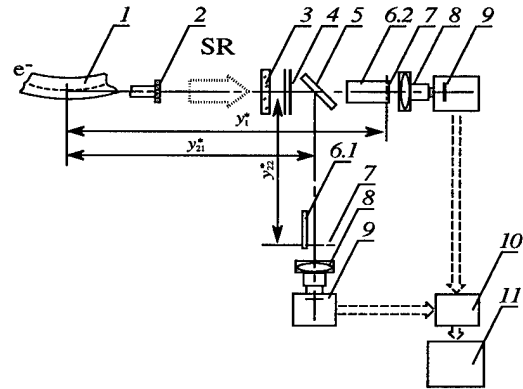
It is worth noting that, according to Eqs. (1) and (2), the SR intensity distribution in the Lloyd's Mirror interference

schemes does not depend on angular divergence of the electron beam (if we neglect the standard SR dependence on the vertical beam divergence, being very weak for long-wave SR, see conditions after Eqs. (1), (2)). With that, the distribution dependence on the beam transverse size takes place at any distance from the "radiation point" (assuming the mirror to be sufficiently large). For reference, as distinct from the case under consideration, intensity distribution in interference patterns of the edge radiation (as well as the distributions of undulator radiation) is known to be very sensitive to the electron beam divergence [2]. Therewith, the distribution dependence on the beam transverse size disappears at large distance ($y^* \gg \sigma_{x,z}/\sigma_{x',z'}$) in this case. The situation is explained by different origination of the interference in the two cases.

III. DETERMINING TRANSVERSE SIZE OF ELECTRON BEAM

An experimental system for measuring the SR intensity distributions in the Lloyd's Mirror interference schemes was installed on Siberia-1 450 MeV electron storage ring (small ring of Kurchatov SR Source, Moscow) in order to determine transverse size of the electron beam (see Figure 2).

The wavelength of the radiation passing through the interference filter was 560 nm at 4 nm bandwidth. Glass plates of 10 cm \times 10 cm size with high-quality surfaces were used as the horizontal and vertical mirrors. The mirrors' reflectivity at the incidence angles used was better than 97 %.



The system allowed one to simultaneously measure the

Figure 2. The system for measuring SR intensity distributions in Lloyd's Mirror interference schemes on the Siberia-1 ring. 1- bending magnet; 2- extraction window; 3- neutral filters; 4- interference filter; 5- semitransparent mirror; 6.1- vertical mirror; 6.2- horizontal mirror; 7- object plane; 8- lens; 9- CCD-matrix camera; 10- interface; 11- computer.

SR intensity distributions in the two "object planes" intersecting the horizontal and vertical mirror as shown in Figure 2. Lenses were used to fit the dimensions of the intensity distributions of interest (i.e., interference patterns) to photo-sensitive windows of the CCD matrices. Optical

magnification was 4.25 in each channel. Dynamic range of the cameras used was approximately 50. The distances from "radiation point" to object planes were $y^*_1 = 202$ cm and $y^*_2 = y^*_{21} + y^*_{22} = 415$ cm. We tried to use larger distance y^* for measurements with vertical mirror in order to make the corresponding interference pattern larger without using large optical magnification: since the horizontal size of the beam was relatively large, the size of the interference pattern in this case appeared too small at $y^*_2 = y^*_1$.

The intensity distribution registered by the first camera with the horizontal mirror is shown in Figure 3 as a half-tone picture (in order to suppress noise, the distribution was partially averaged in horizontal direction). The interference pattern registered agrees qualitatively with the one predicted by Eq. (2).

The fitting of the measured and calculated intensity distributions over σ_{xz} and h_{xz} is illustrated by Figure 4. According to the Figures 4-a and 4-b, the calculated best-fits are in good agreement with the measurement results. The values of the beam sizes corresponding to the best-fits are: $\sigma_x = 1.41 \pm 0.08$ mm (at $h_x = 8.8$ mm) and $\sigma_z = 0.34 \pm 0.02$ mm (at $h_z = 9.1$ mm). We see that $\sigma_x \ll h_x$ and $\sigma_z \ll h_z$, being in agreement with the constraints for Eqs. (1) and (2).

The measurements concerned were performed when the Siberia-1 operated as an injector for the Siberia-2 ring at the energy of $E = 350$ MeV. In agreement with data from other detectors, the vertical beam size appeared to be larger, and the horizontal size little bit smaller in this mode then in the mode when the Siberia-1 operated as light source at $E = 450$ MeV [3].

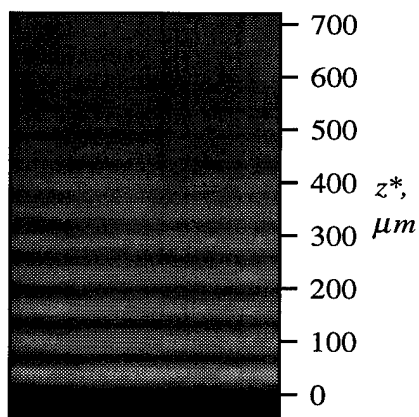


Figure 3. Half-tone representation of the intensity distribution registered by CCD-camera in the case of horizontal mirror. In the case of vertical mirror, the interference pattern was very similar, with the fringes being parallel to the mirror plane.

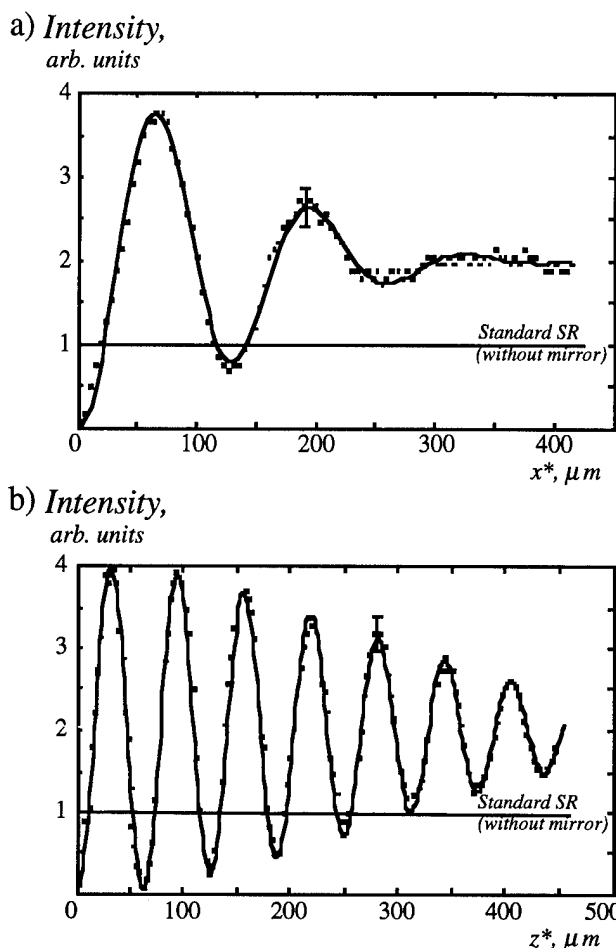


Figure 4. Measured SR intensity distributions for the channel with the vertical (a) and the horizontal (b) mirror (points), and the corresponding best-fits (solid lines). The fitting gives one: $\sigma_x = 1.41 \pm 0.08$ mm and $\sigma_z = 0.34 \pm 0.02$ mm.

IV. ACKNOWLEDGEMENTS

I would like to thank Prof. G.N.Kulipanov (Budker Inst. of Nuclear Physics, Novosibirsk) for very important notes he made on the subject of this work, and the joint team of accelerator physicists from the INP and Kurchatov SR Source, who helped to perform measurements even during the period of very intensive commissioning works on the Siberia-2 ring.

V. REFERENCES

- [1] See, for example, M.Born and E.Wolf, Principles of Optics, 6th ed., Pergamon, Oxford (1980).
- [2] O.Chubar, E.Masunov, "Electron Beam Diagnostics by Means of Edge Radiation", Proceedings of the PAC93, vol.3, p. 2474.
- [3] O.Chubar, "Determining Electron Beam Parameters from Edge Radiation Measurement Results on Siberia-1 Storage Ring", these proceedings.

Charge Balancing Fill Rate Monitor

J.L. Rothman and E.B. Blum

National Synchrotron Light Source, Brookhaven National Laboratory, Upton, New York 11973

Abstract

A fill rate monitor has been developed for the NSLS storage rings to allow machine tuning over a very large dynamic range of beam current. Synchrotron light, focused on a photodiode, produces a signal proportional to the beam current. A charge balancing circuit processes the diode current, creating an output signal proportional to the current injected into the ring. The unit operates linearly over a dynamic range of 120dB and can resolve pulses of injected beam as small as $1\mu\text{A}$.

I. INTRODUCTION

The fill rate monitor is one of the most frequently used diagnostic tools in the NSLS control room, allowing the operator to optimize injection and reduce the time between fills. Previous fill rate monitors have used signals from pickup electrodes (PUEs) or from a DC current transformer (DCCT). A tuned receiver connected to a PUE can measure very small currents, but tends to saturate with large signals. The DCCT tolerates large signals but is too noisy to resolve small changes in current. The new unit combines the best elements of the other systems, providing both high sensitivity and a wide dynamic range.

II. DESIGN

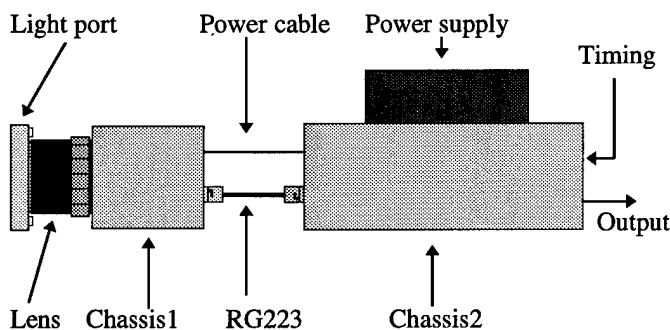


Figure 1: Schematic view of the mechanical design

The mechanical design is shown in figure 1. The lens is a standard video camera lens mounted on the light port via an adapter. It focuses the light into chassis 1 and onto the photodiode. The diode is mounted on a micrometer so the

* Work performed under the auspices of the U.S. Department of Energy

beam spot can be centered. Current from the diode runs through a double shielded cable to the electronics located in chassis 2.

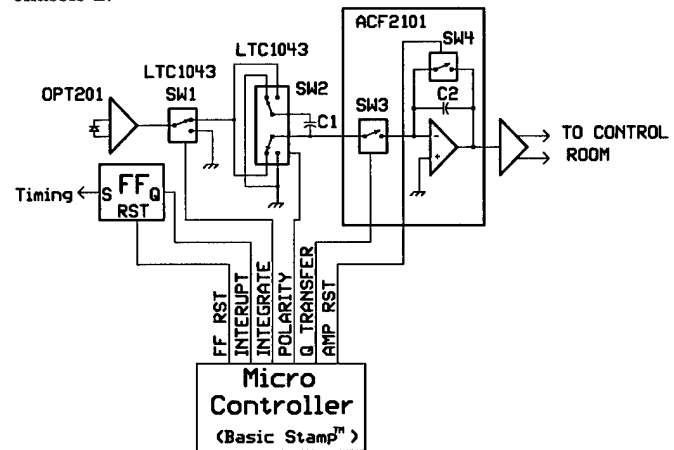


Figure 2: Electronic System diagram

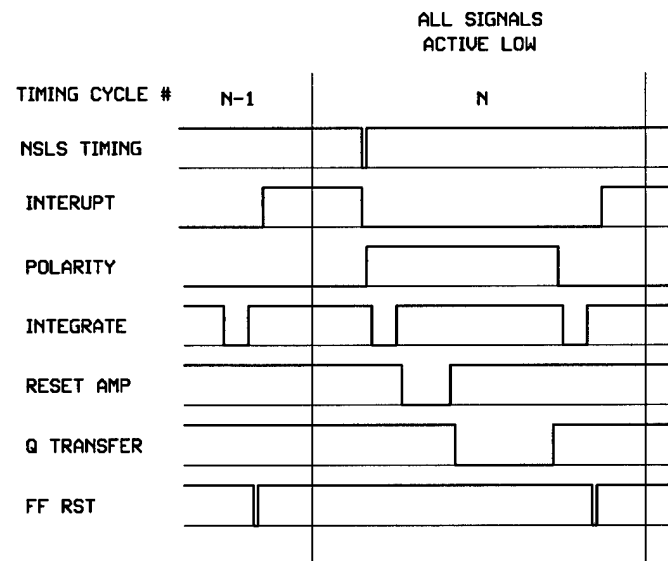


Figure 3: Timing diagram

The electronic system and timing diagrams are shown in figure 2 and figure 3 respectively. At the end of timing cycle N-1, the absolute current in the ring is measured by closing SW1 and integrating the photodiode current on the bottom plate of C1 for 50mS. The interrupt flip flop is then reset in preparation for timing cycle N. A timing pulse sets the flip flop and interrupts the microcontroller 100mS after a shot has been injected into the ring. This allows the beam to damp and

prevents fluctuations in the diode current due to beam motion. The microcontroller then reverses the polarity of SW2. SW1 closes again and integrates the photodiode current on the top plate of C1. The charge remaining on C1 is proportional to the current injected into the ring. At this point SW4 closes, resetting the charge sensitive amplifier. After SW4 opens SW3 closes to transfer the charge from C1 to C2, updating the output signal. Since $C1 = 10\mu\text{F}$ and $C2 = 4.7 \text{ nF}$ the voltage gain = 2100. The output is buffered with a differential driver and transmitted to the control room for display on a digital oscilloscope.

The OPT201[1] is a low noise photodiode and a transimpedance amplifier fabricated on the same chip. In this application it has been configured to provide a current output. SW1 and SW2 are LTC1043 [2] FET switches. C1 is made large to keep the input signals near ground. This makes the switch charge injection less than 1pC, contributing less than 200 μV to the output offset voltage. The ACF2101 [1] is a dual analog integrator also with low noise and low charge injection characteristics.

A Basic StampTM [3] microcontroller sequences the FET switches. Since the Stamp is programmed in a dialect of the Basic programming language, only 11 executable lines of code are required to produce the needed timing signals. Programs are downloaded from a PC via the parallel port.

Variables can be sent back to the PC at run time for debugging purposes, making an emulator unnecessary. The code is stored in an EEPROM so programs can be updated at any time.

III. PERFORMANCE

The resolution as a function of beam current is shown in figure 4. The noise floor is given by:

$$I_N = 1\mu\text{A} * (1 + (I_{\text{BEAM}} \mu\text{A} / 27369))$$

Despite the increase in noise at high currents the monitor can still resolve 37ppm changes in beam current with 850mA in the ring.

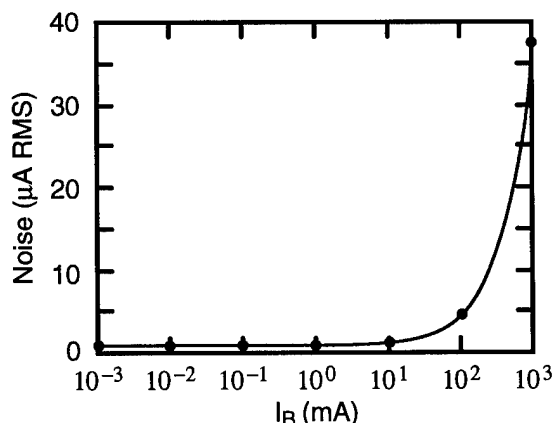


Figure 4: Resolution as a function of beam current

IV. CONCLUSIONS

The charge balancing technique used in this fill rate monitor allows high resolution measurements to be made over a wide range of beam current. The performance can be further enhanced by moving the unit to a beam port that sees less beam motion. Even so, it measures small changes in current much better than previous detectors, opening the possibility of using charge balancing techniques to measure beam lifetime.

VI. REFERENCES

- [1] Burr Brown Corporation, Linear Products, P.O. Box 11400 Tucson, AZ 85734-1400
- [2] Linear Technology Corporation, 1630 McCarthy Blvd, Milpitas, CA 95035
- [3] Parallax, Inc. 3805 Atherton Road, #102, Rocklin, CA 95765

V. ACKNOWLEDGMENTS

Thanks to Henry Link for technical support.

Sensitivity and Offset Calibration for the Beam Position Monitors at the Advanced Photon Source*

Y. Chung, D. Barr, G. Decker, K. Evans, Jr. and E. Kahana
Argonne National Laboratory, Argonne, IL 60439

Abstract

The beam position monitors (BPMs) play a critically important role in commissioning and operation of accelerators. Accurate determination of the offsets relative to the magnetic axis and sensitivities of individual BPMs is thus needed. We will describe in this paper the schemes for calibrating all of the 360 BPMs for sensitivity and offset in the 7-GeV Advanced Photon Source (APS) storage ring and the results. For the sensitivity calibration, a 2-dimensional map of the BPM response in the aluminum vacuum chamber is obtained theoretically, which is combined with the measured nonlinear response of the BPM electronics. A set of 2-dimensional polynomial coefficients is then obtained to approximate the result analytically. The offset calibration of the BPMs is done relative to the magnetic axis of the quadrupoles using the beam. This avoids the problem arising from various mechanical sources as well as the offset in the processing electronics. The measurement results for the resolution and long-term drift of the BPM electronics shows $0.06\text{-}\mu\text{m}/\sqrt{\text{Hz}}$ resolution and $2\text{-}\mu\text{m}/\text{hr}$ drift over a period of 1.5 hrs.

I. INTRODUCTION

For beam position monitoring of the charged particle beam, button-type pickups will be used in the storage ring, injector synchrotron, and insertion devices (IDs) of the Advanced Photon Source (APS). In order to meet the requirements on the accuracy of the measured beam position as shown in Table 1, it is necessary that the beam position monitors (BPMs) are accurately calibrated for the offset and sensitivity.

Table 1: APS Storage Ring BPM Specifications.

First Turn, 1 mA Resolution / Accuracy	200 μm / 500 μm
Stored Beam, Single or Multiple Bunches @ 5 mA Total Resolution / Accuracy	25 μm / 200 μm
Stability, Long Term	$\pm 30 \mu\text{m}$
Dynamic Range, Intensity	$\geq 40 \text{ dB}$
Dynamic Range, Position	$\pm 20 \text{ mm}$

In the past few years, significant effort has gone into implementation of the offset calibration using the external method developed by G. Lambertson [1,2]. This method

requires separate measurements in air and vacuum, since the APS storage ring vacuum chamber is subject to significant deformation under vacuum due to the photon exit channel. For the sensitivity calibration, a different method is needed, such as a wire, antenna, or charged particle beam whose transverse position can be controlled with precision. This approach has met with certain implementation difficulties due to scheduling conflicts with installation and bakeout of the vacuum chambers and relatively high sensitivity of measurement error to the mechanical environment surrounding the BPMs.

An alternative method, which takes advantage of independent powering of the quadrupoles, has been developed for use during the commissioning phase with charged particle beams. From the change in the particle trajectory in the downstream of a quadrupole due to quadrupole strength change, the particle beam offset at the quadrupole relative to the magnetic center can be deduced. The offset of the neighboring BPM can then be determined by comparing the BPM reading and the measured beam offset at the quadrupole. This method has a few advantages over other methods based on laboratory bench measurements or external measurements. First, since this is an end-to-end measurement, all the BPM components between the button electrodes and the digitizers are calibrated as an integrated system. Second, the offsets are calibrated with respect to the magnetic axis adjoining the quadrupoles, and therefore, the calibration includes survey and alignment error of the BPMs and quadrupoles. A possible down side is that this method uses up valuable beam time and the stability of the beam property may not be good during commissioning. As a requirement for this method, the transfer matrices between each quadrupole and each BPM needs to be known. These matrices can be obtained from the lattice model or the lattice functions calculated from it.

Separate from the above procedure for offset determination, measurements need to be made for individual BPMs for mapping between the beam position and the BPM output in the 2-dimensional space [2]. This takes into account the geometric effect of the vacuum chamber and the nonlinear characteristics of BPM electronics. Comparison of the measurement and analytical results on the geometric effect of the vacuum chamber showed good agreement. Therefore, measurements were made only on electronics, whose results were combined with a theoretical model of the vacuum chamber to obtain 2-D polynomial coefficients.

The remainder of this paper will be a theoretical discussion of the beam-based BPM offset determination and error analysis in Section II and a result of measurement in the APS

*Work supported by the U.S. Department of Energy, Office of Basic Energy Sciences, under Contract No. W-31-109-ENG-38.

storage ring in Section III. A summary and discussion are in Section IV.

II. BEAM-BASED BPM OFFSET DETERMINATION

A. Theory

Let us consider a pair consisting of a quadrupole and a BPM in the ring as shown in Fig. 1. The beam offset x_q and angle x'_q with respect to the magnetic axis can change as the beam goes through the quadrupole as written by

$$\begin{pmatrix} x_q \\ x'_q \end{pmatrix}_{out} = \mathbf{M}_q \cdot \begin{pmatrix} x_q \\ x'_q \end{pmatrix}_{in}, \quad (1)$$

where \mathbf{M}_q is the transfer matrix for the quadrupole.

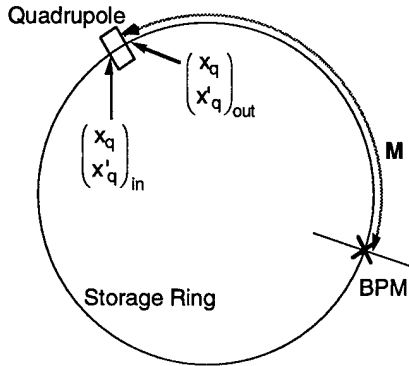


Fig. 1: The transfer matrix \mathbf{M}_{iq} between a quadrupole and a BPM.

Similarly, if we let \mathbf{M}_{iq} be the transfer matrix between the quadrupole and the i -th BPM, we can express the beam position x_i and x'_i at the BPM as

$$\begin{pmatrix} x_i \\ x'_i \end{pmatrix} = \mathbf{M}_{iq} \cdot \begin{pmatrix} x_q \\ x'_q \end{pmatrix}_{out} = \mathbf{M}_{iq} \cdot \mathbf{M}_q \cdot \begin{pmatrix} x_q \\ x'_q \end{pmatrix}_{in}. \quad (2)$$

The transfer matrix \mathbf{M}_{iq} can be obtained from the lattice functions or by multiplying the transfer matrices of all elements between the quadrupole and the BPM. In the following discussion, we will drop the subscript *in* from the notation for simplicity.

On the other hand, the BPM reading x_{bi} is given by

$$x_{bi} = S_i x_i + x_{oi}, \quad (3)$$

where S_i and x_{oi} are the sensitivity and offset of the BPM, respectively. We assume that the nominal value of S_i is 1. In order to obtain S_i and x_{oi} based on Eqs. (2) and (3), we first need to know x_q . Suppose we have a BPM close enough to the quadrupole so that we can write $x_{bi} \approx x_q$, then we have $x_{oi} = x_{bi} - S_i x_q$. In general, x_{oi} can be expressed in terms of the linear combination of x_q 's for two adjacent quadrupoles.

Now, if \mathbf{M}_q is changed by $\Delta\mathbf{M}_q$ through the change in quadrupole strength, Eq. (2) gives for the i -th BPM

$$\begin{pmatrix} \Delta x_{iq} \\ \Delta x'_{iq} \end{pmatrix} = \mathbf{M}_{iq} \cdot \Delta\mathbf{M}_q \cdot \begin{pmatrix} x_q \\ x'_q \end{pmatrix}. \quad (4)$$

Since the BPM does not measure beam angle, we collect only the expressions from Δx_{iq} for M BPMs downstream of the quadrupole and write

$$\Delta\mathbf{x}_q = \mathbf{A}_q \cdot \begin{pmatrix} x_q \\ x'_q \end{pmatrix}, \quad (5)$$

where \mathbf{A}_q is an $M \times 2$ matrix. Each row of \mathbf{A}_q consists of the upper row of the matrices $\mathbf{M}_{iq} \cdot \Delta\mathbf{M}_q$ in Eq. (4) with \mathbf{M}_{iq} evaluated for the quadrupole and the i -th BPM. The solution for x_q and x'_q can be obtained from Eq. (5) using the technique of singular value decomposition (SVD).

If the thin lens approximation is valid, the second column of the matrix \mathbf{A}_q is zero and $\Delta\mathbf{x}_q$ can be expressed in terms of x_q alone. The change in the BPM reading would then be expressed as

$$\Delta x_{biq} = S_i \Delta x_{iq} = -S_i m_{12,iq} \Delta K L_q x_q \quad (i = 1, 2, \dots, M), \quad (6)$$

where ΔK is the quadrupole strength change and

$$m_{12,iq} = \sqrt{\beta_i \beta_q} \sin(\psi_i - \psi_q). \quad (7)$$

The beam angle x'_q is indeterminate in this case. From Eq. (6), x_q is then given by

$$x_q = -\frac{1}{\Delta K L_q} \frac{\Delta x_{biq}}{S_i m_{12,iq}}. \quad (8)$$

B. Error Reduction

From Eq. (8) it is sufficient to measure the beam position change at a single BPM to obtain x_q . However, if the actual lattice is significantly different from the model, the measurement can be sensitive to the phase error and the resulting error in x_q can be quite large. One way to reduce this error is to statistically average out the oscillatory term after squaring the numerators and denominators. That is, we put

$$x_q^2 \approx \frac{1}{(\Delta K L_q)^2} \frac{\sum_i \Delta x_{biq}^2}{\sum_i m_{12,iq}^2}, \quad (9)$$

where we assumed the average of S_i is equal to 1 and the error cancels out after summation over i . The sign of x_q is determined separately by applying Eq. (8) to a few selected BPMs adjacent to the quadrupole for which the betatron phase error is not significant. From Eqs. (7) and (9) and using the identity relation

$$\sin^2 x = \frac{1}{2}(1 - \cos 2x), \quad (10)$$

the effect of the phase error is reduced roughly as $1/M$, where M is the number of BPMs included in the summation.

Once x_q is determined, the BPM sensitivity S_i can be obtained in a similar manner from Eq. (6) as

$$S_i^2 \approx \frac{\sum_q \Delta x_{biq}^2}{\sum_q (\Delta K L_q x_q m_{12,iq})^2}. \quad (11)$$

The summation is done over the quadrupoles.

III. MEASUREMENTS

A. Beam-based Offset Measurement

An electron bunch of typically 1-nC charge with 7-GeV energy is injected from the booster into the storage ring at 1-Hz rate. The beam makes one turn around the ring and is stopped by a scraper at the end of sector 40. Figure 2 shows the vertical orbit change Δy due to the quadrupole strength change in S1B:Q2. The beam offset y_q at the quadrupole was determined to be 0.7 mm, which gave the BPM offset y_o for the nearby S1B:P1 as -0.96 mm. The solid line is the fit to the lattice model.

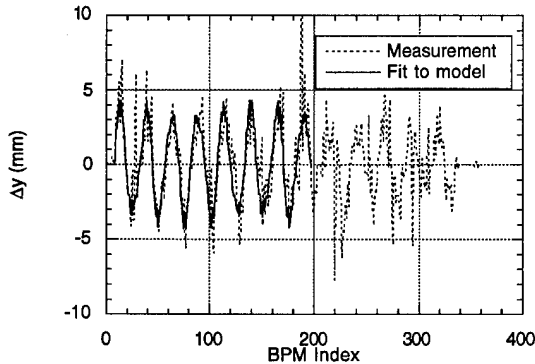


Fig. 2: The vertical orbit change Δy (dotted line) due to the quadrupole strength change in S1B:Q2 in the APS storage ring. The solid line is the fit to model using $y_q = 0.7$ mm. The BPM offset y_o for the nearby S1B:P1 is -0.96 mm.

B. BPM Electronics

The BPM system consists of four button-type electrodes, filter-comparator, monopulse receiver, signal conditioning and digitizing unit (SCDU), memory scanner, beam history module, and timing module [3]. For calibration of the electronics for offset and sensitivity, the SiO_2 cables connecting the buttons and the filter-comparator are replaced with a CW rf source (352 MHz) and four switched attenuators. The beam motion is simulated by changing the gain on the attenuators with 0.125-dB resolution. During the measurements, the attenuators are changed in steps of 0.5 dB in the

low-gain mode and 0.125 dB in the high-gain mode. These correspond to approximately 1 mm and 0.25 mm of beam motion near the center. The response of the monopulse receiver is theoretically given by

$$V_{x,y} = \frac{4}{\pi} \tan^{-1} \left(\frac{D_{x,y}}{\Sigma} \right), \quad (12)$$

where $D_{x,y}$ and Σ are the output of the filter-comparator.

Figure 3 shows examples of BPM electronics in the low- and high-gain modes. The measurement data from each BPM is combined with the theoretical model of the vacuum chamber geometry to derive 2-D polynomial coefficients [2].

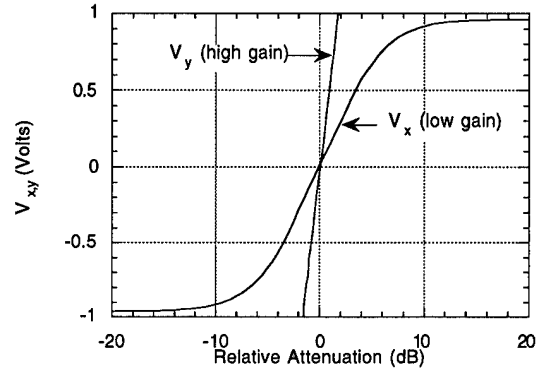


Fig. 3: Measurement on the BPM electronics response using switched attenuators. V_x with low gain and V_y with high gain are shown.

IV. DISCUSSION

In this work, we have discussed methods for calibrating the offset and sensitivity of beam position monitors in the APS storage ring. As operational diagnostic tools and for orbit feedback, BPMs are required to have high resolution and low drift. Results of measurements made at ESRF indicate $0.06\text{-}\mu\text{m}/\sqrt{\text{Hz}}$ resolution and $2\text{-}\mu\text{m}/\text{hr}$ drift over a period of 1.5 hrs with 5 mA of stored beam for the APS [4], which is confirmed through preliminary measurements made on selected BPMs.

V. REFERENCES

- [1] G. R. Lambertson, "Calibration of Position Electrodes Using External Measurements," LSAP Note-5, Lawrence Berkeley Laboratory, May 6, 1987.
- [2] Y. Chung, "Beam Position Monitor Calibration for the Advanced Photon Source," *Proceedings of 1993 IEEE Particle Accelerator Conference*, Washington, D.C., pp. 2304 - 2306, 1993.
- [3] E. Kahana, Y. Chung, A.J. Votaw and F. Lenkszus, "Configuration and Test of the APS Storage Ring Beam Position Monitor Electronics," *Proceedings of 1993 Accelerator Instrumentation Workshop*, Santa Fe, 1993.
- [4] Y. Chung and E. Kahana, "Resolution and Drift Measurements on the Advanced Photon Source Beam Position Monitor," *Proceedings of 1994 Accelerator Instrumentation Workshop*, Vancouver, 1994.

An Sampling Detector for the RHIC BPM Electronics*

W.A. Ryan and T. J. Shea
Brookhaven National Laboratory
Upton, NY 11973

Abstract

The analog detector electronics for the RHIC BPM Instrumentation is described. The detector employs a self-triggered peak detection algorithm for single bunch acquisition of beam position. Optimization of the design for low noise gives excellent position resolution, an internal self-calibration system insures position accuracy to well within the RHIC instrumentation system specification, and switched attenuation and gain insures very broad dynamic range. Design history, current implementation, and test results are described.

I. REQUIREMENTS

The following points, as previously stated [1], summarize the specifications and design philosophy of the analog front end:

1. Single bunch acquisition - bunching frequency is 8.9MHz (112nsec period).
2. Maximum bunch acquisition rate: 78 kHz (the revolution frequency) (12.8μsec period).
3. Position uncertainty at center for entire system (BPM + electronics): <0.13mm.
4. Single bunch resolution for commissioning (single bunch, 10^{10} protons per bunch): <1mm.
For operating storage ($>10^{11}$ protons per bunch, or 10^9 gold ions per bunch): <<0.1mm
5. Bunch-to-bunch coupling: < -60dB
6. Instantaneous Dynamic Range: >17dB.
Programmable attenuation: >30dB.

II. DESIGN APPROACH

The specifications above, when examined closely, require a sensitive, fast and repeatable detector with broadband response.

Broadband response is necessary to obtain single-bunch acquisition with sufficiently small bunch-to-bunch coupling in the 112nsec period between successive bunches. Narrowband detectors are feasible only if a fast switch is used in front of the front end filters to select a specific bunch. However, the trade-offs between switch speed, cost, survivability, and maximum distortion-free amplitude make this impractical.

This presents a problem as most high sensitivity detectors, in fact most RF detectors in general, are narrowband. Most BPM Electronics schemes currently in

use employ narrowband techniques: AM/PMs, the SPS Homodyne detector, and the SSC Log Ratio detector all rely on the ringing response of a narrow bandpass filter to obtain a CW signal for detection. While the output amplitude of these filters is small when compared to the peak amplitude of the BPM output, the reduction in input noise from both the narrow bandwidth of the front end filter and the detector output filter (usually lowpass, with a bandwidth equal to or less than the front end filter) keeps the SNR high.

However, these same filters, with their long ringing response, would induce too much bunch-to-bunch coupling in RHIC to be of any use for single bunch acquisition.

Two designs have been extensively developed for the RHIC BPM Electronics: a broadband synchronous detector, and a self-triggered peak sampling detector.

III. SYNCHRONOUS DETECTION

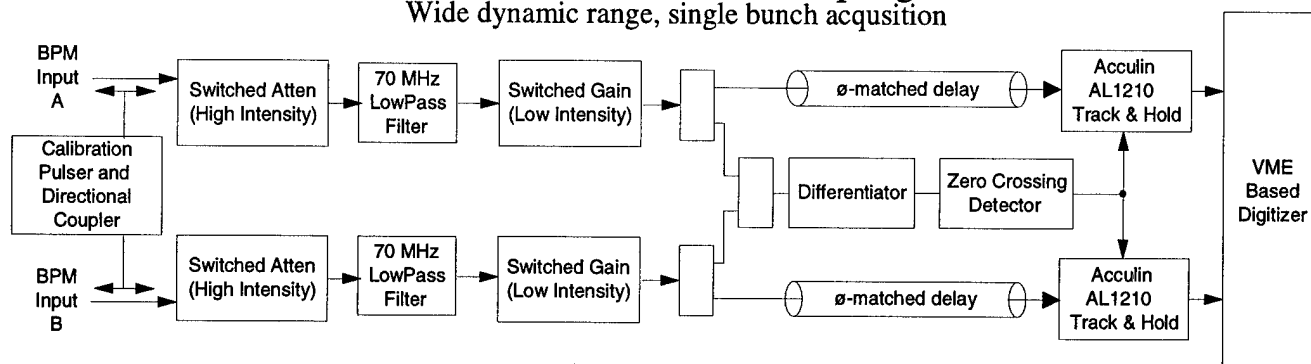
The synchronous, or homodyne, detector has a long history in RF engineering. The version developed by the RHIC instrumentation group [1] used matched 40MHz BW/70MHz center bandpass filters to condition the signal for the detector. These time response of these filters was carefully designed to reduce bunch to bunch coupling, with the bunches separated by 112nsec, to less than 60dBs. The BPM signals were then divided with RF splitters and half of each combined and input into the LO generator chain, which consisted of four Plessey SL532C limiters, a threshold comparator (to eliminate oscillation - a big problem in synchronous detectors, especially when the input signal is not continuous), RF amplifiers and a splitter whose outputs drive the LO of two double-balanced mixers. The filtered BPM signals, from the other outputs of the first two splitters, were connected to the RF mixer inputs through coaxial cable, matched in electrical length with the delay time of the limiter chain. The IF output of the mixers was then lowpass filtered (20MHz BW) and integrated over the length of the bunch response and then digitized.

This design proved to be impractical, inaccurate and expensive. Many problems were discovered trying to improve the linearity of the detector. For instance, we found that the reflected power from the lowpass filter was entering the mixer through the IF port and self-mixing, inducing a strong amplitude-dependent nonlinearity. This was corrected by terminating the IF mixer output and using a Harris high-frequency closed-loop buffer to drive the filters. Even at this point, our parts count was getting high (including 2 pairs of matched filters) and the per channel cost was becoming prohibitive. We then found the integrator was too sensitive to low frequency noise, and replaced it with a Track and

* Work supported by the U.S. Department of Energy

RHIC BPM Electronics - Peak Sampling Detector

Wide dynamic range, single bunch acquisition



Hold sampler. However, consistent operation of the sampler required some form of self-triggering, and at this point we wondered if a Track and Hold sampler could be found with better specifications than the mixer. Both the AD9100 and the Acculin AL1210 had far better linearity than any available mixer and both have sufficient bandwidth to use as the detection element in the BPM electronics.

The synchronous detector design was then abandoned, and we attempted to find a reliable way to use the Track and Hold samplers for peak detection.

IV. PEAK SAMPLING DETECTION

The decision was made to use a 70MHz Bessel lowpass filter on the front end. This reduced the number of matched filter pairs to one, from the two required for the synchronous detector.

Evaluating the Track and Hold samplers, we selected the Acculin. Although the linearity is not quite as good as the Analog Devices part, the AL1210 is much smaller, dissipates far less power, and has over twice the bandwidth (up to 400MHz small signal BW).

Once the samplers were selected, the main design challenge was the generation of a self-trigger signal time-aligned to the input signal maximum to drive the Track and Hold samplers. This is typically accomplished by differentiating the BPM signal (a pulse doublet) and using a zero crossing detector to generate a digital edge correlated to the first peak of the BPM signal.

Building an active differentiator presents several practical problems. Just as an integrator with gain is very sensitive to low frequency noise, a differentiator with gain is very sensitive to high frequency noise. Fortunately, there is sufficient signal amplitude out of the RHIC BPMs to use a passive differentiator and still maintain adequate instantaneous dynamic range. Our passive differentiator is simply a 16pF series capacitor followed by a 50 ohm termination to ground.

The zero crossing detector is made up of an SPT9689 ultrafast comparator wired in a schmitt trigger configuration with a chain of Plessey SL532C limiters on the input. The limiter chain keeps the same peak-to-peak voltage on the

input of the comparator to avoid the dispersion in propagation delay as a function of input amplitude. The dynamic range of the self-trigger, in fact the instantaneous dynamic range of the entire detector, is thus determined by the limiter chain.

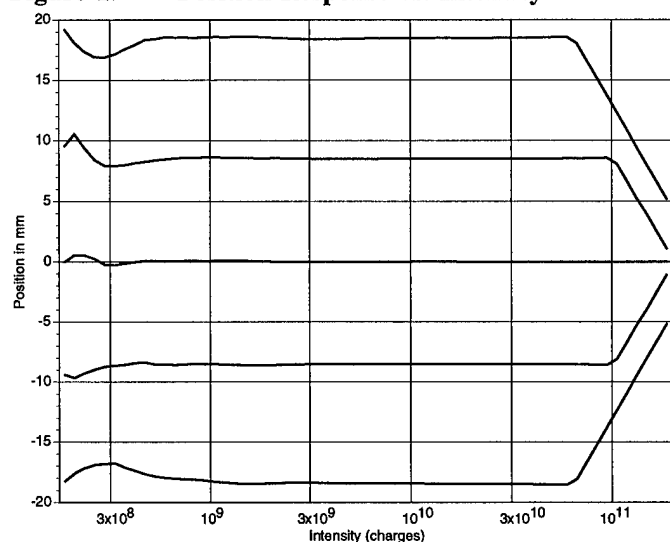
Further timing is performed with an array of one-shots, ECLinPS Lite gates and flip-flops. The circuit is setup to allow the ENABLE gate (all self-triggered detectors must be gated to prevent triggering on random signals) to trigger the Track and Hold samplers and concurrently the digitizer itself if no self-trigger took place within the gated period. In other words, the falling edge of the ENABLE gate will activate the Track and Hold samplers and the timing chain, but only if no self-trigger took place within the time that the ENABLE signal was high. A DATA VALID bit is included to differentiate between self-triggered data and data sampled by the falling edge of the ENABLE gate. This bit is high only if the timing chain was self-triggered by the input signal. The DATA VALID bit is latched and the ADCs are triggered by an ADC_TRIG output signal, also generated by the ECL timing.

V. ADDITIONAL CIRCUITRY

In order to increase the dynamic range of the detector above and beyond the instantaneous dynamic range, switched gain and attenuation have been added to the front end. While -10dB, -20dB and -30dB of attenuation can be switched into either channel independently, due to phase matching constraints the +10dB, +20dB and +30dB of available gain can only be switched into both channels simultaneously.

A pulser and stripline coupler have been designed into the circuit to allow for in-place calibration of the electronics. The coupler allows a matched, pulsed signal to be generated either into the detector or out of the detector into the BPM cables. The "inward" going pulses will permit continuous calibration of the circuit to verify and maintain the position accuracy, while the "outward" going pulses can be reflected off the BPMs and their return can be measured by the detector, which will allow continuity and loss checks of the cabling to be made periodically.

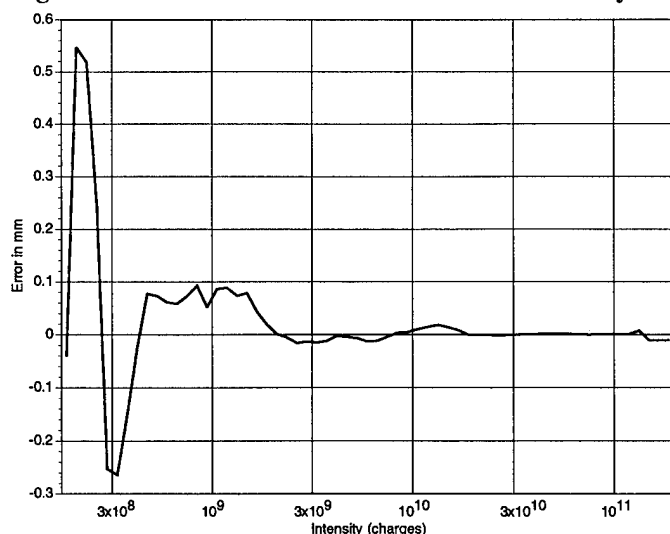
Figure 1. Position Response vs. Intensity



VI. PERFORMANCE

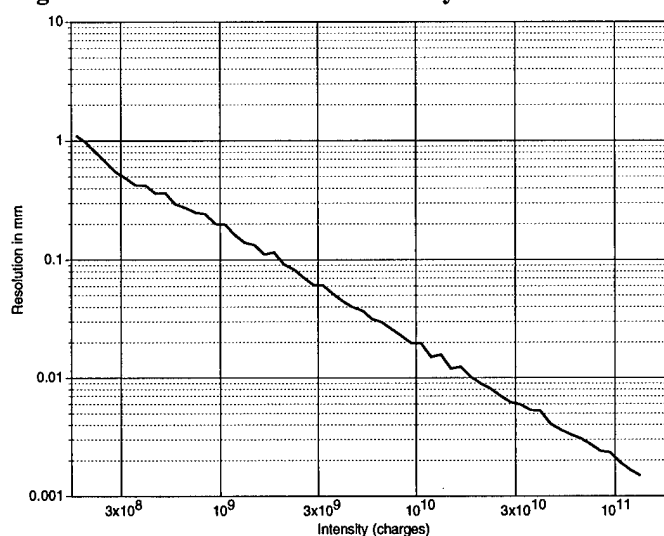
Position response of the detector is shown in Figure 1. The detector shows excellent precision over the RHIC dynamic aperture ($\pm 20\text{mm}$) and has an accurate, full aperture instantaneous dynamic range of greater than 35dB. Combined with the switched attenuation and gain, this would give the detector a full dynamic range of approximately 90dBs, although the accuracy will suffer at higher levels of added gain.

Figure 2. Error on Centered Beam vs. Intensity



Error for centered beam is shown in Figure 2. As can be seen from the graph, the accuracy over the top 30dBs of dynamic range for centered beam is better than $\pm 0.025\text{mm}$. As the beam offset from center increases, this accuracy will decrease, but will remain within spec ($\pm 0.1\text{mm}$) over the full dynamic aperture.

Figure 3. Resolution vs. Intensity



Resolution in mm RMS for centered beam is shown in Figure 3. The obvious linear response without saturation or rolloff indicates the presence of a constant noise source unrelated to the input signal. This source is in fact the injected noise inherent in the track and hold amplifier, which we were unable to reduce. Input noise will only approach this injected noise power when the switched gain is set to its maximum ($+30\text{dBs}$).

VII. FUTURE DIRECTIONS

Calibrator coupling is balanced but amplitude is not as good as predicted. This is most likely due to the small trace size of the coupler striplines, the high sensitivity of the coupling to errors in size and separation of the traces, and the poor homogeneity and accuracy of the dielectric constant of the PCB substrate (FR-4). In future designs, we would like to build the coupler on a separate RT-Duroid substrate.

VIII. ACKNOWLEDGMENTS

Much thanks to John Cupolo, Chris Degen and Bob Sikora for their invaluable assistance.

IX. MORE INFORMATION

For more information, including schematic copies and extended report on this circuit, please contact:

Tony Ryan, BNL, Bldg. 1005S, Upton, NY 11973.

Phone: (516) 282-3858

FAX (516) 282-2588

email: ryan1@bnl.gov

X. REFERENCES

- [1] W.A. Ryan and T.J. Shea, A Prototype BPM Electronics Module for RHIC, Proceedings of the 1995 Particle Accelerator Conference, pp.2310-2312.

RHIC BEAM POSITION MONITOR CHARACTERIZATION*

P.R. Cameron, M.C. Grau, M. Morvillo, T.J. Shea, R.E. Sikora
Brookhaven National Laboratory
Upton, NY 11973

Abstract

Techniques and results of RHIC BPM measurements are presented. These include wire scanner measurements of uncalibrated and calibrated BPM position and roll accuracy, preliminary measurements of the coupling between adjacent striplines to permit in situ offset calibration of the BPM signal cables and electronics, frequency dependence of the location of the BPM electrical center, and antenna measurements of the installed position of the electrical center relative to the cryostat fiducials. We also present results of simulations and measurements of cryogenic signal cable heating, and testing of the cryogenic feedthrus.

I. INTRODUCTION

The RHIC BPM performance requirements, design details, and fabrication techniques are in the literature^{1,2}. Production is underway. The 42 Injection Line BPMs are complete, calibrated, and installed. The first 130 of the 480 RHIC BPMs are complete and ready for installation. The first 20 of these were calibrated with a wire scanner. The remainder of the BPMs will be installed uncalibrated. The precise location of their electrical centers relative to the cryostat fiducials will be determined with an antenna.

II. WIRE SCANNER MEASUREMENTS

The calibration technique previously described¹ yielded the stripline at the hinge where it joins the flange to bring the electrical center into alignment with the mechanical center. Because of the exceptionally good accuracy of the uncalibrated BPMs, it has been possible to refine this

technique with the removal of the nickel bellows spring contact from the end of the contact post. The position of the stripline is now determined by the rigid contact post rather than the bumping operation. This simplifies the calibration procedure, reduces the inductance of the stripline-to-feedthru transition (improving the impedance match), diminishes stripline movement during thermal cycling, and permits baking of the BPM in warm bore regions. The function of the spring contact is now served by the cantilevered stripline, which can be seen in Figure 1. With the stripline thinned to an 0.8 mm hinge where it joins the flange, the spring constant at the contact post is about 0.1 N/micron (8 oz/mil). Typical stripline deflections are about 200 microns. The BPM is calibrated by adjusting the length of the contact posts. Data for the uncalibrated and calibrated positions of the electrical center was taken for 80 BPM measurement planes before the calibration operation was stopped. Sigma of the separation between electrical and mechanical centers is about 100 microns before and 25 microns after calibration.

Unlike position, the roll accuracy of the BPM cannot be calibrated. Data was also taken for 80 measurement planes. Sigma of the difference in orientation of the mechanical and electrical axes of the BPM is about 1 mrad.

To permit the possibility of making offset calibrations of the BPM signal cables and electronics using external means⁴, the observed position of the electrical center when signal is injected on the adjacent orthogonal striplines (instead of the wire) is being measured for all dual plane BPMs, using the setup shown in Figure 2. The transfer function for this measurement can be approximated analytically⁵ to be about 3 dB/mm. Using this transfer function, the data that has been taken on 12 dual plane BPMs has a sigma of about 100

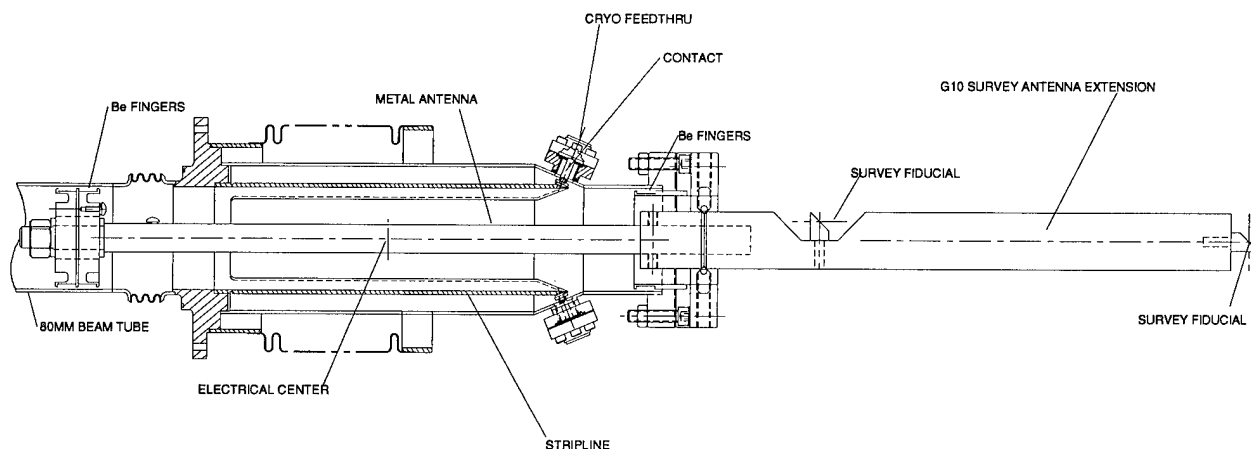


Figure 1. BPM with antenna installed

* Work supported by the U.S. Department of Energy

microns. This agrees well with the sigmas of the uncalibrated position of the electrical center and orientation of the measurement plane about the roll axis using the wire, and suggests that the same construction tolerances govern all three distributions.

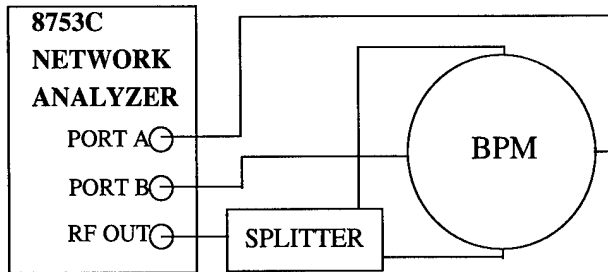


Figure 2. signal injection block diagram

The location of the measured position of the electrical center varies by about 50 microns (.035 dB) over the range from 1 Mhz to 100 Mhz. This variation is attributed to reflections resulting from imperfect terminations and coupling into the room resulting from imperfect shielding. In the wire scanner calibrations the effect of this offset can be eliminated by rotating the BPM 180 degrees. In the antenna measurements this variation will be reduced when the prototype antenna is replaced by the production antenna, which is now being fabricated.

The measured transfer function is about 0.7 dB/mm. The 4 pole Bessel low pass filter in the analog front end of the BPM electronics³ has its 3 dB point at 70 MHz, with a rolloff of 24 dB/octave. Calibrations are done at 50 MHz.

III. ANTENNA MEASUREMENTS

As construction and measurement of BPM/magnet assemblies progressed, the need for direct measurement^{6,7} of the positions of the electrical center of the BPM and the magnetic centers of the quadrupole and sextupole became increasingly clear. To accomplish this in the case of the installed BPM, the antenna shown in Figure 1 is driven by the RF output of a network analyzer, and the ratio of the signals at the BPM ports is used to locate the electrical

center of the BPM. Surveyors using the ManCat system then survey the location of the external fiducials and project back to the hidden location of the electrical center of the antenna, thereby locating the electrical center of the BPM relative to the cryostat fiducials. Antenna measurements have been made on 30 BPM/magnet assemblies. The relative difference between the measured electrical center and the surveyed position of the antenna has a sigma of less than 50 microns. A more absolute measurement is repeatability. Two BPM/magnet assemblies were re-surveyed two months after their initial measurements. The locations of the electrical centers relative to the cryostat fiducials agreed within 50 microns.

IV. CRYOGENIC SIGNAL CABLE

The cryogenic signal cables are stainless steel outer conductor, Tefzel (ETFE) dielectric, silver-plated copper center conductor, with male SMA connectors at both ends. They have been extensively analyzed using a custom program written in LabVIEW. The thermal circuit is shown in Figure 3. The program does a finite difference analysis of heat flow in 1 cm steps along the 122 cm length of the cable. Heat flow occurs because of the thermal conductance of the cable and RF heating from the signal current. Results of a typical analysis are shown in Figure 4. This analysis uses a variable gaussian bunch length convoluted onto the frequency response of the BPM to determine the spectral content of the signal in the cable. Frequency and temperature dependent skin depths and electrical resistivities, and temperature dependent thermal conductivities of the cable and the thermal anchors, are determined at each iteration of the calculation.

Figure 4 shows a plot of the temperature profile along the cable at an intensity of 3×10^{11} charges per bunch and 114 bunches in the machine (RHIC upgrade intensity), with a bunch length of 0.6 nsec and the beam 1 cm off axis. The maximum permissible operating temperature for the cables is around 400 K. It is possible to operate RHIC off-momentum, with the beam displaced as much as 2 cm, and with more high frequency content in the bunch, either because of shorter bunch lengths or bunch structure which is not gaussian. The intensity/bunch length limit for RHIC is set by magnet quenching due to heating of the beam pipe by

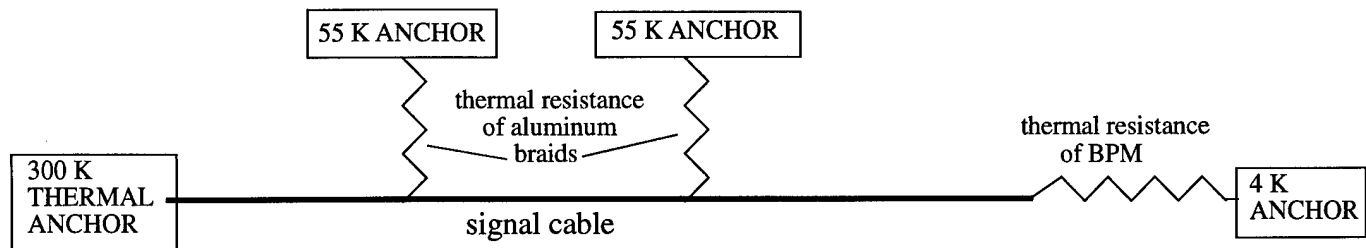


Figure 3. Signal cable thermal circuit

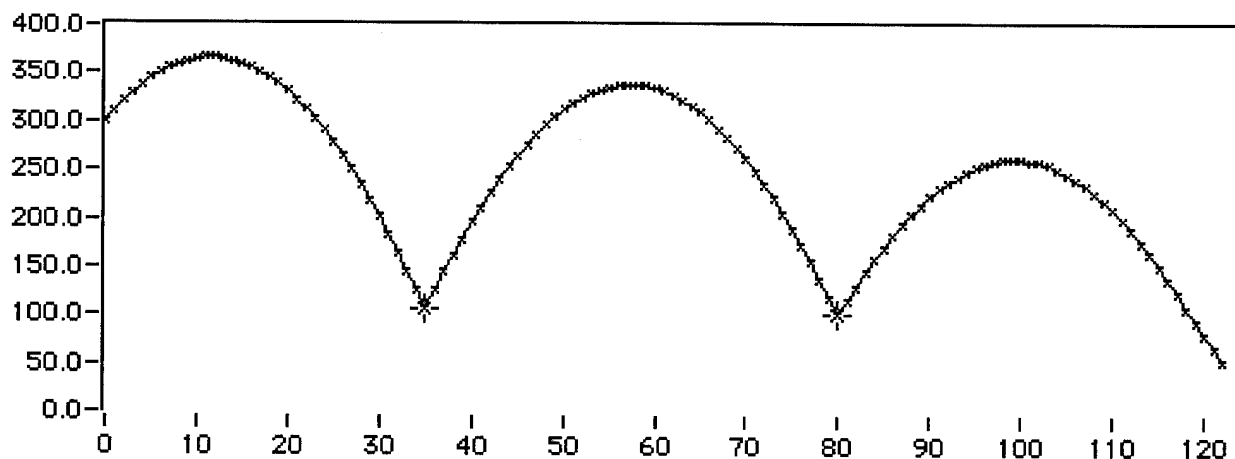


Figure 4. Typical signal cable temperature profile [degrees K vs cm]

the beam image current. Our simulations indicate that in continuous operation, the possibility exists that the signal cables can be overheated before a magnet will quench. In the case of transients, the situation is worse. The time constant for the cable is about 1 degree K/sec. The time constant for the magnet coil is about 0.01 K/sec. Operational constraints must be placed on beam offset and bunch spectral content. This problem remains under study.

Heat load per cable to 4 K at RHIC upgrade intensity and 0.6 nsec bunch length is 170 mW, comprised of 50 mW of conduction and 120 mW of RF heating. Heat load per cable to the 55 K heat shield is 660 mW, 290 mW conduction and 370 mW heating.

Attenuation in the cables is dependent on temperature, and therefore on intensity, position, and bunch length (or more generally the spectral content of the beam). Despite the rather dramatic temperature profile shown in Figure 4, the correction amounts to only about 0.08 dB or 60 microns in this example.

V. CRYOGENIC FEEDTHRU

The 'glass-ceramic' cryogenic feedthru design (which uses lithium silicate glass dielectric doped to match the expansion coefficient of stainless steel) has proven reliable under cryogenic shock testing. About half of the 1400 cryogenic feedthrus have been subject to five shock cycles into liquid nitrogen, followed by vacuum baking at 300 degrees C and UHV leak checking with no failures. This design is more simple, more economical, and has better RF properties than the conventional ceramic/kovar design.

VI. CONCLUSIONS

The exceptionally good accuracy of the uncalibrated BPMs has permitted the refinement of calibration techniques, and contributed to their eventual abandonment in favor of the antenna measurement of the position of the

BPM electrical center. Heating of the cryogenic signal cables might represent a constraint on RHIC operation, and remains under study.

VII. REFERENCES

- [1] P. Cameron et. al., RHIC Beam Position Monitor Assemblies, 1993 IEEE Particle Accelerator Conference, p. 2328.
- [2] Additional information is available on the RHIC Instrumentation Web Server at <http://iguana.rhic.bnl.gov/>
- [3] W.A. Ryan et. al., A Sampling Detector for the RHIC BPM Electronics, these proceedings.
- [4] G.R. Lambertson, Calibration of Position Electrodes Using External Measurements, LSAP Note 5, LBL, 1987.
- [5] R.E. Schafer, Beam Position Monitoring, Accelerator Instrumentation Workshop, Brookhaven, 1989.
- [6] M. Goldman, R. Sikora, and T.J. Shea, Preliminary Studies on a Magneto-Optical Procedure for Aligning RHIC Magnets, 1993 IEEE Particle Accelerator Conference, p. 2916.
- [7] D. Trbojevic et. al., Alignment and Survey of the Elements in RHIC, these proceedings.

DUKE STORAGE RING TUNE MEASUREMENTS SYSTEM USING RAZOR BLADE AND PHOTOMULTIPLIER*

V. N. Litvinenko, B. Burnham, N. Hower, P. Morcombe, and Y. Wu
Duke University, Free Electron Laser Laboratory , Durham, NC 27708-0319 USA

Abstract

We present in this paper the description of the Duke storage ring tune measurements system. An unusual feature of this system is the use of synchrotron radiation to sense oscillation of the electron beam. This system includes a lens, a razor blade placed at the focus and a photomultiplier. Our experience shows that this system can operate on -70 dBm level and detect electron beam oscillations as small as one micron.

I. INTRODUCTION

The 1.1 GeV Duke electron storage ring [1] has four end-of-arc ports for extraction of synchrotron radiation. The visible part of this radiation is used for optical diagnostics of the electron beam. It includes optics (mirrors, lenses, beam-splitters), TV cameras, screens, a dissector with 20 psec resolution, and a number of photomultipliers. Each corner is equipped with a small optical table to mount optical components. We use these elements to build a tune measurements system.

II. TUNE MEASUREMENTS SYSTEM

Schematic of the Duke storage ring tunes measurement system is shown on Fig.1. It is based on surplus equipment:

HP-8443A tracking generator and HP-8553 spectrum analyzer with 110 MHz range. Some parameters of the Duke storage ring are listed in Table 1.

Table 1. Main Parameters of Duke Storage Ring

Operation energy [GeV]	0.2 - 1.1
Ring circumference [m]	107.46
Revolution frequency [MHz]	2.7898
RF frequency [MHz]	178.547
Betatron tunes, Qx and Qy	9.111, 4.180

The excitation part.

The excitation part consists of the tracking generator, 1W amplifier and a transformer attached to two short mismatched BPM striplines. The Duke storage ring has 60 stripline BPMs which do not have electronics. Four BPM striplines are located at 45° with respect to the median plane. They are 2.5 cm long and are shorted at one end. There are two types of BPMs- arc BPMs with 2 cm internal radius and straight section BPMs with 5 cm internal radius. The coupling of these striplines with the electron beam is efficient at very high frequencies (few GHz) where the cost of the tune measurements system is very high.

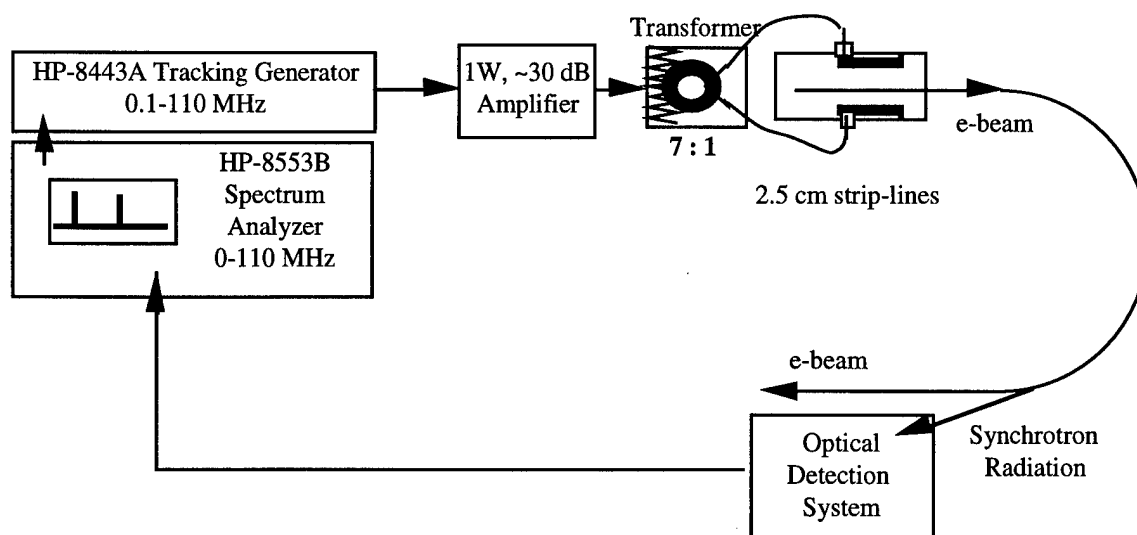


Fig. 1 The Duke Storage Ring Tunes Measurement System

*Work supported by ONR grant #N00014-94-1-0818

We use the pure magnetic coupling at low frequency (<1.5 MHz) in the excitation system. An 1 W, a 30 dB

amplifier is loaded on ferrite 7:1 transformer for better matching. This scheme also improves excitation efficiency at low frequencies by increasing current through the striplines. The transformer is attached to two opposite

striplines to excite a dipole AC magnetic field. The magnetic field is directed at 45° with respect to the median plane and can be used to excite both horizontal and vertical oscillations. The system has a bandwidth of 5 MHz, which is larger than we need. This system excites an electron beam oscillation when the frequency of the tracking generator f_{TG} matches one of betatron frequencies:

$f_{TG} = f_{rev} \cdot \left(N \pm \{Q_{x,y}\} \right)$, where f_{rev} is revolution frequency and $\{Q_{x,y}\}$ is a non-integer part of one of betatron tunes and N is an arbitrary integer number. We use $N=0$ and the most useful tracking generator range for our ring is 200-800 kHz.

The performance of the above system was very satisfactory. This system can excite 1 to 2 mm beam oscillations at 1 GeV when operated at 5 dBm of tracking generator output. We initially used this system in a manual mode in which resonance was determined by the increase in the beam size monitored by a video camera. Later we switched to an automated mode with an optical detector.

The detector part - the razor blade with photomultiplier.

We take advantage of the available visible light to build a simple, elegant, very sensitive and inexpensive system for tune measurements. The schematic of this system is shown on Fig.2. The detection system includes the lens which focuses light emitted by the electron beam on the razor edge. The razor is located on 2D stage. Longitudinal adjustment is used to place the razor exactly at the focal plane, where the image of the electron beam is

created by the lens. This image follows the motion of the electron beam and can be used to detect its oscillations. Transverse adjustment is used to locate the razor edge at the center of beam image. This degree of motion is remotely controlled from the storage ring control room.

The photomultiplier is located behind the razor. Its window and photo-cathode is large enough to detect all light passing the razor blade. The razor blade is installed at 45° and cuts the half of the beam image as shown on Fig. 3. It is natural to use an angle of 45° to be sensitive to both horizontal and vertical oscillations of the electron beam. To adjust the razor on the middle of the beam image we use the DC signal from the photomultiplier: we move the razor blade out to let all light to pass and then move it to the position when the DC signal decreases by a factor of two. There is drastic difference in AC response of the photomultiplier: when the blade is out, the signal from photomultiplier is pure and repeatable; when the blade cuts the image in half, the system becomes very sensitive to small motions of the electron beam.

When the electron beam position oscillates with frequency f_{beam} , horizontally or vertically, it modulates the intensity of the light falling on the photomultiplier. The spectrum of the photomultiplier signal will contain the same frequency shifted by harmonics of the revolution frequency: $f = f_{beam} \pm Nf_{rev}$. The harmonic content depends on the filling pattern of the electron beam and the bandwidth of the photomultiplier.

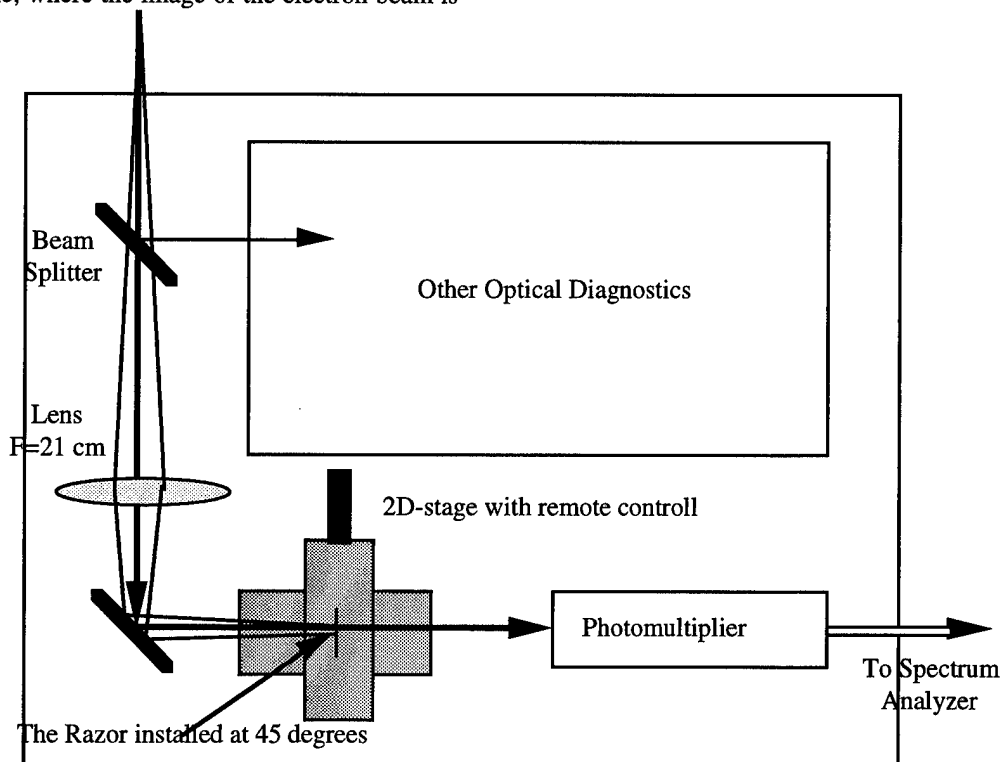


Fig. 2 Optical detection system for tunes measurements.

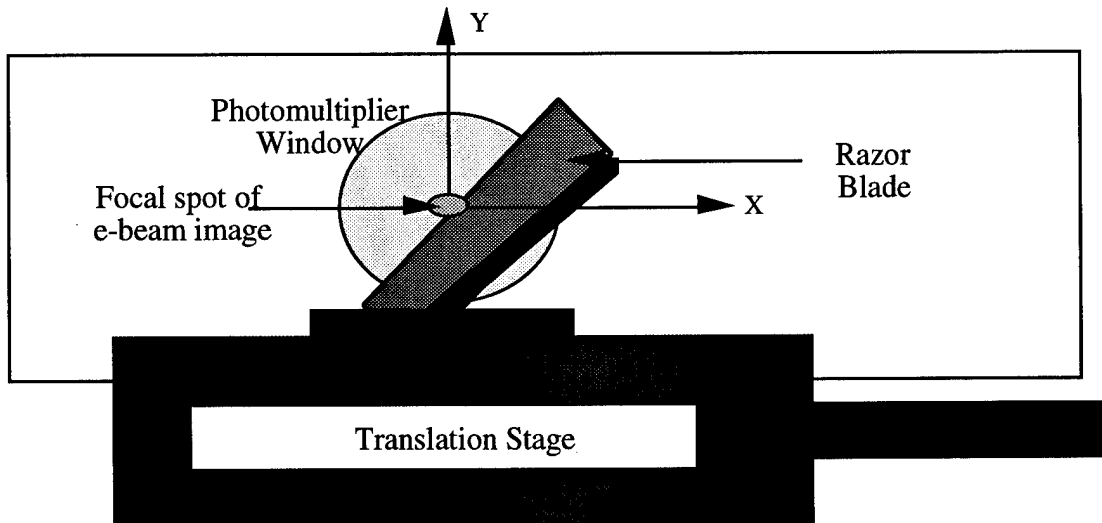


Fig. 3 Ideal positioning of e-beam image on the razor blade for detector of dipole oscillations.

We use the zero-th harmonic whose amplitude is proportional to the average electron beam current and the amplitude of oscillations.

We use a very common 931-A photomultiplier in our system with bandwidth of about 30 MHz. Control of its 1.2 kV high voltage power supply (as well as other photomultipliers) is a part of the storage ring computer control system. Thus, we can always set an optimal operating point of the photomultiplier.

III. CONCLUSIONS

The typical electron beam size in the Duke storage ring is 100-400 microns. It means that oscillations of electron beam with an amplitude of one micron can be detected easily. We tested the performance of the system described above with a wide range of the electron beam current and energies in the Duke storage ring. The system performed perfectly. With 1 kHz bandwidth of the spectrum analyzer, the system has betatron peak 3 dB above the noise level with -70 dBm amplitude (tracking generator output). It means that this system can easily detect an electron beam oscillation as small as 0.5 microns. With -50 dBm signal level, the betatron peaks are very clean without any noticeable noise. The performance is remarkable for a detection system costing less than two thousands dollars.

We are planning further improvements to the detection system, i.e. to make detector self-adjustable using feed-back from a segmented photodiode to control the image position on the blade. In addition, a simple DC feed back system will automatically control the photomultiplier gain. This system (sketched on Fig. 4) would not require any operator assistance: it will provide constant sensitivity in wide range of beam currents (0.01 mA to 1 A) and beam positions (± 1 cm in both directions).

Authors are thankful to Steve Kramer provided for preliminary test of this system at VUV ring (BNL). We would also like to thank Ping Wang, Carl Dickey, Joe Faircloth, Jim Meyer, and Owen Oakeley for helping assembling this system.

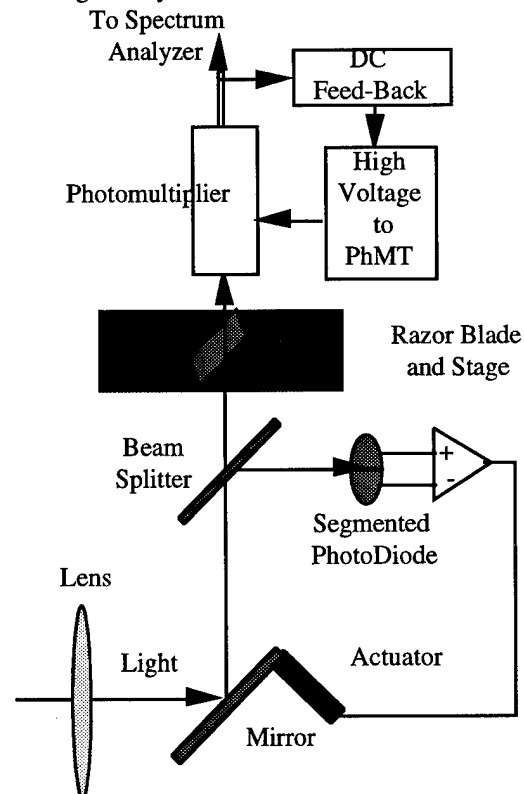


Fig. 4 Self-adjusted detection system.

IV. REFERENCES

- [1] V.N.Litvinenko et al., "Commissioning of the Duke Storage Ring, These Proceedings.

The Development of Beam Current Monitors in the APS*

X. Wang, F. Lenkszus, and E. Rotela

Advanced Photon Source, Argonne National Laboratory
9700 South Cass Avenue, Argonne, Illinois 60439

Abstract

The Advanced Photon Source (APS) is a third-generation 7-GeV synchrotron radiation source. The precision measurement of beam current is a challenging task in high energy accelerators, such as the APS, with a wide range of beam parameters and complicated noise, radiation, and thermal environments. The beam pulses in the APS injector and storage ring have charge ranging from 50pC to 25nC with pulse durations varying from 30ps to 30ns. A total of nine non-intercepting beam current monitors have been installed in the APS facility (excluding those in the linac) for general current measurement. In addition, several independent current monitors with specially designed redundant interlock electronics are installed for personnel safety and machine protection. This paper documents the design and development of current monitors in the APS, discusses the commissioning experience in the past year, and presents the results of recent operations.

I. INTRODUCTION

The Advanced Photon Source, now in the commissioning phase, is a 7-GeV storage ring served by a full-energy injector consisting of an electron/positron linac, a positron accumulator ring (PAR), a 7-GeV booster, and associated beam transfer lines.

Non-intercepting, high-accuracy beam current monitors are required for the measurement of total charge, peak current, average current, lifetime, transfer efficiency, and absolute beam loss. Figure 1 shows the layout of the current monitors in the APS. All current monitors shown have been installed and used extensively to support APS commissioning and operation.

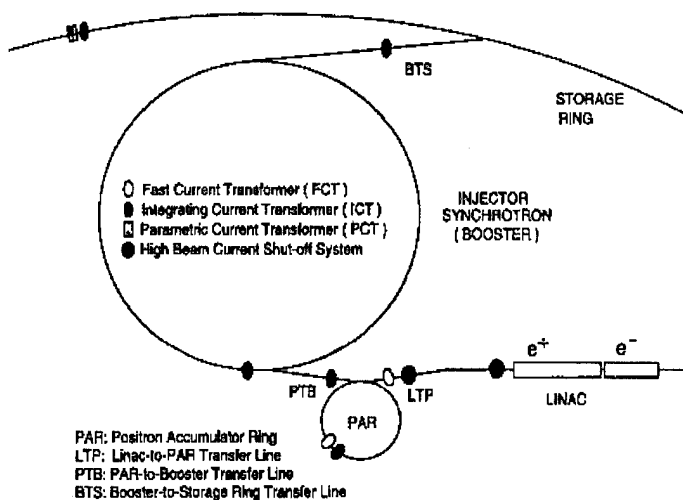


Figure 1: Layout of beam current monitors in the APS

* Work supported by U.S. Department of Energy, Office of Basic Sciences, under Contract No. W-31-109-ENG-38.

II. INJECTOR CURRENT MONITORS

The current monitors in the APS injector are primarily used for measuring total beam charge and transfer efficiency at various locations. The accelerator machine studies and operation require a non-intercepting device that (1) performs real-time measurements with high absolute accuracy, (2) is bipolar so that it can accommodate both electron and positron operations, and (3) has a wide dynamic range up to ± 30 nC with a resolution better than 25pC.

Monitoring of the beam charge/current is based on the use of integrating or fast current transformers (ICTs or FCTs) manufactured by Bergoz and in-house beam current monitoring electronics [1]. The FCT is a passive AC transformer with 1ns rise time. It is used to measure peak current and total charge of the linac 30ns macropulse in the linac-to-PAR (LTP) transfer line. The ICT is a capacitively shorted transformer [2] that stretches a beam bunch of a few tens of picoseconds to an output pulse of around 25 nanoseconds with its area proportional to the total charge of the beam bunch. The signal processing of the ICT output waveform requires a high precision measurement of the voltage \times time area of a very short pulse, which cannot be done by commercially available gated integrators using conventional designs. An ultrafast, high-precision gated integrator [3] has been developed to accurately calculate the transformer's output waveform area and to hold its output DC level proportional to the total beam charge for digitizing. This gated integrator provides fast response and high precision by introducing new design approaches. The various circuit errors usually associated with a high-speed gated integrator are virtually eliminated. Consequently, the relationship between the input and output of the integrator is clearly defined. The integrator is totally bipolar, resettable, and is capable of subtracting the input signal baseline offset within just one timing window, which has been proven extremely useful in processing the current transformer signals and achieving high noise rejection.

The current transformer inside the tunnel is connected to the nearest instrument room via a low-loss Heliax cable. The signal is fed into a single 6U VME current monitoring electronics module, which can be accessed by the control system. The main features of the VME module include a fast gated integrator with automatic baseline subtraction, completely programmable timing circuitry, and an on-board 12-bit A/D converter. The current monitor data acquisition is performed by the APS control system, which is a distributed system consisting of workstations, network servers, and IOCs. Associated operating programs are from the Experimental Physics and Industrial Control System (EPICS). The resulting digital data is converted to beam charge and current information and displayed on the workstation screen. The programs provide mouse-controlled operation for system setup and control.

The same system is used to measure the average current in the PAR and booster. Since there is only one beam bunch in the PAR or booster at a given time, the average current in the rings can be simply obtained by dividing the measured total charge of the single bunch by the ring revolution time.

To use the current monitor as a real-time tuning aid, the buffered ICT raw signals in the rings are made available in the main control room (MCR). For those ICTs too far away from the MCR, the signal is preserved by displaying it on an oscilloscope located in the nearby instrument room. The scope screen is observed by a charge-coupled device (CCD) camera and the video signal is transmitted by optical cable to a screen in the MCR. The scope can be accessed by the MCR via a GPIB bus and the setup can be adjusted on an EPICS screen.

The charge/current monitors described have all been installed and commissioned. Each system was calibrated prior to operation by injecting the test pulses to a single-turn calibration winding of the transformer to simulate the beam pulses of fixed charges. Timing variables for the gated integrator must also be set properly. The gate delay and width were adjusted for each monitor so that the beam pulse falls well within the gate window.

The PAR current monitor data is shown in Fig. 2. The ICT output signal shows a large signal baseline offset relative to the signal amplitude due to small pulse separation (102ns) in the PAR. The offset level changes as beam intensity changes. The high performance of the fast gated integrator is well demonstrated here in the signal bunch charge measurement. As shown in Fig. 2, the signal baseline is subtracted and only one beam bunch signal is integrated within the 100ns gate window. The negative DC level (bottom trace) proportional to the total charge of single electron bunch is digitized for readout.

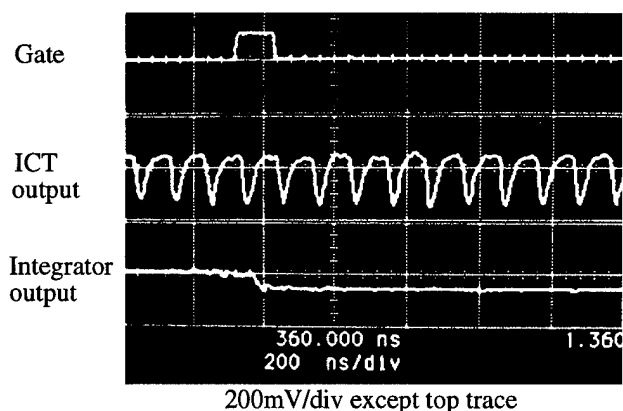


Figure 2: PAR current monitor signals

Figure 3 is an EPICS screen displaying the total beam charges at three different locations. In this case, two linac macrobunches were accumulated in the PAR and then extracted to the PTB transfer line for injection into the booster. The transfer efficiency is near 100%.

Kicker noise has been identified as a major noise contributor to the current monitor signal due to the same arrival time and simple kicker shielding and grounding design. The current

monitor system grounding and shielding method discussed in [4] has helped significantly to reduce the noise pickup. However, the noise level and appearance vary from kicker to kicker depending on the grounding structure and the physical location relative to a specific current transformer. Figure 4 shows the signal from the current monitor in the booster-to-storage ring (BTS) transfer line. The spike is the bunch signal. The underlying wave is noise pickup from the booster extraction kicker. The noise added about 300pC offset to the readout even though the signal was integrated within a very narrow gate window. The problem was resolved by increasing the baseline sampling speed in the gated integrator so that the underlying kicker noise could be subtracted as baseline offset.

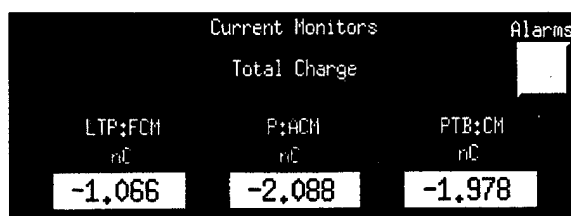


Figure 3: An EPICS screen showing total charges

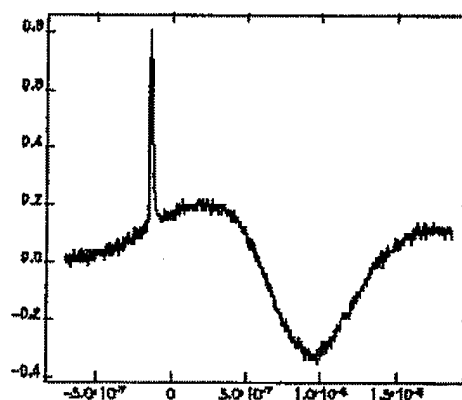


Figure 4: The BTS current monitor signal

The current monitors with specially designed interlock circuitry are also used to provide personnel safety protection in the event of acceleration of excessive beam currents. Two independent high beam current shut-off systems [5] have been installed in the linac and the LTP transfer line as shown in Fig. 1. Beam current is monitored by an FCT and fully redundant supervisory circuits connected to the Access Control Interlock System (ACIS) for beam intensity related shutdowns of the linac. To ensure a high degree of reliability, both systems employ a continuous self-checking function which injects a test pulse to a single-turn test winding after each beam pulse to verify that the system is fully functional. The system is designed to be fail-safe for all possible system faults such as loss of power, open or shorted signal or test cables, loss of external trigger, etc. The capability of the system allows management to define an operational safety envelope that contributes to significantly improved protection at the accelerator.

III. STORAGE RING CURRENT MONITORS

Two current transformers are installed in the storage ring for both average current and injection charge measurements. Average current is measured by Bergoz's parametric current transformer (PCT) with resolution better than $5\mu\text{A}$ and 400mA full scale range. The PCT output is digitized by a high-precision digital voltmeter and read out via GPIB. Single turn injection is monitored by an ICT and the VME module current monitoring electronics described above.

Two current transformers share the same housing and are located in the storage ring sector 35 straight section to avoid synchrotron radiation heating. Since the PCT is sensitive to the nearby stray magnetic fields which could add significant offset to the PCT output, the shield of the housing was very carefully designed. The transformers are completely surrounded by shields, composed of four layers of mu-metal and two layers of copper-plated low carbon steel for wide-range noise shielding. The vacuum chamber is formed by a commercial ceramic break and a welded bellows that protects the ceramic. To limit rf leakage and prevent the housing cavity from ringing with the beam frequency components, the ceramic break is wrapped with metal foil isolated by kapton tape overlapping the vacuum chamber on both sides of the break. In addition, a stainless steel tube with the same aperture as the storage ring vacuum chamber and a 2mm gap at the center is suspended inside the ceramic break and bellows and attached to two end flanges. Total capacitance of the two gaps is around 450pF. Other features of the housing assembly include two built-in heaters for bakeout, a water-cooled transformer support to prevent excessive heating from damaging the transformers, and a thermocouple probe for monitoring the air temperature around the transformers.

Figure 5 shows the PCT data of the APS first stored beam along with an exponential fit. The data fits the exponential extremely well. The monitor detected very low stored beam. No offset errors due to nearby stray magnetic field were observed.

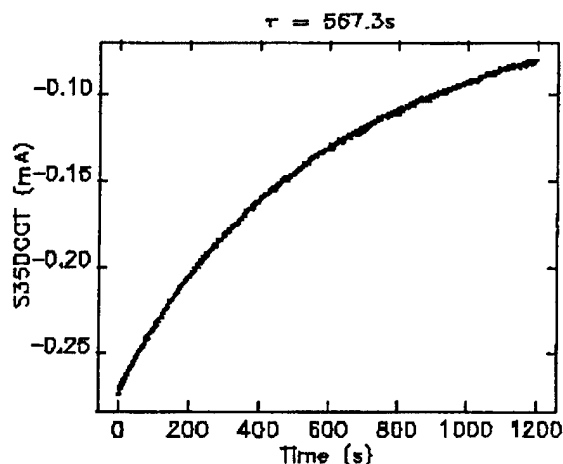


Figure 5: Storage ring PCT data

The storage ring machine protection systems (MPS) [6] are being developed to protect the accelerator components from thermal damage by missteered high-power x-ray beams.

The system consists of a large number of fault sensors. To avoid frequent false or unnecessary machine shut-downs, many trip requests generated by the MPS subsystems require a beam intensity-based decision made in the central MPS summation box. Two independent analog signals proportional to the average beam current and another TTL digital signal indicating minimum beam current status are required to link to the central MPS logic. One analog signal is obtained by applying the PCT output to an absolute value generator that produces output voltage equal in magnitude to the PCT output voltage regardless of the beam polarities. In order to provide the second independent measurement, a new kind of storage ring average current monitor based on the ICT and gated integrator has been developed. The basic concept is to integrate all the bunches in the ring by a fast, high-precision gated integrator to obtain the accumulated total charge. This is accomplished by opening the gate window for exactly one turn (revolution time=3.68 μs). After the gate window is closed, the final output proportional to the average current is sampled and held by a sample-and-hold amplifier which produces a DC output voltage scaled to the same range and sensitivity as the PCT. The output is updated every few turns, which offers the advantage of fast response time over the PCT. The system will be fully tested when the storage ring starts commissioning of multi-bunch accumulation. A full description and test results plus other design features of the MPS current monitor interface system will be presented later.

IV. CONCLUSION

Tremendous progress has been made in commissioning the APS in the past year. The current monitor played an important role in diagnostics support to the commissioning. While the present current monitor designs have been proven sound and adequate, more improvements will be made in the areas of noise reduction and resolution enhancement.

V. REFERENCES

- [1] X. Wang, F. Lenkszus, and E. Rotela, "Design and Commissioning of the APS Beam Charge and Current Monitors," *Proc. of the 6th Accelerator Beam Instrumentation Workshop (BIW)*, Vancouver, B. C., Canada, 1994.
- [2] K. Unser, "Design and Preliminary Tests of a Beam Intensity Monitor for LEP," *Proc. of the 1989 IEEE Particle Accelerator Conference*, Vol. 1, p. 71, 1989.
- [3] X. Wang, "Ultrafast, High Precision Gated Integrator," *Proc. of the 6th BIW*, 1994.
- [4] X. Wang, "Design and Initial Tests of Beam Current Monitoring Systems for the APS Transport Lines," *AIP Conference Proceedings*, No. 281, p. 234-241, 1992.
- [5] X. Wang, M. Knott, and A. Lumpkin, "High Beam Current Shut-Off Systems in the APS linac and Low Energy Transport Line," *Proc. of the 6th BIW*, 1994.
- [6] A. Lumpkin, et al., "Overall Design Concepts for the APS Storage Ring Machine Protection System," these proceedings.

OVERALL DESIGN CONCEPTS FOR THE APS STORAGE RING MACHINE PROTECTION SYSTEM*

A. Lumpkin, R. Fuja, A. Votaw, X. Wang, D. Shu, J. Stepp, N. Arnold,
G. Nawrocki, G. Decker, and Y. Chung

Argonne National Laboratory, 9700 S. Cass Ave., Argonne, IL 60439 USA

Abstract

The basic design and status of the machine protection system for the Advanced Photon Source (APS) storage ring are discussed. The machine is passively safe to the bending magnet sources, but the high power of the insertion devices requires missteering conditions to be identified and the beam aborted in less than one millisecond. The basic aspects of waterflow, temperature, beam position, etc. monitoring are addressed. Initial commissioning of subsystems and sensors is stasured.

I. INTRODUCTION

The Advanced Photon Source (APS) storage ring (SR) will be a third-generation synchrotron radiation user facility and is expected to become operational in late 1996. At 100 mA stored beam current and 7-GeV beam energy, the ring is designed to be passively safe to the 80 bending magnet (BM) radiation sources under normal cooling water flow conditions even to beam missteering [1-3]. Under the same beam conditions, however, the 10-kW x-ray beams from any installed "closed gap" insertion devices, if missteered, pose an immediate threat (in the few-ms timescale) to the extruded aluminum vacuum chamber. The machine protection system (MPS) is based on an array of different types of sensors that will be used to determine if conditions are unacceptable. It would then initiate a fast beam abort by interrupting the low-level rf for the power to the accelerator cavities. The stored beam would then coast inward radially to a scraper and be lost in 300 μ sec. Water flow, vacuum gate valve status, and beam current levels will be initially involved. This will be augmented by beam missteering sensors using selected rf BPM monitors, resistive wire monitors (WMs), and resistive temperature devices (RTDs). A commissioned beam-limit chassis covering the region of the insertion device (ID) chamber is a prerequisite for installation of the first 2.5-m-long undulator.

II. EXPERIMENTAL BACKGROUND AND SENSOR STRATEGIES

The APS presents a challenge both in terms of size, with its 1104-m circumference ring, 80 bending magnet sources, more than 600 controllers of water/temperature, etc., and in the required ms abort time scale if the 10-kW ID beam becomes missteered beyond the accepted limits. It has been calculated that certain areas of the extruded aluminum vacuum chamber could reach unacceptable temperatures if the 10-kW beam

dwelled on it longer than a few ms. Since space limitations preclude a full description of the system, only its key features will be addressed.

The APS MPS system can be divided into roughly three functionally different subsystems: (1) the low-level fault condition sensors, (2) the local MPS logic summation boxes, and (3) the central MPS summation chassis with interface to the fast beam abort system (FBAS) itself. The FBAS method is via a momentary interruption of the storage ring rf system. At this time to address the 1-ms abort response time requirement, the abort command results in the momentary interruption (~ 100 msec) of the low-level rf which is amplified by the high-power rf klystron system. Redundant paths are used, and the beam intensity is monitored by an integrated current transformer (ICT) to verify the beam is below 0.5 mA within the 100-ms time window. Eventually, it is anticipated that a second way to abort the high-power rf will be used should the system sense that the beam current has not reached the low limit in 100 ms.

A. The Low-Level Fault Condition Sensors

A variety of sensors are involved to verify the machine systems are within their prescribed limits. The cooled water flow to all absorbers and temperature (copper metal system), the cooled water flow to the extruded aluminum vacuum chambers (Al water system), and the status of all vacuum gate valves are monitored through a series of 80 VME-based latch cards. Figure 1 shows a schematic of a single sector overview (there are 40 sectors) with a monitoring of flow transducers and thermocouples. The 1-MHz heartbeat is generated in each board and is only interrupted if one of the limits is reached.

An independent water flow and valve status comes from each front end (the UHV section from the accelerator gate valve to the ratchet wall) which includes photon shutters and other apertures.

The threat of the missteered ID beam and even the BM beams for stored currents greater than 100 mA has resulted in a series of devices. The principal protection is by monitoring the beam positions from about 240 of the 360 rf BPMs in the SR. Each dedicated beam limits chassis will cover six BPMs from two adjacent sectors. Although the BPM electronics have single turn capability, the raw output will undergo a 32-turn (~ 100 μ s) average, and this position will be compared to a "warning limit" and an "abort limit." In the latter case, (and if the local ID has a closed gap) the heartbeat from this chassis to the local MPS summation box would be interrupted, resulting in the local MPS heartbeat being interrupted to the main MPS summation box. The FBAS would be activated then, and the beam would coast into the scraper in less than 300 μ s.

*Work supported by the U.S. Department of Energy, Office of Basic Energy Sciences, under Contract No. W-31-109-ENG-38.

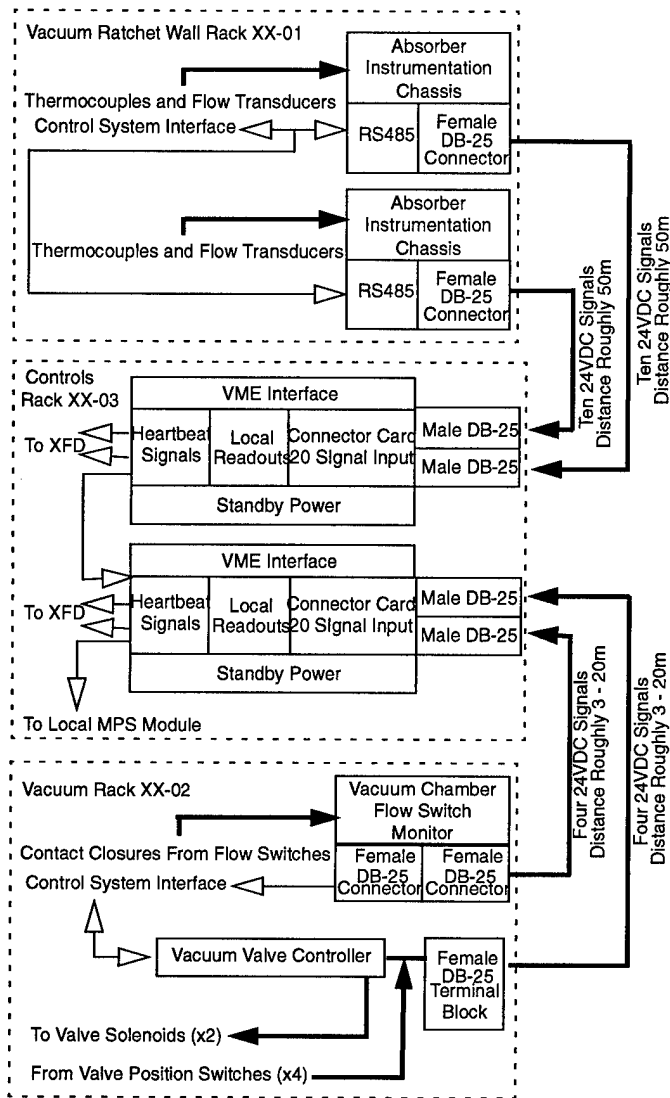


Figure 1: Single sector overview of the water system and vacuum isolation valves to the local VME latch card.

Additional protection from global orbit missteering situations is provided by a small number of resistive wire monitors located above and below the x-ray beam centerline [2]. These are located on the ID front ends which also transport part of one of the two dipole sources in each of the first five sectors of the SR. The temperature change of this wire under x-ray irradiation causes a resistance change which the wire monitor electronics chassis compares to a preset limit. It also has a heartbeat that feeds a local MPS module. This response time-scale is more like tens of ms while a threat from a BM source only is many seconds [3]. Also a series of resistive temperature devices (RTD) will be mounted on the upper and lower wall of each dipole vacuum chamber. A bending magnet beam that is missteered will provide sufficient thermal load so processing electronics can detect the temperature change. The prototype electronics chassis has been built, and the RTD subsystem will be tested in the summer of 1995. This particular protection is planned to be installed prior to test operations above the baseline 100-mA stored beam current.

An additional redundancy is planned by using the beam position information in the orbit feedback systems reflective memory. An independent microprocessor would evaluate positions and even angles to assess beam orbit correctness. This system would be linked to the main MPS module due to the global nature of its data pool.

The local MPS inputs and outputs are summarized in Table 1. There are a few sectors where the eight-channel allotment is exceeded; in those either the sensor heartbeat will be shipped to the next available module or a daughterboard will be developed.

Table 1: Summary of Inputs and Outputs for the Local MPS Module.

8 Inputs Per Local MPS and 1 Output		
Inputs	Total aborts	# Inputs Per Local MPS
Wire Monitors	2	1 in 2
Surface Temp	20	1
Vacuum	20*	1
Water Flow	20*	1
BPMs	20 BM	1
	20 ID	1
XFD	40*	2
Output	1	1

*sum 2 sectors

B. The Local MPS Module

The local MPS module relies on eight fiber receivers for the input 1-MHz heartbeats and uses Altera-based chips to evaluate the incoming channels. Since both Alteras detect the same inputs, a redundancy factor is developed. The module has a VME architecture and is monitored also by EPICS via an I/O connector. The boards are powered by a supply separate from the VME chassis. Since unused inputs are masked in Altera programming, no jumpers are used. One heartbeat is sent on fiber to the main MPS modules. Figure 2 shows a schematic of the module.

C. The Main MPS Module and FBAS Interface

The main MPS module in this phase is comprised of three local modules to cover the heartbeats from the 20 local MPS modules and a decision making card that has an input to the rf pin diode switches. An ICT used as an average current monitor provides input on the low (0.5 mA) or high limit (100 mA) in the ring. Abort requests are ignored if the current level is less than 0.5 mA (as in the early commissioning). Two beam monitor level signals are used.

Aborts are initiated when a heartbeat signal is lost, either of the two beam monitoring analog signals are removed, or the maximum beam current is detected by the analog circuits. The line that requested the abort is latched, the start/stop injection signal is latched low, the rf gates open for 100 ms, and the beam current level logic circuits are activated. If the beam current in the ring has not fallen below 0.5 mA in 100 ms, the rf

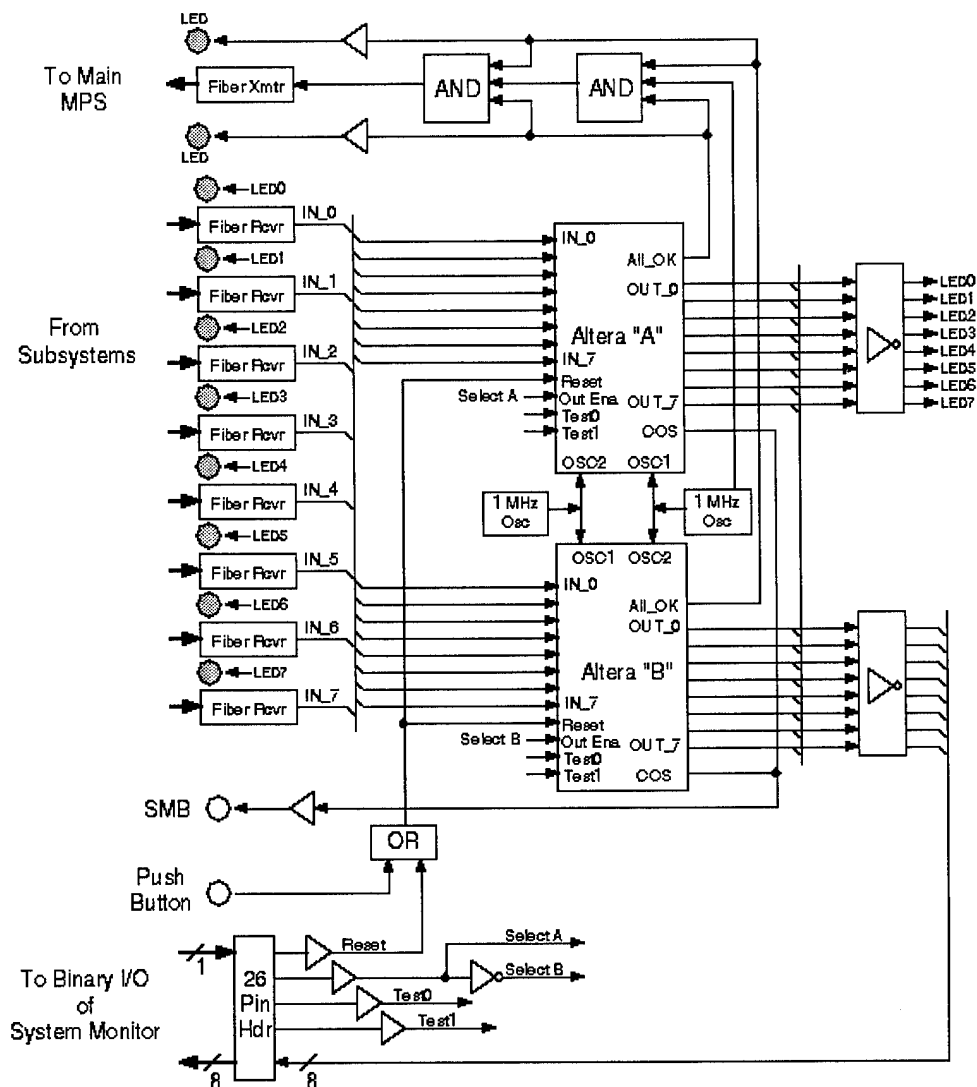


Figure 2: Schematic of the local MPS system module. Each module handles eight inputs and covers two sectors.

gate sensors open until it does. The second rf abort technique would also be activated in the final system implementation.

III. STATUS AND EARLY COMMISSIONING

All local MPS modules, the main MPS module, and rf interface card, the current monitor, and the fiber optic links are installed. The current monitor low limit at 0.5 mA has successfully tripped the rf when the beam exceeded this limit. Single sector water/vacuum valve status has been tested and the front-end monitor system has been linked. The wire monitor test and RTD test are expected this summer. The beam limits chassis is in the final design and test phase and is expected to be tested in May or June 1995. Production of multiple units will follow this summer.

Additional issues of rapid beam vertical instabilities whose average position is within limits, but exceeds the limits for short times, and beam transverse size blowup are being evaluated. The time before damage occurs is much longer, and this relaxation of the response time helps.

IV. SUMMARY

In summary, the APS MPS for the storage ring is being commissioned and validated as the ring is brought into operation. A multilayered defense with redundant channels is used to address the challenge of dealing with missteered beams in third-generation x-ray sources.

V. REFERENCES

- [1] S.L. Kramer, et al., "Vacuum Chamber Thermal Protection for the APS," *Proceedings of the 1989 IEEE PAC*, Vol. 1, p. 586, 1989.
- [2] G. Decker, "Abort Interlock Diagnostics for Protection of APS Vacuum Chamber," *Proceedings of the 1993 IEEE PAC*, Vol. 3, p. 2196, 1993.
- [3] I.-C. Sheng, private communication.

STATUS OF THE SYNCHROTRON RADIATION MONITORS FOR THE APS FACILITY RINGS*

A. Lumpkin and B. Yang

Argonne National Laboratory, 9700 S. Cass Ave., Argonne, IL 60439 USA

Abstract

Initial results from the optical synchrotron radiation (OSR) monitors for the Advanced Photon Source (APS) have been obtained. Data using electron beams on the positron accumulator ring (PAR) at 400 MeV, the injector synchrotron (IS) up to 7-GeV, and the main storage ring (SR) at 4.5 and 7 GeV address both transverse profiles and/or longitudinal bunch length. Recent measurements on OSR transported outside of the PAR and IS enclosures include transverse damping information. Streak camera and photodiode detectors have been used to measure bunch length compression $\sigma_t = 1000$ to 400 ps on the PAR and damping on the IS of $\sigma_t = 200$ to 75 ps. First transverse images have been recorded on the main ring from a single turn and for stored beam.

I. INTRODUCTION

The Advanced Photon Source (APS) [1] includes a 450-MeV positron accumulator ring (PAR), an injector synchrotron (IS) that ramps the beam energy to 7 GeV, and the 7-GeV main storage ring (SR). Characterizations of the beams circulating in these machines have begun using optical synchrotron radiation (OSR) [2]. Images of transverse beam size in all three rings, multiturn data using photomultiplier tubes and photodiodes, and bunch length data using both photodiode and dual-sweep streak camera techniques have been used to support commissioning. The latter are the first of their kind on a circular accelerator in the USA.

In the PAR, estimates of transverse emittance and the tracking of effects of the 12th harmonic cavity on bunch compression have resulted. In the IS both the transverse damping and aspects of longitudinal damping during the ramping cycle have been monitored. For the SR, an initial in-tunnel installation on a bending magnet beam port of a Questar telemicroscope and a charge-coupled device (CCD) camera have allowed the imaging via OSR of the beam on a single-turn and first stored beam. The plans for both OSR and x-ray synchrotron radiation (XSR) monitoring of the beam are outlined. Eventually, both a bending magnet and a "diagnostics undulator" will be used as sources of XSR for beam characterization [3].

II. EXPERIMENTAL BACKGROUND

The parameter spaces of the three rings are sufficiently different to require adjustments to detectors and lenses for each case. The general features are shown in Table 1. The PAR revolution time is the shortest at 102.3 ns with the IS and SR at

1.23 and 3.68 μ s, respectively. For the longer bunch lengths of the PAR, which even after damping would be about $\sigma = 300$ ps, a fast photodiode has been used. At this point a dual-sweep streak camera has been used for both PAR and the IS bunch length dynamics, and it is planned for the SR. The transverse profiles have been obtained via OSR imaging with the camera/lens system focused on the bending magnet source point.

Table 1: APS Parameters for Beam Diagnostics

	PAR	IS	SR
RF Frequency	9.77 or 117 MHz	351.93 MHz	351.93 MHz
Revolution Time	102.3 ns	1.228 μ s	3.68 μ s
No. of Bunches	1	1	1 to 60
Min. Bunch Spacing	---	---	20 ns
Bunch Length (2σ)	30 to 0.6 ns	122 ps	35-100 ps
Min. Avg Beam Current	1.4 mA 1 linac pulse injected	---	0.22 mA for single bunch
Max. Avg Beam Current	33.4 mA 24 linac pulses injected	4.7 mA	5 mA for single bunch
Max. Intensity particles/sec	3.6×10^{10}	3.6×10^{10}	2.2×10^{10} /bunch/mA

A. Transverse Beam Size

In our initial mode, an in-tunnel installation of a lead-shielded CCD camera with remotely controlled zoom lens (16-160 mm focal length) was used. In the PAR, exit ports from two dipole vacuum chambers were utilized, one source point at high energy dispersion and one at low dispersion. More recently, the OSR beams have been transported out of the accelerator enclosure (see Fig. 1), and this has facilitated the use of a fast photodiode, a streak camera, and soon a gated, intensified camera. On this table a CCD camera with a 500-mm focal length lens with a X2 magnifier provides a limiting resolution, $\sigma_{res} \sim 200 \mu$ m. A 450x10 nm band pass filter and a neutral density (ND) filter of ND \sim 2.0 to 3.0 are routinely used.

For the IS, a Questar telemicroscope (model FR1) is located on an optics table in a lab above the IS accelerator tunnel. A series of mirrors brings the OSR to the lens. Four focal lengths ranging from 220 mm to 3100 mm, an ND filter wheel with selection from 0.0 to 2.5 ND, and a 488x1 nm band pass filter are used to adjust the beam spectrum and intensity. At the fully magnified position, the limiting resolution is about $\sigma_{res} = 60 \mu$ m based on tests with an illuminated circular aperture of 12- μ m diameter. A UV-capable Questar has been installed

*Work supported by the U.S. Department of Energy, Office of Basic Energy Sciences, under Contract No. W-31-109-ENG-38.

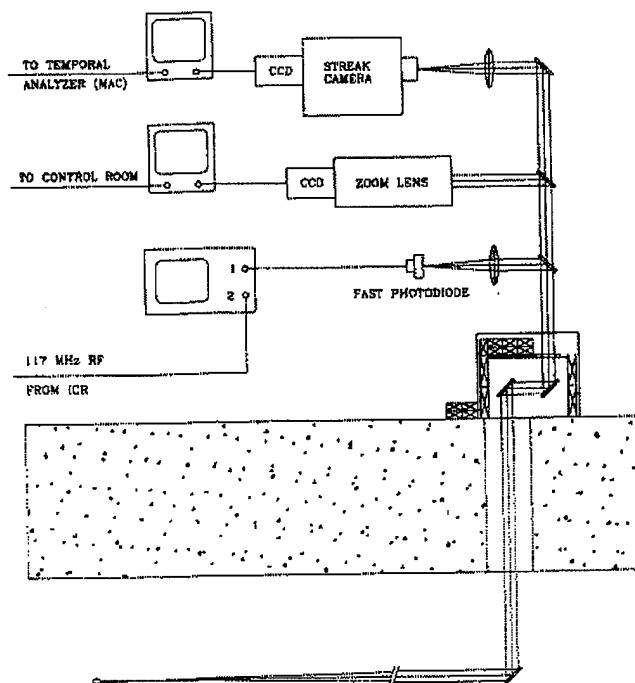


Figure 1: Schematic of OSR transport by mirrors out of the PAR and IS tunnels to detectors on an optics table.

in the SR tunnel on a bending magnet OSR port. The initial in-vacuum moly mirror is water-cooled but may only be used at low stored beam currents in early commissioning. A slotted Glidcop mirror, which will allow the high power, low-divergence angle x-rays to pass through the on-axis slot, will be used in later commissioning.

B. Bunch Length Measurements

In the PAR, the original 30-ns-long linac macropulse is damped to about $\sigma=1$ ns in tens of ms at $E=400$ MeV and the fundamental 9.77-MHz rf cavity at nominal power. Additional compression by a factor of three is obtained by turning on the 12th harmonic cavity (at 117.3 MHz). An Antel photodiode (model AR-S1) with <100 ps rise time, an rf amplifier (10.1-4.2 GHz), and either a Tektronix 11802 digital sampling oscilloscope with a 50 GS/s sampling head or an HP model 54542A 500-MHz BW digitizing oscilloscope were used to record the photodiode signals. The system resolution was observed to be about $\sigma=300$ -350 ps.

Additionally, a Hamamatsu C5680 dual-sweep streak system has been used to provide complementary bunch length information on the PAR as well as on the injector synchrotron. Both rf synchronized or synchroscan and multiple single trigger techniques have been used. These data in the next section are the first measurements using such a technique on a circular accelerator in the USA.

III. RESULTS AND SR PLANS

A. Transverse

For transverse beam size, the results for the three rings are summarized as follows. For the PAR, a damped beam image

profile (see Fig. 2) was measured to have a $\Delta x=3.6$ mm (FWHM). Assuming a Gaussian profile and a camera gamma factor of 0.66, this implies a $\sigma_x \sim 1.2$ mm observed. This would include the contributions of betatron motion ($\beta_x=2.9$ m) and dispersion in this case. This would imply a horizontal emittance $\sigma_{ex} \sim 0.22$ mm mrad as compared to the scaled, theoretical emittance of 0.29 mm mrad at 400 MeV.

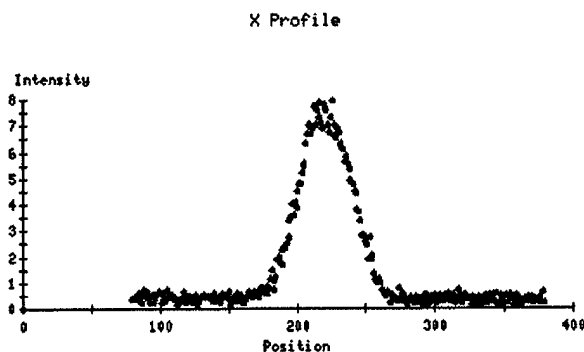


Figure 2: Video image profile of the PAR beam after damping using OSR. The total observed size was $\Delta x=3.6$ mm (FWHM) and $\Delta y=0.6$ mm (FWHM).

For the IS, the reduction of the transverse profile FWHM was observed by capturing a series of digital video image sequences in 33-ms steps. Measurements of the extracted beam emittance in the transport line between the IS and SR have not yet been done.

For the storage ring, we recorded the first OSR image from a bending magnet on March 18, 1995. It is shown in Fig. 3. This was obtained on a single turn at 7-GeV with about 1 nC in the bunch. The first OSR image of a stored beam is shown in Fig. 2 of [4].

B. Longitudinal

Bunch length measurements on the PAR have tracked the stacking, damping, and compression cycle. As shown in Fig. 4, an overlapping of bunch profiles for the photodiode, from early to late in the cycle, are displayed. A phase shift (towards the left) has also been detected. The most intense, negative going signal on the left of the profiles corresponds to a total measured $\sigma_t \sim 600$ ps. The 12th harmonic was not optimized, and the system resolution with the HP digitizing oscilloscope is still convolved. Subsequent streak camera data on a single, damped bunch have shown bunches with $\sigma=400$ ps.

On the IS, the bunch length was tracked during the 230-ms-long energy ramping cycle (400 MeV to 7 GeV) using the dual sweep features of the streak camera. The vertical time axis covered ~ 1500 ps and the horizontal axis covered ~ 100 ms. A DG535 delay generator was used to position the acquisition in the cycle. Figure 5 shows an example in the 35-to-130-ms portion of the cycle. The bunch compression from about 400 ps (FWHM) at the left to 178 ps (FWHM) on the right is obvious. By using a narrower region of interest (1-ms wide), a FWHM of 158 ps ($\sigma_t=67$ ps) is obtained. The wider window integrates over a detectable phase shift which appears to be a part of a relative phase oscillation at 120-Hz frequency.

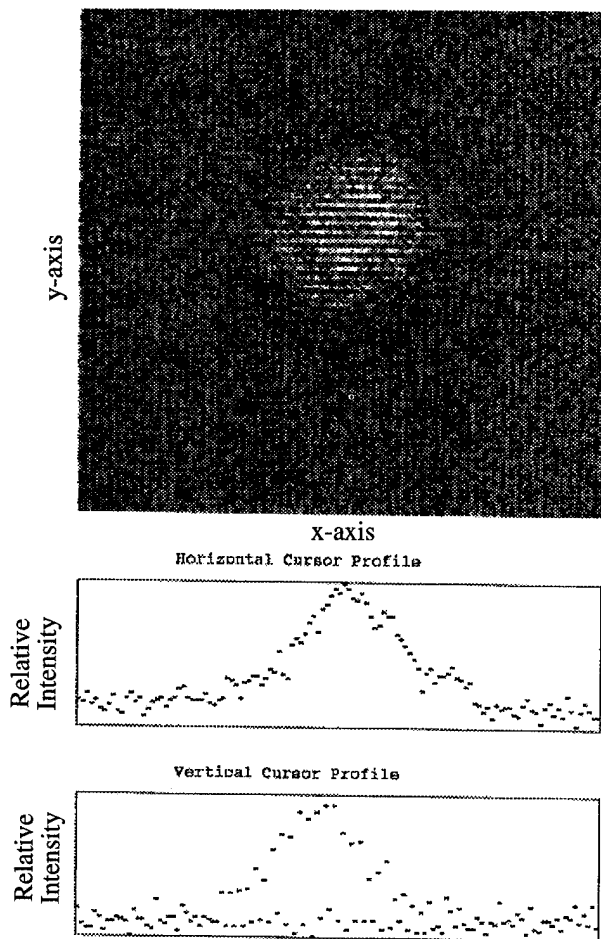


Figure 3: First synchrotron radiation image of the 7-GeV electron beam in the APS main storage ring. These data are from only a single pass.

Further studies addressing single turn, single bunch performance are planned as well as addressing the source of the-120 Hz effect.

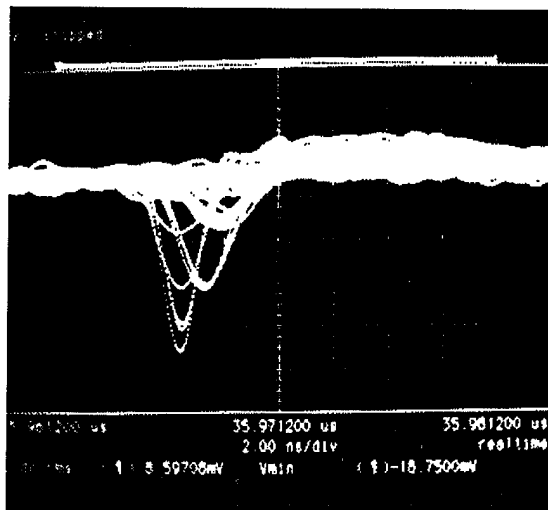


Figure 4: Photodiode data showing the PAR bunch length dynamics during the compression cycle. The final total observed bunch length was about $\sigma=600$ ps in this case. The horizontal scale is 2 ns/division.

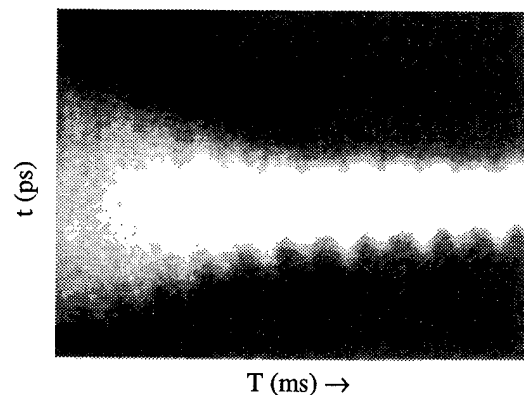


Figure 5: Dual-sweep streak image of the IS bunch length variation during the energy ramping cycle. These data cover from 35 to 130 ms in the ramp cycle on the horizontal axis and 1500 ps on the vertical axis. The bunch length is about 158 ps (FWHM) at the right-hand side.

C. Long-term Plans

Our long-term plans for the storage ring beam characterization include the extension of beam imaging to x-ray synchrotron radiation (XSR) and the use of both the bending magnet source and a diagnostics undulator. The issue of actual beam divergence for various vertical coupling ratios versus the radiation cone divergence is discussed in [3]. We have selected a 1.8-cm period device with a 2.5- to 3.0-m length and a 2- to 3- μ rad cone angle as a primary means of obtaining sensitivity to the baseline 8- μ rad particle beam divergence.

IV. SUMMARY

In summary, we have obtained OSR images of the circulating particle beam (electrons so far) in the three rings at APS. Transverse size, emittance, and bunch length measurements have been obtained and comparison to design objectives has begun. Characterization of the low-emittance SR beams using both OSR and XSR will be a primary objective in the next year.

V. REFERENCES

- [1] D.E. Moncton, E. Crosbie, and G.K. Shenoy "Overview of the Advanced Photon Source," *Rev. Sci. Instruments*, **60** (7), July 1989.
- [2] A.H. Lumpkin, W. Sellyey, and B. Yang, "Proposed Time-resolved Photon/Imaging Diagnostics for the APS," *Proc. of the 1994 European Particle Accelerator Conference*, London, England, Vol. 2, pp. 1687 (1994).
- [3] B. Yang and A.H. Lumpkin, "The Planned Photon Diagnostics Beamlines at the APS," *Proc. of the 1994 Beam Instrumentation Workshop*, Vancouver, B.C., Oct. 2-6, 1994.
- [4] A.H. Lumpkin, et al., "Initial Diagnostics Commissioning Results for the Advanced Photon Source (APS)," these proceedings.

INITIAL DIAGNOSTICS COMMISSIONING RESULTS FOR THE ADVANCED PHOTON SOURCE (APS)*

A. Lumpkin, D. Patterson, X. Wang, E. Kahana, W. Sellyey, A. Votaw, B. Yang, R. Fuja,
W. Berg, M. Borland, L. Emery, G. Decker, and S. Milton
Argonne National Laboratory, 9700 S. Cass Ave., Argonne, IL 60439

Abstract

Principal diagnostics systems have been installed and nearly all have been commissioned on the subsystems of the Advanced Photon Source (APS) facility. Data have been obtained on beam position, beam profile, current, beam loss rate, and synchrotron radiation monitors on both injector rings and most recently the main 7-GeV storage ring. Results for the 150- to 450-MeV electron beams in the accumulator ring, up to 7 GeV in the injector synchrotron, and 4.5 to 7 GeV in the SR will be presented.

I. INTRODUCTION

Significant progress has occurred in the last year at the Advanced Photon Source (APS) project including the beginning of commissioning of all the major subsystems. This process has of course included the commissioning of the primary diagnostics systems for each injector subsystem and the main storage ring. When completed in 1996, the APS will be a synchrotron radiation user facility with one of the world's brightest x-ray sources in the 10-keV to 100-keV regime [1]. Its 200-MeV electron linac, 450-MeV positron linac, positron accumulator ring (PAR), 7-GeV injector synchrotron (IS), 7-GeV storage ring (SR), and undulator test line provide the opportunity for development and demonstration of key particle beam characterization techniques over a wide range of parameter space. A description of the overall status with an emphasis on the diagnostic systems or techniques is provided. More detailed descriptions were provided at EPAC '94 [2,3], in BIW '94 proceedings [4-8], other meetings [9-12], and in proceedings of this conference. Initial measurements have been done with electrons at energies from 250 to 450 MeV and 50 to 400 pC per macrobunch. Operations in single-turn and stored-beam conditions were diagnosed on the PAR, IS, and SR. To date, energy ramping in the IS to 7 GeV has been attained, and beam has been stored at 4.5 GeV and 7 GeV in the SR. The installed diagnostics played a critical role in the early commissioning exercises.

II. EXPERIMENTAL BACKGROUND

Space precludes providing a complete description of the accelerator facilities for the APS but some background information is needed. The baseline electron source is a thermionic gun followed by a 200-MeV linac operating at an rf frequency of 2.8 GHz and a maximum macropulse repetition rate of 60 Hz. The design goals include 14-ps-long micropulses, separated by 350 ps in a 30-ns macropulse with a total macropulse

charge of 50 nC. The 200-MeV linac beam will be focused to a 3-mm spot at the positron-production target. The target yield is about 0.0083 positrons per incident electron with a solid angle of 0.15 sr and an energy range of 8 ± 1.5 MeV. The positrons will then be focused by a pulsed solenoid and about 60% of them will be accelerated to 450 MeV. The 450-MeV positrons are injected into the horizontal phase space of the PAR at a 60-Hz rate. As many as 24 macropulses can be accumulated as a single bunch during each 0.5-s cycle of the PAR. The injector (or booster) synchrotron accelerates the positrons to 7 GeV at which energy they can be extracted and injected into the designated rf bucket of the storage ring. A schematic of the APS accelerators, which lists the number of diagnostic stations, is shown in Fig. 1. All are installed except the diagnostic undulator in the SR. Our group's responsibilities now include the linac diagnostics as well as all other subsystems.

The main design features of the subsystems are listed in [11]. The 20-ns macropulse bunch length and the 200 to 400 pC per macropulse delivered by the linac into the low energy transport (LET) lines between the linac and PAR were measured by the fast current monitor. Macropulse repetition rates of 2 to 10 Hz have been provided with the ultimate design goal being 60 Hz. All experiments to date in the rings have used electrons. Recently a 450-MeV positron beam has been delivered into the LET1 line, and the 8-mA current was measured by the same fast current monitor. [12]

III. INITIAL DIAGNOSTIC RESULTS

The basic charged-particle beam parameters such as beam profile, position, current, beam loss, bunch length, and energy will be addressed. Initial reports have been provided at the 1994 EPAC conference [2] which focused on the early LET1 and PAR results, and the 1994 BIW which added the injector synchrotron results. In this report, samples from the different machines will be given with the most recent data coming from the SR.

A. Beam Profile Monitor

In the early stages of commissioning, one of the key diagnostic systems has been the beam profile monitor based on an Al_2O_3 (Cr) screen material and a standard charge-coupled device (CCD) video camera. Ten intercepting screens on pneumatic actuators are arrayed along the linac and three along the transport line z-axis between the linac and the accumulator ring. There are an additional six viewing screens/cameras in the PAR itself for single-turn tuning, three in the transport line to the IS, five in the IS, and ten in the SR. The system images beam as low as 10 to 30 pC in a macrobunch from the linac. The images are displayed at standard 30-Hz rates on a monitor

* Work supported by the U.S. Department of Energy, Office of Basic Energy Sciences, under Contract No. W-31-109-ENG-38.

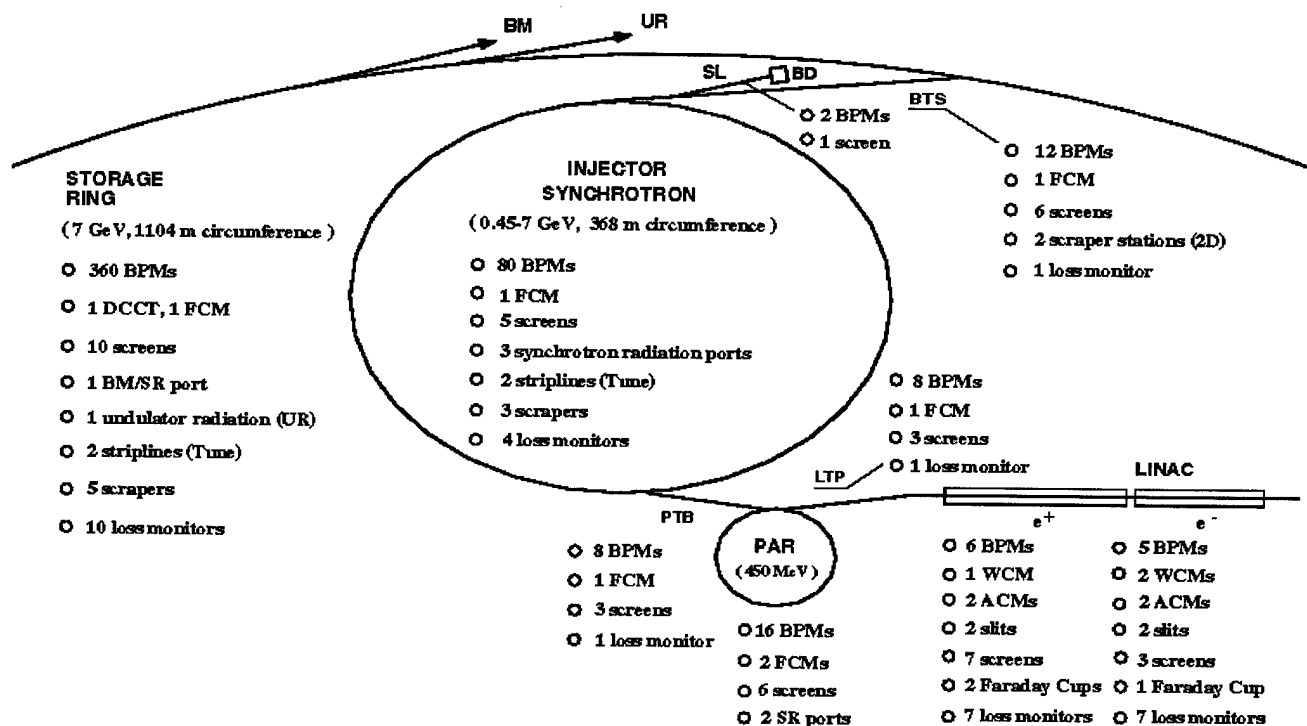


Figure 1: A schematic of the diagnostics system installed or planned for each APS subsystem. Almost all systems are now installed and functional except the undulator system in the SR.

or digitized by a VME-architecture-based video digitizing system linked to a Sun workstation. Figure 2 of [2] shows the pseudo-3D representation of one of the first electron beam bunches injected into the LET1 line. Since the screen is at 45° to the vertical, the ellipticity of the beam is exaggerated in the uncorrected image. The beam size was a few mm (FWHM) in the vertical dimension. During commissioning, beam was readily transported through both the transport lines, the PAR, the 368-m-circumference IS, and the 1104-m-circumference SR using the observed image shapes and positions.

B. Beam Position Monitors

Beam position monitors (BPMs) are installed throughout the accelerators and transport lines. A series of stripline pickup devices are used in the linac, PAR, and the transport lines between the three rings. The processing electronics are designed to provide single macrobunch detection on the linac and transport lines, but require beam to be stored in the PAR. These are addressed in [7,8] and references therein.

In the injector synchrotron, 80 rf BPM stations are composed of 10-mm-diameter pickup buttons in sets of four and storage-ring-like electronics [8]. In early injector synchrotron runs, the initial 400-MeV orbit was closed and corrected as shown in Fig. 4 of [4]. The rms orbit error was corrected from 2 mm to about 0.5 mm using the singular value decomposition (SVD) technique. The booster has now been ramped to 7 GeV. In the SR all 360 rf BPM stations are installed and almost all are responding to beam. The electronics systems have been recently tested on the SR at ESRF and a resolution of $0.06 \mu\text{m}$ per $(\text{Hz})^{1/2}$ has been indicated by scaling from the ESRF to APS standard chamber geometry. An additional factor of three

in sensitivity from the reduced gap of the insertion device (ID) chamber is expected [8]. The electronics also have single turn capability through the AM/PM monopulse receiver so that an early two-sector test at 7-GeV was documented by the beam trajectory measured by the first 18 BPMs.

C. Beam Loss Rate Monitors

The loss rate monitors (LRMs), which cover the entire extent of beamlines and accelerators, are now operational on all subsystems including the SR. A gas-filled coaxial cable acting as an ionization chamber was installed along the length of the transport lines and around the circumference of the PAR, IS, and SR. The gas mixture is 95% Ar and 5% CO_2 , and the voltage across the center conductor to ground is 500 V. A clear effect in loss rate occurs when one beam profile screen in the PAR is removed and its adjacent LRM cable is monitored in a strip-chart-mode on the workstation. A signal change of 0.2 nA was observed with less than 100 pC in the beam [6]. If the arrival time of the signals is viewed on a scope, few-meter axial resolution for losses can be determined. Reference 6 provides more details. Recent data for the SR on 7-GeV beam losses indicate a calculated sensitivity of 13 pC collected charge per pC loss. The minimum observable loss is about 4 pC for this case.

D. Beam Current Monitor

Monitoring of the current/charge in the transport lines and rings is based on the use of fast current transformers manufactured by Bergoz and in-house electronics. The electronics are described in detail by Wang [5]. The current transformer signals are processed through a gated integrator and the output

digitized to provide readouts on the workstation. During commissioning transported electron beams and positron beams from the linac were measured from 50 to 400 pC per macrobunch. In the PAR, both a fast current transformer (FCT) and integrating current transformer (ICT) were used to assess single-turn and stored-beam conditions. Kicker electrical noise interfered with using the FCT raw signal as a turns counter in the early commissioning so a photomultiplier tube (PMT) was used [4]. In the IS, the ICT signal was used to track the charge intensity during the 230-ms ramping cycle to verify ramp performance. In the SR initial data from the ICT and DC current transformer (DCCT) have been obtained. On March 25, 1995, 50 μ A of 4.5-GeV beam was stored, and on April 15, 1995, 100 μ A of 7-GeV beam was stored.

E. Photon Monitors

In each of the three rings at APS at least one bending magnet's synchrotron radiation is viewed by photon detectors. Detection of this radiation can be used to count beam turns or provide a measurement for tune, beam size, and bunch length [13]. A full complement of photon detectors and cameras was planned for radiation analysis. However, initial commissioning involved either a standard, CCD-based video camera and/or a photomultiplier tube (PMT). In the case of the PAR, an early commissioning issue was the large amount of electrical noise in the FCT signal from the nearby kicker magnet system. The PMT also showed noise, but the 300-mV signal from a single bunch/turn was much larger than the noise. The change from six turns in the PAR to thousands occurred in less than an hour with the PMT diagnostic after several shifts of fighting the kicker noise.

For PAR operations at 250 MeV, the lower energy resulted in a transverse damping time which corresponds to 80 to 100 ms. Our standard photon monitor camera easily tracked the progress of such damping in a series of six to eight frames taken 60 ms apart, as reported at EPAC 94 [3]. As a side note, the synchrotron radiation imaging has been very useful during early commissioning, even at low charge (~ 100 pC). We have routinely monitored the beam size in the nonintercepting mode for PAR and IS and recently recorded an image of the first beam stored in the storage ring at 4.5 GeV and at 7 GeV. Figure 2 shows the 7-GeV image which is sub-mm in extent for the horizontal and vertical FWHM. The orbit had not yet been fully corrected. The stored beam current was 100 μ A.

IV. SUMMARY

In summary, key charged-particle beam parameter characterizations are well underway on the APS subsystems. Most of the diagnostic systems are now commissioned and are supporting the injector accelerators and SR commissioning. The formidable tasks of instrumenting the third-generation main storage ring are complete for the primary diagnostics, and the installation of the orbit feedback system, damper systems, and x-ray-based emittance measurements are expected in the coming year.

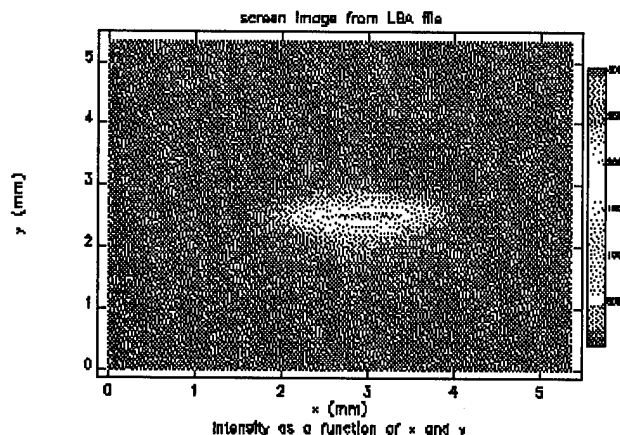


Figure 2: Image via OSR of first stored beam at 7 GeV in the main ring of APS on April 15, 1995. The scales should be multiplied by a factor of two.

V. ACKNOWLEDGMENTS

The authors acknowledge the efforts of the Diagnostics Group technicians and staff who were instrumental in the testing, installation, and checkout activities.

VI. REFERENCES

- [1] D.E. Moncton, et al., "Overview of the Advanced Photon Source," *Rev. Sci. Instrum.*, **60** (7) July 1989.
- [2] A.H. Lumpkin, et al., "Summary Test Results of the Particle Beam Diagnostics for the APS Subsystems," *Proceedings of the 1994 EPAC*, London, England, June 26-July 1, 1994.
- [3] A.H. Lumpkin, et al., "Proposed Time-Resolved Photon/Imaging Diagnostics for the APS," *ibid.*
- [4] A. Lumpkin, et al., "Initial Diagnostics Commissioning Results for the APS Injector Subsystems," *Proc. of the 1994 BIW*, Vancouver, B.C., Oct. 2-6, 1994.
- [5] X. Wang, "Design and Commissioning of the APS Beam Charge and Current Monitors," *ibid.*
- [6] D. Patterson, "Design and Performance of the Beam Loss Monitor System for the Advanced Photon Source," *ibid.*
- [7] W. Sellyey, et al., "Design, Construction, and Wire Calibration of the PAR BPM Striplines," *ibid.*
- [8] Y. Chung, et al., "Resolution and Drift Measurements on the APS Beam Position Monitor," *ibid.*
- [9] J. Hinkson and G. Stover, Eds., *Proc. of the 4th AIW*, Berkeley, CA, AIP No. 281, 1993.
- [10] R. Shafer and M. Plum, Eds., *Proc. of the 5th BIW*, Santa Fe, NM, AIP No. 319, 1993.
- [11] A.H. Lumpkin, et al., "Overview of Charged-Particle Beam Diagnostics for the Advanced Photon Source (APS)," AIP No. 281, p. 150, 1993.
- [12] M. White, et al., "Status of the APS Linac," *Proc. of the 1994 International Linac Conference*, Tsukuba, Japan, Aug. 21-26, 1994.
- [13] A. Lumpkin, et al., "Status of the Synchrotron Radiation Monitors for the APS," these proceedings.

INITIAL TESTS OF THE DUAL-SWEEP STREAK CAMERA SYSTEM PLANNED FOR APS PARTICLE-BEAM DIAGNOSTICS*

A. Lumpkin, B. Yang, and W. Gai

Argonne National Laboratory, 9700 S. Cass, Argonne, IL 60439 USA

W. Cieslik

Hamamatsu Photonic Systems, Bridgewater, NJ 08807 USA

Abstract

Initial tests of a dual-sweep streak system planned for use on the Advanced Photon Source (APS) have been performed using assets of the Argonne Wakefield Accelerator (AWA) facility. The short light pulses from the photoelectric injector drive laser in both the visible ($\lambda=496$ nm, $\Delta t \sim 1.5$ ps (FWHM)), and the ultraviolet ($\lambda=248$ nm, $\Delta t \sim 5$ ps (FWHM)) were used. Both a UV-visible S20 photocathode streak tube and a UV-to-x-ray Au photocathode streak tube were tested. Calibration data with an etalon were also obtained. A sample of dual-sweep streak data using optical synchrotron radiation on the APS injector synchrotron is also presented.

I. INTRODUCTION

The Advanced Photon Source will be a third-generation synchrotron radiation facility for the hard x-ray (10-100 keV) research community. The need to measure and monitor particle and photon beam parameters in the single bunch (10 ps), bunch-to-bunch (3 to 180 ns), and turn-by-turn (3.68 μ s) timescales has resulted in the choice of a dual-sweep streak camera system [1]. Initial laboratory tests with 50- and 80-ps (FWHM) laser diodes were performed. Tests at the Argonne Wakefield Accelerator [2,3] (AWA) using the short-pulsed photoelectric injector drive laser were undertaken to test both UV-visible (S20) and UV-x-ray (Au-based) photocathode streak tubes. The 1.5-ps (FWHM), 496-nm component and the 5-ps (FWHM), 248-nm component were used. Plans to use bremsstrahlung x-rays generated by the linac beam in a short pulsed mode hitting a foil were limited by inadequate photon statistics in the first geometry tried.

II. EXPERIMENTAL BACKGROUND

The initial evaluations of the streak camera were with laser diodes whose bunch lengths were many times longer than the specified camera resolution. The nominal 1.5 ps (FWHM) resolution could be better evaluated with a short bunch in the 1-2 ps regime that was available at the AWA.

The AWA project in its early phase includes an L-band, 20-MeV drive linac with a high brightness photoelectric injector (PEI) capable of delivering 2-MeV, 100-nC, 20-ps (FWHM) bunches to the linac (see Fig. 1). The drive laser for this source is a pulsed laser system constructed jointly by Coherent-Lambda Physics which is described in [3]. A harmonic tripled mode-locked Nd:YAG laser is used to pump the

dye laser. For our test purposes, the laser was adjusted to provide 1-2 ps (FWHM) pulses at 496 nm. Amplification of the subsequent short UV pulses at 248 nm was done in a single stage KrF excimer laser whose observed output pulse length was 4 to 5 ps (FWHM).

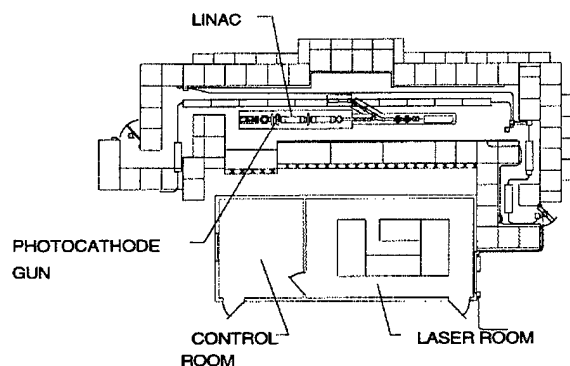


Figure 1: Schematic of the Argonne Wakefield Accelerator Facility. The drive laser and lab, the control room, and the accelerator in the shielded tunnel are indicated.

In our initial setup, as shown in Fig. 2, we used the amplified, 248-nm component from the drive laser system to evaluate the streak camera tubes' resolutions. An autocorrelator that was on-line, but sampling the green component, served as an independent bunch length monitor. The Hamamatsu C5680 with a single-shot fast sweep plug-in unit was aligned to the laser beam. A beam splitter was used to provide both a signal to a photodiode whose output generated an electrical trigger for the camera sweep and a laser beam that was appropriately delayed by transport distance to the entrance slit of the streak tube.

In a second mode, shown in Fig. 3, we split off part of the dye laser component at 496 nm which was also being monitored by the autocorrelator. The autocorrelator monitor nominally indicated bunch lengths of 1 to 2 ps (FWHM) in the baseline operating mode.

Both the UV-visible (S20) photocathode (PC) tube and the Au photocathode tube were evaluated. In the latter case, a quartz window on the front flange allowed UV photons to hit the PC. We also used a front flange with a Be window for the planned test with x-rays. A portable pumping station was used to take the tube pressure to 2×10^{-7} Torr. For both these tests, the camera was positioned off-axis near the end of the linac. Part of the drive laser beam for the PEI was directed to the streak camera.

* Work supported by the U.S. Department of Energy, Office of Basic Energy Sciences, under Contract No. W-31-109-ENG-38.

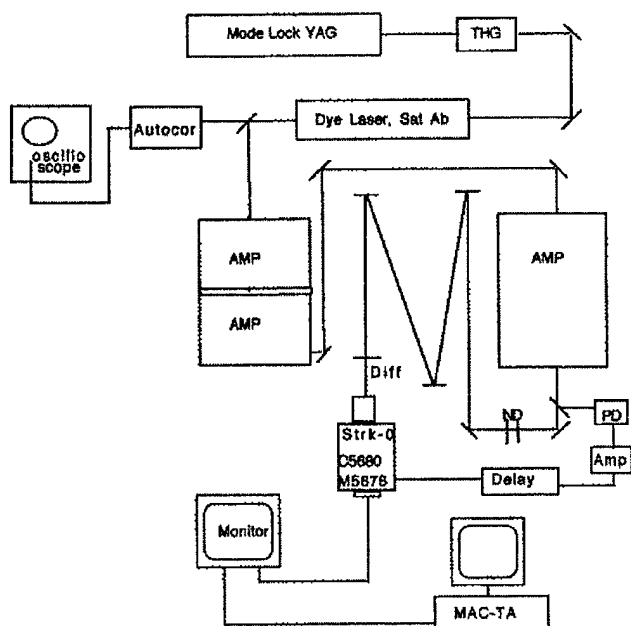


Figure 2: Initial setup for measurements on the amplified UV component (248 nm) of the PEI drive laser.

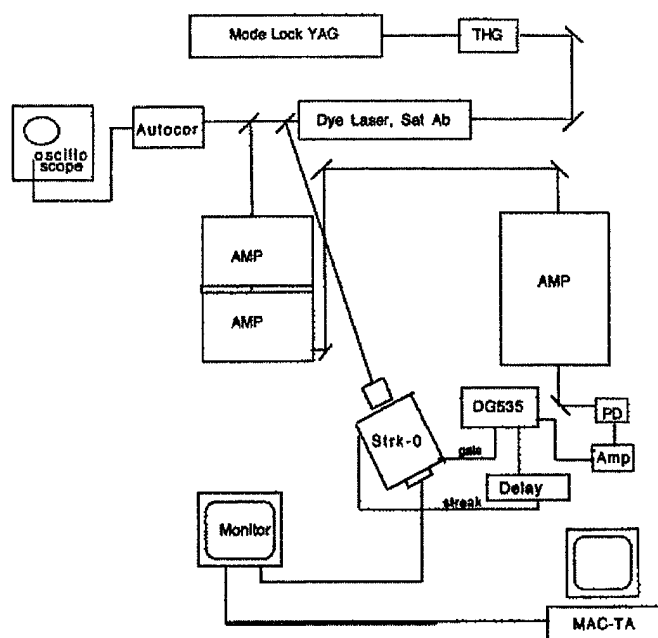


Figure 3: Setup for measurements on the 496-nm wavelength component in the drive laser.

The streak camera's information was readable by a charge-coupled device (CCD) camera, and the video digitized with a Hamamatsu MAC temporal analyzer (TA). The U5568 software program was designed for use with the Macintosh computer and the IQ-V50 frame grabber board. The system also provided remote control of most streak camera functions

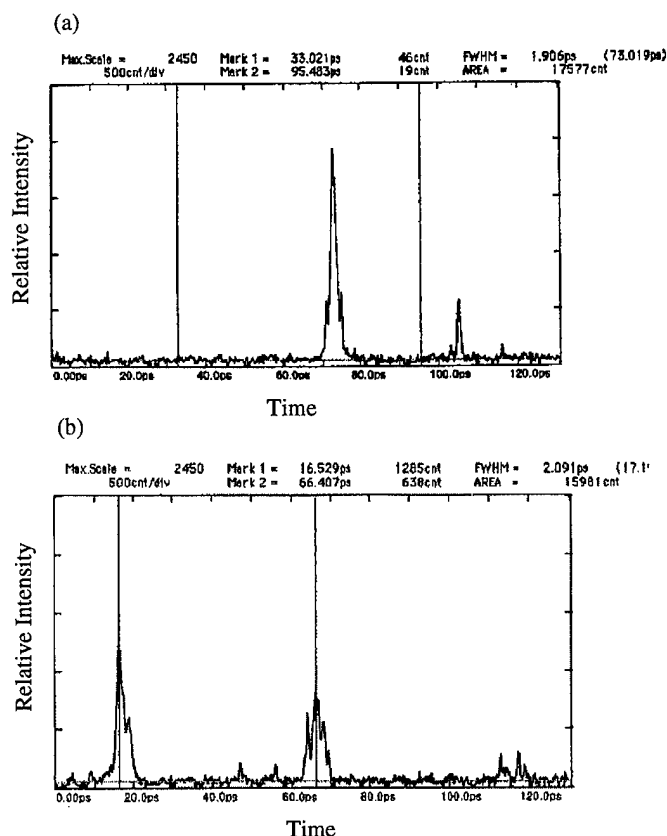


Figure 4: Profiles from streak images of the (a) green component at 1.9 ps (FWHM) and (b) example of 50-ps etalon-based calibration data. The calibration data were similar to the factory calibration since the markers centered on two peaks are 49.9 ps apart based on the calibration file.

through a GPIB interface. The image analysis program was used to provide initial evaluation of streak image position and profiles.

III. PRELIMINARY RESULTS/DISCUSSIONS

The initial measurements were performed on the S20 tube. In Fig. 4, a sample temporal profile from a streak image of the green component is shown. The amplified UV was observed to have a larger FWHM (~ 4.6 ps) bunch length than the green (~ 1.9 ps). The green component when monitored by the autocorrelator provided measurements of 1 to 2 ps, generally.

A second phase of experiments involved the use of an etalon with various spaces between the reflecting surfaces which results in multiple streak images spaced at known separation in time. This information was used to both validate existing calibration files and to generate new files for some plug-in units. In Fig. 4b, the etalon spacing was 50 ps and the reference calibration gave 49.9 ps.

In Fig. 5, test data from the Au photocathode are shown. The focus mode shows the physical extent of the active surface is $80 \mu\text{m} \times 6 \text{ mm}$. Due to the penetrating nature of x-rays, defining slits in front of the PC are not a practical way to control the static spread function of the tube. The limited vertical height of this photocathode addresses this issue. The observed

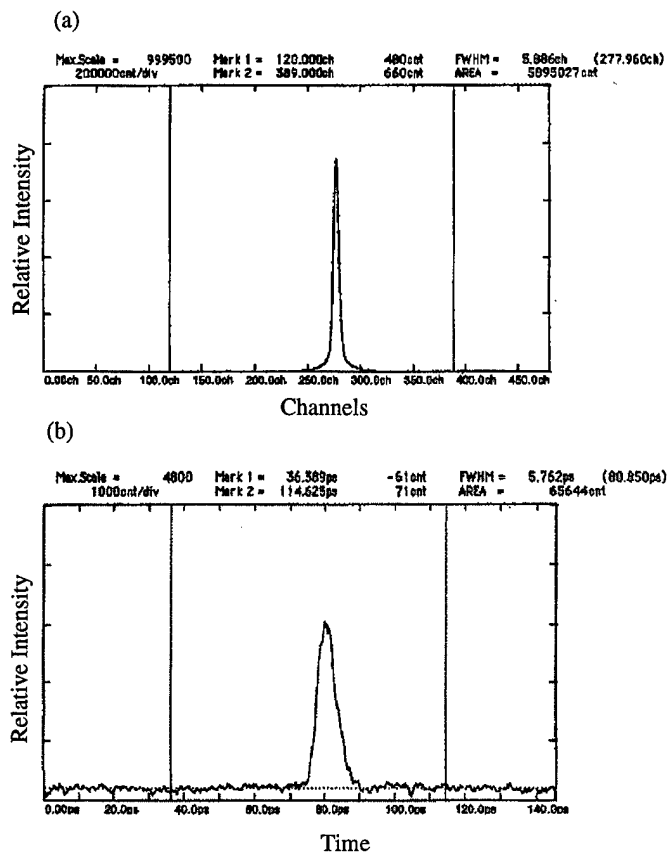


Figure 5: Temporal profiles from the Au-photocathode using the 248-nm laser irradiation: (a) focus mode with 5.9 channels FWHM and (b) streak mode with 5.8 ps (FWHM) result.

streak profile of the UV component when combined with the independent information of the S20 tube was used to determine the UV resolution to be about 2-3 ps (FWHM). In Fig. 5b, a partial laser retuning resulted in a total bunch length of 5.8 ps (FWHM). The initial x-ray tests using the Au PC with the Be window mounted were unsuccessful due to the limited x-rays that could be generated and directed to the streak camera in the available geometry.

A few months later an example of the application to APS was attained with the dual-sweep image of OSR from a bending magnet source in the injector synchrotron. The variation of bunch length during the energy ramping cycle is clearly visible and quantifiable. The damped bunch is about 158 ps (FWHM), or $\sigma=67$ ps as shown on the right-hand side of Fig. 6. The horizontal axis spans ~100 ms and the vertical axis ~1500 ps.

IV. SUMMARY

In summary, the AWA facility drive laser has been used to evaluate streak techniques for short-pulsed photon sources. The pulses are comparable to system resolution and faster than most baseline conditions anticipated on the APS machines. The initial evaluation on the Au photocathode with a short UV bunch was particularly useful. As a side benefit, the elongation of the amplified UV bunch length was quantified, and this will

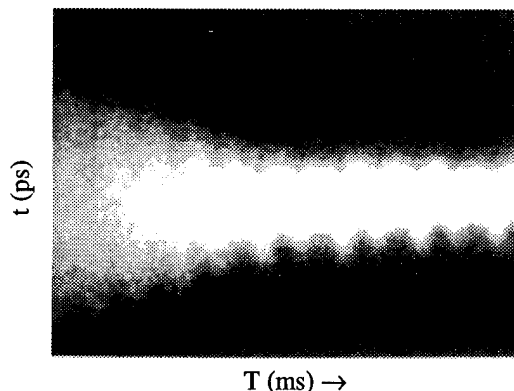


Figure 6: Dual-sweep streak image of the APS injector synchrotron beam (obtained from a bending magnet source).

help in understanding the photoinjector performances. The first application to the APS injector synchrotron was successful in displaying bunch length dynamics, and a series of follow-on experiments on APS rings will be conducted.

V. ACKNOWLEDGEMENTS

The authors acknowledge Dean Walters (ASD/Vacuum Group) for providing a portable pumping station for the x-ray tube and assisting in the vacuum issues. They also acknowledge J. Simpson for providing time on the AWA facility for these tests.

VI. REFERENCES

- [1] A.H. Lumpkin, "Characterization Techniques for the High-Brightness Particle Beam of the APS," *SPIE*, Vol. 2013/3, 1993.
- [2] P. Schoessow, et al., "The Argonne Wakefield Accelerator-Overview and Status," *Proceedings of the 1993 PAC*, p. 2596, Vol. 5, 1993.
- [3] W. Gai, N. Hill, C. Ho, P. Schoessow, and J. Simpson, "The AWA Laser System and Its Laser Pulse Shaper," *Proceedings of the 1993 PAC*, p. 3050, Vol. 4, 1993.

A TRANSVERSE TUNE MONITOR FOR THE FERMILAB MAIN RING

P. J. Chou, B. Fellenz and G. Jackson

Fermi National Accelerator Laboratory*, MS 345, P.O.Box 500, Batavia, IL 60510 USA

ABSTRACT

The transverse tunes of the beam change during the acceleration ramp of the Main Ring. Resonant capacitive pickups were constructed to monitor these tune variations. The detectors were also designed to measure the amplitudes of the beam Schottky signals. Details of the technical design and results of measured beam signal are presented.

I. DESIGN PRINCIPLES

RF frequency drift due to acceleration		
kinetic energy [GeV]	revolution frequency [Hz]	RF frequency [MHz]
8	47417	52.78
150	47746	53.14

Table 1: The frequency changes during the energy ramping for Main Ring.

The operation parameters for Main Ring(MR) are depicted in Table 1. The harmonic number is 1113 for MR. The MR clock signal will be used to mix down the measured beam signal. The clock frequency corresponds to the $n=159$ rotation harmonic line. The detector response has to cover the range of frequency change of $n=159$ betatron sideband due to energy ramping. The fractional tune of the MR is 0.4. We chose to track the positive sideband of the $n=159$ harmonic line, which is 7.558 MHz at 8 GeV and 7.611 MHz at 150 GeV respectively. To enhance the signal to noise ratio, a resonant type of detector was chosen. The 3 dB frequency of detector response was chosen to be 7.558 and 7.611 MHz. The design parameters were set by the above considerations and depicted in Table 2.

f_{center}	7.59 MHz
Q_{load}	125
Q_{unloaded}	250

Table 2: The required parameters for Main Ring tune monitor.

A. Mechanical design and circuit modeling

The layout of the mechanical design[1] is depicted in Figure 1. A diagonally-cut cyclindrical pickup was chosen for its linear response to the beam displacement. The radius of pickup electrode is denoted by b , and the electrode length is denoted by ℓ . The configuration depicted in Figure 1 can be modeled by an electrical circuit as shown in Figure 2. C_p is the coupling capacitance between two electrode plates, C_g is the coupling capacitance between the electrode plate and the vacuum pipe. R_s is the shunt resistance due to the resistive loss of a practical inductor $R_s = Q\ell\omega L$, $Q\ell$ =the quality factor

of inductor, L =inductance, ω =angular frequency.

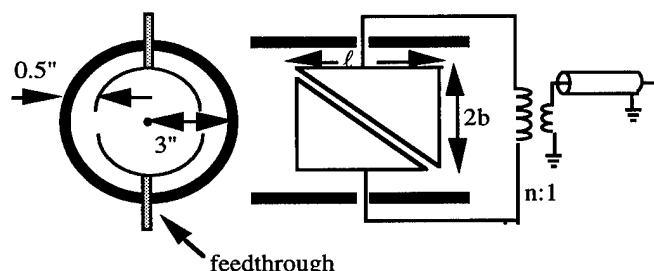


Figure 1: The mechanical layout of MR tune monitor with externally loaded coaxial cable.

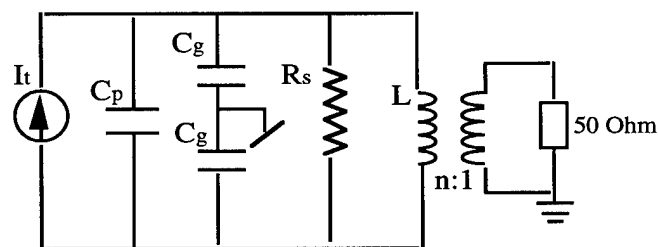


Figure 2: The equivalent circuit model of MR tune monitor.

The circuit shown in Figure 2 can be reduced to an RCL parallel circuit as shown in Figure 3.

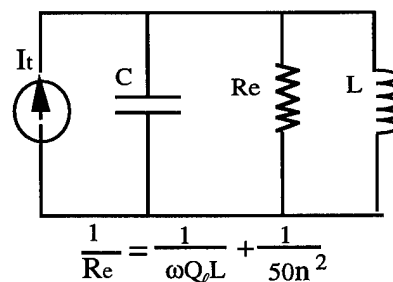


Figure 3: The equivalent circuit of MR tune monitor, $C = C_p + C_g/2$.

To get the maximum output power from the detector, we need to match the load resistance, i.e. $R_e = Q\ell\omega L/2$. For a RCL parallel circuit, the Q factor of the circuit is given by $Q = R/\omega L$. Therefore, the loaded Q factor of equivalent circuit with matched external load is $Q\ell/2$. From Table 2 we conclude that the minimum inductor Q factor has to be larger than 250.

B. Signal analysis in frequency domain

Suppose the particle beam travels along the accelerator with a closed orbit error δy . The beam image current flows along the vacuum pipe. It will have to cross the gap between the vacuum pipe and pickup electrodes when the beam arrives at the upstream and downstream ends of detector. For a

* Operated by Universities Research Association Inc., under contract with the U.S. Department of Energy.

diagonally-cut cylindrical pickup the induced wall currents flow onto the upstream ends of two electrode plates are[2]:

$$I_{T1} = \frac{-I_b(\omega)}{2} \left(1 + \frac{\delta y}{b}\right), I_{B1} = \frac{-I_b(\omega)}{2} \left(1 - \frac{\delta y}{b}\right)$$

The induced wall currents flow onto the downstream ends of two electrode plates are:

$$I_{T2} = -I_{T1}e^{-j\omega\ell/v}, I_{B2} = -I_{B1}e^{-j\omega\ell/v}$$

Hence, the total current flows into the equivalent circuit is:

$$I_t(\omega) = I_{T1} - I_{B1} + I_{T2} - I_{B2}$$

$$\approx -\frac{I_b(\omega) \cdot \delta y}{b} \cdot \frac{j\omega\ell}{v} \left(\text{when } \frac{\omega\ell}{v} \ll 1 \right)$$

The whole detector system is represented by Figure 3. The impedance of the whole system is:

$$Z(\omega) = \frac{j\omega L}{\frac{2}{\omega_0}(\omega_0 - \omega) + \frac{j}{Q_{load}}} \approx \frac{j\omega_0^2 L}{2(\omega_0 - \omega) + j\frac{\omega_0}{Q_{load}}}$$

The voltage across the primary inductor is given by:

$$|V(\omega)| = \frac{\ell \delta y I_b(\omega)}{bvC} \sqrt{\frac{Q_{load}^2}{1 + (Q_{load}/Q_\ell)^2}}$$

Therefore, the voltage across the secondary inductor is[2]:

$$|V_{out}| = \frac{1}{n} |I_t(\omega) Z(\omega)|$$

$$= \frac{\ell \delta y I_b(\omega)}{bv} \sqrt{\frac{R_0 \omega_0 Q_\ell}{C} \frac{Q_{load}}{Q_\ell} \left(1 - \frac{Q_{load}}{Q_\ell}\right)}$$

The detector sensitivity is then given by:

$$S_\perp(\omega) = \frac{|V_{out}|}{\delta y I_b(\omega)} = \frac{\ell}{bv} \sqrt{\frac{R_0 \omega_0 Q_\ell}{C} \frac{Q_{load}}{Q_\ell} \left(1 - \frac{Q_{load}}{Q_\ell}\right)}$$

where ω_0 is the resonant angular frequency, R_0 is cable impedance 50 ohm, v is the speed of particle beam and Q_{load} is the loaded Q factor of the equivalent circuit in Figure 3.

C. Receiver design

The signal processing scheme is described in Figure 4. To make the design simple, we want to utilize the available MR clock signal broacasting around the accelerator. Therefore, the frequency of local oscillator was chosen to be the one of MR reference clock. The distance from the location of detector to the main control room is about 500 fts. Helix cables were

used to minimize the resistive loss and frequency dispersion. Since the MR is running at bunched beam mode, we need to block out the large rf rotation harmonic lines due to beam bunching in order to prevent them from saturating the preamplifier. Because we also want to observe the Schottky signal, which we expect to be very small, a passive lowpass filter with 10 MHz bandwidth was built to minimize the insertion loss and block out the unwanted high frequency signals. Then the signal is divided into two outputs. One is reserved for study purpose, the other is mixed down to the baseband frequency then sent to the main control room. It will be used by the operation crews to monitor the transverse tune of MR and to calibrate the chromaticity values used by the control system.

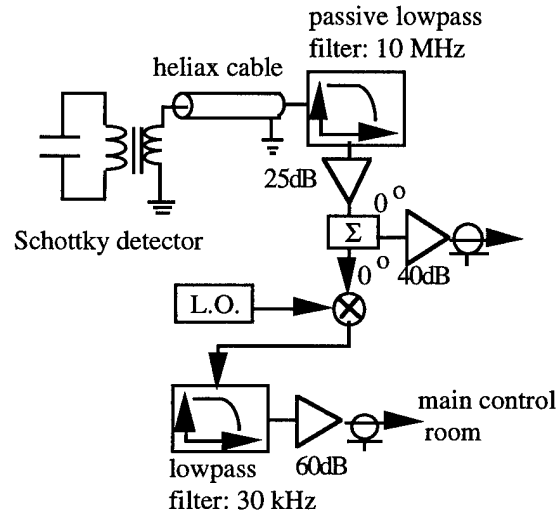


Figure 4: The block diagram of receiver design.

II. BEAM MEASUREMENTS

A. Calibration

The detector sensitivity was measured with both bench and beam measurements. The bench tests were done with the stretched-wire method. The results of the bench measurements are depicted in Figure 5 and 6. The beam measurements were done with the prototype by using bunched beam, depicted in Figure 7. Because of the good agreement between the bench test and beam measurements, no calibration with beam was done for the final model.

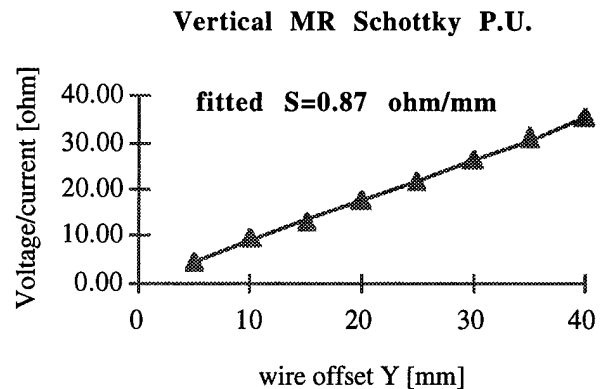


Figure 5: The result of bench calibration for vertical detector.

Horizontal MR Schottky P.U.

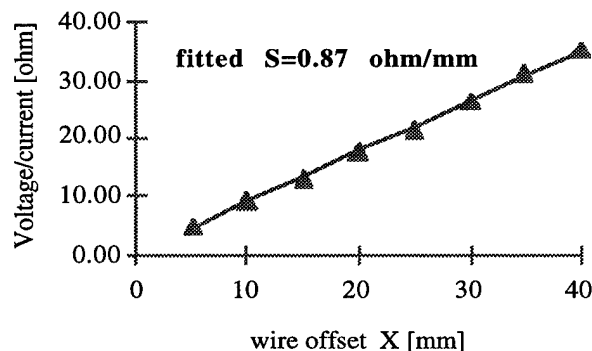


Figure 6: The result of bench calibration for horizontal detector.

Prototype MR Schottky P.U. (beam measurement)

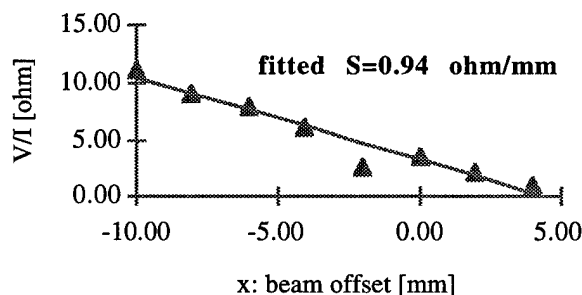


Figure 7: The result of calibration with bunched beam.

B. Beam signal measurements

Bunched beam signals measured right after injection are depicted in Figure 8 and 9. The debunched beam signal was also measured as depicted in Figure 10. The beam size derived from measured debunched beam signal was compared with flying wire profile monitor[3]. The conclusion is that the measured signal is not Schottky signal but coherent signal. The Schottky signal is buried by signal driven by coherent beam motion. Also the detector sensitivity is not high enough to observe the Schottky signal. At least a factor of 10 increase in the detector sensitivity is needed in order to observe the Schottky beam signal.

III. ACKNOWLEDGEMENT

The authors would like to thank E. Jr. Barsotti, A. Hahn and R. Siemann for helpful discussions.

IV. REFERENCES

- [1] Mechanical department/ accelerator division, Fermi drawing number 0450-ME-260541 and 0450-MD-260498.
- [2] R. Siemann, Fermi EXP-155.
- [3] A. Hahn, private communication.

MR horizontal tune

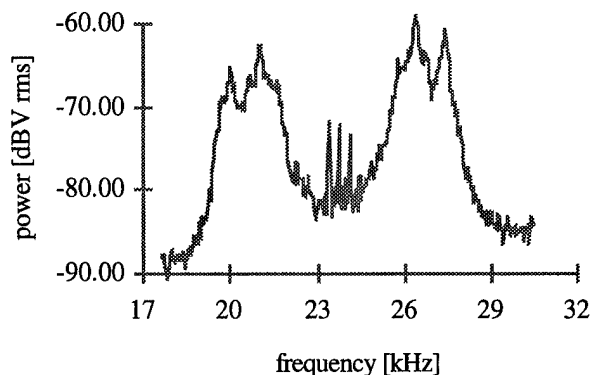


Figure 8: The measured bunched beam signal right after injection.

MR vertical tune

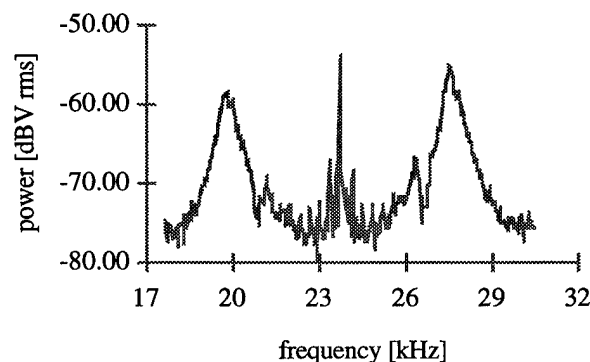


Figure 9: The measured bunched beam signal right after injection.

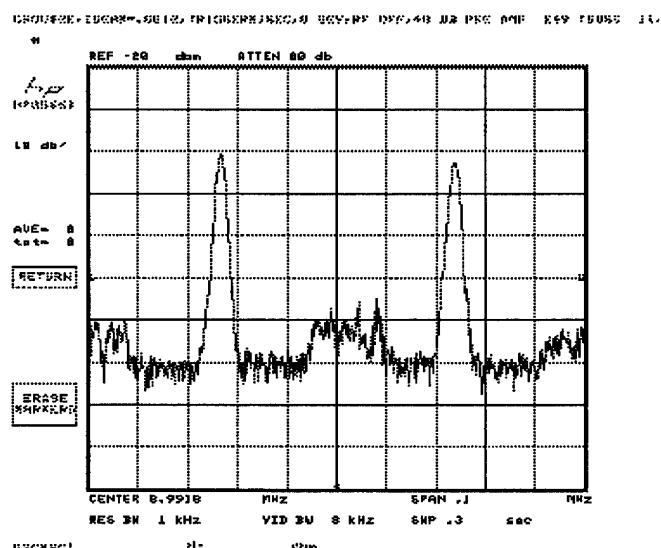


Figure 10: Debunched beam signal measured at the injection energy of MR.

RECALIBRATION OF POSITION MONITORS WITH BEAMS

Kotaro Satoh and Masaki Tejima, National Laboratory for High Energy Physics, Oho 1-1, Tsukuba, Ibaraki 305 Japan

Abstract

This paper proposes a method to find the geometrical center of a position monitor from its beam signals. The method will be useful in accelerators where the optics is very sensitive to the orbit. Beam test results are also presented.

I. INTRODUCTION

A beam position monitor system is operated for two kinds of orbit measurements, a relative measurement and an absolute measurement. The former is to measure the orbit displacement from the initial or standard orbit when some optics perturbation is applied. The latter case is to measure orbit position relative to the geometrical monitor center. This function will be essential for maintaining stable operations in a ring where the optics depends strongly on the orbit, particularly at nonlinear optics elements. The dependence will surely appear in future B-factories, where strong sextupole magnets are installed and a small vertical emittance is required.

The output data from a position monitor system usually shows the orbit position relative to the electric monitor center, not the geometrical center. The electric center, however, may drift due to unpredictable imbalance among output signals from the pick-up electrodes, because they must travel through separate paths, cables, connectors, attenuators, switches, and then are measured by detectors.

This paper proposes a method to estimate the imbalance and to find the geometrical monitor center from four output signals of a pick-up unit. It should be noted, however, that the method is not workable in monitor systems where the number of output signals is less than four, as in an AM/PM system.

II. MODELING OF OUTPUT DATA

Consider a pick-up unit having four electrodes and four processed output data, V_i 's, as shown in Fig.1. The data can be given by

$$V_i = g_i \cdot q \cdot F_i(x, y), \quad i = 1, 2, 3, 4$$

where q measures the beam charge, and x/y are horizontal and vertical displacements of the beam relative to the geometrical monitor center. Functions, $F_i(x, y)$, stand for response of four electrodes, and are normalized as $F_i(0,0)=1$. Hence, the origin of arguments of the response function defines the geometrical center. No symmetry condition is required among the response functions. Quantities, g_i 's, show overall gains of each electrode. Notice that g_i also includes the impedance imbalance through vacuum connectors, and that the present idea can be applied to calibration of a pick-up unit for modeling its response function.

Further analysis is based on two assumptions. One is that the response functions never change, and can be known well by calibration or calculation. Since the response function depends only

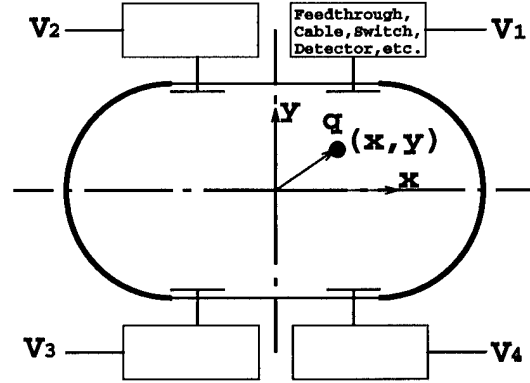


Figure. 1. A model monitor system.

on the geometrical structure of the pick-up unit, this assumption is reasonable. Second assumption is that all of the effects which displace the electric center can be included into g_i 's. The second assumption is acceptable at least in a case when the signals are processed with a narrow frequency-band monitor system.

The objective of the paper is to show a possible way to estimate the gains and to recover the geometrical center.

III. GAIN ESTIMATION

Consider a case when beam positions are measured m times with a pick-up unit, and at each measurement the orbit at the monitor is changed intentionally, for example, with steering magnets. The beam charge may be varied at each measurement although the variation is not important for the gain estimation. Then the data from the i -th electrode at the j -th measurement can be given by,

$$V_{ij} = g_i \cdot q_j \cdot F_i(x_j, y_j).$$

From the fact that only the relative imbalance among the gains contributes to shifting the electric monitor center, g_1 can be always set 1 with a proper scaling factor for the beam charge. This means that there exist only 3 unknown gains, g_2, g_3 and g_4 . At each measurement 3 unknown parameters, q_j, x_j and y_j , are generated, but 4 quantities, V_{1j}, V_{2j}, V_{3j} and V_{4j} , can be measured. After the m -th measurement the number of the unknown parameters is $3+3m$, whereas that of the known parameters is $4m$. When m is larger than 4, the latter number exceeds the former and hence the unknown parameters, including the gains, can be estimated with a nonlinear chi-square method [1].

The present nonlinear model is rewritten as,

$$\begin{aligned} V_{ij} &= g_i \cdot q_j \cdot F_i(x_j, y_j) \equiv V(i, j; \mathbf{a}), \\ i &= 1, \dots, 4, \quad j = 1, \dots, m, \\ \mathbf{a} &= (g_2, g_3, g_4, q_1, x_1, y_1, \dots, q_m, x_m, y_m), \end{aligned}$$

where \mathbf{a} is the array of fitting parameters. The unknown parameters can be estimated by minimizing the chi-square,

$$\chi^2(\mathbf{a}) = \sum_{i=1}^4 \sum_{j=1}^m \frac{[V_{ij} - V(i, j; \mathbf{a})]^2}{\sigma_{ij}^2},$$

where σ_{ij}^2 is the data error of the i -th electrode at the j -th measurement. For simplicity, the data errors are assumed the same as $\sigma_{ij} = \sigma_0$.

The curvature matrix, $[\alpha]$, defined by

$$\alpha_{k\ell} \equiv \frac{1}{2} \frac{\partial^2 \chi^2(\mathbf{a})}{\partial a_k \partial a_\ell}$$

is very important not only for performing the minimization but also for knowing the variance and the covariance of the fitting parameters. The covariant matrix, $[C]$, is just equal to the inverse of the curvature matrix at the minimum point. The diagonal element gives the variance of the estimated parameter in a way that

$$\sigma^2(a_k) = C_{kk} = \alpha_{kk}^{-1},$$

and the off-diagonal element $C_{k\ell}$ shows the correlation between a_k and a_ℓ .

IV. SIMULATION RESULTS

Imagine a circular pipe having four electrodes as shown in Fig.2. This pick-up model has such a pleasant symmetry that all of the response functions can be expressed with only one function, $F_1(x, y)$.

$$\begin{aligned} F_2(x, y) &= F_1(-x, y), & F_3(x, y) &= F_1(-x, -y), \\ F_4(x, y) &= F_1(x, -y). \end{aligned}$$

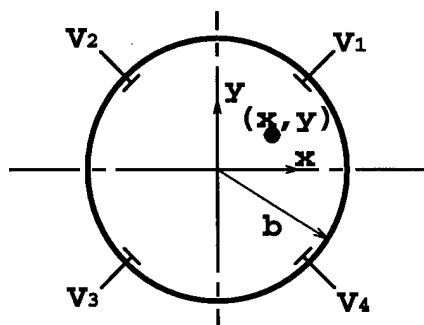


Figure 2. A circular pick-up unit model.

If the electrode dimension is chosen sufficiently small, the response function can be given by the wall current distribution at the electrode location. With a pipe radius b , the response function to the 3-rd order is

$$\begin{aligned} F_1(x, y) &= 1 + \frac{\sqrt{2}}{b}(x + y) + \frac{4}{b^2}xy \\ &\quad + \frac{\sqrt{2}}{b^3}(-x^3 + 3xy^2 - y^3 + 3x^2y). \end{aligned}$$

In simulations, the pipe radius is 50 mm. The first step is to give reasonable values to the gains, and to the charge and displacements at each measurement. The relative gains, g_2, g_3 and g_4 , are typically not far from 1. The unreal measurement is done at 5 or 9 displaced positions, as shown in Fig.3. The charge, q_j , is chosen around 1 with a proper scaling. The second step is to calculate output data from the model monitor with the assumed response functions. Finally estimation of gains and beam parameters at each measurement is carried out, from the simulated data, with the chi-square method. At the same time the variance of the estimated parameter is obtained.

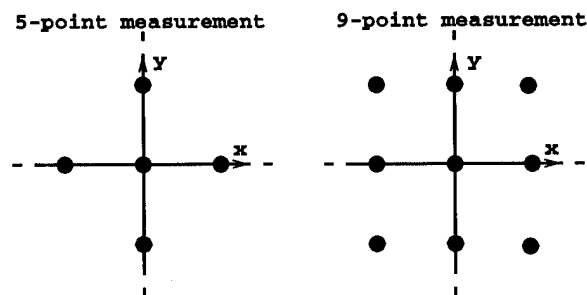


Figure 3. Orbit displacements at the model monitor.

The simulation results are summarized in Table I, which shows values given to relative gains and displacements, and the variance of each parameter. With an expected error of $\sigma_0 < 10^{-3}$, which is estimated from the TRISTAN monitor system, the geometrical center can be found within 100 μm in Case 1 and Case 2. Further improvement can be seen in Case 4 with the nine-point measurement.

Table I

Preset values and simulation results for the variance of the estimated parameters.

Case 1 : m=5					
	g_2	g_3	g_4	q_j	x_j, y_j
preset	1	1	1	1	$\pm 5,0 \text{ mm}$
σ/σ_0	5.5	7.7	5.5	3.9	98
Case 2 : m=5					
	g_2	g_3	g_4	q_j	x_j, y_j
preset	0.9	0.95	1.1	1	$\pm 5,0 \text{ mm}$
σ/σ_0	5.0	7.5	6.1	3.9	100
Case 3 : m=5					
	g_2	g_3	g_4	q_j	x_j, y_j
preset	1	1	1	1	$\pm 1,0 \text{ mm}$
σ/σ_0	25	35	25	18	440
Case 4 : m=9					
	g_2	g_3	g_4	q_j	x_j, y_j
preset	1	1	1	1	$\pm 5,0 \text{ mm}$
σ/σ_0	3.3	4.7	3.3	2.6	63

V. BEAM TEST

The present method was tested with a stripline monitor in TRISTAN. Measurement was done with a single beam, an

electron beam or a positron beam. The configuration of four striplines and the monitor chamber is the same with that of the numerical model. The stripline monitor is 150 mm long, and its inner radius is 42 mm, which is the only necessary parameter for the position estimation.

Each stripline electrode has two output ports for ensuring the signal directivity. The directivities of the four striplines may be different, and also dependent on the beam direction. In this experiment, not only the upstream port signals but also the downstream signals are analyzed.

This test provides an ideal setting to demonstrate the usefulness of the present method. The relative gains are different on the upstream and downstream sides. Due to the variation of the directivities, the range of the relative gains on the downstream side is wider than that of the upstream. Estimation of the beam position can be done with either the upstream or downstream data independently, and the results are compared with each other.

The position measurement was done for 9 different orbits at the monitor. The signal detection was made with a narrow-band detector, sampling a 500MHz frequency component, with the help of a coaxial switch choosing one from 8 output signals.

Test results are summarized in Table II, and shown in Figures 4 and 5. The directivity, the ratio of downstream/upstream, was 17~20 %. The measurement error was not analyzed, but may be the same on the upstream and downstream sides because the signal was detected with the same detector gain. With a typical relative error of 10^{-3} on the upstream side, the measurement error would be $\sim 3 \times 10^{-4}$, which is consistent with the difference between the positions estimated independently from the data on either side. The covariant matrix also shows a strong positive correlation among the estimated positions. This fact can be seen in the figures as an offset between the two sets of estimated positions.

The beam test was so successful that the present method will be surely helpful for finding the geometrical monitor center in future accelerators having the optics extremely sensitive to the orbit, for example, in the KEKB.

References

[1] W. Press, B. Flannery, S. Teukolsky and W. Vetterling, Numerical Recipes (Cambridge University Press).

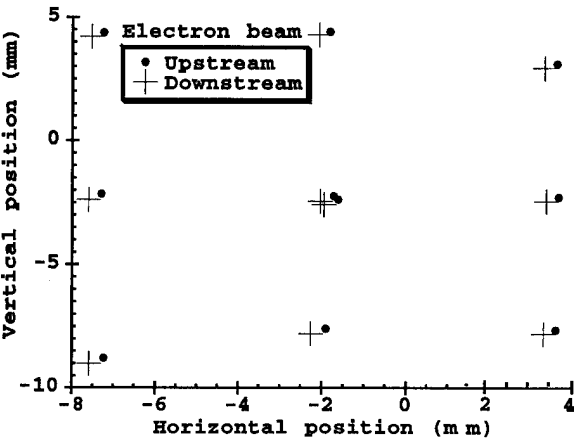


Figure. 4. Estimated positions with an electron beam.

Table II
Estimation for gains and the variance of the fitting parameters in the beam test.

Electron beam					
Upstream					
	g_2	g_3	g_4	q_j	x_j, y_j
fit	1.045	1.031	1.037	~ 0.35	Fig.4
σ/σ_0	10	14	9.2	3.0	160
Downstream					
	g_2	g_3	g_4	q_j	x_j, y_j
fit	1.121	0.987	1.049	~ 0.065	Fig.4
σ/σ_0	57	73	49	3.0	880
Positron beam					
Upstream					
	g_2	g_3	g_4	q_j	x_j, y_j
fit	1.027	1.009	1.039	~ 0.25	Fig.5
σ/σ_0	12	17	12	2.4	200
Downstream					
	g_2	g_3	g_4	q_j	x_j, y_j
fit	1.068	1.043	1.032	~ 0.045	Fig.5
σ/σ_0	70	98	66	2.4	1100

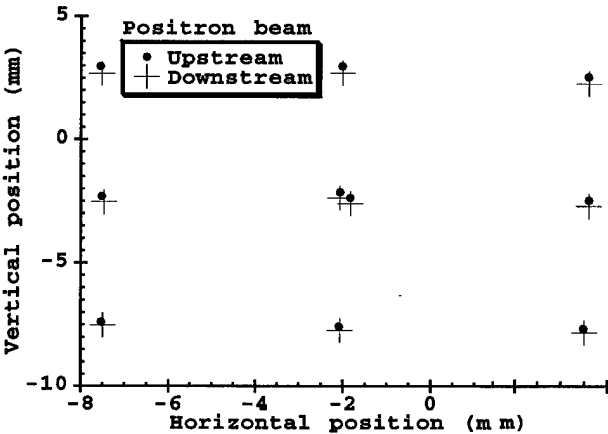


Figure. 5. Estimated positions with a positron beam.

SIMULATION OF PEP-II BEAM POSITION MONITORS*

C.-K. Ng, T. Weiland[†], D. Martin, S. Smith and N. Kurita
Stanford Linear Accelerator Center, Stanford University, Stanford, CA 94309

Abstract

We use MAFIA to analyze the PEP-II button-type beam position monitors (BPMs). Employing proper termination of the BPM into a coaxial cable, the output signal at the BPM can be determined. Thus the issues of sensitivity and power output can be addressed quantitatively, including all transient effects and wakefields. Besides this first quantitative analysis of a true BPM 3D structure, we find that internal resonant modes are a major source of high value narrow-band impedances. These are evaluated and methods are presented to suppress these parasitic resonances below the tolerable limit of multibunch instabilities.

I. INTRODUCTION

There are several issues of concern for the button-type BPMs in the PEP-II [1] vacuum chamber. First, the presence of BPMs in the vacuum chamber contributes significant impedances, broad-band and narrow-band. For broad-band impedance, the contribution of all the BPMs to the total impedance budget can be readily calculated. Narrow-band impedances arise from the formation of resonances or trapped modes in the BPM, which may have detrimental effects on the beams because of coupled-bunch instabilities, and which may produce heating effects above tolerable levels. Second, the power coming out of the cable connected to the BPM should not be too high such that it is within the handling capability of the diagnostic electronics, but not at the expense of losing the signal sensitivity at the frequency of interest which is 1 GHz. Third, the power carried by the trapped modes and by the signal, especially when the beam is offset, may produce considerable heating in the ceramic and metallic walls of the BPM. These issues are closely related to each other, thus increasing the complexity of designing the BPM. In view of these electrical and mechanical requirements, 1.5-cm diameter buttons have been selected for PEP-II BPMs.

II. MAFIA MODELING

The detailed layout of the BPM in the arcs of the PEP-II ring is shown in Fig. 1. Each BPM consists of four buttons, located symmetrically at the top and at the bottom of the vacuum chamber. Each of the High Energy Ring (HER) and Low Energy Ring (LER) contains approximately 198 BPMs in the arcs [1]. There are 92 BPMs in the straight sections of each ring, and the four buttons are located symmetrically at 90° from each other at the circumference of the circular pipe. The BPM button is tapered in such a way that the impedance matches that of a 50 Ω coaxial line. A ceramic ring for vacuum insulation is located near the button region. It has a dielectric constant of about 9.5. The in-

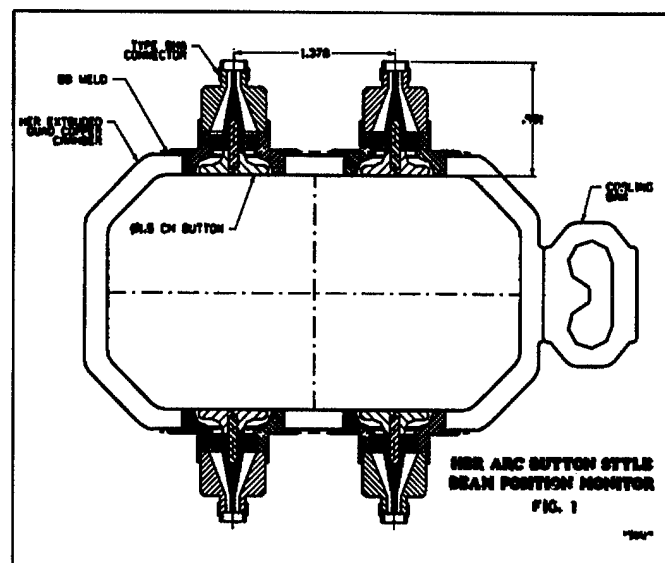


Figure 1. Layout of the 4 buttons of a BPM in the arcs of the HER vacuum chamber.

ner radius of the ceramic ring needs to be adjusted for optimum matching.

The 3D MAFIA model of the BPM is shown in Fig. 2. Because of symmetry, only one quarter of the structure is simulated. One button of the BPM is situated on the top of the vacuum chamber, and it tapers gradually to a coaxial line above. The simulation is done in the time domain, which consists of two kinds of calculations, namely wakefield and port transmission calculations. For wakefield calculation, a rigid beam comes in along the z -direction. It excites electromagnetic fields at the BPM, which in turn act back on the beam. The boundary conditions at the beam entrance and exit planes are set to waveguide boundary conditions so that electromagnetic waves traveling to these boundaries are not reflected. At the top boundary of the coaxial line, it is treated as an outgoing waveguide port, where the transmission of the signal is determined. A two-dimensional eigenvalue problem is first solved to determine the propagating and evanescent modes of the coaxial line. These modes are then loaded at the port in the 3D time domain calculation. Since the beam excites a broad frequency spectrum, a broad-band boundary has to be implemented at the waveguide port.

The impedance of a BPM can be evaluated from the wakefield or its Fourier transform. From the Fourier transform of the wakefield, we can identify potential resonant modes excited in the BPM by the bunch. Since the resolution of narrow resonances in the impedance spectrum depends on the number of sampling points in the wakefield calculation, we calculate the wakefield up to a large distance of $s = 5$ m, where s is the bunch coordinate. The transmission calculation at the port gives us the

*Work supported by the Department of Energy, contract DE-AC03-76SF00515.

[†]Permanent address: University of Technology, FB18, Schlhongortenstr.8, D64289, Darmstadt, Germany.

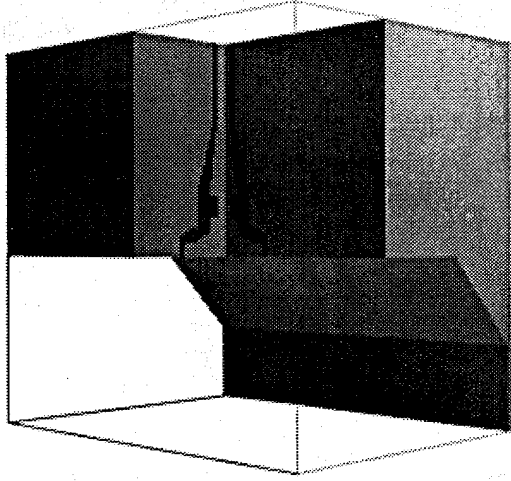


Figure 2. 1/4 MAFIA geometry of the BPM in the vacuum chamber. The button region is cut out for viewing purposes.

value of the outgoing voltage at the end of the coaxial line as a function of time, which corresponds to the signal picked up by the BPM as the beam passes through this region of the vacuum chamber.

III. SIMULATION RESULTS

The high beam current in the PEP-II B-Factor poses stringent requirements on impedances and power deposition. BPMs can generate considerable broad-band and narrow-band impedances. To avoid single-bunch instabilities, the accepted limit of the total broad-band effective impedance for the prescribed PEP-II current is $|Z/n|_{eff} = 0.5 \Omega$ [1], where $n = \omega/\omega_{rev}$ is the harmonic number. It is desirable that BPMs contribute a small fraction to the total broad-band impedance budget. Narrow-band impedances can also be generated as a result of the excitation of trapped modes in the BPMs. Their values have to be controlled below some limits so that coupled-bunch instabilities will not occur. The most serious higher-order mode excited by the beam is the TE_{11} mode with respect to the button axis. Its frequency increases with the decrease in the diameter of the button. The acceptable limit of the narrow-band impedance for avoiding coupled-bunch instabilities is a function of the frequency $f = \omega/2\pi$ of the resonant mode and is given by [2]:

$$\left(\frac{Re[Z]}{k\Omega}\right) < 3.0\left(\frac{\text{GHz}}{f}\right)e^{(\omega\sigma_z/c)^2}, \quad (1)$$

where σ_z is the bunch length which is taken to be 1 cm. It should be noted that the above limit is a conservative estimate since it takes into account of only radiation damping. Other damping mechanisms such as feedback will help suppress the narrow-band resonance. The numerical factor is given for the LER with a current of 3 A, and the limit is inversely proportional to the current. The exponential factor indicates the decay of the beam spectrum at high frequencies.

In the following, we present the numerical results from MAFIA simulations. In our simulations, a Gaussian bunch with $\sigma_z = 1$ cm is used and the total bunch length is $10\sigma_z$'s. For the coaxial port, at the range of frequency of interest, only the TEM

mode propagates. Thus for the output signal at the coaxial line, we only need to consider this mode at the port. The MAFIA results shown in the following figures are normalized to a bunch charge of 1 pC. The numerical results for impedance, power and other relevant quantities for the case with 3 A current (8.3×10^{10} per bunch) are listed in Table 1.

Energy loss by beam		126 W
Power out of one cable		9 W (37 W)*
Transfer impedance at 1 GHz		0.65 Ω
Broad-band impedance, $ Z/n $		0.008 Ω (11 nH)
Narrow-band impedance:	MAFIA	6.5 k Ω at ~ 6.8 GHz
	accepted	3.4 k Ω

Table I

Impedance and power of the 1.5-cm BPM. The beam current is 3 A. The impedances are for all the BPMs in the ring. *The power in the parentheses is that out of the cable which is closest to the beam when it is 1 cm offset from the axis.

(a) Impedances

In Fig. 3, we show the longitudinal wakefield as a function of the beam coordinate s . It can be seen that, for $0 \lesssim s \lesssim 10\sigma$, the wakefield is inductive in nature. The inductance of each BPM is estimated to be 0.04 nH or $|Z/n| = 3.4 \times 10^{-5} \Omega$. The total contribution of all the BPMs is 11 nH or $|Z/n| = 0.008 \Omega$. The total broad-band impedance budget for all the ring elements is estimated to be 0.31 Ω [2], and therefore the BPMs contribute a quite small fraction of it. By integrating the wakefield, the loss parameter of a BPM is found to be 2.7×10^{-3} V/pC. For $N = 8.3 \times 10^{10}$ and a bunch spacing of 1.2 m, this gives a power loss by the beam of 126 W. In Fig. 4, we show the impedance spectrum as a function of frequency. A sharp peak of 25 Ω is seen at around 6.8 GHz, which should be compared with the TE_{11} cutoff frequency of 6.4 GHz of an ideal coaxial waveguide with the button dimensions. The frequency and impedance of the TE_{11} mode are in satisfactory agreement with measurements [3]. The total impedance of all BPMs due to this resonant mode is 6.5 k Ω , which is about twice the accepted value calculated by Eq. 1. This resonance can be suppressed to a small value by introducing asymmetry at the button at the cost of increased mechanical complexity [4]. Since the narrow-band impedance is small compared with the feedback power (~ 100 k Ω) used for damping the RF cavity higher-order modes, we rely on the feedback system to suppress this mode.

(b) Signal and power output

In Fig. 5, we show the output signal of the TEM mode at the coaxial line as a function of time. As the beam is passing the BPM region, it generates a large output signal which then oscillates for some time and then dies off as the beam is gone. The power carried by the signal when the beam is offset by 1 cm is 37 W, which can be handled by the diagnostic electronics. Fig. 6 shows the Fourier transform of the output signal divided by the beam current spectrum. The frequency content of the signal is quite broad-band and there is no evidence of high narrow peaks

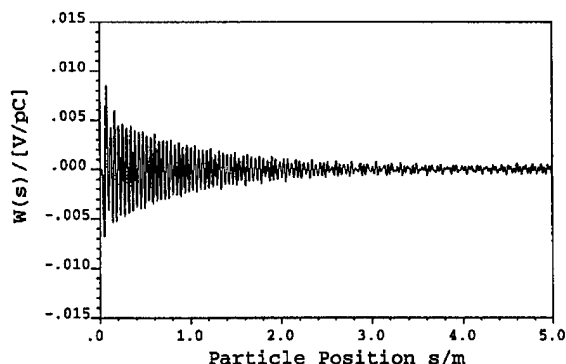


Figure 3. Longitudinal wakefield of the 1.5-cm BPM as a function of the particle position.

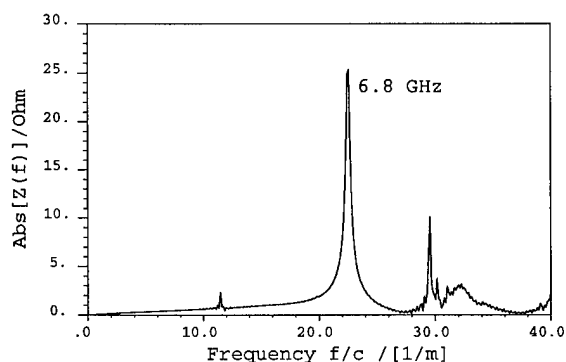


Figure 4. Longitudinal impedance spectrum of the 1.5-cm BPM as a function of the inverse wavelength.

up to 10 GHz. In particular, at 1 GHz, the transfer impedance is 0.65Ω , which is above our minimum requirement of 0.5Ω .

(c) Signal sensitivity

The sensitivity of a BPM is generally determined by the signals picked up by the different monitors when the beam is off center. We define the sensitivity function as:

$$S_i = \frac{1}{d_i} \left(\frac{A - B}{A + B} \right), \quad (2)$$

where i can be either x or y . For S_x , d_x is the offset in the x -direction, and A and B are the signals picked up by the top right and top left monitors respectively. For S_y , d_y is the offset in the y -direction, and A and B are the signals picked up by the right top and right bottom monitors respectively. Fig. 7 shows the sensitivity functions S_x and S_y as functions of frequency. It can be seen that the frequency dependences of S_x and S_y are similar and are extremely flat up to about 5 GHz. Their values at around 1 GHz satisfy our position resolution requirements.

IV. SUMMARY

We have shown that the 1.5-cm button type BPM has the required transfer impedance and signal sensitivity. The broad-band impedance is a small fraction of the ring impedance, and the narrow-band impedance can be suppressed by the feedback system.

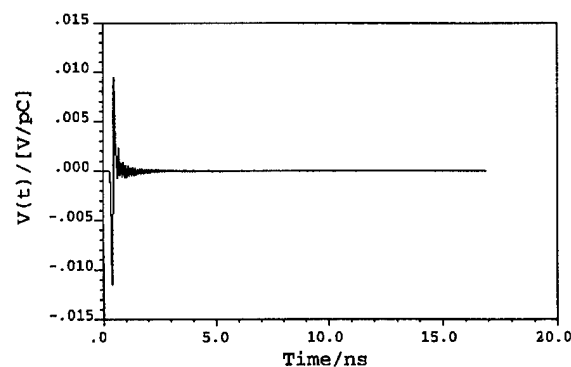


Figure 5. Voltage output of the 1.5-cm BPM at the coaxial line as a function of time.

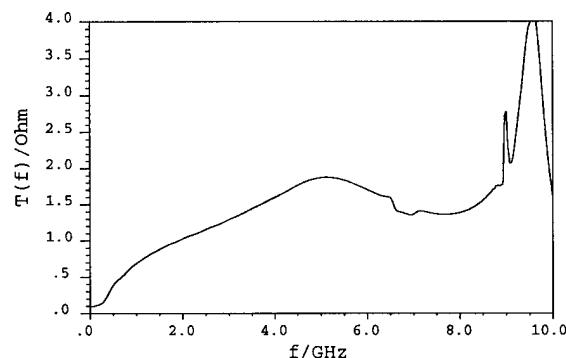


Figure 6. Beam-to-signal transfer function of the 1.5-cm BPM at the coaxial line as a function of frequency.

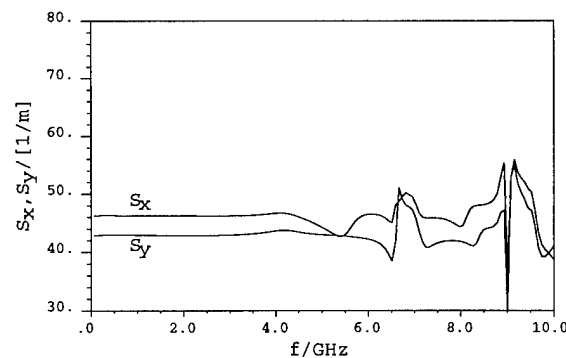


Figure 7. Sensitivity functions of the 1.5-cm BPM as functions of frequency.

Acknowledgements

We would like to thank J. Corlett, S. Heifets, K. Ko, G. Lambertson, M. Nordby, J. Seeman and T. Shintake for many useful discussions.

References

- [1] An Asymmetric B Factory, Conceptual Design Report, LBL-PUB-5379, SLAC-418, CALT-68-1896, UCRL-ID-114055 or UC-IIRPA-93-01, June 1993.
- [2] S. Heifets et. al., Impedance Budget of the PEP-II B-factory, these proceedings.
- [3] J. Corlett, private communication.
- [4] N. Kurita, D. Martin, C.-K. Ng, S. Smith and T. Weiland, Simulation of PEP-II Beam Position Monitors, PEP-II Technical Note No. 87, 1995.

PROTOTYPE BUNCH KILLER SYSTEM AT SRRC

G. J. Jan*, Jenny Chen, C. H. Kuo, T. F. Lin, K. T. Pan, Glory Lin, and K. T. Hsu

Synchrotron Radiation Research Center, Hsinchu 30077, Taiwan

*Department of Electrical Engineering, National Taiwan University, Taipei 10767, Taiwan

ABSTRACT

The prototype bunch killer has been set up at SRRC recently. The system includes two subsystems, the multibunch filling pattern shaping system and single bunch killer system. Gate RF knockout approach is used to shape the filling pattern of multibunch and to obtain a well-defined gap for machine study. The gate processes synchronize with revolution frequency. Widths of the gate signal determine the empty gap of the filling pattern. Beam knockout systems with nanosecond impulse current are also implemented which used to kill the individual electron bunch with bucket addressing capability. The purity of the single bunch is improved by the nanosecond knockout system, despite the difference of the tune and tune spread of the main and parasitic bunches, that lifts the requirement of the narrow tune spread for standard single bunch purification process. The nanosecond knockout technique also applied to kill undesired bunches in the multibunch operation mode. The preliminary results are present.

I. INTRODUCTION

The storage ring of SRRC operates with an 499.654 MHz RF system and has 200 bucket locations. The required filling pattern during operation are dependent on the requirement of users or machine physicists. Multibunch filling and single bunch operations are routine achievable. Even mixed mode operation [1] is supported by existing system also. Multibunch operation modes are the most use mode. Multibunch filling are play an important role for routine operation and beam physics study. Control the filling patterns are highly desirable for various applications, such as to avoid to trap ion. The gate RF knockout technique used to shape the multibunch filling pattern for desired shapes. High purity single bunch is essential for time resolves experiments. Single bunch purity is several percentages after the injection. Since the tune spread of betatron side band are several KHz, it is difficult to kill spurious bunches by using standard resonant excitation of transverse oscillation purification procedure [1,2,3] without make loss of the main bunch at this stage. A novel method that is using impulse generator operates at betatron frequency to purify the single bunch and to kill undesired bunches at multibunch mode also demonstrated.

II. GATE RF KNOCKOUT TECHNIQUES

Gate RF knockout approach is used to shape the filling pattern of multibunch store mode and to obtain a well-defined gap for various applications. The gate process synchronized with revolution frequency. Width of the gate signal determined the length of the empty gap of the filling pattern.

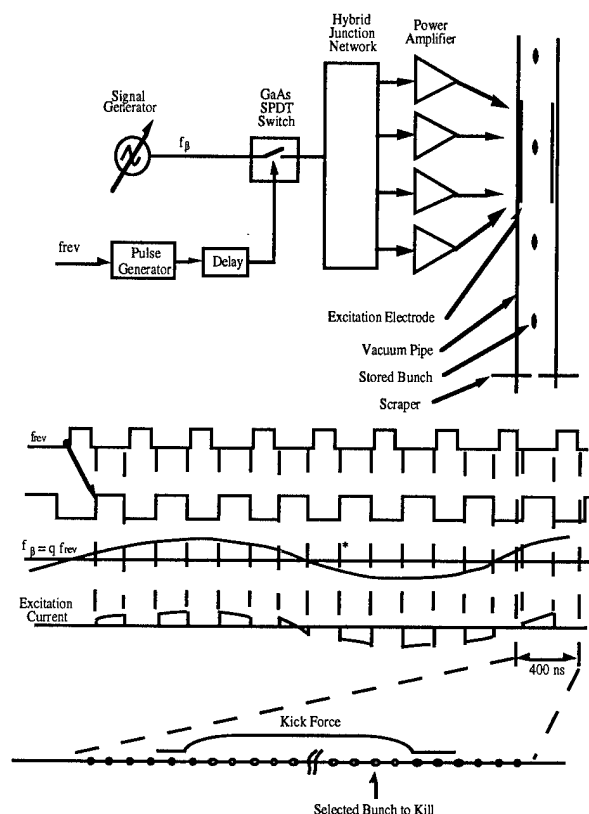


Figure 1. Multibunch filling pattern shaper

Figure 1 shown the functional block diagram of the multibunch filling pattern shaper. The revolution clock f_{rev} is used as reference of the bucket location. The delay unit determines the location of the filling bunches to be kill. The pulse generated by the pulse generator determine the length of bunch train will be kill. Betatron resonance frequency generated by a separate signal generator. The output of signal generator is gate by a GaAs RF switch with 5 nsec rise time. The frequency ranges of the power amplifier are form 10 kHz to 220 MHz with rise time less than 10 nsec. Hence the shaped multibunch will be a rising and falling edge within one to three buckets.

III. NANOSECOND BUNCH KILLER

Beam knockout system with nanosecond impulse current is also implemented which kill the individual electron bunch at specified location. The purity of the single bunch improved by the nanosecond knockout system, despite the difference of the tune and tune spread of the main and parasitic bunches, that lifts the requirement of the narrow tune spread for standard

single bunch purification process. The nanosecond knockout technique is also used to kill undesired bunches in the multibunch operation mode.

The nanosecond bunch killer is shown as figure 2. The gate circuit that is coincident revolution clock and betatron oscillation frequency f_β . The coincident output is delay by a delay generator. The time delay of the delay generator used to address specific bucket to kill. The output of delay trigger signal trigs four sets of impulse generator, two with positive output and two with negative output. The pulse width of the impulse generator is less than 1 nsec, and provide 100 V impulse to 50 ohm load. Four excitation electrodes drive by the output of the impulse generators to exert impulse force to selected bunch.

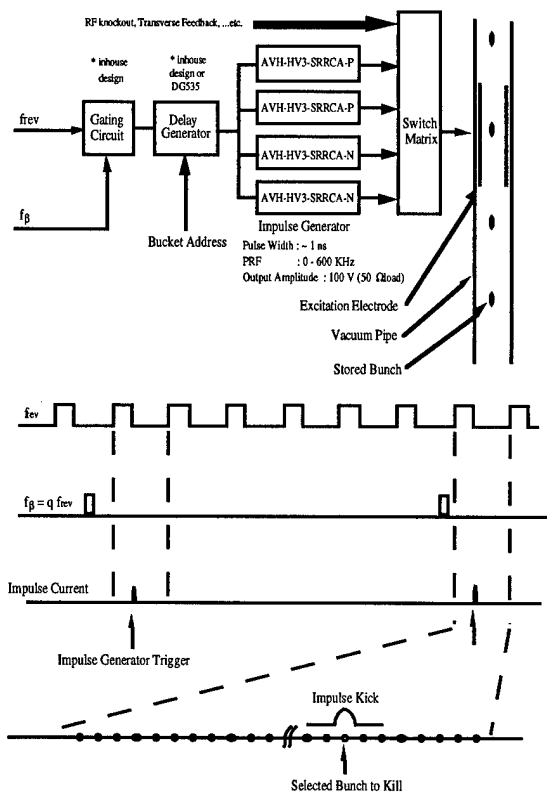
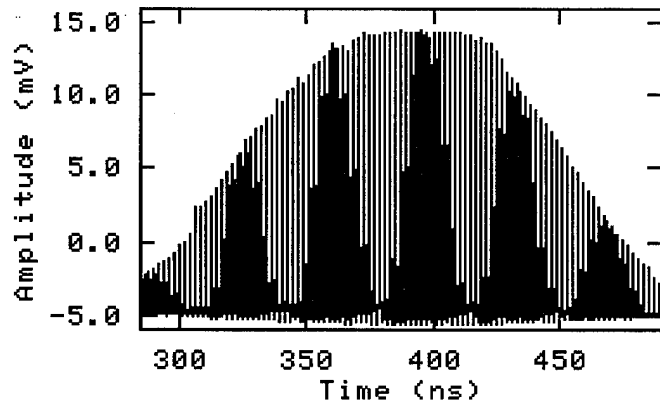


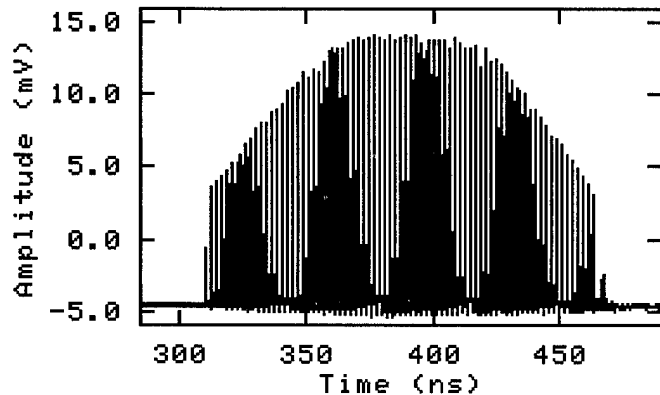
Figure 2. Nanosecond bunch killer

IV. MULTIBUNCH FILLING PATTERN SHAPING

Multibunch filling pattern is reshaped by multibunch bunch killer to desired shape. Figure 3(a) is a designed filling pattern of the storage ring for this study. Edge of both ends cut by bunch killer are shown at figure 3(b). Reduce total beam intensity is the disadvantage of the approach.



(a) Before shaping



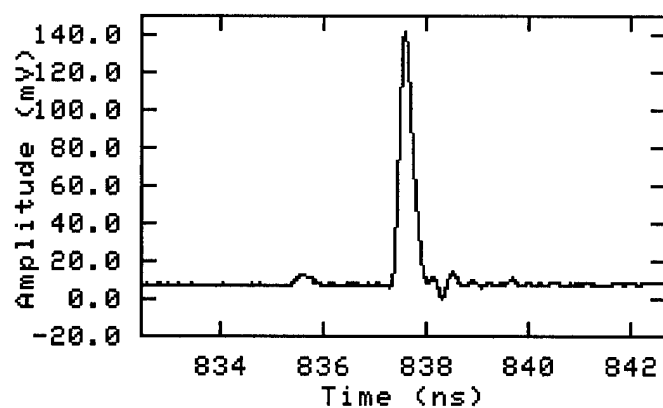
(b) after shaping

Figure 3. Multibunch filling shaping by bunch killer

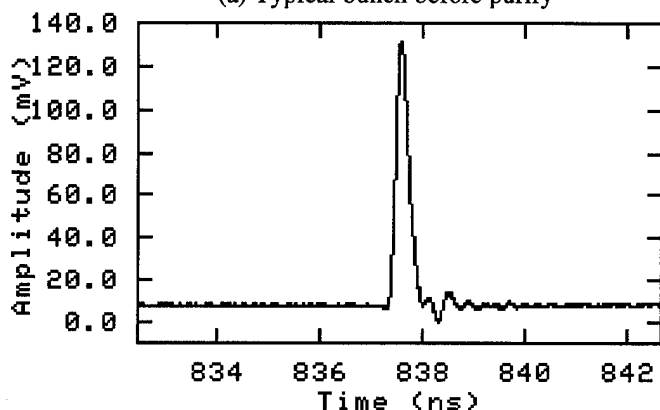
V. SINGLE BUNCH PURIFICATION

High single bunch purity is necessary for time resolved experiments. Single bunch impurity of the storage ring is dependent upon several issues. The injector system can provide a few percentage impurities of single bunch routinely. Single bunch impurity is mainly caused by the timing jitters of the electron gun electronics. Single bunch purity can also deteriorate due to various electron loss mechanisms [4]. Single bunch impurity is improved by RF knockout techniques, which are based upon different betatron frequency of different bunches with different bunch current. When tune spread is too large, this technique is difficult to kill parasitic bunches. Knockout technique by using nanosecond impulse is an alternate to clean satellite bunches.

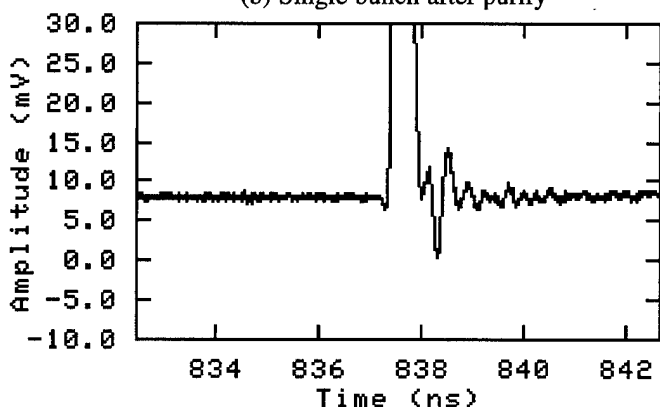
Figure 4(a) is a typical stored single bunch with several percentage residue bunches. At the tail of the main bunches, there are some ringing signals due to the electronic system. The residue bunch before the main bunch is very prominent. Nanosecond bunch killer was used to kill those bunches as shown in Figure 4(b), the enlargement of the detail shown in Figure 4(c). Due to the limited dynamic range of the observation by oscilloscope, the single bunch impurity is estimated to be less than 10^{-3} after purification. To measure very small amounts of single bunch impurity, photon counting for single bunch purity measurement is on the way.



(a) Typical bunch before purify



(b) Single bunch after purify



(c) Enlarge of figure (b)

Figure 4. Single bunch purification by using nanosecond bunch killer

VI. NANOSECOND BUNCH KILLER FOR MULTIBUNCH APPLICATION

Nanosecond bunch killer was used to kill specific bunch at multibunch filling mode shown in figure 6. On the figure, six bunches are removed from a consecutive bunch at multibunch operation mode.

Randomized of multibunch filling pattern by nanosecond bunch killer is possible. Nanosecond bunch killer allows arbitrary sequence of bunches to be killed. This would allow pseudo-random sequences to be generated, affording the

opportunity to add sophisticated system identification techniques to the machine analysis toolkit. Using nanosecond bunch killer to randomize the filling pattern of multibunch operation mode are more efficient than using single bunch injection and with bucket addressing to random the filling pattern of the storage ring.

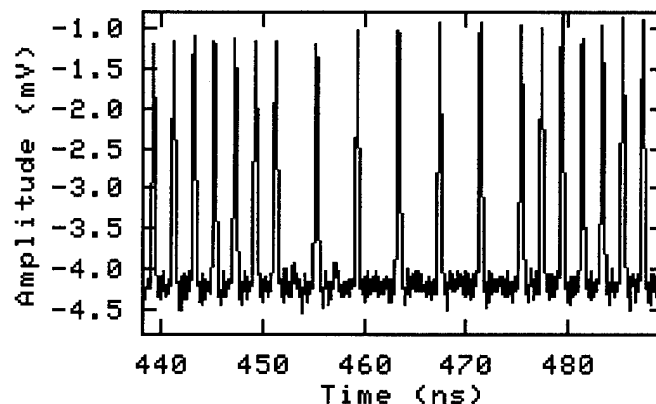


Figure 5. Multibunch filling - selected kill by nanosecond bunch killer

VII. ACKNOWLEDGMENTS

The authors would like to thank the staff of SRRC, especially Dr. K. K. Lin and Dr. T. S. Ueng for their support running the single bunch mode and support various instruments for this study. The encourage from Prof. Y. C. Liu and Dr. Bill Weng are also highly appreciate. The advice by Dr. Jameson is also valuable for this study.

VIII. REFERENCES

- [1] J. L. Revol, et al., "Diagnostics and equipments for single bunch operation at ESRF", The Fourth European Particle Accelerator Conference, 1506 (1994).
- [2] J. L. Revol, E. Plouviez, "The ESRF timing system and single bunch operation", Synchrotron Radiation News, Vol. 7, No. 4, 23 (1994).
- [3] R. J. Nawrocky, et al., "A bunch killer for the NSLS X-ray electron storage ring", IEEE Proceeding of Particle Accelerator Conference 1993, 2145 (1993).
- [4] T. Obina, et al., "Measurement of the longitudinal bunch structure in the Photon Factory position storage ring with a photon counting system", Nucl. Instrum. and Methods A 354, 204 (1995).

Beam diagnostics for the Amsterdam pulse stretcher AmPS.

J.G.Noomen, H.Boer-Rookhuizen, N.Dobbe, J.v.Es, E.Heine,
F.Kroes, J.Kuijt, J.v.d.Laan, A.Poelman, H.Nieuwenkamp, T.Sluijk

NIKHEF-K

p.o.box 41882 1009 DB, Amsterdam, The Netherlands

Abstract

AmPS is an electron storage and pulse stretcher ring operating between 300 and 900 MeV with stored beam currents up to 200 mA. For beam diagnostics the AmPS ring has been provided with 32 stripline beam position monitors, 17 low beam impedance designed screens, a DCCT and 4 synchrotron light ports. In addition 3 scanning wires for injection control, 32 air filled ionisation chambers for beam loss control, a kicker for tune measurements and a harmonic shaker have been implemented. Purpose, design and performance of these devices will be described. The data acquisition for closed orbit correction and tune measurement will be presented as well.

Introduction

The AmPS ring has been constructed for two types of experiments. Physics with a high duty cycle (90%) extracted beam (stretcher mode) and internal target physics (storage mode)[1]. Commissioning started in the middle of 1992 [2]. Meanwhile extracted currents of 10 uA at three turn injection, duty cycles up to 94 % and stored currents of 150 mA have been performed. To obtain these results precise adjustment of the ring parameters is necessary especially in stretcher mode. For this purpose the ring has been provided with adequate diagnostics.

Stripline type beam position monitors

For proper measurement of successive turns a bandwidth of 15 MHz has been chosen since the revolution time of the beam is 0.7 us. For closed orbit correction 32 of these position monitors have been installed (4 per betatron wavelength) Although for closed orbit correction a fast response is not necessary it has been decided for reasons of uniformity to make them all of the fast response type. The data of the 32 monitors are read by a sample (3 us) and hold system and digitized by a 12 bits ADC, 32 channel VME 566 unit. For calculation and execution of an orbit correction a selection of monitors and orbit correctors can be made. This enables the exclusion of badly calibrated or malfunctioning monitors. Due to the high RF frequency in stretcher mode (2856 MHz) [4] the monitors have an over-moded size which should inhibit proper functioning. This has been cured by sandwiching them between RF dampers [5]. However they still suffer from some defects. They have large centre offsets dependent on the inner beam pipe geometry close to the monitor and more nonlinearity than corresponds with the monitor geometry itself. The centre offsets are calibrated by centring the beam in a preceding

quadrupole (by wobbling) one monitor at a time. To make the calibration more straightforward a software tool is under development to center the beam at the same time in all the calibration quadrupoles. This is done by wobbling the quadrupoles individually and calculating the beam offset in the quadrupole from the deviation in a position monitor. Centring the beam in the quadrupoles is then obtained by using the same orbit correction algorithm as exist for the position monitors. In addition this enables us to adjust the closed orbit if too few reliable and calibrated stripline monitors are available.

Beam viewers

A low cost, low impedance beam viewer has been developed. The housing consists of a piece of straight section pipe

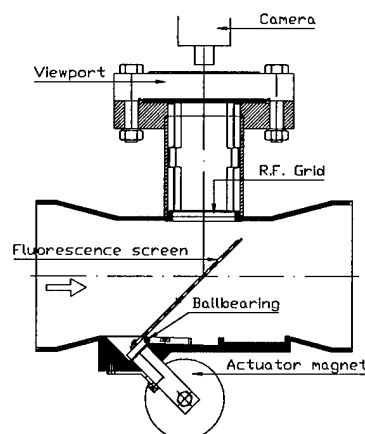


Fig. 1. Beam viewer

which has been squeezed vertically to obtain a quasi elliptical cross section. The actual screen plate is a 6 by 4 cm chromium doped aluminum oxide plate which pivots upon small ball-bearings. If the screen is not used it lies on the bottom of the housing due to its own weight. In this position the disturbance of the beam pipe cross section is minimum and so is the beam impedance. The screen is activated by a magnetic field of a coil outside the vacuum. In this way the dynamical mechanics inside the vacuum are restricted to only the screen plate ball-bearings. A window has been positioned at the upper side. To reduce the beam impedance the entrance of the window pipe has been shielded with a 90 % open s.s. mesh. For global adjustment of the beam position in the ring 16 beam viewers have been installed equally shared along the ring 2 per straight and 2 per curve. One additional beam viewer

has been installed in the injection area.

Synchrotron light ports

Four synchrotron light ports are available. Three at positions with negligible dispersion in the beginning of a curve and one at maximum dispersion in the middle of a curve. They consist simply of a light pipe ending in a window at 83 cm from the light source point. Inside the vacuum in front of the window a 2 mm thick freely expandable quartz plate acts as soft x-ray absorber. Damage of the window by heating up is now prevented. Behind the window outside the vacuum the light beam is deflected by an adjustable mirror to a camera. A lens system on the camera images a light source area of 30 mm horizontal and 24 mm vertical on the light sensitive front-end of the vidicon tube inside the camera. Between mirror and camera is a remotely controlled set of light attenuation filters. The set contains four filters in line with attenuation numbers 3,10,100 and 1000. Any combination of the filters can be put in the light beam. So light attenuation from zero to 65 db can be obtained with 5 db steps. There is no additional light port for alignment. Alignment is done with reference to the magnet pole. Camera and mirror are aligned as one system in a dummy magnet and then replaced to the actual magnet. A computer generated reference frame is superimposed on the light spot image. Due to the absorber the light spot is distorted. This disables high accuracy beam size measurements. Therefore high quality synchrotron ports with a cooled metal mirror inside the vacuum are under development now. Moreover the light of these ports will be transported outside the vault.

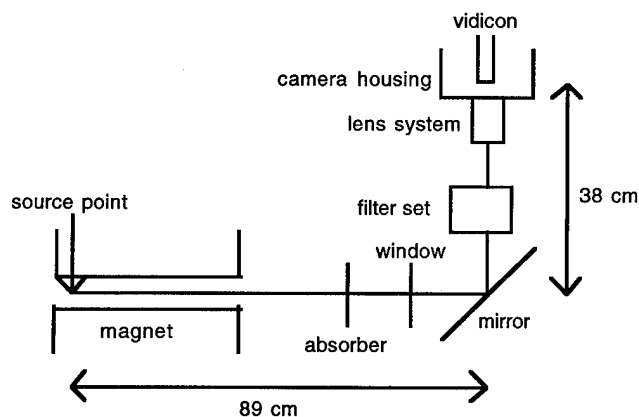


Fig.2 synchrotron light port, schematic lay-out

Scanning wires

For high precision measurement of the injected beam position, wire scanners have been installed. Three in a drift space at the end of the accelerator and three in the injection area. Those at the end of the accelerator are also meant for phase space measurement. Each scanner consists of a horizontal and vertical 50 μm tungsten wire driven across the beam by a stepper motor. One step of the stepper motor is 12.7 μm . A horizontal and vertical beam profile in one scan is performed by a 45 degrees tilted mechanical stroke. So one step is horizontally and vertically 9 μm . The

absolute position reference is a high precision Baume switch. The accuracy of the switch itself is 2 μm . To preserve this high accuracy as position reference the switch is hooked up in a sliding holder kept at center position by a screw spring. The switch is activated when the wires pass

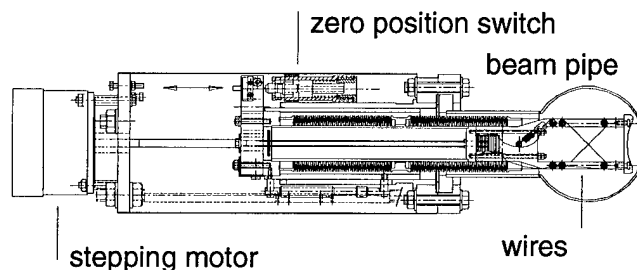


Fig.3 wire scanner

the centre. So at one half scan the switch holder is in center position and the other half scan the holder is taken along with the wire movement. In this way a position accuracy of 0.01 mm is obtained. However due to pulse to pulse beam instabilities the beam position and size accuracy is not better than 0.1 mm. The beam profile measurement is based on secondary emission signal sampling. Each sample covers a complete beam pulse. The sample resolution of the preamplifier located in the vault close to the monitor is 2 fC. However due to interference noise the total resolution is 30 fC. The samples are digitized by a 8 bits ADC and stored in memory. From these data the position of the beam mass center and the beam diameter containing 95 % of the current are calculated. From the three sequential diameters at the end of the accelerator the emittance is calculated. The shape of the beam is shown on a graphic display.

Parametric current transformer

The current in the ring is measured with a commercially available parametric current transformer (PCT)[6]. The PCT is positioned around the beam pipe outside the vacuum close to an aluminum oxide isolation gap in the beam pipe. A copper electrical shield and a u-metal magnetic shield cover the PCT and isolation gap.

Loss monitors

A loss monitor consist of a piece of air filled cable acting as an ionization chamber. These monitors have been positioned all around the ring combined in 32 groups. Each group is read out individually and showed on a graphical bar display.

Tune kicker

The tune is determined from the betatron oscillations induced by injection or by kicking the stored beam with the tune kicker. The betatron oscillations are measured with a stripline position monitor and sampled by a Lecroy 9450 oscilloscope. The oscilloscope has a Built in FFT function which calculates the frequency spectrum and thus the tune

frequency. The kicker consists of four copper rods 1 cm diameter and 50 cm long placed parallel to the beam. In cross section the rods lie on the angular points of a square with horizontal and vertical edges of 6 cm. At one end the rods have been connected through. Each pair of diagonally positioned rods forms a loop. Forcing a current pulse through one of the loops performs a magnetic field with equal horizontal and vertical components. This enables measurement of the horizontal and vertical tune simultaneously. Only a horizontal or vertical magnetic flux is obtained by powering both loops simultaneously.

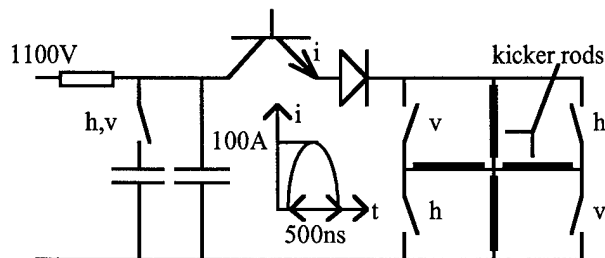


Fig.3. Tune kicker power system, schematic lay-out

Selection between horizontal or vertical flux is obtained by reversing the current in one loop with respect to the other. This is done by activating the switches h or v in fig. 3. A sine shaped current pulse is obtained by discharging a capacitor by a high voltage transistor. The capacitor and high voltage transistor have been positioned in the vault as close to the kicker loops as possible to minimize additional inductance. The capacitor value has been adjusted to make the base length of the current pulse 0.5 μ s which is sufficiently short to fit into the revolution time of 0.7 μ s. At a capacitor voltage of 1100 V is the current amplitude 200 A if both loops are powered. The bending angle at 500MeV is then 0.4 mrad. This corresponds with a betatron oscillation of 2 mm in the curves.

Harmonic shaker

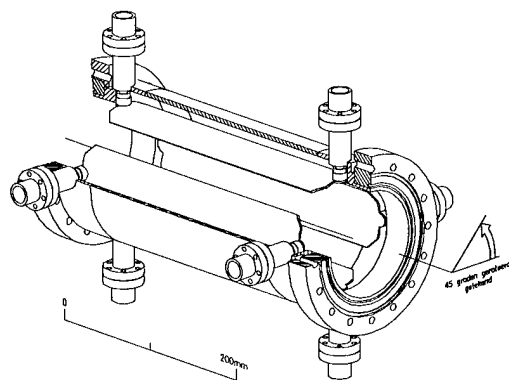


Fig.4 Harmonic shaker

For investigation of stored beam properties also a harmonic shaker has been installed. Since this device will be driven over a wide frequency range the electrodes and connectors have to be well matched to a 50 ohm system. Therefore we

modified the straight type stripline monitor design. The harmonic shaker is actually a straight type stripline monitor with 20 cm long electrodes not short circuited at one end but with connectors at both sides. The position of the excitation electrodes with respect to the beam is similar to the tune kicker. At one end each pair of diagonally positioned electrodes have been connected through creating again two loops. The other ends of the electrodes are transported outside the vault. There one or two loops in series terminated with 50 ohm can be connected onto a transmitter. Similar to the tune kicker horizontal and/or vertical RF fields can be obtained by proper combination of the loops.

Image dissector tube

For bunch length measurements a dissector tube has been ordered [7]. The theoretical bunchlength of AmPS is of the order of 90 ps in storage mode. The resolution of the dissector tube is about 10 ps which makes it suitable for our purpose.

Acknowledgement

The work described in this paper is part of the research program of the National Institute for Nuclear Physics and High Energy Physics (NIKHEF), made possible by financial support from the Foundation for Fundamental Research on Matter (FOM) and the Netherlands Foundation for Scientific Research (NWO).

References

- [1] G.Luijckx et al., The Amsterdam Pulse Stretcher project (AmPS), Proceedings of the IEEE PAC, 1989, Chicago, IL, p 46
- [2] R. Maas et al., The Amsterdam Pulse Stretcher, First commissioning results, IEEE proceedings of the PAC, 1993, Washington D.C., p.1998
- [3] J.Noomen et al., A beam position monitor for AmPS, IEEE proceedings of the PAC, 1991, San Francisco, p. 1148
- [4] F.B.Kroes et al., A fast amplitude and phase modulated RF source for AmPS, IEEE proceedings of the PAC, 1991, San Francisco, p. 684
- [5] J.Noomen et al., An over-moded stripline beam position monitor, IEEE proceedings of the PAC, 1993, Washington D.C., p. 2343
- [6] K.Unser, A torroidal D.C. beam current transformer with high resolution, IEEE proceedings of the PAC, 1981, Washington D.C.
- [7] G.S.brown et al, Measurement of bunch length with a image dissector tube, IEE Trans. Nuc. Sci., NS-30, No. 4, 1983

NON-DESTRUCTIVE BEAM PROFILE MEASURING SYSTEM OBSERVING FLUORESCENCE GENERATED BY CIRCULATING BEAM

T. Kawakubo, E. Kadokura, T. Kubo, KEK, 1, Oho, Tsukuba-shi, Ibaraki-ken, 305,
T. ISHIDA, Mitsubishi and H. Yamaguchi, Tsukuba Meson

The KEK-PS has two sets of non-destructive beam profile monitors (NDPM) in the booster and three sets in the main ring for horizontal and vertical plane, which observe those ions produced by circulating protons hitting the residual gas.[1] The measured beam sizes are always larger than those obtained by the BEAM SCOPE method.[2, 3] It results from the space charge of the circulating proton beam.

In order to eliminate this demerit, the idea of using a luminescence generated by the beam colliding with the residual gas has occurred. This idea, however, is only an idea without measuring [4, 5] or using test equipment to observe the beam at the beam transport line by a CCD camera.[6] It is very hard to observe the time variation of the beam profile (size) in a synchrotron because of the poor S/N ratio.

We inserted an optical shielding in the booster synchrotron ring (proton: 40-500 MeV) with a slit facing the beam. An optical fiber guide is fixed at the end of the slit, led out of the vacuum and connected to a photo-multiplier. A vertical beam profile is obtained by moving the slit vertically without being effected by the electric potential of the circulating beam. The most important factor concerning this method is how to eliminate noise caused by secondary particles generated due to beam loss.

I. EQUIPMENT

Figure 1 shows the measuring system at a straight section of the KEK-PS booster ring. Two slits, having a 0.5mm height, an 80mm width and a 250mm length and a rough surface coated with black plating, are arranged in the vacuum chamber with the symmetry positions to the horizontal beam center. The end of the slit is connected to an optical guide which has an end with the same shape as the slit, and a 1m length comprising of 0.5mm ϕ acrylic fibers. Another end of the optical guide is combined with another optical guide. The combined part of the fiber guide is about 1m in length, and has an end with a 10mm ϕ round shape, which is connected to an acrylic rod of 10mm ϕ and 60mm length supported by a gauge port at a flange of the vacuum chamber. Another end of the acrylic rod at the atmosphere side is connected by an optical fiber guide of 10mm ϕ and 1.5m length, the other end of which is connected to a photo-multiplier.[7] This optical guide system is called a "signal system" for the convenience of explanation.

The same system of the optical fiber guide (called a "blind system") is arranged closely near to the "signal system". The only having a different point concerning the "blind system" from that of the "signal system" is covering

the top end having a rectangular shape with blinds in order to shield any luminescence generated by the beam.

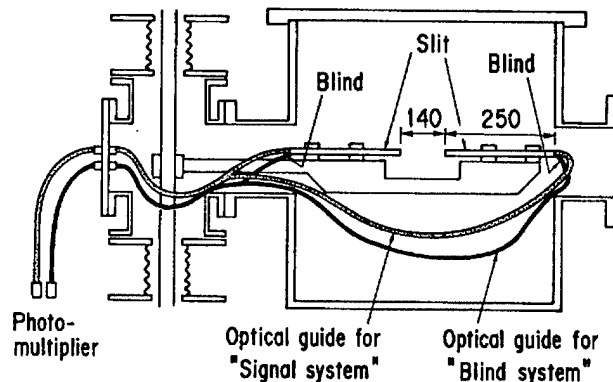


Figure 1: Measuring system to observe the luminescence generated by circulating beam

II. MEASURING

A. Aberration of the beam size

The two slits are set at the same vertical position and moved simultaneously so as to make the observing intensity be double. The largest vertical beam width (ΔY) measured by these slits, which causes an aberration of the beam size, is (see Figure 2)

$$\Delta Y = \frac{2d(a + \Delta x)}{L} + d$$

where d is the slit height, L is the length of the slit, Δx and a are the horizontal distances between the slit end and the designed beam center, and between the designed beam center and the farthest beam position from the slit, respectively. By inserting the dimensions of our monitor ($d=0.5\text{mm}$, $a=72.5\text{mm}$, $L=190\text{mm}$, $\Delta x=50\text{mm}$) into above equation, the aberration of the beam size is found to be $\Delta Y=1.3\text{mm}$.

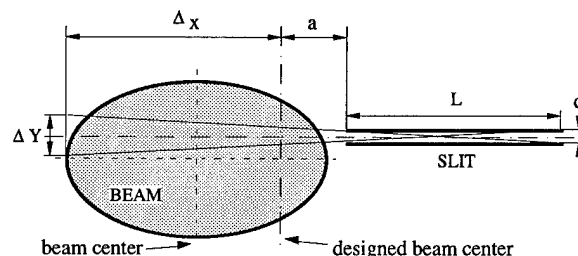


Figure 2: Aberration of the measured beam size due to the slit height

B. Noise and its elimination

The secondary particles generated due to beam loss at the vacuum wall penetrate the optical guide and produce Cherenkov light. The intensity of the light is much greater than the luminescence generated from collisions of the beam into the residual gas, and becomes severe noise. In order to eliminate this noise, the signal of the "blind system" is used. The quantities of Cherenkov light of the "signal system" and the "blind system" might be the same, because they are arranged close to each other. Therefore, the real signal is obtained by subtracting the signal of the "blind system" from that of the "signal system".

C. Block diagram of measuring system

As shown in Figure 3, the electric signals from the "signal system" and the "blind system" are amplified by a pre-amplifier ($Z_{in}=10k\Omega$, $A_{amp}=100$ times) set near to the photo-multipliers, sent to the control room through a 50 Ω coaxial cable, and connected to a subtracting circuit. The output signal of the subtracting circuit is observed by an oscillograph; a photograph is taken upon changing the vertical position of the slits.

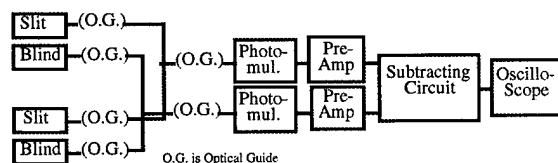


Figure 3: Block diagram of measuring system

D. Vacuum pressure and beam intensity

The S/N ratio is too poor to observe the beam profile under the normal vacuum pressure of 3×10^{-7} Torr at the location of this monitor. However, an observation becomes possible when the nearest ion pump is turned off and the pressure reaches 1.1×10^{-6} Torr one hour later, and under the almost largest intensity of 1.4×10^{12} ppp.

III. MEASURED RESULTS

A. Output signal figure

1. By moving the vertical position of the slits to the upper or lower limit, where no luminescence is injected into the slits, both signals from the pre-amplifiers of the "signal system" and the "blind system" are connected to channel 1 and channel 2 of an oscilloscope, respectively. Since it can be considered that the same intensity of Cherenkov light is generated in both systems under this condition, the two figures of the oscilloscope should agree with each other upon adjusting the bias voltages of the photo-multipliers (see Figure 4).

2. Both signals from the pre-amplifiers are connected to inputs of the subtracting circuit. Figures 5a and 5b show the

averaging figures of 128 shots from the outputs of the subtracting circuit, where the slit position is at the upper limit and at the beam center, respectively. Since the S/N ratio is poor, the effect of noise still remains even at the slit position having the largest intensity of luminescence.

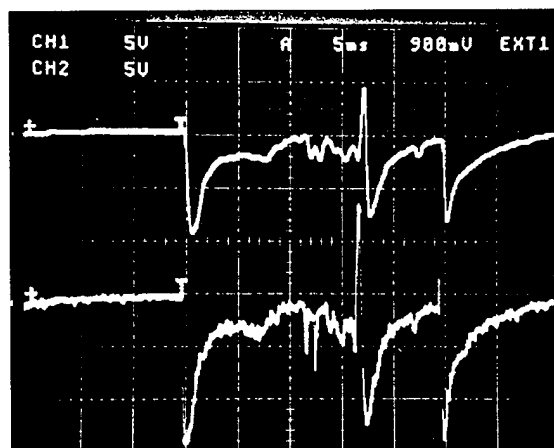


Figure 4: Upper and lower figure are the signals from the "blind system" and the "signal system", respectively, where the vertical position of the slit is set at the upper limit (X: 5ms/d, Y: 5V/d)

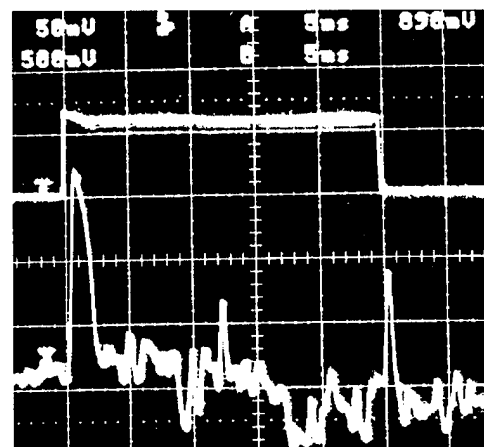


Figure 5a: Upper figure is slow beam intensity of booster, and lower figure is output signal of the subtracting circuit where the slit is set at the upper limit position (by averaging of 128 shots) (X; 5ms/d, Y: 0.5V/d)

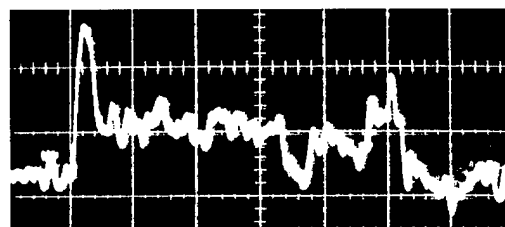


Figure 5b: In the case where the slit is set at the beam center position (by averaging of 128 shots)(Y: 0.5V/d)

B. Time variation of the beam profile

1. By moving the vertical position of slits from the upper limit to the lower limit in steps of 1mm, the output figures during the acceleration period (from 0 to 25ms) at every scraper position were taken by a photograph. By measuring and rearranging the values of the figures at times of 5, 10, 15, 20 and 25ms, beam profiles with the parameters of time are obtained, as shown in Figure 6. The time valuation of the full width of the beam profile at 50% height (FWHH) is taken from Figure 6, and plotted in Figure 7 (Photo NDPM).

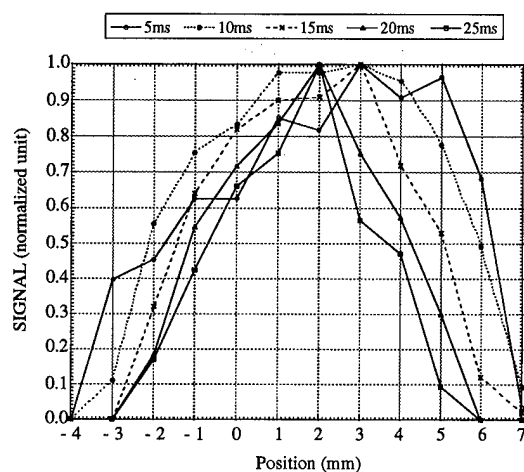


Figure 6: Beam profiles with the parameters of acceleration time from injection to extraction of the booster ring

2. The data measured by the ion collecting NDPM and BEAM SCOPE methods (the measuring system comprising two bump magnets, a scraper and a fast intensity monitor) and calculated adiabatic dumping curve are also plotted in Figure 7. Although the results measured by this monitor (Photo NDPM) and by the BEAM SCOPE are in good agreement with each other, those measured by Ion collecting NDPM are much larger than the others.

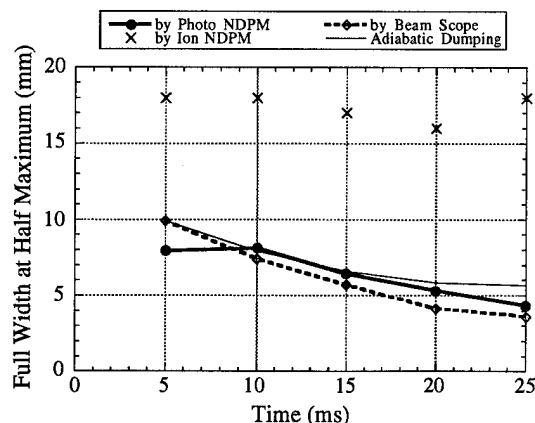


Figure 7: The time valuation of the full width of the beam profile at 50% height (FWHH)

IV. IMPROVEMENT

1. The S/N ratio is not good for taking clear observations. Since noise comes from the Cherenkov light generated by secondary particles penetrating the optical fiber, it can be eliminated by connecting a photo-multiplier to the slit directly without using any optical guides.

2. In this test measurement we adopted an old measuring technique, that is, taking photographs of the figures on an oscilloscope, and measuring the data with a scale. Data-taking, rearrangement and the outputs of the data will soon be automatically done by a computer.

V. REFERENCES

- [1] T. Kawakubo, T. Ishida, E. Kadokura, Y. Ajima, T. Adachi, "Fast data acquisition system of a non-destructive profile monitor for a synchrotron beam by using micro channel plate with multi-anodes", Nucl. Instrum. Meth., A302 (1991) p397-405
- [2] T. Kawakubo, E. Kadokura, T. Ishida, "On the reliability of measured results by non-destructive beam profile monitor", PAC93, Washington, USA, May (1993) p17-20
- [3] T. Adachi, T. Kawakubo, M. Kihara, I. Yamane, C. Ohmori, "Beam profile measurement in the KEK PS booster using pulsed bump magnet and a movable scraper", EPAC94, London, UK, June (1994) p1655-1657
- [4] Tazuo Shoji (Institute of Plasma Physics, Nagoya University), Private communication; He suggested the luminescence generated by the recombination of ion with electrons.
- [5] Kay Wittenburg (DESY), Private communication, F. Hornstra, "A beam induced gas scintillation (BIGS) profile monitor for HERA", DESY, HERA, 89-04, Jan. (1989)
- [6] D. P. Sandoval, et. al., "Video profile monitor diagnostic system for GTA", LA-UR-92-2727 (1992)
- [7] Hamamatsu R5600U-01 (Spectral Response: 300-820nm, Material of Photo cathode: Multialkali, Current Amplification: 1×10^6)

The Closed Orbit Measurement of SRRC Booster During Ramping

T. S. Ueng, K. T. Hsu, K. H. Hwu, K. K. Lin
Synchrotron Radiation Research Center, Hsinchu 300, Taiwan

Abstract

The SRRC booster synchrotron is used to accelerate the electron beam from 50 MeV to 1.3 GeV. The closed orbit of electron beam during ramping was measured. The signals corresponding to the beam positions were picked up by the 23 BPMs around the synchrotron. A control electronic unit was made to control a multiplexer system in order to collect and digitize the signals. During the 50 ms ramping period, the digitized signals were saved into a FIFO in the control electronic unit. Then, these signals were transferred to an IBM/PC for analyzing. The result of measured closed orbits is presented in this report.

1. INTRODUCTION

The booster synchrotron of SRRC was commissioned in 1992. The main purpose of this synchrotron is to accelerate the 50 MeV electron beam extracted from the Linac to 1.3 GeV for the storage ring injection. The lattice is the FODO type, which has circumference of 72 meters and periodicity of 12 [1]. A one turn on axis injection is used. The extraction scheme is to use a 3-bumper magnet system to get the shortest possible closed orbit bump. This will move the beam close to the extraction septum for a fast kicker to kick the beam to the entrance of septum, which will direct the beam to the transport line. At present, the nominal beam current in the synchrotron is about 5 mA for multi-bunch beam and 0.3 mA for single bunch beam. We expect the closed orbit study of this booster synchrotron will provide us the related information about improving the electron beam injection efficiency from the Linac and the extraction efficiency to the transport line, which will thus increase the injection efficiency to the storage ring.

II. THE MEASUREMENT SYSTEM

In the SRRC booster synchrotron, the beam position monitors (BPM) are located in between the dipole and the quadrupole, except one location is used as photon port, see Fig. 1. Thus, there are 23 BPMs mounted around the ring for the beam diagnostics purpose. These BPMs were designed and manufactured originally by Scanditronix AB. The calibration of these BPMs was done at SRRC by K. T. Hsu. The four-button electrodes in the BPM were mount 45 degrees and were connected as two pairs for acquiring the signal. These 23 BPMs can be arranged to collect horizontal

beam position data or vertical beam position data at a time by switching the cables.

The original electronics for the BPMs was basically the same as that developed by ESRF, except a different RF frequency was used at SRRC. In the original Scanditronix's design, 11 BPMs were used for measuring the horizontal beam positions, and 12 used for vertical beam positions. The signal from each BPM button was multiplexed and amplified in an RF-MUX electronics, then fed to a multiplexer-mixer unit. The signal which represents the voltage acquired was displayed with a digital oscilloscope. The selection of BPM signal was done manually.

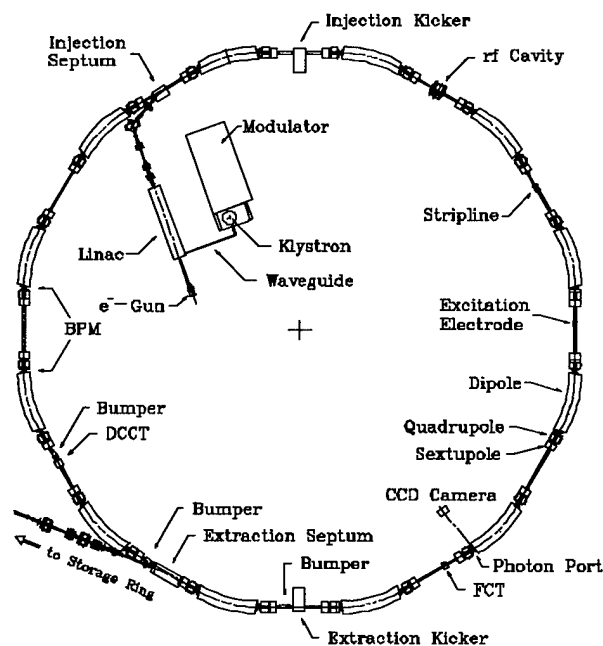


Fig. 1. Brief Layout of SRRC Booster Synchrotron

In order to improve the beam diagnostic capability, an easy and convenient method for studying the behavior of the electron beam closed orbit during ramping was installed in our present beam diagnostic system. The cabling and electronics of the multiplexer system were modified such that the BPM signals can be acquired with an IBM/PC automatically. The block diagram of hardware setup is shown in Fig. 2.

The acquisition time for each pair took about 5 μ sec, thus, each BPM 10 μ sec. The cables from the BPM to the first stage multiplexer were calibrated and trimmed in order to have the same response at the input of the first stage multiplexer. The trigger signal for the acquisition was

coming from the 10 Hz signal of the fast timing system, which was used to monitor and synchronize the magnet families of the synchrotron and also to generate the injection and extraction enable signal for the fast time system. After the timing and trigger circuit receiving the trigger signal, it would also activate the multiplexer system. The acquired signal from the button would pass through the 3-stage multiplexer system to the receiver in the control electronics unit continuously during ramping. After digitizing, the signal was stored in a 16 KW FIFO. This FIFO allowed us to acquire signals for about 80 msec. It covered more than a full ramping cycle, which took about 50 msec. After the FIFO was full, the data was transferred to an IBM/PC to convert it into the beam position for further processing.

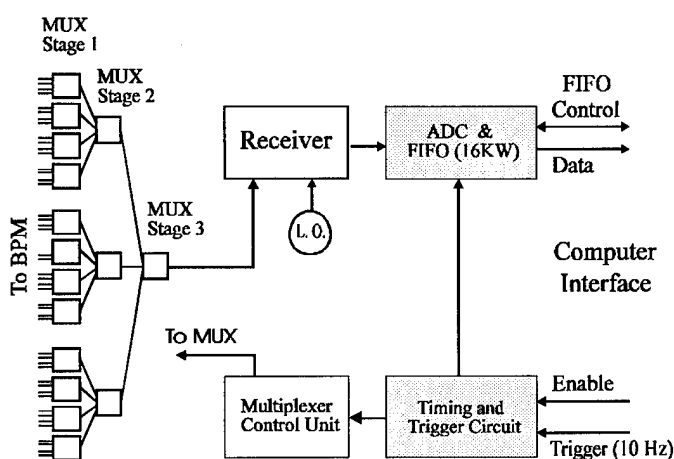


Fig. 2 Block diagram of hardware

III. THE RESULT AND DISCUSSION

With the new beam position acquisition system, we have a first look at the closed orbit of the SRRC synchrotron during ramping. The measurement accuracy is estimated about 250 microns. At present we have measured the horizontal closed orbit with the machine parameters used during routine operation. The closed orbit distortion of electron beam during ramping at some specific time is shown in Fig. 3. During this measurement, the extraction bumpers and kicker were not turned on. From this figure, we suspected that two or three BPMs did not act as expected. But, in general, the bars representing the beam positions give us about 4 periods, which is consistent with our previous measured tune, around 4.15 [2]. At the beginning of ramping, the beam position changed rapidly with time. After ramping for 15 msec these bar charts are shown to have the same shape, which indicates that the beam positions become stable until the next ramping cycle begin. This can also be seen in Fig. 4, where the 3 extraction bumpers were turned on about 47 msec after the ramping cycle began. Thus, it indicates

that the horizontal tune and orbit had no significant change after 15 msec from the injection.

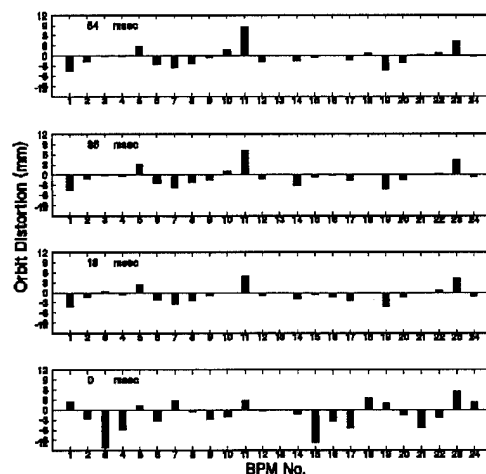


Fig. 3 Closed orbit distortion measured at some specific time during ramping, where the BPM No. 1 is located in the section before the injection septum and the BPM No. 13 is not used.

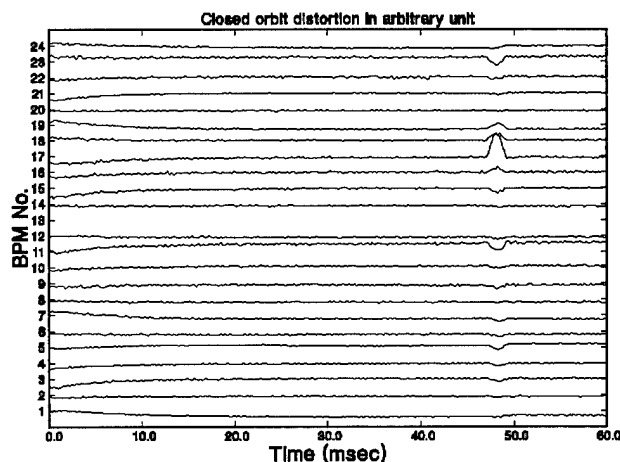


Fig. 4 Closed orbit when all 3 extraction bumpers were on. The tick mark on both sides also marks the center of the orbit of the corresponding BPM. Also, the distance between two ticks is 15 mm.

In Fig. 4, the effect of the 3-bumper magnet system used to move the beam close to the entrance of the extraction septum for extraction is shown, where the beam positions measured by all 23 BPMs from the beginning of ramping until 60 msec are presented. One sees that after the extraction bumpers were turned on, the closed orbit was changed by these 3 bumpers. In the figure, it is clear that a bump was created locally between the first bumper and the third bumper, from BPM 16 to BPM 19. And it does give a very large orbit distortion before the extraction septum, BPM 17. But, it is also seen that there were other bumps measured

by the BPMs, which do not show up when the 3-bumper system were turned off. Thus, these bumps were obviously bumper magnets did not create a simple local bump as originally designed.

We have also varied the parameters of some of the steering correctors and single extraction bumper magnet in order to see how the beam reacts to these changes. We found that the correctors affected the electron beam only at low energy as expected, since only small currents used in the correctors. The beam positions obtained by the BPMs were also qualitatively consistent with the theoretical prediction. As for the bumper, most of the beam positions obtained also agreed qualitatively with the calculation, but some did show an unexpected reaction. It still needs further study.

IV. CONCLUSION

From this measurement we have found that the closed orbit of SRRC's booster synchrotron was somewhat different from what we expected. From the information obtained in this measurement we have considered several improvement in the future. Since the beam position at the beginning of the ramping cycle showed varying with time and different from that at 15 msec after the ramping begin, a best combination of the strength of steering correctors should be found to correct the orbit during this period. This will reduce the beam loss during ramping. At the same time, the parameters, such as phase variation between bumpers and the strength of each bumpers should be optimized in order to create a true local bump in the section between the first and the last bumper magnet. If the beam closed orbit of SRRC

created by the 3 extraction bumpers. In other words, these 3 synchrotron can be optimized and fully controlled, many benefits can be obtained. The most important one is that the Twiss parameters at the exit of the extraction septum can be controlled easily. Thus, the initial condition of the electron beam at the transport line will be known, which will in turn let us tune the electron beam in the transport line much easier and also lead to a better injection efficiency to the storage ring. Meanwhile, a controllable beam closed orbit means we can manipulate the conditions of electron beam. It will provide us more opportunity in studying the beam dynamic behavior.

V. ACKNOWLEDGMENT

The authors would like to show their appreciation to all of the personnel of the injection group of SRRC for their help in setting up the acquisition system and operating the booster synchrotron during the measurement.

VI. REFERENCES

- [1] J. Modeer, Proceedings of the 1993 Particle Accelerator Conference, 2034 (1993)
- [2] K. K. Lin et al., "Performance of SRRC 1.3 GeV electron booster synchrotron", To be published in Nuclear Instruments and Methods in Physics Research, Section A (1995).

Lattice Function Measurement with TBT BPM Data

Ming-Jen Yang, Fermi National Accelerator Laboratory, Batavia, IL 60510 USA

At Fermilab a procedure using data from TBT BPM system to measure the lattice function of a synchrotron has been developed. The betatron oscillation recorded by the BPM system is fitted to obtain beam parameters $x, x', y, y',$ and $\Delta p/p$. These TBT beam parameters (x, x') or (y, y') are fitted to ellipses to obtain the lattice function β, α , and the emittance associated with the betatron amplitude. Fitting the BPM data gives information useful for diagnosing BPM system calibration, noise level and polarity. Other benefits include TBT tune calculation and x-y coupling analysis.

I. Introduction

Single BPM Turn-by-Turn (TBT) beam position data of betatron oscillation is typically used to do FFT tune analysis. Multiple BPM TBT data can be used to go one step further, to the measurement of lattice function. Such procedure has been developed at Fermilab [1] and will be demonstrated here with BPM data taken from Fermilab Main Ring sector D3 & D4 at 150 GeV beam energy. A sketch of BPM layout is shown in Figure 1.

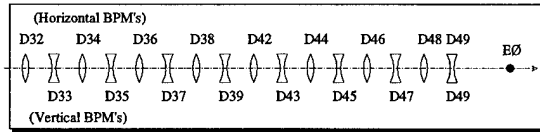


Figure 1: The Layout of BPM's in the D3 & D4 section of Fermilab Main Ring. The horizontal BPM's are indicated above and the vertical BPM's below. The E0 location is the chosen reference location and has no BPM instrumentation.

The procedure fits the BPM data to get the beam parameters x, x' in the horizontal plane, and y, y' in the vertical plane. The fitted TBT beam parameters are in effect coordinates of phase space points which follow elliptical path, as determined by the lattice function. Figure 2 is an example in the horizontal plane. By analyzing these phase space points the lattice function can be calculated. As part

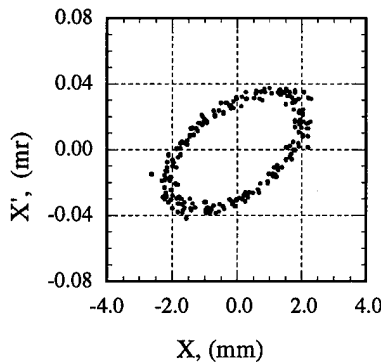


Figure 2: The phase space plot of fitted beam parameters (x, x') at E0. Each point represents one turn of the proton beam. There are a total of 200 consecutive turns on the plot.

of the analysis the deviation from the fit provides useful information either for diagnosing BPM system or for confirming the beam line modeling.

With the normalized phase space it is possible to calculate the TBT tune of the machine with as few as 20 turns of data. Having beam parameters in both planes simultaneously also allows new approach in understanding the local and global x-y coupling effect.

II. The mathematics for analysis

The algorithms used in analyzing the TBT BPM data are quite elementary but are included here to help clarify things that are being discussed here.

A. Fitting for phase space parameters

The beam line transfer matrix between the reference zero-th location and the i-th BPM locations where the data is taken is shown in the equation below:

$$\begin{pmatrix} x_i \\ x_i' \\ \delta \end{pmatrix} = \begin{bmatrix} T_{11}^i & T_{12}^i & T_{13}^i \\ T_{21}^i & T_{22}^i & T_{23}^i \\ 0 & 0 & 1 \end{bmatrix} \begin{pmatrix} x_0 \\ x_0' \\ \delta \end{pmatrix}$$

$\delta (= \Delta p/p)$ is the percentage deviation of the average beam momentum from the reference momentum as determined by the bending field. The inclusion of δ in the fit is necessary to account for the momentum error. The x_0, x_0' , and δ on the right hand side are the beam parameters being fitted at the reference location. The transfer matrix elements are assumed known from beam line model. The fitting is done by minimizing the summed quantity:

$$S = \sum_i (p_i - x_i)^2 = \sum_i (p_i - x_0 \cdot T_{11}^i - x_0' \cdot T_{12}^i - \delta \cdot T_{13}^i)^2$$

The summation index "i" runs through all the BPMs used in the calculation. The " p_i " is the i-th BPM reading. This same process is performed for every turn of beam data.

The horizontal BPM data is fitted for beam parameter x, x' , and $\Delta p/p$ at the reference location. The vertical plane data is fitted for y and y' . The result is then propagated to other BPM location using equation above for calculation of deviations between BPM data and the fitted result.

B. Ellipse and lattice function

To fit for α, β , and ϵ with a given number of data points the procedure starts with normalized phase space coordinate transformation:

$$\begin{pmatrix} X_n \\ Y_n \end{pmatrix} = \begin{pmatrix} x_n / \sqrt{\beta} \\ \sqrt{\beta} \cdot x_n' + \alpha \cdot x_n / \sqrt{\beta} \end{pmatrix}$$

The trajectory will be circular by definition. Re-scale this coordinate space with a factor $1/\sqrt{\beta}$ to get:

$$\begin{pmatrix} U_n \\ V_n \end{pmatrix} = \frac{1}{\sqrt{\beta}} \begin{pmatrix} X_n \\ Y_n \end{pmatrix} = \begin{pmatrix} x_n/\beta \\ x_n' + (\alpha/\beta) \cdot x_n \end{pmatrix} = \begin{pmatrix} a \cdot x_n \\ x_n' + b \cdot x_n \end{pmatrix},$$

where $a = 1/\beta$ and $b = \alpha/\beta$. A circular trajectory in this (U, V) phase space is still expected. Fitting the (U, V) points to the best circular path by minimizing the equation:

$$S = \sum_n [R^2 - (a \cdot x_n)^2 - (x_n' + b \cdot x_n)^2]^2.$$

The summation on "n" is over the number of turns used to fit the phase space ellipse. The value for α , β , and ϵ can be solved accordingly. The ϵ is simply the area enclosed by the ellipse which is $\epsilon = \beta \cdot R^2$, in π -mm-mr.

C. Tune calculation

With fitted lattice function β and α the normalized phase space angle can be calculated cumulatively as:

$$\theta_n = \tan^{-1}[X_n, Y_n] + \Delta\Phi_n,$$

where $\Delta\Phi_n$ is an adjustment in increment of 2π so that θ_n is successively increasing. The TBT tune is simply:

$$\nu_n = \theta_n - \theta_{n-1}.$$

Because of data precision the TBT tune is not expected to be noise free. A more precise estimate of the tune can be obtained by performing a linear fit of θ_n against the turn number. The slope then gives the tune of the machine.

III. Data analysis

For the analysis of the data to be shown here the reference location is chosen to be at the EØ straight at the down stream of M:HPD49, as indicated in Figure 1. Only horizontal data will be shown.

A. Beam parameters from BPM data

The fitting procedure is as outlined in section II.A. Figure 3 is a single turn BPM position data and the position according to the fitted result. The fitted EØ location beam parameters x and x' are already shown in Figure 2 with a total of 200 consecutive turns. The deviation between data and the fit can be a measure of the noise level in the BPM system or a possible error in the known transfer matrix.

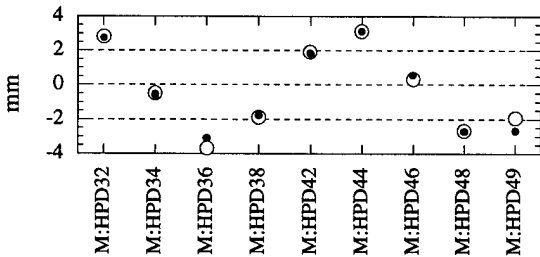


Figure 3: The horizontal BPM position is plotted for each BPM in the beam line. The open circles are the actual BPM data and the solid dots are the calculated beam positions based on the fitted x and x' at EØ.

The deviation statistics is collected and examined in two ways. The "TBT RMS error" is the fit statistics across

all the BPMs for every turn. The "BPM error" is the statistics on individual BPM over a number of turns.

1. TBT RMS error

The each turn Root-Mean-Square deviation of data from the fit is plotted in Figure 4. This error is expected to be independent of the turn number and should be consistent with the expected RMS due to BPM electronics noise and the digitization resolution.

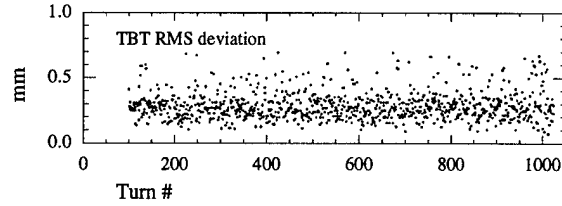


Figure 4: Turn-by-turn RMS deviation of BPM data from the fitted result.

2. BPM deviation error

The individual BPM deviation from the fit is shown in Figure 5. The average of position deviation is expected to be nearly zero and would indicate problems if otherwise. The RMS on the BPM deviation error is shown as the vertical error bars. Generally the RMS in the BPM deviation is a good indicator of individual BPM problems, which could be due to noise, poor calibrations, or even wrong signal polarity.

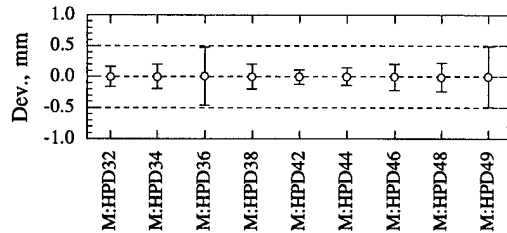


Figure 5: The individual BPM deviation statistics collected for about 200 turns. The open circle represent the average of deviations and error bar is the RMS of the deviation.

B. Fitting the phase space ellipse

It takes five parameters to describe an ellipse, two for the centroid of ellipse in the $x-x'$ space, one for the area of the ellipse, and the last two which has the information on the lattice function α and β . The equations shown in section II.B assumes that ellipse is centered at the origin. By using the average of all data points as origin that assumption is approximately correct and perfect when the number of turns used is beyond 50.

The result of fitting ellipse at EØ location is shown in Figure 6 with the resulted value for ϵ , α , β , and a calculation of the tune list on the right. The lattice function at other BPM location can be constructed by propagating the fitted beam parameters at the EØ reference location using the transfer matrix. The result is plotted in Figure 7. In (a) is the beta function and (b) the alpha function.

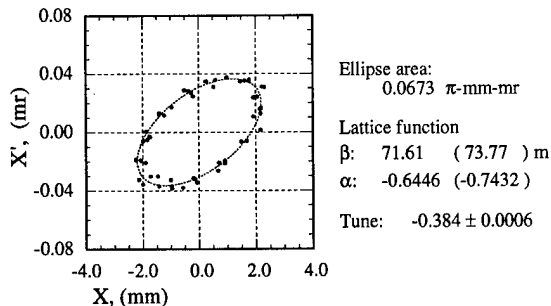


Figure 6: X and X' phase space plot for 50 consecutive turns. The fitted ellipse is shown in dotted lines and the fitted values are shown to the right. The design lattice function is shown enclosed within the parenthesis.

An analytical error analysis is not done because of the algorithm used to fit the ellipse. Instead, the variation of all possible sample of lattice function is used as the estimated error. For example, with "n" number of turns used to fit the lattice function from a data set of "N" total consecutive turns there is a set of (N - n + 1) possible samples. The statistics on this set of possible samples gives the mean and the RMS deviation plotted in Figure 7.

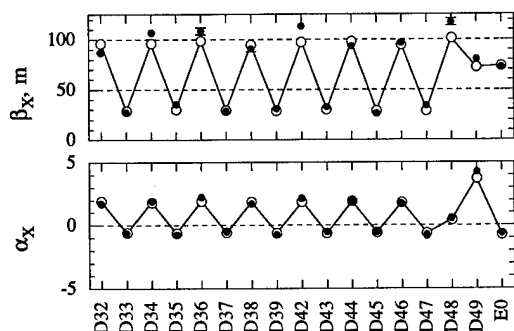


Figure 7: The lattice function at the BPM locations as derived from the data is shown in solid dots. The sigma of the fitted beta distribution is shown as error bars. The open circles with connecting lines are from the SYNCH calculation.

C. Tune calculation

The TBT tune of the machine can be calculated as mentioned in section III.C. However, because of the nature

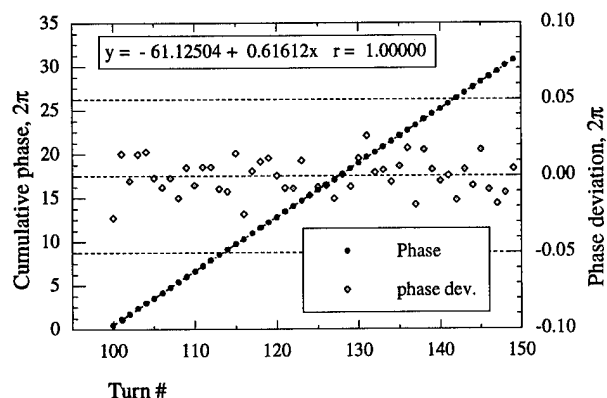


Figure 8: TBT tune calculation. The normalized phase space angles are plotted in solid dots with the vertical scale shown on the left hand side. The phase angle deviations are plotted in open diamonds with the vertical scale shown on the right.

of BPM data noise, a better tune calculation is done by fitting the normalized phase space angle θ_n to the turn number. Figure 8 shows the θ_n and the linear fit result with linear correlation function of 1. The slope gives the horizontal machine tune value of .384. The deviation of θ_n from the linear fit is shown in open diamonds with its values range from -.03 to +.03, in unit of 2π .

Typically this method will need about 30 turns of data to get a resolution of about 1 part in a thousand. The conventional FFT method would require 1024 turns for a comparable accuracy.

D. TBT Dp/p

The beam momentum error $\Delta P/P$ is obtained as part of the fitting procedure to horizontal BPM data and is plotted in Figure 9. This information can be used to correct beam position and angle to account for the $\Delta P/P$ error.

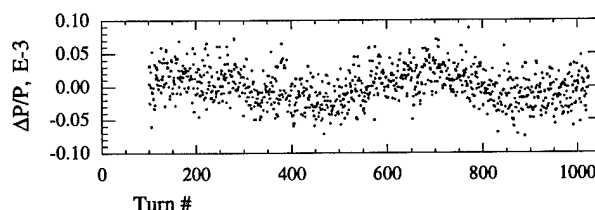


Figure 9: The TBT $\Delta P/P$ from fitting horizontal BPM data.

IV. Conclusion

Knowing the lattice function is important for matching lattice functions between different machines and for the understanding of the machine as well. The technique introduced here provides both the β and α value needed for a complete matching. The measurement can be done within relatively short time. Something no other method of lattice function measurement can do.

The result of this procedure appears reproducible and the procedure possesses some ability of self-diagnosing. It is also inherently susceptible to systematic effect caused by the integrity of data and the use of the bad transfer matrix as well. There is systematic effect associated with fitting the ellipse which has been studied with simulated data. With future improvement to the analysis software the TBT BPM data could be the ideal instrument to machine lattice measurement.

REFERENCES

- [1] MJ Yang, Lattice Function Measurement with TBT BPM Data, FERMILAB-TM-1922, April 1995.

OPTIMAL PLACEMENT OF PROFILE MONITORS IN A MISMATCHED FODO LATTICE*

K. Bertsche, Fermi National Accelerator Laboratory†, P.O. Box 500, Batavia, IL 60510

Abstract

The beam delivered to a circular machine from a beamline must be matched to the machine lattice function in order to avoid emittance dilution. One method of matching is to rely on beam profile measurements at a number of points in the beamline. In this paper we discuss the expected errors associated with various placement options for beam profile monitors. Examples are given from the Low Energy Booster (LEB) to Medium Energy Booster (MEB) transfer line at the Superconducting Super Collider (SSC).

I. INTRODUCTION

Transverse emittance growth arises from three different types of injection mismatch; focusing errors, dispersion errors, and steering errors [1]. For injection into the MEB, it was desired to limit emittance growth from injection mismatches to less than 5%. Since steering errors could have been detected non-invasively with beam profile monitors (BPMs) and dispersion errors would not have caused very much emittance growth due to the small energy spread in the MEB, focusing errors were the greatest concern. Focusing errors could have been detected with destructive single-turn-only measurements in the MEB using beam profile monitors, or could have been minimized by relying on flying wire measurements and tuning the transfer line with multiple injections. But a less invasive and faster method of detecting errors was desired. It was desired to be able to predict and correct focusing errors on the basis of beam profile measurements in the injection line to the MEB. It was also desired to use these same monitors to measure the emittance of the injected beam. At least three monitors are needed for these measurements, since there are three independent beam parameters (α , β , and ϵ).

The LEB-MEB transfer line was designed as a FODO lattice with 90° phase advance per cell. A matching section for α and β at the upstream end of the transfer line was used to accommodate different possible tunes of the LEB. There was no such matching section at the downstream end. In order for beam to be properly matched into the

MEB lattice, it was mismatched to the transfer line lattice (i.e. the beam waists were not at the centers of the quadrupoles, and there were large beta waves along the transfer line). Dispersion was matched by tuning pairs of quadrupoles separated by 180° [2]. In the discussion to follow, it is assumed that the transfer line, downstream of the matching section, has already been tuned to a reference value using a procedure such as that in [3].

It was not obvious *a priori* where was best to place the profile monitors in the transfer line, in part because beam in this line was designed to be mismatched. A number of philosophies exist for placing profile monitors in a lattice. One is to separate the monitors equally in a 2ψ phase diagram, i.e. to space three monitors by 60° in phase. A second approach is to place the monitors regularly in the beamline lattice. A third approach is to separate two monitors by 90° in phase, and to place the third at a separation of 45° from one of the others. Because of the finite resolution of a profile monitor, different placements of profile monitors will lead to different errors in determination of α , β , and ϵ , and errors in α and β will lead to emittance growth.

II. EMITTANCE GROWTH

An amplitude function mismatch of injected beam into a circular machine (i.e. incorrect α and β) causes an emittance growth. Over time, the beam will filament in phase space and assume the β functions of the machine lattice. The beam width at every point in the machine will have grown proportionally by an amount [1; Eq. 7.56]:

$$\frac{\sigma^2}{\sigma_0^2} = 1 + \frac{1}{2} |\det \Delta J| \quad (1)$$

where σ_0 is the initial standard deviation of the beam width, σ is the standard deviation including effects of mismatch, and ΔJ is the error matrix:

$$\Delta J = \begin{pmatrix} \Delta\alpha & \Delta\beta \\ -\Delta\gamma & -\Delta\alpha \end{pmatrix} \quad (2)$$

Using the relations:

$$\beta\gamma = 1 + \alpha^2 \quad (3)$$

and

$$\sigma^2 = \sigma_0^2 \frac{\epsilon}{\epsilon_0} = \sigma_0^2 (1+f) \quad (4)$$

where f is the fractional emittance growth, Eq. (1) may be rewritten to give the emittance growth resulting from this mismatch:

* Work performed at the SSC Laboratory, operated by Universities Research Association, Inc. for the U.S. Department of Energy under Contract No. DE-AC35-89ER40486.

† Operated by the Universities Research Association, Inc. under contract with the U.S. Department of Energy.

$$f = \frac{1}{2} \left| \Delta\alpha^2 - 2 \frac{\alpha}{\beta} \Delta\alpha \Delta\beta + \frac{(1+\alpha^2)}{\beta^2} \Delta\beta^2 \right| \quad (5)$$

$$= \frac{1}{2} \left| \frac{\Delta\beta^2 + (\beta \Delta\alpha - \alpha \Delta\beta)^2}{\beta^2} \right|$$

While Eq. (5) is applicable at any point in the circular machine lattice, it will be convenient for later calculations if it is applied at the center of a quadrupole (e.g. the first quadrupole in the circular machine), where (nominally) $\alpha = 0$. This eliminates troublesome cross-terms involving errors in both α and β and Eq. (5) becomes:

$$f = \frac{1}{2} \left| \Delta\alpha^2 + \frac{\Delta\beta^2}{\beta^2} \right| \quad (6)$$

which can also be interpreted as a relation between the mean emittance growth and the rms errors in α and β of the injected beam, measured at the center of the first quadrupole in the circular machine.

III. BEAM PROPAGATION

For a beam confined in a periodic lattice, the optical transformation between two different longitudinal locations 1 and 2 may be written in terms of the Courant-Snyder parameters α , β , and ψ at the two locations [4]:

$$M_{1 \rightarrow 2} = \begin{pmatrix} \sqrt{\frac{\beta_2}{\beta_1}} \begin{pmatrix} \cos\Delta\psi + \alpha_1 \sin\Delta\psi \\ \alpha_1 \sin\Delta\psi \end{pmatrix} & \sqrt{\beta_1 \beta_2} \sin\Delta\psi \\ \frac{(1+\alpha_1 \alpha_2) \sin\Delta\psi + (\alpha_2 - \alpha_1) \cos\Delta\psi}{\sqrt{\beta_1 \beta_2}} & \sqrt{\frac{\beta_1}{\beta_2}} \begin{pmatrix} \cos\Delta\psi - \alpha_2 \sin\Delta\psi \\ \alpha_2 \sin\Delta\psi \end{pmatrix} \end{pmatrix} \quad (7)$$

This transformation may be calculated in terms of the actual beam parameters (α , β , ψ) or in terms of the reference parameters (α , β , ψ) for a perfectly-tuned beam.

The phase space ellipse of a beam may be defined by a matrix E which may be expressed as [4]:

$$E = \begin{pmatrix} \alpha_x^2 & \alpha_{xx'} \\ \alpha_{xx'} & \alpha_x'^2 \end{pmatrix} = \begin{pmatrix} \sigma_{11} & \sigma_{12} \\ \sigma_{21} & \sigma_{22} \end{pmatrix} = \frac{\varepsilon}{\pi} \begin{pmatrix} \beta & -\alpha \\ -\alpha & \gamma \end{pmatrix} \quad (8)$$

where ε is the un-normalized rms emittance, α_x is the rms beam width in the absence of dispersion, and α , β , γ are the ellipse coefficients, normalized as in Eq. 3.

The beam matrix E evolves from location 1 to location 2 according to the expression:

$$E_2 = M_{1 \rightarrow 2} E_1 M_{1 \rightarrow 2}' \quad (9)$$

Transforming matrix E_1 to E_2 , using Eqs. (7) and (9), and examining the σ_{11} term of E_2 , one finds that a measurement of the beam width at location 2 gives, in terms of the beam parameters at location 1:

$$\sigma_{x2}^2 = \sigma_{x1}^2 m_{11}^2 + 2\sigma_{xx1} m_{11} m_{12} + \sigma_{x1}'^2 m_{12}^2 \quad (10)$$

or, substituting from Eqs. (7) and (8),

$$\sigma_{x2}^2 = \frac{\varepsilon_b \beta_{b1}}{\pi} \frac{\beta_2}{\beta_1} (\cos\Delta\psi + \alpha_1 \sin\Delta\psi)^2$$

$$- \frac{2\varepsilon_b \alpha_{b1}}{\pi} \beta_2 \sin\Delta\psi (\cos\Delta\psi + \alpha_1 \sin\Delta\psi) \quad (11)$$

$$+ \frac{\varepsilon_b (1 + \alpha_{b1}^2)}{\pi \beta_{b1}} \beta_1 \beta_2 \sin^2\Delta\psi$$

Note that the parameters (α , β , ψ) of the beamline (i.e. the parameters for a perfectly-tuned beam which exhibits no emittance growth) have been kept distinct from those of the possibly-mistuned beam (α_b , β_b , ε_b) measured at location 1. We assume that the beamline has been previously tuned very accurately using a procedure similar to that in [3], so that beamline parameters at all points are known to high precision.

IV. MEASUREMENT ERRORS

Eq. (11) may be expanded to first order in the beam parameters (α_b , β_b , ε_b), giving a relation between beam width errors at a point 2 and errors in (α_b , β_b , ε_b) at a remote location 1. Location 1 may be taken to be the center of the first quadrupole in the circular machine, where $\alpha=0$, and location 2 may be taken to be a general point upstream of this in the injection line, giving:

$$\frac{\Delta\sigma_{x2}}{\sigma_{x2}} = \Delta\alpha_{b1} (\sin\Delta\psi \cos\Delta\psi)$$

$$+ \frac{\Delta\beta_{b1}}{\beta_{b1}} \left(\frac{\cos^2\Delta\psi - \sin^2\Delta\psi}{2} \right) + \frac{1}{2} \frac{\Delta\varepsilon_b}{\varepsilon_b} \quad (12)$$

$$= \Delta\alpha_{b1} \left(\frac{\sin(2\Delta\psi)}{2} \right)$$

$$+ \frac{\Delta\beta_{b1}}{\beta_{b1}} \left(\frac{\cos(2\Delta\psi)}{2} \right) + \frac{1}{2} \frac{\Delta\varepsilon_b}{\varepsilon_b}$$

where it has been assumed that the beam parameters at location 1 are nominally those of the reference tune (i.e. tuning errors are assumed to be small).

A similar expression may be written for each of the three profile monitors assumed to be in the transfer line at locations A, B, and C, giving the errors in beam widths at each of the monitors corresponding to injection errors into the circular machine. This may be written as a matrix:

$$\begin{pmatrix} \Delta\sigma_{xA}/\sigma_{xA} \\ \Delta\sigma_{xB}/\sigma_{xB} \\ \Delta\sigma_{xC}/\sigma_{xC} \end{pmatrix} = M \begin{pmatrix} \Delta\alpha_{b1} \\ \Delta\beta_{b1}/\beta_{b1} \\ \Delta\varepsilon_b/\varepsilon_b \end{pmatrix} \quad (13)$$

In practice, one measures the beam widths and wishes to calculate the resultant errors in focusing parameters. Thus the above matrix needs to be inverted:

$$\begin{pmatrix} \Delta\alpha_{bl1} \\ \Delta\beta_{bl1}/\beta_{bl1} \\ \Delta\epsilon_b/\epsilon_b \end{pmatrix} = M^{-1} \begin{pmatrix} \Delta\sigma_{xA}/\sigma_{xA} \\ \Delta\sigma_{xB}/\sigma_{xB} \\ \Delta\sigma_{xC}/\sigma_{xC} \end{pmatrix} \quad (14)$$

This equation may be used to find errors in α , β , or ϵ based on measured deviations in σ . Alternatively, terms may be added in quadrature to give the measurement tolerance of α , β , and ϵ based on the rms measurement precision of σ , and rms α and β tolerances may be combined by use of Eq. (6) to give the resultant mean emittance growth. The placement of profile monitors is optimum when emittance growth and/or emittance measurement tolerance are minimized.

For the case where the fractional error in σ is constant, Eq. (14) depends only on the phase advances, and it can be shown that spacing the profile monitors by 60° is optimal for minimizing both emittance measurement tolerance and emittance growth. But for many situations, including the MEB, this condition is not met. It was believed that measurements with MEB profile monitors would give smaller fractional errors for larger σ , (a fixed absolute error of 0.1mm was assumed below, though in general an error proportional to $\sigma^{1/2}$ would be more realistic [5]).

Since the fractional errors in σ depend on β , Eq. (14) depends on β as well as on phase advance. The equations are highly lattice-dependent, and it is impossible to find a general solution. The matrices in Eqs. (13) and (14) were evaluated and inverted numerically for various placements of profile monitors based on the nominal lattice functions of the LEB-MEB transfer line [2]. The results are shown in Tables 1 and 2. In these tables, focusing (α and β) errors have been converted to mean emittance growth on the basis of Eq. (6). Shown are the mean emittance growth upon injection to the MEB and the rms error in emittance measurement, resulting from an assumed measurement precision of 0.1mm rms in σ at each profile monitor.

Profile Monitor Placement—Horizontal Plane

Placement	ϵ growth	ϵ msmt
Adjacent to quadrupoles	23%	57%
$\sim 60^\circ$ phase separation	14%	27%
$\sim 45^\circ$ and 90° separation	9%	30%
Best location found	8%	30%

Table 1: Comparison of various placements of three horizontal profile monitors in LEB-MEB transfer line.

For the horizontal plane in the LEB-MEB transfer line, placing three beam profile monitors with phase separations of about 45° and 90° gave good measurements, but this arrangement was able to be improved upon slightly by trial and error adjustment of the profile monitor locations.

Profile Monitor Placement—Vertical Plane

Placement	ϵ growth	ϵ msmt
Adjacent to quadrupoles	6%	20%
$\sim 60^\circ$ phase separation	7%	19%
$\sim 45^\circ$ and 90° separation	8%	22%
Best location found	6%	20%

Table 2: Comparison of various placements of three vertical profile monitors in LEB-MEB transfer line.

For the vertical plane, where the reference beam had a different pattern of beta waves in the transfer line, regular lattice locations adjacent to three quadrupoles gave better measurements. Other arrangements of three profile monitors were found which gave roughly the same sensitivity to errors, but no arrangements were found which were better.

In neither plane can α and β be measured to sufficient precision, on the basis of a single measurement, to limit emittance growth to 5%. However, assuming that the errors in measurement of σ at each profile monitor were random, a small number of measurements could have been averaged to statistically reduce these errors to less than 5%.

V. CONCLUSIONS

If measurements of beam σ have constant fractional errors, profile monitors should be placed equally in 2ψ to give the best detection sensitivity for focusing errors; i.e. three monitors should each be separated by 60° in phase. For measurements which do not have constant fractional errors, the best placement depends on the details of the lattice functions. Different placements of profile monitors may be evaluated numerically following the procedure outlined here to find the best arrangement.

VI. REFERENCES

- [1] D.A. Edwards and M.J. Syphers, *An Introduction to the Physics of High Energy Accelerators*, Wiley, 1993.
- [2] N. Mao et al, "Beam Optics of LEB-MEB Transfer Line for Superconducting Super Collider", *Proceedings of the 1993 Particle Accelerator Conference*, Washington, D.C., vol. 1, pp. 333-335.
- [3] K. Bertsche and N. Mao, "Accurate Tuning of 90° Cells in a FODO Lattice", these proceedings.
- [4] K.L. Brown and R. Servranckx, 1990 US Particle Accelerator School class notes.
- [5] K. Bertsche and J. Palkovic, "Beam Profile Measurement in the Presence of Noise", these proceedings.

SSRL Beam Position Monitor Detection Electronics*

J. Sebek, R. Hettel, R. Matheson, R. Ortiz, J. Wachter

Stanford Synchrotron Radiation Laboratory, P.O. Box 4349, Bin 99, Stanford, CA 94309-0210

Abstract

As part of a program to improve its orbit stability SSRL is re-designing its detection electronics for its beam position monitors (BPMs) [1]. The electronics must provide highly reproducible positional information at the low bandwidth required of an orbit feedback system. With available commercial technology, it is now possible to obtain highly resolved turn by turn information so that this electronic module can also be used to measure beam dynamics. The design criteria for this prototype system and performance of the analog section of the processor is discussed.

1 INTRODUCTION

SPEAR is a 3 GeV electron storage ring used for synchrotron radiation. It was originally built as an $e^- - e^+$ collider for high energy physics, and its BPM detection electronics was designed to differentiate between the signals from the two particles. All of the BPM inputs are multiplexed into one large switching matrix and processed by one set of electronics. We are redesigning the electronics to improve processor speed, dynamic range, and resolution. In addition to providing highly resolved positional information under normal operation, the system must be able to detect low current orbits for injection studies, etc.

Table 1: SPEAR BPM Parameters

Energy	E	3	GeV
Radio Frequency	f_{RF}	358.54	MHz
Harmonic Number	h	280	
Revolution Frequency	f_{rev}	1.2805	MHz
Nominal Beam Current	I_{nom}	10-100	mA
Number of BPMs		40	
Resolution		10	μm
Channel Isolation		> 80	dB
Detector SNR @ I_{nom}	SNR	> 126	dB/Hz
Dynamic Range		40	dB

2 BPM SIGNAL SPECTRUM

The periodic nature of the beam in a storage ring means that the signal spectrum on a BPM will be periodic. The spectrum of the 'reference particle' is a sequence of signals at the harmonics of the fundamental frequency, f_{rev} . The amplitudes of the individual harmonics are determined by the frequency response of the pickup electrode. For a bunched beam of many particles in many buckets, the spectrum becomes slightly more complex. Although the locations of the frequencies do not change, their amplitudes now depend on bunch shape and fill pattern. In all cases, the amplitudes of the harmonics incident on the BPM are multiplied by the Fourier transform of the bunch length. For multiple bunch fills, the signals from the various bunches add coherently and modulate the amplitudes of the harmonics with the

Fourier transform of the bucket fill pattern. Since the ring can only contain a finite number of bunches (the harmonic number, h), this modulation repeats with f_{RF} . In particular, all harmonics of f_{RF} carry the information of the DC current of the beam. These are the only harmonics of f_{rev} guaranteed to be non-zero for arbitrary fill patterns.

The spectrum at each harmonic is almost, but not quite a pure frequency. Transverse oscillations of the beam give rise to amplitude modulation of the BPM signals and create betatron sidebands around the f_{rev} harmonics. Longitudinal oscillations give rise to phase modulation and synchrotron sidebands.

3 RF SIGNAL PROCESSING

The periodic nature of a storage ring determined our choice of a harmonic processing system that detects the power in an appropriate frequency bandwidth. Since we determine the beam position by the difference over sum technique, we multiplex the signals as early as possible to minimize errors in the signals due to electronic variations. Our RF processing is designed to provide a high quality, narrow bandwidth signal for our f_{RF} .

3.1 Processing Frequency

For the reasons given above, we process a harmonic of f_{RF} . The decision as to which harmonic to process was a tradeoff of engineering considerations. SPEAR has several BPMs near the RF cavities, where the evanescent fields from these cavities provide a strong beam-independent signal at the RF, so we rejected processing f_{RF} . Although our BPM buttons are more sensitive to the higher beam frequencies, we chose the second RF harmonic, 717.08 MHz, for two reasons. First, our signal processing electronics will be housed in the control room, typically 100 m from the buttons, and attenuation due to the cable length greatly increases with frequency. Second, the size of our beam pipes gives a typical vacuum chamber cutoff frequency of about 1 GHz. Discontinuities and structures in the vacuum chamber support higher order modes at these frequencies that contaminate the fundamental signal on the BPMs produced by the image charges of the beam.

3.2 Signal Multiplexing

The main purpose of the BPM system is to provide highly resolved information about the orbit of the beam. For our vacuum chamber size, resolution of 1 micron beam motion means a variation in the difference signals of about 50 ppm from the 4 buttons of each BPM. The design of the electronics attempts to minimize the potential for systematic errors that could prevent high resolution measurements. Therefore, we have multiplexed as much of the button processing as possible. The current system multiplexes all BPM buttons into a single processor. We will initially commission the new processor with this same arrangement, but then may build more processors to decrease the overall system sampling time.

The BPM signals are multiplexed at the input. Since this is the only part of the circuitry that is not common to all of the buttons, we desire the technology with the most consistent and repeatable characteristics. We favor GaAs FETs over PIN diodes because of the independence of the FET video impedance with respect to signal level. Standard isolation per switch at our processing frequency is less than our desired 80 dB, so our design cascades absorptive switches to achieve the desired isolation. Our 80 dB isolation specification relates to buttons from different monitors;

*Work supported in part by Department of Energy Contract DE-AC03-76SF00515 and Office of Basic Energy Sciences, Division of Chemical Sciences.

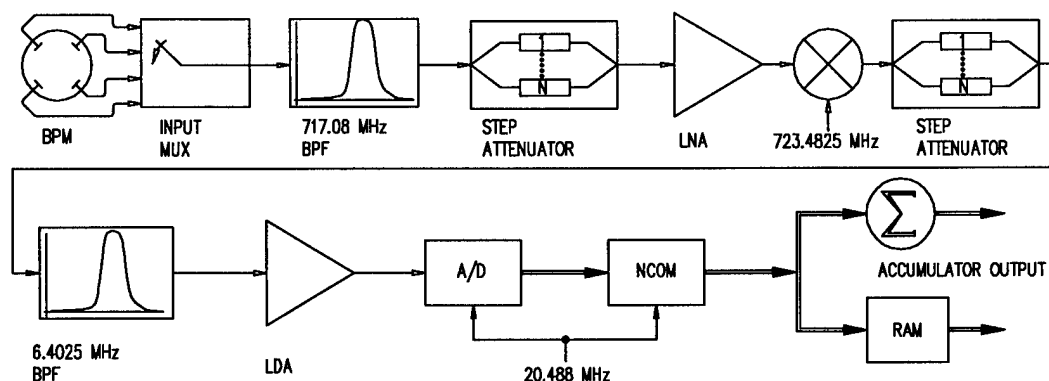


Figure 1: Processor Block Diagram

one 60 dB switch in series should provide sufficient isolation between buttons from a single BPM. Initially, the switches will all be placed in the control room and will be cascaded to provide one final output for the processor. We will also study the feasibility of placing the switches in the ring. If they can be adequately shielded from the radiation, the multiplexer will then require only one high quality signal cable from each BPM to the control room. The only signal paths that will vary from button to button from one BPM will then be a short cable from the button to the multiplexer and the switches themselves. If the switches are placed close to the buttons, we may need to put some inexpensive bandpass filters at the inputs to limit the instantaneous voltage on the switches.

3.3 RF Conditioning

The processor will heterodyne the RF signal down to an f_{IF} of 6.4025 MHz, where its amplitude will be measured. A dielectric resonator band pass filter, a 5 section Chebyshev filter with a 1% bandwidth and 7 dB insertion loss at 717.08 MHz, limits the out of band input power. In order to condition this signal for a 10 dBm image reject mixer, its power level is limited to a maximum value of -10 dBm. We use a combination of a FET step attenuator and a low noise, fixed gain amplifier to keep this level in range. Measurements show that, for our normal operating range of currents, we will always have a -10 dBm signal at the input of our mixer. We chose a fixed gain amplifier and attenuator arrangement because of its overall lower noise figure than that of a variable gain amplifier. We chose a step attenuator over a voltage controlled variable attenuator because we require the more constant attenuation provided by the digital control rather than the fine adjustment offered by variable control. The operating values of the input power were chosen to be well below the amplifier 1 dB compression point and the mixer 3rd order intercept in order to maximize linearity of the system.

4 IF SIGNAL PROCESSING

Our f_{IF} was selected so that, using available commercial technology, we could digitize it directly without sacrificing the resolution of our IF signal. Proper selection of frequency within this range gives us highly resolved, wide bandwidth signals with a minimum of processing overhead.

Recent technological advances have produced monolithic 20 MHz, 12 bit A/Ds at reasonable prices. Therefore we tried to select our f_{IF} below 10 MHz, the frequency above which the A/D performance starts to roll off. The lower f_{IF} , however, the harder it is to reject through filtering the mixer image of the desired frequency. Our RF bandpass filter rejects this image at the input by ~40 dB, but by using an image-reject mixer, we reduce the IF image by another 30 dB. We chose f_{IF} to be 6.4025 MHz as a reasonable compromise where very high quality commer-

cial video opamps and digitizers are available while good image rejection is still possible with simple circuitry.

4.1 Digital Considerations

For any BPM system which is used to control the beam, one needs to digitize the information at some point and pass it on to other elements of the control system. Available technology now makes it reasonable to digitize the signal at the IF. This allows great flexibility in terms of selecting signal bandwidths to optimize SNR, response time, etc., for various applications. In particular, in addition to providing the information needed for our low-bandwidth orbit feedback, this technique allows us to use this processor to detect, with high accuracy, single turn phenomena for machine physics studies. By digitizing the IF, we also have a system with only one non-linear component, the mixer, thereby improving our system linearity.

Since our digital signal processing starts with the IF, we have chosen it, and hence the mixing frequency, to optimize this processing. When Fourier transforming band-limited data, the signal is assumed to be a portion of an infinitely periodic signal. For signals with arbitrary frequency content, this periodic assumption 'contaminates' the transform with non-existent frequency components that are needed to make the sample periodic. To minimize this problem, a 'window' is applied to the data which de-emphasizes the ends of the data sample. This windowing also contaminates the data, but hopefully less than an unwindowed sample. The signals we measure, however, are extremely periodic and we have access to the ultimate system clock, f_{RF} . By making use of this periodicity, we can choose to sample a signal that is periodic with respect to our clock, so that this signal truly is a portion of an infinitely periodic signal. With this method, we get a faithful frequency decomposition of the signal without windowing. Since our signal is coherent while noise is incoherent, N samples per revolution will increase our SNR by \sqrt{N} . Therefore, we chose our digitization frequency as $16f_{rev}$, or 20.488 MHz.

When a perfect periodic signal is digitized, the output codes will have a periodic fixed quantization error. To minimize this error, the digitizer should sample the signal at as many values as possible. This means that the periodicity of the sampler should be as relatively prime as possible to the periodicity of the signal. Based on the criteria of image rejection, analog signal fidelity, periodicity, and digital fidelity, we chose $5f_{rev}$, 6.4025 MHz, as our f_{IF} .

4.2 IF Analog Conditioning

The remainder of the analog processing optimizes the signal for the digitizer. A lumped element band pass filter at 6.4 MHz passes the output of the mixer. This filter needs only act as an anti-aliasing filter for the digital processing that follows, with the nearest aliased frequency of f_{IF} at 14.0855 MHz. We set its

bandwidth to $\sim f_{\text{rev}}$, since we want the ability to observe signals change that quickly. (In fact, we have been very conservative in all of our analog filtering specifications. Since each revolution harmonic carries the same spectral information, we are detecting synchronously with the ring RF, and the button response is essentially constant over the small bandwidths we are considering, the only contamination we would get from aliased signals is a uniform increase or decrease in the detected signals of all buttons. The major danger in this is that two signals may be exactly out of phase and cancel, but contamination on the order of ~ 40 dB would not affect our detection resolution.) In the IF we again use a combination of a digital step attenuator and fixed gain amplifiers. Although there are variable gain video opamps with the same noise performance as fixed gain opamps, we are more confident in keeping the system gain constant with the step attenuators. We use a low distortion, low noise amplifier to boost the IF signal to the 1V nominal input value desired by the digitizer.

4.3 IF Digital Processing

We digitize the data at a high rate to improve the SNR of the system, but it would be very expensive to keep and process the entire Nyquist bandwidth. From a beam dynamics point of view, all desired information is stored within a bandwidth of f_{rev} . Further, since this system is not designed to look for coupled bunch modes, it is not clear what information we would ever need to investigate that happens faster than f_{rev} . We therefore use a digital mixer, the Harris HSP45116 numerically controlled oscillator/modulator (NCOM), to beat our f_{IF} down to baseband once per revolution period.

The NCOM takes as input the stream of 12 bit digital words from the A/D, internally multiplies them with the sine and cosine of f_{IF} , accumulates them 16 samples at a time, and then outputs 16 bit words that represent the amplitudes of the quadrature components (I&Q) of f_{IF} during the previous f_{rev} period. (Its rejection of the other harmonics passed by the anti-aliasing filter is ~ 90 dB.) An AMD29240 32-bit microcontroller accumulates these amplitudes and stores them in DRAM. This sum is the filtered value of f_{IF} , the width of which is determined in software by the number of samples taken. The digital sum is then passed along, in real time, to subsequent processors for orbit calculations and corrections.

The microcontroller will also handle the low level control of the switches and attenuators, and communicate with the rest of the crate via high level commands, which will determine the BPMs that are sampled, the sampling order, and periods. This programmability of the microcontroller allows us to change sampling periods to minimize errors by coordinating the sampling period with, for example, the period of the synchrotron or betatron frequency. The microcontroller can even implement a phase-locked loop on the NCOM that can independently keep the Q signal of each button zeroed to reduce the amount of data needed to transfer to the control system during normal operation.

Although the electronics are primarily designed for orbit measurement that can be used to correct for slow beam motion, the digitization of the IF and the flexibility of the microcontroller allow for accurate single turn information to be output from the electronics. When such information is desired, the microprocessor can be programmed to acquire a large buffer full of turns, then download it to another processor for computations. Because of our choice of processing frequencies, we are able to have a large enough bandwidth in our IF filter to allow turn by turn motion to be observed. One can observe the betatron oscillations by measuring the turn-by-turn amplitude modulation of the data, and can observe the synchrotron oscillations by measuring the phase modulation.

5 SYSTEM TIMING

The timing generation of the system is straightforward. To generate the synchronous signals for our clocks and local oscillators, we divide down either f_{RF} or $2f_{\text{RF}}$. Switching of electrodes will all be done at increments of the revolution period and the processor will sample each electrode for multiples of this fundamental period. These values can, of course, be dynamically changed through software. We plan to package this controller in a format that will interface to a VME environment. Once this decision is finalized, we will use standard interface logic to connect the processor to the control system.

6 SYSTEM TEST RESULTS

We were able to test a prototype version of the analog portion of the processor during SPEAR's 1994 run by parasitically observing signals from one BPM with 55 mA of current in the machine. At this current we required 29 dB attenuation in the signal path to set our IF signal at the 1V level desired by the A/D, so that our measured analog path SNR will hold down to ~ 2 mA. For a 10kHz RBW, our signal measured ~ 70 dB above the noise floor at the IF output. Our signal was clean enough to see the amplitude and phase oscillations on the beam. If we need a greater SNR, we can trade off with the current system dynamic range. We saw no evidence of any problems due to processing at a harmonic of f_{rev} . Direct feedthrough of f_{IF} was ~ 58 dBc, which we feel can be further reduced by addition of appropriate filters. The other noticeable product, probably a mixer IMD was ~ 65 dBc. As discussed earlier, neither of these should be a problem.

We are continuing our development of the processor. Improving commercial technology makes possible increasingly better isolation per multiplexing switch, so we are evaluating new products before we make our final choice. We must still input this signal into the digital processor and program the controller, but based on the results of the beam tests, this work can be done on the bench.

7 REFERENCES

- [1] R. Hettel, J. Corbett, D. Keeley, I. Linscott, D. Mostowfi, J. Sebek, and C. Wermelskirchen, "Digital orbit feedback control for spear," in *IEEE PAC Conf. Proc.*, AIP, 1995.

SINGLE-TURN BEAM POSITION MONITOR FOR THE NSLS VUV ELECTRON STORAGE RING *

R.J. Nawrocky and S.L. Kramer, NSLS, Brookhaven National Laboratory, Upton, NY 11973, USA

Abstract

A "fast" beam position monitor capable of measuring the position of a circulating bunch in the VUV electron storage ring is presently under development. This monitor will collect data at a rate of about 6×10^6 measurements/sec per channel. We describe the design and operation of the monitor and the processing of the acquired data.

I. INTRODUCTION

The NSLS VUV electron storage ring typically operates at 800 MeV with a peak stored current of approximately 800 mA. In the ring, electrons may be stored in any pattern consisting of up to nine bunches (harmonic number $h=9$). The position of the beam orbit is continuously monitored at 24 locations around the ring circumference with dedicated high resolution beam position monitors (RFBPMs) which process rf signals derived from button pick-up electrodes (PUEs) embedded in the machine vacuum chamber wall [1]. These RFBPMs measure beam motion in the frequency range from DC to about 2 kHz, so that their output represents an average position of the beam at the PUEs over many revolutions around the ring.

Since many important phenomena occur at or near the beam revolution frequency, which in the case of the VUV Ring is approximately 5.9 MHz, a single-turn beam position monitor (STBPM) capable of making a position measurement during a single passage of a bunch past a pick-up electrode station or during many successive passages of the same bunch is now under development. In the VUV Ring, STBPMs will be used to study (a). closed orbit fluctuations, (b). correlation between orbit fluctuations, (c). growth and damping rates of transverse instabilities, etc., as well as in the optimization of injection system parameters during routine operations.

The "fast" monitor will process sub-nanosecond wide bipolar PUE pulses with a wideband hybrid network to form sum and difference signals. These signals will be synchronously detected, integrated and then digitized with a very fast A to D converter. Beam position will be calculated by dividing the difference by the sum digitally. Due to the high revolution frequency, data will be collected during the approximately 180 nsec long revolution period on one bunch only. To reduce errors in the data due to additive circuit noise, the output of the integrator will be sampled twice during each period (the second time when there is no signal) and the readings will be subtracted. The "fast" monitor will share the

rf signals from the PUEs with the "slow" BPM. We describe the design and operation of the new monitor.

II. PUE SIGNAL PROCESSING

The voltage signal from a ring PUE for a single bunch (14 mA, shortest bunch length $\sigma_t=162$ psec) circulating in the VUV ring acquired by a real-time oscilloscope is shown in Fig. 1a. The Fourier transform of this waveform in Fig. 1b demonstrates the high frequency response of these electrodes and shows that the spectral content of this signal lies in the range between a few tens MHz and 2 GHz. When the

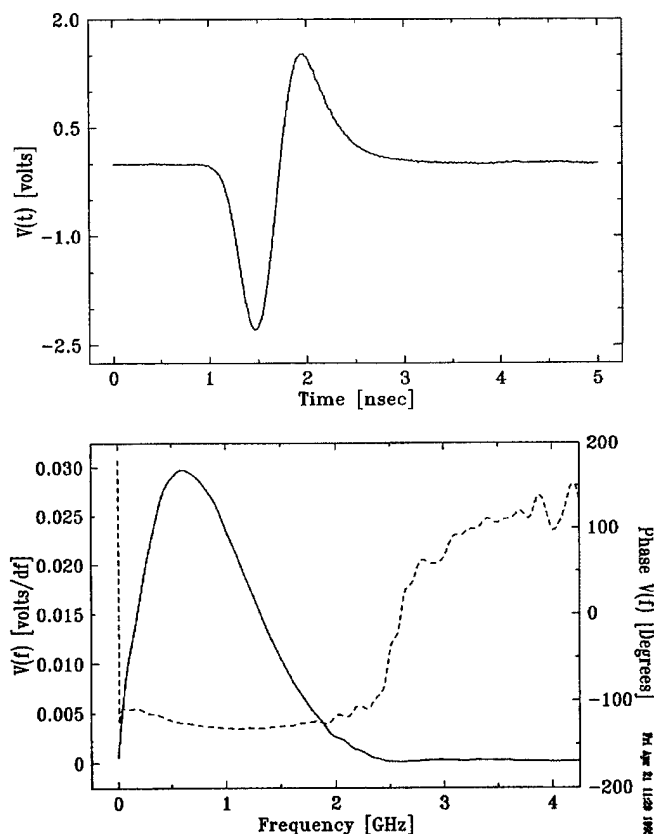


Fig. 1 A PUE signal (a) and its Fourier transform (b)

frequency data is corrected for the current distribution within the bunch, the resulting coupling impedance has a peak at about 900 MHz and a zero at 2.5 GHz.

In order to process a set of four PUE signals and maintain stable gains and offsets, the differencing will be performed directly on the signals, i.e. prior to any amplification, using 180 degree wideband rf hybrids [2]. The present plan is to add directional couplers to the existing broadband signal cables and to provide 10 dB attenuated octave bandwidth signals

*Work performed under the auspices of the U.S. Department of Energy.

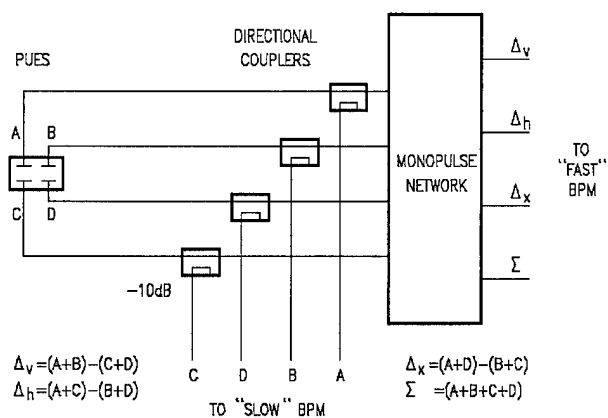


Fig. 2 Fast analog signal processing

centered on 158.66 MHz to the RFBPM while making the broadband signals available to the STBPM. This coupling network and four-way hybrid are shown in Fig. 2. All cables between the PUEs, directional couplers and the hybrid must be carefully matched.

III. STBPM DESIGN

A. Processing Electronics

The front end of the STBPM consists of two channels which simultaneously process the difference and the sum signals from the hybrid network. Each signal is first stretched by a Gaussian filter from < 1 nsec wide to about 10 nsec. The stretched bipolar pulses are synchronously detected, i.e. rectified by a double balanced mixer whose LO input is derived from the sum signal as shown in Fig. 3. The sum signal is processed by several stages of hard limiting before being used as the LO mixer input. The monopolar mixer output is integrated by a fast integrator whose output is sampled by a track and hold (T/H) amplifier. The integrator

is reset after the T/H acquires its output signal level and remains in a reset state until just prior to the start of the next integration period.

In the front end electronics section, some noise is injected into the signal path by the mixer as well as by the integrator reset circuit. This additive noise can be removed from the output by sampling in between signal pulses to yield a noise signal measurement.

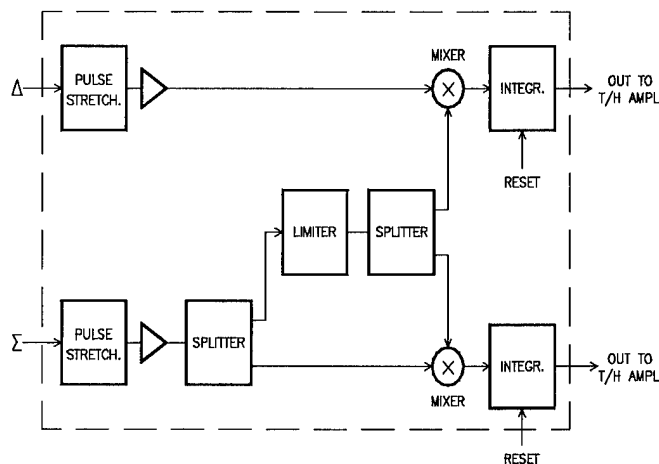


Fig. 3 BPM analog section

B. Analog to Digital Conversion

In each signal channel, the track and hold amplifier (Acculin AL-1210JR) acquires the integrator output signal in less than 10 nsec. This signal level is held by the T/H until it is processed by the 12-bit A/D converter (Datel ADS-119). The A/D output data is ready in less than 80 nsec after the start of conversion. After the completion of the A to D conversion cycle, the data is transferred to a FIFO buffer memory (32 K points/channel). The FIFO is interfaced to a PC-486 processor operating in a VXI environment via VME bus interface.

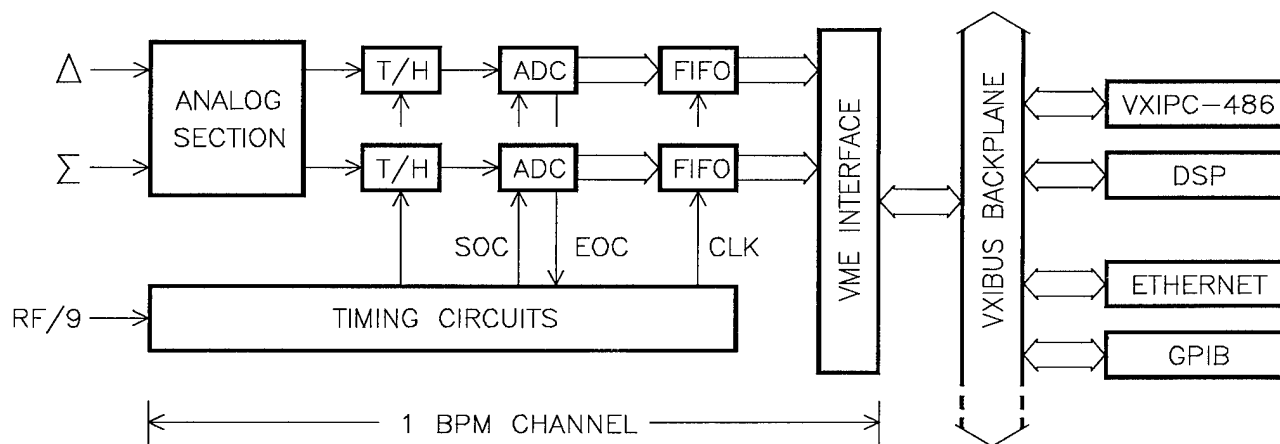


Fig. 4 Block diagram

C. BPM Operation

To describe the basic mode of the monitor operation, we will refer to the block diagram in Fig. 4 and the timing diagram in Fig. 5. In Fig. 4, the Rf/9 input is the master trigger derived from the ring accelerating system 52.88 MHz drive signal. This trigger occurs once every bunch revolution period and is synchronized with the circulating bunch. The integrator reset input, the T/H control signals and the start of conversion pulse (SOC) are derived from the Rf/9 trigger and are appropriately delayed.

At the beginning of a revolution period, as the difference and the sum signals arrive at the inputs of the analog section, the integrator is ready to accept an input. The sum signal is constant in phase whereas the phase of the difference signal depends on the position of the beam relative to the electrical center of the PUEs. Both inputs are equally stretched and synchronously detected as described earlier. The above process detects the phase of the input signal so that the polarity of the sum signal will, for example, always be positive while that of the difference signal may be positive or negative.

Each of the detected signals is integrated and the result is sampled by the T/H and then digitized. To reduce errors in the readings introduced by switching noise in the electronics, the integrator is reset and sampled a second time approximately half-way through the cycle when there is no signal. The second reading is subtracted from the first after digitization. Also, since the difference signals are beam intensity dependent, they must be normalized by dividing by the sum signal which, of course, is also dependent on the intensity.

The above sequence will be started and repeated for as many cycles as commanded by the PC up to maximum available space in the FIFO buffer. The mixer operation is self-correcting for variations in the time of arrival of the input signals and the precision of all other timing signals is not critical in the operation of the monitor.

D. Data Processing

After accumulating a record of data in the FIFO buffer, the microprocessor will read the data, subtract the non-signal noise measurement point from the adjacent signal data point, normalize the difference value with respect to the simultaneously measured sum signal, and then convert these ratios to vertical, horizontal and quadrupole moment values for the bunch, respectively. Each buffer of bunch position measurements will be divided into sub-records of 1K or more data points and processed by the DSP using its built-in FFT processor. (≈ 20 msec. per 1K point FFT). The output will include an average value (closed orbit position) and several spectral peaks. Well defined signals from the betatron oscillations will be tracked as a function of time to determine

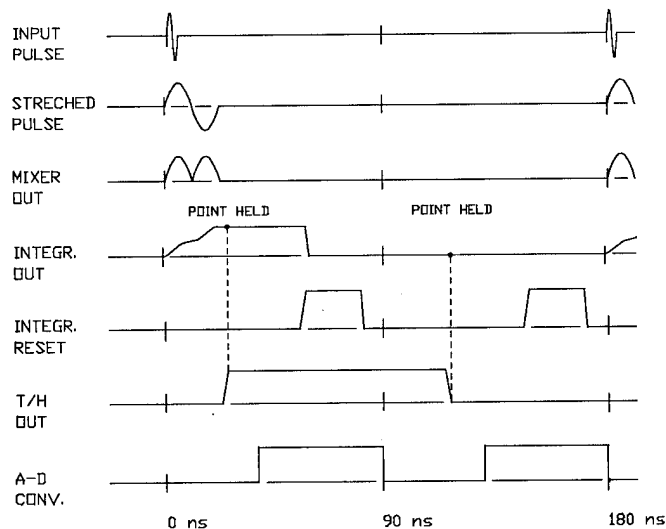


Fig. 5 Timing diagram

their growth and damping rates and the effect of these amplitudes on averaged beam properties. Data obtained via the Ethernet on variation of other system parameters will be used to determine their impact on the amplitudes of these oscillations. Data from the closed orbit micro (from the RFBPMs) will be used to cross-calibrate the average value and to look for slower fluctuations of the closed orbit.

During machine studies periods, a fast bunch kicker will drive the transverse oscillations for linear and non-linear tune measurements and damping rates as a function of system parameters (e.g. chromaticity and sextupole strength). As more STBM channels are installed, the data from PUEs at different azimuthal locations around the ring will be analyzed for simultaneous readings of the closest bunch. This will yield important information on the modal structure of transverse oscillations [3]. If well defined modes are observed, they will allow the source of beam impedance that drives the transverse coupled bunch motion to be more easily studied.

IV. REFERENCES

1. R. Biscardi and J. Bittner, "Switched Detector for Beam Position Monitor", Proceedings of 1989 PAC, IEEE Catalog No.89CH2669-0, Vol.3, pp.1516-19.
2. T. Ring, "Beam Position Monitors For The High Brightness Lattice", Daresbury Laboratory Technical Memo. DL/SCI/TM41A, June 1985.
3. B. Zotter and F. Sacherer, "Transverse Instabilities of Relativistic Particle Beams in Accelerators and Storage Rings", Proceedings of the First International School of Particle Accelerators, Erice, November 1976.

DESIGN OF THE BUTTON BEAM POSITION MONITOR FOR PEP-II*

N. Kurita, D. Martin, S. Smith, C. Ng, M. Nordby, C. Perkins, Stanford Linear Accelerator Center, Stanford University, Stanford, CA 94309 USA

The beam position monitor (BPM) was designed to provide a robust UHV feedthru and a reliable electromagnetic sensor. Stringent resolution requirements at low beam currents, bunch parameters, along with mechanical and chamber requirements produced challenges in the electrical, thermal, and structural design of the BPM's. Numerical modeling and experimental analyses were used to optimize the design. The higher order modes (HOM's) and beam impedance were modeled using MAFIA. Measurements agreed with the calculated 1Ω transfer impedance at the 952 MHz signal processing frequency, and the first two HOM's found in MAFIA. Tests and analysis both showed the button signal power approaching 40 W. Temperature and stress distributions were analyzed using this power loading with ANSYS. An electronic grade CuNi was selected for the BPM to reliably weld into the copper chambers. Pin seal and compressive joints were considered for the insulator vacuum seals. Both glassy ceramic-to-metal and ceramic-to-metal seals were evaluated.

I. INTRODUCTION

The high current and high resolution of the PEP-II B-Factory require a novel design for Beam Position Monitor (BPM). The major design goals are to achieve the resolution and precision requirements, to handle high power due to the bunch and current requirements of the machine, to minimize large discontinuities and subsequent impedances developed from resonances or trapped modes and to serve as a reliable vacuum feedthru. The design represents a compromise between electrical performance and vacuum reliability. Numerical modeling with MAFIA and ANSYS were used to optimize the design for signal performance, impedance and structural reliability.

II. REQUIREMENTS

The PEP-II HER stores 3000 mA of 9 GeV electrons [1]. The BPM's are located 14 inches from the downstream end of every quad chamber. The vacuum chambers are made from octagonal copper extrusion. The BPM's consist of four button-style pick-ups welded symmetrically on the chamber. The individual button pick-

ups are 3.5 cm apart to equalize the x and y position sensitivities.

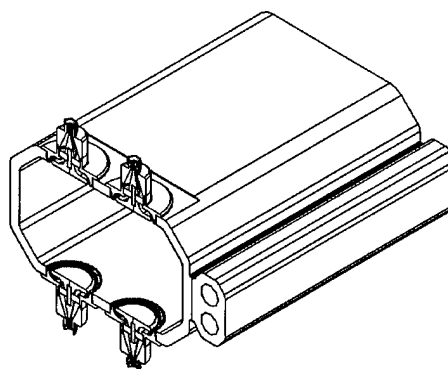


Figure 1:Downstream-End of Quadrupole Chamber.

The feedthru must be compatible with an ultra-high vacuum environment of 3×10^{-9} Torr. It needs to withstand 50 vacuum bakeouts at 200°C and 80,000 cycles from 15°C to 100°C. Vacuum failures occur from damaged or broken feedthrus due to their high profile and vulnerability. The current design addresses this problem by producing a low profile and well protected feedthru.

To meet the scientific needs the following resolution and precision requirements were defined (see table 1).

Parameter	Requirements
Resolution @ Current	15 μm @ 1×10^{10} e-, averaged over a 1000 turns. 1mm @ 5×10^8 e-, single bunch, single turn
Accuracy of measured beam position with respect to quad magnetic center	$\pm 1\text{mm}$ $\sigma < 0.5 \text{ mm}$ single bunch, single turn
Dynamic range, (position)	Meet the above resolution and accuracy spec. for (x,y) within 1 cm of center.
Mechanical Accuracy	0.38 mm
Electrical Accuracy	0.38 mm

Table 1: Operational Requirements

* Work supported by US Department of Energy, contract number DE-AC03-76F00515. Presented at the US Particle Accelerator Conference and International Conference on High-Energy Accelerators (PAC95), Dallas TX, USA, May 1995

III. BPM DESIGN DETAILS

Button and Center Conductor

The BPM's consist of four button style UHV feedthrus. The buttons are 1.5 cm in diameter to provide 1 mm of position resolution at 5×10^8 e⁻. The button is brazed to a molybdenum center conductor. The diameter was optimized using MAFIA to increase sensitivity and decrease the Q of trapped modes[2]. The gap between the button and the housing is 1 mm to minimize the HOM effects without adding excessive capacitance.

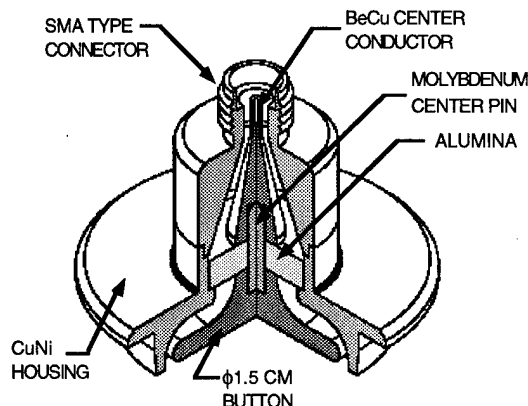


Figure 2: Cut away of a button pick-up

Vacuum Seal-Dielectric Material

The dielectric material most commonly used in BPM's is alumina. SLAC is requiring a minimum of 98% alumina for its thermal conductivity. Previous designs at SLAC and other accelerators typically use a compressive T joint for the ceramic-to-metal seal. However, this type of seal has many discontinuities which can adversely affect the electrical performance or create trapped modes. The current design uses a pin seal joint keeping the discontinuities to a minimum. The pin seal produces an outer diameter compression seal due to the mismatch of thermal expansion coefficients of the materials. The pin seal joint is not as robust as the compressive T joint, but has been proven in other accelerators to have sufficient strength to handle the vacuum load and thermal stresses.

Alumina borosilicate glass or "glassy ceramic" has been shown to be an acceptable alternative dielectric material. The glassy ceramic is an alumina strengthened glass and has a lower dielectric constant. This improves the electrical performance by decreasing the impedance mismatch. The design also eliminates brazing and simplifies the manufacturing process. The vacuum seals are a compressive pin seal between the metal housing and the glassy ceramic and a chemical bond between the glassy ceramic and the molybdenum pin. The major disadvantage is the minimum exposure glassy ceramic BPM's have had in the accelerator environment; however, some have been

operating in positron accumulator at Argonne National Laboratory for about half a year [3].

Vacuum Seal-Welding Feedthru to Quad Chamber

The pick-ups are electron beam (EB) welded into the chamber. This reduces the overall profile of the feedthru, decreases manufacturing tolerances, and fits easily into the chamber space. An electron beam weld minimizes the heat affected zone and increases the control and accuracy of the weld. Several materials were investigated for permeability, mechanical strength, welding and vacuum compatibility. Electronic grade 70/30 "cupronickel" was found to fit all of the requirements.

Copper and nickel are mutually soluble in each other, therefore, copper and cupronickel should produce a reliable weld. Several EB weld tests were performed. No adverse effects from the alloying were found, even during mixing and rewelding of the joint. The permeability of the weld did not increase from its unalloyed state. Welds were subjected to thermal shock tests by elevation of temperature to 250°C followed by immersion into liquid nitrogen. No leaks were observed.

In case of BPM failure, the weld joint of a BPM needs to be removed without contaminating the vacuum chamber. A test of this process was performed by a grinding process and a new BPM mock-up was successfully re-welded to the chamber. The BPM's will be replaced in a clean room.

BPM Cover

To decrease the possibility of failure the BPM's will be protected by a box attached to the BPM support. The cables will also be strain relieved to this box and the raft.

Positional Alignment and Calibration

The quad chamber is mounted directly to the quad magnet at the BPM. Therefore, the chamber and the BPM's move with the quad magnet which reduces inaccuracies due to thermal motion. The 25 μ m motion is primarily due to thermal heating for 100% to 80% beam power causing thermal expansion of the support at the BPM and the bowing of the quad chamber.

Calibration of the BPM's electrical centerline with respect to the mechanical centerline will be performed in the lab using a rod technique and its location with respect to the magnetic centerline will be measured in the tunnel.

IV. NUMERICAL AND EXPERIMENTAL RESULTS

Numerical and experimental data were obtained for electrical, thermal and structural performance. Also, the

transfer impedance of the BPM's was measured experimentally and calculated using MAFIA.

Electrical Measurement and Modeling

A prototype of a 2 cm button was fabricated and electrically tested. The measurements were compared to results from circuit models of three types: lumped capacitance, stripline loaded at center, and radial transmission line and MAFIA.

The button was modeled as a center-tapped strip transmission line of length l , width wl , velocity c , and impedance Z_0 . The load resistance is Z_L . The transfer impedance of this square "button" is given by Eqn. 1,

$$|Z_T(\omega)| = \frac{2gZ_L \sin(\omega l / 2c)}{\sqrt{\cos^2(\omega l / 2c) + (2Z_L / Z_0)^2 \sin^2(\omega l / 2c)}} \quad (1)$$

where g is the transverse geometry factor. A 2 cm button in the HER vacuum chamber has a 1Ω transfer impedance at the 952 MHz operating frequency. At full beam current of 10^{11} e/bunch, with a 1 cm radial position offset, the nearest button will deliver some 40 W of broadband power. Using $ZT = 1\Omega$, Eqn. 2 relates the load current in the 50Ω button termination to the beam current,

$$I_L / I_b = Z_T / Z_L \cong 0.02 \quad (2)$$

and agrees nearly exactly with the -34 dB (952 MHz) bench measurement.

The button possesses significant non-TEM resonances, which appeared in the solution of Maxwell's equations, and the MAFIA simulations. The lowest frequency HOM's are the TE modes when circumferential variations are allowed. The TE_{11} mode occurs at the frequency $f \cong c/2\pi r_0$, calculated at 4.7 GHz. This mode is cutoff in the small diameter output coaxial cable, and is therefore a high-Q resonance. In measurement this was easily observed at 5.73 GHz with a loaded $Q = 21$. Higher TE modes were also clearly present. These modes are strongly driven by the beam, dominating the beam impedance. However, they can be suppressed by introducing asymmetric features into the button. An extreme measure of short circuiting a point on the button circumference decreased the TEM power at 952 MHz by 1 dB, while increasing the total broadband power delivered to the load. Reduction of the button diameter to the present 1.5 cm brought its impedance within the machine's stability requirement.

Thermal/Structural Loading

There are two areas of concern for the thermal stability of the BPM. First, the thermal stability of the feedthru is essential to meet the precision requirements. Second, the resolution requirements at low current results in high power

transfer at full current. As much as 40W delivered out the cable in the TEM mode has been estimated. MAFIA and numerical analysis estimated that 0.16 W is dissipated into concentrated areas of the alumina and 6 W at the interface between the center conductor and the alumina. An additional heat source of 0.25 W/cm^2 was calculated using EGS and FLUKA for scattered SR on the button face. Thermal analysis using ANSYS was performed to determine the temperature distribution in the feedthru. A 3-D analysis verified that the concentrated heat loads in the alumina were negligible and that the primary heat load was at the interface of the center conductor and the alumina. A maximum temperature of 110°C was found on the button.

Thermal stresses were also calculated using ANSYS. Evaluation of the stresses due to heating of the pick-up showed that residual stresses in the compressive seal were needed to maintain a relative margin of safety. An estimate of the residual stresses was calculated assuming all parts are stress free at the softening temperature of cupronickel. Further analysis on power dissipation into the center conductor showed initial values were conservative.

V. CONCLUSIONS

The SLAC button feedthru has been designed to meet the demanding vacuum, reliability and impedance requirements of the PEP-II project. The design was extensively modeled to reveal expected temperature, stress and impedance performance. Trade studies involving material selection, button size, connector type and transition geometry were conducted. Prototypes were fabricated which validated the analyses.

VI. FUTURE WORK

At this time the pre-production order has been placed with several vendors. The feedthrus will be subjected to mechanical and electrical tests. Numerical and experimental analyses on their sensitivity and transfer impedance will also be performed. The production order will be based on a pass-fail evaluation.

VII. REFERENCES

- [1] C. Perkins, et al, "Vacuum System Design for the PEP-II B Factory High Energy Ring", EPAC94 Conference Proceedings, London, World Scientific.
- [2] C-K Ng, et al, "Simulation of PEP-II Beam Position Monitors", these proceedings.
- [3] Personal communication with Dr. Bill Selyey of Argonne National Laboratory.

Study of Fast Energy Electron Beam Profile Monitor System

Ian Hsu, C. I. Yu and C. C. Chu
Institute of Nuclear Science,
National Tsing-Hua University and
Synchrotron Radiation Research Center,
Hsinchu, Taiwan 30043, R. O. C.

ABSTRACT

In the experimental study of accelerator physics, a turn by turn monitoring of the beam profile CAN provide very unique information. In this paper, we proposed a method which may measure a turn by turn electron beam profile through its synchrotron radiation by using a fast photo-diode. Here, we utilized the non-linearity of the response of the photo-diode detector. At high photon intensity, non-linearity occurred due to the saturation of the device. In this paper, we will present the theory and the test experimental results. We had examined this idea by using a modulated He-Ne laser to simulate the synchrotron radiation light. The results agree with our computer simulation results[1]. But the photon power intensity of synchrotron radiation in the storage ring of TLS(Taiwan Light Source) is not sufficient to saturate the photo-diode as what we expected. In order to utilize the idea on the synchrotron radiation, we used an external light source to saturate the photo-diode and the synchrotron radiation be the probe beam. In this paper, the theory and the experiment of the above idea will be discussed.

1. INTRODUCTION

In many accelerator physics experiments, e.g., the coherent damping time measurement and the dynamic aperture study experiments, we like to know the turn by turn variations of the beam positions. Usually, it is accomplished by the button type or the strip line type electrode beam position monitors (BPM). However, the measurements done by these types of BPM only gave us the information of the position of the beam centroid. If the beam centroid motion combined with the decoherence mechanism, the BPM would not be able to distinguish them. That means that by using the BPM, we can not distinguish the coherence damping or the decoherence. In order to distinguish them, we need to monitor the beam profile, simultaneously. For lepton machines, the synchrotron radiation provides a very useful beam profile information. However, to perform a turn by turn beam profile monitor, we need a very fast detecting system. For the speed requirement we need, the commercial photo diode array and the following up electronic system is not available neither a cost reasonable approach. In this paper, we proposed a method to monitor the beam profile by using a fast single photo diode.

2. THEORY

Most P-N silicon photo-diodes are linear (better than 1%) over a wide range of magnitude of the incident power [2]. In linear region, the total photocurrent is independent of the incident photon beam size as long as the total power is the same. At high photon intensity, however, non-linearity is introduced due to the device saturation. Total photocurrent in non-linear region now is not only dependent on the incident total photon power but also dependent upon the photon beam size. This means that in the non-linear region, we can get the photon beam profile information by means of measuring the total photocurrent. A detail discussion has been presented in a previous paper [1].

3. EXPERIMENTS and RESULTS

We used a He-Ne laser to simulate the synchrotron light. The setup of the simulation experiment is shown in figure 1. The power of the He-Ne laser is $1.33mW$, which is sufficient to saturate the photo-diode. We use a functional generator to modulate the He-Ne laser intensity at frequency of $1MHz$. The movable convex lens is used to change the incident photon beam size. The photo-diode (PIN10DI manufactured by UDT) is negatively biased. The output of the photo-diode is then magnified by an amplifier of gain $147V/V$ with output resistance $50ohm$. The CCD camera is used to measure the laser beam size. The results are shown in figure 2. In this figure, we compared the results of two different bias voltage, i.g. $0.3V$ and $0.828V$. We can find that the smaller bias voltage made the saturation easier. We also find that the minimum power intensity to saturate the photo-diode is about $0.3325mW/mm^2$.

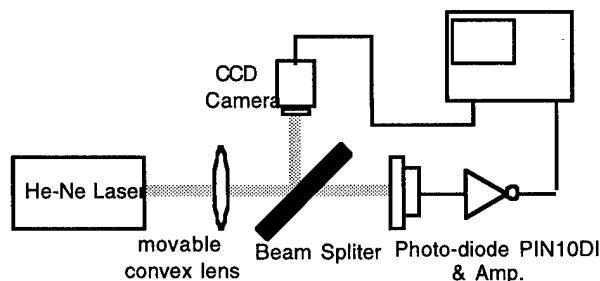


Fig. 1 Experiment Setup

The total photon power of the synchrotron radiation in the storage ring of SRRC is about an order of 10^{-2} (mW) at single bunch mode, with 1mA beam current. The photon beam size is approximately the same order as the He-Ne laser we used in this study ($\sim 0.28\text{-}4\text{mm}^2$). Thus the power intensity is not sufficient to saturate the photo-diode as what we predicted in figure 2.

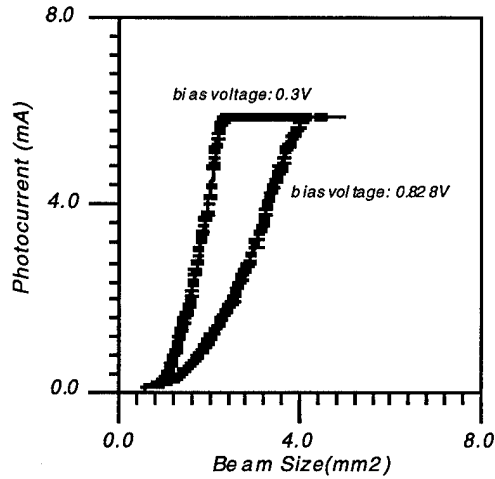


Fig. 2 Plot of the photocurrent vs. incident photon beam size for two bias voltage, 0.3V and 0.828V.

Figure 3 shows the signals of the photo-diode as synchrotron radiation incident on it. From the figure we see that the photo-diode can detect the revolution frequency of the electron beam but fail to sense the beam profile changes. This is due to the low power intensity of the SR as mentioned above.

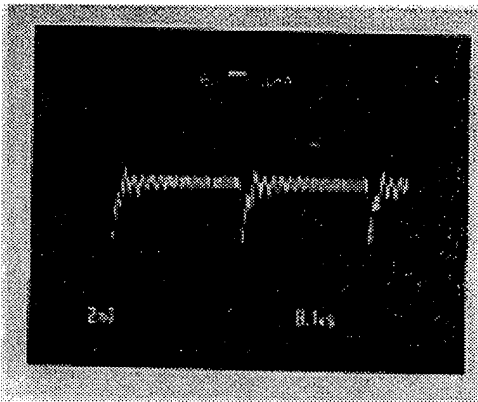


Fig. 3 The response of the photo-diode as the SR of the storage ring in SRRC impinging upon it

To solve this problem, we used an external light source to saturate the photo-diode to sense the beam profile variation of the SR; This variation information indicates the dynamics of the electron beam in the storage ring. The setup of the saturation experiment is shown in figure 4. The power of the saturation beam is

1.09mW and that of the probe beam is the same as before.

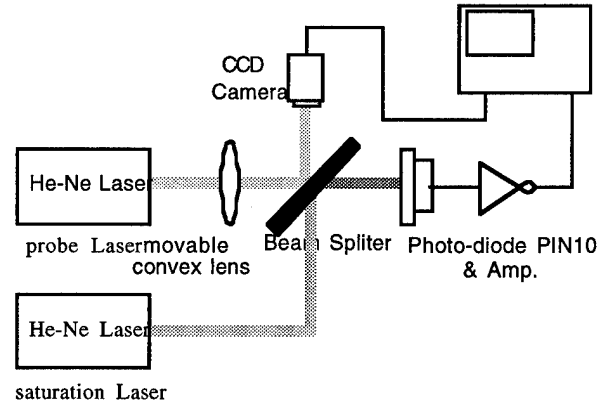


Fig. 4 External light saturation experiment setup

The corresponding beam size vs. the distance between the photo-diode and the convex lens is shown in figure 5. In this experiment we used an anti-reflection coated convex lens with focal lens 17cm. The results of the photocurrent we measured are shown in figure 6. We found an obvious variation of the photocurrent when the beam size was changed. Further, we used filters to change the power intensity of the probe beam. The results is shown in figure 7. The minimum photon power can saturate the photo-diode is about 0.06mW at the beam size of 0.28mm that is about the same as the power intensity of the SR which we are going to use.

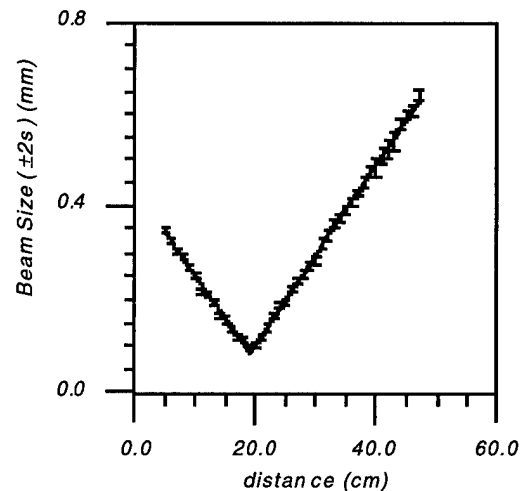


Fig. 5 The corresponding beam size vs. the distance between the photo-diode detector and the movable convex lens.

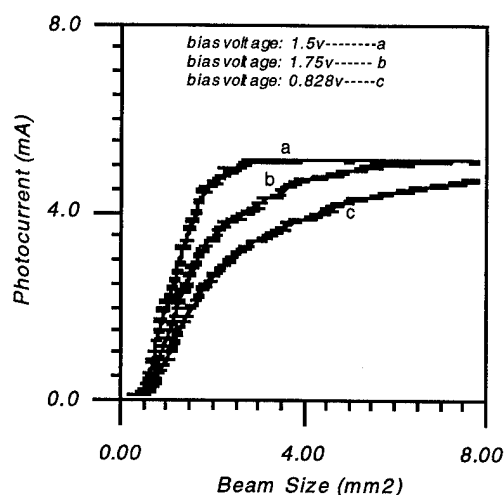


Fig. 6 Plot of the photocurrent vs. photon beam size, three kinds of bias voltage were presented (The power of the saturation beam is 1.09mW , without modulation, that of the probe beam is 1.33mW , 1M Hz modulated by a functional generator)

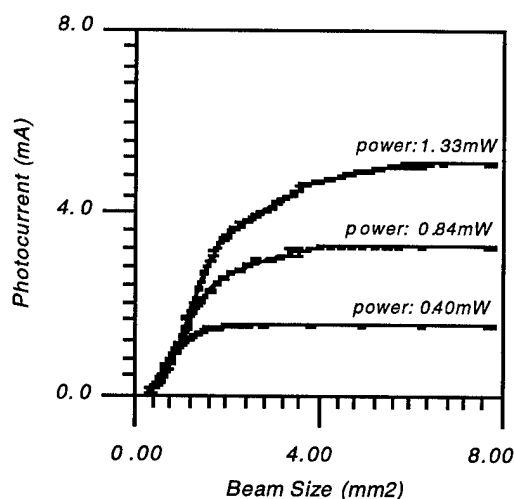


Fig. 7 Plot of the photocurrent vs. photon beam size, for three probe beam power. (The bias voltage was 1.175V . The power of the saturation beam is 1.09mW , without modulation. The probe beam was 1M Hz modulated by a functional generator)

4. DISCUSSIONS

The results from the laser beam experiment prove the feasibility of the idea we first mentioned. That is, we can use the non-linearity of the photo-diode to sense the beam profile variation information as long as the total power of the incident photon is the same.

In the single bunch case, the SR power intensity is, however, too small to saturate the photo-diode as applying the method for sensing the electron beam

profile changes in the storage ring. To solve the problem, we used an external light source to saturate the photo-diode first. In this case the changes of electron beam profile may be detected although the SR intensity is small.

Further, we will search an absorber which can be easily saturated by the SR from the electron beam. The more the absorber is saturated, the larger the transmitted SR is. The differences between the transmitted SR of different power intensity can then be measured by the photo-diode operated at the linear region.

5. ACKNOWLEDGMENTS

We would like to thank Drs. Y. Cheng and K. T. Hsu of SRRC for their help by providing the video amplifier.

6. REFERENCE

- [1] I. Hsu, C. C. Chu and C.I. Yu, "Turn by Turn Beam Profile Monitor by Utilizing the Non-linearity of the Photo-detector", in EPAC'94 Conference Proceedings, London, June 1994, p1649.
- [2] Melles Griot, Optics guides 5, Ch.22.

THE AVERAGE ORBIT SYSTEM UPGRADE FOR THE BROOKHAVEN AGS*

D.J. Ciardullo, J.M. Brennan; Brookhaven National Laboratory, Upton, New York 11973, USA

INTRODUCTION

The flexibility of the AGS to accelerate protons, polarized protons and heavy ions requires average orbit instrumentation capable of performing over a wide range of beam intensity (10^9 to 6×10^{13} charges) and accelerating frequency (1.7MHz to 4.5MHz). In addition, the system must be tolerant of dramatic changes in bunch shape, such as those occurring near transition. Reliability and maintenance issues preclude the use of active electronics within the high radiation environment of the AGS tunnel, prompting the use of remote bunch signal processing. Recently renovated electrostatic beam position detectors will be used to provide both radial and vertical bunch signals from 72 locations around the AGS. The high dynamic range requirement is addressed by using a narrowband *implicit normalization* scheme to provide a linear output with beam position. This paper will describe the basic objectives and design concepts for the AGS Average Orbit system upgrade.

SYSTEM OBJECTIVES

It is desired to build an average orbit measurement system using the recently modified PUE (Pick Up Electrode) detectors currently used for orbit acquisition. The original internal signal wiring in these detectors has been replaced with radiation-hard shielded cable, and new vacuum flanges with coaxial connectors have been installed. These electrostatic detectors exhibit a linear differential response with beam position.

The improved BPM system should be able to operate with one or more bunches in the AGS, over a wide range of bunch lengths (typically 10 nsec to 300 nsec). Since the detectors are electrostatic, the peak amplitude of the bunch signals will vary over a wide range. Although intensities from 10^9 to 6×10^{13} charges appear to imply a dynamic range of ≈ 95 dB, actual peak PUE voltage variations can add another 20dB to this requirement, when the effects of non-zero beam position and bunch signal shape are taken into account.

Concurrent with the dynamic range requirement, the system operates over an RF sweep of 1.7MHz to 4.5 MHz, with PPM (Pulse to Pulse Modulation) compatibility. [PPM would allow the AGS to accelerate alternate types of particles on a pulse by pulse basis]. In addition, maintenance and reliability issues dictate that there be no active electronics located inside the high radiation environment of the AGS ring.

Augmenting its use as an average orbit monitor, the upgrade can also be used to instrument the radial control loop function, adding the flexibility to choose any combination of BPM locations for horizontal position feedback.

DESIGN STRATEGY

The upgrade for the AGS Average Orbit system is divided into three areas; 1. A new PUE signal delivery system; 2. New average orbit processing electronics; and 3. Centralized peripheral

and data acquisition hardware. Figure 1 indicates the locations and functionality for the upgraded hardware. A distributed processing architecture was chosen to minimize the PUE signal cable lengths, the group of four from each detector location being phase matched to within $\pm 5^\circ$.

The design of remote electronics with >95 dB dynamic range implies isolation and filtering requirements calling for a "closed" processing front end to minimize corruption of the low level bunch signals. As such, inputs and outputs other than the PUE signals are fiberoptically coupled for maximum isolation. Processing will be done in the frequency domain, operating on only a single spectral component of the PUE signals. Localized BITE (Built In Test Equipment) circuitry functions to verify proper operation of the remote processing electronics. RF calibration and Local Oscillator (LO) signals are provided by the existing AGS LLRF system, and are shipped to the remote service buildings for distribution. The BITE circuitry provides: 1. Swept-frequency calibration signals and LO; 2. Common-mode amplitude control of the test signals to verify system dynamic range; 3. Differential-mode amplitude control of the test signals to simulate several different beam positions and 4. A zero position reference prior to the start of each AGS cycle.

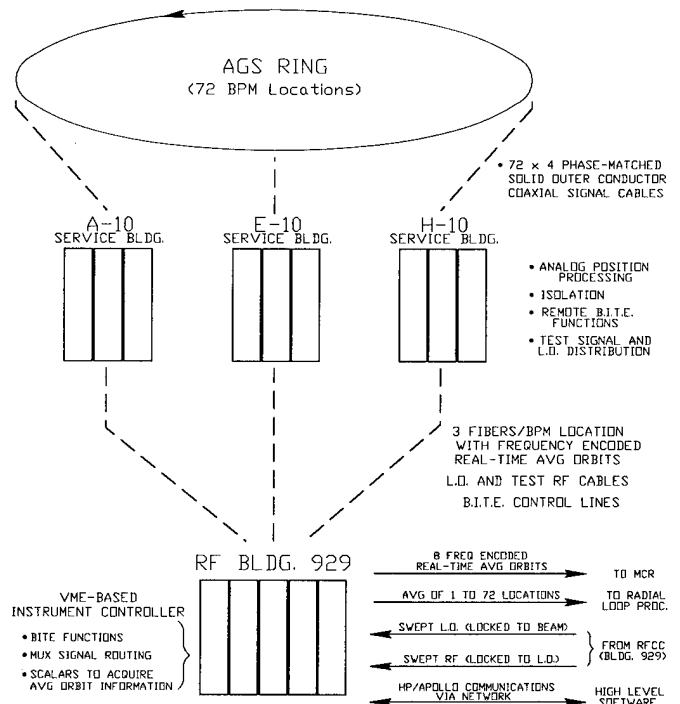


Figure 1. System Overview.

NEW HARDWARE

Design Of A New PUE Signal Delivery System

Figure 2 illustrates the "extended Faraday cage" concept used by the upgrade, necessary to satisfy the contradictory requirements of operating on very low intensity PUE signals using only passive

*Work performed under the auspices of the US Department of Energy.

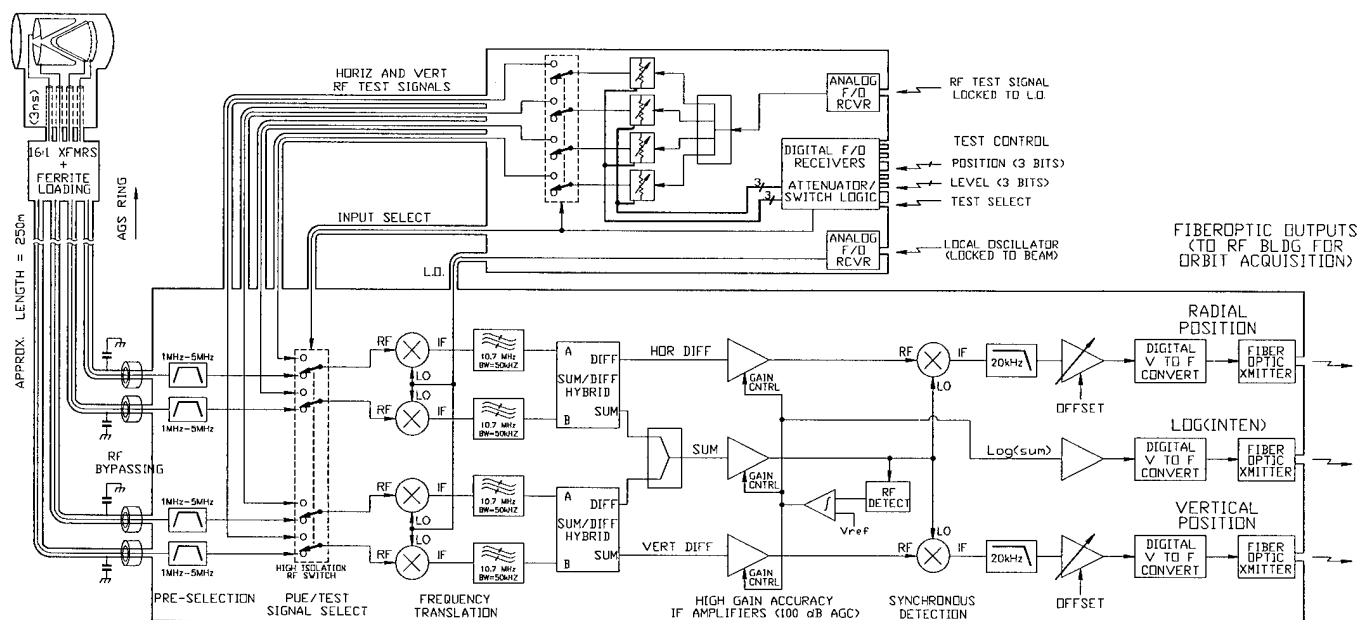


Figure 2. Block Diagram Showing "Extended Faraday Cage" Topology and Implicit Normalization Technique.

electronics in the ring. Of paramount importance is the use of high quality (i.e., low loss, solid shield) coaxial cable, which serves as an extended electrostatic shield from the beampipe to the electronics. Four phase-matched cables from each detector location bring the PUE signals out of the AGS, into three remote service houses for analog processing. All other inputs or outputs to the processing electronics are coupled via fiberoptics to minimize the number of breaks in this "closed system" topology (see Figure 2). Power supplies are "floated" to allow the electronics to be referenced to beampipe potential.

A preliminary design (16:1 and 36:1) for a wideband monofilar autotransformer is currently being tested in the AGS to match the high impedance electrostatic PUEs to commercially available 50Ω coaxial cable. The minimum impedance ratio of this transformer is 16:1 (800Ω to 50Ω), determined by the low end of the rf frequency sweep (1.7MHz). The maximum impedance of the primary is a trade-off between the -3dB response at the low end and signal reduction due to transformer action. The device must be located outside the high B field of the bending magnets (where the vacuum flange of the detectors are located), making necessary a small amount of additional cabling. The capacitance of this extra cable, when added to that of the 3nsec internal BPM lead-out cables, results in a voltage attenuation of approximately 10dB. In addition, these cables are not terminated in their characteristic impedance, and collectively respond to the beam with quarter-wavelength peaking at $\approx 85\text{MHz}$. The transformer assemblies include lossy ferrite beads on the high impedance side to help damp this resonance without increasing the PUE capacitance load.

At the remote end of the cable, a decoupling network is formed by wrapping several turns of the signal cable around a ferrite toroid, then capacitively coupling the shield to earth ground. This helps to suppress any stray rf traveling on the outer conductor of the coax from reaching the electronics housing.

Design Of New Position Processing Electronics

The processing electronics located in the AGS service houses provide localized gain and average orbit processing for 72

BPM detectors, each with dual-plane measurement capability. Average position calculation is carried out using a modified form of sum/difference processing, used in conjunction with a high sensitivity AGC (Automatic Gain Control) circuit. In addition to an uninterrupted flow of average orbit information, this architecture also provides a "comfort" output (the AGC error voltage) which roughly relates to the beam current. Observation of this output gives an indication of whether or not the PUE signal level is sufficient for successful instrument operation. All three analog outputs (horizontal position, vertical position and LogI) are isolated using fiberoptic links with digital frequency modulation. The digital links provide dc and rf signal isolation, very high noise immunity, and protection against the amplitude variations normally associated with standard linearity and attenuation.

Standard heterodyne techniques are used to translate the swept RF component of the bunch signals to a fixed Intermediate Frequency (IF). There are several advantages to doing this; First, position information can be processed narrowband (i.e., at a bandwidth equal to twice the frequency response of the overall BPM system), providing the opportunity to filter wideband noise and f_{rev} frequency components. Secondly, the rf devices used to carry out the position processing need not be broadband. In addition, if the IF is chosen to be an "RF industry standard" frequency (e.g. 10.7 MHz), commercial availability of related rf components increases, significantly reducing their cost.

A block diagram of the implicit normalization technique is included in Figure 2. Due to their somewhat Cos^2 bunch shape, the PUE signals are rich in harmonics of f_{RF} . Since f_{RF} is continuously swept from 1.7MHz to 4.5MHz, some of these harmonics will present themselves as image frequencies and mix back down to the IF, causing interference to the processing circuitry. To remedy this, the IF is chosen to be above f_{RF} , and the PUE signals are low pass filtered to reject frequencies above 4.5MHz. This also limits the peak amplitude of the bunch signals as the machine approaches transition; The PUE signal harmonics (which increase dramatically as the bunch length shortens) are suppressed without affecting f_{RF} , the spectral component used to determine the beam position.

The PUE signal spectrum also includes sidebands at f_{rev} , the AGS revolution frequency. The magnitude of f_{rev} can be relatively large as compared to f_{RF} , especially when the ring is not completely "filled". Since f_{rev} is in close proximity to f_{RF} at the low end of the RF sweep ($f_{rev} \approx 371\text{kHz}$ and f_{RF} sweeps from 1.7MHz to 4.5MHz), it is necessary to reduce the revolution frequency component to avoid saturating the front end amplifiers and confusing the AGC. This is accomplished with the use of a high-pass filter whose passband includes f_{RF} but not f_{rev} .

Following pre-selection, the bunch signals are upconverted, where crystal bandpass filters are used to select the 10.7MHz IF. This passband must be narrow enough to attenuate the revolution frequency sidebands ($\pm 371\text{kHz}$; strongest when the machine is not full), but wide enough to pass the AM sidebands due to beam position movement ($\pm 20\text{ kHz}$). The sum and difference of the IF signals are then taken, resulting in three distinct channels; Horizontal difference, vertical difference and the sum of all four PUE signals.

The amplitude of the SUM channel is maintained at a constant level via 100dB of dynamic gain control. The AGC error signal is used as common feedback to the gain controlled amplifiers of all three channels, dividing the horizontal and vertical differences by the detected sum. The phase of the normalized positions (and hence their sign) are recovered through synchronous detection with the SUM signal. After being low pass filtered and scaled, the analog positions and $\text{Log}\Sigma$ are used to FM modulate three digital fiberoptic transmitters.

Figure 3 shows initial bench test results for the IF/detector section of this processing scheme. The plot assumes a detector sensitivity of 50mm, and illustrates the deviation from expected position due to 0dB and $\pm 1\text{dB}$ IF input ratios (corresponding to 0mm and $\pm 2.875\text{mm}$, respectively).

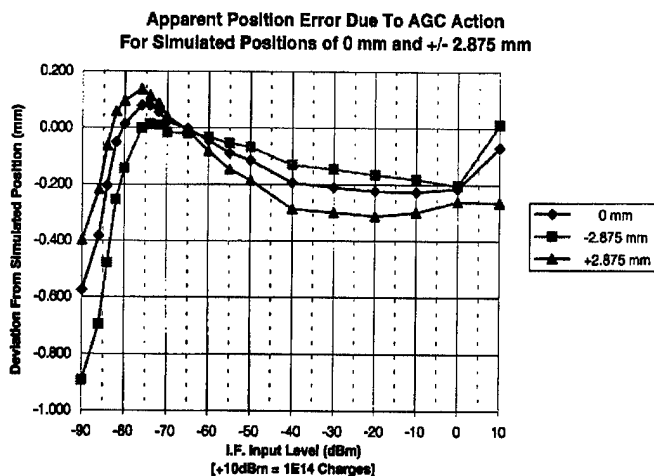


Figure 3. Bench Results For IF/Detector breadboard.

Preliminary results of the implicit normalization method using a pair of actual PUE signals via prototype 16:1 transformers are presented in Figure 4. Trace 1 shows the radial beam position for a full AGS cycle, and is in excellent agreement with the existing AM/PM based position monitor at this BPM location. Trace 2 is the $\text{Log}\Sigma$ output, the AGC error voltage. Actual intensity in the AGS at the time this plot was recorded was 50TP (i.e., 12.5TP per batch), and the PUE signals were attenuated by

76dB before reaching the processing electronics. Note that in actual operation, the processing circuitry will operate on the sum of all four electrodes (rather than just one PUE pair), increasing the voltage to the SUM channel by 6dB.

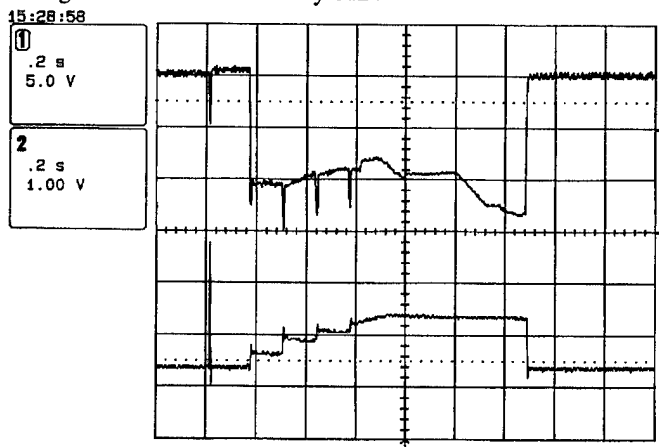


Figure 4. Radial Beam Position and $\text{Log}\Sigma$ Outputs.

Centralized Support Hardware

Peripheral support hardware is centrally located in the RF building, and includes a digital multiplexer (mux) and VME-based Instrument Controller, as well as assorted rf and L.O. distribution amplifiers. The mux is a convenient "tie point" where orbit information from one or more BPM locations can be averaged for the radial control loop function, decreasing its sensitivity to loss of any one particular BPM location. The mux can also be used to route any combination of eight real-time average orbits or $\text{Log}\Sigma$ outputs to the main control room. Finally, the mux provides test accessibility for system troubleshooting.

The Instrument Controller is used to acquire (and make available on the network) the position and $\text{Log}\Sigma$ information from all 72 BPM locations in the AGS. Sample times will be specified as time line events via the high level software. To preserve signal integrity, the controller will receive digital FM orbit data directly, using gated counters (scalars) to input the data. The scalars can also provide additional filtering of the position data by varying the gating interval. In addition to gathering data from the remote processing electronics, the controller will provide control of the mux routing and of the BITE functions used for system test.

CONCLUSION

Initial requirements and design concepts for the AGS average orbit upgrade have been presented. The primary motivation is to seamlessly match the system's dynamic range to that of the AGS, without the need for hardware "changeovers" between runs. To accomplish this, a linear position processing technique based on the concepts of implicit division and AGC has been developed, and initial results presented. The proposed distributed system takes a "laissez-faire" approach to gain control, providing both acquired and real-time orbits.

ACKNOWLEDGEMENT

The authors wish to recognize the rf prototyping talents and helpful suggestions of Siegfried Naase for his work during the breadboarding stage of this project.

FEASIBILITY STUDY OF AN ORBIT FEEDBACK SYSTEM FOR THE KEKB FACILITY

Y. Funakoshi, M. Tejima and H. Ishii, National Laboratory for High Energy Physics (KEK),
1-1 Oho, Tsukuba-shi, Ibaraki-ken, 305 Japan

Abstract

An orbit feedback system is vital for maintaining an optimum collision condition at a B factory where two beams circulate in separate rings. For this purpose the beam-beam deflection technique, pioneered at the SLC[1], may be utilized particularly for detecting an orbit offset at the collision point. To study feasibility of this technique at the KEKB rings we carried out a beam test using a pair of stripline monitors installed in the TRISTAN. The main purpose of the study is to see whether we can detect orbit offsets which are artificially introduced using electro-static separators with sufficient accuracy or not. We succeeded to detect these offsets with enough accuracy using these two beam monitors and have had a confidence that this method will work well also in the KEKB case.

I. INTRODUCTION

A conceptual design of the orbit feedback system for the future B Factory was described in a previous paper[2]. As was shown in this paper, we can detect an orbit offset and a crossing angle by using only two monitors which are located on the both sides of the interaction point (IP) and can measure the position of the two beams separately. Fig. 1 shows the geometry of the two monitors A and B around the IP. The monitors are installed between the IP and the final focus quadrupoles so that we can be free from complexity arising from mechanical position drifts of these magnets. We can get the following expression from measured position data using the monitors;

$$\Delta y_{12} + \Delta y' L = \frac{(y_{1A} - y_{2A}) + (y_{1B} - y_{2B})}{2}, \quad (1)$$

where Δy_{12} denotes the offset at the IP, $\Delta y'$ the beam-beam dipole kick and L a distance between the IP and the monitors, respectively. We assumed that the kick angles of the two beams have the same absolute value and the opposite sign. y_{1A} designates the vertical position of beam 1 at the location of monitor A and so on. With the rigid Gaussian model, the coherent beam-beam kick is given by the Bassetti-Erskine formula[3]. If we assume no horizontal offset and take flat beam limit, the kick is expressed as

$$\Delta y' = -\frac{\sqrt{\pi} N_* r_e}{\gamma \sigma_x} \left[\exp\left(\frac{\Delta y_{12}^2}{4\sigma_x^2}\right) \left\{ 1 - \operatorname{Erf}\left(\frac{\Delta y_{12}}{2\sigma_x}\right) \right\} - \left\{ 1 - \operatorname{Erf}\left(\frac{\Delta y_{12}}{2\sigma_y}\right) \right\} \right], \quad (2)$$

where

$$\operatorname{Erf}(x) = \frac{2}{\sqrt{\pi}} \int_0^x e^{-t^2} dt$$

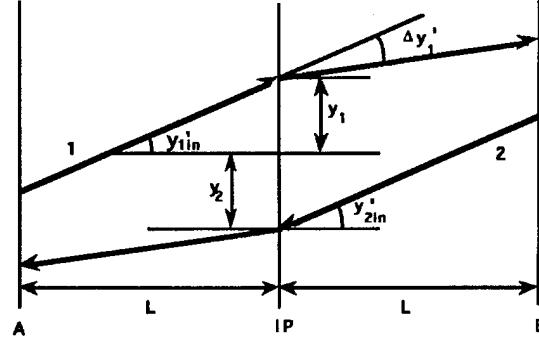


Figure 1. Conceptual Scheme of the Monitor System.

is the error function. In this expression, σ_x and σ_y denotes the horizontal and vertical beam sizes at the IP, respectively. And N_* means the number of particles in the counter-rotating bunch.

In principle, we can know the orbit offset at the IP using equations (1) and (2). A good point of this method is that subtraction of the measured data seen in equation (1) contributes to cancel out spurious offsets which are possibly included in the position data, provided that the offsets are common for the two beams. For example, the effect of a mechanical position oscillation of the monitors can be canceled out. If the offsets included in measured data are different for the two beam, we can not avoid a spurious orbit offset arising from these offsets in the measured data. Even in this case, however, we can know the actual zero-offset point by scanning the orbit offset artificially and fitting the data using (1) and (2). Once the actual zero point is found, the (actual) orbit offset can be obtained as a slip from this zero point. To maintain the optimum collision condition for the orbit offset, we only have to make a feedback loop so that the orbit offset thus obtained is minimized.

II. MONITOR SYSTEM

We newly developed a beam position monitor system for this experiment. We chose stripline type monitors[4], since we have to measure the positions of two beams separately. In addition, the high signal level of the striplines in comparison with button type electrode may also contribute to better position resolution. We employed two monitor chambers with four stripline electrodes. The two monitors are installed around one of the IPs named Nikko. Eight output signals from a monitor chamber are sent to the local control room through its own coaxial cable, and then their signals are selected by RF switches, processed by a common front-end circuit. The signal detector consists of a triple stage super-heterodyne circuit, a synchronous detector and 20bits ADC. A picked up frequency was chosen 521MHz that is the 5267th harmonics of the revolution frequency (99.3KHz).

Table I
Typical machine parameters of the TRISTAN.

Distance between IP and PM [†] (m)	1.65
Emittance, $\varepsilon_y/\varepsilon_x$ (nm)	1.2/80
Beta function at IP, β_y^*/β_x^* (m)	0.04/1.0
Beam size at IP, σ_y^*/σ_x^* (μ m)	6.9/283
Angular divergence, $\sigma_{y'}/\sigma_{x'}$ (μ rad)	173/283
Beam-beam parameter, ξ_y/ξ_x	0.024/0.012
Beta function at PM, $\beta_y^\dagger/\beta_x^\dagger$ (m)	68.1/3.72
Beam size at PM, $\sigma_y^\dagger/\sigma_x^\dagger$ (μ m)	286/546
Bunch length, σ_l (mm)	15

†): Position Monitor

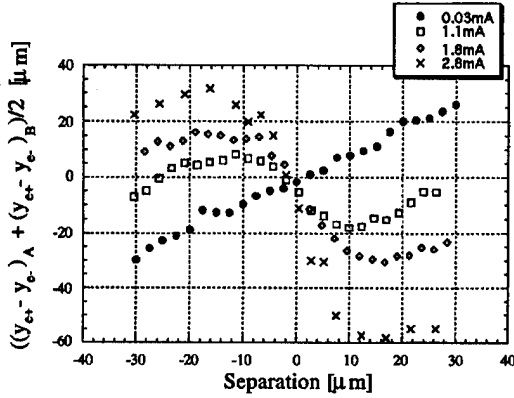


Figure 2. Beam-beam deflection measurement.

With the choice of this pick-up frequency, we aim at obtaining better directivity between the two beam signals. The monitoring system can measure beam position with high resolution of a few micron. We confirmed that this position resolution is actually achieved by seeing reproducibility of the beam position measurements. The overall measuring time is about 3 sec. The time is mainly determined by that necessary for A/D conversion, typical value for which is around 120msec per conversion.

III. EXPERIMENT

The TRISTAN is an electron-positron single ring collider operated at around 30GeV. For the time being, a high energy physics(HEP) experiment is being carried out at 29GeV. The present machine study was done at the same energy and with the same optics as those of the HEP experiment. Typical machine parameters related to the present experiment are shown in Table 1.

The orbit offsets were created using the electro-static separators fed by bi-polar power supplies. The maximum amount of full separation is about $\pm 30\mu\text{m}$. In this study, we employed one electron bunch and another positron bunch and took data at four different beam currents; *i.e.* averaged bunch currents of 0.03, 1.1, 1.8 and 2.8 mA. At each current point, we scanned the offsets at intervals of $2.5\mu\text{m}$ or $5\mu\text{m}$ with recording the beam positions of the two beams. Before we moved from one offset value to the next, we reset the orbit bump and took the beam positions in this situation as the reference values. And when we moved on

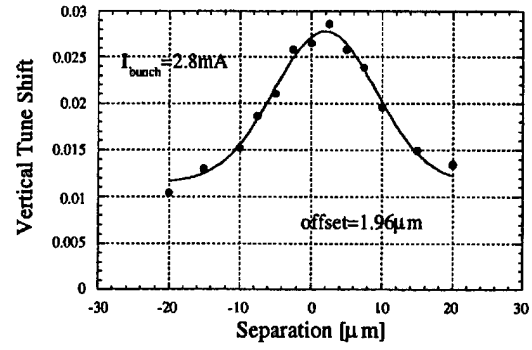


Figure 3. Measurement of the beam-beam tune shift.

to the next offset, we regarded shifts from these reference values as new position data. With this procedure, we can remove possible position offsets different for the two beams, although we found this procedure is not necessary for our experiment. In addition to the position measurements, we also measured beam-beam tune shifts for a cross check.

From the measured position data, we calculated the right hand side of equation (1). Fig. 2 shows results of the offset scans. At the very small beam current of 0.03mA, where the beam-beam effect is almost negligible, the left hand second term of (1) can be ignored and the right hand side should be equal to the offset itself created by the separators. The values obtained at the experiment is roughly equal to the offsets except around 5% disagreement. We used this measurement for calibration of orbit bump height. With high bunch currents the curves in Fig. 2 have negative slopes in a small offset region due to the beam-beam kick. However, with a large offset the beam-beam kick saturates and the slopes come back to positive due to the left hand first term of (1). The curves in Fig. 2 have some offsets in the horizontal and vertical direction in the graph. This means that the two beams have some position offset at the IP, even when the offset artificially introduced by using separators is zero. The horizontal offsets in Fig.2 correspond directly to the position offset at zero artificial offset. The vertical offsets can be attributed to the effects of the beam-beam kick at the zero artificial offset. In this study, we found that the horizontal offset at zero artificial offset is around $2\mu\text{m}$ for these values which are almost the same for there curves. This $2\mu\text{m}$ offset was also observed in the measurement of the beam-beam tune shift, the result of which is shown in Fig. 3. With the scanning method tested here, we found that we can know the position offset at the IP with an accuracy of around $1\mu\text{m}$ which is about 15% of the beam size when the beam-beam parameter is rather large.

We made further corrections for the data plotted in Fig. 2. First, orbit bump height is corrected using the measurement at 0.03mA. Second, we removed the horizontal and vertical offsets of the curves in Fig. 2. Third, beam current change during scanning was corrected. And fourth, the COD changes due to the beam-beam kick were taken into account. This correction is not very large and is about $1.5\mu\text{m}$ at maximum. The corrected data are plotted in Fig. 4. In Fig. 4, theoretical values calculated with (1) and (2) are also shown. In the calculations, we needed the horizontal and vertical beam sizes at the IP. These values were obtained also from the beam-beam tune shift mea-

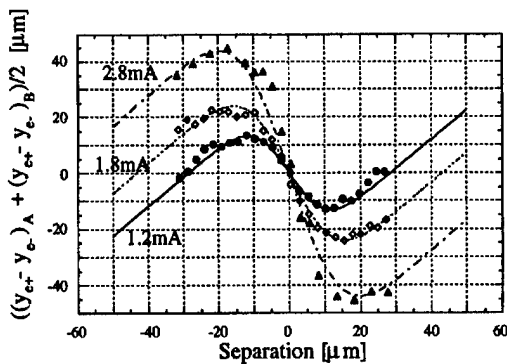


Figure 4. Beam-beam deflection data with some corrections.

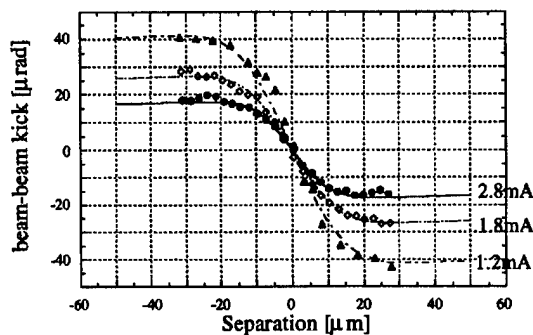


Figure 5. Beam-beam kick as function of the orbit offset.

surement. The horizontal and vertical emittance can be calculated with the beam-beam parameters. As for the beta functions, we employed the calculated values. When we translated the beam-beam tune shift values to the beam-beam parameters, we used so-called Yokoya factors, 1.33 for the horizontal direction and 1.24 for the vertical[5]. The calculated curves seem to well reproduce the measured values.

We can also see the direct relation between the orbit offset and the beam-beam kick angle by using data shown in Fig. 4. As is seen in equation (1), the beam-beam kick can be obtained by subtracting Δy_{12} from the right hand side. Fig. 5 shows the relation thus obtained. Theoretical curves are in good agreement with the measurements, which means that the Bassetti-Erskine formula gives the correct beam-beam force.

IV. CONCLUSION

We investigated feasibility of the beam-beam deflection technique in the ring collider. We tried to see if we can detect the orbit offset of the two beams which are artificially introduced with enough accuracy or not. With a pair of stripline type monitors, we could detect the orbit offset with an accuracy of $1\mu m$ or less particularly when the beam-beam parameters are rather large. Then, we think that this technique is quite feasible for the orbit feedback system of the KEKB.

V. Acknowledgements

We would like to thank A. Hutton for fruitful discussions, who at first drew our attention to this kind of experiment in the TRISTAN. We also wish to thank M. Furman, Y.H. Chin, V. Zie-

mann, N. Toge, N. Hiramatsu and K. Satoh for nice comments and discussions and K. Mori, Y. Suetsugu and K. Hanaoka for assisting with carrying out experiments.

References

- [1] P. Bambade and R. Erickson, SLAC-PUB-3979 (1986).
- [2] Y. Funakoshi, Proceedings of "The state of the art in accelerators, detectors and physics" SLAC-400 (1992).
- [3] M. Bassetti and G.A. Erskine, CERN-ISR-TH/80-06 (1980).
- [4] Y. Funakoshi, M. Tejima, H. Ishii and K. Hanaoka, Proceedings of the 9th Sympo. on Accelerator Science and Technology, 1993, Tsukuba, Japan.
- [5] K. Yokoya, Y. Funakoshi, E. Kikutani, H. Koiso and J. Urakawa, KEK Preprint 89-14(1989).

TURN-BY-TURN BEAM POSITION MEASUREMENT FOR 1.3 GeV BOOSTER SYNCHROTRON

T. S. Ueng, K. T. Hsu, C. S. Fang,
Y. M. Chang, K. K. Lin

Synchrotron Radiation Research Center, Hsinchu 300, Taiwan

Abstract

A prototype turn-by-turn beam position measurement system has been implemented to characterize machine properties of 1.3 GeV booster synchrotron at SRRC. The signals picked up by button electrodes are processed by heterodyne receivers. The output of the receiver is digitized by VXI module with digitizing rate equal to the beam revolution frequency. The beam positions are calculated at embedded VXI controller under HP/UX environment. The performance of the data acquisition system and the measured data are presented.

I. INTRODUCTION

The booster of SRRC is a 10 Hz resonance type machine [1]. The booster accelerates the 50 MeV electron beam injected from Linac to 1.3 GeV in 50 msec. Then, the beam is extracted for storage ring injection. The revolution frequency of the booster is 4.167 MHz, in terms of orbit period 240 nsec. Turn-by-turn beam positions are very important for the beam physics study. The study plan will be concentrated on the beam behavior when it is moved toward a resonant mode. The turn-by-turn beam position measurement system has been implemented recently for the booster synchrotron. The system has 500 kwords memory which can record the beam positions during the whole ramping cycle.

II. BPM ELECTRONICS

Two beam position monitors was used to measure the horizontal or the vertical beam position at current stage. The separation of these beam position monitors is chosen with phase advance near $3\pi/2$. Knowing the beta function and the phase advance between both BPMs, one can calculate the displacement and slope at one of these two BPMs. Thus, the phase space plot can be obtained [2,3].

The processing electronics is a heterodyne receivers. One BPM has two channel receivers as shown in figure 1. The signals picked up by the button electrodes are added and subtracted to obtain the horizontal or vertical beam position signal. The heterodyne receiver filters and amplifies the 500

MHz component of the bunch signal and converts it into a wide bunch signal with the frequency equal to the revolution clock. The output of receiver is sent to multichannel digitizer which is located in VXI crate. The calibration signal is fed into the electronics to measure the loss variation of hybrid junction of different channel and the gain difference of receivers. These variations between different channels are compensated by embedded controller on the VXI crate.

The turn-by-turn beam position measurement electronics can be operated with multi-bunch or single bunch mode. The multi-bunch current can be varied from 1 mA to 5 mA. The bunch train in multi-bunch mode can have different behavior for different bunches. It is not easy to define and analyze the turn-by-turn beam position of the multi-bunch mode. Hence, the turn-by-turn beam position measurement is not desirable for this operation mode. The nominal single bunch current is about 100-300 μA for the booster. The receivers have enough gain to operate in this current range. However, the S/N ratio of the receiver is lower for single bunch operation at current stage. The experiments were performed at multi-bunch mode with bunch train less than 50 nsec.

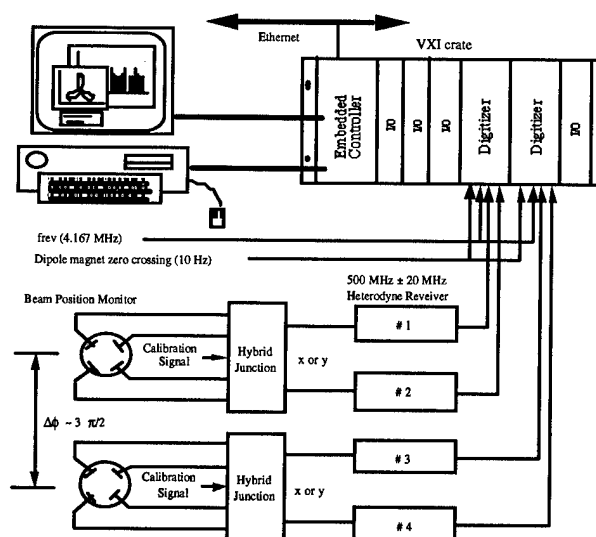


Figure 1. Hardware block diagram

III. DATA ACQUISITION SYSTEM

The data acquisition system is a VXI based system. Two dual-channel 12 bits digitizers are used to digitize bunch signal picked up by the button electrodes. VXI embedded controller is used to initialize digitizers and start the data acquisition operation. After receiving the booster injection trigger signal (10 Hz), the digitizer module starts to convert the beam signal. The acquired signals from button electrodes are filled into the memory of the digitizer with a revolution clock of the booster (4.167 MHz).

The memory depth of the digitizer is 512 Kwords. Maximum record length is about 123 msec. Since the booster has cycling period of 100 msec, the turn-by-turn beam position of the booster can be recorded for full booster cycle. The acquired raw data is normalized and the turn-by-turn beam position is computed by the VXI controller.

The VXI crate controller is a 68040 based embedded controller which running HP/UX operating system. The user interface is developed under X-Windows/Motif environment. The controller communicates with the digitizers via VXI bus by using compiled command system for programmable instruments (C-SCPI).

The raw data, the calculated beam position, the betatron tune and the phase space plot are presented on the screen in interactive basis. The experimental data can also be stored on mass storage devices for off-line analysis.

IV. PRELIMINARY RESULTS

The turn-by-turn beam position measurement system has been used to measure properties of the booster. The slow extraction scheme has been designed for the booster. The extraction system is composed of three bumper magnets, one extraction kicker and one extraction septum. The excitation of bumpers is a 2 msec half-sine pulse current. The pulse for the kicker has a 30 nsec rise time and about 250 nsec flat top width.

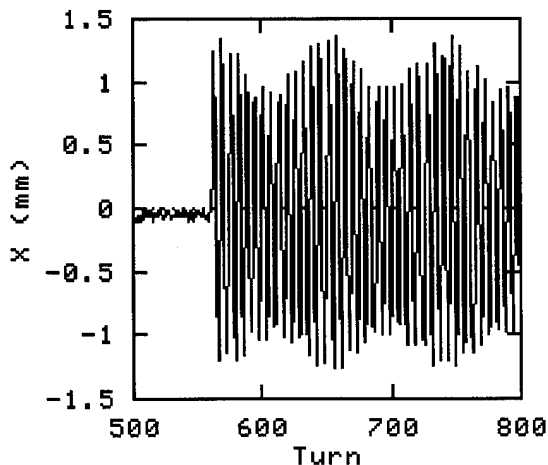


Figure 2: Turn-by-turn beam position at 1.3 GeV with 3 mrad kick

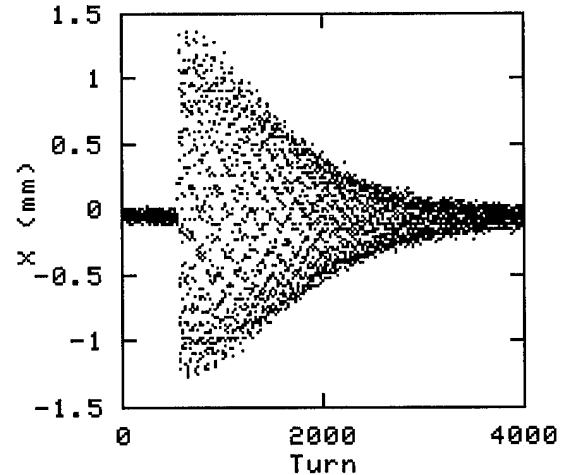


Figure 3: Turn-by-turn beam position at 1.3 GeV

The transverse motion of stored beam can be excited by the extraction kicker. The kicking strength of kicker is about 3 mrad at 1.3 GeV for the nominal extraction setting. Figure 2 shows the beam motion when a 3 mrad kick applied to the stored beam at 1.3 GeV. The coherent and the decoherent processes of the betatron oscillation are clearly observed. The damping effect of betatron oscillation can be seen in figure 3.

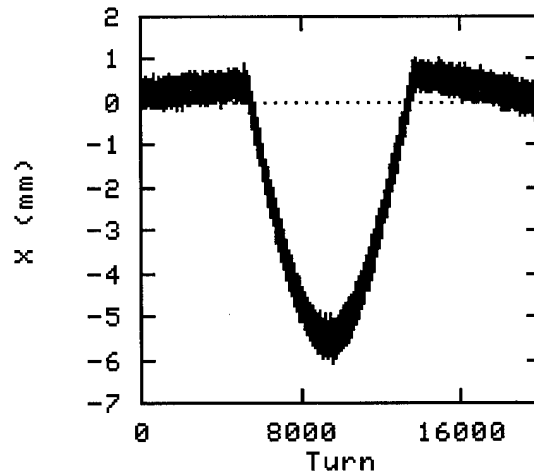


Figure 4: Turn-by-turn beam position change due to the energized of bumper #2 at 1.3 GeV

Another method to observe the disturbed beam motion is to measure the beam position under the kick by the bumper. The extraction bumpers are energized by a 2 msec half-sine pulsed current. With the bumper #2 excited at about half of its nominal strength, the turn-by-turn beam positions measured at BPM location are shown in figure 4. The phase advance between the bumper #2 and the BPM location is

5.8π . As the bumper applies a positive kick in the radial direction, the beam position at BPM is excursive toward the opposite direction.

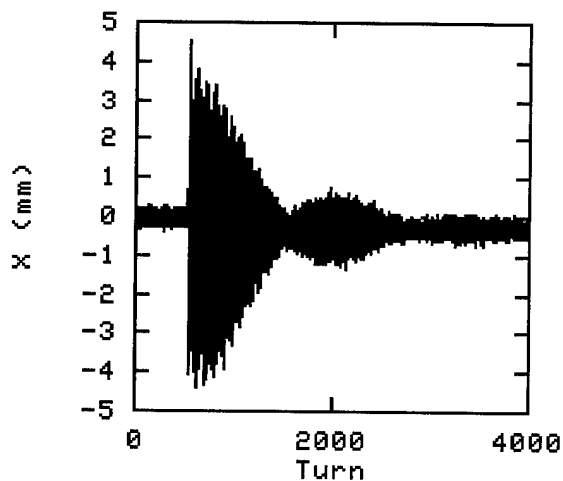


Figure 5. Turn-by-turn beam position of multibunch filling

With a longer bunch train length (> 100 nsec) the result is more complicated than that of short bunch train length. Beside the modulation of synchrotron oscillation, the beating effect during the damping period can also be observed. In figure 5 it shows clearly that the damping as well as excitation for the measurement [4].

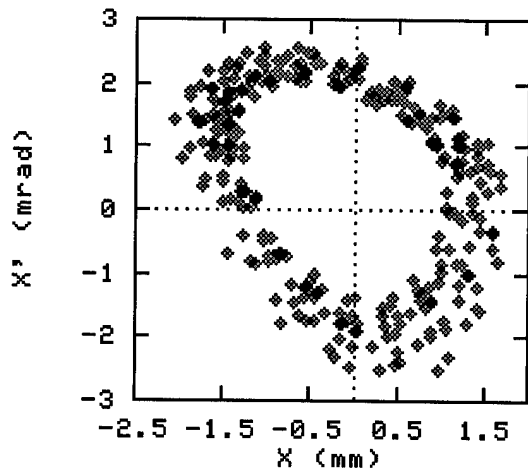


Figure 6. Phase space plot with 3 mrad kick at 1.3 GeV

Using the measured turn-by-turn beam positions at two BPM locations, the phase space plot of 300 turns with 3 mrad kick at 1.3 GeV is constructed and shown in figure 6. There is no significant nonlinearity found in the plot. The size of the ellipse is slightly reduced due to the damping effect of the electron beam.

V. SUMMARY

The prototype turn-by-turn beam position measurement system for the booster has been implemented. The system test and the preliminary experiments are in progress. The system is working for both multi-bunch and single bunch operation modes. One can excite the stored electron beam by the extraction kicker at any energy range to study the behavior of the electron beam dynamically. Upgrading this system to accommodate the sixth dimensional turn-by-turn measurement has been initialized.

VII. ACKNOWLEDGMENTS

The authors would like to thank J. P. Chiou, J. I. Huang, and S. Y. Hsu for their professional skill to operate the Linac and the booster. The help from C. H. Kuo is also appreciated.

VIII. REFERENCES

- [1] K. K. Lin, et al., "Performance of SRRC 1.3 GeV electron booster synchrotron", to be published in Nuclear Instruments and Methods in Physics Research, Section A, 1995.
- [2] E. Crosbie et al., "Non-linear resonance studies at the synchrotron radiation center, Stoughton, Wisconsin", Proceedings of the Particle Accelerator Conference, PAC'91, San Francisco, CA, 1624 (1992).
- [3] J. Liu et al., "Difference resonance study on the electron storage ring Aladdin at SRC", Part. Accel. 41, 1 (1993).
- [4] M. Schürmann, "Preparation of an experiment to investigate nonlinear beam dynamics at the storage ring DELTA", Particle Accelerator Conference PAC'93, 264 (1993).

BEAM POSITION MONITOR FOR THE LNLS UVX SYNCHROTRON LIGHT SOURCE

F.S. Rafael and E. K. C.S. Hayashi, Laboratório Nacional de Luz Síncrotron, Caixa Postal 6192, Campinas, SP 13081-970 Brazil

The beam orbit measuring system for the LNLS UVX ring is presented. The system consists of 24 strip-line beam position monitors and associated electronics. The beam position monitors (BPM's) are capable of detecting down to 10 mA of stored beam current or 100 ns-long LINAC injection pulses (single pulse detection mode) with 0.05 mm resolution. Acquisition electronics is divided into two parts: four fast-acquisition channels for the pulsed mode operation (used during injection) and a single PIN-switch multiplexed channel for CW operation (closed orbit measurement). Experimental results obtained on a characterization bench are presented and compared with theoretical estimates.

I. INTRODUCTION

The LNLS is building a 1.15 GeV electron storage ring. The injector is a 100 MeV, traveling wave LINAC and the RF frequency is 476.000 MHz when accelerated up to final energy. One of important parts of the diagnostic system is the BPM, which is used to measure two important machine characteristics: the path of the pulsed beam during injection and closed orbit in the normal operation modes. These two different requirements led us to construct two separate electronics. Both electronics are discussed in this paper, along with the mechanical characteristics. The main parameters of the LNLS BPM are listed in Table 1

Parameters	Minimum	Maximum	units
Beam current	2	200	mA
Horizontal range	-20	20	mm
Vertical range	-20	20	mm
Resolution	< 0.050		mm
Accuracy	< 0.050		mm
Harmonic frequency	476.000		MHz
LO Frequency	466.000		MHz
Acquisition rate	500		Hz
Pulsed mode			
Pulse length	100	-	ns
Acquisition rate	-	100	Hz

Table 1 - LNLS beam position monitors parameters

II. MECHANICAL CHARACTERISTICS

The BPM is made up of four cylindrical strip-lines of 45° with respect to plane of orbit to avoid synchrotron radiation. The inner diameter is the same as the ring vacuum chamber diameter as is shown schematically in Figure 1. The pick-up length is a compromise between the desired sensibility to measure the pulsed beam from the LINAC and the available physical space.

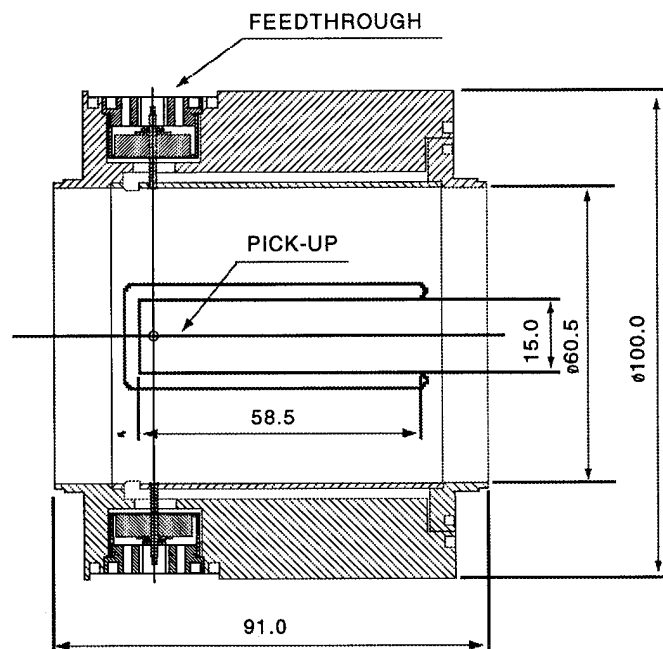


Figure 1a - BPM schematic drawing

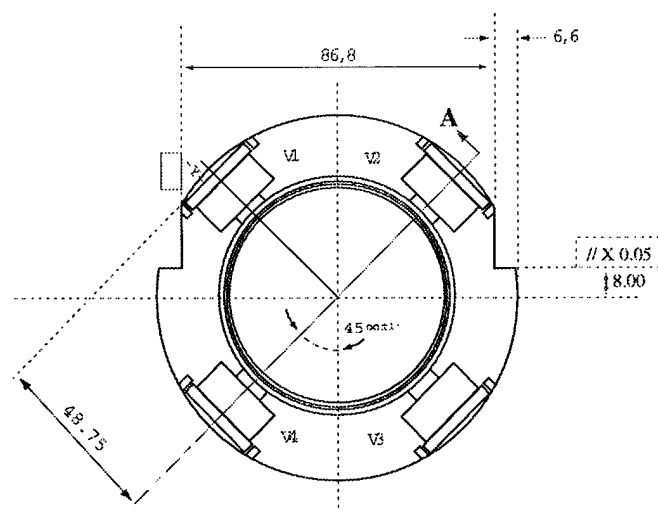


Figure 1b - BPM schematic drawing

The pick-up signals are collected by means of special bakable, vacuum compatible, 50 Ω male-SMA feed-throughs. The feed-throughs are made of stainless steel in order avoid damage after a standard brass SMA-female has been connected to it many times. The feed-through drawing is showing in Figure 2.

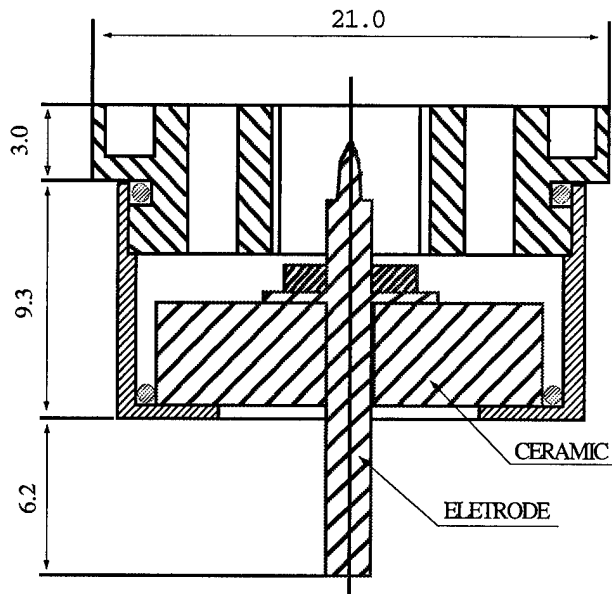


Figure 2 - BPM schematic drawing

III. CHARACTERIZATION BENCH

The characterization bench was specially constructed to move an RF antenna inside the BPM. The maximum resolution is 5 μm in both axes X and Y, and movements are possible using two stepper-motors. The schematic drawing is shown in Figure 3. To minimize electromagnetic interference the bench was placed inside of a shielding box.

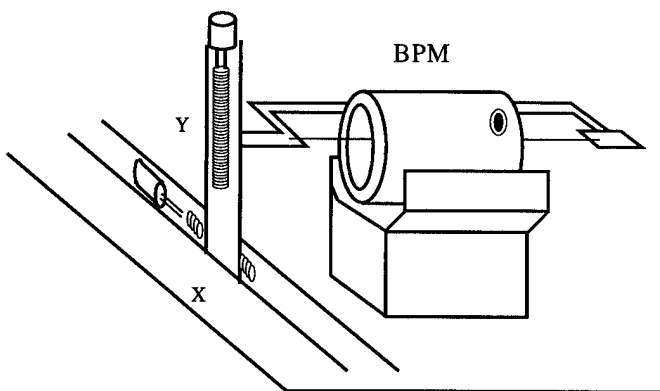


Figure 3 - Characterization bench

In order to detect mechanical zero, a DC voltage is applied to the antenna and the stepper-motors are used to displace the antenna along the horizontal and vertical axes, until it touches either side of the detector's wall. The accuracy of this procedure is limited by the accuracy of the digital rule (0.005 mm) used to determine the position of the antenna. Four semi-rigid 0.141" standard coaxial cables, transfer the signal from the pick-ups to the electronics.

IV. ACQUISITION ELECTRONICS

The RF signals from the pick-ups are equalized separately using 3 dB on-board attenuators and PIN-switches (part number MSWA-2-20, Mini-Circuits) which operate up to 1 GHz with 1.2 dB attenuation @ 500 MHz.

The BPM electronics for the pulse mode operation consists of four fast-acquisition channels. All signals from the switches are selected and amplified simultaneously in four wide-band amplifier, and the pulse recovered by an integrator. A track-hold and a sample-hold circuit, working in conjunction, convert the pulse into a proportional DC signal. The BPM electronic block diagram is shown in Figure 4. This circuit is able to operate, synchronized with the same clock, and at the maximum LINAC repetition rate (30 Hz).

The closed orbit measurement (CW operation) uses a different circuit. The topology adopted is a super-heterodyne tuner with conventional detection. This circuit delivers the X,Y and sums signal (rather than merely four signals proportional to the voltages induced on the antennas) for further processing by a computer. This approach allows shorter acquisition time.

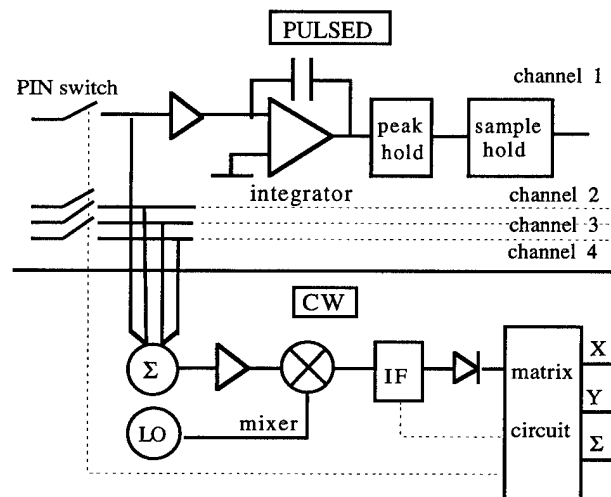


Figure 4 - Electronic block diagram

V. MEASUREMENT RESULTS

Figure 5 shows the absolute value of the measured impedance of a single pick-up as a function of frequency.

$$Z_{pu}(\omega) = \frac{V_{pu}(\omega)}{I(\omega)}$$

Were, $V_{pu}(\omega)$ is the voltage on the antenna and $I(\omega)$ the excitation current. The theoretical value is also shown.

$$|Z_{pu}(\omega)| = \frac{\psi_0}{\pi} \frac{Z_0}{2} \sin\left(\frac{\omega L}{c}\right)$$

Were ψ_0 is half of the angle of the strip-line, Z_0 is strip-line impedance and L the strip-line length.

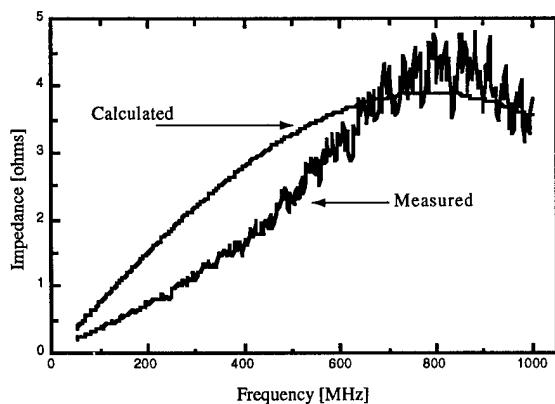


Figure 5 - Impedance response

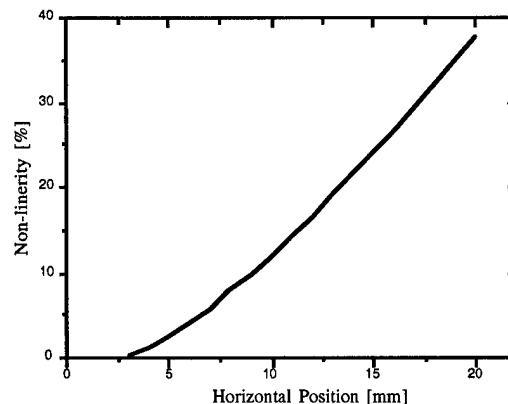


Figure 7 - Non-linearity mapping

The Figure 6 shows the contour lines of functions:

$$V_x(x, y) = \frac{V_2 + V_4 - V_1 - V_3}{V_1 + V_2 + V_3 + V_4}$$

$$V_y(x, y) = \frac{V_1 + V_2 - V_3 - V_4}{V_1 + V_2 + V_3 + V_4}$$

Where V_1 , V_2 , V_3 and V_4 are the voltages induced in the pick-up antennas as shown in the Figure 1 a. These functions were obtained by means of a two-dimensional spline fit to a grid of measured points (step size = 5 mm).

VI. Conclusion

The measurements made in the BPM system constructed at LNLS, show the ability to measure the closed orbit at the desired accuracy. The resolution of the electronic system can be increased for a smaller working region, just by changing the gain of the matrix circuit in the output stage. The non-linearity will be compensated by means of pre-mapping of the monitor cavity as shown before, where the polynomial coefficients, necessary to solve the position equations in the computers were obtained.

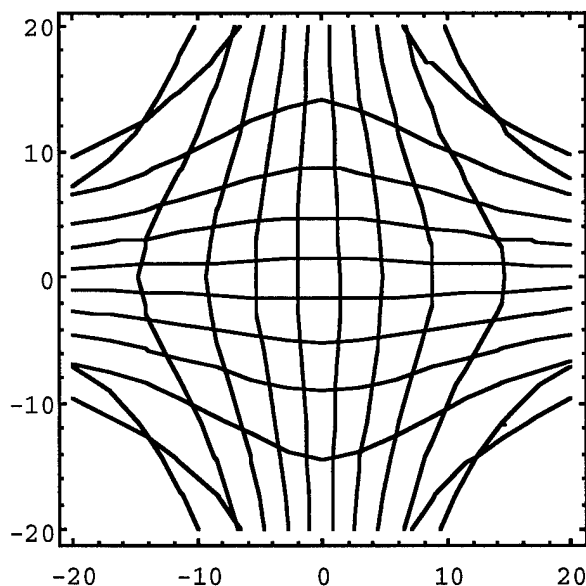


Figure 6 - BPM calibration mapping, showing the relation $(x,y)/(v_x, v_y)$ in an area of 40 X 40 mm

Figure 7 shows the relative deviation (respect straight line) of the horizontal $V_x(x,0)$ as function of position inside the monitors. The graphic shows one side of the monitor in the X direction, and the same is observed in other directions.

Transition Radiation Electron Beam Diagnostic Study At ATF*

X.Z. Qiu, X.J. Wang, K. Batchelor and I. Ben-Zvi National Synchrotron Light Source, Brookhaven National Laboratory Upton, N.Y., 11973

Abstract

Recently we have started a program to develop transition radiation based electron beam diagnostics at the Accelerator Test Facility at Brookhaven National Laboratory. In this paper, we will discuss a technique to estimate the lower limit in electron beam divergence measurement with single foil transition radiation and two-foil transition radiation interferometer. Preliminary experimental data from 4.5 MeV electron beam will be presented.

I. Introduction

Transition radiation occurs when a charged particle crosses the boundary between two media with different dielectric constants. It was first predicted by Ginzburg and Frank in 1946.[1] The first experimental observation of transition radiation was reported in 1959 by Goldsmith and Jelley.[2] Since then, a significant amount of research have been done on transition radiation both experimentally and theoretically.[3]

Because of the strong dependence of transition radiation on the properties of the radiating particle, it is possible to use transition radiation for charge particle beam diagnostics.

In this paper, we will first review the basic physics of transition radiation from a single foil and a two-foil interferometer.

We will then estimate the resolution limit when using transition radiation to measure the divergence of a charged particle beam.

Finally, some preliminary result of transition radiation for 4.5 MeV electrons from the BNL/ATF photocathode injector is presented.

II. Basic theory of optical transition radiation

Transition radiation occurs when a charged particle crosses the boundary of two medium with different dielectric constant.

When a particle with charged e enters a medium from vacuum at 45° incident angle, there will be transition radiation around the direction of specular reflection (backward radiation). Assume $|\epsilon - 1| \gg \gamma^{-2}$, where ϵ is the index of refraction of the medium, the angular intensity distribution in the plane of incidence is given by,[4]

$$\frac{d^2 I}{d\omega d\Omega} = \frac{e^2}{\pi^2 c} \frac{\theta^2}{(\gamma^{-2} + \theta^2)^2} \quad (1)$$

where γ is the Lorentz factor and θ is the angle between the observation direction and the direction of specular reflection.

In the two-foil transition radiation interferometer configuration as shown in Fig.1.

*This manuscript has been authored under contract number DE-AC02-76CH00016 with the U.S. Department of Energy. Accordingly, the U.S. Government retains a non-exclusive, royalty-free license to publish or reproduce the published form of this contribution, or allow others to do so, for U.S. Government purposes.

The forward radiation created when the particle crosses the first foil will interfere with the backward radiation from the second foil, the angular intensity distribution is given by,[4]

$$\frac{d^2 I}{d\omega d\Omega} = \frac{e^2}{\pi^2 c} \frac{\theta^2}{(\gamma^{-2} + \theta^2)^2} \sin^2 \left[\frac{\pi L}{2\lambda} (\gamma^{-2} + \theta^2) \right] \quad (2)$$

where L is the spacing between the foils.

If the transition radiation is created by an ensemble of particles, the angular distribution will be smeared. The divergence of the charged particle beam can be measured by looking at the smearing of the distribution. The divergence can also be measured by looking at the smearing of the spectral distribution at a fixed observation angle. This is called transition radiation spectrometer.[3]

III. Resolution of divergence measurement with transition radiation

The resolution for beam divergence measurement is determined by many factors, for example, the resolution of the detection system and the energy spread of the beam.

For angle $\theta \ll \theta_m$, where $\theta_m = \gamma^{-1}$, the relative intensity varies as,

$$\frac{I(\theta)}{I(\theta_m)} \approx \frac{(\theta\gamma)^2}{4} \quad (3)$$

Assume that our detection system has an intensity resolution of η , then the resolution in divergence due to detection system is,

$$\theta_{min} \approx \sqrt{4\eta} \frac{1}{\gamma} \quad (4)$$

For a 8-bit detection system,

$$\theta_{min} \approx 12.5\% \frac{1}{\gamma} \quad (5)$$

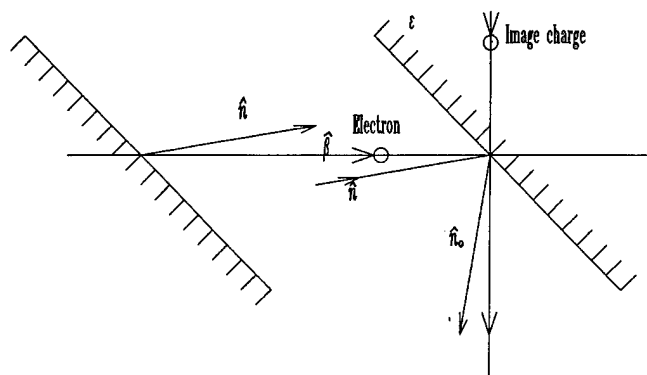


Figure 1. An OTR two-foil interferometer

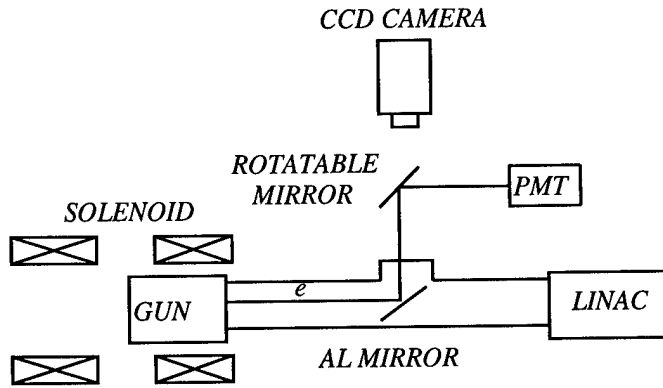


Figure 2. Experimental setup to measure OTR from Low energy electron

The analysis appears to be consistent with the experiment result for single foil transition by Fiorito and Rule.[3] They conclude that beam divergence of the order of 15% of $\theta_m \sim 1/\gamma$ could be measured.

Similar analysis can be performed for two-foil interferometer. We assume the divergence of the beam is a lot smaller than $1/\gamma$ and the observation angle is about $1/\gamma$. We have

$$\theta_{min} \approx \sqrt{\eta} \frac{\gamma \lambda}{\pi L} \quad (6)$$

If we express the inter-foil distance in unit of the formation zone length along the path of the centroid particle,

$$L = k \frac{\lambda \gamma^2}{\pi} \quad (7)$$

where k is a real number. Then,

$$\theta_{min} \approx \frac{\sqrt{\eta}}{k} \frac{1}{\gamma} \quad (8)$$

In principle, an arbitrarily low divergence can be measured by increasing the inter-foil distance. However, as L increases, the spacing between interference maxima and minima will decrease and the resolution of the measurement will be limited by angular resolution.

The resolution in divergence for transition radiation spectrometer should be the same as transition radiation interferometer for the same inter-foil spacing.

Caution has to be taken when choosing the first foil. The thickness has to be chosen in such a way that the change in divergence due to scattering of the particles while the beam passing through the foil is a lot smaller than the intrinsic divergence of the beam.

When very thin foils are used, one still tends to estimate the scattering with formulas for multiple scattering. However, when the average number of scatterings for each passing particle Ω [5] is less than 20, these formulas can no longer be applied. For example, for $1 \mu\text{m}$ thick carbon foil, Ω is only about 2. The region in which $20 \leq \Omega \leq 1$ is called plural scattering. Very little literature is available about this region. Further investigation is needed.

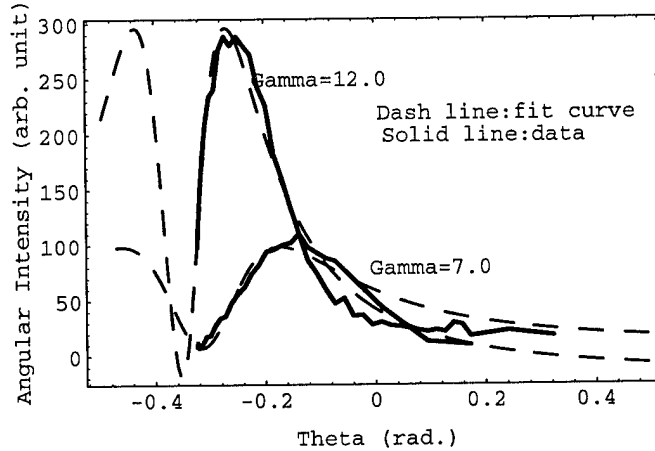


Figure 3. OTR angular distributions with two different RF level of the gun

IV. Experimental result for low energy electron

The Accelerator Test Facility (ATF) at BNL is a users' facility for experiments in accelerator and beam physics. It is equipped with a high brightness photocathode RF-gun, two SLAC linac sections, high-power picosecond pulse lasers. Recently, a new injector was installed to minimize the emittance growth due to spacing charge.

As shown in Fig.2, an aluminum mirror was placed after the electron gun in the path of the electron. A rotatable mirror is placed above the glass window to reflect the transition radiation light into a photo-multiplier tube for detection. The angular distribution of the transition radiation is measured by rotating the mirror.

The angular distributions of transition radiation from electrons produced at two different RF level of the gun is shown in Fig.3. Due to the aperture of the glass window, only one of the two lobes is observed. The data is fitted with (1) to obtain the energy of the electron.

A CCD camera is placed above the window to observe the image of the electron beam. The deflection mirror is rotated to such a position that it would not block the view of the camera. One of the electron beam images is shown in Fig.4. In Fig.5, the density distribution along the vertical and horizontal center lines are plotted.

V. Conclusion

We have estimated the resolution of OTR used to measure the divergence of charged particle beam in terms of the resolution of the detection system. Results of transition radiation from electrons of a few MeV are presented.

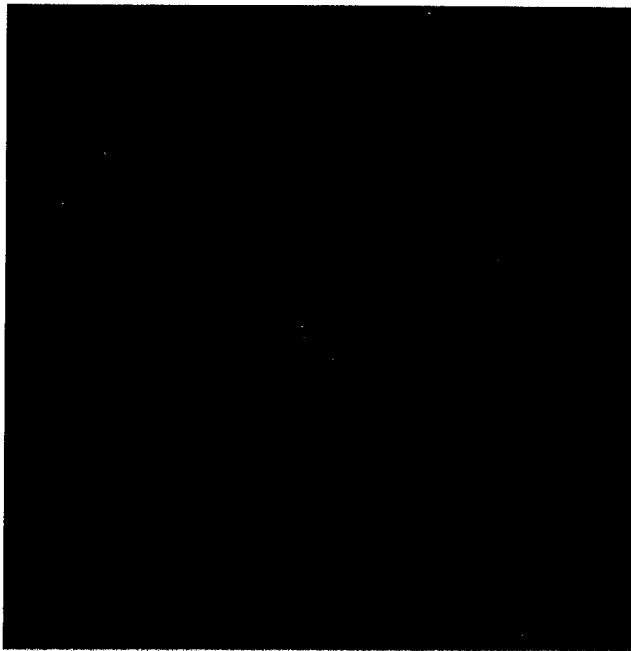


Figure. 4. Distribution of the electron beam density along the center lines

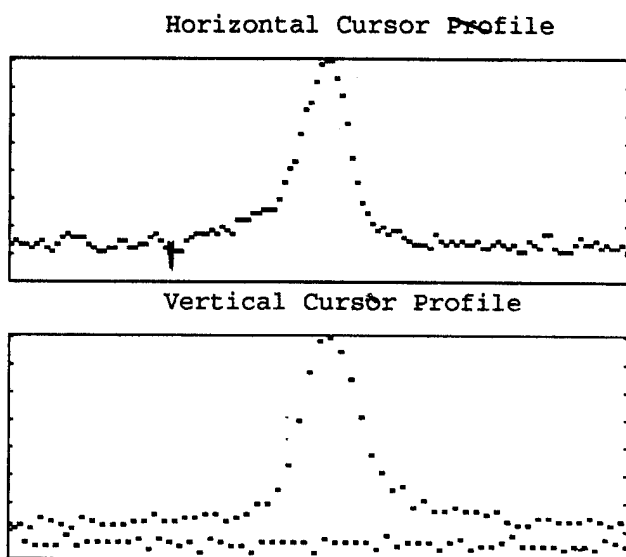


Figure. 5. An image of the electron beam obtained from OTR

VI. Acknowledgements

The authors wish to thank Dr. R. Fernow for providing helpful references on the physics of transition radiation and the entire ATF staff for their continuous support.

References

- [1] V.L. Ginzburg and I.M. Frank, Zh. Exp. Teor. Fiz; **16**, 15 (1946)
- [2] P. Goldsmith and J.V. Jelley, Philosophical Magazine; **4**, 836 (1959)
- [3] R. Fiorito and D. Rule, AIP Conference Proceeding, No.319 (1993)
- [4] L. Wartski, S. Roland, J. Lasalle, M. Bolore, J. Appl. Phys. **46**, 3644(1975)
- [5] G. Lynch and O. Danl, Nucl. Instr. And Meth. **B58**, 6(1991)

MACHINE PARAMETER MEASUREMENT OF THE AMSTERDAM PULSE STRETCHER AmPS

Y. Y. Wu and R. Maas, National Institute for Nuclear and High Energy Physics (NIKHEF),
P.O. Box 41882, 1009 DB Amsterdam, The Netherlands.

Machine parameters (β -functions) have been measured by successively wobbling all the ring quads and observing the subsequent tune changes. As a result a better quadrupole setting has been obtained.

I. INTRODUCTION

The electron pulse stretcher/storage ring AmPS is operational since 1991 [1-3]. Its maximum energy is 800 MeV. The machine routinely delivers extracted beam currents of up to 10 μ A, with a duty factor in excess of 70 %.

In Storage Mode the circulating beam is used in conjunction with an (internal) gas-jet target. By employing beam stacking, stored beam currents of typically 100 mA are accumulated.

The lattice consists of 4 achromatic Curves (each of 21 m length), connected by Straight Sections of 32 m length. In each Curve there are two families of quads; the corresponding quadrupole groups of all four Curves are connected to one common power supply. The quads in the Straight Sections are grouped in pairs (4 per Straight). This set-up, therefore, does not allow the individual control of each of the 68 quadrupoles, necessary to measure the β -functions, see below. In order to be able to vary each quadrupole field by a few percent, each quadrupole has been shunted by a relay-activated resistor ($R_{\text{shunt}}/R_{\text{quad}} = 5\%$).

II. THEORY

A. The concept of the measurement

A gradient error ΔK in a ring quadrupole will cause a betatron tune shift [4]:

$$\Delta v_z = \frac{-1}{4\pi} \int \beta_z(s) \Delta K_z(s) ds, \quad z = x, y \quad (1)$$

Since the betatron function $\beta(s)$ is approximately constant over the length of the quadrupole, (1) can be approximated by:

$$\Delta v_z \approx (-1/4\pi) \beta_z l_q \Delta K_z, \quad z = x, y$$

l_q is the (effective) length of the quadrupole. Thus

$$\beta_z \approx -4\pi \Delta v_z / l_q \Delta K_z, \quad z = x, y \quad (2)$$

In practice, ΔK can be generated by wobbling the quadrupole; by measuring the tune shift Δv , the value of the β -function at the quad location is calculated from (2).

B. The measurement method

The betatron tune is measured by FFT-analysis (using a LeCroy 9450A scope) of a signal from one of the stripline (beam position) monitors. In order to generate a signal, the stored beam is perturbed by a kick (typically 0.2 mrad) administered by an electrostatic fast-kicker ($\tau \sim 500$ ns) [5]. Each measurement consists of two tune measurements: one reference tune measurement, and a measurement when one particular quadrupole shunt is activated (generating $|\Delta K| = 5\%$) – thus eliminating accumulative hysteresis effects of the quads on the tune. This procedure has been carried out for all 68 quadrupoles, and for both transverse planes.

C. Measurement errors

The measurement error of the machine function consists of two parts:

$$\delta\beta / \beta = \delta(\Delta v) / \Delta v + \delta(\Delta K) / (\Delta K) \quad (3)$$

The first term in (3) is the contribution of the tune measurement. The fractional part of the betatron tune is calculated as $v = f/f_r$, with f_r the revolution frequency (1.41 MHz), and f the FFT-analysed signal from a stripline monitor. So,

$$\Delta v = (f_0 - f_{\text{wob}}) / f_r = \Delta f / f_r \quad (4)$$

Here f_{wob} is the frequency when the quadrupole is wobbled, and f_0 is the frequency before wobbling the quadrupole. 20,000 samples were taken for the FFT analysis. The read-out error of the frequency is ~ 1 kHz. The contribution to the measurement error from the tune shift Δv is therefore less than a few percent.

The second term in (3) is the contribution from the uncertainty in the value of the quadrupole shunt resistor. This error is estimated to be about 5%.

The total measurement error of the machine function, therefore, is expected to be within 10%.

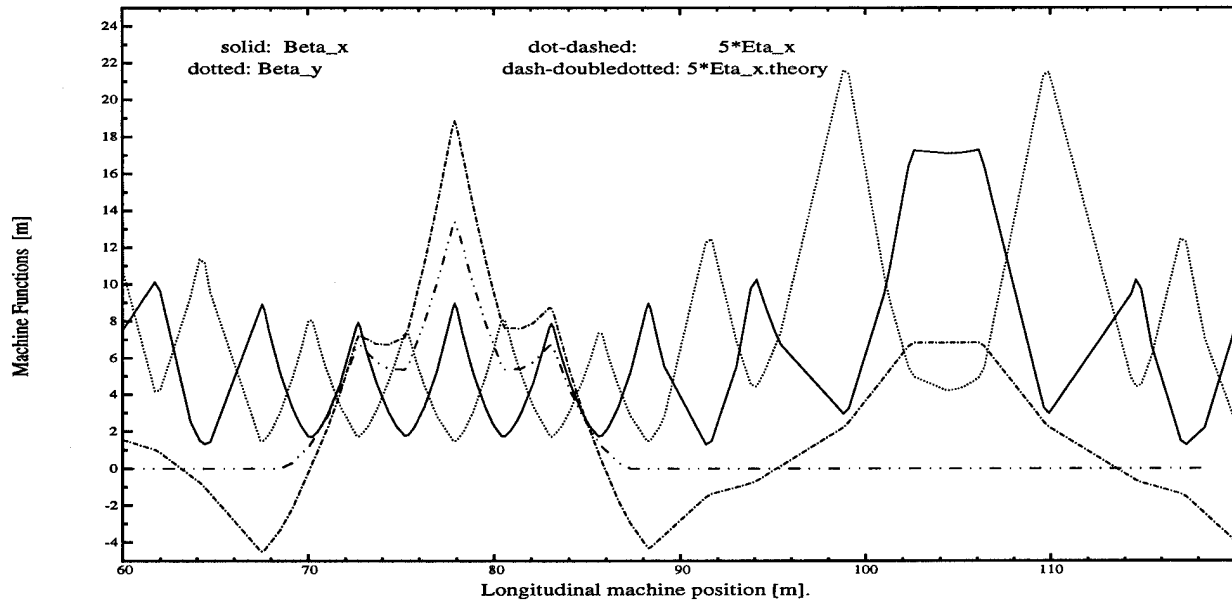


Figure 1: Machine functions for $\Delta v_x = -0.174$ and $\Delta v_y = +0.007$; the tune change is generated by the quadrupoles in the Curved Sections only.

III. OPERATION OF AmPS

When AmPS operates in Stretcher Mode, the horizontal tune is chosen to be close to the third-integer resonance value: $v_x = 8.30$. Past experience showed that the nominal setting of the machine produced a horizontal tune value that deviated substantially from its theoretical value: $\Delta v_x = +0.17$. No such effects were observed for the vertical tune: $\Delta v_y = \sim 0.0$ (these effects occur in both optical modes: Stretcher Mode and Storage Mode).

Simulations show that when *all* quadrupoles are offset by +1.5%, the ensuing tune effects are $\Delta v_x = +0.15$ and $\Delta v_y = +0.14$. Since field integrals of only samples of the quadrupoles have been measured (as opposite of harmonic content, which has been measured [6,7] for all quadrupoles and sextupoles), overall-errors of this magnitude can not entirely be ruled out. Why mainly the horizontal tune deviates from its theoretical value is as yet unclear.

Tune control in AmPS is accomplished by the quads in the Curves only: for small (e.g. $\Delta v \sim 0.015$) variations this method works fine. However, substantial machine function perturbations may occur when one tries to correct the tune deviations mentioned above, see Fig.1: this figure shows β_x , β_y and η_x in case $\Delta v_x = -0.174$ and $\Delta v_y = +0.007$, starting from the 'theoretical' machine setting. In this case the horizontally-focusing quadrupole strength in the Curves has to be reduced by appr. 3%. It

is clearly shown that this procedure can yield non-negligible dispersion values in the Straight Sections. The change in the values of the β -functions is actually much less (e.g. $\Delta \beta_x / \beta_x^{\text{theor}} \approx 5\%$).

IV. MEASUREMENT PROCEDURE

Since the tune shift occurs in both optical modes, the actual measurements have been performed in Storage Mode ($v_x = 8.43$; $v_y = 7.23$). Machine functions have been measured for 5 different sets of quadrupole settings; all these settings produced the 'theoretical' tune values. The details of the 5 sets are summarised in Table 1 (qsh/v are quads in the Straight Sections, qch/v are quads in the Curves).

Table 1 Five data sets used to measure β -functions. Each data set yielded $v_x = 8.43$ and $v_y = 7.23$.

quad	data sets; $\Delta B(q)$ [%]				
	# 1	# 2	# 3	# 4	# 5
qsh	—	-2.0	-1.0	-2.0	-2.0
qsv	—	-1.0	-1.0	-1.0	-1.0
qch	-4.3	-1.1	-1.5	-3.0	-2.3
qcv	-2.1	0.1	0.6	-2.0	-0.3

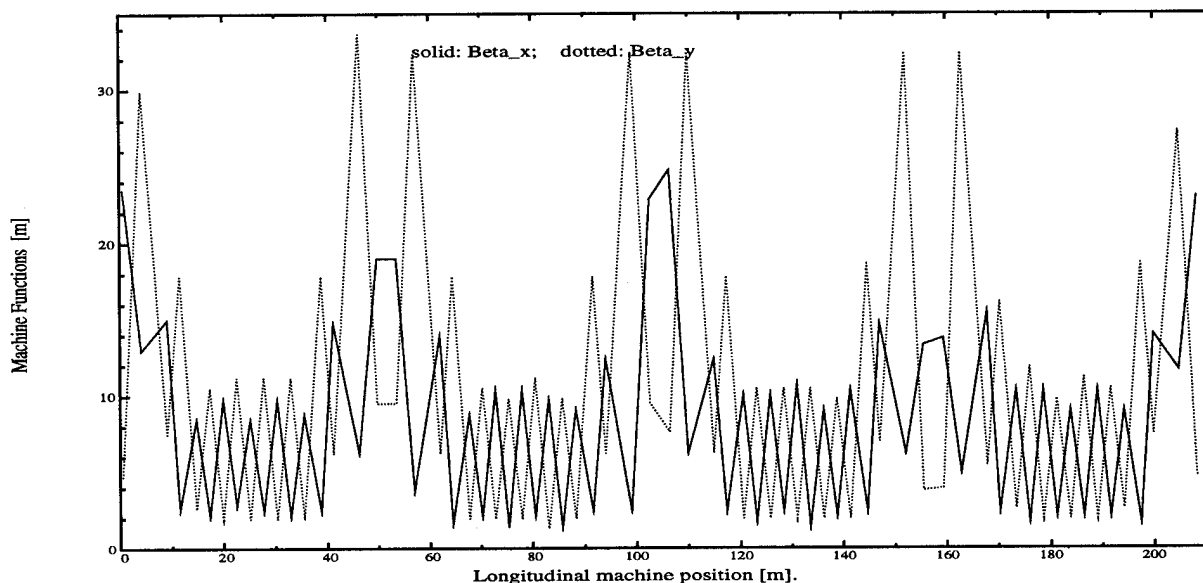


Figure 2: Result of machine function measurement for data set # 2, see Table 1.

Analysis of the results was off-line, so it was not possible to interactively change the settings. Data set # 2 produced the best results, especially with regards to the behaviour of β_x and β_y in the Curves, see Fig. 2.

V. CONCLUSION

Measurement of the machine functions has resulted in a new calibration for the quadrupole settings; with this new setting both the tunes and the machine functions (in both Storage Mode and Stretcher Mode) are now close to their theoretical values.

VI. REFERENCES

- [1] R. Maas and Y.Y. Wu, "Optics of the Amsterdam Pulse Stretcher (AmPS)", Proc. of the IEEE Part. Acc. Conf., Chicago 1989, March 20-23, pp 1698-1700.
- [2] G. Luijckx e.a., "The Amsterdam Pulse Stretcher project (AmPS)", Proc. of the IEEE Part. Acc. Conf., Chicago 1989, March 20-23, pp 46-48.
- [3] G. Luijckx e.a., "The AmPS ring: Actual Performance and Future Plans", this conference.
- [4] M. Sands, "The Physics of Electron Storage Rings", SLAC-121.
- [5] J.G. Noomen e.a., "Beam Diagnostics at the Amsterdam Pulse Stretcher AmPS", this conference.
- [6] H. Boer Rookhuizen e.a., "Magnetic Devices of the Amsterdam Pulse Stretcher Ring AmPS, Proc. of the IEEE Part. Acc. Conf., San Francisco, 1991, pp 2366-2368.
- [7] Y. Wu e.a., "Parametrization of AmPS magnets for the control system", Proc. of the IEEE Part. Acc. Conf., Washington, 1993, pp 1901-1902.

Wire Setup Calibration of Beam Position Monitors

D. Wang, B. Binns, M. Kogan, A. Zolfaghari
Massachusetts Institute of Technology
Bates Linear Accelerator Center
Middleton, MA 01949, USA

ABSTRACT

Many button type and strip line type beam position monitors are employed in the South Hall Ring (SHR) at MIT-Bates. It is desired to calibrate and routinely check the readouts of those monitors by simulating the beam. A wire setup was built to serve this purpose. It consists of a button type beam position monitor body with a wire running through it. To eliminate end-effects both ends are extended with 10 inch long uniform beam pipes. RF matching is carefully performed with ECCOSORB AN 75 microwave absorber forms. The wire is positioned 3 mm offset with respect to the X-pair buttons and symmetric with respect to the Y-pair buttons. Thus the same setup can be used to check both sensitivity and zero-offset.

INTRODUCTION

A number of stripline and button beam position monitors are used in the SHR. The readouts of those beam position monitors change due to zero-drifting of electronic circuits (thermal and/or aging), radiation effects on electronic components, inadequately matched 3-dB hybrids, cable bends, etc., To get reliable data, it is necessary to perform periodic field calibrations and routinely check the zero-offsets and sensitivities of those beam position monitor electronics using rf to simulate the beam.

The normal rf test of the electronics does not calibrate the entire system. We have built a calibration setup with an actual beam position monitor and a wire, excited by rf, to actively simulate the beam.

The SHR is a 0.3-1 GeV, multi-bunch (containing 1812 buckets) electron beam storage ring[1]. The rf frequency of the ring is equal to the rf frequency of the linear accelerator, that is 2856 MHz. Consequently, all beam position monitors operate on this frequency[2][3].

The setup is basically straight forward: a wire running through a button type beam position monitor. The beam position

monitor is stimulated through the wire by a 2856 MHz rf source. The displacement of the wire is a simulation of the beam in an offset position.

DESCRIPTION OF THE FIXTURE

The construction of the wire setup is shown in Fig. 1. The fixture consists of a button type beam position monitor body with 25 cm long uniform extension pipes at both ends. The inner diameter of the monitor and pipes is 60 mm. The function of these pipes is to eliminate the end-effects (local modes' effects). A wire with diameter of 0.5 mm runs through the beam position monitor and the uniform pipes with a displacement of 3 mm from the axial center in the horizontal plane. The wire is tightly stretched to minimize sag and vibration. A dielectric plate with a clearance hole is at both ends to assure good alignment.

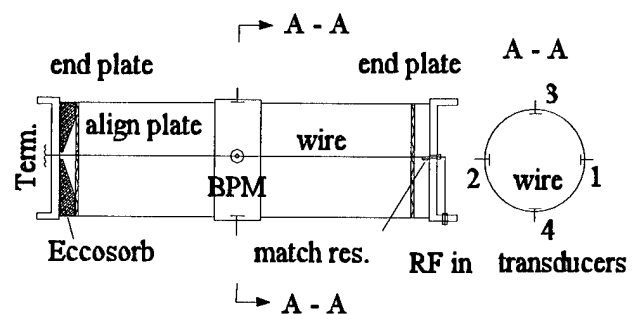


Fig. 1 Construction of the wire setup

An SMA bulkhead feedthrough jack receptacle is mounted on each end-plate, and the wire is soldered to the inner conductor of the SMA bulkhead. One end is the rf input, the other end is terminated with an rf terminator. Because the characteristic impedance of the wire-pipe system is $60 \ln(30/0.5) = 287 \Omega$, parallel and serial resistance matching is needed in order to match

to the outside 50 Ω system. Also, we placed some microwave absorber forms, ECCOSORB AN 75, inside to further improve matching.

RF RELATED CONSIDERATIONS

The beam position monitor rf signal processing block diagram is shown in Fig. 2. The beam induced signals on the transducer pairs (horizontal and vertical) are transmitted to the 90° hybrids. The amplitude difference of these pairs of beam induced signals, which is a function of beam position, is converted to a phase difference by the 90° hybrids. The electronics box processes this phase difference information. The output of the phase detector, which is transmitted to the Central Control Room, is the measurement of the beam position.

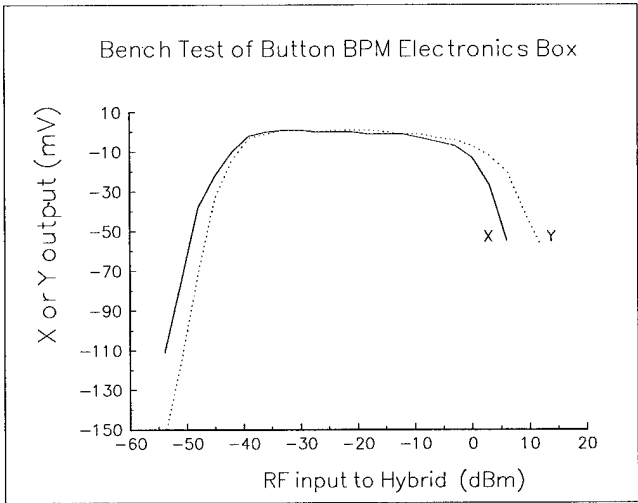


Fig. 3 Dynamic range of the BPM electronics circuit

After the fixture was built we measured the transition, S_{21} , of this wire setup from the input (rf stimulating port) to the output (BPM pickup), which was around -50 dB. Thus, the stimulating rf signal power level should be within the range of 10 dBm to 50 dBm. We set the stimulating rf power level at about 20 dBm, which is easily available.

BENCH TEST AND FIELD OPERATION

To investigate the overall response of the beam position monitor to the displacements of the wire, we did bench measurements using a HP8510B Network Analyzer. Table 1 shows the results.

Table 1: Bench measurements of position sensitivity

displacement of wire (mm)	signal diff. on pair-transducers(dB)	phase diff. converted after hybrid (°)
3	3.7	23.4
6	7.2	43.0
9	10.7	57.1
12	15.4	70.5
15	19.2	77.8

From Table 1 we can see that over the range of half radius of the beam pipe, 1 mm displacement of the wire corresponds with 1.23 dB on average.

One of the advantages of the wire setup calibration over the normal electrical-zeroing by using rf only is that you can

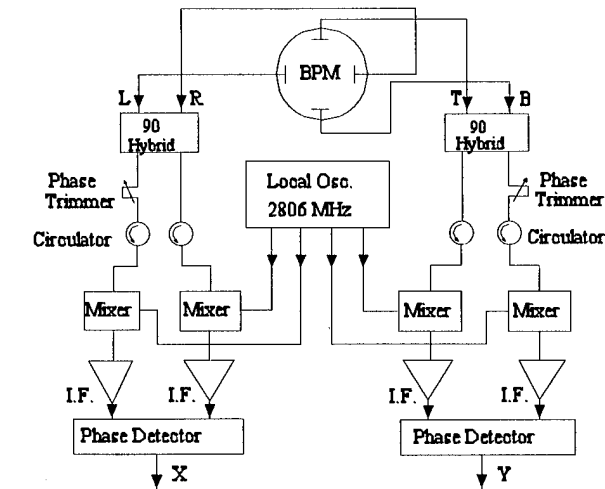


Fig. 2 BPM electronics block diagram

A very important characteristic of the system is the dynamic range, which is determined by the mixers used in the circuits (Mini-Circuits ZEM-4300MH). From the bench measurements, shown in Fig. 3, we note the following: when the rf signal power level to the hybrid is within the range of -40 dBm to 0 dBm, the output of the electronics circuit is only dependent on the phase difference of the input signals to the mixers, and independent of signal amplitude. In other words, the beam position information will not be deteriorated by the beam intensity if the beam induced rf signal power level transmitted to these hybrids is within the above mentioned range.

determine if the signal polarity is correct. For example, in our case we want a positive signal when the beam (wire) goes right or up, and negative when the beam (wire) goes left or down.

Because the wire is positioned 3 mm off center with respect to the horizontal (X) transducers and approximately centered with respect to the vertical (Y) transducers, by swapping X and Y connections we obtain both the sensitivity and the zero-offset of the beam position monitor electronics box under test (see Fig. 1 and 2).

Table 2 lists some sample data on the field operation. Fig. 4 is a scope display of the wire setup field calibration as viewed in the Central Control Room.

Table 2. Sample data of the wire setup calibration

BPM #	*LPM17	*LPM18
Test date	09/27/94	09/27/94
R to 1 (L to 2)	298	335
R to 2 (L to 1)	-325	-274
R to 3 (L to 4)	35	94
R to 4 (L to 3)	-63	-12
Zero-offset(mV)	-14	41
Sens. (mV/mm)	104	102
T to 1 (B to 2)	304	319
T to 2 (B to 1)	-296	-282
T to 3 (B to 4)	54	50
T to 4 (B to 3)	-52	-30
Zero-offset(mV)	1	10
Sens. (mV/mm)	100	100

* LPM17 and LPM18 are the two most important position monitors for SHR operation

ACKNOWLEDGEMENT

The authors would like to thank E. Ihloff, J. Grenham and all others in the Mechanical Group for their support in making the wire setup.

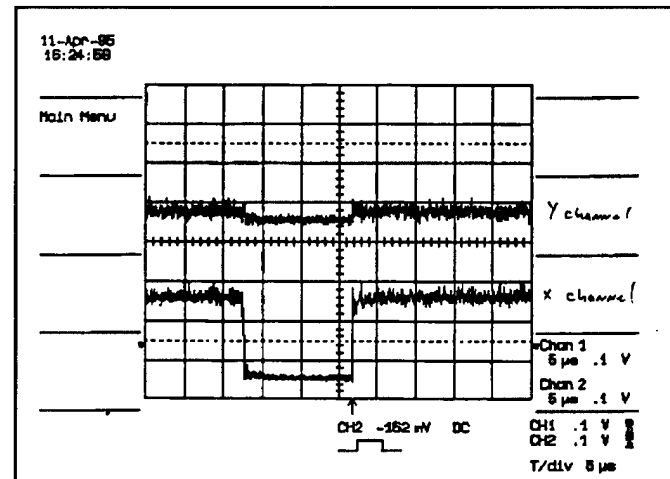


Fig. 4 Wire calibration signal viewed in CCR

REFERENCES

- [1] J. B. Flanz, et al., Proceedings 1989 Particle Accelerator Conference pp34-36 (1989)
- [2] J. B. Flanz, et al., Proceedings 1993 Particle Accelerator Conference pp2331-2333 (1993)
- [3] A. Zolfaghari, C. Sibley, et al., Bates internal reports

BEAM PROFILE DATA ANALYSIS FOR THE RHIC INJECTION LINE *

Ping Zhou
Bldg 830
Brookhaven National Laboratory
Upton, NY 11973

Abstract

Beam profile monitors employing phosphor screens will be used in the beam transfer line from AGS to RHIC, now under construction at BNL, as beam profile monitors. Data analysis procedures are being developed for the transfer line test scheduled for the fall of 1995. In addition to the emittance and Twiss parameters calculation, it will include direct reconstruction of the beam phase space density distribution by using an Abel inversion with the minimal assumption of an elliptically symmetric phase space distribution. The percent emittance comes out of the process naturally.

I. INTRODUCTION

Two dimensional beam profiles will be measured using the video profile system [1] in the RHIC injection line. They will be used to monitor beam quality and measure beam emittance and Twiss parameters for beamline matching. Six flags will be for emittance measurement, though at most four can be used simultaneously, limited by the number of frame grabbers. This will enable us to measure the input beam parameters on a bunch by bunch basis with some redundancy for error checking.

The information on horizontal and vertical coupling extracted from the two dimensional profile directions will be used to identify and in feedback to correct the coupling. If significant coupling is present a complete four dimensional phase space analysis, ignoring the even more complicated additional coupling with the longitudinal dimension, is necessary. A meaningful and reliable complete phase space analysis is impossible by virtue of the number of flags, the necessary measurement accuracy and the complexity of the required analysis. We will assume the coupling effect is negligible after correction and limit the analysis to one dimension at a time.

II. SCATTERING EFFECTS

Going through the flags, beam particles will be scattered. The bulk of the deflection is due to elastic Coulomb scattering from the nuclei within the screen. The distribution of the deflections is roughly Gaussian for small deflections while having greater probability for large-angle scattering[2]. In the limit of thin films where particles' position can be treated as unchanged going through the target, the scattering effect can be easily calculated[3] using a Gaussian scattering angle distribution and a Gaussian beam distribution

$$\epsilon' = \epsilon \sqrt{1 + \beta \Theta^2 / \epsilon}, \quad \alpha' = \frac{\alpha}{\sqrt{1 + \beta \Theta / \epsilon}}$$

*Work performed under the auspices of the U.S. Department of Energy

$$\beta' = \frac{\beta}{\sqrt{1 + \beta \Theta^2 / \epsilon}}, \quad \gamma' = \frac{\gamma + \Theta^2 / \epsilon}{\sqrt{1 + \beta \Theta^2 / \epsilon}}$$

where Θ is the rms deflection angle going through flag. This result can be extended to arbitrary distributions for rms quantities.

With the RHIC injection line parameters, in the worst case the emittance dilution can reach 30% which will greatly affect the accuracy of the measured emittance. Fortunately, scattering effects can be compensated with measurements.

If the beam transfer matrix from flag i to the next flag $i + 1$ is $\begin{pmatrix} T_{11} & T_{12} \\ T_{21} & T_{22} \end{pmatrix}$ then the increase of rms beam width at flag $i + 1$ due to the scattering of flag i follows

$$\Delta \sigma^2 = T_{12}^2 \cdot \Theta^2$$

This effect adds up quadratically from flag to flag. The above equation can be used to obtain each flag's scattering effect by measuring the beam width with and without the flag in front. Thus the effect of scattering on emittance measurement, at least mostly, can be corrected.

III. EMITTANCE CALCULATION

At least three independent measurements are needed to determine α, β, γ and ϵ . The measurements do not necessarily have to be simultaneous. With a very good repeatability from bunch to bunch, they could also be from measurements of multiple bunches with flags at different locations. They could also be measurements with one or more fixed flags but with varying magnet settings.

Emittance and Twiss parameter calculation from beam width measurements is straight forward[4][5]. Basic formula are reproduced here for reference. Details can be found in [4][5] and [6].

The beam width at flag i is related to the parameters at location s_0 as $y_i \equiv w_i^2 = \beta_i \epsilon = \sum_k g_{ik} \cdot a_k$, where $g_{i1} = t_{11}^2$, $g_{i2} = -2t_{11} \cdot t_{12}$, $g_{i3} = t_{12}^2$ with $[t_{ij}]$ being the transfer matrix from s_0 to flag i , and $a_{1,2,3} = \epsilon \beta, \epsilon \alpha, \epsilon \gamma$.

Minimizing

$$\chi^2 = \sum_i \left[\frac{y_i - \sum_k g_{ik} \cdot a_k}{\sigma_i} \right]^2,$$

where σ_i is the rms error in w_i^2 , yields the normal equation for the problem

$$[N_{jk}] [a_k] = [b_j]$$

where

$$N_{jk} = \sum_i \frac{g_{ij} \cdot g_{ik}}{\sigma_i^2}, \quad b_j = \sum_i \frac{g_{ij} \cdot y_i}{\sigma_i^2}$$

The solution is simply

$$(a_j) = [V_{jk}] (b_k)$$

where $[V] = [N]^{-1}$.

The standard error for any dependent variable, $f = f(a_i)$, can be easily calculated with $[V]$:

$$\sigma_f^2 = \sum_i \left(\frac{\partial f}{\partial y_i} \right)^2 \sigma_i^2 = \sum_{m,n} \frac{\partial f}{\partial a_m} \cdot V_{mn} \cdot \frac{\partial f}{\partial a_n}$$

For a_j it is simply $\sigma_{a_j}^2 = V_{jj}$.

The calculations done with artificial profiles for the RHIC injection line show that with 10% rms error in the measured beam widths, the standard error in calculated beam emittance varies from a few percent to above 20% depending on which three flags are used, reflecting on the between-flag betatron phase advances. When two flags are multiples of 180° of betatron phase apart they are images of each other and do not provide independent data. When the phase advance is close to multiples of 180° degrees, theoretically the problem is perfectly solvable, but the result is increasingly sensitive to small errors in beam widths. The phase advance, however, depends on initial beam parameters as well as the transfer line lattice, so what actually turns out in actual measurements may be different from bunch to bunch.

IV. PHASE SPACE DISTRIBUTION

The full property of the beam is characterized by its phase space density distribution. Once the Twiss parameters and emittance are determined, this phase space distribution can be reconstructed from the measured density using Abel transformation technique, and the only underlining assumption needed is that the distribution has elliptical symmetry. Having the 2-dimensional phase space distribution also makes the calculation of partial beam emittance easy and unambiguous. There have been percentage emittance calculations reported with various assumption[5][4]. Elliptical symmetry is the least assumptions needed for this purpose.

A 2-dimensional beam phase space distribution with elliptical symmetry, $\rho(x, x') = \rho(\gamma x^2 + 2\alpha x x' + \beta x'^2)$, can be transformed into a circular distribution in (u, v) space with the transformation

$$\begin{pmatrix} u \\ v \end{pmatrix} = \frac{1}{\sqrt{\beta}} \begin{pmatrix} 1 & 0 \\ \alpha & \beta \end{pmatrix} \begin{pmatrix} x \\ x' \end{pmatrix}$$

The resulting distribution will be $\rho(u^2 + v^2)$. The projection of the phase space distribution is directly related with the measured profile by

$$\int \rho(x, x') dx' = \frac{1}{\sqrt{\beta}} \int \rho(u, v) dv$$

Now $\rho(u, v)$ has circular symmetry, i.e. $\rho(u, v) = \rho(u^2 + v^2)$, and the distribution can be recovered from the projection through inverse Abel transform[7].

For a function with circular symmetry in (x, y) space, $f(x, y) = f(r)$, Abel transforms establish the relation between

the distribution and its projections:

$$f_A(x) = \int_{-\infty}^{\infty} f(r) dy = 2 \int_x^{\infty} \frac{f(r) r dr}{\sqrt{r^2 - x^2}}$$

$$f(r) = -\frac{1}{\pi} \int_r^{\infty} \frac{f_A(x) dx}{\sqrt{x^2 - r^2}}$$

The direct inversion in Eq. 1 involves derivation and integration of a divergent function and therefore is not suited for numerical applications. There are various ways to get around the problem[8], including the filtering of raw data to reduce noise, using transform techniques to avoid the divergence. One can also fit the data to analytical functions based on physical models and carry out the inversion analytically. The latter approach is what we have chosen for its easy control. It reduces the further computation and also serves the noise filtering purpose.

We choose Gaussian weighted Hermite polynomials to expand the beam profile:

$$\rho(x) = \sum_n h_n H_n\left(\frac{x}{\sigma}\right) e^{-\frac{1}{2}\left(\frac{x}{\sigma}\right)^2}$$

Because this set of functions are orthogonal, we can avoid the fitting of parameters thus simplifying the calculation of expansion coefficients. Since the undistorted profile should be symmetric about the center, based on the elliptical phase space distribution assumption, we only need the even orders of Hermite polynomials. The maximum order that has to be used in the expansion, however, is not as small as we might have expected or hoped, even when the profile is close to a Gaussian distribution. This is because errors in the calculation of rms of the profile will introduce many high order components. As a result 10 to 20 terms have to be included usually. Thankfully, the expansion process itself is very fast and high number of terms does not constitute much inefficiency in the overall reconstruction process.

The Abel inversion of the Gaussian weighted Hermite polynomials can be calculated analytically[3]. The values of the functions, their Abel inversions and the fraction of beam inside any radius can all be calculated through recursion relations. The result of the inversion is in the form of

$$\rho(r) = \sum_n a_n r^n e^{-\frac{r^2}{2}}.$$

where r is normalized to the beam rms size.

The reconstructed phase space distribution, with normalized coordinate against the rms beam size, can be directly used to calculate the percentage emittance, or the corresponding beam profile through Abel transform.

The fraction of beam inside a radius R in the (u, v) normalized phase space, is

$$\delta(R) = 2\pi \int_0^R \rho(r) r dr$$

Since R is normalized against rms beam size, the percentage emittance corresponding to δ is simply

$$\epsilon_\delta = R \epsilon$$

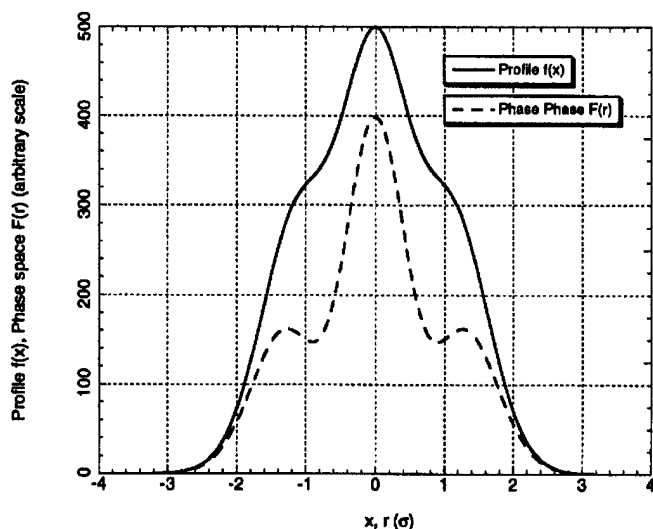


Figure 1. Beam profile and reconstructed phase space distribution.

The fractional beam profile, that of the fraction in the central part of the phase space can also be obtained by Abel transforming $\rho(r)$ with its value set to zero outside $r = R$.

As an example, a beam profile composed of a Gaussian plus a shoulder component is constructed and its corresponding phase space distribution is calculated using the technique described above. They are shown in Fig. 1. The profiles for different fractions of core beam can also be easily extracted. They are shown in Fig. 2 for the example above.

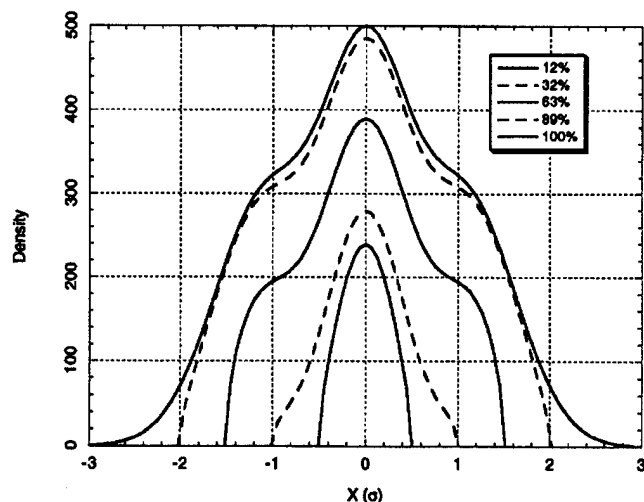


Figure 2. Profiles of various core beam fractions.

In the case where elliptical symmetry assumed throughout this report is lost, the reconstruction of phase space distribution theoretically need infinite number of profile measurements. Except the aspect ratio change that can happen in the beam phase space, the problem is the same as in computed tomography. To reconstruct a 2-dimensional object from all of its projections is the 2-dimensional Radon inversion problem. With the very limited number of beam profiles we can only expect to extract some

coarse features of the phase space distribution using some of the numerical techniques in doing Radon inversion. This has yet to be investigated.

References

- [1] R.L. Witkov. Design of the beam profile monitor system for the rhic injection line. *These proceedings*.
- [2] T. G. Trippe. *Physics Vade Mecum*, chapter 9, page 160. American Institute of Physics, 2nd edition, 1989.
- [3] P. Zhou. Beam profile monitor data analysis. Internal Report RHIC/AP/43, BNL, 1994.
- [4] H. Ploss and L. N. Blumberg. Methods of emittance measurement in external beams using ellipse approximations. Internal Report AGS DIV 68-4, BNL, 1968.
- [5] Kiyokazu Ebihara, et al. Non-destructive emittance measurement of a beam transport line. *Nuclear Instruments and Methods*, 202:403-409, 1982.
- [6] William H. Press, et al. *Numerical Recipes in C*, chapter 15. Cambridge University Press, 2nd edition, 1992.
- [7] R. N. Bracewell. *The Fourier Transform and Its Applications*, chapter 12. McGraw-Hill, 2nd edition, 1986.
- [8] L. M. Smith, et al. Abel inversion using transform techniques. *Journal of Quantitative Spectroscopy and Radiative Transfer*, 39(5):367-373, 1988.

ENERGY SPREAD OF ION BEAMS GENERATED IN MULTICUSP ION SOURCES *

M. Sarstedt, P. Herz, W. B. Kunkel, Y. Lee, K. N. Leung, L. Perkins, D. Pickard, M. Weber, M. D. Williams, Lawrence Berkeley Laboratory, University of California, Berkeley, CA 94720, U.S.A.
E. Hammel, IMS - Ion Microfabrication Systems GmbH, Schreygasse 3, 1020 Vienna, Austria

For the production of future microelectronics devices, various alternate methods are currently being considered to replace the presently used method of lithography with ion beam lithography. One of these methods is the Ion Projection Lithography (IPL), which aims at the possibility of projecting sub-0.25 μm patterns of a stencil mask onto a wafer substrate. In order to keep the chromatic aberrations below 25 nm, an ion source which delivers a beam with energy spread of less than 3 eV is desired. For this application, multicusp ion sources are being considered. We measure the longitudinal energy spread of the plasma ions by using a two-grid electrostatic energy analyzer. The energy spread of the extracted beam is measured by a high-voltage retarding-field energy analyzer. In order to obtain the transverse ion temperature, a parallel-plate scanner is being set up to study the beam emittance. In this paper, comparisons are made for different ion source configurations.

I. INTRODUCTION

For the production of microelectronics devices, lithography, i. e. the projection of structures onto a wafer substrate, plays an important role. However, since the devices are getting smaller, it is foreseeable that the wavelength of light will be too large for future structures.

An alternative method for projecting the structures onto the wafer is Ion Beam Lithography [1], where, instead of light, particle beams are used. The wavelength of the particles depends on their momentum and can be much smaller than in the case of light. The particles can be guided by the well known techniques of electrostatic and magnetic lens systems, which also make their use preferable to that of x-rays.

One of the approaches for Ion Beam Lithography is the Ion Projection Lithography (IPL) [2], which presently is being developed by the Advanced Lithography Group (ALG). According to a design by Ion Microfabrication Systems (IMS), a 10 keV hydrogen or helium ion beam is extracted from an ion source and expanded by a specially designed triode extraction system. With a $\pm 3^\circ$ emission angle, an area of

homogeneity of $60 \times 60 \text{ mm}^2$ is achieved. A condenser lens behind the extraction system allows an additional correction of the overall homogeneity in the beam as well as a mass separation. The beam then falls onto a stencil mask containing the structure that is to be projected onto the wafer. After that an optical column is used to reduce the ion beam before it impinges onto the photoresist surface. Thus, a 5x reduction of the mask pattern can be achieved at the image plane.

This lens system is highly demanding in regard to the ion optical qualities of the beam generated in the source. A high energy spread in the beam would disturb the ion optical qualities of the system and thus also the precision of the projected structures.

The beam is generated in an ion source, consisting of a plasma chamber and a triode extraction system. As plasma generator a multicusp source is considered. A permanent magnet can be installed in the plasma chamber for modification of the plasma potential distribution and for the enhancement of atomic hydrogen ion species [3, 4].

To determine the energy spread generated by the source plasma and the energy spread that is obtained in the process of beam formation, electrostatic energy analyzers are used. The influence of the filter magnets on the energy spread is investigated.

II. EXPERIMENTAL SET-UP

In this experimental investigation, a filament-driven multicusp ion source was used. The source chamber has a diameter and a length of 10 cm and can, in the longitudinal direction, be divided into two sections by the use of a magnetic filter. This filter was originally used to enhance the atomic H^+ in the beam [3] by trapping the cold plasma electrons in the extraction region. However, the filter magnets also influence the potential distribution inside the plasma [4].

In order to determine the influence of the filter magnets on the energy spread, the filters are removable. Additionally, the end-flange of the source is exchangeable, so that later on the plasma can be driven by an rf-discharge as well.

For measurement of the energy spread the transverse and longitudinal components have to be determined separately. For the measurement of the transverse energy spread, a parallel plate slit-slit emittance scanner will be employed. For analyzing the longitudinal energy spread two versions of energy

* This work was supported in part by the Advanced Lithography Group and the US DOE under contract no. DE-AC03-76SF00098.

analyzers can be used. A small, two-grid energy analyzer allows the measurement of the energy distribution of the emitted plasma ions. This analyzer can be attached directly to the first electrode of the source. The measurement of the energy distribution of the accelerated beam can be performed by a high-voltage, retarding-field analyzer, which was built by IMS. This analyzer was used in the measurements described below.

Fig. 1 shows a schematic of the experimental arrangement. The triode extraction system (ES) is mounted to the multicusp ion source (IS). The IMS energy analyzer is placed in 50 cm distance from the extraction system. The beam is collimated and only the central part of the extracted beam contributes to the measurement. Behind the entrance of the energy analyzer a grid for electron suppression is installed. A column of electrodes, connected by a resistor chain, then retards the ion beam. The analyzer plate is tied to source potential. A battery allows a voltage variation on this plate of ± 90 V.

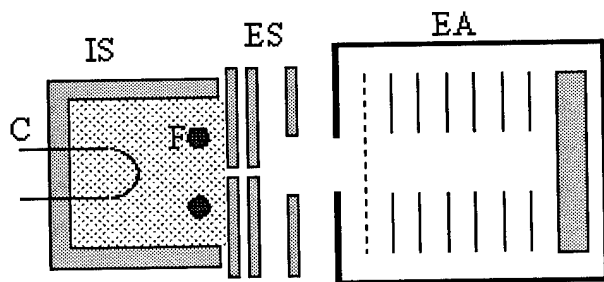


Figure 1: Schematic of the experimental arrangement. A multicusp ion source (IS) with filter magnets (F) is used for filament-driven plasma generation (C). Attached to the source body is the triode extraction system (ES). The high-voltage, retarding-field analyzer (EA) is placed 50 cm behind the extraction system. It consists of an electron suppression grid at the entrance, a column of electrodes for deceleration and an analyzer plate for collection of the ions.

III. EXPERIMENTAL RESULTS

The measurement of the longitudinal energy spread in the accelerated beam was performed on a 5 keV He^+ beam. The beam was formed in a triode extraction system, which was designed by IMS. The beam exits from the extraction system divergent with a very good uniformity.

With the energy analyzer, by applying the retarding field, the integral energy distribution was measured, and from this, by differentiation of the curve, the energy spread (FWHM of the curve) was determined. Figs. 2 and 3 give an example of the measured and calculated data. In this case an arc voltage of 60 V was applied. The first electrode of the extraction system was tied to source potential. No filter magnets were in-

stalled in the plasma chamber. An energy spread of 10.4 eV was determined.

We measured the energy spread for different settings of the arc voltage in the source. Also the influence of the potential of the first electrode of the extraction system (source potential vs. floating potential) was tested. In all these cases the energy spread was approximately 10 eV.

The same measurements were then repeated with the filter magnets installed in the plasma chamber. The energy spread of the beam ions was determined to be approximately 8.7 eV (Fig. 4), which is slightly lower than in the case without the magnetic filter.

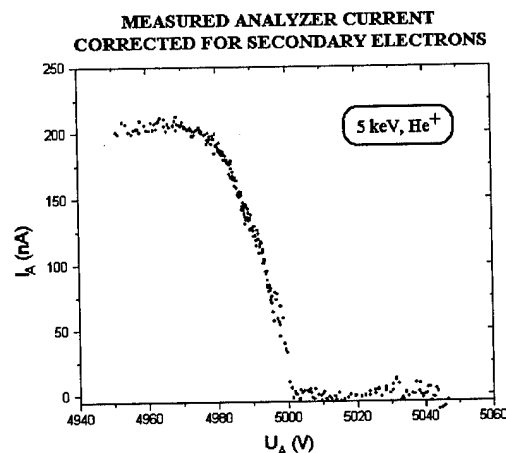


Figure 2: Integral distribution of the energy spread for a 5 keV He^+ beam generated in the filament driven multicusp source with no filter magnets in the source chamber.

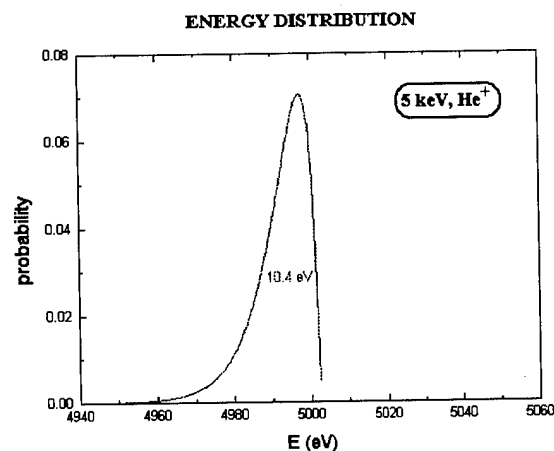
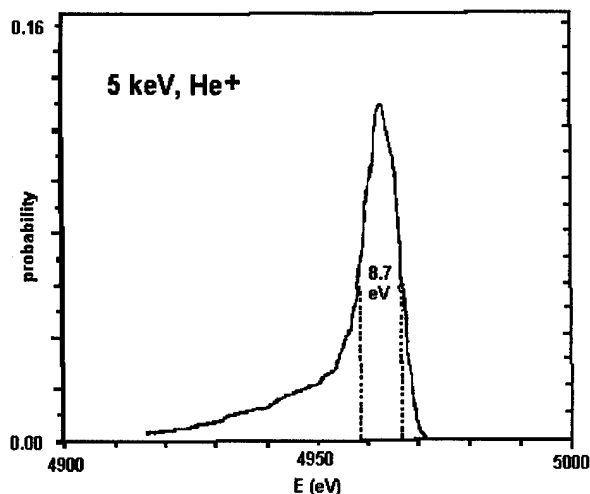


Figure 3: Differentiation of the curve shown in Fig. 2. The energy spread was determined to be in the order of 10 eV.



IV. REFERENCES

- [1] H. Löschner et. al., J. Vac. Sci. Technol. B 11(2), 487 (1993).
- [2] A. Chalupka et. al., J. Vac. Sci. Technol. B12(6), 3513 (1994).
- [3] K. W. Ehlers and K. N. Leung, Rev. Sci. Instrum. 50, 1353 (1979).
- [4] K. W. Ehlers et. al., Appl. Phys. Lett. 41(6), 517 (1982).

Figure 4: Energy spread in a 5 keV He⁺ beam, when the magnetic filters are installed in the ion source.

IV. DISCUSSION

The measurements described above showed an energy spread of the beam ions of 8 to 9 eV with, and 10 to 11 eV without applying the magnetic filter in the plasma chamber of the ion source. This difference can be explained by the change of the axial potential distribution inside the source. As was shown in [4] the introduction of the magnetic filters yields in a region with a relatively flat plasma potential profile in axial direction. The voltage drop in this case is only 1.5 eV, whereas without the filters a potential difference of 3.5 eV could be observed.

The lower energy spread in the case with the magnetic filters can be explained by these former observations. However, there is still a high energy spread in the beam (8 to 10 eV). The cause for this high energy spread is not yet understood. Further investigations are in progress. To obtain information about the energy spread of the ions as they exit from the plasma, at present we are planning to install the two-grid energy analyzer at the first plasma electrode. The transverse energy spread will be determined by means of emittance measurements. Experimental investigation is in progress, results will be presented in the near future.

ACKNOWLEDGMENT

For technical assistance we would like to thank G. J. DeVries, M. Hoff, B. Leonard, C. Matuk, T. McVeigh, L. Mills, and S. Wilde.

A 2 MHz 3-Port Analog Isolation and Fanout Module*

Edward R. Beadle

AGS Department, Brookhaven National Laboratory
Upton, New York 11973-5000 USA

Abstract

A 3-port isolated circuit providing 1:3 fanout, buffering and amplification over a multi-megahertz bandwidth is presented. The circuit accepts a single input and drives 3 independently isolated output channels, up to ± 10 V into 50 ohms. The input and output isolation is supplied via a dual optocoupler, and the power isolation is achieved with DC/DC converters. In each channel, a voltage feedback amplifier is used in combination with the optocoupler to form a transimpedance configuration with the gain-bandwidth product (GBP) set by a pair of resistors. The feedback amplifier linearizes the optocoupler transfer characteristics using a servo technique and also controls the circuit drift, nonlinearity, and bandwidth. The circuit has demonstrated long-term drift of $\pm 0.1\%$ of full scale, and resolution to better than 9 bits. The circuit provides frequency response to true DC with an analog bandwidth variable over a range of <100 kHz to >4 MHz, and a SNR of >55 db in a 1 MHz bandwidth with $<1\%$ THD for a 10 V amplitude sinusoidal input. With few modifications, this design is capable of providing input/output gain and bandwidth in the range of 10 - 50 MHz.

I. INTRODUCTION

In many accelerator based data acquisition systems, signal isolation is a necessary feature so ground loops are avoided. This problem commonly occurs in distributed data acquisition and also in signal distribution from a single point to multiple destinations. Many techniques exist for isolation of analog signals and they are summarized in various places.¹ A common approach is to use voltage-to-frequency converters (VFCs). However, for isolated data transmission of analog signals, because of the digital output, the information bandwidth of VFCs is generally limited to well below their carriers. Further, situations occur where the data must remain in analog form, and although analog fiber optic technology^{2,3,4} is an alternative for new installations, in some cases it is not possible to install fibers, and the existing copper lines must be used. Thus, single package analog isolation amps must be considered. There exists a wide variety of components available from several manufactures, such as Burr-Brown and Analog Devices, but almost all commercially available units have bandwidth below the 100 - 200 kHz range, and many do not isolate the DC power. It is valuable to achieve isolation from the DC power sources so that the system is completely independent of local ground references, and thus the processing

electronics can be located anywhere user demand requires. Addressing the need for a universally applicable 3-port analog isolation fanout/buffer with a DC - 2 MHz bandwidth for signal distribution, the following system was developed.

II. CONCEPT

A picture of the module is shown in figure 1. The form factor is a 10 HP x 3 U x 220 mm eurocard package. This format

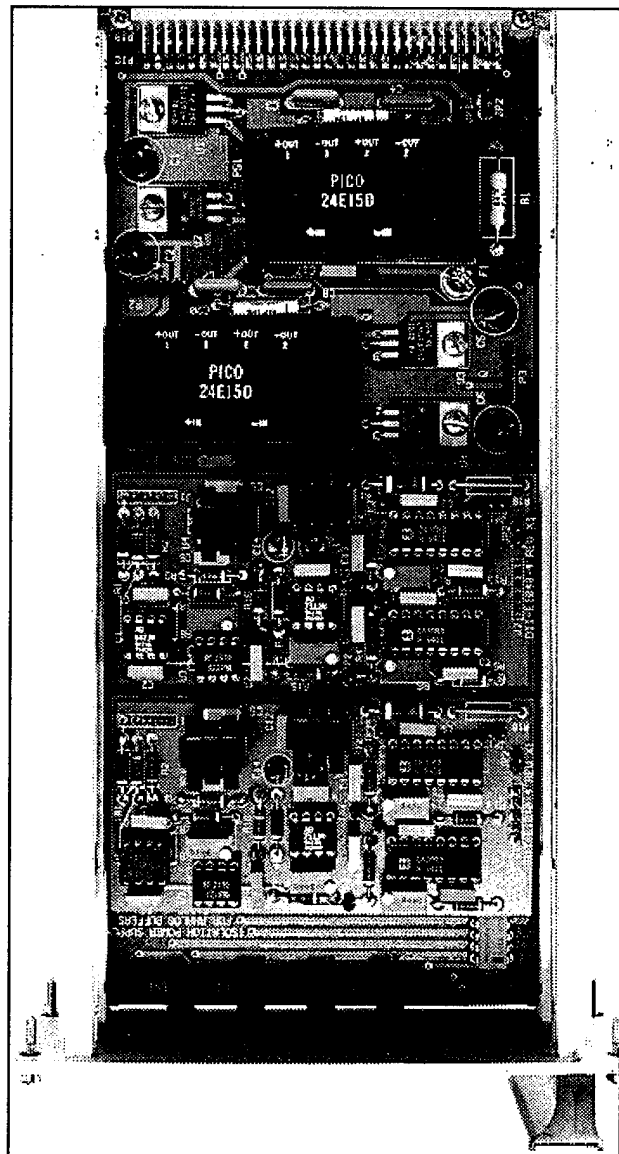


Figure 1. Module populated with 2 of 3 daughter cards

* Work performed under the auspices of the US Dept. of Energy under contract no. DE-AC02-76CH00016.

was selected by considering criteria relating to the application of the circuitry and is not essential to the design. The signal isolation, buffering, and amplification are performed on each daughter card using ± 12 rails. The rail voltages are generated on the host card using 4 DC/DC converters (PICO 24E15D, \$80), which use a common +24 VDC supply. The converters supply an unregulated ± 15 VDC with > 200 mA per output, and switch at nominally 20 - 40 kHz. The converters have internal filtering for noise reduction on the analog supply lines, and were selected based on current output, size and cost. The unregulated converter outputs caused problems when output stages drive large signals into low impedances, so fixed 12V regulators were added to each channel. In addition to regulation, they further reduced the power line ripple and noise seen by the circuitry. One converter powers the input circuit on each of the three daughter cards, and the remaining three each drive the output circuitry of a single daughter card. A common input circuit is replicated on each daughter card to ease the packaging design and simplify the input to output isolation circuitry design. The returns for the input and output circuit power are supplied separately by the signal source and loads. Thus, the DC power for each channel is completely isolated from any local rack or crate grounds. As a result, all the circuit ports, the 3 outputs, input, and local power are pairwise isolated, and true 3-port isolation has been achieved in each channel.

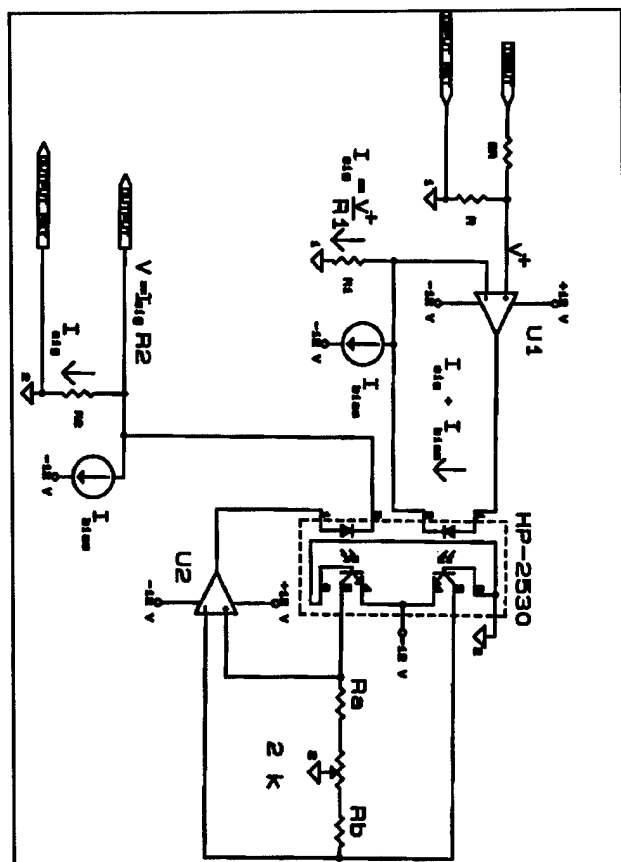


Figure 2. Simplified daughter card schematic

The conceptual design (figure 2) of the daughter card was adapted from a Hewlett-Packard application note⁵ and

consists of an input attenuator, followed by an opamp stage that linearly converts the input voltage to a current, and optically couples it across the isolation barrier. The input signal is recovered by sensing the difference in the D1 and D2 forward currents as a differential voltage using the resistors Ra and Rb and opamp U2. The feedback action of U2 forces the opamp output to move until its differential input is maintained at virtual ground. At this point the diode forward currents match, and assuming matched coupler halves, the collector currents are matched. The signal portion of D2's forward current flows through R2 to generate the output voltage $V_{out} = V_{in}(R2/R1)$. Thus by sizing the ratio of R1 and R2 "noise-free" voltage gain can be achieved. This imbalance does not alter the cancellation properties of the circuit. In the design presented here, gains of up to 10 have been achieved in this way, and higher gains are feasible. The current sources bias the optocouplers into a "linear region", and the exact value of the current selected depends on the input and output swings desired as well as the minimum SNR and maximum distortion tolerable.

III. DETAILED DESIGN

The circuit accepts a 20 Vp-p input and produces a 2 Vp-p swing across the resistor R1. Using a 470 ohm resistor for R1, this sets the diode signal current swing at about 4 mAp-p. Empirically this value was found to produce low distortion ($< 1\%$) and good dynamic range (> 55 db in a 1 MHz bandwidth). For applications requiring less than 20 Vp-p input swings, the attenuator and/or R1 should be set so that the current swing through R1 is in the 2-4 mAp-p range. Larger full-scale swings increase the distortion when the coupler halves have mismatches, and smaller swings reduce the usable dynamic range by limiting the modulation of the optical carrier. The total current flowing in diode D1 is $I_{sig} + I_{bias}$. The I_{sig} component is provided solely by the input signal. Thus, the input amplifier U1 (AD711) acts as a voltage-to-current converter for the input signal and should be able to drive > 20 mA into low impedance loads for good performance. The nonlinear resistance of the LED in the feedback path of U1 does not effect the circuit linearity since, to a good approximation, the current through the diode is linearly related to the non-inverting voltage.

LED bias currents > 5 mA are required to provide good performance, otherwise the SNR is sacrificed for lower distortion. Experimentally, bias currents in the 7 - 10 mA range have been adequate to provide the best trade-offs. The bias currents are generated by Wilson current sources implemented with an RCA CA3083 transistor pack.

Wilson sources were used to get much higher output impedances than achievable with simple two transistor sources. Two transistor sources have output impedances limited to $130/I_{out}$ by the Early Effect, where Wilson sources provide approximately β times more impedance and less sensitivity to β variations⁶. The increased impedance provided by the Wilson sources enabled better bandwidth characteristics when $R1 > 100$ ohms. Each source is independently adjustable to aid circuit matching. Under matched conditions, the nonlinear transfer characteristics of the optocouplers are nulled out by the feedback action of U2, however mismatches between components (i.e.

optocoupler current transfer gain) limit the lower bound on the distortion reduction achievable. However, even this may be compensated for to some degree by selecting the proper ratio of R_a and R_b . In most cases some experimentation is required in selecting the circuit parameters to achieve an optimum balance between maximum distortion, bandwidth, and SNR. For very wideband applications of this circuit, such as extensions to the 10 MHz region, the pole created by R_1 and the capacitances of the opamp and current source begin to limit the useful range of the device and compensation measures may be necessary. Also, different opamps will be necessary to handle the larger bandwidth.

A voltage feedback opamp U2 (PMI OP42), senses the current from one side of the coupler, and develops an output voltage to maintain the virtual ground at its input. The virtual ground is achieved when the U2 output is sufficient to drive D2 such that current coupled through to R_b nulls the differential input of U2. Nominally R_a and R_b are equal so that with the virtual ground condition, the forward currents through each LED are the same (assuming matched optocouplers and bias currents), and thus the current flowing through R_2 is identical to the input circuit's I_{sig} current. Because I_{sig} is linearly dependent on the input voltage, the input and output signals are linearly related by $V_{out} = V_{in}(R_2/R_1)$. However, the current through R_2 is independent of the resistance in that branch, and hence voltage gain for V_{in} can be achieved by increasing the ratio of R_2 to R_1 beyond unity. This is a very low noise way to achieve voltage gain without adding extra components. The mismatch between R_1 and R_2 does not effect the linearity or bandwidth. Further, in some applications an intentional imbalance in R_a and R_b can be introduced to compensate for gain mismatches in the optocouplers, or to add an additional gain control parameters to the circuit.

The optocoupler and U2 opamp combination form a transimpedance amplifier. The feedback amplifier so formed controls the nonlinearity introduced by the optocoupler transfer curves, drift in the operating points, and overall system bandwidth. The current mixing action of the transimpedance amplifier is performed by using the collector resistors R_a and R_b to convert the optocoupler output currents to voltages, and then using U2 to sense the differential signal across R_a and R_b . The collector resistance sets the gain-bandwidth product (GBP) of the transimpedance amplifier at roughly $\alpha R A f$ with a DC open loop gain of $R A \alpha$. The expressions were derived assuming a single-pole opamp model, using α as the current transfer ratio of the coupler, A as the DC open loop gain of the opamp, R as the value of the collector resistor (either R_a or R_b), and f as the unity gain crossover frequency of U2. The expression for the GBP is a loose approximation, but shows the role of the collector resistance. In fact, the increase in the GBP by αR can cause oscillations to occur if U2 is not selected with sufficient phase margin to maintain stability for the desired value of R . Thus careful consideration of the opamp and possible R values is warranted.

The output amplifier (not shown in the schematic) sensing the signal across R_2 , is a fixed gain current boosted amplifier. The amplifier used is the Analog Devices AD711 with an Elantec EL2003 current buffer enclosed in the feedback loop. The output gain is designed at 1.6 which limited the output stage bandwidth to the desired 2 MHz. If wider a bandwidth is required, opamps

like the AD847 can be used to replace the AD711's and OP42. The AD847 has been tested in the circuit and maintains stability. The current driver, EL2003, is used because it provides short circuit proof operation and will typically drive >200 mA into 50 ohms. In addition, locations for back termination resistors have been included for applications requiring them. The circuit has been tested driving cables in excess of 1000 feet.

IV. RESULTS

The circuit was tested for offset and drift. The drift test was performed over several days under loaded output conditions with the input shorted. The drift was measured at $< \pm 10$ mV under laboratory conditions using a strip chart recorder with an ambient temperature range of 15 - 27 degrees Centigrade. Preliminary testing indicates that this drift is note strongly dependent on the ambient temperature, but rather local heating effects in the opto-isolator. The drift was measured after the device experienced a 10 - 15 minute warm-up time. During this time, the output offset drifts approximately 50 mV. Readjustment after this phase using the 2K pot (figure 2) nulled the output.

Frequency domain tests of the circuit's response were made with a network analyzer. The tests showed that the circuit configured for overall unity gain with AD711's achieves a cutoff frequency of approximately 2 MHz for a 1 Vp-p input. Using AD847's a cutoff of approximately 4 MHz is achieved. The noise levels in these implementations were measured using an oscilloscope assuming a peak crest factor of 4, and the results of 5 mVrms (AD711) and 10 mVrms (AD847) were observed. If the optocoupler is changed to one of the faster single units, a bandwidth over 30 MHz can be achieved. We demonstrated this in the lab using the two single HP4562 optocouplers. In this case however circuit balancing is more difficult and drift increases.

V. REFERENCES

1. Beadle, E., "Analog Signal Isolation Techniques", AIP Conference Proceedings No. 281, Berkeley Calif., pp.78-90, (1992). Presented at 1992 Accelerator Instrumentation Workshop.
2. Beadle, E., "Fiber Optics in the BNL Booster Radiation Environment", 1991 Particle Accelerator Conference Proceedings.
3. "Baseband Video Transmission with Low Cost Fiber Optic Components", Tech Brief 104, Optocouplers and Fiber Optics Applications Handbook, Hewlett-Packard.
4. Senior, J., Optical Fiber Communications, Prentice-Hall International, London, (1985).
5. "Linear Applications of Optocouplers", App. Note 951-2, Optocouplers and Fiber Optics Handbook, Hewlett-Packard.
6. Gray and Meyer, Analog Integrated Circuits 2nd Edition Chapter 4, John Wiley & Sons, New York, (1984).

A GENERAL PURPOSE FIBER OPTIC LINK WITH RADIATION RESISTANCE*

Edward R. Beadle
AGS Department, Brookhaven National Laboratory
Upton, New York 11973-5000 USA

Abstract

A general purpose analog fiber optic link transmitting a 2 V_{p-p} input over a passband of .05 Hz to over 25 MHz with a > 50 db dynamic range and < 1 % THD has been developed using previously identified and high volume commercially available radiation resistant components. With few component changes the passband can be extended to over 50 MHz. The basic design, trade-offs, and performance characteristics are presented.

I. INTRODUCTION

In some applications it is necessary to send wide-band analog data, with good fidelity, between two stations separated by several hundred feet. This is particularly true for instrumentation in an accelerator environment, where the sensing equipment can be inside the tunnel, and the processing equipment outside. Aside from the distortion and loss introduced by low cost coaxial cables, this case is further complicated by the possibility of pick-up from environmental noise, and the possible radiation damage of the transmitting electronics. Fiber optics is a viable alternative to the standard coaxial driver, particularly where video bandwidths are concerned. This paper discusses basic design, trade-offs, and performance of one such link developed primarily for the AGS-to-RHIC (ATR) Transfer line profile monitors¹.

II. REQUIREMENTS

For the ATR line profile monitors, 12 complete links are required. The fiber lengths vary from approximately 60 m - 500 m. For each link, the transmission specifications are to provide unity gain over a bandwidth of approximately 6 Hz - 6.5 MHz, with a gain flatness over that band of < +/- 1 db. Further, dynamic range of 50 db, and low THD are also required. Also, because the front end video system of each profile monitor is inside the tunnel, the fiber optic transmitter and fiber must be radiation resistant.

III. BASIC DESIGN

The basic design of the link used components previously found to be radiation in previous testing at the AGS². The cable

selected is Spectran Specialty Optics HCR-series with a 200 micron core. This cable was used in the beam position monitoring system in the AGS Booster and has performed very well over the last 5 years. The fiber has a length-bandwidth product (LBP) of 17 MHz/km at 820 nm. Given worst case fiber length, 500 m, the fiber bandwidth will be about 34 MHz and hence not degrade the video signal. The attenuation introduced by the cable is minimal at 6 db/km as compared to coaxial solutions. The connectors used are SMA in and do not require epoxy polishing to get low loss connections.

The transmit and receive diodes selected are the Hewlett-Packard HFBR 1404/2406 pair (\$40/pr). They are based on InGaAs technology and operate in the 820 nm window. These diodes have also been radiation tested at the AGS and have been used in the Booster for over 5 years. The receiver diode (HFBR2406) has a small signal bandwidth of over 125 MHz.

The transmitter schematic is shown in figure 1. The 75 ohm input resistor is for matching to the source impedance of a video driver. This circuit however can be used with most any matching impedance. The basic circuit is a voltage-to-current (transimpedance amplifier). The RCA CA3083 is used to implement a Wilson current source which provides the dc-bias required by the LED for analog data transmission. Dynamic range and bandwidth are optimized for bias currents of 20 - 25 mA range. The current source is adjusted with a pot in the programming leg of the current source. Since the ideal current source has infinite AC impedance, all of the (low frequency) signal current flows through the resistor R4. The input voltage is scaled to a current by V_i/R_4 . This is where the voltage-to-current conversion occurs. Depending on the application, some peaking across R4 may be desired. The value of R4 can be selected to scale the input voltages of >2 V_{p-p} to fit within the LED current dynamic range. In the system built for the ATR line, R4=100 ohms, the peaking circuit is a series combination of an 820 ohm resistor and 1200 pf capacitor. The opamp selected is the AD847. It was selected based on bandwidth and stability considerations.

To power the transmitter circuit, raw AC is brought into the package, and converted to DC analog rails using a CALEX AC/DC supply. The output is then filtered for use by the circuitry. The CALEX supply is also a proven device in the AGS tunnel, as withstanding radiation doses. However, no quantitative testing has been performed, in qualitative studies they seem to be the power supply of choice based on cost and lifetime. They provide the necessary DC power and require only an AC input which is readily available inside the tunnel at a variety of locations.

Work performed under the auspices of US Dept. of Energy under contract No. DE-AC02-76CH00016.

Packaging the transmitter has been accomplished using a small all aluminum 7"x 7" x 2" chassis. The package concept is such that it is a line replaceable unit (LRU). The chassis is sized such that the entire transmitter assembly can be placed inside a "cubby-hole" along with other instrumentation. The package has been designed to provide indicator lights and test points for quick status checks. Also, access to the control and value of the LED bias current is available without opening the chassis.

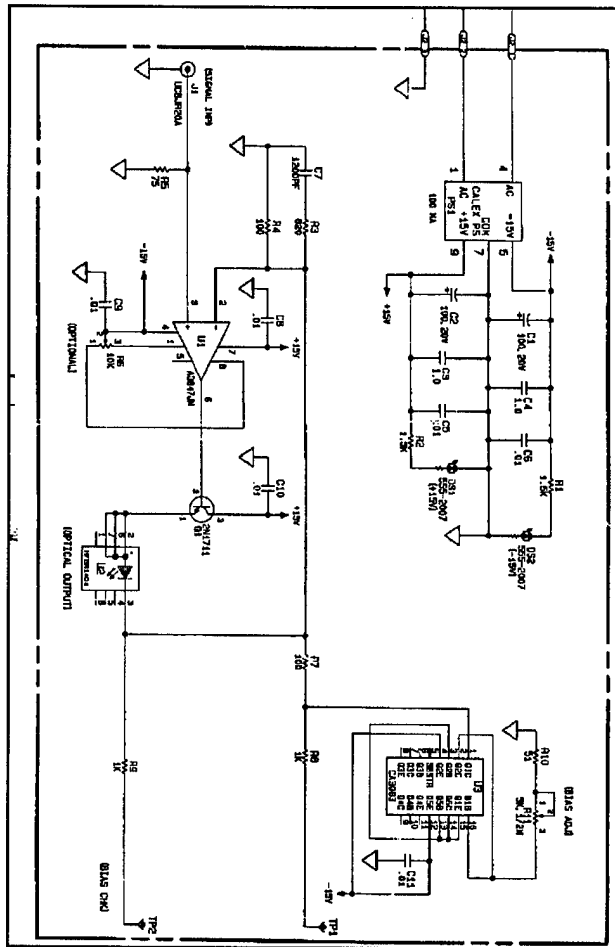


Figure 1. Transmitter schematic.

The receiver circuitry is shown in figure 2. The receivers are centrally located in one of the instrumentation trailers outside the tunnel. Therefore, the receiver circuits have been designed to the more conventional eurocard form factor. Each module is 3 Ux7 HPx220 mm and mates into a slot in a 19" rack mount crate. The crate is powered with a single +/- 15 VDC supply. However, the receivers, unlike the transmitters, require +5 V in addition to the analog rails, so a +5 V regulator has been incorporated onto the board. This lowers the overall part and assembly cost of system, as opposed to adding an additional +5 V supply.

The receiver is the HP HFBR-2406, and is a combination photodiode and analog preamp in one package. The low pass filter following the diode sets the lower corner of the link frequency response, and is used to block the DC offset coming from the receiver photodiode. Across the 330 uF capacitor a good

quality rf capacitor has been placed to reduce the non-ideal behavior of the electrolytic to acceptable levels in wide-band applications. The resistor placed in series with the inverting node of the opamp is important as the capacitance of the AD811 degrades the frequency response. The AD811 was chosen because of the large available output current, and the fact that the bandwidth is nearly independent of the gain. The later reason being the overriding factor. In this application the gain will be varied to compensate for the initial link losses caused by the cable and connectors, and variability in photodiode responsivity from unit-to-unit. Later, some adjustment may be necessary to compensate for some of the radiation induced darkening over the lifetime of the system. However, in the Booster applications which have used this fiber, darkening has not been an issue. The receiver gain, as shown, can be varied over the range of 4.4 to 7.25. However larger ratios can be employed if necessary. The output stage shown has a DC impedance of 75 ohms, and the capacitor serves to reduce the output noise bandwidth. Thus at high frequencies, a 56 ohm impedance is presented to a cable. This is not really a problem as for 75 ohms, it represents a VSWR of 1.5:1, and this is usually acceptable.

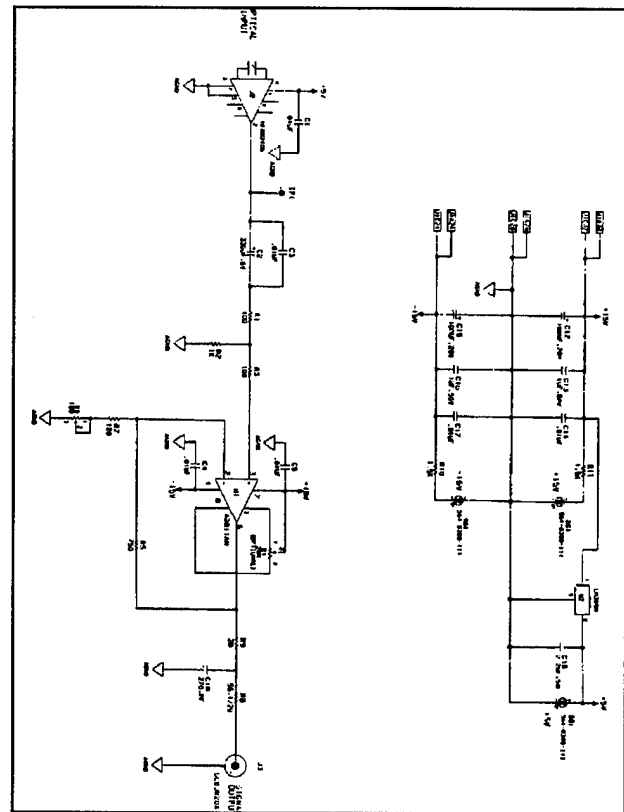


Figure 2. Receiver schematic

IV. PERFORMANCE

The overall system was tested with fibers of lengths 20m, 200 m, 600 m. The frequency response shown in figure 3 is for a 200 m length using 2 Vp-p signal. The receiver was configured with an HFRB-2406, the transmitter bias was 25 mA,

and the value of R6 in the receiver was 67 ohms. The passband is flat (± 0.5 db) over 6 Hz - 12 MHz. The two traces shown are for two samples from the first lot. The difference in the 3 db points (shown as circles) has to do with the parasitics caused by the individual receiver diode packaging and socketing. Since the required bandwidth is below 10 MHz for this application, these effects were not studied further.

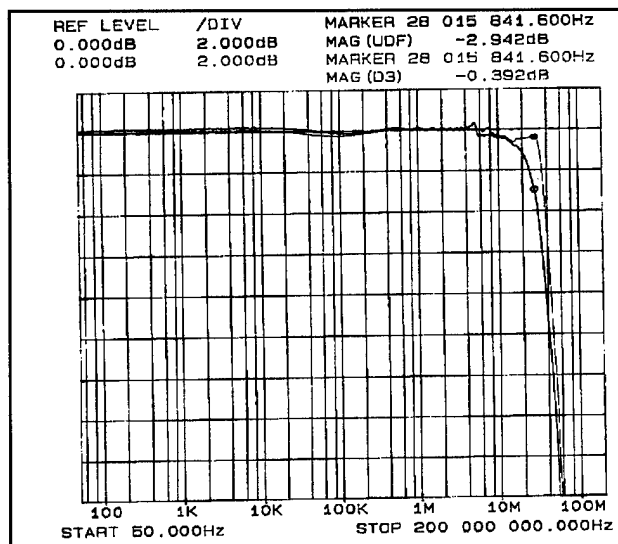
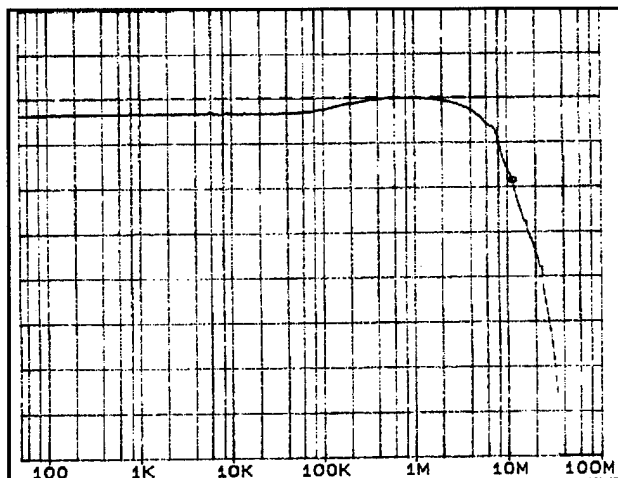


Figure 3. Freq. response of two sample links ($L=200$ m).

In addition we have found that the dc-power level reaching the receiver diode has an effect on the link bandwidth. For example, changing to a 600 m fiber (figure 4) from the 200 m fiber, and using the same transmit and receive pair, the system bandwidth dropped to about 11.5 Mhz. However the gain flatness



to the 6 Mhz stays within the ± 0.5 db range. Note that the scale for figure 4 is the same as figure 3. We believe the cause of this to be the dc-power in the light reaching the receiver causing different capacitance values in the receiver. The dc-power dropped from 75 uW to 46 uW. With less dc-power biasing the PIN receiver, the

diode capacitance is larger, and the causes a lower bandwidth than predicted by the LBP of the fiber alone.

To test the total harmonic distortion (THD) a single tone at 1 Mhz and 2 Vp-p was applied to the transmitter circuit and the receiver output was measured. The resulting THD measured was below .5 %, which corresponds to approximately 50 db dynamic range.

The noise floor was also measured. For this test the transmitter input was terminated in 75 ohms, and the receiver output was measured on an oscilloscope. The gain of the receiver was set such that unity link gain was achieved at 1 Mhz using a 200 m fiber. The tests showed the noise output was less than 2 mV(rms). This minimum signal dynamic range is approximately 53 db. Thus the THD and noise limited dynamic ranges are comparable, implying neither parameter is overdesigned.

As stated in the abstract, the link is capable of providing frequency response beyond 50 Mhz. This assumes adequate illumination of the receiver photodiode. However the peaking has been allowed to increase to about 6-8 db and the passband ripple specification relaxed to ± 1 db. This response was achieved by using the peaking components in the transmitter, and shunting the gain control resistor in the receiver with a capacitor.

V. REFERENCES

1. Witkov, R., "Design of the Beam Profile Monitor for the RHIC Injection Line", see this proceedings.
2. Beadle, E., "Fiber Optics in the BNL Booster Radiation Environment", 1991 PAC Proceedings.

DSP BASED DATA ACQUISITION FOR RHIC*

T. J. Shea, J. Mead, C. M. Degen
Brookhaven National Laboratory
Upton, NY 11973

Abstract

A flexible data acquisition platform has been developed for use in RHIC beam instrumentation systems. By incorporating a floating point digital signal processor (DSP) and standard input/output modules, this system can acquire and process data from a variety of beam diagnostic devices. The DSP performs real time corrections, filtering, and data buffering to greatly reduce control system computation and bandwidth requirements. We will describe the existing hardware and software while emphasizing the compromises required to achieve a flexible yet cost effective system. Applications in several instrumentation systems currently under construction will also be presented.

I. INTRODUCTION

Like other modern accelerators, RHIC will be well instrumented at commissioning^{[1][2]}. Also, the design philosophy embodied in the various beam instrumentation systems places digitizers early in the signal processing chain^[3]. To deal with the resulting data rates, most instrumentation systems will include a digital signal processor followed by a memory buffer that is shared with the control system. This DSP provides the following functionality:

- Filtering that can decrease the data bandwidth to the control system
- Corrections and calculations that decrease the computational load on the control system
- Local circular buffer management to provide a flight recorder
- Software flexibility to present data from various I/O modules in a consistent manner

The decision of how to split functionality between the DSP and the control system is subjective. When allocating functionality to the DSP we use the general guideline that the DSP system is not to be treated as a peer to the control system processors. Rather, the DSP system is viewed as a replacement for hardware that simply provides data to shared memory on a bus slave board. As a result, the DSP board described below is not a bus master, and the software for the example application is limited and simple. In fact, much of this functionality could be obtained with field programmable gate arrays, but the current development tools did not allow the flexibility that we desired. This situation

will change in the future, and for higher bandwidth instrumentation, a hardware dominated system will be considered. So far, our only use of a hardware based system is in the injection profile monitors where commercial image processing boards extract information from four simultaneous video data streams^[4].

II. DSP BOARD DESCRIPTION

This section describes the hardware architecture and performance of the DSP based data acquisition module. The module is physically incorporated on a single width 6U VME standard printed circuit board. It may be installed into a standard VME crate, or as one-half of a VXI module, as has been done for this application. Figure 2 illustrates the block diagram of the design. Listed below are the highlights of the board which will be described in order.

- Motorola DSP96002
- VME/VXI interface
- 4Mbytes Static RAM
- 128Kbytes FLASH memory
- Accepts 4 Industry Pack (IP) Modules

The centerpiece of this module is the Motorola 32 bit floating point DSP. The DSP boasts 16.5 million instructions per second (MIPS), and 49.5 million floating point operations per second (MFLOPS). In addition to its strong performance characteristics, it provides two 32 bit I/O ports, shown as port A and port B in figure 1. These two ports permit independent handling of the raw data input from the Industry Packs (port B), from the post-processed data awaiting upload through VME in the static memory (port A).

The module provides a full 32 bit slave interface which conforms to the IEEE-1014-87 specifications. The necessary VXI registers have also been implemented for compatibility in a VXI environment. The VME bus has full read and limited write access to the Static and FLASH memories. Arbitration for the local bus is performed between the DSP and VME bus with the DSP having higher priority. This priority scheme was chosen to allow the greatest overall DSP performance possible. Due to the asynchronous nature of VME transfers, it remains unaware of this arbitration and only its acknowledge signal is delayed until it can gain access to the local bus.

The on-board memory consists of both static ram and flash memory. The static ram has multiple sources and is packaged in 64 pin zigzag JEDEC standard modules,

* Work supported by the U.S. Department of Energy

permitting easy installation and upgrade. A maximum of four of these memory modules may be installed in sizes of 256kbytes, 512kbytes, or 1Mbyte each. Two size identifying pins on the memory modules themselves allow the hardware to automatically configure itself to the installed size. Since static memory can become expensive the DSP board allows installation of a single 64kbyte memory module for cost sensitive applications, or the installation of four 1Mbyte memory modules for more demanding applications. The on-board flash memory provides a nonvolatile area for program instructions and any necessary permanent coefficients, etc. It provides eight lockable sections, so that a core level program may be locked into a section to prevent inadvertent changes.

What helps makes this board a versatile data acquisition board is its use of a mezzanine cards known as Industry Pack Modules. This interface was developed by Greenspring Computers, and provides a versatile, modular approach for implementing a wide range of I/O, control, interface, analog and digital functions. Up to four of these Industry Pack Modules may be installed on the DSP board while still occupying only one VME slot.

The performance of the DSP board can be characterized by the performance of the DSP itself, along with its I/O throughput with both the SRAM and the Industry Packs. Some performance issues of the DSP itself were listed above, and now the I/O performances of the DSP that were accomplished will be mentioned. On port A of the DSP are the SRAM modules. They are accessed with a single wait state giving a maximum throughput of 42Mbytes/sec, and may have internal access times up to 45ns. On the other port are the Industry Pack Modules. The maximum throughput achieved with the Industry Packs at 8Mhz is 5.3Mbytes/sec. This can be doubled to 10.6Mbytes/sec with a double wide industry pack. The Industry Pack specifications also specifies (preliminary) a 32 Mhz interface, which has been implemented on two of the slots, giving a throughput of 12.8Mbytes/sec. (25.6Mbytes/sec for double wide Industry Pack).

III. APPLICATION EXAMPLES

The number of digitizer channels serviced by a single DSP board depends on the digitizing rate and the complexity of the signal processing algorithm. Examples are summarized in Table 1. The Injection position monitor system is in production and will be commissioned beam in late 1995. A prototype of the collider ring position monitor module has been tested but production will not begin until 1997. A loss monitor module has not yet been constructed. The two variations of position monitor systems will be described. These two systems share the same sampling detector design, but use different digitizers, different timing system interfaces, and run different DSP software. Nevertheless, the results are presented to the control system in identical data structures. In fact, these data structures are

similar to those of the RHIC control system's general purpose digitizers^[5].

Table 1: Typical Data Rates

Application	Digitizer Channels per Module	Peak Digitizer Sample rate (Sa/s)
Injection Line Position monitors	24	30
Ring Position Monitors	4	78k
Ring Loss Monitors	8	20k

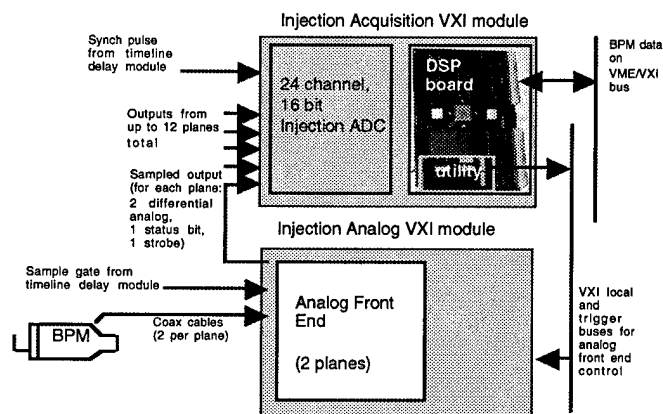


Figure 1. Diagram of Injection Line Modules

A. The Injection Line Position Monitor

The electronics for this system consists of the two VXI modules shown in Figure 2. Because of the low data rate in the injection line, a single DSP board can service multiple analog VXI modules and does not provide any averaging. Software for the injection line application can be summarized with the following routines:

- The acquisition routine runs upon interrupt from the digitizer (about 30 Hz):
 - Raw values are corrected to 3rd order.
 - Position and charge for each bunch are calculated.
 - The buffer pointer and a bunch counter are updated.
 - Results are stored in a circular buffer residing in shared static memory.
- The housekeeping routine is run on interrupt from timing system:
 - Values of the buffer pointer and bunch counter are stored (part of scheme to synchronize buffers of geographically separated modules).

- Changes to settings are read from shared memory and applied.
- If the appropriate bit is set, a self calibration is performed.

B. Collider Ring Position Monitor

Because of the high data rates (turn by turn) of the ring system, a DSP board only services four digitizing channels. Also, the 110 ns bunch spacing in the ring requires that the DSP software be synchronized to the beam synchronous timing system. This special timing interface resides on one Industry Pack while the 4 channel, 16 bit digitizer fits on another. The two planes of analog front end reside in the front of the C-size VXI module. A block diagram of this module is shown in Figure 3. The DSP software for this module can be summarized as follows:

- The acquisition routine runs upon interrupt from the digitizer (about 78 kHz):
 - This routine is similar to injection line acquisition routine, but in addition, the calculated values and their squares are both accumulated.
- The statistics routine is run on interrupt from the timing system (usually at the synchrotron frequency - a few hundred Hz max.):
 - Average and variance of charge and position are calculated.
 - Results are stored in a separate circular buffer.
 - Pointers and counters relating to this circular buffer are updated.
 - The accumulators are cleared in preparation for the next averaging period.
- housekeeping routine is similar to the injection line version

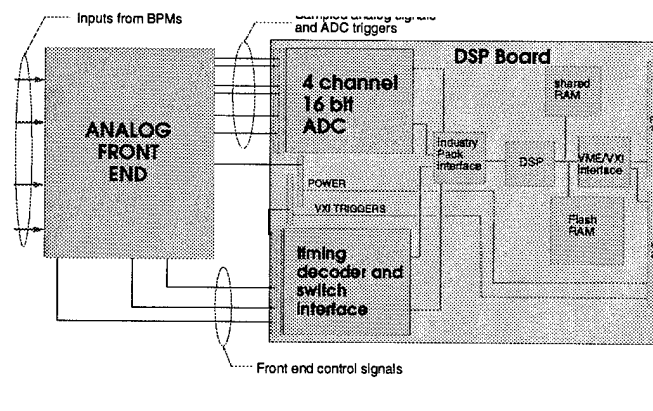


Figure 2. Diagram of Ring Module

IV. FUTURE DIRECTIONS

In addition to investigating competing processors, we are also considering available logic synthesis tools and their viability for higher bandwidth applications. High level

development software may soon allow the DSP to be replaced with field programmable gate arrays.

VXI packaging is proving to be restrictive and expensive for some applications so replacement of the VXI interface by a serial bus connection is being investigated. IEEE-P1394 is a likely candidate and provides the following features:

- 100, 200, or 400 Mbits/s bandwidth
- asynchronous or isochronous data transfer
- simple memory mapped interface (64 bit address)
- maximum of 4.5 meters between nodes is standard - extend to much longer distances with cable upgrades and/or bridges
- cheap (\$50/node)

The evaluation of the P1394 serial bus will proceed as follows:

- Phase 1: existing DSP board will be a test-bed for a 1394 Industry Pack
- Phase 2: new IP carrier board with 1394 built in

V. ACKNOWLEDGMENTS

The authors thank S. Rankowitz and the staff at the BNL Instrumentation Division for producing the DSP board.

VI. REFERENCES

- [1] T. J. Shea, et. al., Beam Instrumentation for the RHIC Sextant Test, Proc. of the Fourth European Particle Accelerator Conference, London (1994).
- [2] RHIC Design Manual, August 1993.
- [3] W. A. Ryan, T. J. Shea, A Sampling Detector for RHIC Position Monitor Electronics, these proceedings.
- [4] R. L. Witkover, Design of the Beam Profile Monitor System for the RHIC Injection Liner, these proceedings.
- [5] R. Michnoff, The RHIC General Purpose Multiplexed Analog to Digital Converter System, these proceedings.

ION-CHAMBER BEAM-LOSS-MONITOR SYSTEM FOR THE LOS ALAMOS MESON PHYSICS FACILITY

M. PLUM, D. BROWN, A. BROWMAN, R. MACEK
Accelerator Operations and Technology Division
Los Alamos National Laboratory, Los Alamos, NM 87545

A new loss monitor system has been designed and installed at the Los Alamos Meson Physics Facility (LAMPF). The detectors are ion chambers filled with N_2 gas. The electronics modules have a threshold range of 1:100, and they can resolve changes in beam loss of about 2% of the threshold settings. They can generate a trip signal in 2 μs if the beam loss is large enough, and if we include the response time of the Fast Protect System, the beam will be shut off in about 37 μs .

I. INTRODUCTION

We needed a new loss-monitor system because the old loss-monitor system was based on photo-multiplier tubes that saturate on the narrow, high-peak-amplitude pulses extracted from the Proton Storage Ring (PSR). Other drawbacks of the old system are 1) the gain of the photo-multiplier tubes change with time, 2) a separate power supply is needed for each detector, 3) it uses a hazardous material (scintillator fluid) that becomes a mixed waste when irradiated, and 4) if a detector must be replaced it must first be recalibrated, which involves spilling the beam. The new system does not suffer from any of these drawbacks. The detectors are ion chambers filled with 160 cm^3 of N_2 gas at 1 std. atm. They do not have the speed of the photo-multiplier tubes (the ion collection time is about 200 μs , compared to the several-nanosecond speed of a photo-multiplier tube), but for our application this is not a problem. The primary purpose of the new system is to protect beam line components from errant beams, but it can also be used as a companion system to a separate, fail-safe loss-monitor system [1], where it can limit the average beam current to prevent errant beams from tripping the fail-safe system used for personnel protection. In this paper we will discuss the design details of the new loss monitor system and describe its performance at our facility.

II. SYSTEM OVERVIEW

A block diagram is shown in Fig. 1. The ion chamber detector, located in the beam tunnel, is connected via long (up to 100 m) coaxial cables to the Current Monitor electronics module and the High Voltage Distribution Unit. The cables are surrounded by solid metal wiring troughs to help reduce noise pickup that could affect the weak signals. The Current Monitor electronics are packaged into single-width NIM modules that fit into a standard NIM bin, which supplies power to the modules. Each NIM bin can hold up to twelve modules, but we use only eleven positions for the Current

Monitors, and reserve the twelfth position for the Fast Protect Interface Module. This latter module is the bridge between the Current Monitor Modules and the Fast Protect System, which quickly (in about 35 μs) shuts off the beam, using electrostatic deflectors at the beginning of the linac, when requested by any one of its many inputs. Some specifications of the system are shown in Table 1.

Other components of the system include a high voltage power supply, set for -2000 V; a High Voltage Distribution Unit; a 5-V floating power supply; and a custom-made Load and Clear Module that is a companion to the LeCroy 4434 scalar CAMAC module used for reading out the Current Monitor module.

The first twenty units have been operating successfully since 1989, and the number in service has been continually expanding since that time.

III. ION CHAMBER DETECTORS

Our ion chambers are custom made by Far West Technology (Model 1054). They are filled with 160 cm^3 of N_2 gas at one std. atm. pressure. We chose this gas type and pressure to minimize the effect of a leaky ion chamber: if the ion chamber leaks, the new gas composition will be 78% N_2 (the natural abundance of nitrogen in air), with a slight pressure decrease to the local pressure of about 3/4 std. atm. Because the gas is still mostly nitrogen, and because the pressure drops just 25%, the response of the system will not change drastically. However, the change is still large enough to detect with a radioactive source. These ion chambers are also the same ones used for the fail-safe ion-chamber system [1], except that we do not add the extra resistors between the high voltage and signal electrodes.

Unlike photo-multiplier tubes, ion chambers do not easily saturate on PSR pulses, and their gains are all practically identical and do not change with age. They are inherently slower devices, but this feature is not a significant drawback in our application.

IV. CURRENT MONITOR MODULES

The function of Current Monitor electronics is to monitor the currents from the ion chamber detectors, and, if the currents

Table 1. Some specifications of the system.

Threshold range	0.1 to 10.0 volts
Ion chamber sensitivity	50 nC/rad
Number in service	68
Speed	About 2 μ s for the electronics, plus another 35 μ s for the Fast Protect System to actually shut off the beam.
Reduced gain mode	Reduces gain by a factor of 10

surpass the threshold settings, to send a trip signal to the Fast Protect Interface electronics. A block diagram is shown in Fig. 2. Current from the ion chamber enters U19, where it is integrated on the 8-nF capacitor, thus generating a voltage on the output of U19. As soon as the output of U19 deviates from zero, U16 turns on the FET Q2, which allows U14 to feed back a current equal to the ion chamber current. The maximum feedback current, I_{MAX} , is proportional to the threshold voltage V_{THR} . As long as the average ion chamber current is less than I_{MAX} , the output of U19 will be maintained close to zero. However, when the ion chamber current exceeds I_{MAX} , U19's output begins to rise, until the comparator U12 fires the one shot U9, which sends a TRIP signal to the Fast Protect System, which shuts off the beam. A signal proportional to the feedback current is used to drive the voltage-to-frequency converter (VFC) U7. A scalar CAMAC module (see Fig. 1) counts the number of pulses from the VFC for one second. The number of counts is therefore proportional to the average current from the ion chamber, which is proportional to the average beam loss. To prevent electrical noise from entering the Current Monitor, the

following signals are brought in or out of the module with optically coupled chips powered by an external floating 5-V power supply: the gain control, the trip status to the control system (FPID), the trip signal to the Interface Module, and the VFC output. For the threshold readback signal we use high-impedance differential inputs on the CAMAC module to reduce ground-loop noise.

A threshold dial on the front panel allows the sensitivity to be varied over a range of 100:1. Front panel LED's indicate the status of the power to the unit and the status of the trip circuitry. A disable button prevents the unit from tripping the interface module, and a gain-reduction button lowers the sensitivity of the unit by a factor of 10 and turns on the gain-reduction LED. The gain-reduction mode can also be set by remote control. A test button injects 60 nA into the front-end circuit to test the module. The output of a buffer amplifier, capable of driving a 50- Ω load, is available on the front and rear panels to monitor the signals from the ion chamber. This buffer circuitry first integrates the ion-chamber signal with a 16- μ s time constant, then amplifies it by a factor of -100. This amplification is important because of the inherently weak signals from the ion chamber. Several other signals are also available on the front panel for diagnostic purposes.

Reaction times of the Current Monitor Module can be as fast as 2 μ s if the beam spills are large enough. If we include the reaction times of the interface module and the fast protect hardware, the total time to shut off the beam is about 37 μ s.

V. THE INTERFACE MODULE

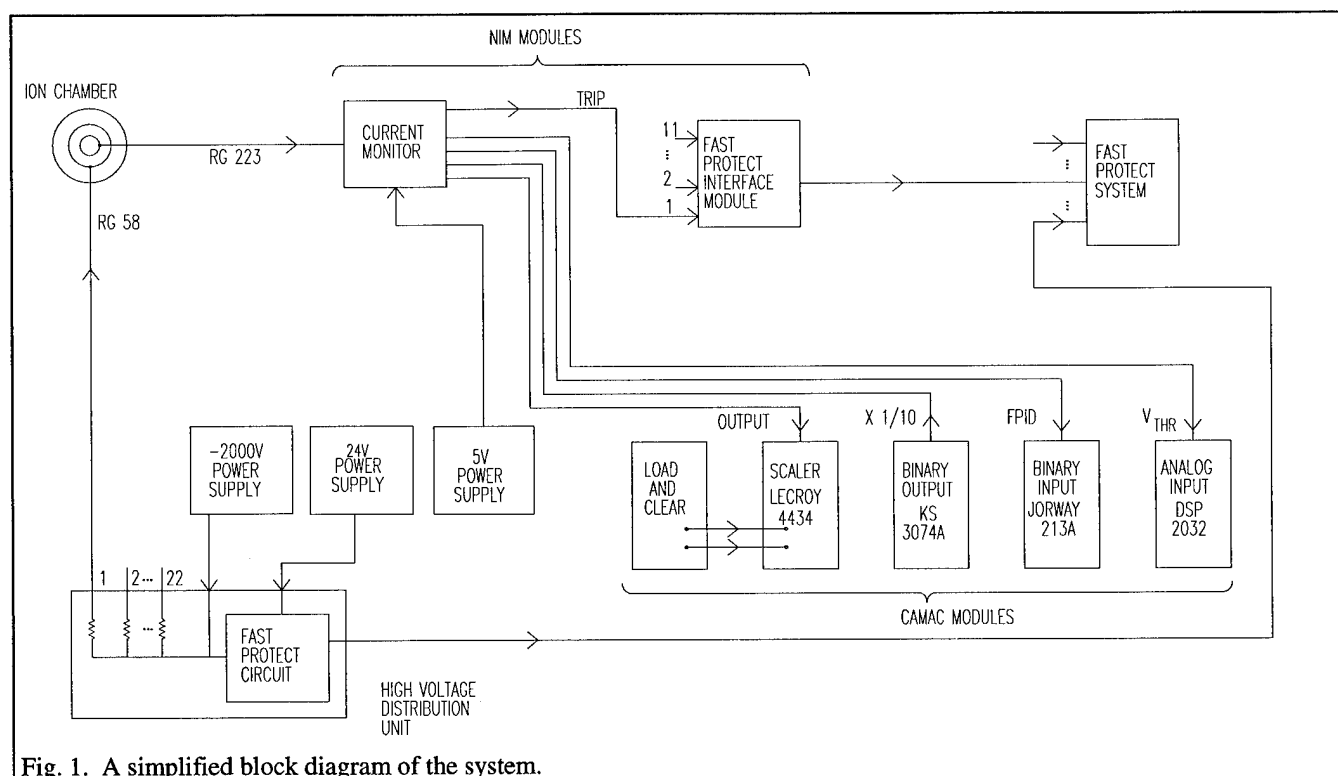


Fig. 1. A simplified block diagram of the system.

The Fast Protect Interface module occupies the twelfth slot of the same NIM bin as the Current Monitors. Each Interface Module receives trip signals from up to eleven Current Monitors. Upon receiving a TRIP signal, it breaks a current loop flowing through the Fast Protect System, which in turn quickly shuts off the beam. DIP switches inside the module allow individual Current Monitor TRIP signals to be disabled. Indicator LEDs on the front panel allow monitoring of the status of each input (disabled or tripped), and the status of the current loop to the Fast Protect System. A push button switch also allows a lamp test.

VI. INTERFACE TO CONTROL SYSTEM

Four different CAMAC modules are used to control and read out the Current Monitor: a binary input module to monitor the status of the Current Monitors, a binary output module to reduce the sensitivity of the Current Monitors by a factor of 10, an analog input module to monitor the thresholds of the current monitors, and a LeCroy 4434 scalar to measure the signal levels from the Current Monitors. Signal-level information is sent to the scalar from VFCs in the Current Monitors, and the scalar is loaded and cleared asynchronously once per second by a custom-made Load and Clear module also located in the CAMAC crate. An update rate of once per second was chosen for convenience, but this is not a limitation of the system. With some hardware changes, it can be as made

as fast as the rep rate of the accelerator.

VII. LOAD AND CLEAR MODULE

These modules are located in the same CAMAC crates as the LeCroy 4434 scalars. Their function is to issue 70-ns-wide load and clear pulses, once each second, to the scalars. Since the scalars are driven by VFCs, the number of counts in one second is proportional to the average voltage, and thereby the average current from the ion chamber.

VIII. HV POWER DISTRIBUTION UNIT

Located in same rack as the current monitor electronics, the function of these units is to distribute -2000 V from the Power Designs model 2K20A high-voltage power supply to the ion chambers. An internal relay circuit will trip the Fast Protect System if the voltage drops below about 1350 V. A green front panel LED indicates current in the loop to the fast protect chassis. This LED will turn off if the high voltage is too low, if there is a problem with the connections to the fast protect chassis, or if there is a problem with the 24 V supplied to the unit.

[1] M. Plum et. al., "Fail-Safe Ion-Chamber Errant Beam Detector Tailored for Personnel Protection", *Proceedings of the 1989 IEEE Particle Accelerator Conference*, March 20-23, 1989.

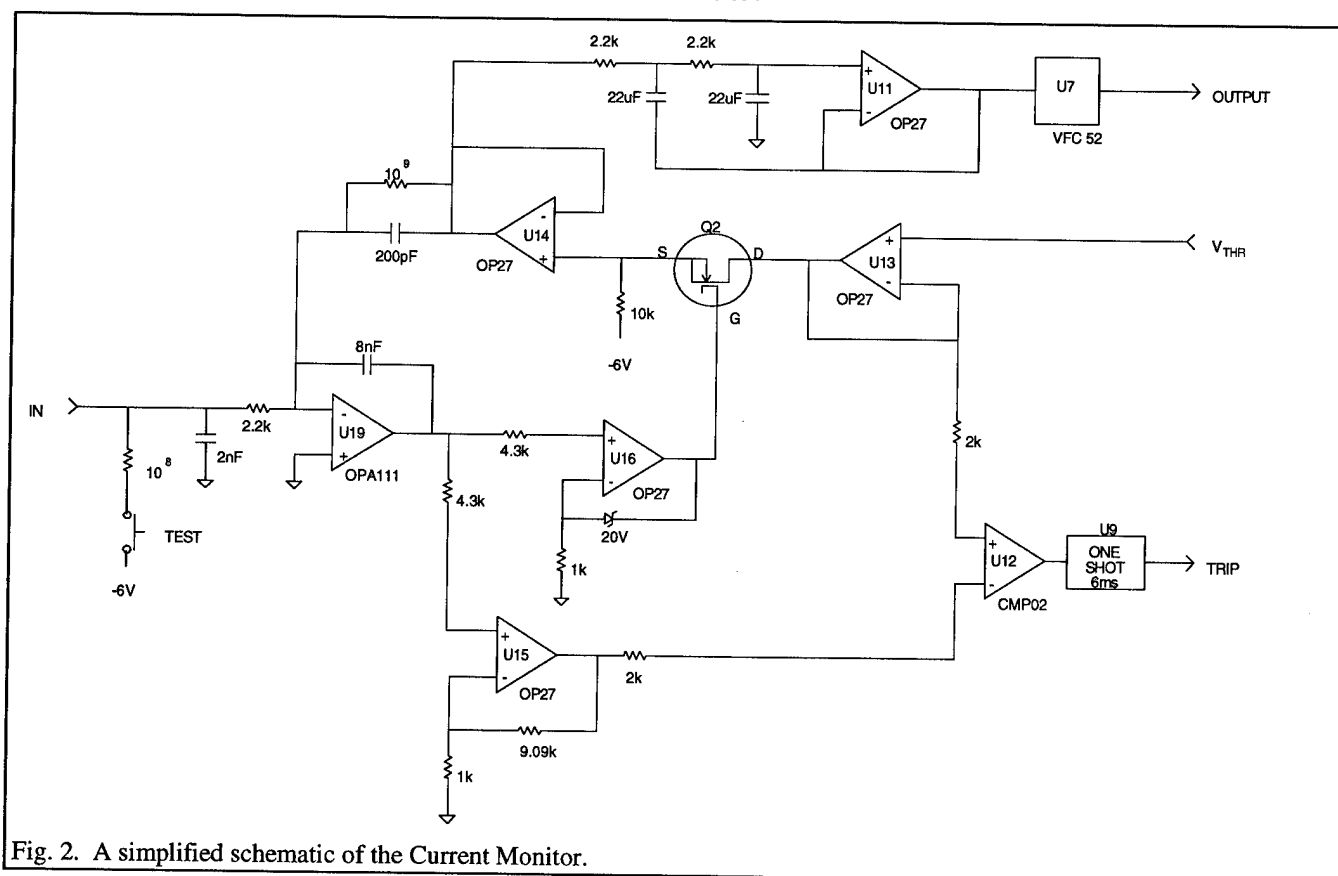


Fig. 2. A simplified schematic of the Current Monitor.

DEVELOPMENT OF BEAM POSITION MONITORS FOR HEAVY ION RECIRCULATORS*

F. J. Deadrick, J. J. Barnard, Lawrence Livermore National Laboratory, Livermore, CA 94550
T. J. Fessenden, LBL, J. W. Meridith, EG&G, and J. Rintamaki, U of Mich.

Work is underway at the Lawrence Livermore National Laboratory to design and build a small-scale, heavy ion recirculating induction accelerator. An essential part of this design work is the development of small non-intercepting diagnostics to measure beam current and position. This paper describes some of this work, with particular emphasis on the development of a small capacitive probe beam position monitor to resolve beam position to the 100 μm level in a 6 cm diameter beam pipe. Initial measured results with an 80 keV potassium ion beam are presented.

I. A HEAVY ION RECIRCULATOR

Heavy ion drivers for Inertial Confinement Fusion (ICF) offer the promise of a cost effective solution to the energy needs of the future [1]. The Lawrence Berkeley Laboratory and the Lawrence Livermore National Laboratory are cooperatively working toward the development of the technology necessary to demonstrate the feasibility of the Heavy Ion Fusion (HIF). LLNL is currently building a small-scale (4m diameter), 4 μs pulse, low-energy (80 keV to 320 keV) K^+ ion recirculating induction accelerator to study the technical problems associated with building a full scale recirculator [2]. Included in this work is the development of a variety of beam diagnostics which will be needed for beam monitoring and control.

II. NON-INTERCEPTING BEAM POSITION MONITORS

Operation in a recirculation mode requires that beam sensing diagnostics do not intercept nor appreciably affect the beam. A wide variety of non-intercepting beam position monitors (BPM) have been devised to sense a beam's image current distribution in the beam pipe wall, the beam's image charge distribution, or the magnetic field produced by the passing beam. They all rely on the fact that the distribution of the current or charge is symmetric when the beam is on axis, however when the beam is off axis, the distribution becomes non uniform and this leads to techniques for determining beam centroid position.

Common BPM resonant tuning techniques used in RF accelerators are not always applicable to induction linacs since the beam is continuous and not RF modulated. A technique which has been successful is to use a resistive wall current monitor where the voltage drop across a resistive break is measured at several points around the circumference of the sensor, and these signals are then

summed and differenced to determine beam position. For this technique to be practical, however, one needs to provide electrical isolation from the beam pipe so that the current image currents flow through the resistance of the break, and azimuthal isolation during the duration of the beam pulse. This is often impractical when the beam current is low and the pulse duration is long, such as the case in our scale model accelerator.

Another technique is to sense the azimuthal magnetic fields produced by the beam current. Berners and Reginato [3] have discussed the design of a small four segment Rogowski BPM for use in the ILSE heavy ion accelerator at LBL. Again, the relatively long beam pulses and low current levels found in our recirculator make this technique difficult to implement if reasonable signal to noise ratios are expected.

Measurement of the charge distribution of the passing beam is a third candidate. Initial calculations show that this diagnostic holds the potential for providing a method of determining beam position with little impact on available space. This paper describes the development of a small non-intercepting capacitive probe beam position monitor which can be inserted inside the evacuated beampipe.

III. CAPACITIVE PROBE PHYSICS MODEL

Consider the design of a diagnostic as illustrated in Fig 1. Here a beam current I_b flowing with a velocity βc will have a charge density λ of $I_b / \beta c$ coul/meter. An equal and opposite sign charge will appear in the inside surface of the beam pipe through which the beam passes. If one considers a C-Probe consisting of a segmented conductive cylinder of length L inserted into the beampipe with a geometry like that shown in Fig 1, charges Q_1 , Q_2 , Q_3 , and Q_4 are induced on the four 90° sections of the conducting surface that surrounds the beam. The problem then

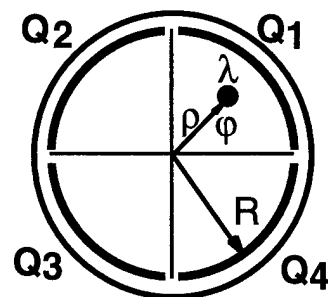


Fig. 1 Sketch of the C-probe problem and geometry

becomes one of finding an expression for the beam position and intensity in terms of the four measurable charges Q_1 , Q_2 , Q_3 , and Q_4 for the general case where the beam is off

* Work performed under the auspices of US DoE by LLNL under contract W-7405-ENG-48.

axis. Here the charge element is a normalized distance ρ off center at an angle ϕ to the horizontal.

There are several methods of solving this field problem. The most customary way is by the method of images wherein an image line-charge of value $-\lambda$ at an angle ϕ and position R/ρ from the origin is assumed. It can be shown that the circle of radius R is an equipotential in the field of the two line charges. The field component normal to the conduction surface gives the distribution of charge around its circumference. From this distribution the total charge on each 90° section can be calculated and the voltage on each section determined. Note we have assumed that the gaps between plates do not significantly change the distribution of charges. One finds the charge on the circumference to be given by

$$\sigma(\vartheta) = \frac{\lambda}{2\pi R} \left[\frac{1-\rho^2}{1+\rho^2-2\rho\cos(\vartheta-\phi)} \right] \quad (1)$$

where $\sigma(\vartheta)$ is the surface charge distribution on the conducting surfaces. Upon integrating this expression over the conducting surface at R (easier using complex variable techniques) one obtains the sum of the four charges $Q_1 + Q_2 + Q_3 + Q_4 = \lambda L$ as expected. Here L is the axial length of the C-probe. The total charge on the first BPM sector is then given by

$$Q_1/L = \frac{\lambda}{2\pi} \int_0^{\pi/2} \frac{1-\rho^2}{1+\rho^2-2\rho\cos(\vartheta-\phi)} d\vartheta \quad (2)$$

Similar expressions exist for the other three sectors.

Consider the following definitions:

$$X \equiv \frac{(Q_1 + Q_4 - Q_2 - Q_3)}{(Q_1 + Q_2 + Q_3 + Q_4)} \quad (3)$$

and

$$Y \equiv \frac{(Q_1 + Q_2 - Q_3 - Q_4)}{(Q_1 + Q_2 + Q_3 + Q_4)} \quad (4)$$

Using the expression for the charge around the circumference given in Eq. (1), and integrating from 0 to $\pi/2$ as in Eq. (2), one finds an expression for the variable X to be given by

$$X = \frac{1}{2\pi} \left\{ 4 \tan^{-1} \left[\frac{1+\rho}{1-\rho} \tan(\pi/4 + \phi/2) \right] + 4 \tan^{-1} \left[\frac{1+\rho}{1-\rho} \tan(\pi/4 - \phi/2) \right] - 2\pi \right\} \quad (5)$$

In terms of the Cartesian coordinates, one finds $X =$

$$\frac{1}{2\pi} \left\{ 4 \tan^{-1} \left[\frac{1+\sqrt{x^2+y^2}}{1-\sqrt{x^2+y^2}} \tan \left(\pi/4 + \frac{\tan^{-1}(y/x)}{2} \right) \right] + 4 \tan^{-1} \left[\frac{1+\sqrt{x^2+y^2}}{1-\sqrt{x^2+y^2}} \tan \left(\pi/4 - \frac{\tan^{-1}(y/x)}{2} \right) \right] - 2\pi \right\} \quad (6)$$

Here x and y are the spatial coordinates divided by the pipe radius R . A similar expression can be found for Y .

One can show that X and Y are zero at the origin. For small values of x and y , or for beams near the center axis,

$$X \approx 4/\pi x; \quad Y \approx 4/\pi y \quad (x, y \ll 1) \quad \text{or} \quad (7)$$

$$x \approx \pi/4 X; \quad y \approx \pi/4 Y.$$

Within the circle $\sqrt{x^2+y^2} = 0.5$, the approximate expressions given above are accurate to better than 7%.

Within $\sqrt{x^2+y^2} = 0.25$ the error becomes less than 2%.

For most situations this should be adequate for determining the beam position within the diagnostic. Needless-to-say, one must multiply the variables x and y by the pipe radius R to obtain the actual offset in centimeters or inches.

Fig. 2. shows a contour plot of both functions X and Y for values from -0.9 to 0.9 in steps of 0.1. Thus for a particular experimental situation, if the values of X and Y are measured, the position of the beam within the pipe and be determined.

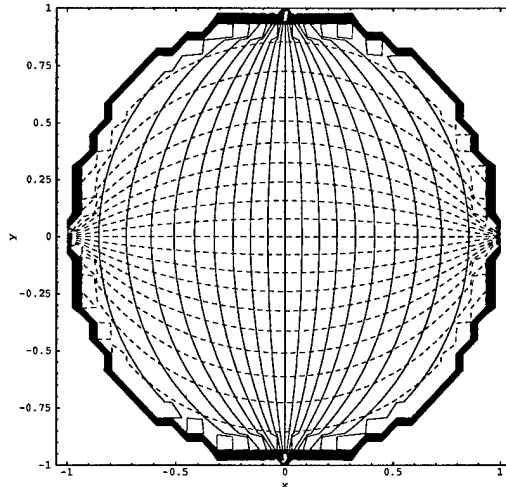


Fig. 2. Contour plots of X and Y . The solid lines are contours of constant X in increments of 0.1. The dotted lines are corresponding contours of constant Y .

IV. ELECTRICAL CONSIDERATIONS

A circuit of the type shown in Fig. 3 will produce signal voltages proportional to X and Y . Here the charge on the four sectors is converted to a voltage signal by the capacitance of the sensor including any external capacitance, C_{ext} . Since the sensor voltage output is inversely proportional to the total system capacitance, it is desirable to locate the buffer amplifiers as close to the sensor as practical.

As an example, the total charge induced on the probe sectors is simply the beam line-charge-density times the axial length of the sector, L . For a sector length of 10 cm, and a 2 mA potassium beam at 80 kV ($\beta=0.002$), we find that approximately 0.33 nC total or 0.083 nC per sector will appear on the plates. If the system capacitance is 1nF, then the voltage on each plate will be near 80 millivolts. Note

that it is especially important to keep the effective capacitance of each of the four circuits extremely well balanced if accurate position information is to be obtained.

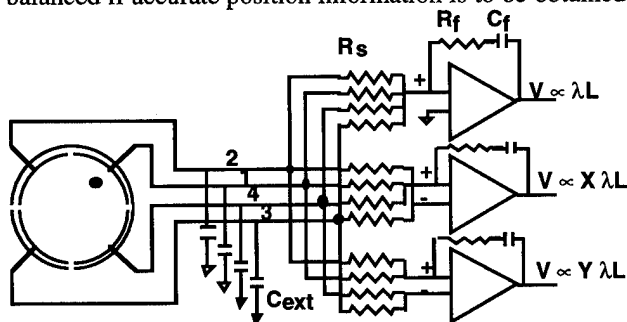


Fig. 3. Monitor circuit to give an electrical output proportional to the total charge, and proportional to the beam displacements in X and Y.

V. TEST RESULTS & CONCLUSIONS

A prototype C-Probe has been built and tested with an ion beam [4]. The sensor element is made on a Macor glass-ceramic cylinder 11.2 cm long by 5.7 cm in diameter. Copper sensor plates are deposited on the inside surface of the cylinder using an electroless plating process. The cylinder fits inside a beampipe which is surrounded by a permanent magnet quadrupole. The intrinsic capacitance of each of the four segments has been measured at 10 pF. However, external cabling used for monitoring and recording the probe signals brought the total capacitance of the circuit up to approximately 2 nF. Fig 4 shows the measured waveforms on each of the four plates due to a 4μs wide, 2 ma K⁺ ion beam pulse.

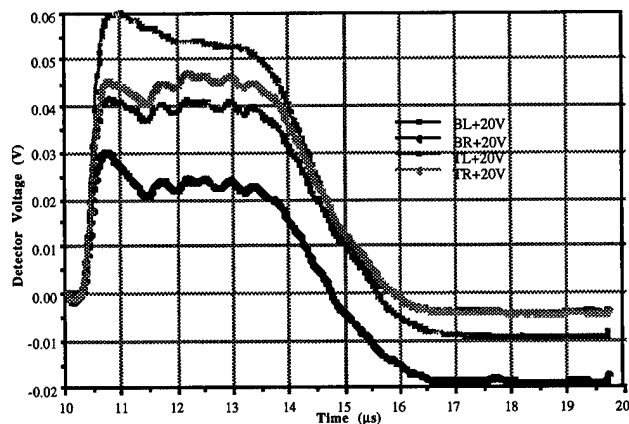


Fig 4. Measured C-Probe plate voltages for a 2.1 ma beam.

Figure 5 shows the waveforms obtained if one numerically adds and subtracts the individual plate voltages as detailed in Fig. 3, where X and Y are proportional to the distance that the ion beam is off axis. By using the *average* values of the voltages during the beam pulse as shown, one can calculate that the beam is off axis by -3.3 mm in the x direction, and +4 mm in the y direction inside a 5.7 cm diameter beampipe. These offset predictions are quite reasonable considering that a final mechanical alignment of the beamline had not been performed prior to these measurements. Beam profile diagnostic instrumentation is

currently being installed to determine absolute beam centroid position. An insitu calibration will be needed to verify the calculated sensitivity factors and balance the analog readout electronics.

Further work certainly remains to turn this diagnostic into a reliable BPM. One of the concerns in using a charge sensitive diagnostic of this type is the affect that stray electrons hitting the sensor plates will have on the plate charge. More importantly the affect of ions hitting the plates is also a factor. We have found that secondary electrons at a ratio of approximately 8 electrons per ion are produced. For this reason a positive bias voltage on the electrodes should be used to re-collect any secondary electrons.

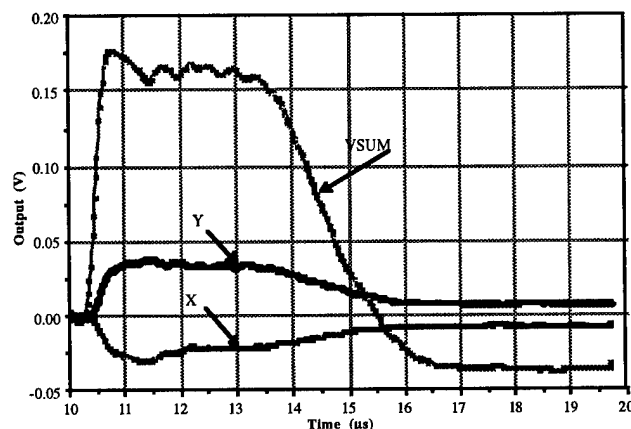


Fig. 5. Processed X & Y offset signals from C-Probe.

Finally, care is needed in the design of the instrumentation electronics. The monitoring circuitry should measure the charge on the capacitors, and not significantly deplete this charge during the beam pulse time. The charge waveforms should return to zero after the beam pulse has passed the sensor.

We find these initial results to be encouraging, and plan to continue the development of this simple diagnostic.

VI. REFERENCES

- [1] J. J. Barnard, et. al., "Study of Recirculating Induction Accelerators as Drivers for Heavy Ion Fusion", Lawrence Livermore National Lab, UCRL-LR-108095, September 21, 1991.
- [2] A. Friedman, et. al., "Progress Toward a Prototype Recirculating Induction Accelerator for Heavy Ion Fusion", This Conference,
- [3] D. Berners and L. Reginato, "Beam Position and Total Current Monitor for Heavy Ion Fusion Beams", Accelerator Instrumentation Fourth Annual Workshop, AIP Conference Proceedings No. 281, Berkeley, CA
- [4] S. Eylon, E. Henestroza and F. Deadrick, "K⁺ Diode for the LLNL Heavy Ion Recirculator Accelerator Experiment", This Conference.

LASER COMPTON POLARIMETRY OF PROTON BEAMS

Arnold Stillman,* Brookhaven National Laboratory, Upton, NY 11973-5000 USA

Abstract

A need exists for non-destructive polarization measurements of the polarized proton beams in the AGS and, in the future, in RHIC. One way to make such measurements is to scatter photons from the polarized beams. Until now, such measurements were impossible because of the extremely low Compton scattering cross section from protons. Modern lasers now can provide enough photons per laser pulse not only to scatter from proton beams but also, at least in RHIC, to analyze their polarization.

I. THEORY

Compton scattering, the elastic scattering of photons from charged particles, has proven useful in polarimeters for electron beams. Laser polarimeters are common at the worlds e^\pm storage rings.[1], [2], [3]. In this method, a laser provides circularly polarized photons which then scatter from the polarized electrons or positrons. Spin-dependent terms in the scattering cross-section cause an asymmetry in the rate of back-scattered photons. This asymmetry depends on the relative orientations of the incoming photon's wave vector and the electron's spin, and so provides the signal proportional to the beam polarization. It would be of great benefit to extend this utility to polarized proton beams, but the cross-section for Compton scattering from protons is small. For polarimetry, it is smaller than the analogous electron cross section by a factor of $(m_e/m_p)^3$, where m_e and m_p are the masses of the electron and proton, respectively. Modern lasers, with their high power densities and pulse energies, stand a chance of making up this difference in rate.

For polarized laser light scattering from polarized electron beams (following the development in [3]), the cross section is [4]

$$d\sigma = \frac{1}{2} r_e^2 \left(\frac{\omega'}{\omega'_0} \right)^2 (\Phi_0 + \Phi_1 + \Phi_2), \quad (1)$$

where

$$\begin{aligned} \Phi_0 &= (1 + \cos^2 \theta') + \frac{1}{m_e} (\omega'_0 - \omega') (1 - \cos \theta') \\ \Phi_1 &= (\xi_1 \cos 2\phi' + \xi_2 \sin 2\phi') \sin^2 \theta' \\ \Phi_2 &= -\xi_3 \frac{1}{m_e} (1 - \cos \theta') \vec{\zeta} \cdot (\vec{k}'_0 \cos \theta' + \vec{k}'). \end{aligned}$$

Here, \vec{k}'_0 , \vec{k}' and ω'_0 , ω' are the wave vectors and frequencies of the initial and final photons, $\vec{\zeta}$ is the electron spin vector, θ' is the scattering angle of the outgoing photon, and ϕ' is the polar angle of the scattered photon with respect to the incoming photon. The primes indicate electron rest frame values, and all expressions are in natural units, so that $\hbar = c = 1$ and $e^2 \approx 1/137$. The laser polarization vector is $\vec{\xi}$, a vector whose three components

are the Stokes parameters ξ_1, ξ_2, ξ_3 . Note that the polarization vector is independent of the spatial axes. This distinction causes the terms that appear in the cross section which are products of a Stokes parameter and a particle spin to be non-invariant. They depend on the spatial orientation of the laser polarization vector. That is, these terms depend on the choice of the scattering plane. When $\xi_3 = \pm 1$, the laser is right or left circularly polarized; ξ_1 and ξ_2 determine the linear polarization. Eq.1 shows that only circularly polarized photons enter into the spin-dependent scattering.

II. The Scattering Rate

To determine the cross section for scattering by protons, it is sufficient merely to substitute m_p for m_e in eq.1. The magnitude of the Compton scattering from protons is much weaker than the scattering from electrons. Indeed, it is lower by a factor of $(m_e/m_p)^3$ since $r_e = e^2/m_e \rightarrow e^2/m_p$ and the term dependent on circular polarization involves a power of $1/m_p$. This is a large reduction, on the order of 10^{-10} . Getting useful statistics from the scattering requires a laser with high energy in a pulse on the order of a bunch length. Such a pulse length, (e.g. 50 ns) is long by modern laser standards, and the energy and power densities necessary are also within reason.

The flux of photons striking a detector due to spin dependent scattering is

$$\dot{n}_\gamma = \mathcal{L} d\sigma(\vec{\zeta}, \vec{\xi}) \quad (2)$$

where \mathcal{L} is the luminosity of the proton-photon interaction area and $d\sigma$ includes only terms which depend on the product of particle spin, $\vec{\xi}$ and laser polarization, $\vec{\zeta}$. It is important to remember that this flux is in addition to the flux of photons from the unpolarized scattering, and that subtracting the large unpolarized background is necessary for successful polarization measurements. The luminosity of the interaction region depends on the overlap of the photon bunch with the charged particle bunch. For laser pulses that are in phase with and smaller than the particle beam bunch length, this luminosity is

$$\mathcal{L} = \frac{NN_\gamma f}{hA} = \frac{N\rho_\gamma \tau_\gamma f}{h} \quad (3)$$

where ρ_γ is the number density of photons in the interaction region, N is the number of protons in the beam, h is the harmonic number, f is the interaction rate, and τ_γ is the laser pulse length. Note that the number of protons per bunch is N/h . The relationship between photon density and photon flux density (i.e. photons/sec/cm²) is $2\pi\rho_\gamma = \lambda'W_\gamma$. Thus, in terms of proton beam and laser parameters, the detector sees a flux of photons

$$\dot{n}_\gamma = \frac{N\tau_\gamma f \lambda W_\gamma d\sigma}{2\pi h}, \quad (4)$$

In laser polarimetry of particle beams, there are two distinct modes of operation[3]. In the *single photon method*, the recurrence of the particle bunches in a storage ring allows a low

*Work performed under the auspices of the U.S. Dept of Energy, Contract No. DE-AC02-76CH00016.

power, high repetition rate laser to generate signal at the rate of about one photon/sec. In the *multi-photon method*, a high power laser generates several thousand signal photons per laser pulse. In the proton beam situation, the scattering is so weak that the multi-photon option requires a laser with energy and power densities that are state-of-the-art. The single-photon method is not an option for proton polarimetry, for reasons which become clear in section III.

To estimate the laser requirements, assume a laser pulse width of 50 ns, a laser energy of 1 eV, a harmonic number h of 1, an interaction rate f (beam revolution freq.) of 100 kHz, and a beam intensity N of 6×10^{13} (the current AGS unpolarized intensity). For a back-scattering rate of 1 kHz, the laser power density must be, in cgs units,

$$W_\gamma \approx 8.8 \times 10^{11} [\text{W/m}^2], \quad (5)$$

deliverable as pulses in phase with the proton bunches. Lasers that generate pulses of this energy density are common, even ones that can sustain kilohertz pulse rates. Much higher power densities are not unusual, but at the expense of lower pulse rates[5], [6], [7]. Note also that, for a beam interaction region of 1 cm^2 area, the polarimeter requirement is for about 4.4 J per pulse. This is not the final word on the laser power requirement, though. Although a laser with an output of 10^{12} W/m^2 would cause count rates of a few kHz, there is a more stringent requirement on the count rate, that of the accuracy of the asymmetry measurement.

III. The Asymmetry Measurement

The relative polarization of the proton beam is proportional to the vertical asymmetry in rates of back scattering by the two distinct photon polarizations, $\xi_3 = \pm 1$. What happens is that photons scatter from the protons in the vertical plane, and these scattering rates differ above and below the horizontal plane. The relative difference between the scattering rates above the plane and below the plane is the asymmetry. For vertically polarized protons denote this asymmetry as [3]

$$A_\uparrow = \frac{d\sigma_+ - d\sigma_-}{d\sigma_+ + d\sigma_-} = \frac{\Phi_2}{\Phi_0} = P_p P_\gamma \cos \phi' F(\theta', \omega'_0), \quad (6)$$

where P_p and P_γ are the polarization components of the proton and photon respectively, and $d\sigma_+$ and $d\sigma_-$ are the right and left helicity photon scattering cross sections. In RHIC, the polarization of the proton bunches alternates with each bunch. This provides an opportunity for reducing systematic errors by making measurements of the total asymmetry,

$$A = (A_\uparrow - A_\downarrow)/2 = \frac{\Phi_2}{\Phi_0}. \quad (7)$$

This measurement, although it achieves a reduction of systematic error, requires the laser to switch polarizations on every other bunch. Automatic polarization switching is possible in the design of the laser. The spacing between the pulses of alternately polarized laser light depends on the sampling scheme for the similarly alternating polarizations of the proton bunches. However, pulse separation times for the laser polarizations are naturally on the order of 4.5 ns [6].

The function $F(\theta', \omega'_0)$ in equation 6 determines the ultimate detectability of the asymmetry. Scaling the photon energy in units of the proton mass, this asymmetry is, from equation 1,

$$\frac{\Phi_2}{\Phi_0} = -\frac{\xi_3(1 - \cos \theta') \vec{\zeta} \cdot (\mathbf{k}'_0 \cos \theta' + \mathbf{k}')}{(1 + \cos^2 \theta') + (\omega'_0 - \omega')(1 - \cos \theta')}. \quad (8)$$

In what follows, it will be convenient to retain these units for the photon energy. Now, since the polarization components of the incoming photon and the proton are $\vec{\xi} = (0, 0, \pm P_\gamma)$ and $\vec{\zeta} = (0, 0, \pm P_p)$ and since, by introducing the azimuth angle, ϕ , $\vec{\zeta} \cdot \mathbf{k}' = \zeta_3 \omega' \sin \theta' \cos \phi$, then

$$F(\theta', \omega'_0) = \frac{\omega' \sin \theta' (1 - \cos \theta')}{(1 + \cos^2 \theta') + (\omega'_0 - \omega')(1 - \cos \theta')}. \quad (9)$$

The angular dependance of this function is at a maximum for scattering angles close to $\theta' = \pi/2$. Assuming placement of detectors at this angle, the energy dependence of F is then

$$F(\pi/2, \omega'_0) = \frac{\omega'}{1 + \omega'_0 - \omega'}. \quad (10)$$

Using the Compton formula,

$$1/\omega' - 1/\omega'_0 = 1 - \cos \theta', \quad (11)$$

yields

$$F(\pi/2, \omega'_0) = \frac{\omega'_0}{1 + \omega'_0 + \omega'^2_0}, \quad (12)$$

which has a maximum at

$$\omega'_0 = 1 \quad (13)$$

if photon energies are measured in units of proton mass. Note that at its maximum, $F = 1/3$, implying that the relative polarization is not simply the asymmetry, A . In fact the absolute polarization of the proton beam is

$$P_p = A/\Pi P_\gamma, \quad (14)$$

where Π is the analyzing power and is defined for beams purely polarized.

The condition $\omega'_0 = 1$ also leads to a relationship between the energy of the particle beam and the input photon wavelength. This relationship exists because the detector is fixed at the optimum scattering angle, and the Compton formula again provides the connection between ω'_0 and E_{beam} . In terms of the rest frame incoming photon energy, ω'_0 , the energy of the lab frame photon, ω_0 is

$$\omega'_0 = 2\gamma\omega_0. \quad (15)$$

Now, explicitly entering the mass scale into equation 13 gives

$$1 = 2\gamma E_\gamma/m = 2E_{beam} E_\gamma/m_p^2 \quad (16)$$

or

$$E_\gamma E_{beam} = m_p^2/2 \quad (17)$$

Using the relationship between the energy of a photon and its wavelength,

$$E_\gamma \lambda = 1.24 [\text{eV} \mu\text{m}] \quad (18)$$

the optimal scattering wavelength, in terms of particle beam parameters, is

$$\lambda = \frac{2.48\gamma}{m_p} [\text{eV}\mu\text{m}]. \quad (19)$$

For RHIC, this wavelength is $\approx 0.5 \times 10^{-3} \text{nm}$. Such photons are too energetic for creation by lasers, so any measurement of polarization must use a less than optimal wavelength. To determine just what the implications on the scattering are of using practical wavelengths, it is necessary to look at the time it takes to make satisfactory polarization measurements.

Suppose the polarization measurement uses high energy visible photons of 300 nm to analyze RHIC beams, then $F(\pi/2, \lambda) \approx 1.7 \times 10^{-6}$. Since $F(\pi/2, \lambda)$ directly determines the degree of asymmetry, this low value requires a large number of interactions to build up the statistics necessary for reasonable precision. In terms of the number of back-scattered photons, the relative accuracy in the asymmetry is [3]

$$\frac{\delta A}{A} = \frac{1}{A\sqrt{2\langle n_A \rangle}}, \quad (20)$$

where $\langle n_A \rangle$ is the number of counts necessary to produce a given accuracy. This number, divided by the production rate, gives the time necessary for a given measurement accuracy. The measurement time for 20% accuracy is,

$$T = \frac{\langle n_A \rangle}{\dot{n}} = \frac{25}{A^2}. \quad (21)$$

For a scattering rate of 1 kHz, the measurement time in Eq. 21 is too long to be workable. It is on the order of 10^4 yr. Some means of enhancing the effectiveness of the counting is necessary. Fortunately, there are real possibilities. The immediate thought that comes to mind is to increase the photon energy, since the dependence of A on λ' goes as $1/\lambda'$, thus, the dependence of $\langle n_A \rangle$ on λ' goes as λ'^2 . Meanwhile, the count rate \dot{n} goes as λ' , so the measurement time for a particular accuracy decreases as λ' decreases. It does not decrease enough though. Optimal photons have a wavelength so much shorter than any possible laser-generated photons that the decrease in measurement time is quite minimal. This goes even for Compton-scattered photons from e-beams or x-rays from undulators[8]. At the present state of the art, there are no photon sources that would provide the necessary intensity of sub-nanometer radiation.

The only reasonable alternative is to use the *sampling method*. This method samples the polarization of the proton beam in a very small area. Focusing the laser spot to sub-millimeter dimensions increases the power density by several orders of magnitude without changing the energy. The laser in [7] delivers 1/3 of the required energy, but 10^{11} the power density. The laser output is then not a limiting factor. However, the count rate of back-scattered photons now goes up substantially, to the GHz range. At a count rate of 100 GHz, and a wavelength of 300 nm, the measurement time to 20% accuracy is now ≈ 165 hrs.

IV. Conclusion

Laser polarimetry of proton beams is difficult, but not impossible. The limitations to accurate measurement of beam polarization is not, surprisingly, the laser output, but the ability

to count back-scattered photons at high rates. This limit arises from the accuracy requirement of the measurement, and the need to spatially sample the polarization of the proton beam. The function $F(\theta', \omega'_0)$ in Eq. 6 has a natural scale set by the mass of the scattering particle. Since the proton mass is so much heavier than the electron, this scale changes by a factor of 2000. This factor decreases even further the already small cross section for Compton scattering from protons. If the interest were only in unpolarized scattering, for a profile monitor, for example, the rates would be quite good. It is the polarimetry requirement, *i.e.* the requirement of a reasonable analyzing power, that makes this measurement difficult. This dependence of the analyzing power on the mass implies a few other things as well. First, laser polarimetry of heavy ions is unfeasible. Second, laser polarimetry of muons is certainly possible, and should give very good results.

Finally, laser polarimetry is inherently non-destructive of the beam and of its polarization. Running a polarimeter for 200 hrs. can be a non-invasive part of the standard operation of an experimental program.

References

- [1] Gustavson, D. B. *et al.*, Nuclear Instr. and Meth., **165**, 177, (1979).
- [2] MacKay, W. W. *et al.* Phys. Rev. D **29**, 11 (1984).
- [3] Placidi, M and Rossmann, R, Nuclear Instr. and Meth., **A274**, 79, (1989).
- [4] Tolhoek, H. A., Rev. Mod. Physics, **28**, 277 (1956).
- [5] S. Watanabe, *et al.* J. Opt. Soc. Am. B, **6**, 1870 (1989).
- [6] M. Mizoguchi, K. Kondo, and S. Watanabe, J. Opt. Soc. Am. B, **9**, 560 (1992).
- [7] Kalashnikov, M. P. *et al.* Laser and Particle Beams **12**, 463, 1994.
- [8] Lucio, A. and Miceli, M., Journal of X-Ray Sci. and Tech., **4**, 247, 1994.

PHASE AND SYNCHRONOUS DETECTOR THEORY AS APPLIED TO BEAM POSITION AND INTENSITY MEASUREMENTS

J. D. Gilpatrick, Los Alamos National Laboratory, Los Alamos, NM 87545 USA

Abstract

A popular signal processing technique for beam position measurements uses the principle of amplitude-modulation-to-phase-modulation (AM/PM) conversion and phase detection. This technique processes position-sensitive beam-image-current probe-signals into output signals that are proportional to the beam's position. These same probe signals may be summed and processed in a different fashion to provide output signals that are proportional to the peak beam current. This paper derives the transfer functions for the AM/PM beam position and peak beam current processors.

I. INTRODUCTION

Presently, there are several techniques that process signals from position-sensitive beam-image-current probes into wide-bandwidth signals proportional to charged particle beam positions and peak current. One of the more popular techniques uses a double balanced mixer (DBM) as a component in a AM/PM beam-position processor and peak beam current or intensity detector [1,2]. The DBM is used as a phase detector in the beam position processor and a synchronous detector in the peak current processor. Fig. 1 and 5 show simplified schematics of these two processors.

The processor initially filters and amplifies opposite probe-lobe signals (e.g., top and bottom lobes) to provide optimum measurement signal-to-noise characteristics. The amplitude ratio of these signals is then converted to a phase difference using an AM/PM circuit. The input signals to the AM/PM circuit are

$$|V_T| \sin(\omega_{RF}t + 0) \quad (1a)$$

and

$$|V_B| \sin(\omega_{RF}t + \pi/2) \quad (1b)$$

where $|V_T|$ and $|V_B|$ are the amplitudes of a specific fundamental or harmonic component of the beam bunching frequency, ω_{RF} . The $\pi/2$ phase delay in the bottom lobe's signal is required for the correct operation of the particular AM/PM circuit realization shown in Fig. 1. The phase difference between the two AM/PM-circuit-output ports, $\Delta\theta$, is

$$\Delta\theta = 2 \arctan(10^{R/20}) - \pi/2 \quad (2)$$

where $R(\text{dB}) = 20 \log(|V_T|/|V_B|)$ [2,3]. This AM/PM output-phase difference is measured by a DBM. Because of the inherent amplitude sensitivity of the DBM to amplitude variations, limiting amplifiers or limiters are used to stabilize the signal amplitudes to the DBM input ports in both the position and peak-current processors. These limiters are key components to an accurate AM/PM beam-position processor

and must have minimal amplitude and phase delay variations throughout their dynamic range. A low pass filter (LPF) between the output amplifier and DBM removes all intermediate frequency (IF) signal components that are generated by limiter output-signals and DBM "mixing" process so that the processor's output signal is only proportional to the beam's position.

In the following analysis, only the DC transfer function will be considered. To add the transient behavior of these circuits, the temporal response of the final multi-pole low-pass-filter must be added to the position- and current-processor output equations.

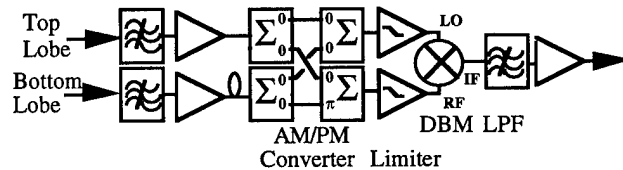


Figure 1: This schematic is a AM/PM beam-position processor. The DBM has two input ports commonly known as the local oscillator (LO) and radio frequency (RF) ports and an output IF port.

II. GENERAL DBM OPERATION

The DBM is a three port device consisting of two transformers whose primary and secondary windings are connected to two input ports and a bridge diode circuit, respectively (see Fig. 2). The DBM output port produces a

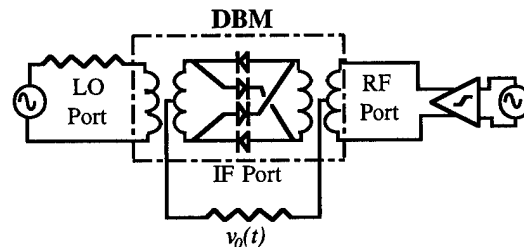


Figure 2: DBM schematic with a limiter amplifier driving the LO port and a terminating resistor across the output IF port.

current through a termination resistor connected between the center taps of the two secondary transformer-windings. As the sign changes on either the LO or RF input ports, currents are conducted through the appropriate diodes in the bridge circuit and through the termination resistor to produce an output voltage, $v_o(t)$.

The LO port is near saturation (as defined by the limiter drive circuitry and the DBM diodes in saturation), the resulting signal provides a square wave switching function described by

$$S(t) = 2 \sum_{n=1}^{\infty} \frac{\sin(n\pi/2)}{n\pi/2} \cos(n\omega_{LO}t + \theta_{LO}). \quad (3)$$

If the RF port is not saturated, its signal is

$$v_{RF}(t) = V_{RF} \cos(\omega_{RF}t + \theta_{RF}). \quad (4)$$

The resultant IF-output-port signal is the multiplication of these two input port signals [4]. Processing at a single frequency (i.e., let $\omega_{LO} = \omega_{RF} = \omega$) and folding the left frequency-domain components into the right components, therefore providing an additional factor of two, the unfiltered IF-output-port signal, $v_0(t)$, is

$$v_0(t) = \frac{8}{\pi} V_{RF} \cos(\omega t + \theta_{RF}) \sum_{n=1}^{\infty} \frac{\sin(n\pi/2)}{n} \cos(n\omega t + \theta_{LO}). \quad (5)$$

By employing a trigonometric identity, the two cosine terms with different arguments in Eq. (5) are separated into sum and difference frequency and phase terms and, $v_0(t)$ becomes

$$v_0(t) = \frac{8}{\pi} V_{RF} \sum_{n=1}^{\infty} \frac{\sin(n\pi/2)}{n} \{ [\cos((\omega - n\omega)t + (\theta_{RF} - \theta_{LO}))] + [\cos((\omega + n\omega)t + \theta_{RF} + \theta_{LO})] \}. \quad (6)$$

Since only the fundamental components are used for the position and peak current processing, and remembering that the LO and RF ports have the same fundamental frequencies, the filtered IF-output-port signal, $v_0(t)$, is

$$v_0(t) = \frac{4}{\pi} V_{RF} \sum_{n=1}^{\infty} \frac{\sin(n\pi/2)}{n} \cos(\theta_{RF} - \theta_{LO}) \quad (7)$$

or

$$v_0(t) = \frac{\beta}{\pi} V_{RF} \cos(\Delta\theta) \quad (8)$$

where $\beta \approx 3.105$ for $n = 1$ to 199.

III. POSITION TRANSFER FUNCTION

Unsaturated DBM RF-Port Case

Fig. 1 shows the beam position processor with limiters connected to the RF- and LO-input DBM ports. To initially simplify the mathematical model, assume that there is no limiter connected to the DBM RF port (i.e., similar to Fig. 5). The position-processor transfer function, $v_{pos}(t)$, is the combination of Eq. (2) and (8) and is

$$v_{pos}(t) = \frac{\beta}{\pi} A_I A_O \alpha V_{RF} \cos[2 \arctan(10^{R/20}) - \pi/2] \quad (9)$$

where α is an dimensionless attenuation circuit-constant and A_I and A_O are the input and output amplifier gains in volts per volts.

Saturated DBM RF-Port Case

However, for the typical realistic position processor, there are limiters for each DBM input port, therefore, Eq. (4) and (5) are rewritten to include the square-wave saturation effect of the limiters so that

$$v_{RF}(t) = 2V_{RF} \sum_{m=1}^{\infty} \frac{\sin(m\pi/2)}{m\pi/2} \sin(m\omega_{RF}t + \theta_{RF}) \quad (10)$$

and

$$v_0(t) = 8V_{RF} \sum_{n=1}^{\infty} \sum_{m=1}^{\infty} \frac{\sin(n\pi/2)}{n\pi/2} \frac{\sin(m\pi/2)}{m\pi/2} \cos(m\omega_{RF}t + \theta_{RF}) \cos(n\omega_{LO}t + \theta_{LO}). \quad (11)$$

The unfiltered DBM-IF-port signal is further simplified by recognizing that Eq. (11) is the convolution of two square waves and can be expressed as a Fourier series. After the same trigonometric identity used between Eq. (5) and (6) is applied, and higher frequency components are removed using a LPF, the filtered DBM-IF-port signal becomes

$$v_0(t) = 2V_{RF} \left\{ \frac{8}{\pi^2} \sum_{n=1}^{\infty} \frac{\sin[(2n-1)(\theta_{LO} - \theta_{RF})]}{(2n-1)^2} \right\}. \quad (12)$$

Fig. 3 shows the triangular waveform as a function of the DBM input-phase difference described by the bracketed portion of Eq. (12) [5].

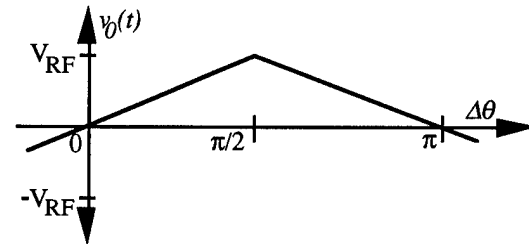


Figure 3: Waveform of $v_0(t)$ in Eq. (12).

Since the AM/PM converter does not allow the phase difference between the two DBM input ports to extend past $\pm\pi/2$, Eq. (12) is further simplified as

$$v_0(t) = \frac{\beta}{\pi} V_{RF} (\Delta\theta) \quad (13)$$

where $\beta = 4$. Therefore, for the saturated DBM-RF-port condition, the position-processor transfer-function equation is

$$v_{pos}(t) = \frac{4}{\pi} A_O \alpha V_{RF} \left[\arctan(10^{R/20}) - \pi/4 \right]. \quad (14)$$

Fig. 4 shows, in practice, how well this model describes the actual circuitry. The circuit parameters α , A_O , and V_{RF} were measured for various input signal ratios, and a nonlinear least squares fit based on Eq. (14) was performed on the measured data. The fit variable was a single multiplier substituted for α , A_O , and V_{RF} . As can be seen, the error between the fit and theory is within a ± 0.1 dB band. The measured centered-beam multiplier for a 1 dB input ratio was 0.76 volts and the fitted equation gave a 0.79 volt multiplier. This difference is within the measurement errors of the circuit parameters used in the multiplier.

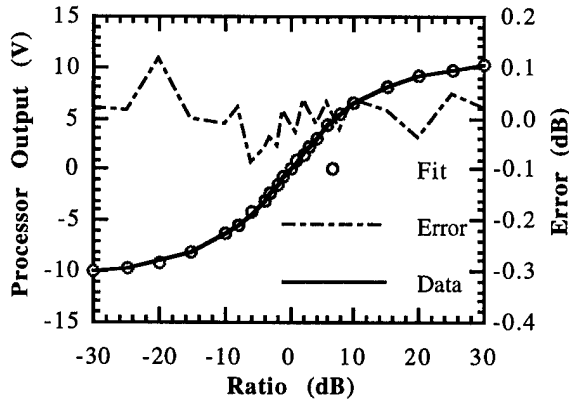


Figure 4: Measured data and fitted theory based on Eq. (14) and the error between the theory and data are plotted as a function of the ratio of opposite-lobe input signals.

Alternate Form

The position-processor transfer function can be further simplified by letting $\phi = \arctan(|V_T|/|V_B|)$ and using another trigonometric identity. The resultant simplification to Eq. (14) is

$$v_{pos}(t) = \frac{4}{\pi} A_O \alpha V_{RF} \arctan \left[\frac{\tan \phi - 1}{\tan \phi + 1} \right]. \quad (15)$$

Substituting for ϕ in Eq. (15), $v_{pos}(t)$ is

$$v_{pos}(t) = \frac{4}{\pi} A_O \alpha V_{RF} \arctan \left(\frac{|V_T| - |V_B|}{|V_T| + |V_B|} \right). \quad (16)$$

For beam positions near the center of the probe, Eq. (15) can be further reduced to

$$v_{pos}(t) = \frac{4}{\pi} A_O \alpha V_{RF} \left(\frac{|V_T| - |V_B|}{|V_T| + |V_B|} \right). \quad (17)$$

As can be seen from Eq. (16) and (17), the AM/PM ratio processing technique is a special case of the more generic "difference-over-sum" (Δ/Σ) processing technique. This AM/PM technique has a larger dynamic range than other Δ/Σ processing techniques due to its inherent larger signal-to-noise characteristics for centered-beam conditions. Other typical Δ/Σ processors have lower signal-to-noise characteristics because most circuit realizations have an amplitude-nulling node or junction within their circuit topology. This nulling junction limits the generic Δ/Σ -processor's dynamic-range for center beam conditions. As can be seen in Fig. 1, the AM/PM position processor does not have an amplitude-nulling junction within its circuit topology, and therefore, has a larger dynamic range than other Δ/Σ processors.

IV. CURRENT TRANSFER FUNCTION

Fig. 5 shows how the DBM is used in a synchronous detector for the peak beam-current processor. There are two major differences between the beam position processor as shown in Fig. 1 and the peak beam current processor. First,

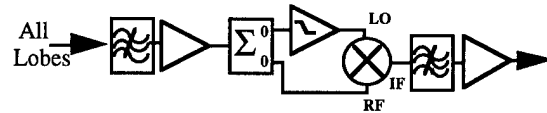


Figure 5: This schematic shows a peak current detector.

the peak current detector uses only a single limiter and, second, the LO and RF DBM ports have 0 or π phase difference between them. This phase shift allows the RF port to act as a linear or synchronous detector for the signal presented to it (i.e., the DBM is a high-frequency full-wave rectifier for the RF-port sinusoidal-signal). The peak-current-processor transfer-function equation is Eq. (8) with $\Delta\theta$ equal to 0 or π , and $V_{RF} = A_I \alpha v_{LOBES} / \sqrt{2}$ where v_{LOBES} is the summation of all probe-lobe signals. The resultant transfer function, $v_{current}(t)$, is

$$v_{current}(t) = \frac{\beta}{\sqrt{2}\pi} A_I A_O \alpha v_{LOBES} \quad (18)$$

where, again, $\beta \approx 3.105$.

V. CONCLUSION

This paper has derived the transfer functions for the AM/PM beam position and peak current processors. The equations were solved for the nonsaturated and saturated DBM-RF-port beam-position-processor. The arctan function's argument, found in the typical saturated RF-port case, is comprised of the ratio of opposite probe lobes. After further simplification, it was found that this AM/PM position-processor circuit is really a special case of the more general "difference-over-sum" processing technique. Finally, the peak-beam-current transfer function was derived.

VI. REFERENCES

- [1] R. E. Shafer, "Beam Position Monitoring," AIP Conference Proceedings 212, Upton, NY, (1989).
- [2] S. P. Jachim, R. C. Webber, and R. E. Shafer, "RF Beam Position Measurement for Fermilab Tevatron," IEEE Trans. Nucl. Sci. **28**, 2323 (1981).
- [3] J. D. Gilpatrick and F. D. Wells, "Double Balance Mixer Operation used as Phase and Synchronous Detectors as Applied to Beam Position and Intensity Measurements," LA-UR-93-1622, AT-3 TECHNICAL NOTE:92-8, July, (1992).
- [4] Solid State Radio Engineering, Krauss, Bostian, Raab, John Wiley & Sons Inc., 1980, p. 188-202.
- [5] Continuous and Discrete Signal and Systems Analysis, McGillen and Cooper, Holt Reinhart and Winston Inc., 1974, p. 101.

Testing Coaxial Switches of BPM using a High-Resolution RF Detector

Takao Ieiri

KEK, National Laboratory for High Energy Physics
Oho 1-1, Tsukuba-shi, Ibaraki-ken, 305 Japan
Internet: IEIRIT@kek.vax.kek.jp

2. RF DETECTOR

ABSTRACT

A high-resolution rf detector has been developed in order to test a coaxial switch used in a beam-position monitor (BPM). The detector with a Digital Multi-Meter (DMM) has an rms resolution of the order of 10^{-6} in short time and a wide linear range of 50 dB. Though detected voltage depends on temperature, it can be compensated by measuring the detector temperature. The insertion loss and its stability of several types of switches were measured at 1.0 GHz using the detector. The normalized positions are kept within $\pm 3 \times 10^{-5}$, which corresponds to about $\pm 1.0 \mu\text{m}$ in a chamber of the KEKB. The detector is useful to evaluate the insertion loss of switches.

1. INTRODUCTION

The beam position is obtained by processing signals from pick-up electrodes. There are two basic methods for the signal processing. One is a parallel process, where the signals are detected at the same time. The other is a multiplexed method, where the signals are multiplexed by a switch and detected by a common detector. Since the multiplexed method has generally better performance on the resolution than the parallel process without considering a real-time measurement, many storage rings employ the multiplexed method [1 - 5].

The TRISTAN MR employs the multiplexed BPM system [6]. About 400 mechanical switches are installed near pick-up electrodes. The picked-up signals are multiplexed by the switch and transferred to a control room via a long coaxial cable. A 380 MHz component of a beam pulse is detected. Measurement errors were noticed in some BPMs, which was mainly caused by a loose contact of a switch. A stability of the contact is reflected in that of the BPM system. When the insertion loss of one port of a switch slightly changes by 0.01 dB (0.1%), for instance, which causes a position change by more than $10 \mu\text{m}$ in the MR.

The KEKB [7] requires about 920 BPMs in the two rings. The stability of a relative beam position rather than an absolute value is strongly demanded. The KEKB will also employ the multiplexed method. The detected frequency is about 1.0 GHz, twice the accelerating frequency. A high-resolution detector is required to detect a change of less than 10^{-4} at 1.0 GHz in order to test the stability of a switch. A network analyzer and/or a spectrum analyzer cannot detect such a small change.

Various techniques are used for linear detection of an rf signal. A most simple method is to use a diode. However, this method has poor linear characteristics and low sensitivity. The synchronous detection is widely used in BPM systems, where an rf signal is converted to a constant amplitude signal using a limiter and is multiplied with an input rf signal. The dynamic range is limited by that of a limiting amplifier. A phase error between the input rf and the limited signal would yield a nonlinearity in the detection.

A simple and precise rf detector has been developed using a DMM. Fig. 1 shows block diagram of the rf detector. The detector consists of a frequency converter, an rms detector and a charge ADC. The frequency converter lowers a frequency of an input rf signal to 455 kHz. Its total gain is 23 dB. The latter two parts are installed in a commercially available DMM (Keithley, 2001). The DMM can measure a signal whose frequency is less than 2 MHz with a resolution of the order of 10^{-6} using an improved rms detector [8]. An rms value of the 455 kHz signal can be obtained by an analog circuit shown in Fig. 1 using the equation of $V_{rms} = \text{Avg}(V_{in}^2 / V_{rms})$. Here, V_{in} is an input voltage to the DMM. Noises caused by the power line can be reduced by locking a measurement cycle to the power line. The DMM is guaranteed that its temperature coefficient is $\pm 5 \times 10^{-5} / ^\circ\text{C}$ [8].

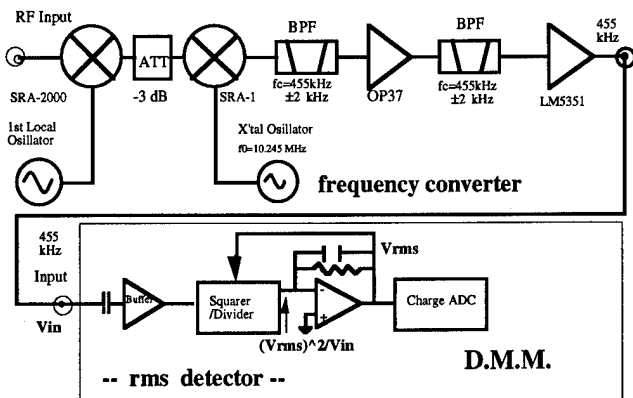


Fig. 1 Block diagram of RF detector.

Since one frequency component of a beam is usually detected, a continuous wave from a signal generator (SG, hp-8648C) is used as a beam signal. The signal is fed to the frequency converter and is read by the DMM. Fig. 2 shows a dynamic response of the detector. Even if the input frequency changes, the detector is available up to 2 GHz by adjusting the frequency of the 1st local oscillator as seen in Fig. 1. The linearity can be obtained from a ratio of two detected voltages between with and without a fixed attenuator of 1 dB. A

linearity of less than ± 0.1 %/dB over the range of 50 dB was obtained.

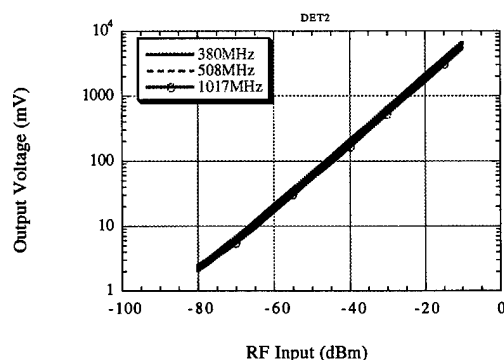


Fig. 2 Dynamic response of the detector.

A short-time stability was tested by measuring repeatedly detected voltages. It took about 5 seconds during a 100 times measurement. Fig. 3 shows the maximum deviation of the rms resolution defined as an rms value divided by an average over several measurements as a function of rf amplitude. The rms resolution seems to be best around -25 dBm, where the rms resolution within the order of 10^{-6} was obtained. When the rf level is low, the stability is worse due to a lower denominator.

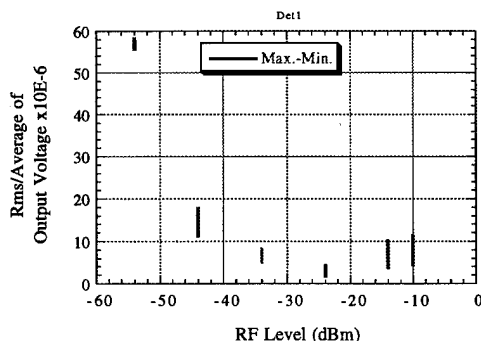


Fig. 3 Rms resolution of the detector as a function of rf level.

A drift of the output voltage was observed during a long time of more than 10 sec. The drift seemed to be very sensitive to the room temperature. In order to see the drift, the temperature on the chassis of the frequency converter was measured with a resolution of 0.01°C and plotted together with detected voltages as seen in Fig. 4. One may notice a linear relation between the output voltage and the detector temperature. This linear relation was obtained when the temperature difference between the room and the detector was almost constant without using an air-conditioner. This may be because that an output level of the SG also depends on the room temperature. The measured temperature dependence of the detected voltage was $3.75 \text{ mV}/^{\circ}\text{C}$ at the rf level of -20 dBm. This temperature dependence seems to be an intrinsic property of semiconductor devices in the converter. However, the dependence was able to be compensated from the measured

temperature (T_d) using a simple linear equation of $V_c = V_m + 3.75T_d$, where V_c and V_m are compensated and measured voltages respectively. The compensated voltages are kept within $\pm 0.35 \text{ mV}$ against a change of 6°C as seen in Fig. 4.

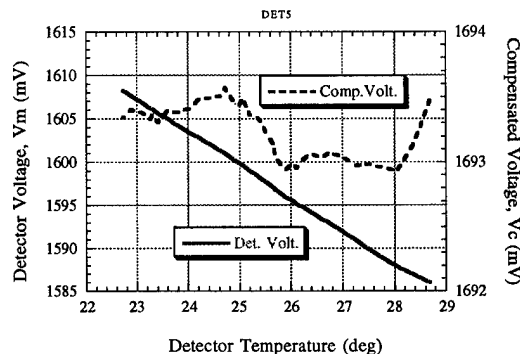


Fig. 4 Detected voltages as a function of the temperature measured at the detector and voltages compensated using the measured temperature.

3. COAXIAL SWITCH

Several types of coaxial switches are commercially available. One may classify the switches into two groups. One is a mechanical type, where a switch is actuated by a coil. There are two types of mechanical switches in air and in mercury evaporation. One may call the two types of switches 'mechanical' and 'mercury' in order to distinguish between them. These switches can be used even for a directly picked-up beam pulse with a high peak voltage. The other is semiconductor devices using a PIN diode and an FET. These semiconductor switches can make faster switching than the mechanical ones, but generally have weak points for a high peak-power pulse and for radiation environment.

The most important performance of a switch for a BPM system is the stability of the insertion loss. Fig. 5 shows an apparatus for measuring the stability. An output signal of the SG is demultiplexed into 4 ways using a power divider and fed to each port of a switch and multiplexed. An isolator is inserted in front of the frequency converter to avoid an effect of a reflection due to impedance mismatch. A multiplexed signal is detected and calculated by a personal computer. One obtains two normalized positions (Δ / Σ)s from four detected voltages as seen in Appendix. It takes about 5 seconds to scan the cycle. The obtained normalized positions do not show real values due to an effect of a cross-talk in the power divider but they are useful enough for measuring the stability. Before a switch was tested, temperature dependence of the apparatus was examined using another power divider instead of a switch. Fig. 6 shows measured normalized positions as a function of the detector temperature. One may notice that the normalized positions are independent of the temperature. The fluctuations are kept within $\pm 3 \times 10^{-5}$ against a change of 4°C . Therefore, this apparatus is useful enough to evaluate the stability of the switches with the resolution of less than 1×10^{-4} .

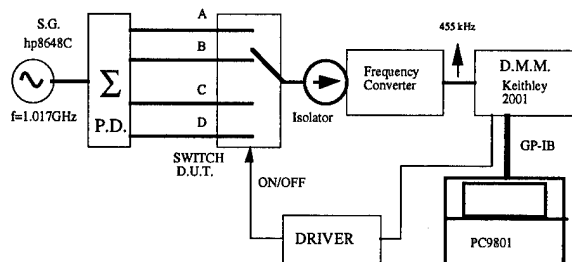


Fig. 5 Apparatus measuring the stability of the insertion loss.

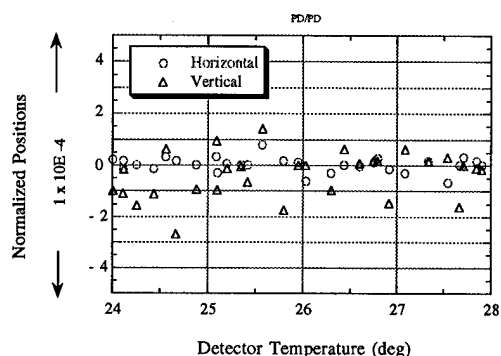


Fig. 6 Measured normalized positions as a function of the detector temperature.

Some switches were tested. An example of histograms of the normalized positions is shown in Fig. 7. They show that maximum deviations are $\pm 3 \times 10^{-5}$, which corresponds a position of $\pm 1 \mu\text{m}$ in case of a chamber with an inner diameter of 100 mm as used in the KEKB. The deviations are comparable to the performance of the apparatus itself.

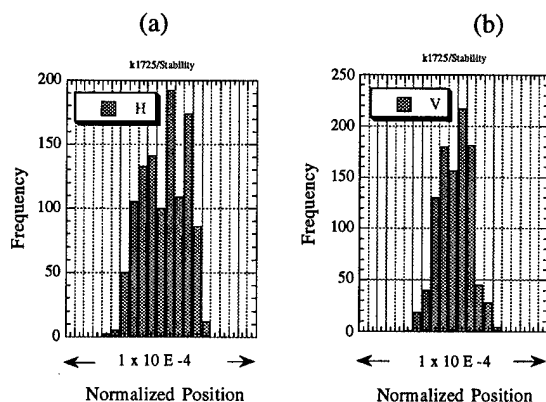


Fig. 7 Histograms of horizontal (a) and vertical (b) normalized positions of a mercury switch with 1000 cycles.

In order to measure an absolute value of the insertion loss, a reliable mechanical switch proved in the stability test was used instead of the power divider because the mechanical switch has the cross-talk of better than 80 dB. The losses can be measured within the accuracy of $\pm 2 \times 10^{-4}$ using temperature-compensated voltages as shown in Fig. 4.

Table 1 shows the measured losses of sampled switches including the loss of the reference switch. The insertion losses of a sampled mechanical switch are the best performance and are well balanced within 0.1%. On the other hand, those of the others are not balanced with more than 0.2%. Since this imbalance yields an offset in the beam position, this measurement will be needed for all switches before installing.

Table 1 Insertion losses of sampled switches measured at 1.0GHz.

Type	Model	Ch1	Ch2	Ch3	Ch4
Mechanical	CS38S(1)	0.9969	0.9972	0.9967	0.9966
Mercury	UCL1G (2)	0.9368	0.9204	0.9289	0.9252
PIN diode	TS503(3)	0.9402	0.9418	0.9419	0.9400
GaAs FET	SW254 (4)	0.8574	0.8564	0.8630	0.8587

(1):Teledyne,USA (2):Sanyu, Japan

(3):Tokimec, Japan (4):Anzac, USA.

Acknowledgement

The author would like to thank colleagues of the KEKB monitor group for useful comments.

REFERENCES

- [1] C. Carman and J.-L. Pellegrin, NIM 113(1973)p.423.
- [2] D. Rice et al., IEEE Trans. Nucl. Sci. NS-30 (1983)p.2190
- [3] R. Biscardi and J. Bittner, Proc. of 89PAC, Chicago, (1989)p.1516.
- [4] F. Loyer and K.Scheidt, Proc. of 92EPAC, (1992)p.1112.
- [5] K. Shinoe et al., Proc. of 93PAC, Washington D.C., (1993)p.2295.
- [6] H. Ishii et al., The 6th Symp. on Accelerator Science and Technology, Tokyo, Japan (1987) p.207.
- [7] S-I. Kurokawa, WPG04 in this conference.
- [8] Keithley, the manual of D.M.M. model 2001.

Appendix

Horizontal and vertical beam positions are obtained by comparing four beam signals named V_A , V_B , V_C and V_D . They are expressed with a linear approximation as

$$X = k_H \cdot \frac{V_A - V_B - V_C + V_D}{V_A + V_B + V_C + V_D} = k_H \cdot \left(\frac{\Delta_H}{\Sigma} \right) \text{ and}$$

$$Y = k_V \cdot \frac{V_A + V_B - V_C - V_D}{V_A + V_B + V_C + V_D} = k_V \cdot \left(\frac{\Delta_V}{\Sigma} \right),$$

where k_H and k_V are position sensitivities determined by a mechanical arrangement of the electrodes. When four electrodes skewed by 45° with the axes are mounted on a chamber wall with a diameter of 100 mm, k_H and k_V are about 35 mm respectively. One may call the (Δ/Σ) s of the above equation normalized positions. The normalized positions are independent of beam intensity.

A BEAM SIZE MONITOR BASED ON APPEARANCE INTENSITIES FOR MULTIPLE GAS IONIZATION*

T. Katsouleas and J. Yoshii, Department of Electrical Engineering-Electrophysics,
University of Southern California, Los Angeles, CA 90089
W. B. Mori, C. Joshi and C. Clayton, Department of Electrical Engineering
University of California, Los Angeles, CA 90024

Abstract

A method of measuring the spot size or bunch length of intense charged particle beams is proposed. The relation between the size (widths and length) of a charged particle beam and the beam's electric field forms the basis for a sub-micron beam size monitor. When the beam passes through a low pressure gas of high Z atoms, the beam field causes multiple ionizations of the gas atoms. The appearance of ionized atoms in a given charge state gives information about the field of the beam and hence its size. Sample calculations show that appearance thresholds can indicate the spot size of round beams with 10 nm accuracy or the bunch length of round or flat beams with up to 10 μm accuracy.

I. INTRODUCTION

Future colliders for high energy physics call for beams of ever smaller dimensions. Recently, two new techniques for measuring sub-micron beams have been tested, a laser interference technique used at the Final Focus Test Beam (FFTB) at Stanford [2] and a time-of-flight technique proposed by a group from Orsay [3]. The scheme we propose here is complementary to these two and can alternatively be used to measure bunch length if spot size is known. Our approach for beam size measurement is a modification of the appearance intensity diagnostic developed for use with lasers [4].

The beam size diagnostic we propose is shown in Figure 1: the focused particle beam passes through a gas cell. The ions produced by tunnel ionization are accelerated by an external electric field to detectors, and the ionization yields are determined. For a round Gaussian beam, the beam spot size can be deduced by relating it to the highest charge state observed. For flat beams this diagnostic provides no data about the small spot size. However, for a known spot size, the appearance of charge states can be used to compute the bunch length of either flat or round beams. We calculate ionization yields by modelling the interaction of the electric field of a round or flat beam with various gases.

II. THEORETICAL MODEL

The rate of change of atoms in each charge state during the passage of the beam is due to ionization by the beam's electric field.

$$\frac{\partial N_j}{\partial t} = w_j N_{j-1} \quad (1)$$

*Work supported by US DOE grant DE-FG03-92ER40745

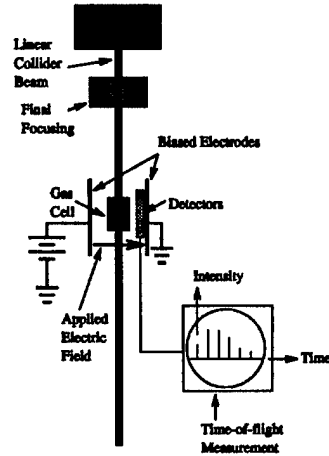


Figure 1. Proposed experimental setup for beam diagnostic.

The N_j represent the fraction of the total gas atoms which are in the j th charge state. The ionization probability, per unit time, is given by the Keldysh formula

$$w_j = w_0 \frac{E_j^{\frac{5}{2}}}{E} e^{-\frac{2E_j^{\frac{3}{2}}}{3E}} \quad (2)$$

where E_j = ionization potential for the j th ionization state, normalized by 13.6 eV; E = transverse beam electric field ($E_r(r)$ for round beams), normalized by the atomic field 5.1453×10^{11} V/m; $w_0 = 1.635 \times 10^5$ /ps. The total ionization yields are obtained by integrating Equations (1) in time.

A. Round beams

The round beam is modelled by a cylindrical bi-Gaussian distribution,

$$N_b(r, z) = N_{b0} e^{-\frac{r^2}{2\sigma_r^2}} e^{-\frac{z^2}{2\sigma_z^2}} \quad (3)$$

where N_{b0} = maximum particle density, σ_r = beam spot size, and σ_z = bunch length. The beam number N_b is related to N_{b0} by

$$N_{b0} = \frac{N_b}{(2\pi)^{\frac{3}{2}} \sigma_r^2 \sigma_z} \quad (4)$$

The radial electric field is found using Gauss' Law, with time dependence brought in through

$$z = c(t - t_p) \quad (5)$$

where t_p is the time when the beam particle density is a maximum.

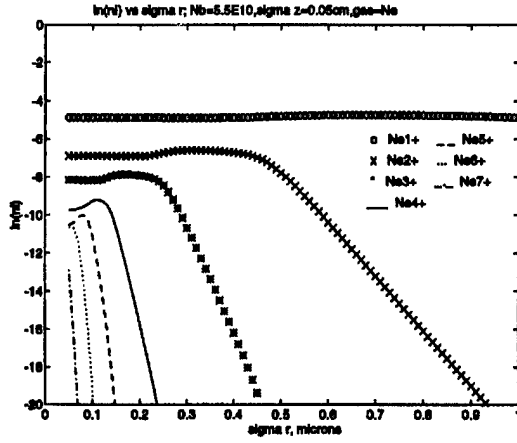


Figure 2. Logarithm of fractional charge state densities for Ne^{1+} through Ne^{8+} vs. σ_r for $N_b = 5.5 \times 10^{10}$ and $\sigma_z = 0.05$ cm.

Eqs. (1) were time-integrated numerically and averaged over r . N_b was taken to be 5.5×10^{10} and the gas sample is assumed to have a radius $r_{max} = 30$ microns for our round beam calculations.

B. Flat beams

The flat beam is modelled by a tri-Gaussian distribution,

$$N_b(x, y, z) = N_{b0} e^{-\frac{x^2}{2\sigma_x^2}} e^{-\frac{y^2}{2\sigma_y^2}} e^{-\frac{z^2}{2\sigma_z^2}} \quad (6)$$

where σ_x = beam width and σ_y = beam height $\ll \sigma_x$; N_{b0} and σ_z are defined as in the round beam case, and the same relation between z and t applies. N_b is related to N_{b0} by

$$N_{b0} = \frac{N_b}{(2\pi)^{\frac{3}{2}} \sigma_x \sigma_y \sigma_z} \quad (7)$$

For these calculations, the beam is treated as a 2-D problem ($\frac{\partial}{\partial z} = 0$). This assumes that the gas cell is shorter than the beam beta functions [6] β_x^* or β_y^* . The gas cell is divided into rectangular boxes of grid sizes δx and δy in the region $-\sigma_x \leq x \leq \sigma_x$, with $\frac{\partial E_y}{\partial x} \ll \frac{E_y}{\delta x}$; over most of the ionization volume $E_x \ll E_y$ and we neglect E_x . Applying Gauss' Law with these approximations allows calculation of E_y . Net ionization yields are obtained by time-integrating Eqs. (1) in each box and summing using a box-based weighting.

III. RESULTS

A. Spot size

Figure 2 plots ionization yields for Ne logarithmically against σ_r for bunch length $\sigma_z = 0.05$ cm. Two points should be noted. First, a charge state will not appear unless σ_r is below some threshold value which allows tunnelling to occur. If σ_r is below the threshold, the ionization yield increases rapidly, then begins to level off. Second, as each successive charge state appears, the yield for the preceding state is decreased by that of the new charge state.

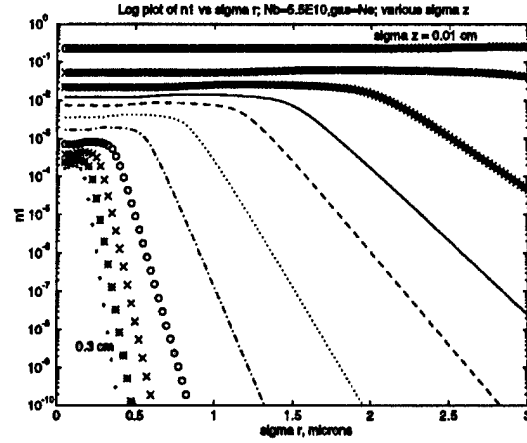


Figure 3. Logarithmic plot showing the variation in ionization yield for Ne^{1+} vs. σ_r as σ_z is varied from 0.01 cm to 0.3 cm. Notice the reduction in N_1 and the threshold value of σ_r for higher values of σ_z . $N_b = 5.5 \times 10^{10}$ in these calculations. The data for the higher charge states show a similar variation.

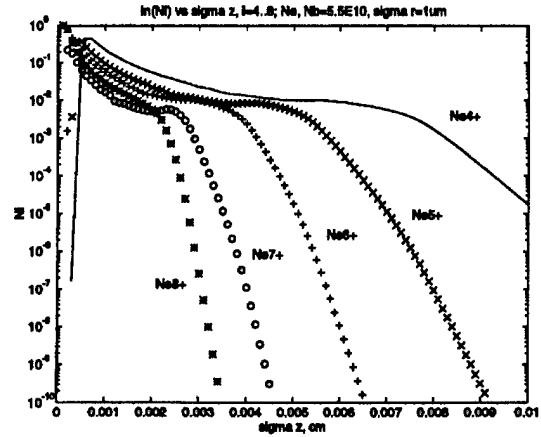


Figure 4. Logarithmic plot of round beam ionization yields for Ne plotted against small values of bunch length. $N_b = 5.5 \times 10^{10}$ and $\sigma_r = 1 \mu\text{m}$. At these small values of σ_z , there are clear appearance thresholds for Ne^{5+} and higher charge states.

It is clear that no significant production of Ne^{2+} occurs until the spot size is below $1 \mu\text{m}$; thus the appearance of Ne^{2+} indicates a spot size below this value. Similarly, the appearance of other charge states gives spot size information from $1 \mu\text{m}$ to $0.07 \mu\text{m}$ with accuracy up to about $0.03 \mu\text{m}$.

To gain some insight into the variation of the ionization yields with σ_z , the calculations were repeated for several values of σ_z ranging from 0.01 cm to 0.3 cm. Figure 3, a logarithmic plot of N_1 vs. σ_r , shows the decrease in N_1 and the lowering of the threshold σ_r below which tunnelling is allowed as σ_z is increased. Although only the data for N_1 are plotted here, the results are similar for the higher charge states.

B. Bunch length

B.1 Round beams

Ne was chosen as the sample gas, with $\sigma_r = 1 \mu\text{m}$. In Figure 4, the bunch lengths are small enough that significant

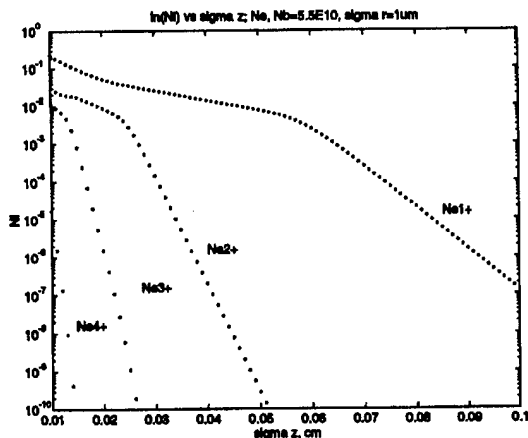


Figure 5. Logarithmic plot of round beam ionization yields for Ne plotted against larger values of bunch length. $N_b = 5.5 \times 10^{10}$ and $\sigma_r = 1 \mu\text{m}$. The appearance thresholds for Ne^{1+} through Ne^{4+} are visible on this scale.

amounts of Ne^{4+} and higher charge states are produced. Figure 5 shows data for longer bunch lengths in the range $0.01 \text{ cm} \leq \sigma_z \leq 0.1 \text{ cm}$. Here, only Ne^{1+} through Ne^{4+} appear in significant numbers. Similar to the data for spot size determination, there are threshold values of bunch length for the appearance of higher charge states. The charge states from Ne^{2+} up give information on bunch lengths ranging from 0.05 cm down to 0.0035 cm with accuracy up to about 0.001 cm.

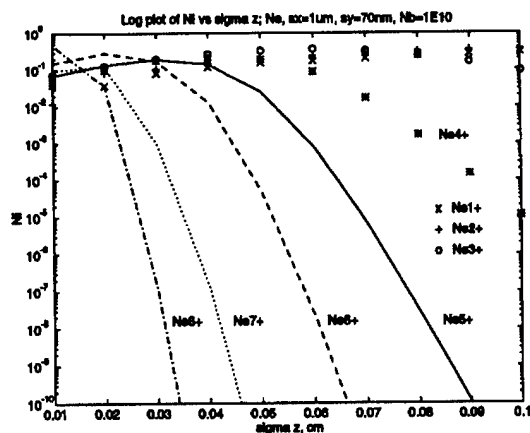


Figure 6. Logarithmic plot of flat beam ionization yields vs. bunch length. The sample gas is Ne, $N_b = 10^{10}$, $\sigma_x = 1 \mu\text{m}$, $\sigma_y = 70 \text{ nm}$. Appearance thresholds for charge states Ne^{5+} and higher are evident.

B.2 Flat beams

The flat beam data were calculated for a beam containing 10^{10} electrons with $\sigma_x = 1 \mu\text{m}$, $\sigma_y = 70 \text{ nm}$, and Ne in the gas cell. These data are shown in Figure 6. As in the round beam case, there are well-defined bunch length thresholds below which charge states will not occur. Bunch length information from 0.09 cm down to about 0.035 cm may be obtained with accuracy up to about 0.01 cm within the limitations of the simplifications made in the calculations.

IV. CONCLUSION

A diagnostic for particle beam size based on field ionization has been described. Calculations of the ionization yields versus spot size for round beams show fairly sharp thresholds for the appearance of the various charge states involved. Similar calculations using different bunch lengths yield curves with the same form, with maxima and threshold spot size decreasing as the bunch length is increased. Plots of ionization yields versus bunch length for both round and flat beams also display thresholds for the appearance of successive charge states. These thresholds can be used to determine the beam size given the beam number and either a known spot size or a known beam length.

An experiment to test this diagnostic could also be useful in atomic physics. Previous tests of DC atomic tunneling theory with lasers [4] have yielded discrepancies between theory and experiment attributed to the AC nature of the laser. As the particle beam does not oscillate, the data obtained through an experiment using the gas cell-beam apparatus described here with beam intensities comparable to those of the laser would be useful in separating the DC and AC effects.

References

- [1] T. Katsouleas *et al.*, "A Beam Size Monitor Based on Appearance Intensities for Multiple Gas Ionization" in *1994 Advanced Accelerator Concepts Conference Proceedings*, 1994.
- [2] B. Schwarzschild, "New Stanford facility squeezes high-energy electron beams," *Physics Today*, vol. 47, no. 7, p. 22, 1994.
- [3] J. Buon *et al.*, "A beam size monitor for the Final Focus Test Beam," *Nuc. Inst. Meth. A*, vol. 306, pp. 93-111, 1991.
- [4] S. Augst *et al.*, "Tunneling Ionization of Noble Gases in a High-Intensity Laser Field," *Phys. Rev. Lett.*, vol. 63, pp. 2212-2215, 1989.
- [5] T. Katsouleas, W. B. Mori, C. Joshi, C. Clayton, "U.S. Plasma Lens Note #002," 1993 (unpublished).
- [6] H. Wiedemann, *Particle Accelerator Physics*, New York: Springer-Verlag, 1993, pp. 159-164.
- [7] W. Barletta, S. Chattopadhyay, P. Chen *et al.*, "Letter of Intent for Plasma Lens Experiments at the Final Focus Test Beam," 1993.

BEAM PROFILE MEASUREMENT IN THE PRESENCE OF NOISE *

K. Bertsche, Fermi National Accelerator Laboratory[†], P.O. Box 500, Batavia, IL 60510 and
J. Palkovic, Deutsches Elektronen-Synchrotron DESY, Notkestraße 85, 22603 Hamburg, Germany

Abstract

In measuring the distribution of a nominally Gaussian beam, it is generally necessary to sample the beam at a number of discrete positions. In the real world, these samples will be somewhat noisy. We present the results of simulations, showing the effects of noise in signal amplitude and noise in sample position on the calculated beam σ , as a function of sample spacing. This has implications for the wire spacing of multiwire profile monitors and for the sampling rate of flying wires and wall current monitors.

I. INTRODUCTION

Many situations occur where one wishes to measure the profile of a beam which is nearly Gaussian and to derive a good estimate of the beam σ . In generating design specifications for beam profile monitors and flying wires at the Superconducting Super Collider (SSC), it was necessary to find a quantitative relationship connecting the various sources of noise and the resultant errors in estimation of beam σ . Since we could not locate any direct treatments of this in the published literature, we decided to generate these relationships with some simple Monte Carlo simulations.

A Gaussian profile follows the relationship:

$$f(x) = A e^{-(x-m)^2/2\sigma^2} \quad (1)$$

which has three degrees of freedom: the amplitude A , the mean m , and the standard deviation σ . Thus, ideally, only three measurements at arbitrary points are necessary to perfectly reconstruct the distribution. But in the real world, noise is present and will lead to uncertainties in the reconstructed parameters. In practice, many more than three points are necessary to provide a good estimate of σ . A rule-of-thumb which has been used in the past is to try to sample at two or three points per σ [1].

II. ESTIMATION METHODS

The error in estimating σ depends greatly on how the estimation is done. Once a profile has been obtained, a

number of options present themselves of calculating the beam's σ . One could simply calculate the mean and standard deviation of the data points [2], but this leads to large errors for sparsely sampled or noisy profiles, because the contributions of points in the tails are overweighted. A much better method is to estimate σ by a least squares fit of the data to a Gaussian [2]. One could also use a "matched filter" approach, where one filters the data by multiplying the Fourier transform of the data by the Fourier transform of the expected profile, e.g. with a Gaussian or quasi-Gaussian profile. One could also "bin" the data, which is a special case of the matched filter approach. (It is equivalent to convolving the data with a rectangular pulse the width of a bin, then re-sampling this signal at points separated by the bin width.)

III. SIMULATIONS

Measurement noise can arise from two sources: noise in sample position (due primarily to mechanical jitter or misalignment) and noise in sample amplitude (due primarily to electrical noise on the signal). Simulations were done of each source separately.

The simulations were done as follows. First, a normalized Gaussian profile was generated with $\sigma=1$. This profile was sampled with a regular sampling grid of 60 points. The center of the sampling grid was randomly aligned (\pm one half of the sample spacing) with respect to the center of the Gaussian profile. Normally-distributed noise in either the sample positions or in the sample amplitudes was added. A Gaussian was fitted to the data by least squares regression (by varying A , m , and σ to minimize the squared errors or the χ^2). The resultant σ was compared to the original σ and the error was tabulated. This procedure was repeated a number of times, and the rms error in estimating σ was calculated for the given sample spacing and noise conditions.

This was repeated for different sample spacing and noise conditions, with the results shown in Figs. 1 and 2. In Fig. 1, amplitude noise was assumed to be independent of the signal amplitude at each sample point, and is normalized to the signal amplitude at the peak of the (theoretical) Gaussian profile. In Fig. 2, position noise is normalized to σ .

IV. DISCUSSION

For the case of noise in signal amplitudes (Fig. 1), the errors for a sampling frequency of one sample per σ are about what one might naively guess. The fractional errors

* Work primarily performed at the SSC Laboratory, operated by Universities Research Association, Inc. for the U.S. Department of Energy under Contract No. DE-AC35-89ER40486.

[†] Operated by the Universities Research Association, Inc. under contract with the U.S. Department of Energy.

in σ are approximately equal to the normalized noise amplitude; i.e. an rms noise level of 1% (-40 dB) of the Gaussian peak causes an rms error of 1% in the estimated value of σ , and so forth.

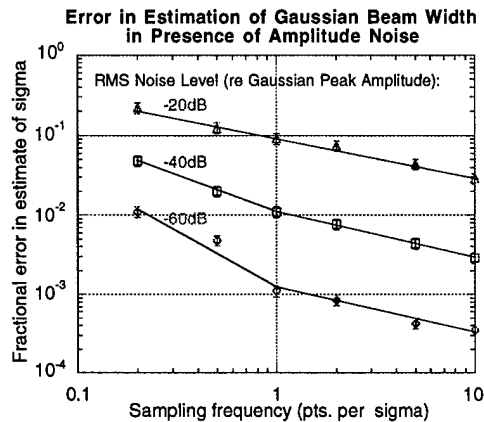


Figure 1: Simulation results of adding noise to signal amplitudes of a sampled Gaussian distribution.

The slope of the curves, for a well-sampled distribution (more than one sample per σ) also makes sense. As the sampling frequency is doubled, more samples are obtained near the peak of the Gaussian. One is effectively getting twice as much signal for the same amount of noise, so the error should drop by a factor of $2^{1/2}$. Thus the slope on a log-log plot should be $1/2$, as is observed.

For a more sparsely-sampled distribution (less than one sample per σ), the slope is greater than this. This is because the sampling is so sparse that sometimes there are NO sample points near the peak of the Gaussian, leading to even larger errors.

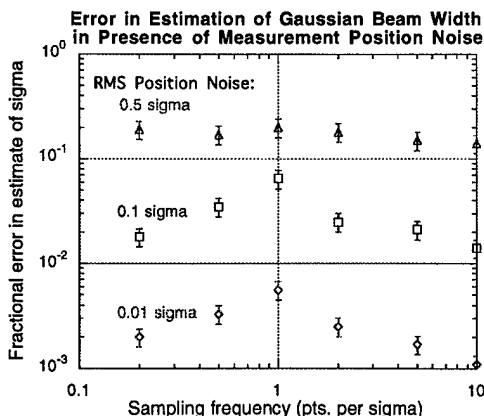


Figure 2: Simulation results of adding noise to sample positions of a sampled Gaussian distribution.

For the case of noise in sample positions (Fig. 2), the slope for a well-sampled distribution should again be $1/2$, for reasons similar to those given above, which is roughly

what is observed. As the sampling frequency is reduced, the estimate of σ is seen to improve. This may be because more of the data points lie in the tails, where noise in sample position has relatively little effect. Thus, even though the signal level is small, the noise is also small and a good estimate results. By this reasoning, noise in sample position will have the most serious effect where the slope of the Gaussian is largest, i.e. at an offset of σ from the peak. Thus it is reasonable that the greatest error in estimating σ occurs at a sampling frequency of around one sample per σ .

V. CONCLUSIONS

It is advisable to sample a Gaussian with at least one sample per σ to keep amplitude noise under control, and preferably with at least two samples per σ to reduce sensitivity to position noise. The rule of thumb of two or three samples per σ seems to be a good one.

For the Medium Energy Booster (MEB) at the SSC, where it was necessary to measure σ to at least a 7% precision, it would have been sufficient to sample the distribution with at least two points per σ , while maintaining a S/N of at least 30dB and a $\pm 0.1 \sigma$ tolerance on sample positions. Specifications for flying wires and beam profile monitors were to be based on this data.

VI. REFERENCES

- [1] Robert Webber, Fermi National Accelerator Laboratory, private communication.
- [2] Particle Data Group, "Review of Particle Properties", *Phys. Rev. D* **50**, 1 Aug. 1994, Part 1, §17, pp. 1275ff.

BEAM SHAPING USING A NEW DIGITAL NOISE GENERATOR

H. Stockhorst, G. Heinrichs, A. Schnase, S. Papureanu, U. Bechstedt, R. Maier, R. Tölle,
Forschungszentrum Jülich GmbH, Germany

A novel digital rf-noise generator [1,2] was used to excite the COSY-beam [3] longitudinally at a certain harmonic of the revolution frequency. Rectangular shaped noise spectra with bandwidths of the order of 10 kHz and frequency resolution of about 6 Hz were used. Beam distributions were measured during shaping and after switching off the noise source in dependence of bandwidth and amplitude of the rf-noise.

I. INTRODUCTION

The application of specifically shaped noise covers a variety of important investigations in accelerator physics, such as beam transfer measurements [4], sensitive measurements of longitudinal beam aperture, controlled beam heating for electron cooling [5] as well as for ultra slow extraction (USE) [6]. The idea behind USE is to move the beam across the resonance by a diffusion process. Firstly, precisely shaped narrow band noise centred on a harmonic of the revolution frequency will be used to transform the initially Gaussian-like distributed beam into a rectangularly shaped distribution. Secondly, to drive the beam towards the resonance, band limited noise, permanently covering the extraction resonance, will be slowly moved across the previously shaped beam distribution. This causes the particles to undertake a random walk within the noise bandwidth thereby filling up any void in longitudinal phase space. Particles reaching the resonance will be extracted from the circulating beam.

II. THE DIGITAL RF-NOISE GENERATOR

Several methods exist to create band limited noise signals. With one exception [7], where the noise spectra are created digitally and a double balanced analog rf mixer is used to convert to the desired revolution harmonic, analog components have been used to build up noise sources. Also, tuneable high quality analog filters are included to reject unwanted frequency components in the spectra [8].

At COSY a new noise generator [1,2] basing completely on digital signal processing technology has been developed. The principal idea bases on the fact that the sequence

$$x(n) = \frac{1}{N} \sum_{s=0}^{N-1} \hat{x}(s) e^{-i2\pi sn/N} \quad (1)$$

represents a complex pseudo random sequence if the random amplitudes $\hat{x}(s)$ are given. For the case of band-limited noise the amplitudes are chosen to be $\hat{x}(s) = A e^{-i\phi(s)}$ for $s_- \leq s \leq s_+$, otherwise zero, with phases $\phi(s)$ uniformly distributed within the interval $[0, 2\pi]$. The constant A is related to the desired discrete power density $S(f) = A^2/(N^2 \Delta f)$ at frequency $f = s\Delta f$ with frequency resolution $\Delta f = 1/(N\Delta t)$. It can be shown [9] that for a sufficiently large sample length N and small Δf the

real or imaginary part of the noise signal, eq. (1), has a nearly Gaussian distribution with zero mean. By applying appropriate trigonometric identities to eq. (1), the real part of the complex noise signal, $x_R(n)$, with a band-limited spectrum centered at frequency f_0 equals to

$$x_R(n) = A \left\{ \cos(2\pi f_0 n \Delta t + \Theta_-(n)) + \cos(2\pi f_0 n \Delta t + \Theta_+(n)) \right\} \quad (2)$$

where the phase sequences $\Theta_-(n)$ and $\Theta_+(n)$ are determined from eq. (1). Thus the noise sequence consists of two phase modulated sequences which can be created by two numerically controlled oscillators (NCO) as shown in the block diagram, fig. 1. Two digital signal processors (DSP) are used to precalculate the desired phase sequences $\Theta_-(n)$ and $\Theta_+(n)$ off-line. The outputs of the NCOs are added and fed to a DAC that produces the analog noise signal. This corresponds to multiply the real signal following from eq. (1) or (2) by the low pass filter transfer function of the DAC.

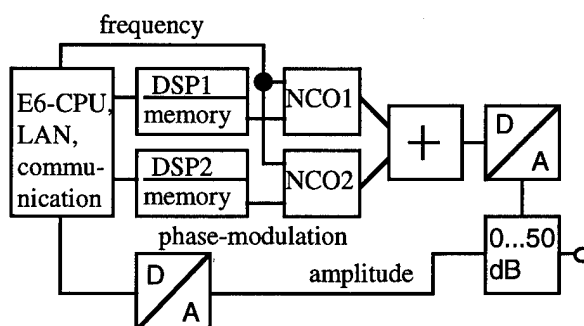


Fig. 1: Lay-out of the noise generator

To achieve a frequency resolution down to 6 Hz, each DSP is linked to a fast local memory bank of 2Mx16 bit size with an access time < 20 ns for storing the phase sequences. A fast sequencer transfers the phase sequences in real time to the NCOs. The clock frequency of 50 MHz allows together with a 32 bit frequency word an adjustment of the center frequency f_0 in 11.6 mHz steps.

The design offers the possibility to tailor sharply band-limited noise spectra of arbitrary shape at center frequencies up to 20 MHz. High resolution components guarantee signal-to-noise ratio better than 60 dB. The bandwidth can be chosen in the wide range from 1 kHz up to 100 kHz. Typical roll-off characteristics of the order of 180 dB/octave are achieved. Two independent digital noise generators are available. Both allow to control the amplitude of the signal and can be triggered by COSY-Control. One module is capable to deliver swept noise with controlled speed < 1 kHz/s. The complete digital design makes the circuit completely predictable, including finite bit resolution. The design has been applied for a patent [10].

III. EXPERIMENTAL RESULTS

Longitudinal beam shaping was studied for debunched beams in flat top of a COSY cycle with approximately one minute flat top length. The experimental test set-up is shown in figure 2.

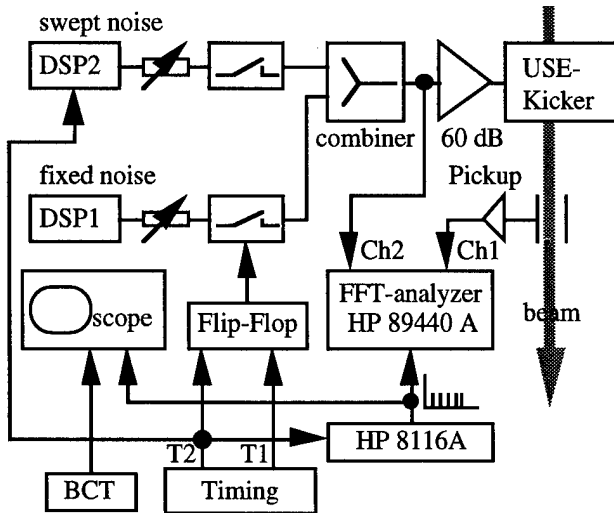


Fig. 2: Experimental test set-up

The timing system delivers two time signals to start (T1) and to stop (T2) the fixed noise (DSP1) for shaping via a Flip-Flop. To measure the beam distribution after applying the noise, the stop signal T2 starts the pulser HP8116A delivering a preset number of pulses which define the instances at which a spectrum is taken by the FFT-analyzer. During the whole cycle the beam current transformer (BCT) as well as the pulses of the HP8116A could be monitored on a scope. By interchanging T1 and T2 measurements during heating were also possible. Swept noise could be applied after shaping by starting DSP2 with trigger T2. Both noise generators could be controlled via a workstation. The combined output of the noise generators was fed to a longitudinal kicker [11] after power amplification.

The response of the beam to the longitudinal excitation was observed with a beam position monitor of COSY [12] in common mode operation. In addition, the beam current was monitored to adjust the noise bandwidth so that no particle losses could occur during beam heating. Figure 3 to 5 show Schottky scans around the third harmonic of the revolution frequency with 5 dB/div and 10 kHz span after 10 s noise excitation for different noise amplitudes. Note, that the upper lines appearing in the figure are due to interference frequencies and are not affected by the noise. The rectangularly shaped noise spectrum of width 4 kHz was centred at the fourth harmonic so that the third harmonic reflects the beam distribution. Figure 3 shows the undisturbed beam spectrum (amplitude 0). The figures demonstrate that the beam shape becomes flattened with increasing noise amplitude. The beam spectrum attains a width of 3 kHz (Fig. 5) as expected according to the equation $\Delta f_m = (m/n) \cdot \Delta f_n$ where n is the harmonic number at which the noise of bandwidth Δf_n is

applied and m denotes the harmonic at which the beam is observed. In this case $m = 3$ and $n = 4$.

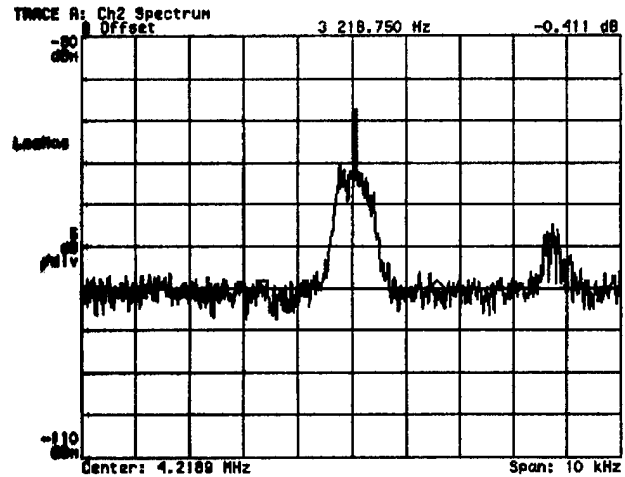


Fig. 3: Schottky scan of the undisturbed beam observed at the 3rd harmonic, 4.219 MHz.

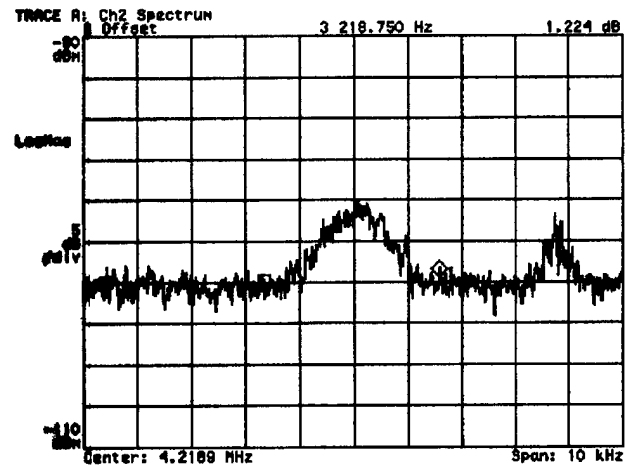


Fig. 4: Schottky scan observed at the 3rd harmonic after shaping with amplitude 2.

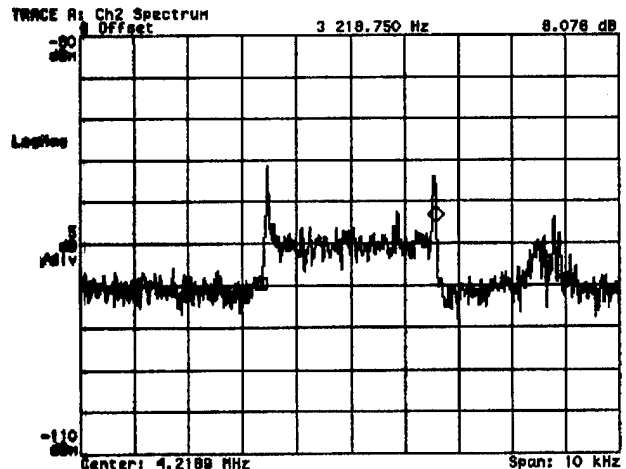


Fig. 5: Schottky scan observed at the 3rd harmonic after shaping with amplitude 8.

The spectrum in fig. 5 is dog-eared indicating an enhancement of particles near the boundary of the distribution. Random walk simulation show that this is due to the sharp edges of the exciting noise spectrum. This enhancement can be reduced by flattening the sharp roll-off of the noise spectrum. On the other hand the sharp edges could be of advantage for fine longitudinal acceptance measurements. In further tests, noise of constant amplitude but different durations had been applied. From this the expected role that duration times amplitude is constant could be derived.

Figure 6 (5 dB/div, span 10 kHz) shows the Schottky scan of the beam distribution at the first harmonic, 1.239 MHz, after 10 s asymmetric noise excitation. The beam was excited at the fourth harmonic, 4.956 MHz, with rectangular shaped noise with a bandwidth of 6 kHz. However, the centre was shifted upwards by 3 kHz.

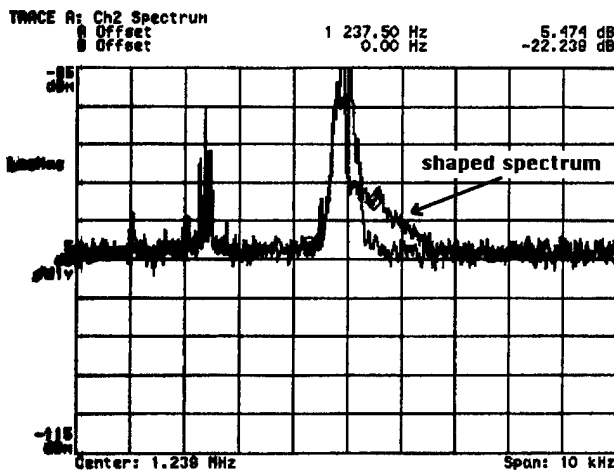


Fig. 6: Schottky scan around the revolution frequency after shaping with 6 kHz noise bandwidth around the 4th harmonic. The noise centre is shifted by +3 kHz.

As expected only particles lying in the right handside of the distribution diffuse into the range of higher momenta. For comparison the figure also contains the spectrum of the undisturbed beam distribution. The low lying lines in the spectrum correspond to interference frequencies.

IV. CONCLUSIONS

The novel narrow-band digital noise generator could be successfully applied for controlled beam shaping. Previous longitudinal beam transfer function measurements [4] using the novel digital rf-synthesizer to excite the beam yielded equivalent results as obtained by applying an analog noise source. This confirms the result following from the current measurements that a frequency resolution of about 6 Hz seems to be sufficient for longitudinal beam shaping applications at COSY. Indeed, a controlled diffusion was observed. It was demonstrated that the diffusion coefficient could have been influenced by the amplitude of the applied noise. Depending on the duration of the excitation and due to the sharp cut-off of the noise spectra the resulting beam distributions exhibit a

steep slope of the edges superimposed with sharp spikes. Thus, stepping the bandwidth of the excitation noise would allow a fine probing of the longitudinal acceptance of the machine. Improved tailored noise spectra for shaping and swept noise spectra to move the shaped beam towards the resonance will be included in the final USE-system at COSY. In order to keep shaping time short low noise amplifiers have to be incorporated.

Finally, due to its completely digital stages the new noise generator outperforms conventional generators in accuracy, stability, tuning range/bandwidth/speed, resolution and signal modulation performance. It is thus not only of interest in accelerator physics but also in the field of communication techniques.

V. REFERENCES

- [1] G. Heinrichs, H. Meuth, H. Stockhorst, A. Schnase., "A Narrow-Band Digital RF-Noise Generator", EPAC 94, London, 1994
- [2] F. -J. Etzkorn, G. Heinrichs, S. Papureanu, A. Schnase, and H. Stockhorst, "Development of the USE-System", IKP Annual Report 1994, Forschungszentrum Jülich
- [3] R. Maier, U. Bechstedt, J. Dietrich, U. Hacker, S. Martin, D. Prasuhn, P. v. Rossen, H. Stockhorst, R. Tölle., "Status of COSY", EPAC 94, London, 1994, ISBN: 981-02-1928-8
- [4] U. Oeftiger, Thesis, "Measurement of beam properties and beam environment in LEAR and COSY using RF excitation methods", Berichte d. Forschungszentrums Jülich, Jül-2977, 1994, ISSN: 0944-2952
- [5] U. Schaaf, "Schottky-Diagnose und BTF-Messungen an gekühlten Strahlen im Schwerionenspeicherring ESR", GSI-91-92, 1991
- [6] S. van der Meer, "Stochastic Extraction, A Low-Ripple Version of Resonant Extraction", CERN/PS/AA 78-6, 1978
- [7] F. Nolden, J. Pinkow, U. Schaaf, M. Steck, "Experiments with Synthetic Coloured Noise at the Heavy Ion Storage Ring ESR", EPAC 92, Berlin, 1992, ISBN: 2-86332-114-5
- [8] G. Molinari, H. Mulder, "The Improved Ultra Slow Extraction Noise System at LEAR", EPAC 94, London, 1994, ISBN: 981-02-1928-8
- [9] G. Heinrichs, Thesis, to be published
- [10] H. Meuth, G. Heinrichs, A. Schnase, H. Stockhorst, "Schmalbandiger arbiträrer HF-Modulations- und Rauschgenerator", PT 1.1185, 1994
- [11] S. Papureanu, H. Meuth, F. -J. Etzkorn, A. Schnase, "Power Tests with the Kickers for Ultraslow Extraction on COSY", IKP Annual Report 1993, Forschungszentrum Jülich
- [12] J. Dietrich, J. Bojowald, K. Doering, N. Dolfus, U. Hacker, H. Labus, H. Lawin, G. Luerken, R. Maier, H. Stockhorst, A. Zumloh, J.-D. Witt, "Beam Diagnostics at COSY-Jülich", EPAC 92, Berlin, 1992, ISBN: 2-86332-114-5

THE RHIC TRANSFER LINE CABLE DATABASE *

E. H. Scholl and T. Satogata

Brookhaven National Laboratory, Upton, New York 11973, USA

Abstract

A cable database was created to facilitate and document installation of cables and wiring in the RHIC project, as well as to provide a data source to track possible wiring and signal problems. The eight tables of this relational database, currently implemented in Sybase, contain information ranging from cable routing to attenuation of individual wires. This database was created in a hierarchical scheme under the assumption that cables contain wires — each instance of a cable has one to many wires associated with it. This scheme allows entry of information pertinent to individual wires while only requiring single entries for each cable. Relationships to other RHIC databases are also discussed.

I. INTRODUCTION AND SCOPE

The RHIC project consists of the pre-existing Booster and AGS as an ion injector complex, the AGS-to-RHIC (ATR) transfer lines and the main RHIC rings. The ongoing construction of the transfer line and collider provides an opportunity to design and fill project databases to track and relate pertinent information regarding the installation of equipment. One such database is the *atr_cable* database, which describes the cabling and wiring of the ATR line of the RHIC project. A separate database to serve this purpose for the main RHIC rings is currently under design.

During construction, a need for an organized, centrally located database to assist in the installation of cables and the “wire-up” of devices was recognized. The original motivation for the *atr_cable* database was to improve and streamline the tracking of signal and ground faults for ATR beam position monitors (BPMs) by the RHIC instrumentation group. The scope has grown, however, and the *atr_cable* database is now being used by all RHIC groups involved in installation of cables and wires in the ATR line.

Cables are defined as the jackets that surround one or many conductors, or wires. Cables and wires are usually, but do not have to be, two different things — in the case of a single-conductor cable, the cable and wire are physically the same. For the purposes of this database, such a single-conductor cable has two separate names, one indicating it is a cable and another indicating it is a wire. There is a one-to-many relationship between cables and wires.

The main objective of the installation section of the database project is two-fold: unique names are needed for the cables and wires in the ATR transfer line, and reports are required for installation. These reports are also used as check lists to record which cables and wires have already been installed. When each cable is pulled and cut for installation, it is labeled with the Brady Cable Labeling system (a small computer that generates labeling sleeves with the unique cable names for permanent tagging)

using data generated from this database. Some individual wires are also labeled in this manner.

II. DATABASE DESIGN

Figure 1 shows the structure of the *atr_cable* database as developed using ERDRAW [1], a graphical extended entity-relationship database tool. The internal compositions and a few sample entries for the two primary tables, Cables and Wires, are shown in Tables I and II respectively.

An entity-relationship (ER) diagram consists of three types of figures: rectangles, rhombi, and arcs. Rectangles represent objects, or “entities”, and are implemented as tables in the database — each table entry, or row, is an object instance. For each entity table, a group of columns is specified as a “primary key” or unique identifier for each table entry. These groups of columns are specified with ** in Tables I and II.

Rhombi in Figure 1 are called “relationships” and represent associations between entities; these too are implemented as database tables. These relationships may be one-to-one, one-to-many or many-to-many mappings. As discussed in the next section, the Found.By relationship is many-to-many and the Implies relationship is one-to-many.

Arcs indicate referential integrity constraints, including key inheritance and update triggers. They further define the relationship between tables through the arc designations. For example, the arc designation *ID* leads to a referential integrity constraint that incorporates the primary key columns of the Keys table into the Cables and Wires tables automatically. Relational database procedures, created automatically by ERDRAW in the SQL language, enforce referential integrity during data entry by allowing entry of data into the Cables and Wires tables only when there is first a corresponding entry in the Keys table.

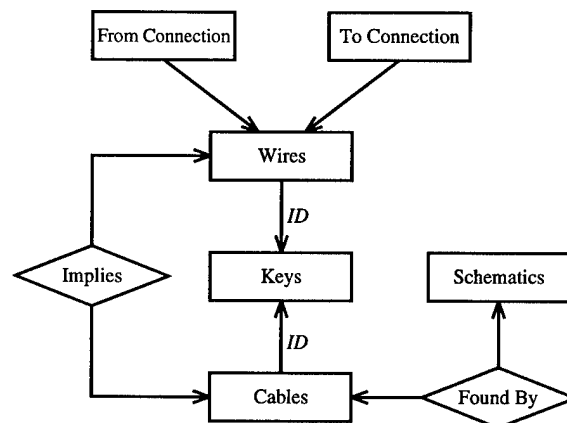


Figure 1. An entity-relationship diagram of the RHIC *atr_cable* database, as diagrammed with ERDRAW. Rectangles represent entity tables while rhombi represent relationship tables. Further details are in sections II and III of the text.

*Work performed under the auspices of the U.S. Department of Energy.

SWN**	CD**	Type*	Length	Total Feet	Attenuation	Reel Number*	Tray	...
...
yd25	c2	1pr#18-600V	41	NULL	NULL	TBD	2	
yd25	c3	3pr#18-600V	41	NULL	NULL	212	3b	
yd26	c1	4pr#18-shld	33	NULL	NULL	TBD	NULL	
...

Table I

The *atr_cable* database Cables table — no null entries are permitted in columns marked with *, and ** demarcated columns (SWN, CD) comprise the table's unique primary key. Each entry represents a single physical cable in the RHIC ATR line with cable-specific attributes.

SWN**	CD**	WD**	Voltage Class	Electrical Length	Status	Remarks	Conductor Size*	Conductor # or Color*
...
yd25	c1	7	TBD	NULL	Installed	NULL	NA	green
yd25	c1	8	TBD	NULL	Installed	NULL	NA	black
yd25	c2	1	TBD	NULL	Not Inst.	NULL	NA	white/blue
...

Table II

The *atr_cable* Wires table. Each entry represents a single wire (conductor or signal-carrying component) within cables in the RHIC ATR line.

III. TABLE DETAILS

The RHIC project has adopted use of a "SiteWide Name" (SWN) as a unique designator for each primary equipment slot; this is different than an equipment serial number which refers to the particular instance of equipment installed within that slot. SiteWide Names are a natural component of unique identifiers for cables and wires, where by convention the SWN of the equipment *from* which the signal carried by the cable or wire travels is used. SiteWide Names also are used as primary indices in many other RHIC databases describing beam optics layout, hardware installation and controls configuration information[2], which provides a consistent language with which to develop the entire RHIC database design.

The Keys table contains two attributes or columns — a SWN and a Cable Designator (CD). The combination of these two attributes results in a unique primary key for each cable in the ATR line; this table thus acts as a base repository for valid primary key designations. The arc-label 'ID' leads to a referential integrity constraint discussed above that incorporates the primary key of the Keys table in the Cables and Wires tables.

The primary key for the Cables table is the same as for the Keys table, a unique combination of SWN and CD. This key thus serves as a singular identifier for every cable within the transfer line complex. The Cables table also contains other information about cables, such as their length in feet, the reel number(s) from which the cables are pulled (a mandatory entry with a default of "TBD" — To Be Determined), and the tray used for installation, as well as others. Table I shows this table with three entries for cables running from Y-line dipole 25.

The primary key for the Wires table includes the primary key from the Keys table, as well as an additional Wire Designator (WD). The WD gives a unique name to each wire or conductor contained within each cable. The WD is the last part of the hierarchical naming scheme, and every table in the database has a reference to either the (SWN, CD) combination to specify a cable, or the (SWN, CD, WD) combination to specify a wire.

Also included in the Wires table is wire-specific information such as voltage class, electrical length, conductor size and color. Table II shows the Wires table, with component wire entries for the cables listed in Table I.

The Implies table is a relationship between the Cables and Wires tables with a one-to-many mapping which provides a direct charting of the relationship between each cable and each wire. This table provides an explicit listing of wires comprising each cable, and serves as another internal consistency check.

The From_ and To_Connection tables provide the most detailed routing information for the wires in the ATR line. These keep track of the specific connections, or spigots, on devices such as bus bars and magnets to and from which a wire leads.

The Schematics table has columns listing which equipment group is responsible for each cable, which schematic number a cable is on (the primary key) as well as the revision and revision date of the given schematic. The Found.By table maintains referential integrity between Cables and Schematics, mapping between a list of cables in the Cables table and the schematics on which the cables are found.

IV. DATABASE USAGE EXAMPLES

After installation, all of the cabling and wiring information for the ATR line will be contained in this database. Data entry is proceeding using the generic Sybase data workbench (dwb) tool[3], and recently the InfoMaker package[4] has been acquired to to implement a form-based data entry system.

As mentioned earlier, this information will be useful in future tracking of signal and ground faults, in conjunction with the wireup database[5]. The wireup database is a repository for a generic wireup scheme describing hierarchical and connection relationships between accelerator subsystems. Using this general scheme in conjunction with the specific instances described in the *atr_cable* database, one can fully trace the routing of all cables and wires in the entire ATR line in an online database.

A simpler example of *atr_cable* database usage is when

a wire comes loose from a connection. Rather than having to find the proper schematic associated with the wire, reconnection can be done simply either by use of the label on that particular wire or with a simple SQL database query. For example, `select * from To.Connection where SWN = yd25 and CD = c2` will respond with a list of all the wire connections for the second cable connected to the magnet named yd25.

Other examples of useful SQL queries to this database include:

1. To find all cables connected to device D:

```
select SiteWideName, CableDesignator
from Cables
where SiteWideName = 'D'
```

2. To list all wires not yet installed:

```
select SiteWideName, CableDesignator,
WireDesignator
from Wires
where Status = 'NI'
```

3. To list all cables on schematic S:

```
select *
from FoundBy
where DrawingNumber = 'S'
```

V. SUMMARY AND CONCLUSIONS

This paper describes the current structure of the *atr_cable* database, including two applications covering installation, and online and offline routing diagnosis. Implementation of data entry and use for cable installation procedures is ongoing. This database is a dynamic system in that the data structures are changing as new requirements arise. As of present, all information requested by installation and instrumentation groups has been implementable within this design. A RHIC cable database based on these tables is currently in design stages.

Acknowledgments

We thank C. Saltmarsh and G. Trahern for helpful discussions and support. Also, many thanks to the discoverer of caffeine without which our lives would be much less stimulated.

VI. REFERENCES

1. V. Markovitz and A. Shoshani, LBL Technical Report LBL-34932, 1993.
2. "ATR Commissioning Software Task Force Report", C. Saltmarsh and G. Trahern eds. RHIC AP Note 53, December 1994.
3. InfoMaker User's Guide, PowerSoft Enterprises, 1994.
4. Transact SQL User's Guide for Sybase SQL Server, Sybase Inc. 1993.
5. T. Satogata, RHIC AP Note 33, November 1994.

Characterization of Beam Position Monitors for Measurement of Second Moment

S. J. Russell, J. D. Gilpatrick, J. F. Power and R. B. Shurter, Los Alamos National Laboratory, Los Alamos, NM 87545 USA

A dual-axis beam position monitor (BPM) consists of four electrodes placed at 90° intervals around the probe aperture. The response signals of these lobes can be expressed as a sum of moments. The first order moment gives the centroid of the beam. The second order moment contains information about the rms size of the beam. It has been shown previously that the second order moment can be used to determine beam emittance [1]. To make this measurement, we must characterize the BPM appropriately. Our approach to this problem is to use a pulsed wire test fixture. By using the principle of superposition, we can build up a diffuse beam by taking the signals from different wire positions and summing them. This is done two ways: first by physically moving a wire about the aperture and building individual distributions, and, second, by taking a two dimensional grid of wire positions versus signal and using a computer to interpolate between the grid points to get arbitrary wire positions and, therefore, distributions. We present the current results of this effort.

I. INTRODUCTION

Here at Los Alamos, we have two photoinjector driven electron linacs. The first is an 8 MeV machine originally built to drive the APEX free electron laser. It has since been moved from its original location and is currently being employed in experiments investigating sub-picosecond bunching of an electron beam. The second is the 20 MeV accelerator for the Advanced Free Electron Laser experiment and has been operating since the summer of 1992.

Photoinjector driven electron accelerators are at the forefront of electron beam technology. They produce beams of unparalleled quality. However, measuring second moment properties of these beams, such as the rms emittance, is very difficult [2]. This is due to their generally non-Gaussian beam distributions. In order to measure the rms emittance, we need an approach that does not require prior knowledge of the beam distribution. Beam position monitors (BPMs) offer such a technique [3].

For us to be able to use BPMs for emittance measurements, we need a method of calibration for measuring the second moment of the BPM signal. Our approach is presented here.

II. CALIBRATION THEORY

The BPMs that we will be using for this measurement were originally built for the AFEL beamline [4]. These are capacitive, or button-style, probes that differentiate the beam bunch

* Work performed under the auspices of the U. S. Department of Energy.

charge distribution that is induced on the probe electrodes.

A. BPM Signal

For the square electrodes, or lobes, of our BPMs, the signal induced by a relativistic beam on the lobe at angular position ϕ is proportional to

$$\begin{aligned} & \{ 2\alpha + 4 \frac{\sin \alpha}{a} (\bar{x} \cos \phi + \bar{y} \sin \phi) \\ & + 2 \frac{\sin 2\alpha}{a^2} \{ [(\sigma_x^2 - \sigma_y^2) + (\bar{x}^2 - \bar{y}^2)] \cos 2\phi \\ & + 2 \langle xy \rangle \sin 2\phi \} + O(\frac{1}{a^3}) \} \end{aligned} \quad (1)$$

The radius of the BPM aperture is a , the angle subtended by the BPM lobe is α , \bar{x} and \bar{y} give the centroid position of the beam and the angled brackets indicate an rms average over the beam distribution. The term $\sigma_x^2 - \sigma_y^2$ is what we are trying to measure. σ_x^2 is equal to the rms average $\langle x^2 \rangle$ in the coordinate system centered on the beam distribution, and similarly for σ_y^2 .

B. Calibration equation

We are interested in extracting the quantity

$$(\sigma_x^2 - \sigma_y^2) + (\bar{x}^2 - \bar{y}^2)$$

from our BPM signals. For a perfect BPM, with four identical lobes at 0, 90, 180 and 270 degrees around the aperture, this term is given by

$$(\sigma_x^2 - \sigma_y^2) + (\bar{x}^2 - \bar{y}^2) = k \frac{S_R + S_L - S_T - S_B}{S_R + S_L + S_T + S_B} \quad (2)$$

where S_R , S_L , S_T and S_B are the signals from the right, left, top and bottom BPM lobes respectively (see Fig. 1) and k is a constant to be determined. However, the lobes of a real BPM will not be identical in general. Each will have a unique subtended angle, α , and a unique aperture radius a . Therefore, equation (2) must be modified to

$$\begin{aligned} & (\sigma_x^2 - \sigma_y^2) + (\bar{x}^2 - \bar{y}^2) \\ & = \frac{c_1 + c_2 S + c_3 \bar{x} (1 - S) + c_4 \bar{y} (1 + S)}{1 + c_5 S} \end{aligned} \quad (3)$$

where S is defined by

$$S \equiv \frac{S_R + S_L - S_T - S_B}{S_R + S_L + S_T + S_B} \quad (4)$$

and the c_i s are constants that need to be determined. This is the goal of our calibration procedure.

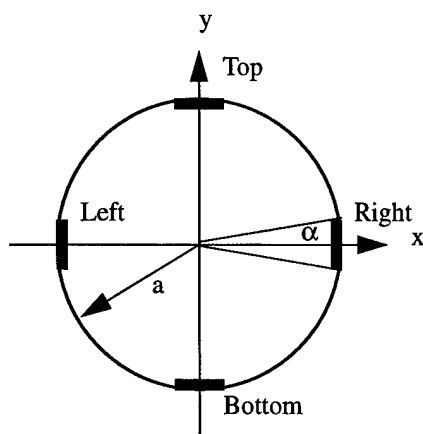


Figure 1: Schematic of BPM.

III. SIMULATING A DIFFUSE BEAM

In order to calibrate a BPM to measure the second moment, we need the ability to input a known beam and look at the lobe response. To do this, we use the pulsed wire setup that calibrates the BPM for centroid measurements [5]. This apparatus uses a thin wire running through the BPM aperture to simulate a $\beta = 1$ beam. A signal is generated on the wire and the responses of the BPM lobes are measured vs. wire location.

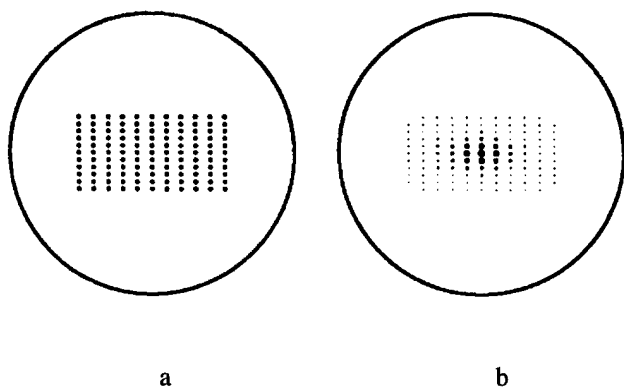


Figure 2: a) Rectangular grid of 121 points within BPM aperture. b) Same grid as in a, but with Gaussian distribution overlaid. The size of the dot indicates the weighting factor.

A. Principle of superposition

A thin wire simulates a beam with zero width. To simulate a diffuse beam we use the principle of superposition. We define a rectangular grid such as that in Fig. 2a. Each grid point represents a wire position for which we can determine the lobe responses. On top of this grid we can superimpose a distribution function, such as a Gaussian (Fig. 2b). By summing the lobe signals, multiplied by their appropriate weighting factor as determined by the distribution function, we can get the response of each of the lobes for the total beam. The total beam is the beam that is created by the "beamlets" of Fig. 2b.

B. Method

To simulate a diffuse beam, we need to determine the lobe response for a given grid point. The obvious way to do this is to move the wire to the desired position and measure its response with the test fixture. However, the signal to noise ratio for a given beam gets better the more wires it contains. With our test stand, we have found that it is generally necessary to use at least 100 wires per simulated beam. As a result, complete calibration of a BPM can take several weeks.

Another way to determine lobe response is to create a map of the BPM such as that in Fig. 3. Using this map, we can interpolate the response for any wire position. This allows us to duplicate the calibration procedure described above with a computer. Instead of weeks, the computer does a complete calibration in a day. Part of our goal is to show that the two methods are effectively the same.

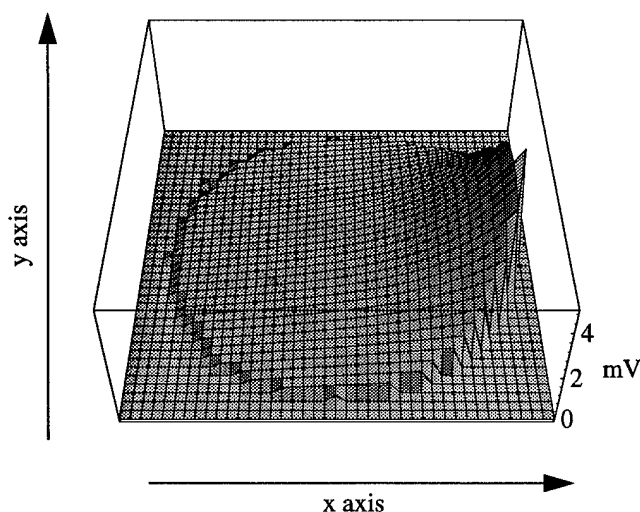


Figure 3: Typical two dimensional map of a BPM lobe response. Center is at $x = 0$, $y = 0$ and grid squares are 0.5 mm on a side. The z axis is the lobe signal for a given wire position in mV.

IV. EXPERIMENTAL RESULTS

To carry out the actual BPM calibration, a number of simulated beams were generated with different σ_x s and σ_y s and known x and y centroid positions.

A. Beam centroid equal to zero

According to the theory, we have five constants to determine to fully characterize the BPM for second moment measurements. The first step is to generate a data set with \bar{x} and \bar{y} equal to zero. Then, we fit the data to the equation

$$\sigma_x^2 - \sigma_y^2 = \frac{c_1 + c_2 S}{1 + c_3 S} \quad (5)$$

where S is the same as defined in (4). Fig. 4 shows the results for data generated using the test stand and for data generated

using the computer model.

The fit to the two sets of data give the following results:

$$c_1 = -2.2, c_2 = 82.2 \text{ and } c_3 = -0.19 \text{ (test stand)}$$

$$c_1 = -2.2, c_2 = 81.9 \text{ and } c_3 = -0.11 \text{ (computer).}$$

These results, for all practical purposes, are the same. (The c_3 term is so small that it could be dropped.)

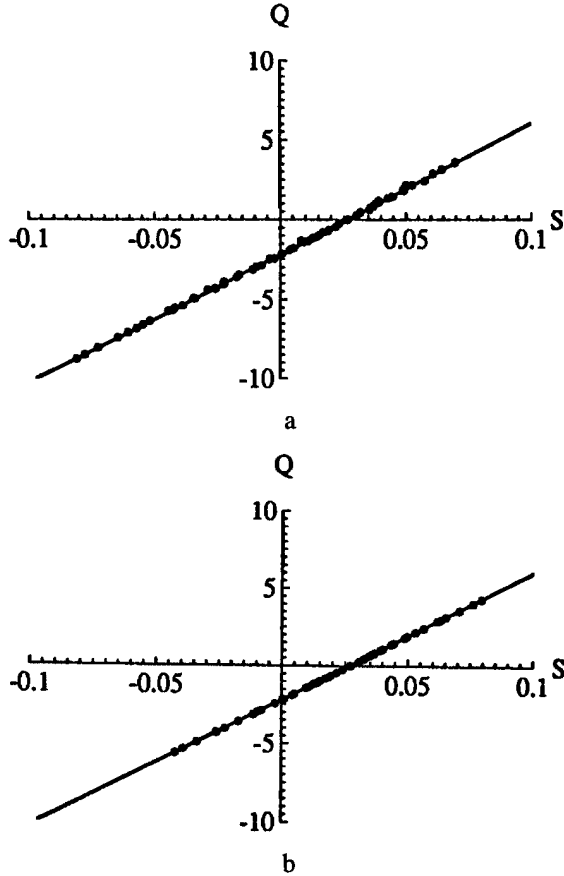


Figure 4: a) Q vs. S generated by test stand where $Q \equiv \sigma_x^2 - \sigma_y^2$ in mm^2 and S is defined by (4). b) Q vs. S generated by computer using interpolation of BPM map. 225 wires were used and a Gaussian distribution was overlaid on the grid for both plots. The solid lines are the fits to the data using (5).

B. Beam centroids nonzero

To determine the remaining two constants, we vary \bar{x} and \bar{y} , generating data sets as in Fig. 4 for each centroid position. Fitting these data sets with (5), we get plots of how c_1 changes with \bar{x} and \bar{y} (Fig. 5). From these, we get

$$c_3 = 0.505 \text{ and } c_4 = 0.054.$$

As of this publication, we have not finished taking data on the test stand for c_3 and c_4 , so comparisons with the computer generated data of Fig. 5 are not available.

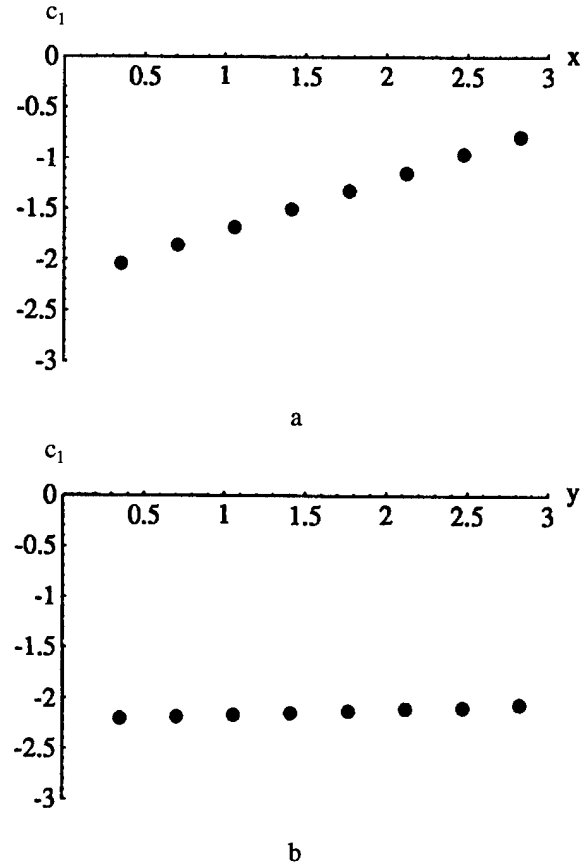


Figure 5: a) c_1 vs. x (in mm) and b) c_1 vs. y (in mm).

V. CONCLUSION

The calibration of our BPMs for second moment measurements is going well. So far, our data fits our model very well and is well understood. In addition, early results indicate that the computer interpolation method is a legitimate approach to speeding up the process.

VI. REFERENCES

- [1] R.H. Miller et al., "Nonintercepting Emittance Monitor," Proc. 12th Int. Conf. on High Energy Accelerators, (Fermilab, 1983), p. 602 (1983).
- [2] Bruce E Carlsten, et. al., "Measuring Emittance of Non-thermalized Electron Beams From Photoinjectors," 14th International Free Electron Laser Conference, Kobe, Japan, August 23-28, 1992, Los Alamos National Laboratory document LA-UR 92 2561
- [3] S. J. Russell and B. E. Carlsten, "Measuring Emittance Using Beam Position Monitors," Proc. of the 1993 Particle Accelerator Conf., p. 2537.
- [4] J. D. Gilpatrick, et. al., "Design and Operation of Button-Probe, Beam-Position Measurements," Proc. of the 1993 Particle Accelerator Conf., p. 2334.
- [5] J. F. Power, et. al., "Characterization of Beam Position Monitors in Two-Dimensions," 16th International LINAC Conf., Ottawa Ontario, CANADA, 1992.

BEAM DIAGNOSTIC SYSTEMS AND THEIR USE IN THE NEW IUCF BEAM LINE *

W. P. Jones, M. Ball, J. Collins, T. Ellison, and B. Hamilton, Indiana University Cyclotron Facility, Bloomington, IN 47401 USA

Abstract

Diagnostic tools developed for and being used in a new 30 m beam line (BL1C) connecting the IUCF high intensity polarized ion source (HIPIOS) with the injector cyclotron are described and the results obtained with them are detailed. These devices include non-intercepting beam position monitors, wire scanners, and beam sweeper systems. Studies of rf beam bunching have been performed using a high bandwidth current readout. Programs have been developed for automatic emittance measurements and beam centering in the beam line.

I. BUNCHER EFFICIENCY TESTS

The combined efficiency of the HIPIOS terminal $f/3$ buncher, the BL1C f buncher, and the $2f/3$ buncher [1] was measured at the end of the beam line, 2 meters upstream of the injector cyclotron inflector magnet. To perform the tests, a water cooled, wide bandwidth stop was installed in the beamline. A dc coupled, FET amplifier was used at the pickup to measure the unbunched, as well as the bunched, beam. The FET amplifier does not discriminate the beam signal, allowing for easier measurements.

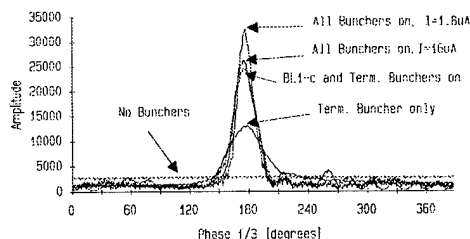


Figure 1. Bunched beam signals compared on a beam stop.

The display in Figure 1 shows the effect of different buncher configurations on the beam. One can see that the terminal buncher is actually more of a prebuncher, and was not designed to bunch the beam into a small phase space. The figure also shows that the tightest bunches occur when using all of the available bunchers and smaller beam currents. When the beam current is increased, the bunching is not quite as sharp and the phase spread increases; space charge effects are suspected. Plans have been made to move the BL1C buncher from its present location to a section further down stream, closer to the injector cyclotron. While this will require more voltage to bunch the beam, it is hoped that the space charge effect can be minimized.

Figure 2 shows the percentage of the total dc beam that is bunched using the different buncher schemes available. The phase acceptance of the injector cyclotron has been measured to

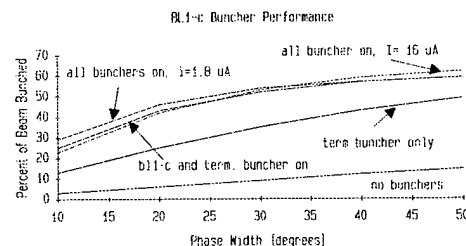


Figure 2. BL1 Buncher Efficiencies

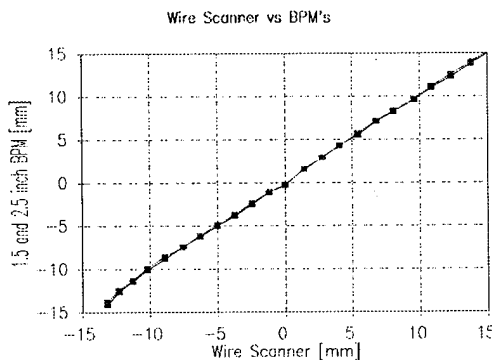


Figure 3. BPM linearity compared to a wire scanner over a 30 mm range.

be 12 degrees. It can be seen that the best bunching obtained was approximately 60 percent. These measurements are consistent with measurements taken under a variety of running conditions.

II. BEAM POSITION MONITOR (BPM) PERFORMANCE

BPM position [2] linearity has been cross-calibrated against a mechanical, spinning wire type beam profile monitor (wire scanner) [3]. A beamline section consisting of a 1.5 inch radius BPM, a wire scanner, and a 2.5 inch radius BPM was incorporated into the initial design for this purpose. In Figure 3, as the beam is moved 30 mm, the wire scanner position output is plotted vs that of the two BPM's. In Figure 4, the difference between the wire scanner and BPM's can be observed. The wire scanner measurement has an accuracy of ± 0.13 mm, with the BPM's having a computer readout resolution of ≈ 0.05 mm. The above data was taken under normal operation conditions with a proton beam current of $20 \mu\text{A}$. The theoretical position resolution at this current is ≈ 0.03 mm. The BPM performance may be limited by the 60 Hz line noise on the interconnecting cables prior to the ADC. This interference can be minimized by analog filters or averaging after digitization, both of which cut system band-

*Work supported in part by the National Science Foundation

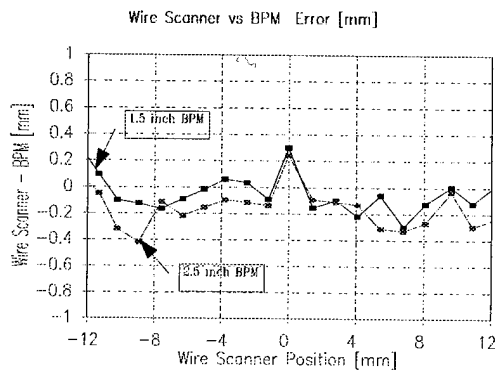


Figure 4. Difference between BPM and wire scanner readings.

width. A better solution would be the use of differential inputs on the ADC.

III. BEAM EMITTANCE MEASUREMENTS

The emittance of the beam at the beginning of the line has been measured using a technique similar to that described by Ross et al. [4]. The output of a wire scanner located 1m downstream of a quadrupole magnet was digitized and recorded as a function of quadrupole magnet current. Programs were written which set the quadrupole polarity, step the quadrupole current through a predetermined range, digitize the wire scanner output, fit the beam width and calculate the emittance. This information is then available as input to beamline modelling software and for the beam sweepers described in section V of this paper. The system measures both horizontal and vertical emittance. A measurement typical of the horizontal results is shown in Figure 5 (where the crosses are the measured data points and the solid line is the result of the fitting algorithm). The horizontal emittances measured are in good agreement with the design values whereas the vertical emittance is approximately 50 % larger than the design goal. Non-linearities in the 15 keV terminal beam line are the suspected source of the problem and studies of the optics of that line are under way to attempt to find a solution.

IV. BEAM CENTERING AND AUTOSTEERING

The beam line has been designed [5] so that steerers and BPMs are located approximately every 90 degrees in betatron phase advance. A program has been written which adjusts the steerers to position the beam to preset values (normally zero) along the length of the beamline. This program is used both to center the beam in the line when first turning systems on and to maintain its position while quadrupole magnets are being adjusted to change focussing conditions. This latter use has proven quite helpful in normal beamline setup. The system routinely maintains the beam's position to ± 1 mm. Figure 6 shows the BPM display for the first two legs of the beam line after the steering program has been run. (At the time these measurements were being made the beam was not being transported all the way to the cyclotron.) The horizontal measurement at BPM 12 was not one that was included in the procedure. (In order to maintain a one to one correspondence between steerer and BPMs one had

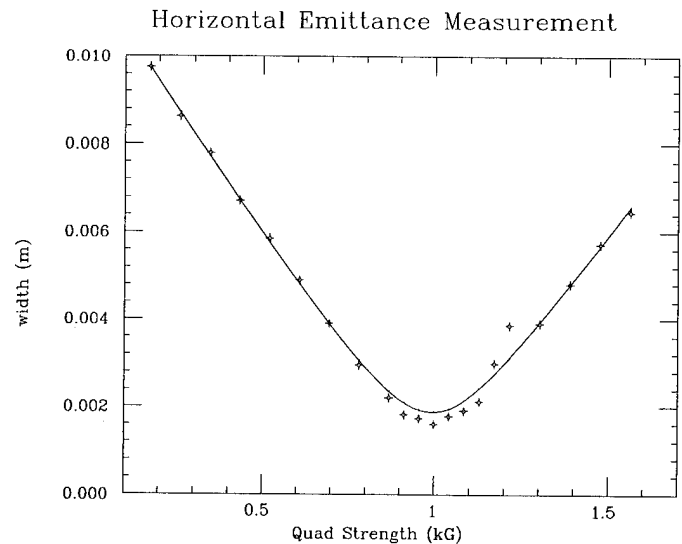


Figure 5. Horizontal Emittance Measurement and fit to data (solid curve).

to be omitted in that section.) BPM 9 is not used because of its proximity to the rf buncher and the resulting noise on its signals.

V. BEAM SWEEPING SYSTEM AND FOCUSING

The information ($\sigma_{11}, \sigma_{22}, r_{12}, \sigma_{33}, \sigma_{44}, r_{34}$) obtained in the emittance measurements can be used to generate the phases and amplitudes for the beam sweeping system's control module. Four 10 Hz modulators can be used to vary the current in four steerers to move the beam centroid around a beam ellipse. This ellipse is scaled down by a factor of 2 or 3 from the phase space ellipse obtained by transforming the measured ellipse through the drift space between the emittance measuring quad and the sweeper system. The BPM system output voltage proportional to peak centroid position provides a measurement of the beam envelope. Using this system it is possible to obtain a display of the beam envelope along the full length of the beam line. The quadrupole magnets can then be adjusted to provide the desired focussing conditions. There are displays showing the location and sharpness of waists in each straight section. Rather than tuning the quadrupoles independently, four linear combinations of quadrupole currents have been defined to provide independent control of the location and sharpness of focus in each plane. With these "combos" and displays of focussing properties, it will be much easier to both adjust the focussing manually and to define algorithms for automatic control.

In the limited development time used to date for this system, it has shown promise as a beam development tool. Further work needs to be done to optimize "combo" coefficients and to calibrate the 10 Hz modulators. Similar "combos" involving the last four quadrupoles in beam line appear to make optimizing injection of the beam into the cyclotron easier than independent tuning of the four quadrupoles. This is also an ongoing development project.

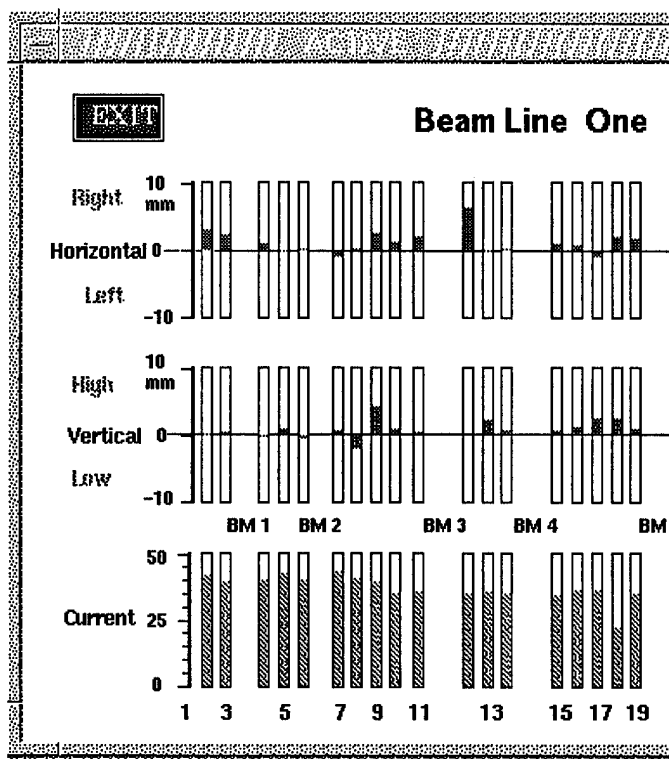


Figure 6. Beam Positions after Automatic Centering.

References

- [1] W.P. Jones, T.J.P. Ellison, M.S. Ball, J.C. Collins, D. DuPlantis, D.L. Friesel, B. Hamilton, J.W. Hicks, and P. Schwandt, "Beam transport system for the IUCF high intensity polarized ion source", Proc. of the 13th Int. Conf., Cyclotrons and Their Applications, Vancouver, 1992.
- [2] Mark Ball, Timothy JP Ellison and Brett J Hamilton, Proc. 1993 Particle Accelerator Conf., p. 2289.
- [3] Beam Profile Monitor Manual, National Electrostatics Corp.
- [4] M.C. Ross, N. Phinney, G. Quickfall, H. Shoaee, and J.C. Shepard, Proc. 1987 Particle Accelerator Conf., p. 725.
- [5] W.P. Jones et al. Beam Line 1C and Beam Line 1: Design and Tuning Procedures, IUCF Internal Report, 1992.

TOMOGRAPHIC METHOD OF EXPERIMENTAL RESEARCH OF PARTICLE DISTRIBUTION IN PHASE SPACE

V.V.Kalashnikov, V.I.Moisseev, V.V.Petrenko
Russian Research Centre "Kurchatov Institute", Moscow, Russia

I. INTRODUCTION

In high-frequency resonant accelerators the criterion of quality of beam dynamics accounts is the set of parameters, which describe a bunch of particles in six-dimensional phase volume. As a rule, experimental methods permit to receive the authentic information only about some parameters, but not about all set. On linear electron accelerator "Fakel" for experimental researches of multidimensional distributions of particles in phase space the method is advanced which in its essence is tomographic.

II. METHOD

The base of method prescribes the work [1], in which the high-frequency field of external generator in one of accelerating sections is used for measurement of dependence of intensity of particles in the bunch of linear electron accelerator particles beam from their phases. The new opportunity was mentioned of research not only one-dimensional particles distributions on phases, but also two-dimensional on longitudinal phase plane [2]. Thus, as well as in work [1], studied distributions are average on many bunches. This approach may be used and for study of two-dimensional distributions of particles on cross phase planes.

Essence of method is the following. Let, for example, electron beam consistently passes through thin dipole magnet, thin quadrupole lens and after collimator falls on current measuring instrument. In utmost case (narrow collimator slot and enough thin dipole magnet) current measuring instrument will registrate beam particles, presenting points of which on phase planes, for example, lie on straight line:

$$x' = -\frac{1}{L} - \frac{eB_1 l_1}{p} \quad (1)$$

where: e - electron charge, p - pulse of particles, B_1 - the magnetic field induction in dipole magnet, l_1 - magnet length ($l_1 \ll p/eB_1$), L - distance from magnet to collimator. Measuring dependence of intensity from field induction B_1 is proection of two-dimensional particles distribution function on $\bar{K} = (1/L, 1)$ direction of phase plane (x, x') , and induction B_1 changes in limits $-B_0 < B_1 < B_0$, where B_0 - induction, when signal from current measuring instrument is equal to zero. The direction \bar{K} is possible to be changed by changing of gradient of induction B_z in quadrupole lens. When gradient in

lens is dB_z/dx , on current measurement instrument the particles fall, presenting points of which on the phase plane (x, x') lie on the straight line:

$$x' = -\left(-\frac{e}{dx} \frac{dB_z}{dx} l_2 + \frac{1}{L}\right)x - \frac{eB_1 l_1}{p} \quad (2)$$

where l_2 is the length of quadrupole lens. Thus, repeating repeatedly the procedure of induction B_1 changing, as it was mentioned before, at various induction gradient dB_z/dx values, it is possible to define the proections of two-dimensional distribution functions of particles on any direction

$$\bar{K}\left(\frac{dB_z}{dx}\right) = \left(e \frac{dB_z}{dx} \frac{l_2}{p} + \frac{1}{L}, 1\right)$$

of plane (x, x') . For two-dimensional distribution functions measurements of particles in plane (y, y') it is necessary to turn the dipole magnet on 90° and to change the current direction in quadrupole lens.

In the installation for two-dimensional distribution functions measurement of particles on phase plane "energy - phase" (E, ϕ) the beam consequently passes through accelerating section, magnetic analyzer and through slot falls on current measurement instrument. This scheme is analogous to previous one. In particular, phase shifter of accelerating section, let's name its diagnostic, is the analogue of dipole magnet, and diagnostic accelerating section - the analogue of quadrupole lens. As a diagnostic section for simplification of processing of experimental results it is convenient to choose the terminal section of accelerator. On the longitudinal phase plane (E, ϕ) with the help of spectrometer and slot the narrow band is allocated, all particles of studied distribution from which fall on current measurement instrument. The measurement of current afterwards spectrometer at various values of phase and amplitude of diagnostic field represents the determination of integrals of studied distribution functions on longitudinal phase plane. We must notice, that the directions on phase planes, along which the profiles of distributions are measured, are determined by amplitudes of diagnostic field, varying inclination of sinusoidal dependence of this field from phase.

III. THE RESULTS OF MEASUREMENTS

Figure 1 shows the examples of particles phase distributions profiles in bunches on (x, x') plane, and figure 2 - the same for longitudinal plane [2]. In both cases the measurements are conducted for beams, accelerated in regimes of stored energy. The measurements were conducted in various moments of current pulses, shown on figures. For beginning of readout of diagnostic section phase it was accepted phase value, appropriate to maximum of intensity in energy spectrum.

The analysis of experimental results has shown:

1. At definite conditions of formation the appearance of bunches-satellites is possible, containing 6-10% of all accelerated electrons.
2. During current pulse the picture of distributions can change. In particular, the reduction of average energy in the bunch during current pulse and increasing of space division of these bunches, that is, appearance of "second beam" is observed.

3. Losses of accelerated beam are maximum in the beginning of current pulse and monotonously decrease to total disappearance at the end of pulse.

The received results allowed to study more deeply the process of accelerated beams formation and, in particular, to find out the role of different variants of operative setup, particles capture on parts of electrodynamic structures with sharp unhomogeneities, breakage of distributions on longitudinal phase plane owing to losses because of cross movement, leading magnetic fields unhomogeneity and other factors.

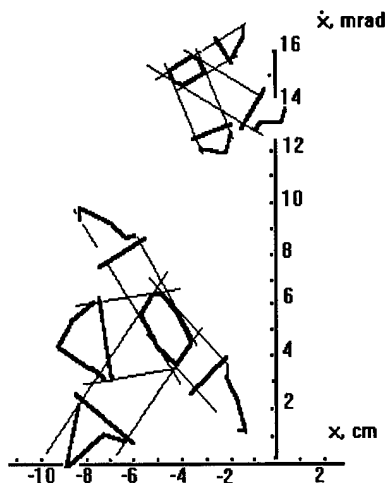


Figure 1. The transverse phase space (x, x') . Four projections locate the main part of beam particle distribution (lower). The rest three projections (upper) give the position of satellite.

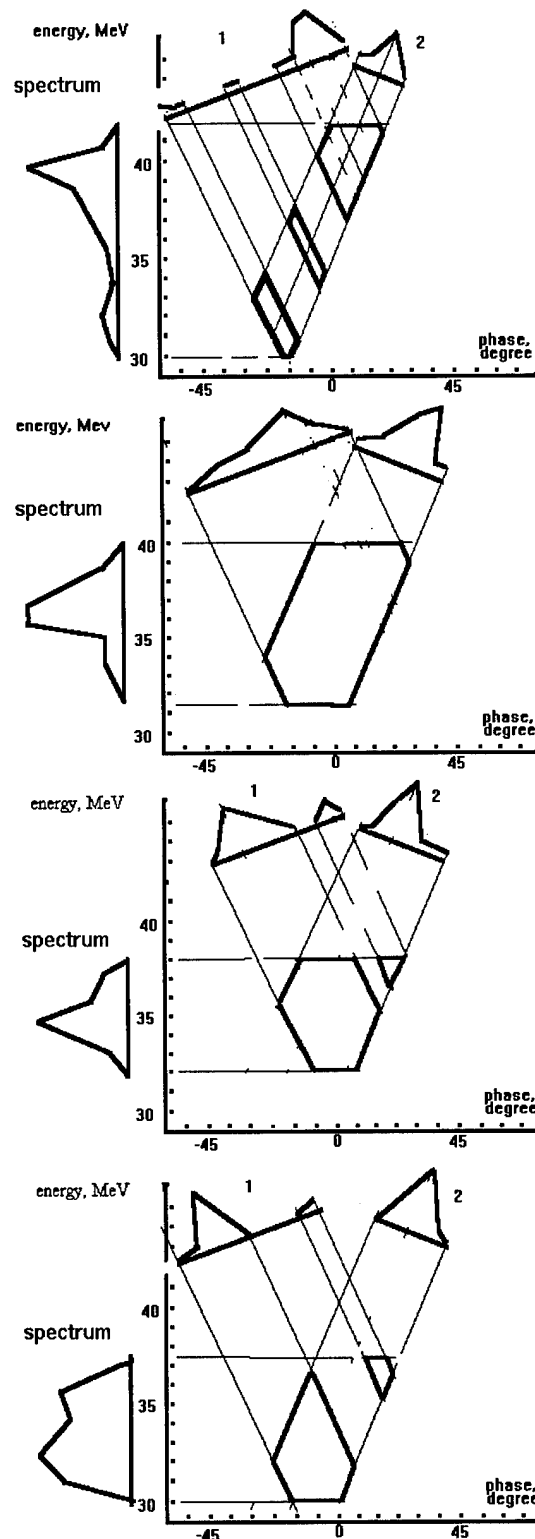


Figure 2. Longitudinal phase space (E, ϕ) . Evolution of beam particle distribution during pulse of beam current: at 25 ns (upper picture), 45 ns, 65 ns and 85 ns (lower picture).

IV. CONCLUSION

The method, considered here, of resonant accelerator bunches research, in its essence, as it already was indicated, is tomographic. In it the role of "layer scanning sources" of bunches is executed in cross planes by dipole and quadrupole magnets, and in longitudinal - by diagnostic section and its phase shifter. Current measuring instrument, installed on output of considered schemes, fixes the integrated value of beam - "beam-sum". This signal with the help of analog-digital converter can be entered in the computer memory. Further, manipulating according to definite laws by analogues of layer scanning sources, it is possible to receive the set of "beam-sums", determining necessary projection distributions.

In the case of restoration distributions in cross plane the task is linear, and in case of longitudinal plane - nonlinear one.

V. REFERENCES

- [1] Gryshaev I.A., Kolosov V.I., Yakimov B.V. and others. Measurements of phase width of electron bunches, accelerated in linear accelerator. -*Pribory i tehnika experimenta*, v.6, pp.30-33.
- [2] Kalashnikov V.V., Moiseev V.I., Petrenko V.V. Experimental investigation of self-consistent longitudinal beam dynamics in transition acceleration mode of linear accelerator "Fakel". -In the book::IX All-Union conference on charged particles accelerators. -Dubna, 1989, v.1, p.453-455.

Design of the Beam Profile Monitor System for the RHIC Injection Line*

R. L. Witkover

AGS Department, Brookhaven National Laboratory
Upton, New York 11973-5000 USA

Abstract

A video profile monitor (VPM) system will be used in the AGS-to-RHIC (ATR) transfer line to acquire single bunches transferred at 30 Hz. An array of 12 video cameras will be connected to 4 frame grabbers through a wide-band mux. Fast VME image processing boards will analyze a 120x120 subset of the image, generated by a 4x4 convolution or an ROI computation and sent over the network during the AGS recycle time. Details of the design, results of lab tests and studies with ion and proton beams will be presented.

I. INTRODUCTION

The VPMs will monitor extracted beam shape and measure profiles with 2.5σ diameters varying from 4.4 to 18 mm. RHIC intensity will range from 10^9 Au⁷⁹ per bunch, to protons at 10^{11} per bunch. Three gold bunches or from 8 - 12 proton bunches will be accelerated each AGS cycle, then individually extracted at 30 Hz. The full AGS intensity of 6×10^{13} per cycle will be carried in the upstream portion of the line where 2 of the VPMs are located. VPMs, or "Flags" will be used because the beam widths are too small for multiwires and single scanning wires can't measure single bunches. By acquiring profiles at 4 locations on each transit the emittance of individual bunches can be measured if low mass screens are used to minimize scattering [1]. All 12 camera outputs are brought to a central frame grabber/image processing location over wideband analog fiber-optic links to preserve resolution.

II. FLAG DESIGN

The flag, mounted at 45°, is inserted to the center of the beam pipe using a 4" stroke pneumatic drive. To simplify alignment and lower cost, the drive and 4" viewing window are mounted on the same 8" conflat flange[2]. Two small windows on either side of the viewing port, angled at the flag, illuminate fiducials on the screen for calibration.

To see a single bunch per frame the phosphor must decay fully in less than 33.3 msec. The screen consists of a 0.002" thick coating of Gadolinium Oxy-sulfide doped with Terbium ($Gd_2O_3:S:Tb$) on a 0.001" aluminum foil substrate with a potassium silicate binder. It fully decays in 2 msec and has good sensitivity. Tests at SLAC [3] indicated no damage at 0.8×10^{18} elec/cm² but flaking was observed at 2.5×10^{18} elec/cm². Similar mechanical failure has been seen at the BNL ATF facility [4]. D.Sagan of CESR [5] pointed out that
*Work performed under the auspices of the U. S. Department of Energy

barium acetate, a binder component used by SLAC (and ATF), is not recommended with a metallic substrate. A screen made without barium acetate appeared to be more durable and was tested in the Booster-to-AGS (BTA) line. Screens made in this way at ATF showed reduced flaking, but less adhesion than the BTA screen, possibly due to a different concentration of potassium silicate. Failure due to beam is not observed at ATF. Because of the lack of lifetime data, screens of 1 mm $Al_2O_3:Cr$ will be used for 2 upstream units exposed to the full AGS intensity. These will not be used during an emittance measurement as they put too much mass into the beam and have long light decay time. The $Gd_2O_3:S:Tb$ flags should have several years lifetime for RHIC beam intensities. Fiducials consisting of 3 holes (0.015" diameter) in a line 1 mm apart, with 5 mm between lines, were made on the $Gd_2O_3:S:Tb$ flags using a numerically controlled laser. Similar patterns for the Al_2O_3 screens were scribed with a pencil.

III. VIDEO CAMERAS

Standard TV cameras operate in "field" mode with odd and even lines acquired over alternate 16.67 msec periods, then interlaced to produce the full frame. The 2 msec beam flash would appear on alternate lines, halving the vertical resolution. The ATR cameras must allow "frame" acquisition, with all lines active for the full period. Other considerations include: resolution, sensitivity, signal-to-noise (S/N) ratio, linearity, pickup uniformity and radiation tolerance.

Vidicon tubes can withstand 10^7 Rad but suffer in uniformity, linearity and sensitivity compared to CCDs. CCDs have a low tolerance to radiation (10^2 to 10^3 Rad) but good uniformity, linearity and sensitivity. Charge Injection Device (CID) arrays can withstand 10^5 Rad but are 1 - 2 f-stops less sensitive and considerably more expensive. CCD cameras will be used in most locations, shielded behind 18" of heavy concrete or, in 5 locations, in 14" pipes inserted into the tunnel walls. In the worst radiation area near the AGS, a CID camera will be used.

A number of CCD cameras and a CID camera were tested using a TV resolution chart. Only relative comparisons were practical since the effect of the lens could not be decoupled from the camera resolution. The CCD camera selected was the Pulnix TM-7CN. The CID camera was the CIDTEK model CID-3710D, with RS-170 option. Both have frame acquisition and can be triggered to synchronize them with the beam, and have S/N ratios in excess of 50 dB to match the 8-bit resolution of the frame grabbers.

IV. OPTICAL DESIGN

The camera will be located as far as practical from the beam to reduce radiation damage, requiring an optical relay to match the flag image to the camera pickup. While the SLAC design[6] using a segment of a parabolic mirror was very elegant, a planar mirror and a single 35 mm-camera lens will be used to simplify alignment. The field of view for each flag is about twice the 2.5σ beam diameter, the actual size depending on the closest lens focal length available. Most locations use a Celestron 500 mm f/5.6 reflector lens but the first flag requires a Celestron 1000 mm f/8 mirror lens. A 400 mm f/5.6 Sigma APO lens will be used at one location with a large beam width. At half of the locations the cameras will be rotated 90° to better match the beam aspect ratio. Since the displays will be digitally regenerated, the correct beam orientation will be re-established by the computer.

Because the beam in the upstream portion of the ATR line will vary over about 3 decades of adjusting the light on the camera is required. A typical lens will only cover a range of about 32:1. Special lenses with graded neutral density center spots have a range of about 3 decades but these motor driven lenses are quite expensive. A simple mechanism was designed using small solenoids to insert up to 4 neutral density (ND) filters between the camera and lens. By choosing these to transmit 50, 25, 10 and 1% of the light, a range of 8000:1 can be covered with a simple digital interface.

The lens and camera and filters sit on an optical rail using commercial optical mounting hardware, allowing precise replacement in the tunnel. The optical rail is on a cradle which pivots in azimuth and elevation about the lens center. Translation along the beam line is also provided.

In most locations the vacuum tee housing the flag will be mounted with the viewing port facing down. This protects the window and mirror from dust and places the camera near the floor where it is more easily shielded. A front surface mirror mounted at 45° on the tee stand base reflects the image normal to the beam line to the tunnel wall where the camera is located. It is adjustable in angle and height and translates in X and Y. Because of local conditions the first two flags require a second mirror.

The optical system will be aligned with a "leveling" laser [7] replacing the camera and lens, which can be precisely reinstalled. Using penta-prisms, which tolerate angular alignment errors, to deflect the beam 90° , and a "hanging" mirror, which self-aligns vertically, the optics can be leveled and squared so the laser reflects back on itself off a mirror placed on the viewing port.

V. SYSTEM RESOLUTION

The overall resolution is limited by: Depth of Field, Camera (H and V) and lens resolution. Phosphor screen grain size, air waves and mechanical vibration, a factor in measuring beams of tens of micron size, are not significant for the ATR beam sizes which range from 4.4 to 17.8 mm diameter.

Depth of field is a factor because the screen is tilted at 45° with the top at a different distance from the lens than the bottom. This matters if the beam is well off center or large. In the latter case, however, finer resolution isn't required. Camera resolution is limited by the number of pixels in the array and the readout electronics bandwidth. The overall resolution was calculated using the manufacturer's data for the cameras and lenses and the parameters of the beam and optical path for each location.

Using an USAF resolution chart, both cameras were tested with the actual lens and distance from the flag. Using the Rayleigh criterion, the measured resolution was about two times worse than calculated. It is not clear what criterion the manufacturers used for their data. However, this is still sufficient as it represents only 4% of the 2.5σ diameter in the worst case. The best resolution measured was $150\mu\text{m}$ over a 3 m optical path. A longer focal length lens would improve this somewhat.

VI. SYSTEM ELECTRONICS

Figure 1 shows a block diagram of the system electronics. The controls to insert the flags and the ND filters is located in the closest of 4 equipment houses. The outputs from the

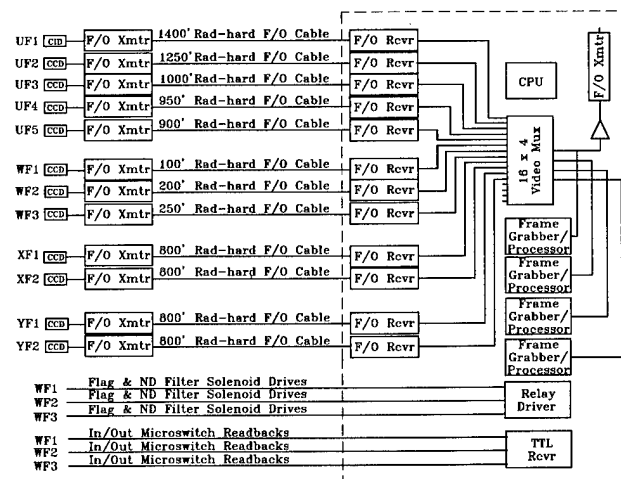


Figure 1. Video profile monitor system electronics

cameras and the synchronizing triggers go to a central location in the 1000P house. Here 2 VME modules, configured as a 16x4 MUX [8], allow any 4 cameras to be multiplexed into the VME based acquisition and processing boards. The cable runs (100' to 1400') could degrade the signal bandwidth and severely limit the horizontal resolution. To prevent this, analog fiber-optic links which are flat to ± 0.5 dB from <1 Hz to over 10 MHz were used. [9]

The acquisition and processing of the video is done using 4 Imaging Technology Inc. IMA-VME-4.0 boards with 4 AMVS-HS Acquisition modules, 2 CMCLU-HS Convolver-Arithmetic modules, and 2 CMHF-H Histogram/Feature Extractor modules. The system runs under VxWorks. It is able to store 48 512x512 frames, plus frames for background subtraction, and computational results. A reduced data mode

allows operation on a 128x128 data subset derived from a 4x4 convolution or a region-of-interest (ROI) set by either the operator or dynamically from the data. The frames will be stored at 30 Hz and processed in the 2 sec AGS recycle period. Computations include: Pixel-by-pixel base frame subtraction, Centroid, H and V projections, and Sum of all pixels. After the data is analyzed the reduced frame and the computational results will be moved to conventional VME memory for off-line network transfer to a work station for display or analysis. Alternatively the full frame data can be sent to VME memory for detailed beam studies or testing the acquisition system.

VII. TESTS WITH BEAM

Early in the design a $\text{Gd}_2\text{O}_2\text{S:Tb}$ screen was tested in the BTA line with Au^{+33} and proton beams. A Sony XC-57 CCD camera with a 385 mm Tele-Athenon lens was used with a 2-mirror optical relay. The optical rail was not used, but the flange with the flag drive and window was similar to the present design. Data was acquired with a Spiricon LBA-100A Laser Beam Analyzer[10] which contains a frame grabber and processor with firmware to generate a 2D or 3D false color display with projection, centroid and computations as well as background subtraction and gaussian fits to the data. It can be controlled from the front panel or a IEEE-488 interface. The

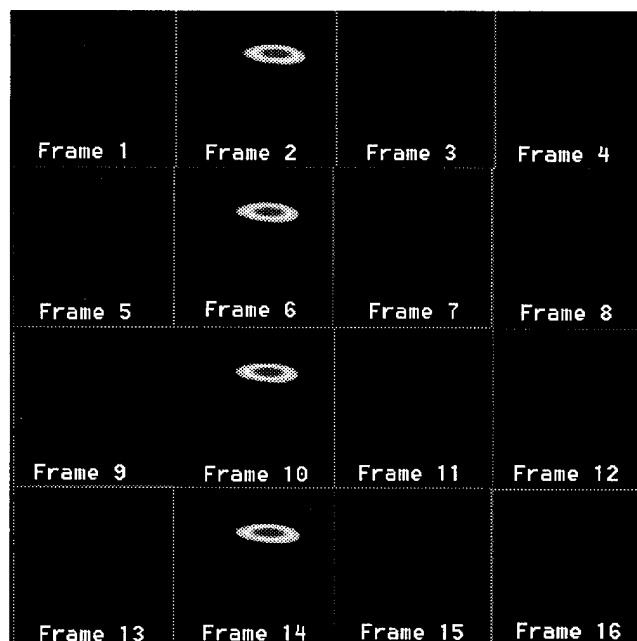


Figure 2. Data from BTA tests. The 30 Hz framing captures the 7.5 Hz beam with no afterglow.

data can be processed at up to 15 Hz on a 120x120 sub-set or full frame at a reduced rate. While the LBA-100A showed great capability as a stand alone unit and performed well in the beam tests, it did not match the control system requirements and could not be used for the final design.

Tests were run over a range of intensities of about 25:1 by adjusting the number of turns in the Booster. At the low end,

injected bunch length was varied for a single turn. The data showed that the response was extremely linear over the intensity range for normal RHIC injection and studies intensities. Higher intensity could not be used due to lack of lens aperture adjustment. The lifetime of the $\text{Gd}_2\text{O}_2\text{S:Tb}$ screen couldn't be established since the camera failed from radiation damage. Thermo-Luminescent Detectors (TLDs) on the camera were removed when the image first began to look "grainy" and read as 130 Rad. Total failure probably occurred within a dose many times this but it was not possible to retrieve the TLDs until long after the camera died. No damage was apparent upon visual inspection of the phosphor screen.

Using the LBA-100A with all computations off, frames were successfully acquired at 30 Hz. Figure 2 clearly shows no residual phosphor glow in the 3 frames between the 7.5 Hz Booster pulses, confirming the light decay rate would be suitable for single bunch measurements in the ATR.

VIII. STATUS

All optical and video components are on hand. A prototype cradle for the optical rail was built and tested and production has begun. The vacuum tees are installed as will be the flag flanges when the phosphor screens are done. The frame grabbers/image processing boards are being tested. The low level code to control the acquisition and perform the analysis is being developed. Full installation will be completed for the first extracted beam tests in the fall of 1995.

ACKNOWLEDGEMENTS

Manny Grau and Joe Guilmette did the mechanical design and engineering. Dave Kipp made the mechanical pieces a working reality. Jack Weinmann and Gene Tombler gave valuable assistance with the TV work. Larry Hoff is the software magician. Michael Goldman's optical advice made it possible to see the light.

- [1] P. Zhou, "Beam Emittance Measurement and Phase Space Distribution", These proceedings.
- [2] Supplied by MDC, Hayward, CA, 94545-1651
- [3] J. Seeman, et. al., Beam Tests of Phosphorescent Screens", Single Pass Collider Memo CN-290, March 5, 1985
- [4] X. J. Wang, private communication, 1993
- [5] D. Sagan, CESR note dated 1/10/88, and private communication, Dec, 1992
- [6] F.-J. Decker, "Beam Size Measurements at High Radiation Levels", Proc. IEEE 1991 Particle Accel. Conf., 91CH3038-7, p1192, (1991)
- [7] P/N M52,202, Edmund Scientific Co., 101 E. Gloucester Pike, Barrington, NJ, 08007
- [8] Cytec Model VM/8x4VID, Cytec Corp., 2555 Baird Road, Pennfield, NY 14526
- [9] E. R. Beadle, "A General Purpose Fiber Optic Link with Radiation Resistance", These proceedings.
- [10] Spiricon Inc., 2600 N. Main, Logan, UT 84321

BEAM INTENSITY OBSERVATION SYSTEM AT SRRC

C. J. Wang, C. H. Kuo, J. S. Chen, J. Chen, K. T. Hsu, and G. J. Jan*
Synchrotron Radiation Research Center
Hsinchu 30077, Taiwan, R. O. C.

* Department of Electrical Engineering, National Taiwan University
Taipei 10764, Taiwan, R. O. C.

ABSTRACTS

Beam intensity and lifetime measurement system have been implemented at SRRC. The average beam intensity is measured by direct current current transformer. The magnet shielding of DCCT is used to reduce stray magnet field interference, then output signal is digitized by high resolution analog to digital converter on VME crate. In order to be compatible with the data refreshing rate of main control system, which is 10 samples per second, all digitized data are filtered and decimated by digital filter to reduce noise level. The adaptive lifetime calculation algorithm are applied to provide fast time response.

I. INTRODUCTION

Beam intensity is a basic machine parameter should be measured at any time. A commercially available high precision DC parametric current transformer (PCT) has been chosen for measuring the beam current. Beam lifetime is also a significant machine parameter of the storage ring. The beam lifetime is calculated by the beam current measured using PCT. The calculation process of beam lifetime requires precise measuring and quick response of the dedicated system. In the following paragraphs, the hardware and software for beam intensity and lifetime measurement system generating desire result are depicted.

II. INTENSITY MONITOR

The intensity monitor is an commercially available parametric current transformer made by Bergoz. The resolution of the sensor is about 1 μ A for 1 second inetgration time. A ceramic break is utilized to couple magnetic field produced by the electron beam on the sensor head. The whole assembled sensor is wrapped by five magnetic shielding layers which are made of highly permeable materials. The shielding effectiveness of the magnetic shield is about 10^3 [1,2,3]. The whole assembled instrument is housed in a Cu-made cover to bypass image current. The ambient magnetic field is about 10 Gauss which is measured by Hall probe.

III. DATA ACQUISITION SYSTEM

The SRRC control system is a two layer hierachical system [4,5]. The upper layer consists of dedicated workstations used as console computers while the lower layer

is integrated by VME-based intelligent local controllers (ILC)[4,5] serving as front end device controllers. Computer systems of both layers are interconnected by Ethernet. Each console layer computer maintains a centrallized control database. Those ILCs refresh transient information of all devices within control database every 100 msec. On one of ILCs, a 16 bit analog-to-digital converting (ADC) channel is used to acquire the current, which is corresponding with beam intensity information, generated by PCT. The necessary hardwares of data acquisition system are shown in figure 1.

The original sampling rate of beam intensity instrument is synchronized with updating rate (10 samples/sec) of main control system, while the sampling rate of new approach is changed to 3.68 KHz.

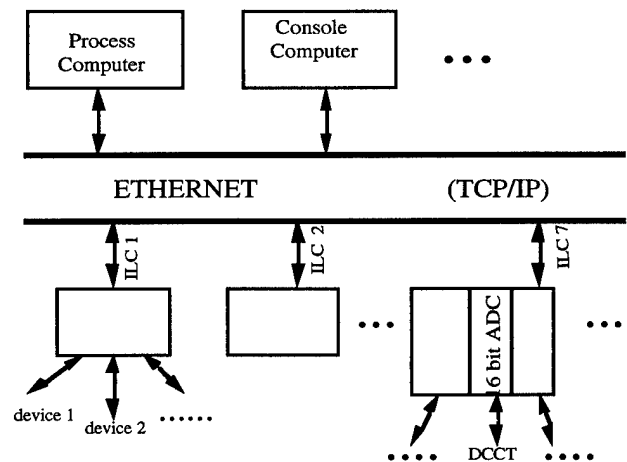


Figure 1. Beam intensity data acquisition block diagram

IV. SIGNAL PROCESSING

The samples obtained by 3.68KHz are reduced to 460 samples per second. A digital filter with respect to decimation is used to reduce noise levels as well as interferences of power systems inherited from the circuitry of ADC. The digital filter is a 20 order low pass finite impulse response (FIR) filter with cutoff frequency at 5 Hz. This process can increase the effective precision of a measurement. Finally filtered values have been decimated to 10 samples per second to fulfill the adopted updating rate of main control

system. The flowchart of implementing softwares is shown in figure 2.

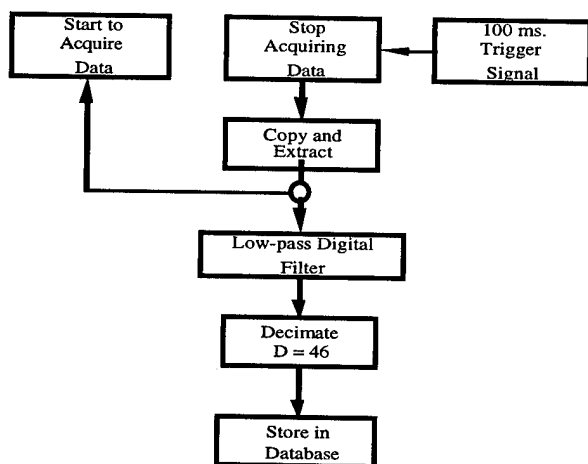
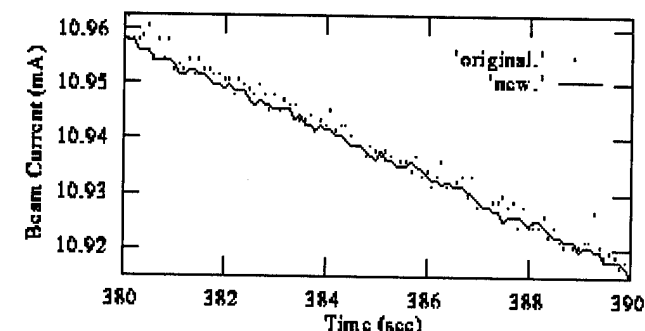
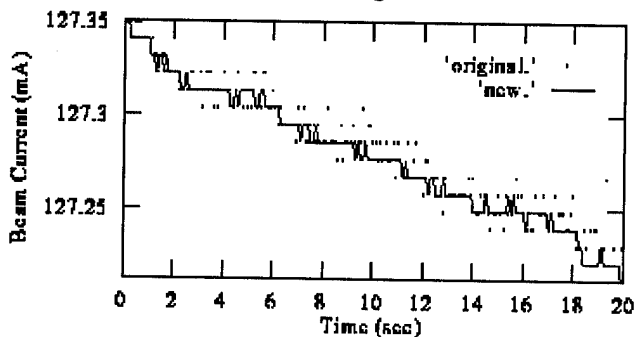


Figure 2. Software flowchart



(a) 60 mA range resolution



(b) 600 mA range resolution

Figure 3. Beam intensity readings

Comparisons between the original measurement system and the new approach can be observed in figure 3. The resolution of PCT can be better than $1 \mu\text{A}$ with 1 second integration time, besides the 1 KHz bandwidth of PCT. Since

the ADC channel is with high bandwidth, the original system is interfered with the line frequency; also due to 10 Hz sampling rate, there are some aliasing effects existed. It is obvious that we can't remove both interferences in old system. The new approach, which resides on the ILC, increases the sampling rate and filters out the interference by the digital filter. As shown in the figure, the peak variation of beam intensity is about $60 \mu\text{A}$ -p. Hence, the new system is much better than the old one.

The resolutions of beam currents generated by new approach are also shown in figure 3. The beam current sensor is with two ranges of full scales (60 mA or 600 mA). From the figure, it is easy to identify that the resolution of beam current is approaching $1 \mu\text{A}$ for 60 mA range and $10 \mu\text{A}$ for 600 mA range.

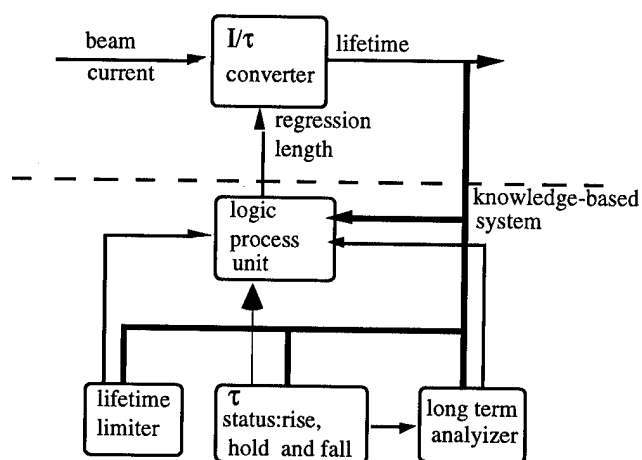


Figure 4. Lifetime calculation algorithm

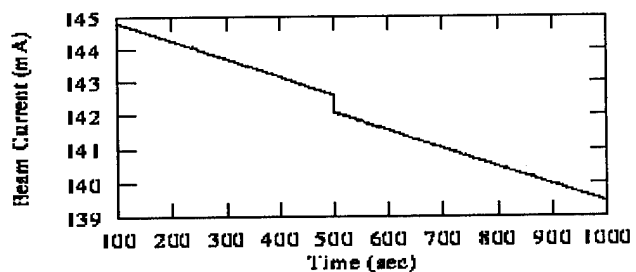
V. LIFE TIME CALCULATION

There are two algorithms have been used to compute beam lifetime. Both algorithms are based on typical regression process.

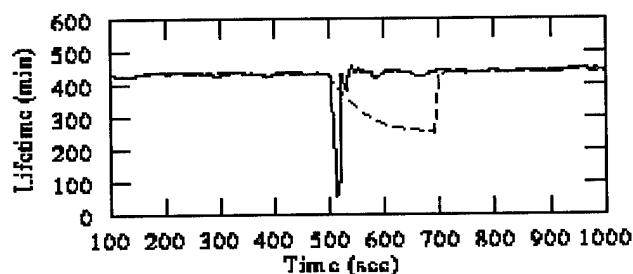
The approach which we currently use is the fixed length regression procedure. This procedure runs on a console level computer, and the regression length is selectable from 100 seconds to 200 seconds. It may happen that the response rate of beam lifetime calculation is not fast enough to show instant changes of beam currents, if longer regression length selected. Another drawback occurs in need of long-term and stable lifetime calculation. In that case, the fluctuating range of lifetime calculation may be enhanced if the selected regression length is not long enough.

The method which is under developing now will be deemed as adaptive and will be done at VME layer in the future. It is shown in figure 4. The new regression length can vary adaptively with respect to time. The longer length of

regression is adaptively applied for the case of needing slow response rate in lifetime calculation, while shorter length of regression is for needing fast response rate category, respectively. Advantages over varied regression length are twofold - one is its fast response time for instant changes of beam currents, shown in figure 5(b); another is smaller fluctuation for long-term and stable lifetime calculation, shown in figure 6(b).

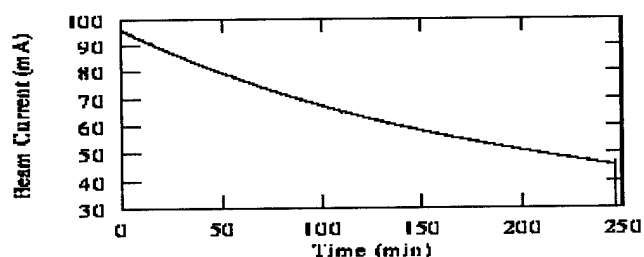


(a) Beam current

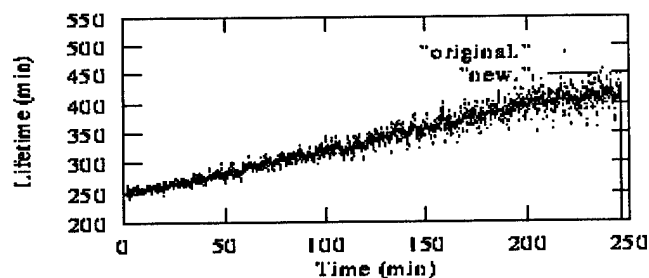


(b) Lifetime calculation

Figure 5. Lifetime calculation with instant beam current drop



(a) Beam current



(b) Lifetime calculation

Figure 6. Long-term lifetime calculation

Comparisons of response times between two methods can also be observed in fig 5(b). The beam current is real beam intensity data, and the sink of beam current is intentionally generated in order to compare performances of both methods of lifetime calculations. The response time of fixed length method is about 200 seconds, while of adaptive regression length method is about 5 seconds. There are some overshooting effects nearby the recovery period in lifetime calculation; those phenomena are nature, and won't affect anything of applications.

VI. CONCLUSIONS

First, speed up the sampling rate of intensity data. Then, sampled raw data are processed by digital signal processing technique to remove the interference inherited from ambience. The lifetime calculation utilizing adaptive regression length method is introduced. Also improvements in precisions of beam intensity observation, and the response time of beam lifetime calculation are demonstrated.

VII. ACKNOWLEDGEMENTS

All authors would like to appreciate those staffs who participated the installation phase; especially Dr. J. R. Chen and Mr. G. Y. Shiung. Encouragements from Director Y. C. Liu and deputy Director Dr. Bill Weng are also valuable.

VIII. REFERENCES

- [1] T. J. Sumner, J. M. Pendlebury, K. F. Smith, "Conventional Magnetic Shielding", J. Phys. D: Appl. Phys. 20 (1987) 1095-1101.
- [2] T. Honda, Y. Sato, T. Katsura, "Beam-Intensity Measurement with a DC Current Transformer at the Photon Factory Storage Ring", Proceedings of the 9th Symposium on Accelerator Science and Technology, October 1993. p 345.
- [3] M. Sugiura, M. Yuasa, T. Kasuga, M. Tobiyama, "Influence of External Magnetic Field on Beam DCCT", Proceedings of the 9th Symposium on Accelerator Science and Technology, October 1993. p342.
- [4] G. J. Jan, et al., "Computer Control and Instrumentation System at the SRR", Nucl. Instr. and Meth. in Phys. Res. A 352 (1994) 33-39.
- [5] C. J. Wang, et al., "The Design Schemes of Graphic User Interface Database and Intelligent Local Controller in the SRR Control System", Nucl. Instr. and Meth. in Phys. Res. A 352 (1994) 300-305.

PERFORMANCE OF THE ADVANCED PHOTON SOURCE (APS) LINAC BEAM POSITION MONITORS (BPMs) WITH LOGARITHMIC AMPLIFIER ELECTRONICS*

R. E. Fuja and M. White

Argonne National Laboratory, 9700 S. Cass Avenue, Argonne, IL 60439 USA

Abstract

This paper discusses the performance of the logarithmic amplifier electronics system used with stripline BPMs to measure electron and positron beam positions at the APS linac. The 2856-MHz, S-band linac accelerates 30-nsec pulses of 1.7 A of electrons to 200 MeV, and focuses them onto a positron conversion target. The resulting 8 mA of positrons are further accelerated to 450 MeV by the positron linac. Beam position resolutions of 50 μm are easily obtainable in both the electron and positron linacs. The resolution of the 12-bit A/D converters limits the ultimate beam positron resolution to between 20 and 30 μm at this time.

I. INTRODUCTION

The APS linac BPM system, in operation for over a year, has been used in the commissioning of both the 200-MeV electron and the 450-MeV positron beams. It consists of stripline pickups and signal processing electronics using logarithmic amplifiers. The system has proven very reliable with only one problem occurring in an A/D section. System stability has not been a problem, and beam can be transported to the end of the linac a few minutes after being turned on.

II. EXPERIMENT

The following data were taken to determine the resolution of the linac BPM system in the presence of pulsed power supply noise. Background on the detectors and the processing electronics is provided.

A. Detectors

Stripline-type BPMs [1], were chosen because they provide -5 dBm of peak signal from the 8-mA positron beam. The BPMs are cylindrical in geometry, and the four striplines are mounted 90 degrees apart. The striplines are 1 inch long and subtend an arc of 1 radian. Their geometry is such that they form 50-Ohm pickups. The measured electrical length of the striplines is 0.21 wavelengths at 2.856 GHz. The average detector sensitivity is 1.73 dB/mm \pm 0.1 dB. Signals from the striplines are transported via 1/4-inch heliax cable to electronics located an average of 85 feet away in the klystron gallery. About 10 dB of signal is lost over this distance.

* Work supported by U.S. Department of Energy, Office of Basic Energy Sciences, under Contract No. W-31-109-ENG-38.

Five BPMs are installed in the electron linac, one downstream of each accelerating structure, and seven BPMs are installed in the positron linac, one downstream of each of the last seven accelerating structures. There are no BPMs downstream of the first two accelerating structures after the target in the positron linac.

B. Electronics

The electronics [2], can be subdivided into two sections, a downconverter section and a logarithmic amplifier section. The downconverter section consists of a 2.856-GHz to 70-MHz downconverter followed by a 70-MHz bandpass filter and amplifier. The bandpass filter stretches the 30-nsec pulse to around 200 nsec and reduces its amplitude by some 13 dB. The overall gain of the downconverter is around 6.2 dB and it has a noise figure of around 7.5 dB. This 70-MHz signal is used as the input to a cascaded chain of logarithmic amplifiers consisting of two Analog Devices AD640s with their video bandwidths set to 7 MHz. The input power to the logarithmic amplifiers is adjusted to -10 dBm for the two different beam intensities in the electron and positron linacs. The sensitivity of the logarithmic amplifier chain is 53 mV/dB \pm 1 mV. The calibration shown in Figure 1 is typical of all logarithmic amplifier sections.

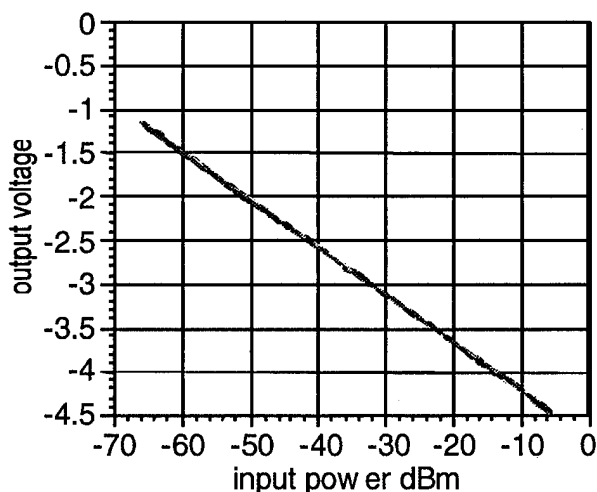


Figure 1: Dynamic ranges of eight different logarithmic amplifier channels. The slope is -54.26 ± 0.6 mV/dBm, and the intercept is at -4.756 ± 0.02 V.

Eight logarithmic amplifier channels are mounted on a single VXI card and process the signals from two BPMs. The VXI card also contains eight sample and hold circuits and eight 12-bit analog-to-digital converters. A specially designed VXI trigger module [3] contains a set of 8-bit programmable delay lines that can be used to select sample times in increments of 5 nsec. Software peak detection by scanning is available for all BPM signals, replacing the more commonly used peak detection circuits.

With a detector sensitivity of 1.73 dB/mm and a logarithmic amplifier sensitivity of 53.3 mV/dB the overall sensitivity of the system becomes 94 mV/mm. The gain of each downconverter channel was adjusted by injecting a 2.856-GHz signal into the cable at the detector end and adjusting the amplitude of the 70-MHz output. Phase shifters at the input to the downconverter enabled the phase between two 70-MHz output signals to be matched. Zeroing the phase shifts was necessary because of coherent noise in the system; 5 mV corresponds to 53 μ m. The signal difference for two typical channels is shown in Figure 2.

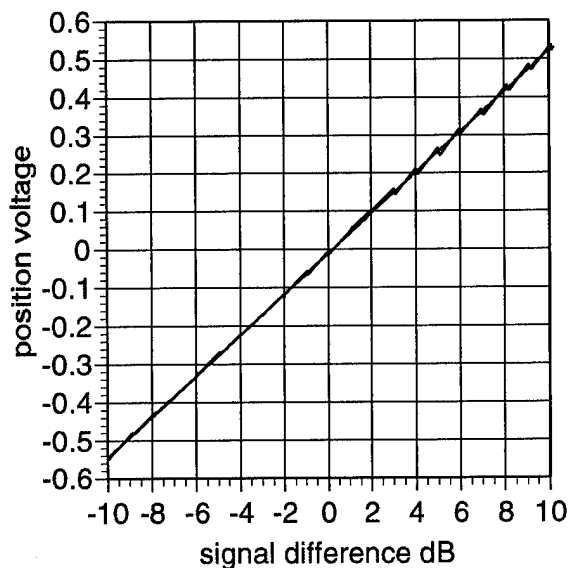


Figure 2: Signal difference between 2 channels for input power levels of -15, -25, and -35 dBm. The slope is 53.31 mV/dB and the offset is -10.2 mV.

III. RESULTS

The results presented below were obtained during a positron studies run and they are the best to date. Typically, operating conditions result in data from selective positron linac BPMs that are up to five times worse. Electron linac BPMs consistently provide good data because the signals are large. The results from positron linac BPMs vary because both electrons and positrons are present in a ratio that depends on the particular transport optimization at the time. The amplitude of the signal they receive depends on the

magnitude of the charge difference between electrons and positrons. The charge of the particle that is present in excess is unknown and must be determined by other means. Figure 3 shows data taken from the BPM located just upstream of the positron target, when 1.06 A of electrons were hitting the target. With 16 samples, the standard deviation of the readings from individual electrodes is 5 to 7 mV and the standard deviation in the difference of two signals is 1 to 2 mV, corresponding to 21.3 μ m. Figure 4 shows BPM data from the detector furthest downstream in the positron linac. Here the intensity reading is 6 mA and represents the magnitude of the sum of the positron and electron currents in the beam. Other measurements made in the low energy transport line after a bending magnet indicate that 4 mA of positrons were present at that time. Here the standard deviation in the position measurement is 3 mV or 33 μ m.

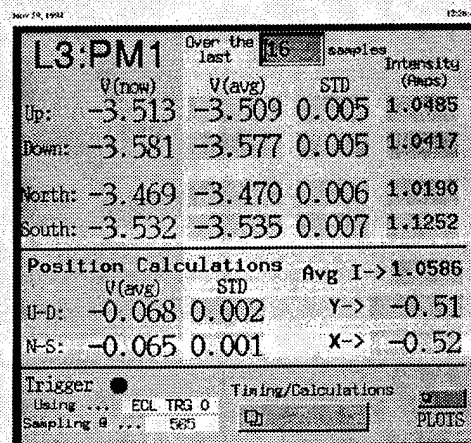


Figure 3: Data taken from the BPM located just upstream of the positron target, when 1.06 A of electrons were hitting the target.

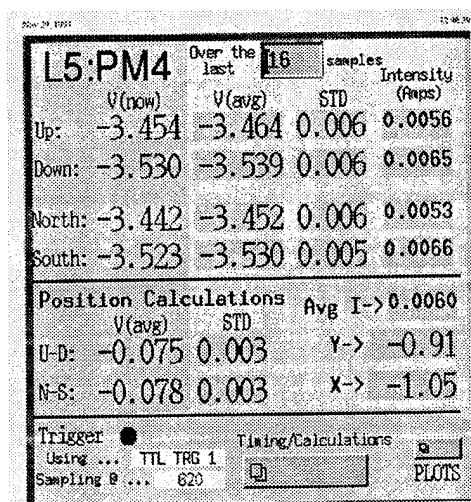


Figure 4: BPM data from the last detector in the positron linac. Here the intensity reading is 6 mA, the magnitude of the sum of the positron and electron currents.

IV. CONCLUSION

With proper phasing of the stripline signals it is not difficult to obtain the results shown. With the signal-to-noise ratio at the input to the logarithmic amplifier circuits approaching 75 dB, resolutions of 1 μm should be possible.

A new BPM system that gives information on the polarity of the charged particle producing the signal (electron or positron) has been worked out, and will provide for much improved positron diagnostics capability [4]. A prototype is under development.

V. ACKNOWLEDGEMENTS

The authors would like to thank C. Gold for his help in the laboratory and in the installation, J. Stephens for his help with the software testing programs, and N. Arnold and K. Ko for developing the control systems and operating screens.

VI. REFERENCES

- [1] R. Shafer, "Beam Position Monitoring," Accelerator Instrumentation, Upton, N.Y., 1989, *AIP Conference Proceedings 212*, pp. 26-58, (1989).
- [2] R. Fuja and Y. Chung, "The APS Linac Beam Position Monitor and Electronics," Proc. of the 4th Accel. Instr. Workshop, Berkeley, CA., October 1992, *AIP Conference Proceedings No. 281*, pp. 248-255 (1993).
- [3] A.E. Grelick, private communication.
- [4] W. Sellyey, private communication.

PRELIMINARY CALCULATIONS ON THE DETERMINATION OF APS PARTICLE-BEAM PARAMETERS BASED ON UNDULATOR RADIATION*

A. Lumpkin, B. Yang, Y. Chung, and R. Dejus

Argonne National Laboratory, 9700 S. Cass Ave., Argonne, IL 60439 USA

G. Voykov⁺⁺ and G. Dattoli

ENEA, Frascati, Italy

Abstract

The potential measurement of particle beam emittance at a third-generation synchrotron radiation facility such as the Advanced Photon Source (APS) by characterizing the observed undulator radiation from an insertion device is considered. The nominal APS particle beam parameters have been used in calculations for insertion devices with periods of $\lambda=3.3$ cm, $\lambda=5.0$ cm (in two configurations), and $\lambda=1.8$ cm. The US program, the MDK1F program, and analytical formulae were used. Sensitivity to variations of emittance by 20% from the nominal value are addressed.

I. INTRODUCTION

The commissioning of the third-generation synchrotron radiation facilities with low natural emittance carries with it the challenge to characterize and monitor the particle beams. One well-established, but somewhat complicated technique is based on the effects of non-ideal beam parameters such as finite transverse emittance and energy spread on the observed undulator radiation (UR). [1-7] The nominal APS parameters including 7-GeV energy, a natural emittance of 8×10^{-9} m rad, a relative energy spread of 0.1%, and a baseline vertical coupling of 10% have been used in evaluating these effects for insertion devices with $\lambda=3.3$ cm, $\lambda=5.0$ cm (in two configurations), and $\lambda=1.8$ cm. Specific calculations using the US program [8] for $\lambda=3.3$ and the MDK1F program [4] for $\lambda=5.0$ cm and 1.8 cm are briefly presented. These calculations were used as a guide to us for designing on-line emittance measurement techniques. Progress in this area has been reported in [6,7].

For the parameter space at APS, and after calculation of effects of particle beam parameters on the standard APS undulator A's radiation, we have developed a plan for a "diagnostic undulator." Some parameters are specifically optimized for the diagnostics tasks. Generally, the UR carries complete information about all first and second moments of particle phase space: beam position, beam direction, beam size, beam divergence, tilt of the emittance ellipse, and other coupling terms. [3-7] A single bending magnet (BM) source addresses beam position and size although the bend plane can introduce uncertainty from energy spread. An undulator should emit more photons than a BM so that faster phenomena (beam instabilities) might be detectable in the 100-ps timescale.

* Work supported by U.S. Department of Energy, Office of Basic Energy Sciences, under Contract No. W-31-109-ENG-38.

⁺⁺ ENEA Frascati Laboratory Guest

II. APS BEAM PARAMETERS AND UNDULATOR CONSIDERATIONS

The nominal APS storage ring particle beam parameters are given in [9]. The natural emittance (8×10^{-9} m rad) and vertical coupling coefficient (10%), the energy (7.0 GeV) and energy spread (0.1%), and beam current (100 mA) are all critical in evaluating the undulator radiation and its strength compared to the nearby bending magnet radiation.

Although not necessarily in the order of priority, design criteria for an undulator have now been developed and for our case they are:

1. Photon energy 20-80 keV to provide phase space resolution of ~ 0.02 - 0.06 nm. This can even address the 1% vertical coupling operations regime.
2. Low magnetic field (≤ 0.2 T) to give low field errors and low trajectory errors.
3. Low undulator parameter, $k < 1.0$ to provide directly calculable undulator properties.
4. Low x-ray power (100 W-400 W) to keep the thermal load of optics manageable.
5. Adequate flux to allow single bunch/single pass measurements. Should be above the BM background continuum by 100 fold.
6. Large aperture to make the system's presence transparent to the storage ring accelerator operations.

In practice, the basic question of what happens to the standard APS undulator A radiation when the finite particle beam emittance is included was previously addressed by a series of calculations using the SHADOW program. [1,2] The angular distribution of the harmonics were clearly changed from the zero- to the APS-emittance cases. An extension of this study was performed using the program US [8] to address the calculated effects for emittance changes of $\pm 20\%$ around the nominal APS value which are briefly reported in the next section. The fundamental problem of sensing the smaller vertical emittance changes with the given asymmetry of the horizontal and vertical emittance (with 10% vertical coupling) remains a challenge experimentally. Absolute intensity and spectral shape of the harmonics remain key features.

A separate question was approached in collaborations between the APS and Frascati groups. The use of interference effects in UR from two undulators separated by a drift space or dispersive section was considered. In addition, the desire to be transparent to the SR operations led us to consider initially a full storage ring vacuum chamber (SRVC) gap of 4 cm. We then chose a calculational regime of period, $\lambda=5.0$ cm, $N=20$,

and $\Delta L = 1.5$ m. The MDK1F [4] program which is based on the Monte Carlo technique was used to address the effects of emittance and energy spread. In this case the formalism also addressed the problem through the standard Twiss parameter (α, β, γ) characterization of particle beams. Initial calculations were carried out on the IBM 3090 at Frascati Lab using APS-like particle-beam parameters. Calculations were again done at the nominal value and at $\pm 20\%$ of that value. Some of these results were presented at EPAC '94 [5], and a few examples are given in Section III. The code was transported to APS in October 1994, and preliminary studies were done on the SUN workstations.

After noting the difficulty in showing significant sensitivity to the small, but critical (to APS) vertical emittance, another tactic was pursued. As parameters were considered, we put more emphasis on making the UR cone angle noticeably smaller than the nominal $8.6 \mu\text{rad}$ of vertical divergence of the APS particle beam at 10% coupling. We focused on criteria to reach a few μrad divergence angles in a reasonable length (3-5 m). The APS straight sections are 5.2 m. We also accepted the fact that the APS would eventually have many smaller gap vacuum chambers, and at that point the diagnostics undulator with a comparable gap would still avoid being the limiting aperture. Parameters explored analytically were a combination of criteria 1-5 with #6 being viewed at a different point in the commissioning cycle. An undulator of 160 periods with $\lambda = 1.8$ cm, and using the third harmonic keV photons gives a cone angle of about $1.7 \mu\text{rad}$ [9].

III. PRELIMINARY RESULTS AND DISCUSSIONS

In this section, a few examples of results from calculations using US, MDK1F, and analytical relationships are presented.

A. US Results

The fundamental question of the finite beam parameter effects on undulator radiation is illustrated in Fig. 1. Figure 1a shows the calculated spectrum from the $\lambda = 3.3$ cm ($K = 0.37$) case with zero emittance, $E = 7.0$ GeV, and 100 mA stored beam current. Its peak brilliance is about 8×10^{21} at the fundamental energy of about 13.1 keV. In Fig. 1b, the nominal emittance is the solid line, and the dashed and dotted curves show the 1.20 times nominal and 0.80 times nominal vertical emittance cases (10% vertical coupling). The peak brilliance is reduced to about 4.4×10^{17} with the intensity at about 13.1 keV further modulated by $\pm 10\%$. The effects are similar, but a little more pronounced for the second and third harmonics. The UR intensity was explored off axis and some minor effects are seen in the lobes at the 10^{11} brilliance level on the $x = 0$ line as shown in Fig. 2. Vertical slices display some effects for the nominal vertical emittance value and variations of $\pm 20\%$ around it.

B. MDK1F Results

For a single undulator with $\lambda = 5.0$ cm, $N = 34$, and $K = 1.48$, calculations with APS-like particle-beam parameters are

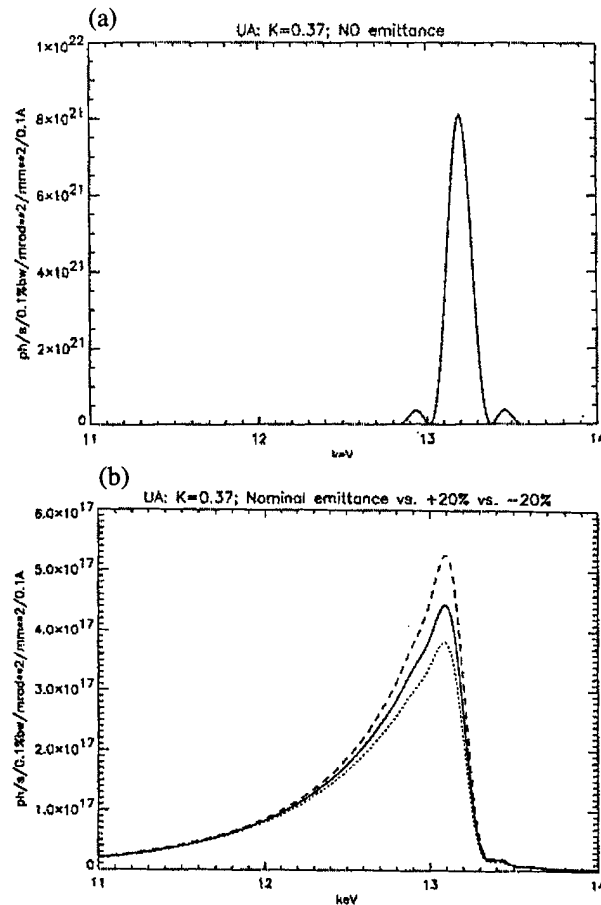


Figure 1: US calculation results for the undulator fundamental spectrum and with $K = 0.37$: (a) zero emittance beam, and (b) an APS nominal emittance (solid line) and for $\pm 20\%$ around the vertical emittance value.

reported in Figs. 1-4 of [5]. It was noted there that the reliability of the analytic approximation decreases at higher harmonics compared to the numerical results in that study.

Another investigation involved the use of MDK1F to assess UR from two 1-meter ($N = 20$) undulators separated by a 1.5-m drift section. The optical klystron configuration shows sensitivity to the energy spread of the particle beam, the larger horizontal emittance, and the small vertical emittance in descending order, respectively. Figure 3 shows the calculated effects of energy spread on the third harmonic spectral intensity plot. The solid curve is for one energy, and the dashed curve has the 0.1% energy spread. The modulation of intensity is visibly reduced. In Fig. 4, the on-axis brilliance is again addressed with an assumed $\beta_{x,y} = 18$ m and $\alpha_{x,y} = 0$. Here the solid curve includes the emittance and no energy spread, and the dashed curve has emittance and the 0.1% energy spread. In the first case, the emittance effect has almost completely obscured the interference patterns even before the energy spread is added. By considering Figs. 3 and 4, one has an idea of the dramatic effect of finite emittance. The test of varying the vertical emittance by 20% was not attempted.

As a follow-up study, the case of the $\lambda = 1.8$ cm period undulator was begun using the MDK1F program ported to the APS computer network and implemented on a Sparc-10 SUN

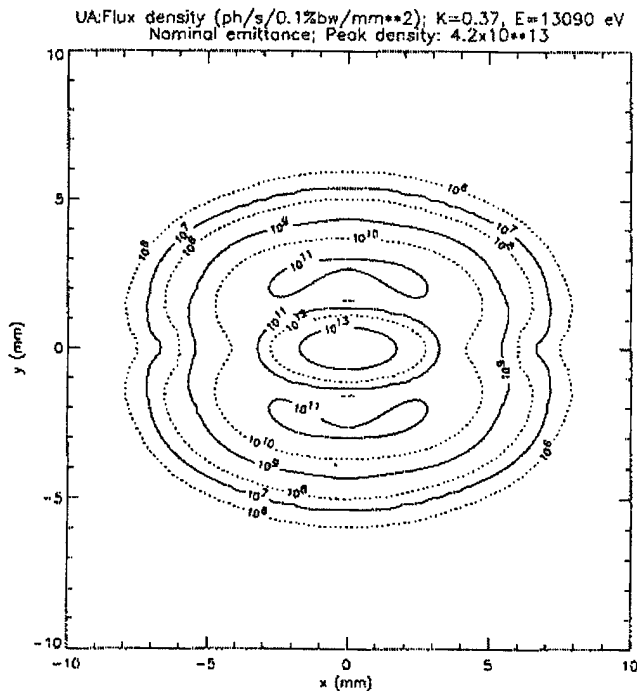


Figure 2: US calculation results in the undulator fundamental spectrum off axis in x and y. The intensity contours are indicated.

workstation. Calculational times in excess of 20 hours for a grid point proved to be impractical, and the code may be tested for calculational speed on the ANL IBM sometime in the future.

C. Other Results

An investigation of central cone flux for the undulator compared to the BM radiation continuum was performed using standard analytical formulae. The undulator fluxes for the first and third harmonic were calculated for periods from 1 to 7 cm

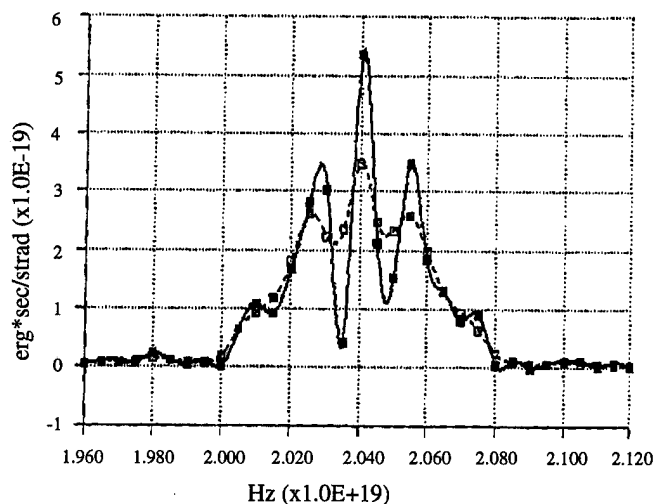


Figure 3: MDK1F results for an optical klystron configuration showing the calculated third harmonic spectral region without (solid) and with (dashed) 0.1% energy spread and no emittance.

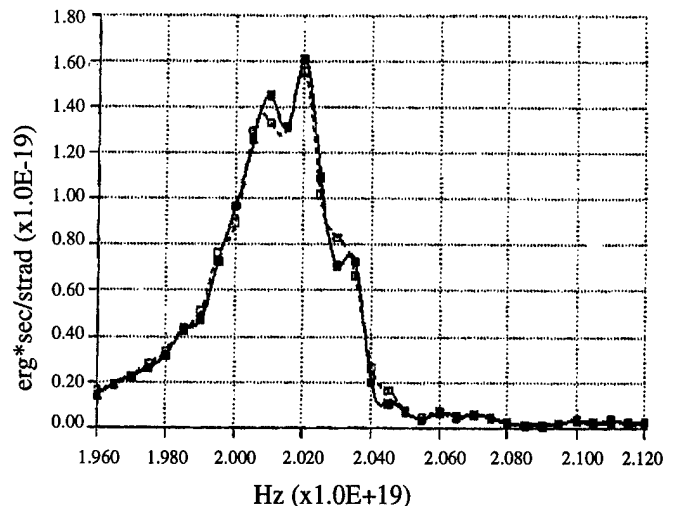


Figure 4: MDK1F results as in Fig. 3 with APS emittance effects added and with (solid) and without (dashed line) 0.1% energy spread.

in the energy range from 1 to 100 keV. We have settled on $\lambda=1.8$ cm, 160 periods, with a fundamental energy at about 25 keV as a good candidate for the undulator. As discussed in [9], the UR cone angle is small compared to the beam divergence, and thus the UR can be used as a sensitive probe.

IV. SUMMARY

In summary, calculations have been performed to assess the effects of APS particle beam parameters on UR. The sensitivities to variations around the nominal value have also been addressed, and these results have provided direction on diagnostics undulator concept designs. Further studies will focus on the $\lambda=1.8$ cm case and exploration of smaller vertical coupling of the APS particle beam.

V. REFERENCES

- [1] B. Lai and F. Cerrini, *Nucl. Inst. and Meth.* **A243**, 337 (1986).
- [2] S. L. Xu, B. Lai, and P. J. Viccaro, "APS Undulator and Wiggler Sources: Monte-Carlo Simulation," ANL/APS/TB-1, Feb. 1992.
- [3] Pascal Ellaume, "Optical Klystron," *Journal de Physique*, Tome 44, PC1-333, Feb. 1983.
- [4] G. Dattoli, L. Giannessi, G. Voykov, *Computers Math. Appl.*, **27**, (6), 63-78 (1994).
- [5] F. Ciocci, G. Dattoli, L. Giannessi, and G. K. Voykov, "Numerical and Analytical Computations of Undulator/Wiggler Radiation," *Proceedings of the 1994 EPAC*, 1241, Vol. 2, 1994.
- [6] Z. Cai, et al., *Rev. Sci. Instrum.* **66**, (2) 1859, Feb. 1995.
- [7] E. Tarazona and P. Ellaume, *ibid.*, 1974.
- [8] R. J. Dejus, Program US (unpublished).
- [9] B. Yang and A. Lumpkin, "The Planned Photon Diagnostics Beamlines at the APS," *Proc. of the 1994 Beam Instrumentation Workshop*, Vancouver, B.C., Oct. 2-6, 1994.

COHERENT SYCHROTRON RADIATION DETECTOR FOR A NON-INVASIVE SUBPICOSECOND BUNCH LENGTH MONITOR*

G. A. Krafft, D. Wang, E. Price, and E. Feldl, Continuous Electron Beam Accelerator Facility,
Newport News, VA, 23606 USA,

D. Porterfield, P. Wood, and T. Crowe, Semiconductor Research Laboratory,
University of Virginia, Charlottesville, VA

A Coherent Synchrotron Radiation (CSR) detector has been developed in a collaboration involving CEBAF and the University of Virginia (UVA) to monitor non-destructively the length of a sub-picosecond bunch with high sensitivity. The monitor employs a state of the art GaAs Schottky whisker diode developed at UVA, which is operated at room temperature at a wavelength of a few hundred microns. The detector is capable of detecting radiation power as low as ten nanowatts, depending on the operating wavelength. In this paper we will describe the details of design specifications, parameter ranges, and features of the monitor and will also report its performance and comparison between the measurement results and calculation. The measurement results will be cross-compared with an independent bunch length measurement using a phase modulation and detection technique.

Following a brief discussion of the need for such a monitor, the following topics will be discussed: brief discussion on the theory of the device and the experimental arrangement, the properties of the Schottky diode detectors which are particularly convenient for our application, a summary of the measurement results, a summary of future plans and improvements to the monitor, and finally, a set of conclusions.

I. Introduction

In order to achieve the smallest energy spread in the extracted CEBAF beam, one would like to set and maintain the bunch length of the beam microbunches as short as possible [1]. The CEBAF injector specification requires the 4σ bunch length to be under 1.2° at 1497 MHz. Routinely, CEBAF achieves 4σ bunch lengths of under 0.6° as measured by an invasive bunch length monitor based on phase transfer function measurements [1,2]. Because the measurement is invasive, it is done only sporadically during beam operations, and does not provide a continuous picture of the beam state. Therefore, CEBAF initiated studies to develop a non-invasive monitor.

In storage rings it is possible to infer the bunch length by using RF "cavities" tuned to harmonics of the fundamental frequency, at high enough frequency that the bunch spectrum is changing as a function of frequency. By observing the power that is radiated into the cavity and by independently measuring the average current, one infers the bunch length from the power and an estimate of the longitudinal form factor [3], assuming the bunch is Gaussian. Longer bunch lengths produce a decrease in the RF current driving the cavity, and less power

coupled out to the RF detector. Typically, the cavity dimensions are of the same order as the bunch length.

In order to apply this idea to a linac beam as at CEBAF, two difficulties must be overcome. First, because the full width bunch length is of order 500 μm , RF detection type monitors must be replaced by something that detects radiation of wavelength of order 500 μm . Assuming that a non-invasive and non-destructive monitor is desired, one is led to explore using the Coherent Synchrotron Radiation emitted from the beam in bends, in the regime of several hundred microns radiation wavelength. The problem of detecting such radiation with low noise has been solved using Schottky barrier diodes developed at the University of Virginia.

Second, the beam distribution is not expected, *a priori*, to be Gaussian in a non-storage ring application. Therefore, a separate calibration measurement must be done in order to obtain the relation between output CSR power and bunch length, which is intimately related to the details of the longitudinal bunch distribution. This can be done at CEBAF because there is an independent method to determine the bunch length.

It should be noted that because the power usually goes down with increasing bunch length, such a monitor provides an operationally useful means of triggering processes that can be used to optimize the bunch length. Once the CSR power falls below a predetermined trip level, the invasive method of bunch length optimization can be invoked to correct the setup.

II. Theory

The CEBAF injector provides beam at 45 MeV. Before being injected into the first linac, the beam is bent horizontally in an injection chicane, which allows the relatively low energy injector beam to be merged with the higher energy recirculated beam. The injection chicane has four dipoles of bend radius 2.6 m, the first of which has a synchrotron radiation port of 1 cm^2 area. The port has a single crystal quartz window; the radiation is collected with reflecting optics and focussed onto the Schottky detector about 10 cm off axis from the port centerline. Fig. 1 gives a theoretical plot of the power through the port for four different values of the bunch length ($4\sigma = 0.4^\circ$, 0.5° , 0.6° , and 0.7°) assuming a Gaussian distribution. It is assumed that the detector bandwidth is 20%, the average current is 100 μA , and the acceptance angle is about 15 mrad. The transition from coherent to incoherent emission occurs at a radiation wavelength of order the bunch length, and gives a power increase of 5×10^5 at long wavelengths.

*Work supported by U.S. D.O.E. contract #DE-AC05-84ER40150

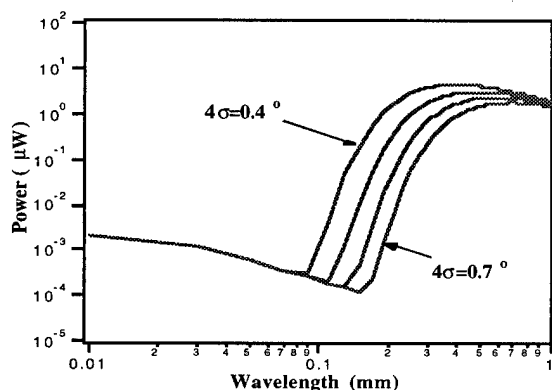


Fig. 1 Plot of Power vs. Wavelength for Injector CSR Port

For a given bunch length, the power peaks at higher levels and shorter wavelengths as the bunch length is made shorter, the total power rising because the emission is rising at shorter wavelengths. If the operating wavelength of the detector is fixed, the power depends very sensitively on the bunch length, more sensitively for larger numbers of electrons per bunch. Therefore, monitoring the CSR power at a fixed wavelength is equivalent to monitoring the bunch length. The optimal wavelength for the detector depends, of course, on the desired bunch length. Finally, it should be noted that the CSR power goes as the current squared, all else remaining constant.

The calculations above were made assuming a Gaussian form factor. Using the data acquired with the invasive bunch length device, one may estimate the longitudinal distribution more precisely and compute the coherent enhancement factor more exactly. Qualitatively, the picture presented above does not change.

III. Schottky Diode Detectors

The Schottky diodes used for these measurements were developed and fabricated by the Semiconductor Device Laboratory of the University of Virginia. They are designed for mixing applications and video detection in the far infrared (about 500 GHz to 3 THz). The diode chip contains several thousand individual circular anode wells in a layer of insulating SiO₂. The anode wells are plated with platinum followed by a top layer of gold. The platinum, in contact with the GaAs epitaxial layer below the SiO₂, form the Schottky diode. Below the epitaxial layer is an n++ GaAs substrate which is soldered to a metal post to form an ohmic contact. This "honey-comb" diode structure was first developed by Young and Irvin [4]. The fabrication and design of these diodes is described in the literature [5,6].

The radiation is coupled to the diode by a four wavelength long wire travelling wave antenna formed from the 1 mil whisker wire that contacts the anode. The antenna length is defined by the distance from the diode to a 90 degree bend which inductively cuts off the remaining length of wire to the induced current. The travelling wave antenna in free space has a symmetric pattern about the axis of the wire. Introducing a 90 de-

gree corner reflector 1.2 wavelengths behind the antenna results in a sharper radiation beam. The corner cube used for these experiments was designed at the Max Planck Institute for Radio Astronomy in Bonn [7]. The radiation is focussed onto the corner cube using an off-axis parabolic mirror (60 mm focal length, Melles Griot 02 POA 019). The performance of whisker contacted diodes as mixers and video detectors versus frequency was investigated by Wood [8]. The video responsivity (V/W) of a diode is inversely proportional to junction capacitance and to frequency. Therefore, the best video detector will have a low junction capacitance, which implies a small anode diameter. The corner cube mounted diode exhibits a wide bandwidth. An external mesh filter was used to achieve a known bandwidth (about 15% to 18% with a very high transmission of 0.93 to 1.00). The mesh filters were a free-standing copper film with cross shaped apertures. A complete description of modelling, fabrication and test results for the mesh filters is discussed by Porterfield, *et al* [9].

A picture of the corner cube and diode assembly is given in Fig. 2, where the scale of the device is seen from the SMA connector on the right side of the cube.

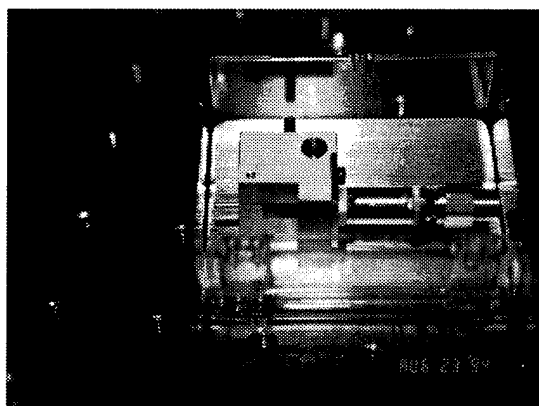


Fig. 2 Corner Cube and Schottky Diode Assembly

IV. Results

Several tests of the CSR diodes have been done. During our first set of tests in February, the CSR signal was observed at the end of a run. After improving the signal amplification and isolating the diodes from damage by ground loops, the coherent emission from the CEBAF bunches was again measured with a new biasing and amplification circuit, and found to be in agreement with expectations given the large radiation spot that was measured.

Fig. 3 gives a plot of CSR power vs. the beam current, along with a fit to the current squared dependence expected for coherent emission.

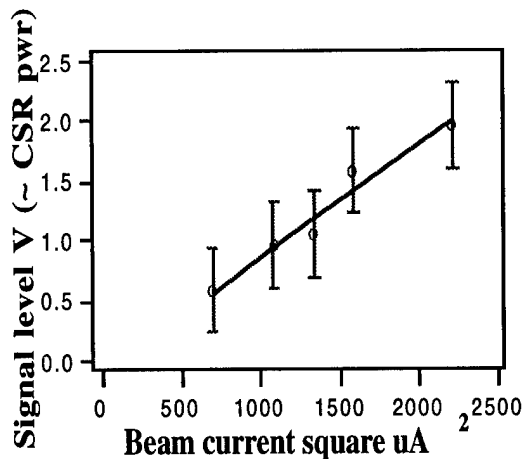


Fig. 3 CSR Power vs. the Square of the Beam Current

In Fig. 4, the fact that the CSR power depends on bunch length is shown. In Fig. 4 the measured CSR power (Schottky diode output voltage) is plotted as a function of the chopper phase of the CEBAF injector. The two curves are for two different diodes operating at wavelengths of $331\mu\text{m}$ and $216\mu\text{m}$. Zero degrees on the chopper gang phase corresponds to the nominal optimized setting yielding minimum bunch length ($4\sigma=0.6^\circ$) as measured by the invasive monitor. If the chopper phase is varied in either direction away from this optimal setting, the invasive monitor shows that the bunch length is increased. As is evident, the CSR power falls on either side of the minimum bunch length configuration, as it should. Given that a 4° change in the chopper phase produces a change of the bunch length from $4\sigma = 0.5^\circ$ to $4\sigma = 1.65^\circ$ as measured by the invasive monitor, a change in the bunch length of 0.1° (200 fsec) is detectable with the $216\mu\text{m}$ diode and a change in bunch length of 0.25° is detectable with the $331\mu\text{m}$ diode. That the $216\mu\text{m}$ diode should be more sensitive for short bunch lengths may be seen from Fig. 1.

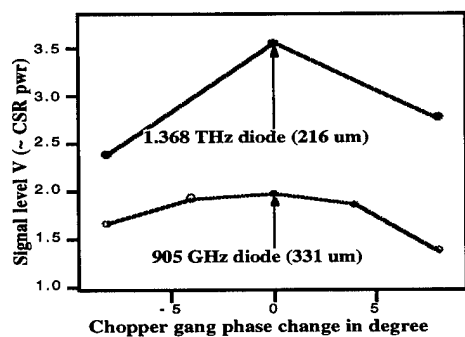


Fig. 4 CSR Power vs. Chopper Phase

V. Future Plans

There are several enhancements that will be pursued in the near term. They are related to computer control and analysis of measurements, coupled with automatic update of the bunching parameters of the injector. An externally triggered A/D card is being purchased to digitize the CSR output signal. In addition, a computer controlled biasing supply is being ac-

quired so that diode validation can be done from the control room. These two additions will produce an operational final monitor. We have run diodes for several hours with no degradation in performance. After a reasonable CSR power trip level is determined, the invasive bunch length monitor will be invoked whenever the power falls too low to correct any bunch length problems that arise. There are well defined correction procedures based on the invasive monitor [10] that can be automated with good results.

Normalization of the measurement is done using standard current monitor cavities [11]. As these are accurate to better than one percent, the normalization should be good to two percent, much smaller than the power changes to be detected. Calibration of the measurement will proceed in the same way as that it occurred for the invasive bunch length measuring system. By systematically changing the bunching parameters it is possible to completely characterize the CSR output as a function of bunch length.

VI. Conclusions

A coherent synchrotron radiation bunch length monitor has been installed in the CEBAF injector. This room temperature device has detected coherent synchrotron radiation at roughly the expected level. We have verified experimentally that the output power varies with the bunch length and that detectors at shorter wavelengths are preferred. We have also verified the high bandwidth of the Schottky detector and used it to study the stringent case of pulsed CEBAF beam, which has very low average power.

VII. References

- [1] G. A. Krafft, "CEBAF Status", *Proc. of the 1994 Linac Conference*, pgs. 3-7
- [2] C. G. Yao, *Proc. of the 1990 Beam Instrumentation Workshop*, AIP Conference Proceedings No. 229, pgs. 254-259
- [3] P. B. Wilson, AIP Conference Proceedings #87, pgs. 460-461 (1981)
- [4] D. T. Young and J. C. Irvin, *Proceedings IEEE*, pgs. 2130-2131 (1965)
- [5] T. W. Crowe, *et al.*, *Proceedings IEEE*, Vol. 80 #11 (1992)
- [6] W. C. B. Peatman and T. W. Crowe, *Int. J. of Infrared and Millimeter Waves*, Vol. 11 #3, pgs. 355-365 (1990)
- [7] H. Krautle, *et al.*, *Infrared Physics*, Vol. 17, pgs. 477-483 (1977)
- [8] P. A. D. Wood, PhD Thesis, University of Virginia (1994)
- [9] D. W. Porterfield, *et al.*, *Applied Optics*, Vol. 33 #25, pgs. 6046-6052 (1994)
- [10] J. A. Jackson and G. A. Krafft, CEBAF TN-92-047 (1992)
- [11] R. Kazimi, *et al.*, these proceedings

A BEAM TEST OF BUTTON-TYPE BEAM POSITION MONITOR FOR THE ATF DAMPING RING

F.Hinode, H.Hayano, M.Tejima, N.Terunuma and J.Urakawa

KEK, National Laboratory for High Energy Physics, 1-1 Oho, Tsukuba-shi, Ibaraki-ken, 305 Japan

The Button-type Beam Position Monitors (BPMs) were fabricated for the ATF damping ring. The BPM was designed to achieve the position resolution less than $5 \mu\text{m}$, and the fabrication of the first 40 BPMs was completed. For this BPM, a beam test was carried out at the 80 MeV injector part of the ATF LINAC. All of bunch signals in multi-bunch beam were clearly observed without any discharge. The calibration of BPMs was also performed to check their offset from the electrical center to the mechanical center and their position detection sensitivity. The result shows a good uniformity of position detection.

I. INTRODUCTION

The ATF [1] is under construction in KEK to study the feasibility for the linear-collider (JLC [2]). The ATF damping ring will be operated at 1.54 GeV with multi-bunch electron beam, which has the vertical emittance of $5 \times 10^{-11} \text{ m}\cdot\text{rad}$. To achieve such a low emittance beam, we must correct the dispersion of the orbit, which is small ($\eta < 2 \text{ mm}$) in the long wiggler section of the damping ring. A precise measurement of the dispersion is indispensable. Usually the actual dispersion is obtained by comparing each closed-orbit distortion under the conditions of different RF frequency ($\Delta f^{\text{RF}} \sim 10 \text{ kHz}$). For this reason, the requirement for the resolution of the BPM is less than $5 \mu\text{m}$ [3]. Furthermore, impedance of the components such as the vacuum chamber can be a source of the single-bunch instability which degrades the beam quality. To avoid such instability, the total longitudinal impedance must be less than about 0.2Ω [1]. Results of wake field calculations indicate that the impedance is very small on the electrode of the button type compared with the directional-coupler type [4]. We therefore selected the button-type electrode for the BPM [5].

II. CONFIGURATION OF BEAM POSITION MONITOR

A. Pickup Electrode

The feedthrough consists of a central conductor with a button electrode, an outer conductor with an SMA connector and an insulator, as shown in Figure 1. The central conductor is made of Kovar and the button electrode is made of stainless steel. Taking into account the impedance, the button shape has a curvature with the same inner radius of the BPM block. The insulator is ceramics Al_2O_3 . The outer conductor with the SMA connector is made of aluminum alloy with titanium joined by a HIP transition. Some electrodes have been tested

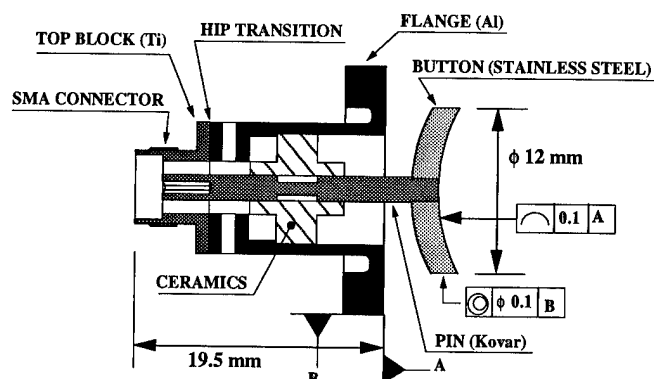


Figure 1: Pickup electrode for the BPM.

for mechanical strength and vacuum leakage. The threshold level of the brazing strength of the central conductor is 60kg against the tensile forces. No vacuum leak occurs after heat-cycle tests from liquid-nitrogen temperature up to 200°C . Furthermore, all of electrodes have been checked concerning to the dielectric strength ($> 1000 \text{ Volts}$).

B. BPM Block

Each BPM is installed at a location near to every quadrupole magnet and sextupole magnet; there are 120 BPMs in the ring. We have already fabricated 40 BPMs in 1994.

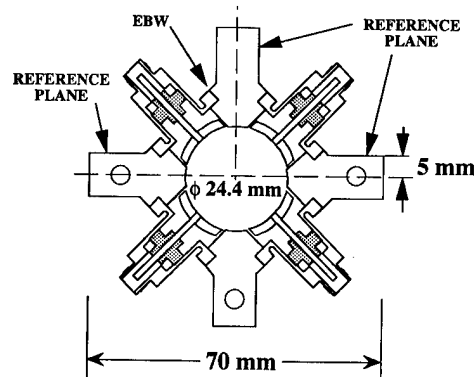


Figure 2: Cross-sectional view of the BPM.

The BPM block was machined from a mass of aluminum alloy, and four pickup electrodes were welded onto the block by the electron beam welding, as shown in Figure 2. It has both horizontal and vertical reference planes, which are used for the alignment of the BPM to the Q magnet. Both planes are also used as a reference for the calibration process to obtain an electrical center of the BPM block. After installation of the vacuum chamber with BPMs to the beam line, the offset of the BPM to the Q magnet will be measured with an accuracy within $50 \mu\text{m}$ by using the reference planes.

III. BEAM TEST

To study the low emittance beam in detail, each bunch signal in the multi-bunch beam should be clearly distinguished. Furthermore, BPMs must be operated stably against 3×10^{10} particles per bunch in maximum. Since the feedthrough of the BPM has a cavity structure, there is a possibility to occur a discharge by the multipacting effect due to resonance fields excited by the wake-field, which is induced by the beam. At the TRISTAN main ring, in fact, such discharge effect, caused by a TE_{11} coaxial mode, was observed on the button-type BPM placed at RF cavity section [6]. The result of a resonance measurement shows that the lowest resonance frequency is 11 GHz, which is consistent with the result calculated by a MAFIA code. According to the calculation of the multipacting zone [7], at such high frequency, the discharge due to the multipacting will not occur, however, it should be checked by the actual beam. To check the performance of the BPM, a beam test was carried out at the 80 MeV injector part of the ATF LINAC.

A. Setup of Beam Test

The setup of the beam test is shown in Figure 3. Electron beam generated at the thermionic gun are accelerated up to 80 MeV and then traverse the wall current monitor (WCM) and the BPM. The BPM is welded to beam ducts which have a length of 70 mm and an inner diameter of 24 mm, and placed at the upstream of the beam dump. The output signal from the BPM is transmitted by RG-213/u cable (~33m) and observed by a sampling oscilloscope (Tektronix 11802, sampling head SD-24). The output signal is attenuated before the oscilloscope due to the small dynamic range of the oscilloscope. The beam current is measured by the WCM. The beam size and the bunch length were measured by a wire-scanner and a streak camera using an optical transition radiation as ϕ 2.2 mm and 20 psec in FWHM, respectively.

B. Beam test by Single-bunch Beam

An observed signal at the single-bunch operation is shown in Figure 4. The peak pulse height is 5 V for 1.6×10^{10} particles. There is a ringing shape at the signal tail. This is

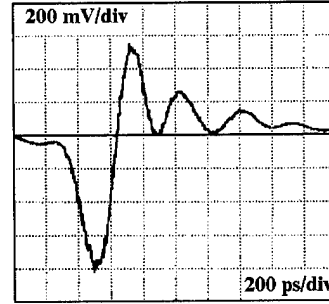


Figure 4: Observed signal of the single-bunch beam.

caused by a multiple reflection of the wall current at the edge of BPM chamber due to the discontinuity. The difference of the inner diameter between the vacuum chamber of LINAC (ϕ 58mm) and the BPM (ϕ 24mm) is 34 mm. However the inner diameter is the same in the damping ring. Therefore it might not be a problem for the actual use. Furthermore, a pickup signal variation for the number of particles was also measured up to 2×10^{10} particles per bunch, and which shows a good linearity. Any discharge such as multipacting was not observed. A beam test with more high intensity beam will be done after the beam commissioning of the beam transport line in this fall.

C. Beam test by Multi-bunch Beam

Figure 5 shows an observed signal for the multi-bunch beam. The bunch spacing is 2.8 nsec. All of bunch signals were clearly observed without any discharge. The signal is almost the same shape as the single-bunch beam. The signal

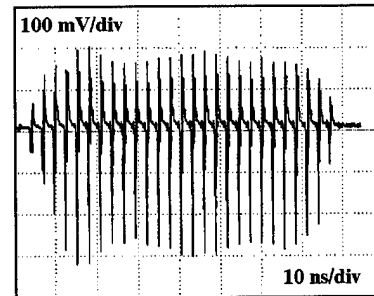


Figure 5: Observed signal of the multi-bunch beam.

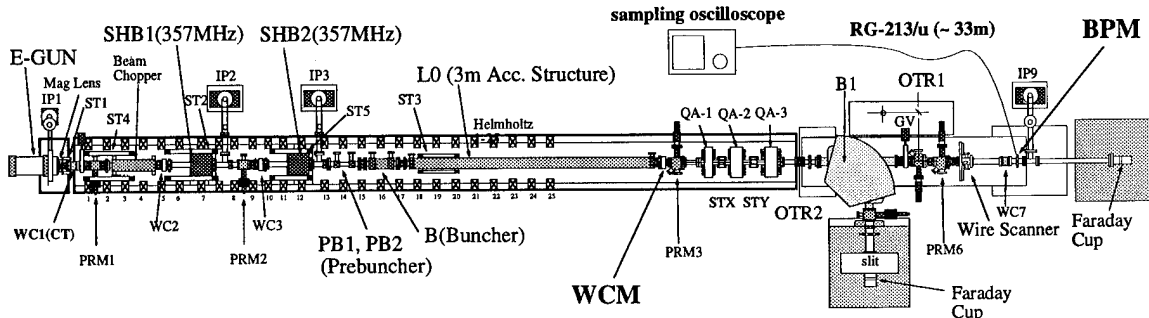


Figure 3: Setup of the beam test.

tail of each bunch is sufficiently small when the next bunch signal arrives.

IV. Electrical Characteristics

A. Capacitance of Electrode

Before and after electrodes were welded on blocks, the capacitance of each electrode was measured using a capacitance meter at a frequency of 800 Hz. The electrical-capacitance values are distributed in the 2.5 ~ 4.7 pF region. Thus, four pickup electrodes with similar capacitance values were grouped and welded on the monitor block to get uniform signals.

B. Mapping for the calibration

Every BPM block was calibrated so as to obtain the offset between the mechanical and the electrical center of the BPM block [1,5]. The mechanical center is defined by the horizontal and vertical reference planes within an accuracy of machining. The electrical center is measured by the following procedure.

The BPM block was mounted on a fixed stage, and a 50 μm diameter tungsten wire was strung coaxially in the BPM block. Both ends of the wire were placed in a V-shaped groove made of ceramics, which was installed on both of the x-y movable stages. The stage has a high positioning accuracy of 0.1 μm . One side of the wire was soldered to the SMA connector. The other end was terminated so as to match into a 50 Ω line; attached 100 g weights provide a constant proper tension. The wire was put in the base position of a gauge, which has the same reference planes of the BPM, and observed directly by a microscope. Thus, the wire was aligned precisely to the mechanical center of the BPM block with an accuracy of 40 μm . The calibration was performed by using a pulse signal with 5 ns rise time. Signal processing is based on the same principle as that for the SLAC/FFTB [8]. The readout electronics, which is a combination of a pulse stretcher amplifier, a Track&Hold ADC and a pulse generator, has a resolution of 5 μm . We measured the four output signals (V_1, V_2, V_3, V_4) induced electrostatically on each electrode due to pulse signals transmitted on the wire. In order to obtain the beam position, the following two calculation steps are performed. The first is a normalization procedure (x', y'), given by

$$x' = k \frac{V_2 - V_4}{V_2 + V_4}, \quad y' = k \frac{V_1 - V_3}{V_1 + V_3},$$

where k is a coefficient of the sensitivity on the position measurement, which depends on the geometry of the monitor chamber. It was obtained by a measurement for each BPM. Secondly, we converted the normalized results to the geometrical position (x, y) according to

$$x = \frac{\sqrt{2}}{2} (x' - y'), \quad y = \frac{\sqrt{2}}{2} (x' + y').$$

In this way, we obtained a relation between the measured position (x, y) and the set position (X, Y) of the wire position for each monitor.

The calibration was performed at 169 points in the central area, which is a 3.6 mm square region with 0.3 mm step. As a result, there was no remarkable distortion in the mapping of all the BPMs. In the central region of ± 0.5 mm, the distortion was less than 10 μm , while it was 100 μm at the point of 1.8 mm away from the center. This distortion is acceptable for our practical use. In the central region, however, it is only 2 % and quite well.

We obtained the distribution of the offsets of the electrical center to the mechanical one from the calibration data. The mean values of the offsets are $X = -19 \mu\text{m}$ and $Y = 58 \mu\text{m}$, and the standard deviations are $\sim 90 \mu\text{m}$ in both directions. The main source of this deviation came from the errors on the manufacture of the BPM block and pickup electrode.

The second fabrication of 40 BPMs and the calibration are now in progress.

V. SUMMARY

The Button-type Beam Position Monitors (BPMs) were fabricated for the ATF damping ring. A beam test of the BPM was carried out at the 80 MeV injector part of the ATF LINAC. All of bunch signals in multi-bunch beam were clearly observed without any discharge up to 2×10^{10} particles per bunch. The calibration of BPMs was also performed and the result shows a good uniformity of position detection.

VI. REFERENCES

- [1] ATF Design and Study Report, to be published as a KEK Internal Report.
- [2] JLC Group, KEK-Report 92-16.
- [3] M. Tejima, Procs. of the SLAC/KEK Linear Collider Workshop on Damping Ring, KEK proceedings 92-6, 1992, p.126~132.
- [4] M. Takao et al., KEK-Report 91-14.
- [5] M. Tejima et al., Proceedings of the 1994 International Linac Conference, Vol. 2, pp. 914-916.
- [6] M. Tejima et al., KEK Preprint 90-183.
- [7] A. J. Hatch, Nucl. Instr. and Meth. 41 (1996) 261-271.
- [8] H. Hayano et al.; KEK Preprint 92-118, H. Hayano et al.; SLAC-PUB-5691.

APPLICATION OF A TRANSVERSE PHASE-SPACE MEASUREMENT TECHNIQUE FOR HIGH-BRIGHTNESS, H^- BEAMS TO THE GTA H^- BEAM*

K. F. Johnson, R.C. Connolly,[†] R.C. Garcia, D.P. Rusthoi, O. R. Sander, D.P. Sandoval, M.A. Shinas, M. Smith, and V.W. Yuan, Los Alamos National Laboratory, Los Alamos, NM 87544 USA

The Ground Test Accelerator (GTA) [1] had the objective of producing a high-brightness, high-current H^- beam. The major components were a 35 keV injector, a Radio Frequency Quadrupole (RFQ), an intertank matching section (IMS), and a drift tube linac (DTL), consisting of 10 modules. A technique for measuring the transverse phase-space of high-power density beams has been developed and tested [2]. This diagnostic has been applied to the GTA H^- beam. Experimental results are compared to the slit and collector technique for transverse phase-space measurements and to simulations.

I. INTRODUCTION

In the commissioning of an accelerator, measurements of the beam's phase-space distributions are made to evaluate the accelerator's performance and to determine the accelerator's operating parameters. A common method of measuring transverse phase-space distributions in charged-particle beams is to intercept the beam with slits, pinhole plates, or wire grids, and to determine the beam distribution after a drift with a parallel-channel collector or fluorescent screen. For high-brightness beams, these measurements should be made near the last optical element to eliminate the space-charge corrections during data analysis. However, the power densities of beams are often too high to allow beam masks, such as slits, to survive the full intensity of the beam.

This paper describes results from a phase-space measurement technique which is applicable to high-brightness H^- beams. It utilizes conventional beam diagnostics combined with the laser induced neutralization diagnostic approach (LINDA) [2]. A small portion of the beam is separated from the full beam by means of photoneutralization with a laser that is upstream from a sweep magnet. Phase-space measurements are made on only the neutralized beam. Because the measured portion of the beam drifts without space charge, the phase-space distribution of the beam at the neutralization point can be inferred accurately from a measurement taken downstream.

*Work supported and funded by the US Department of Defense, Army Strategic Defense Command, under the auspices of the US Department of Energy.

[†]Industrial partner, Grumman Corporate Research Center

II. MEASUREMENT

The LINDA technique as applied to GTA is shown schematically in Fig. 1. A short laser pulse of the appropriate wavelength to neutralize the ions, was passed through the ion beam upstream of a bending magnet. The small fraction of the full beam that was neutralized (H^0 beam) passed through the magnet into the detector (i.e. the slit and collector system). The remaining H^- beam was swept into a beam dump.

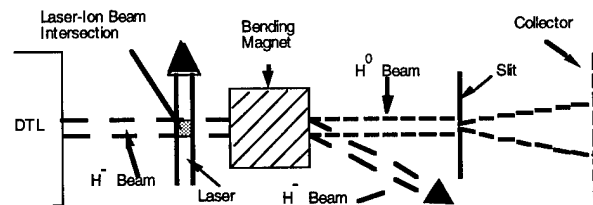


Figure 1: Schematic view of the LINDA technique for measurements of transverse phase-space.

The technique was developed and tested [2] on the Accelerator Test Stand (ATS) [3]. Reference 2 discusses the principles of the neutralization process, the laser characteristics, the geometry of the measurement, the electronics, the data acquisition, and the data analysis for extracting transverse phase-space distributions (e.g. emittances and the Courant-Snyder (CS) parameters).

The measurements of the GTA H^- beam differed from those of the ATS H^- beam primarily in three areas. First, the geometry was improved. The bending magnet was located upstream of the slits instead of its ATS location between the slit and collector. This made interpretation of space charge effects clearer. Second, the ATS measurements were restricted to the horizontal plane. This restriction was removed for the GTA measurements where data were obtained for the horizontal (x) and vertical (y) planes. Third, the bending magnet was an electromagnetic dipole rather than a permanent magnetic dipole as in the ATS measurements. To switch from measurements of the H^0 beam to measurements of the H^- beam the dipole was turned off. The effects of the residual field of the dipole on emittance measurements was negligible.

The GTA measurements were made at the exit of the first GTA Drift Tube linac (DTL) module [4] (output beam energy 3.2 MeV). Transverse phase-space measurements were made with the full H^- beam and with the laser

neutralized beam (H^0 beam). In both cases, the same slit and parallel-channel collector were used and their location with respect to the DTL exit remained fixed. For these set of measurements the average beam current was ≈ 32 mA. The laser neutralization point (see Fig. 1), was ≈ 32 cm upstream of the transverse emittance gear slit. Lastly, data from the two techniques were taken close in time to avoid ambiguities due to changing beam conditions.

III. EXPERIMENTAL RESULTS

The objective of these measurements of the GTA DTL output phase-space distributions was to obtain a more complete data set than was obtained in the ATS experiment. A more complete data set, in term, allows for a more detailed comparison of the LINDA technique and the conventional slit and collector technique. Also a more complete measurement contributes to the understanding of space charge effects in the measurement of the transverse phase-space distributions (emittances).

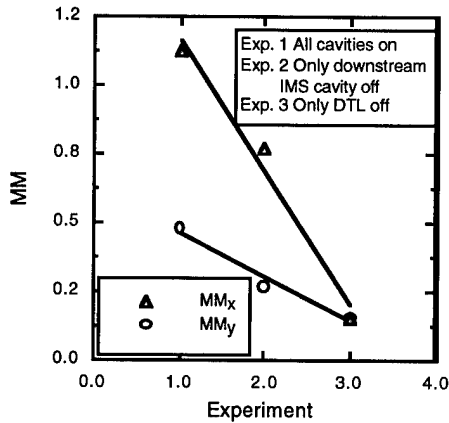


Figure 2: The dependence of the MM (between the two techniques) on the degree of bunching. The lines are meant to guide the eye.

With the accelerator's operating parameters set at their nominal values, repeated emittance measurements were made in the x and y planes with LINDA and the slit and collector techniques. This allowed for reproducibility checks for each technique and for a comparison between techniques. Different criteria were applied in the comparison of the slit and collector (LINDA "off"), technique, which measured the full H^- beam, and the LINDA technique (LINDA "on"), which measured the H^0 beam. The reproducibility of the data was good for each method based on a comparison of the rms normalized emittances, ϵ_x and ϵ_y . ϵ_x and ϵ_y were determined from a beam fraction of 86.5% which corresponds to 4σ if the beam is Gaussian. A beam fraction of 100% includes all of the beam above a 1% background threshold. For LINDA

"off", $\epsilon_x = 0.0186 \pm 0.0013 \pi$ cm mrad and $\epsilon_y = 0.0151 \pm 0.0011 \pi$ cm mrad. For LINDA "on", $\epsilon_x = 0.0158 \pm 0.0011 \pi$ cm mrad and $\epsilon_y = 0.0151 \pm 0.0011 \pi$ cm mrad. These data show a 23% emittance growth in the x-plane over the ≈ 32 cm drift space between the neutralization point and the emittance slit. There was no observed emittance growth in the y-plane.

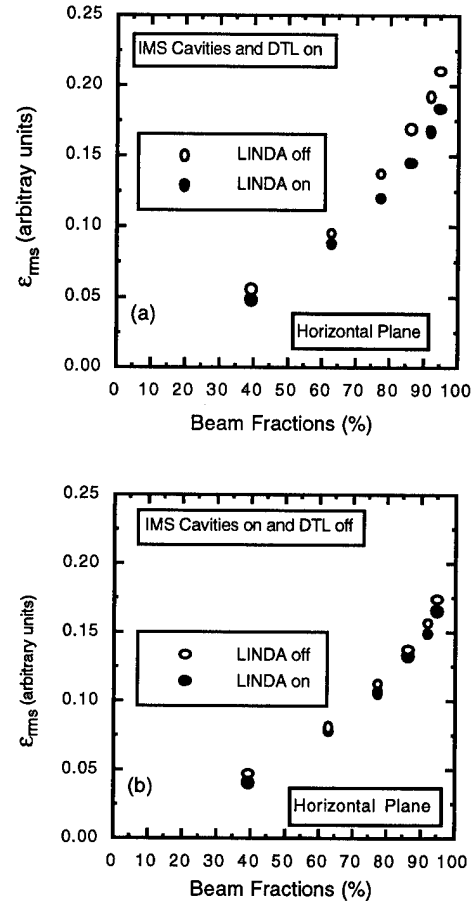


Figure 3: ϵ_{rms} versus the beam fraction used in the calculation of ϵ_{rms} for the LINDA "on" and "off" techniques. (a) All cavities on at nominal settings. (b) The same as (a) with the DTL off.

Another criteria was the mismatch factor MM, which facilitated the comparison of the Courant-Snyder (CS) parameters or beam shape. This criteria was applied in the x-plane where the large emittance growth was observed. For the LINDA "on" (LINDA "off") data the repeatability of measurements was characterized by $MM_x = 0.06$ (0.07). These data indicate little variation in the emittance shape for either technique. However, MM_x varied between ≈ 1.2 and ≈ 1.4 when the two techniques were compared. Although each data set was internally consistent, there was significantly different emittance shapes between data sets.

Using TRACE3D [6], the measured LINDA "off" CS parameters were transported with space charge from the

emittance slit upstream to the laser neutralization point and then transported without space charge downstream to the slit. The resulting CS parameters were compared to the LINDA "on" data giving $MM_x \approx 0.23$ which, although not as small as 0.06, was substantially better than 1.3. These results suggest that space charge plays a significant role over the drift between the neutralization point and the emittance slit.

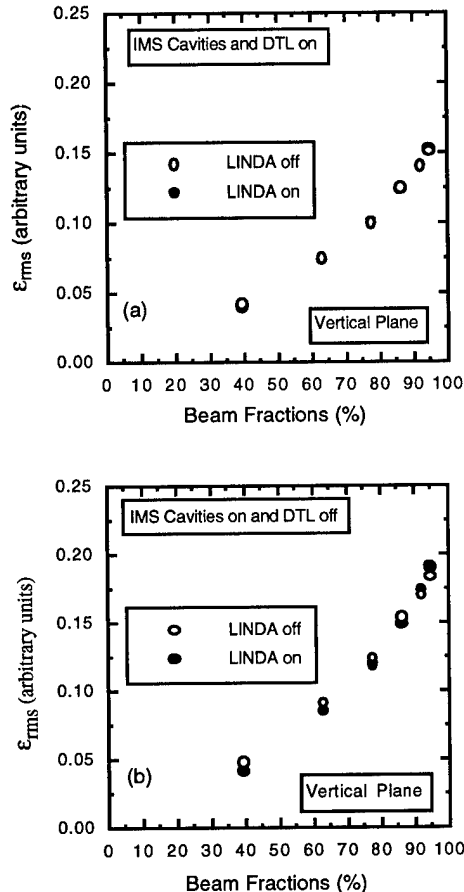


Figure 4: ϵ_{rms} versus the beam fraction used in the calculation of ϵ_{rms} for the LINDA "on" and "off" techniques. (a) All cavities on at nominal settings. (b) The same as (a) with the DTL off.

To further explore the effects of space charge, a set of measurements was performed where the bunch length was varied. In Experiment 1, the IMS buncher cavities and the DTL were operated at their nominal settings. In Experiment 2, the downstream IMS buncher was turned off, allowing the bunch length to increase. To increase the bunch length further, the IMS cavities were set at their nominal operating settings and the DTL was turned off. The expectation was that space charge effects in the emittance measurements should decrease as the bunch length increases. This was confirmed by the MM between the two techniques (see Fig. 2) where MM_x and MM_y

decreased as the bunch length was increased. The effect was considerably larger in the x-plane where MM_x varied by a factor of 10. In the y-plane, MM_y was considerably less sensitive to the bunch length.

Figures 3 and 4 show the sensitivity of ϵ_{rms} on the beam fraction. As the beam fraction increases, more of the halo is included in the determination of ϵ_{rms} . Figure 3(a) shows that, when the bunch length is small, the difference in ϵ_{rms} for LINDA "on" and "off" depends on the amount of halo included in the emittance determination. The two techniques agree if the determination of ϵ_{rms} is restricted to the core of the beam. Figure 3(b) shows that the difference between LINDA "on" and "off" is disappearing as the bunch length grows and space charge effects diminish. This suggests that space charge forces may push some particles into the halo, causing the overall emittance area to grow and the shape to change (Fig. 2), while leaving the core of the bunch largely unchanged [7,8]. Figures 2 and 4 show that, for the y-plane, there is some evidence for a change in the emittance shape but not in area.

IV. CONCLUSIONS

The LINDA technique for measuring transverse phase-space distributions works well. The measurements are repeatable. The differences between the LINDA and the slit and collector techniques are qualitatively understood. Further simulations are needed to explain quantitatively the observed behavior. The differences between the x and y planes may be explainable in terms of the transverse beam sizes and orientation in phase space.

V. REFERENCES

- [1] O.R. Sander, et al., Proc. 1992 Linear Accel. Conf. AECL Research, Chalk River Laboratories Report, AECL-10728 (1992), p. 535
- [2] R.C. Connolly, et al., Nucl. Instr. and Meth., **A312** (1992) 415
- [3] O.R. Sander, et al., Los Alamos National Laboratory report no. LA-CP-89-489 (July 1989)
- [4] K.F. Johnson, et al., Proc. 1993 IEEE Particle Accel. Conf., Washington, DC (May 1993), p. 1669
- [5] J. Guyard and M. Weiss, Proc. 1976 Linear Accel. Conf., Atomic Energy of Canada, AECL-5677 (1976), p. 254
- [6] K. R. Crandall and D.P. Rusthoy, Los Alamos National Laboratory report LA-UR-90-4146 (1990)
- [7] A. Cucchetti, et al., Proc. 1991 IEEE Particle Accel. Conf., San Francisco, CA (May 1991), p. 251
- [8] J.S. O'Connell, et al., Proc. 1993 IEEE Particle Accel. Conf., Washington, DC (May 1993), p. 3657

Precision Intercomparison of Beam Current Monitors at CEBAF*

R. Kazimi, B. Dunham, G.A. Krafft, R. Legg, C. Liang, C. Sinclair, and J. Mammoser, Continuous Electron Beam Accelerator Facility, Newport News, VA 23612 USA

The CEBAF accelerator delivers a CW electron beam at a fundamental frequency of 1497 MHz, with an average beam current up to 200 μ A. Accurate and stable non-intercepting beam current monitors are required for a number of applications. These include setup and control of the accelerator, monitoring of both beam current and beam losses for machine protection and personnel safety purposes, and providing beam current information to the experimental users. Fundamental frequency stainless steel RF cavities have been chosen for these beam current monitors. This paper reports on a precision intercomparison between two such RF cavities, an Unser monitor, and two Faraday cups, all located in the injector area. At the low beam energy in the injector, it is straightforward to verify the high efficiency of the Faraday cups, and the Unser monitor included a wire through it to permit an absolute calibration. The cavity intensity monitors have proven to be capable of stable, high precision monitoring of the beam current.

I. INTRODUCTION

At CEBAF, the electron beam current is monitored at different locations along the machine for several reasons. The beam current is measured at two locations in the injector both as a part of machine setup and for detection of beam condition changes. The machine protection and personnel safety systems rely on current measurements in the injector to set a limit on the amount of beam current input into the rest of the machine. In addition, the machine protection system also compares the beam current in the injector with the current measured at the end of the accelerator to determine and limit beam loss through the machine. Finally, the users in the experimental halls are interested in the measurement of the beam current delivered to their target.

In the injector, two Faraday cups, which also act as beam dumps, are used for current measurements. The personnel and machine protection systems, which need non-intercepting beam current information at all times during the operations, use two fundamental frequency resonant cavity beam current monitors (BCMs) in the injector. For the current measurement at the end of the machine, two BCM cavities are used in conjunction with an Unser monitor. The function of the Unser is to provide absolute calibration for the BCMs. It is difficult and costly to make Faraday cups for high energy and beam power at the end of the machine.

An experiment to determine the calibration factor and accuracy of different current monitors was performed in the injector area. In the following sections we give a brief description of different current monitors used in the experi-

ment, explain the experimental procedure, and present our results.

II. CURRENT MONITORS

Faraday cup 1 is a 100 keV beam dump with a power limit of 100 W. It is a copper plug 3.17 cm long with a re-entrant conical shaped cup 2.84 cm deep with a 1 cm diameter opening. The re-entrant nature of the cup allows all of the beam current to be collected as long as the beam is small and centered in the cup. Faraday cup 2 is a 5 MeV beam dump with a power limit of 1 kW. It is 7 cm long with a similar re-entrant conical shaped cup 6 cm deep and 1.5 cm diameter opening. The cups are water cooled and are designed not to move out of alignment due to heating from the beam. They can be inserted into and pulled out of the beamline remotely from the control room. To have beam on Faraday cup 2, Faraday cup 1 must be retracted; that is, the current cannot be measured at both cups simultaneously.

The Unser monitor [1] is a non-intercepting, parametric dc current transformer with a wide dynamic range and a nominal output of 4 mV per microamp. The monitor is calibrated by passing a known current through a wire inside the beam pipe. It requires extensive magnetic shielding and temperature stabilization to reduce noise and zero drift.

The beam current monitors [2] are stainless steel cylindrical resonant cavities with $Q_L \sim 1500$. The power produced in the cavity as the beam passes through it is measured using an rf power meter, and the current can then be calculated from measured calibration constant.

II. DISCRIPTION OF EXPERIMENT

The current monitor cross calibration test was performed in two phases

A. Phase I

The first phase of the experiment was to calibrate the two Faraday cups. The output current from the Faraday cups is converted to voltage and amplified by I to V amplifiers. Using LABVIEW, a digital controlled precision current source, and a digital voltmeter, the response of I to V amplifiers was mapped for different currents. The results showed very good linear response for both amplifiers.

Next, a pulsed beam was used to scan the Faraday cups in both horizontal and vertical directions. A flat plateau with 3 mm and 5 mm diameter was found at the center of cups 1 and 2, respectively (see figures 1 and 2). Then the efficiency factor for each cup was measured by measuring a pulsed electron beam current while biasing the cups with respect to ground at

Supported by U.S. DOE Contract DE-AC05-84-ER40150

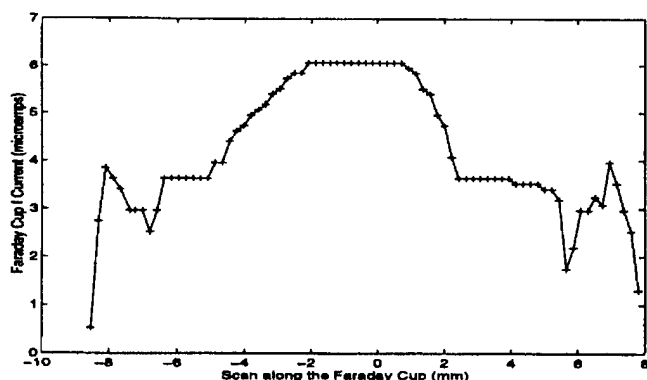


Figure 1: Faraday cup 1 scan.

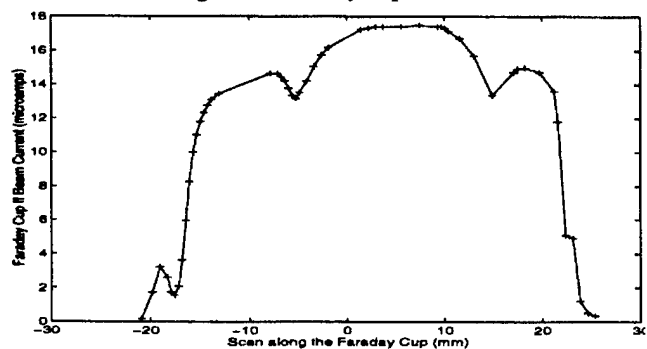


Figure 2: Faraday cup 2 scan.

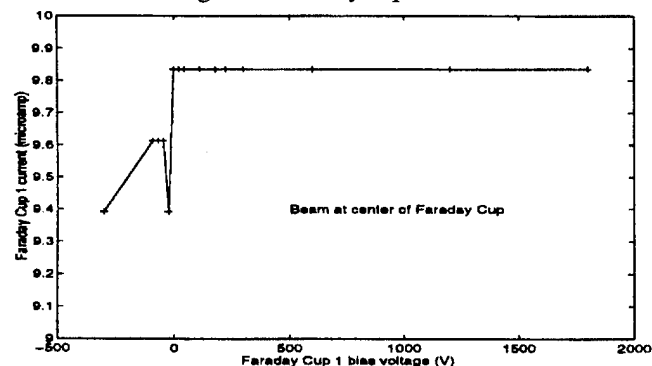


Figure 3: Faraday cup current vs bias voltage

different voltages from -300 V to +18000 V. This experiment showed no significant change of current measured between the biased and unbiased cups when beam was centered in the cups (see figure 3). This measurement confirms essentially 100% collection efficiency for the cups. Therefore, the I to V amplifier response curves can be used to determine the beam current on the Faraday cups.

B. Phase II

In phase II of experiment, the Unser monitor, the BCMs and the Faraday cups were used to measure cw beam current simultaneously. A beam to the second Faraday cup has to pass through the location of Faraday cup 1, the Unser and both BCM monitors in that order. The equivalence of the current signal on both Faraday cups, plus the absence of signals on the beam loss monitors (photomultiplier tubes) in the region between the two cups, indicated no beam loss between the cups. Therefore all current monitors would detect the same current.

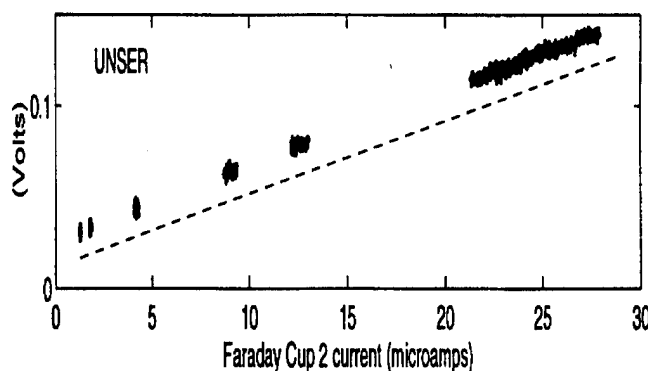
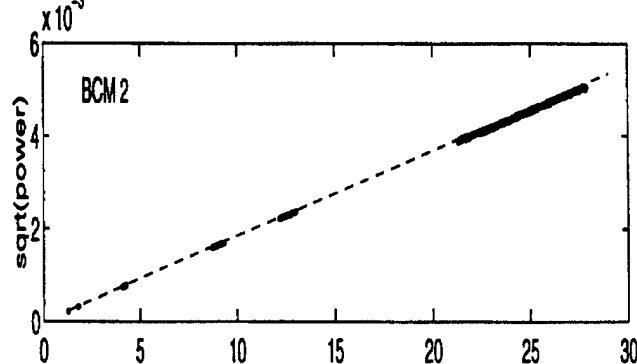
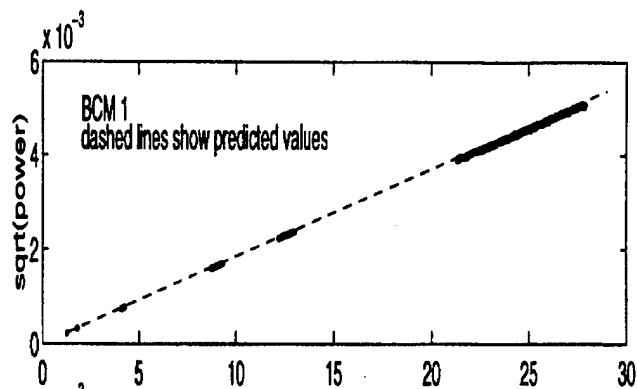


Figure 4: BCM1, BCM2, and Unser voltages vs. FC2 current

Plotting the Unser and the BCMs signals vs. the Faraday cup 2 signal and using Faraday cup 2 calibration curve gave us the calibration factor for the monitors (see figure 4, there are 2677 points in each plot). The dashed lines show the predicted response of the monitor. For the BCM cavities, the predicted lines are based on Q_L , the shunt impedance as calculated using MAFIA, and cable attenuation measurements. For the Unser monitor the predicted line is based on calibration measurement using the calibration wire inside the monitor.

III. ANALYSIS OF THE RESULTS

Table 1 shows the slope and offsets for the best fit and predicted lines for the Unser and the BCM vs. Faraday Cup 2 current. The measured slopes and offsets from beam data obtained in phase II match closely with predicted values. The data also show that the offset value for the Unser was relatively high and changed over time. The reason is that the Unser

monitor is very sensitive to nearby magnetic fields and day to day temperature changes. However, only slope of the Unser response is important to us, since the offset value can be obtained by turning the beam off and measuring the output signal.

The data points for figure 4 were obtained by measurement of the instantaneous signal from the different devices at a rate of approximately 1 Hz. Table 2 lists the values of these fluctuations for each monitor. To obtain the BCM fluctuations independently of the beam noise, a graph of BCM 2 vs BCM1 is plotted and the best linear fit through the data is calculated. The percent difference between BCM 2 values and the fitted line show the level of voltage fluctuations of the BCMs. (see Figure 5).

Table 1

	Phase II Data (Linear Fit)	Predicted results
BCM1 vs FC2	slope: $1.828\text{e-}4 \text{ V}/\mu\text{A}$ offset: $-6.13\text{e-}6 \text{ V}$	$1.853\text{e-}4 \text{ V}/\mu\text{A}$ 0.0 V (MAFIA)
BCM2 vs FC2	slope: $1.820\text{e-}4 \text{ V}/\mu\text{A}$ offset: $-9.16\text{e-}6 \text{ V}$	$1.845\text{e-}4 \text{ V}/\mu\text{A}$ 0.0 V (MAFIA)
Unser vs FC2	slope: $4.11\text{e-}3 \text{ V}/\mu\text{A}$ offset: $2.6\text{e-}2 \text{ V}$	$4.012\text{e-}3 \text{ V}/\mu\text{A}$ $1.2\text{e-}2 \text{ V}$ (Calib. wire)

Table 2

Device	rms fluctuations
Faraday cup 2 current	$0.05 \mu\text{A}$
BCM 1 voltage	0.5%
BCM 2 voltage	0.5%
Unser current	$1.0 \mu\text{A}$

IV. CONCLUSION

This experiment has allowed us to cross compare different current monitoring devices at CEBAF. We have calibrated our Faraday cups by measuring their I to V amplifier responses and demonstrated that there is no secondary emission loss. Using these results we established lossless transmission to Faraday cup 2 and calibrated the rf cavity current monitors and the Unser monitor. These measured calibration factors

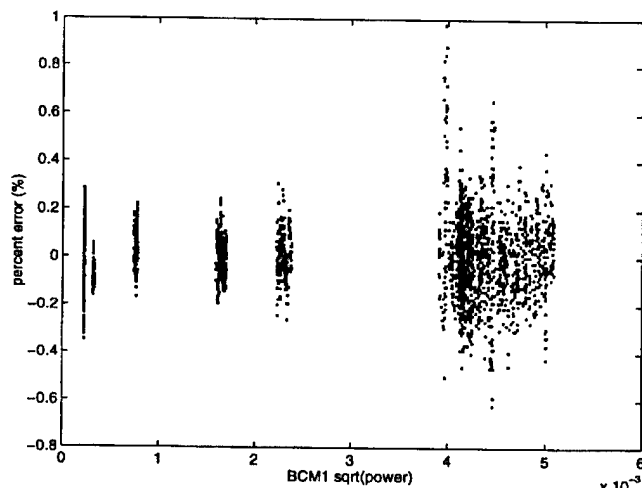


Figure 5: BCM2 vs BCM1 percent difference

agreed well with the predicted values. The results of the study are presently being used for current measurement and for establishing safe operating currents for personnel and machine safety systems. Improvements can be made on increasing the accuracy and reducing the noise level of the monitors. The I to V amplifiers can be redesigned to reduce the noise due to interference and ground loop effects.

Another area of improvement would be to integrate the output signal of the monitors. For safety system purposes, the instantaneous current measurement is important and the accuracy of a few percent is sufficient. The experimental users of the accelerator are more interested in integrated current and high accuracy. We are planning to continue research on this subject and will use lessons learned in future experiments.

V. REFERENCES

- [1] K. B. Unser, The Proceedings of IEEE 1989 Particle Accelerator Conference, p 71.
- [2] R. Ursic, these proceedings.

DAMPED BUTTON ELECTRODE FOR B-FACTORY BPM SYSTEM

T. Obina, T. Shintake, Y. H. Chin and N. Akasaka
KEK:National Laboratory for High Energy Physics,
Oho 1-1, Tsukuba-shi, Ibaraki 305 Japan

Abstract

A new concept of damping of resonances in a button electrode has been proposed and tested in the BPM system for the B-Factory project at KEK (KEKB). Since a very high current beam has to be stored in the machine, even a small resonance in the ring will result in losing a beam due to multi-bunch instabilities. In a conventional button electrode used in BPMs, a TE₁₁₀ mode resonance can be trapped in the gap between the electrode and the vacuum chamber. In order to damp this mode, the diameter of the electrode has been chosen to be small to increase the resonance frequency and to radiate the power into the beam pipe. In addition, an asymmetric structure is applied to extract the EM energy of the TE₁₁₀ mode into the coaxial cable as the propagating TEM mode which has no cut-off frequency. Results of the computer simulations and tests with cold models are reported. The quality factor of the TE₁₁₀ mode was small enough due to the radiation into the beam pipe even in the conventional electrode and the mode coupling effect due to the asymmetric shape was significant on a cavity-like TE₁₁₁ mode.

I. INTRODUCTION

In the KEKB accelerator, the beam current will be of several amperes. Since the number of BPMs amounts to about 450 per ring, possible resonances in the gap is of serious concern to avoid coupled bunch instabilities. On the other hand, it is not necessary to take care very much of VSWR in a wide frequency range, since only 1 GHz component of the beam is detected for the beam position measurements. The resonances in the BPMs can be classified into two categories; one due to a button electrode and another due to a ceramic part that is used for a vacuum seal. In this paper, we mainly focus on the resonances at the button electrode.

II. BPM STRUCTURE

We adopted the N-type vacuum feedthrough because it has an advantage of high power rating and the enough mechanical strength compared to that of the SMA type. Connectors will be brazed to the block of copper chamber.

The small button size has an advantage that can enhance the damping of the TE₁₁₀ mode due to the radiation into the beam chamber. On the other hand, the minimum size of the button is limited to accomplish the required precision of the position measurements, i.e., better than 80 dB in the signal-to-noise ratio at the beam current of 10 mA. We determined the diameter of the button electrode to be 12 mm. The gap distance was determined to be 1 mm to avoid the multipacting discharge.

The structure of the asymmetric BPM is shown in Fig. II. Three faces of the button are cut out to enhance its asymmetry, and are connected to the center conductor with a taper.

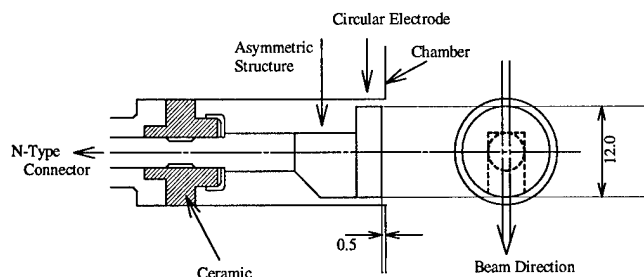


Figure 1. Illustration of the damped BPM. The diameter of the disk is ϕ 12 mm and the gap size is 1 mm. The distance between the electrode surface and the wall is determined to be 0.5 mm to prevent the synchrotron radiation.

III. COMPUTER SIMULATIONS

The damping efficiency of the asymmetric structure has been simulated with the computer code MAFIA. Resonance frequencies and mode patterns (monopole or dipole) are tabulated in Table I.

Table I
Resonance frequency calculated with MAFIA.

frequency[GHz]	mode pattern	location (label in Fig. 4)
1.88	Monopole	
3.96	Monopole	
5.82	Dipole	ceramic (C1)
6.21	Monopole	coaxial (Coax)
7.30	Dipole	button (B1)
7.89	Dipole	ceramic (C2)
8.88	Monopole	

The field pattern of the TE₁₁₀ mode at 7.3 GHz is shown in Fig. 2.

In this model, the BPM is not placed at the chamber wall but at the cylinder that has a magnetic-short boundary at the end.

Among these modes, EM energy of the monopole modes are extracted to the outside of the BPM and have negligible effects on the beam instabilities. The dipole modes under cutoff frequency of the coaxial lines, however, are trapped inside the BPM. The electric field of the dipole mode at 5.8 GHz is localized at the ceramic, so that the coupling between this mode and the beam is small. As shown in Fig. 2, the TE₁₁₀ mode at 7.3 GHz is not effectively converted to TEM modes. The coupling between the two modes can be enhanced by increasing the length of the asymmetric structure. However, this method has a

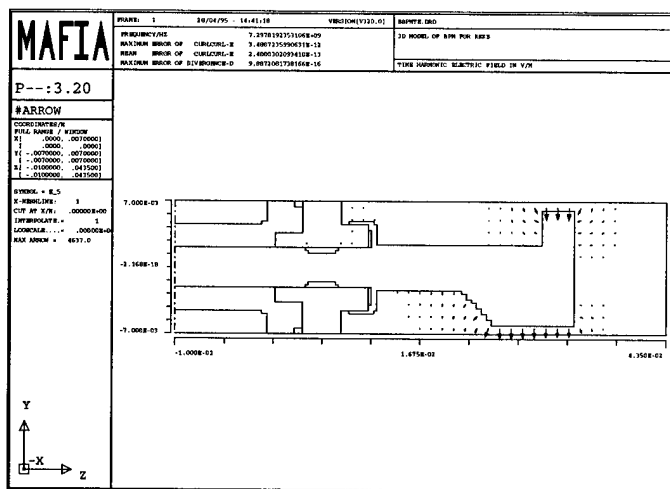


Figure 2. Electric field pattern of the TE110 mode. EM energy is concentrated at the button electrode.

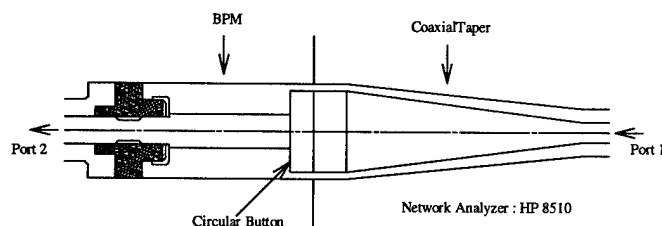


Figure 3. The setup to measure the transmission characteristics of BPM.

disadvantage of the dipole mode at the ceramic penetrating into the beam chamber.

It is difficult to estimate quality factors of the resonance modes from this calculation because this model does not include the radiation into the beam chamber. We calculated the wakefields using the T3 code of MAFIA, and estimated the loss parameters k of the TE110 mode to be 0.4 mV/pC.

IV. EXPERIMENTS AND RESULTS

We measured at first the transmission characteristics (S_{21}) of the electrode with a setup shown in Fig. 3.

The TEM-mode signals are fed to the electrode through a taper. Figure 4 shows the S_{21} response of a conventional circular electrode.

There are two sharp peaks at 6.2 GHz and 8.8 GHz, which are labeled as C1 and C2 in the figure. We measured the S_{21} response without ceramic and found that these peaks are resonances in the ceramic. The difference between the calculation with MAFIA and the measurement is explained by two reasons: one is that the resonance frequency listed in the Table I is the calculation for the damped BPM, and the other is that the measured BPM is not brazed. The peak around 8 GHz, labeled as B1, appears when the button electrode is placed at the off-center position. The broad peak labeled as Coax denotes the resonance of the whole coaxial structure. In this setup, it is difficult to measure

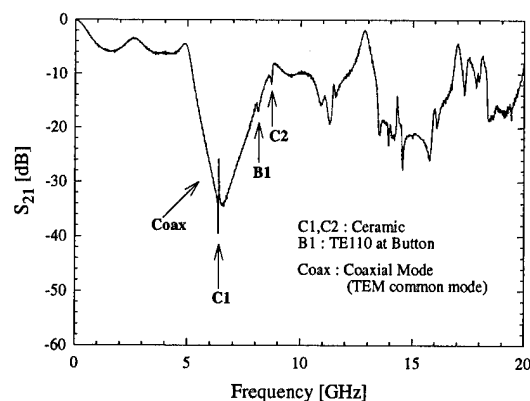


Figure 4. S_{21} measurement of circular BPM.(Network Analyzer HP 8510)

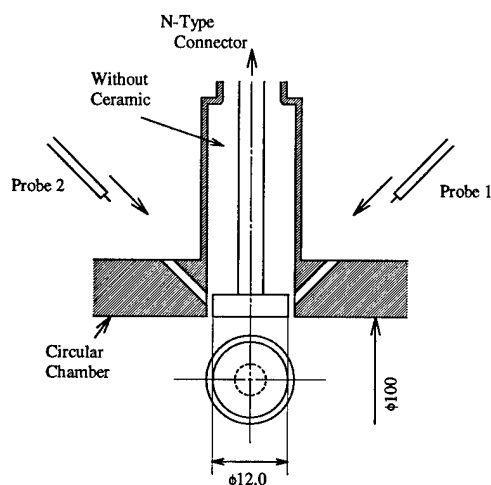


Figure 5. Experimental setup of the TE110 measurement. Two semi-rigid cable is used as an antenna to excite the TE110 mode at the disk. The BPM was mounted on $\phi 100$ mm circular beampipe, at those ends absorbers were loaded.

the quality factor of the TE110 mode resonance because only the coaxial mode can be excited.

Next, we excited the TE110 mode directly with the setup shown in Fig. 5.

Two probes inserted through $\phi 2$ mm holes excite the TE110 mode at the button electrode, while the N-type connector is connected to the matched load. To avoid ceramic resonances, we did not attach the ceramic part during this measurement.

Figure 6 shows the S_{21} spectrum of the circular electrode, where three large peaks are recognized. The first peak around 7.8 GHz, marked as A, is TE110 mode at the electrode. This resonance frequency is consistent with the numerical results of MAFIA. The quality factor of the mode was estimated to be 40. Another measurement with an asymmetric electrode showed a small decrease of the quality factor.

The second peak marked as B in the figure is identified as the TE111 cavity mode inside the BPM. This mode is trapped in a coaxial volume behind the button. The resonance frequency of

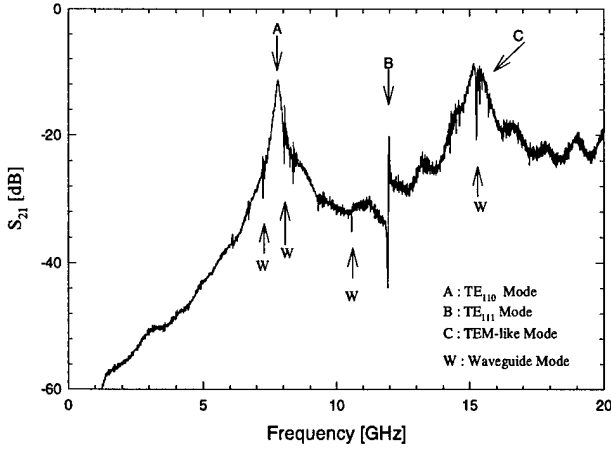


Figure 6. Dipole mode resonance of the circular BPM.

this mode is given by $k = \sqrt{k_z^2 + k_c^2}$, where k is the wave number of the resonance frequency, $\lambda_z (= 2\pi/k_z)$ the wavelength determined by the length of the electrode axis, k_c the cutoff wave number. The quality factor is about 300 with the circular electrode and about 50 with the damped electrode. Since this measurement did not include the ceramic part, the resonance frequency and the quality factor may be different from those of the actual BPM. We will investigate the coupling of this mode to the beam in near future.

The third peak marked as C is the TEM common-mode resonance. This mode is harmless because of its low quality factor and high coupling to the external circuit. There are several sharp peaks marked as W. These frequencies are identified as cutoff frequencies of TM_{nm} modes in a $\phi 100$ mm circular chamber.

V. DISCUSSION

The beam current spectrum and the power spectrum of the KEKB are shown in Fig. 7, for a natural bunch length σ_z of 4 mm. This figure shows that we should avoid resonances in the frequency range below about 15 GHz.

We estimate the growth time of the instability due to the TE110 mode. The R/Q is calculated from the loss factor k calculated with MAFIA and from the relationship [1]

$$k = \frac{\omega_r}{2} \left(\frac{R}{Q} \right) e^{-\omega_r^2 \sigma_t^2}, \quad (1)$$

where ω_r is the resonance frequency and σ_t is the bunch length in units of time. The experimental results show the Q value of the TE110 mode is about 40, leading the peak impedance $R = 1.0 \Omega$ per one BPM (4 buttons). The growth rate of longitudinal coupled bunch instability is given by [2]

$$\tau^{-1} = \frac{\alpha N e^2}{2 E T_0^2 \omega_s} \sum_{p=-\infty}^{\infty} (p \omega_0 + \omega_s) \text{Re}[Z(p \omega_0 + \omega_s)] e^{-\omega_r^2 \sigma_t^2}, \quad (2)$$

where N is the number of electrons (positrons) in the ring and E is the beam energy. The calculated growth time of the instability is 120 ms in the LER and 520 ms in the HER, which are

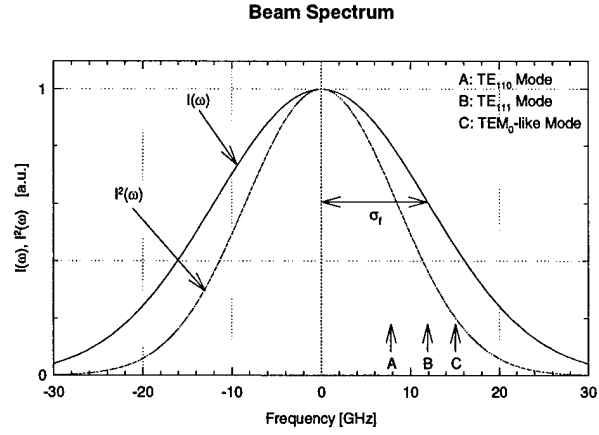


Figure 7. The beam spectrum of KEKB for the natural bunch length $\sigma_z = 4$ mm. The solid line shows the beam current spectrum $I(\omega)$ and the dotted line shows the power spectrum $P(\omega) \propto I^2(\omega)$.

sufficiently larger than the radiation damping time of 43 ms in the LER and 23 ms in the HER.

Though it is possible to enhance the mode mixing between the TE110 mode and the TEM mode by increasing the length of the asymmetric structure, the quality factor was already small enough to prevent the instabilities. Therefore, if we only think of the TE110 mode, we may adopt the circular button in the final design of the KEKB position monitors.

The TE111 mode exists only inside the BPM and it may affect little on the beam impedance, however, the coupling has not been estimated yet. Since the asymmetric structure have good damping effect on the mode, there is still some possibility of using the structure.

At last, we mention about the resonance in the ceramic briefly. Since it is difficult to damp these modes, we will optimize the thickness of the ceramic to detune the resonance from the RF harmonics.

Fabrication tests on brazing the electrode to the copper chamber is in progress. There still remain technical problems in the ceramic feedthrough, i.e., some of the feedthrough had vacuum leakage troubles after the brazing process. We are trying to optimize the detailed structure of ceramic part and sealing metal parts to meet both requirement of the brazing process and the RF impedance issues.

ACKNOWLEDGMENT

The authors wish to thank Dr. Y. Suetsugu who had designed and supported to manufacture the test chamber.

References

- [1] P. B. Wilson, SLAC-PUB-2884, (1987)
- [2] A. W. Chao, AIP Conf. Proc. 105(1983) p.353

BEAM MONITORS FOR THE S-BAND TEST FACILITY

W. Radloff and M. Wendt

Deutsches Elektronen Synchrotron (Desy), Notkestraße 85, D-22603 Hamburg, GERMANY

Abstract

The design of electromagnetic monitors for observation of beam charge and position of single bunches in long bunch trains is presented. With a repetition rate of 50Hz, each of the 125 bunches in the linac's macropulse has to be observed simultaneously. Resistive wall current and button pick-up stations will monitor the beam along the injector. Between the S-band acceleration structures precision stripline pick-ups will be used. Here a one micron position resolution within 16ns bunch-to-bunch spacing may be obtained in combination with well matched broadband rf-electronics.

For future linear colliders these bunch by bunch measurements are required to fulfill the constraints given by advanced beam-based alignment techniques.

I. INTRODUCTION

At Desy's S-Band Test Facility major components for a future Linear Collider layout are studied [1]. These are four 6m long travelling wave accelerating structures (3GHz, 17MV/m) with quadrupole triplets in between, two klystrons (150MW for 3 μ s), two modulators and a position feedback on the accelerating structures.

For commissioning and measurement of essential parameters like *beam current* and *beam orbit*, the Test Facility has to be equipped with *beam monitors*. To study the *bunch trains* behaviour in detail, monitors with enhanced performance are required. Therefore *position*- and *intensity*-monitors should have a single-bunch/single-pass measurement capability. For the investigation of transverse beam motions due to higher order modes (HOM) along the accelerating structures beam position monitors (BPM) with 1 μ m resolution are required. To analyse the HOM-effects, all the bunches in the *same* bunch train (!) have to be measured by the BPM's.

The electrons for the testlinac are served with 50Hz repetition rate by an injector [2]. In the standard operation mode a train of 125 bunches with 16 ns spacing is provided. To reproduce a single bunch in this train by the monitor its system *bandwidth*¹ has to be at least

$$B_{3dB} = f_{h,3dB} - f_{l,3dB} \approx 80 \dots 100\text{MHz}.$$

Other operation modes with 8 (or 24ns) bunch spacing will be studied further and require more (or less) bandwidth. To reach an average current of 300mA, each bunch has to be charged with 4.8nC (3 $\cdot 10^{10}$ e⁻). Out of the thermionic gun the full-width half-maximum (FWHM) *bunch length* is expected to be 2.5ns. Assuming Gaussian particle distributions we get the corresponding 3dB *cutoff frequency* by the relationship $t_{FWHM} f_{3dB} = 0.43$,

for 2.5ns: $f_{3dB} \approx 172\text{MHz}$. Passing the injector, the bunches will be compressed down to 50ps ($\equiv 50^0$ @ 3GHz). Through the linac the bunch length remains constant with less than 10ps ($\equiv 10^0$ @ 3GHz). The corresponding cutoff frequencies are in the order of several 10GHz and the beam excites TM waveguide-modes in the circular vacuum chamber. With its diameter of 32, sometimes 34mm the TM₀₁ cutoff frequency is 7GHz. Above this frequency the beam-to-pick-up signal transfer is "disturbed". As a consequence bunch length measurements with electromagnetic beam monitors are *not* possible everywhere, but only in the injector before the 3 GHz travelling wave buncher cavity (TWB).

In this paper we present the designs for electromagnetic monitors to measure beam position and intensity – and related parameters – along injector and linac.

For the S-band Test Facility two monitor units are developed:

- At the injector a compact *monitor module* was constructed, holding a *resistive wall monitor*, a *inductive monitor* and a *button-BPM*.
- The monitoring in the linac will be done with "*stripline*"-BPM's, and resistive wall monitors as an option.

II. INJECTOR MONITOR MODULE

Four locations along the injector are foreseen for monitor instrumentation, one between the gun and the 125MHz subharmonic buncher cavity (SHB), two between the 125MHz and the 500MHz SHB and a fourth one behind the 3GHz TWB. Three monitors are arranged into a 125mm long piece of vacuum chamber with 34mm diameter:

An electrostatic "button" pick-up, mainly used as a beam position monitor (BPM), a resistive wall monitor and an inductive current transformer. The last two are foreseen for beam current monitoring (CM), but – with little modifications – may be used also as BPM's. As the three monitors have different characteristics (sensitivity, bandwidth, etc.) we have the flexibility to experiment with their signals.

A. Button BPM

The button monitor is an electrostatic device with four round plates, the "buttons", of 19mm diameter. These are fixed on the inner pin of coaxial feedthroughs in symmetric positions around the vacuum chambers cross-section. Denote them *north* (N), *south* (S), *west* (W) and *east* (E). To avoid an aperture reduction at these points the vacuum chamber is made out of a massive block with indentions for the buttons, which have radial shaped inner surfaces on top. The button BPM is very compact and quite simple to manufacture.

The electrical equivalent circuit for a single button is just a capacitive voltage divider loaded with 50 Ω .² The button-to-wall

¹ gaussian-like transfer functions assumed

² for bunches longer than the buttons diameter

capacitance stays constant, while the beam-to-button capacitance varies with the beam-to-button distance (beam position). This causes a highpass-like transfer characteristic, so the output at the feedthrough delivers a totally differentiated impulse when a bunch passes. Wire measurements show a rather “hilly” magnitude response with a lower cutoff frequency of $f_{l,3dB} \approx 100\text{MHz}$ [3]. Beam position measurements can be done simply by comparing the peak amplitudes of two opposite buttons, i.e. W- and E-button for the vertical, N- and S-button for the horizontal axis.

B. Resistive Wall Monitor

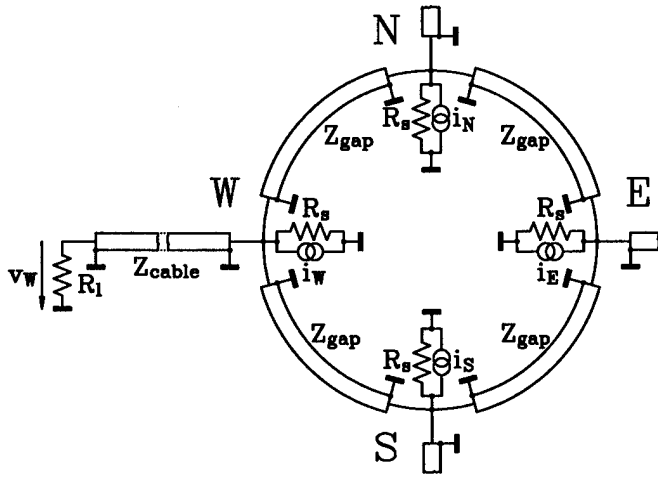


Figure 1. Equivalent circuit of the resistive wall monitors “4-resistor” operation (only one output shown)

The monitor module has a 5mm wide ceramic (Al_2O_3 alumina, $\epsilon_r = 9.7$) gap for the resistive wall monitor. In the “4-resistor operation” we bridge the gap only at the N-, S-, W- and E-positions with high quality rf-chip resistors. Together with the 50Ω “read-out” cables at the same points they form the equivalent circuit shown in Fig. 1. The beam induced wall currents concentrate in the four current sources $i_N + i_S + i_W + i_E = i_{\text{beam}}$. For CM operation the output signals v_N , v_S , v_W and v_E are summed in a broadband power combiner. To analyze the circuit we measured the gaps azimuthal transmission-line parameters by impulse-reflectometry: $Z_{\text{gap},az} \approx 56\Omega$, $\epsilon_{\text{eff}} \approx 3 \dots 4$. Now the monitors upper frequency limit can be estimated from the total gap capacitance³ $C'_{\text{gap}} = \sqrt{\mu_0 \epsilon_0 \epsilon_{\text{eff}}} / Z_{\text{gap},az}$ and the total load resistance. We choose $R_l = Z_{\text{cable}} = R_s = 50\Omega$ which results in 6.25Ω . Together with $C_{\text{gap}} \approx 13.5\text{pF}$ we find $f_{h,3dB} \approx 1.9\text{GHz}$. The monitors lower frequency limit depends on the impedance (inductance) characteristics of the “DC-bypass”. Without a metal-housing this DC-path is often rather long; via cables, shieldings, racks, etc. so that $f_{l,3dB}$ might be quite low, but in some way “undefined”. A metal-housing shields the monitor and delivers a well defined DC-path, but it raises $f_{l,3dB}$. This effect can be reduced with ferrite toroids inside the housing to increase the DC-path’s inductance. In general it is difficult to estimate the lower cutoff frequency, we measure mostly some 100kHz. At $R_l = Z_{\text{cable}} = R_s = Z_{\text{gap}}$ the gaps azimuthal transmission-lines are terminated in their characteristic impedance. In this

³ $C'_{\text{gap}} = C_{\text{gap}}$ per unit length

case no beam position dependence is observable. Analysing the “4-resistor” schematics by varying R_s in a range of typical values we found a beam position dependence of the output signals at frequencies above some 10MHz.

In a “multi-resistor” operation the gap is completely filled with resistors and forms a low impedance ring. Choosing a value that terminates the gaps radial transmission-line impedance results in a very broadband monitor [4]. We compute

$$Z_{\text{gap},rad} = \sqrt{\frac{\mu_0}{\epsilon_0}} \frac{h}{2\pi r} \approx 5\Omega,$$

where r is the gap cylinders central radius and h its height (equivalent to the “length” in beam direction).

In this operation the lower cutoff frequency of the position dependence is given by [5]

$$f_{l,3dB} = \frac{.02775}{L'G'r^2} \approx 130\text{MHz},$$

with $L' = \sqrt{\epsilon_{\text{eff}} \epsilon_0 \mu_0} Z_{\text{gap},az} \approx 350\text{nH/m}$ and $G' \approx 1.6\text{S/m}$.

C. Inductive Monitor

A toroid, made out of a $10 \times .025\text{mm}$ ferrite⁴ bandage, around the ceramic gap couples to the beams magnetic field which produces a proportional flux in it. This is sensed by a single turn of a flat copper wire around the toroid, again four times at the north, south, west and east positions. The delivered broadband signals are impedance matched to 50Ω by rf-transformation, the spectrum ranges from $f_{l,3dB} \approx 30\text{kHz}$ to $f_{h,3dB} \approx 250\text{MHz}$ ($\pm 2\text{dB}$). An extra turn is mounted for calibration purpose. This inductive monitor will be basically used as CM. It is also possible to run as BPM, but its position sensitivity is much lower than that of electrostatic monitors (buttons).

As we use the same ceramic gap for this inductive and for the resistive wall monitor, no extra space is required. Now a metal shielding is mandatory, with the ferrite toroid inside its inductance increases and help to lower the $f_{l,3dB}$ of the resistive wall CM.

D. Signal Processing

For current monitoring the four pick-up signals of each device are summed with commercial power combiners and the resulting signal is transferred via coaxial cables (RG213 quality) into the control room. In case of the BPM’s each button signal is delivered separately there. Later we plan to use delay-lines and broadband combiners to line-up their signals on a single cable. In the control room these signals are switched by a VXI rf-coaxial multiplexer onto a digital oscilloscope for the signal processing. This very simple read-out technique is possible because the number of monitors is small and the required performance is rather moderate (0.5mm position resolution). For the commissioning the instruments are controlled manually, after some experience a computer control (GPIB, HP-VEE or LabView) has to be set up.

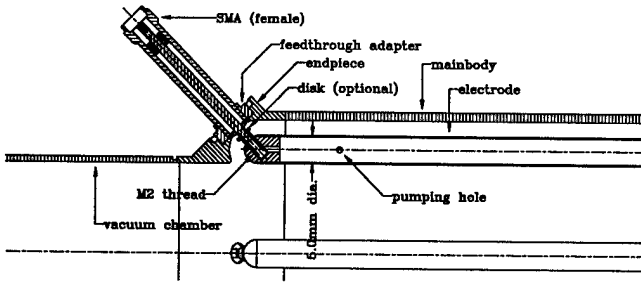


Figure 2. Stripline BPM for the linac (partial view of the longitudinal cut)

III. LINAC BPM

A. Stripline Pick-Up

Heart of the linac instrumentation are the BPM's. As pick-up a stripline monitor with four $\ell_{\text{elec}} = 20\text{cm}$ long tubular electrodes (slotted coaxial-lines made with 5mm dia. $\times 2\text{mm}$ stainless steel tubes) has been developed. The pick-up body is milled and electro-eroded (EDM)⁵ out of three NABE-58 Cu parts which are brazed together. As the monitor fits inside the quadrupole no extra space is required and it is easy to be aligned and calibrated. The pick-up electrodes are fixed at both ends to the center-pin of a 50 Ω vacuum feedthrough. A little disk is used to compensate the stray inductance at the pin-end. This minimizes the reflections on the electrode-to-feedthrough transition. Each electrode acts like a directional-coupler to the beam with the transfer function [6]

$$\frac{v_{\text{out}}(f)}{i_{\text{beam}}(f)} = \frac{k}{c_0 \sqrt{C'_{\text{beam}} C'_{\text{elec}}}} \frac{j \sin \Theta}{\sqrt{1 - k^2 \cos \Theta + j \sin \Theta}}, \quad (1)$$

with $k = C'_{\text{b-e}} / \sqrt{C'_{\text{beam}} C'_{\text{elec}}}$ and $\Theta = 2\pi f \ell_{\text{elec}} / c_0$. With the MAFIA electrostatic solver we found $C'_{\text{elec}} = 66.7\text{pF/m}$ ($\approx 50\Omega$), $C'_{\text{beam}} \approx 15\text{pF/m}$ and the beam-to-electrode capacitance $C'_{\text{b-e}} \approx 1\text{pF/m}$ (centered beam), $\Rightarrow k \approx .035$. The time-domain response to the beam follows as

$$v_{\text{out}} = \frac{k}{2 c_0 \sqrt{C'_{\text{beam}} C'_{\text{elec}}}} [i_{\text{beam}}(t) - i_{\text{beam}}(t - t_{d,\text{PU}})] \quad (2)$$

where $t_{d,\text{PU}} = 2 \ell_{\text{elec}} / c_0 = 1.33\text{ns}$. Further analysis of the pick-ups cross-section leads to the *position sensitivity* of two opposite electrodes: v_W/v_E or $v_N/v_S \approx 2\text{dB/mm}$ around the center.

B. Signal Processing with Comb-Filters

As usual, the signals of two opposite horizontal and vertical electrodes has to be compared to find the beam position with respect to the vacuum chambers center. The *amplitude ratio-to-phase difference* method is a reasonable way to process the broadband signals from the pick-up electrodes. With an analogue *preprocessing* extension (Σ/Δ -hybrid and rf-amplifier) the sensitivity around the origin can be increased [7]. The processing is based on 90 $^\circ$, 3dB-hybrids (directional couplers) and re-

quire continuous wave (CW) sine-signals. As no "memories" are present, the CW can be replaced by a sinus burst signal

$$\tilde{h}(t) = \sin(2\pi f_0 t) \text{ for } -\frac{n}{f_0} \leq t \leq \frac{n}{f_0}, 0 \text{ elsewhere}$$

$$\tilde{H}(f) = j(-1)^n \frac{\sin[2\pi n(f/f_0)]}{\pi f_0[1 - (f/f_0)^2]} \quad (3)$$

of n oscillations, with the frequency matched to the pick-up: $1/f_0 = T_0 = 2 t_{d,\text{PU}}$. For this purpose we designed a sinewave comb-filter, which will be switched between pick-up outputs and signal processing electronics.

The response of this comb-filter to a single bunch signal from the pick-up is a sinewave burst of $n = 4$ oscillations with $f_0 = 375\text{MHz}$. In this way we get a *measurement time* of $4 T_0 = 4/f_0 = 10.67\text{ns}$, which is sufficient to measure the position of every passing bunch within the 16ns bunch-to-bunch spacing. The comb-filter is realized by feeding the pick-ups "quasi"-Dirac⁶ doubled outputs signal (2) through a lowpass pulseformer with a "half"-cosine impulse response:

$$h(t) = \cos(2\pi f_0 t) \text{ for } -\frac{1}{4 f_0} \leq t \leq \frac{1}{4 f_0}, 0 \text{ elsewhere}$$

$$H(f) = \frac{\cos[\pi/2(f/f_0)]}{\pi f_0[1 - (f/f_0)^2]} \quad (4)$$

Its output delivers a single $f_0 = 375\text{MHz}$ sine oscillation as response of (2). With two commercial broadband 4-way power splitters/combiners and some delay-lines we line-up $n=4$ oscillations by splitting and delayed recombining of this single period.

References

- [1] N. Holtkamp; "The S-Band Linear Collider Test Facility", this conference
- [2] M. Schmitz and D. Yeremian; 1994 LINAC, 71-73
- [3] W. Schütte and M. Wendt; DESY HERA 87-05
- [4] R. C. Webber; FNAL TM-1655
- [5] G. C. Schneider; 1987 IEEE PAC, 87CH2387-9, Vol. 1, 664-666
- [6] E. G. Cristal; IEEE Transactions, Vol. MTT-14, No. 7, July, 1966, 337-346
- [7] M. Wendt; 1992 EPAC, Vol. 2, 1127-1129

⁴VAC Vakuumschmelze type Permenorm 3601K2

⁵electrical discharge machining

⁶ $t_{\text{bunch,FWHM}} \ll t_{d,\text{PU}}$ and $f_{h,3\text{dB,bunch}} \gg f_{h,3\text{dB,LP}}$

Low Energy Regime for Optical Transition Radiation Emission

D. Giove, C. De Martinis, M. Pullia and P. Mangili, INFN and University of Milano
LASA, Via F.lli Cervi 201, Segrate (Mi), Italy

Abstract

OTR has been widely investigated in the literature as an electron beam diagnostic tool in the high energy region ($E > 50$ MeV). At lower energy both the model of OTR emission and the experimental observation of the phenomena require a different and more complex approach. Nevertheless the information which can be drawn from OTR spectra at these low energies play a relevant role in new injectors. In this paper we will present and discuss the theoretical work carried out in the last year to provide a suitable background to OTR measurements at energies below 50 MeV.

Introduction

OTR based beam diagnostics are beginning to be used more and more at accelerator facilities around the world. There is a wide spread of data in the high energy region where the phenomena is more relevant. At low energies the situation is quite different for the difficulties in the measure of the emitted radiation, due to its low level, as well as for the lack of an homogeneous approach to the theoretical description of the emission.

The fundamental characteristics of the transition radiation emission shows both a rather complicated relation between a lot of different parameters and the coexistence of different regimes. This latter feature is mainly related to the dependence of the emission from the energy of the charged particles. The emission models used to describe the phenomena at high energies must be deeply modified in order to understand the behavior at lower energies. Moreover, the incidence angle of the beam plays also a relevant role in the characteristics of the emission.

Observation at the focal plane of the detector or at infinite will give different informations, but may results in completely different design of the experimental apparatus.

The purpose of this brief paper is to present and discuss the results of an homogeneous theoretical approach to the model of OTR emission which will include the different regimes and the possible different experimental configurations. We will demonstrate the feasibility of OTR measurements at electron energies of the order of few MeV and we will discuss the most important relations between OTR spectra and beam characteristics.

Analytical treatment

Our aim has been to obtain a general expression for the OTR emission using the simplest and more classic approach based on Maxwell equations and considering all the variables involved. The results obtained are fully compatible with the analytical expressions already available in the literature, but evaluated only for particular conditions⁽¹⁾.

The assumptions which have been considered may be so summarized:

- the materials have been described and modeled according to their macroscopic properties (ϵ, μ) and they are supposed homogeneous and isotropic
- the electron motion has been considered uniform and along a straight path
- the damping of the emitted electromagnetic waves depends only on the conductivity σ of the materials and on the distance from the emission point.

Starting from these hypothesis, we have considered two semi-infinite media with a plane interface between them. The propagation axis forms an angle ψ with the normal to the separation interface. Maxwell equations have been written for such a geometry and with the boundary conditions at the interface which describe the presence of a charged particle and the response of the material to an external electric field.

Computations are quite cumbersome and take into account the presence of fields due to the particle and radiation fields, which arises from the need to satisfy boundary conditions. Electric and magnetic fields may be computed in the two media and symmetry between them may be easily proved. Naming θ the angle between the normal to the interface and the wave vector κ , and ϕ the angle between the projection of the velocity on the interface and the projection of the wave vector κ on the interface, we obtain from the Poynting theorem the complete expression for the emitted radiation (Appendix 1).

The expression so far obtained shows all the dependencies from the different physical parameters involved in a measure: energy of the particle, materials, incidence and observation angles. Nevertheless the formula is rather complex to handle and is still referenced to a model of two semi-infinite planes. It is still possible to use this result also in a more realistic model for the target, i.e. one of finite thickness, providing that the material is a perfect conductor (σ very high).

These expressions are still valid for all the energies and all the geometric arrangements of the experimental setup. It may be shown that the errors introduced by the perfect conductor limit are of the order of 10% (in excess) for incidence angle of 45° , observation in the incidence plane and observation angle less than 0.5 rad. At low energies ($\gamma = 3$) the error percentage may grow up to 100% for observation angles greater than 1 rad. At high energies ($\gamma=100$) the error is negligible.

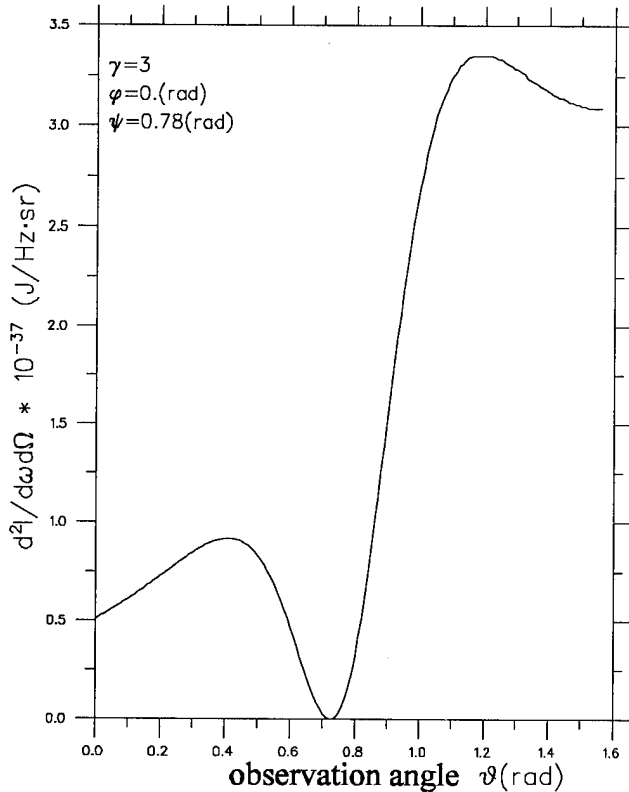


Fig. 1 Distribution of the emitted radiation at $\gamma=3$

Results and discussion

The relations so far obtained can be used to compute the spatial distribution of the radiation emitted from an interface for given conditions of the incident beam and of the detector geometry. This would provide a powerful tool for the design of a good experimental setup for an OTR measure. We have examined such relation in order to outline all the existing relations between the OTR spectra and the characteristics of a beam.

Fig. 1, 2, 3 show the distribution of the emitted radiation at $\phi = 0$ for different values of energy at incidence angles of 0 and 0.78 rad. In the following, we will consider only the so called backward emission, since it is the easiest to observe in diagnostics experiments. The maximum collection of radiation takes place under the following conditions:

- incidence angle centered around 0.78 rad for energies higher than 5 MeV and in the region 0.4-0.78 rad for lower energies (in this region the dependence from the

energy is strong)

- observation angle centered around 0.78 rad for energies higher than 5 MeV and for lower energies with a strong dependence from γ^2 .

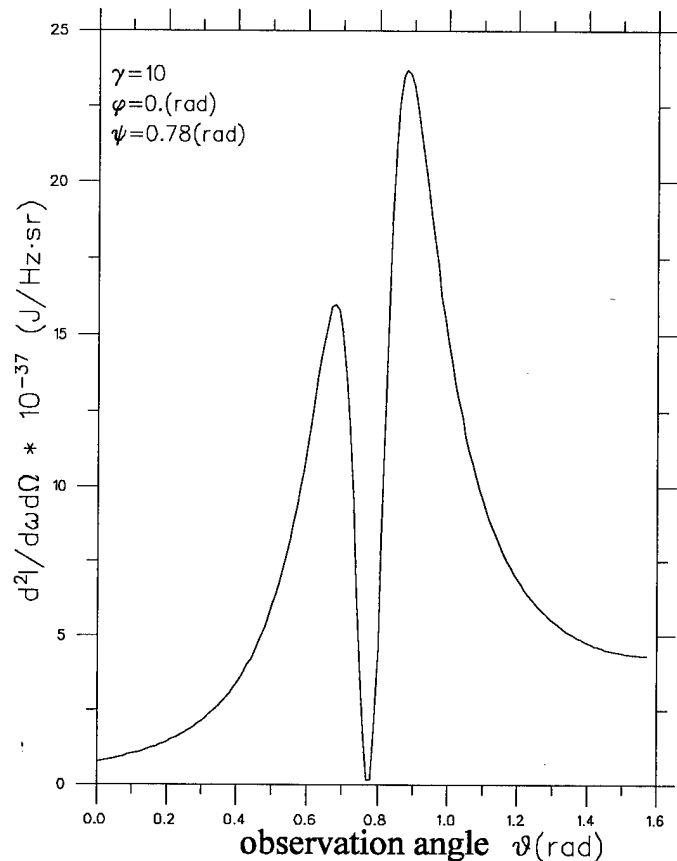


Fig. 2 Distribution of the emitted radiation at $\gamma=10$

These results are particularly interesting since the best geometric arrangement for radiation collection is also the easier from the experimental point of view. In fact the most usual configuration of the target with respect to the beam propagation axis is at 45° , in order to extract the emitted radiation in a simple way from the beam pipe.

The analysis of the relations between the spatial distribution of the emitted radiation and the energy of the beam, has given the following results:

the two characteristics peaks in the OTR spectra presents a maximum of 10% of amplitude unsymmetry with respect to variations in observation angle at energies higher than 10 MeV. At 2-3 MeV the unsymmetry is of the order of 400%. Symmetry is completely maintained with respect to variations in ϕ (fig. 4).

- the distance of the two peaks (Δ) is related to γ of the particle according to different expressions with respect to beam energy and measuring conditions. In particular it may be shown that Δ , at θ fixed, is proportional to $2.8\gamma^1$ and, at ϕ fixed, Δ is proportional to $2.0\gamma^1$ (in the range $\gamma > 20$) and to $1.5\gamma^{1.1}$ (in the range $\gamma < 20$).

The minimum in the emission distribution is related to the

energy of the beam. It may be shown that θ_{\min} overlaps with the reflection axis for $\gamma > 20$ and it is proportional to $0.5 \gamma^{-2}$ for $\gamma < 20$. The amplitude of the maximum peak in the distribution at $\varphi = 0$ is related to γ^2 .

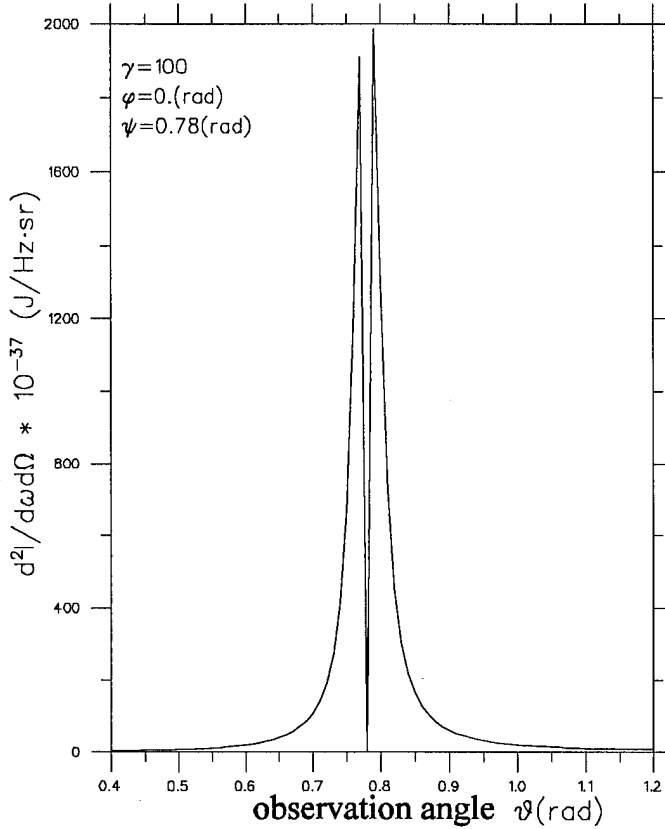


Fig. 3 Distribution of the emitted radiation at $\gamma=100$

As far as the intensity level is concerned our study has shown that at low energy (2-5 MeV) and in the condition of oblique incidence it is impossible to collect informations about spatial distribution. This is due to the large spread of the spectra (fig. 1) with respect to the geometrical constraints of the detector. Nevertheless it is possible to measure the radiation emitted regardless of its distribution.

Appendix 1

$$\frac{dI_{\parallel}}{d\Omega d\omega} = \frac{e^2 \sqrt{\epsilon_1}}{\pi^2 c} \frac{\beta^2 \cos^2 \psi \cos^2 \vartheta_1 |\epsilon_2 - \epsilon_1|^2}{[(1 - \sqrt{\epsilon_1} \sin \vartheta_1 \cos \varphi \beta \sin \psi)^2 - \epsilon_1 \cos^2 \vartheta_1 \beta^2 \cos^2 \psi] \sin^2(\vartheta)^2} \cdot \frac{1}{\left| \frac{\sin^2 \vartheta_1 (1 - \sqrt{\epsilon_1} \sin \vartheta_1 \cos \varphi \beta \sin \psi + (\epsilon_2 - \epsilon_1 \sin^2 \vartheta_1)^{1/2} \beta \cos \psi - \epsilon_1 \beta^2 \cos^2 \psi)}{[1 - \sqrt{\epsilon_1} \sin \vartheta_1 \cos \varphi \beta \sin \psi + (\epsilon_2 - \epsilon_1 \sin^2 \vartheta_1)^{1/2} \beta \cos \psi][(\epsilon_2 \epsilon_1 - \epsilon_1^2 \sin^2 \vartheta_1)^{1/2} + \epsilon_2 \cos \vartheta_1]} - \sqrt{\epsilon_1} \sin \vartheta_1 \cos \varphi \beta \sin \psi (\epsilon_2 - \epsilon_1 \sin^2 \vartheta_1)^{1/2} \beta \cos \psi \right|^2}$$

$$\frac{dI_{\perp}}{d\Omega d\omega} = \frac{e^2 \sqrt{\epsilon_1}}{\pi^2 c} \frac{\beta^6 \cos^4 \psi \sin^2 \vartheta \sin^2 \varphi \cos^2 \vartheta_1 |\epsilon_2 - \epsilon_1|^2}{[(1 - \sqrt{\epsilon_1} \sin \vartheta_1 \cos \varphi \beta \sin \psi)^2 - \epsilon_1 \cos^2 \vartheta_1 \beta^2 \cos^2 \psi]^2} \cdot \left| \frac{1 - \sqrt{\epsilon_1} \sin \vartheta_1 \cos \varphi \beta \sin \psi + (\epsilon_2 - \epsilon_1 \sin^2 \vartheta_1)^{1/2} \beta \cos \psi}{(\epsilon_2 \epsilon_1 - \epsilon_1^2 \sin^2 \vartheta_1)^{1/2} + \epsilon_2 \cos \vartheta_1} \right|^{-2}$$

The measure can be carried out using a normal camera. At higher energies ($\gamma = 10$) it is possible to collect a discrete level of intensity (of the order of 10^{-4} lux and which can be measured using an intensified camera) and the distribution may be analyzed according to the relations so far discussed.

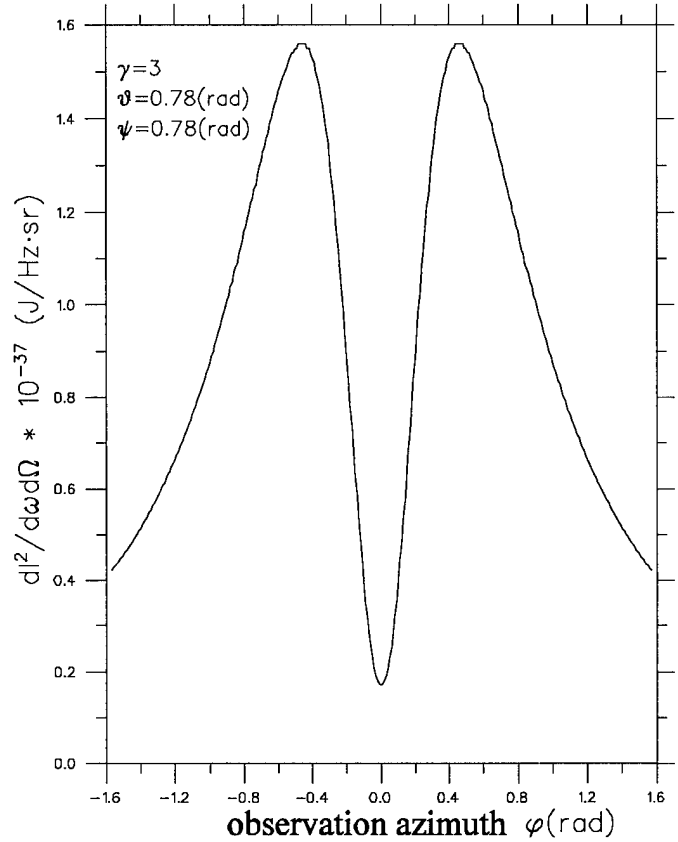


Fig. 4 Distribution of the emitted radiation at $\gamma=3$ vs. azimuth of observation

References

- [1] M. L. Ter Mikaelian, High energy electromagnetic processes in condensed media, ed. Wiley, 1972

RECOVERY OF CTF BEAM SIGNALS FROM A STRONG WAKEFIELD BACKGROUND

Yan Yin , TRIUMF, 4004 Wesbrook Mall, Vancouver, B.C. V6T 2A3, Canada
Elmar Schulte, CERN, CH-1211 Geneva 23, Switzerland
Tord Ekelöf, Uppsala University, P.O.Box 535, S-751 21, Sweden

Abstract

The beam monitor for the CERN Linear Collider Test Facility (CTF) has to work not only with very short pulses (3-50 ps FWHM) at a spacing of 330 ps, but also in a strong wakefield background. A cone-shaped button pickup electrode has been designed and constructed for use with CTF beams and tests have been made using a real time analogue Gaussian filter to recover the beam signals from the strong wakefield signals. As a comparison to the analogue filter, a study has been made to process the data off-line and extract the beam signals using digital filtering based on the wavelet concept.

I. INTRODUCTION

The CERN Linear Collider Test Facility (CTF) is a 4.5-45 MeV linac producing an intense electron beam with the following parameters:

Number of bunches in the train:	1-24
Bunch length (FWHM):	3-50 ps
Bunch repetition rate in the train:	3 GHz
Train repetition rate:	10 Hz
Minimum clear aperture:	40.5 mm

Normally, the bunch spacing is 333 ps and bunch length ≤ 12 ps FWHM. Each bunch contains 5.6×10^{10} electrons, that is a charge of 9 nC. Assuming the bunches have a Gaussian longitudinal distribution, it follows that when rms HW σ is 25 ps, the peak current is 144 A and when σ is 6 ps, the peak current is 598 A^[1].

The CTF beam monitor is intended to measure the intensity and transverse position of each bunch. When the pickup geometric size is comparable to the bunch length, the longitudinal intensity distribution can be recovered by integrating the pickup signal. However, because strong wakefields are present in the CTF, the first task is to extract the beam signal from the wakefield background.

An ordinary button-type electrode senses the signal across the capacitance between the button and the wall. A resonance may occur if the structure of the button and its housing form a cavity. When the bunch length is much longer than the button size, the beam frequency spectrum does not extend up to the resonance frequency, and the resonance is not excited. However, when the bunch length is comparable to the button size, the resonance may be excited, and if it is within the frequency of interest, it may disturb observation of the beam signal. Therefore the pickup has to be carefully designed to avoid such parasitic resonances

A cone-shaped button pickup has been designed to reach this goal; Fig.1 shows the geometry. The pickup electrode is made with a coaxial cone shape and is directly welded into a Kaman feedthrough, which is useable up to 40GHz. The cone shaped pickup has a smooth transition to the feedthrough. The ratio of the cone radius, a , to the outer conductor radius, b , is kept constant at $b/a=2.3$ along the cone axis in order to keep the impedance constant at 50 Ω . In Fig.1, $a=1.8$ mm, $b=3.9$ mm, $a'=0.79$ mm $b'=1.45$ mm (Kaman feedthrough), and the height of the cone is 4 mm.

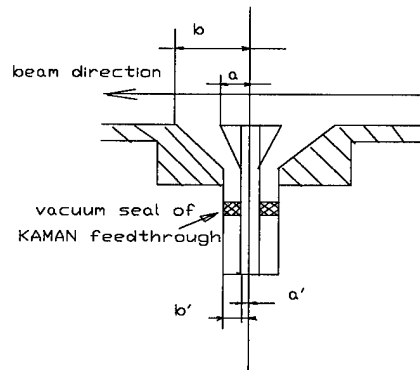


Fig.1 Cross-section of the cone-shaped button pickup.

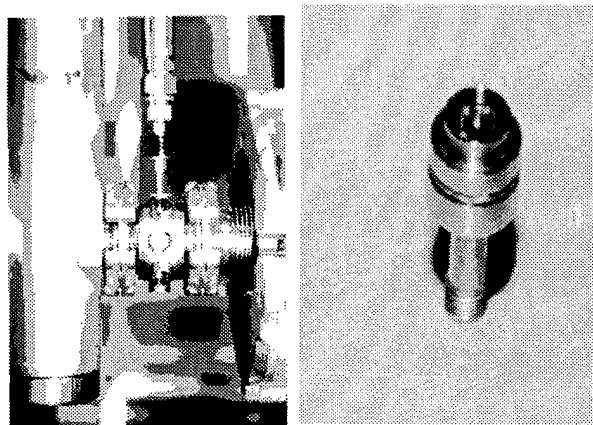


Fig.2 The cone-shaped pickup installed in the CTF (left) and a pickup before being welded into the beam pipe (right).

Two prototype monitors have been made and tested at the CTF. The design calculations and test results have been reported elsewhere^[1]. S_{11} measurements have been made in the time domain to study the resonances of the pickup. Fig.3

shows the synthesized incident pulse at 40 GHz (25 ps FWHM), which is the frequency limit of the network analyzer HP8510, and the reflection from the pickup. The pickup has small resonances at 15 GHz with less than 5% of the original signal amplitude.

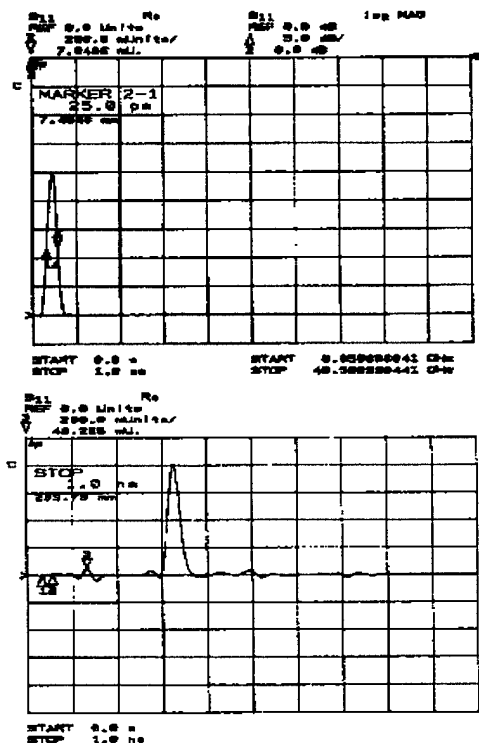


Fig.3. Examples of bench-test results. The top picture is the synthesized input signal, the bottom is the reflected signal from the pickup. (time-scale: 100 ps/div)

The wakefields, introduced into CTF acceleration sections by the very short bunches, escape and run through the smooth beam pipe of the pickup, forming a noisy background. Due to the cutoff frequency of the accelerator exit window, the escaping wakefields are at high frequency, and from the measurements they are above 6 GHz. There are two ways to process the signals. One way is to use analogue Gaussian filters to extract the low-frequency beam signal followed by further electronics to select the signals of each bunch. Another way is to use the wavelet transform to extract beam signals digitally out of the wakefield signal, and calculate the beam position using a computer.

II. GAUSSIAN FILTER

A bunch train signal can be considered as a series of single pulses. We are interested in recovering the signals of each bunch from a messy wakefield in order to measure each bunch's intensity and position. For this application, the behaviour of filters in the time domain and their transient response is more important and convenient for us. We do not need a very selective filter in the frequency domain, because we are not processing a single frequency as an ordinary BPM system does. An ideal Gaussian filter has the following response^[2] to an impulse at $t=0$:

$$f_i(t) = \frac{\Omega_c}{2\sqrt{\pi \ln 2}} \exp - \left[\frac{(\Omega_c t - n\pi / 2)^2}{4 \ln 2} \right]$$

Here Ω_c is the frequency whose amplitude corresponds to the FWHM of the Gaussian filter in the frequency domain, n is the number of cascaded stages, t is time. This impulse response has two remarkable features:

1. The impulse response is identical in shape to the absolute magnitude of the frequency response.
2. No overshoot or ringing is exhibited, giving the Gaussian filter a localization feature in the time domain.

Because two adjacent bunches in the CTF are 330 ps apart, a quasi-Gaussian filter (made by Picosecond Pulse Lab) with a rise time of 100 ps was selected, corresponding to a -3dB bandwidth of 3.5 GHz. The filter is not ideal: although attenuation at 9 GHz is 35 dB, the attenuation at 16 GHz is only 20 dB. The second windows of Figs.4 and 6 show the original signals picked up by the cone button monitor. Figs.5 and 7 show the signals at the output of a Gaussian filter. Although there is some residual high frequency, the tests show that the Gaussian filter has effectively filtered out most of the wakefields.

One does not care about high-frequency resonances such as at 40 GHz if the monitor is only working as a BPM with low frequency. However, when the monitor is used as a longitudinal pickup, it is useful to preserve the high-frequency components. Therefore it should have no ringing. Also, when a digital filter such as a wavelet transform is used, one would like to have a beam signal with all the bandwidth present.

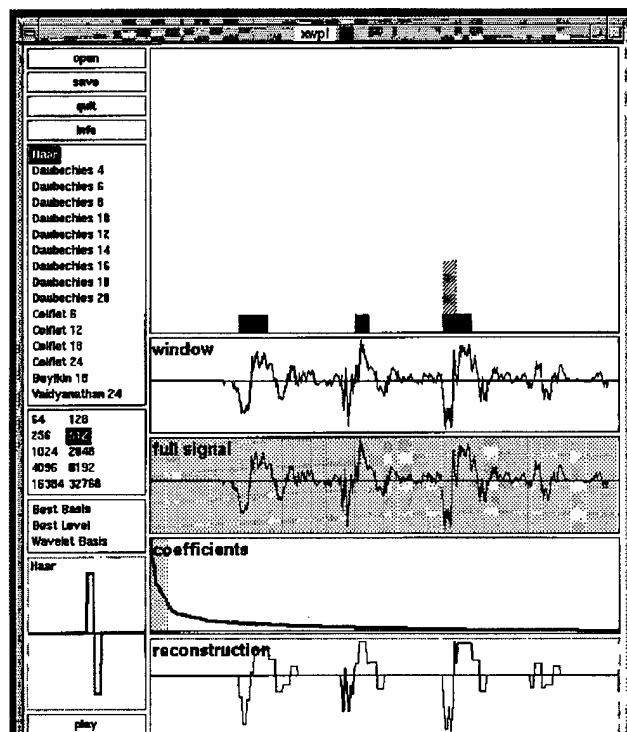


Fig.4 The original 3-bunch beam train signal from the pickup and the 3-bunch signal after the wavelet transform. (1.5 ns full width)

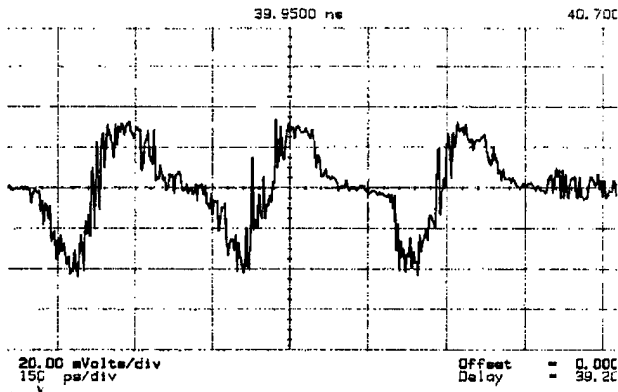


Fig.5 The 3-bunch beam train signal following the Gaussian filter.

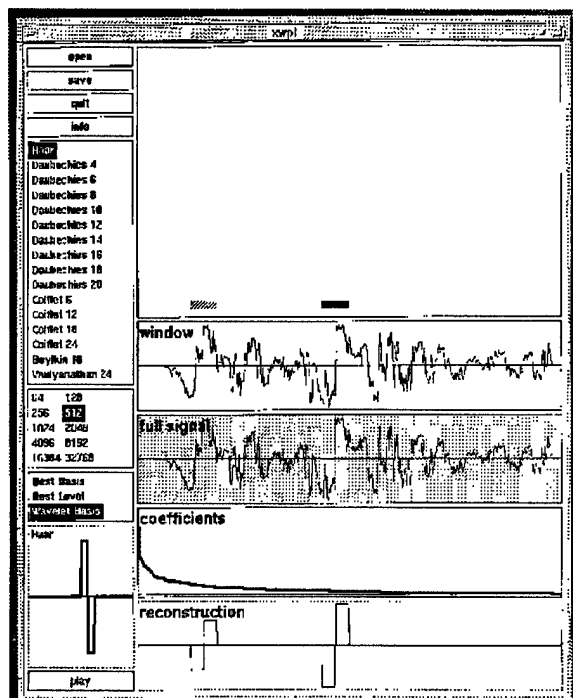


Fig.6 The two-bunch beam train signals picked up by the cone button monitor and the signal extracted with the wavelet transform..(1 ns full width)

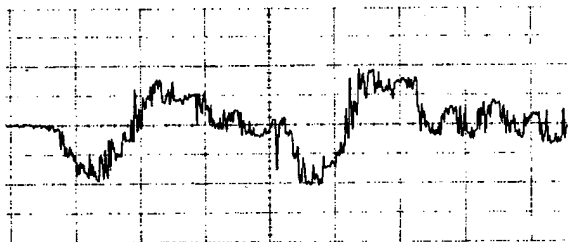


Fig.7 The two-bunch beam train signals at the output of a Gaussian filter. (100 ps/div)

III. WAVELET TRANSFORM

In principle, the wavelet transform is similar to the Fourier transform but with different base functions. The Fourier transform uses \sin and \cos as a set of base functions,

but the wavelet transform uses many other base functions. Because of its localization feature and the large selection of base functions, the wavelet transform can be used as a very good fast digital filter. Wavelet calculations have been done with the computer code XWPL^[3]. The cone-shaped button pickup gives a differentiated beam signal. Among the wavelet base functions provided by XWPL, the Haar function has the greatest similarity to the signals, and has therefore been selected for our calculations.

The wavelet calculation picks the beam signals out of the wakefields and reveals the timing of the bunches as in Fig.4 and Fig.6, where the vertical axis is amplitude, and the horizontal axis is time. Although the beam shape is rough, its amplitude can still be used for position calculation due to the linearity of the transformation.

The fidelity of the wavelet-transformed signal depends on the number of coefficients used. In Fig.4, more coefficients are used than in Fig.6, so the transformed signals more closely approximate to the real beam signals. In Fig.6, only a very few coefficients are used in order to filter out the wakefields and the transformed beam signals become almost like the Haar function itself.

IV. CONCLUSION

Both a Gaussian filter and wavelet transformation can recover certain parts of beam signals from a strong wakefield background. How close the recovered signals are to the real beam signal is still a subject for further study, but for beam position and intensity measurement they are adequate. The Gaussian filter works in a low-frequency range in order to filter out the high-frequency wakefields, but is a real-time analogue device, which is advantageous. On the other hand the wavelet transformation can extract beam signals over the whole measuring frequency range, but with the disadvantage that it is implemented as an off-line digital filter.

V. ACKNOWLEDGMENT

The authors thank Richard Lee (TRIUMF) for help with wavelet calculations, S.Koscielniak and B.Rawnsley for good discussions, and F.Caspers, Jean-Pierre Delahaye (CERN) and many people at CLIC for their contributions and support with this project.

REFERENCE

- [1].Yan Yin, Fritz Caspers, Elmar Schulte (CERN), Tord Ekelöf, Dag Reistad (TSL, Sweden), *Design and Test Results of a Beam Monitor for the CERN Linear Collider Test Facility*, BIW94, Oct. 1994, Vancouver, Canada.
- [2]. Anatol I Zverev, *Handbook of Filter Synthesis*, John Wiley and Sons, Inc. New York, 1967.
- [3]. Fazal Majid, *et al. The XWPL system*, (version 1.3, available by anonymous ftp from [pascal.math.yale.edu](ftp://pascal.math.yale.edu) (128.36.23.1) in the directory /pub/software/xwpl).

A LOW-COST NON-INTERCEPTING BEAM CURRENT AND PHASE MONITOR FOR HEAVY IONS*

J. M. Bogaty and B. E. Clift

Physics Division, Argonne National Laboratory, Argonne, IL 60439

I. INTRODUCTION

A low cost ion beam measurement system has been developed for use at ATLAS [1,2]. The system provides non-destructive phase and intensity measurement of passing ion beam bunches by sensing their electric fields. Bunches traverse a short tubular electrode thereby inducing displacement currents. These currents are brought outside the vacuum jacket where a lumped inductance resonates electrode capacitance at one of the bunching harmonic frequencies. This configuration yields a basic sensitivity of a few hundred millivolts signal per microampere of beam current. Beam induced radiofrequency signals are summed against an offset frequency generated by the master oscillator. The resulting difference frequency conveys beam intensity and bunch phase information which is sent to separate processing channels. One channel utilizes a phase locked loop to stabilize phase readings during microsecond beam drop outs. The other channel uses a linear full-wave active rectifier circuit which converts sine wave signal amplitude to a D.C. voltage

representing beam current. Plans are in progress to install this new diagnostic at several locations in ATLAS which should help shorten the tuning cycle of new ion species.

II. BEAM DETECTION

Figure 1 shows a schematic representation of the prototype beam measurement system in use at ATLAS. The beam pickup electrode design features an external resonant RF tank circuit which can be changed to tune any one of several bunching harmonics. Since the tubular pickup electrode is the only element under vacuum, cost of construction is lower than spiral or helical RF cavities. There is a trade off in beam sensitivity compared to RF cavity designs [3,4] but this is partially offset by using phase locked loops and active bandpass filters to minimize random noise effects. Fourier analysis of bunched beam passing through the pickup electrode was used to determine a general expression for signal amplitude across inductor L_T :

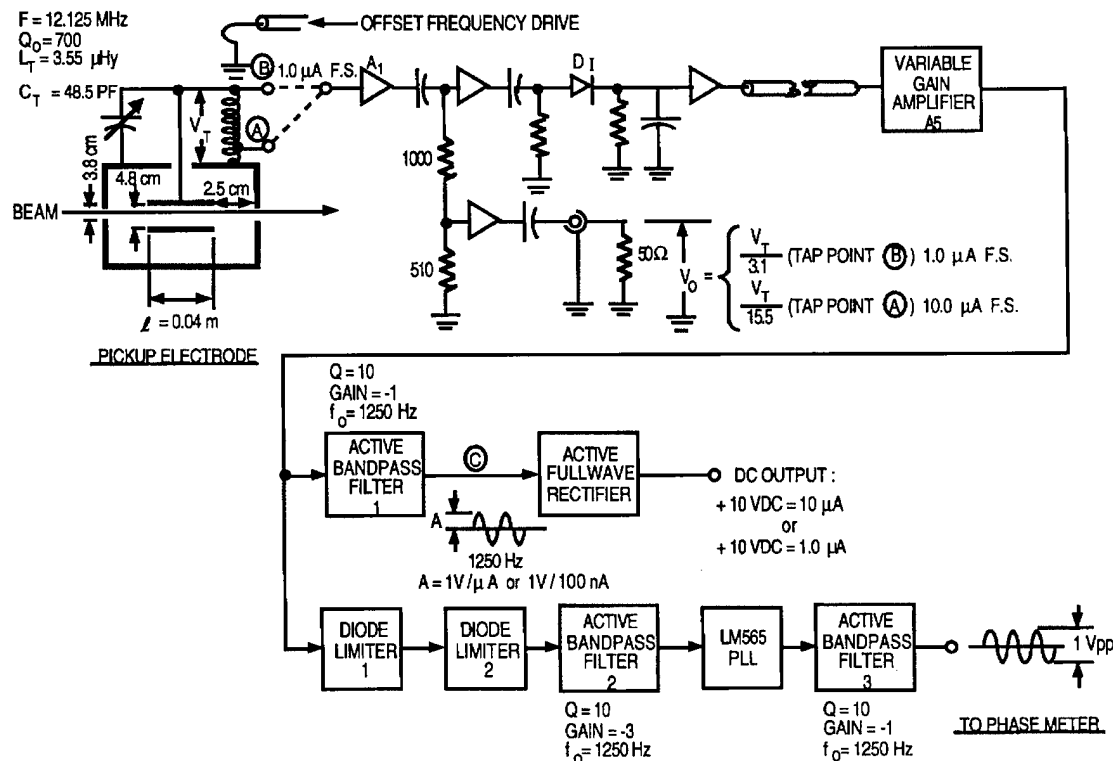


Fig. 1

Figure 1: Prototype Beam Measurement System Schematic.

$$V_T = \frac{2i_{ave}\ell Q_0}{C_T\beta c} \cdot \frac{\sin(N\pi fT)}{(N\pi fT)} \cdot \frac{\sin\left(\frac{N\pi f\ell}{\beta c}\right)}{\left(\frac{N\pi f\ell}{\beta c}\right)} \quad (1)$$

where:

V_T = peak induced signal in volts	(4.26 V)
i_{ave} = average bunched beam current	(10.0 microamperes)
ℓ = pickup electrode length in meters	(0.040 M)
C_T = total capacitance in farads	(48.5x10 ⁻¹² F)
βc = ion beam velocity m/s	(2.55x10 ⁶ m/s)
Q_0 = lightly loaded Q of system	(700)
N = bunching harmonic number	(1)
T = bunch width in sec.	(10 ⁻⁹ sec)
f = bunch repetition rate in Hz	(1.2125x10 ⁷ Hz)

Equation 1 was solved for the ion velocity, bunching, and harmonic number stated. Physical constants such as resonating capacitance and Q value were determined by laboratory measurement. Pickup electrode length " ℓ " was chosen on the basis of available space, beam sensitivity, ion beam velocity, and acceptable response over several bunching harmonics.

III. BEAM SIGNAL PROCESSING

As shown in Eq. 1, the peak value of signal strength " V_T " is equal to 0.42 volts per microampere of bunched beam. We do not critically couple beam induced power out of the resonant electrode, instead, a high input impedance RF buffer amplifier is used to sense voltage " V_T ". Amplifier A_1 can be connected to sense all of the beam induced voltage across L_T , or can be tapped at lower voltage points to accommodate higher beam intensity. Unity gain amplifier A_1 has an input impedance of 1.5 megohms in parallel with 2.0 picofarads, which does not significantly load the electrode's shunt impedance of 0.19 megohm.

Processing the 12 MHz beam signal into a DC voltage requires a two-step procedure to achieve acceptable linearity and dynamic range. Consider the introduction of a high-level RF signal slightly shifted in frequency from the beam. The summed offset and beam signals can then be diode detected to obtain amplitude and phase information. We, in fact, generate an accurate, stable offset signal which is removed from the fundamental frequency of bunching by 1250 Hz. This offset signal is coupled to the beam pick-up electrode and processed by the same circuitry used for beam induced signals. Offset and bunching signals sum together and appear as a low-frequency envelope modulation at the RF detector. This process is represented by the characteristics of two sine waves of slightly different frequency, as their vectors sum through 2 π radians of phase.

$$f(t) = A \sin(\omega t) \pm B \sin(K\omega t) \quad (2)$$

where:

A = amplitude of the beam induced signal

B = amplitude of offset oscillator drive

t = time

K = offset frequency factor = 1.0001031

$\omega = 2\pi f$ (f = 12.125 MHz)

At 100% modulation (A = B) the 1250 Hz modulation envelope will take on the characteristics of a sine squared function.

If we limit the percentage of modulation to 25% or less, the distortion effect becomes negligible and a clean 1250 Hz sine wave results. System parameters are set such that the highest accelerated beam currents result in no more than 25% envelope modulation at the RF detector.

Beam tests were carried out to verify the accuracy of Eq. 1. As maximum sensitivity is desired for this test, we configured buffer amplifier A_1 to sense the total voltage across inductor L_T . Since maximum beam current should not produce more than 25% modulation of RF offset voltage, the magnitude of V_T is set by what the buffer amplifiers can handle. This limited our test beam to a maximum of 1.0 microampere. Figure 2a shows the RF offset voltage level across inductor L_T . Notice that, under zero beam conditions, the peak amplitude of V_T is equal to 4.0 microamperes of beam current. If 1.0 microamperes of beam is present, the peak value of V_T is equal to 4.0 microamperes plus or minus 1.0 microampere, as shown in Fig. 2b. Detector diode D1 recovers the modulation envelope of 1250 Hz. Active bandpass filter number one (ABF1), shown in Fig. 1, has a Q of ten and unity gain. This Q value sets the system bandwidth at 125 Hz for beam intensity measurements. The amplitude of the 1250 Hz sine wave is calibrated at this point by adjusting

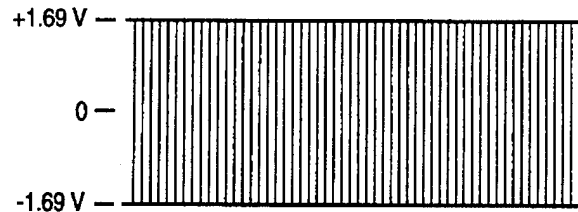


Fig. 2(a)

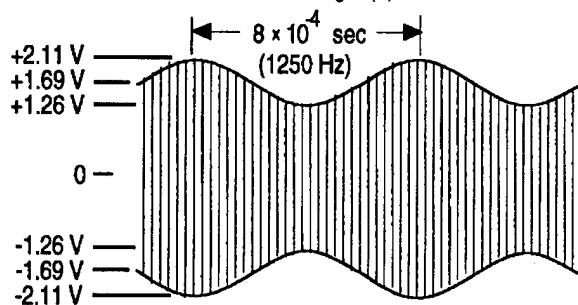


Fig. 2(b)

Figure 2: RF offset voltage level diagram.

the gain of low noise amplifier A₅. Noise voltage amplitude is one millivolt peak to peak at point "C" in Fig. 1, which is equivalent to 50 picoamperes of beam. For 1.0 microampere beams, the signal amplitude at point "C" rises to 20 volts peak to peak. The full wave active rectifier features 1% linearity over the beam intensity range of 1.0 microamperes to 500 picoamperes.

IV. BEAM PHASE MEASUREMENT

Figure 1 shows the beam phase channel consists of two diode limiters, two active band pass filters, and a phase locked loop (PLL). Care was taken to use temperature stable components for the active bandpass filters and PLL voltage controlled oscillator (VCO) circuit. We have used the system for measuring injection phase at the Positive Ion Injector and results have been excellent. We have plans to install two more measuring stations at ATLAS. Phase measurements of accelerated beam exhibit less than 0.5° of jitter over a beam current range of 1.0 microampere to 1.0 nanoamperes. The phase locked loop provides a constant phase signal because its internal VCO is very stable. The free running PLL VCO frequency is always within one hertz of 1250 Hz, therefore the phase error during a millisecond beam drop out is small.

V. SUMMARY

The beam monitor described in this paper is useful for measuring the phase and magnitude of nanoampere ion beams. We plan to improve the sensitivity and noise performance by raising electrode Q and reducing system bandwidth. A future goal is to develop a low cost beam monitor which accurately measures the current and phase of picoampere ion beams. Sensitive, low noise instrumentation will be needed if radioactive beams are developed at ATLAS.

*This work was supported by the U.S. Department of Energy, Nuclear Physics Division, under contract W-31-109-ENG-38.

VI. REFERENCES

- [1] R.C. Pardo, L.M. Bollinger, and K.W. Shepard, Nucl. Instrum. and Methods **B24/25**, 746 (1987).
- [2] L.M. Bollinger, et al., Nucl. Instrum. and Methods **B79**, 753 (1993).
- [3] S. Takeuchi and K.W. Shepard, "A Sensitive Beam-Bunch Phase Detector," Nucl. Instrum. and Methods **227**, 217-219 (1984).
- [4] A.D. Frawley and J.D. Fox, "A Spiral-Resonator Beam Phase Detector," Nucl. Instrum. and Methods **204**, 37-40 (1982).

TRANSVERSE EMITTANCE SYSTEMATICS MEASURED FOR HEAVY-ION BEAMS AT ATLAS

J.A. Nolen, T.A. Barlow*, K.A. Beyer, and K.A. Woody*,
Physics Division, Argonne National Laboratory, Argonne, IL 60439

The horizontal and vertical beam emittances and ellipse parameters are determined at the ATLAS superconducting heavy-ion linac by the well-known method of measuring the beam width at a profile monitor downstream of a quadrupole magnet as a function of the magnet current. Typically six base-to-base beam widths are measured and used in a least-squares fit to an algebraic expression for the three unknown ellipse parameters. The algorithm was derived from the first order matrix equation for the beam sigma matrix transform through the quadrupole singlet and drift to the profile monitor. To date the emittances of five beams from $^{12}\text{C}^{4+}$ to $^{238}\text{U}^{26+}$ have been measured at the entrance of the Positive-ion Injector Linac, yielding normalized values mostly in the range of $0.25\text{--}0.30 \pi \text{ mm-mr}$. These measurements will be extended systematically to several locations to identify possible sources of emittance growth and to develop more systematic beam tuning procedures.

I. INTRODUCTION

The ATLAS superconducting linac delivers a wide variety of heavy ion beams to several experimental areas for basic research in nuclear physics. The chart above in Fig. 1 shows the beams used for research in FY1993.

Most of these beams are produced in the ECR ion source of the Positive-Ion Injector shown in the facility layout in Fig. 2 below. The low energy beamline between the ECR

ion source and the injector linac must be tuned to match the horizontal and vertical emittance ellipses at the linac entrance. The present work is directed towards developing a simple and rapid method of measuring both the transverse emittance envelopes and the ellipse orientation parameters at the linac entrance.

A very simple method of measuring the x- and y- emittances and ellipse parameters is the "three gradient" method discussed, for example, by Qian, et al. [1,2]. The method consists of measuring the x- and y- beam envelope widths at a profile monitor downstream of an adjustable quadrupole magnet, as a function of the quadrupole gradient or current. The basic elements of the method are shown schematically in Fig. 3 below. The scanner which displays the beam profiles at the indicated position is a commercial moving-wire device marketed by the National Electrostatics Corporation. The beam profile displayed as a function of z in Fig. 3 is one calculated from measurements done for one of the beams listed below in Table I.

II. BEAM OPTICS ALGORITHM

The algorithm for extracting the beam parameters from beam width measurements was presented, for example, in reference [2]. We have written a Mathcad routine to process our data assuming the beam can be represented by ellipses in the xx' and yy' transverse planes.

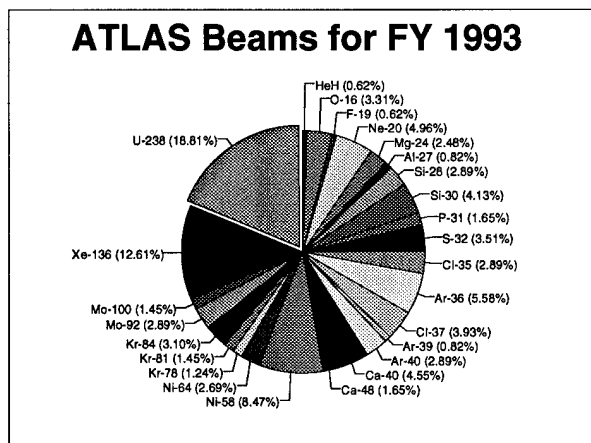


Figure 1. Chart showing the types of ion beams and the relative number of hours that each was used for research in fiscal year 1993.

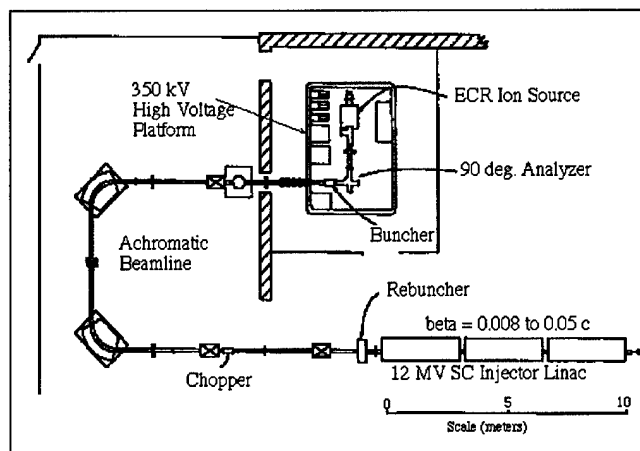


Figure 2. Layout of the Positive-Ion Injector of ATLAS. The emittance measurements reported here were made at the profile monitor located at the Injector Linac entrance, just after the rebuncher in this figure.

*Undergraduate Research Participants, supported by the ANL Division of Educational Programs.

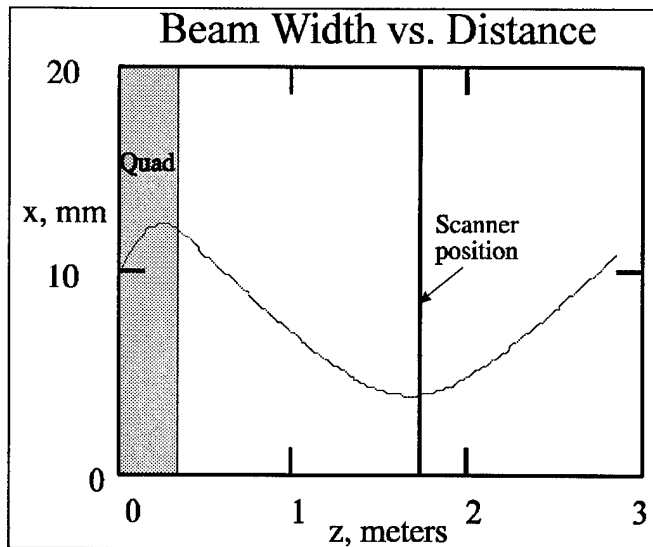


Figure 3. The essential elements of the "quad-drift" or "three-gradient" method of measuring beam emittance envelopes. The actual calculated beam profile vs. distance for one of the cases measured below is shown here.

The beam emittance, ϵ , and the phase space ellipse parameters, in the Courant-Snyder notation, are related by:

$$\epsilon = \gamma \cdot x^2 + 2 \cdot \alpha \cdot x \cdot x' + \beta \cdot x'^2.$$

The Courant-Snyder parameters are also related by:

$$\beta \cdot \gamma - \alpha^2 = 1.$$

Hence, there are three independent parameters to be determined about the beam. The beam ellipse can be expressed in matrix notation as the sigma matrix:

$$\sigma \equiv \epsilon \cdot \begin{pmatrix} \beta & -\alpha \\ -\alpha & \gamma \end{pmatrix}.$$

The matrix equation for propagation of the sigma matrix through a section of beamline represented by the transformation matrix \mathbf{R} is:

$$\sigma_1 = \mathbf{R} \cdot \sigma_0 \cdot \mathbf{R}^T \quad (1)$$

where σ_0 is the initial sigma matrix and σ_1 is the final. For the simple quad-drift geometry used here the transformation matrix (in the focusing plane of the quadrupole) is:

$$\mathbf{R} = \mathbf{D} \cdot \mathbf{Q}_f,$$

with

$$\mathbf{Q}_f = \begin{pmatrix} \cos(kw) & \frac{1}{k} \cdot \sin(kw) \\ -k \cdot \sin(kw) & \cos(kw) \end{pmatrix} \text{ and } \mathbf{D} = \begin{pmatrix} 1 & d \\ 0 & 1 \end{pmatrix}.$$

Using the fact that the beam half-width, x_{\max} , at the scanner location is related to the ellipse parameters by:

$$x_{\max} = \sqrt{\beta \cdot \epsilon},$$

a series of measurements of x_{\max} at the scanner location as a function of the quadrupole strength data can be used with equation (1) to solve for the three independent beam ellipse parameters at the entrance to the quadrupole. If more than three gradients and widths are recorded a least squares fit for the best parameters is done. Typical input and output parameters are presented below. The matrix equations and the least squares fit are done with a Mathcad routine.

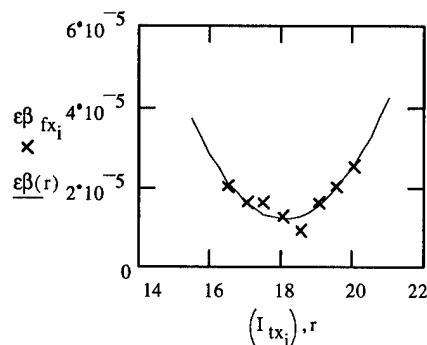
III. RESULTS

A typical array of input data, quadrupole currents and corresponding base-base beam widths in the x-plane are:

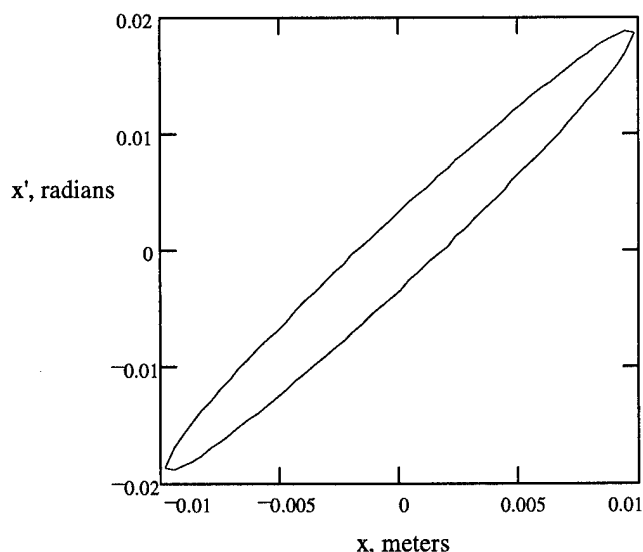
$$\mathbf{I}_x = \begin{pmatrix} 16.5 \\ 17.0 \\ 17.5 \\ 18.0 \\ 18.5 \\ 19.0 \\ 19.5 \\ 20.0 \end{pmatrix} \text{ Amps} \quad \mathbf{X}_{bb} = \begin{pmatrix} 9 \\ 8 \\ 8 \\ 7 \\ 6 \\ 8 \\ 9 \\ 10 \end{pmatrix} \text{ mm.}$$

There are corresponding data for the y-dimension which are not shown here.

The least-squares fit to the parameter $x^2 \equiv \beta \epsilon$ yields the following fit to the data:



And the following plot of the ellipse in the x-plane at the entrance to the quadrupole:



normalized emittance:

$$\epsilon_{nx} := \frac{v}{c} \cdot \epsilon_x$$

$$\epsilon_{nx} = 2.819 \cdot 10^{-7} \pi \text{ m-rad}$$

$$\epsilon_{nx} \cdot 10^6 = 0.282 \pi \text{ mm-mrad}$$

The numerical results for five beams measured with these method are listed in Table I. The values for the x- and y-normalized emittances vary from 0.14-0.54 π mm-mr. This range of values is typical for ECR ion sources [3-8]. These values are also in the range expected due to the axial magnetic fields of such ion sources [6-8]. The smallest emittances from ECR ion sources occur for the lowest and very highest charge states of a given ion type [8].

The sample data in the example above are from the $^{238}\text{U}^{26+}$ beam of Table I. The beam envelope plotted in Fig. 3 is also for this uranium beam. Since these data are for the x-plane, and the quadrupole is focusing in this plane, the tilt of the ellipse shown above at the quadrupole entrance corresponds to a diverging beam.

Table I. Emittances Measured for Five Beams*

Beam	ϵ_x	ϵ_{xn}	ϵ_y	ϵ_{yn}
$^{12}\text{C}^{4+}$	56	0.48	35	0.30
$^{16}\text{O}^{6+}$	22	0.19	16	0.14
$^{130}\text{Te}^{22+}$	32	0.27	28	0.24
$^{208}\text{Pb}^{23+}$	37	0.30	63	0.54
$^{238}\text{U}^{26+}$	33	0.28	34	0.29

*All values in π mm-mr and beam velocities were 0.008c.

The uncertainties on the emittance values given in Table I have not been estimated quantitatively. Currently the largest uncertainties are associated with reading the base-base beam widths from the profile monitors. A qualitative indication of the uncertainties in the emittance values was obtained by randomly changing the beam width data within a range of ± 1 mm and refitting. The variations in the fit results were on the order of 10% or less. Digitization of the analog signals from these monitors will be implemented to permit computer automation of the emittance measuring process.

This work is supported by the U.S. Department of Energy Nuclear Physics Division.

IV. REFERENCES

- [1] Y. Qian and B. Laune, Progress in Research, Texas A&M Cyclotron Inst., (1982)101.
- [2] Y. Qian, et al., Proc. 1994 Int. Linac Conf., Japan, (1994)899.
- [3] N. Chan Tung, et al., Nucl. Instr. Meth. **174** (1980)151.
- [4] Baron, et al., Proc. 7th ECR Workshop, Julich, (1986)25.
- [5] D. J. Clark, roc. 8th ECR Workshop, East Lansing, (1987)433.
- [6] H.L. Hagedoorn, et al., Proc. 8th ECR Workshop, East Lansing, (1987)389.
- [7] Z.-Q. Xie, PhD Thesis, MSU (1989).
- [8] K.A. Harrison and T.A. Antaya, Rev. Sci. Instr. **65**(1994)1138.

Beam Position Monitors in the TESLA Test Facility Linac

R. Lorenz, TU Berlin, Einsteinufer 17, 10587 Berlin

Abstract

The transverse position of the beam in the TTF Linac will be measured using two different types of monitors. For the alignment of the quadrupoles a circular cavity was designed because of the desired resolution of $10 \mu\text{m}$ and the limited longitudinal space. The amplitude of the TM_{110} -mode will be measured in a homodyne receiver, using a signal from the timing system as a reference. Stainless steel prototypes were tested. Furthermore, the single bunch behaviour was measured at the CLIC Test Facility.

Coaxial Striplines will be installed in the experimental area, having a resolution of better than $100 \mu\text{m}$. The averaged position of the whole bunch train or the position of an individual bunch will be measured using the amplitude-to-phase conversion.

Kyocera-feedthroughs welded into a special flange, are replaceable to allow a pre-tuning (by adjusting the coupling after welding).

parameter dimension	at 290 K	target	sensitivity $\pm 1 \text{ mm } \Delta$
radius R_0	115.2 mm	114.77 mm	$\mp 1247 \text{ KHz}$
length l	52.0 mm	51.80 mm	$\pm 79 \text{ KHz}$
beam pipe	39.0 mm	37.85 mm	$\mp 610 \text{ KHz}$
theoret. loss factor $[\frac{\text{V}}{\text{pC}}]$	$k_{110} = 0.242, k_{010} = 0.179$		
theoretical unloaded Q	$Q_{110} = 2965$		
measured frequ. [GHz]	$f_{110} = 1.5133, f_{010} = 1.04$		
measured coupling	$\beta_{110} = 1.31, \beta_{010} = 0.1$		

Table I

Cavity design and measured parameters

I. Introduction

In order to establish a technical basis for a superconducting linear collider the TESLA Test Facility is an essential part of the development of injectors, accelerating cavities, cryostat and new diagnostic techniques.

The transverse position of the beam after the injector will be measured using two different types of monitors. For the alignment of the quadrupoles a single circular cavity was designed because of the limited longitudinal space and the desired resolution of about $10 \mu\text{m}$ in a cold environment (see also [3]). The amplitude of the TM_{110} -mode will be measured in a homodyne receiver, using the seventh harmonic of a 217 MHz timing signal as a reference.

Stripline BPMs will be installed in the experimental area, having a resolution of about $100 \mu\text{m}$. For Injector I (bunch spacing of 4.6 ns) the averaged position of the bunch train will be measured using the amplitude-to-phase conversion.

II. TM_{110} -Cavity

The amplitude of the TM_{110} -mode excited in the cavity by an off-center beam yields a signal proportional to the beam displacement and the bunch charge. Its phase relative to an external reference yields the sign of the displacement. Both polarizations of this mode have to be measured to get the displacement in x and y, respectively. For Injector I this system can measure only an average over the bunch train.

A. Prototype Design

The cavity parameters given in Table I were calculated with URMEL, and the measurements were performed on a stainless steel prototype at room temperature (Fig.1). CrNi was chosen as the cavity material to measure individual bunches spaced at $1 \mu\text{s}$ (Injector II).

After cooling down the structure, the seventh harmonic of 216.7 MHz has to be within the cavity bandwidth to avoid an active tuning system inside the cryostat. The antennae consisting of

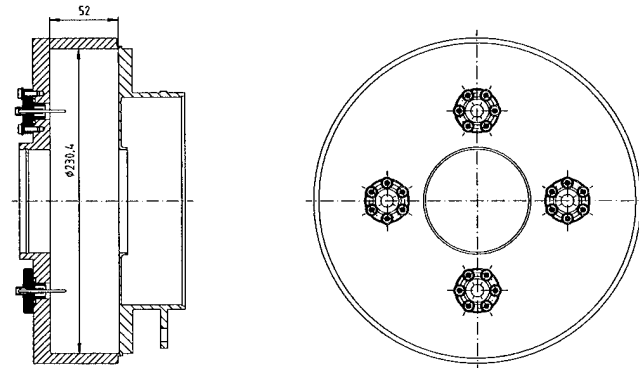


Figure 1. Cavity BPM

B. Estimated Signals

The resolution near the electrical center of the cavity is limited by the thermal noise of the electronics and the excitation of common modes. For a cavity without beam pipes, the voltage of the TM_{110} excited by a beam at a position δ_x vs. the noise voltage can be estimated as

$$\frac{V_{110}(\delta_x)}{V_{\text{noise}}} = \frac{\delta_x \cdot a_{11}}{2J_1^{\text{max}} R_0} \frac{V_{110}^{\text{max}}}{V_{\text{noise}}} = \frac{\delta_x}{J_1^{\text{max}} R_0} \frac{k_{110} \cdot a_{11} \cdot q \cdot T_{\text{tr}}}{\text{NF} \sqrt{Z_0 k_0 T B}}$$

where a_{11} is the first root of J_1 , T_{tr} the transit time factor, $q = 32 \text{ pC}$ the bunch charge, k_{110} the long. lossfactor and R_0 the cavity radius (Table I). For a noise figure of $\text{NF} = 2$, the S/N-ratio in a bandwidth $B = 10 \text{ MHz}$ at 293 K is about $139 \frac{\delta_x}{\mu\text{m}}$.

Since the field maximum of the common modes is on the cavity axis, they will be excited much stronger than the TM_{110} by a beam near the axis. The voltage of the TM_{010} with respect to the TM_{110} and the ratio of the spectral densities at ω_{110} can be estimated as ([1])

$$S_1 = \frac{V_{010}(\omega_{010})}{V_{110}(\omega_{110})} = \frac{1}{\delta_x} \frac{\lambda_{110}}{5.4} \frac{k_{010}}{k_{110}} \approx 27 \cdot \left(\frac{\delta_x}{\text{mm}} \right)^{-1}$$

$$S_2 = \frac{v_{110}(\omega_{110})}{v_{010}(\omega_{110})} \approx \frac{1}{S_1} \frac{Q_{110}}{1 + 2\beta_{110}} \left(1 - \frac{\omega_{010}^2}{\omega_{110}^2} \right) \approx 16 \cdot \frac{\delta_x}{\text{mm}}$$

S_1 gives the required frequency sensitive common-mode rejection - about 69 dB for a displacement of $\delta_x = 10 \mu\text{m}$. But the minimum detectable signal near the electrical center of the cavity is still limited by residual signals at ω_{110} ($S_2 \leq 1$). With a combination of two antennae in a hybrid one gets a field selective filter and a rejection of unwanted common field components at ω_{110} , limited only by the finite isolation of the hybrid between the Σ - and the Δ -port. Finally, we get a theoretical resolution of less than $6 \mu\text{m}$ for 20 dB of isolation.

C. Signal Processing

We adopted a homodyne receiver scheme (Fig.2), where the amplitude of the TM_{110} and a reference are mixed down to DC. The reference-signal is generated by mixing a 217 MHz-signal from the timing system and amplifying the seventh harmonic. When the beam is on the right, the system can be set up to give positive video polarity. The signal changes the phase by 180° when the beam moves to the left, and for a centered beam it becomes zero.

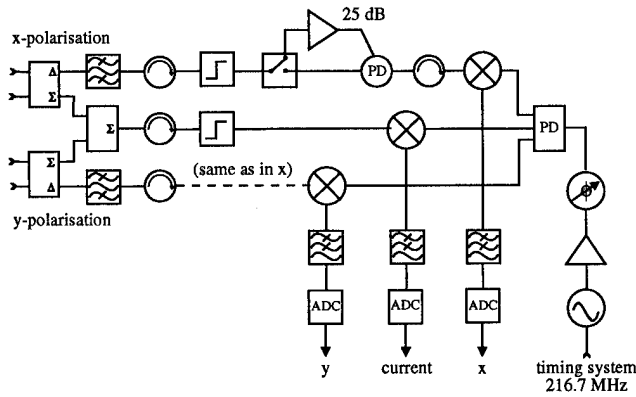


Figure 2. Signal processing scheme for the cavity BPMs

Due to the limited space, the combination of two opposite antennae was realized outside the cryostat. The tubular bandpass filter has a bandwidth of 100 MHz and a stopband attenuation of more than 70 dB, up to 8 GHz. Together with the hybrid and the coupling factors this gives a frequency sensitive common mode rejection of about 100 dB. Because of the finite isolation of the hybrid and between both polarizations of the TM_{110} (asymmetries in the cavity), the full aperture was divided into two measurement ranges.

The LO-RF-isolation of the mixer determines the dynamic range of the electronics. By using a Quadrature IF Mixer, no additional phase stabilization for the reference would be required. An isolator was inserted between the filter and the mixer to reduce reflections and error signals due to second-time mixing.

After passing a low-pass filter and a bipolar video amplifier, the signal may be either viewed directly on an oscilloscope for adjustment, or digitized and used for the quadrupole alignment. All data of the 12-bit ADC-board can be read out between two bunch trains and the normalization will be done in a computer.

D. Test Results

Bench tests were carried out on a stainless steel prototype to determine the resolution near the center and to test the electronics. Therefore the cavity was excited by an antenna, fed by a network analyzer. A resolution of about $5 \mu\text{m}$ was measured in the frequency domain (narrowband) and in the time domain (impulse response) by moving the cavity (Fig.3 and Fig.4, see also [3]).

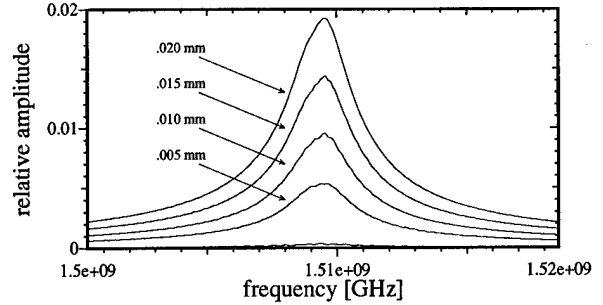


Figure 3. Bench-test - Narrowband output vs. position

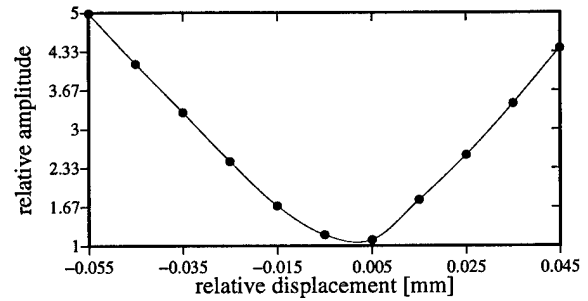


Figure 4. Bench-test - Impulse response vs. position

To get similar responses in a real time domain measurement and for testing the electronics, a pulser ($t_w \approx 370\text{ps}$, $\text{amp} \approx 16\text{V}$) was built to excite the cavity. The filtered Δ -port signal was mixed down to DC and displayed on an oscilloscope triggered by the sum-signal of the hybrid. Since the pulser was not very stable with respect to its amplitude, it was impossible to measure the min. resolution.

In addition, a prototype was tested at the CLIC Test Facility at CERN to demonstrate the principle single bunch response of the monitor and to measure the amplitude of the TM_{110} -mode as a function of the relative beam displacement. Therefore, the BPM was installed in the spectro-meter arm and the beam was moved vertically by changing the current of the steering coil.

Since no LO-signal at 1.51 GHz (phase-related to the beam) was available, four different LO-schemes were tested. In one scheme a 250 MHz-signal from the timing system was fed to a step recovery diode and the 6th harmonic was mixed with the Δ -signal. Figure 5 shows the output of the electronics vs. the relative beam position.

Unfortunately, due to the measurement position, the mechanical setup and some machine parameters it was impossible to measure the minimum detectable signal near the monitor center.

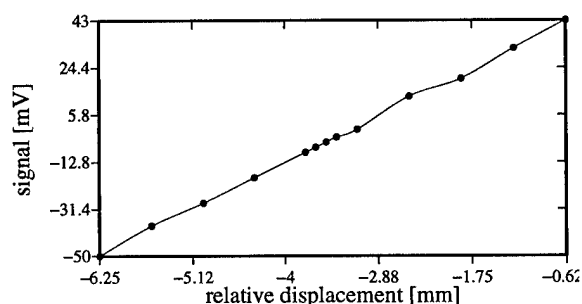
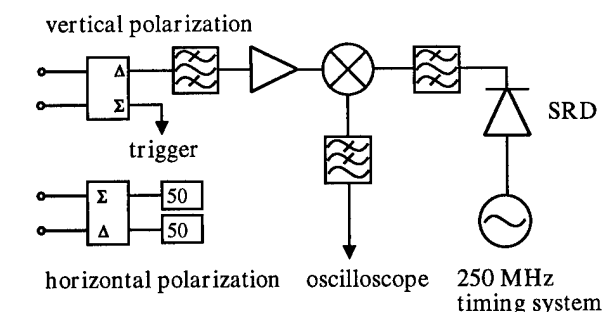


Figure 5. CTF-test - Output versus rel. position

III. Stripline Monitors

Stripline monitors were selected for the experimental area and a temporary beamline because of the relaxed requirements - 100 μm resolution around the center - and the warm location. All monitors will consist of four 50 Ω coaxial striplines, positioned 90 degrees apart in azimuth (Fig.6). The housing for the one in the dipole arm will be slightly modified due to the elliptical beam pipe.

The BPM body is machined from a single block of stainless steel, and four holes and the beam aperture are drilled (similar to the structure described in [4]). Each electrode is 175 mm long, has a geometrical coupling factor of about 2 % and is shortened at the end. To reduce standing waves on the electrode, the transition from the electrode through the feedthrough into the cable was optimized up to 6 GHz. The main distortion is caused by the feedthrough. A prototype was built by DESY-IfH Zeuthen and is under test.

The signal processing electronics have to measure the Δ -signal and the Σ -signal of two opposite electrodes to calculate the position in one direction. Because of the small charge per bunch and the multibunching, an amplitude-to-phase conversion scheme was adopted. Its basic component is a device which transforms the amplitude ratio of two input signals into a phase difference, usually a $\frac{\pi}{2}$ -hybrid. The generation of a normalized output (position versus current) over a wide dynamic range is the main advantage of this system.

Analog electronics will be built by INFN Frascati and a prototype will be tested this summer. The signal coming out of the phase detector may be either viewed directly on an oscilloscope or digitized using a 12-bit ADC-board.

This system will be appropriate to measure individual bunches spaced 1 μs for Injector II, too. Another alternative is to adopt the SLAC-system, where the signals of each electrode are indi-

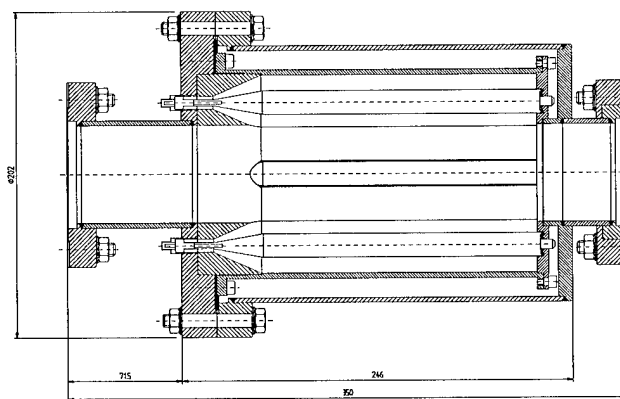


Figure 6. Stripline BPM

vidually stretched, amplified, held at their peak value and then digitized.

IV. Acknowledgements

The author would like to thank DESY-IfH Zeuthen for building several prototypes and the realization of the stripline monitor. Special thanks are extended to Hans Braun from the CLIC/CTF group for his help in the preparation and realization of the tests.

References

- [1] W. Schnell, "Common-mode rejection in resonant microwave position monitors for linear colliders", CLIC note 70, CERN-LEP-RF/88-41
- [2] R. Shafer, "Beam Position Monitoring", AIP Conference Proceedings 212, 1989, pp. 26-58
- [3] R. Lorenz, K. Yezza, "Test results on a Beam Position Monitor Prototype for the TTF", in Conference Proceedings of the EPAC 94, London, July 1994, pp. 1536-1538
- [4] J. Hinkson, K. Rex, "A Wideband Slot-Coupled Beam Sensing Electrode for the Advanced Light Source (ALS)", IEEE Conference Proceedings of the PAC 91, San Francisco, May 1991, pp. 1234-1236

Energy Measurement of Relativistic Electrons by Compton Scattering*

Ian Hsu, C. - C. Chu, C. - I. Yu, C. - I. Chen, A. - T. Lai and Y. - C. Liu[#], P. - K. Tseng, G. - Y. Hsiung, R. - C. Hsu, C. - P. Wang, R. - C. Chen

Institute of Nuclear Science, National Tsing-Hua University and
Synchrotron Radiation Research Center
Hsinchu, Taiwan 30043, R.O.C

ABSTRACT

Measuring the energy of the backscattered photons from laser Compton scattering provided us the energy information of the relativistic electrons in TSL of SRRC. The photon yield, detector efficiency, detector energy calibration, and detector energy resolution would affect the final photon counting rate, and thereby influence the spectrum of the scattered photons. Method of coincidence measurement was applied and was discussed in this paper. The first couple test run results were presented here as well.

1. INTRODUCTION

Compton scattering of laser photons with relativistic electron beam can yield quasi-monochromatic photon beam. This energetic photon beam has applications in the investigation of photonuclear reaction, the calibration of the detectors, medical image, and electron beam diagnostics^[1]. Here we use Compton scattering to measure the electron beam energy in the storage ring of TLS (Taiwan Light Source) of SRRC (Synchrotron Radiation Research Center). The design of the optical system must take the electron beam behavior into consideration to enhance the backscattered photon yield. Optical alignment would obviously affected the photon yield, thereby the optical system should be treated carefully. The backscattered photons were produced within a very short time period since the CO₂ laser was pulsed with 30ns of pulse width. This fact indicated that the HPGe detector used in this system would detect only the background radiation from Bremsstrahlung, which was produced by the collision of the electrons and the residual gases/ions in the vacuum chamber for the most of detecting time. Unfortunately, the contribution of the Bremsstrahlung radiation in obtaining the photon spectrum was comparable to the contribution of the scattered photons. Coincidence measurement would help reducing the background to an acceptable degree.

2. THEORY

The kinematics associated with the scattering is discussed by many papers. The process is shown in figure 1. The scattered photon energy k_2 from laser photons of energy k_1 in lab. frame is^[2]

$$k_2 = \frac{k_1(1 - \beta \cos \theta_1)}{1 - \beta \cos \theta_2 + k_1(1 - \cos \chi)/E_e} \text{ non-head-on} \quad (1.1)$$

$$\text{or } k_2 = \frac{4\gamma^2 k_1}{1 + \frac{4\gamma^2 k_1}{mc^2} + \gamma^2 \theta^2} \text{ head-on} \quad (1.2)$$

where $\chi = \theta_2 - \theta_1$, $\beta = v/c$ with v and c the velocities of the electron and the laser light, θ is the angle between the laser and the scattered photons, and E_e is the electron energy.

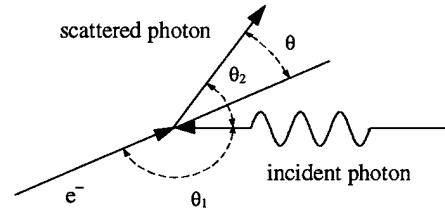


Figure 1 The schematic drawing of the process of Compton scattering

The Klein-Nishina formula shows the differential cross section ds for the head on collision in the electron rest frame. For the lab. frame, after the Lorentz transformation, it is rewritten as^[3]

$$d\sigma = \frac{\pi r_0^2}{2} \frac{m^2}{k_1 E_e^2} \left[\frac{m^4}{4k_1^2 E_e^2} \times \left(\frac{k_2}{E_e - k_2} \right)^2 - \frac{m^2}{k_1 - E_e} \times \left(\frac{k_2}{E_e - k_2} \right) + \frac{E_e - k_2}{E_e} + \frac{E_e}{E_e - k_2} \right] dk_2 \quad (2)$$

where r_0 is the classical electron radius, and m is the electron rest mass. The photon yield Y per pulse is given by

$$Y = \frac{2N_e N_p \sigma d}{A c \tau} \quad (3)$$

where N_e and N_p are the number of electrons and laser photons per pulse, d is the average interaction length, A is the larger one of the transverse beam size of the electron beam and the laser beam, and τ is the longer one of the pulse length of the electron beam and the laser beam. σ is the total cross section of photons and electrons.

3. SYSTEM DESIGN

The very low detection efficiency of HPGe detector at high energy (less than 0.1 relative efficiency at 10MeV) limited the choice for the laser to be employed. A lower energy (and hence the higher detection efficiency) of the backscattered photons was thereby the main criteria. The energy of the backscattered photons was 48.42MeV for a He-Ne laser and 29.49MeV for a Nd:YAG laser. A pulsed CO₂ laser with wavelength $\lambda=10.6\mu\text{m}$ would produced the backscattered photons with maximum energy up to 3.02MeV and therefore made it suitable for this system. Figure 2 indicates the schematic drawing of the experimental setup.

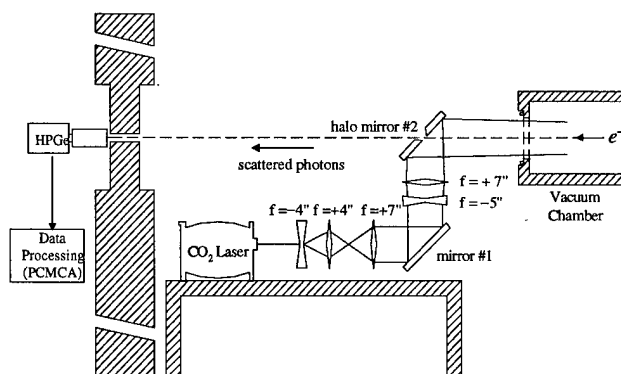


Figure 2 Experimental setup

A. Detector Energy Calibration

The traditional energy calibration using ⁶⁰Co and ¹³⁷Cs as standard sources was not convincible in this case since the energy of the scattered photons was up to 3.02MeV. The energy calibration was carried out through the gamma decay of ²⁴Na, which was the product of neutron activation of Na₂CO₃. The decay energies of ²⁴Na are 1.3684MeV, 2.7536MeV and a sum-peak of 4.122MeV. The spectrum is shown as figure 3.

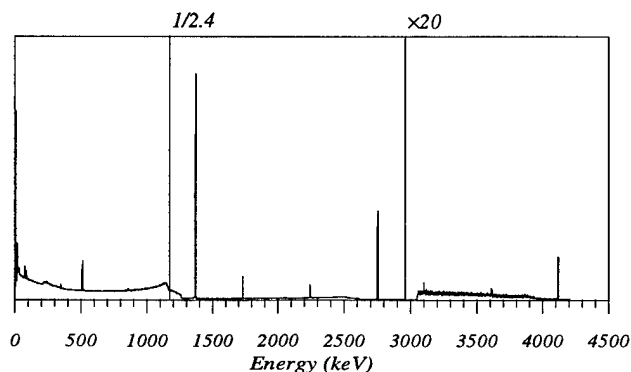


Figure 3 Spectrum of ²⁴Na

B. Optical System

The optical system design in this experiment is also shown in figure 2. The hole in mirror #2 permitted the Compton backscattered photons passing through to the HPGe

detector outside the shielding of the storage ring. This hole would, however, cause the loss of laser photons before their entrance into the vacuum chamber of the storage ring. The beam expander consisting of three ZnSe lenses was therefore designed to alleviate the laser loss on mirror #2. The two ZnSe lenses after the beam expander were thereby to focus the laser within the vacuum chamber, which would lessen the decrease in photon yield as a consequence of the expansion of the laser.

The beam expander could significantly lessen the laser loss; however, it also reduced the photon yield from Compton scattering. This defect was subsequently improved by the focal lenses. How were the magnifying power of the beam expander and the focal length supposed to be for a optimum photon yield? According to the previous study on this experiment^[4], the magnifying power of the beam expander was supposed to be five and the focal length was designed as 4.5m for a optimum photon yield.

C. Coincidence Measurement

The using of a pulsed CO₂ laser for the sake of its higher peak power made the scattered photons be produced periodically with the same frequency of the repetition rate of the CO₂ laser. The pulse width of CO₂ laser was 30ns and therefore the photons was produced within 60ns for each laser pulse. The repetition rate of CO₂ laser was, however, at most 200Hz, i.e., 5ms of period. This information indicated that the photons were produced within a time less than 1.2×10^{-3} % of the total counting time, e.g., for 3 hours total counting time, the photons were produced only about 0.1296 seconds. What the worse was that the directional background of Bremsstrahlung was considerably high in comparison with the backscattered photons. Subsequently, the coincidence measurement became very important. Figure 4 illustrates the concept of coincidence measurement. In this figure, the laser trigger output provided a gate signal which was first shaped and delayed through a logic shaper and delay (Canberra 2055 & Ortec 427A). The signals of the detector were shaped by the linear gate and stretcher (Canberra 1454) as well after passing through the preamplifier and the amplifier. The coincidence gate opened as the gate signal arrived so as to allow the detector's signals to pass through to multichannel analyzer(MCA). Figure 5 is the relative time representation for coincidence measurement and the labels (1) to (4) correspond to the labels in figure 4. In this figure, the time length L is the time delay for gate signal (2). The width of gate signal (2) was such that it covered the drift range of the detector's signal (4).

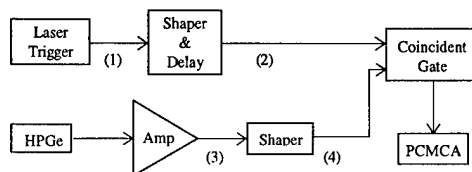


Figure 4 Coincidence measurement system schematic diagram

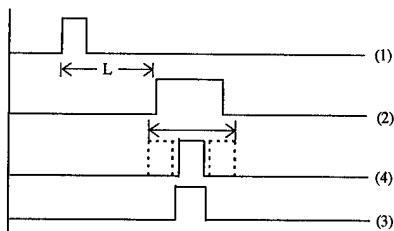


Figure 5 Time representation of coincidence measurement

4. EXPERIMENTAL RESULTS

In this experiment, the beam current of the storage ring of the SRRC was about 2mA to alleviate Bremsstrahlung radiation. Operating under multibunch mode of the storage ring, the number of electron bunches was 200 and the revolution frequency was 2.5MHz. The total counting time in acquiring the spectrum was about 3 hours. Figures 6 and 7 are the spectrum for both the background Bremsstrahlung radiation and the Compton backscattered photons. These figures illustrate the difference between the two kinds of spectrum (Bremsstrahlung and Compton scattering.) Figure 6 illustrates the spectrum obtained under the condition that the magnifying power of the beam expander of the optical system was three, the gate width was 1 μ s, and the collimator's diameter was 3cm; while figure 7 is for the case that the magnifying power was five, the gate width was 3 μ s, and the collimator's diameter was 1cm.

5. DISCUSSIONS

In the case of figure 6, the photon yield was about 9.08cps; while in the case of figure 7, the photon yield was about 10.63cps. This result corresponded to our expectation that the photon yield would be larger if the laser beam were bigger, i.e., less power loss on the halo mirror. Besides, the smaller collimator in figure 7 made the spectrum sharper in higher energy part, just as our previous conclusion under computer simulation.

The method of coincident measurement restricted only one signal passing through one gate opened. The restriction resulted from the 4 μ s shaping time of the amplifier. Since the gate width is less than 5 μ s, it was impossible for more than two signals passing through one gate. Hence our recent work is to enhance the signal counting method and to increase the photon yield.

6. ACKNOWLEDGMENTS

We'd like to thank Drs. Chuan-Jong Tung, Chu-Fang Wang, Lig-Ji Yuan, and Hsiu-Chin Wu of NTHU for their help by lending us their electronics instrumentation in the test stage of our experiment.

7. REFERENCE

[1] Rossmanith and R. Schmidt, Laser Diagnostics in High Energy Accelerators, DESY M-81/24 (1981)

[2] Yamazaki, et al., Generation of Quasimonochromatiz Photon Beams from Compton Back-scattered Laser Light at ETL Electron Storage Ring. *IEEE Trans. Nucl. Sci.* 32 (1985) 3406-3408
 [3] Arutyuanin and V. A. Tumanian, The Compton Effect on Relativistic Electrons and the Possibility of Obtaining High Energy Beams, *Phys. Lett.* 1 April (1963) 176-178
 [4] Ian Hsu, R. - S. Chen, C.- L. Cho, H.- C. Chen, and Y. - C. Liu, "Design study of Laser Compton Scattering with Relativistic Electron to Measure the Electron Beam Energy", *IEEE Particle Accelerator Conference Proceedings*, Vol. 3, (1993) 2151-2153.

* Supported by the National Science Council of R. O. C., Contract NSC81-0417-E-07-545 and SRRC, R. O. C..

Department of Physics, National Tsing-Hua University, Hsinchu, Taiwan 30043, R. O. C..

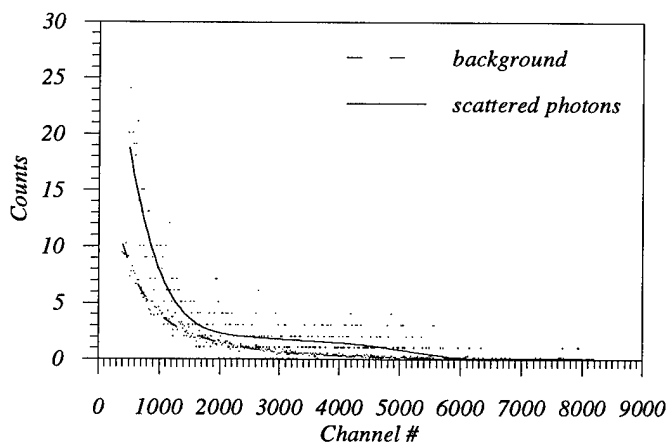


Figure 6 Spectrum with the magnifying power of the beam expander being three.

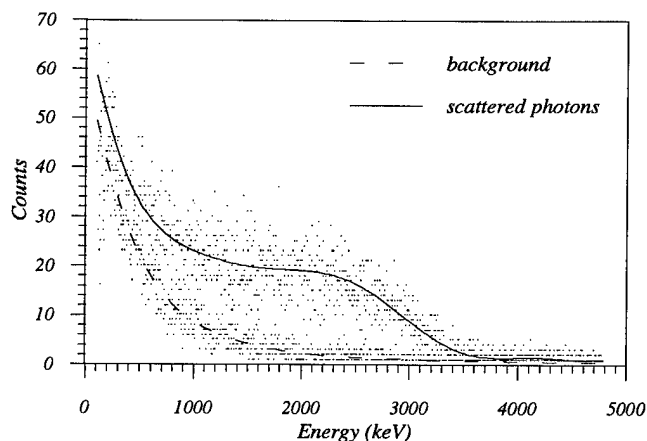


Figure 7 Spectrum with the magnifying power of the beam expander being five.

Tests of a High Resolution Beam Profile Monitor*

J. Norem, J. Dawson, W. Haberichter, R. Lam, L. Reed, X-F. Yang
HEP Division, Argonne National Laboratory, Argonne, IL, 60439, USA

J. Spencer

Stanford Linear Accelerator Center, Stanford University, Stanford, CA, 04309 USA

Abstract

High energy linear colliders require very small beams at the interaction point to produce high luminosities, and these beams must be measured and monitored. We have developed and tested a technique where the profile can be obtained from an extension of pinhole camera optics using thick, single sided collimators and slits. Very high resolutions (a few nm) should be possible. Gamma beams can be obtained from bremsstrahlung, Compton or beamstrahlung radiation. We describe tests of the technique using bremsstrahlung from an 800 MeV electron beam at Bates/MIT, Compton scattered photons from 47 GeV Final Focus Test Beam (FFTB) at SLAC, and other applications, such as linear colliders.

I. Introduction

The next generation of linear colliders will require very high precision diagnostics to be able to tune and maintain the small beams required for high luminosity operation. Present designs require beam spots with a vertical height of $\geq 2 - 4$ nm [1]. The smallest beam spots which have so far been produced and measured have had beam heights, $\sigma = 70$ nm [2].

The proposed system uses non-imaging gamma ray optics to measure the position, profile and width of an electron or positron beam, where the "profile" is the electron distribution folded with the interaction that produces the outgoing photons. Bremsstrahlung, Compton scattering and beamstrahlung from beam-beam collisions, introduce negligible divergence at high energies. The optics are essentially a "pinhole camera" with a single sided collimator and a slit, inclined at a slight angle to the single sided collimator, so a scan along the slit is equivalent to a scan through the penumbra of the first collimator [3].

II. Resolution

The resolution for monochromatic photons is approximately equal to

$$\delta = \sqrt{\lambda L / 2},$$

where λ is the wavelength of the photon, $\sim 10^{-16} - 10^{-17}$ m, and L is the distance between the source and the first collimator, which could be of the order 10 m in the NLC. This would give a measurement resolution of a few nm.

* Work supported by the US Department of Energy, Office of Nuclear and High Energy Physics, Contract W-31-109-ENG-38 and DE-AC03-76SF00515

Assuming targets convert $\sim 1\%$ of the beam energy, 10^{10} e⁻/bunch would yield 10^8 equivalent γ 's in a ~ 1 mm beam at 10 m, giving roughly 500 γ 's through a 5 nm slit. About 1000 photons would be detected, assuming a conversion efficiency of ~ 10 pairs/equivalent γ and 0.2 Cherenkov photons /pair.

III. Experimental Problems

We expect that the primary experimental problems in reaching resolutions in the nm range would be component alignment and backgrounds in the detector. Preliminary measurements using this system, with beams at MIT / Bates and the final focus test beam at the FFTB at SLAC, have demonstrated the system and produced experimental data on alignment techniques and a variety of different background mechanisms.

Operation of this system using 10 MW beams at the Next Linear Collider (NLC) will be complicated by target damage and/or collimator stability. Thin foil bremsstrahlung targets can be moved between beam bunches. Compton scattering from real photons is preferred because it would not require foils, and would provide a photon spectrum peaked at higher energies, giving better resolution. Beamstrahlung, from virtual photons in beam-beam collisions, also provides a useful spectrum as a by product of normal operation, however during tuneup, low intensity beams would produce weak fluxes of long wavelength γ 's. We note that all these processes are intimately related.

Collimators could be protected with absorbers upstream, however they would inevitably heat up and deform. We assume they could be mechanically and thermally isolated from their surroundings. Although useful measurements can be done with single bunches, the use of low expansion mounts should permit essentially continuous operation of this system at high power.

IV. Test Measurements

We tested some aspects of the system at the MIT / Bates 1 GeV electron linear accelerator using a 25 μ m beam defined by collimators and a prototype detector optics to measure the beam profile.

The geometry is shown in Fig. 1. Just before the beam dump, a thin window was used to produce a bremsstrahlung beam with a maximum energy equal to that of the beam, 799.1 MeV. This photon beam was then collimated using a pair of tungsten blocks ground flat on one face and separated by 25 μ m shims. Downstream, we assembled a system consisting

of a single sided collimator and a slit constructed with optically flat tungsten mirrors separated by shims, both remotely controlled by encodermotors with a minimum motion of about $0.1 \mu\text{m}$. These elements, which defined the beam, were followed by a detector which consisted of a pair converter (a 1.25 cm W plate), a Cherenkov radiator (10 cm air), a periscope and camera consisting of an image intensifier and a linear CCD. The collimators were surveyed in using a transit and levels and this alignment was then checked using the beam. In fact, the initial alignment was excellent, so that the first two data pulses straddled the beam centerline.

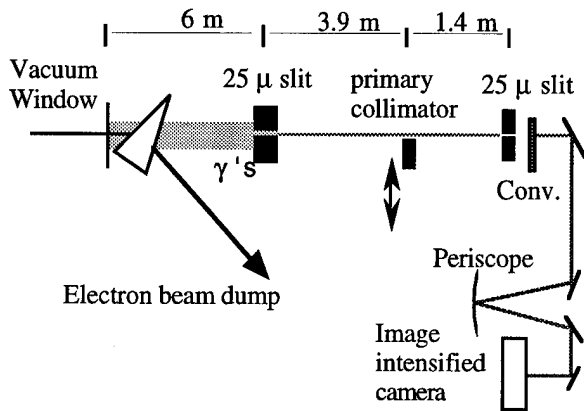


Figure 1. The experimental setup at Bates / MIT.

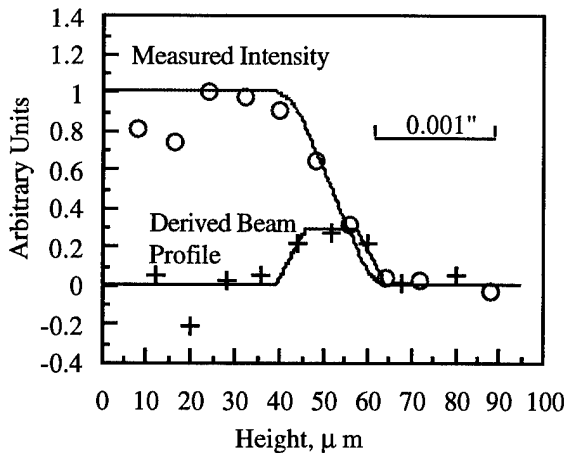


Figure 2. Measured beam profile.

A plot of the beam profile as measured by the system is shown in Fig. 2. As the beam intensity changed somewhat during the run, and we had no precise beam intensity monitor, we normalized the intensity of beam through the slit to the background, which seemed to be roughly proportional to the beam intensity. Since the limiting resolution in this application is $0.1 \mu\text{m}$, the measurements errors are determined by statistics. Profiles are obtained by differentiating the intensity as a function of collimator position. The magnitude of errors due to normalization of the beam intensity, and to statistical error in the signal is difficult to determine independently.

With the beam dumped at the first collimator, it was possible to look at "single" photons in the camera, and thus to normalize the camera sensitivity. Using the primary beam energy and intensity, a calculation of the fringe field of the dump magnet, the radiator thickness, slit widths, and pair conversion and Cherenkov efficiencies calculated by Monte Carlo, we were able to calculate the magnitude of the signal which should be seen in the detectors. The primary uncertainty in this calculation is the initial direction of the electron beam after the $\sim 1.2 \text{ mrad}$ deflection in the fringe field before the gamma converter, which is larger than the divergence of the photon beam from the radiator. We obtained good agreement between the calculated and measured rates.

Scans were also taken with the active stripe of the CCD camera oriented parallel and perpendicular to the detector slit, the latter orientation permitted measurement of the effective width of the Cherenkov source, as well as the distribution of background light. Scans were taken while moving the position the front collimator, and with the beam dumped at the front collimator and the final slit. Typical data are shown in Fig. 3., where the image intensifier was operated with a microchannel plate voltage of 1550 V , which gave about $1/10$ of the maximum gain possible gain. The observed width of a point Cherenkov source should be $\sim l\theta_C/2 = 0.8 \text{ mm}$, where l is the length of the Cherenkov radiator and θ_C is the Cherenkov angle. Both l and θ_C can be controlled by simple adjustments of the light collection optics.

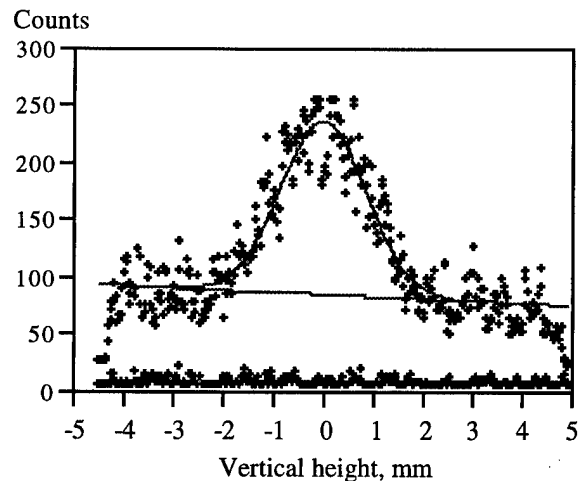


Figure 3. Vertical profile of Cherenkov Source.

V. Backgrounds

At the 800 MeV Bates linac, the primary background seemed to be due to Cherenkov light uncorrelated with the beam transmitted by the slit. Additional shielding around the first collimator and stopping the beam in front of the slit both reduced the background intensity. The source of this background thus seemed to be showers produced at the primary collimator and slit, creating secondaries which produced Cherenkov radiation in the periscope. Because of the geometry of the slit mounting and the volume of the sensitive region of

the periscope, (2 m long and 10 cm in diameter at the largest point), it was difficult to shield this background completely. Reductions of a factor of 10 were obtained however.

At SLAC, measurements will require thick targets in the beam and probably detectors inside the shielding of the FFTB. We have tested a prototype detector inside the shielding of the FFTB using 47 GeV electrons on 0.003" Al flags as target as well as laser Comptons. The image intensifier and CCD were shielded by about 0.05 - 0.10 m of Pb from the Collimator immediately below them that functioned as a beam dump for electrons that lost more than about 1/3 of their energy. Three components were seen: dark current in the CCD, pulses from the image intensifier that seemed to be in time with the photon beam, and photon like pulses that seemed to occur even with the image intensifier gated off. We assume that the last source of background is due to ionization in the structure of the image intensifier. Backgrounds were comparable to dark current with the CCD running at 20°C. With thicker targets, a 0.1 radiation length bremsstrahlung converter, for example, backgrounds would be larger.

VI. Possible Experiments

We hope to be able to measure the size, profile and stability of the Compton conversion spot for SLAC experiment E144 [4] on the FFTB using a system of collimators which will be inserted into the photon dump line downstream of the final focus. This apparatus should also be able to measure the final focus beam spot with a resolution of $\delta \sim 20$ nm.

In principle it should also be possible to use a streak camera to measure the time (or z) dependence of bunch parameters with resolution of perhaps ~ 0.1 ps [5]. Correlations could be studied on a bunch to bunch basis [3]. Comparing measurements made with the apparatus on-axis and off-axis, for example, it should be possible to look at chromatic effects at the final focus, since these would cause the different momenta to focus at different points, producing a larger effective beam width for off axis electrons. Seismic effects have been examined experimentally and should be correctable at the level of 1 - 3 nm [3].

Measurements of plasma focusing should also use this technique, which offers the possibility of time and space resolution comparable with the expected range of nonlinear plasma effects [6].

Since the resolution increases with increasing energy, this technique should also be useful for measurements at the NLC [7]. Bremsstrahlung, Compton scattering or beamstrahlung could be used to produce photons which would give high resolution, with diffraction width of about 5 nm. Assuming targets that convert as much as 5 - 10% of the the beam energy, as many as 20% of electrons produce a photon greater than 100 GeV for 500 GeV collisions, and 10% would have energies greater than 250 GeV for bremsstrahlung. Above 250 GeV, the beamstrahlung spectrum would give typically 2.5 %, and we would expect 25% for Compton scattering from laser

wavelengths selected to avoid pair production. Of all these processes, the latter two are the most practical, due to the difficulty of working with solid targets in highly constrained environments.

A significant complication at NLC energies is that beam power and beam brightness both increase with energy, producing very high power densities on all components, particularly the primary collimator. We should be able to begin to explore some aspects of high power densities on components in FFTB experiments.

It is also interesting to point out, on the 100th anniversary of Roentgen's discovery of X-rays [7], that this radiation was determined to be wavelike and electromagnetic by means of diffraction experiments which showed wavelengths on the order of 10^{-10} m. NLC collider data would involve photon wavelengths of $2 \cdot 10^{-18}$ m, many orders of magnitude shorter than any previous diffraction experiment. We believe it is also interesting to study diffraction phenomena at these wavelengths to verify well understood ideas at these small distances.

VII. Conclusions

This technique offers the possibility of very good spatial resolution at the SLAC / FFTB and NLC, with the added advantage of time resolution compatible with the best streak cameras. Measurements of a variety of correlations, such as chromatic effects, should be possible as well as experiments with plasma focusing. We have made preliminary measurements of beam profiles using non-imaging γ optics with resolutions of a few μm . We have also looked at alignment and backgrounds in realistic beam environments and isolated some sources of background signals.

VIII. Acknowledgements

We would like to thank L. Stinson and the staff of the Bates / MIT linac facility, who effectively built a new test beam facility, helped us set up and survey our equipment. We would also like to thank Mike Saleski and the staff of the Stanford Linear Accelerator Center who helped us install equipment in the Final Focus Test Beam.

IX. References

- [1] R. Palmer, *Annu. Rev. Nucl. Part. Sci.* 40, (1990), 529
- [2] CERN Courier, 34(7), (1994), 15
- [3] J. Norem, J. Dawson, W. Haberichter, R. Lam, L. Reed, X-F. Yang, J. Spencer, *Nucl. Instr. and Meth.* (to be published, 1995).
- [4] K. McDonald, A. Melissinos et al, private communication, 1991
- [5] Hamamatsu Corporation, Bridgewater NJ.
- [6] P. Chen and D. Cline et al. private communication 1993
- [7] J. Spencer et al., *The SLAC NLC Extraction and Diagnostic Line*, these proceedings.
- [8] W. C. Roentgen, *Nature*, 53, (1896), 274

AIRIX ALIGNMENT AND HIGH CURRENT BEAM DIAGNOSTICS

D. Villate, Ch. Bonnafond, A. Devin, E. Merle
Commissariat à l'Energie Atomique
Centre d'Etudes Scientifiques et Techniques d'Aquitaine
B.P.2
33114 LE BARP- FRANCE

II. ALIGNMENT

Abstract

The high performance required for the French Radiographic Hydrotest Facility is tightly connected to the quality of the electron beam. As part of the AIRIX program an Integrated Test Stand named PIVAIR is achieved at CESTA. Many tools have been developed to control and optimize the beam parameters. At first, we describe the alignment technique choosed for PIVAIR. Since AIRIX have essentially time dependant characteristics, all the beam diagnostics are time resolved. Emittance measurement which uses pepper-pot technique associated to a fast scintillator radiator and a gated camera, is described. Non destructive electric diagnostic of the beam position is discussed. We talk about beam profile recording from Cerenkov or Optical Transition Radiation (OTR) radiator. We bring up results of a high resolution energy spectrometer.

I. INTRODUCTION

In the AIRIX project a high current (3.5 kA) beam, generated by the PIVAIR injector at 4 MeV, is then accelerated up to 20 MeV by passing through the 64 cells of an Induction Accelerator. The high focus quality requires small emittance and low energy spread. Stability of the emittance along the accelerator needs in particular carefulness of the mechanical and magnetic alignment and a fine control of beam transport. The goal, to reduce chromatic effect, is to enclose all the magnetic axes of the cells in a 250 μm diameter cylinder with an angle spread lower than 500 μrad . For PIVAIR experiment, emittance measurement is done with pepper-pot technique. The results of this diagnostic, strongly disturbing, have to be analyzed carefully. Beam transport must be controled by non-destructive diagnostics. We use beam position monitor with B-loops to locate the centroid of charges. The objective, on PIVAIR experiment, is to analyze corkscrew, due to chromatic effect, and Beam-Break-Up generated by the accelerating gap in the cells. Radial charge density profile, which gives information about transport quality, is recorded using destructive diagnostic. The energy spread, second cause of chromatic aberrations, must be limited in the $\pm 1\%$ range. Results of the PIVAIR injector and of the first cells are presented.

The discrepancy between mechanical and magnetic axes in each cell is reduced by assembling technique of the different parts and the use of an homogenizer rings mechanically centred in the solenoid.

The aim of alignment procedure is to be able to control the mechanical stability of the accelerator beetween two experiments. In this case, beam axis can no more be used. We developed a prism technique described on the following picture:

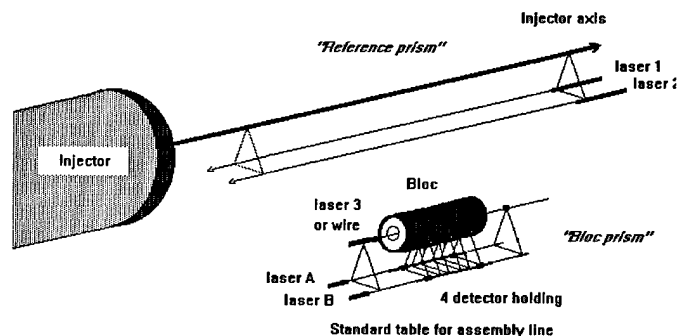


Figure 1: Alignment

Cells are put together on a standard table to be mechanically aligned using laser 3 of a three parallel laser system. The magnetic alignment may be controlled on this table with the stretched wire technique. The "Bloc prism" is defined using four laser (A & B) impacts on XY detector located under the first and fourth cell. The Bloc prism is aligned on "Reference prism" using laser 1 and 2 impacts.

We are currently studying a technique using Hydrostatic Leveling System [1] to control the stability of our reference prism system.

III. EMITTANCE

The emittance has been measured with the pepper-pot technique which was improved since reference [2]. The new CESTA system consists of a 3 mm thick tantalum plate with an array of 1 mm diameter holes and decreasing spacing in the periphery of the mask. The beam is intercepted by this mask and drifted 337 mm to a Bicron 422 scintillator. The beamlet image is recorded with a gated camera (with gating down to 5 ns). This recording gives XY information at a fixed time, during a pulse duration of 60 ns.

The emittance analysis is performed by two techniques. The first is performed by summing the image intensities in "y" and measuring the beamlet widths at 10% of the maximum beamlet intensity. The width is then used to draw a phase space diagram. The area of this diagram is proportional to the emittance defined by the relation.

$$\epsilon_{yx}(90\%) = \frac{\beta\gamma(\text{area. } x)}{\pi}$$

The second technique uses a parametric fit of the beamlets to a Gaussian finding the mean angle x'_c , and corrected angle x' . This fit is used to calculate the rms emittance using the following relations.

$$x^2 = \frac{\sum x_i^2 \sigma_i A_i}{\sum \sigma_i A_i}$$

$$x'^2 = \frac{\sum (x_{ci}'^2 + x_{ci}'^2) \sigma_i A_i}{\sum \sigma_i A_i}$$

$$xx' = \frac{\sum x_i x_{ci}'}{\sum \sigma_i A_i}$$

$$\epsilon_{rms} = 4\beta\gamma \sqrt{\langle x^2 \rangle \langle x'^2 \rangle - \langle xx' \rangle^2}$$

Where x is the hole position, x'_σ is the beamlet angular width, x'_c is the mean angle, $\sigma_i A_i$ is the weight of each beamlet.

The two analysis are quite different and give similar results only for ideal beam $\epsilon_{rms} = \epsilon_{n(100\%)}$. We made some experiments to evaluate error bars. Repetitivity from shot to shot gives only $\pm 2\%$ error. Numerical analysis gives about $\pm 2\%$ error. Correction for nonlinearity in camera recording is in progress. Space charge effect on the drifted beamlets is currently studied. Significant effects are due to pepper-pot mask. We have pointed out a changing of ϵ_{rms} versus mask material. At present, it seems that ϵ_{rms} increases when mask resistivity decreases.

Taking into account this remark, results on PIVAIR experiment are the followings:

PIVAIR	V (MV)	I (kA)	ϵ_{rms} (π .mm.mrad)
Injector	3.8	3.5	1600
Accelerated	4.6	3.5	1600

No emittance increase was measured after four PIVAIR cells.

IV.BEAM POSITION

A. Electrical Beam Position Monitor

Beam transport along the accelerator is controlled by Beam Position Monitor using four loops influenced by the B_θ

field generated by the beam. The object of our development is, in addition to guiding, to measure either corkscrew effect or Beam Break Up (B.B.U) effect. The aim is a range of operation of ± 5 mm round the accelerator axis, an accuracy of ± 0.1 mm and a sensitivity of ± 0.02 mm. The voltage pulse generated by each loop is proportional to the time derivative of current. Analysis of this signal depends on the effect. Beam positioning and corkscrew need only a 60 MHz bandwidth active integrator. At present the 8 bit resolution of the digitizing recorder limits to ± 0.2 mm the accuracy on the absolute position of the beam centroid. Higher accuracy will be reached using Tektronix SCD 1000 scope. B.B.U effect numerical analysis, which needs at least 1 GHz bandwidth, is done by FFT computing. In this case ± 0.02 mm sensitivity is reached.

B. Optical Beam Position Analyser

Transverse beam profile is recorded using Cerenkov or OTR radiators and a gated camera. Numerical analysis includes centroid research and RMS dimensions of the beam.

V. SPECTROMETER

Measurement of absolute energy and energy spread is done using a home made magnetic spectrometer. The principle is based on a 180° deviation obtained with the help of an electromagnet. The magnetic field is measured by a Nuclear Magnetic Resonance probe giving an absolute accuracy around 10^{-5} . Two sheets of 100 optical fibers fit out the analyzing plan. Cerenkov radiation generated by electrons going through each fiber is guided to a streak camera for time analysis.

Picture 2 shows the time evolution of energy at the end of PIVAIR injector recorded with the high resolution sheet ($\Delta E/E = 0.1\%$ over a 0.1 E energy range)

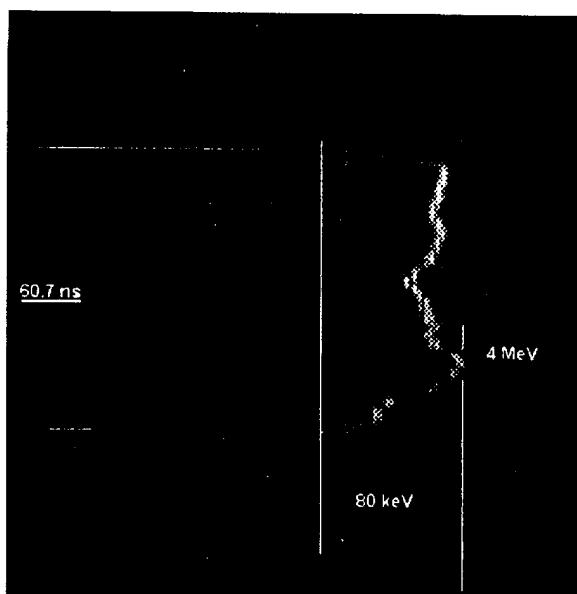


Figure 2 : Injector spectrum

The pictures 3 and 4 present measurements at the end of PIVAIR Accelerator. The second picture shows for comparison an other shoot recorded with the low resolution sheet ($\Delta E/E = 0.5\%$ over an energy range of 0.5 E).

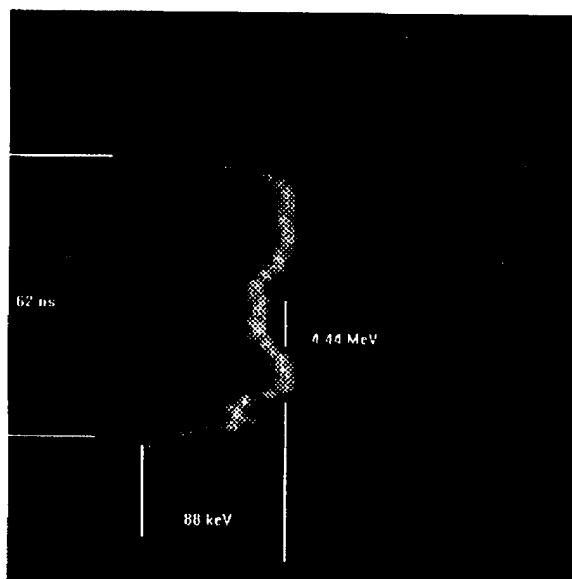


Figure 3 : High resolution at the end of four cells

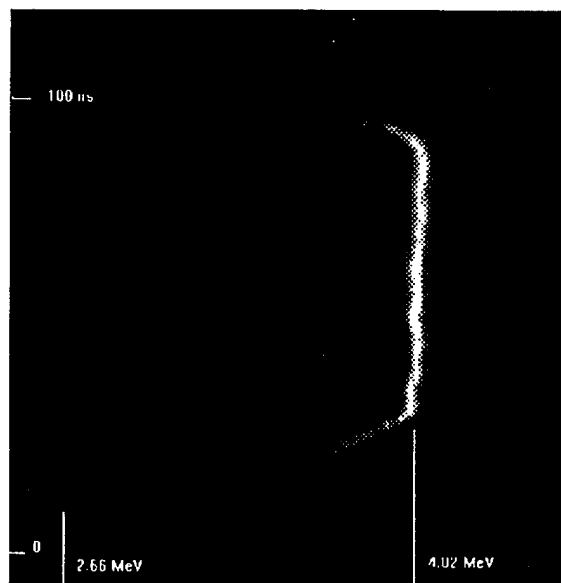


Figure 4 : Exemple of low resolution recording

VI CONCLUSIONS

These diagnostics appear directly connected with the development of the AIRIX program. They aim at analyzing some crucial parameters of the French Radiographic Hydrotest Facility.

VII REFERENCES

- [1] Hydrostatic Leveling System developed by ESRF France
- [2] Diagnostic development for high current electron accelerator at CESTA. J. de Mascureau & al Proceedings of 1993 IEEE Particle Accelerator Conference p 2115-2117

A New Beam Intensity Monitoring System with Wide Dynamic Range for the Holifield Radioactive Ion Beam Facility

M. J. Meigs, D. L. Haynes, C. M. Jones, and C. T. LeCroy
Oak Ridge National Laboratory*, P.O. Box 2008, Oak Ridge, TN 37831-6368 USA

I. ABSTRACT

A new beam intensity monitoring system with a wide dynamic range has been designed, fabricated and tested for use at the Holifield Radioactive Ion Beam Facility (HRIBF). Radioactive ion beams produced with this first generation facility will have intensities much lower than those of stable ions previously injected into the 25URC tandem accelerator and the existing beam current monitoring systems, which have a lower limit of approximately 100 pA, will not be adequate to tune the injection line or accelerator. This paper describes a new system which combines a Faraday cup and a continuous dynode electron multiplier (CDEM) to yield a dynamic range from a few particles per second to greater than a microampere. The CDEM can be biased to count either secondary electrons or Rutherford backscattered ions.

II. INTRODUCTION

The expected low intensities of radioactive ion beams require a new type of diagnostic for use as a tuning aid. Diagnostics presently available in the tandem accelerator and in the experimental beam lines are limited to Faraday cups, beam profile monitors and beam viewers. The logarithmic amplifiers used with the present Faraday cups have a lower limit of about 100 picoamperes while the beam profile monitors may be used with intensities a factor of ten lower. Various phosphors used with the beam viewers have problems with certain beam energies and with producing adequate light for typical cameras. Therefore, the concept for a new beam diagnostic system was developed. The essential design goals were: 1. One universal design to be used throughout the RIB injector, beam lines and tandem accelerator. 2. Primary use as a tuning aid rather than an absolute measure of beam intensity. 3. Beam current measurement range from a few particles per second to at least one microampere.

III. SYSTEM DESCRIPTION

The new diagnostic system uses a Faraday cup for currents greater than one picoampere. The present logarithmic amplifiers will be replaced with Keithley logarithmic amplifiers with a dynamic range of 10^{-12} to 10^{-4} amperes. Another feature of the new system is the ability to amplify the current reading by using the "bad" Faraday cup mode. In this mode, the polarity of the electron suppresser power supply is made positive so that secondary electrons are attracted to the suppresser and the Faraday cup current reading is amplified. The amount of amplification is dependent on the ion beam being measured (species and energy) and the backing material in the Faraday cup. Preliminary tests have used both Cu and Al as backing materials with the highest amplification being observed with Al. Beams of 50 and 300 keV ^{58}Ni and ^{16}O were used with the higher energies yielding the highest amplification. The lowest factor was 5.3 for 50 keV ^{16}O and the highest factor was 12.9 for 300 keV ^{58}Ni . These beams were negative ions, but ion beams of both polarities will be amplified using this method. For either polarity of beam, however, the Faraday cup current measured will be positive.

Beam currents less than one picoampere will be measured by counting either ions or secondary electrons with a CDEM. A metal target will be placed in the beam and the CDEM will count either electrons or Rutherford backscattered ions depending on the intensity of the beam. For ion beam currents less than 10^5 ions per second (16 femtoamperes), the CDEM will be configured so that it will count secondary electrons. The entrance bias in this configuration is a few hundred volts positive which will attract secondary electrons. The total bias for the CDEM is always positive and its value is kept the same in either mode. When the entrance bias is negative by a few hundred volts, electrons, but not Rutherford backscattered ions, are repelled from the entrance. This configuration allows counting in the range 10^4 to 10^7 (1.6 picoamperes) ions per second.

*Managed by Martin Marietta Energy Systems, Inc., under contract No. DE-AC05-84OR21400 with the U.S. Department of Energy.

The submitted manuscript has been authored by a contractor of the U.S. Government under contract No. DE-AC05-84OR21400. Accordingly, the U.S. Government retains a nonexclusive, royalty-free license to publish or reproduce the published form of this contribution, or allow others to do so, for U.S. Government purposes.

The combination of the CDEM in both modes and the Faraday cup allows measurement in the full range of interest for either stable ions or RIBs. Since the intent of these devices is as a tuning aid, exact calibrations for each ion will usually not be performed. The operator will be able to read a rate meter or Faraday cup current to determine the effect of tuning on beam intensity. Other devices will be used to determine the exact intensity of specific radioactive ions.

Figure 1 shows a capacitively coupled CDEM configured for pulse counting. This is the configuration wherever the CDEM is used. For those unfamiliar with CDEMs, a good general description is found in reference 1.

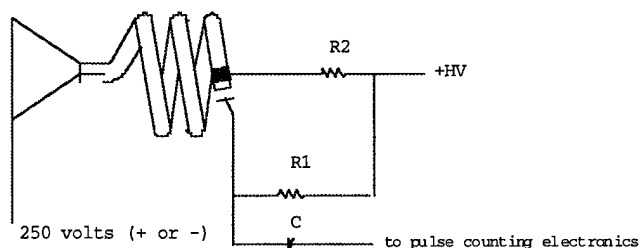


Figure 1. CDEM showing electrical connections for pulse counting.[1]

IV. PROTOTYPE TEST RESULTS

The system description given above provides for an entrance bias on the CDEM for counting either electrons or ions. It should be noted that the same effects can be achieved by biasing the metal target that the beam strikes. It is obvious, however, that the polarity of the target bias would be opposite from the entrance bias for each mode. Since biasing the target can be simpler, this configuration was used for the initial tests. Stable beams from the 25 URC Tandem accelerator injector were used for the tests. Both ^{58}Ni and ^{16}O beams, accelerated to 50 and 300 keV, were used. An example of a measurement of the CDEM count rate as a function of target bias is shown in figure 2. In this measurement, the CDEM bias voltage was maintained at 2500 volts and the intensity of the impinging beam was kept constant for this test. As can be seen, counting in the ion mode reduces the sensitivity of the detector by a factor of approximately 10^3 , which effectively allows an extension of the usable range for the CDEM. It is expected that the change in modes may be accomplished through the control system by operator choice.

The range for the ion-counting mode actually extends into the range for the Faraday cup which allows a calibration for the CDEM counts. Figure 3 shows the ion mode calibration for 300 keV ^{16}O . As can be seen, the count rate is a linear function of the beam intensity until the CDEM saturates.

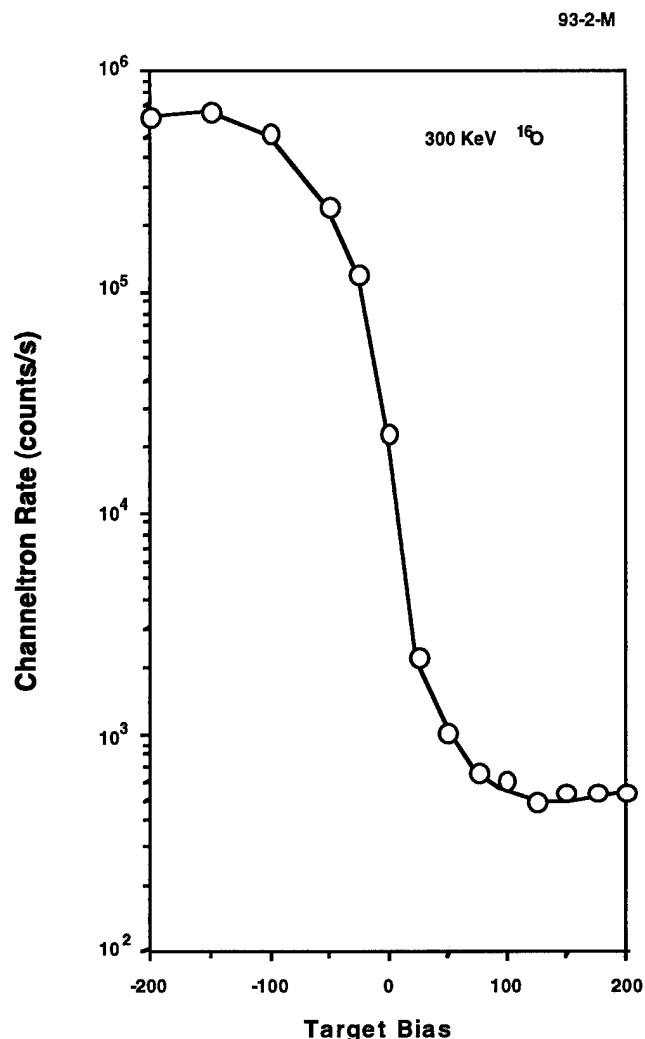


Figure 2. CDEM count rates versus target bias for constant beam.[2]

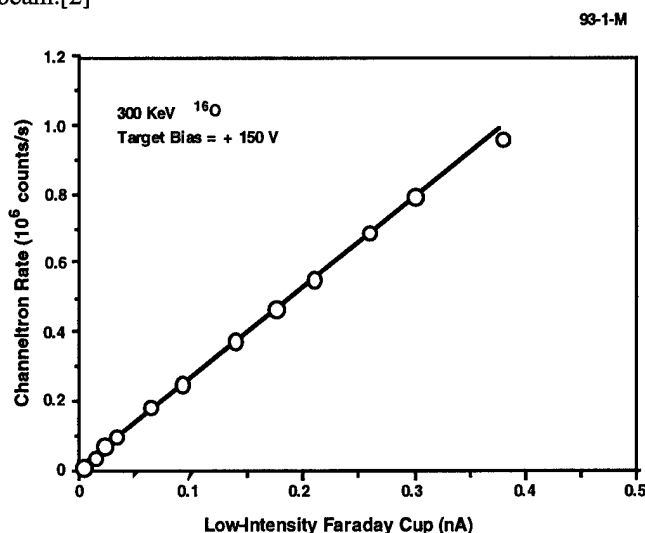


Figure 3. Ion mode calibration for 300 keV ^{16}O . [2]

The efficiency of the detector is dependent on several factors, including ion species, ion energy, and mechanical alignment. For the beam tests depicted in figures 2 and 3, the electron mode efficiency is 50%. That is for every count, an average of two ions have hit the target. In the ion-counting mode, the efficiency is 0.04%. Tests with different species, energies, and alignment show a variation in efficiency from a high of 79% down to a low of 22% for the electron-counting mode, while the ion-counting mode efficiencies range from 0.04% to 0.2%.

Later tests which used a grounded target and a bias on the entrance of the CDEM showed comparable results. The need to bias the entrance of the CDEM rather than the target arose from the requirement to measure radioactive beams. Many radioactive ions are beta emitters and as they are deposited on the target, the betas could confuse the measurement. Therefore a movable target, which is more difficult to bias, was necessary. A movable-belt target system was designed, fabricated, and tested. Figure 4 shows a simplified drawing of this system.

V. Summary and Conclusions

The combination of more sensitive Faraday cups and the CDEM system should allow tuning very low intensity radioactive ions from the RIB injector through the tandem accelerator and on to the user's target. Even though testing has only been done for low energy beams from the stable-ion injector, no significant problems are expected from ion beams at higher energies. A test at higher energies is planned before installation of the new diagnostics throughout the tandem accelerator system.

The new Faraday cup configurations have been installed on the RIB platform and the new stub beam line transporting beams off the platform. Low intensity assemblies for use inside the tandem accelerator will require modification to withstand the SF_6 gas pressure and to fit in the very limited space available. These assemblies will be designed, fabricated, and installed before accelerating RIBs through the tandem accelerator in August 1995.

VI. REFERENCES

- [1] Kurz, Edward A., "Channel Electron Multipliers", American Laboratory, March 1979.
- [2] Channeltron is a registered trademark of the Galileo Electro-Optics Corporation.

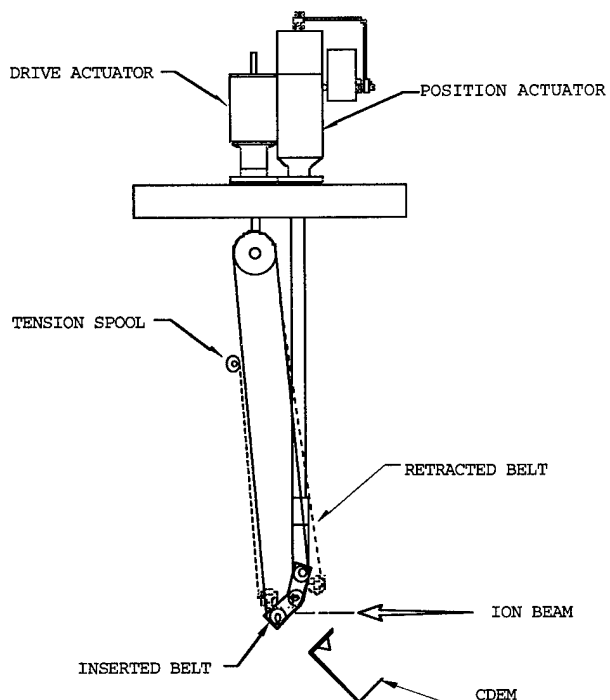


Figure 4. Simplified drawing of the moveable-belt target system.

DIAGNOSTIC BEAM PULSES FOR MONITORING THE SLC LINAC

F.-J. Decker, M. Stanek, H. Smith, F. Tian,
Stanford Linear Accelerator Center*, Stanford University, Stanford, CA 94309 USA

ABSTRACT

The Stanford Linear Collider is a pulsed machine with a repetition rate of 120 Hz. By using fast devices such as kickers and triggers, individual pulses can be modified, measured and diagnosed, and then dumped to avoid any background in the experiment. For more than five years, a diagnostic pulse has been used to kick the beams onto off-axis screens at the end of the linac every 6 seconds. This provides a visual monitor of the beam size and loses about 0.14 % of the rate or two minutes a day. The sensitivity of the linac optics to temperature and phase variations makes it desirable to monitor the phase advance between different locations in order to make local corrections. In principle, the feedback systems can measure the phase advance using the natural jitter of the beam. In practice, the phase jitter of the beam with respect to the rf may dominate the betatron jitter and distort the measurement. By using a large induced betatron oscillation, the two effects can be separated. To improve the monitoring of phase advance, a small kicker at the beginning of the linac is fired every few seconds and the orbit of this particular beam pulse measured and analyzed. The sensitivity, the measured variation and the correction scheme will be discussed.

I. INTRODUCTION

The lattice of the SLC linac can be studied by launching betatron oscillations and comparing the phase advance to the model. Since it takes explicit beam time this task is not done very frequently. This can cause bad setups for example back-phases klystrons, which lead to an oscillating feedback and therefore generate a second generation problem, instead of fixing the original problem. Two solutions are investigated, first to speed up the process, or to get a continuous measurement done by using a small fraction of the beam pulses to monitor the daily behavior. The later one will be discussed by describing the trigger setup, data taking and data analysis, which showed the variations of $\pm 60^\circ$ in betatron phase advance.

*Work supported by the Department of Energy, contract DE-AC03-76SF00515.

II. TRIGGER SETUP

During the last run every hour a kicker was activated in the RTL (ring-to-linac) section. It fired every 6 seconds and this pulse was readout by the linac BPMs. This was exactly one of the pulses which are anyway kick onto the off-axis screens in sector 30 at the end of the linac. The screen spots were disturbed since the beam was half lost on the nearby collimators. The average of 10 kicked and 10 non-kicked orbits was saved as a reference orbits. Since the software routine was put on top of an existing one, the wire macro loop, it wasn't always running. Fig. 1 shows a couple of typical difference orbits over a day.

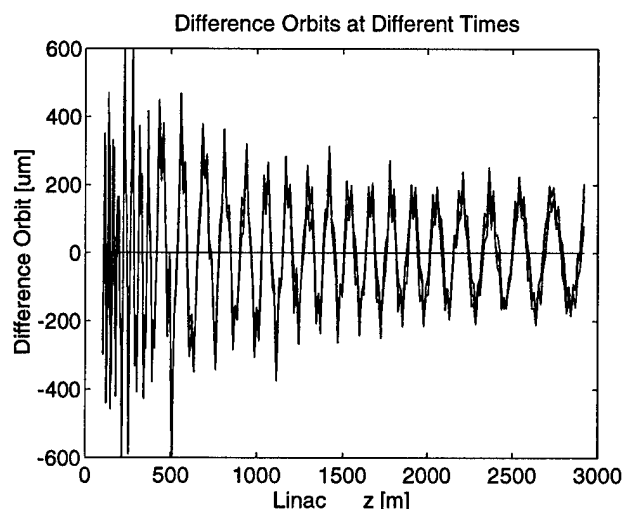


Fig. 1: Betatron oscillations at different times. The different orbits show phase advance changes over the course of a day. At the end the beam is partly lost at collimators and then kicked onto off-axis screens.

III. DATA READOUT

These reference orbits were read out with a small MATLAB program which generated all the differences orbits. By fitting small sections of this oscillation (15 BPMs) to a betatron oscillation, y and y' were generated locally.

The phase advance was calculated with the following formula:

$$\phi = \arctan2(\beta y' + \alpha y, y).$$

Plotting the phase advance versus the length z of the linac, can give some hints of the setup of the lattice and local problems. In Fig. 2 this plot is done for a period when a change in the linac setup from SLC to FFTB occurred. The changes were: Change from a split tune lattice back to SLC-design, less BNS phase offsets, and lower current, plus some not anticipated changes. There is a kink in the top curve (FFTB) near 200 m, which was later found to be the klystron 3-1 with 120° phase offset. The other kink in the middle of Sector 2 in the split tune lattice data is not yet understood.

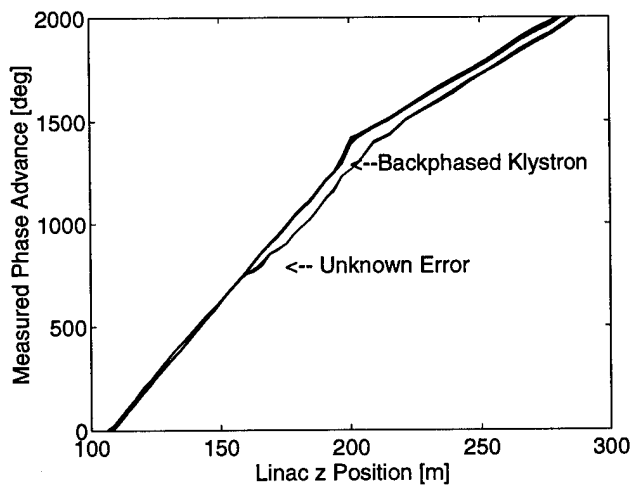


Fig. 2: Betatron phase advance.

The phase advance in the beginning of the linac shows a clear change for data before and after the switch to FFTB. The expected gradual change is overwhelmed by two distinct problems.

The mean phase advance of many days was subtracted and the different phase advance differences for one set up are plotted versus the linac location (Fig. 3). The biggest changes occur in the beginning of the linac. Near 400 m is a place with much less variation, which means that one error is canceling another one. The fast oscillations are coming from a mismatch compared to the average phase (see below).

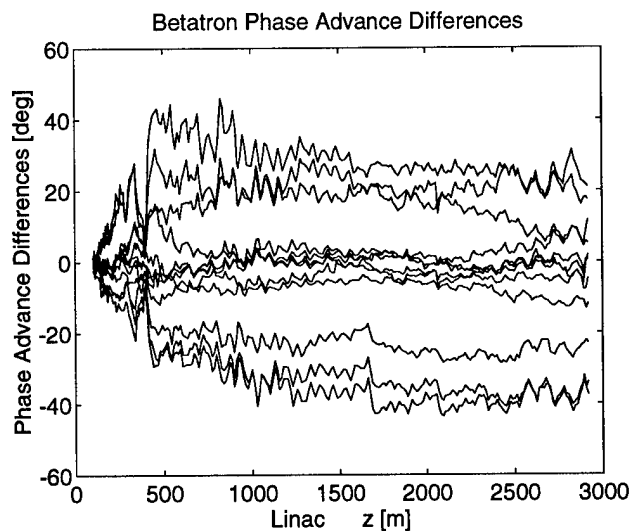


Fig. 3: Phase advance differences for different times. *The phase advance changes mainly in the beginning of the linac up to the first 1000 m, while it stays quite stable afterwards.*

IV. DATA ANALYSIS

A. Temperature variations

Besides looking carefully at the data to localize specific problem region, the data were analyzed for day-night variations. Therefore each BPM was plotted versus time and compared with the outside temperature. The correlation with the temperature can be achieved by calculating the temperature coefficient which is equivalent with the slope of data versus temperature. This method has the advantage that the change can be compared at different day with different temperature swings.

Initial trends of a big correlation in the beginning of the linac, couldn't be confirmed, due to less temperature variation which gave only a non-significant correlation. Later at the end of the FFTB run when the temperature changes were high there was also no correlation. But that time it could have been fixed by a new SLED tuning procedure [1].

B. Comparison to SLC-design lattice

A fixed phase advance from the model for the SLC-design lattice was taken and compared with the measured phase advance to for different time periods. The following observations are initially expected:

1. High current beam loading
 - a) more phase for strong BNS "damping"
 - b) flat for auto-phasing
 - c) less phase for weak BNS
2. Split tune lattice: less phase for e^-
3. good agreement for low current (FFTB).

Figure 4 shows the phase advance difference to the SLC design. The deviations from the expected behavior could come from localized errors. Another fact is that the BNS phase is given to the energy management package, which then lowers the magnet strength a for stronger BNS. This has the effect that the head of the bunch is higher in energy and therefore has a slower phase advance.

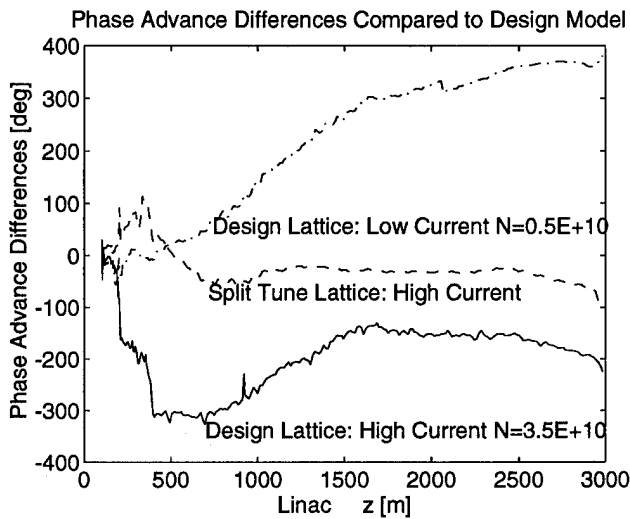


Fig. 4: Three phase advance differences to SLC design. The measurement shows: About 360° change over the length of the linac for FFTB, two big changes in Sector transition 200 m and 400 m where the quadrupole spacing changes by a factor of two for high current design lattice case, and some positive phase for the split tune case.

C. Measurement resolution

The phase differences for ten orbits in a short time span will give the resolution in phase for this method. It is about 5° rms in phase advance over half an hour. Taking the difference of only two phase advances shows some oscillatory behavior in the phase advance, which is an indication of the a mismatch, with different, faster and slower, phase progress than a match case (see Fig. 5).

V. CORRECTION SCHEMES

The first order correction which is envisioned is over the operators. Therefore the off-line code has to get on-line,

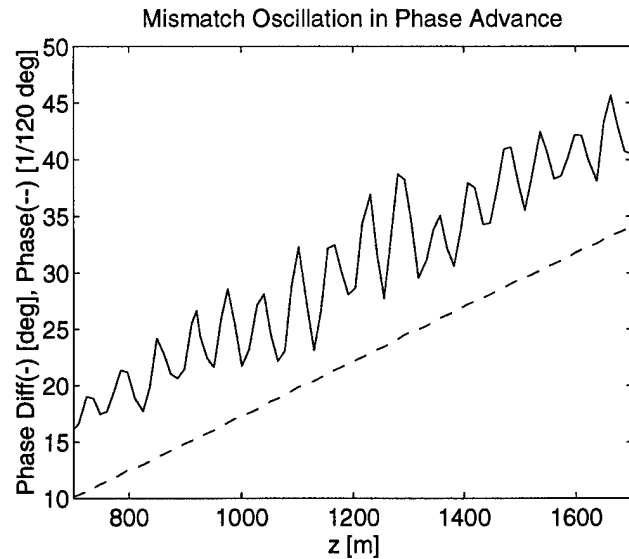


Fig. 5: Phase and phase advance difference.

In the second quarter of the linac the phase advance difference (solid) of two beam pulses shows a $\pm 5^\circ$ oscillation. The 16 oscillations occur during 8 ($=24^\circ \cdot 120/360^\circ$) betatron wave length (dashed) and indicate a mismatch.

that a single phase advance can be compared to a reference phase advance, saved or design (like the reference orbits now). The next step would be to "steer" (adjust) the quadrupoles to that reference, which would be local, comparable to the existing global energy management (LEM). Further steps might be the use of the phase information for steering feedbacks or even the automation of the above procedure via a local LEM feedback.

VI. CONCLUSION

The phase advance difference, measured with diagnostic pulse, is a precise tool to detect any changes or deviations of the order of $\pm 5^\circ$ in betatron phase. The non-invasive character of the diagnostic pulse makes it possible to get that information during the normal colliding beam run. The off-line data processing has to get on-line for the next run.

VII. REFERENCES

- [1] F.-J. Decker et al., *Effects of Temperature Variation on the SLC Linac RF System*, PAC95, Dallas, May 1995.

OBSERVATION OF THERMAL EFFECTS ON THE LEP WIRE SCANNERS

J. Camas, C. Fischer, J.J. Gras, R. Jung, J. Koopman
CERN, European Organisation for Nuclear Research
CH 1211 Geneva 23, Switzerland

Abstract

A new wire scanner was installed in LEP for the 1994 run. It incorporates an improved mechanical design for the wire movement and can accept three mechanisms, two for horizontal and one for vertical scans. Wires of different materials and of various diameters were fixed to new ceramic forks. Viewing ports were installed opposite each wire to allow the direct observation of the wires with a TV camera during a scan. Recordings of the wire resistance and of the light emitted by the wire were made during scans. These observations have provided the first experimental evidence of the various wire heating mechanisms by the beams. The heating due to coupling to the electro-magnetic field generated by the beam exceeds the heating due to particle collisions. An evaluation is made on the behaviour of Carbon and Quartz wires. Conclusions are drawn for defining a safe operating regime.

I. INTRODUCTION

Wire destruction has always been a major concern with wire scanners, particularly with instruments installed on circular lepton machines like LEP, where heating of the wire by the RF fields generated by the short lepton bunches adds to the energy deposited locally by the intercepted particles. In the case of LEP, the RF heating is in fact the major cause of wire destruction. Several studies have been made since the LEP start-up, the latest with direct observation of the wire with a TV camera, in order to better understand the wire heating process so that the beam current limit for safe operation of the instrument could be increased. This is important as the wire scanners are the absolute calibration device for the synchrotron light instruments used continuously in operation [1].

II. HARDWARE EVOLUTION AND STATUS

The original problems and the evolution of the LEP wire scanners are described in Ref. [2,3]. The original forks were part of a common design for LEP and SPS. Similar set-ups in the SPS [4] operate with beams of up to 1.6×10^{13} p, well above the LEP nominal intensity of 6 mA, i.e. 3.3×10^{12} leptons. The vacuum tanks supporting the mechanisms were designed to achieve as low an impedance as possible. The calculated longitudinal loss factor of the tank is equal to 0.1V/pC, of which 0.03V/pC come from the horizontal wire parking cavity. For the originally designed wire scanner a temperature rise of 1420° was estimated from energy deposition in the Carbon fibre at a current of 6 mA [5]. A

refined estimate considering density effects within the wire material brought this down to 1050°. In the first full year of operation, wires were destroyed at much lower currents. On one occasion, the Carbon wire was replaced by a 50 μ m Beryllium wire, which was analysed after its destruction [2]. The analysis showed that the wire had melted towards the extremities, far from the beam impact, at a beam current well below the nominal one. RF energy deposition was suspected and wire resistance measurements were initiated to estimate the average wire temperature increase during a scan. These scans confirmed the RF heating hypothesis, demonstrating the dominance of magnetic coupling to the wire when far from the beam and of electric field coupling when approaching the beam, well before the wire encounters a significant amount of leptons [2]. Two levels of constant temperature were measured when far from the beam, see Fig.1. From the parking position to about 15 mm from the beam, a temperature of 520°/mA was recorded. After the beam traversal, when the beam passed through the loop comprising of the fork and the wire, a second level of 1000°/mA was estimated.

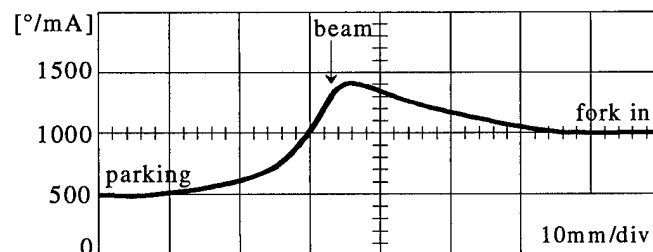


Fig. 1: Wire Temperature evolution during a scan with the original tank and fork set-up at a wire speed of 0.2 m/s.

These levels were thought to result from magnetic coupling of the fork/wire loop to the wakefield in the tank for the first case, and to the magnetic field generated by the beam for the other case. This coupling was strongly reduced by modifying the fork construction by breaking a parasitic loop [3]: see "old#2" fork in Table 1. Temperature levels of 230°/mA and 530°/mA were then measured. The parking temperature was even reduced to 80°/mA for the vertical wires which were better shielded against RF fields. The temperature peak in Fig. 1 corresponds to coupling to the beam electric field and depends on the wire length and on the RF spectrum of the bunch. These hypotheses agreed with observations made where the wire temperature changed at constant current when the bunch length was changed [3]. The beam current limit could then be increased to circulating beams of 3 mA at a wire speed of 0.5 m/s. After analysis, it

was concluded that the current limit could only be further increased by redesigning the vacuum tank to lower the loss factor and the supporting fork to break any remaining current loop and by choosing the wire length below wavelengths present in the beam spectrum. Isolating materials which prevent RF currents from heating the wire were also considered. A new vacuum tank having the elliptical shape of the adjacent chambers and with small parking cavities was designed. Its loss factor is 0.04 V/pC per horizontal parking cavity. Two horizontal and one vertical wire ports were fitted to the tank. They provided the possibility to make scans along three directions (by using inclined wires) and to test various wire materials. Also incorporated were viewing ports to observe the wires with TV cameras: Fig 2.

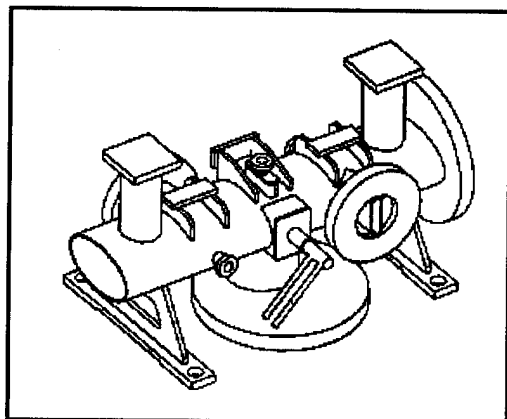


Fig. 2: CAD view of the New Wire Scanner Vacuum Tank: small viewing ports can be seen at the left and top, and flanges for the wire mechanisms at the bottom and right.

The forks were redesigned and made entirely of ceramics, with the possibility to stretch three wires spaced by 6 mm across the aperture: Fig. 3. Carbon wires of 8 and 36 μm and Quartz wires of 33 μm were installed and tested.

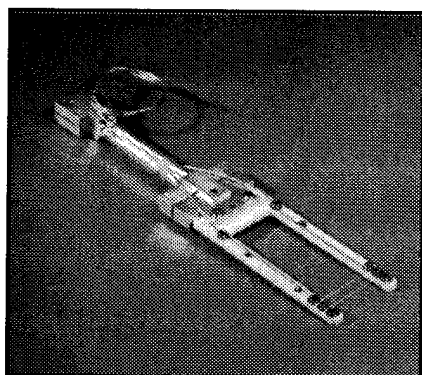


Fig. 3: The new ceramic fork with three wires.

III. TEMPERATURE MEASUREMENT

The temperature is estimated from resistance variations. The Carbon wire is put in the feedback loop of an operational amplifier tuned for zero output with no beam.

This amplifier output is acquired during the scans together with the beam profile measured by a scintillator and the wire position measured with a high precision optical ruler [2]. The results are displayed in real time and saved. The live TV signal is observed during a scan and connected to a video recorder for off-line digitisation. The wire resistivity variation with temperature was estimated. Measurements in an oil bath at low temperature and with a pyrometer at high temperature have been performed. The results are plotted in Fig. 4. Both show a similar negative temperature coefficient. Absolute measurements are difficult, but estimations of temperature variations should be satisfactory up to 1800°C.

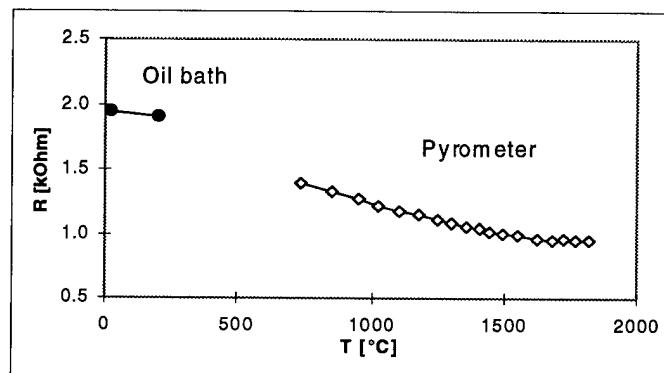


Fig 4: Measured wire resistance variations with temperature.

IV. RESULTS

The temperature measurements during a scan, using the same beam, with old and new tanks and forks, short and long wires show the improvements achieved: Table 1.

Table 1: Normalised average temperature increase of wires

Location	Tank	Fork	Wire length	$\Delta T_{\text{park.}}$	ΔT_{max}
139/ V e ⁻	old	old#2	56mm	80°/mA	620°/mA
140/ H e ⁻	old	old#2	56 mm	200°/mA	640°/mA
160/ H e ⁺	old	old#2	29 mm	30°/mA	520°/mA
161/ V e ⁺	new	new	3 of 29 mm	20°/mA	500°/mA

As a consequence of the new design, the wire heating in the parking position is now negligible and the maximum temperature reached during a scan has decreased confirming the heating by coupling to the electro-magnetic fields. Recordings show again a temperature increase well before reaching the beam and a slow decrease after the traversal. When the wire crosses the beam, the slope of the temperature curve is only slightly changed, indicating that the global temperature increase due to the beam-wire collision is small (Fig. 5). This is consistent with the expected temperature rise for collision losses of 175°/mA, see Section II, on the wire portion hit by the beam (1 mm or 2 mm for the H or V scans) and the induced average resistance variation of the full wire length (29 mm or 56 mm). The latter is very small (in the ratio of the respective lengths when assuming no conduction)

and is much lower than the observed temperature increase when the wire passes inside the beam distribution.

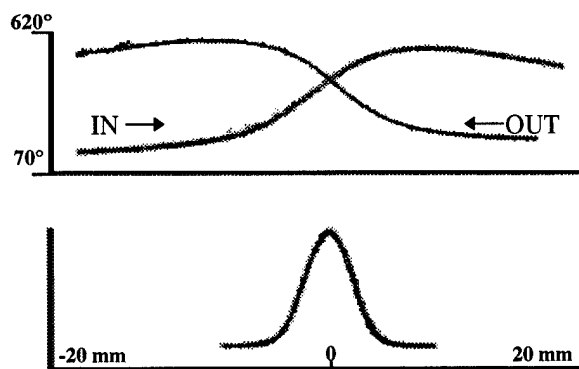


Fig. 5: Resistance/Temperature curves and beam profiles during a full IN and OUT horizontal scan of a 1.2 mA beam.

The video scans confirm the RF heating of the wire. Whatever the position, except perhaps when passing through the beam where the CCD camera saturates, the extremities of the wire are the hottest: Fig 6. The wire average temperature as estimated from the resistance measurement underestimates the peak temperature by more than a factor of two. Similar temperature profiles are obtained by simulations when considering the wire as a dipole in the RF fields generated by the beam along its direction. They confirm also that the long 56 mm wire will heat up more than the shorter 29 mm wire. This dipole type temperature profile is globally helping the wire survival as it has a minimum at the centre where the wire is heated by the collision with the beam. These observations were made primarily with the fork holding three wires: two carbon wires of 8 and 36 μm , and a quartz wire of 33 μm . The 8 μm carbon wire broke at a current of about 1.5 mA and the 36 μm one at 4.3 mA, well above previous limits. The average maximum wire temperature during the scan was in this case about 1750°. The Quartz wire survived these currents despite its lower melting temperature and is still in use. No light emission during scans has so far been seen from either of the Quartz wires.

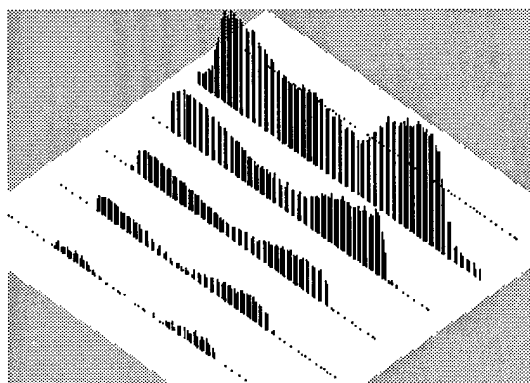


Fig 6: Light emission profile from the 36 μm Carbon wire when approaching a LEP beam of 1.67 mA total intensity. The profiles are taken every 20ms at a wire speed of 0.5 m/s.

V. CONCLUSION

Integrated wire resistance measurements and the observation of light emission from the scanning wires confirm that the major mechanism for wire destruction in lepton storage rings is by RF fields. These fields act on the full wire length far away from the encounter of beam and wire. The induced temperature increase is more than twice that of the estimated heating from beam energy deposition in the central part of the wire. The acceptable current limits are hence reduced for conducting materials like Carbon, and are even lower for Beryllium. These phenomena impose design constraints which can be summarised as follows:

- vacuum tanks with as low loss factors as possible
- wire parking locations connected to the beam pipe with sufficient attenuation for the beam RF spectrum
- wires as short as possible, with a length preferably below the two sigma limit of the bunch wavelength spectrum
- wire supporting forks which effectively break any loop passing through the wire for the magnetic field coupling.

The latest design lowered the integrated temperature increase during a scan to 500°/mA, with wire ends more than a factor of two hotter than the centre. This sets the maximum current limit at 3.7 mA, with a safe current level at 2 mA. Wires made of isolating material, here Quartz, have given the best results for maximum beam current. More experience has to be accumulated to assess their susceptibility to the strong electrical fields generated by high intensity beams, but they withstood scans of beams of more than 4 mA, i.e. more than twice the safe threshold value for Carbon fibres.

Monitoring the thermal behaviour of the wires through resistance measurement and direct video observation has been extremely helpful.

VI. ACKNOWLEDGEMENTS

The new tank was designed by C. Menot and manufactured by the CERN workshops. The loss factors were calculated by P. Valentin. G. Ferioli, J. Mann and J. Provost helped with the resistance and video measurements and J.M. Vouillot with the illustrations.

Their contributions are greatly acknowledged.

VII. REFERENCES

- [1] P. Castro et al.: Comparative precision emittance measurements in LEP, Proc. of EPAC 94, London, 1994
- [2] B. Bouchet et al.: Wire scanners at LEP, Proc. of the 1991 IEEE Acc. Conf., San Francisco, 1991
- [3] J. Camas et al.: High resolution measurements of lepton transverse distributions with the LEP wire scanners, Proc. of the 1993 IEEE Acc. Conf., Washington D.C., 1993
- [4] A. Burns et al.: Wire scanner news from the CERN-SPS, Proc. of the 1989 IEEE Acc. Conf., Chicago, 1989
- [5] C. Fischer et al.: Studies of fast wire scanners for LEP, proc. of the 1988 EPAC, Rome, 1988

CEBAF BEAM LOSS ACCOUNTING

R. Ursic, K. Mahoney, C. Hovater, A. Hutton and C. Sinclair

Continuous Electron Beam Accelerator Facility, 12000 Jefferson Ave. Newport News, VA 23606

Abstract

This paper describes the design and implementation of a beam loss accounting system for the CEBAF electron accelerator. This system samples the beam current throughout the beam path and measures the beam current accurately. Personnel Safety and Machine Protection systems use this system to turn off the beam when hazardous beam losses occur.

INTRODUCTION

In the CEBAF accelerator, superconducting cavities operating at 1497 MHz accelerate electrons to 4 GeV energy in five passes. The nominal beam current is 200 μA in Continuous Wave (CW) mode, with an approximate beam size of 100 μm . An errant beam can produce hazardous amount of radiation in areas where personnel may be present. This is the domain of the Personnel Safety System (PSS). An errant beam with such high power density can also damage the machine components considerably. This is the domain of the Machine Protection System (MPS). In the past, Beam Loss Monitors (BLMs) based on photo-multipliers detected radiation due to beam loss. However, the calibration and auditing of these detectors were prohibitively time consuming. This, along with the need to accurately measure the beam current, necessitated the development of the Beam Loss Accounting (BLA) system. The BLA system measures the beam current using low Q, TM_{010} stainless steel cavities. Two major advantages of the system are the ease of auditability by means of a calibration signal and the need for only a small amount of valuable beam time for verification. Though the PSS and MPS contain systems in addition to the BLA system, this paper concentrates on the BLA aspects only.

PSS AND MPS FUNCTIONS

Personnel Safety System

The PSS protects people from exposure to prompt beam-induced radiation [1]. During normal operations, the PSS issues an active permission signal, which is a 625 kHz square wave. When a fault occurs, the PSS withdraws the permission, causing the removal of the beam at the electron gun. Figure 1 shows the location of the Beam Current Monitors (BCMs) assigned to the PSS. These BCMs serve the following functions:

1. Beam stoppers near the entrance to the experimental halls protect personnel from the beam during access to the experimental areas. When the stoppers are in place, de-energized magnets prevent the beam from going in their direction. Should this safety feature fail, it is conceivable that a beam of high power density may tunnel through the stoppers. The BCMs (EA, A1 and C1) protect the stoppers by causing the termination of the beam when they detect a beam current greater than 1 μA .

2. CEBAF's contractual requirement imposes an operational limit on the beam current. The BCM (I2) ensures that the beam current in the injector does not exceed 190 μA . In addition, the beam dumps in the experimental halls have their own limits on beam current. For halls A and C, these limits are the same as for the injector. For hall B, this limit is 1 μA . BCM (B1) provides this protection.

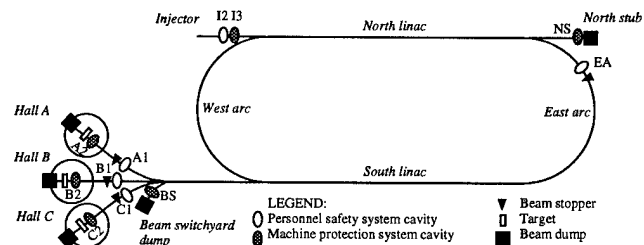


Figure 1: BCM cavities location along the CEBAF beamline.

Machine Protection System

The MPS protects the accelerator and end station equipment from beam related damage. During normal operations, the MPS issues an active permission signal, which is a 5 MHz square wave. When a fault occurs, the MPS withdraws the permission, causing the removal of the beam. Figure 1 shows the locations of the BCMs for machine protection. The BLA system performs the following functions.

1. The BLA system limits the beam current in the injector to 180 μA . This ensures that the MPS will trip before the PSS in all cases.

2. If $i(I3)$, $i(NS)$, ..., represent the beam current values in BCMs at I3, NS, ..., the BLA system calculates the beam loss by computing $i(I3) - i(NS) - i(BS) - i(A2) - i(B2) - i(C2)$. If this value exceeds 2.5 μA , the system will terminate the beam.

3. In case of an instantaneous beam loss, the BLA system will terminate the beam such that the integrated beam loss does not exceed 25000 $\mu\text{A} \cdot \mu\text{s}$. [2,3].

BEAM LOSS ACCOUNTING

Design Criteria

The PSS and the MPS functions described above, though different in some details, have many common features. It is economical both in time and money, to extract and modularize the common functions of the two systems. Thus, the two systems will primarily consist of the same types of devices, with obvious advantages regarding maintainability and testability. A trade off is a small increase in system fragmentation, resulting in increased interconnections.

Each module in the system has a supervisory circuit to ensure safe operation. Upon detecting an error in its operation, a module will generate a fault signal. This fault signal prevents beam from leaving the injector. The system as a whole will have self-test capability and in case of failure, the ability to identify failed modules.

The Cavity

The BCM is a simple pill box cavity, exciting the TM_{010} mode at 1497 MHz. Constructed of stainless steel in order to minimize drifts due to temperature, its Q_0 is approximately 3000 and the geometric shunt impedance is 180 Ω . A stub tuner, mounted on a micrometer, facilitates the frequency adjustment of the cavity. The cavity is available with two or three couplers, depending on the application (figure 2a). The tuning of the cavity is such that its loaded Q is the same in the two coupler configurations. The two coupler cavities are used for the MPS, the three coupler cavities are used in the PSS to provide redundancy.

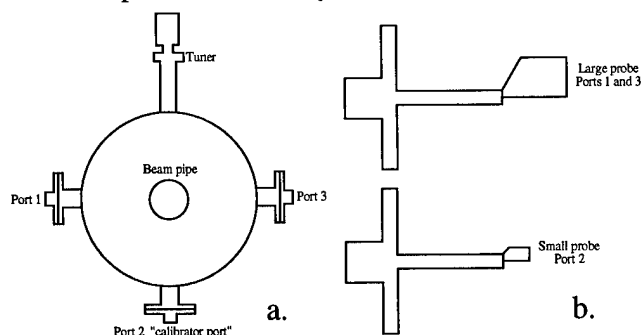


Figure 2: a. The CEBAF beam current monitor pill box cavity, three port configuration. b. Two styles of couplers.

Magnetic field loops situated around the cavity (where magnetic field is the largest), accomplish the coupling in and out of the cavity. The loops, (couplers), mount on 2.75" rotatable conflat flanges and proper coupling is achieved by adjusting the flanges. The couplers are of two styles: a large area loop and a small area loop (figure 2b). The large area loop couples the outgoing beam signal and the small area loop couples the incoming test signal. A cavity with two

couplers has one large area loop and one small area loop. A cavity with three couplers has two large area loops and one small area loop. For a cavity with two couplers, the large area loop couples critically to the cavity. For a cavity with three couplers, each large area loop slightly undercouples to the cavity, in order that their sum couples critically. For all cavities, the small area coupler undercouples to the cavity by 14 dB. As a result, the test source has sufficient isolation and does not disturb the resonance frequency.

Standard Electronic Modules

The 'standard' electronic modules are the down converter, a test source, RMS to DC converter, an equalizer and an integrator. Figure 3 shows the 'standard' configuration.

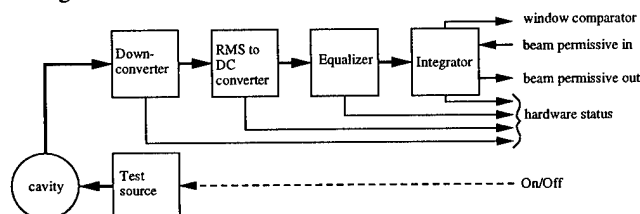


Figure 3: Standard modules and their configuration.

The Down converter shifts the 1497 MHz spectral component of the cavities to 1 MHz. There is a separate down converter for each dynamic range in current: one for 0-10 μA (for use by BCMs of the PSS at the beam stoppers) and one for 0-200 μA . The down converters and the 1497 MHz test source reside close to the cavity in the accelerator tunnel. Such proximity minimizes cable attenuation drifts due to temperature variation. Low loss 10m long 0.5" Heliax cables connect the cavity to the down converter and the test source. The same type of cable connects the down converter to the electronics in the service buildings.

An RMS to DC converter converts the bandpass filtered 1 MHz signal to a baseband signal. This module uses the AD637 RMS to DC converter IC [4], which has excellent linearity and temperature stability.

An equalizer module compensates differences in cable losses. The output of the equalizer scales with the beam current.

All the above modules, except the equalizer, are calibratable in the laboratory and interchangeable with the same type in the field. The equalizer is specific to each BCM and its calibration is *in situ*. However, two identically calibrated equalizers exist for each BCM; the second one acting as a quickly available spare should the first one fail.

The integrator monitors the average beam current or beam loss. When the beam current or beam loss exceeds a preset threshold, the integrator withdraws the permissions.

All modules conform to 3U eurocard standard. The interconnection among modules is through the back plane. Blindmate snap on RF connectors carry the 1497 MHz

signals, while 96-pin DIN connectors carry the baseband and digital signals. Keyed connectors on the modules and the backplane prevent insertion of the modules in the wrong place.

Implementation of the BLA system in PSS

The BLA system for the PSS consists of 4 cavities at the beam stoppers and 1 cavity in the injector. Each cavity has three couplers. The small area coupler connects to the test source. Each large area coupler connects to a downconverter. The reason for two large area couplers is that the PSS requires redundant logic paths and thus two identical electronic systems. Figure 4 shows the PSS logic. The PSS permission from the electronics associated with the BCMs at EA, A1, B1 and C1 go to the injector. At the injector, these permission pass through logic associated with the BCM I2. The latter limit the beam current to 190 μA . For the stopper BCMs two modes of operation exist; one with beam stopper in place and the other without the stopper. For a given mode, faults occur if the beam current in any stopper BCM exceeds 1 μA when the beam stopper is in place. Occurrence of a fault results in the PSS permission going inactive and consequently in the removal of the beam.

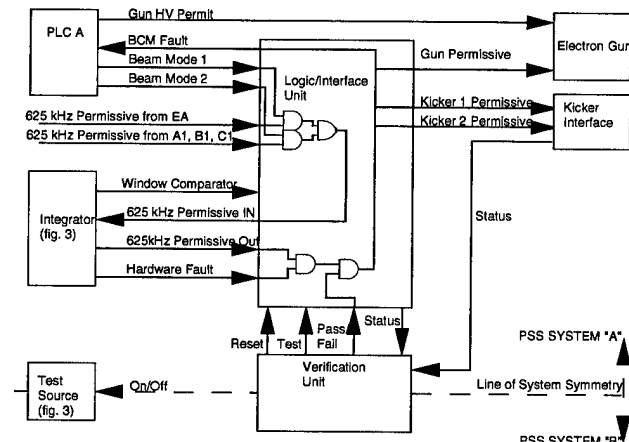


Figure 4: PSS BCM implementation block diagram.

The BLA system for the PSS also contains a verification unit, which is a time sequencing state machine. Through the control system interface to the verification unit, the operators can test the BLA system and remotely reset any BCM.

Implementation of the BLA system in MPS

The BLA system for MPS consists of 6 cavities. Each cavity has two couplers. The small area coupler connects to the test source and the large area coupler connects to a down converter. Cables carry the signals from the down converters to the beam switch yard service building (figure 5). RMS to DC converters process the signals. The MPS implementation requires a slight modification to the standard configuration of figure 3. This modification results in a comparator board that consists of 6 equalizers and a

circuit that calculates the difference between the injector signal and the sum of the other 5 BCM signals. The comparator board has two outputs, each of which goes to an integrator. One output is for the case that the beam current in the injector exceeds 180 μA . The other is for the case that the average beam loss exceeds 2.5 μA or the instantaneous beam loss (above 2.5 μA) exceeds 5000 $\mu\text{A}\cdot\mu\text{s}$. Both outputs force the integrators to withdraw MPS permissions.

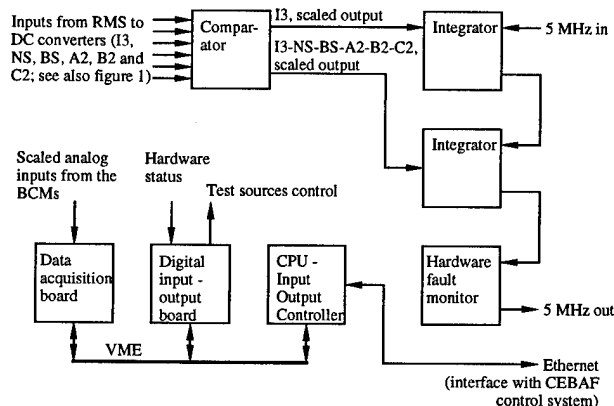


Figure 5: MPS BCM implementation block diagram.

The control system interface to the BLA system of the MPS, permits the operators to initiate and control the self-test sequence, monitor the beam current and hardware status.

CONCLUSION

The BLA system fully conforms to the requirements of both the PSS and the MPS, providing personnel safety and machine protection. Additionally, it will provide an accurate measurement of beam current. A prototype MPS system will be in place during May '95 and the final system will be in place during September '95.

ACKNOWLEDGMENTS

J. Mammoser and D. Ouimette gave valuable technical input during the review phase of the project. K. Jordan developed a detector/integrator module that permitted machine operation during the development of this system. T. Grummel and W. Woodworth provided technical support. H. Areti helped to shape the message flow of this paper.

REFERENCES

- [1] A. Hutton et al., "Beam Current Monitors for Personnel Safety and Machine Protection" Rev. 1/10/95
- [2] C. Sinclair, "Time Response Requirements for the BLM/FSD System", CEBAF-TN-92-046
- [3] C. Sinclair, "Beam Loss Monitor Performance Requirements", CEBAF-TN-94-024
- [4] "AD637 High Precision, Wideband RMS-to-DC Converter", Analog Devices

NANOMETER RESOLUTION BPM USING DAMPED SLOT RESONATOR*

S.C. Hartman

Stanford Linear Accelerator Center, Stanford University, Stanford, CA 94309 USA

T. Shintake and, N. Akasaka

KEK, National Laboratory for High Energy Physics, 1-1 Oho, Tsukuba-shi, Ibaraki 305 JAPAN

A new type of high resolution beam position monitor called the damped slot resonator rf BPM has been installed at the focal point of the FFTB[1]. It is comprised of a cylindrical resonant cavity with a tuned choke joint at the TM_{110} resonance[2]. The BPM has a large dynamic range from the nm to mm range with a minimum resolution of 1 nm. We report on the rf cavity cold tests performance, processing electronics design, and some experimental results obtained in the high energy electron beam line.

I. INTRODUCTION

Precise beam position measurement and control are two of the many important issues in developing technologies for a future linear collider in the TeV region. Typical final focus spot sizes at the interaction point of a few 100 nm horizontally and a few nm vertically pose a considerable challenge for those hoping to sustain collisions on this small scale. Nanometer resolution of the beam position will be

required, a most promising candidate for this application is the rf BPM.

In particular the damped slot resonator design has been chosen to measure the transverse beam position with nanometer resolution in the final focus system of the FFTB.

II. BPM RF CAVITY

The choice of the cavity frequency was dictated by the available space at the FFTB focal point where the real estate is in high demand. X-band is too high and the beam pipe becomes too small, whereas S-band has the opposite problem. The cavity diameter would not fit into the existing vacuum chamber so as a compromise C-band was chosen for the operating frequency.

Technically the most difficult problem is to reject the unwanted noise signal from the beam especially the TM_{010} common mode signal. The common mode is the lowest order TM mode which has a large position independent signal and can be as much as six orders of magnitude larger than the TM_{110} position signal. A rejection gain of 88 dB is necessary in order to be able to sense the position sensitive signal. A damped slot resonator is employed which accomplishes this common mode rejection. The cavity effectively has only a TM_{110} mode.

As can be seen from figure 1, the damped slot resonator is not like a conventional rf cavity. It appears more like a gap in the beam pipe which forms a transmission line on which the beam wakes may propagate radially away from the axis. A choke joint is placed $\lambda_{TM_{110}}/4$ off axis such that the TM_{110} mode is trapped. The structures large slot at the node point of the wall current of the TM_{110} mode, causes most of all the lower and higher order modes to be heavily damped.

Therefore, the pick up antenna are located inside the choke joint where they are only sensitive to the TM_{110} signal whose

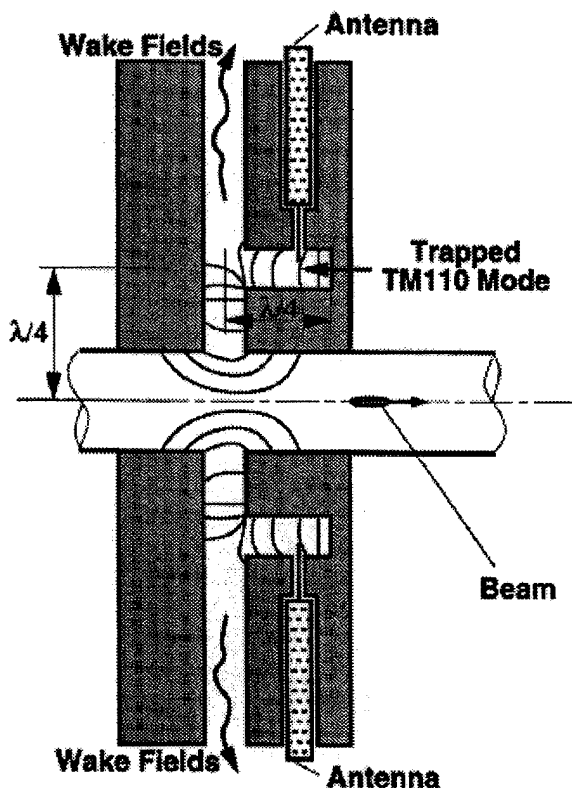


Figure 1. Damped Slot Resonator BPM.

* Work Supported by the Department of Energy, contract DE-AC03-76SF00515

Frequency	5712 MHz
Wavelength	52.5 mm
Cavity Radius	32.0 mm
Slot Radius	15.8 mm
Beam Pipe Radius	5 mm
Slot Height	5 mm
Transit Time Factor	0.99
(R/Q)	12.2 Ω
Shunt Impedance	1.2k Ω/m
Voltage into 50 ohms/nm	14.5 μV @ 1.6 nC

Table 1 BPM Cavity Parameters.

amplitude is proportional to the beam offset from the axis. Table 1. gives the calculated rf cavity parameters and expected performance.

III. RF COLD TEST

The first step in the cold test tuning procedure entailed detuning the common mode by -88 dB. This was accomplished through careful adjustment of the two coupling antenna which are mounted on micro positioners. It was also necessary to add a phase shifter and a variable attenuator to one of the antenna lines to fully cancel the common mode signal which is insensitive to the electron beam offset. Because there is a small amount of leakage of the common mode into the choke joint where the pickup antenna are located it is necessary to pass the two signals through a magic tee looking at the difference signal.

The electron beam was simulated by placing an antenna near the axis of the rf BPM cavity. A network analyzer was used in a transmission through experiment, S_{12} , were the power was radiated from the on axis drive antenna and the difference signal was measured after the magic tee. Due to the low power output of the network analyzer a resonant antenna was used to boost the signal strength by 15 dB. The antenna was mounted on a computer controlled piezo-electric crystal moving stage which was stepped in 20 nm increments for a total of 1 mm. The resulting cavity signal versus antenna offset data was fit to a line which was then subtracted from the data to yield a 20 nm resolution on the cold test bench. The resolution was limited by the low signal power and also the micro seismic mechanical vibrations in the antenna supports. The raw data for the rf cavity signal versus the piezo mover position is plotted in Figure 2. below.

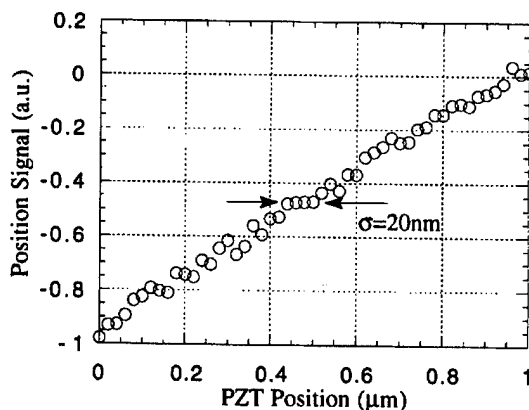


Figure 2. BPM Cavity Response Vs. Piezo Mover Position.

IV. SIGNAL PROCESSING CIRCUIT

The rf detection circuit is shown in figure 3. The rf cavity signal is amplified using a low noise, $NF=0.8\text{dB}$, and high gain, 28 dB, amplifier at 5712 MHz. A remotely controlled variable attenuator, 0-64 dB, is placed at the output of the magic tee to increase the dynamic range of the system and a limiter is placed before the high frequency amplifier for off axis pulse surge protection to the rf circuit. The beam can

be misteered if a sub booster trips off and the beam loses a large amount of energy. The limiter that was used did an excellent job since the beam was misteered by 1mm and the limiter protected the sensitive preamp. After the pre-amp the signal is then mixed down to 500 MHz for transmission out of the FFTB experimental tunnel. This done to avoid large losses and rf pickup noise while transporting a high frequency signal along some 300' plus of cable.

The front end rf processor, the 5712 MHz end, is placed as close to the rf cavity as possible inside the shielding tunnel. Once the cavity signal and the phase reference signal are down converted to 500 MHz they are transported to an external electronics building where the BPM signal is rectified in synchronous detection mixers using the phase reference signal. The signal is then fed into a standard FFTB like NT&H[3] track and hold circuit where it is digitized by a 16 bit digitizer and sent to the SLC control system.

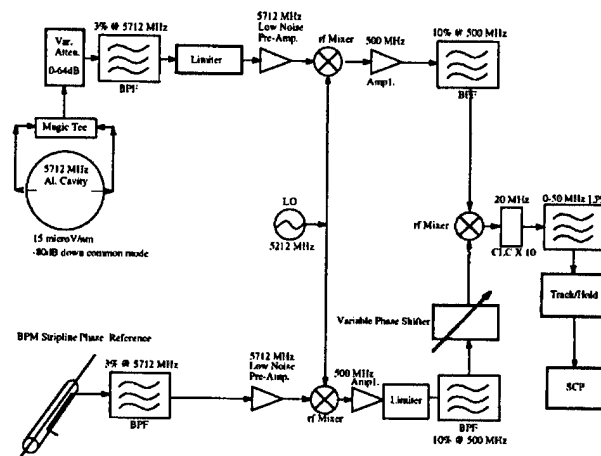


Figure 3 Rf Processing Electronics Block Diagram

The design shows a stripline which is to be used as the phase reference. The stripline is the preferable method of obtaining a phase reference because a 3% bandpass filter at 5712 MHz can be applied to its' broad band spectrum to select the desired phase reference frequency. This gives excellent FM or phase stability referred to the beam. Since the current in the SLC can be measured to less than 1% the induced AM fluctuation can be removed.

The BPM's read back is also sent into a feedback loop which controls a dither coil upstream of the focal point to correct for low frequency < 2 Hz position jitter. However due to the briefness of the FFTB run the loop was not fully commissioned and there is no data available for its performance at this time. It is interesting to note that all of the rf hardware used in the detection circuit is commercially available off the shelf.

Due to experimental difficulties during run time it was necessary to use a different phase reference source other than the stripline. The SLC main linac rf phase reference line operates at 476 MHz so it was necessary to frequency upshift by a factor of 12 to obtain the required phase reference signal. This amplifies any FM or phase jitter noise in the 476MHz signal which adds noise to the BPM signal.

V. EXPERIMENTAL RESULTS

The electron beam intensity throughout the run was kept at 0.7×10^{10} or 1.2 nC in order to have a very low emittance beam, $\gamma\epsilon_y = 2 \times 10^{-6} \text{ m-rad}$, measured at the entrance to the FFTB. The beta function at the focal point is set to, $\beta_y^* = 100 \mu\text{m}$. In order to place the waist longitudinally at the BPM an upstream quadrupole's vertical position is scanned versus the BPM signal. The quadrupole is located at a betatron phase such that when the waist is at the BPM position no correlation is seen. This is repeated for different waist positions until the waist is moved to the BPM longitudinal center. This turns out to be an excellent way to calibrate the waist shift knobs since we know the exact distance from the fringe pattern to the BPM to be 6.5 cm.

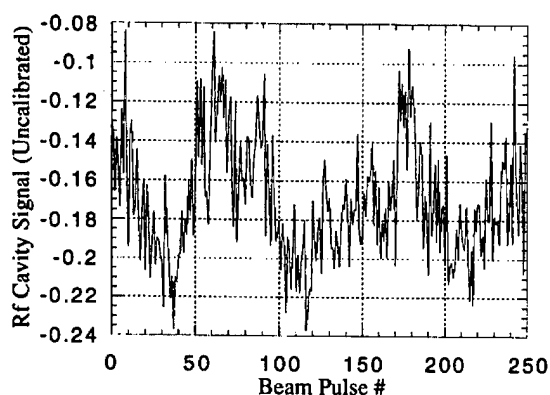


Figure 4. Typical BPM Signal versus Pulse to Pulse

Figure 4 shows a typical position signal read back from the rf BPM when the SLC is running at 30 Hz. One can see the few Hz low frequency jitter of the beam along with a very noisy high frequency component of noise. This noise comes from the FM and AM noise on the phase reference signal and will be corrected for the future FFTB runs by using a stripline BPM as a phase reference source.

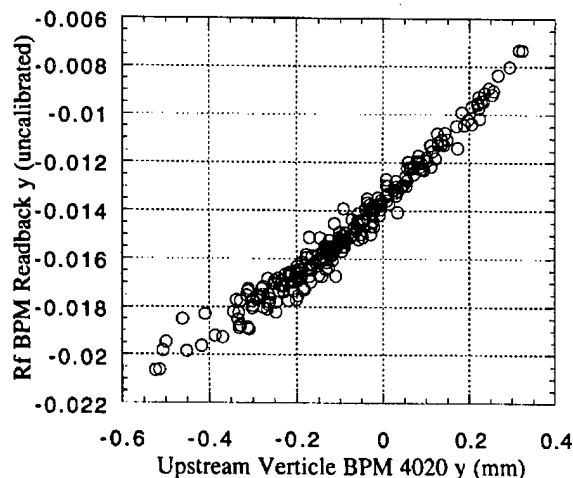


Figure 5. Correlation of rf BPM Vs an upstream Stripline

This will eliminate any FM noise and the AM noise can be normalized out of the signal by using a charge measurement good to less than 1%. Figure 5. shows a typical correlation with an upstream BPM in the FFTB line. Correlations are seen with BPMs as far away as sector 2 in the SLC. Figure 6. shows a calibration scan which is carried out by moving the centroid of the electron beam vertically a known amount at the focal point fitting the result to a line and extracting the scale factor. In the plot below the vertical axis has already been scaled. The plot shows that the BPM "signal" was mis-aligned by 0.6 mm. Note that this does not represent the actual electron beam position only the electrical signals zero point.

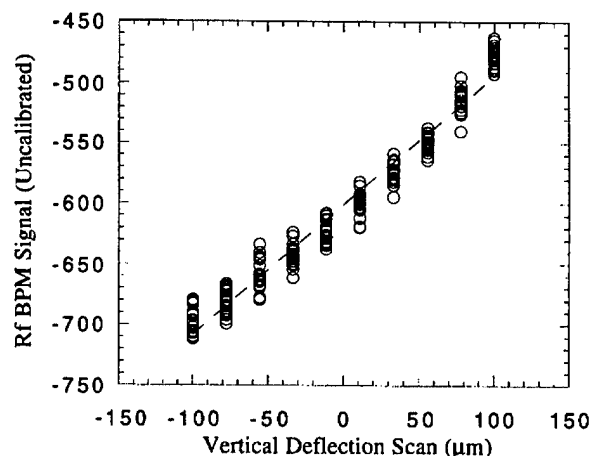


Figure 6. Calibration of Rf BPM Signal

The rf BPM cavity, processing electronics, and data acquisition system have been commissioned. The AM/ FM noise in the phase reference signal produces a large apparent jitter which can be corrected by using a stripline phase reference signal in the next experimental run. The large 0.6 mm offset in the BPM signal will be corrected for the next run via alignment and also by placing the BPM cavity on a vertical mover.

VII. ACKNOWLEDGMENTS

The authors would like to thank P. Corredoura, H. Swartz, G. Dalit, D. Burke, H. Hayano, M. Ross, S. Smith, D. Walz, K. Bouldin, C. Field, P. Tenenbaum, T. Gromme, L. Hendrickson, and S. Cleary.

VIII. REFERENCES

- [1] FFTB Collaboration, "Focusing of Submicron Beams for TeV-Scale e^+e^- Linear Colliders" *Physical Review* **74**,13, 2479-82, (1995)
- [2] T. Shintake "The Choke Mode Cavity", *Jpn. J. Appl. Phys.* Vol. 31 (1992) pp. L1576-L1570 Part 2, No. 11A, 1 Nov. 1992
- [3] H. Hayano *et al*, "High Resolution BPM for FFTB." *Nucl. Inst. Methods* A320:47-52 (1992).

An Automatic Tune-measurement system for the CELSIUS ring.

T. LOFNES

The Svedberg Laboratory, Uppsala, Sweden

Abstract

In CELSIUS [1] the tunes are up till now measured by FFT-analysing the response, at a beam position monitor, of a transverse kick of the beam. This FFT has to be performed over a wide frequency range and requires a high sampling frequency, and thus a large number of samples. By mixing-down the frequency range of interest, with a signal equal to the RF-frequency multiplied by the expected tune, and measure the deviation from the expected tune-value, the FFT can be made with a smaller number of samples and in the same frequency range independently of the RF-frequency. This way the FFT will be calculated faster by the computer, making it possible to measure the Q-values with a higher repetition rate. The set-up of this system and the results will be reported.

1. INTRODUCTION

In CELSIUS the Q-values are presently calculated in approx. 15 seconds. This is done with an FFT, in a digital oscilloscope, that is broadband (0 - 50 MHz) and has a rather high frequency resolution (2kHz / point) For this a sampling frequency of 100 MHz is needed together with 50 k of samples. To decrease the calculation time the number of samples has to be reduced. One way of doing this, without decreasing the frequency resolution, is to mix down the frequency range that contains the betatron sideband to a range close to 0 Hz. This can be done (see Figure 1) by mixing the signal from the pick-up with a frequency equal to $f_{rev} * q_{exp}$, where f_{rev} is the revolution frequency, q is the fractional part of the tune Q and q_{exp} is the expected value of q , and measure the deviation of q from q_{exp} .

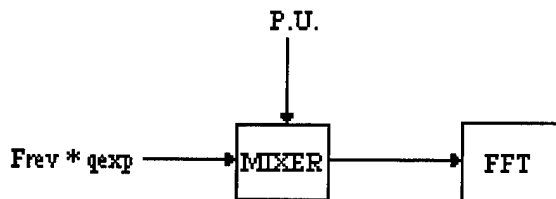


Figure 1

This mixed signal can be analysed by a FFT with a lower sampling frequency (<1MHz) and with less samples (<1000). If f_d is the frequency of this signal the Q-value will be:

$$Q = q_{exp} - f_d / f_{rev} + N$$

where N is the integer part of Q.

With the same oscilloscope the FFT calculation time now will be less than 0.3 seconds.

2. HARDWARE

For each tune-measurement the beam is excited by a magnetic kicker. The resulting oscillation of the beam is measured by an electrostatic beam position monitor. The signal from this pick-up is amplified and low pass filtered and sent to an Image Rejection Mixer together with a signal of frequency $f = f_{rev} * q_{exp} - 50 \text{ kHz}$, which is formed in a Direct Digital Synthesizer (see Figure 2). 50 kHz is subtracted in order to match the 0 - 100 kHz range of the mixer.

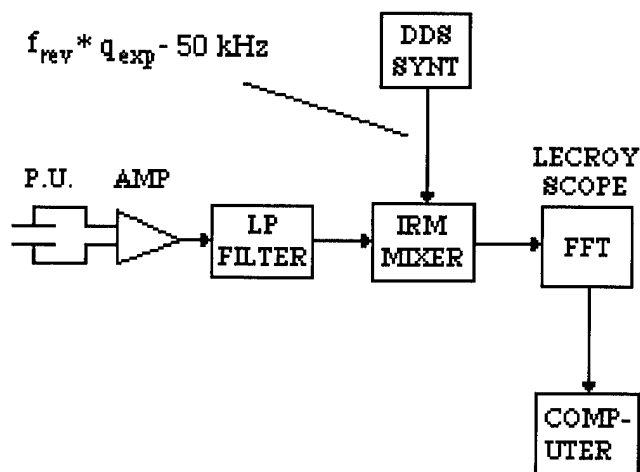


Figure 2. Hardware for the tune measurement system.

The sampling and the FFT calculation of the mixed signal is done by a LeCroy digital oscilloscope and the peak frequency in the FFT spectrum in each measurement is sent to the control computer for tune calculation and automatic correction.

3. RESULTS

Figure 3 and Figure 4 compares broadband FFT with FFT of the downmixed signal.



Figure 3. FFT of a broadband signal from the position monitor. Upper trace: pick-up signal, 10 μ s/div. Lower trace: FFT of upper trace (RF-frequency and 3 betatron sidebands are shown), 100 kHz/div.

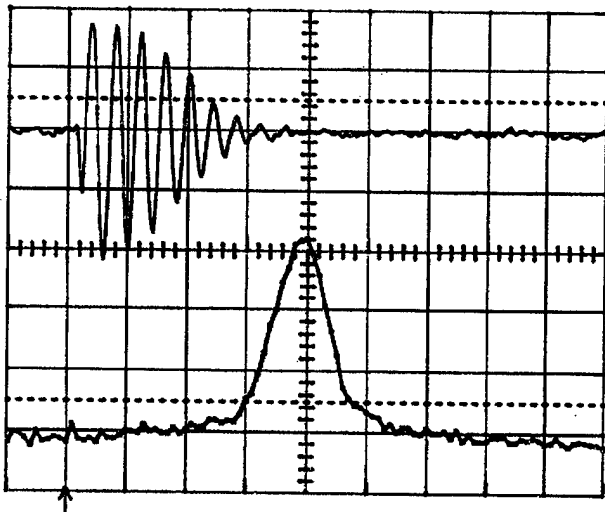


Figure 4. FFT of a downmixed signal. Upper trace: Downmixed signal, 50 μ s/div. Lower trace: FFT of upper trace, 10 kHz/div.

The error in q is estimated to be ± 0.001 in both measurements. With frequency interpolation the error will be even less [2]. The calculation time has been reduced from 15 seconds of the signal shown in Fig. 3 to less than 0.3 seconds

of the signal shown in Fig. 4, and with faster processors the calculation time will be reduced to 3 ms [2].

4. CONCLUSION

With this method it is possible to measure the Q -values at least 2 times per second, which is fast enough in CELSIUS. With more computer power it is possible to do the measurements even faster.

5. REFERENCES

- [1] T. Bergmark et al., Proc. 4th European Particle Accelerator Conference, London, England, 1994, 202
- [2] J. Gonzalez, S. Johnston, and E. Schulte, "Fast Q -measurement for the PS by FFT Analysis", Proc. 4th European Particle Accelerator Conference, London, 1994, 1734.

Software Architecture of the Longitudinal Feedback System for PEP-II, ALS and DAΦNE *

R. Claus, J. Fox, I. Linscott, G. Oxoby, W. Ross, L. Sapozhnikov, D. Teytelman
Stanford Linear Accelerator Center, Stanford, CA, 94309, USA

A. Drago, M. Serio
INFN - LNF, Frascati, Italy

Abstract

We describe the software architecture of the Longitudinal Feedback System being built for the PEP-II B-Factor at SLAC, the ALS light source at LBL and the DAΦNE phi factory at Frascati. This VME/VXI based system utilizes commercially available embedded CPU controller boards running the VxWorks real time operating system. The operator interface for PEP-II and ALS is based on the EPICS control system package. Embedded processors are used to load, monitor and diagnose various components of the system. The feedback function is implemented using digital filtering techniques on a DSP farm residing in the VME crates. The operator interface is written to allow the loading of applications, e.g., accelerator diagnostic functions, system hardware integrity functions, etc., without intervening controller reboots.

1. INTRODUCTION

The Longitudinal FeedBack (LFB) system [1] [2] is intended to be easily portable to various storage rings. In order to accomplish this, its control system software has been made capable of interfacing with the indigenous accelerator control system without too much additional

coding effort. The first guinea pig for the prototype system is the ALS at LBL. The Experimental Physics and Industrial Control System (EPICS) package [3], already in use there for beamline experiment control, was chosen for the operator interface of the first implementation of the device.

2. DATA FLOW

The block diagram of the LFB system hardware is shown in Figure 1. The VXI crate contains the fast front-end and back-end electronics. The VXI standard is being utilized because of its good electromagnetic shielding properties, cooling capacity and system power choices. In the initial incarnation, the control processor is a National Instruments VXIcpu-030 with an internal disk drive. This module also has a GPIB interface, which will be used to tune programmable delay lines that adjust the phase of the input and output signals of the system with respect to the beam timing. After the VXI processor has set up the hardware, it does very little other than periodically checking module status bits in order to gauge the health of the system.

The VME crates are fitted with VSB backplanes. The VME and VSB buses are used as the data and control paths, respectively. Because of the six slot limitation of the VSB standard, there are two 10 slot VME backplanes per VME crate. Five of the VSB slots can contain DSP boards. These boards were designed in-house and contain four 80 MHz AT&T 1610 Digital Signal Processors. Each DSP chip has an associated 16 KB dual-port memory through which it can exchange data with the control processor over the VSB bus. There is one control processor (Force CPU-40s in the initial instance of the system) per VME/VSB backplane pair. Its job is to set up the hardware, load the DSPs with code and retrieve data from the DSP when requested.

Bunch phase-error information derived from a Beam Position Monitor and the master oscillator is sampled at the bunch crossing frequency (500 MHz in the ALS case) with 8 bit resolution. Four samples are packaged together (packetized) along with addressing information from a software programmable look-up table by the Down Sampler Module. It then sends the packets out on four configurable Gigabit serial data links to the VME backplanes. The same data may be sent out over multiple links in order to implement, say, a data spy mode. Data Relay Modules (sometimes called Interface Modules) receive the data and pass it onto the VME bus with 32 bit Read-Modify-Write operations. The Data Relay Module sends the result of the read operation to the Hold Buffer Module in the VXI crate, also over Gigabit serial data links. The Hold Buffer

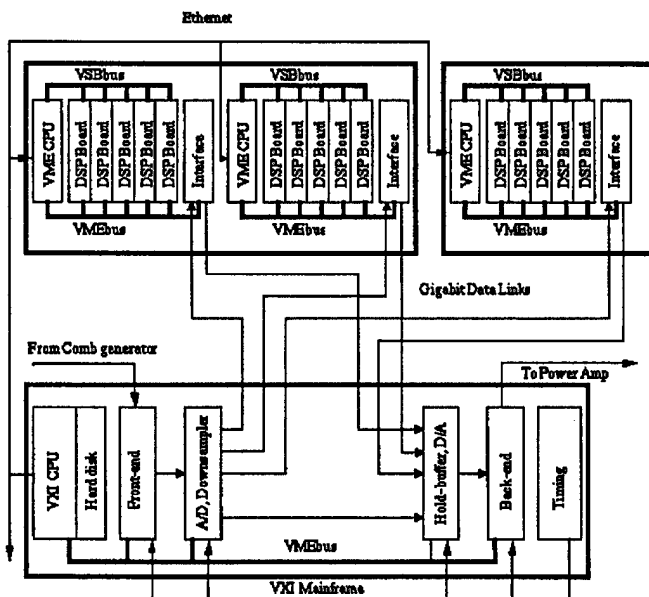


Fig. 1. System Hardware Architecture

*Work supported by Department of Energy contract DE-ACO3-76SF00515

stores the phase correction values in memory locations corresponding to the bunches to which they apply and drives a fast DAC operating at the beam crossing frequency. The analog signal is ultimately sent to the Power Amplifier, which excites the Longitudinal Kicker.

3. ARCHITECTURE

In addition to the normal set of VxWorks and EPICS tasks, several tasks are spawned to implement the LFB control system. As shown in Figure 2, the LFB system consists of three layers of software: the interface to the local machine control system, an LFB system managing layer and an application layer.

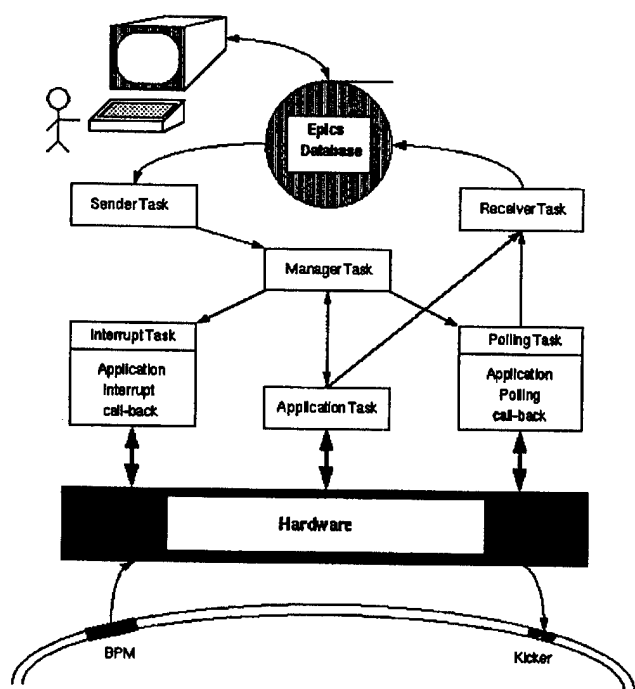


Fig. 2. System software architecture

The top-most level consists of two tasks that provide the interface between EPICS and the heart of the system, tSnd and tRcv. tSnd is responsible for taking operator input and translating it into a local message protocol. tRcv converts system information into messages that are sent to EPICS OPERator Interface (OPI) screens. These two tasks contain all the code (some 4000 fairly repetitive lines) that would need to be replaced in another machine control system environment.

The next layer of software contains the managing task tMgr and its offspring, the interrupt handling task, tInt, and the polling task, tPoll. tMgr receives and interprets messages coming from tSnd. Sometimes this means that it simply passes the message on to one of the subtasks. Legal messages are entered in a dictionary and consist of a message code, a corresponding routine and an argument for that routine. The "Load Application", "Abort Application" and "Quit" messages are always entered into the message dictionary, along with a set of general purpose hardware specific messages. Use of this dictionary concept allows for

great flexibility.

tInt and tPoll provide the services of handling the hardware interrupts and initiating periodic events, respectively. tInt installs an Interrupt Service Routine (ISR) appropriate for the hardware that it handles. The ISR packages the interrupt information into a message packet that is sent to task level code. If an application has registered an interrupt message handler with the interrupt task, then the packets are forwarded to it. This avoids application code writers having to write interrupt level routines, which are difficult to debug.

The tPoll task is often used for checking on the status of the hardware. An application may register a call-back routine with the polling task as well as set the wake-up period. The call-back can then check the hardware for error conditions, look for the existence of certain tasks, etc. The call-back generally sends status information to the tRcv task to inform the operator of the state of the system.

The application layer forms the third layer of software. Applications are loaded and started by the "Load Application" message, after the tMgr task has been established. Applications may add their own messages to the message dictionary. Only one application can run at a time. Applications define what the system does and thus generally contain different code for each of the control processors and the DSPs. Compile-time macro definitions (implemented through the *make* utility) choose the processor specific code when generating object files. Applications can, but do not necessarily have to have an associated DSP executable. Example applications are various hardware diagnostics, e.g., memory tests, bus transfer tests, etc., and digital filter codes, e.g. FIR, IIR, LQG, etc.

DSPs are booted with code loaded into their dual-port RAMs by their controlling processor. They hand-shake with their controlling processor through VSB interrupts and a communications block that they set up at initialization time in their external RAMs. Due to licensing agreements with AT&T, the DSP code assembler can not be bundled with the system like the VxWorks executables can. Thus, the filter coefficients are not part of the DSP code, but are instead loaded through the dual-port RAM using the hand-shake mechanism.

Encoded in three bits of the DSP addressing information of the data is a filter selection code. The DSP code can use this information to select different sets of coefficients in the case of, say, beam grow/damp accelerator experiments, enable/disable data recording, etc.

The filtering algorithms we have implemented in the DSPs typically take around 600 nanoSeconds of execution time and contain some 30 instructions. More time-consuming algorithms could be used if more DSPs were available, up to the limit that can be handled by the four available links on the Down Sampler and Hold Buffer modules. In the ALS case, there are two VME backplanes containing five DSP cards each for a total of 40 DSP chips. Together this corresponds to roughly 2000 MIPS.

All together, the control processor codes comprise some 20000 lines of c-code.

4. EPICS

EPICS [5] is a package with which one can construct an Operator Interface running on a UNIX platform to hardware controlled by code running on embedded computers running the VxWorks Real Time Operating System[4]. It contains many drivers to commercial VME and VXI devices. Communication between different computer platforms is achieved through a distributed database. Several Graphical User Interface (GUI) programs exist with which to build operator screens.

Due to the desire to maintain the portability of the Longitudinal Feedback System to other storage rings, it was decided to avoid becoming heavily EPICS dependent by coding EPICS device drivers for the SLAC-developed hardware. An interface to non-standard software can easily be developed by accessing database records. Some 200 records are used in the LFB system. A small subset of these records are used to cause the tSnd task to wake up and take action. These "events" cause other records to be read and written to the database.

The top-level OPI screen is shown in Figure 3. The triangles are "buttons" that cause another screen to be displayed. Each module in the system has an associated screen.

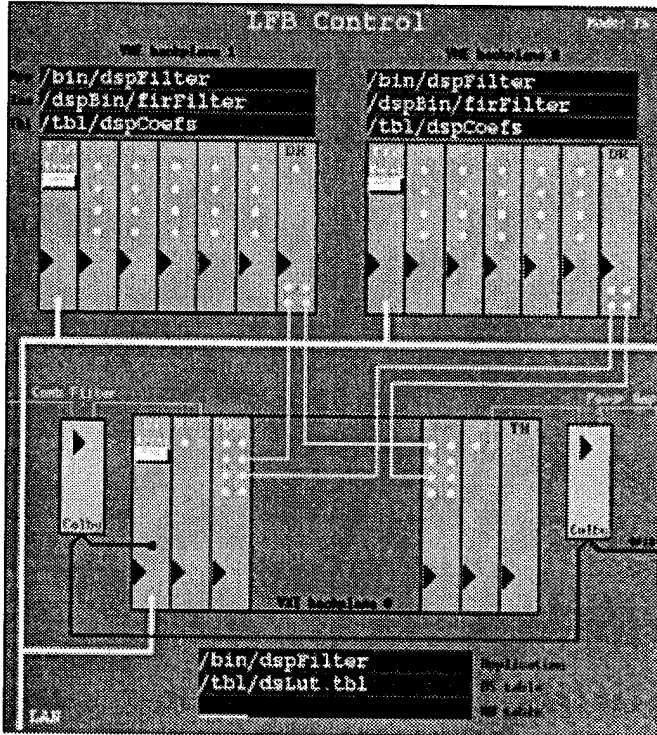


Fig. 3. An EPICS Operator screen

The system has two modes of operation: Full System and Stand-Alone. Stand-Alone mode allows one to use the control processors independently. This is useful when debugging software or hardware. In this case, the processors each have their own EPICS database and can not communicate with one another. This allows multiple users, insofar as tasks can be accomplished with a single processor.

5. CONCLUSION

Software for the control of the Longitudinal Feedback system has been developed. The operator interface of the initial system is based on the EPICS package. The EPICS specific layer is easily replaceable with another control system package so that the system remains portable to other sites.

In the coming months the Longitudinal Feedback system will be completed and installed at the ALS at LBL. By that time, some additional features will have been implemented on the OPI screens to allow for non-expert utilization of the system. Other features will also have been added to enable experts to perform accelerator experiments.

The completed system will constitute a significant advance in the tools available for accelerator control and beam diagnostics.

REFERENCES

- [1] D. Teytelman, et.al. "Operation and Performance of the PEP-II Prototype Longitudinal Damping System at the ALS" this conference
- [2] G. Oxoby, et.al., "Bunch-by-Bunch Longitudinal Feedback System for PEP-II" SLAC-PUB 6520, 1994
- [3] L.R.Dalesio, et.al. in: Proc. (ICALEPCS '93, Berlin, Germany, 1993) Nucl. Instr. and Meth. A 352 eds. W. Busse and M.C. Crowley Milling, (1994) pp.179-184.
- [4] VxWorks is produced by and a registered trademark of Wind River Systems, Inc.
- [5] EPICS is copyrighted by the Regents of the University of California, and the University of Chicago Board of Governors and is used with permission.

Digital I/Q Demodulator*

C. Ziomek and P. Corredoura

Stanford Linear Accelerator Center, Stanford, CA 94309, USA

Abstract

I/Q demodulation is a common and useful RF signal processing technique used in charged-particle accelerators. When implemented with conventional analog RF components, a number of inherent errors can degrade the I/Q Demodulator performance, including gain balance, quadrature-phase balance, DC offsets, impedance match, and carrier leakage. Recent advances in high-speed analog-to-digital converters allow the I/Q demodulator to be implemented digitally, greatly reducing these systematic errors. This paper describes the design of a digital I/Q demodulator that will be applied to the PEP-II B factory.

1. INTRODUCTION

The PEP-II B factory has a number of RF feedback control loops and algorithms that collectively maintain the proper RF field conditions for acceleration and damping of the longitudinal coupled-bunch beam instabilities [1-3]. The setup and operation of the control loops require a method of making very accurate RF measurements of the various signals throughout the RF system for the PEP-II accelerator. These measurements directly affect the operational stability and control for the PEP-II RF system, and thus, must be very precise and time-invariant. It is desired to measure the RF signals with accuracies of 0.1° in phase and 0.1% in amplitude over a dynamic range of approximately 30dB. Resolving the RF amplitude and phase information into their in-phase and quadrature (I/Q) components during demodulation is advantageous because of the symmetry of the I/Q signals and the less-complicated nature of the I/Q electronics. Precision RF measurements for PEP-II shall be accomplished with a digital I/Q demodulator employing a quadrature IF sampling technique.

2. THEORY

The conventional analog I/Q demodulator, shown in figure 1, uses two matched demodulator circuits to convert the RF input signal directly to baseband analog I and Q signals that are subsequently converted to digital data. The functionality of this circuit is based upon the RF input signal being split and mixed with two local oscillator (LO) signals that have a 90° phase shift between them. This 90° phase shift provides the mechanism to distinguish the I and Q components of the RF signal. The mixer outputs are lowpass filtered to remove the high-frequency mixing products, providing baseband analog I and Q signals that are sampled and converted to digital values. The parallel nature of the analog I/Q demodulator requires the two legs to be very closely matched to each other for accurate I/Q measurements. Also, the quadrature phase shift must be exactly 90° at all fre-

quencies. This nature of the conventional analog I/Q detector makes it susceptible to errors associated with gain matching, DC offsets, quadrature phase errors, carrier leakage, and impedance matching. These errors can be difficult to completely eliminate or compensate for, causing RF measurement errors.

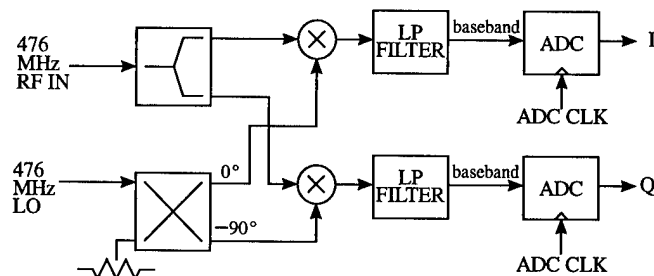


Fig. 1. Conventional Analog I/Q Demodulator.

As an alternative to the analog I/Q demodulator, figure 2 shows a digital I/Q demodulator implementation that inherently improves performance. Within this implementation, the RF input is downconverted to an IF of 4.9 MHz by mixing the RF with a 471.1 MHz LO. The resulting signal is bandpass filtered to remove the high-frequency component that results from mixing and also limit the signal bandwidth to avoid aliasing. Aliasing is discussed in detail in a following section of this paper. The 4.9 MHz IF output is directly sampled with an analog-to-digital converter (ADC) operating at 19.6 MSPS. The time period between consecutive ADC samples is 50.95 ns which corresponds to exactly 90° at the 4.9 MHz IF. The sampled data reflects the amplitude of the original RF signal sampled at 90° intervals. If we define the first sample at 0° as I, the next sample at 90° is Q, the following sample at 180° is -I, the next sample at 270° is -Q, the following sample at 360° is again I, and so on. The ADC output provides a data stream consisting of the repeating pattern of measurements of I, Q, -I, and -Q. The I and Q variables within this digital data stream are separated by a multiplexer that switches every other sample into two parallel digital paths. The sign inversion in each path is removed by multiplying each data stream by +1 and -1 alternately. The resulting outputs correspond to the measured I and Q of the input RF signal.

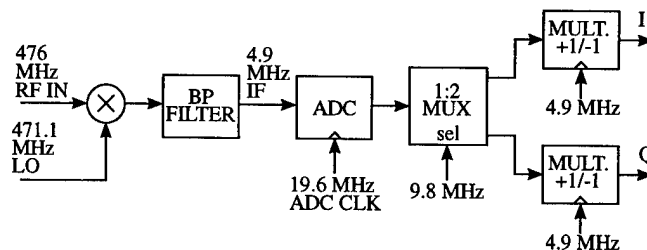


Fig. 2. Digital I/Q Demodulator.

The advantages of the digital I/Q demodulator are significant. The single path for the RF and IF processing insures per-

*Work supported by Department of Energy, contract DE-AC03-76SF00515

fect gain-matching between the two I and Q signals. The two paths are applied to separate circuitry only after they have been converted to digital data. All digital processing can be easily matched for the two signals. The concerns of gain balancing and impedance matching for all the RF and analog components is obviated. Also, because the IF signal is sampled without ever being downconverted to baseband, DC signals are not measured by the demodulator. Consequently, analog DC offsets and drifts do not affect the digital I/Q demodulator. The quadrature phase shift is dependent upon the precise timing of the ADC. The aperture jitter of the selected ADC is inconsequential, and stable clock circuitry have been designed into the PEP-II low level RF (LLRF) system. The one source of error for the digital I/Q demodulator results from the nature of the sampling process. The ADC clock period of 50.95 ns provides an exact 90° phase shift at the center frequency only. Signal frequencies not equal to the center frequency contain a quadrature phase error when measured. For a limited signal bandwidth, this quadrature phase error is maintained at insignificant levels, well below that achievable by conventional means. Narrow-band signals within 5 kHz of the RF carrier are detected with better than 0.05° quadrature error. Signals within the detection bandwidth of the I/Q demodulator (± 50 kHz) are detected with better than 0.5° quadrature error.

3. IMPLEMENTATION

PEP-II requires approximately 20 precision I/Q measurements for each of the eight RF stations. In addition to the I/Q measurements, the amplitudes must be detected for those same 20 RF signals. Consequently an 8-channel I/Q & Amplitude Detector has been designed for PEP-II. The VXIbus form-factor has been chosen for the LLRF system because of the extensive computational requirements. The 8-channel I/Q & Amplitude Detector has been designed as a single-wide C-size VXIbus module. This module includes eight digital I/Q demodulators, eight RF amplitude detectors, extensive digital signal processing circuitry, and the VXIbus interface electronics.

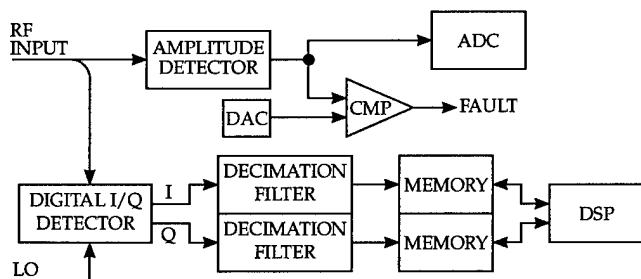


Fig. 3. One Channel of I/Q & Amplitude Detector.

Figure 3 shows a block diagram of one channel of the I/Q & Amplitude Detector module. The RF input, at a level of approximately 1 Watt (+30dBm) is processed in two separate circuits. The majority of the signal power is fed into an RF amplitude detector consisting of a forward-biased rectifying diode. A second matched diode is used to offset the forward bias voltage of the detection diode. This amplitude detector provides about 50 dB of measurement dynamic range and 30 dB of linear dynamic range for amplitude detection. The output

is converted to a digital value for diagnostics and also compared to a fault threshold to indicate overload conditions. A small portion (approximately 1 mW) of the input signal is coupled into the digital I/Q demodulator described earlier. The digital I and Q outputs are processed in digital decimation filters that provide filtering to reduce the data rates from 755 kHz down to as low as 25 Hz. It is significant to note that the data is truly filtered from input bandwidths of a few MHz to output bandwidths as low as 1 Hz in order to avoid any aliasing of the measured data. The data is stored in a history buffer that can be used to display waveforms versus time, or for additional processing with an on-board digital signal processor (DSP). The DSP provides the capability of sophisticated on-board computation, such as converting I and Q to amplitude and phase, performing additional filtering and decimation, and processing data through control algorithms. The net result is a very flexible and powerful instrument for RF signal processing.

The ADC used for direct digital sampling of the IF signal must provide an input bandwidth much greater than the IF frequency (4.9 MHz) and must operate at the required sampling rate of 19.6 MSPS with a vertical resolution of 12 bits. The Comlinear Corporation CLC949, a 12-bit, 20 MSPS ADC, has been selected for the direct I/Q sampling. In order to reduce size and cost of the I/Q demodulator circuitry, a single ADC is used to sample the eight separate IF signals. Figure 4 shows a block diagram of the multiplexing scheme used to process eight IF signals with a single ADC. This multiplexing scheme provides a significant cost savings because the high-performance ADC is a very costly item.

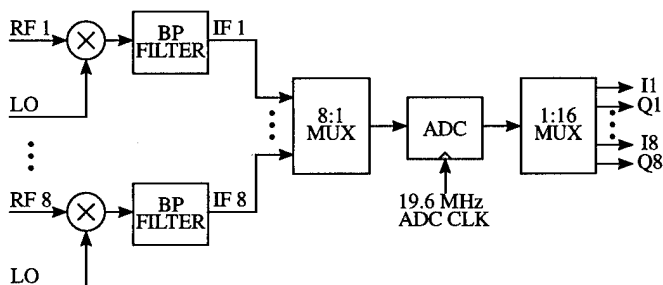


Fig. 4. Applying one ADC to eight I/Q channels.

There is a trade-off associated with using a multiplexer for the eight I/Q demodulators. Without the multiplexer, each channel is sampled at the full 19.6 MSPS, providing unaliased I/Q data with a maximum single-sided bandwidth (SSBW) of approximately 9.7 MHz. Figure 5 shows a graph of the time response of the multiplexed I/Q sampling technique. After sampling a channel twice at the 19.6 MSPS ADC sampling rate, the IF multiplexer is switched to the next channel, which, after allowing the IF signal to settle, is sampled twice also. After cycling through all eight channels, the multiplexer waits an additional 101.9 ns before sampling the first channel again. These extra two clock cycles provide the 180° phase shift to rotate the IF phase to correspond to -I and -Q. The sign inversion, which is necessary to insure insensitivity to analog DC offsets, is removed by the digital +1/-1 multiplier. The resulting time period between consecutive samples for one channel is 1.325 μ s, corresponding to a sample rate of 755 kSPS. This

defines the bandwidth for the bandpass filter that is applied to the IF signal to avoid aliasing during sampling.

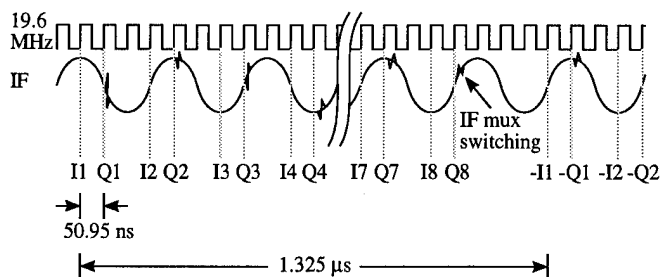


Fig. 5. Time response of I/Q sampling.

Figure 6 shows the frequency response of the I/Q sampling technique. The top graph shows the spectrum of a single IF channel after being mixed with the LO. Note that in order to avoid aliasing in the downconversion process, the SSBW of the RF input must be less than 9.7 MHz. The IF signal is first processed in a narrow-band bandpass filter and then sampled by the ADC. Sampling the IF signal at the 755 kHz sample rate reproduces the filtered IF spectrum at 755 kHz intervals as shown in the middle graph. This indicates that in order to avoid aliasing within the I/Q Demodulator's detection bandwidth of ± 50 kHz, the bandpass filter must limit the SSBW of the IF signal to less than 700 kHz. The bottom plot shows the signal spectrum after being processed by the digital $+1/-1$ multiplier. Multiplication by a repeating pattern of $+1$ and -1 is comparable to mixing the sampled IF signal with a sampled 377.5 kHz sinusoid, which provides a frequency shift of 377.5 kHz. Because this final frequency shift down to baseband is performed digitally, the data does not contain any errors associated with analog DC offsets. Due to the precise nature of digital electronics, all subsequent digital processing does not introduce any errors into the signal data either.

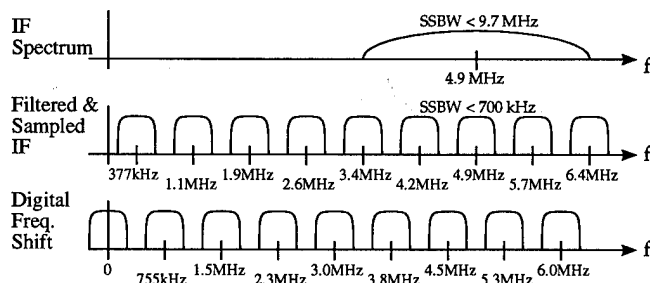


Fig. 6. Frequency response of I/Q sampling.

The dynamic range of the I/Q demodulator is approximately 60 dB. The upper limit is determined by the distortion and compression caused by the downconversion mixer at high RF input power levels. In order to maximize this upper limit, a high-level mixer requiring a $+17$ dBm LO is used. By defining the maximum RF input to be 0 dBm, the distortion due to intermodulation products and gain compression is kept below 0.1%. The high-level mixer also maintains a constant insertion phase for RF inputs below 0 dBm. The lower limit of the dynamic range for the I/Q demodulator is determined by the thermal noise. The noise introduced by the RF circuit is insignificant because its noise bandwidth is limited by the narrow-band anti-aliasing filter. Noise is introduced by the IF buff-

ers, the IF multiplexer, and the ADC. For the I/Q demodulator, the signal-to-noise ratio has been computed to be better than 65 dB.

4. MECHANICAL DESIGN

The mechanical design for the I/Q & Amplitude Detector module is not trivial. The dimensions of a C-size VXIbus module severely limit the physical size of the electronics. In order to maintain adequate shielding and a temperature-controlled environment for the analog (RF/IF) circuitry, an ovenized RF enclosure is required. Surface mount technology is used for the entire analog circuit within the enclosure. This circuit is implemented as a microstrip printed-circuit board (PCB). Figure 7 shows the CAD layout for a single channel of the I/Q & Amplitude Detector electronics. With no through-hole components, the PCB is mounted directly to the bottom of the RF enclosure, providing good thermal and electrical contact. The whole enclosed circuit is heated and regulated at 60°C , which is above the maximum ambient temperature. The constant temperature for the analog electronics maintains constant insertion losses, insertion phases, and return losses for the various components.

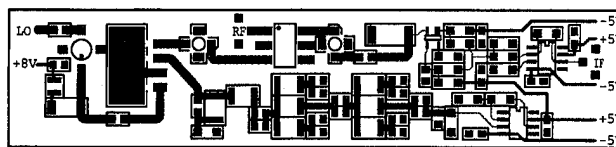


Fig. 7. Microstrip layout of I/Q & Amplitude Detector channel

5. SUMMARY

The I/Q & Amplitude Detector module is a sophisticated electronic instrument that makes use of novel ideas and technology to enable powerful RF measurements and signal processing. The high density of channels per slot and integrated processing power reduce the overhead costs for the PEP-II LLRF system. The performance specifications for the I/Q & Amplitude Detector module can be summarized as follows:

- I/Q Demodulator Dynamic Range: 60 dB
- I/Q Demodulator Accuracy: $\pm 0.1\%$
- I/Q Demodulator Phase Stability: $\pm 0.1^\circ$
- I/Q Demodulator Detection Bandwidth: ± 50 kHz
- Amplitude Detector Dynamic Range: 50 dB
- Amplitude Detector Linear Range: 30 dB
- Amplitude Detector Accuracy: $\pm 1\%$
- Amplitude Detector Detection Bandwidth: ± 5 MHz

6. REFERENCES

- [1] P. Corredoura et. al. "Low Level RF System Design for the PEP-II B Factory", this conference (PAC 95).
- [2] P. Corredoura, L. Sapozhnikov, R. Tighe, "RF Feedback Development for the PEP-II B Factory" Proceedings of the 1994 European Particle Accelerator Conference.
- [3] P. Corredoura "Development of Digital Control for the PEP-II Klystrons" SLAC PEP-II Tech Note #60, 1994.

RF Feedback Simulation Results for PEP-II*

R. Tighe, P. Corredoura, Stanford Linear Accelerator Center, Stanford University, Stanford, CA 94309 USA

Abstract

A model of the RF feedback system for PEP-II has been developed to provide time-domain simulation and frequency-domain analysis of the complete system. The model includes the longitudinal beam dynamics, cavity fundamental resonance, feedback loops, and the nonlinear klystron operating near saturation. Transients from an ion clearing gap and a reference phase modulation from the longitudinal feedback system are also studied. Growth rates are predicted and overall system stability examined.

I. Model Description

The development of a model of the PEP-II RF feedback system and longitudinal dynamics has been described previously[1]. The model has been in use predicting the overall stability of the High Energy Ring (HER) and the Low Energy Ring (LER) RF systems under heavy beam loading[2].

Feedback loops are included, as are the klystron, cavity, and longitudinal dynamics of 36 rigid macro bunches. Three feedback loops are required to stabilize the coupled-bunch oscillations that arise from the detuned cavity fundamental. A direct RF feedback loop, comb filter feedback, and a connection from the bunch-by-bunch longitudinal feedback are required. Signal from the longitudinal feedback is fed to the reference phase shifter to provide additional damping of the low order coupled-bunch modes[3]. Digital components of the feedback system are simulated using the actual system sample rates. Signal propagation delays in the system are also included. Figure 1 is a block diagram of the model.

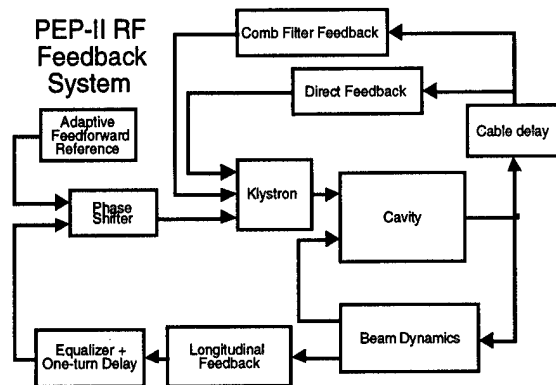


Fig. 1 System Block Diagram

All elements in the model have been discretized to a sample time of 25ns. This allows the model to run using difference equations for the system evolution and is faster than simulating continuous components which require an integration routine for solving. The model is written using MATLAB/Simulink[4] with some components written in C for greater execution speed. Analysis of the system in the frequency domain allows easy configuration, analysis, and optimization of the feedback loops.

II. Klystron Saturation and Bandwidth

An important aspect of the system is the requirement to run the RF stations near saturation to maximize operating efficiency. This leads to reduced AM gain through the klystron and degrades the performance of the RF feedback. Data taken from a typical tube provides a profile of the saturation curve for the klystron used in the simulation. For electrical efficiency it is desirable to run as far into saturation as possible; but not so far as to prevent sufficient amplitude modulation of the klystron power by the feedback system. The desired operating point was chosen to be at 90% of the saturated klystron power. Figure 2 shows the saturation curve used.

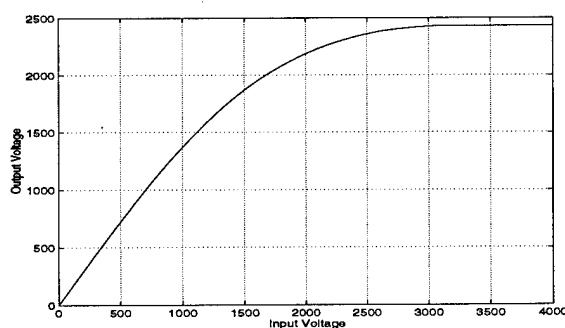


Figure 2. Klystron Saturation Curve

While considering the klystron specifications for use in PEP-II it became necessary to evaluate system stability with tubes of varied parameters. While it is optimal to maintain low group delay and high bandwidth for maximum feedback performance, they come at increased purchase cost. It is therefore important to predict the impact of klystron parameters on system behavior. Klystron bandwidth and delay were varied to quantify the effects on system stability. Table 1 shows simulation results for the LER with 3.15A for two types of tubes at varying levels of saturation. The last column refers to the

*Work supported by U.S. Department of Energy
Contract DE-AC03-76SF00515

damping time of the slowest mode to damp. The table shows that at a higher current the effect of the klystron parameters on stability becomes apparent. It is clear that wider bandwidth and lower group delay are desirable and that the regime where this becomes important will be reached when currents are increased to raise luminosity.

Tube	stable?	Saturation	damping time
BW -3MHz delay- 150ns	YES	None	140 turns
	YES	81%	350 turns
	NO	85%	
BW -6MHz delay- 100ns	YES	None	120 turns
	YES	90%	750 turns

Table 1. Dependence on Klystron Parameters at 3.15A

III. Gap Transients

The HER is to have an ion clearing gap of approximately 5% of the ring circumference. The LER will have its gap partially filled in order to match the beam phase variations in the two rings, maintaining collisions at the interaction point. Figure 3 displays the cavity voltage and phase transients induced by the gap in the HER.

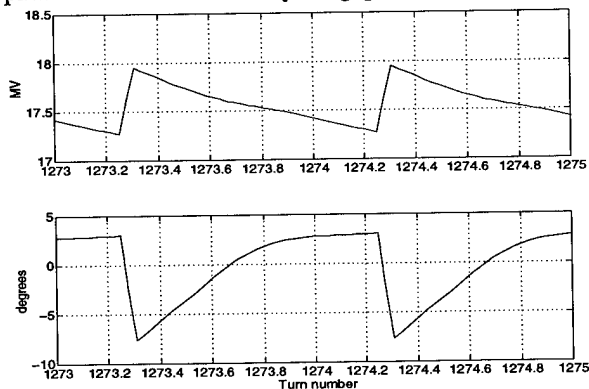


Figure 3. Cavity Voltage Transient

The model confirms the structure of calculated gap transients and allows evaluation of methods to accurately match the transients in the two rings[5].

Without accommodation for the gap transient the feedback would request more than the available power and the klystron would saturate. A procedure will be used to prevent the feedback system from attempting such a compensation.

IV. Feedforward algorithm

An adaptive algorithm has been devised to adjust the station RF reference to track the transient, keeping the klystron power constant. A profile corresponding to 20 MHz samples is generated by sampling the klystron drive over many turns, averaging and modifying the feedforward

values in order to produce a more constant klystron output. The feedforward signal is adapted slowly from turn to turn, and will not interfere with the operation of the feedback loops. Figure 4 shows the envelope of the forward power per cavity during the convergence of the algorithm. The convergence rate may be adjusted as needed.

Figure 5 shows the forward power variation per cavity over two turns both with and without the feedforward in effect. The power variation is reduced to approximately 0.5% with feedforward. Figure 6 shows the station reference signal generated by the feedforward system. This signal combines with the feedback signal to create a nearly constant reference for the klystron, maintaining low power fluctuation despite the gap. The feedforward algorithm will adapt during the filling of the ring and track as the current in the ring decays.

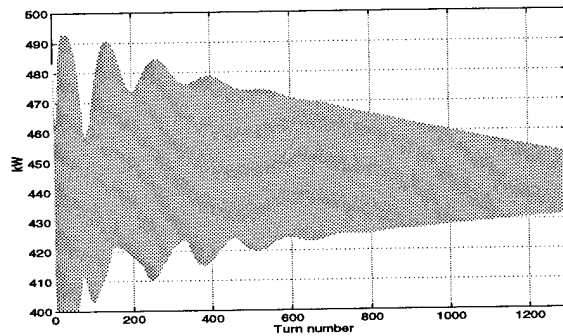


Figure 4. Forward Power Envelope During Adaption

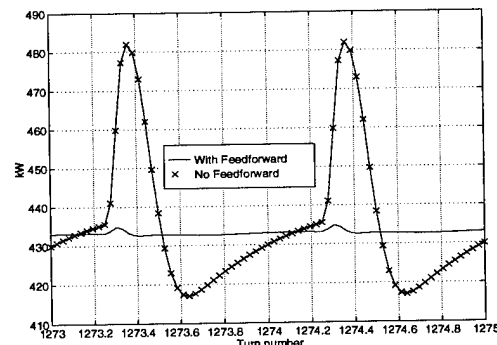


Figure 5. Forward Power Variation, with and without Feedforward.

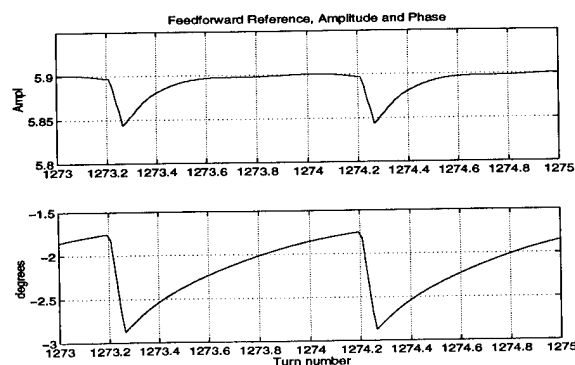


Figure 6. Feedforward Reference Signal

V. Simulation Results

The nominal operating configuration for the LER is to have three klystrons driving six cavities. Table 2 lists the relevant parameters for the nominal LER configuration.

Gap voltage	4.74 MV
Beam current	2.14 A
Synchrotron freq.	4.34 kHz
Detuning freq.	-155 kHz
Revolution freq.	136 kHz
Klystron power per station	2.8 MW
Energy loss per turn	0.87 MV
Momentum compaction	0.00122

Table 2. LER Parameters

Of the 36 bunches, 2 are filled with 60% of the nominal charge which is the typical gap transient matching approach. The maximum klystron power is set to be 10% above the operating point. Startup transients are minimized by calculating and configuring elements with values at or near their steady-state values where possible. Bunch offsets may then be set as desired. The planned injection scheme for the machine will produce small longitudinal disturbances. Figure 6 displays the modal response of the beam oscillations in the nominal LER configuration. All coupled-bunch modes are damped within 500 turns. The less heavily beam-loaded HER is stable as well, with faster damping.

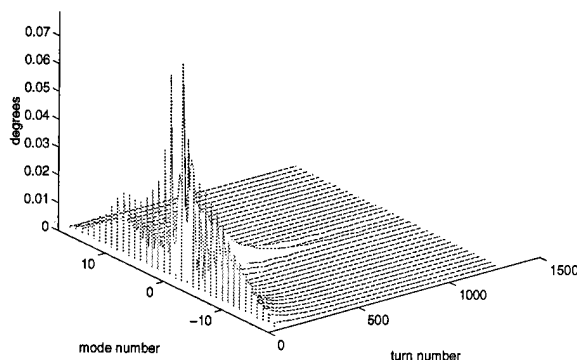


Figure 6. Modal Response of LER Simulation

V. Idle pair parking

Other studies involving the RF feedback system are possible. For example, in the event a ring is temporarily to run with one less than its normal complement of RF stations, that station's cavities must be parked on opposite

sides of the fundamental frequency. These cavities will be tuned such that they are centered between the second and third revolution harmonics to prevent unduly exciting coupled-bunch activity and minimize absorbed beam power. It is useful to examine the signals induced in these unpowered, parked cavities for use in monitoring them to minimize their contribution to the driving impedance. Methods of parked cavity resonant frequency monitoring have been examined using the model.

VI. Other Observations

The presence of the gap may lead to improved system stability due to the decoupling effect through tune spread on the coupled-bunch driving mechanisms. A configuration that is unstable without a gap can become a stable configuration when a gap is introduced. This effect has been observed in the simulation. The full extent of this raising of the stability limit requires further study.

VII. Conclusion

The model has been is use to test components and algorithms as well as to predict the PEP-II RF system behavior in the presence of nonlinearities. The ability to analyze the model in both the time and frequency domains is very powerful, allowing for straightforward configuration of the feedback loops. Both PEP-II rings with gaps and saturating klystrons have been shown to be stable using RF feedback techniques and feedforward compensation.

The model has also proved useful for klystron evaluation, feedforward algorithm testing, and gap transient matching. The model can be readily adapted to represent other storage ring RF systems.

VIII. REFERENCES

- [1] R. Tighe, "RF Feedback Simulation for the PEP-II B Factory", SLAC-PUB-6535, Proceedings of the 1993 Particle Accelerator Conference, pp. 1957-1959.
- [2] P. Corredoura, et al., "Low Level RF System Design for the PEP-II B Factory", these proceedings.
- [3] J.D. Fox, et al., "Feedback Control of Coupled-Bunch Instabilities", Proceedings of the 1993 Particle Accelerator Conference.
- [4] Matlab/Simulink, The Mathworks, Natick, MA 01760 USA
- [5] F. Pederson, "RF Cavity Feedback", B Factories - The State of the Art in Accelerators, Detectors, and Physics", SLAC-400, 1992, pp. 192-207.

TM_{0,1.5,0} MODE CAVITY FOR LONGITUDINAL BUNCH FEEDBACK KICKER

T. Shintake, KEK: National Laboratory for High Energy Physics,
Oho, Tsukuba, Ibaraki 305 Japan

TM_{0,1.5,0} mode cavity has been proposed for a longitudinal kicker of wide band bunch feedback system in B-factory. This is a kind of parallel-plate radial-line power combiner, in its center beams are accelerated or decelerated on axial electric field. In order to improve the power efficiency, the gap width around the beam is made wider than the outer part, as a result the shunt impedance becomes as high as 1.1 k Ω . Because of its simple axial-symmetric structure, we can use well established theory of accelerating cavity and also analyze the HOM problems with minimum ambiguity. There is no floating electrode inside vacuum, it is easy to fabricate and attach cooling water loops.

I. BASIC CONCEPT

The concept of this kicker is shown in Fig. 1. It is basically a kind of power combiner using radial line transformer to connect a number of power amplifiers into one terminal. Beams are accelerated at the center by the longitudinal electric field of combined rf power. There is no actual terminal at the beam center, only the beam absorbs the rf energy, most of the power will be reflected back to the power amplifier and absorbed in the matching resistor (some part of the power heats up solid state in the amplifiers).

In a simple parallel plate radial-line, the wave impedance varies smoothly along the wave propagation, it shows very flat response for wide frequency range[1]. This is very attractive performance for application to fast bunch-by-bunch feedback system. However, the shunt impedance in this radial line is quite low, typically it is less than 100 Ω , thus we need a large amount of rf power to get enough feedback voltage.

In order to improve the power efficiency, we use a step in the radial line as shown in Fig. 1. We choose the position of this step at the first root of the Bessel's function, and the input terminals at the second peak of the Bessel's function. In order to keep this condition, the bandwidth of input rf is somehow limited, this is discussed later. Now, we have TM₀ like mode in this structure. TM₀₁₀ is used to name the dominant mode in a pillbox cavity, whose voltage takes zero at the cavity wall. In the present mode, the voltage takes peak at the maximum radius, therefore we should name it TM_{0,1.5,0} mode (TM_{0,2,0} takes the next zero at the cavity end). The boundary condition at the input terminal is not the "electrical short", but the "magnetic short" which is supported by standing wave in the coaxial cables connected to the power amplifiers.

If we change view point, this structure can be recognized as a pillbox cavity tightly coupled to an external circuit through a parallel plate radial-line. Since the coupling is so tight, the

cavity shows quite low Q-factor, and it can response to rather wide frequency spectrum of feedback signal. It is easy to imagine that if we make the coupling looser (narrows the radial line gap), the external Q-factor becomes higher and we can get higher shunt impedance, but the frequency bandwidth becomes narrow. Therefore, we have to compromise these two issues.

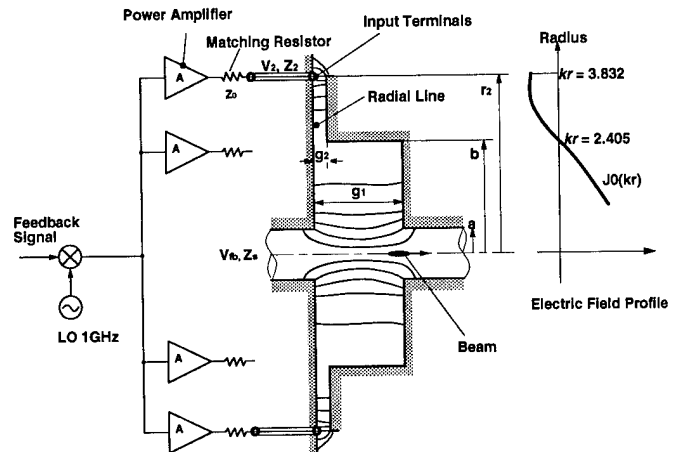


Fig. 1 TM_{0,1.5,0} Mode Longitudinal Kicker

II. BASIC DESIGN PROCEDURE

The design procedure is as follows.

- (1) Choose feedback carrier frequency. It must be high enough to enable the amplitude modulation for wide bandwidth signal, but should be lower than the cut off frequency of beam pipe. Here we choose 1 GHz as a carrier frequency. The radius b and r_2 are determined from its wavelength. Using

$$\begin{aligned} kb &= \rho_{01} = 2.405 \\ kr_2 &= \rho_{11} = 3.832 \end{aligned} \quad (1)$$

we have $b = 115$ mm, $r_2 = 183$ mm. In practical design, we have to determine these parameters on a computer simulation by taking into account beam pipe effect.

- (2) Choose number of amplifier. In order to symmetrically drive the input terminals, distance between terminals must be shorter than the half wavelength. Therefore the number of input terminal must be

$$N > \frac{4\pi r_2}{\lambda} = 2\rho_{11} \approx 8 \quad (2)$$

Here we choose $N = 12$. In practical design, this will be modified to adjust the impedance for microwave absorbers.

(3) Adjust the gap size g_2 to match the TEM-mode impedance in the radial-line to the parallel impedance of the amplifiers. The matching condition becomes,

$$Z_2 = \frac{\zeta_0 g_2}{2\pi r_2} = \frac{50}{N} \quad (3)$$

where ζ is 376.7 Ω . For $N = 12$, Z_2 must be 4.3 Ω , and $g_2 = 12.7$ mm.

(4) Adjust the gap size g_1 to get proper coupling to the beam. The shunt impedance is proportional to square of the gap size, so that larger gap size is desirable. But, too large gap size will lose transit-time factor. From the point of view of frequency bandwidth, lower external Q is desirable, this contradicts with the shunt impedance issue. We have to compromise these factors.

Using the analytical equation of mode properties on TM_{0,1,5,0} mode, the cavity parameters are given by the following equations. The shunt impedance of this cavity is

$$Z_s = \frac{V_{fb}^2}{2P_{in}} = \frac{2\zeta_0 g_2}{\pi r_2} \left[\frac{g_1}{J_0(\rho_{11})g_2} \right]^2 T^2 \quad (4)$$

where T is the transit time factor,

$$T = J_0(ka) \frac{\sin(kg_1/2)}{(kg_1/2)} \quad (5)$$

The input power to get feedback voltage V_{fb} is

$$P_{in} = \frac{V_{fb}^2}{2Z_s} \quad (6)$$

The external Q-factor is,

$$Q_{ext} = \frac{1}{2} \rho_{01} \frac{g_1}{g_2} \quad (7)$$

We choose the gap size $g_1 = 70$ mm, then we have the shunt impedance of 1.33 k Ω . To get 7 kV with this kicker, we need 18 kW input power. In the practical application, we install microwave absorbers in the outer part of vacuums vessel to damp higher order modes. Because they absorb some fraction of the input power, we have to increase the input power to compensate this loading as discussed later.

III. PRACTICAL DESIGN

In the conceptual drawing in Fig. 1, at the input terminal the boundary condition was assumed to be open condition. However, in a practical usage, we need a vacuum vessel and electromagnetic shield outside of this structure. Then the practical design becomes as shown in Fig. 2. Detailed dimensions were determined on computer simulation to tune the resonance at the center frequency of carrier signal of 1 GHz. Figure 3 shows the simulated electric field line plot, where no microwave absorbers were loaded. The calculated electrical performance from this simulation is summarized in Table 1, where the analytically estimated parameters are also listed in parenthesis. The net shunt impedance is lowered due to the loading effect on microwave absorbers, it becomes 1.1 k Ω .

Table-1

Carrier Frequency	f_c	1.0	GHz
Beam Current	I	2.6	A
Feedback Voltage	V_{fb}	7.0	kV
Cavity Dimensions	a	50	mm
	b	124 (113)	mm
	r_2	190 (183)	mm
	g_1	70	mm
	g_2	13	mm
Transit Time Factor	T	0.67 (0.68)	
<i>Without microwave absorber</i>			
Shunt Impedance	Z_s	1.54 (1.33)	k Ω
<i>With microwave absorber</i>			
Number of Power Amp.	N	10	
Shunt Impedance	Z_s	1.1	k Ω
Required Input Power	P_{in}	22.7	kW
Power per Amp.	P_{in}/N	2.3	kW
External Q-factor	Q_{ext}	5.5 (6.5)	
Response Time	τ	1.75	nsec
-3dB Band Width	f_{BW}	182	MHz
Beam Loading Power	P_b	14.8	kW

Note. (values) are analytically estimated.

Here we consider an example application to KEK B-factory[2]. Since the growth rate of the coupled bunch instability in LER (low energy ring) is faster than HER (high energy ring), here we consider LER case. The required feedback voltage per turn can be estimated by

$$V_{fb} = 2gT_{rev}\Delta E \quad (8)$$

where g is damping rate, T_{rev} is beam revolution time, ΔE is energy deviation. If we expect the damping rate 100 s^{-1} (10 msec), this is four times faster than the radiation damping, and energy deviation of 10^{-3} , this is the same order as one sigma of natural energy spread, the required kick voltage per turn becomes 7 kV. Input power of 22.7 kW is enough to generate this kick voltage.

IV. EFFECT OF MICROWAVE ABSORBER

In order to establish $TM_{0,1.5,0}$ mode, the characteristic wave impedance in external volume outside the input terminals should be much higher than the paralleled impedance of amplifiers, which means large volume vacuums vessel is desired. At the same time, every resonances in this volume have to be damped to ensure flat frequency response and avoid additional beam instability due to higher order modes. For the HOM damping, smaller volume is desired. Compromising these issue, here we choose the radius at 240 mm. The characteristic impedance of this volume as a coaxial line is 24.3Ω . We install several microwave absorbers made from SiC material, which are cooled by circulating water.

Now, the amplifiers, the radial line and the coaxial line with microwave absorbers are parallelly connected, we have to modify the number of amplifiers to meet the impedance matching. In order to keep the frequency response as wide as possible, the impedance looking from the cavity must be equal to the parallel impedance of the microwave absorbers and the power amplifiers. Now, the matching condition of eq. (3) becomes,

$$Z_2 = \frac{50}{N} // Z_{\text{absorber}} \quad (9)$$

We find $N=10$ as a best matching solution. The external Q-factor does not change. The shunt impedance becomes $1.1 \text{ k}\Omega$, this is 69 % of initial value.

The power dissipation on the microwave absorber is 13 kW, which is came from the input rf power, and 2.5 kW from multi-bunch beam loading. The single bunch beam loading power was estimated to be 121 W, which will be absorbed in microwave absorber.

V. DISCUSSIONS

Since this kicker utilizes a resonance phenomena to raise the kicker voltage, the bandwidth of frequency response is limited. The external Q-factor of 5.5 is relatively low, but it still limits the bandwidth to 182 MHz (full width at -3 dB point). Because the characteristic response time is 1.75 nsec, for the highest order of multi-bunch mode (π -mode on bunch-to-bunch), the effective kick voltage becomes

$$V = V_b \{1 - \exp(-t_b / \tau)\} = 0.68 V_b \quad (10)$$

This makes the damping time longer, but still 68% of the voltage can effectively kick the beam. This will be quite enough for practical application.

ACKNOWLEDGMENTS

The author would like to thank to Dr. Makoto Tobiyama and Dr. Eiji Kikutani for their useful discussions.

REFERENCES

- [1] R. F. Harrington: Time Harmonic Electromagnetic Fields (McGraw-Hill, Inc., New York, 1961) Chap. 5.
- [2] KEK Accelerator Design Report for KEK B-factory, to be published as KEK report in 1995.

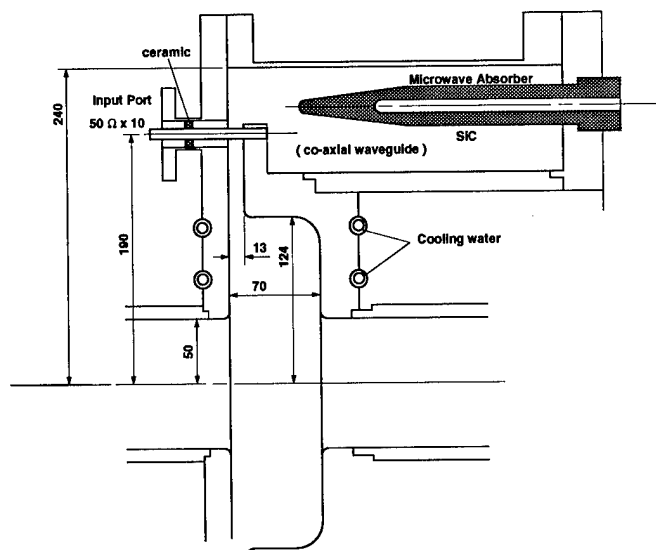


Fig. 2 Longitudinal kicker for B-factory.

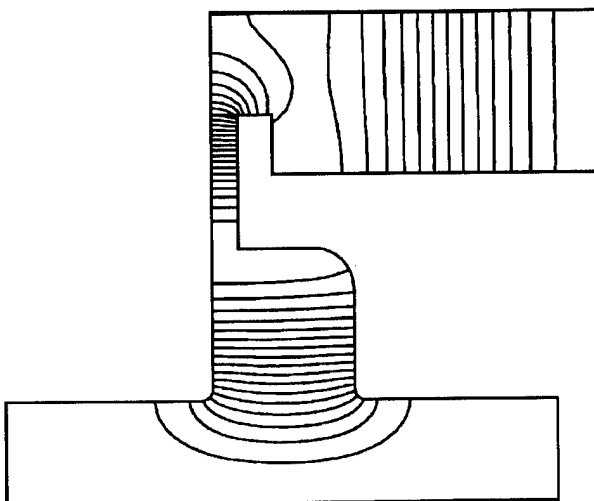


Fig. 3 Electric field line plot of $TM_{0,1.5,0}$ mode.

Low Level RF System Design for the PEP-II B Factory*

P. Corredoura, R. Claus, L. Sapozhnikov, H. Schwarz, R. Tighe, C. Ziomek
Stanford Linear Accelerator Center, Stanford, Ca 94309, USA

Abstract

Heavy beam loading in PEP-II has driven the design of the low level RF system to contain feedback loops similar to those used in proton rings. The RF feedback loops control longitudinal coupled-bunch instabilities caused by the beam interaction with the accelerating mode of the RF cavities by reducing the cavity impedance observed by the beam. The RF system employs a modular design housed in a VXI environment and uses the EPICS control system. Modern control system design and signal processing is used throughout the system. This paper describes the RF system topology and the signal processing used to fulfill the system requirements.

1. INTRODUCTION

As discussed in previous papers [1][2], a fundamental requirement for the PEP-II RF control system is the need to control longitudinal coupled-bunch instabilities caused by the interaction of the beam with the accelerating mode of the RF cavities. This task will be handled by a combination of three feedback loops (Figure 1). The direct loop reduces the growth rate of the most strongly driven modes. The effectiveness of this loop is proportional to the total system group delay and is the reason for specifying a short klystron group delay (<150ns) over the necessary bandwidth (~1 MHz).

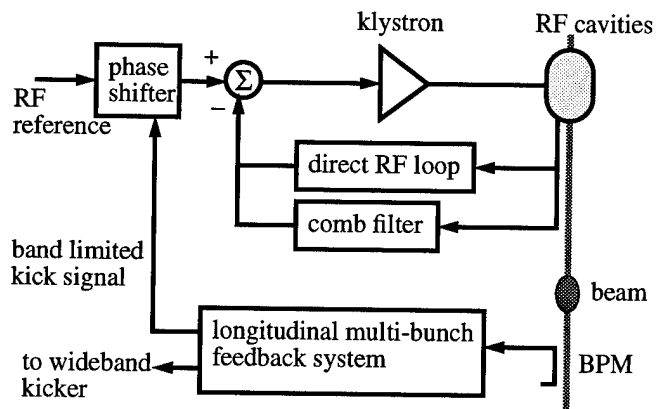


Fig. 1. Block diagram of RF feedback loops planned to control longitudinal instabilities driven by the fundamental mode.

The comb filter loop provides additional gain but only over a narrow band about each synchrotron sideband. The comb loop response operates around the direct loop damped cavity resonance providing gain to synchrotron sidebands over a span of several MHz. Together these two loops bring growth rates down from a few microseconds to several milliseconds.

The longitudinal multi-bunch feedback system will provide the final damping necessary to control the instability [3].

Only a few MHz of the available 500 MHz bandwidth can be passed through the klystron, so a filtered "kick" signal will be transmitted by each RF station. This signal operates through the closed-loop response of the klystron/cavity combination and is therefore very insensitive to system variations. In short the RF system becomes a powerful "sub-woofer" for the multi-bunch feedback system. Simulations show that these three feedback loops will provide a final damping rate of <500 turns in the most demanding 3 Amp. low energy ring (LER) case [4].

2. SYSTEM RF SIGNAL FLOW

The comb filters are implemented digitally as second order IIR filters followed by a 32 tap FIR group delay equalizer and a programmable 1-turn delay with 25 ns resolution. The 476 MHz RF carrier must be quadrature down-converted to baseband before being sampled. We have decided to implement all the RF signal processing at baseband. Figure 3 is a RF signal flow diagram for a PEP-II high energy ring (HER) station. A low energy ring (LER) station contains two cavities.

RF from each cavity is down converted to baseband using an I/Q detector. Each detector produces analog signals proportional to the real (I) and imaginary (Q) components of the RF signal with respect to the reference 476 MHz provided to each detector. To produce a signal proportional to the total station gap voltage, each of the baseband cavity signals must be phase shifted and scaled. This requires a 2-by-2 analog matrix multiplier with programmable coefficients and low group delay (Figure 2). Automated calibration routines will adjust the combining network and remove offsets.

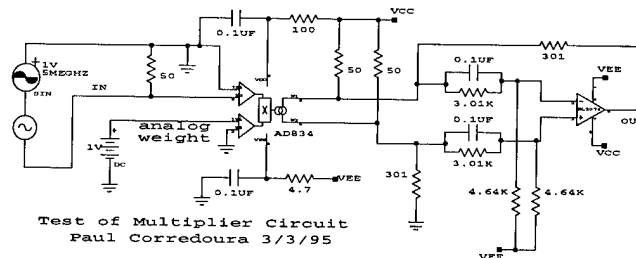


Fig. 2. Schematic of wideband dc-coupled multiplier used in the baseband I/Q modulator. Measured group delay is only 5 ns.

The baseband station gap voltage I/Q signals enter another I/Q modulator to allow adjusting the direct RF feedback loop. A parallel path exists to feed the digital comb filters. Another I/Q modulator follows the comb filters for loop parameter adjustment. Outputs of the two loops are combined and then subtracted from the baseband station RF reference. The reference signal also contains a phase modulation "kick" from the longitudinal multi-bunch feedback system. The I/Q error signals then pass through a PID controller. Lead compensation enhances the performance of the direct RF loop while integration reduces DC errors which directly translate to the 476 MHz system RF carrier.

*Work supported by Department of Energy, contract DE-AC03-76SF00515

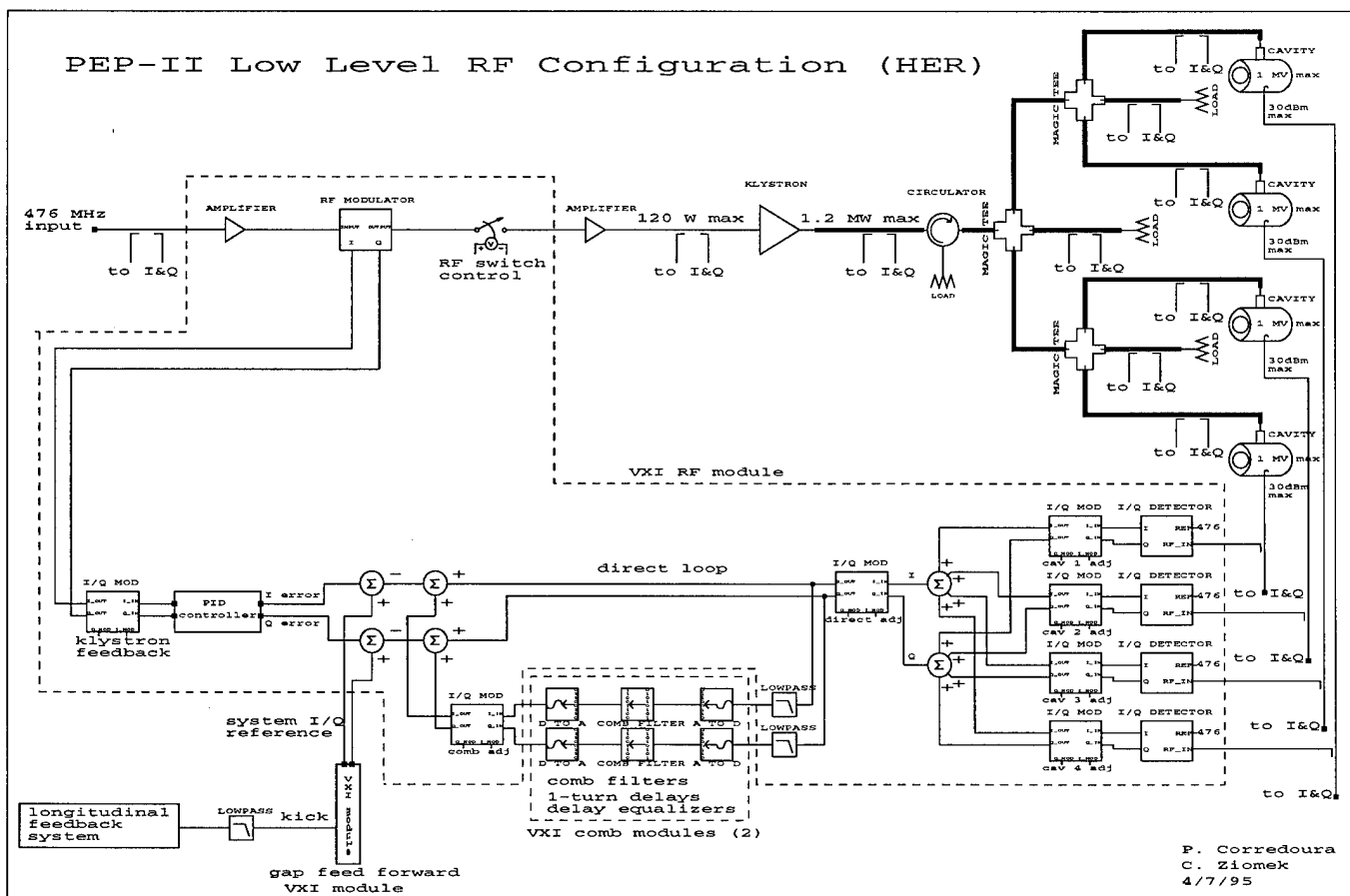


Fig. 3. Block diagram of a HER RF station showing down-conversion to baseband, signal processing and up-conversion to RF.

The signals pass through a final baseband I/Q modulator which is used to implement a digital feedback loop around the up-converter, pre-amplifier and klystron. This loop will be described in detail later in this paper. The final baseband drive signals are next up-converted to 476 MHz using a RF I/Q modulator. High level mixers are used in this device to minimize errors and to allow driving the solid-state klystron pre-amplifier directly. This topology removes the need for a RF limiter to protect the input stage of the solid-state amplifier.

3. ADDITIONAL CONTROL LOOPS

A multi-channel I/Q detector is being developed to create a modular RF measurement and control system [5]. Each channel will be capable of digitally measuring the I/Q components of the RF carrier over a programmable bandwidth producing non-aliased measurements for output rates ranging from 25 Hz to above 50 kHz. Errors will be $<0.05^\circ$ in phase and $<0.1\%$ in amplitude at a 5 kHz data rate. Proposed measurement locations are labeled as "to I&Q" in figure 3. Using this approach it becomes natural to implement digital control for cavity tuners, gap voltage, station phase, and klystron ripple reduction.

Klystron high voltage power supply (HVPS) ripple causes mainly phase modulation, although some amplitude modulation may also be present. The modulation appears at multiples of 60 Hz with the largest component at 720 Hz due to the power supply transformer configuration. This situation lends itself well to a digital control technique known as disturbance

estimation. Since the modulation (disturbance) is composed of several superimposed sinusoids at known frequencies, a state-space error estimator can be designed to track and cancel them [6]. Using digital I/Q information, the output phase and amplitude is calculated, compared to desired values and delivered to two separate state-space disturbance estimators. The estimators converge on the errors which are then subtracted from the system baseband reference. Analysis shows that disturbance reductions of 40 dB are possible.

A simulation of the klystron feedback loop was made using the Simulink control system analysis software package. The superposition of a 720 Hz sinusoid and a step function forms the disturbance for both phase and amplitude. The phase disturbance estimator was augmented with an integration function to track dc errors, this feature is not useful in the amplitude loop. White noise was also injected into each I/Q measurement. The sample rate was 5 kHz. Results of the simulation are shown in figure 4. Note that the 720 Hz phase error is effectively cancelled in 50 ms and the step disturbance is also removed. The amplitude error plot shows cancellation of the 720 Hz while ignoring the step. In each case the convergence rate of the estimators is completely programmable. Slower convergence yields greater noise immunity. In the actual PEP-II implementation the estimators will be designed to track all the necessary power line harmonics.

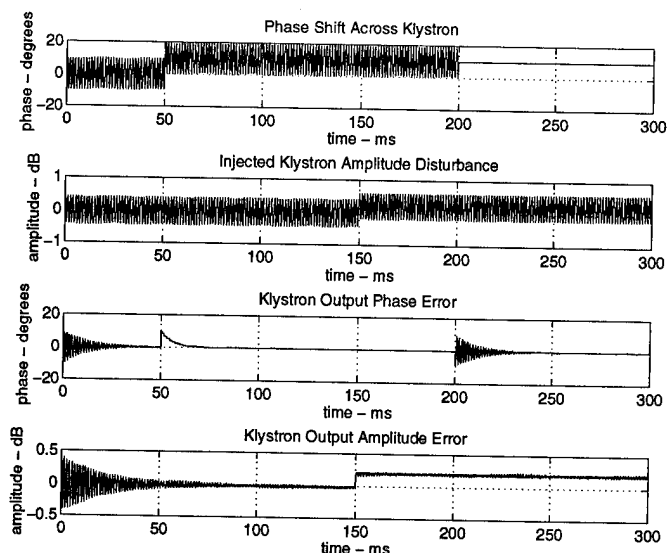


Fig. 4. Simulation of klystron ripple cancellation.

There are several other feedback loops, all of which will be implemented digitally. The baseband station I/Q reference must track the cavity transients caused by the ion clearing gap to prevent the klystron from reaching saturation. An adaptive feed-forward algorithm for minimizing klystron output power variation on a 1-turn basis has been developed and simulated [4]. The algorithm produces a station RF reference which minimizes the variation of the average klystron drive power. The adaption rate is designed to be slow compared to all the feedback loops in the system. In simulation this procedure reduces the klystron output power variations down to a few kW with a 5% beam gap.

The PEP-II klystrons will not contain collectors capable of absorbing the full 2 MW maximum available klystron beam power. A feedback loop measuring the klystron high voltage power supply output and the delivered RF power will be used to program the operating voltage. The goal will be to keep the klystron operating a fixed amount below saturation to insure sufficient AM gain for the RF feedback loops. Electrical efficiency also benefits from this strategy. Since the phase shift across the klystron varies by $\sim 14^\circ/\text{kV}$, the klystron phase loop discussed earlier must be capable of providing a large range of continuous phase shift. With the I/Q topology, phase may be rotated infinitely without discontinuities by simply applying the proper analog weights to the baseband I/Q modulator.

The PEP-II RF control system will also contain the "standard" feedback loops to control gap voltage, station phase and cavity tuners for each station. In addition to minimizing reflected power, the tuner loop must also balance the power delivered to each cavity. Each of these will also be implemented digitally. A major advantage of this approach is that configuring loops or adding new ones becomes a software task - provided that the measurement and control ports are already hardware supported. A programmable I/Q source will be included in the RF module to allow measuring loop responses by injecting white noise or a swept sinusoid. This feature will allow the possibility of automated calibration and remote operation.

4. SYSTEM HARDWARE TOPOLOGY

A PEP-II low-level RF station will be composed mainly of modules in a VXI crate. Like CAMAC, VXI has an addressable data bus and standard power supply voltages. VXI goes further to provide more power supply voltages, larger module size, better shielding and standards for neighboring modules to pass analog and digital information. With the planned baseband signal processing, many system connections can take advantage of the local bus connections effectively eliminating many external connections. Fast interlock functions for window arc detection and excessive klystron reflected power use VXI shared trigger lines to remove RF drive and fire the HVPS crowbar. The VXI module layout planned for PEP-II is shown below in figure 5.

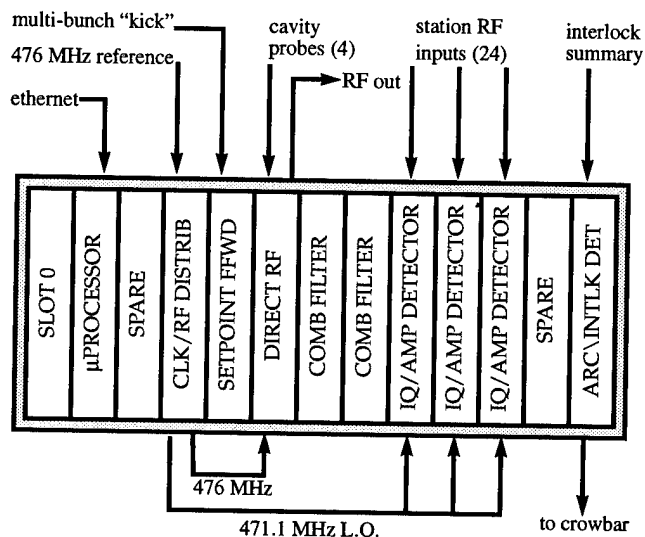


Fig. 5. Planned PEP-II HER VXI Crate Layout.

5. SUMMARY

The PEP-II low-level RF system design described is modern, cost effective and extremely flexible. The system is easily transportable and could be considered for use in other storage rings. Future papers will describe test results as the system is constructed.

6. REFERENCES

- [1] P. Corredoura, L. Sapozhnikov, R. Tighe, "RF Feedback Development for the PEP-II B Factory" Proceedings of the 1994 European Particle Accelerator Conference.
- [2] F. Pedersen, "RF Cavity Feedback", B Factories - The State of the Art in Accelerators, Detectors, and Physics", SLAC-400, November 1992, pp. 192-207.
- [3] J. Fox et al, "Feedback Control of Coupled-Bunch Instabilities", Proceedings of the 1993 IEEE Particle Accelerator Conference.
- [4] R. Tighe, P. Corredoura "RF Feedback Simulation Results for PEP-II", this conference (PAC 95).
- [5] C. Ziomek, P. Corredoura "Digital I/Q Demodulator", this conference (PAC 95).
- [6] P. Corredoura "Development of Digital Control for the PEP-II Klystrons" SLAC PEP-II Tech Note #60, 1994.

EXPERIMENT OF THE RF FEEDBACK USING A PARALLEL COMB FILTER

S. Yoshimoto, E. Ezura, K. Akai and T. Takashima
KEK, National Laboratory for High Energy Physics
1-1, Oho, Tsukuba-shi, Ibaraki-ken, 305, Japan

Abstract

In high beam-current storage rings like KEK B-factory (KEKB) [1], severe coupled-bunch longitudinal instability can be driven by the accelerating mode of significantly detuned RF cavities. The RF feedback with a comb filter, which can reduce the effective cavity impedance at the synchrotron sidebands of the revolution harmonics, is a possible way to damp the instability. This paper describes the results of the experimental RF feedback loop, which includes a N-path filter referred to as a parallel comb filter, a choke mode cavity, and a 1.2 MW klystron. With the feedback, the real part of the cavity impedance was reduced by 16 dB to 24 dB, at the five synchrotron sidebands 100 kHz apart each other.

I. INTRODUCTION

The cavity is detuned to a lower frequency than the RF frequency to compensate the reactive component of the heavy beam loading. This detuning causes the longitudinal coupled-bunch instability by creating the difference in the real part of the cavity impedance at upper and lower sideband of each mode. For KEKB the impedance of the accelerating mode is much higher than that of damped higher order modes (HOM's). Therefore, if the amount of detuning is comparable to or more than the revolution frequency, the accelerating mode would excite more severe instabilities than those by HOM's. For example if the KEKB low energy ring (LER) employs the normal conducting choke mode cavities [2] [3], the amount of detuning frequency is 236 kHz which is over twice as large as the revolution frequency. Figure 1 shows the growth rates of the coupled-bunch instabilities due to the accelerating mode of the choke mode cavities as a function of the beam current, together with the longitudinal radiation damping rate and the expected damping rate by the longitudinal bunch-by-bunch feedback. The first six coupled-bunch modes ($n = -1$ to -6) are so severe that these modes can not be damped by the longitudinal bunch-by-bunch feedback.

In order to cope with the difficulty, a novel three-cavity accelerating system, ARES, has been developing, which consists of an accelerating cavity coupled with a high-Q energy storage cavity through a coupling cavity [4]. Owing to its large stored energy it reduces the amount of detuning by an order of magnitude and can eliminate the coupled-bunch instability associated with the accelerating mode. Another possible means to deal with the problem is to use an RF feedback, which can reduce the cavity impedance seen by the beam at the synchrotron sidebands. As a backup scheme for ARES, we are developing an RF feedback system using a parallel comb filter. This filter enables us to adjust the feedback phase at sideband frequencies even if a frequency-dependent group delay is present around the feedback loop.

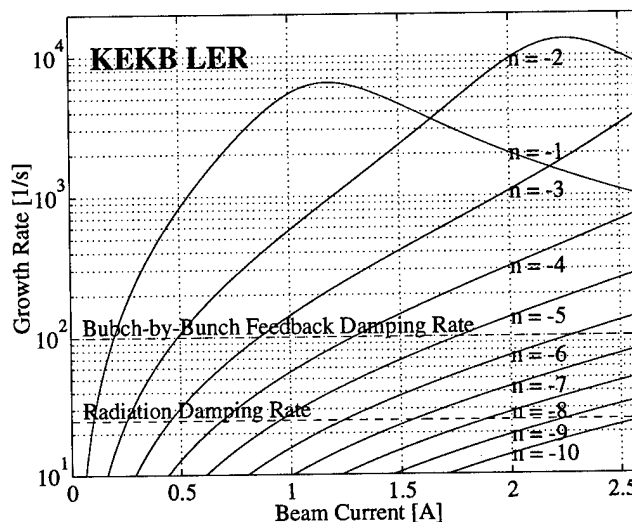


Figure 1. Estimated growth rate of longitudinal coupled-bunch instabilities due to the accelerating mode of choke mode cavities in the KEKB LER.

II. PARALLEL COMB FILTER FEEDBACK

The wide-band RF feedback is necessary to suppress several coupled-bunch modes. The maximum gain and bandwidth, however, are limited by the long group delay around the loop. To solve this problem, a feedback scheme using a comb filter combined with a one-turn delay has been proposed by D. Bousvard [5]. In the KEKB RF system, the feedback loop consists of not only constant group delay elements such as coaxial cables and waveguides, but also frequency-dependent group delay elements such as klystrons and cavities. Hence the phase variation of the feedback loop can be written in the form

$$\theta(\omega) = \theta_d(\omega) + \theta_k(\omega) = -\omega\tau_d + \theta_k(\omega), \quad (1)$$

where $\theta_d(\omega)$ is due to the constant group delay τ_d , and $\theta_k(\omega)$ is due to the frequency-dependent group delay. $\theta_d(\omega)$ is compensated by the one-turn delay feedback, but $\theta_k(\omega)$ is not. One way to compensate for the delay variation is to add a phase equalizer in the feedback path [6] [7]. The other way is to adjust the phase only at the synchrotron sidebands of the revolution harmonics, because we need to reduce the impedance only at these frequencies. This is realized by a N-path filter, each path of which consists of a narrow-band bandpass filter, a phase shifter for compensating the delay variation, and an attenuator for adjusting the loop gain. For convenience this filter is called here a parallel comb filter.

In the application of the RF feedback with a parallel comb filter, the RF signal sampled from the cavity has to be transposed

down to a convenient intermediate frequency before filtering, because it is difficult to realize the high-Q bandpass filter at this frequency range. For this frequency transposition, we developed a single-sideband (SSB) filter using broad-band quadrature hybrids, because the feedback is needed only in the lower side of the RF frequency. The block diagram of the RF feedback system using a parallel comb filter is shown in Figure 2.

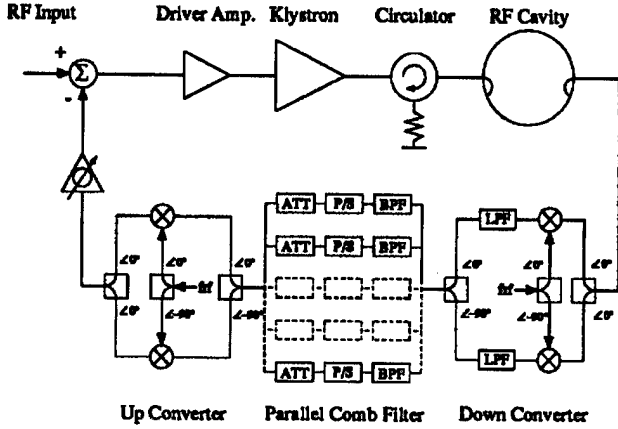


Figure 2. Block diagram of the RF feedback system using a parallel comb filter with frequency transposition by a single-sideband filter.

The transfer function of parallel comb filter can be written as

$$G(s) = \sum_{n=1}^N \frac{2\sigma_n s}{s^2 + 2\sigma_n s + \omega_{0n}^2} e^{j\theta_n(\omega)}, \quad (2)$$

where σ_n and ω_{0n} are the half bandwidth and the center frequency of the n -th filter respectively. For the ideal feedback, the each element of a parallel comb filter is adjusted as follows

- The center frequency of each filter is adjusted to the upper synchrotron sidebands of the revolution harmonics.
- The open loop phase response of the feedback loop is adjusted to zero for each frequency by the phase shifter of each path.

Hence, the center frequency of the n -th filter ω_{0n} is

$$\omega_{0n} = (h - n + \nu_s)\omega_{rev}, \quad n = 1, 2, \dots, N, \quad (3)$$

where h is the harmonic number, ν_s is the synchrotron tune, and ω_{rev} is the angular revolution frequency. By the phase shifter, $\theta_n(\omega)$ is adjusted to

$$\theta_n(\omega) = -(\theta_d(\omega_{0n}) + \theta_k(\omega_{0n})) = \omega_{0n}\tau_d - \theta_k(\omega_{0n}). \quad (4)$$

With this feedback, the real and the imaginary part of the cavity impedance is reduced in a same ratio at ω_{0n} , because the open loop transfer function is a real number. Therefore the real part of impedance seen by the beam is reduced by a factor $(1 + G)$, where G is a loop gain.

III. RESULTS OF MEASUREMENT

We made a preliminary experiment of the RF feedback with a prototype parallel comb filter. Figure 3 shows the experimental setup which includes a parallel comb filter, a choke mode cavity, a 1.2 MW CW klystron, and the constant group delay of 1 μ s mostly due to cables. This value of group delay is comparable to that of the KEKB RF system. As the first step of the experiment, we made a low power measurement. Only a small portion of the klystron output power was extracted with a 55 dB directional coupler, and was fed into the cavity. The detuning frequency and the loaded Q of the cavity were made equal to those used in the instability calculation shown in Fig. 1. The parallel comb filter was comprised of five individual LC bandpass filters arranged with 100 kHz intervals, and each filter has 2 kHz 3 dB-bandwidth. A network analyzer was used to measure the response of each component of the feedback loop to estimate the loop performance, and then the open and closed loop complex transfer responses were measured over a 1 MHz frequency bandwidth.

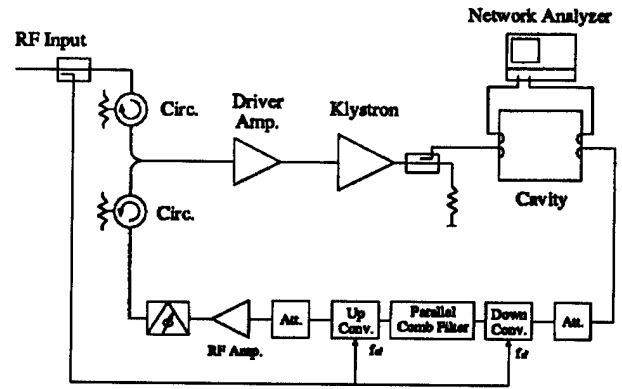


Figure 3. Block diagram of the experimental RF feedback loop which includes a parallel comb filter, a choke mode cavity and a klystron.

Figure 4(a) shows the measured open loop response of the feedback loop. The open loop phase response was adjusted to zero for each frequency by the phase shifter. The unwanted upper sideband of RF frequency was rejected by about 60 dB with the single-sideband filter. We were able to get 29.8 dB of the maximum gain and 25.2 dB of the loop gain with a phase margin 45° over a 1 MHz bandwidth.

The measured closed loop response is shown in Figure 4 (b). The top figure shows the normalized magnitude (broken lines) and the real part (solid lines) of the effective cavity impedance with or without feedback, as a function of normalized frequency $(f - f_{rf})/f_{rev}$. The bottom figure shows the phase response of the cavity with or without feedback. We were able to reduce the real part of the impedance by 16 dB to 24 dB with feedback. Table 1 shows the coupled-bunch mode number, the measured real part of the cavity impedance at the five synchrotron sidebands and the growth time of the coupled bunch instability with or without feedback.

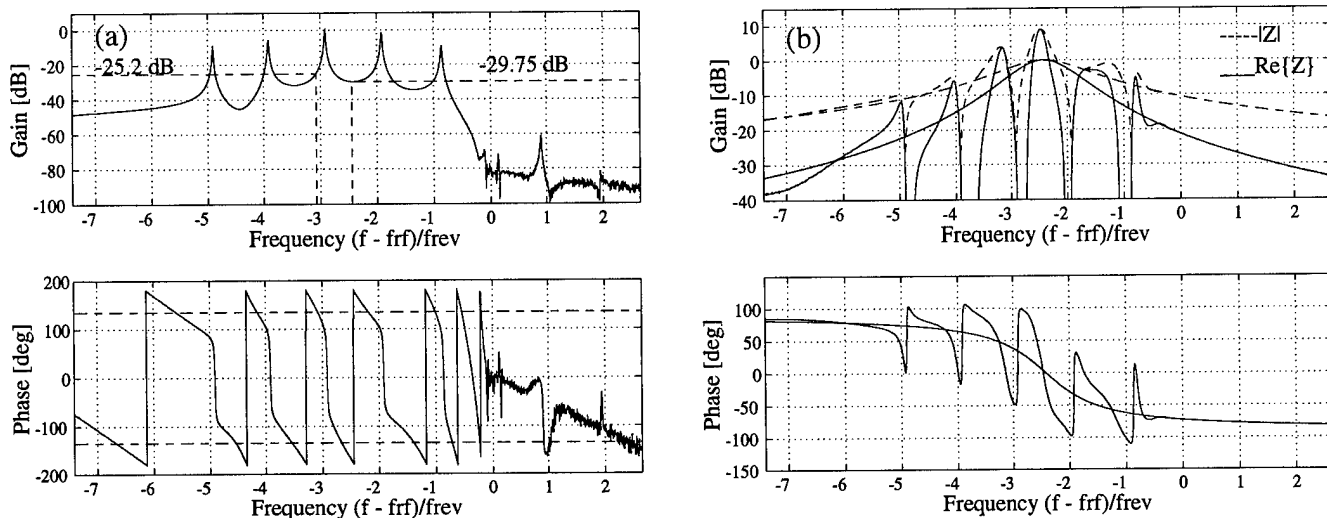


Figure 4. The measured open (a) and the closed (b) loop response as a function of normalized frequency $(f - f_{rf})/f_{rev}$.

Table I

The real part of the impedance and growth time of coupled bunch instabilities with / without parallel comb feedback

Mode	without feedback			with feedback		
	Re{Z ₊ }	Re{Z ₋ }	Growth time	Re{Z ₊ }	Re{Z ₋ }	Growth time
	[kΩ]	[kΩ]	[ms]	[kΩ]	[kΩ]	[ms]
-1	60.36	12.76	0.63	11.27	12.76	-20.16
-2	211.46	7.73	0.15	17.23	7.73	3.15
-3	163.33	5.16	0.19	10.63	5.16	5.48
-4	48.18	3.69	0.67	6.08	3.69	12.55
-5	20.56	2.76	1.68	3.43	2.76	45.18

IV. CONCLUSIONS

We made the experiment on the RF feedback loop, which includes the parallel comb filter, the choke mode cavity and the klystron. The real part of the cavity impedance were reduced by 16 dB to 24 dB at the five synchrotron sidebands 100 kHz apart. If the choke mode cavity is employed in LER, however, the loop gain must be improved by more than 10 db in order to damp the most severe modes ($n = -2, -3$) to a level which can be damped by the bunch-by-bunch feedback system. A feedback simulation shows that 10 dB gain improvement is possible by reducing the bandwidth of the filter to 1 kHz from the present value of 2 kHz. In the next experiment we will try to increase the loop gain up to 35 dB.

V. ACKNOWLEDGEMENTS

The authors would like to thank Professors S. Kurokawa and Y. Yamazaki for their support and helpful discussions.

References

- [1] "KEKB Accelerator Design Report", to be published as a KEK-Report
- [2] T. Kageyama et al. , "Design of a Prototype of RF Cavity for the KEK B-Factor (KEKB)", contributed to the 4th Euro. Part. Accle. Conf., (1994)

- [3] T. Kageyama , "Development of a HOM-Damped Cavity for the KEK B-Factor (KEKB)", WPQ17 in this conference
- [4] Y. Yamazaki et al. , "A Three-Cavity System which suppresses the Coupled-bunch Instability associated with the Accelerating Mode", Part. Accel. Vol. 44, p 107, (1994)
- [5] D. Boussard et al. , "Reduction of the Apparent Impedance of Wide Band Accelerating Cavities by RF Feedback", IEEE Trans. Nucl. Sci. Vol. NS-30, No. 4, 2239 (1983)
- [6] P. Corredoura. , "Klystron Equalization for RF Feedback", SLAC-PUB 6049 (1993)
- [7] P. Corredoura et al. , "RF Feedback Development for the PEP-II B Factor", contributed to the 4th Euro. Part. Accle. Conf., (1994)

DIGITAL TRANSVERSE BEAM DAMPERS FOR THE BROOKHAVEN AGS*

G.A. Smith, V. Castillo, T. Roser, W. Van Asselt, R. Witkover, and V. Wong
Brookhaven National Laboratory, Upton NY

ABSTRACT

A wide band, digital damper system has been developed and is in use at the Brookhaven Alternating Gradient Synchrotron (AGS). The system consists of vertical and horizontal capacitive pickups, analog and digital processing electronics, four 500 Watt wide band power amplifiers, and two pairs of strip line beam kickers. The system is currently used to damp transverse coherent instabilities and injection errors, in both planes, for protons and all species of heavy ions. This paper discusses the system design and operation, particularly with regard to stabilization of the high intensity proton beam. The analog and digital signal processing techniques used to achieve optimum results are discussed. Operational data showing the effect of the damping is presented.

INTRODUCTION

As the AGS moves towards its intensity goal of 60 Tp per cycle, there is an increasing need to reduce the effects of injection errors and transverse coherent instabilities that cause beam loss during acceleration. Active feedback systems, called beam dampers, designed

to reduce these effects, have been installed in both the vertical and horizontal planes and are now being used to maintain beam stability. This system functions by measuring the position of each beam bunch at one point in the ring and calculating a correction signal which it applies as the same bunch passes a strip line deflector located nearly one turn, or 2.5 usecs later.

A previous paper presented a broad view of the AGS damper[1], here the system will only be presented in summary. The focus of this paper is the design and operation of the digital processing architecture and data is shown demonstrating its effectiveness.

SYSTEM DESCRIPTION

A block diagram of one plane of the AGS Damper system is shown in figure 1. It is a wide band, bunch by bunch system with a bandwidth of 20 kHz to 5 Mhz. Beam bunch position is obtained from pairs of capacitive pick up electrodes (PUE) located in the downstream end of the F20 straight section. The 20 to 50 nsec bunch signals (frequency from 3 to 4 Mhz) go to high impedance preamplifiers less than 10 feet from the PUE's. The

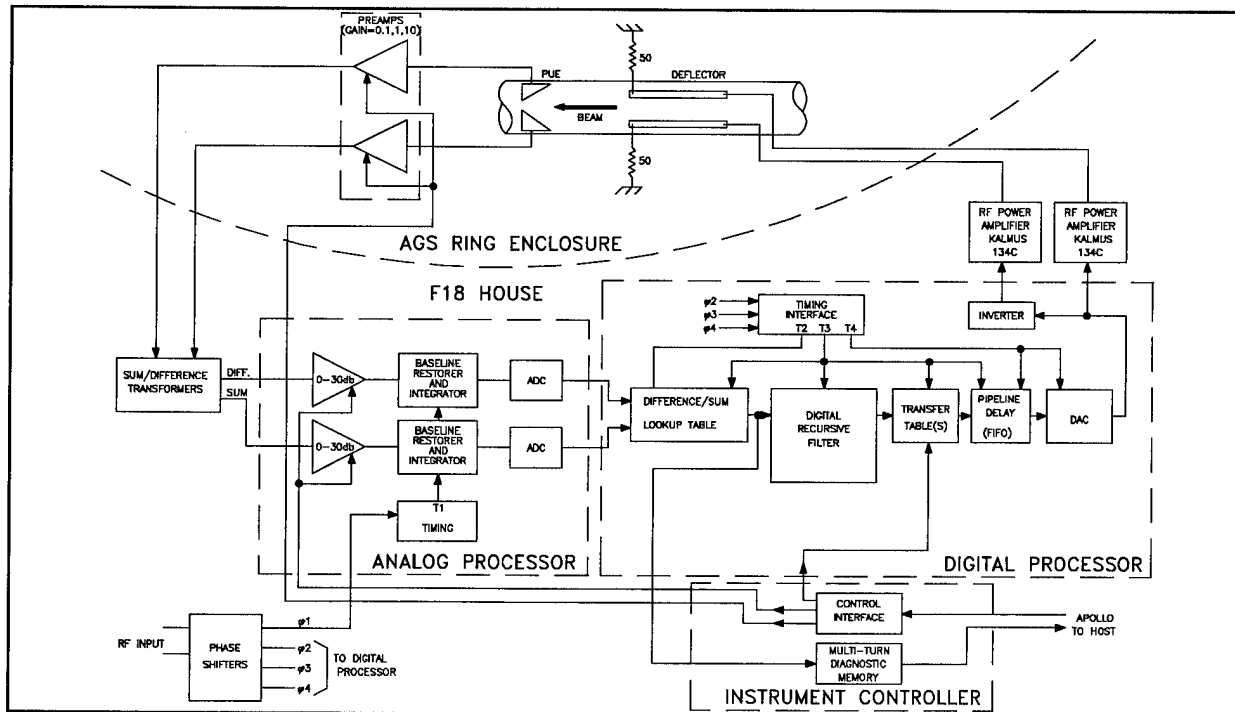


Figure 1 - Block diagram of one plane of the AGS Damper System

*Work performed under the auspices of the U.S. Department of Energy

amplifiers have gains of 10, 1, or 1/10 and impedance match the pulses to 50 Ohm semi-rigid coax that goes to electronics in one of the service buildings in the center of the AGS ring. Hybrid transformers form the sum and difference before the signals go to the analog processor.

In the analog processor, variable gain buffer amplifiers boost the signals another 0 to 30 db before the bunch signals have their base lines restored. This adds back the zero level of the signal lost in the capacitive coupling of the pick up by sampling the input between bunches. Sampling during this interval is done using a clock signal that is locked in frequency and phase with the beam through the entire cycle.

Next, each bunch signal is integrated for one RF clock cycle and the resulting voltage digitized by fast, 8 bit ADC's. Integration is necessary to obtain a centroid that is independent of bunch shape. The integrators used were originally developed for the AGS Booster Damping system[2]. They multiplex two internal integrating channels allowing one full RF period for the result to be acquired and the integrator to be reset.

The digitized sum and difference signals are the inputs of the digital processor. Data is indexed through the system by phased clock signals which are derived from the same source as the BLR clock. A programmable read only memory (PROM), acting as a look up table, generates difference divided by sum. This quotient, which represents the transverse bunch position, is output to a gate array programmed to implement a recursive transfer function using the algorithm discussed below[3][4]. In addition, the quotient is sent to an external memory. This memory is currently capable of storing 16000 turns of bunch data.

Finally, another PROM acts as a final correction signal look-up table. This table contains multiple pages of different transfer functions that can be selected remotely or by specific time events. This transfer tables provide for simple selection of digital gain and dead band options. Several inverse options in this table allow the system to be converted to anti-damping modes so that proper timing can easily be verified. Under the proper conditions the damper in these modes can function as a tune kicker.

Since the signal processing takes less than a revolution period a delay is needed for the correction value before it can be output. This delay is accomplished using a first-in, first-out (FIFO) memory. The FIFO is initialized with blank input bytes prior to strobing in the first data byte. This establishes a ripple through delay, in clock pulses, of input to output. The elegance of using a FIFO for this delay is that phase and frequency of the input and output data are independent.

In the final step the correction value is clocked into an eight bit analog to digital converter (DAC). The resulting analog signal is amplified by 500 Watt RF power amplifiers and applied to 50 Ohm strip line kickers at just the moment that the bunch reaches the strip lines.

THE DIGITAL PROCESSING ALGORITHMS

As the eight bunches circulate in the AGS, coherent motion of their centroids seen at a fixed point describes an ellipse in phase space in each plane, given by the Courant-Snyder invariant:

$$\varepsilon = \pi(\gamma x^2 + 2\alpha x x' + \beta x'^2)$$

where x and x' are the position and angle of the bunch as it passes a point along the orbit and ε is the beam emittance.

The purpose of the damper is to reduce ε . It can do so only by applying a kick (i.e. an angular deflection) to the bunch. The basic problem for the processing algorithm is to determine, for each bunch, the best magnitude and sign for a kick, given the PUE position measurements from one or more previous turns. One difficulty is that the measured positions contain closed orbit beam offsets as well as the coherent motion to be damped. Some filtering is needed to prevent the damper from attempting to correct this slowly changing closed orbit.

A recursive filter algorithm (IIR) has been chosen which acts as a high-pass filter. The recursive nature of the filter allows for the economical inclusion of a very large number of previous turns in determining the value of the constant closed orbit information.

The algorithm chosen implements the following finite difference equation:

$$y(n) - (1 - k)y(n - 1) = x(n) - x(n - 1)$$

where $x(n)$ is the digitized beam position measurement on turn n and $y(n)$ is the output correction. Figure 2 shows a flow graph of the filter which is implemented in a programmable gate array.

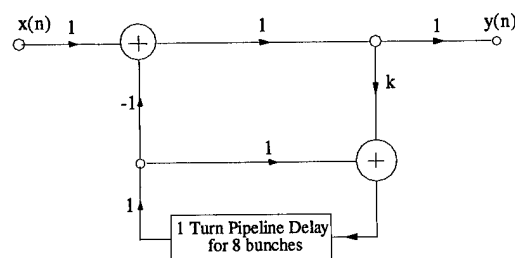


Figure 2 - Flow graph of the recursive filter algorithm with the 8 bunch pipeline delay

The transfer function of this filter for each bunch is:

$$H(z) = \frac{1 - z^{-1}}{1 - (1 - k)z^{-1}}$$

The value of k ($k < 1$) determines the low frequency cutoff. Smaller values of k push the cutoff frequency toward zero. In the AGS Digital damper this value is implemented by a shift register (divide by 2^n) with a choice of $n = 0, 1, 2$ or 3 .

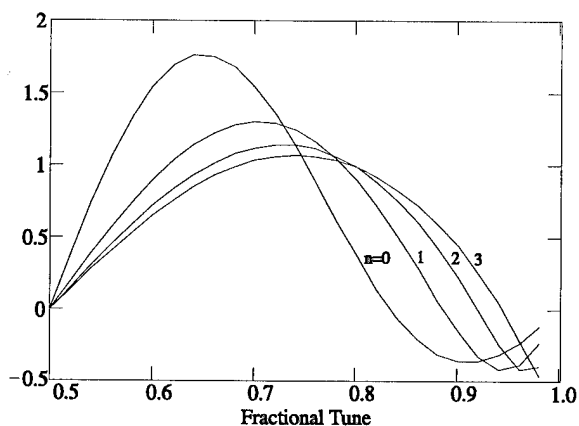


Figure 3 - Effect of the damper in reducing emittance as a function of tune for $n = 0, 1, 2$ and 3 using the PUE at F20.

In the AGS Damper, position data can be taken each revolution from either of two PUEs (in sections F20 or G7). The kick is applied at F20 on the turn following the position measurement. An analysis of the effectiveness of a kick in reducing ϵ shows that sensing and kicking at F20 favors fractional tunes close to 0.75, moving the sensing PUE 60° in betatron phase to G7 still produces a net reduction but favors higher fractional tunes[4]. Figure 3 shows the relative effect of the damper with the recursive filter in reducing beam emittance for $n = 0, 1, 2$ and 3 with the pick-up (PUE) at F20. Choosing larger values of n permits effective damping to extend to higher tunes and still obtain good closed orbit subtraction.

Following the filter is an additional lookup table referred to as the transfer table. This PROM contains up to 15 user selected ways to condition values of $y(n)$ before actually applying them to the output. These functions are used to provide different digital output gains, inversion to cause anti-damping or dead bands of various widths to filter noise.

THE DIAGNOSTIC MEMORY

One benefit of digitizing signals is that they may then be easily stored. One important adjunct to the digital damper system is the capacity to store up to 16,000 turns of position data in both horizontal and vertical planes, triggered by a time event. High level software then parses the data by bunch and can display it or save it for later analysis. While this "diagnostic memory" plays no part in actually damping the beam, it has proved to be an indispensable tool in the ongoing attempt to understand the AGS and in studying the effect of the dampers.

RESULTS

As the AGS has achieved intensities of 60 Tp and higher, the transverse dampers, especially in the vertical plane, have played a critical role. Data showing the effect of the dampers has been elusive however, simply because

the occurrence of instabilities is not very predictable cycle to cycle. One technique that has brought good results uses the AGS Tune Meter Kicker to create some coherence and records with the diagnostic memory the change with damping off and on. Figure 4 shows the results in the vertical plane early in the AGS cycle. In the

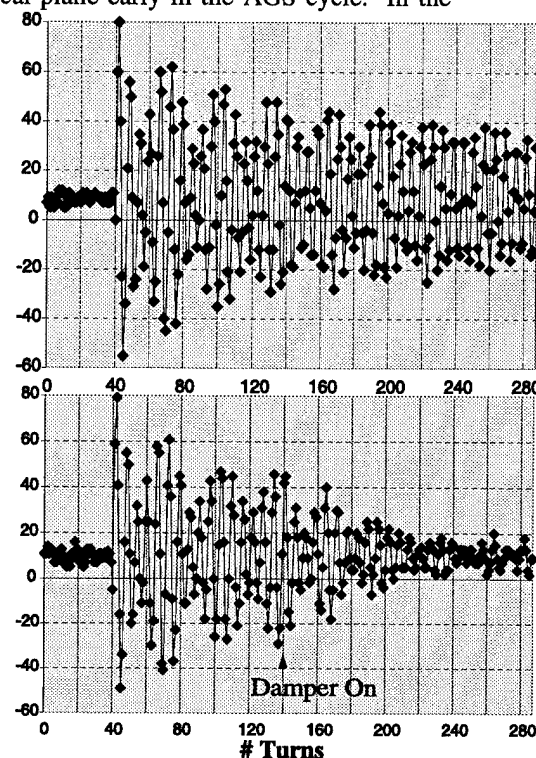


Figure 4 - Effect of damping on the coherence caused by the tune kicker (a) No damping, (b) Damping on 100 turns after tune kick

upper graph, the damper is off. In the lower graph, the damper is gated on at about 300 usecs or 100 turns after the tune kick. Within 100 turns of turn on the coherence caused by the kick is dramatically reduced.

REFERENCES

- [1] G.A. Smith, T. Roser, R. Witkov, V. Wong, Transverse Beam Dampers for the Brookhaven AGS, AIP Conference Proceedings 319, Beam Instrumentation Workshop, Santa Fe, NM 1993, pp309-318.
- [2] D. Russo, M. Brennan, M. Meth, T. Roser, Results from the AGS Booster Transverse Damper Proceedings of the 1993 Particle Accelerator Conference.
- [3] T. Roser, Transverse Damping Algorithms, Accelerator Division Technical Note, AGS/AD/Tech. Note No. 377.
- [4] T. Roser, Recursive Transverse Damping Algorithms, Accelerator Division Technical Note, AGS/AD/Tech. Note No. 398.

DESIGN OF THE PEP-II TRANSVERSE COUPLED-BUNCH FEEDBACK SYSTEM*

W. Barry, J. Byrd, J. Corlett, M. Fahmie, J. Johnson, G. Lambertson, M. Nyman, Lawrence Berkeley Laboratory, Berkeley, CA 94720, and J. Fox, D. Teytelman, Stanford Linear Accelerator Center, Stanford, CA 94309.

The design of a 250 MHz bandwidth, bunch-by-bunch feedback system for controlling transverse coupled-bunch instabilities in the PEP-II Asymmetric B-Factory is described. Relevant system parameters and specifications¹ are discussed along with the design of key system components. In particular, the design of the front-end receivers, baseband processing electronics, and kickers are presented in some detail.

I. INTRODUCTION

The PEP-II B-Factory, now under construction, is a high-luminosity, asymmetric electron-positron collider for studying and determining the origin of CP violation in the B-meson system². The collider basically consists of a 9 GeV high-energy storage ring (HER), and a 3.1 GeV low-energy storage ring (LER). Because of the high average beam currents (1 A HER and 2.14 A LER) in the rings, active feedback systems for controlling longitudinal and transverse coupled-bunch instabilities are required. The storage rings are designed to accommodate a large number of bunches, up to 3316 in buckets separated by 2.1 ns (476 MHz RF). As a result, a broad and dense spectrum of transverse coupled-bunch modes are driven by the higher-order transverse modes of the RF cavities and the transverse resistive-wall impedance. In order to effectively damp and control growth of these modes, a broad-band bunch-by-bunch feedback system, modeled after the ALS transverse feedback system³, has been designed.

Nominally, PEP-II will operate with every other bucket filled and a small ion clearing gap. In this case, the minimum required bandwidth for the feedback system is 119 MHz. However, the feedback electronics have been designed to have a bandwidth of 250 MHz in order to accommodate the possibility of operating the storage rings with every bucket filled. In this paper, the major accelerator parameters which drive the design of the feedback system are discussed as well as the key electronic components of the system.

II. SYSTEM REQUIREMENTS

The transverse feedback systems are conservatively designed to handle a worst-case scenario which assumes a 3 A beam in the LER at a fractional tune

of 0.9 (nominal LER current and tune are 2.14 A and 0.64 respectively). In this case, the fastest growing coupled-bunch mode is the $m = 0$ mode driven by the vertical resistive-wall impedance. Some major accelerator parameters pertinent to the design of the system for this case as well as some resulting feedback system specifications are given in table 1.

Parameter	Description	Value
E	Beam energy	3.1 GeV
f_{rf}	RF frequency	476 MHz
I_b	Average current	3.0 A
f_0	Orbit frequency	136.3 kHz
β_{av}	Average β	10 m
ν_f	Fractional tune	0.9
τ_b	Bunch spacing	4.2 ns
Z_{rw}	R-wall impedance	4.85 M Ω /m
α_0	Growth rate of $m = 0$ mode	3200 sec ⁻¹
$\partial V/\partial x$	Req'd feedback gain	14.6 kV/mm
R_s	Kicker shunt impedance	24 k Ω
P_k	Available kicker power	240 W
V_{max}	Max. available kick	3.4 kV
y_{max}	Max. mode amplitude	0.23 mm
V_{mode}	Voltage to excite y_{max}	71.3 kV-turn
Δf_{min}	Req'd bandpass	13.6 kHz-119 MHz
-	Electronics bandpass	10 kHz-250 MHz
-	Kicker bandpass	DC - 119 MHz
σ_y	Vert. beam size	0.16 mm
-	Req'd dynamic range	23 dB
-	Actual dynamic range	42 dB
y_{os}	Allowable effective orbit offset	1.8 mm

Table 1. Accelerator and feedback system parameters for assumed worst-case transverse coupled-bunch mode.

Several notes to Table 1 are in order. The nominal bunch spacing of 4.2 ns is specified because the machine will operate in this configuration for some period of time. As a result, the kickers, which are simple striplines, have been designed to cover the DC - 119 MHz band because they are more power efficient than shorter versions which would cover the DC - 238 MHz band. However, the remainder of the electronics is designed to cover the 10 kHz - 250 MHz band so that 2.1 ns bunch-spacing operation

*Supported by the US Department of Energy under Contract number DE-AC03-76SF00098 (LBL) and DE-AC03-76SF00515 (SLAC)

can be accommodated by simply installing shorter kickers and possibly additional power amplifiers.

In this worst-case scenario, the maximum controllable mode amplitude (assuming linear feedback) is 0.23 mm for the available kick voltage. Under normal operating conditions, the controllable amplitude is considerably greater. In any case, if the feedback system is operating from the time filling of the storage rings begins, one is hard pressed to identify a mechanism which would cause the accumulated modal voltage of 71.3 kV required to reach the amplitude limit of 0.23 mm. It should also be noted that simulations indicate¹ that any expected injection transients are easily damped by the feedback system. This is because the amplitudes of the normal coupled-bunch modes corresponding to the Fourier decomposition of the transient are extremely small. Injection transients can however produce large transient voltages which can saturate the feedback system. For this reason, damping of injection transients usually starts out in saturated mode where a fixed kick is given to the injected bunch until it is damped to a point where proportional or linear feedback takes over.

As a final note to Table 1, the required dynamic range is based on the requirement that the amplitude of betatron oscillations be damped to 0.1σ . For the case in Table 1, a 23 dB dynamic range is required to cover mode amplitudes ranging from the maximum of 0.23 mm down to $.1\sigma_y = .016$ mm. The actual dynamic range of the system corresponds to that of an 8 bit digital system, 42 dB. From the required and actual dynamic ranges, the maximum allowable effective orbit offset of 1.8 mm can be inferred. This quantity represents a static signal with frequency components at the orbit harmonics which passes through the feedback system reducing the dynamic range available for damping betatron oscillations. The effective orbit offset signal depends on the true closed-orbit offset, various electronic gain imbalances, fill pattern, and the effect of any offset rejection circuitry.

III. FEEDBACK SYSTEM OVERVIEW

The PEP-II transverse feedback system concept matches quite closely that of the current ALS system after which it is modeled³. Therefore, characteristics common to both systems will be described only briefly with more emphasis placed on design issues that are unique to the PEP-II system. The overall feedback system is shown in figure 1. The system utilizes two sets of button pickups, separated by approximately 90 degrees in betatron phase, for detecting beam moment, $I\Delta x$. By summing moment signals from the two pickups in proper proportion, a correction signal that is in quadrature with beam position at the kickers is obtained. This condition results in optimal damping and is adjustable to allow for changes in tune.

The beam moment signals are detected at the third harmonic of the RF (1.428 GHz) in order to exploit the

good sensitivity of the button pickups at this frequency. The signals are then demodulated to baseband with heterodyne receivers that also contain orbit offset rejection circuitry. Baseband processing consists of a system (shown as x and y attenuators) for proportional summing of the two pickup signals and a digital system that provides the necessary pickup-to-kicker timing delay. In addition, the digital electronics features circuitry for changing the sign and gain of the feedback for a single given bunch. This feature is used to trim the charges of single bunches to obtain a uniform fill or kickout an unwanted bunch in its entirety.

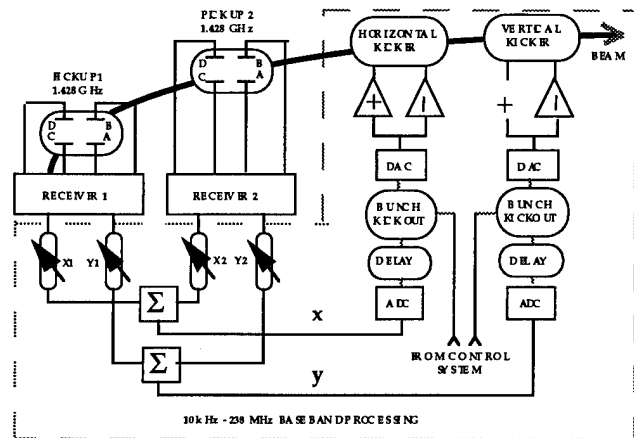


Figure 1. PEP-II transverse feedback system concept.

Finally, separate horizontal and vertical stripline kickers are used to apply the baseband correction kick to the beam. The kicker electrodes are individually driven with opposite polarities by 120 W (minimum), 10 kHz - 250 MHz, solid-state, Class-A, commercial amplifiers. Over most of the band, these amplifiers provide greater than 200 W.

Major components of the PEP-II systems not common to or differing from the present ALS system are the digital electronics and the receivers described below.

IV. RECEIVER DESIGN

The PEP-II transverse feedback system receiver design is shown in figure 2. Beam signals induced on each pickup are first bandpass filtered then differenced and summed in the monopulse comparator to produce true x and y beam moment signals at the 1.428 GHz carrier frequency. Subsequently, these signals are down-converted to baseband using standard heterodyne detection.

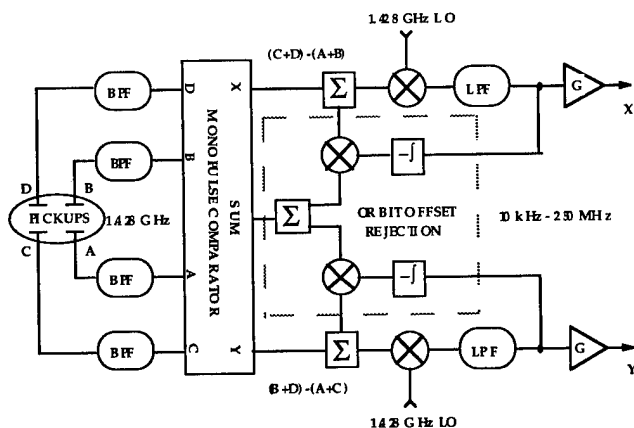


Figure 2. Receiver design.

Of special interest is the orbit offset rejection circuitry in the dashed box. In general, the x and y moment signals contain unwanted components due to static beam orbit offset and, equivalently, imbalances in the gains of the button pickups and the electronics associated with them. These offset signals are independent of the betatron motion and have spectral components only at harmonics of the orbit frequency. In addition, the spectrum of the offset component of the moment signal is, apart from amplitude, identical to that of the signal derived from the sum of all four pickups. Thus, to remove the offset component of the moment signal, some fraction of the sum signal from the comparator is added to or subtracted from it. As shown in figure 2, this process is automated in a feedback loop in order to accommodate changes in closed-orbit offset. Based on an assumed 1 mm closed-orbit offset and worst case 3 dB imbalance in pickup gains, this system must provide 11 dB of offset rejection in order to meet the 1.8 mm effective offset limit set forth in table 1. Early tests of this technique indicate that at least 10 dB of rejection is obtainable.

V. DIGITAL COMPONENTS

The digital components of the system basically consist of a pickup-to-kicker timing delay and circuitry for changing the sign and gain of the feedback for a given bunch. In addition, a digital output of the feedback signals will be available for diagnostic purposes.

For the delay, the baseband signal is sampled at 476 megasamples per second into 8 bit bi-polar digital form and stored in a circular buffer. The buffer is implemented with a fast ECL RAM array and ECLips ECL logic devices. On alternate memory cycles, the RAM is written (into incrementing addresses) with the digitized correction signal then a previously stored value is read out from an offset address. The address offset is programmable and determines the amount of delay applied to the correction signal.

The delayed data is then directed through two parallel paths. In one path, the data remains unaltered. In

the other path, the data undergoes a sign and possible gain change for bunch kickout/trim. A fast multiplexer at the input to a digital-to-analog converter chooses between the normal feedback path and the kickout path on a bunch-by-bunch basis. In this manner, any number of selected bunches may be kicked out or trimmed simultaneously.

VI. CONCLUSION

A broadband feedback system for controlling transverse coupled-bunch instabilities in the PEP-II B-Factor has been designed. The system is modeled after the present ALS transverse system which is presently nearing the completion of a successful commissioning⁴. The design philosophy, as with the ALS system, has been one of simplicity and user friendliness. Given our ALS experience, we look forward to the successful commissioning and operation of the PEP-II systems.

VII. ACKNOWLEDGMENTS

The authors wish to thank the many members of the LBL/SLAC-ALS/PEP-II feedback systems collaboration for many enlightening discussions and useful suggestions.

VIII. REFERENCES

- [1] J. Byrd, "Simulations of the PEP-II Coupled-Bunch Feedback Systems", These Proceedings.
- [2] "PEP-II Conceptual Design Report", LBL-PUB-5379, SLAC-418, CALT-68-1869, UCRL-ID-114055, UC-IRPA-93-01, June, 1993.
- [3] W. Barry, J. Byrd, J. Corlett, J. Hinkson, J. Johnson, and G. Lambertson, "Design of the ALS Transverse Coupled-Bunch Feedback System", Proceedings of the 1993 IEEE Particle Accelerator Conference, Washington DC, May, 1993.
- [4] W. Barry, J. Byrd, J. Corlett, J. Johnson, G. Lambertson, and J. Fox, "Commissioning and Operation of the ALS Transverse Coupled-Bunch Feedback System", These Proceedings.

Simulations of the PEP-II Transverse Coupled-bunch Feedback System*

J. M. Byrd

Lawrence Berkeley Laboratory
Berkeley, CA 94720 USA

Abstract

We report the results of a computer simulation of the PEP-II transverse feedback (TFB) system including single particle transverse beam dynamics and measured RF cavity higher order modes. The simulation addresses issues such as required FB power and gain, noise, bunch offsets, and varying initial bunch conditions. We also summarize a simulation of a proposed mode of operation of the feedback system where selected individual bunches are driven to large amplitudes in order to trim their current.

I. INTRODUCTION

Coupled-bunch instabilities pose one of the problems in operation of high-current, multibunch storage rings such as PEP-II, an asymmetric electron-positron collider with energies of 3.109 and 9 GeV. Electromagnetic wakes excited in vacuum chamber components such as RF cavities couple the oscillations of successive bunches which can lead to exponentially growing oscillations. Because transverse oscillations especially degrade the performance of a collider, a transverse feedback (TFB) system is being designed to damp the oscillations[1]. To help guide the feedback design process and to further understanding of multibunch phenomena, a computer simulation of the oscillations and the corresponding feedback systems has been developed. Instabilities are generally of more concern for the PEP-II low energy ring and thus this paper treats only that case although similar studies have been conducted for the PEP-II high energy ring.

The proposed TFB system is a so-called bunch-by-bunch system which works independently on each bunch. It is very similar to one now in use at the Advanced Light Source (ALS). Implicit in the requirement of acting on each bunch is that the minimum bandwidth of the system be greater than half the bunch frequency, which for PEP-II is 238 MHz. Because the major expense in these systems are the broadband power amplifiers, one of the most important issues in the simulation is to determine if the specified power is adequate to damp the beam under a variety of conditions.

The ability of the TFB to control individual bunches has led to a proposal to use the system as a means of trimming or eliminating individual bunches without affecting other bunches by driving them to large transverse amplitudes where they would encounter aperture restrictions. One issue which arose from previous experience with the ALS system is the nonlinearity of the betatron motion causing decoherence and effectively limiting the amplitude to which the bunch could be driven. The last section of this paper briefly describes a multiparticle/bunch simulation

*This work was supported by the Director, Office of Energy Research, Office of High Energy and Nuclear Physics, High Energy Physics Division, of the U.S. Department of Energy under contract No. DE-AC03-76SF00098.

Symbol	Description	LER Value
E	Beam energy (GeV)	3.109
C	Circumference (m)	2199.318
f_{rf}	RF Freq.	476 MHz
N	No. of bunches	1658
I_0	Beam current (A)	2.14
N_{rf}	No. of RF cells	6
$Q_{x,y}$	x,y β -tron tunes	32.28,35.18
$\langle\beta_{x,y}\rangle$	aver. $\beta_{x,y}$ (m)	10.84,9.95

Table I

PEP-II LER parameters used in the simulations.

including nonlinear effects in both planes which addresses the issue of decoherence with positive feedback gain.

II. BEAM DYNAMICS AND WAKE VOLTAGES

The beam dynamics in this study are simulated using common tracking techniques at a single point in the ring, where difference equations are used to describe the discrete time evolution of the beam oscillations and wake voltages[2], [3]. This approximation is valid for all of the effects we wish to study, especially since most of the wake voltages are localized at the RF cavities. One notable exception is the distributed wake of the resistive wall impedance, which results from the skin effect on the inner vacuum chamber wall. The local approximation for the resistive wall wake is valid when the corresponding growth or damping rate is slow compared to the betatron oscillation period. This condition is true for all cases studied here. Tracking is done in both transverse directions, which we generically label x . The turn-by-turn difference equations for x and x' for a linear lattice are given by

$$x_{i+1} = \cos 2\pi Q_x x_i + \beta_x \sin 2\pi Q_x x'_i (1 - 2\lambda_x) \quad (1)$$

$$x'_{i+1} = -\frac{1}{\beta_x} \sin 2\pi Q_x x_i + \cos 2\pi Q_x x'_i (1 - 2\lambda_x) + \frac{\Re(\tilde{V}_{w,i+1})}{E} \quad (2)$$

where the tracking is assumed to be at a symmetry point with $\beta' = 0$ and zero dispersion. The tunes and β functions are assumed to be constant as a function of amplitude and energy. Amplitude-dependent tunes generally lower the effective coupled-bunch growth rates but in this paper we are restricting ourselves to a worst case scenario with no nonlinearities. The effects of nonlinearities are discussed at the end of this paper with regard to driven motion. Effects of energy oscillations are ignored here. The damping term, λ_x nominally represents

the radiation damping but can be adjusted to approximate coherent damping effects such as head-tail damping and decoherence which the rigid-bunch simulation cannot model.

The transverse wake voltage from dipole HOMs is found by summing the contributions from all previous bunch passages. Tracking of the wake voltage is done by treating it as a complex phasor, \tilde{V}_w . The difference equation for \tilde{V}_w is given by

$$\tilde{V}_{w,i+1} = \tilde{V}_{w,i} e^{(j\omega_r + \frac{\omega_r}{2Q})\Delta t} - j2k_{\perp} q x_{i+1} \quad (3)$$

where k_{\perp} is the transverse loss parameter, ω_r is the angular resonant frequency, and x is the transverse offset at the location of the HOM. The wake voltage is out of phase with the motion and thus does not influence the charge which generated it.

As mentioned above, the resistive wall wake voltage is the only non-localized wake of concern. The approximate localized wake voltage for a round pipe is given by

$$V_{w,rw}(t) = qx \frac{lc}{\pi b^3} \sqrt{\frac{\mu_0 \rho}{\pi}} \frac{1}{\sqrt{t}} \quad (4)$$

where l is the length of the vacuum chamber (usually the ring circumference), ρ the material resistivity, and b the chamber radius. Because the inverse square root time dependence of the wake voltage, it is not possible to use the computational trick in Eq. 3 to advance the wake voltage each discrete time step. The voltage for bunch passage must be remembered and individually recalculated each iteration. Since it is not practical to store all previous wake voltages, we use simply cut off the wake voltage after several turns. The number of turns necessary to adequately simulate the wake voltage was determined empirically by increasing the value until no further change in the observed growth rate was seen, which also was resulted in a growth rate in agreement with the calculated growth rate. The value used was either 4 or 5 turns.

A. Feedback Systems

The TFB system measures a transverse position error and produces the appropriate angular kick to correct the error which is applied to the beam on a subsequent turn. Because the tracking in this simulation is done at only a single point in the ring, we are currently using a linear combination of the transverse position measured on the two previous turns to calculate the correct kick given by

$$V_{fb} = G_{fb} E \left(\frac{x}{\tan \phi_x \beta_x} - \frac{x_{-1}}{\sin \phi_x \beta_x} \right) \quad (5)$$

where G_{fb} is the TFB gain and usually ranges from 0.03–0.3, x and x_{-1} are the positions on the current and previous turns. The FB voltage limits at the maximum amplifier output, which we take here as 2.2 kV.

DC beam offsets at the FB pickups must be reduced by the TFB to maintain the dynamic range of the system. Because the simulation does not explicitly model a filter, beam offsets are simulated by simply assuming that a filter reduces the offset by a factor of 10, which has been shown to be easily achieved.

Freq (MHz)	R_{\perp} ($k\Omega/m$)	Q
1674	0.385	2134
1435	0.342	3955
1311	0.080142	498
1757	0.027283	7129
1588	0.0121	178
1203	0.0103	1588

Table II

Strongest PEP-II RF cavity dipole HOM parameters.

III. RESULTS

A. Multibunch Damping

For the injection scheme of PEP-II, a single bunch out of 1658 is injected with 1/5 the the total bunch charge. For 5 mm maximum offset of the injected charge, the centroid offset is 1 mm. The dipole HOMs used in the simulation are listed in Table II and the resistive wall impedance is $Z_{rw} = 1.53/\sqrt{n} M\Omega/m$, where n is the frequency scaled by the orbit frequency. In addition, a 10% bunch-bunch coupling through the TFB system was used to simulate its finite bandwidth.

The result of an injection transient is shown in Figure 1. Figure 1b shows an expanded view of the other bunches excited by the injected bunch. Figure 1c plots the amplitude of the voltage kick. For most of the transient, amplifier is saturated at its maximum value at the injected bunch but operates proportionally for all other bunches. As a result, the damping of the injected bunch is linear in time until the amplifier comes out of saturation where it becomes exponential. The injected bunch is well-damped before the next injection. The steady-state offset of the damped beam is discussed above and results in a steady-state kick from the amplifier which consumes about half of the available voltage.

B. Single Bunch Kickout

To test whether a single bunch could be driven to large amplitudes by the TFB, we tested the simulation with only a single bunch but using 500-1000 particles/bunch. The transverse distribution was initialized to a Gaussian and a random Gaussian deviate is added to Eqns.1 and 2 according to ref. [2].

The tune spread resulting from the nonlinearity was included in the tracking in a quasi-linear manner by implicitly making the betatron tunes a function of amplitude in the form

$$Q_x(\hat{x}, \hat{y}) = Q_{x0} + k_x \hat{x}^2 + k_{xy} \hat{y}^2 \quad (6)$$

and

$$Q_y(\hat{x}, \hat{y}) = Q_{y0} + k_y \hat{y}^2 + k_{yx} \hat{x}^2 \quad (7)$$

where $\hat{x}^2 = x^2 + (\beta x')^2$. The coefficients k_x , k_{xy} , and k_y are determined from the actual PEP-II lattice[4]. This approach allows us to study the effects of the tune spread without including the effects of the entire lattice and ignores nonlinear dynamics issues.

Particles were considered lost if they exceeded amplitudes of $> 10\sigma$ in either plane. In the simulation, the FB gain was reversed and increase to a large value to destabilize the motion in

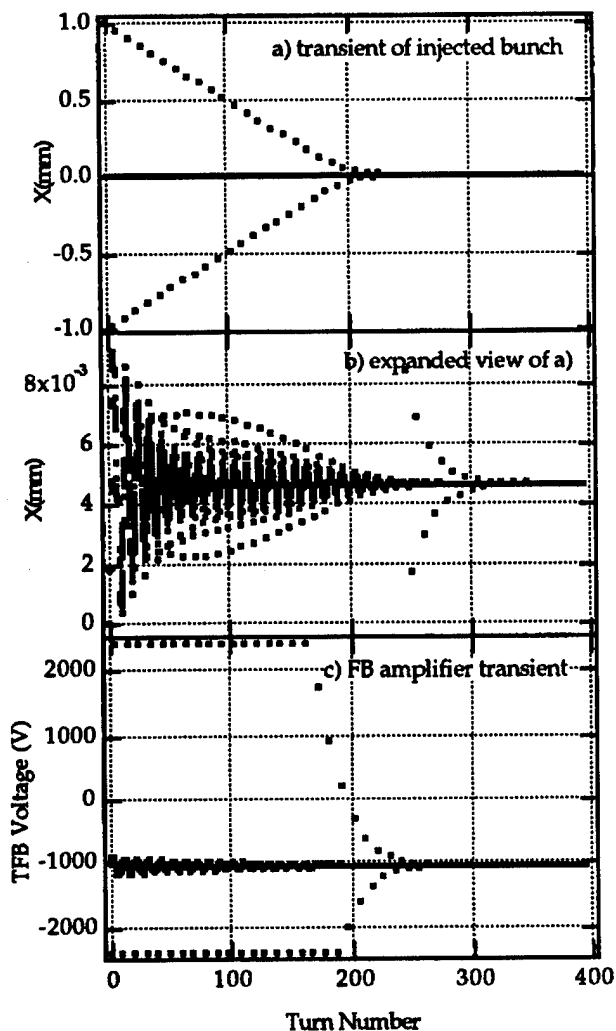


Figure 1. Transient response of beam and TFB at injection. a) Position vs. turn for 1 mm injected bunch. b) Expanded view of a) showing transient of stored bunches. c) Response of TFB showing saturation of injected bunch and DC response from off-set.

the desired plane, while the FB gain remained constant in the other plane. We found that it was possible to drive the bunch vertically and cause controlled beam loss but very difficult to drive a bunch horizontally with the available voltage. This occurs because the larger horizontal beam size allows a larger betatron tune spread than in the vertical plane. The larger tune spread across the bunch causes individual particles to dephase or decohere faster, effectively damping the centroid motion. Because the TFB operates on the centroid position of the bunch, the gain effectively vanishes. The situation is illustrated in Figure 2 which shows the horizontal phase space distribution at 4 stages between 0 and 1600 turns. About 50% of the beam has exceeded an amplitude of 10σ after 1600 turns. The vertical plane shows very little decoherence before it is lost.

IV. CONCLUSIONS

The specifications of PEP-II TFB system are adequate for damping the expected transverse instabilities. Trimming of in-

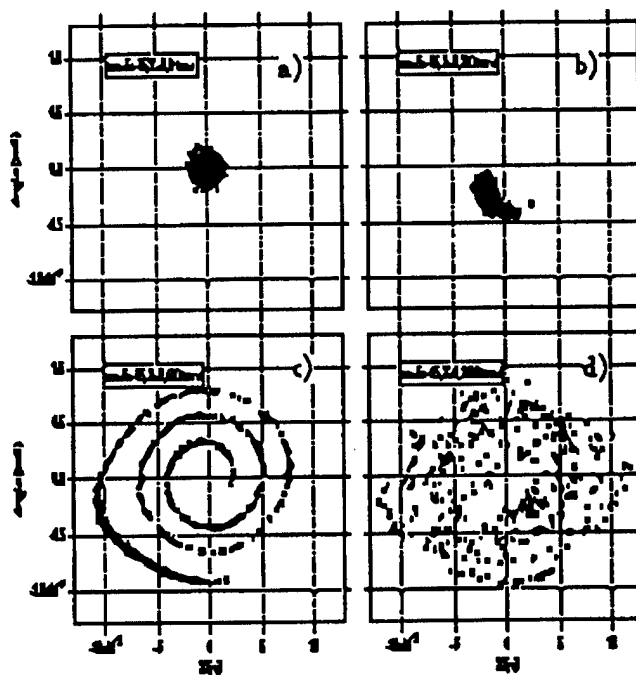


Figure 2. Horizontal phase space distribution (angle vs. position) at 4 stages following initiation of single bunch kickout. After 1600 turns 50% of the beam has exceeded an amplitude of 10σ but there is very little centroid motion.

dividual bunches is feasible if driven in the vertical direction.

References

- [1] W. Barry, et. al., *Design of the PEP-II Transverse Coupled-Bunch Feedback System*, these proceedings.
- [2] R. Siemann, *Computer Models of Instabilities in Electron Storage Rings*, in *The Physics of Particle Accelerators*, AIP Conf. Proc. **127**, 431 (1983).
- [3] K. Thompson, *Transverse and Longitudinal Coupled Bunch Instabilities in Trains of Closely Spaced Bunches*, PAC 1989 (1989).
- [4] E. Forest, et. al., *Sources of amplitude-dependent tune shift in the PEP-II design and their compensation with octupoles*, EPAC 1994, May 1994.

FERMILAB BOOSTER LOW LEVEL RF SYSTEM UPGRADES

Robert C. Webber, Fermi National Accelerator Laboratory,* Batavia, IL 60510 USA

Status of and plans for upgrades to the aging Booster Low Level RF phase and frequency control system are described. The central feature of the new system is replacement of the existing analog voltage controlled oscillator (VCO) with a direct digital synthesizer (DDS) operating directly at the Booster 37-53 Mhz frequency. This eliminates historically chronic problems with VCO frequency drift and setting inaccuracies. Initial implementation consists of the DDS operating under digital signal processor (DSP) control to generate the open loop frequency sweep profile and to close the beam phase-locked frequency loop. Further iterations will bring synchronous phase control, RF station counter-phasing operations at injection and extraction times, and the Booster to Main Ring beam transfer synchronization and phase-lock process under precise and programmable digital control. These improvements will facilitate and provide the enhanced flexibility for features, including new transfer synchronization options, expected to be necessary for continued high intensity operation from now into the Fermilab Main Injector era.

I. INTRODUCTION

The rapid cycling Fermilab Booster operates on a 15 Hz sinusoidal magnetic cycle to accelerate protons from 400 MeV to 8 GeV. At a harmonic number of 84, the Booster rf must sweep from 37.8 to 52.8 Mhz during the 33.3 msec acceleration interval, exhibiting a maximum df/dt of 1.74 Mhz/msec at 4 msec into the cycle. Figure 1 shows selected Booster parameters as a function of time in the cycle. The Low Level RF (LLRF) System provides to the high power systems, each driving one of 17 accelerating cavities, a global rf reference signal at the proper frequency and phase to control beam energy during acceleration and to synchronize bunch-to-bucket transfer of the beam to Main Ring. Programmable feedforward curves and real-time beam feedback signals function within the LLRF to provide stability to the acceleration process and facilitate operator control of radial beam position during the cycle.

II. MOTIVATION FOR THE UPGRADE

The operational LLRF system in Booster today exists in much the same form and utilizes the same hardware as described by Meisner [1], Kerns [2], Jachim [3], and Ducar [4] over the past 16 years. This equipment has served the Booster well for as much as 20 years, but obsolete components now present maintenance problems and the system lacks features and flexibility important for present high intensity operation.

* Work supported by the U.S. Department of Energy under contract No. DE-AC02-76CH03000.

Figure 2 is a functional diagram of the present system.

Specific goals of the current upgrade effort include: 1) elimination of VCO frequency drift with time and temperature, 2) capability of switching between operational states on a machine cycle-by-cycle basis, 3) ability to synchronize a gap in the Booster beam to the extraction kicker for low loss, properly clogged transfer to the Main Ring, 4) built-in programmable flexibility, 5) enhancement of long term operational reliability and maintainability, and 6) improved remote diagnostic features.

III. STATUS

Replacement of the analog VCO frequency source with a more stable and precisely controllable source is key to the merit and success of any upgrade of the Booster LLRF. The feasibility of using a DDS operating directly at the Booster frequency to accelerate beam was demonstrated more than two years ago by Mestha et al.[5,6] In February of this year, the DDS used for that demonstration was revived, coupled with a new digital signal processor, and made to accelerate beam in the Booster once again. This proof-of-principle DSP/DDS frequency source has now been used to operate the Booster for short periods while running for antiproton production. Its use other than for limited periods under closely monitored conditions is precluded, not by performance limitations, rather by lack of suitable interfacing to the Fermilab accelerator

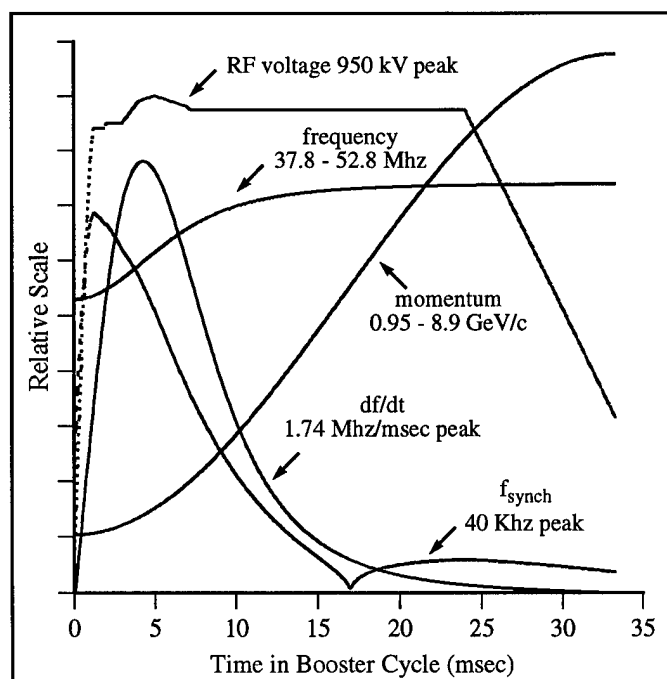


Figure 1: Selected Booster Parameters.

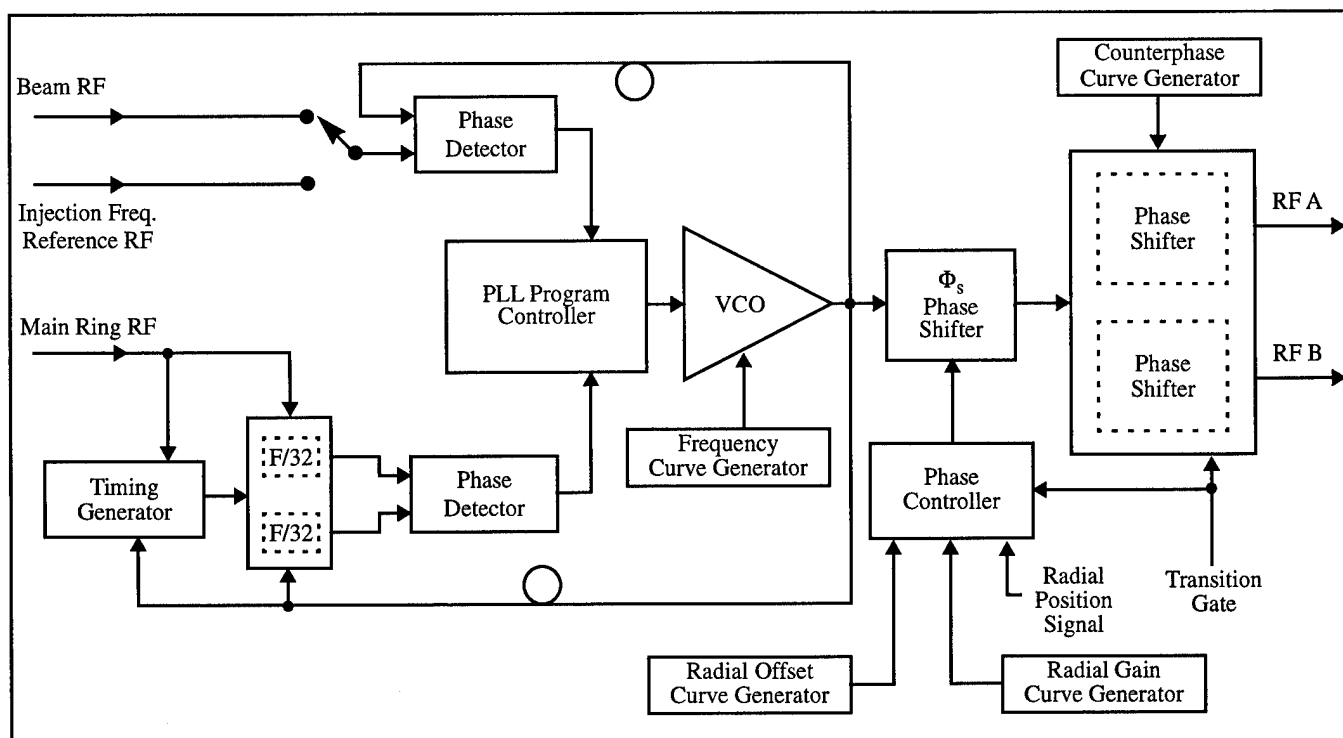


Figure 2: Booster LLRF Block Diagram

control system network (ACNET).

The prototype DSP/DDS frequency source is designed to function within the present LLRF system by simply substituting for the analog VCO and the CAMAC frequency curve generator. Since the LLRF system provides damping of coherent beam phase oscillations by operating the VCO in a beam-referenced phase-locked loop configuration, the DSP/DDS combination is required to meet all performance criteria necessary to stably fulfill that function. The crucial parameters are loop bandwidth and signal transport delay. Given the maximum synchrotron frequency of 40 KHz (Fig. 1), a real-time loop bandwidth of several times that is required, implying correspondingly short signal transport delay times.

As shown in Figure 3, the prototype source is comprised of an Analog Devices ADSP-21020 DSP, a Stanford Telecom STEL-2273A DDS, and two high speed analog to digital convertors (ADCs). A DOS-based computer hosts the software development and program downloading tools. The DSP is used directly as provided on the ADSP 21020 EZ-LAB Evaluation Board. It runs with a clock speed of 25 Mhz. This DSP was available as a result of concurrent Main Ring and Tevatron LLRF improvement efforts utilizing this DSP family. The 2273A DDS is a board level product based on Stanford Telecom's STEL-2173 GaAs numerically controlled oscillator chip. It was selected for this application after DDS products from another manufacturer were tested and observed to exhibit unacceptable phase discontinuities when programmed through certain frequency transitions. Though specified up to 1 Ghz, the DDS is operated with a 576 Mhz clock to minimize the need for high order control bit manipulation and to avoid certain close-in spurious frequency conditions within the Booster frequency range. The output from the 2273A is used

directly with no additional filtering except as provided by the Q of the accelerating cavities. Spurious frequencies as large as -45 dBc are observed out of the DDS, but present no apparent problem to the Booster beam. Presumably the fast frequency sweep prevents any one 'bad' spur from persisting long enough to cause beam blow-up. The ADCs are Analog Devices part AD773 which operates with a 5 cycle pipeline delay. To minimize their contribution to signal transport delay, they are clocked at the full rated speed of 10 Mhz. One ADC processes the fast phase detector signal required for phase-locking operations. Its data is read by the DSP once per microsecond while phase-locking to the beam for acceleration or to a Main Ring rf signal for extraction synchronization. The other ADC is read only once each 15 Hz Booster cycle to provide operator control of the frequency at injection.

An interrupt driven program runs on the DSP to write an

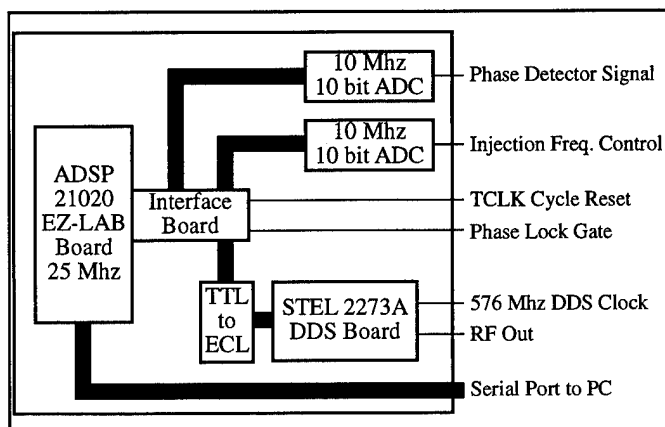


Figure 3: DDS/DSP Prototype Block Diagram

updated frequency setting to the DDS once per microsecond. The Fermilab timing system provides a 15 Hz interrupt to synchronize the frequency sweep to the Booster cycle. Within each cycle, the 21020's internal timer is used to generate regular interrupts every 2 μ sec. A fast interrupt service routine is thereby invoked to step through the pre-calculated frequency table residing in DSP memory and, at two times separated by 1 μ sec, to read and process the digitized phase detector information (for once per microsecond feedback.) Eleven DSP cycles (about 440 nsec) are required to read the ADC, process the information, and write a new setting to the DDS. Including the 0.5 μ sec ADC pipeline, the total feedback signal transport delay from phase detector to change in DDS output frequency is then $< 1 \mu$ sec.

Operating in this manner the DSP/DDS frequency source is able to support a stable phase-locked loop closed loop bandwidth exceeding 150 KHz. Within the framework of the existing LLRF system, it has successfully accelerated beam in the Booster during normal high intensity operations. Acceleration efficiency comparable to that of the analog system was achieved with little fine tuning.

IV. PLANNED SCOPE OF THE UPGRADE

The block architecture of the present system is planned to be maintained as the core of the upgrade. All the existing CAMAC LLRF curve generators and NIM housed RF circuits will be replaced with new hardware built in VXI format. A National Instruments CPU030 running VXWorks will serve as the crate Slot 0 controller and provide the interface to ACNET.

Figure 4 depicts the planned crate layout and individual board functions (compare to Fig. 2). The frequency source DSP provides the Frequency curve generator functionality. A second DSP, on the Phase Controller board, serves the roles of the present Radial Offset, Radial Gain, and Counterphase curve generators. In addition, it is expected that this DSP, perhaps in communication with the other, will provide the horsepower to implement a 'trip plan' type synchronization scheme, as described by Mestha [7], for extraction to Main Ring. The ability to time a gap in the Booster beam to the extraction kicker firing is considered extremely important to

minimize radiation from beam loss during future high intensity, high repetition rate Booster operation.

V. SUMMARY

The proof of principle of using a DDS directly as a frequency source for the Booster has been solidly established. This offers, for the first time in that machine, an opportunity to explore the many benefits that a stable and precise frequency source may provide. A plan has been laid out to design and fabricate the necessary hardware and control system interface required to take full advantage of this opportunity. Much of the new system is expected to be operational by the end of this calendar year. Meanwhile, the prototype remains available for operation within the existing Booster LLRF.

VI. ACKNOWLEDGMENTS

Steve Bjerklie has designed, assembled, and tested the hardware used in the successful prototype. Keith Meisner and Brian Chase, working on the Main Ring and Tevatron LLRF system, have laid much groundwork for this effort and provided valuable guidance in application of the DSP. Acknowledgment is also made of work done by L.K. Mestha, Victor Brouk, Tom Uher et al. at the SSC which forms the basis for the current approach to beam transfer synchronization.

VII. REFERENCES

- [1] Keith G. Meisner et al., "A New Low Level RF System for the Fermilab Booster," IEEE Trans. Nuc. Sci., June, 1979, Vol. NS-26, No. 3, ISSN 0018-9499, pp. 4061-4062, Proceedings of the 1979 Particle Accelerator Conference, San Francisco, CA, March, 1979.
- [2] C. Kerns et al., "New Low-Level RF System for the Fermilab Booster Synchrotron," Proceedings of the 1987 IEEE Particle Accelerator Conference, IEEE Catalog No. 87CH2387-9, pp.619-621.
- [3] Stephen P. Jachim, "A High-Speed Voltage-Controlled Oscillator for the Fermilab Booster Low-Level RF System", IEEE Trans. Nuc. Sci., June, 1979, Vol. NS-26, No. 3, ISSN 0018-9499, pp. 3953-3955, Proceedings of the 1979 Particle Accelerator Conference, San Francisco, CA, March, 1979.
- [4] Robert J. Ducar et al., "A CAMAC Based High-Resolution Repetitive Waveform Generator," IEEE Trans. Nuc. Sci., June, 1979, Vol. NS-26, No. 3, ISSN 0018-9499, pp. 4149-4151, Proceedings of the 1979 Particle Accelerator Conference, San Francisco, CA, March, 1979.
- [5] L.K. Mestha et al., "A Digital Phase Loop for the (SSC) Low Energy Booster," Proceedings of the 1993 Particle Accelerator Conference, IEEE Catalog No. 93CH3279-7, pp.2382-2384.
- [6] L.K. Mestha, "Parasitic Experiments on Fermilab Booster LLRF Systems," SSCL-599, Superconducting Super Collider Laboratory, Dallas, Texas, November, 1992.
- [7] L.K. Mestha, "Phase-Control Scheme for Synchronous Beam Transfer from the Low Energy Booster to the Medium Energy Booster," SSCL-340, Superconducting Super Collider Laboratory, Dallas, Texas, September, 1991.

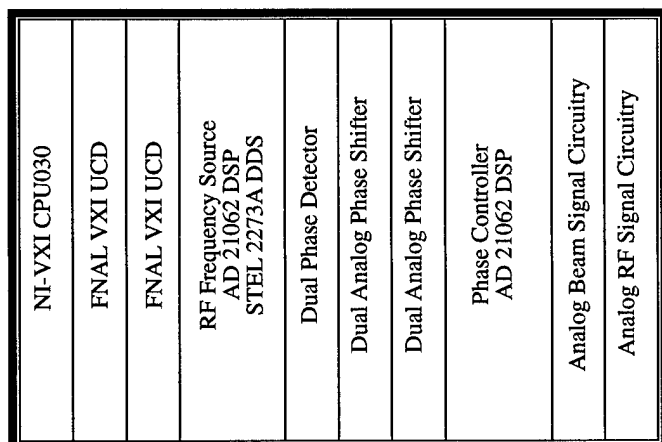


Figure 4: Conceptual Layout of Booster LLRF VXI Crate

ENERGY STABILITY IN A HIGH AVERAGE POWER FEL*

L. Merminga and J. J. Bisognano, CEBAF, 12000 Jefferson Ave, Newport News, VA 23606, USA

Abstract

Recirculating, energy-recovering linacs can be used as driver accelerators for high power FELs. Instabilities which arise from fluctuations of the cavity fields are investigated. Energy changes can cause beam loss on apertures, or, when coupled to M_{56} , phase oscillations. Both effects change the beam induced voltage in the cavities and can lead to unstable variations of the accelerating field. Stability analysis for small perturbations from equilibrium is performed and threshold currents are determined. Design strategies to increase the instability threshold are discussed and the high average power FEL proposed for construction at CEBAF is used as an example.

I. INTRODUCTION

Multipass recirculating, energy-recovering accelerators can be cost-effective and energy-efficient driver accelerators to high-average-power, high-efficiency, low-cost FELs. These accelerators however, are prone to instabilities which arise from fluctuations in energy which in turn cause current loss on apertures, leading to rf field changes and further energy changes. Furthermore, energy fluctuations coupled to compaction factors of non-isochronous arcs can also cause changes in the arrival time of the bunches at the entrance of the linac, leading to further energy changes. These instabilities have been observed experimentally in the energy recovery experiment performed at Los Alamos [1]. Both types of instabilities (longitudinal and beam loss) are analyzed here.

We start with the equivalent circuit model for a cavity, and present the equation that describes the interaction between cavity fields and the beam. Next we perform a stability analysis for small perturbations from equilibrium and we derive expressions for threshold currents for both types of instabilities. As a numerical example we use the design parameters of the high average power FEL proposed for construction at CEBAF. We conclude with a discussion on the role of feedback and we outline plans for future work.

II. EQUIVALENT CIRCUIT MODEL FOR A CAVITY

An rf cavity powered by an rf source (klystron) can be represented by a resonant LCR circuit [2]. The beam in the cavity is represented by a current generator. The interaction of the beam with the cavity fields can be described, to a very good approximation, by the following first order differential equation,

$$\frac{d\tilde{V}_c}{dt} + \frac{\omega_0}{2Q_L}(1 - i \tan \Psi)\tilde{V}_c = \frac{\omega_0 R_L}{2Q_L}(\tilde{I}_g - \tilde{I}_b) \quad (1)$$

where ω_0 is the cavity resonant frequency, Q_L is the loaded Q of the cavity and R_L is the loaded shunt impedance $R_L = (r/Q)Q_L$.

*Work supported by the Virginia Center for Innovative Technology and DOE Contract # DE-AC05-84ER40150.

In arriving at (1) we assume that the cavity voltage, generator and beam current vary as $e^{i\omega t}$, where ω is the rf frequency, and \tilde{V}_c , \tilde{I}_g and \tilde{I}_b are the corresponding complex amplitudes (phasors) in the rotating frame of reference, varying slowly with time. In this equation I_b is equal to the average beam current (in the limit of short bunches) and I_b denotes the magnitude of \tilde{I}_b . Also Ψ is the tuning angle defined by $\tan \Psi = -2Q_L(\omega - \omega_0)/\omega_0$. In steady-state the generator power is given by

$$P_g = \frac{(1 + \beta)}{4\beta} I_g^2 R_L,$$

where β is the cavity coupling coefficient, and can be calculated from $Q_L = Q_0/(1 + \beta)$.

III. STABILITY ANALYSIS

As a concrete example, we take the energy-recovering driver accelerator design of the CEBAF FEL [3]. The generalization is straightforward. We assume that the accelerator consists of a linac with a two-pass recirculation transport. The beam is injected into the linac, accelerated and transported through the first (low energy) arc. It then returns to the linac where it is accelerated for a second time and transported through the second (high energy) arc. A wiggler magnet in the middle of the second arc provides the FEL interaction, as a result of which the beam loses energy and greatly increases its energy spread. The resulting beam is returned into the linac, decelerated for energy recovery through two passes and then transferred into the dump. Therefore, in this model, there are four beams in the linac cavities at any time (two accelerating and two decelerating).

Furthermore, we limit the stability analysis to the linear regime where perturbations from equilibrium are small. This linear approximation is sufficient for determining the stability boundaries of the system and the growth rates of instabilities. Much of our formalism is similar to the analysis of the rf stability in the Los Alamos FEL energy recovery experiment [1].

Two effects may trigger an unstable behavior of the system: beam current loss and shift in the arrival time of each pass at the entrance of the linac. The beam current loss may originate from an energy offset which shifts the beam centroid off its central trajectory and leads to beam scraping on apertures. The phase shift may originate from an energy offset coupled to the finite compaction factors (M_{56}) in the arcs.

We assume that the generator current \tilde{I}_g is constant and is expressed in the polar form $\tilde{I}_g = I_g e^{i\Psi_g}$. We assume that the cavity voltage is perturbed in amplitude and phase, by $\hat{v}(t)$ and $\hat{\phi}(t)$ respectively, therefore

$$\tilde{V}_c = [V_{c0} + \hat{v}(t)]e^{i[\Psi_c + \hat{\phi}(t)]}$$

We now write the expressions for the beams in each of the four passes. We assume that the two accelerating-pass beams (pass 1 and 2) remain unperturbed and express them in polar form as

$\tilde{I}_1 = I_0 e^{i\Psi_1}$, $\tilde{I}_2 = I_0 e^{i\Psi_2}$, where Ψ_1 and Ψ_2 are the beam phases with respect to the phase of the cavity voltage Ψ_c . However there may be energy errors at the end of each pass given by

$$\epsilon_1(t) = V_c(t) \cos[\Psi_c + \hat{\phi}(t) - \Psi_1] - V_{c0} \cos(\Psi_c - \Psi_1) \quad (2)$$

for pass 1 beam, and

$$\epsilon_2(t) = \epsilon_1(t) + V_c(t) \cos[\Psi_c + \hat{\phi}(t) - \Psi_2] - V_{c0} \cos(\Psi_c - \Psi_2) \quad (3)$$

for pass 2 beam, where V_c is the magnitude of \tilde{V}_c . The two decelerating beams can be perturbed both in magnitude and phase

$$\tilde{I}_3 = [I_0 + \hat{i}_3(t)] e^{i[\Psi_3 + \phi_3(t)]}$$

$$\tilde{I}_4 = [I_0 + \hat{i}_4(t)] e^{i[\Psi_4 + \phi_4(t)]}$$

where

$$\hat{i}_3(t) = -b_2 I_0 \epsilon_2(t - \tau_2) \quad (4)$$

$$\phi_3(t) = -h_2 \epsilon_2(t - \tau_2) \quad (5)$$

and $\hat{i}_4(t) = \hat{i}_3(t)$, $\phi_4(t) = \phi_3(t)$. The coefficients h_2 and b_2 are proportional to the compaction factor of the second arc and its momentum aperture respectively, and can be expressed as

$$h_2 = \frac{M_{56}\omega}{cE} \quad (6)$$

where M_{56} is the compaction factor of the arc, ω is the rf frequency, c is the speed of light and E the beam energy around the arc. Similarly, b_2 can be expressed as

$$b_2 = -\frac{\eta_x}{LE} \quad (7)$$

where η_x is the horizontal dispersion (at the maximum point) of the arc, and L is a loss coefficient which characterizes the amount of beam loss; e.g., if 1 mm offset gives rise to 10^{-3} of beam scraping, then $L = 1$ m.

In addition we have taken into account the time τ_2 it takes the electrons to travel around the second arc and through the linac. To simplify the calculations we have assumed that the first arc is isochronous ($h_1=0$) and it has "infinite aperture" ($b_1=0$).

It is assumed that all perturbations imparted to the equilibrium state are small, $\hat{v} \ll V_{c0}$, $\hat{\phi} \ll 1$, $\hat{i}_{3,4} \ll I_0$, $\phi_{3,4} \ll 1$. We can therefore linearize eqs (2), (3) to get

$$\epsilon_1(t) = \hat{v}(t) \cos(\Psi_1) + \hat{\phi} V_{c0} \sin(\Psi_1)$$

$$\epsilon_2(t) = \hat{v}(t) [\cos(\Psi_1) + \cos(\Psi_2)] + \hat{\phi} V_{c0} [\sin(\Psi_1) + \sin(\Psi_2)]$$

where we have set $\Psi_c = 0$, without loss of generality. From eqs (4) and (5) we write $\hat{i}_3(t)$ and $\phi_3(t)$ as

$$\begin{aligned} \hat{i}_3(t) &= -\hat{v}(t - \tau_2) b_2 I_0 (\cos \Psi_1 + \cos \Psi_2) \\ &\quad - \hat{\phi}(t - \tau_2) b_2 I_0 V_{c0} (\sin \Psi_1 + \sin \Psi_2) \end{aligned}$$

$$\begin{aligned} \phi_3(t) &= -\hat{v}(t - \tau_2) h_2 (\cos \Psi_1 + \cos \Psi_2) \\ &\quad - \hat{\phi}(t - \tau_2) h_2 V_{c0} (\sin \Psi_1 + \sin \Psi_2) \end{aligned}$$

Notice that perturbations on both decelerating beams can be expressed in terms of \hat{v} and $\hat{\phi}$ only through a series of nested relations. This is true for any number of passes and the problem at

the end amounts to finding the roots of the determinant of a 2×2 matrix.

Substituting the above equations into the cavity equation (1), separating real and imaginary parts and performing the linearization, we obtain two linear differential equations in \hat{v} and $\hat{\phi}$. To study the stability of the system we assume that $\hat{v}(t)$ and $\hat{\phi}(t)$ vary with time according to e^{st} , $\hat{v}(t) = v(s)e^{st}$, $\hat{\phi}(t) = \phi(s)e^{st}$, to obtain two algebraic equations $MA = 0$, where M is a 2×2 matrix and A is the column vector with v and ϕ as components. The matrix elements of M are

$$\begin{aligned} M_{11} &= s + \frac{\omega_0}{2Q_L} - \frac{\omega_0 R_L}{2Q_L} A_1 e^{-s\tau_2} \\ M_{12} &= V_{c0} \left[\frac{\omega_0}{2Q_L} \tan \Psi - \frac{\omega_0 R_L}{2Q_L} B_1 e^{-s\tau_2} \right] \\ M_{21} &= -\frac{\omega_0}{2Q_L} \tan \Psi + \frac{\omega_0 R_L}{2Q_L} C_1 e^{-s\tau_2} \\ M_{22} &= V_{c0} \left[s + \frac{\omega_0}{2Q_L} + \frac{\omega_0 R_L}{2Q_L} D_1 e^{-s\tau_2} \right] \end{aligned}$$

where

$$\begin{aligned} A_1 &= -I_0 h_2 (\sin \Psi_3 + \sin \Psi_4) (\cos \Psi_1 + \cos \Psi_2) \\ &\quad + I_0 b_2 (\cos \Psi_3 + \cos \Psi_4) (\cos \Psi_1 + \cos \Psi_2) \\ B_1 &= -I_0 h_2 (\sin \Psi_3 + \sin \Psi_4) (\sin \Psi_1 + \sin \Psi_2) \\ &\quad + I_0 b_2 (\cos \Psi_3 + \cos \Psi_4) (\sin \Psi_1 + \sin \Psi_2) \\ C_1 &= -I_0 h_2 (\cos \Psi_3 + \cos \Psi_4) (\cos \Psi_1 + \cos \Psi_2) \\ &\quad - I_0 b_2 (\sin \Psi_3 + \sin \Psi_4) (\cos \Psi_1 + \cos \Psi_2) \\ D_1 &= -I_0 h_2 (\cos \Psi_3 + \cos \Psi_4) (\sin \Psi_1 + \sin \Psi_2) \\ &\quad - I_0 b_2 (\sin \Psi_3 + \sin \Psi_4) (\sin \Psi_1 + \sin \Psi_2) \end{aligned}$$

The determinant of M is then set to zero and the two roots of s are examined. The real parts of the roots will provide the damping or growth rates of perturbations. The imaginary parts of the roots will give the oscillation frequencies relative to the driving rf frequency. If both roots have zero or negative real parts, the system is stable; otherwise the system is unstable. We found that the 415 ns delay in the high-energy arc does not affect the stability boundaries and growth rates significantly, therefore we set $\tau_2=0$, and thus reduced the complexity of the calculation.

Taking this into account, the two roots of s are

$$s = \left(\frac{\omega_0}{2Q_L} \right) \left\{ -1 + \frac{1}{2} I_0 R_L [(h_2 S + b_2 C) \pm \sqrt{Q}] \right\}$$

where

$$Q = \sqrt{(h_2 S + b_2 C)^2 + \frac{4 \tan \Psi}{R_L I_0} (-h_2 C + b_2 S) - \left(\frac{2 \tan \Psi}{R_L I_0} \right)^2}$$

and S and C are defined as

$$\begin{aligned} S &= \sum_{i=1}^2 [\sin(\Psi_i - \Psi_3) + \sin(\Psi_i - \Psi_4)] \\ C &= \sum_{i=1}^2 [\cos(\Psi_i - \Psi_3) + \cos(\Psi_i - \Psi_4)] \end{aligned}$$

From the two roots the one with the positive sign is the limiting one. We can now derive an expression for the threshold current of these instabilities, by setting $s=0$. For the CEBAF FEL parameters, the longitudinal instability threshold current simplifies to

$$I_{th} = \frac{c E}{R_L M_{56} \omega \cos^2 \Psi (S - C \tan \Psi)}$$

where eq.(6) has been used for h_2 . This equation demonstrates possible design strategies for increasing the instability threshold:

1. reducing the shunt impedance of the linac,
2. choosing the off-crest phases such that the S term cancels the $C \tan \Psi$ term,
3. entirely or nearly isochronous arcs, even in the sense of having opposite signs of M_{56} in the two halves of the arc (before and after the wiggler),
4. lowering the rf frequency.

It is worth noting that this expression for the threshold current agrees with the expression derived in reference [4] in its functional dependency on energy, frequency, shunt impedance and compaction factor.

The threshold for the beam loss instability is

$$I_{th} = \frac{2E}{R_L(\eta_x/L)C},$$

where eq. (7) has been used for b_2 .

IV. THE HIGH AVERAGE POWER FEL AT CEBAF: AN EXAMPLE

The driver accelerator for the high average power FEL proposed for construction at CEBAF is a recirculating energy-recovering 200 MeV, 5 mA cw superconducting rf (srf) electron accelerator. The accelerator consists of a 10 MeV injector, a 96 MV srf linac with a two-pass recirculation transport which accelerates the beam to 200 MeV, followed by energy recovery deceleration through two passes to ~ 10 MeV, and then transport to the dump.

Longitudinal dynamics imposes off-crest operation for the four beams, and that in turn implies that the cavities must be operated off resonance to minimize the required generator power. In the baseline design the phases of the four beams are: $\Psi_1 = 1.8^\circ$, $\Psi_2 = -13.5^\circ$, $\Psi_3 = 195.3^\circ$, $\Psi_4 = 180^\circ$, therefore $S = 0.92$ and $C = -3.82$. The optimum tuning angle is -61.5° . For $M_{56} = -0.47$ in the high energy arc, and $E = 200$ MV, h_2 is equal to -7.7×10^{-8} rads/V. Assuming $\eta_x/L \approx 1$, $b_2 = -5 \times 10^{-9}$ A/V. For the above value of h_2 , assuming $b_2 = 0$, the threshold for the longitudinal instability is $130 \mu\text{A}$. On the other hand, for $h_2 = 0$ and the assumed value of b_2 , the threshold for the beam loss instability is 1.4 mA. When both instabilities are present, the threshold is dominated by the longitudinal one and is $130 \mu\text{A}$. Clearly at these design parameters the threshold is less than our design goal, therefore active feedback is required to control the instability. Preliminary analysis indicates that the gain of the rf feedback loop stabilizes the system.

An alternative lattice design has been developed which has opposite signs of M_{56} for the lattice segments entering and leaving the wiggler (so that the total $M_{56} \sim 0$), and the beam phases could be arranged to cancel, therefore on-resonance operation

would be possible. This alternative design is unconditionally stable against the longitudinal instability because $M_{56} \approx 0$ over the second arc. For the alternative design ($\Psi_1 = 13.5^\circ$, $\Psi_2 = 0^\circ$, $\Psi_3 = 193.5^\circ$, $\Psi_4 = 180^\circ$), $S \sim 0$ and $C = -3.9$. However both the baseline and the alternative scenarios have approximately the same beam loss instability threshold.

V. CONCLUSIONS

The above analysis is valid only in the open loop case. The presence of feedback will damp the growth of phase oscillations. Since there is no phase shift induced by the instabilities, we expect that maximum gain is needed at the cavity resonance frequency. Gains of 3000 (70 dB), which are typical in the CEBAF rf control system at these frequencies, will effectively move the threshold well above the 5 mA design current. Future directions include incorporating feedback in our analysis and addressing gain vs bandwidth questions.

VI. Acknowledgments

The authors acknowledge the contributions of S. Benson and G. Neil to this work.

References

- [1] T.-S. Wang and H. Takeda, PAC Proceedings (1987)
- [2] P. B. Wilson, SLAC-PUB-2884, February 1982.
- [3] D. Neuffer et al, these PAC proceedings (1995)
- [4] J. J. Bisognano and M. Fripp, Linac Conf Proc (1988)

AUTOMATED BEAM BASED ALIGNMENT OF THE ALS QUADRUPOLES*

G. Portmann, D. Robin, and L. Schachinger
Lawrence Berkeley Laboratory, Berkeley CA 94720 USA

Abstract

Knowing the electrical offset of the storage ring beam position monitors (BPM) to an adjacent quadrupole magnetic center is important in order to correct the orbit in the ring. We describe a simple, fast and reliable technique to measure the BPM electrical centers relative to the quadrupole magnetic centers. By varying individual quadrupole magnets and observing the effects on the orbit we were able to measure the BPM offsets in half the horizontal and vertical BPMs (48) in the ALS. These offsets were measured to an accuracy of better than $50\mu\text{m}$. The technique is completely automated and takes less than 3 hours for the whole ring.

I. Introduction

In a storage ring it is beneficial to have the beam orbit pass as close as possible to the center of the quadrupole magnets for a variety of reasons. First, if the beam orbit passes through the quadrupole's magnetic center, there is no steering of the orbit from the quadrupole which means that the quadrupole does not generate any orbit distortion or spurious dispersion. Second, if there is some quadrupole power supply jitter, then the amount of the orbit motion caused by the power supply jitter will be minimized. Third, the quadrupole, which is solidly anchored to a massive girder, is less sensitive to thermal effects than is the BPM which is embedded in the relatively flexible aluminum vacuum chamber.

Typically, beam position monitors (BPM) are located near the quadrupole magnets. In order to know precisely where the magnetic center of the quadrupole is, it is necessary to have a direct measurement of the relative offset between the quadrupole's magnetic center and the BPM's electrical center. Knowing of these BPM-to-quadrupole offsets allows one to correct the beam orbit to the magnetic center of the quadrupoles.

At the ALS a beam-based alignment technique has been successfully used to measure the BPM-to-quadrupole offsets of 48 of the 96 BPMs. This process, which takes about 3 hours, measures the offsets to an accuracy of better than $50\mu\text{m}$. The technique has significantly increased the absolute accuracy of the ALS BPMs since some of the measured offsets have been in excess of 1 mm. Analysis of these measurements has also allowed us to identify magnet motion which occurred between measurements.

II. Theory

By changing the strength of an individual quadrupole one can vary the closed orbit of the beam. The change in the closed orbit depends upon how much the beam's closed orbit is offset from the quadrupoles magnetic center. For the case of a perfectly linear

machine without coupling, the effect on the transverse orbit at a location s from a change in the strength of a thin lens quadrupole located at longitudinal position \bar{s} is

$$\Delta x(s) = \left(\frac{\Delta k(\bar{s})x(\bar{s})}{B\rho} \right) \left(\frac{1}{1 - k(\bar{s}) \frac{1}{2B\rho \tan \pi \nu}} \right) \times \frac{\sqrt{\beta(s)}\sqrt{\beta(\bar{s})}}{2 \sin \pi \nu} \cos(\varphi(s) - \varphi(\bar{s}) - \pi \nu). \quad (1)$$

where $\beta(\bar{s})$ and $\beta(s)$ are the beta function at the location of the quadrupole and observation point respectively, $\Delta k(\bar{s})$ is the change in the integrated strength of the quadrupole, $x(\bar{s})$ is the position of the beam orbit in the quadrupole, $B\rho$ is the magnetic rigidity of the beam, ν is the tune of the ring, and $\varphi(\bar{s})$ and $\varphi(s)$ are the betatron phases at the location of the quadrupole and observation point respectively.

From equation 1 one can see that the change in orbit $\Delta x(s)$ from a change in quadrupole strength is a linear function of the offset of the orbit in the quadrupole $x(\bar{s})$. By changing the strength of the quadrupole and observing the change in the orbit at the BPMs one can in principle determine the offset of the orbit in that quadrupole. However in order to compute the offset of the orbit directly from this equation, one needs to know the beta functions, tune and phase advance, as well as the change in quadrupole strength very precisely. Fortunately, the magnetic center of the quadrupole can be located without knowing this information.

It is clear from equation 1 that if the orbit goes through the center of the quadrupole then a subsequent change in the strength of that quadrupole will have no effect on the orbit. Therefore, the center of the that quadrupole can be located by adjusting the beam orbit in that quadrupole to such a position where a variation of that quadrupole's strength will create a minimal distortion of the beam orbit. After placing the beam in the center of the quadrupole, the reading of the adjacent BPM is the relative quadrupole-to-BPM offset. This method was used to determine the BPM-to-quadrupole offsets in the ALS.

In order to use this method one must be able to individually adjust the strength of the quadrupole magnet. It is also important that the BPM is located near in betatron phase to the quadrupole, because even if the beam is passing through the center of the quadrupole it may be passing through at an angle. This angle can produce a large error in our measurement of the offset if the betatron phase is large. Therefore it is only valid to look at BPMs that are located at positions close in phase to the quadrupole. The following section will explain how this technique is implemented in the ALS storage ring.

III. Experimental Technique

The ALS has 3 families of quadrupoles: QF, QD, and QFA. All the quadrupoles in the QF and QD families have individually

*Work supported by the Director, Office of Energy Research, Office of Basic Energy Sciences, Materials Sciences Division, of the U.S. Department of Energy under Contract No. DEAC03-76SF00098

adjustable power supplies. Unfortunately, the quadrupoles in the QFA family are powered in series off one common supply, hence the algorithm described in the previous section will not work for this particular family. It may be possible to adapt the algorithm for magnets powered in series, however this has not yet been attempted at the ALS. Other facilities have used backleg windings, [1], or shunts resistors, [2], to overcome this problem.

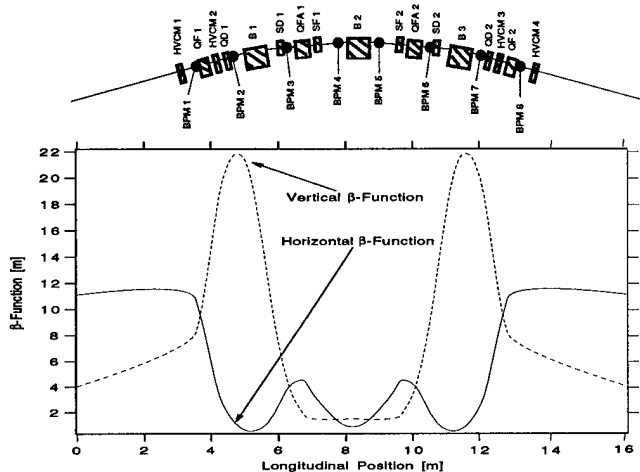


Figure 1. Typical ALS Sector: Layout (Top) and Beta Functions (Bottom)

Each of the 12 sectors in the ALS contains 2 QF, 2 QD and 2 QFA quadrupoles. The layout of a typical sector is shown in Fig. 1. Next to each QF and QD quadrupole is a BPM. (BPM 1 is next to QF1, BPM 2 is next to QD1, BPM 7 is next to QD2, and BPM 8 is next to QF2.) Therefore in each sector one can find the relative quadrupole to BPM offset in four quadrupole-BPM pairs. A typical straight section contains four horizontal correctors (HCM) and four vertical correctors (VCM) which can be used to change the position of the orbit in the quadrupole.

The process of finding the quadrupole center is conceptually very simple. By using any corrector magnet to position the electron beam at different positions in quadrupole magnet, one determines the position which minimizes the orbit distortion when the quadrupole field is varied. This process can be automated using a simple optimization routine. There are basically two steps involved in finding the quadrupole magnet center: first change the orbit in a particular quadrupole, then measure the orbit distortion from varying the quadrupole strength. These steps are repeated several times in order to find the position of the beam orbit which creates the minimum orbit distortion. To measure the orbit distortion due to a quadrupole's strength variation, the difference in closed orbit is measured at two quadrupole setpoints — one below the nominal setpoint and the other above. The merit function for the search is

$$f(\theta_{cm}) = \frac{1}{96} \sum_{i=1}^{96} (x_i(+\Delta k) - x_i(-\Delta k))^2, \quad (2)$$

where θ_{cm} is the strength of the corrector magnet, $x_i(\Delta k)$ is the orbit after changing the quadrupole by Δk , and i is the BPM number. The sum goes from 1 to 96 because the ALS has 96 BPMs.

For example, in order to measure the orbit distortion from a quadrupole in the horizontal plane, one would do the following. First, change the strength of the quadrupole by Δk so that the strength is now $k + \Delta k$ and measure the horizontal orbit in all of the BPMs ($x_i(+\Delta k)$). Then, change the strength to $k - \Delta k$ and again measure the horizontal orbit ($x_i(-\Delta k)$). Finally, compute equation 2.

The ideal size of Δk will be machine-dependent. If Δk is large, the merit function will be "better," i.e. higher signal-to-noise ratio from the BPMs, but the quadrupole hysteresis effects will be large. The hysteresis does not affect the merit function accuracy very much, but it does adversely affect the machine tune since the merit function is computed many times. The change in quadrupole currents for this experiment were chosen based on trial-and-error— ± 3 amps for QF and ± 5 amps for QD. Due to the hysteresis effect, the quadrupoles need to be reconditioned after approximately 16 magnetic centers are found.

In order to find the quadrupole magnet center, one has to find the optimal corrector setting which minimizes equation 2. The functional form of this equation, ignoring high-order effect, is quite easy to find. The position of the orbit in the quadrupole is a linear function of corrector strength (i.e. $x_{QUAD} \propto \theta_{cm}$). From equation 1, the change in the orbit from a quadrupole is proportional to the orbit at the quadrupole (i.e. $x_i(\Delta k) \propto x_{QUAD}$). Therefore, the orbit due to a change in the quadrupole field is directly proportional to the current in the corrector.

$$x_i(\Delta k) \propto \theta_{cm}. \quad (3)$$

Because the merit function, $f(\theta_{cm})$, is a quadratic function of the orbit in the BPM (see equation 2), $f(\theta_{cm})$ will be a quadratic function of corrector strength, θ_{cm} , and thus will be shaped like a parabola

$$f(\theta_{cm}) \propto \theta_{cm}^2. \quad (4)$$

There are a number of ways to find the minimum of this function. Theoretically, one could empirically measure three points and compute the parabola. The problem is that BPM and corrector magnet noise corrupts the merit function calculation. However, by choosing corrector magnet setpoints that are relatively far apart and measuring the merit function at "many" locations, one can obtain a very accurate quadrupole center measurement (see figure 2). At the ALS, by changing the corrector current in discrete steps, approximately .75 amps per step, and performing a least squares fit of seven data points to a parabola, the center of the quadrupole was calculated to an accuracy of at least ± 50 microns.

A gradient search method of finding the minimum of the merit function was briefly tried. However, it was difficult to "fine tune" a gradient method because of BPM and corrector magnet noise. Basically, when performing a gradient search algorithm it is possible for two measurement points (corrector currents) to be very close together, which can produce an erroneous gradient calculation due to measurement noise corrupting the merit function. Since the discrete step, least squares fit methods works so well, the gradient search method was abandoned.

For each quadrupole the vertical and horizontal offsets were measured separately—the vertical was measured first and then

the horizontal. Each quadrupole magnet was paired with the most effective corrector in each plane by examining the phase advance and beta functions in an attempt to maximize the change in orbit at the quadrupole. Due to lattice geometry the effectiveness of the corrector varies with quadrupole family.

A. Example: Sector 3, QF1 and BPM1

Figure 2 shows the experimental results for quadrupole QF1 in sector 3. Here the BPM-to-quadrupole offset determined was between QF1 and BPM1. VCM1 and HCM1 in sector 3 were used to change the orbit vertically and horizontally in QF1 and BPM1. Figure 2 shows the merit function vs. corrector current. The algorithm calculates seven points along the merit function, $f(\theta_{cm})$, guaranteeing that there are three points on either side of the minimum point. The raw data points are depicted as circles in the figure. The solid line is the seven point curve fit to a parabola and the "X" is the minimum of the function. A final data point is taken at the minimum to verify that the minimum has been reached. The data points lie nicely on a parabola which is expected from equation 4.

Figure 2 shows the BPM reading vs. the same corrector currents. As expected, the position at the BPM is a linear function of corrector current. The offset between BPM1 and QF1 is located at the "X" on the dashed line in Figure 2. The BPM data was also fit using the least-squares method to a line to further reduce BPM noise. Thus when the beam was passing through the center of the quadrupole, the BPM read 0.9 mm horizontally and 0.4 mm vertically.

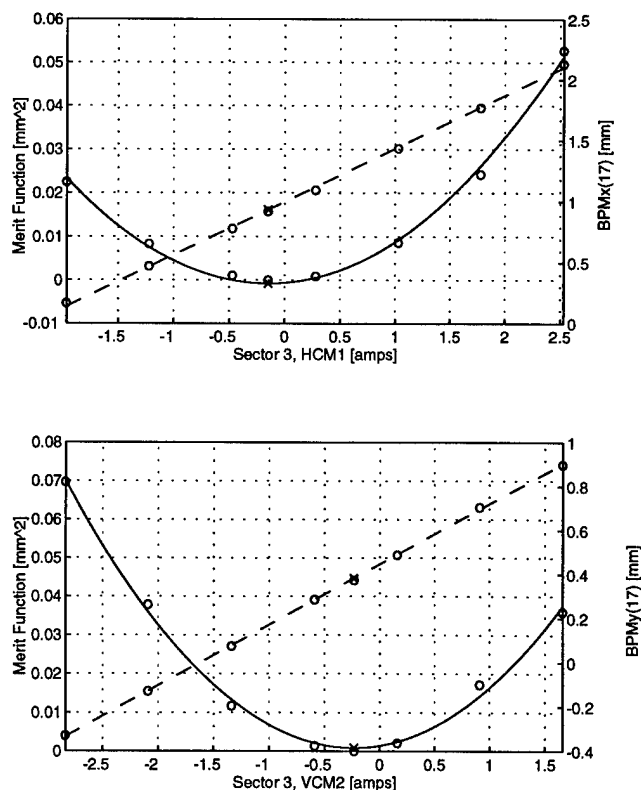


Figure 2. Merit function (solid) and BPM (dashed) values verses corrector strength for QF1 in Sector 3

IV. Conclusion

This method of finding the BPM-to-quadrupole positional offsets has proven to be reliable and relatively fast. The accuracy of the measurement is sensitive to BPM and power supply noise, however, the effects from these error sources can be substantially mitigated by increasing the number of points measured. The number of points and the range of power supply currents used in the corrector and quadrupole magnets are machine dependent, but it is quite easy to adjust these parameters. Since the BPM offsets in the ALS storage ring are typically between .25-1.25 mm, [4], this technique has yielded essential data for correcting the closed orbit in the ALS.

Acknowledgements

The authors would like to thank A. Jackson for his support and encouragement during this study.

References

- [1] I. Barnett et al., "Dynamic Beam Based Alignment" CERN-SL 94-84 (BI).
- [2] P. Rojsel, "A Beam Position Measurement System Using Quadrupole Magnets Magnetic Centra as the Position Reference," Nuc. Inst. Meth. in Phys. Res., 343, (1994).
- [3] M. Sands, "The Physics of Electron Storage Rings: an Introduction", Stanford Linear Accelerator Note, SLAC-121, (1970), 53.
- [4] G. Portmann and D. Robin, "Beam Based Alignment of the Quadrupole Centers in the ALS," LSAP Note-194 (1995).

FIRST RESULTS WITH A NONLINEAR DIGITAL ORBIT FEEDBACK SYSTEM AT THE NSLS *

Eva Bozoki, Aharon Friedman and Susila Ramamoorthy

National Synchrotron Light Source, Brookhaven National Laboratory, Upton, NY 11973

Abstract

We report on the first experimental results with a nonlinear digital orbit feedback system for the NSLS X-ray ring. The system uses the existing RF receivers and orbit corrector magnets (trims) as well as parts of the NSLS control components. The orbit measurement micro was upgraded to a Motorola 68040 CPU in order to achieve the necessary data rate. Filtering and orbit correction calculations are done in a dedicated HP 742 rt micro. The system operates at a 555 Hz data rate, and achieves a bandwidth of 15 – 20 Hz.

I. INTRODUCTION

Orbit stability is an important issue for storage rings, like the ones at the NSLS. Brightness of the photon source and beam lifetime can deteriorate due to even small motions in the beam orbit. The orbit can be stabilized with feedback systems. Digital feedback systems Ref. [1] are very flexible, since the filter and orbit correction algorithms are programmed and any change does not require changes in the hardware. This is a clear advantage over the presently used analog hardware based feedback systems.

II. ORBIT CORRECTION ALGORITHM

In implementing the digital feedback system, we are using the eigenvector decomposition based orbit correction method described in Refs. [2], [3]. This method yields the 'minimum' kick vector required for a desired accuracy of orbit correction.

III. FILTERING

The feedback system and its elements are illustrated in Fig. 1. G represents the effect of the vacuum chamber. It behaves like a single pole low pass filter, with the pole at ≈ 25 Hz: ¹

$$G(s) = \frac{2\pi 25}{s + 2\pi 25} \quad (1)$$

H_{AA} is an "anti aliasing" filter which limits the bandwidth of the signal in order to prevent aliasing (folding) of the signal spectrum after the D/A conversion. It is a low pass filter with a single pole at ≈ 80 Hz:

$$H_{aa}(z) = \frac{2\pi 80}{s + 2\pi 80} \quad (2)$$

$H_d(z) = z^{-3}$ represents the phase delay due to sampling time, computation time and conversion time.

System Overview

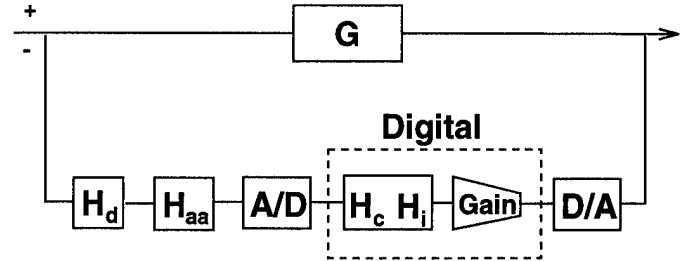


Figure 1. Block diagram of the ring and feedback loop showing the elements of the feedback system.

The H_c filter is designed to compensate for elements in the system G that may be limiting the bandwidth and adding phase retardation to the system. This filter is a high pass filter:

$$H_c(z) = \frac{1}{G(z)} = 8.026 \frac{1 - 0.751z^{-1}}{1 + z^{-1}} \quad (3)$$

H_i is an integrator, which together with the gain is used to limit the bandwidth of the system and to stabilize it.

$$H_i(z) = 1.69 \times 10^{-3} \frac{1 + z^{-1}}{1 - z^{-1}} \quad (4)$$

Note that a pure integrator generates infinite gain at DC. Hence, the correction at DC is absolute.

The closed loop response of this system is

$$T = \frac{G}{1 + g_o G H_{tot}}, \quad \text{where } H_{tot} = H_{aa} H_d H_c H_i, \quad (5)$$

T is plotted as a function of the f frequency on Fig. 2

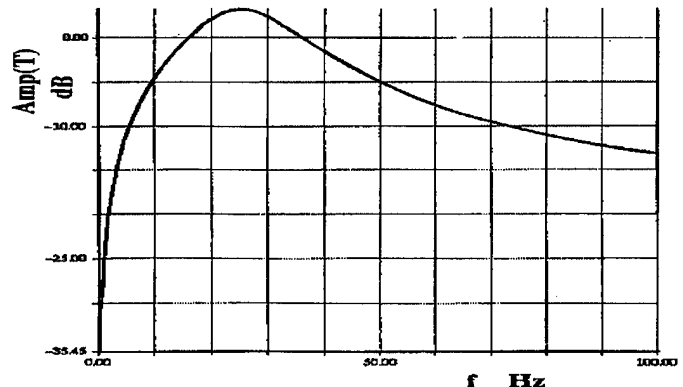


Figure 2. Calculated amplitude response.

*Work performed under the auspices of the U.S. Dept. of Energy under contract no. DE-AC02-76CH00016.

¹In this section $G(s)$ is the Laplace-transform of an $g(t)$ continuous signal ($s = j2\pi f$), and $H(z)$ is the Z-transform of an $h(n)$ discrete signal ($z = \exp(j2\pi f t_s)$), where t_s is the sampling time.

IV. HARDWARE

The feedback system consists of three micros; the HP-742rt CPU based feedback micro, the Motorola-167 CPU based orbit micro and the Motorola-133 CPU based trim micro. The communication between the micros is done by the Bit-3 bus adapter boards through shared memory in the trim and in the orbit micro. The basic layout is shown in Fig. 3.

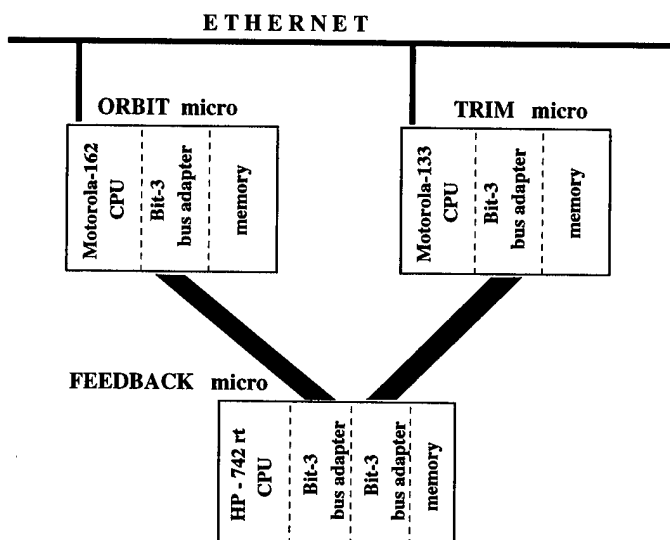


Figure 3. Layout of the feedback system.

The orbit micro samples the PUE data at 555 Hz rate and the data is stored in memory. This memory is mapped by the adapter board to the address space of the feedback micro which calculates the orbit correction and optimizes it. The data communication between the feedback and trim micros is again through memory mapping. The trim micro then controls the power supplies of the orbit corrector magnets. The most computational intensive task is that of the feedback micro. Hence, we chose an HP 742rt, which we estimate to run six times faster than a Motorola 167/162 for this kind of application.

Though the orbit is sampled at 555 Hz rate for the feedback, the data at 32 Hz rate is available for the workstations for existing control programs [4] such as Real Time Orbit, Fast Orbit History, *etc.* Thus the PUE and feedback micros are isolated from the general control network.

To prevent aliasing problem the PUEs are set up with an analog low pass filter.

If it becomes necessary, we will include a control micro in the design to isolate the feedback system from the general control network. The need may arise, since the micros are expected to operate at close to full load and any requests addressed to them on the network may slow them down, reducing the feedback rate.

V. SOFTWARE

The orbit and trim micros use the existing NSLS real time monitor [5]. The programming of the monitor, as well as of the orbit and trim micros were modified such that the feedback micro can place the read points and set point into the shared memory, and that the data collection is synchronized with the feed-

back micro. The PUE readpoints are sampled with 555 Hz for the feedback micro but updated with 32 Hz for general use. A new monitor was written for the feedback micro, based on the HP-RT operating system. The orbit correction code is a modification of the code that was used for orbit correction in Refs. [2], [3]. This is an object oriented code written in C++.

VI. FIRST RESULTS

The feedback system was run successfully on the vertical plane of the NSLS X-ray ring, using all 40 orbit correctors and 48 PUEs. The frequency response of the closed system was measured and compared with the frequency response without feedback. One of the orbit correctors was driven by the output of an HP Dynamic Signal Analyzer in the .1 – 100 Hz frequency region and the amplitude and phase response of one of the PUE's was recorded. The results are shown on Fig. 4.

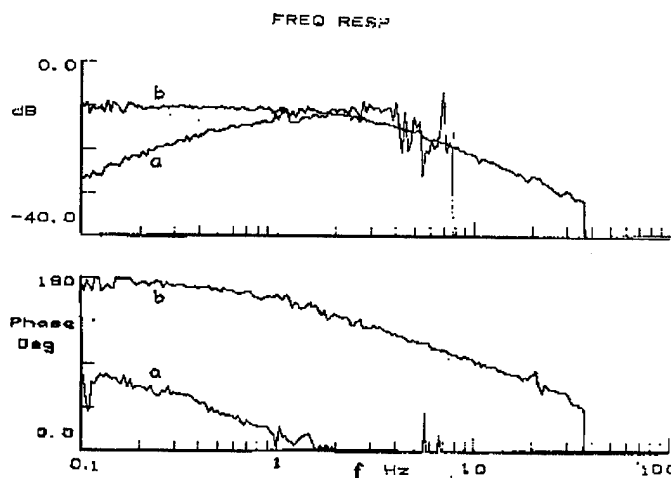


Figure 4. Measured amplitude and phase response.

The DC noise reduction is ≈ 40 db and the effective bandwidth is 15 – 20 Hz with a small noise amplification between 20 – 30 Hz. These results are in good agreement with the calculated closed loop response shown in Fig. 2.

VII. FUTURE PLANS

In order to achieve a higher (1.5 – 2.0 kHz) orbit sampling rate, we will replace the present orbit reading system with Analogic 16-bit, 400 kHz data acquisition boards and 32 channel multiplexers.

We are planning to add a notch filter at 60 Hz in order to effectively suppress a sometimes strong noise at that frequency. In this case the H_{tot} in Eq. (5) is replaced by

$$H_{tot} = H_{aa}H_dH_c(H_i + g_nH_n). \quad (6)$$

The calculated amplitude response of the total closed system with the wide band low pass filter and the notch filter is shown in Fig. 5.

VIII. ACKNOWLEDGEMENT

The authors are grateful to the team of technicians lead by Wayne Rambo for their help.

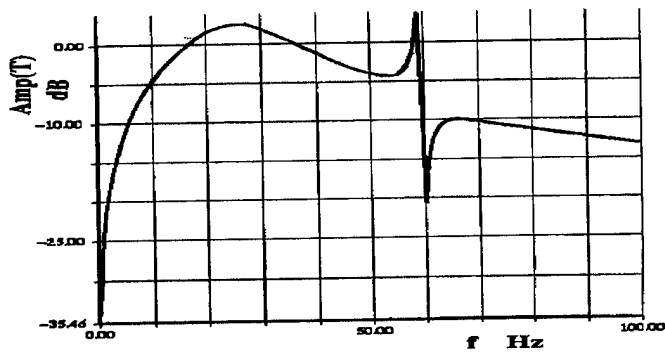


Figure. 5. Calculated amplitude response with notch filter.

References

- [1] A. Friedman and E. Bozoki, "A Digital Feedback System for Transverse Orbit Stabilization," Proc. EPAC, p.1586, 1994.
- [2] E. Bozoki and A. Friedman, "Optimization Method for Orbit Correction in Accelerators," Proc. IEEE PAC, p.105, 1993.
- [3] A. Friedman and E. Bozoki, "Use of Eigen Vectors in Understanding and Correcting Storage Ring Orbits," NIM A, vol. 344, pp. 269-277, 1994.
- [4] J. Smith, S. Ramamoothy, Y. Tang, J. Flannigan, S. Sathe, J. Kean, S. Krinsky, "NSLS Control System Upgrade Status", Proc. IEEE PAC, p.1952, 1993.
- [5] S. Ramamoothy and J. Smith, "NSLS Control Monitor and its Upgrade", Proc. IEEE PAC, p.1849, 1993.

Local Beam Position Feedback Experiments on the ESRF Storage Ring*

Y. Chung, E. Kahana, J. Kirchman, and A. Lumpkin
Argonne National Laboratory, Argonne, IL 60439

J. Meyer, E. Plouviez, K. Scheidt, and E. Taurel
European Synchrotron Radiation Facility, F-38043 Grenoble Cedex, France

A. Ando, S. Sasaki and A. Taketani
SPRING-8 Project Team, Kamigori, Hyogo 678-12, Japan

Abstract

This paper describes the results of local beam position feedback experiments conducted on the ESRF storage ring using digital signal processing (DSP) under the trilateral agreement of collaboration among ESRF, APS, and SPRING-8. Two rf beam position monitors (BPMs) in the upstream and downstream of the insertion device (ID) and two x-ray BPMs in the sixth cell were used to monitor the electron beam and the x-ray beam emitted from the ID, respectively. The local bump coefficients were obtained using the technique of singular value decomposition (SVD) on the global response matrix for the bump magnets and all the available BPMs outside the local bump. The local response matrix was then obtained between the two three-magnet bumps and the position monitors. The data sampling frequency was 4 kHz and a proportional, integral, and derivative (PID) controller was used. The result indicates the closed-loop feedback bandwidth close to 100 Hz and clear attenuation (≈ -40 dB) of the 7-Hz beam motion due to girder vibration resonance. Comparison of the results using the rf BPMs and x-ray BPMs will be also discussed.

I. INTRODUCTION

One of the primary requirements from today's synchrotron light source users is the stringent transverse stability of the x-ray beam emitted from the bending magnets (BMs) and insertion devices (IDs). Correction bandwidth exceeding 100 Hz and long-term drift of less than 10% of the transverse beam size will be routinely expected from the third-generation synchrotron light sources which are characterized by low emittance of the charged particle beam and high brightness of the photon beam.

Sources of beam motion include ground vibration, mechanical vibration of the accelerator subcomponents, thermal effects, and so forth. In order to counteract the effect of these sources, feedback systems that comprise the beam position monitors (BPMs), corrector magnets, and processing units are typically used [1-4]. The beam position feedback systems can largely be divided into global and local feedback systems according to the extent of correction, and DC and AC

feedback systems according to the bandwidth of correction.

In this paper, we will present the results of local AC beam position feedback experiments conducted on the storage ring of the European Synchrotron Radiation Facility (ESRF). The beam position monitor systems consist of two rf BPMs in the straight section for an insertion device (ID) and two x-ray BPMs monitoring the transverse positions of the x-ray beam emanating from the ID. The feedback control is based on digital signal processing (DSP) with the proportional, integral, and derivative (PID) control algorithm. The local bump coefficients are obtained using the technique of singular value decomposition (SVD) of the response matrix for the local correctors and the BPMs outside the bump.

The rest of this paper will consist of a theoretical review of the local beam position feedback with DSP in Section II, description of the experimental setup in Section III, and presentation of the results in Section IV.

II. THEORY

Figure 1 shows the schematic of the local beam position feedback using four corrector magnets for control of both the displacement and angle of the x-ray beam. With two degrees of freedom, this can be done by controlling the positions of the charged particle beam at two locations inside the local bump or of the x-ray beam at two locations in the downstream of the x-ray beamline. The transform between the beam position pair and beam displacement and angle is straightforward. In this work, we do feedback on beam position pairs in the horizontal and vertical planes.

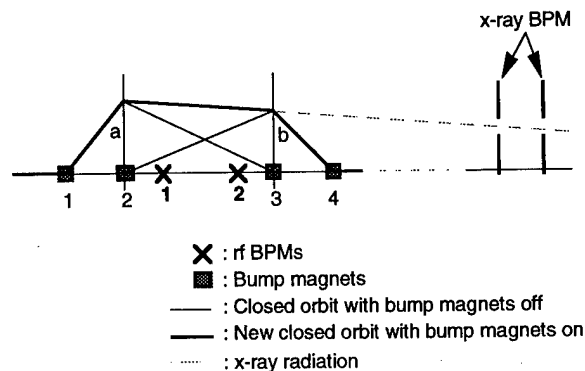


Fig. 1: Schematic of the local beam position feedback using four corrector magnets.

*Work supported by the U.S. Department of Energy, Office of Basic Energy Sciences, under Contract No. W-31-109-ENG-38.

A. Derivation of the Local Bump Coefficients

A four-magnet local bump consists of two independent three-magnet bumps a and b as shown in Fig. 1. The correctors in the bumps must be powered with certain ratios dictated by the lattice functions in order to ensure the locality of the bump. Let θ_1 , θ_2 , θ_3 , and θ_4 be the kick strength on the four correctors, then we have

$$\theta = \begin{pmatrix} \theta_1 \\ \theta_2 \\ \theta_3 \\ \theta_4 \end{pmatrix} = \mathbf{K} \cdot \begin{pmatrix} \theta_a \\ \theta_b \end{pmatrix} = \begin{pmatrix} K_{1a} & 0 \\ K_{2a} & K_{2b} \\ K_{3a} & K_{3b} \\ 0 & K_{4b} \end{pmatrix} \cdot \begin{pmatrix} \theta_a \\ \theta_b \end{pmatrix}, \quad (1)$$

where θ_a and θ_b represent the strength of the a and b bumps, respectively. The beam positions (x_1, x_2) are then related to the bump strengths (θ_a, θ_b) through the 2×2 local response matrix \mathbf{R}_l as

$$\begin{pmatrix} x_1 \\ x_2 \end{pmatrix} = \mathbf{R}_l \cdot \begin{pmatrix} \theta_a \\ \theta_b \end{pmatrix}. \quad (2)$$

The \mathbf{K} matrix in Eq. (1) must satisfy the relation $\mathbf{R}_{gl} \cdot \mathbf{K} = \mathbf{0}$, where \mathbf{R}_{gl} is the response of the global orbit outside the local bump to the bump magnets. The elements are called the local bump coefficients. These coefficients can be expressed in terms of the lattice functions β and ψ of the correctors [5]. Realistically, other factors such as power supply and magnet efficiencies need to be taken into account as well. To simplify the process, an empirical method was employed to determine the coefficients as explained below.

Let us consider the $M \times 3$ response matrix \mathbf{R} for the correctors in a three-magnet bump and the M BPMs outside the bump. The elements are derived from the expression

$$R_{ij} = k_i k_{cj} \frac{\sqrt{\beta_i \beta_{cj}}}{2 \sin(\pi \nu)} \cos(\pi \nu - |\psi_i - \psi_{cj}|), \quad (3)$$

where ν is the tune and k_i and k_{cj} are the coefficients of sensitivity for the BPMs and correctors, respectively. Using the technique of singular value decomposition (SVD) [6,7], \mathbf{R} is written as

$$\mathbf{R} = \mathbf{U} \cdot \mathbf{W} \cdot \mathbf{V}^T, \quad (4)$$

where \mathbf{U} is an $M \times M$ unitary matrix, \mathbf{W} is an $M \times 3$ matrix with off-diagonal elements equal to zero, and \mathbf{V} is a 3×3 unitary matrix. Using Eq. (3), it can be shown that the determinant of the matrix product $\mathbf{R}^T \cdot \mathbf{R}$ is identical to zero. Therefore, at least one singular value in \mathbf{W} should vanish and the corresponding column vector in the matrix \mathbf{V} contains the local bump coefficients. The same procedure is repeated for the other local bump and the \mathbf{K} matrix in Eq. (1) is obtained.

The above procedure was tried in the case of the Advanced Photon Source (APS) storage ring with 360 BPMs. The largest response matrix element is approximately 10

mm/mrad. A random error within ± 0.1 mm/mrad was introduced, and the local bump coefficients were obtained with different numbers of BPMs between 3 and 358, excluding the two BPMs inside the ID local bump. Figure 2 shows the error in the local bump coefficients and the local bump closure expressed as global orbit distortion in mm per mrad of bump strength (θ_a or θ_b).

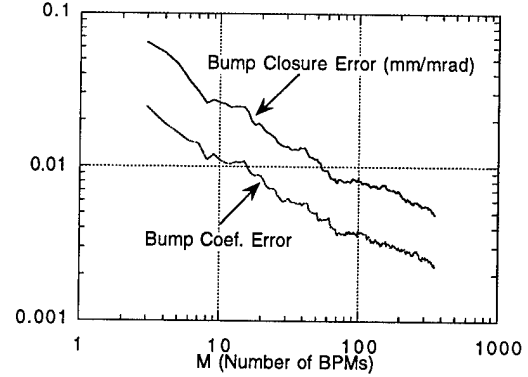


Fig. 2: Application of the SVD-based empirical procedure to the APS storage ring to obtain the local bump coefficients.

B. Digital Signal Processing (DSP)

Schematic of the feedback signal processing for local beam position feedback is shown in Fig. 3. The set points or the references are (s_1, s_2) and the beam positions obtained from the two BPMs are (x_1, x_2) . The difference signals $(s_1 - x_1, s_2 - x_2)$ are passed through the low-pass filters (LPF) and the PID controllers. The DSP computes the corrector strengths θ_j ($1 \leq j \leq 4$) by multiplying the matrix product $\mathbf{K} \cdot \mathbf{R}_l^{-1}$ by the output of the PID controllers. Since $\mathbf{K}_{inv} \cdot \mathbf{K} = \mathbf{1}$, the machine response represented by the matrix product $\mathbf{R}_l \cdot \mathbf{K}_{inv}$ is such that the resulting beam position is equal to the output of the PID controllers. This renders the local beam position feedback into two independent feedback channels for the BPMs.

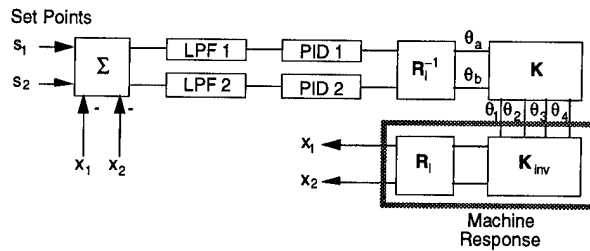


Fig. 3: Schematic of feedback signal processing.

III. EXPERIMENTAL SETUP

The rf BPMs have button-type pickups, which are connected to filter-comparators (FCs) in the tunnel through short cables. The outputs of the FCs, Δ_x , Δ_y , and Σ , are sent to the monopulse receivers in the signal conditioning and digitizing unit (SCDU) housed in the VXI crate. The data is sent to the DSP in the VME crate through the MXI bus. DSP code development, control of operation, and data acquisition is done using a workstation and a PC connected through ethernet. The x-ray BPM analog data is proportional to the

beam position with sensitivity of 10V/mm. This data is digitized by an ADC/DAC board with 12-bit resolution.

The sampling frequency, or number of feedback loops executed per second, was set to 4 kHz. Different low-pass filter (LPF) bandwidth PID controller gains were tried to find the optimal point of operation.

IV. RESULTS

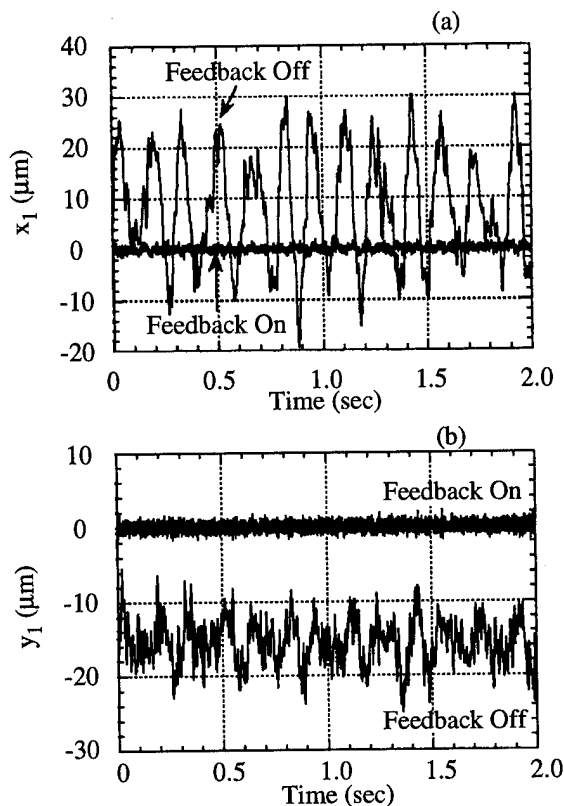


Fig. 4: Beam motion detected by the rf BPMs with feedback on and off in (a) the horizontal plane and (b) the vertical plane. The sampling frequency was 4 kHz, LPF bandwidth was 20 Hz, and the PID gains were: $K_p = 30$, $K_i = 0.3$, $K_d = 0$.

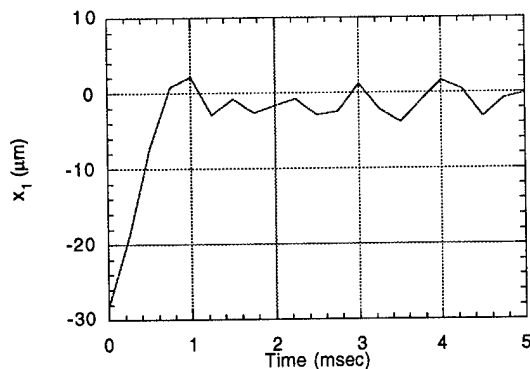


Fig. 5: Impulse response of the feedback system. The rise time is about 600 μ s. The sampling frequency was 4 kHz, LPF bandwidth was 20 Hz, and the PID gains were: $K_p = 20$, $K_i = 0.3$, $K_d = 0$.

Figure 4 shows attenuation of the beam motion in the (a) horizontal and (b) vertical planes. The dominant 7-Hz motion is believed to be due to the ground vibration combined with girder resonance. This beam motion has been successfully arrested by the feedback control. The impulse response of the feedback system shown in Fig. 5 shows a rise time of approximately 500 μ s. We used 4-kHz sampling frequency; 20-Hz LPF bandwidth; and the PID gains $K_p = 20$, $K_i = 0.3$, and $K_d = 0$. The frequency response of the feedback system in the frequency range 0.1 - 1000 Hz is shown in Fig. 6. The bumps near 10 Hz are due to the measurement fluctuation.

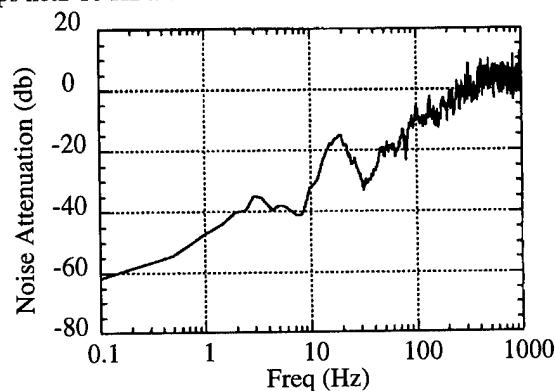


Fig. 6: The frequency response of the feedback system. The feedback parameters are the same as in Fig. 5. The bumps near 10 Hz are due to measurement fluctuations.

V. REFERENCES

- [1] R. O. Hettel, "Beam Steering at the Stanford Synchrotron Radiation Laboratory," *IEEE Trans. Nucl. Sci.*, NS-30, No. 4, p. 2228, 1983.
- [2] R. J. Nawrocky et al., "Automatic Beam Steering in the NSLS Storage Rings Using Closed Orbit Feedback," *Nucl. Instr. and Meth.*, A266, p. 164, 1988.
- [3] Y. Chung, et al., "Closed Orbit Feedback with Digital Signal Processing," *Proceedings of the 1994 European Particle Accelerator Conference*, London, U.K., p. 1592, 1994.
- [4] Y. Chung, et al., "Implementation Status of the Global and Local Beam Position Feedback Systems for the Advanced Photon Source Storage Ring," these proceedings.
- [5] S. Krinsky, et al., "Storage Ring Development at the National Synchrotron Light Source," BNL-46615, p. 58, 1991.
- [6] G. H. Golub and C. Reinsch, "Singular Value Decomposition and Least Squares Solutions," *Numer. Math.* 14, pp. 403-420, 1970, and references therein. Also in J. H. Wilkinson and C. Reinsch, *Linear Algebra*, vol. II of *Handbook for Automatic Computation*, (Springer-Verlag, New York, 1971).
- [7] Y. Chung, G. Decker and K. Evans, Jr., "Closed Orbit Correction Using Singular Value Decomposition of the Response Matrix," *Proceedings of the 1993 IEEE Particle Accelerator Conference*, Washington, D.C., p. 2263, 1993.

Implementation Status of the Global and Local Beam Position Feedback Systems for the Advanced Photon Source Storage Ring*

Y. Chung, D. Barr, G. Decker, J. Galayda, J. Kirchman, F. Lenkszus, A. Lumpkin and A. J. Votaw
Argonne National Laboratory, Argonne, IL 60439

Abstract

The Advanced Photon Source (APS) is implementing an extensive beam position feedback system for both global and local stabilization of particle and photon beams based on digital signal processing. The description and operational experience of the system will be given in this paper. In particular, we will discuss the underlying fundamental principles, hardware layout, controls interface, and automatic software generation for multiple digital signal processors (DSPs) distributed in 20 VME crates around the ring. The feedback system runs at 4-kHz sampling frequency in order to achieve the correction bandwidth of approximately 100 Hz. For the maximum correction efficiency and resolution of conflicts among multiple local feedback systems due to the local bump closure error, the global and local feedback systems are combined into a single unified system. This novel approach is made possible through data sharing among the global and local systems via the fiber-optically networked reflective memories.

I. INTRODUCTION

The Advanced Photon Source (APS) is one of the third-generation synchrotron light sources which are characterized by low emittance of the charged particle beams and high brightness of the photon beams radiated from insertion devices (IDs). In order to take the full advantage of intense synchrotron radiation, the incident intensity, position and angle of the x-ray beam need to be tightly controlled [1-3]. Even though every effort is made to stabilize the electrical and mechanical components of the ring, there will inevitably be residual beam motion primarily caused by the quadrupole vibration.

The sources of vibration include ground vibration, mechanical vibration of the accelerator subcomponents, thermal effects, and so forth. These are manifested in the undesired particle and x-ray beam motion. This results in increased beam size and diluted beam emittance in the short term. An example of the long-term effect is the diurnal changes in the ring circumference and periodic shift of the x-ray beam at the user station [4]. At the APS, the stringent transverse x-ray beam position stability required by the current user community will be achieved through extensive beam position feedback systems with the correction bandwidth exceeding 100 Hz [5].

The APS has 360 rf beam position monitors (BPMs) and 318 corrector magnets distributed around the storage ring, miniature BPMs for ID beamlines, and x-ray BPMs in the front end of x-ray beamlines for global and local orbit feedback. The real-time (AC) feedback systems, which are the main focus of this work, will use a subset of these.

The feedback systems can be largely divided into the global and local feedback systems according to the scope of correction. The global feedback system uses 40 rf BPMs and 38 corrector magnets distributed in 40 sectors. The primary function is to stabilize the selected perturbation modes of the global orbit. The local feedback systems, on the other hand, stabilize the source regions of the x-ray beams locally for angle and displacement.

An ideal local feedback system would not affect the rest of the closed orbit including other local feedback systems. In reality, the global and local feedback systems constantly interact with one another. The effect of global orbit feedback unavoidably interferes with the local feedback. On the other hand, the bump closure error in the local feedback due to bump coefficient error, magnet field error, eddy current effect, etc., causes global orbit perturbation and affects other local feedback systems. If this interaction is too strong, the feedback systems can become ineffective, oscillatory, or even unstable. In order to minimize such effects and maximize the feedback efficiency, it is necessary to decouple the global and local feedback systems.

In this work, we will report on the current status of implementation of the APS orbit feedback systems. The remainder of this paper will be an overview of the feedback algorithm and system description in Section II, system performance test results in Section III, and the current status of system integration in Section IV.

II. FEEDBACK ALGORITHM AND SYSTEM DESCRIPTION

The APS orbit feedback system has the capability to handle multiple local feedback systems for control of the insertion device (ID) and bending magnet (BM) x-ray beamlines and a global feedback system to minimize the global orbit distortion and thus to maintain high beam quality. In this section, we will describe the algorithms governing the operation of these feedback systems [5].

A. Control Algorithm

The signal processing core of the feedback systems is based on digital signal processing (DSP) [6]. The design sampling frequency or the number of feedback loops executed

*Work supported by the U.S. Department of Energy, Office of Basic Energy Sciences, under Contract No. W-31-109-ENG-38.

per second is 4 kHz. Figure 1 shows the schematic of a multichannel digital feedback system. The object to be controlled, or the plant, is represented by the matrix \mathbf{R} . \mathbf{R}_{inv} is the inverse-model matrix that controls coupling of various control points in the plant. In the case of orbit feedback, \mathbf{R} is a composition of the global and local response matrices.

The gain matrix \mathbf{G} comprises the low pass filter (LPF); proportional, integral, and derivative (PID) controller; and any compensation filter (CF) that cancels the undesirable frequency dependence in the plant, such as the effect of the eddy current in the vacuum chamber. \mathbf{H} represents the BPMs.

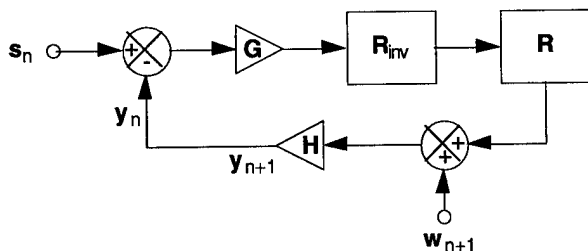


Fig. 1: The schematic diagram of a digital feedback system.

B. Global Orbit Feedback

The global feedback attenuates global orbit distortion by using 40 BPMs and 38 correctors distributed around the ring. One BPM and one corrector per each sector are used, except for sectors 39 and 40 where the correctors were not installed due to space limitation near the injection point. The vacuum chamber at the location of the global corrector is made of thin stainless steel unlike the local feedback systems.

The DSPs and interface boards are installed in twenty VME crates distributed around the ring. Each crate covers two sectors for both the horizontal and vertical planes, an odd sector in the upstream and an even sector in the downstream. A single DSP is assigned per four degrees of freedom.

Since each DSP needs access to the global orbit data at 40 global BPMs, data collected from all 40 sectors needs to be available across the local VME bus. This is done via a dedicated fiber optic network of reflective memories with a data transfer rate of 26 Mbytes/sec. For each degree of freedom, the 40 BPM data are multiplied by a row of the global inverse response matrix obtained using the singular value decomposition (SVD) technique [3,5,7]. Operation of the DSPs is synchronized by an event signal broadcasted from a central 4-kHz clock.

C. Local Orbit Feedback

A local orbit feedback system is based on a four-magnet local bump. The beam positions are detected by two rf BPMs inside the local bump and two x-ray BPMs [2]. This enables control of both the angle and displacement of the x-ray beam.

Four-magnet local bumps can be decomposed into two independent three-magnet local bumps, a and b , and transformation between the bump strengths and the beam positions is straightforward. The locality of the bump can be achieved by powering the bump magnets in certain ratios

determined by local bump coefficients. Empirical derivation of these coefficients is discussed in [8]. The local response matrix \mathbf{R}_l can then be reduced to a 2×2 matrix relating two beam positions and two bump strengths.

Imbalance in the bump coefficients can cause local bump closure error and introduce global orbit distortion. Even though the coefficients are well matched at DC, eddy current effect in the relatively thick (1/2") aluminum vacuum chamber will cause significant bump closure error if orbit perturbation contains components with high enough frequency. This is remedied by global feedback.

D. Decoupling of Global and Local Feedback Systems

In the ideal situation of zero local bump closure error, the local feedback systems are transparent to the rest of the ring. However, the global feedback unavoidably interferes with the operation of the local feedback systems unless the source is localized and does not cause global orbit distortion. In general, orbit perturbation is seen by both the global and local feedback systems, and they will attempt to correct it independently. This can be resolved by decoupling the global and local feedback systems [5]. This unified approach in effect combines the global and local feedback systems, renders the entire system into multiple non-interacting feedback systems, and thus minimizes the interference.

This scheme requires that the local feedback systems take into account the global orbit distortion as well as the local orbit error. This is readily met since the global orbit data is available in all VME crates through the reflective memories.

E. Hardware/Software Configuration and User Interface

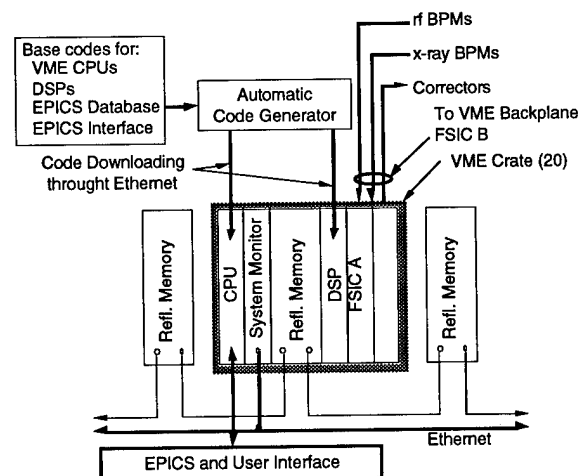


Fig. 2: Operations interface to the orbit feedback system.

Figure 2 shows the operations interface to an orbit feedback system crate. There are a total of 20 such crates, each of which has one VME CPU and multiple DSP boards. Considering the number of processors in the system, it would be impractical and error-prone to write, compile, and link individual codes for each processor. Instead, the codes are generated automatically from base source codes which contain instructions for code generation for different processors. The

command parser is based on the GUS kernel, a script-based interpretive shell developed for streamlined data acquisition and analysis [9]. The compiled codes for the VME CPUs, DSPs, EPICS (Experimental Physics and Industrial Control System) data base, and controls interface are downloaded to the target processors through the ethernet connection. Once the codes begin execution in the processors, the feedback operation, including data sampling and analysis, can be controlled via EPICS and the user interface.

The rf BPMs, x-ray BPMs, and corrector power supplies are interfaced through Feedback System Interface Controller A (FSIC A) and the sisterboard FSIC B in the VME backplane. Reflective memories are used for global orbit data sharing and are networked through fiber optic cables. During feedback operation, the DSPs perform direct data I/O with FSIC A and reflective memory through the local VME bus.

III. SYSTEM PERFORMANCE

The performance of the global feedback system is shown in Fig. 3 in the time and frequency domains using the sampling frequency of 4 kHz, LPF bandwidth of 50Hz, and the PID gains $K_p = 10$, $K_i = 0.5$, and $K_d = 2$. For both tests, the global orbit perturbation was simulated using a single steering error in the ring. In the time domain, the steering error introduced a step impulse at $t = 10$ ms. Comparison of the orbit motion with feedback on and off is shown Fig. 3(a). The response

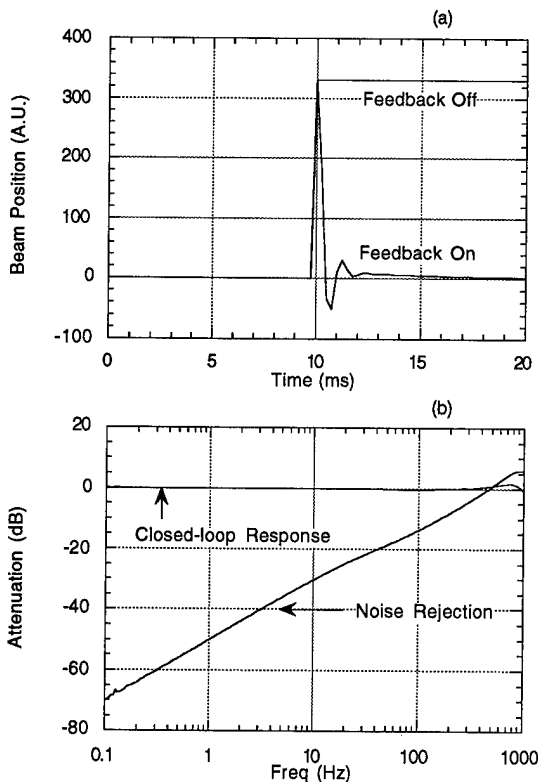


Fig. 3: (a) Impulse response of the global feedback system. (b) Frequency response. The sampling frequency was 4 kHz, LPF bandwidth was 50Hz, and the PID gains were: $K_p = 10$, $K_i = 0.5$, and $K_d = 2$.

time is approximately 500 μ s. The system performance in the frequency domain is shown in Fig. 3(b). The system bandwidth at -6dB noise rejection is 250 Hz. Similar performance results have been obtained from the local feedback system test on the ESRF storage ring [8].

IV. CURRENT STATUS

At this time, the backbone hardware, including the VME crates, VME CPUs, DSPs, reflective memories, and communication network, has been installed and tested. Automatic code generator has been developed to facilitate compiling and downloading of the software for the VME CPUs and DSPs. The performance of the integrated system indicates response time of 500 μ s and correction bandwidth of 250 Hz at -6 dB noise rejection.

The APS storage ring is currently in the commissioning phase. As the ring performance stabilizes in the near future, one or two local feedback systems will be installed on selected x-ray beamlines. With completion of production of the BPM and corrector power supply interface boards expected this fall, the global feedback system will be implemented.

V. REFERENCES

- [1] R. Hettel, "Beam Steering at the Stanford Synchrotron Radiation Laboratory," *IEEE Trans. Nucl. Sci.*, NS-30, No. 4, p. 2228, 1983.
- [2] R. J. Nawrocky et al., "Automatic Beam Steering in the NSLS Storage Rings Using Closed Orbit Feedback," *Nucl. Instr. and Meth.*, A266, p. 164, 1988.
- [3] Y. Chung, et al., "Closed Orbit Feedback with Digital Signal Processing," *Proceedings of the 1994 European Particle Accelerator Conference*, London, U.K., p. 1592, 1994.
- [4] R. Hettel, et al., "Design and Characterization of the SSRL Orbit Feedback System," *Proceedings of the 1994 European Particle Accelerator Conference*, London, U.K., p. 1580, 1994.
- [5] Y. Chung, "A Unified Approach to Global and Local Beam Position Feedback," *Proceedings of the 1994 European Particle Accelerator Conference*, London, U.K., p. 1595, 1994.
- [6] A. Peled and B. Liu, *Digital Signal Processing*, (John Wiley & Sons, 1976).
- [7] Y. Chung, G. Decker and K. Evans, Jr., "Closed Orbit Correction Using Singular Value Decomposition of the Response Matrix," *Proceedings of the 1993 IEEE Particle Accelerator Conference*, Washington, D.C., p. 2263, 1993.
- [8] Y. Chung, et al., "Local Beam Position Feedback Experiments on the ESRF Storage Ring," these proceedings.
- [9] Y. Chung, et al., "Development of GUS for Control Applications at the Advanced Photon Source," *Proceedings of the 1994 European Particle Accelerator Conference*, London, U.K., p. 1794, 1994.

THE RHIC ACCELERATING CAVITY PROTOTYPE TUNER*

A. Ratti, J.M.Brennan, J. Brodowski, E. Onillon, J. Rose
Brookhaven National Laboratory, PO Box 5000, Bldg. 1005, Upton, NY 11973, USA

I. ABSTRACT

The RHIC Accelerating System runs at 26.7 MHz and is required to have an operating range of 85 kHz during the acceleration cycle. Since it also must provide sufficient range to cover manufacturing errors and temperature variation, a requirement of 300 kHz has been specified. A mechanical approach acting on the cavity accelerating gap has been chosen for financial reasons over a ferrite approach. A prototype has been constructed and fully tested on the existing test cavity, using the tuning loop feedback circuitry developed for this task. Results from both the loop response and the power tests of the prototype indicate that this design will successfully meet the performance requirements for the RHIC Accelerating Cavity.

II. INTRODUCTION

The RHIC Accelerating system is responsible for several tasks during the cycle: injection, acceleration, transition crossing and rebucketing, when the beam is handed off to the Storage system, that operates at 196.1 Mhz. At present, a Proof of Principle (PoP) quarterwave cavity with a capacitive load has been built [1] and has provided very useful information. The final Accelerating cavity [2] has been derived from these tests, and is now under construction. Among the tests performed on the PoP cavity are all the tuner measurements that are presented here, both at low level and at high power.

III. TUNING SYSTEM SPECIFICATIONS

The 26 MHz acceleration system needs to tune its frequency to accommodate changes in the beam revolution period during acceleration, and to compensate for beam loading. However the beam loading detune is rather small and has negligible impact on the tuner design; the bulk of the tuning goes into synchronizing with the beam acceleration.

The detuning required for beam loading compensation can be expressed as follows:

$$\Delta f_{rf} = \pm \frac{I_0 \times \cos(\phi_s)}{V_{rf}} \times \frac{R}{Q} \times f_{rf}$$

where ϕ_s is the synchronous angle, I_0 is the average beam current, $R/Q = 60$ is a cavity parameter, and the sign of the shift is positive below transition and negative above. Since the relative low beam intensity and high rf voltage, this frequency change is always less than 1 kHz for RHIC parameters.

The rf frequency, is given by:

$$f_{rf} = \frac{hc}{C} \times \sqrt{1 - \frac{1}{\gamma^2}}$$

where c is the speed of light, C is the RHIC circumference, and $h = 342$ is the chosen harmonic number. At the limit of the speed of light the rf frequency is 26.743 MHz. RHIC will accelerate Gold ions from $\gamma = 12.6$ to $\gamma = 108.4$ and protons from $\gamma = 31.2$ to $\gamma = 268.4$. Since Gold ions are slowest at injection, the lowest rf frequency of operation will be 26.658 MHz. The total frequency range required on this basis is then 85 kHz.

The fastest rate of change of the rf frequency is about 18 kHz per second, for gold ions at the beginning of the acceleration ramp. This sets the specification for the response speed of the tuner.

The tuning loop bandwidth can be specified by assuming an allowable detuning of 0.15 degrees during the magnet ramp, which corresponds to 15 degrees after a 40 dB rf feedback is taken into account. The angular velocity, determined from the maximum frequency sweep rate of 18 kHz/s and the cavity Q , was found to be 1092 r/s in rf cycles. A PSPICE model was then used to determine the loop bandwidth requirement to be > 15 Hz.

IV. THE MECHANICAL CONSTRUCTION OF THE PROTOTYPE TUNER

The mechanical tuner will act directly at the gap, by changing the position of the low voltage electrode. This has many advantages, since it affects the only region of the cavity that will be at both relatively low voltage and current. This makes the construction and cooling of the structure very easy. Another important feature of this structure is the use of only

* Work performed under the auspices of the U.S. Department of Energy.

one small welded bellow which is simple to assemble and very reliable.

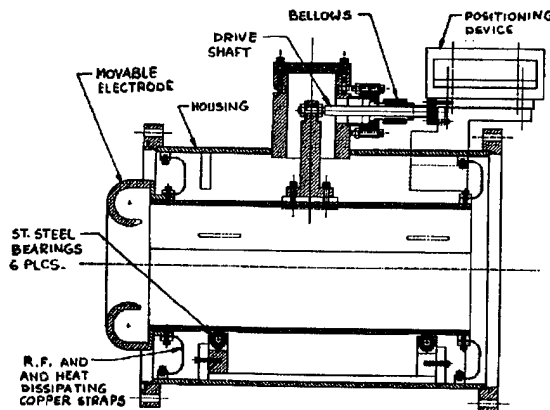


Fig. 1 Prototype mechanical Tuner Assembly

The tuner is made out of an aluminum tank, containing three sets of stainless steel bearings that support an inner cylinder, also made out of aluminum. At one end of this cylinder is mounted a copper tip that is at the low voltage side of the accelerating gap. Grounding copper straps are connected between the gap tip and the outer tank, in order to provide both a good rf ground return and to properly propagate the heat dissipated on this side of the gap. Calculations based upon the code Superfish [1] show that the dissipation at full gap voltage is in the order of 25 Watts which is efficiently carried out by the copper straps. A simplified diagram of the mechanical tuner assembly is shown in Fig. 2.

V. THE FEEDBACK LOOPS AROUND THE TUNER

A linear position stage, driven by a DC motor, moves the mechanical tuner. Two feedback loops are closed around the system (Fig. 2):

- one inner loop around the DC servo system
- one outer loop around the cavity itself

The DC servo system has been chosen to meet the following requirements [2]:

- tuning sensitivity: 11.7 μm
- maximum tuning rate: 18 kHz/s
- time to reach maximum tuning rate: 0.001s
- loop unity gain frequency: > 15 Hz

The inner loop is composed of a digital PID, incorporated in the servo controller; where only the gain part of this is used.

It is a position loop, the input of which being the motor position (encoder signal).

The outer loop filter is composed of a phase advance network, in order to compensate the phase lost due to the mechanical delay. The loop input is the relative phase between the final power amplifier and the cavity voltage, phase which depends on the frequency $\Delta\omega$ by which the cavity is detuned. Its output is used as a input command for the digital PID. A schematic of the studied system is given on Fig. 2.

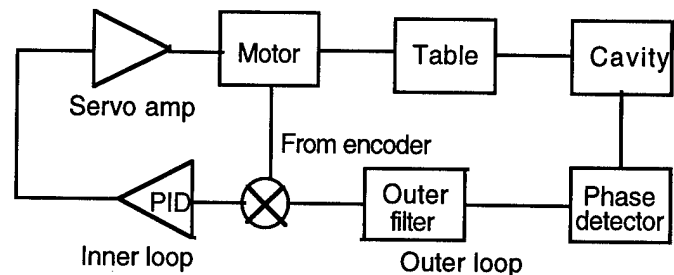


Fig. 2 Schematic of the tuning loops

VI. LOW LEVEL MEASUREMENTS

The system described above was tested at small gap voltages to measure the characteristic response of the system. The open loop measurements show a 35° phase margin and a 8 dB amplitude margin. The 0 dB frequency is 22 Hz. The implementation of the system has shown a 40 Hz mechanical resonance. To avoid exciting it through the tuning loop, a notch filter has been added. Fig. 3 shows the loop measurement result.

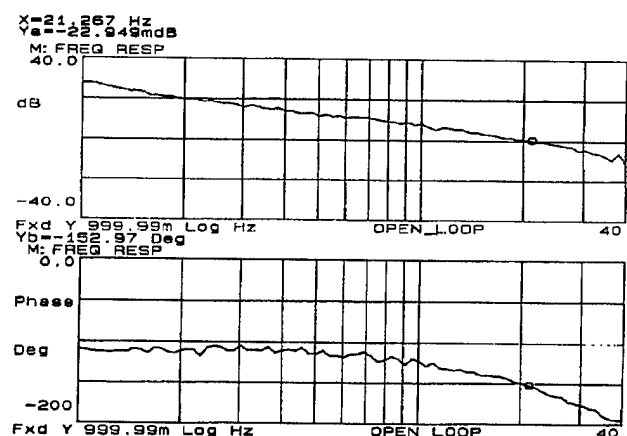


Fig. 3 Measured Open Loop Frequency Response of the Tuning Servo

Static measurements of the cavity resonance have also been done. The tuner changed the natural resonance of the PoP cavity by 273 kHz with its full 2.54 cm travel [2]. This is in excellent agreement with the predictions made with the

Superfish codes. Since the final Accelerating cavity will have a larger gap capacitance, and therefore a more sensitive tuner, this result is very encouraging.

VII. POWER MEASUREMENTS

The PoP system was also run under high power to evaluate the tuner's cooling and high voltage performances. The test cavity was operated at gap voltages around 200 kV in CW for extended periods of time to allow for a full test. Thermocouples installed in a few places inside the tuner were used to monitor the temperature distribution. Preliminary results from testing the cavity with about 30 kW total were consistent with computer modeling [3] and seem to indicate that the cooling of the tuner is adequate. Still, these tests are underway and will be continued until full power is reached.

VIII. CONCLUSIONS

The prototype tuner for the RHIC Accelerating cavity was built and tested both at low and high power. The necessary tuning loops were also developed and used in the setup.

A tuning bandwidth better than 20 Hz was achieved, with a DC gain greater than 20 dB. This meets the requirements for beam dynamics, considering that the Accelerating system will benefit from a 40 dB rf feedback loop.

High power tests indicated that the cooling of the gap electrode has so far been adequate. A stress test of the system,

cycling the tuner many times is planned to insure durability of the device.

To improve the loop performance, a feedforward system which would drive the system according to the frequency ramp could be used. In parallel, the feedback system would remain to correct the static error.

IX. ACKNOWLEDGMENTS

The authors would like to thank the endless support from our technical staff. In particular, Steve Ellerd greatly contributed in the development of all of the electronics, from the loop circuits to the computer programming of the motors; Jeff Aspenleiter was instrumental in assembling the tuner, installing and calibrating the thermocouples and insuring good vacuum and cooling performances.

X. REFERENCES

- [1] J. Rose, et al., "Conceptual Design of the 26 MHz RF System for RHIC", Proceedings of the 1993 Particle Accelerator Conference, Washington, DC USA, p. 1172-4
- [2] J. Rose et al., "Design of the 26.7 MHz Cavity for RHIC" - These Proceedings
- [3] A. Ratti, "Mechanical Tuner Measurements vs. Simulations", informal note, RHIC/RF MTF 2.6.1995

Ramp Tuning of the APS Booster Synchrotron Magnet Power Supplies*

S.V. Milton and J.A. Carwardine

Advanced Photon Source, Argonne National Laboratory
9700 South Cass Avenue, Argonne IL 60439, U.S.A.

Abstract

The acceleration cycle of the Advanced Photon Source (APS) booster synchrotron is completed within 250 ms and is repeated at 2 Hz. The currents in the quadrupole and sextupole magnets must track the dipole current to within tight tolerances if the beam is to remain stable during acceleration. In order to meet the performance specifications, a monitoring system, on-line with the main control system, is used to measure machine performance and adapt power supply reference waveforms from cycle to cycle. The system optimizes the tracking between the power supplies, thus minimizing transient effects and taking care of any slow drifts. Tuning algorithms are described and their performance evaluated. Practical considerations are also discussed.

I. INTRODUCTION

1.1 Description of the Booster

The APS booster synchrotron (booster) raises the energy of a 400-MeV positron or electron beam up to 7 GeV in approximately 230 msec. It is designed to do this at a 2 Hz rate.

The booster employs a classical FODO lattice structure of 292 ramping magnets. Of these magnets there are 68 dipoles, 80 quadrupoles, 64 sextupoles, and 80 correctors. The dipoles are all connected in series and are powered by two 12-phase power supplies operating in a master/slave configuration. The quadrupoles and sextupoles are each separated into two families of equal numbers with each family powered by a separate 12-phase power supply. The correctors are powered with separate bipolar DC/DC convertors.

1.2 Ramp Cycle

With the exception of the correctors, a typical magnet current ramp cycle is shown in Figure 1. At the beginning of the cycle a small DC current is demanded. At an appropriate time, the current begins to ramp up linearly. Injection occurs on the fly 10 - 15 ms after the start of the ramp. The current, and thus energy, continues upward linearly. Extraction occurs approximately 230 ms after injection and is also done on the fly. After extraction, all supplies are ramped back down to zero current.

1.3 Performance/Tracking Tolerances

Tracking tolerances with respect to the dipole must be specified and maintained when beam is present, otherwise the beam transverse tunes will strike destructive resonances. Although one could choose to use a complicated dipole current ramp and force the other power supplies to track this, we choose instead to use a simple linear ramp for the dipoles, quadrupoles, and sextupoles. Due to their importance to the opera-

tion of the machine, we will limit our discussion to only the dipoles and quadrupoles.

The nominal horizontal and vertical transverse tunes of the booster are $Q_h = 11.75$ and $Q_v = 9.80$, respectively. A simple, though somewhat restrictive, performance goal is to maintain the tunes to within $\Delta Q = \pm 0.025$. Neglecting variations in the magnetic properties of the magnets, we then require the ratio of magnet currents to remain very close to constant throughout the energy ramp, with maximum deviations dictated from the above tune tolerances.

The allowable current errors are written simply in terms of the fractional quadrupole strength

$$\frac{\Delta K}{K} = \left(\frac{\Delta I_{quad}}{I_{quad}} - \frac{\Delta I_{dipole}}{I_{dipole}} \right).$$

The tunes vary roughly like $\Delta Q \approx 25\Delta K$. This is true in both horizontal and vertical planes. (The off-diagonal term of the "tune" matrix contributes about a factor of six less than the diagonal term and is neglected in this approximation.) A tracking error of either the dipole or quads will then cause a tune error. The effect is additive. In order to maintain our performance goal we thus require

$$\frac{\Delta I_{q,d}}{I_{q,d}} \leq \frac{1}{50K} \Delta Q_{total} \approx 0.029\Delta Q_{total} \approx \pm 0.14\%.$$

Achieving and then maintaining these tolerances is particularly challenging at injection energies where the current is small and the power supplies are still suffering from turn-on transients. The methods we use to do this are the subject of this paper.

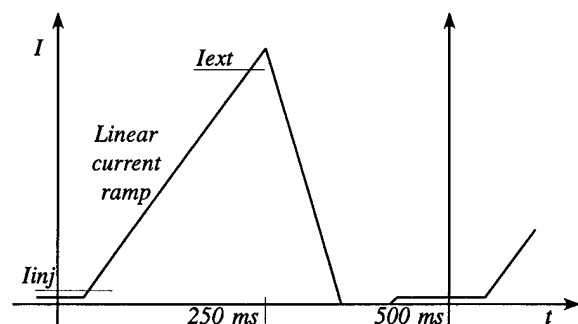


Figure 1: A typical current ramp cycle in the booster.

II. POWER SUPPLY CONFIGURATION AND MONITORING

2.1 Present Configuration

A block diagram of our present power supply control configuration is shown in Figure 2. A more thorough description of

* Work supported by U.S. Department of Energy, Office of Basic Sciences, under Contract No. W-31-109-ENG-38.

its operation and performance can be found in [1]. Only a brief description will be given here.

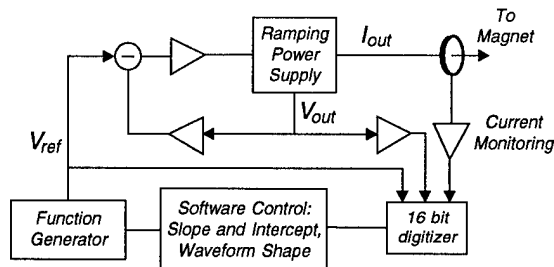


Figure 2: The present power supply control configuration.

Early on in the commissioning of the booster we operated the ramping supply regulators in current-control mode. The bandwidth of this system proved inadequate to achieve the desired fractional current tolerances. Fortunately, cycle-to-cycle repeatability of the supplies was good. We have since switched to operating the supplies in voltage-controlled mode. Taking the L/R time constant out of the loop of the load effectively increased our regulator bandwidth; however, we are still not able to achieve the stated tolerances with hardware feedback alone. Current feedback and the artificial extension of the bandwidth required to achieve and maintain the tolerances is done via software which monitors the output currents shot-to-shot and make fractional changes to the arbitrary function generator (AFG) voltage reference waveforms.

2.2 Monitoring

Success in our tuning methods relies heavily on our capability to accurately measure what the power supplies are doing. Our primary diagnostic technique is direct measurement of their output currents which are monitored in each case with a high stability current transducer. This signal is digitized by a 16-bit Analogic digitizer. The digitized waveforms are made available shot-to-shot to the control system for further processing. We also continually digitize and monitor the AFG voltage reference and power supply output voltage.

III. CURRENT RAMP TUNING AND CONTROL

There are two distinct ways in which we achieve the current ramps we desire: dead-reckoned tailoring (ramp tuning) of the input voltage reference signal and shot-to-shot control of the gross ramp parameters. A linear current ramp within the specified tolerance is first tuned using the methods described below. In this way the input reference effectively becomes the convolution of the desired output voltage with the inverse response function of the supply (no assumption about the linearity of the response is made). After achieving this, the slope and zero current time intercept are maintained, during actual operation, by a separate control program.

3.1 Initial Corrections

Tuning of the ramp tables proceeds in stages. As explained in [1], a nonlinearity is observed in the step response of the power supply. This limits automatic tuning to small corrections about a waveform which already provides reasonable performance. However, even without the nonlinearity, the transient response is still quite complicated and is not fully compensated

by the regulator. We first set about developing reference ramp tables which get the supplies to within $\Delta I/I = \pm 1\%$ of the desired linear ramp. Only then do we apply software correction algorithms. Tuning of the ramps starts with a simple application of $V = L di/dt + Ri$ to a linear current ramp. This is the initial voltage reference signal from which we work.

The ramp linearity is first improved by direct hand tuning of the voltage reference waveforms. Visual inspection of the measured $\Delta I/I$ is used to gauge progress. The hand-corrected waveform is then smoothed to eliminate any discontinuities. Smoothed and unsmoothed voltage reference waveforms for the defocusing quadrupole are shown in Figure 3. Only the first 100 ms of the 250-ms ramp cycle are shown. Beam injection occurs at 25 ms. It can be seen from the figure that the reference waveform is still being used to tune out the turn-on transients of the supply at the time beam is injected.

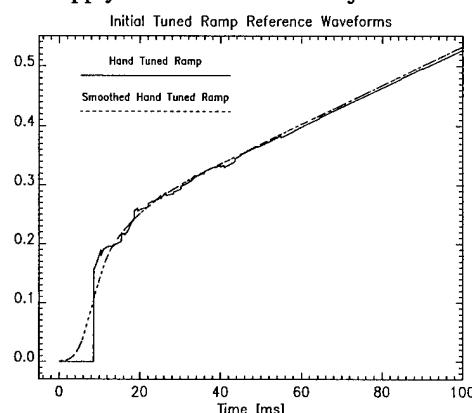


Figure 3: Example of an initial hand-tuned and smoothed voltage reference waveforms.

By tuning in this manner, we are able to routinely achieve a $\Delta I/I \leq 0.5\%$ (Figure 4a). Improvement past this level using hand tuning alone becomes more difficult and time consuming.

3.2 Fine Tuning

Further refinement of the current ramp waveform is done through software feedback. At present, a C-shell script makes calls to a suite of **sdds** (self-describing data set) processing tools [2]. A tool we have created is the **sddsPID** program. Given an input error signal, it returns an output correction signal which is determined by the gains and time constants of proportional, integral, and derivative (PID) terms of the defined software feedback loop. This effectively recreates the PID response normally attributed to a conventional analog regulator. The difference is that we are applying successive feed-forward corrections rather than doing real-time compensation.

The error signal for our loop is the point-by-point difference between the measured current waveform and a linear fit to that waveform. This error signal is first smoothed to get rid of high frequency noise. The **sddsPID** program is then run on the error signal and the output subtracted from the latest voltage reference waveform. This new updated waveform is loaded into the respective AFG. The program **Bcontrol** (see below) is then called upon to maintain the ramp slope and zero current time intercept. The process is repeated until the corrected $\Delta I/I$ is at or below the resolution of the present AFGs.

The results of the software feedback process is shown below in Figures 4a and 4b. In Figure 4a the $\Delta I/I$ signal was the best we were able to obtain by hand tuning and smoothing. Note that there is some 60-Hz ripple in the signal; this is real and believed to be on the voltage reference. Figure 4b is the result of successive iterations of the software current control feedback script. The $\Delta I/I$ signal has been corrected to below $\pm 0.1\%$ during the ~ 230 ms the beam is in the machine (the arrow points to the injection time). The 60-Hz ripple is also no longer visible.

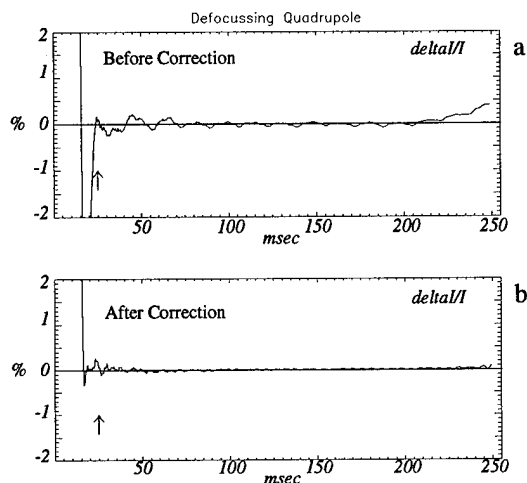


Figure 4: Fractional current errors before and after software feedback correction.

3.3 Maintaining the Slope and Intercept

Once tuned, the current ramp tends to stay within tolerance for long periods of time (days or longer); however, this is only true if the linear fit coefficients are maintained. Of primary importance is the output amplitude of the AFG. By varying this amplitude slightly we can keep the current slope at the desired value independent of slow variations of the line voltage. We must also insure that the quads and dipole all have the same zero current time intercept otherwise the beam transverse tunes will slew with time. **Bcontrol** actively does this control function for us. It monitors the current ramps on a shot-to-shot basis, does a linear fit to the measured current, and adjusts the AFG amplitude and trigger time to maintain the slope and zero current time intercept at the desired values. The values required are first deduced from theory and from magnet measurements. They are then modified as a result of measurement of the beam transverse tunes during ramping.

IV. FURTHER ENHANCEMENTS

4.1 Adaptive Feedback

The method described above still suffers from the fact that the hand-tuned ramps must be very close to optimal before we feel comfortable closing the final control loop. We have also found that occasional adjustments are needed to the control algorithms in order for them to work successfully. We are actively investigating the use of adaptive signal processing to continually determine the inverse response function of the power supply to achieve the desired output waveform. Figure 5 shows the scheme for deriving the inverse voltage response.

The two model blocks shown in the figure are digital filters. The weighting factors for the model under refinement are generated using a minimization routine such as the least-mean squares (LMS) [3] or simplex algorithms.

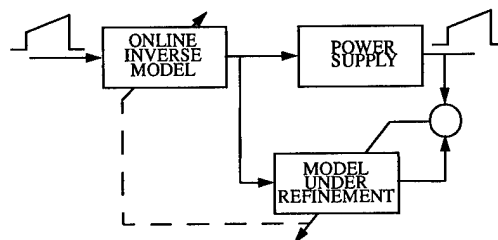


Figure 5: Adaptive Inverse Model Control Scheme.

The adaptive approach has the potential to be more robust than other approaches since it continually updates its model of the inverse response function to whatever subtle changes might occur within the system over time. An accurate forward model of the system has already been created using the LMS algorithm and a finite impulse response filter (FIR).

4.2 Beam-Based Tuning

Of course the beam is the final judge of the quality of the ramp tuning. The ultimate tuning aid would be to use the measured transverse tunes as a function of time during the ramp cycle. To date we have only used the tunes at injection to adjust the ramp reference waveforms.

Since tunes signals are available only when beam is present, tuning with beam can only be supplemental and cannot act as a replacement for the techniques described in this paper. It pays great dividends to be able to confidently tune up the ramps with no beam present using measurements of the supply input and output parameters.

V. SUMMARY

The methods described have proven successful; we routinely and consistently ramp a 400 MeV beam up to 7 GeV in just under 230 msec. Further refinements are being made which will allow full automation of the initial tuning and maintenance of the ramping waveforms.

VI. ACKNOWLEDGEMENTS

We wish to thank D. McGhee of ANL and Dan Wolf and Howie Pfeffer, both from Fermilab, for many fruitful discussions and suggestions. Thanks go to M. Borland for his many tips about programming in the C language. We also would like to thank A. Puttkammer for maintaining and repairing the supplies when some of our initial ramp correction attempts went a little wacky.

VII. REFERENCES

- [1] J.A. Carwardine, S.V. Milton, and D.G. McGhee, "Performance of the Ramping Power Supplies for the APS Booster Synchrotron," these proceedings.
- [2] M. Borland, "A Self-Describing File Protocol for Simulation, Integration and Shared Postprocessors," these proceedings.
- [3] B. Widrow, S. Stearns, *Adaptive Signal Processing*, (Prentice Hall, 1985).

ORBIT STABILITY IMPROVEMENT AT THE NSLS X-RAY RING *

J. Safranek, O. Singh, and L. Solomon

National Synchrotron Light Source, Brookhaven National Laboratory, Upton, NY 11973

Abstract

We describe recent improvements in both the short and long-term orbit stability at the NSLS X-Ray Ring. The short-term stability has been improved by increasing the gain and the bandwidth of the global harmonic feedback systems. The long-term horizontal orbit drift over the course of a fill has been reduced by including the rf-frequency in the orbit feedback. Work is in progress to further reduce orbit drift by compensating for thermally induced mechanical motions of the beam position monitors (BPMs).

I. INTRODUCTION

At the NSLS storage rings, the harmonic based analog global feedback system has provided excellent orbit stability [1]. For most users, the level of this beam stability (short and long-term) has been satisfactory, however, further stabilization is desirable. During the Fall of 1994, the gain and bandwidth of the global feedback systems were increased resulting in significantly reduced short-term orbit fluctuations. The long-term drift in the horizontal orbit has been reduced by up to a factor of 3.6 by varying the rf frequency to eliminate orbit drift proportional to the dispersion.

With the improvements in the global feedback and the addition of the rf frequency feedback, the present limit in orbit stability is the accuracy of the BPMs. The primary limitation in reading the horizontal orbit is the motion of the vacuum chamber at the BPMs due to synchrotron radiation heating. In this paper we describe work to characterize this vacuum chamber motion so that we can compensate for it in the orbit feedbacks. The vacuum chamber moves very little in the vertical plane, so the orbit stability vertically is limited by the variation in BPM processing electronics with stored current. The present BPM electronics are stable to about 10 to 20 μm over the range of operating currents (110 to 250 mA). New BPM electronics with dynamic stability better than 5 μm have been developed recently [2], and we plan to implement these soon for further stabilization of the vertical orbit.

Concurrently, we are developing a new digital orbit feedback system to achieve even better performance [3].

II. IMPROVED GLOBAL FEEDBACK

By increasing the gain and bandwidth of the servo loops for feedback harmonics, the feedback system performance has been enhanced. The improvement can be described by analyzing the overall open-loop-gain and phase responses. Figure 1 shows the gain and phase responses for both the old and new systems. The gain response for the new system (drawn with the solid line) shows a gain increase of 9db (factor of 3), as compared to the old system (drawn with a dotted line). This indicates that the noise

at low frequencies was reduced by an additional factor of 3 when the new system was implemented. The bandwidth is defined as the frequency where gain curve crosses 0 db. The gain curves show that the bandwidth has been increased from 70 Hz to 200 Hz, so the beam noise in this frequency range is reduced. The phase response (shown by solid line in the lower plot) has been modified so that the 45 degree phase margin extends to 200 Hz to meet the stability requirement for the feedback system.

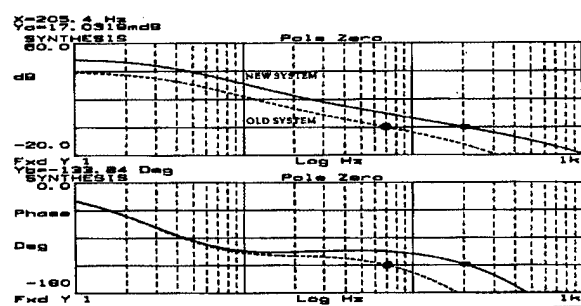


Figure 1. Gain and phase response of the old global feedback compared to the improved high-gain, broad-bandwidth global feedback.

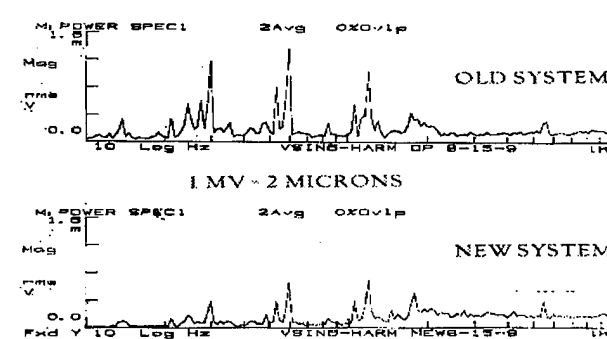


Figure 2. A spectral analysis of a sixth spatial harmonic of the vertical orbit. The new global feedback system shows improved reduction in orbit fluctuations up to 200 Hz.

Figure 2 shows the frequency spectrums for a 6th spatial orbit harmonic in vertical plane. The top trace shows the beam motion harmonic when old feedback was in operation; the bottom trace shows the beam motion harmonic when the new feedback system was in operation (the present operating conditions). The frequency peaks from 1 to 120 Hz have been reduced. The improvement factor at 3 frequencies are listed in table 1.

III. RF FREQUENCY FEEDBACK [4]

The improved gain and bandwidth of the global feedback system primarily reduced orbit motion on time scales less than one

*Work performed under the auspices of the U.S. Department of Energy

Table 1. Improvement seen at different frequencies in orbit noise reduction with the new increased-bandwidth global feedback.

Frequency	Approximate Improvement factor
30 Hz	3
60 Hz	2
120 Hz	1.5

second. We have also made recent progress toward reducing orbit drift on time scales of hours. We noticed that during many fills, much of the horizontal orbit drift had a shape similar to the X-Ray Ring dispersion. For example, the solid line in figure 3 has the largest orbit distortions in the eight dispersion straight sections. This means that we can eliminate this orbit distortion by varying the rf frequency. We have tested a program that changes the rf frequency every five seconds to remove any dispersion-like orbit shift. The change in rf frequency, Δf_{rf} is calculated as follows:

$$\Delta f_{rf} = \frac{(x - x_0) \cdot \frac{dx}{df_{rf}}}{\frac{dx}{df_{rf}} \cdot \frac{dx}{df_{rf}}}$$

where x is the measured orbit, x_0 is the orbit where the synchrotron radiation users want the beam to stay, and $\frac{dx}{df_{rf}}$ is the measured change in orbit with rf frequency (measured with the other global and local orbit feedbacks running). The measured orbit, x , is actually the average of 1280 orbits measured over five seconds. Each five seconds, only 1/5th of the calculated change in f_{rf} is implemented. With all this averaging, the implemented change in the rf frequency for each 5 second step is rarely larger than one bit which is 0.1 Hz and gives about $0.2 \mu m$ change in orbit at the beamline source points. Therefore no appreciable noise is added to the orbit while the long-term drift proportional to the dispersion is eliminated. Figure 3 shows the results of testing the f_{rf} feedback during a studies shift. The rms drift in horizontal orbit was reduced by a factor of 3.6.

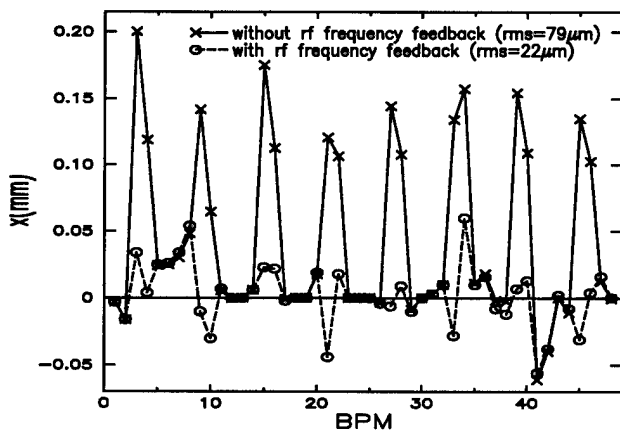


Figure 3. Drift in horizontal orbit over several hours at the 48 BPMs with and without rf frequency feedback. The rf frequency feedback reduced the rms orbit drift by nearly a factor of four during this fill.

The f_{rf} feedback is already running routinely on the NSLS UV Ring. It has run on several fills on the X-Ray Ring, and we plan to put it into regular operations soon.

IV. BPM MOTION MEASUREMENTS [4,5]

As the vacuum chamber heats and expands from synchrotron radiation, the beam position monitors (BPMs) also move [6]. In each superperiod of the X-Ray Ring, a rigid vacuum chamber support near Q4 (see figure 4) fixes the chamber position in all three dimensions. The chamber is free to expand longitudinally between Q4 and the bellows, which are located at the end of the insertion straight section. Several supports between the three-dimensional fixed point and the bellows minimize transverse horizontal and vertical motion while permitting the longitudinal expansion. Despite these supports, the large forces associated with the vacuum chamber expansion lead to significant motion of the vacuum chamber in the transverse horizontal direction in certain locations as well as small vertical motions.

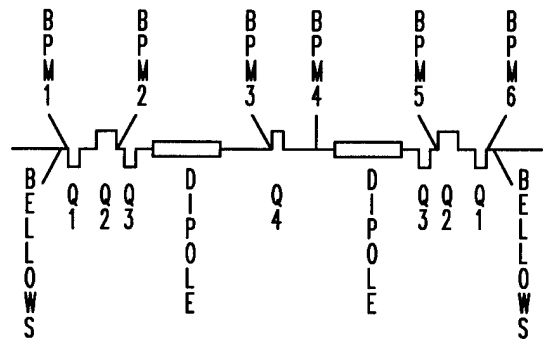


Figure 4. This is a schematic of the layout of one of the 8 superperiods in the X-Ray Ring. The quadrupole, dipole, and BPM locations are shown.

Gauges installed at several BPMs measured the transverse movement of the vacuum chamber. Figure 5 shows the largest measured motion, which was transverse horizontal motion at BPM 5 in the sixth superperiod. The most motion is at BPM 5 in each superperiod, because it is just downstream of the dipole magnet (figure 4) where synchrotron radiation heating is largest. A large chamber movement (about $300 \mu m$ in figure 5) occurs as the ring energy is ramped to 2.584 GeV, when the synchrotron radiation begins heating the chamber. The vacuum chamber is cooled by temperature regulated water, but even with the inlet water temperature held fixed, the outlet water temperature heats 1.8 degrees C from the synchrotron radiation. After the initial large motion which lasts about 10 minutes, there is a slow drift in the chamber position as the synchrotron radiation load decreases due to stored current decay.

Table 2 shows the size of the initial horizontal motion (the first 5 to 10 minutes of the fill) and the subsequent drift in the vacuum chamber over the succeeding hours of the fill for the BPMs measured so far. The limit on the long-term horizontal orbit stability of the X-Ray Ring is set by this vacuum chamber motion, since the orbit motions associated with the feedback

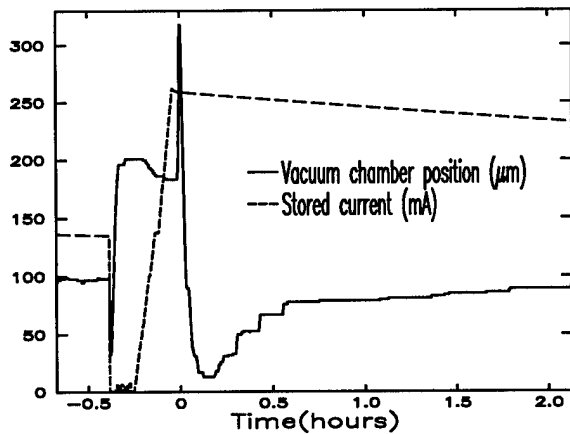


Figure 5. This shows the horizontal motion of the vacuum chamber at BPM 5 in the sixth superperiod as the beam is dumped and refilled. Time zero is the time the ring energy was ramped from injection energy (744 MeV) to operation energy (2.584 GeV).

systems are much smaller. A possibility for removing this limit is compensating for the measured BPM motions by modifying the orbit feedback setpoints as the BPMs move, either in real-time or with a look-up table.

We measured the vertical motion of the vacuum chamber at the two BPMs with the largest measured horizontal motion. Both had initial vertical motions of less than $20 \mu m$. Subsequent vertical motion over the succeeding hours of the fill was even less, and the motion at BPMs where the vacuum chamber sees less synchrotron radiation is expected to be smaller still. At this time, stabilization of the vertical orbit is limited more by the variation of BPM electronics with stored current than by BPM motion.

Table 2. The initial motion is the horizontal movement of the BPM in the first 5 to 10 minutes of the fill. The subsequent motion is the movement in the following several hours of the fill.

BPM	Superperiod	Initial Motion	Subsequent Motion
2	8	$20 \mu m$	$< 10 \mu m$
3	2	$0 \mu m$	$0 \mu m$
4	2	$60 \mu m$	$50 \mu m$
5	1	$90 \mu m$	$60 \mu m$
5	6	$300 \mu m$	$70 \mu m$
5	7	$240 \mu m$	$85 \mu m$
6	7	$40 \mu m$	

V. CONCLUSION

We have reduced short-term orbit fluctuations by as much as a factor of 3 by increasing the gain and bandwidth of the global harmonic feedback system. We have reduced long-term horizontal orbit drift by as much as a factor of 3.6 by using the rf frequency in the orbit feedback. We are pursuing the possibility of further reducing the horizontal orbit drift by compensating for measured

horizontal movement of the vacuum chamber at the beam position monitors. Further reduction in the vertical orbit drift will be achieved when we implement recently developed BPM processing electronics, which have improved dynamic range with stored current.

VI. ACKNOWLEDGEMENTS

The authors appreciate useful discussions with Eric Johnson, Sam Krinsky, and Peter Stefan. Yong Tang and John Smith's help with the computer code for the rf frequency feedback was appreciated. We would like to thank Bob Foxworth, Bob Harrington, Denny Klein, Ed McKenna, Susila Ramamoorthy, and George Stenby for their help with the vacuum chamber motion measurements.

References

- [1] O. Singh, proceedings of the 1993 Particle Accelerator Conference, pg 2254.
- [2] R. Nawrocky, to be published.
- [3] E. Bozoki, A. Friedman, S. Ramamoorthy, these proceedings.
- [4] A. Ropert, AIP Conference Proceedings 315, 1994, pg 69.
- [5] J.A. Balmer, L.A. Welbourne, proceedings of the 1994 European Particle Accelerator Conference, pp 2561-2563.
- [6] E. Johnson, A.M. Fauchet, X. Zhang, Correlation of Photon Beam Motion with Vacuum Chamber Cooling on the NSLS X-Ray Ring, Rev. Sci. Instrum. 63 (1), January, 1992.

DIGITAL ORBIT FEEDBACK COMPENSATION FOR SPEAR*

J. Corbett, R. Hettel, D. Keeley and D. Mostowfi

Stanford Linear Accelerator Center, Stanford University, Stanford, CA 94309
Stanford Synchrotron Radiation Laboratory, Stanford University, Stanford, CA 94309

Abstract

The global orbit feedback system for SPEAR will be upgraded in 1995 to achieve 30-50Hz closed loop bandwidth. In this paper, we discuss issues related to measurements of the corrector frequency response, the DC response matrix, digital compensator design, and the impact of sequential bpm sampling. Results from detailed simulations are included.

1. INTRODUCTION

SPEAR is a 234m synchrotron light source that was originally designed for $e^- e^+$ collider physics. Because of this history, many features built into 3rd generation light sources are not available in SPEAR. The bpm's, for instance, were installed before the modern notions of accelerator impedance were developed, and their geometry was not optimized for high resolution measurements. In addition, many of the magnets are subject to thermal fluctuations, hysteresis, and to ground motion propagating through girder supports. These vibrations lead to electron beam motion in the 1-20Hz range, and diurnal drift of the orbit.

At present, 3-magnet bumps are used in analog servo loops to stabilize each photon beam position at a monitor located 5m to 15m from the source point^[1]. If we also control the electron beam position at the source point, we effectively control the angle of the photon beam. So far, we have stabilized diurnal motion of the electron beam by correcting the orbit with a feedback system operating at ~1min intervals. The next step is to speed up the orbit acquisition in order to control beam motion at several Hz and above. As at other laboratories, the SPEAR system uses either harmonic or eigenvector orbit correction^[2-4] and a 'bump subtraction' algorithm to decouple the global system from the analog servo loops at each photon beamline.

Commissioning the global feedback system exposed some interesting issues peculiar to SPEAR. Many of the vertical corrector magnets, for instance, are located on QF magnets (low β_y), are not optimally located for orbit control, and have only a limited actuator range. In addition, it was found that the bpm readback values depended on the total beam current and the bunch pattern.

Most of these problems have been overcome by a combination of careful machine handling, empirical selection of the eigenvalue cut-off point, and filtering data in the feedback code. As a result, we now have a system that can stabilize the electron beam orbit to ± 100 microns (peak) over a 24hr period. In addition, the corrector currents used in the 3-bump servo loops are 5 to 10 times less than without the global feedback.

*work supported in part by Department of Energy Contract DE-AC03-76SF00515 and Office of Basic Energy Sciences, Division of Chemical Sciences.

Later this year, we will introduce a fast bpm processor to reduce the orbit feedback cycle time to ~1ms and include the photon beam bpm's in the digital control algorithm. In this configuration, we can readily apply a different relative weight on each bpm to adjust for measurement noise, and/or weight each corrector magnet to control the use of individual actuators. The fast feedback system will use a dedicated DSP board in a VME crate to process the orbit information. (See ref. [5] and companion paper [6]) The goal is to stabilize motion at both the electron and photon bpm's with a 30-50Hz closed-loop bandwidth.

In this paper, we will discuss our present approach to compensation of the frequency dependent components of the MIMO (multi-input, multi-output) feedback system. Following the outline of a simple compensator design, we will discuss more challenging aspects of the SPEAR feedback system. The main difficulties are (1) compensation for corrector magnets with different frequency response, (2) delays incurred from sequential bpm sampling, and (3) differences between the measured response matrix and the actual machine response.

2. SYSTEM RESPONSE

Frequency response is presently measured by driving corrector power supplies with a sinusoid (or random) waveform generator and measuring the output at a broadband photon beam position monitor. When the new bpm processor and DSP system come on line, transfer functions between all correctors and bpm's will be evaluated across the complete open loop system.

We expect the transfer functions are dominated by power supply response, eddy currents in the magnet cores, and field penetration into the vacuum chamber. A typical frequency response from one of the 26 vertical correctors wound on a solid core quadrupole is plotted in Fig 1. In this case, a two-pole fit of the Bode plot is indicated. Fits to independent measurements produced close agreement for the low frequency pole (~25Hz) and about 30% difference at the high frequency pole (~250Hz). Since the two pole model only approximates the exact characteristics of the hardware, the final optimization of the compensator design will be the result of empirical tuning. Points above about 300Hz are not indicated in these plots because the phase becomes a non-linear function of drive amplitude.

The DC response to each corrector as measured at each electron and each photon beam bpm forms the response matrix for the feedback algorithm. It is also possible to include the rf frequency in the response matrix to correct DC orbit shifts. The main feedback algorithm consists of first projecting orbit perturbations onto a subset of the eigenvectors from the inverse response matrix (SVD pseudo-inverse) to produce a set of corrector control signals.

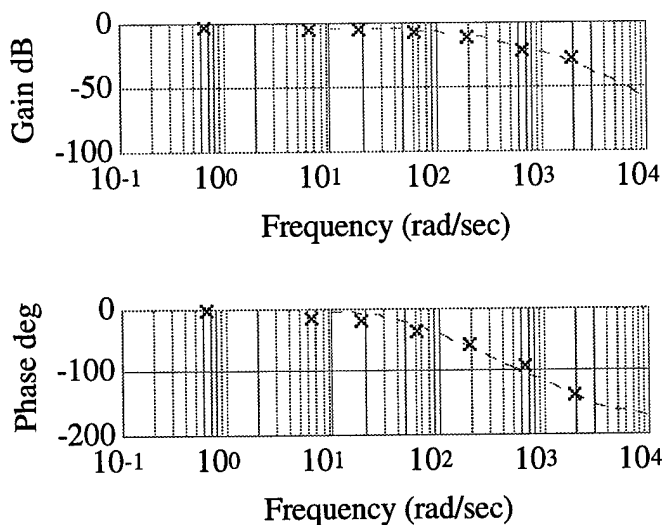


Figure 1 Two-pole fit to measured frequency response of a vertical corrector magnet in SPEAR.

The resulting control signals are then digitally compensated to achieve the desired closed-loop frequency response. Details of the eigenvector cut-off calculation can be found in reference [7].

3. DIGITAL COMPENSATION

Based on the above measurements, a digitally compensated closed-loop Bode plot for a 1kHz sample rate is shown in Fig. 2. For this plot, we included a 1ms computation delay (single cycle) in the open loop transfer function. As discussed in Section 5, there will also be a range of bpm readback delays in the orbit acquisition system. The simple compensator shown here uses a single integrator pole and a single real-axis zero (PI-control) to achieve a closed loop bandwidth of about 25Hz. To avoid excessive actuator drive current, derivative control was not used in this example. A PI compensator simplifies the design and the system behavior while we gain operational experience. A state-space feedback system with optimal gain coefficients will be pursued if simulations show it to provide operational benefits.

In SPEAR, four additional correctors, previously used near the interaction points for collider experiments, exhibit a more broad band frequency response. For reasons discussed in more detail below, we will try to equalize the frequency response of all correctors. In short, equalization filters permit factoring a single frequency-dependent term from the response matrix, and simplify development of the feedback system.

4. DIGITAL FEEDBACK SIMULATOR

A computer simulation program was written by one of the authors (Keeley) to evaluate aspects of the feedback behavior that cannot be characterized analytically. The main features of the simulator are direct integration (Bulirsch-Stoer) of the differential equations representing the analog parts of the system, and difference equations representing the digital parts of the system. The analog part models the

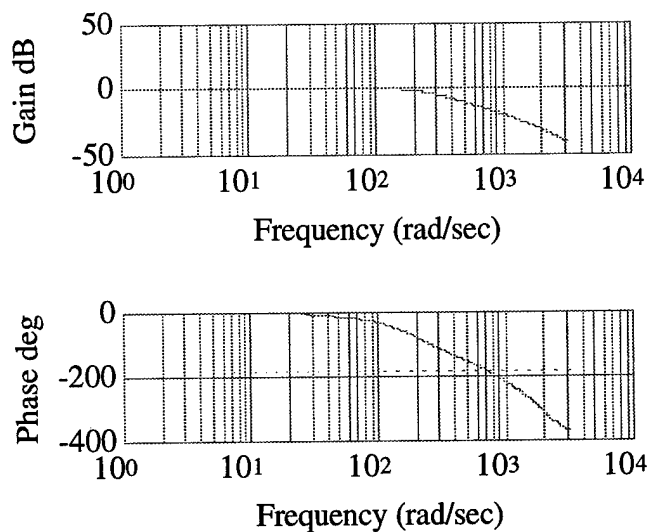


Figure 2 Closed-loop Bode plot with PI compensated corrector magnet.

time dependence of the system response beginning from the discrete inputs to the corrector power supplies, through the corrector magnets, and finally the field penetration into the vacuum chamber. The numerical coefficients for the differential equations are determined from frequency response measurements. We chose to use a differential equation model to permit sampling of the orbit at arbitrary times.

In the simulator, the actuator drive currents are modeled as piecewise constant outputs from the DACs as driven by the digital computer. The orbit is obtained by 'sampling' the ongoing solution of the differential equations for the fields in the vacuum chamber, and using the DC orbit response matrix to compute beam position. The bpm readings are related to the physical orbit through another set of equations representing the transfer function of the bpm's and the bpm processor hardware. This component of the transfer function will be measured directly when the fast bpm processor becomes available.

The digital part of the simulator includes the bpm sampler, the orbit correction calculation, and the digital frequency compensation stage. It is anticipated that the DSP calculation (including voltage to position calculation, matrix multiply, digital filters and I/O) will be less than 1ms.

In general, the response matrix used to calculate the orbit correction need not be the same as the matrix used to simulate the response of the machine to corrector inputs. This feature allows simulation of imperfect response matrix measurements, or systematic changes in the lattice (see section 6).

5. SEQUENTIAL ORBIT SAMPLES

The vertical orbit feedback system on SPEAR will use about 30 electron beam and 10 photon beam position monitors. It is anticipated that the new bpm processor will sample the bpm's sequentially around the ring, with a dwell time of about 10μs (~10 turns) at each button. The time interval for a complete orbit acquisition will be on the order of 1ms, which is close to the desired feedback cycle time.

Note, however, that although the most recent bpm reading will have a delay of $\sim 40\mu\text{s}$, the initial reading will have about 1ms delay.

In practice, the different bpm sample delays produce different open loop transfer functions. Since each corrector drives every bpm in the global feedback system, even an individual compensator for each corrector cannot account for a different sample delay of each bpm. In effect, the closed loop system becomes fully coupled. The coupling implies that if a step is applied to a single bpm readback, the orbit will initially move at *all* the bpms. Simulations of SPEAR show that although the system is typically stable, the transients caused by coupling can be large.

One simple solution is to equalize all the corrector transfer functions, and then design a single compensator that gives a satisfactory step response for the first and the last bpm in the sample sequence. An example of this approach yields the step responses for the first and last bpm as shown in Fig. 3. The corresponding Bode plot for the last bpm sample (one cycle delay only) was shown in Fig. 2.

An alternative approach which is possible with equalized transfer functions is to design a set of 'closed bump' corrector patterns to control each individual bpm. For each corrector pattern, a different frequency compensation can be used to account for the different delay at the particular bpm.

6. RESPONSE MATRIX ERRORS

Simulations have been made to assess problems associated with a response matrix measurement which is an imperfect representation of the machine.[†] BPM noise, corrector hysteresis, or thermal effects for instance, can all lead to a mismatch between the machine response and the measured response matrix.

The feedback simulator has been run using two independent measurements of the response matrix on SPEAR. One matrix is used to simulate the machine response to corrector inputs, and the other (really its pseudo-inverse) is used in the feedback controller. The system is often found to be unstable when the complete set of SVD eigenvectors is used in the control calculations. This is true even when all correctors are assumed to have the same frequency response (or even an 'instantaneous' response, with only a single integrator for DC regulation). The system can be stabilized by using only the dominant 14 or 15 SVD eigenvectors. Interestingly, this number of eigenvectors is roughly the same number of eigenvectors required to correct the orbit to the noise floor^[7].

So far, we have not discovered an analytical way to predict the eigenvector cut-off number for which the system will be stable. Based on optics arguments, however, we found the problem can be eliminated in SPEAR by excluding the 4 bpms nearest to the (former) collider points in the lattice. We suspect that since the bpms and the nearby correctors are separated by $\sim 180^\circ$ phase advance, the feedback is sensitive to response matrix errors in this region.

[†]This condition is different from simulations with numerically 'exact' response matrices that use a reduced number of eigenvectors because now the model and machine eigenvectors are different.

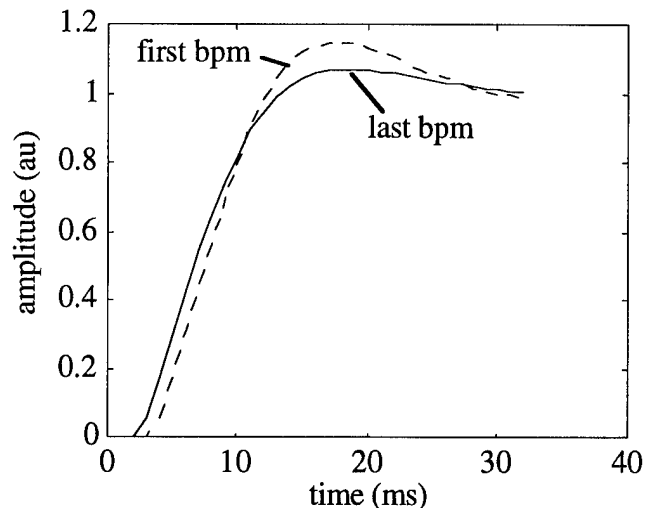


Figure 3 Closed loop step response for first and last bpm in sampling sequence.

If the matrix used in the calculations is exactly the same as the matrix used to simulate the machine, the simulations are always stable, independent of the eigenvector cut-off point.

7. DISCUSSION

In the next development phase with fast data acquisition and fast data processing, the issues of equalizing the correctors and finding a common frequency compensation for the closed loop system will be critical. The operating parameters used in the digital compensation satge will be refined empirically using the on-line system to seek optimum conditions. In particular, the relative weighting for bpms associated with each photon beamline will be adjusted to satisfy user needs. The eigenvalue cut-off value will be adjusted according to results from simulations and experimental observations. Adaptive methods to update the response matrix values used in the controller will be explored.

8. ACKNOWLEDGMENTS

The authors would like to thank Max Cornacchia for encouraging this work. We would also like to thank Ivan Linscott and Jim Sebek for many useful discussions.

9. REFERENCES

- [1] R. O. Hettel, Trans. Nuc. Sci. **NS-30** 2228 (1983).
- [2] L. H. Yu, et al, NIM **A284** 268 (1989).
- [3] A. Friedmann and E. Bozoki, Proc. of Orbit Correction and Analysis Workshop (Brookhaven National. Laboratory, 1993
- [4] Y. Chung, G. Decker and K. Evans, Jr., Proc. 1993 IEEE PAC, Washington D.C., 1993.
- [5] R. Hettel, et al, Proc. 4th European PAC, London, England, June 27-July 1, 1994.
- [6] R. Hettel, et al, these proceedings.
- [7] J. Corbett, D. Keeley, R. Hettel, et al, Proc. 4th European PAC, London, England, June 27-July 1, 1994.

DIGITAL ORBIT FEEDBACK CONTROL FOR SPEAR*

R. Hettel, J. Corbett, D. Keeley, I. Linscott, D. Mostowfi, J. Sebek, and C. Wermelskirchen
Stanford Synchrotron Radiation Laboratory, Stanford, CA 94309

Abstract

A digital orbit feedback system is being developed for SPEAR to improve electron beam stability at photon beam sourcepoints. The first phase implementation of this system operates at 1 minute intervals and stabilizes the horizontal and vertical orbit position to 50 μm rms at beam position monitors. The vertical global system works in tandem with local 50 Hz analog photon beam steering systems to stabilize photon beam position and angle. We are now developing the second phase system which will execute a unified global/local, 30-50 Hz vertical orbit feedback algorithm digitally. In this paper, we discuss design and performance of orbit monitoring, signal processing, and orbit correction components for the digital feedback systems.

I. INTRODUCTION

The SPEAR storage ring presently operates as a second generation light source, having 10 dedicated beamlines with multiple branch lines, and having an emittance of 130 nm-rad at 3 GeV. Orbit instabilities, however, stem from ring components designed in the first generation, nearly 25 years ago, including magnets, supports, vacuum chambers, temperature controls, and power supplies. The dominant instability is a diurnal orbit drift having a peak-to-peak horizontal amplitude of about 1 mm and half as much in the vertical plane. The drift is caused primarily by vacuum chamber and magnet motion (particularly high beta quadrupoles near the colliding beam interaction regions) which is coupled to diurnal temperature and to beam current. In addition, the orbit can shift by a few hundred microns after a beam injection cycle when the 3 GeV ring is ramped down to 2.3 GeV and back. Motion of a few tens of microns can occur as the storage ring temperature stabilizes in the first hour after ramping. Smaller, higher frequency disturbances have electrical and mechanical sources [1].

Our goal is to stabilize the electron beam orbit at the photon beam sourcepoints to 10% of the transverse photon beam size and beam divergence, and to maintain constant flux (to a small fraction of a percent) through restrictive beamline apertures [2]. The most stringent orbit position stability requirements are 80 μm rms horizontally and 20-30 μm rms vertically at focused beamline source points.

For more than a decade SSRL has used local, 3-magnet

* Work supported in part by Department of Energy Contract DE-AC03-76SF00515 and Office of Basic Energy Sciences, Division of Chemical Sciences.

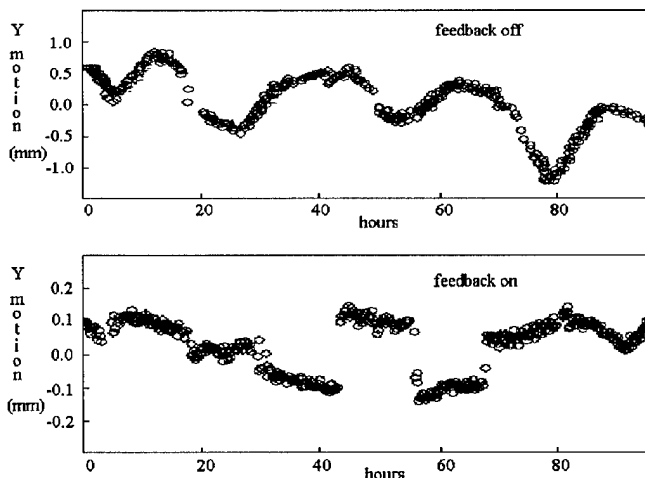


FIGURE 1. Vertical orbit motion at one BPM over 4 days with and without feedback. Step changes occur after each fill and energy ramp cycle. Note change in scale.

bump steering systems to stabilize vertical beam motion at photon beam monitors to the 10 μm level [1]. These feedback systems use analog circuitry and have a 50 Hz bandwidth. They have only a limited stabilizing capacity, however, since they do not correct position and angle independently. Also, large bump currents are sometimes needed to correct disturbances that could be reduced more efficiently with global adjustments.

These local feedback limitations, together with a need for horizontal beam stabilization, have led us develop a global feedback system that uses the singular value decomposition (SVD) method to correct orbit 'eigenvectors' derived from the corrector-beam position monitor (BPM) response matrix [3,4]. The first phase system implementation executes an orbit correction every minute from the main SPEAR computer and has a closed-loop bandwidth of a few mHz. The local 50 Hz steering systems act in concert with the vertical global orbit feedback to stabilize photon beam position and angle. The global system holds the beam stable to better than 100 μm rms at the BPMs (Fig. 1).

We are now developing a unified global/local vertical feedback system that uses digital signal processing (DSP) in a VME environment to achieve 50 μm rms or better stability at electron BPMs, and 10 μm rms stability at photon BPMs. Our goal is to reduce the feedback processing cycle time to ~1 msec to achieve a closed-loop bandwidth of 30-50 Hz. We present simulations of fast feedback performance and discuss digital filter design in a companion paper [5]. In this paper, we consider the design, configuration, and performance

requirements for digital system hardware and software components, focusing primarily on those for the unified vertical system.

II. SYSTEM DESIGN

The principle components of any orbit feedback system include its beam position monitoring, feedback signal processing, and orbit correction systems. We discuss these topics in the following sections.

A. Orbit Monitoring

The phase I feedback system presently uses a system of 20-25 BPMs to sample the electron orbit in SPEAR. All of these are situated in lattice straight sections, most near horizontally focusing QF quadrupoles. Three new monitors [6] were installed within the last two years and several more are scheduled for installation over the next few years, including some near defocusing QD quadrupoles. The increased number of BPMs enhances our ability to detect the orbit and its perturbations, and to control orbit position at the photon beamline source points.

BPM button signals for this system pass through a CAMAC-based PIN diode multiplexer to a single wideband peak-detecting signal processor. The CAMAC μ VAX crate controller computes beam position using the difference-over-sum method, taking BPM response pincushion distortions into account. For orbit feedback operation, we average 10 orbits, each orbit the averaged result of 120 button readings, to obtain rms position noise on the order of 10 μ m. The processor exhibits some beam intensity dependence, so the processing stability over the course of a beam fill is closer to a few tens of microns. An averaged orbit is transmitted over Ethernet to the main control computer database for display and feedback processing about every 5s.

To improve processing speed, signal resolution, and dynamic range for the phase II feedback system, we are building a narrowband heterodyne receiver tuned to the 717.1 MHz (2nd harmonic of the ring rf and 560th revolution harmonic) together with a new multiplexer having superior signal transmission and isolation properties at that frequency [7]. The 717.1 MHz signal is down-converted to the 5th harmonic of the revolution frequency (6.4 MHz) and sampled at 20.48 MHz (16th revolution harmonic) with a 12-bit ADC for one revolution period. The IF is mixed digitally to DC to produce two 16-bit words representing the I (in-phase) and Q (quadrature phase) components of this signal every revolution period. The I and Q signals for each button are then averaged over a programmable number of revolutions and stored in an on-board memory. We expect to be able to acquire a single orbit having 10 μ m processing resolution from 25 BPMs with a single processor in \sim 5ms; acquisition speed may be increased using parallel processors. We are investigating the possibility of altering the programmable phase of the digital mixing frequency on a BPM-by-BPM basis so as to reduce the Q signals to near-zero. This would halve the amount of

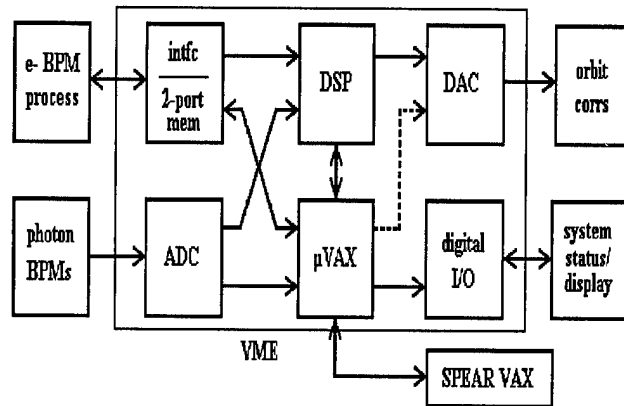


FIGURE 2. VME-based digital orbit feedback system.

transmitted data and eliminate the quadrature sum button signal calculation.

B. Feedback Processing System

Phase I of the global feedback system uses the SPEAR control VAXstation 4000/90 to process orbit information and to update 30 corrector settings in each plane every minute. The control computer communicates with distributed CAMAC μ VAX III crate controllers over Ethernet.

In each correction cycle, a reference orbit is subtracted from the acquired orbit to produce an error orbit which is in turn applied to the feedback algorithm. For the vertical plane, orbit changes at BPMs caused by the fast local steering bumps (responding to global corrections) are subtracted from the error orbit before global feedback processing. This 'bump subtraction' decouples the global system from the local ones.

The phase II vertical system (Fig. 2) employs a unified electron and photon beam digital correction algorithm operating with a 30-50 Hz bandwidth so that analog steering servos can be eliminated. Beam will be stabilized at photon monitors by including those monitors in the response matrix. The control equations for the photon beam monitors are weighted more heavily than those for the electron BPMs so that, following the SVD matrix inversion, the photon monitor error signals can be more tightly constrained. The algorithm will be executed by a VME-based DSP module utilizing the Texas Instruments TMS320C40 DSP (a 32-bit floating-point processor having a 50 ns instruction cycle).

The phase II system will employ up to four parallel 717.1 MHz BPM processors to achieve a feedback cycle time of \sim 1 ms. Button I and Q data from 25 or more BPMs will be transferred over a ribbon cable to a custom VME interface module containing dual-port memory arranged in two pages. One page containing a complete orbit is transferred between the dual-port memory module and the DSP board over the VME bus while the other page is being loaded with new data by the BPM processor for the next feedback cycle. In each feedback cycle (of order 1 ms for vertical 50 Hz bandwidth),

the DSP also acquires sum and difference signals from 10+ photon monitors with a 16-bit ADC. It then converts the integer orbit and photon monitor data to floating-point, calculates the quadrature sum of the I and Q values for each button, computes vertical positions (with a linear approximation for each BPM and photon monitor), and subtracts the reference position vector from the result. Next the DSP multiplies this error vector by the pseudo-inverse response matrix ($\sim 35 \times 30$) to generate correction values for 30 correctors and applies these values to a digital filter algorithm to produce corrector setpoints. These setpoints are converted to integers and sent to the 16-bit DACs. Position monitor signal levels and accumulated changes to corrector setpoints are monitored and the feedback loop is opened if those levels exceed programmed constraints. The whole acquisition and computation cycle takes less than 1 ms. Processing time is reduced if the Q data is reduced to zero by the BPM processor as mentioned above.

A VME μ VAX crate controller must provide BPM button data, calculated x and y position values, and other feedback system parameters acquired within the VME crate to the SPEAR control VAX. This task, as well as special communications tasks for the DSP module, will be handled by the crate controller. The crate controller will normally access this data at 200-300 ms intervals from the dual-ported DSP and BPM processor interface memories. It will compute orbit position using a more accurate polynomial representation of the BPM pincushion response.

C. Orbit Correction

Trim windings on 26 solid iron-core quadrupole magnets in SPEAR are connected to produce most of the horizontal dipole orbit correctors for the vertical feedback system. Four additional "picture frame" magnets located near the colliding beam regions complete the vertical correction set. All correctors are powered by 2 kW bipolar linear supplies. For phase I feedback, 20 of these correctors receive setpoint inputs from both the control computer DAC system and from the local beamline steering systems by means of analog summing junctions. For phase II, the summing junctions will be implemented digitally in the VME feedback system. Orbit correction frequency response is dominated by eddy currents in the magnet core iron and in the aluminum ring vacuum chamber; lead-lag compensation in the feedback processor can extend the response to beyond 50 Hz [1,5]. Compensators are also needed to equalize the responses of the quadrupole and picture frame correctors.

Horizontal correctors are configured using trim windings on 26 of the solid core main bending magnets together with 4 picture frame magnets. Their response is limited to 2 Hz by core and chamber eddy currents.

III. PERFORMANCE AND IMPROVEMENTS

Phase I orbit feedback on SPEAR uses simple integral control to suppress the SPEAR diurnal orbit drift by a factor

of ~ 5 in both planes over a 0.25 mHz bandwidth. Peak orbit excursions have been reduced to the 100 μ m level over the diurnal cycle. Photon beam are vertically stabilized to 10 μ m in a 50 Hz bandwidth at photon monitors by the local steering systems. In addition, we have augmented the vertical corrector-to-BPM response matrix to include the response at the photon monitors; we use an algorithm similar to that planned for the unified system at the top of each fill cycle to steer the photon beamlines with an optimized 'least norm' global corrector pattern. This has reduced local corrector bump excursions for the analog beamline servos by a factor of 5 or more and has reduced overall corrector currents as well.

We believe the performance of the phase I feedback system is limited by several factors, including a lack of BPMs near some beamline source points and at QD sites, non-optimal BPM locations, temperature dependent BPM motion, BPM processing intensity dependence, and imperfect orbit correction patterns caused by magnet hysteresis and lattice nonlinearities (off-center beam position in sextupoles). Lattice nonlinearity and hysteresis can also corrupt measurement of the response matrices and degrade system performance [3,5].

For the 30-50Hz Phase II feedback system, we will add new BPMs, the 717 MHz BPM processor, the VME-based DSP system, and more correctors. We are working to reduce the sources of orbit instabilities by installing more highly regulated main magnet power supplies, developing a new ring lattice to reduce the strengths of the interaction region quadrupoles [8], mechanically stabilizing magnets and BPMs, and realigning the ring. We are investigating temperature control for the SPEAR tunnel, and 3 GeV injection that would eliminate hysteresis due to energy ramping.

IV. ACKNOWLEDGEMENTS

The authors are indebted to M. Cornacchia for encouraging this work, to H.-D. Nuhn for accelerator physics consultation, and the SSRL engineering groups for their support. We also thank Y. Chung from the APS and the accelerator physics staff at NSLS for their contributions.

V. REFERENCES

- [1] R. O. Hettel, IEEE Trans. Nucl. Sci. NS-30 (1983) 2228
- [2] *Synchrotron Radiation Sources - A Primer*, Chap. 13, edited by H. Winick (World Scientific Pub., 1994).
- [3] R. Hettel, et al, Proc. 4th European PAC, London (1994) 1580.
- [4] J. Corbett, D. Keeley, R. Hettel, et al., Proc. 4th European PAC, London (1994) 1583.
- [5] J. Corbett, et al., these proceedings.
- [6] B. Scott, et al., Proc. 4th European PAC, London (1994) 1545.
- [7] J. Sebek, et al., Proc. 4th European PAC, London, 1994, and these proceedings.
- [8] H.-D. Nuhn, Proc. 4th European PAC, London (1994) 642.

BEAM POSITION FEEDBACK SYSTEMS FOR THE PF STORAGE RING

N. Nakamura, K. Haga, T. Honda, T. Kasuga, M. Katoh, Y. Kobayashi, M. Tadano, and M. Yokoyama*
Photon Factory, National Laboratory for High Energy Physics (KEK)

Oho 1-1, Tsukuba-shi, Ibaraki-ken, 305 Japan

*The Institute for Solid State Physics, The University of Tokyo

Roppongi 7-22-1, Minato-Ku, Tokyo, 106 Japan

Two types of fast beam position feedback systems, global and local feedback systems, are proposed for a low-emittance configuration of the 2.5-GeV PF storage ring which will be started in 1997. The global feedback system corrects the closed orbit around the ring and the local feedback system stabilizes the beam positions and angles at insertion devices. Both systems are expected to suppress vibrations up to 50 Hz. For these systems, the beam position monitors will be improved to achieve fast data-taking and high position resolution, and the fast steering magnets and their power supplies will be reinforced. In the feedback control, VMEbus-compatible DSP (digital signal processor) boards will be used for fast computation and a reflective memory network for fast data transfer. In a preliminary test, the global feedback DSP board was confirmed to have a computation performance enough for its purpose.

I. INTRODUCTION

At the Photon Factory (PF), a new configuration of the 2.5-GeV storage ring will start in 1997 to provide more brilliant photon beams for the SR users[1,2]. In the high-brilliance (low-emittance) configuration, the horizontal and vertical beam sizes are reduced by a factor of about two and the beam sensitivity to external disturbances is enhanced because the number and the field strength of the quadrupole magnets are increased. It is easily foreseen that the beam stability will be more important for taking full advantage of the high brilliance.

A global feedback system has been operated since 1987 to mainly suppress a slow orbit drift caused by building distortion[3,4,5]. However, the effective position resolution of the electron (or positron) beam position monitors (BPMs) limiting the system performance is often deteriorated by contact faults of mechanical switches used for multiplexing BPM position signals. Furthermore the present system cannot correct relatively fast orbit fluctuations caused by floor vibrations due to air-conditioners, temperature variations of cooling water, etc. Therefore construction of an improved global feedback system is planned and has to be done in coincidence with the upgrade of the PF storage ring for the high-brilliance configuration. In addition, a local feedback system dedicated to beamlines is proposed for further beam stabilization at insertion devices. It will be constructed by stages after the operation in the high-brilliance configuration starts. This paper will present an overview of the feedback

systems and also report a performance test on a DSP board used for the global feedback control.

II. SYSTEM DESCRIPTION

The global feedback system corrects a vertical closed orbit with a lot of steering magnets, taking position data from all the BPMs. The eigen vector method, used in the present system, will be adopted again as an orbit correction scheme. The local feedback system stabilizes the beam positions and angles for both horizontal and vertical directions at insertion devices, using a local bump generated by four steering magnets. Two BPMs on the sides of an insertion device will be used until a photon beam position monitor applicable to undulator beamlines is developed. Both systems are desired to cover a wide frequency range (0 – 50 Hz), because the orbit fluctuations spread up to 50 Hz[6]. The position measurement error of the systems should be less than 10 μm , 10 – 20 % of the vertical beam sizes at the photon source points in the high-brilliance configuration. Each system component is described below.

A. Beam Position Monitors (BPMs)

Figure 1 shows planned locations of the BPMs in the high-brilliance configuration. The BPMs will be increased from 46 to 65, because quadrupole magnets in the normal-cell section

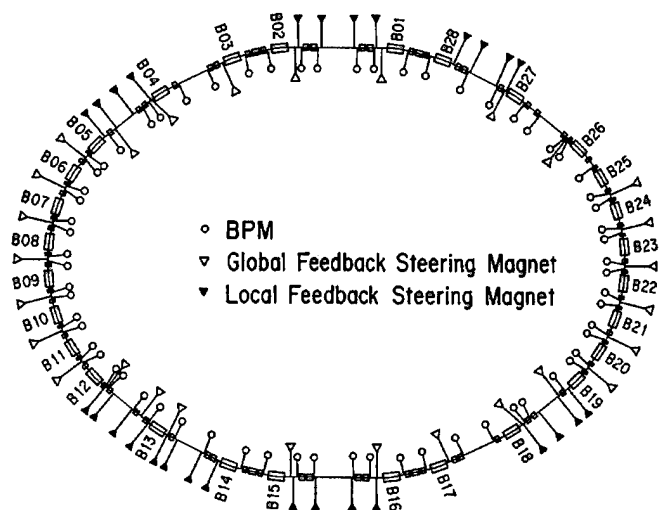


Figure 1: Planned locations of BPMs and steering magnets in the high-brilliance configuration of the PF storage ring

(B05–B12 and B19–B26) are doubled. Forty-one of the BPMs will be reconstructed to match with new vacuum chamber structure of the normal-cell section and the others will be used without any modification. The BPM signal processing electronics will be newly designed so that it can totally satisfy both high position resolution ($< 10 \mu\text{m}$) and fast data-acquisition time ($< 1 \text{ ms}$). Electrical switches will be used as BPM signal multiplexers in place of mechanical switches for improving the switching speed and avoiding deterioration of the effective position resolution due to contact faults. The details of the improved BPM system will be described elsewhere.

B. Steering Magnets and Power Supplies

As shown in Figure 1, twenty-eight vertical steering magnets will be used for the new global feedback system. Twenty of them have been already used for the present global feedback system. The core of the steering magnet is made of 0.35mm-thick silicon steel laminations to obtain good frequency response by reducing the effect of the eddy currents. The power supply is manufactured so that there is no significant deterioration of the frequency response in both gain and phase at least below 100 Hz. For the local feedback system, twenty-eight steering magnets for both horizontal and vertical directions will be additionally installed in seven long straight sections.

C. Control System

Figure 2 shows a design of the feedback control system. Two types of VME crates will be used for the global and local feedback systems. In a global feedback VME crate, a DSP board with two DSPs (the Texas Instruments TMS320C40s) calculates the beam positions from the electrode-voltage data of all the BPMs, writes them to the reflective memory, and computes the coil currents of all the vertical steering magnets. The DSP board is linked with some kinds of I/O boards via a

local I/O bus to control the BPMs and the power supplies of the vertical steering magnets and also connected with a CPU board and a reflective memory board through a VME bus. In a local feedback VME crate, two DSP boards are contained. Each of them has a DSP (the Texas Instruments TMS320C31) to read the beam positions from the reflective memory and to calculate a local bump. A similar DSP board already gave good results in the test of a local feedback system[7]. Since one local feedback VME crate is dedicated to two insertion device beamlines, four crates will be needed in total for seven insertion devices. The CPU board in each VME crate is interfaced with a common UNIX workstation by Ethernet. A DSP program coded on the workstation is downloaded to the DSP board through it.

III. PERFORMANCE TEST OF THE GLOBAL FEEDBACK DSP BOARD

The computation performance of the DSP board with two TMS320C40s[8] for the global feedback was tested by use of a program simulating the global feedback computation (not including the control of the BPMs and the steering magnets). This program consists of the following parts:

- (1) Calculation of Horizontal and vertical positions from electrode-voltage data of the BPMs and quality check of the position data
- (2) Calculation of steering magnet currents from the vertical position data
- (3) Calculation for PID (proportional, integral and derivative) control improving the feedback performance
- (4) Communication of the electrode-voltage data and the horizontal position data between the main and sub DSPs

Figure 3 shows the flow chart of the program. Parts (1), (3) and (4) were coded in C-language and Part (2) in assembly language. Parallel C[9] was used as an optimizing C

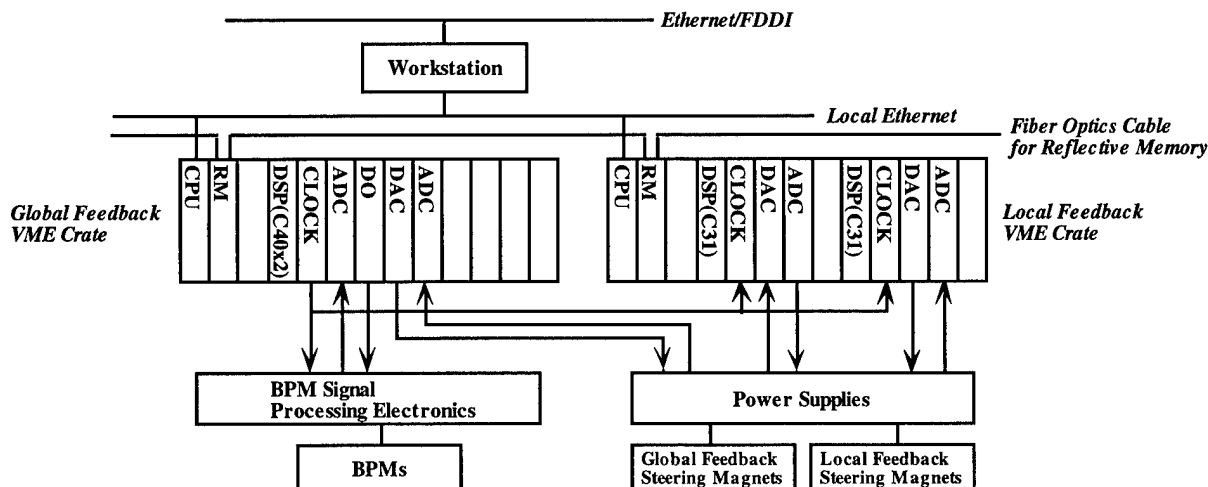


Figure 2: Design of the feedback control system

compiler, assembler and linker to reduce the consumed time for Part (1) by parallel programming of the two DSPs. Part (4) means that the sub DSP has to take the electrode-voltage data from the main DSP directly connected with the outside of the DSP board and return the calculated horizontal position data to it. The communication speed between the two DSPs is 20 MBytes/s except for the software overhead. The program forced the main DSP to change the output voltage of a DAC board before and after one computation cycle. Therefore, the total computation time was easily obtained by observing the DAC output level with an oscilloscope. The consumed time for each part was also measured in the same manner. The result is summarized in Table 1. Since the data-acquisition time of the BPMs is less than 1 ms, the total computation time (555 μ s) is sufficiently short for the global feedback with a planned sampling time of 2 ms. It was also confirmed that the total computation time is almost unchanged in the parallel programming when the horizontal global feedback computation is added to Parts (2) to (4). This suggests that

we can join the horizontal global feedback to the vertical one without a change of the sampling time if necessary.

IV. SUMMARY AND FUTURE WORK

For the high-brilliance configuration, the global and local feedback systems will be constructed to suppress the beam motion below 50 Hz with position resolution better than 10 μ m. In order to achieve the system performance, the BPM system will be improved and the fast steering magnets will be increased with their power supplies. A VME system with DSP and reflective memory boards will be used for the fast feedback control. The computation speed of the DSP board is adequate to the global feedback.

Frequency response measurements will be done for the newly designed vacuum chambers of the normal-cell section, though the frequency response curves of the steering magnet, the power supply and the aluminum vacuum chamber of the straight section were already obtained. Thereafter digital filters will be designed to compensate a considerable phase rotation caused by the time delay of 2 ms sampling and the eddy currents of the vacuum chambers and to equalize the frequency responses of the vacuum chambers. The power supply load and the DSP computation time increased by these digital filters should be experimentally evaluated at the same time. In addition, the data communication with the reflective memory network will be tested.

V. REFERENCES

- [1] M. Katoh, A. Araki, T. Kasuga, Y. Kobayashi and Y. Hori, "The proposed Low Emittance Lattice for the PF Storage Ring", *Proceedings of the 4th European Particle Accelerator Conference*, pp636-638 (1994).
- [2] M. Katoh, Y. Hori, N. Nakamura, H. Kitamura and H. Kobayakawa, "Upgrade of the Photon Factory Storage Ring for a High Brilliance Configuration", *Rev. Sci. Instrum.*, 66, 1892 (1995).
- [3] N. Nakamura, Photon Factory Activity Report #8 R-14 (1990).
- [4] T. Katsura, Y. Kamiya, K. Haga, T. Mitsuhashi, N. Nakamura, M. Katoh, and I. Abe, "Beam position stabilization at the Photon Factory", *Rev. of Sci. Instrum.*, 60, 1507 (1989).
- [5] K. Haga, Y. Kamiya, M. Katoh, T. Katsura, T. Mitsuhashi, and N. Nakamura, "Global Orbit Feedback Systems at the Photon Factory Storage Ring", *Particle Accelerators*, 33, 1795 (1990).
- [6] H. Kobayakawa, "Summary of photon-beam stabilization at the Photon Factory", *Rev. Sci. Instrum.*, 63, 509 (1992).
- [7] N. Nakamura and T. Katsura, "Test of Fast-Digital Beamline Feedback Control", *Proceedings of the 1993 IEEE Particle Accelerator Conference*, pp. 2257-2259.
- [8] *TMS320C4x User's Guide* (Texas Instruments Inc., 1991).
- [9] *Parallel C User Guide* (3L Ltd., 1994).

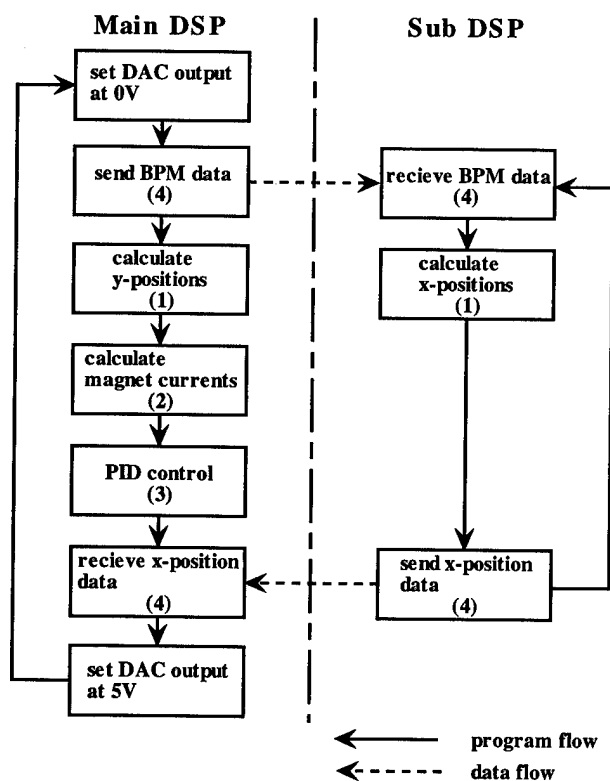


Figure 3: Flow chart of a DSP program simulating the global feedback computation

Table 1. Measured DSP computation time

(1) Position calculation (x&y)	305 μ s
(2) Magnet current calculation (y)	100 μ s
(3) PID control (y)	25 μ s
(4) Data communication	125 μ s
Total	555 μ s

The New Booster Synchronization Loop*

E. Onillon, J.M. Brennan, AGS Department, Brookhaven National Laboratory
Upton, New York 11973-5000 USA

I. INTRODUCTION

The AGS Booster must be synchronized to the AGS rf system before bunch-to-bucket transfer of the beam. The Booster delivers four batches at 7.5 Hz and extraction occurs at full acceleration rate, leaving only 5 ms available for synchronization. An improvement has been made to the synchronization feedback loop. A new loop compensator has been designed using a state variable representation. The three state variables are, beam phase and frequency, and the reference input to the beam control phase loop. The design uses linear quadratic optimum control to achieve greater stability and smaller errors. Lock acquisition, without a transient, is accomplished by a circuit that derives the loop reference from the instantaneous state variable feedback value at loop closing. The reference is brought adiabatically to zero at transfer.

II. DESCRIPTION OF THE LOOP

The synchro system senses the Booster beam phase, with respect to the AGS rf cavity voltage and controls the reference to the Booster phase loop. For 5 ms before beam extraction the radial loop control loop is supplanted by the synchro loop as the beam phase is brought to setpoint for bunch-to-bucket transfer to the AGS. Three challenges confront the synchro system: 1. the Booster is still accelerating at a high rate during the 5 ms in which the synchro operates, 2. the inherent integration in the frequency to phase conversion changes the dynamics of the feedback loop so that the simple proportional feedback used for radial control would not be stable, 3. when the loop is closed the phase is arbitrary so large transients could be imposed on the beam control system, which would cause emittance growth or beam loss.

Number one is overcome by a phase-resolved "moving reference frame" system, implemented with a direct digital synthesizer. The synchronization takes place in the "moving reference frame" where the two machine appear to be at nominally the same frequency. This system is described elsewhere [1,2] and is not part of the improvements discussed herein. The dynamics of the feedback loop are treated differently in the new synchro loop. The conventional lead-lag compensation [3] is replaced with a state variable approach in which an optimal linear quadratic regulator is implemented. By summing proportional feedback on the three

relevant state variables of the system a more stable and higher gain solution is obtained. The variables are respectively proportional to the beam phase ϕ_b , to the phase correction ϕ_r introduced by the radial loop and to the variations $\delta\omega_b$ of the beam frequency. The technique for achieving lock acquisition without transient has also been changed. The previous technique[1,2] employed an intermediate step in which a frequency loop established a specified beat frequency program before the synchro loop was closed. Experience has shown that the reproducibility of the Booster frequency is good enough that the frequency loop is unnecessary. In the new system the transient is avoided by deriving the reference for the synchro loop dynamically from the instantaneous value of the feedback signal at the time of loop closing. This circuit is described in more detail in section 4. below.

III. STATE-SPACE REPRESENTATION

In a first approximation, delays are neglected. We also suppose that the cavity transfer function is equal to one and that we work in the frequency decade 100 Hz to 1 kHz.

In this case, the transfer function between ϕ_r and $\delta\omega_b$ is $\frac{\omega_s^2}{s}$, ω_s being the synchrotron frequency. A diagram of the simplified system is given on fig. 1.

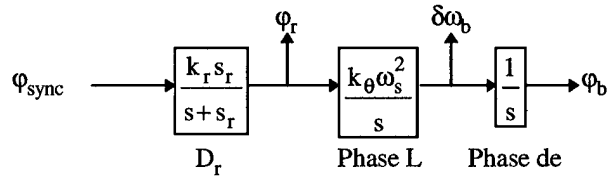


Fig. 1 Simplified schematic

ϕ_{sync} is the command of the synchro loop, D_r represents the radial loop compensator and k_θ the phase shifter gain. We can deduce a state-space representation. Three variables are sufficient to describe our system.

$$X = \begin{bmatrix} x_1 = \phi_b \\ x_2 = \frac{\phi_r}{k_r} \\ x_3 = \frac{\delta\omega_b}{k_\theta \omega_s^2} \end{bmatrix}$$

* Work performed under the auspices of the U.S. Department of Energy.

The command is ϕ_{sync} and we can observe $k_{\text{sync}}\phi_b$, ϕ_r , $k_\omega\delta\omega_b$, with k_{sync} , and k_ω the detector constants.

The observation vector is therefore $Y = \begin{bmatrix} k_{\text{sync}}x_1 \\ k_r x_2 \\ k_\theta\omega_s^2 k_\omega x_3 \end{bmatrix}$.

From the simplified model, it comes out:

$$\begin{cases} \dot{x}_1 = k_\theta\omega_s^2 x_3 \\ \dot{x}_2 = -s_r x_2 + \phi_{\text{sync}} \\ \dot{x}_3 = k_r x_2 \end{cases}$$

We get the following state-space representation:

$$\begin{cases} \dot{X} = \begin{bmatrix} 0 & 0 & k_\theta\omega_s^2 \\ 0 & -s_r & 0 \\ 0 & k_r & 0 \end{bmatrix} X + \begin{bmatrix} 0 \\ 1 \\ 0 \end{bmatrix} \phi_{\text{sync}} \\ Y = \begin{bmatrix} k_{\text{sync}} & 0 & 0 \\ 0 & k_r & 0 \\ 0 & 0 & k_\theta\omega_s^2 k_\omega \end{bmatrix} X \end{cases}$$

A B C

As the rank of the matrix $[B \ A \ A^2 B]$ is 3, we can determine a Linear Quadratic Regulator (LQR), with the following performance index:

$$J = \frac{1}{2} \int_0^{+\infty} (X^T Q X + \phi_{\text{sync}}^T R \phi_{\text{sync}}) dt, \quad Q \text{ minimizing the}$$

deviation in states and R the input energy [4]. The Q and R matrices are chosen by the designer to obtain the desired system dynamic.

Calculations are done using Matlab™. The command of the system will be the difference between the reference signal and a linear combination of the three state variables.

IV. LOCK ACQUISITION

The key to the new lock acquisition system is the observation that the Booster beam frequency is very reproducible. It follows then that the Booster phase can be locked to the AGS reference with negligible discontinuity in frequency, less than 200 Hz (< 1 mm of radius). What remains is to eliminate a discontinuity in phase. This is done by using a track-and-hold circuit to acquire the arbitrary value ϕ_b of the feedback signal at the time of loop closing. A 360 degree phase detector is used to acquire the phase of the beam. See figure 2. The held value becomes the reference to the synchro loop, so that when the loop closes it is already satisfied and there is no transient. Next, the held value from the track-and-hold (in the hold state) is multiplied via a MDAC with a "ramp-down" function to zero. The reference for the synchro loop is ramped down gradually. The

"ramp-down" function is stored in an EPROM and fetched out during the 5 ms period before extraction. Typically a half-cosine function is used because it has zero derivative at the beginning and end, avoiding a frequency transient at the beginning and putting the beam frequency (radius) deviation to zero at extraction.

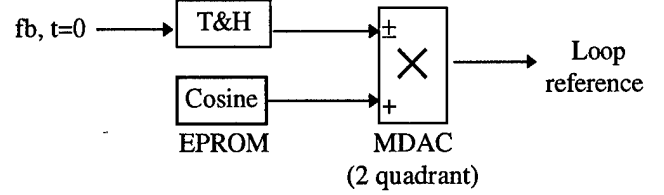


Fig. 2 Lock acquisition system

V. SIMULATIONS

Simulations of the whole system have been performed using the feedback gain values found with the state-space representation described above and with a model including delays and a complete transfer for the phase loop [1]:

$$\frac{\delta\omega_{rf}}{\phi_r} = \frac{k_\theta (s^2 + \omega_s^2) K(\tau'_d s + 1) \left(s + \frac{1}{\tau'_i} \right) e^{-\tau_d s}}{s \left(s^2 + \omega_s^2 \right) \left(\frac{s}{s_c} + 1 \right) + K(\tau'_d s + 1) \left(s + \frac{1}{\tau'_i} \right) e^{-\tau_d s}}$$

In this formula, τ_d is the loop time delay, s_c the cavity response pole, τ'_d and τ'_i parameters of the phase loop compensator and $\delta\omega_{rf}$ the variations of the rf frequency.

The simulation schematic is given on fig. 3.

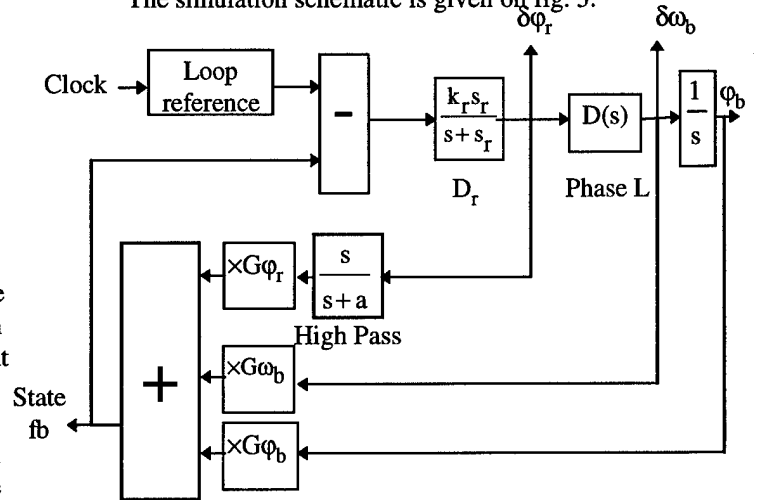


Fig. 3 Simulation schematic

A high pass filter is added on ϕ_r to cut the DC component. G_{ϕ_r} , G_{ϕ_b} , G_{ω_b} are the feedback gains

obtained with the simplified model, divided respectively by k_{sync} , 1 and k_{ω} .

The following results have been obtained with:

$$Q = \begin{bmatrix} 10^4 & 0 & 0 \\ 0 & 10^3 & 0 \\ 0 & 0 & 10^3 \end{bmatrix} \text{ and } R = 8000 \text{ for } \omega_s = 1.4 \text{ kHz.}$$

Voltages proportional to the main signals are plotted on fig. 4.

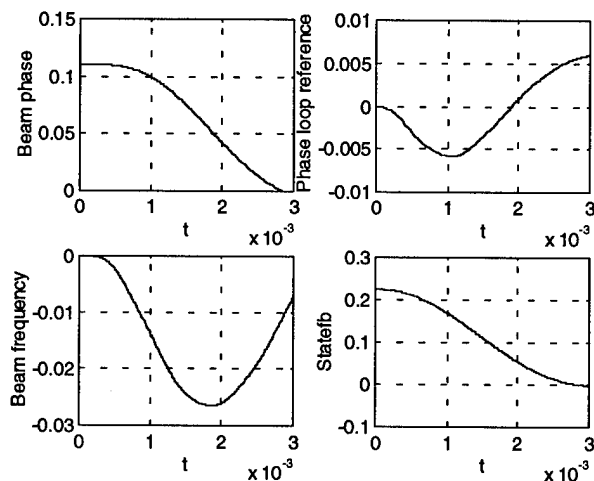


Fig. 4 Simulation results, $\omega_s = 1.4 \text{ kHz}$, $\phi_{b0} = 0.11 \text{ rad}$, $\phi_{r0} = -0.011 \text{ rad}$, $\omega_{b0} = -1.1 \text{ Hz}$.

The phase of the beam follows the cosine function (programmed to go to zero in 3 ms), and, after 3 ms, both the phase and the frequency are equal to zero.

The open loop Bode plot (fig. 5) shows that the system has a 40° phase margin and a 12 dB amplitude margin. The cut off frequency is 1.5 kHz.

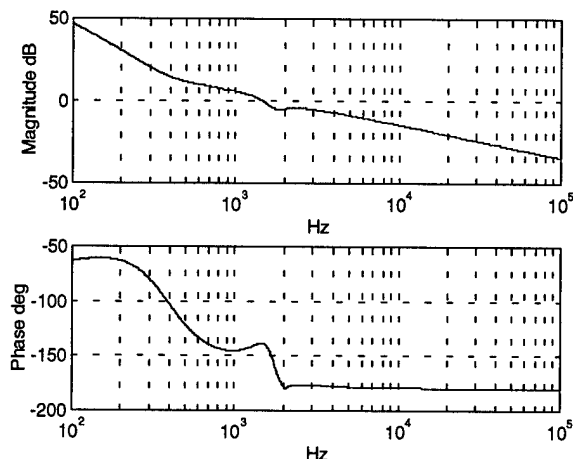


Fig. 5 Open loop, Bode plot

VI. PRACTICAL RESULTS

The three gains in the feedback loop have been realized by using operational amplifiers. The sum of the three channels is subtracted from the reference (cosine function) before being injected back in the system. On fig. 7, the cosine function (top curve) is plotted as well as the synchronous phase for $\omega_s = 1.4 \text{ kHz}$ (bottom curve). The cosine function has been programmed here to go to zero in 3ms. After being held up during 1 ms, the phase goes to zero like its reference in 3 ms and is then held to zero until extraction.

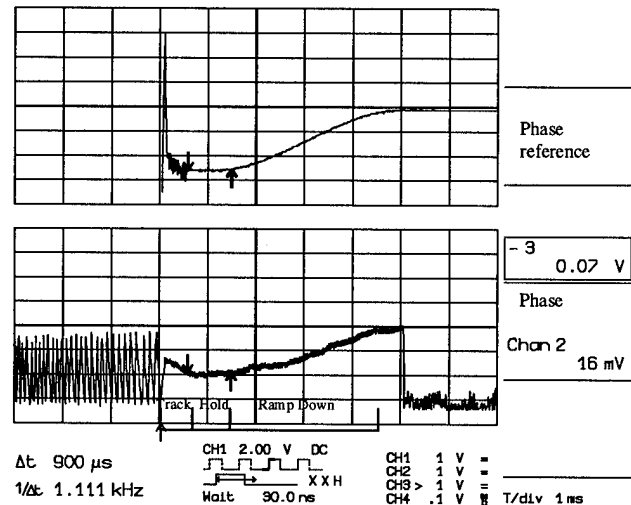


Fig. 6 Synchronous phase measurements

CONCLUSION

The new synchro system allows better synchronization of the Booster bunches to the AGS buckets before transfer between the two machines. State variable feedback and linear quadratic regulator optimization provide good stability margins, high gain, and small transients on the beam. The system has been successfully in operation for all four months on the 1995 high energy physics proton run.

REFERENCES

- [1] RF Beam Control for the AGS Booster, BNL- 52438 Formal Report, J. M. Brennan.
- [2] The RF beam control system for the Brookhaven AGS Booster synchrotron, J. M. Brennan, Conference on High Energy Accelerators, Hamburg, 1992.
- [3] Design of a Ring RF System, D. Boussard, RF CERN Accelerator School proceedings, Oxford.
- [4] Feedback Control of Dynamic Systems, Gene F. Franklin, J. David Powell, Addison-Wesley Publishing Company.

RECENT PROGRESS IN THE DEVELOPMENT OF THE BUNCH FEEDBACK SYSTEMS FOR KEKB

E.Kikutani, T. Kasuga, Y.Minagawa, T.Obina and M.Tobiyama,
National Laboratory for High Energy Physics,
Oho 1-1, Tsukuba-shi, Ibaraki, 305 Japan

Abstract

In KEKB, which is a B-factory project at KEK, the bunch spacing is very short, only 2 ns, and the number of the bunches comes up to about 5000 per ring. In order to cure the instabilities due to the high beam current, we will use bunch feedback systems in KEKB rings. Recently we developed the new position detection system and made a prototype of the signal process system for the feedback systems. Using these tools and accelerating cavities as the kicker we performed an experiment for checking a longitudinal feedback system. The Robinson instability which was intentionally excited was successfully damped with a short damping time.

I. INTRODUCTION

KEKB, a B-factory project at KEK in Japan, is now under construction. In KEKB, the number of bunches per beam is about 5000 and the bunch spacing is only 2 ns. Under this condition it is feared that coupled bunch instabilities due to some impedance sources limit the luminosity. In order to cure these instabilities, we will use powerful bunch feedback systems in both the transverse and longitudinal planes. We have already started the development study of the feedback systems. Up to the present our studies were mainly on the position detection system and the data process system. The results of the studies were published in the papers[1] and [2]. Recently we have improved the performance of the position detection system by increasing the detection frequency. For the data process part, we have designed and made a prototype of a signal process system, which is a 2-tap digital filter realized by a pure hardware logic. In this paper, we report the performance of these newly developed tools and result of the longitudinal feedback experiment at KEK.

II. RECENT PROGRESS OF THE POSITION DETECTION TECHNIQUE

A. 2 GHz as the detection frequency

The front-end part of the bunch feedback system is a simple RF circuit. This circuit inputs the pulses from pickup electrodes and outputs a pulse whose height is proportional to the position of a bunch. As we have explained in the previous paper[2], this output signal is obtained as the phase difference between two (quasi) sinusoidal signals, both in the longitudinal and transverse planes. The frequency of these sinusoidal signals is called the detection frequency. For the longitudinal plane, the detection-frequency component is extracted from the beam signal and its phase is compared with a standard timing signal, which is made from the accelerating RF signal. In the transverse

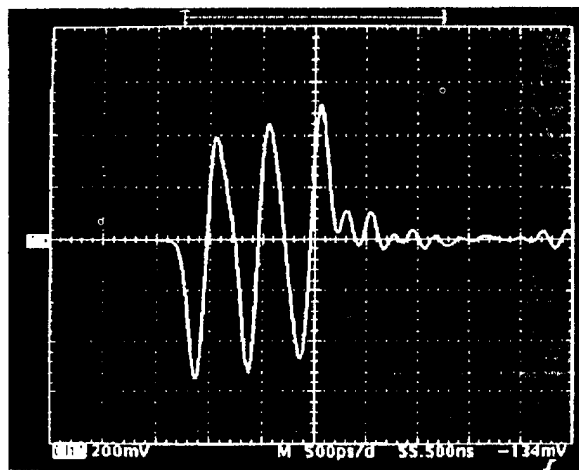


Figure 1. An oscilloscope photo of the pulse train.

plane, we use the AM/PM technique[4]. In this case, the two signals to be compared are obtained from pickups. In both cases, we must use band-pass filters to extract the detection-frequency component out of the beam signal.

We have performed many experiments to develop the front-end part of the feedback systems[1]. There, we used 1.5 GHz as the detection frequency. The main reason why we used this frequency was to avoid RF noises propagating within the beam pipe of a radius of ~ 50 mm. But this frequency is not high enough considering very short bunch spacing, 2 ns, in KEKB. Then, we installed a new set of pickup electrodes attached to a beam pipe with a radius of 35 mm in TRISTAN Accumulation Ring at KEK (AR). With this beam pipe we now can use the detection frequency of 2 GHz. Six button electrodes are used for each plane (longitudinal, horizontal and vertical) then there are 18 electrodes in total. The six pulses are combined by a power combiner to make an input of the front-end circuit. The cables connecting the electrodes and the power combiner are carefully chosen to make a 3-cycle sine-like pulse train. This cable-combiner system works as a low-Q band pass filter effectively. The pulse obtained this technique is shown in Fig. 1. We can catch that the length of the main part of pulse train is only 1.5 ns. With this technique we can measure the position of each bunch independently.

B. Application of the position detection system

One application of the position detection system explained above is mode identification of the coupled bunch instabilities. We made experiments in AR to study various impedances which may cause instabilities. In these experiments, we store a number

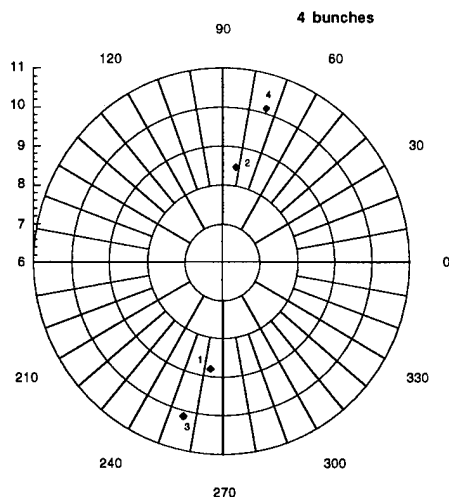


Figure 2. The complex logarithm of the FFT of the oscillation.

of bunches in the ring and observed their oscillations with our position detection system. The output of the front-end circuit is sent to a CAMAC module which packages a 500 MHz flash analog-to-digital converter chip (SONY CXA1276) and 4 kbytes memory (Fast ADC module).

The method of the analysis is as follows. The longitudinal position, that is, the timing of these bunches (here we explain the method by an example of the 4-bunch case) were recorded in the memory over 1024 turns at real time. After data-taking we perform the discrete Fourier transformation on these 4 data, namely, we get 4×512 complex values that are the frequency spectrum of the oscillations. When bunches oscillate we can find peak(s) in these data. Now we pick up the value at the peak and get the complex logarithm of this value. Manifestly the argument of this complex value corresponds to the phase of the bunch oscillation and its absolute value is proportional to the logarithm of the oscillation amplitude. A typical example is shown in Fig. 2. We can easily recognize that 4 points are aligned along a line of 75 degrees and $75+180$ degrees. This means that the mode of coupled bunch oscillation was 2. We know that the accelerating cavity in AR has a higher order mode of 1463.7 MHz from other measurement. This frequency is 1842 times of the revolution frequency of AR. The data strongly suggests that the bunch oscillations correspond to this higher order mode.

III. Prototye 2-tap FIR filter

In our feedback system, the signal process (phase shift by 90 degrees and elimination of DC offset) is done by a 2-tap FIR filter realized by a pure hardware system. As the algorithm of the 2-tap filter has already been given in the paper[3], we will give only a short explanation on the 2-tap digital filter here. In general, the output of an FIR filter is obtained as the linear combination of the data which have been obtained as a time series, $x(1), x(2), \dots$. In the case of two tap filters, the linear combination is a sum of only two terms whose coefficients are 1 and -1. Then the output, y , of the filter is given by

$$y = [x(n_1) - x(n_2)]/2.$$

The filter has the favorite frequency of $1/2(n_1 - n_2)$. Here, the unit of the frequency is the reciprocal of the sampling time, which is, in our case, the revolution period of a ring. By suitably selecting the parameters, n_1 and n_2 (tap positioning), we can obtain various type of the digital filter. In the words of hardware, the filter consists of memory of some depth, a hardware for subtraction operation and a clock circuit for controlling the timing.

In order to realize the filter, a very high-speed circuit is required, because the bunch frequency of KEKB is 508 MHz. For this purpose we are now designing a 2-tap filter board which has high-speed custom IC's (GaAs gate arrays) for de-multiplexing and multiplexing and medium speed 2-tap filter logic on it.

Before the completion of the board, we made a prototype of the 2-tap filter circuit which can work under the bunch frequency of 6.4 MHz. The prototype consists of a 125 MHz analog-to-digital converter chip (Analog Devices AD9002) in front-end, a 40 MHz digital-to-analog converter chip (SONY CXD1171) in back-end and circuitry of a 2-tap digital filter. The digital filter consists of an ALU (SN74HC283) that performs a subtraction operation and memories (HM62832UHP-15) which store the position of bunches through hundreds of turns. The size of memory is 4 kbytes in total. These three components of the filter are packaged in a 1-span CAMAC module. The tap positioning of the 2-tap filtering can be set through the CAMAC command very easily. We found that the 2-tap filter has the desired frequency performance in various tap positionings in bench tests with a network analyzer.

IV. FEEDBACK EXPERIMENT IN AR

A. Experimental procedure

We made an experiment of the longitudinal feedback in AR to check the performance of the position detection system and the 2-tap filter explained above. The basic experimental conditions are summarized in Table I.

Table I
Condition of Experiments.

beam energy	2.5 GeV
circumference/revol. freq.	377 m/795 kHz
beam current	3 ~ 5 mA
synchrotron frequency/ ν_s	20 kHz/0.025

Because the longitudinal kicker is still on the design stage, we used the accelerating cavities as a longitudinal kicker. Due to the narrow bandwidth of the cavity, we can make the experiments only with single bunch. But an experiment with the closed loop of the feedback system is essentially important particularly for checking the performance of the signal process system. In AR there are two RF stations, EAST and WEST, each of which has 4 accelerating cavities. Our kicker was 4 cavities in the WEST. The position detection system and the signal process system sit on the southern part of AR. The processed signal was transferred through a coaxial cable of length of ~ 140 m to the WEST and the accelerating signal was phase-modulated by this processed signal.

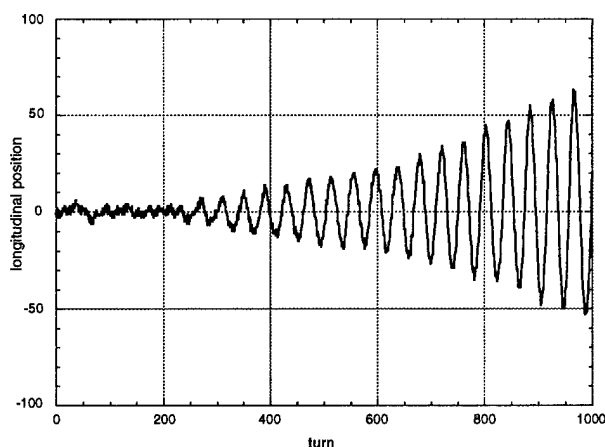


Figure 3. The observed oscillation just after the feedback was turned off. The horizontal axis is the turn number and the vertical axis is the longitudinal position in an arbitrary unit.

The longitudinal oscillation was excited by intentionally shifting the resonant frequency of the cavities to arise the Robinson instability. By tuning the resonant frequency shift, we can control the growth rate of the instability.

The tap positions of the 2-tap filter were chosen to be ($n_1 = 3, n_2 = 22$). The difference of the position, $22 - 3 = 19$, was determined by the condition, $n_1 - n_2 \simeq 1/2\nu_s$. On the other hand, the absolute positions of the taps depend on the delay of the whole feedback loop. We determined the suitable tap positions through this experiment.

B. Result

By setting the tuning angle of the accelerating cavities to be $+10$ degrees, we were able to excite constant longitudinal oscillation. By the measurement with a spectrum analyzer, we found the clean synchrotron side-bands in the both sides of a revolution peak. The power of the side bands were lower than the revolution peak by 30 dB and higher than background level by about 30 dB. When we closed the feedback loop the side-bands disappeared.

Next we increased the tuning angle to the positive direction and found the side-bands appeared again. After that, the gain of the feedback was increased. Then the side bands disappeared again. With these procedure we found that the instability with the growth time of about 0.1 ms could be damped by our feedback system.

We observed the oscillation also by a turn-by-turn position detection system. The front-end circuit of the measurement system was equivalent to that of the feedback system but it was completely independent of the feedback loop. By this system we could observe the change of the oscillation around the moment of feedback on/off. An example of the observed data is shown in Fig. 3. We catch that the oscillation grows with the growth time of about 300 turns or 0.36 ms.

V. SUMMARY

We have developed a new position detection systems for the longitudinal and transverse planes with the detection frequency of 2 GHz. Through the experiments performed in AR, we have

established a bunch-by-bunch position-detection technique even in the bunch frequency of ~ 500 MHz. Applying this technique, we observed the bunch oscillation in AR. When the ring was operated with 4 bunches, we succeeded in identifying the mode of the coupled bunch instability by analyzing the data taken by our system.

The design and the fabrication of the prototype of the 2-tap filter completed recently. The frequency performance was measured in a bench and expected characteristics were obtained. This prototype was actually used in the longitudinal feedback experiment in AR.

The experiment of the longitudinal feedback has also been performed. The kicker for the feedback system was not an actual one but the accelerating cavities. The oscillation was safely damped by the feedback system and the damping time of, roughly, 0.1 ms was obtained. Based on the experiment, we have confirmed that the 2-tap filter system is powerful for the signal processing of the longitudinal bunch feedback systems.

References

- [1] E. Kikutani et al., "Development of Bunch Feedback System for KEKB", Proceedings of the 4-th European Particle Accelerator Conference (EPAC94).
- [2] E. Kikutani et al., "Front-End Electronics for the Bunch Feedback Systems for KEKB", Proceedings of the Beam Instrumentation Workshop (BIW94), Vancouver, Canada, October 2-6, 1994. This paper is also available as KEK Preprint 94-131.
- [3] The feasibility of using the 2-tap FIR filter for the bunch feedback systems was originally discussed by F. Pedersen in Workshop, "Factories with e^+e^- Rings", Benalmadena, Spain, November, 1992. We also discussed the feasibility in the paper, E. Kikutani et al., "Two Tap Digital Filters for the KEKB Bunch Feedback Systems", KEK Report 94-5.
- [4] The AM/PM technique is explained, for example, in the paper by R.E. Shafer, "Beam Position Monitoring", in "AIP Conference Proceedings 212".

60 HZ Beam Motion Reduction at NSLS UV Storage Ring

Om V. Singh

National Synchrotron Light Source, Brookhaven National Laboratory, Upton, NY 11973

I. ABSTRACT

A significant reduction in 60 hz beam motion has been achieved in the UV storage ring. From the wide band harmonic beam motion signal, 60 hz signal is extracted by tuned bandpass filter. This signal is processed by the phase and amplitude adjustment circuits and then, it is fed into the harmonic orbit generation circuits. Several harmonics, near the tune, were cancelled by employing one circuit for each harmonic. The design and description of this experiment is given in this paper. The results showing reduction in beam motion at 60 hz are also provided.

II. INTRODUCTION

Since December 1989, a broad bandwidth, analog global feedback system [1] has been in operation in the UV storage ring at NSLS. This system uses several beam pue's to generate spatial harmonic signals near the betatron tune, and several steering magnets to generate spatial harmonic beam correction signals. Although, this feedback system has provided excellent orbit stability for the users in frequency range from dc to few tens of hertz, there remains higher frequency beam motion, 60 hz in particular. This is due to the fact that the response of the feedback system is limited to around 60 hz frequency. Figure 1 shows the frequency spectrum of the beam motion from 5 hz to 405 hz for one of 24 pues in the UV ring, with global feedback on.

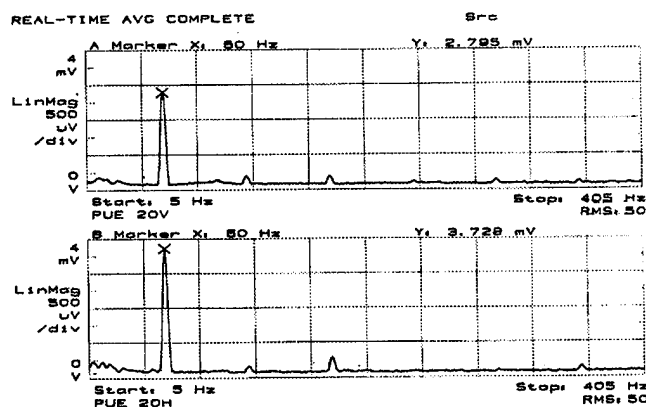


Fig 1 - Beam Motion Frequency Spectrum with Global Feedback On [1mV = 2 microns]

The upper plot is for a vertical pue signal and the lower plot is for a horizontal pue signal at a point near the largest vertical and horizontal betatron function, but not in the global feedback system. As seen in this figure, with the global feedback on, the dominant beam motion remaining is at 60 hz frequency, and there could be a significant improvement in the overall beam motion, if only this frequency of motion was removed or reduced. In the experiment, 60 hz beam motion is reduced by feeding back on the narrow band 60 hz frequency contents at a only few spatial harmonics, near the tune. The experimental set-up is given in figure 2. The wideband harmonic signal, generated by the harmonic orbit synthesize circuits, is passed into a dc block and amplifier circuits, followed by a narrow band 60 hz bandpass filter. This signal is, then, adjusted in amplitude and phase, such that when it is sent to the harmonic orbit generation circuits, the 60 hz motion is cancelled out or minimized.

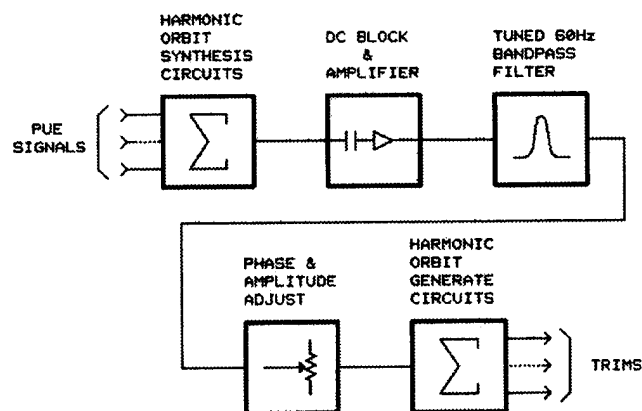


Fig 2 - Block Diagram for experiment setup

III. CIRCUIT DESCRIPTION

Figure 3 shows the circuit diagram for processing dc block and 60 hz filter for harmonic signal. The harmonic signal is received by a differential receiver followed by a dc block amplifier to remove dc component. This signal is amplified by a factor of 20 by an amplifier so that the signal level is high enough for the filter which follows this amplifier. The narrow bandpass filter is a "switched capacitor filter" (MF10 by Maxim)[2], driven by an external 6 khz clock (60 hz x 100). There are two distinct advantages for using this type of filter over the conventional analog type filter: (1) Only few

* Work performed under the auspices of the U.S. Dept. of Energy

discrete components (3 resistors) are required to generate dual 2 pole bandpass filter, (2) the bandpass frequency depends only on the external switching clock and not on the discrete components. The external 6 khz clock is derived by feeding line 60 hz signal into a phase lock loop (XR2212 by Exar)[3] and two counter IC's. This set up provides an excellent 60 hz line tracked bandpass filter and its performance is far superior to the bandpass filter that is built by discrete components which suffers from drift problems. The two traces in Figure 4 indicates that these circuits performed very well. The harmonic signal output, containing broadband beam motion signal, is shown in the upper trace and the 60 hz bandpass filtered signal is shown in the lower trace.

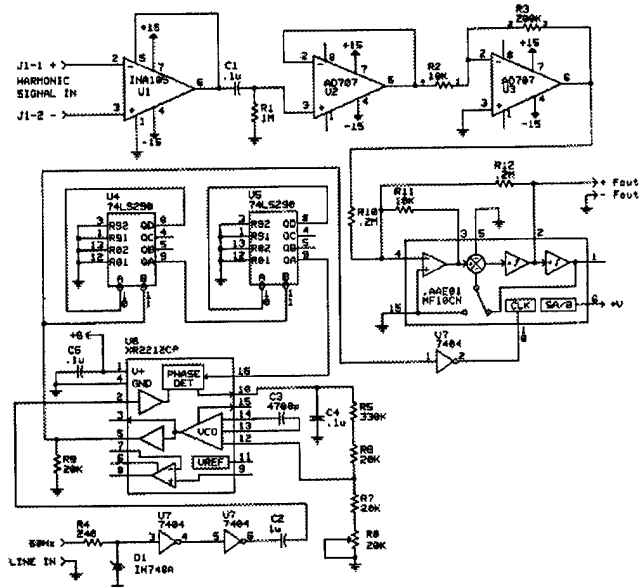


Fig 3 - Circuit diagram - dc block and filter

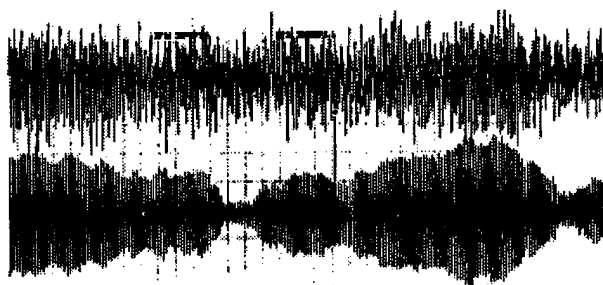


Fig 4 - Harmonic signal (upper trace)
Filtered signal (lower trace)

Figure 5 shows the circuits which provides the phase and amplitude adjustments. There are two cascaded phase adjustment circuits, providing a total of more than 180 degree phase adjustment. The heart of the phase adjust circuit is an operational transconductance amplifier (CA 3080 by RCA)[4]. The transconductance of this device is controlled by a dc bias current and this variable transconductance along

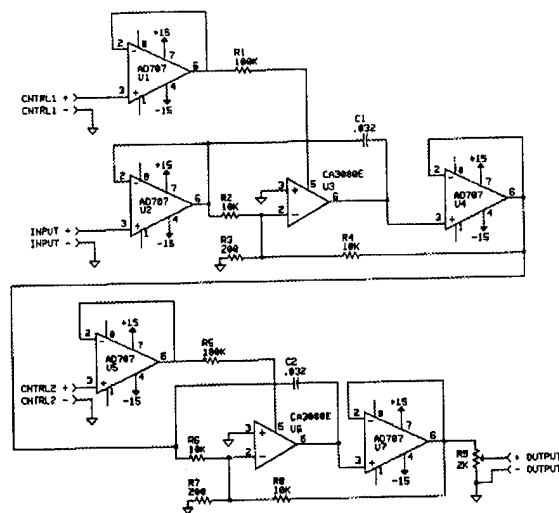


Fig 5 - Phase and amplitude adjustment circuits

with a capacitor provides a phase change without effecting the frequency. A potentiometer at the output provides the amplitude control. To determine the proper phase and amplitude, the signal is added to the broadband harmonic orbit correcting signal; the phase and amplitude of the signal are adjusted, until the 60 hz harmonic is minimized.

IV. RESULTS

The experiment for reducing vertical beam motion was set up to eliminate three harmonics: the average value (dc), cos1 and sin1 (vertical tune=1.2). Figure 6 shows the frequency spectrums taken from 10 hz to 210 hz and provides the improvement results for sin1 harmonic (upper plot) and for photon beam position monitor (lower plot). In both plots, the frequency spectrum before correction is shown by the upper curve (light trace) and the result of applying this correction signal as the lower curve (dark trace). The reduction of the 60 hz signal is > 6 for the harmonic signal and is > 4 for the photon monitor beam position signal.

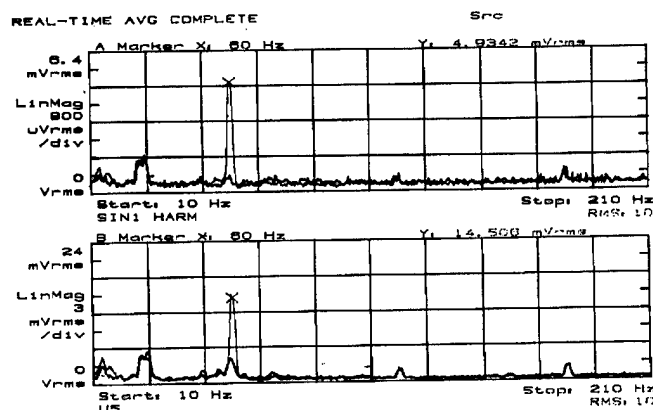


Fig 6 - Improvement results in vertical beam motion

The experiment for reducing horizontal beam motion was set up to eliminate both the sine and cosine 3rd harmonics (horizontal tune=3.14). Figure 7 provides the improvement results for sine3 and cosine3 harmonic. Again, in both plots, the frequency spectrum before correction is shown by the upper curve (light trace) and the result of applying this correction signal as the lower curve (dark trace). The reduction of the 60 hz beam motion is >3 for both harmonics.

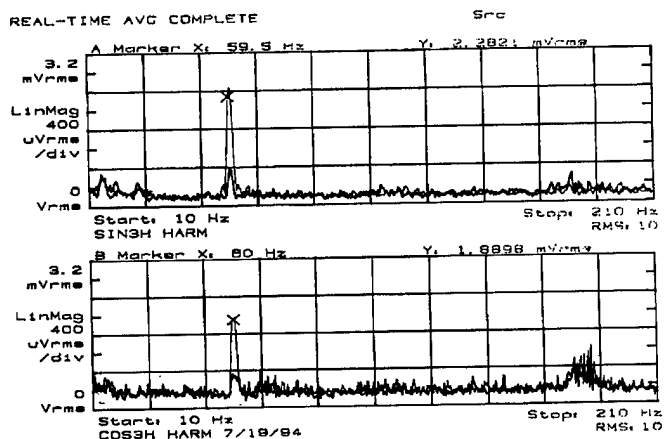


Fig 7 - Improvement results in horizontal beam motion

The beam motion at all horizontal pue's were also measured at 60 hz with and without correction and the data is plotted and is shown in figure 8. The square-mark trace shows the beam motion with correction off and the cross-mark trace shows beam motion with correction on. It is seen that by correcting only two harmonics, large improvements are seen at all the pue's. The signal reduction is greatest in the straight section where the energy dispersion is small and the betatron amplitude is large. At the other points, where the energy

60Hz Correction in VUV Ring (Sin 3H & Cos 3H Harmonics 7-19-94)

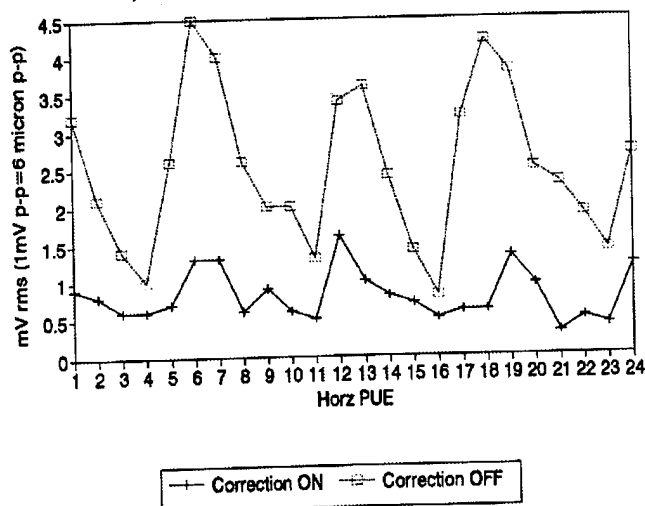


Fig 8 - 60 hz beam motion improvement

dispersion is large, the correction, although significant, is limited.

V. CONCLUSIONS

The use of a narrow bandwidth signal processing system to enhance the gain of the global orbit feedback system was successful in reducing single frequency motion on the beam.

VI. ACKNOWLEDGEMENTS

Author would like to thanks followings: Steve Kramer for his continuous encouragement and useful discussions; Henry J. Link for constructing the prototype and assisting in conducting the experiment; and Jeffrey L. Rothman for his keen discussion in designing phase control circuits.

VII. REFERENCES

- [1]. L.H.Yu et al., "Real Time Closed Orbit Correction System", IEEE Particle Accelerator Conference, Chicago, Ill.(1989)
- [2]. Maxim 1989 Integrated Circuits Data Book.
- [3]. Exar Data Book - Phase locked loops
- [4]. RCA Data Book - I. C. for Linear Application

The CEBAF Fiber Optic Phase Reference System *

K. Crawford, S. Simrock, C. Hovater, A. Krycuk

Continuous Electron Beam Accelerator Facility

12000 Jefferson Avenue, Newport News, Va. 23606-1909 USA

Abstract:

The specified phase stability of the CEBAF RF distribution system is 2.9° rms per linac. Stability is achieved through the use of a temperature and pressure regulated coaxial drive line^[1]. The purpose of the fiber optic phase reference system is to monitor the relative phase at the beginning and ending of this drive line, between linacs, injector and separator to determine drift due to ambient temperature fluctuations. The system utilizes an Ortel 1310 nm single mode laser driving Sumitomo optical fiber to distribute a reference signal at 1497 MHz. The phase of this reference signal is compared to the 1427 MHz (LO) and the 70 MHz (IF) via a 360° phase detector. The detected information is then routed to the CEBAF control system for display with a specified resolution of $\pm 0.2^\circ$ over a 20° phase delta.

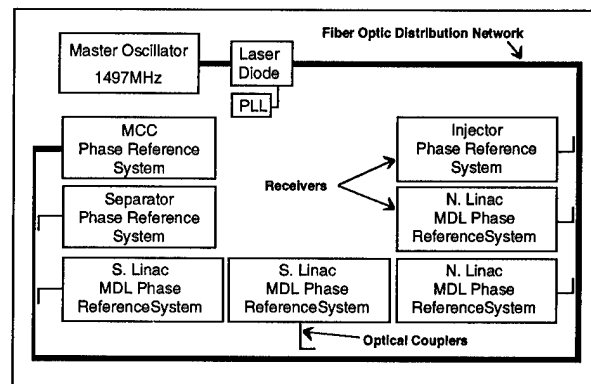
I. INTRODUCTION

The RF control modules for the CEBAF accelerator require that two frequencies, 70 MHz and 1427 MHz, be distributed throughout the accelerator site. This is accomplished in the linacs through the main drive line (MDL). The MDL for each linac consists of 750 ft of 1-5/8" rigid coax line for distribution of the 1427 MHz signal and 1/2" foam filled coax for the 70 MHz. Both lines are encased in a temperature regulated jacket. Proper operation of the multipass beam requires an energy spread of less than 2.5×10^{-5} . This places strict tolerances for the allowed slow phase error or drift. The main contributor to phase drifts is the temperature sensitivity of the 1-5/8" coax line ($6.5^\circ/\text{phase}/^\circ\text{C}$ @ 1427 MHz). In order to meet the phase stability specification it is required to regulate the temperature of the MDL to $\pm 0.1^\circ\text{C}$. In addition to temperature regulation, the 1-5/8" line is also pressurized and regulated to 4 psig to control any phase length changes due to ambient pressure variations. The purpose of the fiber optic phase reference system is to monitor the performance and provide an indication of the phase drifts of the injector, the MDL's of both linacs, and the separator.

II. SYSTEM DESCRIPTION

The fiber optic phase reference system consists of three main sub-systems. These are the laser diode, fiber optic cable distribution network, and the receiver chassis. The laser diode drives the 1497 MHz reference signal through the fiber optic cable distributed throughout the accelerator site. Optical couplers tap off a portion of this reference

signal and route it to receivers located in the injector, both linacs and separator building (Figure 1.). The receivers convert the optical signal into an electrical signal and mix it with 1427 MHz from the MDL. The resultant 70 MHz signal is then mixed with the 70 MHz MDL signal through two four quadrant multipliers configured as a quadrature detector. The phase is derived by a local DSP and passed to the control system through an RS-485 serial link. At present this information is displayed for the operators to make any phase adjustments manually.



Fiber Optic Phase Reference System
Figure 1.

Laser Diode:

The laser diode is a single mode 1310 nm, 5 mW class IIB laser (model 3540A) manufactured by the Ortel Corporation. The distributed feedback laser has a single mode optical line so that dispersive effects are virtually non-existent, allowing higher quality transmission over longer distances. The laser diode chassis incorporates a phase lock loop to maintain the phase within 0.2° . The laser is modulated with 1497 MHz from the master oscillator reference system in the machine control center (MCC).

Fiber Optic Cable Distribution Network:

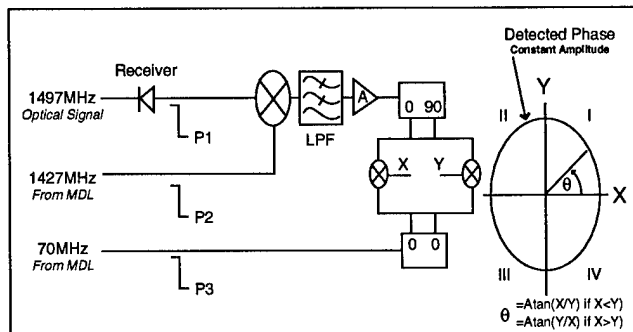
The fiber optic cable used in this system has been developed by the Sumitomo Corporation and has been tested extensively at KEK and JPL^[2,3]. The cable provides a high level of phase stability with regard to temperature by manufacturing the cable such that the clad and the fiber have equal and opposite thermal drifts. To further reduce temperature effects on the fiber cable, the network has been distributed around the site in a 3 ft deep trench encapsulated in a concrete conduit. The fiber run, approximately 1.5 km around the site, exhibits a thermal shift of only $0.12^\circ/\text{phase}/^\circ\text{C}$. The network runs from the machine control center (MCC) to the injector, around the circumference of the accelerator, to the separator building and finally back to the MCC for a final phase comparison.

* Work supported by DOE contract DE-AC05-84ER40150

A combination of Gould and BT&D optical couplers are used to tap off portions of the optical reference signal. The couplers' values were chosen to allow a uniform power representation for each of the six sample points; this compensates for the attenuated signal levels as they are distributed through the 1.5 km of the fiber cable run.

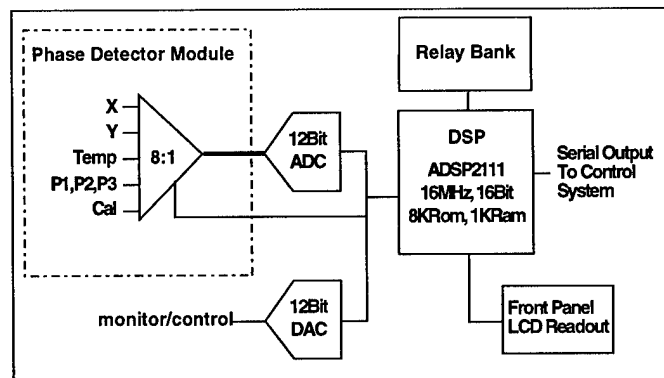
Receiver Chassis:

The receiver is comprised of two main sub-systems. These are the 360° phase detector module (Figure 2.) and the DSP module (Figure 3.).



360° Phase Detector
Figure 2.

The 360° phase detector converts the 1497 MHz modulated laser reference from an optical to an electrical signal using a BT&D model PTD512 receiver diode. The converted signal is mixed with the 1427 MHz signal from the MDL creating a 70 MHz signal. The signal is then filtered to remove all higher frequency components and amplified. The other 70 MHz signal from the MDL is compared to the derived 70 MHz signal to provide phase information. The 360° phase detector is essentially what is known in industry as a quadrature detector and has been used successfully in the CEBAF RF control module^[4]. The derived 70 MHz signal is passed through a 90° hybrid power divider creating two orthogonal signals. The other signal is divided using a normal power divider. The four signals are then fed into two Analog Devices four quadrant multipliers (AD834) that develop the X and Y signals that determine the phase as shown in Figure 2. An important aspect of the design was the care taken to eliminate phase shifts due either to temperature, amplitude drifts, or radio frequency interference (RFI). The circuit is housed within an aluminum enclosure that has a water loop incorporated into it so that the box can be coupled to the CEBAF LCW system to maintain its temperature stability. All electrical components (amplifiers, multipliers) are operated at least 10 dB below their saturation points to keep amplitude modulation to phase modulation, "AM to PM", effects low. The mixer is also operated 5 dB below its LO operation point for similar reasons. RFI shielding has been used extensively to keep out unwanted offsets that can produce errors in the quadrature circuit.



Local DSP
Figure 3.

The main purpose of the DSP module is to acquire the X and Y values of the detector, derive the phase, and deliver the information to the control system. The values acquired from the detector module are: power levels, X and Y voltages, module temperature, and offset values. The DSP used in this system is the ADSP2111 from Analog Devices. The 16 bit DSP reads all of the voltages through a 12 bit ADC providing 2.44 mV/bit with a ± 5 V range. After tuning the quadrature detector gains, this allows for an ideal resolution of $\pm 0.1^\circ$. The use of the local processor provides very fast acquisition of the phase signal to allow signal processing without burdening the control system. The ADSP2111 allows for 2 K program size to be stored in its internal RAM. Coupled with an 8 K EEPROM the processor can run four different programs (operating code, diagnostic code, algorithm code, etc.) or run one 8 K size program with attention placed on rebooting time. The DSP module also provides a local phase and temperature readout through a front panel LCD display. Control features have been incorporated into the system. These include a 12 bit DAC for future phase control/local analog readout and three programmable relays for system interface as well as a real time clock.

III. PERFORMANCE

In order to meet the 0.2° precision for a 20° phase delta, each of the 360° phase detectors requires three areas of attention. Both of the full quadrant multipliers have their input stages tuned to provide balanced maximum signal levels at all four inputs. Two sources, one slightly off frequency, are used to obtain the four quadrant circle. The X and Y components of the circle are acquired and fit to a perfect circle. Compensation coefficients to correct for phase skew, offsets and non-eccentricity are then obtained for use in correction code by the DSP. Finally the DSP routinely issues a calibration sequence to obtain the multiplier/amplifier chain offset values.

IV. CURRENT STATUS

Phase reference systems are installed in the injector and the north linac. They are presently undergoing beta testing. The system is being compared and calibrated against a path length measurement that measures the change in phase down and back of the main drive line. Typical diurnal main drive line drifts are approximately 10° to 20° . Results so far indicate that the laser reference system has some gain errors in the calculation of the MDL phase drifts. In addition to field testing, measurements on the receivers are being made to determine phase drifts due to temperature. Current schedule calls for all systems to be installed by June 1, 1995.

V. REFERENCES

- [1] Krycuk, A, Fugitt, J, Mahoney, K, Simrock, S, "The CEBAF Frequency Distribution System", Particle Accelerator Proceedings, 1991.
- [2] Tanaka, S., Murakami, Y., et al., "Precise Timing Signal Transmission by a New Fiber Optic Cable", KEK Report 90-5, May 1990.
- [3] Primas, L., Lutes, G., Syndor, R., "Stabilized Fiber Optic Frequency Distribution System", TDA Progress Report 42-97, vol. January-March 1989, Jet Propulsion Laboratory, Pasadena, California, pp. 88-97.
- [4] Hovater, C, Fugitt, J, "Analog Techniques in CEBAF's RF Control System", 1988 Linear Accelerator Conference Proceedings, pp. 412-414.

RF SYSTEM MODELING FOR THE HIGH AVERAGE POWER FEL AT CEBAF *

L. Merminga, J. Fugitt, G. Neil and S. Simrock, CEBAF, 12000 Jefferson Ave, Newport News, VA 23606 USA

Abstract

High beam loading and energy recovery compounded by the use of superconducting cavities, which requires tight control of microphonic noise, place stringent constraints on the linac rf system design of the proposed high average power FEL at CEBAF. Longitudinal dynamics imposes off-crest operation, which in turn implies a large tuning angle to minimize power requirements. Amplitude and phase stability requirements are consistent with demonstrated performance at CEBAF. A numerical model of the CEBAF rf control system is presented and the response of the system is examined under large parameter variations, microphonic noise and beam current fluctuations. Studies of the transient behavior lead to a plausible start-up and recovery scenario.

I. RF SYSTEM OVERVIEW

The driver accelerator for the high average power FEL, proposed for construction at CEBAF, is a recirculating energy-recovering 200 MeV, 5 mA cw superconducting rf (SRF) electron accelerator. The accelerator consists of a 10 MeV injector, a 96 MV SRF linac with a two-pass recirculation transport which accelerates the beam to 200 MeV, decelerates it for energy recovery through two passes, and transports it to a ~ 10 MeV dump [1].

Matching of the longitudinal phase space for bunching going into the wiggler and debunching going out of the wiggler and into energy recovery, implies a fairly restrictive set of constraints on the rf voltage, phases of the four beams (two accelerating and two decelerating) with respect to the crest of the rf wave, and arc compaction factors (M_{56}). Phasing of the four beams is such that the resultant beam vector has a strong reactive component; therefore the rf cavities must be operated off resonance to minimize the required generator power. With energy recovery, the generator power that must be supplied to the cavities is greatly reduced to approximately 1.5 kW per cavity, despite accelerating 5 mA by 4 MV.

The rf system provides power for acceleration of the electron beam, and control of the phase and amplitude of the accelerating field. High beam loading, energy recovery and the use of superconducting cavities, which require tight control of microphonic noise, place stringent constraints on the linac rf system design. A dedicated klystron, power amplifier and regulation system for each rf accelerating cavity is required because of the large influence of microphonic noise parametrically modulating the resonant frequency of the superconducting cavity. This modulation is not coherent over the many cavities, and results in random errors in phase and amplitude that can best be corrected by the use of individual rf cavity control systems.

To minimize cost and risk it has been proposed that the CEBAF rf control system [2] be used for the FEL driver accelerator. To

Table I
RF system requirements

Parameter	Requirement
RF power to beam per cavity	1.34 kW
Klystron power per cavity	5 kW
Phase stability (rms)	0.14°
Phase stability (long term)	3°
Gradient stability (rms)	2.8×10^{-4}
Gradient stability (long term)	1.4×10^{-3}
Gradient	8 MV/m
Accelerating phases	1.8°, -13.5°, 195.3°, 180°
Loaded Q	6.6×10^6
Tuning angle	-61.5°

test the control system capabilities and its robustness under the FEL operating conditions, we developed a model of the control system using SIMULINK [3], which numerically integrates the equations of motion of the system. This paper describes the model and presents results of the simulations.

We start with a summary of the FEL rf system requirements for the linac. The cavity equation is presented next and power requirements for the linac at steady-state are derived. RF amplitude and phase control is addressed next. We describe the rf model, discuss its validity and present simulation results which include transient behavior, regulation of microphonics, response to large parameter variation and a start-up/recovery scenario.

II. RF SYSTEM REQUIREMENTS

Table I summarizes the rf system requirements for the linac.

III. STEADY-STATE: POWER REQUIREMENTS

The rf cavity powered by an rf source (klystron) can be represented by a resonant LCR circuit [4]. The beam in the cavity is represented by a current generator. The dynamics of this system can be described, to a very good approximation, by the following first order differential equation,

$$\frac{d\tilde{v}_c}{dt} + \frac{\omega_0}{2Q_L}(1 - i \tan \Psi)\tilde{v}_c = \frac{\omega_0 R_L}{4Q_L}(\tilde{i}_g - \tilde{i}_b) \quad (1)$$

where ω_0 is the cavity resonant frequency, Q_L is the loaded Q of the cavity and R_L is the loaded shunt impedance $R_L = (r/Q)Q_L$. For CEBAF cavities $(r/Q)=480 \Omega$ per cavity. In arriving at (1) we assume that the cavity voltage, generator and beam current vary as $e^{i\omega t}$, where ω is the rf frequency, and \tilde{v}_c , \tilde{i}_g and \tilde{i}_b are the corresponding complex amplitudes, varying slowly with time. For short bunches, $i_b \approx 2I_0$, where I_0 is the average beam current, and i_b denotes the magnitude of \tilde{i}_b . In this equation Ψ is the tuning angle defined by $\tan \Psi = -2Q_L(\omega - \omega_0)/\omega_0$.

*Supported by the Virginia Center for Innovative Technology and DOE Contract # DE-AC05-84ER40150.

The current source \tilde{i}_b is the vector sum of the four beams present in the linac cavities each with an average current of $I_0 = 5\text{mA}$ and phases with respect to the crest of the rf wave, ϕ_k , $k = 1, 2, 3, 4$. Therefore $\tilde{i}_b = 2I_0 \sum_{k=1}^4 e^{i\phi_k}$ or $\tilde{i}_b = 2I_b e^{i\Psi_b}$ where $2I_b$ is the magnitude and Ψ_b the phase of \tilde{i}_b . Similarly we write $\tilde{v}_c = v_c e^{i\Psi_c}$. For convenience the reference phase is taken in the direction of \tilde{v}_c , therefore $\Psi_c = 0$. In steady-state the generator power is given by

$$P_g = \frac{(1 + \beta)}{16\beta} i_g^2 R_L, \quad (2)$$

where β is the cavity coupling coefficient. Using eq. (1) we can express the generator power in terms of Ψ , I_b , Ψ_b and β , and obtain the condition for optimum tuning, $\tan \Psi_{\text{opt}} = (I_b R_L / v_c) \sin \Psi_b$. The generator power at optimum tuning is

$$P_{g0} = \frac{v_c^2}{R_L} \frac{(1 + \beta)}{4\beta} \left[1 + \frac{I_b R_a}{V_c} \cos \Psi_b \right]^2. \quad (3)$$

For the accelerating phases given in Table I, $I_b = 2.33\text{ mA}$ and $\Psi_b = -89^\circ$. For $Q_L = 6.6 \times 10^6$, $Q_0 = 5 \times 10^9$, and $v_c = 4\text{ MV}$, the optimum tuning angle is -61.5° , and the required generator power is equal to 1.34 kW per cavity.

IV. RF AMPLITUDE AND PHASE CONTROL

Several designs exist to control the rf fields in superconducting cavities. The "classical" approach, employed by CEBAF, uses separate control of amplitude and phase. In the CEBAF system the cavity signal at 1497 MHz is downconverted to an IF frequency of 70 MHz where the phase detector and the controllers for amplitude and phase are operated. The amplitude of the accelerating field is determined by a Schottky detector which is operated in its linear range; i.e., the output voltage is proportional to the accelerating field. The fast phase detector uses an analog multiplier. The output signal is proportional to the $\sin(\Delta\phi)$, where $\Delta\phi$ is the phase difference between the rf reference (at 70 MHz) and the frequency-converted field probe (rf signal). Amplitude and phase modulators use analog multipliers at 70 MHz .

The gains and the frequency response of the feedback loops have to be optimized to minimize the residual amplitude and phase noise under steady-state conditions. During tune-up of the accelerator the field stability requirements can be relaxed but the control system must be stable for a wide range of beam loading conditions. The stability over a wide range of parameters determines the robustness of the rf control system. The coupling between the amplitude and phase loop should be minimal for maximum stability (robustness) and minimum residual noise.

Microphonic noise modulates the resonance frequency, which results in the uncontrolled (no feedback) case in rms phase variations of up to 7° and amplitude fluctuations of 0.5% rms (average tuning angle zero) or 8.7% rms (average detuning angle 45°). For the required stability a minimum gain of 40 dB for the phase loop and 50 dB for the amplitude loop is required. The typical microphonic noise frequency range is from 1 Hz to 200 Hz for the CEBAF accelerator.

A. RF Modeling

To simulate the performance of the CEBAF rf control system with FEL operating conditions, we developed a model of the

cavity and low level controls using SIMULINK, a MATLAB program for simulating dynamic systems. Figure 1 is a graphical representation of the rf model of the CEBAF rf control system. Next we give a detailed description of the model.

Equation (1) describes the interaction of the cavity fields with the beam and generator currents. The model includes microphonic noise in the form of sinusoidal modulation of the cavity's resonant frequency, $\delta\omega = \omega_M \sin(\omega_f t)$ where ω_M is the amplitude and ω_f the frequency of the noise. In addition we include the Lorentz-force detuning as another first order equation [5]

$$\tau_m \dot{\Delta\omega} = -\Delta\omega - 2\pi k v_c^2 \quad (4)$$

where $k = 3\text{ Hz}/(\text{MV/m})^2$, v_c is the cavity gradient in MV/m , and τ_m is the mechanical time constant of the cavity, equal to 0.5 msec . The current source is the sum of the generator and beam current. The klystron power is limited to 4 kW (linear range). Outputs of the cavity model are the amplitude and phase of the cavity voltage. The amplitude signal is compared to the amplitude set-point and the normalized error signal is amplified by the loop gain. The loop gain is given by $C(s) = H(s)[1 + G(s)]$ where $H(s)$, $G(s)$ are the transfer functions of the broadband and low-frequency gain respectively, $H(s) = \frac{K_1}{1+sT_1}$, $G(s) = \frac{K_2}{1+sT_2}$, $K_1=100$ and $(2\pi T_1)^{-1} = 1\text{ MHz}$, and $K_2=30$ and $(2\pi T_2)^{-1} = 200\text{ Hz}$. The broadband gain of 100 (up to 1 MHz) is boosted by an additional low-frequency gain of 30 which allows for an error reduction by a factor of 3000 for frequencies up to 200 Hz . However during start-up, the low-frequency gain is turned off since it saturates the modulator drive (to be described later). This combination of broadband and low-frequency gains provides fast settling times in pulsed mode, suppression of microphonics to very low levels, and maintains an energy-gain stability of better than 10^{-3} when the average beam current is increased from low currents to full beam loading. The Bode plot of the system, shown in fig. 2, includes three additional poles at 3 MHz , contributed from the klystron hardware, as well as the cavity pole which occurs at 125 Hz (on resonance). It shows that unity gain is reached at 100 kHz with a phase margin of 50° .

The controller for the phase of the accelerating field employs a vector modulator. The two inputs control the in-phase (real) and quadrature (imaginary) (I/Q control) components of the incident wave. The in-phase input is set to a fixed bias voltage of 5V, while the quadrature input is used to control the cavity phase error. A control voltage range of $\pm 5V$ allows therefore for a phase control range of $\pm 45^\circ$ which is sufficient for the microphonics observed at CEBAF. The vector modulator has the inverse transfer function of the cavity. The amplitude is increased as function of phase as $A/A_0 = \sqrt{1 + \tan^2 \Psi}$ therefore exactly compensating the reduced gradient when the cavity is detuned by an angle Ψ . Phase control by itself stabilizes the amplitude if the origin of the phase noise is purely microphonics, and if the cavity is operated on resonance. The combination of amplitude control and phase control using the quadrature component of the incident wave is identical to I/Q control if the quadrature component of the cavity voltage is zero. In this case the amplitude controller controls only the in-phase component of the incident wave.

B. Validity of Model

To test the validity of the model, it was used to predict the magnitude of induced transients when 200 μA of beam is suddenly turned off. These transient beam loading measurements have been performed at CEBAF and data are available for comparison [6]. The experimentally observed transients were at the 1×10^{-3} level, while the rf model predicted 1.3×10^{-3} . In addition the shape of the beam generated voltage fluctuation is similar and the recovery time is in very good agreement with the data. More extensive studies of the validity of the model are planned.

C. Simulation Results

Extensive simulation studies were carried out to examine the behavior (stability, robustness) of the rf system: Studies of the transient behavior led to a plausible start-up and recovery scenario which is described next. Once steady-state has been established, the system response to large parameter variations was examined. At steady-state, control of microphonic noise and beam current fluctuations were evaluated.

a) Start-up and recovery

The gradients in the cavities are ramped to nominal 8 MV/m. The magnetostrictive tuners maintain on-resonance condition by regulating the phase between incident and transmitted signal to zero. This phase coincides with the tuning angle Ψ for zero beam current. As the beam current is raised slowly, the true tuning angle will change according to eq. (1) of [7], which corresponds to the condition of optimum tuning and is maintained for all beam loading scenarios. It is therefore not necessary to calculate and control the true tuning angle.

b) Response to large parameter variations

We examined the response of the system to the following large, step-function-like perturbations: 1) Change of the tuning angle from -61.5° to -41.5° . 2) Change of the phase of both decelerating beams by $\pm 2^\circ$. 3) Reduction of the beam current of the two decelerating beams by 1%. 4) Reduction of the gradient setpoint by 1%. In all cases we calculated the magnitude of induced transients on the phase and amplitude of the accelerating field. In most cases the induced voltage fluctuations are within the requirements outlined earlier. The system appears to quickly

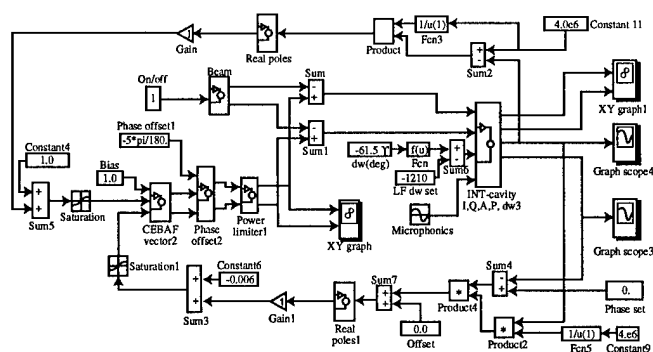


Figure 1. RF control system model

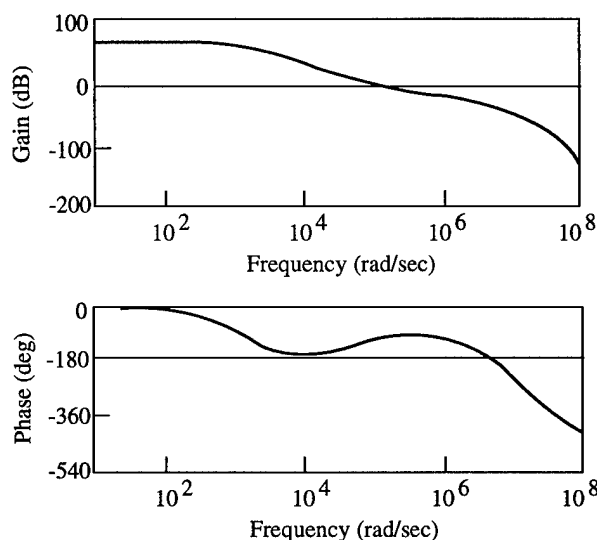


Figure 2. Bode plot of CEBAF's rf control system

recover from the induced perturbation and establish steady-state in less than 0.1 msec (to the 10^{-2} level of error suppression).

c) Control of microphonics and current fluctuations

We observed a reduction of microphonics by a factor of 30 after the low-frequency gain was turned on. At steady-state the phase of the accelerating field fluctuates at the 0.02° level peak-to-peak and the amplitude at the 1×10^{-5} level; therefore the system exceeds performance requirements. Finally we modulated the beam current by 2% peak-to-peak at a frequency of 1 kHz. The response of the system is still dominated by microphonic noise, therefore 2% p-p current fluctuations at 1 kHz are entirely within the range of control of the system.

References

- [1] D. Neuffer et al., these proceedings (1995)
- [2] S. Simrock, proceedings PAC 1991
- [3] SIMULINK, The Mathworks, Inc.
- [4] P. B. Wilson, SLAC-PUB-2884, February 1982
- [5] A. Mosnier, J. Tessier, TESLA 94-16, May 1994
- [6] G. Krafft, S. Simrock, K. Mahoney, proc. PAC 1991
- [7] L. Merminga et al., proceedings PAC 1993

BEAM POSITIONING AND MONITORING IN THE RACETRACK MICROTRON EINDHOVEN

W.H.C. Theuws, R.W. de Leeuw, G.A. Webers, J.I.M. Botman, C.J. Timmermans, H.L. Hagedoorn
Eindhoven University of Technology, Cyclotron Laboratory,
P.O. Box 513, 5600MB Eindhoven, The Netherlands

A scheme to compensate for the effect of misalignments in the racetrack microtron Eindhoven is presented. An array of small dipole magnets will be employed to obtain closed orbits. These dipoles are located at the symmetry axis of the microtron, in the drift space between the two bending magnets. For each orbit a radial stripline beam position monitor (BPM) will be installed in the field free region. The strength of the corrector dipole magnet in the n^{th} orbit is adjusted with the BPM signal in the $(n + 1)^{th}$ orbit. The design of the BPM's is described. It will be shown that a rectangular geometry has a distinct advantage over a conventional circular geometry since it is less dependent on vertical displacements of the beam. Expressions for the difference-over-sum signal are given and compared with that for a circular geometry. Results of measurements performed in a test bench on prototype BPM's are discussed.

I. INTRODUCTION

The aims of the 400 MeV electron storage ring EUTERPE [1] are investigation of charged particle beam dynamics and application of synchrotron radiation. The EUTERPE injection chain consists of a 10 MeV travelling wave linac followed by the 10–75 MeV RaceTrack Microtron Eindhoven (RTME), see figure 1. Some design parameters of RTME are listed in table I. The whole system is currently under construction.

The main components of the electron optical system of the microtron are two 2-sector magnets separated by a drift space [2]. These magnets, which are tilted in their median planes to obtain 180 degrees bending angles, have been designed and constructed, and the magnetic field maps have been measured. Numerical orbit calculations show that it is not possible to obtain simultaneously 180 degrees bending in the horizontal plane for all the different energies. This is caused by the field 'dip', *i.e.* the smooth decrease of the magnetic field towards the centre of the magnets (about 2 % for RTME).

In Section II a scheme to correct for orbit deviations is pre-

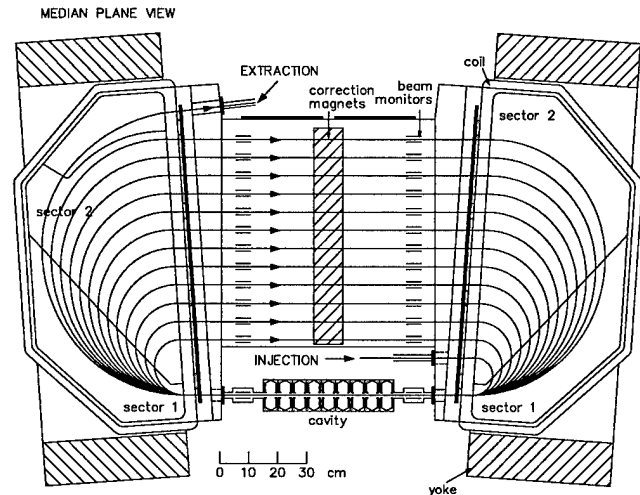


Figure 1. RaceTrack Microtron Eindhoven.

sented. Small dipole magnets will be used to provide an extra bending in the median plane. The signals of stripline BPM's are used to adjust the strength of these magnets. The design of these BPM's is described in Section III. Expressions for the difference-over-sum signal are given both for circular and rectangular geometries. It is shown that a rectangular geometry meets our requirements. In Section IV test bench measurements on prototype BPM's are discussed. Section V gives some concluding remarks.

II. CORRECTION SCHEME

The small deviations from the ideal bending angle of 180 degrees for the different orbits can partly be compensated for by an appropriate choice of the tilt angle of the main bending magnets (4.0 instead of 4.5 degrees). However for each orbit a small residual exit angle remains. Moreover an angular alignment tolerance for the tilt angle of 0.05 mrad would be required, which is far too stringent to be met by mechanical alignment. To compensate both for the residual exit angle as well as the mechanical angular alignment error of approximately 1 mrad an array of small dipole magnets is located halfway the two bending magnets. The magnetic field strengths of these correction magnets can be varied from -400 to 400 Gauss. This range is sufficient for the required bending angles, which are in the order of 10 mrad for the low energies and in the order of a few milliradians for the higher energies.

In RTME we have 14 degrees of freedom, *i.e.* the excitation of 2 bending magnets and 12 correction magnets, to fulfill the condition of closed orbits and the condition of isochronism. We determine these degrees of freedom using numerical orbit cal-

Table I
Design parameters of the microtron.

Injection Energy [MeV]	10
Extraction Energy [MeV]	75
Energy gain per turn [MeV]	5
RF frequency [MHz]	2998
Low field sector [T]	0.51
High field sector [T]	0.60
Tilt angle [degrees]	4.0
Orbit separation [mm]	60.6
Drift length on cavity axis [m]	1.0

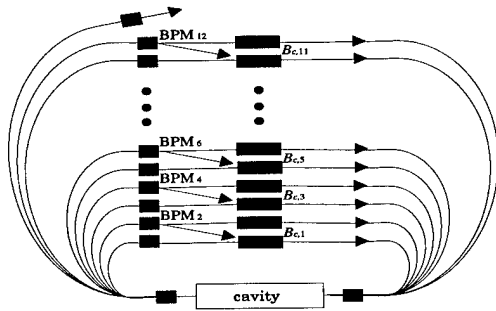


Figure 2. Proposed correction scheme.

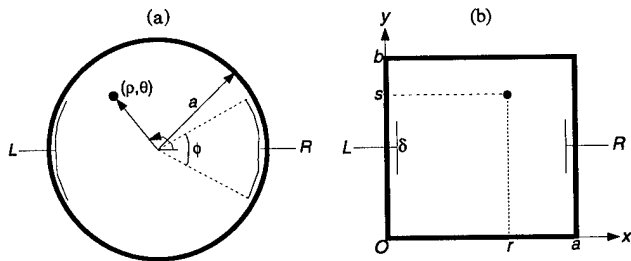


Figure 3. Beam position monitor with circular (a) and rectangular geometry (b).

culations. First we make estimations for the excitations of the main bending magnets. Then a backwards correction procedure is used to determine the excitation of the correction magnets, see figure 2. The beam position with respect to the ideal position in the $(n+1)^{th}$ orbit is used to adjust the magnetic field strength, $B_{c,n}$, of the correction magnet in the n^{th} orbit. This procedure ensures closed orbits. However now the orbit circumferences are slightly changed. Therefore we must check on isochronism. If the condition of isochronism is not fulfilled as optimal as possible new estimations for the excitations of the main bending magnets have to be made, and so on.

This procedure is applicable if the errors in the measured beam positions are smaller than 1 mm.

III. DESIGN OF THE BPM

At the return path of each orbit a small piece of dummy beam pipe will be installed with two striplines facing each other. The striplines act as quarter wave transformers to the accelerating frequency. An extra array of BPM's is employed at the other end of the field free region to be able to measure the residual exit angles of the orbits. For the design of the BPM circular geometries as well as rectangular geometries are regarded, see figure 3.

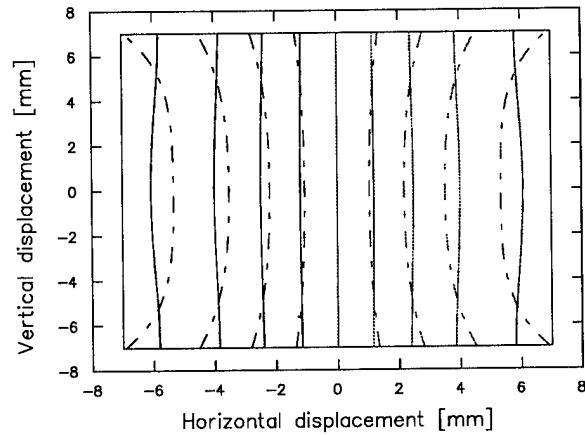


Figure 4. Contour plot of $\frac{R-L}{R+L}$ for the optimal circular (dashed lines) and rectangular geometry (continuous lines). The displacements are given with respect to the centre of the BPM.

The difference-over-sum of the left (L) and right (R) stripline signal only depends on the geometry of the BPM and on the beam position. For a circular geometry the difference-over-sum signal, derived with the two-dimensional Poisson equation, yields [3]:

$$\frac{R-L}{R+L} =$$

$$\frac{\sum_{n=1}^{\infty} \frac{1}{2n-1} \left(\frac{\rho}{a}\right)^{2n-1} \cos(2n-1)\theta \sin(n-\frac{1}{2})\phi}{\frac{\phi}{4} + \sum_{n=1}^{\infty} \frac{1}{2n} \left(\frac{\rho}{a}\right)^{2n} \cos(2n\theta) \sin(n\phi)}, \quad (1)$$

where (ρ, θ) represents the beam position in polar coordinates, a the beam pipe radius and ϕ the angular width of the striplines.

For a rectangular geometry the beam position is represented by (r, s) , the beam pipe dimensions are $a \times b$ and the stripline width is δ . We derived the difference-over-sum signal analogously:

$$\frac{R-L}{R+L} = \frac{\sum_{n=1}^{\infty} A_n \left(\frac{\sinh(\frac{n\pi r}{b})}{\sinh(\frac{n\pi}{b}(a-r))} - 1 \right)}{\sum_{n=1}^{\infty} A_n \left(\frac{\sinh(\frac{n\pi r}{b})}{\sinh(\frac{n\pi}{b}(a-r))} + 1 \right)}, \quad (2)$$

where

$$A_n = \frac{\frac{2 \sin(\frac{n\pi s}{b})}{n\pi} \left(\cos\left(\frac{n\pi(b-\delta)}{2b}\right) - \cos\left(\frac{n\pi(b-\delta)}{2b}\right) \right)}{\frac{\sinh(\frac{n\pi r}{b})}{\sinh(\frac{n\pi}{b}(a-r))} \cosh\left(\frac{n\pi}{b}(a-r)\right) + \cosh\left(\frac{n\pi r}{b}\right)}$$

Since the BPM signals are used for a correction in the horizontal plane we only want to measure horizontal displacements. Therefore we want the signal to be independent of vertical displacements, and linear with and sensitive to horizontal displacements.

For a certain geometry of the BPM these properties can conveniently be visualized by a contour plot [4]. Independency of vertical displacements is expressed by vertical contour lines,

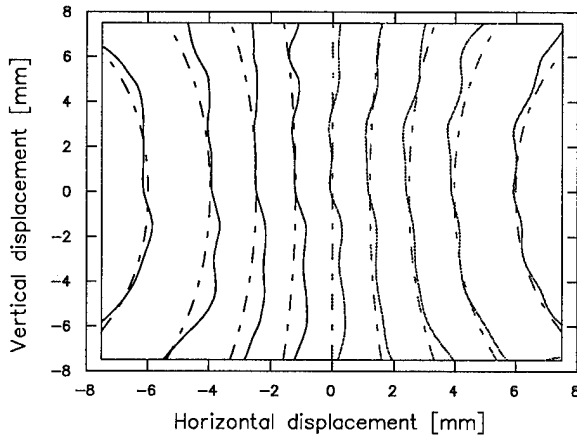


Figure 5. Comparison of measured (continuous lines) with calculated contour plot (dashed lines) for a circular geometry with $a^* = 11.5$ mm and $\phi = 0.70$ rad.

linearity by equidistant contour lines and sensitivity by density of contour lines. The vertical independency can be influenced by the stripline width. Linearity and sensitivity depend on the dimensions of the beam pipe, which are tightly limited by available space and emittance of the electron beam. Hence in practice linearity and sensitivity can hardly be influenced.

The optimal circular BPM is found for $\phi \simeq 1$ rad. For a rectangular geometry the demand of vertical independency can be fulfilled much better, for $\delta \simeq \frac{3}{4}b$, see figure 4.

IV. TEST BENCH MEASUREMENTS

Measurements on prototype BPM's have been performed in a test bench, where the electron beam is represented by a 3 GHz signal on a 1 mm thick copper wire. The stripline signals are measured with calibrated crystal detectors.

A. Circular geometry

A BPM with a radius of 12.5 mm is considered. The striplines have a width of 8 mm, $\phi = 0.64$ rad. From the comparison between measured and calculated contour plot it can be seen that the measurements show a larger sensitivity. However in Eq.(1) the striplines are assumed to be part of the wall. Actually the striplines are both located 1 mm inwards. To compensate for this an *effective radius*, a^* , is introduced. The best match is found for $a^* = 11.5$ mm, see figure 5.

B. Rectangular geometry

For rectangular geometries an effective distance between the striplines (a^*) is introduced. A BPM with $a^* = 20$ mm and $b = 20$ mm, and 3 mm striplines is considered. The measured and calculated contour plot are shown in figure 6. The deviations in the corners of the figure are due to the fact that theory does not account for the finite thickness of the striplines ($\simeq 1$ mm).

V. CONCLUDING REMARKS

Numerical orbit calculations show that the proposed correction scheme is applicable to obtain closed orbits and isochronism in RTME at the same time.

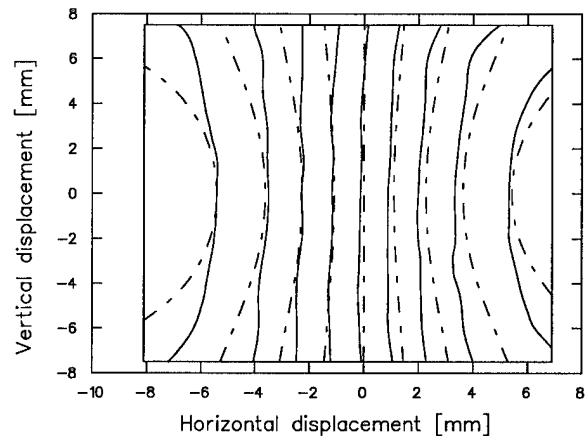


Figure 6. Comparison of measured (continuous lines) with calculated contour plot (dashed lines) for a rectangular geometry.

From the theoretical and experimental investigations it has been found that for our purpose the rectangular geometry is most appropriate since the demand of vertical independency is fulfilled as optimal as possible. For RTME 90 mm long rectangular BPM's ($a = 20$ mm, $b = 20$ mm and $\delta = 15$ mm) will be used to measure the horizontal displacements.

In the beam transport lines of the EUTERPE injection chain we will employ circular BPM's with the same radius as the beam transport lines. The angular width of the striplines will be 1 rad.

The accuracy in the measured beam position is mainly restricted by the measurement accuracy of the stripline signals. The definite detection electronics is still under development. Assuming that both the left and the right signal can be measured with an accuracy of 10 %, the horizontal beam position can be determined within 0.3 mm in the central region of the BPM. Other contributions, such as manufacturing errors and finite width of the electron beam, are estimated to be smaller than 0.3 mm in total.

References

- [1] Botman J.I.M., Boling Xi, Timmermans C.J., Hagedoorn H.L., *The EUTERPE facility*, Rev. of Sci. Instr., vol. 63, no. 1 (1992) 1569.
- [2] Webers G.A., *Design of an electron optical-system for a 75 MeV racetrack microtron*, Ph.D. Thesis, Eindhoven University of Technology (1994).
- [3] Shafer R.E., *Beam position monitoring*, AIP Conf. Proc. 212 (1989) 26.
- [4] Baron A.I., Vogel U., *A method for the calibration of synchrotron beam pick up electrodes*, Rev. of Sci. Instr., vol. 41, no. 12 (1970) 1832.

Multi-Bunch Systems at DESY

Rolf-Dieter Kohaupt
DESY Hamburg, 22607 Hamburg

Abstract

A central problem for the electron machines PETRA, HERA and DORIS is the strong current limitation due to multi-bunch instabilities. The design currents of these machines are a factor of twenty above threshold currents. For the proton machines the beam quality is strongly affected by instabilities. In order to reach the design currents in routine operation of the electron machines very effective multi-bunch feedback systems have been developed. Starting with an intensive theoretical investigation of those systems the technical concept was elaborated.

I. Introduction

The electron machines PETRA, HERA and DORIS have all been equipped with transverse and longitudinal feedback systems. They have worked successfully in routine operation for about two years.

For the proton machine DESY III the observed longitudinal instability has been cured by a longitudinal multi-bunch feedback system based on a completely new concept. The longitudinal bunch deviation is corrected by horizontal kicks at places with large dispersion. Also this system works successfully in routine operation.

For the HERA p ring a transverse multi-bunch feedback system with low noise level has been developed in order to cure the observed instability in this machine. This system will be brought into operation for the next luminosity run period.

II. Review of the Theory

The multi-bunch feedback system was investigated within the theory of discrete systems (1) where the pick-up and the definition systems are explicitly localized. The result is a rigorous description of the multi-bunch theory including feedback systems.

III. Realization of Feedback Systems

The feedback systems are built up according to the following scheme:

1. Pick up
2. Wide band detector
3. Analog digital converter
4. Phase processing (digital filter)
5. Digital analog converter
6. Chain of amplifiers
7. Deflecting devices

The systems have a bandwidth of 5 MHz according to a bunch-to-bunch separation of 96 nsec.

The systems have operated successfully in PETRA, HERA and DORIS. They work in all three directions. In the transverse direction the beam is influenced by ferrite loaded kickers. The

power is 1 kW for each kicker. In the longitudinal direction rf systems with 200 kW peak power feed broad band cavities.

For DESY III the longitudinal bunch deviation is corrected by four horizontal kickers at places with large horizontal dispersion. This system reduces the proton bunch oscillations of 30 degrees to about 1 degree at ejecton energy. The damping line is 30 msec. (2)

For HERA P a transverse multi-bunch feedback system was developed with low-noise e-level detectors and two kickers in each direction. The damping was measured to be around 200 msec. The system will be operated for the next luminosity period.

References

- [1] R. D. Kohaupt, DESY 91-071
- [2] R. D. Kohaupt et al. DESY Report (to be published)

RESULTS OF FINAL FOCUS TEST BEAM*

V. A. Alexandrof, V. Balakin, A. Mikhailichenko,
Budker Institute of Nuclear Physics, Novosibirsk and Protvino, Russia

K. Flöttmann, F. Peters, G.-A. Voss,
Deutsches Elektronen Synchrotron, Hamburg, Germany

V. Bharadwaj, M. Halling, J. A. Holt,
Fermi National Accelerator Laboratory, Batavia, Illinois, U.S.A.

J. Buon, J. Jeanjean, F. LeDiberder, V. Lepeltier, P. Puzo,
Laboratoire de L'Accélérateur Linéaire, Orsay, France

G. Heimlinger, R. Settles, U. Stierlin,

Max-Planck-Institut für Physik, Werner-Heisenberg Institute, Munich, Germany

N. Akasaka, H. Hayano, N. Ishihara, H. Nakayama, K. Oide, T. Shintake, Y. Takeuchi, N. Yamamoto,

National Laboratory for High Energy Physics, Tsukuba, Japan

F. Bulos, D. Burke, R. Field, S. Hartman, R. Helm, J. Irwin, R. Iverson, P. Raimondi, S. Rokni, G. Roy, W.

Spence, P. Tenenbaum, S. R. Wagner, D. Walz, S. Williams,

Stanford Linear Accelerator Center, Stanford, California, U.S.A.

Abstract

The beam experiments of Final Focus Test Beam(FFTB) started in September 1993 at SLAC, and have produced a $1.7 \mu\text{m} \times 75 \text{ nm}$ spot of 46 GeV electron beam. A number of new techniques involving two nanometer spot-size monitors have been developed. Several beam diagnostic/tuning schemes are applied to achieve and maintain the small spot. This experiment opens the way toward the nanometer world for future linear colliders.

I. GOAL OF FFTB

A small spot size is the most important key to enhance the luminosity of an e^+e^- linear collider. Up to now, most plans of future linear colliders at 0.5–1 TeV center of mass assume a vertical spot size below 10 nm either as the standard or upgraded design number. A very flat beam with an aspect ratio more than 100 will be favored to reduce various beam-beam effects at the collision while keeping the luminosity high. The goal of FFTB[1] is to squeeze a high-energy electron beam down to $1 \mu\text{m} \times 60 \text{ nm}$, which is a suitable intermediate step to the future machines. FFTB is located at the end of the SLC Linac on the straight line extended from the SLAC Linac, beyond the beam switch yard. The length of the beam line is about 360 m from the switch yard to the beam dump, and the final focus section with chromaticity correction is 185 m long.

A small spot requires two basic factors—a small emittance and strong focusing (small β -functions). FFTB uses the 46 GeV beam, accelerated by the SLAC Linac, with invariant emittances of $\gamma\epsilon_x \times \gamma\epsilon_y = 30 \times 3 \mu\text{m}^2$, which are the smallest among the existing high energy electron beams. The β -functions at the focal point(FP) of FFTB are $\beta_x^* = 3 \text{ mm}$ and $\beta_y^* = 100 \mu\text{m}$, which are equal to future machines. Such small beta functions inevitably induce high chromaticities in the final lenses. If no chromaticity correction is applied, the spot at the FP becomes 23 times

bigger in horizontal and 34 times in vertical for the design momentum spread of $\Delta p/p = \pm 0.4\%$. Thus special focusing optics with a powerful chromatic correction system are required[2]. The chromaticity correction of FFTB is done by two-family non-interleaved sextupoles, which has become the common base design of future final focus systems. This configuration suppresses the chromatic aberration as shown in Fig. 1, while canceling the major geometric aberrations of the sextupoles with the $-I$ transformer between them. The system minimizes the residual aberrations caused by the finite thickness of the sextupoles and the optical mismatch due to the synchrotron radiation in the dipole magnets between the sextupoles and the final lenses.

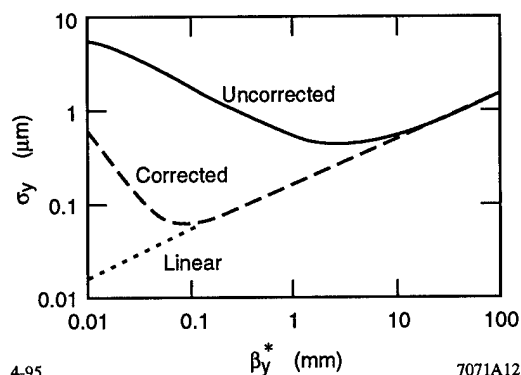


Figure. 1. The vertical spot size of FFTB as a function of the β_y^* . The dashed/solid lines are with/without the chromaticity correction. At the design value $\beta_y^* = 0.1 \text{ mm}$, the spot size becomes nearly the minimum, since below that point, residual aberrations start to dominate.

II. NEW INSTRUMENTATIONS

To achieve the design spot of FFTB, many new instrumentations have been developed and applied. Since most of their fea-

*Work supported by the Department of Energy, contract DE-AC03-76SF00515.

tures will also be necessary for future machines, the development of these devices is an important part of the FFTB project.

A. Magnets and power supplies

Since the β -function peaks at the final three quadrupoles ($\beta_x = 26000$ m, $\beta_y = 11000$ m), the nonlinear components of these magnets should be minimized. The fabrication accuracy of the pole-faces of these magnets are made better than $\pm 2 \mu\text{m}$ [3]. One of the final three quadrupoles has a pole-tip made of perme-dur to achieve the field of 1.4 T. The stability criteria of magnet strength in FFTB is typically 10^{-5} for the dipoles and a few quadrupoles[4]. Thus the power supplies of those magnets are carefully chosen to satisfy the condition. The air in the tunnel of FFTB is simply sealed without air-conditioning. Since the power consumption in the tunnel is small and also constant, this is a good choice to avoid an artificial temperature change due to the air-conditioning itself.

B. Magnet supports

Quadrupoles except the final three lenses are mounted on a magnet mover supported by a pillar made of Anocast artificial stone. This setting satisfies the long-term stability criteria of the vertical motion of each quadrupole, $\Delta y \sim 2 \mu\text{m}$ under the expected temperature change of the tunnel. The heavy final three lenses are supported by a common table with a precision mover[5]. The Laser-Compton monitor is attached to the table to reduce the effect from the possible vibration.

C. Initial alignment

The initial alignment of each component is done in two steps[6]. First, alignment of several "hinge points" is done using the alignment laser extended from Linac as the reference. Second, each magnet is aligned from these hinge points by a laser-tracker. The over-all accuracy of the initial transverse alignment is about $200 \mu\text{m}$ through the FFTB beam line, which is within the adjustable range of the magnet movers by the beam-based alignment.

D. Wire alignment system

The wire alignment system is a unique tool in FFTB to detect the transverse drift of each magnet. All quadrupoles and sextupoles have three sensors attached on two invar plates sit on the median split plane (one on one end, two on the other). The sensor detects the rf signal applied on the wire like a BPM, and the resolution of the transverse wire position is 100 nm with a dynamic range of ± 1.5 mm. A pair of wires are stretched over quasi-straight sections of FFTB, and the three sensors measure the x and y displacements and the rolls of each magnet. The stability of the motion of the magnets detected by the system was typically less than $\pm 5 \mu\text{m}$ in the upstream end of the beam line, and $\pm 15 \mu\text{m}$ in the downstream end, per 24 hours. Besides a periodic day-night variation, a slow drift of $5 \mu\text{m/day}$ is observed. The drift in the electronics and the wire itself were negligibly small.

E. Magnet movers

The magnet mover for the standard quadrupoles and sextupoles is so designed as to match the requirement of the tuning of the FFTB optics[7]. It is used not only in the beam-based

alignment, but also in the lattice diagnostics to create bump orbits, and in the tuning process of the spot size as the multi knob with the sextupoles. This mover consists of three cam shafts independently driven by stepping motors, and the magnet sits on them with wedges. By the combination of the rotation angles of these three cams, the transverse displacement and the roll in x - y plane are controlled independently. The resolution of the motion is $1/3 \mu\text{m}$ and $1 \mu\text{rad}$. The movable range is ± 1.8 mm in x , ± 1.5 mm in y , and ± 5 mrad in roll. The motion is also monitored by linear gauges, and there is neither backlash nor hysteresis.

F. Beam position monitor

The beam position monitor(BPM) of FFTB is designed to detect pulse-to-pulse x - and y - position with a resolution of $1 \mu\text{m}$ at the intensity 1×10^{10} electrons/bunch[8]. Each BPM uses four strip-lines embedded in the gaps of a quadrupole magnet. Thus the BPM measures the beam position in the middle of the quadrupole, which provides an ideal situation for the beam-based alignment. Each strip-line has an independent circuit with an rf booster amplifier before the low-pass filter to reduce the noise level. The calibration of the BPM is done after installation in the quadrupole, at the same time as the measurement of the magnetic center of the quadrupole using a common single wire. The actual resolution of the BPM was verified by the beam using the lattice-diagnostics technique described later, and the result was $\sigma = 1.6 \mu\text{m}$ at $N = 0.7 \times 10^{10}$, which is just equal to the design number.

G. Cavity beam position monitor

The detection of the beam position at the FP is extremely useful in the diagnostics of FFTB. It has many usages: to measure and adjust the R_{34} components of the transfer matrix from a well-established pre-focus to the FP to adjust the waist at the FP; to measure the vibration of the position at the FP to distinguish the position jitter and the spot size in the spot-size monitor; to measure the correlation of the beam-jitter at the FP with upstream or downstream BPMs to analyze the source of the jitter, etc. Therefore a BPM with nanometer pulse-to-pulse resolution is required. The recently developed cavity BPM[9] which detects the excitation of the TM_{110} mode of a single-cell choke-mode cavity at C-band(5712 MHz) has such resolution of 1 nm. This BPM will be fully commissioned in the next run of FFTB.

H. Wire scanners

The wire scanners are the essential tool to measure the beam profile at all locations in FFTB. Even at the FP it is a very powerful tool to adjust the waist in the range $\sigma_y \geq 0.5 \mu\text{m}$. Although the wire scanners of FFTB are basically inherited from SLC[10], several new arrangements were done. One of them is a set of wires with very small tilt angles in the x - y plane. A scanner with a yoke of three wires with angles -0.7° , 0° , $+0.7^\circ$ is installed in one of the pre-focus points where the aspect ratio of the beam is 1:400. This scanner successfully reconstructed the beam sizes in x , y and the tip angle from three apparent spot sizes.

I. Laser-Compton spot-size monitor

The Laser-Compton spot-size monitor[11] measures the modulation of the Compton-scattering rate across an interference fringe of two laser lights produced at the FP. The depth of the modulation corresponds to the spot size at FP. The fringe is produced by a pulsed YAG-laser with $1.06 \mu\text{m}$ wavelength, 10 ns pulse length, 200 mJ/pulse, and 10 pps repetition rate. Since the pitch of the fringe pattern is so rigidly determined by the wavelength of the laser, the measurement of the size by this monitor is direct. This monitor can produce three different fringe patterns with different measuring ranges: $0.8 \mu\text{m} \leq \sigma_x^* \leq 4 \mu\text{m}$, $150 \text{ nm} \leq \sigma_y^* \leq 750 \text{ nm}$, and $40 \text{ nm} \leq \sigma_y^* \leq 200 \text{ nm}$.

J. Ion-Scattering beam-size monitor

The Ion-Scattering beam-size monitor[14] measures the interaction between the electron beam and ions created from the gas injected at the FP. It consists of eight multi channel plates surrounding the FP through a narrow slit which is necessary to reject the ions outside the focal length of $\beta_y^* = 100 \mu\text{m}$. This monitor measures two quantities: the time-of-flight and the azimuthal distribution of the scattered ions. The former tells the larger dimension, and the latter the aspect ratio and the tilt angle of the beam-spot at the FP. This monitor has an advantage in its very wide dynamic range and the insensitivity to the position jitter. Another aspect of this monitor is that the angular distribution involves more information on the beam profile than its sizes such as the beam-tail produced by the wake field.

III. BEAM TUNING TECHNIQUES

A. Beam-based alignment

In order to optimize the tunability and reduce the background for the monitors in FFTB, it is necessary to align strong quadrupole and sextupole magnets with beam-based measurements[12]. Quadrupoles are aligned using a shunt technique, with resolutions from $50 \mu\text{m}$ down to $0.7 \mu\text{m}$. Sextupoles are aligned by moving transversely, looking at the kicks of the orbit observed in the downstream BPMs. The resolution of the residual misalignment of sextupoles by this method was 5 to $20 \mu\text{m}$. All magnets were then moved into aligned positions via the magnet movers with the sub-micron resolution. The beam-based alignment was done in the beginning of every successive run of FFTB.

B. Lattice diagnostics

The amount of the strength error of focusing elements in the FFTB optics must be within a few times 0.1%, otherwise the machine loses the tunability to the design spot size. Thus the detection of the strength error is an important subject prior to the tuning of the machine. For this purpose, a lattice diagnostics with bump orbits is applied. A locally closed bump orbit is created by combining three kicks at quadrupoles, generated by the magnet movers. Then the orbit data from the BPMs up/down stream of the bump orbit contains the information of the strength error of the quadrupoles used in the bump, as well as the calibration errors of BPMs and movers, etc. To separate the strength error from other variables, orbits with multiple bumps are taken and

multi-variable fit is applied. This analysis was able to demonstrate that the FFTB quadrupole strengths were uniform to the required level of 0.1%.

C. Incoming beta match

Because of the limited space in the beam line, the measurement and matching of the incoming phase space is done in the matching section at the entrance of FFTB which has five quadrupoles and two skew quadrupoles[13]. The measurement is done by varying quadrupoles against the beam sizes measured by a wire scanner with three wires x , y , and tilted u . It is possible to determine all 10 parameters of the incoming beam with this method. The matching is done for $\alpha_{x,y}$, $\beta_{x,y}$, and two of x - y coupling coefficients, and the remaining two x - y coupling terms are less relevant to the final spot due to the flatness of the emittances and the spot size. The matching is confirmed at two pre-foci (one for each plane) in the middle of the chromaticity correction sections with the wire scanners. This confirmation was extremely important to tell whether the source of the error in the final spot is, in the incoming beam or in the optics between the pre-foci and the FP.

D. Tuning by multi knobs

After the beam-based alignment, lattice diagnostics, and beta match, the tuning of the spot size is done by scanning several knobs looking at the spot size measured by the spot-size monitors[13], [2]. Since these monitors are located at different focal points, the tuning must be done separately for each monitor. The tuning at one monitor, however, significantly reduces the number of steps of tuning for another monitor. Usually the tuning is done with a beam with reduced momentum spread, $\Delta p/p \leq 0.1\%$ to avoid the mixing of linear and higher order effects. The knobs for the linear terms, such as the waist position, dispersion, and one of the x - y coupling ($x'y'$) are always effective to reduce the spot, but its magnitude depends on the condition. Several iterations are necessary to reach the minimum. These knobs are built by either changing the strength of magnets or combination of the sextupole movers.

FTTB has four strong sextupoles for the chromaticity correction. Each sextupole has the high precision cam-shaft mover. Knobs for the waist motion and linear dispersions in x and y , one of the x - y coupling ($x'y'$ term) can be made by particular combinations of these sextupole movers. According to the high precision, the repeatability, and the hysteresis-free nature of the cam-mover, these mover knobs have advantages on a small-range, repeated scan of the knobs. These knobs were frequently used in the tuning, and after the value of the knob is optimized, their motions were replaced with equivalent changes of the magnet strengths of dipoles, quadrupoles, and skew quadrupoles.

Another effective set of knobs was the nonlinear multi knobs which control four sextupole terms (x'^3 , $x'y'^2$, x'^2y' , y'^3) independently by combining two normal and two skew trim sextupoles.

IV. OBSERVATION OF NANOMETER SPOT

FTTB has run for about seven weeks in four periods since September 1993. The first fringe pattern of the Laser-Compton

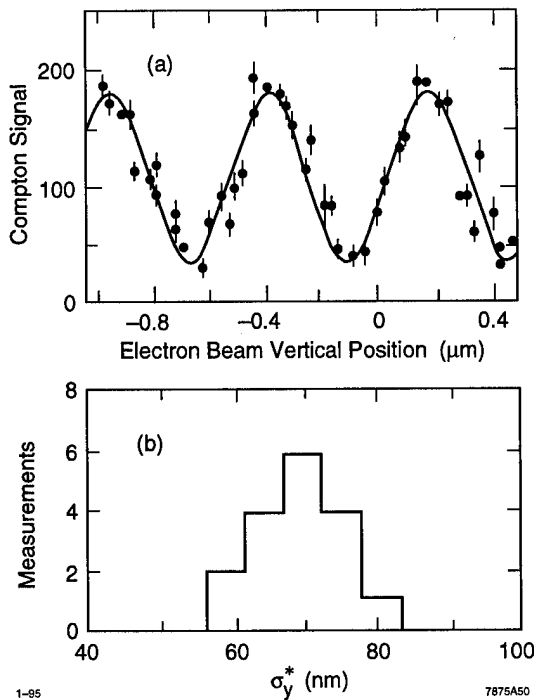


Figure 2. (a) Typical vertical fringe pattern seen by the Laser-Compton monitor. This example corresponds to $\sigma_y^* = 70$ nm. (b) The distribution of the measured in the last 3 hours of the run in May 1994.

monitor was observed in the beginning of April 1994 in horizontal. The small vertical spot around 70 nm was observed in the middle of May 1994[15], [11]. Figure 2 shows the typical fringe pattern seen by the monitor, and also the distribution of the measured spot sizes during the last 3 hours of the run in May 1994. This distribution shows that the beam line of FFTB has the stability of $\sigma_y^* = 70 \pm 7$ nm including the possible fluctuations in the monitor.

The Ion-Scattering monitor was commissioned partly in May 1994, and more totally in September 1994[15], [14]. The spot size determined from the time-of-flight and the azimuthal distribution was typically $1.6 \mu \times 80$ nm, which agrees well with the results of the Laser-Compton monitor. Figure 3 shows a typical azimuthal distribution of the scattered ions observed by the monitor. Taller peaks indicate the higher aspect ratio, *i.e.*, smaller vertical size.

The spot sizes above are obtained with a configuration $\beta_x^* = 10$ mm and $\beta_y^* = 100 \mu\text{m}$ with the incoming emittances around $\gamma\epsilon_x = 30 \mu\text{m}$, $\gamma\epsilon_y = 1 \mu\text{m}$ with the momentum spread $\Delta p/p = \pm 0.1\%$. The horizontal focusing was relaxed to reduce the background signal of the monitor. Although the observed spot sizes were already close to the design number, it was also true that there were non-negligible discrepancies in the vertical sizes between the measured and the expected from the emittance and β_y^* . The discrepancy appeared similar in both spot-size monitors. Figure 4 shows the squared vertical spot size measured by the Laser-Compton monitor versus the incoming vertical emittance. The linear fit Fit-1 in Fig. 4 may suggest an existence of an error source which give an offset to the measured spot size, such as a vibration of the final lenses. The fit with the restriction

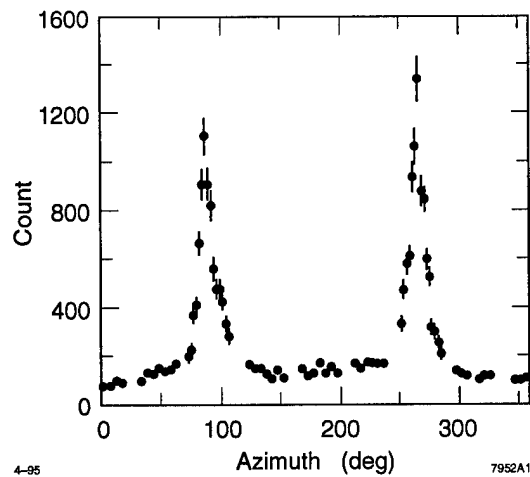


Figure 3. Azimuthal distribution of scattered He ion detected by the Ion-Scattering monitor in September 1994. This distribution corresponds to $1.6 \mu\text{m} \times 80$ nm spot.

at the origin (Fit-2), however, is also possible with the magnitude of the errors. Further experiment such as a measurement of the vibration jitter of the beam using the cavity BPM is necessary to complete our investigation of the results of the spot size.

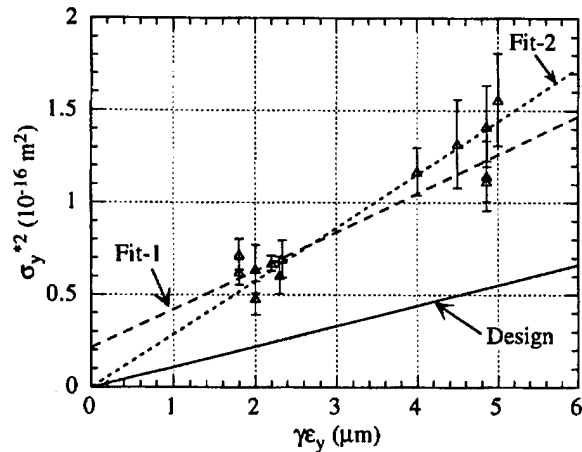


Figure 4. Vertical spot size (squared) versus the incoming vertical emittance. Measured in September 1994 with the Laser-Compton monitor. Fit-1(dashed) is the linear fit to the measured data, Fit-2(dotted) is the linear fit passing the origin, and the solid is the design line.

V. CHROMATIC BEHAVIORS

The chromatic behavior of the FFTB optics is measured in several ways. First we looked at the shift of the vertical waist position at the FP by changing the incoming beam energy. The energy spread of the beam is set small, $\Delta p/p \leq \pm 0.1\%$. If the chromaticity correction works properly as designed, the shift of the waist is minimized within the design bandwidth. Its behavior is shown in Fig. 5 as the solid curve. The shift of the vertical waist position was measured by waist scans with the Laser-Compton monitor in September 1994. First the results shown as squares in Fig. 5 were obtained, which significantly deviate

from the design curve. At that time the lattice diagnostics with multi-bump had been performed and predicted the common calibration error of the quadrupoles relative to the beam energy (to the main dipoles) by -0.73% , i.e., the beam had higher energy offset of $+0.73\%$. The expected shift of the waist with the predicted energy offset becomes the dashed line of Fig 5, which now well agrees with the measured (squares). Then we corrected the energy offset, and re-measured the waist position as shown by crosses in Fig. 5. The results became closer to the design, but still deviated from the design by a small amount. At that time it was found that the vertical sextupoles had been trimmed by about 3% stronger than the design. The trimmed sextupoles give the expected curve as the dot-dashed line in Fig. 5, which agrees with the measurement (crosses) quite well.

The second verification of the chromatic behavior was the measurement of the spot size by changing the momentum spread of the incoming beam through varying the phase-ramp of the Linac. We changed the momentum spread from $\Delta p/p = \pm 0.1\%$ to $\pm 0.5\%$, and the measured vertical spot size at the FP stayed almost constant within the measurement error of about 10%. This shows that the chromaticity correction works, since the bare chromaticity is so large as shown in Fig. 1.

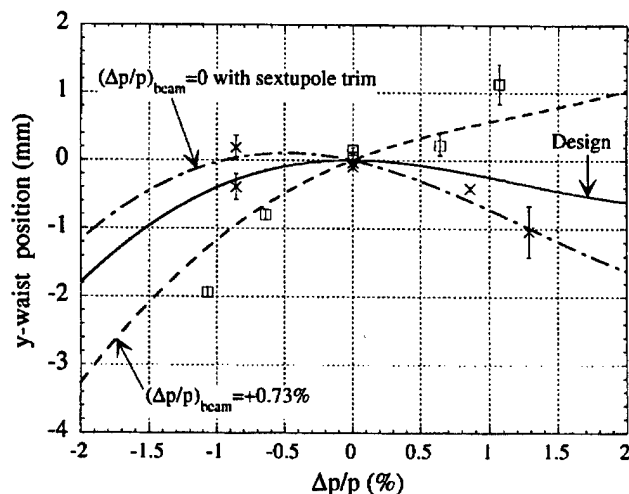


Figure 5. Shift of the vertical waist position as a function of the momentum offset of the incoming beam, measured at the Laser-Compton monitor. Squares are measured before the correction of the beam-energy offset. Dashed line is expected from the energy offset of $+0.73\%$. The crosses are measured after the correction. The dot-dashed is expected from the trimmed values then applied to the sextupoles. The design is shown by the solid line.

References

- [1] M. Berndt *et al.*, Final Focus Test Beam Design Report, SLAC-REF-376(1991).
- [2] K. Oide, SLAC-PUB-4953, in Proceedings of PAC89, Chicago(1989); J. Irwin *et al.*, SLAC-PUB-5539, in Proceedings of PAC91, San Francisco(1991); G. Roy, SLAC-REF-397, Ph.D. thesis(1992).
- [3] H. Nakayama *et al.*, FFTB-94-4(1994).
- [4] F. Bulos *et al.*, SLAC-PUB-5485, in Proceedings of PAC91, San Francisco(1991).
- [5] N. Ishihara *et al.*, KEK-Preprint-92-89, in Proceedings of HEAC92, Hamburg(1992).
- [6] V. E. Bressler *et al.*, SLAC-PUB-6152, in Proceedings of PAC93, Washington DC(1993).
- [7] G. Bowden *et al.*, SLAC-PUB-6132(1993); G. Heimlinger, MPI-PhE 93-13, Ph.D. thesis(1993).
- [8] H. Hayano *et al.*, Nucl. Instrum. Meth. Phys. Res., **A320**(1992)47.
- [9] S. Hartman *et al.*, in these proceedings.
- [10] R. C. Field *et al.*, Nucl. Instrum. Meth. Phys. Res., **A295**(1990)279.
- [11] T. Shintake, Nucl. Instrum. Meth. Phys. Res., **A311**(1992)453; T. Shintake *et al.*, KEK-Preprint-92-65, in Proceedings of HEAC92, Hamburg(1992); T. Shintake *et al.*, KEK-Preprint-94-129(1994).
- [12] P. Tenenbaum *et al.*, in these proceedings; F. Bulos *et al.*, SLAC-PUB-5485, in Proceedings of PAC91, San Francisco(1991).
- [13] P. Tenenbaum *et al.*, in these proceedings.
- [14] J. Buon *et al.*, Nucl. Instrum. Meth. Phys. Res., **A306**(1991)93; P. Puzo *et al.*, LAL-RT-94-08, in Proceedings of EPAC94, London(1994).
- [15] V. Balakin *et al.*, Phys. Rev. Lett. **74**(1995)2479.

COMPARISON OF MEASURED AND CALCULATED DYNAMIC APERTURE

F. Willeke

Deutsches Elektronen-Synchrotron DESY Notkestraße 85, 22607 Hamburg, Germany

Abstract

Dynamic aperture experiments at the Fermilab Main Ring, the TEVATRON, the SPS and HERA are reviewed and compared with simulations. The agreement between experiments with additional strong nonlinearities and corresponding simulations is fairly good, if the relevant parameters are sufficiently well known and included in the model. Direct comparison is more problematic if machines under normal operating conditions with relatively weak non-linear fields are considered. Nevertheless, the agreement is reasonable and discrepancies can be accounted for by known imperfections of the model.

I. INTRODUCTION

Non-linear dynamics in circular accelerators has been studied at many laboratories. The crucial issue for future machines is how well the dynamic aperture can be predicted by calculations. This is important in order to be able to specify the field quality and optimize the design of the magnets.

Particle motion in non-linear fields in accelerators can be described and understood in principle.

The subtle question of predicting the dynamic aperture and long term stability is difficult however.

The greatest problem is the limited knowledge of the system. Accelerators are built as linearly as possible. Non-linearities, apart from the chromatic sextupoles, occur as small imperfections with many sources. It is quite difficult to obtain precise knowledge on these errors. The measurement of magnetic fields with a precision of $\delta B/B \simeq 10^{-4}$ is at the technological limit. In superconducting magnets there are, in addition, persistent currents with slow decay, eddy currents and magnetic coupling between different coils. Furthermore there are the finite permeability of the vacuum components, saturation and remanence effects, and stray fields from injection elements or nearby accelerators. The beam optics is also not perfect, while closed orbit distortions, β -beats, linear coupling and chromaticity modify the dynamics in non-linear fields. Furthermore, the conditions in a real machine are never quite constant. Power supply ripple, ground motion, and vibrations excited by vacuum pumps or coolants cause fast oscillation of the fields seen by the beam. Slow changes are induced by thermal effects or by the variation of the load of the power system.

Accelerators are operated at optimized working points far from major resonances. Then, the effects which determine the dynamic aperture are quite subtle. The border of stability is determined by chaotic motion. Thus the motion becomes unpredictable. Simulation of the motion becomes difficult. Usually one needs to simulate a large number of turns before one can decide upon stability.

Observations involving real beams are multi-particle effects whereas tracking can be performed only with a few particles.

The results of measurements depend on the particle distribution. This is impossible to model exactly. While the structure of the whole phase space is relevant for the stability of a particle beam, tracking can explore only a small fraction. This makes it very difficult to compare numbers directly.

In a real accelerator, additional effects influence the results of measurements. These are tune modulation, collective effects due to space charge, wakefields, beam-ion interaction and intra beam scattering, scattering from the rest gas, interaction with vacuum pumps, noise from rf cavities or damper systems and power supplies.

It is very hard to put all these effects simultaneously into a model.

The experimental strategy under these circumstances has been the following: One started with very simple experiments near strong resonances, which resemble the slow extraction scenario to test experimental equipment and procedures. The next step consisted in the investigation of the dynamic aperture of a machine with controlled strong non-linearities which dominate the non-linear fields. Such experiments have been performed in the FNAL-TEVATRON (1987-1990) and in the CERN-SPS (1986-1988). The importance of power supply ripple and tune modulation was recognized early. These effects have been investigated in the SPS 1988-1993 and in the TEVATRON 1988-1990. The ultimate goal is to study and to understand the real machine as it is operated. This has been addressed in TEVATRON Main Ring studies (1988-1989) and in experiments in the HERA Proton Ring (1994).

II. EXPERIMENTS WITH STRONG, CONTROLLED NON-LINEARITIES

Strong sextupole and octupole fields are turned on, so that the dynamic aperture limit occurs at small amplitudes at which the "natural" small nonlinearities can be neglected. Thus the relevant non-linearities are well under control. In such an experimental set up one has the same qualitative features of non-linear dynamics as in a normal machine, namely amplitude dependent tunes and non-linear resonances for all rational values of the tunes.

Experiments have been performed at the TEVATRON and at the SPS. In the TEVATRON, 16 strong sextupole magnets have been powered to drive the third integer resonance $3Q_x = 97$, whereas in the SPS experiment 8 strong sextupoles are driven such that this resonance is intrinsically canceled.

An important characteristic of a nonlinear system is the tune shift with amplitude. In both experiments the measurements have been compared with simulations. The measured tune shifts with amplitude agree with the simulations within the precision of the measurements [2] [5] [6] [8]. See also Fig. 1.

The comparison of experimental dynamic aperture values with simulations is satisfactory in both studies.

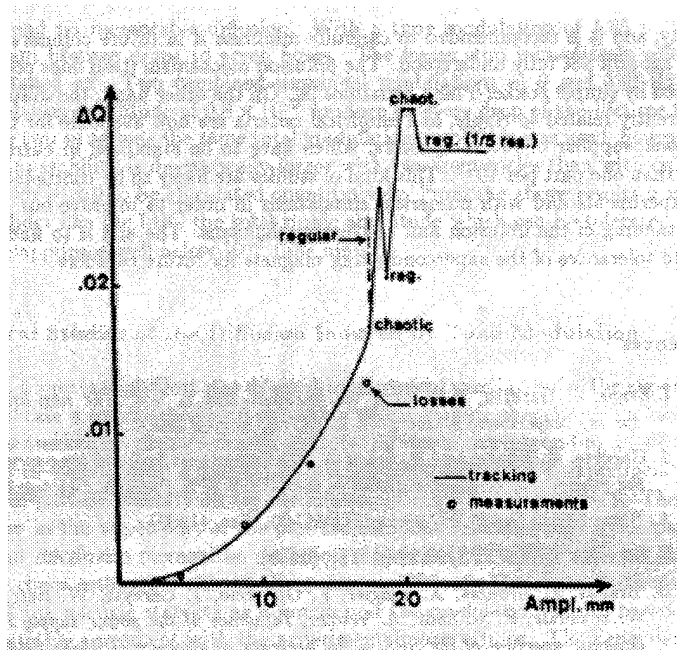


Figure 1. Detuning curves of the SPS Aperture Experiment with strong Sextupoles from [2] [5] (line: tracking, dots: experimental data). Indicated are also the amplitude limits for which losses are observed and the amplitude limit which gives chaotic motion in tracking calculations. They are in good agreement.

In the TEVATRON experiment at 150 GeV , the beam has been heated by applying noise to the beam via the horizontal damper. The available dynamic aperture was filled by this method. The coupling resonance was compensated and the tunes were kept away from the main coupling resonance to avoid the blow up of the emittance in the other plane. The horizontal beam profile was recorded with a wire scanner. Once the available aperture was filled, the beam emittance did not grow any more and the foot width of the profile is identified as the dynamic aperture. The experimental values for various sextupole strengths amount to 63% to 75% of the values obtained from 1000 turn tracking calculations.

In the SPS experiment [2], [5], [12], a bunched pencil beam at 120 GeV was produced by scraping and this beam was kicked horizontally. Once the edge of the beam hit the dynamic aperture, beam losses occurred. The dynamic aperture has been reconstructed from the transverse distribution of the beam and the kick amplitude. The working point was kept away from major resonances ($Q_x = 26.53, Q_y = 27.63$). The results compare well with tracking calculations. In the tracking calculations, a vanishing Lyapunov exponent (see [16]) was considered as the criterion for stability. The values from tracking and experiment agree quite well.

III. EFFECT OF TUNE MODULATION

We know from the theory of nonlinear dynamics that tune modulation creates a side band structure of nonlinear resonances. These sideband resonances may reduce the dynamic aperture. Sidebands may also increase the probability for particles to es-

cape from regions which otherwise would be inside the border of stability. A slow growth of the amplitudes of the particles can be observed, which resembles a diffusion process. The border of stability transforms under these circumstances into a soft transition from quasi-stable motion to fast instability. In simulations, this effect can be made visible by plotting the escape time of a particle versus its initial amplitude (survival plot).

Tune modulation may be caused by power supply ripple, by non-corrected chromaticity or by mechanical vibration of the magnets. It is very difficult to suppress tune modulations below a critical level of $\Delta Q \leq 10^{-4} - 10^{-3}$.

Some experiments have been devoted to exploring this quasi-diffusive behaviour and comparisons have been made with predictions from theory and simulation. Experiments have been carried out in the TEVATRON [11] and in the CERN-SPS [5] [9] [10] [13] [15]. As in the experiments described above, strong controlled nonlinearities have been added to the accelerator fields.

In the TEVATRON experiment, 14 sextupoles have been powered with an intrinsically canceled third integer resonance. The working point was near the resonance $5Q_x=97$. The beam was bunched. The phase of the driving term was adjusted to populate an island in the chain of the 5th order resonance by a horizontal kick. The fraction of the beam trapped in the resonant island gives raise to persistent coherent betatron oscillations, which can be easily detected by a beam position pick-up. The destruction of the regular phase space topology of these islands by tune modulation has been studied. Strong, overlapping side bands cause the trajectories which form island chains to be resolved into a band of chaotic trajectories. This can be observed experimentally by the decay of the coherent betatron oscillation signal, when the particles escape from the island and eventually are uniformly distributed in betatron phase. This behaviour was examined as a function of tune modulation depth and frequency and was compared with an analytical model and with simulations. The experiment confirmed the dependence of the process on tune modulation depth and frequency which was predicted by an analytical model. Strong decay of the coherent signal is observed for parameters for which chaos is predicted. The loss of coherence has also been simulated. The simulations are in excellent agreement with the experimental data. This experiment is a demonstration that the available concepts, methods, and tools are adequate. If the relevant parameters are under control, even subtle effects can be described quantitatively.

In the SPS, diffusion-like behaviour has been discovered in the 1988 sextupole experiments. Beam losses as a function of time have been observed after a scraper has been moved into the beam and has subsequently been retracted by a small amount. The slow losses which developed after the scraper was retracted indicated a diffusion-like growth of oscillation amplitudes. More recently, the experimental studies focused on the role of tune modulation in this process. The same configuration of non-linear fields as in the previously described experiments has been used. In addition, the detuning has been controlled by means of octupole magnets. The experiments have been carried out with a coasting beam. A strong influence on the long term dynamic aperture could be found by applying a tune modulation with a frequency of 9 Hz and with a depth of $1.8 \cdot 10^{-3}$.

Quasi-diffusion constants have been extracted from observation of beam life-time after scraping and subsequent small retraction of the scrapers. The diffusion occurred mainly in the horizontal plane. The diffusion coefficient was enhanced by a factor of 5 – 10 due to this additional tune modulation. In this experiment, the short time dynamic aperture was not affected by the tune modulation. This can also be seen in a simulation study. The tune modulation starts to affect the stability border only if 10^6 or more turns ($t \geq 20 \text{ sec}$) are considered.

An attempt has been made to simulate the diffusion experiment by a computer model [13]. The SPS with its natural and additional strong nonlinearities has been carefully modeled. The corresponding detuning reproduces the experimental values. The measured horizontal distribution of the kicked beam was described by 180 super-particles. The distribution in the vertical and in the longitudinal direction was neglected. The modeled distribution and the detuning can be used to calculate the tune spectrum which agrees well with the measured spectra. If the scraper measurement is simulated using this model, the qualitative features of the beam loss curve versus time are reproduced well. However the losses in the experiment are about three times greater than the simulated ones.

This discrepancy is beyond the range of uncertainty due to imperfect knowledge of parameters such as longitudinal and transverse distribution, kick strength or position of the scraper. Nevertheless the loss mechanism in this experiments could be clarified. According to the simulations, particles in the kicked beam either diffuse outward until they reach the vicinity of a 7th order resonance after which they will be lost quickly or alternatively they will be attracted by an 8th order resonance which is somewhat further inwards and from which no escape could be observed. Beam profile measurements indeed confirm, that particles are diffusing inwards which supports the tracking analysis.

IV. EXPERIMENTS UNDER NOMINAL OPERATING CONDITIONS

The ultimate question is how well one can model an accelerator under normal operating conditions. It has been addressed by two experiments. One of them is the FERMILAB Main Ring study performed in 1988 and 1989 [3] [8]. The other example is the superconducting HERA proton ring with its low injection energy and corresponding large persistent current field errors. Dedicated experiments have been performed recently in 1994 [14].

Here only the short term dynamic aperture is relevant. The machine has a short cycle time of 4sec. The dynamic aperture limitations are only important at 8GeV, an energy at which the beam life-time is dominated by multiple scattering at the rest gas ($\tau = 40 \text{ sec}$). In this way the dynamic aperture is quickly filled with beam. Under the assumption that the phase space is not strongly distorted at the dynamic aperture and that particles beyond the dynamic aperture will be lost quickly, the beam distribution is well defined. The dynamic aperture has been studied by injecting beams of different sizes. If the beam size is too large, it will shrink until all the particles outside the dynamic aperture are lost. If the size is too small, it will grow due to gas scattering until a quasi stationary distribution is reached which extends up to the dynamic aperture.

Another type of measurement was performed by kicking the beam and observing subsequent beam losses. Since the distribution is well defined, the edge of the beam can be reconstructed from the fractional beam loss. The horizontal dynamic aperture obtained in this way is 16.4mm and the value for the vertical one is 13.3mm.

In order to obtain a good model, the field of the dipole magnets has been remeasured carefully. The tracking calculations extended over a period of 35000 turns (the storage time at 8GeV). The horizontal and vertical start amplitudes of the particles have been chosen to be the same. The dynamic aperture values from long term tracking agree with an analysis of Lyapunov exponents. The particles with amplitudes up to about 16mm are stable. Beyond that, chaos is observed in the tracking.

The most recent experiment is the dynamic aperture study in the superconducting HERA proton ring. First crude estimates indicated that the dynamic aperture of the machine was about two times smaller than the values obtained from a very detailed tracking model which took into account the measured non-linear field components of each individual superconducting magnet [17]). In the recent studies, dedicated experiments have been performed for the first time. The dynamic aperture has been measured by two different methods. The beam has been scraped to produce a pencil beam. It was then kicked in the horizontal plane with different strengths. The part of the beam outside the dynamic aperture gave rise to intensity losses from which the dynamic aperture could be reconstructed. In the second type of experiment, the beam was kicked horizontally and the edge of the beam was measured by a restgas ionization beam profile monitor (see Fig. 2). The dynamic aperture obtained by these methods agreed within the errors and amounted to 13mm – 15mm. In Fig. 3, the experimental results are summarized in form of survival plots. In some of the experiments, the working point has been chosen near the main diagonal close to the seventh order resonance ($Q_x = Q_y = .287$). For these values, the dynamic aperture is found significantly lower than for well separated tunes ($Q_x = .285, Q_y = .305$).

In the model calculations the persistent current decay has been taken for each individual magnet in addition to the steady state individual magnet errors. The persistent current decay causes an increase of the spread of the sextupole strength from magnet to magnet. It also changes the global distribution of sextupole strength around the machine since there are two types of magnets which differ in persistent current decay. The knowledge about the exact distribution of sextupole strength is imperfect since only two reference magnets are available from which the sextupole component can be monitored. The model has been optimized by adjusting the detuning. The distribution of sextupole strength has been varied slightly so as to obtain agreement with the measured values. Due to these uncertainties in the sextupole strengths, the calculated dynamic aperture values range from 16.6mm to 18.6mm. The tracking results are shown in a survival plot in Fig. 4.

There is thus a moderate discrepancy between experiment and tracking in the order of (10 – 40)%. An imperfection of the model is that the space charge induced tune shift with its strong amplitude dependence has been omitted. This contribution causes a 20% change to the values due to the sextupoles, but

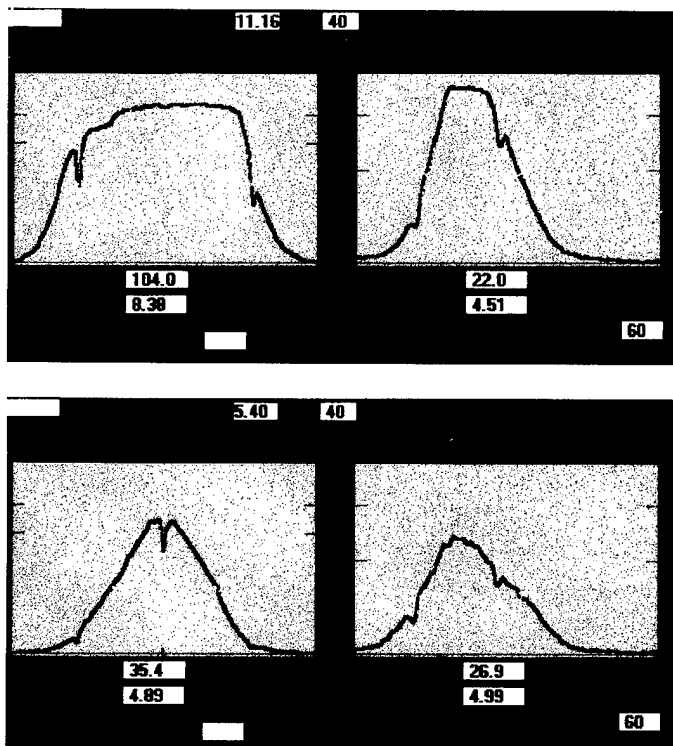


Figure 2. Evolution of Beam Size in HERA after the Beam has been kicked horizontally. The foot width of the beam profiles is interpreted as the projection of the dynamic aperture onto the horizontal and vertical planes respectively. The first profiles are recorded immediately after the kick. The second one is recorded after 8 minutes. The full scale is 36mm .

it cannot be observed by a coherent oscillation of the beam. This additional tune shift with amplitude is strong enough to explain the remaining discrepancies.

What is more striking is the result from a tune modulation experiment. The compensation of existing tune modulation in the order of 10^{-4} by an external source was a big success in beam-beam operation of HERA p at large energies [18]. Background rates could be reduced by a factor of two. Tracking calculations as well as analytic calculations [17] predict that the dynamic aperture is strongly influenced by a tune modulation of depth 10^{-2} with frequencies of $50H_z$ and its multiples. The experimental result is that there is no influence of either adding a tune modulation of 10^{-3} or compensating the existing tune shift of $3 \cdot 10^{-4}$. A possible reason for this result are the 600 chopper power supplies of HERA which were operated at frequencies around 13kHz very close to the betatron tunes. This produced a large level of coherent excitation and emittance growth which overlayed the nonlinear quasi diffusion. After the chopper frequencies have been changed to 16kHz , the level of coherent excitation was reduced by 20db and the emittance growth is reduced by a factor of at least two. Further measurements are planned to clarify the open questions.

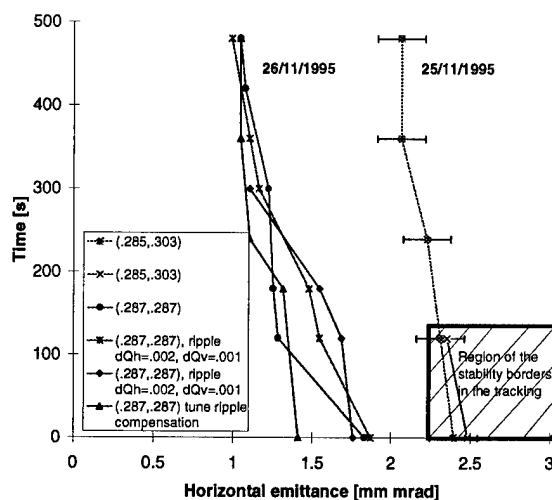


Figure 3. Horizontal Dynamic Aperture of HERA at Injection Energy Derived from Beam Profile Measurements. The box indicates the stability borders obtained by tracking calculations for small variations of closed orbit, ripple and strength of persistent current sextupoles.

V. CONCLUSION

The short term dynamic aperture in experiments with strong, controlled non-linearities is usually well explained by tracking. Good progress has been made in explaining long term effects such as quasi-diffusion and beam life time qualitatively. There are examples for quantitative agreement between experiment and calculations. The dynamic aperture in accelerators under normal conditions agrees reasonably well with predictions if the model is prepared carefully and the experimental conditions are well enough known. There are no results which force the assumption of any yet unknown physics. Discrepancies occur if the modeling of the accelerator and the relevant physics are imperfect.

References

- [1] L. Evans, J. Gareyte, A. Hilaire, W. Scandale, L. Vos, *The Nonlinear Dynamic Aperture Experiment in the SPS* Proceedings of the 1988 European Particle Accelerator Conference, Rome (1988), CERN SPS/88-22(1988)
- [2] J. Gareyte, *Effect of Sextupoles on the Single Particle Dynamics in the CERN SPS*, CERN SPS/88-45(1988)
- [3] R. Gerig, *Main Ring Dynamic Aperture Studies*, FNAL EXP-164 (1989)
- [4] R.E. Gerig L. Michelotti, Y. Chao *Modeling the Behaviour of the FERMILAB Main Ring*, Proceedings of the 1989 Particle Accelerator Conference, Chicago (1989), p 1277-1279
- [5] J. Gareyte, A. Hilaire, F. Schmidt, *Dynamic Aperture and Long Term Particle Stability in the Presence of Strong Sextupoles in the SPS*, Proceedings of the 1989 IEEE Particle Accelerator Conference, Chicago(1989), CERN SPS/89-2(1989)

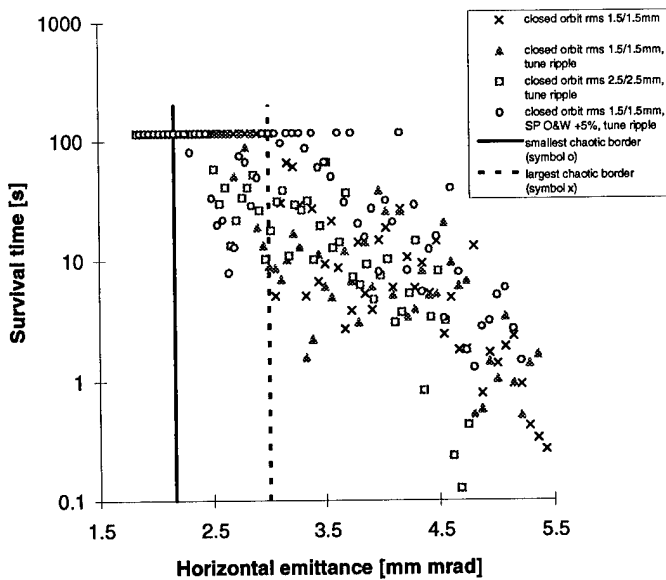


Figure 4. Tracking results for the HERA dynamic aperture studies for small variations of closed orbit, strength of persistent currents and tune modulation. Shown are the survival times in seconds as a function of initial amplitudes. Maximum stable amplitudes for long term tracking agree well with the stability border determined using the Lyapunov method. Tune modulations and variation of sextupole strength have a noticeable influence on the dynamic aperture whereas closed orbit errors are not as important.

[6] L. Merminga et al, *Nonlinear Dynamics Experiments in the TEVATRON*, Proceedings of the 1989 IEEE Particle Accelerator Conference, Chicago (1989), p 1429

[7] L. Merminga, *E778: The Experiment, Basic Results*, Fermilab internal Review of the E778 Experiment 3-16-89 (1989), unpublished

[8] D.A. Edwards and M. J. Syphers, *Review of Beam Dynamics Experiments and Issues in Large Colliders*, Proceedings of the 1989 IEEE Particle Accelerator Conference, Chicago (1989) Vol 3, p 1414-1416

[9] D. Brandt et al, *Influence of Power Supply Ripple on the Dynamic Aperture of the SPS in the Presence of Strong Nonlinear Fields*, Proceedings of the European Particle Accelerator Conference, Nice (1990) Vol 2, p 1438-1440

[10] J. Gareyte, W. Scandale and F. Schmidt, *Review of the Dynamic Aperture Experiment at the CERN SPS*, Proceedings of the Workshop on Nonlinear Problems in Accelerator Physics, Berlin (1992), Inst. Phys. Conf. Ser No 131,

[11] T. Satogata et al, *Driven Response of a Trapped Particle Beam*, Physical Review Letters Vol 68, Number 12, (1992), p 1838-1841

[12] F. Fischer et al, *Recent Results from the Aperture Experiment at the SPS*, Proceedings of the 1993 IEEE Particle Accelerator Conference, Washington D.C. (1993) Vol 3, p246-248

[13] W. Fischer, M. Giovannozzi and F. Schmidt, *Detailed Comparison of Experimental Observations and Computer Tracking for the SPS Dynamic Aperture Experiment*, Pro-

ceedings of the European Particle Accelerator Conference, London (1994) Vol 2, p 950-952

[14] O. Brüning, B. Holzer, W. Fischer, F. Schmidt and F. Willeke, *A Comparison of Measured and Calculated Dynamic Aperture of the HERA Proton Ring at Injection Energy*, DESY-HERA-05-95 (1995)

[15] W. Fischer and F. Schmidt, *Long Term Stability of Chaotic Particles in Hadron Colliders in Simulation and Experiment*, Proceedings of the Workshop on Nonlinear Dynamics, Arcidosso(1994)

[16] F. Schmidt, F. Willeke, F. Zimmermann, *Comparison of Methods to Prove Long Term Stability in Proton Storage Rings*, DESY HERA 91-07(1991), CERN/SL/91-14(AP)

[17] F. Zimmermann, *Comparison of Calculated with Measured Dynamic Aperture*, SLAC-PUB-6504 (June 1994), Proc. of the EPAC94, London (1994) p 327-331

[18] O. Brüning and F. Willeke, this conference

ION EFFECTS IN FUTURE CIRCULAR AND LINEAR ACCELERATORS*

T. O. Raubenheimer

Stanford Linear Accelerator Center, Stanford University, Stanford, CA, 94309

Abstract

In this paper, we discuss ion effects relevant to future storage rings and linear colliders. We first review the conventional ion effects observed in present storage rings and then discuss how these effects will differ in the next generation of rings and linacs. These future accelerators operate in a new regime because of the high current long bunch trains and the very small transverse beam emittances. Usually, storage rings are designed with ion clearing gaps to prevent ion trapping between bunch trains or beam revolutions. Regardless, ions generated within a *single* bunch train can have significant effects. The same is true in transport lines and linacs, where typical vacuum pressures are relatively high. Amongst other effects, we address the tune spreads due to the ions and the resulting filamentation which can severely limit emittance correction techniques in future linear colliders, the bunch-to-bunch coupling due to the ions which can cause a multi-bunch instability with fast growth rates, and the betatron coupling and beam halo creation which limit the vertical emittance and beam lifetimes.

I. INTRODUCTION

Ions are recognized as a potential limitation in electron storage rings where ions generated by beam-gas collisions can become trapped in the negative potential of the beam. The ion density in the beam increases until it is stabilized by neutralization of the beam potential, second ionization, or heating by beam-gas collisions. These trapped ions are observed to cause beam emittance increases, betatron tune shifts and a broadening of the tunes, collective instabilities, and lifetime reductions.

Future storage rings typically have high beam currents and small beam emittances, increasing the deleterious effects of the ions. To avoid ion trapping, most future electron storage rings are designed to include a "gap" in the bunch train. The ions, which are strongly focused by the closely spaced bunches, are over-focused in the gap. The ions become mismatched to the beam and begin executing large amplitude oscillations. Although the ions are still trapped in the negative potential of the beam, because the beam-ion force is very nonlinear, the ion phase space density filaments and becomes irrevocably diluted. Thus the ion density decreases and the ions form a diffuse halo around the beam which does not affect the dynamics.

With a sufficiently large gap, ions are not usually thought to be a limitation. But, many of the future accelerators operate in a new regime with high current, long bunch trains and very small transverse beam emittances. In this case, ions generated and trapped within a *single* bunch train, or, in some cases, within a single bunch, can have significant effects. This is true in transport lines and linacs, where typical vacuum pressures are rela-

tively high, as well as storage rings. It also can be true when free electrons are trapped within a positron bunch.

In the next sections, we will first discuss the relevant ionization processes and then we will describe a few of the important effects. We will consider effects in five colliders that are presently being designed: the PEP-II High Energy Ring for the SLAC B-factory [1], a damping ring [2] for the NLC [3], a future linear collider, and the pre- and main linacs in the NLC for both the NLC-I design (500 GeV center-of-mass) and NLC-II (1 TeV center-of-mass); parameters of the designs are listed in Table 1.

II. IONIZATION AND TRAPPING

In a linac, there are two primary ways in which an ion can be created: collisional ionization and tunneling ionization due to the collective electric field of a bunch. In a storage ring, the tunneling ionization is rarely significant but there are two additional processes due to the synchrotron radiation: photoionization of the residual gas and photoelectrons from the vacuum chamber surface. We will discuss each of these processes in turn.

The cross section for the collisional ionization can be expressed as [4]:

$$\sigma = 4\pi \left(\frac{\hbar}{mc} \right)^2 \beta^2 (C_1 + 2C_2(\ln \beta\gamma - \frac{1}{2})) \quad (1)$$

where C_1 and C_2 depend upon properties of the gas. For CO, a common component of the vacuum, $C_1 = 35$ and $C_2 = 3.7$ and, in the energy range of interest, $\gamma \sim 10^3 \rightarrow 10^6$ and $\sigma_{CO} \sim 1.6 \rightarrow 2.5$ Mbarnes.

In a single bunch, the collisional ionization does not tend to generate significant ion densities. But, the ions are trapped by the bunched beams and significant ion densities can be accumulated along the length of the bunch train, provided that the ions are not over-focused and dispersed between bunches. The condition for trapping is basically the same as that for linear stability in a storage ring [5]:

$$A_{trap} \geq \frac{Nr_p \Delta L}{2\sigma_y(\sigma_x + \sigma_y)} \quad (2)$$

where N is the bunch population, r_p is the classical proton radius, ΔL is the separation between bunches, $\sigma_{x,y}$ are the rms beam sizes, and A_{trap} is the minimum atomic mass that is trapped. Values of A_{trap} are listed in Table 1 for the different designs; the first four designs have significant trapping.

Another method of ion generation is field ionization where the collective electric field of the bunch ionizes the atom or molecule. Field ionization can be divided into two regimes depending upon the strength and temporal duration of the field. In most cases of interest, the field is sufficiently strong and the bunch is sufficiently long that the ionization arises from tunneling ionization. In the notation of Ref. [6], $\gamma \equiv$

*Work supported by the Department of Energy, contracts DE-AC03-76SF00515.

Table 1. Storage Ring and Linac Parameters

	PEP-II HER	NLC DR	NLC-I pre-linac	NLC-I linac	NLC-II linac
Particles/Bunch N [10^{10}]	2.7	0.65	0.65	0.65	1.3
Initial Energy E_0 [GeV]	9	2	2	10	10
β_0 [m]	15	2	13	8	8
$\gamma\epsilon_x$ [10^{-6} m-rad]	850	3	3	5	5
$\gamma\epsilon_y$ [10^{-6} m-rad]	34	0.03	0.03	0.05	0.05
σ_z [mm]	10	4	0.5	0.1	0.1
Bunches n_b	1658	90	90	90	90
Bunch Separation ΔL [m]	1.26	0.42	0.42	0.42	0.42
A_{trap}	0.1	14	2 at 2 GeV 10 at 10 GeV	10 at 10 GeV 50 at 250 GeV	20 at 10 GeV 140 at 500 GeV
$\hat{\mathcal{E}}$ [eV/Å]	0.0003	0.007	0.02 at 2 GeV 0.05 at 10 GeV	0.5 at 10 GeV 1.1 at 250 GeV	1.1 at 10 GeV 2.9 at 500 GeV

$c\sqrt{2m_e E_{ion}}/\sigma_z e\mathcal{E} \ll 1$ where \mathcal{E} is the electric field of the bunch and E_{ion} is the ionization energy.

In the tunneling regime, the transition rate for ionization is approximately [7]:

$$W = 8 \frac{\alpha^3 c E_{ion}}{\lambda_c^2 e\mathcal{E}} \exp\left[-\frac{4}{3} \frac{\alpha}{\lambda_c} \frac{E_{ion}}{e\mathcal{E}}\right] [\text{sec}^{-1}] \quad (3)$$

Because of the exponential factor, this process is very sensitive to the electric field. For example, the time to ionize CO in a 2.9 V/Å electric field is roughly 7 femtoseconds (the static electric field approximation is valid in this case). But, in a field of 1.5 V/Å, the ionization time is roughly 40 picoseconds and there is negligible probability of ionization by a bunch.

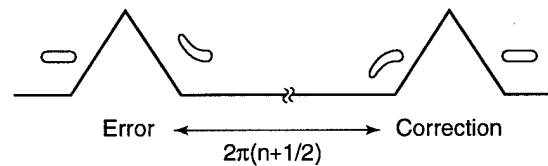
Peak electric fields in the bunches are listed in Table 1. There is no tunneling ionization in the first four designs. However, in the last design, the surrounding gas, within roughly $\pm 2\sigma_{x,y}$ of the beam center, is fully ionized at the end of the linac. There will also be significant tunneling ionization in the collimation, arc, and final focus regions of both the NLC-I and NLC-II designs. In general, trapping is not important where the fields are strong enough for tunneling ionization. Furthermore, because the ions are over-focused and the gas does not fully re-populate between bunches, the ion densities in the trailing bunches will be much lower than that in the leading bunch.

In a storage ring the synchrotron radiation will also ionize the residual gas, forming a swath of ions between the beam and the vacuum chamber wall. In the PEP-II rings and the NLC damping ring, this process yields roughly an order of magnitude more ions than does the collisional ionization. Fortunately, the density of these ions is very low; they will form a halo around the beam without having a significant effect on the beam dynamics.

Finally, the synchrotron radiation will also generate many orders of magnitude more photoelectrons at the chamber wall than ions. These photoelectrons will be accelerated towards the core of a positron beam and may provide a significant coupling between bunches [8].

III. BEAM DYNAMICS

No Filamentation



With Filamentation

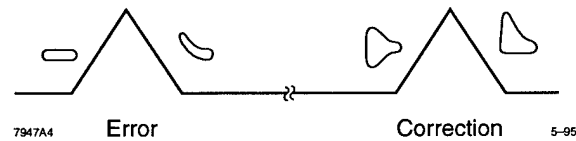


Figure 1. Schematic of emittance correction with and without filamentation (from Ref. [11]).

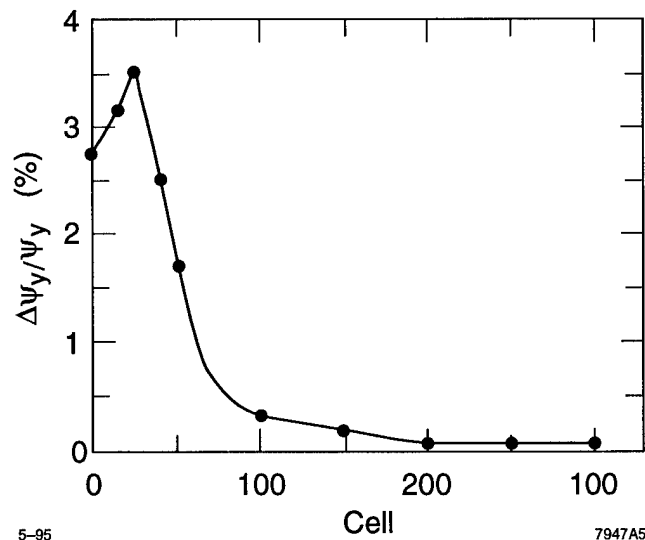


Figure 2. Fraction change in vertical focusing at the end of the bunch train in the NLC-I linac with 1×10^{-8} Torr of CO gas; the linac consists of roughly 300 FODO cells whose length is initially 8 meters and increases to roughly 40 meters by the end of the linac.

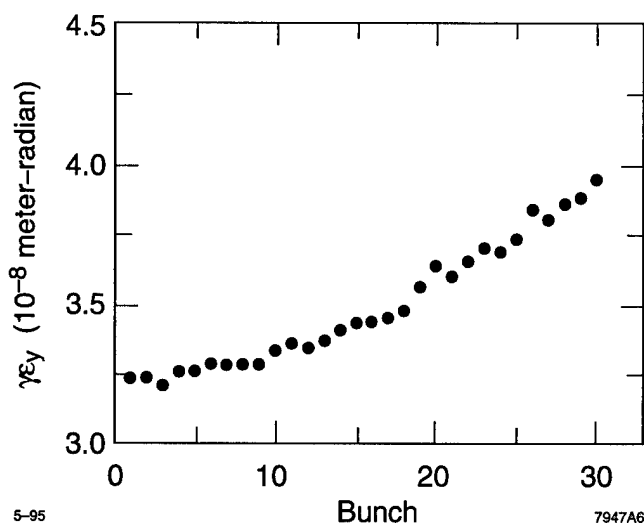


Figure 3. Simulation of emittance correction in the NLC-I pre-linac with a shortened bunch train of 30 bunches and a vacuum pressure of 3×10^{-8} Torr of CO gas; because the ions are trapped, this is equivalent to a vacuum pressure of 1×10^{-8} Torr and a train of 90 bunches.

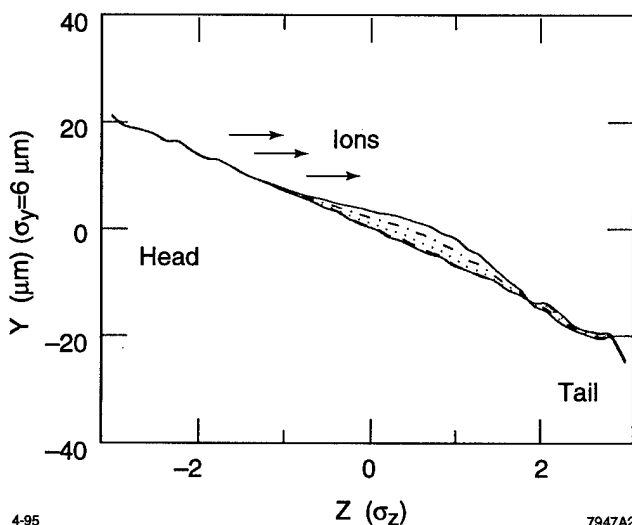


Figure 4. Simulation of electron beam injected with a linear y - z correlation after 0 m (solid), 300 m (dashes), 600 m (dots), 900 m (dash-dot), and 1200 m (solid), in the SLC arc with a vacuum pressure of 3×10^{-4} Torr.

A. Focusing Variation

In a long train of bunches where ions are trapped, the ion density increases linearly along the length of the train. Similarly, in a very dense electron bunch with tunneling ionization, the free electrons are expelled promptly and there is a significant variation of focusing along the bunch due to the increasing ion density.

In a storage ring, the variation in focusing will cause the coherent and incoherent tunes to vary from bunch to bunch. This will provide a Landau damping mechanism for transverse coupled bunch instabilities and could be advantageous.

In a linac, non-local emittance correction has been described as a method of easing the alignment tolerances in future linear

colliders [9] and is being utilized in the Stanford Linear Collider. Unfortunately, the variation in focusing will cause the mismatches and emittance dilutions to filament (phase mix). This has implications for non-local correction of the transverse emittance dilutions as is illustrated schematically in Fig. 1; the filamentation due to the ions will significantly reduce the effectiveness of the correction techniques.

An example of the increased focusing in the NLC-I linac is shown in Fig. 2. With a partial pressure 10^{-8} Torr of CO gas, the vertical focusing is increased by roughly 3% by the end of the bunch train in the beginning of the NLC-I linac. The ion focusing increases as the beam sizes decrease due to the adiabatic damping during acceleration, but, once the ions are over-focused between bunches, the focusing decreases rapidly. In addition, a simulation from the NLC-I pre-linac with emittance correction is shown in Fig. 3. Here, dispersive and wakefield emittance dilutions, introduced by $40 \mu\text{m}$ random Beam Position Monitor (BPM) misalignments, increased the emittance by roughly 100%. Non-local emittance correction was able to reduce the dilution to roughly 10% at the head of the bunch train but was much less effective at the end of the train.

Another effect, related to the variation in focusing, arises if the bunch has a correlation between transverse and longitudinal position such as that due to transverse wakefields or a correlated energy spread and dispersion. In this case, the ions generated by the head of the bunch deflect the tail of the bunch, reducing the offset, but also making it extremely difficult to remove the correlation at a later time. This effect sets a limit on the vacuum pressure in the SLC arcs [10] and will be significant in future colliders with tunneling ionization such as the arcs and final focus of the NLC. The effect is illustrated in Fig. 4 which is a simulation of an electron beam in the SLC arc.

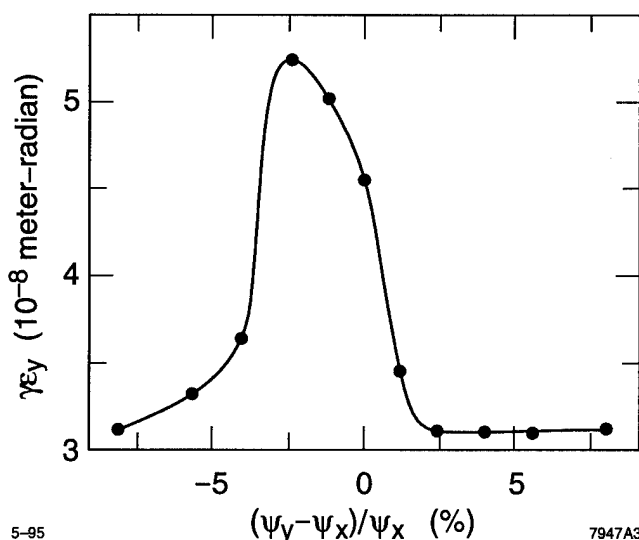


Figure 5. Emittance of the last bunch in the train versus difference between horizontal and vertical focusing in NLC-I pre-linac. This shows the effect of betatron coupling resonance; note that the resonance peak occurs for stronger horizontal focusing because of the additional vertical focusing due to the ions (from Ref. [11]).

B. Nonlinear Resonances and Betatron Coupling

Because the trapped particle distributions are not uniform, they will generate nonlinear electric fields which can drive nonlinear resonances. Assuming a symmetric nonuniform distribution, the lowest order effect is an octupole like coupling resonance driven by the trapped particles. In a flat beam, this can cause an increase in the vertical emittance. The effect has been analyzed for linacs using a simple parametric resonator model [11] and a more complicated analysis has been performed for storage rings [12]; it should be noted that this coupling is very similar to the space charge induced coupling treated in Ref. [13] more than 25 years ago. Finally, Fig. 5 shows results from simulations of the NLC pre-linac. It is straightforward to control the emittance growth by separating the horizontal and vertical phase advances, although higher order resonances can still be important, as discussed subsequently.

In addition to the coupling, the strong nonlinear fields can lead to formation of a beam halo where high order resonances transport particles to large amplitudes. Similar effects are being studied with space charge dominated proton beams [14][15]. Beam halos will lead to a decreased lifetime in a storage ring and cause detector backgrounds in a linear collider.

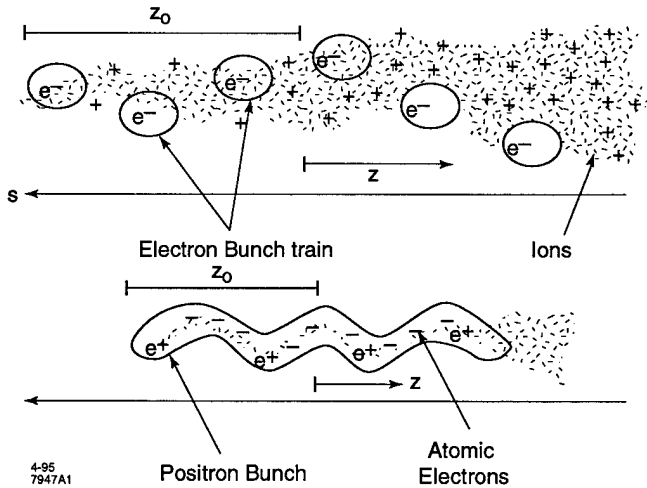


Figure 6. Schematic of fast beam-ion collective instability which can arise due to ion trapping in a long electron bunch train or trapping of free electrons in a positron bunch.

C. Collective Instabilities

Finally, the trapped ions and free electrons can drive collective instabilities. One possible effect arises due to the photoelectrons generated at the vacuum chamber in a positron storage ring. As mentioned, a large number of photoelectrons are created by the synchrotron radiation. These free electrons are accelerated towards the positron beam and can provide a coupling between the bunches. This effect is believed to be the source of a coupled bunch instability observed in the KEK Photon Factory and is described in Ref. [8]; it is presently being evaluated for the PEP-II Low Energy Ring and the NLC positron damping rings.

Another coupled bunch instability can be caused by particles trapped within the beams. The particles oscillate within the potential of the beam and can modulate the transverse beam posi-

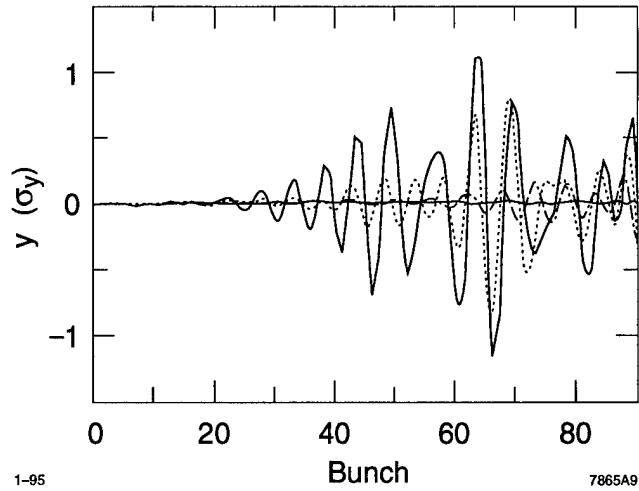


Figure 7. Position of vertical centroids along the electron bunch train after being stored for 0 μ s (solid), 0.67 μ s (dashes), 1.3 μ s (dots), and 2 μ s (solid) in the NLC Damping Ring with a vacuum of 10^{-7} Torr of CO gas; note that the modulation of the electrons goes to roughly σ_y after 2 μ s (from Ref. [16]).

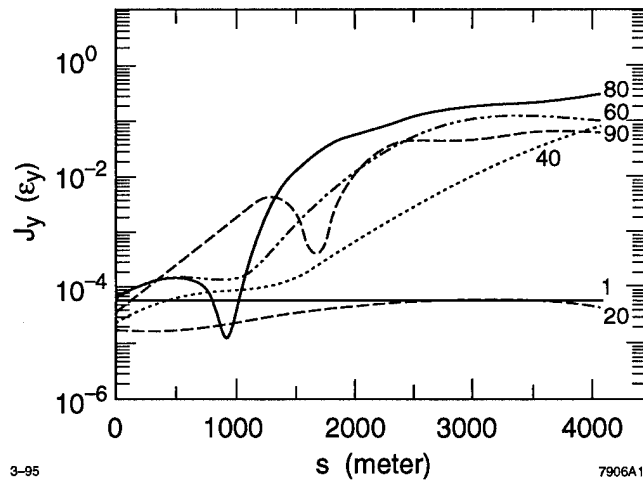


Figure 8. Growth of the action of the vertical centroid for every twentieth bunch in the NLC Damping Ring for a vacuum of 10^{-8} Torr of CO gas; note that the growth saturates at roughly σ_y because of the nonlinearity of the beam-ion force (from Ref. [18]).

tion. The modulation then resonantly drives the trapped particles and exponential growth results. This instability can arise with trapped electrons within a positron bunch or trapped ions within an electron bunch train as is illustrated schematically in Fig. 6.

The nature and analytic treatment of the instability closely resemble the beam break-up instability due to transverse wakefields. It is described in Refs. [16][17] and is summarized in Ref. [18]. The results of macro-particle simulations from the NLC damping ring are shown in Figs. 7 and 8. Because of the high bunch train charge and the very small beam emittances the instability has a very fast growth rate; with a CO partial pressure of 10^{-8} Torr, the bunches are offset by roughly σ_y after 7 μ s. The instability could be a limitation in future linear colliders as well as the SLAC and KEK [19] B-factories. Because the instability growth depends quadratically on the length of the bunch train, the most straightforward solution is to add additional gaps

to the train. Unfortunately, this will not reduce the instability due to free electrons created by tunneling ionization in a positron bunch.

Experiments are being planned to observe this instability at third generation light sources as well as at the Stanford Linear Collider and KEK TRISTAN Accumulator Ring. Finally, this instability is similar to the ion hose instability observed in ion focused high current induction linacs and a similar effect has been seen in the Los Alamos Proton Storage Ring (PSR) where it is believed that the proton beam traps field emission electrons; measurements from the PSR are described in Ref. [20] and the results of simulations are described in Ref. [21].

IV. SUMMARY

We have discussed three effects of trapped particles in future storage rings and linear colliders. Significant ion densities can occur in either a long train of bunches due to collisional ionization and trapping or in very dense bunches due to the tunneling ionization. These ions will cause filamentation, transverse coupling, beam halos, and will drive collective instabilities. These effects arise within the passage of a single train of bunches or, in some cases, in the passage of a single bunch. They arise in storage rings, linacs, and transport lines, and will limit the operation, as well as the acceptable vacuum, in future accelerators.

References

- [1] PEP-II: An Asymmetric B Factory Conceptual Design Report, SLAC-418 (1993).
- [2] T. O. Raubenheimer, et. al., "A Damping Ring Design for the SLAC Next Linear Collider," these proceedings.
- [3] T. O. Raubenheimer, et. al., "Parameters of the SLAC Next Linear Collider," these proceedings.
- [4] F. F. Rieke and W. Prepejchal, "Ionization cross sections of gaseous atoms and molecules for high energy electrons and positrons," *Phys. Rev. A*, **6**: (1972).
- [5] For example see: Y. Baconnier, "Neutralization of accelerator beams by ionization of the residual gas," *Proc. of the 1984 CERN Acc. School*, CERN 85-19 (1985).
- [6] L. V. Keldysh, "Ionization in the Field of a Strong Electromagnetic Wave," *J. Exp. Theor. Phys.*, **47**: 1945 (1965).
- [7] L. D. Landau and E. M. Lifshitz, *Quantum Mechanics: Non-Relativistic Theory*, Pergamon Press (1981).
- [8] K. Ohmi, "Beam and Photoelectron Interactions in Positron Storage Rings," *Submitted to Phys. Rev. Lett.*; KEK-PREPRINT-94-198 (1995).
- [9] T. O. Raubenheimer, "The Preservation of Low Emittance Flat Beams," *Proc. of the 1993 IEEE Part. Acc. Conf.*, Washington D.C. p. 11 (1993).
- [10] P. Emma, T. O. Raubenheimer, F. Zimmermann, "Emittance Dilution by Ions in the SLC Arcs," *Proc. of the Fourth European Particle Acc. Conf.* London, England (1994).
- [11] T. O. Raubenheimer and Pisin Chen, "Ions in the Linacs of Future Linear Colliders," *Proc. of the 1992 Linac Conf.*, Ottawa, Canada, p. 630 (1992).
- [12] P. F. Tavares, "Ion Trapping in Electron Storage Rings," Ph.D. Thesis, University of Campinas (1993).
- [13] B. W. Montague, "Fourth-Order Coupling Resonance Excited by Space Charge Forces in a Synchrotron," CERN 68-38 (1968).
- [14] R. A. Jameson, "Design for Low Beam Loss in Accelerators for Intense Neutron Source Applications," *Proc. 1993 IEEE Part. Acc. Conf.*, Washington, D.C., p. 3926 (1993).
- [15] J. S. O'Connell, et. al., "Beam Halo Formation from Space-Charge Dominated Beams in Uniform Focusing Channels," *Proc. 1993 IEEE Part. Acc. Conf.*, Washington, D.C., p. 3657 (1993).
- [16] T. O. Raubenheimer and F. Zimmermann, "A Fast Beam-Ion Instability in Linear Accelerators and Storage Rings," *Submitted to Phys. Rev. E*, (1995).
- [17] G. Stupakov, T. O. Raubenheimer and F. Zimmermann, "Effect of Ion Decoherence in Fast Beam-Ion Instability," *Submitted to Phys. Rev. E*, (1995).
- [18] F. Zimmermann, T. O. Raubenheimer and G. Stupakov, "A Fast Beam-Ion Instability," these proceedings.
- [19] K. Yokoya, private communication.
- [20] T. Wang, et. al., "Recent Progress on Beam Stability Study in the PSR," these proceedings.
- [21] T. Wang, "Theoretical Study of the Electron-Proton Instability in a Long Proton Pulse," these proceedings.

Nonlinear Wave Phenomena in Coasting Beams

P. L. Colestock, L. K. Spentzouris and F. Ostiguy
Fermi National Accelerator Laboratory[†]
P. O. Box 500, Batavia, IL 60510, USA

Abstract

In beams which are sufficiently close to the linear stability limit, a variety of nonlinear wave phenomena are readily observed which can be used to diagnose aspects of the beam dynamics and the machine impedance. We have found that debunched beams in both the Fermilab Main Ring and the Tevatron are marginally stable to longitudinal oscillations and exhibit nonlinear three-wave coupling as well as nonlinear Landau damping and the formation of soliton-like perturbations. In addition, we have generated classical nonlinear echoes using two-frequency excitation in the Fermilab Accumulator. These phenomena can be used as diagnostic tools to determine diffusion rates in the beam as well as the longitudinal impedance. Moreover, aspects of these effects are likely involved in the approach to equilibrium as a longitudinal instability saturates under the influence of a driving impedance. We present experimental results and analytical models based on perturbation techniques. In addition, we describe particle simulations which model the fully nonlinear evolution of these phenomena.

1 Introduction

In recent years, growing attention has been given to the issue of increasing beam intensity in Fermilab's synchrotrons. However, as these machines have been pushed to operate near their stability limits, they have been observed to be operating under marginally stable conditions.[1] A variety of unstable modes have been identified and suppressed to some degree, however there exists a background level of fluctuations under nominally quiescent conditions whose origins have not been well understood.

To shed further light on these phenomena, an investigation has been underway to determine the driving causes and saturation mechanisms associated with potential instabilities in Fermilab machines using a variety of methods including the well-known beam transfer function technique [2]. In this procedure, an externally-applied sinusoidal voltage is impressed on the beam and the response is monitored with a wall current pickup elsewhere in the ring. The magnitude and phase of the response

is a measure of the beam distribution function and the machine impedance at the excited frequency. For ease of analysis, our efforts have been focussed on the study of longitudinal oscillations in an initially fully debunched beam.

However, under certain conditions, beam transfer function measurements have exhibited nonlinear behavior, indicating a rich variety of wave phenomena not normally considered in the beam transfer function model. In fact, the ease with which these phenomena can be made to occur suggests a ubiquitous presence in any beams which are driven near their stability limits. Moreover, in the course of this study, we have rediscovered a weakly nonlinear coupling phenomenon which has been investigated in other fields, but has not yet been exploited in high energy synchrotrons: beam echoes. Echo phenomena carry the potential as a very useful diagnostic of weak diffusion phenomena in the beam.

In this work we first describe the beam transfer function technique in the context of the Fermilab machines in which these measurements were made. Then we outline a series of experiments carried out to clarify the nature of the observed mode-mode coupling. Next, we describe the observations of longitudinal beam echoes and give an explanation of these phenomena in terms of a weakly-nonlinear mode coupling model. Finally, we report the results of particle simulations which were undertaken to describe the fully nonlinear evolution of the mode coupling. In particular, we wish to shed light on how the beam emittance is affected by the presence of coherent fluctuations and the manner in which an equilibrium state is approached.

2 Experimental Results

In both the Fermilab Main Ring and Tevatron, attempts at measuring beam transfer functions have led to rather complex results[1]. Regarding measurements in the Main Ring, a 5 MHz resonant cavity with a Q of 42 was used as a kicker. In this case, the beam transfer function showed the presence of notches in the response function which presumably correspond to depletion zones in the momentum distribution. In the response, each notch represents a narrow-band resonance which adds a degree of freedom to the longitudinal mode structure. Further investigation showed that the momentum location of the notches was tied to the betatron tune settings in the machine, which implies

[†] Operated by the Universities Research Association, Inc, under contract with the U.S. Department of Energy

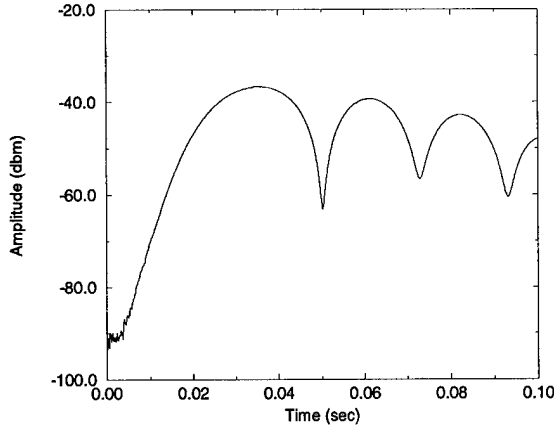


Figure 1: Oscillation of the drive amplitude following a 0.5 msec burst of rf at the $h=106$ harmonic. The current envelope suggests phase rotation.

the notches are the result of transverse resonances which deplete momentum space depending on the level of machine chromaticity. This notion was confirmed by changing tune settings, resulting in a systematic movement of the momentum notches. As a result of these notches, it is expected that the linear stability boundary for longitudinal oscillations is radically altered. In particular, a typical momentum width of a notch was found to be 5% or less of the full momentum spread. The Keil-Schnell stability criterion [3] suggests that such a notch would reduce the stability threshold by over two orders of magnitude.

In an attempt to assess stability in this case, the full spectral response over several revolution harmonics was measured. However, it was found that the response in the Main Ring was significantly nonlinear with no apparent intensity threshold. (Similar results have been previously reported for high intensity coasting beams in the Tevatron albeit with a well-defined threshold condition[4]). A key feature in the response is the observed tendency of the drive frequency to couple primarily downward in frequency. In fact, the coupling to the sidebands was observed to produce a regular cascade to increasingly lower frequencies. In order to further clarify these phenomena, a series of experiments in the time domain was carried out where the kicker cavity was excited for a short period of time, approximately 0.5 msec, using a fast rf gate. It is worthwhile to note that the 5 MHz cavity fields decay in 0.01 msec. The response at the first lower sideband, shown in Fig. 1 shows a characteristic oscillation of the beam current envelope following the excitation pulse suggestive of phase rotation. In addition, lower sidebands showed the same response after a delay proportional to the harmonic spacing relative to the drive frequency. The observed time delay suggests a clear causal relationship in the flow of power from higher harmonics to lower ones and implies that the coupling occurs predominantly across one harmonic at a time. Of note here is the fact that the peak response occurs several harmonics distant from the drive fre-

quency. This characteristic is intrinsic to the beam response and is not a function of the applied power.

3 Parametric Coupling Model

These phenomena are characteristic of classical three-wave, or parametric, coupling which has been studied extensively in plasma physics[5]. Both the single-sided character of the frequency response and the depletion of the pump frequency are well-known effects in this type of resonant coupling. Unique to the beam case is the fact that there exists an infinite collection of longitudinal modes, and hence potential daughter waves, in this periodic system.

The conditions for longitudinal mode coupling can be obtained from the Vlasov equation by a perturbation approach wherein mode-mixing terms are retained in the expansion of the distribution function. Conservation of energy leads to the frequency matching condition, $\omega_n + \omega_k = \omega_m$. If the frequency of the driving wave is Ω_0 , then $\omega_n + \Omega_0 = \omega_m$ must be obeyed in order to have energy transferred into a pair of longitudinal modes. This condition ensures that coupling occurs only downward in frequency. The dispersion relation for parametric coupling of three waves can be shown to be[4]:

$$\nu^2 \int \frac{d\epsilon \frac{\partial f_0}{\partial \epsilon}}{(\omega_m - m\gamma)^2} \int \frac{d\epsilon \frac{\partial f_0}{\partial \epsilon}}{(\omega_n - n\gamma)^2} = \left(\frac{e\omega_0}{2\pi}\right) \cdot \int \frac{d\epsilon \frac{\partial f_0}{\partial \epsilon}}{(\omega_n - n\gamma)(\omega_m - m\gamma)^2} \times \int \frac{d\epsilon \frac{\partial f_0}{\partial \epsilon}}{(\omega_m - m\gamma)(\omega_n - n\gamma)^2} \quad (1)$$

where ν is the growth rate and $\gamma = k_0\epsilon$. We note that the left hand side of Eq. 1 represents the product of linear dispersion relations for modes m and n . Thus, the effect of a small driving amplitude is that the coupling threshold must occur close to the linear mode frequencies. Moreover, the threshold for coupling decreases to zero amplitude as the linear stability boundary is approached. The coupling threshold is found to scale as the inverse fourth power of the momentum spread so that coupling is most likely to occur in notches in the distribution function.

In this analytical model, the pump amplitude was held fixed, however it can be expected that the daughter waves will also have a reaction back on the pump. In simple systems, it has been shown that the exchange of energy between parametrically coupled waves reaches a steady state where all the energy oscillates between the various modes [6]. Indeed the pump may become completely depleted by the presence of strongly-coupled daughter waves. Such a process is likely the cause of the enhanced wave amplitudes at lower sidebands relative to the pump amplitude. With few exceptions, however, the case of a large number of multiple harmonics, including dissipation, has not been treated in the literature [6].

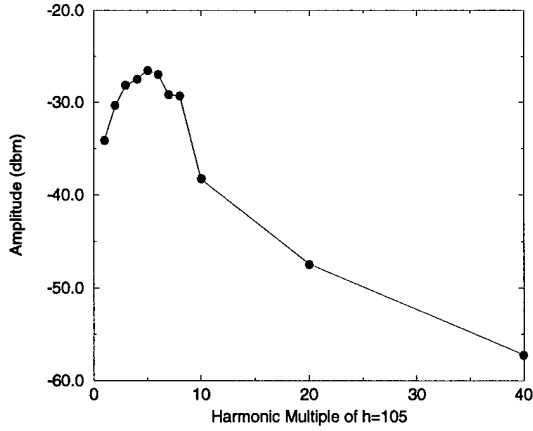


Figure 2: Harmonic spectrum generated in the beam response to impulse excitation at $h=106$. The harmonics shown here are associated with the first lower sideband, $h=105$, excited in the parametric decay.

4 Nonlinear Landau Damping

The oscillatory behavior of the impulse response observed in the Main Ring can be related to a well-known phenomenon in plasma physics known as nonlinear Landau damping[7]. In this process, an initial sinusoidal potential perturbation will cause a portion of the distribution function to become trapped in the potential wells of the wave, namely those particles whose relative energy in the frame moving with the perturbation is sufficiently small. This, of course, causes bunching to occur and the resulting trapped particles will begin to exchange energy coherently with the wave in the form of a rotation in phase space. The steady state condition reached is such that the oscillations of the system decay much more slowly than that expected from simple decoherence through the frequency dispersion of the beam. This is indeed the case, as shown in Fig. 1. Another characteristic of this process is the tendency to generate a rich higher harmonic spectrum as the trapped particles are progressively focussed into tighter and tighter bunches[8]. This feature was also observed, as depicted in Fig. 2. This suggests that wakefields play a role in the evolution of the transient response and we wish to exploit this connection to determine the wakefields themselves.

5 Beam Echoes

One application which arises from the phenomenon of parametric coupling in the time domain is that of beam echoes[9]. Echoes have been found in many other fields[10, 11], but have not yet been applied in the context of synchrotrons, although bunched beam echoes have been investigated theoretically in previous work[12, 13]. The echo phenomenon can be viewed as a nonlinear mixing of two waves propagating in opposite directions around the ring. If a short duration rf excitation is ap-

plied to the beam of the form $\exp(im(\omega_0 + k_0\epsilon)t)$, then the energy dependence of the phase causes the macroscopic perturbation to decay in a Landau damping time. If, however, a second pulse of the form $\exp(-in(\omega_0 + k_0\epsilon)[t - \delta t])$, is applied after a delay δt , by virtue of the amplitude nonlinearity, product perturbations of the form $\exp(i[m - n](\omega_0 + k_0\epsilon)t + in(\omega_0 + k_0\epsilon)\delta t)$, can occur at the difference frequency $(m - n)\omega_0$. These second-order perturbations have the property that the energy dependence can disappear at a $t_E = n/(n - m)\delta t$, which permits the phase-mixing to be undone, resulting in a reconstruction of a portion of the original perturbation.

A complete analysis of this phenomenon for a coasting beam parallels the parametric coupling analysis and leads to an explicit expression for the beam current as an integral over the beam distribution function[9].

$$I_m^{(2)}(t) = imk_0t \left(\frac{e\omega_0}{2\pi}\right)^3 \sum_n \int_{-\infty}^{\infty} d\epsilon \frac{\partial f_0}{\partial \epsilon} \exp(im[\omega_0 + k_0\epsilon]t - in[\omega_0 + k_0\epsilon]\delta t) - \frac{\nu k_0^2 \epsilon_0^2}{3} [m^2 t^3 - n^2 \delta t^3] \quad (2)$$

where n and $n - m$ are the harmonic numbers of the excitation pulses and ν is the longitudinal diffusion coefficient due to scattering or noise. (Wakefield effects have been ignored to simplify the analysis, but may be readily retained). The characteristic echo response is shown in Fig. 3. The first pulse is at the lower harmonic number $n - m$ while the second pulse occurs at harmonic n after a delay δt . At time $t_E = n/(n - m)\delta t$, an echo is observed whose shape is proportional to $\partial f_0 / \partial \epsilon$. If a series of various echo delays are chosen, the amplitude envelope maps out a characteristic shape from which the collision frequency ν can be determined, shown in Fig. 4. Such an experiment was carried out in the Fermilab Antiproton Accumulator yielding a typical momentum diffusion rate of $1/\tau \approx 3hrs^{-1}$, which is consistent with the measured heating rate of the momentum cooling system. Thus it is expected that echo decay can be used to measure very weak diffusion rates in beams.

Once verified, bunched beam echoes hold the promise of permitting measurement of a variety of important diffusion mechanisms, such as beam-beam, intra-beam scattering and noise.

6 Simulations

Simulations of coherent phenomena in coasting beams have been carried out for a number of years and results relevant to our case were first reported in reference 14. The essential physics is contained in the character of the incremental kicks given to the particle's position and energy per turn, relative to the central momentum particle. These may be expressed in the form

$$\delta\theta = -\eta(\epsilon)\epsilon \quad (3)$$

$$\delta\epsilon = \frac{e^2}{(2\pi)^2 E_0} \sum_n e^{in\theta} \int_{-\infty}^{\infty} d\omega Z_{||n}(\omega) e^{-i\omega t} \quad (4)$$

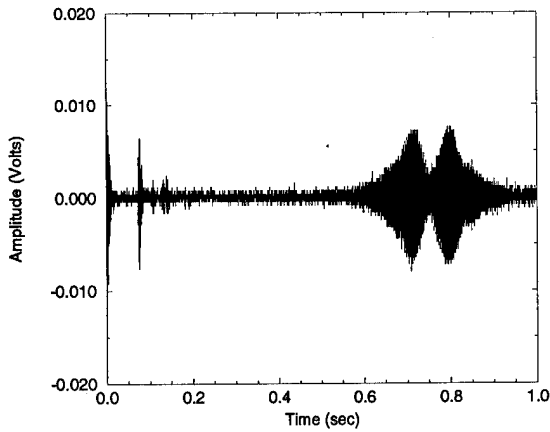


Figure 3: Time evolution of the beam response due to impulse excitation first at $n-m = 9$ followed by $n = 10$ in the Antiproton Accumulator. An echo occurs after a delay $n/(n-m)\delta t$, at the difference harmonic $m = 1$.

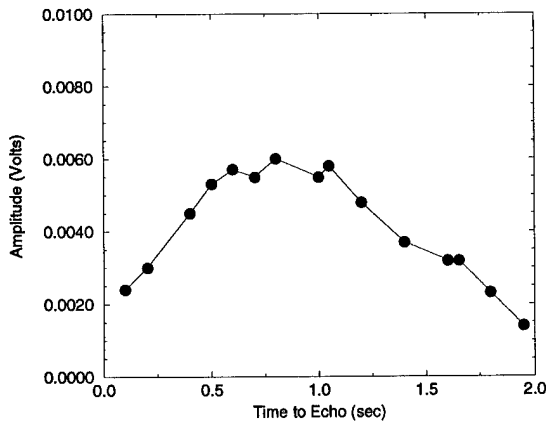


Figure 4: Envelope of the maximum echo amplitude as a function of the applied delay time between excitation pulses. A characteristic decay is observed which depends on weak diffusion processes in the beam.

where $Z_{||}$ is the longitudinal impedance and is the Fourier transform of the wake function given by

$$Z_{||}(\omega) = \int_{-\infty}^{\infty} ds e^{\frac{i\omega}{c}s} W'_0(-s) \quad (5)$$

In our case, only a finite collection of modes play a role and we may considerably reduce computation time by restricting the number of modes included in the wake function. The results for a model impedance at $h=10$ demonstrate the tendency for wave overturning and self-trapping to occur as shown in Fig. 5. A soliton-like structure appears on the low energy side of the distribution function and becomes progressively decelerated in the resulting wakefields. Such behavior has indeed been observed experimentally in the Main Ring[1]. The macroscopic current

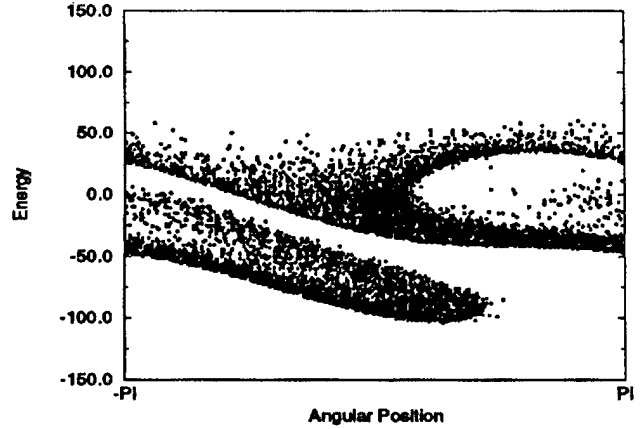


Figure 5: Phase space ($\epsilon-\theta$) diagram of the particle simulation after initial saturation and wave-overturning has taken place. Soliton-like structures have formed on the low energy side of the distribution.

appears to oscillate in a manner similar to that observed in Fig. 1. Each bunch thus formed undergoes further bifurcation until the momentum spread has increased to the point where the beam has become marginally stable. We can associate these effects to the tendency to couple power from the initially unstable frequencies over a wide bandwidth of revolution harmonics which then damp via Landau damping, thereby heating the beam. It is evident from the phase-space pictures that the spectral content shows considerable broadening as the instability approaches saturation.

Simulations have also been used to successfully model the parametric coupling process showing the observed sequential coupling to lower sidebands; moreover, the excitation of echoes has been simulated including the effects of wakefields and diffusion. Work is underway to permit quantitative determination of the machine impedance from the measurements of nonlinear behavior.

7 Summary and Conclusions

We have carried out a series of experiments which have indicated the presence of longitudinal three-wave parametric coupling for beams near marginal stability. The response in the time domain shows a regular causal coupling from high frequency toward lower frequencies, accompanied by wave-overturning and self-trapping of the beam particles.

To explain these effects, we have developed a perturbation model based on the Vlasov equation which explains the single-sided coupling as a manifestation of phase and frequency matching among the coupled modes. In addition, the thresholds for these phenomena are determined by Landau damping rates, which in the case of our observed non-Gaussian distributions, are vanishingly small. In the case of multiple modes, the coupling can proceed as a regular cascade through many harmonics. As such, synchrotrons represent an ideal test bed for studying such coherent phenomena, and the information

can be used, in principle, as a diagnostic to determine machine impedance and other dynamical variables of the device. Work is in progress to quantify the results presented here.

In addition, the phenomenon of beam echoes can be interpreted as a form of parametric coupling and we have observed classic echo formation in our beams. We have derived an expression which relates the observed echo decay to the rate of diffusion in the beam and anticipate that this will become a viable means of characterizing beam diffusion.

Finally, we have invoked a full-particle simulation to study the strongly nonlinear aspects of the mode excitation and saturation. We have identified the onset of nonlinear Landau damping and the formation of soliton-like structures that has been studied in the context of narrow-band instability. We suggest that a form of resonant mode coupling studied here may play a role in the emittance growth of unbunched as well as bunched beams where the coupling occurs among various synchrotron modes. It is also likely that these phenomena are more widespread than previously thought, due in part to the strongly non-Gaussian character of the momentum distribution in our machines.

8 Acknowledgements

The authors would like to acknowledge fruitful discussions with J. Cary, experimental help from G. P. Jackson and S. Asadi and assistance from A. Gerasimov L. Michelotti, J. Holt and J. Beda in carrying out the simulations.

References

- [1] L. K. Spentzouris, P. L. Colestock and F. Ostiguy, this conference
- [2] A. Faltens, E. C. Hartwig, D. Möhl and A. M. Sessler, *8th Int. Conf. on High Energy Accel.*, CERN p 338, (1971).
- [3] E. Keil and W. Schnell, CERN/ISR/TH/RF/ 69-48 (1969)
- [4] P. L. Colestock, G. P. Jackson and L. K. Klamp, *Proc. 3rd Eur. Particle Accelerator Conf*, Berlin, Vol. 1, p. 126 (1992).
- [5] R. Z. Sagdeev, A. A. Galeev, T. M. O'Neil and D. L. Book, *Nonlinear Plasma Theory*, W. A. Benjamin, Inc., New York (1969) and references contained within.
- [6] A. S. Bakai, *Nuclear Fusion*, Vol. 10, p. 53, (1970).
- [7] T. M. O'Neil, *Phys. Fluids*, 8, 12, (1965).
- [8] T. M. O'Neil, J. H. Winfrey and J. H. Malmberg, *Phys. Fluids*, Vol. 14, 6, p. 1204, (1971).
- [9] L. Spentzouris, P. L. Colestock and F. Ostiguy, (submitted for publication).
- [10] E. L. Hahn, *Phys. Rev.*, **80**, 4 (1950).
- [11] R. W. Gould, et. al., *Phys. Rev. Lett.*, **19**, 5, (1967).
- [12] G. V. Stupakov and K. Kauffmann, SSCL-587 (1992).
- [13] N. Mahale, et. al., SSCL-N-817 (1993).
- [14] E. Keil and E. Messerschmid, *Nucl. Inst. and Methods*, Vol. 128, p. 203, (1975).

THE CURE OF MULTIBUNCH INSTABILITIES IN ELETTRA

M. Svandrlík, C. J. Bocchetta, A. Fabris, F. Iazzourene, E. Karantzoulis, R. Nagaoka, C. Pasotti, L. Tosi, R. P. Walker, A. Wrulich, Sincrotrone Trieste, Padriciano 99, 34012 Trieste, Italy

ELETTRA is generally working in a multi-bunch filling mode which gives rise to an instability if a parasitic Higher Order cavity Mode (HOM) is coupled to a multi-bunch oscillation mode. Longitudinal instabilities, even if not destructive, are particular harmful for synchrotron light sources, since they increase the energy variation of the beam and deteriorate in this way the quality of the light spectrum. Multi-bunch instabilities in ELETTRA are cured by tuning the temperatures of the four independent cavities. The effectiveness of the method has been verified by monitoring the spectrum of the SuperESCA beamline. The relation between HOMs and cavity temperature and the variation of this dependence with cavity and machine parameters has been studied. Operational experience and dedicated measurements are presented and compared with theoretical predictions.

I. INTRODUCTION

During operation for users the storage ring is filled in a multibunch mode. Longitudinal Multibunch Instabilities (LMBI) have been studied in ELETTRA already from the beginning of the commissioning and were observed, at injection energy, even at very low currents, i.e. 1 mA. Confirming that LMBI are not destructive, it was possible to store currents as high as 530 mA, and even more, at injection energy (1.0 GeV) [1]. However the expected effects of LMBI on the beam energy variation, on the beam size and stability, and the consequence on the light quality, could be observed.

Beam energy, E	2.0 GeV
Current in normal operation, I_b	200 mA
Nominal RF frequency, f_{RF0}	499.654 MHz
Harmonic number, h	432
Momentum compaction, α	$1.6 \cdot 10^{-3}$
Operating Effective Peak RF voltage, V_{RF}	1.68 MV

Table 1: Relevant ELETTRA parameters.

In case of longitudinal motion the driving source for coupled bunch instabilities is given by the high-Q HOMs of the RF cavities. The instability becomes maximum when a Coupled Bunch Mode (CBM) frequency and a HOM frequency overlap. For small machines like ELETTRA, with high revolution frequency, and for narrow band HOMs it is then possible to tune the HOM away from the CBM frequency and thus reduce the coupling. The experience made during storage ring commissioning shows that the LMBI can be reduced by changing the temperatures of the cavities [2], while changes in the multibunch filling pattern did not bring any improvement. Since ELETTRA cavities are free of damping antennas or loops, a global temperature tuning procedure has been developed.

Transverse Multibunch Instability haven't been observed during machine operation, thus they will not be discussed here.

Dedicated experiments during commissioning showed that temperature tuning is very effective also for them [1].

II. A SYSTEMATIC APPROACH TO TEMPERATURE TUNING OF RF CAVITIES

HOMs' temperature tuning can be effective if the frequencies can be regulated in a wide range and if there is good accuracy in the cavity temperature setting and in the knowledge of the HOM frequency. As it is described in [2], [3], a solution was adopted in the design of the RF cavities for ELETTRA to improve the temperature tuning technique. The high Q, not damped, HOMs' frequency can be shifted by some hundreds of kHz since the cavity temperature can be regulated between 40 and 70 °C. The cavity temperature is stable within ± 0.05 °C. The fundamental mode frequency is kept constant by an external tuning cage.

For a systematic analysis, a pair HOM - CBM can be characterised by a *Critical Temperature*, defined as the cavity temperature for which the frequency of the HOM exactly overlaps the frequency of the CBM, i.e. the coupling is maximised. By calculating this temperature for all harmful HOMs and associating to it the temperature interval where the HOM is strong enough to drive the instability, operating temperature settings for the RF cavities can be found where the coupling HOM-CBM is minimised.

A. The Calculation of the Critical Temperature

The critical temperature $T_{ck,n}$ for the longitudinal HOM L_k and the CBM number n is derived in [4], and is equal to

$$T_{ck,n} = \frac{1}{\tau_{Lk}} \left[(f_{pn} - f_{Lk0}) + \left(\frac{N}{h} - \phi_{Lk} \right) (f_{RF} - f_{RF0}) + \phi_{Lk} \Delta f_{BL} \right] + T_0 \quad (1)$$

f_{Lk0} = frequency of L_k measured at T_0 and at f_{RF0} ;

T_0 = cavity temperature when f_{Lk0} is measured;

$f_{pn} = (pM + n + mQ_s)\omega_0/2\pi$: frequency of CBM number n, with p an integer, M number of bunches, m bunch shape mode (here m=1), Q_s synchrotron tune, $\omega_0/2\pi$ the nominal revolution frequency.

N = ph+n;

τ_{Lk} = f_{Lk} change for unitary temperature change;

ϕ_{Lk} = f_{Lk} change if L_0 mode frequency changes by 1.0 KHz

$\Delta f_{BL} = K_{BL0} I_b / V_g$: L_0 mode frequency shift due to the beam loading, typical ~30 kHz.

Table 2: Definitions used in relation (1); see also [3].

The Critical Temperature (1) depends on the RF frequency f_{RF} , on the beam current I_b and, through Q_s , on the energy E and on the RF voltage V_{RF} . Tab. 3 shows typical values of T_c for different I_b , f_{RF} and E for the harmful HOMs of cavity S3.

HOM	f_{Lk}	CBM	E, GeV	1.0	2.0	2.0	2.0
		n	I_b , mA	1.0	1.0	200.0	200.0
	MHz		f_{RF}	499.654	499.654	499.654	499.644
L1	950	389	Tc1,389	57.8	58.2	56.7	57.8
L3	1421	365	Tc3,365	39.0	39.1	40.5	41.7
L4	1514	12	Tc4,12	70.1	70.3	70.6	71.8
L5	1600	87	Tc5,87	64.2	64.3	65.9	67.2
L9	2073	64	Tc9,64	44.2	43.1	45.2	46.3

Table 3: Calculation of Critical Temperatures for different conditions, for cavity S3.

The largest shifts are caused by I_b and f_{RF} . On the base of these shifts forbidden temperature intervals can be found, as shown in fig. 1 for Cavity S3. A 3dB equivalent bandwidth of the resonance is also included in these intervals.

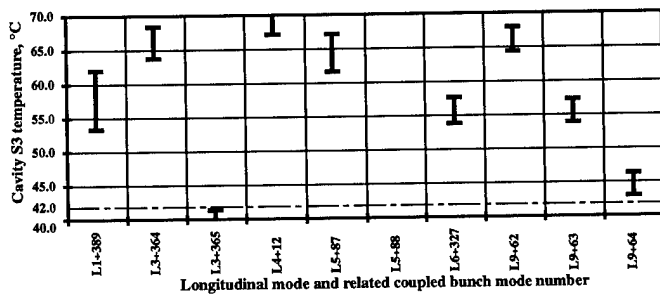


Fig. 1: The forbidden temperature intervals for cavity S3.

The computed values for $T_{ck,n}$ have been verified on the machine. For example, to identify the real value of Tc1,389, at 1.0 GeV a current of 1.0 mA in a uniform filling has been injected and the excitation of the CBM 389 has been measured as a function of cavity S3 temperature. The plot in fig. 2 shows a maximum between 57.6 and 57.9 °C. The computed value in table 3 is 57.8 °C. Also for the other modes a good agreement, with an accuracy of about ± 0.5 °C, was found.

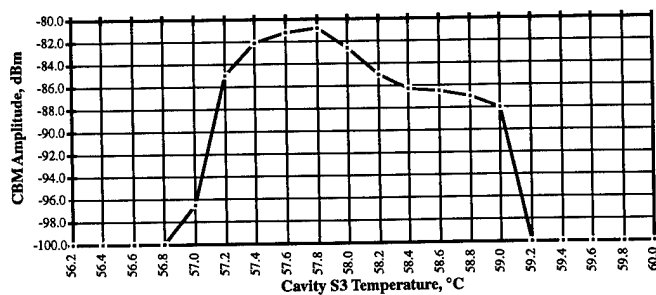


Fig. 2: Measured amplitude of CBM 389 vs. Cavity S3 temp.

There can be a large difference in the critical temperatures for the same pair HOM-CBM among the four cavities, due to the relaxed mechanical tolerances. For example, Tc1,389 is ~ 110 °C for Cavity S2, ~ 65 °C for S8 and ~ 69 °C for S9.

B. Operational Experience

The cavities are normally operated outside the forbidden temperature intervals. Operational experience with currents up to 250 mA at 2.0 GeV shows that this is sufficient to reduce the HOMs' impedance seen at the CB frequency to a value which eliminates the impact of the LMBI. This is not valid for

the mode L1, since the high shunt impedance (851 k Ω) along with the low temperature coefficient ($\tau = -11.5$ kHz/°C) [3] requires a temperature setting far from Tc1,389 to get rid of the instability. Other high shunt impedance modes (L3, L5, L9) have higher τ (40-100 kHz/°C), thus their effect is already cured at a few degrees from Tck,n. The operating temperature for cavity S3 has thus been set around 42.0 °C (fig.1).

The consequence is that the only marked LMBI effect on the machine performance is due to the coupling between the L1 (TM-011) mode and the CBM number 389 becoming strong when the cavity S3 is tuned in the middle of its temperature range, that is, around Tc1,389 for this cavity.

The effect of this interaction has been observed looking at the undulator radiation on the SuperESCA beam line. When cavity S3 is set around 57-58°C large energy oscillations are evident: unacceptable widening of the undulator harmonics is present together with a consistent flux reduction, related to the effective energy spread of the beam produced by the excited LMBI. The typical effect on the fifth harmonic of the undulator spectrum of the L1 HOM exciting CBM 389 is shown in fig. 3. When the cavity is set to bad temperatures the flux is strongly reduced and the harmonic is widened, while setting the cavity to a good temperature (dotted line) the spectrum assumes the wanted profile.

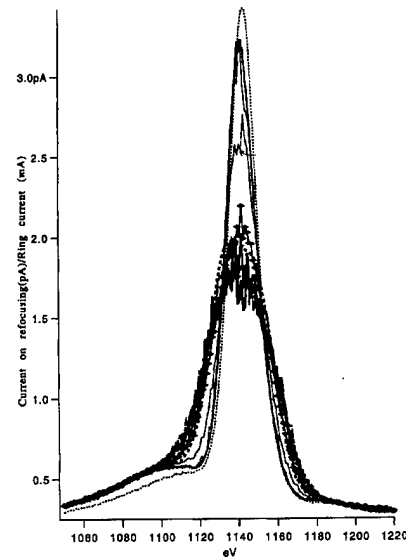


Fig. 3: Effect of the mode L1 on the undulator spectrum.

The second main effect related to LMBI is a Low Frequency beam profile Oscillation (LFO). It is clear that beam profile stability is also of great importance for a light source like ELETTRA. When a cavity is tuned to a temperature at which overlapping between a HOM and a CBM is present, LFOs are present in a typical range from 0 to 30 Hz, depending on the beam current and the energy. At high beam currents a saturation effect seems to be present. The presence of LFOs was found to be insensitive to the beam filling structure, namely once they are excited (i.e. a cavity is tuned to a bad temperature) the LFOs exist under almost any multibunch filling. When the basic longitudinal instability is

suppressed, the LFOs disappear and the beam profile returns stable. This is the situation during operation, with the cavities set 58 °C (S2), 41.5 °C (S3), 45 °C (S8) and 52 °C (S9).

III. THE CB INSTABILITY GROWTH RATES AS A FUNCTION OF CAVITY TEMPERATURE.

The growth rate of a longitudinal coupled bunch instability for a beam current I_b stored in M uniform filled and spaced bunches, for a high- Q cavity HOM can be approximated by

$$1/\tau_{||} = \frac{\alpha I_b}{4\pi Q_s (E/e)} \omega_{pn} \text{Re}(Z_{||}(\omega_{pn})) e^{-\left(\frac{\omega_{pn}}{\omega_0} \frac{\sigma}{R}\right)^2} \quad (2)$$

The impedance of the resonance, for one cavity, is

$$Z_{||}(\omega_{pn}) = \frac{\left(\frac{R}{Q}\right)_{0Lk} \cdot Q_{Lk}}{1 + j Q_{Lk} \left(\frac{\omega_{pn}}{\omega_{Lk}} - \frac{\omega_{Lk}}{\omega_{pn}}\right)} \quad (3)$$

In relation (3) we dropped the summation over all cavities, without a loss of generality. The frequency f_{Lk} of HOM L_k at the generic cavity temperature T and RF frequency f_{RF} and at the beam current I_b can be worked out [4] from relation (1),

$$f_{Lk} = \tau_{Lk}(T - T_0) + \phi_{Lk} [(f_{RF} - f_{RF0}) - \Delta f_{BL}] + f_{Lk0} \quad (4)$$

The ratio $\Omega_{kn} = \omega_{pn}/\omega_{Lk}$ in (3) is then

$$\Omega_{kn} = \frac{\frac{N}{h} f_{RF} + f_s}{\tau_{Lk} \Delta T + \phi_{Lk} [\Delta f_{RF} - \Delta f_{BL}] + f_{Lk0}} \quad (5)$$

with f_{pn} written in terms of f_{RF} and synchrotron frequency f_s . The growth rate (2) becomes then

$$1/\tau_{||} = \frac{\alpha I_b}{4\pi Q_s (E/e)} \frac{\left(\frac{R}{Q}\right)_{0Lk} \cdot Q_{Lk}}{1 + [Q_{Lk} (\Omega_{kn} - 1/\Omega_{kn})]^2} \omega_{pn} e^{-\left(\frac{\omega_{pn}}{\omega_0} \frac{\sigma}{R}\right)^2}$$

which, by relation (5), is a function of T and f_{RF} .

In fig. 4 the computed growth rate for CBM 389 is shown as a function of cavity S3 temperature. It is calculated for a fixed beam current of 150 mA at 2.0 GeV and for the nominal f_{RF} , with the other cavities set to the operation temperatures. The peak is between 56 and 58 °C and corresponds to the

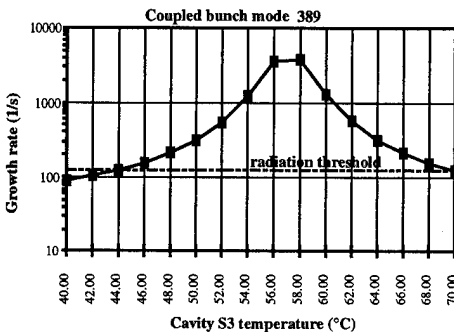


Fig. 4: CBM number 389 growth rate.

critical temperature of the mode L1 for this cavity. It can be observed that around 41.0÷42.0 °C the growth rate reduces below the longitudinal radiation damping threshold.

To correlate the CBM oscillation to the driving impedance at different cavity temperatures, we measured the amplitude of the CBM on a spectrum analyzer. The excited CBM number 389 we are considering here will be present in the beam spectrum as a first order phase modulation sideband ($+f_s$) of the beam harmonic 821. To measure the relative amplitude variation of $+f_s$ at different cavity temperatures we simply took the beam spectrum signal from a capacitive button. The ring was filled with 432 uniform equally spaced bunches, for a total current of 150 mA. The amplitude of the harmonic at f_{RF} was equal to -19.0 dBm. In fig. 5a we can see the plot taken with the cavity tuned close to the critical temperature $T_{c1,389}$ of cavity S3. The amplitude of the $+f_s$ sideband at 949.5857 MHz is large. When the cavity temperature is changed to 42.5 °C the amplitude of the $+f_s$ sideband is reduced by 65.6 dBm, as it is shown in fig. 5b, in agreement with the prediction of fig. 4. Further changing the temperature makes the first order sideband completely disappear.

IV. CONCLUSIONS

The results obtained are consistent with the theoretical expectations. The significant reduction of LMBI obtained by temperature tuning of the RF cavities has allowed a satisfactory routine operation of the machine.

V. REFERENCES

- [1] E. Karantzoulis et al., "Observation of Instabilities in the ELETTRA Storage Ring", in *Proceedings of the Fourth European Particle Accelerator Conference*, London, U.K., June 1994, pp.119-121.
- [2] M. Svandrlik et al., "Investigation of the HOM in the ELETTRA cavities", in *Proceedings of the Fourth European Particle Accelerator Conference*, London, U.K., June 1994, pp. 2134-2136.
- [3] A.Fabris et al., "Operational Performances and Future Upgrades for the ELETTRA RF System", this Conference.
- [4] M. Svandrlik et al., "Systematic RF cavities' Temperature Tuning as a Cure for Multibunch Instabilities", *Sincrotrone Trieste Internal Report*, ST/M-95/1.

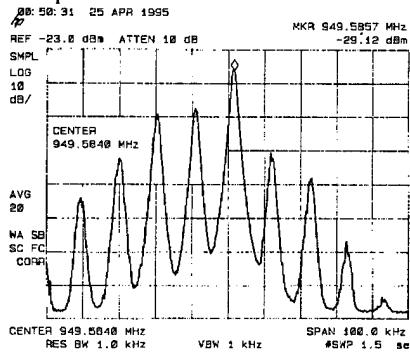


Fig. 5a: CB 389 amplitude, TS3 57 °C.

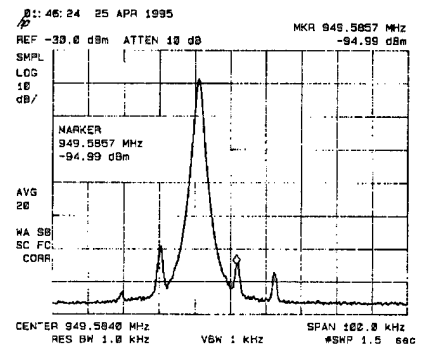


Fig. 5b: CB 389 amplitude, TS3 42.5 °C.

Nonlinear Analyses of Storage Ring Lattices Using One-Turn Maps *

Y.T. Yan, J. Irwin, and T. Chen

Stanford Linear Accelerator Center, Stanford University, Stanford, CA 94309 USA

Abstract

Using normalized one-turn resonance-basis Lie generators in conjunction with an action-angle tracking algorithm (nPB tracking), we have been able to better understand the relationship between the dynamic aperture and lattice nonlinearities. Tunes, tune shifts with amplitude and/or energy, and resonance strengths may be freely changed to probe their individual impact on the dynamic aperture. Fast beam-beam simulations can be performed with the inclusion of nonlinear lattice effects. Examples from studies of the PEP-II lattices are given.

I. INTRODUCTION

Simple lattice element-by-element tracking for dynamic aperture determination is essential but limited by the fact that information is obtained at only one working point and one set of lattice parameters. Furthermore, inadvertent errors in the lattice and control files can remain undetected. To enhance our understanding of lattice nonlinearities and their relationship with the dynamic aperture, we have developed a set of one-turn mapping procedures that allow us to obtain one-turn resonance-basis Lie generators for circular accelerator nonlinear lattice studies.

Contained in the Lie generators are tune-shift and resonance terms of different orders. These terms can be suitably normalized for comparisons among themselves or with those obtained from one of a series of lattices that are under improvement. Furthermore, by directly taking Poisson bracket expansion of the resonance-basis Lie generators to a suitable order to evaluate the turn-by-turn Lie transformations, one not only can achieve a very fast tracking for dynamic aperture determination to obtain swamp plots (dynamic aperture vs. tune), but also can freely change selected tune-shift or resonance terms to probe their individual impact on the dynamic aperture.

In the following sections these one-turn mapping procedures are described and examples for their applications in PEP-II lattice development are presented.

II. The One-Turn Resonance Basis Map

To obtain resonance basis map for a lattice we first extract a one-turn map at a suitable observation position as a Taylor expansion about the on-momentum closed orbit. In general, we include all lattice nonlinearities. However, we can concentrate on a particular lattice module by inserting a linear lattice for the rest of the ring. We usually consider 2-dimensional maps with a parameter δ representing the momentum deviation dp/p . Thus, the Taylor map can be expressed as

$$\vec{Z} = \vec{U}(\vec{z}, \delta) + \mathcal{O}(N+1), \quad (1)$$

where $\mathcal{O}(N+1)$ indicates that the Taylor map is truncated at an order of N , $\vec{z} = (x, p_x, y, p_y)$ is the global or initial phase-space coordinate vector and $\vec{Z} = (X, P_x, Y, P_y)$ is the phase-space coordinate vector after one turn.

Once the one-turn Taylor map is obtained, we make a Floquet transformation such that

$$\vec{Z} = \mathcal{A}^{-1}(\vec{z}, \delta) \mathcal{R}(\vec{z}) e^{f(\vec{z}, \delta)} \mathcal{A}(\vec{z}, \delta) \vec{z} + \mathcal{O}'(N+1), \quad (2)$$

where $\mathcal{R}(\vec{z})$ is one-turn pure rotational map in the 4-dimensional transverse canonical phase-space, and $\mathcal{A}(\vec{z}, \delta)$ and its inverse $\mathcal{A}^{-1}(\vec{z}, \delta)$ are the 4-by-5 matrices that generate the Floquet transformation. The dispersion, η , and the Courant-Snyder parameters, α , β , and γ are all included in $\mathcal{A}(\vec{z}, \delta)$ and $\mathcal{A}^{-1}(\vec{z}, \delta)$. Making the Floquet transformation $\vec{z}_F = \mathcal{A}^{-1}(\vec{z}, \delta) \vec{z}$ and then dropping the subscript F for convenience, one obtains a one-turn map

$$\vec{Z} = \mathcal{R}(\vec{z}) e^{f(\vec{z}, \delta)} \vec{z}. \quad (3)$$

The polynomial $f(\vec{z}, \delta)$ of the Lie transformation in Eq. 3 can be decomposed in a complete basis consisting of the rotational eigen-modes, $\hat{x}_{\pm} = x \mp ip_x = \sqrt{2J_x} e^{\pm i\theta_x}$, $\hat{y}_{\pm} = y \mp ip_y = \sqrt{2J_y} e^{\pm i\theta_y}$, where J_x , J_y , θ_x , and θ_y are action-angle variables. One then obtains

$$f(\vec{z}, \delta) = \sum_{\vec{n}, \vec{m}, p} a_{\vec{n}, \vec{m}, p} (2J_x)^{\frac{n_x}{2}} (2J_y)^{\frac{n_y}{2}} \delta^p \cos(m_x \theta_x + m_y \theta_y + \phi_{\vec{n}, \vec{m}, p}), \quad (4)$$

where the terms with $m_x = m_y = 0$ are the tune shift terms [1]. For convenience, all these tune shift terms are grouped together and represented by $h_T(J_x, J_y, \delta)$. The remaining terms, all with angular variable dependence, are also grouped and represented by $h_R(J_x, J_y, \theta_x, \theta_y, \delta)$. Thus, the one-turn map given by Eq. 3 can be written as

$$\vec{Z} = e^{-i\mu_x J_x - i\mu_y J_y} e^{-h_T(J_x, J_y, \delta) - h_R(\theta_x, J_x, \theta_y, J_y, \delta)} \vec{z}, \quad (5)$$

where we have replaced the rotation $\mathcal{R}(\vec{z})$ with its Lie representation $e^{-i\mu_x J_x - i\mu_y J_y}$, where μ_x and μ_y are the working tunes of the lattice. This is the resonance basis map.

III. NORMALIZATION OF TUNE SHIFT AND RESONANCE COEFFICIENTS

It should be noted that h_T , h_R , and the action coordinates (J_x , J_y) in Eq. 5 have the dimensions of emittance while θ_x , θ_y , and δ are dimensionless. Therefore, the coefficients in the polynomials h_T and h_R have different dimensions. For convenience in directly using these coefficients for calculating and comparing the

*Work supported by the Department of Energy under Contract No. DE-AC03-76SF00515

tune shift and resonance strength of different orders, we introduce a scaling transformation such that $h_T = \epsilon_x \hat{h}_T$, $h_R = \epsilon_x \hat{h}_R$, $J_x = \epsilon_x \hat{J}_x$, and $J_y = \epsilon_x \hat{J}_y$ to obtain the dimensionless one-turn map which, after dropping the symbol $\hat{\cdot}$, is again given by Eq. 5 except with modified coefficient values. Note that ϵ_x is the horizontal emittance, which in PEP-II is 48 nm-rad for the High-Energy Ring (HER) and 64 nm-rad for the the Low-Energy Ring (LER).

In our numerical studies for PEP-II lattices, we set $\epsilon_y = \frac{1}{2}\epsilon_x$ to obtain the required vertical aperture that is sufficient for injection and for vertical blow-up from the beam-beam interaction. Most often we calculate the resonance strength and tune shift along the 10σ (10 times the nominal beam size) ellipse $r_x^2 + \frac{\epsilon_x}{\epsilon_y} r_y^2 = N^2$ with $\frac{\epsilon_x}{\epsilon_y} = 2$ and $N = 10$, where $r_x = \sqrt{2J_x}$, and $r_y = \sqrt{2J_y}$ are radii in the two-dimensional phase-space planes.

A. TUNE SHIFT

Using Hamilton's equations and the effective Hamiltonian h_T in Eq. 5, one can obtain both horizontal (x) and vertical (y) tune shifts as explicit polynomials in the geometric invariants J_x and J_y and the chromatic amplitude δ , given by

$$\Delta\nu_x(J_x, J_y, \delta) = \frac{1}{2\pi} \frac{\partial h_T(J_x, J_y, \delta)}{\partial J_x},$$

and

$$\Delta\nu_y(J_x, J_y, \delta) = \frac{1}{2\pi} \frac{\partial h_T(J_x, J_y, \delta)}{\partial J_y}.$$

To make comparison of tune shift terms of different order, we usually calculate the maximum of each term along the 10σ ellipse.

B. RESONANCES

Since resonance terms (in h_R) of higher orders have larger derivatives, thereby causing larger step-sizes in phase space, we prefer to measure the strength of a resonance term by taking its Poisson bracket (PB) with respect to phase space coordinates J_x, J_y, θ_x , and θ_y . From these PBs we compute the phase-space step [2]

$$|\Delta\vec{z}| = \sqrt{[(r_x \Delta\theta_x)^2 + (\Delta r_x)^2] + \frac{\epsilon_x}{\epsilon_y} [(r_y \Delta\theta_y)^2 + (\Delta r_y)^2]}.$$

We then compute the maximum value of $|\Delta\vec{z}|$ for all possible values of θ_x, θ_y, J_x , and J_y with the constraint $r_x^2 + \frac{\epsilon_x}{\epsilon_y} r_y^2 = N^2$. This maximum is what we call the normalized resonance basis coefficient. $|\Delta\vec{z}| = 1$ means that the corresponding resonance can at most cause a phase-space motion of 1σ in one turn for a particle on the 10σ boundary.

C. A SAMPLE PLOT

Each of the tune shift and resonance terms is uniquely represented by a set of indices (\vec{n}, \vec{m}, p) . For a map of 10^{th} -order, there would be thousands of terms. Although most of the terms are essential to the lattice nonlinear behavior, in search for improvement of the lattice, one only needs to pay attention to a limited number of larger terms. As an example, Figure 1 shows the normalized tune shift and resonance coefficients that are larger than 0.01 for a PEP-II LER bare lattice.

/u1/yan/ler/90_n_int/w12/sbare
Yan, Mon May 15 11:48:56 PDT 1995

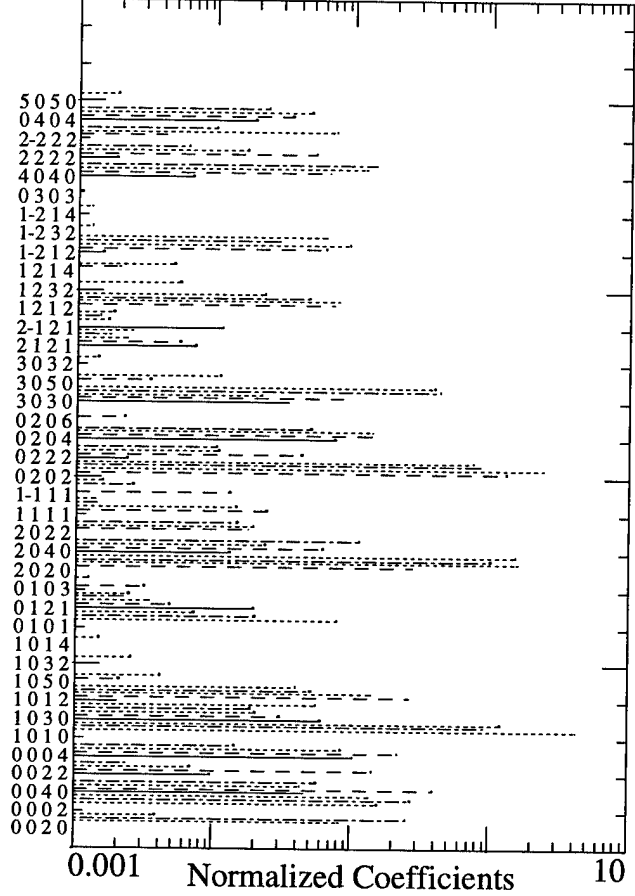


Figure 1. Normalized tune shift and resonance coefficients plotted in log scale horizontally. The vertical axis shows corresponding indices (m_x, m_y, n_x, n_y) for resonances and orders. The corresponding chromatic indices, p 's, are not explicitly shown in the axis but are indicated with line patterns ($p = 0$: solid, 1: dashes, 2: dots, 3: dotdashes, etc).

IV. nPB TRACKING AND ITS RELIABILITY

The normalized tune shift and resonance coefficients described in the last section can help us identify a limited number of terms that would degrade the dynamic aperture. To understand deeper and confirm more precisely their individual impacts on the dynamic aperture, we can freely change the corresponding coefficients and then evaluate the updated resonance basis map to see the change of the dynamic aperture.

To evaluate a resonance basis map, we directly take Poisson bracket expansion of the resonance basis Lie generators to a suitable (n) order and so the name of nPB tracking. The procedure of nPB tracking is basically to perform turn-by-turn tracking of the particle phase-space coordinates. This is done by evaluating the one-turn map given by Eq. 2 followed by an update of the particle momentum deviation (δ) through an accurate but concise time-of-flight map. Note that in evaluating the Lie transformation, the Lie generator, $f = -h_T - h_R$, is kept in the action-angle variable space while the particle phase-space coordinates are always kept in Cartesian coordinates which are considered

as functions of the action-angle variables for the Poisson bracket calculation — this is the key to the fast computational speed of the nPB tracking since all the Sines and Cosines can be calculated only once and stored for repeated turn-by-turn tracking [3].

As to the reliability of the nPB tracking, one may be concerned with the fact that the nPB tracking is not 100% accurate since the map is truncated at a moderate order and not 100% symplectic since one does not carry the Poisson bracket expansion to the infinite order. However, it is well understood that the required accuracy and symplecticity depend on circumstances [4]. For the PEP-II lattice dynamic aperture studies (only 1024 turns needed because of synchrotron radiation damping), from numerous tests we have concluded that a 10^{th} -order map with 3-Poisson-bracket expansion of the Lie transformation is accurate and symplectic enough. It takes about 1 minute with such a 10^{th} -order map, 3PB tracking on a RISC workstation to obtain a dynamic aperture plot at a given working point, which would otherwise have taken a few hours with element-by-element tracking.

V. SWAMP PLOTS FROM nPB TRACKING

The fast computational speed of nPB tracking allows fast calculation of dynamic aperture and so one can obtain a swamp plot for a given lattice in a reasonable time. To obtain a swamp plot with the nPB tracking, one would follow exactly the nPB tracking procedures described in Section IV, except that one would increment the working tunes μ_x and μ_y , while keeping all other terms in the resonance basis map fixed, to obtain dynamic apertures throughout the tune plane. This is equivalent to using element-by-element tracking and inserting an exactly matched linear trombone to switch the working tunes without further changing the lattice. In our practice, we have generally found such swamp plots very informative. They have helped us in evaluating and improving the PEP-II lattices. Occasionally we would check a few spots of a swamp plot against corresponding element-by-element trackings to ensure that there are no surprises.

Some typical PEP-II lattice swamp plots can be found in Ref. [5].

VI. BEAM-BEAM WITH nPB TRACKINGS

The fast speed of the nPB tracking allows one to include the arc lattice as a nonlinear resonance-basis map for beam-beam simulations. To further enhance the tracking speed, one can even drop irrelevant resonance terms. As an example, shown in Figure 2 are the beam tail distributions of the PEP-II HER $\beta_y^* = 2.0\text{cm}$ lattice with and without nonlinear terms in the one-turn map.

VII. SUMMARY

The one-turn mapping procedures described above have been important for PEP-II lattice development. During the course of numerous PEP-II lattice updates, we were able to identify important tune shift and resonance terms that would degrade the dynamic aperture. We then confirmed and understood their individual impacts on the dynamic aperture with nPB tracking and swamp plots, thereby improving the lattice.

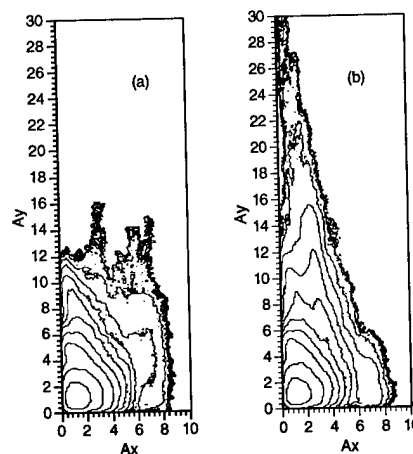


Figure 2. The beam tail distribution of PEP-II HER: (a) with linear lattice, and (b) additionally including tune-shift-with-amplitude terms.

VIII. ACKNOWLEDGEMENT

One of the authors (YTY) thanks John Seeman for his patience in waiting for the development of these non-linear analysis tools for PEP-II lattice studies.

References

- [1] For more accurate tune shift calculation, one should use non-linear normal form.
- [2] J. Irwin, N. Walker, and Y. Yan, "The Application of Lie Algebra Methods to the PEP-II Design," SLAC-PUB-95-6779, in Proc. of the 4th EPAC, p. 899 (1994).
- [3] J. Irwin, T. Chen, and Y. Yan, "A fast tracking method using resonance basis Hamiltonians," SLAC-PBU-95-6727.
- [4] Y.T. Yan, "Application of differential algebra to single-particle dynamics in storage rings", in *Physics of Particle Accelerators*, AIP Conf. Proc. No. 249, edited by M. Month, and M. Diene (AIP, New York, 1992), p. 378.
- [5] Y.T. Yan, *et al.*, "Swamp Plots for Dynamic Aperture Studies of PEP-II Lattices," SLAC-PUB-95-6876, also in these proceedings.

PRECISE DETERMINATION AND COMPARISON OF THE SPS DYNAMIC APERTURE IN EXPERIMENT AND SIMULATION

W. Fischer*, II. Institut für Experimentalphysik, Universität Hamburg, Germany
and

F. Schmidt, CERN, Geneva, Switzerland

Abstract

The combined effect of nonlinear fields and tune ripple can lead to chaotic motion and particle loss in proton accelerators thereby limiting the dynamic aperture of these machines. The SPS Dynamic Aperture Experiment is performed to study a controlled nonlinear machine under the influence of power supply ripple. To this end eight strong sextupoles are used to make the SPS nonlinear. The tune ripple is introduced with one special quadrupole which allows to vary the ripple frequency and depth. In parallel long-term element-by-element tracking is done to investigate its applicability for the estimation of the dynamic aperture of a real accelerator. The influence of non-linear magnetic fields and tune ripple is observed at two working points using a flying wire of $8\mu\text{m}$ diameter. The experimentally determined dynamic aperture is compared with survival plots obtained from the tracking and their differences are discussed.

I. INTRODUCTION

Non-linearities of superconducting magnets, which cannot be completely avoided, may limit the dynamic aperture of accelerators. It is therefore of great interest to predict the stability range due to these non-linearities. The SPS Dynamic Aperture Experiment is used to compare experimental results with tracking which serves as the predictive tool in this study.

After calibrating the instrumentation we have carefully measured the detuning curves as a function of betatron amplitude and compared them with tracking results. An even modest disagreement between the two would cast doubt on the validity of the model.

We will report about measurements and calculations for the dynamic aperture of the SPS with the following machine set up: coasting beam at 120GeV, closed orbit correction with horizontal and vertical rms below 0.3mm, linear coupling compensation up to $|Q_h - Q_v| = 0.002$, momentum spread $\Delta p/p \approx 10^{-3}$, chromaticity in both planes corrected to $\Delta Q/(\Delta p/p) \approx 1$. Strong non-linearities are introduced by 8 powerful sextupoles. The natural tune ripple spectrum contains 7 major lines that add up to a total amplitude of $0.5 \cdot 10^{-4}$. We studied the working points $(Q_h, Q_v) = (26.637, 26.533)$ and $(26.605, 26.538)$ referred to as WP1 and WP2 respectively (see Fig. 1). The artificial tune ripple, introduced by a single quadrupole, had a frequency of 9Hz and an amplitude of $\Delta Q_h = 1.87 \cdot 10^{-3}$ and $\Delta Q_v = 0.55 \cdot 10^{-3}$ at WP1 and WP2 respectively. The ratio of horizontal and vertical ripple depth is $\Delta Q_h/\Delta Q_v = 1.75$. The beam is kicked horizontally until the aperture is reached.

*Supported in part by CERN, Geneva, Switzerland and DESY, Hamburg, Germany.

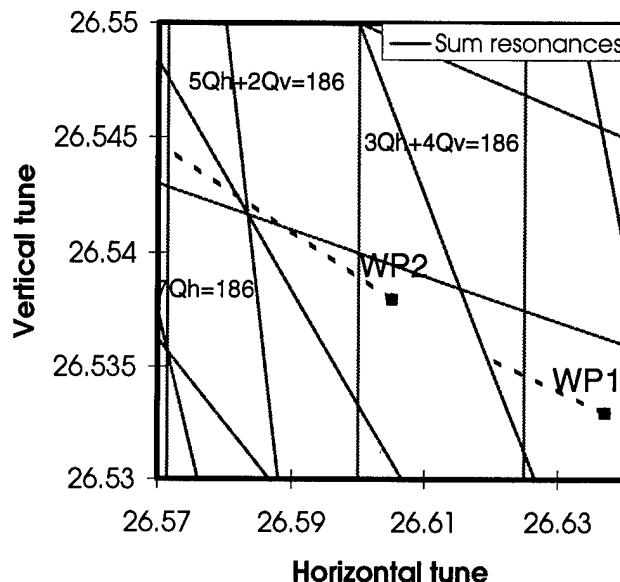


Figure 1. Tune diagram with sum resonances up to order 11 and both working points before and after the kick. The detuning is directed towards smaller horizontal and larger vertical tune values. At the last tune values large scale losses take place.

II. INSTRUMENTATION AND DETUNING

Preconditions for these experiments are an exact knowledge of the applied kickstrength and a high precision of the wire scan readings. The kicker has been calibrated several times and shows a very linear behavior down to small kick amplitudes. Whereas the measurement of 1993 showed a degradation of 10% compared to earlier measurements, the calibration of 1995 showed practically no difference to the measurement of 1993.

The kicked beam is observed by a flying carbon wire of $8\mu\text{m}$ diameter and $0.4\text{m} \cdot \text{s}^{-1}$ speed. The position of the wire can be measured via an opto-electronic ruler with a resolution of $16\mu\text{m}$. The intensity of the kicked beam is reduced by $1.4 \cdot 10^{-4}$ per scan (in and out scan) but no beam blow up can be observed. The kicked beam produces a typical double peak structure in the wire scan profile (Fig. 3). The kick strength calculated from the distance between the peaks agrees within 10% with the kicker calibration. These beam profiles were also compared with scans from flying wires at different locations. The agreement amounts to some 5-10% which also increases our confidence in the knowledge of the β -functions around the ring.

An important test for a nonlinear accelerator model is the dependence of the tunes on the betatron amplitudes. In the SPS the horizontal and vertical detuning is measured as a function of the

horizontal betatron amplitude. The tunes are computed from up to 8192 turns after the kick by FFT and phase advance averaging leading to a precision of $5 \cdot 10^{-4}$ [1]. Fig. 2 shows the comparison of the measured and calculated detuning. The agreement is very good up to large amplitudes and the dependence of the detuning on action ($\frac{x_{max}^2}{2 \times \beta_h}$) is predominantly linear as expected from second order perturbation theory.

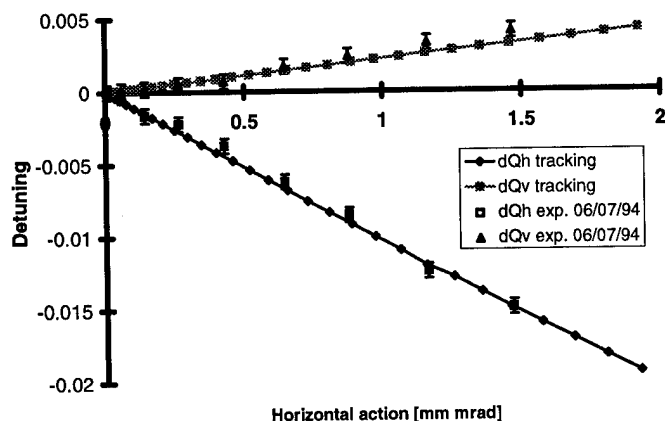


Figure 2. Detuning measured at working point 1.

III. DYNAMIC APERTURE

For practical reasons the dynamic aperture can be defined as stability limit after a certain time interval which may depend on the type of machine and operational considerations. A typical problem is to keep the beam circulating several minutes during the injection period when nonlinearities and beam size are usually at their maximum. In the experiment the observation was done up to 1000s whereas with computer tracking only 345s (15 million turns) could be reached with reasonable computing effort.

A limitation of the SPS experiment is the rather large natural size of the beam before kick. This precludes any fine exploration of the amplitude distribution as is done in tracking. In particular small chaotic regions within an otherwise stable part of the distribution cannot be detected. However the maximum amplitude above which no particle survives after a certain time gives a good measurement of the stability limit.

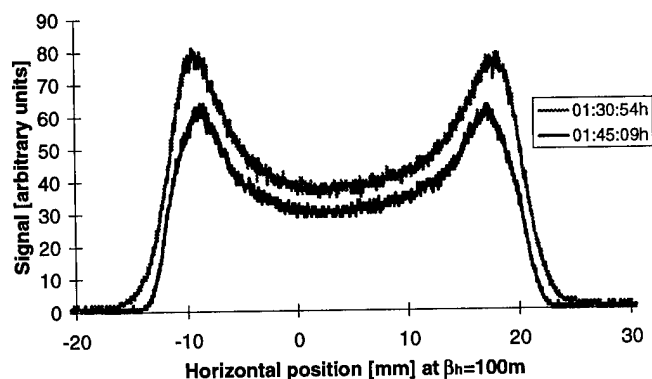


Figure 3. Evolution of the wire scan profile at WP1, tune ripple of 9Hz and $\Delta Q_h = 0.00187$ (#78, no horizontal scraping).

A. Measured

Experimentally, the dynamic aperture is determined from the maximum bottom width of the wire scan profiles (Fig. 3). At the edge of the beam profile $5 \cdot 10^7$ protons (10^{-4} of the intensity) can clearly be detected. In most cases 15 scans have been taken at time intervals of about 1min.

In Fig. 4 four wire scan measurements at WP1 with artificial tune ripple are depicted. These curves have been smoothed and the estimated error bars are shown in case #91. The reproducibility of the experimental results has been found to be within 2% for two measurements under the same conditions but 5 months apart (#62 and #76). Due to the rather large beam size the results depend on the measurement procedure: cases #62 and #76 have been scraped horizontally after kicking, whereas cases #78 and #91 are left unscraped and in addition the latter case has been kept for some extra 15min without artificial tune ripple. Although these cases strongly differ initially, after 345s the differences reduce to about 5%.

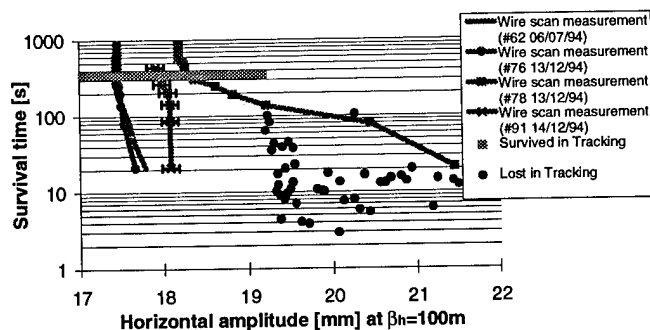


Figure 4. Dynamic aperture at WP1, tune ripple of 9Hz and $\Delta Q_h = 0.00187$.

Fig. 5 shows one of the two cases with natural ripple only. The results of all measured cases are summarized in Tab. I.

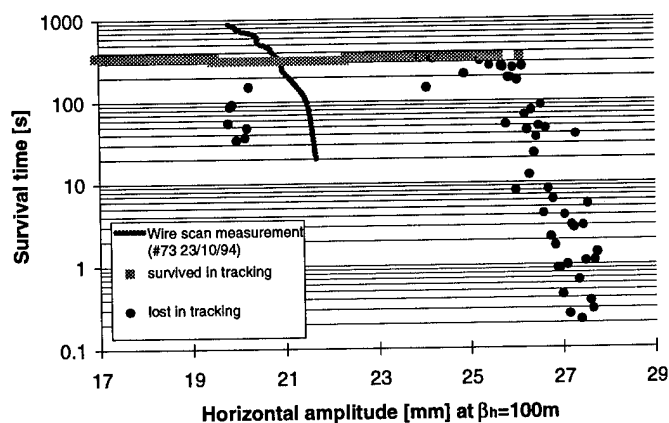


Figure 5. Dynamic aperture at WP2, natural ripple only.

B. Computed

The computer code SIXTRACK [2] has been used for the tracking studies. The model included all sextupoles and horizontal and vertical closed orbit, as well as the tune ripple. Tunes, chromaticities and linear coupling are adjusted similar to what is

Table I

Comparison of measured and computed dynamic aperture. All values are given for $\beta_h = 100\text{m}$. For the onset of chaos there are two values: the larger one is the border above which no regular particles could be found, the lower (in brackets) is the lowest amplitude at which large scale chaotic motion sets in.

case	measured dynamic aperture [mm]	onset of chaos ($2 \cdot 10^5$ turns) [mm]	loss border ($1.5 \cdot 10^7$ turns) [mm]	comparison between measurement and loss border [%]
WP1, natural ripple only	20.0	(15.7) 23.1	24.4	22
WP2, natural ripple only	20.9	(9.8) 23.6	25.7	23
WP1, 9Hz, $\Delta Q_h = 1.87 \cdot 10^{-3}$	17.4	(7.7) 14.3	19.2	10
WP2, 9Hz, $\Delta Q_h = 0.55 \cdot 10^{-3}$	19.5	(7.4) 8.3	22.3	14

measured in the SPS. As the beam is kicked horizontally the particles are tracked with large horizontal displacements. Moreover, a vertical displacements of roughly one σ of the vertical beam size has been considered. In all tracked cases a wide amplitude range could be found (column three in Tab. I) where chaotic (after 200,000 turns) and regular regions alternate. For each chaotic region in that amplitude range a particular sum resonance is found which apparently causes the unstable behavior. In Fig. 4 the lost particles correspond to a coupled 7^{th} order resonance, in Fig. 5 the losses at large amplitudes correspond to the horizontal 7^{th} order resonance and the losses at about 20mm are due to another coupled 7^{th} order resonance (for both cases see Fig. 1).

The dynamic aperture as defined above and computed by long-term tracking is shown in column four in Tab. I. The last column in Tab. I shows the difference in percent between the computed and the measured dynamic aperture. In the cases with additional ripple the difference is about 10% but without ripple this deteriorates by about a factor of two. Moreover in the tracking we find a broad region of apparently regular motion outside of the experimental stability border (not present in the cases with additional ripple). From this we have to conclude that an essential destabilizing effect is missing in our tracking model. A very rough estimate for the scale of this effect is the additional tune ripple because the experimental dynamic aperture without extra tune ripple agrees well with that of the tracking when this ripple is introduced (compare the first two entries in column two with the last two entries in column four of Tab. I). The nature of this effect is still unknown. However, neither some neglected systematic nonlinearities nor extra tune ripple are likely candidates. The former would lead to measurable detuning with amplitude, while for the latter the tune ripple can be understood from measured voltage ripple of the SPS power supplies [3] and in addition it has been measured with good precision with a phase-locked loop.

IV. CONCLUSION

The detuning with amplitude of the SPS with controlled strong sextupoles can be well reproduced with our tracking model. We also know to a good precision the tune ripple induced by power supplies. When an additional and sizeable tune ripple is applied the tracking model gives a value for the dynamic aperture which is about 10% larger than the experimental one. However, the

cases without extra ripple reveal a more prominent difference (larger than 20%) between the theoretical and experimental dynamic aperture. We address this to some neglected and at present unknown effect which should be about as effective as tune ripple of some 10^{-3} .

V. ACKNOWLEDGMENTS

The authors are grateful to all engineers and technicians who helped with the instruments. The operations team and our colleagues in the accelerator physics group are thanked for their cooperation and help. Special thanks to F. McIntosh for his strong support performing the extensive computer simulations and to J. Gareyte for stimulating discussions and reading the manuscript.

References

- [1] W. Fischer et al., "The Million Turn Data Acquisition System BOSC", Proceedings of the 1993 IEEE Particle Accelerator Conference, Washington D.C. (1993).
- [2] F. Schmidt, "SIXTRACK Version 1.2", CERN SL/94-56 (AP) (1994), found in WWW under: <http://hpariel.cern.ch/frs/Documentation/doc.html>.
- [3] P. Burla et al., "Power Supply Ripple Study at the SPS", AIP Conference Proceedings 326 (1995).

Coherency of the Long Range Beam-Beam Interaction in CESR *

Alexander B. Temnykh [†] and James J. Welch, Wilson Lab. Cornell University, Ithaca NY

Introduction

Making more luminosity is the name of the game at CESR these days. Luminosity is proportional to the average beam current I , the vertical tuneshift parameter ξ_y , and inversely proportional to the vertical beta function at the interaction point β_y^* . The main thrust of our efforts is to increase the average beam current by adding more bunches, without losing ground on the other two parameters. This should work as long as the additional bunches can be kept from colliding with each other at the numerous crossing points in the arcs, and the machine hardware is capable of handling higher currents.

The main limitation to the maximum number of bunches the ring can accommodate is due to the long range beam-beam interaction that occurs when the bunches pass by each other in the arcs. Separation can be obtained at these points using electrostatically generated closed orbit distortions known as 'pretzels'. However, the pretzel distortion is proportional to $\sqrt{\beta_x} \cos \phi_x$ and so good separation can be obtained over only the portions of the ring where the cosine term is not small. If crossing points are too close to pretzel nodes the long range beam-beam interaction causes a very short lifetime for the bunches which cross there. Roughly one can collide one train of closely spaced bunches for each integer of the horizontal tune and manage to avoid crossing points near the pretzel nodes. The total length of each train must be limited to some fraction of half the minimum betatron wavelength. For illustration the actual pretzel in a portion of CESR is reproduced in figure 1 together with the beam envelopes and marks at the crossing points. Here we were running with nine trains consisting of two bunches separated by 28 ns.

One may ask when does it actually make sense to increase the number of bunches, given the number and length of the trains is more or less fixed?

There are a few considerations: If the single bunch current is near or above the value for which ξ_y is saturated then luminosity will increase linearly with total beam current, independent of the number of bunches. In this case one may be able to avoid single bunch current limitations by adding more bunches.

If the single bunch current is below the saturation value then it might be better to increase the single bunch current if possible, than to add more bunches, because the luminosity will go up faster than linear. For CESR, saturation occurs at roughly 10 mA/bunch.

Another consideration, which is the main topic of this paper, is if the single bunch current is limited by the long range beam-beam interaction, then it makes sense to try to add more bunches.

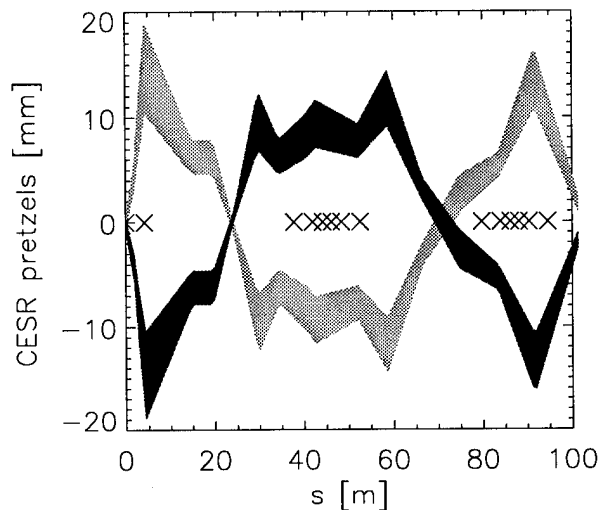


Figure 1: CESR pretzels for e^+ and e^- beams near the main interaction point are shown. The shaded regions represent the beam size $\pm\sigma_x$.

However if the bunches in each train are so close together that the long range beam-beam interactions from successive crossing points add coherently, the effect is the same as if the current were put into a single bunch, and there is no advantage to be gained. A number of machine studies described below quantitatively address the question of coherency and bunch spacing.

This work on coherency follows earlier long range beam-beam studies where we evaluated various phenomenological models ¹ and found that the limiting pretzel increases roughly as the square root of the bunch current.

Whether or not successive interactions are coherent is important because we always desire to reduce the size of the pretzel. Large pretzel causes reduced dynamic aperture, high radiation, poor lifetime, and may reduce ξ_y . To illustrate how the luminosity is related to the coherency of the parasitic beam-beam interactions, consider the following: Suppose we are operating at the highest possible train current I_t , with one bunch per train, and the pretzel amplitude can not be increased. We decide to divide the train current into n equal bunches. If the interactions from the new crossing points act coherently the train current will still be limited to the same value and the luminosity will be unchanged. If the interactions act incoherently we might expect that the net kick due the train current will scale with $\sqrt{n} * I_t/n = I_t/\sqrt{n}$. That is, the interaction strength will be reduced by a factor of

¹A.B. Temnykh, J.J. Welch and D.H. Rice, *The Long Range Beam-Beam Interaction at CESR — Experiments, Simulation and Phenomenology* Proc. Particle Accelerator Conf., 2007 (1993)

$1/\sqrt{n}$ relative to the coherent or $n = 1$ case. This means we can increase the train current and therefore the luminosity by a factor of \sqrt{n} as long as the bunches interact incoherently.

Method and Results

The basic technique we used to study the long range beam-beam interaction was to decrease the pretzel amplitude until the lifetime of a probe bunch dropped to 50 minutes or so. The probe beam consisted of one bunch which was much weaker than the bunches in the drive beam. We would start each measurement set at the highest desirable current in the drive bunches. After the pretzel amplitude was reduced and a limiting value found, some current was removed without changing the magnetic lattice and the measurement repeated. This was done for several different configurations of main bunches and the dependence of pretzel amplitude on current was plotted.

The pretzel amplitude refers to an arbitrary coefficient by which all horizontal electrostatic separators are scaled. For convenience 2000 units is defined so that it generates a ± 2 milliradian crossing angle at the interaction point. In practice the lifetime is essentially independent of pretzel amplitude until the limiting pretzel amplitude is approach. At that point the lifetime changes very rapidly. This fact enables a fairly reproducible value to be obtained for the limiting pretzel even if the beam lifetime is not exactly the same. A typical reproducibility is about 20 pretzel units if there are no changes to the magnetic lattice.

Tune changes and nonreproducible changes to the lattice also affect the measurement of the limiting pretzel amplitude. By optimizing the tune the limiting pretzel can often be reduced by about 100 units. Going back to the same machine configuration on a different day the limiting pretzel could be expected to be within 100 units or so. Within a machine studies session, but after cycling the lattice, the limiting pretzel data had an RMS of about 30 units.

It must be noted that we always chose bunch configurations such that there was no collision at the main interaction point. Such bunches only interact via long range beam-beam interaction. There is some reason to think that if the bunches also had a normal beam-beam interaction they would require even large pretzel as they may have larger tails generated by the normal beam-beam interaction. Thus the limiting pretzel we obtain is probably only a lower bound on an estimate of the limiting pretzel for when the normal beam-beam interaction is included.

Results from three machine studies are reported herein: In the first run we had a single bunch of electrons as the probe bunch against a drive beam of one or two bunches of positrons. The data are plotted in figure 2. The limiting pretzel amplitude obtained when the all the drive beam current is put in a single bunch is not significantly different from that obtained with the charge in two bunches spaced at 14 ns. When the spacing is increased to 28 ns significantly less pretzel was required for the same total drive beam current. In fact, for the pretzel, the limiting drive current in the 28 ns case is between 1.32 and 1.45 times larger than the in the single bunch case — comparable with a factor of

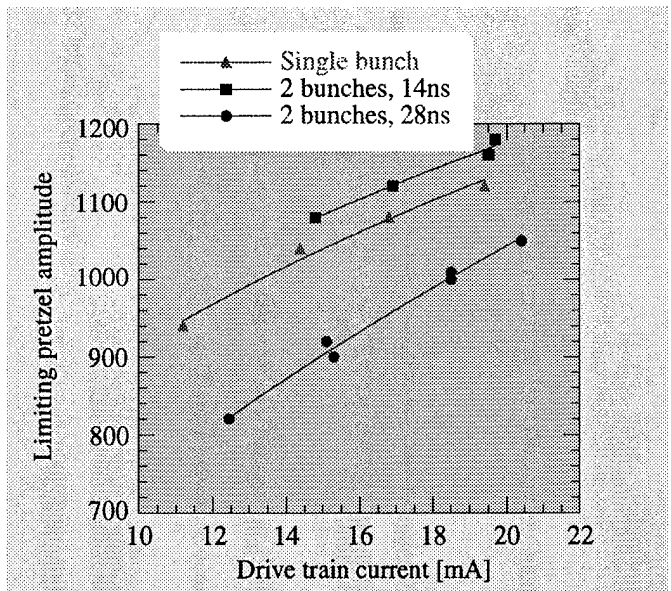


Figure 2: The measured limiting pretzel amplitude (arbitrary units) is plotted against various total drive beam currents. The drive beam consisted either of a single bunch or two bunches separated by either 14 or 28 nanoseconds.

West crossing pts					
	β_x	β_y	ϕ_x	ϕ_y	s
	[m]	[m]	[deg]	[deg]	[m]
0 ns	29.1	6.7	0	0	32.6
14 ns	19.4	11.9	5.0	13.5	26.9
28 ns	12.0	19.5	13.0	21.4	21.0
East crossing pts					
0 ns	32.0	13.5	0	0	34.6
14 ns	23.2	18.3	4.4	7.7	29.5
28 ns	16.3	24.1	10.9	13.4	24.7

Table 1: Crossing points lattice parameters for different spacings of two bunches within a single drive train.

$\sqrt{2}$ expected from the crude scaling law described above.

The lattice parameters for these crossing points are given in table 1. Though the bunch crossings occurs in two places on opposite sides of the ring, the lattice parameters for these places are similar. In both cases the lattice parameters for the 14 ns and 28 ns crossing points are less favourable with respect to the long range beam-beam interaction: larger β_y , more long range tuneshift, less separation distance. So any reduction of the limiting pretzel would plausibly be due to a reduction of the coherency of the vertical kicks received. Thus it appears that with 28 ns spacing there may be incoherency while there is not with 14 ns spacing.

Shorter bunch spacing was the topic of the second machine studies. In this case a single drive bunch was compared against two drive bunches with spacings of 4, 8, and 14 ns. The results are not reproduced here but show no significant differences in

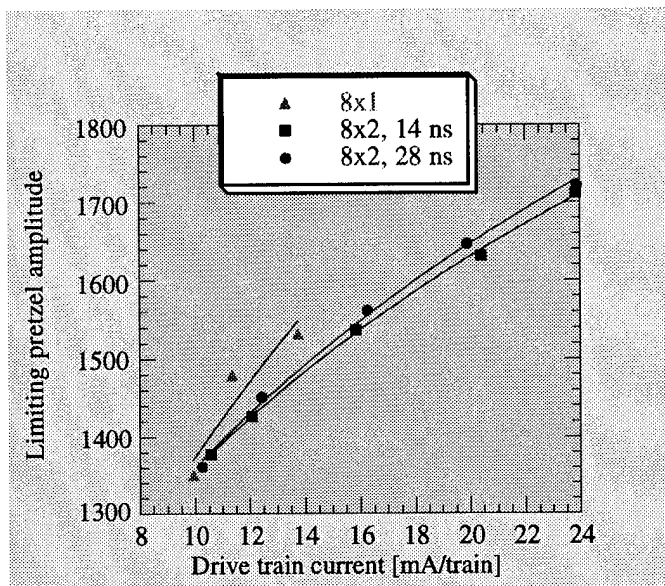


Figure 3: Limiting pretzel amplitude versus total beam current for three configurations of drive beam 8 trains of: 1 bunch, 2 bunches separated by 14 ns, and 2 bunches separated by 28 ns.

the limiting pretzel as a function of total beam current for the various bunch configurations. All are within 100 pretzel units. Thus the parasitic interactions appear to be coherent.

The last machine studies concentrated finding the effects of multiple interactions. Results from a drive beam consisting of 8 trains of single bunches are compared with results obtained from 8 trains of two bunches spaced either 14 or 28 ns. See figure 3. There was no significant difference between the limiting pretzels for the 14 or 28 ns spacing. However, the single bunch trains required substantially more pretzel over a limited and fairly low current range. Here it is not clear if the interactions are coherent.

In none of cases was the vertical beam size noted to change substantially. Beam size was observed to grow when exploring smaller currents and likewise smaller pretzels. In the current regime of interest reduced lifetime was the first deleterious effect observed when reducing the pretzel.

Discussion

It is natural to expect the limiting pretzel amplitude to depend on whether or not kicks are coherent. If the betatron phase advance between successive crossing points is small enough there is little if any cancellation: the kicks add coherently producing the same effect as if they were received at the just one point. Given the results from the 1 train studies we can make a map in the horizontal and vertical phase advance plane showing where incoherent and coherent interactions have been seen (figure 4).

Horizontal phase advance between successive crossing points is a critical factor as it determines the number of σ_x of separation between the beams. We have observed repeatedly that a change in the separation distance of less than σ_x can produce very dramatic changes in the lifetime. Given subsequent crossing points

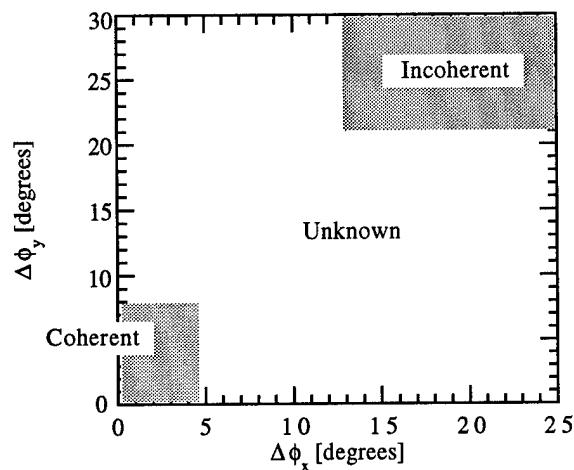


Figure 4: Regions of coherent and incoherent interactions are identified in when plotted against the horizontal and vertical phase advance between successive crossing points.

where the separation at one point is say $6\sigma_x$ and the separation at the other is $5\sigma_x$, it would be consistent with the observations if the $6\sigma_x$ point had essentially no effect on the lifetime. In this case coherency could not be observed.

EFFECT OF QUADRUPOLE NOISE ON THE EMITTANCE GROWTH OF PROTONS IN HERA

T. Sen, O. Brüning, F. Willeke
DESY, 85 Notkestrasse
22603 Hamburg, Germany

Abstract

The emittance growth in HERA at luminosity is about $1\pi\text{mm-mrad/hr}$. Intra-beam scattering and the beam-beam interaction coupled with tune modulation account for only part of the growth. Here we discuss the contribution of random tune fluctuations in the presence of non-linear fields to the emittance growth of protons. At injection energy, a recent experiment with noise deliberately injected into a chain of correction quadrupoles showed no significant effect on the emittance growth and loss rates except at high noise voltages. The results of this experiment are compared with a tracking study. We also present the results of a study done of the emittance growth due to the beam-beam interaction in the presence of tune noise. A future experiment to determine the effects of tune noise on the proton emittance growth rate with colliding beams is planned.

I. DYNAMIC APERTURE AND DIFFUSION AT INJECTION ENERGY

Particles are tracked through the model of the HERA lattice in SIXTRACK with multipolar field errors up to order 10 and without tune modulation. A complete description of the model and tracking procedure can be found in [1]. The chaotic boundary is estimated by examining the evolution of the distance in phase space between two particles which initially differed only in their x coordinate by 10^{-8}mm . A random kick is fed into 8 quadrupoles distributed uniformly around the ring. The amplitude of the kick Δk_0 is chosen so that a constant kick of this magnitude would lead to a tune shift of about 0.0001. We simulate the random kick by an Ornstein-Uhlenbeck process with a well-defined correlation time. The auto-correlation function of the random kick decays exponentially with time constant τ_c and the spectral density of the Ornstein-Uhlenbeck process decreases with the inverse of the frequency squared. The power spectrum drops to half its maximum value at a frequency $f_{1/2} = f_{rev}/(2\pi\tau_c)$, f_{rev} the revolution frequency of HERA is 47.317kHz.

In addition to the onset of chaotic motion, we also look at the diffusion rates of the particles. The diffusion coefficient is calculated by the method of Chirikov [2]. The idea is to calculate an averaged diffusion coefficient over two different time scales which differ by an order of magnitude. For bounded oscillatory motion, the two coefficients so calculated will differ by two or three orders of magnitude while for true diffusive motion, the two coefficients will be quite close, reflecting the underlying scale invariance of diffusive motion.

Without any tune modulation or noise, tracking over 10^5 turns indicates that the chaotic border is at an emittance of $2.90\pi\text{mm-mrad}$. This value is within 10% of that observed in the recent

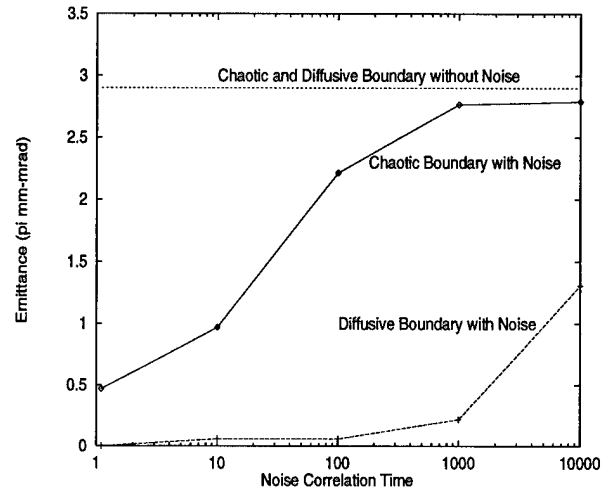


Figure. 1. The chaotic and diffusive boundaries as a function of the noise correlation time.

measurements [1]. The two coefficients D_1 and D_2 averaged over 1000 and 10000 turns respectively, differ by two orders of magnitude for particles launched with an initial emittance of less than $2.90\pi\text{mm-mrad}$ but are close for greater initial emittances. The chaotic border and the diffusive border are thus practically identical in this case. The addition of quadrupole noise separates these two boundaries. With a correlation time $\tau_c = 1.1$ or $f_{1/2} = 6.85\text{kHz}$, the chaotic border is at $0.47\pi\text{mm-mrad}$ while the two diffusion coefficients are nearly the same for all particles implying that all particles are diffusing. This would indicate that there is no absolutely stable region in the beam and that given enough time all particles would be lost. The chaotic boundary increases with the noise correlation time and eventually at $\tau_c = 10,000$ or $f_{1/2} = 0.75\text{Hz}$, the chaotic boundary is at $2.71\pi\text{mm-mrad}$ which is close to the value obtained without any noise. However in all cases with noise, the boundary where diffusion begins is considerably within the chaotic boundary. The diffusive boundary ranges from $0.0\pi\text{mm-mrad}$ at $\tau_c = 1.1$ to $1.3\pi\text{mm-mrad}$ at $\tau_c = 10000$. The dependence of these boundaries on the correlation time can be seen in Figure 1.

II. EXPERIMENTAL RESULTS AT INJECTION

An experiment was performed at the injection energy of 40 GeV where we introduced noise into a chain of correction quadrupoles using a noise source which produced a nearly flat Gaussian noise spectrum with a bandwidth of 10MHz. The closed orbit deviation through these quads was minimized to the extent possible at 2mm rms to avoid dipole noise excitation of the

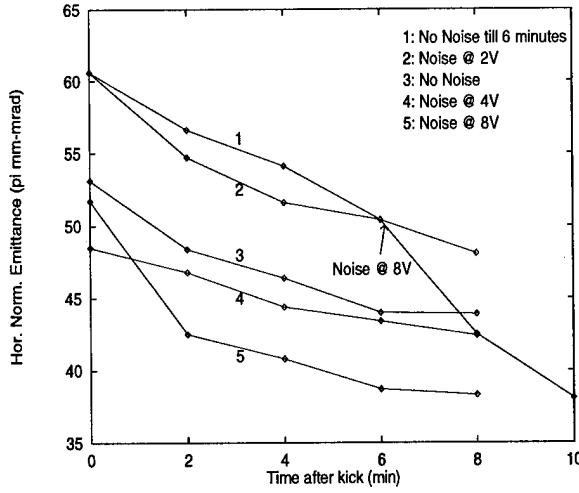


Figure 2. Evolution of the horizontal emittance after a kick to measure the dynamic aperture

beam. The aims were to examine the dependence of the following quantities on the noise voltage: a) the background loss rates, b) dynamic aperture and c) diffusion rates in the beam halo.

Without any external noise and a beam lifetime between 5 to 8 hours, the background rates at two collimators were about 170 and 700 Hz respectively. A noise voltage of 8V peak to peak was applied across the quadrupoles, and this increased the rates at the collimators to about 290 and 1200 Hz respectively. These observations were reproduced three times. We repeated this at a lower noise voltage of 2V but with a new beam. The lifetime of this beam was considerably lower, around 1 hour, and the applied noise made no significant difference to the loss rates.

The dynamic aperture was measured by kicking the beam horizontally with an injection kicker and observing the beam profile with the gas monitor. The outermost particles were kicked to an amplitude larger than the dynamic aperture and are lost so the remaining particles fill up the available dynamic aperture. This was done with five beam fills, twice without noise, initially, and once each with noise voltages of 2V, 4V and 8V across the quadrupoles. The evolution of the normalized horizontal emittance is shown in Figure 2. Clearly noise applied at 8V has a significant impact on the dynamic aperture while the effects of the other noise voltages is somewhat marginal. The fact that the dynamic aperture was reduced shows that a strong noise source can cause the loss of particles in the beam halo.

In the last part of the experiment, scrapers were moved in and out of the beam halo and the loss rates recorded. When the jaws are moved into the beam, the loss rates go up sharply before relaxing down to their previous value and the reverse behaviour is observed when the jaws are moved away from the beam. In this case the application of noise even at 8V did not make a significant difference in the loss rates observed without noise. The beam lifetime for this part of the experiment was also low, between 1 to 2 hours. It turns out [3] that a quantitative estimation of the diffusion rate from these measurements is difficult at injection energy because the observed relaxation does not fit a simple diffusion model. Consequently this was not attempted.

The fact that even a noise voltage of 8V did not change the loss rates at the collimator shows that noise has little effect on particles in the beam halo over short time scales. The dynamic aperture measurements showed however that, on a long time scale, strong noise does remove particles from the halo.

III. DIFFUSION AT COLLISION ENERGY

A study done by Brinkmann [4] showed that there was strong emittance growth due to tune noise when the tunes were close to a non-linear resonance. This growth was surprisingly not strongly dependent on the correlation time of the noise. One can calculate analytically the diffusion due to phase fluctuations in a region of phase space far from strong non-linear resonances. Assuming for simplicity a one dimensional round beam-beam kick, then using a method due to Stupakov [5], we find that the diffusion in action J is

$$D_J = 64\pi^2 \xi^2 J^2 e^{-\beta^* J/\sigma_e^2} \sum_{n=-\infty}^{\infty} K_\psi(n) \left\{ \left[I_0\left(\frac{\beta^* J}{2\sigma_e^2}\right) + I_1\left(\frac{\beta^* J}{2\sigma_e^2}\right) \right]^2 + \frac{1}{2} \sum_{k=1}^{\infty} [I_{k-1} + 2I_k + I_{k+1}]^2 \cos 4\pi k n \nu(J) \right\} \quad (1)$$

where ξ is the linear beam-beam tune spread, β^* is the beta function at the interaction point, σ_e is the rms beam size of the opposing beam, $K_\psi(n)$ is the correlation function of the phase fluctuations, the I_k 's are the modified Bessel functions, all with the same argument, and $\nu(J)$ is the betatron tune at the action J . The crucial observation here is that the first term in curly braces is independent of the betatron tune and shows that even noise of very low frequency can lead to a diffusion in action, one of Brinkmann's observations. The second term is large whenever the noise spectrum is appreciable at sidebands of twice the betatron frequency. At small J , $D_J \sim J^2$ while at large J we find, using the asymptotic expansion for $I_k(J)$, that $D_J \sim J$. However for J sufficiently large, the density of non-linear resonances is large enough that the assumptions of this calculation are not satisfied.

We now discuss the results of a simulation where we studied the interaction of the machine non-linearities with the beam-beam non-linearity in the presence of quadrupole noise. The HERA lattice was modelled by a series of FODO maps with 6 sextupoles and 4 quadrupoles with random kicks distributed between them. The sextupoles were adjusted to give roughly the same tune shifts as observed in the recent measurements [1]. Even then the effect of the sextupoles is quite exaggerated in this model since the diffusive boundary (without any noise) is about half of that obtained with a more realistic model of HERA in section I. However, it serves to emphasize the effects of machine non-linearities on a shorter time scale. We use Brinkmann's rational approximation [4] for the complex error function to speed up the computation of the beam-beam kick.

We follow the evolution of 100 particles for a million turns and calculate the two diffusion coefficients mentioned in section I over intervals of 10^4 and 10^5 turns respectively. With only the

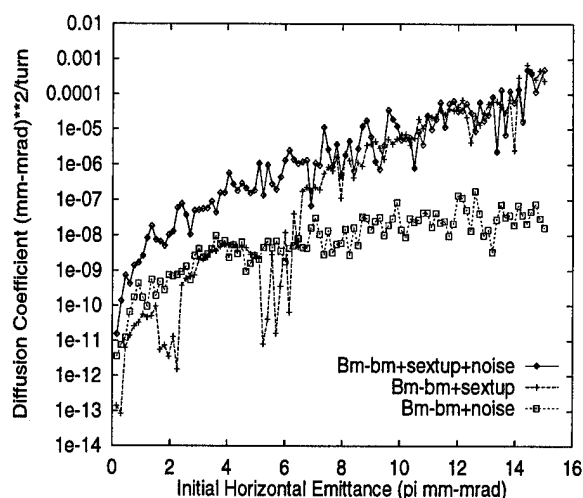


Figure 3. Diffusion coefficient for the horizontal action calculated after a million turns for three cases. The noise correlation time $\tau_c=10,000$.

linear lattice and the beam-beam potential, the two diffusion coefficients differ by two or three orders of magnitude, except in a region between $2.5\pi\text{mm-mrad}$ to $3.5\pi\text{mm-mrad}$, up to an initial emittance of $15\pi\text{mm-mrad}$. There is a dramatic change when we add the sextupoles to the beam-beam kick in the map. There is diffusive motion at all amplitudes. The addition of quadrupole noise to the beam-beam potential also leads to diffusive motion at all amplitudes but with a different amplitude dependence. Finally when both sextupoles and quadrupole noise are included, the diffusion is larger than with either of them alone. These results are shown in Figure 3. To see the effects of very low frequency noise, the correlation time was set to 10,000.

With the beam-beam potential and quadrupole noise the diffusion coefficient is larger at small amplitudes and then appears to saturate. With the beam-beam potential and sextupoles, the diffusion coefficient is smaller (or comparable in some regions) but after an emittance of around $6.0\pi\text{mm-mrad}$, it is larger by orders of magnitude. Thus the sextupoles are the dominant source of diffusion in the tails. With noise of shorter correlation times, the diffusion coefficient increases at all amplitudes.

IV. DISCUSSION

Quadrupole noise can effect the beam in three ways. Firstly there is a linear resonance which occurs if there is noise in the quadrupoles at twice the betatron frequency, i.e. at about 28kHz for the HERA proton beam. It is unlikely that frequencies above 1kHz penetrate into the beam since the inductance and capacitance of the quadrupoles filter out high frequencies and there is additional shielding due to the copper layers in the beam pipe. So the linear resonance is not expected to play a role. Quadrupole noise also causes the phase advance to have a fluctuating component and hence successive non-linear kicks (due to magnets or the opposing beam) occur between partially de-correlated phases. Greater the degree of de-correlation or magnitude of the fluctuating phase, larger will be the diffusive growth. This effect will be dominant at low amplitudes. Finally, the (partially) ran-

dom nature of the kicks can also transport particles into stochastic layers and enhance the rates at which resonances are crossed. This effect will be dominant where the density of non-linear resonances is greatest, i.e. at intermediate amplitudes for the beam-beam kick and large amplitudes for magnetic multipole kicks. This enhancement due to noise could be swamped by other effects such as tune modulation. Bruning [6] has studied diffusion in the tails due to tune modulation. Our results at collision energy show that machine non-linearities also contribute strongly to the diffusion in the tails of the beam. In the core of the beam we find that in addition to intra-beam scattering, quadrupole noise also contributes to diffusion.

We thank M. Bialer for assistance during the experiment, W. Fischer for help with the tracking program SIXTRACK and R. Brinkmann and M. Seidel for useful discussions.

References

- [1] F. Willeke et.al., this conference
- [2] B. Chirikov, *Phys. Rep.*, **52**, pg 263 (1979)
- [3] M. Seidel, private communication
- [4] R. Brinkmann, DESY report HERA 89-24 (1989)
- [5] G.V. Stupakov, SSCL report SSCL-560 (1991)
- [6] O. Bruning, this conference

NONLINEAR MODE COUPLING ANALYSIS IN THE TEVATRON¹

S. Assadi and C.S. Mishra, Fermi National Accelerator Laboratory, Batavia, IL -60510, USA.

Increased demand for higher luminosities from Fermilab proton-antiproton collider requires higher intensities and increased number of bunches. The performance of existing 6x6 and the proposed 36x36 collider is often limited by the non-linear effects arising from beam-beam interactions, in particular for high intensity beams. The tune shifts and spread from increased long range interactions combined with higher order multipoles complicates the frequency spectrum of the particle motions. TEAPOT simulation program is used to generate turn by turn data that could be used in the nonlinear mode spectrums analysis. Bispectral mode analysis is discussed.

I. INTRODUCTION

A ubiquitous feature of high luminosity Tevatron proton-antiproton collider is the presence of nonlinear forces composed of a spectrum of frequencies and wavenumbers (i.e. higher order multipoles sampled by the particles with the largest beam-beam tune shift). Understanding the spatial and temporal structure of the beam dynamics in connection with chromaticity, the dispersion in RF cavities and higher order multipoles remains a daunting goal of nonlinear beam physics. Nonlinear interactions between spatial Fourier components are the key determinant of the wave vector (**k**) spectrum of the fluctuating particles.

The analytic theory of synchro-betatron motions was first studied in connection with chromaticity. The dispersion in RF cavities was found to cause beam loss by coupling, and this effect has been studied analytically and computationally by a number of physicist. However, no experimental evidence of considerable wave-wave coupling of the broadband turbulence has been reported so far. Whereas the standard linear spectral analysis (power spectrum) provides experimental information on the amplitude and phase behavior of the individual Fourier components and the transport induced by fluctuations, it does not give any information about the coupling among different spectral components. The use of the bispectral analysis allows one to discriminate between oscillations spontaneously excited by the beam and those generated by nonlinear coupling.

The purpose of this paper is to introduce a new analysis tool for turbulent or chaotic data to the accelerator physics community. We investigate the combined effect of long range interactions and higher order multipoles to calculate the nonlinearly generated frequency spectrum. In this paper we discuss three cases. First we restrict ourselves to synchro-betatron and betatron-betatron coupling of a single beam with betatron tunes close to 7/12 resonance when higher order multipoles are present. Second, beam-beam

without error fields are considered. Finally beam-beam with multipoles are analyzed. A modified version of thin element tracking program TEAPOT (see paper by C.S. Mishra et al. In these proceedings) has been used to simulate the turn by turn data for Tevatron lattice.

II. ANALYSIS

The bicoherence spectrum has been computed to study the strength of the three-wave coupling contributing to the characteristics of beam-beam coupling in the Tevatron.

The *bicoherency* is defined as

$$b^2(v_1, v_2) = B(v_1, v_2)^2 / [\langle |X_{v_1} X_{v_2}|^2 \rangle P(v)],$$

where $B(v_1, v_2)$ is the bispectrum defined as $B(v_1, v_2) = \langle X_{v_1} X_{v_2} X_{v_1+v_2}^* \rangle$, $P(v)$ the autopower spectrum $P(v) = \langle |X_v|^2 \rangle$, X_v is the Fourier transform of the turn by turn data, $X(t)$ and $\langle \rangle$ means ensemble averaging over many statistically similar realizations. The bicoherency measures the fraction of the fluctuating power at a frequency v which is phase correlated with the spectral components at frequency v_1 and v_2 obeying the summation rule $v = v_1 + v_2$. The bicoherency thus quantifies the degree of coupling among three waves. The bicoherency is bound between 0 and 1: When $b^2(v_1, v_2)$ is equal to 1 then the oscillations at frequency v are completely coupled with frequency components at frequency v_1 and v_2 and completely decoupled for the zero value. The use of the bicoherence as a measure of three-wave coupling is independent of any closure assumptions. The bicoherence is nonzero if there is a statistically significant phase relation between the three modes. Such bispectral analysis has been advanced by Ritz, Powers, and Bengtson for plasma research, and applied in the frequency domain to electrostatic fluctuations [1].

III. SIMULATION RESULTS AND CONCLUSIONS

In order to predict a particle's behavior in the presence of the beam-beam interaction in the Tevatron, modified TEAPOT simulation code was ran under three conditions. The predicted position and phase of a particle after a designated 20000 turns is used to calculate the bicoherencies. In all cases, The base tune for all conditions are $(Q_x, Q_y) = (20.5836, 20.5826)$. The two sextupole families are used to set the chromaticity of the Tevatron

¹ Operated by the University Research Assoc. Inc., under contract with U.S. Dept. of Energy.

to a desired value (minimum chromaticities to keep the beam stable at 900 Gev); the chromaticity setting is adjusted to $\xi_x = 20$ and $\xi_y = 24$. The launched particle has $\Delta P/p = 0.0001$. Beam

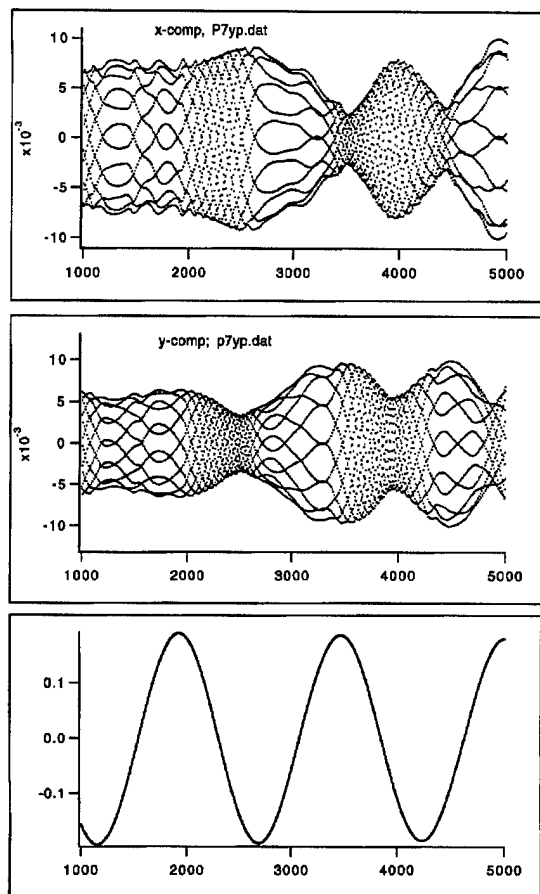


Figure 1.) Small section of the turn by turn plots of a particle with beam-beam is shown. Higher order multipoles are not present. The top plot is the horizontal, the middle plot is the vertical and the lower plot is the synchrotron motion. Clearly the energy exchange between the horizontal and vertical plane during the rise time of the synchronous oscillations is different from the fall.

intensity is $3.0E11$. The initial position and phase is the same for all cases. Figure one shows a small section of the turn by turn data used to calculate the bicoherency. In a first approximation, when the intensity of the opposite beam is relatively low and the tunes are far enough from the low order resonances, the beam-beam effects appear as a nonlinear dependence of the frequencies of transverse oscillations on their amplitude. For larger intensity, or when the tune are close to the low-order resonances, isolated nonlinear resonances, creating a periodic energy exchange between the transverse planes, come into play. This is the regime we have performed the simulations. For still larger intensity, the

resonances can overlap to form stochastic regions where the particle dynamic is diffusive.

Figure 2 shows the normalized phase space plot for the single beam. The only source of nonlinearities is the higher order multipoles. The above standard normalized phase space plot does not show

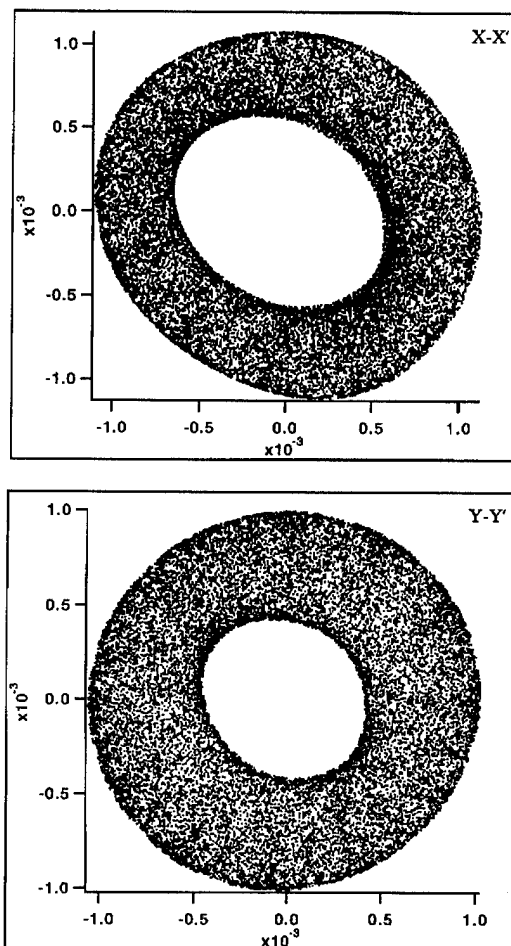


Figure 2). Single beam normalized phase space plots with higher order multipoles is shown.

any structure that could reveal the sources of nonlinearities if any exist. However, Figure 3 shows the calculated bicoherency which clearly shows the three wave coupling. Peak "A" is the only significant nonlinearity observed which is due to the dispersion present in the cavities. This synchro-betatron coupling can be removed from the simulation by removing dispersion. Figure 4 shows the normalized phase-space plot for the beam-beam with the long range kicks. The higher order modes are not present. Twelve island associated with 12 parasitic crossing is observable. This non-linearity is small for small amplitude particles. Figure 5 represent the bicoherency spectrum of beam-beam without the HOM. We observe nonlinearly generated modes due to dispersion

and also along the difference resonance $\nu_H - \nu_V$. Fig. 6 and Fig. 7 show the normalized phase space as higher order multipoles added to the case 2 of Fig. 4 and Fig. 5.

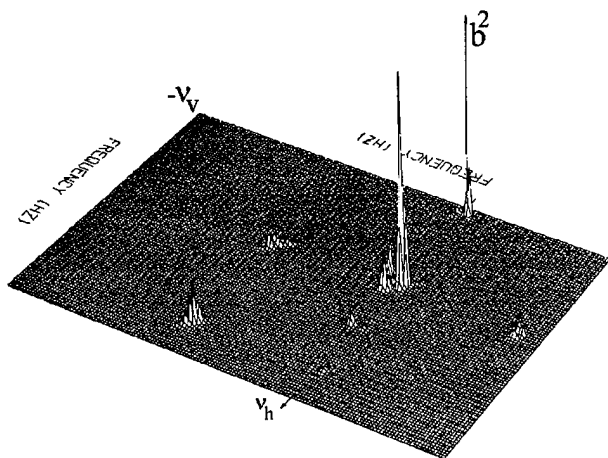


Figure 3) Bicoherence, $b(\nu_1, \nu_2, \nu_3)$ of single beam with all higher order modes present. The horizontal axes denote horiz. and vertical tunes. The vertical axis denotes the bicoherence for $\nu_3 = \nu_1 + \nu_2$. The larger the amplitude, the stronger the nonlinear coupling is.

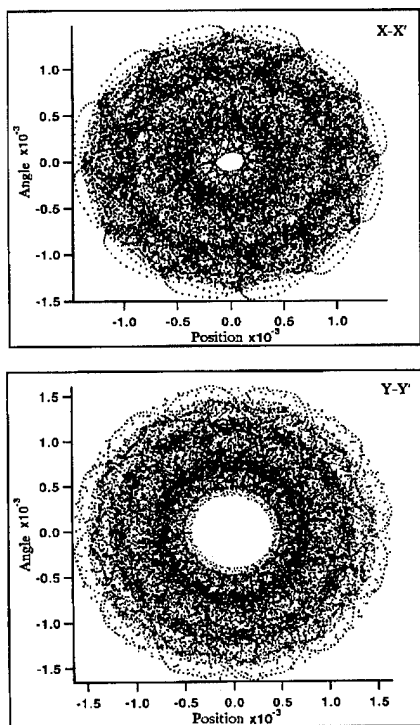


Figure 4) Normalized phase-space plots for beam-beam without higher order multipoles is shown

IV. REFERENCE

- 1) Ch. P. Ritz, et al., Phys. Fluids B I, 153 (1989).

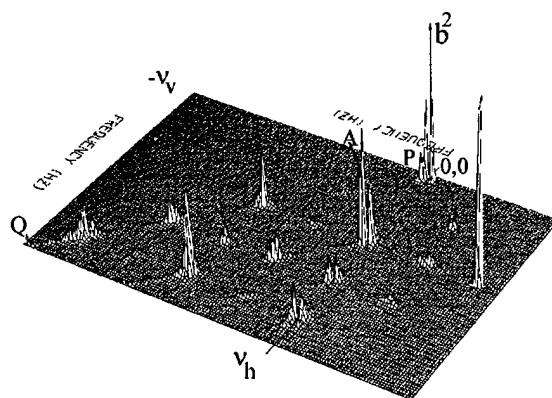


Figure 5) Bicoherence of beam-beam without HOM.

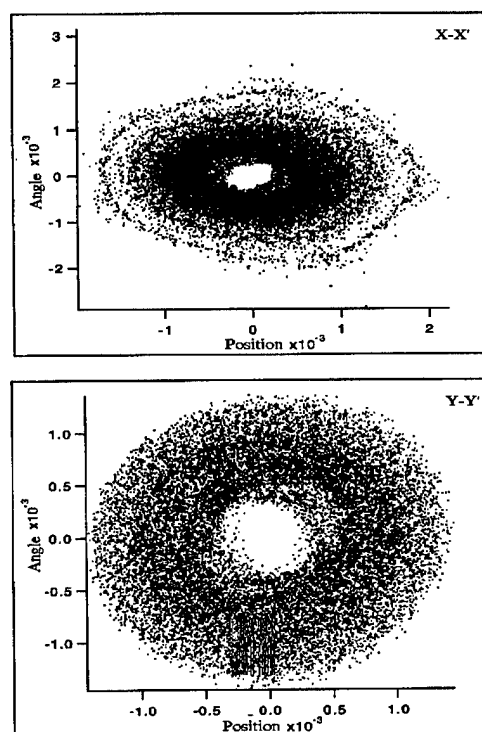


Figure 6) Normalized phase-space plots for beam-beam with higher order multipoles is shown.

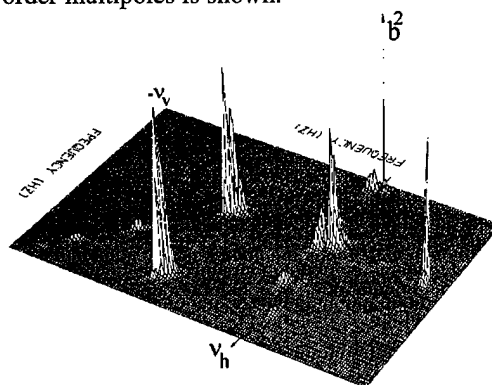


Figure 7) Bicoherence of beam-beam with all higher order multipoles present.

LATTICE DESIGN FOR KEKB COLLIDING RINGS

H. Koiso and K. Oide, National Laboratory for High Energy Physics, Oho, Tsukuba, Ibaraki 305, Japan

Abstract

A lattice consistent with a peak luminosity of $10^{34} \text{ cm}^{-2}\text{s}^{-1}$ is designed for the KEK B-Factory (KEKB). A new unit cell structure with 2.5π phase advance is applied in the arc so as to install the non-interleaved sextupole pairs efficiently. This cell structure also provides a wide range of tunability for the emittance and the momentum compaction factor, while maintaining the $-I$ relation between sextupoles.

I. REQUIREMENTS FOR LATTICE DESIGN

KEKB is a double-ring asymmetric e^+e^- collider at $3.5 \text{ GeV} \times 8 \text{ GeV}$. Basic machine parameters for the goal peak-luminosity of $10^{34} \text{ cm}^{-2}\text{s}^{-1}$ are listed in Table I. The non-interleaved chromaticity correction scheme is essential to satisfy the requirements for the dynamic aperture in KEKB. This scheme uses pairs of identical sextupoles which are connected with a $-I$ transformer in both horizontal and vertical planes. If no other sextupoles exist between paired ones, main transverse nonlinearities of sextupoles are always canceled up to the third order in the Hamiltonian.[1] Thus the transverse dynamic apertures are significantly improved.[2]

	LER	HER
Beam Energy (GeV)	3.5	8.0
Luminosity ($\text{cm}^{-2}\text{s}^{-1}$)	1.0×10^{34}	
Half crossing angle (mrad)	11	
Tune shifts ξ_x/ξ_y	0.039/0.052	
Beta functions β_x^*/β_y^* (m)	0.33/0.01	
Beam current (A)	2.6	1.1
Bunch spacing (m)	0.59	
Particles/bunch	3.3×10^{10}	1.4×10^{10}
Emittances $\varepsilon_x/\varepsilon_y$ (m)	$1.8 \times 10^{-8}/4.3 \times 10^{-10}$	
Bunch length (mm)	4	
Momentum spread	7.1×10^{-4}	6.7×10^{-4}
Synchrotron tune	0.01~0.02	
Momentum compaction	$1 \times 10^{-4} \sim 2 \times 10^{-4}$	
Betatron tunes ν_x/ν_y	45.52/45.08	47.52/43.08
Circumference (m)	3016	

Table I
Machine Parameters of KEKB.

II. DEVELOPMENTS IN BEAM-OPTICAL DESIGN

So far we have tried five types of optics as listed in Table II. These optics have different combinations of cell structures and chromaticity correction schemes. All optics have been designed to give the required values of the horizontal emittance ε_x and

	Injection	Touschek	ν_s
I FODO Cell	bad	bad	bad
NI FODO Cell	good	fair	bad
NI π Cell	excellent	fair	good
NI 2.5π Cell	excellent	good	excellent
NI 2.5π Cell +LCC	excellent	excellent	excellent

Table II

Comparison of performances of cell structures and chromaticity correction schemes for LER. I: interleaved sextupoles, NI: non-interleaved sextupoles, LCC: local chromaticity correction at the interaction region.

the momentum spread σ_δ . Calculations concerning lattice design such as matching of linear optics, optimization of sextupole strengths, particle tracking, etc. have been carried out with a code SAD developed at KEK.[3]

We have compared the performance of these optics in the light of the following requirements: (1) to have a sufficiently large dynamic aperture for the beam injection; (2) also an enough large dynamic aperture for the Touschek lifetime; (3) to give small synchrotron tune ν_s which is necessary to avoid the synchrotron-betatron resonances caused by the lattice nonlinearities and the beam-beam effect. Since σ_δ and the bunch length have been determined, we must adjust the momentum compaction factor α_p to achieve small ν_s . Resulting performances are summarized in Table II and Fig. 1. The second criterion is especially severe for the low energy ring (LER), and thus we will discuss mainly on LER in this paper.

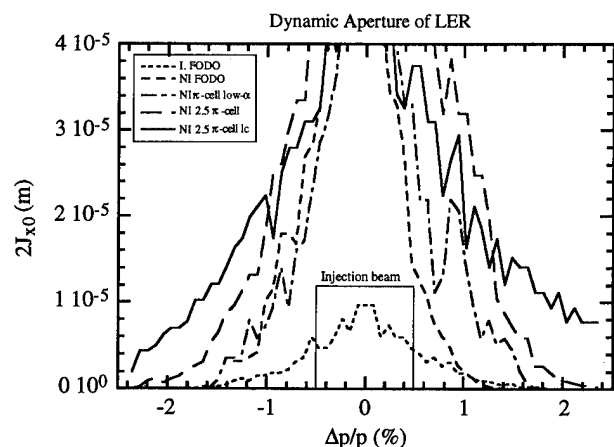


Figure. 1. Dynamic apertures of LER with five types of beam optics.

A. Interleaved $\pi/3$ FODO Cell

We have tried a conventional interleaved chromaticity correction scheme with $\pi/3$ FODO cells, where each quadrupole has a sextupole adjacently. Sextupoles of π phase difference are paired to cancel the lowest order of the transverse nonlinearities. Although we have tried chromaticity corrections with 6, 12, and 24 sextupole families, the dynamic aperture in all cases remains too small to satisfy the requirement. Then we have abandoned the interleaved scheme.

B. Non-interleaved $\pi/2$ FODO Cell

At the first step in designing arcs, we determine the bending radius ρ from the requirement for σ_δ . After fixing ρ , we need two free parameters to give required values of ε_x and α_p . In FODO cells, however, both ε_x and α_p are almost determined by the horizontal tune of the arc ν_x . If we compose arcs with $\varepsilon_x = 1.8 \times 10^{-8} \text{ m}$ of FODO cells, α_p becomes 4 times larger than the required. This means $\nu_s \geq 0.06$, which makes serious shrink of the operating points in the tune space. The anomalous emittance due to the chromaticity can also be serious when ν_s is high.[4] In addition, the accelerating voltage becomes too high to achieve the design bunch length. Then we have rejected FODO cells.

C. Non-interleaved π Cell

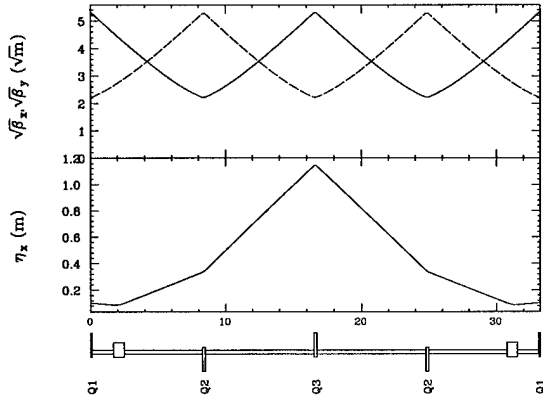


Figure 2. Structure of the π cell for LER. The unlabeled rectangles depict dipoles.

To obtain small α_p , we must reduce the horizontal dispersion η_x in dipoles. We combine two $\pi/2$ FODO cells, merging four dipoles into two, and place the dipoles only where η_x is small, as shown in Fig. 2. We have the positions of dipoles as a free parameter as well as ν_x in this cell, thus we can decrease α_p to be small enough in the LER, keeping the required ε_x .

From the view point of the chromaticity correction, the arc built with π cells has a disadvantage that peaks of η_x are distributed only with $N\pi$ phase difference. This means that if we place sextupole pairs (SF's) for horizontal chromatic corrections only near the η_x peaks, corrections at $(N + 1/2)\pi$ phases become difficult. The packing factor of SF's becomes worse than in the FODO case. Even if we try to place SF's at small η_x points, it is still less effective for $(N + 1/2)\pi$ phases. These situations are undesirable for the chromaticity correction, then the dynamic

apertures in the region of large momentum deviations are not enough satisfactory for the Touschek lifetime.

D. Non-interleaved 2.5π Cell

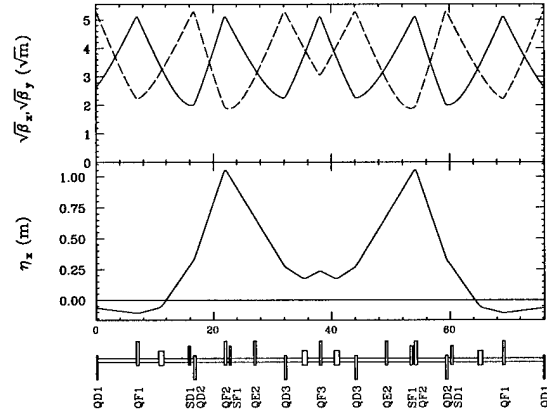


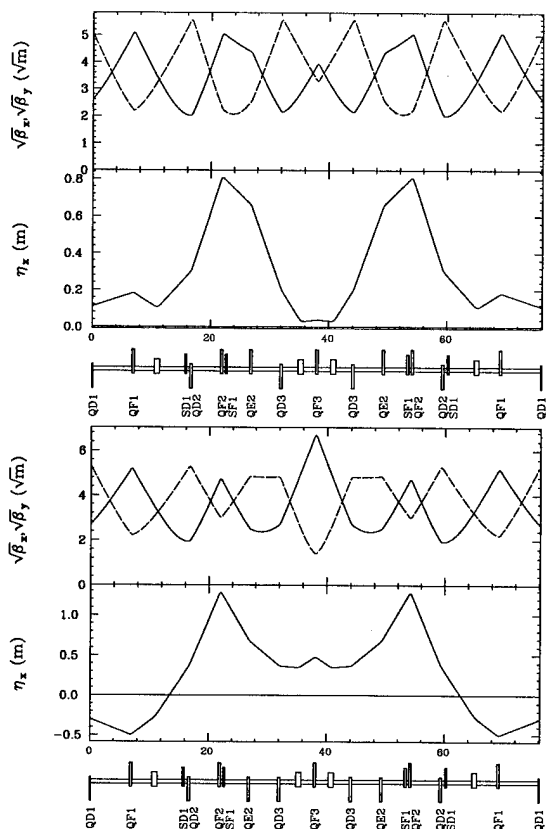
Figure 3. Structure of the 2.5π cell for LER.

A unit cell structure with 2.5π phase advance is created by combining five $\pi/2$ FODO cells and by merging ten dipoles into four. In this cell, dipoles are placed to form two dispersion bumps so that we can keep η_x small at dipoles, similar to the π cell case. By adjusting the positions of dipoles and η_x at the dipoles, we can obtain required values of ε_x and α_p at the same time.

The 2.5π cell enables us to install non-interleaved sextupole pairs effectively. Successive SF (SD) pairs are distributed changing the relative phase of $3\pi/2$. Then chromatic kicks at $N\pi$ and $(N + 1/2)\pi$ phases in both horizontal and vertical planes can be corrected efficiently. The dynamic aperture of the 2.5π cell is significantly improved to satisfy all of the requirements. Higher-order chromaticities still remains because the sextupoles are not sufficiently close to the main chromaticity sources in the interaction region (IR). We can achieve further improvements by localized chromaticity correction in the IR.

The 2.5π cell has another merit on the tunability of ε_x and α_p . In this cell structure, we place non-interleaved sextupoles connected with a 4×4 pseudo $-I$ transformer which has $m_{21} \neq 0$ and $m_{43} \neq 0$ but basically cancels nonlinear kicks by sextupoles. We have confirmed that this pseudo $-I$ transformer brings about as a large dynamic aperture as the perfect $-I$. By allowing $m_{21} \neq 0$ and $m_{43} \neq 0$, two new free parameters become available for tuning. These parameters are utilized by placing two families of quadrupoles (QF2 and QD2) outside the sextupole pairs so that we can change them afterwards to tune α_p , keeping the pseudo $-I$ transformation. Actually we can tune α_p in the range $-1 \times 10^{-4} \leq \alpha_p \leq 4 \times 10^{-4}$ by changing the strengths of QF2's and QD2's by a few percent. During this time, ε_x is kept nearly constant.

On the other hand, it is rather difficult to change ε_x widely only by adjusting the two families of quadrupoles. To cure this restriction, we introduce a new family of quadrupoles QE2 inside the SF pair. By adjusting η_x at dipoles using five free parameters (QF2, QF3, QD2, QD3, and QE2), we can obtain the required tunability, $1.0 \times 10^{-8} \text{ m} \leq \varepsilon_x \leq 3.6 \times 10^{-8} \text{ m}$, while keeping α_p constant and maintaining the pseudo $-I$ condition between the SF's.



Entropy and Emittance Growth*

Patrick G. O'Shea,

Free-electron Laser Laboratory, Box 90319, Duke University, Durham NC 27708 USA

ABSTRACT

In this paper we examine the connection between emittance growth and entropy growth in linear accelerators. We divide emittance growth in to two classes: reversible and irreversible depending on the corresponding entropy change. We propose the general hypothesis that if $\Delta\epsilon > 0$ and $\Delta S = 0$, then the emittance growth may be reversible. We also propose that if $\Delta\epsilon > 0$ and $\Delta S > 0$ then the emittance growth is irreversible. We outline how the concept may be applied to particular cases of relevance e.g. emittance growth and recovery in electron photoinjectors, and wakefield induced emittance growth, where correlations are introduced in the transverse phase space.

INTRODUCTION

The general connection between emittance (ϵ) and entropy (S) was made over two decades ago by Lawson, Lapostolle and Gluckstern [1]. The connection between emittance growth and entropy growth has been mentioned briefly by some authors [2,3].

In classical thermodynamics entropy is defined in two ways [4,5]. Entropy is considered as a macroscopic quantity in equilibrium thermodynamics, or as a microscopic quantity of a statistical ensemble. In macroscopic thermodynamics, entropy, like temperature, cannot be defined for a system that is not in thermal equilibrium. This poses a difficulty when dealing with non thermalized or non equilibrium beam distributions such as those generated in photoinjectors [6].

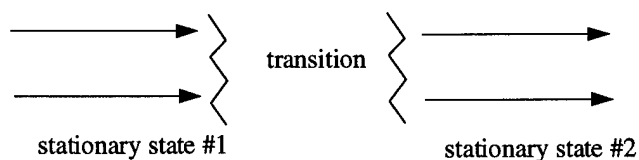


Fig. 1 Macroscopic states of a beam system

We can define both thermodynamic and statistical entropy for equilibrium state #1 or #2 in Fig.1, and consequently the difference in entropy between the two states. In the equilibrium the two definitions lead to identical results. In many cases, the transition i.e. non-equilibrium region, may extend from the cathode to the beam dump [7,8]

DETERMINING THE ENTROPY

In the transition region we must rely on the statistical definition. In the most general sense the statistical entropy of a system can be written, as:⁴

$$S = -k \sum_i f_i \ln(f_i)$$

(1)

where k is Boltzmann's constant, i denotes a microcanonical state of the system, and f_i is the statistical probability of that state and $\sum_i f_i = 1$.

In the case of a beam microbunch with a very large number of particles (N) we can write the sum as an integral by noting that a state corresponds to a six dimensional volume element $A_6 = \delta^6 x$, and the probability is equivalent to the product of A_6 times the distribution function $\rho_6(x, p_x, y, p_y, z, p_z)$. So that:

$$S_6 = -kN \int \rho_6(x) \ln[\rho_6(x)] d^6 x$$

(2)

where $\int \rho_6(x) d^6 x = 1$. To simplify matters for this short paper, and without loss of generality, let us assume a monochromatic beam and consider a 3-D trace space (x, x', ζ) where $x' = dx/dz$ and ζ is the axial coordinate relative to the center of the bunch, and $A_3 = \delta x \delta x' \delta \zeta$. So that the 3-D entropy is given by

$$S_3 = -kN \int \rho_3(x) \ln[\rho_3(x)] d^3 x$$

(3)

We will neglect the numerical subscripts from now on. To deal with beams that are changing energy we can define a normalized entropy S_n as:

$$S_n = -kN \int \rho(x, x', \zeta) \ln \left[\frac{A \rho(x, x', \zeta)}{\beta \gamma} \right] dx dx' d\zeta \quad (4)$$

while keeping A constant, independent of energy.

How do we choose the size of the volume element A ? Let us neglect quantum mechanical limits. We could choose

* Work supported by ONR under contract N00014-91-c-0226

A based on the limits of our ability to make observations on the beam i.e. on the resolution of our instrumentation or on the limits of physical phenomena of interest.

Consider the division of the bunch in to microstates or sub-bunch slices as in Fig. 2.

We divide the bunch into a number of sub-bunches or slices i of axial length $\delta\zeta$ where $\delta\zeta \ll \sigma_b$ the bunch length and ζ_i is the axial coordinate of the i^{th} sub-bunch relative to the centroid of the bunch. Consider each sub-bunch to contain a large number of particles, N_i . The ensemble entropy of the bunch is the sum of the entropies of the sub-bunches i.e. $S = \sum_i S_i$ where S_i is the entropy of the i^{th} sub-bunch. So in

our reduced dimensional space S_i is a 2-D entropy and S is the 3-D entropy.

In general the normalized sub-bunch entropy can be written as:

$$S_{i,n} = kN_i \ln\left(\frac{D_p \pi \tilde{\epsilon}_{i,n} \delta\zeta}{A}\right) \quad (5)$$

where $\tilde{\epsilon}_{i,n}$ is the normalized rms emittance of a sub-bunch, and D_p is a unitless parameter that depends on the shape of the trace space particle distribution. For a K-V distribution $D_{kv} = 4$; for a Gaussian distribution $D_g \approx 5.4$; for a water bag distribution $D_w = 5$. The entropy depends not only on the rms emittance but also on the distribution function.

An entropy change can occur from a change in the emittance, the distribution function or the number of particles in the sub-bunch. Note that changes in N_i correspond to axial migration of particles.

CORRELATED BEAMS

Consider in the case of a beam generated in a an rf photoinjector, in which sub-bunch correlations are introduced by the non uniform axial distribution of the bunch [9]. On scales shorter than $\delta\zeta$ we assume that randomization of the phase space occurs. On scales longer than $\delta\zeta$ we assume that there may be correlations between the phase space and the location in of the slice in the bunch.

The phase space of the i^{th} sub-bunch may be characterized by the emittance $\tilde{\epsilon}_i$, and the Twiss parameters $\hat{\alpha}_i, \hat{\beta}_i, \hat{\gamma}_i$ and $\hat{\alpha}_i^2 + 1 = \hat{\beta}_i \hat{\gamma}_i$. Now envision process where the phase space distribution of beam evolves while each sub-bunch continues to contain the same particles and where the ϵ_i remain constant but where the Twiss parameters change in a ordered fashion i.e. the α_i, β_i , and γ_i maintain some well-defined, well behaved functional relationships such that:

$$\hat{\alpha}_i = \hat{\alpha}(\zeta, z), \hat{\beta}_i = \hat{\beta}(\zeta, z), \text{ and } \hat{\gamma}_i = \hat{\gamma}(\zeta, z) \text{ and } \tilde{\epsilon}_i = \tilde{\epsilon}(\zeta, z)$$

where z is the coordinate of the bunch centroid along the beamline in the laboratory frame.

If the phase space is correlated in ζ , then the forces that determine the phase space evolution must also be correlated in ζ . Other examples of such processes might include single bunch transverse-wakefield induced head to tail kicks, and phase dependent longitudinal and transverse rf effects.

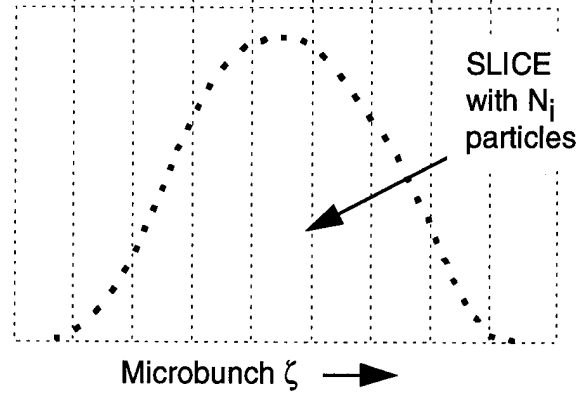


Fig. 2 Division of the bunch in to slices.

Consider a longitudinal density distribution function $p(\zeta)$ independent of z , such that $\int p(\zeta) d\zeta = 1$. If we define the normalized rms emittance of the bunch in the conventional way as:

$$\tilde{\epsilon}_n(z) = \beta \gamma \left[\langle x^2 \rangle \langle x'^2 \rangle - \langle x x' \rangle^2 \right]^{0.5}$$

then:

$$\tilde{\epsilon}_n(z) = \left[\frac{\int \tilde{\epsilon}_n(\zeta, z) \hat{\beta}(\zeta, z) p(\zeta) d\zeta \int \tilde{\epsilon}_n(\zeta, z) \hat{\gamma}(\zeta, z) p(\zeta) d\zeta}{-\left(\int \tilde{\epsilon}_n(\zeta, z) \hat{\alpha}(\zeta, z) p(\zeta) d\zeta \right)^2} \right]^{0.5} \quad (6a)$$

At $z = 0$, i.e. at the cathode, the emittance is the same for all slices, so we can write $\tilde{\epsilon}_n(\zeta, 0) = \tilde{\epsilon}_{s,n}$, where $\tilde{\epsilon}_{s,n}$ is the slice emittance at the cathode. Consider a situation where the emittance of each slice is independent of z . This will be true for linear transverse forces acting on each slice. Then:

$$\tilde{\epsilon}_n(z) = \tilde{\epsilon}_{s,n} \left[\frac{\int \hat{\beta}(\zeta, z) p(\zeta) d\zeta \int \hat{\gamma}(\zeta, z) p(\zeta) d\zeta}{-\left(\int \hat{\alpha}(\zeta, z) p(\zeta) d\zeta \right)^2} \right]^{0.5} = \tilde{\epsilon}_{s,n} C(z) \quad (6b)$$

where we call $C(z)$ the emittance correlation function and $C(0) = 1$ i.e. at the cathode the bunch phase-space is uncorrelated. Because of the properties of the Twiss parameters $C(z) \geq 1$ always. Therefore $\tilde{\epsilon}_n(z) \geq \tilde{\epsilon}_{s,n}$ always.

The value of $C(z)$ is calculable form the beam dynamics. We can write the normalized entropy in this case as :

$$S_n = \sum_i S_{i,n} = \sum_i kN_i \ln\left(\frac{D_p \pi \tilde{\epsilon}_{s,n} \delta\zeta}{A}\right) = kN \ln\left(\frac{D_p \pi \tilde{\epsilon}_{s,n} \delta\zeta}{A}\right) \quad (7)$$

the latter equality when the $\tilde{\epsilon}_{s,n}$ are equal. Note that the entropy of the bunch, unlike the emittance, does not depend

explicitly on the precise details of the of the orientation of the phase space of each slice. Therefore it is possible for $\tilde{\epsilon}_n(z)$ to change i.e. increase or decrease without any change in S_n .

REVERSIBLE AND IRREVERSIBLE PROCESSES

In order for S_n to increase the slice emittances $\tilde{\epsilon}_{s,n}$ must increase. If the $\tilde{\epsilon}_{s,n}$ increase then from eqn. (6), $\tilde{\epsilon}(z)$ will increase irreversibly and $\delta S_n > 0$. Such increase could be the result of non linear space-charge or other forces acting on the beam. Conversely if the $\tilde{\epsilon}_{s,n}$ do not increase then any increase or decrease in $\tilde{\epsilon}(z)$ is a result of changes in $C(z)$ and consequently the process is in principle reversible, and also $\delta S_n = 0$.

In the latter case emittance growth becomes recoverable. This is the case in photoinjectors where solenoidal emittance compensation is used [9]. In this case the combination of self forces and the focusing force combine to introduce correlations into the bunch. It is important to note that in the photoinjector case there is no simple rotation in 6-D phase space that will remove the emittance growth. The correlated emittance growth may be removed by appropriate focusing of the bunch. We have developed an analytic description of the photoinjector emittance compensation process in which $C(z)$ can be calculated [10]. When we have uniform transverse space-charge density in each slice and a well-behaved longitudinal distribution, we see that $C(z)$ will grow and can be brought back down to unity when appropriate focusing forces are applied.

What happens when the correlations implied in eqn. (6) are removed, i.e. $C(z) = 1$ and $\tilde{\epsilon}_n(z) = \tilde{\epsilon}_{s,n}$? Then any further changes in $\tilde{\epsilon}_n(z)$ result from changes in $\tilde{\epsilon}_{s,n}$ and result in changes in S_i and S and are therefore irreversible. The correlations can be lost by axial particle mixing, driven by thermal or space-charge effects. If $C(z) > 1$ and no attempt is made to focus the beam then the correlations will be lost over some longitudinal diffusion distance z_D . When this happens the slice emittances grow to become equal to the bunch emittance and hence the correlation is lost, the entropy grows and the emittance growth becomes irreversible.

Another example is a bunch that experiences a transverse dipole kick such that the magnitude of the displacement is related to the position (ζ) within the bunch. The bunch emittance is increased. The sub-bunch emittances are unchanged. If an equal and opposite kick is applied then the bunch emittance is recovered. If before the correlate emittance growth is removed there are multiple uncorrelated kicks, or if there is particle diffusion, the emittance growth becomes irreversible.

Similar statements can be made about phase dependent rf effects.

In practice we can consider emittance growth to have two components:

1. where $\delta S = 0$

2. where $\delta S > 0$

so that $\delta \tilde{\epsilon}(z)^2 = \delta \tilde{\epsilon}(z)_R^2 + \delta \tilde{\epsilon}(z)_I^2$ where the subscripts R and I stand for reversible and irreversible respectively. In the example of eqn. (6b) we have:

$$\frac{\delta \tilde{\epsilon}_n(z)^2}{\tilde{\epsilon}(z)^2} = \frac{\delta C(z)^2}{C(z)^2} + \frac{\delta \tilde{\epsilon}_{s,n}^2}{\tilde{\epsilon}_{s,n}^2}$$

There is no guarantee that reversible emittance growth can in fact be reversed. The degree of achievable reversibility depends on our ability to apply correlated corrective forces to the bunch.

There are still many unanswered questions about the entropy emittance growth question. In future work we will show how entropy growth can lag behind emittance growth and establish quantitative criteria for the distance scales over which entropy growth occurs. A connection will be made to free-energy concepts.[3,11-13]. We will also generalize our concept to 6-D phase space.

REFERENCES

1. J.D. Lawson, P.M. Lapostolle and R.L. Gluckstern, *Part. Accel.*, **5**, 61 (1973).
2. J.D. Lawson, "The Physics of Charged Particle Beams", Oxford University Press, , Oxford, p. 193 (1988)
3. M. Reiser, "Theory and Design of Charge Particle Beams", Wiley-Interscience, New York, (1994)
4. R.T. Cox, "The Statistical Mechanics of Irreversible Change", The Johns Hopkins Press, Baltimore, (1955)
5. J.D. Fast, "Entropy", McGraw-Hill, New York (1962)
6. B.E. Carlsten, J.C. Goldstein, P.G. O'Shea and E.J. Pitcher, *Nucl. Instr. Meth.*, **A331**, 307 (1993)
7. N. Brown and M. Reiser, *Phys. Plasmas* **2**, 965 (1995)
8. M. Reiser and N. Brown, *Phys. Rev. Lett.*, **74**, 1111 (1995)
9. B.E. Carlsten, *Part. Accel.*, **49**, 27(1995)
10. P.G. O'Shea to be published
11. J. Struckmeier, J. Klabunde, M. Reiser, *Part Accel.* **15**, 47 (1994)
12. T.P. Wangler et al., *IEEE Trans. Nucl. Sc.*, **NS-32** (1985)
13. M. Reiser, *J. Appl. Phys.* **70**, 1919 (1991)

ANALYSIS OF OPTICAL STOCHASTIC COOLING INCLUDING TRANSVERSE EFFECTS *

K.-J. Kim, Lawrence Berkeley Laboratory, Berkeley, CA, 94720 USA

Abstract

The phase space area plays an important role in determining the performance of optical stochastic cooling. Specifically, the number of samples in the beam consists of three factors corresponding to three dimensions, the factor in each dimension being given by the ratio of the total phase space area in that dimension to the radiation wavelength.

I. INTRODUCTION

In microwave stochastic cooling [1], the maximum cooling rate is limited by the number of particles n_s in a so-called "sample", defined to be the subset of particles that can interact with a given particle through the pick-up-amplifier-kicker system. The signal from the particles in the sample, other than that from the particle itself, contribute to the heating term. A smaller value of n_s therefore leads to a faster cooling. If the bandwidth of the pick-up-amplifier-kicker system is denoted by W , n_s is given by the well-known relationship

$$n_s = n \frac{1}{F}. \quad (1)$$

Here, n is the total number of the particles in the beam, $F = TW$, and T is the time duration of the beam. Equation (1) is the statement that the signal due to a given particle appearing at the kicker lasts about $1/W$, and hence only particles within that temporal distance can interact with the given particle. The quantity F is referred to as the number of the samples contained in the beam.

Recently, optical stochastic cooling was proposed to take advantage of the larger bandwidth possible with amplifiers in the optical wavelength region, which could be as high as 10^{13} – 10^{14} Hz [2]. Thus the sample size n_s , and hence the cooling time, would be greatly reduced. A quadrupole undulator and a normal dipole undulator respectively play the role of the pick-up and the kicker in the original scheme in reference[2]. However, the requirement on the beam emittance in that scheme turns out to be very stringent, being about $\lambda\sigma_\delta$ or less, where λ is the wavelength of the radiation used for the cooling and σ_δ is the rms relative energy spread in the beam. The transit time scheme of optical stochastic cooling was proposed to avoid this limitation [3]. In this scheme, normal undulators are employed for both the pick-up and the kicker, and the information on particle coordinates is transmitted via the coordinate-dependent transit time of the particle trajectory between the pick-up and the kicker undulators.

The purpose of this paper is to study the effect of the transverse structure of the radiation field on the cooling performance. To this end, we analyze the transit time scheme of the optical

stochastic cooling in detail, using an approximate model for the undulator radiation to represent the space-time dependence of the undulator field [4]. Our main finding is that the number of samples in the beam F can be written as

$$F = F_L F_{Tx} F_{Ty}, \quad (2)$$

where F_L and F_{Tx} (F_{Ty}) are referred to respectively as the number of the longitudinal and the transverse samples in the $x(y)$ -direction. We find that the number of the samples in each dimension is given by the ratio the total phase space area to the coherent phase space area λ .

The relevance of the transverse structure of the radiation field in optical stochastic cooling was first pointed out in reference[3] based on an intuitive argument. However, the expression for the number of the transverse samples conjectured there—the ratio of the beam size to the coherent mode size—is valid only in the limit of parallel beam.

The expression for F_L as the ratio of the total longitudinal phase space area to the coherent phase space area λ reduces the usual result TW in the long bunch limit. In the short bunch limit, however, F_L becomes the ratio of the beam energy spread to the coherent energy spread. This could have interesting consequences for the cooling of bunched beams.

II. PARTICLES AND FIELDS

Let x_j and x'_j be respectively the position and the angle of the betatron motion of the j th particle as it passes the center of the pick-up undulator, and δ_j its relative energy deviation. The total transverse coordinates are therefore

$$x_{Pj} = x_j + \eta\delta_j, \quad x'_{Pj} = x'_j + \eta'\delta_j, \quad (3)$$

where η and η' are respectively the dispersion and its derivative at the center of the pick-up undulator. In the following, we will be mainly concerned with the behavior in the x -direction where the dispersion occurs. The behavior in the y -direction will become obvious.

Following the work in [3], we choose the betatron transfer matrix between the centers of the pick-up and the kicker undulators to be $-I$, and the dispersion function at the center of the kicker to satisfy the symmetry relation $(\eta_K, \eta'_K) = (\eta, -\eta')$. Thus, the transverse coordinates of the i th particle in the center of the kicker (x_{Ki}, x'_{Ki}) are related to those at the pick-up as follows:

$$x_{Ki} = -x_i + \eta\delta_i, \quad x'_{Ki} = -x'_i - \eta'\delta_i. \quad (4)$$

The path length of the particle trajectory between the centers of the pick-up and the kicker in the linear approximation is given by

$$l_j = l_0 + \Delta l_j = l_0 + 2(\eta x'_{Pj} + Q\delta_j). \quad (5)$$

*This work was supported by the U.S. Department of Energy under Contract No. DE-AC03-76SF00098.

Here, $Q = \eta\eta' + \int_0^{l_0} ds D(s)/\rho(s)$, $D(s)$ being the contribution to the dispersion from the dipole magnets and $\rho(s)$ the radius of the curvature of the particle trajectory[3]. In this paper, the betatron focussing in the undulators is neglected so that particle trajectories are straight. The trajectory of an i th particle in the kicker undulator can therefore be written as

$$x_{Ki}(t) = x_{Ki} + x'_{Ki} z_{Ki}(t), \quad x'_{Ki}(t) = x'_{Ki}. \quad (6)$$

The quantity $z_{Ki}(t)$ in Eq.(6) is the longitudinal coordinate given by:

$$z_{Ki}(t) = \beta_i(1 + x'^2_{Ki}/2)(ct - s_i - \Delta l_i), \quad (7)$$

where β_i is the speed of the i th electron divided by c , c the speed of light, and $s_i = ct_i$ the distance of the i th particle behind the reference particle in the pick-up undulator. It is necessary in Eq.(7) to keep the second order term in the expansion of $\cos x'_{Ki}$ because the leading term is sometimes cancelled out. The constant term l_0 in the path length does not appear in Eq.(7) because the time $t = 0$ is defined to be the moment when the reference particle passes through the center of the kicker undulator.

To find the field produced by the j th electron $E_{Pj}(x; z_P) \exp i\omega(t - t_j)$, where $\omega = 2\pi c/\lambda = kc$, it is sufficient to note the relation at $z_P = 0$ (the center of the pick-up undulator), $E_{Pj}(x; 0) = \exp[ikx'_{Pj}(x - x_{Pj})]E_0(x; 0)$, where E_0 is the field of the reference particle[4]. We will approximate $E_0(x; 0) = \exp(-x^2/4\sigma_r^2)$, where σ_r is the rms mode size at the waist. The field for $z_P \neq 0$ is then obtained by a Fresnel transformation. The resulting expression is further simplified by neglecting the z_P -dependence in the spotsize and the wavefront curvature. The result is then multiplied by the factor $\exp[-(z - c(t - t_j))/4\sigma_C^2]$, where $\sigma_C \simeq N\lambda/\sqrt{2\pi}$, N being the number of the undulator periods. This factor is introduced to account for the fall-off the field strength due to the increase of the spotsize as well as the fact that the relative bandwidth of the undulator radiation is about $1/N$. In this way, we obtain

$$E_{Pj}(x; z_P, t) = E_0 \exp[ikz_P(1 - x'^2/2) - ik(ct - s_j) - \frac{(z_P - ct + s_j)^2}{4\sigma_C^2} + ikx'_j(x - x_j) - \frac{(x - x_j - z_P x'_j)^2}{4\sigma_r^2}] \quad (8)$$

In deriving Eq.(8), we have assumed that the undulator bandwidth, $1/N$, is much larger than both the relative energy spread of the particle beam σ_δ and the line width due to the angular spread, $\gamma^2 x'^2$, where γ is the relativistic factor and x' is the angle at the pick-up or kicker undulator.

We choose the optical ABCD matrix for the pick-up-amplifier-kicker system to be the same as that of the betatron transfer matrix, $-I$, with an amplification factor g . The field at the kicker E_{Kj} is then related to that from the pick-up by $E_{Kj}(x, z, t) = gE_{Pj}(-x, z, t - l_0/c - \Delta s_j/c)$. Here, z is the longitudinal coordinate measured from the center of the kicker undulator.

III. COOLING AND HEATING TERMS

In the kicker undulator, the energy of a particle becomes modified due to the coupling of its transverse motion in the undulator magnetic field and the transverse electric field of the ampli-

fied undulator radiation from the pick-up undulator. The change in the relative energy of the i th particle is

$$\Delta\delta_i = e \frac{gK_u}{2mc^2\gamma^2} Im \sum_j \int dt E_{Pj}(-x_{Ki}(t), z_{Ki}(t), t - \Delta t_i) \times \exp(ik_u z_{Ki}(t) - z_{Ki}^2/4\sigma_L^2). \quad (9)$$

The complex notation for the field is used here with Im implying the imaginary part, and e is the particle charge, m its mass, K_u the undulator deflection parameter, $k_u = 2\pi/\lambda_u$, λ_u the undulator period length, and the trajectory of the i th particle is specified by Eq.(6) and Eq.(7). We are assuming that the undulator strength is tapering out as a Gaussian function with an rms length $\sigma_L \simeq L/\sqrt{2\pi}$. Also note the relation $\sigma_C = (1 - \beta)\sigma_L \simeq \sigma_L/2\gamma^2$. Performing the t -integral, we obtain

$$\Delta\delta_i = G Im \left(\Phi_{ii} + \sum_{j \neq i} \Phi_{ij} \right), \quad (10)$$

where $G = egK_u E_0 L / 2mc^2\gamma^2$, and

$$\Phi_{ij} = \frac{\sigma_r}{\Sigma_{ij}(2)} \exp \left\{ -\frac{k^2 \sigma_L^2 \sigma_r^2 x'^4_{ij}}{8\Sigma_{ij}^2(2)} - ik\Delta l_i - ik(s_i - s_j) - \frac{[(x_{ij} - x'_{ij}(s_i - s_j)\sigma_L/\sigma_C)^2 - x_{ij}^2 - (s_i - s_j)^2 \sigma_r^2/\sigma_C^2]}{8\Sigma_{ij}^2(2)} \right\} \times \exp(i\varphi_{ij}) \quad (11)$$

Here

$$\Sigma_{ij}(2) = \sqrt{\sigma_r^2 + x'^2_{ij}\sigma_L^2/2}, \quad \Sigma_{ij}(1) = \sqrt{\sigma_r^2 + x'^2_{ij}\sigma_L^2}$$

$$l_i = \Delta t_i/c, \quad s_i = t_i/c, \quad x_{ij} = x_{Ki} + x_{Pj} = -x_i + x_j + \eta(\delta_i + \delta_j) \\ x'_{ij} = x'_{Ki} + x'_{Pj} = -x'_i + x'_j + \eta(-\delta_i + \delta_j)$$

The phase term φ_{ij} in the last factor in Eq.(11) is a real quantity with the property $\varphi_{ii} = 0$ and $|\varphi_{ij}| \ll |k(s_i - s_j)|$ for $i \neq j$. The explicit expression of such a phase term will not be important for the following calculations. The change in the average value of δ_i^2 is then

$$\langle \Delta\delta_i^2 \rangle = 2G Im \langle \delta_i \Phi_{11} \rangle + n(G^2/2) \langle \Phi_{12} \Phi_{12}^* \rangle. \quad (12)$$

Here the angular brackets imply taking the average with respect to the variables s_i, δ_i, x_i , and x'_i . We assume that the distribution function in these variables can be factorized into Gaussian functions in each variable, with rms widths $\sigma_z, \sigma_\delta, \sigma_x$, and $\sigma_{x'}$. Since all particles are equivalent, we have arbitrarily chosen two indices, $i = 1$ and $j = 2$. The first term in the above is the cooling term. In obtaining the heating term, the second term in Eq.(12), we have used the fact that the average of the quantity $\Phi_{1j}\Phi_{1j'}^*$ vanishes unless $j = j'$ because of the large, random phase $k(s_j - s_{j'})$.

The cooling term can be evaluated in a closed form as follows:

$$2G Im \langle \delta_1 \Phi_{11} \rangle = -\frac{4kGQ\sigma_\delta^2}{(1 + 2\eta^2\sigma_\delta^2/\sigma_r^2)^{3/2}}$$

$$\exp \left\{ -2k^2 \left[\sigma_x'^2 \eta^2 + \frac{Q^2 \sigma_\delta^2}{1 + 2\eta^2 \sigma_\delta^2 / \sigma_r^2} \right] \right\}. \quad (13)$$

This reproduces the expression derived in reference[3] when $\eta \sigma_\delta \ll \sigma_r$.

The heating term can be written as $n_s G^2/2$, where $n_s = \langle \Phi_{12} \Phi_{12}^* \rangle$ is the number of particles in a sample for optical stochastic cooling. The averaging with respect to variables s_1 and s_2 involves Gaussian integrals. Assuming for simplicity that $\sigma_z \gg \sigma_C$, the result is

$$\langle \Phi_{12} \Phi_{12}^* \rangle = \sigma_C / \sigma_z \times \left\langle \frac{\sigma_r^2}{\Sigma_{12(1)} \Sigma_{12(2)}} \exp \frac{-1}{4} \left\{ \frac{x_{12}^2}{\Sigma_{12(1)}^2} + \frac{x_{12}^2}{\Sigma_{12(2)}^2} + \frac{k^2 \sigma_r^2 \sigma_L^2 x_{12}^4}{\Sigma_{12(2)}^2} \right\} \right\rangle. \quad (14)$$

The rest of the averaging will be carried out approximately by regarding the variables x_{12} and x_{12}' to be independent with Gaussian distributions of widths Σ_x and $\Sigma_{x'}$, respectively. These quantities will be roughly given by $\Sigma_x^2 \approx 2\sigma_x^2 + 2\eta^2 \sigma_\delta^2$ and $\Sigma_{x'}^2 \approx 2\sigma_{x'}^2 + 2\eta^2 \sigma_\delta^2$. Performing the x_{12} -average, we obtain

$$\langle \Phi_{12} \Phi_{12}^* \rangle = \frac{\sigma_C}{\sigma_z} \left\langle \frac{\sigma_r^2 \exp[-(k\sigma_L \sigma_r x_{12}'^2 / 2\Sigma_{12(2)})^2]}{\Sigma_{12(2)} \sqrt{\Sigma_{12(1)}^2 + \Sigma_x^2}} \right\rangle. \quad (15)$$

The final average in the variable x_{12}' can be estimated approximately as follows: First, we assume that the Rayleigh length of the undulator radiation is about σ_L so that

$$\sigma_r \approx \sqrt{\sigma_L / 2k}, \quad \sigma_{r'} \approx 1 / \sqrt{2k\sigma_L} \quad (16)$$

The exponential factor in Eq.(15) can then be written as $\exp(-\xi^2/4(1+\xi))$, where $\xi = \sigma_L^2 x_{12}'^2 / 2\sigma_r^2$. Thus, the average is dominated by the region $\xi \leq 1$. For a rough estimate, therefore, we may set $\xi \approx 0$ everywhere except the exponential function, which we replace by $\exp(-\xi^2/4)$. The average of this term can be expressed in terms of the modified Bessel function $K_{1/4}$. By examining the result, we obtain the following estimate for the heating term:

$$\frac{G^2}{2} n \langle \Phi_{12} \Phi_{12}^* \rangle \equiv \frac{G^2}{2} n_s \approx \frac{\sigma_C}{\sigma_z} \frac{\lambda/2}{2\pi \sqrt{(\sigma_r^2 + \Sigma_x^2)(\sigma_{r'}^2 + \Sigma_{x'}^2)}}. \quad (17)$$

Note here that the quantity $\lambda/2$ in the numerator is the coherent phase space area $2\pi\sigma_r\sigma_{r'}$. Equation (17) is the main result of our analysis in this paper. We consider the meaning of this result in the next section.

IV. THE ROLE OF PHASE SPACE AREA IN LONGITUDINAL AND TRANSVERSE SAMPLES

Comparing Eq.(17) and Eq.(1), we see that the number of samples in the beam F for the present case is indeed in the form of Eq.(2), with $F_L = \sigma_z / \sigma_C$, and

$$F_{Tx} \approx \frac{\sqrt{(\sigma_r^2 + \Sigma_x^2)(\sigma_{r'}^2 + \Sigma_{x'}^2)}}{\sigma_r \sigma_{r'}}. \quad (18)$$

This reduces the conjecture of reference [3], Σ_x / σ_r , in the limit $\beta_x \gg \sigma_L$, where β_x is the beta function of the particle beam in the kicker undulator. However, note that Eq. (18) consists of two factors, the size and the angular factors. The angular factor arises from the fact that two particles with angular separation larger than the coherent mode angle do not interact, and therefore can not both belong to the same sample.

It is clear that n_s will be further reduced by the number of transverse samples in y-direction F_{Ty} , the expression of which will be similar to that of F_{Tx} .

The analysis of previous section gives $F_L \approx \sigma_z / \sigma_C$ because we assumed $\sigma_z \gg \sigma_C$. In analogy to the transverse samples, a more general expression is

$$F_L \approx \frac{2\pi \sqrt{(\sigma_C^2 + \sigma_z^2)(\sigma_C^2 + \sigma_\delta^2)}}{\lambda/2}, \quad (19)$$

where $\sigma_{C\delta} = 1/2k\sigma_C$ is the coherent bandwidth. In the limit $\sigma_z \gg \sigma_C$, $\sigma_{C\delta} \gg \sigma_\delta$, F_L becomes the usual expression σ_z / σ_C . In the opposite limit, $\sigma_z \ll \sigma_C$, $\sigma_{C\delta} \ll \sigma_\delta$, we obtain $F_L = \sigma_\delta / \sigma_{C\delta}$. Thus we find in this case that a faster cooling would be achieved with a narrower bandwidth amplifier. The implication of this conclusion for the cooling of bunched beams will be studied in a future paper.

V. ACKNOWLEDGEMENTS

We thank Sasha Zholents for numerous useful discussions.

References

- [1] For a comprehensive review, see D. Möhl, CERN Accelerator School Report No. CERN 87-03, 453(1987).
- [2] A.A. Mikhailichenko and M.S. Zolotarev, Phys. Rev. Lett., **71**, 4146(1993)
- [3] M.S. Zolotarev, A.A. Zholents, Phys. Rev. E, **50**, 3087(1994).
- [4] K.-J.Kim, SPIE Proceedings, vol 582,2 (1986). For a review, see K.-J.Kim, AIP Conference Proceedings No. 184, 565(1989).

Abe, H. FAP13, 1358
Abe, S. TAQ35, 1608
Abraham, W. WPA01, 902
Abramenko, N. RPR10, RPR15, 1143, 1155
Abramsky, P. WPP11, 1681
Adachi, Toshikazu TPR16, 3275
Adamski, J. FAA27, 248
Adamski, J.L. FAA28, 251
Adolphsen, C. WAG11, RPB03, RPB04, RPC01, RAE03, TPQ17, WAB07, WAC18, 646, 662, 665, 698, 2389, 2989, 3031, 3112
Adolphsen, Chris WAB08, 3034
Afanasiev, O. FAQ06, 1399
Agafonov, A.V. TPR13, TPR14, 3269, 3272
Ahrens, L.A. TAP11, TAP12, TAP13, WAB04, RAQ22, 378, 381, 383, 3022, 3334
Aizatsky, N.I. WPQ22, TPA14, 1773, 3229
Akai, K. FAE09, WPQ08, WPQ09, WPQ17, WPR05, WPR09, RPQ06, WAC08, 1503, 1735, 1738, 1759, 1797, 1806, 2675, 3085
Akasaka, N. RPA20, FAE09, WPQ09, WPQ17, WPR05, WPR09, TPC08, TPC29, TAG01, 1099, 1503, 1738, 1759, 1797, 1806, 2613, 2655, 2742
Akemoto, M. WPR02, WPR03, 1788, 1791
Akimov, V. WAA17, 1263
Akre, J. FAQ24, FAQ25, 1444, 1447
Akre, R. WPR15, WAB12, 1821, 3046
Alessi, J. WPC09, 1013
Alexahin, Y. RAA17, 560
Alexandrof, V.A. TAG01, 2742
Alimov, A. RPA19, 1096
Alimov, A.S. RAR04, 3361
Alinovsky, N.I. TAC06, 143
Allen, C.W. RPA24, 1111
Allen, Christopher K. MPC04, 2324
Allen, J. RAR23, 3406
Allen, L. WPA06, 917
Allen, M.A. WPQ06, 1729
Allen, Ray TPP13, 1645
Alley, R. MPE10, 887
Allison, Paul W. TAE08, 1207
Allison, S. RAE03, 2389
Alonso, Jose R. WPE01, 58
Alton, G.D. MPE05, WPC12, WAQ26, 871, 1022, 1897
Altuna, X. WAP12, WAP13, 464, 467
Amankath, H. RPA26, 1116
Amiranoff, F. WAG07, 634
Anderson, David E. TAE07, 1204
Anderson, K. WAQ22, WAR17, 1888, 1939
Ando, A. RPQ15, 2699
Andreev, V.G. WPP19, 1702
Andreev, V.V. FAC09, 2856
Andriishchin, A. FAQ06, 1399
Anerella, M. TPE04, FAQ04, 1293, 1396
Angerth, B. RPE02, 1999
Ankenbrandt, C. FAG06, 86
Anthouard, Ph. TAE09, 1210
Antonsen, T.M. WAG04, 621
Aoki, T. FAP13, 1358
Arai, S. RPG13, 351
Arbuzov, V. WPP11, 1681
Ardonceanu, J. WAG07, 634
Argyris, J. FAP03, 1328
Arinaga, M. RAB13, 779
Arnold, N. RPA11, RPA14, MPQ08, 1073, 1082, 2467
Asano, K. TPP03, TPP16, 1620, 1652
Ashton, J.R. RPB05, 668
Assadi, S. TAG10, RAP03, WAB01, 2777, 2886, 3016
Asseev, A.A. WAR23, 1955
Assmann, R. RAA19, WAG11, RPB02, 567, 646, 659
Astapov, A.A. RPE13, 2029
Auble, R.L. WAQ26, 1897
Auch, S. RPR06, 1131
Aune, B. WPB22, 998
Ausset, P. WPQ26, 1781
Austin, R.H. FAA19, FAA31, 234, 260
Autin, B. RPC11, WAE09, 722, 2178
Averill, R. RPG05, RAA31, 327, 600
Azorsky, N.I. TAQ34, 1605
Baartman, R. RPG12, WAQ07, WAC20, 348, 1858, 3119
Baba, T. WAQ06, 1855
Babzien, M. MPE11, 890
Backmor, Rudolf TAQ13, 1550
Bailey, J.D. TAP07, TAP08, TAP09, 366, 369, 372
Bailey, R. WAP12, WAP13, RAA11, 464, 467, 548
Bainan, Ding FAA26, 246
Baiod, R. FAP04, FAP06, FAP07, FAP09, MPB06, 1331, 1337, 1340, 1346, 2285
Bak, J.S. RPA06, 1061
Baker, S. WAR19, 1945
Bakker, R. RPG06, 330
Baklakov, B. TAA01, RAR30, 2078, 3424
Balakin, V. TAG01, 2742
Balewski, K. FAR07, 275
Balhan, B. RAA15, 557
Ball, M. TPB24, RAP21, RAP22, WAC12, RAQ23, RAQ24, 2583, 2934, 2937, 3094, 3337, 3340
Ballauff, M. FAR06, 272
Bamblevski, V.P. RPE13, 2029
Bane, K. RPA04, WAC17, 1058, 3109
Bane, K.L.F. RPA20, TPQ16, TPQ17, WAB07, WAC16, WAC18, 1099, 2986, 2989, 3031, 3105, 3112
Bangerter, R.O. WAQ04, 1852
Baptiste, K. TAR03, 801
Baranov, V.I. MPG10, WAR21, 426, 1949
Baranova, L.A. TAP16, 389
Barber, D.P. WPG08, 511
Bardy, J. TAE09, 1210
Barker, D. MPR13, 2265
Barklow, T. RPB01, 656
Barletta, W. TAA28, 2135
Barlow, T.A. TPC13, 2628
Barnard, J. TAR17, 837
Barnard, J.J. TAR14, TPB14, TPR18, 828, 2557, 3278
Barnard, John J. TPR02, 3241
Barnes, P. FAE13, WPQ02, RAQ04, 1515, 1720, 3294
Barov, N. WAG06, WPB11, 631, 976
Barr, D. MPQ03, RPQ16, TPQ19, 2452, 2702, 2992
Barry, W. RAE13, RPQ08, 2423, 2681
Barts, T. MPB10, 2294
Batchelor, K. MPE11, WPB13, RAE09, WXE03, TPB01, 890, 982, 2411, 2432, 2530
Batskikh, G. FAP24, 1387

Batskikh, G.I. RPR07, 1134
 Batygin, Y. WPC01, 1001
 Batygin, Y.K. TPR06, 3251
 Batygin, Yuri K. TPR07, 3254
 Beadle, Edward R. TPB08, TPB09, 2545, 2548
 Beauvais, P.-Y. RAG07, 3173
 Becher, D. MPE05, 871
 Bechstedt, U. TPB20, 2574
 Bechtold, V. FAR06, 272
 Becker, T. FAP02, 1325
 Becker, U. TAQ06, WAE13, 1533, 2190
 Beebe, E. WPC09, 1013
 Behne, D. MPP12, MPP20, 2064, 2075
 Beisel, U. WPA04, 911
 Bekefi, G. TPG14, RPC15, 192, 734
 Belkovets, V. TAC16, 152
 Beloglazov, V.I. TAE14, 1225
 Belomestnykh, S. FAE13, WPP11, RAQ04, RAR18, RAR19, 1515, 1681, 3294, 3391, 3394
 Belov, W. RAQ14, 3315
 Belova, Nadya G. WAA01, 1227
 Belser, C. RAA04, 530
 Belser, F.C. WPQ06, TAA22, 1729, 2129
 Belugin, V.M. RPR07, 1134
 Ben-Zvi, I. MPE11, WPB13, RAE09, WXE03, TPB01, 890, 982, 2411, 2432, 2530
 Benesch, J. FAE12, 1512
 Benjamin, J. TAP11, 378
 Benjegerdes, R. WPA01, FAP17, 902, 1369
 Bennett, L. TAE06, 1201
 Bennett, Lawrence F. TAE07, 1204
 Benson, S. FAG11, FAA25, WPA17, WPC24, 102, 243, 942, 1052
 Benvenuti, C. FAE11, TPP12, 1509, 1642
 Bercher, M. WAG07, 634
 Berenc, T. WPB06, 961
 Berezin, A.K. RAB15, 782
 Berg, J. TAA22, 2129
 Berg, J.S. FAB06, TPQ16, 2804, 2986
 Berg, J. Scott TPQ07, WAC05, 2962, 3076
 Berg, W. RPA11, MPQ10, 1073, 2473
 Berger, D.D. WPQ06, 1729
 Bergher, M. RAP19, 2928
 Berkelman, K. FAE13, 1515
 Bernal, Santiago TAA17, 2117
 Bernard, D. WAG07, 634
 Bernard, M. WPB01, WPB22, 945, 998
 Berridge, S. TAA28, 2135
 Bertagnolli, H. FAR06, 272
 Bertinelli, F. RPE02, 1999
 Bertolini, L. RAA03, 527
 Bertsche, K. TPE05, FAP21, WAQ09, MPQ21, TPB19, 1298, 1381, 1864, 2503, 2572
 Bertuzzi, J.-P. MPP15, 2069
 Bérwald, D. RPR20, 1164
 Berz, Martin MPC09, 2336
 Bessonov, E.G. RAP06, 2895
 Beveridge, J.L. RPG12, 348
 Beyer, K.A. TPC13, 2628
 Bharadwaj, V. MPG02, WAP04, RPC20, RPC21, WPB08, TAG01, 396, 443, 749, 752, 967, 2742
 Bhat, C.M. FAP05, WAR02, TAA12, WAC06, 1334, 1903, 2105, 3079
 Bialowons, W. RPE08, 2017
 Bialy, J. FAR06, 272
 Bickley, M. MPA12, MPR19, 2220, 2276
 Bieniosek, F.M. WAR17, WAR18, 1939, 1942
 Biggs, J. FAP03, 1328
 Billen, J.H. RPR08, RPR09, 1137, 1140
 Billen, James H. MPB16, 2306
 Billing, M. FAE13, FAB12, TPA04, RAQ04, 1515, 2820, 3206, 3294
 Billing, M.G. RAE14, 2426
 Binns, B. WAA16, TPB04, 1260, 2536
 Birukov, I.N. RPR01, 1119
 Biryukov, V.M. MPG10, WAR20, WAR21, 426, 1948, 1949
 Biryukov, Valery WAR24, 1958
 Biscardi, R. TPP06, WPP03, 1626, 1660
 Bisognano, J. FAG11, FAA25, WPA17, 102, 243, 942
 Bisognano, J.J. RPQ11, 2690
 Bisognano, Joseph J. MPC25, RAG12, 2370, 3188
 Bizek, Hana M. RAR27, 3418
 Bjerklie, S. FAG06, 86
 Black, E. FAP03, 1328
 Black, W.M. TAE10, 1213
 Blanchard, R. WAP12, WAP13, 464, 467
 Blas, F. MPG09, 423
 Blaskiewicz, M. TAP11, TAP12, TAP13, WAC24, 378, 381, 383, 3131
 Blaskiewicz, M.M. RAQ22, 3334
 Blastos, J. TPG14, 192
 Blazhevich, S.V. FAG12, 105
 Bleser, E.J. TAP13, WAR13, 383, 1930
 Bloess, D. TPP12, 1642
 Blondel, A. RAA19, 567
 Bloom, E. WAQ15, 1876
 Blosser, H. RPG11, 345
 Bluem, H.P. TAA32, 2141
 Blum, E. FAR10, 284
 Blum, E.B. FAR01, MPQ01, 263, 2450
 Bocchetta, C. FAR06, 272
 Bocchetta, C.J. FAA13, FAR21, TAG05, 222, 309, 2762
 Boehnlein, D. FAG06, 86
 Boer-Rookhuizen, H. MPQ17, 2491
 Boers, Jack E. MPB18, 2312
 Bogacz, A. FAP05, WAR19, RAR17, 1334, 1945, 3388
 Bogacz, S.A. RAB20, TAR20, 790, 843
 Bogard, D. RAG07, 3173
 Bogaty, J.M. TPC12, 2625
 Bogdanovich, B. RPR10, RPR15, TAQ24, 1143, 1155, 1575
 Bogdanovich, B.Yu. TAB13, TAQ23, 125, 1572
 Böge, M. RAP08, 2901
 Bogert, D. MPG01, 391
 Bohl, T. WAP12, WAP13, RAA11, FAE10, 464, 467, 548, 1506
 Bohlen, H. FAE07, 1497
 Bohn, C.L. FAG11, 102
 Bojon, J.-P. RPE06, 2014
 Bolme, G.O. WPA08, RPR19, 923, 1161
 Bolotin, I. WPR19, 1833
 Bolser, C. MPC01, 2317
 Bonati, R. WAR11, 1924
 Bondarev, B.I. RPR07, 1134
 Bongardt, K. TPA01, TPA02,

TPA03, 3197, 3200, 3203
Boni, R. RPA26, 1116
Bonifacio, R. FAA12, 219
Bonin, B. TPP09, 1632
Bonnafond, C. TAE09, 1210
Bonnafond, Ch. TPC17, 2640
Bookwalter, V. MPR13, 2265
Borden, M. RAR23, 3406
Borland, M. FAR11, WAE11, MPQ10, 287, 2184, 2473
Borodich, A.I. TPA15, 3232
Bortnyansky, A. TAA18, 2120
Bosch, R.A. FAR20, 306
Bosotti, A. TAA07, 2093
Bossard, P. MPG09, 423
Bossart, R. RPC10, 719
Bosser, J. RAP23, RAP24, 2940, 2943
Bostic, D. MPP10, 2057
Bothe, W. FAR06, 272
Botman, J.I.M. WAQ19, WAQ20, RPP04, RPQ31, 1882, 1885, 1970, 2738
Bourdon, J.C. WPB22, 998
Boussard, D. FAE10, TPP12, 1506, 1642
Bowden, G.B. RPB04, RPA23, 665, 1108
Bowers, J. WAC17, 3109
Bowling, B. MPR13, 2265
Bowling, B.A. WAE10, 2181
Bowling, S. RPR19, 1161
Boyd, John K. MPC13, 2339
Boyes, John D. TAE07, 1204
Bozoki, Eva RPQ14, 2696
Brabson, B. RAP21, RAQ23, RAQ24, 2934, 3337, 3340
Bracco, R. FAQ19, 1432
Bradley, S. RPG05, 327
Brandt, D. RAA17, RAA20, FAC03, 560, 570, 2841
Brauer, S.O. RPE09, 2020
Braun, A. RPC21, 752
Braun, H. RPC09, RPC10, 716, 719
Brefeld, W. FAA02, FAR07, 195, 275
Brennan, J.M. TAP11, TAP13, FAE05, MPQ30, RPQ17, RPQ25, WAB04, RAQ22, 378, 383, 1489, 2518, 2705, 2723, 3022, 3334
Bricault, P.G. RPG12, RPR02, RPR03, 348, 1122, 1125
Bridges, J.F. WPP16, 1693
Brillson, L.J. FAG11, 102
Brinker, F. FAA02, 195
Brinkmann, R. MPG04, RPB07, RPE08, 406, 674, 2017
Brodowski, J. WPP07, WPQ19, RPQ17, 1669, 1765, 2705
Brogle, R. WAG09, WPC20, 640, 1039
Broome, W. TPP06, 1626
Brouet, M. MPP15, 2069
Brouzet, E. WAP13, 467
Browman, A. TAR12, TPB13, 822, 2554
Brown, B. TPE05, 1298
Brown, B.C. FAP05, FAP06, FAP07, MPB05, MPB06, 1334, 1337, 1340, 2282, 2285
Brown, D. TPB13, 2554
Brown, K. RPC06, MPR13, 707, 2265
Brown, K.A. TPA06, 3212
Brown, Nathan RPR23, 1170
Brown, R. WPC08, 1010
Brown, V.W. WPA08, 923
Bruhweiler, D. RPR20, TPR07, 1164, 3254
Bruhweiler, D.L. TPR08, 3257
Brunelle, P. FAR14, 293
Brunet, J.-C. RPE02, 1999
Brüning, O. TAG09, 2774
Brüning, O.S. MPG07, 420
Brunner, O. WPG09, 514
Bruns, Warner RPA15, RPA16, 1085, 1088
Bryant, P.J. RPG03, 322
Budilin, V. WPR19, 1833
Budnick, J. RAP21, RAQ23, RAQ24, 2934, 3337, 3340
Bugg, W. TAA28, 2135
Bugorsky, A.P. MPG10, 426
Buhler, S. WPB22, 998
Bula, C. TAA28, 2135
Bulfone, D. TPG11, FAR21, 186, 309
Bulos, F. WAQ15, TAG01, 1876, 2742
Bulyak, E. FAR17, TPA12, TPA13, 299, 3223, 3226
Buon, J. RPC20, TAG01, 749, 2742
Burke, D. RPC01, RPC20, TAA08, WXE07, TAG01, 698, 749, 2096, 2444, 2742
Burkhardt, H. WAP12, WAP13, RAA11, 464, 467, 548
Burlet, A. MPP15, 2069
Burnham, B. FAA08, RAA01, RAB22, MPA10, MPA11, MPQ06, FAC20, 213, 524, 796, 2214, 2217, 2461, 2877
Burnside, C. MPP15, 2069
Burov, A. WAB16, WAB17, 3055, 3058
Burrini, D. RAQ05, 3297
Burton, A. RAA15, 557
Bushuyev, A. WPP11, 1681
Bussa, M.P. WAP14, 470
Butteris, J. FAQ32, 1465
Buxton, W.E. MPA19, 2235
Byrd, J. RPC02, MPC01, RAE12, RAE13, RPQ08, TPQ16, 701, 2317, 2420, 2423, 2681, 2986
Byrd, J.M. WXE06, RPQ09, 2441, 2684
Byrne, M. WPR15, 1821
Cable, M.D. TAR14, 828
Cai, Y. RAA22, RAA25, RAA26, RAA27, 576, 585, 588, 591
Cain, T.D. FAG05, 83
Calabrese, R. RAE05, 2399
Calame, J. TAQ17, 1561
Calame, J.P. TAQ18, TAQ19, 1563, 1566
Calder, R. RPE02, 1999
Calish, S. TAR18, 840
Callahan, D.A. TAR14, TPR19, 828, 3282
Callahan, Debra A. TPR01, 3238
Callin, R.S. TAQ28, 1587
Camas, J. TPC21, 2649
Cameron, P. TAA09, 2099
Cameron, P.R. MPQ05, 2458
Campbell, R. WAA16, 1260
Capone, D. FAQ14, 1417
Caporaso, G. RPC16, MPE14, WPC16, WAA19, TAA20, 737, 899, 1027, 1269, 2123
Cappi, R. TAP14, MPG09, 386, 423
Carboni, G. WAP14, 470
Carder, B. WAA19, TAA20, 1269, 2123
Cardman, L. FAG11, WPA17, 102, 942
Cardman, L.S. WPC17, 1030
Cargnello, F. TPG11, 186
Carlier, E. RAA15, 557
Carlsten, Bruce E. WPB15, FAE06, 985, 1494
Carnegie, D.W. TPE08, 1310
Carrigan, D. WAR19, 1945
Carroll, Frank E. FAG04, 80
Carson, J.A. FAP06, FAP07,

1337, 1340
Carter, A. RPG05, 327
Carter, F. FAA08, RPA17, MPA11, 213, 1090, 2217
Caruette, A. TPP11, TPP14, 1639, 1648
Carwardine, J.A. WAA08, RPP03, RPQ18, 1242, 1967, 2708
Caryotakis, G. FAE07, 1497
Casella, R. RPP02, 1964
Caspers, F. RPE02, RAP24, 1999, 2943
Caspi, S. FAQ23, 1441
Cassel, R.L. WAR06, 1915
Castellano, M. TPG11, 186
Castillo, V. RPQ07, 2678
Castle, M. TAQ18, TAQ19, 1563, 1566
Castro, P. RAA20, FAC03, 570, 2841
Catravas, P. TPG14, 192
Caussyn, D.D. RAP21, RAQ23, RAQ24, 2934, 3337, 3340
Cayla, J.N. WPB01, 945
Celata, C.M. TPA10, 3220
Cevenini, F. TPG11, 186
Chae, Y.-C. TAP05, FAB09, 363, 2811
Chae, Yong-Chul TPQ20, TPQ21, RAR24, RAR25, 2995, 2998, 3409, 3412
Chamouard, P.-A. RAG07, 3173
Chan, A. TAR18, 840
Chan, K.C.D. FAA16, TAR12, 228, 822
Chanel, M. RAP24, 2943
Chang, C.H. FAQ26, 1450
Chang, H.P. FAA07, RAA24, TPQ10, 210, 582, 2971
Chang, L.H. FAA04, RAA24, FAQ26, TPQ08, 201, 582, 1450, 2965
Chang, Peace TAR04, 804
Chang, Y.M. MPQ32, 2524
Channell, P. WAC29, 3146
Chao, A. MPC01, WAC17, 2317, 3109
Chao, A.W. WAB09, WAB11, RAQ02, 3037, 3043, 3288
Chao, Alex FAC02, WAB10, 2838, 3040
Charruau, G. WPQ26, 1781
Chattopadhyay, S. TPG07, RPC16, TAA28, 174, 737, 2135
Chautard, F. RPC10, 719
Chavanne, J. TPE10, 1319
Chehab, R. WPB22, 998
Chen, B. WAB20, 3064
Chen, Bo WAB10, 3040
Chen, C.-I. TPC15, 2634
Chen, D. WAR19, 1945
Chen, J.R. FAA07, 210
Chen, J.S. MPR10, TPB29, 2256, 2592
Chen, Jenny MPR10, MPQ16, TPB29, 2256, 2488, 2592
Chen, P. RPC01, TAA28, RAP15, 698, 2135, 2919
Chen, Pisin RAQ18, 3326
Chen, R.-C. TPC15, 2634
Chen, S.C. MPE12, WPB03, WPB04, 893, 951, 954
Chen, T. RAA26, TAG06, RAP09, RAP11, RAP12, WAC17, 588, 2765, 2904, 2910, 2913, 3109
Chen, Y. RPC16, WPC16, WAA19, 737, 1027, 1269
Chen, Yinbao FAA21, RAQ25, RAQ26, 237, 3343, 3346
Cheng, J. TAQ18, TAQ19, 1563, 1566
Cheng, Wen-Hao RAG09, TPR12, 3179, 3266
Cheng, Y. FAA04, FAA07, 201, 210
Chepurinov, A. RPA19, 1096
Chepurinov, A.S. FAG12, RAR04, 105, 3361
Cherenshchikov, S.A. WPA15, WPA16, 938, 939
Chernikov, V.I. WAR09, 1918
Chernogubovsky, M.A. WPP04, 1663
Chertok, I. TPE09, 1316
Chertok, I.L. TAC06, 143
Chesnokov, Yu.A. MPG10, WAR20, WAR21, 426, 1948, 1949
Chester, N.S. FAP06, FAP07, 1337, 1340
Chiang, R. RAQ04, 3294
Chiaveri, E. FAE11, 1509
Chin, A. TPG07, 174
Chin, Y.H. TPC08, WAC07, WAC08, 2613, 3082, 3085
Chiou, T.C. RAB02, RAB08, 761, 773
Chirkov, P.N. FAB02, 2792
Cho, M.H. TAR07, RPA06, TAQ15, 813, 1061, 1556
Cho, Y. TAP05, TPQ22, TPQ23, 363, 3001, 3004
Cho, Y.S. FAA10, 216
Cho, Yanglai RAR25, 3412
Choi, J. TAR07, RPA06, 813, 1061
Choi, Sewan RPP11, 1985
Chojnacki, E. WPB11, WPB12, WPQ02, RAQ04, 976, 979, 1720, 3294
Chou, P.J. MPQ13, WAC09, WAC10, 2479, 3088, 3091
Chou, W. WAP02, WAP03, MPB10, TPQ15, 437, 440, 2294, 2983
Chowdhary, M. MPR14, RAE11, 2268, 2417
Chu, C.C. MPQ26, RAR05, 2515, 3364
Chu, C.-C. TPC15, 2634
Chu, W.T. RAE04, 2394
Chubar, O.V. RAE06, WXE08, 2402, 2447
Chubarov, O. RPA19, 1096
Chubarov, O.V. RAR04, 3361
Chumakov, S.N. TAC06, RPP08, 143, 1979
Chung, K.H. FAA10, 216
Chung, S.C. RAR05, 3364
Chung, Y. MPQ03, MPQ08, TPC03, RPQ15, RPQ16, 2452, 2467, 2598, 2699, 2702
Chupp, W. TPA10, 3220
Church, M. TAR16, 834
Church, Mike RPG07, 333
Ciardullo, D.J. MPQ30, 2518
Cieslik, W. MPQ11, 2476
Ciocci, F. TPG11, 186
Clark, D.C. WPA08, 923
Clark, G.S. RPG12, 348
Clarke, J.A. TPG09, WAC23, 180, 3128
Claus, J. FAP11, 1352
Claus, R. RAE12, RPQ01, RPQ05, 2420, 2660, 2672
Clayton, C. TPB18, 2569
Clayton, C.E. WAG08, RAB01, RAB02, RAB04, RAB05, 637, 758, 761, 767, 770
Clendenin, J. MPE10, WPC21, 887, 1043
Clendenin, J.E. MPE08, WPC18, 877, 1033
Cleveland, E.K. FAG05, 83
Clifft, B.E. TPC12, 2625
Cline, D. TAA28, 2135
Cline, D.B. TAB06, WPG11, RAB20, TAR21, 119, 520, 790,

846

Codutti, A. FAQ19, 1432

Colby, E. WPB05, WPB08, 957, 967

Colestock, P. WPP01, RAP21, WAB01, RAQ24, 1655, 2934, 3016, 3340

Colestock, P.L. TAG04, WAC01, 2757, 3067

Colestock, Patrick L. WAC02, 3070

Collier, P. WAP12, WAP13, RAA10, RAA11, RAA12, RAA13, 464, 467, 545, 548, 551, 554

Collins, J. TPB24, 2583

Colton, E. WAC29, 3146

Coluzza, C. FAR06, 272

Comunian, M. RPC10, 719

Conde, M. WAG06, WPB08, WPB11, 631, 967, 976

Conkling, C.R. MPA16, 2226

Connolly, R. RPR19, WPP07, 1161, 1669

Connolly, R.C. RPR22, TPC06, 1167, 2607

Cooper, R. WAC29, 3146

Cooper, Ronald WPB15, 985

Corbett, J. RPQ21, RPQ22, RAQ17, 2714, 2717, 3323

Corcoran, P. TAE06, 1201

Corlett, J. RPC02, WPR14, MPC01, RAE12, RAE13, RPQ08, TPQ16, 701, 1818, 2317, 2420, 2423, 2681, 2986

Corlett, J.N. WXE06, 2441

Corley, J.P. TAE06, 1201

Cornacchia, M. FAA25, RAA18, RAQ17, 243, 564, 3323

Cornelis, K. WAP12, WAP13, RAA11, RAA17, RAA20, FAC03, 464, 467, 548, 560, 570, 2841

Corredoura, P. RPQ02, RPQ03, RPQ05, 2663, 2666, 2672

Corsini, R. RPC09, RPC11, 716, 722

Corvin, C. TAA16, 2114

Cosso, R. FAE11, 1509

Couillaud, C. RAG06, 3170

Cours, A. RPA11, 1073

Cours, Alexander TAQ16, 1559

Coverdale, C.A. RAB01, 758

Cox, G. WAG06, WPB11, 631, 976

Craddock, M.K. FAB14, 2823

Craddock, W. TAA28, 2135

Crandall, K.R. RPG10, 342

Crane, G. TAR18, 840

Crawford, J. WAP04, 443

Crawford, K. RPQ29, 2732

Cremer, T. FAP20, 1378

Crofford, M. WXE01, 2429

Cromer, K.D. RAP01, 2880

Cros, B. WAG07, 634

Crosbie, E. TAP05, RAA29, RAG05, 363, 597, 3167

Crosbie, E.A. RAR26, 3415

Crowe, T. TPC04, 2601

Cruikshank, P. RPE02, 1999

Cutolo, A. TPG11, 186

Cyvoc, G. MPG09, 423

d'Amico, E.T. RPC12, 725

D'Auria, G. TPG11, FAA13, FAR21, 186, 222, 309

D'Ottavio, T. MPR20, 2279

D'Yachkov, M. WAC20, 3119

Daclon, F. TPG11, FAR21, 186, 309

Dalin, J.-M. RPE02, 1999

Daly, E. TAA22, MPC01, 2129, 2317

Daly, E.F. MPP08, MPP10, MPP12, MPP20, 2051, 2057, 2064, 2075

Dangor, A.E. WAG08, 637

Danilewsky, A.N. FAR06, 272

Danilov, O. TAQ21, 1569

Danly, B.G. MPE12, 893

Darrow, C.B. WAG08, RAB01, 637, 758

Datskov, V.I. MPP01, 2034

Dattoli, G. TPG11, TPC03, 186, 2598

Davies-White, W. RAA04, 530

Davis, P. WPC20, RPA21, RPA22, 1039, 1102, 1105

Dawson, J. WAG09, TPC16, 640, 2637

De Angelis, A. TPG11, 186

De Brion, J.P. RAG06, 3170

de Groen, P. TAQ12, 1547

de Jager, C. RPG06, 330

de Leeuw, R.W. WAQ19, WAQ20, RPP04, RPQ31, 1882, 1885, 1970, 2738

De Martinis, C. TPC10, 2619

De Mascureau, J. TAE09, 1210

De Rijk, G. RAA11, 548

de Rijk, G. WAP12, WAP13, 464, 467

de Wijs, M.C.J. WAQ19, 1882

Deadrick, F. RPC18, TAR17, WPA02, TAE01, 743, 837, 905, 1178

Deadrick, F.J. TAR14, TPB14, 828, 2557

DeBarger, S. FAP16, 1366

Debraine, A. WAG07, 634

Decker, C.D. RAB01, RAB02, 758, 761

Decker, F.J. WAG11, RPB04, WAC17, 646, 665, 3109

Decker, F.-J. RPB02, WPR15, TPC20, RAP15, RAP16, RAP17, WAB05, WAB07, RAQ03, 659, 1821, 2646, 2919, 2922, 2925, 3025, 3031, 3291

Decker, G. FAR13, FAR19, MPQ03, MPQ08, MPQ10, RPQ16, 290, 303, 2452, 2467, 2473, 2702

Decker, Glenn RAR24, 3409

Decking, W. FAA02, FAB01, FAC19, 195, 2789, 2874

DeCobert, J. WAA16, 1260

Degen, C.M. TPB12, 2551

Dehnel, M. WAQ07, 1858

Dehning, B. WAP14, RAA19, 470, 567

Deitinghoff, H. WPA04, RPR06, RPR18, 911, 1131, 1158

Dejus, R. TPC03, 2598

Delahaye, J.P. RPC10, 719

Delahaye, J.-P. RPC09, 716

delaRama, F. TAE01, 1178

Dell, G.F. MPC05, FAB20, 2327, 2829

Dellwo, J. MPE05, WPC12, 871, 1022

Delsart, Ph. TAE09, 1210

Deluen, J.-P. RAA15, 557

Demko, J.A. MPP01, 2034

Den Hartog, P. MPP16, 2072

Deng, D. WAC24, 3131

Deng, D.P. WPP07, WPQ19, 1669, 1765

Deng, D.-P. MPB08, RAQ22, RAR29, 2288, 3334, 3421

Deppe, G. TPP11, 1639

Derenchuk, V. WPC08, RAP22, RAQ24, 1010, 2937, 3340

Desavouret, E. FAP06, FAP07, MPB06, 1337, 1340, 2285

Desmons, M. WPB22, 998

Despe, O. FAQ18, 1429

Deviatilov, V. WAA18, 1266

Devin, A. TAE09, TPC17,

1210, 2640
Dewa, H. FAR08, RPA13, WAQ01, 278, 1079, 1843
Dey, J. WPP08, WPP09, WPP23, RAQ13, 1672, 1675, 1714, 3312
Di Bona, A. WPC23, 1049
Di Crescenzo, J. RAG06, 3170
Dickey, C. FAA08, RPA17, WAA10, MPA11, 213, 1090, 1248, 2217
Dieperink, J. RAA15, 557
Dieulot, J.M. WAG07, 634
Dikansky, N. WPG06, TAR11, 500, 819
Dikansky, N.S. TAC06, WAA17, 143, 1263
DiMarco, J. FAP06, FAP07, 1337, 1340
Dinehart, M.R. WAQ26, 1897
Dinkel, J. WAA05, WAR01, 1236, 1900
Dinkel, J.A. WAA07, 1239
Dipace, A. TPG11, 186
Diviacco, B. FAQ19, 1432
Dobbe, N. MPQ17, 2491
Dobbins, J.A. RAE14, 2426
Dobeck, N. RPP06, 1973
Dobrovodsky, J. TAA18, 2120
Dodson, G. RPG05, 327
Dohlus, M. RPB15, RPB16, TAQ06, WPP05, WAE13, MPC16, 692, 695, 1533, 1666, 2190, 2345
Doinikov, N. MPC21, 2359
Dolbilov, G.V. WAA20, TAQ34, 1272, 1605
Dolique, J.-M. TPR04, TPR05, 3245, 3248
Donald, M. RAA22, 576
Donald, M.H.R. RAA27, 591
Donaldson, A.R. RPB05, WAA11, WAR06, RPP07, 668, 1251, 1915, 1976
Donaldson, T. WAQ15, 1876
Dooling, J.C. RAQ16, 3320
Doolittle, L. MPR13, MPR14, 2265, 2268
Doornbos, J. RPG12, 348
Doose, C. TPE08, 1310
Doria, A. TPG11, 186
Douglas, D. FAA25, WAQ14, 243, 1873
Douglas, D.R. WXE01, 2429
Dovbnya, A.N. WPA15, WPA16, WPB16, 938, 939, 988
Dow, K. RPG05, 327
Dowell, D.H. FAA27, FAA28, WPB20, 248, 251, 992
Dowling, D.T. TAP07, WAQ26, 366, 1897
Doyle, E. FAE07, 1497
Drago, A. RAE12, RPQ01, 2420, 2660
Drees, A. RAA19, 567
Dressler, J. RAA03, 527
Drevlak, M. RPB14, 689
Drury, M. FAE12, 1512
Du, W. FAP01, 1322
Dugardin, F. TAB04, 116
Dunbar, A. WAB04, 3022
Dunham, B. MPR15, TPC07, 2271, 2610
Dunham, B.M. WPC17, 1030
Dunnam, C.R. RAE14, 2426
Dunning, F.B. WPC21, 1043
Durand, R. TPP04, WPQ02, 1623, 1720
Durfee III, C.G. WAG04, 621
Durieu, L. TAP14, 386
Durkin, A.P. RPR07, 1134
Dutto, G. RPG12, MPE03, WAQ07, 348, 864, 1858
Dykes, D.M. WPQ18, WAC22, 1762, 3125
Dylla, F. WPA17, 942
Dylla, H.F. FAG11, FAA25, 102, 243
Early, R. RPC02, 701
East, G. RAP21, RAP22, RAQ23, RAQ24, 2934, 2937, 3337, 3340
Ecklund, S. RPB01, RPC01, 656, 698
Ecklund, S.D. WPC18, 1033
Edighoffer, J. RPA26, 1116
Efimov, S. FAR17, RAA08, 299, 542
Egawa, K. RAA33, 603
Ehrlich, R. FAE13, 1515
Ehrlichmann, H. RPE08, 2017
Eichenberger, C. WAA19, 1269
Eichhorn, K.D. FAR06, 272
Eigenmann, B. FAR06, 272
Einfeld, D. TPG08, FAR06, WPQ24, 177, 272, 1776
Ekelöf, Tord TPC11, 2622
Elias, L.R. FAA29, 254
Elizondo, J. WAA19, TAA20, 1269, 2123
Ellemaume, P. TPE10, 1319
Ellison, M. WPP20, WPP21, RAP21, RAP22, WAC12, RAG10, RAQ23, RAQ24, 1705, 1708, 2934, 2937, 3094, 3182, 3337, 3340
Ellison, T. TPB24, RAP22, 2583, 2937
Elsener, K. WAP14, 470
Emamian, M. FAA08, TAA02, 213, 2081
Emery, L. MPR01, MPB17, MPQ10, 2238, 2309, 2473
Emma, P. WAG11, RPB01, RPC03, RPC06, WAB07, 646, 656, 704, 707, 3031
Emma, Paul WAG01, 606
Emoto, T. TAQ08, 1539
Enchevich, I.B. WPP18, 1699
Engels, O. WPA04, WPA05, 911, 914
Engwall, D. FAG11, WPA17, 102, 942
Enjeti, Prasad N. RPP11, 1985
Enomoto, A. TAQ08, TAQ25, TAA04, 1539, 1578, 2087
Erdman, K. WAQ07, 1858
Eremeev, I.P. FAG10, TAC11, 98, 146
Erg, G.I. FAQ17, 1426
Erickson, R. RPA24, FAP16, 1111, 1366
Ermakov, D. RPA19, 1096
Ermakov, D.I. RAR04, 3361
Erochin, A. FAQ06, 1399
Escallier, J. FAQ03, 1393
Esin, S.K. RPR24, RPR25, RAE08, 1173, 1175, 2408
Estrin, B. WAA17, 1263
Etzkorn, F.J. WPQ26, 1781
Evans Jr., K. MPQ03, 2452
Evans, L.R. FPD04, 40
Everett, M. RAB05, 770
Everett, M.J. RAB04, 767
Evtushenko, Yu.A. FAQ17, 1426
Eyharts, Ph. TAE09, 1210
Eyl, P. TAE09, 1210
Eylon, S. TAR14, WPA02, WPA09, TAE01, TAE11, WAQ04, 828, 905, 926, 1178, 1216, 1852
Ezura, E. FAE09, TPP16, WPQ08, WPQ17, WPR05, WPR09, RPQ06, 1503, 1652, 1735, 1759, 1797, 1806, 2675
Fabris, A. FAR21, WPQ04,

TAG05, 309, 1723, 2762
Fabris, R. FAR21, 309
Fackler, O. RAA03, 527
Fahmie, M. RPQ08, 2681
Fainberg, Ya.B. RAB15, WAA02, WAA03, 782, 1230, 1233
Fallis, M.C. WPR20, 1835
Faltens, A. FAP17, FAP18, TPA10, 1369, 1372, 3220
Fan, T.C. FAQ26, 1450
Fang, C.S. MPQ32, 2524
Fang, S. MPR16, 2273
Fang, S.X. WAB20, 3064
Fang, Si J. FAP05, 1334
Fang, Ye TAR22, 850
Fant, K. WPR08, 1803
Farias, R.H.A. FAP14, 1361
Farkas, Z.D. WPR15, 1821
Farkhondeh, M. RPG05, 327
Farvacque, L. TPG05, 167
Farvid, A. MPP09, 2054
Fateev, A.A. WAA20, TAQ34, 1272, 1605
Fathizadeh, M. TAP05, 363
Faugeras, P. TPE03, 1288
Faugier, A. WAP12, WAP13, RAA11, 464, 467, 548
Faure, J. FAR14, 293
Fawley, W. FAP17, 1369
Fawley, W.M. FAA12, RAB03, FAP18, TPA10, 219, 764, 1372, 3220
Fazio, Michael V. FAE06, 1494
Fedin, O.L. MPG10, 426
Fedotov, A.P. RPR07, 1134
Fedotov, Alexei V. TPR12, 3266
Fedotov, Yu. MPR11, 2259
Feerick, B. WAQ15, 1876
Feldl, E. TPC04, 2601
Feldman, Donald W. WPB15, 985
Fellenz, B. MPQ13, 2479
Feng, W. WAR12, 1927
Feng, W.Q. WAA15, 1257
Ferdinand, R. RPR11, RAG07, 1146, 3173
Ferguson, M. RPP12, 1988
Ferianis, M. TPG11, FAR21, 186, 309
Feroli, F. WAP13, 467
Fernow, Richard MXG03, 53
Ferrario, M. WAC13, 3097
Feschenko, A.V. RAE08, 2408
Fessenden, R.W. TAB17, 131
Fessenden, T. TAR17, 837
Fessenden, T.J. TAR13, TAR14, TPB14, 825, 828, 2557
Fidecaro, G. WAP14, 470
Fieguth, T. WAQ15, 1876
Field, R. TAG01, 2742
Field, R.C. WXE07, 2444
Fietier, N. FAG09, 95
Filatov, B.A. WAA21, 1274
Filtz, M. MPC28, 2373
Fink, C.L. FAG14, 110
Fiorentini, G. WPB10, 973
Firjahn-Andersch, A. WPA03, 908
Fischer, C. RPC14, TPC21, 731, 2649
Fischer, Henk WAB06, 3028
Fischer, W. TAG07, 2768
Fisher, A. TPG14, RAA04, 192, 530
Fitzgerald, D. WPC10, WAC29, RAR23, 1016, 3146, 3406
Fitzgerald, J.B. TPG09, RAE10, 180, 2414
Flanz, J.B. RPE03, 2004
Flechtner, D. WPC19, 1036
Fleckner, K. RPA26, 1116
Fliflet, A.W. TAQ37, 1611
Flood, R. RPP13, 1991
Flora, R. WAE07, 2172
Flöttmann, K. TAA08, TAG01, 2096, 2742
Flynn, G. FAE13, RAR18, 1515, 3391
Fockler, J. WAA19, 1269
Foelsche, H. FAQ15, 1420
Foelsche, H.W. FAP11, 1352
Foley, M. FAG06, WPP01, 86, 1655
Fomin, M. WPP11, 1681
Fong, K. MPR16, 2273
Forest, E. RAA22, RAA25, FAB06, 576, 585, 2804
Forsyth, E.B. WAA15, WAR10, WAR12, 1257, 1921, 1927
Foster, G.W. MPG11, WAP16, TPE05, 428, 473, 1298
Foster, J. WPB06, 961
Foster, W.B. FAP21, 1381
Fouaidy, M. TPP09, TPP11, TPP14, 1632, 1639, 1648
Fougeron, C. WPQ26, 1781
Fowkes, W.R. FAE07, TAQ28, 1497, 1587
Fowler, W. MPG01, 391
Fox, J. RAA04, RAE12, RAE13, RPQ01, RPQ08, 530, 2420, 2423, 2660, 2681
Fox, T. MPR13, 2265
Frachon, D. FAQ17, FAQ18, 1426, 1429
Franks, R.M. WPQ06, 1729
Franzke, B. MPC15, 2342
Freund, A. WAP14, 470
Fricks, R. MPA11, 2217
Friedman, A. TAR14, TAR15, TAR17, FAQ17, TPR19, 828, 831, 837, 1426, 3282
Friedman, Aharon RPQ14, 2696
Friedrich, L. FAR06, 272
Friedsam, H. TAP05, TAA03, 363, 2084
Friesel, D. WPP20, WPP21, RAQ24, 1705, 1708, 3340
Friesel, D.L. RPG08, TAP03, WAQ08, 336, 357, 1861
Frisch, J. WAG11, MPE10, 646, 887
Fu, Shinian FAA21, RAQ25, RAQ26, 237, 3343, 3346
Fugitt, J. FAG11, FAA25, WPA17, RPQ30, 102, 243, 942, 2735
Fuja, R. RPA10, RPA11, MPQ08, MPQ10, 1070, 1073, 2467, 2473
Fuja, R.E. TPC01, 2595
Fujino, T. TPP07, 1629
Fujita, H. FAR08, RPA13, WAQ01, 278, 1079, 1843
Fukuma, H. RAA33, 603
Fukutomi, M. TPP16, 1652
Fullett, K. WAR17, WAR18, 1939, 1942
Funahashi, Y. TPP07, 1629
Funakoshi, Y. MPQ31, WAC08, 2521, 3085
Furman, M. RPC02, TPQ16, 701, 2986
Furman, Miguel A. RAP14, 2916
Furuya, T. TPP03, 1620
Fusellier, J. WAG07, WPB22, 634, 998
Gai, W. WAG06, WPB11, MPQ11, 631, 976, 2476
Galayda, J. RPQ16, 2702
Galayda, John N. MAD02, 4
Gallardo, Juan C. MXG03, WPB21, 53, 995
Gallerano, G.P. TPG11, 186
Gamo, N. TPP03, 1620
Ganetis, G. TPE04, FAQ02,

FAQ03, FAQ04, FAQ15, 1293,
 1390, 1393, 1396, 1420
Ganetis, G.L. TAA09, 2099
Gangeluk, M. WPR13, 1815
Gao, J. RPA03, 1055
Gao, Jie WPQ01, 1717
Garcia, R.C. TPC06, 2607
Gardner, C.J. TAP11, TAP13,
 378, 383
Garnett, R.W. RAG11, 3185
Garoby, R. MPG09, 423
Garosi, F. TPG11, 186
Garrel, N. WAP12, RAA15,
 464, 557
Garren, A. WPG11, 520
Garren, A.A. TAB06, 119
Garvey, J.D. FAP06, FAP07,
 1337, 1340
Garvey, T. WPA14, WPB22,
 935, 998
Gavaggio, R. MPP15, 2069
Gavrilov, N.G. FAQ17, 1426
Gay, T. WPC21, 1043
Gayet, Ph. MPP02, 2037
Geisik, C. WPC10, 1016
Gelato, G. MPG09, 423
Gelfand, N.M. RAB19, 787
Gelfand, Norman M. WAP07,
 452
Geller, J. WAR11, RPP02,
 1924, 1964
Geng, X. MPA01, 2193
Genova, L. RAA04, 530
Georges, J.P. TAB04, 116
Georges, P. WPB01, 945
Geschonke, G. TPP12, 1642
Gevchuk, A. FAR17, 299
Ghiorso, W. TPA10, 3220
Ghosh, A. TPE04, FAQ03,
 FAQ04, 1293, 1393, 1396
Giacuzzo, F. MPP04, 2042
Giannessi, L. TPG11, 186
Giannini, M. TPG11, FAR21,
 186, 309
Gilgenbach, R.M. TAQ32,
 1599
Gillespie, G.H. RPR20, 1164
Gillespie, George H. FAG13,
 MPB14, 107, 2300
Gilpatrick, J.D. RPR19,
 RPR22, TPB16, TPB22, 1161,
 1167, 2563, 2580
Giordano, G. RPC17, 740
Giovannozzi, M. FAC06, 2847
Giove, D. TAA07, TPC10,
 2093, 2619
Giovenale, E. TPG11, 186
Gladkikh, P. FAR17, 299
Glass, H. TPE05, 1298
Glass, H.D. FAP05, FAP06,
 FAP07, MPB05, MPB06, 1334,
 1337, 1340, 2282, 2285
Glazov, A. WPC13, WPR19,
 1025, 1833
Glenn, J.W. TAP13, WAR13,
 383, 1930
Glock, H.-W. RPB15, RPB16,
 692, 695
Glover, E. TPG07, 174
Gluckstern, R. RPA04, 1058
Gluckstern, R.L. TPQ14, 2980
Gluckstern, Robert L.
 RAG09, TPR11, TPR12, RAR12,
 3179, 3263, 3266, 3376
Gluskin, E. TPE06, FAQ17,
 MPP16, 1301, 1426, 2072
Goddard, B. RAA15, 557
Goderre, G. WAP08, 455
Goderre, G.P. WAP05, 446
Godfrey, G. WAQ15, 1876
Godlove, T.F. TAE10, 1213
Godlove, Terry F. TAA17,
 2117
Godot, J.C. RPC10, 719
Goffeney, N. RPC17, 740
Gold, C. RPA10, 1070
Gold, S.H. TAQ37, 1611
Goldberg, D.A. WPQ13, 1747
Goldman, M.A. TAA09, 2099
Goldstein, J.C. FAA16, 228
Golkowski, Cz. TAQ01, 1518
Golubev, I.I. WAA20, 1272
Golubev, V. WPC03, 1004
Goncharov, A.D. TAC06,
 RPP08, 143, 1979
Gonichon, J. MPE12, 893
Gonin, I.V. RPR01, 1119
Goral, J. RPA11, 1073
Gordeeva, M.A. MPG10, 426
Gordon, D. RAB04, RAB05,
 767, 770
Gorelov, D.V. RPR01, 1119
Gorev, V.V. MPE06, 874
Gorin, M.Yu. WAR23, 1955
Gorniker, E. WPP11, 1681
Gorski, A. FAP03, 1328
Goto, A. WPC01, 1001
Gougnaud, F. WPB22, 998
Gournay, J.F. WPB22, 998
Govil, R. TPG07, RAB10, 174,
 776
Gower, E. RPA26, 1116
Graber, J. FAE03, 1478
Gracia, J. RAA04, 530
Granatstein, V.L. TAQ17,
 TAQ18, TAQ19, 1561, 1563,
 1566
Gras, J.J. TPC21, 2649
Grassi, R. FAC06, 2847
Grau, M.C. MPQ05, 2458
Graves, W.S. FAQ13, 1414
Gray, E.R. RAG11, 3185
Green, M. WPG11, 520
Green, M.A. TAB06, 119
Greene, A. TPE04, FAQ03,
 FAQ04, FAQ15, 1293, 1393,
 1396, 1420
Greenly, John B. TAE07,
 1204
Greenwald, Z. FAE13, TPA04,
 1515, 3206
Grelick, A. RPA11, 1073
Grelick, A.E. RPA10, RPA14,
 RPE09, 1070, 1082, 2020
Greth, V.N. WAR20, 1948
Gridasov, V. FAQ06, 1399
Grieser, M. RPR06, 1131
Grigor'ev, Yu.N. RAA07,
 RAQ28, 539, 3349
Grimm, T. RPG11, 345
Grimmer, J. RPE09, 2020
Grishin, V.K. FAG12, FAA14,
 105, 225
Gröbner, O. RPE02, 1999
Gromme, T. RAE03, 2389
Gross, G. WAR06, 1915
Grossberg, P. RAE03, 2389
Grosse-Wiesmann, P. RAA19,
 567
Grote, D. TAR17, TAE01, 837,
 1178
Grote, D.P. TAR13, TAR14,
 TAR15, WPA09, TPR19, 825,
 828, 831, 926, 3282
Grote, H. RAA19, 567
Grudiev, A. MPB09, 2291
Grunder, Hermann A. MAD01,
 1
Gubin, K. WAA17, 1263
Guckel, H. WPE02, 63
Gudkov, K. RPA19, 1096
Gudkov, K.A. FAG12, 105
Guharay, Samar K. MPC04,
 2324
Guidi, V. RAE05, 2399
Guignard, G. RPC09, RPC12,
 RPC13, 716, 725, 728
Guinand, R. RAA15, 557
Guo, H. TAQ17, 1561
Guo, Z. TPQ03, 2955
Gupta, R. TPE04, FAQ04,

FAQ16, TAA09, 1293, 1396,
 1423, 2099
Gupta, R.C. WAP10, 461
Gur'yev, M.P. MPG10, 426
Gurov, G. MPG06, 416
Güsewell, D. MPP02, 2037
Gusinskii, G.M. TAP16, 389
Gustafson, Dick TPE05, 1298
Gustavsson, J. FAA08, 213
Guy, F.W. RPG10, 342
Gyr, M. WAP14, WAQ24, 470,
 1891
Haber, I. TAR15, TPR19, 831,
 3282
Haberichter, W. TPC16, 2637
Habib, Salman RAG01, 3149
Habs, D. RPR06, 1131
Haddock, C. FAQ14, 1417
Haebel, E. TPP12, 1642
Haffmans, A.F. RAG14,
 RAQ20, 3194, 3329
Hafizi, B. TAQ37, 1611
Haga, K. RPQ23, 2720
Hagedoorn, H.L. WAQ19,
 WAQ20, RPP04, RPQ31, 1882,
 1885, 1970, 2738
Hahn, H. TPQ02, 2952
Hahn, K.D. TPA10, 3220
Hahn, U. FAR07, 275
Haimson, J. RPC22, TAQ03,
 755, 1524
Hairapetian, G. WPC20,
 RPA21, RPA22, 1039, 1102,
 1105
Hakota, M. TAQ35, 1608
Hall, P.J. FAP06, FAP07,
 MPB06, 1337, 1340, 2285
Haller, M. FAR06, 272
Halling, M. RPC20, RPC21,
 TAG01, 749, 752, 2742
Hamilton, B. TPB24, RAP21,
 RAP22, RAQ24, 2583, 2934,
 2937, 3340
Hammel, E. TPB07, 2542
Han, Bumsoo TAB09, FAR03,
 122, 269
Han, D.H. WPR11, 1812
Hanna, B. WAR01, 1900
Hanna, S.M. RPA23, 1108
Hanne, G.F. WPC21, 1043
Haouat, G. RAG06, RAG07,
 3170, 3173
Hardek, T. WAC29, 3146
Hardek, T.W. TAQ31, 1596
Harding, D.J. FAP04, FAP05,
 FAP06, FAP07, FAP09, MPB05,
 MPB06, 1331, 1334, 1337,
 1340, 1346, 2282, 2285
Harkay, K. TAP05, TPQ22,
 TPQ23, 363, 3001, 3004
Harrison, M. MPG03, TAA09,
 401, 2099
Harrison, M.A. MPG12, 431
Hartill, D.L. RAE14, 2426
Hartley, R. FAA19, 234
Hartley, R.A. FAA31, 260
Hartman, S. RPB02, RPC20,
 WXE07, TAG01, 659, 749,
 2444, 2742
Hartman, S.C. RPB04, TPC29,
 665, 2655
Hartnagel, H.L. MPC15, 2342
Hartung, W. FAE13, TPA04,
 RAQ04, RAR18, RAR19, 1515,
 3206, 3294, 3391, 3394
Harwood, S.L. WXE01, 2429
Hasegawa, K. RPG09, 339
Haseroth, H. MPG09, 423
Haseroth, H.D. MPG05, 411
Hashimoto, S. FAQ21, 1438
Hathaway, D. MPP12, MPP20,
 2064, 2075
Hawkins, A. WAA16, 1260
Hayakawa, A. WXE07, 2444
Hayano, H. RPA20, WPR03,
 TPC05, TAG01, 1099, 1791,
 2604, 2742
Hayashi, E.K.C.S. MPQ33,
 2527
Hayashi, S. FAP13, 1358
Haynes, D.L. WAQ26, TPC18,
 1897, 2643
Haynes, W. Brian FAE06,
 1494
Hays, S. WAE07, 2172
Hays, T. FAE13, TPP02,
 WPQ02, 1515, 1617, 1720
Hayward, T.D. FAA27, FAA28,
 WPB20, 248, 251, 992
Hedblom, K. WPP20, WPP21,
 WAQ08, RAP21, 1705, 1708,
 1861, 2934
Heese, R. FAR10, 284
Heifets, S. MPC01, MPC08,
 TPQ16, 2317, 2333, 2986
Heifets, S.A. TAA22, MPC02,
 MPC03, MPC18, 2129, 2319,
 2321, 2351
Heim, J. RAA03, 527
Heimlinger, G. TAG01, 2742
Heine, E. TAQ12, MPQ17,
 1547, 2491
Heinrichs, G. TPB20, 2574
Helm, R. RAA22, RPC06,
 RPC07, RPC20, TAA08, TAG01,
 576, 707, 710, 749, 2096,
 2742
Helvajian, H. FAG11, 102
Hemelseoet, G.H. WAE09, 2178
Hémery, J.-Y. TAP14, 386
Hemmer, M.F. TAA09, 2099
Henderson, S. FAE13, 1515
Henderson, T. FAP01, 1322
Hendrickson, L. RAE03, 2389
Hendrickson, L.J. WAG11,
 RPB03, 646, 662
Henestroza, E. RPC16, RPC17,
 RPC19, WPA02, WPA09, TAE01,
 TAE11, MPC01, MPC08, TPA10,
 737, 740, 746, 905, 926,
 1178, 1216, 2317, 2333, 3220
Henke, H. TAQ30, WPQ14,
 WAB11, 1593, 1750, 3043
Henkel, D.P. FAG11, 102
Hentges, M. MPP01, 2034
Herold, W. WPA12, 929
Herr, W. WAP14, WPG09, 470,
 514
Herrup, D.A. TPQ25, TPQ26,
 3007, 3010
Hershcovitch, A. WPC09,
 1013
Herz, P. TPB07, 2542
Hettel, R. MPQ22, RPQ21,
 RPQ22, 2506, 2714, 2717
Heutenik, B. TAQ12, 1547
Heydari, Huschang WAP09,
 458
Higashi, Y. WPQ15, 1753
Higgins, D.S.G. WPQ18, 1762
Higgins, S. MPR13, 2265
Higo, T. FAQ08, WPQ15,
 WPR02, WPR03, 1405, 1753,
 1788, 1791
Higo, Toshiyasu FAE02, 1474
Higuchi, A. RAQ06, 3300
Higuchi, T. TPP07, 1629
Hilaire, A. WAP12, WAP13,
 464, 467
Hill, B.W. RPR20, 1164
Hill, Barrey W. MPB14, 2300
Hill, S.F. WAC21, 3122
Hilleret, N. TPP12, 1642
Himel, T. RAE03, 2389
Hindi, H. RAE12, 2420
Hinode, F. WPQ16, WPR02,
 WPR03, TPC05, 1756, 1788,
 1791, 2604
Hipple, R. WPA01, TAE01,
 902, 1178
Hiramoto, K. TAB03, WPQ21,

113, 1770
Hirano, K. TAQ08, 1539
Hirata, K. RAP02, 2883
Hirata, Y. WPR02, 1788
Hirota, J.I. TAB03, WPQ21, 113, 1770
Hizanidis, K. RAQ01, 3285
Ho, C. WPB11, 976
Ho, C.H. WPB07, 964
Hoag, H. RPA04, WPQ05, 1058, 1726
Hoag, H.A. RPA23, 1108
Hobson, B. RAA03, 527
Hodges, T. RPG12, 348
Hodgkins, D. MPE04, WPA08, 867, 923
Hodgson, J. WPR08, 1803
Hoeflich, J. RAE12, 2420
Hoffstätter, G.H. FAB07, 2807
Hofler, A. MPR13, 2265
Hofmann, A. RAA17, RAA18, RAA20, FAC03, 560, 564, 570, 2841
Hogan, B. TAQ18, TAQ19, 1563, 1566
Hogan, M. FAA23, RPA21, RPA22, 240, 1102, 1105
Hogrefe, R. TPE08, 1310
Hohbach, R. TAQ33, 1602
Holdener, F.R. MPP12, MPP20, TAA22, 2064, 2075, 2129
Holmes, C. WAA19, 1269
Holmes, S. MPG01, 391
Holmes, S.D. WAP01, 434
Holmquist, T. RAE14, 2426
Holsinger, R.F. TPE07, 1305
Holt, J. RPC20, 749
Holt, J.A. WAP01, WAP08, RPC21, TAG01, WAC01, 434, 455, 752, 2742, 3067
Holtkamp, N. FAR06, RPB12, RPB13, RPB15, RPB16, WPA12, WPP05, MPC16, 272, 683, 686, 692, 695, 929, 1666, 2345
Holtzapple, R.L. WXE05, WAB05, WAC04, WAC17, 2438, 3025, 3073, 3109
Honda, T. RPQ23, 2720
Honecker, V. FAR06, 272
Hopster, H. WPC21, 1043
Horan, D. TAP05, RPP12, 363, 1988
Hori, T. WPC22, MPA07, 1046, 2208
Houck, T. RPC16, RPC17, WPC16, 737, 740, 1027
Houck, T.L. TAQ03, 1524
Hovater, C. FAE12, TPC26, RPQ29, 1512, 2652, 2732
Howell, J. TAR08, 816
Hower, N. FAA08, RPA17, TAA02, MPQ06, 213, 1090, 2081, 2461
Hower, Nelson WPA13, 932
Hoyer, E. FAQ24, FAQ25, 1444, 1447
Hoyt, E. MPP09, MPP12, MPP20, 2054, 2064, 2075
Hoyt, M. MPP09, MPP12, MPP20, 2054, 2064, 2075
Hseuh, H.C. TAP11, TAP12, MPP11, 378, 381, 2060
Hsieh, H. RAA05, RPA26, 533, 1116
Hsiung, G.-Y. TPC15, 2634
Hsu, I. TAA28, 2135
Hsu, Ian MPQ26, TPC15, RAR05, 2515, 2634, 3364
Hsu, K.T. FAA04, FAA07, RAA23, RAA24, MPR10, MPQ16, MPQ19, MPQ32, TPB29, TPQ08, TPQ09, TPQ10, 201, 210, 579, 582, 2256, 2488, 2497, 2524, 2592, 2965, 2968, 2971
Hsu, R.-C. TPC15, 2634
Hsu, S.Y. WPB07, 964
Hsue, C.S. RAA24, TAR04, TPQ09, TPQ10, 582, 804, 2968, 2971
Huang, Gloria MPR10, 2256
Huang, H. TPA06, 3212
Huang, J.Y. TPG06, 171
Huang, N. RAA21, WAC27, 573, 3140
Huang, Zhibin FAA21, RAQ25, RAQ26, 237, 3343, 3346
Huang, Zhirong RAQ18, 3326
Huffman, G. FAE07, 1497
Hughes, Thomas P. TAE08, 1207
Hülsmann, P. RPB15, RPB16, 692, 695
Humbert, J. FAP03, 1328
Hümmer, K. FAR06, 272
Humphries, D. FAQ24, FAQ25, 1444, 1447
Hunt, D. MPP13, 2067
Hustache, R. WAP14, 470
Hutson, R. WAC29, 3146
Hutson, R.L. TAR12, 822
Huttel, E. FAR06, 272
Hutton, A. TPC26, 2652
Hwang, J.I. WPB07, 964
Hwang, O.H. TAQ14, 1553
Hwu, K.H. MPQ19, 2497
Iazzourene, F. FAR21, TAG05, 309, 2762
Ieiri, Takao TPB17, 2566
Igarashi, Y. TAQ25, 1578
Igarashi, Z. WPC07, 1007
Ignatyev, A. TAB13, TAQ23, TAQ24, 125, 1572, 1575
Ihloff, E. RPG05, 327
Iida, S. TPP03, 1620
Ikegami, K. WPC07, 1007
Ikegami, M. FAR08, RPA13, WAQ01, 278, 1079, 1843
Ilijinov, A.N. RPR01, 1119
Imai, Y. FAQ08, 1405
Imanishi, A. RPG13, 351
Imel, G.R. TAC12, 149
Inagaki, S. TPP16, 1652
Inaguchi, T. FAQ08, 1405
Ingalls, W. WPC10, 1016
Ingwersen, Pete TAE07, 1204
Inman, T.K. RPA24, 1111
Ino, H. RPG09, 339
Inoue, H. TPP07, 1629
Inoue, M. FAR08, RPA13, RPA18, WPQ21, WAQ01, 278, 1079, 1093, 1770, 1843
Irwin, J. RAA22, RAA25, RAA26, RAA27, RPC01, RPC06, RPC07, RPC08, RPC20, TAA08, TAG01, TAG06, FAC18, RAP09, RAP11, RAP12, 576, 585, 588, 591, 698, 707, 710, 713, 749, 2096, 2742, 2765, 2871, 2904, 2910, 2913
Irwin, John MPC31, 2376
Irwin, M. WPQ13, 1747
Isagawa, S. TPP16, 1652
Ishi, Y. TAP04, TPP03, 360, 1620
Ishida, T. MPQ18, 2494
Ishihara, N. TAG01, 2742
Ishii, H. MPQ31, 2521
Ishkhanov, B. RPA19, 1096
Ishkhanov, B.S. FAG12, FAA14, 105, 225
Issinsky, I.B. WAR09, FAC12, 1918, 2863
Ito, I. TAQ35, 1608
Ito, N. RPG09, 339
Itoh, Y. MPA07, 2208
Ivanov, A. TAC16, 152
Ivanov, A.A. WAR20, 1948
Ivanov, A.S. TAE13, 1222

Ivanov, I.N. WAA20, 1272
Ivanov, P. RAA31, 600
Ivanov, P.M. FAQ17, FAQ18, 1426, 1429
Ivanov, S. WPP05, MPC16, TPQ01, TPQ04, 1666, 2345, 2949, 2958
Ivanov, Yu.D. RPR07, 1134
Ivers, J.D. WPC19, TAE12, 1036, 1219
Iverson, R. RPC20, TAA28, WXE07, TAG01, 749, 2135, 2444, 2742
Iwashita, Y. FAR08, RPA13, RPA18, WPQ21, WAQ01, 278, 1079, 1093, 1770, 1843
Izawa, M. TPP03, WPQ07, WPR04, 1620, 1732, 1794
Jablonka, M. WPA14, WPB22, 935, 998
Jackson, A. FAA03, FAA05, RPC02, 198, 204, 701
Jackson, G. MPG11, WAP16, TPE05, WAR19, MPQ13, RAP20, WAC09, WAC10, 428, 473, 1298, 1945, 2479, 2931, 3088, 3091
Jackson, L.T. RPP01, RPP07, 1961, 1976
Jackson, T. RAA04, FAQ24, 530, 1444
Jacob, J. TPG05, FAR06, 167, 272
Jacobs, K. RPG05, RAA31, 327, 600
Jacquemard, B. WPB22, 998
Jacquet, F. WAG07, 634
Jaeschke, E. RPR06, FAQ12, 1131, 1411
Jaffery, T.S. FAQ32, 1465
Jagger, J. FAP03, 1328
Jain, A. WAP10, TPE04, FAQ03, FAQ04, FAQ16, TAA09, 461, 1293, 1393, 1396, 1423, 2099
Jamison, R.A. RPR20, 1164
Jan, G.J. MPR10, MPQ16, TPB29, 2256, 2488, 2592
Jang, J.S. TPG06, 171
Jarvis, H. WPR15, 1821
Jason, A. WAC29, 3146
Jason, Andrew J. TAE02, 1183
Jayamanna, K. MPE03, WAQ07, 864, 1858
Jean, Benedikt FAG03, 75
Jeanjean, J. RPC20, TAG01, 749, 2742
Jeanneret, B. FAC04, 2844
Jenner, D. WPP20, WPP21, 1705, 1708
Jensen, C. WAR01, 1900
Jensen, C.C. WAA07, 1239
Jensen, D. FAQ08, 1405
Jensen, E. MPG09, 423
Jiang, D.M. RPE10, 2023
Jiang, Shicheng TPR11, 3263
Jiang, W.S. MPP11, 2060
Jiang, Y. FAP01, 1322
Jianjun, Deng FAA26, 246
Jin, K. WPP05, 1666
Jin, L. RAA21, WAC27, 573, 3140
Jinsui, Shi FAA26, 246
Jobe, K. WPR15, 1821
Jobe, R.K. WAB05, 3025
Joffe, D. RPR02, 1122
Joh, Kihun TAB09, FAR03, 122, 269
Johnson, B. WPC21, 1043
Johnson, C. RPC09, 716
Johnson, D. RPG11, 345
Johnson, D.E. TAB06, FAP04, FAP09, FAP10, 119, 1331, 1346, 1349
Johnson, J. WPR14, RAE13, RPQ08, 1818, 2423, 2681
Johnson, J.W. WAQ26, 1897
Johnson, K.F. RPR19, RPR22, TPC06, 1161, 1167, 2607
Johnston, M. WPC21, 1043
Johnstone, C. FAG06, 86
Johnstone, J. WAP01, 434
Joho, W. FAB14, 2823
Joly, J.M. WAG07, WPA14, WPB22, 634, 935, 998
Joly, S. RAG06, 3170
Jones, C.M. TPC18, 2643
Jones, G.S. RPP06, 1973
Jones, R.M. TAA33, MPC03, 2144, 2321
Jones, W.P. TPB24, RAQ24, 2583, 3340
Jongewaard, E. FAE07, 1497
Jonker, M. WAP12, WAP13, RAA11, 464, 467, 548
Jordan, K. FAG11, FAA25, WPA17, 102, 243, 942
Joshi, C. WAG08, WAG09, RAB01, RAB02, RAB03, RAB04, RAB05, WPC20, RPA21, RPA22, TPB18, 637, 640, 758, 761, 764, 767, 770, 1039, 1102, 1105, 2569
Judd, D.L. TAR14, 828
Judkins, J. WPQ10, WPR08, 1741, 1803
Juillard, M. WAG07, WPB22, 634, 998
Junck, K. TPQ28, WAB01, 3013, 3016
Jung, R. TPC21, 2649
Junquera, T. WPB22, TPP09, TPP11, TPP14, 998, 1632, 1639, 1648
Juras, R.C. WAQ26, MPA05, 1897, 2202
Juras, S. TPP12, 1642
Jurgens, T.G. MPB15, 2303
Kachtanov, E. FAQ06, 1399
Kadnikov, A. WAA18, WPR13, MPA04, 1266, 1815, 2199
Kadokura, E. MPQ18, 2494
Kageyama, T. FAE09, WPQ09, WPQ17, WPR05, WPR09, 1503, 1738, 1759, 1797, 1806
Kahana, E. MPQ03, MPQ10, RPQ15, 2452, 2473, 2699
Kahn, S. TPE04, FAQ16, 1293, 1423
Kakigi, S. FAR08, RPA13, WAQ01, 278, 1079, 1843
Kako, E. TPP07, 1629
Kalashnikov, V.V. TPB25, 2586
Kalbreier, W. RAA15, 557
Kalfas, C. RAQ01, 3285
Kaltchev, D. FAB14, 2823
Kamber, I. RPC10, 719
Kaminsky, A. TAC16, 152
Kamiya, Y. FAR09, FAP22, WPQ07, WPR04, 281, 1384, 1732, 1794
Kando, M. FAR08, RPA13, WAQ01, 278, 1079, 1843
Kandrunin, V.N. WPR17, 1827
Kaneda, T. FAP13, 1358
Kang, Kyungwoo TAB09, FAR03, 122, 269
Kang, Woung TAB09, FAR03, 122, 269
Kang, X. TAP03, WPP20, WPP21, RAP21, WAC12, RAG10, RAQ23, RAQ24, 357, 1705, 1708, 2934, 3094, 3182, 3337, 3340
Kang, Y.G. FAR19, FAQ18, 303, 1429
Kang, Y.W. WAG10, WPP16, RPE09, 643, 1693, 2020
Kang, Yoon WPP12, 1684

Kaplan, R. FAE13, WPQ02, 1515, 1720
Karantzoulis, E. FAR21, TAG05, 309, 2762
Karantzoulis, Emanuel MPR12, 2262
Karas', V.I. WAA02, WAA03, 1230, 1233
Karas', Vyacheslav I. WAA01, 1227
Karetnikov, M. RPR10, RPR15, 1143, 1155
Karev, A.I. TAR05, FAP19, WPR17, 807, 1375, 1827
Karl, F.X. TAA09, 2099
Karn, J. MPR15, 2271
Karnaukhov, I. FAR16, FAR17, RAA08, 296, 299, 542
Karpenko, V. TAR17, 837
Karshev, Yu. MPR11, 2259
Kashikin, V. FAR06, 272
Kasuga, T. RPQ23, RPQ26, RAQ06, 2720, 2726, 3300
Katoh, M. RPQ23, 2720
Katoh, T. MPA06, 2205
Katsouleas, T. WAG09, RAB02, RAB08, TAA28, TPB18, 640, 761, 773, 2135, 2569
Kaul, O. FAA02, FAC19, 195, 2874
Kawai, M. RPG09, 339
Kawakubo, T. RAB13, WAR04, MPQ18, 779, 1909, 2494
Kawakubo, Tadamichi TPR16, 3275
Kazarezov, I. WAA17, 1263
Kazimi, R. WXE01, TPC07, 2429, 2610
Keane, J. FAR10, TPP06, 284, 1626
Keeley, D. RPQ21, RPQ22, 2714, 2717
Keffeler, D. TAQ02, 1521
Keffeler, D.R. WPA08, 923
Kehne, D. FAG11, FAA25, WPA17, 102, 243, 942
Keil, E. WPG09, 514
Keith-Monnica, E. WAB04, 3022
Keizer, R. WAP12, 464
Kelley, M.J. FAG11, 102
Kelly, D.R.C. RPE08, 2017
Kelly, E. TPE04, FAQ03, FAQ04, FAQ15, 1293, 1393, 1396, 1420
Kelly, K.W. TAA32, 2141
Kemper, A.H. RPP04, 1970
Kendall, M. RAA03, 527
Kennedy, K. MPP13, 2067
Kerner, T.M. MPA18, 2232
Kerns, C. WPR21, 1838
Kerns, J.A. TAA22, 2129
Kerns, Q. WPR21, 1838
Kerslick, G.S. WPC19, TAE12, TAQ01, 1036, 1219, 1518
Kewisch, J. MPR20, 2279
Khabibouline, T. WPP05, 1666
Khan, S. FAQ12, WAQ17, WAB03, 1411, 1879, 3019
Kheifets, S.A. MPC18, 2351
Khomyakov, E.A. TAE14, 1225
Khrutchinsky, A.A. TPA15, 3232
Kihara, Motohiro TPR16, 3275
Kijima, Y. TPP03, 1620
Kikuchi, M. RAA33, 603
Kikutani, E. RPQ26, 2726
Kikuzawa, N. TPG02, 159
Kim, Byungmun TAB09, FAR03, 122, 269
Kim, C. FAA03, FAA06, 198, 207
Kim, C.H. FAA05, 204
Kim, G.N. TAR07, 813
Kim, J. TAA11, 2102
Kim, J.W. RPR05, FAQ09, RAR21, 1128, 1408, 3400
Kim, Jinsoo TAB09, FAR03, 122, 269
Kim, K. TPE08, 1310
Kim, K.-J. TPG07, TAG13, RAR02, 174, 2786, 3358
Kim, Keeman TAB09, FAR03, 122, 269
Kim, Kwang-Je RAP06, 2895
Kim, S. FAR19, TAP05, FAB09, 303, 363, 2811
Kim, S.H. FAA10, TPE08, 216, 1310
Kim, Sungmyun TAB09, FAR03, 122, 269
Kim, T.H. FAQ08, 1405
Kim, T.Y. FAA10, 216
Kim, Y.S. WPR11, 1812
Kim, Younghee TAB09, FAR03, 122, 269
Kim, Yuri TAB09, FAR03, 122, 269
Kimura, W.D. WAG05, 626
Kindermann, H.P. TPP12, 1642
Kinthead, A.K. TAQ37, 1611
Kinross-Wright, John M. WPB15, 985
Kinsho, M. WPC07, WAQ06, 1007, 1855
Kinter, R. RAB02, 761
Kirbie, H.C. TAR14, 828
Kirby, R. MPE10, MPP09, 887, 2054
Kircher, J. FAR06, 272
Kirchgessner, J. FAE01, FAE13, WPQ02, RAQ04, RAR18, RAR19, 1469, 1515, 1720, 3294, 3391, 3394
Kirchman, J. RPQ15, RPQ16, 2699, 2702
Kirk, Harold G. WPB21, 995
Kiseljov, V.A. RAB15, 782
Kishek, R. TAQ32, 1599
Kishiyama, K. MPP12, MPP20, 2064, 2075
Kiver, A. MPP03, 2040
Kleffner, C.-M. RPR06, 1131
Klein, H. RPB15, RPB16, 692, 695
Klein, W.B. WAE08, 2175
Klem, J. WAP14, 470
Kleman, K.J. WPR01, 1785
Klewe-Nebenius, H. FAR06, 272
Klippert, T. MPP16, 2072
Klopenkov, M. TAA18, 2120
Kneisel, Peter TPP13, 1645
Knobloch, J. FAE13, TPP04, 1515, 1623
Knöchel, A. FAR06, 272
Knuth, T. TPE09, 1316
Ko, I.S. TAR07, RPA06, MPA02, 813, 1061, 2196
Ko, K. RPA04, RPA11, RPA14, TAQ06, WPQ05, WPQ12, WPR07, MPC01, 1058, 1073, 1082, 1533, 1726, 1744, 1800, 2317
Kobayashi, A. FAA30, 257
Kobayashi, T. RAB13, WPQ17, 779, 1759
Kobayashi, Y. FAR09, RPQ23, 281, 2720
Kodaira, M. FAP13, 1358
Koga, A. FAA30, 257
Kogan, M. TPB04, 2536
Kohaupt, Rolf-Dieter RPQ32, 2741
Koike, S. WPQ15, 1753
Koiso, H. TAG11, 2780
Kokoulin, V. WAA17, 1263

Kokura, S. TPP03, 1620
Kolomiets, A.A. TPA05, 3209
Kolonko, J. WPG11, 520
Kolonko, J.J. TAB06, 119
Komarov, V. MPP03, MPR11, 2040, 2259
Komori, K. TPP16, 1652
Konecny, R. WAG06, WPB11, WPB12, 631, 976, 979
Kononenko, S. FAR16, FAR17, RAA08, 296, 299, 542
Konovalov, V.A. RPR07, 1134
Koontz, R. WPR15, 1821
Koopman, J. TPC21, 2649
Korchuganov, V. WAA18, FAP02, 1266, 1325
Korepanov, V.M. WAA21, 1274
Korolev, A.P. TPA05, 3209
Kos, N. RPE02, 1999
Koscielniak, S. RPG12, RAQ15, 348, 3317
Koscielniak, S.R. WAC19, 3115
Koseki, T. FAP22, WPQ07, WPR04, 1384, 1732, 1794
Kößler, V. RPR06, 1131
Kosterin, S.A. FAG12, 105
Kostin, D.V. WPR18, 1830
Kosukhin, V.V. WAA20, 1272
Kot, N. WAA17, 1263
Kotaki, H. WPC22, 1046
Kotov, V.I. MPG10, WAR20, WAR21, 426, 1948, 1949
Kouptsidis, J. RPE08, 2017
Kourbanis, I. WPP08, WPP23, RAQ13, 1672, 1714, 3312
Koutchouk, J.P. RAA17, 560
Koutchouk, J.-P. FAC04, 2844
Kovach, P. TAA18, 2120
Kovachev, V. FAQ14, 1417
Kovalev, V.P. WAA21, 1274
Kowalski, S. RPG05, RAA31, 327, 600
Kozawa, T. RAB13, 779
Kozin, V. FAR17, 299
Kozlov, O.S. WAR09, 1918
Kponou, A. WPC09, 1013
Krafft, G.A. WAQ14, RAE11, WXE01, TPC04, TPC07, 1873, 2417, 2429, 2601, 2610
Krämer, D. TPE09, FAP02, FAQ12, WAQ17, 1316, 1325, 1411, 1879
Kramer, S.L. MPQ23, 2509
Krasnopolsky, V. WPC13, WPR19, 1025, 1833
Krasnykh, A. TAC01, TAC16, 134, 152
Krauter, K. RAE03, 2389
Kravchuk, L.V. RPR24, RPR25, 1173, 1175
Krawczyk, Frank L. MPB16, MPC22, 2306, 2361
Krebs, G. FAB01, 2789
Krejcik, P. WAG11, RPB02, RPC02, WAB07, WAB12, WAC17, 646, 659, 701, 3031, 3046, 3109
Kreps, G. WPP05, 1666
Kriens, W. WPA12, 929
Krietenstein, B. RPB16, TAQ06, 695, 1533
Krinsky, S. FAR10, FAQ17, WXE04, TPQ14, 284, 1426, 2435, 2980
Krishnaswamy, J. FAA19, FAA31, 234, 260
Krivchikov, V.P. TAE14, 1225
Kroc, T. FAG06, 86
Kroes, F. RPG06, TAQ12, MPQ17, 330, 1547, 2491
Krogh, M. WAA19, 1269
Kroll, N. RPA04, 1058
Kroll, N.M. WPQ10, TAA33, 1741, 2144
Kroll, Norman M. WPR10, 1809
Kruijjer, A. TAQ12, 1547
Krüssel, A. FAR06, 272
Krutikhin, S. WPP10, 1678
Krycuk, A. RPQ29, 2732
Krylov, Y. MPA04, 2199
Krylov, Yu. WPR13, 1815
Kuba, A. MPA07, 2208
Kubo, K. WAG12, RPC02, RPA20, WPR03, TPQ16, TPQ17, WAC18, 649, 701, 1099, 1791, 2986, 2989, 3112
Kubo, T. MPQ18, 2494
Kuchar, J. TAP08, 369
Küchler, S. FAP02, 1325
Kudo, M. TPP03, 1620
Kuijt, J. MPQ17, 2491
Kukhtin, V. MPC21, 2359
Kulevoy, T. TAC05, 140
Kulikov, A. RPE14, TAA22, 2032, 2129
Kulikov, A.V. WPC18, 1033
Kulipanov, G.N. FAQ17, 1426
Kumada, M. RPP09, 1982
Kumagai, S. TPP16, 1652
Kumpe, G. FAR06, 272
Kunkel, W.B. TPB07, 2542
Kuo, C. RAA24, 582
Kuo, C.C. FAA04, FAA07, RAA23, TPQ08, TPQ10, 201, 210, 579, 2965, 2971
Kuo, C.H. MPR10, MPQ16, TPB29, 2256, 2488, 2592
Kuo, T. WAQ07, 1858
Kuptsov, I. WPP10, WPP11, 1678, 1681
Kurakin, V.G. WAB14, 3049
Kurennoy, Sergey S. RAR11, RAR12, RAR13, 3373, 3376, 3379
Kurita, N. MPP07, MPP08, TAA22, MPC01, MPQ15, MPQ25, 2048, 2051, 2129, 2317, 2485, 2512
Kurkin, G. WPP11, 1681
Kurkin, Grigori WPR22, 1841
Kurokawa, S.-I. MPA06, 2205
Kurokawa, Shin-ichi WPG04, 491
Kurz, M. RPB15, RPB16, 692, 695
Kusano, J. RPG09, 339
Kushin, V. TAC05, 140
Kushnir, V.A. WPB16, 988
Kustom, R. TAP05, WPP13, WPP14, RPP12, 363, 1687, 1690, 1988
Kustom, R.L. WAG10, 643
Kustom, Robert WPP12, 1684
Kuznetsov, M.I. WPP18, 1699
Kuznetsov, N. FAP02, 1325
Kuznetsov, S. WPR13, MPA04, 1815, 2199
Kuznetsov, V.S. TAE13, 1222
Kvasha, A.I. RPR24, RPR25, 1173, 1175
Kwiatkowski, S. WPP07, WPQ19, 1669, 1765
Kwok, P. TAA28, 2135
Kwon, M. TPG06, WPR11, 171, 1812
Kwon, Y.S. WAQ26, 1897
Labrousche, J. TAE09, 1210
Lacarrere, D. FAE11, 1509
Lackey, J. FAG06, 86
Laclare, J.L. TPG05, 167
Laffin, M. RAA15, 557
Lagniel, J.-M. RPR11, RAG07, 1146, 3173
Lagniel, Jean-Michel TPA17, 3235
Lahti, G. MPR13, MPR14, 2265, 2268

Lai, A.-T. TPC15, 2634
 Lai, C.H. WAG09, 640
 Lai, P. RAB02, TAA28, 761, 2135
 Lal, A. RAB04, RAB05, 767, 770
 Lam, R. TPC16, 2637
 Lambertson, G. MPC01, RAE13, RPQ08, 2317, 2423, 2681
 Lamont, M. WAP12, WAP13, WPG09, RAA11, RAA15, 464, 467, 514, 548, 557
 Lampel, M. RAB03, RPA21, RPA22, 764, 1102, 1105
 Lamzin, E. MPC21, 2359
 Lancaster, C. FAA27, 248
 Lane, S.N. TAP07, 366
 Langdon, A.B. TPR19, 3282
 Langdon, A. Bruce TPR01, 3238
 Langton, J. MPP08, 2051
 Lara, P. MPE04, 867
 Lara, P.D. WPA08, 923
 Larbalestier, D.C. TPE01, 1276
 Lasutin, E.V. FAG12, 105
 Latypov, T. FAP24, 1387
 Lau, W.C. FAA04, 201
 Lau, W.K. RAA23, RAA24, WPB07, TPQ08, TPQ10, 579, 582, 964, 2965, 2971
 Lau, Y.Y. TAQ32, 1599
 Lauer, E. WAA19, 1269
 Launspach, J. TAE09, 1210
 Lauritzen, T. RPE12, 2026
 Laverty, M. MPR16, 2273
 Lavrent'ev, B.M. WAA21, 1274
 Lawrence, G.P. FPD03, 35
 Lawson, W. TAQ17, TAQ18, TAQ19, 1561, 1563, 1566
 Lawton, D. RPG11, 345
 Laxadal, R. WAQ07, 1858
 Laxdal, R.E. WAR15, 1936
 Le Diberder, F. RPC20, 749
 Le Goff, A. TPP09, 1632
 Le Taillandier, P. TAE09, 1210
 Lebedev, A.N. TPR13, 3269
 Lebedev, N.I. WAA20, TAQ34, 1272, 1605
 Lebedev, O.P. WPP02, 1658
 Lebedev, P. TAA01, RAR30, 2078, 3424
 Leblond, B. WPB01, 945
 LeCroy, C.T. TPC18, 2643
 LeDiberder, F. TAG01, 2742
 Lee, Edward P. FAC01, 2835
 Lee, H.S. RPA06, TAQ14, 1061, 1553
 Lee, J.C. FAA07, RAA24, TAR04, TAR06, TPQ09, TPQ10, 210, 582, 804, 810, 2968, 2971
 Lee, P.J. TPE01, 1276
 Lee, S.Y. RPG08, TAP03, WPP20, WPP21, RAP21, WAC12, RAG10, RAQ23, RAQ24, 336, 357, 1705, 1708, 2934, 3094, 3182, 3337, 3340
 Lee, Sangil TAB09, FAR03, 122, 269
 Lee, T. TPG06, TAQ06, WPQ05, 171, 1533, 1726
 Lee, Terry G. TAQ27, 1584
 Lee, Y. TPB07, 2542
 Lee, Y.Y. MXG03, TAP11, WAR13, 53, 378, 1930
 Leemans, W. TPG07, RAB10, WAQ04, TAA28, 174, 776, 1852, 2135
 Legg, R. WAQ14, WXE01, TPC07, 1873, 2429, 2610
 Lehrman, I.S. FAA19, FAA31, 234, 260
 Lemaire, J.-L. RAG07, 3173
 Len, L.K. TAE10, 1213
 Lenci, S. FAE07, 1497
 Lenisa, P. RAE05, 2399
 Lenkszus, F. MPQ07, RPQ16, 2464, 2702
 Lennox, A. FAG06, 86
 Lenz, J.W. RPG10, 342
 Lepeltier, V. RPC20, TAG01, 749, 2742
 Lessner, E. TAP05, FAB09, TPQ22, 363, 2811, 3001
 Letoumelin, R. TAB04, 116
 Letta, P. MPR13, 2265
 Leung, E.M. TAB06, 119
 Leung, K.N. TPB07, 2542
 Levashov, Y. TAA02, 2081
 Levchenko, V.D. WAA02, WAA03, 1230, 1233
 Level, M.-P. FAR14, 293
 Leveling, A. FAG06, 86
 Levichev, E. FAP02, 1325
 Levy, C.D.P. MPE03, 864
 Ley, R. RAP24, 2943
 Leyh, G. WAQ15, 1876
 Leyh, G.E. RPP07, 1976
 Li, D. TAP03, WPA04, WPP20, WPP21, RAP21, WAC12, RAG10, RAQ23, RAQ24, 357, 911, 1705, 1708, 2934, 3094, 3182, 3337, 3340
 Li, H. RPC16, RPC17, RPC19, 737, 740, 746
 Li, N. FAP01, 1322
 Li, Rui WAQ12, MPB11, 1870, 2297
 Li, W.M. RPE10, 2023
 Li, Xiao-Ping RAP25, 2946
 Li, Z. FAG11, FAA25, 102, 243
 Li, Zenghai MPC25, RAG12, 2370, 3188
 Liang, C. TPC07, 2610
 Libault, David TPA17, 3235
 Lien, E. FAE07, 1497
 Limberg, T. RAP08, WAC17, 2901, 3109
 Lin, C.L. MPE12, 893
 Lin, G. TPQ09, 2968
 Lin, Glory MPQ16, 2488
 Lin, K.K. FAA07, MPQ19, MPQ32, 210, 2497, 2524
 Lin, Leon C.-L. WPB03, WPB04, 951, 954
 Lin, Liu FAP14, 1361
 Lin, T.F. TAA14, MPQ16, 2108, 2488
 Lin, X. MPC01, 2317
 Lin, X.E. WPQ12, 1744
 Lin, X.T. RPA04, 1058
 Lin, Xintian E. WPR10, 1809
 Lindner, M. FAQ04, 1396
 Linebarger, W. RPA24, 1111
 Linnecar, T. WAP12, WAP13, FAE10, 464, 467, 1506
 Linnik, A.F. RAB15, 782
 Linscott, I. RAE12, RPQ01, RPQ22, 2420, 2660, 2717
 Liou, R. WAG09, TAA28, 640, 2135
 Lisin, A. MPP10, WAC17, 2057, 3109
 Littlejohn, R.G. RAR02, 3358
 Littmann, B. TAQ30, 1593
 Littmann, Bengt WPP22, 1711
 Litvinenko, V. MPA11, 2217
 Litvinenko, V.N. FAA08, RAA01, RAB22, RPA17, MPA10, MPQ06, FAC20, 213, 524, 796, 1090, 2214, 2461, 2877
 Liu, H. FAG11, WPA17, WAQ11, 102, 942, 1867
 Liu, H.-X. FAA25, 243
 Liu, J. TPP16, WPP20, WPP21, WAC12, 1652, 1705, 1708,

3094
Liu, J.Y. TAP03, RAP21,
 RAG10, RAQ23, RAQ24, 357,
 2934, 3182, 3337, 3340
Liu, W. MPA01, 2193
Liu, Y.C. FAA04, FAA07,
 RAA24, WPB07, 201, 210, 582,
 964
Liu, Y.-C. TPC15, 2634
Liu, Zuping FAQ29, FAQ30,
 1456, 1459
Lo, C.C. TAR03, 801
Lobov, I. MPR11, 2259
Loew, G. RPC01, 698
Loew, G.A. WAG13, 653
Loewen, R. RPA23, 1108
Loewen, R.J. WAG13, 653
Lofnes, T. TPC31, 2658
Long, H. WPA14, 935
Longinotti, D. TAR17, 837
Longinotti, D.B. TAR14, 828
Lopez, F. FAP12, 1355
Lorenz, R. TPC14, 2631
Lou, W. FAB12, 2820
Lou, W.R. TPA04, 3206
Lou, Weiran TAA29, 2138
Louie, W. TAA09, 2099
Loulergue, A. RAG06, 3170
Lovato, Richard WPB15, 985
Lu, J.J. TAQ33, 1602
Lucas, Peter W. WAP06, 449
Luccio, A. FAQ28, 1453
Ludmirsky, E. RAB21, 793
Luger, G. WAE08, 2175
Luijckx, G. RPG06, 330
Lumpkin, A. MPQ08, MPQ09,
 MPQ10, MPQ11, TPC03, RPQ15,
 RPQ16, 2467, 2470, 2473,
 2476, 2598, 2699, 2702
Lund, S. TAR17, 837
Lund, S.M. TAR14, TPR18,
 828, 3278
Luo, G.H. FAA07, RAA24,
 RAR05, 210, 582, 3364
Luo, Gwo-Huei FAA04, 201
Luo, H. MPA01, 2193
Luo, X. FAC04, 2844
Luong, M. TPP09, 1632
Lussignol, Y. WPB22, 998
Lütgert, S. WAE13, 2190
Lykke, Keith R. WPC11, 1019
Lyons, S. TAB17, RPA26, 131,
 1116
Lysenko, W.P. RPR19, RPR22,
 1161, 1167
Maas, R. RPG06, TPB03, 330,
 2533
Maccaferri, R. RAP24, 2943
Macek, R. TPB13, WAC29,
 RAR23, 2554, 3146, 3406
Macek, R.J. TAR12, 822
MacGregor, I. TAR18, 840
Machida, S. TAP04, WPC07,
 WAR05, 360, 1007, 1912
MacKay, W.W. WAC24, RAQ22,
 3131, 3334
MacKenzie, R. RAE03, 2389
MacLachlan, J.A. WAC06,
 3079
Madert, M. RPR06, 1131
Madey, J.M.J. FAA08, RAB22,
 RPA17, FAC20, 213, 796,
 1090, 2877
Madlung, J. WPA03, 908
Madsen, J. RPC09, 716
Madsen, J.H.B. RPC10, 719
Madura, D. WPG11, 520
Madura, D.D. TAB06, 119
Magugumela, M. WPC21, 1043
Mahoney, K. TPC26, 2652
Maier, R. TPB20, 2574
Maines, J. FAQ17, 1426
Mair, R. MPE10, 887
Maïssa, S. TPP09, 1632
Maj, J. WPP13, 1687
Makarov, A. RAQ14, 3315
Mako, F.M. TAE10, 1213
Malakhov, N. TAC16, 152
Maletic, D. RAG14, RAQ20,
 3194, 3329
Malka, V. WAG08, 637
Malone, R. MPE11, 890
Malygin, A.N. RPP08, 1979
Mamaev, G. FAP24, 1387
Mammosser, J. FAE12,
 TPC07, 1512, 2610
Manca, J.J. WPR20, 1835
Manca, J.P.J. WPR20, 1835
Mandrillon, P. FAG09, 95
Mane, V. WAC24, WAC25,
 WAC26, 3131, 3134, 3137
Mangili, P. TPC10, 2619
Manglunki, D. MPG09, 423
Mangra, D. FAR19, 303
Mao, N. WAQ09, 1864
Mapes, M. MPP11, 2060
Margaritondo, G. TPG11, 186
Marhauser, F. WPA05, 914
Mariotti, E. RAE05, 2399
Markiewicz, T. RPC01, 698
Markov, V. FAR17, 299
Marks, S. FAQ24, FAQ25,
 1444, 1447
Marneris, I. WAR11, RPP02,
 1924, 1964
Marone, A. FAQ03, 1393
Marriner, J. WAP01, TPQ28,
 WAB01, 434, 3013, 3016
Marsh, K.A. WAG08, RAB01,
 637, 758
Martens, M. WAP01, 434
Martens, M.A. WAP05,
 WAP08, 446, 455
Marti, F. RPG11, TAP08,
 TAP10, 345, 369, 375
Martin, D. MPQ15, MPQ25,
 2485, 2512
Martin, E.J. RPP06, RPP13,
 1973, 1991
Martin, K. WAE07, 2172
Martin, P. MPG01, 391
Martin, P.S. FAP04, FAP05,
 FAP06, FAP07, FAP09, WAR02,
 TAA12, 1331, 1334, 1337,
 1340, 1346, 1903, 2105
Martini, M. TAP14, WAE09,
 386, 2178
Martlew, B.G. RAE10, 2414
Maruyama, T. MPE10, 887
Marx, M. RPB15, 692
Masalov, V. WPC13, 1025
Mashiko, K. FAR08, RPA13,
 278, 1079
Massarotti, A. TPG11, FAR21,
 WPQ04, 186, 309, 1723
Massoletti, D. FAA05, 204
Mastovsky, I. TPG14, RPC15,
 192, 734
Masunov, E.S. RPR12, 1149
Matheson, R. MPQ22, 2506
Mathewson, A. RPE02, 1999
Matricon, P. WAG07, 634
Matsuda, K. FAR09, 281
Matsumoto, H. WAG12,
 RPA20, WPR03, 649, 1099,
 1791
Matsumoto, S. RPB04, RPA20,
 665, 1099
Matsuoka, M. TPP07, 1629
Mattei, P. RPR11, 1146
Matthews, P.J. WAG10, 643
Matthews, Paul WPP12, 1684
Matthieussent, G. WAG07,
 634
Mattison, T. RPC02, 701
Mattison, T.S. WAR06, 1915
Matveev, Yu. WAA18, 1266
Matyukov, A.V. TAP16, 389
Mau, R. WAP04, 443
Maury, S. RAP23, RAP24,
 2940, 2943

Maury, Stephan RPG07, 333
 May, Lisa M. FAE06, 1494
 May, M. TPE05, FAP09, 1298, 1346
 Mazaheri, G. RPB04, 665
 Mazarakis, M.G. TAE06, 1201
 Mazur, P.O. FAP06, FAP07, 1337, 1340
 McAllister, B. RPG05, 327
 McCormick, D. RPB01, RPB04, 656, 665
 McCrory, E. FAG06, 86
 McCrory, Elliot S. WAP06, 449
 McCune, E. FAE07, 1497
 McDaniel, B.D. RAE14, 2426
 McDaniel, M.R. TAA22, 2129
 McDonald, K.T. TAA28, 2135
 McDonald, M. MPE03, 864
 McDowell, W. TAP05, 363
 McGhee, D. FAR19, TAP05, 303, 363
 McGhee, D.G. RPP03, 1967
 McGinnis, D. WAP01, TPQ26, TPQ28, 434, 3010, 3013
 McIntosh, P.A. MPC19, WAC22, 2353, 3125
 McInturff, A.D. FAQ07, 1402
 McIntyre, Peter M. FAQ31, 1462
 McKee, B. WAC17, 3109
 McManus, A. WAR19, 1945
 McMichael, G.E. TAC12, 149
 McMichael, Gerald E. FAG13, 107
 Mead, J. TPB12, 2551
 Mecklenburg, B. RPC22, TAQ03, 755, 1524
 Meddahl, M. WPG09, RAA17, 514, 560
 Medvedko, A.S. FAQ17, 1426
 Medvedko, E.A. FAQ17, FAQ18, 1426, 1429
 Meigs, M.J. WAQ26, MPA05, TPC18, 1897, 2202, 2643
 Melekhin, V.N. TAR05, FAP19, WPR17, 807, 1375, 1827
 Mencick, M. WPB22, 998
 Mendelsohn, S.L. RPR20, 1164
 Menshikov, L. TAC16, 152
 Méot, F. FAC04, 2844
 Meredith, J. TAR17, 837
 Meredith, J.W. TPB14, 2557
 Merl, R. FAR19, TPE08, 303, 1310
 Merle, E. TAE09, TPC17, 1210, 2640
 Merminga, L. FAG11, FAA25, RPQ11, RPQ30, 102, 243, 2690, 2735
 Mertens, V. RAA15, 557
 Merz, W. RPP13, 1991
 Meshcherov, R. WPC13, 1025
 Meshkov, I. RAP23, RAP24, 2940, 2943
 Metz, H. TAQ19, 1566
 Metzmacher, K. MPG09, 423
 Meuth, H. WPQ26, 1781
 Meyer, J. RPQ15, 2699
 Meyer, S. TAR18, 840
 Meyerer, Thomas WPB21, 995
 Meyerhofer, D.D. TAA28, 2135
 Meyers, T. RPR20, 1164
 Mezi, L. TPG11, 186
 Michailov, S. TPE09, 1316
 Michelato, P. WPC23, 1049
 Michelotti, L. WAP08, 455
 Michelotti, Leo FAB15, 2826
 Michine, A.V. TAB15, 128
 Michnoff, R. MPA17, 2229
 Micklich, B.J. FAG14, 110
 Miertusova, J. MPP04, MPP05, 2042, 2045
 Mikhailichenko, A. TAG01, 2742
 Mikhailichenko, A.A. RAB18, 784
 Mikhailov, V.A. WAR09, FAC12, 1918, 2863
 Milchberg, H.M. WAG04, 621
 Milder, M.L. WPA08, 923
 Milder, Martin L. WPB15, 985
 Miller, H. TAQ11, 1544
 Miller, J.M. TPR18, 3278
 Miller, R. TAB17, RPB02, RPC01, MPE10, RPA04, RPA26, 131, 659, 698, 887, 1058, 1116
 Miller, R.A. WPC18, 1033
 Miller, R.H. WPB13, WXE03, 982, 2432
 Millich, A. WPQ25, 1779
 Milliman, L. FAA27, 248
 Millo, D. FAQ19, 1432
 Mills, F. TAP05, 363
 Mills, G.D. MPE05, WAQ26, 871, 1897
 Milton, B. WAQ07, 1858
 Milton, B.F. FAG07, 89
 Milton, S. MPQ10, 2473
 Milton, S.V. RAA28, FAP12, RPP03, RPQ18, 594, 1355, 1967, 2708
 Mimashi, T. MPA06, 2205
 Minagawa, Y. RPQ26, 2726
 Minamihara, Y. FAQ24, FAQ25, 1444, 1447
 Minato, T. FAQ08, 1405
 Miné, Ph. WAG07, 634
 Minehara, E.J. TPG02, 159
 Mingalev, B. MPC21, 2359
 Minty, M. WAG11, RPC02, RAE03, TPQ16, 646, 701, 2389, 2986
 Minty, M.G. RAA06, RPB03, RAP10, WAB09, WAB12, WAC17, TPA09, 536, 662, 2907, 3037, 3046, 3109, 3217
 Miram, G. FAE07, 1497
 Mirzoev, K. MPP03, 2040
 Mishin, A.V. RPA25, 1114
 Mishra, C.S. FAP06, MPB05, MPB06, TAG10, RAP03, 1337, 2282, 2285, 2777, 2886
 Mishra, S. FAP04, FAP07, 1331, 1340
 Mitchell, M. WPR15, 1821
 Mitra, A.K. TAQ33, 1602
 Mitrochenko, V.V. WPB16, 988
 Mitsuhashi, T. RAQ06, 3300
 Mitsunobu, S. TPP03, 1620
 Miura, T. WPR02, 1788
 Miya, K. RAB13, 779
 Miyahara, Y. FAQ20, FAQ21, RAQ30, 1435, 1438, 3355
 Miyai, Y. TAQ35, 1608
 Miyauchi, Y. FAA30, 257
 Mizumoto, M. RPG09, 339
 Mizuno, A. WPC22, MPA07, 1046, 2208
 Mizuno, H. FAQ08, TAQ29, 1405, 1590
 Mocheshnikov, N. FAR17, 299
 Modena, A. WAG08, 637
 Moe, H. TAP05, 363
 Moe, H.J. RPA07, 1064
 Moffat, D. FAE13, RAQ04, RAR19, 1515, 3294, 3394
 Möhl, D. RAP23, 2940
 Mohr, J. FAR06, 272
 Moi, L. RAE05, 2399
 Moibenko, A. WAE07, 2172
 Moir, David C. TAE08, 1207
 Moiseev, V.A. RPR01, 1119
 Moisseev, V. WPR13, 1815
 Moisseev, V.I. TPB25, 2586
 Mokhov, N.V. RAB19, 787

Mokhtarani, A. FAP06, FAP07, 1337, 1340
Molinari, G. RAP24, 2943
Möller, K.D. FAR06, 272
Møller, S.P. WAP14, 470
Möller, W-D. TPP11, 1639
Molodkin, V. FAR16, FAR17, 296, 299
Montag, C. TAA01, TAA06, RAR30, 2078, 2090, 3424
Montès, B. WAG07, 634
Montjar, B. MPR13, 2265
Moog, E.R. TPE06, 1301
Mora, P. WAG04, WAG07, 621, 634
Morano, R. WAG07, 634
Morcombe, P. FAA08, WAA10, MPA11, MPQ06, 213, 1248, 2217, 2461
Morcombe, Peter WPR22, 1841
Moretti, A. WPA07, 920
Morgan, G. TPE04, FAQ03, FAQ04, FAQ16, 1293, 1393, 1396, 1423
Morgan, J. TAR16, 834
Morgillo, A. FAQ03, 1393
Mori, W.B. WAG09, RAB01, RAB02, RAB08, TPB18, 640, 758, 761, 773, 2569
Mori, Y. TAP04, MPE03, WPC07, WAQ06, WAR05, 360, 864, 1007, 1855, 1912
Morii, Y. TAQ35, 1608
Morillo, J. WAG07, 634
Morpurgo, G. RAA20, FAC03, 570, 2841
Morris, J.T. WAB04, 3022
Mortazavi, P. TPP06, WPQ20, 1626, 1768
Morvillo, M. MPQ05, 2458
Moser, H.O. FAR06, 272
Moshhammer, W. RPC02, 701
Mosko, S.W. TAP07, WAQ26, 366, 1897
Mosnier, A. WPB22, WAC13, 998, 3097
Mostowfi, D. RPQ21, RPQ22, 2714, 2717
Moulin, F. WAG07, 634
Mouton, B. WPB22, 998
Mufel, V.B. TAE14, 1225
Mugge, M. MPP12, MPP20, 2064, 2075
Muggli, P. WAG09, WPC20, 640, 1039
Mulhall, S. FAQ15, TAA09, 1420, 2099
Mulhollan, G. MPE10, WPC21, 887, 1043
Muller, H. FAE13, TPP04, RAR19, 1515, 1623, 3394
Müller, W.F.O. RPB15, 692
Munasypov, R.N. WAA21, 1274
Munneke, B. TAQ12, 1547
Murata, H. RPG09, 339
Muratore, J. TPE04, FAQ02, FAQ03, FAQ04, 1293, 1390, 1393, 1396
Murin, B.P. RPR07, 1134
Murphy, C.T. WAR19, 1945
Murphy, J.B. FAR10, TPQ14, 284, 2980
Murray, S.N. MPE05, 871
Mustafin, E. RAP23, 2940
Myakishev, D. RPA12, 1076
Myakishev, D.G. MPC17, 2348
Myers, S. WPG01, 476
Mytsykov, A. FAR17, 299
Myznikov, K. FAQ06, 1399
Nadji, A. FAR14, 293
Nagaenko, M. FAR06, 272
Nagafuchi, T. FAP13, 1358
Nagai, A. FAA30, 257
Nagai, R. TPG02, 159
Nagaitsev, S. RAP22, 2937
Nagaoka, R. FAR21, TAG05, 309, 2762
Nagatsuka, T. FAP22, WPQ07, 1384, 1732
Nagchaudhuri, A. MPA11, 2217
Naidenov, V.O. TAP16, 389
Naito, F. FAE09, WPQ17, WPR05, WPR09, 1503, 1759, 1797, 1806
Najmudin, Z. WAG08, 637
Nakajima, K. RAB13, TAA28, 779, 2135
Nakamura, N. RPQ23, 2720
Nakamura, T. WAC14, 3100
Nakamura, T.T. MPA06, 2205
Nakanishi, H. RAB13, TPP16, TAA28, 779, 1652, 2135
Nakata, K. TAQ35, 1608
Nakayama, H. WAR03, TAG01, 1906, 2742
Nam, S.H. TPG06, 171
Namkung, W. TAR07, RPA06, TAQ14, TAQ15, MPA02, 813, 1061, 1553, 1556, 2196
Naqvi, S. TAQ01, 1518
Nasonov, N.N. FAG12, 105
Nassiri, A. WPB06, RPA10, WPP16, 961, 1070, 1693
Nath, S. RPR08, RPR09, 1137, 1140
Nath, Subrata WAQ02, 1846
Nation, J.A. WPC19, TAE12, TAQ01, 1036, 1219, 1518
Nattrass, L. TAR17, 837
Nattrass, L.A. TAR14, 828
Nawrocki, G. MPQ08, 2467
Nawrocky, R.J. MPQ23, 2509
Neau, Eugene L. TAE03, 1188
Neil, G. FAA25, WPA17, RPQ30, 243, 942, 2735
Neil, G.R. FAG11, 102
Neil, George R. TAC03, 137
Nelson, D. WAQ15, 1876
Nelson, M. TAR17, 837
Nelson, M.B. TAR14, 828
Nemoshkalenko, V. FAR16, FAR17, 296, 299
Nesemann, H. FAA02, FAC19, 195, 2874
Nesterov, N. TAC05, 140
Nesterov, V.V. WAA11, 1251
Nesterovich, A. RPR10, RPR15, 1143, 1155
Nett, D. TAB17, RPA26, 131, 1116
Neubauer, M. WPQ10, WPR07, WPR08, 1741, 1800, 1803
Neuffer, D. FAG11, WPA17, WAQ11, 102, 942, 1867
Neuffer, D.V. FAA25, 243
Neuffer, David MXG03, 53
Newton, M.A. TAR14, 828
Nezhevenko, O. RPA12, TAQ21, 1076, 1569
Ng, C. WPR07, MPC01, MPQ25, 1800, 2317, 2512
Ng, C.K. TAA28, 2135
Ng, C.-K. WPQ10, WPQ12, MPP07, MPQ15, WAB18, WAC17, 1741, 1744, 2048, 2485, 3061, 3109
Ng, K.Y. RAP21, TPQ12, RAQ23, RAQ24, RAR17, 2934, 2977, 3337, 3340, 3388
Ng, K.-Y. TAR20, 843
Nghiem, P. FAR14, 293
Nguyen, D.C. FAA16, 228
Nicol, T. WPB08, 967
Nielsen, R. TAP05, 363
Nieuwenkamp, H. MPQ17, 2491
Niki, K. RPG13, 351
Nikiforov, S. WPC03, 1004

Niquille, C. WAP13, 467
 Nishi, M. TAB03, WPQ21, 113, 1770
 Nishida, Y. RAB13, TAA28, 779, 2135
 Nishihara, S. FAA30, 257
 Nishimura, H. MPR03, MPR04, 2244, 2247
 Nishimura, Hiroshi WAE04, 2162
 Nobel, R.J. WPA07, 920
 Noda, A. FAR08, RPA13, RPA18, WPQ21, WAQ01, 278, 1079, 1093, 1770, 1843
 Noda, K. TAB03, 113
 Nogiec, J.M. FAP06, FAP07, MPB06, 1337, 1340, 2285
 Noguchi, S. TPP07, 1629
 Nolen, J.A. RPG14, FAQ09, TPC13, RAQ16, 354, 1408, 2628, 3320
 Noomen, J. RPG06, 330
 Noomen, J.G. MPQ17, 2491
 Noonan, J. RPE09, 2020
 Nordberg, E. FAE13, 1515
 Nordby, M. MPP08, MPP12, MPP20, TAA22, MPC01, MPQ25, 2051, 2064, 2075, 2129, 2317, 2512
 Nordby, M.E. MPP07, 2048
 Norek, G. TAP05, 363
 Norem, J. RAA29, TAA28, TPC16, 597, 2135, 2637
 Norris, B.L. WAE02, 2152
 Norton, M. TAA20, 2123
 Norum, B.E. RAP01, 2880
 Norum, Blaine E. RAE07, 2405
 Nosochkov, Y. RAA22, RAA25, RAA27, 576, 585, 591
 Nosyrev, S. WPP10, WPP11, 1678, 1681
 Novikov, A. WPP10, 1678
 Novikov, S.A. WAR09, 1918
 Novikova, T.A. FAA14, 225
 Novokhatsky, A. WAA17, 1263
 Nuhn, H.-D. FAA12, FAA17, 219, 231
 Nusinovich, G.S. TAQ17, 1561
 Nyman, M. RPQ08, 2681
 O'Connor, T. RAA03, 527
 O'Day, S. WAQ22, 1888
 O'Shea, P. FAA08, MPA11, 213, 2217
 O'Shea, P.G. RPA17, TAQ07, 1090, 1536
 O'Shea, Patrick G. WPA13, WPB09, TAG12, 932, 970, 2783
 O'Sullivan, M. RPP13, 1991
 O'Sullivan, M.K. RPP06, 1973
 Obina, T. TPC08, RPQ26, 2613, 2726
 Oerter, B. MPA16, 2226
 Ogata, A. RAB13, TAA28, 779, 2135
 Ogawa, Y. TAA04, 2087
 Ogitsu, T. FAQ02, FAQ08, 1390, 1405
 Oguri, H. RPG09, 339
 Oh, J.S. TAQ15, 1556
 Ohgaki, H. MPR04, 2247
 Ohmi, K. RAP02, 2883
 Ohmori, Chihiro TPR16, 3275
 Ohshita, E. TAQ35, 1608
 Oide, K. RPC20, RPA20, TAA08, WXE07, TAG01, TAG11, WAB20, WAC08, WAC16, 749, 1099, 2096, 2444, 2742, 2780, 3064, 3085, 3105
 Oide, Katsunobu WAB10, 3040
 Okada, M. RPG13, 351
 Okamoto, H. FAR08, RPA13, RPA18, WAQ01, 278, 1079, 1093, 1843
 Okamoto, Hiromi TPR11, 3263
 Okuma, S. FAA30, TAQ35, 257, 1608
 Okumura, Y. RPG09, 339
 Okun, L. FPD05, 45
 Olivieri, D.N. TAR16, 834
 Olsen, D.K. RPG01, TAP07, WAQ26, 312, 366, 1897
 Olsen, J. RAE12, 2420
 Omeich, M. WPA14, WPB22, 935, 998
 Onillon, E. RPQ17, RPQ25, 2705, 2723
 Onishchenko, I.N. RAB15, 782
 Onken, R. WPQ24, 1776
 Ono, M. TPP07, 1629
 Opanasenko, A.N. WPA15, WPA16, 938, 939
 Oren, W. WXE01, 2429
 Oreshnikov, A. TAC05, 140
 Orris, D. TPE05, 1298
 Orris, D.F. FAP06, FAP07, 1337, 1340
 Ortiz, R. MPQ22, 2506
 Osborn, J. FAP01, 1322
 Oshita, E. FAA30, 257
 Ostanin, V.P. RPP08, 1979
 Ostiguy, F. TAG04, 2757
 Ostiguy, Francois WAC02, 3070
 Ostiguy, J.F. WPB08, 967
 Ostiguy, J.-F. TAR20, TPE05, FAP10, FAP21, MPC07, 843, 1298, 1349, 1381, 2330
 Ostojic, R. FAC04, 2844
 Ostroumov, P.N. RPR01, RPR24, RAE08, 1119, 1173, 2408
 Otake, Y. TAQ29, 1590
 Otock, R. TAA11, 2102
 Otock, R.D. RPE09, 2020
 Ottarson, J. TAP08, 369
 Ottaviani, P.L. TPG11, 186
 Oude Velthuis, R.G.J. RPP04, 1970
 Ovchinnikov, V.P. TAE13, 1222
 Owen, H.L. TPG09, 180
 Oxoby, G. RAE12, RPQ01, 2420, 2660
 Ozaki, Y. WXE07, 2444
 Pabst, M. TPA01, TPA02, TPA03, 3197, 3200, 3203
 Pachnik, J.E. FAP06, FAP07, MPB06, 1337, 1340, 2285
 Padamsee, H. FAE13, TPP02, TPP04, WPQ02, RAQ04, RAR18, RAR19, 1515, 1617, 1623, 1720, 3294, 3391, 3394
 Pagani, C. WPB10, WPC23, TAA07, RAQ05, 973, 1049, 2093, 3297
 Pai, C. MPP11, 2060
 Palkovic, J. TPB19, 2572
 Palmer, D. RPA26, 1116
 Palmer, D.T. WPB13, WXE03, 982, 2432
 Palmer, Robert B. MXG03, 53
 Palrang, M. MPP10, 2057
 Pan, K.T. MPQ16, 2488
 Pang, A.W. WPC21, 1043
 Pangos, N. FAR21, MPP05, 309, 2045
 Pankuch, P. TAE06, 1201
 Pantazis, R. MPA11, 2217
 Pantenburg, F.J. FAR06, 272
 Pappas, G.C. WAR10, WAR12, 1921, 1927
 Papureanu, S. RPR06, WPQ26, TPB20, 1131, 1781, 2574
 Paramonov, V.V. WPP17, WPP18, WPP19, 1696, 1699, 1702
 Parazzoli, C. FAA27, 248
 Parazzoli, C.G. FAA28, 251
 Pardo, R.C. WAQ03, 1849
 Park, H.J. WPR11, 1812

Park, Heunggyu TAB09, FAR03, 122, 269
Park, Jongpil TAB09, FAR03, 122, 269
Park, S. RPA21, RPA22, 1102, 1105
Park, S.H. FAA08, RAB22, TAQ14, 213, 796, 1553
Park, S.S. TAQ15, 1556
Park, Sanghyun WPB02, 948
Parkhomchuk, V. TAR11, 819
Parzen, G. FAB03, FAB04, FAB05, 2795, 2798, 2801
Pasotti, C. WPQ04, TAG05, 1723, 2762
Pasquinelli, Ralph J. RAE01, 2379
Patavalis, N. MPR13, 2265
Paterson, E. RPC01, 698
Patteri, P. TPG11, 186
Patterson, D. MPQ10, 2473
Paulson, C.C. RPR20, 1164
Pavlovets, M. TAA18, 2120
Pawlak, T. MPG01, 391
Payet, J. FAR14, 293
Peacock, M.A. RPR20, 1164
Pearson, C. FAE07, 1497
Pearson, Pauline MPR07, 2250
Peck, S. FAE13, 1515
Pedersen, F. MPG09, 423
Peggs, S. MPG12, TAA09, MPC05, FAB20, FAB22, WAC24, WAC25, WAC26, RAQ21, RAQ22, RAR29, 431, 2099, 2327, 2829, 2832, 3131, 3134, 3137, 3331, 3334, 3421
Peggs, S.G. WAP10, 461
Pei, A. TAP03, WPP20, WPP21, RAP21, WAC12, RAG10, RAQ23, RAQ24, 357, 1705, 1708, 2934, 3094, 3182, 3337, 3340
Pei, Yuan Ji RPE10, 2023
Pekeler, M. TPP11, 1639
Pelaia, T.A. RAE14, 2426
Pellegrini, C. FAA23, RAB03, RPA21, RPA22, RAQ17, 240, 764, 1102, 1105, 3323
Pendleton, R. WPR07, WPR16, 1800, 1824
Penicka, M. TAA03, 2084
Pennacchi, R. WPR15, 1821
Perin, R. TPE02, 1282
Perkins, C. RAA04, MPP09, MPP10, MPP12, MPP20, TAA22, MPC01, MPQ25, 530, 2054, 2057, 2064, 2075, 2129, 2317, 2512
Perkins, L. TPB07, 2542
Peschke, C. RPB16, 695
Peters, C. RPC16, RPC18, WPA01, TAE01, FAP17, FAP18, TPA10, 737, 743, 902, 1178, 1369, 1372, 3220
Peters, F. TAG01, 2742
Peterson, K.J. TAP05, 363
Petracca, S. WAE12, 2187
Petrenko, I.I. FAB02, 2792
Petrenko, V. WPR13, 1815
Petrenko, V.V. TPB25, 2586
Petri, H. WPC08, 1010
Petrov, S.P. FAQ17, 1426
Petrov, V. WPP11, 1681
Petrov, V.A. WAA20, TAQ34, 1272, 1605
Petty, L. MPP15, 2069
Pfeffer, H. WAE07, 2172
Pflüger, J. FAR07, 275
Phillips, R. FAE07, 1497
Phinney, N. WAG11, RPB01, RPC01, 646, 656, 698
Phung, B. WPB22, 998
Piaszczyk, C. RPR20, 1164
Plataev, V. TAC16, 152
Pichoff, N. RAG06, RAG07, 3170, 3173
Pickard, D. TPB07, 2542
Pietryka, M. RAA04, WAC17, 530, 3109
Pilat, F. FAQ28, FAB22, 1453, 2832
Pilyar, N. TAC16, 152
Pinto, I.M. WAE12, 2187
Pipersky, P. FAQ24, FAQ25, 1444, 1447
Pirkil, W. WPP07, WPQ19, 1669, 1765
Pirovano, R. TAQ12, 1547
Pisharody, M. FAE13, WPQ02, RAE14, TPA04, RAQ04, RAR18, 1515, 1720, 2426, 3206, 3294, 3391
Piskarev, I. RPA19, 1096
Pitel, Ira J. RPP11, 1985
Placidi, M. RAA19, RPB01, 567, 656
Plass, G. FAG08, 92
Plate, D. FAQ24, FAQ25, 1444, 1447
Plate, S. FAQ15, 1420
Plato, John G. WPB15, 985
Platonov, Yu.P. MPG10, 426
Plesko, M. TPG08, FAA13, FAR06, 177, 222, 272
Plesko, Mark MPR12, 2262
Plotnikov, S. TAC05, 140
Plouviez, E. TPG05, RPQ15, 167, 2699
Plum, M. TPB13, WAC29, RAR22, RAR23, 2554, 3146, 3403, 3406
Podebrad, O. RPB16, 695
Podobedov, B. WAC17, 3109
Poelman, A. MPQ17, 2491
Pogorelsky, I. MPE11, 890
Poilleux, P. WAG07, 634
Poirier, R.L. TAQ33, WPP18, 1602, 1699
Polyakov, V. RAP24, 2943
Poncet, A. RPE02, MPP15, 1999, 2069
Ponds, M. TAQ07, 1536
Poole, J. WPG09, RAA15, WAE03, 514, 557, 2157
Poole, M.W. TPG09, 180
Popik, V.M. FAQ17, 1426
Popov, Yu. TAC16, 152
Popovic, M. FAG06, WPA06, WPA07, WPR21, 86, 917, 920, 1838
Porterfield, D. TPC04, 2601
Portmann, G. FAQ24, RPQ13, FAB01, 1444, 2693, 2789
Potter, James M. FAE06, 1494
Poukey, J.W. TAE06, 1201
Pourre, J.L. TAB04, 116
Power, J. WAG06, WPB11, WPB12, RPR19, 631, 976, 979, 1161
Power, J.F. TPB22, 2580
Powers, T. FAE12, 1512
Powers, Tom TPP13, 1645
Pozdeev, M. TPQ04, 2958
Prabhakar, S. RAE12, 2420
Preble, J. FAE12, 1512
Prelec, K. WPC09, 1013
Prescott, C. MPE10, 887
Price, E. TPC04, 2601
Prieto, P. WAE07, 2172
Primdahl, K. WPP13, WPP14, 1687, 1690
Proch, D. FAE08, TPP11, WPQ24, 1500, 1639, 1776
Prodell, A. TPE04, 1293
Pruyn, J. WPA01, 902
Ptitsin, V.I. RAQ21, 3331
Puchkov, A. RPR10, 1143
Pullia, M. TPC10, 2619
Puntus, V. WPP05, 1666
Puzo, P. RPC20, TAG01, 749,

2742
Qian, Y.L. RPA08, RPA11, 1067, 1073
Qian, Zubao TPP01, 1614
Qin, Q. TPQ03, 2955
Qing, Li FAA26, 246
Qiu, X. MPE11, 890
Qiu, X.Z. RAE09, TPB01, 2411, 2530
Queralt, X. TPG09, 180
Quinn, P.D. RAE10, 2414
Qunell, D. WAR01, 1900
Rackelmann, A. WAC17, 3109
Radloff, W. TPC09, 2616
Radusewicz, P. FAQ08, 1405
Rafael, F.S. MPQ33, 2527
Rago, C. WAC17, 3109
Raimondi, P. WAG11, RPB01, RPC20, TAA08, TAG01, RAP15, RAP16, 646, 656, 749, 2096, 2742, 2919, 2922
Rakowsky, G. FAQ17, WXE04, 1426, 2435
Ramachandran, S. WAR19, 1945
Ramamoorthy, S. MPA15, 2223
Ramamoorthy, Susila MPR07, RPQ14, 2250, 2696
Ramirez, G. WPP03, 1660
Ramirez, J.J. TAE05, TAE06, 1198, 1201
Raparia, D. RAR16, 3385
Rasmussen, J.O. WAQ04, 1852
Rasmussen, N. MPG09, 423
Ratti, A. WPP07, WPQ19, RPQ17, WAC24, 1669, 1765, 2705, 3131
Raubenheimer, T. RPB02, RPC01, RPC03, TPQ16, TPQ17, WAC17, 659, 698, 704, 2986, 2989, 3109
Raubenheimer, T.O. RPC02, TAG03, WAC15, WAC18, RAQ03, 701, 2752, 3102, 3112, 3291
Rauchas, A. TAP05, 363
Ravn, Helge L. MPE02, 858
Razuvakin, V.N. WAA20, 1272
Reece, C. FAE12, 1512
Reece, R.K. TAP11, TAP13, 378, 383
Reed, L. TPC16, 2637
Rees, D. WPA08, TAQ02, TAQ31, 923, 1521, 1596
Reginato, L. RPC16, RPC18, WPA01, TAE01, FAP17, WAQ04, 737, 743, 902, 1178, 1369, 1852
Rehak, M. TPE04, 1293
Reid, J. TAQ11, 1544
Reilly, J. FAE13, WPQ02, 1515, 1720
Reilly, R. WAA05, WAR01, 1236, 1900
Reiser, M. TAE04, TAQ17, TAQ18, TAQ19, TPQ11, 1193, 1561, 1563, 1566, 2974
Reiser, Martin RPR23, TAA17, MPC04, 1170, 2117, 2324
Renieri, A. TPG11, 186
Renken, D. TPP11, 1639
Renner, T. WXE06, 2441
Repnaw, R. RPR06, 1131
Repond, J. RAA29, 597
Repose, G. TAR17, 837
Reusch, M.F. RPR20, TPR08, 1164, 3257
Reuter, E. RAA04, TAA22, 530, 2129
Revol, J.L. TPG05, 167
Reyermier, C. RPE02, 1999
Rhoades, J. WAR19, 1945
Riabko, A. TAP03, WPP20, WPP21, RAP21, WAC12, RAG10, RAQ23, RAQ24, 357, 1705, 1708, 2934, 3094, 3182, 3337, 3340
Rice, D. FAE13, FAB12, 1515, 2820
Rich, D. RAQ23, 3337
Richard, Frank FAC07, 2850
Riche, A.J. MPC24, 2367
Richter, R. FAR21, 309
Rimmer, R. WPR07, WPR14, 1800, 1818
Rimmer, R.A. WPQ06, WPQ13, WPR08, 1729, 1747, 1803
Rindi, A. TPG11, 186
Ringwall, A.D. RPG10, 342
Rinolfi, L. RPC10, 719
Rintamaki, J. TPB14, 2557
Risselada, T. FAC04, 2844
Ritson, D. RAA26, 588
Ritson, D.M. RAA22, RAA27, 576, 591
Riunaud, J.-P. TAP14, 386
Rizawa, T. WPR16, 1824
Robin, D. FAA06, RPC02, RPQ13, FAB01, 207, 701, 2693, 2789
Rode, Claus H. RPE01, 1994
Rodger, E. FAP11, 1352
Rodier, J. WPB22, 998
Rogers, J. FAE13, TPA04, 1515, 3206
Rogers, J.T. RAE14, WAB15, 2426, 3052
Rojak, M. MPB09, 2291
Rokni, S. TAG01, 2742
Romanov, G. MPC16, 2345
Romasko, V.P. WPA15, 938
Rookhuizen, H. Boer RPG06, 330
Root, L. RPG12, WAQ07, 348, 1858
Ropert, A. TPG05, 167
Roques, A. TAE09, 1210
Rose, J. WPP07, WPQ19, RPQ17, WAC24, 1669, 1765, 2705, 3131
Rosel, R. TPG11, 186
Rosenblum, B. WAA19, 1269
Rosenzweig, J. FAA23, WPB05, WPB08, RPA21, RPA22, TAA28, 240, 957, 967, 1102, 1105, 2135
Rosenzweig, J.B. WAG06, MPE13, 631, 896
Roser, T. TAP11, TAP12, TAP13, RPQ07, RAG02, 378, 381, 383, 2678, 3154
Rosing, M. WPB11, 976
Ross, M. RPB01, RPB04, RPC01, WPR15, WAQ15, TAA28, 656, 665, 698, 1821, 1876, 2135
Ross, M.C. WAG11, WAC17, 646, 3109
Ross, W. RAE12, RPQ01, 2420, 2660
Rosßbach, J. FAC19, 2874
Rosßbach, J. TPG12, WAG02, TAA01, TAA06, RAR30, 189, 611, 2078, 2090, 3424
Rossi, C. FAA13, FAR21, 222, 309
Rossmannith, R. FAR07, 275
Rossmannith, Robert RAE07, 2405
Roster, William WAB06, 3028
Rotela, E. MPQ07, 2464
Rotela, R. TAR08, 816
Rothman, J.L. MPQ01, 2450
Roudier, P. WPB22, 998
Roy, G. WAP12, WAP13, RAA11, RAA17, TAG01, 464, 467, 548, 560, 2742
Roybal, W. TAQ02, 1521

Rubbia, C. FAG09, TPG11, 95, 186
Rubin, D. FAE13, RAQ04, 1515, 3294
Rubin, David L. WPG02, 481
Rudenko, V. TAC16, 152
Ruemmler, J. WAR14, 1933
Rufer, C. FAC04, 2844
Ruggiero, A.G. RAG14, RAQ20, 3194, 3329
Ruggiero, F. RPE02, WAE12, 1999, 2187
Ruiz, C. RAG06, RAG07, 3170, 3173
Ruland, Robert E. RPE04, 2009
Rusnak, Brian TPP10, 1636
Russell, A. MPB06, 2285
Russell, A.D. FAP06, FAP07, WAR02, MPB05, 1337, 1340, 1903, 2282
Russell, S.J. TPB22, 2580
Russell, Steven WPB15, 985
Russell, T. RPA11, RPE09, 1073, 2020
Russell, Thomas J. TAQ16, 1559
Rusthoi, D.P. RPR22, TPC06, 1167, 2607
Ruth, R. RPC01, RPA04, 698, 1058
Ruth, R.D. WAG13, TPQ17, 653, 2989
Ruth, Ronald D. WAG03, TAQ26, TAQ27, WAC05, RAQ18, 616, 1581, 1584, 3076, 3326
Ruth, Thomas J. WPE03, 67
Ryan, W.A. MPQ04, 2455
Rybarcyk, L.J. RAG11, 3185
Ryne, Robert D. MPB16, RAG01, 2306, 3149
Ryu, C.M. TAQ14, 1553
Saab, A.H. RPP01, 1961
Saadatmand, K. FAG05, 83
Saba, J. WPQ06, 1729
Saban, R. WAE01, 2147
Sabbi, G.L. RAA20, FAC03, 570, 2841
Sabia, E. TPG11, 186
Sachtschale, R. RPA17, TAQ07, MPA11, 1090, 1536, 2217
Sachtschale, R.J. WAA10, 1248
Sachtshale, R. FAA08, 213
Sackett, J. FAE07, 1497
Saeki, K. FAA30, 257
Saewert, G.W. MPB15, 2303
Sáez, P. MPE10, WPC21, 887, 1043
Safa, H. TPP09, 1632
Safranek, J. FAR02, RPQ19, FAB11, 266, 2711, 2817
Sagan, D. FAE13, TPA04, RAR15, 1515, 3206, 3382
Sagan, David RAP04, 2889
Sah, R. FAG05, 83
Saille, V. TAA32, 2141
Saito, K. TPP07, 1629
Sakae, T. MPE03, 864
Sakai, H. WPQ15, 1753
Sakai, I. WAR05, 1912
Sakaki, H. WPC22, MPA07, 1046, 2208
Sakanaka, S. WPQ16, WPR02, WPR03, RAQ06, 1756, 1788, 1791, 3300
Salah, W. TPR04, 3245
Saltmarsh, C. MPR20, 2279
Sampayan, S. MPE14, WPC16, WAA19, TAA20, 899, 1027, 1269, 2123
Sampson, W. TPE04, FAQ03, FAQ04, 1293, 1393, 1396
Sandberg, J.N. WAR11, RPP02, 1924, 1964
Sander, O.R. RPR19, RPR22, TPC06, 1161, 1167, 2607
Sanders, D.A. RAB20, 790
Sandler, P.H. RAB20, 790
Sandoval, D.P. TPC06, 2607
Sangster, C. TAR17, 837
Sangster, T.C. TAR14, 828
Sannibale, F. RPA26, 1116
Sapozhnikov, L. RAE12, RPQ01, RPQ05, 2420, 2660, 2672
Sapp, W. RPG05, 327
Sarantsev, V.P. TAQ34, 1605
Saraph, G. TAQ19, 1566
Sarau, B. FAA02, 195
Sarstedt, M. TPB07, 2542
Sasaki, S. FAQ21, RPQ15, 1438, 2699
Sasaki, Y. FAP13, 1358
Sass, R. RPB03, RAE03, 662, 2389
Sathe, S. MPR20, 2279
Sato, H. WAR04, WAR05, 1909, 1912
Sato, I. TAQ08, TAQ25, TAA04, 1539, 1578, 2087
Satogata, T. MPR20, TPB21, RAQ22, 2279, 2577, 3334
Satoh, K. WPR02, WAC07, WAC08, 1788, 3082, 3085
Satoh, Kotaro MPQ14, 2482
Satti, J.A. FAP08, 1343
Saulter, Q. WAQ14, 1873
Saury, J.L. WPB22, 998
Sawamura, M. TPG02, 159
Scandale, W. WAP14, FAC04, FAC06, 470, 2844, 2847
Scanlan, R.M. FAQ07, 1402
Schachinger, L. MPR04, RPQ13, 2247, 2693
Schachinger, L.C. TAB06, 119
Schächter, L. WPC19, TAE12, TAQ01, 1036, 1219, 1518
Schaffner, S. MPR13, 2265
Schafstall, P.J. WPA08, 923
Schank, C.V. TPG07, 174
Schaper, J. TPG08, FAR06, 177, 272
Scharlemann, E.T. FAA12, FAA17, 219, 231
Scheidt, K. TPG05, RPQ15, 167, 2699
Schempp, A. WPA03, WPA04, WPA05, RPR06, 908, 911, 914, 1131
Schiffer, John P. RAG04, 3164
Schindl, K. MPG09, 423
Schirm, K.M. FAE11, 1509
Schirmer, D. FAQ12, WAQ17, 1411, 1879
Schlösser, K. FAR06, 272
Schlueter, R. FAQ23, FAQ24, FAQ25, 1441, 1444, 1447
Schlüter, R. FAA17, 231
Schmenk, E.G. TAA32, 2141
Schmickler, H. WAP12, WAP13, RAA10, RAA11, RAA13, 464, 467, 545, 548, 554
Schmidt, C. FAG06, 86
Schmidt, C.W. WPA06, 917
Schmidt, F. TAG07, 2768
Schmidt, R. WPG09, RAA19, 514, 567
Schmieder, R. WPC09, 1013
Schmitz, M. WPA12, 929
Schmor, P. WAQ07, 1858
Schmor, P.W. RPG12, MPE01, MPE03, 348, 853, 864
Schnase, A. WPQ26, TPB20, 1781, 2574
Schneider, G.C. MPG09, 423
Schneider, H.R. RPG12, RPR02, RPR03, 348, 1122,

1125
Schneider, J.D. MPE04, WPA08, 867, 923
Schnell, W. RPC09, 716
Schoenlein, R. TPG07, 174
Schoessow, P. WAG06, WPB11, 631, 976
Scholl, E.H. TPB21, 2577
Scholz, T. RPE02, 1999
Schönauer, H. MPG09, WAQ25, 423, 1894
Schönfeld, Frank WPP22, 1711
Schreiber, S. RPC10, 719
Schreuder, H.W. RPG02, 317
Schulte, Elmar TPC11, 2622
Schultheis, R. MPC15, 2342
Schultz, D. WPC21, WAQ15, 1043, 1876
Schulz, G. FAR06, 272
Schulze, M.E. FAG05, 83
Schumburg, N. RPP02, 1964
Schuppler, S. FAR06, 272
Schwalm, D. RPR06, 1131
Schwandt, P. RAP22, 2937
Schwarz, H. RAA04, WPQ06, WPR07, WPR08, RPQ05, 530, 1729, 1800, 1803, 2672
Schweickert, H. FAR06, 272
Scott, B. RPC02, TPQ16, 701, 2986
Sears, J. FAE13, WPQ02, 1515, 1720
Sebek, J. MPQ22, RPQ22, 2506, 2717
Sedlyarov, I. WPP10, WPP11, 1678, 1681
Seeman, J. RAA27, RPE14, MPP12, MPP20, MPC01, MPC02, 591, 2032, 2064, 2075, 2317, 2319
Seeman, J.T. WPG10, RAA04, TAA22, RAQ03, 517, 530, 2129, 3291
Seeman, John T. WPG03, WAB06, 486, 3028
Segreto, A. TPG11, 186
Seguin, S. RAG06, 3170
Seidel, I. FAR06, 272
Seidl, P. TPA10, 3220
Seidl, Peter RAG03, 3159
Selesnev, V.S. WAR20, 1948
Seleznev, D. TAC05, 140
Sellyey, W. MPQ10, TPQ19, 2473, 2992
Sen, T. TAG09, 2774
Senichev, Yu.V. WPP18, 1699

Sennyu, K. TPP03, 1620
Senyukov, V. TAB13, TAQ23, TAQ24, 125, 1572, 1575
Serafini, L. MPE13, WPB10, WAC13, RAQ05, 896, 973, 3097, 3297
Sereno, N. RPA14, 1082
Sereno, N.S. RPA10, RPA11, 1070, 1073
Serio, M. RAE12, RPQ01, 2420, 2660
Sermes, L. MPG09, 423
Serov, V.L. RPR24, RPR25, 1173, 1175
Sertore, D. WPC23, 1049
Servranckx, R.V. FAB14, 2823
Sessler, A. FAA06, RPC16, RPC17, TAA28, 207, 737, 740, 2135
Sessler, Andrew RAP25, 2946
Sessler, Andrew M. FPD02, 30
Settles, R. TAG01, 2742
Severgin, Y. FAR06, 272
Severgin, Yu. MPC21, RAQ14, 2359, 3315
Sgobba, S. RPE02, 1999
Shalnov, A. TAB13, RPR10, RPR15, TAQ23, TAQ24, 125, 1143, 1155, 1572, 1575
Shapiro, Alan WPB15, TPP10, 985, 1636
Sharma, S. FAR19, TAR08, 303, 816
Sharonov, S.A. FAP06, FAP07, 1337, 1340
Sharp, W. TAR17, 837
Sharp, W.M. TAR13, TAR14, TPR09, 825, 828, 3260
Shatilov, D.N. RAP05, 2892
Shatunov, Yu. RAA31, RAR31, 600, 3427
Shatunov, Yu.M. RAQ21, 3331
Shchedrin, I.S. RPA25, 1114
Shchepunov, V.A. FAC12, 2863
Shcherbakov, A. FAR16, FAR17, RAA08, 296, 299, 542
Shea, D. MPR20, 2279
Shea, T.J. MPQ04, MPQ05, TPB12, WAC24, 2455, 2458, 2551, 3131
Sheehan, J. MPE11, MPA15, 890, 2223
Sheffield, Richard L. MPE09,

882
Shen, Weijun FAQ31, 1462
Sheng, I.C. TAR08, 816
Shenzong, Hu FAA26, 246
Shepard, K.W. RPR05, FAQ09, RAR21, 1128, 1408, 3400
Sheppard, J. RPC01, WAQ15, 698, 1876
Sheppard, R. RPA26, 1116
Sherman, J. MPE04, 867
Sherman, J.D. WPA08, 923
Sherwood, Boyd WPB15, 985
Sheu, R.J. TPQ09, 2968
Sheynin, S. FAP12, 1355
Shibata, H. RAB13, 779
Shiltsev, V. TAA01, TAA21, RAR30, 2078, 2126, 3424
Shimer, D. RAA04, 530
Shimer, D.W. RPP01, 1961
Shinas, M.A. TPC06, 2607
Shinn, M. FAG11, FAA25, WPC24, 102, 243, 1052
Shintake, T. WAG12, RPC20, RPA20, FAE09, WPQ09, WPQ17, WPR05, WPR09, TAA28, WXE07, TPC08, TPC29, RPQ04, TAG01, 649, 749, 1099, 1503, 1738, 1759, 1797, 1806, 2135, 2444, 2613, 2655, 2669, 2742
Shinto, K. WPC07, WAQ06, 1007, 1855
Shirai, T. FAR08, RPA13, RPA18, WAQ01, 278, 1079, 1093, 1843
Shirakata, M. WAR05, 1912
Shishido, T. TPP07, 1629
Shoae, H. WAE10, RAE03, RAE11, 2181, 2389, 2417
Shoji, Y. TAP12, WAR04, WAR05, 381, 1909, 1912
Shpak, A. FAR16, FAR17, 296, 299
Shu, D. MPQ08, 2467
Shu, Q.S. TPP11, TPP14, 1639, 1648
Shukeilo, I. FAR06, 272
Shumakov, A. RPA19, 1096
Shumakov, I.V. RPR07, 1134
Shurina, E. MPB09, 2291
Shurter, R.B. TPB22, 2580
Shvedov, D. WAA18, 1266
Shvedunov, V. RPA19, 1096
Shvedunov, V.I. FAA14, TAR05, FAP19, WPR17, RAQ01, RAR04, 225, 807, 1375, 1827, 3285, 3361

Shvets, G. RAB08, 773
 Shvetsov, V.S. WAA20, TAQ34, 1272, 1605
 Sibley, C. RPG05, 327
 Siemann, R.H. WXE05, RAP10, RAP11, RAP12, WAB12, WAC17, TPA09, 2438, 2907, 2910, 2913, 3046, 3109, 3217
 Sigov, Yu.S. WAA02, WAA03, 1230, 1233
 Sikora, J. TPA04, 3206
 Sikora, J.P. RAE14, 2426
 Sikora, R.E. MPQ05, 2458
 Sim, J. FAP05, 1334
 Sim, J.W. FAP06, FAP07, MPB05, MPB06, 1337, 1340, 2282, 2285
 Simopoulos, C. WXE05, WAB05, WAC04, WAC17, 2438, 3025, 3073, 3109
 Simpson, J. WAG06, WPB11, WPB12, 631, 976, 979
 Simrock, S. RPQ29, RPQ30, 2732, 2735
 Simrock, S.N. MPR14, RAE11, 2268, 2417
 Simrock, Stefan MPB11, 2297
 Sinclair, C. FAG11, FAA25, WPA17, TPC07, TPC26, 102, 243, 942, 2610, 2652
 Sinclair, C.K. WPC17, 1030
 Singh, A. TAQ17, 1561
 Singh, O. FAQ17, MPA15, RPQ19, 1426, 2223, 2711
 Singh, Om V. RPQ27, 2729
 Singleterry Jr., R.C. TAC12, 149
 Sisson, D. TPG14, 192
 Skaritka, J. MPE11, 890
 Skarpaas, K. MPP10, 2057
 Skrinsky, A. MAD04, TAR11, 14, 819
 Skuratov, V. WPR19, 1833
 Slaton, T. WAG11, RPB01, RPB03, 646, 656, 662
 Slaton, Tim WAB08, 3034
 Sloan, T. RAQ23, RAQ24, 3337, 3340
 Sloth, K. TAE10, 1213
 Sluijk, T. TAQ12, MPQ17, 1547, 2491
 Smirnov, A. RAP24, 2943
 Smirnov, A.I. MPG10, 426
 Smirnov, A.V. RPR13, 1152
 Smith, D. FAA27, 248
 Smith, D.L. TAE06, 1201
 Smith, David L. TAE07, 1204
 Smith, G.A. RPQ07, 2678
 Smith, H. WPR15, TPC20, 1821, 2646
 Smith, I. TAE06, 1201
 Smith, J. MPA15, 2223
 Smith, J.D. MPR08, 2253
 Smith, John MPR07, 2250
 Smith, M. RPR22, TPC06, 1167, 2607
 Smith, P. WAQ15, 1876
 Smith, R. WAQ03, 1849
 Smith, S. MPQ15, MPQ25, 2485, 2512
 Smith, S.L. TPG09, RAE10, 180, 2414
 Smith, T.L. WPP16, 1693
 Smithe, D.N. WPC12, 1022
 Snyder, S.L. TAP10, 375
 Snydstrup, L. MPP11, 2060
 Sobczynski, S. RPG05, 327
 Sobenin, N.P. TAR05, FAP19, WPR17, WPR18, 807, 1375, 1827, 1830
 Solnyshkov, D. WPC03, 1004
 Solomon, L. FAQ13, WXE04, RPQ19, 1414, 2435, 2711
 Soloveichik, Yu. MPB09, 2291
 Somersalo, E. FAE08, 1500
 Sommer, M. FAR14, 293
 Somov, L. TAC16, 152
 Song, J.J. RPA10, WPP16, TAA11, 1070, 1693, 2102
 Sotnikov, G.V. RAB15, 782
 Soukas, A. TAP11, WAR11, WAR13, RPP02, 378, 1924, 1930, 1964
 Specka, A. WAG07, 634
 Spence, David WPC11, 1019
 Spence, P. TAE06, 1201
 Spence, W. WAG11, RPC20, TAG01, WAC17, 646, 749, 2742, 3109
 Spence, W.L. RAA06, WAB09, 536, 3037
 Spencer, C. WAQ15, 1876
 Spencer, C.M. FAP16, 1366
 Spencer, J. RPC02, RPC08, TAA28, TPC16, WAC17, 701, 713, 2135, 2637, 3109
 Spencer, J.E. RPB06, 671
 Spentzouris, L.K. TAG04, 2757
 Spentzouris, Linda Klamp WAC02, 3070
 Sprehn, D. WAE13, 2190
 Spyropoulos, B. TAA15, 2111
 Srinivasan-Rao, T. MPE11, 890
 Stanek, M. RPA24, TPC20, 1111, 2646
 Stefan, P.M. WXE04, 2435
 Stege, R. WAG11, RPB04, WAC17, 646, 665, 3109
 Steimel, J. TPQ26, 3010
 Steimel Jr., James M. RAE02, 2384
 Stein, P. TPP11, 1639
 Steinbach, Ch. TAP14, 386
 Steinbock, L. FAR06, 272
 Steinhauser, N. WPQ24, 1776
 Steininger, R. FAR06, 272
 Stelzer, J.E. WPC10, 1016
 Stenz, C. WAG07, 634
 Stepashkin, O. RAP24, 2943
 Stephenson, E. WPC08, 1010
 Stepin, D.L. WPB16, 988
 Stepp, J. MPQ08, 2467
 Stevens Jr., R. MPE04, 867
 Stevens Jr., R.R. WPC10, 1016
 Stevens Jr, Ralph R. WAQ02, 1846
 Stevens, R.R. WPA08, 923
 Stevens, T. MPP13, 2067
 Stevenson, G.R. WAQ24, 1891
 Stevenson, N.R. FAG07, 89
 Stierlin, U. TAG01, 2742
 Still, D. RPC21, 752
 Stillman, A. TPB15, 2560
 Stillman, Arnold MPA09, 2211
 Stirbet, M. TPP12, 1642
 Stockhorst, H. TPB20, 2574
 Stoeffl, W. WPG10, RAA03, MPP12, MPP20, TAA22, MPC01, MPC02, 517, 527, 2064, 2075, 2129, 2317, 2319
 Stoker, J. WPA01, 902
 Stoker, J.D. TAE01, 1178
 Stolyarsky, V.I. TPA15, 3232
 Stolzenburg, C. TPP11, 1639
 Stoner, R. TPG14, 192
 Stovall, J.E. RPR08, RPR09, MPC23, 1137, 1140, 2364
 Stover, G. RAE12, 2420
 Stover, G.D. WAA14, 1254
 Straub, D. FAA08, 213
 Striby, S. RAG06, 3170
 Strohman, C.R. RAE14, 2426
 Strönisch, U. FAP02, 1325
 Strubin, P.M. RPE06, 2014
 Struckmeier, Jürgen FAC10, 2860
 Stuart, M. FAP17, FAP18,

1369, 1372
Studebaker, Jan WPB15, 985
Stupakov, G. MPC01, WAC15, 2317, 3102
Stupakov, G.V. RAQ02, RAQ09, RAQ10, 3288, 3303, 3306
Stupakov, Gennady V. RAR11, RAR12, 3373, 3376
Sturges, Ronald WPB15, 985
Su, J.J. TAA28, 2135
Suberlucq, G. RPC10, 719
Sudan, Ravi N. TAE07, 1204
Sugimoto, M. TPG02, 159
Suk, H. TPQ11, 2974
Sukhina, B. TPE09, 1316
Sukhina, B.N. TAC06, RPP08, 143, 1979
Suller, V.P. TPG09, 180
Sullivan, M. RAA25, 585
Sumbaev, A. TAC16, 152
Sun, D. WPP01, 1655
Sun, Y. FAP01, 1322
Surma, I.V. RAQ01, 3285
Sutter, S. RPA26, 1116
Suzuki, H. FAP13, 1358
Suzuki, S. WPC22, 1046
Suzuki, T. FAA30, TPP07, 257, 1629
Svandrik, M. FAR06, FAR21, WPQ04, TAG05, 272, 309, 1723, 2762
Svinin, M. WPC03, TAA18, 1004, 2120
Svinjin, M.P. TAE13, 1222
Swan, T. RAA03, 527
Swenson, D.A. RPG10, 342
Swenson, D.R. WPC10, 1016
Swift, G. FAA08, RPA17, TAQ07, 213, 1090, 1536
Symon, K. TAP05, RAG05, 363, 3167
Syphers, M. RAP21, RAQ23, RAQ24, 2934, 3337, 3340
Syphers, M.J. TAP13, MPG12, WAB04, 383, 431, 3022
Syresin, E. RAP23, RAP24, 2940, 2943
Sytchev, V. FAQ06, 1399
Sytchevsky, S. MPC21, 2359
Tachibana, S. TPP03, 1620
Tadano, M. RPQ23, 2720
Tadokoro, M. TAB03, 113
Tajima, T. TPP03, 1620
Takagi, A. WPC07, WAQ06, WAR05, 1007, 1855, 1912
Takahashi, T. TPP03, 1620
Takaki, H. FAR09, 281
Takao, M. FAQ20, FAQ21, 1435, 1438
Takashima, T. RPQ06, 2675
Takashina, H. TPP03, 1620
Takatomi, T. WPQ15, 1753
Takeda, H. FAA16, RPR08, RPR09, MPC23, 228, 1137, 1140, 2364
Takeda, Harunori MPB16, 2306
Takeda, O. WAG12, 649
Takeda, Y. RPG13, 351
Taketani, A. RPQ15, 2699
Takeuchi, Y. FAE09, WPQ17, WPR05, WPR09, TAG01, 1503, 1759, 1797, 1806, 2742
Tallerico, P.J. TAR12, TAQ02, 822, 1521
Talman, R. RAP03, 2886
Tambini, U. RAE05, 2399
Tan, J. TPP09, 1632
Tanabe, J. FAP01, 1322
Tanaka, M. WAR13, 1930
Tang, Cha-Mei WPE05, 70
Tang, H. WAG11, RPC01, MPE10, WPC18, WPC21, 646, 698, 887, 1033, 1043
Tang, J. MPR13, 2265
Tang, Y.N. MPR08, 2253
Tani, N. FAP13, 1358
Taniuchi, T. WPC22, 1046
Taniyama, N. TPP03, 1620
Tantawi, S. WPQ05, 1726
Tantawi, S.G. TAQ28, 1587
Tantawi, Sami G. TAQ26, TAQ27, TAA27, 1581, 1584, 2132
Tarabrin, V. TAC16, 152
Tarakanov, M.V. MPG10, WAR20, WAR21, 426, 1948, 1949
Tarassenko, A. RAA08, 542
Tarnetsky, V. RPA12, TAQ21, 1076, 1569
Tarovik, M. RAQ14, 3315
Tatchyn, R. FAP20, FAQ23, 1378, 1441
Tatum, B.A. TAP07, WAQ26, MPA05, 366, 1897, 2202
Taufer, M. FAE11, 1509
Taurel, E. RPQ15, 2699
Taurigna-Quere, M. WPB22, 998
Tauschwitz, A. WAQ04, 1852
Tavares, Pedro F. RAQ29, 3352
Taylor, B. TAR03, 801
Taylor, T. RAA04, FAC04, 530, 2844
Tazzari, S. TPG11, 186
Tazzioli, F. TPG11, WAC13, 186, 3097
Tecimer, M. FAA29, 254
Tecker, F. RAA19, 567
Tejima, M. RAA33, MPQ31, TPC05, 603, 2521, 2604
Tejima, Masaki MPQ14, 2482
Telegin, Yu. FAR17, 299
Temkin, R.J. MPE12, 893
Temnykh, Alexander B. TAG08, 2771
Tenenbaum, P. RPC06, RPC20, TAA08, WXE07, TAG01, 707, 749, 2096, 2444, 2742
Teng, L. RAA29, 597
Teng, L.C. RAR26, 3415
Teng, Lee C. FAB10, 2814
Tenyakov, I. FAP24, 1387
Tepikian, S. TAA09, MPR20, FAB22, 2099, 2279, 2832
Terada, Y. FAP22, WPQ07, 1384, 1732
Terashima, A. FAQ02, 1390
Terekhov, V. MPP03, 2040
Terekhov, V.I. MPG10, WAR20, 426, 1948
Tereshkin, Y. FAP24, 1387
Terrell, R. MPR14, 2268
Terunuma, N. WAR03, TPC05, 1906, 2604
Tessier, J.-M. WAC13, 3097
Teytelman, D. RAE12, RPQ01, RPQ08, 2420, 2660, 2681
Thern, R. TPA06, 3212
Theuws, W. RPQ31, 2738
Theuws, W.H.C. WAQ19, RPP04, 1882, 1970
Thevenot, M. TAE09, 1210
Thieberger, P. TAP11, 378
Thielheim, K.O. RAR09, 3370
Thiery, Y. WPB22, 998
Thivent, M. MPG09, 423
Thomas, M. TPP06, WPQ20, 1626, 1768
Thomas, M.D. TAB17, 131
Thomas, P. WPB01, 945
Thomas, R. TPE04, TAA09, 1293, 2099
Thompson, K. TAP05, RPC01, RPC02, RPA04, FAP03, 363, 698, 701, 1058, 1328
Thompson, K.A. TPQ16, TPQ17, WAC18, 2986, 2989,

3112
Thompson, P. TPE04, FAQ03, FAQ04, FAQ16, 1293, 1393, 1396, 1423
Thorndahl, L. RPC09, 716
Thur, W. RPE12, 2026
Tian, F. WAG11, RPB01, TPC20, WAC17, 646, 656, 2646, 3109
Tiefenback, M. MPR15, 2271
Tiefenback, M.G. WAQ12, 1870
Tieger, D. RPG05, 327
Tigelis, J. RAQ01, 3285
Tighe, R. RPQ03, RPQ05, 2666, 2672
Tigner, M. FAE13, RAQ04, 1515, 3294
Timmer, Carl WPB15, 985
Timmermans, C.J. WAQ19, WAQ20, RPP04, RPQ31, 1882, 1885, 1970, 2738
Timossi, C. MPR03, 2244
Tinsley, D. WAR01, 1900
Titcomb, Ch. MPP02, 2037
Tiunov, A.V. RPR01, RAQ01, RAR04, 1119, 3285, 3361
Tiunov, M. MPB09, 2291
Tkachev, P.L. RAR04, 3361
Tkatchenko, A. FAR14, 293
Tobiyama, M. RPQ26, RAQ06, 2726, 3300
Todd, A.M.M. RPR20, 1164
Todesco, E. FAC06, 2847
Toge, N. RPB01, RAP02, 656, 2883
Tojo, E. RPG13, 351
Tokarev, Yu. WAA17, 1263
Tokuda, N. RPG13, TAP04, 351, 360
Tokumoto, S. TAQ29, WPR02, WPR03, 1590, 1788, 1791
Tölle, R. TPB20, 2574
Tolstun, N.G. TAE13, 1222
Tomimasu, T. FAA30, TAQ35, 257, 1608
Tomlin, R. TPQ26, 3010
Tompkins, J.C. FAP06, FAP07, 1337, 1340
Tongu, E. FAA30, 257
Torre, A. TPG11, 186
Torun, Yagmur MXG03, 53
Tosa, M. TPP16, 1652
Tosello, F. WAP14, 470
Tosi, L. FAA13, FAR21, TAG05, 222, 309, 2762
Tosin, G. FAP14, FAP15, 1361, 1364
Touchi, Y. RPG09, 339
Toyama, T. WAR05, 1912
Trahern, C.G. WAP10, MPR20, 461, 2279
Trakhtenberg, E. FAQ17, MPP16, 1426, 2072
Tran, H.J. RAQ15, 3317
Tran, P. RAQ17, 3323
Tranquille, G. RAP24, 2943
Trantham, K. WPC21, 1043
Travier, C. WPB01, 945
Travish, G. FAA23, RPA21, RPA22, 240, 1102, 1105
Trbojevic, D. WAP10, TAA09, FAB22, WAC25, RAQ22, 461, 2099, 2832, 3134, 3334
Treas, P. TAB17, RPA26, 131, 1116
Tremblay, K. WXE01, 2429
Trenkler, T. FAC04, 2844
Trikalinos, C. RAQ01, 3285
Trimble, D. MPE14, WAA19, TAA20, 899, 1269, 2123
Trombly-Freytag, K. FAP06, FAP07, MPB05, MPB06, 1337, 1340, 2282, 2285
Tronc, D. TAB04, 116
Trotz, S.R. MPE12, 893
Trower, W.P. TAR05, FAP19, WPR17, 807, 1375, 1827
Trzeciak, W.S. FAR20, 306
Tsai, H.J. TPQ10, 2971
Tsang, K.L. FAA07, RAR05, 210, 3364
Tsarik, S.V. MPG10, WAR20, WAR21, 426, 1948, 1949
Tschalaer, C. RPG05, 327
Tseng, P.K. FAA04, 201
Tseng, P.-K. TPC15, 2634
Tsentalovich, E. RPG05, 327
Tsoupas, N. FAP11, 1352
Tsuchiya, K. FAQ02, 1390
Tubaev, M. RPR15, 1155
Tückmantel, J. TPP12, 1642
Tuozzolo, J.E. WAR10, 1921
Tupikov, V.S. RPP08, 1979
Tur, Yu. WPB17, 990
Tur, Yu.D. WPB16, TAE14, 988, 1225
Turchinets, W. RPG05, RAA31, 327, 600
Turner, J. WAG11, RPB01, WAC17, 646, 656, 3109
Turner, J.L. RPB04, 665
Turner, L.R. FAQ17, 1426
Tzeng, K.-C. RAB01, RAB02, 758, 761
Ueda, T. RAB13, 779
Uemura, T. FAQ08, 1405
Ueng, T.S. MPQ19, MPQ32, 2497, 2524
Uesaka, M. RAB13, 779
Ueyama, Y. FAP13, 1358
Uggerhoj, E. WAP14, 470
Uhm, Han S. TAQ04, TAQ05, 1527, 1530
Umezawa, H. TPP07, 1629
Urakawa, J. WPR02, WPR03, WAR03, TPC05, 1788, 1791, 1906, 2604
Ursic, R. TPC26, 2652
Ushkov, V. WPR13, 1815
Uskov, V.V. RAB15, 782
Uythoven, J. TPP12, 1642
v. Blanckenhagen, P. FAR06, 272
v. Es, J. MPQ17, 2491
v. Hartrott, M. WAQ17, 1879
v. Rienen, U. RPB16, 695
Vacca, J.H. RPA07, 1064
Valdez, M. MPR03, 2244
Valentinov, A. MPA04, 2199
Valeri, S. WPC23, 1049
Van Asselt, W. RPQ07, 2678
van Asselt, W.K. WAB04, RAQ22, 3022, 3334
van Bibber, K. MPP12, MPP20, 2064, 2075
v.d. Laan, J. MPQ17, 2491
van der Laan, J. RPG06, 330
van Greevenbroek, H.R.M. WAQ20, 1885
van Oers, W.T.H. MPE03, 864
van Oort, J.M. FAQ07, 1402
van Rooij, M. MPG09, MPP15, 423, 2069
Van Vaerenbergh, P. TPE10, 1319
van Zeijts, J. WAE10, 2181
van Zeijts, Johannes MPR02, MPC20, 2241, 2356
VanAsselt, W. TAP13, 383
Vanecek, D. RPC18, WPA01, TAE01, 743, 902, 1178
Varenne, F. RAP23, RAP24, 2940, 2943
Varfolomeev, A. FAA23, 240
Varisco, G. TAA07, 2093
Vasilevsky, A. MPP03, 2040
Vasiljev, A.A. RPR07, 1134
Vasserman, I. FAQ17, FAQ18, 1426, 1429
Vasserman, S. WAA17, 1263

Vassiliev, L. FAQ06, 1399
Vaziri, K. FAG06, 86
Vella, M.C. FAP18, 1372
Veluri, V.R. RPA07, 1064
Verdier, A. WPG09, RAA17, FAC03, 514, 560, 2841
Verdier, André FAC07, FAC08, 2850, 2853
Verhagen, H. RAA15, 557
Verkooyen, J. TAQ12, 1547
Vescovi, M. RPA26, 1116
Veselov, O. FAQ06, 1399
Veshcherevich, V. WPP10, WPP11, RAR19, 1678, 1681, 3394
Vetter, A.M. FAA27, FAA28, WPB20, 248, 251, 992
Vignola, G. WPG05, RPA26, 495, 1116
Villate, D. TAE09, TPC17, 1210, 2640
Vincent, J. RPG11, 345
Vinokurov, N.A. FAQ17, 1426
Virchenko, Yu.P. RAQ28, 3349
Virostek, S. RPB04, 665
Visintini, R. TPG11, FAR21, 186, 309
Vlieks, A.E. WAG13, RPA23, TAQ26, TAQ27, TAA27, 653, 1108, 1581, 1584, 2132
Vobly, P. MPB09, 2291
Vodopianov, F.A. TAR02, TAQ10, 799, 1542
Voisin, L. TAE09, 1210
Volfbeyn, P. TPG07, RPC15, RAB10, 174, 734, 776
Völker, F. MPG09, 423
von Hahn, R. RPR06, 1131
von Holtey, G. WPG09, 514
Vormann, H. WPA04, 911
Vorogushin, M.F. WPP04, 1663
Voronin, G. WPC03, 1004
Voronin, V.S. TPR13, 3269
Vos, L. RAR07, 3367
Voss, G.-A. TAG01, 2742
Voss, Gustav-Adolf FPD01, 27
Votaw, A. MPQ08, MPQ10, 2467, 2473
Votaw, A.J. RPQ16, 2702
Voykov, G. TPC03, 2598
Vuagnin, G. WAP14, 470
Wachter, J. MPQ22, 2506
Wadlinger, E.A. RPR19, 1161
Wagner, S.R. TAG01, 2742
Wake, M. FAQ32, TPP07, 1465, 1629
Wakisaka, K. FAA30, 257
Wakita, K. FAA30, TAQ35, 257, 1608
Walbridge, D.G.C. FAP06, FAP07, MPB05, MPB06, 1337, 1340, 2282, 2285
Waldschmidt, G. WPB06, 961
Walker, N. RPB01, 656
Walker, R.P. TPG11, FAA13, FAR21, FAQ19, TAG05, 186, 222, 309, 1432, 2762
Wallén, E. RPE02, 1999
Walling, L.S. RPG10, 342
Walters, G.K. WPC21, 1043
Walther, R. WPA12, 929
Walton, J. WAR01, 1900
Walz, D. RPC08, WXE07, TAG01, 713, 2444, 2742
Wan, Weishi MPC09, 2336
Wanderer, P. WAP10, TPE04, FAP11, FAQ02, FAQ04, FAQ16, TAA09, 461, 1293, 1352, 1390, 1396, 1423, 2099
Wanderer, P.J. FAQ03, 1393
Wang, B. MPA01, 2193
Wang, C. MPA01, 2193
Wang, C.J. MPR10, TPB29, 2256, 2592
Wang, C.-P. TPC15, 2634
Wang, Ch. FAA04, RAA24, FAQ26, TPQ08, 201, 582, 1450, 2965
Wang, Chun-xi MPC31, 2376
Wang, Chunxi FAC02, 2838
Wang, D. WAA16, WXE01, TPB04, TPC04, WAC27, 1260, 2429, 2536, 2601, 3140
Wang, D.X. MXG02, 48
Wang, J. RPA04, WAA08, WAA09, 1058, 1242, 1245
Wang, J.G. TAE04, TPQ11, 1193, 2974
Wang, J.M. TPP06, 1626
Wang, J.P. TAA14, 2108
Wang, J.Q. WAB20, 3064
Wang, J.W. WAG13, RPA23, 653, 1108
Wang, L. TAP03, WPP20, WPP21, RAP21, WAC12, WAC27, RAG10, RAQ23, RAQ24, 357, 1705, 1708, 2934, 3094, 3140, 3182, 3337, 3340
Wang, M.H. RAA24, TAR06, TPQ08, TPQ09, TPQ10, 582, 810, 2965, 2968, 2971
Wang, P. FAA08, RPA17, 213, 1090
Wang, Ping WPA13, WPR22, 932, 1841
Wang, Shu-Hong WPG07, 506
Wang, T. WAC29, 3146
Wang, T.S. RAR23, 3406
Wang, Tai-Sen F. WAC28, 3143
Wang, X. MPQ07, MPQ08, MPQ10, 2464, 2467, 2473
Wang, X.J. MPE11, WPB13, RAE09, WXE03, TPB01, 890, 982, 2411, 2432, 2530
Wang, X.-J. TPG14, 192
Wang, X.Q. RPE10, 2023
Wang, Y. TAB17, MPA01, RAP21, 131, 2193, 2934
Wang, Y.L. TAQ08, 1539
Wangler, T.P. RAG11, 3185
Wangler, Thomas P. WAQ02, RAG01, 1846, 3149
Wanzenberg, R. RPB14, 689
Ward, C. TAR17, 837
Warkentien, R. MPA18, 2232
Warner, A. RAQ22, 3334
Warner, D. TAP05, 363
Warnock, R.L. FAB06, 2804
Warnock, Robert L. TPQ07, 2962
Warren, David WPB15, 985
Warwick, A. FAA03, 198
Watson III, William A. WAE05, 2167
Watson, W. WAE10, MPR13, MPR19, 2181, 2265, 2276
Watson, W.A. RAE11, 2417
Webber, Robert C. RPQ10, 2687
Weber, M. TPB07, 2542
Webers, G.A. WAQ19, WAQ20, RPQ31, 1882, 1885, 2738
Wedekind, M. WPC08, 1010
Wehrle, U. FAE10, 1506
Wei, F. FAR21, 309
Wei, J. WAP10, FAB22, WAC24, RAQ22, 461, 2832, 3131, 3334
Wei, Jie RAP25, 2946
Weidemann, A.W. TAA28, 2135
Weihrer, E. TPE09, WAQ17, 1316, 1879
Weiland, T. RPB16, TAQ06, WAE13, MPC01, MPQ15, WAB18, 695, 1533, 2190, 2317, 2485, 3061

Weinberg, J. WAQ15, WAC17, 1876, 3109
Weingarten, W. FAE11, 1509
Weinstein, A. TAR18, 840
Weise, H. RPB08, 677
Weisend, J.G. MPP01, 2034
Weiss, R. RPR22, 1167
Weisse, E. WAP14, WAQ24, 470, 1891
Weisz, S. WAP14, FAC04, 470, 2844
Welch, J. FAE13, 1515
Welch, James J. TAA29, TAG08, FAC14, RAG13, 2138, 2771, 2866, 3191
Welton, R.F. MPE05, WPC12, 871, 1022
Welz, J. MPE03, 864
Wendt, M. TPC09, 2616
Weng, W.T. FAA07, RAA23, RAA24, RAG08, RAR05, 210, 579, 582, 3176, 3364
Wenjun, Zhu FAA26, 246
Wenninger, J. WAP12, RAA11, RAA19, RAA20, 464, 548, 567, 570
Werkema, Steven J. RAR20, 3397
Wermelskirchen, C. RPQ22, 2717
Wesolowski, W. RPA11, 1073
West, C. MPR13, 2265
Westenskow, G. RPC16, RPC17, MPE14, WPC16, TAA28, 737, 740, 899, 1027, 2135
Westenskow, G.A. TAQ03, 1524
Westervelt, R.T. WAE08, 2175
Wetherholt, D. MPR13, 2265
Wharton, K. RAB04, 767
White, K. MPA12, MPR13, 2220, 2265
White, M. TAP05, RPA07, RPA08, RPA10, RPA11, RPA14, TPC01, 363, 1064, 1067, 1070, 1073, 1082, 2595
Whitham, K. TAB17, RPA26, 131, 1116
Whittum, D. RAB13, TAA28, WAC17, 779, 2135, 3109
Widgren, J. FAA08, 213
Wiemerslage, G. MPP16, 2072
Wienands, H.-U. RAA27, 591
Wienands, U. RAA04, TAA22, MPC01, 530, 2129, 2317
Wight, G.W. MPE03, 864
Wildman, D. WPP08, WPP09, WPP23, RAQ13, 1672, 1675, 1714, 3312
Wildner, E. MPG09, WAE09, 423, 2178
Wilkinson, C. WAC29, 3146
Wilkinson, C.A. TAR12, 822
Willeke, F. MPG07, TAG02, TAG09, 420, 2747, 2774
Willen, E. TPE04, FAQ03, FAQ04, FAQ15, FAQ16, 1293, 1393, 1396, 1420, 1423
Williams, C.E. WAQ26, 1897
Williams, G. FAR06, 272
Williams, M.D. TPB07, 2542
Williams, Mel WPB15, 985
Williams, R. TAA28, 2135
Williams, S. TAG01, 2742
Wilson, I. WAG13, RPC09, RPC10, RPC15, 653, 716, 719, 734
Wilson, K. FAR06, 272
Wilson, P. RPC01, RPC02, RPC06, 698, 701, 707
Wilson, P.B. FAE04, TAA33, TPQ16, 1483, 2144, 2986
Winick, H. WPB13, WXE03, 982, 2432
Winje, R.A. FAG05, 83
Winkler, G. MPP02, 2037
Winn, David MXG03, 53
Wise, M. MPR13, 2265
Wiseman, M. FAG11, FAA25, WPA17, 102, 243, 942
Witherspoon, S. WAE10, MPR13, 2181, 2265
Witkover, R. RPQ07, 2678
Witkover, R.L. TPB26, 2589
Witte, K. MPE10, 887
Wolf, Z. FAP16, FAQ08, 1366, 1405
Wolff, D. WAE07, 2172
Wolff, S. RPB09, 680
Wollnik, H. WAQ26, 1897
Wong, J. TAR18, 840
Wong, V. RPQ07, 2678
Woo, B. MPC18, 2351
Wood, P. TPC04, 2601
Wood, R.L. RPR08, RPR09, 1137, 1140
Woodle, M. WPB13, WXE03, 982, 2432
Woodley, M. WAG11, RPB01, RPB03, RPB04, RAE03, 646, 656, 662, 665, 2389
Woods, M. RPC08, 713
Woody, K.A. TPC13, 2628
Wright, D. MPP09, MPP12, MPP20, MPC01, WAC17, 2054, 2064, 2075, 2317, 3109
Wright, E. FAE07, 1497
Wright, E.L. TAQ28, 1587
Wrulich, A. TPG11, FAA13, FAR21, TAG05, 186, 222, 309, 2762
Wu, X. RPG11, 345
Wu, Y. FAA08, RPG06, RAA01, RAA21, RAB22, RPA17, MPA10, MPA11, MPQ06, FAC20, 213, 330, 524, 573, 796, 1090, 2214, 2217, 2461, 2877
Wu, Y.Y. TPB03, 2533
Wu, Ying WPR22, 1841
Wuensch, W. WAG13, RPC09, RPC10, RPC15, 653, 716, 719, 734
Wurtele, J. TAA28, 2135
Wurtele, J.S. RAB08, MPE12, WPB03, WPB04, 773, 893, 951, 954
Wüstefeld, Godehard FAC16, 2868
Wyss, C. TPP12, 1642
Xi, Boling RPP04, 1970
Xiao, A. WAC27, 3140
Xie, Jialin TPG04, 162
Xie, Ming TPG10, 183
Xu, G. RAA21, TPQ03, WAC27, 573, 2955, 3140
Xu, J. MPA01, 2193
Xu, S. MPP16, 2072
Yakimenko, V. TAR11, RAR31, 819, 3427
Yakovlev, V. RPA12, TAQ21, 1076, 1569
Yakovlev, V.P. MPC17, 2348
Yamada, R. MPC07, 2330
Yamada, S. MAD03, 9
Yamaguchi, H. MPQ18, 2494
Yamaguchi, S. TAQ25, 1578
Yamamoto, N. RPC20, MPA06, WXE07, TAG01, 749, 2205, 2444, 2742
Yamane, Isao TPR16, 3275
Yamazaki, Y. FAE09, WPQ08, WPQ09, WPQ17, WPR05, WPR09, 1503, 1735, 1738, 1759, 1797, 1806
Yan, Y. RAA22, 576
Yan, Y.T. RAA26, RAA27, TAG06, 588, 591, 2765
Yanagida, K. WPC22, 1046
Yang, B. MPQ09, MPQ10,

MPQ11, TPC03, 2470, 2473,
 2476, 2598
Yang, J. RAQ17, 3323
Yang, Ming-Jen MPQ20, 2500
Yang, X.-F. TPC16, 2637
Yano, Y. WPC01, 1001
Yaramishev, S.G. TPA05,
 3209
Yarba, V.A. FAP06, FAP07,
 1337, 1340
Yarygin, N. FAQ06, 1399
Yarygin, S.N. WPR18, 1830
Yasumoto, M. FAA30, 257
Yavor, S.Ya. TAP16, 389
Yazynin, I. WAR22, 1952
Yee, D. FAP01, 1322
Yeremian, A.D. WPC18, 1033
Yi, He FAA26, 246
Yifang, Wang TAR22, 850
Yin, Yan TPC11, 2622
Ylä-Oijala, P. FAE08, 1500
Yokomizo, H. WPC22, FAP13,
 MPA07, 1046, 1358, 2208
Yokoya, K. RPA20, WAB20,
 1099, 3064
Yokoyama, M. RPQ23, 2720
Yokoyama, S. FAQ08, 1405
Yonehara, H. FAP13, 1358
Yoon, M. TPG06, WPR11, 171,
 1812
York, R.C. RPG11, 345
York, R.L. WPC10, 1016
Yoshida, Y. RAB13, 779
Yoshihara, K. TPP16, 1652
Yoshii, J. TPB18, 2569
Yoshii, M. TAP04, WPC07,
 WAR05, 360, 1007, 1912
Yoshikawa, H. WPC22,
 MPA07, 1046, 2208
Yoshimoto, S. RPQ06, 2675
Young, E. RAP07, 2898
Young, L.M. RPR08, RPR09,
 1137, 1140
Young, Lloyd M. MPB16, 2306
Yourd, R. FAP01, 1322
Yourd, R.B. RAA05, 533
Yu, C.I. MPQ26, RAR05, 2515,
 3364
Yu, C.-I. TPC15, 2634
Yu, I.H. WPR11, 1812
Yu, S. RPC16, RPC17, RPC18,
 WPA01, TAE01, 737, 740, 743,
 902, 1178
Yu, S.S. RPC19, TAR14,
 WPA09, WAQ04, 746, 828,
 926, 1852
Yu, Y. MPA01, 2193
Yuan, D. WAQ07, 1858
Yuan, V. RPR19, 1161
Yuan, V.W. RPR22, TPC06,
 1167, 2607
Yudin, I.P. MPB19, FAC09,
 2314, 2856
Yugami, N. RAB13, 779
Yuldashev, O.I. MPB19, 2314
Yuldasheva, M.B. MPB19,
 2314
Yule, T.J. FAG14, 110
Yunn, B. WPA17, 942
Yunn, Byung C. MPB11,
 RAQ11, 2297, 3309
Yupinov, Y. MPA04, 2199
Yupinov, Yu. WPR13, 1815
Yurkov, M.V. WAA20, TAQ34,
 1272, 1605
Zako, A. FAA30, 257
Zakutin, V.V. WPA15, TAE14,
 938, 1225
Zangrando, D. TPG11, FAQ19,
 186, 1432
Zante, A. TAB17, RPA26, 131,
 1116
Zaugg, T. WPA08, 923
Zavadtsev, A.A. WPR18, 1830
Zazula, J.M. WAQ24, 1891
Zegenhagen, J. FAR06, 272
Zelenski, A.N. MPE03, 864
Zelinsky, A. FAR17, RAA08,
 299, 542
Zelinsky, A.Yu. RAA07, 539
Zeller, A.F. RPG11, 345
Zenkevich, P. RAP23, 2940
Zenkevich, P.R. TPA05, 3209
Zeno, K. TAP12, 381
Zhan, M. MPA01, 2193
Zhang, C. WPG09, TPQ03, 514,
 2955
Zhang, R. RAB03, RPA21,
 RPA22, 764, 1102, 1105
Zhang, S.Y. TAP13, RAG08,
 TPA08, 383, 3176, 3214
Zhang, W. WAR10, WAC25,
 1921, 3134
Zhang, Zhenhai RAQ25, 3343
Zhao, Aihua FAQ29, FAQ30,
 1456, 1459
Zhao, J. MPA01, 2193
Zhao, S. TAA03, 2084
Zhidkov, E.P. MPB19, 2314
Zhiglo, V.F. WPA15, 938
Zholents, A. RAA03, RAA22,
 FAB01, 527, 576, 2789
Zholents, A.A. RAP05, 2892
Zhou, J. WPB06, TAA11, 961,
 2102
Zhou, Ping TPB05, 2539
Zimmermann, F. WPG10,
 WAG11, RPB01, RPC03, RPC06,
 RPC07, TPQ16, TPQ17, WAB07,
 WAC15, WAC17, 517, 646,
 656, 704, 707, 710, 2986,
 2989, 3031, 3102, 3109
Ziomek, C. TAQ31, RPQ02,
 RPQ05, 1596, 2663, 2672
Zisman, M. MPC01, 2317
Zisman, M.S. RAA03, RAA05,
 527, 533
Zolfaghari, A. RPG05, WAA16,
 TPB04, 327, 1260, 2536
Zolotorev, M. WPG10, RPE14,
 MPC01, MPC08, 517, 2032,
 2317, 2333
Zolotorev, Max TAQ27, 1584
Zotter, B. RAA20, RPC09,
 570, 716
Zubovskiy, V. TAC05, 140
Zwart, T. RPG05, RAA31, 327,
 600
Zyngier, H. TPG01, FAR14,
 155, 293

